Springer Handbook of Nanomaterials

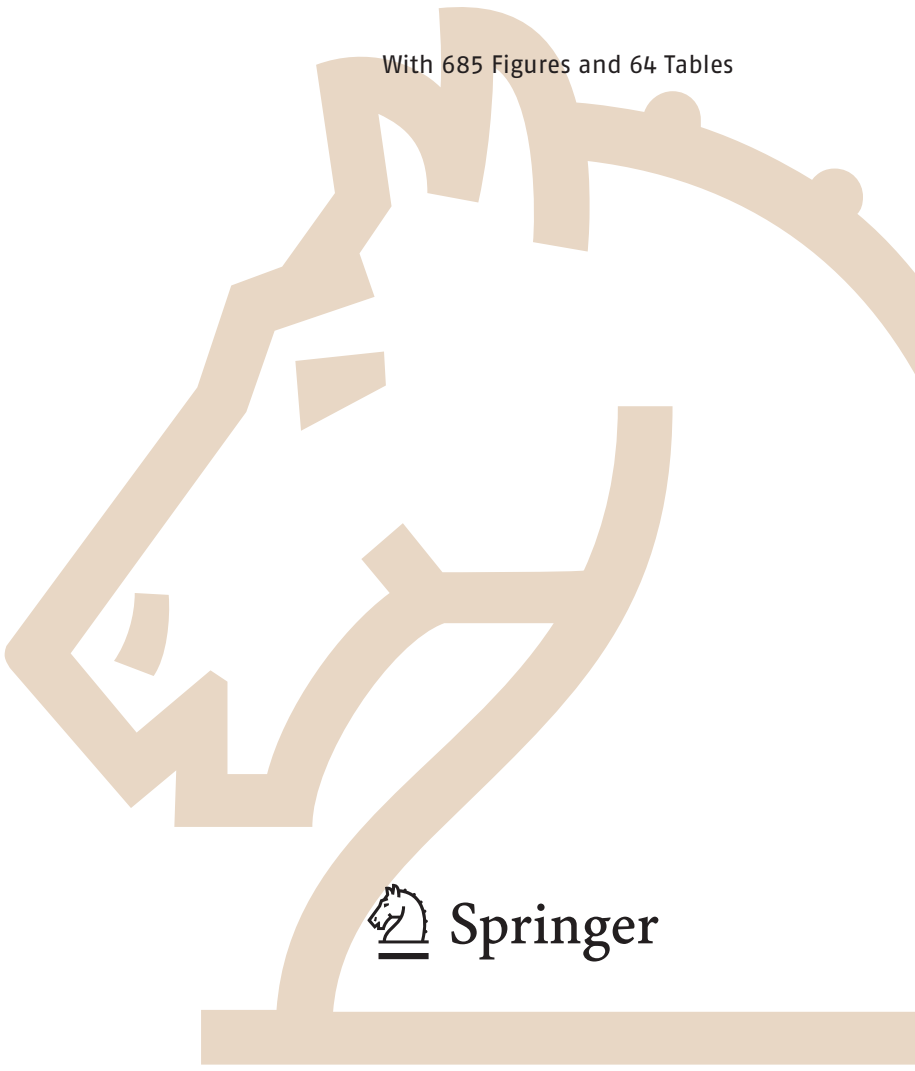
Springer Handbook provides a concise compilation of approved key information on methods of research, general principles, and functional relationships in physical and applied sciences. The world's leading experts in the fields of physics and engineering will be assigned by one or several renowned editors to write the chapters comprising each volume. The content is selected by these experts from Springer sources (books, journals, online content) and other systematic and approved recent publications of scientific and technical information.

The volumes are designed to be useful as readable desk reference book to give a fast and comprehensive overview and easy retrieval of essential reliable key information, including tables, graphs, and bibliographies. References to extensive sources are provided.

Springer Handbook of Nanomaterials

Robert Vajtai (Ed.)

With 685 Figures and 64 Tables



Springer

Editor
Robert Vajtai
Rice University
Department of Mechanical Engineering and Materials Science
6100 Main MS-321
Houston, TX 77005-1827
USA

ISBN: 978-3-642-20594-1 e-ISBN: 978-3-642-20595-8
DOI 10.1007/978-3-642-20595-8
Springer Dordrecht Heidelberg London New York

Library of Congress Control Number: 2013942548

© Springer-Verlag Berlin Heidelberg 2013
This work is subject to copyright. All rights are reserved, whether the whole or part of the material is concerned, specifically the rights of translation, reprinting, reuse of illustrations, recitation, broadcasting, reproduction on microfilm or in any other way, and storage in data banks. Duplication of this publication or parts thereof is permitted only under the provisions of the German Copyright Law of September 9, 1965, in its current version, and permission for use must always be obtained from Springer. Violations are liable to prosecution under the German Copyright Law.
The use of general descriptive names, registered names, trademarks, etc. in this publication does not imply, even in the absence of a specific statement, that such names are exempt from the relevant protective laws and regulations and therefore free for general use.

Production and typesetting: le-tex publishing services GmbH, Leipzig
Senior Manager Springer Handbook: Dr. W. Skolaut, Heidelberg
Typography and layout: schreiberVIS, Seeheim
Illustrations: le-tex publishing services GmbH, Leipzig; Hippmann GbR, Schwarzenbruck
Cover design: eStudio Calamar Steinen, Barcelona
Cover production: WMXDesign GmbH, Heidelberg
Printing and binding: Stürtz GmbH, Würzburg

Printed on acid free paper

Springer is part of Springer Science+Business Media (www.springer.com)

61/3180/YL 5 4 3 2 1 0

Foreword

Nanomaterials are based on structures with characteristic features on the scale of nanometers. This size is small if we compare with normal things around us, but it is not particularly small on the atomic scale. In fact, distances between individual atoms are typically a tenth of a nanometer (an Ångström), so a piece of a material with a side of a nanometer may contain hundreds or even a thousand atoms. Therefore a nanomaterial usually has some resemblance to a bulk material based on the same atoms, but the normal material has been modified to reach superior properties such as higher mechanical strength, different optical and magnetic performance, permeability to a fluid, or something else. Thus nanomaterials may allow us to obtain properties that were previously impossible to achieve, impractical to manufacture, or too expensive for use on a scale large enough to be significant in daily life.

Among the general public, and even the scientific community, nanomaterials are widely perceived as *new* in many different way – newly invented, newly used by human cultures, and newly studied.

In fact, nanomaterials are not new at all. Nature itself is filled with nanofeatures that have evolved in biological systems, one well known example being moths' eyes with nanostructured surfaces that provide antireflection and allow efficient use of feeble light.

Looking at history, we can also see that human beings have been using nanomaterials of various sorts for a very long time. Let us take three examples: nanocarbons, nanometals, and nanoceramics.

Nanocarbons can be created in abundance on the nanometer scale when organic matter burns. Such carbon nanoparticles were used by humans as far back as forty thousand years ago to depict and decorate. The particles were mixed with fat and used for painting in the caves of Altamira and Lascaux in Spain and France, to mention two especially striking and well known cases. This kind of carbon, in principle, is also an essential ingredient in ink and printing paste, and it was used by monastic scribes and by Gutenberg and his followers to make texts of explosive cultural significance and stunning beauty.

Nanometals have also been utilized for thousands of years. An example is the world famous Lycurgus glass cup, now in the holdings of the British Museum. This cup, which was probably created in Rome during the 4th century AD, contains embedded nanoparticles of gold and silver. Because of these particles, the cup normally seems to be a light green color, but it becomes ruby red when light is shone through it. The Lycurgus cup is a wonder of craftsmanship from Antiquity, and it is based on nanotechnology.

Finally, let's consider *nanoceramics*. The world's most widely used artificial material is the nanoceramic cement, which was used extensively by the Romans in constructing buildings, baths and aqueducts. Furthermore, recent archaeological discoveries indicate that the Romans were not the first, that the Macedonians were using cement centuries earlier.



Prof. Claes-Göran Granqvist
Department of Engineering Sciences
Solid State Physics
Uppsala University
Sweden

Even research on nanomaterials is not as new as it seems. The term apparently began appearing in the titles of scientific publications only 15 years ago. But today's *nano* was the subject of an older literature under the term *ultrafine*.

As the examples above indicate, nanomaterials are well rooted in the past. But they are also very much of the future. Let us consider a few specific examples.

Nanocarbons, used for cave painting and the printing of the Gutenberg Bible, are very much in focus today, in the forms of fullerenes, nanotubes and nanodiamonds, all of which offer a multitude of possibilities for future technology. Two-dimensional carbon in the form of graphene has unique properties directly based on quantum physics, and it may have important applications in transparent electronics and elsewhere. Graphane, its hydrogenated cousin, is exciting in its own right.

Nanometals, employed by the Romans to create the amazing Lycurgus glass cup, are the basis today for manifold applications, including thermal collectors that harness the sun's energy and innovative *plasmonic* solar cells. Indeed, *plasmonics* is becoming a household word because of its relevance for light-emitting diodes, sen-

sors and catalysts for chemical reactions, just to mention a few technologies.

Thus many aspects of nanomaterials are indeed truly new and are the subject of intense worldwide interest in today's academic and industrial research laboratories. This *Handbook*, which is a testimony to this growing body of knowledge, presents welcome and authoritative surveys over nanocarbons, nanometals and nanoceramics in its first three parts. Other sections cover nanocomposites and nanoporous materials, as well as organic and biological nanomaterials. Applications and impacts are discussed at the end, together with important questions of toxicology, hazards and safety. These issues are of great importance. We should remember the terrible impact that asbestos – in fact, a natural nanomaterial – had on human health before it was widely banned. We certainly do not want to discover one day that, in our quest for new materials to solve technological problems, we have unleashed another dangerous nanomaterial into the world.

The editor and authors are to be congratulated on the successful completion of this *Handbook of Nanomaterials*. It will surely be a work of great and lasting importance for the scientific community.

Uppsala, November 2012 Prof. Claes G. Granqvist

Foreword



Prof. Neal Lane
Malcolm Gillis University Professor,
Department of Physics and Astronomy,
Senior Fellow,
James A. Baker III Institute for Public Policy
Rice University
Houston, Texas

It has been more than a decade since President Bill Clinton talked about the promise of nanotechnology and the importance of increasing investments in nanoscale science and engineering research in a speech at the California Institute of Technology on January 21, 2000. In his remarks, the President recalled Richard Feynman's American Physical Society talk there in 1959. The following week, in his State of the Union Address, President Clinton announced his *21st Century Research Fund*, a $3 billion budget increase, which included the multiagency national nanotechnology initiative (NNI). The first year's budget allocation to NNI was close to half a billion US$, nearly doubling what the agencies had been spending on nanoscale research; and with the continuous support of succeeding administrations the budget quadrupled in a decade. This strong federal support, initially based on the promise of a revolutionary new technology, was justified by steady scientific and technological advances at the nanometer scale and by the growth of commercial applications, especially in biotechnology and nanoelectronics, offering new ways to tackle disease and new industrial tools and toys. As President Clinton's former science advisor, I am confident that he is as pleased with the progress in nanotechnology as are all of us – inside and outside government – who worked with him to develop and implement the NNI.

One way to define nanotechnology, perhaps, is that it is the knowledge and engineering (design and control) of physical, chemical, and biological systems at the nanometer (10^{-9} m) scale – from the size of individual molecules to dimensions of the order 100 nm. Nanotechnology is, by its nature, a field of synthesis and synergy often requiring physics, chemistry, biology, and almost all areas of engineering in the performance of research and engineering design, for example inventing and optimizing the tools needed to synthesize and manipulate matter at the nanometer scale. As with other new fields, rapid advances in nanotechnology have led to specialization into subdisciplines, one of the most natural and important being *nanomaterials*.

Nanomaterials science and engineering includes the production, properties, and applications of materials at the nanometer scale; it is a part of nanotechnology and at the same time, evidently, a subfield of materials science. The main goal of materials science – macroscopic and nanoscale – is providing new and improved building blocks for engineers in all fields. That said, *nanomaterials* science has distinct features compared to the more mature science and engineering of macroscopic materials, the most salient being its revolutionary nature. New materials and groups of materials with surprising properties continue to be discovered – graphene and topological insulators are two examples from the recent past. As with all exploration at the frontiers of knowledge, it is impossible to predict what discoveries will be made or how those discoveries might lead to applications, commercial or otherwise. But the history of science and technology suggests that some of those advances will surpass all our expectations. Already we are seeing the benefits of nanotechnology in computers and telecommunication devices, computer chips and sensors in automobiles, electric car batteries, medicines and sun creams, tablecloths and socks, tennis rackets, boats, golf clubs – and more. Given the likelihood that ongoing research will yield many more *nanomaterials*, with surprising properties and, at the same time, the continued exponential growth in the number of applications, it seems clear that *nanomaterials* will, at some level, transform most aspects of our lives. It is not too much of a stretch to suggest that President Clinton's policy decision to set up the NNI, which has supported thousands of scientists and engineers working in the field, has indeed helped move us closer to realizing Feynman's prediction – or, perhaps we should say his vision – of a revolutionary new technology. In the world of *nanomaterials* there is still *plenty of room at the bottom* to use Richard Feynman's famous words.

A handbook, by one definition, is a compilation of knowledge about a particular field, collected into a single volume publication that is convenient to use as

a ready reference. Since *nanomaterials* science can now be considered a self-sufficient discipline, a handbook is appropriate and timely. This new *Springer Handbook of Nanomaterials* targets several audiences: researchers working in industry or academia, as well as graduate students studying related fields. The organization of the book follows the usual classification scheme of macroscopic materials science, with information of a materials group – e.g., metals – collected together; other aspects can be followed easily by using the well-developed index.

Putting together a handbook in a new field is a formidable challenge. I would like to congratulate the editor and all of the authors who collaborated to plan, collect materials, and write this important groundbreaking *Springer Handbook of Nanomaterials*.

Houston, January 2013 Neal Lane

Preface

Those who control materials, control technology, stated Eiji Kobayashi, Senior Advisor of Panasonic Corporation, explaining the importance of materials science and engineering. I would translate this quote to *those who control* nano*materials control* nano*technology*; and, considering the effect of the development of nanomaterials and nanotechnology on our global infrastructure, it is not too bold to state that those control technology at large, too. Nanomaterials have a determinant role in many of advanced products around us. Stamp-sized sound recording devices, modern passenger and fighter jets, spaceships and space stations, extreme tall buildings and long bridges, none of these could be created without these marvelous materials. As one could not foresee 50 years ago, the fast development that provided the opportunity for these objects to be realized, now we cannot imagine our life without them.

The editor considers materials science as the knowledge of structure; properties of materials predicted or explained with the help of this knowledge; experimental and theoretical tools designed and established for preparing, characterizing and modifying processes, and last but not least showing application possibilities of the resulted materials. After defining nanomaterials we can simply transpose this description for nanomaterials science. Materials are considered *nanomaterials* when their structure, processing, characterization or application differ from the macroscopic materials and this difference relates to the – normally sub-100 nm – feature size. The *description* of the nanomaterials in this Springer Handbook follows the thorough but concise explanation of the synergy of structure, properties, processing, and applications. Specifically, our aim was to point out the distinction between the properties of bulk and nanomaterials and the reasons for these differences.

To fulfill these goals, we provide a balanced report of the literature of each materials group. The format follows the well-established structure of the Springer Handbooks with chapters as the basic units that are organized into several groups. In each chapter, authors cover materials of their expertise, however, they focus not only on their own work, but report the interesting and important efforts in the community, establishing a balance between references and scientific results reported in tables and figures. We describe nanomaterials in textbook style for newcomers, encyclopedia-like elements and – to follow the fast-space of new results – review or research papers for the experienced reader. Beyond scientific and moral correctness we also look for clarity by concise and easy-to-follow text, well-designed and clear figures which were all professionally drawn by graphics designers.

The book is divided in Parts A to G and covers carbon-based nanomaterials: fullerenes, nanotubes, nanofibers and nanodiamond, noble and common metals and alloys, ceramic materials, crystalline and glassy oxides and other compounds; composites, hybrid structures and solutions as well as porous metals, ceramics and silicon; organic and bio-nanomaterials, bones and fibers and select applications, respectively. This higher level structure conforms to the macroscopic classification of materials and it is composed of chapters. Each chapter is self-consistent and builds up of similar parts, history, definitions, production of the given materials, properties, and applications. All of these parts are richly illustrated and consist of a balanced ratio of important basics and recent results.

My pleasant obligation is to thank all of the help I received in planning and implementing the handbook. First of all, I need to acknowledge the diligent work of the authors in developing the chapters which involves more effort than a review paper, and the reward is not so immediate and evident. Their expertise, energy and time are greatly appreciated. I also would like to thank the advices and help of my colleagues at Rice University and at Rensselaer Polytechnic Institute; as well as Professors Thomas F. George, Bob Curl, Phaedon Avouris, Li Song and Jinquan Wei for keeping contact with many authors. The great workmanship of the Springer publishing team and the continuous support of the managing editors Mayra Castro and Werner Skolaut are also appreciated. I also need to thank my colleagues and friends, Laszlo B. Kish, Claes-Goran Granqvist, Pulickel M. Ajayan and Richard W. Siegel that the collaboration with them oriented me to nanomaterials science. Last, but not least, I thank for the help and pa-

tience of my wife, Agnes, without her I would have not been able to finish this job.

I wish the reader a pleasant and beneficial time when using the Springer Handbook of Nanomaterials, and I hope that it serves as a frequently opened reference work.

Houston, November 2012 Robert Vajtai

About the Editor



Robert Vajtai is a Faculty Fellow at Rice University, Houston, Texas, in the Department of Mechanical Engineering and Materials Science. His expertise covers synthesis, processing, characterization of physical and chemical properties of new, advanced material forms and structures. More specifically Dr. Vajtai's interests are in nanostructured materials, nanocomposites and nanomaterials; as well as their applications in thermal management, energy storage, microelectromechanical systems, sensors and electronic devices.

Dr. Vajtai received his scientific education in physics and his Ph.D. degree in solid-state physics from the University of Szeged (then named Jozsef Attila University), Hungary. From 1987 to 2002 he was a faculty member of the Department of Experimental Physics at the University of Szeged, Hungary. He was rewarded by the Bolyai Fellowship of the Hungarian Academy of Sciences for 1999-2000. He spent sabbaticals as a Fellow of the Swedish Institute in The
glosseintragAAngstrom Laboratory in Uppsala, Sweden, in the years 1998 and 1999; as an Eötvös Fellow at the EPFL in Lausanne, Switzerland in 1995/1996 and visited the Max Planck Institute in Göttingen, Germany, in 1993 via a Max Planck Fellowship. Before moving to Rice University in 2008, Dr. Vajtai spent eight years at the Rensselaer Polytechnic Institute, Troy, New York, where he was a Laboratory Manager at the Rensselaer Nanotechnology Center managing the carbon nanotechnology laboratories.

Dr. Vajtai started his research as a physicist studying laser-metal interaction, melting and oxidation of refractive metals and the nonlinear behavior of the far-from equilibrium processes and systems. Later he developed methods for pulse-probe spectroscopy of biomaterials as well as OH radicals used for the study of organic contamination of the atmosphere by airborne LIDAR systems. His research in materials science started with the synthesis of nanometals and nanosized oxides for the development of sensors. This lead to a new method for the preparation of germanium nanoparticles for building inverse opals used in infrared optical sensing. His most significant contribution is related to the synthesis of different forms of nanocarbons such as carbon nanotubes, graphene and macroscopic systems designed and built from these carbon allotropes, e.g., electromechanical parts and nanotube wires. Recently, his interest extended to various atomically thin layers, hexagonal boron nitride, transition-metal dichalcogenides and oxides.

He has more than 145 journal publications in peer reviewed scientific journals and he delivered numerous invited, keynote and plenary lectures on the topic.

Dr. Vajtai is a passionate teacher, he lectured physics, thermodynamics and electrodynamics courses with hundreds of experimental demonstrations; introductory and advanced courses of materials science. He received several mentoring awards, among those the Siemens-Westinghouse Mentoring Award.

Robert Vajtai is a Faculty Fellow in the Department of Mechanical Engineering & Materials Science at Rice University. He received his undergraduate and Ph.D. degrees from the University of Szeged, then named Jozsef Attila University, Hungary.

List of Authors

Maya Bar-Sadan
Ben-Gurion University
Department of Chemistry
Be'er Sheba , Israel
e-mail: *barsadan@bgu.ac.il*

Giovanni Barcaro
Italian National Research Council
Institute for the Physical and Chemical Processes
Via Giuseppe Moruzzi 1
56124 Pisa, Italy
e-mail: *barcaro@ipcf.cnr.it; giobarc@gmail.com*

Paolo Bettotti
University of Trento
Department of Physics, Nanoscience Laboratory
via Sommarive 14
38123 Povo, Italy
e-mail: *bettotti@science.unitn.it*

Alfredo Caro
Los Alamos National Laboratory
Materials Science and Technology Division
Los Alamos, NM 87544, USA
e-mail: *caro@lanl.gov*

Eunhyea Chung
Korea Institute of Science and Technology (KIST)
Center for Water Resource Cycle
Hwarangno 14-gil 5, Seongbuk-gu
Seoul 136-791, Korea
e-mail: *echung@kist.re.kr*

Suzanne A. Ciftan Hens
ITC/International Technology Center
8100 Brownleigh Road
Raleigh, NC 27617, USA
e-mail: *shens@itc-inc.org*

Vicki L. Colvin
Rice University
Office of Research, Chemistry
6100 Main Str.
Houston, TX 77005, USA
e-mail: *colvin@rice.edu*

Rodolfo Cruz-Silva
Shinshu University
Research Center for Exotic Nanocarbons
Wakasato
380-8553 Nagano, Japan
e-mail: *rcruzsilva@shinshu-u.ac.jp*

Pratap Kumar Deheri
ShayoNano Singapore Pte Ltd.
609969 Singapore
e-mail: *dehe0001@e.ntu.edu.sg*

Libo Deng
University of Manchester
School of Materials
Oxford Road
Manchester, M13 9PL, UK
e-mail: *libo.deng@manchester.ac.uk*

Yi Ding
Shandong University
School of Chemistry and Chemical Engineering
27 South Shan Da Road
Jinan, 250100, China
e-mail: *yding@sdu.edu.cn*

Huanli Dong
Chinese Academy of Sciences
Institute of Chemistry,
Key Laboratory of Organic Solids
Zhongguancun North First Street 2
Beijing, 100190, China
e-mail: *dhl522@iccas.ac.cn*

Mildred S. Dresselhaus
Massachusetts Institute of Technology
Physics; Electrical Engineering
77 Massachusetts Ave
Cambridge, MA 02139, USA
e-mail: *millie@mgm.mit.edu*

Dimple P. Dutta
Bhabha Atomic Research Centre
Chemistry Division
Mumbai, 400085, India
e-mail: *dimpled@barc.gov.in*

Hellmut Eckert
University of Sao Paulo
Department of Physics
Av. Trabalhador Saocarlense 400
Sao Carlos, SP 13566-590, Brazil
e-mail: *eckert@ifsc.usp.br*

Morinobu Endo
Shinshu University
Research Centre for Exotic Nanocarbons
380-8553 Nagano, Japan
e-mail: *endo@endomoribu.shinshu-u.ac.jp*

Adam W. Feinberg
Carnegie Mellon University
Department of Biomedical Engineering
700 Technology Dr.
Pittsburgh, PA 15219, USA
e-mail: *feinberg@andrew.cmu.edu*

Alessandro Fortunelli
IPCF Consiglio Nazionale delle Ricerche (CNR)
via Giuseppe Moruzzi 1
56124 Pisa, Italy
e-mail: *alessandro.fortunelli@cnr.it*

Yogeeswaran Ganesan
Intel Corporation
5200 NE Elam Young Parkway
Hillsboro, OR 97124, USA
e-mail: *yogiganesan@gmail.com*

Wei Gao
Los Alamos National Laboratory
Center for Integrated Nanotechnology
Bikini Atoll Rd
Los Alamos, NM 87545, USA
e-mail: *wei.gaofanyi@gmail.com*

Thomas F. George
University of Missouri-St. Louis
Office of the Chancellor, Center for Nanoscience
One University Boulevard
St. Louis, MO 63121, USA
e-mail: *tfgeorge@umsl.edu*

Lei Gong
University of Manchester
School of Materials
Oxford Road
Manchester, M13 9PL, UK
e-mail: *lei.gong@stud.manchester.ac.uk*

Takuya Hayashi
Shinshu University
Department of Electrical and Electronic Engineering
380-8553 Nagano, Japan
e-mail: *hayashi@endomoribu.shinshu-u.ac.jp*

Wenping Hu
Key Laboratory of Organic Solids
Institute of Chemistry, Chinese Academy of Sciences
Zhongguancun North First Street 2
Beijing, 100190, China
e-mail: *huwp@iccas.ac.cn*

Erik H. Hároz
Rice University
Electrical and Computer Engineering
6100 Main Str.
Houston, TX 77005, USA
e-mail: *enano@rice.edu*

Quentin Jallerat
Carnegie Mellon University
Biomedical Engineering
700 Technology Drive
Pittsburgh, PA 15206, USA
e-mail: *qjallera@andrew.cmu.edu*

Heli Jantunen
University of Oulu
Department of Electrical Engineering
Erkki Koiso-Kanttilankatu 3
Oulu 90014, Finland
e-mail: *heli.jantunen@oulu.fi*

Song Jin
University of Wisconsin-Madison
Department of Chemistry
1101 University Ave.
Madison, WI 53706, USA
e-mail: *jin@chem.wisc.edu*

Kaushik Kalaga
Rice University
Department of Mechanical Enginnering & Materials Science
6100 Main Str.
Houston, TX 77005, USA
e-mail: *kalaga.kaushik@gmail.com*

Ji-Hee Kim
Rice University
Department of Electrical and Computer Engineering
6100 Main Str.
Houston, TX 77005, USA
e-mail: *withphys@gmail.com*

Yoong A. Kim
Shinshu University
Department of Electrical and Electronic Engineering
380-8553 Nagano, Japan
e-mail: *yak@endomoribu.shinshu-u.ac.jp*

Ian A. Kinloch
University of Manchester
School of Materials
Oxford Road
Manchester, M13 9PL, UK
e-mail: *ian.kinloch@manchester.ac.uk*

Imre Kiricsi (deceased)

Junichiro Kono
Rice University
Electrical and Computer Engineering & Physics and Astronomy
6100 Main Str.
Houston, TX 77005, USA
e-mail: *kono@rice.edu*

Krisztián Kordás
University of Oulu
Department of Electrical Engineering
Erkki Koiso-Kanttilankatu 3
Oulu 90570, Finland
e-mail: *lapy@ee.oulu.fi*

Gábor Kozma
University of Szeged
Department of Applied and Environmental Chemistry
Dugonics tér 13
6720 Szeged, Hungary
e-mail: *kozmag@chem.u-szeged.hu*

Jarmo Kukkola
University of Oulu
Department of Electrical Engineering
Erkki Koiso-Kanttilankatu 3
Oulu 90014, Finland
e-mail: *jarmo.kukkola@gmail.com*

Ákos Kukovecz
University of Szeged
Department of Applied and Environmental Chemistry
Rerrich Béla tér 1
Szeged, Hungary
e-mail: *kakos@chem.u-szeged.hu*

Vinod Kumar
Banaras Hindu University
Department of Zoology
Lanka, Varanasi, 221005, India
e-mail: *mail2vinod2@gmail.com*

Zoltán Kónya
University of Szeged
Department of Applied and Environmental Chemistry
Rerrich Bela tér 1
6720 Szeged, Hungary
e-mail: *konya@chem.u-szeged.hu*

Jaesang Lee
Korea Institute of Science and Technology (KIST)
Center for Water Resource Cycle
Hwarangno 14-gil 5
Seoul 136-791, Korea
e-mail: *lee39@kist.re.kr*

Seunghak Lee
Korea Institute of Science and Technology (KIST)
Center for Water Resource Cycle
Hwarangno 14-gil 5
Seoul 136-791, Korea
e-mail: *seunglee@kist.re.kr*

Renat R. Letfullin
Rose-Hulman Institute of Technology
Physics and Optical Engineering
5500 Wabash Avenue
Terre Haute, IN 47803-3999, USA
e-mail: *letfullin@rose-hulman.edu*

Roi Levi
Weizmann Institute of Science
Department of Materials and Interfaces
234 Herzl Street
Rehovot 76100, Israel
e-mail: *roi.levi@weizmann.ac.il*

Zuzanna A. Lewicka
Rice University
Department of Chemistry
6100 Main Street
Houston, TX 77005, USA
e-mail: *zuzannal@rice.edu*

Longtu Li
Tsinghua University
Materials Science & Engineering
Beijing, 100084, China
e-mail: *llt-dms@mail.tsinghua.edu.cn*

Shaily Mahendra
University of California, Los Angeles
Civil and Environmental Engineering
5732 Boelter Hall
Los Angeles, CA 90095, USA
e-mail: *mahendra@seas.ucla.edu*

Balaji P. Mandal
Bhabha Atomic Research Centre
Chemistry Division
Mumbai, 400085, India
e-mail: *bpmandal@barc.gov.i*

Fei Meng
University of Wisconsin-Madison
Department of Chemistry
1101 University Avenue
Madison, WI 53706, USA
e-mail: *fmeng@chem.wisc.edu*

Guowen Meng
Chinese Academy of Sciences
Institute of Solid State Physics
Hefei, Anhui 230031, China
e-mail: *gwmeng@issp.ac.cn*

Younès Messaddeq
Université Laval
Department of Physics
2375, rue de la Terrasse
Québec, Québec G1V 0A6, Canada
e-mail: *younes.messaddeq@copl.ulaval.ca*

Jyri-Pekka Mikkola
Åbo Akademi University
Department of Chemical Engineering
Biskopsgatan 8
Åbo-Turku 20500, Finland
e-mail: *jyri-pekka.mikkola@chem.umu.se;*
jyri-pekka.mikkola@abo.fi

Melinda Mohl
University of Oulu
Department of Electrical Engineering
Erkki Koiso-Kanttilankatu 3
Oulu 90570, Finland
e-mail: *memohl@ee.oulu.fi*

Aarón Morelos-Gómez
Shinshu University
Institute of Carbon Science and Technology
4-17-1 Wakasato
380-8553 Nagano, Japan
e-mail: *amorelos@shinshu-u.ac.jp*

Stephen A. Morin
Harvard University
Chemistry and Chemical Biology
12 Oxford Street
Cambridge, MA 02138, USA
e-mail: *smorin@gmwgroup.harvard.edu*

Marcelo Nalin
Federal University of Sao Carlos
Department of Chemistry
Rodovia Washington Luiz, SP-310
Sao Carlos, Sao Paulo, Brazil
e-mail: *mnalin@ufscar.br*

Sebastien Nanot
Rice University
Electrical and Computer Engineering & Physics and Astronomy
6100 Main Street
Houston, TX 77098, USA
e-mail: *sebastien.nanot@gmail.com*

Rachelle N. Palchesko
Carnegie Mellon University
Biomedical Engineering
Pittsburgh, PA 15219, USA
e-mail: *rachelle@andrew.cmu.edu*

Cary L. Pint
Vanderbilt University
Department of Mechanical Engineering
2301 Vanderbilt Place
Nashville, TN 37215, USA
e-mail: *Cary.L.Pint@vanderbilt.edu*

Gael Poirier
Federal University of Alfenas
Institute of Science and Technology
Rodovia José Aurélio Vilela 11999
Poços de Caldas, MG CEP 37715-400, Brazil
e-mail: *gael.poirier@unifal-mg.edu.br*

Thalappil Pradeep
Indian Institute of Technology Madras
Department of Chemistry
Chennai, 600 036, India
e-mail: *pradeep@iitm.ac.in*

István Pálinkó
University of Szeged
Department of Organic Chemistry
Dóm tér 8
6720 Szeged, Hungary
e-mail: *palinko@chem.u-szeged.hu*

Raju V. Ramanujan
Nanyang Technological University
School of Materials Science and Engineering
50 Nanyang Ave.
639798 Singapore
e-mail: *ramanujan@ntu.edu.sg*

Sundara Ramaprabhu
Indian Institute of Technology, Madras
Department of Physics
Chennai, 600 036, India
e-mail: *ramp@iitm.ac.in*

Jayshree Ramkumar
Bhabha Atomic Research Centre
Analytical Chemistry Division
Mumbai, 400085, India
e-mail: *jrk@barc.gov.in*

Arava L.M. Reddy
Rice University
Department of Mechanical Engineering and Materials Science
6100 Main Str.
Houston, TX 77005, USA
e-mail: *leela@rice.edu*

Vincent C. Reyes
University of California, Los Angeles
Department of Civil and Environmental Engineering
5732 Boelter Hall
Los Angeles, CA 90095, USA
e-mail: *vincecreyes@ ucla.edu*

Sidney J.L. Ribeiro
Sao Paulo State University – UNESP
Institute of Chemistry
Araraquara, SP 14801-970, Brazil
e-mail: *Sidney@iq.unesp.br*

William D. Rice
Los Alamos National Laboratory
National High Magnetic Field Laboratory
Los Alamos, NM 87545, USA
e-mail: *wdrice@lanl.gov*

Silvia H. Santagneli
Sao Paulo State University – UNESP
Institute of Chemistry
Araraquara, SP 14801-970, Brazil
e-mail: *santagneli@iq.unesp.br*

Preeti S. Saxena
Banaras Hindu University
Department of Zoology
Lanka, Varanasi, Uttar Pradesh 221005, India
e-mail: *pssaxena@rediffmail.co*

Olga A. Shenderova
International Technology Center
8100 Brownleigh Road
Raleigh, NC 27617, USA
e-mail: *oshenderova@itc-inc.org*

Rakesh Shukla
Bhabha Atomic Research Centre
Chemistry Division
Mumbai, 400085, India
e-mail: *rakesh@barc.gov.in*

Shashwat Shukla
Nanyang Technological University
639798 Singapore
e-mail: *shas0002@e.ntu.edu.sg*

Theruvakkattil S. Sreeprasad
Kansas State University
Department of Chemical Engineering
1011 Durland Hall
Manhattan, KS 66502, USA
e-mail: *sprasad@k-state.edu*

Anchal Srivastava
Banaras Hindu University
Department of Physics
Lanka, Varanasi, Uttar Pradesh 221005, India
e-mail: *anchalbhu@gmail.com*

Saurabh Srivastava
National Physical Laboratory
Biomedical Instrumentation Section,
New Rajender Nagar, New Delhi 110012, India
e-mail: *saurabhnpl@gmail.com*

Yan Sun
Beihang University (BUAA)
School of Biological Science and Medical Engineering
37 Xueyuan Road, Haidian District
Beijing, 100191, China
e-mail: *sunyan@buaa.edu.cn*

Mária Szabó
University of Szeged
Applied and Environmental Chemistry
1 Rerrich Béle tér
6720 Szeged, Hungary
e-mail: *szmaria@chem.u-szeged.hu*

John M. Szymanski
Carnegie Mellon University
Department of Biomedical Engineering
700 Technology Drive
Pittsburgh, PA 15219, USA
e-mail: *jszymans@andrew.cmu.edu*

András Sápi
University of Szeged
Department of Applied and Environmental Chemistry
1 Rerrich square
6720 Szeged, Hungary
e-mail: *sapia@chem.u-szeged.hu*

Reshef Tenne
Weizmann Institute of Science
Department of Materials and Interfaces
Rehovot 76100, Israel
e-mail: *Reshef.tenne@weizmnn.ac.il*

Humberto Terrones
Pennsylvania State University
Physics Department
S104 Davey Lab
University Park, PA 16802, USA
e-mail: *hzt2@psu.edu*

Mauricio Terrones
Pennsylvania State University
Department of Physics and Materials Science and Engineering
University Park, PA 16802, USA
e-mail: *mut11@psu.edu*

Nicholas A. Thompson
Rice University
Department of Physics & Astronomy
6100 Main Str.
Houston, TX 77005, USA
e-mail: *nt7@rice.edu*

Bipul Tripathi
Banaras Hindu University
Department of Physics
Lanka, Varanasi, Uttar Pradesh 221005, India
e-mail: *bipultripathi@gmail.com*

Ferdinando Tristán López
Shinshu University
Faculty of Engineering, Research Center for Exotic Nanocarbons
380-8553 Nagano, Japan
e-mail: *ftristan@shinshu-u.ac.jp*

Avesh K. Tyagi
Bhabha Atomic Research Centre
Chemistry Division
Mumbai, 400085, India
e-mail: *aktyagi@barc.gov.in*

Géza Tóth
University of Oulu
Department of Electrical Engineering
Erkki Koiso-Kanttilankatu 3
Oulu 90570, Finland
e-mail: *geza@ee.oulu.fi*

Robert Vajtai
Rice University
Department of Mechanical Engineering and Materials Science
6100 Main Str.
Houston, TX 77005-1827, USA
e-mail: *robert.vajtai@rice.edu*

Sofia M. Vega Díaz
Shinshu University
Research Center for Exotic Nanocarbons
380-8553 Nagano, Japan
e-mail: *smvd@shinshu-u.ac.jp*

Aravind Vijayaraghavan
University of Manchester
School of Computer Science
Manchester, M13 9PL, UK
e-mail: *aravind@cs.man.ac.uk*

Xiaohui Wang
Tsinghua University
Department of Materials Science & Engineering
Beijing, 100084, China
e-mail: *wxh@mail.tsinghua.edu.cn*

Xuan Wang
Rice University
Department of Electrica and Computer Engineering
6100 Main Str.
Houston, TX 77005, USA
e-mail: *xw13@rice.edu*

Qiaoling Xu
Chinese Academy of Sciences
Key Laboratory of Materials Physics (CAS), Anhui Key Laboratory of Nanomaterials and Nanostructures
Anhui, 230031, China
e-mail: *qlxu@issp.ac.cn*

Robert J. Young
University of Manchester
School of Materials
Oxford Road
Manchester, M13 9PL, UK
e-mail: *robert.young@manchester.ac.uk*

Ling Zhang
Carnegie Mellon University
Department of Biomedical Engineering
700 Technology Drive
Pittsburgh, PA 15219, USA
e-mail: *zling03@gmail.com*

Shaopeng Zhang
Tsinghua University
Department of Materials Science and Engineering
Beijing, 100084, China
e-mail: *zspthu@gmail.com*

Zhonghua Zhang
Shandong University
School of Materials Science and Engineering
Jingshi Road 17923
Shandong, 250061, China
e-mail: *zh_zhang@sdu.edu.cn*

Contents

Foreword by Claes-Göran Granqvist V
Foreword by Neal Lane VII
List of Abbreviations XXIX

1 **Science and Engineering of Nanomaterials**
Robert Vajtai 1
1.1 History and Definition of Nanomaterials 2
1.2 Formation of Nanomaterials 6
1.3 Properties of Nanomaterials 10
1.4 Typical Applications of Nanomaterials 22
1.5 Concluding Remarks 31
1.6 About the Contents of the Handbook 31
References 31

Part A NanoCarbons

2 **Graphene – Properties and Characterization**
Aravind Vijayaraghavan 39
2.1 Methods of Production 42
2.2 Properties 50
2.3 Characterization 58
2.4 Applications 69
2.5 Conclusions and Outlook 74
References 74

3 **Fullerenes and Beyond: Complexity, Morphology, and Functionality in Closed Carbon Nanostructures**
Humberto Terrones 83
3.1 Geometry and Structural Features of Fullerenes 85
3.2 Methods of Synthesis of Fullerenes and Proposed Growth Models 88
3.3 Physicochemical Properties of Fullerenes 90
3.4 Applications of Fullerenes and Beyond 92
3.5 Conclusions 99
References 99

4 **Single-Walled Carbon Nanotubes**
Sebastien Nanot, Nicholas A. Thompson, Ji-Hee Kim, Xuan Wang, William D. Rice, Erik H. Hároz, Yogeeswaran Ganesan, Cary L. Pint, Junichiro Kono 105
4.1 History 106
4.2 Crystallographic and Electronic Structure 106

4.3 Synthesis 111
4.4 Optical Properties 115
4.5 Transport Properties 123
4.6 Thermal and Mechanical Properties 128
4.7 Concluding Remarks 135
References 135

5 **Multi-Walled Carbon Nanotubes**
Ákos Kukovecz, Gábor Kozma, Zoltán Kónya 147
5.1 Synthesis 148
5.2 Chemistry of MWCNTs 153
5.3 Properties 157
5.4 Selected Applications 163
References 169

6 **Modified Carbon Nanotubes**
Aarón Morelos-Gómez, Ferdinando Tristán López, Rodolfo Cruz-Silva, Sofia M. Vega Díaz, Mauricio Terrones 189
6.1 Doped Carbon Nanotubes 191
6.2 Defects in Carbon Nanotubes 193
6.3 Nanotube Chemical Functionalization 197
6.4 Properties of Modified Carbon Nanotubes 203
6.5 Characterization of Modified Carbon Nanotubes 208
6.6 Applications of Modified Carbon Nanotubes 215
6.7 Toxicity and Biocompatibility 218
6.8 Conclusions 220
6.9 Outlook and Perspectives 221
References 221

7 **Carbon Nanofibers**
Yoong A. Kim, Takuya Hayashi, Morinobu Endo, Mildred S. Dresselhaus 233
7.1 Similarity and Difference Between Carbon Fibers and Carbon Nanofibers 234
7.2 Growth and Structural Modifications of Carbon Nanofibers 238
7.3 Applications of Carbon Nanofibers 251
7.4 Conclusions 257
References 258

8 **Nanodiamonds**
Olga A. Shenderova, Suzanne A. Ciftan Hens 263
8.1 Stability of Diamond at the Nanoscale 264
8.2 Types of Nanodiamonds and Methods of Nanodiamond Synthesis 267
8.3 Detonation Nanodiamond Processing and Modification 278
8.4 Fluorescent Nanodiamonds 284

8.5 Applications of Nanodiamond Particles 285
8.6 Future Directions of Production and Applications 292
References 293

Part B NanoMetals

9 **Noble Metal Nanoparticles**
Theruvakkattil S. Sreeprasad, Thalappil Pradeep 303
9.1 Historical Perspective of Gold and Silver NPs 304
9.2 Diverse Nanostructures 307
9.3 Common Synthetic Routes for the Preparation of Noble Metal NPs 311
9.4 Properties of Noble Metal Nanoparticles 322
9.5 Postsynthetic Tuning of Properties 324
9.6 Functionalized Metal NPs 343
9.7 Applications of Gold and Silver Nanoparticles 347
9.8 New Gold and Silver Materials – Quantum Clusters 363
9.9 Conclusions 366
References 367

10 **Nanostructures of Common Metals**
Melinda Mohl, Krisztián Kordás 389
10.1 Post-Transition Metals 390
10.2 Transition Metals 392
10.3 Concluding Remarks 398
References 399

11 **Alloys on the Nanoscale**
Giovanni Barcaro, Alfredo Caro, Alessandro Fortunelli 409
11.1 Concepts and Principles 411
11.2 Preparation and Synthesis 413
11.3 Characterization of Nanoparticles and Nanoalloys 417
11.4 Properties 424
11.5 Nanostructured Bulk Alloys 450
11.6 Applications 457
11.7 Concluding Remarks 458
References 459

12 **Magnetic Nanostructures: Synthesis, Properties, and Applications**
Shashwat Shukla, Pratap Kumar Deheri, Raju V. Ramanujan 473
12.1 Background 474
12.2 Atomic Origin of Magnetism 475
12.3 Magnetic Length Scales and Origin of Nanomagnetic Behavior 478
12.4 Magnetic Nanostructures 483
12.5 Conclusions 505
References 506

Part C NanoCeramics

13 **Nanocrystalline Functional Oxide Materials**
Rakesh Shukla, Dimple P. Dutta, Jayshree Ramkumar, Balaji P. Mandal, Avesh K. Tyagi 517
13.1 Synthesis Methods 518
13.2 Optical Properties of Oxide Nanomaterials 524
13.3 Sorbent Properties of Oxide Nanomaterials 532
13.4 Catalytic Properties of Oxide Nanomaterials 536
13.5 Oxide Nanomaterials in Ionics 538
13.6 Conclusions 541
References 542

14 **Piezoelectric Nanoceramics**
Xiaohui Wang, Shaopeng Zhang, Longtu Li 553
14.1 Introduction to BSPT 554
14.2 Synthesis of BSPT Nanopowders via Sol–Gel Method 555
14.3 Sintering of BSPT Nanoceramics 556
14.4 Grain Size Effect on the Properties of BSPT Ceramics 563
14.5 Summary 567
References 568

15 **Graphite Oxide**
Wei Gao 571
15.1 Synthesis of Graphite Oxide 572
15.2 Characterization, Chemical Structure and Properties 576
15.3 Applications 589
15.4 Concluding Remarks 592
References 592

16 **Compound Crystals**
Roi Levi, Maya Bar-Sadan, Reshef Tenne 605
16.1 Nanostructures 605
16.2 Synthetic Methods 608
16.3 Physical Properties 618
16.4 Applications 628
16.5 Conclusions 630
References 631

17 **Growth of Nanomaterials by Screw Dislocation**
Fei Meng, Stephen A. Morin, Song Jin 639
17.1 Classical Crystal Growth Theories 640
17.2 Theories for Screw-Dislocation-Driven Growth of Nanomaterials 642
17.3 Structural Characterization of these Nanomaterials 645
17.4 Generality of Dislocation-Driven Nanomaterial Growth 649
17.5 Rational Growth of Dislocation-Driven Nanomaterials – General Strategies 658

17.6 Applications 659
17.7 Summary and Perspectives 660
References 661

18 **Glasses on the Nanoscale**
Hellmut Eckert, Sidney J.L. Ribeiro, Silvia H. Santagneli, Marcelo Nalin, Gael Poirier, Younès Messaddeq 665
18.1 Studying Medium-Range Order in Glasses and Nanoceramics 666
18.2 Nanoceramics 676
18.3 Perspectives and Concluding Remarks 684
References 685

Part D NanoComposites

19 **Carbon in Polymer**
Robert J. Young, Libo Deng, Lei Gong, Ian A. Kinloch 695
19.1 Materials Basics 695
19.2 Carbon Nanotube Composites 702
19.3 Graphene Composites 716
19.4 Conclusions 722
References 722

20 **Nanoparticle Dispersions**
Krisztián Kordás, Jarmo Kukkola, Géza Tóth, Heli Jantunen, Mária Szabó, András Sápi, Ákos Kukovecz, Zoltán Kónya, Jyri-Pekka Mikkola 729
20.1 Stabilization of Nanoparticle Dispersions 730
20.2 Nanoparticle Dispersion in Practice 734
20.3 Dispersions of Carbon Nanomaterials 745
20.4 Drying Dispersions on Surfaces 752
20.5 Concluding Remarks 758
References 758

Part E Nanoporous Materials

21 **Nanoporous Metals**
Yi Ding, Zhonghua Zhang 779
21.1 Preparation of Nanoporous Metals 779
21.2 Properties of Nanoporous Metals 789
21.3 Applications 808
21.4 Concluding Remarks and Prospects 810
References 811

22 **Zeolites**
István Pálinkó, Zoltán Kónya, Ákos Kukovecz, Imre Kiricsi 819
22.1 Common Zeolite Frameworks 822

22.2 Zeolite and Zeolite-Related Molecular Sieves 823
22.3 Natural Zeolites: Occurrence and Formation 825
22.4 Methods of Identification and Characterization 828
22.5 Synthesis of Zeolitic Materials 830
22.6 Ion Exchange, Sorption, and Diffusion in Microporous Materials 836
22.7 Acid–Base Properties of Zeolites 841
22.8 Stability and Modification of Zeolite Structures 843
22.9 Zeolites as Catalysts 846
22.10 Some Special Applications of Zeolites 848
22.11 Conclusions 850
References 850

23 **Porous Anodic Aluminum Oxide**
Qiaoling Xu, Guowen Meng 859
23.1 Background 859
23.2 Preparation of AAO Templates 860
23.3 Nanostructures Constructed in AAO Templates 862
23.4 Conclusions and Outlook 879
References 879

24 **Porous Silicon**
Paolo Bettotti 883
24.1 Basics of Porous Silicon Electrochemistry and Formation Models 884
24.2 Other Etching Methods 886
24.3 Porous Silicon Structural Properties 887
24.4 Light Emission from Porous Silicon 890
24.5 Thermal and Electrical Properties 891
24.6 The Role of the Surface 891
24.7 Applications of Porous Silicon 892
24.8 Conclusions 897
References 898

Part F Organic and Bionanomaterials

25 **Organic Nanomaterials**
Huanli Dong, Wenping Hu 905
25.1 Preparation/Synthesis of Organic Nanomaterials 905
25.2 Properties of Organic Nanomaterials 910
25.3 Applications 925
25.4 Concluding Remarks 930
References 932

26 **Nanocomposites as Bone Implant Material**
Vinod Kumar, Bipul Tripathi, Anchal Srivastava, Preeti S. Saxena 941
26.1 The Quest for a Suitable Bone Implant 942
26.2 Bone 942

26.3 Existing/Conventional Bone Implant Materials and Their Shortcomings 944
26.4 Major Challenges with Existing/Conventional Implant Materials 949
26.5 Nanotechnology and Tissue Engineering 949
26.6 Future Perspectives 965
References 965

27 **Nanofiber Biomaterials**
Rachelle N. Palchesko, Yan Sun, Ling Zhang, John M. Szymanski, Quentin Jallerat, Adam W. Feinberg 977
27.1 Methods of Production 980
27.2 Properties of Nanofiber Biomaterials 986
27.3 Characterization of Nanofiber Biomaterials 993
27.4 Applications 999
27.5 Conclusions and Outlook 1005
References 1006

Part G Applications and Impact

28 **Nanostructured Materials for Energy-Related Applications**
Arava L.M. Reddy, Sundara Ramaprabhu 1013
28.1 Energy-Related Carbon Nanotubes 1013
28.2 CNTs as Support Material for Electrocatalysts in PEMFC 1016
28.3 CNTs as Supercapacitor Electrode Materials 1023
References 1032

29 **Nanomaterials in Civil Engineering**
Jaesang Lee, Seunghak Lee, Eunhyea Chung, Vincent C. Reyes, Shaily Mahendra 1039
29.1 Applications of MNMs in Construction 1041
29.2 Environmental Release of MNMs Used in Construction 1047
29.3 Potential Adverse Biological Impacts and Toxicity Mechanisms 1049
29.4 Mitigation of Environmental and Health Impacts 1052
29.5 Conclusions 1054
References 1055

30 **Plasmonic Nanomaterials for Nanomedicine**
Renat R. Letfullin, Thomas F. George 1063
30.1 Introduction 1063
30.2 Nanooptics – Lorenz–Mie Formalism 1064
30.3 Optical Properties of Gold Nanoparticles in Biological Media 1065
30.4 Kinetics of Heating and Cooling of Nanoparticles 1067
30.5 Spatial Distribution of Temperature Fields Around the Nanoparticle 1076
30.6 New Dynamic Modes in Selective Plasmonic Nanotherapy 1083
References 1095

31 **Carbon Nanotube Membrane Filters**
Anchal Srivastava, Saurabh Srivastava, Kaushik Kalaga 1099
31.1 Types of Filtration 1100
31.2 Mechanisms of Filtration 1101
31.3 Carbon Nanotube Membrane Filters 1102
31.4 Future Research Perspectives 1112
References 1112

32 **Nanomaterial Toxicity, Hazards, and Safety**
Zuzanna A. Lewicka, Vicki L. Colvin 1117
32.1 Engineered Nanomaterials – General Overview 1118
32.2 Occurrence of Engineered Nanoparticles in the Environment 1119
32.3 Effects of Nanoparticles on Organisms 1120
32.4 Nanoparticle Physicochemical Characteristics of Relevance for Toxicology 1124
32.5 Special Case – Sunscreens 1130
32.6 Conclusions 1132
References 1133

Acknowledgements 1143
About the Authors 1145
Detailed Contents 1163
Subject Index 1181

List of Abbreviations

α-SMA	α-smooth muscle actin
p-NP	*p*-nitrophenol
0-D	zero-dimensional
1-D	one-dimensional
2-D	two-dimensional
2-PAM	2-pyridine-aldoxime methiodide
2Q	double-quantum
3-D	three-dimensional
3Q	triple-quantum
4Hop	4-hexadecyloxyphenyl

A

AA	ascorbic acid
AAM	anodized aluminum membrane
AAO	anodic aluminum oxide
AAO	anodized aluminum oxide
AAS	atomic absorption spectroscopy
Ab	antibody
AC	alternating current
Acac	acetylacetone
ACNT	aligned carbon nanotube
ACQ	aggregation-caused quenching
AChE	acetylcholine esterase
ACP	amorphous calcium phosphate
AD	arc discharge
AEE	aggregation-enhanced emission
AES	Auger electron spectroscopy
AES	3-(2-aminoethylaminopropyl)trimethoxysilane
AFC	alkaline fuel cell
AFC	antiferromagnetically coupled
AFM	atomic force microscopy
AIE	aggregation-induced emission
AIEE	aggregation-induced enhanced emission
ALD	atomic layer deposition
AlPO	aluminophosphate
AM	alveolar macrophage
anti-EGFR	anti-epidermal growth factor receptor
AOC	aromatic organic compounds
APC	antigen-presenting cell
APES	aminopropyltrimethoxysilane
APPES	ambient pressure photoelectron spectroscopy
APS	3-aminopropyltrimethoxysilane
APT	atom probe tomography
APTES	(aminopropyl) triethoxysilane
APTS	3-aminopropyltriethoxysilane
AR	analytical reagent
AR	aspect ratio
ARPES	angle-resolved photoemission spectroscopy
ASTM	American Society for Testing and Materials
ATQD	*N*-(4-aminophenyl)-*N*′-(4′-(3-triethoxysilyl-propyl-ureido)phenyl-1,4-quinonenediimine)
ATP	adenosine-5′-triphosphate
ATRP	atom-transfer radical polymerization
AWWA	American Water Works Association

B

BASF	Badische Anilin und Soda Fabrik
bcc	body-centered cubic
BCF	Burton–Cabrera–Frank
BCP	biphasic calcium phosphate
BDAC	benzyldimethylammoniumchloride
BDNF	brain-derived neurotrophic factor
BEP	Brønsted–Evans–Polanyi relations
BES	Office of Basic Energy Sciences
BET	Brunauer–Emmett–Teller
BF	bright field
BFGF	basic fibroblast growth factor
BG	back-gate
BHJ	bulk heterojunction
bioMEMS	biological microelectromechanical system
BMG	bulk metallic glass
BN	boron nitride
BOM	bubble overlapping mode
BP	buckypaper
BPEA	9,10-bis(phenylethynyl)anthracene
BS	black silicon
BSA	bovine serum albumina
BSI	British Standards Institution
BSPP	bis(*p*-sulfonatophenyl) phenylphosphine dihydrate dipotassium
BT	barium titanate
BT	benzenethiol
BTCP	β-tricalcium phosphate

C

C_{16}TAB	hexadecyl trimethyl ammonium bromide
C-PANI	conductive camphorsulfonic acid-doped emeraldine PANI
C3DT	1,3-Propanedithiol
CA	contact angle
CALPHAD	calculation of phase diagrams
CAM	cluster aggregation mode

CBED	convergent-beam electron diffraction
CBEV	coordination-dependent bond-energy variation
CCDB	Cambridge crystallographic data base
CCG	chemically converted graphene
CCT	correlated color temperature
CCVD	catalytic chemical vapor deposition
CD	cyclodextrin
CFR	continuous flow reactor
CHP	cyclohexylpyrrolidone
CHT	chymotrypsin
CIE	International Commission on Illumination
CIP	current in the plane
CMG	chemically modified graphene
CMOS	complementary metal–oxide–semiconductor
CMP	chemical–mechanical planarization
CNF	carbon nanofiber
CNM	carbon nanotube membrane
CNT	carbon nanotube
CN-TFMBE	1-cyano-trans-1,2-bis(3′,5′-bis-trifluoro-methyl-biphenyl)ethylene
CO	cuboctahedron
COD	1,5-cyclooctadiene
COLI	collagen I
COLIV	collagen IV
COST	Cooperation in Science and Technology
COSY	correlation spectroscopy
COT	1,3,5-cyclooctatriene
cp	close packed
CP	coherent phonon
CP	cross polarization
CPP	conduction perpendicular to plane
CPP	current perpendicular to the plane
CPS	collected photo signal
CS	cross section
CS-PCL	chitosan-graft-PCL
CSA	chemical shift anisotropy
CSP	colloidal silver preparation
CT	charge transfer
CTA^+	cetyl-triamine cation
CTA	cetyltrimethylammonium
CTAB	cetyltrimethylammonium bromide
CV	crystal violet
CV	cyclic voltammetry
CVD	chemical vapor deposition
CW	continuous-wave
CuPC	copper phthalocyanine
CuTCNQ	copper tetracyanoquinodimethane

D

D4R	double four ring
DAAQ	1,5-diaminoanthraquinone
DAFC	direct alcohol fuel cell
DAPI	4′,6-diamidino-2-phenylindole
DAPRAL	copolymer of maleic anhydride and α-olefin
DBR	distributed Bragg mirror
DC	dendritic cell
DC	direct current
DCE	1,2-dichloroethane
DD-PTCDI	*N*,*N*′-di(dodecyl)-perylene-3,4,9,10-tetracarboxylic diimide
DDA	discrete dipole approximation
DDAB	didecyldimethylammonium bromide
DDC	*N*,*N*′-dicyclohexylcarbodiimide
DEFC	direct ethanol fuel cell
DEG	diethylene glycol
DF	defluoridation capacity
DF	density function
DFAC	direct formic acid fuel cell
DFT	density functional theory
DFTB	density functional tight binding
DGU	density-gradient ultracentrifugation
DI	deionized
DIC	differential interference contrast
DLC	diamond-like carbon
DLS	dynamic light scattering
DLVO	Derjaguin–Landau–Verwey–Overbeek
DMA	dimethylamide
DMEU	1,3-dimethyl-2-imidazolidinone
DMF	dimethylformamide
DMFC	direct methanol fuel cell
DMPO	5,5-dimethyl-pyrroline *N*-oxide
DMSA	dimercaptosuccinic acid
DMSO	dimethyl sulfoxide
DNA	deoxyribonucleic acid
DND	detonation nanodiamond
DOS	density of states
DOX	doxorubicin
dpa	displacements per atom
DPPTE	1,2-dipalmitoyl-*sn*-glycero-3-phospho-thioethanol
DQ	double quantum
DR	draw ratio
DRG	dorsal root ganglion
DRIFT	diffuse reflectance infrared Fourier-transform
DSC	differential scanning calorimetry
DT	decanethiol
DTAB	dodecyltrimethylammonium bromide
DTE	desaminotyrosyl-tyrosine ethyl ester
DWCNT	double-walled carbon nanotube
DWNT	double-walled nanotubes
Dox	doxorubicin

E

ECD	electrochemical deposition
ECDL	electrochemical double layer

ECELL	environmental cell
ECM	extracellular matrix
ECP	electronically conducting polymer
ECSA	electrochemically active surface area
ED	electrodialysis
ED	electron diffraction
EDAX	energy dispersive analysis
EDC	1-ethyl-3-(3-dimethylaminopropyl)-carbodiimide
EDL	electrical double layer
EDLC	electric double-layer capacitor
EDS	energy-dispersive x-ray spectroscopy
EDTA	ethylenediaminetetraacetic acid
EDX	energy-dispersive x-ray spectroscopy
EELS	electron energy-loss spectroscopy
EFM	electrostatic force microscopy
EG	evaporated gold
EIS	electrochemical impedance spectroscopy
EL	electroluminescence
ELISA	enzyme-linked immuno sorbent assay
EM	electromagnetic
EMI	electromagnetic interference
EOF	electroosmotic flow
EPA	Environmental Protection Agency
EPR	electron paramagnetic resonance
EPS	extracellular polymeric substance
EQE	external quantum efficiency
ESC	embryonic stem cell
ESR	electron spin resonance
ESR	equivalent series resistance
ETEM	environmental TEM
EXAFS	extended x-ray absorption fine structure
ElAP(S)O	element aluminophosphosilicate
EPITH	epithelial cells

F

f-SWCNT	functionalized SWCNT
FABMS	fast atom bombardment mass spectroscopy
FBI	Federal Bureau of Investigation
FBR	fluidized bed reactor
fcc	face-centered cubic
fct	face-centered tetragonal
FDA	Food and Drug Administration
FEB	ferrocene/ethanol/benzylamine
FES	fluctuation-enhanced sensing
FESEM	field emission scanning electron microscope
FET	field-effect transistor
FF	fill factor
FFT	fast Fourier transform
FGO	functionalized GO
FIB	fibrinogen
FIB	focused ion beam
FIPOS	full isolation by porous oxidized silicon
FIT	fluctuation-induced tunneling
FITC	fluorescein isothiocyanate
FLG	few-layer graphene
FMR	ferromagnetic resonance
FN	fibronectin
FND	fluorescent carboxylated HPHT ND
FND	fluorescently enhanced ND
fpRFDR	finite-pulse radio frequency-driven recoupling

G

GMR	giant magnetoresistance
GN	gold nanoparticle
GNC	gold nanoparticle cluster
GNP	gold nanoparticle
GNP	graphite nanoplatelet
GNR	gold nanorod
GNR	graphene nanoribbon
GO	graphene oxide
GOX	glucose oxidase
GSH	glutathione
GTBMD	generalized tight-binding molecular dynamics

H

HA	humic acid
HAADF	high-angle annular dark field
HATU	2-(7-aza-1*H*-benzotriazole-l-yl)-1,1,3,3,-tetramethyluronium hexafluorophosphate
HAZ	heat-affected zone
HC	hexagonal channel
HCCN	highly curved carbon nanostructure
HCI	highly charged ion
hcp	hexagonal close packed
HDA	hexadecylamine
HDD	1,2-hexadecanediol
HDDR	hydrogenation–decomposition–desorption–recombination
HDS	hydrodesulfurization
HDT	hexadecanethiol
HEPES	4-(2-hydroxyethyl)-1-piperazineethane-sulfonic acid
HEV	hybrid electric vehicle
HF	hydrofluoric acid
HG	hydrazinium graphene
HIV	human immunodeficiency virus
HL60	human promyelocytic leukemia
HMDA	hexamethylenediamine
HMO	hydrous manganese dioxide
HMOG	heavy metal oxide glass
HMTA	hexamethylenetetramine
HNS	hot neutron source

HOMO	highest occupied molecular orbital
HOPG	highly oriented pyrolytic graphite
HP	Hall–Petch
HPA	hexylphosphonic acid
HPC-Py	pyrene-labeled hydroxypropyl cellulose
HPHT	high-pressure high-temperature
HPMC	Hydroxypropylmethyl cellulose
HPSMAP	poly(styrene-co-maleic anhydride) carrying pyrene
HSMA	hydrolyzed poly(styrene-co-maleic) anhydrite
h-PSMA	hydrolyzed-poly(styrene-*alt*-maleic anhydride)
HREM	high-resolution electron microscopy
HRN	helical rosette nanotube
HRP	horseradish peroxidase
HRSEM	high-resolution scanning electron microscope
HRTEM	high-resolution transmission electron microscopy
HSA	human serum albumin
hSKMC	human skeletal muscle cell
HTT	heat treatment temperature
HWHM	half-width at half-maximum
HiPCO	high-pressure carbon monoxide

I

IANH	International Alliance for NanoEHS (environment, health, safety)
IC	integrated circuit
ICP	inductively coupled plasma
ICP-MS	inductively coupled plasma mass spectrometry
IE	immersion–electrodeposition
IF	immunofluorescence
IF	inorganic fullerene-like nanoparticle
iFF	isotactic polypropylene
IFSS	interfacial shear strength
Ig	immunoglobulin
IgG	immunoglobulin G
Ih	icosahedron
IKVAV	laminin derived self-assembling peptide
IKVAV-PA	IKVAV polyacrylamide
IL	interleukin
IL	ionic liquid
IMR	intramolecular rotation
INCO	International Nickel Company
INT	inorganic nanotube
IP	iminopyrrole
IPCE	incident photon to charge carrier efficiency
iPSC	induced pluripotent stem cell
IR	infrared
ipr	isolated pentagon rule
ISO	International Standards Organization
ITO	indium tin oxide
IZA	International Zeolite Association

K

KE	Kirkendall effect
KK	Kramers–Kronig

L

LA	longitudinal acoustic
LAM	laminin
LB	Langmuir–Blodgett technique
LB94	van Leeuwen–Baerends
LBL	layer-by-layer
LCD	liquid-crystal display
LDA	local density approximation
LDOS	local density of states
LED	light-emitting diode
LEED	low energy electron diffraction
LIB	lithium-ion battery
LMP	Larson–Miller plot
LN	less noble
LPM	large-pore mordenite
LPS	lipopolysaccharide
LSC	limbal stem cells
LSP	longitudinal surface plasmon
LSPR	localized surface plasmon resonance
LTA	Linde type A
LUMO	lowest unoccupied molecular orbital
LYM	lymphocytes

M

M	metalloid
MA	mechanical alloying
MAE	magnetic anisotropy energy
MALDI-TOF	matrix-assisted laser desorption/ionization-time of flight
MAPO	metalaluminophosphate
MAPSO	metalaluminophosphosilicates
MAS	magic angle spinning
MBE	molecular beam epitaxy
MC	metal cluster
MCFC	molten carbonate fuel cell
MCL	maximum contamination limit
MCS	ethylene glycol monomethyl ether
MD	molecular dynamics
MDA	malondialdehyde
MDA	mercaptodecanoic acid
MEA	membrane electrode assembly
MEMS	microelectromechanical system
MF	mesoflower
MF	microfiltration

MFC	microbial fuel cell
MFI	melt–flow index
MFM	magnetic force microscopy
MGM	metal-graphite multilayer
MHAP	micron particulate hydroxyapatite
ML	monolayer
MN	more noble
MNM	manufactured nanomaterials
MNPM	metallic nanoporous material
MO	methyl orange
MOCVD	metalorganic chemical vapor deposition
MOF	metal-organic framework
MOKE	magneto-optical Kerr effect
MPB	morphotropic phase boundary
MPC	monolayer-protected cluster
MPCF	mesophase pitch-based carbon fiber
MPS	mercaptopropyltrimethoxysilane
MPTMS	mercaptopropyltrimethoxysilane
MR	magnetic resonance
MRAM	magnetic random-access memory
MRI	magnetic resonance imaging
mRNA	messenger RNA
MRR	material removal rate
MRSw	magnetic relaxation switching
MSA	mercaptosuccinic acid
MSC	mesenchymal stem cell
MSE	mercurous sulfate electrode
MTBD	[7-methyl-1,5,7-triazabicyclo[4.4.0]dec-5-ene][bis(perfluoroethylsulfonyl)imide]
MWCNT	multiwalled carbon nanotube
MWNT	multiwalled nanotubes

N

NaBBS	sodiumbutylbenzene sulfonate
NaDDBS	sodium dodecylbenzene sulfonate
NADH	nicotinamide adenine dinucleotide
NaOBS	sodium octylbenzene sulfonate
NaPSS	polystyrene sulfonate sodium salt
NBE	near-band-edge
NC	nanocrystalline
nc-AFM	noncontact AFM
ND	nanodiamond
NDO	ozone-modified nanodiamond
ND-PTCDI	*N*,*N*′-di(nonyldecyl)-perylene-3,4,9,10-tetracarboxylic diimide
NEMS	nanoelectromechanical system
NEUT	neutrophils
NEXAFS	near-edge x-ray absorption fine structure
NF	nanofeatures
NF	nanofiltration
NFA	nanostructured ferritic alloy
NG	natural highly-oriented pyrolytic graphite
NGF	nerve growth factor
NHAP	nanohydroxyapatite
nHAp	nanohydroxyapatite particle
n-HApC	nanohydroxyapatite/chitosan
NHS	*N*-hydroxysuccinimidyl ester
NIOSH	National Institute for Occupational Safety and Health
NIR	near infrared
NM	noble metal
NMP	*N*-methyl-pyrrolidone
Nmpd	*N*-methylpyridinium
Nmpr	*N*-methylpyrrole
NMR	nuclear magnetic resonance
NO-IF	nanooctahedra-IF
NP	nanoparticle
NPG	nanoporous graphite
NPG/GC	NPG supported by glassy carbon electrode
NPGC	nanoporous gold composite
NPM	nanoporous metal
NPNT	nanoporous nanotube
NPS	nanoporous silver
NR	nanorod
NSC	neural stem cell
NSM	nanostructured materials
NT	nanotube
NTS	nanostructured transformable steel
NV	nitrogen-vacancy
NW	nanowire

O

O/F	oxidant-to-fuel
OCP	open-circuit potential
OCT	optical coherence tomography
ODA	octadecylamine
ODE	octadecene
ODF	orientation distribution function
ODPA	octadecylphosphonic acid
ODS	octadecyltrimethoxysilane
ODS	oxide dispersion strengthened
OER	oxygen evolution reaction
OFET	organic field-effect transistor
Oh	octahedron
OL	optical-limiting
OLC	onion-like carbon
OLED	organic light-emitting diode
OPD	O-phenylenediamine
OPH	organophosphorus hydrolase
OPS	oxidized PS
OPV	organic photovoltaic
ORR	oxygen reduction reaction
OSN	organic solvent nanofiltration
OTM	one-temperature model

P

P3HT	poly(3-hexylthiophene)
P3OT	poly(3-octylthiophene)
PA	peptide amphiphile
PA-6	prepared a nylon-6
PAA	poly(acrylic acid)
PABS	polyaminobenzene sulfonic acid
PAFC	phosphoric acid fuel cell
PAGE	polyacrylamide gel electrophoresis
PAH	polycyclic aromatic hydrocarbon
PAN	polyacrylonitrile
PANI	polyaniline
PATS	polythiophene derivatives
PBO	poly(*p*-phenylene benzobisoxazole)
PBS	phosphate buffered saline
PC	pentagonal column
PC	photonic crystal
PC	polycarbonate
PC	principal component
PCA	principal component analysis
PCB	polychlorinated biphenyl
PCE	power conversion efficiency
PCF	photonic crystal fiber
PCL	poly(ε-caprolactone)
PCL-G	PCL-gelatin
PDDA	poly(diallyldimethyl)ammonium chloride
PDDP	1-phenyl-3-((dimethylamino)styryl)-5-((dimethylamino)phenyl)-2-pyrazoline
PDEAEMA	poly(2-diethylaminoethyl methacrylate)
PDGF	platelet-derived growth factor
PDLC	polymer-dispersed liquid-crystal
PDMS	polydimethylsiloxane
PDOS	phonon density of states
PE	photoelectron
PE	polyethylene
PEC	photoelectrochemical
PECVD	plasma-enhanced CVD
PEDOT	poly(3,4-ethylenedioxythiophene)
PEEk	produced poly(ether ether ketone)
PEG	polyethylene glycol
PEI	polyethyleneimine
PEL	permissible occupational exposure limit
PEMFC	proton exchange membrane fuel cell
PEN	Project on Emerging Nanotechnologies
PEO	poly(ethylene oxide)
PES	potential energy surface
PET	polyethylene terephthalate
PFG	pulsed-field-gradient
PFM	piezoelectric force microscopy
PG	PCL–gelatin
PG	proteoglycan
PGA	poly(glycolic acid)
PGLA	copolymer of PGA and PLLA
PGM	platinum group metal
pIh	polyicosahedron
PIPAAm	responsive poly(*N*-isopropylacrylamide)
PL	photoluminescence
PL-PEG	phospholipid polyethylene glycol
PLA	poly-ethylene oxide
PLA	pulsed laser ablation
PLE	photoluminescence excitation
PLGA	poly(lactic-co-glycolic) acid
PLLA	poly(L-lactic) acid
PM	dipropylene glycol monomethylether
PMMA	poly-methyl methacrylate
PMN-PT	$PbMg_{1/3}Nb_{2/3}O_3$-$PbTiO_3$
PmPV	poly(*m*-phenylenevinylene-co-2,5-dioctoxy-*p*-phenylenevinylene)
PN	phosphorus-nitrogen
PNIPAm	poly(*N*-isopropyl acrylamide)
PNP	plasmonic
PP	polypropylene
pp	peak-to-peak
PPCP	1,2,3,4,5-pentaphenyl-1,3-cyclopentadiene
PT	$PbTiO_3$
PPE	poly-*p*-phenyleneethynylene
PPF	propylene fumarate
PPTA	poly phenylene terephthalamide
PPV	poly-*p*-phenylenevinylene
PPy	polypyrrole
PRR	pattern recognition receptor
PS	polystyrene
PS	porous silicon
PS-PFS	poly(styrene-b-ferrocenyldimethylsilane)
PSD	photo signal detector
PSS	poly(sodium 4-styrenesulfonate)
PSS	polystyrene sulfonate
PSU	polysulfonate
PSU	polysulfone
PSVPh	poly(styrene-*co*-vinyl phenol)
Pt-NPG	platinum-decorated nanoporous gold
Pt-NPGL	platinum-plated nanoporous gold leaf
PTCDI	*N*,*N*′-di(propoxyethyl)perylene-3,4,9,10-tetracarboxylic diimide
PTCE	track-etched polycarbonate
PTFE	polytetrafluoroethylene
PU	polyurethane
PV	pervaporation
PV	photovoltaic
PVA	polyvinyl alcohol
PVC	polyvinylchloride
PVD	physical vapor deposition
PVDF	polyvinyldifluoride
PVP	polyvinyl pyrrolidone
PW	plane wave
pzc	point of zero charge

PZN-PT	$PbZn_{1/3}Nb_{2/3}O_3$-$PbTiO_3$
PZT	$Pb(Zr,Ti)O_3$

Q

QC	quantum cluster
QD	quantum dot
QEXAFS	quick EXAFS
QHE	quantum Hall effect

R

R6G	rhodamine 6G
RA	right angle
RBM	radial breathing mode
RCF	rabbit corneal fibroblast
RE	rare-earth
rebar	reinforcement bar
REDOR	rotational echo double resonance
RF	radio frequency
RFDR	radiofrequency-driven recoupling
RFID	radiofrequency identification
RGB	red green blue
RGD	Arg-Gly-Asp
RGO	reduced graphene oxide
rhBMP-2	recombinant human bone morphogenic protein-2
RHE	reversible hydrogen electrode
RIA	radioimmuno assay
RIE	reactive-ion etching
RIR	restriction of intramolecular rotation
RJS	rotary jet spinning
RKKY	Rudermann–Kittel–Kasuya–Yosida
RM	reactive milling
RMS	microscale surface roughness
RNA	ribonucleic acid
RO	reverse osmosis
ROS	reactive oxygen species
RPC	retinal progenitor cells
RRR	redox replacement reaction
RRS	resonant Raman scattering
RT	room temperature
RT-PCR	real-time polymerase chain reaction
R&D	research and development

S

S–W	Stone–Wales
S/L	solid/liquid
SA	sliding angle
SA	solar ablation
SAED	selected-area electron diffraction
SAM	self-assembled monolayer
SANS	small -angle neutron scattering
SAPO	silicoaluminophosphate
SAXS	small-angle x-ray scattering
SBU	secondary building unit
SC	simple cubic
SC	sodium cholate
SCC	stress corrosion cracking
SCE	saturated calomel electrode
SCR	space-charge region
SD	standard deviation
SDBS	sodium dodecylbenzene sulfate
SDCH	samaria-doped ceria
SDS	sodium dodecyl sulfate
SEC	size exclusion chromatography
SEI	solid–electrolyte interphase
SEIRA	surface-enhanced infrared absorption
SEM	scanning electron microscopy
SES	scanning electron spectroscopy
SERS	surface-enhanced Raman scattering
SET	single-electron transistor
SF	silk fibroin
SFF	solid freedom fabrication
SFG	sum-frequency generation
SFM	scanning force microscopy
SGS	spaced superconducting electrode
SHE	standard hydrogen electrode
SIM	structured illumination microscopy
SIMS	secondary-ion mass spectrometry
siRNA	silenced RNA
SL	superlattice
SLS	solution–liquid–solid
SMA	shape-memory alloy
SMAD	solvated metal atom dispersion
SNR	signal-to-noise ratio
SOCT	sodium octanoate
SOFC	solid oxide fuel cell
SOI	silicon-on-insulator
SP	surface plasmon
SP-STM	spin-polarized scanning tunneling microscopy
SPM	scanning probe microscopy
SPM	small-pore mordenite
SPP	surface plasmon polariton
SPR	surface plasmon resonance
SPS	spark plasma sintering
SQ	single quantum
SQUID	superconducting quantum interference device
SRNF	solvent resistant nanofiltration
SS	stainless steel
SSA	specific surface area
SSNMR	solid-state nuclear magnetic resonance
STEM	scanning transmission electron microscopy
STM	scanning tunneling microscopy
STORM	stochastic optical reconstruction microscopy
STS	scanning tunneling spectroscopy
SWCNT	single-walled carbon nanotube

SWNH	single-wall nanohorn
SWNT	single-walled nanotube
SXRD	surface x-ray diffraction
ShdH	Shubnikov–de Haas
Si-MEMS	silicon microelectromechanical system
Si-nc	silicon nanocrystal

T

TA	thioctic acid
TA	transverse acoustic
TAMRA	tetramethylrhodamine
TASA	template-assisted self-assembly
TCNQ	tetracyanoquinodimethane
TCO	transparent conductive oxide
TDABr	tetradodecylammonium bromide
TDDFT	time-dependent density-functional-theory
TDPA	tetradecylphosphonic acid
TE	transition metal element
TEG	tetra(ethylene glycol)
TEM	transmission electron microscopy
TEOS	tetraethyl orthosilicate
TEP	thermoelectric power
TFT	thin-film transistor
TG	top gate
TGA	thermogravimetric analysis
TGA	thioglycolic acid
TGF-β	transforming growth factor
THF	tetrahydrofuran
THPC	tetrakismethyl)phosphonium chloride
TIC	toxic industrial chemical
TIPS	thermally induced phase separation
TL	transition-metal element
TMAH	tetramethylammonium hydroxide
TMR	tunnel magnetoresistance
TNF-α	tumor necrosis factor
TNT	2-methyl-1,3,5-trinitrobenzene
TO	truncated octahedron
TOAB	tetraoctylammonium bromide
TOF	turnover frequency
TOP	trioctylphosphine
TOPO	trioctylphosphine oxide
TPA	tetrapropylammonium
TPD	temperature programmed desorption
TPI	2,4,5-triphenylimidazole
TPL	two-photon luminescence
TPP	1,3,5-triphenyl-2-pyrazoline
TSP	transverse surface plasmon
TSW	Thrower–Stone–Wales
TTCP	tetracalcium phosphate
TWC	three-way catalyst
ThT	thioflavin T

U

UF	ultrafiltration
UHP	ultrahigh pressure
UHV	ultrahigh vacuum
UNCD	ultrananocrystalline diamond
UPD	underpotential deposition
UV	ultraviolet
UV-VIS	ultraviolet-visible
UVR	ultraviolet radiation

V

vdW	van der Waals
VGCF	vapor-grown carbon fiber
VHS	van Hove singularity
VLS	vapor–solid–liquid
VPC	vacuum pyrolysis/carbothermal
VRH	variable range hopping
VS	vapor–solid
VSFG	vibrational sum-frequency generation
VSM	vibrating sample magnetometry
VSS	vapor–solid–solid
Van	vancomycin

W

WAXD	wide angle x-ray diffraction
WC	tungsten carbide
WG	waveguide
WHO	World Health Organization

X

XANES	x-ray absorption near-edge spectroscopy
XAS	x-ray absorption spectroscopy
xc	exchange–correlation
XPS	x-ray photoelectron spectroscopy
XRD	x-ray diffraction

Y

YAB	$YAl_3(BO_3)_4$
YAM	$Y_4Al_2O_9$
Y-CNT	Y-shaped carbon nanotube

Z

ZAP	zone axis pattern
ZHDS	hydroxydodecylsulfate
ZHS	zinc hydroxysulfate
ZLC	zero-length-column
ZSM	zeolite sieve of molecular porosity

1. Science and Engineering of Nanomaterials

Robert Vajtai

Nanomaterials possess different properties compared with macroscopic (bulk) materials built up from the same atoms or compounds. The production routes, characterization, and applications of materials sized on the nanometer scale also differ from the bulk.

In this chapter we define nanomaterials and the specific science that describes them, and collect examples of synthesis and applications of a range of these materials; we also dedicate an extended part of the chapter to material properties, e.g., morphology, mechanical, electrical, magnetic, and optical properties. In both the general and specific parts of the chapter, emphasis is placed on the differences from the bulk phase of the same material and, if possible, the size dependence of the various material properties.

Following the handbook format, the chapter is concise and covers various common properties of nanomaterials and correlations with which nanoscientists work; however, we insert specific parts which have some curiosity value, as well as several aspects of our own research.

1.1 History and Definition of Nanomaterials . 2
1.1.1 History of Nanomaterials 2
1.1.2 Definition of Nanoscale and Nanomaterials 4
1.2 Formation of Nanomaterials 6
1.3 Properties of Nanomaterials 10
1.3.1 Morphology of Nanomaterials 10
1.3.2 Bonds and Structures 10
1.3.3 Mechanical Properties of Nanomaterials 12
1.3.4 Electrical, Magnetic, and Optical Properties 14
1.3.5 Thermal Properties 18
1.3.6 Chemical Properties, Reactivity, and Functionalization 20
1.3.7 Behavior of Nanomaterials in Corrosive Environments 22
1.4 Typical Applications of Nanomaterials 22
1.4.1 Catalysts and Catalyst Templates 26
1.4.2 Energy Conversion and Storage 26
1.4.3 Sensors Based on Nanomaterials 28
1.5 Concluding Remarks 31
1.6 About the Contents of the Handbook 31
References 31

The techniques, recipes, and later science of making and testing tools, artistic objects, and weapons are the main criteria for the characterization and classification of human historical ages – from the Stone Age through the Bronze and Iron Ages to the Silicon Age we are living in. During the history of mankind, the role of nanomaterials has continuously increased, and the growth of this field is accelerating.

In any modern scientific approach, one should design and synthesize materials with a high level of control. The ultimate material design is when one can plan the structure of the produced materials atom by atom, with every defect, bond length, etc. (for example, 60 carbon atoms, or 72, 80, or even a few million, and 80 boron atoms built into a cage similar to carbon fullerene), and synthesis should follow precisely this design.

In this chapter, we collect two sorts of information about nanomaterials. To a lesser extent, the common properties of nanomaterials that are discussed in the following chapters are described, whereas in the main part of the chapter, the features and properties of various groups of materials are discussed. This introductory chapter is more exemplary than universal, and in most cases not detailed. More detailed description of the properties and materials discussed here can be found in the later chapters. For navigation in the handbook please use the extended version of the table of contents and the well-detailed subject index.

1.1 History and Definition of Nanomaterials

In this part of the chapter, we briefly mention several important and interesting events from both ancient and modern ages for nanomaterials production and application. We also present how our fellow scientists and government organizations describe and define nanomaterials.

1.1.1 History of Nanomaterials

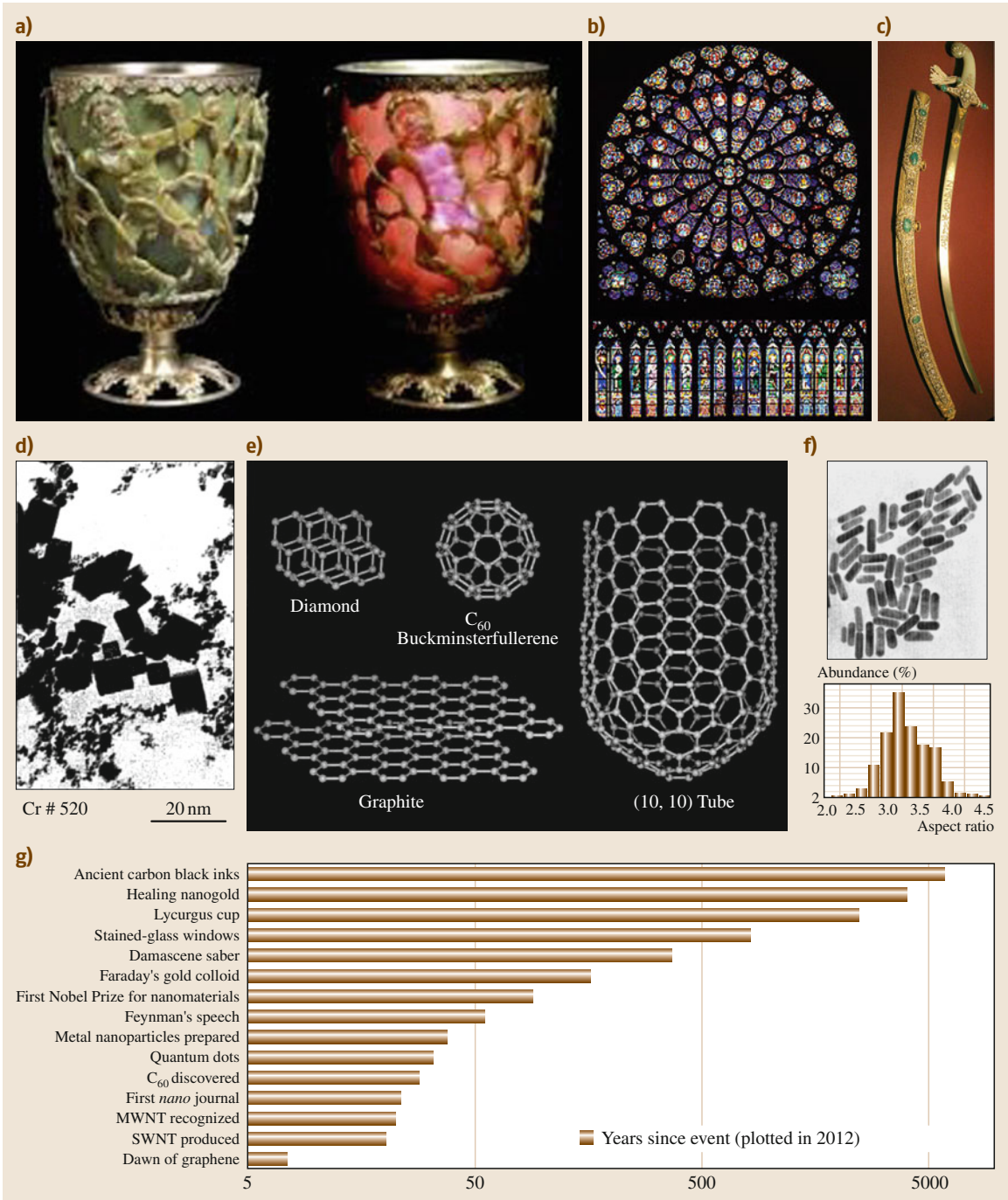
Although we indubitably live not only in the Silicon but also in the beginning of the Nano Age, almost every chapter in this book, as well as most of the comprehensive review papers in the literature, include historical aspects. Usage of nanomaterials remounts to traditional Chinese medicine [1.6], and Mayan [1.7] and medieval Italian paints [1.8]. Nanomaterials such as the colorful and magically healing inks made of colloid-sized (nano) gold particles were also used in artistic applications such as the Lycurgus cup [1.9] and for producing both small and large stained-glass windows for castles and cathedrals.

In Fig. 1.1, we have collected several examples of famous nanomaterials in chronological order (Fig. 1.1a–f). The timescale in Fig. 1.1g shows these mentioned examples and some other important materials as well as important events. Figure 1.1a–c shows pre-modern era examples of nanomaterial applications. The Lycurgus cup (Fig. 1.1a) includes gold nanoparticles which make its color green when we look at it in the usual way, in reflected light, but red in transmitted light [1.9]. Similarly, metal nanoparticles were used in the magnificent south rose window of Notre Dame Cathedral (Fig. 1.1b). The specific nanostructure with cementite nanowires and carbon nanotubes of damascene-style steels (Fig. 1.1c) [1.10] invented in the Mediterranean, and similar techniques used in Sweden, are representative examples of the first manmade engineered nanomaterials [1.10]. Of course, ancient and premodern technologies could not control material properties on the basis of knowledge of nanometer-scale properties; however, the recipes and methods for nanomaterial production were successful enough to provoke admiration and sometimes fear in *scientists* of their age. At the same time, even with our modern knowledge, the admiration for these first craftsmen of nanomaterials still holds.

The history of nanomaterials took an interesting turn in the 20th century. First, the discovery of semiconductor-based transistors [1.11] opened the road for miniaturization and integration of these devices in the first chips [1.12]. In the same decade when the first integrated circuit (IC) was fabricated, Richard Feynman presented his famous lecture [1.13] about the huge information storage capacity of materials if and (as he rather saw it) when one goes to the atomic scale, to store ultimately one bit of information in every atom. He calculated that all of the information stored in the *Encyclopedia Britannica* would fit onto the head of a pin – assuming 120 dpi resolution used in the original print and that the resolution is increased 25 000-fold – without breaking the known rules of physics, and he even envisioned several methods for writing, multiplying, and reading information at that density. In Fig. 1.1d,e, examples of nanomaterials from the last 50 years are displayed. Figure 1.1d shows chromium nanocrystals [1.3] synthesized by the inert gas deposition method [1.3, 14]. Figure 1.1e displays schematics for the newly discovered allotropes of carbon, i. e., nanodiamond, fullerene, nanotubes, and graphene; these materials form such an important part of today's nanomaterial science that at least one chapter in this handbook summarizes knowledge about each of them. Figure 1.1f shows a transmission electron microscopy (TEM) image of gold nanorods and their shape distribution [1.5]; these nanorods are useful in nanomedicine, e.g., for imaging and curing cancer. The bottom part of Fig. 1.1g shows a collection of several historical and novel nanomaterials and related events displayed on a logarithmic scale, dating back from the present to 6000 BC. Even without displaying many important discoveries in the last decades, Nobel and Kavli Prizes awarded for achievements in nanomaterial science, and milestones of commercialization, an obvious exponential acceleration is visible.

Fig. 1.1a–g History of nanomaterial use. **(a–c)** Premodern examples for nanomaterial applications. **(a)** The Lycurgus cup photographed in reflective light and in transmission (after [1.1]). The south rose window of Notre Dame Cathedral in Paris, France. **(c)** Damascus saber (photo Tina Fineberg) (after [1.2]). **(d,e)** Modern-age milestone examples of nanomaterials. **(d)** Metal nanoparticles, Cr shown here, produced by the inert gas deposition technique (after [1.3]); **(e)** allotropes of carbon: nanodiamond, fullerenes, nanotubes, and graphene [1.4]; and **(f)** gold nanorods [1.5]. **(g)** Timescale – measured back from today to 6000 BC on a logarithmic scale – of nanomaterial production and events related to nanomaterials ▶

In this fast-paced and accelerating scientific and engineering nanoworld, one needs to follow several dozen journals which deal with nanomaterials. In this chapter and in the whole *Springer Handbook of Nanomaterials*, we try to provide a compass to identify the most important features.



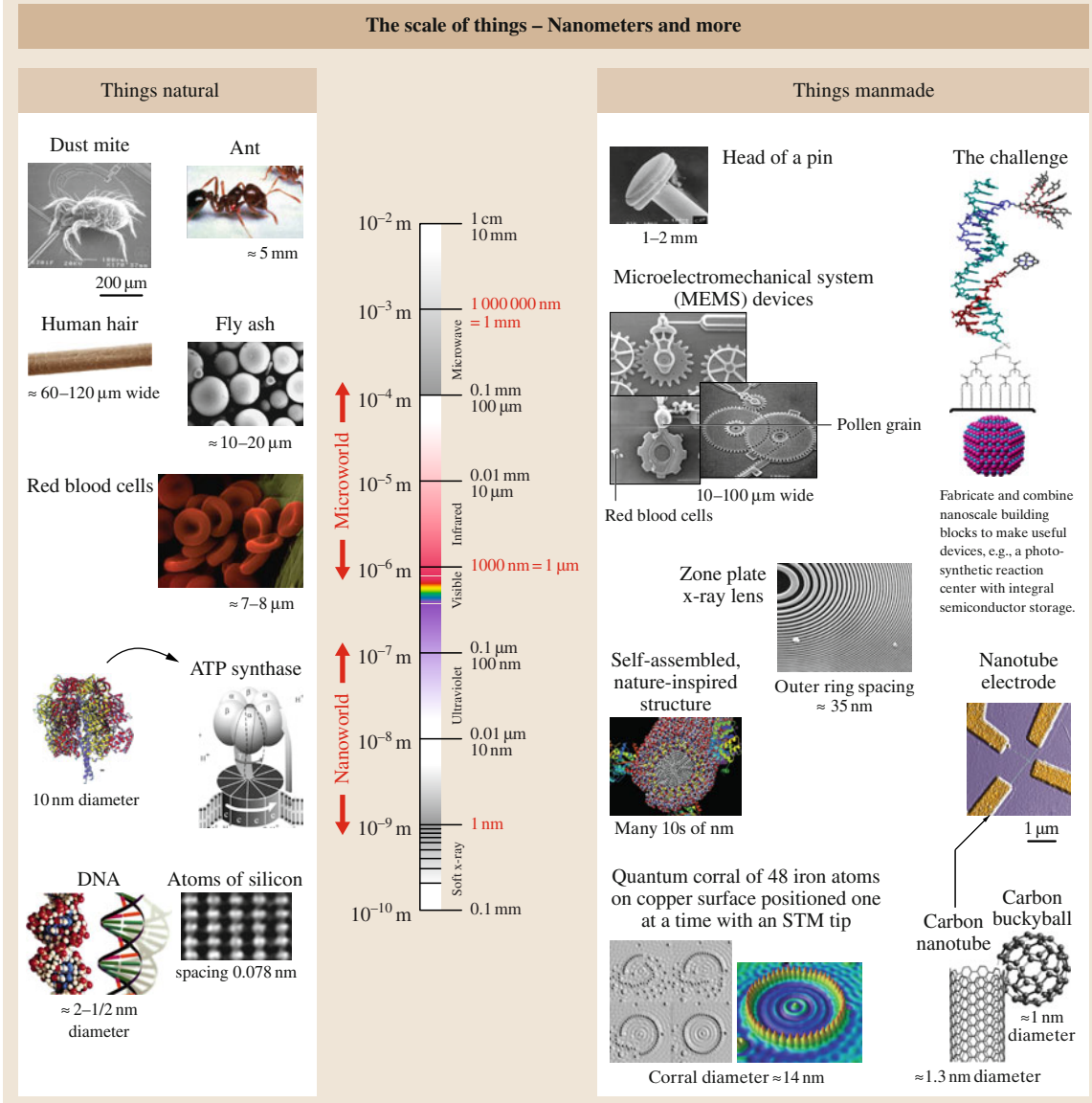


Fig. 1.2 *Scale of things* chart designed by the Office of Basic Energy Sciences (BES) for the US Department of Energy (ATP: adenosine-5′-triphosphate (after [1.15]))

1.1.2 Definition of Nanoscale and Nanomaterials

As mentioned earlier, nanomaterials differ from the corresponding bulk materials in many ways, and this dissimilarity is the reason for the formation of a new discipline that describes the properties and behavior of nanomaterials. To exhibit these unique *nano*properties, materials need to have one, most obvious feature: at least one dimension should be on the nanoscale. In this section, we elaborate what nanoscale means and describe the common properties and features that make nanomaterials different from their well-known macroscopic (bulk) counterparts. We also give definitions of nanosize, nanoscale, and nanostructured materials.

Sizes Are Important: Usual Range of Values

First of all we need to define the size range of structures. The term *nano* comes from Greek and means *dwarf*; when used together with units of physical quantities, it expresses 10^{-9} times smaller than the unit. For nanomaterials, the nanoscale mainly means that length (e.g., size, diameter, edge) is measurable on the nanometer scale. Obviously, other physical quantities, such as area, volume, mass, and energy, may be very far from this particular prefix when we use the corresponding SI units. More exactly, most of the definitions place nanomaterials between the approximate limits of 1 and 100 nm. One nanometer is also equal to 10 Å, using the Angstrom, which is widely used in microscopy and atomic/molecular physics.

In Fig. 1.2, a comparative scale is displayed to show objects with sizes that fall into our common understanding (e.g., ants, pinhead, piece of human hair) to nanomaterials with few-nanometer feature size (e.g., fullerene, nanotube, and DNA (deoxyribonucleic acid)). The figure also shows objects on the intermediate micrometer scale (red blood cells and microelectromechanical systems (MEMSs)), and for comparison with another well-known scale, the different ranges of electromagnetic waves. On this scale, nanomaterials can be positioned between the wavelengths of visible/ultraviolet light and x-ray radiation. Being smaller than the shortest visible wavelengths limits the methods available for determining the shapes of nanomaterials by conventional light microscopy.

Different from Bulk

The most important question is *why* materials on this 1–100 nm scale are distinguished and have their own science and engineering. In the size range below 1 nm we can find molecules, atoms, elementary particles, etc., which are different from the bulk but already have their own disciplines. Multiple atoms or molecules behave differently from individual ones for some obvious reasons; e.g., larger size results in different behavior in collisions with atoms. Other changes with increasing number of atoms in the particle include perturbation of the atomic energy levels leading to energy band structures with fine structure; e.g., the energy difference between neighboring states is $E/2N$, where E is the width of the energy band and N is the number of atoms included. The distinction between molecules and nanomaterials, however, is not sharp. C_{60} is considered a molecule and nanomaterial at the same time, and other large molecules are also used as materials in molecular electronics.

At the other end of the size scale, materials start to be different from bulk below 100 nm size, because the effects of quantum confinement on electrical, thermal, and optical properties become significant at about this size.

Another, very important common feature of nanomaterials (e.g., nanoparticles and nanocrystals) is that they have a very high fraction of their atoms on their surfaces. These atoms behave differently from the ones located inside the object or in ideal bulk crystals (in



Fig. 1.3 Schematic of the top-down and bottom-up nanomaterial production procedures

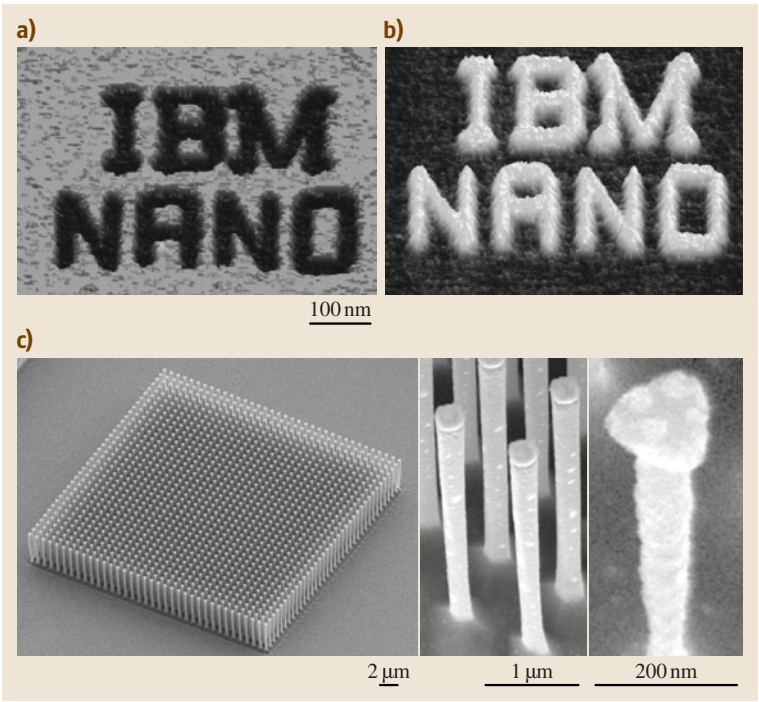


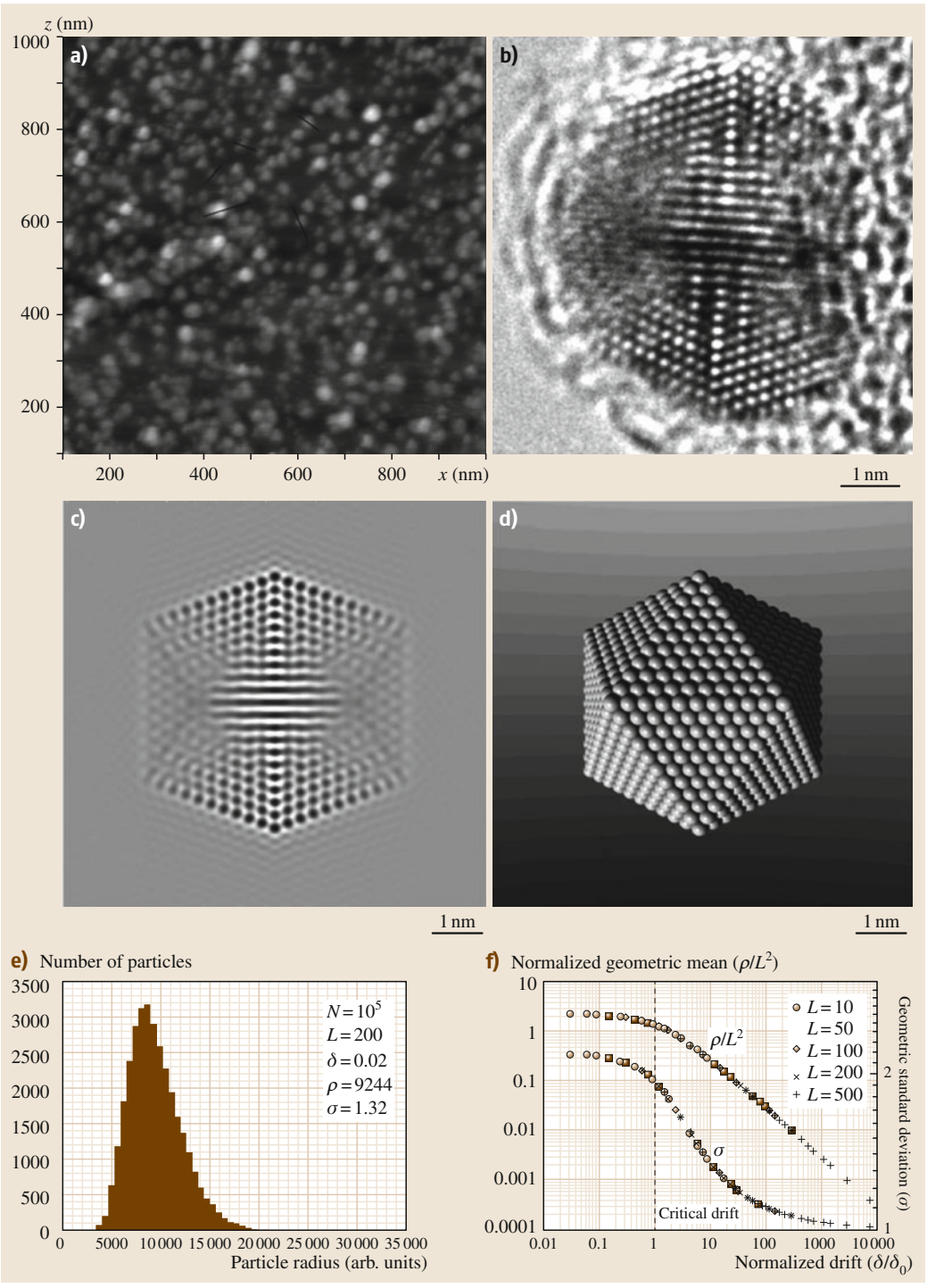
Fig. 1.4a–c Examples of top-down nanostructure fabrication methods. **(a)**,**(b)** Nanoletters generated by direct writing with an AFM tip. **(a)** The *letters* are made of SiO_2 on a silicon wafer. **(b)** Structure after selective etching to remove the oxide [1.16]. **(c)** High-aspect-ratio silicon pillars created by pattern generation by Ga-ion implantation in a focused ion beam (FIB) setup and reactive plasma etching of the wafer [1.17]

fact, the definition of an ideal crystal includes no physical boundary or surface, as the crystal exhibits infinite periodicity) owing to the asymmetrical forces acting on them; there is a force acting on these atoms which is directed into the particle. The integrated effect of the forces on every surface atom provides a surface tension, the related pressure being so high that it can change bond lengths in crystals. Through this, it also changes mechanical, electrical, and thermal properties; e.g., the melting point of small particles can be considerably lower than the bulk value. In the remainder of this chapter we describe in slightly more detail these changes in the physical properties of nanomaterials as a function of feature size; later chapters in this handbook provide more data for individual material groups.

1.2 Formation of Nanomaterials

Formation of nanosized materials – nanoparticles, nanoporous or nanostructured macroscopic materials – is achieved by two basic routes, namely the so-called top-down and bottom-up methods [1.20, 21]. In the former, macroscopic materials are used to fabricate nanomaterials and nanostructures using – typically – very sophisticated methods. In the latter, nanoparticles and other nanomaterials are built up from their ultimate building blocks – atoms and molecules – via self-assembly processes. Figure 1.3 shows a comparative representation of top-down and bottom-up methods. In the top-down method we start from bulk materials and fabricate structures or particles on the nanoscale, analogously to the carving of a sculpture (or many small ones) from a mar-

Fig. 1.5a–f Examples for bottom-up assembly of nanoparticles. **(a–d)** Different representations of an AuPd nanoparticle: **(a)** AFM topography of the surface of the sample covered by the nanoparticles; **(b)** high-resolution transmission electron microscopy (HRTEM) image of an individual nanoparticle; **(c)** HRTEM simulation of the same nanoparticle; **(d)** solid-ball atom model of an icosahedral nanoparticle (after [1.18]). **(e,f)** Explanation of the correlation between particle size distribution and the flow properties of the carrier gas. **(e)** Size distribution at medium inert gas drift conditions; **(f)** size and size distribution as a function of drift intensity (after [1.19]) ▶


z (nm)
1000
800
600
400
200
a)
200
400
600
800
x (nm)
b)
1 nm
c)
1 nm
d)
1 nm
e) Number of particles
3500
3000
2500
2000
1500
1000
500
0
0
5000
10 000
15 000
20 000
25 000
30 000
35 000
Particle radius (arb. units)
N = 10^5
L = 200
δ = 0.02
ρ = 9244
σ = 1.32
f) Normalized geometric mean (ρ/L^2)
10
1
0.1
0.01
0.001
0.0001
0.01
0.1
1
10
100
1000
10 000
Normalized drift (δ/δ0)
ρ/L^2
σ
Critical drift
L = 10
L = 50
L = 100
L = 200
L = 500
2
1
Geometric standard deviation (σ)

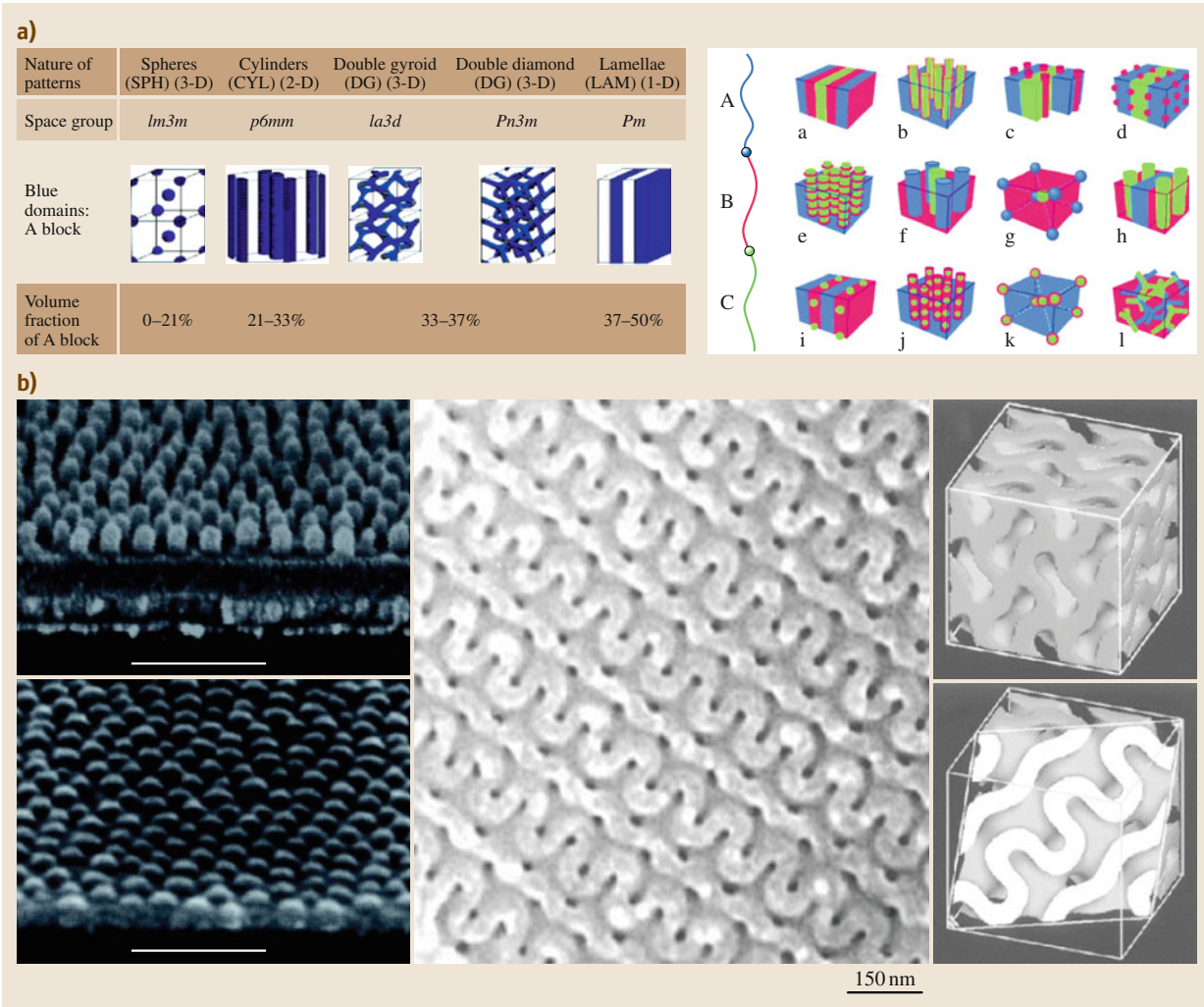


Fig. 1.6a,b Block copolymer self-assembly used in bottom-up and top-down fabrication of nanostructures. **(a)** Schematic showing various block copolymer morphologies; *blue color* represents minority phase, with the matrix surrounding; schematic of a linear triblock copolymer; triblock copolymer structures displayed by *coding colors*. **(b)** SEM image of the Co dot array developed by poly(styrene-b-ferrocenyldimethylsilane) (PS-PFS) BCPs and Ne ion-beam etching (after [1.22–24])

ble boulder; in the bottom-up method we use techniques to build up materials from their component parts, i. e., atoms and molecules, analogously to the building of a cathedral or forming a sculpture from clay.

As procedures used in synthesis and characterization are normally considered parts of nanotechnology rather than nanomaterials science, being discussed in detail in the nanotechnology literature, we only give a very short description for the sake of completeness.

Top-down approaches include evolutionary techniques which are similar to those used in microtechnology of integrated circuit fabrication (e.g., photolithography developed to < 20 nm resolution, nanoimprint lithography) along with several completely new methods [e.g., e-beam and focused ion beam (FIB) lithography, direct writing with atomic force microscopy (AFM), and scanning tunneling microscopy (STM)]. Figure 1.4 shows examples of these revolutionary methods. Figure 1.4a presents a demonstration of nanoscale oxidation of silicon in the shape of letters using an AFM tip [1.16], and the same pattern after etching out the oxide by hydrofluoric acid (HF) (Fig. 1.4b). The

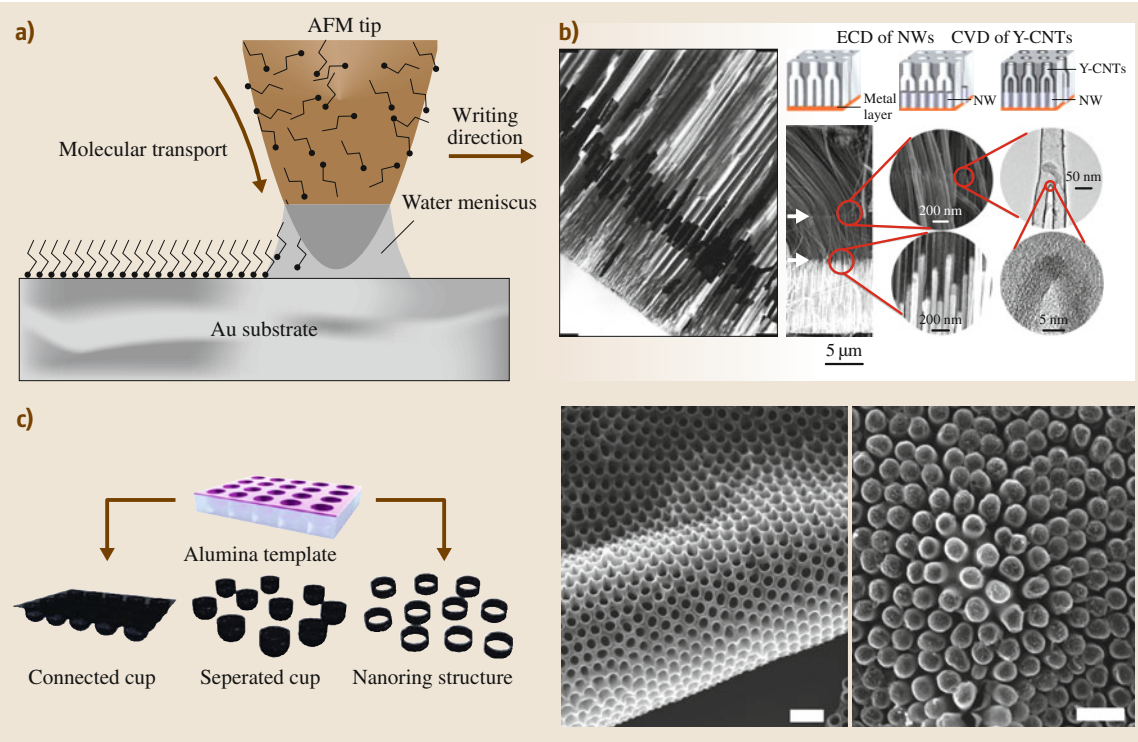


Fig. 1.7a–c Examples of nanomaterial production by methods which merge top-down and bottom-up features. **(a)** Dip-pen nanolithography, AFM structure deposition, and ink self-assembly on the surface (after [1.25]). **(b)** TEM image of gold nanowires grown in an alumina template (after [1.26]); complex shapes and structures generated in predesigned and fabricated alumina template junctions (after [1.27]). **(c)** Schematics of low-aspect-ratio nanocup preparation on alumina template and SEM images of the two sides of the freestanding nanocup layer (ECD: electrochemical deposition; NW: nanowire; Y-CNT: Y-shaped carbon nanotube) (after [1.28])

printing resolution of the letters corresponds to almost 2 000 000 dpi, which is in the range of Feynman's calculations. Figure 1.4c shows high-aspect-ratio structures fabricated by cryogenic plasma etching of gallium ion-implanted regions of a silicon wafer [1.17]. The authors defined the pattern by FIB lithography and used reactive etching, resulting in structures with 65 and 40 nm diameters and 600 nm height (aspect ratio up to 15).

Bottom-up approaches are quite similar to the formation of macroscopic crystals. However, the thermodynamics of the processes involved for nanomaterials differ from the bulk; as we show later, the free energy, chemical potential, phase diagrams, and kinetics of phase transformations are distinct. Nucleation [1.29] and diffusion are the key elements in the formation of particles; however, other parameters, such as forced or natural drift of the carrier gas in the synthesis (Figs. 1.1 and 1.5) of nanoparticles by the inert gas deposition method [1.3, 14, 18, 30, 31], also play a very important role in determining the mean particle size and distribution width [1.19, 32]. One of the most widely used bottom-up methods is chemical vapor deposition (CVD), where nanomaterials *grow* on catalyst layers; references to illustrate such materials can be taken from thousands of related papers for single-walled nanotubes (SWNTs) [1.33, 34], multi-walled nanotubes (MWNTs) [1.35], and *h*-BN [1.36] deposition.

Solution-based methods are governed by the concentration of the components used, the temperature of the reaction, and the amount of surfactant; examples include seed-mediated growth of copper nanoparticles [1.37], synthesis of shape-controlled gold nanoparticles [1.38], and specifically the Kirkendall effect applied for preparation of hollow particles [1.39, 40].

Sonothermal synthesis [1.41] and exfoliation of two-dimensional (2-D) materials – for making nanoma-

terials from bulk – are considered bottom-up methods, as we do not have control over the exact manner of formation or properties of each of the particles via macroscopic equipment or tools.

Another possibility is *to combine the advantages of the bottom-up and top-down* methods. A few such examples are displayed in Figs. 1.6 and 1.7. An interesting way of increasing the resolution of photolithography beyond its physical limitations is by using directed self-assembly and self-orientation of block copolymers [1.42]; structures derived from this technique are displayed in Fig. 1.6. Figure 1.7a shows schematics of dip-pen lithography; in this case, the AFM manipulation is the top-down component while self-assembly of the *printed* materials is the bottom-up component. In the widely used method of membrane-based deposition [1.26], we have control over the shape of the alumina template trough parameters such as the etching time, acid type, and temperature; as examples, nanowire, nanojunction nanocup, and nanoring fabrication are collected in Fig. 1.7b–c.

1.3 Properties of Nanomaterials

When nanomaterials are studied, with few exceptions, the goal of the investigation is to reveal the values of physical properties similar to those used to characterize bulk phases of materials. In most cases though, the values of these properties are very different from those in the bulk, depending on the size and morphology of the nanomaterials; this is similar to the way in which the properties of bulk materials also depend on their crystal system (e.g., face-centered cubic (fcc) versus body-centered cubic (bcc)).

1.3.1 Morphology of Nanomaterials

Not only the overall size, but also the shape of nanomaterials is a factor governing other properties; the aspect ratio, porosity, and surface roughness all change the surface-to-volume ratio and thereby other properties. Shape is such an important property that classification of nanomaterials can be based on their dimensionality or aspect ratio. Figure 1.8 shows schematics of nanomaterials limited to zero, one, two, and three dimensions. Zero-dimensional (0-D) objects have nanometer feature size in every direction; one-dimensional (1-D) objects have nanometer size in two directions but larger, e.g., micrometer, length in the third; two-dimensional (2-D) objects are atomically thin sheets of materials, while three-dimensional (3-D) nanomaterials are nanoporous or nanostructured materials. Figure 1.8b, c, and d show examples of 0-D, 1-D, and 2-D materials, respectively. Quantum dots [1.43], nanoparticles [1.3, 14], and fullerenes [1.44] are 0-D objects; the example shown here is a series of TEM images of iron oxide nanoparticles with particle diameters of 6–13 nm, where the diameter was controlled with 1 nm accuracy [1.45, 46]. The one-dimensional material shown in Fig. 1.8c is a GaAs nanowire mat; the inset shows an individual wire [1.47]. The most famous 1-D materials are the single-walled nanotubes (SWNTs) [1.48,49] and multi-walled carbon nanotubes (MWCNTs) [1.50]. Two-dimensional materials include graphene [1.51], boron nitride (*h*-BN) [1.36], and graphene oxide [1.52]. In Fig. 1.8d, TEM images of BCN of two and three atomic layer thickness are shown [1.53]. Typical 3-D nanostructured materials are nanoporous metals and ceramics, aerogels, and zeolites [1.54]. Figure 1.8e shows Gleiter schematics of different kinds of 3-D materials [1.55], and Fig. 1.8e,f illustrates the self-assembly of microparticles from azobenzene thiol-functionalized nanoparticles [1.56].

1.3.2 Bonds and Structures

The compressive strain in bulk solid materials is relatively small, even in the case of high applied stress, because the bonds in solids are strong and changing their length requires high pressure and a substantial amount of energy. Quite amazingly, the asymmetry caused by the forces near to surface atoms in solids change the bond length of nanomaterials at least on the scale that we are able to achieve by applying outside forces. The importance of the effect of these changes in bond length increases with the surface atom to volume atom ratio (dispersion) and accordingly on the particle size; it is determinant in clusters and nanoparticles at the lower end of the nanoscale, normally between 1–5 nm (about 50–5000 atoms).

Table 1.1 presents a collection of data for bond length relaxation [1.57], data based on references [1.58–70]. It is clear that bond contraction is between 4% and 30%, and, surprisingly for a bulk material scientist, there is a 30% change in the bond length of diamond,

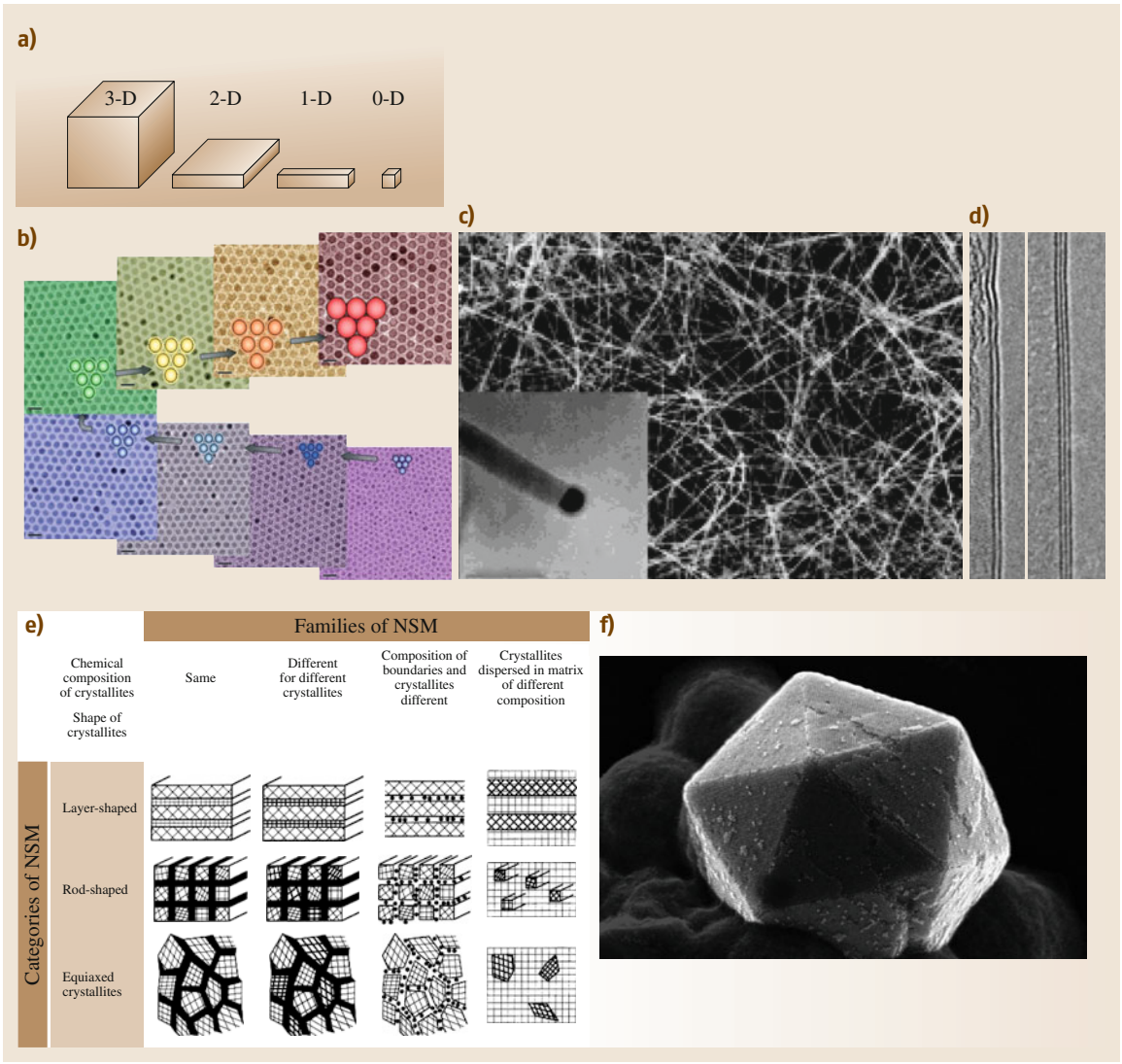


Fig. 1.8a–f Classification of nanomaterials based on their shape, dimensionality, and structure. **(a)** Simple schematics showing 1-D, 2-D, and 3-D nanomaterials. **(b)** 0-D structures: TEM images of iron oxide nanoparticles with particle diameters of 6, 7, 8, 9, 10, 11, 12, and 13 nm (after [1.45, 46]). **(c)** 1-D structures: SEM images of GaAs nanowires with an *inset* of the TEM image of an individual nanowire (after [1.47]). **(d)** 2-D structures: atomic layers (two and three) of BCN (after [1.53]). **(e)** Schematics of classification of different 3-D (bulk-like) nanostructured materials (NSM) (after [1.55]). **(f)** 3-D structure: a microobject built up from self-organized nanoparticles (after [1.56, 71])

too. The table summarizes data for covalent, metallic, and ionic bonds. While the contraction of ionic bonds is slightly less than that for the other two bond types, it is also obvious that the phenomenon is universal for all kinds of bonds. Table 1.1 also names the changes in the physical properties – energy related to bonds, magnetic momentum, and hardness – caused by the bond length contraction and reported in the referenced literature.

Figure 1.9 illustrates how the bond length and bond potential depend on nanoparticle size and shape. Figure 1.9a shows the relative change in the lattice constant for several metal nanoparticles – gold, copper, platinum,

Table 1.1 Bond lengths for typical bonds (covalent, metallic, and ionic) and effect on several physical properties (after [1.57], data from [1.58–70])

Bond nature	Medium	$c_1 = d_1/d$	Effect
Covalent	Diamond {111} [1.72]	0.7	Surface energy decrease
Metallic	Ru [1.73] and Co [1.74]	0.9	
	Re [1.75] (1010) surfaces	0.9	Atomic magnetic momentum is increased by 25–27% [1.76–78]
	Fe-W, Fe-Fe [1.79]	0.88	
	Fe(310) [1.77], N(210) [1.78]	0.88	
	Al(001) [1.80]		Cohesive energy rises by 0.3 eV/bond [1.81]
	Ni, Cu, Ag, Au, Pt and	0.85–0.9	
	Pd dimer bond [1.80]		Single-bond energy increases 2–3-fold [1.80]
	Ti, Zr [1.80]	0.7	
	V [1.80]	0.6	
Ionic	O−Cu(001) [1.82–84]	0.88–0.96	
	O−Cu(110) [1.82, 83]	0.9	
	N−Ti/Cr [1.85]	0.86–0.88	N-TiCr surface is 100% harder that the bulk [1.85]
Extraordinary cases	(Be, Mg) (0001) Zn, Cd and Hg dimer bond [1.80]	>1	No indication of effects on physical properties is yet given

silver, and aluminum – in the size range of 1–20 nm. Figure 1.9b illustrates how the shape and position of the bond potential change for ≈ 15% lattice contraction. The shorter bond length corresponds to a deeper and narrower potential well, resulting in stronger materials and lower thermal expansion. Figure 1.9c shows nanochain formation for gold, in which chain formation is successful, and for copper, in which chains do not form. The bond energy for atoms in the nanometal chain structures is 2–3 times larger than for bulk materials.

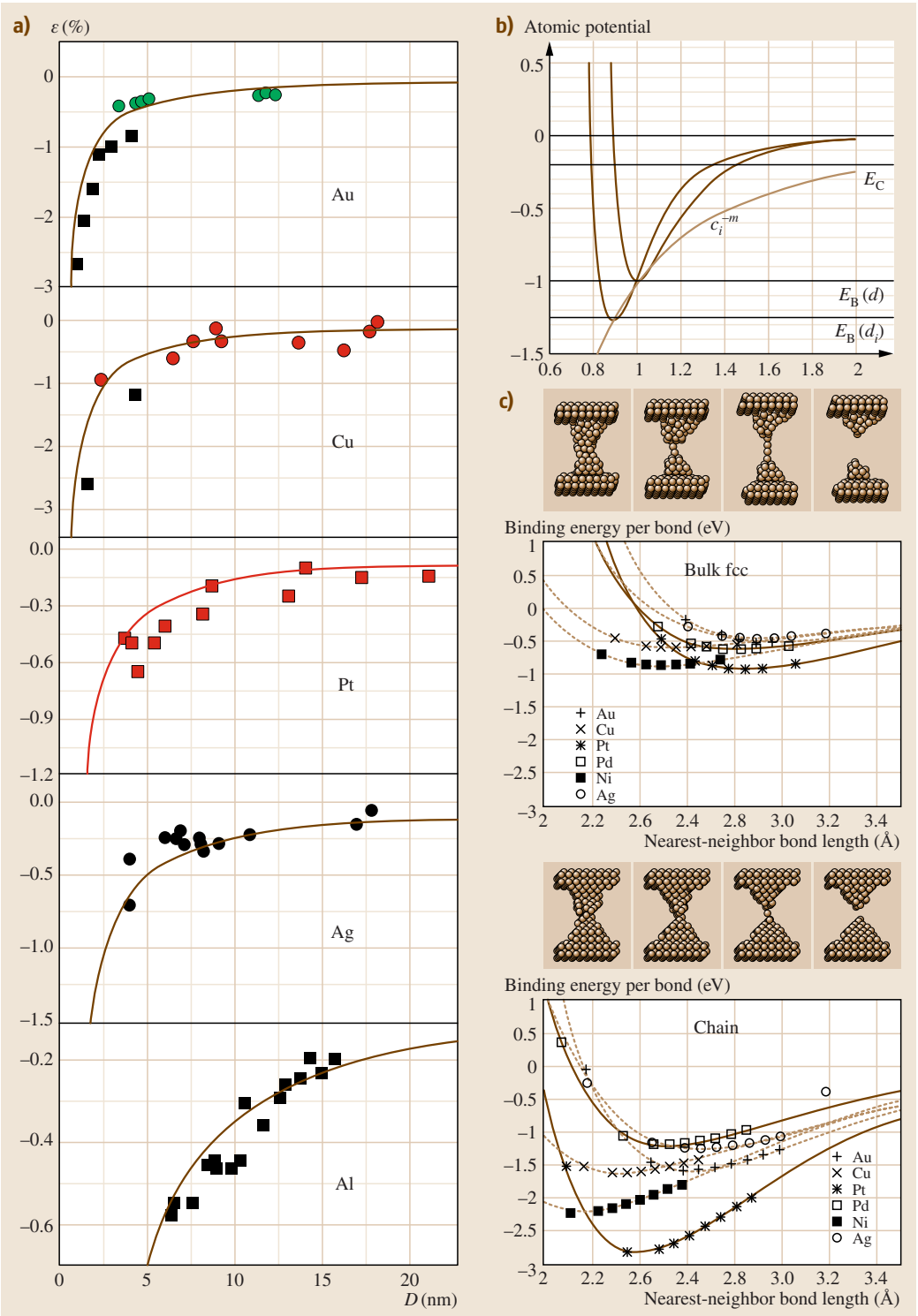
1.3.3 Mechanical Properties of Nanomaterials

Nanomaterials and nanostructured materials have distinct mechanical properties for several reasons: Firstly, the shorter bond length results in stronger and stiffer materials, as mentioned in the previous section; Furthermore, the limited size of the units of the material diminishes the probability of certain defects; e.g., grain boundaries are very rare in small nanoparticles. It is well known that carbon–carbon bonds in the hexagonal lattice of graphite are the strongest ones in any solid, and second only to the N−O bond overall. On the macroscopic scale, however, we do not consider graphite an extraordinarily strong material as its bonds in the *c*-crystal direction are weak, and the lateral strength in the *a*–*b* plane is diminished greatly by the fact that the layer is not continuous, so pulling forces easily disintegrate the crystal. On the nanoscale, the hexagonal sheets of carbon are separated, and strength is measured on individual flakes and domains. The role of point defects in nanomaterials, from the point of view of mechanical strength, is not as critical as for discontinuities in bulk materials. Graphene and carbon nanotubes have high strength and Young's modulus owing to these strong in-plane bonds.

It has been shown that metals with grain structures have an optimum grain size for minimum creep [1.89]; the optimum grain size for most metals is on the few-nanometer scale, corresponding to the limit of Hall–Petch hardening by grain size reduction. Similarly, in the case of ceramics, the maximum Vickers hardness is measured at the optimum grain size that falls in the range of 10–50 nm [1.90, 91].

Figure 1.10 demonstrates several basic mechanical properties of nanomaterials. Figure 1.10a and b show the particle size dependence of hardness for

Fig. 1.9a–c Typical effects of properties of bonds in nanoparticles as a function of particle size. **(a)** Dependence of the bond length on particle diameter for several metals (after [1.86]). **(b)** Increase of the bond energy density with decreasing particle size and the consequently shorter bond length (after [1.57, 87]). **(c)** Bond strength as a function of dimensionality. Chain formation of gold atoms and failure to achieve the same with copper. Binding energies of bulk and atomic 1-D chain structures (after [1.88]) ▶


a)
ε (%)
Au
Cu
Pt
Ag
Al
D (nm)
b) Atomic potential
E_C
c_i^{-m}
$E_B(d)$
$E_B(d_i)$
c)
Binding energy per bond (eV)
Bulk fcc
Au
Cu
Pt
Pd
Ni
Ag
Nearest-neighbor bond length (Å)
Binding energy per bond (eV)
Chain
Au
Cu
Pt
Pd
Ni
Ag
Nearest-neighbor bond length (Å)

metals and intermetallic alloys [1.92], respectively. In the case of metals, there is an obvious trend for the hardness to be 3–10 times higher for the smallest nanoparticles than for those larger than 100 nm, latter is the value corresponding to the bulk material. For the alloys, a trend of increasing hardness is visible for the 100 to ≈ 40 nm range; however, in many cases this trend becomes softening for further diminishing nanoparticle sizes. Figure 1.10c,d shows buckling of carbon nanotubes [1.93–95]. While SWNTs have very high Young's modulus and relatively high stiffness against tensile forces [1.96], they can be deformed by compressive forces, which makes them ideal high-resolution yet gentle and forgiving AFM tips [1.95]. Figure 1.10e,f demonstrates the in-plane mechanical strength of a graphene sheet based on nanoidentation carried out by an AFM tip [1.97].

1.3.4 Electrical, Magnetic, and Optical Properties

Nanoscale materials, especially with dimensionality of zero to two, exhibit intriguing electromagnetic behavior, as the most important effects and properties are derived from the quantum confinement of the wave function of the charge enclosed in the particles. In the nanometer-sized dimensions of the material, the wave function has a limited number of solutions. This results in changes in several electrical properties: with the decreasing feature size the bandgap becomes wider, the conductivity decreases and the density of states decreases. Optical properties change accordingly, as the absorbed and emitted photons depend on the energy difference between the states among the bands or in their fine structure. Beyond this, quasiparticles are generated due to the confined space. An electron–hole pair, i. e., an exciton, carries energy in nanomaterials without motion of net charge. Plasmons, surface plasmons (polaritons), and polarons play a key role in nanomaterial interactions with optical phonons, e.g., causing the color dependence of gold colloids as a function of particle size. Magnetic properties are also governed by the size of the nanomaterials; e.g., superparamagnetic materials exist below the size of the domain size.

Electrical Properties

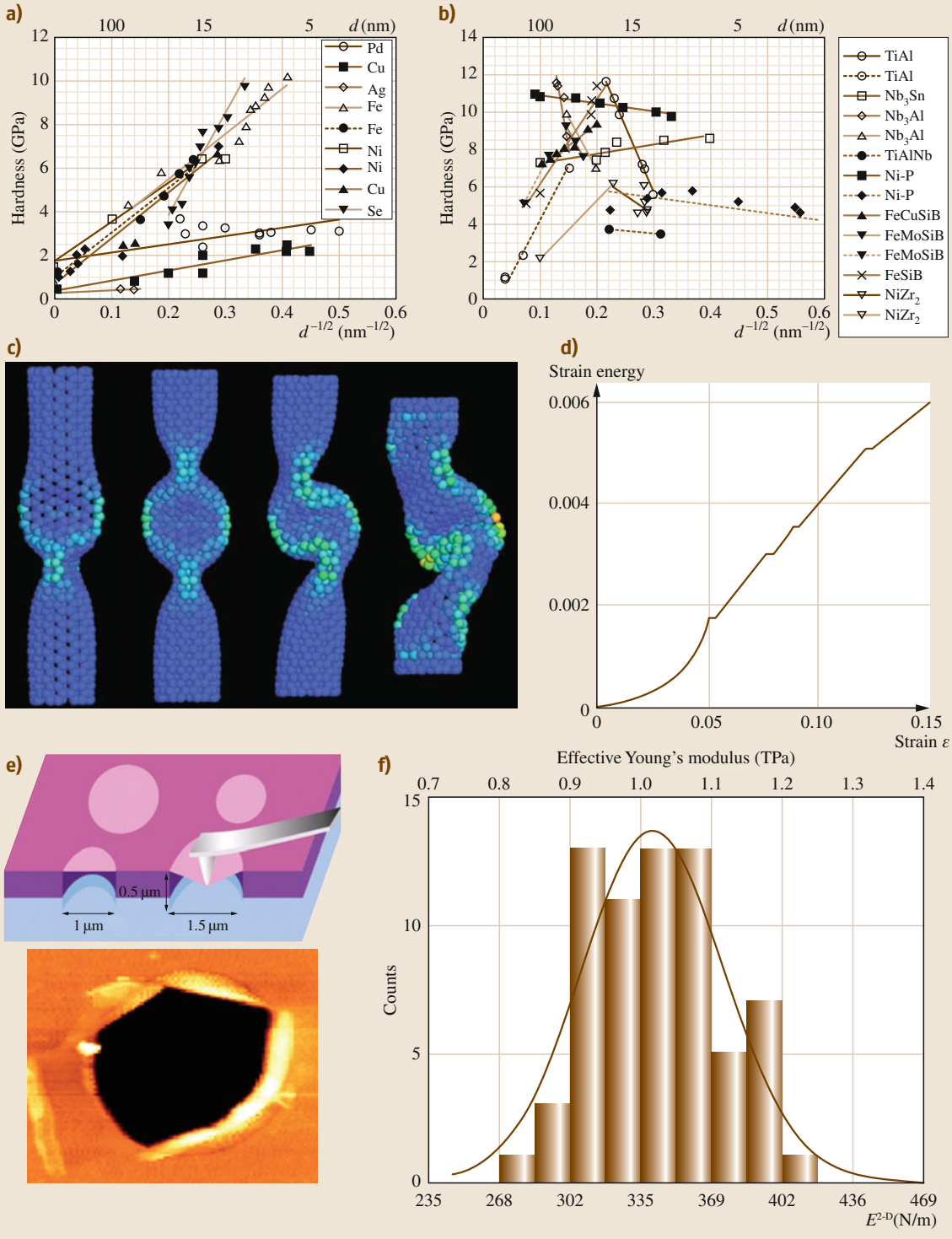
Electrostatic forces play a major role in nanoparticle formation and also have an important effect on nanomaterial properties [1.71]. Most of the larger structures built up from nanomaterials are held together by van der Waals forces. One of the advantages attributed to the high aspect ratio of 1-D structures is the field enhancement of the electrostatic potential, which enables a low turn-on voltage for field emission [1.98, 99].

Nanomaterials, especially 1-D structures such as nanowires and nanotubes, conduct electrical current differently compared with bulk conductors. The limited size in the direction perpendicular to the axis and the atomically organized structure of the 1-D objects – crystals or nanotubes, e.g., molecules – result in weak phonon–charge carrier interaction and ballistic transport. In the ballistic regime of electrical conduction, the resistance does not depend on the length of the conductor but rather on the number of conductance channels used, following Landauer's law [1.100]. Often, there is a single channel, and the quantum nature of the conductance as a function of the number of channels can be demonstrated, e.g., for carbon nanotubes [1.101]. However, in other reports, e.g., on nanotubes used to build field-effect transistors (FETs), the conductance mechanism is considered to be diffusive [1.102].

Another important effect in devices made of nanosized conductors and semiconductors is the Coulomb blockade that occurs when new charge carriers cannot enter the conduction channel while another charge carrier occupies it, as demonstrated for single-molecule devices [1.103]. This phenomenon enables the functioning of single-electron transistors (SETs) even at room temperature [1.104]. SETs are also useful to investigate spin–spin interactions between localized and mobile electrons, i. e., the Kondo effect, more effectively than in macroscopic systems [1.105].

High current-carrying capacity – i. e., no failure caused by electromigration – of individual carbon nanotubes, both single-walled (4×10^9 A cm^2) [1.106] and multi-walled ($> 10^{10}$ A cm^2 at 250 °C) [1.107], and wires made of nanotubes has also been demonstrated. Since carbon atoms are bound into the nanotube by covalent bonds, the charge carriers and high temperature cannot easily move them away from their original location. The state-of-the-art specific conductivity of carbon nanotube

Fig. 1.10a–d Selected mechanical properties of nanomaterials. **(a,b)** Hardness of metals and intermetallic alloys as a function of grain size in nanophase materials (after [1.92]). **(c),(d)** Molecular dynamics computation of the behavior of a carbon nanotube under compressive force. The structure in the strain energy curve corresponds to the modes of buckling (after [1.93–95]). **(e,f)** Measurement and values of the Young's modulus for a suspended graphene sheet on an alumina template by AFM (after [1.97]) ▶


a)
100
15
5
d (nm)
Hardness (GPa)
Pd
Cu
Ag
Fe
Fe
Ni
Ni
Cu
Se
$d^{-1/2}$ ($nm^{-1/2}$)
b)
TiAl
TiAl
Nb_3Sn
Nb_3Al
Nb_3Al
TiAlNb
Ni-P
Ni-P
FeCuSiB
FeMoSiB
FeMoSiB
FeSiB
$NiZr_2$
$NiZr_2$
c)
d)
Strain energy
Strain ε
e)
0.5 µm
1 µm
1.5 µm
f)
Effective Young's modulus (TPa)
Counts
$E^{2\text{-D}}$(N/m)

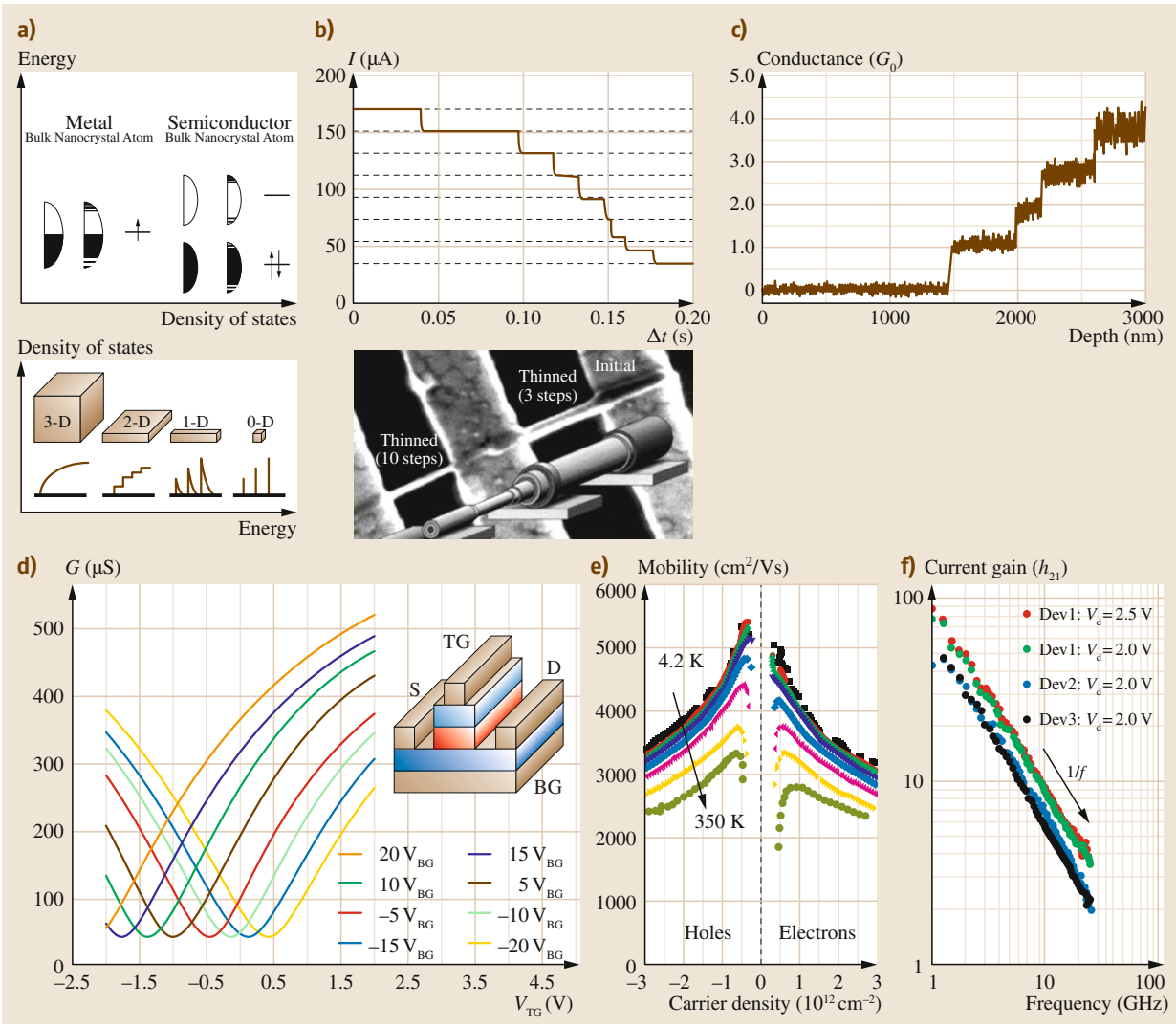


Fig. 1.11a–f Examples for electrical properties of nanomaterials. **(a)** Schematics to represent changes in the DOS of nanomaterials as a function of dimensionality (after [1.109]). **(b)** Quantized decrease of the current when shells of a multi-walled nanotube burned down consecutively and the schematics of the nanotube with partially removed walls (after [1.110]). **(c)** Conductance of carbon nanotubes when a parallel circuit was built from one to four individual tubes. As the voltage was low (100 mV), each nanotube added only one channel to the conductance and the measured values were nG, where n is the number of nanotubes/channels. A larger number of nanotubes resulted in conductance up to 1000 G (after [1.111]). **(d)** Transistor characteristics of a FET device where the active element was a single-layer graphene channel. The figure displays the transconductance, charge carrier mobility, **(e)** and current gain **(f)** as a function of top and bottom gate voltage, carrier density and temperature, frequency and drain voltage, respectively (after [1.112])

fibers surpasses the values for all conventionally applied metallic conductors (Cu, Al, Au, etc.) [1.108].

Figure 1.11 shows a collection of electrical properties. Figure 1.11a shows a schematic of the dependence of the density of states (DOS) on the dimensionality of the nanomaterials; the larger the number of quantum-confined dimensions, the higher the number of discrete states in the DOS [1.109]. Figure 1.11b shows how the

resistance of a carbon nanotube increases as it loses carbon layers from its wall; the resistance, and accordingly the conductivity, also changes in quanta, illustrating the independence of the conductance channels in each layer [1.110]. Results of a similar experiment are shown in Fig. 1.11c. Here, the conductance of a nanotube bundle was measured when one, two, three, and four nanotubes were included sequentially in a circuit including a contact made of mercury [1.111]. In both cases, the size of the quantized steps of the conductance change – following the Landauer law – is equal to G_0. By immersing the nanotube bundle further into the mercury electrode, the authors measured conductance as high as $\approx 1000\ G_0$. In Fig. 1.11d–f, the characteristics of a FET based on a single-layered graphene sheet are shown [1.112]. First, the structure of the device and the conductance as a function of the top gate (TG) voltage are displayed at different back-gate (BG) voltages. The electron and hole mobility were calculated from Hall-effect measurements, being higher than $5000\,\mathrm{cm^2\,V^{-1}\,s^{-1}}$ for low temperatures and carrier densities, and around $3000\,\mathrm{cm^2\,V^{-1}\,s^{-1}}$ at room temperature (RT). The high-frequency behavior of the device shows $1/f$ dependence of the current gain as a function of frequency, and the cutoff frequency is in the range of 100 GHz.

Magnetic Properties

The magnetic properties of nanomaterials depend strongly on the characteristic size, i. e., the diameter of nanoparticles or the grain size of nanostructured material, which is normally small in comparison with the magnetic domain size of the material. The configuration of thin films and few-domain nanoparticles was investigated by *Kittel* [1.113]. Figure 1.12a presents these configurations and the energy density for the various configurations in thin films, showing that (for small size) the single-domain system is energetically favorable. Nanomaterials can be classified according to the type of interaction among the magnetic particles, extending from no interaction in a well-distributed nanoparticle system to strongly interacting nanostructured materials [1.114] (Fig. 1.12b). Ferrofluids consist of particles surrounded by surfactants, capping agents, and solvents, forming an independent system, while alloys with magnetic constituents are strongly correlated.

Superparamagnetic materials behave similarly to paramagnetic materials. However, the magnetization value is considerably higher and the particles keep their magnetization values for a measurable timescale, e.g., several minutes. The magnetization curve of superparamagnetic materials does not show hysteresis, and the exact shape depends on the particle size or its distribution.

By introducing defects into the lattice of carbon, e.g., implanting nitrogen or carbon atoms into nanodiamond, ferromagnetic behavior is observable [1.115]. Also, ferromagnetism is measured on monoatomic cobalt structures at low temperature (10 K), showing the interaction between neighboring atoms [1.116]. During Mackay transformation and Bain transformation, the crystal structure is changing, and the magnetic properties follow the crystal symmetry [1.117], as shown in Fig. 1.12c.

Figure 1.12d shows the grain size dependence of the magnetization of Ni films of different grain sizes, i. e., the magnetization hysteresis loops, the coercive force values, and the relative change in the magnetization [1.118]. In all three cases, the changes are significant below feature size of 10 nm.

Optical Properties

It is a common misbelief that nanomaterials cannot be seen by the naked eye or be detected by optical microscopy. This misbelief is based on the fact that the nanoscale is defined as 1–100 nm while the wavelength of visible light ranges between 400 to 800 nm; however, this scale difference only means that size and shape cannot be resolved by visible-range photons. In fact, there are plenty of interactions between atoms, molecules, and nanomaterials with light, and some of these interactions are applicable to detect the size and morphology of nanomaterials. All of these detection methods need to be first used in parallel with other approaches to measure, e.g., nanoparticle size, and after this *calibration*, the optical method itself can serve as a fast and easy measurement approach. In the case of gold nanoparticles or thin layers of graphene, practiced researchers can tell their size or thickness by eye alone, in the latter case with subnanometer, atomic accuracy. In this section, the main features of the optical properties of nanomaterials are described, while detailed description of these properties for specific nanomaterials is included in the relevant chapters of this handbook.

Optical properties – similarly to the electrical ones – are governed by quantum confinement: the lower dimensionality and smaller size result in a larger energy difference between neighboring discrete energy levels in the DOS, and accordingly higher excitation energy (Fig. 1.13) [1.109]. Inasmuch, the smaller the particle, the shorter the wavelength in the absorption spectrum, and the color shifts from red to blue. This interac-

tion with photons can be interpreted by introducing a quasiparticle known as the surface plasmon (SP) to represent the oscillations in the confined space [1.43]. The absorption spectrum has a maximum when the SP–photon interaction is strongest, at the surface plasmon resonance (SPR) wavelength. The SPR for different nanoparticles depends – beyond the size – also on the material and shape of the nanoparticles. Figure 1.13a demonstrates visible-range colors caused by SPRs of different energy for several basic shapes of gold, silver, and alloy nanoparticles [1.119]. Figure 1.13b shows a particular case from [1.119], where the resonance wavelength shifts when the silver nanoshell particles are coated with a gold layer of increasing thickness. Figure 1.13c presents a silver nanoprism preparation method where the size distribution and accordingly the absorption spectrum are well controlled by the wavelength of light used in the photo-induced reaction. Another interesting phenomenon is the shift in the absorption of gold nanotriangles from 800 nm to 600 nm with the extent of the truncation of the tips [1.120].

Along with other microscopy techniques, the optical property corresponding to Raman scattering [1.121, 122] provides insightful information into the local bonding system of nanomaterials through phonon–photon interactions. It is used for characterizing a wide range of materials from metals to oxides; one of the characteristic examples is its application in studying carbon nanomaterials. Figure 1.13d shows spectra of carbon structures for comparative analysis. Graphene has two characteristic peaks, the ratio of the intensity of the G and G′ peaks depends on the number of layers in the 2-D structure. In the case of carbon nanotubes, the D and G peaks dominate the spectra, while for SWNTs, the radial breathing mode (RBM) is also present and provides information about the diameter and (to some extent) the chirality of the nanotubes. Shifts, shoulders, and new peaks in the spectra can be interpreted as signals caused by defects in the bonds or in the structure.

Fluorescence [1.123] and bandgap photoluminescence are also characteristic properties of nanomaterials, the latter being applied, e.g., to study the diameter and chirality of SWNTs in solutions [1.124, 125]. The schematics of the band structure with the first and second van Hove optical transitions and the measured values on a Kataura plot are displayed in Fig. 1.13e.

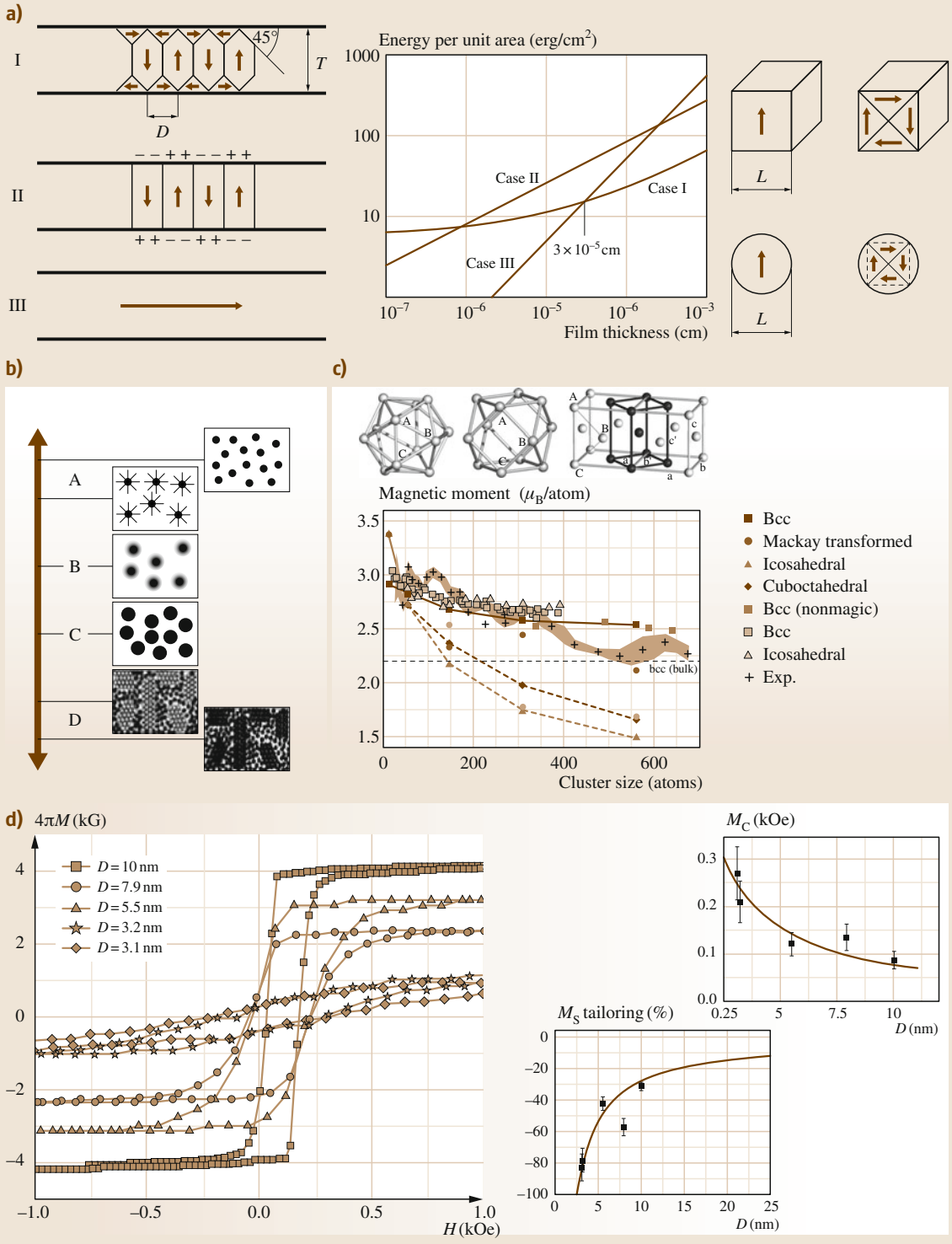
1.3.5 Thermal Properties

Thermal conductivity, specific heat, melting point, and glass-transition temperature are just a few examples of thermal properties that strongly depend on the particle or feature size of nanomaterials. Phase diagrams of nanomaterials depend on the particle size, shape, and even their environment.

The Gibbs–Thomson equation describes the decreasing tendency of melting point with decreasing particle size. For spherical particles, for instance, it predicts that the difference in the melting point has inverse dependence on the diameter of the particle. Figure 1.14a shows the melting point of gold particles as a function of particle size D [1.90, 126]. Below 20 nm the decrease is observable, and for particles smaller than 3 nm the melting temperature decreases by ≈ 600 K. Figure 1.14b illustrates an unusual behavior. In specific cases, indium particles embedded into an aluminum matrix show a melting point increase with decreasing grain size; this exceptional behavior is caused by the interaction with the matrix: here, for smaller grain size, the surface energy of the grain decreases.

Figure 1.14c shows experimental demonstrations of the theoretically predicted, unusually high thermal conductivity [1.127, 128] of carbon nanotubes and graphene, $\approx 6000\,\mathrm{W/(m\,K)}$. Values of thermal conductivity measured on a thick layer of aligned SWNTs range up to $240\,\mathrm{W/(m\,K)}$ in the direction of alignment, and approximately ten times lower in the perpendicular direction. A similar trend was observed for the heat conductivity of aligned carbon nanotube forests [1.129]. For the measurement of thermal conductivity in graphene sheets, the shift in the position of the Raman G peak was investigated. This shift

Fig. 1.12a–d Selected magnetic features in nanomaterials. **(a)** Domain configurations studied by Kittel. For thin films the single-domain configuration has lowest energy for thickness below 300 nm. Several domain configurations for nanoparticles also were suggested in this paper, which was published in 1946 [1.113]. **(b)** Schematics for the main types of nanostructures for magnetic behavior, including independent ultrafine particles (e.g., ferrofluids), core–shell particles with magnetic core, particles as fillers in a matrix, and small crystallites in a noncrystalline matrix (after [1.114]). **(c)** Mackay transformation shows the magnetization changes as a function of crystal structure. Schematics of icosahedron, cuboctahedron, and fcc with inscribed body-centered tetragonal Bain cell and the magnetization as a function of cluster size are displayed (after [1.117]). **(d)** Magnetic hysteresis loops, coercive forces, and relative changes compared with the bulk value for Ni film with different grain sizes is displayed (after [1.118]) ▶


a)
I
II
III
45°
T
D
Energy per unit area (erg/cm²)
1000
100
10
Case II
Case I
Case III
3×10⁻⁵ cm
10⁻⁷
10⁻⁶
10⁻⁵
10⁻⁶
10⁻³
Film thickness (cm)
L
L
b)
A
B
C
D
c)
Magnetic moment (μB/atom)
3.5
3.0
2.5
2.0
1.5
bcc (bulk)
0
200
400
600
Cluster size (atoms)
Bcc
Mackay transformed
Icosahedral
Cuboctahedral
Bcc (nonmagic)
Bcc
Icosahedral
Exp.
d)
4πM (kG)
D = 10 nm
D = 7.9 nm
D = 5.5 nm
D = 3.2 nm
D = 3.1 nm
4
2
0
−2
−4
−1.0
−0.5
0.0
0.5
1.0
H (kOe)
M_C (kOe)
0.3
0.2
0.1
0.0
0.25
5
7.5
10
D (nm)
M_S tailoring (%)
0
−20
−40
−60
−80
−100
0
5
10
15
20
25
D (nm)

corresponds to ≈ 5000 W/(m K) heat conductivity. Another interesting hybrid system is displayed in panel Fig. 1.14d, where covalently bonded carbon nanotube pillars connect parallel graphene sheets to each other. By changing the geometry of this unique system, i. e., the length and separation of the pillars, one can tune for different vertical and lateral thermal conductivities.

1.3.6 Chemical Properties, Reactivity, and Functionalization

Chemical approaches are used in almost all nanomaterial preparation processes. As prepared, nanomaterials have extraordinary properties; however, for many applications they need to be modified, and accordingly further chemical treatment is needed. Some nanomaterials, e.g., fullerenes and nanotubes, can be considered as molecules, and their chemistry is quite well defined. In the case of metallic and ceramic nanomaterials, the reactions and products depend on the size and exact shape of the nanomaterials used. In the narrower definition, we consider only modifications to the strong bonds – covalent, ionic, and metallic – of the materials; in the wider definition, modifications to weak interactions – hydrogen bonding and van der Waals interaction – among parts of the new nanomaterial are also considered. Exchange reactions and chemical transformations of nanoalloys also represent a vast field of nanomaterial chemistry [1.131].

In the scope of this short introduction, a few example reactions are presented, where changes in covalent bonds are dominant. Small pieces of graphene, also called graphene molecules, can be handled by typical methods of organic chemistry; they can be decorated, or connected to each other, and their lateral size can be controllably increased or decreased [1.132]. In Fig. 1.15a, schemes of several graphene molecules are displayed, demonstrating differently sized, bare, and R-functionalized samples. The figure also presents a larger molecule, namely a *nanopropeller*, which is built from three graphene flakes connected to each other. The color of these materials depends on the size of the molecules; with increasing size, the color shifts from blue in the direction of red.

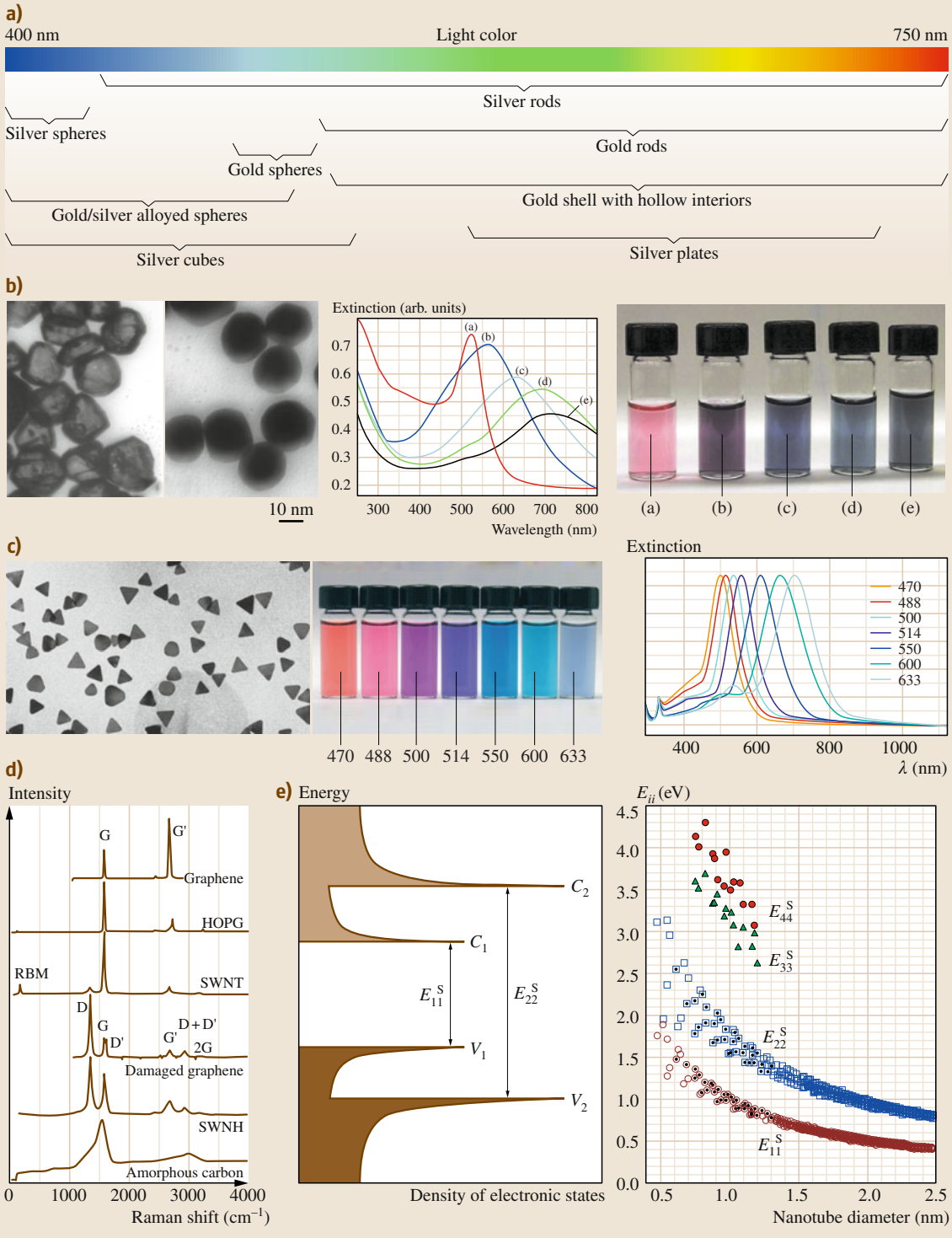
Another example of well-defined molecules which are considered nanomaterials is the fullerenes. These can be modified in two ways: additional atoms are either included inside the cage of the fullerene or added as outside ligands, being called endohedral (inner) and exohedral (outer) fullerenes, respectively. An uncommon example is that of B_{80} [1.133], a fullerene decorated by alkali ligands, which has been suggested for use as an effective hydrogen storage material (Fig. 1.15b) [1.134].

Fig. 1.13a–e Selected optical properties of nanomaterials. **(a)** Typical surface plasmon resonance spectral ranges of silver and gold nanoparticles having various morphologies, compositions, and structures (after [1.119]). **(b)** Ultraviolet-visible (UV-Vis) extinction spectra and photo of solution of silver nanoshells coated with different thicknesses of gold, and solid gold colloids; TEM image of the shell and solid particles (after [1.119]). **(c)** TEM image of silver nanoprisms and extinction spectra of nanoprisms prepared with illumination by various laser wavelengths (after [1.130]). **(d)** Raman shift measured on different types of graphene-related nanocarbons. The main features (RBM and disorder-induced D, D′, and D + D′ bands; first-order Raman-allowed G band; and second-order Raman overtones G′ (2iTO) and 2G) are labeled in some spectra, but the assignment applies to all of them. The analysis of the frequency, line shape, and intensity of these features at different exciting laser wavelengths provides a great deal of information about each respective sp^2 carbon structure (after [1.122]). **(e)** Method for identifying single-walled carbon nanotube diameters by spectrofluorometry (Kataura plots). First and second van Hove optical transitions are displayed as a function of structure for semiconducting nanotubes (after [1.125]) (HOPG: highly oriented pyrolytic graphite; SWNH: single-walled nanohorn) ▶

Carrying out covalent chemistry of SWNTs is necessary for achieving properties important for the formation of composites, preparation of solutions, etc. [1.135]. In most cases, the first chemical reaction aims to break the strong carbon–carbon sp^2 bonds in the sidewalls of the nanotubes by oxidation or fluorination. Afterwards, the attached OH or F groups can be substituted with alkyl or aromatic groups. Figure 1.15 shows different kinds of nanotube reaction products. Various groups can be introduced onto the sidewall or defect locations in the sidewall, or in the cap; surfactants or polymers can be attached to the surface via noncovalent bonds, and the cage of the nanotube can also be filled with different chemicals (in this schematic, C_{60}).

Producing nanotubes with given chirality by direct growth or separation methods is still an underdeveloped area and a challenging task. Functionalization of metallic nanotubes [1.136] with side-groups, which makes them heavier than unfunctionalized semiconductor nanotubes, offers a way for more selective and higher yield separation.

Another important area of nanocarbon chemistry is the oxidation, reduction, and functionalization of


a)
400 nm
Light color
750 nm
Silver rods
Silver spheres
Gold rods
Gold spheres
Gold shell with hollow interiors
Gold/silver alloyed spheres
Silver cubes
Silver plates
b)
10 nm
Extinction (arb. units)
0.7
0.6
0.5
0.4
0.3
0.2
(a)
(b)
(c)
(d)
(e)
300 400 500 600 700 800
Wavelength (nm)
(a) (b) (c) (d) (e)
c)
470 488 500 514 550 600 633
Extinction
470
488
500
514
550
600
633
400 600 800 1000
λ (nm)
d)
Intensity
G
G'
Graphene
HOPG
RBM
SWNT
D
G
D'
D+D'
G'
2G
Damaged graphene
SWNH
Amorphous carbon
0 1000 2000 3000 4000
Raman shift (cm⁻¹)
e)
Energy
C2
C1
E11S
E22S
V1
V2
Density of electronic states
Eii (eV)
4.5
4.0
3.5
3.0
2.5
2.0
1.5
1.0
0.5
0.0
E44S
E33S
E22S
E11S
0.5 1.0 1.5 2.0 2.5
Nanotube diameter (nm)

graphene. Graphite oxide is often produced to aid exfoliation of layers of graphene into graphene oxide (GO), after which reduction procedures are needed to yield graphene as a product (reduced graphene oxide, RGO) [1.137, 138]. Figure 1.15d displays the consecutive steps applied in one of the possible reduction procedures of GO, as well as a photo of the solutions at each step and the C 1s x-ray photoelectron spectroscopy (XPS) peak in the spectra of these materials.

1.3.7 Behavior of Nanomaterials in Corrosive Environments

Some of the ancient and medieval applications of nanomaterials pointed towards corrosion prevention. The Chinese *heiqigu* are black bronze mirrors with a surface coating made of SnO_2 nanoparticles, most probably doped with Cu, Fe, Pb, and Si [1.145,146]. Similarly, as mentioned in Sect. 1.1.1, Mayan blue paint was not only a rare and beautiful color for its time, but also had corrosion resistance and retained its properties for centuries while buried in soil [1.7].

Figure 1.16a shows an example of preventing an aluminum alloy from corroding in an NaCl-containing water environment [1.147]. The scanning electron microscopy (SEM) and TEM images show the morphology of halloysite (aluminosilicate) nanocontainers which hold and release anticorrosion agents, normally polymers, onto the surface when the pH of the environment changes. The photos show extensive surface corrosion of the specimen in a dilute solution when coated without the nanomaterial included but minimal damage in ten times higher concentration salt solution with the filled halloysite additive.

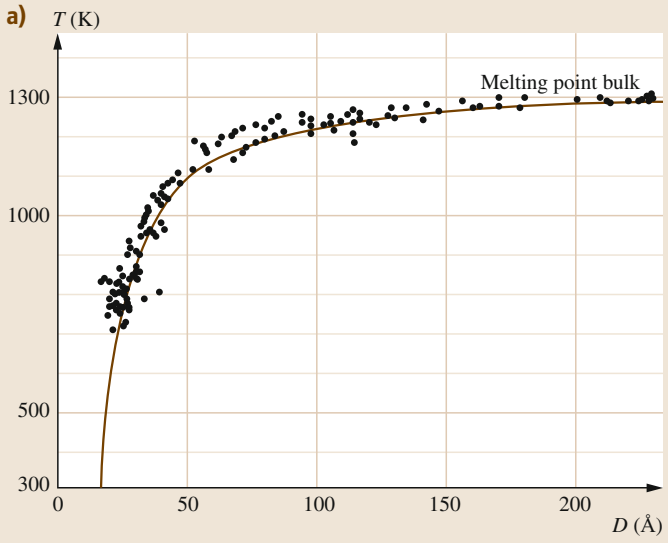
Superalloys are designed and manufactured not only for mechanical strength and creep resistance but also to avoid corrosion in high temperature and harsh environmental conditions. They themselves may or may not consist of nanostructured materials. Figure 1.16b shows an effective nanomaterial coating for corrosion prevention of a Ni superalloy (K52) [1.148] deposited by sputtering a nanostructured layer of the same alloy onto the surface of the specimen. The SEM and TEM images show the morphology of the deposited layer; it has a microgranular structure built up from sub-10 nm particles. The samples were oxidized in air at high temperature, and the oxidation kinetics showed parabolic growth of the oxide layer (Wagner regime) for both the uncoated and coated alloy, however the rate of oxidation was higher for the uncoated sample at all temperatures investigated. The surface of the oxidized sample was coated by nanowire structures, mainly alumina and TiO_2 nanowires, while the uncoated sample had a microgranular oxide layer. In a hot salt environment, the trends were different: the coated sample started to corrode faster, and after an initial fast scaling, the process slowed down.

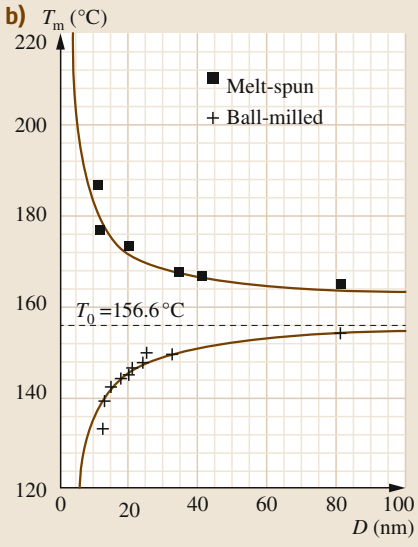
In several cases, nanomaterials exhibit the same or worse corrosion resistance than bulk materials. This effect is mainly attributed to the high concentration of defects in these nanoparticles and nanowires. In [1.149], silver nanowires were investigated, and the authors found faster sulfide formation in nanowires than for bulk silver and that the reaction mechanism was the same.

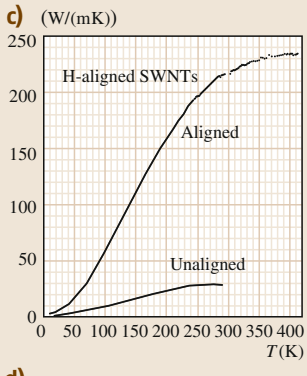
Fig. 1.14a–d Thermal properties of nanomaterials. **(a)** Melting point of gold nanoparticles as a function of size, showing decrease with smaller sizes (after [1.90, 126]). **(b)** Melting point of indium nanograins in aluminum matrix; the direction of deviation from the bulk value depends on the method of preparation (after [1.139]). **(c)** Thermal conductivity of SWNTs and graphene. The thermal conductivity of aligned nanotubes is within an order of magnitude of in-plane values for graphite or diamond (after [1.140, 141]). Raman shift of the G peak position of a graphene sample versus change in total dissipated power. Values calculated for thermal conductivity are higher than for CNTs (after [1.142]). **(d)** Pillared graphene structure proposed originally for hydrogen storage (after [1.143]). Thermal conductivity of the structure along the graphene plane direction is decreased while the vertical thermal conductivity is increased by increasing the number of pillars (after [1.144]) ▶

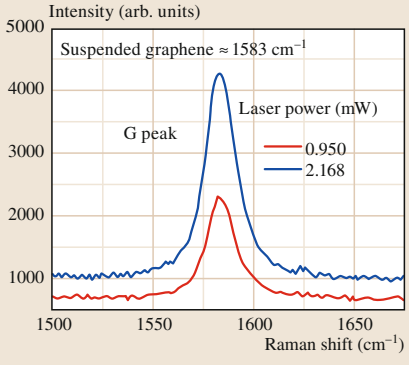
1.4 Typical Applications of Nanomaterials

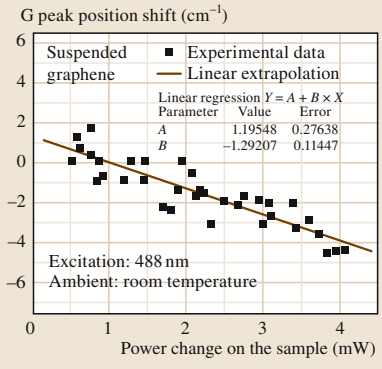
Nanomaterials are not a sanctified object of nanoscience; they have already found applications in a very wide range of engineering fields. From mechanical engineering to bioengineering, we use nanomaterials regularly in our computers, stain-resistant clothes, and suntan creams. Other applications such as nanomaterial-

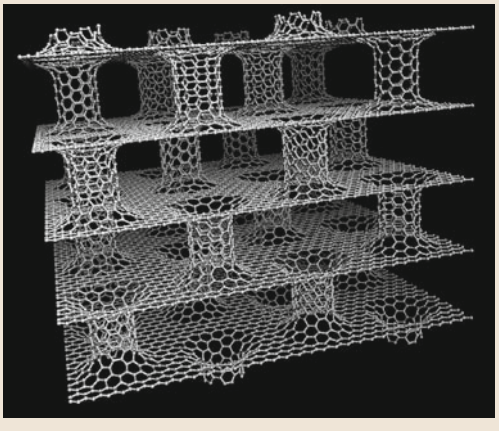

a)
T (K)
Melting point bulk
1300
1000
500
300
0
50
100
150
200
D (Å)

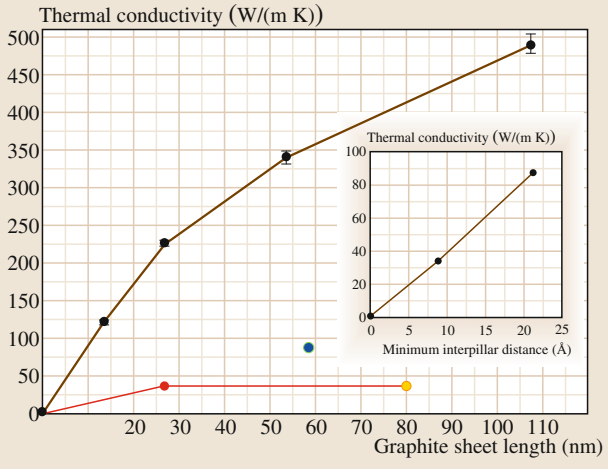

b)
T_m (°C)
Melt-spun
+ Ball-milled
T_0 =156.6 °C
220
200
180
160
140
120
0
20
40
60
80
100
D (nm)


c)
(W/(mK))
H-aligned SWNTs
Aligned
Unaligned
250
200
150
100
50
0
0 50 100 150 200 250 300 350 400
T (K)


Intensity (arb. units)
Suspended graphene ≈ 1583 cm^{-1}
G peak
Laser power (mW)
0.950
2.168
5000
4000
3000
2000
1000
1500
1550
1600
1650
Raman shift (cm^{-1})


G peak position shift (cm^{-1})
Suspended graphene
Experimental data
Linear extrapolation
Linear regression Y = A + B × X
Parameter Value Error
A 1.19548 0.27638
B −1.29207 0.11447
Excitation: 488 nm
Ambient: room temperature
6
4
2
0
−2
−4
−6
0
1
2
3
4
Power change on the sample (mW)


d)


Thermal conductivity (W/(m K))
500
450
400
350
300
250
200
150
100
50
0
20 30 40 50 60 70 80 90 100 110
Graphite sheet length (nm)
Thermal conductivity (W/(m K))
100
80
60
40
20
0
0 5 10 15 20 25
Minimum interpillar distance (Å)

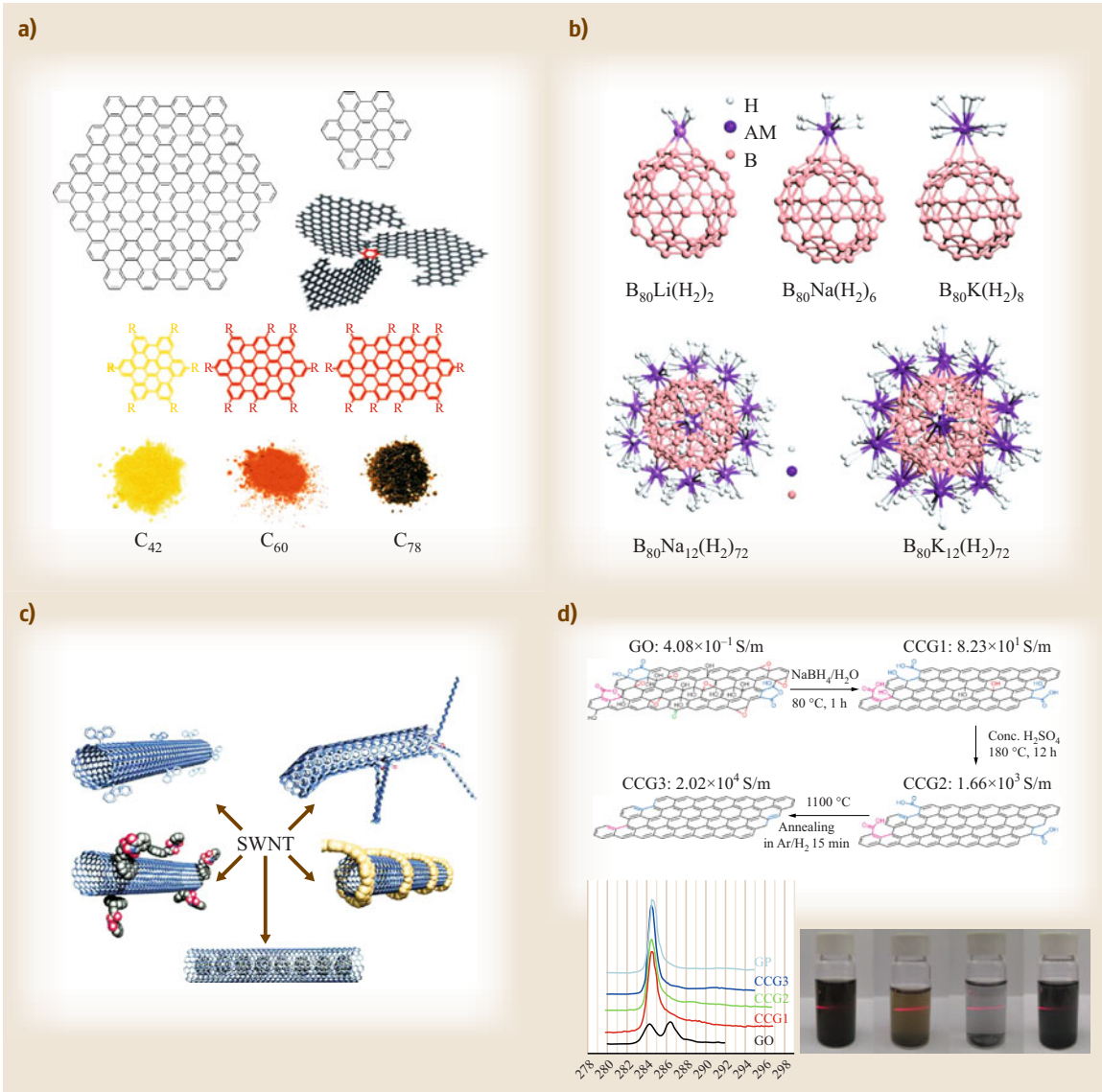


Fig. 1.15a–d Chemical properties of nanomaterials. **(a)** Graphene molecules demonstrating various sizes and shapes. Graphene molecules are mostly 2-D materials; however, they can be organized into larger, 3-D structures; a *nanopropeller* is shown as an example. The size dependence of the color of planar polycyclic aromatic hydrocarbons (PAHs) is also demonstrated (after [1.132]). **(b)** Modifications of the B_{80} molecule by forming complexes with alkali elements. The complexes are suggested as effective hydrogen storage materials up to 11 wt. % capacity (after [1.134]). **(c)** Various ways of functionalization of SWNTs: attaching molecules to the defect locations in the side-walls, connecting molecules by covalent bonds, functionalization with surfactants, functionalization with polymers, and endohedral functionalization with fullerenes (after [1.150]). **(d)** Steps of a GO reduction procedure showing the schematics, the corresponding bonding energies in XPS, and photos of the solutions for each step. The vials contain GO in deionized (DI) water, GO in dimethylformamide (DMF), CCG3 (CCG: chemically converted graphene) in DI water, and CCG3 in DMF from *left to right* (after [1.137])

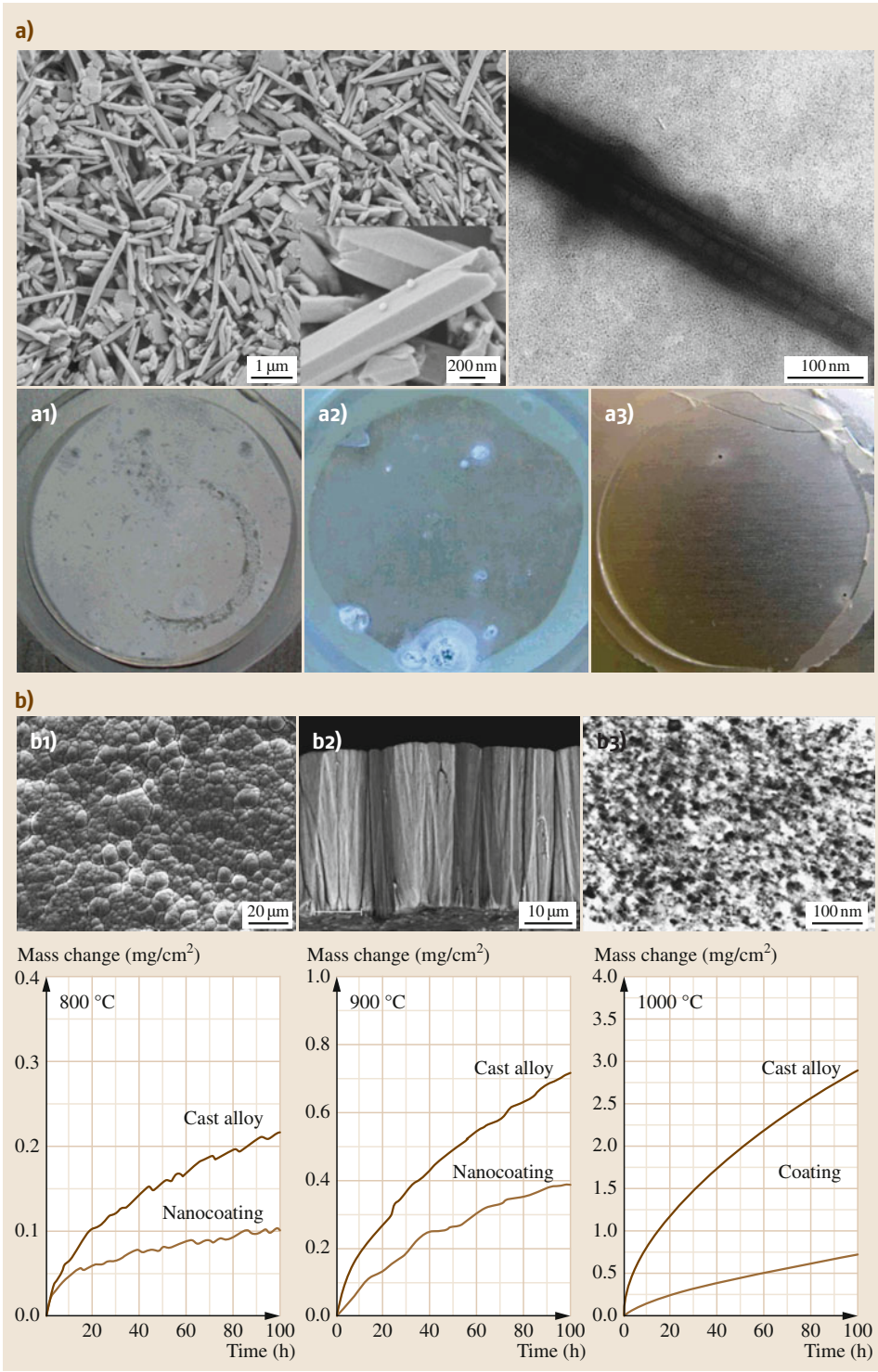


Fig. 1.16a,b Application of nanomaterials for preventing corrosion. **(a)** SEM and TEM images of halloysite nanotube nanocontainers (*top row*). Photos of aluminum specimens after 2 weeks of exposure to corrosive medium (*bottom row*): a1) blank aluminum alloy immersed in 0.3% NaCl, a2) blank aluminum alloy immersed in 0.3% NaCl saturated with 2-mercaptobenzothiazole, and a3) aluminum alloy coated with halloysite-doped sol–gel film after immersion in 3% NaCl solution (after [1.147]). **(b)** *Top row*: Layers of nanostructured materials on its bulk substrate for K52 alloy. SEM images for top b1) and cross-section b2) morphologies are shown along with the TEM showing the structure of the sputtered nanocoating b3). *Bottom row*: Oxidation kinetics of the bulk and coated alloys exhibited faster oxidation rate for the bulk samples at the three temperatures (800 °C, 900 °C, 1000 °C) investigated (after [1.148])

filled composites and medicines released from nanocapsules will soon belong to this category. In scientific communications, a vast number of applications have been proposed in diverse fields. Several chapters in the final part of this handbook are devoted to applications, and in all the other parts, each chapter contains a short section showcasing applications of the nanomaterials considered. Here, we provide only a glimpse on applications, grouped into the categories of catalysts and catalyst templates, nanomaterials in energy conversion, and storage and sensors based on nanomaterials.

1.4.1 Catalysts and Catalyst Templates

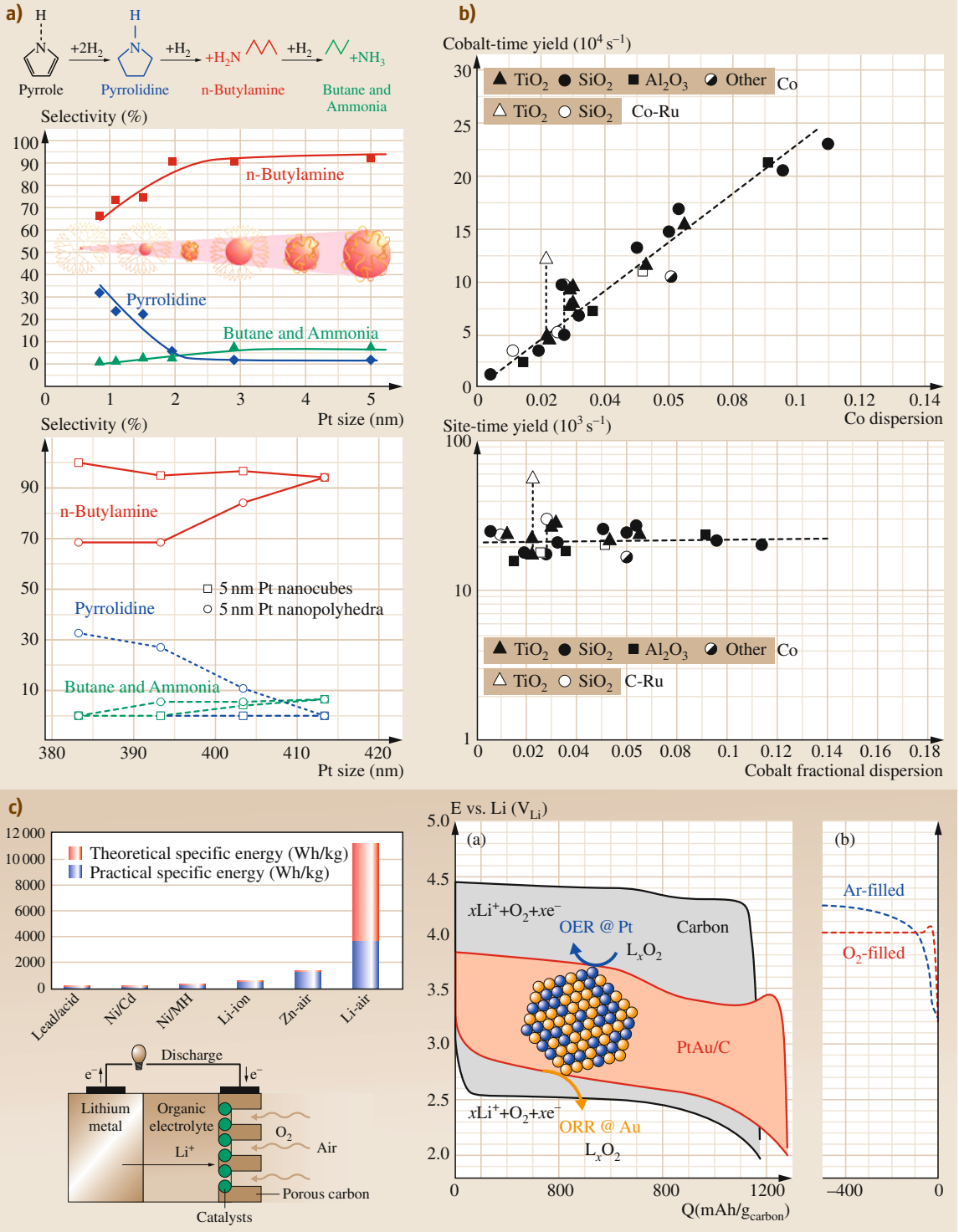
Heterogeneous catalytic reactions need high surface area for obvious reasons, as the process can be realized only at surfaces, and all materials in the volume represent unnecessary weight and cost. There is another reason why nanomaterials can behave differently from their larger-grain counterparts; i. e., they have different selectivity features. In surface catalysis it is well known that different crystal planes and different defect sites on the surface (e.g., steps, kinks) promote different reactions for the same conditions [1.151]. It has also been pointed out that, in homogeneous catalysis, edge and corner atoms play an exceptional role; however, their ratio can change during the reaction, and in fact surface reconfiguration is common [1.155]. In nanomaterials, the number of this kind of defects is naturally higher, depending also on their size and shape, so control of these parameters provides well-regulated reactions in a multichannel process. Figure 1.17a displays an example of how the size and shape of platinum nanoparticles govern the completeness of a pyrrole hydrogenation reaction [1.151]. Figure 1.17b shows how the size of a cobalt catalyst changes the yields of Fischer–Tropsch synthesis [1.152]. The yield is proportional to the dispersion of cobalt atoms, and the site-time yield is accordingly constant, which means that the size of the particles has an important effect; however, it does not change the surface features, so the authors could not find a shape dependence

Figure 1.17c introduces a specific, electrochemical, use of gold–platinum nanocatalyst used in Li–air and Zn–air batteries [1.153]. It is clear that these batteries have much higher specific energy storage capacity than conventionally used ones. The battery works similarly to Li-ion batteries inside, however they have a special porous anode where the air – in some cases oxygen or ozone – enters. Here, a catalyst is needed for efficient conversion of Li ions to lithium oxide during discharging, and lithium oxide to lithium ions during charging of the battery. In the nanosized alloy catalyst the platinum part is responsible for the reduction reaction and the gold part helps the oxidation.

1.4.2 Energy Conversion and Storage

Harvesting clean energy – mainly by converting naturally present energy to electricity – from abundant resources is one of the most important tasks to be accomplished by modern engineering. As clean energy sources (e.g., solar, wind) are not correlated with energy demand in time and non-localized energy sources are needed in transportation, too, efficiency in both energy harvesting and energy storage is necessary. Energy harvesting involves macroscopic equipment, e.g., wind turbines, however in many methods nanomaterials are used to improve efficiency. The two most relevant fields are thermo- and piezoelectric conversion and solar energy conversion by solar cells. Thermoelectric nanomaterials convert thermal energy between two locations at different temperatures. The measure of the efficiency of a material in thermoelectric conversion is the ZT parameter, the ratio of the Seebeck coefficient and the thermal and electrical conductivity of the material. Superlattices are the most efficient conversion devices, however their fabrication is costly and scaling up is complicated. Work has been carried out for efficient use of simpler systems, e.g., silicon nanowires [1.79]. Another way to apply nanomaterials in energy conversion is by using quantum dots – nanoparticles – in solar cells in order to trap more photons or capture more energy from photons [1.156]. Particular cases of

Fig. 1.17a–c Application of nanomaterials as catalysts. **(a)** Pyrrole hydrogenation reaction catalyzed by platinum nanoparticles having different size; the reaction product is a mix of pyrrolidine and *n*-butylamine for small (1–2 nm) particles and mostly *n*-butylamine for larger (3–5 nm) particles; the amount of butane and ammonia slowly increases with increasing particle size (after [1.151]). **(b)** CO conversion time yield and turnover rate in a Fischer–Tropsch reaction as a function of cobalt dispersion [1.152]. **(c)** Energy density for several commonly investigated batteries; schematic of a possible configuration for Li–air or Zn–air battery, showing the location of the catalyst; charge–discharge characteristics of a Li–air cell displaying the role of the PtAu catalyst particle in the reduction and oxidation steps (ORR: oxygen reduction reaction; OER: oxygen evolution reaction) (after [1.153, 154]) ▶


a)
Pyrrole
Pyrrolidine
n-Butylamine
Butane and Ammonia
Selectivity (%)
n-Butylamine
Pyrrolidine
Butane and Ammonia
Pt size (nm)
5 nm Pt nanocubes
5 nm Pt nanopolyhedra
b)
Cobalt-time yield (10^4 s^{-1})
Co
Co-Ru
Co dispersion
Site-time yield (10^3 s^{-1})
C-Ru
Cobalt fractional dispersion
c)
Theoretical specific energy (Wh/kg)
Practical specific energy (Wh/kg)
Lead/acid
Ni/Cd
Ni/MH
Li-ion
Zn-air
Li-air
Discharge
Lithium metal
Organic electrolyte
Air
Porous carbon
Catalysts
E vs. Li (V_{Li})
Carbon
OER @ Pt
PtAu/C
ORR @ Au
Ar-filled
O_2-filled
Q(mAh/g_{carbon})

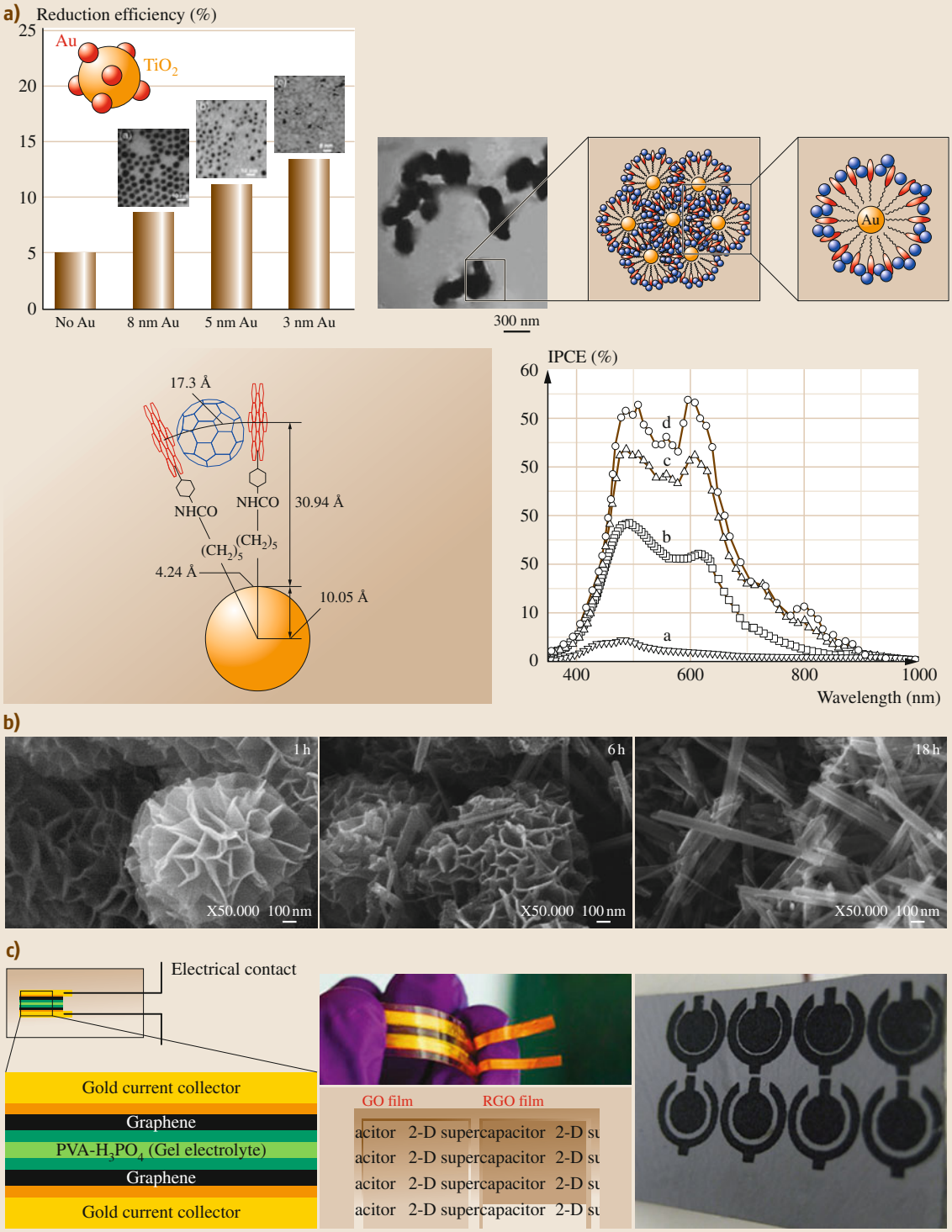
clean energy conversion that use nanomaterials are displayed in Fig. 1.18a. The measurements show a strong dependence of the reduction rate achieved with TiO_2 on the gold particle size; the gold template modifies the Fermi level, and the shift in the Fermi energy increases with decreasing particle size. This reaction is used in photoelectrochemical energy conversion. It was also shown that the solar energy conversion is dependent on the configuration of the optically transparent electrode $(OTE/SnO_2/(H_2PC_nMPC+C_{60})_m)$, where the length of the linker (the number of fullerene molecules) plays the most important role [1.72]. For energy storage, we have collected examples from our previous work in Fig. 1.18b. The SEM images show an MnO_2 structure prepared by hydrothermal synthesis [1.73]. The nanowires obtained have potential applications in supercapacitor devices. We also present an atomically thin, transparent, flexible supercapacitor based on single- or few-layer graphene electrodes. The transparency of the GO and RGO layers are demonstrated placed them onto a printout; here the thickness of the multilayered films was set to $\approx 10\,\text{nm}$ by consecutive dip-coating steps. The last part (Fig. 1.18b) shows a supercapacitor array designed on a monolithic GO piece. Parts of the GO were reduced by a laser beam, and these RGO parts serve as electrodes while the unreduced GO acts as a solid electrolyte.

1.4.3 Sensors Based on Nanomaterials

Nanomaterials are excellent choices for use as active elements of chemical (gas) sensors. To achieve high sensitivity, the material needs to have high dispersion, as surface atoms interact and undergo changes whereas atoms inside the material do not change, meaning that, the higher the surface atom ratio, the larger the relative change in the measured physical property of the material. Similarly to applications as catalysts, in sensors not only the size of the particles is important but also their shape. As the shape, number, and configuration of edge and corner atoms change, further differences occur in the signals measured. Figure 1.19a demonstrates the effect of various shapes when nanoparticles, nanowires, and nanoplatelets of tungsten oxide were used [1.77]. In this case, the nanowires have the highest sensitivity, followed by the platelets and finally the nanoparticles.

Fluctuation-based sensing or fluctuation-enhanced sensing (FES) provides selectivity via investigation of fluctuations in resistance, voltage or current. The method is based on measurement of a signal as a function of time, analysis of this signal, and in most cases fast Fourier transformation (FFT), and finally interpretation of the power spectral density in characteristic frequency ranges to identify the chemical environment [1.78, 81]. This interpretation can be a simple linearization, application of a neural network, or use of principal component analysis (PCA) plots. All these interpretation methods allow selectivity for different gases and for different concentrations. Any kind of sensor can be essentially used with this method; however, sensors made of nanomaterials have the advantage of much stronger FES signals and significantly more information content [1.80, 82, 83]. Carbon nanotubes are especially useful and important building blocks of FES devices, as they can be functionalized with appropriate chemical groups that make them selective for particular materials [1.84]. Functionalization is especially well studied in the case of CNTs for use in biosensors [1.85]. Figure 1.19b displays a print made with a carbon nanotube ink. A similar printing method and ink were used to create the sensors for the devices providing the signals in the lower row. The fluctuation power spectra were measured using a Taguchi-type sensor, and show measurable differences between three different gases compared with a synthetic air reference. The PCA plots demonstrate the sensitivity and selectivity of the printed carbon nanotube sensors. Signals of 30 ppb concentration are shown to be selective for the measured gases.

Fig. 1.18a–c Application of nanomaterials in energy conversion and storage. **(a)** Dependence of photoreduction efficiency of TiO_2 particles on the size of a gold nanoparticle used as a substrate. The smaller the particle, the higher the reduction efficiency. Schemes of $(H_2PC_nMPC+C_{60})_m$ configurations are also displayed. These particles are applicable for photo-induced current; the photocurrent for the visible spectrum is displayed for different configurations of the structure of $OTE/SnO_2/(H_2PC_nMPC+C_{60})_m$ with parameters of $[H_2P]=0.19\,\text{mM}$, $n=15$, $C_n=[C_{60}]=0.38\,\text{mM}$ (after [1.72, 74]). **(b)** Evolution of MnO_2 morphology as a function of the dwell time of hydrothermal synthesis. Supercapacitors prepared with nanowire electrodes have 150–200 F/g specific capacitance (after [1.73]). **(c)** Physical appearance of nanomaterial supercapacitors; transparent, flexible supercapacitor with graphene electrodes (after [1.75]) and laser-defined GO electrode–RGO electrolyte (after [1.76]) (IPCE: incident photon to charge carrier efficiency; PVA: polyvinyl alcohol) ▶


a)
Reduction efficiency (%)
25
20
15
10
5
0
Au
TiO2
No Au
8 nm Au
5 nm Au
3 nm Au
300 nm
Au
17.3 Å
NHCO
NHCO
30.94 Å
(CH2)5
(CH2)5
4.24 Å
10.05 Å
IPCE (%)
60
50
50
50
50
10
0
d
c
b
a
400
600
800
1000
Wavelength (nm)
b)
1 h
X50.000 100 nm
6 h
X50.000 100 nm
18 h
X50.000 100 nm
c)
Electrical contact
Gold current collector
Graphene
PVA-H3PO4 (Gel electrolyte)
Graphene
Gold current collector
GO film
RGO film
acitor 2-D supercapacitor 2-D su
acitor 2-D supercapacitor 2-D su
acitor 2-D supercapacitor 2-D su
acitor 2-D supercapacitor 2-D su

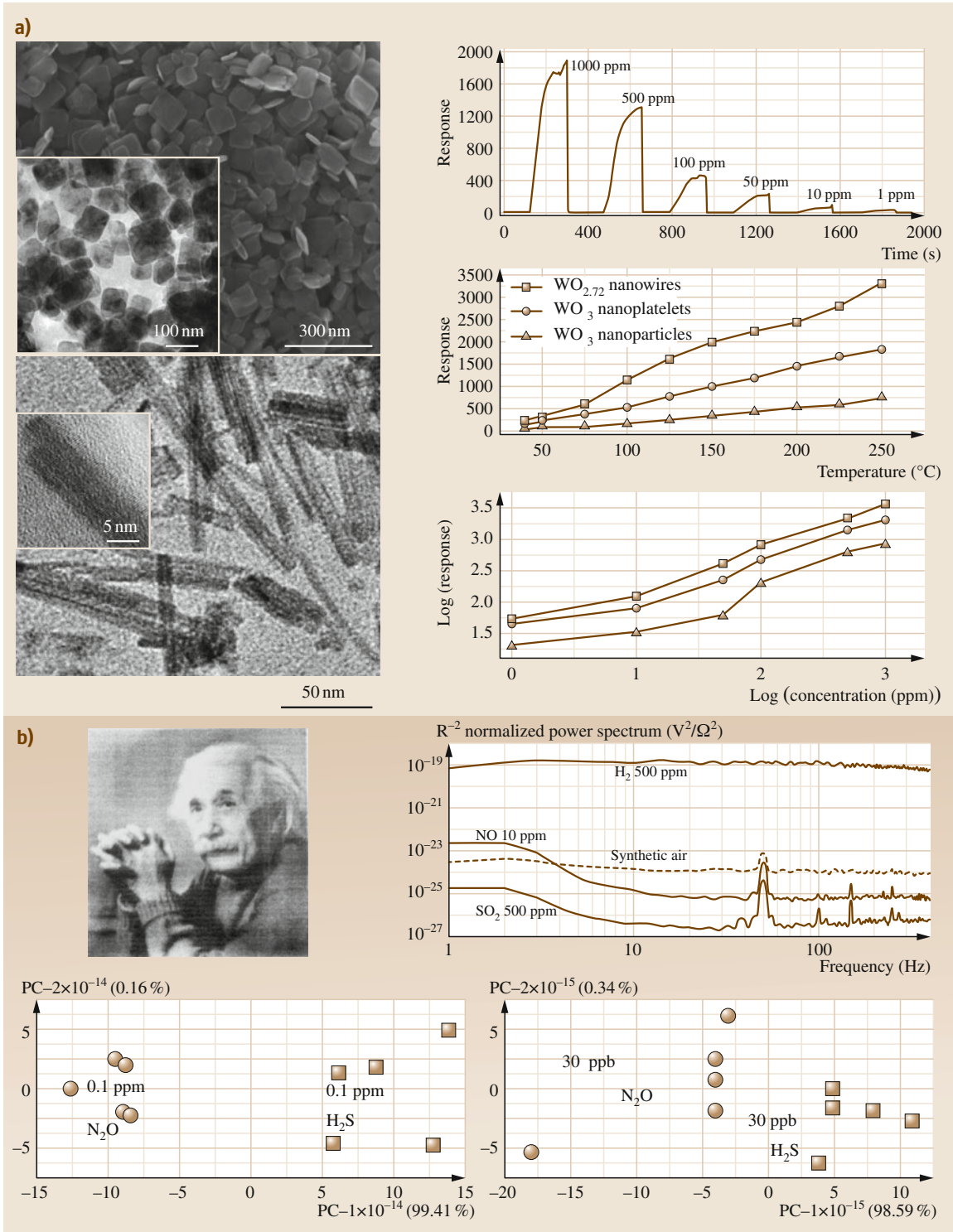

a)
100 nm
300 nm
5 nm
50 nm
Response
1000 ppm
500 ppm
100 ppm
50 ppm
10 ppm
1 ppm
Time (s)
WO2.72 nanowires
WO 3 nanoplatelets
WO 3 nanoparticles
Temperature (°C)
Log (response)
Log (concentration (ppm))
b)
R−2 normalized power spectrum (V2/Ω2)
H2 500 ppm
NO 10 ppm
Synthetic air
SO2 500 ppm
Frequency (Hz)
PC–2×10−14 (0.16 %)
0.1 ppm
N2O
0.1 ppm
H2S
PC–1×10−14 (99.41 %)
PC–2×10−15 (0.34 %)
30 ppb
N2O
30 ppb
H2S
PC–1×10−15 (98.59 %)

Fig. 1.19a,b Application of nanomaterials in sensors. **(a)** SEM and TEM images of tungsten oxide nanoplatelets and TEM of $WO_{2.72}$ nanowires. Measuring different concentrations of H_2S using a nanoplatelet sensor. Gas sensing measurement: sensor signal as a function of H_2S concentration at 250 °C. Comparative graphs showing sensitivity of different nanostructures as a function of temperature and concentration (after [1.77]). **(b)** Demonstration of selectivity achieved by the fluctuation-enhanced sensing method. An image printed using nanotube solution as ink, similar to the ones used to print circuits for sensors (after [1.157]). Linearized spectra measured on thick-film nanoparticle sensors (after [1.81]). PCA plots of FES of N_2O (*circles*) and H_2S (*squares*) measured with an MWCNT sensor showing both sensitivity and selectivity (PC: principal component) (after [1.83]) ◀

1.5 Concluding Remarks

Nanomaterials differ in many regards from their macroscopic – bulk – allotropes, and accordingly they call for special scientific and engineering approaches. The large number of scientific articles, encyclopedias, and handbooks in related topics, as well as textbooks and full courses, show the growing importance of this field.

In this chapter we could give only a glimpse of the numerous unique and interesting, mainly universal properties of nanosized materials. This similarity of properties of materials as a function of their characteristic size clearly shows that nanomaterials represent a one-of-a-kind, coherent group of materials. The later chapters in this handbook elaborate on the synthesis, specific properties, and applications of the various material groups. Our main objective in this chapter was to collect and present material properties in a way that would introduce novice readers to a new topic, and at the same time serve as a reference for the everyday work of well-established scientists and engineers.

1.6 About the Contents of the Handbook

The structure of the handbook follows the classification of important material groups. Part A describes carbon-based nanomaterials from fullerenes to nanotubes and nanofibers, as well as nanodiamonds. Part B introduces noble and common metals and alloys. Part C describes ceramic materials, crystalline and glassy oxides, and other compounds. Part D describes composites and hybrid structures where nanomaterials serve as fillers and building blocks, as well as solutions, so-called nanoinks. Part E deals with porous nanomaterials, metals, ceramics, and silicon. Part F presents examples of organic and bio-nanomaterials, bones, and fibers. Finally, Part G contains several chapters on the topics of applications in nanomedicine, civil engineering, toxicology, and hazards, as well as energy harvesting and energy storage.

References

1.1 E. Rzepka: Raman scattering (2009) http://www.raman-scattering.eu/raman/index.php

1.2 H. Fountain: Antique Nanotubes, The New York Times, November 28 (2006), available online at http://www.nytimes.com/2006/11/28/science/28observ.Html?_r=1

1.3 C.G. Granqvist, R.A. Buhrman: Ultrafine metal particles, J. Appl. Phys. **47**(5), 2200–2219 (1976)

1.4 M.S. Dresselhaus, C. Dresselhaus, P.C. Eklund: *Science of Fullerenes and Carbon Nanotubes* (Academic, San Diego 1995)

1.5 M.B. Mohamed, V. Volkov, S. Link, M.A. El-Sayed: The 'lightning' gold nanorods: Fluorescence enhancement of over a million compared to the gold metal, Chem. Phys. Lett. **317**(6), 517–523 (2000)

1.6 M.A. Peiyan, F.U. Zhengyi, S.U. Yanli, M.A. Jingjing: The nano pulverization of traditional Chinese medicine Liuwei Dihuang, J. Wuhan Univ. Technol. Mater. Sci. Ed. **21**(2), 105–108 (2006)

1.7 M. José-Yacaman, L. Rendón, J. Arenas, M.C.S. Puche: Maya blue paint: An ancient nanostructured material, Science **273**(5272), 223–225 (1996)

1.8 G. Padeletti, P. Fermo: How the masters in Umbria, Italy, generated and used nanoparticles in art fabrication during the Renaissance period, Appl. Phys. A **76**(4), 515–525 (2003)

1.9 M.-C. Daniel, D. Astruc: Gold nanoparticles: Assembly, supramolecular chemistry, quantum-size-related properties, and applications toward biology, catalysis, and nanotechnology, Chem. Rev. **104**(1), 293–346 (2003)

1.10 M. Reibold, P. Paufler, A.A. Levin, W. Kochmann, N. Patzke, D.C. Meyer: Materials: Carbon nanotubes in an ancient Damascus sabre, Nature **444**(7117), 286–286 (2006)

1.11 J. Bardeen, W.H. Brattain: The transistor, a semiconductor triode, Phys. Rev. **74**(2), 230–231 (1948)

1.12 J.S. Kilby: Invention of integrated-circuit, IEEE Trans. Electron Devices **23**(7), 648–654 (1976)

1.13 R.P. Feynman: There's plenty of room at the bottom, Eng. Sci. **23**(5), 22–36 (1960)

1.14 R.W. Siegel, S. Ramasamy, H. Hahn, Z.Q. Li, T. Lu, R. Gronsky: Synthesis, characterization, and properties of nanophase TiO_2, J. Mater. Res. **3**(6), 1367–1372 (1988)

1.15 Office of Basic Energy Sciences (BES): *The Scale of Things* (US Department of Energy, Washington D.C. 2006), available online at http://science.energy.gov/bes/news-and-resources/scale-of-things-chart/

1.16 P. Avouris, R. Martel, T. Hertel, R. Sandstrom: AFM-tip-induced and current-induced local oxidation of silicon and metals, Appl. Phys. A **66**, S659–S667 (1998)

1.17 N. Chekurov, K. Grigoras, A. Peltonen, S. Franssila, I. Tittonen: The fabrication of silicon nanostructures by local gallium implantation and cryogenic deep reactive ion etching, Nanotechnology **20**(6), 065307 (2009)

1.18 E. Perez-Tijerina, M.A. Gracia-Pinilla, S. Mejia-Rosales, U. Ortiz-Mendez, A. Torres, M. Jose-Yacaman: Highly size-controlled synthesis of Au/Pd nanoparticles by inert-gas condensation, Faraday Discuss. **138**, 353–362 (2008)

1.19 L.B. Kiss, J. Söderlund, G.A. Niklasson, C.G. Granqvist: The real origin of lognormal size distributions of nanoparticles in vapor growth processes, Nanostruct. Mater. **12**(1–4), 327–332 (1999)

1.20 D.D. Majumder, R. Banerjee, C. Ulrichs, I. Mewis, A. Goswami: Nano-materials: Science of bottom-up and top-down, IETE Tech. Rev. **24**(1), 9–25 (2007)

1.21 K. Ariga, J.P. Hill, M.V. Lee, A. Vinu, R. Charvet, S. Acharya: Challenges and breakthroughs in recent research on self-assembly, Sci. Technol. Adv. Mater. **9**(1), 014109 (2008)

1.22 C. Park, J. Yoon, E.L. Thomas: Enabling nanotechnology with self assembled block copolymer patterns, Polymer **44**(22), 6725–6760 (2003)

1.23 F.S. Bates, G.H. Fredrickson: Block copolymers – designer soft materials, Phys. Today **52**(2), 32–38 (1999)

1.24 J.Y. Cheng, C.A. Ross, V.Z.H. Chan, E.L. Thomas, R.G.H. Lammertink, G.J. Vancso: Formation of a cobalt magnetic dot array via block copolymer lithography, Adv. Mater. **13**(15), 1174–1178 (2001)

1.25 R.D. Piner, J. Zhu, F. Xu, S.H. Hong, C.A. Mirkin: "Dip-pen" nanolithography, Science **283**(5402), 661–663 (1999)

1.26 C.R. Martin: Membrane-based synthesis of nanomaterials, Chem. Mater. **8**(8), 1739–1746 (1996)

1.27 G.W. Meng, F.M. Han, X.L. Zhao, B.S. Chen, D.C. Yang, J.X. Liu, Q.L. Xu, M.G. Kong, X.G. Zhu, Y.J. Jung, Y.J. Yang, Z.Q. Chu, M. Ye, S. Kar, R. Vajtai, P.M. Ajayan: A general synthetic approach to interconnected nanowire/nanotube and nanotube/nanowire/nanotube heterojunctions with branched topology, Angew. Chem. Int. Ed. **48**(39), 7166–7170 (2009)

1.28 H. Chun, M.G. Hahm, Y. Homma, R. Meritz, K. Kuramochi, L. Menon, L. Ci, P.M. Ajayan, Y.J. Jung: Engineering low-aspect ratio carbon nanostructures: Nanocups, nanorings, and nanocontainers, ACS Nano **3**(5), 1274–1278 (2009)

1.29 A.R. Tao, S. Habas, P.D. Yang: Shape control of colloidal metal nanocrystals, Small **4**(3), 310–325 (2008)

1.30 J. Banhart: Manufacture, characterisation and application of cellular metals and metal foams, Progress Mater. Sci. **46**(6), 559–632 (2001)

1.31 C. Suryanarayana: Nanocrystalline materials, Int. Mater. Rev. **40**(2), 41–64 (1995)

1.32 J. Soderlund, L.B. Kiss, G.A. Niklasson, C.G. Granqvist: Lognormal size distributions in particle growth processes without coagulation, Phys. Rev. Lett. **80**(11), 2386–2388 (1998)

1.33 K. Hata, D.N. Futaba, K. Mizuno, T. Namai, M. Yumura, S. Iijima: Water-assisted highly efficient synthesis of impurity-free single-waited carbon nanotubes, Science **306**(5700), 1362–1364 (2004)

1.34 H.W. Zhu, C.L. Xu, D.H. Wu, B.Q. Wei, R. Vajtai, P.M. Ajayan: Direct synthesis of long single-walled carbon nanotube strands, Science **296**(5569), 884–886 (2002)

1.35 B.Q. Wei, R. Vajtai, Y. Jung, J. Ward, R. Zhang, G. Ramanath, P.M. Ajayan: Organized assembly of carbon nanotubes – cunning refinements help to customize the architecture of nanotube structures, Nature **416**(6880), 495–496 (2002)

1.36 L. Song, L. Ci, H. Lu, P.B. Sorokin, C. Jin, J. Ni, A.G. Kvashnin, D.G. Kvashnin, J. Lou, B.I. Yakobson, P.M. Ajayan: Large scale growth and characterization of atomic hexagonal boron nitride layers, Nano Lett. **10**(8), 3209–3215 (2010)

1.37 B. Nikoobakht, M.A. El-Sayed: Preparation and growth mechanism of gold nanorods (NRs) using seed-mediated growth method, Chem. Mater. **15**(10), 1957–1962 (2003)

1.38 M. Grzelczak, J. Perez-Juste, P. Mulvaney, L.M. Liz-Marzan: Shape control in gold nanoparticle synthesis, Chem. Soc. Rev. **37**(9), 1783–1791 (2008)

1.39 Y.D. Yin, R.M. Rioux, C.K. Erdonmez, S. Hughes, G.A. Somorjai, A.P. Alivisatos: Formation of hollow nanocrystals through the nanoscale Kirkendall effect, Science **304**(5671), 711–714 (2004)

1.40 H.J. Fan, U. Gosele, M. Zacharias: Formation of nanotubes and hollow nanoparticles based on Kirkendall and diffusion processes: A review, Small **3**(10), 1660–1671 (2007)

1.41 A. Gedanken: Using sonochemistry for the fabrication of nanomaterials, Ultrason. Sonochem. **11**(2), 47–55 (2004)

1.42 C.J. Hawker, T.P. Russell: Block copolymer lithography: Merging "bottom-up" with "top-down" processes, MRS Bulletin **30**(12), 952–966 (2005)

1.43 N.J. Halas, S. Lal, W.S. Chang, S. Link, P. Nordlander: Plasmons in strongly coupled metallic nanostructures, Chem. Rev. **111**(6), 3913–3961 (2011)

1.44 H.W. Kroto, J.R. Heath, S.C. O'Brien, R.F. Curl, R.E. Smalley: C_{60}: Buckminsterfullerene, Nature **318**(6042), 162–163 (1985)

1.45 J. Park, J. Joo, S.G. Kwon, Y. Jang, T. Hyeon: Synthesis of monodisperse spherical nanocrystals, Angew. Chem. Int. Ed. **46**(25), 4630–4660 (2007)

1.46 J. Park, E. Lee, N.-M. Hwang, M. Kang, S.C. Kim, Y. Hwang, J.-G. Park, H.-J. Noh, J.-Y. Kim, J.-H. Park, T. Hyeon: One-nanometer-scale size-controlled synthesis of monodisperse magnetic iron oxide nanoparticles, Angew. Chem. Int. Ed. **44**(19), 2872–2877 (2005)

1.47 X.F. Duan, C.M. Lieber: General synthesis of compound semiconductor nanowires, Adv. Mater. **12**(4), 298–302 (2000)

1.48 S. Iijima, T. Ichihashi: Single-shell carbon nanotubes of 1-nm diameter, Nature **363**(6430), 603–605 (1993)

1.49 D.S. Bethune, C.H. Kiang, M.S. Devries, G. Gorman, R. Savoy, J. Vazquez, R. Beyers: Cobalt-catalyzed growth of carbon nanotubes with single-atomic-layerwalls, Nature **363**(6430), 605–607 (1993)

1.50 S. Iijima: Helical microtubules of graphitic carbon, Nature **354**(6348), 56–58 (1991)

1.51 A.K. Geim, K.S. Novoselov: The rise of graphene, Nat. Mater. **6**(3), 183–191 (2007)

1.52 S. Park, R.S. Ruoff: Chemical methods for the production of graphenes, Nat. Nanotechnol. **4**(4), 217–224 (2009)

1.53 L. Ci, L. Song, C.H. Jin, D. Jariwala, D.X. Wu, Y.J. Li, A. Srivastava, Z.F. Wang, K. Storr, L. Balicas, F. Liu, P.M. Ajayan: Atomic layers of hybridized boron nitride and graphene domains, Nat. Mater. **9**(5), 430–435 (2010)

1.54 J. Zhu, Z. Konya, V.F. Puntes, I. Kiricsi, C.X. Miao, J.W. Ager, A.P. Alivisatos, G.A. Somorjai: Encapsulation of metal (Au, Ag, Pt) nanoparticles into the mesoporous SBA-15 structure, Langmuir **19**(10), 4396–4401 (2003)

1.55 H. Gleiter: Nanostructured materials: Basic concepts and microstructure, Acta Mater. **48**(1), 1–29 (2000)

1.56 K.J.M. Bishop, C.E. Wilmer, S. Soh, B.A. Grzybowski: Nanoscale forces and their uses in self-assembly, Small **5**(14), 1600–1630 (2009)

1.57 C.Q. Sun, B.K. Tay, X.T. Zeng, S. Li, T.P. Chen, J. Zhou, H.L. Bai, E.Y. Jiang: Bond-order-bond-length-bond-strength (bond-OLS) correlation mechanism for the shape-and-size dependence of a nanosolid, J. Phys. D **14**(34), 7781–7795 (2002)

1.58 T. Halicioglu: Calculation of surface energies for low index planes of diamond, Surface Sci. **259**(1–2), L714–L718 (1991)

1.59 A. Baraldi, S. Lizzit, G. Comelli, G. Paolucci: Oxygen adsorption and ordering on Ru (10$\bar{1}$0), Phys. Rev. B **63**(11), 115410 (2001)

1.60 H. Over, G. Kleinle, G. Ertl, W. Moritz, K.H. Ernst, H. Wohlgemuth, K. Christmann, E. Schwarz: A leed structural-analysis of the Co(1010) surface, Surface Sci. **254**(1–3), L469–L474 (1991)

1.61 H.L. Davis, D.M. Zehner: Structure of the clean re(1010) surface, J. Vac. Sci. Technol. **17**(1), 190–193 (1980)

1.62 X. Qian, W. Hubner: First-principles calculation of structural and magnetic properties for Fe monolayers and bilayers on W(110), Phys. Rev. B **60**(23), 16192–16197 (1999)

1.63 W.T. Geng, A.J. Freeman, R.Q. Wu: Magnetism at high-index transition-metal surfaces and the effect of metalloid impurities: Ni(210), Phys. Rev. B **63**(6), 064427 (2001)

1.64 W.T. Geng, M. Kim, A.J. Freeman: Multilayer relaxation and magnetism of a high-index transition metal surface: Fe(310), Phys. Rev. B **63**(24), 245401 (2001)

1.65 I.P. Batra: Lattice-relaxation in aluminum monolayers, J. Vac. Sci. Technol. Vac. Surf. and Films **3**(3), 1603–1606 (1985)

1.66 P.J. Feibelman: Relaxation of hcp(0001) surfaces: A chemical view, Phys. Rev. B **53**(20), 13740–13746 (1996)

1.67 C.Q. Sun: O-Cu(001): I. Binding the signatures of LEED, STM and PES in a bond-forming way, Surf. Rev. and Lett. **8**(3–4), 367–402 (2001)

1.68 C.Q. Sun: O-Cu(001): Ii. Vleed quantification of the four-stage Cu_3O_2 bonding kinetics, Surf. Rev. Lett. **8**(6), 703–734 (2001)

1.69 C.Q. Sun: Time-resolved vleed from the O-Cu(001): Atomic processes of oxidation, Vacuum **48**(6), 525–530 (1997)

1.70 C.Q. Sun, B.K. Tay, S.P. Lau, X.W. Sun, X.T. Zeng, S. Li, H.L. Bai, H. Liu, Z.H. Liu, E.Y. Jiang: Bond contraction and lone pair interaction at nitride surfaces, J. Appl. Phys. **90**(5), 2615–2617 (2001)

1.71 D.A. Walker, B. Kowalczyk, M.O. de la Cruz, B.A. Grzybowski: Electrostatics at the nanoscale, Nanoscale **3**(4), 1316 (2011)

1.72 P.V. Kamat: Meeting the clean energy demand: Nanostructure architectures for solar energy conversion, J. Phys. Chem. C **111**(7), 2834–2860 (2007)

1.73 V. Subramanian, H.W. Zhu, R. Vajtai, P.M. Ajayan, B.Q. Wei: Hydrothermal synthesis and pseudocapac-

itance properties of MnO_2 nanostructures, J. Phys. Chem. B **109**(43), 20207–20214 (2005)

1.74 T. Hasobe, H. Imahori, P.V. Kamat, T.K. Ahn, S.K. Kim, D. Kim, A. Fujimoto, T. Hirakawa, S. Fukuzumi: Photovoltaic cells using composite nanoclusters of porphyrins and fullerenes with gold nanoparticles, J. Am. Chem. Soc. **127**(4), 1216–1228 (2005)

1.75 J.J. Yoo, K. Balakrishnan, J.S. Huang, V. Meunier, B.G. Sumpter, A. Srivastava, M. Conway, A.L.M. Reddy, J. Yu, R. Vajtai, P.M. Ajayan: Ultrathin planar graphene supercapacitors, Nano Lett. **11**(4), 1423–1427 (2011)

1.76 W. Gao, N. Singh, L. Song, Z. Liu, A.L.M. Reddy, L.J. Ci, R. Vajtai, Q. Zhang, B.Q. Wei, P.M. Ajayan: Direct laser writing of micro-supercapacitors on hydrated graphite oxide films, Nat. Nanotechnol. **6**(8), 496–500 (2011)

1.77 C.S. Rout, M. Hegde, C.N.R. Rao: H2s sensors based on tungsten oxide nanostructures, Sens. Actuator B **128**(2), 488–493 (2008)

1.78 L.B. Kish, R. Vajtai, C.G. Granqvist: Extracting information from noise spectra of chemical sensors: Single sensor electronic noses and tongues, Sensor Actuat or B **71**(1–2), 55–59 (2000)

1.79 A.I. Boukai, Y. Bunimovich, J. Tahir-Kheli, J.K. Yu, W.A. Goddard, J.R. Heath: Silicon nanowires as efficient thermoelectric materials, Nature **451**(7175), 168–171 (2008)

1.80 H. Haspel, R. Ionescu, P. Heszler, A. Kukovecz, Z. Konya, Z. Gingl, J. Maklin, T. Mustonen, K. Kordas, R. Vajtai, P.M. Ajayan: Fluctuation enhanced gas sensing on functionalized carbon nanotube thin films, Phys. Status Solidi (b) **245**(10), 2339–2342 (2008)

1.81 L.B. Kish, Y.F. Li, J.L. Solis, W.H. Marlow, R. Vajtai, C.G. Granqvist, V. Lantto, J.M. Smulko, G. Schmera: Detecting harmful gases using fluctuation-enhanced sensing with taguchi sensors, IEEE Sens. J. **5**(4), 671–676 (2005)

1.82 J. Maklin, T. Mustonen, N. Halonen, G. Toth, K. Kordas, J. Vahakangas, H. Moilanen, A. Kukovecz, Z. Konya, H. Haspel, Z. Gingl, P. Heszler, R. Vajtai, P.M. Ajayan: Inkjet printed resistive and chemical-fet carbon nanotube gas sensors, Phys. Status Solidi (b) **245**(10), 2335–2338 (2008)

1.83 D. Molnar, P. Heszler, R. Mingesz, Z. Gingl, A. Kukovecz, Z. Konya, H. Haspel, M. Mohl, A. Sapi, I. Kiricsi, K. Kordas, J. Maklin, N. Halonen, G. Toth, H. Moilanen, S. Roth, R. Vajtai, P.M. Ajayan, Y. Pouillon, A. Rubio: Increasing chemical selectivity of carbon nanotube-based sensors by fluctuation-enhanced sensing, Fluct. Noise Lett. **9**(3), 277–287 (2010)

1.84 Á. Kukovecz, D. Molnár, K. Kordás, Z. Gingl, H. Moilanen, R. Mingesz, Z. Kónya, J. Mäklin, N. Halonen, G. Tóth, H. Haspel, P. Heszler, M. Mohl, A. Sápi, S. Roth, R. Vajtai, P.M. Ajayan, Y. Pouillon, A. Rubio, I. Kiricsi: Carbon nanotube based sensors and fluctuation enhanced sensing, Phys. Status Solidi (c) **7**(3–4), 1217–1221 (2010)

1.85 J. Wang: Carbon-nanotube based electrochemical biosensors: A review, Electroanalysis **17**(1), 7–14 (2005)

1.86 Q. Jiang, L.H. Liang, D.S. Zhao: Lattice contraction and surface stress of fcc nanocrystals, J. Phys. Chem. B **105**(27), 6275–6277 (2001)

1.87 Q.S. Chang, X.W. Sun, B.K. Tay, S.P. Lau, H.T. Huang, S. Li: Dielectric suppression and its effect on photoabsorption of nanometric semiconductors, J. Phys. D **34**(15), 2359 (2001)

1.88 S.R. Bahn, K.W. Jacobsen: Chain formation of metal atoms, Phys. Rev. Lett. **87**(26), 266101 (2001)

1.89 E. Arzt: Overview no. 130 – size effects in materials due to microstructural and dimensional constraints: A comparative review, Acta Mater. **46**(16), 5611–5626 (1998)

1.90 R.A. Andrievski: Size-dependent effects in properties of nanostructured materials, Rev. Adv. Mater. Sci. **21**(2), 107–133 (2009)

1.91 N. Dubrovinskaia, V.L. Solozhenko, N. Miyajima, V. Dmitriev, O.O. Kurakevych, L. Dubrovinsky: Superhard nanocomposite of dense polymorphs of boron nitride: Noncarbon material has reached diamond hardness, Appl. Phys. Lett. **90**(10), 101912–1–101912–3 (2007)

1.92 R.W. Siegel, G.E. Fougere: Mechanical properties of nanophase metals, Nanostruct. Mater. **6**(1–4), 205–216 (1995)

1.93 B.I. Yakobson, P. Avouris: Mechanical properties of carbon nanotubes, Carbon Nanotub. **80**, 287–327 (2001)

1.94 B.I. Yakobson, C.J. Brabec, J. Bernholc: Nanomechanics of carbon tubes: Instabilities beyond linear response, Phys. Rev. Lett. **76**(14), 2511–2514 (1996)

1.95 B.I. Yakobson, R.E. Smalley: Fullerene nanotubes: C-1000000 and beyond, Am. Sci. **85**(4), 324–337 (1997)

1.96 M.M.J. Treacy, T.W. Ebbesen, J.M. Gibson: Exceptionally high young's modulus observed for individual carbon nanotubes, Nature **381**(6584), 678–680 (1996)

1.97 C. Lee, X.D. Wei, J.W. Kysar, J. Hone: Measurement of the elastic properties and intrinsic strength of monolayer graphene, Science **321**(5887), 385–388 (2008)

1.98 W.A. Deheer, A. Chatelain, D. Ugarte: A carbon nanotube field-emission electron source, Science **270**(5239), 1179–1180 (1995)

1.99 Y.N. Xia, P.D. Yang, Y.G. Sun, Y.Y. Wu, B. Mayers, B. Gates, Y.D. Yin, F. Kim, Y.Q. Yan: One-dimensional nanostructures: Synthesis, characterization, and applications, Adv. Mater. **15**(5), 353–389 (2003)

1.100 R. Landauer: Electrical resistance of disordered one-dimensional lattices, Philos. Mag. **21**(172), 863–867 (1970)

1.101 C.T. White, T.N. Todorov: Carbon nanotubes as long ballistic conductors, Nature **393**(6682), 240–242 (1998)

1.102 R. Martel, T. Schmidt, H.R. Shea, T. Hertel, P. Avouris: Single- and multi-wall carbon nanotube field-effect transistors, Appl. Phys. Lett. **73**(17), 2447–2449 (1998)

1.103 J. Park, A.N. Pasupathy, J.I. Goldsmith, C. Chang, Y. Yaish, J.R. Petta, M. Rinkoski, J.P. Sethna, H.D. Abruna, P.L. McEuen, D.C. Ralph: Coulomb blockade and the Kondo effect in single-atom transistors, Nature **417**(6890), 722–725 (2002)

1.104 H.W.C. Postma, T. Teepen, Z. Yao, M. Grifoni, C. Dekker: Carbon nanotube single-electron transistors at room temperature, Science **293**(5527), 76–79 (2001)

1.105 D. Goldhaber-Gordon, H. Shtrikman, D. Mahalu, D. Abusch-Magder, U. Meirav, M.A. Kastner: Kondo effect in a single-electron transistor, Nature **391**(6663), 156–159 (1998)

1.106 A. Javey, P.F. Qi, Q. Wang, H.J. Dai: Ten- to 50-nm-long quasi-ballistic carbon nanotube devices obtained without complex lithography, Proc. Nat. Acad. Sci. USA **101**(37), 13408–13410 (2004)

1.107 B.Q. Wei, R. Vajtai, P.M. Ajayan: Reliability and current carrying capacity of carbon nanotubes, Appl. Phys. Lett. **79**(8), 1172–1174 (2001)

1.108 Y. Zhao, J.Q. Wei, R. Vajtai, P.M. Ajayan, E.V. Barrera: Iodine doped carbon nanotube cables exceeding specific electrical conductivity of metals, Sci. Rep. **1**(83), 1–5 (2011)

1.109 A.P. Alivisatos: Semiconductor clusters, nanocrystals, and quantum dots, Science **271**(5251), 933–937 (1996)

1.110 P. Avouris, J. Appenzeller, R. Martel, S.J. Wind: Carbon nanotube electronics, Proc. IEEE **91**(11), 1772–1784 (2003)

1.111 P. Poncharal, S. Frank, Z.L. Wang, W.A. de Heer: Conductance quantization in multiwalled carbon nanotubes, Eur. Phys. J. D **9**(1–4), 77–79 (1999)

1.112 P. Avouris: Graphene: Electronic and photonic properties and devices, Nano Lett. **10**(11), 4285–4294 (2010)

1.113 C. Kittel: Theory of the structure of ferromagnetic domains in films and small particles, Phys. Rev. **70**(11–1), 965–971 (1946)

1.114 D.L. Leslie-Pelecky, R.D. Rieke: Magnetic properties of nanostructured materials, Chem. Mater. **8**(8), 1770–1783 (1996)

1.115 S. Talapatra, P.G. Ganesan, T. Kim, R. Vajtai, M. Huang, M. Shima, G. Ramanath, D. Srivastava, S.C. Deevi, P.M. Ajayan: Irradiation-induced magnetism in carbon nanostructures, Phys. Rev. Lett. **95**(9), 097201 (2005)

1.116 P. Gambardella, A. Dallmeyer, K. Maiti, M.C. Malagoli, W. Eberhardt, K. Kern, C. Carbone: Ferromagnetism in one-dimensional monatomic metal chains, Nature **416**(6878), 301–304 (2002)

1.117 G. Rollmann, M.E. Gruner, A. Hucht, R. Meyer, P. Entel, M.L. Tiago, J.R. Chelikowsky: Shellwise mackay transformation in iron nanoclusters, Phys. Rev. Lett. **99**(8), 083402 (2007)

1.118 W.H. Zhong, C.Q. Sun, S. Li: Size effect on the magnetism of nanocrystalline Ni films at ambient temperature, Solid State Commun. **130**(9), 603–606 (2004)

1.119 Y.G. Sun, Y.N. Xia: Gold and silver nanoparticles: A class of chromophores with colors tunable in the range from 400 to 750 nm, Analyst **128**(6), 686–691 (2003)

1.120 K.L. Kelly, E. Coronado, L.L. Zhao, G.C. Schatz: The optical properties of metal nanoparticles: The influence of size, shape, and dielectric environment, J. Phys. Chem. B **107**(3), 668–677 (2003)

1.121 M.S. Dresselhaus, G. Dresselhaus, R. Saito, A. Jorio: Raman spectroscopy of carbon nanotubes, Phys. Rep.-Rev. Soc. Phys. Lett. **409**(2), 47–99 (2005)

1.122 M.S. Dresselhaus, A. Jorio, M. Hofmann, G. Dresselhaus, R. Saito: Perspectives on carbon nanotubes and graphene raman spectroscopy, Nano Lett. **10**(3), 751–758 (2010)

1.123 B.K. Gupta, P. Thanikaivelan, T.N. Narayanan, L. Song, W. Gao, T. Hayashi, A. Leela Mohana Reddy, A. Saha, V. Shanker, M. Endo, A.A. Martí, P.M. Ajayan: Optical bifunctionality of europium-complexed luminescent graphene nanosheets, Nano Lett. **11**(12), 5227–5233 (2011)

1.124 M.J. O'Connell, S.M. Bachilo, C.B. Huffman, V.C. Moore, M.S. Strano, E.H. Haroz, K.L. Rialon, P.J. Boul, W.H. Noon, C. Kittrell, J.P. Ma, R.H. Hauge, R.B. Weisman, R.E. Smalley: Band gap fluorescence from individual single-walled carbon nanotubes, Science **297**(5581), 593–596 (2002)

1.125 R.B. Weisman, S.M. Bachilo: Dependence of optical transition energies on structure for single-walled carbon nanotubes in aqueous suspension: An empirical Kataura plot, Nano Lett. **3**(9), 1235–1238 (2003)

1.126 P. Buffat, J.P. Borel: Size effect on the melting temperature of gold particles, Phys. Rev. A **13**(6), 2287–2298 (1976)

1.127 S. Berber, Y.K. Kwon, D. Tomanek: Unusually high thermal conductivity of carbon nanotubes, Phys. Rev. Lett. **84**(20), 4613–4616 (2000)

1.128 J. Hone, M. Whitney, C. Piskoti, A. Zettl: Thermal conductivity of single-walled carbon nanotubes, Phys. Rev. B **59**(4), R2514–R2516 (1999)

1.129 T. Borca-Tasciuc, S. Vafaei, D.A. Borca-Tasciuc, B.Q. Wei, R. Vajtai, P.M. Ajayan: Anisotropic thermal diffusivity of aligned multiwall carbon nanotube arrays, J. Appl. Phys. **98**(5), 054309–054303–6 (2005)

1.130 C. Xue, C.A. Mirkin: pH-switchable silver nanoprism growth pathways, Angew. Chem. Int. Ed. **46**(12), 2036–2038 (2007)

1.131 G.D. Moon, S. Ko, Y. Min, J. Zeng, Y. Xia, U. Jeong: Chemical transformations of nanostructured materials, Nano Today **6**(2), 186–203 (2011)

1.132 A.C. Grimsdale, K. Mullen: The chemistry of organic nanomaterials, Angew. Chem. Int. Ed. **44**(35), 5592–5629 (2005)

1.133 N.G. Szwacki, A. Sadrzadeh, B.I. Yakobson: B-80 fullerene: An ab initio prediction of geometry, stability, and electronic structure, Phys. Rev. Lett. **98**(16), 166804–1–166804–4 (2007)

1.134 Y. Li, G. Zhou, J. Li, B.-L. Gu, W. Duan: Alkali-metal-doped B_{80} as high-capacity hydrogen storage media, J. Phys. Chem. C **112**(49), 19268–19271 (2008)

1.135 J.L. Bahr, J.M. Tour: Covalent chemistry of single-wall carbon nanotubes, J. Mater. Chem. **12**(7), 1952–1958 (2002)

1.136 D. Wunderlich, F. Hauke, A. Hirsch: Preferred functionalization of metallic and small-diameter single walled carbon nanotubes via reductive alkylation, J. Mater. Chem. **18**(13), 1493–1497 (2008)

1.137 W. Gao, L.B. Alemany, L. Ci, P.M. Ajayan: New insights into the structure and reduction of graphite oxide, Nat. Chem. **1**(5), 403–408 (2009)

1.138 D.R. Dreyer, S. Park, C.W. Bielawski, R.S. Ruoff: The chemistry of graphene oxide, Chem. Soc. Rev. **39**(1), 228–240 (2010)

1.139 K. Lu, Z.H. Jin: Melting and superheating of low-dimensional materials, Curr. Opin. Solid State Mater. Sci. **5**(1), 39–44 (2001)

1.140 J. Hone, M.C. Llaguno, M.J. Biercuk, A.T. Johnson, B. Batlogg, Z. Benes, J.E. Fischer: Thermal properties of carbon nanotubes and nanotube-based materials, Appl. Phys. A **74**(3), 339–343 (2002)

1.141 J. Hone, M.C. Llaguno, N.M. Nemes, A.T. Johnson, J.E. Fischer, D.A. Walters, M.J. Casavant, J. Schmidt, R.E. Smalley: Electrical and thermal transport properties of magnetically aligned single walt carbon nanotube films, Appl. Phys. Lett. **77**(5), 666–668 (2000)

1.142 A.A. Balandin, S. Ghosh, W.Z. Bao, I. Calizo, D. Teweldebrhan, F. Miao, C.N. Lau: Superior thermal conductivity of single-layer graphene, Nano Lett. **8**(3), 902–907 (2008)

1.143 G.K. Dimitrakakis, E. Tylianakis, G.E. Froudakis: Pillared graphene: A new 3-d network nanostructure for enhanced hydrogen storage, Nano Lett. **8**(10), 3166–3170 (2008)

1.144 V. Varshney, S.S. Patnaik, A.K. Roy, G. Froudakis, B.L. Farmer: Modeling of thermal transport in pillared-graphene architectures, ACS Nano **4**(2), 1153–1161 (2010)

1.145 G.D. Smith, R.J.H. Clark: Raman microscopy in archaeological science, J. Archaeol. Sci. **31**(8), 1137–1160 (2004)

1.146 C. Wang, B. Lu, J. Zuo, S. Zhang, S. Tan, M. Suzuki, W.T. Chase: Structural and elemental analysis on the nanocrystalline SnO_2 in the surface of ancient chinese black mirrors, Nanostruct. Mater. **5**(4), 489–496 (1995)

1.147 D.G. Shchukin, S.V. Lamaka, K.A. Yasakau, M.L. Zheludkevich, M.G.S. Ferreira, H. Mohwald: Active anticorrosion coatings with halloysite nanocontainers, J. Phys. Chem. C **112**(4), 958–964 (2008)

1.148 F. Wang, X. Tian, Q. Li, L. Li, X. Peng: Oxidation and hot corrosion behavior of sputtered nanocrystalline coating of superalloy K52, Thin Solid Films **516**(16), 5740–5747 (2008)

1.149 J.L. Elechiguerra, L. Larios-Lopez, C. Liu, D. Garcia-Gutierrez, A. Camacho-Bragado, M.J. Yacaman: Corrosion at the nanoscale: The case of silver nanowires and nanoparticles, Chem. Mater. **17**(24), 6042–6052 (2005)

1.150 A. Hirsch: Functionalization of single-walled carbon nanotubes, Angew. Chem. Int. Ed. **41**(11), 1853–1859 (2002)

1.151 Y. Li, G.A. Somorjai: Nanoscale advances in catalysis and energy applications, Nano Lett. **10**(7), 2289–2295 (2010)

1.152 E. Iglesia: Design, synthesis, and use of cobalt-based Fischer-Tropsch synthesis catalysts, Appl. Catal. A **161**(1–2), 59–78 (1997)

1.153 J.-S. Lee, S. Tai Kim, R. Cao, N.-S. Choi, M. Liu, K.T. Lee, J. Cho: Metal-air batteries with high energy density: Li-air versus Zn-air, Adv. Energy Mater. **1**(1), 34–50 (2011)

1.154 Y.C. Lu, Z.C. Xu, H.A. Gasteiger, S. Chen, K. Hamad-Schifferli, Y. Shao-Horn: Platinum-gold nanoparticles: A highly active bifunctional electrocatalyst for rechargeable lithium-air batteries, J. Ame. Chem. Soc. **132**(35), 12170–12171 (2010)

1.155 C. Burda, X. Chen, R. Narayanan, M.A. El-Sayed: Chemistry and properties of nanocrystals of different shapes, Chem. Rev. **105**(4), 1025–1102 (2005)

1.156 A.J. Nozik: Nanoscience and nanostructures for photovoltaics and solar fuels, Nano Lett. **10**(8), 2735–2741 (2010)

1.157 K. Kordas, T. Mustonen, G. Toth, H. Jantunen, M. Lajunen, C. Soldano, S. Talapatra, S. Kar, R. Vajtai, P.M. Ajayan: Inkjet printing of electrically conductive patterns of carbon nanotubes, Small **2**(8–9), 1021–1025 (2006)

Part A NanoCarbons

2 Graphene – Properties and Characterization
Aravind Vijayaraghavan, Manchester, UK

3 Fullerenes and Beyond: Complexity, Morphology, and Functionality in Closed Carbon Nanostructures
Humberto Terrones, University Park, USA

4 Single-Walled Carbon Nanotubes
Sebastien Nanot, Houston, USA
Nicholas A. Thompson, Houston, USA
Ji-Hee Kim, Houston, USA
Xuan Wang, Houston, USA
William D. Rice, Los Alamos, USA
Erik H. Hároz, Houston, USA
Yogeeswaran Ganesan, Hillsboro, USA
Cary L. Pint, Nashville, USA
Junichiro Kono, Houston, USA

5 Multi-Walled Carbon Nanotubes
Ákos Kukovecz, Szeged, Hungary
Gábor Kozma, Szeged, Hungary
Zoltán Kónya, Szeged, Hungary

6 Modified Carbon Nanotubes
Aarón Morelos-Gómez, Nagano, Japan
Ferdinando Tristán López, Nagano, Japan
Rodolfo Cruz-Silva, Nagano, Japan
Sofia M. Vega Díaz, Nagano, Japan
Mauricio Terrones, University Park, USA

7 Carbon Nanofibers
Yoong A. Kim, Nagano, Japan
Takuya Hayashi, Nagano, Japan
Morinobu Endo, Nagano, Japan
Mildred S. Dresselhaus, Cambridge, USA

8 Nanodiamonds
Olga A. Shenderova, Raleigh, USA
Suzanne A. Ciftan Hens, Raleigh, USA

2. Graphene – Properties and Characterization

Aravind Vijayaraghavan

Graphene is the two-dimensional allotrope of carbon, consisting of a hexagonal arrangement of carbon atoms on a single plane. This chapter explores the history of graphene, as the theoretical building block for other carbon allotropes as well as its rise as a material in its own right in recent years. Graphene can be fabricated by different methods including mechanical exfoliation, chemical vapor deposition, and decomposition of SiC, although bulk-quantity production of pristine graphene remains a challenge. The atomic and electronic structure of graphene is described, highlighting the strong correlation in graphene between structure and properties, as is the case with other carbon allotropes. Graphene exhibits a number of unique and superlative electronic and optical properties. The intrinsic properties of graphene can be tailored by nanofabrication, chemistry, electromagnetic fields, etc. Various applications of graphene have been proposed in electronic, optoelectronic, and mechanical products. In addition, graphene has emerged as a candidate in chemical, biochemical, and biological applications. Derivatives of graphene such as graphene oxide or graphane are also of interest in terms of both fundamental properties and applications.

2.1 **Methods of Production** 42
2.1.1 Micromechanical Cleavage of Graphite (Scotch Tape Technique) 42
2.1.2 Chemical Vapor Deposition (CVD) 43
2.1.3 Decomposition of Carbides 44
2.1.4 Exfoliation by a Solvent 46
2.1.5 Synthetic Production Route 49
2.1.6 Graphene Nanoribbon (GNR)..... 49
2.1.7 Derivatives of Graphene..... 50
2.2 **Properties** 50
2.2.1 Structure and Physical Properties ... 50
2.2.2 Mechanical Properties..... 51
2.2.3 Electronic Properties..... 52
2.2.4 Optical Properties..... 55
2.2.5 Thermal and Thermoelectric Properties 56
2.2.6 Chemical Properties..... 56
2.2.7 Properties of Graphene Derivatives. 57
2.3 **Characterization** 58
2.3.1 Optical Characterization 58
2.3.2 Transmission Electron Microscopy... 58
2.3.3 Scanning Probe Techniques 60
2.3.4 Angle-Resolved Photoemission Spectroscopy (ARPES)..... 60
2.3.5 Raman Spectroscopy..... 61
2.3.6 Electrical Characterization 63
2.3.7 Photocurrent Microscopy..... 69
2.4 **Applications** 69
2.4.1 Structural and Electrical Composites 69
2.4.2 Transparent Conducting Films..... 69
2.4.3 Sensors 72
2.4.4 Electronic Applications..... 73
2.4.5 Photonics and Optoelectronics..... 74
2.5 **Conclusions and Outlook** 74
References 74

As a three-dimensional (3-D) material, carbon exists as three predominant allotropes: diamond, graphite, and amorphous carbon (historically knows as carbon black). These are distinguished by their crystalline structure and the hybridization of the carbon atoms therein. Carbon atoms in diamond are all sp^3 hybridized and arranged in diamond cubic structure which comprises two interpenetrating face-centered cubic (fcc) lattices. Graphite has a layered structure, where the sp^2 hybridized carbon atoms are arranged in a hexagonal

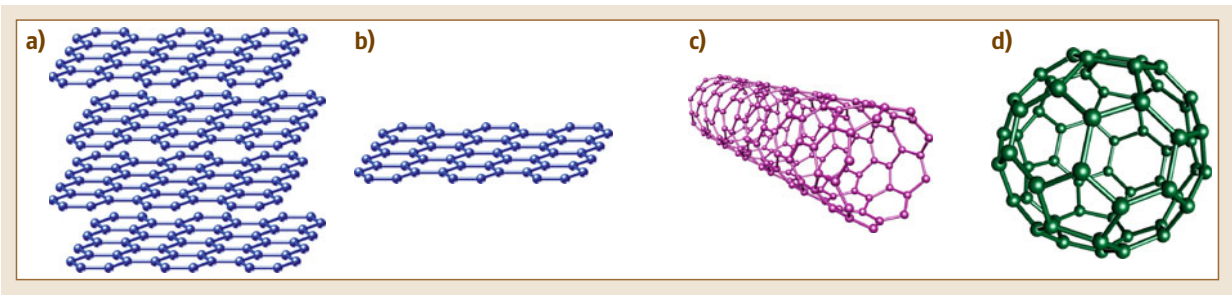


Fig. 2.1a–d Allotropes of sp^2 carbon: **(a)** graphite (3-D), **(b)** graphene (2-D), **(c)** carbon nanotube (1-D), and **(d)** fullerene (0-D) (courtesy K.S. Novoselov)

lattice in each plane, while the planes themselves are AB (Bernal) stacked and held together by van der Waals forces. Amorphous carbon, as the name indicates, does not have long-range crystalline order, although locally the atoms are bound together covalently and comprise a mix of sp^2 and sp^3 carbons. While diamond can be reduced in size to the nanoscale to form nanodiamond, it is graphite that can be truly reduced to lower-dimensional allotropes. A single layer of graphite is defined as graphene, the topic of this chapter. Graphene has been used as the building block to conceptually visualize carbon allotropes such as graphite, carbon nanotubes, and fullerenes; it was believed that such a freestanding, two-dimensional (2-D) structure would not be stable. Carbon nanotubes (CNT) form its one-dimensional (1-D) counterpart, while fullerenes are the zero-dimensional (0-D) allotropes. These various forms of carbon are summarized in Fig. 2.1. It is important to note that CNTs or fullerenes are not unique structures, but rather describe a family of structures, which are described in detail in subsequent chapters. Nonetheless, their structure and properties are all derived from graphene.

Despite serving as the fundamental building block for these carbon allotropes, graphene remained a concept until 2004. It was substantially predated by its related allotropes, fullerenes being discovered and described in 1985 [2.1], while carbon nanotubes were synthesized and their atomic structure elucidated in 1991 [2.2]. The term "graphene" was coined in 1987 [2.3], to describe one of the two alternating layers in graphite intercalation compounds (GIC), the other layer being the intercalating agent. It was postulated that independent, freestanding graphene would not become a physical reality since it would voluntarily transform into a more stable allotrope in an attempt to minimize its surface energy. Supported monolayers of carbon, however, had been previously synthesized and described, including epitaxial graphene which has been known since the 1970s. Chemical derivatives of graphite such as graphite oxide can be traced back to the 1950s and can exist as single layers (graphene oxide), although these are not truly two-dimensional layers due to out-of-plane atoms which stabilize their structure.

Since graphene occurs naturally as a constituent of bulk graphite, it appeared to be the logical place to start the hunt for freestanding graphene. This effort culminated in the successful exfoliation of a single sheet of carbon atoms by *Andre Geim* and *Kostya Novoselov* at the University of Manchester in 2004 [2.4], using a technique referred to as micromechanical cleavage, or colloquially, the Scotch tape method. This discovery and the subsequent investigations into the properties of graphene were rewarded with the Nobel Prize in Physics in 2010 for Geim and Novoselov. The existence of graphene, however, does not contradict the physics that predicted that it could not exist. It was discovered that graphene is not truly flat; there exist atomic-scale ripples in the carbon sheet, which accommodate the excess surface energy, thereby stabilizing the 2-D structure of graphene. For this reason, it might be argued that graphene is a quasi-2-D material. However, it has been shown to exhibit a range of properties that are unique to 2-D physics, and therefore graphene will be identified as a 2-D material for the rest of this chapter, without qualification.

A surge of research into the structure and properties of graphene ensued, and graphene did not disappoint. Almost immediately, an anomalous quantum Hall effect was reported in graphene, which also serves as direct experimental evidence for the electrons in graphene behaving as massless Dirac fermions, confirming theoretical predictions. Graphene yielded record high values for various properties, such as tensile strength, car-

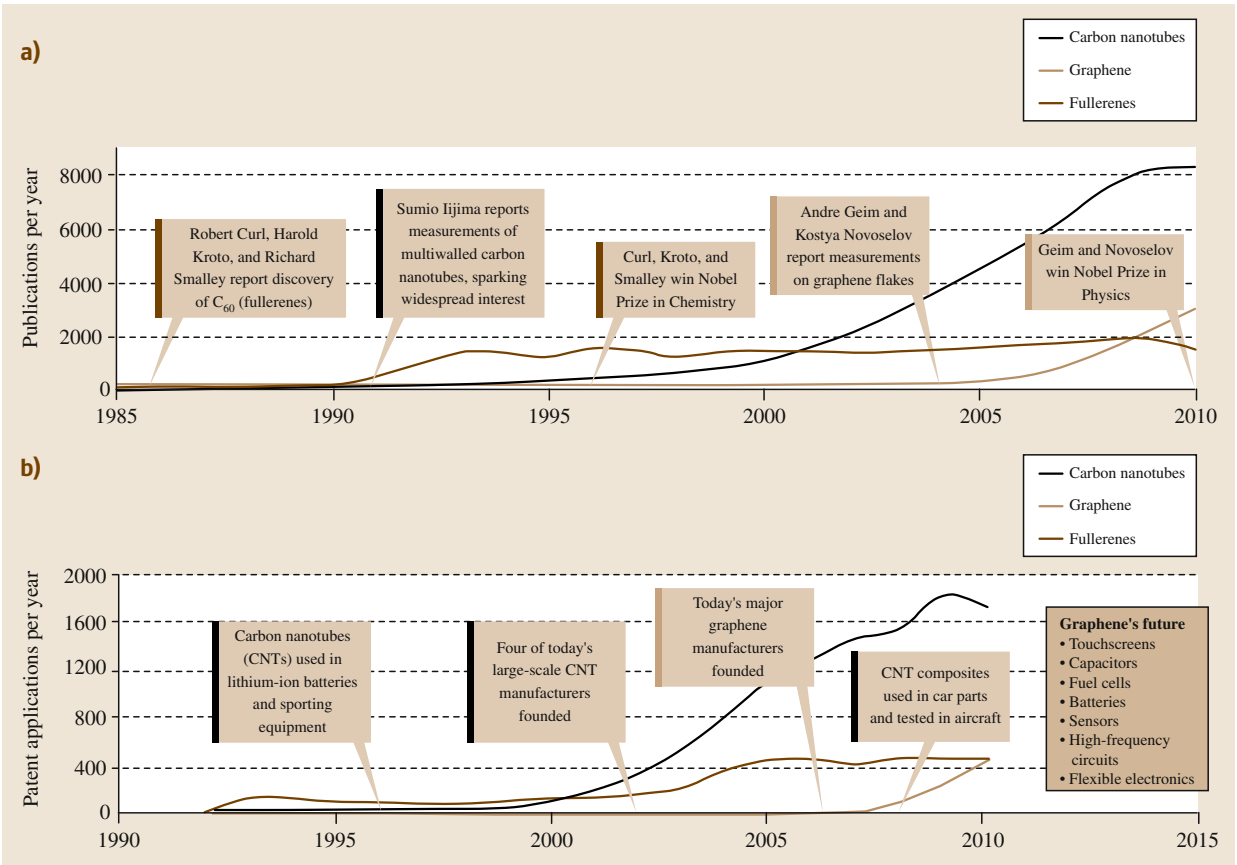


Fig. 2.2a,b Time line of nanocarbon allotropes and the **(a)** number of publications and **(b)** number of patent applications per year on each topic (after [2.5])

rier mobility, thermoelectric power, etc. Scientists have also succeeded in transferring epitaxial graphene from its native metal or silicon carbide substrate onto other substrates of interest or as freestanding structures. Since the early 1990s, carbon nanotubes have been described as *rolled-up graphene sheets*. This description has come full circle, with the recent unzipping of carbon nanotubes to yield graphene. While the number of publications on carbon nanotubes has leveled off in recent years at about 8000 papers per year, the publications on graphene are only just starting their exponential growth at a rate faster than that which was enjoyed by carbon nanotubes in their first few years (Fig. 2.2; over 3000 papers were published in the field of graphene in 2010 [2.5]). A similar trend is also observed in patent applications based on carbon nanotubes and graphene.

Any chapter on graphene would not be complete without discussion of its other, quasi-2-D derivatives based on the fundamental graphene structure. Perhaps the most interesting of these is the case where two graphene layers are AB stacked to form a bilayer. Unlike graphene, which has zero electronic bandgap and is therefore a quasimetal, this bilayer structure can have a bandgap. A bandgap is critical for electronic applications, and one of the most active areas of research in graphene is currently the generation of a stable, true, electronic bandgap in graphene. The oxidized derivative, graphene oxide (GO), has been alluded to before, and serves as a useful intermediate in a chemical route for graphite exfoliation. Hydrogenated graphene, christened graphane, and fluorinated graphene or fluorographene have been recently produced and characterized.

2.1 Methods of Production

Historically, graphene supported on substrates such as metals and SiC was synthesized first; however, such graphene was not liberated from the substrate support to form a truly two-dimensional structure. Freestanding graphene was not a reality until the ground-breaking publication of Novoselov and Geim in 2004. Consequently, this micromechanical cleavage method is presented first, followed by the epitaxial synthesis of graphene as well as chemical vapor deposition on metallic substrates. Graphene can also be exfoliated from graphite by sonochemical means in a solvent, followed by a purification step to extract the monolayers. Recently, islands of nanographene have also been synthesized by chemical routes, and this bottom-up approach is discussed. Finally, separate sections are devoted to production of graphene nanoribbons (GNR) and derivatives of graphene.

2.1.1 Micromechanical Cleavage of Graphite (Scotch Tape Technique)

Micromechanical cleavage (or exfoliation), as the name implies, refers to thinning down of graphite by mechanically reducing the number of layers in a repeated fashion. Graphite is known to cleave preferentially along the interlayer direction where layers are held together by weak van der Waals forces, rather than across the strong covalent bonds that bind the atoms within a layer. The most common procedure to accomplish this is using adhesive tape. Attaching a thick graphite flake to adhesive tape on both its exposed faces, and then peeling the two pieces of tape apart, results in two thinner flakes of graphite, stuck to each of the adhesive tape pieces. Repeating this process a sufficient number of times would in principle result in a single sheet of carbon atoms, i. e., graphene, adhered to the adhesive tape. This is still not freestanding graphene, since it is supported by the tape, and must be transferred to a suitable weakly coupling substrate or suspended across supports. The genericized Scotch trademark for transparent adhesive tape has subsequently lent its name to the micromechanical exfoliation of graphite. Different variations of this method exist.

One of the earliest such efforts was undertaken by *Fernandez-Moran*, who succeeded in thinning graphite down to ≈ 15 layers (5 nm) over a millimeter size, to serve as a support membrane for transmission electron microscopy [2.6]. This result remained relatively unknown outside the electron microscopy community, until the interest of condensed matter physicists turned to graphene and other lower-dimensional carbons. The first successful thinning down of graphite to its monolayer graphene form involved a wet/dry method [2.4]. The surface of highly oriented pyrolytic graphite (HOPG) was first patterned into square mesas, which were pressed into wet photoresist. After baking, the mesas attached to the now dry photoresist, and could be detached from the bulk of the HOPG. Scotch tape was used to repeatedly peel off layers of graphite from the mesas, thinning them down, until only very thin layers remained in the photoresist. The photoresist was then dissolved in acetone to release these thin flakes, which float on the solvent surface. The flakes were collected onto Si/SiO_2 wafer pieces dipped into the solvent. Thicker flakes adhering to the silicon could be cleaned off by sonication in 2-propanol, while thinner flakes were reported to adhere strongly to the substrate due to capillary forces.

In the resultant sample, the flakes of graphene, bilayer graphene, and few-layer graphene (FLG) must be distinguished from among a sea of flakes of various thicknesses. Fortunately, at certain thicknesses of the SiO_2 layer that covers the silicon wafer, for example, 300 nm, the interference contrast generated by graphene flakes on the surface makes them relatively easy to spot and identify by optical microscopy. A trained eye can, in fact, distinguish between graphene, bilayer graphene, and thicker flakes. This is described in detail in Sect. 2.2.4 on optical properties of graphene. Figure 2.3 shows the appearance of micromechanically cleaved graphene flakes of different thicknesses in an optical microscope [2.7], atomic force microscope (AFM) [2.8], and transmission electron microscope (TEM) [2.9]. These, along with Raman spectral mapping, are routinely used to characterize graphene flakes, and are described in Sect. 2.3 dedicated to graphene characterization.

The procedure has since evolved into a completely dry technique. It has been shown that rubbing the freshly cleaved surface of a layered material such as graphite on another solid surface results in a variety of flakes, among which monolayer flakes can be invariably found [2.8]. Alternatively, HOPG is mechanically cleaved repeatedly between two pieces of adhesive tape until the surface of the tape is covered by a layer of relatively thin graphite [2.10]. No specific criterion exists at the time of writing for the optimum degree of such exfoliation. Researchers rely

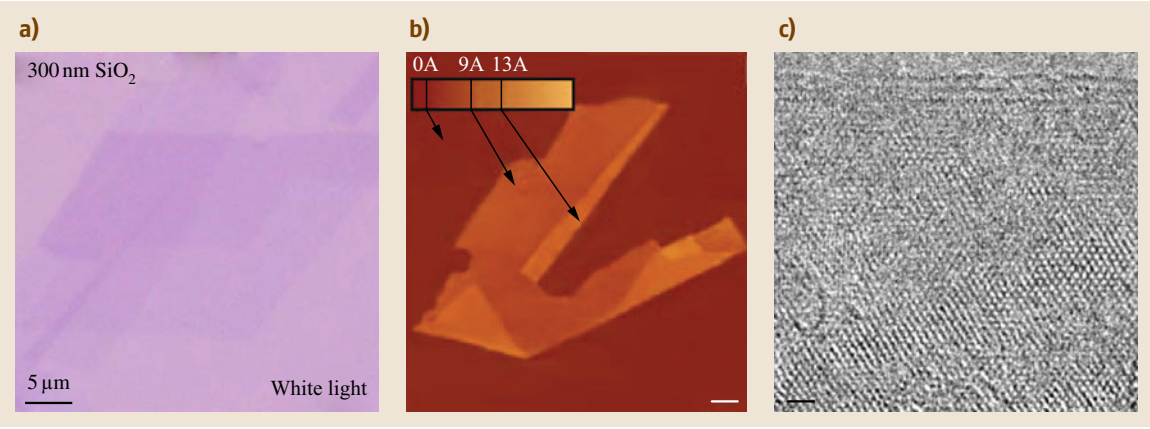


Fig. 2.3a–c Monolayer graphene flake as seen in **(a)** an optical microscope [2.7], **(b)** an atomic force microscope [2.8], and **(c)** a transmission electron microscope (after [2.9])

on personal experience or historic parameters specific to their laboratory to carry out this procedure. Once a satisfactory degree of exfoliation has been accomplished with the adhesive tape, it is pressed against the surface of a desired substrate, such as Si/SiO_2 wafer. Again, various scientist-specific parameters exist for this process, such as duration, force, application and peeling-off procedure, etc. At the end of this procedure, the surface of the graphene as well as the substrate is often contaminated with adhesive residue from the tape, which has been shown to limit the carrier mobility in the graphene flake. Efforts to remove this residue have included annealing at 200 °C in a reducing atmosphere of Ar and H_2 [2.11], annealing in vacuum at 280 °C [2.12], and current-induced Joule heating after graphene device fabrication [2.13]. Variations such as applying an electric field perpendicular to the substrate during the transfer from the adhesive tape have also been explored [2.14]. Covalent linkers such as perfluorophenylazide between graphene and SiO_2 have been explored to aid in the exfoliation process to increase monolayer yield [2.15]. The residue issue can also be completely avoided by evaporating a thin film of gold on the HOPG surface prior to the transfer step, to avoid direct contact between the adhesive and the graphene [2.16]. The gold can be subsequently dissolved in a suitable etchant without affecting the graphene. The lack of standardization is indicative of the early stage of current graphene research, and is perhaps an indication that micromechanical exfoliation is not destined to evolve into a large-scale or industrial method for graphene production. Competing techniques, discussed subsequently, have reached much higher degrees of standardization and reproducibility, albeit with drawbacks of their own.

It should be noted that the *best quality* of graphene currently available is indisputably that produced by micromechanical cleavage, where the graphene quality is defined in terms of crystalline domain size, number of defects, carrier mobility, etc. The choice of initial graphite material having large grain size, using freshly cleaved graphite for further exfoliation, and the cleanliness and quality of the adhesive tape and SiO_2 substrate are all variables which significantly affect the quality of the final flakes obtained. Flakes of graphene hundreds of µm across are routinely produced in laboratories all over the world by this method, predominantly for fundamental research purposes. In some cases, millimeter-size flakes have also been reported. While this method has not matured for commercial applications, ventures such as Graphene Industries have been established to sell micromechanically cleaved graphene flakes.

2.1.2 Chemical Vapor Deposition (CVD)

The study of the deposition of thin graphitic layers on metal substrates by CVD dates back to the late 1960s [2.17, 18]. One of the motivations for this was in fact to eliminate the formation of graphitic structures on metals such as platinum which results in degradation of catalytic activity. CVD is currently the preferred route for large-scale fabrication of carbon nanotubes, and therefore has generated substantial excitement as a potential method for large-scale production of graphene. In general, this involves thermal decomposition of

gaseous hydrocarbon sources followed by dissolution and recrystallization of the cracked carbon on the surface of metallic substrates. The solubility of carbon in various metals, such as rhodium, ruthenium, iridium, and rhenium, has been measured [2.19], along with the observation that excess carbon dissolved in such metals at high temperatures can segregate as graphite on the surface upon cooling. Various metallic substrates and carbon feedstock have been explored in the effort to grow monolayer graphene, and some of the significant developments are mentioned next.

As early as 1991, monolayer graphene was grown on Pt(111) by hydrocarbon decomposition at 800 °C [2.20], resulting in islands of 20–30 nm size distributed uniformly over the surface. Upon annealing at higher temperatures, the graphene was found to accumulate into large, regularly shaped islands on terraces and step edges. Recently, a variation in which a beam of methane molecules with high kinetic energy (670 meV) impacting a Pt(111) surface at 890 K resulted in large domains of monolayer graphene covering the entire Pt surface [2.21]. Ni soon followed, requiring a minimum temperature of 600 °C, and monolayer graphite on Ni(111) was shown to have an arrangement whereby one carbon atom in a unit cell of the graphite overlayer is located at the on-top site of the topmost Ni atoms, while another carbon atom exists at the fcc hollow site [2.22]. Carbon has been shown to segregate on the surface of Ru(0001) as monolayer graphene [2.23], when annealed at 1400 K. STM reveals a (11×11) structure with good rotational alignment and structural perfection, a well-defined periodicity of ≈ 30 Å, and large domain sizes exceeding 100 μm. Graphene has also been grown by thermal decomposition of benzene on Ir(111) [2.24].

At present, the two predominant metallic substrates for CVD graphene growth are Ni and Cu. Large-size (cm^2) films of monolayer and few-layer graphene have been grown on Ni [2.25], with monolayer regions as large as 20 μm in size. Cu does even better, and predominantly monolayer graphene covering many cm^2 is grown in various laboratories using methane CVD [2.26]. The solubility of C in Cu appears to make the process self-limiting, and at most 5% of the surface is covered by small islands of bilayer graphene. Most importantly, methods have been developed to detach these films from the metallic substrate and transfer them intact onto dielectric substrate (Fig. 2.4), where they can be lithographically patterned and processed for electronic or optical applications [2.25]. In another variation, graphene is grown on a thin copper film on arbitrary substrates, and the Cu dewets and evaporates during the growth process itself, leaving behind the graphene film intact on the substrate [2.27]. The first truly large-area production of graphene has recently been reported using a continuous CVD deposition and transfer process [2.28].

In general, for substrates with small lattice mismatch (< 1%) such as Co(0001) and Ni(111), commensurate superstructures are formed, while substrates with larger mismatches such as Pt(111), Ir(111), and Ru(0001) yield incommensurate moiré superstructures. The first graphene monolayer on the metal surface has strong interaction with the substrate, and the spacing between the two is much shorter than between two layers of graphite (3.35 Å). For the case of Ru it is 1.45 Å, and for Ni it is 2.11 Å.

2.1.3 Decomposition of Carbides

The second substrate-supported route for graphene production involves thermal decomposition of surface layers of carbides such as SiC. About 250 different crystal structure of SiC are known, but α-SiC is the most commonly encountered polymorph and, until recently, the primary focus of epitaxial graphene growth. α-SiC has a hexagonal crystal structure, similar to wurtzite. The (0001) (Si) and $(000\bar{1})$ (C) faces of 6H-(α-SiC) [2.29–31] and 4C-(α-SiC) [2.32] have been shown suitable for the growth of epitaxial graphene.

6H-(α-SiC) is first cleaned for 20 min at 850 °C under a Si flux to prevent Si sublimation during the cleaning step. At higher annealing temperatures in ultrahigh vacuum (UHV), the surface of SiC undergoes various reconstructions, until the graphitization temperature when the surface graphene layers form. The Si surface of the hexagonal SiC undergoes the following reconstructions: 3×3 at 850 °C under Si flux, $\sqrt{3}\times\sqrt{3}R30°$ below 1000 °C, $6\sqrt{3}\times6\sqrt{3}R30°$ (6R3) at 1150 °C, and graphitization at 1350 °C. On this face, the C atoms are in epitaxy with the SiC underneath after graphitization. The surface is passivated by the first C layer, the interface extends to two C layers, and subsequent C layers are decoupled from the substrate and exhibit the properties of graphene. Graphitization occurs at 1150 °C on the C face of the hexagonal SiC, and the C layer occurs on a SiC 2×2 native reconstruction. This reconstruction saturates the dangling bond states, so that the first C layer already exhibits graphene properties. However, this C layer is no longer epitaxial with the underlying SiC, so the long-range order of the SiC substrate no longer imposes itself upon the

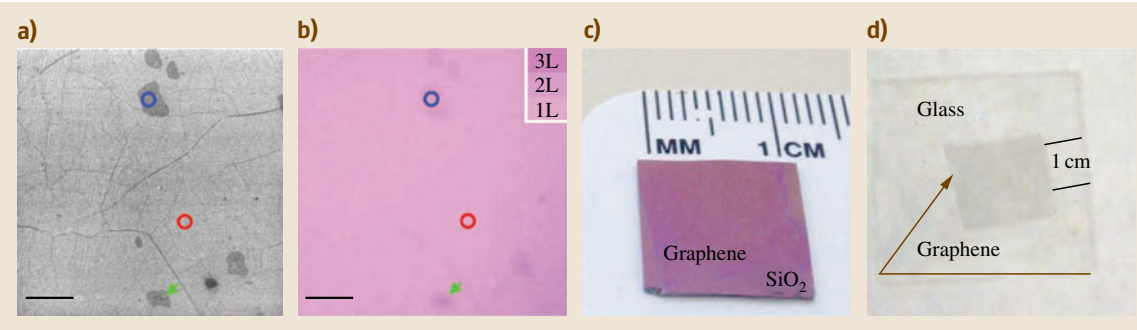


Fig. 2.4a–d Graphene films transferred onto **(a)** a SiO_2/Si substrate and **(b)** a glass plate. **(c)** Scanning electron micrograph (SEM) image of graphene transferred onto SiO_2/Si (285 nm-thick oxide layer), showing wrinkles as well as two- and three-layer regions. **(d)** Optical microscope image of the same regions as in **(c)** (after [2.26])

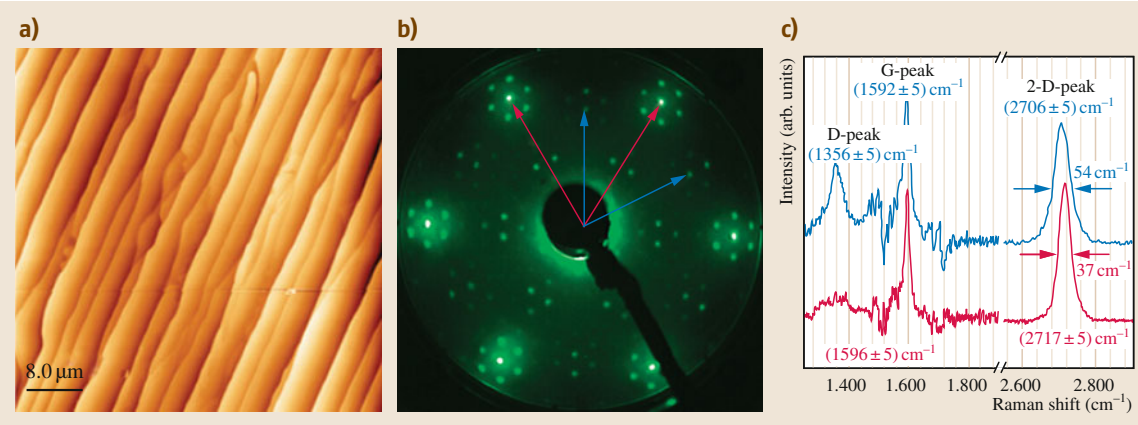


Fig. 2.5 **(a)** AFM image of graphene on 6H-SiC(0001) formed by annealing in Ar ($p = 900$ mbar, $T = 1650$ °C). **(b)** Low energy electron diffraction (LEED) pattern at 74 eV showing the diffraction spots due to the SiC(0001) substrate (*blue arrows*) and the graphene lattice (*red arrows*). The extra spots are due to the $(6\sqrt{3}\times 6\sqrt{3})$ interface layer. **(c)** Comparison of Raman spectra of Ar-grown (*red*) and UHV-grown (*blue*) epitaxial graphene (after [2.33])

C layer. Therefore, it has not been possible to accomplish both long-range ordering as well as decoupling from the surface simultaneously using 6H-(α-SiC). Epitaxial graphene has also been grown on SiC(0001) in Ar atmosphere [2.33], at close to atmospheric pressure and a significantly higher annealing temperature of 1650 °C, resulting in morphologically and electronically superior graphene compared with vacuum annealing (Fig. 2.5).

Perhaps the greatest limitation of SiC as a substrate for graphene growth is cost. α-SiC wafers are relatively expensive, at about USD 300 for a 50 mm wafer. Cubic 3C-SiC (β-SIC), however, can be grown directly on the surface of Si wafers of 300 mm and larger, and is therefore a more commercially viable substrate. It was believed that, due to its cubic structure, β-SiC would be unsuitable for graphene growth. However, recently scientists have succeeded in growing graphene on the Si-rich (100) surface of β-SiC by a series of annealing cycles with temperature increasing from 1200 to 1550 K [2.34]. They found that the strong lattice mismatch between graphene and underlying SiC results in very weak coupling similar to the $(000\bar{1})$ C face of α-SiC. However, it was found that graphene growth on β-SiC was guided along the [110] crystallographic direction despite the lattice mismatch, raising hopes that both substrate–graphene decoupling as well as substrate-guided large domain size might be simultaneously achievable after further process optimization and characterization of graphene on β-SiC.

Ribbons of graphene, a few nanometers wide, develop an electronic bandgap due to confinement effects, which is absent in larger dimensions of graphene, which is a zero-bandgap semimetal. The importance and methods of inducing a bandgap in graphene are discussed later. Here, we briefly discuss how SiC decomposition can be used to grow graphene nanoribbons [2.35]. It is known that the (0001) face of both 6H and 4C α-SiC with vicinal miscuts towards $\langle 1\bar{1}00\rangle$ displays bunching of parallel steps into $(1\bar{1}0n)$ nanofacets up to 4–5 unit cells in height and oriented at an angle of $\approx 25°$ to the basal plane. The α-SiC $(000\bar{1})$ face generally does not show preferential orientation for nanofacets, but step-bunched $(1\bar{1}0n)$ nanofacets can be induced by suitable pretreatment. It has also been observed that graphene grown on the (0001) and $(000\bar{1})$ faces of α-SiC are continuous over these steps. Controlled facets can be achieved by conventional photolithography and microfabrication. Few-layer graphene is shown to grow selectively on these facets. Facets of other crystallographic orientations are possible, and it is expected that the graphene quality, properties, and growth mechanism will depend significantly on the crystallographic surface. However, these preliminary results indicate that, with further research and optimization, the ideal facets and growth conditions might be determined for large-scale controlled growth of graphene nanoribbons.

Interestingly, there was significant research into the growth and characterization of graphene on other metal carbides [2.36–38], such as TiC, TaC, and HfC, as early as the 1980s. Then, it was referred to as *monolayer graphite*. Graphene has been grown on the (100) and (111) faces of these carbides by heating them to 1700 K in UHV. As with SiC, graphene nanoribbons as narrow as 1.3 nm with well-defined edge structure have been grown, for instance, on TiC (755) surface [2.39]. In all these cases, a significant degree of hybridization between the graphene π-electrons and the electronic bands of the substrate carbide was reported, similar to some of the crystallographic faces of SiC. Despite the revelation that the graphene is significantly decoupled from certain other SiC faces, similar exploration into other metallic carbides remains pending.

2.1.4 Exfoliation by a Solvent

Exfoliation of graphene from graphite involves overcoming the interlayer van der Waals bonds. This is the same interaction in play between individual CNTs in a bundle. Just as ultrasonication in a solvent has been used to overcome this weak force and separate and disperse individual CNTs from a bundle, it has also been used to individualize graphene layers from graphite. This process can be facilitated if the interlayer attraction can be compromised by intercalates. The resultant flakes of graphene in a solvent can be stabilized to prevent aggregation, and separated into fractions which are enriched in particular graphene thicknesses.

Graphite Intercalation Compounds

Due to the nature of hybridization of carbon atoms in graphite, it is capable of reactivity involving incorporation of atoms, ions, or molecules in its lattice while leaving its basic structure unchanged. Such graphite intercalation compounds (GIC) [2.40] may be broadly classified into those with homopolar bonding and polar bonding. Graphite oxide (GO) and graphite fluoride (GF) are examples of homopolar bonding, while potassium-, rhodium- and cesium-graphite are examples of polar bonding. GICs were well studied as early as the 1950s and are a staple of chemistry textbooks. Here, we restrict our discussion to exfoliation of GICs, in particular graphite oxide, and its reduction to graphene, which has been achieved with varying degrees of success. A family of GICs with interhalogen compounds offers control over the stage of intercalation and subsequently the layer distribution in the resultant graphene.

Graphite can be oxidized to GO in various ways. In the *modified Staudenmaier method* [2.41] a mixture of 97% sulfuric acid and fuming nitric acid is cooled down to 5 °C in an ice bath, graphite in flake or powder form is added, followed by repeated additions of potassium perchlorate every hour over a period of 3 days. The resulting solution, sometimes referred to as graphitic acid, is filtered and washed until the pH of the filtrate reaches 5 or more. The *Brodie method* [2.41] is identical, except that only nitric acid is used, and the potassium perchlorate is added every hour for 3 h. In the *Hummers method* [2.42, 43], graphite is oxidized in a mixture of concentrated sulfuric acid, sodium nitrate, and potassium permanganate at 45 °C for 2 h. At this stage, the material is often referred to as *expandable graphite*, reasons for which are explained in the next section. In the *electrochemical method* [2.41], a graphite sheet electrode is anodically polarized in perchloric acid with a platinum wire as counterelectrode. When dried, the above methods result in a powder consisting of graphite oxide flakes. Graphite fluoride has also been used as a starting point for graphene dispersions. Graphite can be fluorinated under fluo-

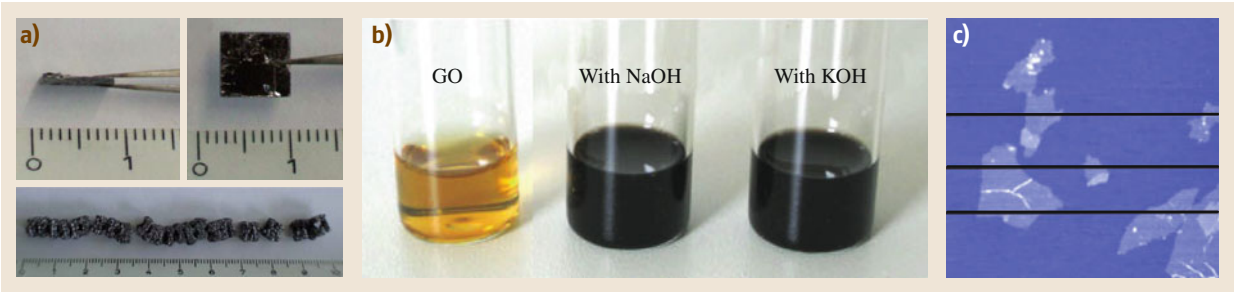


Fig. 2.6 **(a)** HOPG before (*top*) and after (*bottom*) oxidation and expansion (after [2.45]). **(b)** Deoxygenation of exfoliated GO under alkaline conditions (after [2.46]). **(c)** AFM image of exfoliated monolayer graphene oxide sheets (after [2.47])

rine pressure of 200 mmHg, in a temperature range of 375–640 °C [2.44].

Interhalogen compounds such as IBr and ICl also form GICs, offering control over the stage of intercalation. Stage I GIC refers to intercalation of every layer of graphite, while stage II GICs only have every second layer of graphite intercalated, and stage III GICs have every third layer intercalated, etc. As discussed in subsequent sections, bilayer and trilayer graphene are electronically distinct from monolayer graphene and in certain instances, such as semiconductor electronics, might prove superior to monolayer graphene. Exfoliation of graphene from stage II and stage III GICs has been shown to yield solutions of predominantly bilayer and trilayer graphene [2.48], and is currently the only large-scale route available to synthesize these multilayer graphenes.

From GIC to Graphene

Usually, the next step involves expansion of intercalated graphite by decomposing and expelling the intercalate. Rapid annealing of expandable graphite to 1050 °C generates high-pressure gaseous decomposition products which force the individual layers apart. This results in a $\approx$ 100-fold expansion in the interlayer spacing in graphite, and the material is now referred to as expanded graphite (Fig. 2.6a) [2.45, 47]. Similarly, interhalogen GICs can be expanded by expelling the entrapped intercalants.

Expanded graphite or graphite oxide is dispersed in a solvent by ultrasonication, resulting in graphene or GO solutions, respectively. In the case of GO, the predominant product in solution is monolayer GO, while stage II and III GICs of interhalogen compounds yield solutions of predominantly bilayer and trilayer graphenes. Alternatively, GO can be intercalated and exfoliated, for instance, by tributylammonium cations [2.49]. The phenol, carbonyl, and epoxy groups resulting from the oxidation of graphite ensured colloidal stability in polar solvents [2.50]. Polymers, surfactants, DNA, etc. can be used to provide additional stabilization of the GO flakes in colloidal suspension. Edge-selective diazonium functionalization [2.51] has also been demonstrated as a way to stabilize high-concentration graphene solutions without the stabilizing agents perturbing the bulk structure of the graphene sheets.

Exfoliated GO can be subsequently reduced to yield reduced GO. It cannot be referred to as graphene at this stage due to the incomplete nature of the reduction process. One route involves reduction in water with hydrazine hydrate [2.52, 53] or dimethylhydrazine [2.54]. A reduced GO suspension can also be obtained by heating the exfoliated GO suspension under strongly alkaline conditions by addition of NaOH at 50–90 °C (Fig. 2.6b) [2.46]. Alternately, the flakes can be deposited in a substrate and reduced by hydrazine vapors or hydrogen plasma [2.55]. All these methods result in the formation of unsaturated and conjugated carbon atoms, which results in electrical conductivity and Raman signatures intermediate between those of GO and pristine graphene.

GF can be reacted with *n*-butyl and *n*-hexyl lithium reagents in hexane at 0 °C. The alkyl lithium reagent replaces the fluorine functionalization during this process. The product can then be dispersed in ethanol by sonication. The alkyl functionalization, followed by a subsequent annealing step, partially restores the pristine graphene structure similar to reduced GO [2.56]. A one-step electrochemical approach has been demonstrated to form ionic liquid functionalized graphite sheets, which are then exfoliated into functionalized graphene dispersed in polar aprotic solvents [2.57].

It is also possible to exfoliate noncovalent GICs to yield graphene flakes that do not suffer the disadvantage

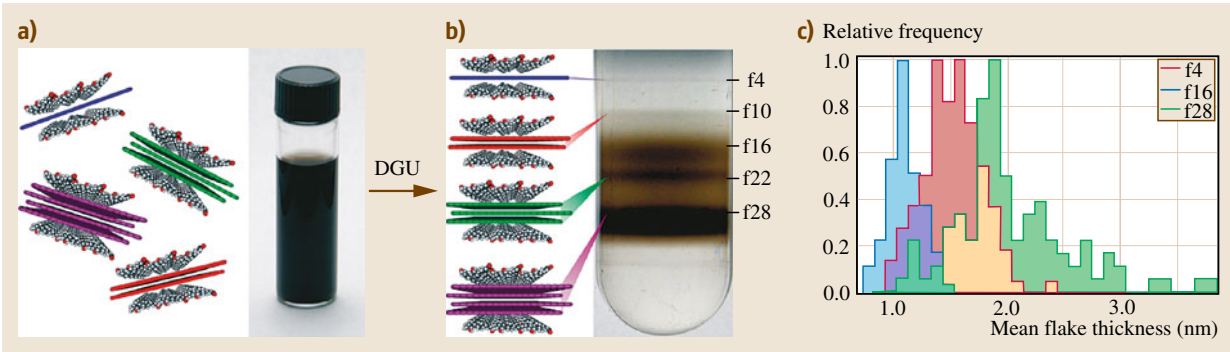


Fig. 2.7 (**a**) Schematic illustration of ordered sodium cholate encapsulation of graphene sheets and a photograph of an unsorted aqueous graphene suspension with graphene loading of ≈ 0.1 mg/ml. (**b**) Photograph of a centrifuge tube following DGU marked with the main bands of monodisperse graphene. (**c**) Mean flake thickness histogram measured by AFM of sorted graphene taken from the locations marked in panel (**b**) (after [2.59])

of high defect density; for instance, alkali-metal GICs have been shown to readily and spontaneously exfoliate in *N*-methyl-pyrrolidone (NMP), yielding a stable solution of negatively charged graphene sheets. Graphene can also be noncovalently functionalized and exfoliated with 1-pyrenecarboxylic acid by continuous sonication in water [2.58]. Interhalogen compounds do not covalently functionalize the graphite upon intercalation, and therefore the resultant solution is one of pure graphene, without any need for further reduction or reconversion.

Exfoliation Without Intercalation

In an effort to avoid disruption to the desirable structure and properties of graphene, efforts have been undertaken to directly exfoliate and disperse graphite in a solvent by ultrasonication, as has been successfully demonstrated for debundling CNTs. Systematic study has been undertaken in the case of CNTs to explore their solubility in various solvents without the assistance of stabilizing agents such as surfactants. It has emerged that certain solvents such as *N*-methyl-pyrrolidone and *N*,*N*-dimethylamide (DMA) are ideally suited to dissolve CNTs in significant concentration [2.60]. Dissolution of CNTs in aqueous media is only possible using stabilizing surfactants; however, these solutions have emerged as the premier option among researchers, since the adsorbed surfactants can be easily desorbed or disintegrated if and when required.

Sieved graphite powder was dispersed in NMP by bath sonication. The macroscopic particles and aggregates were sedimented by mild centrifugation (500–2000 rpm), resulting in a homogeneous dark dispersion which was found to contain a high fraction of monolayer and few-layer graphene flakes [2.61]. Other solvents such as DMA, γ-butyrolactone, and 1,3-dimethyl-2-imidazolidinone yield similar results. The procedure has been adopted successfully for using water as solvent, in the presence of sodium dodecylbenzene sulfonate or sodium cholate as stabilizing surfactant [2.62]. The predominant drawback of this process lies in the fact that the sonication breaks up the graphene into particularly small fragments, with the monolayer flakes having lateral dimensions of, on average, 100 nm. This is similar to the case of CNTs, where sonication appears to cut them down to ≈ 200 nm [2.63]. The aqueous graphene dispersion can now be processed by density-gradient ultracentrifugation (DGU) using iodixanol as density medium to yield fractions enriched in particular graphene thicknesses (Fig. 2.7) [2.59]. Highly enriched solutions of monolayer and bilayer graphene with the above size limitation are now available for research purposes from commercial sources such as Nanointegris, but not yet in industrial quantity.

Single- and few-layer graphene sheets with sizes up to 0.1 mm have been fabricated by quenching hot graphite in ammonium hydrogen carbonate aqueous solution [2.64]. Few-layer graphene has also been produced by immersing and intercalating graphite in supercritical CO_2 for 30 min followed by rapidly depressurizing the supercritical fluid to expand and exfoliate the graphite [2.65]. The expanding CO_2 gas containing the graphene flakes was collected directly in an aqueous solution containing stabilizing surfactant to avoid aggregation. Other supercritical fluids, such as ethanol, NMP, and DMF, can also be used to exfoliate graphite into graphene [2.66].

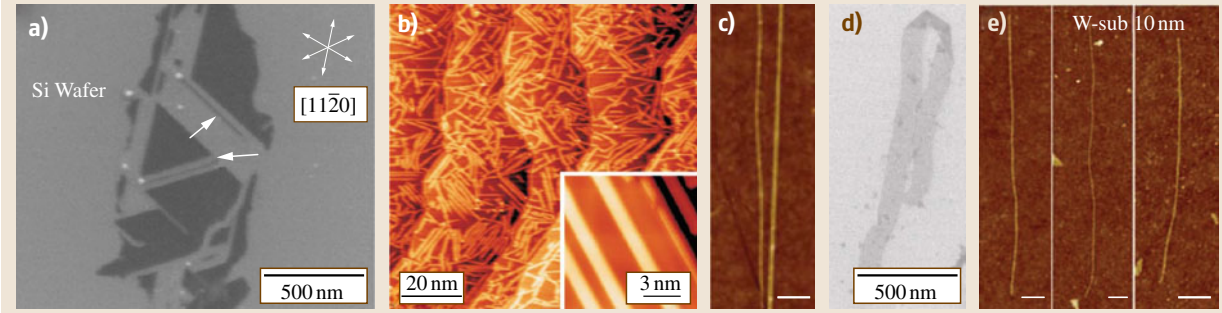


Fig. 2.8a–e Graphene nanoribbons formed by various means. **(a)** Nanoparticle cutting (after [2.67]); **(b)** synthesized from polyphenylene precursors (after [2.68]); **(c)** etching of carbon nanotubes embedded in a polymer (after [2.69]); **(d)** unzipping of carbon nanotubes (after [2.70]); **(e)** chemical exfoliation in DCE with PmPV (after [2.71])

2.1.5 Synthetic Production Route

If the reduction of bulk graphite into graphene is viewed as a top-down approach, then the chemical synthesis of graphene from smaller aromatic hydrocarbons will constitute the bottom-up approach. If graphene is regarded as a polycyclic aromatic hydrocarbon (PAH), one of the largest of these synthesized involves 222 carbon atoms or 37 benzene units in a hexagonal structure, 3 nm in diameter [2.72], from an oligophenylene precursor which was planarized by oxidative cyclohydrogenation. These structures have also shown a high tendency to self-assemble on surfaces [2.73] and could potentially act as precursors for larger synthetic graphene.

2.1.6 Graphene Nanoribbon (GNR)

The techniques described here have been suitably modified and developed with particular focus on forming very narrow ribbons of graphene with widths of tens of nanometers and with well-defined edge structure and orientation (Fig. 2.8). This is of particular importance in electronic applications, since such nanoribbons of graphene are one of the means to engineer an electronic bandgap in otherwise gapless graphene, as discussed in detail in Sect. 2.3.6. Once graphene flakes have been deposited onto a substrate, nanoribbons can be fabricated on it using standard and nonconventional lithography and etching processes, such as electron-beam lithography [2.74] and nanowire lithography [2.75], respectively.

Nickel [2.76] and silver [2.77] nanoparticles have been shown to act as a *knife* for cutting patterns in surface graphite layers of HOPG. The cutting proceeds via catalytic hydrogenation of the graphene lattice, and preferentially along crystallographic directions. The particles can become deflected into proceeding along a different direction if they come within close proximity of each other, of defects in the graphene lattice, or of previously formed cuts. The result is a complex pattern of cuts which border various well-defined shapes of the surface graphene layers, including instances where two parallel cuts result in a narrow ribbon between them. These shapes can be transferred onto arbitrary substrates using the mechanical exfoliation methods described earlier [2.67]. The graphene can also be cut into ribbons after they have been transferred onto any arbitrary substrate [2.78].

Expanded graphite was dispersed in a 1,2-dichloroethane (DCE) solution containing a polymer poly(*m*-phenylenevinylene-co-2,5-dioctoxy-*p*-phenylenevinylene) (PmPV) by sonication for 30 min followed by centrifugation to remove larger aggregates. The supernatant after sonication was shown to contain an appreciable fraction of graphene nanoribbons and related morphologies such as ribbons with kinks, bends, and nonparallel sides [2.71]. The exact mechanism or variation to the liquid-phase exfoliation procedures described earlier that results in the significant yield of nanoribbons in this case is not clearly understood.

Graphene nanoribbons, 8–12 nm in length and 2–3 nm width, have also been synthesized by surface-assisted coupling of molecular precursors into linear polyphenylenes and their subsequent cyclohydrogenation [2.68].

CNTs have been described as rolled-up graphene sheets, and now graphene nanoribbons have been made from unraveling CNTs. Oxidized nanoribbons were obtained by suspending CNTs in concentrated sulfuric acid followed by treatment with 500 wt.% $KMnO_4$ for

1 h at 22 °C and 1 h at 55–70 °C. The process, described as CNT unzipping, could occur as a linear longitudinal cut or in a spiral manner depending on the chirality of the CNT [2.70]. CNTs have also been converted to GNR by controlled plasma etching of CNTs that are partially embedded in a polymer film [2.69].

2.1.7 Derivatives of Graphene

Graphane, a fully saturated hydrocarbon derived from graphene, with formula CH, was predicted to be stable based on first-principles total-energy calculations [2.79]. Experimentally, it was later shown that graphene can be hydrogenated and converted to graphane using a low-pressure (0.1 mbar) hydrogen-argon mixture (10% H_2) with direct-current (DC) plasma for 2 h [2.80]. The hydrogenation is stable but reversible, and the graphane can be reconverted to graphene by annealing at 450 °C in Ar atmosphere for 24 h. The reconverted graphene, however, contains remnant defects just as vacancies and oxygenated or hydrogenated carbon atoms. In the case of substrate-supported graphene, only one side is hydrogenated, while both sides can be hydrogenated in the case of suspended graphene.

Graphene can also be fluorinated with xenon difluoride. When one side is exposed, F coverage saturates at 25% (C_4F), whereas fluorination of both sides results in perfluorographene [2.81] and fluorographene [2.82], which are the nonstoichiometric and stoichiometric variations. Nonstoichiometric and multilayered fluorographene can also be exfoliated from graphite fluoride [2.56, 83]. Hydrazine treatment has been shown to reverse the fluorination.

2.2 Properties

While its very existence as a freestanding two-dimensional material is a feather in graphene's cap, it is the properties of graphene that make it the truly exceptional material that has stoked feverish research in this field. The individual properties of pristine graphene are discussed first, while the properties of graphene derivatives such as GO, graphane, and fluorographene are discussed in the final section.

2.2.1 Structure and Physical Properties

Graphene shares most of its structure and physical properties with graphite, its parent material. The carbon atoms are arranged in a two-dimensional hexagonal lattice (Fig. 2.9b), which can also be constructed as two interpenetrating triangular sublattices, which takes particular significance in bilayer and other multilayer graphenes. The carbon atoms are sp^2 hybridized, and the in-plane carbon–carbon bond length is $a = 1.42$ Å. The remaining p-orbital is oriented perpendicular to the plane of carbon atoms and delocalizes to form the π (valence) and π^* (conduction) electronic bands which are discussed in detail in Sect. 2.2.3. The carbon layers are usually stacked in an ABAB (Bernal) stacking; however, in certain few-layer graphenes such as that grown by CVD, the layers are rotated with respect to this standard arrangement. The interplane spacing is 3.45 Å. A staggered ABCABC (rhombohedral) arrangement is also possible, but has not been realized by any of the graphene production routes.

Two-dimensional structures such as graphene have been postulated to be intrinsically unstable, and according to the Mermin–Wagner theorem [2.84], long-wavelength fluctuations destroy the long-range order of 2-D crystals. Even 2-D crystals embedded in 3-D space have a tendency to crumple. The puzzling stability of suspended 2-D graphene sheets has been attributed to intrinsic microscopic undulations in which the surface normal varies by several degrees and the out-of-plane deformation reaches 1 nm [2.9, 85]. This observation by TEM is discussed further in Sect. 2.3.2 and also conforms to atomistic Monte Carlo simulations. Similar corrugation has also been reported on graphene supported on SiO_2 substrates, where it is a superposition of intrinsic rippling as well as extrinsic undulations imposed by the substrate surface morphology [2.86]. Periodic ripples have also been observed on weakly coupled graphene monolayers on substrates such as Ru(0001) [2.87]. Corrugations in substrate-supported graphene are primarily observed by STM and are discussed further in Sect. 2.3.3. In addition to ripples, substrate-supported graphene also exhibits ubiquitous wrinkles which could be several nanometers in width. Scrolling has been occasionally observed at the edges of graphene flakes, both suspended [2.88] and substrate supported [2.89], and this appears to rely on the fabrication method. Scrolling occurs when graphene is

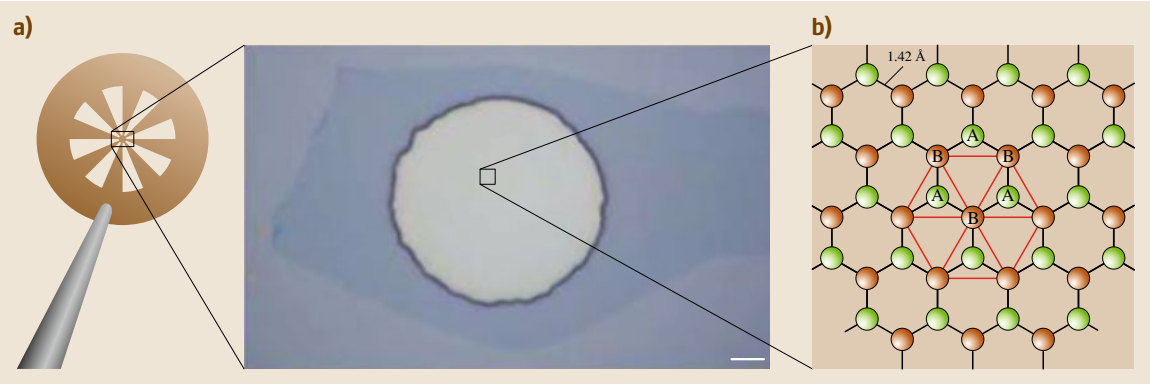


Fig. 2.9 **(a)** SEM of graphene suspended over a macroscopic hole of a Cu TEM grid (after [2.90]). **(b)** Structure of graphene (after [2.92])

subjected to liquid-phase processing during microfabrication, while its solid-phase or gas-phase processing appears to avoid this [2.90], and it is possible to obtain large free-standing sheets of monolayer graphene (Fig. 2.9a). The ripples in graphene also result in perturbations in the electronic structure, and many electronic and chemical properties of graphene have been attributed to these ripples, rather than being intrinsic to graphene. However, it has been shown that graphene deposited on atomically flat terraces of cleaved mica surfaces is flat down to the atomic scale [2.91]. The height variation observed by AFM was less than 25 pm, and such *ultraflat* graphene is expected to permit exploration of various intrinsic physical and chemical properties of graphene.

2.2.2 Mechanical Properties

Carbon materials have made it a habit of setting records for their intrinsic mechanical properties. Diamond is the hardest known natural material, and is assigned a grade of 10 (highest) on the Mohs scale of mineral hardness [2.93]. Similarly, the record for tensile strength has been held by CNTs; a Young's modulus of 1 TPa and tensile strength of 150 GPa coupled with elongation to failure as high as 20% have been experimentally reported [2.94].

The earliest experimental indication for the extraordinary stiffness of graphene was the observation that graphene *beams* supported on only one end do not scroll or fold, quite unlike the papery or cloth-like appearance of graphene. If the effective thickness of monolayer graphene is estimated to be 0.23 Å from elastic theory, a bending rigidity of 1.1 eV [2.85], and a Young's modulus of 22 eV/Å^2 from the elastic modulus of bulk graphite [2.95], the lengths of unsupported graphene observed in TEM samples have been 10^6 times larger than its effective thickness. Suspended graphene can gain additional thickness from large-scale corrugations by a factor of $(H/a)^2$, where H is the characteristic height of the corrugations. In addition to supporting its own weight, suspended graphene has been shown to support significant extra load such as copper nanoparticles [2.90], as well as surviving accidental shocks such as during handing.

Direct measurements of the elastic properties of graphene have been conducted by nanoindentation of suspended graphene layers in an AFM [2.96, 97]. Details of the measurement technique are found in Sect. 2.3.3. Measurements conducted on few-layer graphene of less than 8 nm thickness yielded spring constants of 1–5 N/m. A Young's modulus of 0.5 TPa was extracted by fitting the data to a model for doubly clamped beams under tension. For measurements on monolayer graphene, the force–displacement characteristics yield second- and third-order elastic stiffness of 340 and −690 N/m, respectively. The breaking strength was found to be 42 N/m, which represents the intrinsic strength of a defect-free sheet. This corresponds to Young's modulus $E = 1.0$ TPa, third-order elastic stiffness of 2.0 TPa, and intrinsic strength of 130 GPa. These figures mean that graphene is the strongest material ever measured.

Nonlinear finite elasticity theory for graphene resonators for both electrostatic and electrodynamic cases has been developed and agrees well with experiments on graphene resonators [2.98]. The dynamic response of clamped graphene resonators resembles that of coupled

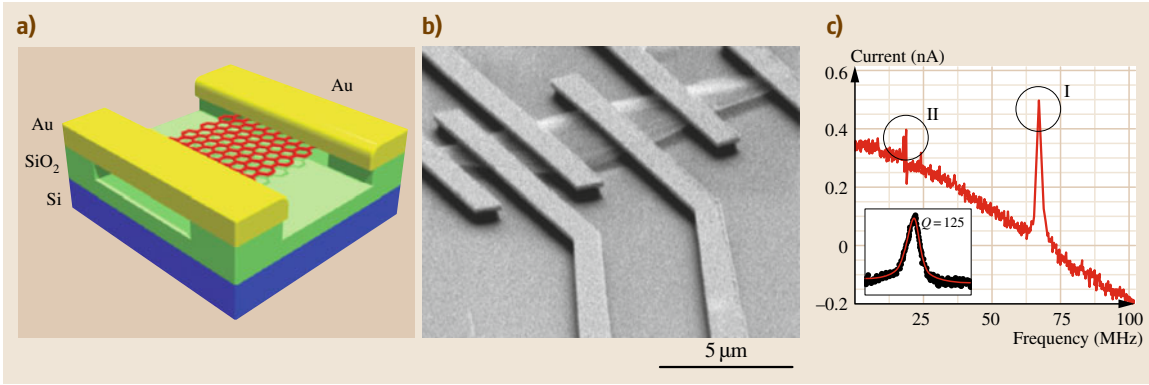


Fig. 2.10 **(a)** Schematic of graphene resonator, with electrostatic actuation and electrical readout. **(b)** SEM image of such a resonator. **(c)** The graphene resonance (I) at 65 MHz. Resonances of metal beams (II) are also visible below 25 MHz. *Inset*: the graphene resonance at low driving power, and Lorentzian fit (*red line*) with $Q = 125$ (after [2.102])

Duffing-type resonators. Similarly, a continuum plate model for the vibration of multilayered graphene sheets, including the van der Waals (vdW) interaction between the layers, suggests that the lowest natural frequencies are identical for various numbers of layered graphenes. Higher resonance frequencies, however, depend on the vdW interaction and are different for different layered graphenes [2.99]. In general, natural resonance frequencies in the THz regime are expected for graphene resonators, due to the combination of their extreme thinness and extraordinary stiffness. Experimentally, the mechanical vibrations in electrostatically actuated graphene resonators have been imaged by a special modification of atomic force microscopy [2.100]. Resonance frequencies in the tens of MHz have been recorded in graphene resonators (Fig. 2.10), with quality factors as high as 4000 at room temperature [2.101] and 10 000 at 5 K [2.102].

2.2.3 Electronic Properties

Electronically, monolayer, bilayer, and trilayer graphene are electronically distinct materials. Beyond three layers, graphene's electronic properties tend towards those of bulk graphite. In certain aspects, graphene of up 10 layers might exhibit deviation in electronic properties from bulk graphite and could be referred to as graphene, but beyond 10 layers all graphenes are indistinguishable from graphite.

Monolayer Graphene

The electronic structure of graphene was first described in 1946 [2.103], as a theoretical building block to describe graphite. The valence and conduction bands of graphene are conical valleys that touch at the high-symmetry K and K′ points of the Brillouin zone. Near these points, the energy varies linearly with the magnitude of momentum, i. e., follows a linear dispersion relation. In neutral graphene, this point of intersection coincides with the charge neutrality point, and is referred to as the Dirac point.

In every other material known to condensed matter physicists, the electrons behave as and can be described by the Schrödinger equation. In graphene, on the other hand, electrons have been shown to behave as relativistic particles, and should be described by the Dirac equation [2.104–106]. The interaction of electrons with the periodic potential of the graphene hexagonal lattice results in quasiparticles, which can be viewed as electrons devoid of their rest mass m_0 and therefore called massless Dirac fermions. The linear energy dispersion means that the speed of electrons in graphene is a constant, independent of momentum, as in the case of the speed of photons. The velocity of electrons in graphene is $\approx 10^6$ m/s, about 300 times slower than the speed of light (photons).

The electronic states near the Dirac point are composed of states belonging to the two graphene sublattices, and as a result the quasiparticles possess pseudospin, similar to the electron's spin [2.107, 108]. As a result, these Dirac fermions are said to be chiral. Another relativistic feature of these quasiparticles is the Klein paradox [2.107], wherein they tunnel through a potential barrier of any height and width with a transmission probability of 1 or without a reflected component. As a result, electrons in graphene

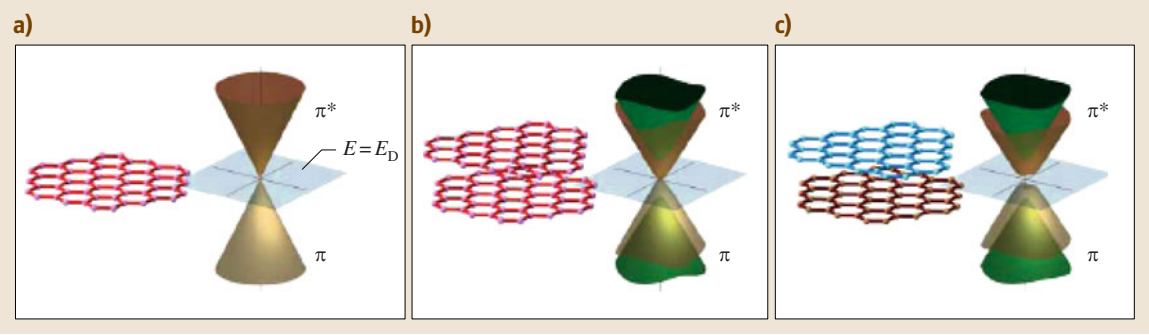


Fig. 2.11a–c Electronic structure of **(a)** monolayer, **(b)** symmetric bilayer, and **(c)** asymmetric bilayer of graphene (after [2.109])

can propagate over (relatively) vast distances of the order of microns through the graphene lattice, even in the presence of lattice defects or other external perturbing potentials [2.4].

Bilayer Graphene

If the hexagonal atomic structure of graphene is composed of nonidentical elements, such as in boron nitride, the lateral in-plane symmetry is broken and a large bandgap is formed between the π and π* states. This is the case in bilayer graphene, where the AB (Bernal) stacking between the two graphene renders the two carbon atoms inequivalent and results in two graphene sublattices. As a result, the unit cell of bilayer graphene contains four atoms, and two additional bands result (π and π* states). If the inversion symmetry between the two layers is broken, then an energy gap between the low-energy valence and conduction bands forms at the Dirac point (Fig. 2.11).

The first experimental demonstration of this effect was performed on bilayer graphene synthesized on SiC (6H, (0001) orientation) [2.109]. The as-grown graphene is n-doped due to the depletion of the substrate's dopant carriers. At low temperature, the SiC dopant electrons are frozen out and the substrate acts as a nearly perfect insulator while the excess electrons in graphene retain their high mobility. In this case, the symmetry of the bilayers is broken by the dipole field created between the depletion layer of the SiC and the accumulation of charge on the graphene layer next to the interface. Further n-type doping can be introduced by deposition of potassium atoms onto the vacuum side, which donate their lone valence electrons to the graphene layer, forming another dipole. The binding energy–momentum dispersion relation of π, π*, and σ states along high-symmetry directions was measured by angle-resolved photoemission spectroscopy (ARPES) (Fig. 2.12). The relative potential of the top and bottom graphene layers is varied by changing the doping level by potassium adsorption. An apparent gap at the K point appears in the as-prepared graphene, disappearing and reappearing with increasing level of K doping.

The electronic gap in bilayer graphene can thus be controlled by applying an external transverse electric field, such as by a gate bias, making it the only known semiconductor material with a tunable energy gap. Using a tight-binding model, the value of the gap was extracted as a function of electron density, showing that it can be tuned to values larger than 0.2 eV, using fields of ≈ 1 V/m.

The two key semiconductor parameters, the electronic bandgap and carrier doping concentration, can also be independently tuned by using a dual-gate configuration. Reliable determination of the bilayer bandgap has been carried out in such a configuration using infrared microscopy [2.110]. Figure 2.13 shows the gate-modulated bilayer absorption spectra at the charge neutrality point. The two features present in the spectra, a peak below 300 meV and a dip around 400 meV, arise from different optical transitions between the bilayer electronic bands. Transition I shows pronounced gate tunability up to 250 meV at 3 V/nm, since it accounts for the bandgap-induced spectral response.

By examining the electronic band structure of graphene around the K point within a tight-binding approach, it has been shown that a single graphene layer is a zero-gap semiconductor with a linear Dirac-like spectrum around the Fermi energy, while graphite shows semimetallic behavior with band overlap of about 41 meV. Bilayer graphene has a parabolic band structure around the Fermi energy and is a semimetal like graphite; however, the band overlap is only 0.16 meV.

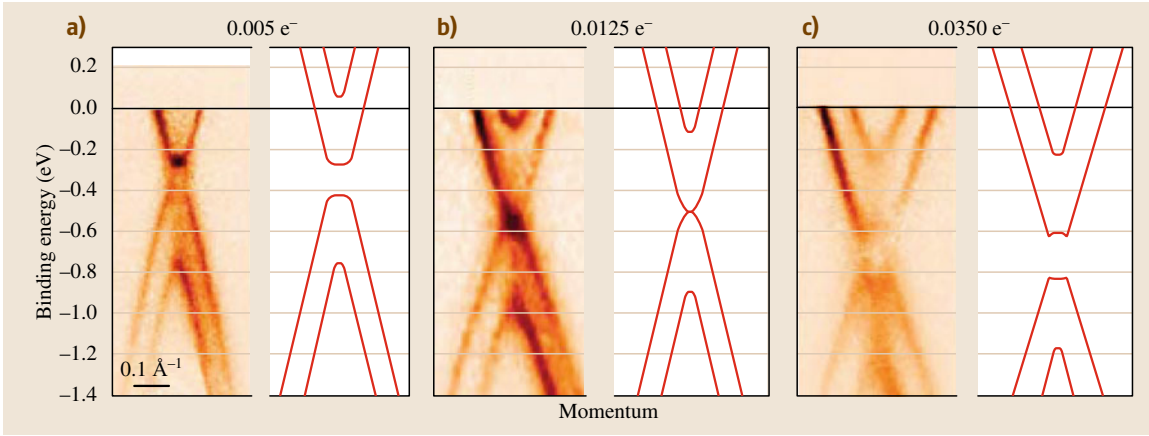


Fig. 2.12a–c Evolution of gap closing and reopening by changing the doping level by potassium adsorption. Experimental and theoretical bands (*solid lines*) for **(a)** as-prepared graphene bilayers and **b**,**c** with progressive adsorption of potassium are shown. The number of doping electrons per unit cell, estimated from the relative size of the Fermi surface, is indicated at the top of each panel (after [2.109])

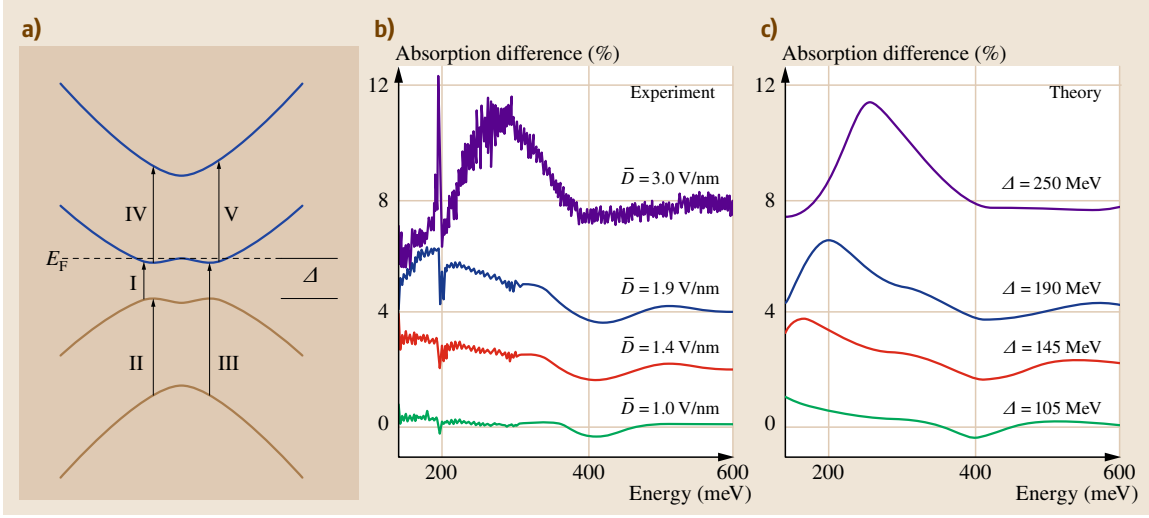


Fig. 2.13a–c Infrared spectroscopy to probe bilayer energy gap opening at strong electrical gating. **(a)** Allowed optical transitions between different subbands of a graphene bilayers. **(b)** Gate-induced absorption spectra at the charge neutrality point for different applied displacement fields $\bar{D}$. *Curves* are offset from zero for clarity. **(c)** Theoretical prediction of gate-induced absorption spectra based on a tight-binding model where the bandgap value is taken as an adjustable parameter. The fit provides an accurate determination of the gate-tunable bandgap at strong electrical gating (after [2.110])

This overlap increases with the number of graphene layers, and for 11 or more layers it is smaller than 10%.

Superconductivity

Andreev reflection at a metal–superconductor junction involving graphene is fundamentally different from normal metals [2.111]. In weakly doped graphene, electron–hole conversion involves electrons from the conduction band being converted into a hole from the valence band. This interband conversion is associated with specular reflection instead of the retroreflection found in normal metals where electron–hole conversion occurs within the conduction band (Fig. 2.14). The Josephson effect has also been experimentally stud-

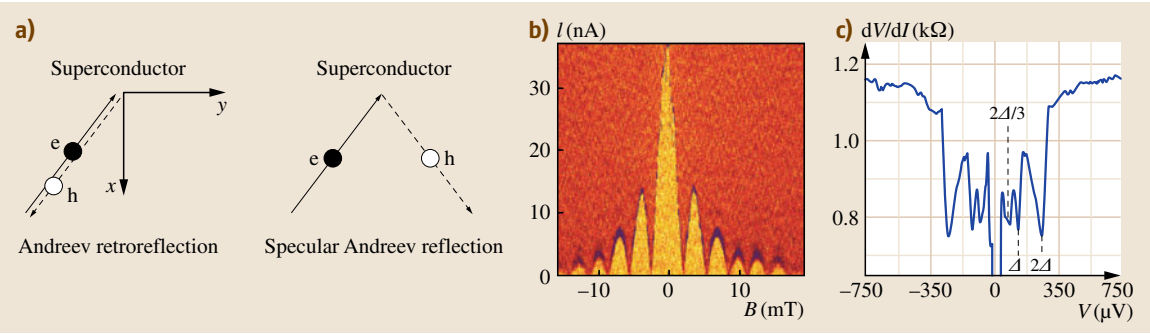


Fig. 2.14 **(a)** Andreev retroreflection (*left*) at the interface between a normal metal and a superconductor, and specular Andreev reflection (*right*) at the interface between undoped graphene and a superconductor. *Arrows* indicate the direction of the velocity, and *solid* or *dashed lines* distinguish whether the particle is a negatively charged electron (e) or a positively charged hole (h) (after [2.111]). **(b)** Josephson effect in graphene: $\mathrm{d}V/\mathrm{d}I(I, B)$ at $T = 30\,\mathrm{mK}$ (*yellow-orange* is zero, that is, the supercurrent region, and *red* corresponds to finite $\mathrm{d}V/\mathrm{d}I$) (after [2.112]). **(c)** $\mathrm{d}V/\mathrm{d}I$ versus V, showing multiple Andreev reflection dips below the superconducting energy gap. The dips in $\mathrm{d}V/\mathrm{d}I$ occur at values of $V = 2\Delta/en$, where n is an integer number (after [2.112])

ied in macroscopic junctions consisting of a graphene layer contacted by two closely spaced superconducting electrodes (SGS) [2.112, 113]. A supercurrent is observed, which can be carried either by electrons in the conduction band or by holes in the valance band, as determined by the gate voltage. A finite supercurrent is also observed at zero charge density at the charge neutrality point, indicating phase-coherent electronic transport at the Dirac point. The diffusive junction model has been shown to yield quantitative agreement with experiments [2.114], while a ballistic SGS model is inconsistent with the data. This is attributed to potential fluctuations in graphene due to the influence of the substrate as well as metallic leads. Crossed Andreev reflection in graphene–superconductor–graphene junctions [2.115] and Andreev reflection in graphene nanoribbons [2.116] have been theoretically investigated, but experimental confirmation remains pending.

2.2.4 Optical Properties

Successful exfoliation of monolayer graphene depends on the recognition of the optical properties of graphene more than the exfoliation procedure [2.7]. The choice of 300 nm-thick SiO_2 on Si substrate allowed optical identification of the exfoliated monolayer graphene, which would otherwise have been invisible and not practically detectable; for instance, only flakes thicker than ten layers can be found in white light on top of 200 nm SiO_2, which also marks the commonly accepted transition from graphene to bulk graphite. The contrast of a graphene flake depends not only on the SiO_2 thickness but also on the wavelength λ of light used. Figure 2.15 summarizes the expected contrast as a function of SiO_2 thickness as well as wavelength of monochromatic illumination, derived using Fresnel theory. It was also inferred that the complex refractive index of graphene is the same as that of bulk graphite, $n = 2.6 - 1.3\mathrm{i}$, which is independent of λ. This can be explained by the fact that the optical response of graphite with the electric field parallel to graphene planes is dominated by the in-plane electromagnetic response. Since changes in the light intensity due to graphene are relatively minor, the observed contrast can be used to determine the number of graphene layers.

The absorbance of light by monolayer and bilayer graphene has been measured to be 2.3 and 4.6%, respectively, in the visual regime (450–750 nm), and this extends linearity up to five layers. The optical transparency of noninteracting graphene is solely determined by the fine structure constant of quantum electrodynamics ($\alpha = e^2/\hbar c = 1/137$), which describes the coupling between light and relativistic electrons [2.117, 118]. This is because, as discussed in the previous section, the electrons in graphene behave as relativistic Dirac particles and electron–electron Coulomb interactions can be neglected. The high-frequency (dynamic) conductivity G for Dirac fermions in graphene is a universal constant equal to $e^2/4\hbar$. The universal G implies that observable quantities such as graphene's optical transmittance T and reflectance R are also universal

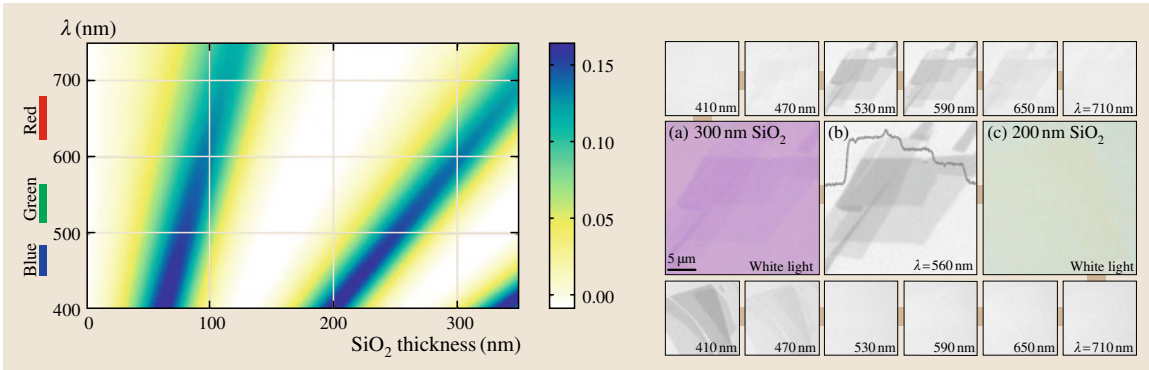


Fig. 2.15 *Left*: Color plot of contrast as a function of wavelength and SiO_2 thickness. The *color scale* on the *right* shows the expected contrast. *Right*: Graphene crystallites on 300 nm SiO_2 imaged with white light (*panel a*), green light, and another graphene sample on 200 nm SiO_2 imaged with white light (*panel c*). Single-layer graphene is clearly visible in the *left image* (*panel a*), but even three layers are indiscernible on the *right* (*panel c*). Image sizes are $25 \times 25\,\mu m^2$. *Top* and *bottom* panels show the same flakes as in (*panel a*) and (*panel c*), respectively, but illuminated through various narrow bandpass filters with bandwidth of ≈ 10 nm (after [2.7])

and given by $T \equiv (1 + 2\pi G/c)^{-2} = (1 + 1/2\pi\alpha)^{-2}$ and $R \equiv 1/4\pi^2\alpha^2 T$ for normal light incidence. This yields graphene's opacity $(1 - T) \approx \pi\alpha = 2.3\%$.

2.2.5 Thermal and Thermoelectric Properties

CNTs are known to have very high thermal conductivity K with the experimentally determined value of $K \approx 3000\,W/(m\,K)$ at room temperature for an individual multi-walled CNT [2.119] and $K \approx 3500\,W/(m\,K)$ for an individual single-walled CNT [2.120]. These values exceed those of the best bulk crystalline thermal conductor, diamond, which has thermal conductivity in the range $K = 1000–2200\,W/(m\,K)$ [2.121].

The first experimental determination of the thermal conductivity of suspended monolayer graphene pegged the value at $5300\,W/(m\,K)$ and a phonon mean free path of 775 nm near room temperature [2.122], which was extracted from the dependence of the Raman G peak frequency on the excitation laser power and independently measured G peak temperature coefficient. Interestingly, this value is higher than the bulk graphite limit of $K \approx 2000\,W/(m\,K)$ [2.123]. It has been experimentally shown that the room-temperature thermal conductivity decreases from ≈ 2800 to $\approx 1300\,W/(m\,K)$ as the number of graphene layers in few-layer graphene (FLG) increases from two to four [2.124]. The observed evolution from two-dimensional graphene to bulk graphite is explained by the cross-plane coupling of the low-energy phonons and changes in the phonon Umklapp scattering, since more states are available for scattering owing to the increased number of phonon branches.

The thermoelectric power (TEP) is the voltage developed across a sample when a constant temperature gradient is applied. TEP of $80\,\mu V/K$ was recently measured in graphene at room temperature (300 K) [2.125]. Similar to the quantum Hall effect in electronic transport, quantized TEP has also been observed in graphene at high magnetic fields [2.125]. The TEP can be tuned in graphene, even to negative values, under the application of a gate bias or chemical potential [2.126]. Very large TEP values have been predicted for graphene nanoribbons, for instance, $4\,mV/K$ for a 1.6 nm-wide ribbon [2.127]. In comparison, the highest value experimentally reported so far is $850\,\mu V/K$ for two-dimensional electron gases in $SrTi_2O_3$ heterostructures [2.128], while only a few $\mu V/K$ has been reported for bulk graphite [2.123]. The TEP power of SWNTs has been theoretically and experimentally shown to be $60\,\mu V/K$ [2.129], inferior to that of graphene. A giant thermoelectric coefficient of $30\,mV/K$ was reported in a nanostructure consisting of metallic electrodes periodically patterned over graphene, deposited on a silicon dioxide substrate [2.130].

2.2.6 Chemical Properties

The chemistry of graphene is dominated entirely by its surface, since every carbon atom is a surface atom twice over, forming a part of two surfaces. For nanorib-

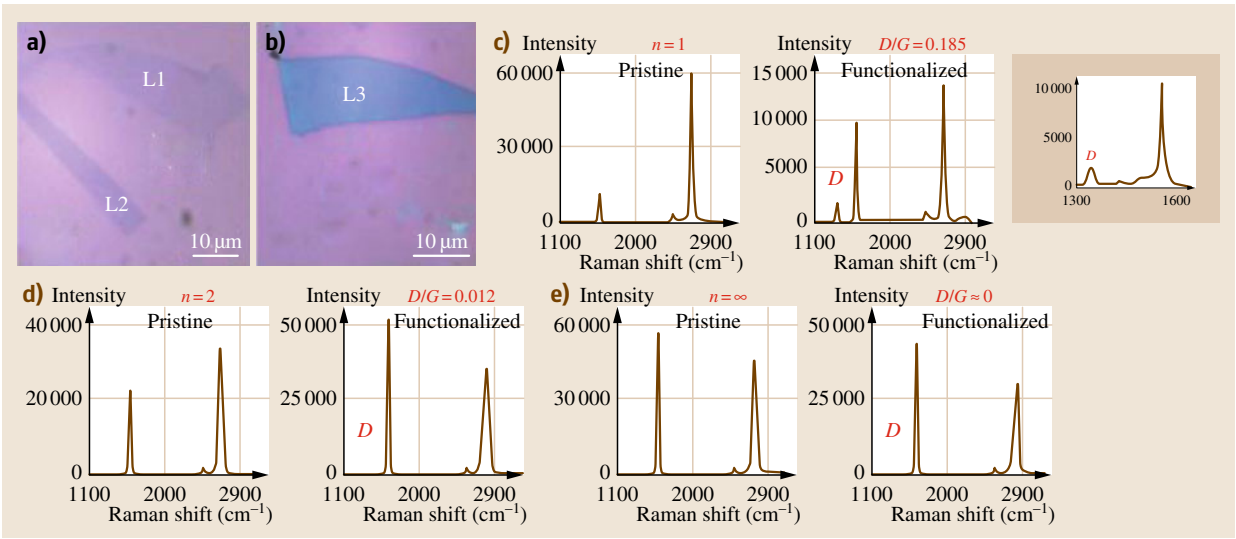


Fig. 2.16 **(a)** Microscopic images of single-layer (*right*), bilayer (*left*), and **(b)** multilayer ($n \approx \infty$) graphene. **(c–e)** Raman spectra of pristine (*left*) and functionalized (*right*) sheets: **(c)** spot L1 on single sheet with *inset* showing expanded 1300–1700 cm^{-1} region, **(d)** spot L2 on bilayer, and **(e)** spot L3 on multilayer ($n \approx \infty$, graphite). There is no D peak for the pristine samples (*left spectra*). The D/G ratio after reaction of single layer (0.185) is about 15 times higher than that for a bilayer (0.012) and greater for other multilayers (≈ 0). Reactions all performed at 35 °C with 17 mM 4-nitrobenzene diazonium water with 1 wt.% sodium dodecyl sulfate (SDS) (after [2.131])

bons of graphene, the edges play an increasing role in determining their reactivity.

It has been shown that, for electron transfer chemistries, single graphene sheets are almost 10 times more reactive than bilayer or multilayer graphene (Fig. 2.16) according to the relative intensity of the disorder (D) peak in the Raman spectrum examined before and after chemical reaction [2.131, 132]. Substrate-induced doping of the graphene resulting in electron-rich regions has been proposed to explain this trend. The effect of doping is greatest in monolayers because the screening length in the *c*-axis in graphite and graphene is only 5 Å, comparable to the interlayer spacing of 3.5 Å [2.133, 134]. Similarly, the reactivity of edges is at least two times higher than the reactivity of the bulk graphene sheet [2.131]. Predictions based on Gerischer–Marcus electron transfer theory and tight-binding approximations predict that armchair and zigzag graphene nanoribbons (GNRs) have opposite trends in reactivity, with the former increasing with width and the latter decreasing. In zigzag ribbons the major reactivity contribution comes from edge states [2.135]. This reactivity trend for zigzag GNR is reversed for very narrow ribbons due to the presence of large semiconducting gaps with correspondingly low reactivities.

Graphene can be readily functionalized through diazonium or nitrene [2.136] reactions, which can introduce reactive species covalently linked to graphene. These groups then serve as templates for further chemistry and grafting of functional groups, for instance, through an azide linker. Chemical functionalization of graphene can be monitored through its effect on the conductivity of graphene, serving as a means to control the electrical transport properties of graphene [2.137, 138]. Furthermore, p-doped and n-doped regions in graphene can be generated by suitably functionalizing them, for instance, with diazonium salts and polyethylene imine, respectively [2.139]. Such chemical modification can also be performed on different parts of a single sheet to form p–n junctions in graphene [2.140].

2.2.7 Properties of Graphene Derivatives

Graphane was theoretically predicted to take one of two configurations: a *chair* conformer with the hydrogen atoms alternating on both sides of the plane for the two graphene sublattices, and a *boat* conformer with the hydrogen atoms alternating in pairs [2.79]. These chair and boat conformers have a direct electronic bandgap of 3.5 and 3.7 eV, respectively. Graphane is a com-

pletely insulating material; its resistivity changes by two orders of magnitude with decreasing temperature from 300 to 4 K, and its carrier mobility decreases to $\approx 10\,\mathrm{cm}^2/(\mathrm{V\,s})$ at liquid-helium temperatures for typical carrier concentrations of $10^{12}\,\mathrm{cm}^{-2}$ [2.80].

Similarly, fluorographene [2.82] is a high-quality insulator with large optical bandgap of $> 3\,\mathrm{eV}$ and room-temperature resistivity of $> 10^{12}\,\Omega$. The Young's modulus of fluorographene was measured to be 0.3 TPa, which is about 30% the stiffness of graphene. Similarly, fluorination reduces graphene's intrinsic breaking strength by 2.5 times. However, fluorographene is able to sustain the same ultimate strain of 15% as graphene. Fluorographene is also strongly hydrophobic, and can be considered the two-dimensional equivalent of Teflon.

2.3 Characterization

Each of the properties discussed in the previous section has to be measured and correlated using multiple characterization techniques, which are discussed in this section; for instance, electronic properties of graphene have to be independently verified by ARPES, optical spectroscopy, and electronic transport. This is essential, since just one measurement, for instance, electronic transport, might not be able to sufficiently distinguish between an electronic bandgap and a mobility gap. Similarly, mechanical properties have to be confirmed by a combination of tensile testing, electromechanical resonance, and Raman spectroscopy.

2.3.1 Optical Characterization

Based on the optical properties of graphene discussed in an earlier section, and the fact that green light is most comfortable for the eyes, optimal SiO_2 thicknesses of 90 and 280 nm can be recommended [2.7]. Similarly, it has been shown that graphene can be observed on 50 nm Si_3N_4 using blue light and on 90 nm poly-methyl methacrylate (PMMA) using white light [2.7]. Optical contrast can similarly be used to identify graphene oxide on Si/SiO_2 substrates, as well as to visualize its conversion to reduced GO upon annealing, since both the effective index of refraction and the effective extinction coefficient increase [2.141].

Rayleigh scattering can identify the number of graphene layers as well as probe their dielectric constant [2.142]. Rayleigh imaging relies on elastically scattered incident photons, while Raman spectroscopy, which is discussed later, collects inelastically scattered photons. For graphene on Si/SiO_2 substrate, under white-light illumination combined with interferometric detection, the contrast can be tailored by adjusting the SiO_2 thickness and the light modulations depend strongly on the graphene thickness. Up to six layers, the graphene behaves as a superposition of single sheets and the monochromatic contrast increases linearly.

2.3.2 Transmission Electron Microscopy

Transmission electron microscopy (TEM) is one of the most direct observation techniques to elucidate the structure of graphene. High-resolution TEM can resolve individual carbon atoms as well as adatoms, defects, and other anomalies in graphene (Fig. 2.17) [2.88]. The high-energy electrons in a TEM can also be used to engineer defects such as vacancies, cause edge reconstructions and graphene sublimation, as well as observe them in situ [2.10]. Various techniques have been developed to transfer micromechanically cleaved graphene flakes onto TEM grids. If folds occur in the transferred graphene flake, observation of the folded edge can yield information about the number of layers in the graphene flake [2.9]; a monolayer fold edge turns up as a single dark line, while a bilayer fold edge appears as two dark lines and so on, in analogy to single-walled and multi-walled carbon nanotubes. In addition, nanobeam electron diffraction (Fig. 2.17) can also be used to quantify the layering in graphene [2.9]. Monolayer graphene can be distinguished from higher-layered graphenes by the anomalous intensity ratio of the diffraction peaks; its $0\bar{1}10$ peaks being more intense than the $1\bar{2}10$ peaks. When measured as a function of incidence angle, it probes the whole 3-D reciprocal space. The total (integrated) intensity of the $0\bar{1}10$ and $1\bar{2}10$ peaks of monolayer graphene varies weakly with tilt angle and no minima in intensity are observed, since the intensities in reciprocal space for monolayer graphene are continuous rods. In contrast, the total intensity of bilayer graphene diffraction peaks varies strongly with tilt angle, including minima at certain angles where some peaks vanish [2.143]. However, while the total intensity in monolayer graphene only decreases slightly, significant peak broadening is observed with increasing tilt angle. This effect is most pronounced in monolayers, and decreases with increasing thickness of the graphene flake. This is attributed to nanoscale corrugations in 2-D

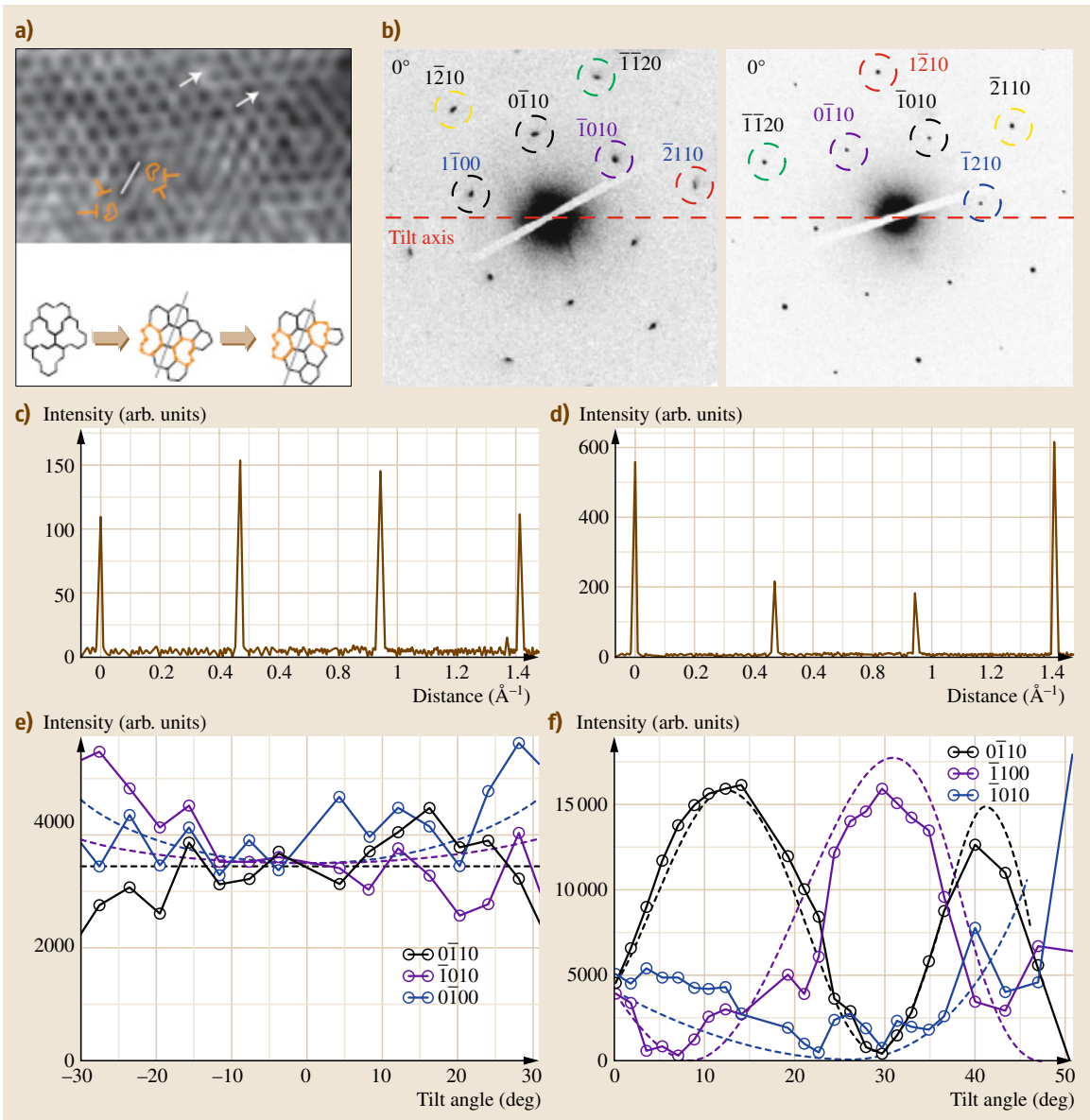


Fig. 2.17 **(a)** Atomic-resolution TEM of graphene (after [2.88]). **(b)** Nanobeam electron diffraction patterns of monolayer and bilayer graphene. Relative intensities of 1$\bar{1}$00 and 1$\bar{2}$10 peaks in **(c)** monolayer and **(d)** bilayer graphene. Variation of intensity of the 1$\bar{1}$00 peaks with tilt angle for **(e)** monolayer and **(f)** bilayer graphene (after [2.143])

graphene, with the surface normal deviating on average by ±5° in monolayers and ±2° in bilayers. Considering that the spatial extent of these corrugations cannot be drastically smaller than the coherence length of the diffracted electrons and that a large number of orientations should be included within the submicron electron beam in order to yield a smooth Gaussian shape of the diffraction peak, it is estimated that the corrugations occur on length scales of 10–25 nm. This nanoscale corrugation extending into the third dimension squares the existence of 2-D graphene with the theoretical prediction that perfect 2-D atomic crystals cannot exist.

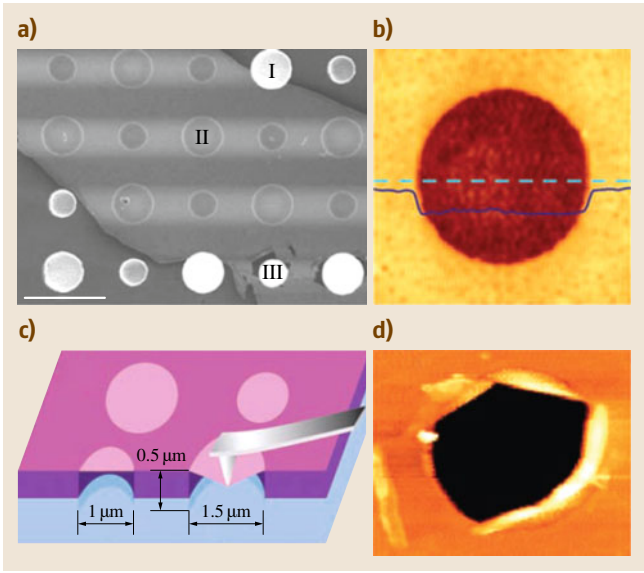


Fig. 2.18a–d Images of suspended graphene membranes. **(a)** Scanning electron micrograph of a large graphene flake spanning an array of circular holes (1 and 1.5 µm in diameter). *Area I* shows a hole partially covered by graphene, *area II* is fully covered, and *area III* is fractured from indentation. *Scale bar* 3 µm. **(b)** Noncontact AFM image of one membrane, 1.5 µm in diameter. The *solid blue line* is a height profile along the *dashed line*. The step height at the edge of the membrane is 2.5 nm. **(c)** Schematic of nanoindentation on suspended graphene membrane. **(d)** AFM image of fractured membrane (after [2.96])

2.3.3 Scanning Probe Techniques

Scanning probe techniques discussed here in the context of graphene characterization include atomic force microscopy (AFM), electrostatic force microscopy (EFM), and scanning tunneling microscopy (STM) and spectroscopy (STS).

AFM in tapping mode is commonly used to measure the thickness of graphene flakes on substrates; however, the correlation between measured thickness and actual thickness as well as number of layers is challenging [2.144]. Electrostatic interactions between the tip and the graphene, adsorbed moisture, and incorrect choice of AFM parameters such as free amplitude values can all influence the final measured thickness of a graphene flake. Therefore, while using AFM to characterize graphene flakes, an internal reference such as a fold in the flake, or a second characterization tool such as Raman spectroscopy, is often used to correlate the measured thickness and number of layers, and this process needs to be repeated at least for every different substrate and processing conditions involved in the graphene preparation.

In addition, AFM is used to measure the flatness of graphene on various substrates, and it is revealed that ultraflat graphene can be obtained on mica surface [2.91] with standard deviation of height and height correlation length of 24.1 pm and 2 nm, respectively, compared with 154 pm and 22 nm, respectively, for SiO_2 substrate. AFM can also be used in nanoindentation mode to probe the stiffness of suspended graphene (Fig. 2.18) [2.96]. This technique has the advantage that the sample geometry can be precisely defined and the sheet is clamped around the entire hole circumference; a Young's modulus of 1 TPa and intrinsic breaking strength of 42 N/m have been measured. EFM has been used to confirm that the surface potential of few-layer graphene increases with film thickness, approaching bulk graphite values for five or more layers [2.145]. This is a measure of the extent of the electrostatic interaction between graphene and the substrate, and the screening of these perturbations by underlying graphene layers.

STM can image graphene with atomic resolution, and the correlation of the graphene hexagonal lattice to the direction of the edge of an exfoliated flake reveals the orientation of the edge as being either armchair or zigzag [2.146]. It has been shown that, in mechanically exfoliated graphene flakes, a majority of edges follow either of these orientations and intersect at angles that are multiples of 30°. STM imaging of graphene grown epitaxially on SiC [2.147] or metallic substrates [2.20, 23, 87, 148] reveals the superlattice structure and the extent of coupling between the graphene and substrate. STM can also be used to locate and characterize point defects in the graphene lattice [2.149, 150]. STS can be used to probe the atomically resolved local electronic structure of graphene [2.147, 151, 152]. A prominent gap in the tunneling spectrum unique to graphene has been observed and attributed to a phonon-mediated inelastic tunneling process.

2.3.4 Angle-Resolved Photoemission Spectroscopy (ARPES)

ARPES is a direct experimental technique that has measured the electronic density of states in graphene with both energy and momentum information. The shape of the π and π^* bands near E_F at the K-point from ARPES reveals the transition from 2-D to bulk character from one to four layers of graphene [2.153]. Fermi velocities and effective masses of the electrons

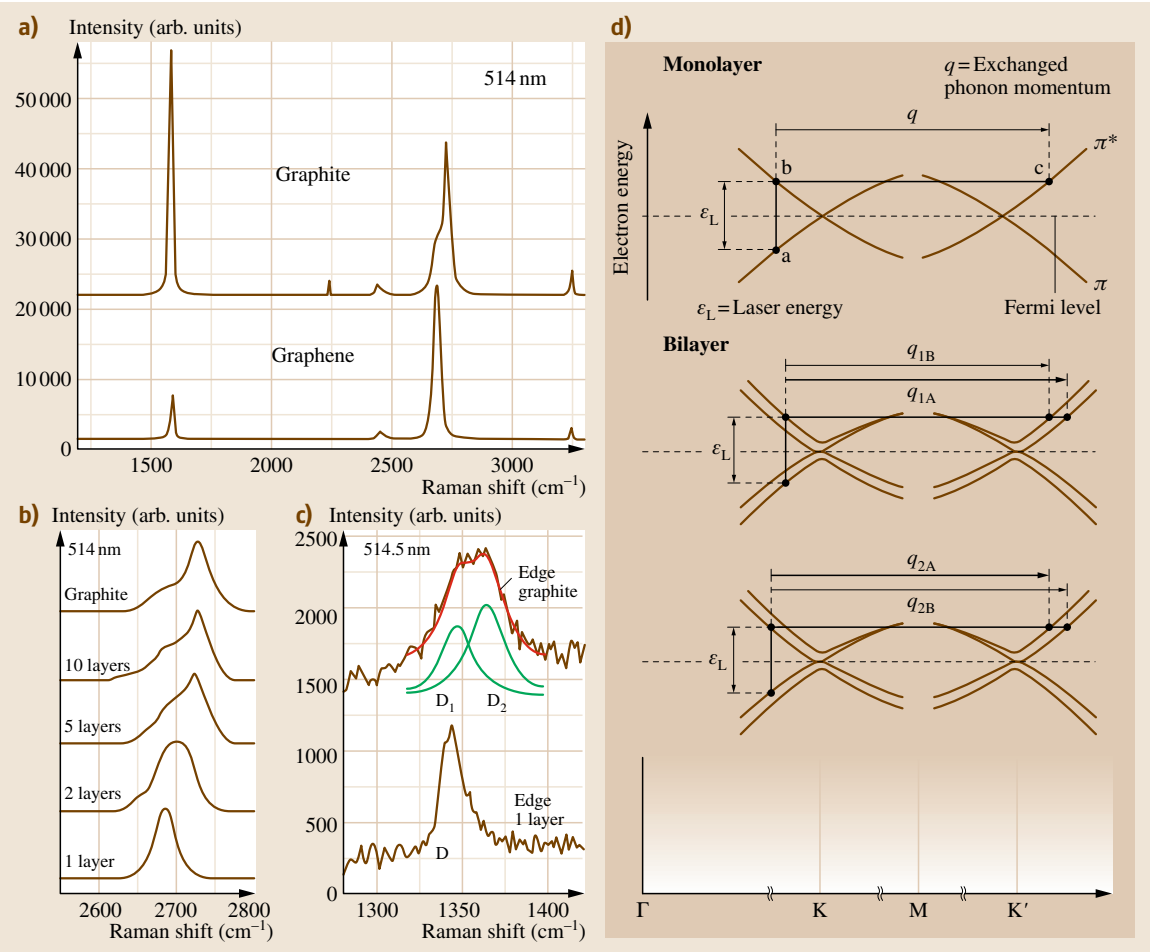


Fig. 2.19 **(a)** Comparison between Raman spectra of graphene and graphite. **(b)** Evolution of 2D peak shape with number of layers of AB-stacked graphene. **(c)** Comparison of D peak between graphene and graphite. **(d)** Scattering processing causing the 2D peak components in monolayer and bilayer graphene (after [2.156])

can also be measured. ARPES on epitaxial AB-stacked bilayer graphene on SiC has revealed that the magnitude of the gap between the valance and conduction bands can be varied by controlling the carrier density, for instance, with a transverse electric field. On the other hand, APRES also reveals that individual graphene layers of multilayer graphene grown on SiC(000$\bar{1}$) behave as decoupled monolayers with independent linearly dispersed bands at the K-point [2.154]. ARPES also allows studies of electron–electron, electron–phonon, and electron–plasmon interactions, and indicates that all three must be considered on an equal footing in understanding the quasiparticle dynamics in graphene [2.155]. Ab initio simulations of the ARPES intensity spectra of graphene has been able to reproduce key experimental observations including the indication of a mismatch between the upper and lower halves of the Dirac cone.

2.3.5 Raman Spectroscopy

The three significant Raman spectral features in graphene are the G peak at $\approx 1580\,\mathrm{cm}^{-1}$, the D peak at $\approx 1350\,\mathrm{cm}^{-1}$, and the 2D peak at $\approx 2700\,\mathrm{cm}^{-1}$, as seen in Fig. 2.19 [2.156]. The G peak is due to the E_{2g} mode, i. e., in-plane vibrations of the carbon atoms. The D peak and 2D peak are strongly dispersive, with excitation energy due to the Kohn anomaly at the K-point, while the G peak is not.

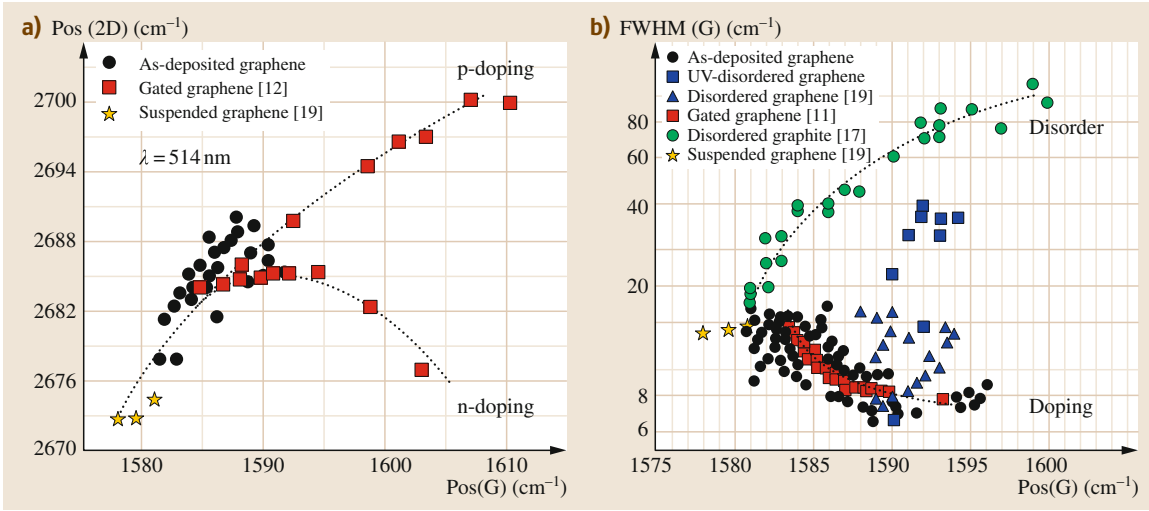


Fig. 2.20 **(a)** Pos(G) as a function of Pos(2D) for as-deposited graphene and gated graphene. **(b)** Pos(G) as a function of FWHM(G) for as-deposited graphene, compared with disordered graphene, disordered graphite, and gated graphene. The *dotted lines* are only a guide to the eye (after [2.159])

The 2D peak is the second order of the zone-boundary phonons and therefore does not require defects. For monolayer and few-layer graphene, the 2D peak serves as a fingerprint for identification [2.156]. In general, the 2D peak of graphite has four components: 2-D_{1B}, 2-D_{1A}, 2-D_{2A}, and 2-D_{2B}. Monolayer graphene has a single sharp 2D peak, dominated by the 2-D_{1A} component. In bilayer graphene, the 2-D_{1A} and 2-D_{2A} peaks have higher relative intensity compared with the other two, and the 2D peak appears up-shifted and broader compared with monolayer graphene. In monolayer graphene, there is only one phonon satisfying the double-resonance conditions for the 2D Raman peak. In bilayer graphene, the interaction between graphene layers causes the π and π^* electronic bands to split into four bands. According to density functional theory dipole matrix elements, the incident light couples more strongly to two among four possible optical transitions (Fig. 2.19). The excited electrons can be scattered by phonons with momenta q_{1B}, q_{1A}, q_{2A}, and q_{2B}. The corresponding processes for holes are associated to identical phonon momenta, resulting in four components to the 2D peak of bilayer graphene. As the number of layers further increases, the $2D_1$ peaks reduce in intensity, and beyond five layers, it resembles the 2D peak of bulk graphite. It is also important to note here that non-AB stacked graphene, such as multilayer CVD graphene, also shows a single 2D peak [2.157, 158]. However, this can be distinguished from monolayer graphene by its full-width at half-maximum (FWHM) of 50 cm^{-1}, which is twice that of monolayer graphene.

A similar observation can also be made for the D peak [2.156]. The D peak of monolayer graphene is a single sharp peak, while in bulk graphite it can be resolved into two peaks, D_1 and D_2. The D peak is observed in defective graphene, and prominently at the edges of graphene flakes. In carbon nanotubes, confinement and curvature split the two degenerate modes of the G peak into G^+ and G^- components, whereas only one G peak is observed in graphene. The D peak arises from a double-resonance process involving electron scattering by zone-boundary phonons as well as defects in graphene. Since these do not satisfy the Raman selection rule, they do not occur in the Raman spectra of defect-free graphene. A similar process involving intravalley scattering gives rise to a D′ peak at $\approx 1620\,\mathrm{cm}^{-1}$ in defective graphene.

The Raman spectrum of graphene also responds to doping, i. e., changes in the Fermi surface of graphene [2.160, 161]. Graphene can be doped intentionally or unintentionally, by electron transfer from adsorbed chemical species, and by modulation of the electronic band structure by a gate voltage or interaction with the substrate. The G peak upshifts for both hole and electron doping. The position of the 2D peak, however, decreases monotonically with increasing electron concentration or decreasing hole concentration,

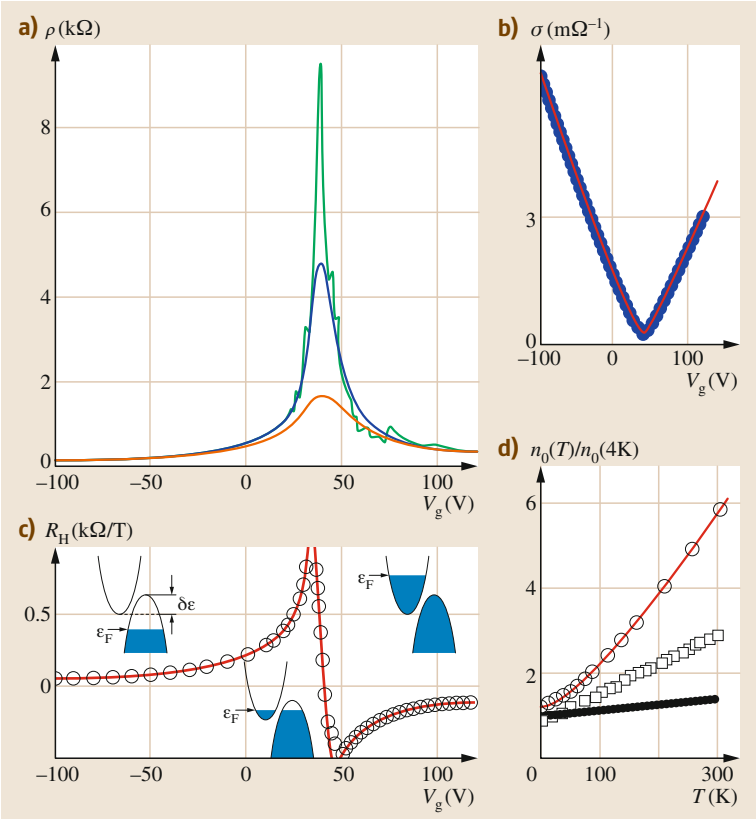


Fig. 2.21a–d Field effect in few-layer graphene. **(a)** Typical dependences of graphene's resistivity ρ on gate voltage for different temperatures ($T = 5$, 70, and 300 K for *top to bottom curves*, respectively). **(b)** Example of changes to the film's conductivity $\sigma = 1/\rho$ (V_g) obtained by inverting the 70 K curve (*dots*). **(c)** Hall coefficient R_H versus V_g for the same film at $T = 5$ K. **(d)** Temperature dependence of carrier concentration n_0 in the mixed state for the film in **(a)** (*open circles*), a thicker FLG film (*squares*), and multilayer graphene ($d \approx 5$ nm, *solid circles*). *Red curves* in **b**–**d** are the dependences calculated from the model of a 2-D semimetal illustrated by *insets* in **(c)** (after [2.4])

and the 2D peak can be used to distinguish between electron and hole doping. The changes in the G peak position are related to the nonadiabatic Kohn anomaly at the Γ point, while the shift in the 2D peak position is due to electron–electron scattering in addition to electron–phonon scattering. Taken together, a plot of 2D versus G peak positions can be used to distinguish between electron and hole doping in graphene (Fig. 2.20a) [2.159]. Doping trends can also be observed in the FWHM and intensities of Raman peaks. Raman peaks in graphene can also be shifted by biaxial strain induced, for example, by interaction with the substrate [2.162, 163]. It has been proposed that the correlation between normalized shift of 2D and G peak positions, i. e., $\Delta 2D/2D_0$ and $\Delta G/G_0$, where 2-D_0 and G_0 are the peak positions for undoped graphene, indicates whether the shift arises from doping or strain [2.164]. When $\Delta 2D/2D_0$ versus $\Delta G/G_0$ is plotted from Raman spectra obtained at a number of points on a graphene samples, a linear fit with slope close to 1.58 ± 0.18 indicates that strain plays a predominant role, while a smaller slope indicates increasing influence of doping. Highly doped samples yield a slope of < 1. In another approach, if the plot of FWHM versus position of the G peak is monotonically decreasing, it is related to doping, while if it is monotonically increasing, it is caused by strain or disorder (Fig. 2.20b) [2.161]. Under uniaxial strain, the G peak splits into two bands, G^+ and G^-, analogous to the effect of curvature on the G peak of carbon nanotubes [2.165].

2.3.6 Electrical Characterization

The first electrical characterization of graphene was carried out on micromechanically cleaved few-layer graphene flakes (Fig. 2.21) [2.4]. The sheet resistivity ρ of FLG flakes varies with applied gate voltage V_g, exhibiting a sharp peak of several kiloohms and decaying to $\approx 100\,\Omega$ at high V_g. The conductivity $\sigma = 1/\rho$ increases linearly with V_g on either side of the resistivity peak (conductivity valley). The Hall coefficient R_H reverses sign at the same V_G as the resistivity peak. This resembles an ambipolar semiconducting

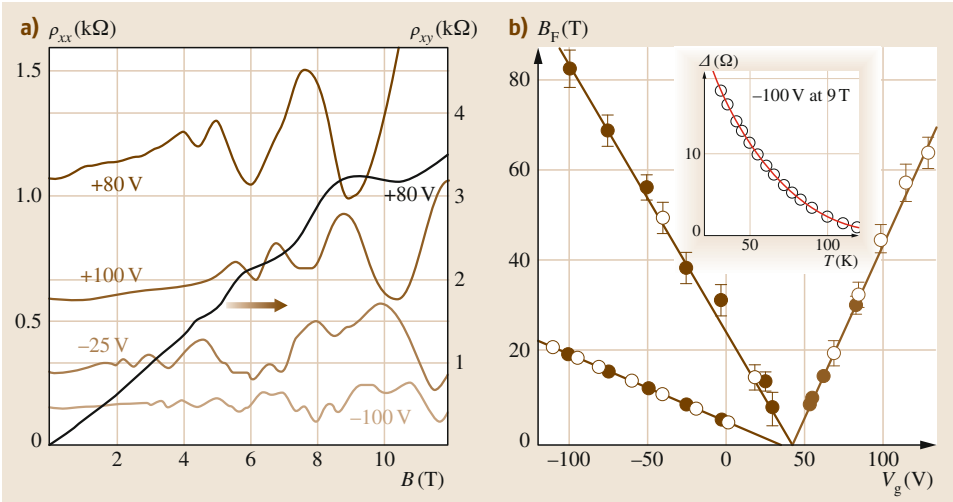


Fig. 2.22 **(a)** Examples of ShdH oscillations in a graphene device for different gate voltages; $T = 3$ K, and B is the magnetic field. **(b)** Dependence of the frequency of ShdH oscillations B_F on gate voltage. *Solid* and *open symbols* are for samples with $\delta\varepsilon \approx 6$ and 20 meV, respectively. *Solid lines* are guides to the eye. The *inset* shows an example of the temperature dependence of amplitude % of ShdH oscillations (*circles*) (after [2.4])

field-effect transistor (FET), except that there is no zero-conductance region since there is no bandgap. This tunability of conductivity is achieved by transforming the graphene by electric-field doping from a completely electron to completely hole conductor, passing through a mixed state where both electrons and holes contribute equally. This behavior holds true for monolayer graphene as well as undoped bilayer graphene; however, doped bilayer graphene has an intrinsic bandgap and will be discussed subsequently. In both the electron and hole regions, R_H decreases with increasing carrier concentration as $1/ne$ as expected, and the resistivity follows the standard $\rho = 1/ne\mu$ relation, where μ is the carrier mobility. Also significant is the minimum conductivity of graphene at the charge neutrality point (σ_{min}), which has been shown to be about $4e^2/h$. This σ_{min} is not related to the physics of the Dirac point singularity, but instead related to charge-density inhomogeneities (electron–hole puddles) induced by the substrate or charged impurities [2.166, 167]. Invariably, the position of the charge neutrality point (ρ peak) is shifted to large positive V_G, leaving the ungated graphene as a hole metal. This large shift is attributed to unintentional doping of the graphene by adsorbed species such as water. The peak position can also be shifted by intentional doping [2.166] or removal of dopants by thermal or current-induced annealing [2.13], but such charged impurities do not affect σ_{min}. The mobility and minimum conductivity also decrease as a result of defects, which can be induced in a controlled fashion to study this effect, for instance, by ion irradiation [2.168] or exposure to atomic hydrogen [2.169].

The earliest determination of carrier mobility by field-effect and magnetoresistance measurements in few-layer graphene yielded $\approx 10\,000\,\mathrm{cm}^2/(\mathrm{V\,s})$, which was independent of the absolute temperature, indicating that it was limited by scattering defects. For multilayer graphene, the mobility reached $15\,000\,\mathrm{cm}^2/(\mathrm{V\,s})$ at 300 K and $60\,000\,\mathrm{cm}^2/(\mathrm{V\,s})$ at 4 K. Substrate-induced charge puddles are significantly reduced in suspended graphene, and low-temperature mobility approaching $200\,000\,\mathrm{cm}^2/(\mathrm{V\,s})$ has been reported [2.170, 171]. In such devices, the conductivity of suspended graphene at the Dirac point is strongly temperature dependent and approaches ballistic values at liquid-helium temperatures [2.171].

Graphene flakes also exhibit pronounced Shubnikov–de Haas (ShdH) oscillations in both longitudinal resistivity ρ_{xx} and Hall resistivity ρ_{xy} (Fig. 2.22). The oscillations depend only on the perpendicular component of the magnetic field $B\cos\Theta$, where Θ is the angle between the magnetic field and the graphene. The frequency of the SsdH oscillations B_F depends linearly on V_G, indicating that the Fermi energies ε_F of holes and electrons are proportional to their concentration n. This is different from the 3-D dependence ε_F proportional

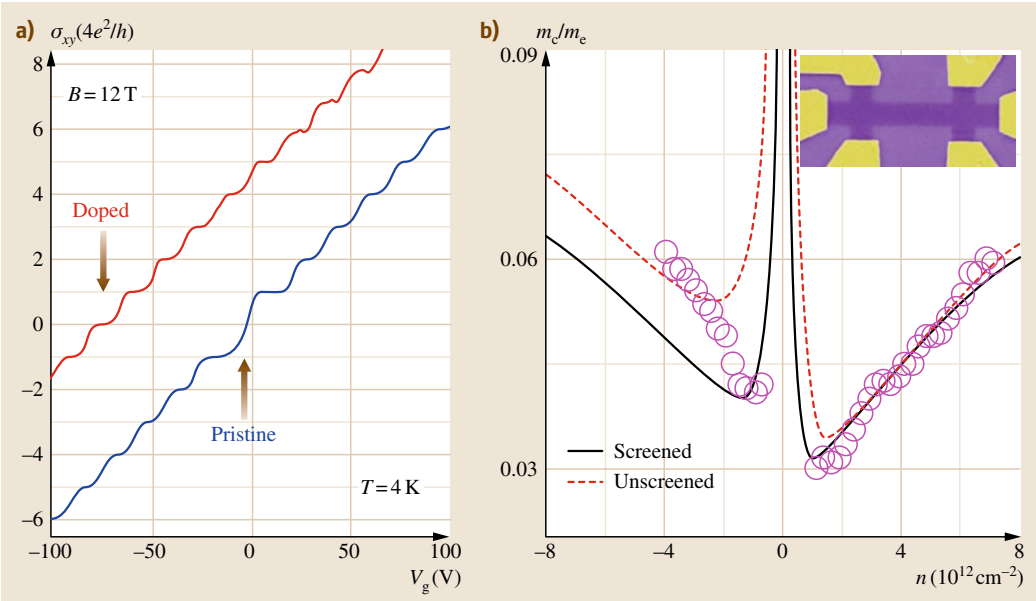


Fig. 2.23 **(a)** Measured Hall conductivity of pristine (undoped) and chemically doped bilayer graphene ($n_0 \approx 5.4\times10^{12}\,cm^{-2}$), showing a comparison of the QHE in both systems. **(b)** Cyclotron mass versus n, normalized to the free electron mass m_e. Experimental data are shown as *open circles*. The *inset* shows an electron micrograph (*in false color*) of the Hall bar device with a graphene ribbon width of 1 μm (after [2.172])

to $n^{2/3}$, proving the 2-D nature of charge carriers in graphene.

QHE has been observed in graphene even at room temperature, since the electrons suffer little scattering due to their relativistic nature and have a large cyclotron gap which exceeds the thermal energy k_BT by a factor of 10.

Under the influence of strong magnetic field, electrons in a two-dimensional system such as graphene develop strong Coulomb interactions between them, leading to correlated states of matter such as a fractional quantum Hall liquid. This collective behavior in graphene was predicted to yield the fractional quantum Hall effect (FQHE); however, due to prevalent disorder effects, observation of this remained elusive in early measurements. The FQHE was eventually reported in suspended graphene devices when a plateau at filling factor $\nu = 1/3$ was observed above a magnetic field as low as 2 T [2.173, 174]. An insulating state was also observed at magnetic fields $B > 5$ T and filling factors $\nu < 0.15$, which has been attributed to symmetry breaking of the zeroth Landau level by electron–electron interaction.

The first electron transport measurement of the tunable bandgap in bilayer graphene was conducted on micromechanically cleaved graphene on an oxidized silicon wafer (300 nm SiO_2) [2.172]. The silicon substrate was used as a back gate to modulate the carrier density n, while doping from adsorbed NH_3 on the exposed graphene surface was used to mimic a top gate and open a bandgap corresponding to a fixed electron density n_0. Under applied magnetic field, a plateau at zero Hall conductivity $\sigma_{xy} = 0$ occurs in biased bilayer graphene, as a result of the gap opened between the valence and conduction bands. Plateaus at $\sigma_{xy} = 4Ne^2/h$ occur as expected, including at $N = 0$ (Fig. 2.23a). This is the standard integer QHE that is expected for an ambipolar semiconductor with energy gap larger than the cyclotron energy. This plateau is absent in monolayer and unbiased bilayer graphene, which show an anomalous double step of $8e^2/h$ at $n = 0$, indicative of the metallic state at the charge neutrality point. A huge peak in the longitudinal resistivity ρ_{xx} at $n = 0$ was also observed, exceeding 150 kΩ at 4 K compared with 6 kΩ for the unbiased case. From Shubnikov–de Haas measurements, the cyclotron mass, m_c, in biased bilayer graphene is found to be an asymmetric function of the carrier density, which is a clear signature of a bandgap (Fig. 2.23b). Measurements with dual-gated bilayer graphene have also confirmed these results [2.175].

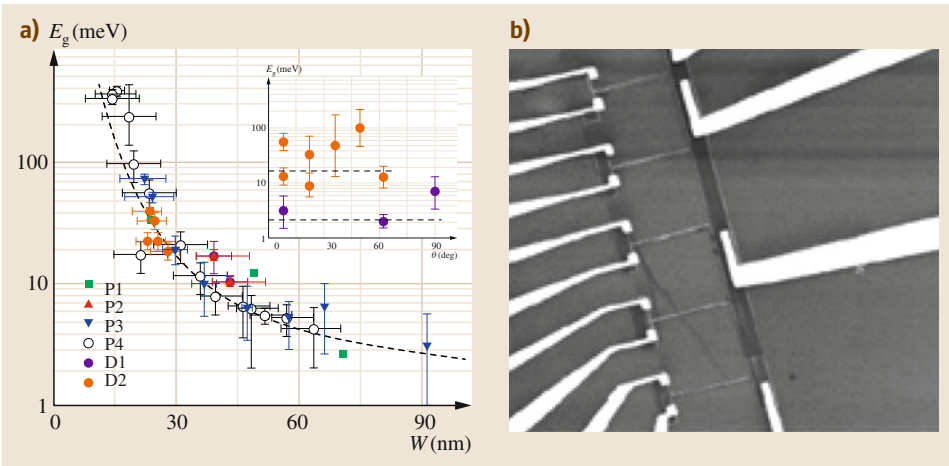


Fig. 2.24 **(a)** SEM image of a set of graphene nanoribbon devices of varying width. **(b)** Dependence of energy gap on ribbon width and orientation (*inset*). *Dashed line* shows the predicted empirical scaling (after [2.177])

Due to the linear dispersion relation in graphene, intrinsic electron scattering by acoustic phonons is independent of carrier density and only contributed 30 Ω to the room-temperature resistivity of graphene. This would yield an intrinsic mobility of 2×10^5 cm^2/(V s) at carrier density of 1×10^2/cm^2, which would be make it the highest known mobility, superior to those of InSb and semiconducting single-walled carbon nanotubes. However, a strong temperature dependence of mobility is observed in substrate-supported graphene devices, suggestive of extrinsic scattering, which limits the mobility to about 4×10^4 cm^2/(V s) [2.176].

Various approaches have been proposed to increase the performance of graphene devices, in particular to reduce impurity scattering and enhance mobility. Ultrahigh current density-induced removal of adsorbents, photoresist, or e-beam resist residue can be used to clean graphene in situ during transport measurements [2.13]. A parylene-coated SiO_2 substrate used as a dielectric stack for back-gating yields a stable charge neutrality point and low hysteresis [2.178], since the hydrophobic nature of the parylene surface suppresses moisture-related doping and charge-injection effects and yields mobilities of up to 10 000 cm^2/(V s). Similar results have been achieved by utilizing an organic polymer buffer between graphene and conventional top-gate dielectrics [2.179]. It was demonstrated that merely changing the dielectric to a high-k dielectric or media does not increase the carrier mobility beyond $\approx$ 10 000 cm^2/(V s), suggesting that Coulomb scattering is not the dominant limitation beyond this regime [2.180]. Phonon scattering or resonant scatterers with energy close to the Dirac point have been proposed as alternate mechanisms.

As discussed previously, another route to opening a bandgap in graphene is to exploit lateral confinement of charge carriers in a graphene nanoribbon, which creates an energy gap near the charge neutrality point [2.177]. Graphene nanoribbons of varying widths and different crystallographic orientations have been fabricated by lithographic patterning of monolayer exfoliated graphene (Fig. 2.24). An energy gap is observed for narrow ribbons, which scales inversely with ribbon width. Energy gaps in excess of 100 meV were observed for widths less than 20 nm, which could have potential technological relevance. It has also been shown that edge states do not contribute to the dominant electrical noise at low frequencies for nanoribbons as narrow as 20 nm [2.181]. However, the lack of a well-defined crystallographic structure of lithographically etched edges means that the effect of orientation is not observed in the bandgap produced in such nanoribbons.

It is also possible to fabricate quantum dot (QD) devices entirely out of graphene using a similar lithographic procedure [2.182–184]. Such a device consists of a graphene island connected to the source and drain via two narrow graphene constrictions and three fully tunable graphene lateral gates (Fig. 2.25). Larger QDs ($>$ 100 nm) show conventional single-electron transistor characteristics, with periodic Coulomb blockade peaks. For smaller QDs, the peaks become strongly nonperiodic, indicating a strong contribution from quantum confinement. The narrow constrictions remain conductive and show a confinement gap of $\approx$ 0.5 eV. This can be extended to a double QD system (Fig. 2.25) where the coupling of the dots to the leads and between the dots is tuned by graphene in-plane gates [2.185]. This structure has been proposed for the realization of

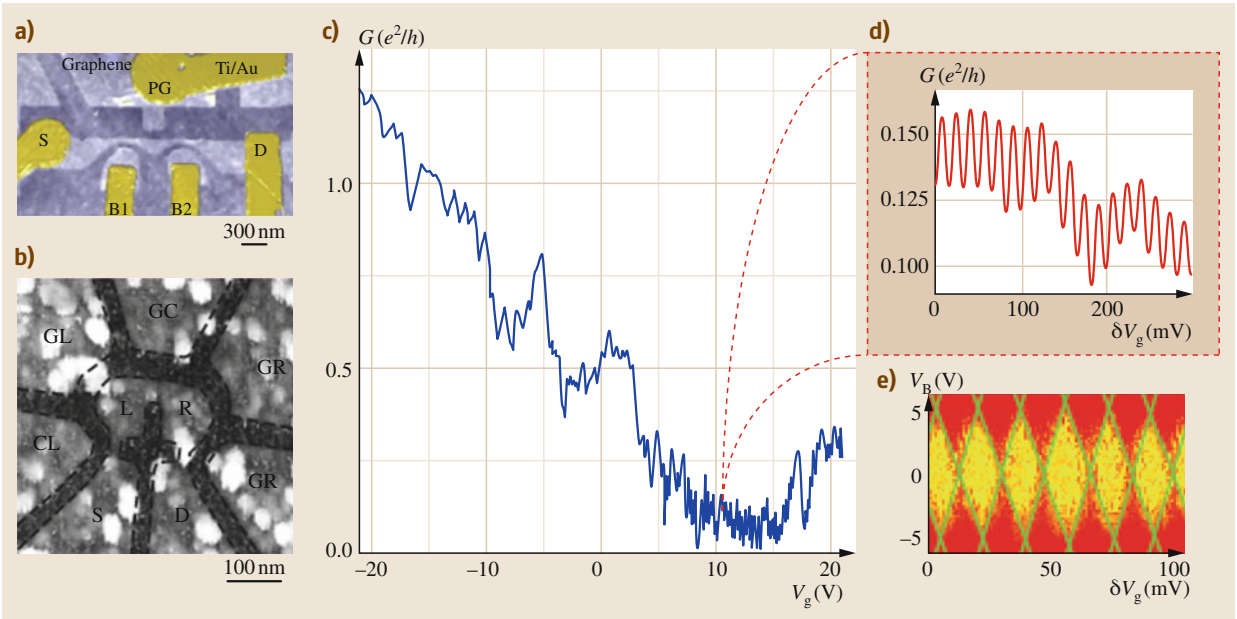


Fig. 2.25 **(a)** SEM of an all-graphene single quantum dot device (after [2.184]). **(b)** SEM of an all-graphene double quantum dot device (after [2.185]). **(c)** Conductance of a graphene single QD device over a wide range of gate voltages at $T = 4\,\mathrm{K}$. **(d)** Zoom in to low-conductance region showing Coulomb blockade oscillations (after [2.182]). **(e)** Coulomb diamonds showing differential conductance as a function of gate voltage and drains–source bias

spin qubits from graphene QDs [2.186]. It has been shown that, in an array of many qubits, it is possible to couple any two of them via Heisenberg exchange while the others are decoupled by detuning. This unique feature is a direct consequence of the quasirelativistic nature of carriers in graphene.

One of the important considerations in electronic device performance is the signal-to-noise ratio, where usually the low-frequency $1/f$ noise dominates. In monolayer graphene, the $1/f$ noise follows Hooge's empirical relation with a noise level comparable to carbon nanotube and bulk semiconductor devices. However, in bilayer graphene, the $1/f$ noise is strongly suppressed and obeys a unique dependence on carrier density, due to effective screening of carrier scattering by external impurities [2.134]. In monolayer graphene, the noise amplitude is minimum at the Dirac point and increases with increasing carrier density. However, in bilayer graphene, the noise amplitude achieves a maximum at the Dirac point and decreases with increasing carrier density. In both cases, the noise is independent of carrier type.

In an effort to realize commercial viability of graphene electronics, reduced graphene oxide (RGO) has been explored as an alternative to pristine monolayer graphene. However, measurements in individual monolayer RGO flakes have yielded conductivities ranging between 0.05 and 2 S/cm and field-effect mobilities of $2–200\,\mathrm{cm^2/(V\,s)}$ at room temperature. Conductivity decreases by up to three orders of magnitude when measured down to 4 K, following a $T^{-1/3}$ dependence, suggesting variable-range hopping conduction between regions of highly reduced (nearly pristine) graphene islands separated by defective or poorly reduced regions.

Spintronics

When graphene devices are fabricated with ferromagnetic electrodes, such as the soft magnetic NiFe or Co, it is possible to inject spin-polarized current into the graphene. A thin Al_2O_3 or MgO tunnel barrier is used at the ferromagnet–graphene interface. High-quality graphene enjoys ballistic transport with spin relaxation lengths between 1.5 and 2 µm even at room temperature, which is only weakly dependent on charge density [2.187]. The switching fields of the electrodes can be controlled by in-plane shape anisotropy. Graphene spin valves have been constructed using ei-

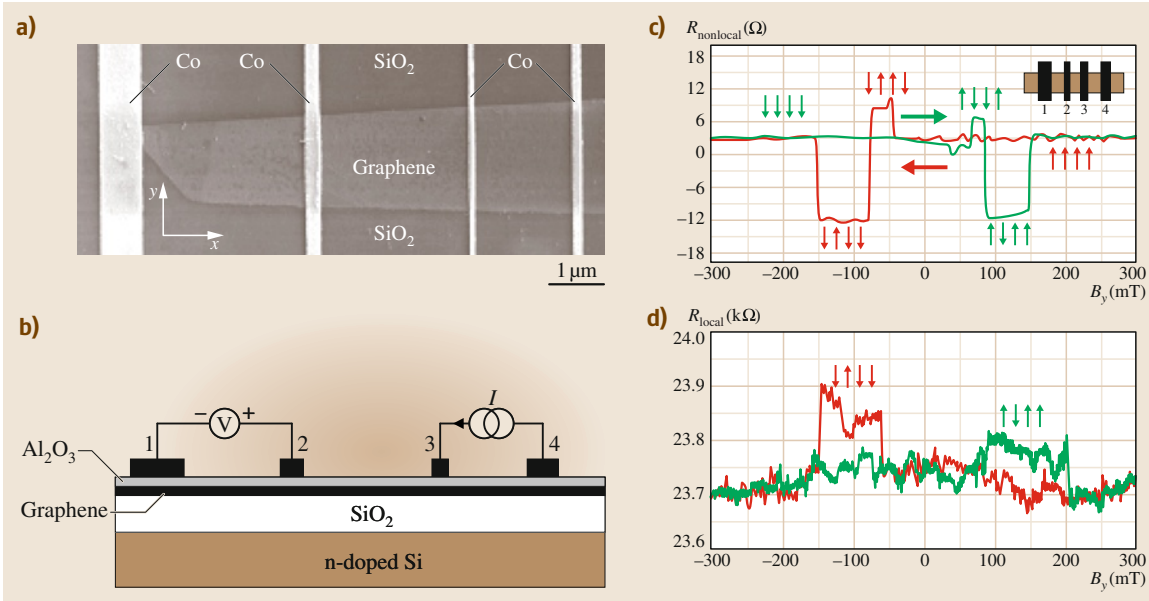


Fig. 2.26a–d Spin transport in a four-terminal spin valve device. **(a)** Scanning electron micrograph of a four-terminal single-layer graphene spin valve. **(b)** The nonlocal spin valve geometry. A current I is injected from electrode 3 through the Al_2O_3 barrier into graphene and is extracted at contact 4. The voltage difference is measured between contacts 2 and 1. **(c)** Nonlocal spin valve signal for device 1 at 4.2 K. The sweep directions of the magnetic field are indicated (*red* or *green arrows*). **(d)** A two-terminal local spin valve signal (measured between contacts 2 and 3) of about 60 V is measured at 4.2 K (after [2.187])

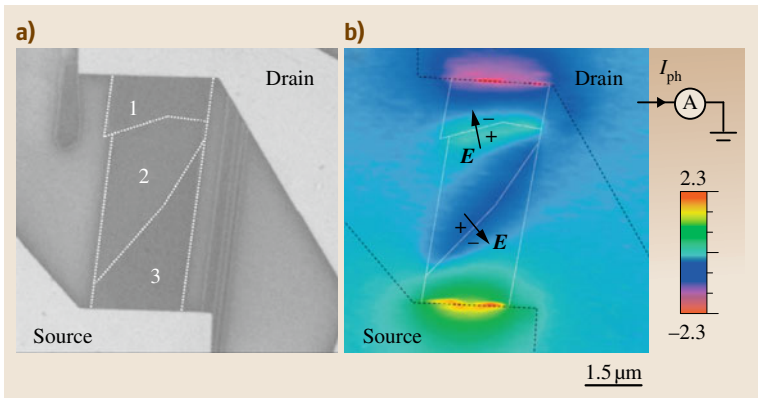


Fig. 2.27 **(a)** SEM image of the device. Region 2 consists of single-layer graphene, and regions 1 and 3 are multilayer. **(b)** Photocurrent image recorded in the p-type conduction regime. *Black dashed lines* indicate the edges of the source and drain electrodes. The *white dotted lines* mark the interfaces between single- and multi-layer graphene (after [2.190])

ther a local [2.188] or nonlocal [2.187, 189] geometry, and clear bipolar spin signal has been observed which is indicative of the relative magnetization directions of the electrodes (Fig. 2.26), and magnetoresistance of up to 12% has been reported in local geometry. In addition, Henle-type spin precession has also been reported, and a sign reversal in the spin signal can be achieved by applying an orthogonal switching magnetic field. The nonlocal spin-valve signal changes magnitude and sign with back-gate voltage, and is observed up to $T = 300$ K [2.189].

An alternative configuration, comprising a graphene monolayer sandwiched between two ferromagnetic layers, involves spin-polarized conduction perpendicular to the plane of the graphene in a conduction perpendicular to plane (CPP) geometry [2.191]. Graphene

was sufficient to reduce the exchange coupling between the magnetic electrodes. in a NiFe/Au/graphene/NiFe stack, the graphene channels the spin current perpendicular to the plane and thus produces an enhanced magnetoresistance effect compared with a simple stack without the graphene.

2.3.7 Photocurrent Microscopy

The channel potential distribution in a graphene field-effect transistor can be imaged by scanning photocurrent imaging (Fig. 2.27) [2.190, 192]. When graphene is contacted to a metal, it is doped by the metal due to the work-function mismatch. The potential step between the graphene that is p-doped by a Ti-Pd-Au contact and bulk graphene with no gate bias was estimated to be 45 meV. When light is shone on such potential steps which occur close to each contact, excited electron–hole pairs can be split by the potential gradient, leading to a photocurrent. At negative gate bias, before the flat-band condition, the graphene forms a p–p^+–p channel. In the flat-band condition, the influence of the metal electrodes was measured to extend up to 450 nm into the graphene channel. For positive gate biases beyond the Dirac point, the graphene forms a p–n–p channel, and when light is focused on the p–n junction, an external responsivity of 0.001 A/W was measured. Scanning photocurrent microscopy has also revealed potential gradients occurring at monolayer–multilayer graphene interfaces [2.190].

2.4 Applications

While the field of experimental graphene research is still in its early years, graphene's potential for applications is already evident. Graphene is currently under evaluation for a wide range of applications, which will benefit from its unique combination of excellent mechanical, electronic, optical, and chemical properties. Commercial viability of most applications is severely limited by the limited options available for large-scale production of graphene. As a case study, graphene was proposed as an excellent transparent conductor with potential for replacing indium tin oxide (ITO), but it was not possible to pursue this application commercially until a roll-to-roll fabrication process for graphene was recently developed. Other applications, particularly in electronic devices, are critically dependent on breakthroughs in wafer-scale, complementary metal–oxide–semiconductor (CMOS)-compatible integration of individual graphene electronic devices.

2.4.1 Structural and Electrical Composites

The remarkable mechanical properties of graphene coupled with its high electrical and thermal conductivity suggest that it would be ideal for use in composite materials for structural as well as electronic applications. This potential has been enhanced by recent advances in solution-phase dispersion of graphene oxide (GO) and graphene, even down to highly monolayer-enriched graphene solutions. Graphene oxide-polystyrene composites show a low percolation threshold of ≈ 0.1 vol. % for room-temperature electrical conductivity and ≈ 0.1 S/m at 1 vol. %, which is sufficient for many electrical applications [2.54]. Such composites show ambipolar field-effect behavior with electron and hole mobilities of 0.2 and 0.7 $cm^2/(V\,s)$, respectively [2.193]. GO-silica composites have been fabricated by spin-coating GO-impregnated silica sols to yield transparent conducting composite films [2.194]. Layered GO-polymer composites have been fabricated by layer-by-layer (LBL) assembly, taking advantage of electrostatic interactions between anionic GO sheets and cationic polymer [2.43]. Graphene oxide composites with poly(3-hexylthiophene) (P3HT) and poly(3-octylthiophene) (P3OT) have been demonstrated as a superior active layer in organic photovoltaics [2.195], while TiO_2-graphene composite has been demonstrated as a high-performance photocatalyst [2.196]. Composites of functionalized graphene derived from GO with polymers such as PMMA, poly(acrylonitrile), and poly(acrylic acid) show the best performance in terms of Young's modulus, glass-transition temperature, ultimate strength, and thermal degradation [2.197]. Composites of graphene with metal nanoparticles (Au, Pt, and Pd) have also been produced, and the graphene-Pt composite has been demonstrated as a catalyst in direct methanol fuel cells [2.198].

2.4.2 Transparent Conducting Films

Thin films of graphene have been deposited from solution-phase graphene with controllable thickness from a single monolayer to several layers over large areas (Fig. 2.28) [2.199]. The thickness of the film de-

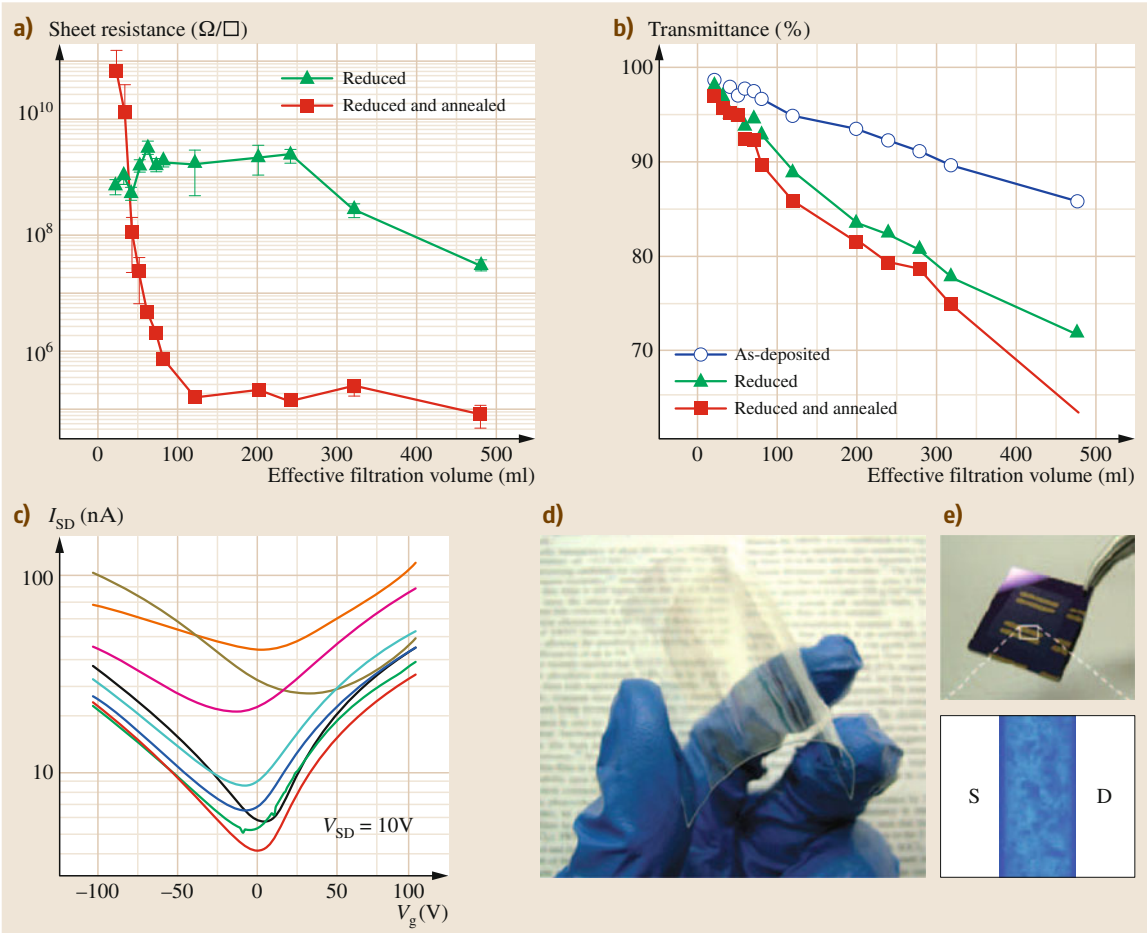


Fig. 2.28a–e Electrical and optical properties of reduced GO thin films. Sheet resistance **(a)** and transmittance **(b)** at $\lambda = 550$ nm as a function of filtration volume for reduced GO thin films. *Plots* are shown for thin films with different reduction steps. The sheet resistance for as-deposited GO thin films is out of scale. **(c)** Source–drain current as a function of gate voltage for 20 ml films measured at different temperatures in vacuum. **(d)** Photograph of GO thin films on filtration on a plastic substrate. **(e)** Optical micrograph of the actual device. The channel consists of several reduced GO sheets percolating across the source (S) and drain (D) electrodes. The channel length is 21 μm (after [2.199])

termines its conductivity, transparency, and mechanical integrity, making it suitable for various applications. Electronic properties can be tuned from graphene-like ambipolar field-effect behavior for the thinnest films to graphite-like semimetal conductivity for thicker films. Flow-based deposition, vacuum filtration, and layer-by-layer assembly are among the techniques used to deposit graphene thin films from solution. However, the predominant part of solution-phase research has involved reduced [2.200] or functionalized derivatives of graphene oxide, rather than pristine graphene.

Graphene conducting thin films are targeted at replacing indium tin oxide (ITO); however, it has so far been unable to match ITO's combination of 100 Ω per square sheet resistance at 90% transparency. Solution-processed reduced GO can be deposited as thin films of controllable thickness by Langmuir–Blodgett LBL deposition [2.201], and can achieve sheet resistance of 1 kΩ/□ per square at 90% transparency. Such films have been demonstrated as transparent conductive anodes for inorganic, organic, and dye-sensitized photovoltaic cells, but the short-circuit current and fill factor are still lower than those of control devices us-

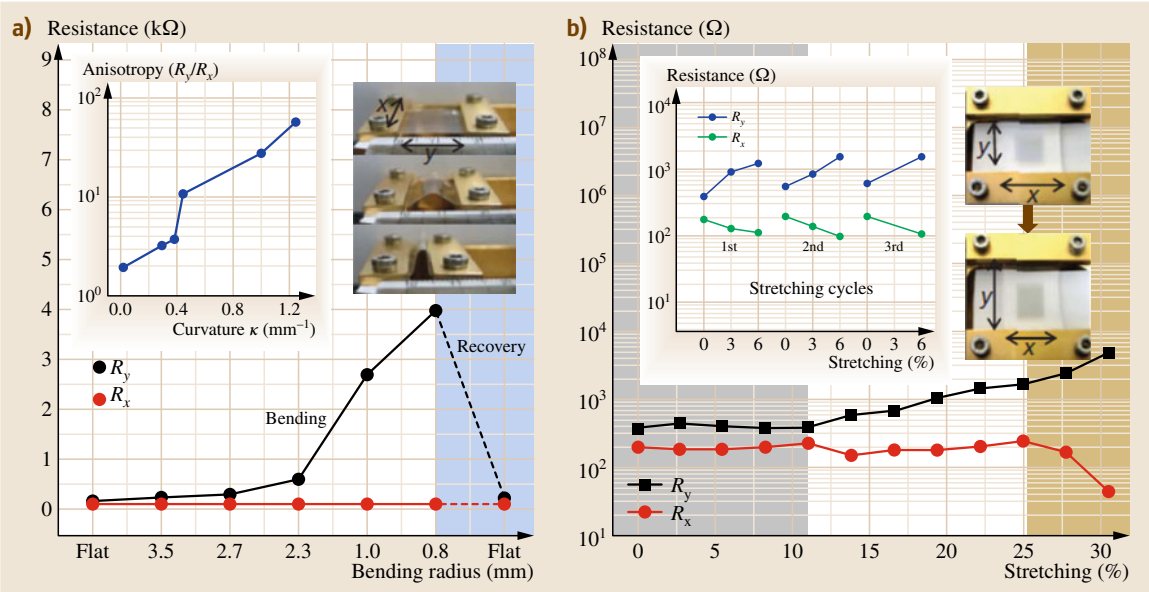


Fig. 2.29 **(a)** Variation in resistance of a graphene film transferred to a ≈ 0.3 mm-thick polydimethylsiloxane (PDMS)/polyethylene terephthalate (PET) substrate for different bending radii. The *left inset* shows the anisotropy in four-probe resistance, measured as the ratio R_y/R_x of the resistances parallel and perpendicular to the bending direction y. The *right inset* shows the bending process. **(b)** Resistance of a graphene film transferred to a PDMS substrate isotropically stretched by ≈ 12%. The *left inset* shows the case in which the graphene film is transferred to an unstretched PDMS substrate. The *right inset* shows the movement of holding stages and the consequent change in shape of the graphene film (after [2.204])

ing ITO [2.202,203]. However, they do have advantages such as tunable wettability, high chemical and thermal stability, and flexibility.

Pristine graphene films grown by chemical vapor deposition (CVD) on Ni or Cu substrates and transferred by a wet process can achieve ≈ 280 Ω per square at ≈ 80% transparency, but still fall short of ITO's benchmark. Still, the films show high electron mobility of 3700 cm^2/(V s) and exhibit the half-integer quantum Hall effect typical of high-quality graphene, which cannot be accomplished with reduced or functionalized GO (Fig. 2.29). Most importantly, the graphene films can recover its original resistance after being stretched by up to 6% and the resistance shows little variation up to bending radius of 2.3 mm, corresponding to tensile strain of 6.5%. This gives graphene films a significant advantage over ITO for applications in flexible electronics [2.204, 205]. A roll-to-roll dry transfer process has been developed for up to 30 inch monolayer (ML) graphene grown on Cu, yielding films with 97.4% transparency and 125 Ω per square sheet resistance (Fig. 2.30). The conductivity of graphene can be further improved by doping, for example, p-doping with HNO_3, and resistance as low as 30 Ω per square can be achieved at 90% transparency, making graphene a strong potential candidate for ITO replacement, particularly in flexible electronics [2.28].

Solution-processed graphene as well as CVD graphene have been demonstrated as electrodes for organic light-emitting diodes [2.206]. This, combined with graphene-based field-effect transistors and graphene transparent conducting electrodes, allows for fabrication of fully flexible and transparent touchscreen displays.

Graphene can be used as an electrode for polymer-dispersed liquid-crystal (PDLC) devices, for example, as a *smart window*. Light passing through the liquid crystal/polymer is strongly scattered, resulting in a milky film. If the liquid crystal's refractive index is close to that of the polymer, an electric field in the transverse direction causes the liquid crystals to align in the direction of light propagation, resulting in a transparent state [2.207].

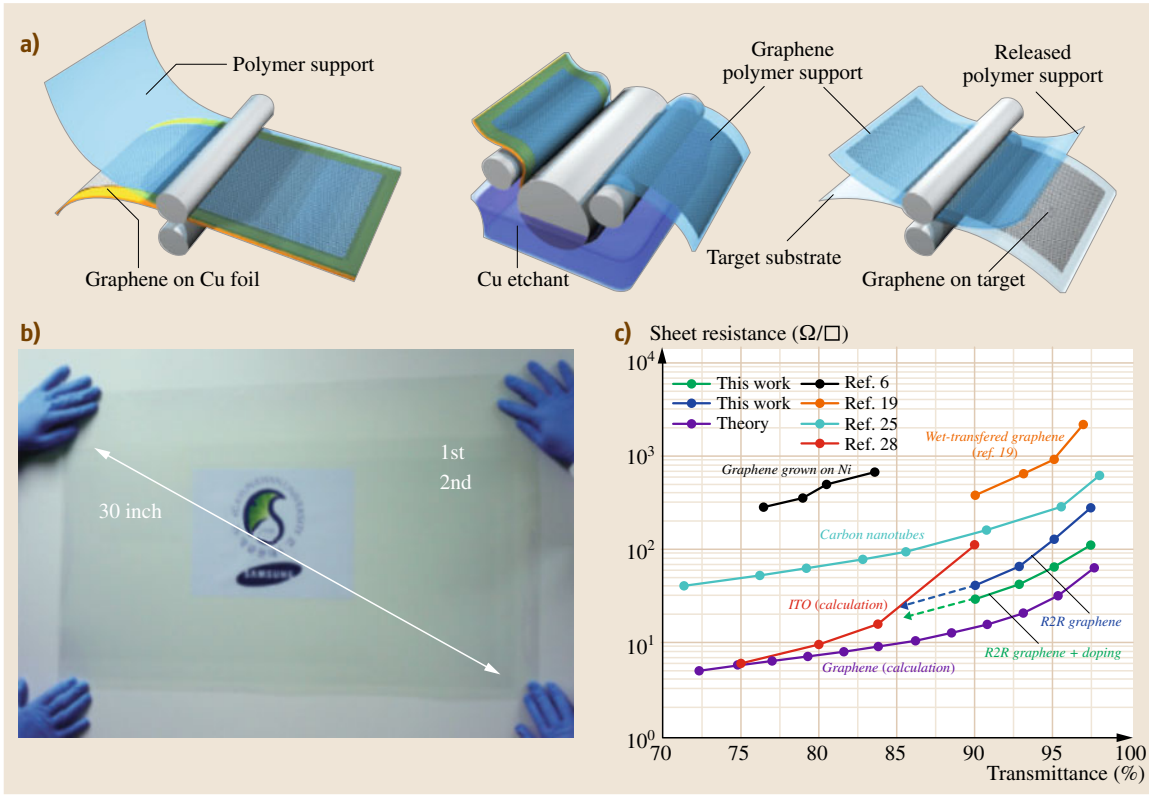


Fig. 2.30 **(a)** Schematic of roll-based production of graphene films grown on a copper foil. The process includes adhesion of polymer supports, copper etching (rinsing), and dry transfer printing onto a target substrate. **(b)** A transparent ultralarge-area graphene film transferred onto a 35 inch PET sheet. **(c)** Comparison of sheet resistance from this research and transmittance plots taken from other publications. The *dashed arrows* indicate the expected sheet resistances at lower transmittance (after [2.28])

2.4.3 Sensors

The ultimate detection limit of any chemical sensor is the ability to detect individual molecules of a desired species (Fig. 2.31). The exceptionally low-noise electronic characteristics of graphene allow for such single-molecule sensitivity [2.208]. Adsorbed gas molecules change the local carrier concentration one electron at a time, which can be detected as stepwise changes in device resistance.

Depending on the nature of the adsorbed species, the graphene can be either electron doped (NH_3) or hole doped (H_2O, NO_2). As there is no gap in the graphene density of states, even a small mismatch in chemical potential to the adsorbate is sufficient to provide an active donor or acceptor level, whereas in semiconductors, the chemical potential mismatch has to exceed half the gap energy to achieve doping [2.209]. Therefore, graphene sensors are expected to be more sensitive than conventional semiconductor sensors.

Reduced graphene oxide-based devices have shown parts-per-billion sensitivity to chemical warfare agents and explosives [2.210], and parts-per-million sensitivity to gasses such as NO_2 and NH_3 [2.211]. Reduced GO-based sensors have also been demonstrated in surface acoustic wave configuration, with parts-per-million sensitivity to H_2 and CO [2.212]. Electrolyte-gated graphene devices have been demonstrated as pH and biomolecule sensors with picomolar sensitivity [2.213].

Suspended graphene resonators can be electrically or optically actuated and detected, with fundamental mode frequencies in the MHz range [2.214]. Molecular structural mechanics modeling has shown that the principle frequency vibrations of monolayer graphene are sensitive to added mass of $\approx 10^{-6}$ fg [2.215]. Mass sensitivity of ≈ 2 zg has been experimentally demonstrated

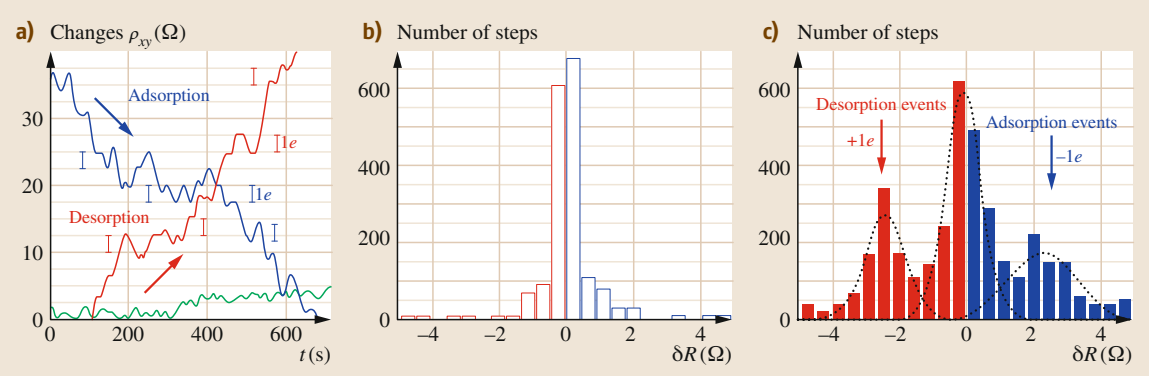


Fig. 2.31a–c Single-molecule detection. **(a)** Examples of changes in Hall resistivity observed near the neutrality point ($|n| < 10^{11}$ cm^{-2}) during adsorption of strongly diluted NO_2 (*blue curve*) and its desorption in vacuum at 50 °C (*red curve*). The *green curve* is a reference – the same device thoroughly annealed and then exposed to pure He. The curves are for a three-layer device in $B = 10$ T. The *grid lines* correspond to changes in ρ_{xy} caused by adding one electron charge e ($\delta R \approx 2.5\,\Omega$), as calibrated in independent measurements by varying V_g. **(b–c)** Statistical distribution of step heights δR in this device without its exposure to NO_2 (in helium) **(b)** and during a slow desorption of NO_2 **(c)**. For this analysis, all changes in ρ_{xy} larger than 0.5 Ω and quicker than 10 s (lock-in time constant was 1 s, making the response time ≈ 6 s) were recorded as individual steps (after [2.208])

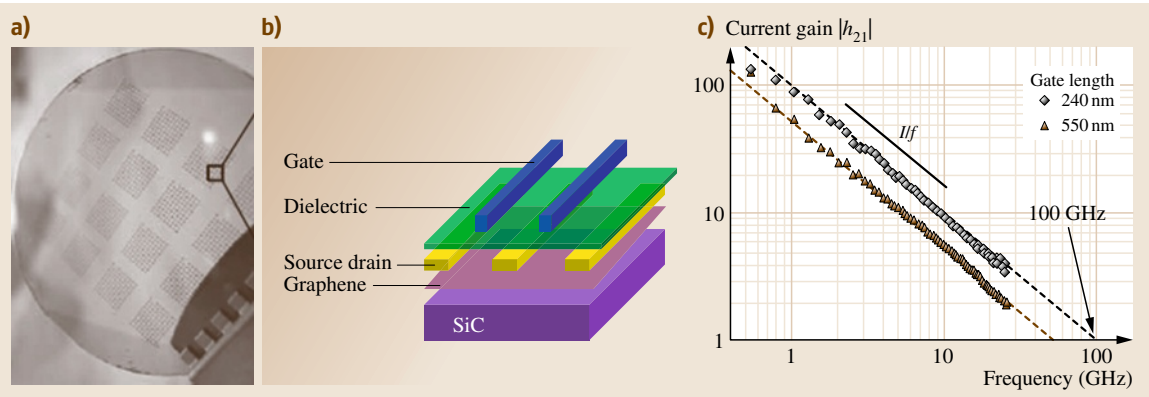


Fig. 2.32 **(a)** Image of devices fabricated on a 2 inch graphene wafer and **(b)** schematic cross-sectional view of a top-gated graphene FET. **(c)** Measured small-signal current gain $|h_{21}|$ as a function of frequency f for a 240 nm gate (◇) and a 550 gate (△) graphene FET at $V_D = 2.5$ V. Cutoff frequencies, f_T, were 53 and 100 GHz for the 550 and 240 nm devices, respectively (after [2.216])

using graphene resonators with a high quality factor of 14 000 at low temperature [2.102].

2.4.4 Electronic Applications

Charge carriers in graphene have very high mobility, which is not significantly affected by doping, leading to ballistic transport on a submicron scale even at room temperature. This is a much sought-after characteristic for the next generation of electronic materials, since it would allow for very fast switching times, perhaps less than 10^{-13} s. The low on–off ratio (< 100) in gapless graphene is not a fundamental limitation for high-frequency operation. Transistors fabricated on epitaxial graphene on SiC have achieved a cutoff frequency of 100 GHz (Fig. 2.32) [2.216], and those fabricated on conventional Si/SiO_2 substrates have reached a cutoff frequency of 26 GHz [2.217].

Large-scale integration of graphene devices can be achieved either by conventional top-down fabrication

in the case of epitaxial graphene on SiC [2.218], or CVD graphene grown on metallic substrates and transferred to dielectric substrates. In the case of solution-phase graphene, bottom-up approaches such as dielectrophoretic trapping can achieve similar ultralarge-scale integration densities [2.219].

2.4.5 Photonics and Optoelectronics

Graphene enjoys broadband absorption of light, and therefore does not suffer from the *long-wavelength limit* of semiconductors, which become transparent at incident energies smaller than their bandgap. As a result, graphene-based photodetectors have been demonstrated to work over a much broader wavelength range. The photoresponse does not degrade for optical intensity modulations up to 40 GHz, with ultrafast response due to the high carrier mobility in graphene [2.220]. Graphene can also be used as the nonlinear saturable absorber in mode-locking for ultrafast laser systems, which turns a continuous wave into a train of ultrafast optical pulses [2.221, 222]. Graphene dispersions have been used as wideband optical limiters covering the visible and infrared regions of the spectrum [2.223].

2.5 Conclusions and Outlook

The field of graphene research is still very much in its early stages, with a majority of researchers devoted to exploring the fundamental properties of graphene. Not only is graphene a new material; it is also quite literally a new dimension of possibilities. A lot of mystery still surrounds this exciting new material, and often one finds that theoretical predictions are well ahead of experimental data in an emerging field such as this. Exciting physics that only occurs in two dimensions and that was previously inaccessible in experiments is now being sought, and new results are published regularly. Now that graphene has laid to rest the question of whether two-dimensional materials can exist in a stable self-supported form, researchers have started the hunt for other such 2-D materials. Boron nitride is one of the candidates to attract significant attention, particularly for its potential in combination with graphene.

Only recently, applications of the extraordinary properties of graphene have been experimentally demonstrated, and a still greater number of potential applications are still on the drawing board. In fact, only recently has bulk production of graphene in sheet or solution form been achieved, but the economies of scale are still unfavorable for mass application. The commercial prospects of graphene remain unexplored, but it is hoped that, in the near future, the substantial research and investment into graphene will be vindicated. However, for a scientist motivated by the quest for new knowledge and understanding, graphene continues to reap rich rewards, as evidenced by the numerous results included here that were only published for the very first time during the duration of writing this chapter.

Lastly, it should be noted that graphene is a rapidly evolving field, and since the writing of this chapter, a large number of papers have been published covering every aspect discussed here. In many cases, these subsequent publications have added new knowledge about graphene, or provided better or even a different understanding of known phenomena. Consequently, the information compiled in this chapter should serve as a starting point for the reader to further investigate the properties, characterization and applications of graphene by referring to the latest publications.

References

2.1 H.W. Kroto, J.R. Heath, S.C. Obrien, R.F. Curl, R.E. Smalley: C-60 – buckminsterfullerene, Nature **318**, 162–163 (1985)

2.2 S. Iijima: Helical microtubules of graphitic carbon, Nature **354**, 56–58 (1991)

2.3 S. Mouras, A. Hamm, D. Djurado, J.-C. Cousseins: *Synthesis of First Stage Graphite Intercalation Compounds with Fluorides* (Paris, Gauthier-Villars 1987)

2.4 K.S. Novoselov, A.K. Geim, S.V. Morozov, D. Jiang, Y. Zhang, S.V. Dubonos, I.V. Grigorieva, A.A. Firsov: Electric field effect in atomically thin carbon films, Science **306**, 666–669 (2004)

2.5 R.V. Noorden: The trials of new carbon, Nature **469**, 14–16 (2011)

2.6 H. Fernandez-Moran: Single-crystals of graphite and of mica as specimen supports for electron microscopy, J. Appl. Phys. **31**, 1840 (1960)

2.7 P. Blake, E.W. Hill, A.H.C. Neto, K.S. Novoselov, D. Jiang, R. Yang, T.J. Booth, A.K. Geim: Making graphene visible, Appl. Phys. Lett. **91**, 063124–1–063124–3 (2007)

2.8 K.S. Novoselov, D. Jiang, F. Schedin, T.J. Booth, V.V. Khotkevich, S.V. Morozov, A.K. Geim: Two-dimensional atomic crystals, Proc. Natl. Acad. Sci. USA **102**, 10451–10453 (2005)

2.9 J.C. Meyer, A.K. Geim, M.I. Katsnelson, K.S. Novoselov, T.J. Booth, S. Roth: The structure of suspended graphene sheets, Nature **446**, 60–63 (2007)

2.10 J.Y. Huang, F. Ding, B.I. Yakobson, P. Lu, L. Qi, J. Li: In situ observation of graphene sublimation and multilayer edge reconstructions, Proc. Natl. Acad. Sci. **106**, 10103–10108 (2009)

2.11 M. Ishigami, J.H. Chen, W.G. Cullen, M.S. Fuhrer, E.D. Williams: Atomic structure of graphene on SiO_2, Nano Lett. **7**, 1643–1648 (2007)

2.12 E. Stolyarova, K.T. Rim, S. Ryu, J. Maultzsch, P. Kim, L.E. Brus, T.F. Heinz, M.S. Hybertsen, G.W. Flynn: High-resolution scanning tunneling microscopy imaging of mesoscopic graphene sheets on an insulating surface, Proc. Natl. Acad. Sci. **104**, 9209–9212 (2007)

2.13 J. Moser, A. Barreiro, A. Bachtold: Current-induced cleaning of graphene, Appl. Phys. Lett. **91**, 163513 (2007)

2.14 A.N. Sidorov, M.M. Yazdanpanah, R. Jalilian, P.J. Ouseph, R.W. Cohn, G.U. Sumanasekera: Electrostatic deposition of graphene, Nanotechnology **18**, 135301 (2007)

2.15 L.-H. Liu, M. Yan: Simple Method for the covalent immobilization of graphene, Nano Lett. **9**, 3375–3378 (2009)

2.16 L. Song, L.J. Ci, W. Gao, P.M. Ajayan: Transfer printing of graphene using gold film, ACS Nano **3**, 1353–1356 (2009)

2.17 J.W. May: Platinum surface LEED rings, Surf. Sci. **17**, 267–270 (1969)

2.18 B. Lang: A LEED study of the deposition of carbon on platinum crystal surfaces, Surf. Sci. **53**, 317–329 (1975)

2.19 W.J. Arnoult, R.B. Mclellan: The solubility of carbon in rhodium ruthenium, iridium and rhenium, Scr. Metall. **6**, 1013–1018 (1972)

2.20 T.A. Land, T. Michely, R.J. Behm, J.C. Hemminger, G. Comsa: STM investigation of single layer graphite structures produced on Pt(111) by hydrocarbon decomposition, Surf. Sci. **264**, 261–270 (1992)

2.21 H. Ueta, M. Saida, C. Nakai, Y. Yamada, M. Sasaki, S. Yamamoto: Highly oriented monolayer graphite formation on Pt(111) by a supersonic methane beam, Surf. Sci. **560**, 183–190 (2004)

2.22 Y. Gamo, A. Nagashima, M. Wakabayashi, M. Terai, C. Oshima: Atomic structure of monolayer graphite formed on Ni(111), Surf. Sci. **374**, 61–64 (1997)

2.23 S. Marchini, S. Gunther, J. Wintterlin: Scanning tunneling microscopy of graphene on Ru(0001), Phys. Rev. B **76**, 075429 (2007)

2.24 I. Makarenko, A. Titkov, Z. Waqar, P. Dumas, E. Rut'kov, N. Gall': Structural properties of a monolayer graphite film on the (111)Ir surface, Phys. Solid State **49**, 371–376 (2007)

2.25 A. Reina, X. Jia, J. Ho, D. Nezich, H. Son, V. Bulovic, M.S. Dresselhaus, J. Kong: Large area, few-layer graphene films on arbitrary substrates by chemical vapor deposition, Nano Lett. **9**, 30–35 (2009)

2.26 X. Li, W. Cai, J. An, S. Kim, J. Nah, D. Yang, R. Piner, A. Velamakanni, I. Jung, E. Tutuc, S.K. Banerjee, L. Colombo, R.S. Ruoff: Large-area synthesis of high-quality and uniform graphene films on copper foils, Science **324**, 1312–1314 (2009)

2.27 A. Ismach, C. Druzgalski, S. Penwell, A. Schwartzberg, M. Zheng, A. Javey, J. Bokor, Y. Zhang: Direct chemical vapor deposition of graphene on dielectric surfaces, Nano Lett. **10**, 1542–1548 (2010)

2.28 S. Bae, H. Kim, Y. Lee, X. Xu, J.-S. Park, Y. Zheng, J. Balakrishnan, T. Lei, H. Ri Kim, Y.I. Song, Y.-J. Kim, K.S. Kim, B. Ozyilmaz, J.-H. Ahn, B.H. Hong, S. Iijima: Roll-to-roll production of 30-inch graphene films for transparent electrodes, Nat. Nanotechnol. **5**, 574–578 (2010)

2.29 C. Virojanadara, M. Syväjarvi, R. Yakimova, L.I. Johansson, A.A. Zakharov, T. Balasubramanian: Homogeneous large-area graphene layer growth on 6H-SiC(0001), Phys. Rev. B **78**, 245403 (2008)

2.30 E. Rollings, G.H. Gweon, S.Y. Zhou, B.S. Mun, J.L. Mcchesney, B.S. Hussain, A.V. Fedorov, P.N. First, W.A. de Heer, A. Lanzara: Synthesis and characterization of atomically thin graphite films on a silicon carbide substrate, J. Phys. Chem. Solids **67**, 2172–2177 (2006)

2.31 J. Penuelas, A. Ouerghi, D. Lucot, C. David, J. Gierak, H. Estrade-Szwarckopf, C. Andreazza-Vignolle: Surface morphology and characterization of thin graphene films on SiC vicinal substrate, Phys. Rev. B **79**, 033408 (2009)

2.32 J. Hass, R. Feng, T. Li, X. Li, Z. Zong, W.A. de Heer, P.N. First, E.H. Conrad, C.A. Jeffrey, C. Berger: Highly ordered graphene for two dimensional electronics, Appl. Phys. Lett. **89**, 143106–1–143106–3 (2006)

2.33 K.V. Emtsev, A. Bostwick, K. Horn, J. Jobst, G.L. Kellogg, L. Ley, J.L. McChesney, T. Ohta, S.A. Reshanov, J. Rohrl, E. Rotenberg, A.K. Schmid, D. Waldmann, H.B. Weber, T. Seyller: Towards wafer-size graphene layers by atmospheric pressure graphitization of silicon carbide, Nat. Mater. **8**, 203–207 (2009)

2.34 V.Y. Aristov, G. Urbanik, K. Kummer, D.V. Vyalikh, O.V. Molodtsova, A.B. Preobrajenski, A.A. Zakharov, C. Hess, T. Hänke, B. Büchner, I. Vobornik, J. Fujii, G. Panaccione, Y.A. Ossipyan, M. Knupfer: Graphene synthesis on cubic SiC/Si wafers. Perspectives for mass production of graphene-based electronic devices, Nano Lett. **10**, 992–995 (2010)

2.35 M. Sprinkle, M. Ruan, X. Wu, Y. Hu, M. Rubio-Roy, J. Hankinson, C. Berger, W.A. de Heer: Scalable templated growth of graphene nanoribbons on SiC, Nat. Nanotechnol. **5**, 727 (2010)

2.36 T. Aizawa, R. Souda, S. Otani, Y. Ishizawa, C. Oshima: Bond softening in monolayer graphite formed on transition-metal carbide surfaces, Phys. Rev. B **42**, 11469 (1990)

2.37 B.S. Itchkawitz, P.F. Lyman, G.W. Ownby, D.M. Zehner: Monolayer graphite on TaC(111): Electronic band structure, Surf. Sci. **318**, 395–402 (1994)

2.38 T. Aizawa, R. Souda, S. Otani, Y. Ishizawa, C. Oshima: Anomalous bond of monolayer graphite on transition-metal carbide surfaces, Phys. Rev. Lett. **64**, 768 (1990)

2.39 T. Tanaka, A. Tajima, R. Moriizumi, M. Hosoda, R. Ohno, E. Rokuta, C. Oshima, S. Otani: Carbon nano-ribbons and their edge phonons, Solid State Commun. **123**, 33–36 (2002)

2.40 M.S. Dresselhaus, G. Dresselhaus: Intercalation compounds of graphite, Adv. Phys. **30**, 139–326 (1981)

2.41 T. Nakajima, Y. Matsuo: Formation process and structure of graphite oxide, Carbon **32**, 469–475 (1994)

2.42 W.S. Hummers, R.E. Offeman: Preparation of graphitic oxide, J. Am. Chem. Soc. **80**, 1339 (1958)

2.43 N.I. Kovtyukhova, P.J. Ollivier, B.R. Martin, T.E. Mallouk, S.A. Chizhik, E.V. Buzaneva, A.D. Gorchinskiy: Layer-by-layer assembly of ultrathin composite films from micron-sized graphite oxide sheets and polycations, Chem. Mater. **11**, 771–778 (1999)

2.44 Y. Kita, N. Watanabe, Y. Fujii: Chemical composition and crystal structure of graphite fluoride, J. Am. Chem. Soc. **101**, 3832–3841 (1979)

2.45 S. Malik, A. Vijayaraghavan, R. Erni, K. Ariga, I. Khalakhan, J.P. Hill: High purity graphenes prepared by a chemical intercalation method, Nanoscale **2**, 2139–2143 (2010)

2.46 X. Fan, W. Peng, Y. Li, X. Li, S. Wang, G. Zhang, F. Zhang: Deoxygenation of exfoliated graphite oxide under alkaline conditions: A green route to graphene preparation, Adv. Mater. **20**, 4490–4493 (2008)

2.47 S. Park, R.S. Ruoff: Chemical methods for the production of graphenes, Nat. Nanotechnol. **4**, 217–224 (2009)

2.48 C.-J. Shih, A. Vijayaraghavan, R. Krishnan, R. Sharma, J.-H. Han, M.-H. Ham, Z. Jin, S. Lin, G.L.C. Paulus, N.F. Reuel, Q.H. Wang, D. Blankschtein, M.S. Strano: Bi- and trilayer graphene solutions, Nat. Nanotechnol. **6**(7), 439–445 (2011)

2.49 P.K. Ang, S. Wang, Q. Bao, J.T.L. Thong, K.P. Loh: High-throughput synthesis of graphene by intercalation-exfoliation of graphite oxide and study of ionic screening in graphene transistor, ACS Nano **3**, 3587–3594 (2009)

2.50 J.I. Paredes, S. Villar-Rodil, A. Martiínez-Alonso, J.M.D. Tascón: Graphene oxide dispersions in organic solvents, Langmuir **24**, 10560–10564 (2008)

2.51 Z. Sun, S.-I. Kohama, Z. Zhang, J. Lomeda, J. Tour: Soluble graphene through edge-selective functionalization, Nano Res. **3**, 117–125 (2010)

2.52 V.C. Tung, M.J. Allen, Y. Yang, R.B. Kaner: High-throughput solution processing of large-scale graphene, Nat. Nanotechnol. **4**, 25–29 (2009)

2.53 S. Stankovich, D.A. Dikin, R.D. Piner, K.A. Kohlhaas, A. Kleinhammes, Y. Jia, Y. Wu, S.T. Nguyen, R.S. Ruoff: Synthesis of graphene-based nanosheets via chemical reduction of exfoliated graphite oxide, Carbon **45**, 1558–1565 (2007)

2.54 S. Stankovich, D.A. Dikin, G.H.B. Dommett, K.M. Kohlhaas, E.J. Zimney, E.A. Stach, R.D. Piner, S.T. Nguyen, R.S. Ruoff: Graphene-based composite materials, Nature **442**, 282–286 (2006)

2.55 C. Gómez-Navarro, R.T. Weitz, A.M. Bittner, M. Scolari, A. Mews, M. Burghard, K. Kern: Electronic transport properties of individual chemically reduced graphene oxide sheets, Nano Lett. **7**, 3499–3503 (2007)

2.56 K.A. Worsley, P. Ramesh, S.K. Mandal, S. Niyogi, M.E. Itkis, R.C. Haddon: Soluble graphene derived from graphite fluoride, Chem. Phys. Lett. **445**, 51–56 (2007)

2.57 N. Liu, F. Luo, H. Wu, Y. Liu, C. Zhang, J. Chen: One-step ionic-liquid-assisted electrochemical synthesis of ionic-liquid-functionalized graphene sheets directly from graphite, Adv. Funct. Mater. **18**, 1518–1525 (2008)

2.58 X. An, T. Simmons, R. Shah, C. Wolfe, K.M. Lewis, M. Washington, S.K. Nayak, S. Talapatra, S. Kar: Stable aqueous dispersions of noncovalently functionalized graphene from graphite and their multifunctional high-performance applications, Nano Lett. **10**, 4295–4301 (2010)

2.59 A.A. Green, M.C. Hersam: Solution phase production of graphene with controlled thickness via density differentiation, Nano Lett. **9**, 4031–4036 (2009)

2.60 S.D. Bergin, V. Nicolosi, P.V. Streich, S. Giordani, Z. Sun, A.H. Windle, P. Ryan, N.P.P. Niraj, Z.-T.T. Wang, L. Carpenter, W.J. Blau, J.J. Boland, J.P. Hamilton, J.N. Coleman: Towards solutions of single-walled carbon nanotubes in common solvents, Adv. Mater. **20**, 1876–1881 (2008)

2.61 Y. Hernandez, V. Nicolosi, M. Lotya, F.M. Blighe, Z. Sun, S. De, I.T. McGovern, B. Holland, M. Byrne, Y.K. Gun'Ko, J.J. Boland, P. Niraj, G. Duesberg, S. Krishnamurthy, R. Goodhue, J. Hutchison, V. Scardaci, A.C. Ferrari, J.N. Coleman: High-yield production of graphene by liquid-phase exfoliation of graphite, Nat. Nanotechnol. **3**, 563–568 (2008)

2.62 M. Lotya, Y. Hernandez, P.J. King, R.J. Smith, V. Nicolosi, L.S. Karlsson, F.M. Blighe, S. De, Z. Wang, I.T. McGovern, G.S. Duesberg, J.N. Coleman: Liquid phase production of graphene by exfoliation of graphite in surfactant/water solutions, J. Am. Chem. Soc. **131**, 3611–3620 (2009)

2.63 F. Hennrich, R. Krupke, K. Arnold, J.A. Rojas Stutz, S. Lebedkin, T. Koch, T. Schimmel, M.M. Kappes: The mechanism of cavitation-induced scission of single-walled carbon nanotubes, J. Phys. Chem. B **111**, 1932–1937 (2007)

2.64 Y.B. Tang, C.S. Lee, Z.H. Chen, G.D. Yuan, Z.H. Kang, L.B. Luo, H.S. Song, Y. Liu, Z.B. He, W.J. Zhang, I. Bello, S.T. Lee: High-quality graphenes via a facile quenching method for field-effect transistors, Nano Lett. **9**, 1374–1377 (2009)

2.65 N.-W. Pu, C.-A. Wang, Y. Sung, Y.-M. Liu, M.-D. Ger: Production of few-layer graphene by supercritical C02 exfoliation of graphite, Mater. Lett. **63**, 1987–1989 (2009)

2.66 D. Rangappa, K. Sone, M. Wang, U. Gautam, D. Golberg, H. Itoh, M. Ichihara, I. Honma: Rapid and direct conversion of graphite crystals into high-yielding, good-quality graphene by supercritical fluid exfoliation, Chem. Eur. J. **16**, 6488–6494 (2010)

2.67 C. Lijie, S. Li, J. Deep, A.L. Elias, G. Wei, T. Mauricio, M.A. Pulickel: Graphene shape control by multistage cutting and transfer, Adv. Mater. **21**, 1–5 (2009)

2.68 J. Cai, P. Ruffieux, R. Jaafar, M. Bieri, T. Braun, S. Blankenburg, M. Muoth, A.P. Seitsonen, M. Saleh, X. Feng, K. Müllen, R. Fasel: Atomically precise bottom-up fabrication of graphene nanoribbons, Nature **466**, 470–473 (2010)

2.69 L. Jiao, L. Zhang, X. Wang, G. Diankov, H. Dai: Narrow graphene nanoribbons from carbon nanotubes, Nature **458**, 877–880 (2009)

2.70 D.V. Kosynkin, A.L. Higginbotham, A. Sinitskii, J.R. Lomeda, A. Dimiev, B.K. Price, J.M. Tour: Longitudinal unzipping of carbon nanotubes to form graphene nanoribbons, Nature **458**, 872–876 (2009)

2.71 X. Li, X. Wang, L. Zhang, S. Lee, H. Dai: Chemically derived, ultrasmooth graphene nanoribbon semiconductors, Science **319**, 1229–1232 (2008)

2.72 C.D. Simpson, J.D. Brand, A.J. Berresheim, L. Przybilla, H.J. Räder, K. Müllen: Synthesis of a giant 222 carbon graphite sheet, Chem. Eur. J. **8**, 1424–1429 (2002)

2.73 H.J. Räder, A. Rouhanipour, A.M. Talarico, V. Palermo, P. Samori, K. Müllen: Processing of giant graphene molecules by soft-landing mass spectrometry, Nat. Mater. **5**, 276–280 (2006)

2.74 C. Stampfer, J. Güttinger, S. Hellmüller, F. Molitor, K. Ensslin, T. Ihn: Energy gaps in etched graphene nanoribbons, Phys. Rev. Lett. **102**, 056403 (2009)

2.75 J. Bai, X. Duan, Y. Huang: Rational fabrication of graphene nanoribbons using a nanowire etch mask, Nano Lett. **9**, 2083–2087 (2009)

2.76 L. Ci, Z. Xu, L. Wang, W. Gao, F. Ding, K. Kelly, B. Yakobson, P. Ajayan: Controlled nanocutting of graphene, Nano Res. **1**, 116–122 (2008)

2.77 N. Severin, S. Kirstein, I.M. Sokolov, J.P. Rabe: Rapid trench channeling of graphenes with catalytic silver nanoparticles, Nano Lett. **9**, 457–461 (2009)

2.78 L.C. Campos, V.R. Manfrinato, J.D. Sanchez-Yamagishi, J. Kong, P. Jarillo-Herrero: Anisotropic etching and nanoribbon formation in single-layer graphene, Nano Lett. **9**, 2600–2604 (2009)

2.79 J.O. Sofo, A.S. Chaudhari, G.D. Barber: Graphane: A two-dimensional hydrocarbon, Phys. Rev. B **75**, 153401 (2007)

2.80 D.C. Elias, R.R. Nair, T.M.G. Mohiuddin, S.V. Morozov, P. Blake, M.P. Halsall, A.C. Ferrari, D.W. Boukhvalov, M.I. Katsnelson, A.K. Geim, K.S. Novoselov: Control of graphene's properties by reversible hydrogenation: Evidence for graphane, Science **323**, 610–613 (2009)

2.81 J.T. Robinson, J.S. Burgess, C.E. Junkermeier, S.C. Badescu, T.L. Reinecke, F.K. Perkins, M.K. Zalalutdniov, J.W. Baldwin, J.C. Culbertson, P.E. Sheehan, E.S. Snow: Properties of fluorinated graphene films, Nano Lett. **10**, 3001–3005 (2010)

2.82 R.R. Nair, W. Ren, R. Jalil, I. Riaz, V.G. Kravets, L. Britnell, P. Blake, F. Schedin, A.S. Mayorov, S. Yuan, M.I. Katsnelson, H.-M. Cheng, W. Strupinski, L.G. Bulusheva, A.V. Okotrub, I.V. Grigorieva, A.N. Grigorenko, K.S. Novoselov, A.K. Geim: Fluorographene: A two-dimensional counterpart of teflon, Small **6**, 2877–2884 (2010)

2.83 F. Withers, M. Dubois, A.K. Savchenko: Electron properties of fluorinated single-layer graphene transistors, Phys. Rev. B **82**, 073403 (2010)

2.84 N.D. Mermin: Crystalline order in two dimensions, Phys. Rev. **176**, 250 (1968)

2.85 A. Fasolino, J.H. Los, M.I. Katsnelson: Intrinsic ripples in graphene, Nat. Mater. **6**, 858–861 (2007)

2.86 V. Geringer, M. Liebmann, T. Echtermeyer, S. Runte, M. Schmidt, R. Rückamp, M.C. Lemme, M. Morgenstern: Intrinsic and extrinsic corrugation of monolayer graphene deposited on SiO_2, Phys. Rev. Lett. **102**, 076102 (2009)

2.87 A.L.V. de Parga, F. Calleja, B. Borca, M.C.G. Passeggi Jr., J.J. Hinarejos, F. Guinea, R. Miranda: Periodically rippled graphene: Growth and spatially resolved electronic structure, Phys. Rev. Lett. **100**, 056807 (2008)

2.88 M.H. Gass, U. Bangert, A.L. Bleloch, P. Wang, R.R. Nair, A.K. Geim: Free-standing graphene at atomic resolution, Nat. Nanotechnol. **3**, 676–681 (2008)

2.89 X. Xie, L. Ju, X. Feng, Y. Sun, R. Zhou, K. Liu, S. Fan, Q. Li, K. Jiang: Controlled fabrication of high-quality carbon nanoscrolls from monolayer graphene, Nano Lett. **9**, 2565–2570 (2009)

2.90 T.J. Booth, P. Blake, R.R. Nair, D. Jiang, E.W. Hill, U. Bangert, A. Bleloch, M. Gass, K.S. Novoselov, M.I. Katsnelson, A.K. Geim: Macroscopic graphene membranes and their extraordinary stiffness, Nano Lett. **8**, 2442–2446 (2008)

2.91 C.H. Lui, L. Liu, K.F. Mak, G.W. Flynn, T.F. Heinz: Ultraflat graphene, Nature **462**, 339–341 (2009)

2.92 A. Geim, A. MacDonald: Graphene: Exploring carbon flatland, Phys. Today **60**, 35–41 (2007)
2.93 D. Tabor: Mohs's Hardness Scale – A physical interpretation, Proc. Phys. Soc. B **67**, 249 (1954)
2.94 P.M. Ajayan: Nanotubes from carbon, Chem. Rev. **99**, 1787–1799 (1999)
2.95 O.L. Blakslee, D.G. Proctor, E.J. Seldin, G.B. Spence, T. Weng: Elastic constants of compression-annealed pyrolytic graphite, J. Appl. Phys. **41**, 3373–3382 (1970)
2.96 C. Lee, X. Wei, J.W. Kysar, J. Hone: Measurement of the elastic properties and intrinsic strength of monolayer graphene, Science **321**, 385–388 (2008)
2.97 M. Poot, H.S.J. van der Zant: Nanomechanical properties of few-layer graphene membranes, Appl. Phys. Lett. **92**, 063111–063113 (2008)
2.98 J. Atalaya, A. Isacsson, J.M. Kinaret: Continuum elastic modeling of graphene resonators, Nano Lett. **8**, 4196–4200 (2008)
2.99 X.Q. He, S. Kitipornchai, K.M. Liew: Resonance analysis of multilayered graphene sheets used as nanoscale resonators, Nanotechnology **16**, 2086 (2005)
2.100 D. Garcia-Sanchez, A.M. van der Zande, A.S. Paulo, B. Lassagne, P.L. McEuen, A. Bachtold: Imaging mechanical vibrations in suspended graphene sheets, Nano Lett. **8**, 1399–1403 (2008)
2.101 J.T. Robinson, M. Zalalutdinov, J.W. Baldwin, E.S. Snow, Z. Wei, P. Sheehan, B.H. Houston: Wafer-scale reduced graphene oxide films for nanomechanical devices, Nano Lett. **8**, 3441–3445 (2008)
2.102 C. Chen, S. Rosenblatt, K.I. Bolotin, W. Kalb, P. Kim, I. Kymissis, H.L. Stormer, T.F. Heinz, J. Hone: Performance of monolayer graphene nanomechanical resonators with electrical readout, Nat. Nanotechnol. **4**, 861–867 (2009)
2.103 P.R. Wallace: The band theory of graphite, Phys. Rev. **71**, 622 (1947)
2.104 K.S. Novoselov, A.K. Geim, S.V. Morozov, D. Jiang, M.I. Katsnelson, I.V. Grigorieva, S.V. Dubonos, A.A. Firsov: Two-dimensional gas of massless Dirac fermions in graphene, Nature **438**, 197–200 (2005)
2.105 M.I. Katsnelson, K.S. Novoselov: Graphene: New bridge between condensed matter physics and quantum electrodynamics, Solid State Commun. **143**, 3–13 (2007)
2.106 Y. Zhang, Y.-W. Tan, H.L. Stormer, P. Kim: Experimental observation of the quantum Hall effect and Berry's phase in graphene, Nature **438**, 201–204 (2005)
2.107 M.I. Katsnelson, K.S. Novoselov, A.K. Geim: Chiral tunnelling and the Klein paradox in graphene, Nat. Phys. **2**, 620–625 (2006)
2.108 I. Brihuega, P. Mallet, C. Bena, S. Bose, C. Michaelis, L. Vitali, F. Varchon, L. Magaud, K. Kern, J.Y. Veuillen: Quasiparticle chirality in epitaxial graphene probed at the nanometer scale, Phys. Rev. Lett. **101**, 206802 (2008)
2.109 T. Ohta, A. Bostwick, T. Seyller, K. Horn, E. Rotenberg: Controlling the electronic structure of bilayer graphene, Science **313**, 951–954 (2006)
2.110 Y. Zhang, T.-T. Tang, C. Girit, Z. Hao, M.C. Martin, A. Zettl, M.F. Crommie, Y.R. Shen, F. Wang: Direct observation of a widely tunable bandgap in bilayer graphene, Nature **459**, 820–823 (2009)
2.111 C.W.J. Beenakker: Specular Andreev reflection in graphene, Phys. Rev. Lett. **97**, 067007 (2006)
2.112 H.B. Heersche, P. Jarillo-Herrero, J.B. Oostinga, L.M.K. Vandersypen, A.F. Morpurgo: Bipolar supercurrent in graphene, Nature **446**, 56–59 (2007)
2.113 H.B. Heersche, P. Jarillo-Herrero, J.B. Oostinga, L.M.K. Vandersypen, A.F. Morpurgo: Induced superconductivity in graphene, Solid State Commun. **143**, 72–76 (2007)
2.114 X. Du, I. Skachko, E.Y. Andrei: Josephson current and multiple Andreev reflections in graphene SNS junctions, Phys. Rev. B **77**, 184507 (2008)
2.115 J. Cayssol: Crossed andreev reflection in a graphene bipolar transistor, Phys. Rev. Lett. **100**, 147001 (2008)
2.116 D. Rainis, F. Taddei, F. Dolcini, M. Polini, R. Fazio: Andreev reflection in graphene nanoribbons, Phys. Rev. B **79**, 115131 (2009)
2.117 D.E. Sheehy, J. Schmalian: Optical transparency of graphene as determined by the fine-structure constant, Phys. Rev. B **80**, 193411 (2009)
2.118 R.R. Nair, P. Blake, A.N. Grigorenko, K.S. Novoselov, T.J. Booth, T. Stauber, N.M.R. Peres, A.K. Geim: Fine structure constant defines visual transparency of graphene, Science **320**, 1308 (2008)
2.119 P. Kim, L. Shi, A. Majumdar, P.L. McEuen: Thermal transport measurements of individual multiwalled nanotubes, Phys. Rev. Lett. **87**, 215502 (2001)
2.120 E. Pop, D. Mann, Q. Wang, K. Goodson, H. Dai: Thermal conductance of an individual single-wall carbon nanotube above room temperature, Nano Lett. **6**, 96–100 (2005)
2.121 A.V. Sukhadolau, E.V. Ivakin, V.G. Ralchenko, A.V. Khomich, A.V. Vlasov, A.F. Popovich: Thermal conductivity of CVD diamond at elevated temperatures, Diam. Relat. Mater. **14**, 589–593 (2005)
2.122 A.A. Balandin, S. Ghosh, W. Bao, I. Calizo, D. Teweldebrhan, F. Miao, C.N. Lau: Superior thermal conductivity of single-layer graphene, Nano Lett. **8**, 902–907 (2008)
2.123 W.W. Tyler, A.C. Wilson: Thermal conductivity, electrical resistivity, and thermoelectric power of graphite, Phys. Rev. **89**, 870 (1953)
2.124 S. Ghosh, W. Bao, D.L. Nika, S. Subrina, E.P. Pokatilov, C.N. Lau, A.A. Balandin: Dimensional crossover of thermal transport in few-layer graphene, Nat. Mater. **9**, 555–558 (2010)
2.125 Y.M. Zuev, W. Chang, P. Kim: Thermoelectric and magnetothermoelectric transport measurements of graphene, Phys. Rev. Lett. **102**, 096807 (2009)
2.126 P. Wei, W. Bao, Y. Pu, C.N. Lau, J. Shi: Anomalous thermoelectric transport of dirac par-

ticles in graphene, Phys. Rev. Lett. **102**, 166808 (2009)
2.127 Y. Ouyang, J. Guo: A theoretical study on thermoelectric properties of graphene nanoribbons, Appl. Phys. Lett. **94**, 263107–1–263107–4 (2009)
2.128 H. Ohta, S. Kim, Y. Mune, T. Mizoguchi, K. Nomura, S. Ohta, T. Nomura, Y. Nakanishi, Y. Ikuhara, M. Hirano, H. Hosono, K. Koumoto: Giant thermoelectric Seebeck coefficient of a two-dimensional electron gas in $SrTiO_3$, Nat. Mater. **6**, 129–134 (2007)
2.129 J. Hone, I. Ellwood, M. Muno, A. Mizel, M.L. Cohen, A. Zettl, A.G. Rinzler, R.E. Smalley: Thermoelectric power of single-walled carbon nanotubes, Phys. Rev. Lett. **80**, 1042 (1998)
2.130 D. Dragoman, M. Dragoman: Giant thermoelectric effect in graphene, Appl. Phys. Lett. **91**, 203116–203116–3 (2007)
2.131 R. Sharma, J.H. Baik, C.J. Perera, M.S. Strano: Anomalously large reactivity of single graphene layers and edges toward electron transfer chemistries, Nano Lett. **10**, 398–405 (2010)
2.132 F.M. Koehler, A. Jacobsen, K. Ensslin, C. Stampfer, W.J. Stark: Selective chemical modification of graphene surfaces: Distinction between single- and bilayer graphene, Small **6**, 1125–1130 (2010)
2.133 L. Pietronero, S. Strässler, H.R. Zeller, M.J. Rice: Charge distribution in c direction in lamellar graphite acceptor intercalation compounds, Phys. Rev. Lett. **41**, 763 (1978)
2.134 Y.-M. Lin, P. Avouris: Strong suppression of electrical noise in bilayer graphene nanodevices, Nano Lett. **8**, 2119–2125 (2008)
2.135 R. Sharma, N. Nair, M.S. Strano: Structure-reactivity relationships for graphene nanoribbons, J. Phys. Chem. C **113**, 14771–14777 (2009)
2.136 H. He, C. Gao: General approach to individually dispersed, highly soluble, and conductive graphene nanosheets functionalized by nitrene chemistry, Chem. Mat. **22**, 5054–5064 (2010)
2.137 A. Sinitskii, A. Dimiev, D.A. Corley, A.A. Fursina, D.V. Kosynkin, J.M. Tour: Kinetics of diazonium functionalization of chemically converted graphene nanoribbons, ACS Nano **4**, 1949–1954 (2010)
2.138 E. Bekyarova, M.E. Itkis, P. Ramesh, C. Berger, M. Sprinkle, W.A. de Heer, R.C. Haddon: Chemical modification of epitaxial graphene: Spontaneous grafting of aryl groups, J. Am. Chem. Soc. **131**, 1336–1337 (2009)
2.139 D.B. Farmer, R. Golizadeh-Mojarad, V. Perebeinos, Y.-M. Lin, G.S. Tulevski, J.C. Tsang, P. Avouris: Chemical doping and electron-hole conduction asymmetry in graphene devices, Nano Lett. **9**, 388–392 (2008)
2.140 D.B. Farmer, Y.-M. Lin, A. Afzali-Ardakani, P. Avouris: Behavior of a chemically doped graphene junction, Appl. Phys. Lett. **94**, 213106–213106–3 (2009)
2.141 I. Jung, M. Pelton, R. Piner, D.A. Dikin, S. Stankovich, S. Watcharotone, M. Hausner, R.S. Ruoff: Simple approach for high-contrast optical imaging and characterization of graphene-based sheets, Nano Lett. **7**, 3569–3575 (2007)
2.142 C. Casiraghi, A. Hartschuh, E. Lidorikis, H. Qian, H. Harutyunyan, T. Gokus, K.S. Novoselov, A.C. Ferrari: Rayleigh imaging of graphene and graphene layers, Nano Lett. **7**, 2711–2717 (2007)
2.143 J.C. Meyer, A.K. Geim, M.I. Katsnelson, K.S. Novoselov, D. Obergfell, S. Roth, C. Girit, A. Zettl: On the roughness of single- and bi-layer graphene membranes, Solid State Commun. **143**, 101–109 (2007)
2.144 P. Nemes-Incze, Z. Osváth, K. Kamarás, L.P. Biró: Anomalies in thickness measurements of graphene and few layer graphite crystals by tapping mode atomic force microscopy, Carbon **46**, 1435–1442 (2008)
2.145 S.S. Datta, D.R. Strachan, E.J. Mele, A.T.C. Johnson: Surface potentials and layer charge distributions in few-layer graphene films, Nano Lett. **9**, 7–11 (2009)
2.146 S. Neubeck, Y.M. You, Z.H. Ni, P. Blake, Z.X. Shen, A.K. Geim, K.S. Novoselov: Direct determination of the crystallographic orientation of graphene edges by atomic resolution imaging, Appl. Phys. Lett. **97**, 053110–053113 (2010)
2.147 P. Lauffer, K.V. Emtsev, R. Graupner, T. Seyller, L. Ley, S.A. Reshanov, H.B. Weber: Atomic and electronic structure of few-layer graphene on SiC(0001) studied with scanning tunneling microscopy and spectroscopy, Phys. Rev. B **77**, 155426 (2008)
2.148 D.E. Starr, E.M. Pazhetnov, A.I. Stadnichenko, A.I. Boronin, S.K. Shaikhutdinov: Carbon films grown on Pt(111) as supports for model gold catalysts, Surf. Sci. **600**, 2688–2695 (2006)
2.149 H. Amara, S. Latil, V. Meunier, P. Lambin, J.C. Charlier: Scanning tunneling microscopy fingerprints of point defects in graphene: A theoretical prediction, Phys. Rev. B **76**, 115423 (2007)
2.150 J.R. Hahn, H. Kang, S. Song, I.C. Jeon: Observation of charge enhancement induced by graphite atomic vacancy: A comparative STM and AFM study, Phys. Rev. B **53**, R1725 (1996)
2.151 V.W. Brar, Y. Zhang, Y. Yayon, T. Ohta, J.L. McChesney, A. Bostwick, E. Rotenberg, K. Horn, M.F. Crommie: Scanning tunneling spectroscopy of inhomogeneous electronic structure in monolayer and bilayer graphene on SiC, Appl. Phys. Lett. **91**, 122102–122103 (2007)
2.152 Y. Zhang, V.W. Brar, F. Wang, C. Girit, Y. Yayon, M. Panlasigui, A. Zettl, M.F. Crommie: Giant phonon-induced conductance in scanning tunnelling spectroscopy of gate-tunable graphene, Nat. Phys. **4**, 627–630 (2008)
2.153 T. Ohta, A. Bostwick, J.L. McChesney, T. Seyller, K. Horn, E. Rotenberg: Interlayer interaction and electronic screening in multilayer graphene investigated with angle-resolved photoemission

spectroscopy, Phys. Rev. Lett. **98**, 206802–206804 (2007)
2.154 M. Sprinkle, D. Siegel, Y. Hu, J. Hicks, A. Tejeda, A. Taleb-Ibrahimi, P. Le Fèvre, F. Bertran, S. Vizzini, H. Enriquez, S. Chiang, P. Soukiassian, C. Berger, W.A. de Heer, A. Lanzara, E.H. Conrad: First direct observation of a nearly ideal graphene band structure, Phys. Rev. Lett. **103**, 226803 (2009)
2.155 A. Bostwick, T. Ohta, T. Seyller, K. Horn, E. Rotenberg: Quasiparticle dynamics in graphene, Nat. Phys. **3**, 36–40 (2007)
2.156 A.C. Ferrari, J.C. Meyer, V. Scardaci, C. Casiraghi, M. Lazzeri, F. Mauri, S. Piscanec, D. Jiang, K.S. Novoselov, S. Roth, A.K. Geim: Raman spectrum of graphene and graphene layers, Phys. Rev. Lett. **97**, 187401 (2006)
2.157 A.N. Obraztsov, A.V. Tyurnina, E.A. Obraztsova, A.A. Zolotukhin, B. Liu, K.-C. Chin, A.T.S. Wee: Raman scattering characterization of CVD graphite films, Carbon **46**, 963–968 (2008)
2.158 J. Rohrl, M. Hundhausen, K.V. Emtsev, T. Seyller, R. Graupner, L. Ley: Raman spectra of epitaxial graphene on SiC(0001), Appl. Phys. Lett. **92**, 201918–1–201918–3 (2008)
2.159 C. Casiraghi: Probing disorder and charged impurities in graphene by Raman spectroscopy, Physica Status Solidi (RRL) – Rapid Res. Lett. **3**, 175–177 (2009)
2.160 A. Das, S. Pisana, B. Chakraborty, S. Piscanec, S.K. Saha, U.V. Waghmare, K.S. Novoselov, H.R. Krishnamurthy, A.K. Geim, A.C. Ferrari, A.K. Sood: Monitoring dopants by Raman scattering in an electrochemically top-gated graphene transistor, Nat. Nanotechnol. **3**, 210–215 (2008)
2.161 C. Casiraghi, S. Pisana, K.S. Novoselov, A.K. Geim, A.C. Ferrari: Raman fingerprint of charged impurities in graphene, Appl. Phys. Lett. **91**, 233108/1–233108/3 (2007)
2.162 T. Yu, Z. Ni, C. Du, Y. You, Y. Wang, Z. Shen: Raman mapping investigation of graphene on transparent flexible substrate: The strain effect, J. Phys. Chem. C **112**, 12602–12605 (2008)
2.163 J.E. Proctor, E. Gregoryanz, K.S. Novoselov, M. Lotya, J.N. Coleman, M.P. Halsall: High-pressure Raman spectroscopy of graphene, Phys. Rev. B **80**, 073408 (2009)
2.164 M. Bruna, A. Vaira, A. Battiato, E. Vittone, S. Borini: Graphene strain tuning by control of the substrate surface chemistry, Appl. Phys. Lett. **97**, 021911–021913 (2010)
2.165 T.M.G. Mohiuddin, A. Lombardo, R.R. Nair, A. Bonetti, G. Savini, R. Jalil, N. Bonini, D.M. Basko, C. Galiotis, N. Marzari, K.S. Novoselov, A.K. Geim, A.C. Ferrari: Uniaxial strain in graphene by Raman spectroscopy: G peak splitting, Grüneisen parameters, and sample orientation, Phys. Rev. B **79**, 205433 (2009)
2.166 J.H. Chen, C. Jang, S. Adam, M.S. Fuhrer, E.D. Williams, M. Ishigami: Charged-impurity scattering in graphene, Nat. Phys. **4**, 377–381 (2008)
2.167 Y.W. Tan, Y. Zhang, K. Bolotin, Y. Zhao, S. Adam, E.H. Hwang, S.D. Sarma, H.L. Stormer, P. Kim: Measurement of scattering rate and minimum conductivity in graphene, Phys. Rev. Lett. **99**, 246803–246804 (2007)
2.168 J.-H. Chen, W.G. Cullen, C. Jang, M.S. Fuhrer, E.D. Williams: Defect scattering in graphene, Phys. Rev. Lett. **102**, 236805 (2009)
2.169 Z.H. Ni, L.A. Ponomarenko, R.R. Nair, R. Yang, S. Anissimova, I.V. Grigorieva, F. Schedin, P. Blake, Z.X. Shen, E.H. Hill, K.S. Novoselov, A.K. Geim: On resonant scatterers as a factor limiting carrier mobility in graphene, Nano Lett. **10**, 3868–3872 (2010)
2.170 K.I. Bolotin, K.J. Sikes, Z. Jiang, M. Klima, G. Fudenberg, J. Hone, P. Kim, H.L. Stormer: Ultrahigh electron mobility in suspended graphene, Solid State Commun. **146**, 351–355 (2008)
2.171 X. Du, I. Skachko, A. Barker, E.Y. Andrei: Approaching ballistic transport in suspended graphene, Nat. Nanotechnol. **3**, 491–495 (2008)
2.172 E.V. Castro, K.S. Novoselov, S.V. Morozov, N.M.R. Peres, J.M.B.L. dos Santos, J. Nilsson, F. Guinea, A.K. Geim, A.H.C. Neto: Biased bilayer graphene: Semiconductor with a gap tunable by the electric field effect, Phys. Rev. Lett. **99**, 216802 (2007)
2.173 X. Du, I. Skachko, F. Duerr, A. Luican, E.Y. Andrei: Fractional quantum Hall effect and insulating phase of Dirac electrons in graphene, Nature **462**, 192–195 (2009)
2.174 K.I. Bolotin, F. Ghahari, M.D. Shulman, H.L. Stormer, P. Kim: Observation of the fractional quantum Hall effect in graphene, Nature **462**, 196–199 (2009)
2.175 J.B. Oostinga, H.B. Heersche, X. Liu, A.F. Morpurgo, L.M.K. Vandersypen: Gate-induced insulating state in bilayer graphene devices, Nat. Mater. **7**, 151–157 (2008)
2.176 J.-H. Chen, C. Jang, S. Xiao, M. Ishigami, M.S. Fuhrer: Intrinsic and extrinsic performance limits of graphene devices on SiO_2, Nat. Nanotechnol. **3**, 206–209 (2008)
2.177 M.Y. Han, B. Özyilmaz, Y. Zhang, P. Kim: Energy band-gap engineering of graphene nanoribbons, Phys. Rev. Lett. **98**, 206805 (2007)
2.178 S.S. Sabri, P.L. Levesque, C.M. Aguirre, J. Guillemette, R. Martel, T. Szkopek: Graphene field effect transistors with parylene gate dielectric, Appl. Phys. Lett. **95**, 242104–242104–3 (2009)
2.179 D.B. Farmer, H.-Y. Chiu, Y.-M. Lin, K.A. Jenkins, F. Xia, P. Avouris: Utilization of a buffered dielectric to achieve high field-effect carrier mobility in graphene transistors, Nano Lett. **9**, 4474–4478 (2009)
2.180 L.A. Ponomarenko, R. Yang, T.M. Mohiuddin, M.I. Katsnelson, K.S. Novoselov, S.V. Morozov,

A.A. Zhukov, F. Schedin, E.W. Hill, A.K. Geim: Effect of a high- kappa environment on charge carrier mobility in graphene, Phys. Rev. Lett. **102**, 206603 (2009)

2.181 Z. Chen, Y.-M. Lin, M.J. Rooks, P. Avouris: Graphene nano-ribbon electronics, Physica E **40**, 228–232 (2007)

2.182 L.A. Ponomarenko, F. Schedin, M.I. Katsnelson, R. Yang, E.W. Hill, K.S. Novoselov, A.K. Geim: Chaotic dirac billiard in graphene quantum dots, Science **320**, 356–358 (2008)

2.183 C. Stampfer, J. Guttinger, F. Molitor, D. Graf, T. Ihn, K. Ensslin: Tunable Coulomb blockade in nanostructured graphene, Appl. Phys. Lett. **92**, 012102–012103 (2008)

2.184 C. Stampfer, E. Schurtenberger, F. Molitor, J. Güttinger, T. Ihn, K. Ensslin: Tunable graphene single electron transistor, Nano Lett. **8**, 2378–2383 (2008)

2.185 F. Molitor, S. Droscher, J. Guttinger, A. Jacobsen, C. Stampfer, T. Ihn, K. Ensslin: Transport through graphene double dots, Appl. Phys. Lett. **94**, 222107–222107–3 (2009)

2.186 B. Trauzettel, D.V. Bulaev, D. Loss, G. Burkard: Spin qubits in graphene quantum dots, Nat. Phys. **3**, 192–196 (2007)

2.187 N. Tombros, C. Jozsa, M. Popinciuc, H.T. Jonkman, B.J.V. Wees: Electronic spin transport and spin precession in single graphene layers at room temperature, Nature **448**, 571–574 (2007)

2.188 E.W. Hill, A.K. Geim, K. Novoselov, F. Schedin, P. Blake: Graphene spin valve devices, IEEE Trans. Magn. **42**, 2694–2696 (2006)

2.189 S. Cho, Y.-F. Chen, M.S. Fuhrer: Gate-tunable graphene spin valve, Appl. Phys. Lett. **91**, 123105 (2007)

2.190 T. Mueller, F. Xia, M. Freitag, J. Tsang, P. Avouris: Role of contacts in graphene transistors: A scanning photocurrent study, Phys. Rev. B **79**, 245430 (2009)

2.191 T.M.G. Mohiuddin, E. Hill, D. Elias, A. Zhukov, K. Novoselov, A. Geim: Graphene in multilayered CPP spin valves, IEEE Trans. Magn. **44**, 2624–2627 (2008)

2.192 F. Xia, T. Mueller, R. Golizadeh-Mojarad, M. Freitag, Y.-M. Lin, J. Tsang, V. Perebeinos, P. Avouris: Photocurrent imaging and efficient photon detection in a graphene transistor, Nano Lett. **9**, 1039–1044 (2009)

2.193 G. Eda, M. Chhowalla: Graphene-based composite thin films for electronics, Nano Lett. **9**, 814–818 (2009)

2.194 S. Watcharotone, D.A. Dikin, S. Stankovich, R. Piner, I. Jung, G.H.B. Dommett, G. Evmenenko, S.-E. Wu, S.-F. Chen, C.-P. Liu, S.T. Nguyen, R.S. Ruoff: Graphene-silica composite thin films as transparent conductors, Nano Lett. **7**, 1888–1892 (2007)

2.195 Z. Liu, Q. Liu, Y. Huang, Y. Ma, S. Yin, X. Zhang, W. Sun, Y. Chen: Organic photovoltaic devices based on a novel acceptor material: Graphene, Adv. Mater. **20**, 3924–3930 (2008)

2.196 H. Zhang, X. Lv, Y. Li, Y. Wang, J. Li: P25-graphene composite as a high performance photocatalyst, ACS Nano **4**, 380–386 (2009)

2.197 T. Ramanathan, A.A. Abdala, S. Stankovich, D.A. Dikin, M. Herrera Alonso, R.D. Piner, D.H. Adamson, H.C. Schniepp, X. Chen, R.S. Ruoff, S.T. Nguyen, I.A. Aksay, R.K. Prud'Homme, L.C. Brinson: Functionalized graphene sheets for polymer nanocomposites, Nat. Nanotechnol. **3**, 327–331 (2008)

2.198 C. Xu, X. Wang, J.W. Zhu: Graphene-Metal Particle Nanocomposites, J. Phys. Chem. C **112**, 19841–19845 (2008)

2.199 G. Eda, G. Fanchini, M. Chhowalla: Large-area ultrathin films of reduced graphene oxide as a transparent and flexible electronic material, Nat. Nanotechnol. **3**, 270–274 (2008)

2.200 C. Mattevi, G. Eda, S. Agnoli, S. Miller, K.A. Mkhoyan, O. Celik, D. Mastrogiovanni, G. Granozzi, E. Garfunkel, M. Chhowalla: Evolution of electrical, chemical, and structural properties of transparent and conducting chemically derived graphene thin films, Adv. Funct. Mater. **19**, 2577–2583 (2009)

2.201 X. Li, G. Zhang, X. Bai, X. Sun, X. Wang, E. Wang, H. Dai: Highly conducting graphene sheets and Langmuir–Blodgett films, Nat. Nanotechnol. **3**, 538–542 (2008)

2.202 J. Wu, H.A. Becerril, Z. Bao, Z. Liu, Y. Chen, P. Peumans: Organic solar cells with solution-processed graphene transparent electrodes, Appl. Phys. Lett. **92**, 263302–263303 (2008)

2.203 X. Wang, L. Zhi, K. Mullen: Transparent, conductive graphene electrodes for dye-sensitized solar cells, Nano Lett. **8**, 323–327 (2007)

2.204 K.S. Kim, Y. Zhao, H. Jang, S.Y. Lee, J.M. Kim, K.S. Kim, J.-H. Ahn, P. Kim, J.-Y. Choi, B.H. Hong: Large-scale pattern growth of graphene films for stretchable transparent electrodes, Nature **457**, 706–710 (2009)

2.205 X. Li, Y. Zhu, W. Cai, M. Borysiak, B. Han, D. Chen, R.D. Piner, L. Colombo, R.S. Ruoff: Transfer of large-area graphene films for high-performance transparent conductive electrodes, Nano Lett. **9**, 4359–4363 (2009)

2.206 J. Wu, M. Agrawal, H.A. Becerril, Z. Bao, Z. Liu, Y. Chen, P. Peumans: Organic light-emitting diodes on solution-processed graphene transparent electrodes, ACS Nano **4**, 43–48 (2010)

2.207 F. Bonaccorso, Z. Sun, T. Hasan, A.C. Ferrari: Graphene photonics and optoelectronics, Nat. Photonics **4**, 611–622 (2010)

2.208 F. Schedin, A.K. Geim, S.V. Morozov, E.W. Hill, P. Blake, M.I. Katsnelson, K.S. Novoselov: Detection of individual gas molecules adsorbed on graphene, Nat. Mater. **6**, 652–655 (2007)

2.209 T.O. Wehling, K.S. Novoselov, S.V. Morozov, E.E. Vdovin, M.I. Katsnelson, A.K. Geim, A.I. Lichtenstein: Molecular doping of graphene, Nano Lett. **8**, 173–177 (2007)

2.210 J.T. Robinson, F.K. Perkins, E.S. Snow, Z. Wei, P.E. Sheehan: Reduced graphene oxide molecular sensors, Nano Lett. **8**, 3137–3140 (2008)

2.211 J.D. Fowler, M.J. Allen, V.C. Tung, Y. Yang, R.B. Kaner, B.H. Weiller: Practical chemical sensors from chemically derived graphene, ACS Nano **3**, 301–306 (2009)

2.212 R. Arsat, M. Breedon, M. Shafiei, P.G. Spizziri, S. Gilje, R.B. Kaner, K. Kalantar-zadeh, W. Wlodarski: Graphene-like nano-sheets for surface acoustic wave gas sensor applications, Chem. Phys. Lett. **467**, 344–347 (2009)

2.213 Y. Ohno, K. Maehashi, Y. Yamashiro, K. Matsumoto: Electrolyte-gated graphene field-effect transistors for detecting pH and protein adsorption, Nano Lett. **9**, 3318–3322 (2009)

2.214 J.S. Bunch, A.M. van der Zande, S.S. Verbridge, I.W. Frank, D.M. Tanenbaum, J.M. Parpia, H.G. Craighead, P.L. McEuen: Electromechanical resonators from graphene sheets, Science **315**, 490–493 (2007)

2.215 A. Sakhaee-Pour, M.T. Ahmadian, A. Vafai: Applications of single-layered graphene sheets as mass sensors and atomistic dust detectors, Solid State Commun. **145**, 168–172 (2008)

2.216 Y.-M. Lin, C. Dimitrakopoulos, K.A. Jenkins, D.B. Farmer, H.-Y. Chiu, A. Grill, P. Avouris: 100-GHz transistors from wafer-scale epitaxial graphene, Science **327**, 662 (2010)

2.217 Y.-M. Lin, K.A. Jenkins, A. Valdes-Garcia, J.P. Small, D.B. Farmer, P. Avouris: Operation of graphene transistors at gigahertz frequencies, Nano Lett. **9**, 422–426 (2008)

2.218 J. Kedzierski, H. Pei-Lan, P. Healey, P. Wyatt, C. Keast: Epitaxial graphene transistors on SiC substrates, IEEE T. Electron. Dev. **55**, 2078–2085 (2008)

2.219 A. Vijayaraghavan, C. Sciascia, S. Dehm, A. Lombardo, A. Bonetti, A.C. Ferrari, R. Krupke: Dielectrophoretic assembly of high-density arrays of individual graphene devices for rapid screening, ACS Nano **3**, 1729–1734 (2009)

2.220 F. Xia, T. Mueller, Y.-M. Lin, A. Valdes-Garcia, P. Avouris: Ultrafast graphene photodetector, Nat. Nanotechnol. **4**, 839–843 (2009)

2.221 Q. Bao, H. Zhang, Y. Wang, Z. Ni, Y. Yan, Z.X. Shen, K.P. Loh, D.Y. Tang: Atomic-layer graphene as a saturable absorber for ultrafast pulsed lasers, Adv. Funct. Mater. **19**, 3077–3083 (2009)

2.222 T. Hasan, Z. Sun, F. Wang, F. Bonaccorso, P.H. Tan, A.G. Rozhin, A.C. Ferrari: Nanotube–polymer composites for ultrafast photonics, Adv. Mater. **21**, 3874–3899 (2009)

2.223 J. Wang, Y. Hernandez, M. Lotya, J.N. Coleman, W.J. Blau: Broadband nonlinear optical response of graphene dispersions, Adv. Mater. **21**, 2430–2435 (2009)

3. Fullerenes and Beyond: Complexity, Morphology, and Functionality in Closed Carbon Nanostructures

Humberto Terrones

The discovery of buckminsterfullerene 25 years ago opened a new field in materials science in which different disciplines such as physics, chemistry, medicine, mathematics, and engineering came together. This discovery is a clear example of what we now call nanoscience, thus having important implications for several applications in what is known as the nanotechnology of carbon materials. In this chapter, a revision of the most important advances in this area, involving the multidisciplinarity of the field, is given. Special emphasis is given to the geometry, production methods, physicochemical behavior, applications, future perspectives, and the relationship to other layered materials such as graphene, boron nitride, and metal chalcogenides.

3.1 **Geometry and Structural Features of Fullerenes** 85
3.1.1 The Mathematics of Closed Carbon Nanostructures 85
3.1.2 Carbon Nanostructures with Zero, Positive, and Negative Gaussian Curvature ... 85
3.1.3 Classical and Nonclassical Fullerenes 86
3.2 **Methods of Synthesis of Fullerenes and Proposed Growth Models** 88
3.2.1 Fullerenes by Laser Vaporization Method 88
3.2.2 Fullerenes by Arc Discharge 88
3.2.3 Fullerenes by Pyrolysis 88
3.2.4 Fullerenes by Combustion in Flames 89
3.2.5 Fullerenes Under Electron Beam Irradiation Inside a Transmission Electron Microscope (TEM) 89
3.2.6 Fullerenes by Concentrated Solar Flux 89
3.2.7 Proposed Mechanisms for Fullerene Growth and Formation 89
3.3 **Physicochemical Properties of Fullerenes** 90
3.3.1 Mechanical Properties and Phases of Fullerene Crystals 90
3.3.2 Electrical Properties and Superconductivity of Fullerites 91
3.3.3 Chemical Properties of Fullerenes ... 91
3.4 **Applications of Fullerenes and Beyond** ... 92
3.4.1 Fullerenes and Health 92
3.4.2 Fullerenes in Solar Cells 92
3.4.3 Nested Fullerenes: Carbon Onions .. 92
3.4.4 Fullerene Peapods and Fullerene Coalescence 94
3.4.5 High-Genus Fullerenes 97
3.4.6 Inorganic Fullerenes (BN, MoS_2, NbS_2, etc.) 97
3.4.7 Nanodiamond 98
3.5 **Conclusions** 99
References 99

Twenty-five years after the discovery of buckminsterfullerene or C_{60} [3.1], the field has matured, and besides the fundamental science involved, different applications have been found and others are waiting to be discovered. Eleven years after the discovery of C_{60}, the Nobel Prize in Chemistry was awarded to Harold Kroto, Robert Curl, and Richard Smalley; According to the ISI Web of Knowledge [3.2] the original manuscript of *Kroto* and colleagues [3.1] has been cited around 7000 times by other scientific papers, and the term *fullerene* appears in more than 14 000 scientific publications. Not only C_{60} has been recognized as im-

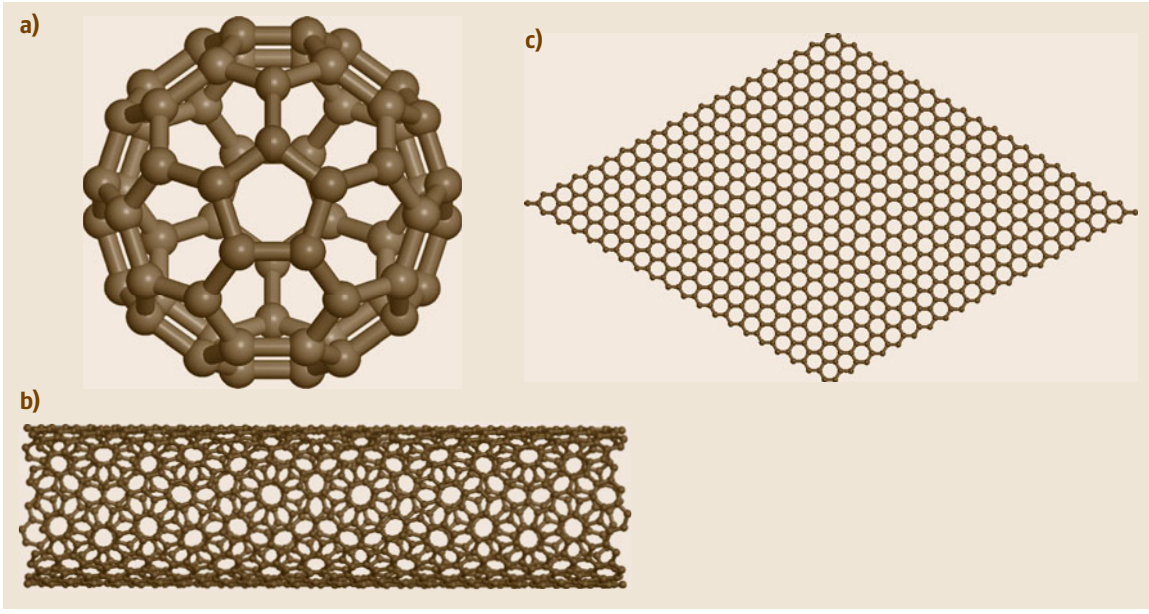


Fig. 3.1 **(a)** Buckminsterfullerene or C_{60}, **(b)** carbon nanotube, and **(c)** graphene piece

portant; other carbon nanostructure discoveries such as nanotubes [3.3, 4] have accumulated more than 10 000 citations in the scientific literature. Moreover, *André Geim* and *Konstantin Novoselov* were awarded the Nobel Prize in Physics in 2010 for the first experiments with few-layer graphite and graphene (a single layer of graphite, one atom thick), the flat cousin of C_{60} [3.5, 6] (Fig. 3.1).

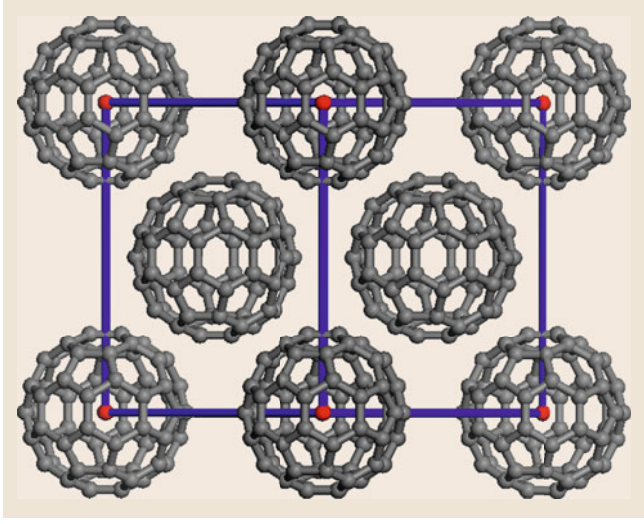


Fig. 3.2 The face-centered cubic (fcc) cell of fullerite of C_{60}

However, there are more carbon nanostructures that need to be studied further, such as carbon onions (the bigger cousins of fullerenes) [3.7] and porous carbons [3.8]. In addition, fullerene research has opened a new field in nanoscience which involves layered materials such as boron nitride, molybdenum sulfide, tungsten sulfide, and other metal chalcogenides [3.9–14]. Even thin layers of metal oxides such as zinc oxide have been studied theoretically as layered structures due to their high stability and possible magnetic behavior [3.15].

Although the discovery of C_{60} as a spherical icosahedral (I_h) carbon molecule was reported in 1985 [3.1], other researchers thought about it before. *Schultz* in 1965 showed the possibility of having different kinds of carbon hydrogenated cages, among them the I_h truncated icosahedron of C_{60} [3.16]. In 1970, *Osawa* published a paper in the Japanese journal *Kagaku* showing that C_{60} was a possible structure [3.17]. Orville L. Chapman started the first experiments towards chemical synthesis of C_{60} at the beginning of the 1980s, before the discovery of C_{60}.

What really pushed the field of fullerenes forward was the method to synthesize large amounts of C_{60} published by *Krätschmer* and colleagues in 1990 [3.18] using an electric arc discharge. At the same time, it was also found that C_{60} crystallized in a face-centered cubic lattice (Fig. 3.2), forming a molecular crystal in

which the C_{60} molecules exhibit disorder because they are rotating.

C_{60} illustrates the multidisciplinarity of nanoscience, involving topics in different fields mentioned herein such as new composite materials for more efficient solar cells, virus inhibition, superconductivity, lithium-ion batteries, drug delivery, nanoelectronics, etc. All these show the amazing world of carbon and represent the tip of the iceberg of new carbon materials for the 21st century and beyond.

3.1 Geometry and Structural Features of Fullerenes

Perhaps the most interesting features of C_{60} are its round shape and its high symmetry (I_h). In this section, the geometry and mathematics of different possibilities for sp^2 nanostructures, including fullerenes, are presented, emphasizing the versatility of carbon to generate different shapes. The concept of Gaussian curvature is introduced in the context of graphite nanostructures, and the possibilities of nonclassical fullerenes are discussed. It is worth saying that the possibilities for carbon to form different nanoarchitectures are enormous, and it is up to researchers to try to find new ways to synthesize them.

3.1.1 The Mathematics of Closed Carbon Nanostructures

Buckminsterfullerene, or C_{60}, is just one case in which a nanostructure can acquire curvature to avoid dangling bonds and become more stable. There are other cases such as carbon onions [3.7], inorganic onions of MoS_2 or WS_2 [3.11, 12], and carbon nanotubes [3.3, 4]. However, to better understand the role of curvature in layered materials, we have to consider the restrictions imposed by mathematics.

It turns out that we live in a three-dimensional space (3-D) and all our atoms form structures in this space (space–time is not considered in our approach); therefore, everything that exists does so in this 3-D space. In 3-D space there are just three geometries: Euclidean, spherical, and hyperbolic, so nature is restricted to these geometries to form everything which surrounds us.

Euclidean or planar geometry is the one most commonly taught in schools, and one of its main features is that no curvature is present (everything is flat), for example. If we measure the interior angles of a triangle on a flat surface, they will add to exactly 180°. However, this is not the case for the other two geometries. If a triangle is drawn on the surface of an orange, its interior angles will measure more than 180°, and if we do the same experiment on the surface of a horse saddle or a seaweed the interior angles of the triangle will add to less than 180°. Nature uses this, and that is why, at different levels of complexity, different shapes are observed in which not just Euclidean geometry is valid.

Another characteristic of 3-D space is that the surfaces immersed in it exhibit just two principal curvatures (C_1 and C_2). The product of these curvatures is called the *Gaussian curvature* K ($K = C_1C_2$) and the average is called the *mean curvature* $H = (C_1 + C_2)/2$. According to the sign of the Gaussian curvature we can identify the geometry to which a particular point on a surface belongs. In the case of Euclidean geometry, both or one of the principal curvatures is zero and therefore $K = 0$. On the surface of a sphere, all the points possess principal curvatures with the same sign, and thus the Gaussian curvature is always positive everywhere. In hyperbolic geometry, the principal curvatures have different signs, and thus their product is always negative; this means that the points are saddle points and curve in opposite directions. In nature, at different levels of complexity, including the atomic level, it is possible to identify objects with zero, positive, and negative Gaussian curvature.

3.1.2 Carbon Nanostructures with Zero, Positive, and Negative Gaussian Curvature

Graphite is as a crystal formed by carbon atoms forming hexagonal layers and belongs to space group $P63/mmc$. One single layer of graphite is called graphene. In graphene, both principal curvatures are zero, thus belonging to the Euclidean geometry. However, if in a small piece of graphene, 12 pentagonal rings of carbon are introduced, then C_{60} can be formed. In C_{60}, both principal curvatures are positive, and it thus belongs to spherical geometry (Fig. 3.3a,b). A graphene sheet can also be bent to form a tube (a single carbon walled nanotube) and thus will show curvature (one of the principal curvatures is not zero and is the inverse of the radius of the tube $C_1 = 1/r$, where r is the radius of

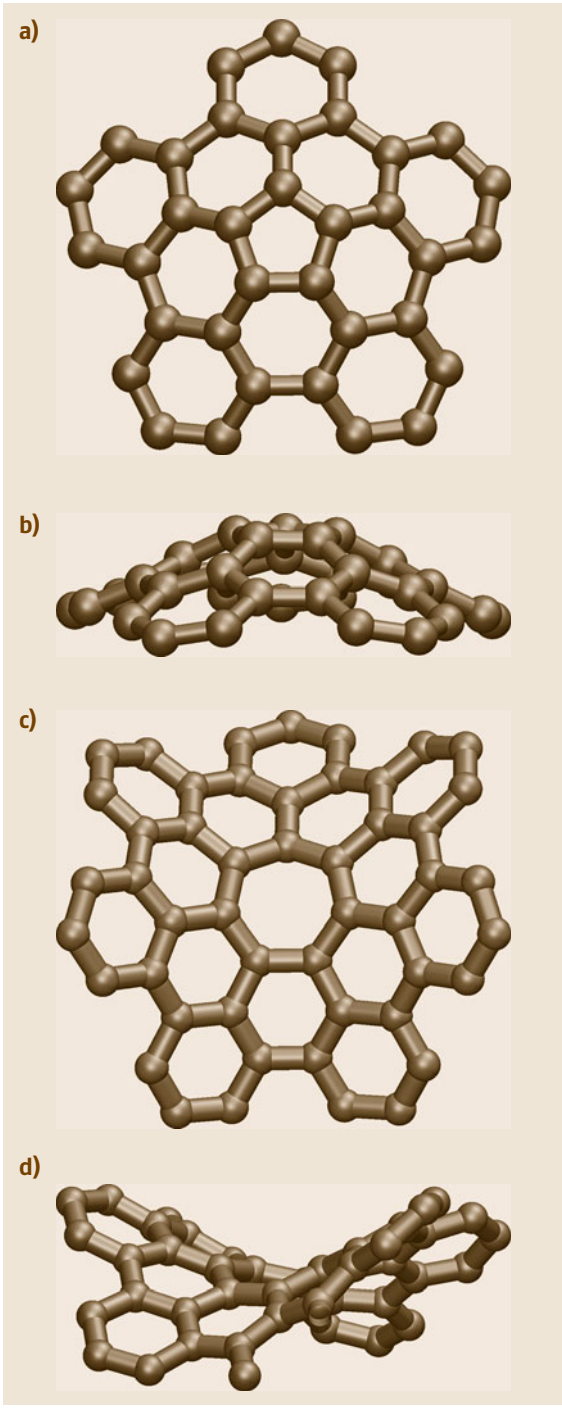


Fig. 3.3 **(a)** Introduction of one pentagon in a graphitic piece induces positive Gaussian curvature (*up view*). **(b)** Side view of **(a)**. **(c)** Introduction of a heptagon in a graphitic piece induces negative Gaussian curvature (*up view*). **(d)** Side view of **(c)** ◀

the nanotube); however, the total Gaussian curvature is zero, because one of the principal curvatures is zero at all points ($K = 0$). Therefore, the carbon nanotube belongs to Euclidean geometry. To confirm this, a triangle drawn on a sheet of paper will have the same interior angles if the sheet is rolled up to form a tube, since the paper cannot be deformed like rubber.

Structures with hyperbolic geometry have been proposed [3.8, 19–22] by the introduction of carbon rings with more than six carbon atoms, heptagons, octagons, and so on (Figs. 3.3c,d, 3.4). These periodic arrangements, with holes that divide space into two congruent regions, have been called schwarzites in honor of the German mathematician *Hermann Amandus Schwarz* (1843–1921) who was the first to find that negative curvature arrangements can produce periodic surfaces with zero mean curvature everywhere [3.23]. Mathematicians have defined a minimal surface as a surface that exhibits zero mean curvature at all points; therefore, minimal surfaces are surfaces formed by symmetric saddle points. Schwarzites are topological representations of minimal surfaces at the atomic level.

Considering Euler's Law, the Gauss–Bonnet theorem, and that in graphitic sp^2 structures every carbon atom is shared by three faces and every edge is shared by two faces, one has $2n_4 + n_5 - n_7 - 2n_8 = 12(1 - g)$, where n_4, n_5, n_7, and n_8 are the number of squares, pentagonal, heptagonal, and octagonal rings of carbon in the nanostructure and g is the genus or number of handles in the graphitic arrangement. A sphere has genus zero (no handles), and a torus has genus 1 (one handle). The equation above can be applied to closed graphitic structures; that is, they do not exhibit boundaries. In the case of C_{60} and other classical fullerenes, there are just 12 pentagons (no squares, no heptagons, and no octagons) so $g = 0$, which is the same genus as the sphere.

In the case of the infinitely periodic schwarzites the genus per primitive cell is greater than or equal to 3. As the genus increases, the structure becomes more complex, as can be seen in Sect. 3.4.5 of this chapter, devoted to high-genus fullerenes.

3.1.3 Classical and Nonclassical Fullerenes

A fullerene can be defined as a closed carbon shell in which each carbon atom is shared by three neighbors.

Classical fullerenes contain hexagonal rings and, as we have seen, 12 pentagonal rings of carbon (Fig. 3.5a–c). The pentagons are responsible for introducing the positive Gaussian curvature that characterizes fullerenes. Twelve pentagons are needed to achieve the closure of the structure, thus having exactly the angular deficit of the sphere (4π).

Nonclassical fullerenes exhibit rings with fewer or more than six carbon atoms, such as squares or heptagons. For each heptagon included, an additional pentagon is needed to compensate for the negative Gaussian curvature of the heptagon (Fig. 3.5d). Fullerenes in which there are six squares can also be considered as nonclassical.

Experimentally it is found that the most abundant fullerene is C_{60} or buckminsterfullerene, synthesized by *Kroto* and colleagues in 1985 using a laser and a graphite target [3.1]; C_{70} and higher fullerenes can also be obtained using this technique. A different way for synthesizing fullerenes is by electric arc discharge, which was used by *Krätschmer* and colleagues in 1990, leading to the discovery of fullerite (the solid form of C_{60}), which is composed of a molecular crystal formed by C_{60} molecules arranged in a face-centered cubic (fcc) structure (Fig. 3.2) [3.18]. Other fullerenes were synthesized afterwards, such as C_{76}, C_{84}, C_{90}, etc. [3.24]. The truncated icosahedral structure (I_h) of C_{60} and the elongated shape of C_{70} have been confirmed by ^{13}C nuclear magnetic resonance (NMR) spectroscopy [3.25, 26].

Despite the existence of 1812 possible ways of forming a classical fullerene with 60 carbon atoms, the most stable and symmetric is the I_h isomer. The number of isomers increases exponentially as the number of carbon atoms increases (Table 3.1). For nonclassical isomers with one heptagon the number of isomers increases even more [3.27].

One feature that makes C_{60} stable is that every pentagon is isolated from the others by hexagons, lead-

Table 3.1 Number of classical and nonclassical isomers with one heptagonal ring of carbon

No. of atoms	Classical isomers	Nonclassical isomers with one heptagon
60	1812	36 295
62	2385	56 950
64	3465	87 425
66	4478	132 586
68	6332	197 218
70	8149	289 921

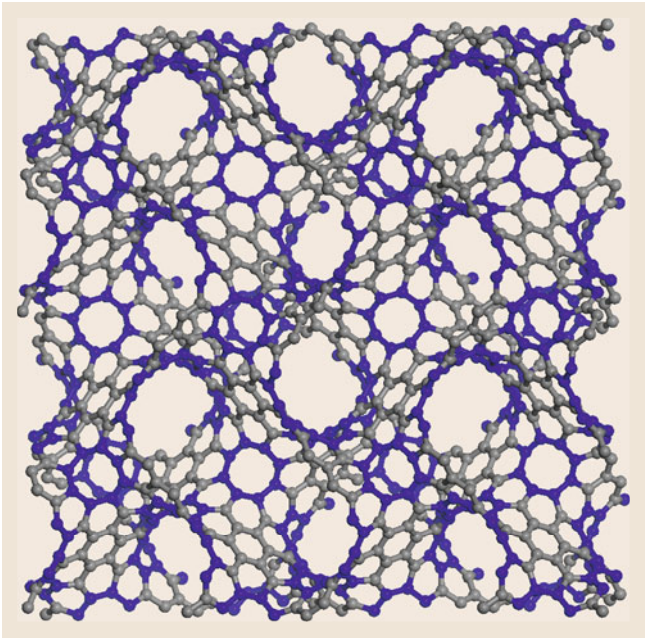


Fig. 3.4 Slice of a G-surface schwarzite with negative Gaussian curvature. The octagonal rings of carbon are formed by the *darker* atoms

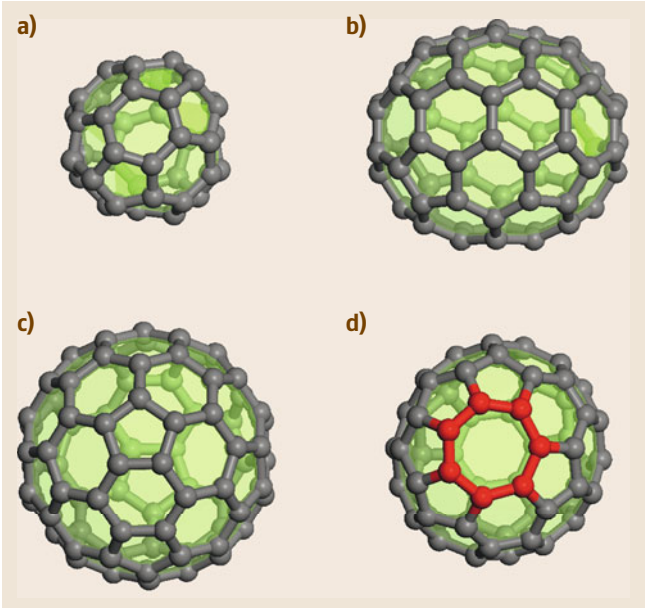


Fig. 3.5 **(a)** Classical C_{40} fullerene with T_d symmetry. **(b)** Classical C_{70} fullerene with D_{5h} symmetry. **(c)** Classical C_{80} fullerene with I_h symmetry. **(d)** Nonclassical C_{62} fullerene with 1 heptagon (*in color*) and 13 pentagons

ing to the isolated pentagon rule (ipr) in fullerenes; therefore, fullerenes with adjacent pentagons cost more energy [3.28]. The next classical fullerene that exhibits isolated pentagons is C_{70} with D_{5h} symmetry, which also has been identified experimentally [3.1,25,26]. For classical fullerenes with fewer than 60 carbon atoms there are no isolated pentagons, which is one of the reasons why they are not very stable [3.28].

3.2 Methods of Synthesis of Fullerenes and Proposed Growth Models

In this section different methods for obtaining C_{60} and other fullerenes are discussed. Most of the methods to produce C_{60} involve very high temperatures (around 4000 °C), such as laser vaporization and arc discharge, because these deal with solid graphite. However, there are other methods which work at lower temperatures such as pyrolysis and electron irradiation, which work with carbon sources that are easier to decompose at lower temperatures. In the case of pyrolysis, an organic compound is used, and in the case of electron irradiation, graphene is used. Certainly, the atmosphere in which the experiments are carried out plays an important role in fullerene formation to avoid undesirable reactions with other elements. To date, the formation mechanisms are not well understood, so different models that have been proposed are reviewed.

3.2.1 Fullerenes by Laser Vaporization Method

The first experiments studying vaporization of carbon clusters by a laser were carried out by *Rohlfing* et al. in 1984, revealing that only carbon clusters with an even number of atoms are formed when the number of atoms is greater than 40 [3.29].

These authors did not identify the structure of C_{60} nor of the other fullerenes. In 1985 the molecule was first identified as a very special cluster of 60 carbon atoms exhibiting the shape of a soccer ball [3.1]. This experiment consisted in using a Nd:YAG laser pulse against a graphite target under a helium atmosphere to decrease the reactivity of the carbon atoms. The molecule was detected by a mass spectrometer. It is noteworthy to say that, when the helium pressure was about 760 Torr, another strong signal corresponding to C_{70} was identified. Unfortunately, these laser experiments produced small amounts of C_{60} and other fullerenes, which prevented scientists from identifying their exact structure and physicochemical properties. Other laser experiments have also led to synthesis of C_{60}, for example, the use of a CO_2 laser to heat benzene molecules for production of C_{60} [3.30].

3.2.2 Fullerenes by Arc Discharge

In 1990, another method to synthesize fullerenes was reported by *Krätschmer* et al. using an electric arc-discharge apparatus with graphite rods attached at both sides of the electrodes under an inert gas atmosphere to avoid reactions [3.18]. The amount of C_{60} obtained by this method was enough to dissolve it in benzene and crystallize it. Although Krätschmer and colleagues reported that the C_{60} crystals had hexagonal close packing, it was found that the real crystals exhibit face-centered cubic (fcc) structure. Since this method could produce high yields of C_{60}, a huge explosion of scientific articles studying its physical and chemical properties appeared. This method became the standard to produce higher fullerenes [3.24] and also carbon nanotubes [3.4].

Another high-temperature method related to arc discharge for producing C_{60} and higher fullerenes involves a hybrid plasma in which a radiofrequency plasma and a direct-current (DC) arc jet operated together can produce vaporization of carbon and the support of the hot region required [3.31].

3.2.3 Fullerenes by Pyrolysis

In the laser irradiation and arc-discharge procedures, the temperatures involved are very high, of the order of 4000 °C, so at a certain stage it becomes difficult to control or study the fullerene formation processes. Several attempts to decrease the temperature and improve control of all the parameters have been reported using lower temperatures and hydrocarbons as carbon precursors (which decompose at lower temperature than graphite). In 1993, a method for producing C_{60} and C_{70} consisting of pyrolysis of naphthalene at 1000 °C was reported [3.32]. Pyrolysis of other organic precursors such as binaphthyl and oligonaphthylene at 1100 °C has

also led to formation of C_{60} [3.33]. Synthesis of C_{60} at 700 °C by reduction of CO_2 with metallic lithium has also been achieved [3.34]. Furthermore, C_{60}, C_{70}, and higher fullerenes have been obtained by pyrolysis of defective single-walled carbon nanotubes at 1200 °C [3.35].

3.2.4 Fullerenes by Combustion in Flames

C_{60} and C_{70} can also be found in flames of hydrocarbons such as benzene in which the C_{60}/C_{70} ratio depends on the temperature, pressure, and carbon/oxygen ratio [3.36–38]. In 1997, *Richter* and colleagues found higher fullerenes including C_{60} and C_{70} such as C_{76}, C_{78}, C_{80}, C_{84}, C_{86}, C_{88}, C_{90}, C_{92}, C_{94}, C_{96}, C_{98}, C_{100}, C_{102}, and C_{108} in flames of benzene/oxygen/argon at pressures of around 40 Torr; These authors compared the soot of flames and that of the arc discharge and found that the abundances of higher fullerenes in the soot from flames were higher than that of the arc discharge [3.39]. It is noteworthy that flame-generated soot which contains fullerenes is formed by transformation of polycyclic aromatic hydrocarbons [3.40].

3.2.5 Fullerenes Under Electron Beam Irradiation Inside a Transmission Electron Microscope (TEM)

As we have seen in the previous synthesis methods for fullerenes, there should be a carbon source that needs to be rearranged or excited to form a metastable nanostructure such as a fullerene. Using an aberration-corrected high-resolution transmission electron microscope working at 80 keV it is possible to observe rearrangement of the carbon atoms of graphene (a single layer of graphite) to form a fullerene [3.41] (Fig. 3.6). In this case, pentagonal rings of carbon at the edges of graphene trigger the positive Gaussian curvature needed to form a ball-shaped structure, and then closure is achieved by avoidance of dangling bonds. It is not clear from this observation that the isomer formed is that of C_{60} I_h, C_{70} D_{5h}, or another fullerene. However, what is clear is that fullerenes can form under the right conditions under electron beam irradiation.

3.2.6 Fullerenes by Concentrated Solar Flux

Solar radiation can be concentrated and controlled to build furnaces which can achieve high temperatures (around 3000 °C) and thereby vaporize graphite to form fullerenes [3.42, 43]. Although this method involves high temperatures as in arc discharge and laser ablation, it can be scaled to increase the yield [3.44].

3.2.7 Proposed Mechanisms for Fullerene Growth and Formation

Although there are different methods for producing fullerenes, their formation is not well understood. Although avoiding dangling bonds may be the driving force for formation of carbon cages, there remain unanswered questions regarding the formation or growth mechanisms of fullerenes. The first attempts to ex-

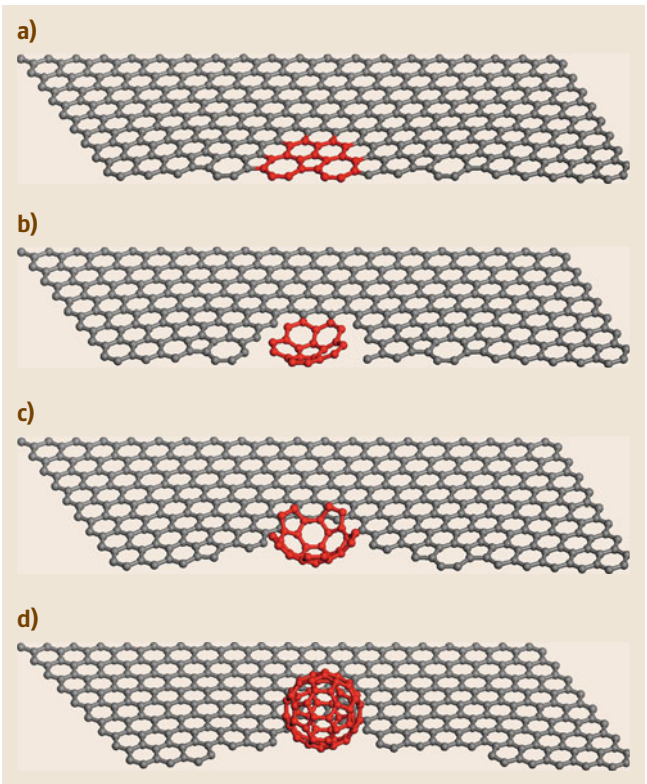


Fig. 3.6a–d Sequence of formation of C_{60} from graphene by electron irradiation: **(a)** The five–seven defects at the edges introduce the local curvature and reactivity. **(b)** Pentagonal and additional hexagonal rings separate from the defective graphene sheet. **(c)** The fullerene grows due to its reactivity (dangling bonds) by addition of carbon atoms ejected by the electron irradiation process from the graphene sheet. **(d)** The process is complete when the fullerene molecule closes itself, satisfying all dangling bonds

plain the formation and growth of fullerenes were the pentagon road, the fullerene road, and ring coalescence [3.45].

The Pentagon Road for Fullerene Formation

This process considers the formation of linear chains which become rings that form pentagons of carbon in the gas phase. These are responsible for the positive Gaussian curvature of the structure, forming a cup-like arrangement, until the 12 isolated pentagons are produced for the closure [3.46].

If extra pentagons (more than 12) are introduced, spirals of carbon can be formed and graphitic onions can be produced [3.47]. Different sizes of fullerenes can be formed in this way, but only those that possess isolated pentagons prevail. C_{60} I_h and C_{70} D_{5h} both exhibit isolated pentagons. This route does not take into account the possibility of generating nonclassical fullerenes [3.27].

The Fullerene Road

Heath [3.48] suggested that the formation of fullerenes in the gas phase consists of four steps:

1. Growth of carbon chains up to lengths of C_{10}
2. Growth from chains into monocyclic rings (C_{10}–C_{20})
3. Production and growth of three-dimensional reactive carbon networks (C_{20}–C_{40})
4. Growth of small fullerene cages (with more than 40 atoms) via closed shells in which there are adjacent pentagonal rings of carbon which constitute active sites for addition of dimers until C_{60} and C_{70} as well as higher fullerenes are formed.

The Importance of Carbon Rings in Fullerene Formation

McElvany and colleagues used Fourier-transform mass spectrometry (FTMS) to study the reaction of cyclical carbon–oxide molecules C_{18}, C_{24}, and C_{30}, finding that these ring structures coalesce to form C_{60}^+ and C_{70}^+ [3.49]. In fact, the importance of carbon rings in the formation of fullerenes has been addressed experimentally by different groups.

Von Helden and coworkers showed experimentally that fullerenes can be formed in the gas phase by a three-stage process: from linear chains of carbon atoms to planar rings and then to fullerenes accompanied by evaporation of small carbon fragments C_1 or C_3 for odd systems and C_2 for even systems [3.50]. *Hunter* and coworkers studied the annealing of nonfullerene C_{60}^+ cluster ions, finding that these, when fragmented, form C_{60} fullerenes and monocyclic rings. These rings are very stable and constitute another nonspheroidal form of carbon [3.51]. *Pope* et al. proposed a mechanism which uses polycyclic aromatic hydrocarbons to form C_{60} and C_{70} in flames [3.52].

Some theoretical models involve carbon dimer additions to small nonclassical fullerenes during a very fast reaction at high temperature in arc-discharge synthesis [3.27]. It is noteworthy that closed cages of fullerenes, both classical and nonclassical, should have an even number of carbon atoms, more than 20 (with the exception of 22).

3.3 Physicochemical Properties of Fullerenes

Working with fullerenes involves studying their crystals, known as fullerites, and obviously the molecules themselves. In this section the physical properties reviewed are those of the fullerites, studying their structure, different phases, and electronic behavior. Regarding their chemical properties, isolated fullerene molecules interact with other elements or compounds, forming new ones which might have important applications in the future.

3.3.1 Mechanical Properties and Phases of Fullerene Crystals

Fullerites are formed by crystallization of fullerenes. As we have seen, *Krätschmer* and colleagues in their original paper reported that C_{60} crystals, under normal conditions, exhibited hexagonal close-packing (hcp) structure [3.18]; however, the actual packing of fullerite (crystals of C_{60}) is face-centered cubic (fcc) with cell parameter of 14.198 Å, and the molecules exhibit orientational disorder [3.53]. When the temperature is decreased to 294 K, the C_{60} molecules become ordered (no rotation) and the fcc phase changes to a simple cubic (SC) phase [3.53].

C_{60} fullerite is stable at hydrostatic pressures of 20 GPa, but when the pressure is nonhydrostatic, changes are produced, lowering the symmetry of C_{60} crystals [3.54]. *Regueiro* and colleagues found that nonhydrostatic pressure on fullerite can lead to polycrystalline diamond at room temperature [3.55]. Fullerite is

a semiconductor with band gap of 1.5 eV [3.56], and although pressure induces changes in the gap of fullerite, a metallic phase is not observed [3.57]. At pressures of the order of 5 GPa and temperatures of 400 °C, a new fcc phase is observed. Increasing the temperature to 800 °C, a rhombohedral phase is found [3.58]. The compression behavior of fullerite and its phase diagram have been discussed in detail by *Sundqvist* [3.59]. C_{70} also possesses different phases such as fcc, hcp, and monoclinic [3.60]. Certainly, investigation in crystals obtained from other fullerenes, considering doping, should continue to identify new applications, possibly in electronics.

3.3.2 Electrical Properties and Superconductivity of Fullerites

Despite the semiconducting nature of fullerite crystals with band gap around 1.5 eV [3.56, 61], films of C_{60} and C_{70} doped with alkali metals (Rb, K, or Cs) are conducting [3.62]. In the AC_{60} fullerite phases, where *A* is Rb, K, or Cs, linkage due to [2 + 2] cycloaddition between the C_{60} molecules is observed, causing a 9% reduction of the cell parameters in one direction and thus resulting in polymerization of the C_{60} molecules in one direction [3.63, 64].

However, superconductivity has been observed at low temperatures. C_{60} fullerite doped with potassium atoms exhibits a superconducting temperature of 18 K [3.65]. According to Rietveld analysis of x-ray diffraction data, the superconducting phase K_3C_{60} corresponds to a fcc lattice with potassium atoms occupying interstitial sites [3.66].

The superconducting temperature can be increased to 28 K when using Rb [3.67] and up to 33 K when using cesium and rubidium together [3.68]. The electronic structure, conductivity, and superconductivity of alkali metal-doped C_{60} have been studied and reviewed thoroughly by *Haddon* [3.69]. To explain the superconductivity in fulleride systems (fullerite crystals doped with metal atoms) the electron–phonon coupling has been studied theoretically [3.70]. Superconductivity at 8.4 K of C_{60} doped with calcium has also been reported [3.71]. Cesium-doped fullerenes can reach superconducting temperatures of up to 40 K [3.72, 73].

In 2010, *Ganin* and coworkers isolated a phase of a Cs_3C_{60} crystal which shows magnetic semiconducting behavior at ambient pressure and superconducting behavior under pressure [3.74].

3.3.3 Chemical Properties of Fullerenes

C_{60} and higher fullerenes have opened a new chemistry in which the fullerenes behave as a superatom. In the early stages of fullerene research, *Taylor* and *Walton* recognized the importance of C_{60} and C_{70} as reactive species that can undergo several chemical reactions [3.75]. In C_{60} there is an alternation of bonds, which plays an important role in chemical reactions: There are 30 (6–6) bonds at the junctions between two six-member rings with bond length of ca. 1.38 Å. These bonds have a double-bond character. On the other hand, there are 60 bonds between adjacent pentagons and hexagons (6–5) with length around 1.45 Å. The introduction of one double bond between a hexagon and a pentagon costs energy (around 8.5 kcal/mol) [3.76, 77]. Therefore, through these double bonds, C_{60} can interact with other atoms or molecules. Early electrochemical experiments showed that oxidation of C_{60} and C_{70} is difficult to achieve, but they can be reduced with multiple one-electron reduction steps [3.78]. Via Birch reduction, C_{60} can be hydrogenated to obtain $C_{60}H_{36}$ [3.79].

Suzuki and coworkers were able to add phenol groups to C_{60} to form fulleroids C_{61} and C_{66} [3.80]. Different groups have made important contributions in the study of cycloaddition reactions of C_{60} [3.81–84].

The reactivity of C_{60}, as described by *Diederich* and *Thilgen*, consists of a strained electron-deficient polyalkene with localized double bonds [3.77]. C_{60} reacts with transition metals such as iridium, ruthenium, osmium, rhenium, palladium, and platinum through these double bonds [3.85, 86]. Halogenation reactions with fluorine, chlorine, and bromine have also been achieved [3.86].

The basics of C_{60} chemistry with applications in materials science have been studied and reviewed by *Prato* [3.87]. Among these applications of C_{60} are the incorporation of C_{60} into polymers for photoconductive devices, thin films with C_{60}, and electrooptical devices. It is no exaggeration to say that fullerenes have their own chemistry which certainly will find a future in different applications such as health and energy.

3.4 Applications of Fullerenes and Beyond

One of the expectations of nanotechnology is to help in solving problems related to health, energy, and the environment. In this context, fullerene researchers have made important contributions that show the potential of these amazing molecules. In this section, some of the most relevant advances are presented. In addition, it is fair to say that fullerenes have also opened other fundamental research areas with related materials such as carbon onions, which consist of nested fullerenes, fullerene peapods, high-genus fullerenes, inorganic fullerenes made of metal chalcogenides, and nanodiamonds. The potential of these nanostructures is discussed in the next sections.

3.4.1 Fullerenes and Health

As a multidisciplinary activity, one of the aims of nanoscience and nanotechnology is to help in solving some human health problems. Since 1993, extensive research has been carried out on use of C_{60} as a virucidal compound to inhibit human immunodeficiency virus (HIV) enzymes [3.88–90].

In vivo experiments in rats have been carried out with water-soluble fullerenes, showing that they are not acutely toxic. Fullerenes distribute rapidly in many tissues and thus may be useful for drug delivery applications [3.91]. Research into functionalized fullerenes in water has led to important achievements such as the interaction of organofullerenes with DNA, proteins, and living cells, their photochemical properties, radical quenching, and hydrophobicity [3.92].

Among the applications that fullerene derivatives might have in biological systems are as antioxidants and neuroprotective agents, antiapoptotic activity, DNA photocleavage, enzyme inhibition, antimicrobial activity, osteoporosis therapy, antifullerene monoclonal antibodies, contrast agents and radiotracers, and gene transfection agents [3.93]. Also, fullerenes might help in inhibiting allergic responses [3.94].

Cytotoxic mechanisms of C_{60} and its derivatives have also been studied in detail [3.95, 96].

3.4.2 Fullerenes in Solar Cells

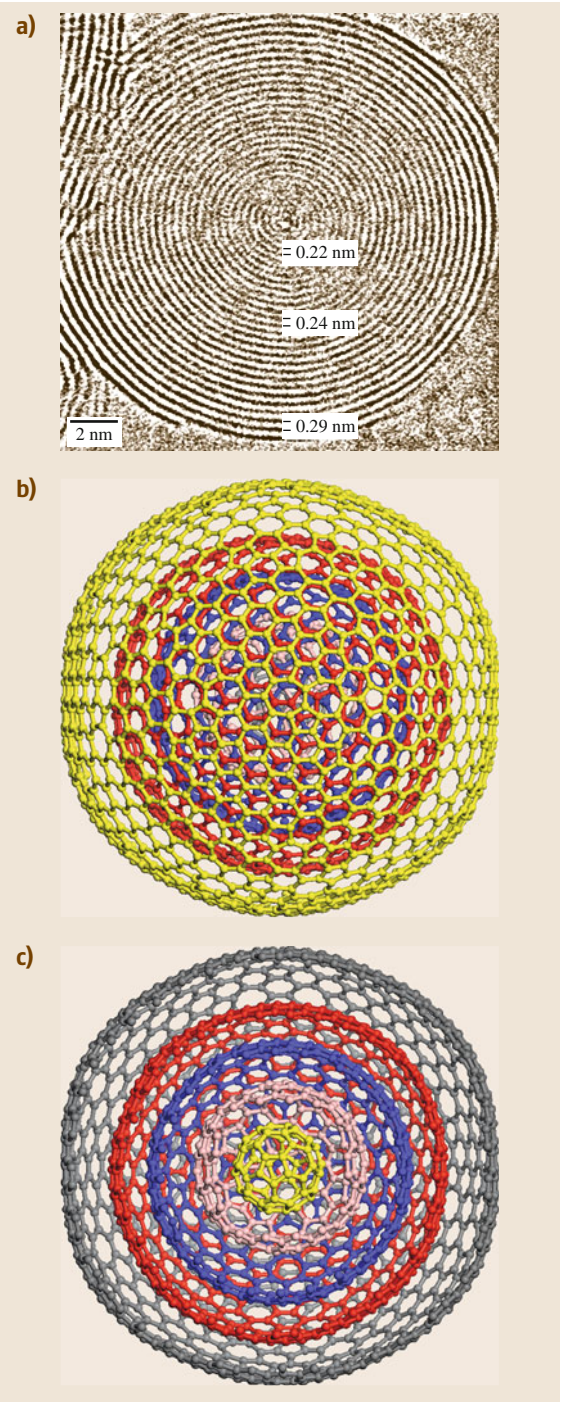
An important advancement in solar cell design has been made using the bulk heterojunction approach in which a donor-type conjugated polymer is blended with an acceptor fullerene. In this context, highly soluble fullerene derivatives such as methanofullerene [6,6]-phenyl C_{61}-butyric acidmethyl ester, a new azafulleroid, and a ketolactam quasifullerene have been synthesized for use as electron acceptors in plastic solar cells. It has been found that the open-circuit voltage in the solar cells is directly related to the acceptor strength of the fullerenes [3.97], so plastic solar cells including fullerenes might have a future as new solar cell devices [3.98]. *Wienk* et al. have shown that methano[70]fullerene, based on C_{70} fullerenes, can be used in plastic solar cells with power conversion efficiency (PCE) of 3% [3.99]. Photovoltaic solar cells with PCE of 1.45% have been also obtained using a mixture of porphyrin nanoclusters with C_{60} and gold nanoparticles [3.100]. *Imahori* and *Fukuzumi* used just porphyrins and C_{60} to produce a photovoltaic cell with PCE of 1% [3.101]. Endohedral fullerenes such as trimetallic nitride inside the C_{80} I_h fullerene, $Lu_3N@C_{80}$, have been used in polymer solar cells as an electron acceptor with PCE of more than 4% [3.102]. The performance of inverted solar cells using ZnO nanoparticles as the electron selective layer can be improved from 3.7% to 4.5% after modification with a C_{60} self-assembled monolayer [3.103]. *Troshin* et al., prepared 27 derivatives of C_{60} and C_{70} for use in plastic solar cells, finding that the PCE varies from as little as (0.02%) to considerably high (4.1%) [3.104]. Use of alkene dithiols in semiconducting polymer solar cells with C_{60} derivatives increases the PCE from 2.8% to 5.5% [3.105]. Solar cells based on semiconducting polymers and C_{60} fullerene derivatives (tandem solar cells) can achieve PCE of the order of 6.7% [3.106].

Hatakeyama and colleagues used fullerene C_{60} inside single-walled carbon nanotubes (fullerene peapods) to increase the efficiency of infrared photovoltaic solar cells [3.107]. Polymer photodetectors made with polymers and C_{60} derivatives exhibit spectral responses from 300 up to 1350 nm and can substitute photodetectors based on inorganic materials [3.108].

3.4.3 Nested Fullerenes: Carbon Onions

As a byproduct of electric arc-discharge experiments, it is common to find, besides carbon nanotubes and C_{60}, polyhedral particles of carbon which look like nested or matryoshka-like fullerenes formed by giant fullerenes one inside the other (Figs. 3.7, 3.8). In 1980, *Iijima* reported high-resolution TEM studies of nested carbon structures [3.109] and in 1987 recognized the possi-

bility of having C_{60} in the most interior shell of these onions [3.110].



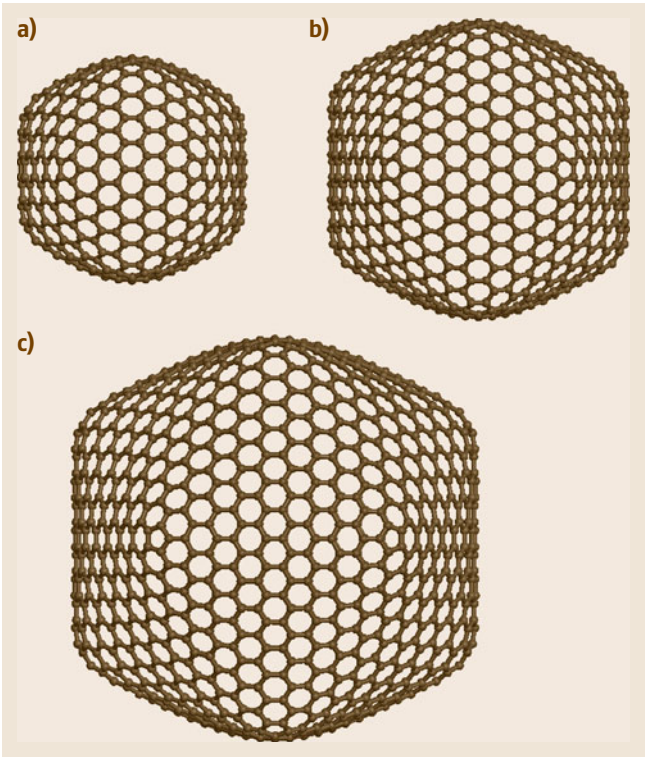


Fig. 3.7a–c Giant icosahedral (I_h) fullerenes: **(a)** C_{540}, **(b)** C_{960}, and **(c)** C_{1500}

Ugarte found that, by irradiating amorphous carbon with the electron beam of a transmission electron microscope, quasispherical carbon onions were produced in situ [3.7, 112, 113]. The high sphericity attracted the attention of researchers, since in most cases, polyhedral graphitic particles exhibit facets. A model which explained the sphericity of carbon onions through the introduction of pentagonal and heptagonal rings of carbon was proposed by *Terrones* et al. (Fig. 3.8) [3.114–116]. These spherical onions compete in terms of stability with classical fullerenes [3.117].

Another important observation of spherical carbon onions consisted in the formation of diamond inside

Fig. 3.8 **(a)** Carbon onion obtained by electron irradiation and heating. The graphitic distances inside the onion are shorter than outside due to pressure effects (after [3.111], courtesy of Elsevier). **(b)** Model of a carbon onion in which the sphericity of the nanostructure is obtained by the addition of heptagon–pentagon pairs of carbon: *the Terrones model*. **(c)** Cut of the onion shown in **(c)** depicting the several nested fullerenes ◀

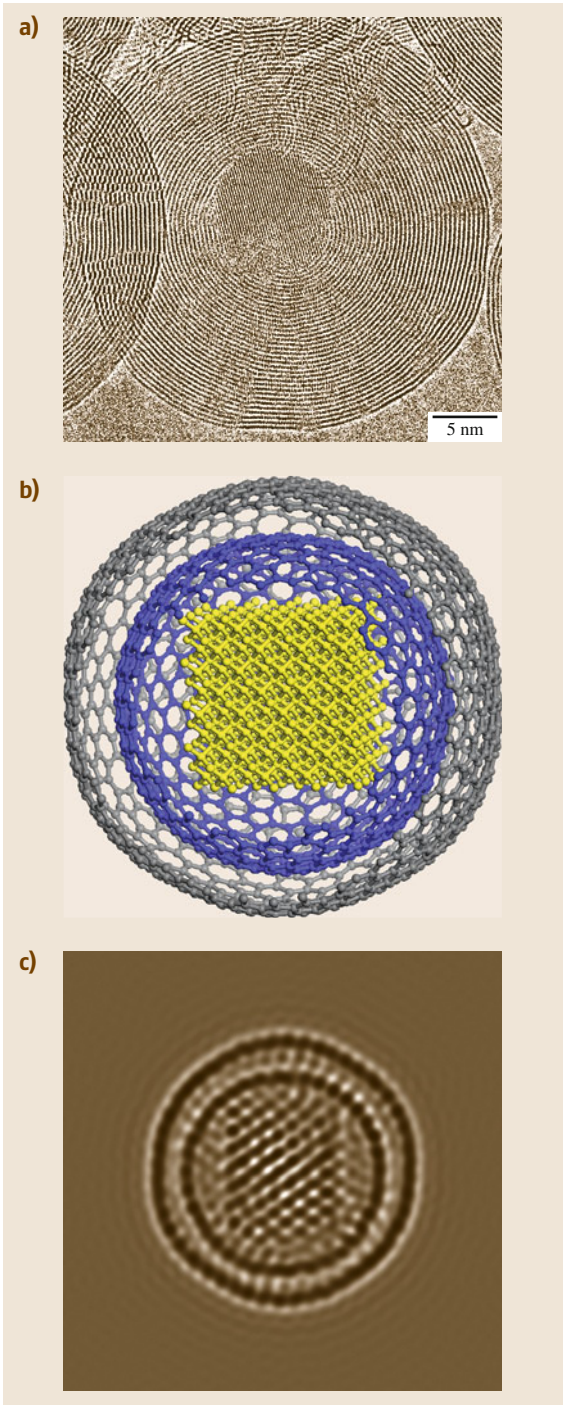


Fig. 3.9 **(a)** Carbon onion with diamond grown at the center (after [3.118]). **(b)** Model of a two-shell carbon onion with diamond inside. **(c)** Simulation of a high-resolution TEM image of the onion shown in **(b)**, in which the diamond lattice can be resolved ▶

them under transmission electron microscope action (Fig. 3.9). Therefore, it is possible to grow nanodiamond inside carbon onions. The pressure inside carbon onions and electron irradiation help the diamond formation. In Fig. 3.9b,c a molecular model of a carbon onion with diamond inside and a high-resolution image simulation are shown [3.111, 118, 119].

Although these higher nested fullerenes require more study, important advances have been reported. Recently, it was found that carbon onions exhibit excellent properties as supercapacitors [3.120].

Chemical vapor deposition processes at temperatures between 750 °C and 850 °C have also been used to produce considerable amounts of carbon onions with diameters of 400–2000 nm [3.121–124].

Other applications of carbon onions include: Use as x-ray target materials prepared with lanthanum carbide and lanthanum hexaboride [3.125], for electrodes in Li-ion batteries [3.126] and broadband wave absorbers in the GHz and THz regions [3.127]. When filled with nickel, using the electric arc-discharge technique, good electromagnetic absorbers in the 2–18 GHz range can be obtained [3.128].

A new electron field emitter has been produced by attaching a single carbon onion to the tip of a tungsten nanowire. This new kind of emitter can sustain large emission currents of more than 100 μA and possesses long-term emission stability [3.129].

In the biological area, the toxicity of carbon onions used as contrast agents when filled with lanthanide carbides has been assessed, showing that it is similar to or lower than that of TiO_2 nanoparticles [3.130]. Gold nanoparticles attached to carbon onions could be used for immobilizing biomolecules or as biomolecule sensors [3.131]. Iron–cobalt nanoparticles inside carbon shells have been made soluble in water and tested in magnetic resonance imaging in rabbits, with applications also in photothermal treatment using magnetic fields [3.132].

3.4.4 Fullerene Peapods and Fullerene Coalescence

It has been found that, during the laser evaporation process to form single-walled carbon nanotubes, C_{60} can also be generated and introduced inside single-walled carbon nanotubes, thus forming a nanopeapod

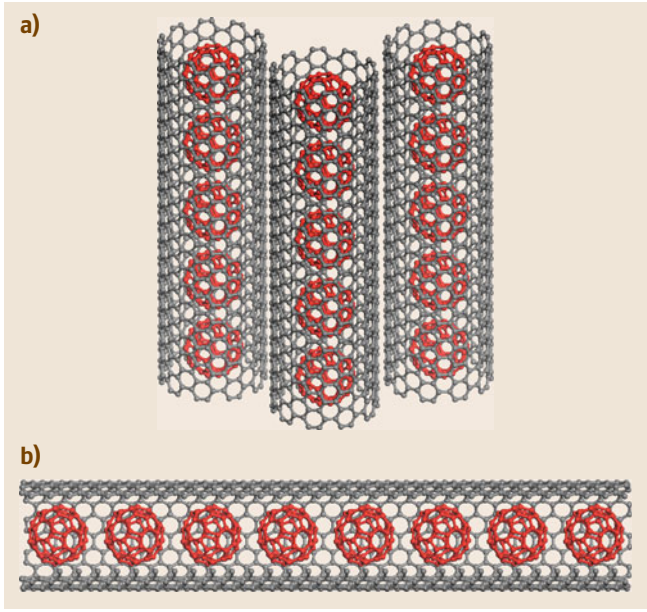


Fig. 3.10 **(a)** Carbon nanotubes with C_{60} inside *fullerene peapods*. **(b)** Cut of a carbon nanotube showing the C_{60} molecules inside ▶

(Fig. 3.10) [3.133–136]. *Luzzi* and *Smith* proposed that C_{60} accumulates on the surface of the nanotubes and enters via defects, forming linear van der Waals chains of molecules, which can coalesce to create an inner tube (Figs. 3.11, 3.12) [3.136].

Evidence of coalescence reactions in C_{60} and C_{70} has been reported by *Yeretzian* and coworkers [3.138]. Coalescence of C_{60} with negative Gaussian curvature, preserving the sp^2 bonding, has been used to propose theoretical models of icosahedral aperiodic arrangements in 3-D [3.139].

Scanning tunneling microscopy (STM) and scanning tunneling spectroscopy (STS) have revealed electronic modulation effects due to the chain arrangement of C_{60} molecules inside single-walled carbon nanotubes (SWCNT) [3.140]. High yields of fullerene peapods can be generated by sublimation methods, including the introduction of C_{70} molecules [3.141, 142]. Raman spectroscopy has been used to study the fullerene coalescence process inside a SWCNT, proposing that the coalescence leads to zigzag inner nanotube formation [3.143].

Theoretical studies have shown that, depending on the C_{60} orientation of the molecules (inside the nanotubes), the inner tube can be metallic or semiconducting [3.137]. The electrochemical properties of fullerene peopods are dominated by their capacitive charging, without any distinct Faradaic processes, and is similar to that of empty single-walled carbon nanotubes [3.144]. Gadolinium metallofullerene $Gd@C_{82}$ has been synthesized by arc discharge and introduced inside SWCNTs using a sealed glass ampule at 500 °C, thus producing a metallofullerene one-dimensional crystal inside SWCNTs in which the Gd atom might transfer charge to the fullerene and to the SWCNT [3.145]. A metallofullerene is a fullerene which encapsulates a metal atom.

Praseodymium and scandium atoms inside C_{80} ($PrSc@C_{80}$) have been encapsulated inside a SWCNT and identified using electron microscopy techniques

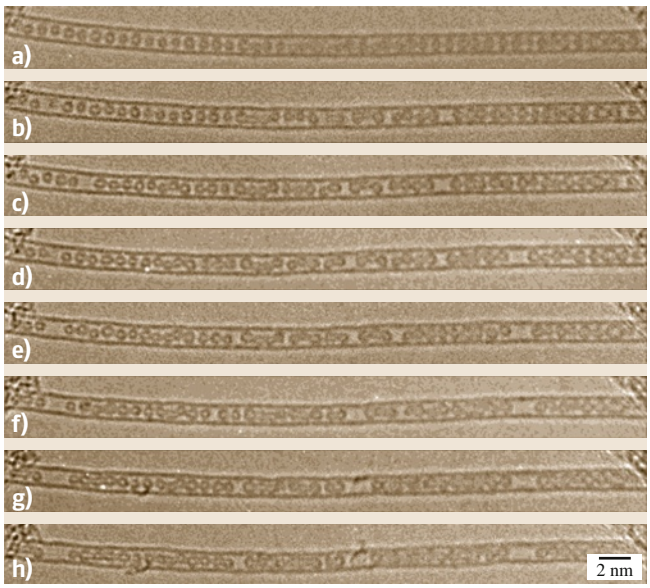


Fig. 3.11a–h Sequence of TEM micrographs showing irradiation-induced coalescence of C_{60} within the lumen of an isolated SWNT. **(a)** Starting configuration after a minimal electron dose. **(b–h)** Consecutive images recorded at 60–90 s intervals. Damage to the fullerenes occurs by knock-on ejection of carbon atoms, resulting in structural reconfiguration into corrugated tubules that are ca. 5–7 Å in diameter. These tubules exhibit regions of negative curvature that may be associated with the formation of heptagonal rings acting to link the discrete molecules together. Pronounced damage to the SWNT is also visible beginning in **(c)**, but its damage rate is appreciably slower because of curvature effects. Therefore, C_{60}–C_{60} fusion predominates over C_{60}–SWNT fusion (after [3.137], courtesy of ACS) ▶

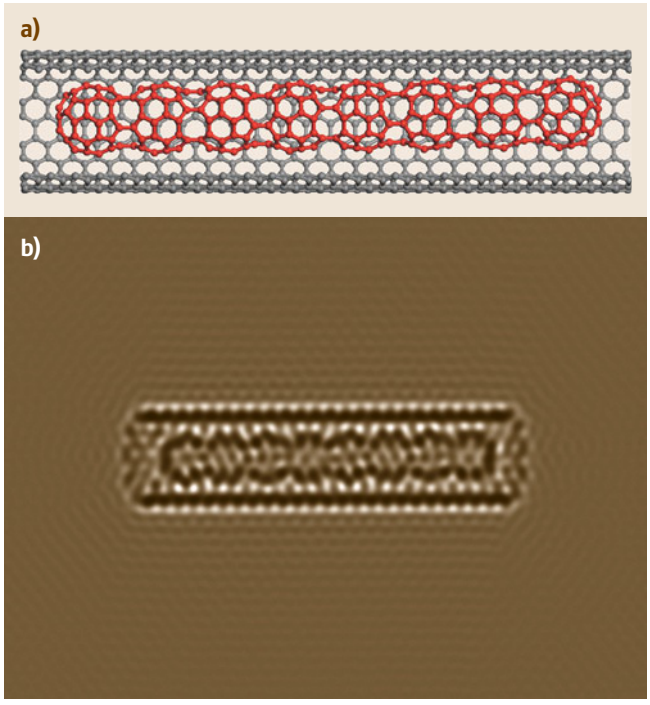


Fig. 3.12 **(a)** Carbon nanotube with coalesced C_{60} molecules forming a corrugated nanotube. **(b)** Simulation of a high-resolution TEM image of a carbon nanotube with a corrugated tube inside formed by fullerene coalescence

such as high-angle annular dark-field and electron energy-loss spectroscopy (EELS) [3.146].



Fig. 3.13 Model of a nanotorus formed by C_{60} coalescence through the presence of octagonal rings of carbon

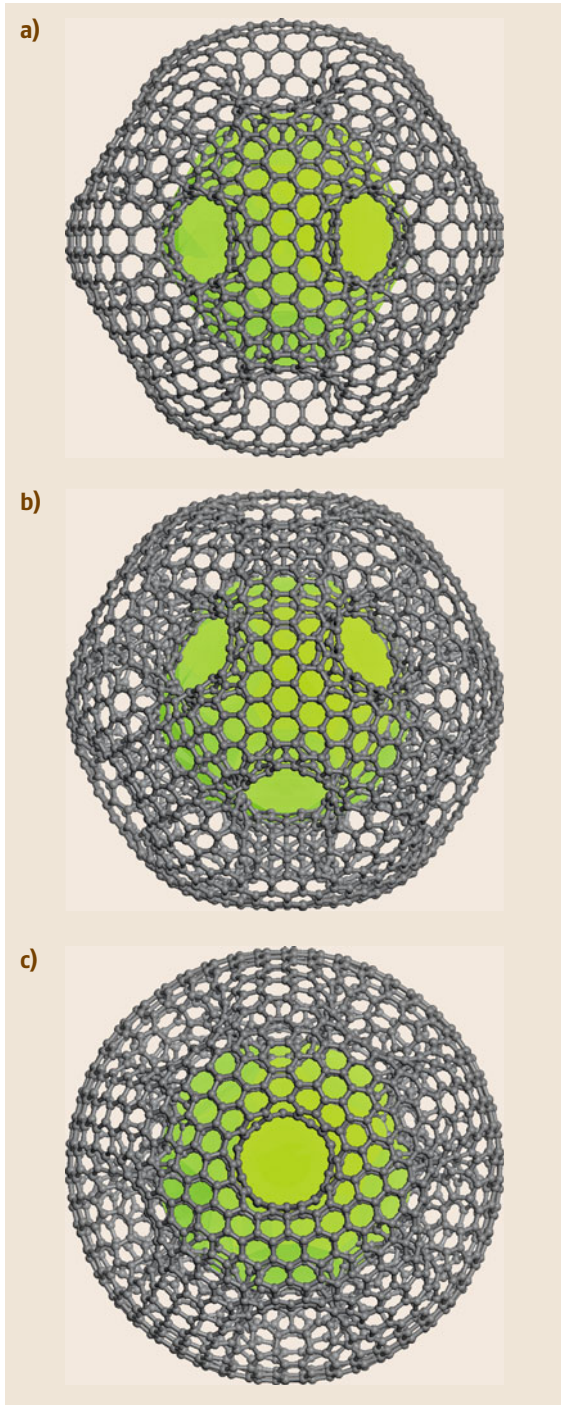


Fig. 3.14a–c Holey fullerene with genus 11, icosahedral I_h symmetry, and 2040 carbon atoms: **(a)** twofold axis view, **(b)** threefold axis view, and **(c)** fivefold axis view

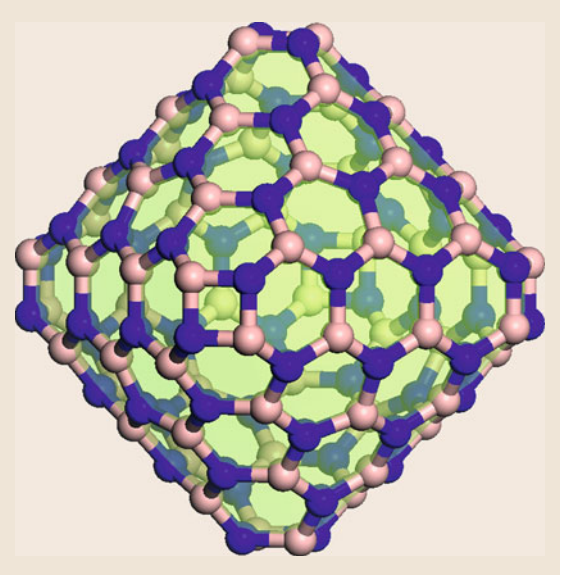


Fig. 3.15 Boron nitride cage $B_{64}N_{64}$ with T_d symmetry

3.4.5 High-Genus Fullerenes

As has been seen in the previous section, fullerenes can coalesce and form one-dimensional (1-D) chains or nanotubes; however, another possibility is formation of toroidal structures (Fig. 3.13), which can respond to a magnetic field, exhibiting an induced magnetic moment, depending on the orientation of the C_{60} molecules [3.147]. For the case of coalesced toroidal C_{60} molecules the genus g is 1, the same as for a donut.

More complex architectures can be proposed by coalescing larger fullerenes, starting from onion-like structures; for example, a genus-11 holey fullerene with I_h symmetry can be constructed by coalescing a I_h C_{500} and a I_h C_{240} fullerene [3.148] (Fig. 3.14). Closed nanotubes up to genus 21 have been proposed [3.148]. Using a tight-binding approach, the electronic properties of these complex fullerenes can be calculated, finding that their holes behave as active sites for attachment of molecules or foreign atoms [3.149], which can be used as molecular sensors or for hydrogen storage [3.150]. Different families of high-genus fullerenes have been proposed and classified according to their geometrical features [3.151].

3.4.6 Inorganic Fullerenes (BN, MoS_2, NbS_2, etc.)

Graphite and graphene are not the only layered materials; there are others such as boron nitride (BN) and molybdenum, tungsten, and rhenium disulfides. Hexagonal BN is composed of hexagonal flat layers with hexagonal rings of alternating boron and nitrogen atoms. In the case of BN fullerenes, six squares are required to close the structure and preserve the stoichiometry (Fig. 3.15). Octahedral BN nested fullerenes (up to three layers) have been found by electron irradiation [3.152].

Theoretical calculations have been performed on octahedral BN fullerenes [3.153]. Closed-tip boron nitride nanotubes have been found in electric-arc discharge made out of BN inside tantalum rods [3.154] and tungsten rods [3.9]. The tip of these tubes might exhibit half

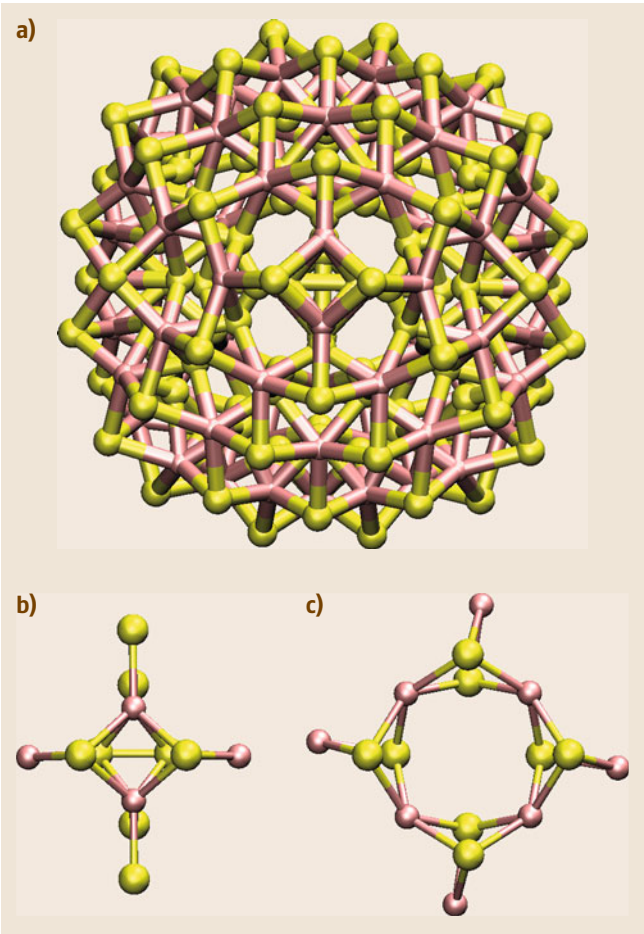


Fig. 3.16 **(a)** Molybdenum sulfide cage $Mo_{64}S_{128}$ with T_d symmetry. **(b)** Stoichiometry-preserving defects in metal chalcogenide layers: square-like defect responsible for the positive Gaussian curvature. **(c)** Octagonal-like defect responsible for the negative Gaussian curvature (*smaller atoms* are the metal atoms)

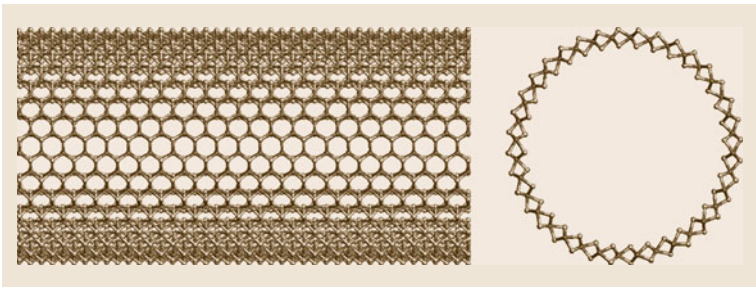


Fig. 3.17 Tungsten sulfide WS_2 (18,18) armchair nanotube

a BN fullerene [3.155]. Pentagonal rings can be stable in BN fullerenes if there is a nitrogen excess [3.155].

Tenne and coworkers found that metal chalcogenides can acquire curvature to form fullerene-like structures and nanotubes [3.12] (Figs. 3.16, 3.17). In fact, WS_2 fullerenes can be used as solid lubricants [3.156]. The curvature in these systems requires a square-like defect for positive Gaussian curvature and an octagon-like defect for negative Gaussian curvature [3.157]. These fullerene-like structures could exhibit octahedral symmetry (T_d point group) and possess six square-like defects (Fig. 3.16).

3.4.7 Nanodiamond

Nanodiamonds are small clusters of sp^3 carbon in which each atom is connected covalently to four nearest neighbors, except for the boundary atoms. It has been shown in this chapter that fullerite under high pressure and high temperature becomes diamond and also that carbon onions undergo a phase transformation into diamond [3.158]. Following *Shenderova* et al., there are two large groups of nanodiamond: The first group involves nanodiamonds as a final product obtained from methods such as electron irradiation of carbon onions, ultrananocrystalline diamond films, and ultradispersed diamond obtained from detonation synthesis [3.159]; The other group involves nanodiamonds which are the result of interrupting the process of growth of micro- or macrodiamonds [3.158]. It is worth mentioning that there is diamond in interstellar space found in meteorites [3.159, 160]. Approximately 10–20% of interstellar carbon is in the form of nanodiamonds.

The fluorescence properties of nanodiamonds enable their use as biological markers, which might have application in the future for tumor targeting [3.161]. In this context, it has been found that nanodiamonds of sizes between 2 and 10 nm are not toxic [3.162].

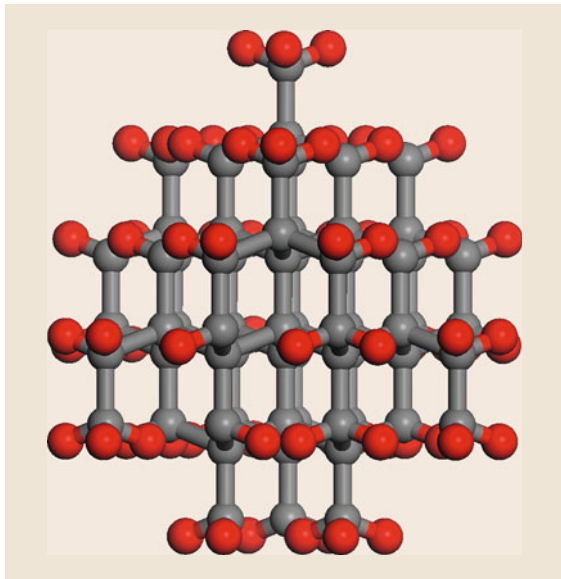


Fig. 3.18 Nanodiamond saturated with hydrogen

First-principles calculations indicate that the nanodiamond surface can be reconstructed by sp^2 bonding, forming a kind of hybrid between a fullerene and diamond, having diamond in the interior and a fullerene on the surface [3.163].

Diamonoids are a variant of carbon cage molecules made of sp^3 carbon saturated with hydrogen (Fig. 3.18). Among these molecules are: adamantane ($C_{10}H_{16}$), iceane ($C_{12}H_{18}$), diamantane ($C_{14}H_{20}$), triamantane ($C_{18}H_{20}$), pentamantane ($C_{25}H_{30}$), and superadamantane ($C_{35}H_{36}$). Larger diamonoids have been isolated from petroleum and might have applications in biology as well as electronics and field emission [3.164].

3.5 Conclusions

Buckminsterfullerene opened the field of carbon nanostructures, strengthened nanoscience and nanotechnology, and brought about a new way of doing science involving multidisciplinarity. The whole spectrum of new applications for layered nanomaterials is very promising, and certainly the novel building blocks for advanced materials in the 21st century will include fullerenes, carbon nanotubes, graphene, graphene nanoribbons, carbon onions, porous carbons, boron nitride nanoribbons, and metal chalcogenide nanostructures. The idea of producing, out of any bulk material, a thin layer, one atom thick, and curving it in different ways, opens new avenues in advanced architectures. New characterization techniques and new tools will have to be developed to make full use of them.

These nanomaterials will play an essential role in the immediate challenges such as efficient energy production, environmental remediation, and health problems. It is no coincidence that two carbon nanostructures, C_{60} and graphene, have been awarded two Nobel Prizes in two different fields.

References

3.1 H.W. Kroto, J.R. Heath, C.O. O'Brien, R.F. Curl, R.E. Smalley: C_{60}: Buckminsterfullerene, Nature **318**(6042), 162–163 (1985)

3.2 The Institute for Scientific Information web page: http://apps.isiknowledge.com/ (last accessed December 2010)

3.3 A. Oberlin, M. Endo, T. Koyama: Filamentous growth of carbon through benzene decomposition, J. Cryst. Growth **32**(3), 335–349 (1976)

3.4 S. Iijima: Helical microtubules of graphitic carbon, Nature **354**(6348), 56–58 (1991)

3.5 K.S. Novoselov, A.K. Geim, S.V. Morozov, D. Jiang, Y. Zhang, S.V. Dubonos, I.V. Grigorieva, A.A. Firsov: Electric field effect in atomically thin carbon films, Science **306**(5296), 666–669 (2004)

3.6 K.S. Novoselov, A.K. Geim, S.V. Morozov, D. Jiang, M.I. Katsnelson, I.V. Grigorieva, S.V. Dubonos, A.A. Firsov: Two-dimensional gas of massless Dirac fermions in graphene, Nature **438**(7065), 197–200 (2005)

3.7 D. Ugarte: Curling and closure of graphitic networks under electron-beam irradiation, Nature **359**(6397), 707–709 (1992)

3.8 A.L. Mackay, H. Terrones: Diamond from graphite, Nature **352**(6338), 762–762 (1991)

3.9 N.G. Chopra, R.J. Luyken, K. Cherrey, V.H. Crespi, M.L. Cohen, S.G. Louie, A. Zettl: Boron-nitride nanotubes, Science **269**(5226), 966–967 (1995)

3.10 Y.Q. Zhu, W.K. Hsu, N. Grobert, B.H. Chang, M. Terrones, H. Terrones, H.W. Kroto, D.R.M. Walton, B.Q. Wei: Production of WS_2 nanotubes, Chem. Mater. **12**(5), 1190–1194 (2000)

3.11 R. Tenne, L. Margulis, M. Genut, G. Hodes: Polyhedral and cylindrical structures of tungsten disulfide, Nature **360**(6403), 444–446 (1992)

3.12 L. Margulis, G. Salitra, R. Tenne, M. Talianker: Nested fullerene-like structures, Nature **365**(6442), 113–114 (1993)

3.13 G. Seifert, H. Terrones, M. Terrones, G. Jungnickel, T. Frauenheim: Structure and electronic properties of MoS_2 nanotubes, Phys. Rev. Lett. **85**(1), 146–149 (2000)

3.14 K.S. Coleman, J. Sloan, N.A. Hanson, G. Brown, G.P. Clancy, M. Terrones, H. Terrones, M.L.H. Green: The formation of ReS_2 inorganic fullerene-like structures containing Re-4 parallelogram units and metal–metal bonds, J. Am. Chem. Soc. **124**(39), 11580–11581 (2002)

3.15 A.R. Botello-Mendez, F. Lopez-Urias, M. Terrones, H. Terrones: Magnetic behavior in zinc oxide zigzag nanoribbons, Nano Lett. **8**(6), 1562–1565 (2008)

3.16 H.P. Schultz: Topological organic chemistry: Polyhedranes and prismanes, J. Org. Chem. **30**(5), 1361–1364 (1965)

3.17 E. Osawa: Kagaku (Kyoto) **25**, 854-863 (1970) (in Japanese); The original conjecture of a stable C_{60} molecule, Chem. Abstr. **74**, 75698v (1971)

3.18 W. Krätschmer, L.D. Lamb, K. Fostiropoulos, D.R. Huffman: Solid C-60 – A new form of carbon, Nature **347**(6291), 354–358 (1990)

3.19 H. Terrones, A.L. Mackay: The geometry of hypothetical curved graphite structures, Carbon **30**(8), 1251–1260 (1992)

3.20 T. Lenosky, X. Gonze, M. Teter, V. Elser: Energetics of negatively curved graphitic carbon, Nature **355**(6358), 333–335 (1992)

3.21 D. Vanderbilt, J. Tersoff: Negative-curvature fullerene analog of C_{60}, Phys. Rev. Lett. **68**(4), 511–513 (1992)

3.22 M. O'Keeffe, G.B. Adams, O.F. Sankey: Predicted new low-energy forms of carbon, Phys. Rev. Lett. **68**(15), 2325–2328 (1992)

3.23 H.A. Schwarz: *Gesammelte Mathematische Abhandlungen* (Springer, Berlin 1890), in German

3.24 F. Diederich, R. Ettl, Y. Rubin, R.L. Whetten, R. Beck, M. Alvarez, S. Anz, D. Sensharma, F. Wudl, K.C. Khe-

mani, A. Koch: The higher fullerenes – Isolation and characterization of C_{76}, C_{84}, C_{90}, C_{94}, and $C_{70}O$, an oxide of D_{5h}-C_{70}, Science **252**(5005), 548–551 (1991)

3.25 R. Taylor, J.P. Hare, A.K. Abdulsada, H.W. Kroto: Isolation, separation and characterization of the fullerenes C-60 and C-70 – The 3rd form of carbon, Chem. Commun.(20), 1423–1424 (1990)

3.26 H.W. Kroto, A.W. Allaf, S.P. Balm: C_{60} – Buckminsterfullerene, Chem. Rev. **91**(6), 1213–1235 (1991)

3.27 E. Hernandez, P. Ordejon, H. Terrones: Fullerene growth and the role of nonclassical isomers, Phys. Rev. B **63**(19), 193403 (2001)

3.28 P.W. Fowler, D.E. Manolopoulos: *An Atlas of Fullerenes* (Clarendon, Oxford 1995)

3.29 E.A. Rohlfing, D.M. Cox, A. Kaldor: Production and Characterization of supersonic carbon clusters beam, J. Chem. Phys. **81**(7), 3322–3330 (1984)

3.30 S. Petcu, M. Cauchetier, X. Armand, I. Voicu, R. Alexandrescu: Formation of fullerenes in the laser-pyrolysis of benzene, Combust. Flame **122**(4), 500 (2000)

3.31 K. Yoshie, S. Kasuya, K. Egushi, T. Yoshida: Novel method for C_{60} synthesis: A thermal plasma at atmospheric pressure, Appl. Phys. Lett. **61**(23), 2782 (1992)

3.32 R. Taylor, G.J. Langley, H.W. Kroto, D.R.M. Walton: Formation of C_{60} by pyrolysis of naphthalene, Nature **366**(6457), 728–731 (1993)

3.33 K.Y. Amsharov, K. Simeonov, M. Jansen: Formation of fullerenes by pyrolysis of 1,2-binaphthyl and 1,3-oligonaphthylene, Carbon **45**(2), 337–343 (2007)

3.34 C.L. Chen, Z.S. Lou: Formation of C-60 by reduction of CO_2, J. Supercrit. Fluid. **50**(1), 42–45 (2009)

3.35 A. Koshio, M. Yudasaka, M. Ozawa, S. Iijima: Fullerene formation via pyrolysis of ragged single-wall carbon nanotubes, Nano Lett. **2**(9), 995–997 (2002)

3.36 J.B. Howard, J.T. McKinnon, Y. Makarovsky, A.L. Lafleur, M.E. Johnson: Fullerenes C_{60} and C_{70} in flames, Nature **352**(6331), 139–141 (1991)

3.37 J.B. Howard, J.T. McKinnon, M.E. Johnson, Y. Makarovsky, A.L. Lafleur: Production of C_{60} and C_{70} fullerenes in benzene-oxygen flames, J. Phys. Chem. **96**(16), 6657–6662 (1992)

3.38 J.T. McKinnon, W.L. Bell, R.M. Barkley: Combustion synthesis of fullerenes, Combust. Flame **88**(1), 102–112 (1992)

3.39 H. Richter, A.J. Labrocca, W.J. Grieco, K. Taghizadeh, A.L. Lafleur, J.B. Howard: Generation of higher fullerenes in flames, J. Phys. Chem. B **101**(9), 1556–1560 (1997)

3.40 P.T.A. Reilly, R.A. Gieray, W.B. Whitten, J.M. Ramsey: Fullerene evolution in flame-generated soot, J. Am. Chem. Soc. **122**(47), 11596 (2000)

3.41 A. Chuvilin, U. Kaiser, E. Bichoutskaia, N.A. Besley, A.N. Khlobystov: Direct transformation of graphene to fullerene, Nat. Chem. **2**(6), 450–453 (2010)

3.42 L.P.F. Chibante, A. Thess, J.M. Alford, M.D. Diener, R.E. Smalley: Solar generation of the fullerenes, J. Phys. Chem. **97**(34), 8696–8700 (1993)

3.43 C.L. Fields, J.R. Pitts, M.J. Hale, C. Bingham, A. Lewandowski, D.E. King: Formation of fullerenes in highly concentrated solar flux, J. Phys. Chem. **97**(34), 8701–8702 (1993)

3.44 T. Guillard, G. Flamant, J.F. Robert, B. Rivoire, J. Giral, D. Laplaze: Scale up of a solar reactor for fullerene and nanotube synthesis, J. Solar Energy Eng. Trans. ASME **124**(1), 22–27 (2002)

3.45 N.S. Goroff: Mechanism of fullerene formation, Acc. Chem. Res. **29**(2), 77–83 (1996)

3.46 R.F. Curl, R.E. Smalley: Fullerenes, Sci. Am. **265**(4), 54 (1991)

3.47 H.W. Kroto, K. Mackay: The formation of quasi-icosahedral spiral shell carbon particles, Nature **331**(6154), 328–331 (1988)

3.48 J.R. Heath: Synthesis of C_{60} from small Carbon Clusters. In: *Fullerenes*, ACS Symposium Ser., ed. by G.S. Hammond, V.J. Kuck (Am. Chem. Soc, Washington 1992) pp. 1–23

3.49 S.W. McElvany, M.M. Ross, N.S. Goroff, F. Diederich: Cyclocarbon coalescence – Mechanisms for tailor made fullerene formation, Science **259**(5101), 1594–1596 (1993)

3.50 G. Von Helden, N.G. Gotts, M.T. Bowers: Experimental evidence for the formation of fullerenes by collisional heating of carbon rings in the gas phase, Nature **363**(6424), 60–63 (1993), see papers of these authors for evidence smaller fullerenes

3.51 J. Hunter, J. Fye, M.F. Jarrold: Annealing C-60+ synthesis of fullerenes and large carbon rings, Science **260**(5109), 784–786 (1993)

3.52 C.J. Pope, J.A. Marr, J.B. Howard: Chemistry of fullerenes C-60 and C-70 formation in flames, J. Phys. Chem. **97**(42), 11001–11013 (1993)

3.53 W.I.F. David, R.M. Ibberson, J.C. Matthewman, K. Prassides, T.J.S. Dennis, J.P. Hare, H.W. Kroto, R. Taylor, D.R.M. Walton: Crystal-structure and bonding of ordered C_{60}, Nature **353**(6340), 147–149 (1991)

3.54 S.J. Duclos, K. Brister, R.C. Haddon, A.R. Kortan, F.A. Thiel: Effects of pressure and stress on C_{60} fullerite to 20 GPA, Nature **351**(6325), 380–382 (1991)

3.55 M.N. Regueiro, P. Monceau, J.L. Hodeau: Crushing C_{60} to diamond at room-temperature, Nature **355**(6357), 237–239 (1992)

3.56 S. Saito, A. Oshiyama: Cohesive mechanism and energy-bands of solid C_{60}, Phys. Rev. Lett. **66**(20), 2637–2640 (1991)

3.57 M.N. Regueiro, P. Monceau, A. Rassat, P. Bernier, A. Zahab: Absence of a metallic phase at high-pressures in C_{60}, Nature **354**(6351), 289–291 (1991)

3.58 Y. Iwasa, T. Arima, R.M. Fleming, T. Siegrist, O. Zhou, R.C. Haddon, L.J. Rothberg, K.B. Lyons, H.L. Carter, A.F. Hebard, R. Tycko, G. Dabbagh, J.J. Krajewski, G.A. Thomas, T. Yagi: New phases of C-60 synthe-

sized at high-pressure, Science **264**(5165), 1570–1572 (1994)
3.59 B. Sundqvist: Fullerenes under high pressures, Adv. Phys. **48**(1), 1–134 (1999)
3.60 M.A. Verheijen, H. Meekes, G. Meijer, P. Bennema, J.L. Deboer, S. Vansmaalen, G. Vantendeloo, S. Amelinckx, S. Muto, J. Vanlanduyt: The structure of different phases of pure C-70 crystals, Chem. Phys. **166**(1/2), 287–297 (1992)
3.61 J.H. Weaver, J.L. Martins, T. Komeda, Y. Chen, T.R. Ohno, G.H. Kroll, N. Troullier, R.E. Haufler, R.E. Smalley: Electronic-structure of solid C_{60} – Experiment and theory, Phys. Rev. Lett. **66**(13), 1741–1744 (1991)
3.62 R.C. Haddon, A.F. Hebard, M.J. Rosseinsky, D.W. Murphy, S.J. Duclos, K.B. Lyons, B. Miller, J.M. Rosamilia, R.M. Fleming, A.R. Kortan, S.H. Glarum, A.V. Makhija, A.J. Muller, R.H. Eick, S.M. Zahurak, R. Tycko, G. Dabbagh, F.A. Thiel: Conducting films of C_{60} and C_{70} by alkali-metal doping, Nature **350**(6316), 320–322 (1991)
3.63 P.W. Stephens, G. Bortel, G. Faigel, M. Tegze, A. Janossy, S. Pekker, G. Oszlanyi, L. Forro: Polymeric fullerene chains in RbC_{60} and KC_{60}, Nature **370**(6491), 636–639 (1994)
3.64 O. Chauvet, G. Oszlanyi, L. Forro, P.W. Stephens, M. Tegze, G. Faigel, A. Janossy: Quasi-one-dimensional electronic-structure in orthorhombic RbC_{60}, Phys. Rev. Lett. **72**(17), 2721–2724 (1994)
3.65 A.F. Hebard, M.J. Rosseinsky, R.C. Haddon, D.W. Murphy, S.H. Glarum, T.T.M. Palstra, A.P. Ramirez, A.R. Kortan: Superconductivity at 18-K in potassium-doped C-60, Nature **350**(6319), 600–601 (1991)
3.66 P.W. Stephens, L. Mihaly, P.L. Lee, R.L. Whetten, S.M. Huang, R. Kaner, F. Deiderich, K. Holczer: Structure of single-phase superconducting K_3C_{60}, Nature **351**(6328), 632–634 (1991)
3.67 M.J. Rosseinsky, A.P. Ramirez, S.H. Glarum, D.W. Murphy, R.C. Haddon, A.F. Hebard, T.T.M. Palstra, A.R. Kortan, S.M. Zahurak, A.V. Makhija: Superconductivity at 28 K in Rb_xC_{60}, Phys. Rev. Lett. **66**(21), 2830–2832 (1991)
3.68 K. Tanigaki, T.W. Ebbesen, S. Saito, J. Mizuki, J.S. Tsai, Y. Kubo, S. Kuroshima: Superconductivity at 33-K in $Cs_xRb_yC_{60}$, Nature **352**(6332), 222–223 (1991)
3.69 R.C. Haddon: Electronic-structure, conductivity, and superconductivity of alkali-metal doped C-60, Acc. Chem. Res. **25**(3), 127–133 (1992)
3.70 O. Gunnarsson: Superconductivity in fullerides, Rev. Mod. Phys. **69**(2), 575–606 (1997)
3.71 A.R. Kortan, N. Kopylov, S. Glarum, E.M. Gyorgy, A.P. Ramirez, R.M. Fleming, F.A. Thiel, R.C. Haddon: Superconductivity at 8.4-K in calcium-doped C-60, Nature **355**(6360), 529–532 (1992)
3.72 T.T.M. Palstra, O. Zhou, Y. Iwasa, P.E. Sulewski, R.M. Fleming, B.R. Zegarski: Superconductivity at 40 K in cesium doped C-60, Solid State Commun. **93**(4), 327–330 (1995)
3.73 A.Y. Ganin, Y. Takabayashi, Y.Z. Khimyak, S. Margadonna, A. Tamai, M.J. Rosseinsky, K. Prassides: Bulk superconductivity at 38 K in a molecular system, Nat. Mater. **7**(5), 367–371 (2008)
3.74 A.Y. Ganin, Y. Takabayashi, P. Jeglič, D. Arčon, A. Potočnik, P.J. Baker, Y. Ohishi, M.T. McDonald, M.D. Tzirakis, A. McLennan, G.R. Darling, M. Takata, M.J. Rosseinsky, K. Prassides: Polymorphism control of superconductivity and magnetism in Cs_3C_{60} close to the Mott transition, Nature **466**(7303), 221–225 (2010)
3.75 R. Taylor, D.R.M. Walton: The Chemistry of fullerenes, Nature **363**(6431), 685–693 (1993)
3.76 N. Matsuzawa, D.A. Dixon, T. Fukunaga: Semiempirical calculations of dihydrogenated Buckminsterfullerenes, $C_{60}H$, J. Phys. Chem. **96**(19), 7594–7604 (1992)
3.77 F. Diederich, C. Thilgen: Covalent fullerene chemistry, Science **271**(5247), 317–323 (1996)
3.78 P.M. Allemand, A. Koch, F. Wudl, Y. Rubin, F. Diederich, M.M. Alvarez, S.J. Anz, R.L. Whetten: 2 different fullerenes have the same cyclic voltammetry, J. Am. Chem. Soc. **113**(3), 1050–1051 (1991)
3.79 R.E. Haufler, J. Conceicao, L.P.F. Chibante, Y. Chai, N.E. Byrne, S. Flanagan, M.M. Haley, S.C. Obrien, C. Pan, Z. Xiao, W.E. Billups, M.A. Ciufolini, R.H. Hauge, J.L. Margrave, L.J. Wilson, R.F. Curl, R.E. Smalley: Efficient production of C_{60} (Buckminsterfullerene), $C_{60}H_{36}$, and the solvated buckide ion, J. Phys. Chem. **94**(24), 8634–8636 (1990)
3.80 T. Suzuki, K.C. Khemani, F. Wudl, O. Almarsson: Systematic inflation of Buckminsterfullerene C_{60} – Synthesis of diphenyl fulleroids C_{61} and C_{66}, Science **254**(5035), 1186–1188 (1991)
3.81 F. Wudl: The chemical properties of Buckminsterfullerene (C-60) and the birth and infancy of fulleroids, Acc. Chem. Res. **25**(3), 157–161 (1992)
3.82 M. Prato, T. Suzuki, H. Foroundian, Q. Li, K. Kheman, F. Wudl, J. Leonetti, R.D. Little, T. White, B. Rickborn, S. Yamago, E. Nakamura: [3+2] and [2+4] cycloadditions of C_{60}, J. Am. Chem. Soc. **115**(4), 1594–1595 (1993)
3.83 A. Hirsch: Addition-reactions of Buckminsterfullerene (C-60), Synthesis **8**, 895–913 (1995)
3.84 M. Prato, M. Maggini: Fulleropyrrolidines: A family of full-fledged fullerene derivatives, Acc. Chem. Res. **31**(9), 519–526 (1998)
3.85 A.L. Balch, V.J. Catalano, J.W. Lee, M.M. Olmstead: Supramolecular aggregation of an .eta.2-C(60)) iridium complex involving phenyl chelation of the fullerene, J. Am. Chem. Soc. **114**(13), 5455–5457 (1992)
3.86 A. Hirsch, M. Brettreich: *Fullerenes: Chemistry and Reactions* (Wiley-VCH, Weinheim 2005)
3.87 M. Prato: [60] Fullerene chemistry for materials science applications, J. Mater. Chem. **7**(7), 1097 (1997)

3.88 R.F. Schinazi, R. Sijbesma, G. Srdanov, C.L. Hill, F. Wudl: Synthesis and virucidal activity of a water-soluble, configurationally stable, derivatized C_{60} Fullerene, Antimicrob. Agents Chemother. **37**(8), 1707–1710 (1993)

3.89 S.H. Friedman, D.L. Decamp, R.P. Sijbesma, G. Srdanov, F. Wudl, G.L. Kenyon: Inhibition of the HIV-1 protease by fullerene derivatives-model-building studies and experimental verification, J. Am. Chem. Soc. **115**(15), 6506–6509 (1993)

3.90 R. Sijbesma, G. Srdanov, F. Wudl, J.A. Castoro, C. Wilkins, S.H. Friedman, D.L. Decamp, G.L. Kenyon: Synthesis of a fullerene derivative for the inhibition of HIV enzymes, J. Am. Chem. Soc. **115**(15), 6510–6512 (1993)

3.91 S. Yamago, H. Tokuyama, E. Nakamura, S. Kikuchi, K. Sueki, H. Nakahara, S. Enomoto, F. Ambe: In-vivo biological behavior of water-miscible fullerene-C-14 labeling absorption, distribution, excretion and acute toxicity, Chem. Biol. **2**(6), 385–389 (1995)

3.92 E. Nakamura, H. Isobe: Functionalized fullerenes in water. The first 10 years of their chemistry, biology, and nanoscience, Acc. Chem. Res. **36**(11), 807–815 (2003)

3.93 S. Bosi, T. Da Ros, G. Spalluto, M. Prato: Fullerene derivatives: An attractive tool for biological applications, Eur. J. Med. Chem. **38**(11/12), 913–923 (2003)

3.94 J.J. Ryan, H.R. Bateman, A. Stover, G. Gomez, S.K. Norton, W. Zhao, L.B. Schwartz, R. Lenk, C.L. Kepley: Fullerene nanomaterials inhibit the allergic response, J. Immunol. **179**(1), 665–672 (2007)

3.95 A. Isakovic, Z. Markovic, B. Todorovic-Markovic, N. Mikolic, S. Vranjes-Djuric, M. Mirkovic, M. Dramicanins, L. Harhaji, N. Raicevic, Z. Nikolic, V. Trajkovic: Distinct cytotoxic mechanisms of pristine versus hydroxylated fullerene, Toxicol. Sci. **91**(1), 173–183 (2006)

3.96 C.M. Sayes, A.A. Marchione, K.L. Reed, D.B. Warheit: Comparative pulmonary toxicity assessments of C-60 water suspensions in rats: Few differences in fullerene toxicity in vivo in contrast profiles, Nano Lett. **7**(8), 2399–2406 (2007)

3.97 C.J. Brabec, A. Cravino, D. Meissner, N.S. Sariciftci, T. Fromherz, M.T. Rispens, L. Sanchez, J.C. Hummelen: Origin of the open circuit voltage of plastic solar cells, Adv. Funct. Mater. **11**(5), 374–380 (2001)

3.98 S.E. Shaheen, C.J. Brabec, N.S. Sariciftci, F. Padinger, T. Fromherz, J.C. Hummelen: 2.5% efficient organic plastic solar cells, Appl. Phys. Lett. **78**(6), 841–843 (2001)

3.99 M.M. Wienk, J.M. Kroon, W.J.H. Verhees, J. Knol, J.C. Hummelen, P.A. van Hal, R.A.J. Janssen: Efficient methano[70]fullerene/MDMO-PPV bulk heterojunction photovoltaic cells, Angew. Chem. Int. Ed. **42**(29), 3371–3375 (2003)

3.100 T. Hasobe, H. Imahori, P.V. Kamat, T.K. Ahn, S.K. Kim, D. Kim, A. Fujimoto, T. Hirakawa, S. Fukuzumi: Photovoltaic cells using composite nanoclusters of porphyrins and fullerenes with gold nanoparticles, J. Am. Chem. Soc. **127**(4), 1216–1228 (2005)

3.101 H. Imahori, S. Fukuzumi: Porphyrin- and fullerene-based molecular photovoltaic devices, Adv. Funct. Mater. **14**(6), 525–536 (2004)

3.102 R.B. Ross, C.M. Cardona, D.M. Guldi, S.G. Sankaranarayanan, M.O. Reese, N. Kopidakis, J. Peet, B. Walker, G.C. Bazan, E. Van Keuren, B.C. Holloway, M. Drees: Endohedral fullerenes for organic photovoltaic devices, Nat. Mater. **8**(3), 208–212 (2009)

3.103 S.K. Hau, H.L. Yip, H. Ma, A.K.Y. Jen: High performance ambient processed inverted polymer solar cells through interfacial modification with a fullerene self-assembled monolayer, Appl. Phys. Lett. **93**(23), 233304 (2008)

3.104 P.A. Troshin, H. Hoppe, J. Renz, M. Egginger, J.Y. Mayorova, A.E. Goryochev, A.S. Peregudov, R.N. Lyubovskaya, G. Gobsch, N.S. Sariciftci, V.F. Razumov: Material solubility-photovoltaic performance relationship in the design of novel fullerene derivatives for bulk heterojunction solar cells, Adv. Funct. Mater. **19**, 779–788 (2009)

3.105 J. Peet, J.Y. Kim, N.E. Coates, W.L. Ma, D. Moses, A.J. Heeger, G.C. Bazan: Efficiency enhancement in low-bandgap polymer solar cells by processing with alkane dithiols, Nat. Mater. **6**, 497–500 (2007)

3.106 J.Y. Kim, K. Lee, N.E. Coates, D. Moses, T.Q. Nguyen, M. Dante, A.J. Heeger: Efficient tandem polymer solar cells fabricated by all-solution processing, Science **317**(5835), 222–225 (2007)

3.107 R. Hatakeyama, Y.F. Li, T.Y. Kato, T. Kaneko: Infrared photovoltaic solar cells based on C-60 fullerene encapsulated single-walled carbon nanotubes, Appl. Phys. Lett. **97**(1), 013104 (2010)

3.108 X. Gong, M.H. Tong, Y.J. Xia, W.Z. Cai, J.S. Moon, Y. Cao, G. Yu, C.L. Shieh, B. Nilsson, A.J. Heeger: High-detectivity polymer photodetectors with spectral response from 300 nm to 1450 nm, Science **325**(5948), 1665–1667 (2009)

3.109 S. Iijima: Direct observation of the tetrahedral bonding in graphitized carbon-black by high-resolution electron-microscopy, J. Cryst. Growth **50**(3), 675–683 (1980)

3.110 S. Iijima: The 60-carbon cluster has been revealed, J. Phys. Chem. **91**(13), 3466–3467 (1987)

3.111 F. Banhart, T. Fuller, P. Redlich, P.M. Ajayan: The formation, annealing and self-compression of carbon onions under electron irradiation, Chem. Phys. Lett. **269**(3/4), 349–355 (1997)

3.112 D. Ugarte: Formation mechanism of quasi-spherical carbon particles induced by electron-bombardment, Chem. Phys. Lett. **207**(4–6), 473–479 (1993)

3.113 W.A. Deheer, D. Ugarte: Carbon onions produced by heat-treatment of carbon soot and their relation to the 217.5 nm interstellar absorption feature, Chem. Phys. Lett. **207**(4/6), 480–486 (1993)

3.114 M. Terrones, H. Terrones: The role of defects in graphitic structures, Fuller. Sci. Technol. **4**(3), 517–533 (1996)

3.115 H. Terrones, M. Terrones: The transformation of polyhedral particles into graphitic onions, J. Phys. Chem. Solids **58**(11), 1789–1796 (1997)

3.116 M. Terrones, G. Terrones, H. Terrones: Structure, chirality, and formation of giant icosahedral fullerenes and spherical graphitic onions, Struct. Chem. **13**(3/4), 373–384 (2002)

3.117 M.I. Heggie, M. Terrones, B.R. Eggen, G. Jungnickel, R. Jones, C.D. Latham, P.R. Briddon, H. Terrones: Quantitative density-functional study of nested fullerenes, Phys. Rev. B **57**(21), 13339–13342 (1998)

3.118 F. Banhart, P.M. Ajayan: Carbon onions as nanoscopic pressure cells for diamond formation, Nature **382**(6590), 433–435 (1996)

3.119 A. Gómez-Rodríguez, L.M. Beltrán-Del-Río, R. Herrera-Becerra: SimulaTEM: Multislice simulations for general objects, Ultramicroscopy **110**(2), 95–104 (2010)

3.120 D. Pech, M. Brunet, H. Durou, P.H. Huang, V. Mochalin, Y. Gogotsi, P. Simon: Ultrahigh-power micrometre-sized supercapacitors based on onion-like carbon, Nat. Nanotechnol. **5**(9), 651–654 (2010)

3.121 K.C. Hwang: Recent progress in the preparation and application of carbon nanocapsules, J. Phys. D **43**(37), 374001 (2010)

3.122 J.Y. Miao, D.W. Hwang, K.V. Narasimhulu, P.I. Lin, Y.T. Chen, S.H. Lin, L.P. Hwang: Synthesis and properties of carbon nanospheres grown by CVD using kaolin supported transition metal catalysts, Carbon **42**, 813 (2004)

3.123 H.C. Wu, C.T. Hong, H.T. Chiu, Y.Y. Li: Continuous synthesis of carbon spheres by a non-catalyst vertical chemical vapor deposition, Diam. Relat. Mater. **18**, 601 (2009)

3.124 Z.J. Yi, G. Chao, W.K. Hsu, Y. Zhu, A. Huczko, M. Bystrzejewski, M. Roe, C.Y. Lee, S. Acquah, H. Kroto, D.R.M. Walton: Large-scale synthesis and characterization of carbon spheres prepared by direct pyrolysis of hydrocarbons, Carbon, **43**, 1944 (2005)

3.125 M. Namura, I. Waki, Y. Sato, G. Yamamoto, A. Okubo, H. Kimura, N. Osaka, K. Motomiya, T. Hashida, B. Jeyadevan, K. Tohji: Preparation and characterization of lanthanum carbide encapsulated carbon nanocapsule/lanthanum hexaboride nanocomposites, Mater. Lett. **63**(15), 1307–1310 (2009)

3.126 H. Wang, T. Abe, S. Maruyama, Y. Iriyama, Z. Ogumi, K. Yoshikawa: Graphitized carbon nanobeads with an onion texture as a lithium-ion battery negative electrode for high-rate use, Adv. Mater. **17**(23), 2857–2860 (2005)

3.127 P.P. Kuzhir, D.S. Bychanok, S.A. Maksimenko, A.V. Gusinski, O.V. Ruhavets, V.L. Kuznetsov, S.I. Moseenkov, C. Jones, O. Shenderova, P. Lambin: Onion-like carbon based polymer composite films in microwaves, Solid State Sci. **11**(10), 1762–1767 (2008)

3.128 X.F. Zhang, X.L. Dong, H. Huang, Y.Y. Liu, W.N. Wang, X.G. Zhu, B. Lv, J.P. Lei, C.G. Lee: Microwave absorption properties of the carbon-coated nickel nanocapsules, Appl. Phys. Lett. **89**, 053115 (2006)

3.129 M.-S. Wang, D. Golberg, Y. Bando: Carbon "onions" as point electron sources, ACS Nano **4**(8), 4396–4402 (2010)

3.130 M. Uo, K. Tamura, Y. Sato, A. Yokoyama, F. Watari, Y. Totsuka, K. Tohji: The cytotoxicity of metal-encapsulating carbon nanocapsules, Small **1**(8/9), 816–819 (2005)

3.131 R.J. Cui, C. Liu, J. Shen, D. Gao, J.-J. Zhu, H.-Y. Chen: Gold nanoparticle–colloidal carbon nanosphere hybrid material: Preparation, characterization, and application for an amplified electrochemical immunoassay, Adv. Funct. Mater. **18**(15), 2197–2204 (2008)

3.132 W.S. Seo, J.H. Lee, X. Sun, Y. Suzuki, D. Mann, Z. Liu, M. Terashima, P.C. Yang, M.V. McConnell, D.G. Nishimura, H. Dai: FeCo/graphitic-shell nanocrystals as advanced magnetic-resonance-imaging and near-infrared agents, Nat. Mater. **5**, 971–976 (2006)

3.133 B.W. Smith, M. Monthioux, D.E. Luzzi: Encapsulated C-60 in carbon nanotubes, Nature **396**(6709), 323–324 (1998)

3.134 B. Burteaux, A. Claye, B.W. Smith, M. Monthioux, D.E. Luzzi, J.E. Fischer: Abundance of encapsulated C-60 in single-wall carbon nanotubes, Chem. Phys. Lett. **310**(1/2), 21–24 (1999)

3.135 B.W. Smith, M. Monthioux, D.E. Luzzi: Carbon nanotube encapsulated fullerenes: A unique class of hybrid materials, Chem. Phys. Lett. **315**(1/2), 31–36 (1999)

3.136 B.W. Smith, D.E. Luzzi: Formation mechanism of fullerene peapods and coaxial tubes: A path to large scale synthesis, Chem. Phys. Lett. **321**(1/2), 169–174 (2000)

3.137 E. Hernandez, V. Meunier, B.W. Smith, R. Rurali, H. Terrones, M.B. Nardelli, M. Terrones, D.E. Luzzi, J.C. Charlier: Fullerene coalescence in nanopeapods: A path to novel tubular carbon, Nano Lett. **3**(8), 1037–1042 (2003)

3.138 C. Yeretzian, K. Hansen, F. Diederich, R.L. Whetten: Coalescence reactions of fullerenes, Nature **359**(6390), 44–47 (1992)

3.139 J.L. Aragon, H. Terrones, D. Romeu: Model for icosahedral aperiodic graphite structures, Phys. Rev. B **48**(11), 8409 (1993)

3.140 D.J. Hornbaker, S.J. Kahng, S. Misra, B.W. Smith, A.T. Johnson, E.J. Mele, D.E. Luzzi, A. Yazdani: Mapping the one-dimensional electronic states of nanotube peapod structures, Science **295**(5556), 828–831 (2002)

3.141 H. Kataura, Y. Maniwa, T. Kodama, K. Kikuchi, K. Hirahara, K. Suenaga, S. Iijima, S. Suzuki, Y. Achiba,

W. Krätschmer: High-yield fullerene encapsulation in single-wall carbon nanotubes, Synth. Met. **121**(1/3 Special Issue), 1195–1196 (2001)

3.142 H. Kataura, Y. Maniwa, M. Abe, A. Fujiwara, T. Kodama, K. Kikuchi, H. Imahori, Y. Misaki, S. Suzuki, Y. Achiba: Optical properties of fullerene and non-fullerene peapods, Appl. Phys. A **74**(3), 349–354 (2002)

3.143 S. Bandow, T. Hiraoka, T. Yumura, K. Hirahara, H. Shinohara, S. Iijima: Raman scattering study on fullerene derived intermediates formed within single-wall carbon nanotube: From peapod to double-wall carbon nanotube, Chem. Phys. Lett. **384**(4/6), 320–325 (2004)

3.144 L. Kavan, L. Dunsch, H. Kataura: In situ Vis-NIR and Raman spectroelectrochemistry at fullerene peapods, Chem. Phys. Lett. **361**(1/2), 79–85 (2002)

3.145 K. Hirahara, K. Suenaga, S. Bandow, H. Kato, T. Okazaki, H. Shinohara, S. Iijima: One-dimensional metallofullerene crystal generated inside single-walled carbon nanotubes, Phys. Rev. Lett. **85**, 5384–5387 (2000)

3.146 R.J. Nicholls, K. Sader, J.H. Warner, S.R. Plant, K. Porfyrakis, P.D. Nellist, G.A.D. Briggs, D.J.H. Cockayne: Direct imaging and chemical identification of the encapsulated metal atoms in bimetallic endofullerene peapods, ACS Nano **4**(7), 3943–3948 (2010)

3.147 J.A. Rodriguez-Manzo, F. Lopez-Urias, M. Terrones, H. Terrones: Magnetism in corrugated carbon nanotori: The importance of symmetry, defects, and negative curvature, Nano Lett. **4**(11), 2179–2183 (2004)

3.148 H. Terrones, M. Terrones: Quasiperiodic icosahedral graphite sheets and high-genus fullerenes with nonpositive Gaussian curvature, Phys. Rev. B **55**(15), 9969–9974 (1997)

3.149 J.L. Ricardochavez, J. Dorantesdavila, M. Terrones, H. Terrones: Electronic properties of fullerenes with nonpositive Gaussian curvature: Finite zeolites, Phys. Rev. B **56**(19), 12143–12146 (1997)

3.150 P. Kowalczyk, R. Holyst, M. Terrones, H. Terrones: Hydrogen storage in nanoporous carbon materials: Myth and facts, Phys. Chem. Chem. Phys. **9**(15), 1786–1792 (2007)

3.151 C. Chuang, B.Y. Jin: Systematics of high-genus fullerenes, J. Chem. Inform. Model. **49**(7), 1664–1668 (2009)

3.152 D. Golberg, Y. Bando, O. Stephan, K. Kurashima: Octahedral boron nitride fullerenes formed by electron beam irradiation, Appl. Phys. Lett. **73**(17), 2441–2443 (1998)

3.153 S.S. Alexandre, M.S.C. Mazzoni, H. Chacham: Stability, geometry, and electronic structure of the boron nitride $B_{36}N_{36}$ fullerene, Appl. Phys. Lett. **75**(1), 61–63 (1999)

3.154 M. Terrones, W.K. Hsu, H. Terrones, J.P. Zhang, S. Ramos, J.P. Hare, R. Castillo, K. Prassides, A.K. Cheetham, H.W. Kroto, D.R.M. Walton: Metal particle catalysed production of nanoscale BN structures, Chem. Phys. Lett. **259**(5/6), 568–573 (1996)

3.155 P.W. Fowler, K.M. Rogers, G. Seifert, M. Terrones, H. Terrones: Pentagonal rings and nitrogen excess in fullerene-based BN cages and nanotube caps, Chem. Phys. Lett. **299**(5), 359–367 (1999)

3.156 L. Rapoport, Y. Bilik, Y. Feldman, M. Homyonfer, S.R. Cohen, R. Tenne: Hollow nanoparticles of WS_2 as potential solid-state lubricants, Nature **387**(6635), 791–793 (1997)

3.157 G. Seifert, H. Terrones, M. Terrones, G. Jungnickel, T. Frauenheim: Structure and electronic properties of MoS_2 nanotubes, Phys. Rev. Lett. **85**(1), 146–149 (2000)

3.158 O.A. Shenderova, V.V. Zhirnov, D.W. Brenner: Carbon nanostructures, Crit. Rev. Solid State Mater. Sci. **27**(3/4), 227–356 (2002)

3.159 T.L. Daulton, D.D. Eisenhour, T.J. Bernatowicz, R.S. Lewis, P.R. Buseck: Genesis of presolar diamonds: Comparative high-resolution transmission electron microscopy study of meteoritic and terrestrial nano-diamonds, Geochim. Cosmochim. Acta **60**(23), 4853–4872 (1996)

3.160 L.J. Allamandola, S.A. Sandford, A.G.G.M. Tielens, T.M. Herbst: Diamonds in dense molecular clouds – A challenge to the standard interstellar-medium paradigm, Science **260**(5104), 64–66 (1993)

3.161 C.C. Fu, H.Y. Lee, K. Chen, T.S. Lim, H.Y. Wu, P.K. Lin, P.K. Wei, P.H. Tsao, H.C. Chang, W. Fann: Characterization and application of single fluorescent nanodiamonds as cellular biomarkers, Proc. Natl. Acad. Sci. USA **104**(3), 727–732 (2007)

3.162 A.M. Schrand, H.J. Huang, C. Carlson, J.J. Schlager, E. Osawa, S.M. Hussain, L.M. Dai: Are diamond nanoparticles cytotoxic?, J. Phys. Chem. B **111**(1), 2–7 (2007)

3.163 J.Y. Raty, G. Galli, C. Bostedt, T.W. van Buuren, L.J. Terminello: Quantum confinement and fullerenelike surface reconstructions in nanodiamonds, Phys. Rev. Lett. **90**(3), 037401 (2003)

3.164 J.E. Dahl, S.G. Liu, R.M.K. Carlson: Isolation and structure of higher diamondoids, nanometer-sized diamond molecules, Science **299**(5603), 96–99 (2003)

4. Single-Walled Carbon Nanotubes

Sebastien Nanot, Nicholas A. Thompson, Ji-Hee Kim, Xuan Wang, William D. Rice, Erik H. Hároz, Yogeeswaran Ganesan, Cary L. Pint, Junichiro Kono

Single-walled carbon nanotubes (SWCNTs) are hollow, long cylinders with extremely large aspect ratios, made of one atomic sheet of carbon atoms in a honeycomb lattice. They possess extraordinary thermal, mechanical, and electrical properties and are considered as one of the most promising nanomaterials for applications and basic research. This chapter describes the structural, electronic, vibrational, optical, transport, mechanical, and thermal properties of these unusual one-dimensional (1-D) nanomaterials. The crystallographic (Sect. 4.2.1), electronic (Sect. 4.2.2), vibrational (Sect. 4.2.3), optical (Sect. 4.4), transport (Sect. 4.5), thermal (Sect. 4.6.1), and mechanical (Sect. 4.6.2) properties of these unusual 1-D nanomaterials will be outlined. In addition, we will provide an overview of the various methods developed for synthesizing SWCNTs in Sect. 4.3.

Even after more than two decades of extensive basic studies since their discovery, carbon nanotubes continue to surprise researchers with potential new applications and interesting discoveries of novel phenomena and properties. Because of an enormous thrust towards finding practical applications, carbon nanotube research is actively being pursued in diverse areas including energy storage, molecular electronics, nanomechanical devices, composites, and chemical and bio-sensing.

Structurally, carbon nanotubes are made up of sp^2-bonded carbon atoms, like graphite, and can be conceptually viewed as rolled-up sheets of single-layer graphite, or graphene. Their diameter typically lies in the nanometer range while their length often exceeds microns, sometimes centimeters, thus making them 1-D nanostructures. Depending on the number of tubes that are arranged concentrically, carbon nanotubes are further classified into single-walled and multi-walled nanotubes. Single-walled carbon nanotubes, the subject of this chapter, are especially interesting. They are ideal materials in which to explore one-dimensional physics and strong Coulomb correlations. In addition, their cylindrical topology allows them to exhibit nonintuitive quantum phenomena when placed in a parallel magnetic field, due to the Aharonov–Bohm effect. A number of research groups have found exotic many-body effects through a variety of transport, optical, magnetic, and photoemission experiments.

Their electronic properties are very sensitive to their microscopic atomic arrangements and symmetry, covering a wide spectrum of energy scales. They can be either metallic or semiconducting with varying band gaps, depending on their diameter and chirality. Semiconducting nanotubes are particularly promising for photonic device applications with their diameter-dependent, direct band gaps, while metallic tubes are considered to be ideal candidates for a variety of electronic applications such as nanocircuit components and power transmission cables.

4.1 **History** 106

4.2 **Crystallographic and Electronic Structure** 106
4.2.1 Crystallographic Structure 106
4.2.2 Electronic Dispersion 107
4.2.3 Phonon Dispersion 109

4.3 **Synthesis** 111
4.3.1 Substrate-Free Growth Techniques . 112
4.3.2 Substrate-Bound Growth Technique 113
4.3.3 Growth Mechanisms 114

4.4 **Optical Properties** 115
4.4.1 Optical Absorption and Photoluminescence 116

4.4.2 Raman Spectroscopy 118
4.4.3 Resonant Rayleigh Spectroscopy 119
4.4.4 Ultrafast Spectroscopy 120
4.4.5 Excitonic Effects 121
4.5 **Transport Properties** 123
4.6 **Thermal and Mechanical Properties** 128
4.6.1 Thermal Properties 128
4.6.2 Mechanical Properties 130
4.7 **Concluding Remarks** 135
References 135

4.1 History

This chapter summarizes some of the basic properties of carbon nanotubes (CNTs), one of the most ideal realizations of one-dimensional (1-D) systems available today. Since their discovery [4.1], much attention has been given to their unique structure and properties that are promising for a wide range of applications and fundamental physical and chemical studies [4.2–5]. These hollow crystals of sp^2-bonded carbon atoms have exhibited a variety of extraordinary thermal, mechanical, and electrical properties and phenomena, fascinating scientists and engineers in diverse disciplines. Even after more than two decades of extensive basic studies since their discovery, they continue to surprise researchers through exciting discoveries of phenomena and properties as well as novel potential applications, including energy storage, molecular electronics, nanomechanical devices, composites, and chemical and bio-sensing.

The diameters of carbon nanotubes are in the nanometer range while their lengths are typically microns and often millimeters, corresponding to aspect ratios of millions, especially in single-walled carbon nanotubes (SWCNTs), the most prominent member of the carbon nanotube family. A typical SWCNT has a diameter of ≈ 1 nm and consists of just one atomic sheet, which can be pictured as a rolled-up version of graphene, i. e., a honey-comb lattice of sp^2-bonded carbon atoms. The one-dimensionality of SWCNTs is attractive, allowing researchers to explore exotic 1-D physics in the quantum regime [4.6] and new functionalities in optoelectronic devices [4.7, 8]. The strong 1-D confinement of electrons and phonons results in unique anisotropic effects in various properties, e.g., polarization-dependent Raman scattering [4.9] and optical absorption [4.10–12], large magnetic susceptibility anisotropies [4.13–17], and anisotropic terahertz dynamic conductivities [4.18–21].

One of the most striking properties of SWCNTs is their chirality-dependent metallicity. Namely, depending on their microscopic atomic arrangements and symmetry, a SWCNT can be either metallic or semiconducting. A subtle structural difference leads to opening or closing of a band gap, which is also tunable by a magnetic field applied parallel to the tube axis via the Aharonov–Bohm effect [4.10, 22–25]. Semiconducting nanotubes are particularly promising for photonic device applications with their diameter-dependent, direct band gaps, while metallic tubes are considered to be ideal candidates for a variety of electronic and electrical applications ranging from nano-circuit wires to power transmission cables.

4.2 Crystallographic and Electronic Structure

A SWCNT can be viewed as a graphene sheet rolled into a cylinder which is terminated by two half-fullerene caps. The diameter of these species typically ranges from 0.7 to 2.5 nm, and their aspect ratio can be as high as 10^4–10^5. This very strong confinement along their circumference make them behave like 1-D materials. The purpose of this section is to describe the crystallographic and electronic structure of SWCNTs, which will be used throughout the text. For a more detailed study we refer the reader to some of the many published books [4.2, 5, 26–28].

4.2.1 Crystallographic Structure

To give a formal description of the crystal structure of a SWCNT, it is easiest to first consider its parent material, graphene. Graphene is a monolayer of sp^2-hybridized carbon atoms arranged in a honeycomb

lattice. Its unit cell is defined by the primitive vectors $\boldsymbol{a}_1$ and $\boldsymbol{a}_2$ (bottom right of Fig. 4.1, for a review see [4.29]). Each SWCNT is then indicated by a *chiral vector* $\boldsymbol{C}_h$, which specifies the two atoms of the graphene sheet which are identified upon formation of the tube (see the points O and A in Fig. 4.1). The chiral vector is defined with respect to the graphene primitive vectors as

$$\boldsymbol{C}_h \equiv n\boldsymbol{a}_1 + m\boldsymbol{a}_2 \equiv (n, m)\,, \tag{4.1}$$

where n and m are integers such that $0 \leq m \leq n$. When we express the chiral vector $\boldsymbol{C}_h$ in the form (n, m), we call it the *chiral index*. These two terms should be regarded as synonymous. The angle θ formed between $\boldsymbol{C}_h$ and $\boldsymbol{a}_1$ is a quantity of great importance for determining the electronic properties of the SWCNT; it is called the *chiral angle*, and is defined through

$$\cos\theta = \frac{\boldsymbol{C}_h \cdot \boldsymbol{a}_1}{|\boldsymbol{C}_h|\,|\boldsymbol{a}_1|} = \frac{2n+m}{2\sqrt{n^2+m^2+nm}}\,. \tag{4.2}$$

The nanotube diameter can be computed from the chiral vector by

$$d_t = |\boldsymbol{C}_h|/\pi = \frac{a_{\mathrm{C-C}}}{\pi}\sqrt{3(m^2+mn+n^2)}\,, \tag{4.3}$$

where $a_{\mathrm{C-C}} \approx 1.44$ Å is the nearest neighbor distance between carbon atoms in graphene.

SWCNTs can be classified into three main types:

1. *Armchair* nanotubes for which $n = m$ (i. e. $\boldsymbol{C}_h = (n, n)$)
2. *Zig-zag* nanotubes for which $m = 0$ (i. e. $\boldsymbol{C}_h = (n, 0)$)
3. *Chiral* nanotubes ($n \neq m \neq 0$) whose mirror images have a different structure and display different properties, for example in circular dichroism.

Armchair and zigzag nanotubes (having the highest symmetry) (Fig. 4.1b) are named after the shape of their cross section along $\boldsymbol{C}_h$. All three of these different structures will display various physical properties and their distinction will be of prime importance for their electronic structure, phonon dispersion and optical properties.

4.2.2 Electronic Dispersion

Single-walled carbon nanotubes can be either metals or semiconductors depending on their chirality (Sect. 4.2.1). Their metallicity can be deduced from purely geometrical considerations related to their chiral angle. Similar conclusions can be drawn from

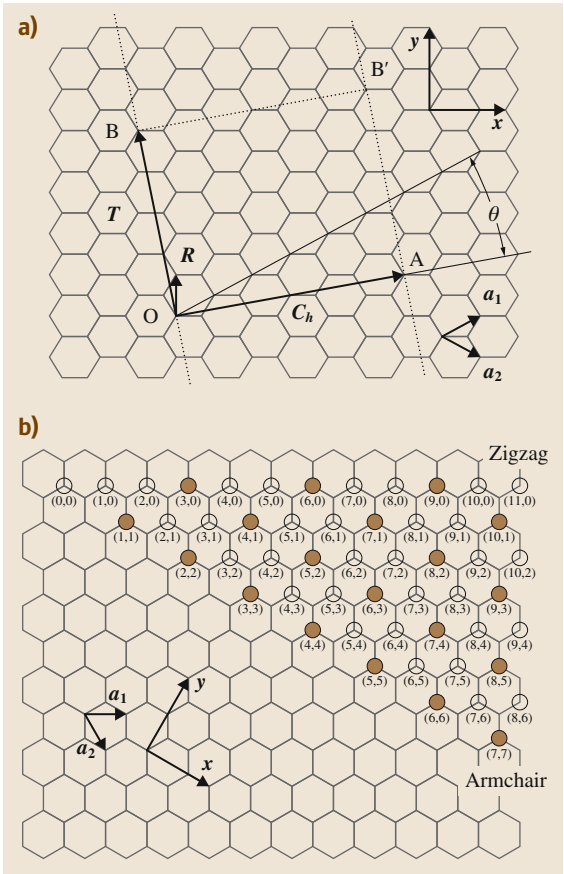


Fig. 4.1 **(a)** The unrolled hexagonal lattice of a nanotube. When we connect sites O–A, and B–B′, a nanotube can be constructed. $\boldsymbol{OA}$ and $\boldsymbol{OB}$ define the chiral vector $\boldsymbol{C}_h$ and the translational vector $\boldsymbol{T}$ of the nanotube, respectively. The rectangle OAB′B defines the unit cell for the nanotube. The vector $\boldsymbol{R}$ denotes a symmetry vector. **(b)** The hexagonal lattice of all possible (n, m) species formed by rolling the $(0, 0)$ point onto (n, m). The empty circles are semiconducting (n, m), $(\nu = \pm 1)$. The filled circles represent *metallic*, $\nu = 0$ (n, m) species. (After [4.26])

tight-binding models of graphene [4.30, 31] or $\boldsymbol{k}\cdot\boldsymbol{p}$ formalism for low energy bands [4.32], although the precise band structure of (very) small diameter nanotubes necessitates more complex calculations which include curvature effects, second neighbor interactions, or the use of ab initio methods [4.33].

The electronic properties of graphene have been studied extensively [4.29], so here we will only describe the properties useful for deducing the nanotube band structure. The graphene reciprocal lattice is hexagonal

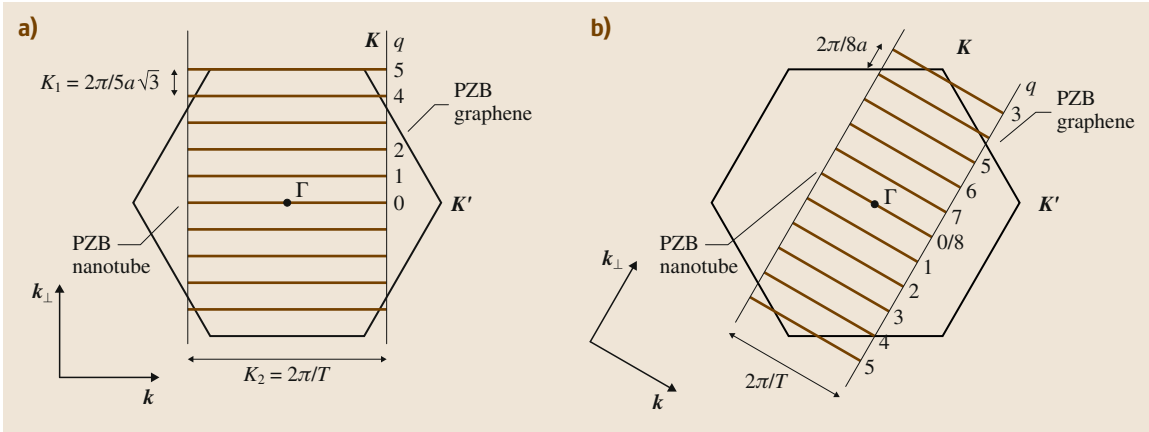


Fig. 4.2a,b First Brillouin zone and quantized vectors of **(a)** an armchair nanotube (5,5) and **(b)** a zigzag nanotube (8,0) with rotational indices q corresponding to the zone folding method indices. PZB = 1st Brillouin zone (After [4.35])

and the (nonequivalent) points K and K′ at the corners of the first Brillouin zone (called *Dirac points*) are of particular importance for its electronic properties. The valence and conduction band meet only at the Dirac points [4.34], making graphene a zero bandgap semiconductor. Moreover, its dispersion is linear close to these points and hence low energy carriers behave like massless, chiral Dirac fermions. As a consequence, its electronic dispersion near the Dirac points is well described by

$$E(\delta k) = \pm\hbar v_F \delta k \,, \tag{4.4}$$

where $v_F = \sqrt{3}\gamma_0 a/2\hbar \approx 9.5\times10^5$ m/s is the electron Fermi velocity, $\gamma_0 = 2.9$ eV is the nearest neighbor hopping energy, $a = |\boldsymbol{a}_1| = |\boldsymbol{a}_2| = 2.49$ Å and δk is the wavevector with origin at either the K or K′ point.

The periodicity condition introduced on the wavefunctions along the circumference of carbon nanotubes induces a quantization along their axes. As a consequence, they are quasi-1-D systems with only specific $\boldsymbol{k}$ vectors allowed along the circumference and the base vector parallel to the axis, as illustrated in Fig. 4.2. The mono-electronic dispersion relation can be directly deduced from graphene by using the *zone folding method*, which imposes the periodic boundary condition $\psi(x + n\boldsymbol{C}_h) = \psi(x)$ on graphene. The continuous graphene wavevector is replaced by a *half-quantized* new vector (continuous along the nanotube axis and quantized along the circumference). As can be seen from Fig. 4.2, a specific (n, m) nanotube will be metallic if an authorized subband crosses the K point or semiconducting otherwise. Simple geometric considerations related the chiral vector $\boldsymbol{C}_h$ allows one to deduce that the condition for a nanotube to be metallic is $n - m = 3\ell(\ell \in \mathbb{N})$ [4.30,31,33]. If we define $\nu \equiv n - m$ mod 3, we can see that $\nu = 0$ if the nanotube is metallic and $\nu = \pm1$ if it is a semiconductor. Hence one-third of all possible carbon nanotube species are expected to be metallic.

Using (4.4), one can deduce the band structures close to the K points through the $\boldsymbol{k}\cdot\boldsymbol{p}$ formalism [4.32]

$$E_q(k) = \pm\gamma_0\sqrt{\left(q - \frac{\nu}{3}\right)^2 + \left(\frac{kd_t}{2}\right)^2}\,. \tag{4.5}$$

Noticeably:

- Metallic nanotubes have a linear dispersion and massless charge carriers, just as their parent material graphene
- Semiconducting nanotubes have a band gap $E_g = 2\gamma_0 a_{C-C}/d_t \approx 0.839\,\text{eV}\cdot\text{nm}/d_t$.

A complete band structure can be deduced by folding the tight-binding dispersion of graphene [4.30, 31, 33]. This is shown for a representative metallic armchair nanotube and a semiconducting zigzag nanotube of similar diameters in Fig. 4.3. Due to symmetries of the K and K′ points, all subbands are doubly degenerate. The corresponding density of states (Fig. 4.4) is constant in the metallic bands and presents van Hove singularities typical of 1-D systems at the onset of each new subband.

These considerations are sufficient for nanotubes with large diameter. However, for small diameter nanotubes, one has to consider the distortions of the

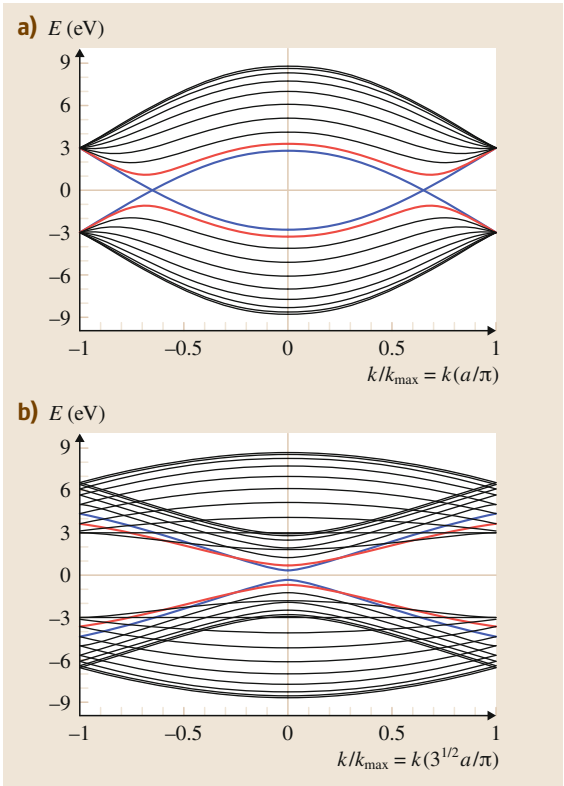


Fig. 4.3a,b Electronic dispersion of **(a)** a metallic (9,9) armchair nanotube and **(b)** a semiconducting (16,0) zigzag nanotube. Both nanotubes have similar diameter $d_t \approx 1.2\,\text{nm}$

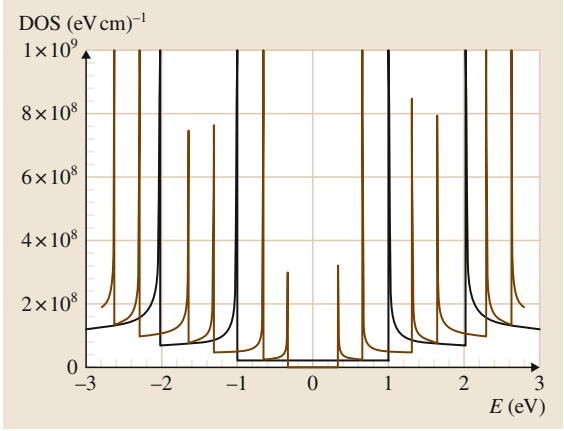


Fig. 4.4 Density of states (DOS) of the same SWCNTs as above; a metallic (9,9) armchair nanotube (*black curve*) and a semiconducting (16,0) zigzag nanotube (*dark-brown curve*)

hexagonal lattice due to curvature [4.31, 36] and that graphene dispersion is not linear at the high energies where new subbands appear (i. e., (4.4) and (4.5) are no longer valid, due to trigonal warping effects). These become of particular importance for optical experiments and low temperature transport measurements. Important considerations are:

- Armchair (n, n) nanotubes are the only truly metallic nanotubes.
- Other nanotubes satisfying $n - m \mod 3 = 0$ but $n \neq m$ develop a small band gap (typically on the order of some tens of meV) and the degeneracy between higher energy subbands is lifted.
- Semiconducting nanotubes develop a chirality dependent band gap (with a term proportional to $\cos(3\theta)$).

4.2.3 Phonon Dispersion

Atomic vibrational motions of carbon nanotubes are very similar to those of graphene but due to their cylindrical symmetry they are separated into radial *breathing* modes (along the radial axis), transverse modes (along the azimuth angle axis), and longitudinal modes (along the length axis) [4.37]. The phonon band structure has been calculated by various methods including zone folding [4.38, 39], constant force [4.40, 41], tight-binding [4.42, 43] and ab initio methods [4.44–46]. Similar to the electronic structure, the phonon dispersion in SWCNTs is quantized and exhibits singularities specific to their 1-D nature.

Due to its honeycomb lattice containing two atoms in each unit cell, graphene phonon dispersion contains six modes, with two types of transverse and one type of longitudinal motions; hence three acoustic and three optical modes. There are two main consequences when wrapping a graphene sheet into an SWCNT. First, it introduces a periodic boundary condition along the circumference, which quantizes the corresponding wavevector. As a result, the 2-D graphene phonon modes are further split into a large number of subbands. If the SWCNT contains 2N atoms per unit cell, there are 6N phonon modes in total, many of which are degenerated (Fig. 4.5b,c [4.45]). The second consequence is that the curvature makes its three fundamental atomic motions different from those of graphene. Hence, the SWCNT phonon modes can be viewed as a mixture of 2-D graphene phonon modes [4.37]. The effect of such symmetry difference is significant for lower frequency modes. For instance, there are four acoustic modes in-

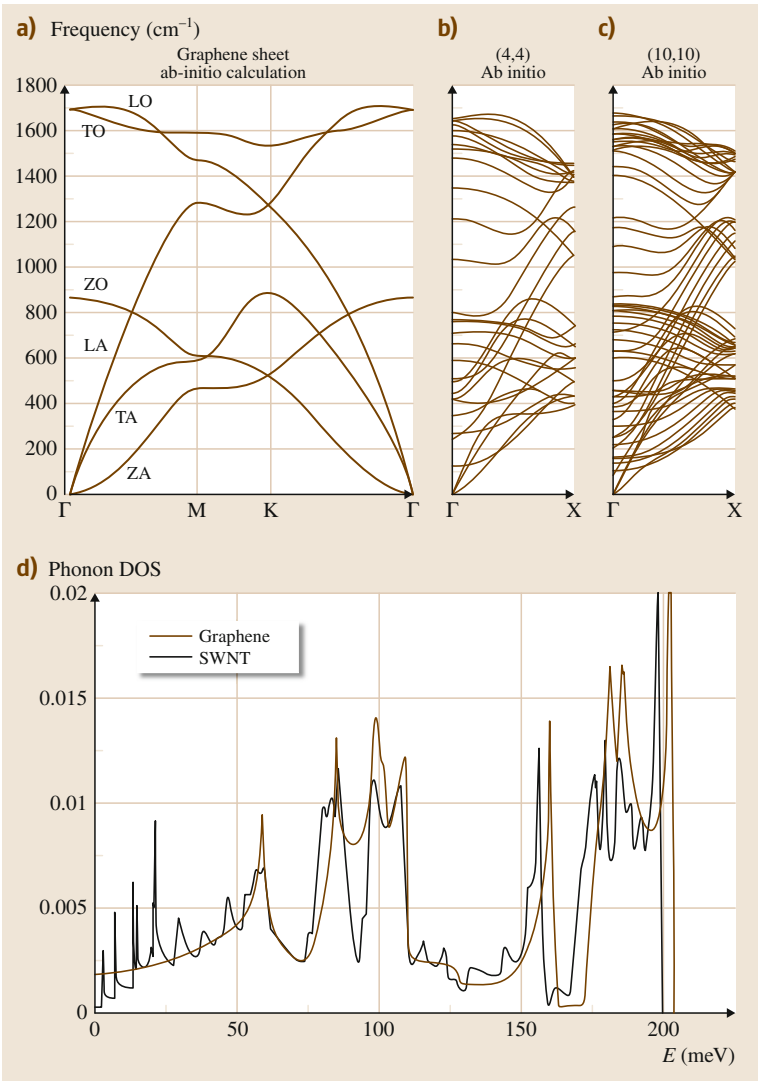


Fig. 4.5 (**a**). Ab initio dispersion relations for the (4,4) (**b**), and the (10,10) (**c**) nanotubes. In (**c**) and (**d**), *thicker lines* are used to mark two special branches: the acoustic band is a twiston mode (torsional shape vibrations), the other (with finite frequency γ) is the breathing mode. (**d**) Phonon density of states of an isolated (10,10) SWCNT (*solid line*), compared to a 2-D graphene sheet. ((**a–c**) after [4.45], (**d**) after [4.48])

stead of three (Fig. 4.5b,c [4.47]; also see Fig. 4.25a for a larger view):

- A *longitudinal acoustic* (LA) mode, corresponding to motion of the atoms along the tube axis (similar to the LA mode in graphene).
- Two degenerate *transverse acoustic* (TA) modes, corresponding to atomic displacements perpendicular to the nanotube axis (a combination of in-plane and out-of plane TA modes in graphene).
- A *twist mode*, corresponding to a torsion of the tube around its axis (similar to the in-plane TA modes in graphene).

The *radial breathing mode* (RBM) is another important low-frequency mode, corresponding to radial expansion-contraction of the nanotube. It is similar to the out-of plane TA mode in graphene with zero energy at the center of the Brillouin zone, but becomes a mode with a finite energy due to the curvature. To first order, the energy of the RBM mode is inversely proportional to the diameter of the tube and presents chiral angle dependencies similar to electronic subbands [4.44].

Figure 4.5d shows the calculated phonon density of states of a (10, 10) tube and a graphene sheet side by side [4.49]. One of the main features is that the

SWCNT phonon density of states has a number of sharp peaks (van Hove singularities) due to its 1-D structure. Such a difference is more profound at lower frequencies than higher frequencies, because low frequency phonon modes are more reflective of the symmetry of carbon nanotubes, while higher frequency modes are more reflective of carbon–carbon bonding. For this nanotube the calculated energy of RBM mode is 21.7 meV while the first van Hove singularity appears at about 2.5 meV. Van Hove singularities have been observed by neutron scattering experiments [4.48], thus confirming theoretical calculation.

When carbon nanotubes are bundled together, the intertube interaction will introduce dispersion along the transverse (intertube) direction. This will reduce the density of phonon states at low frequency, which has profound effect on the thermal properties of SWCNTs [4.49]. However, the heterogeneous nature of carbon nanotube bundles make theoretical calculation difficult. Figure 4.6 shows a tight-binding calculation for the case of graphite-like SWCNT bundles [4.50]. It can be seen that the intertube acoustic modes have fairly flat dispersion and the overall phonon frequencies are much less than those of intratube modes. Consequently, these modes should have very low Debye temperature

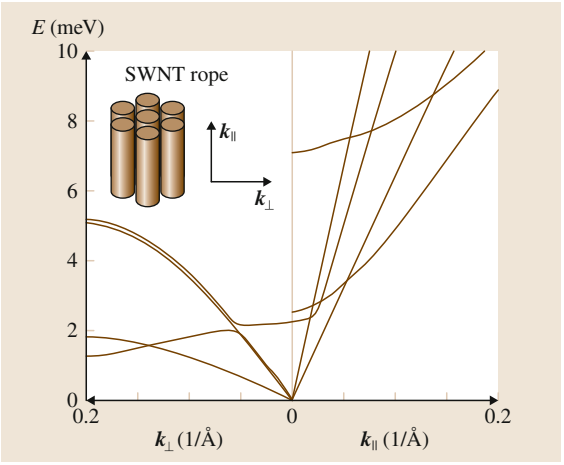


Fig. 4.6 Calculated low-energy phonon band structure of a SWNT bundle, for the case of graphite-like (*strong*) coupling

Θ_D and their contributions are only significant at very low temperature. The intratube modes are also different from those for SWCNT showing a shift in frequency, which mostly affects low frequency modes or small diameter SWCNTs [4.37, 51].

4.3 Synthesis

Over 20 years after the first batches of carbon nanotubes (CNTs) were synthesized and documented as such [4.1], CNTs continue on a steady trajectory toward industrial applications while many of the remaining challenges of growth continued to be ironed out. Whereas CNT growth has been a dynamic topical area for the past few decades, the gap between readily available products incorporating CNTs and the progression of studies in this area remains significant. In recent years, it has been estimated that the capacity for production of multi-walled CNTs could be as high as 300 to/yr, whereas that of single-walled CNTs could be as high as 7 to/yr [4.52]. However, the challenge required to further push production levels is to build a global market for CNT-based products that will instigate further scale-up production based on cost, safety, and material performance, and to develop understanding of CNT growth that will aid in the design of cheaper, more efficient synthesis techniques. One drawback to industry is that many of the largest potential CNT markets require specific homogenous properties, even though most large-scale CNT synthesis techniques yield mixtures of CNTs with different diameters and physical properties. This motivates research efforts continuing in the area of CNT growth to understand how to tighten the CNT diameter and property distribution by building a strong understanding of the growth processes and mechanisms. However, there is still a market even for wide-distribution multi-walled CNTs that can be produced at low cost in bulk quantities for their use as structural enhancers in materials.

The purpose of this section is to introduce the reader to the different techniques utilized to synthesize carbon nanotubes in addition to the different types of carbon nanotubes that can be produced using these methods. The caveat to this section is that the sheer breadth of techniques utilized in CNT growth makes it challenging to present a unified picture of CNT growth processes explaining every observation made thus far. A myriad of unique processes and systems have been utilized to grow CNTs, often reporting conflicting mechanistic results. Therefore, this section will focus on the ideas that have been accepted and have the capability to apply broadly to the vast majority of growth techniques discussed.

4.3.1 Substrate-Free Growth Techniques

In general, one can separate the growth of CNTs into two different categories: substrate-free CNT growth and substrate-bound CNT growth. By far, substrate-free CNT growth processes make up the majority of the large-scale industrial efforts due to the ease of scaling such techniques to implement continuous processes as opposed to operating using batch processes. From a historical perspective, two primary techniques have built the foundation of substrate-free CNT growth processes, which are (i) arc discharge [4.55, 56] and (ii) laser ablation [4.57]. In an arc discharge growth process, illustrated in Fig. 4.7a, two graphite electrodes are utilized in a chamber with an inert gas. A DC power supply is connected across the two electrodes (or rods) that passes electric current through the electrode configuration. This creates a discharge that consumes one of the electrodes and leaves a deposit on the other electrode that contains carbon nanomaterials that can vary in composition depending on the specific conditions utilized. One can tune the process to produce primarily multi-walled CNTs using two standard graphite electrodes to a process that produces single-walled CNTs using metal catalysts such as Ni, Fe, Mo, or Co doped into the electrode. Arc discharge is the most straightforward approach to synthesize carbon nanotubes, but its application as a large-scale production technique suffers due to the moderate yield of CNTs (often between 30–50%) amidst a variety of other carbons that requires one to employ post-process separation techniques to achieve well-defined samples. However, arc discharge processes predate carbon nanotubes and were readily employed in the synthesis of carbon whiskers and C_{60} decades before the report by Iijima in 1991 [4.58]. It is suggested that processes to form carbon materials using arc discharge date back to the 1960s, and closer analysis of the soot in these materials would have revealed carbon nanotubes.

Laser ablation growth of CNTs (Fig. 4.7b), on the other hand, is a process whereby the energy is supplied to the graphite target using either a continuous wave or pulsed laser, in comparison to a DC power supply in arc discharge. In laser ablation growth, the laser hits a hot target, which typically involves graphite with a catalytic metal (Ni, Fe, Co, etc.) doped into it, and vaporizes the target. Downstream of the target, a water-cooled condenser collects the product of the vaporized carbon/metal mixture that is carried using a flow of inert gas, such as Ar. Laser ablation processes can also be tuned to yield either single-walled CNTs or multi-walled CNTs based on the variation of parameters in the growth process such as the laser wavelength, laser power, laser pulse duration, furnace temperature, and graphite target composition. In particular, a low metal : graphite ratio in the target and a high furnace temperature (typically ≈ 1200 °C) is generally associated with good quality crystalline single-walled CNTs, whereas greater amounts of metal yields multi-walled CNTs, and lower furnace temperatures compromise crystallinity of the CNT tube walls. Today, laser ablation and arc discharge processes are still employed readily in the research lab, although industry scale-up efforts have typically not incorporated these techniques due to the *batch-by-batch* nature of these processes and the common difficulty of getting mixtures of CNTs and amorphous carbons, metals, or fullerenes. However, significant progress has been made in utilizing processes such as laser ablation to yield controllable double-walled CNTs with moderately small diameters (2–3 nm) compared to other techniques.

Aside from these techniques, there are a myriad of other processes that have been developed and adopted for substrate-free CNT synthesis. Many of these techniques represent a form of chemical vapor deposition

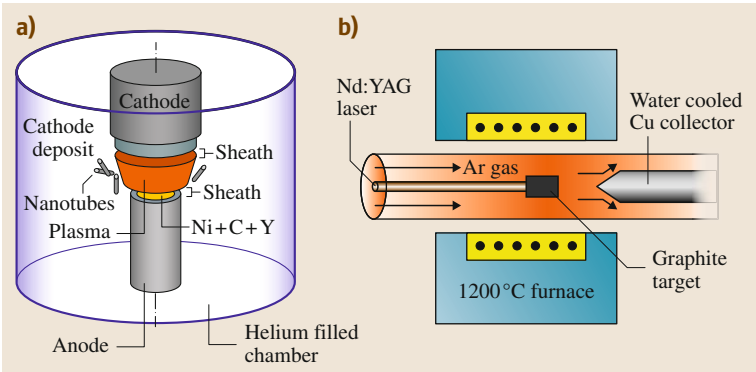


Fig. 4.7a,b Illustration of **(a)** an arc-discharge apparatus and **(b)** a laser ablation apparatus for growing carbon nanotubes. (**(a)** After [4.53]. **(b)** After [4.54])

(CVD) that can be scalable to large areas or can produce bulk quantities using cost-effective continuous processing. Generally, CVD techniques for CNT growth involve the reaction of a feedstock gas that contains carbon with nanoscale metal catalyst particles inside a heated reaction zone. For substrate-free synthesis processes, the metal is typically supplied during the process. Two notable processes that have proved capable of industrial-scale production are the HiPco process and fluidized bed CVD. The HiPco process was first designed at Rice University, with reports as early as 2001 documenting lab-scale SWNT production at 0.45 g/day [4.59]. The HiPco process is a form of CVD where an organometallic compound, such as $Fe(CO)_5$, is fed into a reaction zone at high pressures (up to 50 atm) and high temperatures (900–1100 °C). This process causes the organometallic compound to decompose into small, nanoscale metal clusters that catalyze the CO disproportionation reaction to form by-products of CO_2 and single-walled CNTs. Although additional processes for synthesizing single-walled CNTs have been developed on an industrial front in recent years, much of the widespread CNT research efforts over the past decade can be attributed to the HiPco process.

In addition to HiPco, another key CVD-based process that has demonstrated significant potential for large-scale production is the fluidized bed CVD (FB-CVD) process [4.62]. In this process, illustrated in Fig. 4.8, feedstock gases and catalyst material are fed into the reaction zone forming CNTs that are then collected in a continuous fashion. In some cases, the FB-CVD process involves two distinct reaction zones whereby a *catalyst* precursor reacts in the first zone forming the catalytic material, and this then flows downstream to the reaction zone where the CNTs form through reaction with this catalytic material. The benefit of this process is that the catalyst source is continuous, enabling the development of highly scalable CNTs with controllable properties in many cases. However, the drawback to FB-CVD is often the excess metal present in the CNTs that can be difficult to remove, and the difficulty achieving the level of precision in growth processes that can be comparable to fixed substrate-based CNT growth techniques.

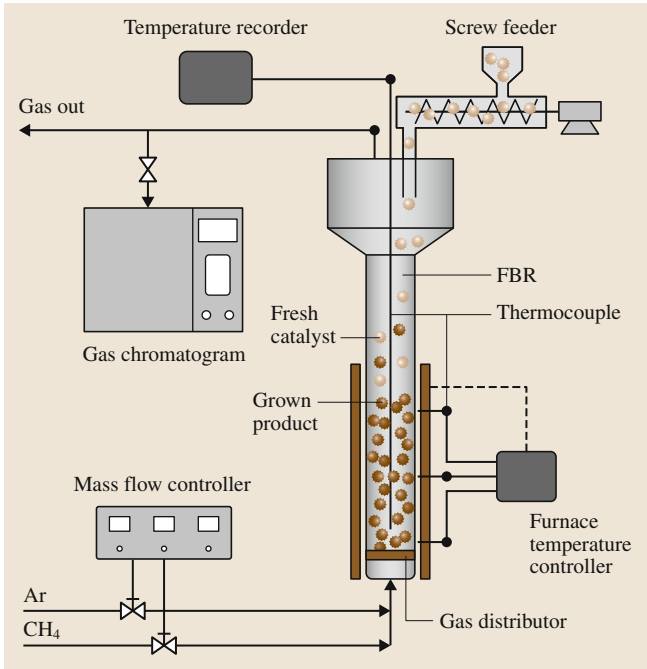


Fig. 4.8 Schematic diagram of a fluidized bed chemical vapor deposition system. (After [4.60])

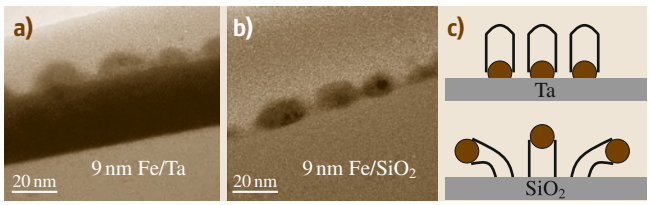


Fig. 4.9 **(a,b)** TEM images of catalyst particles that grow CNTs supported on Ta and SiO_2. **(c)** Schematic showing how the substrate supporting the particles dictate whether tip growth (SiO_2) or base growth (Ta) is achieved. (After [4.61])

4.3.2 Substrate-Bound Growth Technique

Whereas substrate-free growth techniques have been the medium for bridging the CNT synthesis effort to the industrial marketplace, substrate-bound CNT growth represents a growth form that is more tailored to electronics or specialized fields. Substrate-based CNT growth is almost always based on variations of the CVD growth technique and involves a substrate that usually supports both the CNTs formed during growth in addition to the catalyst material that grows the CNTs. In substrate-bound CVD growth, there are two types of growth modes that are well-accepted, which are (i) *base-growth* where growth of CNTs occurs while the layer of catalyst nanoparticles remains at the interface with the growth substrate, and (ii) *tip-growth*, where the catalyst nanoparticles lift off the substrate and are supported by the growing CNT during the growth process (Fig. 4.9). In a typical substrate-bound CNT growth ex-

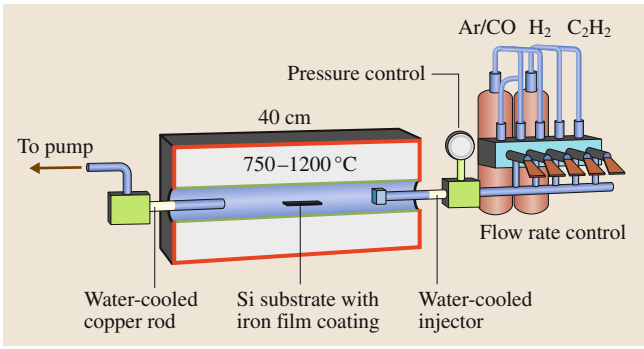


Fig. 4.10 Schematic of thermal CVD system setup generally utilized in aligned CNT growth (courtesy Atomic Physics, Göteborg University)

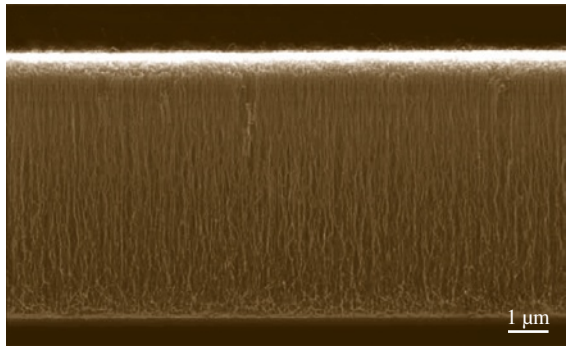


Fig. 4.11 SEM image of a vertically aligned carbon nanotube array (after [4.65])

periment using thermal CVD, the substrate containing the catalyst is placed into a heated zone, and a flow of carbon feedstock initiates the nucleation and growth of the CNTs. Variations of this process include plasma-enhanced CVD [4.63] and hot-filament CVD [4.64], where the plasma or hot filament act as energy sources to form reactive species for catalytic growth that would otherwise not form in a thermal CVD environment. A general illustration of a thermal CVD system utilized in these sort of experiments in shown in Fig. 4.10.

One of the most remarkable observations for the substrate-based growth of CNTs was the notion that a thin, uniform layer of catalytic material can be deposited onto the surface of a substrate, and the growth from this catalytic layer can result in self-oriented, aligned arrays of CNTs. Whereas this was initially shown for multi-walled CNTs in 1999 [4.66], by 2004 a few groups had demonstrated this for single-walled CNTs as well [4.67, 68]. One of the most notable observations early-on was that the addition of a small amount of H_2O during the catalytic reaction in addition to the carbon feedstock can accelerate the growth process dramatically, yielding millimeter-scale single-walled CNT arrays that grow in 10 min or less. Since the CNTs produced in this novel synthetic approach – which themselves are only a few nanometers in diameter – can be greater than a centimeter [4.69] in length and grown in structures where alignment is inherent from the stage of growth, these materials drew excitement from researchers. Figure 4.11 shows an SEM image of a short CNT forest where the individual CNT bundles are visible. In particular, substrate-free growth techniques such as arc discharge, laser ablation, or HiPco yield tangled CNTs that have submicron lengths. The challenge that remains for these materials is that substrate-based aligned CNTs are produced in a batch process using high temperatures that is not amenable to scalable production. Additionally, the limitations of many growth processes to specific substrates, such as alumina, have created roadblocks to the diverse applications envisioned for these materials. Recent efforts have made progress in growth of CNTs on conductive Cu substrates and at low temperatures [4.70], but a better understanding of the mechanisms behind CNT growth needs to be elucidated prior to large-scale advances in these areas. Fortunately, aligned CNT arrays have emerged as excellent test-beds to analyze the mechanistic aspects of CNT growth. Unlike most substrate-free CNT growth processes, aligned CNTs nucleate at virtually the same time and are uninhibited in many cases by significant steric hindrances that can alter the catalytic properties of randomly aligned materials. Therefore, one can use aligned CNT growth to probe quantitative and bulk-scale characteristics of the CNT growth and termination mechanisms that are relevant to all CNT growth processes.

4.3.3 Growth Mechanisms

The identification of specific mechanisms related to CNT growth remains controversial due to the wide variety of observations in growth processes that a single, unified mechanism would have to explain. However, it has been most readily accepted that CNT growth occurs via a vapor–solid–solid (VSS) model or a vapor–liquid–solid (VLS) model that has been readily employed for catalyst-based synthetic processes of other nanomaterials. In some cases for high temperature ($> 900\,^{\circ}C$) CNT growth, it is expected that the catalyst particles are in liquid phase whereas in lower temperature processes ($< 700\,^{\circ}C$) it is expected that catalyst particles

exist as a solid. It should be noted that the fast growth rates observed in CNT array growth can be modeled using diffusion parameters relevant to solids [4.71]. In these simple models, the hydrocarbon feedstock reacts with the catalyst particle and provides carbon that diffuses to the catalyst particle. In the initial phases of growth, a carbon cap precipitates on the surface of the particle and lifts off to result in CNT nucleation. Following nucleation, a constant carbon flux to the particle leads to the diffusion of carbon through the particle and to the edges of the growing CNT. In the simplest theoretical case, this becomes a steady-state system where a constant flux of carbon is supplied to the particle and the nanotube grows at a constant rate. However, from an experimental perspective, carbon nanotube synthetic processes terminate at some point, which is still not completely understood. This is believed to be a function of a process of *carbon overcoating* where amorphous carbon builds up on the catalyst particle and, over time, renders it inactive in growing CNTs. TEM studies have identified that morphology changes of the catalyst in the form of Ostwald ripening or other kinetic processes that occur due to the high free energy of catalyst nanoparticles and their exposure to the high temperature growth conditions may play a key role in termination processes as well, especially when the catalyst is supported by a solid surface [4.72].

Theoretical models of this process, one which is illustrated in Fig. 4.12, have been able to unify the interplay between multi-walled and single-walled CNT growth through the simple concept of carbon flux that

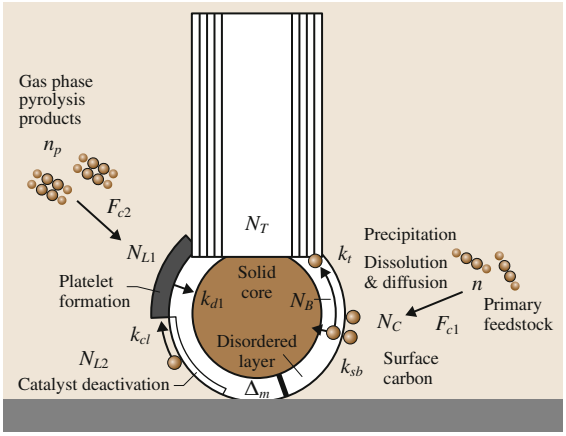


Fig. 4.12 Schematic showing the complex processes occurring during the catalytic growth of CNTs based on a model from *Puretzky* et al. (After [4.73])

is incident on the particle [4.71]. In a carbon starved environment (where the carbon flux is smaller than the diffusion rate), the result will be the nucleation of CNTs with only one wall whose outer diameter matches the particle size. Greater flux of carbon will result in the formation of multiple walls in the CNT. Whereas these ideas may oversimplify the challenges in understanding CNT synthetic processes, it is hoped that some unified model will emerge in the future that can establish a connection between the variable processes and systems used in CNT growth and the mechanisms that are at play in dictating nucleation, growth, and termination of CNTs.

4.4 Optical Properties

Because of their diameter-dependent direct band gaps, SWCNTs are promising for next-generation optoelectronic components. At the same time, their one-dimensionality is ideal for the study of 1-D excitons, whose properties remain largely unexplored despite predictions that they should behave very differently from excitons in higher dimensions [4.74, 75]. However, intrinsic optical properties of individual SWCNTs were difficult to probe for many years because of the effects of bundling and resulting tube-tube interactions in typical ensemble samples. During the past decade, much progress has been made in optical studies of SWCNTs, stimulated in part by the 2002 discovery of band gap photoluminescence (PL) from individually suspended SWCNTs in aqueous solution [4.76]. These samples have created opportunities to perform spectroscopy of individual nanotubes of specific chiralities, allowing exploration of their intrinsic optical properties. PL excitation (PLE) spectroscopy [4.77–88], Raman spectroscopy [4.89–110], ultrafast optical spectroscopy [4.111–140], micro- and nano-spectroscopy [4.141–163], and magneto-optical spectroscopy [4.11, 15, 17, 156, 157, 164–170] of individualized SWCNTs are currently under investigation, revealing fundamental properties of 1-D excitons and phonons.

Due to the strong 1-D quantum confinement, photo-created electron–hole pairs form excitons, i. e., hydro-

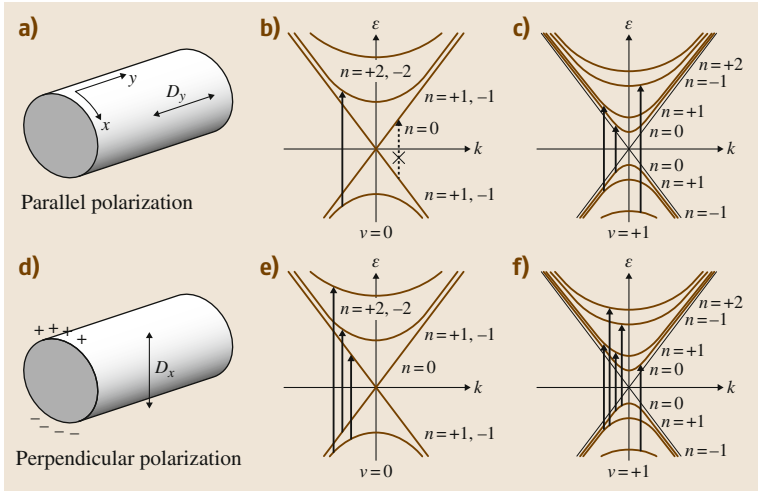


Fig. 4.13 (a–c) Incident light polarized parallel to SWCNT axis for a metallic SWCNT and a semiconducting SWCNT with allowed transitions indicated ($\Delta n = 0$). (d–f) Incident light polarized perpendicular to SWCNT axis for a metallic and semiconducting SWCNT with allowed transitions indicated ($\Delta n = \pm 1$). (After [4.23])

genic, Coulomb-bound electron–hole pairs [4.171]. In fact, in an ideal 1-D system, the binding energy of excitons has long been known to be infinite [4.172, 173]. Later, the binding energies of excitons in SWCNTs were experimentally determined to be hundreds of meV [4.174, 175], a significant fraction of their bare band gap, making SWCNTs one of the first systems in which to investigate excitons in the 1-D quantum limit.

4.4.1 Optical Absorption and Photoluminescence

Interband optical properties of SWCNTs arise from their structure-dependent attributes such as diameter and chiral angle as well as their electronic type (i. e., metallic or semiconducting). Therefore, optical spectroscopy provides a powerful tool for determining these attributes and their distributions in a given macroscopic sample.

First we will summarize the selection rules for interband absorption and emission in SWCNTs. If the photon momenta are small compared to the crystal momentum of the Bloch electrons, then approximate conservation of total linear momentum disallows *horizontal transitions*. Hence only *vertical transitions* are observed.

As in any solid, only vertical transitions are possible due to conservation of total linear momentum. This is because the photon momenta are small compared to the crystal momentum of the Bloch electrons. In the case of 1-D systems like SWCNTs, only transitions between states with nearly equal linear momenta along the tube axis are allowed. Since valence and conduction subbands in SWCNTs can be indexed by their angular momentum along the tube axis [4.23] (Fig. 4.13), angular momentum conservation must be considered for optical absorption and emission. Light polarized parallel to the tube axis does not have any angular momentum, and thus only transitions between states having equal angular momentum (i. e., the same subband index) are allowed for this polarization. In contrast, light polarized perpendicular to the tube axis can impart angular momentum to the circumference of the tube. This is visualized by thinking of the equal mixture of right- and left-handed circularly polarized light that comprises this polarization configuration; left-handed (σ_-) light changes angular momentum by -1 and right-handed (σ_+) by $+1$. The perpendicular polarization, therefore, allows for transitions between states with a change in angular momentum of ± 1. However, there is a strong depolarization effect for a perpendicular optical field [4.10, 176, 177], which suppresses absorption, making these optical transitions difficult to observe.

Experimentally, absorption spectroscopy is the simplest way to understand the basic characteristics of interband optical transitions in SWCNTs [4.76, 178–180]. Optical transitions occur between the valence and conduction bands, following the selection rules described before. The transitions are illustrated in Fig. 4.14. Because the transitions between states in the valence band vary in a precise way with the tube diameter in the optical regime, nanotubes were quickly identified as excellent candidates for optoelectronic applications. The interband transitions in SWCNTs reflect the underlying crystal symmetry of the nanotube. Since most synthesized SWCNTs have diameters ranging

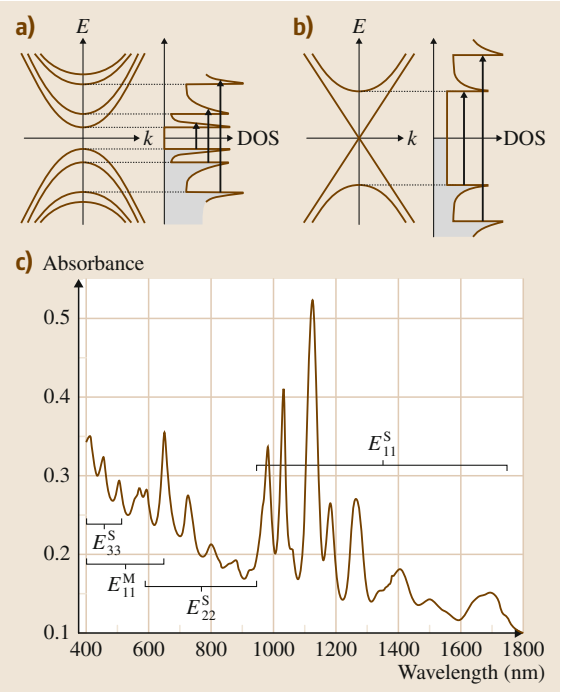


Fig. 4.14 Energy band diagram and density of states for **(a)** the E_{11}, E_{22}, and E_{33} transitions for semiconducting nanotubes, and **(b)** the E_{11} and E_{22} transitions for metallic nanotubes. The occupied states are expressed by the *gray color*. **(c)** Optical absorption spectrum of HiPco SWCNTs in a wide energy range from UV to IR. (Note that the first (second) of the subscripts of E_{ii} refers to the conduction (valence) subband index.) (After [4.8])

from 0.5 to 1.5 nm, the E_{11} and E_{22} transitions range from 800 meV to 3 eV. With increasing purity and individualization, higher-order transitions (up to E_{66}) have been observed, as well as phonon side-bands.

Figure 4.14c shows an optical absorption spectrum for HiPco SWCNTs, displaying four absorption bands:

1. E_{11} transition in semiconducting tubes
2. E_{22} transition in semiconducting tubes
3. E_{11} transition in metallic tubes
4. E_{33} transition in metallic tubes.

Within each band, there are multiple absorption peaks, coming from different (n, m) species present in the sample. It is therefore difficult to determine the (n, m) distribution quantitatively, unless the sample is highly enriched in a single (n, m) species. However, the intensity ratio between absorption peaks of metallic tubes and absorption peaks of semiconducting tubes

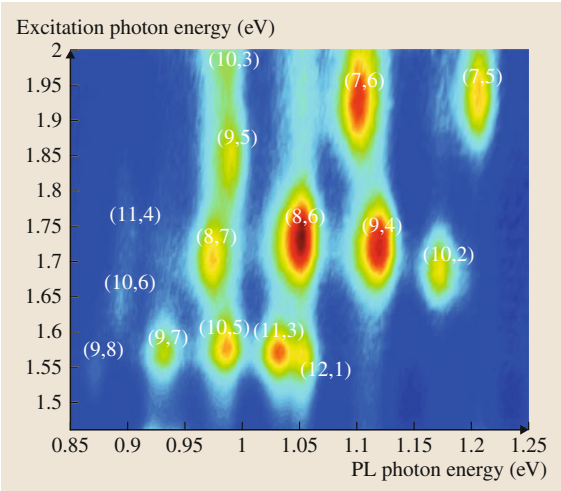


Fig. 4.15 Typical PLE map for HiPco nanotubes suspended in aqueous SDS. (After [4.8])

allows a qualitative estimate of the population ratio between these two types.

In the process of photoluminescence (PL), a high energy photon is absorbed by the medium and then a lower-energy photon is emitted. The excited state in a SWCNT can, in principle, be any high energy state or anywhere in the continuum, but due to enhanced absorption, a resonance appears when the E_{22} transition is excited and emission comes from E_{11} transitions. This effect was first observed in SWCNTs by O'Connel et al., and it quickly became one of the most common characterization tools for nanotube materials. In a typical PL experiment, the sample is excited by a range of visible wavelengths, and the luminescence is measured over a range of near-infrared wavelengths. Plotting the measured light intensity against the emission and excitation wavelengths creates a *photoluminescence excitation* (PLE) map (Fig. 4.15). Contrary to absorption spectroscopy, this technique is not useful for probing metallic (and small band gap) nanotubes but has the advantage of being sensitive enough to assign chiralities of semiconducting nanotubes, as illustrated in Fig. 4.15. It has proven to be ideal for measuring large quantities of materials, especially when combined with other spectroscopic tools (e.g., resonant Raman and absorption), and provides statistical information which cannot be obtained with electron microscopy. In addition, PL experiments have been used to obtain an understanding of excitonic states associated with the 1-D nature and the fourfold degeneracy of the electronic band structure of these semiconductors.

4.4.2 Raman Spectroscopy

As a consequence of their unique 1-D band structure, resonant Raman scattering spectroscopy serves as a powerful technique for the characterization and study of carbon nanotubes. A variant of normal Raman scattering, resonant Raman scattering (RRS) measures the intensity and energy of incident photons that are inelastically scattered off matter. The change in energy of the scattered photon relative to the energy of the incident photon corresponds to a quantum of the material under investigation, in this case a vibrational or phonon mode of an SWCNT. The resonant aspect of the technique comes from the use of excitation laser energies that coincide with real optical transitions of the SWCNT, resulting in a resonant enhancement effect that increases the Raman scattering probability from about 1 in 10^7 to approximately 1 in 10^3. The unique combination of the resonant nature of this technique with the highly anisotropic structure of carbon nanotubes allows for unconventional uses of vibrational Raman scattering to provide information on bulk and individual mechanical, electronic, and solution properties of these materials. One specific advantage of RRS over other optical methods is its ability to examine both semiconducting and metallic types of SWCNTs, regardless of aggregation state, doping, or number of defects.

The most widely used and intense Raman-active vibrational modes used for studying and characterizing carbon nanotubes are shown in Fig. 4.16. The lowest frequency mode (≈ 100–$400\,\mathrm{cm}^{-1}$) appears only in carbon nanotubes and fullerene structures and is known as the radial breathing mode (RBM) [4.181,182] (Sect. 4.2.3). It is an isotropic stretching vibration occurring in the radial direction perpendicular to the tube axis. Since its frequency varies inversely with nanotube diameter [4.181], it serves as one of the most common methods for optically determining the tube diameter of a particular SWCNT species.

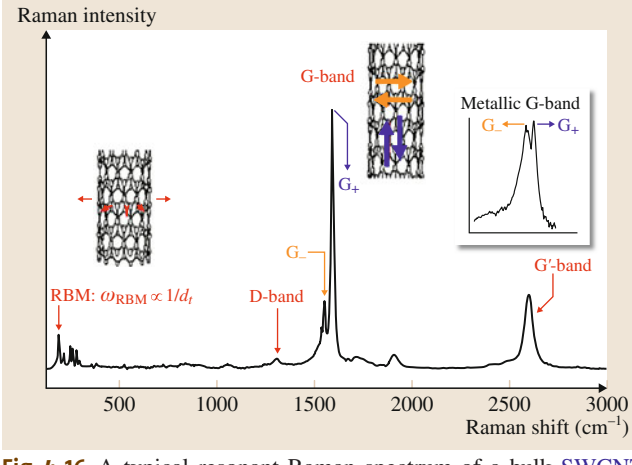


Fig. 4.16 A typical resonant Raman spectrum of a bulk SWCNT sample, taken at 785 nm excitation, for SWCNTs produced at Rice University. The spectrum illustrates the primary vibrational modes observed for SWCNTs, namely the RBM, D-band, G-band and G′-band

When such data is taken using a tunable laser source, the excitation energy dependence of specific RBMs can be determined. The energy at which the RBM Raman intensity reaches a maximum corresponds to the incident and scattered photon resonances with the SWCNT optical transition. As a result both diameter and optical transition energy can be determined from RBM Raman measurements allowing for assignment of RBM Raman features to specific (n, m) SWCNT structures [4.90–93, 97]. Once the optical transition energies are known for individualized SWCNTs, RBM intensity excitation profile data can be used to determine aggregation state [4.183] and even relative (n, m) abundance [4.109, 184–186].

The G-band vibration, centered at 1550–$1600\,\mathrm{cm}^{-1}$, is another very intense vibration and is common to all sp^2-hybridized carbon [1,2]. It is an in-plane, C−C stretching mode which is isotropic in graphene but anisotropic in carbon nanotubes due to the curvature-induced inequality of the two bond-displacement directions which causes the phonon to split into two, the G^+ and G^- peaks. Because of the splitting of the G-band into two separate but related modes, the overall line shape and intensity of the G-band can identify whether the tubes undergoing resonance with the excitation laser are metallic or semiconducting, as shown in Fig. 4.16 [4.103, 181, 187–190]. Furthermore, shifts in the G-band frequency can be observed due to doping via charge transfer resulting in the so-called *Eklund shift* [4.191]. With the application of uniaxial mechanical strain, the effective spring constants in each bond displacement direction can be further modified causing shifts in both G^+ and G^- frequencies as well as shifts in the observed optical transition energies, making the G-band a sensitive monitor of mechanical strain [4.192].

Another important mode is the D-band phonon, an out-of-plane bending mode with frequency $1300\,\mathrm{cm}^{-1}$ [4.181, 182]. This mode is normally Raman-inactive in pristine or perfect sp^2-carbon due to symmetry considerations, however, when the translational symmetry of the extended structure of graphene, graphite, or a car-

bon nanotube is broken by some sort of disorder, the D-band becomes Raman active and its intensity generally increases with the degree of disorder. This is why the D-band is often referred to as the *disorder* or *defect* peak in graphitic-like materials. This disorder can be actual bond dislocation defects, chemical functional groups, physisorbed molecular species, charge transfer complexes, etc., i. e., anything that can cause a localization of electron density in the otherwise delocalized π-bonding network.

Lastly, the G′-band (2600–2700 cm^{-1}), also common to all sp^2-hybridized carbon, is a dispersive, second-order Raman mode highly sensitive to small changes in electronic and vibrational structure [4.182]. Specifically, the excitation dependence of the G′-band can be used to measure the dispersion of the optical transition under resonance, an important characteristic for understanding electronic band structure. Such *mapping* of the G′-band excitation profile allowed the first experimental confirmation of the trigonal warping effect in the electronic density-of-states [4.194].

Raman scattering provides information only about the crystal structure of carbon nanotubes. However, when combined with the resonance effect, the intensity of the scattered photons can provide quantitative information about the electronic, aggregation, chemical, and mechanical states of carbon nanotubes. Such information is invaluable to future research tasked with turning these molecules into macroscopic materials with tailor-made properties.

4.4.3 Resonant Rayleigh Spectroscopy

Resonant Rayleigh scattering or resonant elastic light scattering has recently become a popular tool for the optical study and rapid characterization of nanotube samples [4.195–197]. This technique can rapidly identify excited states in both metallic and semiconducting SWCNTs due to its high scattering intensity when combined with a broadband, tunable excitation source. *Sfeir* et al. [4.195] made initial observations of scattering peaks in the excitation spectra consistent with expected optical transitions for both semiconducting and metallic species. In particular, the excitation spectra of metallic SWCNTs exhibited peak splitting which were attributed to trigonal warping of the graphene Brillouin zone. In subsequent studies by *Sfeir* et al. [4.196] and *Berciaud* et al. [4.193], individual nanotubes were structurally identified using electron beam diffraction via transmission electron microscopy prior to Rayleigh scattering measurements, allowing a direct assignment of optical

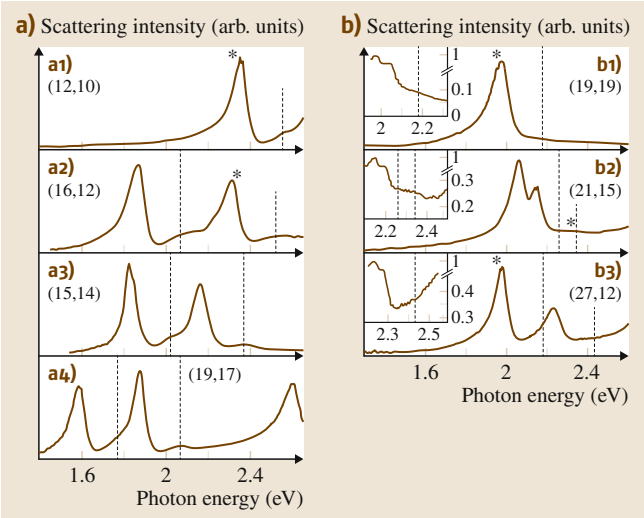


Fig. 4.17a,b Rayleigh scattering excitation spectra of **(a)** specific semiconducting and **(b)** metallic single-walled carbon nanotube chiralities. *Vertical dashed lines* indicate the energy position at which phonon sidebands are expected. *Insets* **(b)** are magnifications of the energy regions where phonon sidebands are expected, revealing no apparent feature. (After [4.193])

spectra obtained via resonant Rayleigh scattering to individual (n, m) species, as shown in Fig. 4.17. Semiconducting features were assigned to E^{S}_{33} and E^{S}_{44} excitonic optical transitions, while those of metallic SWCNTs were attributed to those of E^{M}_{11}. In addition, spectra of semiconducting SWCNTs show smaller, higher-energy features, located ≈ 200 meV above the main excitonic optical transition peak, attributed to phonon sidebands.

More recently, *Liu* et al. [4.197] combined electron beam diffraction with in situ Rayleigh scattering to measure 206 optical transitions of (n, m)-identified nanotubes. In particular, for nanotubes spanning diameters 1.4–4.7 nm, optical transitions were measured for semiconducting species ranging from E^{S}_{33} up to E^{S}_{77}, and for metallic species ranging from E^{M}_{11} up to E^{M}_{33}. From this broad range of data collected via Rayleigh scattering spectroscopy along with existing E^{S}_{11} and E^{S}_{22} data collected via photoluminescence excitation spectroscopy, an empirical equation was produced to predict optical transition energies with appropriate (n, m)- and E_{ii}-dependent parameters, providing a predictive tool for assigning measured optical spectra to specific SWCNT chiralities over a broad range of experimentally relevant energies.

One particularly useful application of Rayleigh scattering spectroscopy is the wide-scale characterization of

many nanotubes simultaneously [4.198]. Using a wide-field laser illumination in a dark-field microscope geometry and refractive-index-matching, Joh et al. were able to Rayleigh image entire chips containing many different SWCNT species as a function of laser excitation energy. Combined with atomic force microscopy (AFM), this improvement in experimental setup allows not only the identification of nanotube growth but also the rapid determination of optical spectrum and diameter from Rayleigh scattering and AFM measurements, respectively, facilitating assignment to specific (n, m) structures [4.198].

4.4.4 Ultrafast Spectroscopy

Ultrafast spectroscopy allows the interrogation of carrier and phonon dynamics in condensed matter systems. As the rise and relaxation times of these ultrafast phenomena are on the order of 1 ps, they can be observed by using femtosecond laser pulses. One of the most popular tools for this is time-resolved pump-probe measurements. When a strong optical pump pulse from a femtosecond laser generates electron–hole pairs, the concomitant changes in the properties of the material (e.g., Raman scattering, absorption, and reflectivity) are detected by a weaker probe pulse, and the delay is controlled by the experimenter.

Time-resolved pump-probe spectroscopy is a suitable method for measuring carrier dynamics, such as distribution functions and relaxation mechanisms. Using this method, one can explore carrier dephasing processes, carrier–carrier scattering, carrier–phonon scattering, and radiative and nonradiative recombination processes [4.111, 113, 115, 123, 199–202].

Figure 4.18 shows typical differential transmission ($\Delta T/T_0$) signals as a function of delay between pump and probe pulse. Two traces taken at 0.89 eV (1393 nm) and 1.60 eV (775 nm) correspond to E_{11} and E_{22} ranges, respectively. In both cases, a positive differential transmission is consistent with band filling, and the shorter decay time is explained by a nonradiative intraband relaxation process [4.203]. The slower decay time only found in the E_{11} range ($h\nu = 0.89$ eV in Fig. 4.18) can be explained as a radiative interband recombination, because the signal is resonantly enhanced when the photon energy is consistent with an interband absorption peak [4.111, 113, 200].

Coherent phonon (CP) spectroscopy is a powerful characterization tool, especially for SWCNTs. It allows direct measurement of excited state phonon dynamics in the time domain, including phase information and dephasing time. This information cannot be directly obtained via Raman spectroscopy. CP spectroscopy has several more advantages over Raman spectroscopy, including high resolution and narrow linewidths, no Rayleigh scattering, and no photoluminescence. Hence it allows characterization of metallic as well as semiconducting nanotubes, whereas PLE is incapable of characterizing metallic nanotubes.

Since the observation of coherent phonons in SWCNTs by *Gambetta* et al., many studies of the RBM and G-mode coherent phonons in SWCNTs have been published [4.129, 130, 134, 135, 137, 204, 205]. Figure 4.19a shows a coherent phonon oscillation signal in the time-domain [4.137]. To determine the frequencies of the excited lattice vibrations, one can perform a fast Fourier transformation (FFT) of the time-domain oscillations, such as is shown in Fig. 4.19b. The multiple peaks in the lower frequencies correspond to the RBM, which indicates that the SWCNT sample contains several chiralities that are resonantly excited at 840 nm (1.48 eV) [4.130]. Since the CP spectrum has high resolution, the peaks can be used to accurately determine the chiral index of the SWCNTs [4.206].

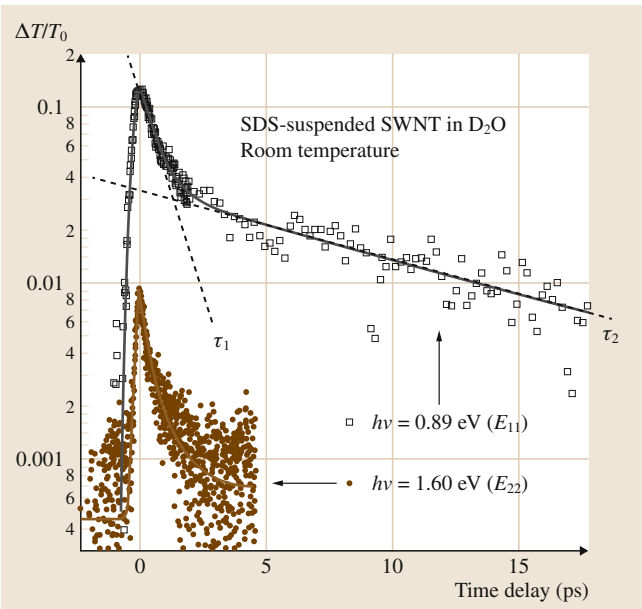


Fig. 4.18 Ultrafast pump-probe data at two wavelengths, corresponding to first and second subband transitions. A very fast single decay is seen in the second subband case while two decay components ($\tau_1 \approx 770$ fs and $\tau_2 \approx 10$ ps) are clearly seen in the first subband case. *Solid lines* show Gaussian and exponential fits in the appropriate delay regimes. (After [4.113])

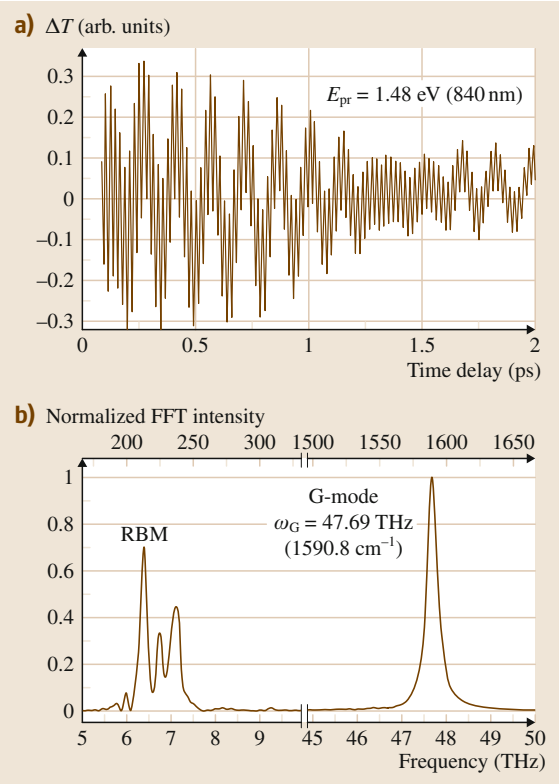


Fig. 4.19 **(a)** Transmitted intensity modulations due to coherent phonon oscillations in SWCNTs, which were extracted from the pump-probe signal for pump and probe energies of 1.55 eV (800 nm, E_{pu}) and 1.48 eV (840 nm, E_{pr}), respectively. The beating pattern arises from superposition of the CP oscillations from the RBM and G-mode. **(b)** Corresponding Fourier-transformed spectrum showing radial-breathing modes (RBMs) at 6.0–7.5 THz (200–250 cm^{-1}) and G-mode phonons at 47.69 THz (1590.8 cm^{-1}). (After [4.137])

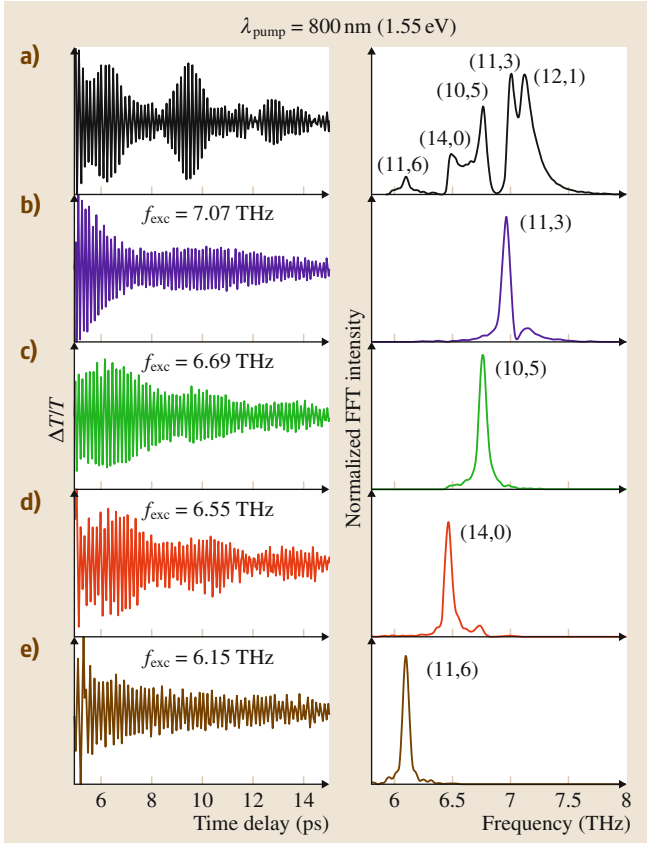


Fig. 4.20 **(a)** *Left*: time-domain transmission modulations of the probe due to coherent RBM vibrations in ensemble SWCNT solution generated using standard pump-probe techniques without pulse shaping. **(a)** *Right*: Fourier transformation of time-domain oscillations with chirality-assigned peaks. **(b–e)** *Left*: time-domain coherent RBM oscillations selectively excited by multiple pulse trains via pulse shaping with corresponding repetition rates of 6.15, 6.55, 6.69, and 7.07 THz. **(b–e)** *Right*: Fourier transformations of corresponding oscillations, with their dominant nanotube chirality (n, m) indicated. (After [4.134])

The peak at 47.69 THz (1590.8 cm^{-1}) corresponds to G-mode phonons of SWCNTs. With regard to the G-mode, *Kim* et al. recently presented a clear picture for the dephasing of G-band phonons by random frequency modulation via interaction with the RBM through anharmonicity [4.136, 137].

Using a pulse-shaping technique [4.207], chiral-selective excitation has been achieved for studying the physical properties of single-chirality SWCNTs [4.134]. Figure 4.20a shows typical CP oscillations (Fig. 4.20a, *left*) and their Fourier transformed spectrum (Fig. 4.20a, *right*). By introducing multiple pulse trains with different repetition rates (7.07–6.15 THz), a coherent RBM oscillation is selectively excited, as shown in Fig. 4.20b–e, respectively. For instance, by choosing a pump repetition rate of 7.07 THz, the (11,3) nanotubes can be excited selectively, as shown in Fig. 4.20b. Note that the accuracy of selectivity depends on the number of pulses in the tailored pulse train.

4.4.5 Excitonic Effects

1-D Coulomb interaction differs significantly from systems with other dimensions. For example, the ex-

citon binding energy becomes infinite in an ideal 1-D electron–hole system [4.172, 173, 208]. In addition, the Sommerfeld factor, the ratio of the exciton continuum to the free electron–hole pair above the band edge, has been shown to be less than 1 in 1-D systems [4.74, 75]. 1-D excitons in SWCNTs [4.209] seem to be even more peculiar. Early experimental PLE results (e.g., [4.80]) indicated that interband excitation energies are *higher* than those expected from band structure calculations based on simple tight-binding models. This blue shift is totally against our conventional wisdom that excitonic binding should red shift the excitation energy from the band edge. Ando's pioneering theoretical work [4.210, 211] indicates that there is a significant blue shift from the single-particle band gap (which is what tight-binding calculations yield) due to quasi-particle corrections. This blue shift is expected to exceed the excitonic binding energy, and thus, the net effect is a blue shift. A number of more recent theoretical studies [4.177, 212–229] not only confirmed these predictions and provided estimates for the exciton binding energies but also raised an array of new issues, questions, and predictions, including the intrinsic radiative lifetimes, the existence of *dark* excitons, and the stability of excitons in metallic carbon nanotubes. Two-photon PLE studies [4.174, 175] have successfully determined the exciton binding energies to be very large (300–500 meV). Excitonic signatures have also been detected in absorption spectra of metallic nanotubes [4.180]. Furthermore, recent temperature-dependent magneto-optical studies have provided new insight into the excitonic fine structure in SWCNTs [4.165–169], including the direct measurement of dark-bright splitting values in individual SWCNTs [4.156, 157].

The existence of two equivalent valleys in momentum space, K and K' valleys, combined with strong short-range Coulomb interactions (intervalley mixing and exchange), produces an intriguing excitonic fine structure in SWCNTs [4.223, 231]. There are four combinations of lowest-energy excitons: two are direct excitons formed by linear combinations of KK and $K'K'$ electron–hole pairs and two are indirect excitons that are created by indirect $K'K$ and KK' electron–hole pairs. The latter are finite momentum exciton states that require a phonon-assisted transition to be optically created. Direct excitons are zero momentum states, which facilitates optical absorption and emission. However, the mixing of the KK and $K'K'$ transitions produces two wavefunctions that have opposite parity under transformations about the axis perpendicular to the tube (sometimes referred to as the U symmetry axis). The lower (s-like, often called the $1g$ state) exciton state has even symmetry, while the upper state (p-like, $1u$ state) has odd symmetry. Since a photon will only couple with a state with odd parity (system overall has even parity), the upper state is optically active (*bright*) and the lower state is inactive (*dark*), which is a unique scenario whereby the lowest state is not the emissive one [4.214, 217, 219, 221–223, 231]. The $n = 2$ orbitals of the E_{11} exciton reverse the ordering of even and odd symmetry, such that the $2u$ (odd symmetry) has a lower energy than the $2g$ (even) state.

Experimentalists have exploited these symmetry-based transition rules to investigate SWCNT excitons. Since only the $1u$ exciton state couples to the light field by way of one photon, and $2g$ couples only using two photons, one can excite one-photon dark states and monitor the $1u$ luminescence (Fig. 4.21) [4.174, 175]. Using the difference between the excitation energy for E_{11}^{2g} and the emission energy of E_{11}^{1u} and assuming

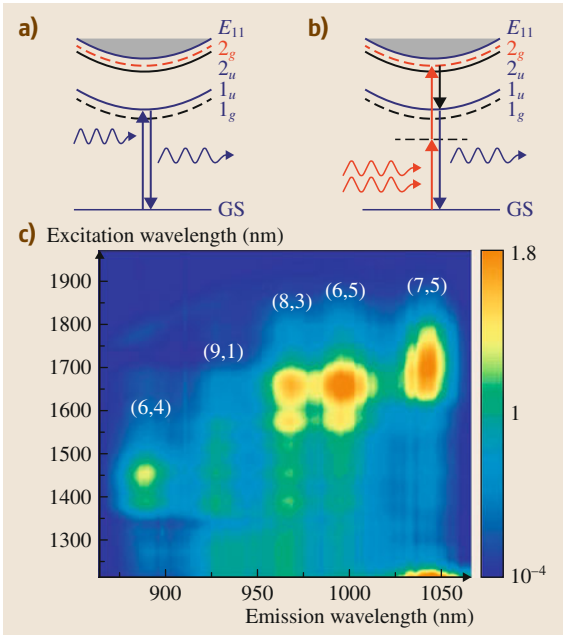


Fig. 4.21 **(a)** One photon can couple to the $1u$ state both as an excitation and emission. **(b)** Two photons can access even parity states, like $1g$ or $2g$. In two-photon spectroscopy, two photons excite a dark state while the bright, luminescent $1u$ state is monitored. **(c)** Experimental contour map of the PL intensity as a function of two-photon excitation (y-axis) versus one-photon emission (x-axis). (After [4.230])

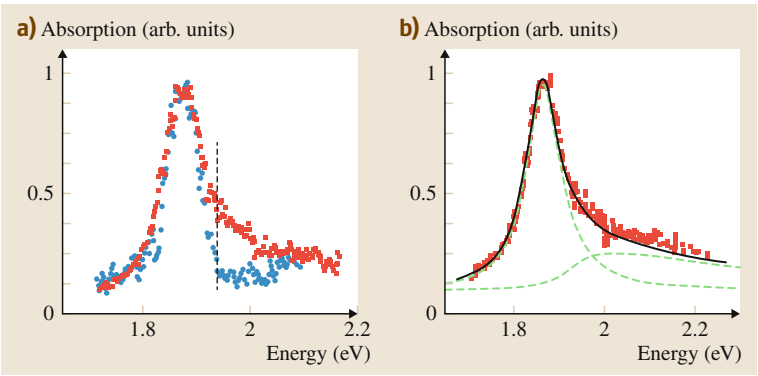


Fig. 4.22 **(a)** Absorption spectrum of a (21,21) metallic nanotube (*red symbols*) and a (16,15) semiconducting SWCNT (*blue symbols*), after a slight shift in energy and adjustment in strength. In the armchair nanotube, absorption from the continuum transitions is apparent in the high-energy wing. From the threshold of the continuum absorption (*dashed line*), we estimate an exciton binding energy of 50 meV. **(b)** Comparison of the theory (*black solid line*) for the optical transition in a metallic nanotube. The absorption can be decomposed into the dominant exciton contribution and a continuum contribution (*green dashed lines*). (After [4.233])

a hydrogenic model, the exciton binding energy was estimated to be ~ 300 to 400 meV for $0.6 < d_t < 0.9$ nm SWCNTs and showed a linear dependence on the inverse of the diameter [4.232]. Furthermore, the tubular nature of SWCNT crystal structure allows a magnetic field applied parallel to the tube axis to induce non-intuitive quantum phenomena. Such a magnetic field breaks time reversal symmetry and adds an Aharonov–Bohm phase to the electronic wavefunction, which mixes the lowest-energy bright and dark exciton states. In particular, a series of recent experiments [4.156, 157, 165–169] demonstrated that such a symmetry-breaking magnetic field can dramatically *brighten* the dark state. Namely, the PL intensity increases, or *brightens*, with magnetic field and the amount of brightening decreases with temperature. This phenomenon, magnetic brightening, can be understood as a consequence of interplay between the strong intervalley Coulomb mixing and field-induced lifting of valley degeneracy.

Contrary to the situation of semiconducting SWCNTs, excitonic properties of metallic SWCNTs have been poorly explored [4.186], although they are expected to provide a novel system for the study of electron–hole pairs in the presence of degenerate 1-D electrons. Unlike *conventional* 1-D metals, the lowest van Hove singularity (VHS) peak in the conduction-band is unoccupied in metallic SWCNT, allowing one to create excitons into an interacting 1-D electron system by resonantly pumping the lowest 1-D VHS peak. The created excitons should show unique dephasing and energy relaxation dynamics, the correct understanding of which should provide significant new insight into many-body dynamics in femtosecond time scales. Screening does takes place in metallic SWCNTs, but only weakly, allowing for exciton binding energies to reach 50 meV, as measured by direct optical absorption of a single metallic SWCNT [4.233], shown in Fig. 4.22. Unlike graphene, transitions in metallic SWCNTs cannot occur between the linear bands that form the Dirac cone at K and K', as discussed earlier. Instead, like semiconducting SWCNTs, the lowest allowed transition occurs between the highest valence van Hove singularity the lowest conduction one. This transition is heavily modified by the large exciton binding energy creating Lorentzian-like transitions that are similar to the semiconducting SWCNTs. Since the absorption is from excitons and not a free plasmon resonance like most metals, metallic SWCNTs scatter the visible light that they do not absorb [4.234].

4.5 Transport Properties

Electronic transport properties of carbon nanotubes were studied intensively very soon after their discovery. A wide variety of CNT systems have been studied, including ropes, networks, and films. Numerous effects typical of polymer matrices, classical crystals, and disordered materials have been observed in these bulk systems. Some of the key parameters governing transport are the sample quality and the nature and number of nanotube-nanotube and nanotube-electrode junctions. In this section, a brief presentation of nanotube films is given to illustrate the complexity induced by the combination of these parameters; the main part is dedicated

to individual nanotubes, where a better understanding has been achieved, to illustrate the strong distinction between metallic and semiconducting nanotubes and some of the most important parameters to describe their device operation.

SWCNT films or *mats* are formed by randomly or partially oriented SWCNT bundles. In some respects, such a network is similar to an amorphous metal system with conductive tubes or bundles as the metallic islands separated by energy or spacial barriers. As a result, the DC transport is primarily determined by intertube transport within bundles or interbundle transport, while the 1-D intratube transport nature is buried [4.235].

The DC conductivity of SWCNTs is metallic at high temperatures, increasing linearly with decreasing temperature [4.236]. However, at lower temperatures, the DC conductivity reaches a maximum and starts to decrease with decreasing temperature. Such nonmetallic behavior is usually explained by either variable range hopping (VRH) [4.237, 238] or fluctuation-induced tunneling (FIT) [4.239, 240]. But it is still not clear whether such behavior is mainly due to weak interbundle connections, localization by impurities, defects, or frozen semiconducting tubes within bundles [4.235]. Other experimental techniques such as magnetoresistance measurements [4.237, 238] and AC conductivity measurements [4.241, 242] are also used to explore the transport mechanism in SWNT films.

Studied as *individual nano-objects*, both metallic and semiconducting nanotubes have provided much insight and are still explored as both ideal one-dimensional mesoscopic systems [4.243–246] and potential building blocks for electronic applications [4.247–251]. Metallic nanotubes have charge carriers with very high mobilities near the Dirac point, and current densities as high as 25 μA can be carried by a single nanotube [4.252], making them much larger than copper for the same cross-section. Moreover, due to the strong Coulomb interaction in one-dimensional metals, electron–electron correlations become important and their properties become described by the Tommonaga–Lüttinger liquid model [4.253]. On the other end, the chirality dependence of semiconducting nanotube band gaps have allowed to study many device properties ranging from single-electron transistors [4.254] to Schottky [4.255] and p-n diodes [4.251] and are showing a very high sensitivity to the environment or external excitations (optical, magnetic) expected to give rise, combined with their mechanical strength, to highly robust detectors.

In most of the numerous reports in the literature, individual nanotubes are directly contacted by two metallic electrodes and a third nearby electrode is used to apply an electrostatic field (Fig. 4.23), as proposed since the first transport measurements in 1997 and 1998 [4.243, 247–249]. This three-terminal (transistor) configuration allows the direct determination of the metallicity of the nanotubes (Sect. 4.2.2) by measuring the resistance or current-voltage characteristics of the device as a function of the potential applied through the third electrode (called gate). The detailed fabrication procedure varies a lot depending on the expected outcomes: devices are obtained by either depositing nanotubes from dispersions or directly growing them on a substrate; electrodes can be deposited on top of the nanotubes, or they can lie on top of them; typically the substrate is highly-doped silicon (which will be used as the gate electrode) over which a thermal oxide is grown (Fig. 4.23); as a consequence, the SWCNT can be suspended or directly in contact with the substrate.

Most basic electronic properties can be clarified by considering the effect of an external potential to the doping level of the nanotube, and the transport characteristics of a 1-D system. This second aspect can be given by the Landauer formula of the two terminal resistance [4.256]. The two-terminal conductance of a 1-D system, is given by

$$G = \frac{4e^2}{h} \sum_i \int \overline{T}_i(E) \left(-\frac{\partial f[(E - E_F)/k_B T]}{\partial E} \right) \mathrm{d}E \,, \tag{4.6}$$

where the total conductance is given by the sum at the Fermi energy E_F of all subbands with index i of transmission $\overline{T}_i(E)$, and $f(E)$ is the Fermi distribution. The prefactor 4 is due to the subband spin and orbital degeneracies.

The modulation of the nanotube doping by the gate voltage can be obtained by considering the electrostatic equilibrium at a given gate potential. The carbon nanotube is capacitively coupled to the gate electrode and charges are injected in both of them. This charge injection will induce a change in the electrochemical potential of the nanotube through a density-of-states term [4.257, 258] and can be expressed as (for low source–drain voltage and neglecting temperature broadening)

$$E_F = eV_g - e^2 \frac{\int_0^{E_F} \rho(E)\,\mathrm{d}E}{C_g} \,, \tag{4.7}$$

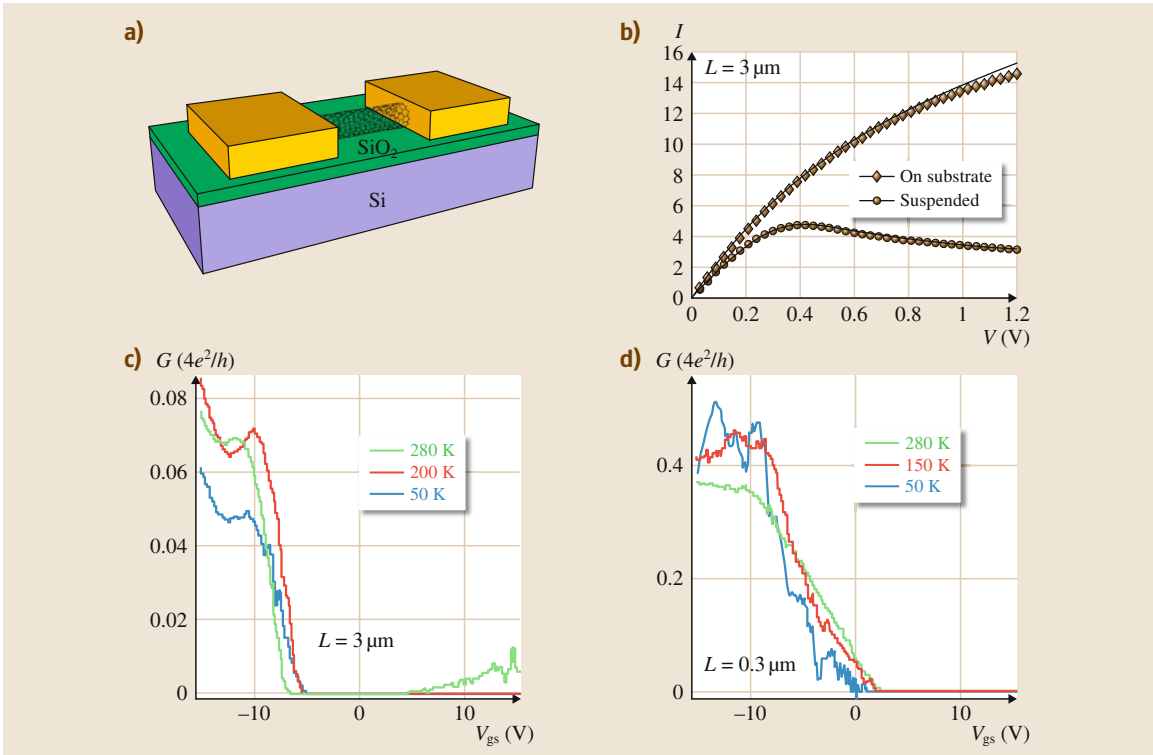


Fig. 4.23 **(a)** Schematic of the typical transistor configuration used to measure individual carbon nanotube transport properties. **(b)** $I(V)$ characteristic at high voltage of a long carbon nanotube device with comparison between a nanotube on substrate and suspended. (After [4.252]). **(c)** Conductance G (at low source-drain bias V_{ds}) versus gate voltage V_{gs} for a 3 µm long SWCNT device recorded at various temperatures. **(d)** G versus V_{gs} for a 300 nm long tube section on the same tube as for **(c)** at various T. (**(c,d)** after [4.245])

with V_g the potential applied between the gate and the source–drain electrodes, C_g the electrostatic (geometric) capacitance and $\rho(E)$ the density of states integrated from the center of the band gap (or the Dirac point) to the Fermi energy. In this specific expression, the Dirac point is assumed to be at $V_g(E_F = 0) = 0\,V$. However, in most devices, due to charge traps and doping from the oxide or impurities, an hysteresis in the gate dependence [4.259] and a threshold voltage ($V_g(E_F = 0) = V_{th}$) will appear [4.260, 261].

From these two equations, one can see that the conductance depends on the transmission of electrons through the whole device at the Fermi energy controlled by the gate voltage. Hence, different nanotubes will exhibit clear gate dependencies even at room temperature:

- Semiconducting nanotubes will exhibit field-effect transistors type behaviors with on/off ratios of many orders of magnitude, since there is no subband available near E_F. They will exhibit diode type current-voltage characteristics. The most common reported behavior is unipolar with a p-doping of the nanotube attributed to adsorbates on the nanotube surface [4.249] (Fig. 4.23c,d) and effects from the substrate (or the electrodes); however, ambipolar devices are now commonly achieved [4.262].
- The small band gap carbon nanotubes will only show a small dip, since the band gap energy is comparable to the thermal energy and the tails of the Fermi distribution are within the valence or conduction band.
- Metallic nanotubes will only show very weak (or no) gate voltage dependence since they will be less sensitive to the gate voltage (due to finite density-of-states everywhere) and the number of subbands will remain constant over a large energy range; and they typically exhibit linear I–V curves before saturation.

The various transport regimes described by (4.6) are governed by the transmission of the whole device including the tube, but also the contacts. The minimum conductance is then given by the ballistic regime where $\overline{T}_i(E) = 1$ and gives a quantized conductance of $G_{\text{bal}} = \frac{4e^2}{h}$ for each subband. This corresponds to a resistance of 6.5 kΩ. At room temperature, additional resistance is due to incoherent addition of nonperfect contact transmission and diffusive centers in the nanotube, this is the *classical regime*. At low temperature, coherent effects dominate and quantum dot regimes or localization effects develop; these regimes are referred as *quantum transport* or *mesoscopic regimes*. Ballistic resistance has been demonstrated for metallic carbon nanotubes up to room temperature [4.244,263], whereas semiconducting nanotubes do not exactly reach this value [4.245, 263] (Fig. 4.23c,d).

Impressive progress has been made in the understanding and reduction of the contact contribution to the resistance. Different metals have been used to contact nanotubes with the most common being gold, titanium, palladium and platinum. A first barrier can form at the interface between the metal and the nanotube due to bad wetting of the nanotube in the metal; this interface will be governed by the cleanliness and contaminations of the interface and by the overlap between the metal-nanotube wavefunctions [4.28]. A low, ohmic contact resistance is typically obtained by using top electrodes made of palladium or gold and/or by annealing the device. Another route to achieve near perfect contacts consists in direct growth on top of the contacts [4.245], or using nano-welding (*burying* the nanotube in the contact). Moreover, in the case of semiconductors, even with a good interface a Schottky barrier can form depending on the band alignment [4.255, 264]. The matching of the metal and nanotube work function has been shown to provide a good approximation of this barrier height, although charge transfer at the interface must be considered for a precise understanding. These barriers have been shown to govern the field-effect properties of nanotube transistors and yield to a very high sensitivity of these devices to the environment. As an example, a good p-type contact will be obtained for a metal with a high work function, but a good interface is also necessary. As a consequence, titanium will be a bad choice due to its work function lying in the center of the nanotube band gap, but platinum also, due to a poor contact and the formation of additional barriers; whereas palladium will satisfy both conditions.

Obviously, the intrinsic resistance of the nanotube will also contribute to the overall measured value. In the classical case, the two main contributions come from scattering by disorder and phonons. The origin of disorder is often complex to assign and scattering can be due to lattice defects (vacancies, impurities, ...), mechanical deformations and potential fluctuations induced by adsorbates and the substrate [4.261]. A backscattering mechanism can be distinguished between intervalley (from K to K') or intravalley scattering and will be associated with short-range and long-range disorder, respectively. It has been theoretically [4.261] shown that metallic nanotubes are insensitive to the first type of scattering and they exhibit lower intrinsic resistance than semiconducting nanotubes. Scattering will also occur with acoustic phonons at low source–drain bias. In metallic and clean (doped) semiconducting nanotubes the I–V curves are linear at low-bias; and mobilities higher than 100 000 $\text{cm}^2/(\text{V s})$ and ballistic transport for short distance between contacts have been demonstrated [4.244, 252, 263]. At higher voltage, the resistance will start saturating due to interaction with optical phonons (around $\hbar\omega_0 \simeq 160$ meV) and the maximum current carried by a single tube will be as high as 25 μA (Fig. 4.23b). For suspended nanotubes, a negative differential conductance can even be observed due to heating induced by hot phonons (Fig. 4.23b). This higher current limit can be overcome only for contact distances shorter than the optical phonon mean-free path around 10 nm [4.265].

At lower temperature, coherent addition of the scattering contributions and coherent transmission at the electrode interface must be considered. Moreover, the effect of confinement and electron–electron interaction becomes important and some of these effects might even need to be considered up to room temperature. A large variety of phenomena have been observed depending on the metallicity, the transmission at the contacts and the nature, density and strength of the scattering centers in the nanotubes. Detailed reviews provide an extensive description of such quantum phenomena from both the theoretical [4.28,261] and experimental point of views; we can summarize some of the consensus achieved by dividing these mesoscopic results in three main effects:

- Correlated electrons in 1-D metals are not described by a Fermi liquid of weakly interacting fermions, but as a correlated ground state called a *Lüttinger liquid*. Spin and charge propagate as two independent bosonic modes and different power law dependencies of the tunneling density of state and conductance are expected. This law will depend on

the bias voltage range, temperature, the nature of the contacts (to the end or the bulk of the nanotubes) and will depend on the Lüttinger liquid parameter, $g \approx 0.22$ for SWCNTs [4.36, 266]. Although such measurements are difficult to assign univoquely, experimental power laws have been demonstrated to be consistent with theory [4.253, 267].

- When the presence of scatterers becomes too important, the mean-free path is given by static scatterers; as the temperature decreases the coherence length increases and coherent back-scattering takes place: this is the so-called *localization regime*. Both weak and strong localization can occur depending wether disorder or electron interactions dominate. Magneto-resistance measurements allow unique assignment of these regimes, and, in the case of individual SWCNTs, weak localization is intimately related to Lüttinger liquid behaviors; this is not the case for small bundles or MWCNTs, where Fermi liquid behaviors are observed.
- When no (or very few, weak) scattering centers are present, the coherent response is dominated by the reflection and transmission at the contacts. The behavior can vary from *Coulomb blockade* [4.243, 247, 269], where nanotubes behave like single-electron transistors when contacts are transmit poorly, to *Fabry–Perot type* interferences [4.244, 263], where the system behaves like an electron waveguide when contacts are almost transparent. Both regimes are characterized by very strong oscillations of the conductance, as illustrated in Fig. 4.24. In the first case, the finite length of the nanotube induces a supplementary quantization of the wavevector and forms of a zero-dimensional system (right inset), while in the second case, constructive and destructive interferences of the wavefunction occur (left inset). Interestingly, in both cases, the induced wavevector quantization is given by $\Delta k = \pi/L$. The quantum dot regime exhibits more complex V_g and V_b dependency due to degeneracy lifting induced by the mutual interaction between added charges leading to spin-orbit coupling. Magnetoresistance measurements have been very useful to probe such effects in detail [4.269].

One of the current challenges in the field consists in exploiting the properties of single nanotube devices to large-scale applications and much progress has been made in building more and more complex structures using individual nanotubes, and also controlling bulk samples by using for example aligned growth or chirality sorted films. These structures have been exploited in numerous configurations and for various applications. For example, large-scale logic and analog electronic structures, microwave and radio-frequency operation, proximity effects from superconducting or ferromagnetic electrodes have been demonstrated. It is also worth noticing that transport measurements have also been coupled with other experimental configurations and a very rich literature has also arisen regarding photovoltaic detection and electroluminescence, nano-electromechanical resonators, and scanning tunneling spectroscopies. All this has contributed to a deeper understanding of the mechanisms described above, but also demonstrated the wide range of potential applications of carbon nanotube especially for (mass or chemical) sensors and optoelectronics [4.8, 270].

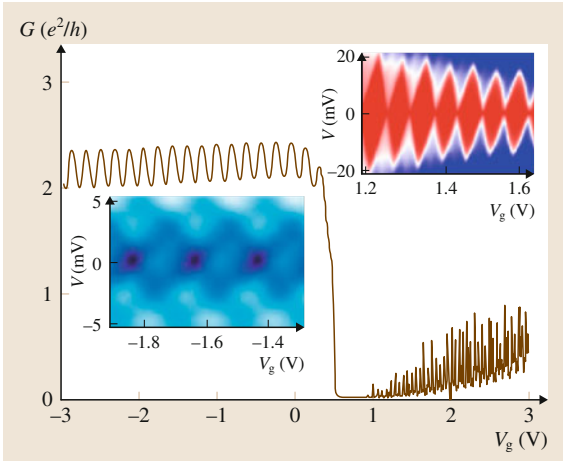


Fig. 4.24 Gate dependent conductance of a suspended, ultra-clean small band gap carbon nanotube at $T = 300$ mK. The almost transparent contacts in the p-doping regime exhibits a Fabry–Perot pattern. *Left inset*: shows conductance while varying bias and gate voltage (*dark blue*: $2e^2/h$, *bright white*: $4e^2/h$). In the n doping regime, Schottky barrier and lower transmission at the contacts induce a Coulomb blockade regime. *Right inset*: Coulomb diamonds. (After [4.268])

4.6 Thermal and Mechanical Properties

Since their discovery, it has been expected that SWCNTs would have remarkable thermal and mechanical properties. This is because of the hexagonal arrangement of carbon atoms and the nature of the sp^2 carbon bond. We will first present a brief introduction to the basic thermal properties of carbon nanotubes and then describe their mechanical properties, where a much larger consensus has been achieved.

4.6.1 Thermal Properties

Specific Heat

The specific heat C_v of graphite arises from phonon and electronic contributions as

$$C_v = C_{\mathrm{ph}} + C_{\mathrm{el}} \,. \tag{4.8}$$

The phonon contribution to the specific heat can be calculated by

$$C_{\mathrm{ph}} = \int_0^{\omega_{\max}} k_{\mathrm{B}} \left(\frac{\hbar\omega}{k_{\mathrm{B}}T}\right)^2 \frac{\exp\left(\frac{\hbar\omega}{k_{\mathrm{B}}T}\right)\rho(\omega)}{\left[\exp\left(\frac{\hbar\omega}{k_{\mathrm{B}}T}\right)-1\right]^2}\,\mathrm{d}\omega \,, \tag{4.9}$$

where $\rho(\omega)$ is the phonon density of states and $\omega_{\max}$ is the highest phonon energy of the material. For $T \ll \Theta_{\mathrm{D}}$ (where Θ_{D} is the Debye temperature), only acoustic phonon modes are populated. If an acoustic phonon mode in d-dimensions follows an $\omega \propto k^{\alpha}$ dispersion, then according to (4.9), the corresponding specific heat should obey $C_{\mathrm{ph}} \propto T^{d/\alpha}$ [4.47].

Figure 4.25a highlights the low frequency phonon modes of SWCNTs [4.37]. All acoustic phonon modes show linear dispersion and high phonon velocities. For example, for a (10,10) tube, $v_{\mathrm{LA}} = 24\,\mathrm{km/s}$, $v_{\mathrm{TA}} = 9\,\mathrm{km/s}$, and $v_{\mathrm{twist}} = 15\,\mathrm{km/s}$. Thus, for each acoustic phonon mode, C_{ph} shows a linear relation to temperature given by [4.271]

$$C_{\mathrm{ph}} = \frac{\pi k_{\mathrm{B}}^2 T}{\hbar v_{\mathrm{ph}} \rho_{\mathrm{m}}} \,, \tag{4.10}$$

where ρ_{m} is the linear mass density and v_{ph} is the phonon speed.

The electronic contribution to C_v can be evaluated by [4.271]

$$C_{\mathrm{el}} = \Omega \int_0^{\infty} (E - E_F) \frac{\mathrm{d}f}{\mathrm{d}T} N(E)\,\mathrm{d}E \,, \tag{4.11}$$

where f is the Fermi–Dirac function and Ω is the d-dimensional volume. For undoped metallic CNTs, $N(E)$ is a constant below the first van Hove singularities which implies that C_{el} also linear with temperature for $T \ll \hbar v_{\mathrm{F}}/k_{\mathrm{B}}R$:

$$C_{\mathrm{el}} = \frac{\pi k_{\mathrm{B}}^2 T}{\hbar v_{\mathrm{F}} \rho_{\mathrm{m}}} \,, \tag{4.12}$$

where v_{F} is the Fermi velocity. According to (4.10) and (4.12), the ratio between C_{ph} and C_{el} is

$$\frac{C_{\mathrm{ph}}}{C_{\mathrm{el}}} \approx \frac{v_{\mathrm{ph}}}{v_{\mathrm{F}}} \approx 10^2 \,. \tag{4.13}$$

As a result, the electronic contribution to the specific heat can be ignored. For an undoped semiconducting SWCNT, C_{el} is even smaller and should decay more rapidly with decreasing temperature. However, if the tubes are doped above the van Hove singularity, then C_{el} could be significantly enhanced.

Figure 4.25b shows the measured heat capacity of SWCNTs with a highlight of their low temperature behavior [4.272]. The temperature dependence is also compared with other carbon materials. Briefly, the heat capacity of SWCNTs is smaller than graphene due to the reduction of density of phonons by *subband* splitting (see Fig. 4.25a inset). On the other hand, it is higher than graphite, whose low frequency phonons are further quenched by graphite inter-layer interactions. However, this discrepancy is amended when SWCNTs are tightly bundled due to the inter-tube bundling effect (Fig. 4.6). The low temperature behavior of the heat capacity could be well fitted by taking into account this bundling effect and also the lowest subband mode contribution (Fig. 4.25c). The fitting parameters are also close to the theoretically calculated phonon spectrum.

Thermal Conductivity

In this section, we will only consider diagonal elements of the thermal conductivity matrix

$$\kappa_{zz} = \sum c v_z^2 \tau \,, \tag{4.14}$$

where c is the specific heat, v_z is the group velocity, τ the relaxation time of a given phonon state, and the sum is over all phonon states. For $T \ll \Theta_{\mathrm{D}}$, the relaxation time is determined by scattering off impurities, defects, and sample boundaries, and is roughly constant. Therefore the low-temperature thermal conductivity should follow the same temperature dependence as the specific heat. But due to the weight factor $v_z^2\tau$, certain phonon

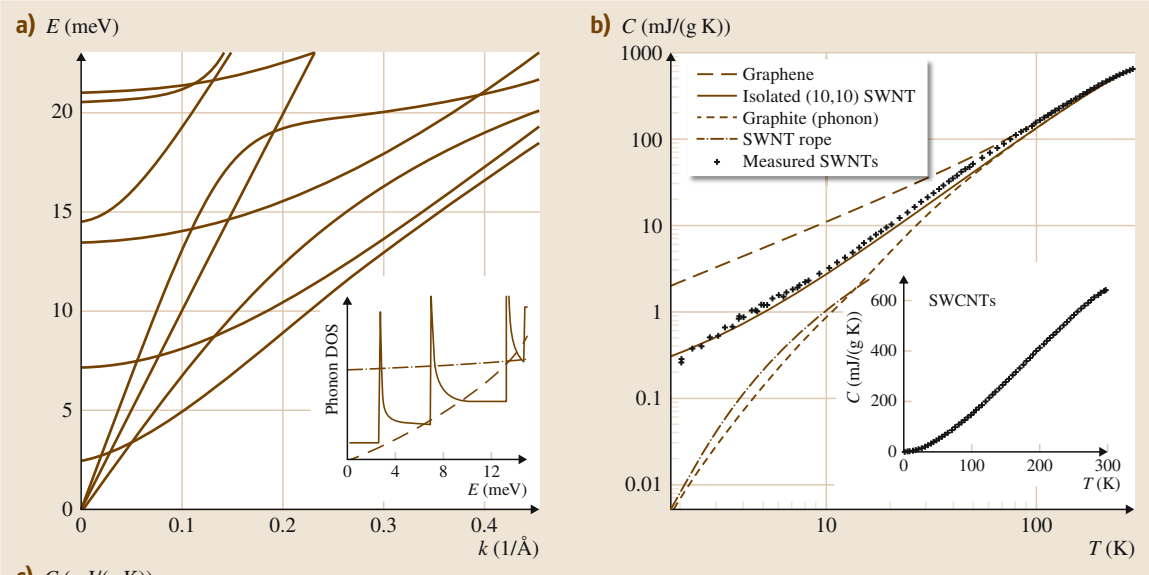


Fig. 4.25 **(a)** Low-energy phonon band structure of an isolated (10,10) SWCNT. The *inset* shows the low-energy phonon density of states, compared to those of 2-D graphene (*dash-dotted line*) and 3-D graphite (*dashed line*). (After [4.37]). **(b)** Measured specific heat of SWCNTs, compared to predictions for the specific heat of isolated (10,10) tubes, SWCNT ropes, a graphene layer and graphite. **(c)** Measured specific heat of SWCNTs compared to a two-band model with transverse dispersion (*inset*). (After [4.272])

modes with higher v_z and τ should contribute more. κ is bounded by the 1-D ballistic transport limit. For each phonon mode, the quantum of thermal conductance is [4.47]

$$G_{th} = \frac{\pi^2 k_B T}{3\,h}\,, \tag{4.15}$$

and therefore the effective thermal conductivity is

$$\kappa_{eff} = G_{th}\frac{L}{\pi d_t \delta d}\,, \tag{4.16}$$

where L is the length of the carbon nanotube, d_t is its diameter, and δd is the effective thickness that the phonon propagates over, which is usually assumed to be the distance between two graphite layers. At very low temperature, only four acoustic branches contribute to κ. As the temperature increases, more *subbands* are populated and thus κ will increase more rapidly until τ starts to decrease due to phonon scattering. When $T \gg \Theta_D$, Umklapp scattering between zone boundary phonons will significantly reduce τ and consequently reduce κ [4.273]. So there should be a turning point in $\kappa(T)$, where it reaches its maximum. Since CNTs have a very high Debye temperature and their 1-D structure reduces Umklapp scattering due to deficiency in conserving momentum and energy, the turning point should be at a fairly high temperature.

In metallic or doped SWCNTs, electron systems also contribute to the thermal conductivity. Principally, the electronic thermal conductivity κ_{el} can be determined from electronic conductivity by the Wiedemann–Franz law

$$\frac{\kappa_{el}}{\sigma} \approx L_0\,, \tag{4.17}$$

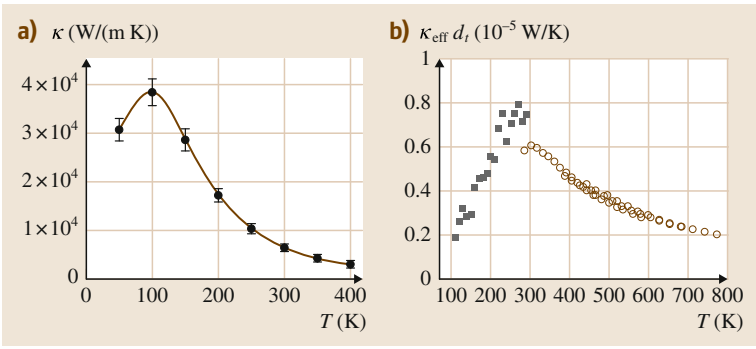


Fig. 4.26 **(a)** Calculated thermal conductivity of an isolated (10,10) SWCNT, as a function of temperature. **(b)** Measured diameter-adjusted thermal conductivity ($\kappa_{\text{eff}} d_t$, see (4.16)) of an isolated SWNT, as a function of temperature. Since the diameters of the tubes range from 1 to 3 nm, the maximum value of kappa is several thousands W/(m K) (■: *Yu* et al. [4.273]; ○: this work). (After [4.274])

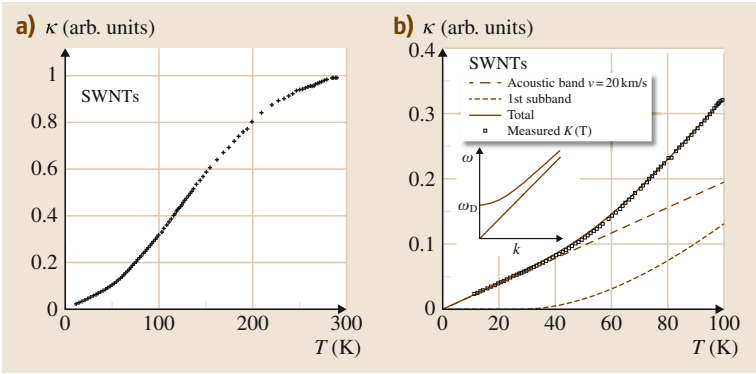


Fig. 4.27 **(a)** Thermal conductivity of a bulk sample of SWNTs below room temperature. **(b)** Highlight of the low temperature part fitted by two-band model. (After [4.275])

where the Lorenz number $L_0 = 2.45 \cdot 10^8 (\text{V/K})^2$ and σ is the electronic conductivity. The estimated κ_{el} is usually one or two orders of magnitude smaller than κ_{ph} and therefore can be ignored in most cases.

As shown in Fig. 4.26a the thermal conductivity of SWCNT has been predicted as high as 40 000 W/(m K) at its maximum and 3600 W/(m K) at room temperature [4.274]. On the other hand, the measured κ peaks around one order of magnitude lower a few thousandths of a watt per millikelvin W/(m K) as shown in Fig. 4.26b [4.276, 277], probably due to imperfections or short tube length [4.278]. When tubes are bundled or formed into a CNT network, κ will decrease strongly depending on the sample's morphology. The reduction may be attributed to a quench of phonon modes by intertube interactions, analogous to the effect on C_{ph}. This effect should be more significant for well-aligned CNT fibers or MWCNT devices [4.279]. Another reason is the weak transport at tube–tube junctions. It has been predicted that in a random network, κ would obey [4.280]

$$\kappa \backsim \rho^2 L^2 \,, \tag{4.18}$$

where ρ is the density of tubes in the network. This opens the possibility to tune the thermal conductivity of a SWCNT device from a good thermal conductor to a good thermal insulator [4.281].

Figure 4.27 shows a measured κ as function of temperature for a SWCNT network [4.275]. In this case, the effect of the intertube junction on κ is treated as a reduction of the phonon relaxation time τ. Consequently, the turning point of κ shifts to a higher temperature while its temperature dependency still reflects the 1-D nature of a CNT. The $\kappa(T)$ curve could be fit by considering the four acoustic phonon modes and the first subband mode (Fig. 4.27b). However, the fitting parameters are slightly different from those by fitting to heating capacity. The difference may be attributed to the weight factor $v^2\tau$ in κ.

4.6.2 Mechanical Properties

SWCNTs lack the multiple cylindrical nesting of MWCNTs and are expected to be stiffer due to curvature effects [4.282]. Over the past couple of decades, SWCNTs have attracted a considerable amount of interest owing to their extraordinary mechanical properties,

such as their ability to sustain large deformations, their excellent stiffness, and high strength. Additionally, most conventional synthesis techniques result in SWCNTs arranged in ropes with a close-packed stacking, thus forming high performance self-assembled fibers on the nanoscale.

Elastic Properties

Overney et al. were the first to report on the structural rigidity of carbon nanotubes [4.284]. The authors used an empirical Keating Hamiltonian with parameters determined from first principles in order to model SWCNTs consisting of 100, 200, and 400 atoms. It was later pointed out by *Treacy* et al. that their results implied a Young's modulus in the range of 1.5–5.0 TPa [4.285]. *Lu* performed an extensive study of the elastic properties of SWCNTs (Table 4.1) and SWCNT ropes using an empirical force constant model [4.283]. The Young's modulus, E, for the materials was extracted from the second derivative of the ab initio strain energy with respect to the axial strain, $\partial^2 E/\partial\varepsilon^2$. The tensile Young's modulus (≈ 1 TPa, a value which is in good agreement with the C_{11} elastic constant of graphite) and the torsion shear modulus of individual SWCNTs were found to be comparable to that of diamond and that of a graphitic sheet, while the bulk modulus was found to be smaller. Their elastic moduli were shown to be insensitive to structural details such as the chirality and radius. One must bear in mind that in order to deduce properties such as SWCNT Young's modulus, it is required to adopt a convention for the effective nanotube thickness. Lu chose the interlayer separation of graphite (0.34 nm, now a widely accepted convention) as the SWCNT wall thickness in his calculations. Assuming the extent of π orbitals (≈ 0.066 nm) to be the thickness, as *Yakobson* et al. had proposed earlier, can result in rather spectacular values of the SWCNT Young's modulus (≈ 5 TPa) [4.286]. Lu's study of SWCNT ropes, each assumed to be composed of 100–500 armchair SWNTs of uniform size arranged in hexagonal order, found them to be soft along the basal plane but very stiff along the axial direction. Their Young's moduli (average ≈ 0.6 TPa) were found to be about one-half that of diamond, values that decreased with nanotube radius. An alternate method that was based on the energy per-surface area rather than per-volume was used to deduce the SWCNT Young's modulus [4.287]. The authors used a nonorthogonal tight-binding scheme for their calculations and reported a surface Young's modulus of 0.42 TPa-nm (1.2 TPa) with only a slight dependence on diameter for SWCNTs with a diameter > 0.7 nm.

Interestingly, while SWCNTs can be highly rigid in the axial direction (as is evident from the high tensile Young's modulus values), they can experience considerable structural instability under compression, torsion, or bending in the radial direction [4.288]. Yakobson et al. modeled the buckling of SWNTs exposed to axial compression, with the atomic interaction modeled using the Tersoff–Brenner potential [4.289, 290]. They found

Table 4.1 Elastic coefficients and moduli of selective single-walled nanotubes. (n, m) are the chiral indices, R is the radius in nm, C_{11} and C_{33} are the elastic constants along the basal plane and the axial direction, respectively. B, Y, M are bulk, Young's, and shear moduli in units of TPa and ν is the Poisson ratio. Experimental values for the graphite and the diamond are listed for comparison. (After [4.283])

(n_1, n_2)	R (nm)	C_{11}	C_{33}	B (TPa)	Y (TPa)	M (TPa)	ν
(5,5)	0.34	0.397	1.054	0.191	0.971	0.436	0.280
(6,4)	0.34	0.397	1.054	0.191	0.972	0.437	0.280
(7,3)	0.35	0.397	1.055	0.190	0.973	0.454	0.280
(8,2)	0.36	0.397	1.057	0.190	0.974	0.452	0.280
(9,1)	0.37	0.396	1.058	0.191	0.974	0.465	0.280
(10,0)	0.39	0.396	1.058	0.190	0.975	0.451	0.280
(10,10)	0.68	0.398	1.054	0.191	0.972	0.457	0.278
(50,50)	3.39	0.399	1.054	0.192	0.972	0.458	0.278
(100,100)	6.78	0.399	1.054	0.192	0.972	0.462	0.277
(200,200)	13.5	0.399	1.054	0.192	0.972	0.478	0.277
Graphite along the basal plane		1.6	–	0.0083	1.02	0.44	0.16
Graphite along the C axis		–	0.036	0.0083	0.0365	0.004	0.012
Diamond along the cube axis		1.07	1.07	0.442	1.063	0.5758	0.1041

that nanotubes subject to large deformations reversibly switched into four different morphological patterns with each one corresponding to an abrupt release of energy and a singularity in the strain energy versus strain curve (Fig. 4.26). The authors' simulations of bending and torsion resulted in SWCNT cross-section collapses and similar observations of changes in energy with the increase in bending angle and azimuthal angle, between the tube ends, respectively. Cross-section collapses and flattening can also occur in SWCNT ropes owing to van der Waal's attractive forces between the tubes. *Tersoff* and *Ruoff* studied the deformation pattern of SWCNTs in ropes and concluded that rigid tubes with diameters < 1 nm deform insignificantly while those with diameters > 2.5 nm flatten against each other thus forming a honeycomb-like structure [4.291].

Strength and Plasticity

Quantum mechanical calculations predict that defect-free single-walled carbon nanotubes possess tensile strengths greater than 100 GPa (i. e., close to the theoretical strength viz. $E/10$ GPa) and failure strains as high as 15–30% depending upon chirality [4.293, 294]. Yakobson et al., used molecular dynamics (MD) simulations to perform high-strain-rate tensile tests (in the range of 100 MHz) on SWCNTs and found that stretching simply elongated the hexagons in the tube walls, until at the critical point an atomic disorder suddenly nucleated: one or a few C−C bonds broke almost simultaneously, and the resulting *holes* in the tube walls became crack precursors. While the fractures propagated very quickly along the circumference of the tubes, the nanotubes themselves did not break completely in half but were separated into two parts connected by a monoatomic carbon chain [4.288]. Under compression, classical MD simulations have shown a SWCNT to also be remarkably resilient, sustaining strains as high as 15% with no signs of brittleness, plasticity, or atomic rearrangements [4.295].

Theoretical predictions, however, have constantly emphasized the important role played by defects, the loading rate, and temperature on the strength of a SWCNT [4.296]. Defects often become incorporated into the SWCNT structure during purification or dispersion. Also, the mode of CNT synthesis plays an important role in determining the nature and distribution of defects, with low temperature catalytic chemical vapor deposition (CVD) grown nanotubes typically having a more defect laden structure when compared to nanotubes grown via other techniques such as laser vaporization and arc discharge (AD). The presence of

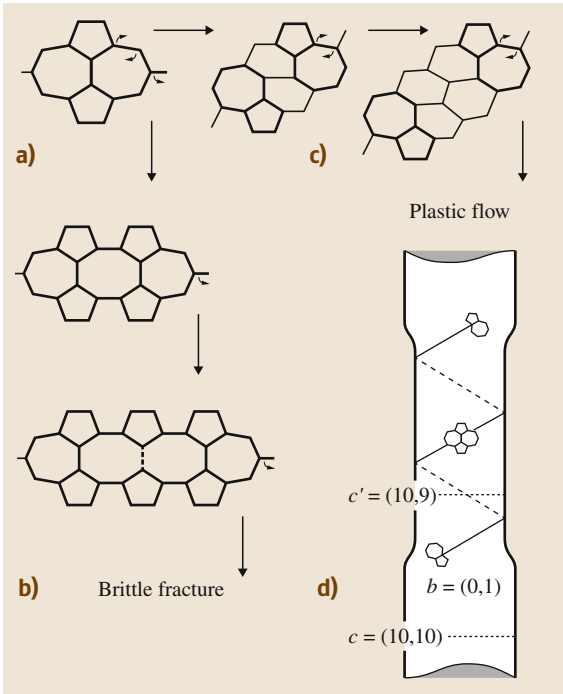


Fig. 4.28 Stone–Wales (S–W) transformations of an equatorially oriented bond into a vertical position creates a nucleus of relaxation (*top left corner*). It evolves further as either a crack (brittle fracture route, *left column*) or as a couple of dislocations gliding away along the spiral slip plane (plastic yield, *top row*). In both cases only S–W rotations are required as elementary steps. The stepwise change of the nanotube diameter reflects the change of chirality (*bottom right image*). (After [4.292])

defects on the nanotube wall can considerably degrade the strength of a SWCNT. Belytschko et al. observed a drop in the failure stress from 93 GPa to 74 GPa upon the incorporation of a single atom defect on a zigzag SWCNT wall. The failure strains were also found to drop from 15.5% to 10% [4.293]. *Sammalkorpi* et al. used MD simulations to study how vacancies affect the Young's modulus and tensile strength of SWCNTs [4.297]. They found that while the Young's modulus depended weakly on the vacancy concentration (a relatively high defect density of one vacancy per 50 Å resulted in about a 3% decrease in the Young's modulus), the SWCNT tensile strength could degrade by $\approx 40\%$ (actual value chirality dependent) if vacancies were present on their walls.

With regard to the deformation of SWCNTs in static or slow tension conditions, an interesting phenomenon

was uncovered by quantum molecular dynamics simulations and dislocation theory: a mechanical relaxation step that occurs via a bond rotation known as a Stone–Wales (S–W) transformation (Fig. 4.28) [4.298]. It leads to the formation of the lowest energy defect, a cluster of two pentagons and heptagons 5/7/7/5 on the SWCNT wall. In a lattice of hexagons this represents a dislocation dipole, which explains its formation under high tension. At high temperatures, 5/7/7/5 defects in SWNTs of a certain chirality, can separate into two 5,7 pairs that glide away from each other in a spiral path, leaving in their wake a plastically deformed nanotube with an altered chirality. In contrast, a competing mechanism of evolution, which does not require thermal activation, occurs at a high strain level as a sequence of direct brittle bond-breaking steps leading to formation of disordered cracks and large open rings, which results in the brittle failure of a SWCNT (Fig. 4.28) [4.292, 299]. Thus, while all SWCNTs behave in a brittle fashion at high strains and low temperatures, at high temperatures and low strains, SWCNTs of a certain chirality can be completely or partially ductile. This has been observed in a (10,10) armchair nanotube with a 5/7/7/5 defect under axial tension. At a strain value close to 15% and temperature of about 1300 K, nucleation of large open rings occurred (brittle relaxation), while at a strain value $\approx 3\%$ and at a temperature of about 3000 K, 5/7 defect motion resulted in plastic flow [4.300]. It has been suggested that an axially compressed SWCNT would also deform plastically via S–W defect based mechanism [4.292]. Interestingly, Srivastava et al., who employed a quantum generalized tight binding molecular dynamics (GTBMD) scheme to study SWNTs under compression, observed an alternate mechanism of plastic deformation in which SWCNT bonding geometry collapsed from a graphitic sp^2 to a localized diamond-like sp^3 reconstruction [4.301, 302]. The computed critical strain for such a collapse for a (8,0) zigzag SWNT was $\approx 12\%$, a value considerably lower that than the elastic limit computed using classical MD simulations (Fig. 4.29).

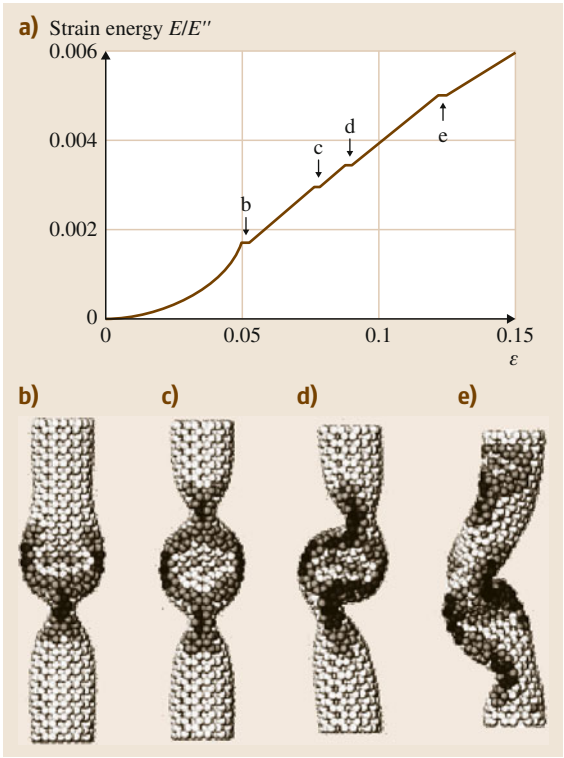


Fig. 4.29a–e MD-simulated nanotube of length 6 nm, diameter 1 nm, and armchair helicity (7,7) under axial compression. The strain energy displays four singularities **b**, **c**, **d**, **e** as shown in strain energy (normalized to its second derivative) versus strain (ε) curve corresponding to shape changes **(a)**; at $\varepsilon = 0.05$ the cylinder buckles into the pattern **(b)**, displaying two identical flattenings, *fins*, perpendicular to each other. Further increasing strain enhances this pattern gradually until at $\varepsilon = 0.076$ the tube switches to a three-fin pattern **(c)**, which still possesses a straight axis. On buckling sideways at $\varepsilon = 0.09$ the flattenings serve as hinges, and only a plane of symmetry is preserved **(d)**4. At $\varepsilon = 0.13$ **(e)** an entirely squashed asymmetric nanotube. (After [4.286])

Mechanical Characterization

Owing to their small size and the magnitude of the forces involved, the mechanical characterization of individual SWCNTs is extremely challenging. There are thus only a handful of reports that deal with characterization of individual SWCNTs, with many of them relying on the electrical breakdown of MWCNTs for SWCNT generation. However, numerous studies focus on the properties of SWCNT ropes. Using an atomic force microscope (AFM) based deflection technique, *Salvetat* et al. measured the vertical deflection of SWCNT ropes bridging holes on a porous alumina membrane (Fig. 4.30) [4.303]. The ropes were modeled as beams, with a term describing sliding between tubes (shear) comprising the ropes being included in the expression for mechanical deformation

$$\delta = \delta_B + \delta_S = FL^3/192EI + f_s FL/4GA\,,$$

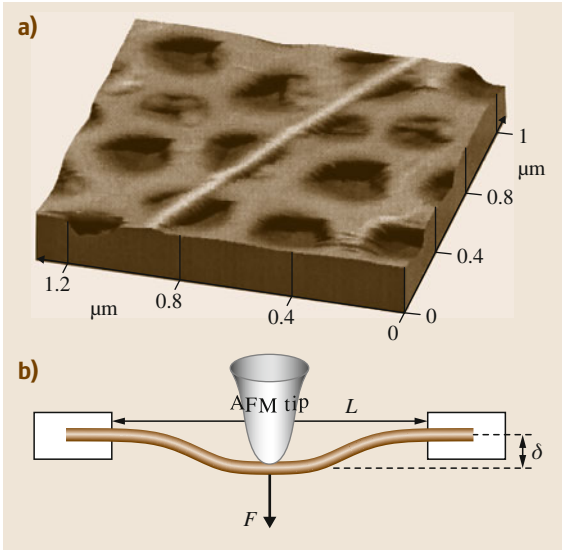


Fig. 4.30 **(a)** AFM image of a SWNT rope adhered to the polished alumina ultrafiltration membrane, with a portion bridging a pore. **(b)** The AFM is used to apply a load to the nanobeam and to determine directly the resulting deflection. (After [4.303])

where F is the concentrated load, δ_B and δ_S are the deflections due to bending and shear deformation respectively, L is the suspended length, E is the elastic modulus, f_s is the shape factor (equal to 10/9 for a cylindrical beam), G is the shear modulus, I is the second moment of area of the beam and A is the cross-sectional area. Deflections of small diameter long ropes, for which shearing was assumed to be negligible, were used to compute Young's modulus (measured to be about 1 TPa), while the deflection of thick ropes was used to compute the intertube shear modulus G measured as ≈ 1 GPa. *Walters* et al. also studied the elastic properties of freely suspended SWCNT ropes by inducing large elastic strains using an AFM tip operating in the lateral force mode [4.304]. By modeling the stretched ropes as elastic strings (instead of beams), the authors were able to derive an expression for the force F exerted on the tube by the AFM tip

$$F = 2T\sin(\theta) = 2T\frac{2x}{L} \approx \frac{8kx^3}{L_0} ,$$

where T is the tension in the string, L_0 its equilibrium length, k the spring constant, and x the lateral deflection in the middle. Assuming a Young's modulus of 1.25 TPa for SWCNTs, they deduced that close-packed nanotube ropes would have a yield strength exceeding 45.67 GPa (corresponding to a 5.8% strain). *Yu* et al. subjected 15 SWCNT ropes to tensile loading using a nanostressing stage (two opposing AFM tips) operated inside an SEM chamber [4.305]. Force versus strain data were obtained for 8 ropes, with the highest strain value observed being 5.3%. By examining the fragments left on the AFM tips post failure, the authors deduced that only the SWCNTs along the periphery of the ropes were load bearing. They were thus able to ascertain the average breaking strength of SWNTs along the perimeter of each rope, viz. 13 to 52 GPa. The corresponding Young's moduli were determined to be in the range of 320 to 1470 GPa. The mechanical properties of SWCNT bundles in compression were studied by Chesnokov et al.sa, who subjected them to quasi-hydrostatic pressure using a piston-cylinder setup. The bundles were found to undergo a reversible deformation up to a pressure of 3 GPa [4.306]. Tang et al. used a diamond anvil cell to subject SWCNT bundles to hydrostatic pressure and observed that the SWCNTs were linearly elastic up to 1.5 GPa at room temperature. The volume compressibility, measured via in situ synchrotron x-ray diffraction, was determined to be 0.024 GPa^{-1} [4.307].

Krishnan et al. estimated the stiffness of individual SWCNTs by observing their freestanding room temperature vibrations in a TEM [4.308]. The nanotube lengths and tip vibration amplitudes were estimated directly from the digital micrographs. The nanotubes were modeled as stochastically driven resonators (i. e., they were assumed to be vibrating beams) and their Young's moduli estimated from their Gaussian vibrational profile whose standard deviation is given by

$$\sigma^2 = 0.8486\frac{L^3 k_B T}{YWG(W^2+G^2)} ,$$

where L is the cantilevered beam's length (SWNT length), G is the graphite interlayer spacing, W is the SWCNT diameter, T the temperature and Y the Young's modulus. Micrographs of 27 nanotubes in the diameter range 1.0–1.5 nm were measured to yield an average Young's modulus of $1.3+0.4/-0.6$ TPa. *Wang* et al. directly tested the mechanical response of SWCNTs by subjecting them to tensile loads using an AFM within a TEM setup [4.309]. The SWCNTs for the experiments were formed in situ by subjecting MWNTs to large voltage biases. The tubes were found to exhibit fracture strengths ranging from 25 to 100 GPa. SWCNTs with relatively higher strength possessed visibly perfect

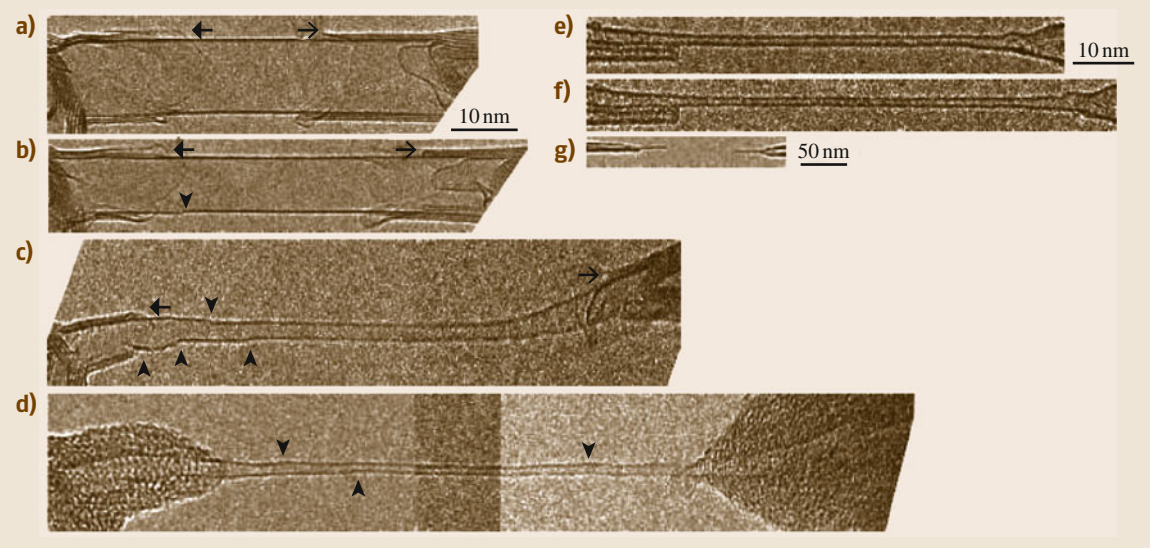


Fig. 4.31 In situ tensile elongation of individual SWNTs viewed in a HRTEM. **(a–d)** Tensile elongation of a SWNT under a constant bias of 2.3 V (images are all scaled to the same magnification). *Arrowheads* mark kinks, *arrows* indicate features at the ends of the nanotube that are almost unchanged during elongation; e.g., tensile elongation of a SWCNT at room temperature without bias (**(e–g)** are scaled to the same magnification). (After [4.310])

shell structures while the significant strength reduction in low-strength samples was attributed to clearly identifiable shell structural defects. *Huang* et al. observed *superplasticity* in a SWCNT (Fig. 4.31) [4.310]. The nanotube was subjected to a tensile load and at failure, found to be 91 nm long, showing an elongation of 280% with its diameter reduced 15-fold, from 12 to 0.8 nm. Since the deformation occurred at a bias of about 2.3 V, the temperature in the middle of the SWCNT was estimated to be more than 2000 °C. This superplastic deformation was assumed to be the result of the nucleation and motion of kinks (possibly 5/7 pairs) as well as atom diffusion. In contrast, tensile-pulling experiments conducted at room temperature with no bias showed in SWCNTs failing at a tensile strain of less than 15%.

4.7 Concluding Remarks

Single-walled carbon nanotubes have been extensively studied and immense progress has been made in their basic understanding, demonstrating the potential of nanoscience in general. A good understanding of their basic properties has been reached, but direct evidences of some fundamental processes are still lacking; for example, spin-charge separation expected in Lüttinger liquids.

The feasibility of nanotube applications lies directly between basic and technical questions. For example, nanotube photodetectors and emitters (or even lasers) would be of great tunability and could potentially cover large wavelength ranges. Efforts are being made to obtain purer, single chirality semiconductors material in large quantities, and to understand the mechanisms limiting their light emission.

References

4.1 S. Iijima: Helical microtubules of graphitic carbon, Nature **354**(6348), 56–58 (1991)

4.2 M.S. Dresselhaus, G. Dresselhaus, P. Avouris (eds.): *Carbon Nanotubes: Synthesis, Structure, Properties,*

and Applications, Topics in Applied Physics, Vol. 80 (Springer, Berlin, Heidelberg 2001)
4.3 S. Reich, C. Thomsen, J. Maultzsch: *Carbon Nanotubes: Basic Concepts and Physical Properties* (Wiley-VCH, Weinheim 2004)
4.4 M.J. O'Connell (Ed.): *Carbon Nanotubes: Properties and Applications* (CRC, Boca Raton 2006)
4.5 A. Jorio, G. Dresselhaus, M.S. Dresselhaus (Eds.): *Carbon Nanotubes: Advanced Topics in the Synthesis, Structure, Properties and Applications*, Topics in Applied Physics, Vol. 111 (Springer, Berlin, Heidelberg 2008)
4.6 T. Giamarchi: *Quantum Physics in One Dimension* (Oxford Univ. Press, Oxford 2004)
4.7 P. Avouris, M. Freitag, V. Perebeinos: Carbon-nanotube photonics and optoelectronics, Nat. Photonics **2**, 341–350 (2008)
4.8 S. Nanot, E.H. Hároz, J.-H. Kim, R.H. Hauge, J. Kono: Optoelectronic properties of single-wall carbon nanotubes, Adv. Mater. **24**, 4977–4994 (2012)
4.9 M.S. Dresselhaus, A. Jorio, M. Hofmann, G. Dresselhaus, R. Saito: Perspectives on carbon nanotubes and graphene Raman spectroscopy, Nano Lett. **10**, 751–758 (2010)
4.10 H. Ajiki, T. Ando: Aharonov–Bohm effect in carbon nanotubes, Physica B **201**, 349–352 (1994)
4.11 M.F. Islam, D.E. Milkie, C.L. Kane, A.G. Yodh, J.M. Kikkawa: Direct measurement of the polarized optical absorption cross section of single-wall carbon nanotubes, Phys. Rev. Lett. **93**, 037404 (2004)
4.12 Y. Murakami, E. Einarsson, T. Edamura, S. Maruyama: Polarization dependence of the optical absorption of single-walled carbon nanotubes, Phys. Rev. Lett. **94**, 087402 (2005)
4.13 H. Ajiki, T. Ando: Magnetic properties of carbon nanotubes, J. Phys. Soc. Jpn. **62**, 2470–2480 (1993)
4.14 J.P. Lu: Novel magnetic properties of carbon nanotubes, Phys. Rev. Lett. **74**, 1123–1126 (1995)
4.15 S. Zaric, G.N. Ostojic, J. Kono, J. Shaver, V.C. Moore, R.H. Hauge, R.E. Smalley, X. Wei: Estimation of magnetic susceptibility anisotropy of carbon nanotubes using magneto-photoluminescence, Nano Lett. **4**, 2219–2221 (2004)
4.16 M.F. Islam, D.E. Milkie, O.N. Torrens, A.G. Yodh, J.M. Kikkawa: Magnetic heterogeneity and alignment of single wall carbon nanotubes, Phys. Rev. B **71**, 201401 (2005)
4.17 T.A. Searles, Y. Imanaka, T. Takamasu, H. Ajiki, J.A. Fagan, E.K. Hobbie, J. Kono: Large anisotropy in the magnetic susceptibility of metallic carbon nanotubes, Phys. Rev. Lett. **105**, 017403 (2010)
4.18 T.-I. Jeon, K.-J. Kim, C. Kang, S.-J. Oh, J.-H. Son, K.H. An, D.J. Bae, Y.H. Lee: Terahertz conductivity of anisotropic single walled carbon nanotube films, Appl. Phys. Lett. **80**, 3403–3405 (2002)
4.19 L. Ren, C.L. Pint, L.G. Booshehri, W.D. Rice, X. Wang, D.J. Hilton, K. Takeya, I. Kawayama, M. Tonouchi, R.H. Hauge, J. Kono: Carbon nanotube terahertz polarizer, Nano Lett. **9**, 2610–2613 (2009)
4.20 J. Kyoung, E.-Y. Jang, M.D. Lima, H.-R. Park, R.-O. Robls, X. Lepro, Y.-H. Kim, R.H. Baughman, D.-S. Kim: A reel-wound carbon nanotube polarizer for terahertz frequencies, Nano Lett. **11**, 4227–4231 (2011)
4.21 L. Ren, C.L. Pint, T. Arikawa, K. Takeya, I. Kawayama, M. Tonouchi, R.H. Hauge, J. Kono: Broadband terahertz polarizers with ideal performance based on aligned carbon nanotube stacks, Nano Lett. **12**, 787–790 (2012)
4.22 H. Ajiki, T. Ando: Electronic states of carbon nanotubes, J. Phys. Soc. Jpn. **62**, 1255–1266 (1993)
4.23 T. Ando: Theory of electronic states and transport in carbon nanotubes, J. Phys. Soc. Jpn. **74**, 777–817 (2005)
4.24 J. Kono, S. Roche: Magnetic properties. In: *Carbon Nanotubes: Properties and Applications*, ed. by M.J. O'Connell (CRC, Boca Raton 2006), 119–151
4.25 J. Kono, R.J. Nicholas, S. Roche: High magnetic field phenomena in carbon nanotubes. In: *Carbon Nanotubes: Advanced Topics in the Synthesis, Structure, Properties and Applications*, ed. by A. Jorio, G. Dresselhaus, M.S. Dresselhaus (Springer, Berlin, Heidelberg 2008), 393–421
4.26 R. Saito, G. Dresselhaus, M.S. Dresselhaus: *Physical Properties of Carbon Nanotubes* (Imperial College Press, London 1998)
4.27 A. Loiseau, P. Launois, P. Petit, S. Roche, J.-P. Salvetat (eds.): *Understanding Carbon Nanotubes: From Basics to Application*, Lecture Notes in Physics, Vol. 677 (Springer, Berlin, Heidelberg 2006)
4.28 F. Léonard: *The Physics of Carbon Nanotube Devices* (William Andrew, Norwich 2009)
4.29 A.H. Castro Neto, F. Guinea, N.M.R. Peres, K.S. Novoselov, A.K. Geim: The electronic properties of graphene, Rev. Mod. Phys. **81**(1), 109 (2009)
4.30 R. Saito, M. Fujita, G. Dresselhaus, M.S. Dresselhaus: Electronic structure of chiral graphene tubules, Appl. Phys. Lett. **60**, 2204–2206 (1992)
4.31 N. Hamada, S. Sawada, A. Oshiyama: New one-dimensional conductors: Graphitic microtubules, Phys. Rev. Lett. **68**, 1579–1581 (1992)
4.32 H. Ajiki, T. Ando: Electronic states of carbon nanotubes, J. Phys. Soc. Jpn. **62**, 1255–1266 (1993)
4.33 J.W. Mintmire, B.I. Dunlap, C.T. White: Are fullerene tubules metallic?, Phys. Rev. Lett. **68**, 631–634 (1992)
4.34 P.R. Wallace: The band theory of graphite, Phys. Rev. **71**(9), 622–634 (1947)
4.35 B. Bourlon: Physique Interfeuillet Dans Les Nanotubes de Carbone Multifeuillets. Ph.D. Thesis (Université Paris VI, Paris 2005)
4.36 C. Kane, L. Balents, M.P.A. Fisher: Coulomb interactions and mesoscopic effects in carbon nanotubes, Phys. Rev. Lett. **79**, 5086–5089 (1997)
4.37 M.S. Dresselhaus, P.C. Eklund: Phonons in carbon nanotubes, Adv. Phys. **49**(6), 705–814 (2000)

4.38 R.A. Jishi, L. Venkataraman, M.S. Dresselhaus, G. Dresselhaus: Phonon modes in carbon nanotubules, Chem. Phys. Lett. **209**(1/2), 77–82 (1993)

4.39 P.C. Eklund, J.M. Holden, R.A. Jishi: Phonon modes in carbon nanotubules, Carbon **33**(7), 959–972 (1995)

4.40 R. Saito, T. Takeya, T. Kimura, G. Dresselhaus, M.S. Dresselhaus: Raman intensity of single-wall carbon nanotubes, Phys. Rev. B **57**, 4145–4153 (1998)

4.41 O. Dubay, G. Kresse: Accurate density functional calculations for the phonon dispersion relations of graphite layer and carbon nanotubes, Phys. Rev. B **67**, 035401 (2003)

4.42 J. Yu, R.K. Kalia, P. Vashishta: Phonons in graphitic tubules: A tight-binding molecular dynamics study, J. Chem. Phys. **103**, 6697 (1995)

4.43 M. Menon, E. Richter, K.R. Subbaswamy: Structural and vibrational properties of fullerenes and nanotubes in a nonorthogonal tight-binding scheme, J. Chem. Phys. **104**(15), 5875–5882 (1996)

4.44 J. Kürti, G. Kresse, H. Kuzmany: First-principles calculations of the radial breathing mode of single-wall carbon nanotubes, Phys. Rev. B **58**, R8869–R8872 (1998)

4.45 D. Sánchez-Portal, E. Artacho, J.M. Soler, A. Rubio, P. Ordejón: *Ab initio* structural, elastic, and vibrational properties of carbon nanotubes, Phys. Rev. B **59**, 12678–12688 (1999)

4.46 L.-H. Ye, B.-G. Liu, D.-S. Wang, R. Han: *Ab initio* phonon dispersions of single-wall carbon nanotubes, Phys. Rev. B **69**, 235409 (2004)

4.47 J. Hone: Phonons and thermal properties of carbon nanotubes. In: *Carbon Nanotubes*, Topics in Applied Physics, Vol. 80, ed. by M. Dresselhaus, G. Dresselhaus, P. Avouris (Springer, Berlin, Heidelberg 2001) pp. 273–286

4.48 S. Rols, Z. Benes, E. Anglaret, J.L. Sauvajol, P. Papanek, J.E. Fischer, G. Coddens, H. Schober, A.J. Dianoux: Phonon density of states of single-wall carbon nanotubes, Phys. Rev. Lett. **85**, 5222–5225 (2000)

4.49 J. Hone: Carbon nanotubes: Thermal properties. In: *Dekker Encyclopedia of Nanoscience and Nanotechnology*, ed. by J.A. Schwarz, C.I. Contescu, K. Putyera (Marcel Dekker, New York 2004) pp. 603–610

4.50 A. Mizel, L.X. Benedict, M.L. Cohen, S.G. Louie, A. Zettl, N.K. Budraa, W.P. Beyermann: Analysis of the low-temperature specific heat of multiwalled carbon nanotubes and carbon nanotube ropes, Phys. Rev. B **60**, 3264–3270 (1999)

4.51 D. Kahn, J.P. Lu: Vibrational modes of carbon nanotubes and nanoropes, Phys. Rev. B **60**, 6535–6540 (1999)

4.52 P. Eklund, P.A.R. Blackmon, A.J. Hart, J. Kong, P. Bhabendra, A. Rao, A. Rinzler: *International Assessment of Research and Development on Carbon Nanotubes: Manufacturing and Applications* (World Technology Evaluation Center, Arlington 2007), available online at http://www.wtec.org/cnm/

4.53 M. Kundrapu, J. Li, A. Shashurin, M. Keidar: A model of carbon nanotube synthesis in arc discharge plasmas, J. Phys. D **45**, 315305 (2012)

4.54 T. Guo, P. Nikolaev, A. Thess, D.T. Colbert, R.E. Smalley: Catalytic growth of single-walled nanotubes by laser vaporization, Chem. Phys. Lett. **243**, 49–54 (1995)

4.55 T.W. Ebbesen, P.M. Ajayan: Large-scale synthesis of carbon nanotubes, Nature **358**(6383), 220–222 (1992)

4.56 D.S. Bethune, C.H. Kiang, M.S. Devries, G. Gorman, R. Savoy, J. Vazquez, R. Beyers: Cobalt-catalysed growth of carbon nanotubes with single-atomic-layer walls, Nature **363**(6430), 605–607 (1993)

4.57 T. Guo, P. Nikolaev, A. Thess, D.T. Colbert, R.E. Smalley: Catalytic growth of single-walled manotubes by laser vaporization, Chem. Phys. Lett. **243**(1/2), 49–54 (1995)

4.58 B.I. Yakobson, R.E. Smalley: Fullerene nanotubes: $C_{1000000}$ and beyond, Am. Sci. **85**(4), 324–337 (1997)

4.59 M.J. Bronikowski, P.A. Willis, D.T. Colbert, K.A. Smith, R.E. Smalley: Gas-phase production of carbon single-walled nanotubes from carbon monoxide via the HiPco process: A parametric study, J. Vac. Sci. Technol. A **19**(4), 1800–1805 (2001)

4.60 Y. Liu, W.Z. Qian, Q. Zhang, G.Q. Ning, G.H. Luo, Y. Wang, D.Z. Wang, F. Wei: Synthesis of high-quality, double-walled carbon nanotubes in a fluidized bed reactor, Chem. Eng. Technol. **32**(1), 73–79 (2009)

4.61 Y. Wang, B. Li, P.S. Ho, Z. Yao, L. Shi: Effect of supporting layer on growth of carbon nanotubes by thermal chemical vapor deposition, Appl. Phys. Lett. **89**, 183113 (2006)

4.62 R. Philippe, A. Moranqais, M. Corrias, B. Caussat, Y. Kihn, P. Kalck, D. Plee, P. Gaillard, D. Bernard, P. Serp: Catalytic production of carbon nanotubes by fluidized-bed CVD, Chem. Vap. Depos. **13**(9), 447–457 (2007)

4.63 M. Meyyappan: A review of plasma enhanced chemical vapour deposition of carbon nanotubes, J. Phys. D **42**(21), 15 (2009)

4.64 Y.Q. Xu, E. Flor, H. Schmidt, R.E. Smalley, R.H. Hauge: Effects of atomic hydrogen and active carbon species in 1 mm vertically aligned single-walled carbon nanotube growth, Appl. Phys. Lett. **89**(12), 3 (2006)

4.65 C.L. Pint, G.B. Bozzolo, R. Hauge: Catalyst design for carbon nanotube growth using atomistic modeling, Nanotechnology **19**, 405704 (2008)

4.66 S.S. Fan, M.G. Chapline, N.R. Franklin, T.W. Tombler, A.M. Cassell, H.J. Dai: Self-oriented regular arrays of carbon nanotubes and their field emission properties, Science **283**(5401), 512–514 (1999)

4.67 K. Hata, D.N. Futaba, K. Mizuno, T. Namai, M. Yumura, S. Iijima: Water-assisted highly efficient synthesis of impurity-free single-walled carbon nanotubes, Science **306**(5700), 1362–1364 (2004)

4.68 Y. Murakami, S. Chiashi, Y. Miyauchi, M.H. Hu, M. Ogura, T. Okubo, S. Maruyama: Growth of ver-

tically aligned single-walled carbon nanotube films on quartz substrates and their optical anisotropy, Chem. Phys. Lett. **385**(3/4), 298–303 (2004)
4.69 S. Yasuda, D.N. Futaba, T. Yamada, J. Satou, A. Shibuya, H. Takai, K. Arakawa, M. Yumura, K. Hata: Improved and large area single-walled carbon nanotube forest growth by controlling the gas flow direction, ACS Nano **3**(12), 4164–4170 (2009)
4.70 G.D. Nessim, M. Seita, K.P. O'Brien, A.J. Hart, R.K. Bonaparte, R.R. Mitchell, C.V. Thompson: Low temperature synthesis of vertically aligned carbon nanotubes with electrical contact to metallic substrates enabled by thermal decomposition of the carbon feedstock, Nano Lett. **9**(10), 3398–3405 (2009)
4.71 R.F. Wood, S. Pannala, J.C. Wells, A.A. Puretzky, D.B. Geohegan: Simple model of the interrelation between single- and multiwall carbon nanotube growth rates for the CVD process, Phys. Rev. B **75**(23), 8 (2007)
4.72 S.M. Kim, C.L. Pint, P.B. Amama, D.N. Zakharov, R.H. Hauge, B. Maruyama, E.A. Stach: Evolution in catalyst morphology leads to carbon nanotube growth termination, J. Phys. Chem. Lett. **1**(6), 918–922 (2010)
4.73 A.A. Puretzky, D.B. Geohegan, S. Jesse, I.N. Ivanov, G. Eres: In situ measurements and modeling of carbon nanotube array growth kinetics during chemical vapor deposition, Appl. Phys. A **81**, 223–240 (2005)
4.74 T. Ogawa, T. Takagahara: Interband absorption spectra and Sommerfeld factors of a one-dimensional electron-hole system, Phys. Rev. B **43**, 14325–14328 (1991)
4.75 T. Ogawa, T. Takagahara: Optical absorption and Sommerfeld factors of one-dimensional semiconductors: An exact treatment of excitonic effects, Phys. Rev. B **44**, 8138–8156 (1991)
4.76 M.J. O'Connell, S.M. Bachilo, C.B. Huffman, V.C. Moore, M.S. Strano, E.H. Hároz, K.L. Rialon, P.J. Boul, W.H. Noon, C. Kittrell, J. Ma, R.H. Hauge, R.B. Weisman, R.E. Smalley: Band gap fluorescence from individual single-walled carbon nanotubes, Science **297**, 593–596 (2002)
4.77 S.M. Bachilo, M.S. Strano, C. Kittrell, R.H. Hauge, R.E. Smalley, R.B. Weisman: Structure-assigned optical spectra of single-walled carbon nanotubes, Science **298**, 2361–2366 (2002)
4.78 S. Lebedkin, F. Hennrich, T. Skipa, M.M. Kappes: Near-infrared photoluminescence of single-walled carbon nanotubes prepared by the laser vaporization method, J. Phys. Chem. B **107**, 1949–1956 (2003)
4.79 J. Lefebvre, Y. Homma, P. Finnie: Bright band gap photoluminescence from unprocessed single-walled carbon nanotubes, Phys. Rev. Lett. **90**, 217401 (2003)
4.80 R.B. Weisman, S.M. Bachilo: Dependence of optical transition energies on structure for single-walled carbon nanotubes in aqueous suspension: An empirical Kataura plot, Nano Lett. **3**, 1235–1238 (2003)
4.81 Y. Miyauchi, S. Chiashi, Y. Murakami, Y. Hayashida, S. Maruyama: Fluorescence spectroscopy of single-walled carbon nanotubes synthesized from alcohol, Chem. Phys. Lett. **387**, 198–203 (2004)
4.82 O.N. Torrens, D.E. Milkie, M. Zheng, J.M. Kikkawa: Photoluminescence from intertube carrier migration in single-walled carbon nanotube bundles, Nano Lett. **6**, 2864–2867 (2006)
4.83 P.H. Tan, A.G. Rozhin, T. Hasan, P. Hu, V. Scardaci, W.I. Milne, A.C. Ferrari: Photoluminescence spectroscopy of carbon nanotube bundles: Evidence for exciton energy transfer, Phys. Rev. Lett. **99**, 137402 (2007)
4.84 O. Kiowski, K. Arnold, S. Lebedkin, F. Hennrich, M.M. Kappes: Direct observation of deep excitonic states in the photoluminescence spectra of single-walled carbon nanotubes, Phys. Rev. Lett. **99**, 237402 (2007)
4.85 O.N. Torrens, M. Zheng, J.M. Kikkawa: Energy of *k*-momentum dark excitons in carbon nanotubes by optical spectroscopy, Phys. Rev. Lett. **101**(15), 157401 (2008)
4.86 Y. Murakami, J. Kono: Nonlinear photoluminescence excitation spectroscopy of carbon nanotubes: Exploring the upper density limit of one-dimensional excitons, Phys. Rev. Lett. **102**, 037401 (2009)
4.87 Y. Murakami, J. Kono: Existence of an upper limit on the density of excitons in carbon nanotubes by diffusion-limited exciton–exciton annihilation: Experiment and theory, Phys. Rev. B **80**, 035432 (2009)
4.88 J.A. Fagan, J.Y. Huh, J.R. Simpson, J.L. Blackburn, J.M. Holt, B.A. Larsen, A.R. Hight Walker: Separation of empty and water-filled single-wall carbon nanotubes, ACS Nano **5**, 3943–3953 (2011)
4.89 A. Jorio, A.G. Souza Filho, G. Dresselhaus, M.S. Dresselhaus, A.K. Swan, M.S. Ünlü, B.B. Goldberg, M.A. Pimenta, J.H. Hafner, C.M. Lieber, R. Saito: *G*-band resonant Raman study of 62 isolated single-wall carbon nanotubes, Phys. Rev. B **65**, 155412 (2002)
4.90 H. Telg, J. Maultzsch, S. Reich, F. Hennrich, C. Thomsen: Chirality distribution and transition energies of carbon nanotubes, Phys. Rev. Lett. **93**, 177401 (2004)
4.91 S.K. Doorn, D.A. Heller, P.W. Barone, M.L. Usrey, M.S. Strano: Resonant Raman excitation profiles of individually dispersed single walled carbon nanotubes in solution, Appl. Phys. A **78**, 1147–1155 (2004)
4.92 C. Fantini, A. Jorio, M. Souza, M.S. Strano, M.S. Dresselhaus, M.A. Pimenta: Optical transition energies for carbon nanotubes from resonant Raman spectroscopy: Environment and temperature effects, Phys. Rev. Lett. **93**, 147406 (2004)
4.93 J. Maultzsch, H. Telg, S. Reich, C. Thomsen: Radial breathing mode of single-walled carbon nanotubes: Optical transition energies and chiral-index assignment, Phys. Rev. B **72**, 205438 (2005)

4.94 S.K. Doorn, M.J. O'Connell, L. Zheng, Y.T. Zhu, S. Huang, J. Liu: Raman spectral imaging of a carbon nanotube intramolecular junction, Phys. Rev. Lett. **94**, 016802 (2005)

4.95 J. Jiang, R. Saito, A. Grüneis, S.G. Chou, G.G. Samsonidze, A. Jorio, G. Dresselhaus, M.S. Dresselhaus: Intensity of the resonance Raman excitation spectra of single-wall carbon nanotubes, Phys. Rev. B **71**, 205420 (2005)

4.96 J.C. Meyer, M. Paillet, T. Michel, A. Moréac, A. Neumann, G.S. Duesberg, S. Roth, J.-L. Sauvajol: Raman modes of index-identified freestanding single-walled carbon nanotubes, Phys. Rev. Lett. **95**, 217401 (2005)

4.97 A. Jorio, C. Fantini, M.A. Pimenta, R.B. Capaz, G.G. Samsonidze, G. Dresselhaus, M.S. Dresselhaus, J. Jiang, N. Kobayashi, A. Grüneis, R. Saito: Resonance Raman spectroscopy (n,m)-dependent effects in small-diameter single-wall carbon nanotubes, Phys. Rev. B **71**, 075401 (2005)

4.98 M. Paillet, T. Michel, J.C. Meyer, V.N. Popov, L. Henrard, S. Roth, J.-L. Sauvajol: Raman active phonons of identified semiconducting single-walled carbon nanotubes, Phys. Rev. Lett. **96**, 257401 (2006)

4.99 H. Son, A. Reina, G.G. Samsonidze, R. Saito, A. Jorio, M.S. Dresselhaus, J. Kong: Raman characterization of electronic transition energies of metallic single-wall carbon nanotubes, Phys. Rev. B **74**, 073406 (2006)

4.100 Y. Yin, A.N. Vamivakas, A.G. Walsh, S.B. Cronin, M.S. Ünlü, B.B. Goldberg, A.K. Swan: Optical determination of electron-phonon coupling in carbon nanotubes, Phys. Rev. Lett. **98**, 037404 (2007)

4.101 F. Wang, W. Liu, Y. Wu, M.Y. Sfeir, L. Huang, J. Hone, S. O'Brien, L.E. Brus, T.F. Heinz, Y.R. Shen: Multiphonon Raman scattering from individual single-walled carbon nanotubes, Phys. Rev. Lett. **98**, 047402 (2007)

4.102 K.T. Nguyen, A. Gaur, M. Shim: Fano lineshape and phonon softening in single isolated metallic carbon nanotubes, Phys. Rev. Lett. **98**, 145504 (2007)

4.103 Y. Wu, J. Maultzsch, E. Knoesel, B. Chandra, M. Huang, M.Y. Sfeir, L.E. Brus, J. Hone, T.F. Heinz: Variable electron-phonon coupling in isolated metallic carbon nanotubes observed by Raman scattering, Phys. Rev. Lett. **99**, 027402 (2007)

4.104 H. Farhat, H. Son, G.G. Samsonidze, S. Reich, M.S. Dresselhaus, J. Kong: Phonon softening in individual metallic carbon nanotubes due to the Kohn anomaly, Phys. Rev. Lett. **99**, 145506 (2007)

4.105 J.C. Tsang, M. Freitag, V. Perebeinos, J. Liu, P. Avouris: Doping and phonon renormalization in carbon nanotubes, Nat. Nanotechnol. **2**, 725–730 (2007)

4.106 M. Oron-Carl, R. Krupke: Raman spectroscopic evidence for hot-phonon generation in electrically biased carbon nanotubes, Phys. Rev. Lett. **100**, 127401 (2008)

4.107 M. Fouquet, H. Telg, J. Maultzsch, Y. Wu, B. Chandra, J. Hone, T.F. Heinz, C. Thomsen: Longitudinal optical phonons in metallic and semiconducting carbon nanotubes, Phys. Rev. Lett. **102**, 075501 (2009)

4.108 T. Michel, M. Paillet, D. Nakabayashi, M. Picher, V. Jourdain, J.C. Meyer, A.A. Zahab, J.-L. Sauvajol: Indexing of individual single-walled carbon nanotubes from Raman spectroscopy, Phys. Rev. B **80**, 245416 (2009)

4.109 E.H. Hároz, W.D. Rice, B.Y. Lu, S. Ghosh, R.H. Hauge, R.B. Weisman, S.K. Doorn, J. Kono: Enrichment of armchair carbon nanotubes via density gradient ultracentrifugation: Raman spectroscopy evidence, ACS Nano **4**, 1955–1962 (2010)

4.110 J.G. Duque, H. Chen, A.K. Swan, A.P. Shreve, S. Kilina, S. Tretiak, X. Tu, M. Zheng, S.K. Doorn: Violation of the Condon approximation in semiconducting carbon nanotubes, ACS Nano **5**, 5233–5241 (2011)

4.111 G.N. Ostojic, S. Zaric, J. Kono, M.S. Strano, V.C. Moore, R.H. Hauge, R.E. Smalley: Interband recombination dynamics of resonantly-excited single-walled carbon nanotubes, Phys. Rev. Lett. **92**, 117402 (2004)

4.112 L. Huang, H.N. Pedrosa, T.D. Krauss: Ultrafast ground-state recovery of single-walled carbon nanotubes, Phys. Rev. Lett. **93**, 017403 (2004)

4.113 J. Kono, G.N. Ostojic, S. Zaric, M.S. Strano, V.C. Moore, J. Shaver, R.H. Hauge, R.E. Smalley: Ultrafast optical spectroscopy of micelle-suspended single-walled carbon nanotubes, Appl. Phys. A **78**, 1093–1098 (2004)

4.114 A. Hagen, G. Moos, V. Talalaev, T. Hertel: Electronic structure and dynamics of optically excited single-wall carbon nanotubes, Appl. Phys. A **78**, 1137 (2004)

4.115 Y.-Z. Ma, J. Stenger, J. Zimmerman, S.M. Bachilo, R.E. Smalley, R.B. Weisman, G.R. Fleming: Ultrafast carrier dynamics in single-walled carbon nanotubes probed by femtosecond spectroscopy, J. Chem. Phys. **120**, 3368 (2004)

4.116 F. Wang, G. Dukovic, L.E. Brus, T.F. Heinz: Time-resolved fluorescence in carbon nanotubes and its implication for radiative lifetimes, Phys. Rev. Lett. **92**, 177402 (2004)

4.117 R.J. Ellingson, C. Engtrakul, M. Jones, M. Samec, G. Rumbles, A.J. Nozik, M.J. Heben: Ultrafast photoresponse of metallic and semiconducting single-wall carbon nanotubes, Phys. Rev. B **71**, 115444 (2005)

4.118 S. Reich, M. Dworzak, A. Hoffmann, C. Thomsen, M.S. Strano: Excited-state carrier lifetime in single-walled carbon nanotubes, Phys. Rev. B **71**, 033402 (2005)

4.119 F. Wang, G. Dukovic, E. Knoesel, L.E. Brus, T.F. Heinz: Observation of rapid Auger recombination in optically excited semiconducting carbon nanotubes, Phys. Rev. B **70**, 241403 (2004)

4.120 A. Maeda, S. Matsumoto, H. Kishida, T. Takenobu, Y. Iwasa, M. Shiraishi, M. Ata, H. Okamoto: Large optical nonlinearity of semiconducting single-walled carbon nanotubes under resonant excitations, Phys. Rev. Lett. **94**, 047404 (2005)

4.121 C.-X. Sheng, Z.V. Vardeny, B. Dalton, R.H. Baughman: Exciton dynamics in single-walled nanotubes: Transient photoinduced dichroism and polarized emission, Phys. Rev. B **71**, 125427 (2005)

4.122 S.G. Chou, F. Plentz, J. Jiang, R. Saito, D. Nezich, H.B. Ribeiro, A. Jorio, M.A. Pimenta, G.G. Samsonidze, A.P. Santos, M. Zheng, G.B. Onoa, E.D. Semke, G. Dresselhaus, M.S. Dresselhaus: Phonon-assisted excitonic recombination channels observed in DNA-wrapped carbon nanotubes using photoluminescence spectroscopy, Phys. Rev. Lett. **94**, 127402 (2005)

4.123 Y.-Z. Ma, L. Valkunas, S.L. Dexheimer, S.M. Bachilo, G.R. Fleming: Femtosecond spectroscopy of optical excitations in single-walled carbon nanotubes: Evidence for exciton-exciton annihilation, Phys. Rev. Lett. **94**, 157402 (2005)

4.124 C. Manzoni, A. Gambetta, E. Menna, M. Meneghetti, G. Lanzani, G. Cerullo: Intersubband exciton relaxation dynamics in single-walled carbon nanotubes, Phys. Rev. Lett. **94**, 207401 (2005)

4.125 J.S. Lauret, C. Voisin, S. Berger, G. Cassabois, C. Delalande, P. Roussignol, L. Goux-Capes, A. Filoramo: Environmental effects on the carrier dynamics in carbon nanotubes, Phys. Rev. B **72**, 113413 (2005)

4.126 A. Hagen, M. Steiner, M.B. Raschke, C. Lienau, T. Hertel, H. Qian, A.J. Meixner, A. Hartschuh: Exponential decay lifetimes of excitons in individual single-walled carbon nanotubes, Phys. Rev. Lett. **95**, 197401 (2005)

4.127 S.G. Chou, M.F. DeCamp, J. Jiang, G.G. Samsonidze, E.B. Barros, F. Plentz, A. Jorio, M. Zheng, G.B. Onoa, E.D. Semke, A. Tokmakoff, R. Saito, G. Dresselhaus, M.S. Dresselhaus: Phonon-assisted exciton relaxation dynamics for a (6,5)-enriched DNA-wrapped single-walled carbon nanotube sample, Phys. Rev. B **72**, 195415 (2005)

4.128 G.N. Ostojic, S. Zaric, J. Kono, V.C. Moore, R.H. Hauge, R.E. Smalley: Stability of high-density one-dimensional excitons in carbon nanotubes under high laser excitation, Phys. Rev. Lett. **94**, 097401 (2005)

4.129 A. Gambetta, C. Manzoni, E. Menna, M. Meneghetti, G. Cerullo, G. Lanzani, S. Tretiak, A. Piryatinski, A. Saxena, R.L. Martin, A.R. Bishop: Real-time observation of nonlinear coherent phonon dynamics in single-walled carbon nanotubes, Nat. Phys. **2**, 515–520 (2006)

4.130 Y.-S. Lim, K.-J. Yee, J.-H. Kim, J. Shaver, E.H. Hároz, J. Kono, S.K. Doorn, R.H. Hauge, R.E. Smalley: Coherent lattice vibrations in carbon nanotubes, Nano Lett. **6**, 2696–2700 (2006)

4.131 Y. Hashimoto, Y. Murakami, S. Maruyama, J. Kono: Anisotropic decay dynamics of photoexcited aligned carbon nanotube bundles, Phys. Rev. B **75**, 245408 (2007)

4.132 D. Song, F. Wang, G. Dukovic, M. Zheng, E.D. Semke, L.E. Brus, T.F. Heinz: Direct measurement of the lifetime of optical phonons in single-walled carbon nanotubes, Phys. Rev. Lett. **100**, 225503 (2008)

4.133 K. Kang, T. Ozel, D.G. Cahill, M. Shim: Optical phonon lifetimes in single-walled carbon nanotubes by time-resolved Raman scattering, Nano Lett. **8**, 4642–4647 (2008)

4.134 J.-H. Kim, K.-J. Han, N.-J. Kim, K.-J. Yee, Y.-S. Lim, G.D. Sanders, C.J. Stanton, L.G. Booshehri, E.H. Hároz, J. Kono: Chirality-selective excitations of coherent phonons in carbon nanotubes by femtosecond optical pulses, Phys. Rev. Lett. **102**, 037402 (2009)

4.135 L. Lüer, C. Gadermaier, J. Crochet, T. Hertel, D. Brida, G. Lanzani: Coherent phonon dynamics in semiconducting carbon nanotubes: A quantitative study of electron-phonon coupling, Phys. Rev. Lett. **102**, 127401 (2009)

4.136 I. Chatzakis, H. Yan, D. Song, S. Berciaud, T.F. Heinz: Temperature dependence of the anharmonic decay of optical phonons in carbon nanotubes and graphite, Phys. Rev. B **83**, 205411 (2011)

4.137 J.-H. Kim, K.-J. Yee, Y.-S. Lim, L.G. Booshehri, E.H. Hároz, J. Kono: Optical phonon dephasing in single-walled carbon nanotubes probed via impulsive stimulated Raman scattering, Phys. Rev. B **86**, 161415(R) (2011)

4.138 D.T. Nguyen, C. Voisin, P. Roussignol, C. Roquelet, J.S. Lauret, G. Cassabois: Elastic exciton–exciton scattering in photoexcited carbon nanotubes, Phys. Rev. Lett. **107**, 127401 (2011)

4.139 S.M. Santos, B. Yuma, S. Berciaud, J. Shaver, M. Gallart, P. Gilliot, L. Cognet, B. Lounis: All-optical trion generation in single-walled carbon nanotubes, Phys. Rev. Lett. **107**, 187401 (2011)

4.140 J.J. Crochet, S. Hoseinkhani, L. Lüer, T. Hertel, S.K. Doorn, G. Lanzani: Free-carrier generation in aggregates of single-wall carbon nanotubes by photoexcitation in the ultraviolet regime, Phys. Rev. Lett. **107**, 257402 (2011)

4.141 M. Freitag, Y. Martin, J.A. Misewich, R. Martel, P. Avouris: Photoconductivity of single carbon nanotubes, Nano Lett. **3**, 1067–1071 (2003)

4.142 A. Hartschuh, E.J. Sánchez, X.S. Xie, L. Novotny: High-resolution near-field raman microscopy of single-walled carbon nanotubes, Phys. Rev. Lett. **90**, 095503 (2003)

4.143 J.A. Misewich, R. Martel, P. Avouris, J.C. Tsang, S. Heinze, J. Tersoff: Electrically induced optical emission from a carbon nanotube FET, Science **300**, 783–786 (2003)

4.144 A. Hartschuh, H.N. Pedrosa, L. Novotny, T.D. Krauss: Simultaneous fluorescence and Raman scattering

from single carbon nanotubes, Science **301**, 1354–1356 (2003)
4.145 J. Lefebvre, J.M. Fraser, P. Finnie, Y. Homma: Photoluminescence from an individual single-walled carbon nanotube, Phys. Rev. B **69**, 075403 (2004)
4.146 H. Htoon, M.J. O'Connell, P.J. Cox, S.K. Doorn, V.I. Klimov: Low temperature emission spectra of individual single-walled carbon nanotubes: Multiplicity of subspecies within single-species nanotube ensembles, Phys. Rev. Lett. **93**, 027401 (2004)
4.147 K. Matsuda, Y. Kanemitsu, K. Irie, T. Saiki, T. Someya, Y. Miyauchi, S. Maruyama: Photoluminescence intermittency in an individual single-walled carbon nanotube at room temperature, Appl. Phys. Lett. **86**, 123116 (2005)
4.148 K. Balasubramanian, M. Burghard, K. Kern, M. Scolari, A. Mews: Photocurrent imaging of charge transport barriers in carbon nanotube devices, Nano Lett. **5**, 507–510 (2005)
4.149 H. Htoon, M.J. O'Connell, S.K. Doorn, V.I. Klimov: Single carbon nanotubes probed by photoluminescence excitation spectroscopy: The role of phonon-assisted transitions, Phys. Rev. Lett. **94**, 127403 (2005)
4.150 J.U. Lee: Photovoltaic effect in ideal carbon nanotube diodes, Appl. Phys. Lett. **87**, 073101 (2005)
4.151 J. Chen, V. Perebeinos, M. Freitag, J. Tsang, Q. Fu, J. Liu, P. Avouris: Bright infrared emission from electrically induced excitons in carbon nanotubes, Science **310**, 1171–1174 (2005)
4.152 J.U. Lee, P.J. Codella, M. Pietrzykowski: Direct probe of excitonic and continuum transitions in the photocurrent spectroscopy of individual carbon nanotube p-n diodes, Appl. Phys. Lett. **90**, 053103 (2007)
4.153 L. Cognet, D.A. Tsyboulski, J.-D.R. Rocha, C.D. Doyle, J.M. Tour, R.B. Weisman: Stepwise quenching of exciton fluorescence in carbon nanotubes by single-molecule reactions, Science **316**, 1465–1468 (2007)
4.154 A. Högele, C. Galland, M. Winger, A. Imamoğlu: Photon antibunching in the photoluminescence spectra of a single carbon nanotube, Phys. Rev. Lett. **100**, 217401 (2008)
4.155 C. Galland, A. Högele, H.E. Türeci, A. Imamoğlu: Non-Markovian decoherence of localized nanotube excitons by acoustic phonons, Phys. Rev. Lett. **101**, 067402 (2008)
4.156 A. Srivastava, H. Htoon, V.I. Klimov, J. Kono: Direct observation of dark excitons in individual carbon nanotubes: Inhomogeneity in the exchange splitting, Phys. Rev. Lett. **101**, 087402 (2008)
4.157 R. Matsunaga, K. Matsuda, Y. Kanemitsu: Evidence for dark excitons in a single carbon nanotube due to the Aharonov–Bohm effect, Phys. Rev. Lett. **101**, 147404 (2008)
4.158 K. Matsuda, T. Inoue, Y. Murakami, S. Maruyama, Y. Kanemitsu: Exciton dephasing and multiexciton recombinations in a single carbon nanotube, Phys. Rev. B **77**, 033406 (2008)
4.159 N.M. Gabor, Z. Zhong, K. Bosnick, J. Park, P.L. McEuen: Extremely efficient multiple electron-hole pair generation in carbon nanotube photodiodes, Science **325**, 1367–1371 (2009)
4.160 M. Steiner, M. Freitag, V. Perebeinos, A. Naumov, J.P. Small, A.A. Bol, P. Avouris: Gate-variable light absorption and emission in a semiconducting carbon nanotube, Nano Lett. **9**, 3477–3481 (2009)
4.161 R. Matsunaga, Y. Miyauchi, K. Matsuda, Y. Kanemitsu: Symmetry-induced nonequilibrium distributions of bright and dark exciton states in single carbon nanotubes, Phys. Rev. B **80**, 115436 (2009)
4.162 M. Freitag, M. Steiner, A. Naumov, J.P. Small, A.A. Bol, V. Perebeinos, P. Avouris: Carbon nanotube photo- and electroluminescence in longitudinal electric fields, ACS Nano **3**, 3744–3748 (2009)
4.163 S. Moritsubo, T. Murai, T. Shimada, Y. Murakami, S. Chiashi, S. Maruyama, Y.K. Kato: Exciton diffusion in air-suspended single-walled carbon nanotubes, Phys. Rev. Lett. **104**, 247402 (2010)
4.164 S. Zaric, G.N. Ostojic, J. Kono, J. Shaver, V.C. Moore, M.S. Strano, R.H. Hauge, R.E. Smalley, X. Wei: Optical signatures of the Aharonov–Bohm phase in single-walled carbon nanotubes, Science **304**, 1129–1131 (2004)
4.165 S. Zaric, G.N. Ostojic, J. Shaver, J. Kono, O. Portugall, P.H. Frings, G.L.J.A. Rikken, M. Furis, S.A. Crooker, X. Wei, V.C. Moore, R.H. Hauge, R.E. Smalley: Excitons in carbon nanotubes with broken time-reversal symmetry, Phys. Rev. Lett. **96**, 016406 (2006)
4.166 J. Shaver, J. Kono, O. Portugall, V. Krstic, G.L.J.A. Rikken, Y. Miyauchi, S. Maruyama, V. Perebeinos: Magnetic brightening of carbon nanotube photoluminescence through symmetry breaking, Nano Lett. **7**, 1851–1855 (2007)
4.167 I.B. Mortimer, R.J. Nicholas: Role of bright and dark excitons in the temperature-dependent photoluminescence of carbon nanotubes, Phys. Rev. Lett. **98**, 027404 (2007)
4.168 J. Shaver, J. Kono: Temperature dependent magneto-photoluminescence spectroscopy of carbon nanotubes: Evidence for dark excitons, Laser Photonics Rev. **1**, 260–274 (2007)
4.169 J. Shaver, S.A. Crooker, J.A. Fagan, E.K. Hobbie, N. Ubrig, O. Portugall, V. Perebeinos, P. Avouris, J. Kono: Magneto-optical spectroscopy of highly-aligned carbon nanotubes: Identifying the role of threading magnetic flux, Phys. Rev. B **78**, 081402 (2008)
4.170 J. Shaver, A.N.G. Parra-Vasquez, S. Hansel, O. Portugall, C.H. Mielke, M. von Ortenberg, R.H. Hauge, M. Pasquali, J. Kono: Alignment dynamics of carbon nanotubes in pulsed ultrahigh magnetic fields, ACS Nano **3**, 131 (2009)
4.171 R.S. Knox: *Theory of Excitons*, Solid State Physics, Vol. 5 (Academic, New York 1963)

4.172 R. Loudon: One-dimensional hydrogen atom, Am. J. Phys. **27**, 649 (1959)

4.173 R.J. Elliot, R. Loudon: Theory of the absorption edge in semiconductors in a high magnetic field, J. Phys. Chem. Solids **15**, 196–207 (1960)

4.174 F. Wang, G. Dukovic, L.E. Brus, T.F. Heinz: The optical resonances in carbon nanotubes arise from excitons, Science **308**, 838 (2005)

4.175 J. Maultzsch, R. Pomraenke, S. Reich, E. Chang, D. Prezzi, A. Ruini, E. Molinari, M.S. Strano, C. Thomsen, C. Lienau: Exciton binding energies in carbon nanotubes from two-photon photoluminescence, Phys. Rev. B **72**, 241402 (2005)

4.176 S. Uryu, T. Ando: Exciton absorption of perpendicularly polarized light in carbon nanotubes, Phys. Rev. B **74**, 155411 (2006)

4.177 S. Uryu, T. Ando: Cross-polarized exciton absorption in carbon nanotubes with Aharonov–Bohm flux, Phys. Rev. B **76**, 115420 (2007)

4.178 H. Kataura, Y. Kumazawa, Y. Maniwa, I. Umezu, S. Suzuki, Y. Ohtsuka, Y. Achiba: Optical properties of single-wall carbon nanotubes, Synth. Met. **103**, 2555–2558 (1999)

4.179 S. Berciaud, L. Cognet, P. Poulin, R.B. Weisman, B. Lounis: Absorption spectroscopy of individual single-walled carbon nanotubes, Nano Lett. **7**, 1203–1207 (2007)

4.180 F. Wang, D.J. Cho, B. Kessler, J. Deslippe, P.J. Schuck, S.G. Louie, A. Zettl, T.F. Heinz, Y.R. Shen: Observation of excitons in one-dimensional metallic single-walled carbon nanotubes, Phys. Rev. Lett. **99**, 227401 (2007)

4.181 A.M. Rao, E. Richter, S. Bandow, B. Chase, P.C. Eklund, K.A. Williams, S. Fang, K.R. Subbaswamy, M. Menon, A. Thess, R.E. Smalley, G. Dresselhaus, M.S. Dresselhaus: Diameter-selective Raman scattering from virbrational modes in carbon nanotubes, Science **275**, 187–191 (1997)

4.182 A. Jorio, M.S. Dresselhaus, R. Saito, G.F. Dresselhaus: *Raman Spectroscopy in Graphene Related Systems* (Wiley-VCH, Weinheim 2011)

4.183 M.J. O'Connell, S. Sivaram, S.K. Doorn: Near-infrared resonance Raman excitation profile studies of single-walled carbon nanotube intertube interactions: A direct comparison of bundled and individually dispersed HiPco nanotubes, Phys. Rev. B **69**, 235415 (2004)

4.184 A. Jorio, A.P. Santos, H.B. Ribeiro, C. Fantini, M. Souza, J.P.M. Viera, C.A. Furtado, J. Jiang, R. Saito, L. Balzano, D.E. Resasco, M.A. Pimenta: Quantifying carbon-nanotube species with resonance Raman scattering, Phys. Rev. B **72**, 075207 (2005)

4.185 H. Telg, J. Maultzsch, C. Thomsen: Raman Intensities of the Radial-Breathing Mode in Carbon Nanotubes: The Exciton-Phonon Coupling as a Function of ($n1$,$n2$), J. Nanophoton. **4**, 041660 (2012)

4.186 E.H. Hároz, J.G. Duque, X. Tu, M. Zheng, A.R. Hight Walker, R.H. Hauge, S.K. Doorn, J. Kono: Fundamental optical processes in armchair carbon nanotubes, Nanoscale **5**(4), 1411–1411 (2012)

4.187 M.A. Pimenta, A. Marucci, S.A. Empedocles, M.G. Bawendi, E.B. Hanlon, A.M. Rao, P.C. Eklund, R.E. Smalley, G. Dresselhaus, M.S. Dresselhaus: Raman modes of metallic carbon nanotubes, Phys. Rev. B **58**(24), R16016–R16019 (1998)

4.188 S.D.M. Brown, A. Jorio, M.S. Dresselhaus, G. Dresselhaus: Observations of the D-band feature in the Raman spectra of carbon nanotubes, Phys. Rev. B **64**(7), 073403 (2001)

4.189 S. Piscanec, M. Lazzeri, J. Robertson, A.C. Ferrari, F. Mauri: Optical phonons in carbon nanotubes: Kohn anomalies, Peierls distortions, and dynamic effects, Phys. Rev. B **75**(3), 035427 (2007)

4.190 E.H. Hároz, J.G. Duque, W.D. Rice, C.G. Densmore, J. Kono, S.K. Doorn: Resonant Raman spectroscopy of armchair carbon nanotubes: Absence of broad G^- feature, Phys. Rev. B **84**(12), 121403 (2011)

4.191 A.M. Rao, P.C. Eklund, S. Bandow, A. Thess, R.E. Smalley: Evidence for charge transfer in doped carbon nanotube bundles from Raman scattering, Nature **388**, 257 (1997)

4.192 S.B. Cronin, A.K. Swan, M.S. Ünlü, B.B. Goldberg, M.S. Dresselhaus, M. Tinkham: Resonant Raman spectroscopy of individual metallic and semiconducting single-wall carbon nanotubes under uniaxial strain, Phys. Rev. B **72**, 035425 (2005)

4.193 S. Berciaud, C. Voisin, H. Yan, B. Chandra, R. Caldwell, Y. Shan, L.E. Brus, J. Hone, T.F. Heinz: Excitons and high-order optical transitions in individual carbon nanotubes: A Rayleigh scattering spectroscopy study, Phys. Rev. B **81**, 041414 (2010)

4.194 A.G. Souza Filho, A. Jorio, G.G. Samsonidze, G. Dresselhaus, M.S. Dresselhaus, A.K. Swan, M.S. Ünlü, B.B. Goldberg, R. Saito, J.H. Hafner, C.M. Lieber, M.A. Pimenta: Probing the electronic trigonal warping effect in inidividual single-wall carbon nanotubes using phonon spectra, Chem. Phys. Lett. **354**, 62–68 (2002)

4.195 M.Y. Sfeir, F. Wang, L. Huang, C.C. Chuang, J. Hone, S.P. O'Brien, T.F. Heinz, L.E. Brus: Probing electronic transitions in individual carbon nanotubes by Rayleigh scattering, Science **306**, 1540 (2004)

4.196 M.Y. Sfeir, T. Beetz, F. Wang, L. Huang, X.M.H. Huang, M. Huang, J. Hone, S. O'Brien, J.A. Misewich, T.F. Heinz, L. Wu, Y. Zhu, L.E. Brus: Optical spectroscopy of individual single-walled carbon nanotubes of defined chiral structure, Science **312**, 554–556 (2006)

4.197 K. Liu, J. Deslippe, F. Xiao, R.B. Capaz, X. Hong, S. Aloni, A. Zettl, W. Wang, X. Bai, S.G. Louie, E. Wang, F. Wang: An atlas of carbon nanotube optical transitions, Nat. Nanotechnol. **7**, 325–329 (2012)

4.198 D.Y. Joh, L.H. Herman, S.-Y. Ju, J. Kinder, M.A. Segal, J.N. Johnson, G.K.L. Chan, J. Park: On-chip Rayleigh

imaging and spectroscopy of carbon nanotubes, Nano Lett. **11**, 1–7 (2011)
4.199 T. Hertel, G. Moos: Electron–phonon interaction in single-wall carbon nanotubes: A time-domain study, Phys. Rev. Lett. **84**, 5002 (2000)
4.200 J.-H. Kim, J. Park, B.Y. Lee, D. Lee, K.-J. Yee, Y.-S. Lim, L.G. Booshehri, E.H. Hároz, J. Kono, S.-H. Baik: Polarization anisotropy of transient carrier and phonon dynamics in carbon nanotubes, J. Appl. Phys. **105**, 103506 (2009)
4.201 J. Wang, M.W. Graham, Y.-Z. Ma, G.R. Fleming, R.A. Kaindl: Ultrafast spectroscopy of midinfrared internal exciton transitions in seperated single-walled carbon nanotubes, Phys. Rev. Lett. **104**, 177401 (2010)
4.202 B. Gao, G.B. Hartland, L. Huang: Transient absorption spectroscopy and imaging of individual chirality-assigned single-walled carbon nanotubes, ACS Nano **6**, 5083 (2012)
4.203 J.S. Lauret, C. Voisin, G. Cassabois, C. Delalande, P. Roussignol, O. Jost, L. Capes: Ultrafast carrier dynamics in single-wall carbon nanotubes, Phys. Rev. Lett. **90**, 057404 (2003)
4.204 K. Kato, K. Ishioka, M. Kitajima, J. Tang, R. Saito, H. Petek: Coherent phonon anisotropy in aligned single-walled carbon nanotubes, Nano Lett. **8**, 3102–3108 (2008)
4.205 L.G. Booshehri, C.L. Pint, G.D. Sanders, L. Ren, C. Sun, E.H. Hároz, J.-H. Kim, K.-J. Yee, Y.-S. Lim, R.H. Hauge, C.J. Stanton, J. Kono: Polarization dependence of coherent phonon generation and detection in highly-aligned single-walled carbon nanotubes, Phys. Rev. B **83**, 195411 (2011)
4.206 Y.-S. Lim, K.-J. Yee, J.-H. Kim, E.H. Hároz, J. Shaver, J. Kono, S.K. Doorn, R.H. Hauge, R.E. Smalley: Chirality assignment of micelle-suspended single-walled carbon nanotubes using coherent phonon oscillations, J. Korean Phys. Soc. **51**, 306 (2007)
4.207 A.M. Weiner, J.P. Heritage, E.M. Kirschner: High-resolution femtosecond pulse shaping, J. Opt. Soc. Am. B **5**(8), 1563 (1988)
4.208 R.J. Elliot, R. Loudon: Theory of fine structure on the absorption edge in semiconductors, J. Phys. Chem. Solids **8**, 382–388 (1959)
4.209 M.S. Dresselhaus, G. Dresselhaus, R. Saito, A. Jorio: Exciton photophysics of carbon nanotubes, Annu. Rev. Phys. Chem. **58**, 719–747 (2007)
4.210 T. Ando: Excitons in carbon nanotubes, J. Phys. Soc. Jpn. **66**, 1066–1073 (1997)
4.211 T. Ando: Excitons in carbon nanotubes revisited: Dependence on diameter, Aharonov–Bohm flux, and strain, J. Phys. Soc. Jpn. **73**, 3351–3363 (2004)
4.212 T.G. Pedersen: Variational approach to excitons in carbon nanotubes, Phys. Rev. B **67**, 073401 (2003)
4.213 C.L. Kane, E.J. Mele: Ratio problem in single carbon nanotube fluorescence spectroscopy, Phys. Rev. Lett. **90**, 207401 (2003)
4.214 C.D. Spataru, S. Ismail-Beigi, L.X. Benedict, S.G. Louie: Excitonic effects and optical spectra of single-walled carbon nanotubes, Phys. Rev. Lett. **92**, 077402 (2004)
4.215 E. Chang, G. Bussi, A. Ruini, E. Molinari: Excitons in carbon nanotubes: An *ab initio* symmetry-based approach, Phys. Rev. Lett. **92**, 196401 (2004)
4.216 T.G. Pederson: Exciton effects in carbon nanotubes, Carbon **42**, 1007 (2004)
4.217 V. Perebeinos, J. Tersoff, P. Avouris: Scaling of excitons in carbon nanotubes, Phys. Rev. Lett. **92**, 257402 (2004)
4.218 C.L. Kane, E.J. Mele: Electron interactions and scaling relations for optical excitations in carbon nanotubes, Phys. Rev. Lett. **93**, 197402 (2004)
4.219 H. Zhao, S. Mazumdar: Electron–electron interaction effects on the optical excitations of semiconducting single-walled carbon nanotubes, Phys. Rev. Lett. **93**, 157402 (2004)
4.220 E. Chang, G. Bussi, A. Ruini, E. Molinari: First-principles approach for the calculation of optical properties of one-dimensional systems with helical symmetry: The case of carbon nanotubes, Phys. Rev. B **72**, 195423 (2005)
4.221 V. Perebeinos, J. Tersoff, P. Avouris: Radiative lifetime of excitons in carbon nanotubes, Nano Lett. **5**, 2495–2499 (2005)
4.222 C.D. Spataru, S. Ismail-Beigi, R.B. Capaz, S.G. Louie: Theory and *ab initio* calculation of radiative lifetime of excitons in semiconducting carbon nanotubes, Phys. Rev. Lett. **95**, 247402 (2005)
4.223 T. Ando: Effects of valley mixing and exchange on excitons in carbon nanotubes with Aharonov–Bohm flux, J. Phys. Soc. Jpn. **75**, 024707 (2006)
4.224 J. Deslippe, C.D. Spataru, D. Prendergast, S.G. Louie: Bound excitons in metallic single-walled carbon nanotubes, Nano Lett. **7**, 1626–1630 (2007)
4.225 S. Kilina, S. Tretiak, S.K. Doorn, Z. Luo, F. Papadimitrakopoulos, A. Piryatinski, A. Saxena, A.R. Bishop: Cross-polarized excitons in carbon nanotubes, Proc. Natl. Acad. Sci. USA **105**, 6797–6802 (2008)
4.226 S. Uryu, T. Ando: Excitons in metallic carbon nanotubes with Aharonov–Bohm flux, Phys. Rev. B **77**, 205407 (2008)
4.227 P.T. Araujo, A. Jorio, M.S. Dresselhaus, K. Sato, R. Saito: Diameter dependence of the dielectric constant for the excitonic transition energy of single-wall carbon nanotubes, Phys. Rev. Lett. **103**, 146802 (2009)
4.228 T. Ando: Environment effects on excitons in semiconducting carbon nanotubes, J. Phys. Soc. Jpn. **79**, 024706 (2010)
4.229 A.R.T. Nugraha, R. Saito, K. Sato, P.T. Araujo, A. Jorio, M.S. Dresselhaus: Dielectric constant model for environmental effects on the exciton energies of single wall carbon nanotubes, Appl. Phys. Lett. **97**, 091905 (2010)

4.230 J. Maultzsch, H. Telg, S. Reich, C. Thomsen: Radial breathing mode of single-walled carbon nanotubes: Optical transition energies and chiral-index assignment, Phys. Rev. B **72**, 205438 (2005)

4.231 E. Chang, D. Prezzi, A. Ruini, E. Molinari: Dark excitons in carbon nanotubes, Phys. Rev. B (2012), in press

4.232 G. Dukovic, F. Wang, D. Song, M.Y. Sfeir, T.F. Heinz, L.E. Brus: Structural dependence of excitonic optical transitions and band-gap energies in carbon nanotubes, Nano Lett. **5**, 2314–2318 (2005)

4.233 F. Wang, D.J. Cho, B. Kessler, J. Deslippe, P.J. Schuck, S.G. Louie, A. Zettl, T.F. Heinz, Y.R. Shen: Observation of excitons in one-dimensional metallic single-walled carbon nanotubes, Phys. Rev. Lett. **99**, 227401 (2007)

4.234 E.H. Hároz, J.G. Duque, B.Y. Lu, P. Nikolaev, S. Arepalli, R.H. Hauge, S.K. Doorn, J. Kono: Unique origin of colors of armchair carbon nanotubes, J. Am. Chem. Soc. **134**, 4461–4464 (2011)

4.235 A.B. Kaiser: Electronic transport properties of conducting polymers and carbon nanotubes, Rep. Prog. Phys. **64**(1), 1 (2000)

4.236 J.E. Fischer, H. Dai, A. Thess, R. Lee, N.M. Hanjani, D.L. Dehaas, R.E. Smalley: Metallic resistivity in crystalline ropes of single-wall carbon nanotubes, Phys. Rev. B **55**, R4921–R4924 (1997)

4.237 G.T. Kim, E.S. Choi, D.C. Kim, D.S. Suh, Y.W. Park, K. Liu, G. Duesberg, S. Roth: Magnetoresistance of an entangled single-wall carbon-nanotube network, Phys. Rev. B **58**, 16064–16069 (1998)

4.238 Y. Yosida, I. Oguro: Variable range hopping conduction in bulk samples composed of single-walled carbon nanotubes, J. Appl. Phys. **86**(2), 999–1003 (1999)

4.239 M.S. Fuhrer, M.L. Cohen, A. Zettl, V. Crespi: Localization in single-walled carbon nanotubes, Solid State Commun. **109**(2), 105–109 (1998)

4.240 P. Pipinys, A. Kiveris: Phonon-assisted tunnelling in electrical conductivity of individual carbon nanotubes and networks ones, Physica B **403**(19/20), 3730–3733 (2008)

4.241 A.B. Kaiser, K.J. Challis, G.C. McIntosh, G.T. Kim, H.Y. Yu, J.G. Park, S.H. Jhang, Y.W. Park: Frequency and field dependent conductivity of carbon nanotube networks, Curr. Appl. Phys. **2**(2), 163–166 (2002)

4.242 H. Xu, S. Zhang, S.M. Anlage, L. Hu, G. Grüner: Frequency- and electric-field-dependent conductivity of single-walled carbon nanotube networks of varying density, Phys. Rev. B **77**, 075418 (2008)

4.243 M. Bockrath, D.H. Cobden, P.L. McEuen, N.G. Chopra, A. Zettl, A. Thess, R.E. Smalley: Single-electron transport in ropes of carbon nanotubes, Science **275**, 1922–1925 (1997)

4.244 W. Liang, M. Bockrath, D. Bozovic, J.H. Hafner, M. Tinkham, H. Park: Fabry–Perot interference in a nanotube electron waveguide, Nature **411**, 665 (2001)

4.245 A. Javey, J. Guo, Q. Wang, M. Lundstrom, H. Dai: Ballistic carbon nanotube field-effect transistors, Nature **424**, 654 (2003)

4.246 D.H. Cobden, M. Bockrath, P.L. McEuen, A.G. Rinzler, R.E. Smalley: Spin splitting and even-odd effects in carbon nanotubes, Phys. Rev. Lett. **81**, 681–684 (1998)

4.247 S.J. Tans, M.H. Devoret, H. Dai, A. Thess, R.E. Smalley, L.J. Geerligs, C. Dekker: Individual single-wall carbon nanotubes as quantum wires, Nature **386**, 474–477 (1997)

4.248 S.J. Tans, A.R.M. Verschueren, C. Dekker: Room-temperature transistor based on a single carbon nanotube, Nature **393**, 49–52 (1998)

4.249 R. Martel, T. Schmidt, H.R. Shea, T. Hertel, P. Avouris: Single- and multi-wall carbon nanotube field-effect transistors, Appl. Phys. Lett. **73**(17), 2447–2449 (1998)

4.250 S.J. Kang, C. Kocabas, T. Ozel, M. Shim, N. Pimparkar, M.A. Alam, S.V. Rotkin, J.A. Rogers: High-performance electronics using dense, perfectly aligned arrays of single-walled carbon nanotubes, Nat. Nanotechnol. **2**, 230–236 (2007)

4.251 J.U. Lee, P.P. Gipp, C.M. Heller: Carbon nanotube p-n junction diodes, Appl. Phys. Lett. **85**, 145 (2004)

4.252 E. Pop, D. Mann, J. Cao, Q. Wang, K. Goodson, H. Dai: Negative differential conductance and hot phonons in suspended nanotube molecular wires, Phys. Rev. Lett. **95**, 155505 (2005)

4.253 M. Bockrath, D.H. Cobden, J. Lu, A.G. Rinzler, R.E. Smalley, L. Balents, P.L. McEuen: Luttinger liquid behavior in carbon nanotubes, Nature **397**, 598 (1999)

4.254 H.W.C. Postma, T. Teepen, Z. Yao, M. Grifoni, C. Dekker: Carbon nanotube single-electron transistors at room temperature, Science **293**, 76–79 (2001)

4.255 S. Heinze, J. Tersoff, R. Martel, V. Derycke, J. Appenzeller, P. Avouris: Carbon nanotubes as Schottky barrier transistors, Phys. Rev. Lett. **89**, 106801 (2002)

4.256 S. Datta: *Electronic Transport in Mesoscopic Systems* (Cambridge Univ. Press, Cambridge 1995)

4.257 H. Mathieu: *Physique des Semiconducteurs et des Composants électroniques* (Dunod, Paris 2001)

4.258 M. Krüger, M.R. Buitelaar, T. Nussbaumer, C. Schönenberger, L. Forró: Electrochemical carbon nanotube field-effect transistor, Appl. Phys. Lett. **78**(9), 1291–1293 (2001)

4.259 W. Kim, A. Javey, O. Vermesh, Q. Wang, Y. Li, H. Dai: Hysteresis caused by water molecules in carbon nanotube field-effect transistors, Nano Lett. **3**(2), 193–198 (2003)

4.260 J. Guo, S. Goasguen, M. Lundstrom, S. Datta: Metal–insulator–semiconductor electrostatics of carbon nanotubes, Appl. Phys. Lett. **81**(8), 1486–1488 (2002)

4.261 J.-C. Charlier, X. Blase, S. Roche: Electronic and transport properties of nanotubes, Rev. Mod. Phys. **79**, 677–732 (2007)

4.262 R. Martel, V. Derycke, C. Lavoie, J. Appenzeller, K.K. Chan, J. Tersoff, P. Avouris: Ambipolar electrical transport in semiconducting single-wall carbon nanotubes, Phys. Rev. Lett. **87**, 256805 (2001)

4.263 J. Kong, E. Yenilmez, T.W. Tombler, W. Kim, H. Dai, R.B. Laughlin, L. Liu, C.S. Jayanthi, S.Y. Wu: Quantum interference and ballistic transmission in nanotube electron waveguides, Phys. Rev. Lett. **87**, 106801 (2001)

4.264 F. Léonard, J. Tersoff: Role of Fermi-level pinning in nanotube Schottky diodes, Phys. Rev. Lett. **84**(20), 4693–4696 (2000)

4.265 A. Javey, P. Qi, Q. Wang, H. Dai: Ten- to 50-nm-long quasi-ballistic carbon nanotubes devices obtained without complex lithography, Proc. Natl. Acad. Sci. USA **101**, 13408–13410 (2004)

4.266 R. Egger, A.O. Gogolin: Effective low-energy theory for correlated carbon nanotubes, Phys. Rev. Lett. **79**, 5082 (1997)

4.267 Z. Yao, H.W.C. Postma, L. Balents, C. Dekker: Carbon nanotube intramolecular junctions, Nature **402**, 273 (1999)

4.268 J. Cao, Q. Wang, M. Rolandi, H. Dai: Aharonov–Bohm interference and beating in single-walled carbon-nanotube interferrometers, Phys. Rev. Lett. **93**, 216803 (2004)

4.269 E.D. Minot, Y. Yaish, V. Sazonova, P.L. McEuen: Determination of electron orbital magnetic moments in carbon nanotubes, Nature **428**, 536–539 (2004)

4.270 P. Avouris, Z. Chen, V. Perebeinos: Carbon-based electronics, Nat. Nanotechnol. **2**, 605–615 (2007)

4.271 L.X. Benedict, S.G. Louie, M.L. Cohen: Heat capacity of carbon nanotubes, Solid State Commun. **100**(3), 177–180 (1996)

4.272 J. Hone, B. Batlogg, Z. Benes, A.T. Johnson, J.E. Fischer: Quantized phonon spectrum of single-wall carbon nanotubes, Science **289**(5485), 1730–1733 (2000)

4.273 J. Heremans, C.P. Beetz: Thermal conductivity and thermopower of vapor-grown graphite fibers, Phys. Rev. B **32**, 1981–1986 (1985)

4.274 S. Berber, Y.-K. Kwon, D. Tománek: Unusually high thermal conductivity of carbon nanotubes, Phys. Rev. Lett. **84**, 4613–4616 (2000)

4.275 J. Hone, M. Whitney, C. Piskoti, A. Zettl: Thermal conductivity of single-walled carbon nanotubes, Phys. Rev. B **59**, R2514–R2516 (1999)

4.276 E. Pop, D. Mann, Q. Wang, K. Goodson, H. Dai: Thermal conductance of an individual single-wall carbon nanotube above room temperature, Nano Lett. **6**(1), 96–100 (2006)

4.277 C. Yu, L. Shi, Z. Yao, D. Li, A. Majumdar: Thermal conductance and thermopower of an individual single-wall carbon nanotube, Nano Lett. **5**(9), 1842–1846 (2005)

4.278 N. Mingo, D.A. Broido: Carbon nanotube ballistic thermal conductance and its limits, Phys. Rev. Lett. **95**, 096105 (2005)

4.279 P. Kim, L. Shi, A. Majumdar, P.L. McEuen: Thermal transport measurements of individual multiwalled nanotubes, Phys. Rev. Lett. **87**, 215502 (2001)

4.280 A.N. Volkov, L.V. Zhigilei: Scaling laws and mesoscopic modeling of thermal conductivity in carbon nanotube materials, Phys. Rev. Lett. **104**, 215902 (2010)

4.281 R.S. Prasher, X.J. Hu, Y. Chalopin, N. Mingo, K. Lofgreen, S. Volz, F. Cleri, P. Keblinski: Turning carbon nanotubes from exceptional heat conductors into insulators, Phys. Rev. Lett. **102**, 105901 (2009)

4.282 C.F. Cornwell, L.T. Wille: Elastic properties of single-walled carbon nanotubes in compression, Solid State Commun. **101**, 555–558 (1997)

4.283 J.P. Lu: Elastic properties of carbon nanotubes and nanoropes, Phys. Rev. Lett. **79**, 1297–1300 (1997)

4.284 G. Overney, W. Zhong, D. Tomanek: Structural rigidity and low-frequency vibrational-modes of long carbon tubules, Z. Phys. D **27**, 93–96 (1993)

4.285 M.M.J. Treacy, T.W. Ebbesen, J.M. Gibson: Exceptionally high young's modulus observed for individual carbon nanotubes, Nature **381**, 678–680 (1996)

4.286 B.I. Yakobson, C.J. Brabec, J. Bernholc: Nanomechanics of carbon tubes: Instabilities beyond linear range, Phys. Rev. Lett. **76**, 2511–2514 (1996)

4.287 E. Hernandez, C. Goze, A. Rubio: Elastic properties of C and $B_xC_yN_z$ composite nanotubes, Phys. Rev. Lett. **80**, 4502–4505 (1998)

4.288 B.I. Yakobson, C.J. Brabec, J. Bernholc: Structural mechanics of carbon nanotubes: From continuum elasticity to atomistic fracture, J. Comput.-Aided Mater. Des. **3**, 173–182 (1996)

4.289 J. Tersoff: Empirical interatomic potential for carbon, with applications to amorphous carbon, Phys. Rev. Lett. **61**, 2879–2882 (1988)

4.290 D.W. Brenner: Empirical potential for hydrocarbons for use in simulating the chemical vapor deposition of diamond films, Phys. Rev. B **42**, 9458–9471 (1990)

4.291 J. Tersoff, R.S. Ruoff: Structural-properties of a carbon nanotube crystal, Phys. Rev. Lett. **73**, 676–679 (1994)

4.292 B.I. Yakobson: Mechanical relaxation and "intramolecular plasticity" in carbon nanotubes, Appl. Phys. Lett. **72**, 918–920 (1998)

4.293 T. Belytschko, S.P. Xiao, G.C. Schatz, R.S. Ruoff: Simulation of the fracture of nanotubes, Phys. Rev. B **65**, 235430–1–235430–8 (2002)

4.294 S. Ogata, Y. Shibutani: Ideal tensile strength and band gap of single-walled carbon nanotubes, Phys. Rev. B **68**, 165409–1–165409–4 (2003)

4.295 J. Bernholc, C. Brabec, M. Buongiorno Nardelli, A. Maiti, C.M. Roland, B.I. Yakobson: Theory of growth and mechanical properties of nanotubes, Appl. Phys. A **67**, 39–46 (1998)

4.296 T. Dumitrica, M. Hua, B.I. Yakobson: Symmetry-, time-, and temperature-dependent strength of carbon nanotubes, PNAS **103**, 6105–6109 (2006)

4.297 M. Sammalkorpi, A. Krasheninnikov, A. Kuronen, K. Nordlund, K. Kaski: Mechanical properties of carbon nanotubes with vacancies and related defects, Phys. Rev. B **70**, 245416–1–245416–8 (2004)
4.298 A.J. Stone, D.J. Wales: Theoretical-studies of icosahedral C_{60} and some related species, Chem. Phys. Lett. **128**, 501–503 (1986)
4.299 T. Dumitrica, T. Belytschko, B.I. Yakobson: Bond-breaking bifurcation states in carbon nanotube fracture, J. Chem. Phys. **118**, 9485–9488 (2003)
4.300 M. Buongiorno Nardelli, B.I. Yakobson, J. Bernholc: Brittle and ductile behavior in carbon nanotubes, Phys. Rev. Lett. **81**, 4656–4659 (1998)
4.301 M. Menon, E. Richter, K.R. Subbaswamy: Structural and vibrational properties of fullerenes and nanotubes in a nonorthogonal tight-binding scheme, J. Chem. Phys. **104**, 5875–5882 (1996)
4.302 D. Srivastava, M. Menon, K. Cho: Nanoplasticity of single-wall carbon nanotubes under uniaxial compression, Phys. Rev. Lett. **83**, 2973–2976 (1999)
4.303 J.-P. Salvetat, G.A.D. Briggs, J.-M. Bonard, R.R. Bacsa, A.J. Kulik, T. Stöckli, N.A. Burnham, L. Forró: Elastic and shear moduli of single-walled carbon nanotube, Phys. Rev. Lett. **82**(5), 944–947 (1999)
4.304 D.A. Walters, L.M. Ericson, M.J. Casavant, J. Liu, D.T. Colbert, K.A. Smith, R.E. Smalley: Elastic strain of freely suspended single-wall carbon nanotube ropes, Appl. Phys. Lett. **74**, 3803–3805 (1999)
4.305 M.-F. Yu, B.S. Files, S. Arepalli, R.S. Ruoff: Tensile loading of ropes of single wall carbon nanotubes and their mechanical properties, Phys. Rev. Lett. **84**, 5552–5555 (2000)
4.306 S.A. Chesnokov, V.A. Nalimova, A.G. Rinzler, R.E. Smalley, J.E. Fischer: Mechanical energy storage in carbon nanotube springs, Phys. Rev. Lett. **82**, 343–346 (1999)
4.307 J. Tang, L.C. Qin, T. Sasaki, M. Yudasaka, A. Matsushita, S. Iijima: Compressibility and polygonization of single-walled carbon nanotubes under hydrostatic pressure, Phys. Rev. Lett. **85**, 1887–1889 (2000)
4.308 A. Krishnan, E. Dujardin, T.W. Ebbessen, P.N. Yianilos, M.M.J. Treacy: Young's modulus of single-walled nanotubes, Phys. Rev. B **58**, 14013–14019 (1998)
4.309 M.-S. Wang, D. Golberg, Y. Bando: Tensile tests on individual single-walled carbon nanotubes: Linking nanotube strength with its defects, Adv. Mater. **22**, 4071–4075 (2010)
4.310 J.Y. Huang, S. Chen, Z.Q. Wang, K. Kempa, Y.M. Wang, S.H. Jo, G. Chen, M.S. Dresselhaus, Z.F. Ren: Superplastic carbon nanotubes, Nature **439**, 281 (2006)

5. Multi-Walled Carbon Nanotubes

Ákos Kukovecz, Gábor Kozma, Zoltán Kónya

Multi-walled carbon nanotubes (MWCNTs) are elongated cylindrical nanoobjects made of sp^2 carbon. Their diameter is 3–30 nm and they can grow several cm long, thus their aspect ratio can vary between 10 and ten million. They can be distinguished from single-walled carbon nanotubes on the basis of their multi-walled Russian-doll structure and rigidity, and from carbon nanofibers on the basis of their different wall structure, smaller outer diameter, and hollow interior. This chapter introduces MWCNT synthesis methods, discusses the chemistry and properties of multi-walled carbon nanotubes, and gives examples of their application. References to single-walled carbon nanotubes (SWNT) are kept at a minimum.

5.1 **Synthesis** 148
5.1.1 Arc Discharge 148
5.1.2 Laser Ablation 149
5.1.3 CCVD Methods 149
5.1.4 Exotic MWCNT Synthesis Methods 150
5.1.5 MWCNT Formation Mechanism – Current Understanding 151
5.1.6 Industrial Production 152
5.1.7 Quality Assessment 153

5.2 **Chemistry of MWCNTs** 153
5.2.1 Purification of Raw MWCNTs Obtained by Various Methods 154
5.2.2 MWCNT Functionalization 155

5.3 **Properties** 157
5.3.1 Mechanical Properties 159
5.3.2 Electromagnetic Properties 159
5.3.3 Thermal Properties 160
5.3.4 Spectroscopic Properties 160
5.3.5 Health and Environmental Issues 162

5.4 **Selected Applications** 163
5.4.1 MWCNT Membranes, Filtration, and Adsorption 164
5.4.2 MWCNTs in Catalysis 166
5.4.3 MWCNT Composites 167
5.4.4 Other Selected MWCNT Applications 168

References 169

Multi-walled carbon nanotubes (MWCNTs) are elongated hollow cylindrical nanoobjects made of sp^2 carbon. Their diameter is 3–30 nm and they can grow several cm long, thus their aspect ratio can vary between 10 and ten million. The wall thickness of a MWCNT is fairly constant along the axis, and therefore the inner channel is straight. This channel is not directly accessible from the outside because the ends of perfect MWCNTs are capped by half fullerene spheres; however, it can be accessed by opening the nanotube using, e.g., oxidation, milling or ion beam treatment. MWCNT-specific reviews have been written by *Forró* and *Schonenberger* [5.1], *Andrews* et al. [5.2], and more recently by *Lehman* et al. [5.3].

The credit for discovering multi-walled carbon nanotubes is given to Sumio Iijima, who in 1991 reported on carbon microtubulii found as by-products in the Krätschmer electronic arc discharge reactor used for fullerene synthesis.

Multi-walled carbon nanotubes can be distinguished clearly from single-walled and double-walled carbon nanotubes on the basis of (i) their larger diameter and (ii) their Raman spectrum. The distinction between MWCNTs and carbon nanofibers relies on the well-defined structure of carbon nanotubes: any elongated carbonaceous object with diameter below ~500 nm that does not feature a carbon nanotube structure is a carbon nanofiber (CNF). In principle, a multi-walled carbon nanotube consists of as many giant molecules as the number of its walls, and each molecule is as long as the nanotube itself. On the other hand, CNFs consist of entities (graphitic platelets) significantly smaller than

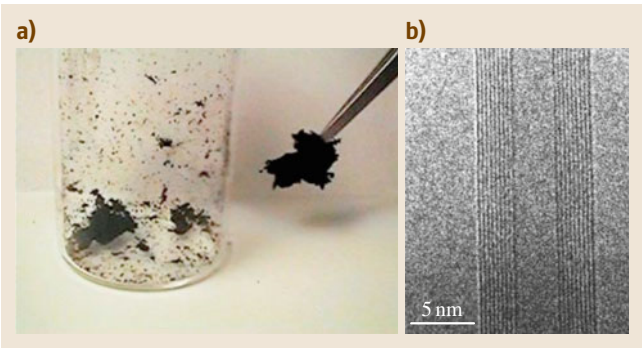


Fig. 5.1 (a) Typical appearance of as-synthesized multi-walled carbon nanotubes macroscopically and (b) in a high-resolution TEM image

the fiber itself, held together by secondary bonding forces and arranged in various ways including standing columns, herring-bone structures with and without a hollow inner channel, and even spirals.

Graphite is a three-dimensional (3-D) material consisting of several two-dimensional (2-D) layers (graphene sheets) of hexagons of sp^2 carbon atoms arranged into a hexagonal honeycomb lattice. Single-walled carbon nanotubes (SWCNTs) can be derived by rolling up a long, thin strip of hexagons cut out of a graphene sheet to make the opposite long edges meet.

Multi-walled carbon nanotubes are assemblies of several SWCNTs arranged in a coaxial Russian-doll structure, each single-walled nanotube corresponding to one wall of the MWCNT. The wall-to-wall distance is 0.340 nm, slightly larger than the sheet-to-sheet distance in graphite (0.335 nm) [5.4] (Fig. 5.1). A major difference between MWCNTs and SWCNTs is that the former are stiff, rigid, rod-like structures whereas single-walled carbon nanotubes are flexible.

5.1 Synthesis

Although the original discovery of multi-walled carbon nanotubes (MWCNTs) was recently credited [5.5] to *Radushkevich* and *Lukyanovich* [5.6] in 1952, it is without doubt that the current *carbon nanotube boom* in materials science was initiated by the 1991 paper of Iijima on *helical microtubules of graphitic carbon* [5.7] and the subsequent discovery of single-walled nanotubes (SWNTs) in 1993 independently by *Iijima* and *Ichihashi* [5.8] and *Bethune* et al. [5.9].

Multi-walled and single-walled carbon nanotubes can be prepared using the same general techniques tuned towards one or the other tube type. A broad variety of synthesis methods have been developed in the past 20 years, and now MWCNT synthesis is a well-established process that has successfully been scaled up to a commercial level. Catalytic chemical vapor deposition (CVD) is the most feasible and widespread synthesis method today; however, arc discharge and laser ablation must also be mentioned.

5.1.1 Arc Discharge

Arc discharge carbon nanotube synthesis reactors operate by igniting an electric arc (60–100 A across a potential drop of 25 V) between two graphite electrodes in a gaseous atmosphere (typically an argon/hydrogen mixture). The temperature in an electric discharge may reach as high as 4000 °C, and a plasma is formed. The electrode material evaporates and condenses as filamentous carbon product on the cathode which contains carbon nanotubes. Using this method, successful fullerene (1990) [5.10] and carbon nanotube synthesis (1991) [5.7] were performed.

Lozovik and *Popov* [5.11] divided the operation mode of electric discharge systems into a noisy and a quiet one. Continuous transition between the two modes can be simply regulated by changing the current density. It was found that high current density and low inert gas pressure results in the formation of fullerenes, while for low current density and high pressure, nanoparticles and nanotubes are predominately formed. *Ebbessen* and *Ajayan* [5.12] developed the technique to make it suitable for large-scale production. Helium is run through the reactor at a controlled rate and pressure. The anode graphite rod may contain a drilled hole filled with metal catalyst. This is necessary for arc discharge production of single-walled carbon nanotubes, but the right catalyst can promote MWCNT formation as well.

The crystallinity of arc-discharge-synthesized MWCNTs can be improved by increasing the hydrogen content of the chamber gas, or doing the synthesis in liquid nitrogen [5.13] or in a magnetic field [5.14]. The productivity of the method can be improved by optimizing the quenching process [5.15, 16] or by applying the plasma-rotating arc discharge technique [5.17].

Advantages of the arc discharge method are its simplicity and versatility in terms of carbon source material

and catalyst. Its major disadvantages are the high energy consumption, low potential for industrial up-scaling, and the necessity for postproduction purification steps. The product formed on the cathode is composed of various types of carbonaceous matter, including nanotubes, fullerenes, carbonaceous nanoparticles, and catalyst.

5.1.2 Laser Ablation

Laser ablation is the method that started the nanocarbon revolution back in the 1980s. Curl, Kroto, and Smalley used this process to synthesize fullerenes in their pioneering experiment. When a laser beam is used for evaporating a carbon target, generally containing transition metals as catalyst component, similar processes take place as in arc discharge [5.18]. In a typical laser ablation experiment, the second harmonic of a Nd:YAG laser pulse is focused onto a graphite target containing 1–2 at.% catalyst metal [5.19–21]. The target is kept in an inert gas flow, and the system is heated to 800–1400 °C by an electric furnace. The laser evaporates the target into a plasma in which carbon nanotubes are formed. The produced nanotubes are swept by the inert gas stream onto a cold finger collector and removed periodically from the reactor. Laser ablation is unsuitable for mass production. On the other hand, it yields very high-quality nanotubes, and therefore it has been the synthetic method of choice for many fundamental studies.

5.1.3 CCVD Methods

CCVD stands for *catalytic chemical vapor deposition*. Although CVD is also a valid term in general, CCVD should be preferred when discussing carbon nanotube synthesis because all CVD-based CNT production methods rely on a catalyst. In a general CCVD synthesis, a volatile carbon source (hydrocarbons, alcohols, CO, etc.) is introduced into a reactor, where it is decomposed on a suitable catalyst (transition metal) surface and its carbon content is recrystallized in carbon nanotube form. Both single-walled and multi-walled carbon nanotubes can be produced by CCVD. The mechanisms for CCVD MWCNT growth have been reviewed by *Bajwa* et al. [5.22].

CCVD can be realized in many practical designs. The catalysis can be homogeneous (carbon source and catalyst are both volatile) or heterogeneous (catalyst is supported in the solid phase). The metal catalyst can be pre-made (metallic nanoparticles deposited on the support) or can form in situ from a volatile organometallic compound such as ferrocene in a homogeneous catalytic reaction or from thin metallic films or impregnated metallic compounds in heterogeneous catalytic synthesis. Energy for the carbon source decomposition can be supplied as heat, microwaves or plasma. Thermal CCVD methods utilize either conventional heating methods such as a tube furnace or in situ heating as in hot-filament CCVD synthesis.

Advantages of the CCVD method include cost efficiency, scalability, continuous operation, and relatively low (500–800 °C) operating temperature. Combined with the ability to yield aligned nanotubes that grow in predesigned patterns only, this latter property renders CCVD a good candidate for integration with the silicon-based semiconductor industry. Notable disadvantages of the CCVD method are the lower quality (more defects in the wall structure and more carbonaceous contamination deposit) of the synthesized nanotubes and the necessity for a postsynthetic purification step in which the catalyst and/or catalyst support are removed.

The first successful experiments on the preparation of multi-walled nanotubes (MWNTs) by and *Ivanov* [5.23] were followed by hundreds of modified or new procedures. On the basis of these experiments, several fundamental principles were concluded. In most cases the syntheses are carried out at high temperature, applying a stream of carbon source diluted with inert compounds such as nitrogen, argon, etc. The experimental setup consists of a high-temperature oven in which the catalysts are placed onto a highly resistant ceramic or metal plate.

The nature and yield of the deposit obtained in the reaction are controlled by varying different parameters such as the nature of the metals and the supports, the hydrocarbon sources, the gas flows, the reaction temperature, the reaction time, etc. By selecting the proper conditions, both the physical (e.g., length, shape, diameter) and chemical properties (e.g., number of defects, graphitization) of the MWNTs can be designed in advance. For catalyst preparation, various methods are applied, such as impregnation, ion exchange, and mechanical grinding of the support and the metal components. The activity of catalyst samples prepared in different ways shows dependence on the nature of the catalyst support (silica of different pore diameter, zeolites of various structures) and on the pH of the solution used during the synthesis of the catalyst samples. Supported Co [5.24], Ni [5.25], and Fe [5.26] catalysts were found to be the most active in CVD. When other elements (e.g., Cu, Cr, Mn) are used, only a negligible amount of carbon nano-

tubes (NTs) is formed. As far as the catalyst support is concerned, its quality is of considerable importance. While Si-, Mg-, and Al-containing materials (silica, alumina, zeolites, magnesia) prove to be applicable as supports, the different forms of carbon (graphite, activated carbon) are not suitable for NT production. These results suggest that the support has a peculiar role in the reaction. The hydrocarbons most frequently used are acetylene, ethylene, and benzene because of their high carbon content. It was also shown that, generally, increasing the reaction time results in the formation of larger amounts of amorphous carbon due to deactivation of catalytic sites. Determining the optimal reaction temperature is a very complicated task since several requirements come into conflict: while high temperature favors proper graphitization, the homogeneous pyrolysis of the hydrocarbon becomes excessive above a certain temperature depending on the carbon source used. Moreover, the metals and supports demand different temperature ranges.

Nanotubes of helical shape have been produced using particular catalyst preparation methods [5.27, 28]. Silica and alumina supported Co catalysts proved to give a large amount of helical tubes in the decomposition of acetylene at 700 °C [5.29]. According to results obtained over catalysts prepared by impregnation, the quality of the tubes strongly depends on the pH of the initial solution and on the pretreatment applied during catalyst preparation. Those samples which contain acidic centers on the surface show low activity. Formation of carbon nanotubes is observed over catalysts produced from solutions of pH $\geq$7. Although catalyst activity increases in parallel with the basicity of the solution, selectivity towards helical carbon nanotubes increases suddenly when the catalyst surface has neutral character. The presence of acidic OH groups on the silica support probably hinders carbon nanotube formation and side-reactions which do not involve carbon deposition become dominant [5.30].

With further pH increase, the amount of spiral nanotubes becomes significantly higher. A possible explanation for this phenomenon is that the solubility of Co-acetate is good at low pH, and therefore particles formed on the silica surface are symmetric. Consequently, the catalytic centers are symmetric too. With increasing pH, precipitation of $Co(OH)_2$ begins, and some particles get onto the surface of the catalyst support in a solid, probably asymmetric form. Presumably, these asymmetric particles contain regions of different catalytic activity, which can help in forming carbon nanotubes of helical shape. Note that the formation of spiral carbon nanotubes was observed only in catalytic processes [5.31].

It is important to note here that, according to our current understanding of the catalyst state in carbon nanotube growth, a liquid-catalyst phase favors CNT growth whereas a solid catalyst phase hinders it [5.32]. Since a liquid surface is not asymmetric, the role that any asymmetric catalyst particle could play in spiral carbon nanotube growth is still heavily debated.

Arrays of aligned multi-walled nanotubes have been synthesized for use in flat-panel display applications. *Thess* et al. [5.18] succeeded in producing more than 70% of single-walled nanotubes by condensation of a laser-vaporized carbon–nickel–cobalt mixture at 1200 °C. In parallel, iron particles embedded in mesoporous silica were used for large-scale synthesis of aligned MWNTs [5.33]. One of the most promising methods was reported by *Ren* et al. [5.34], where aligned carbon nanotubes were grown over areas up to square centimeters on nickel-coated glass below 700 °C using a special plasma-enhanced hot-filament chemical vapor decomposition. *Dai*'s group [5.35] presented synthesis of massive arrays of length-controlled carbon nanotubes that are self-oriented on patterned porous and plain silicon substrate. The main points in this method are the use of CVD for nanotube production, the catalytic particle size control by special substrate design, and the positioning of the array by patterning. *Forró*'s group [5.36] produced patterned nanotube films using microcontact printing of pure transition-metal (Fe, Ni, Co) catalysts and their mixtures.

5.1.4 Exotic MWCNT Synthesis Methods

Besides the demonstrated methods, there are peculiar procedures applied for synthesis of MWNTs such as growth from Ni phtalocyanine deposited on a quartz plate by vacuum chemical vapor decomposition [5.37], production of carbon tubes on Ni particles using 2-methyl-1,2′-naphthyl ketone [5.38] at temperatures between 600 and 1000 °C, pyrolytic decomposition of propylene using uniform and straight channels of anodic alumina film as a template [5.39], and many others.

Carbon nanotubes are not only damaged in mechanochemical reactions – they can also be formed in such manner. *Chen* et al. milled 99.8% pure crystalline hexagonal graphite powder in a Fritsch pulverisette "0" vibration mill in 300 kPa Ar atmosphere for 150 h [5.40] at ambient temperature. The end product of the milling was a disordered nanoporous structure which did not

contain any nanotubes. However, by annealing this material in 1 cm^3/min N_2 flow for 8 h at 1400 °C, they were able to prepare multi-walled carbon nanotubes over 1 μm in length [5.41]. They explained this finding by assuming that the milled material provided nanotube nucleation sites for the growth of SWCNTs and then for MWCNTs via fast surface diffusion of carbon material along the external (0 0 2) surfaces [5.42].

Trace amounts of carbon nanotubes were identified by *Wilson* et al. in the end product of hexagonal graphite rod milled for 80 h in 2 bar Ar atmosphere and annealed for 6 h at 1400 °C in 30 cm^3/min Ar flow [5.43].

Li et al. have converted 400 mesh, 99.9% pure natural graphite powder into carbon nanotubes directly in the mill by grinding the material for 15 h in Ar atmosphere in a GN2 high-energy ball machine [5.44]. They explain their success based on the special physics of their GN2 instrument, which provides both shear stress and normal stress to the milled powders. However, their results should be treated with caution since there is some discrepancy in the paper concerning the diameter of the nanotubes. Both 80–400 nm (which is too large to be accepted as a carbon nanotube) and 10–50 nm (which is acceptable for a CNT) are reported. They do show a high-resolution transmission electron microscopy (HRTEM) image of an apparently tubular object measuring ≈ 8 nm in diameter, but even this does not provide unambiguous proof because of focusing issues. In a follow-up paper [5.45], the same authors managed to prove the successful synthesis of curled graphite layers and ropes, so in principle, unmistakable evidence for CNT formation could appear in the near future.

Highly curved carbon nanostructures (HCCNs) – potential CNT precursors – were prepared by milling homogeneous mixtures of graphite powder and soot in a shaker mill in air atmosphere [5.46]. The HCCNs were 4–10 nm in diameter and 20 nm in length. HCCNs resembling half-nanotubes 3–6 nm in diameter could also be produced by ball milling highly ordered pyrolytic graphene using tungsten carbide (WC) milling medium [5.47].

MWCNTs can be synthesized by vapor-phase growth methods characterized by the lack of substrate in the pyrolysis chamber. Metallocenes serve as the catalyst precursor, while aliphatic or aromatic hydrocarbons or metallocenes provide the necessary carbon material [5.48]. Product quality is determined by the pyrolysis temperature, gas flow rates, and concentration ratios [5.49]. The main advantage of metallocene-based pyrolytic methods is that they are relatively easy to scale up; the main disadvantage is the high metallocene cost and the inevitable inclusion of metallic nanoparticles in the produced nanotubes [5.50].

5.1.5 MWCNT Formation Mechanism – Current Understanding

We refer to a recent review by *Nessim* for a detailed account of MWCNT growth mechanism theories [5.51]. It is sufficient to say here that, at the beginning, three basic mechanisms were proposed for the growth of multishell nanotubes: shell-by-shell growth [5.24, 52], curling of graphite sheets [5.53], and simultaneous growth of all shells [5.54].

In the shell-by-shell model, each concentric shell results from carbon adsorption onto the surface of the preceding outer shell. Nevertheless, as discussed in several papers [5.55], carbon atoms and microclusters can be adsorbed onto the surface of nanoparticles only at temperature less than 200 K. This temperature is not sufficient to cleave and reform the bonds between the carbon atoms and hence to form a newer graphitic shell on the external surface. As a result, the growth mechanism for a carbon nanoparticle based on physical adsorption of carbon species onto a graphitic surface is impossible. Since shell-by-shell growth of carbon nanotubes is analogous to the case of nanoparticles, this mechanism is somewhat doubtful.

Another possibility for the shell-by-shell mechanism is that each shell starts growing from the nanotube base attached to the substrate [5.56]. Assuming this possibility, the outer shell could stop growing before reaching the nanotube tip. However, HRTEM results showed that the outer wall of the nanotubes is closed in almost every case.

Another proposed mechanism was the rolling up of large graphite sheets along the lines of sp^3 defects forming nanotubes. However, such a graphite sheet is a parallelogram [5.57] in shape with an acute angle of 30°. It is almost impossible to roll up this sheet into a nanotube with equal number of shells along the length of the nanotube. Scanning tunneling microscopy did not reveal the sheet edges [5.58], which should be found on the surface with the roll structure. Moreover, different walls of MWNTs were found to have different helicity, proving that the nanotubes cannot be formed from a single graphite sheet.

Finally, the third model, i. e., simultaneous growth of all walls, remained as the only possibility for the formation of MWNTs. However, it has to be taken into consideration that up to now there is no proper

Table 5.1 Nonexclusive list of currently operating MWCNT production capacities in the world. Capacity data were obtained from the open literature or from personal communication with the manufacturer

Company	Plant location	Capacity (t/year)
Bayer MaterialScience	Leverkusen, Germany	200
Bayer MaterialScience	Laufenburg, Germany	60
Nanocyl	Belgium	400
CNano	China	500
Arkema	Lacq, France	20
Arkema	Mont, France	400 (startup in 2011)
NanothinX	Rio Patras, Greece	1
Cheap Tubes Inc.	Brattleboro, USA	50
Arry Nano	Hong Kong, China	7
Carbon Nano Materials R&D Center	Chengdu, China	30
Carbon NT&F 21	Steinbrunn, Austria	10
NanoLab	Waltham, USA	20
C-Polymer GmbH	Tresdorf, Austria	10

explanation of the step-by-step growth mechanism of multi-walled nanotube formation.

It is postulated that the formation and growth of nanotubes are an extension of other known processes in which graphitic structures are formed over metal surfaces at temperature below 1000 °C from carbon. It is also very obvious that the shape of the graphitic carbon produced depends on the chemical properties and the physical dimensions of the metal particles. The most efficient metals were found to be Fe, Co, and Ni. The peculiar ability of the mentioned metals to form graphitic carbon layers is thought to be related to a combination of different factors. These include their catalytic activity towards the decomposition of carbon compounds, the possibility to form unstable carbides, and finally the speed of carbon diffusion in the metal particle, which must be extremely rapid. *Derbyshire* et al. showed that, over thin metal foils, carbon dissolves to form a solid solution [5.59]. After cooling, the carbon precipitates onto the surface, forming a continuous thin film of highly crystalline graphite parallel to the metal surface. The high crystallinity obtained in a very short time shows that carbon atoms are extremely mobile and able to move easily over and through the metal.

When the size of the metal is in the range of microns, instead of graphite the carbon is produced as filaments of similar diameter. *Baker* and *Harris* [5.60] proposed a general scheme for the formation of such thin graphitic carbon structures on metal surfaces. In this proposal, the metal particles are supported on a substrate and either strong or weak metal–support interaction is assumed. In the first case, the carbon fiber grows upwards from the metal particles, which remain attached to the substrate. This is the so-called *extrusion* mechanism. In the case of weak metal–support interaction, the particle is detached from the substrate and moves to the head of the fiber, labeled the *tip-growth* mechanism.

A detailed investigation has been reported on the influence of support and metals on the quality and quantity of carbon nanotubes produced by catalytic decomposition of acetylene. The authors attributed an exceptionally important role to the size and nature of the metal particles and additionally to the alloy phase generation during the reaction. In opposition to the case of single metal particles, the carbon dissolves easily in this alloy phase, which results in an increase of one order of magnitude in the nanotube yield.

5.1.6 Industrial Production

Multi-walled carbon nanotube production is neither difficult nor particularly costly with today's continuous CCVD processes, provided that the multivariate laboratory processes are scaled up adequately [5.61]. Therefore, is seems very likely that the third decade of multi-walled carbon nanotubes will be about commercial products. Global demand for nanotubes was expected to expand rapidly from a small base to more than US $200 million in 2009. Current forecasts assign a 25% annual growth rate to CNTs, with the market expected to be worth US $2 billion within 10 years.

Known major MWCNT synthesis capacities worldwide are summarized in Table 5.1. These plants all

use modified proprietary CCVD processes, but differ considerably in their chemical engineering solutions and also in the characteristics of their final product. Although reproducible product quality can be expected from each individual manufacturer, the lack of MWCNT quality standards still makes it difficult to develop any supplier-independent carbon nanotube applications.

Summarizing, global MWCNT production capacity is now over 1700 metric t/year. Comparing this with the annual production capacity of, e.g., platinum (130 metric t/year), cocaine (865 metric t/year) or gold (2300 metric t/year) makes it evident that multi-walled carbon nanotubes have certainly made it up the innovation chain from laboratory curiosity to a commercial product of their own. It is even more interesting to realize that the global polyacrylonitrile (PAN)-based carbon nanofiber production capacity was only one order of magnitude larger (25 000 metric t/year) in 2006.

5.1.7 Quality Assessment

Contemporary synthesis methods are unable to yield pure multi-walled carbon nanotubes in macroscopic amounts in the chemical sense of the word *pure*, meaning that any random sample taken from the material should have exactly the same composition, exhibit the same features, and contain the same molecules/crystals as any other sample. The major reasons behind the chemical heterogeneity of MWCNTs are:

- Differences due to the unequal chirality of the MWCNT walls
- Differences due to the varying length, diameter, and number of walls between tubes
- Differences between the crystallinity of the walls, number of defects, presence of open tube ends, and radial micro/mesopores
- Functionalization of the nanotube surface and/or inner channel
- Presence of carbonaceous contaminants (e.g., condensed polyaromatic hydrocarbons) on the walls
- Presence of amorphous carbon particles separated from the nanotubes
- Presence of catalyst support particles
- Metallic impurities (catalyst particles) either embedded into the MWCNT or deposited on the nanotube wall or deposited on the catalyst support particles
- Technological contamination resulting from, e.g., washing or functionalization steps.

The most important characterization method of MWCNTs is transmission electron microscopy (TEM). TEM sample preparation methods were reviewed by *Caplovicova* et al. [5.62], whereas TEM analysis is discussed by many authors [5.63–65]. Care must be exercised to avoid misinterpreting TEM images because of artifacts originating from the carbon films used on TEM grids [5.66]. Very nice science can be done when MWCNT modification studies are undertaken in situ in a TEM instrument [5.67–71]. Low-magnification (× 10–60k) TEM images can be used to measure nanotube length distributions and to assess the ratio of non-nanotube impurities by counting nanotubes and irregular objects (e.g., amorphous carbon or catalyst support) per unit area. Normal TEM and scanning electron microscopy (SEM) can also be used for determining tube outer diameter distributions [5.72–74]. The number of walls, the diameter of the inner channel, and the crystallinity of the walls are measured in high-resolution TEM (HRTEM) images [5.75]. The presence of noncarbonaceous impurities can be quantified by classical analytical methods, x-ray fluorescence [5.76], energy-dispersive x-ray spectroscopy combined with TEM or SEM [5.77], magnetic methods [5.78] or neutron activation analysis [5.79]. The amount of amorphous carbon debris is derived from Raman spectroscopy [5.80] or thermogravimetry [5.81, 82]. The amount of condensed aromatic contaminants stacking to the walls can be quantified by extracting these impurities from the nanotubes and performing comparative spectroscopic measurements on the solution or on the nanotubes themselves [5.83, 84].

5.2 Chemistry of MWCNTs

The chemistry of multi-walled carbon nanotubes focuses on the purification and functionalization of the material. Concepts from fullerene, SWCNT, and graphite chemistry are generally applicable to MWCNTs as well, provided that MWCNT-specific characteristics are taken into account.

5.2.1 Purification of Raw MWCNTs Obtained by Various Methods

The purification of MWCNTs has been developed in parallel with the synthesis methods [5.85]. Some recent reviews on this topic are available from *Hou* et al. [5.86] and *Matlhoko* et al. [5.87]. Summarizing, liquid-phase oxidation followed by acid leaching appears to be a good overall solution for most CVD-grown nanotubes. *Alvizo-Paez* et al. suggested an efficient soft purification procedure that is recommended for applications where keeping the nanotube structure intact is mandatory [5.88].

Removal of Catalysts and Catalyst Supports

For production of MWCNTs by catalytic decomposition of hydrocarbons, supported metal catalysts are generally used. The most frequently applied metals are Co, Fe, and Ni or their mixtures [5.89, 90]. Supported metal catalysts are prepared by impregnating the surface of an oxide-like support (such as silica, alumina or zeolites) with a solution of the given metal salts. Zeolite and silica supports can be separated from the carbon product by leaching the primary product in hydrofluoric acid (38–40%) for 48 h under vigorous stirring followed by filtration and washing [5.27,91]. The resulting wet cake contains various forms of carbons as discussed above. When alumina is the support, its extraction differs from those previously described. A sodium hydroxide solution is used instead of HF solution, since alumina can be easily dissolved in concentrated hydroxide solution. The most economical method is growth of MWCNTs on a water-soluble support, e.g., the *wash and go* method where transition metals supported on NaCl are used as CCVD catalysts [5.92].

Upon treatment of the catalyst–carbon mixture, the metal component of the catalysts is generally also transferred into the solution. If not, further treatment in diluted mineral acid solution is recommended [5.93]. It should be mentioned that metal particles encapsulated into the carbon nanotubes remain intact after this treatment. For their removal, we should first open the nanotubes, which are generally produced with closed ends. MWCNTs can be uncapped by oxidation [5.94] and by treatment in a molten LiCl–KCl eutectic [5.95].

Removal of Amorphous Carbon

There are chemical and physical methods to purify samples of carbon nanotubes containing by-product carbon material. The chemical methods generally result in products of higher purity but often modify the starting material irreversibly.

In order to remove amorphous carbon, the catalyst-free material can be either oxidized or reduced [5.96]. Reduction is generally performed in hydrogen atmosphere at elevated temperature (above 800 °C). Oxidation of carbon forming irregular structures can be performed either in gas or in liquid phase. Gas-phase oxidation occurs at 500 °C in air. In 210 min, such treatment results in carbon nanotubes of purity higher than 95%. Instead of air, oxygen or ozone can also be used. When purification is carried out in solution, use of an acidic (0.5 M sulfuric acid) $KMnO_4$ solution (0.3 M) is recommended. After 1 h of reaction at 80 °C, carbon nanotubes of 95% purity are obtained. Other liquid-phase oxidation processes rely on conc. HNO_3 treatment [5.83], H_2SO_4/HNO_3, $NH_4S_2O_8$, H_2O_2, ozone, and chlorine water [5.97,98]. Oxidative digestion procedures can be intensified by microwave treatment [5.99–101] or ultrasound. Ultrasound at 300 kHz generates less structural damage in MWCNTs than the common 20–35 kHz range [5.102]. *Wang* et al. reported on the simultaneous cutting and oxidative purification of MWCNTs in molten KNO_3 (MWCNT : $KNO_3 = 1 : 40$ by mass, 340–420 °C, 12 h) [5.103]. It is important to realize that oxidative purification procedures generate functionalized carbonaceous debris which should be removed by aqueous bases before subsequent processing steps [5.84]. Alternatively, debris gasification in CO_2 atmosphere at 525 °C can also be applied [5.104].

Methods that deliberately functionalize the nanotubes are also utilized. Bromination [5.105, 106], 1,3-dipolar cycloaddition of azomethine ylides [5.107], and even HNO_3 oxidation [5.108, 109] can be considered. Functionalization renders the MWCNTs soluble and thus facilitates their separation from contaminants. Reduction or high-temperature annealing should be used after purification to get the original MWCNT structure back.

MWCNTs can be purified in situ by a post plasma-enhanced CVD (PECVD) hydrogen plasma treatment, which removes both metallic impurities and residual carbonaceous particles [5.110]. Precisely controlled oxidation in air can burn out amorphous carbon without damaging the nanotubes [5.111]; For example, a 450 °C, 180 s treatment can be applied to purify vertically aligned MWCNT forests [5.112].

In some instances these treatments lead to uncapping of nanotubes, which are therefore ready to be filled

with gases or metals. Some chemical functionalization, such as implantation by hydroxyl, carboxyl, etc. groups, can also take place.

Centrifugal separation is generally applied for further purification of nanotubes. First, a dilute aqueous NT solution is prepared and an appropriate amount (0.1%) of an ionic surfactant such as benzalkonium chloride is sonicated in an ultrasonic bath for 4–6 h. Then, the colloidal suspension is centrifuged, first at 2000 g in order to separate large carbon particles ($d = 50–80$ nm) followed by a second step at 20 000 g in order to precipitate nanospheres with $d < 50$ nm. The result is a product with NTs of 70% purity.

Microfiltration separation is appropriate for soots containing a higher yield of NT, since the nanoparticles easily contaminate the membrane filter. Therefore, centrifugal purification is usually applied before microfiltration. First the soot is soaked in CS_2 to remove fullerenes and other soluble materials from the sample. The next step is to disperse the material in water containing 0.1% surfactant, followed by agitation in an ultrasonic bath. The suspension is then filtered on a 0.2 μm-pore-size membrane filter. The NTs are caught by the filter.

Ultimately, MWCNTs can be purified by size exclusion chromatography (SEC) as well [5.113]. In addition to the removal of catalysts and amorphous carbon, length separation can also be achieved [5.114]. Electrophoretic methods have recently been introduced to separate different MWCNTs from each other [5.115].

Opening Up of Carbon Nanotubes

The simplest method to open nanotubes is their oxidative treatment. It is well known that graphite oxidizes primarily at defects of the hexagonal lattice to create etch pits. When such defect sites are present in the wall of the nanotubes, they become the center of preferential etching. However, nanotubes have additional structural features such as high curvature and helicity, and may contain five- and seven-membered rings, which modify the initiation and also the propagation of oxidation. Particularly for MWNTs, the oxidation tends to start near the tips, providing a mechanism for opening the tubes. Oxidation proceeds layer by layer, resulting in thinner tubes. Once the tip is removed, the strain induced by the distribution of pentagons is no longer there. The concentric layers of MWNTs do not react at the same rate, since each shell has its own tip. It follows that the inner shells might persist longer than the outer ones. Therefore, different oxidation rates are assumed for oxidation of an open MWNT.

Upon treatment, carbon nanotubes are refluxed in concentrated HNO_3, H_2SO_4 or $KMnO_4$ solution, or at room temperature in superacidic HF/BF_3 solution, or even in aqueous solution of OsO_4 or OsO_4–$NaIO_4$ for 24 h until their originally capped ends open up [5.116]. Treatment in acidified $KMnO_4$ solution seems to be a somewhat better procedure. The advantage of HF/BF_3 treatment is that it is carried out at room temperature. As mentioned before, oxidative treatment of nanotubes results not only in nanotubes open at their tips, but also nanotubes that are thinner in diameter [5.117]. The extent of the thinning depends on the duration of treatment. A further consequence of oxidative treatment is partial functionalization of the tubes; i. e., the nanotubes become covered with carboxyl or hydroxyl groups at their ends. These functional groups make the NTs partially soluble. The number or concentration of the inserted carboxyl groups can be estimated by simple acid–base titration. The concentration of the surface acid groups on nanotubes opened by various oxidants is in the range of $2\times10^{20}–10\times10^{20}$ sites per gram of nanotube [5.118].

Improving Graphitization

Annealing MWCNTs at very high temperatures (up to 3000 °C) in an inert atmosphere improves their quality [5.119] by favoring the formation of graphitic structures over those of less stable carbon species, including sp^3 defect sites [5.120]. This has been explicitly demonstrated by *Kanyo* et al., who measured ethanol adsorption excess isotherms on CCVD-synthesized MWCNT surfaces annealed between 1000–1400 °C and demonstrated the conversion of the mostly hydrophilic, functionalized starting material into a hydrophobic, graphitic nanotube structure at high temperature [5.121]. Annealing at 1000 °C in NH_3 atmosphere improved the hydrogen storage capacity of MWCNTs from 0.39 wt% to 2.9 wt% at 6.89 MPa [5.122].

5.2.2 MWCNT Functionalization

Multi-walled and single-walled carbon nanotubes exhibit some very similar chemical properties; therefore, approaches discussed for SWCNTs can also be attempted for MWCNT functionalization. The most important difference is that, due to their larger outer diameter and consequently lower curvature, MWCNTs are less reactive than their single-walled counterparts.

The chemical properties of carbon nanotubes are governed by three factors:

1. The sp^2 hybridization of the carbon atoms arranged into hexagonal rings to form the nanotube walls and the distortion of these hybrid orbitals due to curvature-induced strain (quantitatively characterized by the pyramidalization angle) [5.123, 124]
2. The π orbital misalignment between adjacent carbon atom pairs [5.125, 126]
3. The presence of sp^3 defect sites in the walls.

Both the pyramidalization angle and the π orbital misalignment angle scale inversely with the tube diameter; therefore, there is a direct correlation between nanotube diameter and addition reaction affinity [5.127].

On the other hand, MWCNTs are often found to be readily transformable in chemical reactions. This is due to the fact that most MWCNTs are synthesized by CCVD methods and thus their outer surface features a high sp^3 defect concentration. These defects serve as bridgeheads for further chemical transformations and may facilitate the solubilization of MWCNTs and the preparation of homogeneous MWCNT dispersions in polymer matrices.

Functionalization reviews are available from, e.g., *Musso* et al. [5.128] and *Karousis* et al. [5.129]. The chapter by *Hauke* and *Hirsch* is particularly comprehensive about the covalent functionalization of carbon nanotubes [5.130].

Noncovalent Functionalization

MWCNTs exhibit high affinity towards long-chain organic molecules to form noncovalent adducts where the nanotube is wrapped into the chains of the partner molecule. Such adducts are relatively easy to prepare from the chemical point of view, but require careful MWCNT disentanglement and product separation techniques to provide meaningful results. Noncovalent functionalization agents tested with MWCNTs include DNA [5.131, 132], proteins [5.133], enzymes [5.134, 135], dendrimers [5.136], β-cyclodextrins [5.137, 138], porphyrins [5.139], dyes [5.140], and various polymers [5.141–152].

Water-soluble porphyrins can be used to form electron donor–acceptor nanohybrids with carbon nanotubes. The stability of radical ion pairs was better for MWCNTs (5.8 μs) than for corresponding SWCNT-based systems (0.5 μs) [5.153–155]. The attachment of surfactants is considered as noncovalent functionalization and is discussed in Sect. 5.3. Reaction partners for noncovalent MWCNT functionalization are usually prepared before the reaction. However, *Tang* and *Xu* reported on the synthesis of water-soluble MWCNT–poly(phenylacetylenes) prepared by in situ polymerization of phenylacetylene [5.156].

Covalent Functionalization

Functionalization methods developed for graphene and single-walled carbon nanotubes can be adapted for forming functional groups on MWCNT walls, which exhibit reactivities falling between these two extremes. It should be noted that MWCNTs are often covered by amorphous carbon and polycondensed aromatic hydrocarbon fragments after synthesis. Since these are more reactive than the nanotubes themselves, failure to remove these contaminants prior to functionalization can easily result in overestimation of the extent of nanotube functionalization.

Although even sonication in water can create oxygen-containing functional groups (hydroxide, carbonyl, carboxyl) on the nanotube surface [5.157], these groups are mostly formed during the oxidative purification of the MWCNTs as discussed in Sect. 5.2.1. This method can be varied extensively, starting from the simplest HNO_3 digestion up to the asymmetric end functionalization of MWCNTs which was achieved by embedding a vertically aligned MWCNT array in a protective polystyrene matrix, oxidizing their tips with water plasma, and floating the assembly on the top of a reactive solution [5.158]. Carboxylated MWCNTs can be converted to open nucleophilic chemistry routes [5.106, 159] or coupled with ionic materials such as 1-hydroxyethyl-3-hexyl imidazolium chloride [5.160, 161] or zwitterion intermediates [5.162].

Direct sidewall addition reactions reported to work on MWCNTs include epoxidation [5.163], [2 + 1] cycloaddition [5.164], Prato reaction [5.136, 165–169], [4 + 2] cycloaddition (also known as Diels–Alder reaction) [5.170–172], and Friedel–Crafts-type acylation [5.173]. Reductive alkylation under Birch conditions is also possible on MWCNTs [5.174].

Radical chemistry can be used to graft polymers onto MWCNTs [5.175]. Benzoyl peroxide is a possible carbon-centered free radical initiator that was shown to activate poly(oxyalkylene)amines [5.176]. Oxygen-centered free radicals are generated from hydrogen peroxide and can introduce OH, COOH, and quinone groups onto the nanotubes [5.177]. MWCNT–liquid crystal nanocomposites were prepared by exploiting electron transfer from lithium naphthalene radical

anion to the MWCNT surface [5.178]. Nitroxide-mediated radical polymerization of 4-vinylpyridine and sodium 4-styrenesulfonate was demonstrated to yield water-soluble, covalently bonded MWCNT–polymer adducts [5.179].

Mechanochemical Functionalization

The simplest mechanochemical CNT functionalization reactions are adduct formations in which nanotubes are mixed with potential modifiers and milled vigorously in a high-energy vibrating mill. Successful nanotube functionalization with DNA [5.180, 181] gave MWCNT–DNA complexes with a remarkable 5 mg/ml water solubility. The literature on covalent mechanochemical functionalization is somewhat underdeveloped, most probably because of the broad variety of wet chemical functionalization techniques available [5.182]. Nevertheless, the improved chemical reactivity [5.183] of strained sites in MWCNTs can be very efficiently utilized in mechanochemical reactions as well.

The general synthesis strategy is to mix CNTs with adequate functional group precursor molecules and then let the high-energy ball impacts initiate reactions between the partners. The technique was developed by *Kónya* et al., who milled MWCNTs in reactive atmospheres such as CO, Cl_2, NH_3, $COCl_2$, H_2S, and CH_3SH using a low-impact vibration mill for 100 h [5.184, 185]. The resulting material was covered with simple functional groups which can be used as bridgeheads for subsequent derivatization reactions. Further applications of this concept include the functionalization of SWCNTs with the alkyl halides trifluoromethane, trichloromethane, tetrachloroethylene, and hexafluoroprene [5.186], and the synthesis of water-soluble *nanotubols* by ball-milling SWCNTs with KOH [5.187].

Filling of MWCNTs

Opened MWCNTs can be filled using capillary forces provided that the surface tension of the filling medium is not above 200 mN/m [5.188, 189]. Successful reports on using metals [5.190–192], metal oxides [5.193–197], nitrates [5.198], and chlorides [5.199] are available in the literature. Some of these species can be reduced within the nanotube by H_2 gas flow into the corresponding metallic nanowires [5.118, 200, 201].

Nanoparticles on MWCNTs

Metallic nanoparticles and semiconducting quantum dots can both be mounted successfully on MWCNTs. To decorate MWCNTs with gold nanoparticles, carboxyl groups are first formed by oxidation. Treatment with NaOH converts these into carboxylate ions that can be alkylated with 2-bromoethanethiol to yield MWCNT-SH derivatives. Both premade and in situ-synthesized gold nanoparticles can react readily with these derivatives [5.202–204].

To anchor quantum dots to MWCNTs, *Pan* et al. first created carboxylic acid functionalities on MWCNTs and then converted the surface to an amine-decorated one by reacting the carboxyl groups with ethylenediamine [5.205]. CdSe quantum dots functionalized by mercaptoacetic acid were then reacted with the amine groups and thus anchored onto the MWCNT surface. CdTe quantum dots could also be attached to the nanotube by the same method using *para*-phenylenediamine as a linker molecule [5.206]. The direct link between the quantum dot and the nanotube quenches the CdTe photoluminescence. However, by using a poly(2-dimethylaminoethyl)methacrylate coating and subsequent quantum dot anchoring, the luminescent properties can be retained. The same strategy could also be applied for synthesis of MWCNTs decorated with magnetic Fe_3O_4 nanoparticles [5.207].

Covering MWCNTs with inorganic nanoparticles is an emerging field with huge application potential in photocatalysis and sensorics. Nanocomposites of multi-walled carbon nanotubes with hydroxyapatite [5.208], TiO_2 [5.209–211], rare-earth fluorides [5.212], SnO_2 [5.213–215], ZnO [5.216], V_2O_5 [5.217], Bi_2O_3 [5.218], WO_3 [5.219], and WS_2 [5.220] are typical examples of this material type. Although sol–gel methods make it very easy to synthesize such MWCNT–oxide mixtures, ensuring that the inorganic particles are indeed decorating the nanotubes instead of forming a separate phase is very difficult.

5.3 Properties

As-synthesized multi-walled carbon nanotubes appear as fluffy black powder with a very low apparent density between 0.03 g/cm^3 and 0.22 g/cm^3. The skeletal density of MWCNTs was measured to be 1.74 g/cm^3 in 2009 [5.221]. Today, skeletal densities of 2.1 g/cm^3 are usually reported. MWCNTs are agglomerated after synthesis and can be separated by physical methods [5.222]. Purification and functionalization in solu-

tion result in an agglomerated, dense material which is difficult to disperse again even by using high-energy ultrasonic horns. The solubility of MWCNTs is very low in all liquids, and the stacking of MWCNTs caused by the high (500 eV/μm) tube–tube van der Waals interaction energy [5.223] makes creating stable solutions a very challenging task. Actually, the term *solution* should not be used for MWCNTs at all. Rather, multi-walled carbon nanotubes form colloidal solid/liquid (S/L) dispersions in solvents, and therefore MWCNT *solutions* should be referred to as sols [5.224].

The stability of MWCNT dispersions in water can be increased by several methods including (i) shortening of the nanotubes [5.225], (ii) surface functionalization (e.g., 1.2 mg/ml MWCNT in water [5.162]), and (iii) use of surfactant molecules. Stable dispersions of untreated multi-walled carbon nanotubes feature concentrations below 0.05 mg/ml in water, whereas carboxy-functionalized MWCNTs can be dissolved up to 0.5 mg/ml. The redox pair ammonium persulfate/diethanolamine can be used to prepare MWCNT dispersions stable in water up to 4 days [5.226]. The choice of the functional group largely affects the solubility. *Shen* et al. reported that amino-functionalized MWCNTs get cross-linked through diamine connecting units to form large, insoluble aggregates, whereas carboxylic acid functionalities improve dispersibility in water [5.227]. Ester derivatives of MWCNTs are soluble in chloroform, and their solubility depends on the chain length of the attached aliphatic groups [5.228]. Surfactant molecules frequently used for improving carbon nanotube dispersibility are sodium dodecyl sulfate (SDS) [5.229, 230], sodium dodecylbenzene sulfate (SDBS) [5.231], octyl phenol ethoxylate (Triton X-100) [5.232], hexadecyltrimethylammonium bromide (CTAB) [5.233], poly(diallyldimethylammonium) chloride [5.157], and poly(methyl methacrylate) derivatives [5.234]. Inorganic compatibilization agents are also used. *Loginov* et al. reported MWCNT concentrations up to 0.5 wt% in water when using laponite [5.235]. Very high nanotube concentrations (up to 10 mg/ml) can be reached by simultaneously functionalizing the nanotube surface (e.g., acyl chloride activation) and applying a surfactant and/or wrapping agent such as a small peptide or even the simple amino acid lysine [5.236]. *Madni* et al. utilized reversible noncovalent functionalization to achieve 1 wt% MWCNT (approximately 1 mg/ml) by using a 1:1 mixture of a cationic (dodecyltrimethylammonium bromide, DTAB) and an anionic (sodium octanoate, SOCT) surfactant [5.237]. Even higher concentrations (7.4 mg/ml and 29.2 mg/ml, respectively) were reported for irreversible noncovalent functionalization of MWCNTs by using hydrolyzed poly(styrene-co-maleic anhydride) carrying pyrene (HPSMAP) [5.238] or hydrolyzed poly(styrene-co-maleic) anhydrite (HSMA) [5.239]. Nonaqueous solvents are also used for carbon nanotube dispersion [5.224]. Since surfactants are not always utilized in this case, the properties of the solvent are critical. Slightly polar organic solvents with surface tension close to 40 mJ/m^2 are known to work well. Surfactants specifically designed to facilitate dispersion of MWCNTs in nonpolar sol-solvents used in sol–gel synthesis have appeared recently in the literature; For example, the surfactant dabcosil stearate contains a stearate-based 18-carbon alkyl chain as an anion and a silsesquioxane containing a bridged, positively charged 1,4-diazoniabicyclo[2.2.2]octane group [5.240].

The specific surface area (A_S) of MWCNTs with both ends opened is determined by the number of walls N roughly as $A_S = 2360/N$ [m^2/g]. The cavity of open MWCNTs is available for adsorption governed by capillary condensation (unlike in SWCNTs, where micropore filling is dominant) [5.241]. MWCNTs with one open end have a hysteresis-free adsorption–desorption profile, in agreement with theoretical predictions [5.242]. Although this makes nanotubes good candidates for nanoscale gas cylinders, reactors [5.243] or templates [5.244–246] for other one-dimensional nanomaterials, the majority of MWCNT samples are capped at both ends. The measured specific surface area of closed MWCNTs is 190–350 m^2/g, depending on the number of walls, the purity of the sample, and the ratio of opened to closed nanotubes. *Peigney* et al. published correlation charts useful for theoretical prediction of MWCNT specific surface area [5.247]. The pore system of capped MWCNTs is characterized by adsorption in 20–40 nm aggregated pores, which are actually intertube openings between relatively loosely attached nanotubes [5.248]. In practical applications, MWCNTs behave as mesoporous materials with mesopore volume of 0.5–2.0 cm^3/g.

The x-ray diffraction profile of MWCNTs is dominated by the (002) peak (indexed on the basis of the hexagonal close-packed graphite unit cell) which probes the interwall spacing. This peak is found at $2\theta = 26°$ when measured with Cu K_α radiation and is broadened because of the finite number of walls and their curvature. The (100), (004), and (110) peaks are usually noticeable at 44°, 53°, and 78°, respectively [5.249]. X-ray diffraction (XRD) is not considered to be a major characterization technique for MWCNTs, mostly because the measured profiles

are often complicated by the signal of leftover catalyst impurities. However, the ability of XRD to measure the interlayer spacing rendered it very important for all interwall filling studies [5.250, 251], most importantly Li^+ intercalation [5.252] and H_2 storage [5.253] measurements. Moreover, advanced x-ray diffraction methods can provide information about the crystal structure of aligned MWCNT forests [5.254].

5.3.1 Mechanical Properties

In principle, the mechanical properties of MWCNTs in the axial direction are exceptional, with Young's modulus in the TPa range [5.255] and tensile strength of 60 GPa [5.256]. MWCNTs are softer in the radial direction, as indicated by a radial Young's modulus of 30 GPa [5.257] and up to 40% radial deformability [5.258]. On the basis of direct TEM observation, *Demczyk* et al. calculated the Young's modulus and tensile strength to be 0.8 TPa and 0.15 TPa, respectively [5.68]. It is important to note that (i) the cross-sectional area of MWCNT is not reduced before mechanical failure, and (ii) the outermost shell is the only load-bearing element, because of the ultralow friction between the MWCNT walls [5.259]. The friction during the cyclic telescopic motion of MWCNTs was found to be less than 1.4×10^{-15} N/atom by *Kis* et al. [5.260]. Defects decrease the strength of the individual shells but improve the load transfer between walls [5.261], therefore exhibiting a complex overall effect on the mechanical properties of MWCNTs. The locally probed Young's modulus of coiled MWCNTs is comparable to that of straight nanotubes [5.262].

The spring constant of MWCNT cantilevers can be as small as 0.001 N/m and was found to be tunable by adjusting the length of the nanotube [5.263]. Carbon nanocoils can be elongated to 42% of their original length and behave like an elastic spring with spring constant of 0.12 N/m in the low-strain region [5.264]. The fundamental resonance frequency of coiled MWCNTs ranges from 100 to 400 MHz, which can be exploited in creating resonators sensitive to mass changes in the sub-attogram range [5.265].

The low radial strength of MWCNTs makes it relatively easy to modify them by mechanical forces. The most evident macroscopic effect of ball milling is the fast increase of the apparent sample density. In a low-energy vibrational mill, the originally fluffy and thin ($\rho_{appar} = 0.07\,g/cm^3$) starting MWCNT material was transformed into a dense black powder ($\rho_{appar} = 0.38\,g/cm^3$) after ≈ 1 h of milling and kept this form until the end of the experiment [5.266]. It is generally agreed that this thickening is due to the loss of air trapped within the intertube spaces of the nanotube aggregates. Disentanglement of CNTs by ball milling is an alternative to ultrasonication and chemical treatment [5.267–269]. *Wang* et al. compared several disentanglement methods including ball milling and found that only chemical treatment can give truly separated, individual nanotubes [5.222]. *Willems* and coworkers have also confirmed that MWCNTs synthesized on MgO-supported transition-metal catalysts by chemical vapor deposition cannot be separated by ball milling [5.270]. They observed that oxidative treatment before the milling makes the nanotubes more liable to mechanical cutting and subsequent separation, and explained this finding based on the weakening of the nanotube wall structure at sites where oxygen-containing functional groups were formed.

The end morphology of milled carbon nanotubes is an important topic of its own. All reports agree that nanotubes with open tips appear during milling. However, a more detailed investigation by *Konya*'s group revealed that a considerable amount of tube ends have partially or completely collapsed openings [5.271]. Kinks are known to develop in carbon nanotubes during bending, with strain energy concentrated in the kink area [5.272, 273]. The concentration of strain energy in the kink area weakens the material strength of the nanotube and therefore is the preferred site to break.

5.3.2 Electromagnetic Properties

The electronic properties of individual MWCNTs have not yet been studied as extensively as those of single-walled nanotubes [5.274–277]. The longitudinal polarizability of MWCNTs is given by the sum of the polarizabilities of the constituent tubes. The transverse response is dominated by the outer layers [5.278]. It is generally accepted that the helicity of the outermost wall determines the properties of the MWCNTs at low bias and temperature [5.279–281]. This is why *Collins* et al. have succeeded in burning the outermost metallic walls of MWCNTs by passing a large current through the tube and ending up with semiconductor-only nanotubes [5.282, 283]. The interesting feature here is that the inner walls of MWCNTs do not necessarily feature the same helicity, and shell-to-shell interactions are nonnegligible. In fact, such interactions are thought to be responsible for the significantly lower resistance of MWCNTs with a large number of walls [5.284, 285]. The electrical current

conductivity of arc-discharge-synthesized MWCNTs is 10^4 S/m [5.12] and that of annealed CVD MWCNTs is 2×10^5 S/cm [5.286], which renders them useful for lightweight wire and cable applications (compare with 59.6×10^6 S/m for pure copper). Electrical conductivity in the longitudinal direction is an order of magnitude higher than in the transverse direction [5.287].

MWCNTs can support extremely high current densities and tolerate very high temperatures. The early measurements of *Kaneto* et al. indicated that more than 10^6 A/cm^2 can flow through an individual nanotube [5.288]. Plasma-enhanced CVD-derived MWCNTs have pushed this limit up to 10^8 A/cm^2 [5.289], and *Zettl*'s group verified that MWCNTs can maintain up to 2×10^8 A/cm^2 even at 3200 K [5.290].

The magnetic moment of MWCNTs is a controversial topic because of the lack of standardized, metal-catalyst-free nanotube samples [5.291]. On the other hand, the magnetic properties of the embedded transition-metal particles can be studied well [5.292]. *Wang* et al. recently reported on giant magnetic moment enhancement of nickel nanoparticles in MWCNTs [5.293]. The magnetoresistance [5.294,295] of MWCNTs is negative and can be described adequately by conventional weak localization theory [5.280]. Electronic states near the energy gap have an orbital magnetic moment larger than the Bohr magneton [5.296].

The ^{13}C nuclear magnetic resonance (NMR) signal of MWCNTs broadens roughly proportionally with the number of walls [5.297], which makes direct NMR observations on multi-walled carbon nanotubes difficult. On the other hand, NMR has been successfully utilized for monitoring H_2 [5.298] and Xe [5.299, 300] adsorption on MWCNTs and also for verifying functionalization reactions performed with simple functional groups such as $-NH_2$ [5.301] as well as with organic partners, e.g., octadecylamine [5.302], polyisoprene [5.303], poly(ε-caprolactone) [5.304], and [4 + 2] Diels–Alder cycloaddition reagents [5.305].

The electron paramagnetic resonance (EPR or ESR) spectrum of MWCNTs is characteristically different from that of SWCNTs because the latter exhibit a double peak linked to spin-charged separation, whereas MWCNTs have a single narrow asymmetric peak [5.306] with splitting factor of $g = 2.2529$ and peak-to-peak (pp) line width of $\Delta H(\mathrm{pp}) = 890$ G [5.307]. Actual MWCNT electron spin resonance (ESR) measurements have exhibited considerable variation in their results depending on the extent of metallic impurity removal, size distribution, and doping effects [5.308–310]. Nevertheless, ESR has been successfully used to study MWCNT synthesis [5.311], purification [5.312], and modification [5.313]. Both the g-value and the ESR line width increased after thermal annealing [5.314, 315].

5.3.3 Thermal Properties

We refer to the work of *Dresselhaus* and *Eklund* for a treatise on phonons in carbon nanotubes [5.316]. The thermal conductivity of aligned MWCNT films was found to be 15–25 W/(m K) when measured with the 3ω technique [5.317, 318]. By taking the volume filling fraction into account, this number translates to an effective average thermal conductivity of 200 W/(m K) for MWCNTs [5.287]. Recently *Gaillard* et al. reported on measuring thermal conductivities between 180 and 220 W/(m K) for MWCNT carpets by using time-resolved laser pyrometry [5.319]. Measurements performed on individual multi-walled carbon nanotubes yielded thermal conductivities around 650–830 W/(m K) for supported [5.320] and over 3000 W/(m K) for free-standing suspended [5.321] MWCNTs at room temperature, respectively. These findings were confirmed by theoretical calculations [5.322] and independent experiments [5.323]. *Chiu* et al. found phonon transport in MWCNTs to be ballistic and were able to determine the thermal conductance quantum (6×10^{-6} W/K) and the phonon mean free path (220 nm) as well [5.324]. *Yan* et al. reported that strong intertube coupling in MWCNTs could be responsible for low thermal conductivity [5.325]. The specific heat of MWCNTs was analyzed by several authors and found to be similar to that of graphite but influenced heavily by the arrangement of the nanotubes (e.g., aligned nanotubes, ropes, etc.) [5.326]. A 0.6 vol% suspension of MWCNTs in water was found to increase the thermal conductivity of water by up to 38% [5.327, 328]. In a study comparing the thermal conductivity enhancement of several nanofluids, *Hwang* et al. reported on an increase of up to 11.3% at a volume fraction of 0.01 [5.329].

5.3.4 Spectroscopic Properties

Raman spectroscopy has rapidly become a pivotal technique for studying carbon nanotubes [5.330–338], especially for SWCNTs. The Raman spectrum of MWCNTs is dominated by two peaks: the G band (E_{2g}) at 1590 cm^{-1}, which corresponds to tangential stretching C−C vibrations in the nanotube wall plane (in graphite a single peak at 1582 cm^{-1} is found), and

the D band at 1350 cm^{-1}, which originates from a double resonance process [5.339, 340] and is attributed to the presence of amorphous disordered carbon. It should be emphasized that the D band is not a good measure of nanotube wall defects; rather, its intensity is proportional to the amount of amorphous carbon in the system [5.341, 342]. Nevertheless, measuring the intensity ratio of the D and G bands is a widely accepted method of assessing the general purity of a multi-walled carbon nanotube sample [5.343]. The radial breathing mode, a distinctive feature of single-walled carbon nanotubes, is visible in double-walled carbon nanotubes but is usually not observed in MWCNTs [5.344, 345]. Micro-Raman measurements on highly crystalline hydrogen direct-current (DC) arc discharge multi-walled carbon nanotubes indicated the existence of another peak characteristic of MWCNTs at 1840 cm^{-1} [5.346], which was tentatively attributed to the presence of short carbon chains within the nanotubes [5.347, 348] or interconnecting nanotube surfaces [5.349]. The G′ peak originates from two-phonon scattering phenomena around the K point (feature at approximately 2700 cm^{-1}) and around the M point (approximately 2730 cm^{-1}) in the Brillouin zone [5.350]. Several additional peaks of very low intensity can be identified in high-quality MWCNT Raman spectra below 500 cm^{-1}. These were associated with the radial breathing modes of the thinnest inner walls.

The optical spectrum of MWCNTs from the ultraviolet (UV) to the infrared range is different from SWCNTs insofar as it does not depend on the chirality of the outermost shell, but rather, the reflectivity is determined by the topology of the bulk nanotube phase and the polarization orientation with respect to the applied field [5.351]. A model for the dielectric function developed from Maxwell's equations is available from *Garcia-Vidal* et al. [5.352]. *Kamarás* et al. provide comprehensive broadband optical characterization of various carbons including MWCNTs [5.353]. A π plasmon near 5 eV determines the optical absorption of MWCNTs. MWCNTs exhibit optical limiting properties in the visible and infrared range. *Sun* et al. reported limiting thresholds of 1, 5, and 13 J/cm^2 at 532, 700, and 1064 nm, respectively [5.354]. An interesting consequence of the MWCNT optical properties is the existence of the world's darkest material, a low-density aligned MWCNT array synthesized by Ajayan's group which has an integrated total reflectance of 0.45% [5.355]. Photoluminescence from MWCNTs was reported by *Brennan* et al. even though theoretical expectations favored nonradiative decay because of intershell coupling effects [5.356, 357]. Although later studies confirmed the possibility of photoluminescence (PL) from isolated [5.358] or thiol-functionalized standalone MWCNTs [5.359], it is far more common to dope multi-walled carbon nanotubes with quantum dots [5.360, 361] or metal complexes [5.362–364] to achieve photoluminescence. It should also be noted here that MWCNTs were shown to quench the PL effect of certain quantum dot [5.365] and polymer [5.366] composites; therefore, care must always be exercised when evaluating MWCNT photoluminescence measurements.

The infrared spectrum of MWCNTs can be measured in transmission by, e.g., mixing the nanotubes into KBr pellets or in reflection–absorption geometry using a gold mirror as sample holder. Some claimed MWCNT-specific infrared (IR) spectral features include the 1445 cm^{-1} peak [5.367], the G band (1584 cm^{-1}), and the D band (1200 cm^{-1}) [5.368]. Additional peaks associated with O−H vibrations (1600 and 3450 cm^{-1}), carboxylic groups (1725 cm^{-1}), and C−H stretching vibrations (close to 3000 cm^{-1}) are also frequently observable in the spectra, even though they correspond to defects and impurities rather than the MWCNT structure itself. The most important use of infrared spectroscopy in MWCNT research is the characterization of surface functionalization [5.369–372].

Photoelectron spectroscopy of MWCNTs revealed that their work function (4.3 eV) is lower than that of highly oriented pyrolytic graphite (4.4 eV). Surface functionalization which disrupts the π conjugation and introduces surface dipole moments can increase the work function up to 5.1 eV [5.373, 374]. x-Ray photoelectron spectroscopy is well suited for studying MWCNTs and has been used for monitoring MWCNT doping [5.375], purification [5.105], surface functionalization [5.376, 377], and nanoparticle deposition [5.378].

Broadband dielectric spectroscopy is scarcely used on pure MWCNTs. On the other hand, dielectric spectra provide excellent information about MWCNT dispersions either in solution [5.379] or in polymers [5.380]. The most important field of application here is the identification of a percolating MWCNT network [5.381, 382], which is important for, e.g., conductive nanocomposites [5.383] or electromagnetic shielding [5.384, 385].

Terahertz spectroscopy is an emerging new characterization tool today [5.386, 387]. The THz refractive index decreases and the absorption coefficient increases with increasing frequency [5.388]. Since the terahertz

spectrum is sensitive to the MWCNT morphology (number of walls, length, etc.), *Parrott* et al. were able to distinguish between two MWCNTs on the basis of their THz spectra alone [5.389].

5.3.5 Health and Environmental Issues

There have been an increasing number of scientific publications from the research community at large that address one type of nanomaterial in particular, i. e., carbon nanotubes, and seek to determine if they biologically behave like asbestos; That is, if inhaled, are carbon nanotubes likely to cause irreparable and fatal effects such as those associated with asbestos exposure [5.390]? The effects of asbestos include severe lung fibrosis or scarring and lung cancer, including cancer of the lining of the lungs or pleura called mesothelioma.

More precisely, the major biological processes associated with particle-induced lung injuries are summarized below. After toxic dust inhalation, particles can be either translocated or cleared. Particles that reach the alveolar epithelial surface can stimulate alveolar macrophages (AM) but also epithelial cells (EPITH) to release several factors attracting leukocytes such as neutrophils (NEUT) and lymphocytes (LYM) into the lung. The activated alveolar macrophages and neutrophils produce a burden of oxidants and proteases that injure the alveolar wall. Oxidants can also induce cellular and DNA damage leading to cancer. Leukocytes also release growth factors and cytokines that stimulate lung fibroblasts to proliferate, with a subsequent accumulation of extracellular matrix. The net result is an expansion of mesenchymal cells and an accumulation of connective tissue matrix which characterize lung fibrosis [5.391]. Details of these processes can be understood by knowing the potential pathways of CNTs after inhalation [5.392].

The question of the comparison between carbon nanotubes and asbestos arises for several reasons. Some varieties of carbon nanotubes are similar in shape to asbestos fibers, and like asbestos, some varieties of carbon nanotubes have been shown in laboratory studies to persist in the lungs of laboratory animals. Some animal studies have even shown effects similar to those of asbestos; For example, an in situ study on the fibrogenic activity of carbon black and single-walled carbon nanotubes revealed that only SWCNTs caused (i) interstitial fibrotic lesions in the lungs of rats, (ii) significant increases in lung platelet-derived growth factor (PDGF) messenger RNA (mRNA) levels, and (iii) formation of unique carbon bridge structures between alveolar macrophages in situ. These differences between carbon black nanoparticles and SWCNTs suggest that the fibrogenic activity of SWCNTs is due to factors that make them unique from carbon black nanoparticles, including their unique shape or the presence of contaminating metal catalysts used in the manufacturing process. Finally, carbon bridge structures that form between macrophages are likely due to the unique structural characteristics of SWCNTs.

The question of whether carbon nanotubes pose a toxicological hazard has been investigated since at least 2003 [5.393]. A challenge has been in determining whether carbon nanotube materials used in the workplace have the same characteristics as those associated with biological responses in laboratory studies. Earlier studies used materials with high levels of other forms of carbon such as carbon black and high levels of metal catalyst. *Petersen* and *Henry* recently reviewed the methodological considerations relevant for testing the ecotoxicity of carbon nanotubes [5.394].

Carbon nanotubes can vary widely in diameter, length, number of layers, and structures. They can also vary widely in surface composition, since certain carbon nanotubes may be *coated* with specific metals or other materials in order to perform specific functions. Also, they can clump together or agglomerate, which can affect their potential for settling in the lungs if inhaled, their ability to penetrate the body's membranes and consequently move from the lungs to other organs, and their interaction with cells and tissues. Such variations bring an additional degree of complexity to risk assessment analysis for carbon nanotubes.

In 2005, National Institute for Occupational Safety and Health (NIOSH) researchers showed that aspiration of single-walled carbon nanotubes in mice caused progressive fibrosis and granuloma formation [5.395]. (Fibrosis and granuloma reduce the gas-exchange area of the lung, thus making breathing difficult.) It is estimated that 1 month of exposure to carbon nanotubes at the airborne concentration of $5\,mg/m^3$ of air would yield an equivalent dose in workers to that causing fibrosis in the mouse. This $5\,mg/m^3$ concentration is sometimes reported on material safety datasheets as a manufacturer's suggested exposure limit for carbon nanotubes and is based on the permissible occupational exposure limit (PEL) for graphite, whose most commonly known use is as a powder for manufacturing pencils. However, the findings reported by NIOSH in 2005 suggest that, on the basis of the effects seen in the laboratory studies, it might not be appropriate to use the graphite PEL for carbon nanotubes. In fact, BSI British

Standards Published Document PD 6699-2, 2007 *Guide to safe handling and disposal of manufactured nanomaterials* suggests setting a benchmark exposure limit for nanoscale fibers longer than 5 μm to one-tenth of the PEL for asbestos, that is at 0.01 fibers per cubic centimeter. However, this benchmark exposure limit, described as a *pragmatic guidance level only*, was not rigorously developed and is derived *on the assumption that the hazard potential of the nanoparticle form is greater than the large particle form.*

A British study found that long (that is, longer than 20 μm) multi-walled carbon nanotubes exhibit asbestos-like response in the form of injury to the linings of the body cavity in laboratory mice, while short and tangled multi-walled carbon nanotubes do not [5.396]. A Japanese study reported that multi-walled carbon nanotubes were more potent in causing mesothelioma than asbestos in laboratory mice genetically modified to be prone to cancer [5.397].

Even though most contemporary studies focus on the adverse effects of carbon nanotubes in the respiratory tract, it is important to realize that the human toxicity of CNTs in general is also a heavily debated issue today. On the one hand, CNTs are anticipated to revolutionize nanomedicine as drug carriers or nanosurgery devices, but on the other hand, it is also possible that they represent a toxic hazard themselves. The 2010 review of *Firme* and *Bandaru* elaborates these questions in detail [5.398]. At the general cellular level the potential targets and payload effects of CNTs are summarized below.

Either receptor-mediated endocytosis or nanopenetration, which is functionalization dependent, are suggested as possible mechanisms for CNT interactions with cells. Although preliminary studies have probed the targeting capability of CNTs vis-à-vis distinct organelles, the mechanism of excretion is as yet unknown.

Unfortunately, in vitro toxicity results for CNTs studied using different cell types remain inconsistent because all studies used different nanotubes and did not compare CNT toxicity between cell types. A possible intravenous route of CNT circulation after injection is as follows:

1. Contact with flowing red blood cells and plasma, and with vascular endothelium
2. Interaction with contractile fibers of the heart wall
3. Ingestion into alveolar capillaries (lung) and travel through the arteries via the heart
4. Localization to the kidneys for excretion in urine
5. Interaction with cells of the ureter and urethra
6. Delivery close to tumor sites for CNT action (i. e., drug and gene delivery).

As CNTs move into the interstitial space of tissue, excess fluids, along with CNTs, are collected into the (7) lymphatic system and recycled back into the blood to complete the circuit. The effect of CNT interactions at (8) the blood–brain barrier is still unknown.

Interestingly, the final conclusion of Firme and Bandaru on the biomedical applicability of carbon nanotubes is actually positive. They suggest that the safety concerns regarding CNTs can be ameliorated. In this context, it is important to put the known hazards of CNTs into perspective. The average person consumes an estimated 5000 to 300 000 particles/cm^3 daily due to incidental nanoparticles from the ambient environment. The safe systemic dose of CNTs, if it can be made to conform to such numbers, would then make current toxicity reports on biological risk seem overestimated. Only through a relative comparison can one understand the dangers of functionalized CNT administration against other treatment options. If the queries raised to date can be satisfactorily answered in their favor, then use of CNTs in biomedicine may indeed be feasible. The Janus-like behavior of CNTs in human medicine was elaborated in even more detail in the 2009 review paper of *Shvedova* et al. on nanotube pulmonary toxicity versus potential medical applications [5.399].

5.4 Selected Applications

Whereas interesting and new scientific results are published continuously in all CNT application fields, these fields are not equally feasible for commercialization [5.400]; For example, single-CNT electronic devices are not even close to mass production, even though they make splendid use of the unique properties of nanotubes. On the other hand, it is very easy to synthesize large quantities of heterogeneous catalysts based on CNT supports, but it is questionable whether the usage of expensive carbon nanotubes is justified over other, cheaper alternative high-surface-area carbonaceous materials.

A possible classification of CNT applications is offered in Fig. 5.2. From the commercial point of view, pursuing goals selected from the top-right quadrant appears to be more justified than going after ones located

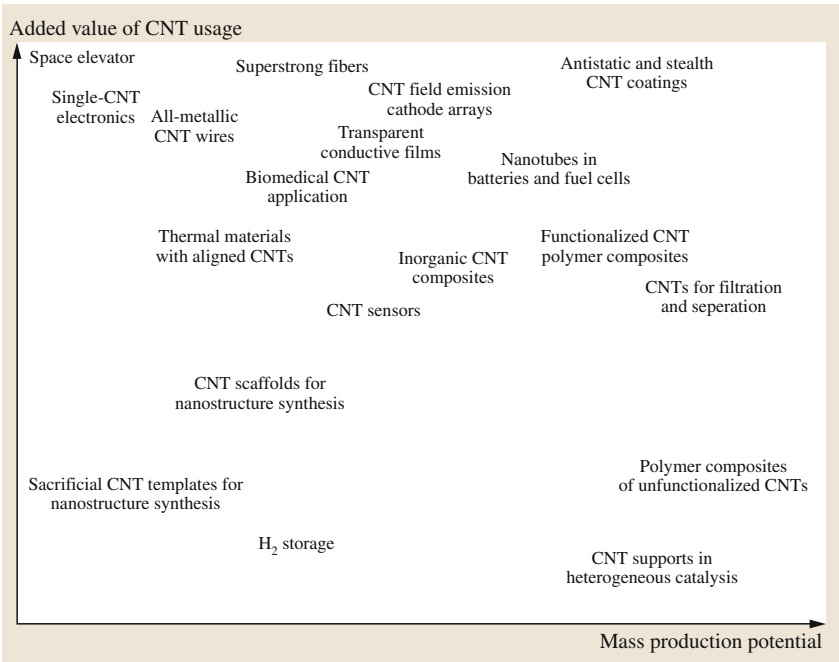


Fig. 5.2 Overview of potential carbon nanotube applications from a commercial feasibility point of view

in the bottom-left quadrant. It is impossible to give full coverage of all MWCNT applications here; therefore, only certain areas are discussed to give an overview of the field.

5.4.1 MWCNT Membranes, Filtration, and Adsorption

Their high aspect ratio as well as chemical and mechanical stability render carbon nanotubes applicable for filtering tasks. In fact, filtration may well be one of the areas where the commercial application of nanotubes is feasible. The simplest CNT filter is a layered self-supporting nanotube film made by the dead-end filtration of a CNT suspension (Fig. 5.3b). We have demonstrated that the specific cake resistance and the gas permeability of the resulting buckypaper are independent of the type of solvent for papers thicker than 150 μm [5.401]. The SEM apparent pore diameter distribution of buckypapers made from CVD-grown MWCNTs is log-normal. The mean pore diameter can be tuned between 24 and 39 nm by changing the length of the nanotubes (Fig. 5.3a) [5.73]. More complex filter architectures can be achieved by adding a second porous layer onto the buckypaper. This was realized by covering the CNT mat with Teflon using pulsed laser deposition (Fig. 5.3c). The diffusion properties of the resulting structure were governed solely by the porosity of the buckypaper [5.401]. We have measured the effective diffusivity (D_{eff}) of six common laboratory gases through MWCNT buckypaper at a pressure difference of 101 325 Pa. Results fell into the $3-12\times10^{-9}$ mol s/kg range and correlated with the kinetic diameter of the gases (Fig. 5.3g) [5.401], in agreement with previous literature results [5.402].

Filter performance can be improved by (i) cross-linking the nanotubes, (ii) controlling the filter geometry precisely or (iii) exploiting selective adsorption phenomena taking place on the nanotube surface. An and Song entangled CNTs by amide bonding and shaped the material into filter form using polydimethylsiloxane (PDMS) molding and vacuum filtering to realize a carbon-nanotube-based microdialysis chip filter [5.403]. Other synthesis alternatives leading to interlinked CNT networks include polyurea functionalization [5.404] and [2 + 1] cycloaddition [5.405].

Pursuing the second alternative for filter enhancement, we were able to construct macroscopic hollow-cylinder filters consisting of radially aligned carbon nanotubes and demonstrated their application potential by eliminating heavy hydrocarbons from petroleum and by filtering *Escherichia coli* bacteria from water [5.406]. *Chen* and *Wang* tested the nicotine and tar removal efficiency of oxidized carbon nanotube filters

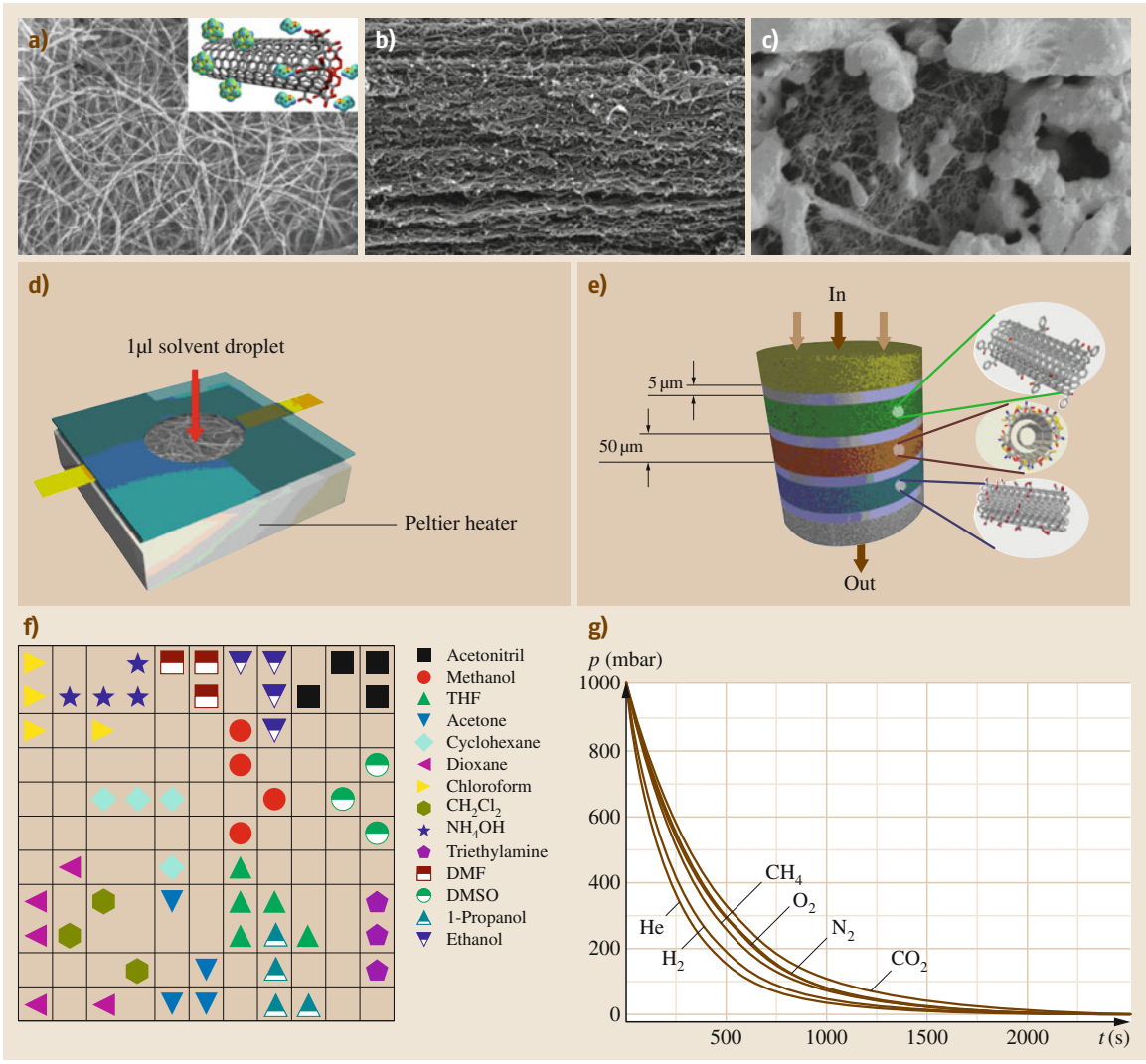


Fig. 5.3a–g Top **(a)** and side **(b)** SEM views of a MWCNT buckypaper. The *inset* in **(a)** demonstrates the selective adsorption of cyclohexane on unfunctionalized and ethanol on functionalized nanotube surfaces. **(c)** Laser-ablated porous Teflon coating on buckypaper. **(d)** Conceptual devices for measuring evaporation profiles and **(e)** multi-gas sensor response using buckypaper. **(f)** Kohonen clustering of certain organic solvents based on their evaporation profile (THF: tetrahydrofurane; DMF: dimethylformamide; DMSO: dimethyl sulfoxide) and and **(g)** gas permeability of a MWCNT buckypaper for several common laboratory gases

from mainstream cigarette smoke and suggested that 20–30 mg CNT per cigarette could be enough to remove most of the nicotine and tar [5.407]. Although the price of carbon nanotubes is dropping continuously, the cheap commercial availability of nanotube-only filters may still be well in the future. However, highly cost-effective devices can be realized by combining the superior filtering/adsorption abilities of CNTs with, e.g., proven polymer membrane technology. MWCNT-coated cellulose fiber filters exhibited filtration efficiencies exceeding 99% for airborne fine particles even at very low (0.07 mg/cm^2) nanotube coverages [5.408]. *Basheer* et al. constructed a micro solid-phase extraction device by heat-sealing 6 mg MWCNTs into a porous

polypropylene membrane sheet. The device showed superior organophosphorus pesticide enrichment performance in sewage sludge sample analysis [5.409]. The applicability of carbon nanotubes in solid-phase extraction units was confirmed for polybrominated diphenyl ethers [5.410], benzodiazepine residues [5.411], and drugs spiked in urine [5.412] as well.

MWCNTs show some promise as heavy-metal ion adsorbents. Since the sorption is heavily dependent on the nanotube functionalization, temperature, pH, ionic strength of the solution, etc., it is possible to tune MWCNT adsorbents towards selected ions. The sorption behavior of ^{243}Am [5.413], Ni^{2+} [5.407], Pb^{2+} [5.414–416], Cu^{2+} [5.415–417], Zn^{2+} [5.415, 416], and Cd^{2+} [5.416] on MWCNTs has been published so far. Moreover, MWCNTs can be combined with MnO_2 to remove Pb^{2+} and Cd^{2+} [5.418], with titanate nanotubes to remove Pb^{2+} and Cu^{2+} [5.419], and with iron/iron oxide to adsorb Ni^{2+}, Sr^{2+}, and Cu^{2+} [5.420].

There is a huge and largely untapped potential in exploiting selective adsorption phenomena taking place in the pores of buckypaper made of functionalized CNTs. Carbon nanotubes are inherently somewhat hydrophilic, with a water contact angle of less than 86° [5.421]. Moreover, the widely utilized oxidative purification method renders the nanotube surface definitely hydrophilic, as could be demonstrated by measuring adsorption excess isotherms in the cyclohexane–ethanol–nanotube system (Fig. 5.3a, *inset*) [5.121]. A truly hydrophobic CNT surface is best achieved by high-temperature annealing of a purified nanotube sample. The selectivity of the adsorption phenomenon can be enhanced by taking a step further than hydrophilic–hydrophobic balance and increasing the affinity of the nanotube membrane towards a specific molecule via covalent functionalization [5.422].

Recently, we examined the adsorption and evaporation behavior of certain liquid analytes in MWCNT membranes in detail [5.423]. We found that the electrical resistance of MWCNT buckypaper as a function of time changes in a pattern characteristic of a liquid dropped onto a heated nanotube membrane (Fig. 5.3d). The measured *evaporation profiles* of the analytes could be classified correctly by a Kohonen self-organizing map-type artificial neural network (Fig. 5.3f), therefore making qualitative identification of liquid analytes possible from sample amounts comparable to typical gas chromatography (GC) experiments. It should be noted here that carbon nanotubes were also tested successfully as conventional stationary phases of GC columns by several groups [5.424, 425]. For a complete review of CNTs in analytical science we refer to *Valcarcel* et al. [5.426].

5.4.2 MWCNTs in Catalysis

Their relatively high specific surface area (typically 100–500 m^2/g) and heat stability render carbon nanotubes a suitable support material for heterogeneous catalysis. Even though the idea itself [5.427] was suggested as early as 1994, research in this direction was sporadic because of the high cost of CNTs. We refer to the review of *Serp* et al. [5.428] for developments until 2003 and to *Georgakilas* et al. for a review of the rich chemistry of attaching metallic and semiconductor nanoparticles to carbon nanotubes, a prerequisite for granting them catalytic activity [5.204].

The fundamental issue when using CNTs as heterogeneous catalytic supports is producing a sufficiently pure nanotube sample. Some important scientific achievements of the last few years have made it possible to grow very clean nanotubes [5.429]; however, these methods have not yet matured to an industrial production level. At a commercial scale, carbon nanotubes are solely manufactured today by variations of the catalytic chemical vapor deposition method. The resulting samples are considered *clean* if their catalyst impurity (typically transition metals iron or cobalt) content is below 2 wt%, which is actually well within the metal loading range of several commercial supported catalysts used by the chemical industry. Sometimes the metal content cannot be removed even by very aggressive purification schemes [5.79]. Even though the metal contamination is usually inactivated by the covering carbonaceous layers, it is considered bad practice in heterogeneous catalysis to work with a support containing an ill-defined amount of potentially active species in ill-defined chemical condition.

It is also debatable from the application point of view whether heterogeneous catalysis is indeed a field where the high cost of using carbon nanotubes instead of other supports is justified today. Noble metals supported on CNTs certainly perform well in fuel-cell applications [5.430] because of the low charge-transfer reaction resistance of the interface and also in traditional C=C bond hydrogenation reactions [5.431]. Carbon nanotube supports are generally resistant to coke formation because of their low acidity [5.432], but this statement holds for other carbon species as well. On the other hand, Pt and/or Pd catalysts supported on CNTs do not appear to outperform the correspond-

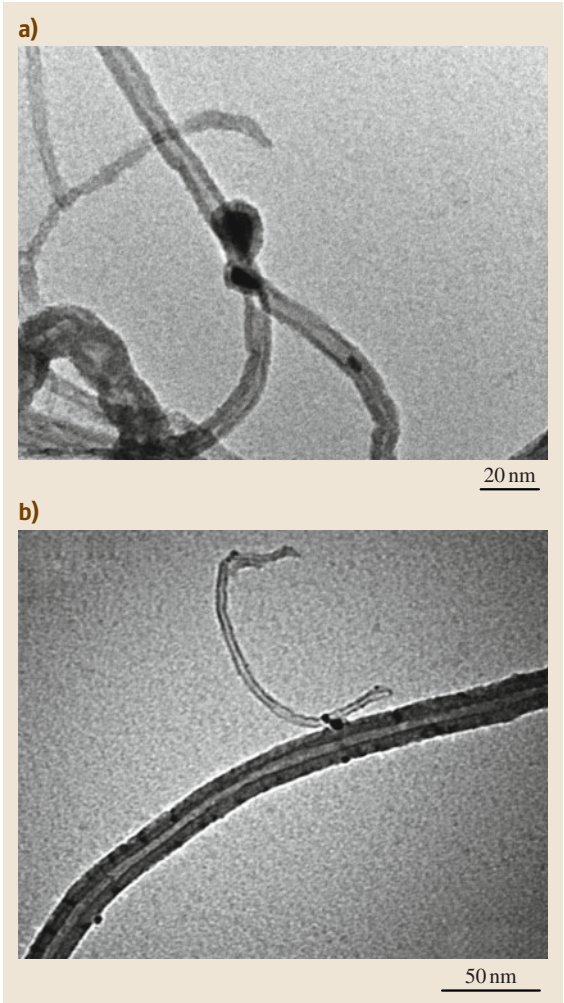


Fig. 5.4a,b TEM images of a tube-on-tube MWCNT branch synthesized by the double CCVD method developed by *Kiricsi* et al. **(a)** and **(b)** depict a typical Y branch and a typical parent-child relationship, respectively. (After [5.435])

ing carbon black or carbon microfiber supports with comparable noble-metal nanoparticle dispersions in continuous industrial hydrogenation/dehydrogenation processes [5.433]. The most promising development in this field is the recent discovery of a huge synergetic effect between Rh nanoparticles confined inside carbon nanotubes and the nanotube host itself in the conversion of CO and H_2 to ethanol [5.434].

Papers on using carbon nanotube supports for other mainstream heterogeneous catalytic processes such as reforming, hydrodesulfurization, isomerization, oxidation, and Fischer–Tropsch synthesis [5.436–438] are available but not abundant. Moreover, these reports have yet to prove that the usage of carbon nanotubes truly improves the performance of the already well-known active functions.

Carbon nanotubes have a morphological advantage over traditional porous supports such as carbon black or silica: in a CNT matrix there are no bottled pores or dead ends [5.439]. Therefore, the full surface of the nanotube forest is available for reaction, and the pressure drop on the catalyst bed can be kept very low, which in turn means that theoretically the reactor could run at very high space velocities. The catalytic community is still waiting for a breakthrough which would exploit this advantage on an industrial level.

There is one heterogeneous catalytic application, however, where the use of carbon nanotubes is a prerequisite for success, i. e., growing CNTs on a CNT support to obtain a branched nanotube network. This method was developed by us and is characteristically different from the one-step reactions tuned towards a high yield of Y-junctions [5.440]. We discovered that it is possible to impregnate chemical vapor deposition (CVD)-grown carbon nanotubes by a second transition-metal precursor molecule and repeat the CVD reaction [5.435] to get an interconnected nanotube network assembled through metal nanoparticle joints (Fig. 5.4). The diameter ratio of the parent and the child nanotube can be controlled by tuning the CVD reaction conditions.

5.4.3 MWCNT Composites

MWCNTs are extensively used and tested as polymer additives to improve mechanical properties, fire retardancy, electromagnetic shielding, thermal conductivity, etc. The majority of MWCNTs commercially produced today are purchased by polymer composite manufacturers and used in end-user products such as golf clubs, boat hulls, and structural plastics. Some of the best MWCNT composites available today do not use the MWCNTs as primary reinforcement elements; rather, the function of the nanotubes is to promote load transfer from the matrix to the reinforcement material (e.g., a Kevlar or carbon fiber textile). The following factors must be kept under rigorous control in order to create high-performance MWCNT–polymer nanocomposites:

1. Pretreatment of the nanotubes [5.441]
2. Disentanglement and homogeneous distribution of the nanotubes in the matrix [5.442]

3. Orientation of the nanotubes in the composite [5.443, 444]
4. High-quality synthesis of the polymer matrix itself, i. e., no air bubbles, correct usage of additives, etc.

It is actually quite difficult to meet all these criteria, which is probably the reason why the quality of MWCNT–polymer nanocomposites reported in the literature is very heterogeneous. Polymer nanocomposites are regularly reviewed in detail [5.445–455].

Inorganic composites of carbon nanotubes is a field where rapid expansion took place recently. This is because several widely used technological and construction materials (ceramics, semiconductors, steel) are processed under such demanding conditions that it is difficult to find a carbon-based modifier compatible with the technology. Their exceptional mechanical properties, heat stability, and low chemical reactivity render carbon nanotubes suitable candidates for such a role. Similarly to the case of CNT-reinforced polymers [5.446] and CNT-based biomaterials [5.456], the biggest challenge is interfacing the nanotubes to the inorganic matrix [5.457, 458]. MWCNT–SnO_2 composites are utilized as sensors [5.213, 214, 459, 459] and Li^+ battery anodes [5.215, 460–462], MWCNT-TiO_2 materials as photocatalysts [5.210, 463, 464], and MWCNT–ZnO as promoted catalyst [5.465], photocatalyst [5.466, 467], or sensor [5.468, 469].

We have shown that mixing MWCNTs into the precursor solution of the mesoporous silicate MCM-41 results in a composite material with tailored pore structure and controlled surface chemical properties [5.470]. It was also shown by Raman spectroscopy and x-ray photoelectron spectroscopy (XPS) that there exists a special interface region between nanotubes and SnO_x or VO_x in their sol–gel-derived composites [5.471]. A 5–10 wt% CNT loading is enough to improve the electrical conductivity of a ceramic matrix by 5–8 orders of magnitude, and it generally improves the mechanical properties of ceramics as well [5.472]. However, a lot remains to be discovered in this field; For example, adding 10 wt% MWCNTs to a borosilicate glass matrix will worsen the load-bearing but improve the wear-resistant properties of the glass [5.473].

Little attention has been devoted to nanotube–metal composites in the literature so far, even though the possibility of synthesizing such structures has been demonstrated for titanium [5.474], copper [5.475], cobalt [5.476], aluminum [5.477], magnesium [5.478], and iron [5.479]. This latter finding is especially interesting, since in a recent paper *Paufler* et al. reported on the discovery of carbon nanotubes in a 17th century Damascus steel sword [5.480]. We expect to see major advances in the applications of CNT–metal composites in the coming years.

5.4.4 Other Selected MWCNT Applications

The excellent thermal conductivity of MWCNTs can be exploited in creating nanotube heat sinks, thermal interface materials [5.481], and heat-conductive polymer nanocomposites [5.482]. MWCNT films can be used as scalable temperature sensors with temperature coefficient of resistance around $-7\times10^{-4}\,K^{-1}$ for unmodified films [5.483]. *Smajda* et al. demonstrated that the temperature sensitivity of MWCNT buckypapers can be improved by depositing pyroelectric crystals (e.g., $CsNO_3$ or $LiNbO_3$) on the nanotubes [5.484].

Vertically aligned MWCNT arrays can serve as directional adhesives mimicking the famous gecko foothair effect [5.485, 486].

MWCNTs are very well suited to serve as a basis for biosensors, because they are electrically conductive, can be functionalized, and can act as an immobilization matrix formed into diverse macroscopic shapes of controlled porosity [5.487, 488]. MWCNT-based biosensors have been created for the detection of, e.g., reduced nicotinamide adenine dinucleotide (NADH) [5.489], glucose [5.490], organophosphorus nerve agents [5.491] and pesticides [5.492], cholesterol [5.493, 494], H_2O_2 [5.495, 496], phenolics [5.497, 498], serotonin and dopamine [5.499], acetaminophen and tyramine [5.500], tetracycline [5.501], and even bacteria [5.502].

Early in the nanotube era, MWCNTs were seriously considered for pharmaceutical applications, including cell membrane channels and drug delivery systems [5.168, 503–506]. Even though such applications are technically possible, the current controversies around the human health effects of carbon nanotubes will make a MWCNT-based human drug delivery breakthrough very difficult in the near future. On the other hand, MWCNTs promote cell adhesion and proliferation (e.g., L-929 mouse fibroblast cells and C2C12 mouse myoblastic cells). Therefore, MWCNTs may play an important role in future tissue engineering and neural cell scaffolding applications, which may eventually lead to more complex bionanotechnological systems [5.507–511].

We conclude this chapter by discussing some electronic applications of MWCNTs. Due to the differences between the band structure of SWCNTs and MWCNTs

and also because of the lack of reliable bandgap engineering and separation procedures for MWCNTs, individual-tube-based device applications, which are so important for SWCNTs, are not very relevant for multi-walled carbon nanotubes. Rather, their electronic applications exploit their light weight, good conductivity, relatively low price, low growth temperature, high current tolerance, and field-emission properties. MWCNTs are therefore utilized as electric cables and interconnects [5.512–514], transparent conductive films [5.515–517], Li^+ ion battery electrodes [5.518–524], field-emission light sources [5.525, 526], inkjet-printed circuits [5.527, 528], and sensors [5.529]. A stimulating recent development is the report of a very high-performance lithium ion capacitor based on NiO-nanoparticle-containing nitrogen-doped MWCNTs that features 3500 mAh/g capacity and cycle life greater than 10 000 times [5.530].

References

5.1 L. Forro, C. Schonenberger: Physical properties of multi-wall nanotubes, Carbon Nanotubes **80**, 329–390 (2001)

5.2 R. Andrews, D. Jacques, D.L. Qian, T. Rantell: Multi-wall carbon nanotubes, synthesis and application, Acc. Chem. Res. **35**(12), 1008–1017 (2002)

5.3 J.H. Lehman, M. Terrones, E. Mansfield, K.E. Hurst, V. Meunier: Evaluating the characteristics of multiwall carbon nanotubes, Carbon **49**(8), 2581–2602 (2011)

5.4 P.M. Ajayan: Nanotubes from carbon, Chem. Rev. **99**(7), 1787–1799 (1999)

5.5 M. Monthioux, E. Flahaut, J.P. Cleuziou: Hybrid carbon nanotubes, strategy, progress, and perspectives, J. Mater. Res. **21**(11), 2774–2793 (2006)

5.6 L.V. Radushkevich, V.M. Lukyanovich: Carbon structure formed under thermal decomposition of carbon monoxid on iron, Zh. Fiz. Khim. **26**, 88–95 (1952)

5.7 S. Iijima: Helical microtubules of graphitic carbon, Nature **354**(6348), 56–58 (1991)

5.8 S. Iijima, T. Ichihashi: Single-shell carbon nanotubes of 1-nm diameter, Nature **363**(6430), 603–605 (1993)

5.9 D.S. Bethune, C.H. Kiang, M.S. Devries, G. Gorman, R. Savoy, J. Vazquez, R. Beyers: Cobalt-catalyzed growth of carbon nanotubes with single-atomic-layerwalls, Nature **363**(6430), 605–607 (1993)

5.10 W. Krätschmer, L.D. Lamb, K. Fostiropoulos, D.R. Huffman: C_{60}: A new form of carbon, Nature **347**, 354–358 (1990)

5.11 Y.E. Lozovik, A.M. Popov: Formation and growth of carbon nanostructures, fullerenes, nanoparticles, nanotubes and cones, Usp. Fiz. Nauk. **167**(7), 751–774 (1997)

5.12 T.W. Ebbesen, P.M. Ajayan: Large-scale synthesis of carbon nanotubes, Nature **358**(6383), 220–222 (1992)

5.13 S.H. Jung, M.R. Kim, S.H. Jeong, S.U. Kim, O.J. Lee, K.H. Lee, J.-H. Suh, C.-K. Park: High-yield synthesis of multi-walled carbon nanotubes by arc discharge in liquid nitrogen, Appl. Phys. A **76**(2), 285–286 (2003)

5.14 K. Anazawa, K. Shimotani, C. Manabe, H. Watanabe, M. Shimizu: High-purity carbon nanotubes synthesis method by an arc discharging in magnetic field, Appl. Phys. Lett. **81**(4), 739–741 (2002)

5.15 N. Hatta, K. Murata: Very long graphitic nanotubules synthesized by plasma-decomposition of benzene, Chem. Phys. Lett. 21, **217**(4), 398–402 (1994)

5.16 D.T. Colbert, J. Zhang, S.M. McClure, P. Nikolaev, Z. Chen, J.H. Hafner, D.W. Owens, P.G. Kotula, C.B. Carter, J.H. Weaver, A.G. Rinzler, R.E. Smalley: Growth and sintering of fullerene nanotubes, Science **266**(5188), 1218–1222 (1994)

5.17 S.J. Lee, H.K. Baik, J.E. Yoo, J.H. Han: Large scale synthesis of carbon nanotubes by plasma rotating arc discharge technique, Diam. Relat. Mater. **11**(3–6), 914–947 (2002)

5.18 A. Thess, R. Lee, P. Nikolaev, H. Dai, P. Petit, J. Robert, C. Xu, Y.H. Lee, S.G. Kim, A.G. Rinzler, D.T. Colbert, G.E. Scuseria, D. Tomanek, J.E. Fischer, R.E. Smalley: Crystalline ropes of metallic carbon nanotubes, Science **273**(5274), 483–487 (1996)

5.19 T. Guo, P. Nikolaev, A. Thess, D.T. Colbert, R.E. Smalley: Catalytic growth of single-walled nanotubes by laser vaporization, Chem. Phys. Lett. **243**(1/2), 49–54 (1995)

5.20 S. Iijima, T. Wakabayashi, Y. Achiba: Structures of carbon soot prepared by laser ablation, J. Phys. Chem. **100**(14), 5839–5843 (1996)

5.21 T. Wakabayashi, D. Kasuya, H. Shiromaru, S. Suzuki, K. Kikuchi, Y.Z. Achiba: Towards the selective formation of specific isomers of fullerenes: T- and p dependence in the yield of various isomers of C_{60}–C_{84}, Phys. D **40**, 414–417 (1997)

5.22 N. Bajwa, X.S. Li, P.M. Ajayan, R. Vajtai: Mechanisms for catalytic CVD growth of multiwalled carbon nanotubes, J. Nanosci. Nanotechnol. **8**(11), 6054–6064 (2008)

5.23 V. Ivanov, J.B. Nagy, P. Lambin, A. Lucas, X.B. Zhang, X.F. Zhang, D. Bernaerts, G. Van Tendeloo, S. Amelinckx, J. Van Landuyt: The study of carbon nanotubules produced by catalytic method, Chem. Phys. Lett. **223**(4), 329–335 (1994)

5.24 M. Endo, H.W. Kroto: Formation of carbon nanofibers, J. Phys. Chem. **96**(17), 6941–6944 (1992)

5.25 M. Yudasaka, R. Kikuchi, T. Matsui, Y. Ohki, S. Yoshimura, E. Ota: Specific conditions for Ni catalyzed carbon nanotube growth by chemical-vapor-deposition, Appl. Phys. Lett. **67**(17), 2477–2479 (1995)

5.26 K. Hernadi, A. Fonseca, J.B. Nagy, D. Bernaerts, A.A. Lucas: Fe-catalyzed carbon nanotube formation, Carbon **34**(10), 1249–1257 (1996)

5.27 K. Hernadi, A. Fonseca, P. Piedigrosso, M. Delvaux, J.B. Nagy, D. Bernaerts, D. Riga: Carbon nanotubes production over Co/silica catalysts, Catal. Lett. **48**(3–4), 229–238 (1997)

5.28 H.Q. Hou, Z. Jun, F. Weller, A. Greiner: Large-scale synthesis and characterization of helically coiled carbon nanotubes by use of $Fe(C0)_5$ as floating catalyst precursor, Chem. Mater. **15**(16), 3170–3175 (2003)

5.29 J. Liu, A.T. Harris: Synthesis of coiled carbon nanotubes on Co/Al_20_3 catalysts in a fluidised-bed, J. Nanopart. Res. **12**(2), 645–653 (2010)

5.30 D. Fejes, K. Hernadi: A review of the properties and CVD synthesis of coiled carbon nanotubes, Materials **3**(4), 2618–2642 (2010)

5.31 T. Somanathan, A. Pandurangan: Helical multi-walled carbon nanotubes (*h*-MWCNTs) synthesized by catalytic chemical vapor deposition, New Carbon Mater. **25**(3), 175–180 (2010)

5.32 A.R. Harutyunyan, T. Tokune, E. Mora: Liquid as a required catalyst phase for carbon single-walled nanotube growth, Appl. Phys. Lett. **87**(5), 051919 (2005)

5.33 W.Z. Li, S.S. Xie, L.X. Qian, B.H. Chang, B.S. Zou, W.Y. Zhou, R.A. Zhao, G. Wang: Large-scale synthesis of aligned carbon nanotubes, Science **274**(5293), 1701–1703 (1996)

5.34 Z.F. Ren, Z.P. Huang, J.W. Xu, J.H. Wang, P. Bush, M.P. Siegal, P.N. Provencio: Synthesis of large arrays of well-aligned carbon nanotubes on glass, Science **282**(5391), 1105–1107 (1998)

5.35 S.S. Fan, M.G. Chapline, N.R. Franklin, T.W. Tombler, A.M. Cassell, H.J. Dai: Self-oriented regular arrays of carbon nanotubes and their field emission properties, Science **283**(5401), 512–514 (1999)

5.36 H. Kind, J.M. Bonard, C. Emmenegger, L.O. Nilsson, K. Hernadi, E. Maillard-Schaller, L. Schlappbach, L. Forro, K. Kern: Patterned films of nanotubes using microcontact printing of catalysts, Adv. Mater. **11**(15), 1285 (1999)

5.37 M. Yudasaka, R. Kikuchi, Y. Ohki, S. Yoshimura: Nitrogen-containing carbon nanotube growth from Ni phthalocyanine by chemical vapor deposition, Carbon **35**(2), 195–201 (1997)

5.38 M. Yudasaka, R. Kikuchi, T. Matsui, Y. Ohki, E. Ota, S. Yoshimura: Graphite film formation by chemical vapor deposition on Ni coated sapphire, Carbon **34**(6), 763–767 (1996)

5.39 T. Kyotani, L.F. Tsai, A. Tomita: Preparation of ultrafine carbon tubes in nanochannels of an anodic aluminum oxide film, Chem. Mater. **8**(8), 2109–2113 (1996)

5.40 D. Chen, L. Chen, S. Liu, C.X. Ma, D.M. Chen, L.B. Wang: Microstructure and hydrogen storage property of Mg/MWNTs composites, J. Alloys Compd. **372**(1/2), 231–237 (2004)

5.41 D.M. Chen, T. Ichikawa, H. Fujii, N. Ogita, M. Udagawa, Y. Kitano, E. Tanabe: Unusual hydrogen absorption properties in graphite mechanically milled under various hydrogen pressures up to 6 MPa, J. Alloy Compd. **354**(1/2), L5–L9 (2003)

5.42 L.T. Chadderton, Y. Chen: Nanotube growth by surface diffusion, Phys. Lett. A **263**(4–6), 401–405 (1999)

5.43 D.E. Smeulders, A.S. Milev, G.S.K. Kannangara, M.A. Wilson: Rod milling and thermal annealing of graphite: Passing the equilibrium barrier, J. Mater Sci. **40**(3), 655–662 (2005)

5.44 Y. Li, X.B. Zhang, X.Y. Tao, J.M. Xu, W.Z. Huang, J.H. Luo, Z.Q. Luo, T. Li, F. Liu, Y. Bao, H.J. Geise: Mass production of high-quality multi-walled carbon nanotube bundles on a Ni/Mo/Mg0 catalyst, Carbon **43**(2), 295–301 (2005)

5.45 J.L. Li, L.J. Wang, G.Z. Bai, W. Jiang: Carbon tubes produced during high-energy ball milling process, Scr. Mater. **54**(1), 93–97 (2006)

5.46 M. Drofenik, D. Makovec, A. Košak, M. Kristl: Synthesis of carbon nanostructures with mechanical alloying. In: *Progress in Advanced Materials and Processes*, ed. by D.P. Uskokovic, S.K. Milonjic, D.J. Rakovic (Trans Tech., Zurich-Uetikon 2004) pp. 213–217

5.47 J.Y. Huang: HRTEM and EELS studies of defects structure and amorphous-like graphite induced by ball-milling, Acta Mater. **47**(6), 1801–1808 (1999)

5.48 T.M. Keller, S.B. Qadri: Ferrocenylethynylbenzenes as precursors to in situ synthesis of carbon nanotube and Fe nanoparticle compositions, Chem. Mater. **16**(6), 1091–1097 (2004)

5.49 C.N.R. Rao, A. Govindaraj, R. Sen, B.C. Satishkumar: Synthesis of multi-walled and single-walled nanotubes, aligned- nanotube bundles and nanorods by employing organometallic precursors, Mater. Res. Innov. **2**(3), 128–141 (1998)

5.50 R. Sen, A. Govindaraj, C.N.R. Rao: Carbon nanotubes by the metallocene route, Chem. Phys. Lett. **267**(3–4), 276–280 (1997)

5.51 G.D. Nessim: Properties, synthesis, and growth mechanisms of carbon nanotubes with special focus on thermal chemical vapor deposition, Nanoscale **2**(8), 1306–1323 (2010)

5.52 D. Ugarte: Morphology and structure of graphitic soot particles generated in arc-discharge C_{60} production, Chem. Phys. Lett. **198**(6), 596–602 (1992)

5.53 A.V. Eletskii, B.M. Smirnov: Fullerenes and the structure of carbon, Usp Fiz Nauk. **165**, 977–1009 (1995)

5.54 Y. Saito, T. Yoshikawa, M. Inagaki, M. Tomita, T. Hayashi: Growth and structure of graphitic tubules and polyhedral particles in arc-discharge, Chem. Phys. Lett. **204**(3–4), 277–282 (1993)

5.55 Y.E. Lozovik, A.M. Popov: Carbon spheric nanoparticles – possible formation mechanism, Phys. Lett. A **189**(1/2), 127–130 (1994)

5.56 P.M. Ajayan, T. Ichihashi, S. Iijima: Distribution of pentagons and shapes in carbon nanotubes and nanoparticles, Chem. Phys. Lett. **202**(5), 384–388 (1993)

5.57 T.W. Ebbesen, P.M. Ajayan, H. Hiura, K. Tanigaki: Purification of nanotubes, Nature **367**(6463), 519 (1994)

5.58 M.H. Ge, K. Sattler: Scanning-tunneling-microscopy of vapor-phase grown nanotubes of carbon, J. Phys. Chem. Solids **54**(12), 1871–1877 (1993)

5.59 F.J. Derbyshire, A.E.B. Presland, D.L. Trimm: Graphite formation by dissolution-precipitation of carbon in cobalt, nickel and iron, Carbon **13**(2), 111–113 (1975)

5.60 R.T.K. Baker, P.S. Harris: Formation of filamentous carbon. In: *Chemistry and Physics of Carbon*, ed. by P.L. Walker (Marcel Dekker, New York 1978) p. 83

5.61 S. Santangelo, C. Milone, M. Lanza, A. Pistone, G. Messina, G. Faggio: Scaling laws for multi-walled carbon nanotube growth by catalyzed chemical vapor deposition, J. Nanosci. Nanotechnol. **10**(2), 1286–1295 (2010)

5.62 M. Caplovicova, T. Danis, D. Buc, L. Caplovic, J. Janik, I. Bello: An alternative approach to carbon nanotube sample preparation for TEM investigation, Ultramicroscopy **107**(8), 692–697 (2007)

5.63 P. Ramesh, K. Sato, Y. Ozeki, M. Yoshikawa, N. Kishi, T. Sugai, H. Shinohara: Microscopic characterization of thin-multiwall carbon nanotubes synthesized by catalytic CVD method with mesoporous silica, Nano **1**(3), 207–212 (2006)

5.64 K. Molhave, S.B. Gudnason, A.T. Pedersen, C.H. Clausen, A. Horsewell, P. Boggild: Transmission electron microscopy study of individual carbon nanotube breakdown caused by Joule heating in air, Nano Lett. **6**(8), 1663–1668 (2006)

5.65 S.P. Sharma, S.C. Lakkad: Morphology study of carbon nanospecies grown on carbon fibers by thermal CVD technique, Surf. Coat Technol. **203**(10–11), 1329–1335 (2009)

5.66 R.F. Klie, D. Ciuparu, L. Pfefferle, Y. Zhu: Multi-walled carbon nanotubes on amorphous carbon films, Carbon **42**(10), 1953–1957 (2004)

5.67 K. Asaka, M. Karita, Y. Saito: Joining of multiwall carbon nanotubes for the end-contact configuration by applying electric current, Mater. Lett. **65**(12), 1832–1834 (2011)

5.68 B.G. Demczyk, Y.M. Wang, J. Cumings, M. Hetman, W. Han, A. Zettl, R.O. Ritchie: Direct mechanical measurement of the tensile strength and elastic modulus of multiwalled carbon nanotubes, Mater. Sci. Eng. A **334**(1/2), 173–178 (2002)

5.69 T. Kuzumaki, Y. Mitsuda: Dynamic measurement of electrical conductivity of carbon nanotubes during mechanical deformation by nanoprobe manipulation in transmission electron microscopy, Appl. Phys. Lett. **85**(7), 1250–1252 (2004)

5.70 H. Watanabe, Y. Hisada, S. Mukainakano, N. Tanaka: In situ observation of the initial growth process of carbon nanotubes by time-resolved high resolution transmission electron microscopy, J. Microscopy-Oxford **203**, 40–46 (2001)

5.71 Z. Xu, X.D. Bai, E.G. Wang: Geometrical enhancement of field emission of individual nanotubes studied by in situ transmission electron microscopy, Appl. Phys. Lett. **88**(13), 133107 (2006)

5.72 C.L. Cheung, A. Kurtz, H. Park, C.M. Lieber: Diameter-controlled synthesis of carbon nanotubes, J. Phys. Chem. B **106**(10), 2429–2433 (2002)

5.73 A. Kukovecz, R. Smajda, Z. Kónya, I. Kiricsi: Controlling the pore diameter distribution of multi-wall carbon nanotube buckypapers, Carbon **45**, 1696–1698 (2007)

5.74 J. Loos, N. Grossiord, C.E. Koning, O. Regev: On the fate of carbon nanotubes, morphological characterisations, Compos. Sci. Technol. **67**(5), 783–788 (2007)

5.75 T. Yaguchi, T. Sato, T. Kamino, Y. Taniguchi, K. Motomiya, K. Tohji, A. Kasuya: A method for characterizing carbon nanotubes, J. Electron Microsc. **50**(4), 321–324 (2001)

5.76 L.P. Biro, N.Q. Khanh, Z. Vertesy, Z.E. Horvath, Z. Osvath, A. Koos, J. Gyulai, A. Kocsonya, Z. Konya, X.B. Zhang, G. Van Tendeloo, A. Fonseca, J.B. Nagy: Catalyst traces and other impurities in chemically purified carbon nanotubes grown by CVD, Mater. Sci. Eng. C **19**(1/2), 9–13 (2002)

5.77 R.B. Mathur, S. Seth, C. Lal, R. Rao, B.P. Singh, T.L. Dhami, A.M. Rao: Co-synthesis, purification and characterization of single- and multi-walled carbon nanotubes using the electric arc method, Carbon **45**(1), 132–140 (2007)

5.78 E. Pellicer, A.B. Gonzalez-Guerrero, J. Nogues, L.M. Lechuga, E. Mendoza: Assessment of catalyst particle removal in multi-wall carbon nanotubes by highly sensitive magnetic measurements, Carbon **47**(3), 758–763 (2009)

5.79 T. Braun, H. Rausch, L.P. Biro, L. Konya, I. Kiricsi: Determination of traces of elemental impurities in single walled (SWNT) and multi walled (MWNT) pristine and purified carbon nanotubes by instrumental neutron activation analysis, J. Radioanal. Nucl. Chem. **262**(1), 31–34 (2004)

5.80 S. Osswald, M. Havel, Y. Gogotsi: Monitoring oxidation of multiwalled carbon nanotubes by Raman spectroscopy, J. Raman Spectroscopy **38**(6), 728–736 (2007)

5.81 E. Mansfield, A. Kar, S.A. Hooker: Applications of TGA in quality control of SWCNTs, Anal. Bioanal. Chem. **396**(3), 1071–1077 (2010)

5.82 R. Schönfelder, F. Avilés, A. Bachmatiuk, J.V. Cauich-Rodriguez, M. Knupfer, B. Büchner, M.H. Rümmeli: On the merits of Raman spectroscopy and ther-

mogravimetric analysis to asses carbon nanotube structural modifications, Appl. Phys. A **106**(4), 843–852 (2012)
5.83 L. Stobinski, B. Lesiak, L. Kover, J. Toth, S. Biniak, G. Trykowski, J. Judek: Multiwall carbon nanotubes purification and oxidation by nitric acid studied by the FTIR, and electron spectroscopy methods, J. Alloy Compd. **501**(1), 77–84 (2010)
5.84 R. Verdejo, S. Lamoriniere, B. Cottam, A. Bismarck, M. Shaffer: Removal of oxidation debris from multi-walled carbon nanotubes, Chem. Commun.(5), 513–515 (2007)
5.85 G.S. Duesberg, J. Muster, H.J. Byrne, S. Roth, M. Burghard: Towards processing of carbon nanotubes for technical applications, Appl. Phys. A **69**(3), 269–274 (1999)
5.86 P.X. Hou, C. Liu, H.M. Cheng: Purification of carbon nanotubes, Carbon **46**(15), 2003–2025 (2008)
5.87 L. Matlhoko, S.K. Pillai, M. Moodley, W.G. Augustyn, S.S. Ray: A comparison of purification procedures for multi-walled carbon nanotubes produced by chemical vapour deposition, J. Nanosci. Nanotechnol. **9**(9), 5431–5435 (2009)
5.88 E.R. Alvizo-Paez, J.M. Romo-Herrera, H. Terrones, M. Terrones, J. Ruiz-Garcia, J.L. Hernandez-Lopez: Soft purification of N-doped and undoped multi-wall carbon nanotubes, Nanotechnology **19**(15), 155701–01–155701–06 (2008)
5.89 A. Kukovecz, Z. Konya, N. Nagaraju, I. Willems, A. Tamasi, A. Fonseca, J.B. Nagy, I. Kiricsi: Catalytic synthesis of carbon nanotubes over Co, Fe and Ni containing conventional and sol-gel silica-aluminas, Phys. Chem. Chem. Phys. **2**(13), 3071–3076 (2000)
5.90 H. Kathyayini, N. Nagaraju, A. Fonseca, J.B. Nagy: Catalytic activity of Fe, Co and Fe/Co supported on Ca and Mg oxides, hydroxides and carbonates in the synthesis of carbon nanotubes, J. Mol. Catal. A **223**(1/2), 129–136 (2004)
5.91 K. Hernadi, A. Fonseca, J.B. Nagy, D. Bernaerts, J. Riga, A. Lucas: Catalytic synthesis and purification of carbon nanotubes, Synth. Met. **77**(1–3), 31–34 (1996)
5.92 A. Szabo, D. Mehn, Z. Konya, A. Fonseca, J.B. Nagy: "Wash and go", sodium chloride as an easily removable catalyst support for the synthesis of carbon nanotubes, PhysChemCommun. **6**, 40–41 (2003)
5.93 A. Jamrozik, M. Mazurkiewicz, A. Małolepszy, L. Stobiłski, K. Matlak, J. Korecki, K.J. Kurzydńowski, K. Burda: Mössbauer spectroscopy analysis of iron compounds in carboxylated multiwall carbon nanotubes and their ammonium salt, Physica Status Solidi A **208**(8), 1783–1786 (2011)
5.94 Q.L. Li, D.X. Yuan, B. Guan, D.M. Lin, X.F. Wang: Removal of metal catalyst in multi-walled carbon nanotubes with combination of Air and Hydrogen annealing followed by acid treatment, J. Nanosci. Nanotechnol. **8**(11), 5807–5812 (2008)
5.95 X.K. Li, G.M. Yuan, A. Brown, A. Westwood, R. Brydson, B. Rand: The removal of encapsulated catalyst particles from carbon nanotubes using molten salts, Carbon **44**(9), 1699–1705 (2006)
5.96 T.W. Ebbesen: Carbon nanotubes, Annu. Rev. Mater. Sci. **24**, 235–264 (1994)
5.97 J.M. Yuan, X.H. Chen, Z.F. Fan, X.G. Yang, Z.H. Chen: An easy method for purifying multi-walled carbon nanotubes by chlorine oxidation, Carbon **46**(9), 1266–1269 (2008)
5.98 K.A. Wepasnick, B.A. Smith, K.E. Schrote, H.K. Wilson, S.R. Diegelmann, D.H. Fairbrother: Surface and structural characterization of multi-walled carbon nanotubes following different oxidative treatments, Carbon **49**(1), 24–36 (2011)
5.99 C.M. Chen, M. Chen, F.C. Leu, S.Y. Hsu, S.C. Wang, S.C. Shi: Purification of multi-walled carbon nanotubes by microwave digestion method, Diam. Relat. Mater. **13**(4–8), 1182–1186 (2004)
5.100 F.H. Ko, C.Y. Lee, C.J. Ko, T.C. Chu: Purification of multi-walled carbon nanotubes through microwave heating of nitric acid in a closed vessel, Carbon **43**(4), 727–733 (2005)
5.101 C.M. Chen, M. Chen, Y.W. Peng, H.W. Yu, C.F. Chen: High efficiency microwave digestion purification of multi-walled carbon nanotubes synthesized by thermal chemical vapor deposition, Thin Solid Films **498**(1/2), 202–205 (2006)
5.102 G. Cravotto, D. Garella, E.C. Gaudino, F. Turci, S. Bertarione, G. Agostini, F. Cesano, D. Scarano: Rapid purification/oxidation of multi-walled carbon nanotubes under 300 kHz-ultrasound and microwave irradiation, New J. Chem. **35**(4), 915–919 (2011)
5.103 Y.H. Wang, J.H. Zhang, J.B. Zang, E.B. Ge, H. Huang: Etching and cutting of multi-walled carbon nanotubes in molten nitrate, Corrosion Sci. **53**(11), 3764–3770 (2011)
5.104 S. Delpeux, K. Szostak, E. Frackowiak, F. Beguin: An efficient two-step process for producing. opened multi-walled carbon nanotubes of high-purity, Chem. Phys. Lett. **404**(4–6), 374–378 (2005)
5.105 P.X. Hou, S. Bai, Q.H. Yang, C. Liu, H.M. Cheng: Multi-step purification of carbon nanotubes, Carbon **40**(1), 81–85 (2002)
5.106 S. Hanelt, J.F. Friedrich, G. Orts-Gil, A. Meyer-Plath: Study of Lewis acid catalyzed chemical bromination and bromoalkylation of multi-walled carbon nanotubes, Carbon **50**(3), 1373–1385 (2012)
5.107 N. Tagmatarchis, A. Zattoni, P. Reschiglian, M. Prato: Separation and purification of functionalised water-soluble multi-walled carbon nanotubes by flow field-flow fractionation, Carbon **43**(9), 1984–1989 (2005)
5.108 M. Pumera, B. Smid, K. Veltruska: Influence of nitric acid treatment of carbon nanotubes on their physico-chemical properties, J. Nanosci. Nanotechnol. **9**(4), 2671–2676 (2009)

5.109 P. Canete-Rosales, V. Ortega, A. Alvarez-Lueje, S. Bollo, M. Gonzalez, A. Anson, M.T. Martínez: Influence of size and oxidative treatments of multi-walled carbon nanotubes on their electrocatalytic properties, Electrochim. Acta. **62**, 163–171 (2012)

5.110 M. Kang, Y. Kim, H. Jeon: In-situ hydrogen and oxygen plasma purification of carbon nanotubes, J. Korean Phys. Soc. **39**(6), 1072–1075 (2001)

5.111 X.G. Sun, X.S. Zeng: An investigation on the purification of multiwall carbon nanotubes by oxidation in air, New Carbon Mater. **19**(1), 65–68 (2004)

5.112 I.Y.Y. Bu, K. Hou, D. Engstrom: Industrial compatible re-growth of vertically aligned multiwall carbon nanotubes by ultrafast pure oxygen purification process, Diam. Relat. Mater. **20**(5–6), 746–751 (2011)

5.113 G.S. Duesberg, M. Burghard, J. Muster, G. Philipp, S. Roth: Separation of carbon nanotubes by size exclusion chromatography, Chem. Commun. **7**(3), 435–436 (1998)

5.114 G.S. Duesberg, W. Blau, H.J. Byrne, J. Muster, M. Burghard, S. Roth: Chromatography of carbon nanotubes, Synth. Met. **103**(1–3), 2484–2485 (1999)

5.115 C.H. Wei, T.Y. Wei, C.H. Liang, F.C. Tai: The separation of different conducting multi-walled carbon nanotubes by AC dielectrophoresis, Diam. Relat. Mater. **18**(2–3), 332–336 (2009)

5.116 D.Y. Kim, C.M. Yang, Y.S. Park, K.K. Kim, S.Y. Jeong, J.H. Han, Y.H. Lee: Characterization of thin multi-walled carbon nanotubes synthesized by catalytic chemical vapor deposition, Chem. Phys. Lett. **413**(1–3), 135–141 (2005)

5.117 N. Yao, V. Lordi, S.X.C. Ma, E. Dujardin, A. Krishnan, M.M.J. Treacy, T.W. Ebbesen: Structure and oxidation patterns of carbon nanotubes, J. Mater. Res. **13**(9), 2432–2437 (1998)

5.118 B.C. Satishkumar, A. Govindaraj, J. Mofokeng, G.N. Subbanna, C.N.R. Rao: Novel experiments with carbon nanotubes, opening, filling, closing and functionalizing nanotubes, J. Phys. B **29**(21), 4925–4934 (1996)

5.119 J. Zhao, Y.Z. Zhang, Y.J. Su, X.L. Huang, L.M. Wei, E.S.W. Kong, Y. Zhang: Structural improvement of CVD multi-walled carbon nanotubes by a rapid annealing process, Diam. Relat. Mater. **25**, 242–248 (2012)

5.120 R. Andrews, D. Jacques, D. Qian, E.C. Dickey: Purification and structural annealing of multiwalled carbon nanotubes at graphitization temperatures, Carbon **39**(11), 1681–1687 (2001)

5.121 T. Kanyo, Z. Konya, A. Kukovecz, F. Berger, I. Dekany, I. Kiricsi: Quantitative characterization of hydrophilic-hydrophobic properties of MWNTs surfaces, Langmuir **20**(5), 1656–1661 (2004)

5.122 K.Y. Lin, J.K. Chang, C.Y. Chen, W.T. Tsai: Effects of heat treatment on materials characteristics and hydrogen storage capability of multi-wall carbon nanotubes, Diam. Relat. Mater. **18**(2–3), 553–556 (2009)

5.123 R.C. Haddon: Pi-electrons in 3 dimensions, Acc. Chem. Res. **21**(6), 243–249 (1988)

5.124 Z.F. Chen, W. Thiel, A. Hirsch: Reactivity of the convex and concave surfaces of single-walled carbon nanotubes (SWCNTs) towards addition reactions, dependence on the carbon-atom pyramidalization, ChemPhysChem. **4**(1), 93 (2003)

5.125 S. Niyogi, M.A. Hamon, H. Hu, B. Zhao, P. Bhowmik, R. Sen, M.E. Itkis, R.C. Haddon: Chemistry of single-walled carbon nanotubes, Acc. Chem. Res. **35**(12), 1105–1113 (2002)

5.126 M.A. Hamon, M.E. Itkis, S. Niyogi, T. Alvaraez, C. Kuper, M. Menon, R.C. Haddon: Effect of rehybridization on the electronic structure of single-walled carbon nanotubes, J. Am. Chem. Soc. **123**(45), 11292–11293 (2001)

5.127 G.S. Zheng, Z. Wang, S. Irle, K. Morokuma: Origin of the linear relationship between CH_2/NH/O-SWNT reaction energies and sidewall curvature: Armchair nanotubes, J. Am Chem. Soc. **128**(47), 15117–15126 (2006)

5.128 S. Musso, S. Porro, M. Vinante, L. Vanzetti, R. Ploeger, M. Giorcelli, B. Possetti, F. Trotta, C. Pederzolli, A. Tagliaferro: Modification of MWNTs obtained by thermal-CVD, Diam. Relat. Mater. **16**(4–7), 1183–1187 (2007)

5.129 N. Karousis, N. Tagmatarchis, D. Tasis: Current progress on the chemical modification of carbon nanotubes, Chem. Rev. **110**(9), 5366–5397 (2010)

5.130 F. Hauke, A. Hirsch: Covalent functionalization of carbon nanotubes. In: *Carbon Nanotubes and Related Structures*, ed. by D.M. Guldi, N. Martin (Wiley-VCH, Weinheim 2010) pp. 135–198

5.131 H. Takahashi, S. Numao, S. Bandow, S. Iijima: AFM imaging of wrapped multiwall carbon nanotube in DNA, Chem. Phys. Lett. **418**(4–6), 535–539 (2006)

5.132 V. Sanz, E. Borowiak, P. Lukanov, A.M. Galibert, E. Flahaut, H.M. Coley, S.R.P. Silva, J. McFadden: Optimising DNA binding to carbon nanotubes by non-covalent methods, Carbon **49**(5), 1775–1781 (2011)

5.133 J. Du, C. Ge, Y. Liu, R. Bai, D. Li, Y. Yang, L. Liao, C. Chen: The interaction of serum proteins with carbon nanotubes depend on the physicochemical properties of nanotubes, J. Nanosci. Nanotechnol. **11**(11), 10102–10110 (2011)

5.134 H.T. Zhao, H.X. Ju: Multilayer membranes for glucose biosensing via layer-by-layer assembly of multi-wall carbon nanotubes and glucose oxidase, Anal. Biochem. **350**(1), 138–144 (2006)

5.135 K.M. Manesh, H.T. Kim, P. Santhosh, A.I. Gopalan, K.P. Lee: A novel glucose biosensor based on immobilization of glucose oxidase into multiwall carbon nanotubes-polyelectrolyte-loaded electrospun nanofibrous membrane, Biosens. Bioelectron. **23**(6), 771–779 (2008)

5.136 A. Garcia, M.A. Herrero, S. Frein, R. Deschenaux, R. Munoz, I. Bustero, F. Toma, M. Prato: Synthesis

of dendrimer–carbon nanotube conjugates, Physica Status Solidi A **205**(6), 1402–1407 (2008)
5.137 K.S. Liu, H.G. Fu, Y. Xie, L.L. Zhang, K. Pan, W. Zhou: Assembly of beta-cyclodextrins acting as molecular bricks onto multiwall carbon nanotubes, J. Phys. Chem. C **112**(4), 951–957 (2008)
5.138 B. Leger, S. Menuel, D. Landy, J.F. Blach, E. Monflier, A. Ponchel: Noncovalent functionalization of multiwall carbon nanotubes by methylated-beta-cyclodextrins modified by a triazole group, Chem. Commun. **46**(39), 7382–7384 (2010)
5.139 E.V. Basiuk, V.A. Basiuk, P. Santiago, I. Puente-Lee: Noncovalent functionalization of carbon nanotubes with porphyrins, meso-tetraphenylporphine and its transition metal complexes, J. Nanosci. Nanotechnol. **7**(4–5), 1530–1538 (2007)
5.140 D.Y. Zheng, C.G. Hu, Y.F. Peng, W.Q. Yue, S.S. Hu: Noncovalently functionalized water-soluble multiwall-nanotubes through azocarmine B and their application in nitric oxide sensor, Electrochem. Commun. **10**(1), 90–94 (2008)
5.141 P. Petrov, F. Stassin, C. Pagnoulle, R. Jerome: Noncovalent functionalization of multi-walled carbon nanotubes by pyrene containing polymers, Chem. Commun.(23), 2904–2905 (2003)
5.142 V.A. Sinani, M.K. Gheith, A.A. Yaroslavov, A.A. Rakhnyanskaya, K. Sun, A.A. Mamedov, J.P. Wicksted, N.A. Kotov: Aqueous dispersions of single-wall and multiwall carbon nanotubes with designed amphiphilic polycations, J. Am Chem. Soc. **127**(10), 3463–3472 (2005)
5.143 A.H. Liu, I. Honma, M. Ichihara, H.S. Zhou: Poly(acrylicacid)-wrapped multi-walled carbon nanotubes composite solubilization in water, definitive spectroscopic properties, Nanotechnology **17**(12), 2845–2849 (2006)
5.144 M.N. Zhang, L. Su, L.Q. Mao: Surfactant functionalization of carbon nanotubes (CNTs) for layer-by-layer assembling of CNT multi-layer films and fabrication of gold nanoparticle/CNT nanohybrid, Carbon **44**(2), 276–283 (2006)
5.145 P.C. Ma, J.K. Kim, B.Z. Tang: Effects of silane functionalization on the properties of carbon nanotube/epoxy nanocomposites, Compos. Sci. Technol. **67**(14), 2965–2972 (2007)
5.146 Z.M. Wang, Q.C. Liu, H. Zhu, H.F. Liu, Y.M. Chen, M.S. Yang: Dispersing multi-walled carbon nanotubes with water-soluble block copolymers and their use as supports for metal nanoparticles, Carbon **45**(2), 285–292 (2007)
5.147 C.Y. Hu, H.L. Liao, F.Y. Li, J.H. Xiang, W.K. Li, S.W. Duo, M.S. Li: Noncovalent functionalization of multi-walled carbon nanotubes with siloxane polyether copolymer, Mater. Lett. **62**(17–18), 2585–2588 (2008)
5.148 L.X. Xu, Z.B. Ye, Q.Z. Cui, Z.Y. Gu: Noncovalent nonspecific functionalization and solubilization of multi-walled carbon nanotubes at high concentrations with a hyperbranched polyethylene, Macromol. Chem. Phys. **210**(24), 2194–2202 (2009)
5.149 S.S. Mahapatra, S.K. Yadav, J.W. Cho: Synthesis and characterization of multi-walled carbon nanotubes functionalized with hyperbranched poly(urea-urethane), J. Nanosci. Nanotechnol. **10**(12), 8244–8253 (2010)
5.150 Y.Y. Huang, Y.D. Zheng, W.H. Song, Y.X. Ma, J. Wu, L.Z. Fan: Poly(vinyl pyrrolidone) wrapped multi-walled carbon nanotube/poly(vinyl alcohol) composite hydrogels, Compos. Part A **42**(10), 1398–1405 (2011)
5.151 S.A. Ntim, O. Sae-Khow, F.A. Witzmann, S. Mitra: Effects of polymer wrapping and covalent functionalization on the stability of MWCNT in aqueous dispersions, J. Colloid Interface Sci. **355**(2), 383–388 (2011)
5.152 A.B. Zhang, M. Tang, J.F. Luan, J.Y. Li: Noncovalent functionalization of multi-walled carbon nanotubes with amphiphilic polymers containing pyrene pendants, Mater. Lett. **67**(1), 283–285 (2012)
5.153 C. Ehli, G.M.A. Rahman, N. Jux, D. Balbinot, D.M. Guldi, F. Paolucci, M. Melle-Franco, F. Zerbetto, S. Campidelli, M. Prato: Interactions in single wall carbon nanotubes/pyrene/porphyrin nanohybrids, J. Am Chem. Soc. **128**(34), 11222–11231 (2006)
5.154 D.M. Guldi, G.M.A. Rahman, N. Jux, D. Balbinot, U. Hartnagel, N. Tagmatarchis, M. Prato: Functional single-wall carbon nanotube nanohybrids-associating SWNTs with water-soluble enzyme model systems, J. Am Chem. Soc. **127**(27), 9830–9838 (2005)
5.155 D.M. Guldi, G.M.A. Rahman, N. Jux, D. Balbinot, N. Tagmatarchis, M. Prato: Multiwalled carbon nanotubes in donor-acceptor nanohybrids – towards long-lived electron transfer products, Chem. Commun.(15), 2038–2040 (2005)
5.156 B.Z. Tang, H.Y. Xu: Preparation, alignment, and optical properties of soluble poly(phenylacetylene)-wrapped carbon nanotubes, Macromolecules **32**(8), 2569–2576 (1999)
5.157 D.Q. Yang, J.F. Rochette, E. Sacher: Functionalization of multiwalled carbon nanotubes by mild aqueous sonication, J. Phys. Chem. B **109**(16), 7788–7794 (2005)
5.158 N. Chopra, M. Majumder, B.J. Hinds: Bifunctional carbon nanotubes by sidewall protection, Adv. Funct. Mater. **15**(5), 858–864 (2005)
5.159 D. Goldman, J.P. Lellouche: An easy method for the production of functional polypyrrole/MWCNT, and polycarbazole/MWCNT. composites using nucleophilic multi-walled carbon nanotubes, Carbon **48**(14), 4170–4177 (2010)
5.160 B. Yu, F. Zhou, G. Liu, Y. Liang, W.T.S. Huck, W.M. Liu: The electrolyte switchable solubility of multi-walled carbon nanotube/ionic liquid (MWCNT/IL) hybrids, Chem. Commun.(22), 2356–2358 (2006)

5.161 M.J. Park, J.K. Lee, B.S. Lee, Y.W. Lee, I.S. Choi, S.G. Lee: Covalent modification of multiwalled carbon nanotubes with imidazolium-based ionic liquids, effect of anions on solubility, Chem. Mater. **18**(6), 1546–1551 (2006)

5.162 W. Zhang, J.K. Sprafke, M.L. Ma, E.Y. Tsui, S.A. Sydlik, G.C. Rutledge, T.M. Swager: Modular functionalization of carbon nanotubes and fullerenes, J. Am. Chem. Soc. **131**(24), 8446–8454 (2009)

5.163 Q.F. Cheng, B. Wang, C. Zhang, Z.Y. Liang: Functionalized carbon-nanotube sheet/bismaleimide nanocomposites, mechanical and electrical performance beyond carbon-fiber composites, Small **6**(6), 763–767 (2010)

5.164 M.J. Moghaddam, S. Taylor, M. Gao, S.M. Huang, L.M. Dai, M.J. McCall: Highly efficient binding of DNA on the sidewalls and tips of carbon nanotubes using photochemistry, Nano Lett. **4**(1), 89–93 (2004)

5.165 F.G. Brunetti, M.A. Herrero, J.D.M. Munoz, S. Giordani, A. Diaz-Ortiz, S. Filippone, G. Ruaro, M. Meneghetti, M. Prato, E. Vázquez: Reversible microwave-assisted cycloaddition of aziridines to carbon nanotubes, J. Am. Chem. Soc. **129**(47), 14580–14581 (2007)

5.166 V. Georoakilas, A.B. Bourlinos, R. Zboril, C. Trapalis: Synthesis, characterization and aspects of superhydrophobic functionalized carbon nanotubes, Chem. Mater. **20**(9), 2884–2886 (2008)

5.167 J.X. Li, H. Grennberg: Microwave-assisted covalent sidewall functionalization of multiwalled carbon nanotubes, Chemistry **12**(14), 3869–3875 (2006)

5.168 G. Pastorin, W. Wu, S. Wieckowski, J.P. Briand, K. Kostarelos, M. Prato, M. Prato, A. Bianco: Double functionalisation of carbon nanotubes for multimodal drug delivery, Chem. Commun.(11), 1182–1184 (2006)

5.169 M. Prato, K. Kostarelos, A. Bianco: Functionalized carbon nanotubes in drug design and discovery, Acc. Chem. Res. **41**(1), 60–68 (2008)

5.170 A. Gergely, J. Telegdi, E. Meszaros, Z. Paszti, G. Tarkanyi, F.H. Kármán, E. Kálmán: Modification of multi-walled carbon nanotubes by Diels–Alder and Sandmeyer reactions, J. Nanosci. Nanotechnol. **7**(8), 2795–2807 (2007)

5.171 H. Hayden, Y.K. Gun'ko, T.S. Perova: Chemical modification of multi-walled carbon nanotubes using a tetrazine derivative, Chem. Phys. Lett. **435**(1–3), 84–89 (2007)

5.172 G. Sakellariou, H. Ji, J.W. Mays, N. Hadjichristidis, D. Baskaran: Controlled covalent functionalization of multiwalled carbon nanotubes using [4+2] cycloaddition of benzocyclobutenes, Chem. Mater. **19**(26), 6370–6372 (2007)

5.173 H.J. Lee, S.W. Han, Y.D. Kwon, L.S. Tan, J.B. Baek: Functionalization of multi-walled carbon nanotubes with various 4-substituted benzoic acids in mild polyphosphoric acid/phosphorous pentoxide, Carbon **46**(14), 1850–1859 (2008)

5.174 J.J. Stephenson, A.K. Sadana, A.L. Higginbotham, J.M. Tour: Highly functionalized and soluble multiwalled carbon nanotubes by reductive alkylation and arylation: The Billups reaction, Chem. Mater. **18**(19), 4658–4661 (2006)

5.175 S.B. Oh, H.L. Kim, J.H. Chang, Y.W. Lee, J.H. Han, S.S. An, S.W. Joo, H.K. Kim, I.S. Choi, H.J. Paik: Facile covalent attachment of well-defined poly(*t*-butyl acrylate) on carbon nanotubes via radical addition reaction, J. Nanosci. Nanotechnol. **8**(9), 4598–4602 (2008)

5.176 S.H. Liao, C.Y. Yen, C.H. Hung, C.C. Weng, M.C. Tsai, Y.F. Lin, C.-C.M. Ma, S.J. Lee: One-step functionalization of carbon nanotubes by free-radical modification for the preparation of nanocomposite bipolar plates in polymer electrolyte membrane fuel cells, J. Mater. Chem. **18**(33), 3993–4002 (2008)

5.177 W. Li, Y. Bai, Y.K. Zhang, M.L. Sun, R.M. Cheng, X.C. Xu, Y.W. Chen, Y.J. Mo: Effect of hydroxyl radical on the structure of multi-walled carbon nanotubes, Synth. Met. **155**(3), 509–515 (2005)

5.178 X.H. Chen, X.L. Wu, J.G. Zou, J.P. Wan: A convenient route to modified multiwall carbon nanotubes with liquid crystal molecules via covalent functionalization, J. Appl. Polym. Sci. **124**(4), 3399–3406 (2012)

5.179 X.D. Zhao, W.R. Lin, N.H. Song, X.F. Chen, X.H. Fan, Q.F. Zhou: Water soluble multi-walled carbon nanotubes prepared via nitroxide-mediated radical polymerization, J. Mater. Chem. **16**(47), 4619–4625 (2006)

5.180 D. Nepal, S. Samal, K.E. Geckeler: The first fullerene-terminated soluble poly(azomethine) rotaxane, Macromolecules **36**, 3800–3802 (2003)

5.181 D. Nepal, J.I. Sohn, W.K. Aicher, S. Lee, K.E. Geckeler: Supramolecular conjugates of carbon nanotubes and DNA by a solid-state reaction, Biomacromolecules **6**(6), 2919–2922 (2005)

5.182 D. Tasis, N. Tagmatarchis, A. Bianco, M. Prato: Chemistry of carbon nanotubes, Chem. Rev. **106**(3), 1105–1136 (2006)

5.183 K.D. Ausman, H.W. Rohrs, M.F. Yu, R.S. Ruoff: Nanostressing and mechanochemistry, Nanotechnology **10**(3), 258–262 (1999)

5.184 Z. Kónya, I. Vesselenyi, K. Niesz, A. Kukovecz, A. Demortier, A. Fonseca, J. Delhalle, Z. Mekhalif, J.B. Nagy, A.A. Koós, Z. Osváth, A. Kocsonya, L.P. Biró, I. Kiricsi: Large scale production of short functionalized carbon nanotubes, Chem. Phys. Lett. **360**(5–6), 429–435 (2002)

5.185 K. Niesz, I. Vesselenyi, D. Mehn, Z. Konya, I. Kiricsi: Carbon nanotubes – on the eve of success?. In: *Materials Science, Testing and Informatics* (Trans Tech, Zurich-Uetikon 2005) pp. 141–146

5.186 R. Barthos, D. Mehn, A. Demortier, N. Pierard, Y. Morciaux, G. Demortier, A. Fonseca, J.B. Nagy: Functionalization of single-walled carbon nanotubes by using alkyl-halides, Carbon **43**(2), 321–325 (2005)

5.187 H.L. Pan, L.Q. Liu, Z.X. Guo, L.M. Dai, F.S. Zhang, D.B. Zhu: Carbon nanotubols from mechanochemical reaction, Nano Lett. **3**(1), 29–32 (2003)
5.188 E. Dujardin, T.W. Ebbesen, H. Hiura, K. Tanigaki: Capillarity and wetting of carbon nanotubes, Science **265**(5180), 1850–1852 (1994)
5.189 T.W. Ebbesen: Wetting, filling and decorating carbon nanotubes, J. Phys. Chem. Solids **57**(6–8), 951–955 (1996)
5.190 P.M. Ajayan, S. Iijima: Capillarity-induced filling of carbon nanotubes, Nature **361**(6410), 333–334 (1993)
5.191 A. Chu, J. Cook, R.J.R. Heesom, J.L. Hutchison, M.L.H. Green, J. Sloan: Filling of carbon nanotubes with silver, gold, and gold chloride, Chem. Mater. **8**(12), 2751–2754 (1996)
5.192 Y.K. Chen, A. Chu, J. Cook, M.L.H. Green, P.J.F. Harris, R. Heesom, M. Humphries, J. Sloan, S.C. Tsang, J.F.C. Turner: Synthesis of carbon nanotubes containing metal oxides and metals of the d-block and f-block transition metals and related studies, J. Mater. Chem. **7**(3), 545–549 (1997)
5.193 S.C. Tsang, P.J.F. Harris, M.L.H. Green: Thinning and opening of carbon nanotubes by oxidation using carbon-dioxide, Nature **362**(6420), 520–522 (1993)
5.194 P.M. Ajayan, O. Stephan, P. Redlich, C. Colliex: Carbon nanotubes as removable templates for metal-oxide nanocomposites and nanostructures, Nature **375**(6532), 564–567 (1995)
5.195 B.C. Satishkumar, A. Govindaraj, E.M. Vogl, L. Basumallick, C.N.R. Rao: Oxide nanotubes prepared using carbon nanotubes as templates, J. Mater. Res. **12**(3), 604–606 (1997)
5.196 C.N.R. Rao, B.C. Satishkumar, A. Govindaraj: Zirconia nanotubes, Chem. Commun. **21**(16), 1581–1582 (1997)
5.197 B.C. Satishkumar, A. Govindaraj, M. Nath, C.N.R. Rao: Synthesis of metal oxide nanorods using carbon nanotubes as templates, J. Mater. Chem. **10**(9), 2115–2219 (2000)
5.198 D. Ugarte, T. Stockli, J.M. Bonard, A. Chatelain, W.A. de Heer: Filling carbon nanotubes, Appl. Phys. A **67**(1), 101–105 (1998)
5.199 J. Sloan, J. Cook, A. Chu, M. Zwiefka-Sibley, M.L.H. Green, J.L. Hutchison: Selective deposition of UCl_4 and $(KCl)_x(UCl)_y$ inside carbon nanotubes using eutectic and noneutectic mixtures of UCl_4 with KCl, J. Solid State Chem. **140**(1), 83–90 (1998)
5.200 J. Sloan, J. Hammer, M. Zwiefka-Sibley, M.L.H. Green: The opening and filling of single walled carbon nanotubes (SWTs), Chem. Commun. **7**(3), 347–348 (1998)
5.201 J. Sloan, D.M. Wright, H.G. Woo, S. Bailey, G. Brown, A.P.E. York, K.S. Coleman, J.L. Hutchison, M.L.H. Green: Capillarity and silver nanowire formation observed in single walled carbon nanotubes, Chem. Commun.(8), 699–700 (1999)
5.202 J.P. Hu, J.H. Shi, S.P. Li, Y.J. Qin, Z.X. Guo, Y.L. Song, D.B. Zhu: Efficient method to functionalize carbon nanotubes with thiol groups and fabricate gold nanocomposites, Chem. Phys. Lett. **401**(4–6), 352–356 (2005)
5.203 G.G. Wildgoose, C.E. Banks, R.G. Compton: Metal nanopartictes and related materials supported on carbon nanotubes, methods and applications, Small **2**(2), 182–193 (2006)
5.204 V. Georgakilas, D. Gournis, V. Tzitzios, L. Pasquato, D.M. Guldi, M. Prato: Decorating carbon nanotubes with metal or semiconductor nanoparticles, J. Mater. Chem. **17**(26), 2679–2694 (2007)
5.205 B.F. Pan, D.X. Cui, R. He, F. Gao, Y.F. Zhang: Covalent attachment of quantum dot on carbon nanotubes, Chem. Phys. Lett. **417**(4–6), 419–424 (2006)
5.206 W.W. Li, C. Gao, H.F. Qian, J.C. Ren, D.Y. Yan: Multiamino-functionalized carbon nanotubes and their applications in loading quantum dots and magnetic nanoparticles, J. Mater. Chem. **16**(19), 1852–1859 (2006)
5.207 C. Gao, W.W. Li, H. Morimoto, Y. Nagaoka, T. Maekawa: Magnetic carbon nanotubes, synthesis by electrostatic self-assembly approach and application in biomanipulations, J. Phys. Chem. B **110**(14), 7213–7220 (2006)
5.208 Y. Xiao, T. Gong, S.B. Zhou: The functionalization of multi-walled carbon nanotubes by in situ deposition of hydroxyapatite, Biomaterials **31**(19), 5182–5190 (2010)
5.209 A. Jitianu, T. Cacciaguerra, R. Benoit, S. Delpeux, F. Beguin, S. Bonnamy: Synthesis and characterization of carbon nanotubes – TiO_2 nanocomposites, Carbon **42**(5–6), 1147–1151 (2004)
5.210 W.D. Wang, P. Serp, P. Kalck, J.L. Faria: Photocatalytic degradation of phenol on MWNT, and titania composite catalysts prepared by a modified sol–gel method, Appl. Catal. B **56**(4), 305–312 (2005)
5.211 B. Gao, G.Z. Chen, G.L. Puma: Carbon nanotubes/titanium dioxide ($CNTs/TiO_2$) nanocomposites prepared by conventional and novel surfactant wrapping sol–gel methods exhibiting enhanced photocatalytic activity, Appl. B Catal. **89**(3–4), 503–509 (2009)
5.212 X.W. Wei, J. Xu, X.H. Song, Y.H. Ni, P. Zhang, C.J. Xia, G.C. Zhao, Z.S. Yang: Multi-walled carbon nanotubes coated with rare earth fluoride EuF_3 and TbF_3 nanoparticles, Mater. Res. Bull. **41**(1), 92–98 (2006)
5.213 Y.J. Chen, C.L. Zhu, T.H. Wang: The enhanced ethanol sensing properties of multi-walled carbon nanotubes/SnO_2 core/shell nanostructures, Nanotechnology **17**(12), 3012–3017 (2006)
5.214 Y.L. Liu, H.F. Yang, Y. Yang, Z.M. Liu, G.L. Shen, R.Q. Yu: Gas sensing properties of tin dioxide coated onto multi-walled carbon nanotubes, Thin Solid Films **497**(1/2), 355–360 (2006)
5.215 Z.H. Wen, Q. Wang, Q. Zhang, J.H. Li: In situ growth of mesoporous SnO_2 on multiwalled carbon nanotubes, a novel composite with porous-tube structure as anode for lithium batteries, Adv. Funct. Mater. **17**(15), 2772–2778 (2007)

5.216 G. Guo, J. Guo, D. Tao, W.C.H. Choy, L. Zhao, W. Qian, Z. Wang: A. Simple method to prepare multi-walled carbon nanotube/ZnO nanoparticle composites, Appl. Phys. A **89**(2), 525–528 (2007)

5.217 G.M. Wu, A.R. Wang, M.X. Zhang, H.Y. Yang, B. Zhou, J. Shen: Investigation on properties of V_2O_5–MWCNTs composites as cathode materials, J. Sol-Gel Sci Technol. **46**(1), 79–85 (2008)

5.218 R. Jain, R. Sharma: Novel bismuth/multi-walled carbon nanotubes-based electrochemical sensor for the determination of neuroprotective drug cilostazol, J. Appl. Electrochem. **42**(5), 341–348 (2012)

5.219 C. Bittencourt, A. Felten, E.H. Espinosa, R. Ionescu, E. Llobet, X. Corteig, J.J. Pireaux: WO_3 films modified with functionalised multi-wall carbon nanotubes: Morphological compositional and gas response studies, Sens. Actuators B **115**(1), 33–41 (2006)

5.220 R.L.D. Whitby, W.K. Hsu, C.B. Boothroyd, H.W. Kroto, D.R.M. Walton: Tungsten disulphide coated multi-walled carbon nanotubes, Chem. Phys. Lett. **359**(1/2), 121–126 (2002)

5.221 S.H. Kim, G.W. Mulholland, M.R. Zachariah: Density measurement of size selected multiwalled carbon nanotubes by mobility-mass characterization, Carbon **47**(5), 1297–1302 (2009)

5.222 J. Wang, M. Musameh, Y.H. Lin: Solubilization of carbon nanotubes by Nafion toward the preparation of amperometric biosensors, J. Am. Chem. Soc. **125**(9), 2408–2409 (2003)

5.223 L.A. Girifalco, M. Hodak, R.S. Lee: Carbon nanotubes, buckyballs, ropes, and a universal graphitic potential, Phys. Rev. B **62**(19), 13104–13110 (2000)

5.224 G.X. Sun, Z.P. Liu, G.M. Chen: Dispersion of pristine multi-walled carbon nanotubes in common organic solvents, Nano **5**(2), 103–109 (2010)

5.225 D.H. Marsh, G.A. Rance, M.H. Zaka, R.J. Whitby, A.N. Khlobystov: Comparison of the stability of multiwalled carbon nanotube dispersions in water, Phys. Chem. Chem. Phys. **9**(40), 5490–5496 (2007)

5.226 P. Liu, T.M. Wang: Concise route to water-soluble multi-walled carbon nanotubes, Current Nanosci. **6**(1), 54–58 (2010)

5.227 J.D. Shen, W.S. Huang, L.P. Wu, Y.Z. Hu, M.X. Ye: Study on amino-functionalized multiwalled carbon nanotubes, Mater. Sci. Eng. A **464**(1/2), 151–156 (2007)

5.228 S.P. Li, Y.J. Qin, J.H. Shi, Z.X. Guo, L. Yongfang, D.B. Zhu: Electrical properties of soluble carbon nanotube/polymer composite films, Chem. Mater. **17**(1), 130–135 (2005)

5.229 J.R. Yu, N. Grossiord, C.E. Koning, J. Loos: Controlling the dispersion of multi-wall carbon nanotubes in aqueous surfactant solution, Carbon **45**(3), 618–623 (2007)

5.230 W.H. Duan, Q. Wang, F. Collins: Dispersion of carbon nanotubes with SDS surfactants: A study from a binding energy perspective, Chem. Sci. **2**(7), 1407–1413 (2011)

5.231 M.F. Islam, E. Rojas, D.M. Bergey, A.T. Johnson, A.G. Yodh: High weight fraction surfactant solubilization of single-wall carbon nanotubes in water, Nano Lett. **3**(2), 269–273 (2003)

5.232 H. Wang, W. Zhou, D.L. Ho, K.I. Winey, J.E. Fischer, C.J. Glinka, E.K. Hobbie: Dispersing single-walled carbon nanotubes with surfactants: A small angle neutron scattering study, Nano Lett. **4**(9), 1789–1793 (2004)

5.233 A.G. Ryabenko, T.V. Dorofeeva, G.I. Zvereva: UV-VIS-NIR spectroscopy study of sensitivity of single-wall carbon nanotubes to chemical processing and Vander-Waals SWNT/SWNT interaction. Verification of the SWNT content measurements by absorption spectroscopy, Carbon **42**(8–9), 1523–1535 (2004)

5.234 S. Meuer, L. Braun, R. Zentel: Pyrene containing polymers for the non-covalent functionalization of carbon nanotubes, Macromol. Chem. Phys. **210**(18), 1528–1535 (2009)

5.235 M. Loginov, N. Lebovka, E. Vorobiev: Laponite assisted dispersion of carbon nanotubes in water, J. Colloid Interface Sci. **365**(1), 127–136 (2012)

5.236 N.T. Hu, G.D. Dang, H.W. Zhou, J. Jing, C.H. Chen: Efficient direct water dispersion of multi-walled carbon nanotubes by functionalization with lysine, Mater. Lett. **61**(30), 5285–5287 (2007)

5.237 I. Madni, C.Y. Hwang, S.D. Park, Y.H. Choa, H.T. Kim: Mixed surfactant system for stable suspension of multiwalled carbon nanotubes, Colloids Surf. A **358**(1–3), 101–107 (2010)

5.238 C.H. Xue, R.J. Zhou, M.M. Shi, Y. Gao, G. Wu, X.B. Zhang, H.Z. Chen, M. Wang: The preparation of highly water-soluble multi-walled carbon nanotubes by irreversible noncovalent functionalization with a pyrene-carrying polymer, Nanotechnology **19**(21), 215604 (2008)

5.239 C.H. Xue, M.M. Shi, Q.X. Yan, Z. Shao, Y. Gao, G. Wu, X.B. Zhang, Y. Yang, H.Z. Chen, M. Wang: Preparation of water-soluble multi-walled carbon nanotubes by polymer dispersant assisted exfoliation, Nanotechnology **19**(11), 115605 (2008)

5.240 P.R. Silva, V.O. Almeida, G.B. Machado, E.V. Benvenutti, T.M.H. Costa, M.R. Gallas: Surfactant-based dispersant for multiwall carbon nanotubes to prepare ceramic composites by a sol-gel method, Langmuir **28**(2), 1447–1452 (2012)

5.241 Q.H. Yang, P.X. Hou, S. Bai, M.Z. Wang, H.M. Cheng: Adsorption and capillarity of nitrogen in aggregated multi-walled carbon nanotubes, Chem. Phys. Lett. **345**(1/2), 18–24 (2001)

5.242 S. Inoue, N. Ichikuni, T. Suzuki, T. Uematsu, K. Kaneko: Capillary condensation of N_2 on multi-wall carbon nanotubes, J. Phys. Chem. B **102**(24), 4689–4692 (1998)

5.243 D. Ugarte, A. Chatelain, W.A. deHeer: Nanocapillarity and chemistry in carbon nanotubes, Science **274**(5294), 1897–1899 (1996)

5.244 W.Q. Han, S.S. Fan, Q.Q. Li, B.L. Gu, X.B. Zhang, W.A. Yu: Synthesis of silicon nitride nanorods using carbon nanotube as a template, Appl. Phys. Lett. **71**(16), 2271–2273 (1997)

5.245 W.Q. Han, S.S. Fan, Q.Q. Li, Y.D. Hu: Synthesis of gallium nitride nanorods through a carbon nanotube-confined reaction, Science **277**(5330), 1287–1289 (1997)

5.246 Y.Q. Zhu, W.K. Hsu, H.W. Kroto, D.R.M. Walton: Carbon nanotube template promoted growth of NbS_2 nanotubes/nanorods, Chem. Commun.(21), 2184–2185 (2001)

5.247 A. Peigney, C. Laurent, E. Flahaut, R.R. Bacsa, A. Rousset: Specific surface area of carbon nanotubes and bundles of carbon nanotubes, Carbon **39**(4), 507–514 (2001)

5.248 E. Alain, Y.F. Yin, T.J. Mays, B. McEnaney: Molecular simulation and measurement of adsorption in porous carbon nanotubes, Stud. Surf. Sci. **128**, 313–322 (2000)

5.249 W.K. Hsu, S. Firth, P. Redlich, M. Terrones, H. Terrones, Y.Q. Zhu, N. Grobert, A. Schilder, R.J.H. Clark, H.W. Kroto, D.R.M. Walton: Boron-doping effects in carbon nanotubes, J. Mater. Chem. **10**(6), 1425–1429 (2000)

5.250 W.K. Hsu, W.Z. Li, Y.Q. Zhu, N. Grobert, M. Terrones, H. Terrones, H. Terrones, N. Yao, J.P. Zhang, S. Firth, R.J.H. Clark, A.K. Cheetham, J.P. Hare, H.W. Kroto, D.R.M. Walton: KCl crystallization within the space between carbon nanotube walls, Chem. Phys. Lett. **317**(1/2), 77–82 (2000)

5.251 K. Rana, A. Sil, S. Ray: Modification of the structure of multi-walled carbon nanotubes by choice of catalyst and their electro-chemical behavior, Mater. Chem. Phys. **120**(2–3), 484–489 (2010)

5.252 G. Maurin, C. Bousquet, F. Henn, P. Bernier, R. Almairac, B. Simon: Electrochemical intercalation of lithium into multiwall carbon nanotubes, Chem. Phys. Lett. **312**(1), 14–18 (1999)

5.253 X.B. Wu, P. Chen, J. Lin, K.L. Tan: Hydrogen uptake by carbon nanotubes, Internat. J. Hydrogen Energy **25**(3), 261–265 (2000)

5.254 H. Furuta, T. Kawaharamura, M. Furuta, K. Kawabata, T. Hirao, T. Komukai, K. Yoshihara, Y. Shimomoto, T. Oguchi: Crystal structure analysis of multiwalled carbon nanotube forests by newly developed cross-sectional X-ray diffraction measurement, Appl. Phys. Express **3**, 105101 (2010)

5.255 M.M.J. Treacy, T.W. Ebbesen, J.M. Gibson: Exceptionally high Young's modulus observed for individual carbon nanotubes, Nature **381**(6584), 678–680 (1996)

5.256 M.F. Yu, O. Lourie, M.J. Dyer, K. Moloni, T.F. Kelly, R.S. Ruoff: Strength and breaking mechanism of multiwalled carbon nanotubes under tensile load, Science **287**(5453), 637–640 (2000)

5.257 I. Palaci, S. Fedrigo, H. Brune, C. Klinke, M. Chen, E. Riedo: Radial elasticity of multiwalled carbon nanotubes, Phys. Rev. Lett. **94**(17), 170401 (2005)

5.258 M.F. Yu, T. Kowalewski, R.S. Ruoff: Investigation of the radial deformability of individual carbon nanotubes under controlled indentation force, Phys. Rev. Lett. **85**(7), 1456–1459 (2000)

5.259 M. Huhtala, A.V. Krasheninnikov, J. Aittoniemi, S.J. Stuart, K. Nordlund, K. Kaski: Improved mechanical load transfer between shells of multiwalled carbon nanotubes, Phys. Rev. B **70**(4), 045404–01–045404–08 (2004)

5.260 A. Kis, K. Jensen, S. Aloni, W. Mickelson, A. Zettl: Interlayer forces and ultralow sliding friction in multiwalled carbon nanotubes, Phys. Rev. Lett. **97**(2), 025501 (2006)

5.261 M. Locascio, B. Peng, P. Zapol, Y. Zhu, S. Li, T. Belytschko, H.D. Espinosa: Tailoring the load carrying capacity of MWCNTs through inter-shell atomic bridging, Exp. Mech. **49**(2), 169–182 (2009)

5.262 A. Volodin, M. Ahlskog, E. Seynaeve, C. Van Haesendonck, A. Fonseca, J.B. Nagy: Imaging the elastic properties of coiled carbon nanotubes with atomic force microscopy, Phys. Rev. Lett. **84**(15), 3342–3345 (2000)

5.263 S. Kwon, H. Park, H.C. Shim, H.W. Lee, Y.K. Kwak, S. Kim: Experimental determination of the spring constant of an individual multiwalled carbon nanotube cantilever using fluorescence measurement, Appl. Phys. Lett. **95**(1), 013110–01–013110–03 (2009)

5.264 X.Q. Chen, S.L. Zhang, D.A. Dikin, W.Q. Ding, R.S. Ruoff, L.J. Pan, Y. Nakayama: Mechanics of a carbon nanocoil, Nano Lett. **3**(9), 1299–1304 (2003)

5.265 A. Volodin, D. Buntinx, M. Ahlskog, A. Fonseca, J.B. Nagy, C. Van Haesendonck: Coiled carbon nanotubes as self-sensing mechanical resonators, Nano Lett. **4**(9), 1775–1779 (2004)

5.266 A. Kukovecz, T. Kanyo, Z. Kónya, I. Kiricsi: Long-time low-impact ball milling of multi-wall carbon nanotubes, Carbon **43**(5), 994–1000 (2005)

5.267 H. Machida, S. Honda, S. Ohkura, K. Oura, H. Inakura, M. Katayama: Improvement in field emission uniformity from screen-printed double-walled carbon nanotube paste by grinding, Jpn. J. Appl. Phys. 1 **45**(2A), 1044–1046 (2006)

5.268 J. Hahn, J.E. Yoo, J. Han, H.B. Kwon, J.S. Suh: Field emission from the film of the finely black core material dispersed arc discharge, Carbon **43**(5), 937–943 (2005)

5.269 J. Hilding, E.A. Grulke, Z.G. Zhang, F. Lockwood: Dispersion of carbon nanotubes in liquids, J. Dispers. Sci. Technol. **24**(1), 1–41 (2003)

5.270 I. Willems, Z. Konya, A. Fonseca, J.B. Nagy: Heterogeneous catalytic production and mechanical resistance of nanotubes prepared on magnesium oxide supported Co-based catalysts, Appl. Catal. A 10, **229**(1/2), 229–233 (2002)

5.271 Z. Konya, J. Zhu, K. Niesz, D. Mehn, I. Kiricsi: End morphology of ball milled carbon nanotubes, Carbon **42**(10), 2001–2008 (2004)

5.272 S. Iijima, C. Brabec, A. Maiti, J. Bernholc: Structural flexibility of carbon nanotubes, J. Chem. Phys. **104**(5), 2089–2092 (1996)

5.273 M.R. Falvo, G.J. Clary, R.M. Taylor, V. Chi, F.P. Brooks, S. Washburn, R. Superfine: Bending and buckling of carbon nanotubes under large strain, Nature **389**(6651), 582–584 (1997)

5.274 P.L. McEuen, J.Y. Park: Electron transport in single-walled carbon nanotubes, MRS Bulletin **29**(4), 272–275 (2004)

5.275 Y. Awano, S. Sato, D. Kondo, M. Ohfuti, A. Kawabata, M. Nihei, N. Yokoyama: Carbon nanotube via interconnect technologies: Size-classified catalyst nanoparticles and low-resistance ohmic contact formation, Phys. Status Solidi (a) **203**(14), 3611–3616 (2006)

5.276 H. Kajiura, A. Nandyala, A. Bezryadin: Quasi-ballistic electron transport in as-produced and annealed multiwall carbon nanotubes, Carbon **43**(6), 1317–1319 (2005)

5.277 G.D. Nessim, M. Seita, K.P. O'Brien, A.J. Hart, R.K. Bonaparte, R.R. Mitchell, C.V. Thompson: Low temperature synthesis of vertically aligned carbon nanotubes with electrical contact to metallic substrates enabled by thermal decomposition of the carbon feedstock, Nano Lett. **9**(10), 3398–3405 (2009)

5.278 B. Kozinsky, N. Marzari: Static dielectric properties of carbon nanotubes from first principles, Phys. Rev. Lett. **96**(16), 166801–01–166801–04 (2006)

5.279 S. Frank, P. Poncharal, Z.L. Wang, W.A. de Heer: Carbon nanotube quantum resistors, Science **280**(5370), 1744–1746 (1998)

5.280 A. Bachtold, C. Strunk, J.P. Salvetat, J.M. Bonard, L. Forro, T. Nussbaumer, C. Schönenberger: Aharonov–Bohm oscillations in carbon nanotubes, Nature **397**(6721), 673–675 (1999)

5.281 C. Schonenberger, A. Bachtold, C. Strunk, J.P. Salvetat, L. Forro: Interference and Interaction in multi-wall carbon nanotubes, Appl. Phys. A **69**(3), 283–295 (1999)

5.282 P.C. Collins, M.S. Arnold, P. Avouris: Engineering carbon nanotubes and nanotube circuits using electrical breakdown, Science **292**(5517), 706–709 (2001)

5.283 P.G. Collins, P. Avouris: Multishell conduction in multiwalled carbon nanotubes, Appl. Phys. A **74**(3), 329–332 (2002)

5.284 A. Naeemi, J.D. Meindl: Compact physical models for multiwall carbon-nanotube interconnects, IEEE Electron. Device Lett. **27**(5), 338–340 (2006)

5.285 H.J. Li, W.G. Lu, J.J. Li, X.D. Bai, C.Z. Gu: Multichannel ballistic transport in multiwall carbon nanotubes, Phys. Rev. Lett. **95**(8), 086601–01–086601–04 (2005)

5.286 D. Mattia, M.P. Rossi, B.M. Kim, G. Korneva, H.H. Bau, Y. Gogotsi: Effect of graphitization on the wettability and electrical conductivity of CVD-carbon nanotubes and films, J. Phys. Chem. B **110**(20), 9850–9855 (2006)

5.287 D.J. Yang, S.G. Wang, Q. Zhang, P.J. Sellin, G. Chen: Thermal and electrical transport in multi-walled carbon nanotubes, Phys. Lett. A **329**(3), 207–213 (2004)

5.288 K. Kaneto, M. Tsuruta, G. Sakai, W.Y. Cho, Y. Ando: Electrical conductivities of multi-wall carbon nano tubes, Synth. Met. **103**(1–3), 2543–2546 (1999)

5.289 W.I. Milne, K.B.K. Teo, M. Chhowalla, G.A.J. Amaratunga, S.B. Lee, D.G. Hasko, H. Ahmed, O. Groening, P. Legagneux, L. Gangloff, J.P. Schnell, G. Pirio, D. Pribat, M. Castignolles, A. Loiseau, V. Semet, V. Thien Binh: Electrical and field emission investigation of individual carbon nanotubes from plasma enhanced chemical vapour deposition, Diam. Relat. Mater. **12**(3–7), 422–428 (2003)

5.290 G.E. Begtrup, K.G. Ray, B.M. Kessler, T.D. Yuzvinsky, H. Garcia, A. Zettl: Probing nanoscale solids at thermal extremes, Phys. Rev. Lett. **99**(15), 155901–01–155901–04 (2007)

5.291 J.W. Jang, K.W. Lee, C.E. Lee, T.J. Lee, C.J. Lee, S.C. Lyu: Magnetic properties of Fe catalysts included in carbon nanotubes, Phys. Status Solidi (b) **241**(7), 1605–1608 (2004)

5.292 V.P. Arya, V. Prasad, P.S.A. Kumar: Magnetic properties of iron particles embedded in multiwall carbon nanotubes, J. Nanosci. Nanotechnol. **9**(9), 5406–5410 (2009)

5.293 J. Wang, P. Beeli, Y. Ren, G.M. Zhao: Giant magnetic moment enhancement of nickel nanoparticles embedded in multiwalled carbon nanotubes, Phys. Rev. B **82**(19), 193410–01–193410–04 (2010)

5.294 X. Hoffer, C. Klinke, J.M. Bonard, L. Gravier, J.E. Wegrowe: Spin-dependent magnetoresistance in multiwall carbon nanotubes, Europhys. Lett. **67**(1), 103–109 (2004)

5.295 R.M. Langford, M.J. Thornton, T.X. Wang, W. Blau, B. Lassagne, B. Raquet: Magnetoresistance and spin diffusion in multi-wall carbon nanotubes, Microelectron. Eng. **84**(5–8), 1593–1595 (2007)

5.296 E.D. Minot, Y. Yaish, V. Sazonova, P.L. McEuen: Determination of electron orbital magnetic moments in carbon nanotubes, Nature **428**(6982), 536–539 (2004)

5.297 M. Yamamoto, M. Koshino, T. Ando: Electric and magnetic response of multi-wall carbon nanotubes, J. Phys. Soc. Jpn. **77**(8), 084705–01–084705–04 (2008)

5.298 I.S. Yu, J. Lee, S. Lee: NMR of hydrogen adsorbed on carbon nanotubes, Physica B **329**, 421–422 (2003)

5.299 C.F.M. Clewett, T. Pietrass: ^{129}Xe and ^{131}Xe NMR of gas adsorption on single- and multi-walled carbon nanotubes, J. Phys. Chem. B **109**(38), 17907–17912 (2005)

5.300 K.V. Romanenko, A. Fonseca, S. Dumonteil, J.B. Nagy, J.D.B. de Lacaillerie, O.B. Lapina, J. Fraissard: ^{129}Xe NMR study of Xe adsorption on multiwall

carbon nanotubes, Solid State Nucl. Magn. Res. **28**(2–4), 135–141 (2005)
5.301 M.G. Ruther, F. Frehill, J.E. O'Brien, A.I. Minett, W.J. Blau, J.G. Vos, M. Panhuis: Characterization of covalent functionalized carbon nanotubes, J. Phys. Chem. B **108**(28), 9665–9668 (2004)
5.302 M. Xu, Q.H. Huang, Q. Chen, P.S. Guo, Z. Sun: Synthesis and characterization of octadecylamine grafted multi-walled carbon nanotubes, Chem. Phys. Lett. **375**(5–6), 598–604 (2003)
5.303 J.C. Yu, B. Tonpheng, G. Grobner, O. Andersson: A MWCNT/polyisoprene composite reinforced by an effective load transfer reflected in the extent of polymer coating, Macromolecules **45**(6), 2841–2849 (2012)
5.304 S. Rana, H.J. Yoo, J.W. Cho, B.C. Chun, J.S. Park: Functionalization of multi-walled carbon nanotubes with poly(epsilon-caprolactone) using click chemistry, J. Appl. Polymer Sci. **119**(1), 31–37 (2011)
5.305 D. Priftis, G. Sakellariou, D. Baskaran, J.W. Mays, N. Hadjichristidis: Polymer grafted Janus multiwalled carbon nanotubes, Soft Matter. **5**(21), 4272–4278 (2009)
5.306 A. De Martino, R. Egger, K. Hallberg, C.A. Balseiro: Spin–orbit coupling and electron spin resonance theory for carbon nanotubes, Phys. Rev. Lett. **88**(20), 206402–01–206402–04 (2002)
5.307 I.I. Geru, Y.I. Prylutskyy, V. Koroli: Inhomogeneous EPR-line broadening of carbon nanotubes, Metallofiz. Nov. Tekhnol. **32**(7), 871–876 (2010)
5.308 V. Likodimos, S. Glenis, N. Guskos, C.L. Lin: Magnetic and electronic properties of multiwall carbon nanotubes, Phys. Rev. B **68**(4), 045417–01–045417–06 (2003)
5.309 P. Szroeder, F. Rozpłoch, W. Marciniak: Two-temperature EPR measurements of multi-walled carbon nanotubes, Interfacial Effects and Novel Properties of Nanomaterials, Vol. 94, ed. by W. Lojkowski, J.R. Blizzard (Trans Tech Publications, Zürich 2003) pp. 275–278
5.310 L.W. Chang, J.T. Lue: Magnetic properties of multiwalled carbon nanotubes, J. Nanosci. Nanotechnol. **9**(3), 1956–1963 (2009)
5.311 A.S. Kotosonov, D.V. Shilo, A.P. Moravskii: Magnetic properties of carbon nanotubes produced by the arc-discharge method under different conditions, Phys. Solid State **44**(4), 666–667 (2002)
5.312 T. Pietrass, J.L. Dewald, C.F. Clewett, D. Tierney, A.V. Ellis, S. Dias, A. Alvarado, L. Sandoval, S. Tai, S.A. Curran: Electron spin resonance and Raman scattering spectroscopy of multi-walled carbon nanotubes: A function of acid treatment, J. Nanosci. Nanotechnol. **6**(1), 135–140 (2006)
5.313 F. Beuneu, C. l'Huillier, J.P. Salvetat, J.M. Bonard, L. Forro: Modification of multiwall carbon nanotubes by electron irradiation, an ESR study, Phys. Rev. B **59**(8), 5945–5949 (1999)
5.314 S. Ishii, N. Aoki, K. Miyamoto, N. Oguri, K. Horiuchi, Y. Ochiai: Cesr in multi walled carbon nanotubes, Physica E **17**(1–4), 386–388 (2003)
5.315 S.D. Mhlanga, E.N. Nxumalo, N. Coville, V.V. Srinivasu: Nitrogen doping of CVD multiwalled carbon nanotubes, observation of a large *g*-factor shift, Mater. Chem. Phys. **130**(3), 1182–1186 (2011)
5.316 M.S. Dresselhaus, P.C. Eklund: Phonons in carbon nanotubes, Adv. Phys. **49**(6), 705–814 (2000)
5.317 W. Yi, L. Lu, D.L. Zhang, Z.W. Pan, S.S. Xie: Linear specific heat of carbon nanotubes, Phys. Rev. B **59**(14), R9015–R8 (1999)
5.318 J.C. Lasjaunias: Thermal properties of carbon nanotubes, C. r. Phys. **4**(9), 1047–1054 (2003)
5.319 M. Gaillard, H. Mbitsi, A. Petit, E. Amin-Chalhoub, C. Boulmer-Leborgne, N. Semmar, E. Millon, J. Mathias, S. Kouassi: Electrical and thermal characterization of carbon nanotube films, J. Vac. Sci. Technol. B **29**(4), 1805 (2011)
5.320 T.Y. Choi, D. Poulikakos, J. Tharian, U. Sennhauser: Measurement of thermal conductivity of individual multiwalled carbon nanotubes by the 3-omega method, Appl. Phys. Lett. **87**(1), 013108–01–013108–03 (2005)
5.321 P. Kim, L. Shi, A. Majumdar, P.L. McEuen: Thermal transport measurements of individual multiwalled nanotubes, Phys. Rev. Lett. **8721**(21), 215502–01–215502–04 (2001)
5.322 R. Prasher: Thermal boundary resistance and thermal conductivity of multiwalled carbon nanotubes, Phys. Rev. B **77**(7), 075424–01–075424–11 (2008)
5.323 M. Fujii, X. Zhang, H.Q. Xie, H. Ago, K. Takahashi, T. Ikuta, H. Abe, T. Shimizu: Measuring the thermal conductivity of a single carbon nanotube, Phys. Rev. Lett. **95**(6), 065502 (2005)
5.324 H.Y. Chiu, V.V. Deshpande, H.W.C. Postma, C.N. Lau, C. Miko, L. Forro, M. Bockrath: Ballistic phonon thermal transport in multiwalled carbon nanotubes, Phys. Rev. Lett. **95**(22), 226101 (2005)
5.325 X.H. Yan, Y. Xiao, Z.M. Li: Effects of intertube coupling and tube chirality on thermal transport of carbon nanotubes, J. Appl. Phys. **99**(12), 124305–01–124305–04 (2006)
5.326 C. Masarapu, L.L. Henry, B.Q. Wei: Specific heat of aligned multiwalled carbon nanotubes, Nanotechnology **16**(9), 1490–1494 (2005)
5.327 M.J. Assael, C.F. Chen, I. Metaxa, W.A. Wakeham: Thermal conductivity of suspensions of carbon nanotubes in water, Int. J. Thermophys. **25**(4), 971–985 (2004)
5.328 B.H. Kim, G.P. Peterson: Effect of morphology of carbon nanotubes on thermal conductivity enhancement of nanofluids, J. Thermophys. Heat Transf. **21**(3), 451–459 (2007)
5.329 Y.J. Hwang, Y.C. Ahn, H.S. Shin, C.G. Lee, G.T. Kim, H.S. Park: Investigation on characteristics of thermal conductivity enhancement of nanofluids, Curr. Appl. Phys. **6**(6), 1068–1071 (2006)

5.330 W.S. Bacsa, D. Ugarte, A. Chatelain, W.A. Deheer: High-resolution electron-microscopy and inelastic light-scattering of purified multishelled carbon nanotubes, Phys. Rev. B **50**(20), 15473–15476 (1994)

5.331 F. Bommeli, L. Degiorgi, P. Wachter, W.S. Bacsa, W.A. deHeer, L. Forro: The optical response of carbon nanotubes, Synth. Met. **86**(1–3), 2307–2308 (1997)

5.332 H. Hiura, T.W. Ebbesen, K. Tanigaki, H. Takahashi: Raman studies of carbon nanotubes, Chem. Phys. Lett. **202**(6), 509–512 (1993)

5.333 J.M. Holden, Z. Ping, X.X. Bi, P.C. Eklund, S.J. Bandow, R.A. Jishi, K. Daschowdhury, G. Dresselhaus, M.S. Dresselhaus: Raman-scattering from nanoscale carbons generated in a cobalt-catalyzed carbon plasma, Chem. Phys. Lett. **220**(3–5), 186–191 (1994)

5.334 P.V. Huong, R. Cavagnat, P.M. Ajayan, O. Stephan: Temperature-dependent vibrational-spectra of carbon nanotubes, Phys. Rev. B **51**(15), 10048–10051 (1995)

5.335 H. Jantoljak, J.P. Salvetat, L. Forro, C. Thomsen: Low-energy Raman-active phonons of multiwalled carbon nanotubes, Appl. Phys. A **67**(1), 113–116 (1998)

5.336 R.A. Jishi, L. Venkataraman, M.S. Dresselhaus, G. Dresselhaus: Phonon modes in carbon nanotubules, Chem. Phys. Lett. **209**(1/2), 77–82 (1993)

5.337 J. Kastner, T. Pichler, H. Kuzmany, S. Curran, W. Blau, D.N. Weldon, M. Delamesiere, S. Draper, H. Zandbergen, M. Delamesiere, S. Draper, H. Zandbergen: Resonance Raman and infrared-spectroscopy of carbon nanotubues, Chem. Phys. Lett. **221**(1/2), 53–58 (1994)

5.338 K. Tanaka, T. Sato, T. Yamabe, K. Okahara, K. Uchida, M. Yumura, M. Niino, H. Ohshima, S. Kurik: Electronic-properties of carbon nanotube, Chem. Phys. Lett. **223**(1/2), 65–68 (1994)

5.339 R. Saito, A. Jorio, A.G. Souza, G. Dresselhaus, M.S. Dresselhaus, M.A. Pimenta: Probing phonon dispersion relations of graphite by double resonance Raman scattering, Phys. Rev. Lett. **88**(2), 027401–01–027401–04 (2002)

5.340 J. Kurti, V. Zolyomi, A. Gruneis, H. Kuzmany: Double resonant Raman phenomena enhanced by van Hove singularities in single-wall carbon nanotubes, Phys. Rev. B **65**(16), 165433 (2002)

5.341 S.M. Bose, S. Gayen, S.N. Behera: Theory of the tangential G-band feature in the Raman spectra of metallic carbon nanotubes, Phys. Rev. B **72**(15), 153402–01–153402–04 (2005)

5.342 S. Osswald, E. Flahaut, H. Ye, Y. Gogotsi: Elimination of D-band in Raman spectra of double-wall carbon nanotubes by oxidation, Chem. Phys. Lett. **402**(4–6), 422–427 (2005)

5.343 R.A. DiLeo, B.J. Landi, R.P. Raffaelle: Purity assessment of multiwalled carbon nanotubes by Raman spectroscopy, J. Appl. Phys. **101**(6), 064307–01–064307–05 (2007)

5.344 H. Kuzmany, W. Plank, R. Pfeiffer, F. Simon: Raman scattering from double-walled carbon nanotubes, J. Raman Spectroscopy **39**(2), 134–140 (2008)

5.345 R. Pfeiffer, F. Simon, H. Kuzmany, V.N. Popov: Fine structure of the radial breathing mode of double-wall carbon nanotubes, Phys. Rev. B **72**(16), 161404(R)–01–161404(R)–04 (2005)

5.346 Y. Ando, X. Zhao, H. Shimoyama: Structure analysis of purified multiwalled carbon nanotubes, Carbon **39**(4), 569–574 (2001)

5.347 M. Endo, Y.A. Kim, T. Hayashi, H. Muramatsu, M. Terrones, R. Saito, F. Villalpando-Paez, S.G. Chou, M.S. Dresselhaus: Nanotube coalescence-inducing mode: A novel vibrational mode in carbon systems, Small **2**(8/9), 1031–1106 (2006)

5.348 C. Fantini, E. Cruz, A. Jorio, M. Terrones, H. Terrones, G. Van Lier, J.-C. Charlier, M.S. Dresselhaus, R. Saito, Y.A. Kim, T. Hayashi, H. Muramatsu, M. Endo, M.A. Pimenta: Resonance Raman study of linear carbon chains formed by the heat treatment of double-wall carbon nanotubes, Phys. Rev. B **73**(19), 1934081–1934084 (2006)

5.349 M. Jinno, Y. Ando, S. Bandow, J. Fan, M. Yudasaka, S. Iijima: Raman scattering study for heat-treated carbon nanotubes, the origin of approximate to 1855 cm^{-1} Raman band, Chem. Phys. Lett. **418**(1–3), 109–114 (2006)

5.350 N. Chakrapani, S. Curran, B.Q. Wei, P.M. Ajayan, A. Carrillo, R.S. Kane: Spectral fingerprinting of structural defects in plasma-treated carbon nanotubes, J. Mater. Res. **18**(10), 2515–2521 (2003)

5.351 R. Saito, G. Dresselhaus, M.S. Dresselhaus: Electronic-structure of double-layer graphene tubules, J. Appl. Phys. **73**(2), 494–500 (1993)

5.352 F.J. GarciaVidal, J.M. Pitarke, J.B. Pendry: Effective medium theory of the optical properties of aligned carbon nanotubes, Phys. Rev. Lett. **78**(22), 4289–4292 (1997)

5.353 K. Kamarás, Á. Pekker, M. Bruckner, F. Borondics, A.G. Rinzler, D.B. Tanner, M.E. Itkis, R.C. Haddon, Y. Tan, D.E. Resasco: Wide-range optical spectra of carbon nanotubes: A comparative study, Phys. Status Solidi (b) **245**(10), 2229–2232 (2008)

5.354 X. Sun, R.Q. Yu, G.Q. Xu, T.S.A. Hor, W. Ji: Broadband optical limiting with multiwalled carbon nanotubes, Appl. Phys. Lett. **73**(25), 3632–3634 (1998)

5.355 Z.P. Yang, L.J. Ci, J.A. Bur, S.Y. Lin, P.M. Ajayan: Experimental observation of an extremely dark material made by a low-density nanotube array, Nano Lett. **8**(2), 446–451 (2008)

5.356 M.E. Brennan, J.N. Coleman, A. Drury, B. Lahr, T. Kobayashi, W.J. Blau: Nonlinear photoluminescence from van Hove singularities in multiwalled carbon nanotubes, Opt. Lett. **28**(4), 266–268 (2003)

5.357 M.E. Brennan, J.N. Coleman, M.I.H. Panhuis, L. Marty, H.J. Byrne, W.J. Blau: Nonlinear photoluminescence in multiwall carbon nanotubes, Synth. Met. **119**(1–3), 641–642 (2001)

5.358 M. Reyes-Reyes, E. Segura-Cardenas, A.Y. Gorbatchev, R. Lopez-Sandoval: Infrared photoluminescence of composite films containing quasi-isolated multiwalled carbon nanotubes and carbon nanoshells, J. Nanosci. Nanotechnol. **10**(7), 4352–4356 (2010)
5.359 L. Minati, G. Speranza, I. Bernagozzi, S. Torrengo, A. Chiasera, M. Ferrari: Luminescent short thiol-functionalized multi-wall carbon nanotubes, Diam. Relat. Mater. **20**(7), 1046–1049 (2011)
5.360 P. Baviskar, P. Chavan, N. Kalyankar, B. Sankapal: Decoration of CdS nanoparticles on MWCNT's by simple solution chemistry, Appl. Surf. Sci. **258**(19), 7536–7539 (2012)
5.361 N. Jia, Q. Lian, Z. Tian, X. Duan, M. Yin, L. Jing, S. Chen, H. Shen, M. Gao: Decorating multi-walled carbon nanotubes with quantum dots for construction of multi-color fluorescent nanoprobes, Nanotechnology **21**(4), 045606 (2010)
5.362 E.C. Dickey, C.A. Grimes, M.K. Jain, K.G. Ong, D. Qian, P.D. Kichambare, R. Andrews, D. Jacques: Visible photoluminescence from ruthenium-doped multiwall carbon nanotubes, Appl. Phys. Lett. **79**(24), 4022–4024 (2001)
5.363 H.X. Wu, W.M. Cao, J. Wang, H. Yang, S.P. Yang: Coating multi-walled carbon nanotubes with rare-earth complexes by an in situ synthetic method, Nanotechnology **19**(34), 345701–01–345701–05 (2008)
5.364 C.B. Chen, H. Zhang, N. Du, B. Zhang, Y. Wu, D. Shi, D. Yang: Magnetic-fluorescent nanohybrids of carbon nanotubes coated with Eu, Gd Co-doped LaF_3 as a multimodal imaging probe, J. Colloid and Interface Sci. **367**, 61–66 (2012)
5.365 M. Olek, T. Busgen, M. Hilgendorff, M. Giersig: Quantum dot modified multiwall carbon nanotubes, J. Phys. Chem. B **110**(26), 12901–12904 (2006)
5.366 N.A. Nismy, K. Jayawardena, A. Adikaari, S.R.P. Silva: Photoluminescence quenching in carbon nanotube-polymer/fullerene films, carbon nanotubes as exciton dissociation centres in organic photovoltaics, Adv. Mater. **23**(33), 3796–3800 (2011)
5.367 A. Misra, P.K. Tyagi, P. Rai, D.S. Misra: FTIR spectroscopy of multiwalled carbon nanotubes: A simple approach to study the nitrogen doping, J. Nanosci. Nanotechnol. **7**(6), 1820–1823 (2007)
5.368 N. Kouklin, M. Tzolov, D. Straus, A. Yin, J.M. Xu: Infrared absorption properties of carbon nanotubes synthesized by chemical vapor deposition, Appl. Phys. Lett. **85**(19), 4463–4465 (2004)
5.369 N.F. Yudanov, A.V. Okotrub, Y.V. Shubin, L.I. Yudanova, L.G. Bulusheva, A.L. Chuvilin, J.M. Bonard: Fluorination of arc-produced carbon material containing multiwall nanotubes, Chem. Mater. **14**(4), 1472–1476 (2002)
5.370 T. Saito, K. Matsushige, K. Tanaka: Chemical treatment and modification of multi-walled carbon nanotubes, Physica B **323**(1–4), 280–283 (2002)
5.371 L.Q. Liu, Y.J. Qin, Z.X. Guo, D.B. Zhu: Reduction of solubilized multi-walled carbon nanotubes, Carbon **41**(2), 331–335 (2003)
5.372 M.E. Lipinska, S.L.H. Rebelo, M.F.R. Pereira, J. Gomes, C. Freire, J.L. Figueiredo: New insights into the functionalization of multi-walled carbon nanotubes with aniline derivatives, Carbon **50**(9), 3280–3294 (2012)
5.373 H. Ago, T. Kugler, F. Cacialli, K. Petritsch, R.H. Friend, W.R. Salaneck, Y. Ono, T. Yamabe, K. Tanaka: Work-function of purified and oxidised carbon nanotubes, Synth. Met. **103**(1–3), 2494–2495 (1999)
5.374 H. Ago, T. Kugler, F. Cacialli, W.R. Salaneck, M.S.P. Shaffer, A.H. Windle, R.H. Friend: Work functions and surface functional groups of multiwall carbon nanotubes, J. Phys. Chem. B **103**(38), 8116–8121 (1999)
5.375 C.P. Ewels, M. Glerup: Nitrogen doping in carbon nanotubes, J. Nanosci. Nanotechnol. **5**(9), 1345–1363 (2005)
5.376 T.I.T. Okpalugo, P. Papakonstantinou, H. Murphy, J. McLaughlin, N.M.D. Brown: High resolution XPS characterization of chemical functionalised MWCNTs and SWCNTs, Carbon **43**(1), 153–161 (2005)
5.377 W. Xia, Y. Wang, R. Bergstrasser, S. Kundu, M. Muhler: Surface characterization of oxygen-functionalized multi-walled carbon nanotubes by high-resolution X-ray photoelectron spectroscopy and temperature-programmed desorption, Appl. Surf. Sci. **254**(1), 247–250 (2007)
5.378 X.R. Ye, Y.H. Lin, C.M. Wang, M.H. Engelhard, Y. Wang, C.M. Wai: Supercritical fluid synthesis and characterization of catalytic metal nanoparticles on carbon nanotubes, J. Mater. Chem. **14**(5), 908–913 (2004)
5.379 X.M. Liu, J.L. Spencer, A.B. Kaiser, W.M. Arnold: Electric-field oriented carbon nanotubes in different dielectric solvents, Curr. Appl. Phys. **4**(2–4), 125–128 (2004)
5.380 B.K. Zhu, S.H. Xie, Z.K. Xu, Y.Y. Xu: Preparation and properties of the polyimide/multi-walled carbon nanotubes (MWNTs) nanocomposites, Compos. Sci. Technol. **66**(3–4), 548–554 (2006)
5.381 C.A. Martin, J.K.W. Sandler, M.S.P. Shaffer, M.K. Schwarz, W. Bauhofer, K. Schulte, A.H. Windle: Formation of percolating networks in multi-wall carbon-nanotube-epoxy composites, Compos. Sci. Technol. **64**(15), 2309–2316 (2004)
5.382 L. Wang, Z.M. Dang: Carbon nanotube composites with high dielectric constant at low percolation threshold, Appl. Phys. Lett. **87**(4), 042903–01–042903–03 (2005)
5.383 I. Alig, D. Lellinger, M. Engel, T. Skipa, P. Potschke: Destruction and formation of a conductive carbon nanotube network in polymer melts: In-line experiments, Polymer **49**(7), 1902–1909 (2008)
5.384 I.N. Mazov, V. Kuznetsov, S. Moseenkov, A. Usoltseva, A. Romanenko, O. Anikeeva, T. Buryakov,

P. Kuzhir, S. Maksimenko, D. Bychanok, J. Macutkevic, D. Seliuta, G. Valusis, J. Banys, P. Lambin: Electromagnetic shielding properties of MWCNT/PMMA composites in K_a-band, Phys. Status Solidi (b) **246**(11–12), 2662–2666 (2009)

5.385 I.M. De Rosa, A. Dinescu, F. Sarasini, M.S. Sarto, A. Tamburrano: Effect of short carbon fibers and MWCNTs on microwave absorbing properties of polyester composites containing nickel-coated carbon fibers, Compos. Sci. Technol. **70**(1), 102–109 (2010)

5.386 R. Rungsawang, V.G. Geethamma, E.P.J. Parrott, D.A. Ritchie, E.M. Terentjev: Terahertz spectroscopy of carbon nanotubes embedded in a deformable rubber, J. Appl. Phys. **103**(12), 123503–01–123503–04 (2008)

5.387 J.A. Berres, G.W. Hanson: Multiwall carbon nanotubes at RF-THz frequencies, scattering, shielding, effective conductivity, and power dissipation, IEEE Trans. Antennas Propag. **59**(8), 3098–3103 (2011)

5.388 T.F. Su, B. Yu, P.Y. Han, Y.L. Li, W. Li, G.Z. Zhao, C.R. Gong: Study on Terahertz spectra of multiwalled carbon nanotubes, Spectrosc. Spectr. Anal. **29**(11), 3154–3157 (2009)

5.389 E.P.J. Parrott, J.A. Zeitler, J. McGregor, S.P. Oei, W.I. Milne, J.P. Tessonnier, D.S. Su, R. Schlögl, L.F. Gladden: The use of Terahertz spectroscopy as a sensitive probe in discriminating the electronic properties of structurally similar multi-walled carbon nanotubes, Adv. Mater. **21**(38–39), 3953–3957 (2009)

5.390 V.C. Sanchez, J.R. Pietruska, N.R. Miselis, R.H. Hurt, A.B. Kane: Biopersistence and potential adverse health impacts of fibrous nanomaterials, what have we learned from asbestos?, Nanomed. Nanobiotechnol. **1**(5), 511–529 (2009)

5.391 J. Muller, F. Huaux, D. Lison: Respiratory toxicity of carbon nanotubes, how worried should we be?, Carbon **44**(6), 1048–1056 (2006)

5.392 A.K. Jain, N.K. Mehra, N. Lodhi, V. Dubey, D.K. Mishra, P.K. Jain, N.K. Jain: Carbon nanotubes and their toxicity, Nanotoxicology **1**(3), 167–197 (2007)

5.393 J. Muller, F. Huaux, N. Moreau, P. Misson, J.F. Heilier, M. Delos, M. Arras, A. Fonseca, J.B. Nagy, D. Lison: Respiratory toxicity of multi-wall carbon nanotubes, Toxicol. Appl. Pharmacol. **207**(3), 221–231 (2005)

5.394 E.J. Petersen, T.B. Henry: Methodological considerations for testing the ecotoxicity of carbon nanotubes and fullerenes, Rev. Environ. Toxicol. Chem. **31**(1), 60–72 (2012)

5.395 A.A. Shvedova, E.R. Kisin, R. Mercer, A.R. Murray, V.J. Johnson, A.I. Potapovich, Y.Y. Tyurina, O. Gorelik, S. Arepalli, D. Schwegler-Berry, A.F. Hubbs, J. Antonini, D.E. Evans, B.K. Ku, D. Ramsey, A. Maynard, V.E. Kagan, V. Castranova, P. Baron: Unusual inflammatory and fibrogenic pulmonary responses to single-walled carbon nanotubes in mice, J. Am. Physiol. Lung Cell. Mol. Physiol. **289**(5), L698–L708 (2005)

5.396 C.A. Poland, R. Duffin, I. Kinloch, A. Maynard, W.A. Wallace, A. Seaton, V. Stone, S. Brown, W. Macnee, K. Donaldson: Carbon nanotubes introduced into the abdominal cavity of mice show asbestos-like pathogenicity in a pilot study, Nat. Nanotechnol. **3**(7), 423–428 (2008)

5.397 T.A. Takagi, A. Hirose, T. Nishimura, N. Fukumori, A. Ogata, N. Ohashi, S. Kitajima, J. Kanno: Induction of mesothelioma in p53+/− mouse by intraperitoneal application of multi-wall carbon nanotube, J. Toxicological Sciences **33**(1), 105–116 (2008)

5.398 C.P. Firme, P.R. Bandaru: Toxicity issues in the application of carbon nanotubes to biological systems, Nanomed. Nanotechnol. Biol. Med. **6**(2), 245–256 (2010)

5.399 A.A. Shvedova, E.R. Kisin, D. Porter, P. Schulte, V.E. Kagan, B. Fadeel, V. Castranova: Mechanisms of pulmonary toxicity and medical applications of carbon nanotubes: Two faces of Janus?, Pharmacol. Ther. **121**(2), 192–204 (2009)

5.400 M. Endo, M.S. Strano, P.M. Ajayan: Potential applications of carbon nanotubes. In: *Carbon Nanotubes*, Topics in Applied Physics, Vol. 111, ed. by A. Jorio, G. Dresselhaus, M.S. Dresselhaus (Springer, Berlin 2008) pp. 13–61

5.401 R. Smajda, A. Kukovecz, Z. Konya, I. Kiricsi: Structure and gas permeability of multi-wall carbon nanotube buckypapers, Carbon **45**(6), 1176–1184 (2007)

5.402 S.M. Cooper, B.A. Cruden, M. Meyyappan, R. Raju, S. Roy: Gas transport characteristics through a carbon nanotubule, Nano Lett. **4**(2), 377–381 (2004)

5.403 Y.H. An, S.M. Song: Fabrication of a CNT filter for a microdialysis chip, Mol. Cell. Toxicol. **2**(4), 279–284 (2006)

5.404 C. Gao, Y.Z. Jin, H. Kong, R.L. Whitby, S.F. Acquah, G.Y. Chen, H. Qian, A. Hartschuh, S.R. Silva, S. Henley, P. Fearon, H.W. Kroto, D.R. Walton: Polyurea-functionalized multiwalled carbon nanotubes, synthesis, morphology, and Raman spectroscopy, J. Phys. Chem. B **109**(24), 11925–11932 (2005)

5.405 M. Holzinger, J. Steinmetz, D. Samaille, M. Glerup, M. Paillet, P. Bernier, L. Ley, R. Graupner: [2+1] cycloaddition for cross-linking SWCNTs, Carbon **42**(5–6), 941–947 (2004)

5.406 A. Srivastava, O.N. Srivastava, S. Talapatra, R. Vajtai, P.M. Ajayan: Carbon nanotube filters, Nat. Mater. **3**(9), 610–614 (2004)

5.407 C.L. Chen, X.K. Wang: Adsorption of Ni(II) from aqueous solution using oxidized multiwall carbon nanotubes, Ind. Eng. Chem. Res. **45**(26), 9144–9149 (2006)

5.408 G. Viswanathan, D.B. Kane, P.J. Lipowicz: High efficiency fine particulate filtration using carbon nanotube coatings, Adv. Mater. **16**(22), 2045–2049 (2004)

5.409 C. Basheer, A.A. Ainedhary, B.S.M. Rao, S. Valliyaveettil, H.K. Lee: Development and application of porous membrane-protected carbon nanotube micro-solid-phase extraction combined with gas chromatography/mass spectrometry, Anal. Chem. **78**(8), 2853–2858 (2006)

5.410 J.X. Wang, D.Q. Jiang, Z.Y. Gu, X.P. Yan: Multiwalled carbon nanotubes coated fibers for solid-phase microextraction of polybrominated diphenyl ethers in water and milk samples before gas chromatography with electron-capture detection, J. Chromatogr. A **1137**(1), 8–14 (2006)

5.411 L.P. Wang, H.X. Zhao, Y.M. Qiu, Z.Q. Zhou: Determination of four benzodiazepine residues in pork using multiwalled carbon nanotube solid-phase extraction and gas chromatography-mass spectrometry, J. Chromatogr. A **1136**(1), 99–105 (2006)

5.412 B. Pan, B.S. Xing: Adsorption mechanisms of organic chemicals on carbon nanotubes, Environ. Sci. Technol. **42**(24), 9005–9013 (2008)

5.413 X.K. Wang, C.L. Chen, W.P. Hu, A.P. Ding, D. Xu, X. Zhou: Carbon nanotubes, Environ. Sci. Technol. **39**(8), 2856–2860 (2005)

5.414 C.P. Li, Y.J. Zhang, X.C. Wang, J. Zhao, W. Chen: Removal and recovery of lead (II) ions from contaminated licorice extracts using oxidized multi-walled carbon nanotubes, J. Nanosci. Nanotechnol. **11**(11), 9731–9736 (2011)

5.415 K. Pyrzynska, A. Stafiej: Sorption behavior of Cu(II), Pb(II), and Zn(II) onto carbon nanotubes, Solvent Extr. Ion Exchange **30**(1), 41–53 (2012)

5.416 M.A. Salam, G. Al-Zhrani, S.A. Kosa: Simultaneous removal of copper(II), lead(II), zinc(II) and cadmium(II) from aqueous solutions by multi-walled carbon nanotubes, C. r. Chim. **15**(5), 398–408 (2012)

5.417 M. Soylak, O. Ercan: Selective separation and preconcentration of copper (II) in environmental samples by the solid phase extraction on multi-walled carbon nanotubes, J. Hazard. Mater. **168**(2–3), 1527–1531 (2009)

5.418 B.W. Yang, Q.J. Gong, L.P. Zhao, H. Sun, N.N. Ren, J.X. Qin, J. Xu, H.Y. Yang: Preconcentration and determination of lead and cadmium in water samples with a MnO_2 coated carbon nanotubes by using ETAAS, Desalination **278**(1–3), 65–69 (2011)

5.419 R.A. Doong, L.F. Chiang: Coupled removal of organic compounds and heavy metals by titanate/carbon nanotube composites, Water Sci. Technol. **58**(10), 1985–1992 (2008)

5.420 H. Wang, N. Yan, Y. Li, X.H. Zhou, J. Chen, B.X. Yu, M. Gong, Q.W. Chen: Fe nanoparticle-functionalized multi-walled carbon nanotubes, one-pot synthesis and their applications in magnetic removal of heavy metal ions, J. Mater. Chem. **22**(18), 9230–9236 (2012)

5.421 H. Liu, J. Zhai, L. Jiang: Wetting and anti-wetting on aligned carbon nanotube films, Soft Matter. **2**(10), 811–821 (2006)

5.422 S. Banerjee, T. Hemraj-Benny, S.S. Wong: Covalent surface chemistry of single-walled carbon nanotubes, Adv. Mater. **17**(1), 17–29 (2005)

5.423 R. Smajda, A. Kukovecz, H. Haspel, Z. Konya, R. Rajko, I. Kiricsi: *Buckypaper Gas Chromatograph, Evaporation Profile Based Identification of Liquid Analytes Using Multi-Wall Carbon Nanotube Films, SZTE-KNRET Annual Report (2008)*, ed. by Gabor Szabó (Univ. of Szeged, Szeged 2008)

5.424 L.M. Yuan, C.X. Ren, L. Li, P. Ai, Z.H. Yan, M. Zi, Z.Y. Li: Single-walled carbon nanotubes used as stationary phase in GC, Anal. Chem. **78**(18), 6384–6390 (2006)

5.425 M. Karwa, S. Mitra: Gas chromatography on self-assembled single-walled carbon nanotubes, Anal. Chem. **78**(6), 2064–2070 (2006)

5.426 M. Valcarcel, S. Cardenas, B.M. Simonet: Role of carbon nanotubes in analytical science, Anal. Chem. **79**(13), 4788–4797 (2007)

5.427 J.M. Planeix, N. Coustel, B. Coq, V. Brotons, P.S. Kumbhar, R. Dutartre, P. Geneste, P. Bernier, P.H. Ajayan: Application of carbon nanotubes as supports in heterogeneous catalysis, J. Am. Chem. Soc. **116**(17), 7935–7936 (1994)

5.428 P. Serp, M. Corrias, P. Kalck: Carbon nanotubes and nanofibers in catalysis, Appl. Catal. A **253**(2), 337–358 (2003)

5.429 K. Hata, D.N. Futaba, K. Mizuno, T. Namai, M. Yumura, S. Iijima: Water-assisted highly efficient synthesis of impurity-free single-waited carbon nanotubes, Science **306**(5700), 1362–1364 (2004)

5.430 G. Girishkumar, M. Rettker, R. Underhile, D. Binz, K. Vinodgopal, P. McGinn, P. Kamat: Single-wall carbon nanotube-based proton exchange membrane assembly for hydrogen fuel cells, Langmuir **21**(18), 8487–8494 (2005)

5.431 T. Onoe, S. Iwamoto, M. Inoue: Synthesis and activity of the Pt catalyst supported on CNT, Catal. Commun. **8**(4), 701–706 (2007)

5.432 B. Pawelec, V. La Parola, R.M. Navarro, S. Murcia-Mascaros, J.L.G. Fierro: On the origin of the high performance of MWNT-supported PtPd catalysts for the hydrogenation of aromatics, Carbon **44**(1), 84–98 (2006)

5.433 E. Auer, A. Freund, J. Pietsch, T. Tacke: Carbons as supports for industrial precious metal catalysts, Appl. Catal. A **173**(2), 259–271 (1998)

5.434 X.L. Pan, Z.L. Fan, W. Chen, Y.J. Ding, H.Y. Luo, X.H. Bao: Enhanced ethanol production inside carbon-nanotube reactors containing catalytic particles, Nat. Mater. **6**(7), 507–511 (2007)

5.435 I. Kiricsi, Z. Konya, K. Niesz, A. Koos, L.P. Biro: Synthesis procedures for production of carbon nanotube junctions. In: *Nanotechnology*, Proc. SPIE, Vol. 5118, ed. by R. Vajtai, X. Aymerich, L.B. Kish, A. Rubio (SPIE, Maspalomas 2003) pp. 280–287

5.436 B. Pietruszka, F. Di Gregorio, N. Keller, V. Keller: High-efficiency WO_3/carbon nanotubes for olefin

skeletal isomerization, Catal. Today **102**, 94–100 (2005)
5.437 G. Ovejero, J.L. Sotelo, A. Rodriguez, C. Diaz, R. Sanz, J. Garcia: Platinum catalyst on multiwalled carbon nanotubes for the catalytic wet air oxidation of phenol, Ind. Eng. Chem. Res. **46**(20), 6449–6455 (2007)
5.438 M.C. Bahome, L.L. Jewell, D. Hildebrandt, D. Glasser, N.J. Coville: Fischer–Tropsch synthesis over iron catalysts supported on carbon nanotubes, Appl. Catal. A **287**(1), 60–67 (2005)
5.439 M.J. Ledoux, C. Pham-Huu: Carbon nanostructures with macroscopic shaping for catalytic applications, Catal. Today **102**, 2–14 (2005)
5.440 J.F. AuBuchon, L.H. Chen, C. Daraio, S.H. Jin: Multibranching carbon nanotubes via self-seeded catalysts, Nano Lett. **6**(2), 324–328 (2006)
5.441 S. Bose, R.A. Khare, P. Moldenaers: Assessing the strengths and weaknesses of various types of pretreatments of carbon nanotubes on the properties of polymer/carbon nanotubes composites: A critical review, Polymer **51**(5), 975–993 (2010)
5.442 P. Verge, S. Benali, L. Bonnaud, A. Minoia, M. Mainil, R. Lazzaroni, P. Dubois: Unpredictable dispersion states of MWNTs in HDPE: A comparative and comprehensive study, Euro. Polymer J. **48**(4), 677–683 (2012)
5.443 X.L. Xie, Y.W. Mai, X.P. Zhou: Dispersion and alignment of carbon nanotubes in polymer matrix, a review, Mater. Sci. Eng. R **49**(4), 89–112 (2005)
5.444 A. Dombovari, N. Halonen, A. Sapi, M. Szabo, G. Toth, J. Maklin, K. Kordas, J. Juceti, H. Jantusen, A. Kukovecz, Z. Konya: Moderate anisotropy in the electrical conductivity of bulk MWCNT/epoxy composites, Carbon **48**(7), 1918–1925 (2010)
5.445 J.N. Coleman, U. Khan, W.J. Blau, Y.K. Gun'ko: Small but strong: A review of the mechanical properties of carbon nanotube-polymer composites, Carbon **44**(9), 1624–1652 (2006)
5.446 J.N. Coleman, U. Khan, Y.K. Gun'ko: Mechanical reinforcement of polymers using carbon nanotubes, Adv. Mater. **18**(6), 689–706 (2006)
5.447 M. Moniruzzaman, K.I. Winey: Polymer nanocomposites containing carbon nanotubes, Macromolecules **39**(16), 5194–5205 (2006)
5.448 W. Bauhofer, J.Z. Kovacs: A review and analysis of electrical percolation in carbon nanotube polymer composites, Compos. Sci. Technol. **69**(10), 1486–1498 (2009)
5.449 M.T. Byrne, Y.K. Gun'ko: Recent advances in research on carbon nanotube-polymer composites, Adv. Mater. **22**(15), 1672–1688 (2010)
5.450 T.W. Chou, L.M. Gao, E.T. Thostenson, Z.G. Zhang, J.H. Byun: An assessment of the science and technology of carbon nanotube-based fibers and composites, Compos. Sci. Technol. **70**(1), 1–19 (2010)
5.451 P.C. Ma, N.A. Siddiqui, G. Marom, J.K. Kim: Dispersion and functionalization of carbon nanotubes for polymer-based nanocomposites, a review, Compos. A **41**(10), 1345–1367 (2010)
5.452 H. Qian, E.S. Greenhalgh, M.S.P. Shaffer, A. Bismarck: Carbon nanotube-based hierarchical composites: A review, J. Mater. Chem. **20**(23), 4751–4762 (2010)
5.453 N.G. Sahoo, S. Rana, J.W. Cho, L. Li, S.H. Chan: Polymer nanocomposites based on functionalized carbon nanotubes, Prog. Polym. Sci. **35**(7), 837–867 (2010)
5.454 Z. Spitalsky, D. Tasis, K. Papagelis, C. Galiotis: Carbon nanotube-polymer composites, chemistry, processing, mechanical and electrical properties, Prog. Polym. Sci. **35**(3), 357–401 (2010)
5.455 D.D.L. Chung: Carbon materials for structural self-sensing, electromagnetic shielding and thermal interfacing, Carbon **50**(9), 3342–3353 (2012)
5.456 S.K. Smart, A.I. Cassady, G.Q. Lu, D.J. Martin: The biocompatibility of carbon nanotubes, Carbon **44**(6), 1034–1047 (2006)
5.457 G.D. Zhan, J.D. Kuntz, J.L. Wan, A.K. Mukherjee: Single-wall carbon nanotubes as attractive toughening agents in alumina-based nanocomposites, Nat. Mater. **2**(1), 38–42 (2003)
5.458 G.L. Hwang, K.C. Hwang: Carbon nanotube reinforced ceramics, J. Mater. Chem. **11**(6), 1722–1725 (2001)
5.459 F.F. Zhang, X.L. Wang, C.X. Li, X.H. Li, Q. Wan, Y.Z. Xian, L.T. Jin, K. Yamamoto: Assay for uric acid level in rat striatum by a reagentless biosensor based on functionalized multi-wall carbon nanotubes with tin oxide, Anal. Bioanal. Chem. **382**(6), 1368–1373 (2005)
5.460 Z.Y. Wang, G. Chen, D.G. Xia: Coating of multi-walled carbon nanotube with SnO_2 films of controlled thickness and its application for Li-ion battery, J. Power Sources **184**(2), 432–436 (2008)
5.461 G.D. Du, C. Zhong, P. Zhang, Z.P. Guo, Z.X. Chen, H.K. Liu: Tin dioxide/carbon nanotube composites with high uniform SnO_2 loading as anode materials for lithium ion batteries, Electrochim. Acta **55**(7), 2582–2586 (2010)
5.462 L. Noerochim, J.Z. Wang, S.L. Chou, H.J. Li, H.K. Liu: SnO_2-coated multiwall carbon nanotube composite anode materials for rechargeable lithium-ion batteries, Electrochim. Acta **56**(1), 314–320 (2010)
5.463 W.D. Wang, P. Serp, P. Kalck, J.L. Faria: Visible light photodegradation of phenol on MWNT-TiO_2 composite catalysts prepared by a modified sol-gel method, J. Mol. Catal. A **235**(1/2), 194–199 (2005)
5.464 M. Daranyi, T. Csesznok, A. Kukovecz, Z. Konya, I. Kiricsi, P.M. Ajayan, R. Vajtai: Layer-by-layer assembly of TiO_2 nanowire/carbon nanotube films and characterization of their photocatalytic activity, Nanotechnology **22**(19), 195701 (2011)
5.465 X. Dong, H.B. Zhang, G.D. Lin, Y.Z. Yuan, K.R. Tsai: Highly active CNT-promoted Cu-ZnO-Al_2O_3 catalyst

for methanol synthesis from $H_2/CO/CO_2$, Catal. Lett. **85**(3–4), 237–246 (2003)
5.466 L.Q. Jiang, L. Gao: Fabrication and characterization of ZnO-coated multi-walled carbon nanotubes with enhanced photocatalytic activity, Mater. Chem. Phys. **91**(2–3), 313–316 (2005)
5.467 L.P. Zhu, G.H. Liao, W.Y. Huang, L.L. Ma, Y. Yang, Y. Yu, S.Y. Fu: Preparation, characterization and photocatalytic properties of ZnO-coated multi-walled carbon nanotubes, Mater. Sci. Eng. B **163**(3), 194–198 (2009)
5.468 Y.T. Wang, L. Yu, Z.Q. Zhu, J. Zhang, J.Z. Zhu: Novel uric acid sensor based on enzyme electrode modified by ZnO nanoparticles and multiwall carbon nanotubes, Anal. Lett. **42**(5), 775–789 (2009)
5.469 C.H. Zhang, G.F. Wang, M. Liu, Y.H. Feng, Z.D. Zhang, B. Fang: A hydroxylamine electrochemical sensor based on electrodeposition of porous ZnO nanofilms onto carbon nanotubes films modified electrode, Electrochim. Acta **55**(8), 2835–2840 (2010)
5.470 A. Kukovecz, T. Kanyo, Z. Konya, I. Kiricsi: Morphological characterization of mesoporous silicate-carbon nanocomposites, Microporous Mesoporous Mater. **80**(1–3), 85–94 (2005)
5.471 R. Smajda, Z. Gyori, A. Sapi, M. Veres, A. Oszko, J. Kis-Csitari, A. Kukovecz, Z. Konya, I. Kiricsi: Spectroscopic studies on self-supporting multi-wall carbon nanotube based composite films for sensor applications, J. Mol. Struct. **834**, 471–476 (2007)
5.472 C. Balazsi, B. Fenyi, N. Hegman, Z. Kover, F. Weber, Z. Vertesy, Z. Konya, I. Kiricsi, L.P. Biro, P. Arato: Development of CNT/Si_3N_4 composites with improved mechanical and electrical properties, Compos. B **37**(6), 418–424 (2006)
5.473 A.R. Boccaccini, B.J.C. Thomas, G. Brusatin, P. Colombo: Mechanical and electrical properties of hot-pressed borosilicate glass matrix composites containing multi-wall carbon nanotubes, J. Mater. Sci. **42**(6), 2030–2036 (2007)
5.474 T. Kuzumaki, O. Ujiie, H. Ichinose, K. Ito: Mechanical characteristics and preparation of carbon nanotube fiber-reinforced Ti composite, Adv. Engrg. Mater. **2**(7), 416–418 (2000)
5.475 W.X. Chen, J.P. Tu, L.Y. Wang, H.Y. Gan, Z.D. Xu, X.B. Zhang: Tribological application of carbon nanotubes in a metal-based composite coating and composites, Carbon **41**(2), 215–222 (2003)
5.476 X.H. Chen, J.T. Xia, J.C. Peng, W.Z. Li, S.S. Xie: Carbon-nanotube metal-matrix composites prepared by electroless plating, Compos. Sci. Technol. **60**(2), 301–306 (2000)
5.477 J.H. Jang, K.S. Han: Fabrication of graphite nanofibers reinforced metal matrix composites by powder metallurgy and their mechanical and physical characteristics, J. Compos. Mater. **41**(12), 1431–1443 (2007)
5.478 E. Carreno-Morelli, J. Yang, E. Couteau, K. Hernadi, J.W. Seo, C. Bonjour, L. Forró, R. Schaller: Carbon nanotube/magnesium composites, Phys. Status Solidi (a) **201**(8), R53–R55 (2004)
5.479 A. Goyal, D.A. Wiegand, F.J. Owens, Z. Iqbal: Synthesis of carbide-free, high strength iron-carbon nanotube composite by in situ nanotube growth, Chem. Phys. Lett. **442**(4–6), 365–371 (2007)
5.480 M. Reibold, P. Paufler, A.A. Levin, W. Kochmann, N. Patzke, D.C. Meyer: Materials – Carbon nanotubes in an ancient Damascus sabre, Nature **444**(7117), 286 (2006)
5.481 H.Y. Chen, M.H. Chen, J.T. Di, G. Xu, H.B. Li, Q.W. Li: Architecting three-dimensional networks in carbon nanotube buckypapers for thermal interface materials, J. Phys. Chem. C **116**(6), 3903–3909 (2012)
5.482 Z.D. Han, A. Fina: Thermal conductivity of carbon nanotubes and their polymer nanocomposites: A review, Prog. Polym. Sci. **36**(7), 914–944 (2011)
5.483 A. Di Bartolomeo, M. Sarno, F. Giubileo, C. Altavilla, L. Iemmo, S. Piano, F. Bobba, M. Longobardi, A. Scarfato, D. Sannino, A.M. Cucolo, P. Ciambelli: Multiwalled carbon nanotube films as small-sized temperature sensors, J. Appl. Phys. **105**(6), 064518 (2009)
5.484 A. Kukovecz, R. Smajda, M. Oze, H. Haspel, Z. Konya, I. Kiricsi: Pyroelectric temperature sensitization of multi-wall carbon nanotube papers, Carbon **46**(9), 1262–1265 (2008)
5.485 W. Zhou, Y. Huang, B. Liu, J. Wu, K.C. Hwang, B.Q. Wei: Adhesion between carbon nanotubes and substrate: Mimicking the gecko foot-hair, Nano **2**(3), 175–179 (2007)
5.486 Y.M. Fu, P. Zhang: Peeling off carbon nanotubes from rigid substrates, an exact model, J. Adhes. Sci. Technol. **25**(10), 1061–1072 (2011)
5.487 S. Sotiropoulou, N.A. Chaniotakis: Carbon nanotube array-based biosensor, Anal. Bioanal. Chem. **375**(1), 103–105 (2003)
5.488 A. Merkoçi, M. Pumera, X. Llopis, B. Pérez, M. del Valle, S. Alegret: New materials for electrochemical sensing VI: Carbon nanotubes, TrAC-Trends Anal. Chem. **24**(9), 826–838 (2005)
5.489 M. Musameh, J. Wang, A. Merkoçi, Y.H. Lin: Low-potential stable NADH detection at carbon-nanotube-modified glassy carbon electrodes, Electrochem. Commun. **4**(10), 743–746 (2002)
5.490 J.S. Ye, Y. Wen, W.D. Zhang, L.M. Gan, G.Q. Xu, F.S. Sheu: Nonenzymatic glucose detection using multi-walled carbon nanotube electrodes, Electrochem. Commun. **6**(1), 66–70 (2004)
5.491 K.A. Joshi, J. Tang, R. Haddon, J. Wang, W. Chen, A. Mulchandani: A disposable biosensor for organophosphorus nerve agents based on carbon nanotubes modified thick film strip electrode, Electroanalysis **17**(1), 54–58 (2005)
5.492 R. Xue, T.F. Kang, L.P. Lu, S.Y. Cheng: Immobilization of acetylcholinesterase via biocompatible interface of silk fibroin for detection of organophosphate

and carbamate pesticides, Appl. Surface Sci. **258**(16), 6040–6045 (2012)
5.493 G. Li, J.M. Liao, G.Q. Hu, N.Z. Ma, P.J. Wu: Study of carbon nanotube modified biosensor for monitoring total cholesterol in blood, Biosens. Bioelectron. **20**(10), 2140–2144 (2005)
5.494 X.C. Tan, M.J. LI, P.X. Cai, L.J. Luo, X.Y. Zou: An amperometric cholesterol biosensor based on multiwalled carbon nanotubes and organically modified sol-gel/chitosan hybrid composite film, Anal. Biochem. **337**(1), 111–120 (2005)
5.495 G.C. Zhao, Z.Z. Yin, L. Zhang, X.W. Wei: Direct electrochemistry of cytochrome C on a multi-walled carbon nanotubes modified electrode and its electrocatalytic activity for the reduction of H_2O_2, Electrochem. Commun. **7**(3), 256–260 (2005)
5.496 L. Qian, X.R. Yang: Composite film of carbon nanotubes and chitosan for preparation of amperometric hydrogen peroxide biosensor, Talanta **68**(3), 721–727 (2006)
5.497 L.J. Liu, F. Zhang, F.N. Xi, X.F. Lin: Highly sensitive biosensor based on bionanomultilayer with water-soluble multiwall carbon nanotubes for determination of phenolics, Biosens. Bioelectron. **24**(2), 306–312 (2008)
5.498 S. Hashemnia, S. Khayatzadeh, M. Hashemnia: Electrochemical detection of phenolic compounds using composite film of multiwall carbon nanotube/surfactants/tyrosinase on a carbon paste electrode, J. Solid State Electrochem. **16**(2), 473–479 (2012)
5.499 S.K. Kim, S. Jeon: Simultaneous determination of serotonin and dopamine at the PEDOP/MWCNTs-Pd nanoparticle modified glassy carbon electrode, J. Nanosci. Nanotechnol. **12**(3), 1903–1909 (2012)
5.500 J.B. Raoof, R. Ojani, M. Baghayeri, M. Amiri-Aref: Application of a glassy carbon electrode modified with functionalized multi-walled carbon nanotubes as a sensor device for simultaneous determination of acetaminophen and tyramine, Anal. Methods **4**(6), 1579–1587 (2012)
5.501 L. Zhou, D.J. Li, L. Gai, J.P. Wang, Y.B. Li: Electrochemical aptasensor for the detection of tetracycline with multi-walled carbon nanotubes amplification, Sens. Actuators B **162**(1), 201–208 (2012)
5.502 R. Singh, R. Verma, G. Sumana, A.K. Srivastava, S. Sood, R.K. Gupta, B.D. Malhotra: Nanobiocomposite platform based on polyaniline-iron oxide-carbon nanotubes for bacterial detection, Bioelectrochemistry **86**, 30–37 (2012)
5.503 M. Foldvari, M. Bagonluri: Carbon nanotubes as functional excipients for nanomedicines, II. Drug delivery and biocompatibility issues, Nanomed-Nanotechnol. Biol. Med. **4**(3), 183–200 (2008)
5.504 Y. Rosen, N.M. Elman: Carbon nanotubes in drug delivery, focus on infectious diseases, Expert Opinion Drug Delivery **6**(5), 517–530 (2009)
5.505 J.S. Im, B.C. Bai, Y.S. Lee: The effect of carbon nanotubes on drug delivery in an electro-sensitive transdermal drug delivery system, Biomaterials **31**(6), 1414–1419 (2010)
5.506 E. Mehdipoor, M. Adeli, M. Bavadi, P. Sasanpour, B. Rashidian: A possible anticancer drug delivery system based on carbon nanotube-dendrimer hybrid nanomaterials, J. Mater. Chem. **21**(39), 15456–15463 (2011)
5.507 N. Aoki, T. Akasaka, F. Watari, A. Yokoyama: Carbon nanotubes as scaffolds for cell culture and effect on cellular functions, Dent. Mater. J. **26**(2), 178–185 (2007)
5.508 A.R. Boccaccini, F. Chicatun, J. Cho, O. Bretcanu, J.A. Roether, S. Novak, Q.Z. Chen: Carbon nanotube coatings on bioglass-based tissue engineering scaffolds, Adv. Funct. Mater. **17**(15), 2815–2822 (2007)
5.509 P. Galvan-Garcia, E.W. Keefer, F. Yang, M. Zhang, S. Fang, A.A. Zakhidov, R.H. Baughman, M.I. Romero: Robust cell migration and neuronal growth on pristine carbon nanotube sheets and yarns, J. Biomaterials Science-Polymer Edition **18**(10), 1245–1261 (2007)
5.510 S. Mwenifumbo, M.S. Shaffer, M.M. Stevens: Exploring cellular behaviour with multi-walled carbon nanotube constructs, J. Mater. Chem. **17**(19), 1894–1902 (2007)
5.511 J.A. Rojas-Chapana, M. Giersig: Multi-walled carbon nanotubes and metallic nanoparticles and their application in biomedicine, J. Nanosci. Nanotechnol. **6**(2), 316–321 (2006)
5.512 G.F. Close, S. Yasuda, B.C. Paul, S. Fujita, H.S.P. Wong: Measurement of subnanosecond delay through multiwall carbon-nanotube local interconnects in a CMOS integrated circuit, IEEE Trans. Electron Devices **56**(1), 43–49 (2009)
5.513 E.P. Li, X.C. Wei, A.C. Cangellaris, E.X. Liu, Y.J. Zhang, M. D'Amore, J. Kim, T. Sudo: Progress review of electromagnetic compatibility analysis technologies for packages, printed circuit boards, and novel interconnects, IEEE. Trans. Electromagn. Compat. **52**(2), 248–265 (2010)
5.514 A. Naeemi, J.D. Meindl: Performance modeling for single- and multiwall carbon nanotubes as signal and power interconnects in gigascale systems, IEEE. Trans Electron Devices **55**(10), 2574–2582 (2008)
5.515 M.R.S. Castro, H.K. Schmidt: Preparation and characterization of low- and high-adherent transparent multi-walled carbon nanotube thin films, Mater. Chem. Phys. **111**(2–3), 317–321 (2008)
5.516 R.A. Hatton, A.J. Miller, S.R.P. Silva: Carbon nanotubes, a multi-functional material for organic optoelectronics, J. Mater. Chem. **18**(11), 1183–1192 (2008)
5.517 R. Ulbricht, S.B. Lee, X.M. Jiang, K. Inoue, M. Zhang, S.L. Fang, R.H. Baughman, A.A. Zakhidov: Transparent carbon nanotube sheets as 3-D charge collectors

in organic solar cells, Sol. Energy Mater. Sol. Cells **91**(5), 416–419 (2007)
5.518 K. Sheem, Y.H. Lee, H.S. Lim: High-density positive electrodes containing carbon nanotubes for use in Li-ion cells, J. Power Sources **158**(2), 1425–1430 (2006)
5.519 Y. Zhang, X.G. Zhang, H.L. Zhang, Z.G. Zhao, F. Li, C. Liu, H.M. Cheng: Composite anode material of silicon/graphite/carbon nanotubes for Li-ion batteries, Electrochim. Acta. **51**(23), 4994–5000 (2006)
5.520 B.J. Landi, R.A. Dileo, C.M. Schauerman, C.D. Cress, M.J. Ganter, R.P. Raffaelle: Multi-walled carbon nanotube paper anodes for lithium ion batteries, J. Nanosci. Nanotechnol. **9**(6), 3406–3410 (2009)
5.521 C. Masarapu, V. Subramanian, H.W. Zhu, B.Q. Wei: Long-cycle electrochemical behavior of multiwall carbon nanotubes synthesized on stainless steel in Li ion batteries, Adv. Funct. Mater. **19**(7), 1008–1014 (2009)
5.522 L. Kavan, R. Bacsa, M. Tunckol, P. Serp, S.M. Zakeeruddin, F. Le Formal, M. Zukalova, M. Graetzel: Multi-walled carbon nanotubes functionalized by carboxylic groups: Activation of TiO_2 (anatase) and phosphate olivines ($LiMnPO_4$, $LiFePO_4$) for electrochemical Li-storage, J. Power Sources **195**(16), 5360–5369 (2010)
5.523 I. Lahiri, S.W. Oh, J.Y. Hwang, S. Cho, Y.K. Sun, R. Banerjee, W. Choi: High capacity and excellent stability of lithium ion battery anode using interface-controlled binder-free multiwall carbon nanotubes grown on copper, ACS Nano. **4**(6), 3440–3446 (2010)
5.524 W. Wang, P.N. Kumta: Nanostructured hybrid silicon/carbon nanotube heterostructures: Reversible high-capacity lithium-ion anodes, Acs Nano. **4**(4), 2233–2241 (2010)
5.525 J.T. Li, W. Lei, X.B. Zhang, B.P. Wang, L. Ba: Field emission of vertically-aligned carbon nanotube arrays grown on porous silicon substrate, Solid-State Electron. **48**(12), 2147–2151 (2004)
5.526 J.T. Li, W. Lei, X.B. Zhang, X.D. Zhou, Q.L. Wang, Y.N. Zhang, B.P. Wang: Field emission characteristic of screen-printed carbon nanotube cathode, Appl. Surface Sci. **220**(1–4), 96–104 (2003)
5.527 K. Kordás, T. Mustonen, G. Tóth, H. Jantunen, M. Lajunen, C. Soldano, S. Talapatra, S. Kar, R. Vajtai, P.M. Ajayan: Inkjet printing of electrically conductive patterns of carbon nanotubes, Small **2**(8–9), 1021–1025 (2006)
5.528 M.I.H. Panhuis, A. Heurtematte, W.R. Small, V.N. Paunov: Inkjet printed water sensitive transparent films from natural gum-carbon nanotube composites, Soft Matter. **3**(7), 840–843 (2007)
5.529 H. Haspel, R. Ionescu, P. Heszler, A. Kukovecz, Z. Konya, Z. Gingl, J. Mäklin, T. Mustonen, K. Kordas, R. Vajtai, P.M. Ajayan: Fluctuation enhanced gas sensing on functionalized carbon nanotube thin films, Phys. Status Solidi (b) **245**(10), 2339–2342 (2008)
5.530 W.H. Shin, H.M. Jeong, B.G. Kim, J.K. Kang, J.W. Choi: Nitrogen-doped multiwall carbon nanotubes for lithium storage with extremely high capacity, Nano Lett. **12**(5), 2283–2288 (2012)

6. Modified Carbon Nanotubes

Aarón Morelos-Gómez, Ferdinando Tristán López, Rodolfo Cruz-Silva, Sofia M. Vega Díaz, Mauricio Terrones

It is well known that carbon nanotubes possess outstanding electrical and mechanical properties, and if they are modified these properties can be improved or other novel characteristics can appear. In addition, these modified carbon nanotubes, being different from their pure counterparts, now require additional studies to assess their toxicity and biocompatibility.

Generally speaking, carbon nanotubes can be classified as single-, double- or multi-walled, and each type can be modified; For example, these tubular structures can be doped with foreign atoms, incorporate structural defects, and/or be functionalized with different molecules. These local modifications greatly modify their electronic and chemical properties, and can be understood by using a variety of microscopy and spectroscopy techniques.

In Sect. 6.1, we describe the general concepts and synthesis for the main doping types. In Sect. 6.2, we focus on the different types of defects that can be introduced into nanotubes so as to modify their physicochemical properties. Section 6.3 discusses the categories of nanotube chemical functionalization and their resulting effects. The electrochemical properties of modified carbon nanotubes are an important topic that needs further investigation, and Sect. 6.4 reviews the latest advances in this area. The characterization techniques mainly used to study modified carbon nanotubes are reviewed in Sect. 6.5. Some applications of modified carbon nanotubes are described in Sect. 6.6. Finally, aspects of the toxicity and biocompatibility of modified carbon nanotubes are presented in Sect. 6.7. The chapter finally provides an outlook and perspectives in the field.

6.1 **Doped Carbon Nanotubes** 191
6.1.1 Endohedral Doping 192
6.1.2 Exohedral Doping 192
6.1.3 In-Plane Doping 193
6.2 **Defects in Carbon Nanotubes** 193
6.3 **Nanotube Chemical Functionalization** 197
6.3.1 Covalent Modification 197
6.3.2 Functionalization of Carbon Nanotubes via $\pi-\pi$ Interactions 200
6.3.3 Electrostatic Functionalization of Carbon Nanotubes 201
6.4 **Properties of Modified Carbon Nanotubes** 203
6.4.1 Electrical Properties of Modified Tubes 203
6.4.2 Electrochemistry of Modified Nanotubes 203
6.5 **Characterization of Modified Carbon Nanotubes** 208
6.5.1 Transmission Electron Microscopy 208
6.5.2 Atomic Force Microscopy and Scanning Transmission Microscopy 209
6.5.3 Electron Energy Loss Spectroscopy (EELS) 211
6.5.4 X-Ray Photoelectron Spectroscopy 212
6.5.5 Raman Spectroscopy 212
6.5.6 Thermogravimetric Analysis 214
6.6 **Applications of Modified Carbon Nanotubes** 215
6.7 **Toxicity and Biocompatibility** 218
6.8 **Conclusions** 220
6.9 **Outlook and Perspectives** 221
References 221

In recent years, it has been demonstrated that modified carbon nanotubes exhibit novel and fascinating properties that could be used in the fabrication of composites, electronic devices, and biomedical applications.

In order for them to be used in these devices and applications, it is important to make them more compatible with different molecules, atoms, cells, or even clusters.

Although great advances in carbon nanoscience and nanotechnology have been achieved over the last 20 years, there is still more work to be done, and this chapter intends to present current research so that novel ideas and applications can be developed based on the modification of carbon nanotubes (CNTs).

The nanocarbon world is vast and novel. Carbon nanostructures have appeared over the last two decades. Nanocarbon cages (also known as fullerenes) were first observed in 1985 [6.2] and synthesized in bulk in 1990 [6.3]. Soon afterwards, other nanocarbon forms known as nanotubes were identified by *Iijima* [6.4], although some previous observations in the 1970s reported synthesis of carbon nanotubes using the chemical vapor deposition method developed by *Endo* et al. [6.5]. More recently and at the beginning of this century, flat layers of graphene were successfully isolated [6.6] and their electronic properties were measured [6.7, 8]. The search for new forms of carbon continued, and very recently, graphene nanoribbons were also synthesized and produced using different routes [6.9]. Therefore, it is clear that carbon is extremely versatile and can be shaped into any nanomorphology.

To date, the most prolific scientific carbon field has been dedicated to carbon nanotubes. However, graphene and graphene nanoribbons are also gaining importance day by day. In particular, carbon nanotubes possess fascinating electronic, optical, and mechanical properties depending on their geometry (diameter and chirality) [6.10, 11]. These tubular structures can be categorized into three groups as a function of the number of concentric layers they contain (Fig. 6.1): single-walled carbon nanotubes (SWCNTs), double-walled carbon nanotubes (DWCNTs), and multi-walled carbon nanotubes (MWCNTs). All these tubular cat-

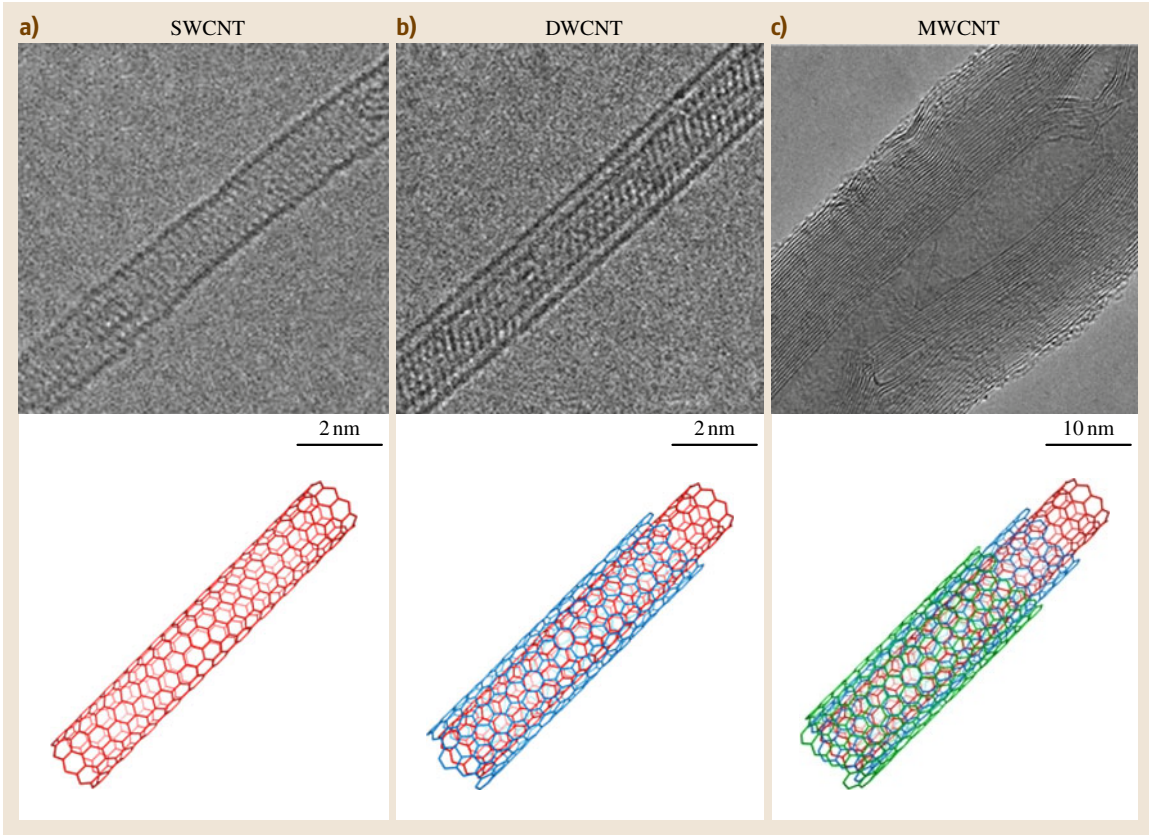


Fig. 6.1a–c High-resolution transmission electron microscopy (HRTEM) images and molecular models of: **(a)** single-walled (SWCNT), **(b)** double-walled (DWCNT), and **(c)** multiwalled (MWCNT) carbon nanotubes (after [6.1])

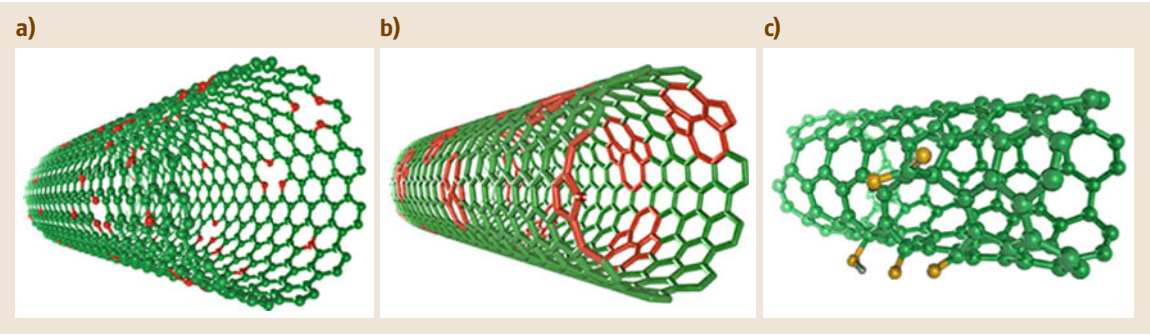


Fig. 6.2a–c Sketches showing the different ways of chemically modifying carbon nanotubes. The routes are mainly divided into **(a)** doping, **(b)** defect introduction, and **(c)** functionalization

egories are relatively stable and can exhibit extreme chemical surface inertness, which can be modified by introducing defects or by anchoring moieties in their crystalline structure. This chemical modification process can occur through three main routes (Fig. 6.2):

1. Nanotube doping
2. Defect introduction and
3. Nanotube functionalization.

These routes open up the opportunity to tailor the electronic, vibrational, chemical, and mechanical properties of carbon nanotubes.

We will also show in this chapter that modified carbon nanotubes possess outstanding properties when compared to pure carbon nanotubes, and it is foreseen that these systems will develop further nanotube science, and will eventually transform the potential applications of carbon nanotubes into real-world technology.

6.1 Doped Carbon Nanotubes

In this section we review three main doping categories: (a) exohedral doping or intercalation, (b) endohedral doping or encapsulation, and (c) in-plane or substitutional doping. By definition, in-plane doping is a covalent functionalization, whereas the endohedral and exohedral kinds of doping can be either covalent or noncovalent functionalization (Fig. 6.3). Due to the nanotube curvature, it is expected that exohedral covalent functionalization will be more favorable when compared with the endohedral counterpart because the outer surface (convex) is more reactive than the inner surface (concave). Using surface science terminology, covalent and noncovalent functionalization are also termed chemisorption and physisorption, respectively.

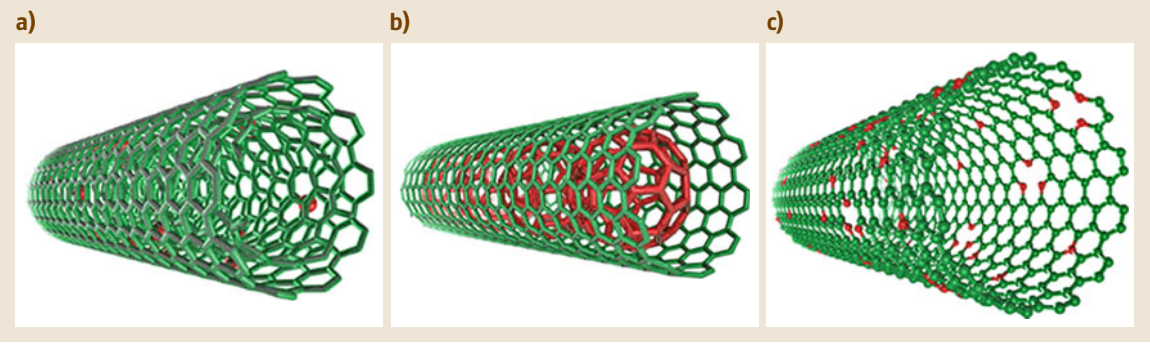


Fig. 6.3a–c Molecular models illustrating the possible sites and different doping types in carbon nanotubes: **(a)** exohedral doping or intercalation, **(b)** endohedral doping or encapsulation, and **(c)** in-plane or substitutional doping

6.1.1 Endohedral Doping

The possibility of filling the core (*endohedral doping*) of these one-dimensional (1-D) structures with atoms or molecules is attractive for scientists because both storage and transport of molecular species at the nanoscale are of great interest, especially in biology for drug delivery and as models for biochemical processes. This field started with the theoretical work of *Pederson* and *Broughton* [6.12] claiming the nanocapillarity of carbon nanotubes. From the experimental standpoint, *Ajayan* et al. [6.13] were the first to report the filling of MWCNTs with lead or lead oxide, by heating the tubes in air together with metallic lead. There is extensive work related to the filling of carbon nanotubes, which has been reviewed elsewhere [6.14–16].

Filling of carbon nanotubes has been of historical importance in nanotube science. It was the attempt to fill the core of MWCNTs with pure transition metals such as Ni, Co, and Fe that resulted in the production of SWCNTs using the arc discharge technique [6.17, 18]. Five years later, the first reports relating to the successful filling of SWCNTs with C_{60} molecules were presented by *Smith* et al. [6.19] and *Sloan* et al. [6.20]. The remarkable properties of these endohedrally doped systems led to fast development in use of the 1-D structure of SWCNTs to prepare a large variety of filled nanotube systems (Fig. 6.3b). The natural attempt was to use the unique 1-D tubular morphology as the template for preparing a new generation of very small-diameter wires or to prepare quasi-1-D superconductors using alkali metals as fillers. Heavy metals such as Ru, Bi, Au, Pt, Pd, and Ag have also been inserted in the nanotube cavity [6.20,21]. In addition, a variety of other metals have been filled within MWCNTs, such as Re, Pb, Cr, Ge, Cu, FeCo, FePt, FeNi, and Fe_3C [6.22–35]. In addition, different compounds such as halides and oxides have also been introduced into SWCNTs [6.36].

The discovery of C_{60}@SWCNTs (also called fullerene peapods; Figs. 6.3b, 6.4a) is another very important advance in carbon nanotube science. The control and high yield of C_{60} filling could lead to double-walled carbon nanotubes (DWCNTs) after heat treatments (Fig. 6.4b). Furthermore, this system allowed the observation in real time using an electronic microscope of nanoscale phenomena such as dimerization, diffusion, and coalescence [6.37,38]. Subsequently, 1-D crystals were synthesized using encapsulation of metallofullerenes [6.39].

Bundles of as-prepared carbon nanotubes (SWCNTs, DWCNTs or MWCNTs) can serve as a host lattice for different chemical moieties. The electronic properties can be tailored by doping with electron-donating or electron-accepting guest atoms and small molecules, which reside in the interstitial channels. Endohedral doping is expected to substantially increase the density of free charge carriers (electrons or holes) and thereby enhance the electrical and thermal conductivity in SWCNT bundles.

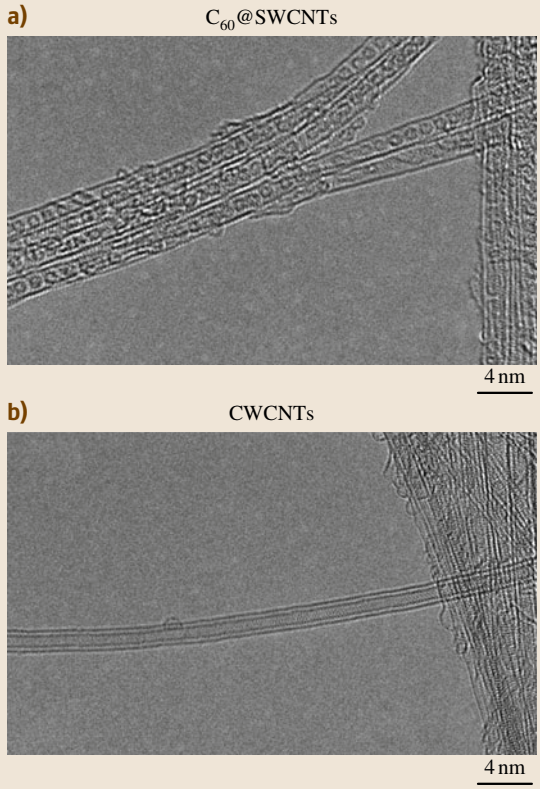


Fig. 6.4a,b HRTEM images of: **(a)** peapods, consisting of C_{60} molecules encapsulated inside SWCNTs, and **(b)** a DWCNT resulting from heat treatment of peapod samples at 1700 °C in Ar atmosphere (courtesy of M. Endo, T. Hayashi, H. Muramatsu)

6.1.2 Exohedral Doping

Intercalated alkali metal atoms (*exohedral doping*) act as electron donors, and this charge transfer weakens the C−C bonds in the SWCNTs, as electrons have been known to soften the C−C bond in all sp^2-bonded carbon materials [6.40, 41]. Acceptor halogens (e.g., $CHCl_3$, Br_2) were found to stiffen the C−C bonds. This kind of

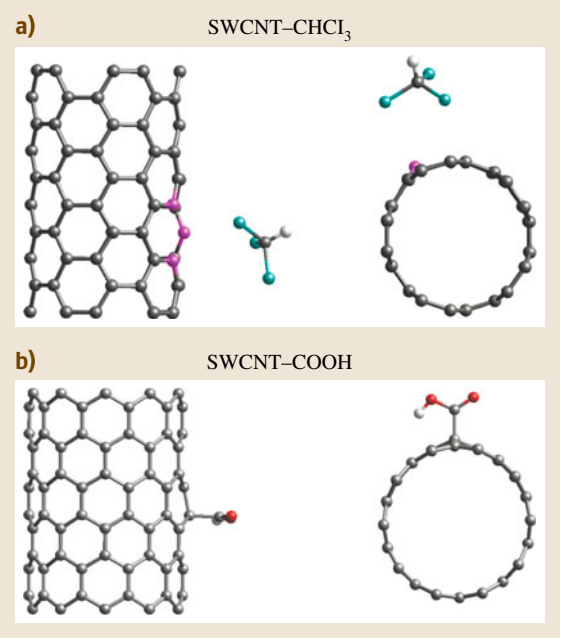


Fig. 6.5a,b Molecular models: **(a)** $CHCl_3$ molecule physisorbed to a N-doped SWCNT (side view and cross section), **(b)** COOH group chemisorbed to a SWCNT (side view and cross section; courtesy of E. Gracia-Espino)

doping is noncovalent, and such carbon nanotube samples can be easily undoped by heat treatments at high temperatures. The atomic structure of the nanotubes is not affected in this process (Fig. 6.5a), but the electronic structure is strongly affected.

Exohedral doping can also be covalent (functionalization), which can modify the nanotube wall to a great extent depending on the concentration of the dopant molecules. There are several routes for covalently attaching moieties onto the surface of carbon nanotubes, but one of the most simple covalent functionalization is carboxylation of the nanotubes (Fig. 6.5b). The charge plots for the local densities of states coming from the half-occupied levels indicate that charges are mainly located around the functional groups (Fig. 6.5b) [6.42]. The carboxylic acid group (COOH) is considered the prototype chemical group for achieving covalent functionalization of carbon nanotube because the carbon atom is covalently bonded to the tube while the −OH group can be exchanged for other chemical groups using standard chemical reactions via a coupling agent. This approach allows one to attach more complex molecules such as amino acids and DNA, and other groups such as amine and amide [6.43].

Optical absorption spectra of doped SWCNT thin films can provide insight into which electronic states are primarily influenced by the charge transfer interaction with the dopants. *Kazaoui* et al. [6.44] have separately monitored the doping behavior of semiconducting and metallic SWCNTs in a combined optical absorption and direct-current (DC) resistance measurement study. Both electron acceptors (Br_2, I_2) and donors (K, Cs) were used as dopants, with controlled stoichiometry. Disappearance of absorption bands at 0.68 and 1.2 eV (assigned to semiconductor SWCNTs) and at 1.8 eV (assigned to metallic SWCNTs) in pristine SWCNTs with a concomitant decrease in the electrical resistance upon doping has been attributed to electron depletion from, or filling of, specific bands in semiconducting or metallic SWCNTs.

6.1.3 In-Plane Doping

Both structural and electronic properties of the nanotubes are highly affected by substitutional (*in-plane*) doping. In this process one or more heteroatoms (defects) are added to the nanotube lattice (Fig. 6.3c), thus breaking the translational symmetry of the lattice. Both the number of electrons and the size of the heteroatom play an important role in determining the physical properties (structure, morphology, and electronic) of the doped structures. In the following section we discuss in detail this doping process, focusing mainly on boron- (B-), nitrogen (N-), boron-nitrogen- (BN-), and phosphorous-nitrogen- (PN-) doped carbon nanotubes.

6.2 Defects in Carbon Nanotubes

Defects are crucial in tailoring the physicochemical properties of carbon nanotubes. They can significantly affect the morphology and functionality of tubes. Unfortunately, it is still extremely difficult to identify accurately and quantitatively the type of defects contained in carbon nanotubes (SWCNTs and MWCNTs). The most common defects are classified as:

1. Structural defects
2. Topological defects or heptagon–pentagon pair (Thrower–Stone–Wales)-type transformations

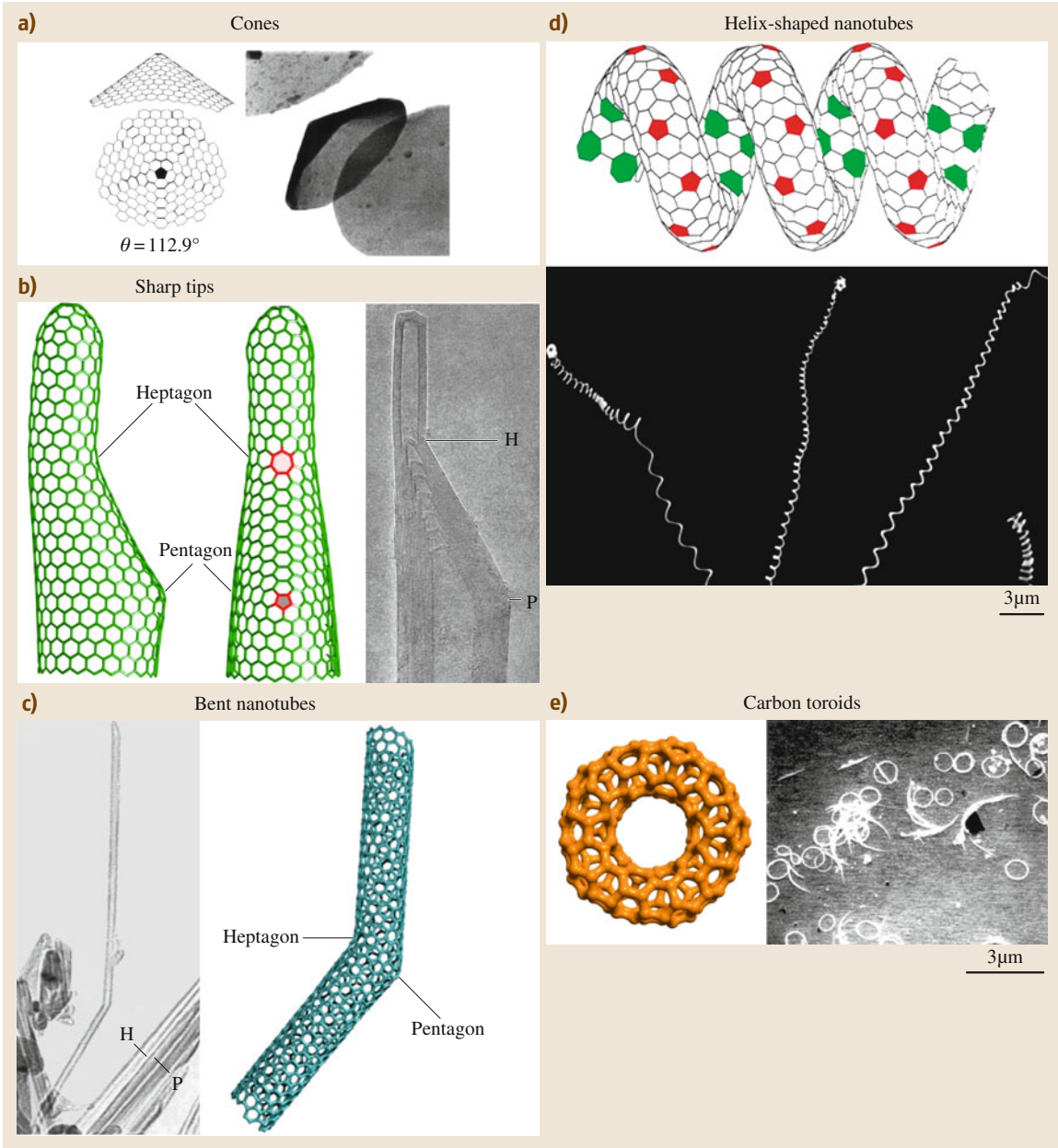


Fig. 6.6a–e TEM images and molecular models of different types of structural defects in sp^2-hybridized carbon. **(a)** Graphitic cone constructed by adding one pentagon in graphene, a molecular model and an experimental TEM image of such cones are shown for clarity (model courtesy of M. Endo, experimental image courtesy of T.W. Ebbesen; *Krishnan* et al. [6.45]). **(b)** High-resolution image of a nanotube tip displaying the influence of a pentagon and heptagon. The image shows the molecular models, and a HRTEM image of such structure has been reported (after [6.46]). **(c)** TEM image of a 30° bent MWCNT and molecular model of a bent nanotube created by adding a pentagon–heptagon pair. **(d)** Molecular model of a helix-shaped CNT showing the presence of pentagons and heptagons (after [6.47]) and experimental images of carbon helices produced by the CVD process of triazine over cobalt oxide substrates. **(e)** Molecular model of a toroidal carbon and experimental SEM image of toroidal carbons obtained by the IBM group (after [6.48])

3. Narrow-diameter tubes or collapsed tubes
4. Interstitials, edges, and adatoms (Fig. 6.6).

It is noteworthy that heptagons, pentagons, heptagon–pentagon pairs, and collapsed tubes preserve the sp^2-hybridized lattice, whereas interstitials, adatoms, and vacancies do not. It is envisaged that defects could be controlled so as to design novel types of morphologies in carbon nanotubes, including helicoidal tubules, toroids, etc. (Fig. 6.6). These structures will then possess specific sites that could be very sensitive to different molecules or certain polymer chains:

1. *Structural defects* are imperfections that significantly modify the overall curvature of the tube. These defects include pentagons, heptagons, and octagons, and are embedded in the sp^2-hybridized carbon lattice; for example, if an individual pentagon is embedded in a graphene sheet, a nanocone is obtained (Fig. 6.6a). It has also been demonstrated that heptagons introduce negative curvature and pentagons positive curvature to a graphene sheet (Fig. 6.6b). A bent nanotube exhibiting a 30° angle could also be explained by the presence of a pentagon on one side and a heptagon on the opposite side (Fig. 6.6c). It is clear that the reactivity of pentagons, heptagons or octagons with specific acceptor or donor molecules will be different, and further research is needed to determine their interactions from a theoretical and experimental standpoint (Fig. 6.6).

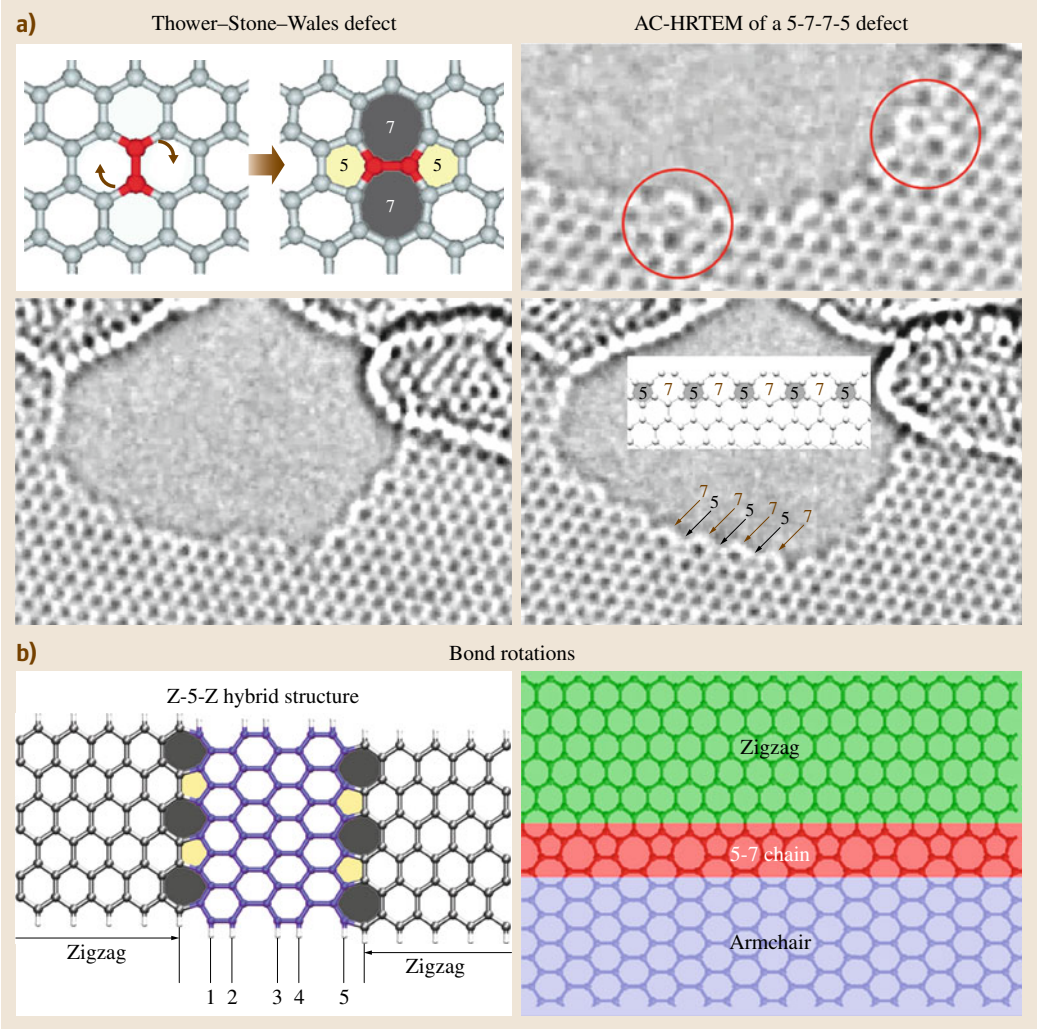


Fig. 6.7 **(a)** Molecular model of the Thrower–Stone–Wales defect transforming four hexagons into two pentagons and two heptagons. Next and below the model, HRTEM images showing experimentally created 5–7–7–5 defects and 5–7–5–7–5–7–5–7 lines (HRTEM images from [6.49]). **(b)** Molecular models of hybrid graphene ribbons connecting a zigzag ribbon with an armchair ribbon

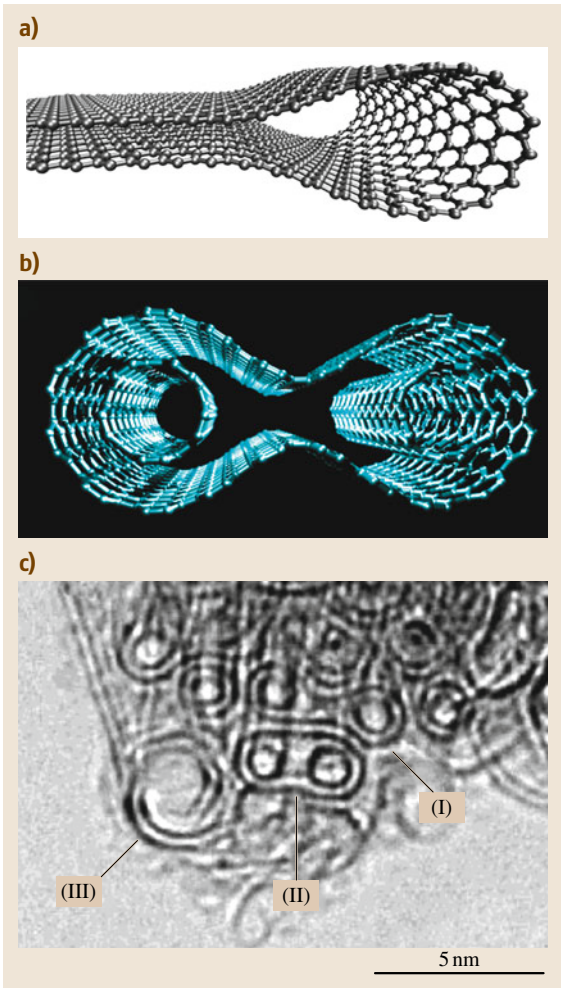


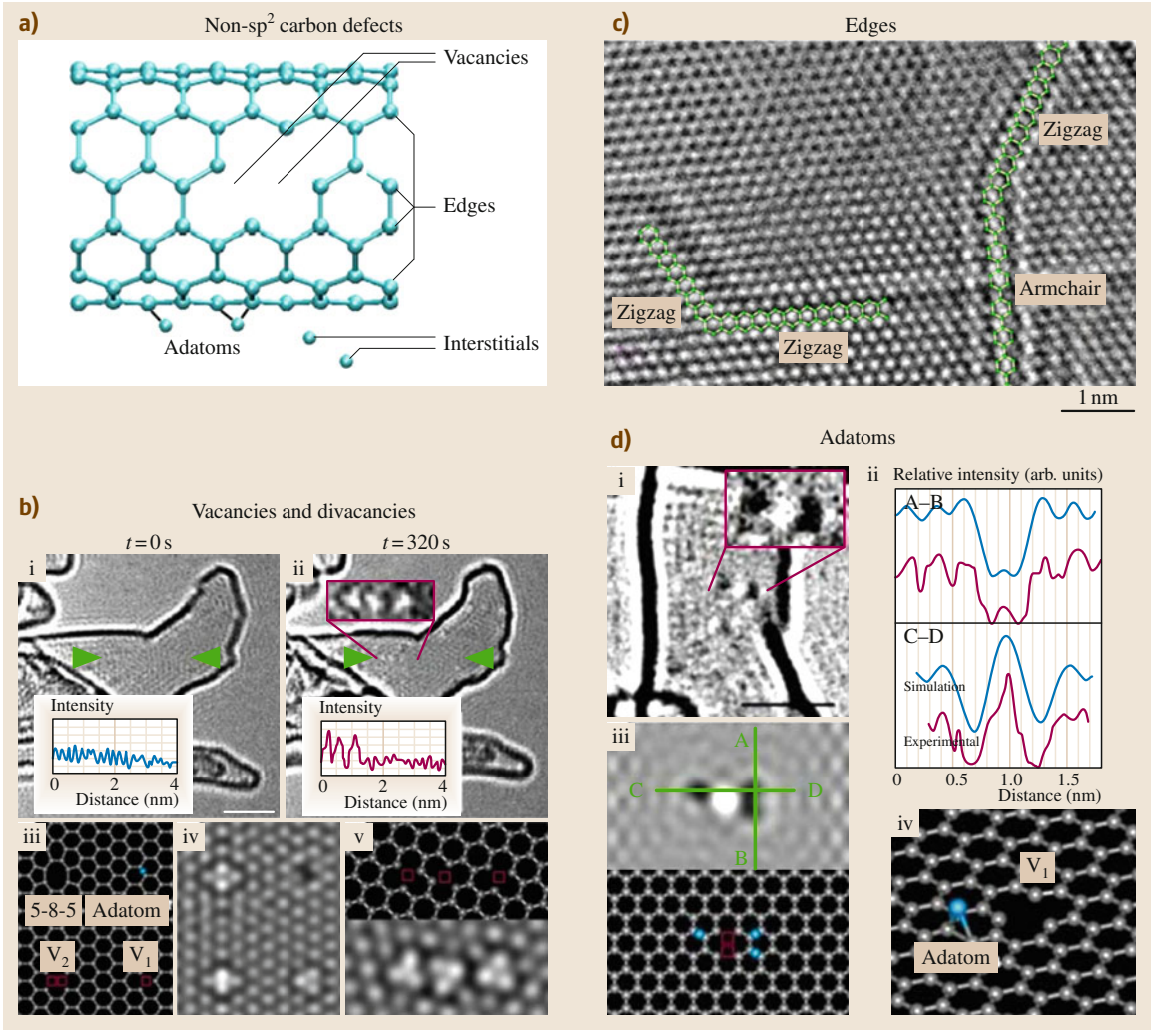
Fig. 6.8 **(a)** Molecular model of one segment of a collapsed CNT showing high strain and deformation of the p_z orbital. **(b)** Collapsed nanotube with two narrow-diameter tubes inside (binocular-like structure). **(c)** HRTEM image of the model shown in **(b)**

2. *Topological defects or bond rotations* occur on nanotube surfaces and do not result in significant changes in the overall curvature of the tubule. In particular, these defects could be 5–7–7–5 pairs embedded in the hexagonal network (Fig. 6.7) or Thrower–Stone–Wales (TSW)-type defects [6.50, 51] that could be created by rotating a carbon–carbon bond by 90° within four neighboring hexagons, thus resulting in the transformation of two pentagons and two heptagons [6.52, 53].

Fig. 6.9 **(a)** Molecular model of the different types of non-sp^2 defects in graphene: vacancies interstitials, adatoms, edges, and interstitials. **(b)** Experimental images showing the creation of vacancies in graphitic materials (i, ii) and ii-*inset*, molecular models and HRTEM image simulations are also shown for clarity **(iii–v)**; after *Hashimoto* et al. [6.54]. **(c)** HRTEM image of graphene edges exhibiting zigzag and armchair edges, obtained by applying Joule heating on individual graphene nanoribbons inside the HRTEM [6.55]; **(di,dii)** HRTEM image of adatoms on a graphitic surface (*darker contrast spots*); **(diii,iv)** HRTEM simulations and models of different configurations of adatoms on the surface of graphene that correspond to the experimental observations (after *Hashimoto* [6.54]) ►

It is noteworthy that the electronic and chemical properties of these 5–7 or 5–7–7–5 pairs (Fig. 6.7) are different from the structural defects, and their reactivity and detection need to be investigated theoretically and experimentally. Recently, *Zettl* and coworkers were able to observe directly 5–7 and TSW-type defects on isolated graphene surfaces using aberration-corrected transmission electron microscopy (Fig. 6.7); see also the movies in the supplementary material of [6.49].

3. *Narrow-diameter nanotubes or collapsed nanotubes* could be observed in large diameter nanotubes (Fig. 6.8a). Their chemical reactivity and electronic properties have not been investigated in detail. Narrow or highly curved nanotubes (usually < 1 nm diameter) would also be more reactive when compared with a flat graphene sheet (the π orbitals would be distorted in highly curved regions). A hybrid structure including a collapsed nanotube and narrow-diameter tubes (binocular-like) is depicted in Fig. 6.8b,c. At present, nanotube chemistry requires better understanding of these defects in order to induce and control strong (or weaker) covalent (or $\pi-\pi$) interactions with other molecules, atoms or clusters.
4. *Non-sp^2 carbon defects* are caused by the presence of highly reactive carbon atoms such as dangling bonds, carbon chains, interstitials (free atoms trapped between SWCNTs or between graphene sheets), edges (open nanotubes), adatoms, and vacancies (Fig. 6.9). These defects are usually observed by high-resolution transmission electron microscopy (HRTEM), when the adsorbed atoms on these reactive sites are removed by the electron beam energy.



6.3 Nanotube Chemical Functionalization

MWCNTs and SWCNTs have resulted in important discoveries in the area of chemistry and materials science over recent years. These nanoscale tubular structures possess tremendous strength [6.56] and extreme aspect ratio, and are excellent thermal and electrical conductors [6.57]. Carbon nanotubes promise to have a large number of potential applications, and some progress is being made towards commercial applications. However, it is apparent that chemical modification of SWCNTs and MWCNTs will be necessary to achieve some of these applications. An important issue is to improve their dispersion and compatibility either in water-based solutions for biological and medical applications [6.58], or in a polymer matrix to create polymer composites with enhanced electrical and mechanical properties [6.59–61].

6.3.1 Covalent Modification

Various covalent functionalization strategies have been reported:

1. Defect site creation, and functionalization from the defect sites [6.62]
2. Creation of carboxylic acids on the end caps of carbon nanotubes and subsequent derivatization from the acids [6.63, 64]
3. Covalent sidewall functionalization [6.56].

In particular, covalent functionalization of SWCNTs has been accomplished using three different approaches: thermally activated chemistry, electrochemical modification, and photochemical functionalization [6.65]. Although covalent functionalization methods have also been developed for MWCNTs [6.66], fewer investigations have been devoted to this type of nanotube.

Oxidation and Subsequent Nanotube Functionalization

There are many reports in literature related to successful chemistry with carbon nanotubes involving treatment under oxidizing conditions, such as sonication in mixtures of sulfuric and nitric acids, or treatments with sulfuric acid/hydrogen peroxide [6.67, 68], potassium permanganate in acidic solution [6.69] or potassium dichromate/sulfuric acid. These processes also help to remove unwanted carbonaceous materials from raw nanotube samples. In addition, these processes can be used to shorten carbon nanotubes. Such shortening leaves carbon nanotubes with open ends decorated with an indeterminate number of oxygenated functionalities (Fig. 6.10) such as carboxylic acids, anhydrides, quinones, and esters. Such functionalities can also be introduced by treating carbon nanotubes with ozone [6.70–73]. The distribution of these functionalities has not been well characterized; they are presumed to exist primarily at the ends of nanotubes and at sites along the sidewalls, where increased curvature results in increased reactivity [6.74]. The concept of higher reactivity at defect sites such as pentagon–heptagon pairs called Thrower–Stone–Wales type defects, sp^3-hybridized defects, and vacancies in the nanotube lattice, or sites of increased curvature (especially end caps and kinks), has been described in literature [6.75], as well as the increased reactiv-

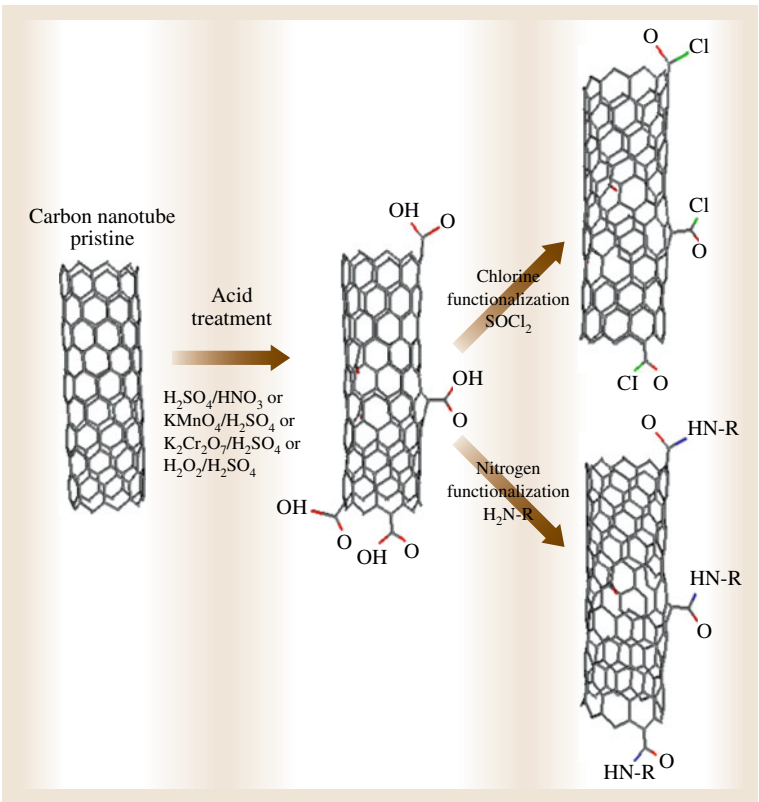


Fig. 6.10 Schematic representation of the oxidation process in a carbon nanotube, and two possible routes of functionalization

ity of smaller-diameter SWCNTs [6.76]. Functional groups created in this manner (carboxylic acid, ketone, alcohol, ester groups, etc.) can be removed by heating the samples in a vacuum or inert atmosphere [primarily esters and quinones based on infrared (IR) absorption frequencies], thus leaving the nanotube walls almost intact. It is noteworthy that the presence of carboxylic acid functionalities in carbon nanotubes provides a large number of possibilities for achieving chemical modifications.

Fluorination

Fluorination is a process that involves addition of fluorine atoms onto the surface of carbon nanotubes, thus causing significant alteration of their properties [6.78]. A possible route involves treatment of CNTs with hydrazine, or alkyl-magnesium bromides or alkyl-lithium reagents to yield alkylated CNTs which are later fluorinated. Other fluorination processes have been reported via aryl diazonium salts, carbenes, nitrenes, organic radicals, etc. These fluorinated CNTs are now sold commercially [6.79]. Fluorinated CNTs result in significant changes in the spectroscopic properties [ultraviolet (UV)/Vis/near infrared (NIR) absorption and Raman scattering], thermogravimetric analysis (TGA), and enhanced solubility in organic solvents (2-propanol, 2-butanol, *n*-pentanol, *n*-hexanol, mixtures of acetone and water, etc.) [6.80]. Covalent functionalization such as fluorination appears to have strong effects on the electrical conductivity of functionalized materials, which greatly differs from that of pristine carbon nanotubes. It has been reported that the thermodynamic stability of fluorinated SWNTs decreases with tube diameter, meaning that the dissociation energy of the C−F bonds increases as the diameter decreases. C−F bonds were also found to be covalent (with bond length ranging from 1.41 to 1.45 Å). Fluorinated carbon nanotubes have found some applications in the fabrication of cathodes, electrochemical cells, etc., but further studies on different degrees of fluorination should be carried out. It is believed that it is possible to tune the electronic and chemical properties of nanotubes by synthesizing fluorinated tubes with different concentrations of F atoms on their surfaces and ends.

Aryl Diazonium Chemistry

Diazonium compounds are organic compounds whose functional group is represented as $R-N_2H^+X$, in which R could be any organic compound and X an inorganic or organic anion. The importance of these salts in carbon nanotube functionalization is that they can form an

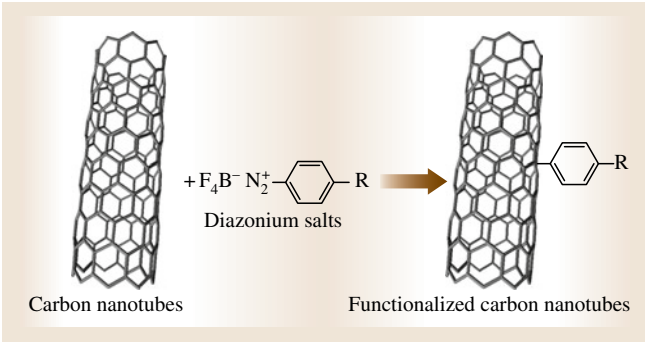


Fig. 6.11 Scheme for functionalization of carbon nanotube with diazonium salts

aryl radical that can then efficiently react with the walls of carbon nanotubes. The chemical activity of aryl di-

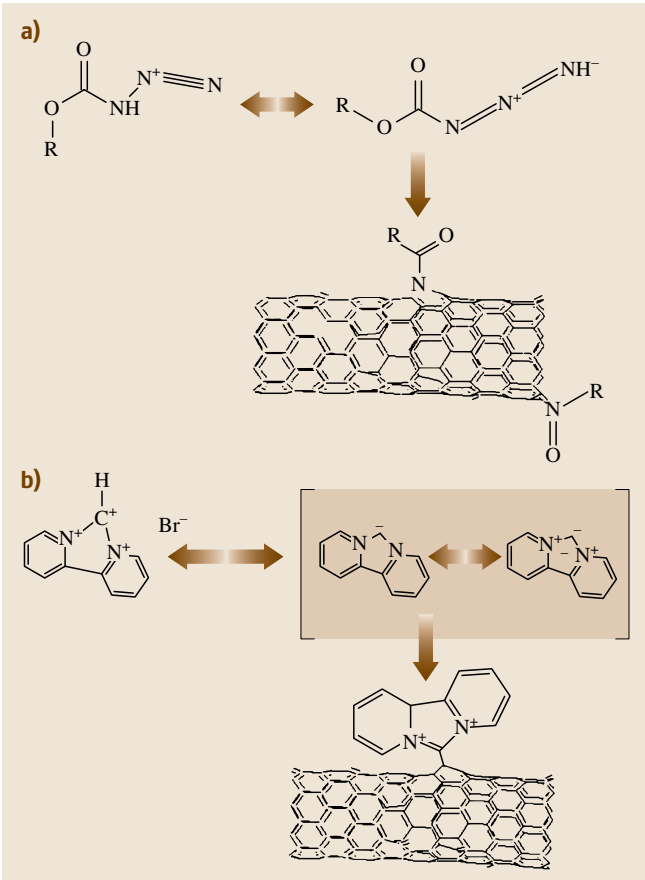


Fig. 6.12a,b Schematic description of functionalization techniques: **(a)** cycloaddition of nitrenes and **(b)** nucleophilic carbene functionalization (after [6.77])

azonium salts with highly oriented pyrolytic graphite (HOPG) and other carbon surfaces has been demonstrated [6.62]. This reaction presumably occurs when the diazonium salt is added to the nanotube suspension. An electron is then injected into the diazo functionality, liberating N_2 and forming a reactive aryl radical, which immediately reacts with the carbon nanotube sidewalls as shown in Fig. 6.11 [6.81]. These methods can be very versatile, since aryl diazonium salts can bear a wide variety of substituents to decorate carbon nanotubes with different functionalization groups. This method could also be scaled up.

Carbenes and Nitrenes

Nitrenes (R–N:) are analogs of carbenes. These compounds are considered electrophile reagents which can add carbon–carbon double bonds. Nanotube functionalization with nitrenes proceeds by thermolysis of alkyl azidoformates (Fig. 6.12a). The same reaction mechanism is followed during functionalization of carbon nanotubes by carbenes. First, nucleophilic carbene is formed by deprotonation of imidizolinium cation, and second, one negative charge per attached moiety is transferred to the nanotube (Fig. 6.12b), thus obtaining functionalized carbon nanotubes [6.82, 83].

6.3.2 Functionalization of Carbon Nanotubes via $\pi-\pi$ Interactions

A great number of routes to noncovalent modification of carbon nanotubes have been reported. In this way, the original tubular structure is preserved and the technique does not damage the surface of the CNTs. Noncovalent carbon nanotube functionalization strategies can be classified into two groups: (a) via $\pi-\pi$ interactions, or (b) by electrostatic interactions. In the following paragraphs both strategies are explained and many examples are given to illustrate them (Fig. 6.13).

Since nanotube covalent functionalization may significantly alter the robustness of the system as well as its optical, electrical, and thermal properties, noncovalent nanotube functionalization approaches should be exploited [6.84]. Functionalization via $\pi-\pi$ interactions relies on the interactions established between carbon nanotubes and nonpolar molecules when these molecules contain aromatic rings or C=C bonds. These interactions could be very stable [6.85] and are caused by $\pi-\pi$ stacking. This stacking was originally proposed as an explanation for the attractive interaction existing between molecules containing π orbitals in the absence of spectroscopic evidence for highest occupied molecular orbital (HOMO)–lowest unoccupied molecular orbital (LUMO) interactions [6.77]. A $\pi-\pi$ interaction is an electrostatic interaction in which the offset and/or orientation of the π orbitals on opposing molecules maximize the $\sigma-\pi$ attractive interactions while minimizing the opposing $\pi-\pi$ repulsive interactions. Such interactions with CNTs can be surprisingly strong, depending on the molecules, and even capable of withstanding temperatures $> 400\,^{\circ}C$ [6.86]. Since these interactions do not cause significant effects on the electrical and mechanical properties of

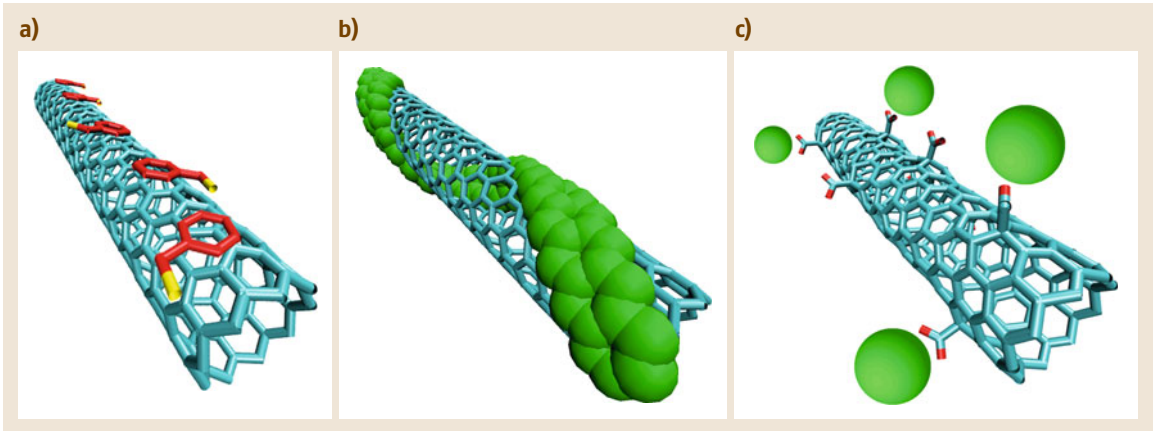


Fig. 6.13a–c Schematic models showing functionalization through **(a)** $\pi-\pi$ interactions with individual molecules; **(b)** wrapping functionalization with long chain-like molecules, thus leading to electrostatic interactions; and **(c)** electrostatic interactions established between molecules or clusters with functional sites available on carbon nanotube surface

Table 6.1 Examples to illustrate the $\pi-\pi$ interactions for functionalization of carbon nanotubes

Compound	Via	CNT type	Achievement/Purpose	References
Amines	Micelle formation	SWCNT	Increase solubilization/ immobilization of proteins	[6.87]
Polystyrene sulfonate sodium salt	Wrapping	SWCNT	Enhance solubilization/breaking bundles	[6.88]
N-succinimidyl-1-pyrenebutanoate	Micelle formation	SWCNT	Immobilization of proteins (ferritin, streptavidin)	[6.89]
Poly(*m*-phenylene-co-2,5-dioctoxy-*p*-phenylene-vinylene) (PmPV, 2)	Wrapping in organic solvents	SWCNT	Enhancing optoelectronic properties	[6.87, 90, 91]
Pyrene and porphyrin derivative	Micelle formation	SWCNT	Development of electron donor–acceptor nanohybrids	[6.92–94]
Pyrene derivatives with nanoparticles (Zn, CdSe)	Micelle formation	SWCNT	Developing field effect transistors	[6.95, 96]
Pyrenecyclodextrin derivatives	Micelle formation	SWCNT	Developing field effect transistors	[6.97]
Pyrene and naphthalene	Micelle formation	SWCNT	Enhance solubility, SWNT polyelectrolyte analog preparation	[6.98]
Pyrene-labeled hydroxypropyl cellulose (HPC-Py)	Micelle formation	MWCNT	Biosensors	[6.99]
Hydrolyzed-poly(styrene-*alt*-maleic anhydride) (h-PSMA)	Wrapping	SWCNT, MWCNT	Further functionalization (polyethyleneimine and gold nanoparticles)	[6.100]
Benzyl mercaptan	Micelle formation	MWCNT	Further functionalization (Pt nanoparticles)	[6.101]
Nucleotide bases [DNA (single and double stranded), poly(rC) and poly(rG)]	Wrapping	SWCNT	UV-Vis optical properties	[6.102]

CNTs, these functionalization methods have attracted considerable attention of numerous scientists in order to obtain novel functional carbon nanomaterials. Table 6.1 presents some examples of this kind of functionalization.

A number of routes to noncovalent modification of carbon nanotubes have been reported, including polymer wrapping and adsorption [6.87, 88, 103], adsorption of amines [6.104] and molecules with large π-systems [6.89], complexation with organometallic compounds [6.105], and radiofrequency glow-discharge plasma modification [6.106]. Table 6.1 presents several examples related to the type of functionalization. This strategy can be applied not only to SWCNTs but also to MWCNTs and possibly graphene. From the examples described in Table 6.1, it is worth mentioning that the main objective of functionalization in most cases is to enhance the solubilization of the carbon nanotubes in polar solvents for further applications. These surface moieties act as effective anchoring sites on the CNT surface and can be used to adsorb other functional molecules, clusters or nanoparticles.

6.3.3 Electrostatic Functionalization of Carbon Nanotubes

To functionalize CNTs electrostatically, first it is necessary to modify the nanotube surface to create some active sites. These active sites can be obtained by covalent functionalization or molecular adsorption via $\pi-\pi$ interactions. This first functionalization step will then allow electrostatic interactions with different molecules, thus enhancing its adsorption on the surface of carbon nanotubes. For example, CNTs functionalized with oxygen functional groups, mainly carboxylic groups [6.107], could then be decorated with different molecules via electrostatic functionalization. In Table 6.2, various examples of different types of electrostatic functionalization routes are presented to illustrate the wide spectrum of possibilities to synthe-

Table 6.2 Examples of electrostatic functionalization of different carbon nanotubes

Functionalization with	Via	CNT type	Achievement/purpose	References
Polyethylene glycol (PEG)	Solution-based chemistry	SWCNT	Increase solubility	[6.108]
Long-chain alyphatic amines	Solution-based chemistry	SWCNT	Increase solubility	[6.109]
Hyperbranched PEI	Solution-based chemistry	MWCNT	Further functionalization Bovine serum albumina (BSA)	[6.110]
Porphyrins (H2P8- and/or ZnP8-)	Solution-based chemistry	SWCNT wrapped with poly[(vinylbenzyl)trimethylammonium chloride] (PVBTAn+)	Improving photocurrent generation	[6.111]
DNA	Solution-based chemistry	SWCNT-NH_3^+; MWCNT-NH_3^+; SWCNT Lys-NH_3^+	Gene delivery vectors	[6.112]
Thioglycolic acid (TGA)-capped CdTe nanoparticles	Solution-based chemistry	SWCNT/pyrene+, MWCNT/pyrene+	Electron donor–acceptor nanohybrids	[6.113]
Poly(dimethyldiallylammonium chloride) (PDDA)	Solution-based chemistry/ Layer by layer (LbL) technique	MWCNT-PSSn−	Further functionalization (magnetic nanoparticles)	[6.114]
Magnetic iron oxide (Fe_3O_4) nanoparticles	Solution-based chemistry	MWCNT grafted with poly(2-diethyl-aminoethyl methacrylate) (PDEAEMA)	Magnetic cell formation	[6.115]
Polystyrene sulfonate sodium salt (PSS),poly(dimethyldiallyl-ammoniumchloride) (PDDA)	Solution-based chemistry/LbL	SWCNT-pyrene+; SWCNT-pyrene−	Further functionalization	[6.116]
Poly(ethyleneimine) (PEI), poly(acrylic acid) (PAA)	Solution-based chemistry/LbL	SWCNT-polyamphiphiles; MWCNT-polyamphiphiles	Further functionalization	[6.117]
Glucose oxidase (GOX), poly(diallyldimethylammonium chloride) (PDDA)	Solution-based chemistry/LbL	MWCNT (surface carboxylate groups)	Amperometric glucose biosensors	[6.118]
RNA	Solution-based chemistry	SWCNT modified with hexamethylene-diamine (HMDA) and poly(diallyl-dimethylammonium)chloride (PDDA) [PDDA-HMDA-SWCNT]	Carriers of biologically active molecules	[6.119]
Pt nanoparticles	Solution-based chemistry	SWCNT (carboxylate groups on the surface)	Catalysts	[6.120]

size different functional materials for different specific applications.

It is noteworthy that electrostatic functionalization of carbon nanotubes is normally carried out by synthetic or natural polyelectrolytes such as polyethyleneimine (PEI) [6.110, 117], polystyrene sulfonate sodium salt (NaPSS) [6.117], deoxyribonucleic acid (DNA), different proteins [6.111, 112, 118], etc. This is due to the fact that these molecules have the possibility to have high charge density, thus allowing an increase of anchoring points on the CNT surface. Due to the possibility of using polyelectrolytes of natural origin, this functionalization is ideal to produce biocompatible CNTs for further biomedical applications [6.112, 118]. Electrostatic functionalization also enables decoration of CNTs with different metallic nanoparticles or functional molecules for use in the fabrication of efficient sensors and even catalysts [6.111, 113, 115, 120].

Functionalization of carbon nanotubes while preserving their structural integrity opens a wide range of novel applications, especially if doped carbon nanotubes are used. This kind of soft physical chemistry helps to preserve carbon nanotube properties, thus enhancing and expanding their fields of application.

6.4 Properties of Modified Carbon Nanotubes

This section shows that CNTs are sensitive to any modification of their crystalline lattice. Changes in their atomic structure could result in different electrical, mechanical, and chemical properties. Even if they do not exhibit any covalent modification, their interaction with foreign molecules may also affect the way they behave.

6.4.1 Electrical Properties of Modified Tubes

Nitrogen-doped carbon nanotubes (CN_x) may have higher conductivity than carbon nanotubes, originating from the isolated pair of electrons introduced by the substitutional doping of nitrogen which is conjugated with π orbitals [6.121, 122]. This π interaction is capable of converting a semiconducting (zigzag) carbon nanotube to metallic by introducing electronic states at or close to the Fermi level. Experimental measurements have shown that nitrogen-doped SWCNTs require less energy to excite carriers into the conduction band [6.123]. Mats of CN_x could exhibit electrical conductivities in the range of ca. $200–450\,\Omega^{-1}\,\mathrm{cm}^{-1}$. In addition, the conductivity could be tailored according to the doping concentration within the CNTs (Fig. 6.14a,b) [6.124]. These N-doped CNTs could exhibit larger third-order susceptibility and better ultrafast saturable absorption of visible light when compared with undoped CNTs. This phenomenon is caused by the high density of π electrons in the system.

Doping carbon nanotubes with boron introduces hole-type charge carriers. Although these defects will increase the electron scattering density, they could lead to enhanced conductivity values by lowering the resistivity by an order of magnitude (7.4×10^{-7}–$7.7\times10^{-6}\,\Omega\,\mathrm{m}$) when compared with pure carbon MWCNTs (5.33×10^{-6}–$1.9\times10^{-5}\,\Omega\,\mathrm{m}$) (Fig. 6.14c) [6.125–128]. These B-doped CNTs possess a low temperature dependence of resistivity; it is thought that close to 0 K the total number of conduction channels increased with the number of conduction carriers (hole carriers induced by boron doping) [6.129]. The optical absorption spectra of the boron-doped SWCNTs indicate the presence of a new peak at ca. 0.4 eV, which is assigned to the valence band of a new acceptor band caused in-plane doping of boron within the SWCNTs [6.130].

When intercalating iodine in SWCNT mats, the resistance at 300 K may be reduced by a factor of ≈ 40 (compared with the pristine sample). Here, iodine atoms increase the concentration of mobile holes in the π-electron bands of the nanotubes (Fig. 6.14d) [6.131]. In addition, iodine-doped DWCNT cables have shown lower resistivity values ($1.5\times10^{-7}\,\Omega\,\mathrm{m}$) compared with their undoped counterparts ($5\times10^{-7}\,\Omega\,\mathrm{m}$). In addition, the doped systems have lower specific conductivity ($1.96\times10^{4}\,\mathrm{S\,m^2/kg}$) when compared with aluminum or copper, and similar current capacity to copper ($104–105\,\mathrm{A/cm^2}$) [6.132]. The conductivity of fluorinated SWCNTs has also been studied, and the results show that it differs dramatically from that of pristine SWCNTs; a sample of pristine SWCNTs was reported to have resistance of $10–15\,\Omega$, whereas fluorinated SWCNTs displayed resistance $> 20\,\mathrm{M\Omega}$ [6.78].

6.4.2 Electrochemistry of Modified Nanotubes

Due to the excellent electronic properties of carbon nanotubes and their reactivity after modification, their electrochemical properties and applications have been studied. These modifications may be classified into redox enzyme interactions, metal nanoparticle anchoring, doping, conductive polymer doping, covalent modification, and intercalation.

Redox-Enzyme-Modified Carbon Nanotubes

High-surface-area carbon materials have long been used as a conductive matrix for redox enzyme immobilization to enable use of this carbon–enzyme nanocomposite as a transductor in electrochemical sensors. The small diameter of SWCNTs means that this material is capable of being in close contact with the active site of several oxidoreductases, thus exhibiting enhanced electron transfer when compared with flat carbon surfaces such as HOPG and carbon paste electrodes. Among different enzymes, laccases, peroxidases, glucose oxidase, alcohol oxidase, cholesterol oxidase [6.133], and many others have been reported to interact well with CNTs. Recently, the possibility of using carbon nanotube composites with redox enzymes not only in sensors but also in fuel cells has attracted great attention. Figure 6.15a shows a potential biofuel cell configuration using modified carbon nanotube electrodes. By using redox mediators, both the anode and cathode could be constructed with carbon nanotubes and redox enzymes. Over recent years, direct electron transfer between redox enzymes and carbon electrodes has been studied. Direct electron

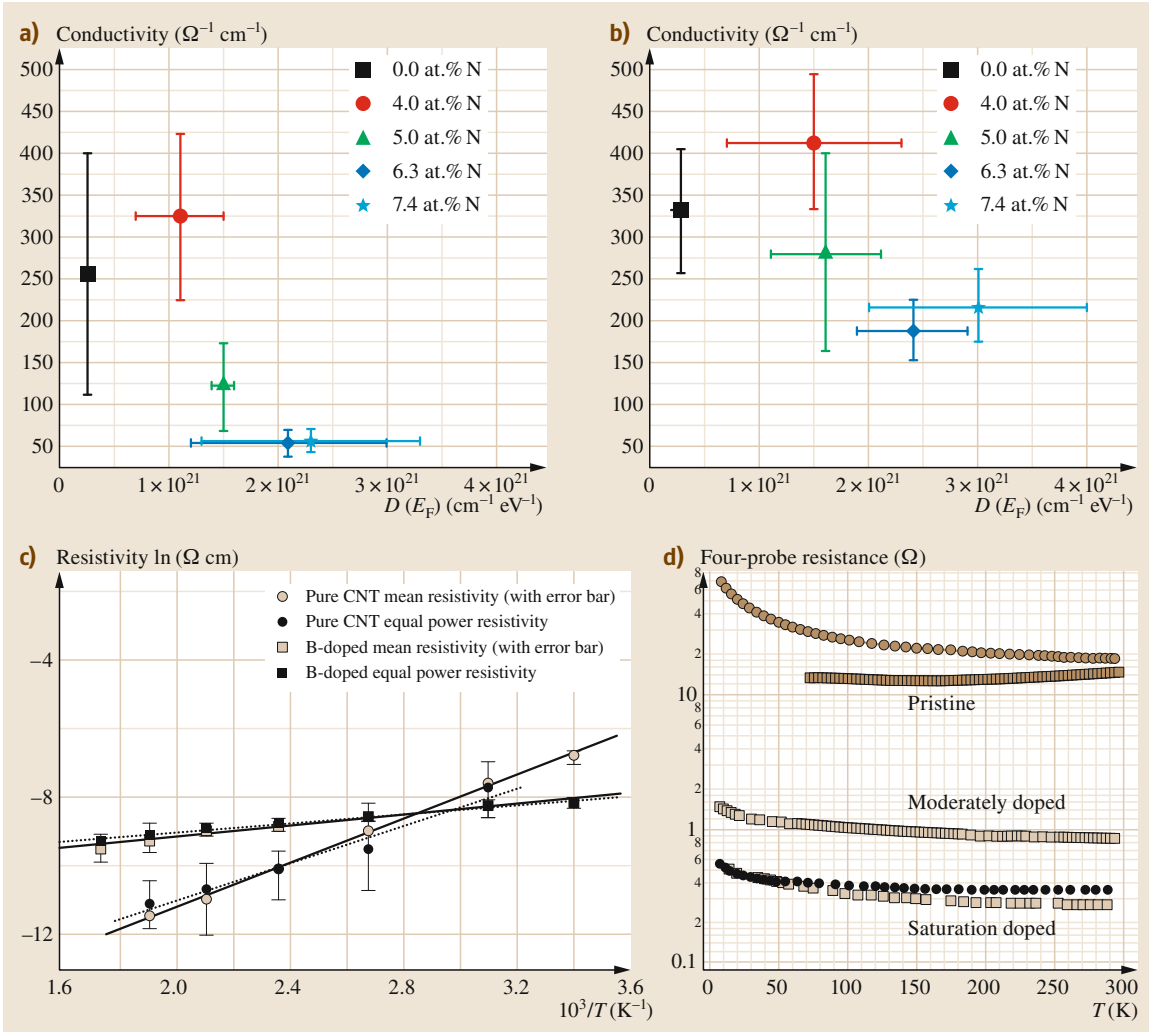


Fig. 6.14a–d Plots of conductivity versus density of states, $D(E_F)$, at the Fermi level of N-doped CNT mats that are **(a)** acid treated and **(b)** pristine (after [6.124]). **(c)** Resistivity versus temperature of pure and boron-doped MWCNTs (after [6.128]) and **(d)** resistivity versus temperature of pristine and iodine-doped SWCNTs (after [6.131])

transfer should result in higher available potential, but the high charge-transfer resistance limits the power available of these devices. *Rivas* and *Rubianes* [6.134] reported direct electron transfer from glucose oxidase to CNTs, and its application to glucose biosensors. These authors found excellent response of glucose oxidase with low interference from compounds such as uric acid and acetaminophen. The results indicate that nanotubes could also improve the specificity of the electrochemical oxidation of some compounds. Other authors have demonstrated that cytochrome C peroxidase could be immobilized in polyaniline (PANI)/MWCNT electrodes by electrochemical oxidation followed by adsorption [6.135]. It was shown that these composite electrodes exhibit direct electron transfer as well as bioelectrocatalytic activity towards hydrogen peroxide. Subsequently, Liu et al. managed to immobilize glucose oxidase on PANI–Fe_3O_4–CNT electrodes. The modification of these nanotubes is rather complex because it involves an electroactive biomolecule, a conductive polymer, and a metal oxide. However, the electrochemical response towards glucose oxidation was very

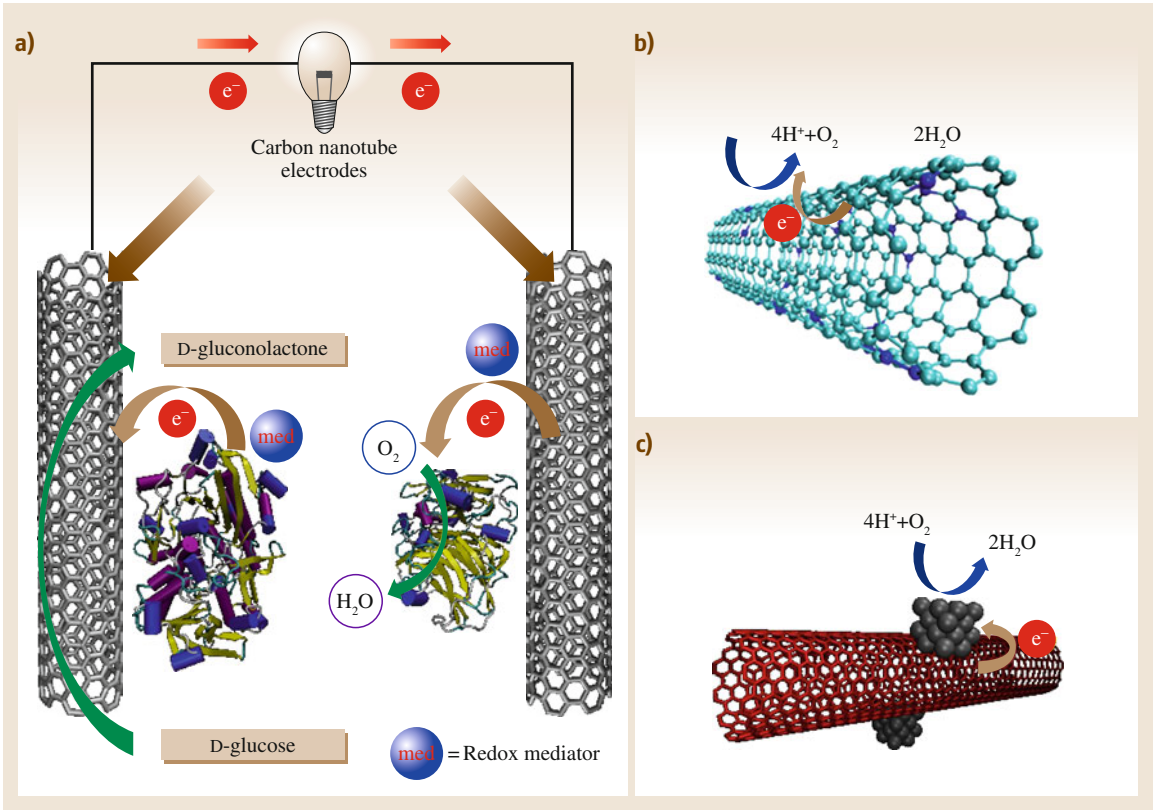


Fig. 6.15 **(a)** Typical biofuel cell configuration using carbon nanotube electrodes modified with redox enzymes. On the *left*, a carbon nanotube modified with glucose oxidase catalyzes the oxidation of glucose to yield gluconolactone. On the *right*, a SWCNT modified with laccase catalyzes the reduction of oxygen to water. **(b)** Scheme for oxygen reduction on the surface of a nitrogen-doped CNT. The doping sites work as electrocatalytically active sites that promote oxygen reduction. **(c)** CNT decorated with Pt nanoparticles. The metal nanoparticle has electrocatalytically active surfaces that promote reduction of oxygen to water. Electron transfer is mediated through the metal nanoparticle

efficient, and the electrode material displayed good dispersibility in water and superparamagnetic properties, an important issue from the biomedical point of view. *Chen* and *Lu* [6.136] assembled hemoglobin using a mixture of polyelectrolytes and a surfactant. The electrochemical response was studied by cyclic voltammetry, and the assembled material showed enhanced reduction of hydrogen peroxide. Table 6.3 presents some of the redox enzyme–carbon nanotube assembly systems that have been studied.

Metal Nanoparticle Modified Carbon Nanotubes

Carbon nanotubes are electrically conductive nanomaterials, with relatively high surface area and robust mechanical properties. For these reasons, carbon nanotubes have potential applications as an electrode support for electrocatalytically active metal nanoparticles (NPs). Various metal nanoparticles could catalyze the electrochemical oxidation/reduction of chemical compounds and efficiently transfer charge to electrically conductive supports. Electrodes made of carbon nanotubes and metal nanoparticles might find direct application in fuel cell technologies (Fig. 6.15c). In this context, *Che* et al. [6.137] used graphitic carbon nanotubes prepared using a template method to support Pt/Ru nanoparticles that showed electrocatalytic activity towards O_2 reduction and methanol oxidation. Later, MWCNTs prepared by chemical vapor deposition (CVD) were decorated with platinum nanoparticles by *Liu* et al. [6.138]. The Pt-coated nanotubes showed a typical cyclic voltammetry reduction peak for oxy-

Table 6.3 Examples of redox-enzyme-modified carbon nanotubes with electrochemical applications

Type of nanotubes	Redox enzyme	Notes	References
SWCNT	GO_x	Composite with Pt NP, sensitive to glucose	[6.139]
Shortened HiPCO SWCNT	Microperoxidase-11	High electron transfer without redox mediator	[6.140]
MWCNT	Glucose dehydrogenase	Modified with chitosan. Sensitive to nicotinamide adenine dinucleotide (NADH)	[6.141]
SWCNT	Glucose oxidase	Enzyme adsorbed to the nanotube	[6.142]
MWCNT	Glucose oxidase	Cetyltrimethylammonium bromide (CTAB) added as dispersing agent	[6.143]
SWCNT	Myoglobin and horseradish peroxidase	Enzymes bound to the tip of the nanotubes. H_2O_2 sensitivity	[6.144]
Shortened SWCNT	Flavin adenine dinucleotide (not an enzyme but redox cofactor) and apo-glucose oxidase	Glucose electrocatalytic activity regained by the enzyme	[6.145]
MWCNT	Acetylcholinesterase	Organophosphorous pesticides and nerve agent electrochemical sensor developed	[6.146]
MWCNT	Glucose oxidase	Chitosan-coated carbon nanotubes. Direct electron transfer achieved	[6.147]
MWCNT	Horseradish peroxidase	Direct electron transfer and hydrogen peroxide electrochemical sensitivity achieved	[6.148]
MWCNT	Glucose oxidase	Nafion was used as carbon nanotube modifier	[6.149]
MWCNT	Hemoglobin	Hybrid composite films containing gold nanoparticles. H_2O_2 sensitivity achieved	[6.150]
MWCNT	Several hemoproteins: horseradish peroxidase, hemoglobin, myoglobin, and cytochrome C	Surfactant-modified carbon nanotubes	[6.151]
MWCNT	Lactate oxidase, polyphenol oxidase, and alcohol dehydrogenase	MWCNT paste prepared with mineral oil. Biosensors with high selectivity were prepared	[6.152]
MWCNT	Glucose oxidase	Nanotubes modified with aminopropyltriethoxy silane	[6.153]
MWCNT	Horseradish peroxidase, myoglobin, and cytochrome C	MWCNT paste with ionic liquid	[6.154]
CN_x-MWCNT	Glucose oxidase	Improved electron transfer than MWCNT	[6.155]
SWCNT-carbon fiber electrode	Laccase	Good O_2 reduction activity. Microbiofuel cell constructed	[6.156]
MWCNT	Laccase	Poly(L-lysine) layer-by-layer modified nanotubes	[6.157]
MWCNT	Laccase	Ascorbate/O_2 biofuel cell developed	[6.158]

gen reduction, and the Pt–MWCNT composites were evaluated in real fuel cells, showing good performance with high exchange current density and low DC resistance. Indeed, compared with carbon black, CNTs exhibit higher electrical conductivities due to their high aspect ratio and degree of crystallinity. To increase the electrode efficiency, MWCNTs grown on carbon fibers were used as support for Pt nanoparticles, and their electrochemical behavior was characterized by cyclic voltammetry. These reports opened a field related to the use of CNTs in fuel cell technologies. Table 6.4 presents some publications related to the decoration of carbon nanotubes with metal nanoparticles and their use for electrocatalytic applications.

Doped Carbon Nanotubes

Increase of the nitrogen content in CNTs also increases their capacitance, because the number of active sites for electron transfer increases (Fig. 6.15b) [6.124]. It has been suggested that the pyridinic sites may act as reducing points within CNTs [6.159]. Nitrogen-doped carbon nanotubes exhibit enhanced catalytic activity for oxygen reduction in fuel cells; this process follows a four-electron pathway. The advantage of N-doped CNTs is that they have exceptional resistance to CO poisoning and selectivity, when compared with Pt-based systems [6.160, 161]. Doped nanotubes have also shown higher electron transfer to redox enzymes when compared with pure CNTs. Nitrogen- [6.155] and

Table 6.4 Publications related to decoration of carbon nanotubes with different metal nanoparticles and their electrocatalytic performance

Type of CCNT and metallic NP	Reaction	Notes	References
MWCNT-PtRu	Proton exchange membrane fuel cell (PEMFC)	Good resistance to CO poisoning	[6.163]
MWCNT-PtSn	Ethanol oxidation	NPs 2.7 nm mean particle diameter	[6.164]
MWCNT-Pt	Methanol oxidation	Microwave-assisted polyol synthesis. NPs 2–6 nm diameter	[6.165]
MWCNT-Pt, Pd, and Rh	O_2 reduction	NPs 3–5 nm diameter	[6.166]
MWCNT-Pt	Methanol oxidation	Pt NPs deposited by electrochemical reduction	[6.167]
MWCNT-Pt	Methanol oxidation	NPs 2–4 nm diameter	[6.168]
MWCNT-Pd	Hydrazine oxidation	Potentiostatic deposition	[6.169]
SWCNT bundles-Pt	Methanol oxidation	5 nm-diameter NPs	[6.170]
SWCNT-Pt	Methanol oxidation	Transparent electrocatalytically active electrode	[6.171]
MWCNT-Pt	Hydrogen electrochemical absorption/desorption	NPs diameter less than 5 nm	[6.172]
MWCNT-Pt	PEMFC	Microwave-assisted synthesis, 3 nm diameter	[6.173]
MWCNT-PtRu	Direct methanol fuel cell (DMFC)	Improved stability as compared with Pt NPs	[6.174]
SWCNT-Pt	O_2 reduction	Higher electron transfer rate than commercial carbon black/Pt electrocatalyst	[6.175]
MWCNT-Ag	Methanol oxidation in alkaline media	Electrodeposited on modified MWCNTs	[6.176]
CN_x-Pt	DMFC	Pt NPs, 2 nm in diameter, deposited by sputtering	[6.177]
MWCNT-Pt	Methanol oxidation	Deposition on MWCNT defects	[6.178]
Nitrogen-doped CCNT-Pt	Methanol oxidation	Nanotubes grown by template method	[6.179]
MWCNTs-Pd	Formic acid oxidation	Functionalized carbon nanotubes	[6.180]
MWCNT-PtFe	Methanol oxidation	Higher activity than similar MWCNT-Pt electrodes	[6.181]
CN_x-Pt	Methanol oxidation	Pt nanoparticles 3–9 nm diameter	[6.182]
MWCNT-Pd	Formaldehyde oxidation	Iodinated MWCNTs as support. NPs 5–10 nm diameter	[6.183]
MWCNT-Cu-PtFe	DMFC and O_2 reduction	Improved methanol tolerance	[6.184]
MWCNT-PtCo MWCNT-PtMn	Methanol oxidation	Electrochemical deposition, NPs 100–200 nm diameter	[6.185]
MWCNT-PtCo	DMFC	PtCo hollow NPs 10–20 nm diameter	[6.186]

boron-doped [6.162] CNTs have been assembled with glucose oxidase; here, better sensitivity and increased linear response were found, making these nanotubes excellent candidates for direct electrochemistry with redox enzymes.

Conductive Polymer-Doped Nanotubes

Not only conducting polymers but also hybrid coatings of conductive polymer–inorganic materials have been employed to modify the electrochemical response of CNTs; for instance, phosphomolybdate/polypyrrole (PPy) and phosphomolybdate/poly(3,4-ethylenedioxythiophene) (PEDOT) coatings have been deposited on CNTs by adsorption followed by electrochemical oxidation. The process was repeated several times to achieve a layered structure. The resulting composite revealed high electrocatalytic activity towards reduction of bromate ion. Polyaniline (PANI)-coated MWCNTs have been prepared by electrochemical oxidation in the presence of amine-modified MWCNTs [6.187]. This composite showed good electrochemical response in amperometric detection of celecoxib, a nonsteroidal anti-inflammatory drug. This improved response is attributed to both an increase of electrochemical available area and promoted adsorption of the drug on the polyaniline-modified electrode. By simple mixing of a colloidal dispersion of PANI nanofibers and water-dispersable MWCNTs, composite electrodes were prepared by *Yang* et al. [6.188]; the composite exhibits great capability for detecting DNA hybridization. When using redox probes it has been shown that the composite has improved electron transfer ability when compared

with PANI or MWCNT alone, and the redox activity of PANI plays a key role in the regeneration and stability of the biosensor. *Hu* et al. have also examined the electrochemical response of PANI/MWCNT–poly(sodium 4-styrenesulfonate) (PSS) composite electrodes, prepared by layer-by-layer self-assembly [6.189]. These authors showed that anionic MWCNT–PSS could dope cationic polyaniline, and that the technique could be used to construct electrodes in a reliable way. Composite electrodes of DWCNT/PEDOT:PSS were studied by *Kalbáč* et al. [6.190], and they found that, after mixing DWCNTs with the conductive polymer, the Raman bands of the carbon nanotube shifted whereas those of the polymer remained intact. By using in situ Raman spectroelectrochemistry, it was shown that the CNTs change their electronic conformation as a function of the potential charge. It is also noteworthy that electrochemical synthesis of PEDOT in the presence of MWCNTs results in composite electrodes with lower charge transfer impedance, lower internal resistance, and superior capacitive response. These improved electrical properties result in faster response and better coloration efficiency in electrochromic devices.

Covalently Modified Nanotubes

Modification of CNTs with either electroactive or non-electroactive molecules by covalent bonding results in alteration of their electrochemical response. Recently, MWCNTs were modified by covalent bonding with neutral red [6.191], a nitrogen-containing polycyclic compound which can behave as a redox mediator. These nanotubes showed better electrochemical transfer to glucose oxidase and were employed to construct biosensors. The covalent bonding between the redox mediator and the MWCNTs improves its long-term stability. In a similar approach, MWCNTs were modified with thionine in order to increase its electrocatalytic activity towards hydrogen peroxide reduction [6.192]. Due to the covalent bonding, the electrochemical response decreased by less than 5% over 150 days of use. Sidewall-functionalized aminated MWCNTs were also immobilized on silicon surfaces via a carbodiimide reaction, and the electrochemical properties were evaluated by scanning electrochemical microscopy, with and without redox mediators. In this case, the MWCNTs enabled efficient electrical communication between the silicon surface and the redox probe in solution [6.179].

Electrochemical Intercalation of Nanotubes

Lithium ions have been intercalated between MWCNTs, exhibiting a reversible capacity that is sensitive to the processing conditions; the obtained values are between 100 and 400 mA h/g [6.193]. In addition, by intercalating Li within the hollow cores of SWCNTs, it is possible to obtain a high reversible capacity of 1000 mA h/g [6.194], the observed saturation Li/C ratio for shortened SWCNTs being ca. $LiC_{3.35}$ [6.194, 195]. Here, Li ions may be located on the outer surfaces of the CNT; however, the results are enhanced when the carbon nanotubes are shortened, leaving open tips available for intercalation of Li ions within the cores, since Li ions display a diameter of 0.7 Å and SWCNTs exhibit larger diameters of 1.3–1.6 nm. Li ions could diffuse through defect sites created by oxidation into the cores of the CNTs, thus causing a lower irreversible capacity due to the difficulty for Li ions to deintercalate [6.194, 196].

6.5 Characterization of Modified Carbon Nanotubes

Once carbon nanotubes have been modified, it is important to monitor the resulting changes. For this reason, the most commonly used techniques used to characterize CNTs are discussed in this section. These techniques mainly consist of transmission electron microscopy (TEM), atomic force microscopy (AFM), scanning transmission microscopy (STM), electron energy loss spectroscopy (EELS), x-ray photoelectron spectroscopy (XPS), Raman spectroscopy, and thermogravimetric analysis (TGA).

6.5.1 Transmission Electron Microscopy

This technique enables direct observation of the walls of the carbon nanotube, capable of showing how crystalline or defective they are. This can be observed by the straightness of the walls, as the presence of defects in the carbon nanotube introduces variations in the local curvature within the nanotube lattice; for example, nitrogen-doped MWCNTs tend to create compartments within the hollow cores, resembling

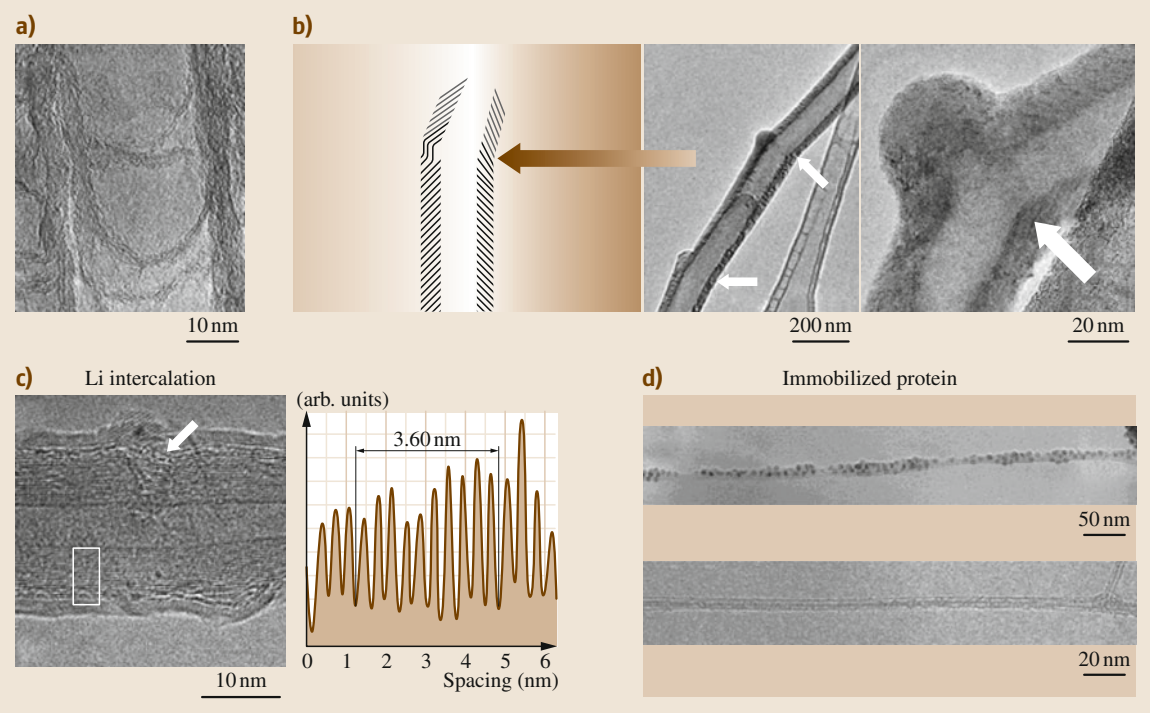


Fig. 6.16a–d TEM images of: **(a)** nitrogen-doped CNT with internal compartments resembling a bamboo-type morphology (after [6.122]); **(b)** sulfur-doped MWCNT with an extruding kink (after [6.197]); **(c)** effect of Li intercalation in a MWCNT, showing an increase in the interlayer spacing within the nanotube walls (after [6.198]); and **(d)** immobilized protein on the surface of a SWCNT (after [6.89])

a *bamboo-like* morphology (Fig. 6.16a) [6.122]. In addition, sulfur atoms have been reported to cause deformation of the tubular layers and the presence of branches (Fig. 6.16b) [6.197]. It is also possible to observe an increase in the interlayer spacings within the concentric walls of a MWCNT caused by alkali-metal intercalation. In this case, Li intercalation exhibits an interlayer spacing increase from 3.4 to 3.6 Å (Fig. 6.16c) [6.198].

TEM can also allow visualization of macromolecules such as polymers and proteins on the surface of carbon nanotubes. In this context, metal-containing proteins such as ferritin and streptavidin–Au conjugates have been observed as dark spots corresponding to the nanoparticles that are contained within the proteins (Fig. 6.16d) [6.89]. Regarding polymers, it is possible to visualize the wetting of the carbon nanotube walls with an amorphous-like polymer layer [6.199, 200].

6.5.2 Atomic Force Microscopy and Scanning Transmission Microscopy

AFM allows visualization of the morphology or phase changes within the surface of a sample. In this technique, a sharp tip approaches the desired surface and could be in full contact or tapping at a specific frequency. This tool has been used to visualize anchoring of biomolecules such as proteins and DNA onto carbon nanotubes. Proteins such as ferritin and streptavidin–Au conjugates appear as clusters under AFM [6.89]. DNA wrapped around MWCNTs could be observed as thin strands on the surface of the tube, where the nanotubes exhibit a nonsmooth surface due to the wrapping of DNA strands (Fig. 6.17a,b) [6.201].

Scanning transmission microscopy (STM) measures the electric potential differences across the surface of the sample and has been used to identify atomic de-

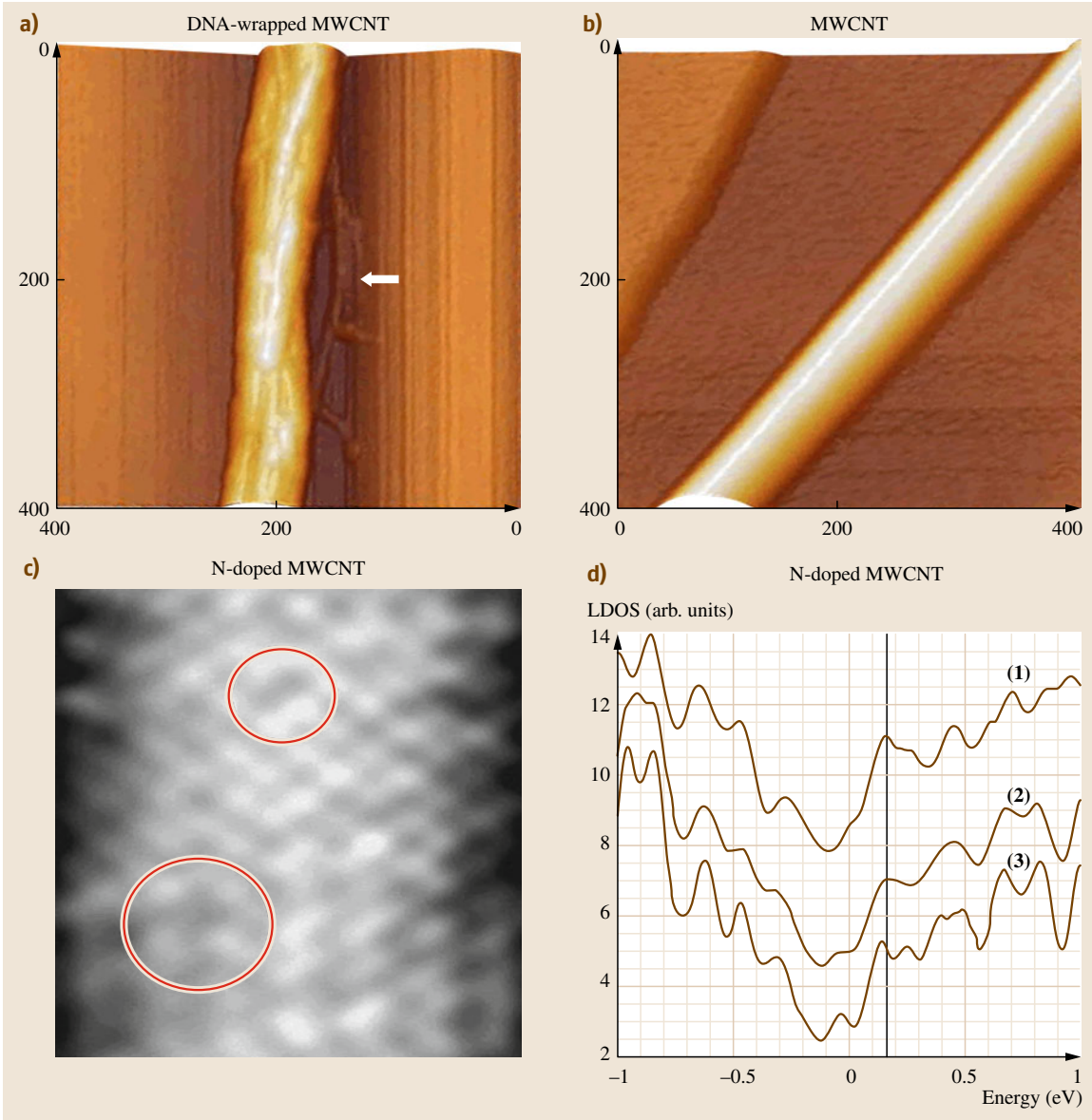


Fig. 6.17a–d Tapping-mode AFM images of **(a)** DNA strands wrapping a MWCNT and **(b)** a pure MWCNT (after [6.201]). **(c)** STM image of vacancies in a N-doped MWCNT caused by pyridine-like sites, and **(d)** scanning tunneling spectra taken at different sites of a nitrogen-doped MWCNT showing peaks located at ca. 0.18 eV in the conduction band (*vertical line*; after [6.122])

fects in carbon nanotubes. In particular, it has been used for nitrogen-doped CNT, where vacancies corresponding to pyridinic-type nitrogen atoms have been identified (Fig. 6.17c) [6.121]. When using the spectroscopy mode (STS), this technique can also provide information related to the local density of states (LDOS) near the Fermi level. The technique has been used for nitrogen- and boron-doped CNTs, which exhibit characteristic spectra when compared to their undoped counterparts. Nitrogen (Fig. 6.17d) and boron

atoms result in donor and acceptor states, respectively [6.121, 202].

6.5.3 Electron Energy Loss Spectroscopy (EELS)

When a ray of fast electrons is aimed at a sample and these electrons are scattered, some may suffer inelastic scattering and be randomly deflected. The amount of energy lost during the excitation of an electron from the inner electronic shell of an atom can then be determined. It is noteworthy that each element exhibits a unique energy loss for this type of inelastic interaction. EELS can therefore provide information related to the elemental composition of modified nanotubes; for example, boron- and nitrogen-doped CNTs have been analyzed by EELS [6.130, 205]. When a SWCNT is doped with boron near the C1s $\rightarrow \pi^*$ resonance lo-

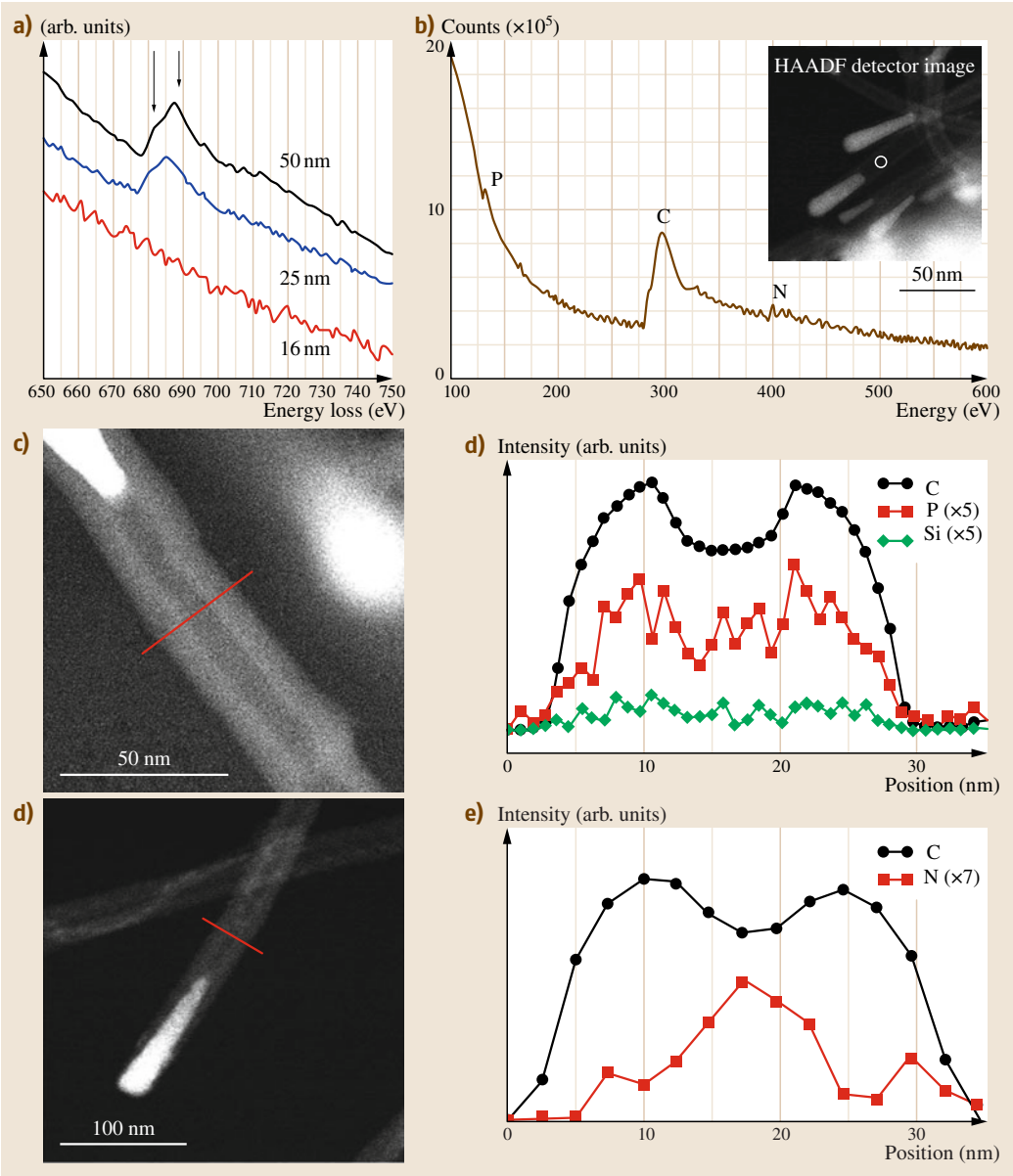


Fig. 6.18a,b EEL spectra of **(a)** diameter selectivity of SWCNT fluorination (after [6.203]). **(b)** PN-doped MWCNT (HAADF – High angle annular dark field) (after [6.204]). **(d,f)** Elemental line scans using EELS of a PN-doped MWCNT: **(d)** C and P signals, and **(f)** C and N signals. **(c,e)** Scanning TEM image of the respective CNT and **(d,f)** elemental line scans

cated at ca. 284 eV, the B1s ionization edge (π^*) can be observed at ca. 192 eV, showing that the B atoms are incorporated into the lattice [6.130]. For nitrogen-doped systems, the N-*K* edge shows the presence of trivalent nitrogen (401–403 eV) and pyridine-type sites ($\approx$ 399 eV) [6.205]. EELS has also been used to observe covalent ($\approx$ 685 eV) and ionic ($\approx$ 690 eV) bonding in fluorinated MWCNTs (Fig. 6.18a) [6.203]. In addition, EELS has been used to study heterodoped nanotubes such as phosphorus-nitrogen (PN)-doped MWCNTs (Fig. 6.18b). Here, the presence of phosphorus atoms was confirmed by the ionization edge located at ca. 130 eV [6.204]. Furthermore, EELS has been used to determine whether alkali metals intercalated in MWCNTs and SWCNT bundles, calculated by the ratio of the spectral intensity of $I_{\text{alkali}}/I_{\text{C}}$ (alkali/carbon) [6.206, 207].

EELS in conjunction with TEM has been used to elucidate the elemental distribution in carbon nanotubes; for example, the following metal compounds encapsulated inside nanotubes have been detected: Fe_3P [6.204], Fe_3C, and FeO_x [6.226]. For nonmetallic elements it has been used for CNTs doped with fluorine [6.203] and nitrogen [6.211], and PN heterodoping (Fig. 6.18c,d) [6.204]. This technique has also been used for mapping sulfur in thiol group functionalization [6.227].

6.5.4 X-Ray Photoelectron Spectroscopy

X-ray photoelectron spectroscopy (XPS) consists of irradiating samples with a focused x-ray beam. The change in kinetic energy of the photoemitted electrons from the top surface of the sample (ca. 10–100 Å in depth) can be recorded using an energy analyzer. XPS is able to measure the elemental composition, chemical states, and electronic states of the elements present in the samples. This tool is capable of showing the elements and the types of bonds that are present in pristine or modified CNTs. Using this technique, one can determine the degree of crystallinity of CNT samples by studying the sp^2 C=C (284.3 eV) bonding; the less sp^3 C−C (285.2 eV) bonds in the sample, the higher the degree of crystallinity of the CNTs [6.208–212]. Using this technique, it is also possible to identify C−N bonds by analyzing the C1s signal for C−N (2863 eV) and C=N (285.6 eV) [6.213]. From the N1s signal it is possible to determine substitutional (400.5 eV), pyridine-like (398.5 eV), and quaternary (401.2 eV) nitrogen, as well as nitrogen oxide (405 eV) [6.159, 214, 220–222, 224, 225]. When carbon nanotubes are fluorinated, they exhibit fluorine peaks corresponding to semi-ionic (6862 eV) and covalent (688.7 eV) C−F bonds [6.101, 219, 228], and the C1s signal shows a variety of C−F (291.2 eV), $C-F_2$ (292.9 eV), and $C-F_3$ (294.6 eV) bonds [6.219]. When carbon nanotubes are oxidized, the presence of several C−O bonds may be monitored in the C1s region: C−O (286.5 eV), C=O (2873 eV), −COO (288.8 eV), O−C=O (288.5 eV), and O−COO (290.3 eV). Similarly, by analyzing the O1s signal, one can identify O=C (531.7 eV), O−C (533.3 eV), and O−COO (534.4 eV) functional groups [6.208–210, 212, 215–217]. In addition, from survey spectra it is possible to obtain the elemental concentration present in the entire sample [6.159, 214, 223, 229]. Table 6.5 summarizes the binding energies of different elements that have been reported in literature for different types of modified CNTs.

Table 6.5 Reported bonds within modified carbon nanotubes measured by x-ray photoelectron spectroscopy

Element	Bond type	eV	References
C	C=C	284.3	[6.208–212]
	C−C	285.2	[6.208–210, 212]
	C=N	285.6	[6.213]
	C−N	286.3	[6.213]
	C−O	286.5	[6.208, 210, 214–216]
	C=O	287.3	[6.208–210, 215, 217]
	O−C=O	288.5	[6.209, 216]
	COO	288.8	[6.208, 210, 215, 217]
	O−COO	290.3	[6.208]
	C−F	291.2	[6.218, 219]
	$C-F_2$	292.9	[6.219]
	$C-F_3$	294.6	[6.219]
N	Pyridinic	398.5	[6.159, 214, 220–223]
	Substitutional	400.5	[6.214, 220, 221, 224, 225]
	Quaternary	401.2	[6.159, 214, 222]
	Nitrogen oxide	405	[6.159, 214]
O	O=C	531.74	[6.208, 209, 215–217]
	O−C	533.3	[6.208, 209, 215–217]
	O−COO	534.4	[6.215]
F	Semiionic	686.2	[6.218, 219]
	Covalent	688.7	[6.218, 219]

6.5.5 Raman Spectroscopy

Raman scattering consists of inelastic scattering in which:

1. An electron is excited so that it *jumps* from the valence band to the conduction band by adsorbing a photon
2. The excited electron may suffer scattering from the emission or absorption of phonons, and
3. A photon can then be emitted due to the relaxation of an electron back to the valence band.

Some characteristic Raman signals have been ascribed to SWCNTs and MWCNTs. In particular, the radial breathing mode (RBM) which is caused by a radial vibration mode ($100–500\,cm^{-1}$) is used to determine the nanotube diameter of SWCNTs. The G-band corresponds to tangential vibrations and is located at ca. $1500–1605\,cm^{-1}$. This band is related to the degree of crystallinity of graphite-like materials. The D-band arises from disorder present within the carbon hexagonal lattice; this peak is located at ca. $1250–1350\,cm^{-1}$. The G′-band (D-band overtone) (ca. $250–2900\,cm^{-1}$) arises from a two-phonon, intervalley second-order Raman scattering process and may be observed from defect-free sp^2-hybridized carbons. The D-band and G′-band are very sensitive to the laser excitation energy [6.230, 231].

Introduction of disorder into nanotubes will reduce their crystal symmetry; here, phonon modes at the Γ point can be allowed, and phonon modes within the Brillouin zone may participate in a double resonance process, all of which may cause broadening of the Raman peaks [6.232, 233]. In particular, for carbon nanotubes containing a large concentration of defects, the scattering cross section might increase, as well as the double-resonant Raman modes in the first-order spectra.

The description of double resonance establishes that the G-band phonon wavevectors are closer to the Γ point than those of the D-band [6.234]. With low defect concentration the phonon wavevectors are in the range of $0.1–0.3\,\pi/a_0$ (where a_0 is the length of the graphene lattice vectors), independent of the nanotube chirality. However, at high defect concentrations, these phonon wavevectors are large when compared with those observed at the Γ point. Therefore, when the defect concentration is large enough, the separation distance between defects becomes similar to the D-band phonons.

The G′-band [also known as the two-dimensional (2-D) band by some authors] is highly sensitive to modifications in sp^2-hybridized carbon structures, including nanotube diameter and structural changes induced by doping [6.235, 236]. In particular, it has been observed that a lower-frequency peak next to the G′-band arises due to the presence of defects in SWCNTs, and depending on the band shifts, one can determine whether the defect introduces acceptors or donors in SWCNT samples (Fig. 6.19a) [6.236, 237]. This low-frequency G′-band has been used to study phosphorus- and nitrogen-doped SWCNTs. This mode is known as G'_D (where "D" stands for defect), and the frequency difference between the undoped G′, called G'_P (where "P" stands for pristine) and the G'_D band ($\omega_{G'P}-\omega_{G'D}$) is negative for p-doped (electron acceptor atoms) SWCNTs but positive for n-doped (electron donor atoms) SWCNTs [6.237, 238]. In addition, the frequency splitting $\omega_{G'P}-\omega_{G'D}$ exhibits a certain range of values depending upon the dopant; $\approx 31–33\,cm^{-1}$ corresponds to phosphorus, $\approx 35–40\,cm^{-1}$ corresponds to nitrogen, and $\approx 41–45\,cm^{-1}$ corresponds to silicon (Fig. 6.19b). Furthermore, the $I_{G'D}/I_{G'P}$ ratio has been used to study SWCNTs doped with nitrogen, phosphorus, and silicon, and the results show that this ratio increases when the amount of dopant per carbon atom increases within the structure (Fig. 6.19c) [6.239].

Various authors use the ratio of the relative intensities of the D-band and G-band (I_D/I_G) to obtain the degree of crystallinity of samples. Higher ratios are related to higher content of defects; for example, this relationship has been widely used to study the air and acid oxidation process of MWCNTs, showing that I_D/I_G increases with higher oxidation temperatures and that this ratio also increases when the acid treatment reaction time is longer. In this way, it was determined that the acid treatment is a strong nanotube oxidizer [6.240]. Other comparisons using different acid solutions to oxidize MWCNTs revealed that NH_4OH/H_2O_2 is a very strong agent [6.216]. For nitrogen-doped MWCNTs, the I_D/I_G ratio increases when the content of substitutional and pyridinic nitrogen increases [6.224]. A similar increase has also been observed when increasing the amount of dopants in phosphorus-doped SWCNTs [6.238], nitrogen-doped MWCNTs (Fig. 6.19d) [6.123, 234], nitrogen-doped DWCNTs [6.241], and boron-doped MWCNTs [6.127], and in fluorination of SWCNTs [6.237] and dichlorocarbene functionalization of SWCNTs (Fig. 6.19e) [6.242]. This ratio has also been used to monitor the anchorage of Pt nanoparticles onto oxidized MWCNTs, revealing that the ratio decreases with this anchorage of NPs since these particles prefer to adsorb at defective sites [6.243]. In addition, the ratio between the D-band and G′-band ($I_D/I_{G'}$) has been used to study the degree of functionalization of SWCNTs [6.244, 245]. In particular, for

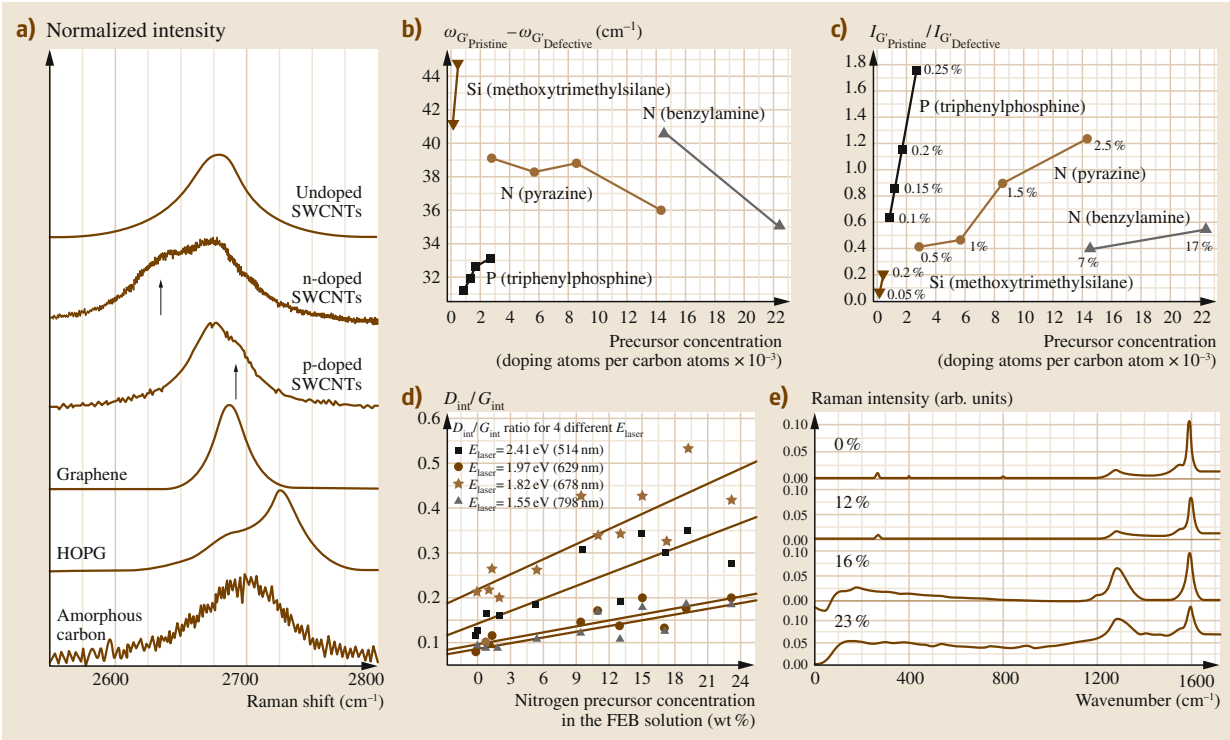


Fig. 6.19 **(a)** G′-band of different carbon nanostructures; here the doping of SWCNTs with boron and nitrogen: a new upshift occurs for p-type doping (nitrogen atoms in SWCNTs), and a new downshift is observed for n-type doping (nitrogen atoms in SWCNTs; after [6.237]). Different precursors have been used to induce nitrogen, phosphorus, and silicon doping in SWCNTs, and the Raman spectra exhibit G-band shifts **(b)** as well as intensity variations **(c)**, that are characteristic of each precursor used to prepare the SWCNT samples (after [6.239]). **(d)** Modifications of CNTs due to nitrogen doping (FEB – ferrocene/ethanol/benzylamine) (after [6.123]) and **(e)** dichlorocarbene functionalization of CNTs (after [6.242])

boron-doped CNTs the relative intensities D/D* and G/D* (where D* is the second-order mode) increase with the density of defects [6.246].

The position of the modes has also been used to determine other types of modifications of CNTs; for example, when intercalating K and Li in SWCNTs, there is a downshift of the tangential phonon mode, and this shift appears to be reversible. This is due to electron–phonon coupling and/or local disorder in the dopant distribution [6.247]. Raman spectroscopy has also been used to monitor the oxidation process (e.g., carboxyl functionalization) by the observation of upshifts in the Raman modes [6.248].

6.5.6 Thermogravimetric Analysis

In thermogravimetric analysis (TGA), the weight loss is monitored as the sample is heated in a specific atmosphere. Generally, carbon nanotubes are subjected to thermal oxidation monitored by TGA in order to observe variations in their reactivity as a function of temperature. Nitrogen-doped SWCNTs have shown a lower thermal decomposition temperature compared with pristine SWCNTs [6.123]. It has also been observed that nitrogen- and boron-doped DWCNTs decompose at lower temperature compared with pure carbon DWCNTs (Fig. 6.20a) [6.249]. If carbon nanotubes are functionalized with polymers, TGA may provide evidence of different compounds burning at different temperatures, a fact that is consistent with the presence of polymers (Fig. 6.20b) [6.200]. The degree of functionalization has also been studied by TGA, where a greater amount of weight loss is usually attributed to side functional groups anchored on the surface of CNTs [6.223].

Different types of CNTs can result from different growth processes and conditions; the number of de-

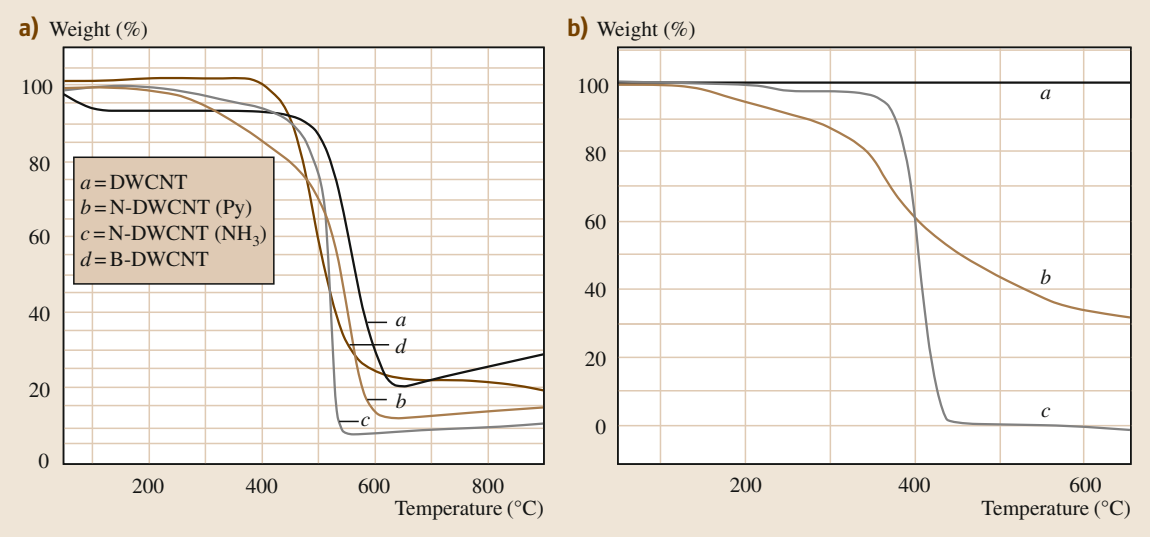


Fig. 6.20a,b TGA plots of **(a)** pristine DWCNTs, and N- and B-doped DWCNTs in which the doped tubes exhibit a lower thermal decomposition temperature in air when compared with pure DWCNTs (after [6.249]). **(b)** MWCNTs functionalized with polystyrene (PS) showing greater weight loss (in nitrogen) caused by the presence of the polymer; (**a**) purified MWCNT, (**b**) MWCNT/PS, and (**c**) only polystyrene (after [6.200])

fects or side-groups may then vary. Therefore, TGA can be used to identify samples with a large number or defects or functional groups. In addition, high-temperature thermal annealing (e.g., 1500–2500 °C) of CNTs can be used to reduce the number of defects and increase the degree of crystallinity of the samples. This structural transition from defective CNTs to highly crystalline CNTs has been studied by TGA. Here, the thermal decomposition temperature increases with higher thermal annealing temperatures. In addition, if there is a mixture of unannealed and annealed CNTs within the same sample, the resulting TGA plot is the sum of each separate TGA curve [6.250].

6.6 Applications of Modified Carbon Nanotubes

Modified CNTs can exhibit good electrical and chemical properties, and for this reason they have been used as electrodes for diverse applications such as in capacitors, fuel cells, solar cells, electron field-emission sensors, etc. In biology, modified CNTs are used as biomarkers, protein or microbial sensors, drug delivery agents for cancer treatments, etc. In this section, these applications are summarized.

In the case of electronic devices, N-doped CNTs can exhibit enhanced electron field emission, and this emission can be further improved if a high concentration of nitrogen atoms is located at the tip of the CNT, because these foreign atoms induce a well-known peak near the Fermi level [6.121, 122]. Experimentally, N-doped CNTs have exhibited relatively high emission currents ($10\,\mathrm{mA/cm^2}$) at fields of ca. $3\,\mathrm{V/\mu m}$ [6.251]. If a high degree of nitrogen defects are introduced into CNTs, the structure will exhibit lower potential barriers for electron field emission [6.252]. As previously discussed, this kind of doped CNTs also exhibits good catalytic activity for oxygen reduction in fuel cells, and has revealed good selectivity in the presence of methanol (Fig. 6.21a,b) [6.161, 222] and higher capacitance when compared with undoped CNTs (Fig. 6.21c) [6.124].

Modified CNTs have also been used to fabricate sensors. In a theoretical work, when a carbon nanotube exhibits –COOH groups, a hydrogen bond could appear with acetone, as observed by *Robinson* et al. [6.253]. This suggests that a functional oxygen group on a carbon nanotube may be useful to

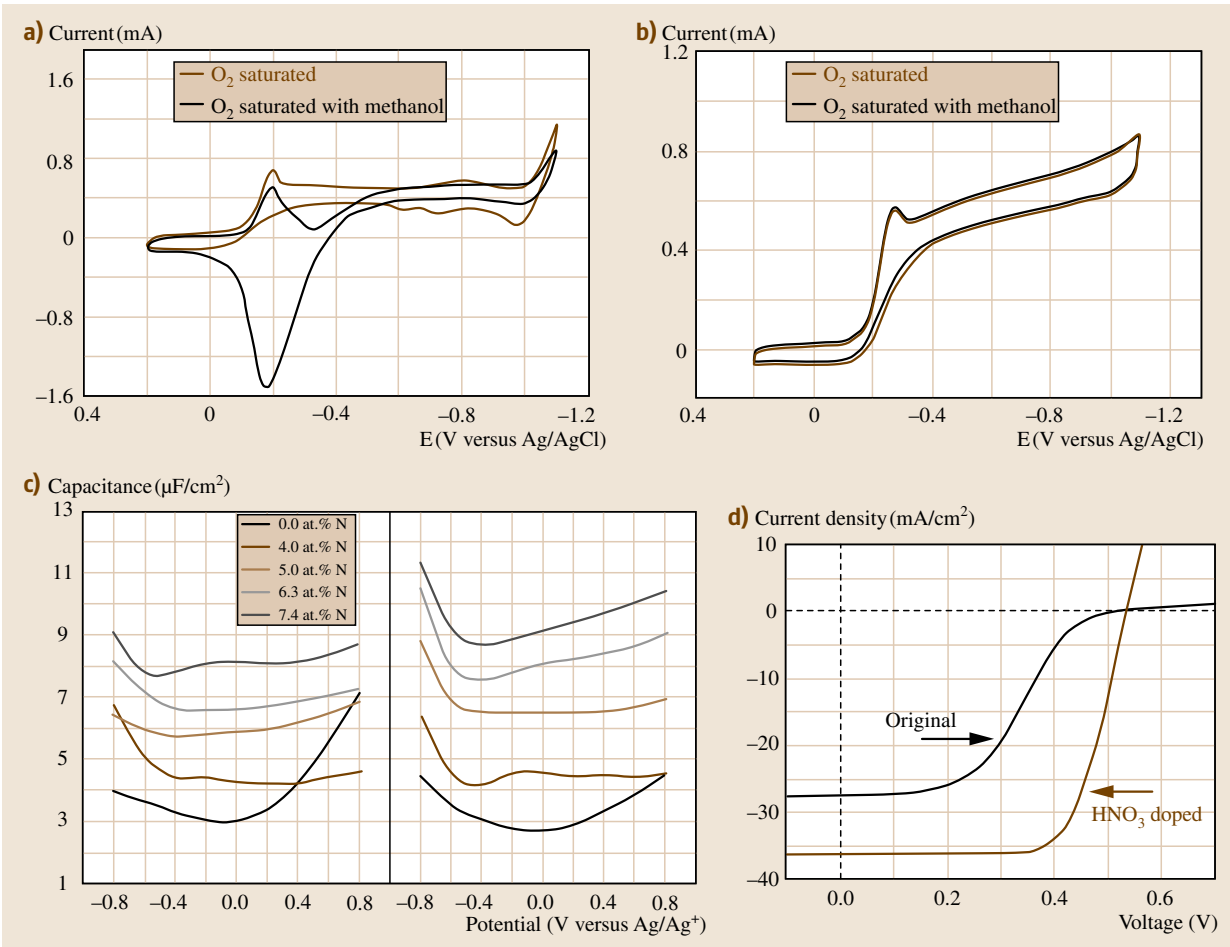
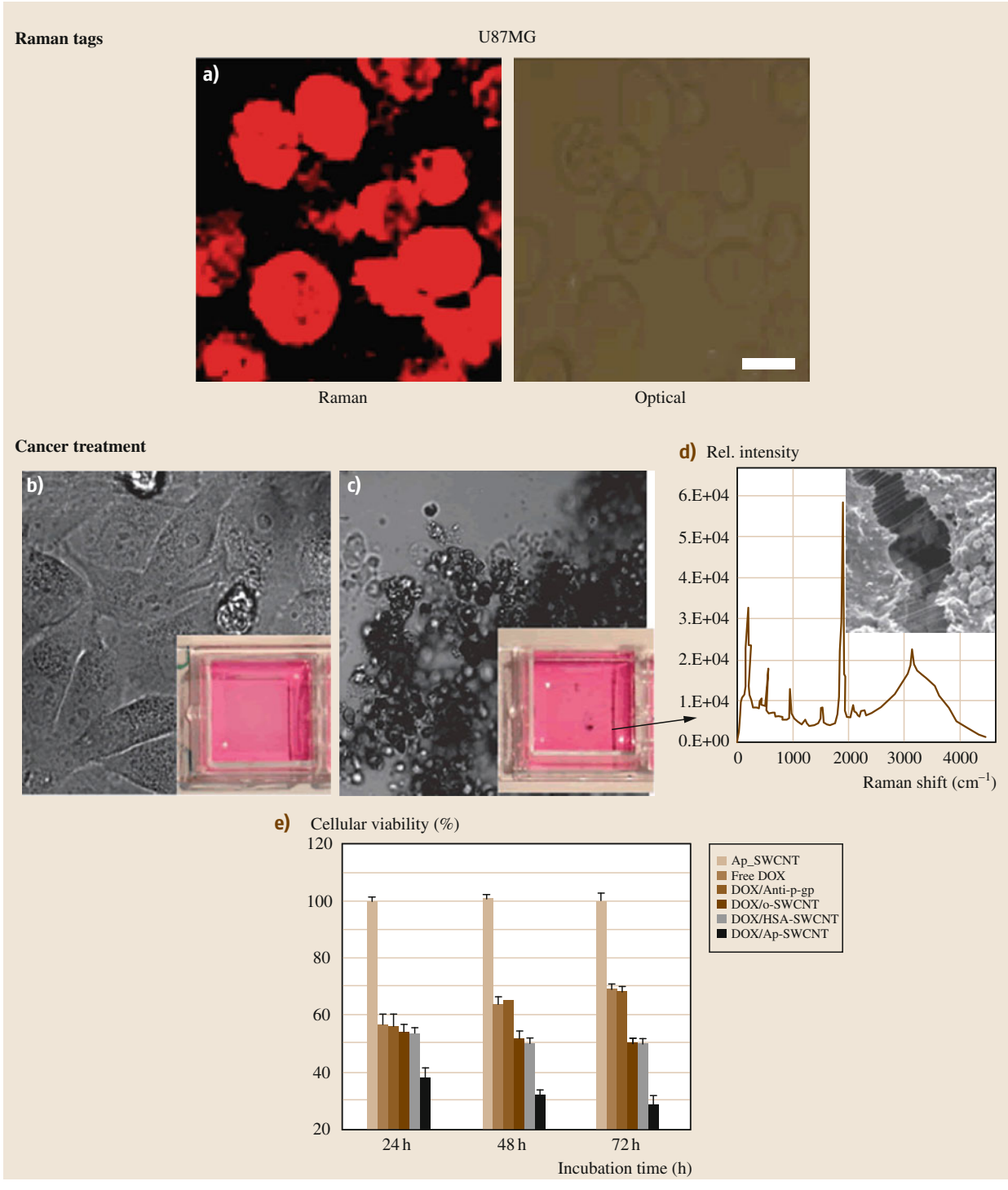


Fig. 6.21a–d Oxygen reduction observed by **(a)** Pt-C/glassy carbon, and **(b)** N-doped CNTs/glassy carbon electrodes. N-doped CNTs exhibit excellent selectivity in the presence of methanol (after [6.161]). **(c)** Enhanced capacitance by N-doped CNT mats that have been acid treated (*left*); untreated or pristine tubes are also shown for comparison (*right*; after [6.124]). **(d)** Improved short-circuit current density and filling factor obtained after treating CNTs with HNO_3 (after [6.258])

sense polar molecules. Regarding doping of carbon nanotubes with boron and nitrogen, it has been demonstrated that, when sensing CO and H_2O, boron-doped sites exhibit chemical adsorption whereas nitrogenated sites exhibit physical adsorption [6.254]. In another study, pyridine-like sites promoted chemisorption of molecules with OH groups [6.255]. When CNTs are doped with P there is a greater affinity towards acceptor molecules, and when CNTs are codoped with P and N atoms, the affinity towards donor molecules becomes strong, an effect caused by a partial positive charge located at the phosphorus atom [6.256].

Fig. 6.22 **(a)** Modified SWCNTs used as Raman tags in U87MG cancer cells (after [6.259]). NIR irradiation of HeLa cells **(b)** without uptake and **(c)** with uptake of DNA-SWCNTs; *insets* show photographs of cell solutions after NIR irradiation. Only after taking up DNA-SWCNTs do the HeLa cells die and aggregate. **(d)** Raman spectrum and SEM image showing the presence of SWCNTs within the cells (after [6.260]). **(e)** Viability of K562R leukemia cells treated with Ap-SWCNTs, free DOX, DOX/anti-P-gp, DOX/o-SWCNTs, DOX/HSA-SWCNTs, and DOX/Ap-SWCNTs at different incubation times (HSA – human serum albumin; Ap – antibody of P-gp) (after [6.261]) ▶


Raman tags
U87MG
a)
Raman
Optical
Cancer treatment
b)
c)
d) Rel. intensity
6.E+04
5.E+04
4.E+04
3.E+04
2.E+04
1.E+04
0.E+00
0
1000
2000
3000
4000
Raman shift (cm−1)
e) Cellular viability (%)
120
100
80
60
40
20
24 h
48 h
72 h
Incubation time (h)
Ap_SWCNT
Free DOX
DOX/Anti-p-gp
DOX/o-SWCNT
DOX/HSA-SWCNT
DOX/Ap-SWCNT

Experimentally, nitrogen-doped CNTs are capable of sensing acetone, ethanol, gasoline, chloroform, and ammonia. These devices show fast response on the order of tenths of a second [6.255]. In addition, sensors fabricated using SWCNTs covered with polyelectrolytes (nafion–ethanol or poly(sodium 4-styrene sulfonate)) and soaked on cotton fibers could efficiently detect albumin, a protein found in blood [6.257].

It has been observed that acid treatments shorten CNTs and functionalize their surface with carboxylic groups, thus allowing fabrication of homogeneous composites used in solar cells [6.262]. These kinds of CNTs have shown higher current densities than undoped CNTs [6.263]. In addition, fluorinated MWCNTs have been shown to improve the power conversion efficiency [6.262, 264]. Functionalization of CNTs is widely used to enhance the efficiency of solar cells, particularly of Si-based solar cells (Fig. 6.21d) [6.258]. CdSe nanoparticles have also been covalently anchored to carboxyl-functionalized SWCNTs and used for solar cell devices; the materials showed enhanced optical absorption [6.265].

In biological applications, it is important to modify CNTs in order for them to be dispersed in water suspension. Therefore, CNTs have been oxidized and wrapped with hydrophilic polymers [6.266–268], for example, with proteins, DNA, phospholipids, etc. [6.260, 269, 270]. Cycloadditions can also be carried out with azides [6.271, 272] or other dipolar compounds [6.273, 274]. These types of modified CNTs have been used as protein sensors [6.109, 275, 276] and as Raman tags able to detect low concentrations of analytes and biomarkers of human autoimmune diseases (Fig. 6.22a) [6.259].

Phospholipid polyethylene glycol (PL-PEG)-modified SWCNTs have been used for near-infrared imaging in mice, in which the intrinsic near-infrared photoluminescence is detected at a low dose [6.277]. These conjugated systems can also be used as sensors in biological systems in which electron transfer between oxidative enzymes and the electrode surface takes place [6.140, 278, 279]. Finally, CNTs modified with chitosan have been used as microbial sensors, displaying higher sensitivity compared with a pure graphite electrode [6.280].

When functionalizing SWCNTs with specific proteins, they may be used to carry drugs to specific cells. It has been shown that SWCNTs modified with streptavidin are capable of penetrating human promyelocytic leukemia (HL60) cells and human T cells via endocytosis. However, streptavidin itself cannot enter the cells [6.281]. In another study, polyethylene glycol-modified SWCNTs loaded with doxorubicin (DOX) showed enhanced therapeutic efficacy and lower toxicity compared with DOX alone; when the DOX loaded on SWCNTs reaches the tumor cells, it is released due to the slightly acidic environment [6.282]. In addition, phospholipid polyethylene glycol moieties with folic acid terminal group have been attached to SWCNTs. These systems could then selectively enter cancer cells; once inside the cells, they can be irradiated with NIR lasers in order to heat the local environment, thus killing only cancer cells (Fig. 6.22b–d) [6.260]. It has also been found that P-glycoprotein-functionalized SWCNTs loaded with doxorubicin express 2.4-fold higher cytotoxicity with significant cell proliferation suppression towards K562R leukemia cells ($p < 0.05$) (Fig. 6.22e) [6.261].

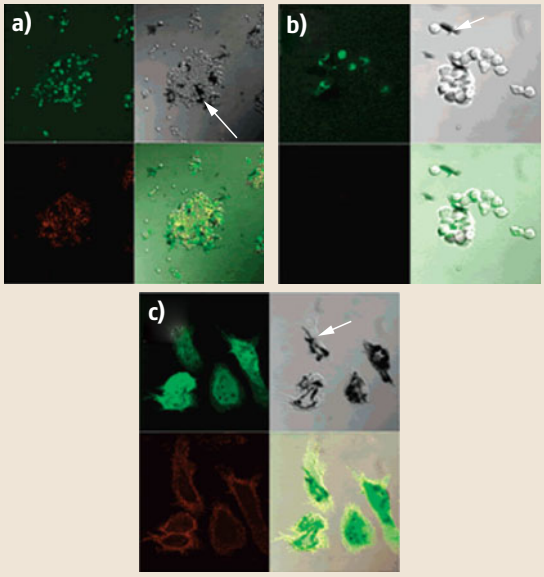
6.7 Toxicity and Biocompatibility

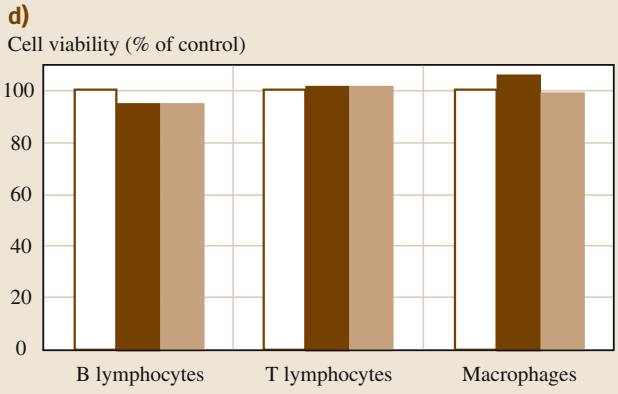
The toxicity of CNTs has been studied for several years and is still not completely understood; this is because it depends on how the carbon nanotubes are modified either on their surface via functional groups (oxidation, doping, functionalization) or via external entities decorating them (phospholipids, nanoparticles).

Regarding the toxicity of CNTs in mice, there have been several studies showing that as-produced CNTs could be toxic when inhaled, affecting their lungs [6.286–289]. However, in vivo studies have shown that SWCNTs functionalized with polyethylene glycol intravenously injected into mice are excreted from the body, and no mortality was observed during the study [6.270]. In particular, hydroxylated SWCNTs

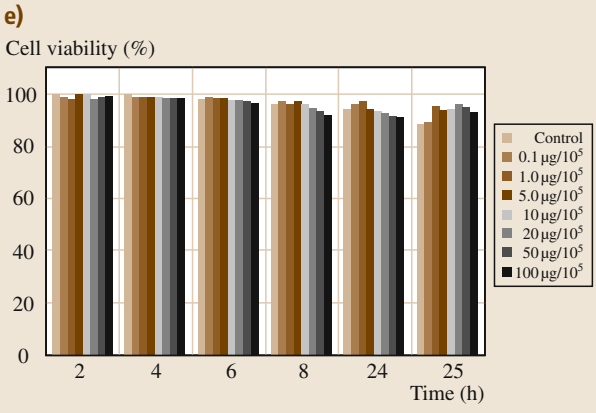
Fig. 6.23 **(a)** B lymphocytes, **(b)** T lymphocytes, and **(c)** macrophages in presence of SWCNTs functionalized by 1,3-dipolar cycloaddition reaction (f-SWCNT); only the macrophages exhibit these f-SWCNT within the cytoplasm. **(d)** Cell viability of immune cells in presence of f-SWCNT without any effect (after [6.283]). **(e)** Nitrogen-doped and **(f)** undoped MWCNTs: cell viability of *Entamoeba histolytica*; here, the N-doped MWCNTs exhibited a higher degree of biocompatibility compared with undoped MWCNTs (after [6.284]). **(g)** Pristine SWCNTs biodegrade by oxidation with horseradish peroxidase with low concentrations of H_2O_2 ($\approx 40\,\mu m$), after **(h)** 8 and **(i)** 12 weeks. The material is highly biodegraded after 12 weeks (after [6.285]) ▶

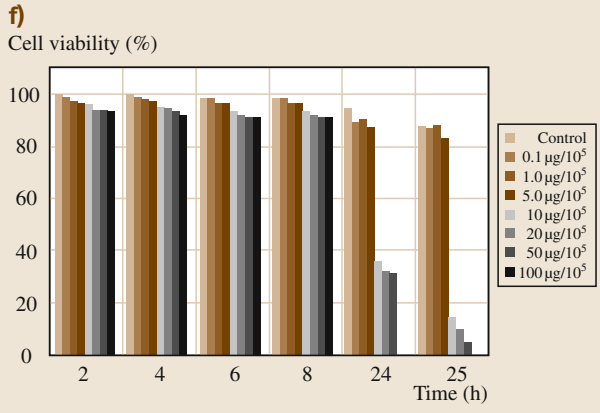
Primary immune cells



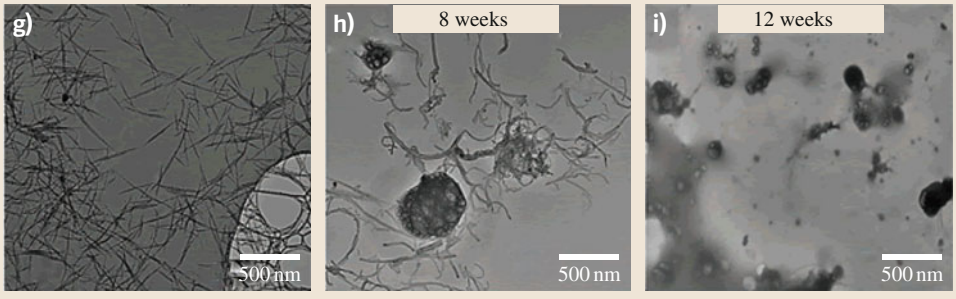


Entamoeba histolytica





Enzymatic biodegradation



tend to aggregate in the kidney, stomach, and bones of mice, being excreted via the renal route [6.290]. On the other hand, other studies have demonstrated that crystalline CNTs exhibit a lower degree of toxicity in mice compared with CNTs possessing structural defects (dangling bonds) and functionalities [6.291]. It is becoming more evident that the agglomeration and length of CNTs could affect their toxicity [6.286–289]. However, if CNTs are adequately modified, they may not be toxic [6.267, 281, 283, 292].

In vitro studies have also been carried out to understand how specific cell lines behave in the presence of modified CNTs. Human dermal fibroblasts have shown lower cytotoxicity with phenyl-SO_3H-functionalized SWCNTs. In addition, these modified SWCNTs did not exhibit any change in metabolic activity [6.293]. CNTs modified by the 1,3-dipolar cycloaddition reaction have been shown to be nontoxic to immunoregulatory cells, and PEG-functionalized CNTs obtained using an oxidation/amidation procedure cause secretion of proinflammatory cytokines by macrophages (Fig. 6.23a–d) [6.283]. Regarding the toxicity of nitrogen-doped MWCNTs, they have been shown to be nontoxic for cultures of *Entamoeba histolytica*, however undoped MWCNTs exhibited the opposite effect (Fig. 6.23e,f) [6.284]. Furthermore, Ag nanoparticles have been anchored on hydroxyl-functionalized and N-doped MWCNTs and tested for biocompatibility. Although isolated Ag nanoparticles exhibit toxic activity, Ag nanoparticles anchored on N-doped and hydroxylated MWCNTs did not have significant effects on cellular functions [6.294]. A different study showed that metalloproteins could be more immobilized on acid-treated N-doped CNTs, possibly due to hydrogen bonds established between amino acid chains from the proteins and carboxyl functional groups of the carbon nanotubes [6.295]. For biomedical applications it is also important to know if CNTs are biodegradable. In this context, it has been observed that acid-treated SWCNTs could be degraded by enzymes with low concentration of H_2O_2; this biodegradation takes several weeks to accomplish (Fig. 6.23g–i) [6.285, 296].

6.8 Conclusions

Carbon nanotubes can be modified by doping with foreign atoms, incorporation of structural defects, and/or functionalization with different molecules. Doping can be endohedral (filling the tube core), exohedral (by intercalation of alkali metals among tubes), or in-plane (one or more heteroatoms being placed within the nanotube lattice). Structural defects include:

1. Introduction of pentagons, heptagons or octagons, changing the curvature of the structure
2. Bond rotations creating 5–7 pairs or Thrower–Stone–Wales (TSW) defects
3. Non-sp^2 defects such as adatoms, vacancies, edges, and interstitials, and
4. Curvature effects observed in narrow-diameter or collapsed nanotubes.

Functionalization of CNTs could be achieved via covalent modification, $\pi-\pi$ interactions, or electrostatic interactions. Covalent modifications occur via oxidation, fluorination, aryl diazonium chemistry, azomethine ylides, reduction, carbenes, nitrenes, and radicals. $\pi-\pi$ interactions are observed when nonpolar molecules with aromatic rings or C=C bonds interact with the surface of carbon nanotubes. Finally, electrostatic interactions can be enhanced by covalent functionalization in order to induce different charge on the tubes' surface.

Due to the local modification of the carbon nanotubes, they suffer significant changes in their electrical and chemical properties. The electrical properties can show an increase in electrical conductivity by electrons or holes. When CNTs are doped with conductive polymers or covalent bonding with redox mediators, they can exhibit faster response and higher electrochemical activity.

To improve understanding of how these modifications affect carbon nanotubes, several characterization techniques need to be used. The most common are high-resolution transmission electron microscopy (HRTEM) to view the atomic lattice, atomic force microscopy (AFM) to visualize the topography or phase differences, scanning transmission microscopy (STM) to improve understanding of how the electrons are distributed on the surface, electron energy loss spectroscopy (EELS) to study the charge distribution and the type of bonds involved in certain regions, x-ray photoelectron spectroscopy (XPS) to provide information related to the bonding environment within the surface, Raman spectroscopy to reveal the vibrational modes of carbon

nanotubes, and thermogravimetric analysis (TGA) to determine the thermal reaction weight loss under different atmospheres.

To decrease the toxicity of carbon nanotubes, they can be modified to improve their dispersibility and prevent agglomeration; some CNTs with covalent functionalization, cycloaddition, and doping have also shown lower toxicity. Many studies show that, with appropriate modification, carbon nanotubes can be made more biocompatible.

6.9 Outlook and Perspectives

CNTs possess fascinating electrical and mechanical properties, and they are good candidates to be used in composites, and electronic and biomedical devices. Regarding electron field emission, N-doped CNTs are expected to exhibit good performance [6.251, 252]. Electronic sensors could also be fabricated, and these devices could efficiently sense various vapors or gases [6.253–257]. Similarly, modified CNTs could be used in biological sensors [6.259, 275, 276, 280] and solar cells with higher power conversion efficiency and better optical absorption [6.258, 262–265].

In biology and medicine, modified CNTs have been demonstrated to be useful in near-infrared imaging [6.277], investigation of the electron transfer properties of proteins, enzymes, and microbes [6.140, 278–280], drug delivery [6.281, 282], and even cancer treatments [6.270]. Regarding their toxicological aspects and biocompatibility, further investigations are needed, since their morphological, structural, and chemical properties appear to determine how they interact with cells and tissues [6.261, 281, 282]. Several studies have demonstrated that modified CNTs are less toxic compared with undoped (pristine) CNTs [6.283, 292, 293, 295]. Furthermore, modified CNTs could be efficiently biodegraded by certain enzymes [6.285, 296]. This result ensures that CNTs will not have a long-term presence in biological systems.

Due to the increasing number of applications and commercial products based on CNTs, it is also important to improve their characterization techniques and identify more precisely their surface functionalities and precise reactivity. By increasing the spatial resolution of current instruments, one could detect and quantify (at atomic scale) the type of dopant (or functional groups) on the surface of CNTs. Based on these improved characterization techniques, one could then start setting up standards for carbon nanotubes. In this way, various applications could then be realized worldwide.

References

6.1 K. Fujisawa, K. Komiyama, H. Muramatsu, D. Shimamoto, T. Tojo, Y.A. Kim, T. Hayashi, M. Endo, K. Oshida, M. Terrones, M.S. Dresselhaus: Chirality-dependent transport in double-walled carbon nanotube assemblies: The role of inner tubes, ACS Nano **5**, 7547–7554 (2001)

6.2 H.W. Kroto, J.R. Heath, S.C. O'Brien, R.F. Curl, R.E. Smalley: C_{60}: Buckminsterfullerene, Nature **318**, 162–163 (1985)

6.3 W. Krätschmer, L.D. Lamb, K. Fostiropoulos, D.R. Huffman: Solid C_{60}: A new form of carbon, Nature **347**, 354–358 (1990)

6.4 S. Iijima: Helical microtubules of graphitic carbon, Nature **354**, 56–58 (1991)

6.5 A. Oberlin, M. Endo, T. Koyama: Filamentous growth of carbon through benzene decomposition, J. Cryst. Growth **32**, 335–349 (1976)

6.6 K.S. Novoselov, A.K. Geim, S.V. Morozov, D. Jiang, Y. Zhang, S.V. Dubonos, I.V. Grigorieva, A.A. Firsov: Electric field effect in atomically thin carbon films, Science **306**, 666 (2004)

6.7 K.S. Novoselov, A.K. Geim, S.V. Morozov, D. Jiang, M.I. Katsnelson, I.V. Grigorieva, S.V. Dubonos, A.A. Firsov: Two-dimensional gas of massless Dirac fermions in graphene, Nature **438**, 197 (2005)

6.8 Y. Zhang, Y.-W. Tan, H.L. Stormer, P. Kim: Experimental observation of the quantum Hall effect and Berry's phase in graphene, Nature **438**, 201 (2005)

6.9 M. Terrones, A.R. Botello-Méndez, J. Campos-Delgado, F. López-Urías, Y.I. Vega-Cantú, F.J. Rodríguez-Macías, A.L. Elias, E. Muñoz-Sandoval, A.G. Cano-Márquez, J.-C. Charlier, H. Terrones: Graphene and graphite nanoribbons: Morphology, properties, synthesis, defects and applications, Nano Today **5**, 351–372 (2010)

6.10 M. Terrones: Science and technology of the twenty-first century: Synthesis, properties, and applications of carbon nanotubes, Annu. Rev. Mater. Res. **33**, 419 (2003)

6.11 M.S. Dresselhaus, G. Dresselhaus, P.C. Eklund: *Science of Fullerenes and Carbon Nanotubes* (Academic, New York 1996)

6.12 M.R. Pederson, J.Q. Broughton: Nanocapillarity in fullerene tubules, Phys. Rev. Lett. **69**, 2689 (1992)

6.13 P.M. Ajayan, T.W. Ebessen, T. Ichihashi, S. Ijima, K. Tanigaki, H. Hiura: Opening carbon nanotube with oxygen and implication for filling, Nature **362**, 522 (1993)

6.14 M. Terrones, N. Grobert, W.K. Hsu, Y.Q. Zhu, W.B. Hu, H. Terrones, J.P. Hare, H.W. Kroto, D.R.M. Walton: Advances in the creation of filled nanotubes and novel nanowires, Mater. Res. Soc. Bull. **24**, 43 (1999)

6.15 M. Monthioux: Filling single-wall carbon nanotubes, Carbon **40**, 1809 (2002)

6.16 Z.Y. Wang, Z.B. Zhao, J.S. Qiu: Development of filling carbon nanotubes, Prog. Chem. **18**, 563 (2006)

6.17 S. Ijima, T. Ichihashi: Single-shell carbon nanotubes of 1 nm diameter, Nature **363**, 603 (1993)

6.18 D.S. Bethune, C.H. Kiang, M.S. DeVries, G. Gorman, R. Savoy, J. Vazquez, R. Beyers: Cobalt-catalyzed growth of carbon nanotubes with single-atomic-layer walls, Nature **363**, 605 (1993)

6.19 B.W. Smith, M. Monthioux, D.E. Luzzi: Encapsulated C_{60} in carbon nanotubes, Nature **296**, 323 (1998)

6.20 J. Sloan, J. Hammer, M.Z. Sibley, M.L.H. Green: The opening and filling of single walled carbon nanotubes (SWNTs), Chem. Commun. **3**, 347 (1998)

6.21 A. Govindaraj, B.C. Satishkumar, M. Nath, C.N. Rao: Metal nanowires and intercalated metal layers in single-walled carbon nanotube bundles, Chem. Mater. **12**, 205 (2000)

6.22 Y.K. Chen, A. Chu, J. Cook, M.L.H. Green, P.J.F. Harris, R. Heesom, M. Humphries, J. Sloan, S.C. Tsang, J.F.C. Turner: Synthesis of carbon nanotubes containing metal oxides and metals of the d-block and f-block transition metals and related studies, J. Mater. Chem. **7**, 545–550 (1997)

6.23 P.M. Ajayan, T.W. Ebbesen, T. Ichihashi, S. Ijima, K. Tanigaki, H. Hiura: Opening carbon nanotubes with oxygen and implications for filling, Nature **362**, 522–525 (1993)

6.24 B.K. Pradhan, T. Kyotani, A. Tomita: Nickel nanowires of 4 nm diameter in the cavity of carbon nanotubes, Chem. Commun. **4**, 1317–1318 (1999)

6.25 N. Grobert, W.K. Hsu, Y.Q. Zhu, J.P. Hare, H.W. Kroto, D.R.M. Walton, M. Terrones, H. Terrones, P. Redlich, M. Rühle, R. Escudero, F. Morales: Enhanced magnetic coercivities in Fe nanowires, Appl. Phys. Lett. **75**, 3363–3365 (1999)

6.26 T. Mül, D. Elefant, A. Graff, R. Kozhuharova, A. Leonhardt, I. Mönch, M. Ritschel, P. Simon, S. Groudeva-Zotova, C.M. Schneider: Magnetic properties of aligned Fe-filled carbon nanotubes, J. Appl. Phys. **93**, 7894–7896 (2003)

6.27 S. Liu, J. Zhu, Y. Mastai, I. Felner, A. Gedanken: Preparation and characteristics of carbon nanotubes filled with cobalt, Chem. Mater. **12**, 2205–2211 (2000)

6.28 G.Y. Zhang, E.G. Wang: Cu-filled carbon nanotubes by simultaneous plasma-assisted copper incorporation, Appl. Phys. Lett. **82**, 1926–1928 (2003)

6.29 A.L. Elías, J.A. Rodríguez-Manzo, M.R. McCartney, D. Golberg, A. Zamudio, S.E. Baltazar, F. López-Urías, E. Muñoz-Sandoval, L. Gu, C.C. Tang, D.J. Smith, Y. Bando, H. Terrones, M. Terrones: Production and characterization of single-crystal FeCo nanowires inside carbon nanotubes, Nano Lett. **5**, 467–472 (2005)

6.30 D.C. Lee, F.V. Mikulec, B.A. Korgel: Carbon nanotube synthesis in supercritical toluene, J. Am. Chem. Soc. **126**, 4951–4957 (2004)

6.31 N. Grobert, M. Mayne, M. Terrones, J. Sloan, R.E. Dunin-Borkowski, R. Kamalakaran, T. Seeger, H. Terrones, M. Rühle, D.R.M. Walton, H.W. Kroto, J.L. Hutchison: Alloy nanowires: Invar inside carbon nanotubes, Chem. Commun. **5**, 471–472 (2001)

6.32 S.C. Tsang, P.J.F. Harris, M.L.H. Green: Thinning and opening of carbon nanotubes by oxidation using carbon dioxide, Nature **362**, 520–522 (1993)

6.33 A. Morelos-Gomez, F. Lopez-Urias, E. Muñoz-Sandoval, C.L. Dennis, R.D. Shull, H. Terrones, M. Terrones: Controlling high coercivities of ferromagnetic nanowires encapsulated in carbon nanotubes, J. Mater. Chem. **20**, 5906–5914 (2010)

6.34 J. Sloan, M. Terrones, S. Nufer, S. Friedrichs, S.R. Bailey, H.G. Woo, M. Ruhle, J.L. Hutchison, M.J.H. Green: Metastable one-dimensional $AgCl_{1-x}I_x$ solid-solution wurzite "tunnel" crystals formed within single-walled carbon nanotubes, J. Am. Chem. Soc. **124**, 2116–2117 (2002)

6.35 J. Sloan, D.M. Wright, H.G. Woo, S.R. Bailey, G. Brown, A.P.E. York, K.S. Coleman, J.L. Hutchison, M.L.H. Green: Capillarity and silver nanowire formation observed in single walled carbon nanotubes, Chem. Commun. **700**, 699 (1999)

6.36 R.R. Meyer, J. Sloan, R.E. Dunin-Borkowski, A. Kirkland, M.C. Novotny, S.R. Bailey, J.L. Hutchison, M.L.H. Green: Discrete atom imaging of one-dimensional crystals formed within single-walled carbon nanotubes, Science **289**, 1324–1326 (2000)

6.37 D.E. Luzzi, B.W. Smith: Carbon cage structures in single wall carbon nanotubes: **A new class of materials, Carbon **38**, 1751 (2000)

6.38 E. Hernandez, V. Meunier, B.W. Smith, R. Rurali, H. Terrones, M. Buongiorno, N. Nardelli, M. Terrones, D.E. Luzzi, J.C. Charlier: Fullerene coalescence in nanopeapods: A path to novel tubular carbon, Nano Lett. **3**, 1037 (2003)

6.39 K. Hirahara, K. Suenaga, S. Bandow, H. Kato, T. Okazaki, H. Shinohara, S. Ijima: One-dimensional metallofullerene crystal generated inside single-walled carbon nanotubes, Phys. Rev. Lett. **85**, 5384 (2000)

6.40 M.S. Dresselhaus, G. Dresselhaus: Intercalation compounds of graphite, Adv. Phys. **30**, 139 (1981)

6.41 A.M. Rao, P.C. Eklund, S. Bandow, A. Thess, R.E. Smalley: Evidence for charge transfer in doped carbon nanotube bundles from Raman scattering, Nature **388**, 257 (1997)

6.42 M.V. Veloso, A.G. Souza Filho, J. Mendes Filho, S.B. Fagan, R. Mota: Ab initio study of covalently functionalized carbon nanotubes, Chem. Phys. Lett. **430**, 71 (2006)

6.43 T. Ramanathan, F.T. Fischer, R.S. Ruo, L.C. Brinson: Amino-functionalized carbon nanotubes for binding to polymers and biological systems, Chem. Mater. **17**, 1290 (2005)

6.44 S. Kazaoui, N. Minami, R. Jacquemin, H. Kataura, Y. Achiba: Amphoteric doping of single-wall carbon-nanotube thin films as probed by optical adsorption spectroscopy, Phys. Rev. B **60**, 13339 (1999)

6.45 A. Krishnan, E. Dujardin, M.M.J. Treacy, J. Hugdahl, S. Lynum, T.W. Ebbesen: Graphitic cones and the nucleation of curved carbon surfaces, Nature **388**, 451–454 (1997)

6.46 S. Iijima, T. Ichihashi, Y. Ando: Pentagons, heptagons, and negative curvature in graphitic microtubule growth, Nature **356**, 776–778 (1992)

6.47 S. Itoh, S. Ihara, J. Kitakami: Toroidal form of carbon C_{360}, Phys. Rev. B **47**, 1703–1704 (1993)

6.48 R. Martel, H.R. Shea, P. Avouris: Rings of single-walled carbon nanotubes, Nature **398**, 299 (1999)

6.49 C.O. Girit, J.C. Meyer, R. Erni, M.D. Rossell, C. Kisielowski, L. Yang, C.-H. Park, M.F. Crommie, M.L. Cohen, S.G. Louie, A. Zettl: Graphene at the edge: Stability and dynamics, Science **323**, 1705–1708 (2009)

6.50 P.A. Thrower: Study of defects in graphite by transmission electron microscopy, Chem. Phys. Carbon **5**, 217–319 (1969)

6.51 A. Stone, D. Wales: Theoretical studies of icosahedral C_{60} and some related species, Chem. Phys. Lett. **128**, 501–503 (1986)

6.52 M. Terrones, G. Terrones, H. Terrones: Structure, chirality, and formation of giant icosahedral fullerenes and spherical graphitic onions, J. Struct. Chem. **13**, 373–384 (2002)

6.53 M. Terrones, H. Terrones: The role of defects in graphitic structures, Fuller. Sci. Technol. **4**, 517–533 (1996)

6.54 A. Hashimoto, K. Suenaga, A. Gloter, K. Urita, S. Iijima: Direct evidence for atomic defects in graphene layers, Nature **430**, 870–873 (2004)

6.55 X. Jia, M. Hofmann, V. Meunier, B.G. Sumpter, J. Campos-Delgado, J.M. Romo-Herrera, J. Kong, M. Terrones, M.S. Dresselhaus: Controlled formation of sharp edge zigzag and armchair edges in graphitic nanoribbons, Science **323**, 1701–1705 (2009)

6.56 M.-F. Yu, B.S. Files, S. Arepalli, R.S. Ruoff: Tensile loading of ropes of single wall carbon nanotubes and their mechanical properties, Phys. Rev. Lett. **84**, 5552–5555 (2000)

6.57 A.M. Rao, A. Jorio, M.A. Pimenta, M.S.S. Dantas, R. Saito, G. Dresselhaus, M.S. Dresselhaus: Polarized raman study of aligned multiwalled carbon nanotubes, Phys. Rev. Lett. **84**, 1820–1823 (2000)

6.58 L.J. Bahr, J.M. Tour: Covalent chemistry of single-wall carbon nanotubes, J. Mater. Chem. **12**, 1952–1958 (2002)

6.59 E. Kymakis, I. Alexandou, G.A.J. Amaratunga: Single-walled carbon nanotube-polymer composites: Electrical, optical and structural investigation, Synth. Met. **127**, 59–62 (2002)

6.60 J. Sandler, M.S.P. Shaffer, T. Prasse, W. Bauhofer, K. Schulte, A.H. Windle: Development of a dispersion process for carbon nanotubes in an epoxy matrix and the resulting electrical properties, Polymer **40**, 5967–5971 (1999)

6.61 J.N. Coleman, U. Khan, W.J. Blau, Y.K. Gun'ko: Small but strong: A review of the mechanical properties of carbon nanotube-polymer composites, Carbon **44**, 1624–1652 (2006)

6.62 K. Fu, W. Huang, Y. Lin, L.A. Riddle, D.F.L. Carroll, Y.-P. Sun: Defunctionalization of functionalized carbon nanotubes, Nano Lett. **1**, 439–441 (2001)

6.63 M.A. Hamon, H. Hui, P. Bhowmik, H.M.E. Itkis, R.C. Haddon: Ester-functionalized soluble single-walled carbon nanotubes, Appl. Phys. A **74**, 333–338 (2002)

6.64 S.S. Wong, E. Joselevich, A.T. Woolley, C.L. Cheung, C.M. Lieber: Covalently functionalized nanotubes as nanometre-sized probes in chemistry and biology, Nature **394**, 52–55 (1998)

6.65 K. Balasubramanian, M. Burghard: Chemically functionalized carbon nanotubes, Small **1**, 180–192 (2005)

6.66 T. Sainsbury, D. Fitzmaurice: Templated assembly of semiconductor and insulator nanoparticles at the surface of covalently modified multiwalled carbon nanotubes, Chem. Mater. **16**, 3780–3790 (2004)

6.67 J. Liu, A.G. Rinzler, H. Dai, J.H. Hafner, R.K. Bradley, P.J. Boul, A. Lu, T. Iverson, K. Shelimov, C.B. Huffman, F. Macias-Rodriguez, Y.-S. Shon, T.R. Lee, D.T. Colbert, R.E. Smalley: Fullerene pipes, Science **280**, 1253–1256 (1998)

6.68 A.G. Rinzler, J. Liu, H. Dai, P. Nikolaev, C.B. Huffman, F.J. Rodriguez-Macias, P.J. Boul, A.H. Lu, D. Heymann, D.T. Colbert, R.S. Lee, J.E. Fischer, A.M. Rao, P.C. Eklund, R.E. Smalley: Large-scale purification of single-wall carbon nanotubes: Process, product, and characterization, Appl. Phys. A **67**, 29–37 (1998)

6.69 H. Hiura, T.W. Ebbesen, K. Tanigaki: Opening and purification of carbon nanotubes in high yields, Adv. Mater. **7**, 275–276 (1995)

6.70 D.B. Mawhinney, V. Naumenko, A. Kuznetsova, J.T. Yates Jr., J. Liu, R.E. Smalley: Infrared spectral evidence for the etching of carbon nanotubes: Ozone oxidation at 298 K, J. Am. Chem. Soc. **122**, 2383–2384 (2000)

6.71 D.B. Mawhinney, V. Naumenko, A. Kuznetsova, J.T. Yates Jr., J. Liu, R.E. Smalley: Surface defects site density on single walled carbon nanotubes by titration, Chem. Phys. Lett. **324**, 213–216 (2000)

6.72 A. Kuznetsova, I. Popova, J.T. Yates Jr., M.J. Bronikowski, C.B. Huffman, J. Liu, R.E. Smalley, H.H. Hwu,

J.G. Chen: Oxygen-containing functional groups on single-wall carbon nanotubes: NEXAFS and vibrational spectroscopic studies, J. Am. Chem. Soc. **123**, 10699–10704 (2001)
6.73 J.P. Deng, C.Y. Mou, C.C. Han: Oxidation of fullerenes by ozone, Fuller. Sci. Technol. **5**, 1033 (1997)
6.74 Y. Chen, R.C. Haddon, S. Fang, A.M. Rao, P.C. Eklund, W.H. Lee, E.C. Dickey, E.A. Grulke, J.C. Pendergrass, A. Chavan, B.E. Haley, R.E. Smalley: Chemical attachment of organic functional groups to single-walled carbon nanotube material, J. Mater. Res. **13**, 2423–2431 (1998)
6.75 S. Banerjee, T. Hemraj-Benny, S.S. Wong: Covalent surface chemistry of single-walled carbon nanotubes, Adv. Mater. **17**, 17–29 (2005)
6.76 W. Zhou, Y.H. Ooi, R. Russo, P. Papanek, D.E. Luzzi, J.E. Fischer, M.J. Bronikowski, P.A. Willis, R.E. Smalley: Structural characterization and diameter-dependent oxidative stability of single wall carbon nanotubes synthesized by the catalytic decomposition CO, Chem. Phys. Lett. **350**, 6–14 (2001)
6.77 C.A. Hunter, J.K.M. Sanders: The nature of .pi-.pi. interactions, J. Am. Chem. Soc. **112**, 5525 (1990)
6.78 E.T. Mickelson, C.B. Huffman, A.G. Rinzler, R.E. Smalley, R.H. Hauge, J.L. Margrave: Fluorination of single-wall carbon nanotubes, Chem. Phys. Lett. **296**, 188–194 (1998)
6.79 M. Maggini, G. Scorrano, M. Prato: Addition of azomethine ylides to C_{60}: Synthesis, characterization, and functionalization of fullerene pyrrolidines, J. Am. Chem. Soc. **115**, 9798–9799 (1993)
6.80 E.T. Mickelson, I.W. Chiang, J.L. Zimmerman, P.J. Boul, J. Lozano, J. Liu, R.E. Smalley, R.H. Hauge, J.L. Margrave: Solvation of fluorinated single-wall carbon nanotubes in alcohol solvents, J. Phys. Chem. B **103**, 4318–4322 (1999)
6.81 C.A. Dyke, J.M. Tour: Unbundled and highly functionalized carbon nanotubes from aqueous reactions, Nano Lett. **3**, 1215–1218 (2003)
6.82 M. Holzinger, O. Vostrowsky, A. Hirsch, F. Hennrich, M. Kappes, R. Weiss, F. Jellen: Sidewall functionalization of carbon nanotubes, Angew. Chem. Int. Ed. **40**, 4002–4005 (2001)
6.83 M. Holzinger, J. Abraham, P. Whelan, R. Graupner, L. Ley, F. Hennrich, M. Kappes, A. Hirsch: Functionalization of single-walled carbon nanotubes with (R)-Oxycarbonyl nitrenes, J. Am. Chem. Soc. **125**, 8566–8580 (2003)
6.84 S. Peng, K. Cho: Chemical control of nanotube electronics, Nanotechnology **11**, 57 (2000)
6.85 A. Hirsch: Functionalization of single-walled carbon nanotubes, Angew. Chem. Int. Ed. **41**, 1853 (2002)
6.86 Y. Lee, H.J. Song, H.S. Shin, H.J. Shin, H.C. Choi: Spontaneous formation of transition-metal nanoparticles on single-walled carbon nanotubes anchored wiht conjugated molecules, Small **1**, 975 (2005)
6.87 A. Star, J.F. Stoddart, D. Steuerman, M. Diehl, A. Boukai, E.W. Wong, X. Yang, S.-W. Chung, H. Choi, J.R. Heath: Preparation and properties of polymer-wrapped single-walled carbon nanotubes, Angew. Chem. Int. Ed. **40**(9), 1721–1725 (2001)
6.88 M.J. O'Connell, P.J. Boul, L.M. Ericson, C.B. Huffman, Y. Huang, E.H. Haroz, K.D. Ausman, R.E. Smalley: Reversible water-solubilization of single-walled carbon nanotubes by polymer wrapping, Chem. Phys. Lett. **342**, 265–271 (2001)
6.89 R.J. Chen, Y. Zhang, D. Wang, H. Dai: Noncovalent sidewall functionalization of single-walled carbon nanotubes for protein immobilization, J. Am. Chem. Soc. **123**, 3838–3839 (2001)
6.90 S.A. Curran, P.M. Ajayan, W.J. Blau, D.L. Carroll, J.N. Coleman, A.B. Dalton, A.P. Davey, A. Drury, B. McCarthy, S. Maier, A. Strevens: A composite from Poly(*m*-phenylenevinylene-*co*-2,5-dioctoxy-*p*-phenylenevinylene) and carbon nanotubes: A novel material for molecular optoelectronics, Adv. Mater. **10**, 1091–1093 (1998)
6.91 J.N. Coleman, A.B. Dalton, S. Curran, A. Rubio, A.P. Davey, A. Drury, B. McCarthy, B. Lahr, P.M. Ajayan, S. Roth, R.C. Barklie, W.J. Blau: Phase separation of carbon nanotubes and turbostratic graphite using a functional organic polymer, Adv. Mater. **12**, 213–216 (2000)
6.92 D.M. Guldi, G.M.A. Rahman, F. Zerbetto, M. Prato: Carbon nanotubes in electron donor-acceptor nanocomposites, Acc. Chem. Res. **38**, 871 (2005)
6.93 D.M. Guldi, G.M.A. Rahman, N. Jux, N. Tagmatarchis, M. Prato: Integrating single-wall carbon nanotubes into donor-accepto nanohybrids, Angew. Chem. Int. Ed. **43**, 5526–5530 (2004)
6.94 C. Ehli, G.M.A. Rahman, N. Jux, D. Balbinot, D.M. Guldi, F. Paolucci, M. Marcaccio, D. Paolucci, M. Melle-Franco, F. Zerbetto, S. Campidelli, M.J. Prato: Interactions in single wall carbon nanotubes/pyrene/porphyrin, J. Am. Chem. Soc. **128**, 11222 (2006)
6.95 D.S. Hecht, R.J.A. Ramirez, M. Briman, E. Artukovic, K.S. Chichak, J.F. Stoddart, G. Gruner: Bioinspired detection of light using a porphyrin-sensitized single-wall nanotube field effect transistor, Nano Lett. **6**, 2031–2036 (2006)
6.96 L. Hu, Y.-L. Zhao, K. Ryu, C. Zhou, J.F. Stoddart, G. Gruner: Light-induced charge transfer in pyrene/CdSe SWNT hybrids, Adv. Mater. **20**, 939 (2008)
6.97 Y.-L. Zhao, L. Hu, J.F. Stoddart, G. Gruner: Pyrenecyclodextrin-decorated single-walled carbon nanotube field-effect transistors as chemical sensors, Adv. Mater. **20**, 1910–1915 (2008)
6.98 H. Paloniemi, T. Aaritalo, T. Laiho, H. Liuke, N. Kocharova, K. Haapakka, F. Terzi, R. Seeber, J. Lukkari: Water-soluble full-length single-wall carbon nanotube polyelectrolytes: Preparation and

characterization, J. Phys. Chem. B **109**, 8634–8642 (2005)
6.99 Q. Yang, L. Shuai, J. Zhou, F. Lu, X. Pan: Functionalization of multiwalled carbon nanotubes by pyrene-labeled hydroxypropyl cellulose, J. Phys. Chem. B **112**, 12934–12939 (2008)
6.100 A.D. Stroock, R.S. Kane, M. Weck, S.J. Metallo, G.M. Whitesides: Synthesis of free-standing quasi-two-dimensional polymers, Langmuir **10**, 2466–2472 (2003)
6.101 D.-Q. Yang, B. Hennequin, E. Sacher: XPS demonstration of π–π interaction between benzyl mercaptan and multiwalled carbon nanotubes and their use in the adhesion of Pt nanoparticles, Chem. Mater. **18**, 5033 (2006)
6.102 V.A. Karachevtsev, A.M. Plokhotnichenko, M.V. Karachevtsev, V.S. Leontiev: Decrease of carbon nanotube UV light absorption induced by π–π stacking interaction with nucelotide bases, Carbon **48**, 3682–3691 (2010)
6.103 M. Shim, A. Javey, N. Wong, S. Kam, H. Dai: Polymer functionalization for air-stable n-type carbon nanotube field-effect transistors, J. Am. Chem. Soc. **123**, 11512–11513 (2001)
6.104 J. Kong, H. Dai: Full and modulated chemical gating of individual carbon nanotubes by organic amine compounds, J. Phys. Chem. B **105**, 2890–2893 (2001)
6.105 S. Banerjee, S.S. Wong: Functionalziation of carbon nanotubes with a metal-containing molecular complex, Nano Lett. **2**, 49–53 (2002)
6.106 Q. Chen, L. Dai, M. Gao, S. Huang, A. Mau: Plasma activation of carbon nanotubes for chemical modification, J. Phys. Chem. B **105**, 618–622 (2001)
6.107 J. Chen, M.A. Hamon, H. Hu, Y. Chen, A.M. Rao, P.C. Eklund, R.C. Haddon: Solution properties of single-walled carbon nanotubes, Science **282**, 95 (1998)
6.108 K.A.S. Fernando, Y. Lin, Y.P. Sun: High aqueous solubility of functionalized single-walled carbon nanotubes, Langmuir **20**, 4777–4778 (2004)
6.109 J. Chen, A.M. Rao, S. Lyuksyutov, M.E. Itkis, M.A. Hamon, H. Hu, R.W. Cohn, P.C. Eklund, D.T. Colbert, R.E. Smalley, R.C. Haddon: Dissolution of full-length single-walled carbon nanotubes, J. Phys. Chem. B **105**, 2525–2528 (2001)
6.110 M.-L. Chen, M.-L. Chen, X.-W. Chen, J.-H. Wang: Functionalization of MWNTs with hyperbranched PEI for highly selective isolation of BSA, Macromol. Biosci. **10**, 906 (2010)
6.111 G.M.A. Rahman, A. Troeger, V. Sgobba, D.M. Guldi, N. Jux, D. Balbino, M.N. Tchoul, W.T. Ford, A. Mateo-Alonso, M. Prato: Improving photocurrent generation: Supramolecularly and covalently functionalized single-wall carbon nanotubes-polymer/porphyrin donor-acceptor nanohybrids, Chem. A Eur. J. **14**, 8837–8846 (2008)
6.112 R. Singh, D. Pantarotto, D. McCarthy, O. Chaloin, J. Hoebeke, C.D. Partidos, J.-P. Briand, M. Prato, A. Bianco, K. Kostarelos: Binding and condensation of plasmid DNA onto functionalized carbon nanotubes: Toward the construction of nanotube-based gene delivery vectors, J. Am. Chem. Soc. **127**, 4388–4396 (2005)
6.113 D.M. Guldi, G.M.A. Rahman, V. Sgobba, N.A. Kotov, D. Bonifazi, M. Prato: CNT-CdTe versatile donor-acceptor nanohybrids, J. Am. Chem. Soc. **128**, 2315–2323 (2006)
6.114 M.A. Correa-Duarte, M. Grzelczak, V. Salgueirino-Maceira, M. Giersig, L.M. Liz-Marzan, M. Farle, K. Sierazdki, R. Diaz: Alignment of carbon nanotubes under low magnetic fields through attachment of magnetic nanoparticles, J. Phys. Chem. B **109**, 19060–19063 (2005)
6.115 C. Gao, W. Li, H. Morimoto, Y. Nagaoka, T. Maekawa: Magnetic carbon nanotubes: Synthesis by electrostatic self-assembly approach and application in biomanipulations, J. Phys. Chem. B **110**, 7213–7220 (2006)
6.116 A.B. Artyukhin, O. Bakajin, P. Stroeve, A. Noy: Layer-by-layer electrostatic self-assembly of polyelectrolyte nanoshells on individual carbon nanotube templates, Langmuir **20**, 1442–1448 (2004)
6.117 A. Carrillo, J.A. Swartz, J.M. Gamba, R.S. Kane, N. Chakrapani, B. Wei, P.M. Ajayan: Noncovalent functionalization of graphite and carbon nanotubes with polymer multilayers and gold nanoparticles, Nano Lett. **3**, 1437 (2003)
6.118 G. Liu, Y. Lin: Amperometric glucose biosensor based on self-assembling glucose oxidase on carbon nanotubes, Electrochem. Commun. **8**, 251–256 (2006)
6.119 R. Krajcik, A. Jung, A. Hirsch, W. Neuhuber, O. Zolk: Functionalization of carbon nanotubes enable non-covalent binding and intracellular delivery of small interfering RNA for efficient knock-down of genes, Biochem. Biophys. Res. Commun. **369**, 595–602 (2008)
6.120 V. Lordi, N. Yao, J. Wei: Method for supporting platinum on single-walled carbon nanotubes for a selective hdrogenation catalyst, Chem. Mater. **13**, 733–737 (2001)
6.121 R. Czerw, M. Terrones, J.-C. Charlier, X. Blase, B. Foley, R. Kamalakaran, N. Grobert, H. Terrones, D. Teklea, P.M. Ajayan, W. Blau, M. Rühle, D.L. Carroll: Identification of electron donor states in N-doped carbon nanotubes, Nano Lett. **1**, 457–460 (2001)
6.122 M. Terrones, P.M. Ajayan, F. Banhart, X. Blase, D.L. Carroll, J.C. Charlier, R. Czerw, B. Foley, N. Grobert, R. Kamalakaran, P. Kohler-Redlich, M. Ruhle, T. Seeger, H. Terrones: N-doping and coalescence of carbon nanotubes: Synthesis and electronic properties, Appl. Phys. A **74**, 355–361 (2002)
6.123 F. Villalpando-Paez, A. Zamudio, A.L. Elias, H. Son, E.B. Barros, S.G. Chou, Y.A. Kim, H. Muramatsu,

T. Hayashi, J. Kong, H. Terrones, G. Dresselhaus, M. Endo, M. Terrones, M.S. Dresselhaus: Synthesis and characterization of long strands of nitrogen-doped single-walled carbon nanotubes, Chem. Phys. Lett. **424**, 345–352 (2006)

6.124 J.D. Wiggins-Camacho, K.J. Stevenson: Effect of nitrogen concentration on capacitance, density of states, electronic conductivity, and morphology of N-doped carbon nanotube electrodes, J. Phys. Chem. C **113**, 19082–19090 (2009)

6.125 Y. Miyamoto, A. Rubio, S.G. Louie, M.L. Cohen: Electronic properties of tubule forms of hexagonal BC_3, Phys. Rev. B **50**, 18360 (1994)

6.126 M. Terrones, W.K. Hsu, A. Schilder, H. Terrones, N. Grobert, J.P. Hare, Y.Q. Zhu, M. Schwoerer, K. Prassides, H.W. Kroto, D.R.M. Walton: Novel nanotubes and encapsulated nanowires, Appl. Phys. A **66**, 307–317 (1998)

6.127 W.K. Hsu, S. Firth, P. Redlich, M. Terrones, H. Terrones, Y.Q. Zhu, N. Grobert, A. Schilder, R.J.H. Clark, H.W. Kroto, D.R.M. Walton: Boron-doping effects in carbon nanotubes, J. Mater. Chem **10**, 1425–1429 (2000)

6.128 B. Wei, R. Spolenak, P. Kohler-Redlich, M. Rühle, E. Arzt: Electrical transport in pure and boron-doped carbon nanotubes, Appl. Phys. Lett. **74**, 3149–3151 (1999)

6.129 S. Ishii, T. Watanabe, S. Ueda, S. Tsuda, T. Yamaguchi, Y. Takano: Resistivity reduction of boron-doped multiwalled carbon nanotubes synthesized from a methanol solution containing boric acid, Appl. Phys. Lett. **92**, 202116 (2008)

6.130 E. Borowiak-Palen, T. Pichler, A. Graff, R.J. Kalenczuk, M. Knupfer, J. Fink: Synthesis and electronic properties of B-doped single wall carbon nanotubes, Carbon **42**, 1123–1126 (2004)

6.131 L. Grigorian, K.A. Williams, S. Fang, G.U. Sumanasekera, A.L. Loper, E.C. Dickey, S.J. Pennycook, P.C. Eklund: Reversible intercalation of charged iodine chains into carbon nanotube ropes, Phys. Rev. Lett. **80**, 5560–5563 (1998)

6.132 Y. Zhao, J. Wei, R. Vajtai, P.M. Ajayan, E.V. Barrera: Iodine doped carbon nanotube cables exceeding specific electrical conductivity of metals, Sci. Rep. **1**, 83 (2011)

6.133 M.L. Guo, J.H. Chen, J. Li, L.H. Nie, S.Z. Yao: Carbon nanotubes-based amperometric cholesterol biosensor fabricated through layer-by-layer technique, Electroanalysis **16**, 1992–1998 (2004)

6.134 M.D. Rubianes, G.A. Rivas: Carbon nanotubes paste electrode, Electrochem. Commun. **5**, 689–694 (2003)

6.135 K.-P. Lee, A.I. Gopalan, S. Komathi: Direct electrochemistry of cytochrome c and biosensing for hydrogen peroxide on polyaniline grafted multiwalled carbon nanotube electrode, Sens. Actuators B **141**, 518–525 (2009)

6.136 L. Chen, G. Lu: Direct electrochemistry and electrocatalysis of hybrid film assembled by polyelectrolyte–surfactant polymer, carbon nanotubes and hemoglobin, J. Electroanal. Chem. **597**, 51–59 (2006)

6.137 G. Che, B.B. Lakshmi, E.R. Fisher, C.R. Martin: Carbon nanotubule membranes for electrochemical energy storage and production, Nature **393**, 346–349 (1998)

6.138 Z. Liu, X. Lin, J.Y. Lee, W. Zhang, M. Han, L.M. Gan: Preparation and characterization of platinum-based electrocatalysts on multiwalled carbon nanotubes for proton exchange membrane fuel cells, Langmuir **18**, 4054–4060 (2002)

6.139 S. Hrapovic, Y. Liu, K.B. Male, J.H.T. Luong: Electrochemical biosensing platforms using platinum nanoparticles and carbon nanotubes, Anal. Chem. **76**, 1083–1088 (2004)

6.140 J.J. Gooding, R. Wibowo, J. Liu, W. Yang, D. Losic, S. Orbons, F.J. Mearns, J.G. Shapter, D.B. Hibbert: Protein electrochemistry using aligned carbon nanotube arrays, J. Am. Chem. Soc. **125**, 9006–9007 (2003)

6.141 M. Zhang, A. Smith, W. Gorski: Carbon nanotube-chitosan system for electrochemical sensing based on dehydrogenase enzymes, Anal. Chem. **76**, 5045–5050 (2004)

6.142 B.R. Azamian, J.J. Davis, K.S. Coleman, C.B. Bagshaw, M.L.H. Green: Bioelectrochemical single-walled carbon nanotubes, J. Am. Chem. Soc. **124**, 12664–12665 (2002)

6.143 C. Cai, J. Chen: Direct electron transfer of glucose oxidase promoted by carbon nanotubes, Anal. Biochem. **332**, 75–83 (2004)

6.144 X. Yu, D. Chattopadhyay, I. Galeska, F. Papadimitrakopoulos, J.F. Rusling: Peroxidase activity of enzymes bound to the ends of single-wall carbon nanotube forest electrodes, Electrochem. Commun. **5**, 408–411 (2003)

6.145 F. Patolsky, Y. Weizmann, I. Willner: Long-range electrical contacting of redox enzymes by SWCNT connectors, Angew. Chem. Int. Ed. **43**, 2113–2117 (2004)

6.146 G. Liu, Y. Lin: Biosensor based on self-assembling acetylcholinesterase on carbon nanotubes for flow injection/amperometric detection of organophosphate pesticides and nerve agents, Anal. Chem. **78**, 835–843 (2006)

6.147 Y. Liu, M. Wang, F. Zhao, Z. Xu, S. Dong: The direct electron transfer of glucose oxidase and glucose biosensor based on carbon nanotubes/chitosan matrix, Biosens. Bioelectron. **21**, 984–988 (2005)

6.148 Y.-D. Zhao, W.-D. Zhang, H. Chen, Q.-M. Luo, S.F.Y. Li: Direct electrochemistry of horseradish peroxidase at carbon nanotube powder microelectrode, Sens. Actuators B **87**, 168 (2002)

6.149 Y.-C. Tsai, S.-C. Li, J.-M. Chen: Cast thin film biosensor design based on a nafion backbone, a multiwalled carbon nanotube conduit, and a glucose oxidase function, Langmuir **21**, 3653–3658 (2005)

6.150 S. Chen, R. Yuan, Y. Chai, L. Zhang, N. Wang, X. Li: Amperometric third-generation hydrogen peroxide biosensor based on the immobilization of hemoglobin on multiwall carbon nanotubes and gold colloidal nanoparticles, Biosens. Bioelectron. **22**, 1268–1274 (2007)

6.151 Y. Yan, W. Zheng, M. Zhang, L. Wang, L. Su, L. Mao: Bioelectrochemically functional nanohybrids through Co-assembling of proteins and surfactants onto carbon nanotubes: Facilitated electron transfer of assembled proteins with enhanced faradic response, Langmuir **21**, 6560–6566 (2005)

6.152 M.D. Rubianes, G.A. Rivas: Enzymatic biosensors based on carbon nanotubes paste electrodes electroanalysis, Electroanalysis **17**, 73–78 (2005)

6.153 J.H.T. Luong, S. Hrapovic, D. Wang, F. Benseba, B. Simard: Solubilization of multiwall carbon nanotubes by 3-aminopropyltriethoxysilane towards the fabrication of electrochemical biosensors with promoted electron transfer, Electroanalysis **16**, 132–139 (2004)

6.154 P. Du, S. Liu, P. Wu, C. Cai: Preparation and characterization of room temperature ionic liquid/single-walled carbon nanotube nanocomposites and their application to the direct electrochemistry of heme-containing proteins/enzymes, Electrochim. Acta **52**, 6534–6547 (2007)

6.155 S. Deng, G. Jian, J. Lei, Z. Hu, H. Ju: A glucose biosensor based on direct electrochemistry of glucose oxidase immobilized on nitrogen-doped carbon nanotubes, Biosens. Bioelectron. **25**, 373–377 (2009)

6.156 X. Li, H. Zhou, P. Yu, L. Su, T. Ohsaka, L. Mao: A miniature glucose/O_2 biofuel cell with single-walled carbon nanotubes-modified carbon fiber microelectrodes as the substrate, Electrochem. Commun. **10**, 851–854 (2008)

6.157 L. Deng, L. Shang, Y. Wang, T. Wang, H. Chen, S. Dong: Multilayer structured carbon nanotubes/poly-l-lysine/laccase composite cathode for glucose/O_2 biofuel cell, Electrochem. Commun. **10**, 1012–1015 (2008)

6.158 W. Zheng, H.M. Zhou, Y.F. Zheng, N. Wang: A comparative study on electrochemistry of laccase at two kinds of carbon nanotubes and its application for biofuel cell, Chem. Phys. Lett. **457**, 381–385 (2008)

6.159 S. Maldonado, S. Morin, K.J. Stevenson: Structure, composition, and chemical reactivity of carbon nanotubes by selective nitrogen doping, Carbon **44**, 1429–1437 (2006)

6.160 K. Gong, F. Du, Z. Xia, M. Durstock, L. Dai: Nitrogen-doped carbon nanotube arrays with high electrocatalytic activity for oxygen reduction, Science **323**, 760–764 (2009)

6.161 Z. Wang, R. Jia, J. Zheng, J. Zhao, L. Li, J. Song, Z. Zhu: Nitrogen-promoted self-assembly of n-doped carbon nanotubes and their intrinsic catalysis for oxygen reduction in fuel cells, ACS Nano **5**, 1677–1684 (2011)

6.162 C. Deng, J. Chen, X. Chen, C. Xiao, L. Nie, S. Yao: Direct electrochemistry of glucose oxidase and biosensing for glucose based on boron-doped carbon nanotubes modified electrode, Biosens. Bioelectron. **23**, 1272–1277 (2008)

6.163 L. Yan-hui, C. Jun-Feng, D. Jun, M. Zong-Qiang, X. Cai-Lu, W. De-Hai: Effect of Pt/Ru supported by carbon nanotubes on the ability of PEMFC to resist CO poisoning, J. Inorg. Mater. **19**, 629–633 (2004)

6.164 X. Zhao, W. Li, L. Jiang, W. Zhou, Q. Xin, B. Yi, G. Sun: Multi-wall carbon nanotube supported Pt-Sn nanoparticles as an anode catalyst for the direct ethanol fuel cell, Carbon **42**, 3263–3265 (2004)

6.165 Z. Liu, J.Y. Lee, W. Chen, M. Han, L.M. Gan: Physical and electrochemical characterizations of microwave-assisted polyol preparation of carbon-supported PtRu nanoparticles, Langmuir **20**, 181–187 (2003)

6.166 X.-R. Ye, Y. Lin, C. Wang, M.H. Engelhard, Y. Wang, C.M. Wai: Supercritical fluid synthesis and characterization of catalytic metal nanoparticles on carbon nanotubes, J. Mater. Chem. **14**, 908–913 (2004)

6.167 Z. He, J. Chen, D. Liu, H. Tang, W. Deng, Y. Kuang: Deposition and electrocatalytic properties of platinum nanoparticles on carbon nanotubes for methanol electrooxidation, Mater. Chem. Phys. **85**, 396–401 (2004)

6.168 T. Matsumoto, T. Komatsu, H. Nakano, K. Arai, Y. Nagashima, E. Yoo, T. Yamazki, M. Kijima, H. Shimizu, Y. Takasawa, J. Nakamura: Efficent usage of highly dispersed Pt on carbon nanotubes for electrode catalysts of polymer electrolyte fuel cells, Catal. Today **90**, 277–281 (2004)

6.169 D.-J. Guo, H.-L. Li: Electrochemical synthesis of Pd nanoparticles on functional MWNT surfaces, Electrochem. Commun. **6**, 999–1003 (2004)

6.170 D.-J. Guo, H.-L. Li: High dispersion and electrocatalytic properties of Pt nanoparticles onSWNT bundles, J. Electroanal. Chem. **573**, 197–202 (2004)

6.171 G. Girishkumar, K. Vinodgopal, V.P. Kamat: Carbon nanostructures in portable fuel cells: Single-walled carbon nanotube electrode for methanol oxidation and oxygen reduction, J. Phys. Chem. B **108**, 19960–19966 (2004)

6.172 Y. Xing: Synthesis and eletrochemical characterization of uniformly-dipsrsed high loading Pt nanoparticles on sonochemically-treated carbon nanotubes, J. Phys. Chem. B **108**, 19255–19259 (2004)

6.173 Z.Q. Tian, S.P. Jiang, Y.M. Liang, P.K. Shen: Synthesis and characterization of platinum catalysts on multiwalled carbon nanotubes by intermittent microwave irradiation for fuel cell applications, J. Phys. Chem. B **110**, 5343–5350 (2006)

6.174 J. Prabhuram, T.S. Zhao, Z.K. Tang, R. Chen, Z.X. Liang: Multiwalled carbon nanotube supported

PtRu for the anode of direct methanol fuel cells, J. Phys. Chem. B **110**, 5245–5252 (2006)
6.175 A. Kongkanand, S. Kuwabata, G. Girishkumar, P. Kamata: Single-wall carbon nanotubes supported platinum nanoparticles with improved electrocatalytic activity for oxygen reduction reaction, Langmuir **22**, 2392–2396 (2006)
6.176 D.J. Guo, H.L. Li: Highly dispersed Ag nanoparticles on functional MWNT surfaces for methanol oxidation in alkaline solution, Carbon **43**, 1259–1264 (2005)
6.177 C.-L. Sun, L.-C. Chen, M.-C. Su, L.-S. Hong, O. Chyan, C.-Y. Hsu, K.-H. Chen, T.-F. Chang, L. Chang: Ultrafine platinum nanoparticles uniformly dispersed on arrayed CN_x nanotubes with high electrochemical activity, Chem. Mater. **17**, 3749–3753 (2005)
6.178 J. Chen, M. Wang, B. Liu, Z. Fan, K. Cui, Y. Kuang: Platinum catalysts prepared with functional carbon nanotube defects and its improved catalytic performance for methanol oxidation, J. Phys. Chem. B **110**, 11775–11779 (2006)
6.179 T. Maiyalagan, B. Viswanathan, U. Varadaraju: Nitrogen containing carbon nanotubes as supports for Pt – Alternate anodes for fuel cell applications, Electrochem. Commun. **7**, 905–912 (2005)
6.180 S. Yang, X. Zhang, H. Mi, X. Ye: Pd nanoparticles supported on functionlized multi-walled carbon nanotubes (MWCNTs) and electrooxidation for formic acid, J. Power Sources **175**, 26–32 (2008)
6.181 J. Xu, K. Hua, G. Sun, C. Wang, X. Lv, Y. Wang: Electrooxidation of methanol on carbon nanotubes supported Pt-Fe alloy electrode, Electrochem. Commun. **8**, 982–986 (2006)
6.182 B. Yue, Y. Ma, H. Tao, L. Yu, G. Jian, X. Wang, X. Wang, Y. Lu, Z. Hu: CN_x nanotubes as catalyst support to immobilize platinum nanoparticles for methanol oxidation, J. Mater. Chem. **18**, 1747–1750 (2008)
6.183 G.-Y. Gao, D.-J. Guo, H.-L. Li: Electrocatalytic oxidation of formaldehyde on palladium nanoparticles supported on multi-walled carbon nanotubes, J. Power Sources **162**, 1094–1098 (2006)
6.184 H. Wang, J. Liang, L. Zhu, F. Peng, H. Yu, J. Yang: High oxygen-reduction-activity and methanol-tolerance cathode catalyst Cu-PtFe-CNTs for direct methanol duel cells, Fuel Cells **10**, 99–105 (2010)
6.185 C. Xu, Y. Su, L. Tan, Z. Liu, J. Zhang, S. Chen, S.P. Jiang: Electrodeposited PtCo and PtMn electrocalysts for methanol and ethanol electrooxidation of direct alcohol fuel cells, Electrochim. Acta **54**, 6322–6326 (2009)
6.186 D.-J. Guo, S.-K. Cui: Hollow PtCo nanospheres supported on multi-walled carbon nanotubes for methanol electrooxidation, J. Colloid Interface Sci. **340**, 53 (2009)
6.187 K.M. Manesh, P. Santhosh, S. Komathi, N.H. Kim, J.W. Park, A.I. Gopalan, K.-P. Lee: Electrochemical detection of celecoxib at a polyaniline grafted multiwall carbon nanotubes modified electrode, Anal. Chim. Acta **626**, 1–9 (2008)
6.188 T. Yang, N. Zhou, Y. Zhang, W. Zhang, K. Jiao, G. Li: Synergistically improved sensitivity for the detection of specific DNA sequences using polyaniline nanofibers and multi-walled carbon nanotubes composites, Biosens. Bioelectron. **24**, 2165–2170 (2009)
6.189 Z. Hu, J. Xu, Y. Tian, R. Peng, Y. Xian, Q. Ran, L. Jin: Layer-by-layer assembly of poly(sodium 4-styrenesulfonate) wrapped multiwalled carbon nanotubes with polyaniline nanofibers and its electrochemistry, Carbon **48**, 3729–3736 (2010)
6.190 M. Kalbáč, L. Kavan, L. Dunsch: Controlled doping of double walled carbon nanotubes and conducting polymers in a composite: An in situ Raman spectroelectrochemical study, Compos. Sci. Technol. **69**, 1553–1557 (2009)
6.191 D.R.S. Jeykumari, S.S. Narayanan: A novel nanobiocomposite based glucose biosensor using neutral red functionalized carbon nanotubes, Biosens. Bioelectron. **23**, 1404–1411 (2008)
6.192 D.R.S. Jeykumari, S. Ramaprabhu, S.S. Narayanan: A thionine functionalized multiwalled carbon nanotube modified electrode for the determination of hydrogen peroxide, Carbon **45**, 1340–1353 (2007)
6.193 E. Frackowiak, S. Gautier, H. Gaucher, S. Bonnamy, F. Beguin: Electrochemical storage of lithium in multiwalled carbon nanotubes, Carbon **37**, 61 (1999)
6.194 B. Gao, A. Kleinhammes, X.P. Tang, C. Bower, L. Fleming, Y. Wu, O. Zhou: Electrochemical intercalation of single-walled carbon nanotubes with lithium, Chem. Phys. Lett. **307**, 153–157 (1999)
6.195 H. Shimoda, B. Gao, X.P. Tang, A. Kleinhammes, L. Fleming, Y. Wu, O. Zhou: Lithium intercalation into opened single-wall carbon nanotubes: Storage capacity and electronic properties, Phys. Rev. Lett. **88**, 015502 (2002)
6.196 Z.-H. Yang, H. Wu: Electrochemical intercalation of lithium into carbon nanotube, Solid State Ion. **143**, 173–180 (2001)
6.197 J.M. Romo-Herrera, B.G. Sumpter, D.A. Cullen, H. Terrones, E. Cruz-Silva, D.J. Smith, V. Meunier, M. Terrones: An atomistic branching mechanism for carbon nanotubes: Sulfure as the triggering agent, Angew. Chem. Int. Ed. **47**, 2948–2953 (2008)
6.198 Y. Liu, H. Zheng, X.H. Liu, S. Huang, T. Zhu, J. Wang, A. Kushima, N.S. Hudak, X. Huang, S. Zhang, S.X. Mao, X. Qian, J. Li, J.Y. Huang: Lithiation-induced embrittlement of multiwalled carbon nanotubes, ACS Nano **5**, 7245–7253 (2011)
6.199 Y. Lin, D.E. Hill, J. Bentley, L.F. Allard, Y.-P. Sun: Characterization of functionalized single-walled carbon nanotubes at individual nanotube-thin bundle level, J. Phys. Chem. B **107**, 10453–10457 (2003)
6.200 H.-X. Wu, R. Tong, X.-Q. Qiu, H.-F. Yang, Y.-H. Lin, R.-F. Cai, S.-X. Qian: Functionalization of multi-

walled carbon nanotubes with polystyrene under atom transfer radical polymerization conditions, Carbon **45**, 152–159 (2007)
6.201 H. Takahashi, S. Numao, S. Bandow, S. Iijima: AFM imaging of wrapped multiwall carbon nanotube in DNA, Chem. Phys. Lett. **418**, 535–539 (2006)
6.202 D.L. Carroll, P. Redlich, X. Blase, J.-C. Charlier, S. Curran, P.M. Ajayan, S. Roth, M. Rühle: Effects of nanodomain formation on the electronic structure of doped carbon nanotubes, Phys. Rev. Lett. **81**, 2332–2335 (1998)
6.203 T. Hayashi, M. Terrones, C. Scheu, Y.A. Kim, M. Rühle, T. Nakajima, M. Endo: NanoTeflons: Structure and EELS Characterization of Fluorinated Carbon Nanotubes and Nanofibers, Nano Lett. **2**, 491–496 (2002)
6.204 E. Cruz-Silva, D.A. Cullen, L. Gu, J.M. Romo-Herrera, E. Muñoz-Sandoval, F. López-Urías, B.G. Sumpter, V. Meunier, J.-C. Charlier, D.J. Smith, H. Terrones, M. Terrones: Heterodoped nanotubes: Theory, synthesis, and characterization of phosphorus nitrogen doped multiwalled carbon nanotubes, ACS Nano **2**, 441–448 (2008)
6.205 M. Terrones, H. Terrones, N. Grobert, W.K. Hsu, Y.Q. Zhu, J.P. Hare, H.W. Kroto, D.R.M. Walton, P. Kohler-Redlich, M. Rühle, J.P. Zhang, A.K. Cheetham: Efficient route to large arrays of CN_X nanofibers by pyrolysis of ferrocene/melamine mixtures, Appl. Phys. Lett. **75**, 3932–3934 (1999)
6.206 S. Suzuki, M. Tomita: Observation of potassium-intercalated carbon nanotubes and their valence-band excitation spectra, J. Appl. Phys. **79**, 3739 (1996)
6.207 S. Suzuki, C. Bower, O. Zhou: In-situ TEM and EELS studies of alkali-metal intercalation with single-walled carbon nanotubes, Chem. Phys. Lett. **285**, 230–234 (1998)
6.208 T.I.T. Okpalugo, P. Papakonstantinou, H. Murphy, J. McLaughlin, N.M.D. Brown: High resolution XPS characterization of chemical functionalized MWCNTs and SWCNTs, Carbon **43**, 153–161 (2005)
6.209 W.-J. Chou, C.-C. Wang, C.-Y. Chen: The Improvement of electrical property of multiwalled carbon nanotubes with plasma modification and chemical oxidation in the polymer matrix, J. Inorg. Organomet. Polym. **19**, 234–242 (2009)
6.210 H. Ago, T. Kugler, F. Cacialli, W.R. Salaneck, M.S.P. Shaffer, A.H. Windle, R.H. Friend: Work functions and surface functional groups of multiwall carbon nanotubes, J. Phys. Chem. B **103**, 8116–8121 (1999)
6.211 K. Ghosh, M. Kumar, T. Maruyama, Y. Ando: Tailoring the field emission property of nitrogen-doped carbon nanotubes by controlling the graphitic/pyridinic substitution, Carbon **48**, 191–200 (2010)
6.212 A. Velamakanni, C.W. Magnuson, K.J. Ganesh, Y. Zhu, J. An, P.J. Ferreira, R.S. Ruoff: Site-specific deposition of Au nanoparticles in CNT Films by chemical bonding, ACS Nano **4**, 540–546 (2010)
6.213 H.C. Choi, S.Y. Bae, W.-S. Jang, J. Park, H.J. Song, H.-J. Shin, H. Jung, J.-P. Ahn: Release of N_2 from the carbon nanotubes via high-temperature annealing, J. Phys. Chem. B **109**, 1683–1688 (2005)
6.214 S. Kundu, T.C. Nagaiah, W. Xia, Y. Wang, S.V. Dommele, J.H. Bitter, M. Santa, G. Grundmeier, M. Bron, W. Schuhmann, M. Muhler: Electrocatalytic activity and stability of nitrogen-containing carbon nanotubes in the oxygen reduction reaction, J. Phys. Chem. C **113**, 14302–14310 (2009)
6.215 Y. Xing, L. Li, C.C. Chusuei, R.V. Hull: Sonochemical oxidation of multiwalled carbon nanotubes, Langmuir **21**, 4185–4190 (2005)
6.216 V. Datsyuk, M. Kalyva, K. Papagelis, J. Parthenios, D. Tasis, A. Siokou, I. Kallitsisa, C. Galiotis: Chemical oxidation of multiwalled carbon nanotubes, Carbon **46**, 833–840 (2008)
6.217 S. Kundu, Y. Wang, W. Xia, M. Muhler: Thermal stability and reducibility of oxygen-containing functional groups on multiwalled carbon nanotube surfaces: A quantitative high-resolution XPS and TPD/TPR study, J. Phys. Chem. C **112**, 16869–16878 (2008)
6.218 C.-M. Yang, K.H. An, J.S. Park, K.A. Park, S.C. Lim, S.-H. Cho, Y.S. Lee, W. Park, C.Y. Park, Y.H. Lee: Preferential etching of metallic single-walled carbon nanotubes with small diameter by fluorine gas, Phys. Rev. B **73**, 075419 (2006)
6.219 K.H. An, J.G. Heo, K.G. Jeon, D.J. Bae, C. Jo, C.W. Yang, C.-Y. Park, Y.H. Lee, Y.S. Lee, Y.S. Chung: X-ray photoemission spectroscopy study of fluorinated single-walled carbon nanotubes, Appl. Phys. Lett. **80**(22), 4235–4237 (2002)
6.220 J. Liu, S. Webster, D.L. Carroll: Highly aligned coiled nitrogen-doped carbon nanotubes synthesized by injection-assisted chemical vapor deposition, Appl. Phys. Lett. **88**, 213119 (2006)
6.221 R. Sen, B.C. Satishkumar, A. Govindaraj, K.R. Harikumar, M.K. Renganathan, C.N.R. Rao: Nitrogen-containing carbon nanotubes, J. Mater. Chem. **7**, 2335–2337 (1997)
6.222 Z. Chen, D. Higgins, H. Tao, R.S. Hsu, Z. Chen: Highly active nitrogen-doped carbon nanotubes for oxygen reduction reaction in fuel cell applications, J. Phys. Chem. C **113**, 21008–21013 (2009)
6.223 C. Gao, H. He, L. Zhou, X. Zheng, Y. Zhang: Scalable functional group engineering of carbon nanotubes by improved one-step nitrene chemistry, Chem. Mater. **21**, 360–370 (2009)
6.224 L.G. Bulusheva, A.V. Okotrub, I.A. Kinloch, I.P. Asanov, A.G. Kurenya, A.G. Kudashov, X. Chen, H. Song: Effect of nitrogen doping on Raman spectra of multi-walled carbon nanotubes, Phys. Status Solidi (b) **245**, 1971–1974 (2008)
6.225 M. Terrones, P. Redlich, N. Grobert, S. Trasobares, W.-K. Hsu, H. Terrones, Y.-Q. Zhu, J.P. Hare, C.L. Reeves, A.K. Cheetham, M. Rühle, H.W. Kroto, D.R.M. Walton: Carbon nitride nanocomposites: For-

mation of aligned C_xN_y nanofibers, Adv. Mater. **11**, 655–658 (1999)
6.226 M.J. Behr, K.A. Mkhoyan, E.S. Aydil: Orientation and morphological evolution of catalyst nanoparticles during carbon nanotube growth, ACS Nano **4**, 5087–5094 (2010)
6.227 J. Čech, S.A. Curran, D. Zhang, J.L. Dewald, A. Avadhanula, M. Kandadai, S. Roth: Functionalization of multi-walled carbon nanotubes: Direct proof of sidewall thiolation, Phys. Status Solidi (b) **243**, 3221–3225 (2006)
6.228 N.O.V. Plank, L. Jiang, R. Cheung: Fluorination of carbon nanotubes in CF_4 plasma, Appl. Phys. Lett. **83**, 2426–2428 (2003)
6.229 W. Xia, X. Chen, S. Kundu, X. Wang, G. Grundmeier, Y. Wang, M. Bron, W. Schuhmann, M. Muhler: Chemical vapor synthesis of secondary carbon nanotubes catalyzed by iron nanoparticles electrodeposited on primary carbon nanotubes, Surf. Coating Technol. **201**, 9232–9237 (2007)
6.230 M.S. Dresselhaus, G. Dresselhaus, R. Saito, A. Jorio: Raman spectroscopy of carbon nanotubes, Phys. Rep. **409**, 47–99 (2005)
6.231 M.S. Dresselhaus, G. Dresselhaus, A. Jorio, A.G. Souza Filho, R. Saito: Review Raman spectroscopy on isolated single wall carbon nanotubes, Carbon **40**, 2043–2061 (2002)
6.232 M.H. Brodsky: Raman scattering in amorphous semiconductors. In: *Light Scattering in Solids I: Introductory Concepts*, Topics in Applied Physics, Vol. 8, 2nd edn., ed. by M. Cardona (Springer, Berlin 1983) p. 205
6.233 R.S. Berg, P.Y. Yu: Resonant Raman study of intrinsic defect modes in electron- and neutron-irradiated GaAs, Phys. Rev. B **35**, 2205 (1987)
6.234 J. Maultzsch, S. Reich, C. Thomsen: Raman scattering in carbon nanotubes revisited, Phys. Rev. B **65**, 233402 (2002)
6.235 A.G.S. Filho, A. Jorio, G.G. Samsonidze, G. Dresselhaus, M.A. Pimenta, M.S. Dresselhaus, A.K. Swan, M.S. Unlu, B.B. Goldberg, R. Saito: Competing spring constant versus double resonance effects on the properties of dispersive modes in isolated single-wall carbon nanotubes, Phys. Rev. B **67**, 035427 (2003)
6.236 I.O. Maciel, M.A. Pimenta, M. Terrones, H. Terrones, J. Campos-Delgado, A. Jorio: The two peaks G band in carbon nanotubes, Phys. Status Solidi (b) **245**(10), 2197–2200 (2008)
6.237 I.O. Maciel, N. Anderson, M.A. Pimenta, A. Hartschuh, H. Qian, M. Terrones, H. Terrones, J. Campos-Delgado, A.M. Rao, L. Novotny, A. Jorio: Electron and phonon renormalization near charged defects in carbon nanotubes, Nat. Mater. **7**, 878–883 (2008)
6.238 I.O. Maciel, J. Campos-Delgado, E. Cruz-Silva, M.A. Pimenta, B.G. Sumpter, V. Meunier, F. Lopez-Urias, E. Munoz-Sandoval, H. Terrones, M. Terrones, A. Jorio: Synthesis, electronic structure, and Raman scattering of phosphorus-doped single-wall carbon nanotubes, Nano Lett. **9**, 2267–2272 (2009)
6.239 J. Campos-Delgado, I.O. Maciel, D.A. Cullen, D.J. Smith, A. Jorio, M.A. Pimenta, H. Terrones, M. Terrones: Chemical vapor deposition synthesis of N-, P-, and Si-doped single-walled carbon nanotubes, ACS Nano **4**, 1696–1702 (2010)
6.240 S. Osswald, M. Havel, Y. Gogotsi: Monitoring oxidation of multiwalled carbon nanotubes by Raman spectroscopy, J. Raman Spectrosc. **38**, 728–736 (2007)
6.241 K.-Y. Chuna, H. Sang Lee, C.J. Lee: Nitrogen doping effects on the structure behavior and the field emission performance of double-walled carbon nanotubes, Carbon **47**, 169–177 (2009)
6.242 H. Hu, B. Zhao, M.A. Hamon, K. Kamaras, M.E. Itkis, R.C. Haddon: Sidewall functionalization of single-walled carbon nanotubes by addition of dichlorocarbene, J. Am. Chem. Soc. **125**, 14893–14900 (2003)
6.243 S.J. Kim, Y.J. Park, E.J. Ra, K.K. Kim, K.H. An, Y.H. Lee, J.Y. Choi, C.H. Park, S.K. Doo, M.H. Park, C.W. Yang: Defect-induced loading of Pt nanoparticles on carbon nanotubes, Appl. Phys. Lett. **90**, 023114 (2007)
6.244 A.E. Porter, M. Gass, J.S. Bendall, K. Muller, A. Goode, J.N. Skepper, P.A. Midgley, M. Welland: Uptake of noncytotoxic acid-treated single-walled carbon nanotubes into the cytoplasm of human macrophage cells, ACS Nano **3**, 1485–1492 (2009)
6.245 C.A. Dyke, J.M. Tour: Solvent-free functionalization of carbon nanotubes, J. Am. Chem. Soc. **125**, 1156–1157 (2003)
6.246 J. Maultzsch, S. Reich, C. Thomsen, S. Webster, R. Czerw, D.L. Carroll, S.M.C. Vieira, P.R. Birkett, C.A. Rego: Raman characterization of boron-doped multiwalled carbon nanotubes, Appl. Phys. Lett. **81**, 2647–2649 (2002)
6.247 A. Claye, S. Rahman, J.E. Fischer, A. Sirenko, G.U. Sumanasekera, P.C. Eklund: In situ Raman scattering studies of alkali-doped single wall carbon nanotubes, Chem. Phys. Lett. **333**, 16–22 (2001)
6.248 H. Kuzmany, A. Kukovecz, F. Simon, M. Holzweber, C. Kramberger, T. Pichler: Functionalization of carbon nanotubes, Synth. Met. **141**, 113–122 (2004)
6.249 L.S. Panchakarla, A. Govindaraj, C.N.R. Rao: Nitrogen- and boron-doped double-walled carbon nanotubes, ACS Nano **1**, 494–500 (2007)
6.250 D. Bom, R. Andrews, D. Jacques, J. Anthony, B. Chen, M.S. Meier, J.P. Selegue: Thermogravimetric analysis of the oxidation of multiwalled carbon nanotubes: Evidence for the role of defect sites in carbon nanotube chemistry, Nano Lett. **2**, 615–619 (2002)
6.251 P. Ghosh, M. Zamri, M. Subramanian, T. Soga, T. Jimbo, R. Katoh, M. Tanemura: Bamboo-shaped aligned CN_x nanotubes synthesized using single feedstock at different temperatures and study of their field electron emission, J. Phys. D **41**, 155405 (2008)

6.252 R.C. Che, L.-M. Peng, M.S. Wang: Electron side-emission from corrugated CN_x nanotubes, Appl. Phys. Lett. **85**, 4753–4755 (2004)

6.253 J.A. Robinson, E.S. Snow, S.C. Badescu, T.L. Reinecke, F.K. Perkins: Role of defects in single-walled carbon nanotube chemical sensors, Nano Lett. **6**, 1747 (2006)

6.254 S. Peng, K. Cho: Ab initio study of doped carbon nanotube sensors, Nano Lett. **3**, 513–517 (2003)

6.255 F. Villalpando-Páez, A.H. Romero, E. Muñoz-Sandoval, L.M. Martínez, H. Terrones, M. Terrones: Fabrication of vapor and gas sensors using films of aligned CN_x nanotubes, Chem. Phys. Lett. **386**, 137 (2004)

6.256 E. Cruz-Silva, F. Lopez-Urias, E. Muñoz-Sandoval, B.G. Sumpter, H. Terrones, J.-C. Charlier, V. Meunier, M. Terrones: Phosphorus and phosphorus–nitrogen doped carbon nanotubes for ultrasensitive and selective molecular detection, Nanoscale **3**, 1008–1013 (2011)

6.257 B.S. Shim, W. Chen, C. Doty, C. Xu, N.A. Kotov: Smart electronic yarns and wearable fabrics for human biomonitoring made by carbon nanotube coating with polyelectrolytes, Nano Lett. **2008**(8), 4151–4157 (2008)

6.258 Y. Jia, A. Cao, X. Bai, Z. Li, L. Zhang, N. Guo, J. Wei, K. Wang, H. Zhu, D. Wu, P.M. Ajayan: Achieving high efficiency silicon-carbon nanotube heterojunction solar cells by acid doping, Nano Lett. **11**, 1901–1905 (2011)

6.259 Z. Chen, S.M. Tabakman, A.P. Goodwin, M.G. Kattah, D. Daranciang, X. Wang, G. Zhang, X. Li, Z. Liu, P.J. Utz, K. Jiang, S. Fan, H. Dai: Protein microarrays with carbon nanotubes as multi-color Raman labels, Nat. Biotechnol. **26**, 1285–1292 (2008)

6.260 N.W.S. Kam, M. O'Connell, J.A. Wisdom, H. Dai: Carbon nanotubes as multifunctional biological transporters and near-infrared agents for selective cancer cell destruction, Proc. Natl. Acad. Sci. USA **102**, 11600–11605 (2005)

6.261 R. Li, R. Wu, L. Zhao, M. Wu, L. Yang, H. Zou: P-Glycoprotein antibody functionalized carbon nanotube overcomes the multidrug resistance of human leukemia cells, ACS Nano **4**, 1399–1408 (2010)

6.262 B. Pradhan, S.K. Batabyal, A.J. Pal: Functionalized carbon nanotubes in donor/acceptor-type photovoltaic devices, Appl. Phys. Lett. **88**, 093106 (2006)

6.263 S.-R. Jang, R. Vittal, K.-J. Kim: Incorporation of functionalized single-wall carbon nanotubes in dye-sensitized TiO_2 solar cells, Langmuir **20**, 9807–9810 (2004)

6.264 A.J. Miller, R.A. Hatton, S.R.P. Silva: Interpenetrating multiwall carbon nanotube electrodes for organic solar cells, Appl. Phys. Lett. **89**, 133117 (2006)

6.265 B.J. Landi, S.L. Castro, H.J. Ruf, C.M. Evans, S.G. Bailey, R.P. Raffaelle: CdSe quantum dot-single wall carbon nanotube complexes for polymeric solar cells, Sol. Energy Mater. Sol. Cells **87**, 733–746 (2005)

6.266 Z. Liu, X. Sun, N. Nakayama, H. Dai: Supramolecular chemistry on water-soluble carbon nanotubes for drug loading and delivery, ACS Nano **1**, 50–56 (2007)

6.267 M.L. Schipper, N. Nakayama-Ratchford, C.R. Davis, N.W.S. Kam, P. Chu, Z. Liu, X. Sun, H. Dai, S.S. Gambhir: A pilot toxicology study of single-walled carbon nanotubes in a small sample of mice, Nat. Nanotechnol. **3**, 216–221 (2008)

6.268 L. Zeng, L.B. Alemany, C.L. Edwards, A.R. Barron: Demonstration of covalent sidewall functionalization of single wall carbon nanotubes by NMR spectroscopy: Side chain length dependence on the observation of the sidewall sp^3 carbons, Nano Res. **1**, 72–88 (2008)

6.269 Z. Liu, S. Tabakman, K. Welsher, H. Dai: Carbon nanotubes in biology and medicine: In vitro and in vivo detection, imaging and drug delivery, Nano Res. **2**, 85–120 (2009)

6.270 Z. Liu, C. Davis, W. Cai, L. He, X. Chen, H. Dai: Circulation and long-term fate of functionalized, biocompatible single-walled carbon nanotubes in mice probed by Raman spectroscopy, Proc. Natl. Acad. Sci. USA **105**, 1410–1415 (2008)

6.271 K. Lee, L. Li, L. Dai: Asymmetric end-functionalization of multi-walled carbon nanotubes, J. Am. Chem. Soc. **127**, 4122–4123 (2005)

6.272 M.J. Moghaddam, S. Taylor, M. Gao, S. Huang, L. Dai, M. McCall: Highly efficient binding of DNA on the sidewalls and tips of carbon nanotubes using photochemistry, Nano Lett. **4**, 89–93 (2004)

6.273 V. Georgakilas, K. Kordatos, M. Prato, D.M. Guldi, M. Holzinger, A. Hirsch: Organic functionalization of carbon nanotubes, J. Am. Chem. Soc. **124**, 760–761 (2002)

6.274 N. Tagmatarchis, M. Prato: Functionalization of carbon nanotubes via 1,3-dipolar cycloadditions, J. Mater. Chem. **14**, 437–439 (2004)

6.275 R.J. Chen, S. Bangsaruntip, K.A. Drouvalakis, N.W.S. Kam, M. Shim, Y. Li, W. Kim, P.J. Utz, H. Dai: Noncovalent functionalization of carbon nanotubes for highly specific electronic biosensors, Proc. Natl. Acad. Sci. USA **100**, 4984–4989 (2003)

6.276 R.J. Chen, H.C. Choi, A. Bangsaruntip, E. Yenilmez, X. Tang, Q. Wang, Y.L. Chang, H. Dai: An investigation of the mechanisms of electronic sensing of protein adsorption on carbon nanotube devices, J. Am. Chem. Soc. **126**, 1563–1568 (2004)

6.277 K. Welsher, Z. Liu, S.P. Sherlock, J.T. Robinson, Z. Chen, D. Daranciang, H.J. Dai: A route to brightly fluorescent carbon nanotubes for near-infrared imaging in mice, Nat. Nanotechnol. **4**, 773 (2009)

6.278 M.E. Ghica, C.M.A. Brett: The influence of carbon nanotubes and polyazine redox mediators on the performance of amperometric enzyme biosensors, Microchim. Acta **170**, 257 (2010)

6.279 Q. Yang, Y. Qu, Y. Bo, Y. Wen, S. Huang: Biosensor for atrazin based on aligned carbon nanotubes modi-

fied with glucose oxidase, Microchim. Acta **168**, 197 (2010)
6.280 D.O. Demirkol, S. Timur: Chitosan matrices modified with carbon nanotubes for use in mediated microbial biosensing, Microchim. Acta **173**, 537–542 (2011)
6.281 N.W.S. Kam, T.C. Jessop, P.A. Wender, H.J. Dai: Nanotube molecular transporters: Internalization of carbon nanotube-protein conjugates into mammalian cells, J. Am. Chem. Soc. **126**, 6850 (2004)
6.282 Z. Liu, A.C. Fan, K. Rakhra, S. Sherlock, A. Goodwin, X.Y. Chen, Q.W. Yang, D.W. Felsher, H.J. Dai: Supramolecular stacking of doxorubicin on carbon nanotubes for in vivo cancer therapy, Angew. Chem. Int. Ed. **48**, 7668 (2009)
6.283 H. Dumortier, S. Lacotte, G. Pastorin, R. Marega, W. Wu, D. Bonifazi, J.P. Briand, M. Prato, S. Muller, A. Bianco: Functionalized carbon nanotubes are non-cytotoxic and preserve the functionality of primary immune cells, Nano Lett. **6**, 1522–1528 (2006)
6.284 A.L. Elias, J.C. Carrero-Sanchez, H. Terrones, M. Endo, J.P. Laclette, M. Terrones: Viability studies of pure carbon- and nitrogen-doped nanotubes with entamoeba histolytica: From amoebicidal to biocompatible structures, Small **3**, 1723–1729 (2007)
6.285 B.L. Allen, P.D. Kichambare, P. Gou, I.I. Vlasova, A.A. Kapralov, N. Konduru, V.E. Kagan, A. Star: Biodegradation of single-walled carbon nanotubes through enzymatic catalysis, Nano Lett. **8**, 3899–3903 (2008)
6.286 C.W. Lam, J.T. James, R. McCluskey, R.L. Hunter: Pulmonary toxicity of single-wall carbon nanotubes in mice 7 and 90 days after intratracheal instillation, Toxicol. Lett. **77**, 126–134 (2004)
6.287 D.B. Warheit, B.R. Laurence, K.L. Reed, D.H. Roach, G.A.M. Reynolds, T.R. Webb: Comparative pulmonary toxicity assessment of single-wall carbon nanotubes in rats, Toxicol. Lett. **77**, 117–125 (2004)
6.288 A.A. Shvedova, E.R. Kisin, R. Mercer, A.R. Murray, V.J. Johnson, A.I. Potapovich, Y.Y. Tyurina, O. Gorelik, S. Arepalli, D. Schwegler-Berry, A.F. Hubbs, J. Antonini, D.E. Evans, B.-K. Ku, D. Ramsey, A. Maynard, V.E. Kagan, V. Castanova, P. Baron: Unusual inflammatory and fibrogenic pulmonary responses to single-walled carbon nanotubes in mice, Am. J. Physiol. Lung Cell. Mol. Physiol. **289**, L698–L708 (2005)
6.289 J. Muller, F. Huaux, N. Moreau, P. Misson, J.F. Heilier, M. Delos, M. Arras, A. Fonseca, J.B. Nagy, D. Lison: Respiratory toxicity of multi-wall carbon nanotubes, Toxicol. Appl. Pharmacol. **207**, 221–231 (2005)
6.290 H.F. Wang, J. Wang, X.Y. Deng, H.F. Sun, Z.J. Shi, Z.N. Gu, Y.F. Liu, Y.L. Zhao: Biodistribution of carbon single-wall carbon nanotubes in mice, J. Nanosci. Nanotechnol. **4**, 1019 (2004)
6.291 S. Koyama, Y.A. Kim, T. Hayashi, K. Takeuchi, C. Fujii, N. Kuroiwaa, H. Koyama, T. Tsukahara, M. Endo: In vivo immunological toxicity in mice of carbon nanotubes with impurities, Carbon **47**, 1365–1372 (2009)
6.292 P. Wu, X. Chen, N. Hu, U.C. Tam, O. Blixt, A. Zettl, C.R. Bertozzi: Biocompatible carbon nanotubes generated by functionalization with glycodendrimers, Angew. Chem. Int. Ed. **47**, 5022–5025 (2008)
6.293 C.M. Sayes, F. Liang, J.L. Hudson, J. Mendez, W. Guo, J.M. Beach, V.C. Moore, C.D. Doyle, J.L. West, W.E. Billups, K.D. Ausman, V.L. Colvin: Functionalization density dependence of single-walled carbon nanotubes cytotoxicity in vitro, Toxicol. Lett. **161**, 135–142 (2006)
6.294 A.B. Castle, E. Gracia-Espino, C. Nieto-Delgado, H. Terrones, M. Terrones, S. Hussain: Hydroxyl-functionalized and N-doped multiwalled carbon nanotubes decorated with silver nanoparticles preserve cellular function, ACS Nano **5**, 2458–2466 (2011)
6.295 H.J. Burch, S.A. Contera, M.R.R. de Planque, N. Grobert, J.F. Ryan: Doping of carbon nanotubes with nitrogen improves protein coverage whilst retaining correct conformation, Nanotechnology **19**, 384001 (2008)
6.296 V.E. Kagan, N.V. Konduru, W.H. Feng, B.L. Allen, J. Conroy, Y. Volkov, I.I. Vlasova, N.A. Belikova, N. Yanamala, A. Kapralov, Y.Y. Tyurina, J.W. Shi, E.R. Kisin, A.R. Murray, J. Franks, D. Stolz, P.P. Gou, J. Klein-Seetharaman, B. Fadeel, A. Star, A.A. Shvedova: Carbon nanotubes degraded by neutrophil myeloperoxidase induce less pulmonary inflammation, Nat. Nanotechnol. **5**, 354 (2010)

7. Carbon Nanofibers

Yoong A. Kim, Takuya Hayashi, Morinobu Endo, Mildred S. Dresselhaus

Carbon nanofibers are sp^2-based linear, noncontinuous filaments that are different from carbon fibers, which are continuous with diameter of several micrometers. This chapter provides a review on the growth, structural properties, and practical applications of carbon nanofibers as compared with those of conventional carbon fibers. Carbon nanofibers can be produced via catalytic chemical vapor deposition (CVD) as well as the combination of electrospinning of organic polymer and thermal treatment. The amount of commercially available carbon nanofiber worldwide is ca. 500 t/year. Carbon nanofibers exhibit high specific area, flexibility, and superstrength due to their nanosized diameter, which allows them to be used in electrode materials of energy storage devices, hybrid-type filler in carbon-fiber-reinforced plastics, and bone tissue scaffold. It is envisaged that carbon nanofibers will be key materials of green science and technology through a close combination with carbon fibers and carbon nanotubes.

7.1 **Similarity and Difference Between Carbon Fibers and Carbon Nanofibers** 234
7.1.1 Basic Concepts 234
7.1.2 Synthesis and Properties of Carbon Fibers 235
7.1.3 Vapor-Grown Carbon Fibers 236

7.2 **Growth and Structural Modifications of Carbon Nanofibers** 238
7.2.1 Catalytically Grown Cup-Stacked Type 238
7.2.2 Catalytically Grown Platelet Type 241
7.2.3 Electrospun Carbon Nanofibers 244
7.2.4 Electrospun Porous Carbon Nanofibers 249

7.3 **Applications of Carbon Nanofibers** 251
7.3.1 Electrode Material in Lithium-Ion Secondary Batteries 251
7.3.2 Electrode Material for Supercapacitors 253
7.3.3 Supporting Material for Metal Nanoparticles 256
7.3.4 Bone Tissue Scaffold 257

7.4 **Conclusions** 257

References 258

Carbon nanofibers could be defined as sp^2-based linear filaments with diameter of ca. 100 nm that are characterized by flexibility and their aspect ratio (above 100). Materials in fiber form are of great practical and scientific importance. The combination of high specific area, flexibility, and high mechanical strength allows nanofibers to be used in our daily life as well as in fabrication of tough composites for vehicle and aerospace applications. However, carbon nanofibers should be distinguished from conventional carbon fibers [7.1–3] and vapor-grown carbon fibers (VGCFs) [7.4–10] in their small diameter (Fig. 7.1). Conventional carbon fibers and VGCFs have diameters of several micrometers (Fig. 7.1c,d). In addition, carbon nanofibers are different from well-known carbon nanotubes [7.5, 11–14]. Carbon nanofibers can be grown by passing carbon feedstock over nanosized metal particles at high temperature [7.4–10], which is very similar to the growth conditions for carbon nanotubes. However, their geometry is different from concentric carbon nanotubes containing an entire hollow core, because they can be visualized as consisting of regularly stacked, truncated conical or planar layers along the filament length [7.15–18].

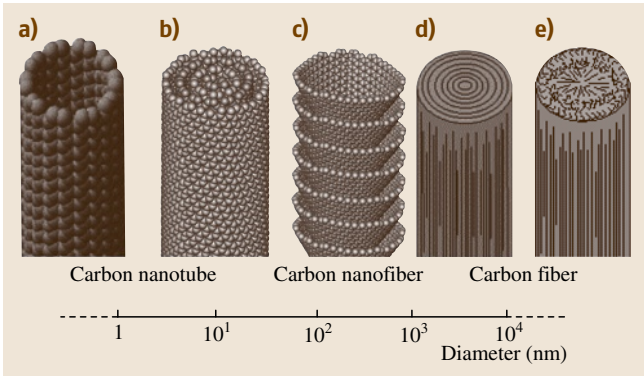


Fig. 7.1 Schematic comparison of the diameter dimensions on a log scale for various types of fibrous carbon materials

This unique structure endows them with semiconducting behavior [7.19] and chemically active end planes on both the inner and outer surfaces of the nanofibers, thereby making them useful as supporting materials for catalysts [7.20], reinforcing fillers in polymeric composites [7.21], hybrid-type fillers in carbon-fiber-reinforced plastics [7.22–24], and photocurrent generators in photochemical cells [7.25, 26].

Alternatively, carbon nanofibers can be fabricated by the right combination of electrospinning of organic polymers and thermal treatment in an inert atmosphere. The electrospinning technique has been considered to be one of the advanced fiber formation techniques from polymer solution by using electrostatic forces [7.27–30]. Nanofibers produced by electrospinning exhibit noticeably different properties, such as nanosized diameter, high surface area, and thin web morphology, which make them applicable for fabrication of high-performance nanocomposites, tissue scaffolds, and energy storage devices [7.31–37].

Within this context, intensive studies on the synthesis, characterization, and possible applications of carbon nanofibers have been carried out during the last decade. In this chapter, we review their synthesis techniques and interesting textural properties, as well as promising applications of carbon nanofibers that have been developed over the past 10 years.

7.1 Similarity and Difference Between Carbon Fibers and Carbon Nanofibers

Since carbon nanofibers could be considered as a one-dimensional (1-D) form of carbon, their structure and properties are closely related to those of other forms of carbon, especially to crystalline three-dimensional graphite, turbostratic carbons, and to their constituent two-dimensional (2-D) layers. Therefore, several forms of conventional carbon materials should be mentioned in terms of their similarities and differences relative to carbon nanofibers. Especially, direct comparison should be made between fibrous carbon materials, because carbon fibers act as a bridge between carbon nanofibers and conventional bulk carbon materials. In this section, the structures of carbon fibers as well as VGCFs are described, with strong emphasis on the similarities and differences of these 1-D carbon materials.

7.1.1 Basic Concepts

Carbon fibers represent an important class of graphite-related materials that are closely related to carbon nanofibers with regard to structure and properties. Carbon fibers have been studied scientifically since the late 1950s, and fabricated industrially since 1963. They are now becoming a technologically and commercially important material in aerospace, construction, sports, electronic device, and automobile industries. The global carbon fiber market has now grown to about 12 500 t/year of product, after 40 years of continuous research and development (R&D) work [7.1–3]. Carbon fibers are defined as a filamentary form of carbon with an aspect ratio (length/diameter) greater than 100. Probably, the earliest documented carbon fibers are the bamboo-char filaments made by Edison for use in the first incandescent light bulb in 1880. With time, carbon fibers were replaced by more robust tungsten filaments in light bulb applications, and consequently carbon fiber R&D vanished at that early time. However, in the late 1950s, carbon fibers once again became important because of the aggressive demand from the aerospace industry for lightweight, strong composite materials, in which carbon fibers are used as a reinforcement agent in conjunction with plastics, metals, ceramics, and bulk carbon materials. The specific strength (strength/weight) and specific modulus (stiffness/weight) of carbon-fiber-reinforced composites explain their importance as engineering materials,

due to the high performance of their carbon fiber constituents.

Since the temperature and pressure necessary to prepare a carbon fiber from the liquid phase is at the triple point ($T = 4100\,\mathrm{K}$, $p = 123\,\mathrm{kbar}$), it would be almost impossible to prepare carbon fibers from the melt under industrial processing conditions. Carbon fibers are therefore prepared from organic precursors. This preparation is generally done in three steps, including stabilization of a precursor fiber in air (at $\approx 300\,^{\circ}\mathrm{C}$), carbonization at $\approx 1100\,^{\circ}\mathrm{C}$, and subsequent graphitization (at $> 2500\,^{\circ}\mathrm{C}$). Fibers undergoing only the first two steps are commonly called *carbon fibers*, while fibers undergoing all three steps are called *graphite fibers*. Carbon fibers are generally used for their high strength, while graphite fibers are used for their high modulus. Historically, Bacon's graphite whisker (Fig. 7.2) has demonstrated the highest mechanical properties of a carbon fiber (with regard to both strength and modulus), comparable to the ideal value for a graphite network [7.38]. Graphitic whiskers were grown under conditions near the triple point of graphite. Then, a structural model was proposed in which layers consisting of graphene sheets are wound around the axis as if rolling up a carpet. These whiskers were used as the performance target in the early stages of carbon-fiber technology, even though they have never been produced on a large scale.

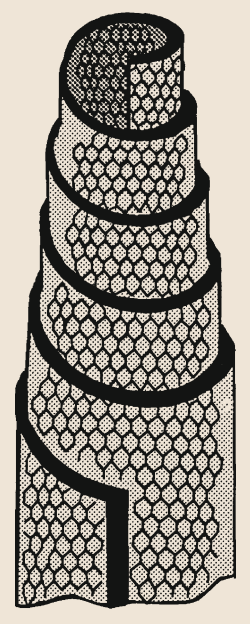


Fig. 7.2 Model for graphite whiskers grown by direct-current (DC) arc discharge of graphite electrodes. Whiskers were reported to have a carpet-rolling structure of graphite sheets with high mechanical strength and modulus along the fiber axis, similar to the ideal values of a graphene sheet

7.1.2 Synthesis and Properties of Carbon Fibers

Scanning electron microscopy (SEM) images together with schematic structural models are shown in Fig. 7.3 for typical carbon fibers: a high-strength polyacrylonitrile (PAN)-based fiber (Fig. 7.3a), a high-modulus PAN-based fiber (Fig. 7.3b), and a mesophase pitch-based carbon fiber (MPCF) (Fig. 7.3c) [7.38, 39]. The PAN-based fibers consist of small sp^2-carbon structural units preferentially aligned with the carbon hexagonal segments parallel to the fiber axis. This orientation is responsible for the high tensile strength of PAN-based carbon fibers [7.40]. By varying the processing conditions (e.g., oxidation conditions, choice of precursor material, and especially by increasing the heat treatment temperature) of PAN fibers, better alignment of the graphene layers can be achieved (structural model of Fig. 7.3b), thus leading to stiffer, higher-modulus PAN fibers, but with lower strength [7.39]. PAN-based fibers are one of the typical hard carbons. MPCFs consist of well-aligned graphitic layers arranged nearly parallel to the fiber axis, and this high degree of preferred orientation is responsible for their high modulus or stiffness as well as their relatively high graphitizability. The structures described above give rise to different physical properties, although each type of fiber features hexagonal carbon networks, possessing the strongest covalent bonds in nature (C–C bonds). These strong interatomic bonds lie in sheets essentially parallel to the fiber axis and are responsible for the high mechanical performance of these carbon fibers.

Referring to Fig. 7.4a, we see that PAN-based fibers have high strength and MPCFs have high modulus, while VGCFs provide mainly ultrahigh-modulus materials [7.4, 41]. In this figure we also observe isotropic pitch-based (general grade) fibers, exhibiting much lower modulus and strength, but widely used in composites with cement matrix for construction due to their low cost and high chemical stability. Figure 7.4b demonstrates a direct indication of the differences in the mechanical properties of various carbon fibers, from low-modulus high-strength to high-modulus low-strength fibers, from the lower left to the upper right in the photograph, where a yarn containing 500 fibers was initially placed in a horizontal position. These fibers are combined with other materials in order to design suitable mechanical properties, and the fibers are used as a filler for various advanced composite materials. To obtain high performance in carbon and graphite fibers, it is very important to control the

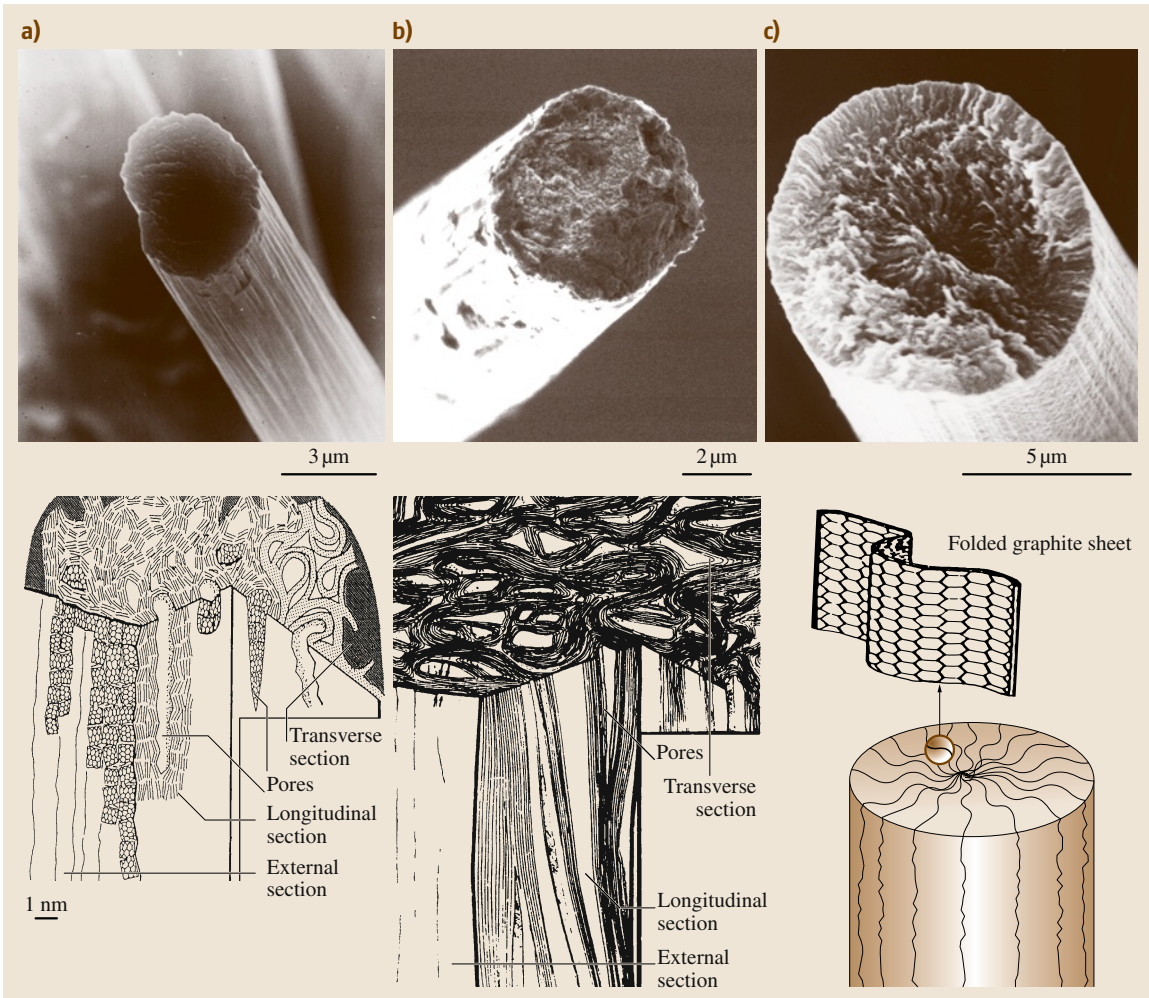


Fig. 7.3a–c SEM micrographs of three types of carbon fibers and corresponding structural models: **(a)** high-strength PAN-based fiber, **(b)** high-modulus PAN-based fiber, and **(c)** a mesophase pitch-based fiber. In the *second row*, for each fiber type, a schematic diagram of the fiber structure is shown

microstructure and nanostructure by selecting the appropriate organic precursor as well as the processing conditions.

7.1.3 Vapor-Grown Carbon Fibers

VGCFs have a very special structure like annular rings on a tree (Fig. 7.5a) and are synthesized by a somewhat different formation process than that used to produce PAN-based and MPCFs. In particular, VGCFs are not prepared from a fibrous precursor, but rather from hydrocarbon gas, using a catalytic growth process outlined in Fig. 7.5b [7.5–10]. Ultrafine transition-metal particles, such as iron particles with diameter less than 10 nm, are dispersed on a ceramic substrate, and a hydrocarbon, such as benzene diluted with hydrogen gas, is introduced at temperatures of about 1100 °C. Hydrocarbon decomposition takes place on the catalytic particle, leading to continuous carbon uptake by the catalytic particle and continuous output by the particle of well-organized tubular filaments of hexagonal sp^2 carbon. The rapid growth rate of several tens of µm/min, which is 106 times faster than that observed for the growth of common metal whiskers [7.37], enables production of commercially viable quantities of VGCFs. Evidence in support of this growth model is provided

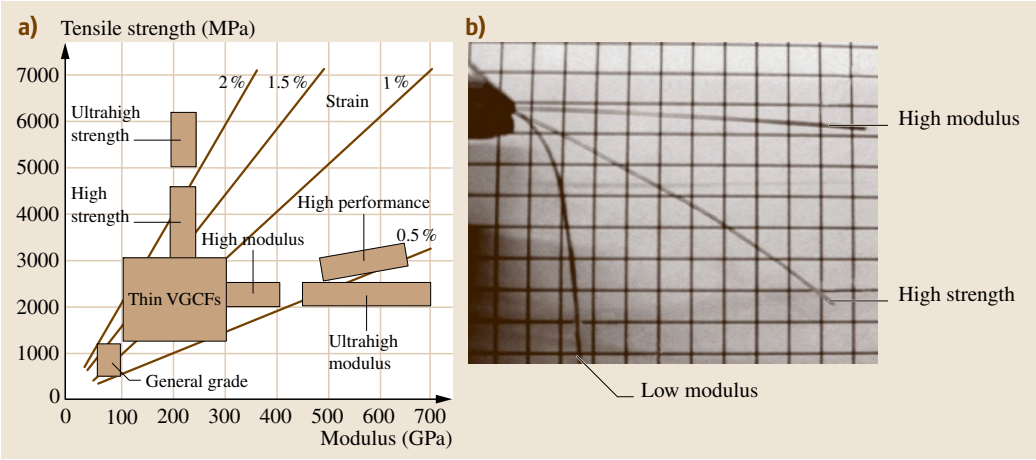


Fig. 7.4 (a) Mechanical properties of various kinds of carbon and graphite fibers, and (b) direct comparison of the mechanical properties for high-strength and high-modulus fibers. A low-modulus fiber droops under its own weight, whereas high-modulus fibers do not

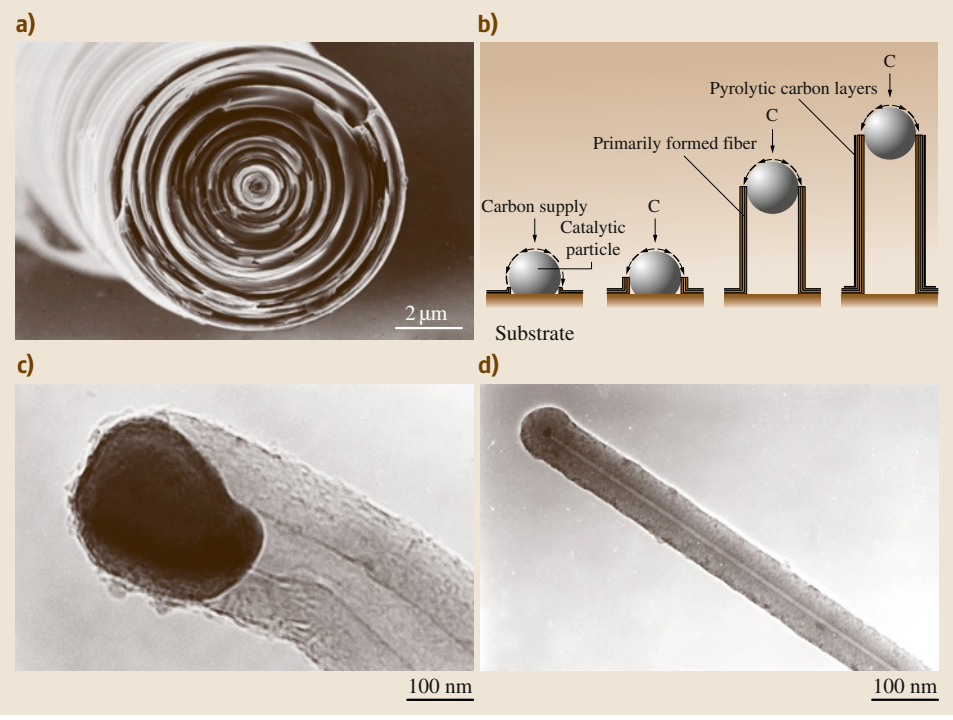


Fig. 7.5 (a) SEM image of vapor-grown carbon fibers, (b) suggested growth mechanism of VGCFs using ultrafine catalytic metal particles, (c) very early stage of tubule growth in which the catalytic particle is still active, promoting elongation. The primary tubule thus formed acts as a core for vapor-grown fibers. (d) The fiber is obtained through a thickening process, such as pyrolytic deposition of carbon layers on the primary tubule. The encapsulated catalytic particle can be seen at the tip of the hollow core

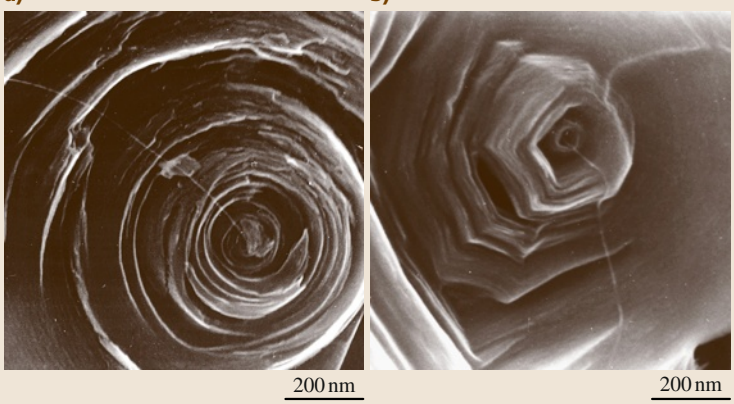


Fig. 7.6 (a) Carbon nanotube exposed at the broken end of a vapor-grown carbon fiber: (a) as grown, and (b) heat-treated at 3000 °C. The sample is fractured by pulverization, and the core diameter is ≈ 5 nm. These images suggest a structural discontinuity between the nanotube core of the fiber and the CVD-deposited carbon layers, and also show the strong mechanical properties of the nanotube core, which maintains its form after breakage

by the presence of catalytic particles at the tips of the resulting VGCFs (Fig. 7.5c) [7.38]. The primary hollow tubule is first formed by the catalytic process (with a diameter of less than several nanometers), and the tubule is then thickened by a successive chemical vapor deposition (CVD) process, corresponding to deposition of pyrolytic carbon layers on the primary tubular core (Fig. 7.5d).

Interestingly, at the center of the annular ring structure, we can clearly observe an extruded carbon nanotube (with diameter ≈ 5 nm) (Fig. 7.6a), which serves as a template for growing the thicker carbon fiber [7.42]. This tubular core implies a discontinuity in the structure between the core and the thickened periphery of the carbon fiber. Such a discontinuity in the structure is retained even after heat treatment at temperatures as high as 3000 °C. This graphitization process introduces a fully developed graphite structure in the peripheral region of a VGCF, exhibiting a polygonal shape (Fig. 7.6b).

7.2 Growth and Structural Modifications of Carbon Nanofibers

This section presents how carbon nanofibers are fabricated, and their morphological and physicochemical modifications by post treatments are presented in relation to their microstructure. We give an overview of two different synthetic methods: the catalytic chemical vapor deposition method, and the combination of electrospinning with subsequent thermal treatment.

7.2.1 Catalytically Grown Cup-Stacked Type

A catalytic thermal chemical vapor deposition synthesis method has been extensively investigated as a promising method for large-scale production of carbon nanotubes and carbon nanofibers [7.43–45]. Through precise control of the synthesis conditions, it is possible to tailor the diameter, crystallinity, and also orientation of the cone angle with respect to the fiber axis [7.46–48]. Carbon nanofibers with a large hollow core and a large portion of open edges at the outer surface and also in the inner channels, due to the truncated graphene cone morphology (cup-stacked), are characterized in terms of their microstructure, oxidation behavior, and also graphitizability, and are compared with those of conventional tubular types of carbon nanofibers. These structural characteristics as well as their potential low production cost using a floating reactant production system may make it possible to use such carbon nanofibers in the fabrication of absorbent materials, catalyst supports, field emitters, gas storage components, and composite materials.

Field-emission scanning electron microscopy (FE-SEM) and transmission electron microscopy (TEM) images at low magnification (Fig. 7.7a,b) reveal relatively long and straight carbon nanofibers with a hollow core along the fiber length (Fig. 7.7c), which exhibit diameters ranging from 50 to 150 nm and lengths up to 200 μm. One of the main characteristics of these fibers is a large hollow core, as compared with conventional tubular-type nanofibers. In addition, we can find some differences in the ratio of the outer

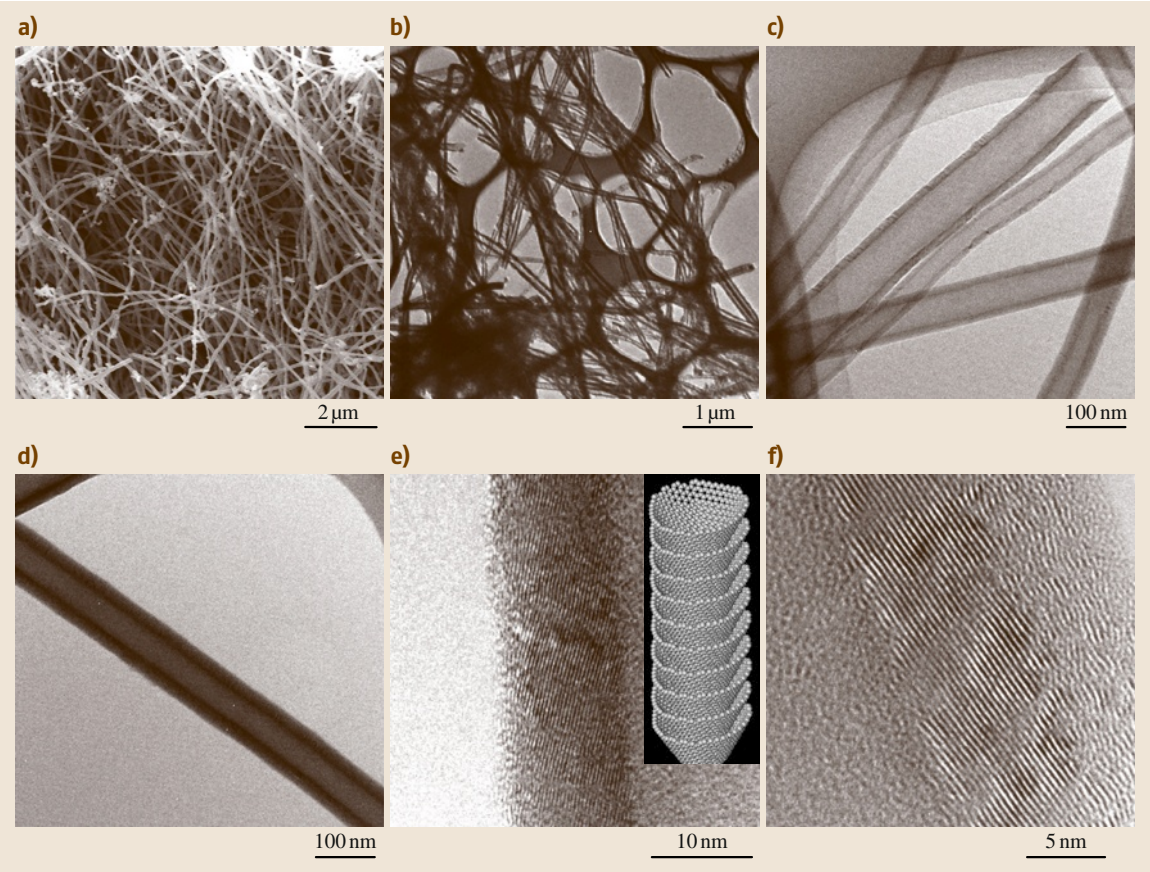
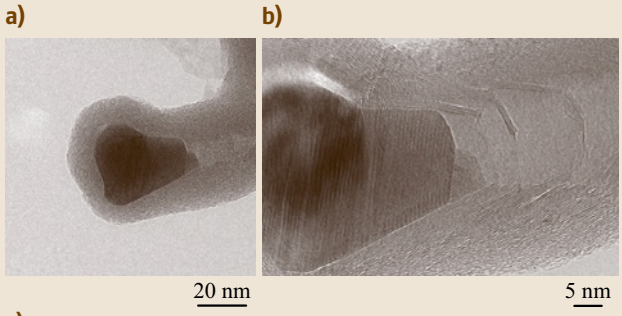


Fig. 7.7 **(a)** FE-SEM image of nanofibers showing a long and straight morphology; **(b)** TEM image of nanofibers with a hollow core at low resolution; **(c)** TEM image of uncoated nanofibers with a large hollow core; **(d)** TEM image of coated nanofibers with a large hollow core; **(e)** HRTEM image of an uncoated nanofiber (*inset* shows a schematic model of a carbon nanofiber); **(f)** HRTEM image of a coated nanofiber

diameter to the inner diameter, i.e., the wall thickness of the carbon nanofibers, as shown in the TEM images of Fig. 7.7c,d. To study these differences in detail, high-resolution TEM (HRTEM) studies have been carried out for these two types of samples. One type of nanofiber shows a truncated cone microstructure (Fig. 7.7e), whereas the other type of nanofiber contains a certain portion of amorphous carbon (coated structure) (Fig. 7.7f). The truncated cone angle (cup) with regard to the fiber axis, measured by electron diffraction (ED), taking the fast Fourier transform (FFT) of several TEM images, lies mainly between 45° and 80°. The observation of (110) planes of graphite might be due to a superposition of conical graphene sheets with ABAB stacking. In terms of the growth mechanism, uncoated nanofibers (Fig. 7.7e), consisting of stacked conical graphene sheets, are primarily formed by catalytic effects, while the outer part of the coated nanofiber (Fig. 7.7f) corresponds to amorphous carbon deposited during the secondary thickening growth process.

To understand the unique properties of these novel nanofibers, such as a large hollow core and a conical morphology, it is indispensable to mention the morphology of the catalytic metal particles used in the growth process. It has been clearly shown that the microstructure of the nanofibers is determined by the shape of the metal particle at the tip of the fiber (Fig. 7.8a,b). Carbon derived from the decomposition of hydrocarbons dissolved in the metal particle might precipitate as graphitic carbon. This carbon replication from metal particles results in the formation of stacked truncated cones, which grow graphitic nanofibers [7.48]. Along



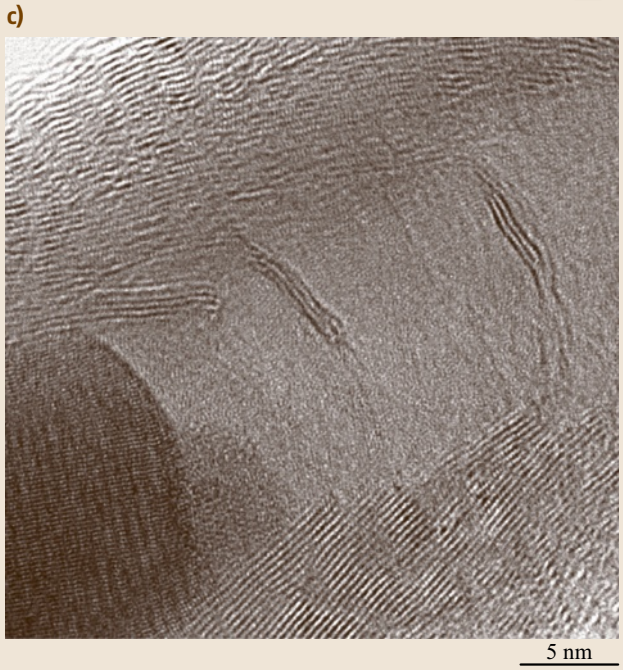


Fig. 7.8 **(a)** HRTEM image of a typical metal particle at the tip of the nanofibers; **(b)** and **(c)** enlarged HRTEM images. (Note that the truncated conical graphene sheets replicate the shape of the rear part of the metal particle)

the fiber axis (Fig. 7.8c), there are some disordered and wavy regions, which might be due to the relaxation of carbon layers as a result of cooling [7.49]. Based on this study, it is possible to say that the size of the metal particle in the growth direction of the fiber is directly related to the size of the hollow core, which is also determined by the composition of the catalytic particle, the type of carbon feedstock, and the reaction temperature.

The outer and also inner surfaces of the nanofiber have to be covered entirely by open edges, i.e., the end face of the graphitic conical sheets from the point of view of the growth mechanism. Practically, the deposition of amorphous carbon on the catalytically induced graphitic carbon phase, which is unavoidable in the synthetic process of nanofibers, and also the possible formation of loops between adjacent conical graphene sheets might deteriorate the total chemical and physical reactivity of the nanofibers. To solve this problem, an air oxidation process is applied to prepare nanofibers with an increased fraction of open edge sites. Figure 7.9a shows Raman spectra for oxidized uncoated nanofibers (Fig. 7.7c,e) at different temperatures. Modification of the surface of the nanofiber starts at 520 °C, and then the optimal oxidation temperature is found to be at 530 °C for our experimental conditions, based on a decreased half-width at half-maximum (HWHM) and intensity of the D peak at 1355 cm^{-1} (the defect mode), the appearance of a shoulder peak at 1620 cm^{-1}, and also a decreased relative intensity (I_D/I_G). When oxidized at 540 °C, structural disruption might occur, due to severe oxidation, based on an increased intensity of the D peak and also a large value of the relative intensity ($I_D/I_G = 0.9674$). For the case of an optimally modified sample (530 °C), consistent fiber morphology (Fig. 7.9b) and a somewhat decreased wall thickness (Fig. 7.9c) are observed, accompanying an increase in the specific surface area from 49.67 to 146.47 m^2/g.

The graphitization process is known as one of the most efficient ways to modify the microstructure of carbons [7.50, 51]. TEM images of graphitized nanofibers are shown in Fig. 7.10. The most interesting change caused by the graphitization process is a morphological transformation from a smooth-walled tubule type to a reversing sawtooth type with regular pitch (Fig. 7.10a,b,d). The other features of the graphitized nanofibers are the formation of long links along the outer and inner sides of the fibers at regular pitch intervals (closure of open cups on both sides) and loop formation between neighboring conical sheets (Fig. 7.10c,e), resulting in the formation of triangle-type nanomaterials (Fig. 7.10f). Also, the morphologies of the graphitized samples are strongly affected by the microstructure of the starting materials (Fig. 7.10b from an uncoated nanofiber and Fig. 7.10d from a coated nanofiber). For the graphitization mechanism, the decrease in interlayer spacing [from 3.45 to 3.395 Å, based on x-ray diffraction (XRD) analysis] is smaller than that of CVD-based carbon materials. In fact, the number of loops increases with increasing heat treatment temperature. Therefore, the formation of loops in both the inner and outer surfaces of the nanofiber might retard the three-dimensional stacking ordering caused by mass transformation, and also give indirect evidence

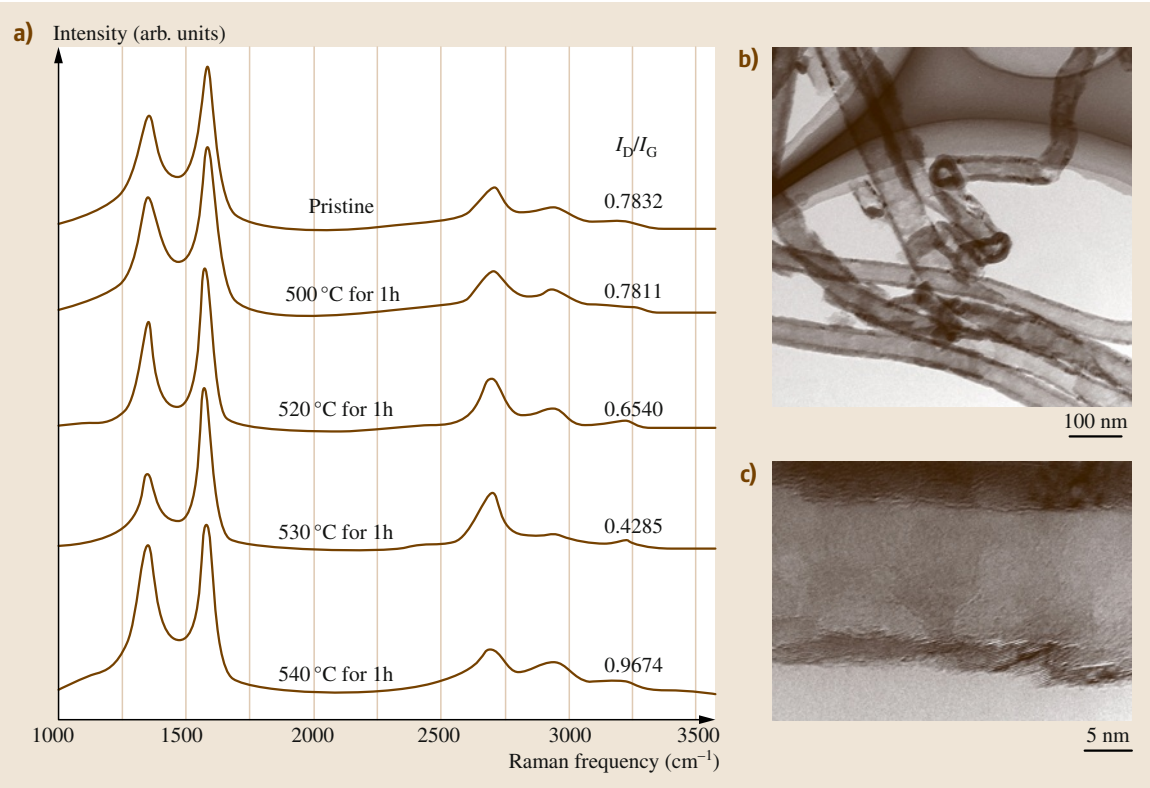


Fig. 7.9 **(a)** Raman spectra of nanofibers oxidized at different temperatures in air atmosphere for 1 h (I_D/I_G is the relative intensity ratio of the G peak over the D peak). **(b)** TEM image of nanofiber morphology for experimental condition at 530 °C, **(c)** high resolution TEM image of nanofiber showing decrease in wall thickness, and an increase in specific surface area

for the carbonization and graphitization mechanism of hard carbon materials.

7.2.2 Catalytically Grown Platelet Type

SEM and TEM studies reveal that carbon nanofibers have the form of short rods (Fig. 7.11a) with semirectangular cross-sectional morphology (inset to Fig. 7.11a). Moreover, crystalline graphene layers are stacked regularly along the length direction of the carbon nanofiber (Fig. 7.11b), the accessible surface area of which is fully covered with chemically active end planes. When an undoped sample was thermally treated in argon at 2200 °C and 2500 °C, the active edges were structurally converted to energetically stable multiloops (Fig. 7.11c). For the undoped sample, multiloop formation was not clearly observed at 1900 °C. In contrast, we clearly observed formation of multiloops in a boron-doped sample treated at 1900 °C. In addition, the B-doped sample treated at 2500 °C (Fig. 7.11f) had a higher number of multiloops than did the corresponding undoped sample (Fig. 7.11d). Therefore, we assume that B atoms play an important role in loop formation, leading to changes in the surface morphology of carbon nanofibers during high-temperature thermal treatment.

We carried out x-ray diffraction (Fig. 7.12a,b) and Raman spectroscopy (Fig. 7.12c,d) studies to investigate the changes in the structure of carbon nanofibers that result from high-temperature thermal treatment in the presence of B atoms. The sharp (002) line for the as-grown sample indicates the relatively high crystallinity of the catalytically grown carbon nanofibers (Fig. 7.12a). As the heat treatment temperature is increased for the undoped sample, the (002) line shifts to higher angles. The decreased HWHM of the D band (defect-induced mode) at 1350 cm^{-1} and the G band (E_{2g2} graphitic mode) at 1580 cm^{-1}, as well as decreased R value (intensity of the D band/intensity of

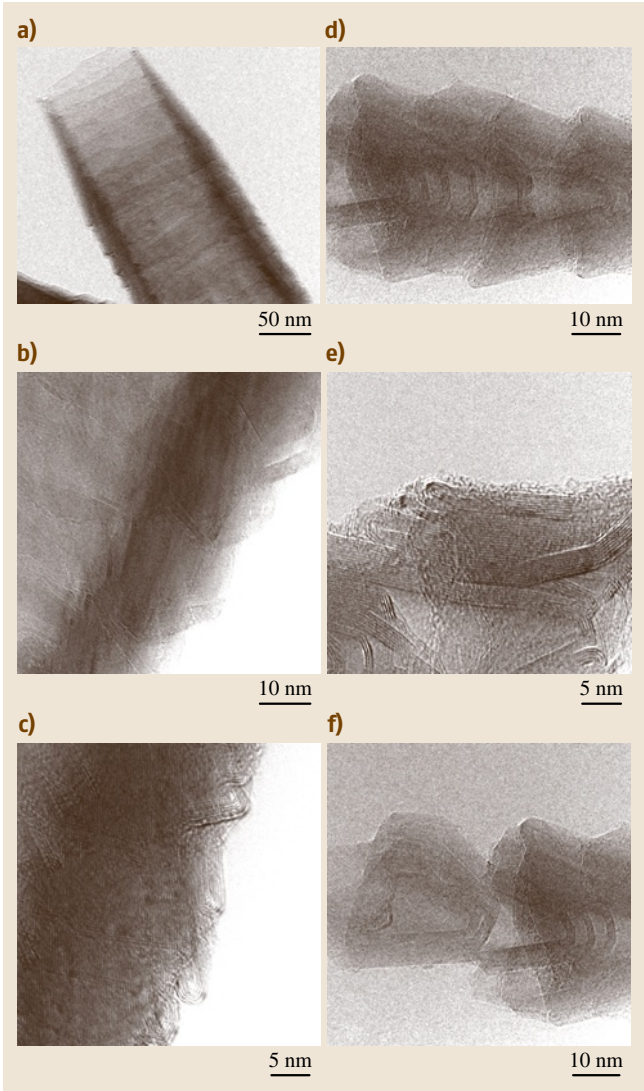


Fig. 7.10 (a), (b), (c) HRTEM images of a graphitized uncoated nanofiber [starting material is uncoated nanofiber (Fig. 7.1c,e)]; (d), (e), (f) HRTEM images of a graphitized coated nanofiber

the G band) in the Raman spectra (Fig. 7.12c and Table 7.1) indicate that the structure of the undoped carbon nanofibers was improved by the high-temperature thermal treatment. Even though the undoped nanofibers were thermally treated at 2500 °C in argon, there was no splitting of the (101) and (100) lines in the x-ray diffraction patterns; furthermore, no distinctive reduction in the intensity of the D band was observed in the Raman spectrum for the undoped sample. This result can be explained by the formation of stable multiloops on the outer surface of the carbon nanofibers (TEM images in Fig. 7.11), which effectively inhibited three-dimensional stacking [7.52]. In the case of B-doped carbon nanofibers, we observed highly improved structures upon thermal treatment at high temperatures (Fig. 7.12b, and lower value of interlayer spacing in Table 7.1), reflecting the fact that B atoms are graphitization accelerators in carbon materials. Recently, it was reported that resonance Raman spectroscopy is extremely sensitive to the end planes in graphitic nanoribbons [7.53]. It is well known that the Raman line at 1620 cm^{-1} in the as-grown sample originates from the end planes in carbon materials [7.54]. With increasing thermal treatment temperature, the Raman line at 1620 cm^{-1} disappears, which is consistent with the formation of energetically stable multiloops at the end planes. However, the high intensity of the D and D′ bands as well as the high R values observed for B-doped samples (Fig. 7.12d) strongly indicate that the B atoms were incorporated into the sp^2 carbon network via substitution for carbon, because the B–C distance is slightly larger than the C–C distance [7.55]. Notably, the higher value of the HWHM of the G band (Table 7.1) (which is intrinsically related to phonon lifetime) indicates that the B atoms incorporated into the carbon network create optical defects. In addition, we have confirmed the presence of substitutional incorporation of B into carbon fibers by using x-ray photoelectron spectroscopy.

To evaluate the physical changes in the B-doped carbon nanofibers, we measured their electrical resistivity in the bulk state using a four-point probe method (Fig. 7.13a). After pouring a specific amount of the carbon nanofibers into the sample holder, we measured the volumetric resistivity at a nanotube mass density of 1.23 g/cm^3. Generally, B-doped samples exhibited improved electrical conductivity compared with undoped samples. It is noteworthy that the electrical resistivity in the bulk state is determined by both the contact resistivity between fibers and the intrinsic resistivity of individual fibers. Therefore, we measured the electrical resistivity of a freestanding individual nanofiber using methods described in the relevant literature [7.56, 57]. After spin-coating a nanofiber suspension onto Au/Ti electrodes, we confirmed using FE-SEM that an individual fiber had bridged the electrode gap (500 nm). We then obtained the intrinsic resistivity of an individual nanofiber from a linear current–voltage relation up to 1 V. As shown in Fig. 7.13b, the electrical resistivity at room temperature of the individual as-grown

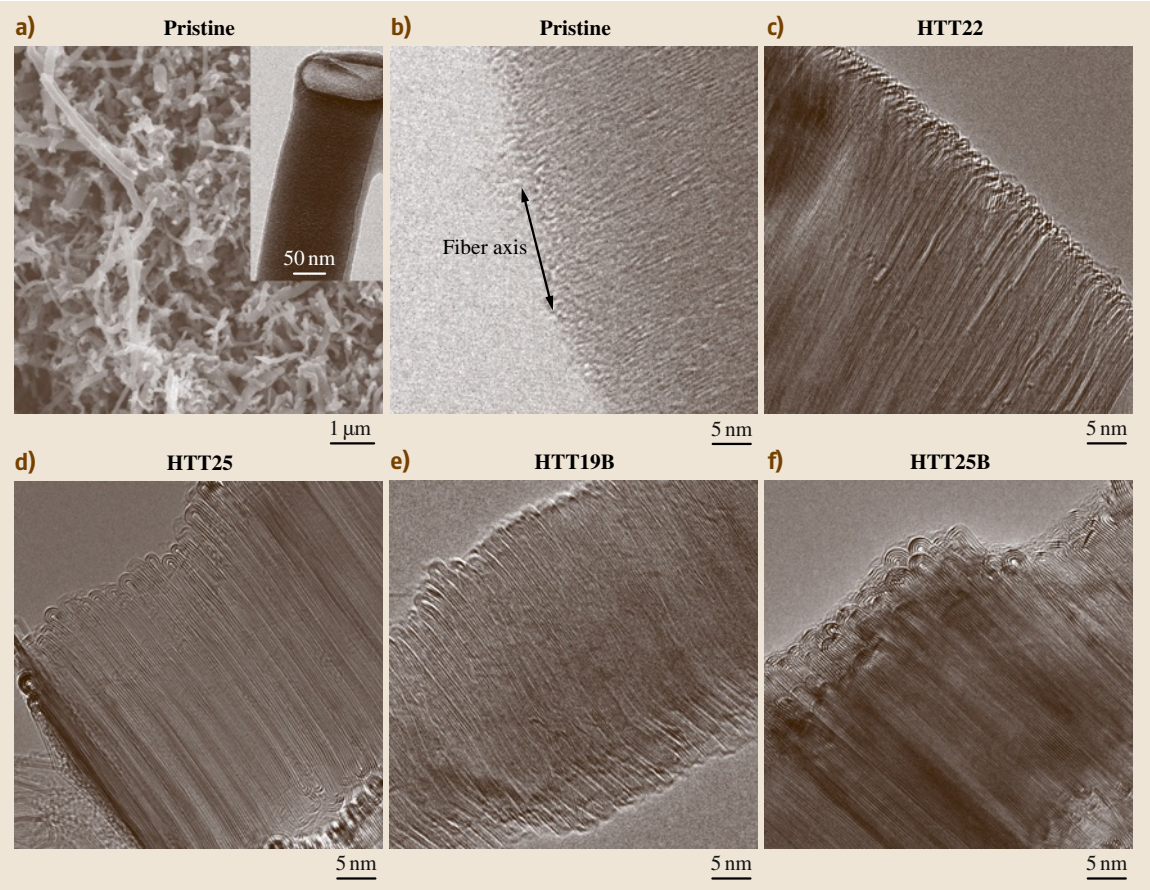


Fig. 7.11 **(a)** SEM and **(b)** TEM images of as-grown platelet-type carbon nanofibers. *Inset* shows the semirectangular cross-sectional morphology of the carbon nanofibers. Note that the crystalline graphene layers are stacked regularly along the length of the carbon nanofiber, the accessible surface area of which is covered with active edges. TEM images of samples thermally treated at **(c)** 2200 °C and **(d)** 2500 °C without B, and at **(e)** 1900 °C and **(f)** 2500 °C in the presence of B

carbon nanofiber was extremely high (≈ 280 kΩ) compared with an arc-based multi-walled carbon nanotube (≈ 2.4 kΩ) [7.58]. This result can be explained by the peculiar platelet-like morphology of the nanofibers investigated in the present study: the current flow between graphene layers in graphite (along the fiber length direction) is six times lower than that in the graphene plane (*a*-axis) [7.59]. Although no general relationship between thermal treatment temperature and the electrical resistivity of an individual fiber was observed (possibly due to the inhomogeneous diameter distribution), we confirmed that the substituted B atoms in the carbon nanofibers lowered the Fermi level, thus increasing the electrical conductivity of the carbon nanofibers.

In addition, we evaluated the effectiveness of the B-doped carbon nanofibers as an anode material for high-rate lithium-ion batteries (LIBs). We demonstrated that the substituted B atoms improve the electrical conductivity as well as give rise to multiloop formation, producing an outer surface that is stable against (or inert to) electrolytes. Figure 7.14a,b shows the voltage profiles of the second discharging/charging cycle for carbon nanofibers prepared under different conditions. The increased proportion of the lithium discharge/charge plateau below 0.2 V with increasing thermal treatment temperature (Fig. 7.14a) and B doping (Fig. 7.14b) indicates that Li insertion/desertion was the main mechanism and that the structural

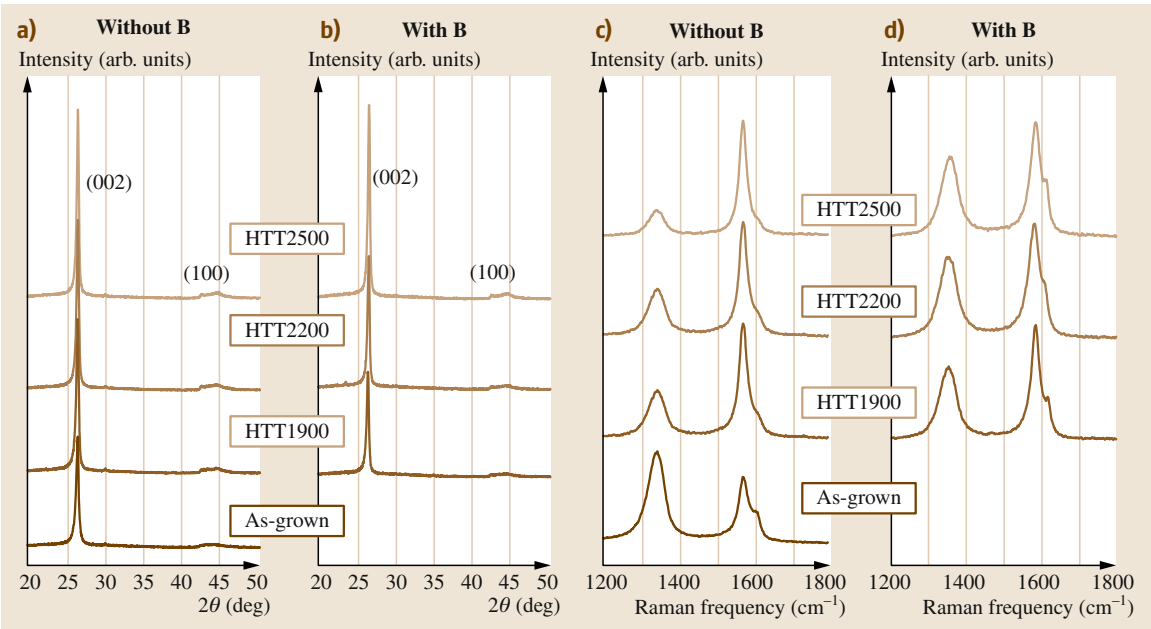


Fig. 7.12a–d X-ray diffraction patterns of carbon nanofibers: **(a)** without boron, and **(b)** with boron; Raman spectra of carbon nanofibers: **(c)** without boron, and **(d)** with boron. From *bottom* to *top*, results are shown for the as-grown sample and samples thermally treated at 1900 °C, 2200 °C, and 2500 °C

Table 7.1 Raman and crystallographic factors of undoped and boron-doped platelet-type carbon nanofibers

	HWHM of the G band (cm^{-1})	*R* value[a)]	2θ(°)	d_{002} (nm)[b)]	L_c (nm)[b)]
Pristine	34.97	1.390	26.430	3.369	18.02
HTT1900	30.97	0.417	26.498	3.361	21.51
HTT2200	25.43	0.250	26.520	3.358	24.20
HTT2500	24.72	0.241	26.528	3.357	25.31
HTT1900B	31.25	0.654	26.458	3.366	24.67
HTT2200B	36.15	0.724	26.523	3.353	28.74
HTT2500B	36.08	0.705	26.566	3.352	29.82

a) *R* value is the intensity of the D band divided by the intensity of the G band,
b) d_{002} and L_c are obtained using the Scherrer's formula

integrity was improved. The large amount of Li adsorption onto B-substituted planar carbon materials has been theoretically confirmed by molecular-orbital calculations [7.60]; this improved Li adsorption is one reason for the improved discharge capacity of the B-doped carbon nanofibers, since B atoms act as an electron acceptor and induce redistribution of the π-electrons within loops. In addition, we found that the capacity of the B-doped carbon nanofibers degraded to a lesser extent at high discharge current density (Fig. 7.14c,d) compared with undoped samples. In other words, substituted B atoms within carbon nanofibers enhanced the electrical conductivity of individual carbon nanofibers as well as forming loop-ended surfaces that were stable against (or inert to) electrolytes.

7.2.3 Electrospun Carbon Nanofibers

Polyacrylonitrile (PAN) polymer in dimethylformamide (DMF) can be easily transformed into white-colored nanofiber web using our electrospinning conditions (Fig. 7.15a), because PAN has been widely used as a precursor for conventional carbon fibers. The con-

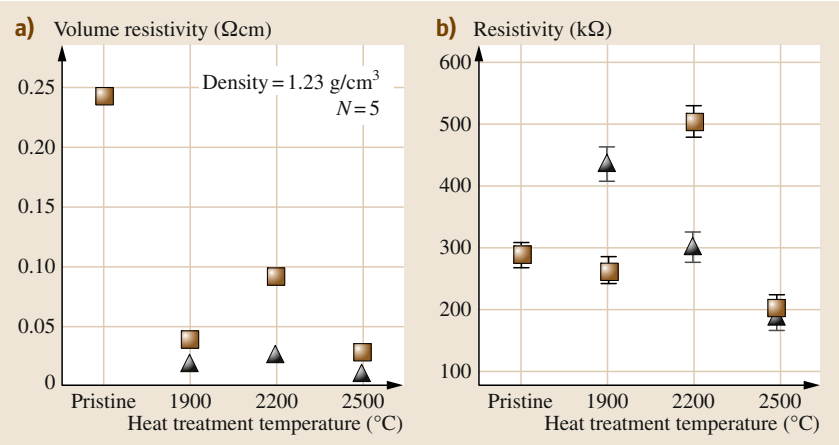


Fig. 7.13 **(a)** Variations in volumetric resistivity of carbon nanofibers at density of 1.23 g/cm^3, and **(b)** electrical resistivity of an individual carbon nanofiber; *rectangles* denote as-grown and thermally treated undoped carbon nanofibers, while *triangles* denote boron-doped carbon nanofibers

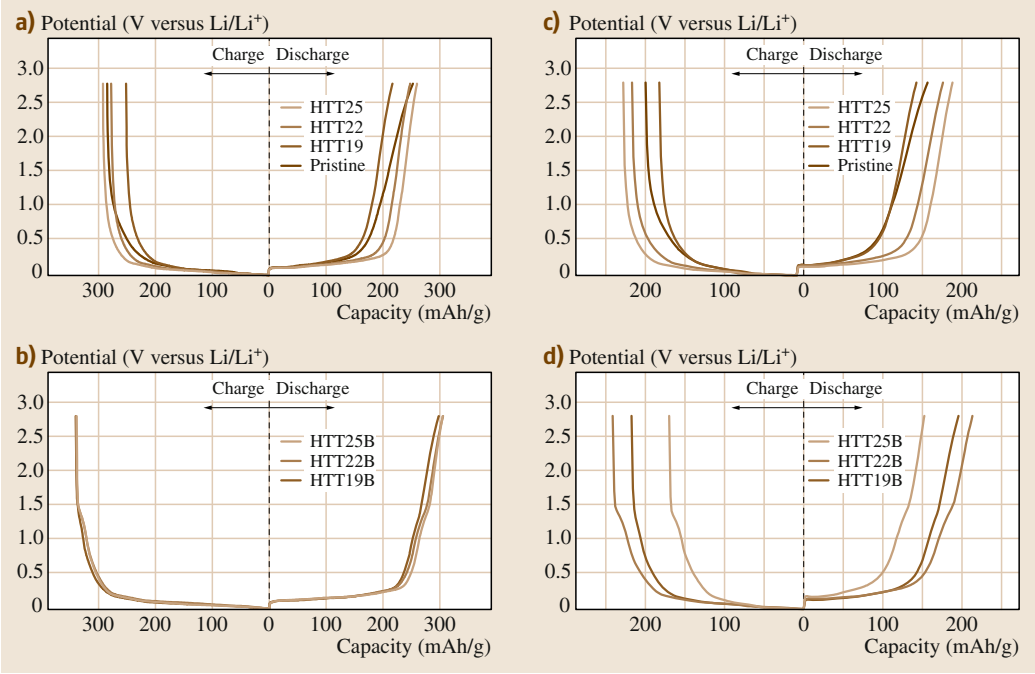


Fig. 7.14a–d Change in potential profile during the second discharging/charging cycle in the range of 0–2.8 V for current densities of **(a,b)** 30 and **(c,d)** 100 mA/g

version of a PAN nanofiber to a carbon nanofiber involves stabilization and carbonization. Air stabilization of electrospun nanofiber (≈ 280 °C for 1 h under controlled air circulation) is accompanied by a change in color from white to reddish brown (Fig. 7.15b). Finally, when an air-stabilized nanofiber web was thermally treated at 1000 °C in an inert atmosphere (e.g., argon or nitrogen gas), the obtained black-colored carbon nanofiber web (Fig. 7.15c) exhibited a relatively high carbon yield (up to 40–50%). This oxidative stabilization is considered to be due to the introduction of thermosetting properties to the spun organic fibers, and involves oxygen uptake and subsequent complex chemical and physical reactions occurring on multiple time and temperature scales [7.61, 62]. Thus, the accessible surface area of a precursor will be the determining

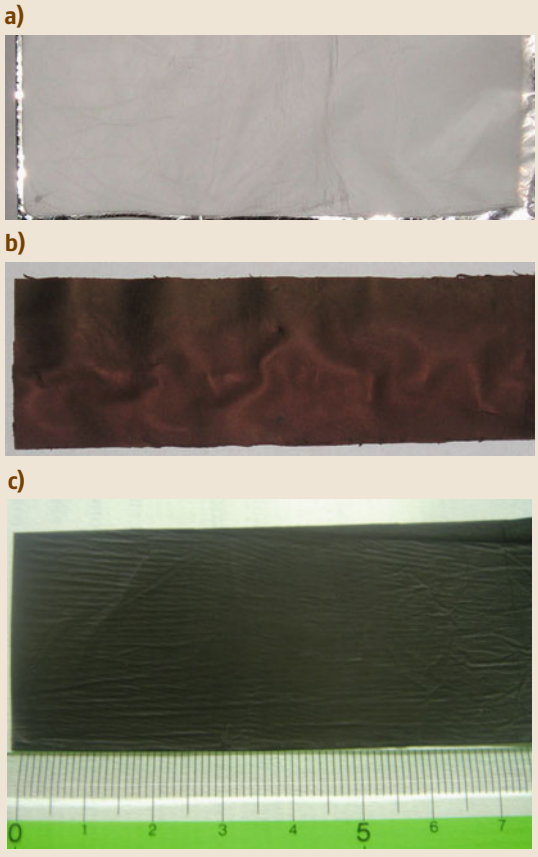


Fig. 7.15a–c Photographs of PAN-derived **(a)** electrospun nanofiber web (*light-gray color*), **(b)** air-stabilized web (*dark-brown color*), and web thermally treated at 700 °C (*black color*). It is noteworthy that air stabilization is a critical step for obtaining dimensional stability of nanofibers

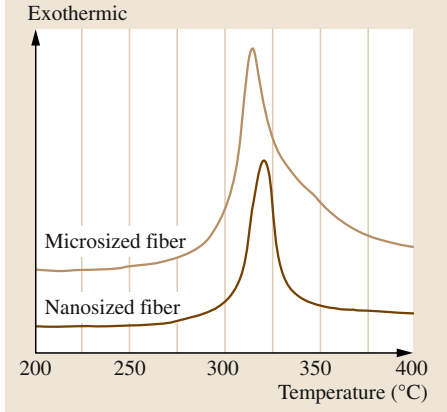


Fig. 7.16 Differential thermal analysis graphs of microsized and nanosized fibers in air atmosphere, respectively (heating rate 10 °C/min)

factor in terms of the chemical kinetics. To understand the oxidation behaviors in detail, differential thermal analysis was carried out for both microsized and nanosized fibers in air atmosphere (Fig. 7.16). Both samples exhibited single exothermic peaks at around 320 °C, corresponding to oxygen uptake and the subsequent complex chemical reactions [7.61, 62]. The relatively sharp peak for the electrospun sample indicates that the oxygen-induced chemical reactions in nanosized fibers occur quickly at a specific temperature, as expected. Therefore, the theoretically twofold higher accessible surface area (as derived from the nanosized diameters) as compared with the microsized fibers (≈ 10 μm) is quite favorable in decreasing the air stabilization time by a factor of two, because oxygen is believed to diffuse from the outer surface of fibers kinetically. For our experimental conditions, optimally air-stabilized nanofiber was *flameproof* when the oxygen content was 8–10%.

FE-SEM images of electrospun PAN nanofibers (Fig. 7.17a,b) exhibit a very long and straight fibrous morphology with uniform diameters ranging from 200 to 300 nm (average 250 nm). In addition, nanofibers are partially aligned along the winding direction. When thermally treated at 700 °C, morphological changes from straight to undulated fibers (Fig. 7.17c,d) are caused by large weight loss (up to 30–40%) accompanied by gas evolution (e.g., CO, CO_2, H_2O etc.). For thermally treated nanofiber webs at 1000 °C (Fig. 7.17e,f), 1500 °C, 2000 °C, and 2500 °C, there were no large changes in macromorphology, as in typical nongraphitizable carbon materials. When thermally treated up to 2800 °C (Fig. 7.17g,h), the main changes are a morphological transformation from a round to facetted cross-sectional morphology and from a smooth to wrinkled surface, mainly due to large density changes resulting from the liberation of heteroatoms and densification of carbon atoms (see the specific gravity change from 0.690 to 1.999 in Table 7.2). It is well known that the structural development of conventional carbon materials during thermal treatment is a thermally activated kinetic process [7.63]. When considering the morphological changes of our nanosized fibers kinetically, compared with microsized ones, no large structural changes on isothermal treatment at 2500 °C and 2800 °C for various holding times ranging from 10 to 10–60 min are observed for our

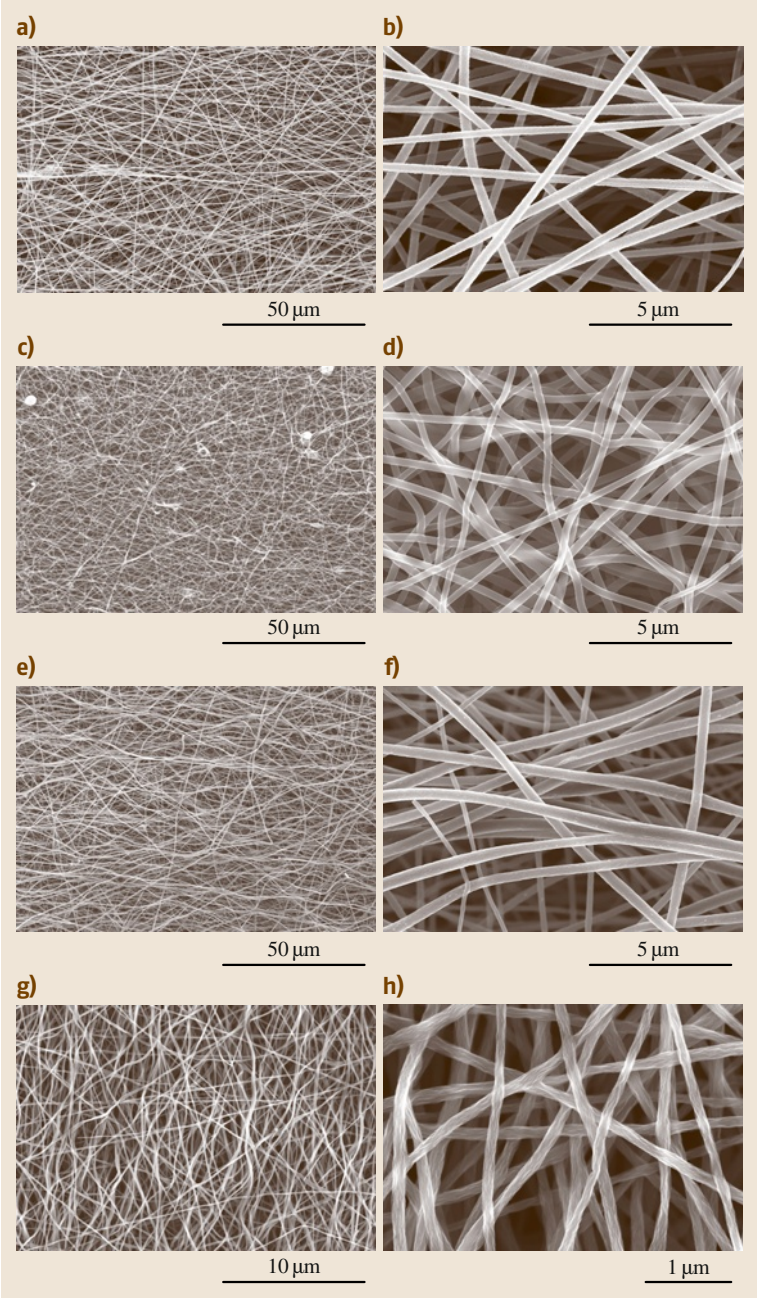


Fig. 7.17a–h FE-SEM images of (**a**,**b**) electrospun nanofibers thermally treated at (**c**,**d**) 700 °C, (**e**,**f**) 1000 °C, and (**g**,**h**) 2800 °C at different resolutions

electrospun nanofibers, because thermal energy is fully transferred to the inner part of the nanosized fibers within a short time. As a result, high-purity carbon nanofibers can be fabricated without disrupting the fiber morphology through the controlled combination of electrospinning and thermal treatment, even when the electrospun nanofiber web is thermally treated up to 2800 °C.

The variations of structural changes on thermal treatment of electrospun nanofibers as a function

Table 7.2 Structural parameters and electrical conductivity for PAN-derived carbon nanofibers as a function of heat treatment temperature (HTT)

HTT (°C)	d_{002} (nm)[a]	L_c (nm)[a]	R value (I_D/I_G)[b]	Electrical conductivity (S/cm)	Specific gravity[c]
700	0.361	0.470	3.81	–	0.690
1000	0.362	0.498	3.41	2.193	–
1500	0.363	0.530	1.51	14.86	–
2000	0.359	0.777	1.31	55.41	–
2500	0.350	1.424	0.93	–	–
2800	0.341	5.274	0.29	20.15	1.998

[a] Average interlayer spacing (d_{002}) and crystallite size (L_c) obtained by x-ray measurements using the Bragg and Scherrer formulae
[b] R is the intensity of D band divided by the intensity of G band from Raman spectra
[c] Specific gravity measured by Sartorius (Genius)

of heat treatment temperature have been studied by x-ray diffraction and microprobe Raman spectroscopy (Fig. 7.18a,b). The x-ray patterns near $2\theta = 25°$ corresponding to the (002) layers of the graphite sharpen, and move to slightly higher angles for the sample at 2500 °C. In the Raman spectra (Fig. 7.18a), the increased intensity and decreased HWHM of the G band (E_{2g2} graphitic mode) at 1580 cm^{-1}, and also the decreased intensity and HWHM of the D band at 1355 cm^{-1} (defect-induced mode), with increasing thermal treatment temperature indicate the sequential structural development [7.64]. Even when thermally treated at 2800 °C, the absence of (100) and (004) lines (Fig. 7.18b) and the presence of D band and the appearance of D′ band (1620 cm^{-1}) (Fig. 7.18a) indicate that PAN-derived nanofibers are typically nongraphitizable carbon. Structural parameters including electrical conductivity and specific gravity are summarized in Table 7.2. Even though no large changes are observed in the structural parameters (interlayer spacing and crystallite size) by x-ray diffraction for samples heat treated between 1000 °C and 1500 °C, it is noteworthy that large changes in the R value (from Raman spectra) occurred for the same samples. In addition, an abrupt increase in electrical conductivity, by more than one order of magnitude, occurs in this region. This inconsistency results from the different analytical techniques used, because XRD provides average bulk structural information whereas Raman studies provide structural information within the optical skin depth (≈ 10 nm). Thus, it is possible to say that carbonization occurs from the outer surface to the inner part kinet-

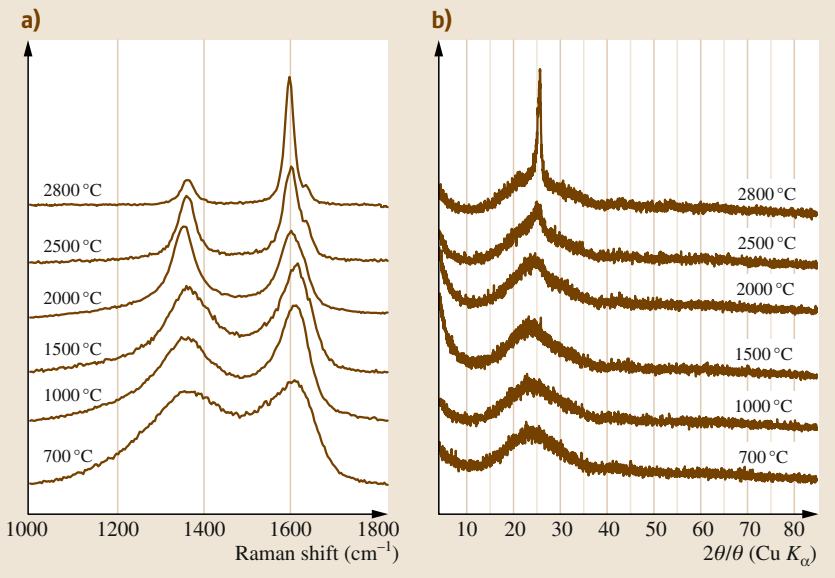


Fig. 7.18 (**a**) Raman spectra and (**b**) x-ray diffraction characterization of thermally treated nanofibers at various temperatures in the range 700–2800 °C

ically. Even though nanofiber web thermally treated at 2800 °C exhibits a relatively well-developed texture, the greatly decreased electrical conductivity (from 55.41 to 20.15 S/cm) is thought to be due to contact points between nanofibers due to abrupt volume changes. These structural parameters are not independent, but rather are interdependent. As a result, their very low graphitization ability, resulting from the intrinsic nature of the PAN polymer and their small diameter, is closely related to the electrochemical properties of the resulting electrochemical devices.

7.2.4 Electrospun Porous Carbon Nanofibers

Porous carbon materials have attracted much attention because of their versatile applications in catalysis, sensors, electronic devices, gas or liquid separation, and storage [7.65–70]. The conventional process for the production of porous carbon materials requires a pore creation step (so-called activation), which involves complex chemical and physical phenomena occurring on multiple time and temperature scales and is also expensive [7.71]. Against this background, intensive studies have been carried out to identify controllable and cost-effective synthetic routes such as the template method and use of polymer blends. The template technique has been utilized as a powerful tool to control pore sizes exactly in the nano to macro range [7.72–74]. The alternative for obtaining porous carbon materials is melt-spinning of immiscible polymer blends with subsequent thermal treatment [7.75–77]. In recent years, electrospinning has been shown to be a simple but powerful technique for preparation of functional nanofibers with submicrometer diameter [7.78]. There have been a few reports on preparation of electrospun carbon nanofibers from pure PAN [7.79–84], because PAN is a well-known precursor for conventional microsized carbon fibers [7.1–3]. Also, synthesis of fibrous carbons with a single and continuous hollow core has been reported by different groups using melt-spinning [7.85] and the co-electrospinning [7.86] of immiscible polymer blends with subsequent thermal treatments.

Thus, it is possible to fabricate porous but nanosized fibrous carbon materials in web form through nanofiber formation using the recently highlighted method of electrospinning of two immiscible polymer solutions and subsequent thermal treatment at 1000 °C in an inert atmosphere. Use of the electrospinning method enables production of nanosized (≈ 400 nm) organic fibers containing two separate phases (sea and islands in cross-section) in web (or sheet) form, where the continuous phase (or sea) transforms into pore walls (or the skeleton of the nanofiber) and the discontinuous phase (or islands) forms multiple hollow pores that develop along the fiber length through thermal decomposition when thermally treated at 1000 °C.

Polymer blend solutions can be prepared by dissolving two or more different polymers in solvent, where phase separation into sea–island features occurs due to the intrinsic nature (e.g., interfacial tension, viscosity, elasticity) of the polymers [7.87]. Such stable emulsion-like polymer blend solutions are prepared by judicious selection of the two types of polymers, their blend ratios, and the solvent; the continuous phase (or sea) consists of PAN solution, and the homogeneously dispersed island-like phase consists of polymethylmethacrylate (PMMA) solution. Empirically, to understand the resulting morphological changes with the blend ratios and the nature of the constituent polymers, we have carried out viscosity and surface tension measurements for the polymer blends. All solutions showed shear-thinning behavior due to increasing orientation of drops along the flow direction at increasing shear rates. Also, the viscosity increased when the volume fraction of PAN in the blend solutions increased. Interestingly, we obtained lower surface tension for PAN solution (5.195 mN/m) than for PMMA solution (8.843 mN/m). Thus, the surface tension of our constituent polymers is thought to be the most important factor determining the cross-sectional morphology of the electrospun organic nanofibers. As a result, the low-surface-tension polymer (PAN) occupies the continuous phase (or sea) while the high-surface-tension polymer (PMMA) forms the discontinuous phase (or islands).

Thus, we were able to obtain homogeneous and long organic nanofibers in the form of a thin white web through use of optimized electrospinning conditions. The conversion of an organic nanofiber into a carbon nanofiber involves stabilization and thermal treatment steps. Air stabilization of electrospun nanofibers, which involves complex chemical reactions such as three-dimensional cross-linking, is accompanied by a change in color from white to reddish brown. Finally, by thermally treating the air-stabilized fibers, we obtain a black web consisting of fibrous carbon containing multiple hollow cores.

As shown in Fig. 7.19a–c, the electrospun organic nanofibers exhibit a smooth outer surface, a long fibrous morphology, and a homogeneous diameter distribution in the range 200–400 nm. The higher the fraction of

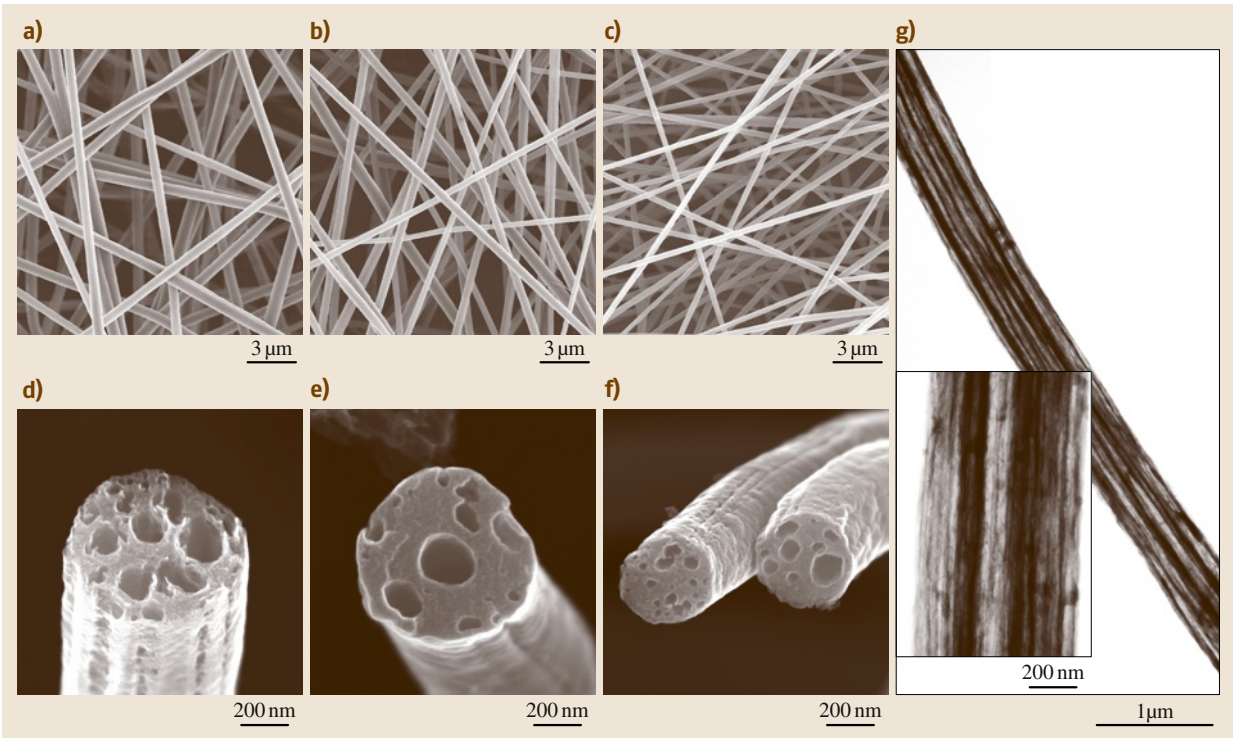


Fig. 7.19 **(a–c)** Macromorphologies of electrospun polymeric nanofibers containing two polymer phases (PAN/PMMA = **(a)** 5/5, **(b)** 7/3, and **(c)** 9/1), and cross-sectional FE-SEM images of nanofibers thermally treated at 1000 °C (PAN/PMMA = **(d)** 5/5, **(e)** 7/3, and **(f)** 9/1). **(g)** TEM image of the sample shown in **(d)** (PAN/PMMA = 5/5), showing linearly developed multiple hollow cores along the fiber length (*inset* shows a magnified TEM image)

PAN polymer, the smaller the diameter of the obtained nanofibers, basically due to their high ability to form fibers (or spinnability). Here it is noted that an electrospun organic single nanofiber consists of two phases, namely the discontinuous and long rod-like PMMA phase and the continuous PAN phase. Then, we carried out studies of the air stabilization of electrospun nanofiber web at 280 °C for 1 h under controlled air circulation, which is critical to sustain their fibrous morphology through the introduction of dimensional stability. Therefore, the fibrous morphology is not disrupted by the following thermal treatment step at 1000 °C in an inert atmosphere, as in the case of conventional PAN-based carbon fiber. Since the elongated PMMA phase decomposes (or disappears) without carbon residue and the continuous PAN phase was easily transformed into carbon (≈ 40–50%) during thermal treatment, we successfully created multiple hollow cores within a single carbon fiber. As shown by the cross-sectional SEM images of carbon fibers thermally treated at 1000 °C in Fig. 7.19d–f, multiple hollow cores were present in a single carbon fiber. Interestingly, the number of hollow cores increased with increasing PMMA concentration. In addition, low-resolution TEM images (Fig. 7.19g) indicated that the long but discontinuous multiple hollow cores are well developed along the fiber length. Thus, we are able to control the diameter, number, and length of hollow cores in a single carbon nanofiber using well-known polymer chemistry knowledge. Finally, the rugged surface morphology of the thermally treated carbon nanofibers (Fig. 7.19d–f) is believed to be the combined result of abrupt gas evolution of both polymers and also the carbon densification process. Therefore, it is expected that the blend ratio of the constituent polymers will greatly affect the patterns of pore creation as well as the porosity of the carbon nanofibers.

On detailed TEM study after thermal treatment at 2800 °C, the outer surface of all samples was

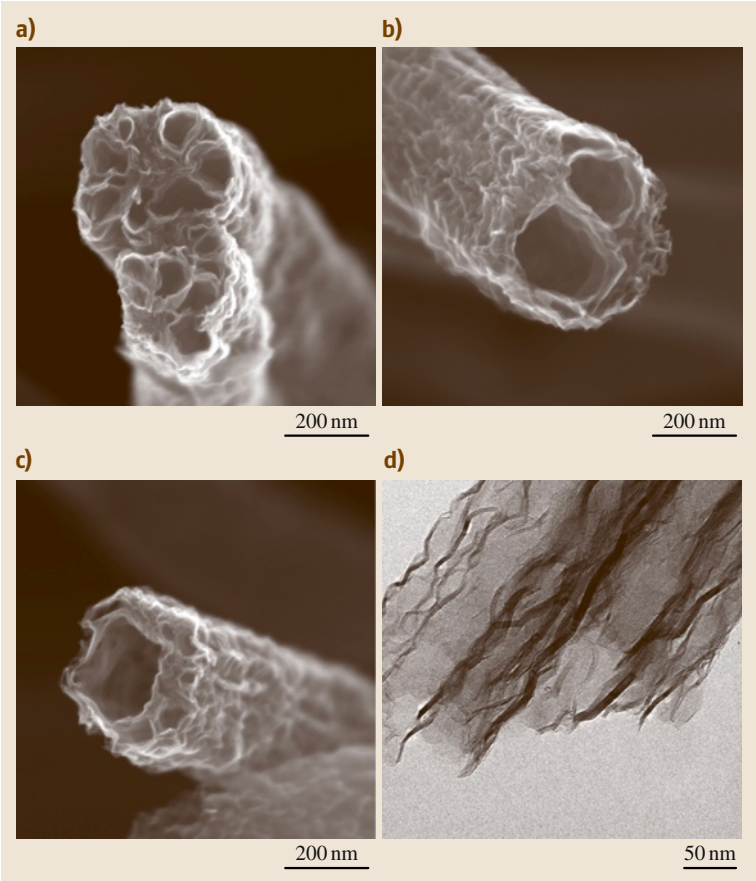


Fig. 7.20a–d Cross-sectional images of nanofibers thermally treated at 2800 °C (PAN/PMMA = **(a)** 5/5, **(b)** 7/3, and **(c)** 9/1); **(d)** TEM image of the sample shown in **(a)**, showing multicore wall structurally developed through thermal treatment

transformed from relatively rugged to largely irregular because of the large changes in real density resulting from the high-temperature treatment. It is interesting to note that the multiple hollow cores in a single fiber did not collapse (Fig. 7.20a–c) and that the pore walls/skeletons (≈ 10 nm), consisting of ca. 15 graphene sheets, were crystalline on the short range but undulated along the fiber length (Fig. 7.20d).

7.3 Applications of Carbon Nanofibers

The particular characteristics of carbon nanofibers due to their small dimension, excellent physicochemical properties, and relatively low cost make them useful in versatile applications ranging from multifunctional composites, electrode materials for supercapacitors, anode electrodes or additives for lithium-ion batteries, supporting materials for metal particles, to bone tissue scaffolds. In this section, we present some of the important applications of carbon nanofibers.

7.3.1 Electrode Material in Lithium-Ion Secondary Batteries

Since sp^2-based carbon materials were adopted as anode materials in commercialized lithium-ion batteries (LIBs) to solve safety problems, various types of carbon textures have been examined to improve the specific energy and power density of batteries [7.88–92]. The capacity as well as cyclic performance of LIBs strongly depend on the carbon texture due to the very different

lithium-ion (Li^+) insertion and desertion mechanisms. More recently, development of high-power LIBs has been required to meet growing demand for use in lighter electronic portable devices and hybrid electric vehicles (HEV). Thus, intensive study has been focused on nanosized carbon materials as promising materials for storing Li^+, because they show increased capacity as an active material and also improved cyclic characteristics when used as an additive to anode and cathode materials [7.93–100].

Through the right combination of the electrospinning technique and thermal treatment process, dimensionally thin, mechanically tough, electrically conductive web-based electrodes consisting of interconnected nanofibers with a diameter in the range 200–300 nm have been fabricated. No binder or conductive filler (e.g., polyvinylidene fluoride, carbon black) was used in the fabrication of the active electrode, to enable evaluation of the anodic performance of the electrospun carbon nanofiber web. Therefore, the thin web in combination with their expected good mechanical and electrical properties makes them very attractive for fabrication of anode materials in thin polymer LIBs. Figure 7.21 shows voltage profiles for nanofiber webs thermally treated at 700 °C, 1000 °C, and 2800 °C. Even though carbon nanofibers thermally treated at 700 °C and 1000 °C have large Li^+ storage capacity of 510 and 1000 mAh/g, their reversible capacities are 300 and 450 mAh/g, respectively. Their large irreversible capacities (≈ 500 mAh/g) are closely related to electrolyte decomposition and the formation of a solid electrolyte interphase at ≈ 0.8 V [7.101]. However, after the second cycle, relatively stable reversible capacity could be obtained. Nanofiber web thermally treated at 2800 °C exhibits a reproducible discharge/charge plateau at about 0.2 V (stage formation) and provides a reversible capacity of 130 mAh/g. As mentioned above, thermally treated PAN polymer could be characterized as a typical nongraphitic carbon, and thus has low discharge capacity due to its low crystallinity. It is noteworthy that carbon nanofibers thermally treated at 1000 °C have reversible capacity of 450 mAh/g, which is larger than both the theoretical value for graphite (372 mAh/g) and the value of 300 mAh/g for carbon nanofiber thermally treated at 700 °C.

Very recently, *Yoon* et al. [7.102] reported high capacity of 431 mAh/g for highly crystalline carbon nanofibers through the catalytic chemical vapor deposition method by carrying out a systematic study of the anodic behaviors of very different crystalline and textured carbon nanofibers. Also, relatively crystalline carbon nanofibers obtained by applying direct-current (DC) high voltage to a mist of 2-propanol showed a large reversible capacity of ≈ 340 mAh/g [7.103]. It is not clear why the reversible capacity of our carbon nanofiber thermally treated at 1000 °C exhibited the largest reversible capacity of 450 mAh/g as compared with various carbon nanofibers including microsized PAN carbon fiber (≈ 220 mAh/g) [7.104]. One possible explanation is that the nanosized fiber morphology invokes different carbonization behavior including gas

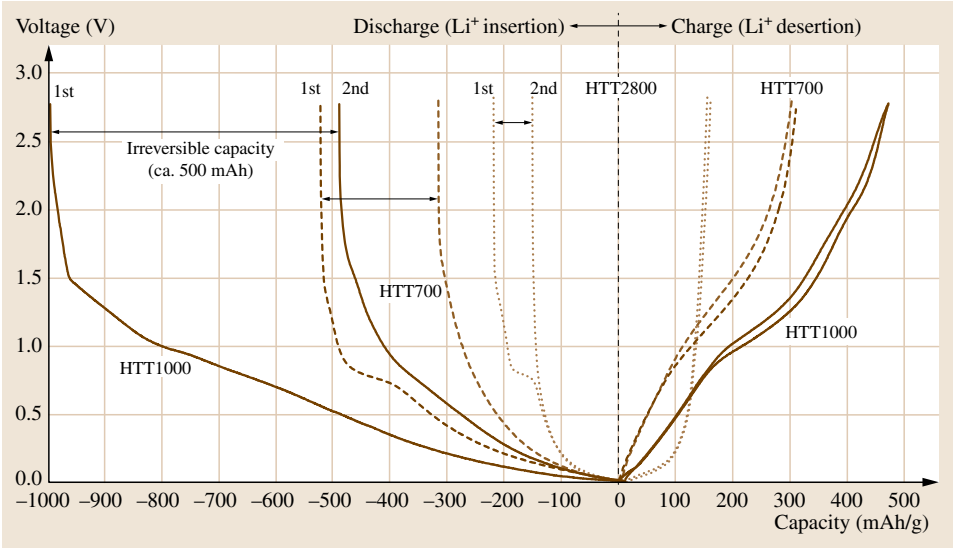


Fig. 7.21 Charge–discharge curves for nanofiber webs thermally treated at 700 °C, 1000 °C, and 2800 °C (current density 30 mA/g, second cycle)

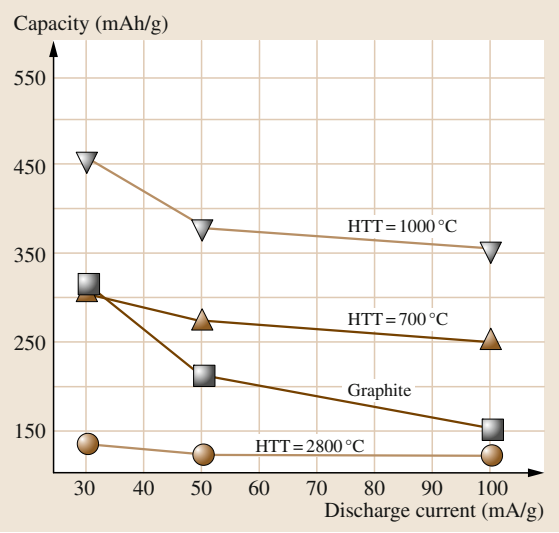


Fig. 7.22 Variation of reversible capacities (rate capability) for nanofiber webs thermally treated at 700 °C, 1000 °C, and 2800 °C at different discharge current densities of 30, 50, and 100 mA/g ◀

evolution and pore development and thereby different surface properties when compared with microsized polymeric materials. In other words, the higher reversible capacity (up to 450 mAh/g) is expected to originate from the peculiar microtexture of carbon nanofibers thermally treated at 1000 °C, e.g., the highly disordered structure, defects, and dangling bonds. Thus, Li ions are inserted/deserted into and out of carbon nanofibers by a doping/dedoping process, because we could not observe any distinct redox peaks from the derivative voltage profiles (not shown here). This takes into account that a nanofiber web treated at low temperature (700 °C and 1000 °C) with constant and slightly inclined charge potential profiles is quite suitable for electronic portable device and HEV applications due to easy distinction of the the remaining battery capacity. In addition, when considering the battery rate capability (30, 50, and 100 mA/g) of samples thermally treated at 700 °C, 1000 °C, and 2800 °C (Fig. 7.22), there was no large degradation of capacity as a function of discharge current density compared with conventional graphite. In other words, this result confirms that the Li^+ diffusion path within anode materials is greatly reduced due to the small diameter of the carbon nanofibers.

7.3.2 Electrode Material for Supercapacitors

Supercapacitors have been intensively investigated as a main and/or backup energy storage systems, because they are able to carry high power and, furthermore, to have a long lifecycle [7.105]. Their double-layer capacitances strongly depend on the types and forms of the electrode materials. Against this background, various forms and textures of porous carbon have been examined as possible electrode materials for supercapacitors [7.106–111]. Among these, carbon nanotubes have attracted lots of attention, because they have large accessible surface area, based on their nanosized diameter, and relatively high electrical conductivity, which makes them very promising as efficient electrode materials for use in high-power supercapacitors [7.112–116]. Currently, their intrinsic problems, such as the limited amount of available charge and high cost, combined with their low effective specific surface area, limit practical use of carbon nanotubes as the electrode material in supercapacitors.

Another route to the fabrication of fibrous carbon as the electrode material for supercapacitors, based on electrospinning and subsequent steam activation, has been reported [7.33]. The preparation process involves fiber formation from a PAN polymer solution using electrostatic force. The technical reason for selecting PAN as a precursor was the good electrospinnability of PAN polymer solution and the relatively high carbon yield. The subsequent physical activation to increase the specific surface area or to create pores by subjecting air-stabilized carbon to steam at high temperature involves complex chemical and physical phenomena occurring on multiple time and temperature scales, and this step was known to be difficult in terms of controlling the pore size and surface properties of the obtained carbon materials, as well as being time consuming [7.117–119].

When considering their versatile promising applications in catalysis, electrochemical energy storage systems, and gas or liquid separation and storage, a simple and effective technique for decreasing the fiber diameter of ≈ 100 nm and also creating effective pores in a controllable fashion has to be developed to maximize the intrinsic 1-D functions (e.g., large accessible surface area and enhanced electrical and mechanical properties). Here we report a method for preparing porous, smaller-sized fibrous carbon in thin web form with the help of zinc chloride. Specifically, zinc chloride decreases the fiber diameter from 350 to 200 nm during electrospinning, enhances the reaction rate catalytically during air stabilization, and effectively creates suitable pores on the outer surface of smaller-sized (≈ 100 nm) carbon

nanofibers during thermal treatment. Also, dimensionally thin but flexible, an electrically conductive black web consisting of physically entangled, long carbon nanofibers enabled us to fabricate highly pure and self-sustained electrodes, without using binder or conductive materials; furthermore, the suitably developed micropores as well as the large external surface directly contributed to good capacitive behavior of supercapacitors.

The resultant black web, consisting of porous and long carbon nanofibers with diameter of 100 nm, was cut into a rectangular (2.25 × 2.25 cm) shape, and then attached to nickel plates to evaluate the capacitive performance based on a two-electrode system. The electrochemical properties of the carbon nanofiber web electrodes were studied by cyclic voltammetry in 6 M KOH aqueous solution as an electrolyte. Typical cyclic voltammograms (CVs) at 10–200 mV/s scan rate are shown in Fig. 7.23. The CVs were recorded in the potential range between 0 and 0.9 V, where no obvious redox peaks originating from the functional groups are observed. It is well known that CVs for an ideal double-layer capacitor are characterized by a perfectly rectangular-shaped profile [7.105]. For our samples, the CV profiles deviated from this ideal shape, but the shape of the curve is still satisfactory, even at the high scan rate used. However, the relatively broad feature in the CV of all samples could be considered as a side-reaction closely related to the intrinsic nitrogen functionalities derived from the parent PAN and also oxygen functional groups formed by zinc chloride.

When the zinc chloride was increased from 1% to 5%, the specific capacitances, calculated from CV curves, increase from 120 to 140 F/g without any distinct changes in the shape of the CV profiles (Fig. 7.24a), indicating not only a reduction in the equivalent series resistance of the nanofiber web electrode, but also a reduction in the hindrance of ion penetration into the pores. The specific capacitance of our sample was higher than that of freestanding multi-walled carbon nanotubes in KOH medium (≈ 113 F/g) [7.112]. In addition, the samples showed relatively high rate capability (Fig. 7.24a). In other words, the sample exhibited good capacitive behavior with low diffusive limitation compared with conventional activated carbon materials, which could be explained by the highly intermingled porous nanofiber network providing an easily available electrode–electrolyte interface to form an electric double layer.

We measured the alternating-current (AC) impedance spectra (Nyquist plot) (Fig. 7.24b), because this technique enables one to distinguish the resistance and capacitance of devices. The impedances nearest to the origin were determined at high frequencies. This plot consists of three main regions (inset to Fig. 7.24b):

(I) A semicircular arc representing the resistance and capacitance of the contact between the electrode and current collector, and the resistance of the porous electrode itself.
(II) Another, small semicircular arc corresponding to the movement of electrons across the electrical double layer.
(III) A (near-vertical) straight line at low frequency, suggesting blocking electrode behavior. This very

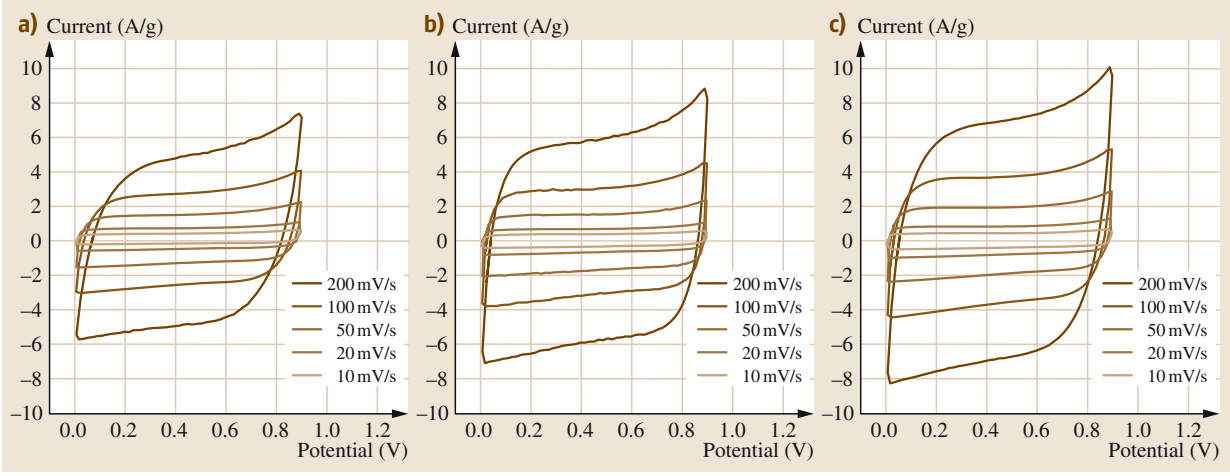


Fig. 7.23a–c Cyclic voltammograms of zinc-chloride-activated porous carbon nanofibers; **(a)** 1 wt %, **(b)** 3 wt %, and **(c)** 5 wt % zinc-chloride-activated porous nanofiber webs in 6 M KOH solution at different sweep rates

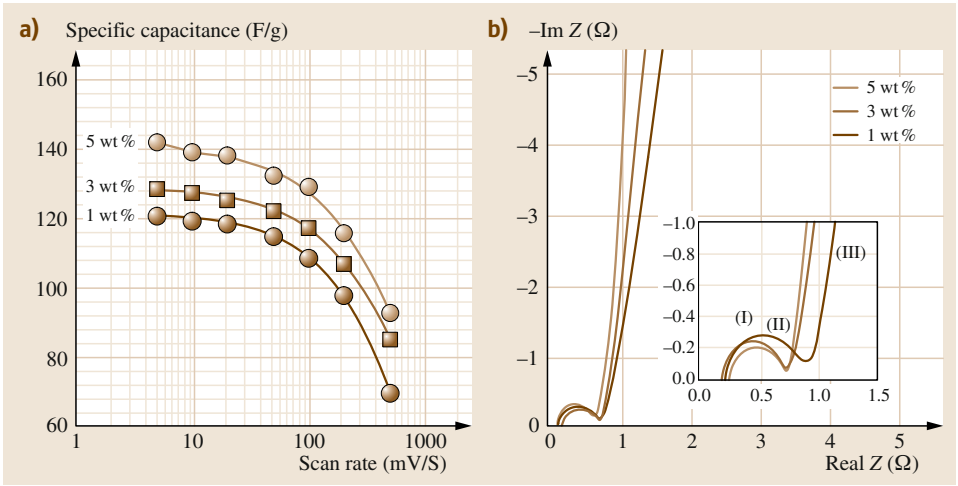


Fig. 7.24 **(a)** Gravimetric capacitances of all samples in 6 M KOH at different sweep rates, **(b)** complex-plane impedance plots of zinc-chloride-activated porous nanofiber-based electrodes (AC signal level 10 mV; frequency range 10 mHz to 100 kHz)

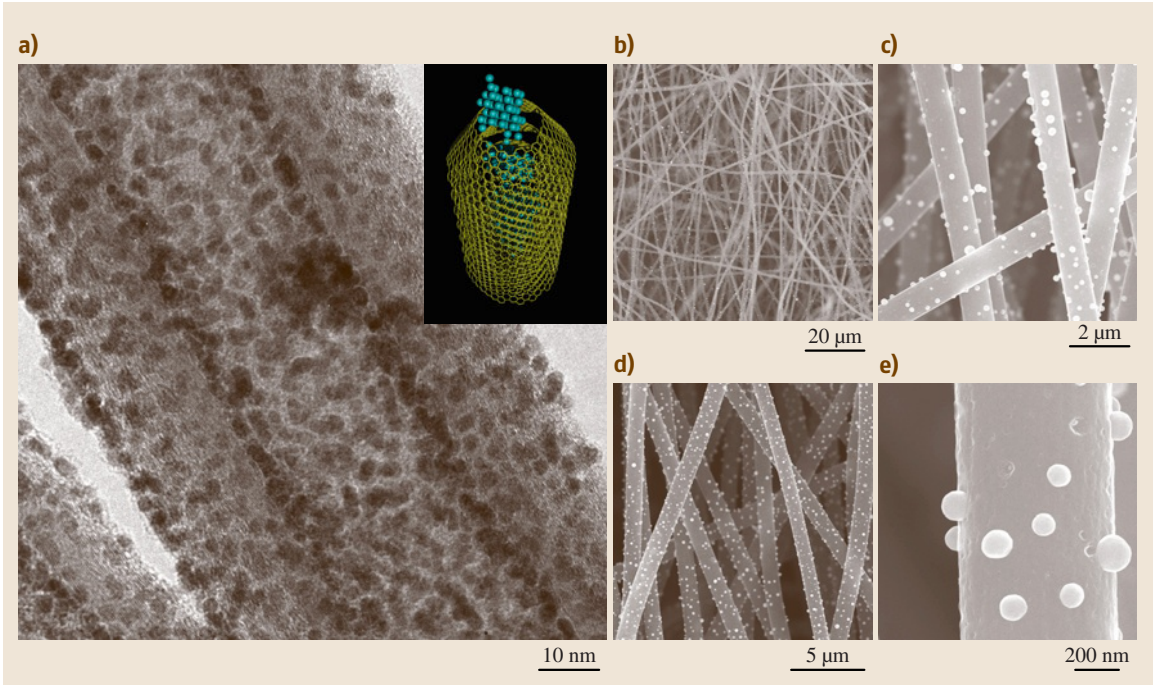


Fig. 7.25 **(a)** HRTEM image exhibiting high dispersion of Pt nanoparticles only on the surface of a carbon nanofiber. **(b–e)** SEM images of electrospun-based carbon nanofibers at different resolutions. Note that spherical palladium particles homogeneously cover the outer surface of the carbon nanofibers

steep spike shows that the kinetics of the diffusion of ions in the solution as well as the adsorption of ions onto the electrode surface occur swiftly. Therefore, the Warburg impedance, representing the diffusion of ions in pores and in the electrolyte, is unnoticeable.

The values I and II (inset of Fig. 7.24b) gradually decrease with increasing zinc chloride content from 1 wt % to 5 wt %, respectively. Electrolyte accessibility becomes greater for the larger pores, while the ions will not enter the smallest pores. Thus, lower resistance is associated with better electrolyte pore accessibility. In

the case of the sample with 5 wt % added zinc chloride, the pore density is higher than for the others, which is why the capacitive behavior appears at lower resistance.

7.3.3 Supporting Material for Metal Nanoparticles

For a decade, nanocarbon materials have been widely studied as catalyst supports for use in heterogeneous catalysis due to their unique morphology and reactivity [7.120–122]. It is well known that the basic properties of impregnated catalyst are strongly affected by the impregnation method, microstructure, surface reactivity, and the metal precursor [7.123, 124]. Among these factors, appropriate morphology and nanostructure of the support is considered to be the main factor enabling the production of a well-dispersed nanoparticle catalyst as in Fig. 7.25.

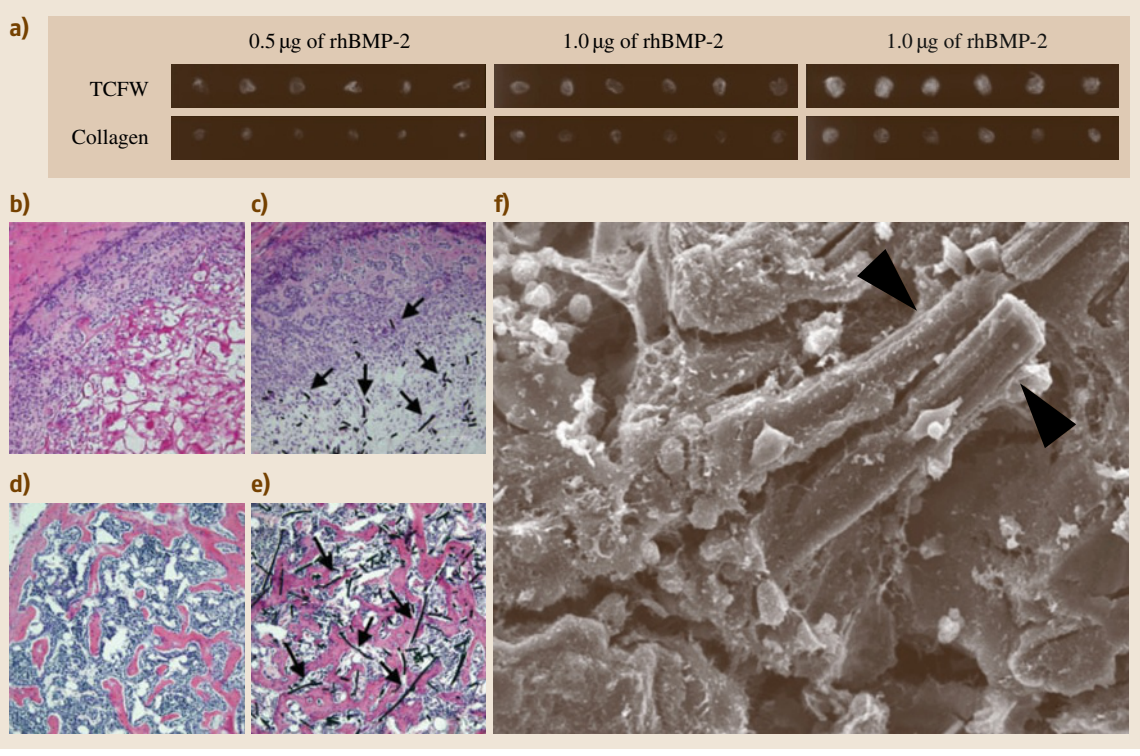


Fig. 7.26a–f Ectopic bone formation in the dorsal muscle of mice. **(a)** X-ray images of ectopic bone formed by rhBMP-2/carbon nanofiber web and rhBMP-2/collagen implants. Three weeks later, bone trabecular shadows were observed in all of the carbon nanofiber web and collagen implants with 0.5, 1 or 5 mg rhBMP-2. The bone trabecular shadows were clear and large and corresponded to the rhBMP-2 dosage in both groups. At each dose, the shadows of the carbon nanofiber web group were larger than those of the collagen group. **(b–e)** Bone formation of the carbon nanofiber web and collagen implants with 5 mg rhBMP-2. At 1 week, both the rhBMP-2/collagen **(b)** and rhBMP-2/carbon nanofiber web **(c)** showed the presence of immature bone matrix in the peripheral zone of the implants. The maturity of the collagen and carbon nanofiber web groups was the same. At 3 weeks, both the rhBMP-2/collagen **(d)** and rhBMP-2/carbon nanofiber web **(e)** specimens demonstrated normal-appearing bone with thick trabecular and hematopoietic marrow. Mature trabecular of the carbon nanofiber web group was thicker than in the collagen group. The collagen sheets were absorbed, but the carbon nanofibers remained and were in dense contact with the bone matrix. Hematoxylin and eosin staining. *Scale bar*: 200 mm. *Arrows*: carbon fibers. **(f)** SEM image of tissue sections containing the carbon nanofiber web with 5 mg rhBMP-2 at 3 weeks after operation. The carbon fibers were directly integrated into the new bone and adhered closely to the bone matrix with no intervening space. *Scale bar*: 10 mm. *Arrow heads*: carbon nanofibers

Efficient impregnation of Pt nanoparticles (outer diameter < 3 nm) into carbon nanofibers has been reported [7.125]. The method involves dispersion of the nanofibers in H_2PtCl_6, followed by low-temperature annealing. The Pt particle deposition is homogeneous, and can be controlled selectively on the outer or internal core using the hydrophobic nature of the material (Fig. 7.25a). Since the activity of the Pt nanoparticles on the fibers is high, this material could find application in efficient catalysts and allied biological devices. Alternatively, carbon nanofibers containing palladium nanoparticles have been prepared simply by electrospinning polymer solution containing palladium chloride and subsequent thermal treatment in argon [7.126]. It has been demonstrated that palladium oxide formed during air stabilization transforms into nanoparticles through an interaction with the carbon material. Since the palladium nanoparticles homogeneously covering the outer surface of the nanofibers (Fig. 7.25b–e) are small enough to have high catalytic activity, this material could find application in efficient catalysts and hydrogen sensors.

7.3.4 Bone Tissue Scaffold

At present, the most popular scaffold is type I collagen [7.127–129], which is often used in clinical applications [7.130, 131]. However, use of collagen leads to certain problems such as the possibility of disease transfer or immunogenic reactions due to xenogenicity [7.132–134]. Further, the soft nature of collagen does not allow it to preserve its shape in the body. Actually, carbon fibers have been used for tendon repair in clinical settings [7.135, 136], but they are too thick for use in cell or cytokine therapy for tissue regeneration. If creation of a three-dimensional web consisting of carbon fibers with a nanostructure is possible, it may serve as a promising new scaffold biomaterial for tissue regeneration. Thus, by using the electrospinning method, a carbon nanofiber web consisting of high-purity carbon was examined as a bone tissue scaffold [7.35]. The carbon nanofiber web consists of high-purity carbon with a very small amount of functional groups. It is considered to be safe in the living body even when present at high levels. In vivo implantation for a short time period resulted in little inflammatory reaction of the surrounding tissue, indicating that this material is highly biocompatible. Examination of the interface between the carbon fibers and bone matrix by using FE-SEM revealed that the carbon fibers directly adhered to the bone itself without any intervening space being integrated into the bone matrix, indicating high bone tissue compatibility. Recombinant human bone morphogenic protein-2 (rhBMP-2)/nanofiber web composite implants could induce ectopic new bone formation effectively when tested in vivo and could repair large bone defects orthotopically (Fig. 7.26). It is envisaged that the nanofiber web is a promising scaffold material candidate for use in bone regeneration therapy and represents a prominent advance in technology for enhancement of bone repair. We also expect that such carbon-nanofiber-derived scaffold systems will play a major role in regeneration therapy for various tissues in future clinical applications.

7.4 Conclusions

The 19th century can be remembered as the iron age, while the 20th century is recognized as being founded on silicon technology. Now, much attention is being paid to fibrous nanocarbon materials as one of the promising candidates that could revolutionize technology in the 21st century. Carbon nanofibers differ from conventional carbon fibers in their nanosized diameter and from carbon nanotubes in their intrinsic geometry. Thus, they could be visualized as connecting bridges between molecular and macro materials. However, some challenges have to be solved in order to speed up industrial use of carbon nanofibers. The first challenge is large-scale synthesis of defect-free carbon nanofibers at low cost. Secondly, it is important to control the diameter and length of carbon nanofibers. The final and most important challenge is how to manipulate (or disperse) such nanosized entangled fluffy materials in order to fabricate novel multifunctional materials. It is envisaged that various carbon-nanofiber-based products will be seen in less than 10 years.

References

7.1 J.B. Donnet, R.C. Bansal: *Carbon Fibers* (Marcel Dekker, New York 1984)
7.2 L.H. Peebles: *Carbon Fibers* (CRC, Boca Raton 1994)
7.3 D.D.L. Chung: *Carbon Fiber Composites* (Butterworth Heinemann, Boston 1994)
7.4 M.S. Dresselhaus, G. Dresselhaus, K. Sugihara, I.L. Spain, H.A. Goldberg: *Graphite Fiber and Filaments* (Springer, Berlin Heidelberg 1988)
7.5 A. Oberlin, M. Endo, T. Koyama: Filamentous growth of carbon through benzene decomposition, J. Cryst. Growth **32**, 335–349 (1976)
7.6 R.T.K. Baker: Catalytic growth of carbon filaments, Carbon **27**, 315–323 (1989)
7.7 G.G. Tibbetts: Why are carbon filaments tubular?, J. Cryst. Growth **66**, 632–637 (1984)
7.8 M. Endo: Grow carbon fibers in the vapor phase, Chem. Technol. **18**, 568–576 (1988)
7.9 N.M. Rodriguez: A review of catalytically grown carbon nanofibers, J. Mater. Res. **8**, 3233–3250 (1993)
7.10 G.G. Tibbetts: Vapor-grown carbon fibers: Status and prospects, Carbon **27**, 745–747 (1989)
7.11 S. Iijima: Helical microtubules of graphitic carbon, Nature **354**, 56–58 (1991)
7.12 M.S. Dresselhaus, G. Dresselhaus, P. Eklund: *Science of Fullerenes and Carbon Nanotubes* (Academic, New York 1996)
7.13 R. Saito, G. Dresselhaus, D.S. Dresselhaus: *Physical Properties of Carbon Nanotubes* (Imperial College Press, London 1998)
7.14 T.W. Ebbesen: *Carbon Nanotubes: Preparation and Properties* (CRC, London 1997)
7.15 N.M. Rodriguez, A. Chambers, R.T.K. Baker: Catalytic engineering of carbon nanostructures, Langmuir **11**, 3862–3866 (1995)
7.16 M. Endo, Y.A. Kim, T. Fukai, T. Hayashi, K. Oshida, M. Terrones, T. Yanagisawa, S. Higaki, M.S. Dresselhaus: Structural characterization of cup-stacked type nanofibers with an entire hollow core, Appl. Phys. Lett. **80**, 1267–1269 (2002)
7.17 S.H. Yoon, S. Lim, Y. Song, Y. Ota, W.M. Qiao, A. Tanaka, I. Mochida: KOH activation of carbon nanofibers, Carbon **42**, 1723–1729 (2004)
7.18 S.H. Yoon, C.W. Park, H.J. Yang, Y. Korai, I. Mochida, R.T.K. Baker, N.M. Rodriguez: Novel carbon nanofibers of high graphitization as anodic materials for lithium ion secondary batteries, Carbon **42**, 21–32 (2004)
7.19 Q.F. Liu, W.C. Ren, Z.G. Cheng: Semiconducting properties of cup-stacked carbon nanotubes, Carbon **47**, 731–736 (2009)
7.20 M. Endo, Y.A. Kim, M. Ezaka, K. Osada, T. Yanagisawa, T. Hayashi, M. Terrones, M.S. Dresselhaus: Selective and efficient impregnation of metal nanoparticles on cup-stacked-type nanofibers, Nano Lett. **3**, 723–726 (2003)
7.21 Y.K. Choi, Y. Gotoh, K.I. Sugimoto, S.M. Song, T. Yanagisawa, M. Endo: Processing and characterization of epoxy nanocomposites reinforced by cup-stacked carbon nanotubes, Polymer **46**, 11489–11498 (2005)
7.22 T. Yokozeki, Y. Iwahori, S. Ishiwata: Matrix cracking behaviors in carbon fiber/epoxy laminates filled with cup-stacked carbon nanotubes (CSCNTs), Compos. A: Appl. Sci. Manuf. **38**, 917–924 (2007)
7.23 T. Yokozeki, Y. Iwahori, S. Ishiwata, K. Enomoto: Mechanical properties of CFRP laminates manufactured from unidirectional prepregs using CSCNT-dispersed epoxy, Compos. A: Appl. Sci. Manuf. **38**, 2121–2130 (2007)
7.24 T. Yokozeki, Y. Iwahori, M. Ishibashi, T. Yanagisawa, K. Imai, M. Arai, T. Takayashi, K. Enomoto: Fracture toughness improvement of CFRP laminates by dispersion of cup-stacked carbon nanotubes, Compos. Sci. Technol. **69**, 2268–2273 (2009)
7.25 K. Saito, M. Ohtani, F. Fukuzumi: Electron-transfer reduction of cup-stacked carbon nanotubes affording cup-shaped carbons with controlled diameter and size, J. Am. Chem. Soc. **128**, 14216–14217 (2006)
7.26 T. Hasobe, H. Murata, P.V. Kamat: Photoelectrochemistry of stacked-cup carbon nanotube film: Tube-length dependence and charge transfer with excited porphyrin, J. Phys. Chem. C **111**, 16626–16634 (2007)
7.27 S. Ramakrishna, K. Fujihara, W.-E. Teo, T.-C. Lim, Z. Ma: *An Introduction to Electrospinning and Nanofibers* (World Scientific, Singapore 2005)
7.28 D.H. Renecker, A.L. Yarine, H. Fong, S. Koombhongse: Bending instability of electrically charged liquid jets of polymer solutions in electrospinning, J. Appl. Phys. **87**, 4531 (2000)
7.29 Y.M. Shin, M.M. Hohman, G.C. Martin: Processing and microstructural characterization of porous biocompatible protein polymer thin films, Polymer **40**, 7397–7407 (1999)
7.30 I.D. Norris, M.M. Shaker, F.K. Ko, A.G. MacDiarmid: Electrostatic fabrication of ultrafine conducting fibers: polyaniline/polyethylene oxide blends, Synth. Met. **114**, 109–114 (2000)
7.31 F. Ko, Y. Gogotsi, A. Ali, N. Naguib, H. Ye, G. Yang, C. Li, P. Willis: Electrospinning of continuous carbon nanotube-filled nanofiber yarns, Adv. Mater. **15**, 1161–1165 (2003)
7.32 C. Vozzi, C.J. Flaim, F. Bianchi, A. Ahluwalia, S. Bhatia: Microfabricated PLGA scaffolds: a comparative study for application to tissue engineering, Mater. Sci. Eng. **20**, 43–47 (2002)
7.33 C. Kim, K.S. Yang: Electrochemical properties of carbon nanofiber web as an electrode for supercapacitor prepared by electrospinning, Appl. Phys. Lett. **83**, 1216–1218 (2003)

7.34 R. Dersch, M. Steinhart, U. Boudriot, A. Greiner, J.H. Wendorff: Nanoprocessing of polymers: applications in medicine, sensors, catalysis, photonics, Polym. Adv. Technol. **16**, 276–282 (2005)

7.35 K. Aoki, Y. Usui, N. Narita, N. Ogiwara, N. Iashigaki, K. Nakamura, H. Kato, K. Sano, N. Ogiwara, K. Kametani, C. Kim, S. Taruta, Y.A. Kim, M. Endo, N. Saito: A thin carbon fiber web as a scaffold for bone tissue regeneration, Small **5**, 1540–1546 (2009)

7.36 C. Kim, K.S. Yang, M. Kojima, K. Yoshida, Y.J. Kim, Y.A. Kim, M. Endo: Fabrication of electrospun-derived carbon nanofiber web for the anode material of lithium-ion secondary batteries, Adv. Funct. Mater. **16**, 2393–2397 (2006)

7.37 R. Bacon: Production of graphite whiskers, J. Appl. Phys. **31**, 283–290 (1960)

7.38 M. Endo, R. Saito, M.S. Dresselhaus, G. Dresselhaus: From carbon fibers to carbon nanotubes. In: *Carbon Nanotubes*, ed. by T.W. Ebbesen (CRC, New York 1997) pp. 35–105

7.39 A. Oberlin: High-resolution TEM studies of carbonization and graphitization, Chem. Phys. Carbon **22**, 1–135 (1989)

7.40 L.H. Peebles, Y.G. Yanovsky, A.G. Sirota, V.V. Bogdanov, P.M. Levit: Mechanical properties of carbon fibers. In: *Carbon Fibers*, ed. by J.B. Donnet (Marcel Dekker, New York 1998) pp. 311–370

7.41 M. Endo, Y.A. Kim, T. Hayashi, K. Nishimura, T. Matushita, K. Miyashita, M.S. Dresselhaus: Vapor-grown carbon fibers (VGCFs): basic properties and battery application, Carbon **39**, 1287–1297 (2001)

7.42 M. Endo, K. Takeuchi, K. Kobori, K. Takahashi, H.W. Kroto, A. Sarkar: Pyrolytic carbon nanotubes from vapor-grown carbon fibers, Carbon **33**, 873–881 (1995)

7.43 H.J. Dai, A.G. Rinzler, P. Nikolaev, A. Thess, D.T. Colbert, R.E. Smalley: Single-wall nanotubes produced by metal-catalyzed disproportionation of carbon monoxide, Chem. Phys. Lett. **260**, 471–475 (1996)

7.44 C.N.R. Rao, R. Sen, B.C. Satisshkumar, A. Govindaraj: Large aligned-nanotube bundles from ferrocene pyrolysis, Chem. Commun. **15**, 1525–1526 (1998)

7.45 R. Andrews, D. Jacques, A.M. Rao, F. Derbyshire, D. Qian, X. Fan, E.C. Dickey, J. Chen: Continuous production of aligned carbon nanotubes: a step closer to commercial realization, Chem. Phys. Lett. **303**, 467–474 (1999)

7.46 R. Kamalakaran, M. Terrones, T. Seeger, P. Kohler-Redlich, M. Ruhle, Y.A. Kim, T. Hayashi, M. Endo: Synthesis of thick and crystalline nanotube arrays by spray pyrolysis, Appl. Phys. Lett. **77**, 3385–3387 (2000)

7.47 M. Endo, Y.A. Kim, Y. Fukai, T. Hayashi, M. Terrones, H. Terrones, M.S. Dresselhaus: Comparison study of semi-crystalline and highly crystalline multiwalled carbon nanotubes, Appl. Phys. Lett. **79**, 1531–1533 (2001)

7.48 H. Terrones, T. Hayashi, M. Munoz-Navia, M. Terrones, Y.A. Kim, N. Grobert, R. Kamalakaran, J. Dorantes-Davila, R. Escudero, M.S. Dresselhaus, M. Endo: Graphitic cones in palladium catalysed carbon nanofibers, Chem. Phys. Lett. **343**, 241–250 (2001)

7.49 J.F. Despres, E. Daguerre, K. Lafdi: Flexibility of graphene layers in carbon nanotubes, Carbon **33**, 87–89 (1995)

7.50 M. Kosaka, T.W. Ebbesen, H. Hiura, K. Tanigaki: Annealing effect on carbon nanotubes. An ESR study, Chem. Phys. Lett. **233**, 47–51 (1995)

7.51 M. Endo, K. Nishimura, Y.A. Kim, K. Hakamada, T. Matushita, M.S. Dresselhaus, G. Dresselhaus: Raman spectroscopic characterization of submicron vapor-grown carbon fibers and carbon nanofibers obtained by pyrolyzing hydrocarbons, J. Mater. Res. **14**, 4474–4477 (1999)

7.52 M. Endo, Y.A. Kim, T. Hayashi, T. Yanagisawa, H. Muramatsu, M. Ezaka, H. Terrones, M. Terrones, M.S. Dresselhaus: Microstructural changes induced in stacked cup carbon nanofibers by heat treatment, Carbon **41**, 1941–1947 (2003)

7.53 J. Campos-Delgado, H. Farhat, Y.A. Kim, A. Reina, J. Kong, M. Endo, H. Muramatsu, T. Hayashi, H. Terrones, M. Terrones, M.S. Dresselhaus: Resonant Raman study on bulk and isolated graphitic nanoribbons, Small **5**, 2698–2702 (2009)

7.54 G. Katagiri, H. Ishida, A. Ishitani: Raman spectra of graphite edge planes, Carbon **26**, 565–571 (1988)

7.55 M. Endo, T. Hayashi, S.H. Hong, T. Enoki, M.S. Dresselhaus: Scanning tunneling microscope study of boron-doped highly oriented pyrolytic graphite, J. Appl. Phys. **90**, 5670–5674 (2001)

7.56 P.G. Collins, M. Hersam, M. Arnold, R. Martel, P. Avouris: Current saturation and electrical breakdown in multiwalled carbon nanotubes, Phys. Rev. Lett. **86**, 3128–3131 (2001)

7.57 A.P. Graham, G.S. Duesberg, R.V. Seidel, M. Liebau, E. Unger, W. Pamler, F. Kreupl, W. Hoenlein: Carbon nanotubes for microelectronics?, Small **1**, 382–390 (2005)

7.58 B.Q. Wei, R. Vajtai, P.M. Ajayan: Reliability and current carrying capacity of carbon nanotubes, Appl. Phys. Lett. **79**, 1172–1174 (2001)

7.59 B.T. Kelly: *Physics of Graphite* (Springer, New York 1981)

7.60 N. Kurita, M. Endo: Molecular orbital calculations on electronic and Li-adsorption properties of sulfur-, phosphorus- and silicon-substituted disordered carbons, Carbon **40**, 253–260 (2002)

7.61 H. Jiang, C. Wu, A. Zhang, P. Yang: Structural characteristics of polyacrylonitrile (PAN) fibers during oxidative stabilization, Compos. Sci. Technol. **29**, 33–44 (1987)

7.62 H. Ogawa, K. Saito: Oxidation behavior of polyacrylonitrile fibers evaluated by new stabilization index, Carbon **33**, 783–788 (1995)

7.63 P.L. Walker: *Chemistry and Physics of Carbon* (Marcel Dekker, New York 1971)
7.64 R.J. Nemanichi, S.A. Solin: First- and second-order Raman scattering from finite-size crystals of graphite, Phys. Rev. B **20**, 392–401 (1970)
7.65 K. Kaneko, J. Imai: Adsorption of NO_2 on activated carbon fibers, Carbon **27**, 954–955 (1989)
7.66 S.H. Joo, S.J. Choi, I.W. Oh, J.Y. Kwak, Z. Liu, O. Terasaki, R. Ryoo: Ordered nanoporous arrays of carbon supporting high dispersions of platinum nanoparticles, Nature **412**, 169–172 (2001)
7.67 L. Schlapbach, A. Zuttel: Hydrogen-storage materials for mobile applications, Nature **414**, 353–358 (2001)
7.68 M. Terrones: Science and technology of the twenty-first century: synthesis, propertypes, and applications of carbon nanotubes, Annu. Rev. Mater. Res. **33**, 419–501 (2003)
7.69 E. Bekyarova, V. Murata, M. Yudasaka, D. Kasuya, S. Iijima, H. Tanaka, K. Kaneko: Single-wall nanostructured carbon for methane storage, J. Phys. Chem. B **107**, 4681–4684 (2003)
7.70 H. Take, T. Matsumoto, K. Yoshino: Anodic properties of porous carbon with periodic nanostructure, Synth. Met. **135–136**, 731–732 (2003)
7.71 R.C. Bansal, J.B. Donnet, H.F. Stoeckli: *Active Carbon* (Marcel Dekker, New York 1988)
7.72 Z. Yang, Y. Xia, R. Mokaya: Zeolite ZSM-5 with unique supermicropores synthesized using mesoporous carbon as a template, Adv. Mater. **16**, 727–732 (2004)
7.73 J.W. Lee, S.J. Han, T.H. Hyeon: Synthesis of new nanoporous carbon materials using nanostructured silica materials as templates, J. Mater. Chem. **14**, 478–486 (2004)
7.74 A.B. Fuertes: A low-cost synthetic route to mesoporous carbons with narrow pore size distributions and tunable porosity through silica xerogel templates, Chem. Mater. **16**, 449–455 (2004)
7.75 J. Ozaki, N. Endo, W. Ohizumi, K. Igarashi, M. Nakahara, A. Oya: Novel preparation method for the production of mesoporous carbon fiber from a polymer blend, Carbon **35**, 1031–1033 (1997)
7.76 A. Oya, N. Kasahara: Preparation of thin carbon fibers from phenol–formaldehyde polymer microbeads dispersed in polyethylene matrix, Carbon **38**, 1141–1144 (2000)
7.77 D. Hulicova, F. Sato, K. Okabe, M. Koishi, A. Oya: An attempt to prepare carbon nanotubes by the spinning of microcapsules, Carbon **39**, 1438–1442 (2001)
7.78 Z.-M. Huang, Y.-Z. Zhang, M. Kotaki, S. Ramakrishn: A review on polymer nanofibers by electrospinning and their applications in nanocomposites, Compos. Sci. Technol. **63**, 2223–2253 (2003)
7.79 Y. Wang, S. Serrano, J.J. Santiago-Aviles: Conductivity measurement of electrospun PAN-based carbon nanofiber, J. Mater. Sci. Lett. **21**, 1055–1057 (2002)
7.80 Y. Wang, J.J. Santiago-Aviles, R. Furlan, I. Ramos: Pyrolysis temperature and time dependence of electrical conductivity evolution for electrostatically generated carbon nanofibers, IEEE Trans. Nanotechnol. **2**, 39–43 (2003)
7.81 Y. Wang, S. Serrano, J.J. Santiago-Aviles: Raman characterization of carbon nanofibers prepared using electrospinning, Synth. Met. **138**, 423–427 (2003)
7.82 S.Y. Gu, J. Ren, Q.L. Wu: Preparation and structures of electrospun PAN nanofibers as a precursor of carbon nanofibers, Synth. Met. **155**, 157–161 (2005)
7.83 S.Y. Gu, J. Ren, G.J. Vancso: Process optimization and empirical modeling for electrospun polyacrylonitrile (PAN) nanofiber precursor of carbon nanofibers, Eur. Polym. J. **41**, 2559–2568 (2005)
7.84 D. Lai, Y. Xia: Electrospinning of nanofibers: reinventing the wheel, Adv. Mater. **16**, 1151–1170 (2004)
7.85 D. Hulicova, K. Hosoi, S. Kuroda, H. Abe, A. Oya: Carbon nanotubes prepared by spinning and carbonizing fine core-shell polymer microspheres, Adv. Mater. **14**, 452–455 (2002)
7.86 E. Zussman, A.L. Yarin, A.V. Brazilevsky, R. Avrahami, M. Feldman: Electrospun PAN/PMMA-derived carbon nanotubes, Adv. Mater. **18**, 348–353 (2006)
7.87 J. Brandrup, E.H. Immergut, E.A. Grulke, D. Bloch: *Polymer Handbook* (Wiley, New York 2005)
7.88 M. Winter, J.O. Besenhard, M.E. Spahar, P. Novak: Electrode materials for rechargeable lithium batteries, Adv. Mater. **10**, 725–763 (1998)
7.89 T.D. Burchell: *Carbon Materials for Advanced Technologies* (Elsevier, Amsterdam 1999)
7.90 M. Endo, C. Kim, K. Nishimura, T. Fujino, K. Miyashita: Recent development of carbon materials for Li ion batteries, Carbon **38**, 183–197 (2000)
7.91 E. Frackowiak, F. Beguin: Electrochemical storage of energy in carbon nanotubes and nanostructured carbons, Carbon **40**, 1775–1787 (2002)
7.92 E. Yasuda, M. Inagaki, K. Kaneko, M. Endo, A. Oya, Y. Tanabe: *Carbon Alloy* (Elsevier, Amsterdam 2003)
7.93 V.A. Nalimova, D.E. Sklovsky, G.N. Bondarenko, H. Alvergnat-Gaucher, S. Bonnamy, F. Beguin: Lithium interaction with carbon nanotubes, Synth. Met. **88**, 89–93 (1997)
7.94 B. Gao, A. Kleinhammes, X.P. Tang, C. Bower, L. Fleming, Y. Wu, O. Zhou: Electrochemical intercalation of single-walled carbon nanotubes with lithium, Chem. Phys. Lett. **307**, 153–157 (1999)
7.95 F. Leroux, K. Metenier, S. Gautier, E. Frackowiak, S. Bonnamy, F. Beguin: Electrochemical insertion of lithium in catalytic multi-walled carbon nanotubes, J. Power Source **81–82**, 317–322 (1999)
7.96 A.S. Claye, J.E. Fischer, C.B. Huffman, A.G. Rinzler, R.E. Smalley: Solid-state electrochemistry of the Li single wall carbon nanotube system, J. Electrochem. Soc. **147**, 2845–2852 (2000)
7.97 R.S. Morris, B.G. Dixon, T. Gennett, R. Raffaelle, M.J. Heben: High-energy, rechargeable Li-ion battery based on carbon nanotube technology, J. Power Source **138**, 277–280 (2004)
7.98 G.L. Che, B.B. Lakshmi, E.R. Fisher, C.R. Martin: Carbon nanotubule membranes for electrochemical

energy storage and production, Nature **393**, 346–349 (1998)
7.99 M. Endo, Y.A. Kim, T. Hayashi, K. Nishimura, T. Matushita, K. Miyashita, M.S. Dresselhaus: Vapor-grown carbon fibers (VGCFs): Basic properties and their battery applications, Carbon **39**, 1287–1297 (2001)
7.100 C. Sotowa, G. Origi, M. Takeuchi, Y. Nishimura, K. Takeuchi, I.Y. Jang, Y.J. Kim, T. Hayashi, Y.A. Kim, M. Endo, M.S. Dresselhaus: The reinforcing effect of combined carbon nanotubes and acetylene blacks on the cathode electrode of lithium ion batteries, ChemSusChem **1**, 911–915 (2008)
7.101 F. Fong, K. Sacken, J.R. Dahn: Studies of lithium intercalation into carbons using nonaqueous electrochemical cells, J. Electrochem. Soc. **137**, 2009–2013 (1990)
7.102 S.H. Yoon, C.W. Park, H.J. Yang, Y. Korai, I. Mochida, R.T.K. Baker, N.M. Rodriguez: Novel carbon nanofibers of high graphitization as anodic materials for lithium ion secondary batteries, Carbon **42**, 21–32 (2004)
7.103 T. Doi, A. Fukuda, Y. Iriyama, T. Abe, Z. Ogumi, K. Nakagawa, T. Ando: Low-temperature synthesis of graphitized nanofibers for reversible lithium-ion insertion/extraction, Electrochem. Commun. **7**, 10–13 (2005)
7.104 J.K. Lee, K.W. An, J.B. Ju, B.W. Cho, W.I. Cho, D. Park, K.S. Yun: Electrochemical properties of PAN-based carbon fibers as anodes for rechargeable lithium ion batteries, Carbon **39**, 1299–1305 (2001)
7.105 B.E. Conway: *Electrochemical Supercapacitors-Scientific Fundamentals and Technological Applications* (Kluwer, New York 1999)
7.106 A.G. Pandolfo, A.F. Hollenkamp: Carbon properties and their role in supercapacitors, J. Power Source **157**, 11–27 (2006)
7.107 A. Yoshida, I. Tanahashi, A. Nishino: Effect of concentration of surface acidic functional groups on electric double-layer properties of activated carbon fibers, Carbon **28**, 611–615 (1990)
7.108 A. Nishino: Capacitors: operating principles, current market and technical trends, J. Power Source **60**, 137–147 (1990)
7.109 J.P. Zheng: Ruthenium oxide-carbon composite electrodes for electrochemical capacitors, Electrochem. Solid-State Lett. **2**, 359–361 (1999)
7.110 E. Frackowiak, F. Béguin: Carbon materials for the electrochemical storage of energy in capacitors, Carbon **39**, 937–950 (2001)
7.111 M. Endo, T. Maeda, T. Takeda, Y.J. Kim, K. Koshiba, H. Hara, M.S. Dresselhaus: Capacitance and pore-size distribution in aqueous and nonaqueous electrolytes using various activated carbon electrodes, J. Electrochem. Soc. **148**, A910–A914 (2001)
7.112 C. Niu, E.K. Sichel, R. Hoch, D. Moy, H. Tennent: High power electrochemical capacitors based on carbon nanotube electrodes, Appl. Phys. Lett. **70**, 1480–1482 (1997)
7.113 C.Y. Liu, A.J. Bard, F. Wudl, I. Weitz, J.R. Heath: Electrochemical characterization of films of single-walled carbon nanotubes and their possible application in supercapacitors, Electrochem. Solid State Lett. **2**, 577–578 (1999)
7.114 E. Frackowiak, K. Metenier, V. Bertagna, F. Béguin: Supercapacitor electrodes from multiwalled carbon nanotubes, Appl. Phys. Lett. **77**, 2421–2423 (2000)
7.115 K.H. An, W.S. Kim, Y.S. Park, Y.C. Choi, S.M. Lee, D.C. Chung, D.J. Bae, S.C. Lim, Y.H. Lee: Supercapacitors using single-walled carbon nanotube electrodes, Adv. Mater. **13**, 497–500 (2001)
7.116 E. Frackowiak, F. Béguin: Electrochemical storage of energy in carbon nanotubes and nanostructured carbons, Carbon **40**, 1775–1787 (2002)
7.117 Z. Yie, C.L. Mangun, J. Economy: Preparation of fibrous porous materials by chemical activation: 1. $ZnCl_2$ activation of polymer-coated fibers, Carbon **40**, 1181–1191 (2002)
7.118 N. Yalcin, V. Sevinc: Studies of the surface area and porosity of activated carbons prepared from rice husks, Carbon **38**, 1943–1945 (2000)
7.119 A. Huidobro, A.C. Pastor, F. Rodriguez-Reinoso: Preparation of activated carbon cloth from viscous rayon: Part IV. Chemical activation, Carbon **39**, 389–398 (2001)
7.120 J.M. Planeix, N. Coustel, B. Coq, V. Brotons, P.S. Kumbhar, R. Dutartre: Application of carbon nanotubes as supports in heterogeneous catalysis, J. Am. Chem. Soc. **116**, 7935–7936 (1994)
7.121 W. Li, C. Liang, J. Qiu, W. Zhou, H. Han, Z. Wei, G. Sun, Q. Xin: Carbon nanotubes as support for cathode catalyst of a direct methanol fuel cell, Carbon **40**, 791–794 (2002)
7.122 H.C. Choi, M. Shim, S. Bangsaruntip, H. Dai: Spontaneous reduction of metal ions on the sidewalls of carbon nanotubes, J. Am. Chem. Soc. **124**, 9058–9059 (2002)
7.123 L.R. Radovic, F. Rodriguez-Reinoso: Carbon materials in catalysis, Chem. Phys. Carbon **25**, 243–358 (1997)
7.124 M.C. Roman-Martinez, D. Cazoria-Amoros, A. Linares-Solano, C. Salinas-Martinez De Lecea, H. Yamashita, M. Anpo: Metal-support interaction in Pt/C catalysts. Influence of the support surface chemistry and the metal precursor, Carbon **33**, 3–13 (1995)
7.125 M. Endo, Y.A. Kim, M. Ezaka, K. Osada, T. Yanagisawa, T. Hayashi, M. Terrones, M.S. Dresselhaus: Selective and efficient impregnation of metal nanoparticles on cup-stacked-type nanofibers, Nano Lett. **3**, 723–726 (2003)
7.126 C. Kim, Y.A. Kim, J.H. Kim, M. Kataoka, M. Endo: Self-assembled palladium nanoparticles on carbon nanofibers, Nanotechnology **19**, 145602 (2008)
7.127 K.A. Faraj, T.H. van Kuppevelt, W.F. Daamen: Construction of collagen scaffolds that mimic the

three-dimensional architecture of specific tissues, Tissue Eng. **13**, 2387–2394 (2007)
7.128 M.T. Valarmathi, M.J. Yost, R.L. Goodwin, J.D. Potts: The influence of proepicardial cells on the osteogenic potential of marrow stromal cells in a three-dimensional tubular scaffold, Biomaterials **29**, 2203–2216 (2008)
7.129 J. Glowacki, S. Mizuno: Collagen scaffolds for tissue engineering, Biopolymers **89**, 338–344 (2008)
7.130 A. Atala, S.B. Bauer, S. Soker, J.J. Yoo, A.B. Retik: Tissue-engineered autologous bladders for patients needing cystoplasty, Lancet **367**, 1241–1246 (2006)
7.131 J.C. Chachques, J.C. Trainini, N. Lago, O.H. Masoli, J.L. Barisani, M. Cortes-Morichetti, O. Schussler, A. Carpentier: Myocardial assistance by grafting a new bioartificial upgraded myocardium (MAGNUM clinical trial): one year follow-up, Cell Transplant. **16**, 927–934 (2007)
7.132 F. DeLustro, J. Dasch, J. Keefe, L. Ellingsworth: Immune responses to allogeneic and xenogeneic implants of collagen and collagen derivatives, Clin. Orthop. Relat. Res. **260**, 263–279 (1990)
7.133 D. Butler: Last chance to stop and think on risks of xenotransplants, Nature **391**, 320–324 (1998)
7.134 F.H. Bach, J.A. Fishman, N. Daniels, J. Proimos, B. Anderson, C.B. Carpenter, L. Forrow, S.C. Robson, H.V. Fineberg: Uncertainty in xenotransplantation: individual benefit versus collective risk, Nat. Med. **4**, 141–144 (1998)
7.135 J.R. Parsons, A.B. Weiss, R.S. Schenk, H. Alexander, F. Pavlisko: Long-term follow-up of achilles tendon repair with an absorbable polymer carbon fiber composite, Foot Ankle. **9**, 179–184 (1989)
7.136 T. Visuri, O. Kiviluoto, M. Eskelin: Carbon fiber for repair of the rotator cuff. A 4-year follow-up of 14 cases, Acta Orthop. Scand. **62**, 356–359 (1991)

8. Nanodiamonds

Olga A. Shenderova, Suzanne A. Ciftan Hens

This chapter presents a brief survey of the different classes of nanodiamond particles and a comparison of their purity, structure, and physical properties. The primary focus of this chapter is on nanodiamond particles produced by detonation shock wave-assisted synthesis, thus harnessing the energy of explosives. Selected applications of nanodiamond particles are discussed, including for polishing, as a filler material for nanocomposites, in drug delivery, and for chemical vapor deposition of diamond films.

8.1 **Stability of Diamond at the Nanoscale** 264
8.2 **Types of Nanodiamonds and Methods of Nanodiamond Synthesis** 267
8.2.1 Nanodiamond Produced by Detonation Shock Wave-Assisted Synthesis 270
8.2.2 Survey of Laboratory-Scale Methods of Nanodiamond Synthesis 275
8.3 **Detonation Nanodiamond Processing and Modification** 278
8.3.1 Postsynthesis Processing 278
8.3.2 Nanodiamond Deagglomeration and Fractionation 279
8.3.3 ND Surface Functionalization 280
8.4 **Fluorescent Nanodiamonds** 284
8.5 **Applications of Nanodiamond Particles** 285
8.5.1 Nanodiamond in Polishing Applications 285
8.5.2 ND Applications in Composites 286
8.5.3 Biomedical Applications 288
8.5.4 Nanodiamonds for Seeding 290
8.6 **Future Directions of Production and Applications** 292
References 293

Nanostructured diamond particles were first synthesized at the beginning of the 1960s using the energy of explosives. Diamond powders in the form of micrometer-sized single particles with nanocrystalline structure were produced using shock wave compression of carbon materials (graphite, carbon black) mixed with catalyst by *DeCarli* and *Jamieson* [8.1]. The size of the primary grains in the polycrystalline particles was about 10–20 nm. The product has been commercially available since the 1970s and since then has been widely used in the polishing industry. An alternative approach for producing diamond powder with a characteristic size of primary particles of ≈ 4–5 nm, from the carbon contained in high-energy explosives themselves, was invented in the former USSR [8.2], but this material remained essentially unknown to the rest of the world until the end of the 1980s [8.3]. While these so-called detonation nanodiamonds (DND) have diameters of 4–5 nm, they tend to aggregate, and typical commercial suspensions of DND contain larger aggregates, up to several hundred nanometers in size (which can withstand ultrasonic treatment). While DND was produced in quantities by the tons in the former USSR, the material did not penetrate the world market. Nanodiamond particles have become an object of keen scientific interest all over the world only within the last 5–6 years. The reason for this is fourfold. First, colloidal suspensions of individual nanodiamond particles of only 4–5 nm in size (so-called single-digit nanodiamond) recently became available [8.4]. Second, the production of nanodiamond particles containing specific impurity defects that allow for photoluminescent particles seems poised to revolutionize biological imaging and quantum optics applications [8.5, 6]. Third, the chemical reactivity of

the nanodiamond (ND) surface that allows it to participate in a wide range of chemical reactions and its ability to easily modify surface chemical groups [8.7] permit NDs to be readily used in many applications. Fourth, ND is reported to have the lowest toxicity among all known carbon nanoparticles [8.8, 9].

The availability of single-digit ND particles produced by detonation of explosives in kilogram quantities has opened broad prospective applications of NDs in composites and nanolubricants, and as drug delivery vehicles. Indeed, the specific surface area of ND particles with 4 and 30 nm diameter is 428 and 57 m^2/g, respectively, making a noticeable sevenfold difference in the adsorbing and loading capacity of the nanoparticles. The availability of single-digit ND particles is also important for biomedical applications for delivery of biologically active molecules, for example, through the blood–brain barrier [8.10].

A central focus of many research groups remains the controlled production of nitrogen-vacancy (NV) centers in nanoscale diamond. Due to the strong optical transition, single defects can be detected using a fluorescence microscope. The spin state of the negatively charged NV centers can be polarized by optical pumping and can be manipulated using electron paramagnetic resonance (EPR), permitting the implementation of efficient single-photon emitters for quantum information processing [8.5] or magnetic sensors with nanoscale resolution [8.6]. Single color centers show outstandingly high photostability, even at room temperature [8.11]. Bright photoluminescent NDs were produced using high-pressure high-temperature (HPHT) diamond, containing 10–300 ppm of native substitutional nitrogen defects (N_s), ground to nanosized particles [8.11, 12], and irradiated with energetic particles (electrons, protons, etc.) to create vacancies.

The two major breakthroughs, i. e., production of nanodiamond particles 4–5 nm in size and nanodiamond particles containing impurity defects exhibiting stable luminescence and unique spin properties, are related to nanodiamond particles synthesized by different techniques: detonation of explosives and grinding of HPHT diamond, respectively. Thus, these two important characteristics are not available through a single synthesis route. Synthesis of NDs a few nanometers in size with specific color centers remains elusive.

For a newcomer to the field, there is a baffling array of types of nanodiamond particles available for research. Besides the detonation of explosives technique, diamond with characteristic sizes encompassing several nanometers has also been synthesized by other methods, particularly by chlorination of carbides [8.13], ion irradiation of graphite [8.14], electron irradiation of carbon onions [8.15], laser ablation of carbon precursors [8.16], and in the vapor phase in a substrate-free low-pressure microwave-plasma chemical vapor deposition (CVD) reactor [8.17]. Moreover, astronomical observations suggest that nanodiamonds are present in the protoplanetary disks of certain types of stars [8.18, 19]. The origins of these cosmic sources are still under investigation.

A central goal of this chapter is to present a brief survey of the different classes of nanodiamond particles and provide a comparison of their purity, structure, and physical properties. Another purpose of the chapter is to review applications where unique properties of ND particles provide significant benefits, such as biomedical applications, nanocomposites, and as seeding material for growth of diamond films.

8.1 Stability of Diamond at the Nanoscale

It is well known that graphite is the most stable form of carbon at ambient temperatures and pressures, and that diamond is metastable. The energy difference between the two phases is only 0.02 eV/atom. However, because of the high activation barrier for the phase transition ($\approx$ 0.4 eV/atom), very high temperatures and pressures and/or the use of a catalyst are required to realize the phase transformation. At the nanoscale, however, the carbon phase diagram must also include cluster size as a third parameter (in addition to pressure and temperature) because the Gibbs free energy depends on the surface energy, which leads to changes in the phase diagram [8.20, 21] (Fig. 8.1). The authors [8.20] report better agreement with calculations for experimental shock pressure–volume and temperature data using a *nanocarbon phase diagram* than those obtained with a bulk carbon equation of state. The results also suggest that carbon particles, of the order of 10^3–10^4 atoms, can exist in the liquid state at lower temperatures than bulk carbon (Fig. 8.1). *Danilenko* [8.21] applied the phase diagram for the nanocarbon phases to a detailed elaboration of the mechanism of DND formation, which is described in a later section. *Chevrot* et al. [8.22] performed

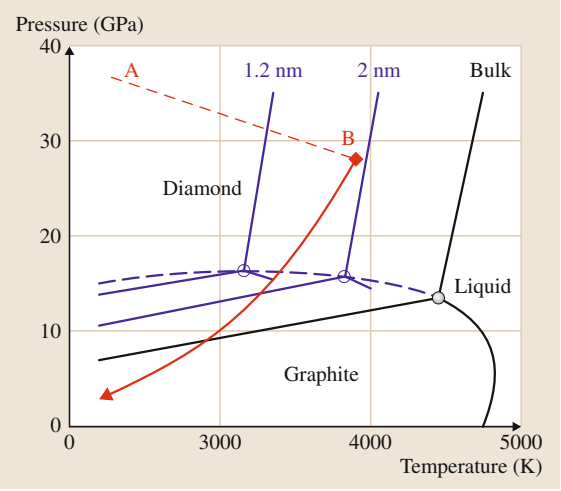


Fig. 8.1 Phase diagrams for bulk and nanoscale (*blue lines*) carbon. *Red lines* demonstrate a pressure–temperature trajectory in a detonation wave during synthesis of detonation nanodiamond (for the composition RDX/TNT 64%/36%). A corresponds to the shock compression of the explosives (chemical peak), AB corresponds to decomposition of explosive molecules, and B is the termination of decomposition (the Jouguet point) (after [8.21])

a molecular dynamics study of carbon nanoparticles of different sizes in sp^2 and sp^3 starting configurations under high-temperature (1000–7000 K) and high-pressure (2–45 GPa) conditions. For finite-size clusters, the transition line between the graphite and the diamond structure was shifted to higher pressures as the size of the cluster decreased, supporting the findings by Viecelli et al. and Danilenko.

The relative phase stability of carbon nanoparticles has been a focus of numerous theoretical and computational studies. First, *Badziag* et al. [8.23] using simple atomistic models predicted that, between 3 and 6 nm, diamond clusters become more stable than their graphitic counterparts. Later it was discovered that morphology plays a very important role in cluster stability in terms of surface reconstructions and appearance of sp^2 carbon fragments [8.24–27]. While the bare (nonfunctionalized) surfaces of cubic crystals exhibit structures similar to bulk diamond, the surfaces of octahedral, cuboctahedral, and spherical clusters show a transition from sp^3 to sp^2 bonding. The preferential exfoliation of the (111) surfaces begins for clusters in the subnanometer size range and promotes the cluster transition to endo-fullerenes for small clusters (≈tens of atoms) and onion-like shells with diamond cores (bucky-diamond) for larger clusters [8.25]. Large ND clusters (≈ 1–3.3 nm) of various shapes with less than 76% surface graphitization are likely to be stable in the diamond structure, possessing a thin (either single- or double-layer) graphitic shell [8.28]. Importantly, the simulations imply a strong correlation between structure, shape, and the sign of electrostatic potential, with bare carbon (100) surfaces exhibiting a positive electrostatic potential, and significant regions of (111) surface graphitization exhibiting a negative electrostatic potential. These theoretical findings imply that bare ND particles with reconstructed surfaces will be prone to aggregation due to electrostatic interactions between particles (assuming that the ND particles have no surface functional groups).

Barnard et al., analyzing carbon structures, identified two important size regimes, where sp^2 to sp^3 or sp^3 to sp^2 phase transitions may be readily expected [8.29]. As the system size for the carbon particles is increased, the most stable carbon form at the nanoscale changes from fullerene to onions to bucky-diamond to nanodiamond to graphite. For smaller particles the crossover between fullerenic particles and nanodiamond may be expected at 1.5–2 nm, and for larger particles, the crossover in stability between nanodiamond and nanographite may be expected at around 5–10 nm in diameter.

The surface of sp^3 clusters must be either stabilized via termination with some functional groups or reconstructed into sp^2 carbon. Therefore, in addition to size and shape, the stability of carbon nanoparticles also depends on their surface terminations. *Raty* and *Galli* [8.30] used first-principles calculations to examine the relative stability of nanodiamond as a function of hydrogen coverage for different particle sizes. Their results indicated that, when the size of diamond is about 3 nm and larger, bucky-diamonds (Fig. 8.2a) are energetically preferred over hydrogenated nanodiamonds. Hydrogen-terminated nanodiamonds with sizes < 1.5 nm (known as diamondoids) are stable molecules that occur naturally in oil [8.31].

First results of modeling of nanodiamonds terminated with oxygen [8.32] and nitrogen-containing functional groups [8.33] showed complex behavior where different groups favored different nanodiamond facets depending upon the temperature, the environment of the particle, as well as the size and morphology of the nanodiamonds.

Currently, different structural models of nanodiamond particles have been suggested for detonation ND (Fig. 8.2). In the earliest models, the diamond nanoclus-

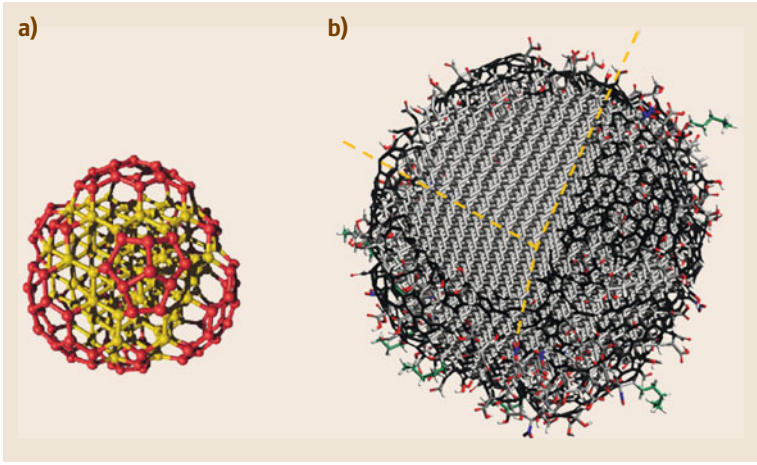


Fig. 8.2a,b Structural models of nanodiamond clusters. Bare surface of diamond clusters experiences surface reconstruction resulting in a cluster with a diamond core and a fullerene-like shell: bucky-diamond **(a)**. *Red-colored atoms* are sp^2 carbon atoms. Schematic model illustrating the structure of a single ≈ 5 nm nanodiamond after oxidative purification **(b)**. The diamond core is covered by a layer of surface functional groups which stabilize the particle by terminating the dangling bonds. The surface can also be stabilized by the conversion of sp^3 carbon to sp^2 carbon (shown in *black*). (**(a)** Courtesy of G. Galli, Lawrence Livermore National Laboratory. **(b)** Courtesy of V. Mochalin, Drexel University)

ter was considered to consist of a crystalline diamond core coated by an onion-like carbon or amorphous carbon shell (core–shell model) [8.34, 35]. The models were derived based on experimental data obtained from x-ray diffraction and small-angle x-ray scattering of DND of different levels of purification. Later models suggested the presence of an intermediate layer between the perfect nanodiamond core and the sp^2 shell, resulting in a three-layer model of DND particles [8.36–38]. However, these models did not take into account surface functional groups present on DND due to different oxidation treatments of detonation soot [8.38, 39]. In the latest core–shell model it is considered that carbon atoms with dangling bonds on the outer surface are bonded to functional groups [8.40]. Additional characteristic features of the DND not included in the model are nitrogen impurities (up to 2–3 wt %) which can form complexes in the core of DND particles [8.41, 42] and the presence of twins and grain boundaries in the crystallites (Fig. 8.3b). The latter can be responsible for the broadening of the x-ray diffraction peaks earlier attributed to disordered sp^3 carbon.

The DND models which originated from the experimental observations listed above assumed a spherical shape of DND particles, based on the earliest low-resolution transmission electron microscopy (TEM) observations of aggregates of DND [8.46]. Graphiti-

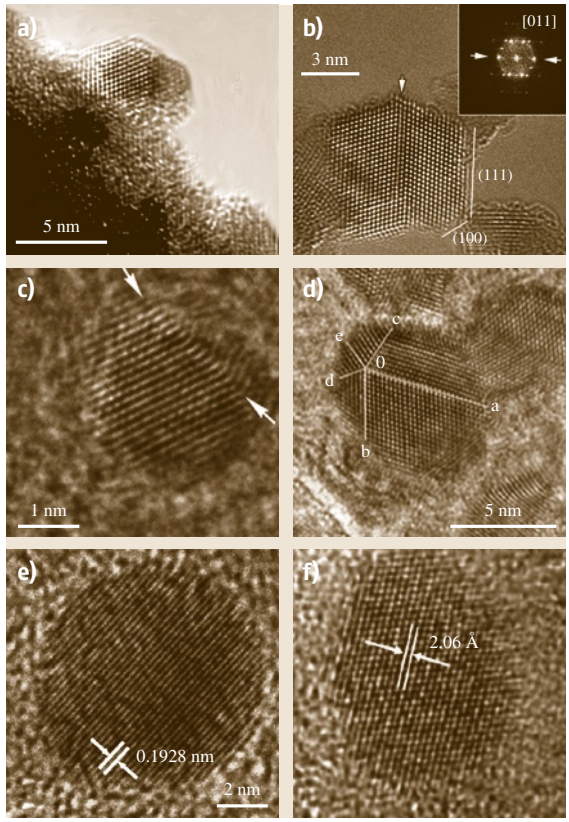


Fig. 8.3a–f HRTEM images of a polyhedral particle of detonation nanodiamond (DND) **(a)**. A faceted DND made up of a highly ordered diamond core (the inset with a fast Fourier transform of the micrograph confirms this) **(b)**. Nanodiamonds synthesized by pulsed laser irradiation. A single-crystal structure **(c)** and multiply twinning structure **(d)**. A spherical diamond in a carbide matrix synthesized by carbide chlorination process **(e)**. A spherical HPHT ND particle obtained by high-energy ball-milling **(f)** (after **(a)** [8.43]; **(c,d)** [8.41, 44]; **(e)** [8.45]; **(f)** [8.12]) ▶

zation of the DND surface that might be initiated by the high-energy electron beam during TEM observations [8.47] also contributes to the impression of the ND particles having spherical shapes. However, using a nondestructive high-vacuum aberration-corrected electron microscope, *Iakoubovskii* et al. demonstrated that DND grains could have crystalline structure with negligible fractions of nondiamond carbon [8.47]. These findings are consistent with earlier reports by *Tyler* et al. [8.43, 48] on clear diamond facets of individual polyhedral DND particles obtained by electrodeposition of ozone-purified DND on Mo tips [8.43] (Fig. 8.3a). Recently, Turner confirmed the absence of sp^2 carbon phase on small fractions of ozone-purified DND (Fig. 8.3b).

The survey of the existing DND models indicates that currently there is still no full agreement on the DND structure. Since the authors have studied differently synthesized and processed DND particles, it is quite possible that a single model cannot describe all kinds of NDs, and probably different models should be applied depending on the manufacturing and purification methods. Nevertheless, a model illustrating the most common and important features, suggested by Mochalin et al., is illustrated in Fig. 8.2b. This model includes an almost perfect crystalline structure of the diamond grain, the presence of surface functional groups and their variability, the presence of sp^2 carbon (sometime negligible fraction), and spherical or polyhedral shape of the particle.

Nanodiamond particles produced by other methods also have specific features; For example, *Hu* et al. [8.44] reported that, for nanodiamonds synthesized by pulsed laser irradiation, a preferred structure for smaller particles is a single-crystal structure (Fig. 8.3c), while for larger particles a multiply twinning structure was observed (Fig. 8.3d). The authors conclude, based on thermodynamic calculation, that the multiply twinning structure is more stable than the single-crystal structure in a certain size range. *Welz* et al. reported spherical shapes of nanodiamond particles in a carbide matrix synthesized by the carbide chlorination process [8.45] (Fig. 8.3e). Figure 8.3f demonstrates a spherical, free of sp^2 carbon particle of HPHT ND ground by high-energy ball-milling to the sub-10 nm size range [8.12]. Thus, ND shape and composition to a large extent depend on the method of synthesis and postsynthesis processing.

8.2 Types of Nanodiamonds and Methods of Nanodiamond Synthesis

Diamond structures at the nanoscale (the length scale of approximately 1–100 nm) include pure-phase diamond films, diamond particles, recently fabricated one-dimensional (1-D) diamond nanorods, and two-dimensional (2-D) diamond nanoplatelets. Nanoscale diamond structures of different dimensions have been reviewed in several publications [8.48, 49]. A focus of the current chapter is zero-dimensional nanodiamond, e.g., nanoparticles.

ND particles can be conveniently categorized into three groups according to the size of their primary particles (Fig. 8.4): nanocrystalline particles, ultrananocrystalline particles, and diamondoids. Characteristic sizes of nanocrystalline particles encompass the size range of tens of nanometers, while sizes of primary particles of ultrananocrystalline diamond are within several nanometers [8.49]. Diamondoids are well-defined hydrogen-terminated molecular forms consisting of several tens of carbon atoms with characteristic sizes $\approx$ 1–2 nm [8.31]. While a choice of 10 nm as the margin between two classes of nanodiamonds seems arbitrary, it reflects a difference in properties of the resulting products using diamond nanoparticles of different sizes. As pointed out in the Introduction, the specific surface areas of ND particles with 4 and 30 nm diameter make a noticeable sevenfold difference in the adsorbing and loading capacity of the nanoparticles. The term "single-digit ND" coined by *Osawa* [8.4] seems to be gaining broader acceptance in the community for sub-10 nm ND particles, rather than *ultrananocrystalline* ND particles.

The class of nanocrystalline diamond particles includes subgroups of monocrystalline and polycrystalline particles (Fig. 8.4). Monocrystalline nanoparticles include ND particles processed from HPHT synthetic diamond as well as from natural diamond powders, commercially available with smallest average particle size around 20 nm (produced, for example, by Microdiamant AG). Polycrystalline nanodiamond powder is processed from micrometer-sized polycrystalline diamond particles obtained by shock compression of graphite mixed with metals [8.1] (DuPont de Nemours's

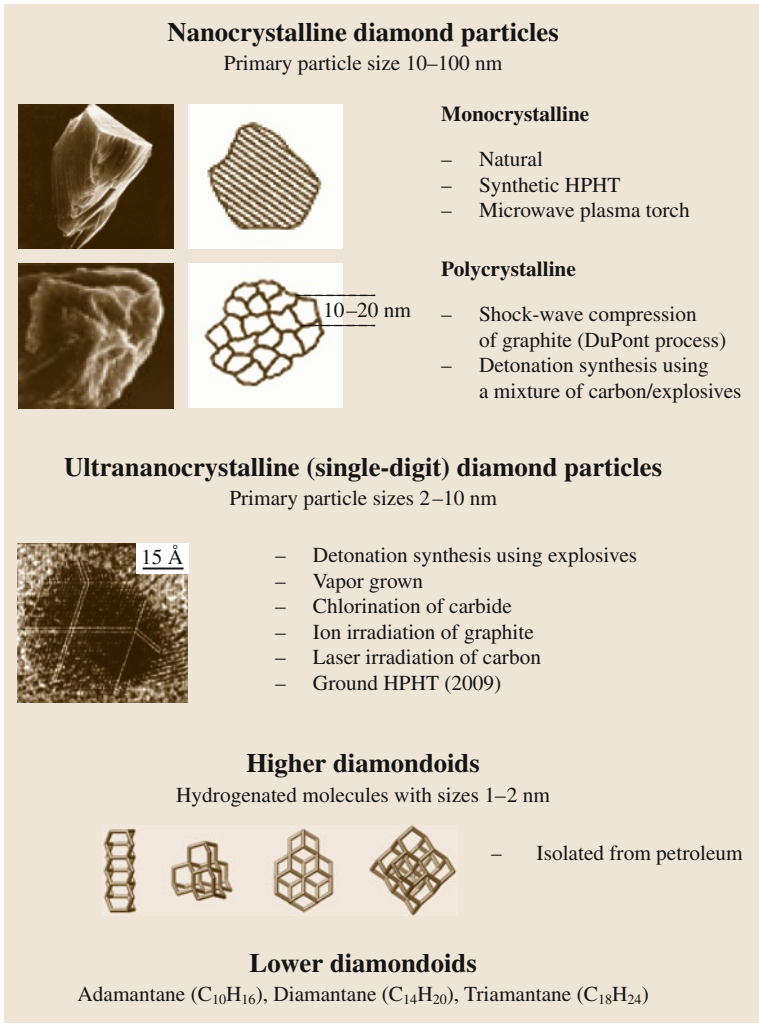


Fig. 8.4 Summary of the types of nanoscale diamond particles and molecular forms (low diamondoids) according to the primary particle size. (Pictures of nanocrystalline diamond courtesy of Microdiamant AG, Switzerland. Pictures of UNCD single particles courtesy of T.L. Daulton, Naval Research Laboratory.) Examples of higher diamondoids from petroleum, 1–2 nm hydrogen-terminated diamond molecules (*left to right*): rod-shaped [1212]pentamantane $C_{26}H_{32}$, pyramid-shaped [1(2,3)4]pentamantane $C_{26}H_{32}$, irregular disc-shaped [121321]heptamantane $C_{30}H_{34}$, octahedral [1231241(2)3]decamantane $C_{35}H_{36}$ (courtesy of ChevronTexaco MolecularDiamond Technologies)

method) or by detonation of a mixture of graphite and explosives (Tacii). Polycrystalline particles consist of nanometer-sized diamond grains (≈ 10–20 nm). The finest diamond fraction produced by micronizing followed by grading has an average size of an individual particle of ≈ 25 nm (Microdiamant AG).

Out of several types of ultrananocrystalline diamond particles (Fig. 8.4), only detonation ND, obtained by the detonation of solid explosives in an inert atmosphere, has been commercialized on a large scale. The average size of primary detonation ND particles produced by most vendors lies in the range of 3.5–6 nm. Recently, single-digit nanodiamond produced by laser ablation of carbon precursors has became commercially available (Ray Technologies). Details on the methods of synthesis of other single-digit nanodiamond particles are provided in the next section.

Higher diamondoids (Fig. 8.4) are highly rigid, well-defined hydrogen-terminated diamond species [8.31, 50]. With more than three crystal diamond cages, higher diamondoids are intermediate in size to the adamantane molecule, the smallest species of H-terminated cubic diamond containing only 10 carbon atoms, and ultrananocrystalline diamond particles with sizes more than 3 nm as described above. Higher diamondoids are extracted from petroleum as diamond molecules in the form of nanometer-sized rods, helices, discs, pyramids, etc. [8.31,51]. So far it has not been possible to synthesize higher diamondoids except anti-tetramantane, a tetramantane isomer [8.50]. By comparison, lower diamon-

doids (adamantane, diadamantane and triadamantane), extracted from crude oil much earlier than larger members of the diamondoid series, are currently available in kilogram quantities [8.50] and can be synthesized.

Figure 8.5 summarizes commercially available ND particles based on their method of synthesis. Major classes of commercial ND are those made by *static* and *dynamic* synthesis. While ND made by static synthesis is 1–2 orders of magnitude more expensive than ND made by dynamic synthesis, this material is a primary material for production of photoluminescent ND particles. ND made by static synthesis can be HPHT ND type Ib, with substitutional nitrogen (N_s) concentration 1–300 ppm. ND produced from natural diamond type Ia (N_s concentration up to 3000 ppm) is also available. Irradiation by high-energy particles of type Ib ND causes formation of NV centers with red emission, while ND from diamond Ia demonstrates green luminescence originating from the formation of N–V–N centers after irradiation and annealing. A large subgroup of nanodiamond is produced via *dynamic synthesis*, harnessing the energy of explosives and different carbon-containing precursor materials. Three classes of dynamically synthesized NDs are manufactured on an industrial scale (Fig. 8.6):

1. NDs produced by direct phase transformation of graphite induced by an external shock wave (the DuPont method) [8.1].
2. NDs produced from a mixture of a carbon precursor and explosives [8.52].
3. NDs produced from the carbon contained in high-energy explosives (so-called detonation ND (DND), or ultradispersed diamond [8.53, 54]. Such explosive compounds simultaneously serve as sources of energy and carbon.

Depending on the precursor material used in dynamic synthesis, NDs with primary crystal sizes between 4 and 25 nm can be synthesized. Slurries of 4 nm individual DND particles or slurries of polycrystalline NDs synthesized from graphite and graphite/hexogen precursors with average aggregate size of 20–30 nm are commercially available.

While the first publications on laser irradiation of graphite precursors in liquids appeared a decade ago [8.16], ND produced using a laser became commercially available (in small quantities) only recently (Ray Technologies Inc.). Primary particle size, as reported by the vendor, ranges between 2 and 10 nm. Aggregate size in water suspensions is about 100 nm. At the moment, this type of ND is two orders of magnitude more expensive than detonation ND.

Sections below provide more details on manufacturing of ND by dynamic synthesis, followed by a brief survey of methods of synthesis of ND particles produced on laboratory scale.

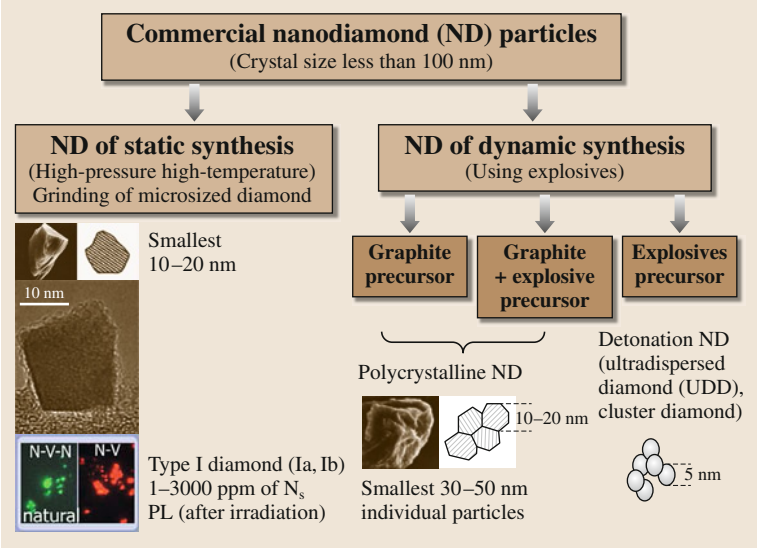


Fig. 8.5 Summary of types of commercial nanodiamonds (PL – photoluminescent)

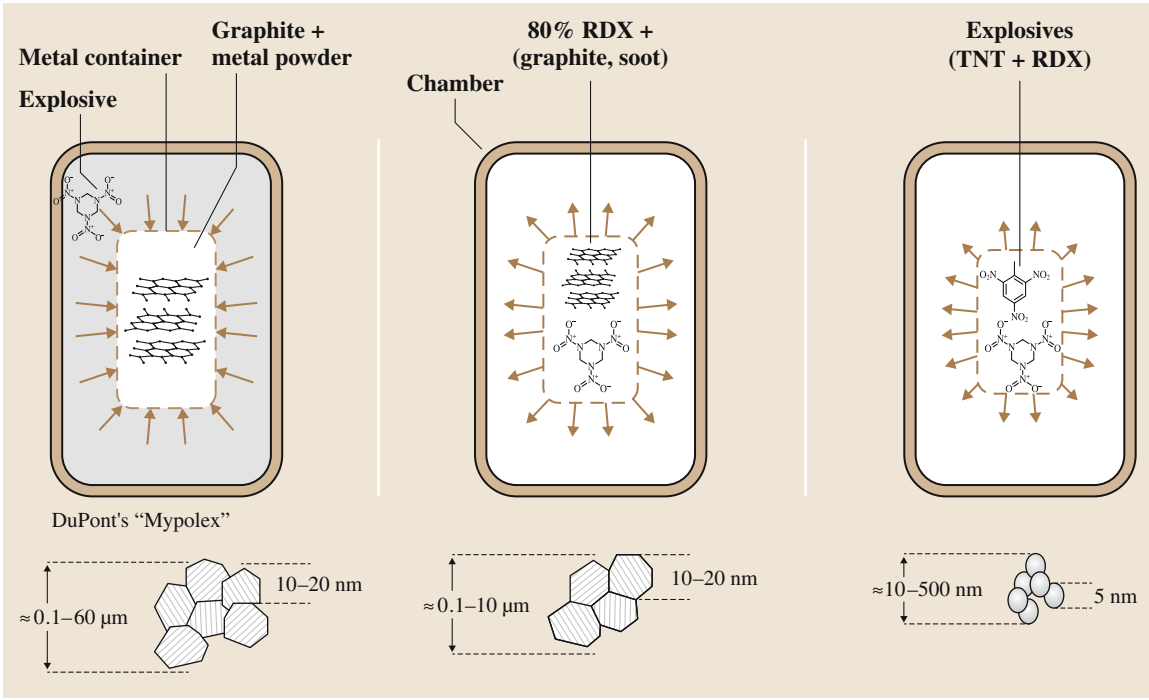


Fig. 8.6 Classes of nanodiamonds produced by detonation shock wave-assisted synthesis on an industrial scale

8.2.1 Nanodiamond Produced by Detonation Shock Wave-Assisted Synthesis

Below, we briefly survey methods of synthesis and characteristics (crystal size, morphology) of the three classes of dynamically synthesized NDs manufactured on industrial scale (Fig. 8.6).

Nanodiamond Produced by Shock Conversion of Graphite

Synthesis of polycrystalline diamond particles produced by direct phase transformation of graphite induced by an *external* plain shock wave was first reported by *DeCarli* and *Jamieson* [8.1] and patented by *DeCarli* [8.55]. A patent by Cowan et al. (1968, assigned to DuPont de Nemours Co.) provided a means for significant increase of diamond yield during shock wave transformation of graphite by mixing graphite with cooling media. In 1976, this technology was commercialized by DuPont, producing microcrystalline diamond powder under the tradename Mypolex [8.56]. In parallel, studies of the formation of diamond in shock-loaded graphite were taking place in the former USSR at the VNIITF Institute (Snezhinsk) [8.56]. Diamond production by the shock synthesis technique in spherical and cylindrical enclosures was first demonstrated in 1962 (2% diamond yield), followed by experiments with mixtures of graphite or soot with metals, resulting in 20% yield of diamond product (1963) [8.2, 56].

More specifically, under suitable conditions, explosively produced shock waves can create high-pressure (≈ 20–200 GPa), high-temperature (> 2000 K) conditions in confined volumes (Fig. 8.6) for a sufficient duration to achieve partial conversion of graphite into nanometer-sized diamond grains (≈ 20 nm); these grains compact into micrometer-sized, polycrystalline particles. Copper is mixed with graphite in this process to provide fast heat dissipation at the high temperatures reached during the explosion, which will avoid transformation of the diamond back to graphite [8.57]. Diamond powder with characteristic sizes of particles in the submicrometer range can be processed from micrometer-sized polycrystalline diamond particles obtained by shock synthesis. Polycrystalline diamond particles are tougher than monocrystalline diamond microparticles (natural or produced by HPHT) and are widely used in fine polishing applications. It is important to note that agglomerate-free suspensions of

nanocrystalline diamond particles (for both monocrystalline and polycrystalline forms) in water and oil are commercially available (Microdiamant AG, Lengwil, Switzerland).

Nanodiamond Produced from Carbon Precursor/Explosive Mixture

NDs produced by another dynamic method, detonation of a mixture of a carbon precursor (graphite or carbon black) and explosives, is much less well known in the community. This approach was invented at the Institute of Problems of Chemical Physics, Russian Academy of Sciences, Chernogolovka [8.58] and registered under the trademark DALAN (the Russian acronym for detonation diamonds of the Academy of Sciences). *Tatsii* [8.52] summarized the data on the production of DALAN ND from three types of precursors: mixture of hexagen (RDX) and carbon black (charge density 1.34–1.39 g/cm^3), RDX and graphite (charge density 1.61–1.67 g/cm^3), and gunpowder/carbon/RDX (charge density 1.67–1.75 g/cm^3). The concentration of carbon precursor materials can be varied between 5 and 35%. The detonation pressure measured by dynamic methods (in the Chapman–Jouguet plane) was about 27.5–14.5 GPa. It was concluded that the diamond powders synthesized from graphite consist of 1–3 μm particles of lamellar shape with different phase compositions (diamond, lonsdaleite, and graphite) and grain sizes. The particles of diamond powder synthesized from carbon black are aggregates consisting of 20–80 nm grains of cubic-phase diamond exhibiting either round or polyhedral shape. The particles of diamond extracted from the solid detonation products of the gunpowder/carbon black/RDX mixture are single-phase particles having homogeneous grain structure with grain size of mainly 1–3 nm. These smaller grains form spherule-shaped aggregates. These findings demonstrate the key role of the carbon precursor material in the phase composition and the primary particle size of the resulting products. Currently, polycrystalline diamond produced from graphite/RDX mixture is a valuable commercial product for polishing applications. While micrometer-sized particles (1–10 μm) with narrow size distribution are in greatest demand, the fractions of polycrystalline diamond with sub-100 nm particle sizes are also utilized.

Nanodiamond Produced from High-Energy Explosives

A method of production of ND from the carbon contained in high-energy explosives (detonation ND) was developed in the former USSR in the 1960s [8.2]. The conversion of the carbon-containing explosive compounds into diamond occurs by firing the explosives in a detonation chamber [8.53]. The resultant product is a mixture of diamond particles with primary particle size of 4–5 nm, other carbon allotropes, and metallic impurities. A wide variety of explosive materials may be used. A typical explosive mixture is 2-methyl-1,3,5-trinitrobenzene (TNT) and hexogen (in the proportion 40 : 60) composed of C, N, O, and H with a negative oxygen balance, so that free nonoxidized carbon is present in the system. The explosion takes place in an inert medium of either gas (N_2, CO_2, Ar, or another medium that can be under pressure) or water (ice), called *dry* or *wet* synthesis, respectively. The medium acts as a coolant.

The product of detonation synthesis, called detonation soot or diamond blend, contains 40–80 wt % diamond phase depending on the detonation conditions [8.54]. The carbon yield is 4–10% of the weight of the explosive charge, depending on the cooling media.

Danilenko proposed the mechanism of nanodiamond formation during detonation [8.21, 56, 59]. The initial shock wave created by a detonator compresses the high-explosive material, heating it and causing chemical decomposition, thereby releasing enormous amounts of energy in a fraction of a microsecond. The detonation wave includes (Fig. 8.7) a shock wave, a zone of detonation-induced decomposition of ex-

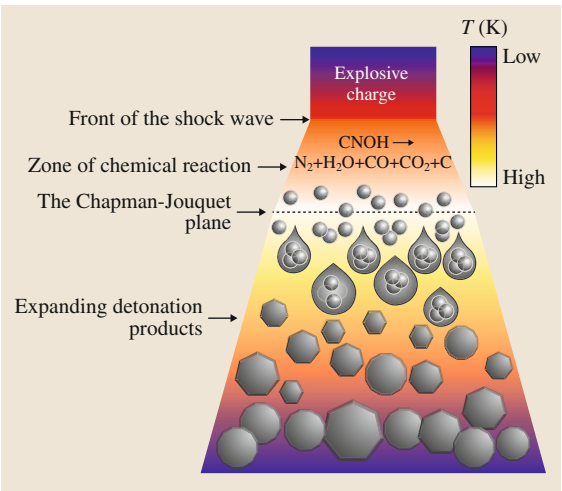


Fig. 8.7 Schematic of the detonation wave propagation and formation of detonation nanodiamonds from nanocarbon droplets (as described in [8.21]) (courtesy of V. Mochalin, Drexel University)

plosive molecules (a zone of chemical reaction), and a zone of expanding detonation products. The zones of chemical reaction and expanding detonation products are shown for the so-called composition B explosive in the corresponding phase diagram (Fig. 8.1, red lines) [8.21]. Decomposition of explosive molecules with the formation of free carbon (for an explosive with negative oxygen balance) proceeds according to

$$\mathrm{CNOH} \rightarrow \mathrm{N_2} + \mathrm{H_2O} + \mathrm{CO} + \mathrm{CO_2} + \mathrm{C}$$

In Fig. 8.1, point B corresponds to the termination of the decomposition (the Jouguet point). It can be seen in Fig. 8.1 that the $P-T$ values at the Jouguet point do not reach the region of liquid carbon in the bulk carbon phase diagram, while conditions for the existence of liquid carbon can be achieved in the phase diagram for nanoscale carbon. Importantly, the Jouguet point of several powerful explosives is located in the region of liquid carbon in the nanocarbon phase diagrams, as confirmed by calculations of two different groups [8.20, 21, 60]. Pressures and temperatures at the Jouguet point (point A in Fig. 8.1) are not high enough to produce liquid bulk carbon, but they are high enough to produce liquid carbon at the nanoscale (Fig. 8.1). The region of liquid carbon is shifted to lower temperatures for nanocarbon, and the region of nanodiamond stability is slightly shifted to higher pressures (Fig. 8.1). Thus, it is suggested that nanodiamond is formed by homogeneous nucleation in the volume of supersaturated carbon vapor via condensation and crystallization of liquid carbon (Fig. 8.7). First, after decomposition of the explosive molecules (during ≈ 1 ns), primary carbon embryos (< 2 nm in size) are formed in the zone of chemical reaction (during ≈ 10 ns), followed by their coagulation into carbon droplets > 2 nm in size along the isentrope of expanding detonation products above 16.5 GPa (this stage lasts $\approx 10^2 - 10^3$ ns). Finally, nanodiamond particles are formed by crystallization of the liquid carbon droplets along the isentrope of expanding detonation products in the region 9–16.5 GPa (duration of this stage $> 10^3$ ns).

A mechanism for DND formation through crystallization of liquid carbon droplets formed from free carbon was also described in the work by *Viecelli* and *Ree* [8.60], who demonstrated that the Chapman–Jouguet states of all of the explosives fall in the liquid-phase region for carbon clusters with fewer than approximately 1000 atoms.

Further details on synthesis of DND can be found in books [8.49, 54, 59, 61] and reviews [8.7, 48, 62–64]. Recently, DND synthesis was revisited by several groups with the purpose of addressing new demands on this material. Major focuses for novel approaches for DND synthesis are as follows:

1. Further reduction of the primary particle size
2. Control of the level of aggregation of DND at the synthesis stage
3. Increased sp^3 carbon content in detonation soot (in terms of reduction of noncarbon elements and sp^2 carbon on DND particle surfaces)
4. Doping of DND during synthesis, including control of the amount of substitutional nitrogen in the diamond core.

Reducing DND primary particle size down to the range of 1–3 nm may further increase their capability for penetrating cells and organelle membranes, including nuclear pores. ND particles with sizes ≈ 2 nm and smaller show quantum confinement effects [8.65]. Thus, synthesis of small particles would open perspectives for the development of diamond quantum dots. An increase of the ND specific surface area to a level comparable to that for carbon nanotubes would bring ND to the stage of perspective materials for hydrogen storage, catalyst support, fuel cells, and other applications.

In principle, the x-ray diffraction (XRD) data on the size distribution of primary DND particles within detonation soot, as reported in a limited number of publications [8.53, 66], include 2 nm peaks. It was reported by the *Dolmatov* group [8.66] that his novel method of using reducing agents (for example, urea, ammonia) in water cooling media allows preservation of the DND fraction with primary particle size less than 3 nm along with a *typical* fraction of 5 nm primary particles. In general, production of several classes of DND with average primary particle sizes from the 2 to 10 nm size range (for example, classes with 2–3, 4–5, and 10 nm average sizes) would be beneficial for various applications.

Also, a method reported in [8.66] using reducing agents provides the benefits of increased DND yield from soot (by 2–5 wt %) and overall yield of soot itself (by 100%) [8.66] as well as an increased carbon content (up to 96 mass %) within the DND particle composition, where the total content of C, H, N, and O corresponds to 100 mass %. A possible mechanism of action of the reducing agents in the cooling media is suggested to be as follows [8.66]: In the presence of reducing agents, the oxidants (the detonation products CO_2, H_2O, O_2, NO_2, N_2O_3) interact primarily with the reducing agents, instead of oxidizing the carbon and particularly DND. This increases the yield of detonation soot and DND and quantitatively changes their

elemental composition, including carbon. Besides, the presence of readily oxidizable reducing agents among the detonation products helps to reduce graphitization of DND. Besides, the smallest amount of incombustible impurities (0.1–0.3 wt %) was found in DND synthesized in the presence of urotropine. This is due to the fact that urotropine is a strong complexing agent and captures impurities (metals Fe, Ni, Cr, Cu, Ti, etc.) to form soluble complexes which are easy to remove by subsequent chemical purification, i. e., treatment with nitric acid.

Another question is related to the possibility of optimizing the detonation process to produce mostly isolated primary particles and only small-size aggregates in the detonation soot. This would significantly reduce the cost of the final DND product. In fact, it has been recognized that dry DND synthesis results in smaller primary DND particle sizes and smaller average aggregate sizes as compared with wet synthesis. Another factor that influences the aggregation of DND during synthesis is the mass of the charge and the ratio between the masses of the charge and wet cooling media used [8.59].

Tailoring of DND electronic and optical properties for specific applications can be done at the stage of synthesis by development of different combinations of explosive materials with possible solid dopants, as well as using nontraditional cooling media (both gaseous and liquid) with possible additives to alter the DND composition (both bulk defects/doping content and surface groups). The possibility to control the N content by proper choice of the precursor material is discussed in the next section.

Structure of Different Types of Dynamically Synthesized Nanodiamonds

Recently, *Shenderova* et al. [8.67] carried out a thorough comparative analysis of the structure and composition of ND made by dynamic synthesis using the three major methods described above. Polycrystalline diamond from Microdiamant (produced by shock wave conversion of graphite) and from Real-Dzerzinsk (obtained from a graphite/RDX mixture), as well as detonation ND synthesized from different explosives were studied. Aggregates with sizes below 100 nm were chosen for the investigation. The phase composition and size distribution of the nanodiamond crystallites in the ND powders were analyzed by x-ray diffraction (XRD) and small-angle x-ray scattering (SAXS). For all samples, the diamond phase in the XRD patterns dominated. However, the presence of various amounts of graphitic carbon was also observed (peak at $\approx 26.9°$), being most pronounced in ND from Microdiamant. The diamond 111 diffraction peak was nonsymmetric due to overlap of the diamond 111 and graphite 101 peaks. The dimensions of the diamond crystallites were estimated from the Debye–Scherrer formula and were approximately 13.6 nm for the 111 reflection and 9.6 nm for the 110 peak for ND produced from graphite/RDX, 8 nm for ND obtained from graphite, and 4 nm for DND produced from explosives. A very rough estimation of the possible lonsdaleite grain size in Microdiamant's ND gives ≈ 2.4 nm.

For all samples the crystal size of the dominant fraction determined by SAXS was larger than the size determined from the broadening of the Bragg peaks. This difference originates in the different principles used for size determination in the two techniques. The width of the Bragg peaks in a XRD pattern reflects the size of so-called *coherently scattering domains*, which is usually smaller than (rarely equal to) the entire particle size. SAXS is based on the electron density contrast between the scatterer and the surrounding medium, thus providing information about the overall size of a nanodiamond particle. The discrepancy in the crystal size determined by the two techniques reflects the fact that diamond particles consist of several crystallites within a single grain.

The SAXS data for the ND from graphite sample showed a bimodal size distribution of the particles with peaks (diameters) at ≈ 6 nm (possibly graphite or lonsdaleite) and at ≈ 23 nm. The size distribution for the ND from graphite/RDX mixture possessed a relatively broad size distribution centered at ≈ 34 nm. Finally, the size distribution of the nanodiamonds produced from explosives (TNT/RDX and TNT/HNS) was typical for detonation nanodiamonds: the main peak showed diameters around 6 nm and a broad tail stretching out to larger sizes.

Figure 8.8 shows high-resolution TEM (HRTEM) images of the different ND samples. ND produced from graphite contained only abundant large, rounded or elongated diamond particles without a clear morphology (Fig. 8.8a). These structures often consist of agglomerates of smaller particles and show the presence of large amounts of defects in the diamond lattice. These particles can also be found in ND produced from a graphite/RDX mixture, but in combination with rounded or well-faceted polyhedral and truncated octahedral particles with low-index facets (Fig. 8.8b,c). The smaller DND particles below 6 nm in diameter show mainly (111) and (100) facets typical for small

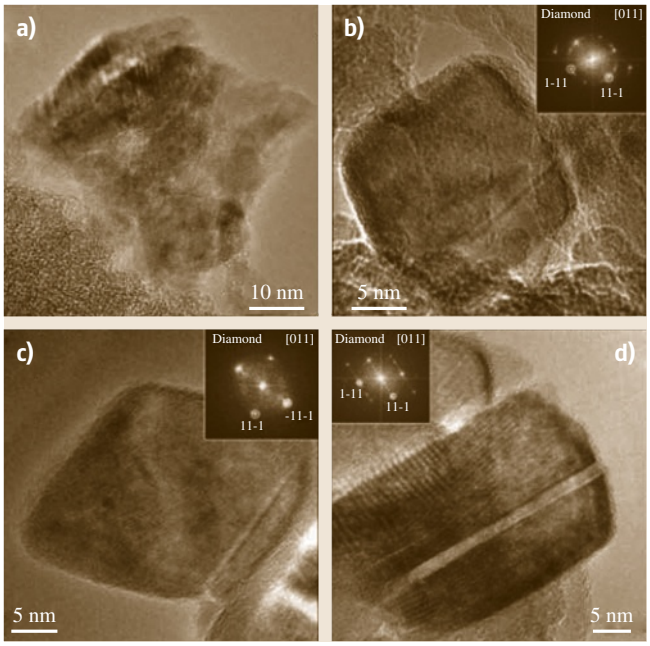


Fig. 8.8a–d HRTEM images of ND synthesized by shock compression of graphite **(a)** and by detonation of graphite/RDX mixture **(b–d)** (after [8.67])

DND particles (Fig. 8.9a); larger particles also show higher-index facets (Fig. 8.9b). These particles show the presence of coherent $\Sigma = 3$ (111) twinning, common for detonation ND. Large, multiply twinned particles with diameters up to 100 nm can be found occasionally in DND samples (Fig. 8.9c).

Raman spectra of the samples were acquired in the range of 1200–1700 cm^{-1} (Fig. 8.10). Typically the first-order Raman spectrum of highly purified DND consists of two peaks. The first one is located in the vicinity of 1332.5 cm^{-1} and corresponds to the vibrational mode of a diamond lattice from the center of its Brillouin zone. The origin of the second one observed at 1630 cm^{-1} is still a subject of debate. When an abundance of sp^2-bonded carbon clusters is present in the ND, another two peaks characteristic for sp^2 carbon appear between 1350 and 1380 cm^{-1} (the D-band) and 1580–1610 cm^{-1} (the G-band). The G-band and D-band, obscuring the diamond peak in the ND produced from graphite, indicate a high content of sp^2-bonded carbon in this sample. Large primary particles of the ND produced from graphite/RDX are not influenced by the phonon confinement effect, and the diamond line position is actually not shifted from the 1332.5 cm^{-1} position characteristic for the bulk material. All samples of detonation-type synthesis demonstrate a shift in the diamond Raman line down to 1328.5 cm^{-1}, which is explained by the phonon confinement effect observed for small nanocrystals [8.68].

Besides the morphological characteristics, of particular interest is the investigation of the effect of the type of synthesis on N content, N location in the ND core, and its ability to form optically active centers through the creation of complexes with vacancies. A scheme of the carbon-containing precursors for the three major methods of dynamic synthesis of nanodiamonds and factors influencing the nitrogen content in the produced nanodiamond material is presented in Fig. 8.11. In ND synthesis using explosives, N is an integral part of the high-energy explosive compounds. It can also be present as an impurity or an intentional dopant in graphite (or other carbon-containing materials) in the methods of dynamic synthesis involving bulk carbon precursors for ND production. The nitrogen content in

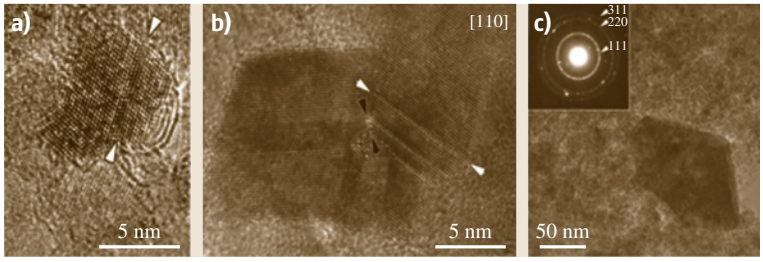


Fig. 8.9a–c HRTEM images of ND synthesized by detonation of TNT/RDX explosives. **(a)** The main fraction of DND particles has particle size close to 6 nm. Twinning is frequently observed in these small particles, with all visible twinning occurring along a (111) twin plane (examples of twin planes are indicated by *white arrows* in **(a)** and **(b)**). **(b)** Larger, multiple-twinned ND particle. An incoherent region is indicated by *black arrows*. **(c)** A rarely observed 100 nm octahedral particle. The *inset* electron diffraction ring pattern is typical for all DND samples and clearly evidences the cubic diamond crystal structure of all of the nanoparticles (after **(a)**[8.41], **(b,c)** [8.42])

the ND samples measured using combustion analysis indicated that the N concentration in the ND produced from a mixture of TNT/RDX explosives was higher than 2–2.5 wt %, that made from TNT/HNS was lower than 1%, and in ND made from graphite and graphite/RDX mixture it was lower than 0.5%. Thus, variations in the type of explosives can provide variation in the N content in the final ND product. It is possible that the N–N units of RDX (Fig. 8.11) contribute to enhanced N aggregation in the ND core, if they are not completely destroyed during detonation and are incorporated into the ND core as neighboring nitrogen atoms. Substituting RDX with HNS significantly reduces the N content. These issues require further study. Thus, variations in the type of explosives can be used together with the addition of other carbon precursor materials (for example, combination of graphite and HNS) to achieve the desired N content.

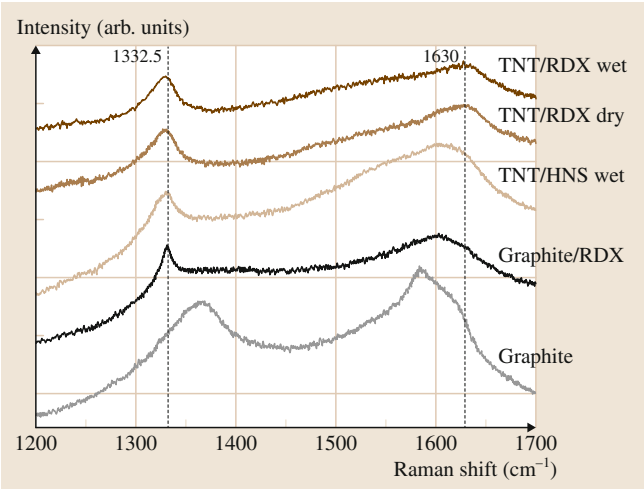


Fig. 8.10 Raman spectra of dynamically synthesized ND samples (courtesy of I. Vlasov, General Institute of Physics, Moscow)

8.2.2 Survey of Laboratory-Scale Methods of Nanodiamond Synthesis

There are numerous reports on experimental observations of nanosized diamond, summarized in [8.48, 49]. In this section we provide a brief overview of nanodiamond particles synthesized on laboratory scale.

Milling of HPHT Microdiamond

The shape of diamond nanoparticles obtained by ball-milling of micrometer-sized HPHT or natural diamond particles typically have sharp edges and on HRTEM look like shattered glass particles [8.12]. Remarkably, ND particles with rounded shapes and particle sizes below 10 nm were recently obtained by a group of researches starting with HPHT diamond [8.12]. The reported method is an important breakthrough in the production of single-digit ND containing NV centers, as it was demonstrated by the authors through processing of type Ib diamond. The initial raw material was a highly crystalline synthetic micrometer diamond powder (from Element Six) containing 80–100 mesh (150–190 μm) blocky, very uniformly shaped cubocta-

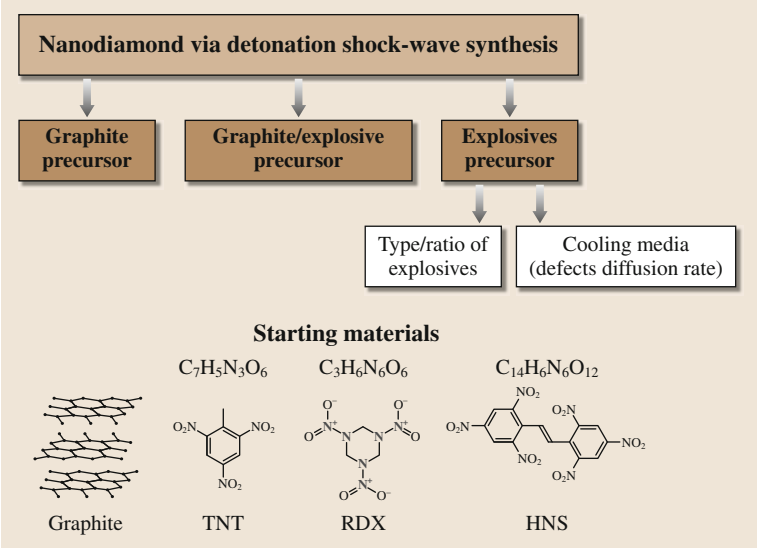


Fig. 8.11 A scheme of the carbon-containing precursors for the three major methods of dynamic synthesis of nanodiamonds and factors influencing the nitrogen content in the produced nanodiamond material

hedral diamond crystals. The first step included nitrogen jet milling micronization resulting in a powder with 97% of particles having sizes below 2 μm. Then an aliquot was ball-milled under argon using a planetary ball mill (Vario-Planetary Mill, Pulverisette 4; Fritsch, Germany), with 10 mm balls made of WC-Co cemented carbide for 24 h of effective grinding time. Nanodiamonds appeared as deformed polygons with quasispherical shape and an aspect ratio in the range 1.13–1.75. The overall yield of this method is about 15 wt % of the microdiamond mass converted into sub-10 nm diamond nanoparticles. The authors attribute the success of the production of the quasispherical particles to the complex loading regimes of the Vario planetary mill as compared with regular planetary mills.

HPHT Synthesis

While a particular class of nanodiamonds is obtained as a commercial byproduct of HPHT synthesis, there are laboratory studies of HPHT conversion of exotic carbon forms to nanodiamond. The HPHT process requires approximately 6 GPa pressure and 1500 °C to convert graphite powder into diamond in the presence of a catalyst. The use of exotic precursor materials such as fullerenes [8.69] as well as carbon nanotubes [8.70] allows much lower temperatures and externally applied pressures as compared with the use of graphite in order to synthesize diamond; for example, the transformation of buckyballs to diamond at high static pressure can be done at room temperature and does not require a catalyst at all [8.69]. Another group of authors reported the conversion of fullerenes to diamond under *moderate* conditions of 5.0–5.5 GPa and 1400 °C [8.71]. Carbon nanotubes have been converted to diamond at 4.5 GPa and 1300 °C using NiMnCo catalyst [8.70]. Based on HRTEM observations, the authors suggest that under HPHT conditions the tubular structures collapse and broken graphitic shells curl up and close into spheroidal networks to eliminate the dangling bonds at the edges.

Multi-walled carbon nanotubes were heated by a laser in a diamond anvil cell to above 17 GPa and 2500 K [8.72]. The recovered product consisted of nanosized octahedral crystals (diamond) of less than 50 nm. The tubular structure completely changed to granular, and the grain sizes corresponded to the diameter of the nanotubes. The grain size of the diamond suggests that the transformation took place by direct conversion of nanotubes, which might provide a means to control diamond size by choice of the multi-walled nanotube (MWNT) size.

An interesting implementation of HPHT treatment was reported by *Soltamova* et al. Sintering experiments were carried out on detonation ND with average particle size of 4.5 nm at temperatures of 1500–1700 °C and pressure of 6–7 GPa. According to the results of x-ray diffraction, the average size of the primary particles became 8.5 nm after sintering. When the sintering temperature is above 800 °C, vacancies start to diffuse. The presence of a significant amount of nitrogen-vacancy (NV) centers was detected in 10 μm aggregates using pulsed EPR [8.73]. The formation of NV centers can be possibly attributed to the combination of 1) elimination of surface paramagnetic centers and 2) vacancy diffusion from the high temperature of the process.

Nanodiamond Particles Synthesis Based on the CVD Technique

Frenklach and coworkers [8.74] studied the nucleation and growth of nanodiamond powder directly from the vapor phase in a substrate-free low-pressure microwave-plasma chemical vapor deposition (CVD) reactor. The particles were collected downstream of the reaction zone on a filter within the tubular flow reactor and were subjected to a wet oxidation to remove nondiamond carbon. The homogeneous diamond nucleation took place when dichloromethane– and trichloroethylene–oxygen mixtures were used as source material. The particles formed had crystalline shapes with average particle size around 50 nm. A mixture of diamond polytypes were observed in the powder.

Frenklach et al. [8.17] also studied the effects of heteroatom addition on the nucleation of solid carbon in a low-pressure plasma reactor. Addition of diborane (B_2H_6) resulted in substantial production of diamond particles, 5–450 nm in diameter, under the same conditions that show no diamond formation without the presence of diborane. The observed yield of the oxidation-resistant powder produced in boron-containing mixtures reached 1.3 mg/h. It was found that nanodiamonds in the CVD residue have an abundance of linear twins and star-twin microstructures consistent with radial (isotropic) gas-phase growth conditions. Studies of diamond nucleation directly from an activated gas phase have important implications in revealing mechanisms of interstellar dust formation.

Another example of homogeneous diamond nucleation in the gas phase is laser-induced decomposition of C_2H_4 at low pressures and temperatures that results in diamond powder formation with grain diameters of 6 nm–18 μm. According to the authors, the high-purity

homogeneously nucleated diamond nanoparticles had spherical and faceted morphology [8.75].

Ting et al. [8.76] developed a synthesis method for nanodiamond particles with 25–50 nm diameters using a microwave plasma torch system operating at near-atmospheric pressure. Gas mixtures of CH_4 with Ar or N_2 were used for ND particle synthesis, with Ar or N_2 serving as catalysts. Higher flow rate of Ar and N_2 or greater pressure in the reaction chamber produced larger nanoparticles.

The CVD technique was recently used for production of electrically conductive nanodiamond in particulate form by CVD growth of boron-doped nanodiamond films around a dielectric core of diamond nanoparticles [8.77]. Production of electroconductive boron-doped nanodiamond particles can be very beneficial and can find broad applications in high-surface-area carbon electrode materials for electroanalysis, electrochemical double-layer capacitors, storage materials for batteries, as a possible electrocatalyst support material for fuel cells, stationary support for liquid chromatography, and other applications [8.77].

Methods Using Radiation and High-Energetic Particles

Another group of methods for nanodiamond formation include direct transformation of carbon solids to nanodiamond. Recent experiments have shown that heavy-ion or electron irradiation induces nucleation of diamond crystallites inside concentric nested carbon fullerenes [8.15, 78]. High-energy electron irradiation (1.2 MeV, $> 10^{24}$ e/cm^2; ≈ 100 dpa) was successfully used to convert the cores of concentric-shell graphitic onions into nanometer-size diamonds at irradiation temperatures above 900 K [8.15]. These experiments were performed in situ in an electron microscope, which allowed continuous observation of the formation process. A strong compression in the interior of the onion was inferred from the observed reduction in spacing between adjacent concentric shells during irradiation. Ion-beam irradiation of carbon solids also resulted in formation of nanodiamond [8.78]. Irradiation with Ne^+ (3 MeV, 4×10^{19} cm^{-2}; ≈ 600 dpa) at temperatures between 700 and 1100 °C converted graphitic carbon soot into nanometer-size diamonds [8.78]. Again, the diamonds were found to nucleate in the cores of graphitic onions that developed under irradiation. The increased diamond yield as compared with e-beam irradiation is explained by the higher displacement cross-section, the higher energy transfer, and the higher total beam current on the specimen. Other carbon materials can also be transformed to nanodiamond by using a MeV electron or ion beams. ND nucleation occurs inside graphite under ion irradiation at ambient temperature when implanted with Kr^+ ions (350 MeV, 6×10^{12} cm^{-2}) [8.14]. The residue of the ion-irradiated graphite was found to contain nanodiamonds with average diameter of 7.5 nm. Another example of nanodiamond formation includes irradiation of highly oriented pyrolytic graphite surfaces using a highly charged ion (HCI) [8.79].

Laser-Assisted Synthesis of Nanodiamond Particles

Generation of nanoparticles by laser ablation in liquids is a relatively new approach that has been actively explored during the last decade [8.80]. It has a number of important advantages over conventional multistep chemical synthesis methods that introduce contamination from the intermediate reactants and/or produce agglomerated structures with degraded functionality. The direct laser ablation eliminates the need for chemical precursors and enables generation of *clean* nanoparticles. Due to the highly nonequilibrium nature of the laser ablation process, the structure and composition of nanoparticles produced by laser ablation can be very far from the equilibrium ones, opening an exciting range of opportunities for generation of novel nanostructures with unique properties.

Nanocrystalline diamond has also been produced by pulsed laser ablation using a graphite target along with water or acetone as the liquid medium [8.80]. The authors suggested that OH groups formed from the oxygen-containing liquids etched nondiamond carbon species from the surface, thereby allowing diamond to form preferentially. Diamond nanocrystals have been produced by pulsed laser ablation of graphite at room temperature and pressure in two liquids (water and cyclohexane) by *Pearce* et al. [8.81]. The nanodiamond formation was attributed to the extreme temperature/pressure conditions created by collapse of bubbles. The sequence of processes in laser ablation of liquids is likely to include explosive decomposition of the overheated surface region of the absorbing target, ejection of clusters and vapor into the surrounding liquid, mixing of the ejected ablation plume with the liquid and bringing the liquid to boiling or supercritical states, and growth and solidification of the nanoparticles under conditions of fast quenching. The final size, structure, and composition of the produced nanoparticles are defined by the heat and mass transfer occurring under highly nonequilibrium, quickly evolving conditions that are poorly understood at this time. Nanodiamond par-

ticles have been also synthesized from fine particles of carbon black exposed to intense laser irradiation [8.82]. Similarly, the transformation from carbon nanotubes to carbon onions and then to nanodiamond as a result of laser irradiation has been reported [8.83].

Diamond Synthesis Using Ultrasound Cavitation

The temperatures and pressures required for synthesis of diamond material can be achieved by different means, including ultrasound cavitation as a result of the rapid collapse of cavitation bubbles generated in a suitable liquid medium [8.84]. Depending upon the cavitation conditions, the pressure and temperature inside the cavity at the moment of collapse may reach extremely high instantaneous values: $\approx 10^5 - 10^6$ bar and 1000 K, respectively [8.85]. Two research groups reported the formation of nanostructured [8.86] and monocrystalline [8.87] micrometer-sized diamond particles. Cavitation destruction of benzene resulted in production of particles consisting of aggregates of nanocrystallites of 10–30 nm in size [8.86]. Micrometer-sized diamond crystals (5–10 μm) were produced by the cavitation synthesis method from a suspension of powdered graphite (100–200 μm) in organic liquid [8.87]. The major factor influencing the diamond yield in the cavitation process was the composition of the cavitation medium. The diamond yield was about 10% of the initial graphite weight. As cavitation fluids, a series of aromatic C–H–O oligomers with low saturated vapor pressure and high boiling temperatures were used.

Carbide-Derived Diamond

Selective etching of carbides is an attractive technique for the synthesis of various carbon structures including nanocrystalline diamond [8.13, 45, 88]. Carbon produced by extraction of metals from carbides is called carbide-derived carbon [8.88]. As summarized in [8.88], leaching in supercritical water, high-temperature treatment in halogens, vacuum decomposition, and other methods can be used to remove metals from carbides to produce carbon coatings or bulk and powdered carbon. In principle, chlorination of carbides for the production of carbon-based materials and, particularly, nanoporous carbon is a relatively mature technology that has been commercialized. However, the synthesis of nanocrystalline diamond by this technique [8.13] is a recent achievement. Particularly, during extraction of silicon from silicon carbide or metal carbide using chlorine-containing gases at ambient pressure and temperatures not exceeding 1000 °C [8.45], nanocrystalline diamond with average crystallite size of 5 nm was formed. Nanocrystalline diamond is usually surrounded by amorphous carbon.

8.3 Detonation Nanodiamond Processing and Modification

The three major steps in the conversion of carbon-containing explosives to DND products include synthesis, postsynthesis processing, and modification, which are discussed in detail in the following sections. Postsynthesis processing includes purification of detonation soot from metallic impurities and nondiamond carbon and is typically performed in conjunction with detonation soot synthesis by the same vendor. The result of the processing is DND of a certain purity (presently at a level of incombustible impurity content 0.5–5 wt % depending on the vendor) that is available on a large scale (thousands of kilograms). DND treatments, tentatively called modification, can include additional deep purification, surface functionalization toward specific applications, and deagglomeration or size fractionation. In the last 3–4 years, the development of approaches for DND modifications has been the major focus of research activity. Although initially DND modifications were performed on a small scale, currently these steps are being implemented on a large scale at DND production centers [8.89]. Of primary importance is the method of disintegration of nanodiamond aggregates by stirred-media milling with micrometer-sized ceramic beads as suggested by *Osawa* and coworkers [8.90], resulting in diamond slurries containing primary 4–5 nm DND particles. This single-digit DND immediately attracted the attention of a relatively large number of researchers working in the area of nanoscale materials, as demonstrated by recent publications [8.91].

8.3.1 Postsynthesis Processing

The development of DND products of ultrahigh purity remains an important goal for many applications. In addition to the diamond phase, the detonation soot contains both graphite-like structures (25–55 wt %) and incombustible impurities (metals and their oxides – 1–8 wt %) [8.92]. The metal impurities orig-

inate from the detonator and from the walls of the detonation chamber. After typical purification steps, powders of DND can be considered a composite consisting of different forms of carbon (≈ 80–89%), nitrogen (≈ 2–3%), hydrogen (≈ 0.5–1.5%), oxygen (up to ≈ 10%), and an incombustible residue (≈ 0.5–8%) [8.62]. The carbon phase consists of a mixture of diamond (90–99%) and nondiamond carbon (1–10%).

Both nondiamond carbon and metallic, incombustible impurities can be located externally or internally relative to the tight DND aggregates. In order to remove the internal metal impurities and internal nondiamond carbon, tight DND agglomerates should be disintegrated. Currently, detonation soot can be industrially purified to a level of remaining incombustible impurities of about 0.5–0.6 wt %. In general, methods of DND purification as well as DND purity vary from vendor to vendor [8.62]. *Classical* purification methods, based upon the use of liquid oxidizers for the removal of metallic impurities, include sulfuric acid, a mixture of sulfuric and nitric acids, hydrochloric acid, potassium dichromate in sulfuric acid, as well as other schemes. A brief review on the numerous methods of detonation soot purification developed in the former USSR is provided in [8.93]. For the oxidation of sp^2 carbons, the purification schemes include KOH/KNO_3, Na_2O_2, CrO_3/H_2SO_4, HNO_3/H_2O_2 under pressure, mixtures of concentrated sulfuric and perchloric acids, and other approaches [8.62]. To remove noncarbon impurities, the chemically purified product is subjected, in some cases, to an additional purification process using ion-exchange and membrane technologies. Currently, the majority of DND vendors use strong liquid oxidizers at elevated temperatures and pressures. However, liquid-phase purification is both hazardous and costly, contributing up to 40% of the product cost. Alternatively, DND can be very effectively purified from nondiamond carbon in a more environmentally friendly manner by a gas-phase treatment using ozone at elevated temperatures [8.94] to eliminate the need for use of corrosive liquid oxidizers. Ozone is generated using corona discharge at the input of the reactor and is destroyed at the output of the gas flow. Ozone oxidation is more efficient for sp^2 carbon oxidation than oxygen. Such ozone-modified nanodiamonds (NDO) were found to have a number of distinctive characteristics. The size of polydispersed NDO in water suspensions is about 160–180 nm, as measured by dynamic light scattering technique. This number is the smallest average size reported for commercially available polydispersed unfractionated DND. In addition, the content of the primary, polyhedrally shaped, faceted particles with size of 3–5 nm in the polydispersed NDO is substantially higher than that of acid-purified DNDs. The NDO hydrosols were found to possess a very low pH (1.6–2 for 10% hydrosol) and low negative zeta potential (−50 mV for polydispersed sample and down to −100 mV for 20–30 nm fraction) and to feature a constant zeta potential (≈−40 to −50 mV) over a wide pH range of 2–12, apparently due to enrichment of the surface with oxygen-containing strong-acid groups. HRTEM imaging of NDO particles demonstrated low sp^2 content, and electron energy-loss spectroscopy (EELS) studies demonstrated lower content of sp^2 carbon in NDO as compared with ND purified using etching in hydrogen, as well as with other types of DND [8.95].

Several efforts have been made to purify DND by oxidation of detonation soot with air at elevated temperatures. The method allowed for a significant decrease in the nondiamond carbon content. *Larionova* et al. purified DND using soot treatment with air at 380–440 °C for several hours [8.96]. Soot purification through a combination of liquid oxidizers and air treatment at temperatures up to 600 °C was reported by *Mitev* et al. [8.97]. *Osswald* et al. [8.98] demonstrated that for soot the optimal temperature for the heat treatment in air within several hours is 400–430 °C.

8.3.2 Nanodiamond Deagglomeration and Fractionation

DND obtained from commercial vendors often requires additional processing and modification, since the content of incombustible impurities and nondiamond carbon can be too high, with an average aggregate size that is too large and with surface chemistry that is not suitable for a specific application. Poor colloidal stability of commercially available DND powders after liquid dispersion is a common problem. Besides, there is no universal material called *detonation nanodiamond*, since materials properties are specific to the synthesis and postsynthesis purification methods adopted by the vendor. As a means to improve the quality of the DND product, methods of fractionation and deaggregation are discussed below.

While the primary DND particle size is 4–5 nm, the primary particles form tightly and loosely bound aggregates. Typical commercial polydispersed ND suspensions that are subjected to powerful ultrasound treatments routinely exhibit 200–400 nm average aggregate sizes, which are unbreakable by the ultrasonic

treatment. An approach to effectively separate the particles to achieve a narrow size distribution is centrifugal fractionation [8.89, 99, 100]. Importantly, DND suspensions must possess high colloidal stability for centrifugal fractionation. It is not possible to fractionate an unstable suspension.

DND fractionation has several attractive aspects. First, it is a contamination-free approach as compared, for example, with bead milling, which introduces impurities from the ceramic beads which require further purification [8.4]. It is also convenient to be able to fractionate DND into different, narrow size distributions for different niche applications; for example, only DND with aggregate sizes of more than 100 nm can form photonic structures that diffract light in the visible region [8.101]. Finally, after deep purification or treatment with ozone/air, the content of DND with small-sized aggregates can be significantly increased and the production of suspensions with small fractions of pure DND without added contaminants becomes economically feasible. In fact, suspensions of 5 wt % of 25 nm-size DND fraction in water have been produced using the fractionation method [8.89]. Importantly, it is possible to extract only primary DND particles by centrifugal fractionation, including ultracentrifugation [8.102].

Deagglomeration of nanodiamond aggregates into individual primary particles is an important goal for a variety of applications. Methods of mechanical deagglomeration of DND dispersion in suspensions by stirred-media milling [8.4] or bead-assisted sonic disintegration [8.103] were developed, and suspensions of individual 4–5 nm DND particles have been produced.

Undesirable side-effects from bead milling include contamination with the bead material and generation of graphitic layers on the particle surface [8.4]. Attempts to purify bead-milled DND with liquid oxidizers led to aggregation of the primary particles [8.4]. Fortunately, by optimizing the bead-milling process, it is possible to minimize the contamination by the bead-milling media to below 0.2%. Purification from the bead-milled material using NaOH solution in water was considered [8.104] as well as molten NaOH. In addition, amorphous carbon and metal contaminants confined within DND aggregates and released during bead milling also need to be removed from the resulting suspension of primary particles. Nevertheless, production in kilogram quantities of this so-called Nanoamando nanodiamond has been started. Nanoamando has become a very popular nanodiamond material for biomedical research and has permitted successful development of applications.

A novel method of ND deaggregation by salt- or sugar-assisted dry milling was recently explored and yielded 5–20 nm ND particles with much fewer impurities than the bead-milling method [8.105].

Several other methods have been proposed for DND deagglomeration. *Xu* et al. developed a two-step deagglomeration procedure that included graphitization of byproducts of detonation in N_2 atmosphere at 1000 °C for 1 h followed by their oxidation with air at 450 °C for several hours [8.106]. The final powdered product contained at least 50% DND with particle size of less than 50 nm. *Krueger* reported using DND reduced in borane (accompanied by ultrasonic treatment), resulting in significantly smaller-sized aggregates [8.107]. Treatment of DND powder in an atmospheric pressure plasma also reduced the average DND aggregate size by ≈ 20% [8.108].

A concern that requires thorough study is the possible reagglomeration of single-digit DND or small-sized fractions subjected to further surface functionalization or drying for storage. Typically, during drying of ND from water and other solvents, ND aggregation is further increased due to capillary forces pulling together individual particles. Attractive van der Waals forces also play a major role in particle agglomeration. Agglomeration during drying makes ND functionalization more difficult, since it often requires dry starting ND material. *Puzyr* and *Bondar* has developed a modification based upon sonication-assisted treatment of ND in NaCl solution [8.109], which results in purification of the ND and possibly the incorporation of Na^+ ions into the ND surface. The attractive feature of the NaCl treatment method of ND modification [8.109] is the possibility of drying NDs from a hydrosol to a powder form with subsequent resuspension without agglomeration. DND powder with average aggregate size ≈ 40 nm after dispersion in water was obtained through this method.

8.3.3 ND Surface Functionalization

Among the two main types of nanodiamonds, i. e., DND and HPHT ND, DND are unique in their diversity of surface chemical functional groups generated in the detonation process. DND particles consist of a surface containing a wide variety of chemical functional groups surrounding a diamond core. This chemical *soup* may include well-known groups such as carboxylic acids, esters, ethers, lactones, and amines. While the diversity

of these functional groups is large, the density of surface groups as a function of particle size is also large. The DND primary particle size is small (≈ 4–5 nm), and thus they have a large surface area-to-volume ratio. For HPHT ND, the nanoscale diamond powders are in the size range of 25–30 nm. Therefore, the amount of functional chemical groups per unit mass of DND exceeds by several times the functionalization capacity of nanoscale diamond powders. DNDs may be thought of as solid-phase chemical libraries; they are solvent-accessible, highly dense, and chemically rich arrays positioned on a physically and chemically stable diamond platform. Conveniently, this chemical array can also be readily modified using standard wet chemical synthesis. Also, the hydrophilic nature of DNDs is important in applying these particles for applications in chemistry and biology. In fact, DNDs readily adsorb water from air, which requires the use of vacuum desorption Fourier-transform infrared (FTIR) spectroscopy to unmask chemical functional groups that are located at the same frequency as water groups [8.110]. Water and dimethylsulfoxide (DMSO) are excellent solvents for DNDs and allow for stable, highly concentrated colloidal suspensions. It is well known that DNDs function as an adsorbent, collecting toxins (enterosorbents), proteins, peptides, polysaccharides, antibodies, nucleic acids, viruses, and bacteria.

There are several processing steps that may be taken in chemically modifying nanodiamonds. For nanodiamonds of detonation origin, soot is initially produced in the synthesis. To obtain DNDs, the soot is purified to remove metallic and nondiamond carbon contaminants. Purification procedures are optimized to produce nanoparticles that have a high density of charge, in order to form stable colloidal suspensions. To further improve the colloidal stability, enrichment of carboxylic acid groups on the nanodiamond surface can be achieved by oxidation with ozone or by thermal annealing in air at temperatures above 400 °C [8.98]. This treatment yields solutions with a negative zeta potential. Conversely, DND surfaces may be reduced to enrich the surface with hydroxyl chemical groups using either borane or lithium aluminum hydride [8.110, 111], producing positive zeta potentials.

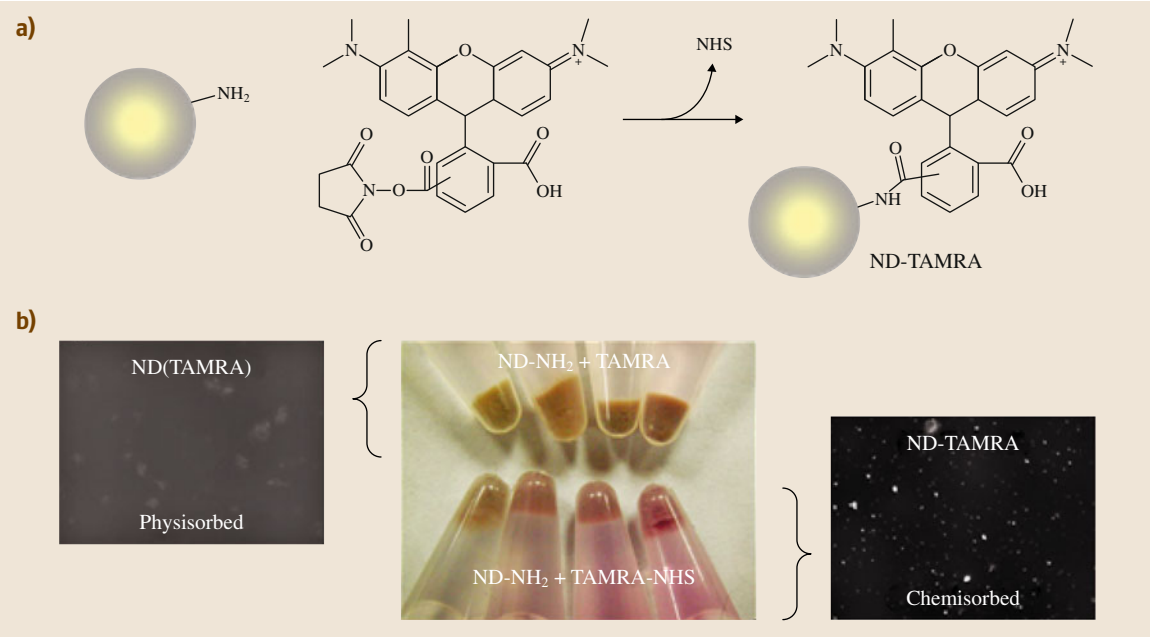


Fig. 8.12a,b Results from labeling nanodiamond with TAMRA fluorescent dye. **(a)** Schematic of the reaction of aminated nanodiamond with the succinimidyl ester of TAMRA dye **(b)**. Eppendorf tubes after thorough rinsing of the ND pellet with water using aminated ND (ND-NH_2) and either TAMRA dye alone (*top row*) or reactive TAMRA-NHS (NHS – *N*-hydroxysuccinimidyl ester) (*bottom row*). Photographs of strongly photoluminescent dye on ND (*right*) and physisorbed dye (*left*) taken with a fluorescent microscope using illumination with green light

Covalent Bonding

In recent years, extensive chemical synthesis has been done on nanodiamonds [8.112]. As compared with DNDs, chemical modification of HPHT NDs is more difficult. Some reaction chemistries for HPHT NDs that have been used include radical chemistry conjugation using small molecules to conjugate aromatic-NO_2 surface groups [8.113, 114] and carboxylic acids [8.115]. Fluorine surfaces on nanodiamond films can be created by photolysis [8.116] or by cold plasma with fluorine gases [8.117]. Fluorinated HPHT nanodiamond particles may be converted to alkyl, amino, and amino acid derivatives [8.118].

For DND, standard wet chemical synthesis methods are available for grafting chemical groups onto its surface. One of the most useful nanodiamond conjugates is aminated ND. Several different pathways have been used to create aminated DND. In one method, silanization of ND-OH using aminopropyltrimethoxysilane (APES) produced aminated ND for attaching peptides [8.111], biotin [8.107], dyes [8.119], and protein-capturing aminophenylboronic acid [8.120]. A second method to produce aminated DND (Fig. 8.13), used standard wet chemical synthesis that required four reaction steps. This method produced aminated ND that was colloidally stable in water and was used to bond biotin and TAMRA (tetramethylrhodamine) dye moieties with their succinimidyl ester conjugates, producing stable amide linkages [8.110]. The third method for amination requires only a two-step reaction from ND-COOH, whereby the COOH is converted to an acyl chloride and then reacted with octadecylamine. Surprisingly, this modified DND was fluorescent blue in hydrophobic solvents [8.121].

Loh et al. showed that the Suzuki coupling reaction can be used to prepare biaryl-functionalized DNDs. Initially, a bromophenyldiazonium salt is coupled onto the hydrogenated DND surface, producing a bromophenyl DND synthon. This synthon undergoes Suzuki coupling with an aryl boronic acid moiety, resulting in a biaryl-functionalized compound. The broad applicability of this reaction means that it is used to prepare drugs for pharmaceuticals and for attaching different aryl moieties, such as fluorescent dyes, onto a range of substrates. Here the coupling was used to graft a functionalized fluorescent dye using the reaction of a commercially available pyrene boronic acid derivative to a bromophenyl-functionalized DND. The Suzuki reaction can also improve the colloidal stability of DNDs in organic solvents, since they

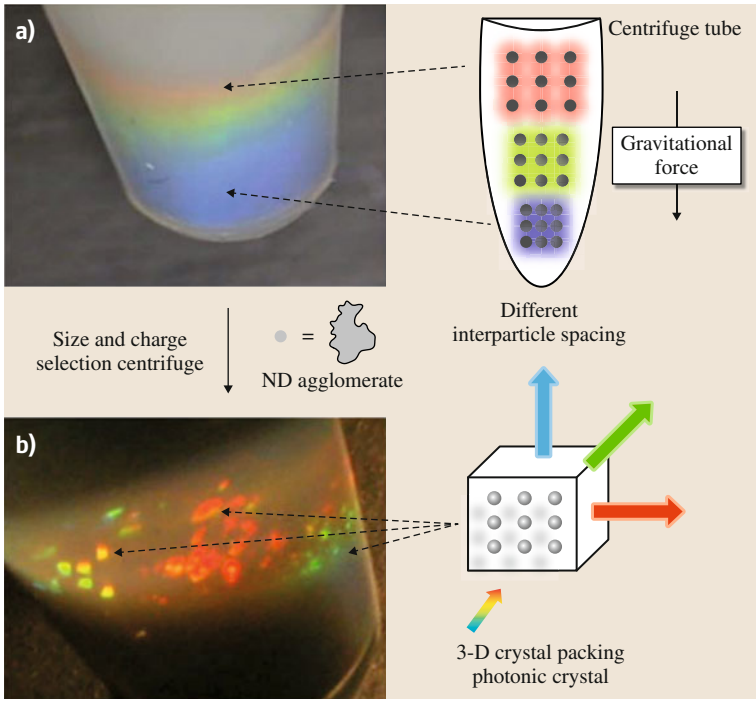


Fig. 8.13a,b Photographs showing that nanodiamonds form a rainbow pattern of colors that is dependent upon the interparticle spacing: wide spacing (*red band*) or close spacing (*blue band*) **(a)**. Continued washing by centrifugation produces discrete, bright, millimeter-sized photonic crystals that are ordered in 3-D space **(b)**

readily form hydrophobic aryl compounds, such as trifluoromethylaryl-functionalized DND for colloidal stability in ethanol and hexane [8.122].

Recently, Krueger et al. have been successful in using several standard wet chemical synthetic methods applied to nanodiamonds after some surface conversion of sp^2 character [8.112]. These reactions are adopted from carbon nanotube and fullerene chemistry, based upon the reactivity of the C – H bond from sp^2-functionalized carbon surfaces. Initially, nanodiamonds are produced by thermal annealing (DND and HPHT) or ball-milling (DND) nanodiamonds. These arylation reactions include (briefly):

1. C – C coupling reactions with aryl diazonium compounds [8.123]
2. 1,3-Dipolar cycloaddition using the Prato reaction [8.124]
3. Cycloaddition using the Diels–Alder reaction [8.125]
4. *Click* chemistry using the product from the diazotization of primary amines [8.126].

These reactions are described in more detail here. In the first reaction, *Krueger* et al. used the diamond C=C of sp^2 carbons of thermally annealed DNDs to prepare DNDs bearing either hydrophilic (COOH, SO_3H) or hydrophobic (NO_2, CH_2CH_2Br) groups by using suitably substituted anilines that were converted to their reactive diazo salt. These aryl-functionalized groups formed stable colloidal suspensions in water (COOH, SO_3H) and acetone (NO_2, CH_2CH_2Br). Importantly, the aryl-COOH-functionalized DND is stable in phosphate-buffered saline. This unique property of nanodiamond paves the way for realizing biomedical applications with DND [8.123].

In the second reaction, Krueger et al. demonstrated a general approach for DND surface grafting by using the Prato reaction in which a pyrrolidine ring as the linking moiety is formed in the presence of sp^2 carbons from the DND surface. This is a versatile reaction that allows grafting of both alkyl and aromatic side-chains that can be achieved under mild conditions. This reaction uses sarcosine (*N*-methylglycine) and a number of aldehydes to generate azomethine ylides in situ. The 1,3-cycloaddition reaction produced a variety of substituted pyrrolidine rings, including rings with oligoethyleneglycol chains, aromatic moieties, and reactive groups such as the cyano group [8.124].

In the third reaction, Krueger et al. used the classic Diels–Alder cycloaddition reaction using *o*-quinodimethane, which acts as a diene, on the πC=C bond of sp^2 carbons of DND. This reaction is simple and allows for another method for conjugating DND surfaces with many different substitution patterns. In one example, a thiol-functionalized product was used to conjugate Oregon Green dye which carried a maleimide group by using the maleimide-thiol reaction onto the DND surface [8.125].

In the fourth reaction, Krueger et al. used the popular *click* chemistry carried out with the sp^2 surface of nanodiamonds, which allowed for both high product yield and reactivity under aqueous conditions. It was demonstrated that the addition of sp^2 surfaces on HPHT ND and DND (by either thermal annealing or mechanical milling) increases the surface coverage of reactive groups useful for *click* chemistry reactions. Similar to previous work, a diazotization reaction was used to bind the diamond surface, whereby the primary amine was *para*-substituted with either an azide or an alkyne [8.123]. Next, the *click* reaction proceeded using the coupling of the azide/alkyne. An orthogonally functionalized DND, modified with two different reactive groups (COOH and alkyne), was used to conjugate differently colored dyes. First, the COOH was used to produce an amide bond to bind Oregon Green, which was followed by a *click* reaction of the ND-alkyne to the azide of TAMRA [8.126].

Polymeric reactions on the ND surface have been achieved with a number of different methods. Using thermally annealed HPHT NDs, Chang et al. functionalized the sp^2 carbon layer with polymers using a radical initiator in under 10 min using ultrasonication and microwave heating. The oligomer side-chains on the HPHT NDs were either hydrophilic (amines, carboxylic acids) or hydrophobic (alkyls, phenyl) [8.127]. Copolymers of methyl methacrylate, styrene, and an acrylamide were grafted on NDs using ferrocene [8.128]. Hydrophobic and hydrophilic polymer brushes have been prepared by atom-transfer radical polymerization from the carboxylated DND and methacrylate esters [8.129]. These polymer brushes provide exceptional properties to DNDs, which have a low number of reactive sites for the high surface area.

Noncovalent Binding

DND surfaces have been modified by electrostatic binding. Due to the charged nature of DNDs, attachment by electrostatics alone can be achieved for small molecule dyes [8.108] and proteins such as insulin [8.130]. When condensation does not occur on its own, additives can be used to facilitate the binding; for example,

small molecules can be condensed onto DNDs with the addition of salts for the chemotherapeutic drugs doxorubicin [8.91, 131] and 10-hydroxycamptothecin [8.132]. This mechanism of binding allows for the release of the drugs under certain ionic conditions. In addition to using salts, charged polymers can be used. DNDs have been adsorbed with cationic polymers, such as poly-L-lysine, to negatively charged DND. The advantage of using poly-L-lysine is that it enriches the DND surface with a high density of amine groups, commonly used for biofunctionalization chemistries; for example, succinimidyl ester conjugate dyes and proteins may be chemically linked to these amine groups on the DND surface [8.133, 134]. Heterofunctional linkers have also been used to bind the cytochrome c protein to poly-L-lysine-coated DND, providing up to two molecules of protein for a 5 nm particle [8.133]. In addition, polycationic polyethylenimine was used to condense silenced RNA (siRNA) onto DNDs [8.135], whereas cationic polylysine-coated [8.134] or a methacrylate cationic polymer brush [8.136] was used to adsorb DNA plasmids.

8.4 Fluorescent Nanodiamonds

The presence of nitrogen-vacancy (NV) centers – a nitrogen atom next to a vacancy – in nanodiamond leads to useful fluorescence properties. A central focus of many research groups remains the controlled production of nitrogen-vacancy centers in nanoscale diamond. Due to the strong optical transition, single defects can be detected using a fluorescence microscope. The spin state of the negatively charged NV centers permits the implementation of efficient single-photon emitters for quantum information processing [8.5] or magnetic sensors with nanoscale resolution [8.6]. Single color centers show outstandingly high photostability, even at room temperature [8.11]. Thus, on-demand production of NV centers in nanodiamond is important for several emerging applications such as quantum information, nanoscale sensing, and photoluminescent markers for microscopy.

NV centers can be created by irradiating nanodiamond with high-energy particles (electrons, protons, helium ions), followed by vacuum annealing at 600–800 °C [8.11]. Irradiation forms vacancies in the diamond structure, and during annealing these vacancies migrate and get trapped by the nitrogen atoms that are always present in diamond. Two types of NV centers are formed – neutral (NV^0) and negatively charged (NV^-) – and these have different emission spectra. The NV^- center is of particular interest because it has a $S = 1$ spin ground state that can be spin-polarized by optical pumping and manipulated using electron paramagnetic resonance (EPR). Moreover, it has a long spin coherence time [8.5]. Fluorescent NV centers in isotopically clean diamond are of particular interest for quantum computing [8.137], while NV centers in nanodiamond are also being investigated for applications in high-resolution magnetic sensing [8.6, 138, 139], fluorescence resonance energy transfer [8.140], and biomedical imaging [8.11].

The development of bright photoluminescent nanodiamonds has been mostly done on materials produced by high-pressure high-temperature synthesis [8.11, 12] containing up to hundreds of parts per million of native substitutional nitrogen, which are then crushed down to nanosized particles, including single-digit nanodiamonds [8.12]. While the concentration of the fluorescent NV defects produced by electron irradiation does not depend on the size of the nanocrystals [8.141], the fraction of NV^- defects produced by the same technique decreases with the size of the nanodiamond [8.142], presumably due to electron traps located at the surface.

While 7 nm HPHT ND particles have been obtained on laboratory scale [8.12], 20 nm particles are the only commercially available fraction of HPHT ND (for example, from Van Mopes, Co.). Cost is also an important factor in nanodiamond particle applications. Cost of HPHT ND ground to nanometer sizes is an order of magnitude higher than that of deagglomerated detonation nanodiamond.

Up to now, nanodiamond synthesized from explosives was not amongst the preferred candidates for imaging applications based on NV centers. Recently, intermittent luminescence originating from NV centers was observed in individual pristine 5 nm detonation nanodiamonds (DND) produced from TNT/hexogen precursor [8.139]. Stable luminescence has also recently been detected from NV centers trapped in larger (> 20 nm) nanodiamonds produced from TNT/hexogen [8.42] and graphite/hexogen [8.67] precursors. These results suggest that various factors (such as the amount of nitrogen in the precursors and the cooling

conditions) have a role in the nitrogen incorporation into the nanodiamond core and in possible in situ formation of NV centers. Size-related proximity of surface defects and the presence of numerous internal defects might contribute to the low fluorescence intensity of nanodiamond produced from explosives. This is supported by the demonstration of a very high content (up to 1%) of NV defects in detonation nanodiamond after sintering at $T = 800\,^{\circ}\mathrm{C}$ and $P = 6\,\mathrm{GPa}$ [8.143], enlarging nanodiamond sizes.

Fluorescent particles can also be produced by linking [8.110] or adsorbing [8.133] various fluorophores onto nanodiamond. Fluorophore-conjugated nanodiamond can travel through cellular compartments of varying pH without degradation of the surface-conjugated fluorophore or alteration of cell viability over extended periods of time [8.144]. Bright-blue fluorescent nanodiamond was recently produced via covalent linking of octadecylamine to carboxylic groups on the nanodiamond surface [8.121].

Fluorescent nanodiamonds combine the advantages of semiconductor quantum dots (small size, high photostability, bright multicolor fluorescence) with biocompatibility, nontoxicity, and rich surface chemistry, which means that they have the potential to revolutionize in vivo imaging applications [8.11, 145, 146].

8.5 Applications of Nanodiamond Particles

The market for nanodiamond particles has been expanding rapidly worldwide following the release of previously tightly held information by the former USSR related to detonation nanodiamonds. Consumption of DND is still largely centered around many of the core applications identified in the former USSR: additives to galvanic coatings, polishing and lubricant additives [8.48, 62]. Marketing has made industries around the world aware of the applications where DND provides benefit through enhancement of material properties in a wide range of applications. Below we survey selected applications which benefit from the property of nanodiamond as a superhard additive as well as its biocompatibility, nontoxicity, and rich surface chemistry. This survey is far from being comprehensive and is intended to provide a flavor of this rapidly growing field.

8.5.1 Nanodiamond in Polishing Applications

Polycrystalline diamond particles produced by shock conversion of graphite or detonation of a graphite/RDX mixture have been steadily consumed for several decades as micrometer-sized particles for lapping and polishing. In this capacity micrometer-sized diamond is indispensable despite its high cost (more than US $ 6/g), providing a high removal rate during polishing of hard carbide and nitrate substrates for microelectronic devices. For the fine finish polishing, requiring abrasives of sub-100 nm size, much less expensive colloidal silica is widely used. It was recently reported, however, that a combination of colloidal silica and nanosized diamond particles can provide the most beneficial effect through an increase in polishing rates, leading to a reduction in production time and surface finish better than 4 Å (Nanodiamond Product, Ltd., Ireland [8.147]). Since the amount of nanodiamond added is low ($\approx 10\%$), the cost of the synergistic composition is increased insignificantly; For example, *An* et al. [8.147] investigated the effect of addition of nanosized diamond slurry (grain size 25 nm) into conventional KOH-based colloidal silica slurry for chemical–mechanical planarization (CMP) of SiC materials. Addition of the nanodiamond slurry resulted in surface roughness of R_a $R_a \approx 2.2$ Å (after 1 h of polishing) as compared with 5.9 Å when colloidal silica alone was used. Moreover, addition of a strong oxidizer NaOCl into the ND–silica composition resulted in a material removal rate (MRR) of 0.3 mg/h (versus 0.06 mg/h in the slurry without NaOCl) and $R_a \approx 1.08$ Å. The improvement in the R_a and MRR after addition of ND particles can be explained as follows. Colloidal silica acts as a wet-chemical surface oxidizer that generates a SiO_2 layer on the SiC surface and etches the surface to reveal the damaged layer from mechanical polishing. The nanodiamond particles remove (abrade) the silica layer, increasing the MRR, and polish the damaged layer revealed by KOH-based colloidal silica slurry, decreasing R_a. Addition of NaOCl further enhances the chemical reaction on the SiC surface with KOH-based colloidal silica, producing a much thicker SiO_2 layer which can be efficiently removed by ND particles. Nanodiamond Products, Ltd. report that nanodiamond additive to colloidal silica enhances production of electronic substrate materials such as sapphire, silicon carbide (4H/6H

polytypes), silicon nitride, and gallium nitride, lithium niobate, gallium arsenide, calcium fluoride windows, fiber-optical bundle ends for greater data transmission, liquid-crystal displays (LCD), and light-emitting diode (LED)/organic LED (OLED) displays. The addition of a nanodiamond slurry to existing colloidal solutions is also used for metallographic polishing.

8.5.2 ND Applications in Composites

A broad area of application of nanodiamonds utilizing their high chemical inertness and superhardness is incorporation of DND into different matrixes and production of composites. Numerous applications of DND-based nanocomposites are under development, including wear-resistant additives to metal coatings; antifriction additives to lubricants and oils; polymer nanocomposites and coatings with enhanced strength, impact resistance, and scratch resistance; and nanocomposites with improved thermal stability and thermal conductivity. An example of nontraditional applications includes demonstration that nanodiamond particles in a polydimethylsiloxane matrix attain very pronounced photoluminescent when irradiated with a flux of MeV protons [8.148]. This suggests application of the ND-polymer coatings as fluorescence-induced indicators of acquired proton dose, for example, by spacecraft that is exposed to irradiation of protons. Other examples include fabrication of novel composites of carbon nanotubes incorporated into a nanodiamond matrix [8.149, 150], photonic structures made of DND [8.151], and DND-based ultraviolet (UV)-protection coatings and sunscreens [8.152]. Also, DNDs serve as a source material for production of onion-like carbon (OLC) by high-temperature annealing of DND in an inert atmosphere. Recently it was demonstrated that OLCs are strong absorbers of electromagnetic (EM) radiation from the gigahertz, to terahertz, to visible spectral ranges, providing efficient EM interference (EMI) shielding [8.153, 154].

Borjanovich et al. studied irradiation with 2 MeV proton beams of pure poly(dimethylsiloxane) (PDMS) polymer and PDMS-detonation nanodiamond (PDMS-DND) composite with 1 wt % of DND [8.155]. Based on spectroscopic analysis of vibrational dynamics, it was concluded that structural degradation of PDMS-DND composites takes place at an order of magnitude higher fluence than for pure PDMS, indicating the potential of using DND-based polymer composites for application in high-radiation environments. The appearance of strong photoluminescence following irradiation was more pronounced for PDMS-DND composites as compared with pure PDMS. *Gupta* et al. reported a decrease of damage of single-walled carbon nanotubes (SWCNT) by gamma irradiation when they were mixed with nanodiamond particles, providing a healing effect to SWCNT (possibly by charge transfer and dangling-bond formation and passivation) [8.156].

Several nanoadditives can be incorporated into a matrix simultaneously. Formation of ND/carbon nanotube (CNT) composites produced by codeposition of CNT and ND from a suspension was demonstrated [8.149,150]. At certain ND/CNT weight ratios, it was possible to form large-area ND/CNT films that adhered strongly to a substrate with uniformly distributed multi-walled carbon nanotubes (MWCNTs) within a ND matrix. Nanodiamond particles were also used to disperse carbon nanotubes, allowing the formation of their stable colloidal suspensions. It was demonstrated that NDs stabilize CNTs in organic solutions that are commonly used for polymer films, coatings, and composites. Thus, the development of nanocomposites may be facilitated with the addition of NDs that serve as both a dispersive and filler material. It was demonstrated that a urethane film with added NDs showed greater dispersivity of CNTs as compared with the CNT-containing film without NDs [8.150]. *Prasad* et al. fabricated polyvinyl alcohol-based composites with simultaneous addition of CNT and ND and observed a synergistic effect with a 400% increase in stiffness and hardness of the resulting composites, as compared with those obtained with single nanocarbon reinforcements [8.157].

Addition of DND to polymers provides an increase in their mechanical strength, wear resistance, and heat-ageing resistance [8.62, 158]. Highly effective coatings based on incorporation of DND into fluoroelastomers and polysiloxanes have been developed, and the elastic strengths of rubbers based on polyisoprene, butadiene-styrene, butadiene-nitrile, and natural rubbers were considerably improved; for example, fluoroelastomers filled with DND particles showed an increase in the tensile modulus at 100% elongation (from 280% to 480%) and in the conditional rupture strength (from 8.5 MPa to 92 MPa and from 15.7 MPa to 173 MPa, respectively). According to [8.62], addition of DND into the rubbers decreases attrition wear by an average of 3–5 times and increases rupture strength by 30%. Based upon experiments conducted on several polymer materials [poly(methyl methacrylate), benzocyclobutene, polyimide] with 1–2% by mass of nanodiamond particles incorporated, the thermal stability of the materials increased by at least 30 °C [8.152].

In the most recent publications, incorporation of octadecylamine-functionalized nanodiamond into a biodegradable polymer, poly(L-lactic acid) (PLLA), intended for a bone scaffold material application, resulted in a significant increase in hardness and Young's modulus of the composites [8.159]. Addition of 10 wt % of ND-ODA (ODA – octadecylamine) resulted in a more than 200% increase in Young's modulus and 800% increase in hardness, bringing the nanocomposite properties close to those of human cortical bone. *Neitzel* et al. studied the mechanical and thermal properties of ND–epoxy composites at high content of ND [8.160]. Composites with 25 vol % ND showed an increase in Young's modulus (up to 470%) and hardness (up to 300%) as compared with neat epoxy. Significant increases in the scratch resistance and thermal conductivity of the composites were observed as well.

However, addition of nanofillers into a matrix does not necessary produce a positive effect. *Comet* et al. [8.161] reported an attempt to enclose diamond nanoparticles produced by detonation into a Kevlar matrix (40 wt % diamond). The hydrogen interactions between carboxylic groups on the ND surface and the amide groups of Kevlar destroyed the *rod-like* structure and the classical three-dimensional organization of this polymer, reducing the macroscopic hardness of Kevlar doped by nanodiamonds by approximately a factor of two as compared with pure Kevlar.

Electrochemical deposition of DND together with metals using standard galvanic equipment has been demonstrated to be beneficial in a variety of applications for coatings of components of transportation units, tools for electronics, electrical engineering, medicine, and the watch and jewelry industry [8.158]. The advantages of adding DND to galvanic coatings include increases in wear resistance (2–13 times depending on the metal) and microhardness (maybe up to 2 times depending on the metal), an increase in corrosion resistance (2–6 times depending on the metal), a decrease in porosity (pores can be completely eliminated depending on the metal), a significant decrease of friction coefficient, considerable improvement of adhesion and cohesion, and high throwing power of electrolyte. According to reports [8.158], the service life of products is increased by 2–10 times, even when the coating thickness is decreased by a factor of 2–3. The strengthening effect is observed for coatings of many metals, including silver, gold, and platinum. In particular, DND is most widely used in strengthening chromium coatings deposited using an electrolytic process. In this process, DND-containing additives are added to the chrome-plating electrolyte without any modification of the standard production line. Such coatings increase by a few times the operating life of molds, high-precision bearing surfaces, and other similar components [8.158]. Interestingly, it was recently demonstrated that the best result in terms of the microhardness for coatings prepared by the hard chromium plating method has been achieved using Nanoamando, i. e., nanodiamond particles deagglomerated to individual primary particles [8.162].

A different approach for production of DND–metal matrix composites was reported by *Nunes* et al., who suggested a novel material design for nuclear fusion reactors based on Cu-diamond and W-diamond nanocomposites [8.163]. The proposed design involves the production of W/W-diamond/Cu-diamond/Cu functionally graded material. W, W-diamond, Cu-diamond, and Cu nanostructured composite powders were produced independently by mechanical alloying and subsequently consolidated/welded through spark plasma sintering.

A wide variety of nanomaterials in powder and colloidal forms have emerged as potential antifriction and antiwear additives to different classes of base lubricants [8.164]. Detonation nanodiamonds with 4–5 nm primary particle size and spherical shape seem to be among the most promising candidates as additives to such lubricants. Until recently, detonation soot, which is a mixture of graphite and nanodiamond particles, has been the predominant material of this class used as an additive to lubricants [8.165]. It was assumed that the combination of nanodiamond and the graphite phase is beneficial since graphite on its own has lubricating properties, while DND contributes by polishing of asperities on friction surfaces and thus reducing friction. Concerns regarding use of DND alone without a protective sp^2 shell were related to the abrasive nature of diamond powder. To a large extent the absence of positive results on using purified DND in lubricant applications was related to the fact that until recently DND was available only as a polydispersed material. However, studies by *Ivanov* et al. [8.166–168] demonstrated successful application of purified DND for enhanced tribological performance of greases and oils when used as synergistic compositions with other additives. Specifically, *Ivanov* et al. demonstrated that a combination of DND with ultradispersed polytetrafluoroethylene (PTFE) particles provides excellent lubrication properties in mineral oils of class I and greases, well exceeding those for soot and when using PTFE additives alone [8.166]. Besides 90% improvement in friction coefficient and 100% decrease in a wear spot,

extreme pressure to failure was increased up to 7 times for poly-α-olefin oil-based compositions [8.167, 168].

8.5.3 Biomedical Applications

The toxicity of particles on the nanoscale depends upon many factors, including particle size, surface chemical groups, shape, and hydrophilicity [8.169–172]. The physicochemical properties of nanodiamonds for biomedical applications have been outlined [8.64]. Diamond particles consist of a stable, nonreactive, diamond core that is biologically compatible and nonreactive. On the other hand, more commonly used nanoparticles such as quantum dots have a toxic core, so they are modified, for example, with silica coatings, to prevent toxicity. One potential route for nanodiamond toxicity is the lack of biological clearance [8.159, 173], when their particle size is too large, for example. Also, the advantageous hydrophilic property of NDs can cause a toxicological response since NDs are likely to interact with biomolecules, which may also prevent biological clearance. In addition, surface functional groups that aid in the hydrophilicity of DNDs may chemically react with or bind biological targets, or cause ND agglomeration; these reactions may be detrimental to biomolecules or biological processing. Furthermore, the surface chemistry may produce destructive chemical species, such as reactive oxygen species [8.174], which would be biologically harmful. Postprocessing is aimed at removing harmful species, such as metallic and amorphous carbon impurities, by treating DNDs with HCl and other acids, for example. On the other hand, HPHT NDs are produced with fewer impurities, so less extensive postprocessing is needed. Chemical reactions on the surface of NDs are aimed at functionality and biocompatibility; for example, the chemical modification of ND surfaces with polymeric coatings [8.175] is expected to minimize surface binding of nontargeted biological entities such as proteins, nucleic acids, cells, etc. The chemistry of DNDs is rapidly becoming more sophisticated; thus, only time is required before they are widely used in biomedical applications.

NDs have been evaluated for cytotoxicity both in vitro and in vivo. Biocompatibility studies of nanodiamonds have been summarized [8.64]. Briefly, there are a number of in vitro assays to assess cell health after exposure to nanoparticles; for example, DNDs were found to be noncytotoxic in a variety of different cell lines using in vitro approaches, including morphological imaging, cell viability, and reactive oxygen species production; it was found that DNDs do not illicit inflammation or cytotoxic responses by the cell [8.8, 9, 64]. In addition to the lack of inflammation, DNA fragmentation assays also showed that DNDs were not cytotoxic [8.91, 131]. Similarly, fluorescent carboxylated HPHT NDs (FND) do not reduce cell viability or protein expression in lung cells [8.176]. Imaging studies of fluorescently labeled DNDs detailed the uptake of particles by cells, remaining stable through translocations of endosomes and lysozomes without affecting cell viability [8.144].

The primary particles of DNDs are small (4–5 nm) and round, so would be expected to have good biological clearance. In one recent study, DND agglomerates that were broken down to the primary particles did exhibit whole-body clearance in mice [8.119]. Conversely, HPHT NDs are usually modified to decrease their size and made round instead of their naturally crystalline shape. On intravenous injection into mice, larger, 50 nm HPHT NDs that were not milled for spherical shape (Advapowder Co., China), and appeared crystalline with sharp edges and side, were found to be retained in the liver, spleen, and lung after 28 days [8.173]. HPHT NDs, 100 nm size but from a different source (Element Six), were fed or microinjected with fluorescently enhanced NDs (FND) [8.177] to worms (*Caenorhabditis elegans*). The NDs did not appear to affect their stress, reproductivity, or longevity. Only FNDs coated with dextran or bovine serum albumin (BSA) are taken up by intestinal cells, while tracking of the FNDs could be done continuously and through the next generation [8.178].

Studies by *Dolmatov* have shown that DNDs prolonged the life and improved the health of mice, dogs, and humans with cancer, presumably by adsorption of free radicals as well as other toxins [8.158]. A summary of in vivo studies with DNDs has been tabulated [8.64]. In vivo studies have shown limited toxicity; however, safety in humans cannot be determined from animal models.

Specific Applications

Use of NDs as substrates for delivery has been investigated for vaccine and drug delivery, immunoassays, antimicrobial agents, and biosensor development. The solid platform of NDs has been used for drug delivery of the chemotherapeutic drug doxorubicin (Dox), which showed good activity, while limiting the toxicity of the drug. More recently, *Li* et al. showed that DNDs could be used as carriers for the chemotherapeutic drug 10-hydroxycamptothecin; its release can be effected by lowering the pH of the media, while this combination

demonstrated that the complex has higher efficacy than the drug alone [8.132].

The study of drug delivery by NDs using Dox is extensive. Physisorption of Dox on carboxylated DNDs was achieved by electrostatics that could be released in the presence of excess salt [8.91]. In addition, a ND/Dox polymeric patch system was developed to allow for site-specific delivery of Dox, being shown to be biocompatible and biofunctional [8.131]. Furthermore, the most recent work by Ho et al. has shown that the ND/Dox complex is safe in mice and allows for slow release of Dox, increasing the blood circulation half-life by tenfold while decreasing the toxicity. Toxicity was monitored by a decrease in the inflammatory response, as compared with high doses of Dox delivered alone. DND transport was monitored through the kidneys, spleen, and liver; whole-body clearance was found for the smaller ND particles ($\approx 4–5$ nm) [8.119].

HPHT NDs are effective substrates for antigen delivery of mussel adhesive protein, a protein for which it is difficult to illicit an immune response. Thus, use of NDs may allow development of a surgical adhesive or a corrosion inhibitor [8.179]. In addition, DNDs are able to complex and stabilize an antibody (transforming growth factor), preserving the antibody's activity, while releasing it from its nanoparticle carrier in a physiological environment [8.180].

For gene or vaccine delivery, NDs have the ability to stabilize DNA without causing damage, as compared with traditionally used heavy-metal nanoparticles. The usefulness of DND as a general, robust solid-phase support was demonstrated in experiments using the Bio-Rad PDS-1000/He instrument for the delivery of bioactive molecules to yeast, fall armyworms, and bananas [8.134]. In comparison with other cell delivery methods (not including the nanofountain detailed below), biolistic delivery can target cells with bioactive molecules over a wide range of velocities and distances. As compared with gold nanoparticles, NDs as biolistic delivery platforms are beneficial because they are less toxic, nonexplosive, nonvolatile, water soluble, and less costly. One example included use of ND-assisted ballistic delivery of diphenylcyclopropenone, an ethylene antagonist, which was used to prevent ripening of bananas. In a second example, DNA was delivered to bacterial cells using the same method [8.134]. The immobilization of DNA onto NDs led to its use in plasmid delivery via ballistic bombardment.

DNDs may be used for therapeutic delivery of silence RNA (siRNA), which is expected to be beneficial for knocking out deleterious genes. The polyanion RNA was electrostatically bound to the DND carrier using a polycationic mediator, polyethylenimine. As compared with the typically used liposomal siRNA delivery vehicle, the DND hybrid complex as a whole was capable of a similar cell transfection efficiency causing gene knockdown of green fluorescent protein, while being nearly noncytotoxic, unlike liposomal siRNA delivery vehicles [8.135].

DNDs can also be used for gene delivery due to the stabilization of a DND/plasmid complex, which also promotes transfection efficiency. In this case, methacrylate cationic polymer brushes, widely used to mediate gene delivery, were grafted onto DNDs by atom-transfer radical polymerization. These particles were found to be good carriers for plasmid DNA, preventing enzymatic degradation of the plasmid, while effectively transfecting cells and allowing for imaging of the innate fluorescence of DNDs by scanning confocal microscopy [8.136].

Although ND can be used as a platform for therapeutics, its ease of chemical modification also provides controlled design of chemical therapies; For example, the development of a ND–gadolinium complex was found useful for magnetic resonance imaging that increases the image contrast by tenfold as compared with Gd used alone [8.181].

DND in Healthcare Products

Nanodiamonds are also considered for cosmetics and healthcare applications due to their ability to bond with biological materials, improving the durability and robustness of a composition. The Environmental Working Group lists a number of cosmetic products currently on the market containing diamond powder, including nail polishes, nail treatments, anti-aging formulation, and facial cleanser. The diamond powder is listed in the formulations as a material with low hazard score (1 out of 10); For example, *Sung* et al. hypothesize that nanodiamonds dispersed in a biologically acceptable carrier and bonded with biological materials may offer improvement when applied in various cosmetics and cleansers [8.182]. As cleansers, NDs have specifically been studied for antimicrobial and antifungal properties. For antimicrobial applications, NDs loaded with lysozyme have been evaluated since this enzyme cleaves bacterial cell walls. The adsorption capacity of carboxylated HPHT NDs was used to make a ND/lysozyme complex based upon electrostatics. The activity of the lysozyme was found to be 60% with ND surface coverage of 50% [8.183], while Raman mapping showed that the enzyme retained its func-

tionality [8.184]. Thus, NDs can act as a solid-phase platform for lysozyme to provide a reusable antimicrobial substrate to treat surfaces or solutions, for example.

Another potential application of nanodiamonds in healthcare products is protection from ultraviolet radiation (UVR) [8.185]. DND has high refractive index (≈ 2.4) and efficiently scatters light. Attenuation of UVR by DND can be enhanced due to the absorption by the sp^2 carbons on the DND surface. In addition, many lattice defects and impurities found in natural and synthetic diamonds absorb UVR [8.186], contributing to the radiation attenuation. DND is a very attractive candidate as a physical sunscreen due to its biocompatible, nontoxic properties and excellent physical strength.

As a seed material for CVD diamond growth, DND particles play an important role in the development of medical implants [8.187, 188]. Seeding with DND allows coatings with small grain size and, therefore, smooth surfaces that are important for medical implant applications.

Carbon- and clay-containing adsorbents are commonly used to bind ingested toxins in medical and pharmacological industries. However, their use can be potentially fatal to both animals and humans [8.189, 190, 190, 191]. As a remedy after accidental ingestion of mycotoxins, which are low-molecular-weight byproducts of mold growth, enterosorbents are used to specifically bind the toxins while remaining biocompatible, well dispersed in aqueous solution, and stable for transportation and administration. Currently, enterosorbents that are safe and practical are not readily available [8.191]. DNDs are considered as potential enterosorbents for binding a group of mycotoxins called aflotoxins, because of their high biocompatibility, small size, large surface area, rich surface chemistry, inexpensive production, and variety of available samples. A positive zeta potential is the main property that contributes to the greatest aflotoxin adsorption onto DNDs [8.192]. At 0.1 wt % concentration of DND in water slurries, the two samples with adsorptive capacities of over 100 mg of aflotoxin/kg of ND were purified detonation NDs, being 185 and 300 nm in size with surface charges of +47 and +18, respectively. It would be desirable to further control the ND surface chemistry, determine their optimal concentrations, and reduce the size of the ND aggregates useful for applications in low-pH environments such as the stomach.

Biosensors and Biochips

DNDs may be used as a solid-phase capture probe for physisorption of biological molecules. Early research showed that DND nanoparticles are capable of adsorbing recombinant apoobelin and luciferase proteins [8.193]. It has been found that DNDs have tenfold greater binding capacity for the protein lysozyme as compared with traditional chromatographic substrate, nanosilica, which is probably due to the greater surface area of porous nanodiamond [8.194].

Bioactive substrates or biosensors can be fabricated by collection of DNDs by electrophoresis; For example, it was demonstrated that collection of DND onto a support is possible by electrophoresis. In this application, biotinylated nanodiamond conjugate probe (ND-biotin) was used to capture its target (streptavidin) [8.110]. In a more sophisticated and precise approach for ND array patterning, the application of direct-write nanopatterning was used with a DND ink, whereby the DND was conjugated to a fluorophore. This nanofountain instrument demonstrated that it is possible to insert DND probes into single cells, thus paving the way for systematic studies of drug or DNA therapeutics in biomedicine. It could also be used to create DND-probe-based arrays for biochip sensors [8.195].

As an ultimate platform, DND agglomerated particles are capable of forming ordered assemblies by centrifugation. With a narrow size fraction of DND (≈ 150 nm), centrifugation causes ordering of the particles along the centrifuge tube. At the top, the interparticle distance is large, resulting in a red color, and at the bottom the interparticle spacing is smallest, causing a blue color (Fig. 8.13). This results in a rainbow of colors along the length of an Eppendorf tube. Analogous to these rainbows, further centrifugation caused a three-dimensional crystallization of similar interparticle spacing for a particular color, producing photonic crystals that were millimeters in size and very bright [8.151]. These ordered DND particle assemblies may have applications in biodiagnostics, providing a colorimetric signal for the presence or absence of targeted biomolecules. In addition, their robust chemical and physical properties also may be exploited to advance the biosensor field [8.64].

8.5.4 Nanodiamonds for Seeding

Diamond film growth by chemical vapor deposition (CVD) has been under investigation since before 1975 [8.196]. One aspect of this research is the use of diamond seed crystals to increase the rate of growth. The use of HPHT nanodiamonds as seeds began in the late 1990s, but their large size produced nonuniformity in the diamond film. In 2003, seeding from nanodi-

amonds of detonation origin was shown to produce superior films. Use of DNDs as the seeding material has continued since this time [8.197]. Recently, laboratories that grow diamond films have begun procuring DND slurries from facilities that specialize in DND technologies, and these partnerships have greatly improved the development of DND seeding slurries.

To produce uniform diamond films, the DND must be of small particle size and evenly distributed on the substrate of interest. To achieve this goal, deagglomeration of particles is required, bead-milling is often used to break down primary particle agglomerates [8.90], and a colloidal suspension of the DND particles is needed. In the last few years, advances in DND deagglomeration and fractionation have produced seeding slurries with consistent properties. Williams et al. have developed methods for improving the nucleation density of nanocrystalline diamond film growth using bead-milled DND that is processed to form stable aqueous colloidal solutions of primary particles. This colloid was applied to various substrates to yield a high density of individually spaced diamond nanoparticles (greater than 10^{11} cm^{-2}) [8.187, 188].

As a cost-effective, commercial product, DND seeding slurries are initially formed by centrifugal fractionation [8.100], which eliminates sp^2 formation and zirconia impurities produced by milling. It has been found that the most effective solvent for producing colloidal DND suspensions for seeding is dimethylsulfoxide (DMSO) [8.198] (Fig. 8.14a). The most striking properties of DMSO are best illustrated using unfractionated DND *Standard* product (with 250 nm agglomerate sizes), which contains 1.4 wt % of incombustible metallic impurities. (It should be noted that only purified DND is used for commercial seeding applications.) DMSO produces colloidal suspensions of Standard DND, whereas suspensions in water readily sediment. For DND slurries in DMSO, addition of methanol produces a colloidal solution that is readily fractionated. This is surprising since DND in methanol alone readily sediments. Centrifugal fractionation of Standard DND is efficient using high concentrations of DND (3% w/v) in DMSO and effectively produces small particles (48 nm average size) at high concentration (0.9% w/v). Thus, centrifugation alone can be used to isolate small DNDs, while ball-milling requires purification steps. For our purified and fractionated 100 nm DND product, superior results are obtained starting with higher DND concentrations (up to 3.5%) for the centrifugation step, producing particles that are smaller (25 nm) and at higher concentrations ($\approx$ 0.5%). An example of successful seeding is shown in Fig. 8.14b. There exists one caveat, however, in that only DNDs with positive zeta potentials are stable in DMSO. Thus, negatively charged or air-treated DNDs cannot be processed with this solvent. As compared with water suspensions, DMSO allows for smaller, more concentrated, more stable dispersions of DNDs [8.199].

DMSO can also be useful in retaining the DND size after removing the solvent to produce powders. DNDs

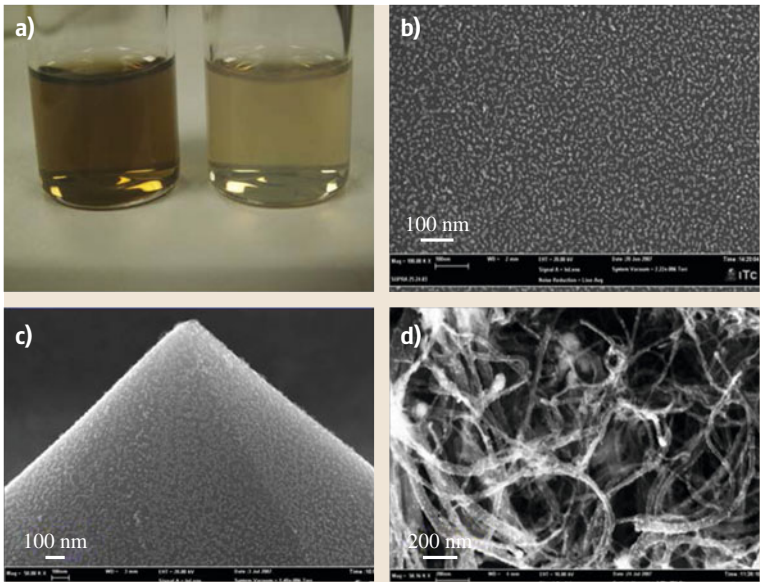


Fig. 8.14a–d Photographs showing detonation nanodiamond seeding. The colloidal solutions for seeding are transparent for high concentrations (*left*) and lower concentrations (*right*) **(a)**. Scanning electron microscopy (SEM) image of seeding on a silicon substrate using ND opal seeds **(b)**. SEM images of seeding carried out on highly structured substrates such as silicon field tips **(c)** and carbon nanotubes **(d)**

dried from DMSO retain their small size when reconstituted in DMSO or in water, whereas DNDs dried from water result in agglomerated particles that are approximately twice as large in diameter. In addition, a 10 vol. % volume fraction of DMSO added to water before drying prevented agglomeration [8.199].

Starting with purified DNDs, a rapid collection process for small, pure DND particles is possible using DNDs in DMSO suspensions. However, seeding with alcohols allows for rapid drying of substrates, so the addition of alcohols to the DMSO seeding slurry has proven successful. The effectiveness of seeding on Si was compared by varying:

1. The fractionation solvent (DMSO or DMSO/MeOH)
2. The solvent composition of the seeding slurry solution (DMSO or DMSO/MeOH)
3. The concentration of DND in the slurry.

The most successful seeding, which consists of discretely spaced, small DND particles (some are 5 nm), was obtained from polydispersed DNDs that are (1) fractionated from DMSO, and (2) seeded by sonication using DMSO/MeOH slurries in a 1 : 1 ratio (Fig. 8.14b) [8.199].

DND seeding is possible on different materials, such as metals, and on highly structured objects, including carbon nanotubes and silicon tips (Fig. 8.14c,d) [8.199]. Thus DND, as a seed material for CVD diamond growth, is important for many applications, from machines to medical implants [8.187, 188]. Different types of carbon coatings [among them diamond-like carbon (DLC) and diamond] deposited on the surface of implants increase implant biocompatibility and hemocompatibility, and serve the role of a barrier against corrosion [8.200]. Nanocrystalline (NC) and ultrananocrystalline diamond (UNCD) coatings on suitable substrates are promising materials for medical orthopedic implants, for example, hip and knee joint implants [8.201], and for coating of certain components of artificial heart valves [8.202, 203] due to their extremely high chemical inertness, surface smoothness, and good adhesion of the coatings to the substrate. These films are able to coat complex geometrical shapes with good conformal accuracy and with smooth surfaces to produce hermetic bioinert protective coatings, or to provide surfaces for cell grafting through appropriate functionalization. However, recent studies have shown that diamond powders are not bioinactive at the molecular level; they affect cellular gene expression and inhibit stress, such as oxidative, cellular, and genotoxic [8.204]. UNCD is a more suitable material than silicon for fabrication of biological microelectromechanical systems (bioMEMS); For example, in the case of a Si microchip implantable in the eye as the main component of an artificial retina to restore sight to people blinded by retina degeneration, Si cannot survive long-term implantation, while UNCD bioinert encapsulation can successfully replace the Si microchip implantation in the eye [8.205].

8.6 Future Directions of Production and Applications

Compared with many other nanomaterials, DND produced by detonation of explosives is relatively expensive since it has not experienced production scale-up to large volumes. As with any market, a high price is a factor that will inhibit widespread use in the marketplace. Even at the current purity and particle size, particularly for bulk manufacturing, with a 50% reduction in price the demand for DND would increase dramatically [8.206]. Recent advances in separation and fractionation methods of DNDs have led to the current availability of 50, 20, and 5 nm particle sizes. As the material meets the demands of specific uses, the increased production volume of these smaller-sized fractions will open up new markets and expand existing ones; For example, the recent availability of single-digit ND particles, produced by detonation of explosives in kilogram quantities [8.4], has opened broad perspectives for the application of ND in composites and nanolubricants. Other prospective applications include the use of DND in polymers, sunscreens, and galvanic coatings. Although new technologies are providing the means to increase the production of small-sized fractions in larger volumes, the method of production of the initial soot has largely remained the same for the past 30 years. Other methods of ND synthesis, such as laser-assisted synthesis [8.80], are intended to be useful for large-scale production. In addition, breaking of HPHT diamond into sub-10 nm particles is an important breakthrough for applications in quantum optics and luminescent markers. Both approaches, DND deagglomeration and HPHT ND milling, require further development of inexpensive processing meth-

ods so that single-digit NDs will be affordable for large-scale production and applications. Furthermore, production of electroconductive (i. e., boron-doped) nanodiamond particles during their synthesis would be very useful for broad applications in high-surface-area carbon electrode materials in electroanalysis and energy storage applications. If inexpensive methods of HPHT ND milling are developed, grinding of electrically conductive HPHT diamond will be advantageous also.

Nanodiamond's large and reactive surface area enables a broad range of modifications without compromising its superior chemically inert, physically strong diamond core. Recent achievements in the functionalization of NDs have led to a whole new range of applications, and this topic remains an object of intense research. Thus, it can be concluded that a *golden age* of diamond particles has begun, which will lead us to rapid, widespread use in both commodity products and brilliant materials of the future.

References

8.1 P.S. DeCarli, J.C. Jamieson: Formation of diamond by explosive shock, Science **133**(3467), 1821–1822 (1961)

8.2 V.V. Danilenko: On the history of the discovery of nanodiamond synthesis, Phys. Solid State **46**(4), 595–599 (2004)

8.3 N.R. Greiner, D.S. Phillips, J.D. Johnson, F. Volk: Diamonds in detonation soot, Nature **333**, 440–442 (1988)

8.4 E. Osawa: Recent progress and perspectives in single-digit nanodiamond, Diam. Relat. Mater. **16**(12), 2018–2022 (2007)

8.5 F. Jelezko, T. Gaebel, I. Popa, A. Gruber, J. Wrachtrup: Observation of coherent oscillations in a single electron spin, Phys. Rev. Lett. **92**(7), 076401–076405 (2004)

8.6 G. Balasubramanian, I.Y. Chan, R. Kolesov, M. Al-Hmoud, J. Tisler, C. Shin, C. Kim, A. Wojcik, P.R. Hemmer, A. Krueger, T. Hanke, A. Leitenstorfer, R. Bratschitsch, F. Jelezko, J. Wrachtrup: Nanoscale imaging magnetometry with diamond spins under ambient conditions, Nature **455**, 648–651 (2008)

8.7 A. Krueger: Diamond nanoparticles: Jewels for chemistry and physics, Adv. Mater. **20**(12), 2445–2449 (2008)

8.8 A.M. Schrand, H.J. Huang, C. Carlson, J.J. Schlager, E. Omacr Sawa, S.M. Hussain, L. Dai: Are diamond nanoparticles cytotoxic?, J. Phys. Chem. B **111**(1), 2–7 (2007)

8.9 A.M. Schrand, L. Dai, J.J. Schlager, S.M. Hussain, E. Osawa: Differential biocompatibility of carbon nanotubes and nanodiamonds, Diam. Relat. Mater. **16**(12), 2118–2123 (2007)

8.10 J.A. Chang, Y. Jallouli, A. Barras, N. Dupont, D. Betbeder: Drug delivery to the brain using colloidal carriers, Prog. Brain Res. **180**, 3–17 (2009)

8.11 Y.-R. Chang, H.-Y. Lee, K. Chen, C.-C. Chang, D.-S. Tsai, C.-C. Fu, T.-S. Lim, Y.-K. Tzeng, C.-Y. Fang, C.-C. Han, H.-C. Chang, W. Fann: Mass production and dynamic imaging of fluorescent nanodiamonds, Nat. Nanotechnol. **3**, 284–288 (2008)

8.12 J.-P. Boudou, P.A. Curmi, F. Jelezko, J. Wrachtrup, P. Aubert, M. Sennour, G. Balasubramanian, R. Reuter, A. Thorel, E. Gaffet: High yield fabrication of fluorescent nanodiamonds, Nanotechnology **20**, 235602 (2009)

8.13 Y. Gogotsi, S. Welz, D.A. Ersoy, M.J. McNallan: Conversion of silicon carbide to crystalline diamond-structured carbon at ambient pressure, Nature **411**, 283–287 (2001)

8.14 T.L. Daulton, M.A. Kirk, R.S. Lewis, L.E. Rehn: Production of nanodiamonds by high-energy ion irradiation of graphite at room temperature, Nucl. Instrum. Methods Phys. Res. B **175**, 12–18 (2001)

8.15 F. Banhart, P.M. Ajayan: Carbon onion as nanoscopic pressure cell for diamond formation, Nature, **382**, 433–437 (1996)

8.16 G.W. Yang, J.B. Wang, Q.X. Liu: Preparation of nanocrystalline diamonds using pulsed laser induced reactive quenching, J. Phys. D **10**, 7923–7928 (1998)

8.17 M. Frenklach, W. Howard, D. Huang, J. Yuan, K.E. Spear, R. Koba: Induced nucleation of diamond powder, Appl. Phys. Lett. **59**(5), 546–548 (1991)

8.18 O. Guillois, G. Ledoux, C. Reynaud: Diamond infrared emission bands in circumstellar media, Astrophys. J. **521**, L133–L136 (1999)

8.19 M. Goto, T. Henning, A. Kouchi, H. Takami, Y. Hayano, T. Usuda, N. Takato, H. Terada, S. Oya, C. Jäger, A.C. Andersen: Spatially resolved 3 µm spectroscopy of Elias 1: Origin of diamonds in protoplanetary disks, Astrophys. J. **693**, 610–616 (2009)

8.20 J.A. Viecelli, S. Bastea, J.N. Glosli, F.H. Ree: Phase transformations of nanometer size carbon particles in shocked hydrocarbons and explosives, J. Chem. Phys. **115**, 2730–2735 (2001)

8.21 V.V. Danilenko: Nanocarbon phase diagram and conditions for detonation nanodiamond formation. In: *Synthesis, Properties and Applications of Ultrananocrystalline Diamond*, NATO Sci. Ser. II, Math. Phys. Chem., Vol. 192, ed. by D.M. Gruen, O.A. Shenderova, A.Y. Vul' (Springer, Dordrecht 2005)

8.22 G. Chevrot, E. Bourasseau, N. Pineau, J.-B. Maillet: Molecular dynamics simulations of nanocarbons at high pressure and temperature, Carbon **47**, 3392–3402 (2009)

8.23 P. Badziag, W.S. Verwoerd, W.P. Ellis, N.R. Greiner: Nanometre-sized diamonds are more stable than graphite, Nature **343**, 244–245 (1990)

8.24 N.W. Winter, F.H. Ree: Carbon particle phase stability as a function of size, J. Comput.-Aided Mater. Des. **5**, 279–294 (1998)

8.25 A.S. Barnard, S.P. Russo, I.K. Snook: Structural relaxation and relative stability of nanodiamond morphologies, Diam. Relat. Mater. **12**, 1867–1873 (2003)

8.26 A.S. Barnard, S.P. Russo, I.K. Snook: Size dependent phase stability of carbon nanoparticles: Nanodiamond versus fullerenes, J. Chem. Phys. **118**, 5094–5098 (2003)

8.27 A.S. Barnard, S.P. Russo, I.K. Snook: Ab initio modelling of stability of nanodiamond morphologies, Philos. Mag. Lett. **83**, 39–42 (2003)

8.28 A.S. Barnard, M. Sternberg: Crystallinity and surface electrostatics of diamond nanocrystals, J. Mater. Chem. **17**, 4811–4819 (2007)

8.29 A.S. Barnard, S.P. Russo, I.K. Snook: Coexistence of bucky diamond with nanodiamond and fullerene carbon phases, Phys. Rev. B, **68**, 73406–73410 (2003)

8.30 J.Y. Raty, G. Galli: Ultradispersivity of diamond at the nanoscale, Nat. Mater. **2**(12), 792–795 (2003)

8.31 J.E. Dahl, S.G. Liu, R.M.K. Carlson: Isolation and structure of higher diamondoids nanometer-sized diamond molecules, Science **299**, 96–102 (2003)

8.32 L. Lai, A.S. Barnard: Modeling the thermostability of surface functionalisation by oxygen, hydroxyl, and water on nanodiamonds, Nanoscale **3**, 2566–2575 (2011)

8.33 L. Lai, A.S. Barnard: Stability of nanodiamond surfaces exposed to N, NH, and NH_2, J. Phys. Chem. C **115**, 6218–6228 (2011)

8.34 A.E. Aleksenskii, M.V. Baidakova, A.Y. Vul', V.I. Siklitskii: The structure of diamond nanoclusters, Phys. Solid State **41**, 668–671 (1999)

8.35 O.O. Mykhaylyk, Y.M. Solonin, D.N. Batchelder, R.J. Brydson: Transformation of nanodiamond into carbon onions: A comparative study by high-resolution transmission electron microscopy, electron energy-loss spectroscopy, x-ray diffraction, small-angle x-ray scattering, and ultraviolet Raman spectroscopy, J. Appl. Phys. **97**(7), 074302 (2005)

8.36 L. Hawelek, A. Brodka, J.C. Dore, V. Honkimaki, S. Tomita, A. Burian: Structural studies of nanodiamond by high-energy X-ray diffraction, Diam. Relat. Mater. **17**, 1186–1193 (2008)

8.37 I.I. Kulakova: Chemistry of nanodiamond surface, Solid State. Phys. **46**(4), 621–629 (2004)

8.38 M. Baidakova, A. Vul': New prospects and frontiers of nanodiamond clusters, J. Phys. D: Appl. Phys. **40**(20), 6300–6311 (2007)

8.39 V.L. Kuznetsov, Y.V. Butenko: Diamond phase transitions. In: *Ultra-Nanocrystalline Diamond: Syntheses, Properties and Applications*, ed. by O. Shenderova, D. Gruen (Andrew, New York 2006) pp. 405–463

8.40 A. Aleksenskiy, M. Baidakova, V. Osipov, A. Vul': The fundamental properties and characteristics of nanodiamonds. In: *Nanodiamonds*, ed. by D. Ho (Springer, New York 2010) pp. 55–79

8.41 S. Turner, O.I. Lebedev, O. Shenderova, I.I. Vasov, J. Verbeeck, G.V. Tendeloo: Determination of size, morphology and nitrogen impurity location in treated detonation nanodiamond by transmission electron microscopy, Adv. Funct. Mater. **19**(13), 2116–2124 (2009)

8.42 I.I. Vlasov, O. Shenderova, S. Turner, I.I. Vlasov, O. Shenderova, S. Turner, O.I. Lebedev, A.A. Basov, I. Sildos, M. Rahn, A.A. Shiryaev, G. Van Tendeloo: Nitrogen and luminescent nitrogen-vacancy defects in detonation nanodiamond, Small **6**(5), 687–694 (2010)

8.43 T. Tyler, V.V. Zhirnov, A.V. Kvit, D. Kang, J.J. Hren: Electron emission from diamond nanoparticles on metal tips, Appl. Phys. Lett. **82**(17), 2904–2906 (2003)

8.44 S. Hu, J. Sun, X. Du, F. Tian, L. Jiang: The formation of multiply twinning structure and photoluminescence of well-dispersed nanodiamonds produced by pulsed-laser irradiation, Diam. Relat. Mater. **17**, 142–146 (2008)

8.45 S. Welz, Y. Gogotsi, M.J. McNallan: Nucleation, growth, and graphitization of diamond nanocrystals during chlorination of carbides, J. Appl. Phys. **93**, 4207 (2003)

8.46 P.W. Chen, Y.S. Ding, Q. Chen, F.L. Huang, S.R. Yun: Spherical nanometer-sized diamond obtain from detonation, Diamond Rel. Mater. **9**, 1722–1729 (2000)

8.47 K. Iakoubovskii, K. Mitsuishi, K. Furuya: High-resolution electron microscopy of detonation nanodiamond, Nanotechnology **19**, 155705–155710 (2008)

8.48 O.A. Shenderova, V.V. Zhirnov, D.W. Brenner: Carbon nanostructures, Crit. Rev. Solid State **27**, 227–356 (2002)

8.49 O. Shenderova, D. Gruen (Eds.): *Ultrananocrystalline Diamond* (William Andrew, Norwich 2006)

8.50 H. Schwertfeger, A.A. Fokin, P.R. Schreiner: Diamonds are a chemist's best friend: Diamondoid chemistry beyond adamantane, Angew. Chem. Int. Ed. **47**, 1022–1036 (2008)

8.51 R.M.K. Carlson, J.E.P. Dahl, S.G. Liu: Diamond molecules found in petroleum. In: *Synthesis, Properties and Applications of Ultrananocrystalline Diamond*, NATO Sci. Ser. II, Math. Phys. Chem., Vol. 192, ed. by D.M Gruen, O.A. Shenderova, A.Y. Vul' (Springer, Dordrecht 2005)

8.52 V.F. Tatsii, A.V. Bochko, G.S. Oleinik: Structure and properties of dalan detonation diamonds, Combust. Explos. Shock Waves **45**(1), 95–103 (2009)

8.53 V.V. Danilenko: *Synthesis and Sintering of Diamond by Explosion* (Moscow, Energoatomizdat 2003)

8.54 V.Y. Dolmatov: *Detonation synthesis ultradispersed diamonds (Russian edition)* (Saint-Petersburg State Polytechnic Univ., Saint-Petersburg 2003)

8.55 P.S. DeCarli: Method of making diamond, US Patent 3238019 (1966)

8.56 V.V. Danilenko: On the discovery of detonation nanodiamond. In: *Ultrananocrystalline Diamond*, ed. by O.A. Shenderova, D.M. Gruen (William Andrew, Norwich 2006) pp. 335–344

8.57 G.R. Cowan, N.J. Woodbury, B.W. Dunnington, P. Wood, A.H. Holtzman: Process for synthesizing diamond, US Patent 3401019 (1968)

8.58 G.A. Adadurov, A.V. Baluev, O.N. Breusov, V.N. Drobyshev, A.I. Rogacheva, A.M. Sapegin, V.F. Tatsii: Some properties of diamonds produced by an explosive method, Izv. Akad. Nauk SSSR Ser. Neorg. Mater. **13**(4), 649–653 (1977)

8.59 V.V. Danilenko: *Explosion Physics, Technique, Technology* (Moscow, Energoatomizdat 2010)

8.60 J.A. Viecelli, F.H. Ree: Carbon particle phase transformation kinetics in detonation waves, J. Appl. Phys. **88**, 683–690 (2000)

8.61 A.L. Vereschagin: *Properties of Detonation Nanodiamonds* (Barnaul State Technical Univ., Altay Region 2005)

8.62 V.Y. Dolmatov: Detonation synthesis ultradispersed diamonds: Properties and applications, Russ. Chem. Rev. **70**, 607–626 (2001)

8.63 K.B. Holt: Diamond at the nanoscale: Applications of diamond nanoparticles from cellular biomarkers to quantum computing, Philos. Trans. R. Soc. A **365**, 2845–2861 (2007)

8.64 A.M. Schrand, S.A. Hens, O.A. Shenderova: Nanodiamond particles: Properties and perspectives for bioapplications, Crit. Rev. Solid State Mater. Sci. **34**(1), 18–74 (2009)

8.65 J.Y. Raty, G. Galli, C. Bostedt, T.W. Van Buuren, L.J. Terminello: Quantum confinement and fullerenelike surface reconstructions in nanodiamonds, Phys. Rev. Lett. **90**, 037401 (2003)

8.66 G.S. Yur'ev, V.Y. Dolmatov: X-ray diffraction study of detonation nanodiamonds, J. Superhard Mater. **32**(5), 29–50 (2010)

8.67 O. Shenderova, I. Vlasov, S. Turner, G. Van Tendeloo, S.B. Orlinskii, A.A. Shiryaev, A.A. Khomich, S.N. Sulyanov, F. Jelezko, J. Wrachtrup: Nitrogen control in nanodiamond produced by detonation shock-wave-assisted synthesis, J. Phys. Chem. C **115**, 14014–14024 (2011)

8.68 J.W. Ager, D.K. Veirs, G.M. Rosenblatt: Spatially resolved Raman studies of diamond films grown by chemical vapor deposition, Phys. Rev. B **43**, 6491 (1991)

8.69 M. Núñez-Regueiro, P. Monceau, J.-L. Hodeau: Crushing C_60 to diamond at room temperature, Nature **355**, 237–239 (1992)

8.70 L.M. Cao, C.X. Gao, H.P. Sun, G.T. Zou, Z. Zhang, X.Y. Zhang, M. He, M. Zhang, Y.C. Li, J. Zhang, D.Y. Dai, L.L. Sun, W.K. Wang: Synthesis of diamond from carbon nanotubes under high pressure and high temperature, Carbon **39**, 311–317 (2001)

8.71 Y.Z. Ma, G.T. Zou, H.B. Yang, J.F. Meng: Conversion of fullerenes to diamond under high pressure and high temperature, Appl. Phys. Lett. **65**, 822–826 (1994)

8.72 H. Yusa: Nanocrystalline diamond directly transformed from carbon nanotubes under high pressure, Diam. Relat. Mater. **11**, 87–91 (2002)

8.73 A.A. Soltamova, I.V. Ilyin, F.M. Shakhov, S.V. Kidalov, A.Y. Vul, B.V. Yavkin, G.V. Mamin, S.B. Orlinskii, P.G. Baranov: Electron paramagnetic resonance detection of the giant concentration of nitrogen vacancy defects in sintered detonation nanodiamonds, JETP Lett. **92**(2), 106–110 (2010)

8.74 M. Frenklach, R. Kematick, D. Huang, W. Howard, K.E. Spear, A.W. Phelps, R. Koba: Homogeneous nucleation of diamond powder in the gas phase, J. Appl. Phys. **66**, 395–399 (1989)

8.75 P.R. Buerki, S. Leutwyler: Homogeneous nucleation of diamond powder by CO_2 laser-driven reactions, J. Appl. Phys. **69**, 3739–3745 (1991)

8.76 C.C. Ting, T. Young, C.S. Jwo: Fabrication of diamond nanopowder using microwave plasma torch technique, Int. J. Adv. Manuf. Technol. **34**, 316–322 (2007)

8.77 A. Ay, V.M. Swope, G.M. Swain: The physicochemical and electrochemical properties of 100 and 500 nm diameter diamond powders coated with boron-doped nanocrystalline diamond, J. Electrochem. Soc. **155**(10), B1013–B1022 (2008)

8.78 P. Wesolowski, Y. Lyutovich, F. Banhart, H.D. Carstanjen, H. Kronmüller: Formation of diamond in carbon onions under MeV ion irradiation, Appl. Phys. Lett. **71**, 1948–1951 (1997)

8.79 T. Meguro, M. Hida, M. Suzuki, Y. Koguchi, H. Takai, Y. Yamamoto, K. Maeda, Y. Aoyagi: Creation of nanodiamonds by single impacts of highly charged ions upon graphite, Appl. Phys. Lett. **79**, 3866–3870 (2001)

8.80 G.W. Yang: Laser ablation in liquids: Applications in the synthesis of nanocrystals, Progr. Mater. Sci. **52**, 648–698 (2007)

8.81 S.R.J. Pearce, S.J. Henley, F. Claeyssens, P.W. May, K.R. Hallam, J.A. Smith, K.N. Rosser: Production of nanocrystalline diamond by laser ablation at the solid/liquid interface, Diam. Relat. Mater. **13**, 661–665 (2004)

8.82 V.D. Fedoseev, V.L. Bukhovets, I.G. Varshavskaya, A.V. Lavrentev, B.V. Derjaguin: Transition of graphite into diamond in a solid state under the atmospheric pressure, Carbon **21**, 237–243 (1983)

8.83 B. Wei, J. Zhang, J. Liang, D. Wu: The mechanism of phase transformation from carbon nanotube to diamond, Carbon **36**, 997–1002 (1998)

8.84 H.G. Flynn: Method and means for converting graphite to diamond, US Patent 4563341 (1986)

8.85 C.E. Brennen: *Cavitation and Bubble Dynamics* (Oxford Univ., Oxford 1995)

8.86 E.M. Galimov, S. Kudin, V.N. Skorobogatski, V.G. Plotnichenko, O.L. Bondarev, B.G. Zarubin, V.V. Strazdovskii, A.S. Aronin, A.V. Fisenko, I.V. Bykov: Experimental corroboration of the synthesis of diamond in the cavitation process, Dokl. Phys. **49**, 150–156 (2004)

8.87 A.K. Khachatryan, S. Aloyan, P.W. May, R. Sargsyan, V.A. Khachatryan, V.S. Baghdasaryan: Graphite-to-diamond transformation induced by ultrasonic cavitation, Diam. Relat. Mater. **17**(6), 931–937 (2008)

8.88 A. Nikitin, Y. Gogotsi: Nanostructured carbide-derived carbon. In: *Encyclopedia of Nanoscience and Nanotechnology*, Vol. 7, ed. by H.S. Nalwa (American Scientific, Valencia 2004) pp. 553–574

8.89 I. Larionova, V. Kuznetsov, A. Frolov, O. Shenderova, S. Moseenkov, I. Mazov: Properties of individual fractions of detonation nanodiamond, Diam. Relat. Mater. **15**, 1804–1808 (2006)

8.90 A. Krüger, M. Ozawa, F. Kataoka, T. Fujino, Y. Suzuki, A.E. Aleksenskii, A.Y. Vul', E. Osawa: Unusually tight aggregation in detonation nanodiamond: Identification and disintegration, Carbon **43**(8), 1722–1730 (2005)

8.91 H. Huang, E. Pierstorff, E. Osawa, D. Ho: Active nanodiamond hydrogels for chemotherapeutic delivery, Nano Lett. **7**, 3305–3314 (2007)

8.92 V.Y. Dolmatov: Detonation nanodiamonds: Synthesis, structure properties and applications, Usp. Khim. **76**(4), 375–397 (2007)

8.93 I. Petrov, O. Shenderova: History of Russian patents on detonation nanodiamonds. In: *Ultrananocrystalline Diamond*, ed. by O.A. Shenderova, D.M. Gruen (William Andrew, Norwich 2006) pp. 559–589

8.94 I. Petrov, O. Shenderova, V. Grishko, V. Grichko, T. Tyler, G. Cunningham, G. Mcguire: Detonation nanodiamonds simultaneously purified and modified by gas treatment, Diam. Relat. Mater. **16**, 2098–2103 (2007)

8.95 O. Shenderova, A. Koscheev, N. Zaripov, I. Petrov, Y. Skryabin, P. Detkov, S. Turner, G. Van Tendeloo: Surface chemistry and properties of ozone-purified detonation nanodiamonds, J. Phys. Chem. C **115**, 9827–9837 (2011)

8.96 I.S. Larionova, I.N. Molostov, L.S. Kulagina, V.F. Komarov: Method of purification of synthetic ultradispersed diamonds, Patent RU 2168462 (1999)

8.97 D. Mitev, R. Dimitrova, M. Spassova, C. Minchev, S. Stavrev: Surface peculiarities of detonation nanodiamonds in dependence of fabrication and purification methods, Diam. Relat. Mater. **16**, 776 (2007)

8.98 S. Osswald, G. Yushin, V. Mochalin, S.O. Kucheyev, Y. Gogotsi: Control of sp^2/sp^3 carbon ratio and surface chemistry of nanodiamond powders by selective oxidation in air, J. Am. Chem. Soc. **128**(35), 11635–11642 (2006)

8.99 S.I. Chukhaeva, P. Detkov, A. Tkachenko, A. Toropov: Physicochemical properties of fractions isolated from ultradispersed diamonds, Superhard Mater. **4**, 29–36 (1998)

8.100 O. Shenderova, I. Petrov, J. Walsh, V. Grichko, V. Grichko, T. Tyler: Modification of detonation nanodiamonds by heat treatment in air, Diam. Relat. Mater. **15**(11/12), 1799–1803 (2006)

8.101 V. Grichko, O. Shenderova: Nanodiamond designing the bioplatform. In: *Ultrananocrystalline Diamond: Synthesis, Properties, and Applications*, ed. by O.A Shenderova, D.M. Gruen (William-Andrew, Norwich 2006) pp. 529–557

8.102 Y. Morita, T. Takimoto, H. Yamanaka, K. Kumekawa, S. Morino, S. Aonuma, T. Kimura, N. Komatsu: A facile and scalable process for size-controllable separation of nanodiamond particles as small as 4 nm, Small **4**, 2154–2160 (2008)

8.103 M. Ozawa, M. Inaguma, M. Takahashi, F. Kataoka, A. Kruger, E. Osawa: Preparation and behavior of brownish, clear nanodiamond colloids, Adv. Mater. **19**, 1201 (2007)

8.104 H.J. Huang, L.M. Dai, D.H. Wang, L.S. Tan, E. Osawa: Large-scale self-assembly of dispersed nanodiamonds, J. Mater. Chem. **18**, 1347–1355 (2008)

8.105 A. Pentecost, S. Gour, V. Mochalin, I. Knoke, Y. Gogotsi: De-aggregation of nanodiamond powders using salt- and sugar-assisted milling, ACS Appl. Mater. Interfaces **2**(11), 3289–3294 (2010)

8.106 K. Xu, Q.J. Xue: A new method for deaggregation of nanodiamond from explosive detonation: Graphitization-oxidation method, Phys. Solid State **46**, 649–650 (2004)

8.107 A. Krueger, J. Stegk, Y. Liang, L. Lu, G. Jarre: Biotinylated nanodiamond: Simple and efficient functionalization of detonation diamond, Langmuir **24**, 4200–4204 (2008)

8.108 N. Gibson, O. Shenderova, T.J.M. Luo, S. Moseenkov, V. Bondar, A. Puzyr, K. Purtov, Z. Fitzgerald, D.W. Brenner: Colloidal stability of modified nanodiamond particles, Diam. Relat. Mater. **18**(4), 620–626 (2009)

8.109 V.S. Bondar, A.P. Puzyr: Nanodiamonds for biological investigations, Phys. Solid State **46**(4), 716–719 (2004)

8.110 S.C. Hens, G. Cunningham, T. Tyler, S. Moseenkov, V. Kuznetsov, O. Shenderova: Nanodiamond bioconjugate probes and their collection by electrophoresis, Diam. Relat. Mater. **17**(11), 1858–1866 (2008)

8.111 A. Krueger, Y.J. Liang, G. Jarre, J. Stegk: Surface functionalization of detonation diamond suitable for biological applications, J. Mater. Chem. **16**(24), 2322–2328 (2006)

8.112 Y.L. Zhong, K.P. Loh: The chemistry of C–H bond activation on diamond, Chem. Asian J. **5**(7), 1532–1540 (2010)

8.113 T. Tsubota, S. Tanii, S. Ida, M. Nagata, Y. Matsumoto: Chemical modification of diamond surface with various carboxylic acids by radical reaction in liquid phase, Diam. Relat. Mater. **13**(4–8), 1093–1097 (2004)

8.114 T. Tsubota, T. Ohno, H. Yoshida, K. Kusakabe: Introduction of molecules containing a NO_2 group on diamond surface by using radical reaction in liquid phase, Diam. Relat. Mater. **15**(4–8), 668–672 (2006)

8.115 Y. Liu, V.N. Khabashesku, N.J. Halas: Fluorinated nanodiamond as a wet chemistry precursor for diamond coatings covalently bonded to glass surface, J. Am. Chem. Soc. **127**(11), 3712–3713 (2005)

8.116 T. Nakamura, M. Hasegawa, K. Tsugawa, T. Ohana, M. Ishihara, Y. Koga: Photochemical modification of nanodiamond films with perfluorooctyl functionalities, Diam. Relat. Mater. **15**(4–8), 678–681 (2006)

8.117 M.A. Ray, O. Shenderova, W. Hook, A. Martin, V. Grishko, T. Tyler, G.B. Cunningham, G. McGuire: Cold plasma functionalization of nanodiamond particles, Diam. Relat. Mater. **15**(11/12), 1809–1812 (2006)

8.118 Y. Liu, Z.N. Gu, J.L. Margrave, V.N. Khabashesku: Functionalization of nanoscale diamond powder: Fluoro-, alkyl-, amino- and amino acid-nanodiamond derivatives, Chem. Mater. **16**(20), 3924–3930 (2004)

8.119 E.K. Chow, X.Q. Zhang, M. Chen, R. Lam, E. Robinson, H.J. Huang, D. Schaffer, E. Osawa, A. Goga, D. Ho: Nanodiamond therapeutic delivery agents mediate enhanced chemoresistant tumor treatment, Sci. Transl. Med. **3**(73), 10 (2011)

8.120 W.S. Yeap, Y.Y. Tan, K.P. Loh: Using detonation nanodiamond for the specific capture of glycoproteins, Anal. Chem. **80**, 4659–4665 (2008)

8.121 V.N. Mochalin, Y. Gogotsi: Wet chemistry route to hydrophobic blue fluorescent nanodiamond, J. Am. Chem. Soc. **131**(13), 4594 (2009)

8.122 W.S. Yeap, S.M. Chen, K.P. Loh: Detonation nanodiamond: An organic platform for the Suzuki coupling of organic molecules, Langmuir **25**(1), 185–191 (2009)

8.123 Y.J. Liang, T. Meinhardt, G. Jarre, M. Ozawa, P. Vrdoljak, A. Schöll, F. Reinert, A. Krueger: Deagglomeration and surface modification of thermally annealed nanoscale diamond, J. Colloid Interface Sci. **354**(1), 23–30 (2011)

8.124 D. Lang, A. Krueger: The Prato reaction on nanodiamond: Surface functionalization by formation of pyrrolidine rings, Diam. Relat. Mater. **20**(2), 101–104 (2011)

8.125 G. Jarre, Y.J. Liang, P. Betz, D. Lang, A. Krueger: Playing the surface game – Diels–Alder reactions on diamond nanoparticles, Chem. Commun. **47**(1), 544–546 (2011)

8.126 T. Meinhardt, D. Lang, H. Dill, A. Krueger: Pushing the functionality of diamond nanoparticles to new horizons: Orthogonally functionalized nanodiamond using click chemistry, Adv. Funct. Mater. **21**(3), 494–500 (2011)

8.127 I.P. Chang, K.C. Hwang, J.A.A. Ho, C.C. Lin, R.J.R. Hwu, J.C. Horng: Facile surface functionalization of nanodiamonds, Langmuir **26**(5), 3685–3689 (2010)

8.128 I. Cha, K. Shirai, K. Fujiki, T. Yamauchi, N. Tsubokawa: Suface grafting of polymers onto nanodiamond by ligand-exchange reaction of ferrocene moieties of polymers with polycondensed aromatic rings of the surface, Diam. Relat. Mater. **20**(3), 439–444 (2011)

8.129 L. Li, J.L. Davidson, C.M. Lukehart: Surface functionalization of nanodiamond particles via atom transfer radical polymerization, Carbon **44**(11), 2308–2315 (2006)

8.130 R.A. Shimkunas, E. Robinson, R. Lam, S. Lu, X.Y. Xu, X.Q. Zhang, H.J. Huang, E. Osawa, D. Ho: Nanodiamond-insulin complexes as pH-dependent protein delivery vehicles, Biomaterials **30**(29), 5720–5728 (2009)

8.131 H.J. Huang, E. Pierstorff, E. Osawa, D. Ho: Protein-mediated assembly of nanodiamond hydrogels into a biocompatible and biofunctional multilayer nanofilm, ACS Nano **2**, 203–212 (2008)

8.132 J. Li, Y. Zhu, W. Li, X. Zhang, Y. Peng, Q. Huang: Nanodiamonds as intracellular transporters of chemotherapeutic drug, Biomaterials **31**(32), 8410–8418 (2010)

8.133 L.C. Huang, H.C. Chang: Adsorption and immobilization of cytochrome c on nanodiamonds, Langmuir **20**(14), 5879–5884 (2004)

8.134 V. Grichko, V. Grishko, O. Shenderova: Nanodiamond bullets and their biological targets, Nanobiotechnology **2**, 37–42 (2007)

8.135 M. Chen, X.Q. Zhang, H.B. Man, R. Lam, E.K. Chow, D.A. Ho: Nanodiamond vectors functionalized with polyethylenimine for siRNA delivery, J. Phys. Chem. Lett. **1**(21), 3167–3171 (2010)

8.136 P. Zhang, J.H. Yang, W.C. Li, W. Wang, C.J. Liu, M. Griffith, W.G. Liu: Cationic polymer brush grafted-nanodiamond via atom transfer radical polymerization for enhanced gene delivery and bioimaging, J. Mater. Chem. **21**, 7755–7764 (2011)

8.137 P. Neumann, J. Beck, M. Steiner, F. Rempp, H. Fedder, P.R. Hemmer, J. Wrachtrup, F. Jelezko: Single-shot readout of a single nuclear spin, Science **329**, 542–544 (2010)

8.138 J.R. Maze, P.L. Stanwix, J.S. Hodges, S. Hong, J.M. Taylor, P. Cappellaro, L. Jiang, M.V. Gurudev Dutt, E. Togan, A.S. Zibrov, A. Yacoby, R.L. Walsworth, M.D. Lukin: Nanoscale magnetic sensing with an individual electronic spin in diamond, Nature **455**, 644–647 (2008)

8.139 C. Bradac, T. Gaebel, N. Naidoo, M. Sellars, J. Twamley, L. Brown, A. Barnard, T. Plakhotnik, A. Zvyagin, J. Rabeau: Observation and control of blinking nitrogen-vacancy centres in discrete nanodiamonds, Nat. Nanotechnol. **5**, 345–349 (2010)

8.140 J. Tisler, R. Reuter, A. Lammle, F. Jelezko, G. Balasubramanian, P.R. Hemmer, F. Reinhard, J. Wrachtrup: Highly efficient FRET from a single nitrogen-vacancy center in nanodiamonds to a single organic molecule, ACS Nano **5**, 7893–7898 (2011)

8.141 J. Tisler, G. Balasubramanian, B. Naydenov, R. Kolesov, B. Grotz, R. Reuter, J.-P. Boudou, P.A. Curmi, M. Sennour, A. Thorel, M. Börsch, K. Aulenbacher, R. Erdmann, P.R. Hemmer, F. Jelezko, J. Wrachtrup: Fluorescence and spin properties of defects in single digit nanodiamonds, ACS Nano **3**, 1959–1965 (2009)

8.142 L. Rondin, G. Dantelle, A. Slablab, F. Grosshans, F. Treussart, P. Bergonzo, S. Perruchas, T. Gacoin, M. Chaigneau, H.C. Chang: Surface-induced charge state conversion of nitrogen-vacancy defects in nanodiamonds, Phys. Rev. B **82**, 115449 (2010)

8.143 P.G. Baranov, A.A. Soltamova, D.O. Tolmachev, N.G. Romanov, R.A. Babunts, F.M. Shakhov, S.V. Kidalov, A.Y. Vul', G.V. Mamin, S.B. Orlinskii, N.I. Silkin: Enormously high concentrations of fluorescent nitrogen-vacancy centers fabricated by sintering of detonation nanodiamonds, Small **7**, 1533–1537 (2011)

8.144 A.M. Schrand, J.B. Lin, S.C. Hens, S.M. Hussain: Temporal and mechanistic tracking of cellular uptake dynamics with novel surface fluorophore-bound nanodiamonds, Nanoscale **3**(2), 435–445 (2010)

8.145 O. Faklaris, V. Joshi, T. Irinopoulou, P. Tauc, M. Sennour, H. Girard, C. Gesset, J.-C. Arnault, A. Thorel, J.-P. Boudou, P.A. Curmi, F. Treussar: Photoluminescent diamond nanoparticles for cell labeling: Study of the uptake mechanism in mammalian cells, ACS Nano **3**, 3955–3962 (2009)

8.146 L.P. McGuinness, Y. Yan, A. Stacey, D.A. Simpson, L.T. Hall, D. Maclaurin, S. Prawer, P. Mulvaney, J. Wrachtrup, F. Caruso, R.E. Scholten, L.C.L. Hollenberg: Quantum measurement and orientation tracking of fluorescent nanodiamonds inside living cells, Nat. Nanotechnol. **6**, 358–363 (2011)

8.147 J.H. An, G.S. Lee, W.J. Lee, B.C. Shin, J.D. Seo, K.R. Ku, H.D. Seo, H.D. Jeong: Effect of process parameters on material removal rate in chemical mechanical polishing of 6H-SiC(0001), Mater. Sci. Forum **600–603**, 831–837 (2008)

8.148 V. Borjanović, W.G. Lawrence, S. Hens, M. Jakšić, I. Zamboni, C. Edson, I. Vlasov, O. Shenderova, G.E. McGuire: Effect of proton irradiation on photoluminescent properties of PDMS–nanodiamond composites, Nanotechnology **19**(50), 509901–509909 (2008)

8.149 O. Shenderova, C. Jones, V. Borjanović, S. Hens, G. Cunningham, S. Moseenkov, V. Kuznetsov, G. McGuire: Detonation nanodiamond and onion-like carbon: Applications in composites, Phys. Status Solidi A **205**(9), 2245–2251 (2008)

8.150 S. Hens, G. Cunningham, G. McGuire, O. Shenderova: Nanodiamond-assisted dispersion of carbon nanotubes and hybrid nanocarbon-based composites, Nanosci. Nanotechnol. Lett. **3**(1), 75–82 (2011)

8.151 V. Grichko, T. Tyler, V. Grishko, O. Shenderova: Nanodiamond particles forming photonic structures, Nanotechnology **19**(22), 225201–225207 (2008)

8.152 O. Shenderova, T. Tyler, G. Cunningham, M. Ray, J. Walsh, M. Casulli, S. Hens, G. McGuire, V. Kuznetsov, S. Lipa: Nanodiamond and onion-like carbon polymer nanocomposites, Diam. Relat. Mater **16**(4/7), 1213–1217 (2007)

8.153 J. Macutkevic, D. Seliuta, G. Valusis, J. Banys, V. Kuznetsov, S. Moseenkov, O. Shenderova: High dielectric permittivity of percolative composites based on onion-like carbon, Appl. Phys. Lett. **95**(11), 112901–112905 (2009)

8.154 O. Shenderova, V. Grishko, G. Cunningham, S. Moseenkov, G. McGuire, V. Kuznetsov: Onion-like carbon for terahertz electromagnetic shielding, Diam. Rel. Mater. **17**(4/5), 462–466 (2008)

8.155 V. Borjanović, L. Bistričić, I. Vlasov, K. Furić, I. Zamboni, M. Jakšić, O. Shenderova: Influence of proton irradiation on the structure and stability of poly(dimethylsiloxane) and poly(dimethylsiloxane)–nanodiamond composite, J. Vac. Sci. Technol. B **27**, 2396–2404 (2009)

8.156 S. Gupta, A.M. Scuttler, J. Farmer: Novel nanocarbon hybrids of single-walled carbon nanotubes and dispersed nanodiamond: Structure and hierarchical defects evolution irradiated with gamma rays, J. Appl. Phys. **107**(10), 104308–104318 (2010)

8.157 K.E. Prasad, B. Das, U. Maitra, U. Ramamurty, C.N.R. Rao: Extraordinary synergy in the mechanical properties of polymer matrix composites reinforced with two nanocarbons, Proc. Natl. Acad. Sci. USA **106**(32), 13186–13189 (2009)

8.158 V.Y. Dolmatov: Applications of Detonation Nanodiamond. In: *Ultrananocrystalline Diamond*, ed. by O.A. Shenderova, D.M. Gruen (William Andrew, Norwich 2006) pp. 513–527

8.159 Q.W. Zhang, V.N. Mochalin, I. Neitzel, I.Y. Knoke, J. Han, C.A. Klug, J.G. Zhou, P.I. Lelkes, Y. Gogotsi: Fluorescent PLLA-nanodiamond composites for bone tissue engineering, Biomaterials **32**(1), 87–94 (2011)

8.160 I. Neitzel, V. Mochalin, I. Knoke, G.R. Palmese, Y. Gogotsi: Mechanical properties of epoxy composites with high contents of nanodiamond, Compos. Sci. Technol. **71**(6), 710–716 (2011)

8.161 M. Comet, V. Pichot, B. Siegert, F. Britz, D. Spitzer: Detonation nanodiamonds for doping Kevlar, J. Nanosci. Nanotechnol. **10**(7), 4286–4292 (2010)

8.162 G.K. Burkat, V.Y. Dolmatov, E. Osawa, E.K. Orlova: A study of properties of chromium-diamond coatings using nanodiamonds from various producers, J. Superhard. Mater. **32**(2), 98–111 (2010)

8.163 D. Nunes, V. Livramento, U.V. Mardolcar, J.B. Correia, P.A. Carvalho: W-diamond/Cu-diamond nanostruc-

tured composites for fusion devices, J. Nucl. Mater. **426**, 115–119 (2012)
8.164 J.M. Martin, N. Ohmae (Eds.): *Nanolubricants* (Wiley, New York 2008)
8.165 V.Y. Dolmatov: Detonation nanodiamonds in oils and lubricants, J. Superhard Mater. **32**(1), 14–20 (2010)
8.166 M.G. Ivanov, V.V. Kharlamov, V.M. Buznik, D.M. Ivanov, S.G. Pavlushko, A.K. Tsvetnikov: Tribological properties of the grease containing polytetrafluorethylene and ultrafine diamond, Friction Wear **25**(1), 99–105 (2004)
8.167 M.G. Ivanov, S.V. Pavlyshko, D.M. Ivanov, I. Petrov, O. Shenderova: Synergistic compositions of colloidal nanodiamond as lubricant-additive, J. Vac. Sci. Technol. B **28**, 869–878 (2010)
8.168 M.G. Ivanov, S.V. Pavlyshko, D.M. Ivanov, I. Petrov, G. McGuire, O. Shenderova: Nanodiamonds particles as additives in lubricants, Mater. Res. Soc. Symp. Proc., Vol. 1203 (2009), 1203-J17-16
8.169 E. Oh, J.B. Delehanty, K.E. Sapsford, K. Susumu, R. Goswami, J.B. Blanco-Canosa, P.E. Dawson, J. Granek, M. Shoff, Q. Zhang, P.L. Goering, A. Huston, I.L. Medintz: Cellular uptake and fate of PEGylated gold nanoparticles is dependent on both cell-penetration peptides and particle size, ACS Nano **5**(8), 6434–6448 (2011)
8.170 V.L. Colvin: The potential environmental impact of engineered nanomaterials, Nat. Biotechnol. **21**(10), 1166–1170 (2003)
8.171 L. Braydich-Stolle, S. Hussain, J.J. Schlager, M.C. Hofmann: In vitro cytotoxicity of nanoparticles in mammalian germline stem cells, Toxicol. Sci. **88**(2), 412–419 (2005)
8.172 S.M. Hussain, K.L. Hess, J.M. Gearhart, K.T. Geiss, J.J. Schlager: In vitro toxicity of nanoparticles in BRL 3A rat liver cells, Toxicol. In Vitro **19**(7), 975–983 (2005)
8.173 Y. Yuan, Y. Chen, J.-H. Liu, H. Wang, Y. Liu: Biodistribution and fate of nanodiamonds in vivo, Diam. Relat. Mater. **18**(1), 95–100 (2009)
8.174 A. Nel, T. Xia, L. Madler, N. Li: Toxic potential of materials at the nanolevel, Science **311**(5761), 622–627 (2006)
8.175 L. Zhao, T. Takimoto, M. Ito, N. Kitagawa, T. Kimura, N. Komatsu: Chromatographic separation of highly soluble diamond nanoparticles prepared by polyglycerol grafting, Angew. Chem. Int. Ed. **50**(6), 1388–1392 (2011)
8.176 K.K. Liu, C.L. Cheng, C.C. Chang, J.I. Chao: Biocompatible and detectable carboxylated nanodiamond on human cell, Nanotechnology **18**, 32 (2007)
8.177 H.-C. Chang: *Development and Use of Fluorescent Nanodiamonds as Cellular Markers* (Springer, New York 2009)
8.178 N. Mohan, C.S. Chen, H.H. Hsieh, Y.C. Wu, H.C. Chang: In vivo imaging and toxicity assessments of fluorescent nanodiamonds in *Caenorhabditis elegans*, Nano Lett. **10**(9), 3692–3699 (2010)
8.179 N. Kossovsky, A. Gelman, H.J. Hnatyszyn, S. Rajguru, R.L. Garrell, S. Torbati, S.S. Freitas, G.M. Chow: Surface-modified diamond nanoparticles as antigen delivery vehicles, Bioconjug. Chem. **6**(5), 507–511 (1995)
8.180 A.H. Smith, E.M. Robinson, X.Q. Zhang, E.K. Chow, Y. Lin, E. Osawa, J.Z. Xi, D.A. Ho: Triggered release of therapeutic antibodies from nanodiamond complexes, Nanoscale **3**(7), 2844–2848 (2011)
8.181 L.M. Manus, D.J. Mastarone, E.A. Waters, X.Q. Zhang, E.A. Schultz-Sikma, K.W. MacRenaris, D. Ho, T.J. Meade: Gd(III)-nanodiamond conjugates for MRI contrast enhancement, Nano Lett. **10**(2), 484–489 (2010)
8.182 C.-M. Sung, M. Sung, E. Sung: Healthcare and cosmetic compositions containing nanodiamond, US Patent 7294340 (2007)
8.183 T.T.B. Nguyen, H.C. Chang, V.W.K. Wu: Adsorption and hydrolytic activity of lysozyme on diamond nanocrystallites, Diam. Relat. Mater. **16**(4–7), 872–876 (2007)
8.184 E. Perevedentseva, C.Y. Cheng, P.H. Chung, J.S. Tu, Y.H. Hsieh, C.L. Cheng: The interaction of the protein lysozyme with bacteria *E. coli* observed using nanodiamond labelling, Nanotechnology **18**, 31 (2007)
8.185 O. Shenderova, V. Grichko, S. Hens, J. Walsh: Detonation nanodiamonds as UV radiation filter, Diam. Relat. Mater. **16**(12), 2003–2008 (2007)
8.186 A.M. Zaitsev: *Optical Properties of Diamond* (Springer, Berlin, Heidelberg 2001)
8.187 M. Daenen, O.A. Williams, J. D'Haen, K. Haenen, M. Nesladek: Seeding growth and characterization of nanocrystalline diamond films on various substrates, Phys. Status Solidi (a) **203**(12), 3005–3010 (2006)
8.188 O.A. Williams, O. Douheret, M. Daenen, K. Haenen, E. Osawa, M. Takahashi: Enhanced diamond nucleation on monodispersed nanocrystalline diamond, Chem. Phys. Lett. **445**(4–6), 255–258 (2007)
8.189 V.N. Anisimov, M.A. Zabezhinski, I.G. Popovich, A.I. Lieberman, J.L. Shmidt: Prevention of spontaneous and chemically-induced carcinogenesis using activated carbon fiber adsorbent. I. Effect of the activated carbon fiber adsorbent 'Aqualen' on spontaneous carcinogenesis and life-span in mice, Cancer Lett. **126**(1), 23–28 (1998)
8.190 V.N. Anisimov, M.A. Zabezhinski, I.G. Popovich, L.M. Berstein, I.G. Kovalenko, A.I. Lieberman, J.L. Shmidt: Prevention of spontaneous and chemically induced carcinogenesis using activated carbon fiber adsorbent. III. Inhibitory effect of the activated carbon fiber adsorbent 'Aqualen' on 1,2-dimethylhydrazine-induced intestinal carcinogenesis in rats, Cancer Lett. **138**(1/2), 27–35 (1999)

8.191 T.D. Phillips: Dietary clay in the chemoprevention of aflatoxin-induced disease, Toxicol. Sci. **52**(2), 118–126 (1999)
8.192 N. Gibson, O. Shenderova, A. Puzyr, K. Purtov, V. Grichko, T.J.M. Luo, Z. Fitgerald, V. Bondar, D. Brenner: Nanodiamonds for Detoxification, Tech. Dig. 2007 NSTI NanoTechnology Conf., Vol. 8 (2007) pp. 713–716
8.193 V.S. Bondar, I.O. Pozdnyakova, A.P. Puzyr: Applications of nanodiamonds for separation and purification of proteins, Phys. Solid State **46**(4), 758–760 (2004)
8.194 V.W.K. Wu: Adsorption reaction constants between nanosilica/nanodiamond and lysozyme molecule at pH = 11.0, Chem. Lett. **35**(12), 1380–1381 (2006)
8.195 O. Loh, R. Lam, M. Chen, N. Moldovan, H.J. Huang, D. Ho, H.D. Espinosa: Nanofountain-probe-based high-resolution patterning and single-cell injection of functionalized nanodiamonds, Small **5**(14), 1667–1674 (2009)
8.196 R.C. Devries: Synthesis of diamond under metastable conditions, Annu. Rev. Mater. Sci. **17**, 161–187 (1987)
8.197 J.E. Butler, A.V. Sumant: The CVD of nanodiamond materials, Chem. Vapor Depos. **14**(7/8), 145–160 (2008)
8.198 S. Hens, S. Wallen, O. Shenderova: *Nanodiamond fractionation and products thereof*, US Patent Application, Vol. 7569205 (International Technology Center, 2009)
8.199 O. Shenderova, S. Hens, G. McGuire: Seeding slurries based on detonation nanodiamond in DMSO, Diam. Relat. Mater. **19**(2/3), 260–267 (2010)
8.200 R. Hauert: A review of modified DLC coatings for biological applications, Diam. Relat. Mater. **12**(3/7), 583–589 (2003)
8.201 M. Amaral, C.S. Abreu: Biotribological performace of NCD coated Si_3N_4–bioglass composites, Diam. Relat. Mater. **16**(4/7), 790–795 (2007)
8.202 S. Mitura, A. Mitura, P. Niedzielski, P. Couvrat: Nanocrystalline diamond coatings, Chaos Solitons Fractals **10**(12), 2165–2176 (1999)
8.203 P. Bajaj, D. Akin, A. Gupta, D. Sherman, B. Shi, O. Auciello, R. Bashir: Ultrananocrystalline diamond film as an optimal cell interface for biomedical applications, Biomed. Microdevices **9**(6), 787–794 (2007)
8.204 K. Bakowicz-Mitura, G. Bartosz, S. Mitura: Influence of diamond powder particles on human gene expression, Surf. Coat. Technol. **201**(13), 6131–6135 (2007)
8.205 X.C. Xiao, J. Wang, C. Liu, J.A. Carlisle, B. Mech, R. Greenberg, D. Guven, R. Freda, M.S. Humayun, J. Weiland, O. Auciello: In vitro and in vivo evaluation of ultrananocrystalline diamond for coating of implantable retinal microchips, J. Biomed. Mater. Res. B **77**(2), 273–281 (2006)
8.206 V.V. Danilenko: Nanodiamonds: Problems and prospects, J. Superhard Mater. **32**(5), 301–310 (2009)

Part B NanoMet

Part B NanoMetals

9 Noble Metal Nanoparticles
Theruvakkattil S. Sreeprasad, Manhattan, USA
Thalappil Pradeep, Chennai, India

10 Nanostructures of Common Metals
Melinda Mohl, Oulu, Finland
Krisztián Kordás, Oulu, Finland

11 Alloys on the Nanoscale
Giovanni Barcaro, Pisa, Italy
Alfredo Caro, Los Alamos, USA
Alessandro Fortunelli, Pisa, Italy

12 Magnetic Nanostructures: Synthesis, Properties, and Applications
Shashwat Shukla, Singapore, Singapore
Pratap Kumar Deheri, Singapore, Singapore
Raju V. Ramanujan, Singapore, Singapore

9. Noble Metal Nanoparticles

Theruvakkattil S. Sreeprasad, Thalappil Pradeep

Noble metal nanoparticles in general and their gold and silver analogs in particular are attracting huge interest from the scientific community owing to their fabulous properties and diversity of applications. Mankind has been fascinated by gold and silver since prehistoric times, and applications of their nanoparticles have attracted attention for millennia, although understanding phenomena at the nanoscale is very recent. Nanoscale analogs are being explored due to their unusual functional attributes quite unlike the bulk. As research in this area moves forward, scientists are discovering novel application possibilities. Tunability of properties by varying size, shape, composition, or local environment presents them with unusual capabilities. By manipulating the chemical composition of the materials at the nanoscale, their electrical, chemical, optical, and other properties can be manipulated precisely. In this chapter, an overview of their history, diversity, strategies of synthesis, and optical properties is presented. The specialized methods employed for synthesis of anisotropic nanosystems are also discussed. Approaches to modulate the properties of these systems postsynthetically either through chemical reactions or by the formation of superstructures via assembly are also covered. Methodologies for fabricating functionalized nanomaterials are also discussed. Various proposed applications of such materials are pointed out. A glimpse into a newly emerging category of noble metal nanosystems called quantum clusters is also given.

9.1 **Historical Perspective of Gold and Silver NPs** 304

9.2 **Diverse Nanostructures** 307
9.2.1 Physical and Chemical Methods 308
9.2.2 General Issues of Concern 309

9.3 **Common Synthetic Routes for the Preparation of Noble Metal NPs** ... 311
9.3.1 Solution Phase Routes by Chemical Reduction 311
9.3.2 The Most Common Methods for Gold NPs 312
9.3.3 Specialized Synthetic Strategies – Anisotropic NPs 314

9.4 **Properties of Noble Metal Nanoparticles** . 322

9.5 **Postsynthetic Tuning of Properties** 324
9.5.1 Tuning Properties Through Chemical Reactions 324
9.5.2 Modification of Properties – Formation of Superstructures 331

9.6 **Functionalized Metal NPs** 343
9.6.1 Core–Shell Nanoparticles 343

9.7 **Applications of Gold and Silver Nanoparticles** 347
9.7.1 Water Purification 348
9.7.2 Bioconjugation and Labeling 357
9.7.3 Optical Contrast Agents 357
9.7.4 Photothermal Therapy 358
9.7.5 Cancer Cell Imaging 359
9.7.6 Surface-Enhanced Raman Scattering Substrates 360
9.7.7 Superhydrophobic Surfaces 360
9.7.8 Mercury Sensor 361
9.7.9 Infrared Absorbing Material 362
9.7.10 Plasmonic Waveguides 362
9.7.11 Biosensors 362
9.7.12 Photovoltaic Devices 362

9.8 **New Gold and Silver Materials – Quantum Clusters** 363

9.9 **Conclusions** 366

References 367

Noble metals are those metals which are resistant to corrosion and oxidation in moist air. The list contains ruthenium, rhodium, palladium, silver, osmium, iridium, platinum, and gold, in order of atomic number. Many of them are also precious as they are of poor abundance in the Earth's crust. Noble metal nanoparticles (NPs), especially of gold (Au) and silver (Ag), have been intensely explored by the scientific community owing to their spectacular properties. The *noble* nature of these NPs compared with other NPs, for example, transition metal NPs such as iron, nickel, or cobalt, as well as their lesser cytotoxicity make them attractive candidates for biological and environmental applications. A large proportion of the study of noble metal NPs is done with Au and Ag NPs. Therefore, Au and Ag NPs can be taken as examples to demonstrate the relevance and diversity of the area of NPs in general.

9.1 Historical Perspective of Gold and Silver NPs

From time immemorial, three metals, namely gold, silver, and copper, were used extensively by mankind. In fact, it is certain that these were the metals first used by human beings, since they are found in the native state. Even before the invention of gold coins in Egypt around 3400 BC, these metals were used as primitive money, hence the name *coinage metals*. The origin of the names *gold* and *silver* has long history. Different words are used in different languages to represent gold. Most of them simply mean *yellow* (*metal*), which comes from its appearance; for example, the Latin name *aurum* means yellow. This word is believed to have been coined from the ancient Roman word *aurora* or *ausosa*, meaning morning glow. The word is said to have its origin in the Sanskrit word *hari*, meaning *yellow*. In Slavic languages, gold was referred to as *золото* (*zlato*), having connections with the Indo-European word *sol* (sun). The present-day name *gold* is believed to have Germanic origin (*goud* in Dutch). The root of the word *gold* is believed to be from *gelwa*, meaning again yellow, which is connected to the Sanskrit word *jval*, meaning *to shine*. Hence, the word *gold* really means *the yellow shining metal*. Silver also has a rich history and it is also known by different names. It has different but very similar names in Dutch (*zilver*), German (*Silber*), and Anglo-Saxon (*seolfor*). In Greek, silver is known as *argyros* and in Latin as *argentums*, which in turn are closely related. The Italian (*argento*) and French (*argent*) names are also similar. However, the Spanish use a totally different name for silver: *plata*.

Gold and silver NPs have a rich history in science, where they were used for both esthetic and medicinal purposes [9.1]. A mixture of gold salts with molten glass was used by medieval artisans to produce tiny gold colloids having a rich ruby color, and their varieties were exploited for coloration of glass, ceramics, and pottery. The great alchemist and founder of modern medicine, Paracelsus (1493–1541), developed many highly successful treatments from metallic minerals, including gold. In China, people cook their rice with a gold coin in order to help replenish gold in their bodies. Colloidal gold has been incorporated into glasses and vases to give them color. The oldest of these is the fourth century AD Lycurgus cup made by the Romans (one piece is kept in the British Museum in London) (Fig. 9.1). The cup appears red in transmitted light (if a light source is held within the cup) and appears green in reflected light (if the light source is outside). Modern chemical analysis shows that the glass is not much different from that used today. However, it contains very small amounts of gold (about 40 ppm) and silver (about 300 ppm) in the form of mixed Au-Ag NPs of approximately 70 nm diameter. *Purple of Cassius*, a pink pigment commonly used in the seventeenth century, is also now known to be a combination of gold particles and tin dioxide.

The Egyptians used gold for mental, bodily, and spiritual purification [9.2], and the medicinal use of gold can be traced back to China in 2500 BC. In ancient times, Egyptians used gold in dentistry as well. In the Indian medical system called *Ayurveda*, gold is used in several preparations. One popular preparation is called *Saraswatharishtam*, prescribed for memory enhancement. Gold is also added in certain medicinal preparations for babies, in order to enhance their mental capability. All these preparations use finely ground gold along with herbs.

The curative power of gold is well documented from antiquity. Until the Middle Ages, gold was used as a cure for various diseases such as heart and venereal problems, dysentery, epilepsy, and tumors, as documented in a book written by Francisci Antonii in 1618 [9.1]. The use of *soluble gold* for diagnosis of syphilis is also documented [9.1]. In his book of 1676,

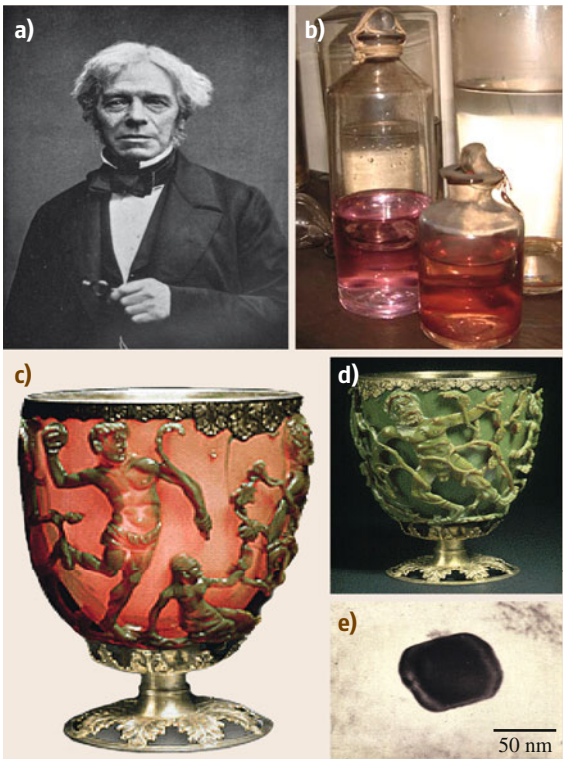


Fig. 9.1 **(a)** Michael Faraday (after [9.3]). **(b)** Faraday's gold preserved at the Royal Institution of Great Britain (after [9.4]). **(c,d)** The Lycurgus cup made from glass appears red in transmitted light and green in reflected light (after [9.5]). **(e)** The 70 nm Au-Ag alloy NPs found in the glass of the Lycurgus cup, as seen in a transmission electron micrograph (after [9.5])

Johann Kunckels mentioned a form of gold which he addressed as *drinkable gold that contains metallic gold in a neutral, slightly pink solution that exerts curative properties for several diseases* [9.1]. In this book, he even foresaw the possibility of the existence of gold in a form that is not visible to the human eye. It was also reported in 1718 by Hans Heinrich that the stability of *drinkable gold* can be increased by a special combination with boiled starch [9.1].

During this period, gold was used for coloring fabrics as well. In 1794 Mrs. Fuhlame reported that she had dyed silk with colloidal gold, which is documented in her book *An Essay on Combustion with a View to a New Art of Dying and Painting*. The different colors exhibited by different *drinkable gold preparations* were explained by Jeremias Benjamin Richters in 1818 [9.1]. He hypothesized that *pink or purple solutions contain gold in the finest degree of subdivision, whereas yellow solutions are found when these fine particles have aggregated* [9.1].

Systematic chemical synthesis of colloidal NPs was pioneered by Michael Faraday in 1857, when he observed the formation of a pure form of deep-red-colored colloidal gold by the reduction of an aqueous solution of chloroaurate ($AuCl_4^-$) using phosphorus in CS_2 in a two-phase system [9.6] (the word *colloid* itself was nonexistent at the time of Faraday's work). This is considered to have been a major step in the development of nanotechnology. He found that colloidal gold had special optical and electrical properties. In this study, he also investigated the optical properties of thin films prepared from dried colloidal solutions. He observed a reversible color change from bluish-purple to green upon pressurizing the films. In 1861, *Graham* coined the word *colloid* from the French word *colle* [9.7]. Following Faraday, a large number of experimental methods have been reported for synthesis of gold NPs (GNPs). This is dealt with in a separate section.

Similar to gold, silver has also been used for thousands of years in various fields. As explained earlier, it is Au-Ag NPs which are responsible for the color of the Lycurgus cup. However, the major use of silver historically was in the medicinal field and as an antimicrobial/disinfectant agent. Silver vessels were used to keep water and other liquids fresh by the Greeks [9.8]. The writings of *Herodotus*, the Greek philosopher and historian, date the use of silver to before the birth of Christ [9.9]. Silver urns were used for storage of wine to prevent spoilage in the Roman Empire. A similar use of silver is mentioned in ancient Egyptian writings also. Although most ancient civilizations were not fully aware of the antibacterial properties of silver, it was widely accepted that addition of silver to water would increase clarity, reduce odor, and improve the taste as well [9.10]. In ancient civilizations (especially the Greek and Roman Empires), Ag was used for various applications because of its well-known medical, preservative, and restorative powers [9.8, 10]. The germicidal power of silver was also known during these times [9.11]. Before modern germicides and antibiotics were discovered, the old civilizations understood that disease-causing pathogens would not survive in the presence of silver. Hence, silver was used in dishware, drinking vessels, and eating utensils [9.11]. Rich families of those periods stored and ate their food from silver vessels to prevent bacteria from growing. This is perhaps the reason for the phrase, *born with a silver spoon*, indicating traditional wealth. Vikings had knowledge

of the antialgal effects of silver. They applied strings of silver and copper below the water-line on the hull of their ships to prevent growth of algae and barnacles. The same methodology is used on modern ships as well [9.12].

Hippocrates, the father of modern medicine, promoted the use of silver by writing about the beneficial healing and antidisease properties of silver in his book [9.13]; he also recommended the use of finely powdered silver formulations for various ailment conditions such as ulcers and wounds [9.14]. Alexander the Great was advised by Aristotle to boil and store water in silver vessels to eradicate waterborne diseases [9.15]. Ancient Indian civilizations also had knowledge of the medicinal powers of silver. In Ayurvedic medicine, silver was used (in small amounts) as a tonic and rejuvenating agent for patients incapacitated by age or disease. Silver was also used as an eyedrop for ophthalmic problems [9.16], for various infections [9.17], and sometimes internally for diseases such as gonorrhea, epilepsy, common cold, and tropical sprue [9.11, 18]. Colloidal silver preparations (CSP) were used to treat or prevent gonorrhea and gonorrheal conjunctivitis [9.19]. It was also used in pure silver tongue scrapers as part of dental maintenance and for other oral disease conditions. Silver was widely used for the treatment of heart problems, blood purification, and other conditions, especially in the Middle East. Silver needles have been used for acupuncture by physicians of Chinese medicine over the years.

Silver also found applications in many other medical therapies and devices, including bone prostheses, ophthalmic surgery, treatments for venereal disease, and veterinary medicine [9.10]. The use of silver pins to fuse bones, silver wire to suture wounds, silver powder on ulcerations, and silver foil to protect wounds against infection was reported by ancient surgeons. In Egypt, skeletons where silver pins were used to repair bones via surgical procedures were found to support this [9.15]. As early as the late thirteenth century, it is reported that Lanfranc utilized silver tubes for introduction of food beyond fistula [9.20]. However, Paracelsus is credited to be the pioneer of the use of metals for medical applications. In his hermetic and alchemical writings, he associated silver with the development of brain activities. In 1617 Fabricius of Aquapendente, used a small silver tube to feed patients suffering from tetanus [9.21]. In 1884, Crede, a German obstetrician, popularized administering 1% silver nitrate solution to newborns to prevent ophthalmia neonatorum [9.22, 23]. It is also documented that he even used finely divided silver powder also for medical applications in 1896, which can be considered as the first proper medicinal use of colloidal silver [9.24, 25]. It is also documented that, during the mid-nineteenth century, silver wire structures were used to reduce septic complications [9.20]. Even in the late eighteenth century, William Halsted used silver wire for hernia operations and silver foil to prevent wound-related infections [9.26]. It is documented that, during the late 1800s and early 1900s, silver was frequently used as a medicine. During ancient times, it was understood that several metal salts and compounds have strong germicidal properties. However, it was also proved that silver alone has both strong germicidal properties and low or no toxicity to humans, which increased the use of silver-based preparations. The colloidal state is known to be the most effective form among other formulations because colloidal silver does not have the caustic properties of salts (such as $AgNO_3$) and it also demonstrated a high level of activity at very low concentrations [9.24]. Although it was established that colloidal silver was superior in this regard, the use of silver nitrate continued for a long time [9.24].

Scientific and methodological study of the antibacterial effects of metals against bacteria and lower life forms was carried out by Ravelin (1869) and in a more detailed manner by Karl Wilhelm von Nägeli, a Swiss botanist who discovered chromosomes (he named them *cytoblasts*) [9.13]. *Nägeli* reported that even low concentrations (9.2×10^{-9} and 5.5×10^{-6} M) of extremely fine silver, copper, as well as other metal hydrosols have toxic effects on *Spirogyra* and *Aspergillus niger* spores, respectively. The term *oligodynamic effect* was coined by him to explain this phenomenon [9.13]. In early twentieth century the germicidal properties of colloidal silver were popularized by Henry Crookes. He even stated in his book [9.11, 24] that:

> *silver in the colloidal state is highly germicidal, quite harmless to humans and absolutely nontoxic. Rather than in a chemical compound, the silver in the colloidal state may be applied in a much more concentrated form, with correspondingly better results. All virus, fungus, bacterium, streptococcus, staphylococcus, and other pathogenic organisms are killed in three or four minutes upon contact. There are no side effects whatsoever from the highest concentrations.*

Long before the introduction of antibiotics, colloidal silver had been known and used as a bactericide for at least 1200 years [9.15]. Also, it is reported that in

World War I, when antibiotics has not yet been discovered, silver formulations were used to prevent and treat infections, as antiseptics [9.27], as eyedrops to prevent conjunctivitis, etc. Silver compounds were used in dermatology to treat certain skin conditions, such as corns and warts [9.28]. In the early 1900s, silver foil dressings were used for wounds. These dressings were used extensively until just after World War II and were listed in the Physician's Desk Reference until 1955 [9.27]. However, with the introduction of antibiotics in the 1940s, the use of silver as an antimicrobial agent diminished. Still, silver holds an edge over antibiotics, since bacteria do not generally develop resistance to silver unless they have a very thick wall that does not absorb it [9.10].

In 1889, *Frens* and *Overbeek* [9.29] and *Lea* [9.30] accomplished a major landmark in chemistry by preparing silver colloid for the first time through reduction of silver nitrate using ferrous sulfate and consequent protection of colloidal particles with citrate ions. A huge interest in colloidal silver followed this, and a large number of researchers worked on the antibacterial properties of silver in the early twentieth century. Research work was initiated to use silver for water purification as well. In 1928, Katadyn of Switzerland developed a silver-impregnated ceramic gravity-fed water filter termed *Katadyn silver*. This was utilized as an antibacterial water filter in remote areas where clean water was not readily available by various agencies and militaries around the world [9.31]. In another instance, in a Federal Bureau of Investigation (FBI) declassified document 100-93211.247 dated December 21, 1949 and declassified on September 9, 2004, the use of silver for converting sea water to fresh water is quoted. This document illustrates that during World War II the US Navy used the services of Alexander Goetz, then Associate Professor of Physics at the California Institute of Technology, for generating drinking water. The document says *he helped perfect the process for converting sea water into fresh water by the use of silverized carbon pellets* [9.32]. Throughout the twentieth century, the popularity of silver salts continued to grow and several silver-based products were also commercialized (Katadyn, Argyrol, Movidyn, Tetrasil, Alagon, etc.) [9.33]. Silver in the supported form was also used to disinfect water. Zero-valent silver was immobilized on activated carbon in 1966 by *Renn* for disinfection of water [9.34]. Silver has also been used in space programs since the Apollo missions to sterilize recycled water. The same practice continues, and silver ion-exchange materials are still being used in space stations and space shuttles to recycle water.

As this historical perspective illustrates, gold and silver have been used for a large number of applications in several fields. However, until the last century, most applications were restricted to their medicinal value or antimicrobial activity. Catalysis is another area where silver found application in the early twentieth century. A few examples where noble metals were used as catalysts include silver-based catalysis of methanol to formaldehyde [9.35] and ethylene to ethylene oxide [9.36].

9.2 Diverse Nanostructures

The size and shape-dependent variation in properties of matter at the nanoscale is one of the most fascinating aspects of nanoscience. Hence, various parameters which directly affect the intrinsic properties of such materials [9.37–40] must be thoroughly understood. Nanomaterials can be broadly classified into four groups depending upon the confinement: (a) zero-dimensional (0-D), (b) one-dimensional (1-D), (c) two-dimensional (2-D), and (d) three-dimensional (3-D) nanomaterials. Similarly, based on geometry, they can be classified into isotropic and anisotropic NPs.

Gold and silver nanosystems are interesting because of the diversity that they exhibit. They are found in different shapes. Spherical NPs, quantum dots, and the newest excitement in the subnano regime called *quantum clusters* are all included in isotropic nanosystems, since they have no specific direction of growth and no difference in properties in different directions. They are generally considered to be 0-D nanosystems. However, materials of 1-D and 2-D NPs, and most 3-D nanosystems, which usually have a specific direction of growth and confinement of electronic motion along specific axes, are included in anisotropic NPs. Anisotropic NPs comprise a plethora of nanostructures such as nanorods (NRs) [9.41–43], nanowires (NWs) [9.44–46], nanotubes [9.47] (which can be collectively termed as 1-D); triangles [9.48, 49], plates and sheets [9.50, 51], ribbons or helices [9.52, 53], nanobelts [9.54, 55], nanocombs [9.56], nanorattles [9.57] etc. (belonging to 2-D), and pyramids [9.58, 59], stars [9.60, 61], flowers [9.62–65], multipods [9.66, 67], nanourchins [9.68, 69], tad-

poles [9.70, 71], nanocages [9.72, 73], nanorice [9.74, 75], nanocorn [9.76], nanoboxes [9.77, 78], nanocubes [9.79], triangular nanoframes [9.80], nanodumbbells [9.81], etc. (belonging to 3-D).

Noble metal nanosystems are attracting intense research efforts due to their diverse properties and exceptional tunability in properties. The size, surface, and shape dependence of the physical, optical, and electronic properties of anisotropic nanomaterials make them fascinating components in modern materials research. These properties of these systems are dealt with in a separate section. However, the most important step in utilizing these properties is to synthesize these materials with precise control over their size and shape. Specialized synthetic strategies are needed to make them with precise control over size and shape. These synthetic methods, at least in some cases, should have the flexibility to be expanded for possible commercial exploitation, if suitable applications are found. In this section, the most common methods used for synthesis of noble metal nanomaterials are briefly discussed.

9.2.1 Physical and Chemical Methods

General methods of synthesis can be broadly divided into two categories: physical and chemical routes. In the former approach, bulk material or constituents of the desired nanomaterial are taken and formulate systematic conditions by which nanomaterials are formed. Since the methods of synthesis start from bulk materials, they are called *top-down* approaches. This method includes the following techniques:

1. High-energy ball milling: Nanoscale powders are produced by milling bulk materials.
2. Wire explosion: Used to produce conducting nanomaterials such as metals. A sudden high current pulse is supplied resulting in an explosion.
3. Arc discharge: Alternating current (AC) or direct current (DC) arcs are used to evaporate materials.
4. Inert-gas condensation: Particle growth is achieved by condensing evaporated atoms in a matrix.
5. Laser ablation: High-energy laser to induce evaporation.
6. Ion sputtering: Impact using high energy ions (usually rare gases) cause evaporation.

By controlling the environment in which evaporation happens, we can control the composition of the resulting material. For example, if evaporation of metals occurs in the presence of oxygen, oxides can be produced. These methods can effectively manufacture large quantities of materials. However, these methods can only produce materials with large particle size variation.

In chemical methods, which will be described in more detail later, a range of techniques is used. In all of these, nanomaterials are made starting from atoms generated from ions, in solution, and are assembled to make nanomaterials. As the synthesis initiates from atoms, these methods are also called *bottom-up* approaches. Several methods come under this category:

1. Chemical reduction: Metal ions are reduced using reducing agents to create atoms.
2. Electrochemical synthesis: Electrochemical reduction or oxidation reactions.
3. Photochemical synthesis: Chemical processes assisted by light.
4. Sonochemical routes: Chemical reaction system done with the aid of ultrasound.
5. Solvothermal synthesis: Chemical processes in a closed system using solvents at lower temperatures.
6. Interfacial synthesis: An organic–aqueous interface is created to make nanomaterials.
7. Micelles and microemulsions: Producing nanomaterials by using oil-in-water or water-in-oil emulsions, or cavities of micelles or reverse micelles.
8. Biological methods: Biomolecules or living cells being used as synthetic reactors.
9. Thermolysis (e.g., pyrolysis, spray pyrolysis) strategies: Reactions in flames and thermal decomposition.
10. Arrested precipitation (mainly for semiconductors and oxides): Desired material is precipitated from an organometallic precursor solution.
11. Hybrid methods: More than one of the methods described above is used in a systematic combination to produce complex structures.
12. Solvated metal atom dispersion (SMAD): Nanoparticles are synthesized from metal vapors deposited in solid matrices of solvents, which upon heating evaporates to create the nanostructure. Synthesis of protected clusters is also possible if a capping agent is present in the solvent used.

Since NPs are made up of atoms, a two-phase colloidal system can be categorized in terms of the dispersed phase and the dispersion medium. The dispersed phase and the dispersion medium can be gas, liquid, or solid, except for the combination *gas in gas*. Therefore, NPs dispersed in an amorphous solid is a colloidal

system and consequently a *nanofluid*. A dispersion of nanomaterials in a fluid medium is generally referred to as *nanofluid*. Here, the fluid is a liquid at ordinary conditions of temperature and pressure, and hence supercritical fluids and gases as the dispersion phase can be omitted. However, it is worth mentioning that the synthesis of NPs in media such as solid matrices [9.82] and supercritical fluids [9.83] is a highly advanced research area. From the historical perspective discussed above, it is also important to remember that some of the early applications of NPs were in the form of particles embedded in glasses. Supercritical fluids are attracting a great deal of interest currently. Generally these fluids are mostly termed as colloids. The nanomaterials so prepared can be in the form of a fluid or solid. In many cases, applications of these materials will be in the form of solutions or dispersions, called nanofluids. They may also be used as powders, often referred to as nanomaterials. Particle films, pastes, emulsions, and many other forms may also be used.

9.2.2 General Issues of Concern

For devising a synthetic strategy, several factors of interest should be taken into account.

Thermal Stability

NPs being metastable systems will transform to stable materials having global energy minima in the free energy landscape. Thus, they will transform back to the bulk form at infinite time. Mostly, the time involved has no practical consequence. For example, *Faraday*'s colloids, made in 1856 (and reported in 1857), are still stable [9.6]. In other words, even though the bulk metal is more stable, the comparison is similar to that comparing the stability of graphite in comparison with diamond. Although diamond is metastable, it will not become graphite at normal conditions of temperature and pressure even in a millennium. Diamond-to-graphite transformation kinetics is very slow and hence insignificant under normal conditions. The situation of NPs in suitable media is analogous and is referred to as *kinetic stability*.

Dispersibility in Diverse Media

An NP usually has two entities: a core, which can be ceramic, metallic, or polymeric, and a thin shell, which also can be ionic, molecular, polymeric, ceramic, or metallic (Fig. 9.2). For this review, the core is always a noble metal which governs the properties of the NPs. The shell which is usually used to provide a protective

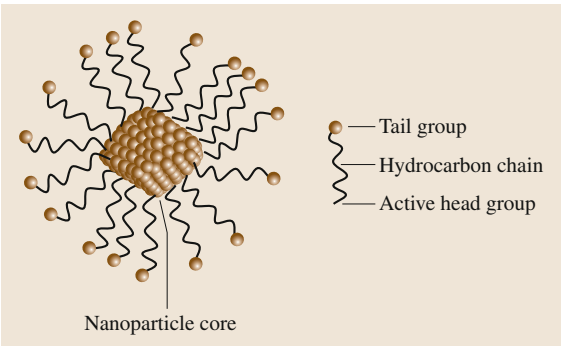


Fig. 9.2 Schematic of an NP with metallic core and organic shell. The shell may also be an extended solid such as SiO_2

layer is important in a number of applications such as those utilizing the luminescence of the particles. Moreover, the chemical nature of the shell determines the dispersibility of a NP.

Generally, the molecular shell will have a characteristic chemical affinity to the core due to its specific atoms or groups. In the case of a metal NP such as gold, for example, the metal can bind with a sulfur atom of the thiolate (−SR) group, a common protecting ligand, to form a protecting shell. Such a bond present on the surface of the NP is termed a protective monolayer or capping layer, and the NP is called a protected or capped NP. The chemical link so formed renders thermal stability to the system. The weaker the bond, the more easily it desorbs from the surface of the NP and hence the NP will be less stable. Therefore, the binding between metal and the active head group binding on the ligand is an important parameter influencing the thermal stability of the nanosystem.

It must be emphasized that the shell need not be a molecule. In specific examples, the shell will be an inherent part of the core, like in the case of silica NPs. Here, the surface will have a layer of hydroxyl groups and hence the particles can be easily suspended in water. A hydrocarbon monolayer in contrast can disperse the particle in organic solvents. In a similar manner, Au NPs can be made hydrophilic or hydrophobic. For reactive NPs such as copper, the surface is susceptible to oxidation and when the particles are exposed to air, a layer of oxide will form over the surface.

Depending upon the medium, the tail group can change its nature especially for end groups such as −COOH, $-NH_2$, −OH, etc. These groups will change form depending on the pH of the medium. In acidic media, the COOH group, for example (in the case

of a −COOH-terminated monolayer), will not become ionized and will remain as −COOH, whereas in alkaline media it will become transformed into −COO− by losing H^+. These surface charge modifications play an important role in applications such as drug delivery. Sometimes, the pH changes can affect the core as well.

Nanoparticles prepared by diverse routes and covered by a variety of activators and dispersants [9.84] such as laurate salts ($CH_3(CH_2)_{10}COO-X$), oleic acid ($CH_3(CH_2)_7CH=CH(CH_2)_7COOH$), etc., and dispersed in different media such as transformer oil, water, ethylene glycol, etc., were used for early conductivity studies [9.85]. Generally, surface functionalization is done so that the NP surface is friendly to the medium in which NPs are dispersed. The core–shell structure of an NP system is not limited to spherical particles. The very same general structure may be considered for anisotropic structures such as NRs, nanotubes, nanoshells, etc., where a chemically compatible shell is put around the nanosystem to make it go into the solution, biological environment, etc.

Chemical Compatibility and Ease of Surface Manipulation

When NPs of the same core size are considered for several applications, the above parameters attain significance. The synthetic conditions determine the size, shape, and properties of NPs as to be expected from a method producing metastable systems. Kinetically, an NP is always trapped in a local minimum of free energy, and the synthetic parameters are crucial in deciding the final product. Hence, to get uniformly the desired core size, it is essential to follow the same experimental conditions. Usually, this poses limitations in the adaptability of the system to various chemicals and conditions.

Post-synthetically, solvent compatibility can be modulated by changing the monolayer on the NPs. This process is often termed the ligand exchange, in which one monolayer of ligand molecules present on the NP surface are exchanged with another one in the medium. This exchange process usually results in equilibrium between the molecules in the adsorbed and free states. Repetition of this process a few times can complete the exchange process.

Chemical modification of the monolayer is similar to solution chemistry with simple molecules. Utilizing the chemistry of monolayers, suitable post-synthetic changes are made on NPs. For example, by employing functional group chemistry, a given monolayer can be polymerized or can be included into a polymeric matrix. This can be achieved via chemical, thermal, and photochemical processes. In specific cases, post-synthetic modification can result in the entrapment of nanosystems inside the cavity of a large molecule so that the nanosystem can be transferred into a suitable medium. The use of dendrimers and cyclodextrins are examples of this kind of chemistry.

Size Control and Monodispersity

An ideal synthetic strategy should produce particles of a given size distribution through a simple process. A narrow size distribution is always desired. Post-synthetic processes are utilized if a methodology fails to generate particles with a narrow size distribution. This involves selecting particles of interest or converting one system to another. However, post-synthetic methods also have their own advantages and disadvantages.

When a methodology produces of a variety of sizes in the as-synthesized particles, selection of a given size can be done by post-synthetic approaches. Several such processes exist. The first is size exclusion chromatography. Here, the mixture of NPs is passed through a size-selective stationary phase (e.g., a gel) having definite pore sizes. The applied eluent (solvent) elutes the material as a function of size. Agarose and Sephadex are the two common media used. The next method involves solvent-selective precipitation. In this method, by progressively changing the polarity of the medium from low to high, larger particles are forced to precipitate from the mixture. One disadvantage is that the stability of the material in different solvents may vary. However, by repeating this process, precise control over the size of the resulting NP is possible. Digestive ripening is also used to obtain monodisperse samples. In this method, the NP is digested with the protecting agent used during the synthesis at elevated temperatures. Smaller sized particles become consumed during the ripening process. Ostwald ripening or particle coarsening is a similar process where the as-prepared particles are allowed to age for a finite period during which large particles grow at the expense of smaller particles, narrowing the particle size distribution. This may be achieved along with temperature cycling.

9.3 Common Synthetic Routes for the Preparation of Noble Metal NPs

This section outlines the various strategies applied for synthesis of noble metal NPs. The discussion will mostly pertain to conventional spherical NPs. Synthesis of other shapes are extensions of some of these methods and a brief description of some of these will also be provided without going into the details.

9.3.1 Solution Phase Routes by Chemical Reduction

Metal atoms produced by the reduction of metal ions can upon aggregation produce NPs. The growth of these aggregates can be arrested at a desired stage by the use of protecting agents. A general reduction reaction can be represented as

$$M^{n+} + n\,e^- \rightarrow M^0\,. \tag{9.1}$$

Instead of supplying the electron directly, the oxidation of the reducing agent results in the production of electrons bringing about the reductions.

$$Red^{m-} \rightarrow Oxi^{(m-n)-} + n\,e^-\,, \tag{9.2}$$

where the reducing species (reducing agent) having a finite charge loses some specific amount of charge and becomes oxidized. It is important to mention that both the metal and the reductant may not contain any distinct charge and those mentioned are only nominal. The net reaction

$$M^{n+} + Red^{m-} \rightarrow M^0 + Oxi^{(m-n)-} \tag{9.3}$$

and its feasibility depends on the thermodynamics of the process, which in turn is governed by the electrochemical potentials of the corresponding half-cell reactions (standard reduction potentials). The sum of the reduction potentials (with their signs) of reactions (9.1) and (9.2) gives a net positive value, thus the process is thermodynamically feasible. This implies a net negative free energy change of $\Delta G = -nFE$, where ΔG is the free energy change of the reaction (9.3), n is the number of electrons involved, F is the Faraday constant, and E is the electrochemical potential of the reaction (9.3). Since the potential must be taken at the appropriate conditions, E must be considered not E^o. Thermodynamically feasible reactions have negative ΔG.

When the ions present in the solution are in complex form, the reduction potentials are not the only criteria that determine the feasibility of reduction. Ions present in complex form will have different potential compared to bare ions. For example, simple Au^{3+} (as in $[AuCl_4]^-$) can be reduced using mild reducing agents such as carboxylates or alcohols. However, in the presence of excess thiol this is not possible. The formation of metal thiolates makes the reduction of these complexes and reduction will only take place with strong reducing agents such as borohydride. In the presence of gold metal particles, reduction with mild reducing agents is possible, since the reduction occurs on the surface of gold. The reduction of gold ions by ascorbic acid in the presence of gold seeds during the preparation of GNRs (discussed below) is an example.

A molecule or ion itself can act both as the reducing agent and as the capping agent as in the case of citrate, amines, alcohols, thiols, etc. Reduction and the subsequent stabilization action of trisodium citrate for making Au NPs is the best example. In the recent past, several such examples have been reported where a variety of amines, alcohols, thiols, complex ions, etc., were used. Since alcohols are not good protecting agents, polyols containing a larger number of hydroxyl groups per molecule are used, which effectively chelate (multiply coordinate) the metal ions. A summary of the specific reduction processes employed is presented in Table 9.1.

Strong Reducing Agents

Reduction of metals with a large negative reduction potential is very difficult and demands careful control of the reaction conditions. The use of a strong reducing agent can minimize the solvent and other reactants present. For example, the presence of water should be avoided if the reagent is very strong to avoid the following reaction

$$2H_2O + 2e^- \rightarrow H_2 + 2OH^-\,. \tag{9.4}$$

The standard reduction potential of this reaction is -0.828 V. Solvated electrons are the most powerful reducing agents. They can be prepared in the laboratory by dissolving alkali metals in aprotic solvents like diethylether or tetrahydrofuran in the presence of excess complexing agents such as crown ether. The reaction can be depicted as

$$M + 2(15\text{-crown-5}) = M^+(15\text{-crown-5})_2\,e^-\,. \tag{9.5}$$

However, in the presence of smaller amounts of complexing agent, an alkalide (the alkali metal anion) will be formed [9.86],

$$2M + (15\text{-crown-5}) = M^+(15\text{-crown-5})M^-\,. \tag{9.6}$$

Since the thermal stability of the above reagents is less, the reactions should be done at lower tempera-

Table 9.1 Summary of various solution-phase reduction processes employed to make metal NPs

Method	Metal/reducing agent	Example	References
1. $NaBH_4$ route	Metal ion/BH_4^-	Au, Ag	[9.88, 89]
2. Amine route	Metal ion/APS[a], AES[b]	Ag	[9.90]
3. Polyol route	Metal ion/ethylene glycol	Ag, Pd	[9.91]
4. Citrate route	Metal ion/Cit^{3-}	Au, Ag	[9.6, 92]
5. Polyvinylpyrrolidone route	Metal ion/PVP[c]	Pd	[9.93]

[a] APS: 3-aminopropyltrimethoxysilane
[b] AES: 3-(2-aminoethylaminopropyl)trimethoxysilane
[c] PVP: polyvinylpyrrolidone

tures. This approach has been successfully employed for the synthesis of several nanocrystalline metals and alloys [9.87].

Trialkylborohydrides ($ABEt_3H$, A = Li, Na, K) are another class of strong reducing agents. Some methods utilizing aralkyl aluminum as the reducing agent have also been reported. A variety of transition metal NPs have been synthesized through the use of strong reducing agents [9.87, 94].

9.3.2 The Most Common Methods for Gold NPs

Two of the most common methods used for the synthesis of GNPs, namely the citrate route and the Brust method, are described in detail in this section. Other common methods for the preparation of metallic NPs are also briefly discussed.

The Citrate Route

This method also known as the Turkevich method [9.95], is the most used and easy-to-use method for the synthesis of colloidal gold NPs having a mean diameter of ≈ 15 nm. In this approach, the reducing agent used, sodium citrate (other reducing agents, such as amino acids, have also been employed successfully), also acts as the stabilizing agent, reducing Au^{3+} ions to atoms and subsequent aggregation results in the formations of NPs at elevated temperature. The NPs produced via this method are mostly monodisperse and spherical with a diameter of around 10–20 nm. The reduction in the amount of sodium citrate can increase the size of the resulting NPs. In 1973 *Frens* modified this method to obtain Au NPs of predetermined size by varying the trisodium citrate to gold ratio [9.96]. Transmission electron microscopy (TEM) images of the particles obtained by this method are shown in Fig. 9.3.

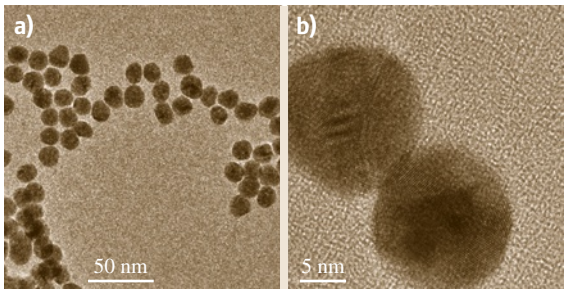


Fig. 9.3a,b TEM images of Au@citrate prepared by the citrate reduction method with average particle diameter of 15 nm. **(a)** low magnification and **(b)** higher magnification, lattice resolved image

Covering citrate-protected particles with various molecules or ceramics such as silica, can enable the NPs to be taken out of the solution, and redispersed. Since these particles can be good starting points for various investigations in biology and materials science, this approach is widely practiced [9.97].

Brust–Schiffrin Reduction

The Brust–Schiffrin method [9.98] involves phase transfer of $[AuCl_4]^-$ from the aqueous phase to the organic phase by a phase-transfer reagent, tetraoctyl ammonium bromide, and subsequent reduction of it at the interface by $NaBH_4$ in the presence of a thiol, resulting in the production of thiolate (RS−)-protected GNPs having a very small core diameter (range 1–5 nm). Variation of the Au/thiol ratio used in the synthesis can bring about a change in core dimension. A smaller Au/thiol ratio (a higher thiol concentration) produces smaller particles. The main advantage of the process is that the synthesized Au NPs can be repeatedly isolated and redispersed in organic solvents without aggregation or decomposition. The NPs can be taken out of the medium and dried, and the powder can be stored for a long time and can again be redispersed. Figure 9.4

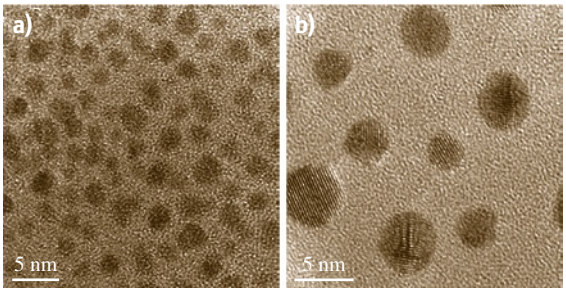


Fig. 9.4a,b Typical TEM images of Au@ODT NPs, prepared by the Brust method. Particles of 3 nm diameter are observed. **(a)** low magnification and **(b)** lattice resolved image showing single crystalline nature of most of the particles (courtesy T. Pradeep)

shows the representative image of NPs obtained in such a synthesis with a 1 : 2 Au : S ratio.

Another main advantage of this approach is that functionalization of the particles formed is feasible by using functionalized thiols during the synthesis. Alternately functionalization can be realized via exchange reaction (described earlier), where one kind of thiol or another ligand is exchanged with that on the NP surface. These NPs, often referred to as monolayer-protected clusters (MPCs), have been extensively reviewed [9.99, 100]. Several ways exist to conduct the synthesis. Using acid [9.101] for phase transfer helps to avoid phase-transfer catalyst impurity in the ensemble. The high degree of monodispersity can induce two-dimensionally-ordered lattices on a TEM grid. Digestive ripening (discussed earlier) [9.102] has been employed to reduce the particle size distribution in the Brust method. After this, the resulting particles with a narrow size distribution arrange to give 2-D and 3-D superstructures [9.103].

Similar superstructures can be produced with silver as well. Here, a variety of reducing agents can be used instead of $NaBH_4$ and the synthesis can be achieved without phase transfer. Several reports exist on the preparation of water-soluble NPs, synthesized using water-soluble thiols such as glutathione [9.104] and mercaptosuccinic acid (MSA) [9.105]. Reduction of the Au–thiolate complex in methanol by $NaBH_4$ in water is the important step during the reaction. The NP being insoluble in methanol precipitates out. This is washed repeatedly using methanol and is redispersed in water. Clusters formed using MSA are known to form well-arranged superlattices (SLs) [9.106]. Glutathione is known to produce a variety of molecular clusters starting from Au_8 to Au_{39}, which can be size separated using polyacrylamide gel electrophoresis (PAGE) [9.107].

Electrochemical Reduction

Chemical reduction is the most extensively investigated and employed method for making nanomaterials. However, various other methods have also been employed for the synthesis of special nanosystems. Electrochemical reduction where the metal is dissolved at the anode and the metal ion formed is reduced at the cathode is one of the prominent ones. To avoid the deposition of the resulting NP on the cathode (leading to electroplating), the process is done in the presence of a stabilizer. Nanoparticles of palladium (Pd) of 4.8 nm diameter have been synthesized by this approach by passing 0.1 mA cm^2 current at 1 V in a 0.1 M tetraoctylammonium bromide (TOAB) solution in 4 : 1 acetonitrile : tetrahydrofuran (THF) mixture [9.108]. The resultant NPs, which precipitated out could be redispersed in THF or toluene. A similar methodology can be used for other metals such as silver [9.109] and also for the preparation of GNRs [9.110].

Radiolytic Reduction

Reduction under various radiations such as visible, ultraviolet (UV), x-rays, and γ-rays is another method for synthesizing NPs. Metal salts solutions are irradiated in presence of stabilizing agents. In photoreduction with gamma rays, various species are generated in the medium, depending on the photon energy absorbed. In an aqueous solution, H_2, $H^\bullet$, H_2O_2, OH, and e^- are produced by radiolysis of water. Nitrous oxide in the medium scavenges the electrons generated, which further generates OH− and $OH^\bullet$ [9.111].

$$N_2O + e^-(aq) + H_2O \rightarrow N_2 + OH^- + OH^\bullet \,. \quad (9.7)$$

Alcohols react with the formed radical according to the following reaction

$$CH_3OH + OH^\bullet \rightarrow H_2O + {}^\bullet CH_2OH \quad (9.8)$$

$$CH_3OH + H^\bullet \rightarrow H_2 + {}^\bullet CH_2OH \,. \quad (9.9)$$

The $^\bullet CH_2OH$ radical in the reaction mixture acts as the reducing agent according to the equation

$$M^{n+} + n\,{}^\bullet CH_2OH \rightarrow M + nCH_2O + nH^+ \,. \quad (9.10)$$

The reduced metal and formaldehyde are the final products of the reaction and if the solvated electron itself can be used, the reduction is more powerful. Nanoparticles of Au [9.112], Ag [9.113], Cu [9.114], and Co [9.115] have been synthesized using this methodology. This approach is especially useful for the preparation of complex structures such as core–shell particles, where a metal core is coated with a shell of another metal. A few examples are Au@Ag [9.116], Au@Pt [9.117],

Pt@Au [9.117], Au@Pb [9.118], etc. Radiolysis is done on a mixture of a metal NP and aqueous metal ion using a ^{60}Co source. The surface of metal NPs become charged due to the transfer of electrons from the generated radicals. These NPs thus reduce the metal ions which are deposited on the surface of the NPs, resulting in core–shell geometry. Using a similar strategy, the size of Au NPs (repeated radiolysis) were modulated [9.119].

Thermal Decomposition of Organometallics

Decomposition of corresponding metal carbonyls by heating in an inert solvent at elevated temperature in the presence of a suitable stabilizing agent is another way to produce metal NPs. For example, heating $Co_2(CO)_8$ in decalin at 130–170 °C can produce Co NPs [9.120]. Usually, nitrogen-containing polymers are used as stabilizers in the reaction. It is known that the stabilizer will form metal cluster macromolecules, where these polymers act as a complexing agent. The particle size can be controlled by varying the functionality of the polymer. Various NPs made up of Fe [9.121], Ni, Cr, Mo, and W [9.122,123], as well as alloy NPs have been prepared by employing different polymers. It is to be noted that the ligands should be selected with care as they should be stable at high temperatures. A new metastable Co phase (ε-Co) obtained through the use of this method has also been reported [9.124]. The stabilizer used in the reaction was trioctylphosphine oxide (TOPO), and in the absence of TOPO this phase was not formed. The formations of various kinetically stabilized shapes have been studied in detail [9.125,126]. Mixtures of carbonyls and other organometallic reagents were used to prepare FePt [9.127] and CoPt [9.128] alloy and core–shell NPs. Thermal decomposition of metalloalkenes is also known to form NPs [9.129, 130]. Various ligands such as 1,5-cyclooctadiene (COD), 1,3,5-cyclooctatriene (COT), dibenzylidene, and cyclooctenyl ($C_8H_{13}-$) have been used in various syntheses. Some examples of NPs synthesized through the use of this approach include Co, Ni, Ru, Pd, and Pt NPs, Co and Ni NRs, and CoPt, CoRu, CoRh, and RuPt nanoalloys.

Microwave-Assisted Synthesis

A microwave-assisted approach has been abundantly employed for the synthesis of a variety of organic and inorganic materials. This method can be utilized for both synthesis and processing aspects [9.131]. This method is less time-consuming and heating is achieved from within. Usually the mixture to be irradiated is placed inside a domestic microwave oven working at a frequency of 2450 MHz and the mixture is stirred. In the case of metals, the metal ion and the reducing agent in a suitable solvent are placed in the oven and especially in the case of Au and Ag, this approach is known to form highly monodisperse NP samples (when compared to thermal reduction) [9.132]. Polyols are one of the most effective reductants for metal ions using microwave irradiation and the process is often referred to as the microwave polyol process [9.133]. Microwave irradiation of a mixture of poly(vinylpyrrolidone) (PVP), ethylene glycol, NaOH, and H_2PtCl_6 in water resulted in the formation of 2–4 nm Pt NPs [9.134]. A similar strategy was employed for the synthesis of 6 nm diameter Ni NPs as well [9.135]. This synthesis methodology can be automated by adapting it to continuous-flow reactors [9.136]. An excellent review on microwave-based methods for NP fabrications is available in the literature [9.137].

Sonolysis

Ultrasound (typically at 20 kHz) irradiation of the reaction mixture is utilized for the synthesis of NPs in this methodology. Here NP formation here is termed cavitation, which involves the implosion of cavities of very small dimensions on nanosecond timescales. This leads to the formation of local hot spots of very high temperature in the range of 5000 K. The reactant (a precursor species like organometallics) becomes trapped in this and is decomposed at this temperature. The products are instantaneously quenched by the surrounding solvent medium, resulting in the formation of amorphous NPs. A variety of transition metal NPs has been synthesized using this strategy [9.138]. Sonolysis of $Fe(CO)_5$ in decane in the presence of oleic acid resulted in the formation of 8 nm oleic acid protected Fe NPs [9.136]. Alloy NPs can be also prepared by this method. This approach has also been reviewed in [9.139].

9.3.3 Specialized Synthetic Strategies – Anisotropic NPs

As discussed earlier, specialized strategies are needed to synthesize nanosystems of various shapes with control over size and shape. Most of these are either an adaptation or modification of the methods described above. However, specific molecular interactions or templates can be used to facilitate shape-selective synthesis. It has been found that metal ions can be reduced via radiolytic [9.140] and photochemical [9.141,142] methods. NPs of various morphologies such as rods, triangles, hexagons, etc., can be generated using the photochem-

ical method [9.141, 142]. Template-assisted [9.143] methods have been used to make 1-D nanostructures with uniform size and controllable physical dimensions. The galvanic displacement reaction [9.144] is another method to make GNPs and their hybrid forms. This method has been widely used to produce nanostructures with different morphologies, including plates, cubic nanoboxes, cubic nanocages, nanorings, nanoboxes, single-walled nanotubes, and multi-walled nanoshells or nanotubes [9.145, 146]. Many other techniques such as sonolysis [9.147], microwave-assisted synthesis [9.148, 149], the hydrothermal method [9.150], etc., are being used to make gold and silver NPs. All the above-mentioned methods come under the category of bottom-up approaches for synthesizing NPs. The following section describes some of the important strategies employed in this regard. Only brief descriptions are given.

Seed-Mediated Growth Method

This is one of the most widely used strategies for the synthesis of anisotropic NPs of gold and silver. It is a modified version of Zsigmondy's *nuclear* method [9.151], which involves two steps. However, the seed-mediated method usually produces larger NPs of size 30–100 nm. This was first demonstrated by *Brown* and *Nathan* [9.152]. The first step involves the synthesis of *seed NPs* by reduction of metal salts in the presence of stabilizing agents. Usually this is carried out by using a strong reducing agent such as sodium borohydride ($NaBH_4$). It must be noted that the seed need not always be a metal NP. Subsequently in the second step growth of seed NPs into the desired shape happens in a growth solution containing excess metal ions, a surfactant or shaping agent, and a mild reducing agent. Here, the reduction of metal salts is facilitated on the surface of the seed NPs, and due to the presence of the surfactant molecules which form suitable templates, the growth happens to yield NPs of the desired morphology.

Murphy et al. devised various strategies based on the seed-mediated growth approach to make NPs of various shapes [9.153, 154]. Noble metal NPs of diverse structures such as rods [9.155], wires [9.156], triangles [9.157], stars [9.158], flowers [9.159, 160], etc., can be synthesized using this method. Tuning of size is possible by varying the amount of seed NPs added to the growth solution. This strategy has been successfully used for the synthesis of GNRs. The presence of external agents such as molecules or ions can influence the growth direction and can result in the formation of a different morphology. For example, the presence of iodide ion in the growth solution during the synthesis of GNRs, results in the formation of triangular nanoprisms [9.161]. Iodide ions adsorbs on gold seeds to suppress the growth along the Au(111) direction, leading to the formation of Au(111)-faced triangular nanoprisms. Even the counter-ion present on the surfactant used can influence the morphology. When the counter-anions on cetyltrimethylammonium bromide (CTAB) were replaced with chloride ions (instead of the original bromide), a rice-shaped NP formed instead of rods. The concentration of surfactant molecules is another parameter that affects the shape, since the shape of the micelles formed by the surfactant during the growth changes with the concentration. A method developed by *Mirkin* et al. [9.48] is an excellent example for this concentration dependence; they synthesized nanoprisms by changing the parameters in seed mediated synthesis. This involves a three-step growth process where gold seed NPs of ≈ 5 nm were added into the growth solution containing the capping agent CTAB, gold ions, a reducing agent (ascorbic acid), and NaOH, resulting in the formation of gold nanoprisms in very good yield. Synthesis required a saturated CTAB solution for good yield with uniform morphology.

Seedless Synthesis: Modification of Seed-Mediated Synthesis

Seedless synthesis is a slight modification of the above-mentioned method. In the above method, the purity of the seeds determines the quality of the resulting structures. Hence, *Pradeep* et al. [9.162] and *Jana* [9.163] separately showed that gold nanostructures can also be formed without the presence of the seeds. Jana illustrated that, without the use of seeds, near-monodisperse gold and silver NRs, spheroids, NWs, platelets, or cubes of 4–50 nm dimension and controllable aspect ratio (AR), can be prepared by introducing a mixture of strong and weak reducing agents into the micellar solution of a metal salt. Here, the strong reducing agent initiates nucleation and the weak reducing agent induces the NP growth [9.163]. This strategy was found to be extendable to semiconductors as well. *Pradeep* et al. studied the role of sodium borohydride ($NaBH_4$) in the formation of GNRs [9.162]. They found that addition of a calculated amount of $NaBH_4$ directly into the growth solution leads to the formation of uniform GNRs. They also studied the formation of GNRs with various seeds of metals of widely differing crystal structures, and understood that there is no variation in the properties of the GNRs formed. The role of $NaBH_4$ in the growth of

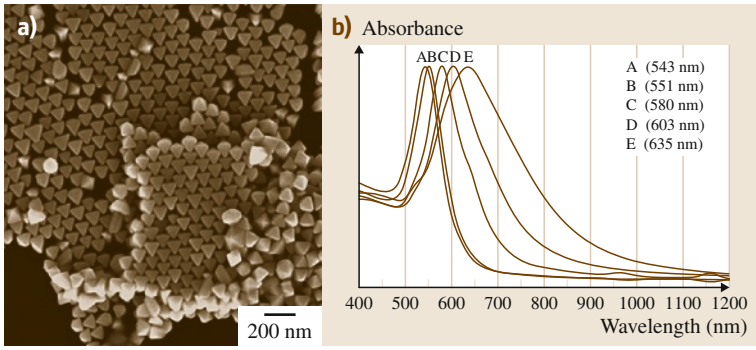


Fig. 9.5 **(a)** Scanning electron microscopy (SEM) image of octahedral gold nanocrystals. The imaged regions show extensive self-assembled structures. **(b)** UV/Vis absorption spectra of octahedral NPs of different sizes. Maximum absorbance of the spectra has been normalized (after [9.150])

GNRs, which was not well understood in earlier reports, was investigated in detail. They found that there is a relation between the longitudinal plasmon peak and the concentration of $NaBH_4$. To validate this further, the observed dependence was compared with the dependence of the residual concentration of $NaBH_4$ in the seed solution left over from the growth solution after the GNR growth. It was suggested that the addition of $NaBH_4$ leads to in situ formation of the seed particles, which enables the growth of GNRs.

Biological Synthesis

As an alternative to the use of chemicals, biological synthesis was advertised as a safe and ecofriendly approach for synthesis of GNPs. Here, the NPs are synthesized using organisms ranging from bacteria to fungi, various parts of plants, biological extracts, etc. One important advantage of this method is that it yields NPs capped with biological entities, which consequently have improved biocompatibility so that they can be used in many biomedical applications. Noble metal NPs of various shapes such as triangles, wires, spheres, plates, etc., have been synthesized via this method. A classical example is the high yield synthesis of thin, flat, single-crystalline gold nanotriangles (NTs) by the reduction of aqueous chloroaurate ions ($[AuCl_4]^-$) using an extract of the lemongrass plant (*Cymbopogon flexuosus*) [9.164]. The reducing agent in the reaction was found to be *aldoses* (reducing sugars) present in the lemongrass extract. Similar examples of Au NP preparation using extracts of tamarind leaf [9.165], *Cinnamomum zeylanicum* leaf [9.166], the unicellular green algae *Chlorella vulgaris* [9.167], *Rhodopseudomonas capsulata*, are available in the literature.

Hydro/Solvothermal Synthesis

This method involves the synthesis of NPs in a solvent at elevated temperatures under high pressure in an autoclave. The solvent (in most cases water) acts both as a catalyst and occasionally as a component of solid phases. Since several other solvents, including water, can be used for the synthesis this approach is generally termed solvothermal synthesis [9.168]. In hydrothermal processes, initial properties of water can be modified by introducing additives. This is a versatile strategy where various solvent systems such as polar solvents (e.g., aqueous solutions containing HF, or other acids or bases to modulate pH) or nonpolar solvents (e.g., pure, supercritical) are used for the dissolution–recrystallization process. Various nanostructures have been synthesized using this approach. The hydrothermal reaction of an aqueous solution of $HAuCl_4$, trisodium citrate and CTAB has been reported to produce octahedral gold nanocrystals (Fig. 9.5a) [9.150]. Gold octahedra with varying average sizes were synthesized by heating the different reactants at 110 °C for different time periods. Evidence of the formation of differently sized octahedra was seen in the absorption spectra where the surface plasmon resonance (SPR) band shifted from 543 to 635 nm (Fig. 9.5b). Structurally, the octahedra are bounded by specifically bound by (111) facets [9.150]. Technologically important nanostructures composed of Pd–Cd having high hydrogen storage capacity were also synthesized by this method. Here, various nanostructures with varying concentrations of Cd were grown directly on a solid substrate [9.169]. Because the method is low cost and environmentally friendly where substrates are at comparatively lower temperatures it is advantageous for the creation of diverse nanostructures on temperature-sensitive substrates.

Galvanic Replacement Reactions

This method (also called electroless plating) was introduced by *Brenner* and *Riddell* [9.170]. In this method the spontaneous reduction of metal ions to metallic particles and films occurs at equilibrium in the absence

of an external electric field. Due to its ease of operation, this method has attracted wide attention. It is highly versatile and can be used to make a wide range of metal/substrate combinations, including metal-on-metal, metal-on-semiconductor, and metal-on-insulator types. This is particularly important in the area of electronics with regard to metal deposition on a circuit board, for example. The process, *electroless deposition* includes three fundamentally different mechanisms such autocatalytic, substrate catalyzed, and galvanic displacement (immersion) processes in which the galvanic displacement reaction proceeds in an entirely different manner and the deposition is carried out in the absence of an external reducing agent.

Galvanic replacement reactions are single-step reactions that work depending on the differences in the standard electrode potentials of various elements, leading to deposition of the more noble element and dissolution of the less noble component. The electrons for the reduction are derived from the valance-band electrons of the substrate (Fig. 9.6a). Until the permeation of oxidized substrate ion into the solution though the metals film stops, the reaction will continue. The formation of a dielectric layer of oxidized substrate that hinders the electron transfer can also arrest the reaction. There are several advantages with this approach. For example, most synthetic processes use surfactants to obtain anisotropic nanostructures with smooth surfaces. However, attachment of surfactant molecules on the surface is not desirable for many applications. The presence of surfactants usually increases the electrical resistance, hence limits the use of these NPs as conductive components in electronics. Electroless deposition avoids the use of surfactant molecules whereby the NPs can be directly utilized without loss of electrical properties.

Preparation of pristine Ag nanoplates on semiconducting GaAs wafers (Fig. 9.6b) has been reported [9.171] through a galvanic reaction between an aqueous solution of $AgNO_3$ and GaAs (9.11). A droplet of aqueous solution of $AgNO_3$ was added on a GaAs wafer (treated with aqueous hydrofluoric acid solution) to grow silver micro/nanostructures via the galvanic reaction

$$12AgNO_3 + 2GaAs + 6H_2O \rightarrow 12Ag + Ga_2O_3 + As_2O_3 + 12HNO_3 . \quad (9.11)$$

Controlling the concentration of $AgNO_3$ resulted in the tuning of the morphological parameters of the Ag nanoplates. At high concentration of $AgNO_3$, thicker Ag nanoplates were obtained. Electrons for the reduction are provided by the germanium–germanium bonds leading to the formation of Ag(s) from Ag^+ and Ga(s) becomes oxidized during the process via a redox reaction.

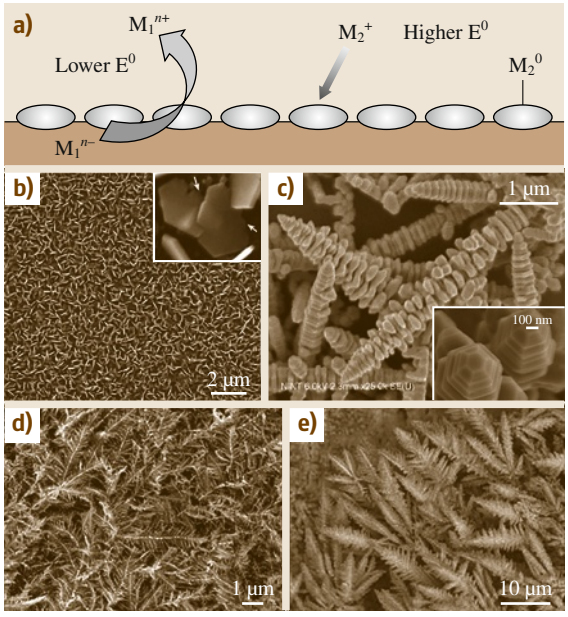


Fig. 9.6 **(a)** Schematic of galvanic displacement reaction. **(b)** SEM image of Ag nanoplates formed on the surface of n-type (110) GaAs wafer. **(c)** Silver nanoinukshuks prepared by immersing n-type Ge(100) in aqueous $AgNO_3$ solution. *Inset* shows a close-up view of facets on the tips of silver metallic nanoinukshuks. SEM images of silver **(d)** and gold **(e)** dendrites formed on zinc plates. (**(b,e)** after [9.171–174])

An unusual variety of Ag nanostructures called nanoinukshuks (Fig. 9.6c), was synthesized by immersing n-type Ge(100) in aqueous $AgNO_3$ solution [9.172]. When the Ag^+ ion concentration reached 1 mM, nanoinukshuks were obtained at room temperature on flat or rough, oxidized germanium surfaces. The nanoinukshuks were composed of 300 nm-diameter stacked hexagons, which can grow perpendicular to the (111) planes of the silver hexagons. Synthesis was carried out with different Ag salts, such as $AgClO_4$ and $Ag(CH_3CO_2)$. With $AgSO_4$, flat dendritic structures formed. A close-up view of the tip of the nanoinukshuks is given in Fig. 9.6c. Gold dendritic nanostructures can also be synthesized using $HAuCl_4$, H_2O, and zinc through this methodology. Dendritic structures formed by immersing a Zn plate in a container with $HAuCl_4$ solution at room temperature and ambient pressure (Fig. 9.6e) [9.173].

The same strategy can be employed for preparing Ag dendritic nanostructures as well (Fig. 9.6d) [9.174].

Hollow metal nanostructures can also be produced in this way. The structure can be made hollow or have porous walls. This change can be brought about by using a less active metal salt precursor. A wide variety of gold-based hollow nanostructures of different morphologies, including cubic nanoboxes, cubic nanocages, nanorings, nanoboxes, single-walled nanotubes, and multi-walled nanoshells or nanotubes [9.175–177] have been synthesized using this strategy. More details of these reactions is given in the discussion of the reactivity of these anisotropic systems in Sect. 9.5.1.

Photochemical Synthesis

As described in previously, the reduction of metal salt precursors can also be carried out by radiolytic and photochemical methods. Here, there is no eternal reducing agent involved and radiation becomes absorbed regardless of the light-absorbing solutes and products. Also, the number of reducing equivalents generated by radiation being known exactly, the rate of the reduction reaction can be accurately determined. This methodology does not require any specific and expensive instrument. All this makes this approach highly attractive for synthesis on metallic nanostructures.

Rod-shaped NPs were the first anisotropic NPs to be synthesized by reduction of metal salt by UV irradiation [9.178]. Here, a rod-like micelle formed by hexadecyltrimethylammonium chloride becomes embedded by $AuCl_4$, and the reduction of these ions to Au^0 is achieved through photochemical irradiation ($\lambda_{max} = 253.7\,nm$). However, synthesizing uniform, AR-controlled rods is difficult because an increase in length of NRs will always result in an increase in spherical NP impurities. *Yang* et al. [9.179] reported an improved methodology which produces NRs with well-controlled AR. This method was similar to the electrochemical method described earlier and the reaction mixture had the surfactant CTAB and tetradodecylammonium bromide and the precursor $HAuCl_4 \cdot 3H_2O$. The reduction was achieved by photoirradiation for 30 h ($\lambda_{max} = 254\,nm$, $I = 420\,\mu W/cm^2$). During the process, acetone and cyclohexane were used for loosening the micellar structure. However, additionally, silver nitrate was used in this process to control the AR of the NRs. Also, an increase in the silver ion concentration led to a decrease in the AR of the NRs and when the silver ion was absent a large number of spherical particles formed.

Photo-induced methods have found useful the preparation of large quantities of silver nanoprisms in high yield in the form of a colloidal suspension as well [9.180]. The as-synthesized colloids had distinctive optical properties that directly relate to the shape. The first step of the reaction includes the synthesis of spherical silver particles from an aqueous solution of $AgNO_3$ using $NaBH_4$ in the presence of trisodium citrate. A stabilizing agent, bis(*p*-sulfonatophenyl) phenylphosphine dihydrate dipotassium (BSPP) was introduced dropwise into the reaction mixture. The mixture was irradiated with a conventional fluorescent light. The edge length of the nanoprisms in this process was found to be tunable to 30–120 nm range [9.181]. Using dual beam illumination of the NPs, the growth can be controlled, and the process is believed to be driven by surface plasmon excitations. Depending on the wavelength of the illumination, the plasmon excitations lead to the fusion of nanoprisms. The bimodal growth process observed occurs through an edge-selective particle fusion mechanism, with four type 1 nanoprisms coming together in stepwise manner to form a type 2 nanoprism (Fig. 9.7). GNPs of various morphologies such as triangular or hexagonal shapes can be generated using the photoreduction method by mixing Au^{3+} with sodium oxalate and a reducing agent, in aqueous solution under illumination by a mercury lamp for more than 10 min. The size of the GNPs varies from 25 to 200 nm, mainly depending on the duration of light illumination and the concentration of sodium oxalate [9.182].

Electrochemical Synthesis

This is a modification of the process described above, developed to create anisotropy in the formed structures. The electrochemical method was first proposed by *Reetz* and *Helbig* in 1994 [9.108]. They demonstrated that by adjusting current density, highly size-selective NPs can be synthesized via an electrochemical reduction method. Diverse nanostructures such as cubes, rods, triangles, plates, etc., have been synthesized by this method [9.183]. It has many advantages over other methods since it has a lower processing temperature and low cost, requires modest equipment, and offers good control of size, shape, and morphology. The experimental setup (Fig. 9.8) for the electrolytic process includes a two-electrode setup for 50–250 ml electrolyte solutions in which the sacrificial anode consists of the bulk metal to be transformed into a metal colloid. In a two-electrode setup, GNRs were recently synthesized in high yield [9.184]. In this process, gold and platinum

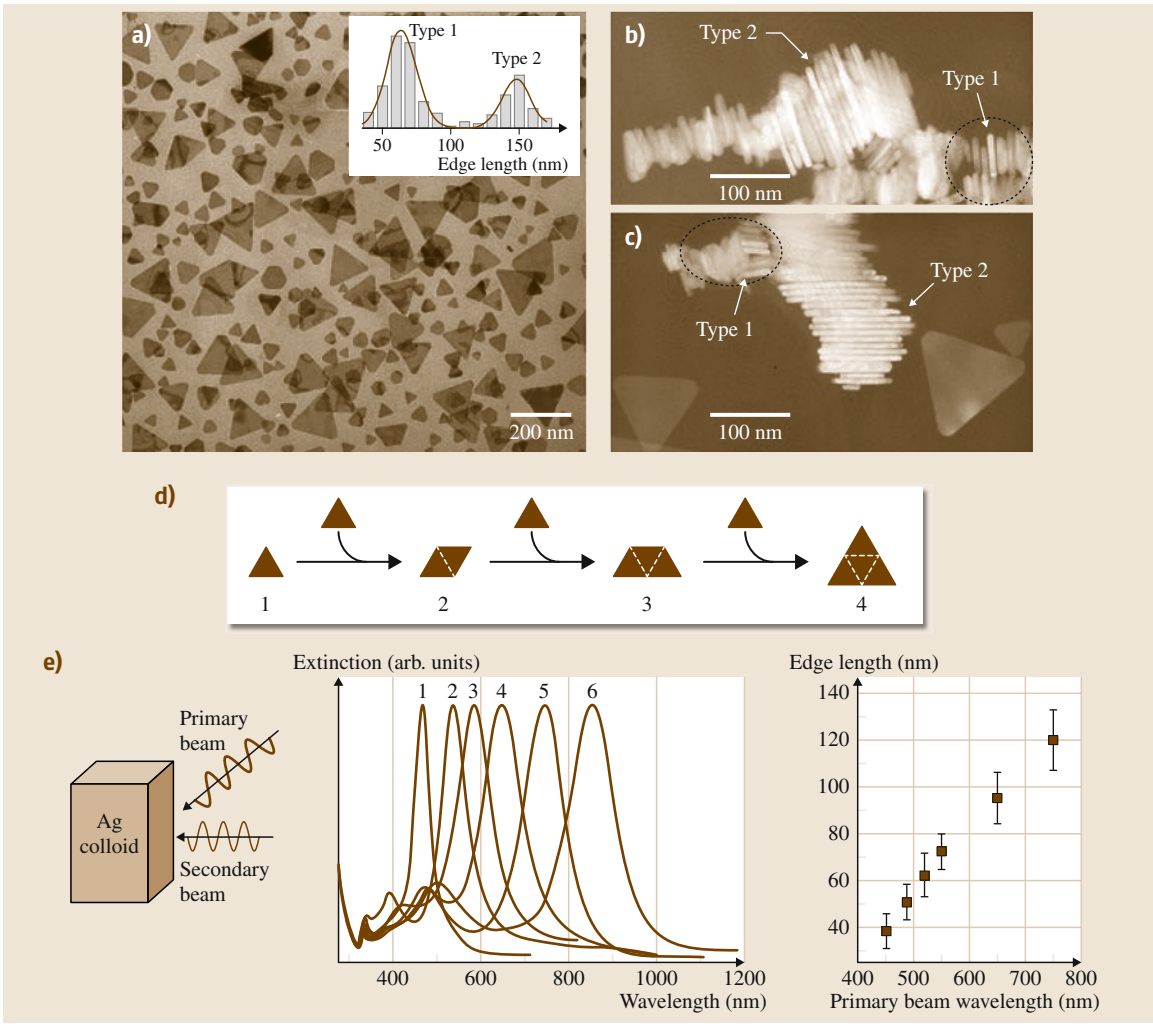


Fig. 9.7a–e Bimodal growth of Ag nanoprisms. **(a)** TEM image of a sample of Ag nanoprisms formed using single-beam excitation; *inset* histograms used to characterize the size distribution as bimodal. **(b,c)** SEM images of nanoprism stacks showing that nanoprisms have nearly identical thicknesses. **(d)** Schematic diagram of the proposed light-induced fusion growth of Ag nanoprisms. **(e)** *Left*: schematic diagram of dual-beam excitation. *Middle*: the optical spectra (normalized) for six different-size nanoprisms prepared by varying the primary excitation wavelength. *Right*: the edge lengths as a function of the primary excitation wavelength (after [9.181])

plates were used as the anode and cathode, respectively. The electrolytic solution had a mixture of a cationic surfactant or stabilizing agent and a cosurfactant, and the electrodes were immersed in it. During electrolysis, bulk gold metal is oxidized at the anode, and the metal cations at the interfacial region of the cathodic surface are reduced, and in the presence of the capping agent, form GNRs. GNRs with various ARs can be synthesized by this method.

Highly monodisperse gold nanocubes can be synthesized by an electrochemical method, using a surfactant solution and acetone [9.185]. Here also a two-electrode setup with gold and platinum plates as the anode and cathode is used. These electrodes are placed vertically face-to-face inside the cell, separated by Teflon spacers in an aqueous solution of CTAB and a much more hydrophobic cationic cosurfactant, tetradecyltrimethylammonium bromide. Acetone was

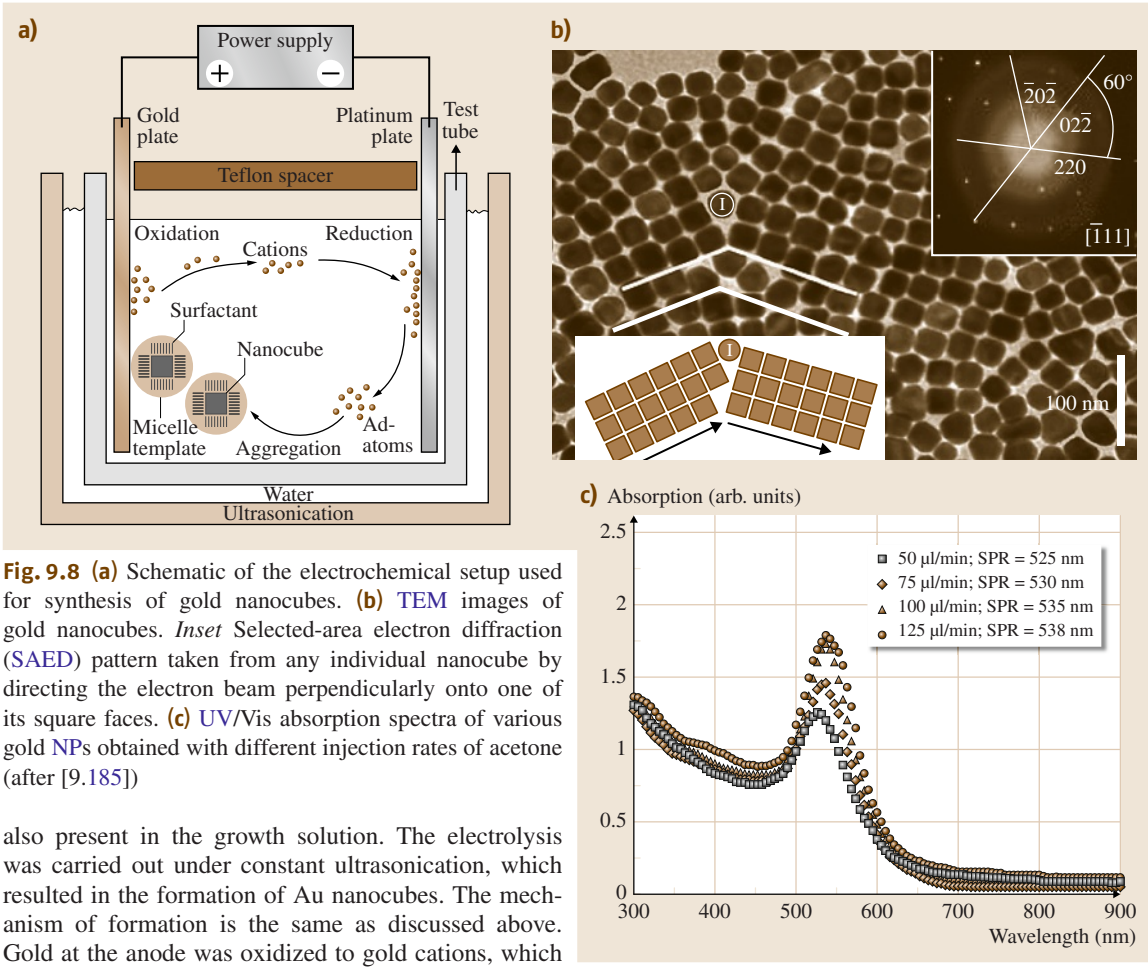


Fig. 9.8 **(a)** Schematic of the electrochemical setup used for synthesis of gold nanocubes. **(b)** TEM images of gold nanocubes. *Inset* Selected-area electron diffraction (SAED) pattern taken from any individual nanocube by directing the electron beam perpendicularly onto one of its square faces. **(c)** UV/Vis absorption spectra of various gold NPs obtained with different injection rates of acetone (after [9.185])

also present in the growth solution. The electrolysis was carried out under constant ultrasonication, which resulted in the formation of Au nanocubes. The mechanism of formation is the same as discussed above. Gold at the anode was oxidized to gold cations, which then migrated to the cathode, where reduction occurred with the formation of gold adatoms (Fig. 9.8a). These adatoms were trapped by the surfactant to form nanocubes (Fig. 9.8b). The surfactant, which doubles as the electrolyte and the stabilizer, also forms a micelle template to control the size and shape of the NPs. The rate of injection of acetone was found to influence the shape of the NP formed. Spherical NPs were formed at lower concentrations of acetone. As the amount of acetone increased a red-shift was observed in the UV/Vis absorption spectra (Fig. 9.8c) of gold nanostructures.

Synthesis of GNRs has also been carried out via an electrochemical method using a simple two-electrode cell [9.186]. In this process, a gold metal plate acts as the anode and a platinum plate as the cathode. A cationic surfactant, CTAB, and a rod-inducing cosurfactant were used as the electrolyte. Using a standard three-electrode cell with a potentiostat, a platinum foil counter electrode, and a saturated calomel electrode, platinum nanothorns were synthesized electrochemically at room temperature [9.187]. Here, platinum nanothorns (Fig. 9.9) were electrodeposited on glassy carbon substrate in 2 mM K_2PtCl_6 and 0.5 M H_2SO_4 solution by applying a square wave potential between −0.20 and 0.80 V at 10 Hz for 20 min.

Using a templateless, surfactantless, electrochemical method, single-crystalline Ag dendrites were fabricated on a Ni/Cu substrate by [9.188, 189]. The applied potential controlled the morphology and geometry of the Ag particles. The morphology changed from Ag polyhedrons to Ag dendrites, which preferentially grow along the directions in a fractal mode, upon decreasing the potential from −0.4 to −2.0 V [9.190].

Template Mediated Synthesis

Recently, the template-mediated synthesis of 1-D nanostructures with uniform size and controllable physical dimensions has attracted a great deal of interest. The advantages of this method over other methods are: ease of fabrication, adaptability to various compositions of materials, low cost, and high throughput [9.190, 192, 193].

Usually, nanoporous polycarbonate or alumina are used as the template. Metals from which NP is to be synthesized (Au, Ag etc.) are electrochemically deposited in the template structure. First, a small amount of Ag or Cu is sputtered on the template to make a conductive film for electrodeposition. Subsequently, metal is electrochemically deposited onto the conductive template. The template is removed by selective dissolution in the presence of a polymeric stabilizer (e.g., PVP), and the nanostructures are dispersed either in water or an organic medium by means of sonication. Template-mediated synthesis of GNRs is shown in Fig. 9.10. By controlling the pore size of the template, the diameters of synthesized structures can be controlled [9.194]. Similarly, by regulating the amount of metal deposited, the length of the structures can be controlled [9.191].

Other Methods

Gold and silver NPs can also be synthesized via top-down approaches. Nanosphere lithography [9.195] is a powerful tool to produce NP arrays with controlled shape, size, and interparticle spacing. This approach uses self-assembled polystyrene nanospheres as templates. Diverse nanostructures such as disks, chains, triangles, rings, etc., have been fabricated using this method [9.195]. The atomic force microscopy (AFM)-based soft lithographic technique called dip-pen nanolithography [9.196] can produce layers on Au and in combination with wet chemical etching is able to fabricate various nanostructures such as dots, lines, rings, triangles, etc., with nanoscale precision. GNPs have been generated using other top-down strategies such as photolithography, electron beam lithography, etc. [9.197]. However, these processes follow expensive synthetic pathways and are industrially nonscalable. Hence, bottom-up approaches are far more popular for synthesis of NPs.

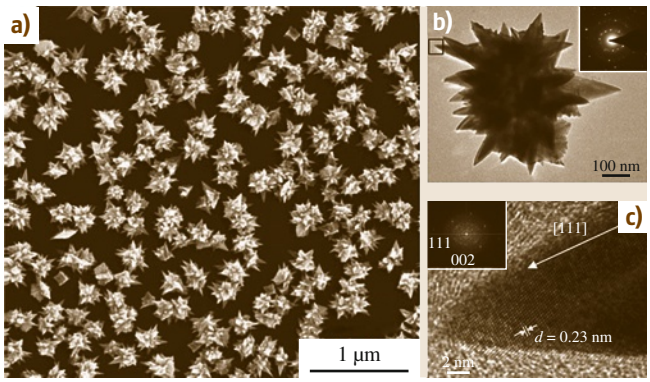


Fig. 9.9 (a) Large area SEM image of platinum nanothorns. TEM images of the platinum nanothorn (b,c) with the corresponding selected area diffraction (SAED) pattern and fast Fourier transform (FFT) in the *insets* (after [9.187])

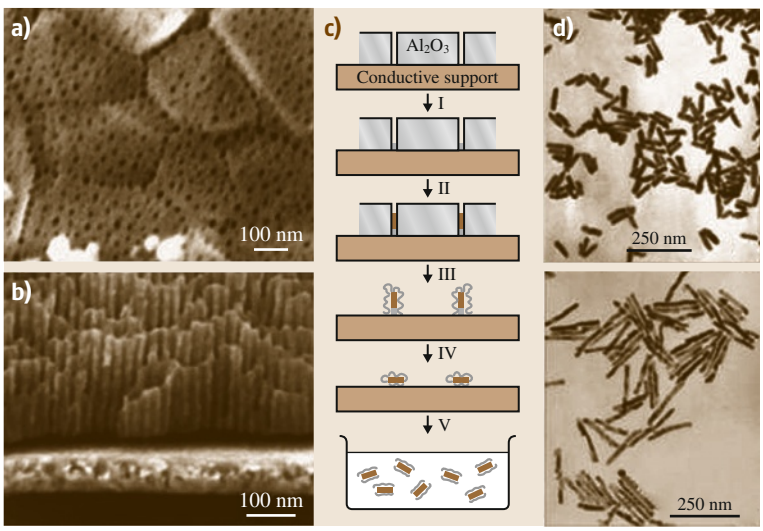


Fig. 9.10 (a,b) Field-emission SEM (FESEM) images of an alumina membrane. (c) Schematic representation of the successive stages during formation of GNRs via the template method. (d) TEM micrographs of GNRs obtained by the template method (after [9.191])

9.4 Properties of Noble Metal Nanoparticles

Noble metal NPs have received a great deal of attention for many applications due to their extraordinary properties. The spatial confinement of electrons controls the physical and chemical properties of NPs. GNPs are classic systems though which the properties of noble metal NPs can be understood. Properties of GNPs can be varied by altering the size, shape, degree of aggregation, and local environment. They exhibit characteristic colors and unusual optical properties that strongly depend on their size, shape, and the dielectric constant of the surrounding medium. The characteristic wine-red color of spherical GNPs stems from a phenomenon termed localized surface plasmon resonance (LSPR) [9.199, 200]. When electromagnetic radiation of an appropriate wavelength interacts with a metallic nanostructure, the conduction electrons near a metal–dielectric interface will be excited and undergo a collective oscillation relative to the lattice of positive nuclei with the frequency of the incoming light resulting in LSPR (Fig. 9.11). A momentary electric field is generated on the surface of the NP as a result of the oscillations. This can extend into the dielectric over nanometer length scale and hence can give rise to an enhancement of the incident field by several orders of magnitude, resulting in novel properties of NPs. One of the first investigations of the interaction between NPs and light was done by Faraday in the nineteenth century on his gold colloid.

A complete theory to understand plasmon resonance absorption and color of metal colloids in solution was developed by *Gustav Mie* in 1908 when he studied the theory behind the scattering and absorption of electromagnetic radiation by a sphere [9.201]. In its original form, Mie's theory was able to explain the spectral properties of spherical particles. The theory showed that the total extinction cross-section comprises contributions from the scattering and absorption cross-sections, i. e., the extinction cross-section, $\sigma_{\text{ext}} = \sigma_{\text{abs}} + \sigma_{\text{scat}}$ (absorption cross-section + scattering cross-section). When the size of the NP is smaller than the wavelength of light ($\lambda \gg 2r$, where r is the radius of the NPs), Mie's theory reduces to [9.202–204]

$$\sigma_{\text{ext}}(\omega) = 9\frac{\omega}{c}\varepsilon_{\text{m}}^{3/2} V \frac{\varepsilon_2(\omega)}{[\varepsilon_1(\omega)+2\varepsilon_{\text{m}}]^2+\varepsilon_2(\omega)^2}\,, \tag{9.12}$$

where V is the volume of the particle [$(4\pi/3)r^3$], ω is the angular frequency of the exciting light, c is the velocity of light, ε_{m} is the dielectric function of the surrounding medium of the NPs, and ε_1 and ε_2 are the real and imaginary parts of the dielectric function of the NPs, respectively, i. e., $\varepsilon(\omega) = \varepsilon_1(\omega) + \text{i}\varepsilon_2(\omega)$. The condition for resonance is $\varepsilon_1(\omega) = -2\varepsilon m$, if ε_2 is small and is a weak function of ω. For Au NPs in air, this can happen around $\lambda = 520$ nm [9.205].

In order to explain the properties of other shapes (oblate and prolate spheroidal particles), in 1912 *Gans* remodeled Mie's theory and predicted two well-defined, distinct surface plasmon modes for these metal NPs [9.206]. It is important to note that the details of the LSPR response of metal nanostructures depend on

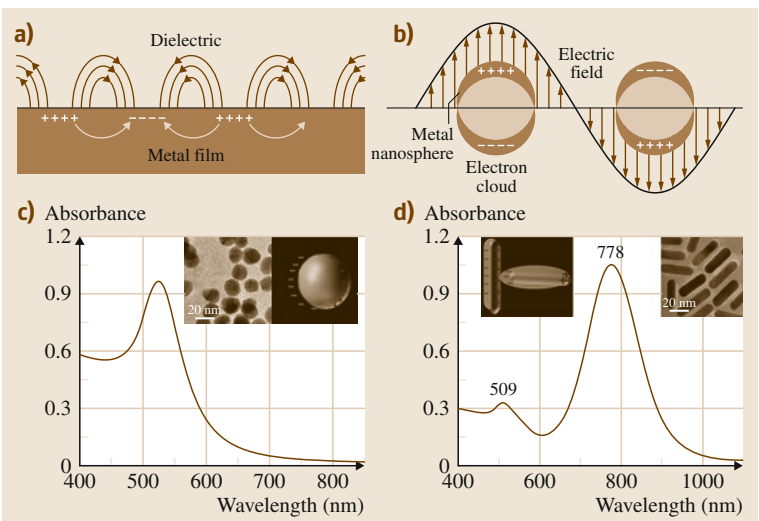


Fig. 9.11 **(a)** Propagation of surface plasmons on a metal surface. **(b)** Localized surface plasmons in metal nanospheres (after [9.198]). **(c,d)** Absorption spectra of gold nanospheres and NR, respectively. Corresponding TEM images of spherical and rod-shaped GNPs are shown in the *inset*

different variables such as size, shape, environment, dielectric function, effective mass, and electron density. GNRs are classical examples to demonstrate the shape-dependent LSPR properties. Unlike nanospheres (which have only one well-defined resonance peak), GNRs in their optical spectrum exhibit two bands in the visible/near-infrared (NIR) regions (Fig. 9.11). According to theoretical calculations, the first band near 530 nm (called transverse LSPR) is due to electron oscillation perpendicular to the long axis of the NR and the other one, appearing at a longer wavelength (called longitudinal LSPR mod) is assigned to an oscillation parallel to the long axis (Fig. 9.11). For anisotropic NPs like disks and triangular prisms, LSPRs are split into distinctive dipole and quadrupole plasmon modes [9.207].

The advent of new spectroscopic techniques has resulted in the capability to use surface plasmons for imaging single NPs. *Sonnichsen* et al. have developed a fast and flexible technique using total internal reflection spectroscopy to measure the optical scattering spectra of single metallic NPs [9.208]. By embedding noble metal NPs in an electrooptical material such as a liquid crystal, which induces a spectral shift of the particle's plasmon resonance by applying an electric field, the same group later showed that single NP scattering can be measured [9.209]. Using a similar method based on single-particle scattering, biomolecular recognition has also been proposed [9.210]. By this technique, GNRs were used as nonbleaching plasmon-based orientation sensors recently [9.211]. The polarized light scattering from individual GNRs was monitored in a dark-field microscope, and through observation of the rotational diffusion of gold rods attached to a glass surface, it was demonstrated that their orientation as a function of time can be determined [9.211]. This property was used for probing protein–membrane interaction as well [9.212]. Using plasmon spectroscopy, *Mulvaney* et al. recently showed that chemical reactions on single molecules can be probed [9.213]. They investigated the kinetics of atomic deposition onto a single gold nanocrystal. The electron injection and extraction during a redox reaction involving the oxidation of ascorbic acid on a gold nanocrystal surface was also monitored. Hence, for the first time it was established that direct measurement of the rates of redox catalysis on single nanocrystals is possible. It was established that 2-D array detectors would enable the acquisition of spectra from pixels along a line in the field of view and using push-broom scanning technology, 2-D hyperspectral images can be obtained [9.214]. *Becker* et al. selectively measured spectra of up to 20 plasmonic NPs per exposure using an electronically addressable mask [9.215]. However, a condition such that only a few NPs are present within the field of view was maintained throughout the measurements. Here for the first time they used single-particle spectroscopy to monitor the growth process of GNPs [9.215]. Using a grating monochromator to select a 2 nm spectral band for dark-field illumination, *Liu* et al. were able to achieve high-resolution imaging [9.216]. Au plasmonic NPs (PNPs) and NWs were imaged with relatively high spectral resolution and exposure time of 2 s per band. SPR plasmon resonance can result in a huge enhancement in the local electric field around the GNP surfaces [9.200, 217]. The local electric field around the NP surfaces can get a huge enhancement due to SPR [9.200, 217]. At the tip of a metal NP or a rough metallic surface, a highly localized and strong electric field can develop due to the interaction between the electromagnetic field and the free electrons. This results in the creation of a large electric field at the sharp tips or vertices of the NPs, leading to an enhancement in the Raman scattering cross-section by several orders of magnitude [9.218, 219]. This effect, known as surface-enhanced Raman scattering (SERS), was first observed by *Fleischman* et al. in 1974 [9.220]. This huge enhancement enables single-molecule spectroscopy, and the SERS activity depends on different parameters such as the size and shape of the NPs, the dielectric environment, the wavelength of the excitation light source, and the interparticle spacing between the NPs [9.221]. Shape dependence can be explained well by considering different GNPs. Gold mesoflowers [9.160] and triangles [9.157] were found to have higher SERS activity compared to their spherical analogs, owing to the higher electric field generated at the tips and edges of these NPs.

Chemical reactivity of NPs is also dependent on their surface area. These NPs are made-up of tens to several thousands of atoms. Each NP has a hybrid electronic structure having aspects of both discrete energy levels as in atoms or molecules and the band structure seen in metals. At considerably lower size regimes, i. e., below 2 nm, gold and silver NPs lose their metallic character substantially and start to exhibit molecular-like transitions under ambient conditions. Size ranges below 2 nm will not have the continuous band structure like bulk gold, and hence very small NPs (< 2 nm) do not possess continuous band structure like bulk gold and will start to demonstrate fascinating electronic properties. This aspect is briefly described in a later section (Sect. 9.8). Noble metals are considered to be the most

inert of all metallic elements. However, gold and silver NPs are known to show very good catalytic activity. In 1987, *Haruta* found that, when deposited on metal oxide supports, Au NPs smaller than 10 nm have high degree of catalytic activity [9.222]. They were found to be excellent in converting toxic carbon monoxide into carbon dioxide at room temperature. Moreover, due to their nontoxic nature and high surface-to-volume ratio, noble metal NPs were found to be excellent candidates as catalysts for a variety of chemical reactions including hydrogenation, CO oxidation, selective oxidation, and nucleophilic additions [9.223, 224].

9.5 Postsynthetic Tuning of Properties

Tuning the properties of nanosystems is usually done during synthesis. Postsynthetically, properties can be tuned via chemical interactions or through assembly. Nanosystems that interact with chemical entities can result in either reactions or organization. Before using any system in practical applications, the reactivity of the system must be studied thoroughly. Reactions can lead to size changes, shape or morphology changes, or composite formation. All this will result in changes in properties, and through precise control over the reaction conditions, we can tune the resultant properties. Small molecular interactions can sometimes result in self-organization as well. Self-organization can sometimes result in the creation of new superstructures with novel or enhanced properties. The resultant properties can be regulated by controlling self-organization. Considerable efforts have been dedicated to this, and some of these are reviewed below.

9.5.1 Tuning Properties Through Chemical Reactions

Postsynthetic chemical transformations of nanostructures through controlled reactions are attracting growing interest. Through this method we can greatly diversify the composition of the material, or sometimes it can result in the formation of novel structures consisting of multiple components, which may not be possible through direct synthetic processes [9.225–227]. The high mechanical stress generated during the transformations enables the creation of novel structures [9.228]. The main chemical transformation reactions frequently employed in nanosystems are redox reactions and ion-exchange reactions. Redox reactions, especially galvanic displacement reactions, are some of the most studied reactions for bringing about chemical transformation in metallic nanosystems [9.229]. The reactivity of spherical NPs has been extensively reviewed [9.1, 230–232]. Hence, this section mainly concentrates on nonspherical, anisotropic particles. Moreover, the inherent diversity in the surface structure of anisotropic NPs gives us an additional tool to regulate the reaction of these NPs and the resultant properties. Change in size or shape can greatly influence change in properties. A review of efforts that have been made to tune properties postsynthetically is presented below.

Reactions of Gold Nanorods

GNRs belong to the most studied class of 1-D nanosystems and can be taken as the best example to illustrate the reactivity of 1-D nanosystems. Optical properties of metallic NPs that originate from SPR have many application possibilities. The absorption cross-section of NPs, being orders of magnitude stronger than the strongest absorbing molecules, can impart intense color to the suspensions. In the case of isotropic spherical GNPs, a single, strong SPR absorption band in the visible region around 520 nm is observed. In contrast, anisotropic GNPs can have several plasmon resonance modes spreading from the visible to NIR region due to various excitation modes. The absorption in the NIR region has both therapeutic and imaging applications in tissues, because in this range of wavelengths, biomaterials do not have significant absorption. Hence anisotropic NPs have applications in biochemical sensors [9.233], biological imaging, and medical therapeutics [9.234]. The UV/Vis spectrum of GNRs has two characteristic maxima [9.235]. The first one, called the transverse surface plasmon resonance (TSP), is located around 520 nm and originates from the oscillation of electrons along the breadth of the NR. The second maximum is due to the longitudinal surface plasmon (LSP) resonance and is due to the oscillation of the electron cloud along the length of the NR, appearing at a longer wavelength. This band will shift to a higher wavelength region with an increase in AR (length/breadth). As mentioned earlier, the exceptional tunability of the photophysical properties of GNRs gives them an edge over their isotropic counterparts. This aspect is illustrated in Fig. 9.12. Doubling the diameter of a spherical NP only results in a minimal change in the spectral position. The sizes of GNRs are represented by a term called the AR

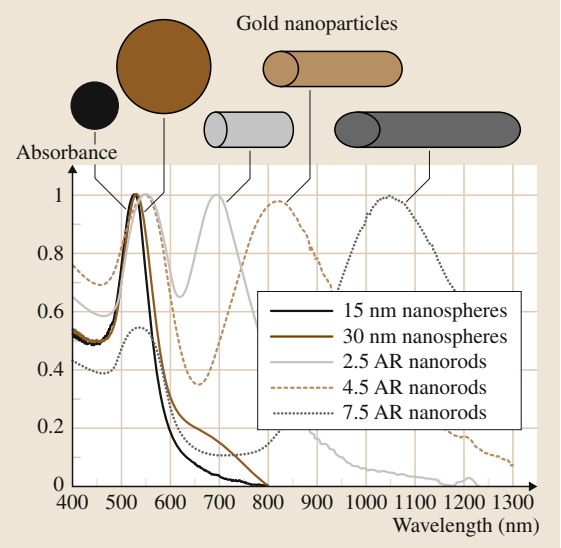


Fig. 9.12 UV/Vis spectra of spherical and rod-shaped GNPs indicating the tunability of anisotropic NRs (after [9.236])

which is the length divided by the breadth of the NR. A change in the AR of GNRs will change the spectrum considerably, and absorption can be tuned throughout the UV/Vis/NIR window [9.236].

The surface structures of isotropic and anisotropic GNPs differ drastically from each other. GNRs especially have an anisotropic crystal structure and have different fractions of atoms at edges, faces, and tips. Spherical GNPs are generally composed of either {111} or {100}. Usually {110} facets will be absent owing to their inherent instability compared with the other two low-index planes [9.237, 238]. However, in GNRs, the rod axis will be oriented along the {001} direction and the side faces are composed of {110} [9.239]. The tips will be mainly composed of {111} and {100} facets [9.239]. Recently, it was found that high-index planes such as {250} also can be present on GNRs [9.240].

CTAB, the surfactant used in synthesis of GNRs, has high affinity towards the {110} surface and will preferentially stabilize {110} planes, giving anisotropic surface structures for GNRs [9.239]. Due to the anisotropy of the surface crystal structure, the distribution of surfactant on the surface is also anisotropic. Due to the presence of {110} facets, the distribution of CTAB on the side faces is thicker compared with on the tips. This gives an additional tool to control the reactivity of GNRs. Incoming species attack the end faces first, and reaction starts from the tip of the NRs. *Jana* et al. studied the reactivity of gold spheroids and NRs prepared in the presence of silver nitrate ($AgNO_3$) with cyanide and persulfate [9.241]. They showed that, in the presence of cyanide, dissolution of GNRs (AR 2–5) occurs. They also found that the reaction starts at the tips and that throughout the reaction the width remains constant, leading to the formation of lower-aspect-ratio NRs. The reaction leads to the formation of spheres, which also ultimately dissolve. Time-dependent UV/Vis spectroscopy showed progressive dampening of LSP and a blue-shift indicating the decrease in the AR of NRs. After some time, only the TSP was seen, indicating the transformation of rod-shaped NPs into spheres. After the completion of the reaction, no feature pertaining to gold nanostructures remained, indicating complete dissolution of the GNRs. No clear mechanism of reaction was proposed. The reactivity of GNRs prepared in the absence of $AgNO_3$ was examined as well [9.242]. Here the reactivity was found to be different. Instead of decreasing the AR, dissolution occurred at various spots along the side edges. During the reaction, various pits were formed on the side faces but the length of the NRs remained the same. Here also, no mechanism was put forward for this anomalous behavior of long NRs prepared in the absence of $AgNO_3$.

Charge-induced instabilities of GNRs were also studied [9.243]. They found that shape changes can be introduced in metallic NRs through double-layer charging. They found that addition of electrons in the form of reducing agents such as sodium borohydride ($NaBH_4$) or ascorbic acid (AA) can induce size and shape changes in small metallic NRs. Introduction of small quantities of electron densities resulted in red-shift of the surface plasmon band, and the end caps of the rods underwent increased faceting. Charge-induced faceting results in the creation of the lower-energy {111} facets. They found that more sharp edges are formed during the process. This is explained as an unusual example of Le Chatelier's principle in action. At crystallographic discontinuities, the particle electric field will be the highest. These edges can provide hot spots for driving hydrogen evolution, which catalyzes the discharge of the GNR double layer. In the presence of higher electron densities, the Rayleigh threshold is crossed and the rods fragment into clouds of smaller spheres. By the formation of spherical NPs which have predominant {111} facets, the formation of the more stable crystal facets results in the surface stress being relieved in a favorable pathway.

Reshaping GNRs by thermal treatment is also reported in [9.244]. It was found that, with increase in

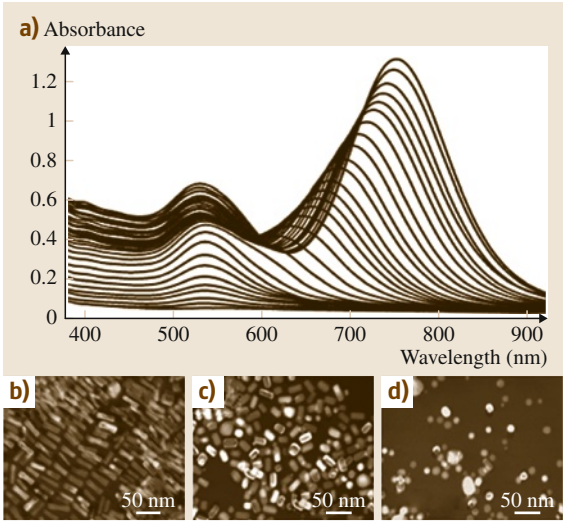


Fig. 9.13a–d Oxidation of GNRs. **(a)** UV/Vis spectra acquired every 1 min. TEM images of **(b)** initial GNRs, **(c)** shortened NRs, and **(d)** spherical particles formed due to oxidation (after [9.247])

temperature, the length of the NR decreases, resulting in decrease of the mean AR of the NRs in solution. Heating the dried NRs on the TEM grid itself did not produce a similar shape change. Hence, it was concluded that the relative instability is due to the instability of micelles capping the NRs. The calculated activation energy needed for the thermal decomposition of the micelles was found to be 21.0 ± 1.0 kcal/mol. A photon-induced shape transition process was reported by *Chang* et al. [9.245]. NRs were exposed to laser lines of two different frequencies, 532 and 1064 nm, and it was found that, due to photoannealing, rod-to-sphere conversion occurred. In the case of 1064 nm, new *ϕ-shaped* structures formed. A shape change of NRs induced by femtosecond and nanosecond laser pulses has been reported by *Link* and *El-Sayed* as well [9.246].

A mild oxidation method using O_2 which results in continuous selective shortening of GNRs was reported by *Tsung* et al. [9.247]. Figure 9.13a shows the UV/Vis spectral changes accompanying the oxidation. The LSP blue-shifts and decreases in intensity with oxidation, while the TSP remains at 520 nm and decreases in intensity, pointing to shortening of the GNRs. As further oxidation happens, the LSP disappears and only the TSP is seen, pointing to the formation of spherical NPs. Subsequently, oxidization also occurs, as demonstrated by the disappearance of the TSP. Similar observations were seen by TEM as well (Fig. 9.13b–d). The rate of oxidation can be controlled by manipulating the temperature and acid concentration. At the same time, a strategy to fine-tune the AR of GNRs using Cu^{2+} was devised by *Pradeep* et al. [9.248]. The advantage of the reaction was that it can be stopped at any point of time by simply removing the heating device, and the NR of desired AR can be obtained (Fig. 9.14). It was also found that the reaction can be controlled in such a way that it starts from either the tip or the rod body by adjusting the presence or absence of the surfactant [9.248].

Spatially directed oxidation of GNRs by the Au(III)–CTAB complex has also been reported [9.249] through a redox reaction between Au^0 and $[AuCl_4]^-$. Oxidation preferentially occurs at surface sites with higher curvature such as the tips of the NRs. This peculiar oxidation was attributed to the differences in the flux of micelles to highly curved and flat surfaces of GNRs. Morphological transformation of GNRs induced by iodide formed in situ by the reaction between potassium iodide and copper chloride was reported by *Wang* et al. [9.250]. It was found that the thus-formed iodide could fuse GNRs in the side-by-side mode, which in turn can result in morphological transformation of GNRs to spheres. Characteristic changes in the absorption spectra with the decrease of AR, such as blue-shift of the LSP band, red-shift of the TSP band, as well as a broadening of both of these bands, were seen. They proposed this methodology for quantification of iodide without the interference of elements such as F^-, Cl^-, and Br^-, etc.

Curvature-directed oxidation of GNRs and gold pyramids was investigated by *Kou* et al. [9.251]. Oxidation was found to happen selectively at surface sites with high curvature. By varying the amount of H_2O_2 and HCl, the oxidation rate can be controlled. The oxidation rate increased in the order: CTBAB-stabilized Au bipyramids, CTBAB-stabilized GNRs, CTAB-stabilized GNRs. Through this method, the LSP band can be precisely controlled from 650 to 1300 nm. Overgrowth of different metals on GNR was also investigated [9.252]. They found that, depending upon the metal used, either single-crystalline or polycrystalline shells will grow on GNRs. In the case of Au and Ag, single-crystalline thin shells were formed, and for Pd the shell was polycrystalline. This was attributed to the lattice mismatch between Au and Pd. Because of the anisotropic surface structure, the competition between the overgrowth on different surface facets resulted in highly anisotropic overgrowth. Due to the strong interaction between the {110} facet and CTAB, {110} was less accessible for overgrowth compared with the {111} and {100} facets. Hence, anisotropic overgrowth occurs,

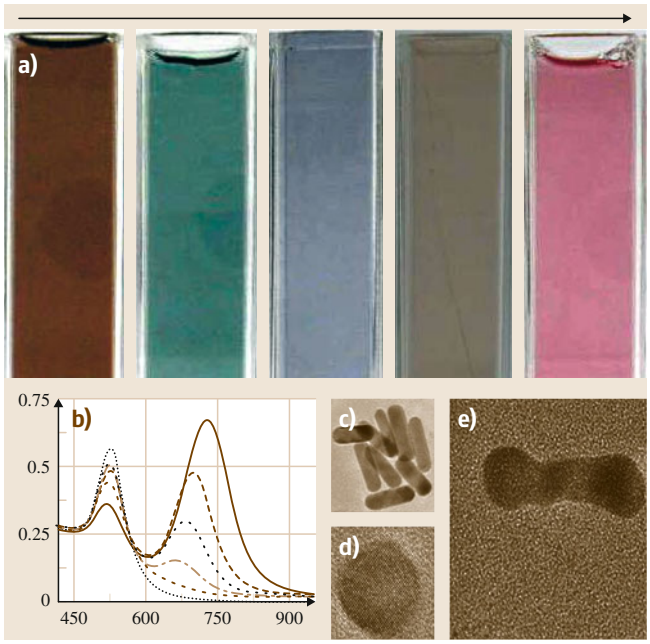


Fig. 9.14 **(a)** Reaction mixture at different time intervals of reaction, depiction of color changes. **(b)** Time-dependent UV/Vis spectra of reaction (*y*-axis: extinction (O.D.), *y*-axis: wavelength (nm)). **(c–e)** TEM images of the NR, nanosphere, and intermediate structure. Formation of GNRs with various aspect ratios is evident from **(b)** (after [9.248]) ▶

and this results in the formation of dumbbell-shaped NRs.

Transverse overgrowth of GNRs by the attachment of thiol-containing molecules such as glutathione and cysteine onto their ends was reported [9.254]. It was found that, as the concentration of the Au precursor increased, the shape underwent a gradual change from rods, peanuts, and truncated octahedra to faceted spheres. The attachment of glutathione and cysteine onto the end faces blocks longitudinal growth and allows growth on the side faces, resulting in an increase of diameter while retaining the length constant. This was also found to be excellent for tailoring the plasmonic characteristics of the GNRs. By combining the selective shortening and controlled transverse overgrowth, *Ni* et al. devised a strategy to tune the LSP band of GNRs [9.255]. GNRs were used as the seed for making silver nanostructures, utilizing the anisotropic surface structure [9.253]. Both homogeneous and anisotropic coatings of Ag were created. This resulted in the formation of an *orange slice-like* shape for the Au@Ag nanocrystal. Figure 9.15 shows the UV/Vis extinction spectra during the formation of the Ag shell. The inset image shows SEM images of the structures formed. The preferential growth of the {110} facets was found to be the primary reason for the formation of the structure. Two neighboring {110} facets among the four present on the side faces grow faster compared with the others. The strong stabilization of CTAB onto the {110} facets of Ag and the minimization of the overall surface energy were given as the reasons for this selective growth. *Carbó-Argibay* et al. reported a chemical method for sharpening the GNRs which results in the rod to octahedron shape transition [9.256]. Rods with sharp tips and strongly faceted lateral faces were formed first. Later, they transformed into octahedrons. The growth rates on different facets were found to be different, following the order: {111} < {110} < {100}. This is believed to be due to the preferential attachment of poly(vinyl pyrrolidone) (PVP) to different body-centered cubic (bcc) facets, which alters the surface energies.

Competing growth of the Pd shell between {110} and {100} facets on the side faces of GNRs, which resulted in the formation of rectangular Pd/Au bimetallic NRs, was reported by *Xiang* et al. [9.257]. The surface energy of the {110} facet is higher compared with that of {100}. Hence, a driving force to minimize

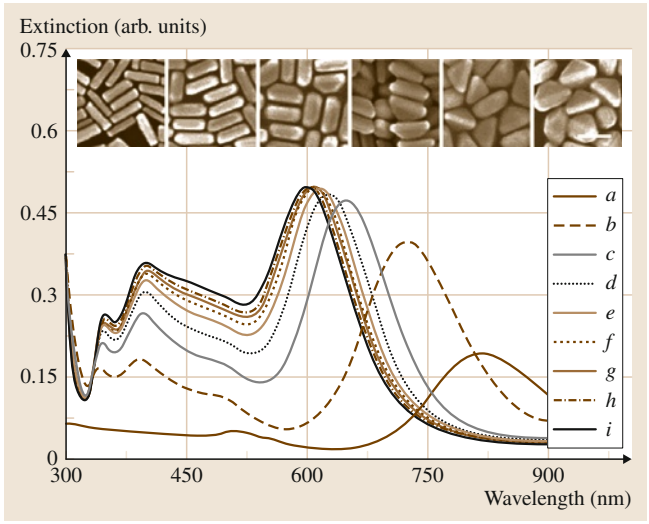


Fig. 9.15 UV/Vis extinction spectra during the formation of the Ag shell after seed addition at: (*a*) 0 min, (*b*) 2 min, (*c*) 4 min, (*d*) 6 min, (*e*) 8 min, (*f*) 10 min, (*g*) 12 min, (*h*) 14 min, and (*i*) 30 min. *Inserts*: SEM images showing intermediate shapes of the Au@Ag nanocrystals during the growth process (after [9.253])

the overall surface energy by changing the morphology exists. As a result, palladium grows faster along the {110} planes than along the {100} planes. This in turn produces an enlargement of the {100} surfaces by sacrificing {110}. After some time, {110} facets disappear and a rectangular Pd shell terminated with four {100} side surfaces is formed, as illustrated in Fig. 9.16. GNRs were used as a template for synthesis of other anisotropic structures as well. *Obare* et al. used polystyrene and silica-coated GNRs as templates for creating hollow nanotubes [9.258]. Silica-coated GNRs (AR 13) were coated with polystyrene. Dissolution of the GNR core by the use of KCN resulted in the formation of hollow nanotubes.

Other Common Reactions on Noble Metal Nanostructures: Examples

As was discussed earlier, there is keen interest in enhancing the properties of anisotropic nanosystems by carefully engineering their structure and composition. Of the many strategies employed, galvanic replacement reactions deserve special mention. The high tunability and versatility, and the possibility to study alloying and dealloying in metallic nanostructures give these reactions utmost importance in postsynthetic design of nanosystems. Galvanic reactions are spontaneous reactions occurring when the atoms of one metal react with ions of another metal having a different electrochemical potential, whereby the metal atoms having lesser reduction potential are oxidized and dissolved into the solution, while the metal ions are reduced. Through this methodology, versatile structures such as hollow NPs, alloyed nanostructures with controllable elemental composition, and nanosystems with tunable optical properties have been created [9.259, 260]. Figure 9.17 shows such a reaction done on truncated Ag nanocubes. Another advantage of the galvanic replacement reaction is the controllability of the final morphology, which closely resembles the starting template.

Galvanic replacement reactions of Ag nanocubes have been well studied. With $HAuCl_4$, Ag nanocubes are reported to show interesting galvanic reactions. The reaction can be divided into two half-reactions as follows: The half-reaction showing dissolution of metal at the anode is (standard hydrogen electrode (SHE)

$$Ag^{+}_{aq} + e^{-}_{aq} \rightarrow Ag_s (0.80\,V \text{ versus SHE}) . \qquad (9.13)$$

The half-reaction showing reduction/deposition of the metal ions at the cathode is

$$Au^{3+}_{aq} + 3e^{-}_{aq} \rightarrow Au_s (1.50\,V \text{ versus SHE}) . \qquad (9.14)$$

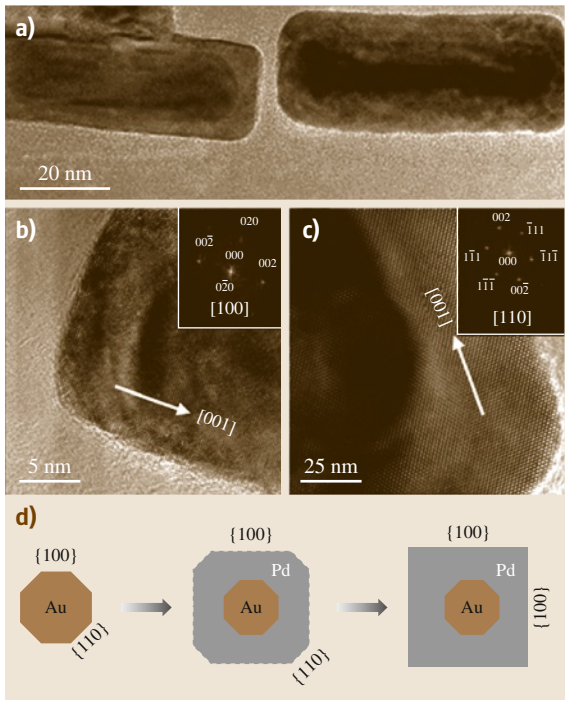


Fig. 9.16 **(a)** Low-resolution TEM image of single bimetallic NRs. High-resolution TEM images of bimetallic NRs when the electron beam is aligned in the [001] **(b)** and [011] **(c)** directions, showing the distribution of the atoms on the {001} and {111} faces, respectively. *Insets* show the corresponding FFT transform images. **(d)** Cross-section showing the morphology transition from pure GNRs to Pd/Au bimetallic NRs (after [9.257])

Hence, the total reaction is

$$Au^{3+}_{aq} + 3Ag^{0}_{aq} \rightarrow Au_s + 3Ag^{+}_{aq} . \qquad (9.15)$$

These equations are valid only at standard conditions (at 25 °C). A change in temperature to 100 °C, the presence of Cl^- ions, and other nonstandard conditions can affect the potentials [9.261, 262].

Starting with a variety of shape-controlled nanomaterials as templates, hollow nanostructures of a variety of materials with well-defined and controllable sizes and shapes have been reported through galvanic reactions. Reaction between Ag nanocubes and $HAuCl_4$ where hollow nanostructures are formed has been reported [9.175]. The reaction was done at 100 °C to avoid deposition of AgCl on the surface of the nanostructures formed. Time-dependent SEM analysis showed that small pits formed on the surface of the cubes, first mainly at defect sites. As the reaction continued, these

pits expanded into the interior of the nanocubes, resulting in hollow structures. It was also found that, by controlling the reaction parameters, different structures such as nanocages, nanoboxes, etc., could be generated using this methodology. The creation of nanocages with controllable pores was possible when different facets were present on the surface of the starting Ag nanocubes [9.263]. Galvanic reaction on 42 nm Ag nanocubes with truncated corners having six {100} facets and eight {111} facets, and some {110} facets at the truncated parts, resulted in the formation of final pores selectively on the {111} facets at the corners. After the replacement reaction, the pores found at all eight corners (consisting of {111} facets) were uniform in size and shape. The facet-selective reactivity observed is explained as being due to the preferential binding of PVP to {100} facets of Ag compared with {111} facets, thereby making the {111} surface more exposed for reactions.

Galvanic reactions normally preserve the morphology of the starting materials. However, when the facet-selective reaction was started with 24 nm spherical Ag particles, this morphology changed to octahedrons [9.266]. Starting Ag particles had {111} and {100} facets. As discussed above, the pitting reaction happened on the {111} facet and deposition of Au on the {100} facet. Due to the smaller size of the particles, this resulted in a change in morphology. A similar transition was seen in the case of 11 nm Ag spheres as well [9.267]. Similar reactions are also applicable for polycrystalline materials [9.268–270].

Hollow nanotubes can also be made using an analogous method. Ag NWs having five twin-planes along the length of the wire together with a pentagonal cross-section were treated with $HAuCl_4$ [9.271]. Multi-walled structures such as nanorattles, multi-walled nanoshells, and multi-walled nanotubes can be made using this reaction [9.77, 271]. By electroplating, a thin layer of pure Ag was coated on the surface of Au-Ag alloy particles, and the consequent reaction resulted in multi-walled structures. Using a comparable strategy, a single-step, large-scale methodology for the production of nanoframes of different morphologies was reported by *Sun* et al. [9.77].

The difference in surface energies between common facets of face-centered cubic (fcc) metals were used for fabricating hollow Au-Ag octahedrons containing GNRs [9.272]. The difference in surface energy resulted in an uneven growth rate and a complete change in the morphology. GNRs to begin with had {111}, {100}, and {110} facets. After deposition of Ag, all the rods

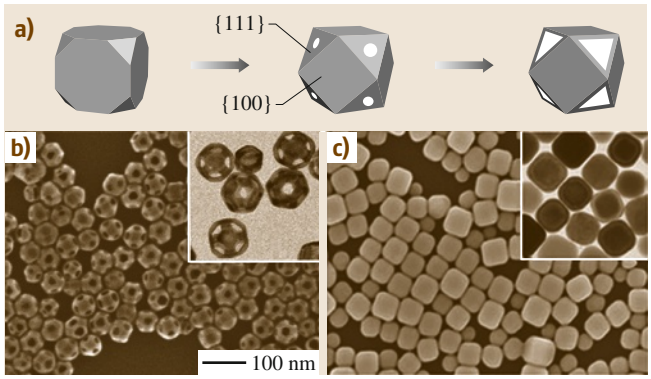


Fig. 9.17 **(a)** Schematic showing the morphological changes during the different stages of the galvanic replacement reaction with truncated Ag nanocubes. **(b)** SEM (with TEM *inset*) of truncated Ag nanocubes. **(c)** SEM (with TEM *inset*) of Au nanocubes with rounded edges (after [9.264])

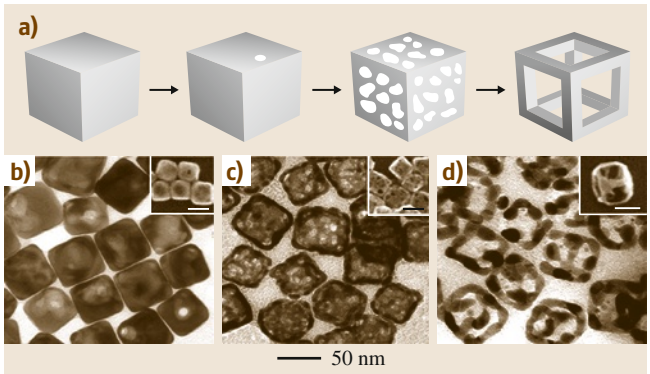


Fig. 9.18 **(a)** Schematic summarizing the formation of cubic Au nanoframes by treating Ag nanocubes with $HAuCl_4$ to form Au-Ag nanoboxes **(b)**, and then etching with ferric nitrate to form thin-walled nanoboxes, **(c)** and eventually cubic nanoframes **(d)**. *Inset scale bars* are 50 nm (after [9.265])

transformed into Au@Ag octahedrons capped by {111} facets. When the resultant particles were treated with excess $HAuCl_4$, hollow Au-Ag octahedra containing GNRs were formed. A similar reaction has been observed out in organic media as well.

Galvanic reactions of Pd NRs with $HAuCl_4$ did not produce hollow structures. Instead, solid tadpole-like structures having a Pd tail and an Au head were formed [9.273]. As the reaction proceeded, Au was deposited first at one end and then both ends. The selective deposition was attributed to electron–electron repulsion, which pushes the electrons generated during Pd oxidation to either ends of the rod, resulting in the

reduction of Au^{3+}. After some time, the Au head increased in size and eventually fell off the structures. A similar study of polycrystalline Pd rods resulted in a nonrandom alloy with an Au-rich core and a Pd-rich shell. A similar morphology was formed when Co NRs were treated with Au precursors as well [9.274].

Introduction of a wet etchant such as ferric nitrate ($Fe(NO_3)_3$) can influence the galvanic reaction between Au and Ag [9.276, 277]. This enables removal of Ag without deposition of Au, resulting in better control of wall thickness, composition, and resultant optical properties. Ag nanocubes were treated with $HAuCl_4$ first, which resulted in the formation of small pits. On treatment with $Fe(NO_3)_3$ solution, thin-walled nanoboxes were formed. As the concentration of $Fe(NO_3)_3$ added increased, the thin-walled nanoboxes were converted to nanoframes. This transition was attributed to the higher susceptibility of {100} facet towards etching (Fig. 9.18).

Due to their catalytic applications galvanic replacement of Ag nanocubes with Pt and Pd precursors have been well studied [9.278]. Reaction between 50 nm Ag cubes and Pt precursor resulted in hollow structures with rough exterior. This was attributed to the lack of miscibility between Pt and Ag at the reaction temperature (100 °C), but when the reaction was done with Pd, the surface of the structures formed was smooth. However, the reaction never went beyond the nanobox stage. When the galvanic reaction was done with two or more metal ions, the order of addition was found to influence the resultant morphology [9.78]. In the case of Au and Pd reaction with Ag nanostructures, addition of Pd before Au resulted in products with large pores. However, first reaction with Au and subsequent reaction with Pd resulted in solid walls. In the case of Au, there was a difference in reactivity between $[AuCl_4]^-$ and $[AuCl_2]^-$. The striking difference between Au(I) and Au(III) was the early disappearance of the pinhole in the case of Au(I), due to the larger amount of Au deposited for the same amount of Ag being dissolved. Structure-wise, in the case of Au(I), the walls of the nanocages were thicker compared with those formed for Au(III).

An epitaxial growth process by which Au nanooctahedra were changed to Pd and Ag nanocubes was reported by *Fan* et al. [9.279]. Au nanooctahedra were used as seeds, and through the use of a seed-mediated growth method, shape transition was realized. The formation of an asymmetric hollow structure from a heterometallic NR by partial galvanic reaction was demonstrated by *Seo* and *Song* [9.275]. They found that asymmetric single-hollow or symmetric double-hollow

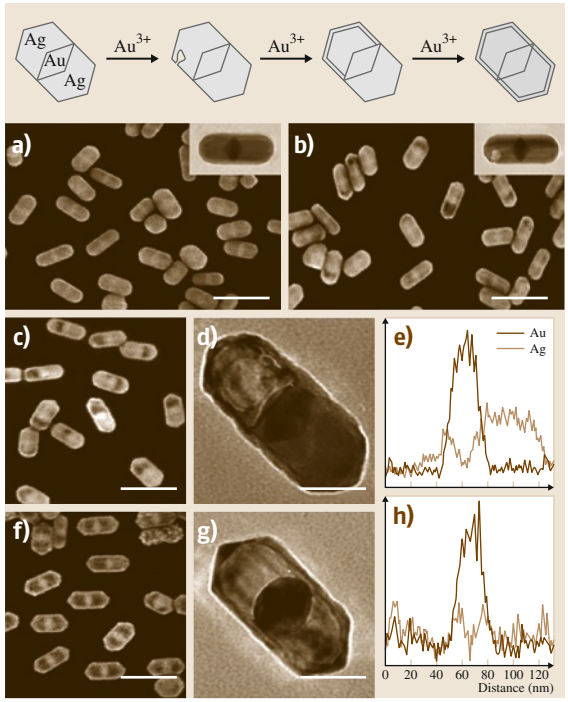


Fig. 9.19a–h Schematic representation of the galvanic replacement in Ag-Au-Ag heterometallic NR. SEM and TEM (*insets*) images of **(a)** original heterometallic NR and **(b–d)**, **(f)**, and **(g)** hollow structures at different concentrations of Au^{3+}. **(e,h)** Energy-dispersive x-ray spectroscopy (EDAX) line profiles along the long axes of the hollow structures (after [9.275])

NRs could be generated from Ag-Au-Ag heterometallic NRs. The breaking of symmetry was a result of random pit formation on the Ag end. The reaction scheme and the structures formed are shown in Fig. 9.19. Production of triangular gold nanorings by galvanic replacement reaction of ultrasonically synthesized Ag nanoplates was reported by *Jiang* et al. [9.280]. The nanoplates and nanorings were highly single crystalline and had (111) planes as the basal planes.

The diffusivity difference between metals can give rise to the formation of hollow structures by a phenomenon known as the Kirkendall effect (KE). If the inner material diffuses outwards faster than the rate at which the outer material diffuses inwards, voids will form. In nanosystems, such an effect can result in the formation of hollow structures. Several reports exist in this regard [9.267, 281–284]. Recent studies reveal that the formation of some of the hollow structures discussed above through galvanic replacement reactions can also

have a contribution from the KE [9.283]. Reaction between cobalt nanocrystals in solution with oxygen and either sulfur or selenium can result in the formation of hollow nanocrystals through the KE [9.281]. Recently, a size-dependent nanoscale KE observed during the oxidation of nickel NPs was reported by *Railsback* et al. [9.285]. Depending upon the size of the NP, either single-pored or multipored NiO nanostructures were formed. It was found that the fast self-diffusion of Ni compared with its rate of diffusion through the NiO shell resulted in the single-pore structure. When the diffusion was not fast enough, multiple pores resulted.

9.5.2 Modification of Properties – Formation of Superstructures

Tapping the incredible properties exhibited by NPs into useful applications is challenging when one is working with individual NPs. Assembling them into well-arranged superstructures is one of the ways to make use of these systems in modern day science and technology. Assemblies of NPs are important for many fruitful applications. Functionalization of noble metal NPs is comparatively easier and this makes them attractive candidates for making diverse superstructures. Creation of their one, two, or three-dimensional assembled structures can enhance the properties or can sometimes give rise to novel improved properties due to the effective coupling of different domains. Noble metals (mainly gold and silver) owing to their biocompatibility, tunable optical properties, and easy synthesis, have been extensively used to create superstructures that are useful in studying various properties including SERS, metal–insulator transitions, interplasmon coupling, etc.

Assembly can be brought about by using molecular linkers, templates, or spacers in well-organized periodic one, two- or three-dimensional superstructures. For spherical NPs solid superstructures called particle crystals or SLs [9.286–288] can be generated via bottom-up or top-down approaches. A high degree of monodispersity is the prerequisite for making such SLs over a long range. The changes in properties of individual NPs in the collection can be understood by studying these structures. For example, changes in optical properties such as interplasmon coupling and changes in transport properties including metal–insulator transitions, etc., can be understood in a better way by studying the properties of SLs [9.286]. Various strategies such as electrostatic self-assembly, solvent evaporation on a substrate, self-organization at interfaces, covalent and hydrogen bonding, biochemical interaction, van der

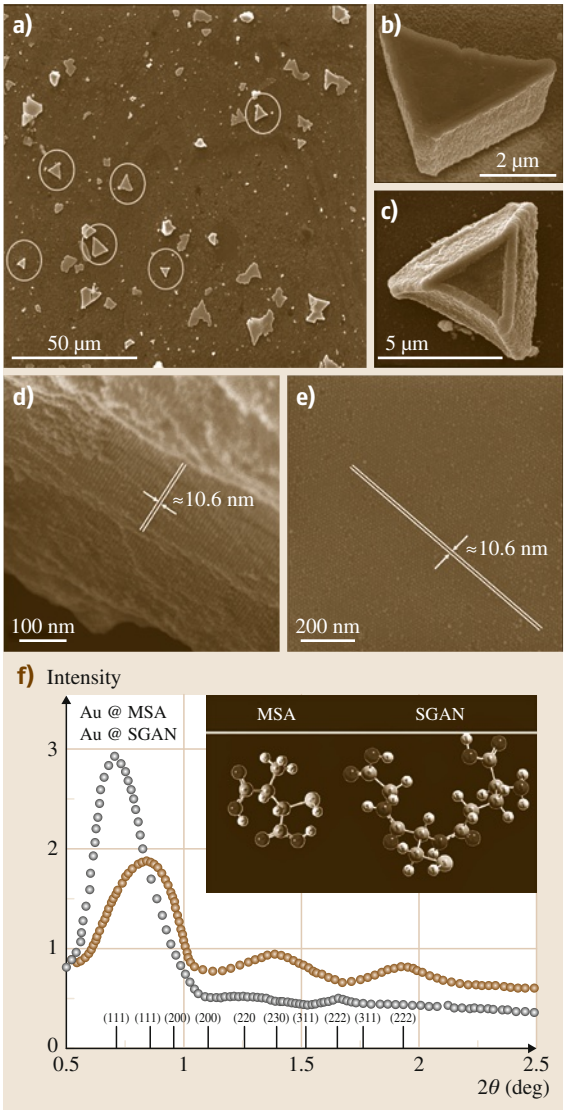


Fig. 9.20 **(a–e)** SEM images of superlattices made of GNPs at various magnifications. **(d,e)** Clear images of large area ordered arrays of NPs. **(f)** Small-angle x-ray scattering showing the regular array of atoms in SLs. From the authors' laboratory

Waals and dipole interactions, etc. [9.289], have been utilized to create SLs of GNPs. Several well-written reviews are available on this topic [9.289, 290].

Digestive ripening, the SMAD method, and hydrogen-bonding methods are used extensively to create SLs [9.289]. Thiol-protected GNPs synthesized by the SMAD process upon digestive ripening will

spontaneously form 2-D and 3-D SL crystals via self-organization. Changing the pH of the solution by the addition of acid (pH ≈ 2) resulted in the organization of MSA acid-protected GNPs into beautiful 3-D structures [9.287, 291]. The formation of hydrogen bonding between the dicarboxylic acid moieties present on the adjacent NPs drive the assembly formation. Formation of a brown mirror-like appearance on the air/water interface after a few days indicates SL formation [9.292]. Diverse morphologies such as triangles, hexagons, etc., were adopted during the crystal formation. Some representative SLs formed by these interactions are shown in Fig. 9.20.

Spherical particles that are isotropic will experience the same interactions in all directions in a 3-D assembly and the resultant effect as well as collective properties will be the same. Only the extent of interaction and hence the change in properties will vary depending upon the dimensionality of the assembly. Unlike isotropic NPs, the inherent anisotropy of anisotropic NPs adds a directional dependence on the assembly and the consequent interactions between NPs. A variety of factors plays seminal roles in assembling NPs in an ordered manner, without the formation of complex 3-D aggregates. The following section reviews different assemblies of various nanostructures and various forces inducing such assemblies.

Assembly of Gold Nanorods

The crystal structure and crystallographic planes present on the NP surface plays important part in regulating their assembly. Unlike spherical NPs, which have an isotropic crystal structure entirely composed of either ⟨111⟩ or ⟨100⟩ planes, the surface structure of anisotropic NPs are different. GNRds are classical examples of this anisotropic surface crystal structure. The GNR surface is highly anisotropic consisting of different facets (Fig. 9.21a,b) [9.239]. The edges (side faces) of GNRs are constructed by ⟨110⟩, and their tips consists of either ⟨111⟩ or ⟨100⟩ facets [9.239]. Due to this anisotropic crystal structure, the distribution of surfactant molecules (the CTAB bilayer coverage) on the surface of GNRs will also be anisotropic, and the bilayer will be thicker on the side faces due to the higher affinity of CTAB towards ⟨110⟩ facets. A lattice-resolved image of a GNR showing the specific planes is given in Fig. 9.21b.

Anisotropy in the crystal structure and in surface reactivity can be used as tools for selective functionalization of GNRs to bring about specific interactions between GNRs leading to different types of assembled structures. Because the tips of GNRs are less populated with CTAB they are more susceptible to functionalization strategies and can thus can trigger end-to-end interactions to form linear chains where GNRs are connected in an end-to-end fashion. The shape anisotropy of GNRs opens up another type of linear assembly where the sides of the NRs interact with each other (termed as side-to-side assembly). The free energy of bilayer stabilization between CTAB molecules is 6 kJ/mol per two methylene groups and hence the removal of CTAB from the side faces is rather difficult [9.293]. Hence, to bring about the functionalization of this face, rigorous procedures must be followed. The possible interactions and different kinds of resultant assemblies are pictorially depicted in Fig. 9.21c. Theoretical studies have established that side-by-side assembly leads to a blue-shift in the UV/Vis spectrum, whereas end-to-end assembly imparts a red-shift [9.294]. The extent of the shift in the spectra depends on the extent of assembly. For example, in a 2-D or 3-D assembly where multiple interactions are present, the resultant shift can be a combination of all of these interactions.

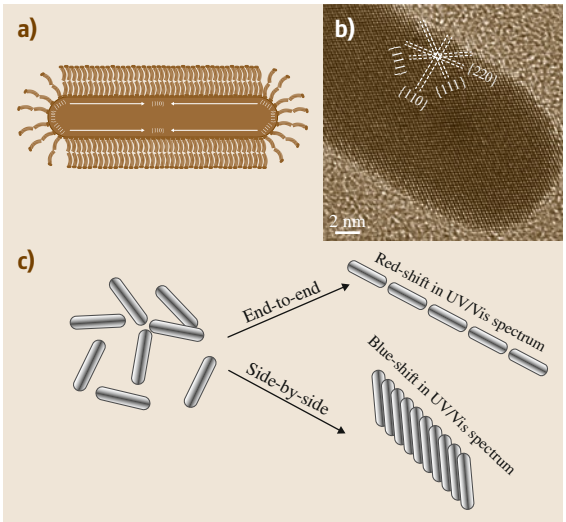


Fig. 9.21 **(a)** Schematic of a single GNR. **(b)** High-resolution TEM (HRTEM) image showing the different crystal planes and lattice structure. **(c)** Schematic showing the different ways of arranging the NRs

Spontaneous assembly without any external aid is often called self-assembly. GNRs are known to self-assemble under optimum conditions such as concentration, pH, ionic strength, etc. Controlling the interactions between the constituents can lead to mod-

ification of self-assembly. Generally, environmental conditions such as pH and ionic strength are modulated for this purpose. Then the process will be termed *programmed self-assembly*. The assembly process can be controlled by chemical modifications or functionalizations as well. Surface functionalization of GNRs with specific molecular groups can result in precisely programmed self-assembled structures. Due to its simplicity, versatility, and low cost, programmed self-assembly with functionalized NRs is used extensively for nanofabrication purposes. One of the disadvantages of this strategy is that it normally produces ordered structures with small area and does not allow control over the design or interparticle distance in the NR architecture. Also, once triggered, further manipulation of the assembly is rather difficult. However, a better understanding of the system and the advent of new techniques are helping us to overcome these limitations. Programmed assembly can be brought about using a wide variety of operating forces, by changing the functionalizing molecules. The operating forces involved in the assembly can be covalent, hydrogen bonding, electrostatic, biochemical interaction, van der Waals, dipole interactions, etc.

The following section illustrates a brief review about the different kinds of assemblies and the operating forces leading to the assembly, taking GNRs as the example.

Self-Assembly of Gold Nanorods upon Solvent Evaporation

GNR suspensions are stabilized due to the electrostatic repulsion between the head groups of CTAB (the stabilizing bilayer) on adjacent rods avoiding aggregation. Removing excess surfactant by centrifugation and at optimum concentration, pH and ionic strength, the hydrophobic–hydrophobic interaction between the CTAB tails can compensate the electrostatic repulsion facilitating the assembly of NRs where the distance between the NRs depends on the compensation of the above-mentioned interactions. Therefore, NRs form assembled structures with an optimum separation between NRs upon solvent evaporation, with all forces being compensated. In 2000 *Nikoobakht* et al. made one of the first attempts to study the self-assembly of GNRs [9.295]. GNRs prepared by electrochemical methods (AR $\approx$ 4.6) were centrifuged at 14 000 rpm and were resuspended in water. The sample was diluted to an optical density of 1.5–1.7. A 1 : 1 solution of the above suspension and 0.1 M NaCl solution was made and was dropcasted onto a TEM grid as shown in the inset of Fig. 9.22. Long-range (over micrometer areas) 1-D, 2-D, and 3-D assemblies of GNRs were formed on the grid upon solvent evaporation. Here the electrolyte (NaCl) was used to form the assembly. Later it was found that even without the use of electrolyte, removal of excess CTAB can result in self-assembly at appropriate NR concentrations [9.293]. It is also reported that liquid-crystalline assemblies of large-aspect-ratio GNRs will form when the as-prepared rods are centrifuged to remove associated spherical particles and are redispersed in an optimum concentration of CTAB (1–100 mM). The assembly was studied in detail using UV/Vis and small-angle x-ray scattering (SAXS) measurements.

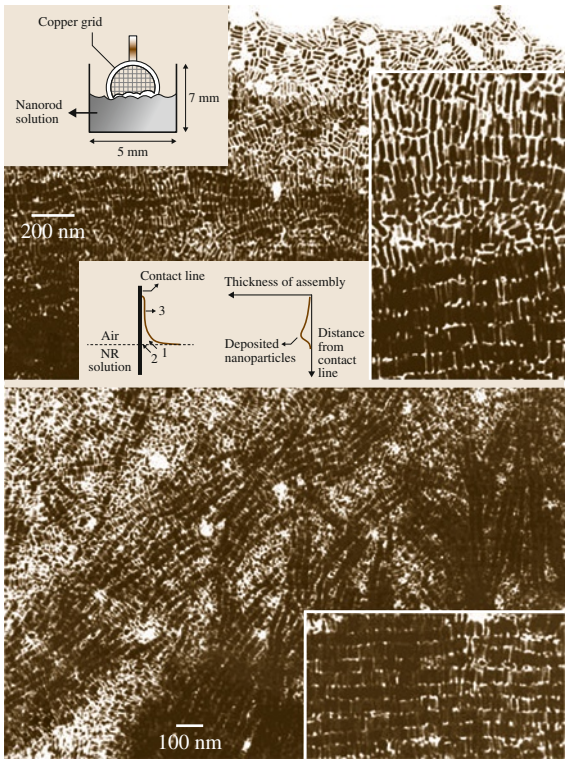


Fig. 9.22 Electron micrograph showing border of the self-assemblies. The thickness increases from *top* to *bottom*. The *insets* show magnified parts of the assembly. *Inset top left*: scheme of the deposition method (after [9.295])

Assembly Involving Biological Interaction and Bio-Recognition

Functional entities in biology are almost entirely assembled structures and the operating forces involved are very specific. GNRs have been assembled using such

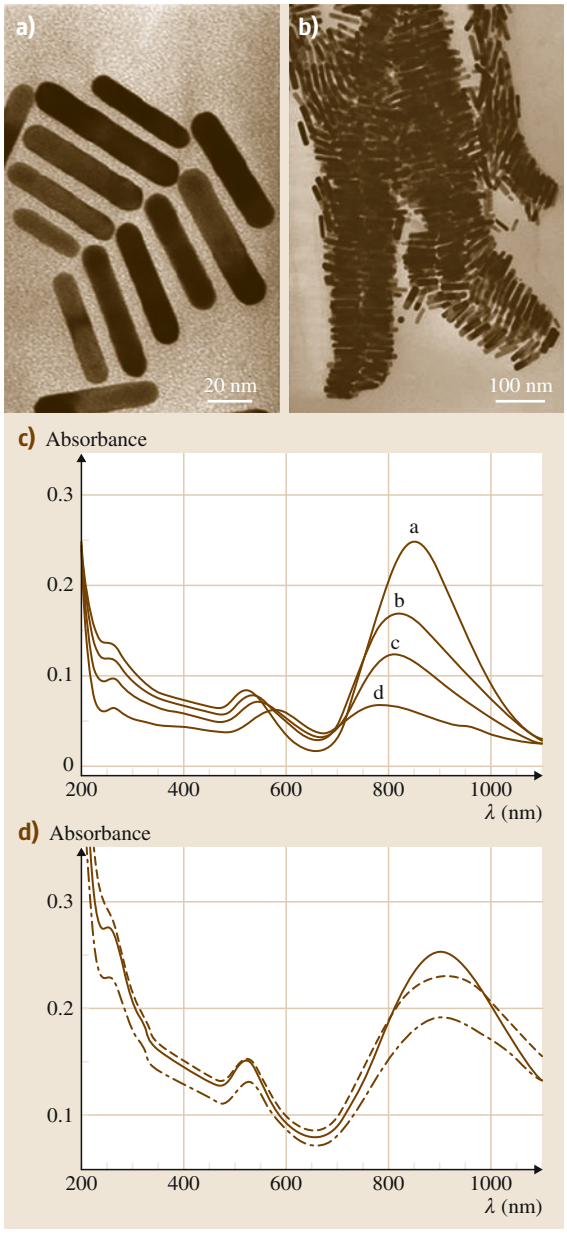


Fig. 9.23a–d TEM images of bundles of DNA-linked GNRs. The three-strand **(a)** and two-strand **(b)** DNA linking systems. UV/Vis spectra of **(c)** a suspension of non-complementary DNA functionalized NRs and **(d)** the two-strand NR system before (*solid line*) and after (*dash-dotted line*) duplexation at 25 °C. The *dashed curve* represents the spectrum after melting the DNA above 60 °C (after [9.296])

interactions as well. The first effort in this direction was made by *Dujardin* et al. [9.296]. In this work, NRs were functionalized with thiolated DNAs. Assembled structures were formed upon addition of duplex DNA into the above mixture. Figure 9.23a,b shows TEM images of the assembled structures and the associated UV/Vis spectral changes during the assembly (Fig. 9.23c,d).

End-to-end assembly of GNRs, surface-functionalized with mercaptoalkyloligonucleotide, was brought about by the addition of a target oligonucleotide [9.297]. Here, the thiol groups in the mercaptoalkyloligonucleotide binds to the ends of the NRs, which further assemble in end-to-end fashion through hybridization with the target oligonucleotide. *Chang* et al. utilized the specific binding of an antibody to an antigen to form an oriented assembly of GNRs in solution through a biomolecular recognition system [9.298]. In this work, thioctic acid (TA), used as a binding agent, was made to specifically self-assemble onto GNR tips. The conjugation of TA with various immunoglobulins (Ig) or other biomolecules resulted in the GNR to assemble. *Wang* et al. utilized a similar strategy to detect proteins such as IgG [9.299]. Compared to the spherical counterparts (detection limit 0.1 μg/ml), an enhanced detection limit of 60 ng/ml was shown by the NR assembly.

The biotin–streptavidin interaction is one of the most specific and strongest noncovalent interactions known in biology. Utilizing this interaction, a preferential end-to-end assembly of GNRs was fabricated. First, GNRs were surface-functionalized with biotin disulfide and the subsequent addition of the streptavidin linker gave GNRs assembled preferentially in end-to-end fashion [9.300]. A simple and versatile approach for end-to-end assembly of GNRs was reported by *Huang* et al. This strategy involved the specific molecular recognition between thymine-rich (T-rich) oligonucleotides and mercury(II). The high specificity of the oligonucleotide improved the selectivity of the process [9.301].

Assembly Involving Covalent Bonding

Longitudinal assemblies of GNRs were fabricated by the interaction of GNRs and α,ω-alkanedithiols of varying chain lengths, and the mechanism, structure, as well as changes in properties were investigated using absorption spectroscopy and TEM by *Thomas* et al. [9.302]. A decrease in the longitudinal plasmon absorption was observed upon addition of dithiols. The simultaneous appearance of a new red-shifted band above a critical dithiol concentration resulting from the interplasmon

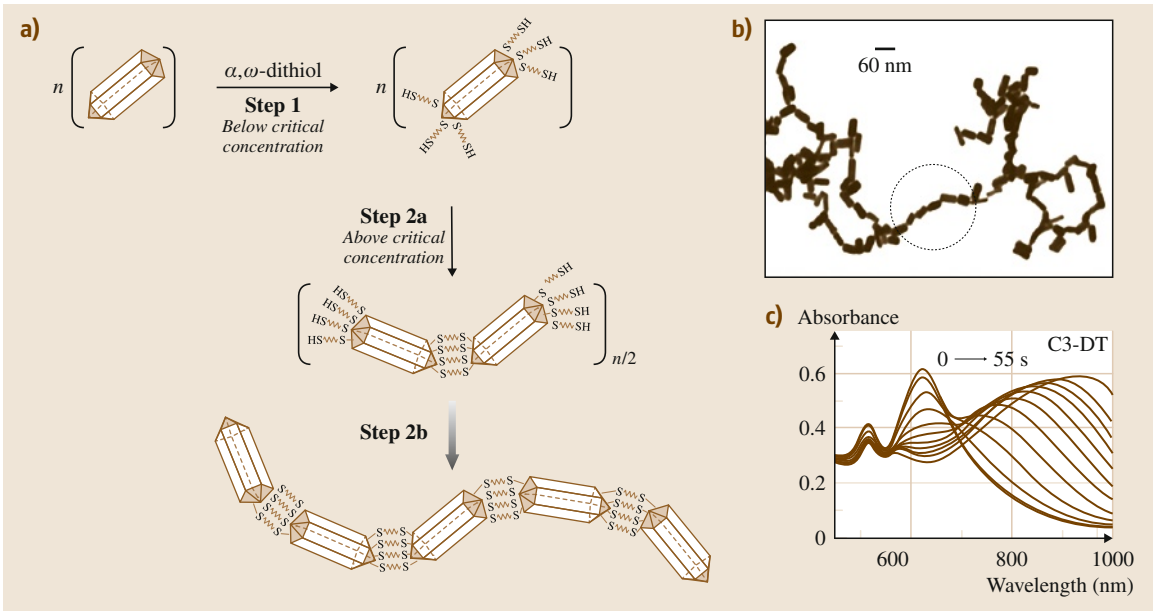


Fig. 9.24 **(a)** Schematic of the general mechanism of GNR nanochain formation due to electrostatic interaction of cysteine and glutathione. **(b)** Transmission electron micrograph of nanochains. **(c)** 1,3-Propanedithiol (C3-DT) (0.83 μM) to Au NR of AR 2.2 at a time interval of 5 s (after [9.302])

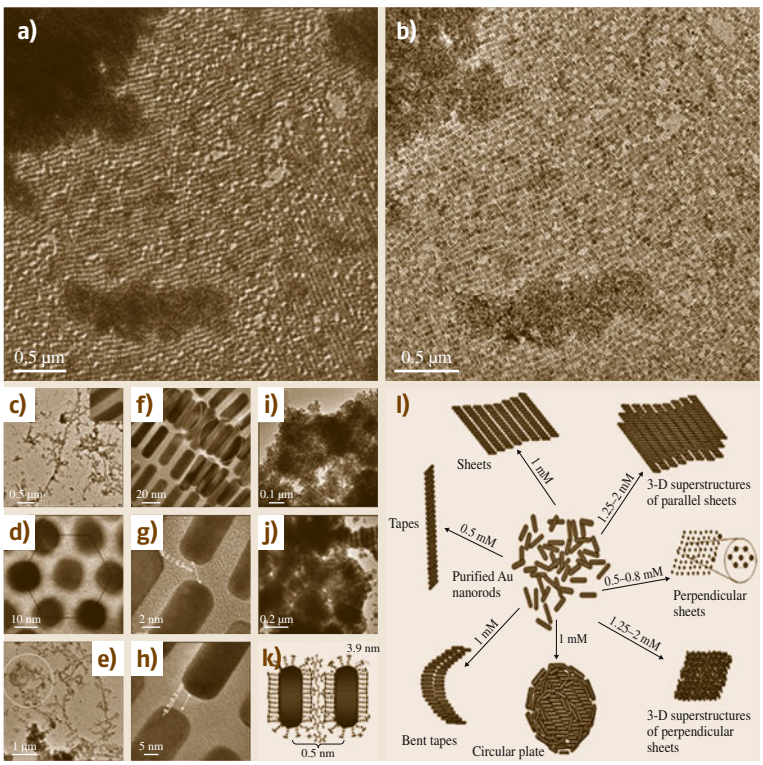


Fig. 9.25a–l TEM images taken in the **(a)** low MAG and **(b)** MAG I modes of the same area, showing self-assembly of NRs, induced by DMSA. Different self-assembled structures obtained at different concentrations of DMSA; **(c)** a parallel assembly of NRs leading to a tape-like structure, **(d)** high-magnification image of perpendicularly oriented assembly showing the hexagonal nature of the rods, **(e)** circular structures and bent tapes, and **(f)** magnified portion of the same assembly showing the staggered configuration of NRs in the same plane. The NRs in the top layer (*circled*) are located in the grooves of the bottom layer. **(g,h)** High magnification images showing the spacing between the NR in a monolayer. TEM images of 3-D superstructures formed by **(i)** perpendicular orientation and **(j)** parallel orientation with respect to substrate. **(k)** Schematic showing the mechanism of the self-assembly. **(l)** Cartoon representation of various superstructures formed from Au NRs in the presence of different concentrations of DMSA. From the authors' laboratory (after [9.303])

coupling in the assembled NRs was also observed. The presence of clear isosbestic points in the time-dependent absorption spectrum, and TEM investigations proved the formation of dimers, indicating the existence of a dimerization step in the chain-up process. It was also understood that the process is not diffusion controlled but activation controlled with large activation energy [9.302].

Assembly Through Hydrogen Bonding

The cooperative intermolecular hydrogen bond formed between two thioacids anchored onto the end faces of GNRs was utilized to precisely control the longitudinal assembly and modulate the plasmon coupling. Adjusting the concentration of thioacids added into the mixture resulted in the modulation of plasmon band positions. An increase in concentration of thioacids produced a plasmon shift to a higher wavelength. Precise tuning of the optoelectronic properties is possible through this method [9.304]. Recently, hydrogen-bonding-directed assembly of GNRs in aqueous solution was investigated by *Ni* et al. [9.305]. Theoretical as well as experimental investigations of the mechanism behind the formation of end-to-end assemblies of GNRs modified with bifunctional linking molecule were made in this study.

Assembly Through Electrostatic Forces

Electrostatic interactions are one of the most common forces encountered in the living world and in assemblies. Electrostatic forces between amino acids anchored onto GNR surfaces were utilized to assemble NRs [9.306]. Two thiol containing amino acids, namely cysteine and glutathione were added to the GNR solution. Due to the thiol-gold affinity, they became anchored onto the GNR end faces and the electrostatic interaction between adjacent amino acids on separate GNRs resulted in the preferential longitudinal assembly (Fig. 9.24). This was manifested by a red-shift of the LSP. This change in the plasmonic characteristics was used for specific detection of cysteine and glutathione at micromolar concentrations. Gold bipyramids and rods were assembled into different types of nanonecklaces using a similar methodology by *Zhang* et al. [9.307].

The time-dependent shift in LSP at a specific concentration of assembly-inducing agents was always constant and it was not precisely controllable in any of the above methods. *Kawamura* et al. reported a more controllable fabrication method for GNRs assembly, in which the shift of the LSP can be stopped at a desired point to obtain a stable suspension with a desired absorption range [9.308]. A gradual red-shift of the LSP was observed upon addition of sodium citrate to GNRs, which can be stopped at any point simply by the addition of CTAB to the reaction mixture. The preferential adsorption of citrate anions onto the end faces of the GNRs, which results the neutralizations of the surface charge of the GNR ends, triggers the end-to-end assembly of the GNRs. High AR GNRs (AR of 16) assembled in an end-to-end fashion upon decreasing the CTAB concentration and the assembled GNRs became welded at their connecting points upon a further decrease of the CTAB concentration [9.308]. A pH-dependent self-assembly of GNRs into ordered structures using adipic acid was reported by *Orendorff* et al. [9.309]. Here, the electrostatic interactions between the cationic surfactant bilayer around the NRs and the negatively charged deprotonated adipic acid result in pH-dependent self-assembly of the NRs into 2-D ordered structures. A similar but more refined strategy to assemble GNRs into 1-D, 2-D, and 3-D superstructures was reported by the authors of this chapter (Fig. 9.25). The addition of dimercaptosuccinic acid (DMSA) to the NR solution-induced self-assembly of the latter into 1-D *tape-like*, 2-D *sheet-like*, and 3-D *SL-like* structures depending on the DMSA concentration. A smectic structure where the NR long axes are parallel to each other was found to be followed throughout the assembly process. Different parameters that determine the quality of the assembly including DMSA concentration, pH, and monodispersity of the sample were studied. Immediately after the addition of DMSA to the NR solution, UV/Vis spectral changes were observed. The peak position was found to be stable (after the initial shift) even after 24 h of incubation. A gradual shift was observed for the LSP, while the TSP remained unchanged. An increase in concentration of DMSA resulted in an increased red-shift. There was a marginal increase in width of the LSP as well. At lower concentrations, a longitudinal assembly formed was transformed into a lateral assembly upon increase of the DMSA concentration. As the concentration was increased, the assembly changed from 1-D *tape-like* to 2-D *sheet-like*, and finally to 3-D *SL-like* structures. Perpendicular arrangement of NRs (NR long axis perpendicular to the TEM grid) was also seen at places. At lower pH (below the pK_a of DMSA) where DMSA molecules are not ionized no assembly was produced. Detailed investigation indicated that charge neutralization of the NRs by the carboxylic group of DMSA was found to be the principal reason for such an assembly, while the mercapto groups render additional stability to

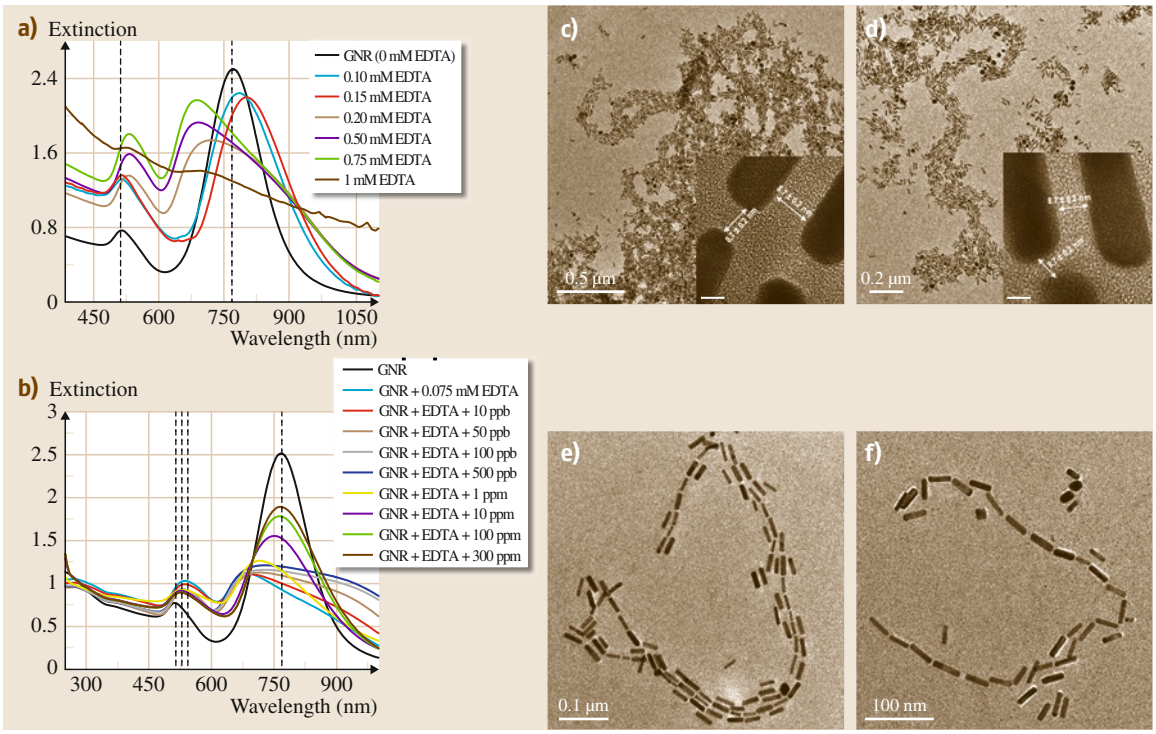


Fig. 9.26a–f UV/Vis spectral changes of the assembly **(a)** and disassembly **(b)** processes. TEM images of assembly and disassembly by EDTA–Pb^{2+} interaction **(c–f)**. From the authors' laboratory (after [9.303])

the superstructure. A mechanistic model of the assembly has also been proposed [9.310].

Electrostatic assemblies are difficult to manipulate once they have been formed. However, recently a strategy for the reversible assembly and disassembly of GNRs was also devised [9.303] A labile ligand ethylenediaminetetraacetic acid (EDTA) was used. The disassembly followed a peculiar pattern by forming bundled chains and then single chains before forming discrete NRs. It was also observed that the assembled structures are highly SERS in nature and through use of the disassembly method SERS activity can be tuned. Figure 9.26 illustrates the UV/Vis spectral changes of the assembly (Fig. 9.26a) and disassembly (Fig. 9.26b) process. The TEM images of the disassembly also can be seen (Fig. 9.26c–f) [9.303].

Gold Nanorod Assembly Involving van der Waals and Dipole Interaction

Changing the hydrophilic nature of the GNR surface (due to the presence by of CTAB) to hydrophobic by treating with mercaptopropyltrimethoxysilane (MPS) and subsequently octadecyltrimethoxysilane (ODS) can induce formation of assembled structures. Well-ordered 2-D or 3-D superstructures of hydrophobic NRs on a substrate by solvent evaporation technique was reported by *Mitamura* et al. [9.311]. The concentration of the NRs controlled the 2-D assemblies and at lower concentration, the NRs assembled parallel to the substrate. Upon increasing the concentration, NRs started to stand on the substrate to form perpendicular assemblies forming hexagonal arrays. 3-D assemblies with a hexagonal close-packed structure due to their side-by-side interaction leading to lamellar structure (over small range) were observed when the NR sample was converted into a solid state.

Nakashima et al. devised a strategy to prepare surface-directed, lateral or perpendicular GNR assemblies [9.312]. This was achieved by anchoring a homemade peptide, 1,2-dipalmitoyl-*sn*-glycero-3-phosphothioethanol (DPPTE) onto the GNR surface. The drying method and the hydrophilic or hydrophobic nature of the Si surface influenced the form of self-assembled superstructures (Fig. 9.27). Driven by intermolecular interactions of surface-anchored lipids, the GNR–DPPTE hybrid formed characteristic 1-D and 2-D self-assemblies

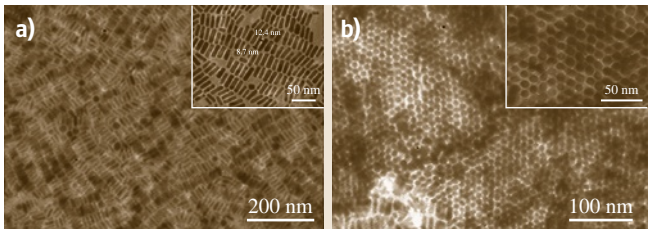


Fig. 9.27a,b TEM images of assemblies of hydrophobic GNRs arranged **(a)** parallel and **(b)** perpendicular to the substrate. *Insets* are the corresponding high magnification images (after [9.311])

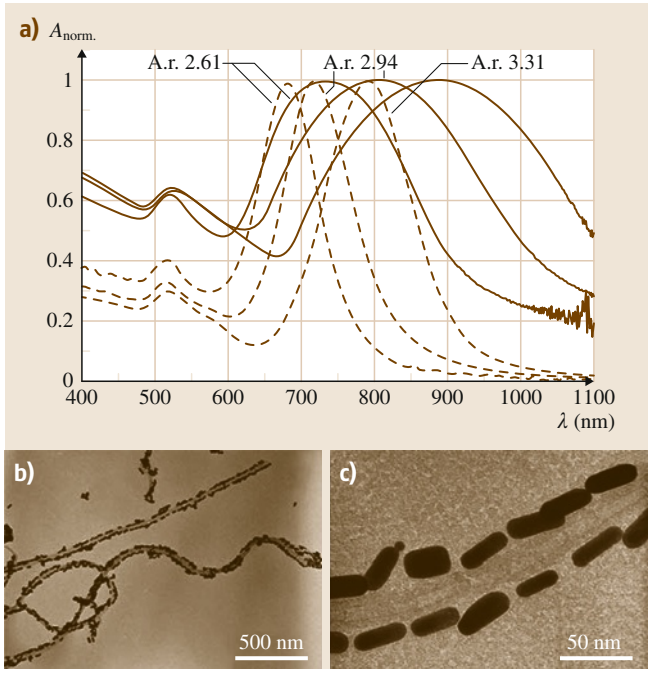


Fig. 9.28 **(a)** UV/Vis spectral changes and TEM images of GNRs (average AR 2.94) assembled on MWNTs (average diameter 30 nm) at different magnifications **(b,c)**

upon controlled drying process. Solvent evaporation from the sample drop in combination with interfacial hydrophilicity or hydrophobicity induced a variety of self-assembled structures. *Walker* and *Gupta* reported a reversible, pH-dependent strategy to form end-to-end assembly of GNRs functionalized with disulfide-modified poly(L-glutamic acid) [9.313].

Changes in pH of the medium-induced corresponding changes in the secondary conformation.

Recently, GNRs were assembled, disassembled, and reassembled by *Chan* et al. who used a bis(terpyridine)–metal connectivity [9.314]. A special molecular moiety (disulfide-modified terpyridine)2–M(II) (M = Fe or Cd) was used as interconnectors to form end-to-end linear and branched assembly of GNRs into multicomponent structures. Basic conditions destabilized the prepared (terpyridine)2–M(II) complexes and the addition of NaOH resulted in disassembly. When Cd was used to induce the assembly, the complexes formed were labile and the resultant assembly was also found to be labile. At low concentrations of Cd, assemblies were formed and in the presence of excess Cd(II) ions, they disassembled. Upon addition of Fe(II) to this disassembled system, they again reassembled into end-to-end chains. This also could also again be disassembled by a mere change in the pH as mentioned above [9.314].

Assembly on Templates

Assembly of NPs on templates is a widely utilized strategy. *Correa-Duarte* et al. was the first group to form GNR superstructures via this approach [9.315]. Multi-walled carbon nanotubes (MWNT) were used as the templates in this work. First the CTAB covering on the GNRs was interchanged with PVP. Then, MWNTs were coated with a polyelectrolyte, mainly polystyrene sulfonate (PSS), followed by poly(diallyldimethyl)ammonium chloride (PDDA). This wrapping resulted in the production of adsorption sites on the carbon nanotubes (CNTs) where GNRs could be deposited electrostatically. A preferential end-to-end assembly of GNRs, forming a string-like alignment (Fig. 9.28) resulted through this method. A broadened absorption feature exhibited by the superstructures indicated the formation of end-to-end assembly and the resultant plasmon coupling between neighboring NRs. It was also noted that these NRs can serve as a label to monitor the alignment of CNTs within polymer films [9.315, 316]. Using drying droplets as the templates, rings of NRs were fabricated by *Zubarev* and *Khanal* [9.317]. A simple and quantitative model for the formation of GNR rings was also described. Here, condensed water droplets from humid air on the surface of nonpolar solvents acted as templates for the spontaneous assembly of hybrid gold–polymer core–shell NRs.

Pradeep et al. reported the use of microgels as a template for a solution-phase method for assembling NRs into a hexagonal pattern [9.318]. First, poly(*N*-isopropyl acrylamide) (PNIPAm) microgels coated with GNRs were synthesized. For this purpose, microgels loaded with CTAB-coated GNPs of 4–5 nm size (used as seed particles) were added to the growth solution used for the seed-mediated growth method for GNRs. This helped in achieving the required population of

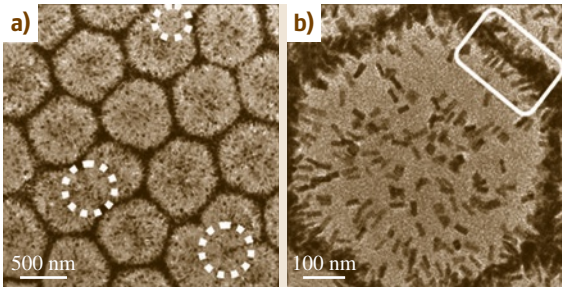


Fig. 9.29a,b TEM images of the GNR-PNIPAm composite. **(a)** Large-area image of the hexagonal pattern with defect sites marked with *dashed circles*. **(b)** Higher magnification image of a single cell of the hexagonal pattern confirming that the anisotropic structures sitting on the microgels are GNRs. From the authors' laboratory (after [9.318])

NRs on the microgels (Fig. 9.29a,b). These NR-loaded microgels were allowed to self-assemble to obtain a hexagonal pattern (Fig. 9.29c,d). Similar experiments performed with NP-coated or prefabricated NR-coated microgels did not give such hexagonal patterns because of the reduced number density of NPs. The interpenetration and interlocking of the NR structures were thought to be the reason for the formation of these patterns [9.318]. *Fava* et al. made use of the affinity of NRs for PNIPAm-based microgels for their sequestering by cationic, anionic, and close-to-neutral-state microgels [9.319]. Cationic, anionic, or near neutral microgels were fabricated by adjusting the pH of the solution. Sequestration of GNRs occurred independently of the charge of the microgels when added to the above solutions. This indicates that electrostatic interactions alone do not govern the loading of microgels with NRs. Electrostatic interactions and subsequent coating of silica with controllable thickness was used to assemble GNRs by *Wang* et al. [9.320].

Assembly on Substrates

Assembly of nanostructures on suitable substrates has the extra edge that it can be directly used for applications. *Mieszawska* et al. reported a methodology for directly growing highly aligned GNRs on a NH_2-functionalized Si(100) substrate with a remarkable degree of parallel alignment over large areas [9.321]. When a similar reaction was carried out on amorphous glass no assembled structure was observed, which pointed towards the importance of having a crystalline structure. However, throughout the sample, the alignment direction varied and no direct correlation between the arrangement of Si atoms and GNR assembly was seen. Hence it was concluded that the crystallinity of the substrate will not affect the direction of assembly. The exact mechanism of the assembly is still not well understood. Control experiments with mercaptopropyltrimethoxysilane (MPTMS) – and (aminopropyl) triethoxysilane (APTES) functionalized, or bare Si(100) did not produce any assembled structures, which indicates the importance of surface chemistry. However, the exact role of the amidation reaction in the alignment is not yet clear. *Mieszawska* et al. observed alignment on acetic and succinic acid surfaces implying the minimal role played by surface hydrophobicity [9.321]. End-to-end alignment of phosphatidylcholine-passivated GNRs adsorbed on polyanion-modified glass substrates were demonstrated by *Yamada* et al. [9.322]. *Zhang* and *Imae* successfully used a patterned silicon substrate with hydrophobic stripes for growing gold NR SLs [9.323]. Perpendicular SLs were also fabricated by this method. The most important factor governing the assembly was the substrate surface. GNRs should be either positively attracted or at least not repelled by hydrophobic surfaces in order to obtain a well-defined assembly. GNRs stayed in solution when the silicon substrate was hydrophilic. Another important criterion was the monodispersity of the sample devoid of particles without shape difference. *Zareie* et al. reported a protocol to directly grow end-to-end assembled long chains on a substrate embedded with a mixed self-assembled monolayer (SAM) that had been functionalized with streptavidin [9.324]. Assemblies extending over a micrometer in length with 5 nm inter-rod separation were obtained by this process.

Assembling by Polymer Tethering

A novel strategy where self-organization of GNRs into a predefined pattern by attaching multiple polymer arms termed *pom-poms* was reported by *Kumacheva* et al. [9.319, 325, 326]. NRs that are end-terminated with polystyrene (PS) when dispersed in dimethylformamide (DMF)/water mixtures tend to self-assemble into higher-order structures. The length and distribution of the PS molecules between the ends and the longitudinal facets of the NRs controls the ordering. Changing the structure of the polymer pom-poms also can modulate the assembly. Depending upon the variation in the molecular weight of the polymers and their relative location on the long side of the NRs, various kinds of NR assemblies namely bundles, bundled chains, and chains involving side-by-side and end-to-end assembly were generated. By changing the concentration of

water in the system, one form of assembly can be changed to another one. It was also understood that the evolution of the self-assembled structures of GNRs end-terminated with PS occurs through competition between side-to-side and end-to-end assemblies. This competition is due to the difference in solubilities of the PS and CTAB-coated metal blocks in the solvent mixture. The tendency to side-to-side aggregation was found to be dominant over most of the compositional range. The above tendency was reduced at high DMF or water content and at very low THF/DMF weight ratios [9.319, 325, 326].

Layer-by-Layer Assembly of Gold Nanorods into Gold Nanorod Films

Yun et al. recently developed a protocol for assembling GNRs into 2-D arrays at a water/hexane interface without the aid of any linker molecule [9.327]. In this method, aggregates of GNRs with a relatively clean surface and controlled NR density were obtained and the film thickness can also be controlled systematically. Because GNRs are hydrophilic, they have a contact angle of $< 90°$ at a water/hexane interface and they will always remain in the aqueous phase. However, when their contact angle is approximately equal to 90°, these particles start to adsorb to the water/hexane interface. A medium with high dielectric constant can separate the charged particles from each other. However, the introduction of a miscible solvent with lower dielectric constant will result in a decrease in the dielectric constant of the medium. Consequently, the surface charge of the particles will also be decreased as a function of the amount of miscible solvent added. When ethanol (with a lower dielectric constant) is added to the water/hexane interface, the surface charge density of the NRs decreases and the NRs are brought to the interface. The reduction in the interfacial energy at the water/oil interface upon the reduction of the dielectric constant of water is the driving force for this entrapment of the NRs. The thickness-dependent SERS activity of the resultant films (when molecules adsorbed on these NR films) has been investigated, and it was found that NR films have an order of magnitude stronger SERS enhancement compared to nanosphere films under similar experimental conditions [9.327].

Gold Nanorod Assembly by Surface Anchored Crown Ethers

Surface anchored crown ethers (end-functionalized) on GNRs were used to induce assembly of GNRs where the addition of specific metal ions resulted in the assembly formation. The approach was reported by *Nakashima* et al. [9.328]. They synthesized two thiol-modified crown ethers, 2-((6-mercaptohexyl)oxy)methyl-15-crown-5 (15-crown-5-SH) and 2-((6-mercaptohexyl)oxy)methyl-12-crown-4 (12-crown-4-SH) and the synthesized crown ethers were added to purified NR dispersions. Covalent attachment of these crown ethers onto the end faces of the NRs through the thiol moieties is possible. In the presence of metal ions corresponding to the anchored crown ethers, assembly of the GNRs resulted. The concentrations of crown ethers and cations added controlled the structure of the GNR aggregates assembled (side-to-side and end-to-end fashion). UV/Vis spectra demonstrated the corresponding changes and the intensity of the longitudinal absorption of the NRs gradually decreased, and the peak was initially red-shifted and then blue-shifted. Potassium ions (K^+) can form a 2 : 1 sandwich complex between the 15-crown-5 moiety, leading to assembly formation and resultant coupling of the plasmon absorbance, in turn leading to changes in the spectral features. This was used for specific detection of metal ions.

Gold Nanorod Assembly Induced by a Magnetic Field

Magnetic field-induced assembly of GNRs is possible by imparting magnetic characteristics to GNRs. For this, Pt-doped GNRs (Fig. 9.30a) were homogeneously coated with metallic Ni through hydrazine reduction in aqueous solutions. This resulted in a quasi-epitaxial growth of an Ni shell on the GNRs (Fig. 9.30b) [9.329]. Since Pt has a much higher redox potential, it will become reduced first compared to nickel. Upon reduction Pt forms small nuclei which act as a *nucleation agent*, on which Ni can be catalytically reduced. When the Ni-coated GNRs (Au@Ni NR) were allowed to dry on a TEM grid under the influence of an external magnetic field (0.2 T), the NRs became aligned in a chain-like structure in the direction of the applied field (Fig. 9.30c). However, the orientation of individual rods within the chains was not found to be the same and coexistence of both *side-to-side* and *end-to-end* assemblies was observed, pointing towards the complex magnetic response of the system [9.329].

Assembly of Various Anisotropic Nanostructures of Silver

Compared to gold, anisotropic silver NPs are more diverse. The main limitation in the case of Ag anisotropic particles is the difficulty to synthesize of them in

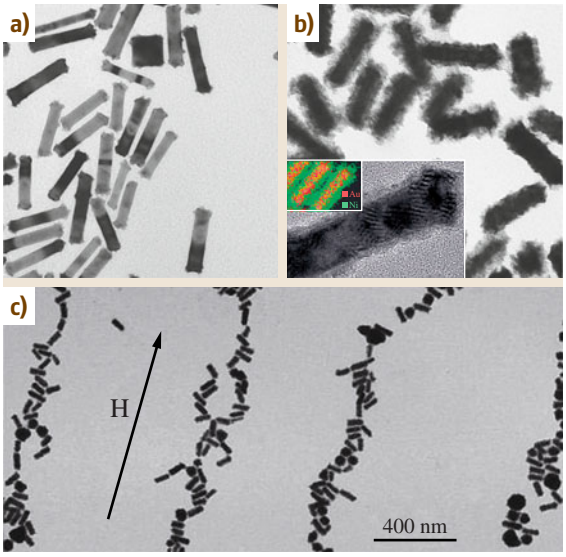


Fig. 9.30a–c Large area TEM of **(a)** GNRs after tip-coating with platinum and **(b)** nickel coated GNRS in the absence of magnetic field. *Inset* shows a high magnification image of a single Au@Ni NR and STEM-EDAX (STEM: scanning TEM) analysis of Au@Ni NRs, showing the relative distribution of the elements (Au = *red*; Ni = *green*). **(c)** Au@Ni NRs, dried on the TEM grid under an external magnetic field (0.2 T) (after [9.329])

a monodisperse fashion. The presence of a surfactant that caps the nanostructures formed and avoids their aggregation is common in all synthetic methodologies, and hence surfactant-induced assembly of these structures upon solvent evaporation is highly feasible. *Jana* et al. devised a seed-mediated growth approach for preparation of silver NRs with varied ARs [9.330]. The approach was very similar to that used for making GNRs. A spontaneous self-assembly process assisted by solvent evaporation was observed upon shape separation of these NRs, resulting in a 2-D smectic liquid-crystal-like superstructure (Fig. 9.31a,b). Recently, a new method to produce monodisperse size-controlled faceted pentagonal silver NRs by thermal regrowth of decahedral silver NPs using citrate as the reducing agent was reported by *Pietrobon* et al. [9.43]. The resultant structures were highly monodisperse and showed a great tendency to self-assemble into smectic mesophases such as densely packed rafts and 3-D arrays when the dispersions dried (Fig. 9.31c–h). It was also noted that the fivefold symmetry of the constituent NRs is always overridden by the long-range hexagonal order within the layers [9.43].

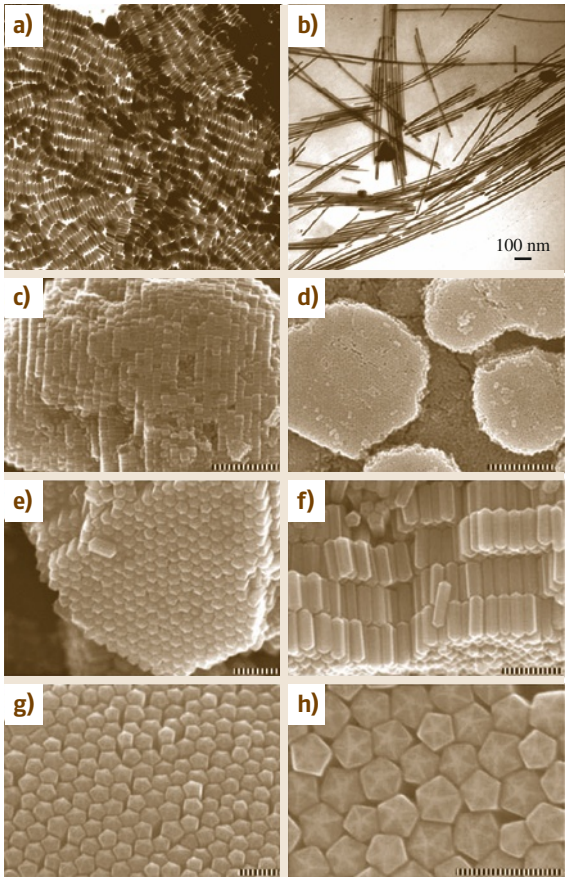


Fig. 9.31a–h TEM image of shape-separated **(a)** silver NRs self-assembled on TEM grids and **(b)** silver NWs. **(c–f)** SEM images of self-assembled packing of monodisperse faceted pentagonal rod AgNRs with different aspect ratio forming 3-D superlattices. **(g,h)** show the top view of the assembly (**(a,b)** after *Jana* et al. [9.330] and **(c–f)** after [9.43])

The Langmuir–Blodgett (LB) technique is one of the most widely used methods to assemble a large area monolayer of nanosystems. Nanowires (NWs) with ≈ 50 nm diameter and 2–3 μm length were assembled into a large area of about 20 cm^2 by *Tao* et al. using this approach (Fig. 9.32) [9.331]. First, the PVP capping of the as-prepared NWs was replaced with 1-hexadecanethiol ligands to make them hydrophobic.

These NWs were then redispersed in chloroform, followed by transferal onto a water surface of the LB trough and were then assembled by the LB method. Large area, side-by-side aligned NWs resembling the nematic 2-D ordering of a liquid crystal were obtained.

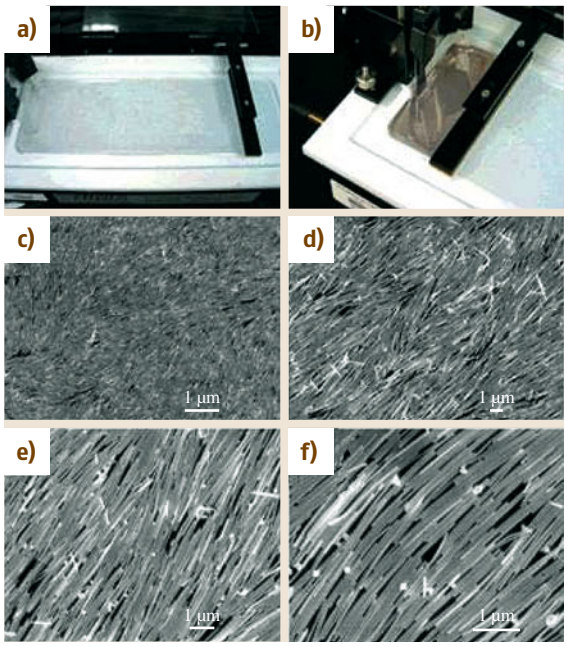


Fig. 9.32 (a,b) Photographs of LB NW assembly process at different compression stages. (c–f) SEM images (at different magnifications) of the silver NW monolayer deposited on a silicon wafer (after [9.333])

An alternating extinction pattern was exhibited by these aligned NW areas when the sample was rotated every 45° [9.331]. The same group, following a similar methodology, was able to create novel SL architectures composed of different polyhedral building blocks, including truncated cubes, cuboctahedra, and octahedra of Ag nanocrystals [9.332]. In the superstructures formed, the packing and the dimensions were determined by the choice of the nanocrystal building block. For example, truncated cubes formed a square lattice by assembling in a face-to-face manner. However, cuboctahedra (which are comparatively more truncated polyhedral particles) assembled to make a rhombohedral unit cell, formed by shearing of the square lattice [9.332].

Bae et al. recently reported the assembly of Ag nanoprisms (Fig. 9.33a,b) [9.334]. They were able to assemble the prisms with anisotropic orientation and studied the orientation-dependent properties of these assemblies [9.334]. *Rycenga* et al. reported an interesting strategy to assemble Ag nanocubes by selective functionalization of each face [9.332]. They prepared five distinct SAM-modified Ag nanocubes from the possible combinations of hydrophobic and hydrophilic faces and these were assembled into four different nanostructures and one microstructure (Fig. 9.33c–f). The mechanism of the assembly was explained on the basis of hydrophobic interaction and solvation-free energy. Figure 9.33c depicts the methodology adopted for selective functionalization of the Ag cube faces. The selective functionalization was carried out by protecting the Ag nanocube, faces which are in direct contact with

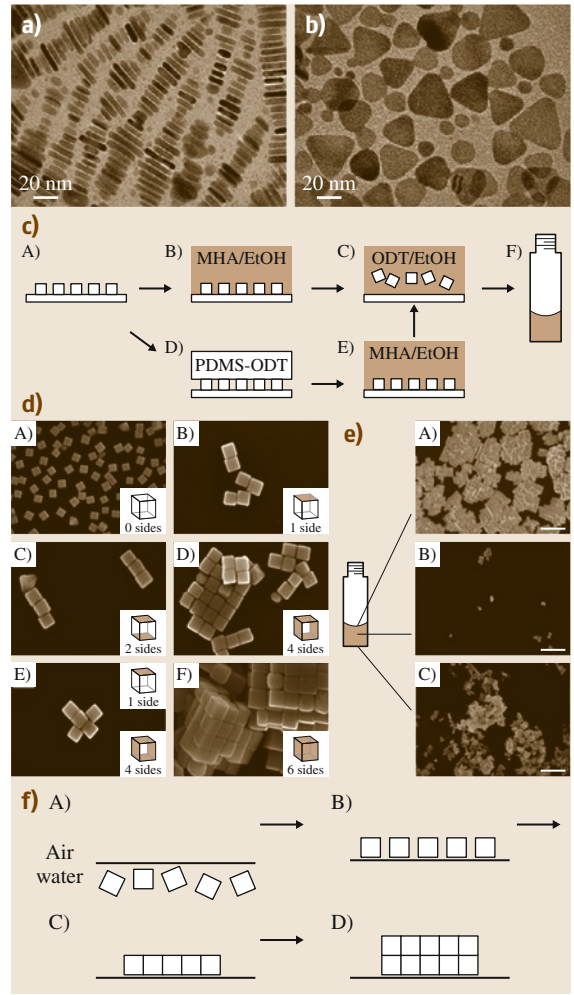


Fig. 9.33a–f TEM images of assembly A (a) and B (b) (after *Bae* et al. [9.332]). (c) A schematic representation of specific functionalization of Ag nanocube faces. (d) SEM images of Ag nanocubes and the assemblies depending upon the functionalization. (e) SEM images of ODT-functionalized Ag nanocubes sampled at different parts in a reaction vessel. (f) Schematics depicting the mechanism of formation of self-assembly at the air–water interfaces (after [9.332])

a clean Si substrate, and the free faces were functionalized sequentially with solutions of alkanethiols, and polydimethylsiloxane (PDMS) inked with alkanethiols. Nanocubes that were not functionalized did not show any tendency to assemble. Single face functionalization of the nanocube with hydrophobic octadecanethiol (ODT), resulted in the formation of dimers, joined at the hydrophobic faces in order to try and move this face away from water. Nanocubes with two opposing faces functionalized with ODT formed linear chains.

When four faces of the nanocubes were functionalized with ODT, a sheet-like superstructure was obtained. Upon mixing Ag nanocubes with four hydrophobic faces and one hydrophobic face (1 : 4 ratio), star-shaped structures were obtained. When all six faces were functionalized, they formed 3-D SLs. Figure 9.33f schematically illustrates the self-assembly process of Ag nanocubes, completely functionalized with a hydrophobic SAM, at the air–water interface [9.332].

9.6 Functionalized Metal NPs

The adding of more functional capabilities and preparing functionalized nanomaterials has received considerable attention in the recent past. The main strategies for functionalization are ligand exchange reaction, using modified thiol as the capping agent in the Brust method or adding more components to the system such as making core–shell structures. In this section, various methods employed for the functionalization of monolayer-protected NPs and various approaches for the synthesis of functional core–shell particles are discussed. The presence of thiol end groups on the ligand have been utilized to anchor various photoactive molecules such as derivatives of porphyrenes [9.336], fullerenes [9.337], pyrenes [9.338], stilbenes [9.339], fluorenes [9.340], resorcinarenes [9.341], azobenzenes [9.342], etc., on the surface of GNPs.

GNPs having a double shell structure with the inner shell made of spiropyran have been used to control the photo-controlled binding and release of the outer shell of amino acids [9.343]. In the absence of light, spiropyran moieties exist as closed-rings (a nonpolar colorless form). Upon irradiation of light, spiropyran changes to the highly polar, colored merocyanine form. This merocyanine (the open ring form) can complex with amino acids to form the second layer (Fig. 9.34). Thus, this system can be used for the light-mediated binding and release of amino acid derivatives.

In specific cases, the attachment of a fluorescent moiety onto the surface of NPs was found to alter the fluorescence intensity. For example, attachment of pyrenemethylamine on GNPs found to increase in the fluorescence of pyrene [9.343]. Generally, metals quench the fluorescence and the observed trend was different. This difference was explained as follows. The binding of nitrogen onto gold suppresses the electron transfer between the nitrogen and the pyrene ring (Fig. 9.35), which results in enhanced fluorescence.

9.6.1 Core–Shell Nanoparticles

Particles with a well-defined core and a shell (both in the nanometer regime) are called core–shell NPs. They have found applicability in diverse fields such as pharmaceuticals, chemical engineering, biology, optics, drug delivery, and many other related areas in addition to chemistry. Recent years have seen large efforts

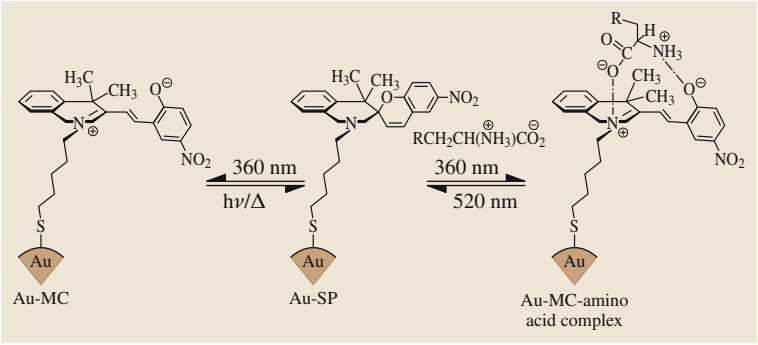


Fig. 9.34 Reversible binding of amino acids with spiropyran-capped GNPs (MC: metal cluster) (after [9.335])

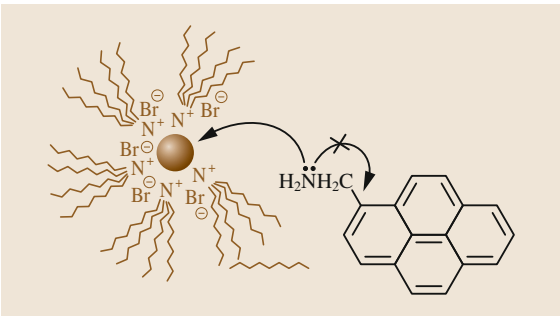


Fig. 9.35 Gold NP-assisted enhancement of fluorescence in pyrenemethylamine. Due to the attachment of nitrogen onto the NPs, conjugation between the lone pair on nitrogen and the pyrene ring is blocked. This is indicated by an *arrow with a cross mark* (after [9.343])

to develop core–shell colloidal NPs with tailored structural, optical, surface, and other properties [9.344, 345]. The formation of a protecting shell to the core imparts several functional attributes to these hybrid structures. They are:

1. Solubility and stability
2. Monodispersity in size
3. Ease of self-assembly
4. Core and shell processability
5. Applications in catalytic, magnetic, chemical, and biological fields, as well as in nanoscale electronics and optics.

A brief description of the diversity of core–shell systems involving noble metals is presented below.

Metal–Metal Oxide Core–Shell NPs

The scientific community has shown tremendous interest in this category of NPs, and these are among the most widely studied core–shell nanosystems. As discussed in an earlier section, the intense color exhibited by metallic NPs can be varied by controlling the size of these NPs. However, the chance of aggregation is a major problem associated with their handling. Making core–shell structures is one of most efficient ways to overcome this difficulty. Various strategies such as coating with silica [9.346], titania [9.347], zirconia [9.348], and maghemite [9.349] have been reported in this direction. A procedure to prepare silica-coated nanosized metal NPs was reported by *Liz-Marzán* et al.. This procedure is applicable for various metals such as Au, Ag, and CdS [9.350]. The approach involves the use of 3-aminopropyltrimethoxysilane (APS), the silane coupling agent, which can bind to the NP surface. This also

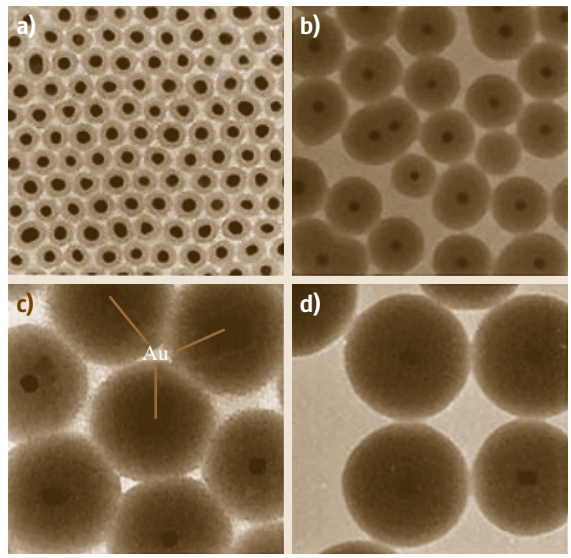


Fig. 9.36a–d TEM images of silica-coated GNPs. The shell thicknesses are **(a)** 10 nm, **(b)** 23 nm, **(c)** 58 nm, and **(d)** 83 nm (after [9.344])

acts as an anchor point for chemical deposition of silica (SiO_3^{2-}).

In this method, the shell thickness of the silica can be controlled (from 10–83 nm) and according to the thickness, the absorption characteristics are also tunable [9.344]. TEM images of Au@SiO_2 NPs with different shell thicknesses synthesized using the above method are shown in Fig. 9.36. Methodologies for the creation of various other inorganic coatings such as zirconia, yttrium basic carbonate, titania, titanium nitride, and Fe_2O_3 are available in the literature. Factors such as the size and shape of the core particles and the relative ratios of the reactants can control the thickness of the shell. *Liz-Marzán* et al. prepared TiO_2-coated Ag NPs by simultaneous reduction of Ag^+ and condensation of titanium butoxide [9.347]. As an extension to this methodology, ZrO_2- and TiO_2-coated Au and Ag NPs were prepared later [9.348].

A single-pot method for the synthesis of Pt–maghemite (Fe_2O_3) core–shell NPs where the reduction of platinum acetylacetonate in octyl ether produces Pt NPs and subsequent thermal decomposition of iron pentacarbonyl creates layers of iron oxide on the surface was reported recently [9.349]. The complexation of a negatively charged titanium(IV) bis(ammonium lactate) dihydroxide with poly(dimethyldiallylammonium hydroxide) was used for coating Au NPs with titania by *Mayya* et al. [9.351].

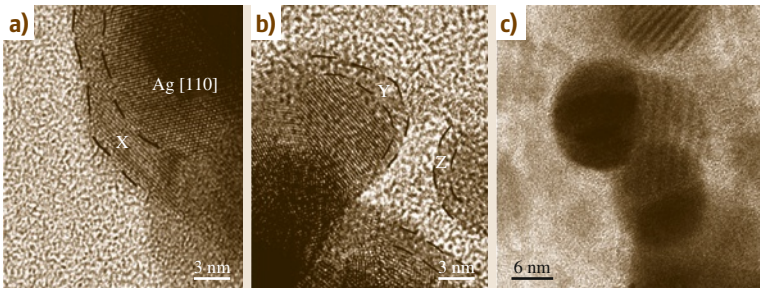


Fig. 9.37 HRTEM images of $Ag@ZrO_2$ core–shell NPs functionalized with a stearate monolayer (after [9.352])

Reverse micelle and sol–gel techniques are also employed for synthesis of metal–metal oxide core–shell NPs. The inorganic coatings around the NPs modify the optical properties of the systems in addition to stabilizing them against coalescence. The core–shell geometry also allows shell functionalization using appropriate organic monolayers [9.352] for better redispersibility and ease of handling. High-resolution TEM images of a stearate-functionalized $Ag@ZrO_2$ core–shell NP are shown in Fig. 9.37. Although the organic monolayer build-up around the ZrO_2 shell is not clearly seen, the distinct core–shell geometry is visible from the image.

A special approach to synthesize $Au@SiO_2$ core–shell NPs by incorporating a mercaptosilane at the core–shell interface was devised by *Chen* and *Katz*, who exploited the strong interaction between thiols and gold [9.353]. They achieved the highest degree of functional group organization at the core–shell interface. Recently, Wang et al. synthesized Au–SiO_2 inverse opals by colloidal crystal templating.

Bimetallic Core–Shell NPs

Due to the high demand for catalysis, a large number of bimetallic core–shell NPs has been synthesized lately. Some important examples are the synthesis of Au-Pt core–shell alloys by the simultaneous reduction of chloroauric acid and chloroplatinic acid by *Henglein* [9.117], a single-step procedure for the synthesis of Au-Pt core–shell NPS by *Yonezawa* and *Toshima* [9.354], the synthesis of Au core–Pt shell NPs by simultaneous reduction of $PtCl_6^{2-}$ in aqueous gold sol by *Schmid* et al. [9.355], etc. The synthesis of a variety of bimetallic systems including Ag/Cd, Ag/Pb, and Ag/In by a γ-irradiation-based approach was reported as early as 1980 by *Henglein* [9.117]. Synthesis of Ag-Au core–shell NPs by *Mulvaney* et al. [9.356] and *Link* et al. (NPs of 17–25nm size) are also available in the literature [9.357]. *Kim* et al. synthesized Au-Ag core–shell NPs and studied their optical characteristics such as linear extinction and resonant hyper-Rayleigh scattering [9.358].

The optical behavior and stability of Ag core–Co shell NPs was studied by *Sobal* et al. They showed that the core–shell particles exhibit an optical behavior distinct from the individual components, and the presence of a noble metal also protects the Co shell against oxidation [9.359]. *Cai* et al. developed a low-temperature synthetic protocol for Cu@Au core–shell NPs [9.360]. The formation of core–shell alloy NPs resulted in a good voltammetric response of Cu, which was utilized for electrochemical DNA hybridization detection assays. The oxidative peak current of the Cu colloid is much higher than that of Au of the same size and quantity. The coating of a layer of Au on the Cu core helped to protect the Cu from oxidative degradation and can also provide an active surface for immobilization of oligonucleotides. The synthesis of dumbbell-shaped Au-Ag core–shell NRs by seed-mediated growth under alkaline conditions was reported by *Huang* and *Matijevic* [9.361]. This method uses GNRs as seeds in the presence of Ag and ascorbate ions. Ag ions that are reduced by ascorbate are deposited on the surface of the Au NRs to form dumbbell-shaped Au-Ag core–shell NRs. Recently, the synthesis of Au-Ag core–shell NPs using tyrosine as a pH-dependent reducing agent was reported by *Sastry* et al. [9.362].

Semiconductor Core–Shell NPs

Similarly to metallic NPs, semiconductor nanocrystals also exhibit interesting size-dependent optical properties (fluorescence) due to the confinement of electronic wave functions. However, in order to obtain highly luminescent nanocrystals, their surface must be precisely controlled. The presence of a large number of surface defects (e.g., nonstoichiometry, unsaturated bonds, etc.) can have a large impact on their luminescence. Core–shell-type semiconductor NPs or quantum dots demonstrate novel properties that make them attractive for various applications. The photoluminescence quantum

yield can be increased by covering the nanocrystallites with higher-band-gap inorganic material, which passivates the surface nonradiative recombination sites. Moreover, compared to their organic analogs, NPs covered with inorganic composite materials are much sturdier and more stable. *Yang* et al. reported the off-resonance optical nonlinearities of Au@CdS core–shell NPs, embedded in $BaTiO_3$ thin films [9.363]. Due to their large third-order nonlinearities and ultrafast nonlinear optical response, semiconductor NPs are attracting a great deal of attention.

Polymer-Coated Core–Shell NPs

Polymer-coated core–shell NPs have found application possibilities in diverse fields ranging from catalysis to industry where these NPs are used in making additives, paints, and pigments, etc. There are mainly two classes of synthetic methodologies for polymer capping of NPs, namely: (a) polymerization at the NP surface, and (b) adsorption of preformed polymer onto the NP cores. The most common methods used for the preparation of polymer core–shell structures are:

1. Monomer adsorption onto NPs followed by polymerization [9.360, 365–367]
2. Heterocoagulation polymerization [9.364]
3. Emulsion polymerization [9.368, 369].

The colloidal particles themselves or an external initiator added to the reaction mixture can catalyze the polymerization. Using a pretreatment method, *Huang* and *Matijevic* [9.361] reported the synthesis of polydivinylbenzene coated silica particles. Following a similar strategy, polydivinylbenzene–poly(vinylbenzyl chloride) copolymers, poly(vinylbenzyl chloride), and double shells of polydivinylbenzene and poly(vinylbenzyl chloride) were also synthesized. In specific cases, where cores consist of dyes, polymer coating of the particles allowed the dyes to be retained inside the nanocores because the polymer shells are permeable only to small inorganic ions and not to big dye molecules. As was mentioned before, polymerization can also take place in the presence of catalytically active cores.

Several factors affect the thickness of the polymer coating: the contact time with the core, the type of core employed, and the nature of the polymer [9.360]. *Feldheim* et al. reported an excellent strategy for the synthesis of polymer-coated NPs [9.364] where the particles in the pores of a membrane were trapped and aligned by vacuum filtration. Then, inside the pore, the monomers were polymerized. Through this method, polypyrrole coated Au NPs can be prepared; corresponding TEM images are shown in Fig. 9.38. Figure 9.38b illustrates the increased shell thickness as a result of the change in the monomer for the polymer shell. Hence, this methodology allows control of the thickness and composition of the polymer coating. Generally for most of these polymerization reactions, the thickness of the coating depends on the polymerization time. Heterocoagulation of small particles with larger ones assisted with heating is another widely used method for preparing polymer coating. Through this method, polystyrene cores coated with a uniform layer of polybutylmethacrylate have been prepared.

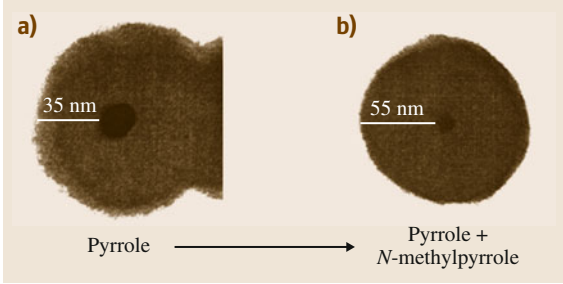


Fig. 9.38a,b TEM of polypyrrole-capped Au NPs **(a)** and with further increase in shell thickness by polymerization with poly(*N*-methylpyrrole) **(b)** (after [9.364])

The third technique, emulsion polymerization, has been widely employed for the synthesis of polymer-capped core–shell NPs. The important feature of this approach is that NPs of different size regime (from sub-nanometer to micrometer-sized organic and inorganic particles) can be coated with polymer. Polymerization of styrene and/or methacrylic acid in emulsions of oleic acid resulted in the formation of a uniform polymer layer around the metal core. Compared to uncoated particles, the polymer-coated particles are highly etch-resistant and can be easily centrifuged and redispersed. These NPs can be made in the form of thin films through the use of self-assembly techniques. The layer-by-layer (LbL) templating strategy is commonly used for this. Here, a polymer solution (having an opposite charge to that on the particles) in excess of that required for saturation adsorption is added to the colloidal dispersion. The polymer adsorbs onto the NPs through electrostatic interactions.

9.7 Applications of Gold and Silver Nanoparticles

The unique properties exhibited by gold and silver NPs such as SPR, SERS, nonlinear optical properties, quantized charging effect, etc., have been utilized for a variety of applications in the areas of biolabeling, bioimaging, sensors, catalysis, nanodevices, nanoelectronics, etc. [9.1, 154, 370, 371]. Although noble metal NPs have a long history as materials for many therapeutic applications, the advancements in the area of nanochemistry have broadened their potential in various biomedical applications. Apart from their biocompatibility, unique properties, and ease of functionalization with various biological molecules, noble metal NPs have been used for targeting and delivery of therapeutic doses of drugs to cancer cells. The large extinction cross-sections and tunable optical absorption of NPs such as NRs, NTs, nanocages, etc., in the NIR region (a wavelength region where blood and tissues are relatively transparent to radiation) make them good candidates for diagnosis and many other medical applications. The strong SPR of metal NPs enables imaging of individual particle locations with the use of various optical microscopic techniques such as dark-field optical and two-photon luminescence (TPL) microscopy [9.372]. GNRs and nanocages are ideal candidates for cancer cell imaging due to their tunable SPR peaks and scattering in the near infrared. The usefulness of gold nanocages as optical contrast agents has been demonstrated by optical coherence tomography (OCT) imaging [9.144]. They are the perfect raw material for robust and rapid diagnostic testing for many diseases. Living cells are highly sensitive to temperature, and increases of a few degrees can lead to cell death. NIR absorption and related photothermal effect are other important features of anisotropic GNPs [9.144, 370]. Compared with other nonmetallic photothermal absorbers, GNPs enable dual imaging/therapy functions. It has been demonstrated that several anisotropic nanomaterials such as NRs, NTs, nanocages, nanoshells, nanostars, etc., can be used for photothermal therapy [9.144, 370].

Gold and silver NPs have been found to be useful for optical limiting applications as well. Optical limiters have found applicability in fields including sensor and eye protection, optical communications, and optical information processing. Optical bistable materials are useful for functions such as logic gating and pattern recognition in optical computers. The applicability of Au, Ag, and Au-Ag alloy nanosystems for optical limiting applications was investigated in 2000 [9.373]. Initially, octanethiol and octadecanethiol-protected Au, Ag, and Au-Ag alloy NPs were synthesized, and optical nonlinearity was induced by 35 ps pulses at 532 nm. The samples were investigated using the Z-scan technique. It was found that they behaved either as saturable absorbers or reverse saturable absorbers, depending on the intensity of excitation. It was also found that Au and Ag NPs show nearly the same efficiency for optical limiting; however, the alloy clusters were found to be less efficient in limiting and were less photostable. An explanation based on the electron dynamics of the excited-state species was given for the behavior observed [9.373].

Gold and silver NPs have attracted considerable attention due to their high SERS [9.217, 374] activity, thus possessing strong advantages for the detection of molecules. They have been found to be useful for many applications in trace analysis of pesticides, biomolecules, bacteria, viruses, specific antigens, glucose, DNA, explosive materials, etc. [9.375]. Recently, it has been found that silica-coated GNPs can enhance the sensitivity of this method, and even detection of adsorbed hydrogen is possible with such materials [9.376]. Single-molecule detection is possible using SERS, and several protein and nucleic acid biosensors have been designed using this property of GNPs [9.375].

The properties of GNPs such as intense SPR and scattering of visible light have also been used for sensing applications. A variety of schemes based on the LSPR of GNPs have been developed for sensing organic vapors [9.377]. A composite material made of GNPs with pH-sensitive polymers has been used in a variety of pH-sensing schemes. GNP-based technologies are showing great promise in providing solutions to a number of environmentally important issues. They are highly promising for sensing and removal of heavy metal ions from water [9.378]. GNP-based colorimetric sensors have been widely used in this direction, overcoming some of the limitations of conventional methods because these assays do not use organic solvents, light-sensitive dye molecules, or sophisticated instrumentation. GNRs are capable of quick and selective sensing of mercury in tap water samples at the ppt level [9.379]. The selectivity and sensitivity towards mercury are due to the amalgamation of mercury and gold. Complete removal of mercury from water can be done by using GNPs supported on alumina [9.380].

Catalysis by active oxide-supported gold, silver, platinum, and palladium NPs is an ever-expanding area,

and a large number of new catalytic systems for various reactions have been widely exploited for many applications. GNPs can oxidize highly toxic CO to far less toxic carbon dioxide [9.222, 380]. More recent investigations have shown that GNPs adsorbed and dispersed on an oxide support can be used as an efficient catalyst for hydrogenation of unsaturated substrates [9.1]. Thus, shape and crystal structure differences can lead to different catalytic rates [9.381]. In homogeneous catalysis, *Narayanan* and *El-Sayed* demonstrated that shapes with more corners and edge atoms have higher reactivity than similar NPs with fewer corner and edge atoms [9.382]. Catalytically active bimetallic gold–palladium NPs proved to degrade organic pesticides effectively [9.383]. GNPs are also used in solar cells to improve the efficiency, as the GNPs enhance the optical absorption in the range of visible light [9.1]. It has been recognized that NIR absorbing films made from GNPs can be used as an alternative to reflective coatings for blocking infrared (IR) radiation. NP-based approaches are highly desirable, being more economically viable than other methods. Certain nanomaterials have been used for the development of IR filters. Using a prototypical device, *Pradeep* and *Sajanlal* have demonstrated that the NIR-IR absorption exhibited by gold MFs can absorb a significant amount of heat, thereby reducing the temperature rise in an enclosure exposed to daylight [9.160]. A few of these application possibilities are described in detail in the following section.

9.7.1 Water Purification

Among all these application possibilities, water purification remains one of the most important fields of application for any material. Noble metal NPs have also found tremendous possibilities in this arena as well. A specific review on this topic was discussed by the author in recent work, where a description about the important events during last 200 years in the area of drinking water purification was presented [9.23]. This section gives an overview about the use of noble metal NPs for the removal and detection of severely toxic contaminants including pesticides, halogenated organics, heavy metals, and microorganisms found in drinking water.

Degradation and/or Removal of Pesticides with Noble Metal NPs

The chemistry of noble metals (even in bulk form) for catalytic synthesis of organic compounds is well documented. However, their reactivity with halogenated hydrocarbons was not explored until recently. The first example for a metal (here, a transition metal) interacting with halogenated organics was initiated following the discovery that zero-valent iron catalyzed degradation of halogenated aliphatics [9.384]. Similarly, there were attempts to study the degradation of halocarbons [9.385] by using other reactive metals such as magnesium, tin, and zinc. However, until 1998, noble metals were never thought to be attacked by halocarbons. Noble metals had very low reactivity. However, later investigations revealed that in colloidal state noble metals are reactive. It was postulated in early 1998, based on absorption studies of silver colloid with oxygen and carbon tetrachloride, that carbon tetrachloride induces oxidation of silver colloid in a manner similar to oxygen [9.386]. Another study concluded that the degradation of noble metal clusters can be done by chlorine radicals produced by UV irradiation of halogenated organics [9.387]. It was also suggested that many organosulfur compounds adsorb on noble metal NP surfaces [9.388] and carbon disulfide undergoes dissociation on silver surfaces.

In early 2003, the first detailed report, from the authors' group, appeared on the interaction of noble metal NPs with halocarbons [9.389]. In a manner strikingly similar to the reaction of other metals with halocarbons, nanoscale noble metals also react with halocarbons. Through reductive dehalogenation, the reaction leads to the formation of metal halide. An important thing to be noted is the formation of amorphous carbon in this process [9.389], and harmful that the reaction proceeds efficiently at room temperature [9.389]. The reaction of noble metal NPs with halocarbons could be considered as a classic example of the particle size-based reactivity of metals [9.389] as noble metals in bulk form are not attacked by halocarbons.

Using a number of spectroscopic techniques, this reaction was studied to understand the reaction mechanism [9.389]. It was observed that plasmon intensity in the absorption spectrum gradually decreases without any shift in the plasmon peak position. When the reaction product obtained at the end of the reaction was analyzed using x-ray diffraction (XRD), features were similar to AgCl. Thus the conversion of metal to metal halide was confirmed. In the Raman spectra, broad G and D-band signatures of the amorphous carbon centered at 1550 and 1288 cm^{-1} was seen, pointing towards the formation of amorphous carbon.

Gas chromatographic and IR spectroscopic measurements also confirmed the complete mineralization of the halocarbon, as there were no reaction prod-

ucts. A reaction mechanism was suggested that depends on the spectroscopic observations [9.389]. We can represent the reductive dehalogenation of carbon tetrachloride as

$$4\mathrm{Ag} + \mathrm{CCl_4} \rightarrow 4\mathrm{AgCl} + \mathrm{C} \quad \Delta H = 1.2\,\mathrm{kJ/mol}\,.$$

We can also consider the reaction from an electrochemical standpoint as

$$\begin{aligned} \mathrm{Ag} &\rightarrow \mathrm{Ag^+} + \mathrm{e} \\ &\Delta E_{\mathrm{OXDN}} = -0.80\,\mathrm{V} \\ \mathrm{CCl_4} + \mathrm{H^+} + 2\mathrm{e} &\rightarrow \mathrm{CHCl_3} + \mathrm{Cl^-} \\ &\Delta E_{\mathrm{RDCN}} = +0.67\,\mathrm{V} \\ \mathrm{CHCl_3} + \mathrm{H^+} + 2\mathrm{e} &\rightarrow \mathrm{CH_2Cl_2} + \mathrm{Cl^-} \\ &\Delta E_{\mathrm{RDCN}} = +0.56\,\mathrm{V}\,. \end{aligned}$$

The excess surface energy of the NPs is the reason behind the reaction proceeding at the nanodimension. This is very helpful in overcoming the thermochemical barrier and the reductive dehalogenation reaction is exothermic [9.389]. After understanding the mineralization of halocarbons, the research was extended to the field of pesticides. They are another important family of halogenated organics. Pesticides such as endosulfan [9.390] and chlorpyrifos [9.391,392] belong to halogenated organic family, and malathion [9.391, 392] is an organophosphate type pesticide.

When the pesticides interacted with gold and silver NPs, their spectroscopic behaviors were different. A decrease in plasmonic absorption intensity was observed when endosulfan reacted on gold. There was the emergence of an additional peak at higher wavelengths as well [9.393]. This was due to adsorbate binding onto the NP surface, thereby leading to particle aggregation. IR measurement on the residue obtained after the adsorption process showed a substantially broadened signature of the pesticide. There were significant changes in the feature at 1192 $\mathrm{cm^{-1}}$ (Si=O bond) and negligible changes in the feature at 750 $\mathrm{cm^{-1}}$. This indicated that the interaction largely occurs through the sulfur. The reverse was the case with endosulfan and silver. The plasmon absorption did not change significantly in the case of endosulfan on silver surfaces. The IR spectrum of the residue obtained after the reaction was analyzed and the adsorption of endosulfan onto silver surface was confirmed.

The heterogeneous adsorption of pesticides onto NP surfaces was one of the major aspects of the reaction chemistry [9.391]. For removal of pesticides from solution, noble metal NPs supported on alumina were found to be very effective. When the input concentration was 50 ppb, using alumina-supported noble metal NPs, pesticides could be completely removed from the aqueous phase. The complete removal was confirmed using gas chromatography, which did not show any significant signature of pesticides [9.391]. It is very clear that the chemistry of supported noble metal NPs can comfortably be utilized for the complete removal of most of the pesticides from drinking water whether they are organochlorine (e.g., simazine, lindane, atrazine, etc.) or organosulfur pesticides (e.g., triazophos, quinalphos, etc.), or contain nitrogen-based functional groups (e.g., carbaryl, carbofuran, monocrotophos, etc.). This versatility of noble metal NPs in removing a wide variety of pesticides makes them an attractive candidate for drinking water purification. The strong attachment of NPs on substrates such as alumina can ensure the stability of the supported hybrid structures and can ensure that the NPs will not be released into water under the conditions used in water purifiers.

Detection of Pesticides in Drinking Water with Noble Metal NPs

Ultralow concentration sensing of pesticides in drinking water is as important as it is to remove these toxic pesticides. A large number of water resources across the world are becoming severely polluted by the widespread, large-scale use of different pesticides. Hence, it is imperative to develop rapid, sensitive, and selective detection protocols for detecting such molecules [9.394,395]. Several protocols have been put forward for ultralow-concentration detection of pesticides during the past 25 years [9.396]. Methods such as chromatography, mass spectrometry, and biosensors are some of most practiced methods for this and they offer high sensitivity and selectivity. However, the high sophistication, amount of time required to evaluate the data are the main limitations when considered for common use.

Nanomaterials are expected to contribute in this area as well by developing rapid and facile measurement methods based on nanomaterial chemistry [9.397]. Oligonucleotide-modified GNPs are being used for the biomolecular colorimetric detection of polynucleotides at ultralow concentrations [9.306]. Unlike materials chosen as adsorbents where a higher surface area is a prerequisite, the substrate used for contaminant detection should produce a large change in the surface with adsorbate interaction and a consequent manifestation in reliable spectroscopic signatures. Another important aspect about contaminant detection is the se-

lectivity. This can be ensured by choosing appropriate nanomaterials and functionalizing them with suitable ligands. A good example regarding selective detection of cysteine and glutathione at micromolar concentrations using GNR is described in more detail in another section (Sect. 9.5.2) [9.306].

Two general strategies have been employed for the ultralow-concentration detection of pesticides using GNPs:

1. Variation in the principal properties of a functional group attached to the noble metal NP surface in the presence of organic molecules. This approach has not yet been utilized for the detection of pesticides in drinking water. However, the nature of the molecules detected being similar, this technique can be modified for detection of pesticides as well. Europium ions (Eu^{3+}) when anchored on the surface of a GNP are known to show enhanced fluorescence intensity [9.398, 399]. The interaction of organophosphorus molecules with this will result in the fluorescence being quenched. Organophosphorus molecules tend to bind with GNPs, resulting in the release of Eu^{3+} ions. In another study, a zirconium–phosphate-terminated surface was fabricated by treating GNPs supported on silica gel with zirconium (Zr^{4+}) and $POCl_3$ [9.400, 401]. This surface demonstrated a strong affinity towards organophosphorus compounds. The resultant interaction induced visible changes in the optical properties of the GNPs. In another approach, paraoxon was detected using GNPs functionalized with an antibody specific to paraoxon [9.402]. The electrochemical properties of the system were modified upon interaction with paraoxon. Low concentrations (at ppb level) were detected in this method. Using a metalloenzyme, organophosphorus hydrolase (OPH), which can hydrolyze a large variety of organophosphate pesticides and neurotoxins, an ultralow-concentration detection strategy was devised recently [9.403]. GNPs were functionalized with OPH enzyme. Later fluorophore molecules were positioned at the OPH active sites. These fluorophore molecules were released upon addition of organophosphorus compounds, resulting in changes in the fluorescence intensity. Enzyme-mediated hydrolysis of acetylthiocholine can generate species with reducing capabilities, and Au NPs can be synthesized using this [9.404]. The presence of toxic organic molecules can hinder the catalytic activity of the enzyme, acetylcholine esterase (AChE). This inhibition of the enzyme can result in quenching Au NP production due to the unavailability of the reducing agent. This quenching can even be effected by nanomolar concentrations of toxic organic molecules. The resultant changes are manifested in the optical properties of the GNPs. A similar reaction will result in changes in electrochemical currents as well. Au NPs functionalized with AChE were used to hydrolysis acetylthiocholine, and the reaction was utilized as a pesticide sensor through measurement of the electrochemical current, which depends on the extent of formation of thiocholine in the presence of pesticides [9.405]. A summary of efforts related to the use of biomolecular immobilized Au NPs for electrochemical sensing can be found in a recent review article [9.406]. The enzyme is known to catalyze conversion of acetylcholine chloride in the following way [9.407]:

$$\text{Acetylcholine} + H_2O \xrightarrow{\text{AChE}} \text{acetic acid} + \text{chloine}\,.$$

As discussed above, the presence of organophosphorus pesticide molecules inhibit the activity of AChE to hydrolyze Ach. An attenuation of light when AChE is covalently bound onto GNP surfaces which can be correlated with the pesticide concentration manifests this inhibition [9.408]. The dephosphorylation by 2-pyridine-aldoxime methiodide (2-PAM) can reactivate AChE. Thus the sensor can be reused for many operations. Detection of pesticides in the ppb limit is possible by this method. A correlation between the shift in plasmon wavelength of Ag NPs and the pesticide concentration was also used to detect pesticides [9.409]. Indoxyl, a product of the reaction of certain organophosphorus compounds and indole is fluorescent in nature. Indole anchored on the Au NP surface was reacted with organophosphorus pesticides and the fluorescence (resulting from the indoxyl formation) was utilized for the pesticide detection [9.410]. A ppt level detection was reported by this method.

2. Interaction with pesticides results in changes in the optical properties of noble metal NPs. Chemistry at the nanolevel is extremely sensitive. Hence, even at ultralow concentrations, the interaction between pesticides and NPs brings about considerable changes in properties. The interaction of an endosulfan–noble metal NP system can be followed spectroscopically by using different techniques such as the UV/Vis absorption spectrum, the Fourier

transform IR (FTIR) spectrum, etc., which use the changes in the signatures of the NPs to detect the presence of pesticide on NP surfaces. One of the easiest ways is to observe sensitive color changes of the solution [9.393]. Colorimetric methods are simple, user-friendly, and comparatively less sophisticated. Moreover, the intensity of the color change is nearly quantitative. Reports suggest that the colorimetric detection of pesticides at a concentration level of 1 ppm (this is more than 100 times the permissible levels) is possible. To take nanochemistry-based methods to the levels relevant to drinking water, different strategies have been employed. One of the most established approaches is salt-induced aggregation of noble metal NPs in the presence of pesticide [9.411, 412]. Studies showed exceptional colorimetric changes due to pesticides at low concentrations in a salt-induced aggregation method, which can be easily followed by absorption measurements. A recent study indicated that chlorpyrifos induces severe aggregation to GNP-Na_2SO_4 solution, and this results in the change in the solution color and thus absorption characteristics [9.411]. Figure 9.39a shows the UV/Vis spectral changes and the corresponding color changes. The fast response time and simplicity of the method points to the on-field adaptability of the process [9.411]. A change in the SPR band position and the intensity of humic acid-protected silver NPs were utilized for detection of herbicides. However, these changes were observed only at high concentrations of herbicides [9.413].

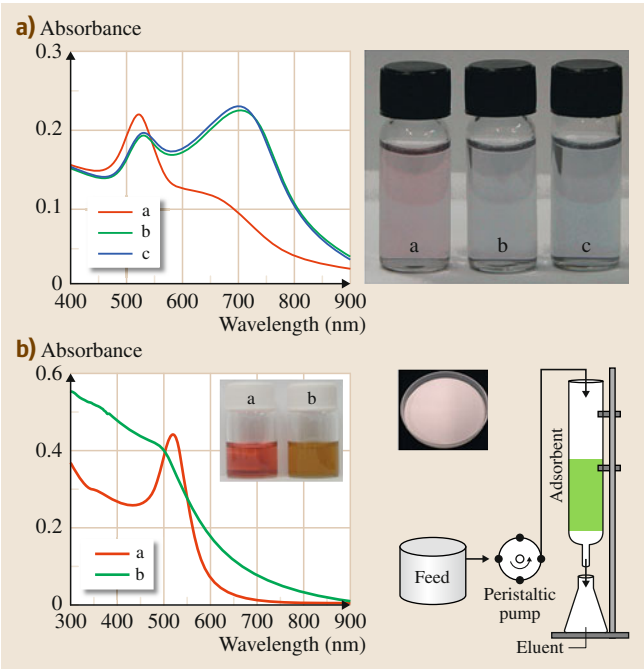


Fig. 9.39 (a) UV/Vis spectra of Au@citrate/Na_2SO_4 mixture before and after the addition of chlorpyrifos-spiked water. (a) Au@citrate/Na_2SO_4 mixture, (b) 20 ppb and (c) 25 ppb chlorpyrifos in Au@citrate/Na_2SO_4 mixture. The corresponding photographs are also shown. From the authors' laboratory. **(b)** UV/Vis spectra of GNPs (a) before and (b) after mercury treatment. *Inset*: Photograph of gold nanoparticles and mercury treated GNPs. Schematic of the down-flow column apparatus used is also shown. From the authors' laboratory (after [9.381, 414])

In addition to the above-mentioned two general approaches, the enhancement of Raman signals in the presence of noble metal NPs has been extensively utilized for detection of organic molecules. A dye molecule, rhodamine 6G, where very low concentration (equal to single rhodamine 6G molecule) detection through an SERS-based method is the most studied example [9.414–417]. Recent investigations indicated higher Raman signal enhancements in the presence of anisotropic gold and silver nanostructures, which can lead to the detection of ultralow concentrations of organic molecules [9.418, 419]. Using the Langmuir–Blodgett assembly of anisotropic nanostructures, the detection limit can be further improved [9.331]. This is discussed in more detail in another section (Sect. 9.7.6). Molecular level details about the interaction between proteins and DNA interactions were studied using this method recently [9.420]. Another study revealed the feasibility of using humic acid-protected GNPs for the detection of organic contaminants [9.421]. The high affinity of humic acid (HA) towards a variety of organic molecules and the low background SERS spectrum of HA (the spectrum is relatively weak in absolute intensity) also helps in the detection process.

Chemistry of Heavy Metal Ions with Noble Metal NPs

Sequestration of heavy metals is considered to be one of the most interesting application areas of noble metal NPs in drinking water purification. The pioneering studies regarding the interaction of metal ions with noble metal NPs were carried out in the early 1990s [9.386] and indicated that many of the previously known properties of metals do not hold true as the size goes down to the nanometer regime.

As the size of the particle increases, the redox potential of a microelectrode becomes more positive

$$Ag_n \rightarrow Ag_n^+ + e^- .$$

For a free silver atom ($n = 1$), the reduction potential is -1.8 V. However when $n \rightarrow \infty$ (for conventional silver electrodes) the potential reaches a value of 0.799 V [9.422]. Such drastic size-dependent changes in electrochemical properties will have high impact in the interaction of these NPs with pesticides and heavy metals in water. The conversion of Ag clusters into colloidal metal particles catalyzed by Cu^{2+} illustrates this effect. The reaction follows the following scheme [9.423]

$$Ag_n + Cu^{2+} \rightarrow Ag_{n-1} + Ag^+ + Cu ,$$

followed by similar reaction of Ag_{n-1},

$$Cu^+ + Ag_{n+m} \rightarrow Cu^{2+} + Ag_{n+m}^- Ag^+ + Ag_{n+m}^- \rightarrow Ag_{n+m+1} .$$

Here, the cluster containing n atoms is depicted as Ag_n, and Ag_{n+m} correspond to a colloidal particle composed of $n + m$ atoms. Aggregation of unstable clusters results in the formation of colloidal particles. The reaction becomes feasible due to the rather negative potential of silver clusters. The reaction can be followed by the disappearance of the absorption feature of clusters and an increase in the intensity of the 380 nm band of metallic silver. A similar study on the interaction of Cd^{2+} with 4 nm colloidal silver particles is also available [9.424]. In this reaction, 1-hydroxyethylmethyl radicals generated radiolytically in a mixed solvent system (acetone + 2-propanol) results in the production of colloidal cadmium via electron transfer. An absorption feature corresponding to colloidal cadmium starts to appear around 250–280 nm, confirming this reduction. A concurrent red-shift was observed for the silver plasmon band (375–383 nm). Another study about the interaction between Ag NPs (0.25 mM in water) with Cd^{2+} solution (0.02 mM) reported the appearance of a separate absorption feature around the 550–600 nm region [9.425]. It is worth noting that in both studies, the size of the silver NPs remained constant. However, different spectral observations were made in the two methods. One method did not show any change after the addition of metal ions, while the other showed an instantaneous appearance of a new feature. Similar observations were seen in the case of other metal ions as well.

Several adsorbent systems including activated carbon [9.426], polyethyleneimine-modified cellulose [9.427], functionalized membranes [9.428], silica [9.429], and graphene [9.430] have been employed for the removal of mercury from drinking water. All good adsorbents should have an extremely high metal adsorption capacity, minimum contamination of the water (e.g., minimum ion exchange), zero desorption under environmental conditions, and economic adaptability.

During the sequestration of heavy metals from drinking water by NPs, the adsorption chemistry plays an important role. Depending on the phase stability two metals can exist as an alloy with varying compositions. For example, gold and mercury can exist as Au_3Hg, AuHg, and $AuHg_3$. Therefore, for 1 g of Au, a maximum adsorption of 3.05 g of Hg is possible. Hence, utilizing the alloy formation, a high efficiency adsorption process can be devised. Zero-valent iron was the first system where metal alloying induced sequestration of heavy metals was reported [9.431]. However, surface corrosion can reduce the capacity of iron to alloy with heavy metals. The use of noble metal NPs for this concept pointed towards the large possibility of these NPs in water purification [9.380]. An increased adsorption capacity of 4.065 g/g of gold is reported when mercury was reduced to the zero-valent state followed by alloying with GNPs. The mechanism of the reaction was studied using various techniques. Microscopic images demonstrated an increase in the size of the NPs upon addition of Hg. An amorphous layer of mercury was also observed around the NPs. In the absorption spectrum, a shift in the plasmon position along with a significant modification in the peak shape was observed (Fig. 9.38b). An X-ray diffractogram confirmed the formation of an alloy Au_3Hg phase. Quantitatively 738 mg gold can be used to decontaminate 3500 l of 1 ppm mercury [9.380].

Silver NPs have enhanced ability to function as a reducing agent for mercury and can exist with mercury in different phases as an alloy as well. Surface plasmon of Ag NPs experiences a blue-shift along with a decrease in intensity immediately upon introduction of Hg^{2+} ions. The partial oxidation of Ag NPs to silver ions results in the decrease in plasmon intensity whereas the shift can be due to the incorporation of mercury into the silver NPs [9.432, 433]. Aqueous mercury NP solutions are reported to exhibit a plasmon absorption band below 300 nm [9.434]. Hg-Ag alloy NPs synthesized via simultaneous reduction with sodium borohydride showed a plasmon in the region of 300–400 nm [9.435].

Silver NPs (average size 60–80 nm) prepared by the Turkevich method (discussed earlier) are known to show a tremendous growth in size up to over 600 nm upon mercury incorporation. This was attributed to the

nucleation of reduced mercury on the silver surface. Energy-dispersive x-ray analysis confirmed the homogeneous distribution of mercury on the silver NPs. The edges of the particles had a slightly higher concentration of Hg compared to the center. The surface adsorbed mercury atoms might diffuse rapidly into the silver core, resulting in a very fast disappearance of the silver plasmon band. In order to understand this, the reaction needs to be analyzed thermodynamically. The reduction reaction is

$$\begin{aligned} \mathrm{Ag} &\rightarrow \mathrm{Ag}^{+} + \mathrm{e}^{-} & E^{\circ}_{\mathrm{OXDN}} &= -0.8\,\mathrm{V} \\ \mathrm{Hg}^{2+} + 2\mathrm{e}^{-} &\rightarrow \mathrm{Hg} & E^{\circ}_{\mathrm{RDN}} &= 0.85\,\mathrm{V} \\ 2\mathrm{Ag} + \mathrm{Hg}^{2+} &\rightarrow \mathrm{Hg} + 2\mathrm{Ag}^{+} & E^{\circ} &= 0.05\,\mathrm{V}\,. \end{aligned}$$

According to the potential in bulk scale, this reaction is thermodynamically feasible. However, as discussed earlier, the conditions are different in the nanoregime. At atomic scale, the $\mathrm{Ag}^{+}|\mathrm{Ag}$ (atom) cell has a reduction potential of $-1.80\,\mathrm{V}$. Hence it is reasonable to think that the reduction potential of the silver NP is likely to be much less than 0.8 V, which creates a strong driving force for the galvanic reaction to occur. The difference in the reduction potential of silver NPs and in the bulk state can be understood from the Ag-HCl system [9.436]. Silver in bulk form will not react with HCl. However, silver NPs prepared by the sodium borohydride reduction method demonstrate an unusually high reactivity with HCl. The plasmon band of silver NPs vanishes after the addition of HCl, confirming the dissolution. A white residue obtained after the reaction of silver NPs with HCl (AgCl) confirmed this.

This result can also be understood from the reaction

$$\begin{aligned} &\mathrm{Ag(s)} + \mathrm{H}^{+} + \mathrm{Cl}^{-} \rightarrow \mathrm{AgCl(s)} + \tfrac{1}{2}\mathrm{H}_2 \\ &E^{\circ} = -0.22\,\mathrm{V}\,. \end{aligned}$$

Hence, with bulk silver, there is no driving force for the reaction. However, at the nanoscale, the feasibility of the reaction points to the continuous increase of the reducing nature of the silver as the size reaches the nanoregime. Utilizing the ability of silver NPs to reduce a number of heavy metals, a variety of alloy NPs (e.g., Ag-Hg bimetallic NPs) have been prepared. Similarly Pd-Ag and Pt-Ag NPs [9.437] have also been synthesized using galvanic etching.

Recently, the authors' group has carried out extensive studies on the mechanism of Hg removal by silver NPs. A detailed study of the chemical interaction of heavy metal ions such as Hg(II), Hg(I), Pb(II), and Cd(II) with naked and protected silver NPs was carried out [9.438]. Silver NPs protected by citrate (Ag@citrate, 30 nm average diameter) and MSA (Ag@MSA, 8 nm) were taken as the model nanosystems. With the help of various spectroscopic and microscopic techniques, it was concluded that the metal ions interact with both the core of the NPs and the functional groups of the capping agents, especially carboxylic acid functionalities (Fig. 9.40). It was also observed that both NPs studied were able reduce Hg(II) and Hg(I) ions to metallic mercury, because of the feasibility of the redox reaction, and that no reduction occurred for Cd(II) and Pb(II). It was concluded that the reduction of Hg(I) and Hg(II) ions was by electrons supplied by the core silver atoms of the NPs at lower metal ion concentrations. At higher concentrations, the metal ions were chemically bonded to the carboxylate groups of the citrate and MSA, in turn, forming sulfides.

Using this same basic chemistry, a practical silver NP-based adsorbent for removal of Hg(II) from water was developed by the authors of this chapter [9.439]. The NPs were supported on alumina and its efficiency in removing Hg(II) from water was demonstrated. The study was also extended to novel noble metal nanosystems known as quantum clusters (discussed later in Sect. 9.8). The interaction of novel unsupported and supported MSA-protected clusters such as Ag_7 and Ag_8 with Hg(II), Cd(II), and Pb(II) in water at different concentrations was investigated [9.440]. It was understood that the interaction with these clusters is similar to that for corresponding larger NPs. It was concluded that Hg(II) was reduced to metallic mercury by both supported and unsupported clusters, due to the feasibility of the redox reaction discussed above, whereas no reduction happened for Cd(II) and Pb(II). This interaction resulted in the disappearance of the luminescence of the cluster, which may aid in sensing Hg(II). The metal ions were chemically bonded to the carboxylate groups of MSA at lower concentration, and due to this chemical affinity of the ligands and the lower silver content per cluster compared with the number of carboxylate groups, Hg(II) was not reduced at these lower concentrations.

Detection of Heavy Metals in Drinking Water with Noble Metal NPs

The maximum contamination limit (MCL) for various contaminants in drinking water was reviewed recently and MCLs for various contaminants were reduced. For example, the MCL for lead has been changed from 15 to 10 ppb and the MCL for arsenic has been revised from 50 to 10 ppb. Various methodologies for the detection

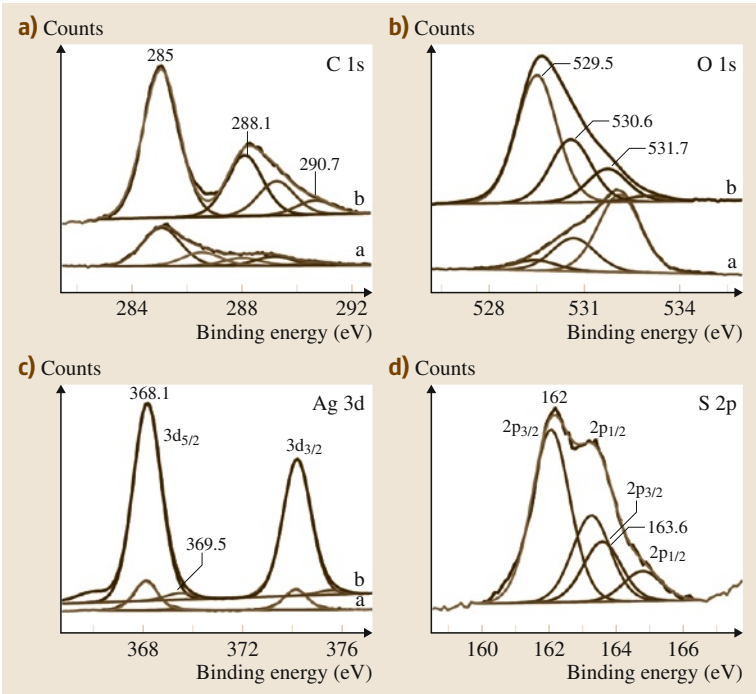


Fig. 9.40a–d X-ray photoelectron spectroscopy (XPS) spectra in the **(a)** C 1s, **(b)** O 1s, and **(c)** Ag 3d of Ag@citrate and Ag@MSA and **(d)** S 2p region of Ag@MSA. Traces (a) and (b) in **(a–c)** are due to Ag@citrate and Ag@MSA, respectively. From the authors' laboratory (after [9.439])

of mercury [9.441], arsenic [9.442], lead [9.443], and anions [9.444] are available. Similar to the methodology adopted for the detection of pesticides, there are two possible ways to detect metal ions by noble metal NPs.

Colorimetric Detection. Noble metal NPs can anchor various types of ligands on the surface and can intercede in several ligand-mediated reactions. Moreover, this anchoring or functionalization of metal surfaces generally results in sensitive changes in their optical properties [9.445]. Heavy metals can be detected using surface functionalized NPs [9.446]. Biomolecule-functionalized GNPs were used for this application recently. The interaction between metal ion and nucleotide, for example the Hg^{2+}-promoted formation of thymine–thymine base pairs [9.447, 448], was used for detection. Based on this interaction a scanometric device involving the use of an oligonucleotide chip array for the low concentration detection of metal ions was reported [9.449]. The aggregation of Au NPs functionalized with a DNA strand due to the hybridization action of enzymes in the presence of a substrate is another example of a similar approach [9.450–453]. The presence of specific metal ions can hinder the hybridization by catalytic cleavage of the substrate. Hence upon addition of metal ions, the aggregates of GNPs become disengaged. This method has a detection limit of 100 ppb. Peptide-functionalized Au NPs were also utilized for colorimetric detection of Hg^{2+} and Pb^{2+} at the ppb level (distinct color changes for the two ions), via a similar methodology [9.454]. The peptide (Flg-A3 peptide with specific sequence, -Asp-Tyr-Lys-Asp-Asp-Asp-Asp-Lys-Pro-Ala-Tyr-Ser-Ser-Gly-Pro-Ala-Pro-Pro-Met-Pro-Pro-Phe-) was anchored on NP surfaces which also acted as the stabilizing agent due to its negative charge. The aromatic, charged, and hydroxyl groups in the peptide sequence distinguish heavy metal ions leading to plasmon shifts in the absorption spectrum-based nanomolar detection. Metal ion-induced assembly of GNPs in the presence of carboxylated peptide (tyrosine containing peptide NH_2-Leu-Aib-Tyr-OMe) was also used for the ppm level detection of various metal ions [9.455]. Simple colorimetric approaches based on the specific action of DNA enzymes towards metal ions (e.g., Cu^{2+} and Zn^{2+}) have also been also utilized for the targeted detection of metal ions [9.456, 457].

The mechanism of colorimetric detection usually depends on the complexation of ligands functionalized onto noble metal NP surfaces with specific metal ions. This results in observable optical changes at concentra-

tions in the ppm level. Various ligands such as gallic acid (Pb^{2+}), cysteine (Hg^{2+}, Cu^{2+}) [9.458], and mercaptoundecanoic acid (Pb^{2+}, Cd^{2+}, Hg^{2+}) [9.459] have been employed for this purpose.

The chemistry of metal NPs can also be utilized for the removal of heavy metals. The alloy formation between the metals gives rise to notable changes in the optical properties of noble metal NPs (as was discussed earlier) [9.379, 380]. Aggregation of Au NP surfaces modified by carboxylate groups can be induced by Hg^{2+} and pyridinedicarboxylic acid, leading to a colorimetric response [9.460, 461], fluorescence quenching [9.462], and enhancement of hyper-Rayleigh scattering intensity [9.463]. The selectivity of metal ions depends on the choice of carboxylate group. Generally, 3-mercaptopropionic acid [9.460, 461, 463], adenosine monophosphate [9.460], and mercaptoundecanoic acid [9.462] are used.

SERS-Based Detection. Utilizing the SERS activity of noble metal NPs, trace quantities of contaminants in drinking water can be detected. As was explained earlier (Sect. 9.4), the large electric field generation near the metal surface due to the collective oscillations of conduction electrons with the incident light leads to signal amplification. Charge transfer between the chemisorbed species and the metal surface leads to electronic transitions from the highest occupied molecular orbital (HOMO) the to lowest unoccupied molecular orbital (LUMO). Excellent reviews on SERS can be found in the literature [9.464]. Various attributes of SERS such as size-dependent SERS activity [9.415], single-molecule detection [9.416], and enhanced activity from assembled nanostructures [9.465] can be utilized for detection of contaminant molecules in drinking water. A recent study demonstrated the shape dependency of SERS-based concentration detection of arsenic in drinking water [9.466]. A detailed description of this is given in a later section (Sect. 9.7.6). Alterations in the conformation of DNA can inhibit their binding capacity to NP surface. This difference in binding capacity induced by Hg^{2+} on thymine-rich single-strand DNA tagged with a fluorescent dye was used for the detection of Hg^{2+}. NPs aggregated upon addition salt when DNA (which can prevent this aggregation) was not anchored on the surface leading to the detection [9.467]. It was also understood that Hg^{2+} can catalyze the formation of stable duplex DNA from single-strand DNA-functionalized GNPs through thymine–Hg^{2+}–thymine linkage [9.468]. This temperature-dependent process can be modulated by controlling the extent of thymine–thymine mismatch. Surface modification of Au NPs with suitable molecules can result in enhanced metal ion capacity [9.469]. Raman vibrational modes are extremely sensitive towards the heavy metal coordination, which will become enhanced upon coupling with noble metal NPs.

Ultralow quantities of anions can be detected using SERS-based protocols. Perchlorate, thiocyanate, and cyanide ions have been detected using positively charged silver NPs protected by amino and amide groups which are immobilized on the silica surface [9.470].

Chemistry of Microorganisms with Noble Metal NPs

Silver, in zero-valent and ionic form, is known to possess antimicrobial effects [9.471–475]. As is illustrated in the historical perspective as well, it has been widely used as a common disinfectant for surgical masks [9.476], textile fibers [9.477], wound dressing [9.478], etc. Several scientific studies have been undertaken to understand the mechanism of this effect, and there exist a number of reviews regarding this [9.479–484]. Here, some important aspects of NP chemistry with microorganisms, that are relevant to drinking water purification are summarized.

Toxic effects of Ag NPs on a broad spectrum of microorganisms, including *Escherichia coli* [9.471, 474, 475, 484–486], *Pseudomonas aeruginosa* [9.484], *Vibrio cholera* [9.484], *Bacillus subtilis*, and the human immunodeficiency virus (HIV)-1 [9.487] are well documented. Before going into the mode of action of Ag NPs, it is important to understand the biocidal activity of silver ions. The precise mechanism behind the effect is not fully understood. However, protein inactivation and loss of replication ability of DNA are suggested as the route cause for this effect based on certain key observations:

1. When cells are subjected to external stimuli like heat, they will try to protect the DNA by forming a defense around the nucleus [9.488]. However, this defense mechanism cannot withstand certain external stimuli, which will result in denaturation of the DNA (loss of replication ability). When Ag ions were injected to *E. coli* and *Staphylococcus aureus,* a similar observation was made[9.489]. DNA condensation resulting from the formation of protective layers around the DNA was observed in this investigation [9.489]. A large-scale movement in the cellular components when encountering Ag ions

points to the capability of the cell to protect itself against external stimuli.
2. Studies indicated that the interaction of silver ions with the sulfur present in many proteins leads to protein inactivation [9.490]. It was also observed that external addition of sulfur-containing compounds led to neutralization of the antibacterial activity of silver. This confirmed the interaction between sulfur and silver.

The effectiveness of Ag ions is closely related to the nature of the charges on the cell surface (due to the presence of various functional groups) and the antibacterial composition. For example, if the antibacterial composition and charge on the cell surface are negative, the contact between these two entities will be minimal due to repulsion [9.491]. Silver can absorb oxygen in atomic form and this has been widely utilized for many organic reactions such as conversion of methanol to formaldehyde [9.492]. Also, bulk silver in water enriched with oxygen is known to oxidatively destroy microorganisms [9.493]. Cell viability is maintained by cellular membranes and in the case of gram-negative bacteria such as *E. coli*, the cellular permeability is controlled by a lipopolysaccharide (LPS) layer on the outer surface of the cellular membrane. The saturated fatty acids on LPS bind to the negative ions present on the membrane backbone. This renders LSPs to have high affinity towards cations. This allows the permeation of polycationic antibiotics into the cytoplasm. Also, cations such as Mg^{2+} and Ca^{2+} can act as electrostatic linkers to bind adjacent LPS chains [9.494]. However, this also makes LSPs to be highly susceptible towards cations and it has been reported that even simple cations can bind to LSP and can induce weakness in the membrane's backbone, leading to disintegration of the membrane and can lead to loss of cellular viability [9.494]. Now the effect of Ag NPs on microorganisms can be looked at.

The severe and irreparable damage caused by silver NPs to the cellular membrane [9.474, 485, 495] leading to the accumulation of NPs in the cytoplasm [9.474] has been investigated in detail. The damage these Ag NPs bring to cells stems from this and is not due to their toxicity [9.485]. This can be easily understood by the significant amount of pits formed after treatment. Another requirement of Ag NPs to have good biocidal activity is that they should be supported to have a considerable amount of antibacterial effects. Generally, cellular proteins, which help cells to guard against metal toxicity, bind to the NP surface, leading to the aggregation of NPs. In this aggregated state the NPs become immobile [9.474]. The size of the NP particle plays an important role in the permeation of NPs into the cell, and small NPs are expected to penetrate across the cell membrane easily [9.484, 485]. Consequently, the biocidal activity of Ag NPs is also dependent on their size and shape. For example, compared to NRs and spherical particles, triangular nanoplates were found to have more activity. The crystal structure of the surface of the NPs can also influence the activity. It is understood that bacteria will interact more with high atom density (111) crystal planes [9.484]. Hence, a crystal with a larger number of (111) planes will demonstrate higher antibacterial activity [9.485].

The formation of superoxide (detected by the dismutation activity of superoxide dismutase) has been also proposed to be a reason for the antibacterial activity. It was also found that the addition of dismutase resulted in a reduction in antibacterial activity [9.496].

Another opinion suggests that the chemistry of silver ions is important in the antibacterial effect of silver NPs. Study showed that oxidized silver NPs are nontoxic towards *E. coli* strains, pointing towards the importance of chemisorbed Ag^{+} ions in determining silver NP toxicity [9.486].

Studies showed that Ag NPs interact with the glycoproteins of HIV-1 and particles greater than 10 nm attach to the viral envelope. HIV cell infection also occurs due to the binding of glycoproteins with receptor sites on host cells. The sulfur-bearing residues on the protein surface actively participate in the binding process with Ag NPs and make the glycoprotiens incapable of binding with host cells, deactivating the HIV virus [9.487].

The stabilization of Ag NPs in organic media such as plastics, oils, etc., is also important to attain optimum antibacterial action. There are two major approaches for this:

1. Synthesis of organic-soluble Ag NPs via different methods, for example, polymerization of benzylthiocyanate on silver NPs [9.497].
2. Preparing Ag NPs directly in vegetable oil by reduction of the metal salt by oxidative drying process in oils [9.498].

Ag NPs and their antibacterial properties have also been utilized for making bacteriostatic separation membranes [9.499–501]. Biofouling and inability to remove viruses are recurring problems in many membrane-based technologies. Thus, Ag NPs can contribute greatly to this area and incorporation of Ag NPs

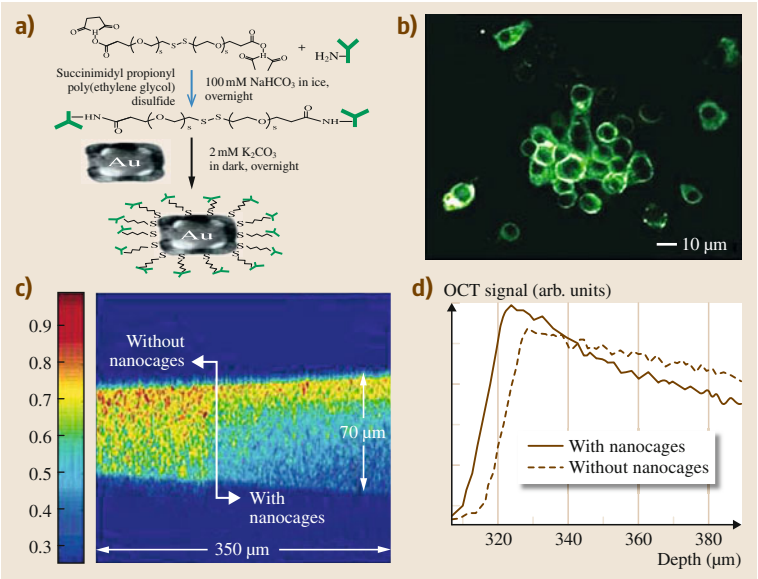


Fig. 9.41 **(a)** Schematic illustration of the protocol used to conjugate antibodies to the surface of Au nanocages. **(b)** Fluorescence image of SK-BR-3 cells whose surfaces were treated with anti-HER_2 antibodies, followed by incubation with fluorescence-labeled IgG. **(c)** OCT image of a gelatin phantom embedded with TiO_2; the concentration of TiO_2 was controlled at 1 mg/mL to mimic the background scattering of soft tissues. **(d)** OCT signals on log scale as a function of depth (after [9.503])

onto the membrane solves both problems. The loading can be done via two processes namely, addition of silver in zero-valent form or reduction of silver ions in the membrane casting solution. Addition of Ag NPs improved the bioresistance as well as the permeability [9.500]. Investigations pointed out that the biocidal properties of silver NP loaded membranes are due to the leaching of Ag^+ ions from the NPs [9.502].

Size and shape-dependent physical and chemical properties of anisotropic nanomaterials make them attractive candidates for various applications. The higher efficiency of these particles over spherical NPs has been demonstrated in various applications. Hence, a few of the important applications of different kinds of anisotropic nanostructures are mentioned below. This section does not provide a comprehensive review of the literature.

9.7.2 Bioconjugation and Labeling

Functionalization of NPs with biological entities can increase their biocompatibility and thus improve their utility for targeting cancer cells. *Hafner* et al. stabilized, conjugated to antibodies, and characterized GNRs for biological applications. To this end, the stabilizing surfactant bilayer surrounding GNRs was replaced with thiol-terminated methoxypoly(ethylene glycol). Bioconjugation of GNRs was carried out using a heterobifunctional crosslinker and the antibody activity was confirmed by a strip plate assay. Antibody-functionalized NRs were conjugated to murine macrophage cells by *Cortie* et al. [9.504] to study their photothermal properties. Bioconjugation of GNRs with phosphatidylcholine for controlled release of plasmid DNA by NIR radiation was reported by *Takahasi* et al. [9.505]. Nanocages made of gold were also bioconjugated with entities including antibodies, nucleic acids, and small-molecule inhibitors. These were used to target cancer cells for early-stage diagnostics and thermal therapy of tumors [9.506]. Figure 9.41a shows a schematic illustration of the procedure used to conjugate antibodies onto the surface of Au nanocages. The molecular specific binding of these cages were tested on breast cancer cell line SK-BR-3, which overexpresses epidermal growth factor receptor 2 (EGFR2 or HER2) [9.506]. The monoclonal anti-HER2 antibody from a mouse was anchored onto cancer cells by incubating the cells and the antibody. Secondary antibodies (anti-mouse immunoglobulin G, IgG) were immobilized on gold nanocages in a buffer solution (Fig. 9.41). When the two solutions came into contact, SK-BR-3 cells conjugated with anti-HER2 antibodies became anchored on the cages. A uniform green color, indicating homogeneous distribution of the primary anti-HER2 antibody on the cell surface, was seen in the fluorescence image (Fig. 9.41b).

9.7.3 Optical Contrast Agents

Anisotropic noble metal NPs are ideal candidates as contrast agents for NIR imaging applications due to

their strong SPR, biocompatibility, ease of bioconjugation, and large scattering cross-section [9.506, 507]. The strong, tunable SPR features in the NIR region and smaller size of Au nanocages make them attractive contrast agents [9.506]. Gold nanocages were used as optical contrast agents in the OCT imaging on phantom samples. OCT imaging (Fig. 9.41c) was conducted using a 7 fs Ti:sapphire laser with a wavelength of 825 nm and a bandwidth of 155 nm. The presence of Au nanocages significantly improved the spectroscopic imaging contrast for tissues. The high absorption cross-section (2.9×10^{-20} m^2 at 800 nm) exhibited by the Au nanocages was about five orders of magnitude stronger than the conventional dye indocyanine green. This emphasizes the usefulness of these structures for OCT imaging. Figure 9.41d shows the log of the OCT signal as a function of depth.

9.7.4 Photothermal Therapy

Living cells being extremely temperature sensitive can be adversely affected by an increase of a few degrees and can even lead to cell death. Anisotropic NPs with NIR absorption can be used for photothermal therapy where heat is generated by plasmonic absorption [9.509, 510]. Moreover, these particles can function as dual imaging/therapy capable entities. Several anisotropic NPs including NRs, nanocages, nanoshells, and nanostars have demonstrated a good NIR absorbing capacity which can be used for photothermal therapy [9.259, 504, 506, 508, 511–516]. Selective bioconjugation of Au nanocages can cause targeted delivery of these systems into cancer cells where they can produce a local temperature rise that can provide a therapeutic effect on cancer cells [9.260, 503, 506, 508, 511, 512, 514]. As mentioned in Sect. 9.7.2, the large absorption cross-sections of Au nanocages can aid these structures to covert absorbed photons into phonons. This results in an increase in the temperature of the system. Using an ultrafast laser-induced heating process, Ag nanocages can create extremely high lattice temperatures [9.514]. Such therapy is less invasive than chemotherapy or surgery and holds strong promise as a novel form of cancer treatment. *Xia* et al. demonstrated the photothermal destruction of breast cancer cells in vitro using immunotargeted Au nanocages [9.259]. Gold nanocages (with an average edge length of 65 ± 7 nm and an absorption peak at 800 nm) were conjugated with anti-HER2, which enabled the specific targeting of breast cancer cells (SK-BR-3) [9.508, 513, 514]. When the targeted cells were irradiated with a pulsed NIR laser, photothermal heating resulted in cell death. Treatment conditions such as the power density, the duration of laser exposure, and the response time after irradiation can be varied to achieve effective destruction of cancer cells. Cells targeted with Au nanocages responded immediately to laser irradiation, and irreversible cellular damage occurred at power densities greater than 1.6 W/cm^2 (Fig. 9.42). As the time of exposure increased, more and more cell death was observed.

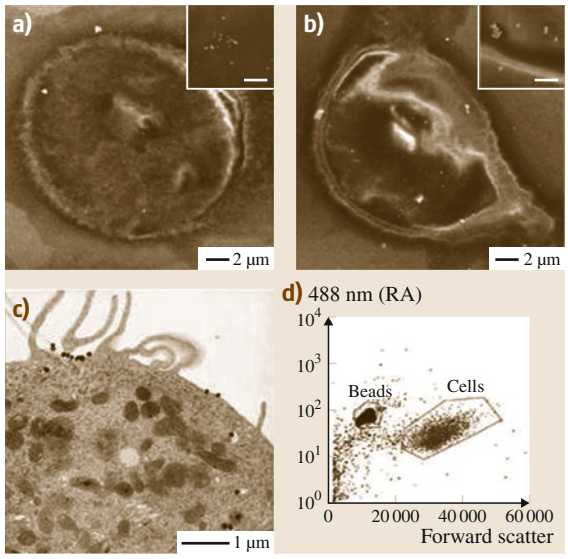


Fig. 9.42a–d SEM images of SK-BR-3 cells targeted with immuno-Au nanospheres **(a)** and nanocages **(b)**. SEM images at higher magnification (*insets*) reveal that the *bright spots* in the SEM images are indeed nanospheres and nanocages, respectively. The *scale bar* in the *insets* represents 500 nm. **(c)** TEM image of a microtomed SK-BR-3 cell conjugated with immuno Au nanocages. **(d)** Typical flow cytometry graph indicating how the forward scatter (*x*-axis) and right angle (RA) scatter (*y*-axis) can be used to differentiate the size difference between beads and cells (after [9.508])

Salem et al. demonstrated a novel nonviral gene therapy approach using multisegmented metal NRs [9.517, 518]. Cancer treatment can make use of NTs as well. Hyperthermic treatments can be carried out using NTs, which also possess large NIR absorption. Because the surface of NTs is flat, it facilitates high contact between the NTs and cancer cells, which in turn helps to reduce the required exposure time. Hence even at low dosage NTs can be effectively delivered into cancer cells, and the low dosage reduces the metal toxicity as well.

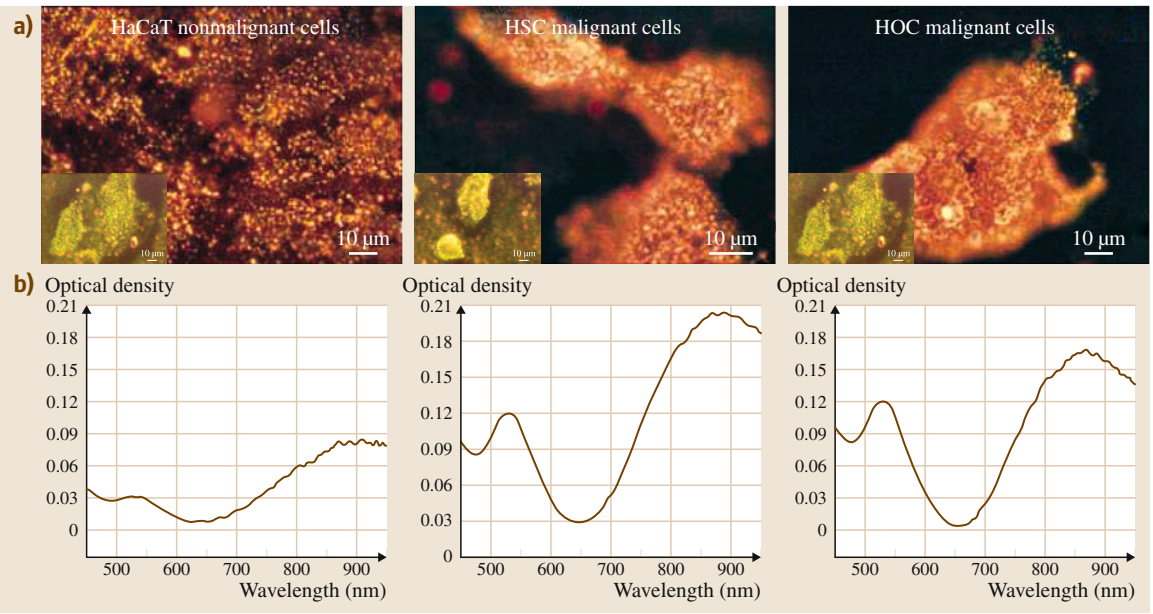


Fig. 9.43 **(a)** Light scattering images of anti-EGFR conjugated Au NRs after incubation with cells for 30 min at room temperature. **(b)** Average extinction spectra of anti-EGFR conjugated Au NRs from 20 different single cells for each kind. *Insets* show the corresponding light scattering images of anti-EGFR-Au nanospheres after incubation with cells for 30 min at room temperature (after [9.519])

9.7.5 Cancer Cell Imaging

Using dark-field optical microscopy and TPL microscopy, individual anisotropic NPs can be imaged due to the strong SPR exhibited by them. They are ideal candidates for biomedical imaging because of the large scattering cross-section [9.510]. GNRs in particular, are well suited for cancer cell imaging due to their strong absorption and scattering in the NIR region (650–900 nm) [9.509, 510, 517–523]. *Huang* et al. used GNRs functionalized with negatively charged PSS for cancer cell imaging [9.519]. The PSS coated GNRs on mixing with an antibody solution in 4-(2-hydroxyethyl)-1-piperazineethanesulfonic acid (HEPES) buffer, conjugated with anti-epidermal growth factor receptor (anti-EGFR) monoclonal antibodies. Two malignant cells, namely HOC 313 clone 8 and HSC 3, and one nonmalignant Ha-Cat cell were used in the experiment. The anti-EGFR antibody-conjugated NRs showed higher affinity to malignant cells due to the over-expressed EGFR on the cytoplasmic membrane and bound specifically to the surface of the malignant-type cells. The light scattering images of anti-EGFR-conjugated GNRs after binding to malignant and nonmalignant cells are shown in Fig. 9.43. The dominant orange color in the image corresponds to the surface plasmonic enhancement of the longitudinal oscillation in the NIR of GNR. After antibody conjugation, GNRs only interact with the malignant cells. The nature of the interaction is distinguished by light scattering imaging; Fig. 9.43 shows the quantity of NRs bound to the cell. From the extinction spectra, it is clear that the cancerous cells with nanocages have twice the intensity compared to noncancerous cells. The difference in interaction of anti-EGFR-conjugated GNRs with malignant (target specific) and nonmalignant (nonspecific random) cells gives rise to this difference in intensity. *Wang* et al. showed that GNRs, when excited at appropriate wavelengths (corresponding to LSPR peak position) using a two-photon scheme, can produce a luminescence signal 58 times stronger than the fluorescence signal from a rhodamine molecule [9.524]. *Durr* et al. used GNRs as contrast agents for imaging of cancer cells and the huge TPL of GNRs was found to be excellent for this application [9.525]. Gold nanocages are also known to exhibit a broad two-photon photoluminescence band (from 450 to 650 nm) when excited by a 800 nm Ti:sapphire laser. Use of Au nanocages as optical imaging agents for two-photon microscopy has recently been demonstrated by *Xia* et al., who

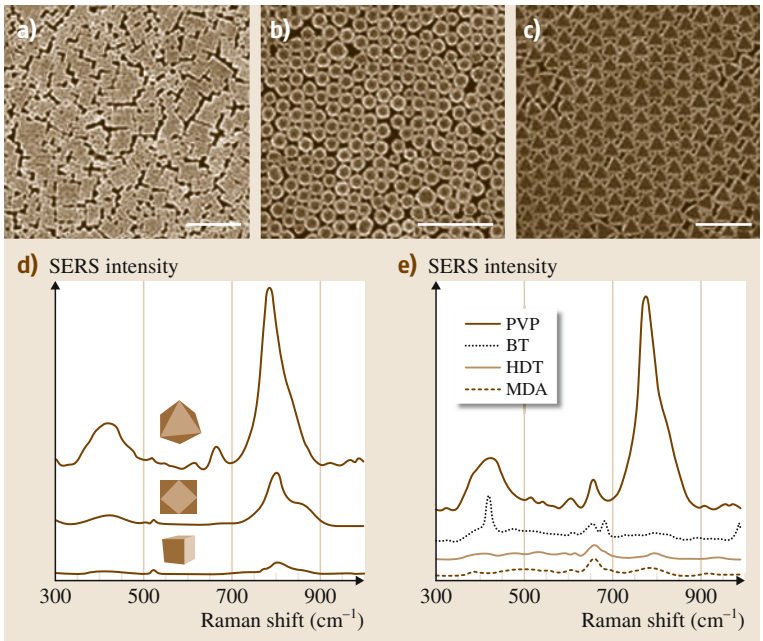


Fig. 9.44a–e SEM images showing closely packed films of the three nanocrystal shapes: **(a)** cubes, **(b)** cuboctahedra, and **(c)** octahedra; *scale bars* are 1 μm. **(d)** SERS spectra collected on LB films of each of the nanocrystal shapes of 10^{-6} M arsenate solution. Peaks at 800 and 425 cm^{-1} can be assigned to Na_2HAsO_4. **(e)** SERS response of octahedra LB arrays coated with various organic species: benzenethiol (BT), hexadecanethiol (HDT), mercaptodecanoic acid (MDA), and PVP (after [9.466])

directly examined the uptake of antibody-conjugated and PEGylated Au nanocages by U87MGwtEGFR cells [9.512].

9.7.6 Surface-Enhanced Raman Scattering Substrates

Ultrahigh sensitivity and specificity are the marked features of SERS. So it is a well-established technique and an attractive tool for trace level chemical detection. An excellent number of fine reviews are available on this topic in the literature [9.414, 417, 464, 526–534]. The SERS signal sensitivity strongly depends on the shape of the NPs [9.526, 527] This technique can be used for the detection of arsenate and arsenite in aqueous solutions with a detection limit of 1 ppb (Fig. 9.44d), an order of magnitude below the standard set by the World Health Organization (WHO) [9.466, 535]. Yang et al. successfully demonstrated this by using LB assemblies of various polyhedral Ag nanocrystals (Fig. 9.44a–c), made by a polyol process. Octahedra LB arrays coated with various organic species such as benzenethiol, hexadecanethiol, and mercaptodecanoic acid have very good SERS response, as is shown in Fig. 9.44e. We know that contaminated ground water becomes a curse to public health in most developing nations. So there is a need for a reliable and simple device to detect arsenic in ground water. This SERS substrate has proven to be a good solution for the above crisis. It is reliable, reproducible, highly portable, and could be easily implemented for field detection. Another SERS substrate NP that exhibits strong SERS activity is AuNF. By packaging RhB@AuNF particles with denatured BSACE94 molecules the AuNF particles could be developed into Raman-active tags, whose application in living cells was demonstrated by using the RAW264.7 macrophage cell line [9.536, 537].

Real-time detection of biomolecules using SERS has also been reported [9.528–530]. It is known that SERS activity varies depending on several factors. For example, *Nogami* et al. reported that triangular plates having sharper corners and edges have higher SERS activity [9.531]. Similarly, silver nanoplates in aggregated form have higher SERS activity than single-form ones due to strong electromagnetic coupling between neighboring nanoplates [9.51, 538]. When we consider anisotropic metal NPs, it is clear that their unusual LSPR properties and sharp corners on the surface are the factors contributing to higher SERS activity. These sharp corners can create a more localized electric field in comparison with spherical particles [9.535, 537].

9.7.7 Superhydrophobic Surfaces

The wettability of a surface depends on the chemical composition and morphology of that surface.

Some surfaces have a very high water repellency. The creation of a local geometry with a large geometric area relative to the projected area or the use of roughness combined with hydrophobic coatings can result in increased surface hydrophobicity. Such superhydrophobic surfaces have many advantages. Water droplets that are in contact with such surfaces (contact angle $> 150°$) form nearly spherical beads. They are self-cleaning surfaces in which contaminants of any type, whether inorganic or organic, adhere to water droplets and will be removed when the water droplets roll off. Superhydrophobic surfaces can be made by using anisotropic nanomaterials. A single-crystalline Ag dendritic film (thickness $\approx 10\,\mu m$) when functionalized with a SAM of n-dodecanethiol can form a superhydrophobic surface with a contact angle of $154.5 \pm 1.0°$ and a tilt angle lower than 2° [9.188]. From contact angle measurements, we can infer that the presence of Ag crystallites on the substrate increases hydrophobicity compared with substrates without Ag crystallites (Fig. 9.45). We can grow Ag nanoplates on GaAs substrates by direct reaction between aqueous solutions of $AgNO_3$ and the GaAs surface, and it then shows the Lotus effect [9.189]. These Ag nanoplates can be coated with 1-hexadecanethiol molecules to decrease the surface energy of Ag plates. One of the major advantages of this methodology is that we can change the wettability of such a surface. This is done by controlling the dimensions and nanoscale surface roughness of individual nanoplates using appropriate variation of the reaction conditions.

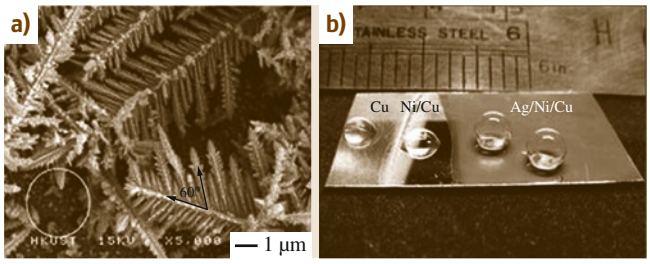


Fig. 9.45 **(a)** SEM image of Ag crystallites. **(b)** Photograph of water droplets on the Ag dendritic film surface, Ni surface, and Cu surface. All surfaces were modified with *n*-dodecanethiol (after [9.188])

9.7.8 Mercury Sensor

Mercury, a highly toxic pollutant which is harmful to the environment, is released from various sources such as power plants, burning fossil fuels, etc. Exposure to high Hg can harm our organs and affect the immune system. So it is important to monitor Hg levels in aquatic ecosystems. Owing to the amalgamation of gold and mercury, GNRs can selectively detect the presence of mercury in tap water samples at the ppt level [9.379]. The main highlight of this method is that it is very fast and the entire sensing process takes place in less than 10 min, with no sample separation and even ultralow levels of Hg can be detected very easily. The amalgamation process of Hg with GNRs is schematically represented in Fig. 9.46. Mercury was added into the growth solution during the synthesis of GNRs and it was found that the AR of the GNRs is inversely propor-

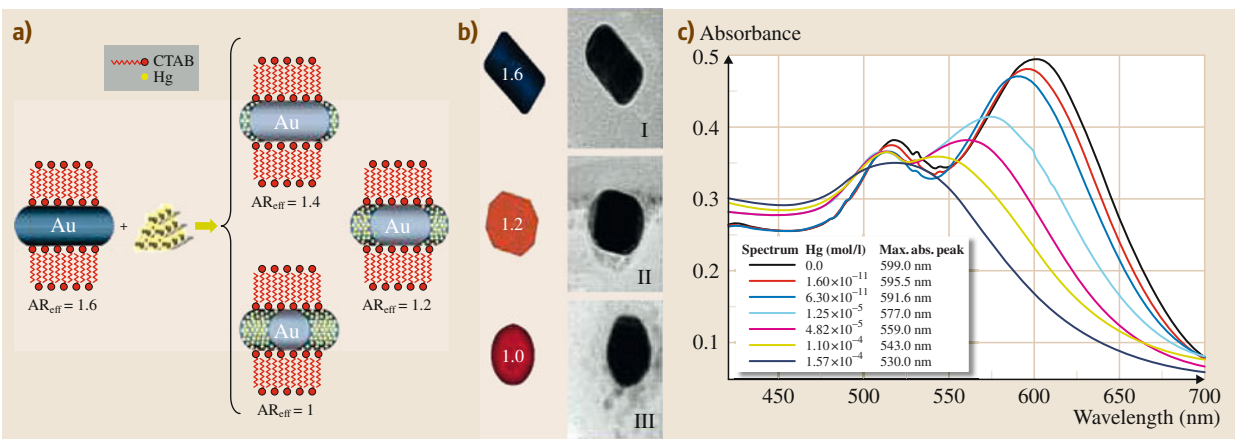


Fig. 9.46 **(a)** Schematic representation of the amalgamation of Hg with GNRs. **(b)** TEM images of GNRs in the absence and the presence of Hg. (I) no Hg, (II) 1.25×10^{-5} M, and (III) $1.57-4$ M of Hg^{2+}. **(c)** UV/Vis absorption shift in the concentration range between 1.6×10^{-11} and 6.3×10^{-11} M of Hg(II) (after [9.379])

tional to the concentration of Hg^{2+} at constant $NaBH_4$ concentration. A quantitative analysis can be made by connecting the wavelength shift and the mercury concentration (Fig. 9.46). The detection limit of Hg in tap water for this method was 6.6×10^{-13} g/l.

9.7.9 Infrared Absorbing Material

NIR absorbing films based on gold can be effectively used for blocking IR radiation. NP-based methods have a high efficiency and are economically more viable compared to other methods. Thus they can be used as an alternative way of blocking IR rays instead of reflective coatings. We can develop IR filters using nanomaterials with NIR-IR absorption capacity. Using a prototypical device, it was demonstrated that gold mesoflowers (MFs) can be successfully used to reduce the temperature rise in an enclosure exposed to daylight [9.539]. They were able to absorb a significant portion of heat. Along with a blank glass substrate as the control, a monolayer and a bilayer of MF-coated glass slides were used to take the heat absorption measurements. Results showed that the MF-coated glass (monolayer) gave an average temperature inside the cardboard box which was lower by 2 °C, whereas the bilayer coated substrate showed a reduction of 4.3 °C compared to the blank glass substrate. In future this can lead to the application of such NIR absorbing materials to make heat absorbing optical coating of windows [9.419, 539].

9.7.10 Plasmonic Waveguides

Another application of nanomaterials is in the area of photonic devices. They can have the role of waveguides if we carefully fabricate them to guide electromagnetic energy. This can be realized with lateral mode confinement below the diffraction limit of light, which is not possible through conventional waveguides or photonic crystals. Chains of closely spaced metal NPs that convert the optical mode into nonradiating surface plasmons can be prepared through electron beam lithography or self-assembly techniques. *Maier* et al. experimentally demonstrated that closely spaced silver NRs can guide electromagnetic energy from a localized subwavelength source to a localized detector over a distance of about 0.5 μm [9.540]. The waveguide structures have individual AgNRs (90 nm – long and 30 nm × 30 nm width/thickness) with spacing of 50 nm between adjacent particles. An increase in near-field coupling between the particles was created due to the perpendicular orientation of the NRs (long axis) with respect to waveguide chain axis. The waveguides used the tip of a scanning near-field optical microscope. For this, a dye laser (wavelength of 570 nm) corresponding to the single-particle resonance was used. The energy transfer through the waveguide was probed using fluorescent nanospheres made up of carboxyl-coated polystyrene. Fluorescent nanospheres placed on top of a waveguide at a distance from the excitation source became excited (illustrated by the dye emission from the fluorescent particle) by the local excitation given to the NR, which proves the propagation of these excitons along the NR array. The study demonstrated that energy attenuation lengths of several hundred nanometers is possible through nanostructure arrays pointing towards the utility of these plasmon waveguides as functional end-structures in integrated optical devices [9.540].

9.7.11 Biosensors

Anisotropic NPs with strong SPR features, which are greatly influenced by the changes in local environment, can be used for sensing [9.541]. GNRs with high-value shape factor (surface curvature), are ideal candidates for plasmon sensing. A multiplex biosensor assay for different targets was constructed using GNRs by *Yu* and *Irudayaraj* [9.542]. GNRs of different ARs were conjugated with the IgG of humans, rabbits, and mice using the 11-mercaptoundecanoic acid linker. The shifts in SPR wavelengths of these NRs were used to probe their coupling with respective complements (anti-IgGs). Detection of multiplex surface markers of breast cancer cells by the use of antibody-conjugated GNR molecular probes also employs a similar strategy [9.543]. A glucose sensor based on the layered superstructure of gold nanooctahedra was demonstrated by *Choi* et al. [9.544]. The superstructure was fabricated via a molecularly mediated assembly approach. Compared to spherical particles/glucose oxidase (GOx) system, the single-layered Au nanooctahedra/GOx system exhibited a greater voltammetric response under same conditions pointing towards the dependence of the sensor activity on the shape of the Au particles used. The Au nanooctahedra-based glucose biosensor demonstrated a high level of sensitivity in the range of 0.349 μA/mM and fast response (within few seconds) with a wide response range (between 0.125–12 mM) [9.544].

9.7.12 Photovoltaic Devices

Photovoltaic devices consisting of nanocrystals rely on the electron acceptor capability of constituent NPs from

conjugated polymers. However, the limitation of electron extraction through the nanocrystal is a big problem of photovoltaic devices made with spherical nanocrystals [9.39, 40]. The use of anisotropic structures (e.g. NRs) instead of spherical nanocrystals can give significantly higher efficiencies because of the smaller number of interparticle hops necessary for electrons to leave the device [9.545]. Generally, either TiO_2 [9.546] or ZnO [9.547] NPs are used for this application. Recent studies indicate that noble metal nanosystems can be also used for this application. Incorporation of noble metal NPs are reported to increase the efficiency of solar cells containing ZnO [9.548] and TiO_2 [9.549, 550] nanomaterials. The overall transport properties of the system will become modified by the incorporation this nanophase into the composite. Moreover, this will also permit optical tunability by adjusting the size of the metal NPs present. The overall absorption of light is also believed to be enhanced by the presence of noble metals.

Hasobe et al. pioneered works in this direction in 2003 [9.551]. Organic solar cells containing self-organized porphyrin (donor), fullerene (acceptor), and SnO_2 electrodes containing Au NPs were prepared. A large enhancement in the photoelectrochemical performance and a broader photoresponse in the visible and IR ranges were demonstrated by the Au NP containing cells. A self-assembled composite of Au NP and porphyrin was used for photovoltaic applications by *Yamada* et al. [9.552]. *Kim* and *Carroll* did a detailed study regarding the enhancement of poly(3-octylthiophene)/fullerene bulk heterojunction photovoltaic devices by gold and silver NPs [9.553]. *Derkacs* et al. reported an increase in the efficiency of amorphous-silicon solar cells by metallic NPs [9.554]. Others have reported similar enhancement in the case of polymer-based voltaic cells [9.555,556]. Dye-sensitized solar cells (both iodide/triiodide electrolyte-based and solid-state) made up of core–shell $Au-SiO_2$ NPs, which help in plasmon-enhanced light absorption leading to enhanced photocurrent and efficiency have been demonstrated by *Brown* et al. [9.557]. *Yildiz* et al. reported a solar cell consisting of oligoaniline crosslinked Au/CdS NP arrays on electrodes with enhanced photocurrent efficiency [9.558]. *Isikawa* et al. investigated the effect of the SPR of Ag NPs on dye-sensitized solar cells [9.559]. An increased photovoltaic efficiency for tandem ultrathin-film organic photovoltaic cells was found by the incorporation of Ag NPs [9.560].

9.8 New Gold and Silver Materials – Quantum Clusters

The dimensions of noble metal NPs are decreasing. In the very recent past, subnanometer particles and their associated properties have attracted intense interest. Quantum clusters (QCs) are a new class of materials made up of a few to tens of atoms, giving core sizes below 1 nm, which exhibit unusual physical and chemical properties due to their molecule-like nature [9.561,562]. QCs act as a bridge between molecular and NP behaviors, and they possess properties that are entirely different from both of these size regimes. They possess an intermediate chemical composition between the bulk and molecular regimes, with an electronic band structure modified into discrete electronic states as a result of quantum confinement. Just as in the nanometer regime, the subnanometer regime is also dominated by optical properties. While it was absorption for the former, it is luminescence for the latter. QCs exhibit strong and core size-dependent, tunable photoluminescence properties. They show characteristic absorption features and are also photostable. The quantum yield of gold QCs is several orders of magnitude higher than that of bulk gold. The photoluminescence, photostability, and biocompatibility exhibited by gold QCs make them potential materials for use in many biorelated applications such as labeling, cell imaging, drug delivery, detection, etc. [9.562]. Coupled with the possibility of chemical functionalization and due to the absence of cytotoxicity, these materials are beginning to enter biomaterials; the possibility that such clusters can directly nucleate in proteins expands the scope of this application. The clusters that have been investigated using the tools of gas-phase spectroscopy are now being made in the condensed phase. Adaptation of the properties of gas-phase clusters to their condensed-phase analogs will enrich this area in the years to come. Newer spectroscopy and mass spectrometry tools would enable the exploration of these novel properties. Several of the phenomena exhibited by such materials cannot be fully studied without comprehensive theoretical calculations. Newer insights are expected on the structure, properties, and dynamics of these systems from such studies. Although several types of cluster have been synthesized,

very few have been fully characterized by crystallography (Au_{25}, Au_{40}, Au_{102}).

Monolayer-protected gold QCs can be synthesized by various methods [9.561, 563]. They can be directly synthesized from precursor ions (Au^{3+}), which are reduced by a reducing agent (e.g., $NaBH_4$) in the presence of stabilizing ligands such as thiols, amino acids, proteins, dendrimers, etc. [9.562, 564]. A series of glutathione-capped gold QCs have been synthesized by reducing gold ions in the presence of glutathione, followed by their separation using the polyacrylamide gel electrophoresis method. A new QC can be made from another QC by treating it with the appropriate ligands. QCs are also synthesized by core etching processes [9.563]. In this process, core etching of NPs using appropriate ligands such as dendrimers, thiols, Au^{3+} ions, etc., results in the formation of QCs. Gold clusters are also highly stable at ambient conditions.

Recently our group devised a strategy for synthesis of Au QCs with the aid of cyclodextrin (Fig. 9.47b) [9.564]. They showed interesting solvent-dependent luminescence, indicating a large number of applications in sensing and security. In the case of gold QCs, the electronic bands resolve into discrete energy levels which resemble those of molecules; hence, they can be treated as molecular entities. For example, Au_{25} shows multiple molecular-like transitions in its optical spectrum [9.565]. The luminescence quantum yield of synthesized gold QCs ranges from 0.1 to 25%. Although the mechanism of luminescence in QCs is not fully known, it is believed that the emission originates from radiative intraband transitions within the sp bands, across the HOMO–LUMO gap. As the size of the cluster decreases, the spacing between the discrete states increases, which leads to a blue-shift in the emission of smaller QCs as compared with their larger analogs. Since QCs are biocompatible and luminescent, they are promising candidates for biorelated applications such as targeted imaging of cancer cells, biolabeling, drug delivery, etc. [9.561, 566]. Recently, the cluster formation process inside a protein was studied using various spectroscopic techniques [9.567]. These clusters can easily be conjugated with biological molecules, further enhancing their application potential. Most of the metal quantum clusters emit in the NIR region and hence they can be used for two-photon imaging with IR excitation [9.563]. Two-photon emission of Au_{25} observed at 830 nm with excitation at 1290 nm can be useful for two-photon imaging [9.561]. QCs also exhibit electroluminescence at room temperature and hence provide facile routes to produce strong single-photon emitters [9.561]. The luminescence of gold QCs is exploited for metal ion sensing [9.568]. Fluorescent gold QCs can be used to sense mercury(II) based on fluorescence quenching through Hg(II)-induced aggregations [9.569]. Quantum clusters are very good catalysts [9.561]. As the crystal structures of QCs are known, it is possible to correlate the particle structure with catalytic properties. It was found that metal oxide (e.g., Fe_2O_3, TiO_2)-supported gold QCs show higher catalytic activity and yield compared with unsupported QCs [9.561].

Silver analogs of these fascinating materials, however, are more reactive compared to their gold counterparts. Hence, comparatively fewer reports exist. Nevertheless, diverse methods have been reported for the preparation of Ag clusters [9.570] and most of them are highly luminescent in both solution and the solid state. The pioneering effort in this direction was done via gas-phase and low-temperature matrix-isolation methods [9.571, 572]. The formation of excited Ag_2 and Ag_3 clusters and the resulting chemiluminescence during Ag condensation with Ar has also been reported [9.573]. Nonluminescent silver clusters have been synthesized in frozen solutions and zeolites [9.574]. Diverse methods such as radiolytic reduction [9.575, 576], sonochemical synthesis [9.577, 578], chemical reduction [9.579–583], photoreduction [9.584], etc. have also been employed for synthesis of Ag clusters. A solid-state route for synthesis of Ag_9 clusters was recently reported by *Pradeep* et al. (Fig. 9.47a) [9.579]. The same group also made silver clusters by following an interfacial method (Fig. 9.47c) [9.585, 586].

Due to the higher reactivity of silver clusters, they are prone to aggregation and the resultant growth to form larger clusters/NPs. Usually this problem is avoided by using some preformed templates or capping agents to synthesize stable entities [9.587]. Both organic and inorganic scaffolds are being used for this purpose. Organic scaffolds for fluorescent silver QCs were first employed by the group of *Dickson* in 2002, who employed dendrimers as scaffolds [9.588]. Since then, several organic scaffolds such as dendrimers, polymers, short molecules containing both carboxylic groups and thiols groups, DNA, proteins, and peptides have all been employed for this purpose. *Kumacheva* et al. employed poly(*N*-isopropylacrylamide-acrylic acid-2-hydroxyethyl acrylate) microgel particles as a scaffold for preparing luminescent silver QCs [9.584]. The use of acrylates for synthesis of small silver QCs, which do not exhibit fluorescence, by applying γ radiation was reported earlier by *Ershov* and *Henglein* [9.589]. It has also been reported that, as compared with small poly-

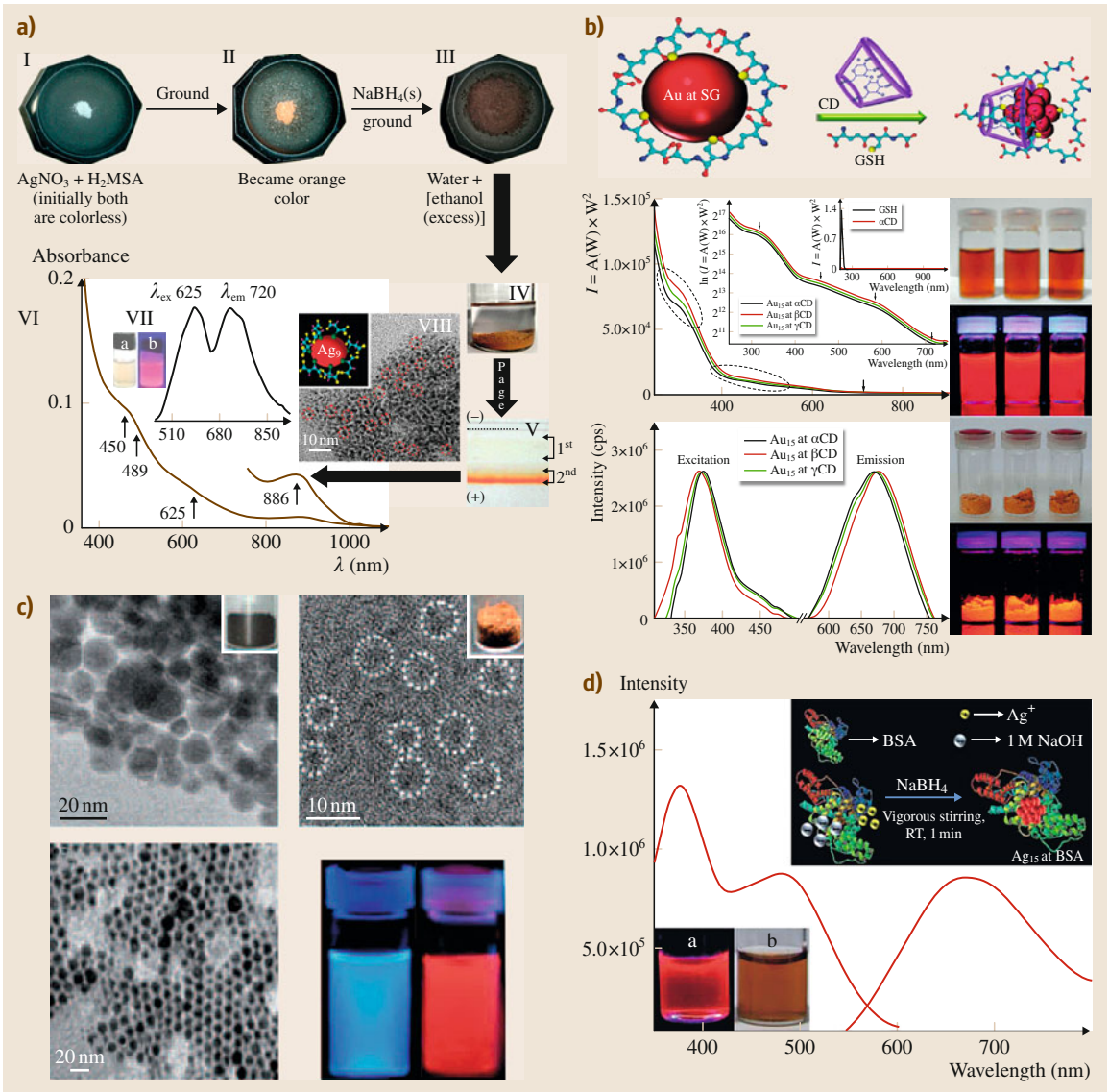


Fig. 9.47 **(a)** Scheme of preparation of Ag clusters synthesized through solid-state route and their characterization. **(b)** Au clusters synthesized using cyclodextrin, UV/Vis spectrum, and luminescence (CD: cyclodextrin; GSH: glutathione). **(c)** TEM image of Ag clusters synthesized by interfacial etching method and photograph showing the luminescence. **(d)** Scheme for the preparation of BSA-protected silver clusters and their luminescence characterization. From the authors' laboratory

mers, a high density of COOH-groups is better for the formation of fluorescent silver QCs [9.590]. Recently, small molecules having carboxylic or thiol functionalities were also used for synthesis of small clusters. Molecules such as captopril and glutathione [9.591], and dihydrolipoic acid [9.592] are reported to produce silver clusters with weak fluorescence. *Pradeep* and *Bhaskara Rao* used MSA as a scaffold for the preparation of Ag_7 and Ag_8 QCs via interfacial etching of large NPs in several aqueous/organic biphasic systems [9.586]. Ag_9 clusters have been synthesized using a solid-state route as well [9.579].

The use of biomolecules as scaffolds is a step towards developing green chemistry protocols for making quantum clusters, and it also enables the clusters to permeate into cells. Due to their luminescence property, molecular events such as replication of DNA and other genomic events happening inside cells can be visualized, measured, and tracked. Linear oligonucleotides having 12 bases were reported to be excellent scaffolds for preparation of Ag clusters [9.593–596]. It was also reported that, of these bases, Ag has more affinity towards cytosine [9.597] and guanine [9.598] residues. Efforts to use proteins as scaffolds for silver clusters due to the high affinity of silver to proteins have also been reported. Enzymes such as bovine pancreatic a-chymotrypsin (CHT) were used as templates for preparation of fluorescent silver clusters [9.599]. Cluster preparation by photoreduction in the presence of thioflavin T (ThT) has also been reported [9.600]. Synthetic oligopeptides also are being used for the preparation of silver clusters [9.601, 602]. A supramolecular hydrogel made up of dipeptides was also employed for synthesis of Ag clusters [9.603]. Proteins are also very actively used as scaffolds. Similar to dendrimers, the cage effect of the protein stabilizes the clusters and enhances their optical properties. Recently, *Liu* et al. synthesized BSA-protected Au and Au@Ag clusters using a sonochemical approach [9.578]. A protocol using BSA as the template for synthesis of Ag clusters was developed by our group recently (Fig. 9.47d) [9.604]. The conversion of Ag@citrate NPs to luminescent quantum clusters was also reported by our group [9.605]. The chemical synthesis of these systems has advanced tremendously. It is possible to create precisely controlled alloy clusters (Ag_7Au_6) through chemical means, as illustrated by our group very recently [9.606].

Inorganic templates such as glasses have also been used for preparing quantum clusters. This involves several steps. The first step involves doping of the glass with Ag^+, followed by activation by external means in the second step. The activation can be done through laser irradiation [9.607, 608], synchrotron irradiation [9.609], thermal annealing, or controlled quenching of the melt [9.571]. Zeolites have also been employed for synthesis of clusters [9.610, 611]. Here also, activation can be done by various means including heat treatment [9.612], UV light excitation [9.611], and two-photon excitation [9.613].

The application possibilities of these new nanosystems are enormous, and their exploration is in its infancy. One of the most obvious applications of these systems is in biology, especially in bioimaging [9.563, 568, 614, 615]. They have shown tremendous promise in catalysis as well [9.616–618]. These materials have been investigated for use in water purification as well. Their reactivity with heavy metals was recently explored by our group, and it was proved that the chemistry is essentially similar to that of corresponding larger NPs [9.440]. It has been demonstrated that such clusters are useful for detecting heavy metals in water as well [9.619]. The feasibility of using these materials in composites for novel applications such as antibacterial scaffolds has also been explored [9.620]. However, the authors feel that these materials are going to make a large impact in many fields, including water purification, ultrasmall sensors, diagnosis, and therapy.

9.9 Conclusions

Nanomaterials in general and noble metal NPs in particular are interesting materials for a large number of applications. This chapter illustrates the potential of noble metal NPs in various fields. The diversity and tunable properties of noble metal NPs make them superior over other categories of NPs for several key applications. In comparison with other nanoscale systems, noble metal NPs are much more stable and exhibit much less cytotoxicity. Hence, the applicability of these NPs is far greater than that of other nanosystems, especially in biology. However, most properties of many of these nanosystems, especially the anisotropic analogs, have been studied only to a limited extent, and more work is needed to understand them better. There are many promising avenues in terms of their medical and material science applications, and consistent efforts are needed to bring these to reality. The properties of gold and silver NPs and clusters are extremely sensitive to their size and shape. Detailed understanding is possible only through precise computational analyses. Rapid and sensitive responses of these NPs would be useful for developing new sensing devices. Recent research and understanding of the use of various gold and silver NPs in cancer diagnostics and therapy have already provided a platform for the development of clinical applications in the near future. A better understanding of the kinetics and dynamics of the evolution of a single NP and the development

of a more precise kinetic theory to provide an insight into the influence of various parameters on the growth of NPs under a range of conditions are also desirable. Before using these nanosystems for various applications, especially in biology and for clinical purposes, a thorough evaluation of the cytotoxicity of NPs as a function of their size, shape, and surface coating is needed.

References

9.1 M.-C. Daniel, D. Astruc: Gold nanoparticles: Assembly, supramolecular chemistry, quantum-size-related properties, and applications toward biology, catalysis, and nanotechnology, Chem. Rev. **104**(1), 293–346 (2003)

9.2 A. Moores, F. Goettmann: The plasmon band in noble metal nanoparticles: An introduction to theory and applications, New J. Chem. **30**(8), 1121–1132 (2006)

9.3 Faraday 2, http://faradayclubaward.org/wp-content/uploads/2012/08/Michael_Faraday.jpg

9.4 The Royal Institution of Great Britain, http://www.rigb.org/rimain/heritage/faradaypage.jsp

9.5 Lycurgus cup, British Museum http://www.britishmuseum.org/explore/highlights/highlight_objects/pe_mla/t/the_lycurgus_cup.aspx

9.6 M. Faraday: The Bakerian lecture: Experimental relations of gold (and other metals) to light, Philos. Trans. R. Soc. **147**, 145–181 (1857)

9.7 T. Graham: Liquid diffusion applied to analysis, Philos. Trans. R. Soc. **151**, 183–224 (1861)

9.8 Salt Lake Metals: *Antibacterial effects of silver* (Salt Lake Metals, Salt Lake City 2011), available online at http://www.saltlakemetals.com/Silver_Antibacterial.htm

9.9 Herodotus: *The History of Herodotus, translated by George Rawlinson* (Mille Tre, Vienna 2010), 1858, e-book

9.10 A.B.G. Lansdown: Silver I: Its antibacterial properties and mechanism of action, J. Wound Care **11**(4), 125–130 (2002)

9.11 A.B. Searle: *The Use of Colloids in Health and Disease* (Constable, London 1920)

9.12 E.J. Laubusch: *Water Quality and Treatment*, 3rd edn. (McGraw-Hill, New York 1971)

9.13 A.B.G. Lansdown: Silver in health care: Antimicrobial effects and safety in use, Curr. Probl. Dermatol. **33**, 17–34 (2006)

9.14 P.C. Grammaticos, A. Diamantis: Useful known and unknown views of the father of modern medicine, Hippocrates and his teacher Democritus, Hell. J. Nucl. Med. **11**(1), 2–4 (2008)

9.15 A.D. Russell, W.B. Hugo, G.P. Ellis, D.K. Luscombe: Antimicrobial activity and action of silver, Prog. Med. Chem. **31**, 351–370 (1994)

9.16 A.L. Roe: Collosol argentum and its ophthalmic uses, Br. Med. J. **1**(2820), 104 (1915)

9.17 C.E.A. Macleod: Electric metallic colloids and their therapeutical applications, Lancet **179**(4614), 322–323 (1912)

9.18 W.A. Hollis: Eighty-first Annual Meeting of the British Medical Association President's address, Br. Med. J. **2**(2759), 1282–1302 (1913)

9.19 M.C. Fung, D.L. Bowen: Silver products for medical indications: Risk-benefit assessment, Clin. Toxicol. **34**(1), 119–126 (1996)

9.20 I.M. Rutkow: *The History of Surgery in the United States* (Jeremy Norman, New York 1988)

9.21 G. Cresci, J. Mellinger: The history of nonsurgical enteral tube feeding access, Nutr. Clin. Pract. **21**(5), 522–528 (2006)

9.22 S. Simeon: On the prevention of blindness by the ophthalmia of the new-born, Lancet **132**(3392), 412–413 (1888)

9.23 T. Pradeep, Anshup: Noble metal nanoparticles for water purification: A critical review, Thin Solid Films **517**(24), 6441–6478 (2009)

9.24 A. Searle: *The Use of Metal Colloids in Health and Disease* (Sutton, New York 1919)

9.25 H. Bechhold: *Colloids in Biology and Medicine, translated by J.G.M. Bullow* (Van Nostrand, New York 1919)

9.26 O. Michael: P. William Stewart Halsted: His life and contributions to surgery, Lancet Oncol. **8**(3), 256–265 (2007)

9.27 Physician's Desk Reference: About herbs: Colloidal silver (Memorial Sloan-Kettering Cancer Center, New York 2012), available online at http://www.mskcc.org/cancer-care/herb/colloidal-silver

9.28 P.L. Drake, E. Pribitkin, W. Weber: *Colloidal Silver Products* (National Center for Complementary and Alternative Medicine, Bethesda 2006), available online at http://nccam.nih.gov/health/silver/

9.29 G. Frens, J.T.G. Overbeek: Carey Lea's colloidal silver, Colloid Polym. Sci. **233**(1), 922–929 (1969)

9.30 M.C. Lea: Allotropic forms of silver, Am. J. Sci. **37**, 476 (1889)

9.31 M. Peter-Varbanets, C. Zurbrügg, C. Swartz, W. Pronk: Decentralized systems for potable water and the potential of membrane technology, Water Res. **43**(2), 245–265 (2009)

9.32 V. Goetsch: *Free Online Colloidal Silver Ebook* (Synergenesis, Coker Creek 2010), available at http://wishgranted.com/colloidal_silver_pages_breif_history.htm

9.33 G.A. Krause: Patent 2046467 (7 July 1936) available online at http://books.google.co.in/patents/US2046467

9.34 C.E. Renn: Method of disinfecting potable water, Patent 3268444 (1966)

9.35 O. Blank: German Patent No. DRP 228697 (1910)
9.36 T.E. Lefort: French Patent No. 729952 (27 March 1931)
9.37 H. Wang, D.W. Brandl, P. Nordlander, N.J. Halas: Plasmonic nanostructures: Artificial molecules, Acc. Chem. Res. **40**(1), 53–62 (2006)
9.38 M.A. El-Sayed: Small is different: Shape-, size-, and composition-dependent properties of some colloidal semiconductor nanocrystals, Acc. Chem. Res. **37**(5), 326–333 (2004)
9.39 A.R. Tao, S. Habas, P. Yang: Shape control of colloidal metal nanocrystals, Small **4**(3), 310–325 (2008)
9.40 M.P. Pileni: Control of the size and shape of inorganic nanocrystals at various scales from nano to macrodomains, J. Phys. Chem. C **111**(26), 9019–9038 (2007)
9.41 J. Perez-Juste, I. Pastoriza-Santos, L.M. Liz-Marzán, P. Mulvaney: Gold nanorods: Synthesis, characterization and applications, Coord. Chem. Rev. **249**(17/18), 1870–1901 (2005)
9.42 S. Guo, S. Dong, E. Wang: Rectangular silver nanorods: Controlled preparation, liquid liquid interface assembly, and application in surface-enhanced Raman scattering, Cryst. Growth Des. **9**(1), 372–377 (2008)
9.43 B. Pietrobon, M. McEachran, V. Kitaev: Synthesis of size-controlled faceted pentagonal silver nanorods with tunable plasmonic properties and self-assembly of these nanorods, Am. Chem. Soc. Nano **3**(1), 21–26 (2008)
9.44 H.M. Chen, R.-S. Liu, K. Asakura, L.-Y. Jang, J.-F. Lee: Controlling length of gold nanowires with large-scale: X-ray absorption spectroscopy approaches to the growth process, J. Phys. Chem. C **111**(50), 18550–18557 (2007)
9.45 S.E. Hunyadi, C.J. Murphy: Bimetallic silver-gold nanowires: Fabrication and use in surface-enhanced Raman scattering, J. Mater. Chem. **16**(40), 3929–3935 (2006)
9.46 D. Zhang, L. Qi, J. Yang, J. Ma, H. Cheng, L. Huang: Wet chemical synthesis of silver nanowire thin films at ambient temperature, Chem. Mater. **16**(5), 872–876 (2004)
9.47 J. Hu, T.W. Odom, C.M. Lieber: Chemistry and physics in one dimension: Synthesis and properties of nanowires and nanotubes, Acc. Chem. Res. **32**(5), 435–445 (1999)
9.48 J.E. Millstone, S. Park, K.L. Shuford, L. Qin, G.C. Schatz, C.A. Mirkin: Observation of a quadrupole plasmon mode for a colloidal solution of gold nanoprisms, J. Am. Chem. Soc. **127**(15), 5312–5313 (2005)
9.49 Y. He, G. Shi: Surface plasmon resonances of silver triangle nanoplates: Graphic assignments of resonance modes and linear fittings of resonance peaks, J. Phys. Chem. B **109**(37), 17503–17511 (2005)
9.50 C. Kan, X. Zhu, G. Wang: Single-crystalline gold microplates: Synthesis, characterization, and thermal stability, J. Phys. Chem. B **110**(10), 4651–4656 (2006)
9.51 X. Zou, S. Dong: Surface-enhanced Raman scattering studies on aggregated silver nanoplates in aqueous solution, J. Phys. Chem. B **110**(43), 21545–21550 (2006)
9.52 A. Swami, A. Kumar, P.R. Selvakannan, S. Mandal, R. Pasricha, M. Sastry: Highly oriented gold nanoribbons by the reduction of aqueous chloroaurate ions by hexadecylaniline langmuir monolayers, Chem. Mater. **15**(1), 17–19 (2002)
9.53 C. Zhan, J. Wang, J. Yuan, H. Gong, Y. Liu, M. Liu: Synthesis of right- and left-handed silver nanohelices with a racemic gelator, Langmuir **19**(22), 9440–9445 (2003)
9.54 Y. Chen, S. Milenkovic, A.W. Hassel: Arrays of isooriented gold nanobelts, Nano Lett. **8**(2), 737–742 (2008)
9.55 Y. Sun, B. Mayers, Y. Xia: Transformation of silver nanospheres into nanobelts and triangular nanoplates through a thermal process, Nano Lett. **3**(5), 675–679 (2003)
9.56 N. Zhao, Y. Wei, N. Sun, Q. Chen, J. Bai, L. Zhou, Y. Qin, M. Li, L. Qi: Controlled synthesis of gold nanobelts and nanocombs in aqueous mixed surfactant solutions, Langmuir **24**(3), 991–998 (2008)
9.57 Y. Khalavka, J. Becker, C. Sönnichsen: Synthesis of rod-shaped gold nanorattles with improved plasmon sensitivity and catalytic activity, J. Am. Chem. Soc. **131**(5), 1871–1875 (2009)
9.58 J. Burgin, M. Liu, P. Guyot-Sionnest: Dielectric sensing with deposited gold bipyramids, J. Phys. Chem. C **112**(49), 19279–19282 (2008)
9.59 J. Henzie, E.-S. Kwak, T.W. Odom: Mesoscale metallic pyramids with nanoscale tips, Nano Lett. **5**(7), 1199–1202 (2005)
9.60 C.L. Nehl, H. Liao, J.H. Hafner: Optical properties of star-shaped gold nanoparticles, Nano Lett. **6**(4), 683–688 (2006)
9.61 J.L. Burt, J.L. Elechiguerra, J. Reyes-Gasga, J.M. Montejano-Carrizales, M. Jose-Yacaman: Beyond Archimedean solids: Star polyhedral gold nanocrystals, J. Cryst. Growth **285**(4), 681–691 (2005)
9.62 P.R. Sajanlal, T.S. Sreeprasad, A.S. Nair, T. Pradeep: Wires, plates, flowers, needles, and core shells: Diverse nanostructures of gold using polyaniline templates, Langmuir **24**(9), 4607–4614 (2008)
9.63 B.K. Jena, C.R. Raj: Seedless, surfactantless room temperature synthesis of single crystalline fluorescent gold nanoflowers with pronounced SERS and electrocatalytic activity, Chem. Mater. **20**(11), 3546–3548 (2008)
9.64 B.K. Jena, C.R. Raj: Synthesis of flower-like gold nanoparticles and their electrocatalytic activity towards the oxidation of methanol and the reduction of oxygen, Langmuir **23**(7), 4064–4070 (2007)
9.65 M.S. Bakshi, F. Possmayer, N.O. Petersen: Role of different phospholipids in the synthesis of pearl-necklace-type gold silver bimetallic nanoparticles

as bioconjugate materials, J. Phys. Chem. C **111**(38), 14113–14124 (2007)
9.66 E. Hao, R.C. Bailey, G.C. Schatz, J.T. Hupp, S. Li: Synthesis and optical properties of "branched" gold nanocrystals, Nano Lett. **4**(2), 327–330 (2004)
9.67 H.M. Chen, C.F. Hsin, R.-S. Liu, J.-F. Lee, L.-Y. Jang: Synthesis and characterization of multi-pod-shaped gold/silver nanostructures, J. Phys. Chem. C **111**(16), 5909–5914 (2007)
9.68 O.M. Bakr, B.H. Wunsch, F. Stellacci: High-yield synthesis of multi-branched urchin-like gold nanoparticles, Chem. Mater. **18**(14), 3297–3301 (2006)
9.69 S. D'Agostino, F. Della Sala: Silver nanourchins in plasmonics: Theoretical investigation on the optical properties of the branches, J. Phys. Chem. C **115**(24), 11934–11940 (2011)
9.70 J. Hu, Y. Zhang, B. Liu, J. Liu, H. Zhou, Y. Xu, Y. Jiang, Z. Yang, Z.-Q. Tian: Synthesis and properties of tadpole-shaped gold nanoparticles, J. Am. Chem. Soc. **126**(31), 9470–9471 (2004)
9.71 L. Tian, M.T. Ng, N. Venkatram, W. Ji, J.J. Vittal: Tadpole-shaped $AgInSe_2$ nanocrystals from a single molecular precursor and its nonlinear optical properties, Cryst. Growth Des. **10**(3), 1237–1242 (2010)
9.72 S.E. Skrabalak, L. Au, X. Li, Y. Xia: Facile synthesis of Ag nanocubes and Au nanocages, Nat. Protoc. **2**(9), 2182–2190 (2007)
9.73 M. Hu, J. Chen, M. Marquez, Y. Xia, G.V. Hartland: Correlated rayleigh scattering spectroscopy and scanning electron microscopy studies of Au Ag bimetallic nanoboxes and nanocages, J. Phys. Chem. C **111**(34), 12558–12565 (2007)
9.74 C.E. Talley, J.B. Jackson, C. Oubre, N.K. Grady, C.W. Hollars, S.M. Lane, T.R. Huser, P. Nordlander, N.J. Halas: Surface-enhanced Raman scattering from individual Au nanoparticles and nanoparticle dimer substrates, Nano Lett. **5**(8), 1569–1574 (2005)
9.75 H. Wang, D.W. Brandl, F. Le, P. Nordlander, N.J. Halas: Nanorice: A hybrid plasmonic nanostructure, Nano Lett. **6**(4), 827–832 (2006)
9.76 T. Teranishi, Y. Inoue, M. Nakaya, Y. Oumi, T. Sano: Nanoacorns: Anisotropically phase-segregated copd sulfide nanoparticles, J. Am. Chem. Soc. **126**(32), 9914–9915 (2004)
9.77 Y. Sun, B.T. Mayers, Y. Xia: Template-engaged replacement reaction: A one-step approach to the large-scale synthesis of metal nanostructures with hollow interiors, Nano Lett. **2**(5), 481–485 (2002)
9.78 C.M. Cobley, D.J. Campbell, Y. Xia: Tailoring the optical and catalytic properties of gold-silver nanoboxes and nanocages by introducing palladium, Adv. Mater. **20**(4), 748–752 (2008)
9.79 R. Gunawidjaja, S. Peleshanko, H. Ko, V.V. Tsukruk: Bimetallic nanocobs: Decorating silver nanowires with gold nanoparticles, Adv. Mater. **20**(8), 1544–1549 (2008)
9.80 G.S. Metraux, Y.C. Cao, R. Jin, C.A. Mirkin: Triangular nanoframes made of gold and silver, Nano Lett. **3**(4), 519–522 (2003)
9.81 C.-C. Huang, Z. Yang, H.-T. Chang: Synthesis of dumbbell-shaped Au Ag core shell nanorods by seed-mediated growth under alkaline conditions, Langmuir **20**(15), 6089–6092 (2004)
9.82 J.D. Swalen, D.L. Allara, J.D. Andrade, E.A. Chandross, S. Garoff, J. Israelachvili, T.J. McCarthy, R. Murray, R.F. Pease, J.F. Raboldt, K.J. Wynne: Molecular monolayers and films. A panel report for the materials sciences division of the department of energy, Langmuir **3**(6), 932–950 (1987)
9.83 K.S. Morley, P.C. Marr, P.B. Webb, A.R. Berry, F.J. Allison, G. Moldovan, P.D. Brown, S.M. Howdle: Clean preparation of nanoparticulate metals in porous supports: A supercritical route, J. Mater. Chem. **12**(6), 1898–1905 (2002)
9.84 Y. Xuan, Q. Li: Heat transfer enhancement of nanofluids, Int. J. Heat Fluid Flow **21**(1), 58–64 (2000)
9.85 X. Wang, X. Xu, S.U.S. Choi: Thermal conductivity of nanoparticle-fluid mixture, J. Thermophys. Heat Transf. **13**(4), 474–480 (1999)
9.86 M.G. DaGue, J.S. Landers, H.L. Lewis, J.L. Dye: Alkali metal anions and trapped electrons formed by evaporating metal ammonia solutions which contain cryptands, Chem. Phys. Lett. **66**(1), 169–182 (1979)
9.87 J.L. Dye, K.-L. Tsai: Small alloy particles formed by co-reduction of soluble precursors with alkalides or electrides in aprotic solvents, Faraday Discuss. **92**, 45–55 (1991)
9.88 B.A. Korgel, S. Fullam, S. Connolly, D. Fitzmaurice: Assembly and self-organization of silver nanocrystal superlattices: Ordered soft spheres, J. Phys. Chem. B **102**(43), 8379–8388 (1998)
9.89 G.B. Birrell, K.K. Hedberg, O.H. Griffith: Pitfalls of immunogold labeling: Analysis by light microscopy, transmission electron microscopy, and photoelectron microscopy, J. Histochem. Cytochem. **35**(8), 843–853 (1987)
9.90 A. Frattini, N. Pellegri, D. Nicastro, O. de Sanctis: Effect of amine groups in the synthesis of Ag nanoparticles using aminosilanes, Mater. Chem. Phys. **94**(1), 148–152 (2005)
9.91 F. Bonet, S. Grugeon, R. Herrera Urbina, K. Tekaia-Elhsissen, J.M. Tarascon: In situ deposition of silver and palladium nanoparticles prepared by the polyol process, and their performance as catalytic converters of automobile exhaust gases, Solid State Sci. **4**(5), 665–670 (2002)
9.92 P.V. Kamat, M. Flumiani, G.V. Hartland: Picosecond dynamics of silver nanoclusters. Photoejection of electrons and fragmentation, J. Phys. Chem. B **102**(17), 3123–3128 (1998)
9.93 T. Teranishi, M. Miyake: Size control of palladium nanoparticles and their crystal structures, Chem. Mater. **10**(2), 594–600 (1998)

9.94 H. Bönnemann, R.A. Brand, W. Brijoux, H.W. Hofstadt, M. Frerichs, V. Kempter, W. Maus-Friedrichs, N. Matoussevitch, K.S. Nagabhushana, F. Voigts, V. Caps: Air stable Fe and Fe–Co magnetic fluids – synthesis and characterization, Appl. Organomet. Chem. **19**(6), 790–796 (2005)

9.95 J. Turkevich, P.C. Stevenson, J. Hillier: A study of the nucleation and growth processes in the synthesis of colloidal gold, Discuss. Faraday Soc. **11**, 55–75 (1951)

9.96 G. Frens: Controlled nucleation for the regulation of the particle size in monodisperse gold suspensions, Nat. Phys. Sci. **241**(105), 20–22 (1973)

9.97 B.V. Enüstün, J. Turkevich: Coagulation of colloidal gold, J. Am. Chem. Soc. **85**(21), 3317–3328 (1963)

9.98 M. Brust, M. Walker, D. Bethell, D.J. Schiffrin, R. Whyman: Synthesis of thiol-derivatized gold nanoparticles in a two-phase liquid-liquid system, J. Chem. Soc. Chem. Commun. **7**, 801–802 (1994)

9.99 A.C. Templeton, W.P. Wuelfing, R.W. Murray: Monolayer-protected cluster molecules, Acc. Chem. Res. **33**(1), 27–36 (1999)

9.100 N. Sandhyarani, T. Pradeep: Current understanding of the structure, phase transitions and dynamics of self-assembled monolayers on two- and three-dimensional surfaces, Int. Rev. Phys. Chem. **22**(2), 221–262 (2003)

9.101 K. Vijaya Sarathy, G.U. Kulkarni, C.N.R. Rao: A novel method of preparing thiol-derivatised nanoparticles of gold, platinum and silver forming superstructures, Chem. Commun. **6**, 537–538 (1997)

9.102 B.L.V. Prasad, S.I. Stoeva, C.M. Sorensen, K.J. Klabunde: Digestive-ripening agents for gold nanoparticles: Alternatives to thiols, Chem. Mater. **15**(4), 935–942 (2003)

9.103 A. Taleb, C. Petit, M.P. Pileni: Optical properties of self-assembled 2-D and 3-D superlattices of silver nanoparticles, J. Phys. Chem. B **102**(12), 2214–2220 (1998)

9.104 T.G. Schaaff, G. Knight, M.N. Shafigullin, R.F. Borkman, R.L. Whetten: Isolation and selected properties of a 10.4 kDa gold: Glutathione cluster compound, J. Phys. Chem. B **102**(52), 10643–10646 (1998)

9.105 S. Chen, K. Kimura: Synthesis and characterization of carboxylate-modified gold nanoparticle powders dispersible in water, Langmuir **15**(4), 1075–1082 (1999)

9.106 K. Kimura, S. Sato, H. Yao: Particle crystals of surface modified gold nanoparticles grown from water, Chem. Lett. **30**(4), 372–373 (2001)

9.107 Y. Negishi, K. Nobusada, T. Tsukuda: Glutathione-protected gold clusters revisited: Bridging the gap between gold(i) thiolate complexes and thiolate-protected gold nanocrystals, J. Am. Chem. Soc. **127**(14), 5261–5270 (2005)

9.108 M.T. Reetz, W. Helbig: Size-selective synthesis of nanostructured transition metal clusters, J. Am. Chem. Soc. **116**(16), 7401–7402 (1994)

9.109 L. Rodriguez-Sanchez, M.C. Blanco, M.A. López-Quintela: Electrochemical synthesis of silver nanoparticles, J. Phys. Chem. B **104**(41), 9683–9688 (2000)

9.110 M.B. Mohamed, Z.L. Wang, M.A. El-Sayed: Temperature-dependent size-controlled nucleation and growth of gold nanoclusters, J. Phys. Chem. A **103**(49), 10255–10259 (1999)

9.111 I.G. Draganic, Z.D. Draganic: *The Radiolysis of Water* (Academic, New York 1971)

9.112 A. Henglein: Radiolytic preparation of ultrafine colloidal gold particles in aqueous solution: Optical spectrum, controlled growth, and some chemical reactions, Langmuir **15**(20), 6738–6744 (1999)

9.113 S. Wang, H. Xin: Fractal and dendritic growth of metallic Ag aggregated from different kinds of gamma-irradiated solutions, J. Phys. Chem. B **104**(24), 5681–5685 (2000)

9.114 A. Henglein: Formation and absorption spectrum of copper nanoparticles from the radiolytic reduction of $Cu(CN)_2$, J. Phys. Chem. B **104**(6), 1206–1211 (2000)

9.115 B.G. Ershov, N.L. Sukhov, E. Janata: Formation, absorption spectrum, and chemical reactions of nanosized colloidal cobalt in aqueous solution, J. Phys. Chem. B **104**(26), 6138–6142 (2000)

9.116 J.H. Hodak, A. Henglein, G.V. Hartland: Photophysics of nanometer sized metal particles: Electron-phonon coupling and coherent excitation of breathing vibrational modes, J. Phys. Chem. B **104**(43), 9954–9965 (2000)

9.117 A. Henglein: Preparation and optical aborption spectra of Au core Pt shell and Pt core Au shell colloidal nanoparticles in aqueous solution, J. Phys. Chem. B **104**(10), 2201–2203 (2000)

9.118 P. Mulvaney, M. Giersig, A. Henglein: Surface chemistry of colloidal gold: Deposition of lead and accompanying optical effects, J. Phys. Chem. **96**(25), 10419–10424 (1992)

9.119 A. Henglein, D. Meisel: Radiolytic control of the size of colloidal gold nanoparticles, Langmuir **14**(26), 7392–7396 (1998)

9.120 Y. Kato, S. Sugimoto, K. Shinohara, N. Tezuka, T. Kagotani, K. Inomata: Magnetic properties and microwave absorption properties of polymer-protected cobalt nanoparticles, Mater. Trans. Jpn. Inst. Met. **43**(3), 406–409 (2002)

9.121 T.W. Smith, D. Wychick: Colloidal iron dispersions prepared via the polymer-catalyzed decomposition of iron pentacarbonyl, J. Phys. Chem. **84**(12), 1621–1629 (1980)

9.122 J. Van Wonterghem, S. Mørup, S. Charles, S. Wells, J.R. Villadsen: Formation and chemical stability of metallic glass particles prepared by thermolysis of $Fe(CO)_5$, Hyperfine Interact. **27**(1), 333–336 (1986)

9.123 J. van Wonterghem, S. Mørup, S.W. Charles, S. Wells, J.R. Villadsen: Formation of a metallic glass by thermal decomposition of Fe $(CO)_5$, Phys. Rev. Lett. **55**(4), 410 (1985)

9.124 D.P. Dinega, M.G. Bawendi: A solution-phase chemical approach to a new crystal structure of cobalt, Angew. Chem. Int. Ed. **38**(12), 1788–1791 (1999)

9.125 V.F. Puntes, K.M. Krishnan, A.P. Alivisatos: Colloidal nanocrystal shape and size control: The case of cobalt, Science **291**(5511), 2115–2117 (2001)

9.126 V.F. Puntes, D. Zanchet, C.K. Erdonmez, A.P. Alivisatos: Synthesis of hcp-co nanodisks, J. Am. Chem. Soc. **124**(43), 12874–12880 (2002)

9.127 S. Sun, C.B. Murray, D. Weller, L. Folks, A. Moser: Monodisperse FePt nanoparticles and ferromagnetic FePt nanocrystal superlattices, Science **287**(5460), 1989–1992 (2000)

9.128 J.-I. Park, J. Cheon: Synthesis of solid solutio- and core–shell-type cobaltplatinum magnetic nanoparticles via transmetalation reactions, J. Am. Chem. Soc. **123**(24), 5743–5746 (2001)

9.129 C. Amiens, D. de Caro, B. Chaudret, J.S. Bradley, R. Mazel, C. Roucau: Selective synthesis, characterization, and spectroscopic studies on a novel class of reduced platinum and palladium particles stabilized by carbonyl and phosphine ligands, J. Am. Chem. Soc. **115**(24), 11638–11639 (1993)

9.130 F. Dumestre, B. Chaudret, C. Amiens, M.-C. Fromen, M.-J. Casanove, P. Renaud, P. Zurcher: Shape control of thermodynamically stable cobalt nanorods through organometallic chemistry, Angew. Chem. Int. Ed. **41**(22), 4286–4289 (2002)

9.131 K.J. Rao, B. Vaidhyanathan, M. Ganguli, P.A. Ramakrishnan: Synthesis of inorganic solids using microwaves, Chem. Mater. **11**(4), 882–895 (1999)

9.132 I. Pastoriza-Santos, L.M. Liz-Marzán: Formation of PVP-protected metal nanoparticles in DMF, Langmuir **18**(7), 2888–2894 (2002)

9.133 F. Fievet, J.P. Lagier, M. Figlarz: Preparing monodisperse metal powders in micrometer and submicrometer sizes by the polyol process, MRS Bulletin **24**, 29 (1989)

9.134 W. Yu, W. Tu, H. Liu: Synthesis of nanoscale platinum colloids by microwave dielectric heating, Langmuir **15**(1), 6–9 (1998)

9.135 M. Tsuji, M. Hashimoto, T. Tsuji: Fast preparation of nano-sized nickel particles under microwave irradiation without using catalyst for nucleation, Chem. Lett. **31**(12), 1232–1233 (2002)

9.136 W. Tu, H. Liu: Continuous synthesis of colloidal metal nanoclusters by microwave irradiation, Chem. Mater. **12**(2), 564–567 (2000)

9.137 B.L. Cushing, V.L. Kolesnichenko, C.J. O'Connor: Recent advances in the liquid-phase syntheses of inorganic nanoparticles, Chem. Rev. **104**(9), 3893–3946 (2004)

9.138 K.S. Suslick, S.-B. Choe, A.A. Cichowlas, M.W. Grinstaff: Sonochemical synthesis of amorphous iron, Nature **353**(6343), 414–416 (1991)

9.139 G. Aharon: Using sonochemistry for the fabrication of nanomaterials, Ultrason. Sonochem. **11**(2), 47–55 (2004)

9.140 K. Dick, T. Dhanasekaran, Z. Zhang, D. Meisel: Size-dependent melting of silica-encapsulated gold nanoparticles, J. Am. Chem. Soc. **124**(10), 2312–2317 (2002)

9.141 S. Eustis, H.-Y. Hsu, M.A. El-Sayed: Gold nanoparticle formation from photochemical reduction of Au^{3+} by continuous excitation in colloidal solutions. A proposed molecular mechanism, J. Phys. Chem. B **109**(11), 4811–4815 (2005)

9.142 F. Kim, J.H. Song, P. Yang: Photochemical synthesis of gold nanorods, J. Am. Chem. Soc. **124**(48), 14316–14317 (2002)

9.143 M.R. Jones, K.D. Osberg, R.J. Macfarlane, M.R. Langille, C.A. Mirkin: Templated techniques for the synthesis and assembly of plasmonic nanostructures, Chem. Rev. **111**(6), 3736–3827 (2011)

9.144 S.E. Skrabalak, J. Chen, Y. Sun, X. Lu, L. Au, C.M. Cobley, Y. Xia: Gold nanocages: Synthesis, properties, and applications, Acc. Chem. Res. **41**(12), 1587–1595 (2008)

9.145 B. Wiley, Y. Sun, J. Chen, H. Cang, Z.-Y. Li, X. Li, Y. Xia: Shape-controlled synthesis of silver and gold nanostructures, MRS Bulletin **30**(5), 356–361 (2005)

9.146 K. An, T. Hyeon: Synthesis and biomedical applications of hollow nanostructures, Nano Today **4**(4), 359–373 (2009)

9.147 C.-H. Su, P.-L. Wu, C.-S. Yeh: Sonochemical synthesis of well-dispersed gold nanoparticles at the ice temperature, J. Phys. Chem. B **107**(51), 14240–14243 (2003)

9.148 Y.-J. Zhu, X.-L. Hu: Microwave-polyol preparation of single-crystalline gold nanorods and nanowires, Chem. Lett. **32**(12), 1140–1141 (2003)

9.149 S. Horikoshi, H. Abe, T. Sumi, K. Torigoe, H. Sakai, N. Serpone, M. Abe: Microwave frequency effect in the formation of Au nanocolloids in polar and nonpolar solvents, Nanoscale **3**(4), 1697–1702 (2011)

9.150 C.-C. Chang, H.-L. Wu, C.-H. Kuo, M.H. Huang: Hydrothermal synthesis of monodispersed octahedral gold nanocrystals with five different size ranges and their self-assembled structures, Chem. Mater. **20**(24), 7570–7574 (2008)

9.151 R. Gans: Form of ultramicroscopic particles of silver, Ann. Phys. **47**, 270–284 (1915)

9.152 K.R. Brown, M.J. Natan: Hydroxylamine seeding of colloidal Au nanoparticles in solution and on surfaces, Langmuir **14**(4), 726–728 (1998)

9.153 N.R. Jana, L. Gearheart, C.J. Murphy: Seed-mediated growth approach for shape-controlled synthesis of spheroidal and rod-like gold nanoparticles using a surfactant template, Adv. Mater. **13**(18), 1389–1393 (2001)

9.154 C.J. Murphy, A.M. Gole, J.W. Stone, P.N. Sisco, A.M. Alkilany, E.C. Goldsmith, S.C. Baxter: Gold nanoparticles in biology: Beyond toxicity to cellular imaging, Acc. Chem. Res. **41**(12), 1721–1730 (2008)

9.155 B. Nikoobakht, M.A. El-Sayed: Preparation and growth mechanism of gold nanorods (NRs) us-

ing seed-mediated growth method, Chem. Mater. **15**(10), 1957–1962 (2003)
9.156 X. Lu, M.S. Yavuz, H.-Y. Tuan, B.A. Korgel, Y. Xia: Ultrathin gold nanowires can be obtained by reducing polymeric strands of oleylamine-AuCl complexes formed via aurophilic interaction, J. Am. Chem. Soc. **130**(28), 8900–8901 (2008)
9.157 P.R. Sajanlal, T. Pradeep: Electric-field-assisted growth of highly uniform and oriented gold nanotriangles on conducting glass substrates, Adv. Mater. **20**(5), 980–983 (2008)
9.158 F. Hao, C.L. Nehl, J.H. Hafner, P. Nordlander: Plasmon resonances of a gold nanostar, Nano Lett. **7**(3), 729–732 (2007)
9.159 Z. Wang, J. Zhang, J.M. Ekman, P.J.A. Kenis, Y. Lu: DNA-mediated control of metal nanoparticle shape: One-pot synthesis and cellular uptake of highly stable and functional gold nanoflowers, Nano Lett. **10**(5), 1886–1891 (2010)
9.160 P.R. Sajanlal, T. Pradeep: Mesoflowers: A new class of highly efficient surface-enhanced Raman active and infrared-absorbing materials, Nano Res. **2**(4), 306–320 (2009)
9.161 T.H. Ha, H.-J. Koo, B.H. Chung: Shape-controlled syntheses of gold nanoprisms and nanorods influenced by specific adsorption of halide ions, J. Phys. Chem. C **111**(3), 1123–1130 (2006)
9.162 A. Samal, T.S. Sreeprasad, T. Pradeep: Investigation of the role of $NaBH_4$ in the chemical synthesis of gold nanorods, J. Nanopart. Res. **12**(5), 1777–1786 (2010)
9.163 N.R. Jana: Gram-scale synthesis of soluble, near-monodisperse gold nanorods and other anisotropic nanoparticles, Small **1**(8/9), 875–882 (2005)
9.164 S.S. Shankar, A. Rai, B. Ankamwar, A. Singh, A. Ahmad, M. Sastry: Biological synthesis of triangular gold nanoprisms, Nat. Mater. **3**(7), 482–488 (2004)
9.165 B. Ankamwar, M. Chaudhary, M. Sastry: Gold nanotriangles biologically synthesized using tamarind leaf extract and potential application in vapor sensing, Synth. React. Inorg. Met.-Org. Nano-Met. Chem. **35**(1), 19–26 (2005)
9.166 S.L. Smitha, D. Philip, K.G. Gopchandran: Green synthesis of gold nanoparticles using *Cinnamomum zeylanicum* leaf broth, Spectrochim. Acta A **74**(3), 735–739 (2009)
9.167 M. Hosea, B. Greene, R. McPherson, M. Henzl, M.D. Alexander, D.W. Darnall: Accumulation of elemental gold on the alga *Chlorella vulgaris*, Inorg. Chim. Acta **123**(3), 161–165 (1986)
9.168 C. Lu, L. Qi, J. Yang, L. Tang, D. Zhang, J. Ma: Hydrothermal growth of large-scale micropatterned arrays of ultralong zno nanowires and nanobelts on zinc substrate, Chem. Commun. **33**, 3551–3553 (2006)
9.169 B.D. Adams, G. Wu, S. Nigro, A. Chen: Facile synthesis of Pd-Cd nanostructures with high capacity for hydrogen storage, J. Am. Chem. Soc. **131**(20), 6930–6931 (2009)
9.170 A.R. Brenner, G.E. Riddell: Nickel plating on steel by chemical reduction, J. Res. Natl. Bur. Standard **37**, 31–34 (1946)
9.171 Y. Sun: Direct growth of dense, pristine metal nanoplates with well-controlled dimensions on semiconductor substrates, Chem. Mater. **19**(24), 5845–5847 (2007)
9.172 M. Aizawa, A.M. Cooper, M. Malac, J.M. Buriak: Silver nano-inukshuks on germanium, Nano Lett. **5**(5), 815–819 (2005)
9.173 J. Fang, H. You, P. Kong, Y. Yi, X. Song, B. Ding: Dendritic silver nanostructure growth and evolution in replacement reaction, Cryst. Growth Des. **7**(5), 864–867 (2007)
9.174 J.X. Fang, X.N. Ma, H.H. Cai, X.P. Song, B.J. Ding: Nanoparticle-aggregated 3-D monocrystalline gold dendritic nanostructures, Nanotechnology **17**(23), 5841 (2006)
9.175 Y. Sun, Y. Xia: Mechanistic study on the replacement reaction between silver nanostructures and chloroauric acid in aqueous medium, J. Am. Chem. Soc. **126**(12), 3892–3901 (2004)
9.176 L. Au, Y. Chen, F. Zhou, P. Camargo, B. Lim, Z.-Y. Li, D. Ginger, Y. Xia: Synthesis and optical properties of cubic gold nanoframes, Nano Res. **1**(6), 441–449 (2008)
9.177 Y. Sun, Y. Xia: Multiple-walled nanotubes made of metals, Adv. Mater. **16**(3), 264–268 (2004)
9.178 K. Esumi, K. Matsuhisa, K. Torigoe: Preparation of rodlike gold particles by UV irradiation using cationic micelles as a template, Langmuir **11**(9), 3285–3287 (1995)
9.179 F. Kim, J.H. Song, P. Yang: Photochemical synthesis of gold nanorods, J. Am. Chem. Soc. **124**(48), 14316–14317 (2002)
9.180 R. Jin, Y. Cao, C.A. Mirkin, K.L. Kelly, G.C. Schatz, J.G. Zheng: Photoinduced conversion of silver nanospheres to nanoprisms, Science **294**(5548), 1901–1903 (2001)
9.181 R. Jin, Y. Charles Cao, E. Hao, G.S. Metraux, G.C. Schatz, C.A. Mirkin: Controlling anisotropic nanoparticle growth through plasmon excitation, Nature **425**(6957), 487–490 (2003)
9.182 W.-C. Huang, Y.-C. Chen: Photochemical synthesis of polygonal gold nanoparticles, J. Nanopart. Res. **10**(4), 697–702 (2008)
9.183 P.R. Sajanlal, T.S. Sreeprasad, A.K. Samal, T. Pradeep: Anisotropic nanomaterials: Structure, growth, assembly, and functions, Nano Rev. **2**, 5883 (2011)
9.184 Y.-Y. Yu, S.-S. Chang, C.-L. Lee, C.R.C. Wang: Gold nanorods: Electrochemical synthesis and optical properties, J. Phys. Chem. B **101**(34), 6661–6664 (1997)
9.185 C.-J. Huang, P.-H. Chiu, Y.-H. Wang, W.R. Chen, T.H. Meen: Synthesis of the gold nanocubes by elec-

trochemical technique, J. Electrochem. Soc. **153**(8), D129–D133 (2006)
9.186 S.-S. Yu, C.-L. Chang Lee, C.R.C. Wang: Gold nanorods: Electrochemical synthesis and optical properties, J. Phys. Chem. B **101**(34), 6661–6664 (1997)
9.187 N. Tian, Z.-Y. Zhou, S.-G. Sun, L. Cui, B. Ren, Z.-Q. Tian: Electrochemical preparation of platinum nanothorn assemblies with high surface enhanced Raman scattering activity, Chem. Commun. **39**, 4090–4092 (2006)
9.188 C. Gu, T.-Y. Zhang: Electrochemical synthesis of silver polyhedrons and dendritic films with superhydrophobic surfaces, Langmuir **24**(20), 12010–12016 (2008)
9.189 Y. Sun, R. Qiao: Facile tuning of superhydrophobic states with Ag nanoplates, Nano Res. **1**(4), 292–302 (2008)
9.190 C.R. Martin: Nanomaterials: A membrane-based synthetic approach, Science **266**(5193), 1961–1966 (1994)
9.191 B.M.I. van der Zande, M.R. Böhmer, L.G.J. Fokkink, C. Schönenberger: Colloidal dispersions of gold rods: Synthesis and optical properties, Langmuir **16**(2), 451–458 (1999)
9.192 H.-W. Liang, S. Liu, S.-H. Yu: Controlled synthesis of one-dimensional inorganic nanostructures using pre-existing one-dimensional nanostructures as templates, Adv. Mater. **22**(35), 3925–3937 (2010)
9.193 G. Meng, F. Han, X. Zhao, B. Chen, D. Yang, J. Liu, Q. Xu, M. Kong, X. Zhu, Y.J. Jung, Y. Yang, Z. Chu, M. Ye, S. Kar, R. Vajtai, P.M. Ajayan: A general synthetic approach to interconnected nanowire/nanotube and nanotube/nanowire/nanotube heterojunctions with branched topology, Angew. Chem. Int. Ed. **48**(39), 7166–7170 (2009)
9.194 J.C. Hulteen, C.R. Martin: A general template-based method for the preparation of nanomaterials, J. Mater. Chem. **7**(7), 1075–1087 (1997)
9.195 J.P. Camden, J.A. Dieringer, J. Zhao, R.P. Van Duyne: Controlled plasmonic nanostructures for surface-enhanced spectroscopy and sensing, Acc. Chem. Res. **41**(12), 1653–1661 (2008)
9.196 K. Salaita, Y. Wang, C.A. Mirkin: Applications of dip-pen nanolithography, Nat. Nano **2**(3), 145–155 (2007)
9.197 G.M. Wallraff, W.D. Hinsberg: Lithographic imaging techniques for the formation of nanoscopic features, Chem. Rev. **99**(7), 1801–1822 (1999)
9.198 X. Lu, M. Rycenga, S.E. Skrabalak, B. Wiley, Y. Xia: Chemical synthesis of novel plasmonic nanoparticles, Annu. Rev. Phys. Chem. **60**(1), 167–192 (2009)
9.199 P.K. Jain, X. Huang, I.H. El-Sayed, M.A. El-Sayed: Noble metals on the nanoscale: Optical and photothermal properties and some applications in imaging, sensing, biology, and medicine, Acc. Chem. Res. **41**(12), 1578–1586 (2008)
9.200 K.A. Willets, D.R.P. Van: Localized surface plasmon resonance spectroscopy and sensing, Annu. Rev. Phys. Chem. **58**, 267–297 (2007)
9.201 G. Mie: Beiträge zur Optik trüber Medien speziell kolloidaler Metallösungen, Ann. Phys. **25**, 377–445 (1908)
9.202 E. Hutter, J.H. Fendler: Exploitation of localized surface plasmon resonance, Adv. Mater. **16**(19), 1685–1706 (2004)
9.203 U. Kreibig, M. Vollmer: *Optical Properties of Metal Clusters* (Springer, Berlin, Heidelberg 1995)
9.204 S. Link, M.A. El-Sayed: Shape and size dependence of radiative, non-radiative and photothermal properties of gold nanocrystals, Int. Rev. Phys. Chem. **19**(3), 409–453 (2000)
9.205 S. Link, M.A. El-Sayed: Size and temperature dependence of the plasmon absorption of colloidal gold nanoparticles, J. Phys. Chem. B **103**(21), 4212–4217 (1999)
9.206 R. Gans: Über die Form ultramikroskopischer Goldteilchen, Ann. Phys. **342**, 881 (1912)
9.207 J. Nelayah, M. Kociak, O. Stephan, F.J. Garcia de Abajo, M. Tence, L. Henrard, D. Taverna, I. Pastoriza-Santos, L.M. Liz-Marzán, C. Colliex: Mapping surface plasmons on a single metallic nanoparticle, Nat. Phys. **3**(5), 348–353 (2007)
9.208 C. Sönnichsen, S. Geier, N.E. Hecker, G. von Plessen, J. Feldmann, H. Ditlbacher, B. Lamprecht, J.R. Krenn, F.R. Aussenegg, V.Z.H. Chan, J.P. Spatz, M. Möller: Spectroscopy of single metallic nanoparticles using total internal reflection microscopy, Appl. Phys. Lett. **77**(19), 2949–2951 (2000)
9.209 J. Müller, C. Sönnichsen, H. von Poschinger, G. von Plessen, T.A. Klar, J. Feldmann: Electrically controlled light scattering with single metal nanoparticles, Appl. Phys. Lett. **81**(1), 171–173 (2002)
9.210 G. Raschke, S. Kowarik, T. Franzl, C. Sönnichsen, T.A. Klar, J. Feldmann, A. Nichtl, K. Kärzinger: Biomolecular recognition based on single gold nanoparticle light scattering, Nano Lett. **3**(7), 935–938 (2003)
9.211 C. Sönnichsen, A.P. Alivisatos: Gold nanorods as novel nonbleaching plasmon-based orientation sensors for polarized single-particle microscopy, Nano Lett. **5**(2), 301–304 (2004)
9.212 C.L. Baciu, J. Becker, A. Janshoff, C. Sönnichsen: Protein membrane interaction probed by single plasmonic nanoparticles, Nano Lett. **8**(6), 1724–1728 (2008)
9.213 C. Novo, A.M. Funston, P. Mulvaney: Direct observation of chemical reactions on single gold nanocrystals using surface plasmon spectroscopy, Nat. Nano **3**(10), 598–602 (2008)
9.214 M.J. Crow, G. Grant, J.M. Provenzale, A. Wax: Molecular imaging and quantitative measurement of epidermal growth factor receptor expression in live cancer cells using immunolabeled gold nanoparticles, Am. J. Roentgenol. **192**(4), 1021–1028 (2009)

9.215 J. Becker, O. Schubert, C. Sönnichsen: Gold nanoparticle growth monitored in situ using a novel fast optical single-particle spectroscopy method, Nano Lett. **7**(6), 1664–1669 (2007)

9.216 G. Liu, J. Doll, L. Lee: High-speed multispectral imaging of nanoplasmonic array, Opt. Express **13**(21), 8520–8525 (2005)

9.217 G.C. Schatz: Theoretical studies of surface enhanced Raman scattering, Acc. Chem. Res. **17**(10), 370–376 (1984)

9.218 P.R. Sajanlal, C. SubRamaniam, P. Sasanpour, B. Rashidian, T. Pradeep: Electric field enhancement and concomitant Raman spectral effects at the edges of a nanometre-thin gold mesotriangle, J. Mater. Chem. **20**(11), 2108–2113 (2010)

9.219 J. Zhao, A.O. Pinchuk, J.M. McMahon, S. Li, L.K. Ausman, A.L. Atkinson, G.C. Schatz: Methods for describing the electromagnetic properties of silver and gold nanoparticles, Acc. Chem. Res. **41**(12), 1710–1720 (2008)

9.220 M. Fleischmann, P.J. Hendra, A.J. McQuillan: Raman spectra of pyridine adsorbed at a silver electrode, Chem. Phys. Lett. **26**(2), 163–166 (1974)

9.221 M.D. Porter, R.J. Lipert, L.M. Siperko, G. Wang, R. Narayanan: SERS as a bioassay platform: Fundamentals, design, and applications, Chem. Soc. Rev. **37**(5), 1001–1011 (2008)

9.222 M. Haruta, T. Kobayashi, H. Sano, N. Yamada: Novel gold catalysts for the oxidation of carbon monoxide at a temperature far below 0 °C, Chem. Lett. **2**, 405–408 (1987)

9.223 J. Xiao, L. Qi: Surfactant-assisted, shape-controlled synthesis of gold nanocrystals, Nanoscale **3**(4), 1383–1396 (2011)

9.224 O. Vaughan: A golden opportunity, Nat. Nanotechnol. **5**(1), 5–7 (2010)

9.225 G.D. Moon, S. Ko, Y. Xia, U. Jeong: Chemical transformations in ultrathin chalcogenide nanowires, Am. Chem. Soc. Nano **4**(4), 2307–2319 (2010)

9.226 R.D. Robinson, B. Sadtler, D.O. Demchenko, C.K. Erdonmez, L.-W. Wang, A.P. Alivisatos: Spontaneous superlattice formation in nanorods through partial cation exchange, Science **317**(5836), 355–358 (2007)

9.227 L. Dloczik, R. Könenkamp: Nanostructure transfer in semiconductors by ion exchange, Nano Lett. **3**(5), 651–653 (2003)

9.228 A.E. Henkes, R.E. Schaak: Trioctylphosphine: A general phosphorus source for the low-temperature conversion of metals into metal phosphides, Chem. Mater. **19**(17), 4234–4242 (2007)

9.229 C.M. Cobley, Y. Xia: Engineering the properties of metal nanostructures via galvanic replacement reactions, Mater. Sci. Eng. Rep. **70**, 44–62 (2011)

9.230 M. Chen, D.W. Goodman: Catalytically active gold: From nanoparticles to ultrathin films, Acc. Chem. Res. **39**(10), 739–746 (2006)

9.231 M.A. El-Sayed: Some interesting properties of metals confined in time and nanometer space of different shapes, Acc. Chem. Res. **34**(4), 257–264 (2001)

9.232 P.K. Jain, X. Huang, I.H. El-Sayed, M.A. El-Sayed: Noble metals on the nanoscale: Optical and photothermal properties and some applications in imaging, sensing, biology, and medicine, Acc. Chem. Res. **41**(12), 1578–1586 (2008)

9.233 C.A. Mirkin, R.L. Letsinger, R.C. Mucic, J.J. Storhoff: A DNA-based method for rationally assembling nanoparticles into macroscopic materials, Nature **382**(6592), 607–609 (1996)

9.234 L.R. Hirsch, R.J. Stafford, J.A. Bankson, S.R. Sershen, B. Rivera, R.E. Price, J.D. Hazle, N.J. Halas, J.L. West: Nanoshell-mediated near-infrared thermal therapy of tumors under magnetic resonance guidance, Proc. Natl. Acad. Sci. USA **100**(23), 13549–13554 (2003)

9.235 Y.Y. Yu, S.-S. Chang, C.-L. Lee, C.R.C. Wang: Gold nanorods: Electrochemical synthesis and optical properties, J. Phys. Chem. B **101**(34), 6661–6664 (1997)

9.236 S. Eustis, M.A. El-Sayed: Why gold nanoparticles are more precious than pretty gold: Noble metal surface plasmon resonance and its enhancement of the radiative and nonradiative properties of nanocrystals of different shapes, Chem. Soc. Rev. **35**(3), 209–217 (2006)

9.237 B.D. Todd, R.M. Lynden-Bell: Surface and bulk properties of metals modelled with Sutton–Chen potentials, Surf. Sci. **281**(1/2), 191–206 (1993)

9.238 J. Uppenbrink, R.L. Johnston, J.N. Murrell: Modeling transition metal surfaces with empirical potentials, Surf. Sci. **304**(1/2), 223–236 (1994)

9.239 Z.L. Wang, R.P. Gao, B. Nikoobakht, M.A. El-Sayed: Surface reconstruction of the unstable {110} surface in gold nanorods, J. Phys. Chem. B **104**(23), 5417–5420 (2000)

9.240 E. Carbó-Argibay, B. Rodríguez-González, S. Gómez-Graña, A. Guerrero-Martínez, I. Pastoriza-Santos, J. Pérez-Juste, L.M. Liz-Marzán: The crystalline structure of gold nanorods revisited: Evidence for higher-index lateral facets, Angew. Chem. Int. Ed. **49**(49), 9397–9400 (2010)

9.241 N.R. Jana, L. Gearheart, S.O. Obare, C.J. Murphy: Anisotropic chemical reactivity of gold spheroids and nanorods, Langmuir **18**(3), 922–927 (2002)

9.242 N.R. Jana, L. Gearheart, C.J. Murphy: Wet chemical synthesis of high aspect ratio cylindrical gold nanorods, J. Phys. Chem. B **105**(19), 4065–4067 (2001)

9.243 C. Novo, P. Mulvaney: Charge-induced Rayleigh instabilities in small gold rods, Nano Lett. **7**(2), 520–524 (2007)

9.244 M.B. Mohamed, K.Z. Ismail, S. Link, M.A. El-Sayed: Thermal reshaping of gold nanorods in micelles, J. Phys. Chem. B **102**(47), 9370–9374 (1998)

9.245 S.-S. Chang, C.-W. Shih, C.-D. Chen, W.-C. Lai, C.R.C. Wang: The shape transition of gold nanorods, Langmuir **15**(3), 701–709 (1999)

9.246 S. Link, M.A. El-Sayed: Shape and size dependence of radiative, non-radiative and photothermal properties of gold nanocrystals, Int. Rev. Phys. Chem. **19**(3), 409–453 (2000)

9.247 C.-K. Tsung, X. Kou, Q. Shi, J. Zhang, M.H. Yeung, J. Wang, G.D. Stucky: Selective shortening of single-crystalline gold nanorods by mild oxidation, J. Am. Chem. Soc. **128**(16), 5352–5353 (2006)

9.248 T.S. Sreeprasad, A.K. Samal, T. Pradeep: Body- or tip-controlled reactivity of gold nanorods and their conversion to particles through other anisotropic structures, Langmuir **23**(18), 9463–9471 (2007)

9.249 J. Rodriguez-Fernandez, J. Perez-Juste, P. Mulvaney, L.M. Liz-Marzán: Spatially-directed oxidation of gold nanoparticles by Au(III)-CTAB complexes, J. Phys. Chem. B **109**(30), 14257–14261 (2005)

9.250 J. Wang, Y.F. Li, C.Z. Huang: Identification of iodine-induced morphological transformation of gold nanorods, J. Phys. Chem. C **112**(31), 11691–11695 (2008)

9.251 X. Kou, W. Ni, C.-K. Tsung, K. Chan, H.-Q. Lin, G.D. Stucky, J. Wang: Growth of gold bipyramids with improved yield and their curvature-directed oxidation, Small **3**(12), 2103–2113 (2007)

9.252 J.H. Song, F. Kim, D. Kim, P. Yang: Crystal overgrowth on gold nanorods: Tuning the shape, facet, aspect ratio, and composition of the nanorods, Chemistry **11**(3), 910–916 (2005)

9.253 Y. Xiang, X. Wu, D. Liu, Z. Li, W. Chu, L. Feng, K. Zhang, W. Zhou, S. Xie: Gold nanorod-seeded growth of silver nanostructures: From homogeneous coating to anisotropic coating, Langmuir **24**(7), 3465–3470 (2008)

9.254 X. Kou, S. Zhang, Z. Yang, C.-K. Tsung, G.D. Stucky, L. Sun, J. Wang, C. Yan: Glutathione- and cysteine-induced transverse overgrowth on gold nanorods, J. Am. Chem. Soc. **129**(20), 6402–6404 (2007)

9.255 W. Ni, X. Kou, Z. Yang, J. Wang: Tailoring longitudinal surface plasmon wavelengths, scattering and absorption cross sections of gold nanorods, Am. Chem. Soc. Nano **2**(4), 677–686 (2008)

9.256 E. Carbó-Argibay, B. Rodríguez-González, J. Pacifico, I. Pastoriza-Santos, J. Pérez-Juste, L.M. Liz-Marzán: Chemical sharpening of gold nanorods: The rod-to-octahedron transition, Angew. Chem. Int. Ed. **46**(47), 8983–8987 (2007)

9.257 Y. Xiang, X. Wu, D. Liu, X. Jiang, W. Chu, Z. Li, Y. Ma, W. Zhou, S. Xie: Formation of rectangularly shaped Pd/Au bimetallic nanorods: Evidence for competing growth of the Pd shell between the {110} and {100} side facets of Au nanorods, Nano Lett. **6**(10), 2290–2294 (2006)

9.258 S.O. Obare, N.R. Jana, C.J. Murphy: Preparation of polystyrene- and silica-coated gold nanorods and their use as templates for the synthesis of hollow nanotubes, Nano Lett. **1**(11), 601–603 (2001)

9.259 S.E. Skrabalak, J. Chen, L. Au, X. Lu, X. Li, Y. Xia: Gold nanocages for biomedical applications, Adv. Mater. **19**(20), 3177–3184 (2007)

9.260 E. Prodan, C. Radloff, N.J. Halas, P. Nordlander: A hybridization model for the plasmon response of complex nanostructures, Science **302**(5644), 419–422 (2003)

9.261 A. Dursun, D.V. Pugh, S.G. Corcoran: Dealloying of Ag-Au alloys in halide-containing electrolytes, J. Electrochem. Soc. **150**(7), B355–B360 (2003)

9.262 J. Greeley, J.K. Nørskov: Electrochemical dissolution of surface alloys in acids: Thermodynamic trends from first-principles calculations, Electrochim. Acta **52**(19), 5829–5836 (2007)

9.263 J. Chen, J.M. McLellan, A. Siekkinen, Y. Xiong, Z.-Y. Li, Y. Xia: Facile synthesis of goldsilver nanocages with controllable pores on the surface, J. Am. Chem. Soc. **128**(46), 14776–14777 (2006)

9.264 S.E. Skrabalak, J. Chen, Y. Sun, X. Lu, L. Au, C.M. Cobley, Y. Xia: Gold nanocages: Synthesis, properties, and applications, Acc. Chem. Res. **41**(12), 1587–1595 (2008)

9.265 C.M. Cobley, Y. Xia: Engineering the properties of metal nanostructures via galvanic replacement reactions, Mater. Sci. Eng. Rep. **70**(3/6), 44–62 (2010)

9.266 M.H. Kim, X. Lu, B. Wiley, E.P. Lee, Y. Xia: Morphological evolution of single-crystal Ag nanospheres during the galvanic replacement reaction with HAuCl(4), J. Phys. Chem. C **112**(21), 7872–7876 (2008)

9.267 Y. Yin, C. Erdonmez, S. Aloni, A.P. Alivisatos: Faceting of nanocrystals during chemical transformation: From solid silver spheres to hollow gold octahedra, J. Am. Chem. Soc. **128**(39), 12671–12673 (2006)

9.268 Y. Yin, Z.-Y. Li, Z. Zhong, B. Gates, Y. Xia, S. Venkateswaran: Synthesis and characterization of stable aqueous dispersions of silver nanoparticles through the tollens process, J. Mater. Chem. **12**(3), 522–527 (2002)

9.269 A. Pyatenko, M. Yamaguchi, M. Suzuki: Synthesis of spherical silver nanoparticles with controllable sizes in aqueous solutions, J. Phys. Chem. C **111**(22), 7910–7917 (2007)

9.270 Y. Sun, Y. Xia: Alloying and dealloying processes involved in the preparation of metal nanoshells through a galvanic replacement reaction, Nano Lett. **3**(11), 1569–1572 (2003)

9.271 Y. Sun, B. Wiley, Z.-Y. Li, Y. Xia: Synthesis and optical properties of nanorattles and multiple-walled nanoshells/nanotubes made of metal alloys, J. Am. Chem. Soc. **126**(30), 9399–9406 (2004)

9.272 E.C. Cho, P.H.C. Camargo, Y. Xia: Synthesis and characterization of noble-metal nanostructures containing gold nanorods in the center, Adv. Mater. **22**(6), 744–748 (2010)

9.273 P.H.C. Camargo, Y. Xiong, L. Ji, J.M. Zuo, Y. Xia: Facile synthesis of tadpole-like nanostructures consisting of Au heads and Pd tails, J. Am. Chem. Soc. **129**(50), 15452–15453 (2007)

9.274 F. Wetz, K. Soulantica, A. Falqui, M. Respaud, E. Snoeck, B. Chaudret: Hybrid Co–Au nanorods:

Controlling Au nucleation and location, Angew. Chem. **119**(37), 7209–7211 (2007)
9.275 D. Seo, H. Song: Asymmetric hollow nanorod formation through a partial galvanic replacement reaction, J. Am. Chem. Soc. **131**(51), 18210–18211 (2009)
9.276 X. Lu, L. Au, J. McLellan, Z.-Y. Li, M. Marquez, Y. Xia: Fabrication of cubic nanocages and nanoframes by dealloying Au/Ag alloy nanoboxes with an aqueous etchant based on $Fe(NO_3)_3$ or NH_4OH, Nano Lett. **7**(6), 1764–1769 (2007)
9.277 R.C. Newman, K. Sieradzki: Metallic corrosion, Science **263**(5154), 1708–1709 (1994)
9.278 J. Chen, B. Wiley, J. McLellan, Y. Xiong, Z.-Y. Li, Y. Xia: Optical properties of PdAg and PtAg nanoboxes synthesized via galvanic replacement reactions, Nano Lett. **5**(10), 2058–2062 (2005)
9.279 F.-R. Fan, D.-Y. Liu, Y.-F. Wu, S. Duan, Z.-X. Xie, Z.-Y. Jiang, Z.-Q. Tian: Epitaxial growth of heterogeneous metal nanocrystals: From gold nanooctahedra to palladium and silver nanocubes, J. Am. Chem. Soc. **130**(22), 6949–6951 (2008)
9.280 L.-P. Jiang, S. Xu, J.-M. Zhu, J.-R. Zhang, J.-J. Zhu, H.-Y. Chen: Ultrasonic-assisted synthesis of monodisperse single-crystalline silver nanoplates and gold nanorings, Inorg. Chem. **43**(19), 5877–5883 (2004)
9.281 Y. Yin, R.M. Rioux, C.K. Erdonmez, S. Hughes, G.A. Somorjai, A.P. Alivisatos: Formation of hollow nanocrystals through the nanoscale Kirkendall effect, Science **304**(5671), 711–714 (2004)
9.282 H.J. Fan, M. Knez, R. Scholz, K. Nielsch, E. Pippel, D. Hesse, M. Zacharias, U. Gösele: Monocrystalline spinel nanotube fabrication based on the Kirkendall effect, Nat. Mater. **5**(8), 627–631 (2006)
9.283 H.J. Fan, U. Gösele, M. Zacharias: Formation of nanotubes and hollow nanoparticles based on Kirkendall and diffusion processes: A review, Small **3**(10), 1660–1671 (2007)
9.284 A. Cabot, R.K. Smith, Y. Yin, H. Zheng, B.R.M. Reinhard, H. Liu, A.P. Alivisatos: Sulfidation of cadmium at the nanoscale, Am. Chem. Soc. Nano **2**(7), 1452–1458 (2008)
9.285 J.G. Railsback, A.C. Johnston-Peck, J. Wang, J.B. Tracy: Size-dependent nanoscale Kirkendall effect during the oxidation of nickel nanoparticles, Am. Chem. Soc. Nano **4**(4), 1913–1920 (2010)
9.286 C.B. Murray, C.R. Kagan, M.G. Bawendi: Synthesis and characterization of monodisperse nanocrystals and close-packed nanocrystal assemblies, Annu. Rev. Mater. Sci. **30**, 545–610 (2000)
9.287 N. Nishida, E.S. Shibu, H. Yao, T. Oonishi, K. Kimura, T. Pradeep: Fluorescent gold nanoparticle superlattices, Adv. Mater. **20**(24), 4719–4723 (2008)
9.288 E.S. Shibu, K. Kimura, T. Pradeep: Gold nanoparticle superlattices: Novel surface enhanced Raman scattering active substrates, Chem. Mater. **21**(16), 3773–3781 (2009)
9.289 B.L.V. Prasad, C.M. Sorensen, K.J. Klabunde: Gold nanoparticle superlattices, Chem. Soc. Rev. **37**(9), 1871–1883 (2008)
9.290 K. Kimura, T. Pradeep: Functional noble metal nanoparticle superlattices grown at interfaces, Phys. Chem. Chem. Phys. **13**(43), 19214–19225 (2011)
9.291 E.S. Shibu, J. Cyriac, T. Pradeep, J. Chakrabarti: Gold nanoparticle superlattices as functional solids for concomitant conductivity and SERS tuning, Nanoscale **3**(3), 1066–1072 (2011)
9.292 E.S. Shibu, M.A.H. Muhammed, K. Kimura, T. Pradeep: Fluorescent superlattices of gold nanoparticles: A new class of functional materials, Nano Res. **2**(3), 220–234 (2009)
9.293 C.J. Murphy, T.K. Sau, A.M. Gole, C.J. Orendorff, J. Gao, L. Gou, S.E. Hunyadi, T. Li: Anisotropic metal nanoparticles: Synthesis, assembly, and optical applications, J. Phys. Chem. B **109**(29), 13857–13870 (2005)
9.294 P.K. Jain, S. Eustis, M.A. El-Sayed: Plasmon coupling in nanorod assemblies: Optical absorption, discrete dipole approximation simulation, and exciton-coupling model, J. Phys. Chem. B **110**(37), 18243–18253 (2006)
9.295 B. Nikoobakht, Z.L. Wang, M.A. El-Sayed: Self-assembly of gold nanorods, J. Phys. Chem. B **104**(36), 8635–8640 (2000)
9.296 E. Dujardin, S. Mann, L.-B. Hsin, C.R.C. Wang: DNA-driven self-assembly of gold nanorods, Chem. Commun. **14**, 1264–1265 (2001)
9.297 B. Pan, L. Ao, F. Gao, H. Tian, R. He, D. Cui: End-to-end self-assembly and colorimetric characterization of gold nanorods and nanospheres via oligonucleotide hybridization, Nanotechnology **9**, 1776 (2005)
9.298 J.-Y. Chang, H. Wu, H. Chen, Y.-C. Ling, W. Tan: Oriented assembly of Au nanorods using biorecognition system, Chem. Commun. **8**, 1092–1094 (2005)
9.299 C. Wang, Y. Chen, T. Wang, Z. Ma, Z. Su: Biorecognition-driven self-assembly of gold nanorods: A rapid and sensitive approach toward antibody sensing, Chem. Mater. **19**(24), 5809–5811 (2007)
9.300 K.K. Caswell, J.N. Wilson, U.H.F. Bunz, C.J. Murphy: Preferential end-to-end assembly of gold nanorods by biotin-streptavidin connectors, J. Am. Chem. Soc. **125**(46), 13914–13915 (2003)
9.301 Y. Wang, Y.F. Li, J. Wang, Y. Sang, C.Z. Huang: End-to-end assembly of gold nanorods by means of oligonucleotide-mercury(II) molecular recognition, Chem. Commun. **46**(8), 1332–1334 (2010)
9.302 S.T.S. Joseph, B.I. Ipe, P. Pramod, K.G. Thomas: Gold nanorods to nanochains: Mechanistic investigations on their longitudinal assembly using α,ω-alkanedithiols and interplasmon coupling, J. Phys. Chem. B **110**(1), 150–157 (2005)
9.303 T.S. Sreeprasad, T. Pradeep: Reversible assembly and disassembly of gold nanorods induced by EDTA and

its application in SERS tuning, Langmuir **27**(7), 3381–3390 (2011)
9.304 K.G. Thomas, S. Barazzouk, B.I. Ipe, S.T.S. Joseph, P.V. Kamat: Uniaxial plasmon coupling through longitudinal self-assembly of gold nanorods, J. Phys. Chem. B **108**(35), 13066–13068 (2004)
9.305 W. Ni, R.A. Mosquera, J. Pérez-Juste, L.M. Liz-Marzán: Evidence for hydrogen-bonding-directed assembly of gold nanorods in aqueous solution, J. Phys. Chem. Lett. **1**(8), 1181–1185 (2010)
9.306 P.K. Sudeep, S.T.S. Joseph, K.G. Thomas: Selective detection of cysteine and glutathione using gold nanorods, J. Am. Chem. Soc. **127**(18), 6516–6517 (2005)
9.307 S. Zhang, X. Kou, Z. Yang, Q. Shi, G.D. Stucky, L. Sun, J. Wang, C. Yan: Nanonecklaces assembled from gold rods, spheres, and bipyramids, Chem. Commun. **18**, 1816–1818 (2007)
9.308 G. Kawamura, Y. Yang, M. Nogami: End-to-end assembly of CTAB-stabilized gold nanorods by citrate anions, J. Phys. Chem. C **112**(29), 10632–10636 (2008)
9.309 C.J. Orendorff, P.L. Hankins, C.J. Murphy: pH-triggered assembly of gold nanorods, Langmuir **21**(5), 2022–2026 (2005)
9.310 T.S. Sreeprasad, A.K. Samal, T. Pradeep: One-, two-, and three-dimensional superstructures of gold nanorods induced by dimercaptosuccinic acid, Langmuir **24**(9), 4589–4599 (2008)
9.311 K. Mitamura, T. Imae, N. Saito, O. Takai: Fabrication and self-assembly of hydrophobic gold nanorods, J. Phys. Chem. B **111**(30), 8891–8898 (2007)
9.312 H. Nakashima, K. Furukawa, Y. Kashimura, K. Torimitsu: Self-assembly of gold nanorods induced by intermolecular interactions of surface-anchored lipids, Langmuir **24**(11), 5654–5658 (2008)
9.313 D.A. Walker, V.K. Gupta: Reversible end-to-end assembly of gold nanorods using a disulfide-modified polypeptide, Nanotechnology **43**, 435603 (2008)
9.314 Y.-T. Chan, S. Li, C.N. Moorefield, P. Wang, C.D. Shreiner, G.R. Newkome: Self-assembly, disassembly, and reassembly of gold nanorods mediated by bis(terpyridine)–metal connectivity, Chemistry **16**(14), 4164–4168 (2010)
9.315 M.A. Correa-Duarte, J. Pérez-Juste, A. Sánchez-Iglesias, M. Giersig, L.M. Liz-Marzán: Aligning Au nanorods by using carbon nanotubes as templates, Angew. Chem. Int. Ed. **44**(28), 4375–4378 (2005)
9.316 M.A. Correa-Duarte, L.M. Liz-Marzán: Carbon nanotubes as templates for one-dimensional nanoparticle assemblies, J. Mater. Chem. **16**(1), 22–25 (2006)
9.317 B.P. Khanal, E.R. Zubarev: Rings of nanorods, Angew. Chem. Int. Ed. **46**(13), 2195–2198 (2007)
9.318 V.R.R. Kumar, A.K. Samal, T.S. Sreeprasad, T. Pradeep: Gold nanorods grown on microgels leading to hexagonal nanostructures, Langmuir **23**(17), 8667–8669 (2007)
9.319 D. Fava, Z. Nie, M.A. Winnik, E. Kumacheva: Evolution of self-assembled structures of polymer-terminated gold nanorods in selective solvents, Adv. Mater. **20**(22), 4318–4322 (2008)
9.320 C. Wang, Y. Chen, T. Wang, Z. Ma, Z. Su: Monodispersed gold nanorod-embedded silica particles as novel Raman labels for biosensing, Adv. Funct. Mater. **18**(2), 355–361 (2008)
9.321 A.J. Mieszawska, G.W. Slawinski, F.P. Zamborini: Directing the growth of highly aligned gold nanorods through a surface chemical amidation reaction, J. Am. Chem. Soc. **128**(17), 5622–5623 (2006)
9.322 K. Honda, Y. Niidome, N. Nakashima, H. Kawazumi, S. Yamada: End-to-end assemblies of gold nanorods adsorbed on a glass substrate modified with polyanion polymers, Chem. Lett. **35**(8), 854–855 (2006)
9.323 X. Zhang, T. Imae: Perpendicular superlattice growth of hydrophobic gold nanorods on patterned silicon substrates via evaporation-induced self-assembling, J. Phys. Chem. C **113**(15), 5947–5951 (2009)
9.324 M.H. Zareie, X. Xu, M.B. Cortie: In situ organization of gold nanorods on mixed self-assembled-monolayer substrates, Small **3**(1), 139–145 (2007)
9.325 Z. Nie, D. Fava, M. Rubinstein, E. Kumacheva: Supramolecular assembly of gold nanorods end-terminated with polymerpom-poms: Effect of pom-pom structure on the association modes, J. Am. Chem. Soc. **130**(11), 3683–3689 (2008)
9.326 Z. Nie, D. Fava, E. Kumacheva, S. Zou, G.C. Walker, M. Rubinstein: Self-assembly of metal-polymer analogues of amphiphilic triblock copolymers, Nat. Mater. **6**(8), 609–614 (2007)
9.327 S. Yun, Y.-K. Park, S.K. Kim, S. Park: Linker-molecule-free gold nanorod layer-by-layer films for surface-enhanced Raman scattering, Anal. Chem. **79**(22), 8584–8589 (2007)
9.328 H. Nakashima, K. Furukawa, Y. Kashimura, K. Torimitsu: Anisotropic assembly of gold nanorods assisted by selective ion recognition of surface-anchored crown ether derivatives, Chem. Commun. **10**, 1080–1082 (2007)
9.329 M. Grzelczak, B. Rodríguez-González, J. Pérez-Juste, L.M. Liz-Marzán: Quasi-epitaxial growth of Ni nanoshells on Au nanorods, Adv. Mater. **19**(17), 2262–2266 (2007)
9.330 N.R. Jana, L. Gearheart, C.J. Murphy: Wet chemical synthesis of silver nanorods and nanowires of controllable aspect ratio, Chem. Commun. **7**, 617–618 (2001)
9.331 A. Tao, F. Kim, C. Hess, J. Goldberger, R. He, Y. Sun, Y. Xia, P. Yang: Langmuir–Blodgett silver nanowire monolayers for molecular sensing using surface-enhanced Raman spectroscopy, Nano Lett. **3**(9), 1229–1233 (2003)
9.332 M. Rycenga, J. McLellan, Y. Xia: Controlling the assembly of silver nanocubes through selective functionalization of their faces, Adv. Mater. **20**(12), 2416–2420 (2008)

9.333 A. Tao, P. Sinsermsuksakul, P. Yang: Tunable plasmonic lattices of silver nanocrystals, Nat. Nano **2**(7), 435–440 (2007)

9.334 Y. Bae, N.H. Kim, M. Kim, K.Y. Lee, S.W. Han: Anisotropic assembly of Ag nanoprisms, J. Am. Chem. Soc. **130**(16), 5432–5433 (2008)

9.335 B.I. Ipe, S. Mahima, K.G. Thomas: Light-induced modulation of self-assembly on spiropyran-capped gold nanoparticles: A potential system for the controlled release of amino acid derivatives, J. Am. Chem. Soc. **125**(24), 7174–7175 (2003)

9.336 H. Imahori, M. Arimura, T. Hanada, Y. Nishimura, I. Yamazaki, Y. Sakata, S. Fukuzumi: Photoactive three-dimensional monolayers: Porphyrin-alkanethiolate-stabilized gold clusters, J. Am. Chem. Soc. **123**(2), 335–336 (2000)

9.337 H. Fujihara, H. Nakai: Fullerenethiolate-functionalized gold nanoparticles: A new class of surface-confined metal-C_{60} nanocomposites, Langmuir **17**(21), 6393–6395 (2001)

9.338 T. Wang, D. Zhang, W. Xu, J. Yang, R. Han, D. Zhu: Preparation, characterization, and photophysical properties of alkanethiols with pyrene units-capped gold nanoparticles: Unusual fluorescence enhancement for the aged solutions of these gold nanoparticles, Langmuir **18**(5), 1840–1848 (2002)

9.339 J. Zhang, J.K. Whitesell, M.A. Fox: Photoreactivity of self-assembled monolayers of azobenzene or stilbene derivatives capped on colloidal gold clusters, Chem. Mater. **13**(7), 2323–2331 (2001)

9.340 T. Gu, T. Ye, J.D. Simon, J.K. Whitesell, M.A. Fox: Subpicosecond transient dynamics in gold nanoparticles encapsulated by a fluorophore-terminated monolayer, J. Phys. Chem. B **107**(8), 1765–1771 (2003)

9.341 R. BalasubRamanian, B. Kim, S.L. Tripp, X. Wang, M. Lieberman, A. Wei: Dispersion and stability studies of resorcinarene-encapsulated gold nanoparticles, Langmuir **18**(9), 3676–3681 (2002)

9.342 A. Manna, P.-L. Chen, H. Akiyama, T.-X. Wei, K. Tamada, W. Knoll: Optimized photoisomerization on gold nanoparticles capped by unsymmetrical azobenzene disulfides, Chem. Mater. **15**(1), 20–28 (2002)

9.343 K.G. Thomas, P.V. Kamat: Making gold nanoparticles glow: Enhanced emission from a surface-bound fluoroprobe, J. Am. Chem. Soc. **122**(11), 2655–2656 (2000)

9.344 L.M. Liz-Marzán, M. Giersig, P. Mulvaney: Synthesis of nanosized gold-silica core-shell particles, Langmuir **12**(18), 4329–4335 (1996)

9.345 R. Davies, G.A. Schurr, P. Meenan, R.D. Nelson, H.E. Bergna, C.A.S. Brevett, R.H. Goldbaum: Engineered particle surfaces, Adv. Mater. **10**(15), 1264–1270 (1998)

9.346 L.M. Liz-Marzán, M. Giersig, P. Mulvaney: Homogeneous silica coating of vitreophobic colloids, Chem. Commun. **6**, 731–732 (1996)

9.347 I. Pastoriza-Santos, D.S. Koktysh, A.A. Mamedov, M. Giersig, N.A. Kotov, L.M. Liz-Marzán: One-pot synthesis of Ag@TiO_2 core-shell nanoparticles and their layer-by-layer assembly, Langmuir **16**(6), 2731–2735 (2000)

9.348 R.T. Tom, A.S. Nair, N. Singh, M. Aslam, C.L. Nagendra, R. Philip, K. Vijayamohanan, T. Pradeep: Freely dispersible Au@TiO_2, Au@ZrO_2, Ag@TiO_2, and Ag@ZrO_2 core-shell nanoparticles: One-step synthesis, characterization, spectroscopy, and optical limiting properties, Langmuir **19**(8), 3439–3445 (2003)

9.349 X. Teng, D. Black, N.J. Watkins, Y. Gao, H. Yang: Platinum-maghemite core-shell nanoparticles using a sequential synthesis, Nano Lett. **3**(2), 261–264 (2003)

9.350 P. Mulvaney, L.M. Liz-Marzán, M. Giersig, T. Ung: Silica encapsulation of quantum dots and metal clusters, J. Mater. Chem. **10**(6), 1259–1270 (2000)

9.351 K.S. Mayya, D.I. Gittins, F. Caruso: Gold-titania core-shell nanoparticles by polyelectrolyte complexation with a titania precursor, Chem. Mater. **13**(11), 3833–3836 (2001)

9.352 A.S. Nair, T. Pradeep, I. MacLaren: An investigation of the structure of stearate monolayers on Au@ZrO_2 and Ag@ZrO_2 core-shell nanoparticles, J. Mater. Chem. **14**(5), 857–862 (2004)

9.353 M.M.Y. Chen, A. Katz: Synthesis and characterization of gold-silica nanoparticles incorporating a mercaptosilane core-shell interface, Langmuir **18**(22), 8566–8572 (2002)

9.354 T. Yonezawa, N. Toshima: Polymer- and micelle-protected gold/platinum bimetallic systems. Preparation, application to catalysis for visible-light-induced hydrogen evolution, and analysis of formation process with optical methods, J. Mol. Catal. **83**(1-2), 167–181 (1993)

9.355 G. Schmid, A. Lehnert, J.-O. Malm, J.-O. Bovin: Ligand-stabilized bimetallic colloids identified by HRTEM and EDX, Angew. Chem. Int. Ed. **30**(7), 874–876 (1991)

9.356 P. Mulvaney, M. Giersig, A. Henglein: Electrochemistry of multilayer colloids: Preparation and absorption spectrum of gold-coated silver particles, J. Phys. Chem. **97**(27), 7061–7064 (1993)

9.357 S. Link, C. Burda, Z. Wang, M. El-Sayed: Electron dynamics in gold and gold-silver alloy nanoparticles: The influence of a nonequilibrium electron distribution and the size dependence of the electron? Phonon relaxation, J. Chem. Phys. **111**(3), 1255 (1999)

9.358 Y. Kim, R.C. Johnson, J. Li, J.T. Hupp, G.C. Schatz: Synthesis, linear extinction, and preliminary resonant hyper-Rayleigh scattering studies of gold-core/silver-shell nanoparticles: Comparisons of theory and experiment, Chem. Phys. Lett. **352**(5/6), 421–428 (2002)

9.359 N.S. Sobal, M. Hilgendorff, H. Möhwald, M. Giersig, M. Spasova, T. Radetic, M. Farle: Synthesis and

structure of colloidal bimetallic nanocrystals: The non-alloying system Ag/Co, Nano Lett. **2**(6), 621–624 (2002)
9.360 H. Cai, N. Zhu, Y. Jiang, P. He, Y. Fang: Cu@Au alloy nanoparticle as oligonucleotides labels for electrochemical stripping detection of DNA hybridization, Biosens. Bioelectron. **18**(11), 1311–1319 (2003)
9.361 C.-L. Huang, E. Matijevic: Coating of uniform inorganic particles with polymers: III. Polypyrrole on different metal oxides, J. Mater. Res. **10**(05), 1327–1336 (1995)
9.362 M. Sastry, A. Swami, S. Mandal, P.R. Selvakannan: New approaches to the synthesis of anisotropic, core-shell and hollow metal nanostructures, J. Mater. Chem. **15**(31), 3161–3174 (2005)
9.363 Y. Yang, J. Shi, H. Chen, S. Dai, Y. Liu: Enhanced off-resonance optical nonlinearities of Au@CdS core-shell nanoparticles embedded in $BaTiO_3$ thin films, Chem. Phys. Lett. **370**(1-2), 1–6 (2003)
9.364 S.M. Marinakos, J.P. Novak, L.C. Brousseau, A.B. House, E.M. Edeki, J.C. Feldhaus, D.L. Feldheim: Gold particles as templates for the synthesis of hollow polymer capsules. Control of capsule dimensions and guest encapsulation, J. Am. Chem. Soc. **121**(37), 8518–8522 (1999)
9.365 I. Mekis, D.V. Talapin, A. Kornowski, M. Haase, H. Weller: One-pot synthesis of highly luminescent CdSe/CdS core-shell nanocrystals via organometallic and "greener" chemical approaches, J. Phys. Chem. B **107**(30), 7454–7462 (2003)
9.366 S.M. Marinakos, L.C. Brousseau, A. Jones, D.L. Feldheim: Template synthesis of one-dimensional Au, Au-poly(pyrrole), and poly(pyrrole) nanoparticle arrays, Chem. Mater. **10**(5), 1214–1219 (1998)
9.367 S.M. Marinakos, D.A. Shultz, D.L. Feldheim: Gold nanoparticles as templates for the synthesis of hollow nanometer-sized conductive polymer capsules, Adv. Mater. **11**(1), 34–37 (1999)
9.368 R. Ottewill, A. Schofield, J. Waters, N. Williams: Preparation of core-shell polymer colloid particles by encapsulation, Colloid Polym. Sci. **275**(3), 274–283 (1997)
9.369 L. Quaroni, G. Chumanov: Preparation of polymer-coated functionalized silver nanoparticles, J. Am. Chem. Soc. **121**(45), 10642–10643 (1999)
9.370 P.K. Jain, X. Huang, I.H. El-Sayed, M.A. El-Sayed: Noble metals on the nanoscale: Optical and photothermal properties and some applications in imaging, sensing, biology, and medicine, Acc. Chem. Res. **41**(12), 1578–1586 (2008)
9.371 R.A. Sperling, G.P. Rivera, F. Zhang, M. Zanella, W.J. Parak: Biological applications of gold nanoparticles, Chem. Soc. Rev. **37**(9), 1896–1908 (2008)
9.372 H. Wang, T.B. Huff, D.A. Zweifel, W. He, P.S. Low, A. Wei, J.-X. Cheng: In vitro and in vivo two-photon luminescence imaging of single gold nanorods, Proc. Natl. Acad. Sci. USA **102**(44), 15752–15756 (2005)
9.373 R. Philip, G.R. Kumar, N. Sandhyarani, T. Pradeep: Picosecond optical nonlinearity in monolayer-protected gold, silver, and gold-silver alloy nanoclusters, Phys. Rev. B **62**(19), 13160–13166 (2000)
9.374 A. Campion, P. Kambhampati: Surface-enhanced Raman scattering, Chem. Soc. Rev. **27**(4), 241–250 (1998)
9.375 M.J. Banholzer, J.E. Millstone, L. Qin, C.A. Mirkin: Rationally designed nanostructures for surface-enhanced Raman spectroscopy, Chem. Soc. Rev. **37**(5), 885–897 (2008)
9.376 J.F. Li, Y.F. Huang, Y. Ding, Z.L. Yang, S.B. Li, X.S. Zhou, F.R. Fan, W. Zhang, Z.Y. Zhou, D.Y. Wu, B. Ren, Z.L. Wang, Z.Q. Tian: Shell-isolated nanoparticle-enhanced Raman spectroscopy, Nature **464**(7287), 392–395 (2010)
9.377 K.M. Mayer, J.H. Hafner: Localized surface plasmon resonance sensors, Chem. Rev. **111**(6), 3828–3857 (2011)
9.378 G. Aragay, J. Pons, A. Merkoçi: Recent trends in macro-, micro-, and nanomaterial-based tools and strategies for heavy-metal detection, Chem. Rev. **111**(5), 3433–3458 (2011)
9.379 M. Rex, F.E. Hernandez, A.D. Campiglia: Pushing the limits of mercury sensors with gold nanorods, Anal. Chem. **78**(2), 445–451 (2005)
9.380 K.P. Lisha, Anshup, T. Pradeep: Towards a practical solution for removing inorganic mercury from drinking water using gold nanoparticles, Gold Bull. **42**(2), 144–152 (2009)
9.381 S. Eustis, M.A. El-Sayed: Why gold nanoparticles are more precious than pretty gold: Noble metal surface plasmon resonance and its enhancement of the radiative and nonradiative properties of nanocrystals of different shapes, Chem. Soc. Rev. **35**(3), 209–217 (2006)
9.382 R. Narayanan, M.A. El-Sayed: Catalysis with transition metal nanoparticles in colloidal solution: Nanoparticle shape dependence and stability, J. Phys. Chem. B **109**(26), 12663–12676 (2005)
9.383 H. Yu, X. Wang, H. Sun, M. Huo: Photocatalytic degradation of malathion in aqueous solution using an Au-Pd-TiO_2 nanotube film, J. Hazard. Mater. **184**(1-3), 753–758 (2010)
9.384 F.H. Rhodes, J.T. Carty: The corrosion of certain metals by carbon tetrachloride, Ind. Eng. Chem. **17**(9), 909–911 (1925)
9.385 T. Boronina, K.J. Klabunde, G. Sergeev: Destruction of organohalides in water using metal particles: Carbon tetrachloride/water reactions with magnesium, tin, and zinc, Environ. Sci. Technol. **29**(6), 1511–1517 (1995)
9.386 A. Henglein: Colloidal silver nanoparticles: Photochemical preparation and interaction with O_2, CCl_4, and some metal ions, Chem. Mater. **10**(1), 444–450 (1998)

9.387 N. Sandhyarani, T. Pradeep: Oxidation of alkanethiol monolayers on gold cluster surfaces, Chem. Phys. Lett. **338**(1), 33–36 (2001)

9.388 A. Henglein, D. Meisel: Spectrophotometric observations of the adsorption of organosulfur compounds on colloidal silver nanoparticles, J. Phys. Chem. B **102**(43), 8364–8366 (1998)

9.389 A.S. Nair, T. Pradeep: Halocarbon mineralization and catalytic destruction by metal nanoparticles, Curr. Sci. **84**, 1560–1564 (2003)

9.390 A. Sreekumaran Nair, R.T. Tom, T. Pradeep: Detection and extraction of endosulfan by metal nanoparticles, J. Environ. Mon. **5**(2), 363–365 (2003)

9.391 A.S. Nair, T. Pradeep: Extraction of chlorpyrifos and malathion from water by metal nanoparticles, J. Nanosci. Nanotechnol. **7**(6), 1871–1877 (2007)

9.392 T. Pradeep, A.S. Nair: A method of preparing purified water from water containing pesticides (chlorpyrifos and malatheon) and purified water prepared by the said method, Indian Patent Ser., Vol. 200767 (2006)

9.393 A.S. Nair, R.T. Tom, T. Pradeep: Detection and extraction of endosulfan by metal nanoparticles, J. Environ. Mon. **5**(2), 363–365 (2003)

9.394 D.L. Illman: Water analysis in the developing world, Anal. Chem. **78**(15), 5266–5272 (2006)

9.395 S.D. Richardson: Water analysis: Emerging contaminants and current issues, Anal. Chem. **79**(12), 4295–4324 (2007)

9.396 S. Andreescu, J.-L. Marty: Twenty years research in cholinesterase biosensors: From basic research to practical applications, Biomol. Eng. **23**(1), 1–15 (2006)

9.397 X.J. Huang, Y.K. Choi: Chemical sensors based on nanostructured materials, Sens. Actuators B **122**(2), 659–671 (2007)

9.398 D.J. Lewis, T.M. Day, J.V. MacPherson, Z. Pikramenou: Luminescent nanobeads: Attachment of surface reactive Eu(III) complexes to gold nanoparticles, Chem. Commun. **13**, 1433–1435 (2006)

9.399 S.S.R. Dasary, U.S. Rai, H. Yu, Y. Anjaneyulu, M. Dubey, P.C. Ray: Gold nanoparticle based surface enhanced fluorescence for detection of organophosphorus agents, Chem. Phys. Lett. **460**(1-3), 187–190 (2008)

9.400 J.D.S. Newman, J.M. Roberts, G.J. Blanchard: Optical organophosphate sensor based upon gold nanoparticle functionalized fumed silica gel, Anal. Chem. **79**(9), 3448–3454 (2007)

9.401 J.D.S. Newman, J.M. Roberts, G.J. Blanchard: Optical organophosphate/phosphonate sensor based upon gold nanoparticle functionalized quartz, Anal. Chim. Acta **602**(1), 101–107 (2007)

9.402 S.-Q. Hu, J.-W. Xie, Q.-H. Xu, K.-T. Rong, G.-L. Shen, R.-Q. Yu: A label-free electrochemical immunosensor based on gold nanoparticles for detection of paraoxon, Talanta **61**(6), 769–777 (2003)

9.403 D.P. Dumas, H.D. Durst, W.G. Landis, F.M. Raushel, J.R. Wild: Inactivation of organophosphorus nerve agents by the phosphotriesterase from pseudomonas diminuta, Arch. Biochem. Biophys. **277**(1), 155–159 (1990)

9.404 V. Pavlov, Y. Xiao, I. Willner: Inhibition of the acetycholine esterase-stimulated growth of Au nanoparticles: Nanotechnology-based sensing of nerve gases, Nano Lett. **5**(4), 649–653 (2005)

9.405 D. Du, J. Ding, Y. Tao, X. Chen: Application of chemisorption/desorption process of thiocholine for pesticide detection based on acetylcholinesterase biosensor, Sens. Actuators B **134**(2), 908–912 (2008)

9.406 J.M. Pingarrón, P. Yáñez-Sedeño, A. González-Cortés: Gold nanoparticle-based electrochemical biosensors, Electrochim. Acta **53**(19), 5848–5866 (2008)

9.407 K.A. Hassal: *The Biochemistry and Use of Pesticides* (Wiley, New York 1990)

9.408 T.J. Lin, K.T. Huang, C.Y. Liu: Determination of organophosphorous pesticides by a novel biosensor based on localized surface plasmon resonance, Biosens. Bioelectron. **22**(4), 513–518 (2006)

9.409 Rajan, S. Chand, B.D. Gupta: Surface plasmon resonance based fiber-optic sensor for the detection of pesticide, Sens. Actuators B **123**(2), 661–666 (2007)

9.410 X. Sun, K. Xia, B. Liu: Design of fluorescent self-assembled multilayers and interfacial sensing for organophosphorus pesticides, Talanta **76**(4), 747–751 (2008)

9.411 K.P. Lisha, Anshup, T. Pradeep: Enhanced visual detection of pesticides using gold nanoparticles, J. Environ. Sci. Health B **44**(7), 697–705 (2009)

9.412 C. Burns, W.U. Spendel, S. Puckett, G.E. Pacey: Solution ionic strength effect on gold nanoparticle solution color transition, Talanta **69**(4), 873–876 (2006)

9.413 S.T. Dubas, V. Pimpan: Humic acid assisted synthesis of silver nanoparticles and its application to herbicide detection, Mater. Lett. **62**(17/18), 2661–2663 (2008)

9.414 K. Kneipp, H. Kneipp, I. Itzkan, R.R. Dasari, M.S. Feld: Ultrasensitive chemical analysis by Raman spectroscopy, Chem. Rev. **99**(10), 2957–2976 (1999)

9.415 M. Moskovits: Surface-enhanced spectroscopy, Rev. Mod. Phys. **57**(3), 783–826 (1985)

9.416 K. Kneipp, Y. Wang, H. Kneipp, L.T. Perelman, I. Itzkan, R.R. Dasari, M.S. Feld: Single molecule detection using surface-enhanced Raman scattering (SERS), Phys. Rev. Lett. **78**(9), 1667–1670 (1997)

9.417 S. Nie, S.R. Emory: Probing single molecules and single nanoparticles by surface-enhanced Raman scattering, Science **275**(5303), 1102–1106 (1997)

9.418 V.S. Tiwari, T. Oleg, G.K. Darbha, W. Hardy, J.P. Singh, P.C. Ray: Non-resonance SERS effects of silver colloids with different shapes, Chem. Phys. Lett. **446**(1–3), 77–82 (2007)

9.419 P.R. Sajanlal, T. Pradeep: Electric-field-assisted growth of highly uniform and oriented gold nanotriangles on conducting glass substrates, Adv. Mater. **20**(5), 980–983 (2008)

9.420 A.J. Bonham, G. Braun, I. Pavel, M. Moskovits, N.O. Reich: Detection of sequence-specific protein-DNA interactions via surface enhanced resonance Raman scattering, J. Am. Chem. Soc. **129**(47), 14572–14573 (2007)

9.421 R.A. Alvarez-Puebla, J.D.S. dos Santos, R.F. Aroca: Sers detection of environmental pollutants in humic acid-gold nanoparticle composite materials, Analyst **132**(12), 1210–1214 (2007)

9.422 A. Henglein: Physicochemical properties of small metal particles in solution: "Microelectrode" Reactions, chemisorption, composite metal particles, and the atom-to-metal transition, J. Phys. Chem. **97**(21), 5457–5471 (1993)

9.423 A. Henglein: Non-metallic silver clusters in aqueous solution: Stabilization and chemical reactions, Chem. Phys. Lett. **154**(5), 473–476 (1989)

9.424 A. Henglein, P. Mulvaney, T. Linnert, A. Holzwarth: Surface chemistry of colloidal silver: Reduction of adsorbed cadmium(2+) ions and accompanying optical effects, J. Phys. Chem. **96**(6), 2411–2414 (1992)

9.425 Y. Liu, C.Y. Liu, L.B. Chen, Z.Y. Zhang: Adsorption of cations onto the surfaces of silver nanoparticles, J. Colloid Interface Sci. **257**(2), 188–194 (2003)

9.426 C. Namasivayam, K. Periasamy: Bicarbonate-treated peanut hull carbon for mercury(II) removal from aqueous solution, Water Res. **27**(11), 1663–1668 (1993)

9.427 R.R. Navarro, K. Sumi, N. Fujii, M. Matsumura: Mercury removal from wastewater using porous cellulose carrier modified with polyethyleneimine, Water Res. **30**(10), 2488–2494 (1996)

9.428 V. Smuleac, D.A. Butterfield, S.K. Sikdar, R.S. Varma, D. Bhattacharyya: Polythiol-functionalized alumina membranes for mercury capture, J. Membr. Sci. **251**(1/2), 169–178 (2005)

9.429 S.M. Evangelista, E. DeOliveira, G.R. Castro, L.F. Zara, A.G.S. Prado: Hexagonal mesoporous silica modified with 2-mercaptothiazoline for removing mercury from water solution, Surf. Sci. **601**(10), 2194–2202 (2007)

9.430 T.S. Sreeprasad, S.M. Maliyekkal, K.P. Lisha, T. Pradeep: Reduced graphene oxide"metal/metal oxide composites: Facile synthesis and application in water purification, J. Hazard. Mater. **186**(1), 921–931 (2011)

9.431 X.-Q. Li, W.-X. Zhang: Iron nanoparticles: The core-shell structure and unique properties for Ni(II) sequestration, Langmuir **22**(10), 4638–4642 (2006)

9.432 T. Morris, H. Copeland, E. McLinden, S. Wilson, G. Szulczewski: The effects of mercury adsorption on the optical response of size-selected gold and silver nanoparticles, Langmuir **18**(20), 7261–7264 (2002)

9.433 L. Katsikas, M. Gutiérrez, A. Henglein: Bimetallic colloids: Silver and mercury, J. Phys. Chem. **100**(27), 11203–11206 (1996)

9.434 J.A. Creighton, D.G. Eadon: Ultraviolet-visible absorption spectra of the colloidal metallic elements, J. Chem. Soc. Faraday Trans. **87**(24), 3881–3891 (1991)

9.435 A. Henglein, C. Brancewicz: Absorption spectra and reactions of colloidal bimetallic nanoparticles containing mercury, Chem. Mater. **9**(10), 2164–2167 (1997)

9.436 L. Li, Y.J. Zhu: High chemical reactivity of silver nanoparticles toward hydrochloric acid, J. Colloid Interface Sci. **303**(2), 415–418 (2006)

9.437 J. Chen, B. Wiley, J. McLellan, Y. Xiong, Z.Y. Li, Y. Xia: Optical properties of Pd-Ag and Pt-Ag nanoboxes synthesized via galvanic replacement reactions, Nano Lett. **5**(10), 2058–2062 (2005)

9.438 M.S. Bootharaju, T. Pradeep: Uptake of toxic metal ions from water by naked and monolayer protected silver nanoparticles: An x-ray photoelectron spectroscopic investigation, J. Phys. Chem. C **114**(18), 8328–8336 (2010)

9.439 E. Sumesh, M.S. Bootharaju, Anshup, T. Pradeep: A practical silver nanoparticle-based adsorbent for the removal of Hg^{2+} from water, J. Hazard. Mater. **189**(1/2), 450–457 (2011)

9.440 M.S. Bootharaju, T. Pradeep: Investigation into the reactivity of unsupported and supported Ag_7 and Ag_8 clusters with toxic metal ions, Langmuir **27**(13), 8134–8143 (2011)

9.441 E.M. Nolan, S.J. Lippard: Tools and tactics for the optical detection of mercuric ion, Chem. Rev. **108**(9), 3443–3480 (2008)

9.442 D. Melamed: Monitoring arsenic in the environment: A review of science and technologies with the potential for field measurements, Anal. Chim. Acta **532**(1), 1–13 (2005)

9.443 M.d.G.A. Korn, J.B. de Andrade, D.S. de Jesus, V.A. Lemos, M.L.S.F. Bandeira, W.N.L. dos Santos, M.A. Bezerra, F.A.C. Amorim, A.S. Souza, S.L.C. Ferreira: Separation and preconcentration procedures for the determination of lead using spectrometric techniques: A review, Talanta **69**(1), 16–24 (2006)

9.444 P.A. Mosier-Boss, S.H. Lieberman: Detection of anions by normal Raman spectroscopy and surface-enhanced Raman spectroscopy of cationic-coated substrates, Appl. Spectrosc. **57**(9), 1129–1137 (2003)

9.445 J.J. Storhoff, A.A. Lazarides, R.C. Mucic, C.A. Mirkin, R.L. Letsinger, G.C. Schatz: What controls the optical properties of DNA-linked gold nanoparticle assemblies?, J. Am. Chem. Soc. **122**(19), 4640–4650 (2000)

9.446 Y. Lu, J. Liu: Smart nanomaterials inspired by biology: Dynamic assembly of error-free nanomaterials in response to multiple chemical and biological stimuli, Acc. Chem. Res. **40**(5), 315–323 (2007)

9.447 A. Ono, H. Togashi: Highly selective oligonucleotide-based sensor for mercury(II) in aqueous solutions, Angew. Chem. Int. Ed. **43**(33), 4300–4302 (2004)

9.448 J.-S. Lee, M.S. Han, C.A. Mirkin: Colorimetric detection of mercuric ion (Hg^{2+}) in aqueous media using DNA-functionalized gold nanoparticles, Angew. Chem. Int. Ed. **46**(22), 4093–4096 (2007)

9.449 J.-S. Lee, C.A. Mirkin: Chip-based scanometric detection of mercuric ion using DNA-functionalized gold nanoparticles, Anal. Chem. **80**(17), 6805–6808 (2008)

9.450 J. Liu, Y. Lu: A colorimetric lead biosensor using DNAzyme-directed assembly of gold nanoparticles, J. Am. Chem. Soc. **125**(22), 6642–6643 (2003)

9.451 J. Liu, Y. Lu: Accelerated color change of gold nanoparticles assembled by DNAzymes for simple and fast colorimetric Pb^{2+} detection, J. Am. Chem. Soc. **126**(39), 12298–12305 (2004)

9.452 J. Liu, Y. Lu: Stimuli-responsive disassembly of nanoparticle aggregates for light-up colorimetric sensing, J. Am. Chem. Soc. **127**(36), 12677–12683 (2005)

9.453 Z. Wang, J.H. Lee, Y. Lu: Label-free colorimetric detection of lead ions with a nanomolar detection limit and tunable dynamic range by using gold nanoparticles and DNAzyme, Adv. Mater. **20**(17), 3263–3267 (2008)

9.454 J.M. Slocik, J.S. Zabinski, D.M. Phillips, R.R. Naik: Colorimetric response of peptide-functionalized gold nanoparticles to metal ions, Small **4**(5), 548–551 (2008)

9.455 S. Si, M. Raula, T.K. Paira, T.K. Mandal: Reversible self-assembly of carboxylated peptide-functionalized gold nanoparticles driven by metal-ion coordination, ChemPhysChem **9**(11), 1578–1584 (2008)

9.456 B. Cuenoud, J.W. Szostak: A DNA metalloenzyme with DNA ligase activity, Nature **375**(6532), 611–614 (1995)

9.457 S.W. Santoro, G.F. Joyce, K. Sakthivel, S. Gramatikova, C.F. Barbas: RNA cleavage by a DNA enzyme with extended chemical functionality, J. Am. Chem. Soc. **122**(11), 2433–2439 (2000)

9.458 S.-Y. Lin, S.-H. Wu, C.-H. Chen: A simple strategy for prompt visual sensing by gold nanoparticles: General applications of interparticle hydrogen bonds, Angew. Chem. Int. Ed. **45**(30), 4948–4951 (2006)

9.459 Y. Kim, R.C. Johnson, J.T. Hupp: Gold nanoparticle-based sensing of spectroscopically silent heavy metal ions, Nano Lett. **1**(4), 165–167 (2001)

9.460 C.-J. Yu, W.-L. Tseng: Colorimetric detection of mercury(II) in a high-salinity solution using gold nanoparticles capped with 3-mercaptopropionate acid and adenosine monophosphate, Langmuir **24**(21), 12717–12722 (2008)

9.461 C.-C. Huang, H.-T. Chang: Parameters for selective colorimetric sensing of mercury(II) in aqueous solutions using mercaptopropionic acid-modified gold nanoparticles, Chem. Commun. **12**, 1215–1217 (2007)

9.462 C.-C. Huang, Z. Yang, K.-H. Lee, H.-T. Chang: Synthesis of highly fluorescent gold nanoparticles for sensing mercury(II), Angew. Chem. Int. Ed. **46**(36), 6824–6828 (2007)

9.463 G.K. Darbha, A.K. Singh, U.S. Rai, E. Yu, H. Yu, P. Chandra Ray: Selective detection of mercury (II) ion using nonlinear optical properties of gold nanoparticles, J. Am. Chem. Soc. **130**(25), 8038–8043 (2008)

9.464 A. Campion, P. Kambhampati: Surface-enhanced Raman scattering, Chem. Soc. Rev. **27**(4), 241–250 (1998)

9.465 A.M. Michaels, J. Jiang, L. Brus: Ag nanocrystal junctions as the site for surface-enhanced Raman scattering of single rhodamine 6G molecules, J. Phys. Chem. B **104**(50), 11965–11971 (2000)

9.466 M. Mulvihill, A. Tao, K. Benjauthrit, J. Arnold, P. Yang: Surface-enhanced Raman spectroscopy for trace arsenic detection in contaminated water, Angew. Chem. Int. Ed. **47**(34), 6456–6460 (2008)

9.467 H. Li, L. Rothberg: Colorimetric detection of DNA sequences based on electrostatic interactions with unmodified gold nanoparticles, Proc. Natl. Acad. Sci. USA **101**(39), 14036–14039 (2004)

9.468 X. Xue, F. Wang, X. Liu: One-step, room temperature, colorimetric detection of mercury (Hg^{2+}) using DNA/nanoparticle conjugates, J. Am. Chem. Soc. **130**(11), 3244–3245 (2008)

9.469 V.M. Zamarion, R.A. Timm, K. Araki, H.E. Toma: Ultrasensitive SERS nanoprobes for hazardous metal ions based on trimercaptotriazine-modified gold nanoparticles, Inorg. Chem. **47**(8), 2934–2936 (2008)

9.470 S. Tan, M. Erol, S. Sukhishvili, H. Du: Substrates with discretely immobilized silver nanoparticles for ultrasensitive detection of anions in water using surface-enhanced Raman scattering, Langmuir **24**(9), 4765–4771 (2008)

9.471 P. Jain, T. Pradeep: Potential of silver nanoparticle-coated polyurethane foam as an antibacterial water filter, Biotechnol. Bioeng. **90**(1), 59–63 (2005)

9.472 T.J. Berger, J.A. Spadaro, S.E. Chapin, R.O. Becker: Electrically generated silver ions: Quantitative effects on bacterial and mammalian cells, Antimicrob. Agents Chemother. **9**(2), 357–358 (1976)

9.473 C. Aymonier, U. Schlotterbeck, L. Antonietti, P. Zacharias, R. Thomann, J.C. Tiller, S. Mecking: Hybrids of silver nanoparticles with amphiphilic hyperbranched macromolecules exhibiting antimicrobial properties, Chem. Commun. **24**, 3018–3019 (2002)

9.474 I. Sondi, B. Salopek-Sondi: Silver nanoparticles as antimicrobial agent: A case study on e. Coli as a model for gram-negative bacteria, J. Colloid Interface Sci. **275**(1), 177–182 (2004)

9.475 V. Sambhy, M.M. MacBride, B.R. Peterson, A. Sen: Silver bromide nanoparticle/polymer composites: Dual action tunable antimicrobial materials, J. Am. Chem. Soc. **128**(30), 9798–9808 (2006)

9.476 Y. Li, P. Leung, L. Yao, Q.W. Song, E. Newton: Antimicrobial effect of surgical masks coated with nanoparticles, J. Hosp. Infect. **62**(1), 58–63 (2006)

9.477 S.T. Dubas, P. Kumlangdudsana, P. Potiyaraj: Layer-by-layer deposition of antimicrobial silver nanoparticles on textile fibers, Colloid. Surf. A **289**(1–3), 105–109 (2006)

9.478 T. Maneerung, S. Tokura, R. Rujiravanit: Impregnation of silver nanoparticles into bacterial cellulose for antimicrobial wound dressing, Carbohydr. Polym. **72**(1), 43–51 (2008)

9.479 S. Silver: Bacterial silver resistance: Molecular biology and uses and misuses of silver compounds, FEMS Microbiol. Rev. **27**(2/3), 341–353 (2003)

9.480 S. Silver, L. Phung, G. Silver: Silver as biocides in burn and wound dressings and bacterial resistance to silver compounds, J. Ind. Microbiol. Biotechnol. **33**(7), 627–634 (2006)

9.481 A. Neal: What can be inferred from bacterium-nanoparticle interactions about the potential consequences of environmental exposure to nanoparticles?, Ecotoxicology **17**(5), 362–371 (2008)

9.482 M. Rai, A. Yadav, A. Gade: Silver nanoparticles as a new generation of antimicrobials, Biotechnol. Adv. **27**(1), 76–83 (2009)

9.483 V.K. Sharma, R.A. Yngard, Y. Lin: Silver nanoparticles: Green synthesis and their antimicrobial activities, Adv. Colloid Interf. Sci. **145**(1/2), 83–96 (2009)

9.484 J.R. Morones, J.L. Elechiguerra, A. Camacho, K. Holt, J.B. Kouri, J.T Ramírez, M.J. Yacaman: The bactericidal effect of silver nanoparticles, Nanotechnology **16**(10), 2346 (2005)

9.485 S. Pal, Y.K. Tak, J.M. Song: Does the antibacterial activity of silver nanoparticles depend on the shape of the nanoparticle? A study of the gram-negative bacterium *Escherichia coli*, Appl. Environ. Microbiol. **73**(6), 1712–1720 (2007)

9.486 C.-N. Lok, C.-M. Ho, R. Chen, Q.-Y. He, W.-Y. Yu, H. Sun, P. Tam, J.-F. Chiu, C.-M. Che: Silver nanoparticles: Partial oxidation and antibacterial activities, J. Biol. Inorg. Chem. **12**(4), 527–534 (2007)

9.487 J. Elechiguerra, J. Burt, J. Morones, A. Camacho-Bragado, X. Gao, H. Lara, M. Yacaman: Interaction of silver nanoparticles with HIV-1, J. Nanobiotechnol. **3**(1), 6 (2005)

9.488 L. Nover, K.D. Scharf, D. Neumann: Formation of cytoplasmic heat shock granules in tomato cell cultures and leaves, Mol. Cell. Biol. **3**(9), 1648–1655 (1983)

9.489 Q.L. Feng, J. Wu, G.Q. Chen, F.Z. Cui, T.N. Kim, J.O. Kim: A mechanistic study of the antibacterial effect of silver ions on *Escherichia coli* and *Staphylococcus aureus*, J. Biomed. Mater. Res. **52**(4), 662–668 (2000)

9.490 S.Y. Liau, D.C. Read, W.J. Pugh, J.R. Furr, A.D. Russell: Interaction of silver nitrate with readily identifiable groups: Relationship to the antibacterial action of silver ions, Lett. Appl. Microbiol. **25**(4), 279–283 (1997)

9.491 T. Hamouda, J.R. Baker: Antimicrobial mechanism of action of surfactant lipid preparations in enteric gram-negative bacilli, J. Appl. Microbiol. **89**(3), 397–403 (2000)

9.492 I.E. Wachs, R.J. Madix: The oxidation of methanol on a silver (110) catalyst, Surf. Sci. **76**(2), 531–558 (1978)

9.493 R.L. Davies, S.F. Etris: The development and functions of silver in water purification and disease control, Catal. Today **36**(1), 107–114 (1997)

9.494 M. Vaara: Agents that increase the permeability of the outer membrane, Microbiol. Rev. **56**(3), 395–411 (1992)

9.495 S.K. Gogoi, P. Gopinath, A. Paul, A. Ramesh, S.S. Ghosh, A. Chattopadhyay: Green fluorescent protein-expressing *Escherichia coli* as a model system for investigating the antimicrobial activities of silver nanoparticles, Langmuir **22**(22), 9322–9328 (2006)

9.496 Q. Chang, L. Yan, M. Chen, H. He, J. Qu: Bactericidal mechanism of Ag/Al_2O_3 against *Escherichia coli*, Langmuir **23**(22), 11197–11199 (2007)

9.497 V.R.R. Kumar, T. Pradeep: Polymerization of benzylthiocyanate on silver nanoparticles and the formation of polymer coated nanoparticles, J. Mater. Chem. **16**(9), 837–841 (2006)

9.498 A. Kumar, P.K. Vemula, P.M. Ajayan, G. John: Silver-nanoparticle-embedded antimicrobial paints based on vegetable oil, Nat. Mater. **7**(3), 236–241 (2008)

9.499 L. Zhenyu, H. Huimin, S. Tiecun, Y. Fan, Z. Wei, W. Ce, K.M. Sanjeev: Facile synthesis of single-crystal and controllable sized silver nanoparticles on the surfaces of polyacrylonitrile nanofibres, Nanotechnology **17**(3), 917 (2006)

9.500 W.L. Chou, D.G. Yu, M.C. Yang: The preparation and characterization of silver-loading cellulose acetate hollow fiber membrane for water treatment, Polym. Adv. Technol. **16**(8), 600–607 (2005)

9.501 W.K. Son, J.H. Youk, T.S. Lee, W.H. Park: Preparation of antimicrobial ultrafine cellulose acetate fibers with silver nanoparticles, Macromol. Rapid Commun. **25**(18), 1632–1637 (2004)

9.502 K. Zodrow, L. Brunet, S. Mahendra, D. Li, A. Zhang, Q. Li, P.J.J. Alvarez: Polysulfone ultrafiltration membranes impregnated with silver nanoparticles show improved biofouling resistance and virus removal, Water Res. **43**(3), 715–723 (2009)

9.503 J. Chen, F. Saeki, B.J. Wiley, H. Cang, M.J. Cobb, Z.-Y. Li, L. Au, H. Zhang, M.B. Kimmey, X. Li, Y. Xia: Gold nanocages: Bioconjugation and their potential use as optical imaging contrast agents, Nano Lett. **5**(3), 473–477 (2005)

9.504 D. Pissuwan, S. Valenzuela, M. Killingsworth, X. Xu, M. Cortie: Targeted destruction of murine macrophage cells with bioconjugated gold nanorods, J. Nanopart. Res. **9**(6), 1109–1124 (2007)

9.505 H. Takahashi, Y. Niidome, S. Yamada: Controlled release of plasmid DNA from gold nanorods induced by pulsed near-infrared light, Chem. Commun. **17**, 2247–2249 (2005)

9.506 J. Chen, M. Yang, Q. Zhang, E.C. Cho, C.M. Cobley, C. Kim, C. Glaus, L.V. Wang, M.J. Welch, Y. Xia: Gold nanocages: A novel class of multifunctional nanomaterials for theranostic applications, Adv. Funct. Mater. **20**(21), 3684–3694 (2010)

9.507 X. Huang, S. Neretina, M.A. El-Sayed: Gold nanorods: From synthesis and properties to biological and biomedical applications, Adv. Mater. **21**(48), 4880–4910 (2009)

9.508 L. Au, D. Zheng, F. Zhou, Z.-Y. Li, X. Li, Y. Xia: A quantitative study on the photothermal effect of immuno gold nanocages targeted to breast cancer cells, Am. Chem. Soc. Nano **2**(8), 1645–1652 (2008)

9.509 M. Hu, J. Chen, Z.-Y. Li, L. Au, G.V. Hartland, X. Li, M. Marquez, Y. Xia: Gold nanostructures: Engineering their plasmonic properties for biomedical applications, Chem. Soc. Rev. **35**(11), 1084–1094 (2006)

9.510 P.K. Jain, K.S. Lee, I.H. El-Sayed, M.A. El-Sayed: Calculated absorption and scattering properties of gold nanoparticles of different size, shape, and composition: Applications in biological imaging and biomedicine, J. Phys. Chem. B **110**(14), 7238–7248 (2006)

9.511 H. Liao, J.H. Hafner: Gold nanorod bioconjugates, Chem. Mater. **17**(18), 4636–4641 (2005)

9.512 L. Au, Q. Zhang, C.M. Cobley, M. Gidding, A.G. Schwartz, J. Chen, Y. Xia: Quantifying the cellular uptake of antibody-conjugated Au nanocages by two-photon microscopy and inductively coupled plasma mass spectrometry, Am. Chem. Soc. Nano **4**(1), 35–42 (2009)

9.513 C. Hrelescu, T.K. Sau, A.L. Rogach, F. Jäckel, J. Feldmann: Single gold nanostars enhance Raman scattering, Appl. Phys. Lett. **94**, 153113 (2009)

9.514 M. Hu, H. Petrova, J. Chen, J.M. McLellan, A.R. Siekkinen, M. Marquez, X. Li, Y. Xia, G.V. Hartland: Ultrafast laser studies of the photothermal properties of gold nanocages, J. Phys. Chem. B **110**(4), 1520–1524 (2006)

9.515 H. Liao, C.L. Nehl, J.H. Hafner: Biomedical applications of plasmon resonant metal nanoparticles, Nanomedicine **1**(2), 201–208 (2006)

9.516 C.M. Cobley, L. Au, J. Chen, Y. Xia: Targeting gold nanocages to cancer cells for photothermal destruction and drug delivery, Exp. Opin. Drug Deliv. **7**(5), 577–587 (2010)

9.517 A.K. Salem, P.C. Searson, K.W. Leong: Multifunctional nanorods for gene delivery, Nat. Mater. **2**(10), 668–671 (2003)

9.518 A.K. Salem, C.F. Hung, T.W. Kim, T.C. Wu, P.C. Searson, K.W. Leong: Multi-component nanorods for vaccination applications, Nanotechnology **16**(4), 484 (2005)

9.519 X. Huang, I.H. El-Sayed, W. Qian, M.A. El-Sayed: Cancer cell imaging and photothermal therapy in the near-infrared region by using gold nanorods, J. Am. Chem. Soc. **128**(6), 2115–2120 (2006)

9.520 S. Link, M.A. El-Sayed: Optical properties and ultrafast dynamics of metallic nanocrystals, Annu. Rev. Phys. Chem. **54**(1), 331–366 (2003)

9.521 A.R. Lowery, A.M. Gobin, E.S. Day, N.J. Halas: Immunonanoshells for targeted photothermal ablation of tumor cells, Int. J. Nanomed. **1**(2), 1–6 (2006)

9.522 M.B. Mohamed, T.S. Ahmadi, S. Link, M. Braun, M.A. El-Sayed: Hot electron and phonon dynamics of gold nanoparticles embedded in a gel matrix, Chem. Phys. Lett. **343**(1/2), 55–63 (2001)

9.523 C.J. Murphy, A.M. Gole, J.W. Stone, P.N. Sisco, A.M. Alkilany, E.C. Goldsmith, S.C. Baxter: Gold nanoparticles in biology: Beyond toxicity to cellular imaging, Acc. Chem. Res. **41**(12), 1721–1730 (2008)

9.524 H. Wang, T.B. Huff, D.A. Zweifel, W. He, P.S. Low, A. Wei, J.-X. Cheng: In vitro and in vivo two-photon luminescence imaging of single gold nanorods, Proc. Natl. Acad. Sci. USA **102**(44), 15752–15756 (2005)

9.525 N.J. Durr, T. Larson, D.K. Smith, B.A. Korgel, K. Sokolov, A. Ben-Yakar: Two-photon luminescence imaging of cancer cells using molecularly targeted gold nanorods, Nano Lett. **7**(4), 941–945 (2007)

9.526 C.J. Orendorff, A. Gole, T.K. Sau, C.J. Murphy: Surface-enhanced Raman spectroscopy of self-assembled monolayers: Sandwich architecture and nanoparticle shape dependence, Anal. Chem. **77**(10), 3261–3266 (2005)

9.527 J.Q. Hu, Q. Chen, Z.X. Xie, G.B. Han, R.H. Wang, B. Ren, Y. Zhang, Z.L. Yang, Z.Q. Tian: A simple and effective route for the synthesis of crystalline silver nanorods and nanowires, Adv. Funct. Mater. **14**(2), 183–189 (2004)

9.528 H. Wang, C.S. Levin, N.J. Halas: Nanosphere arrays with controlled sub-10-nm gaps as surface-enhanced Raman spectroscopy substrates, J. Am. Chem. Soc. **127**(43), 14992–14993 (2005)

9.529 P.D. O'Neal, G.L. Coté, M. Motamedi, J. Chen, W.-C. Lin: Feasibility study using surface-enhanced Raman spectroscopy for the quantitative detection of excitatory amino acids, SPIE Proc. **8**, 33–39 (2003)

9.530 R. Sulk, C. Chan, J. Guicheteau, C. Gomez, J.B.B. Heyns, R. Corcoran, K. Carron: Surface-enhanced Raman assays (SERA): Measurement of bilirubin and salicylate, J. Raman Spectrosc. **30**(9), 853–859 (1999)

9.531 Y. Yang, S. Matsubara, L. Xiong, T. Hayakawa, M. Nogami: Solvothermal synthesis of multiple shapes of silver nanoparticles and their SERS properties, J. Phys. Chem. C **111**(26), 9095–9104 (2007)

9.532 L. Rocks, K. Faulds, D. Graham: Rationally designed SERS active silica coated silver nanoparticles, Chem. Commun. **47**(15), 4415–4417 (2011)

9.533 M.J. Banholzer, J.E. Millstone, L. Qin, C.A. Mirkin: Rationally designed nanostructures for surface-enhanced Raman spectroscopy, Chem. Soc. Rev. **37**(5), 885–897 (2008)

9.534 K.A. Willets, R.P. Van Duyne: Localized surface plasmon resonance spectroscopy and sensing, Annu. Rev. Phys. Chem. **58**(1), 267–297 (2007)

9.535 J.J. Mock, M. Barbic, D.R. Smith, D.A. Schultz, S. Schultz: Shape effects in plasmon resonance of individual colloidal silver nanoparticles, J. Chem. Phys. **116**(15), 6755–6759 (2002)

9.536 J. Xie, Q. Zhang, J.Y. Lee, D.I.C. Wang: The synthesis of SERS-active gold nanoflower tags for in vivo applications, Am. Chem. Soc. Nano **2**(12), 2473–2480 (2008)

9.537 E. Hao: Electromagnetic fields around silver nanoparticles and dimers, J. Chem. Phys. **120**(1), 357 (2004)

9.538 Y. Wang, X. Zou, W. Ren, W. Wang, E. Wang: Effect of silver nanoplates on Raman spectra of p-aminothiophenol assembled on smooth macroscopic gold and silver surface, J. Phys. Chem. C **111**(8), 3259–3265 (2007)

9.539 P. Sajanlal, T. Pradeep: Mesoflowers: A new class of highly efficient surface-enhanced Raman active and infrared-absorbing materials, Nano Res. **2**(4), 306–320 (2009)

9.540 S.A. Maier, P.G. Kik, H.A. Atwater, S. Meltzer, E. Harel, B.E. Koel, A.A.G. Requicha: Local detection of electromagnetic energy transport below the diffraction limit in metal nanoparticle plasmon waveguides, Nat. Mater. **2**(4), 229–232 (2003)

9.541 K. Aslan, J.R. Lakowicz, C.D. Geddes: Plasmon light scattering in biology and medicine: New sensing approaches, visions and perspectives, Curr. Opin. Chem. Biol. **9**(5), 538–544 (2005)

9.542 C. Yu, J. Irudayaraj: Quantitative evaluation of sensitivity and selectivity of multiplex nanoSPR biosensor assays, Biophys. J. **93**(10), 3684–3692 (2007)

9.543 C. Yu, H. Nakshatri, J. Irudayaraj: Identity profiling of cell surface markers by multiplex gold nanorod probes, Nano Lett. **7**(8), 2300–2306 (2007)

9.544 X.-J. Huang, C.-C. Li, B. Gu, J.-H. Kim, S.-O. Cho, Y.-K. Choi: Controlled molecularly mediated assembly of gold nanooctahedra for a glucose biosensor, J. Phys. Chem. C **112**(10), 3605–3611 (2008)

9.545 M.-C. Daniel, D. Astruc: Gold nanoparticles: Assembly, supramolecular chemistry, quantum-size-related properties, and applications toward biology, catalysis, and nanotechnology, Chem. Rev. **104**(1), 293–346 (2004)

9.546 Q. Wei, K. Hirota, K. Tajima, K. Hashimoto: Design and synthesis of TiO_2 nanorod assemblies and their application for photovoltaic devices, Chem. Mater. **18**(21), 5080–5087 (2006)

9.547 J. Xiaohui, W. Feng, K. Varutt, T. Hori, A. Fujii, M. Ozaki: Fabrication of oriented ZnO nanopillar self-assemblies and their application for photovoltaic devices, Nanotechnology **19**(43), 435706 (2008)

9.548 V. Dhas, S. Muduli, W. Lee, S. Han, S. Ogale: Enhanced conversion efficiency in dye-sensitized solar cells based on zno bifunctional nanoflowers loaded with gold nanoparticles, Appl. Phys. Lett. **93**(24), 243108 (2008)

9.549 E. Pedrueza, J.L. Valdés, V. Chirvony, R. Abargues, J. Hernández-Saz, M. Herrera, S.I. Molina, J.P. Martínez-Pastor: Novel method of preparation of gold-nanoparticle-doped TiO_2 and SiO_2 plasmonic thin films: Optical characterization and comparison with Maxwell–Garnett modeling, Adv. Funct. Mater. **21**(18), 3502–3507 (2011)

9.550 J. Chen, Y. Zou, Y. Li, X. Zhou, J. Zhang, X. Li, X. Xiao, Y. Lin: Improving the photoelectrochemical performance of polythiophene sensitized TiO_2 electrode by modification with gold nanoparticles, Chem. Phys. Lett. **460**(1–3), 168–172 (2008)

9.551 T. Hasobe, H. Imahori, P.V. Kamat, S. Fukuzumi: Quaternary self-organization of porphyrin and fullerene units by clusterization with gold nanoparticles on SnO_2 electrodes for organic solar cells, J. Am. Chem. Soc. **125**(49), 14962–14963 (2003)

9.552 S. Yamada, T. Tasaki, T. Akiyama, N. Terasaki, S. Nitahara: Gold nanoparticle–porphyrin self-assembled multistructures for photoelectric conversion, Thin Solid Films **438/439**(0), 70–74 (2003)

9.553 K. Kim, D.L. Carroll: Roles of Au and Ag nanoparticles in efficiency enhancement of poly(3-octylthiophene)/C_{60} bulk heterojunction photovoltaic devices, Appl. Phys. Lett. **87**(20), 203113 (2005)

9.554 D. Derkacs, S.H. Lim, P. Matheu, W. Mar, E.T. Yu: Improved performance of amorphous silicon solar cells via scattering from surface plasmon polaritons in nearby metallic nanoparticles, Appl. Phys. Lett. **89**(9), 093103 (2006)

9.555 S.W. Tong, C.F. Zhang, C.Y. Jiang, G. Liu, Q.D. Ling, E.T. Kang, D.S.H. Chan, C. Zhu: Improvement in the hole collection of polymer solar cells by utilizing gold nanoparticle buffer layer, Chem. Phys. Lett. **453**(1–3), 73–76 (2008)

9.556 J. Yang, J. You, C.-C. Chen, W.-C. Hsu, H.-R. Tan, X.W. Zhang, Z. Hong, Y. Yang: Plasmonic polymer tandem solar cell, Am. Chem. Soc. Nano **5**(8), 6210–6217 (2011)

9.557 M.D. Brown, T. Suteewong, R.S.S. Kumar, V. D'Innocenzo, A. Petrozza, M.M. Lee, U. Wiesner, H.J. Snaith: Plasmonic dye-sensitized solar cells using core–shell metal–insulator nanoparticles, Nano Lett. **11**(2), 438–445 (2010)

9.558 H.B. Yildiz, R. Tel-Vered, I. Willner: Solar cells with enhanced photocurrent efficiencies using oligoaniline-crosslinked Au/CdS nanoparticles arrays on electrodes, Adv. Funct. Mater. **18**(21), 3497–3505 (2008)

9.559 K. Ishikawa, C.-J. Wen, K. Yamada, T. Okubo: The photocurrent of dye-sensitized solar cells enhanced by the surface plasmon resonance, J. Chem. Eng. Jpn. **37**(5), 645–649 (2004)

9.560 B. Rand, P. Peumans, S. Forrest: Long-range absorption enhancement in organic tandem thin-film

solar cells containing silver nanoclusters, J. Appl. Phys. **96**(12), 7519 (2004)
9.561 A.P. Demchenko, M.A.H. Muhammed, T. Pradeep: Luminescent quantum clusters of gold as bio-labels, Springer Ser. Fluoresc. **9**, 333–353 (2010)
9.562 J. Zheng, P.R. Nicovich, R.M. Dickson: Highly fluorescent noble-metal quantum dots, Annu. Rev. Phys. Chem. **58**, 409–431 (2007)
9.563 M.A.H. Muhammed, P.K. Verma, S.K. Pal, A. Retnakumari, M. Koyakutty, S. Nair, T. Pradeep: Luminescent quantum clusters of gold in bulk by albumin-induced core etching of nanoparticles: Metal ion sensing, metal-enhanced luminescence, and biolabeling, Chemistry **16**(33), 10103–10112 (2010)
9.564 E.S. Shibu, T. Pradeep: Quantum clusters in cavities: Trapped Au_{15} in cyclodextrins, Chem. Mater. **23**(4), 989–999 (2011)
9.565 E.S. Shibu, M.A.H. Muhammed, T. Tsukuda, T. Pradeep: Ligand exchange of $Au_{25}SG_{18}$ leading to functionalized gold clusters: Spectroscopy, kinetics, and luminescence, J. Phys. Chem. C **112**(32), 12168–12176 (2008)
9.566 P.L. Xavier, K. Chaudhari, P.K. Verma, S.K. Pal, T. Pradeep: Luminescent quantum clusters of gold in transferrin family protein, lactoferrin exhibiting FRET, Nanoscale **2**(12), 2769–2776 (2010)
9.567 K. Chaudhari, P.L. Xavier, T. Pradeep: Understanding the evolution of luminescent gold quantum clusters in protein templates, Am. Chem. Soc. Nano **5**(11), 8816–8827 (2011)
9.568 M.A.H. Muhammed, P.K. Verma, S.K. Pal, R.C.A. Kumar, S. Paul, R.V. Omkumar, T. Pradeep: Bright, NIR-emitting Au_{23} from Au_{25}: Characterization and applications including biolabeling, Chemistry **15**(39), 10110–10120 (2009)
9.569 C.-C. Huang, Z. Yang, K.-H. Lee, H.-T. Chang: Synthesis of highly fluorescent gold nanoparticles for sensing mercury(II), Angew. Chem. **119**(36), 6948–6952 (2007)
9.570 I. Diez, R.H.A. Ras: Fluorescent silver nanoclusters, Nanoscale **3**(5), 1963–1970 (2011)
9.571 G.A. Ozin, H. Huber: Cryophotoclustering techniques for synthesizing very small, naked silver clusters Ag_n of known size (where $n = 2–5$). The molecular metal cluster-bulk metal particle interface, Inorg. Chem. **17**(1), 155–163 (1978)
9.572 W. Harbich, S. Fedrigo, J. Buttet: The optical absorption spectra of small silver clusters ($n = 5–11$) embedded in argon matrices, Chem. Phys. Lett. **195**(5-6), 613–617 (1992)
9.573 W. Schulze, I. Rabin, G. Ertl: Formation of light-emitting Ag_2 and Ag_3 species in the course of condensation of Ag atoms with Ar, ChemPhysChem **5**(3), 403–407 (2004)
9.574 A.D. Stevens, M.C.R. Symons: Spectroscopic studies of silver(0) centres formed radiolytically in water-ethanol solvents at 4 and 77 K, J. Chem. Soc. Faraday Trans. I **85**(6), 1439–1450 (1989)
9.575 S. Liu, F. Lu, J.-J. Zhu: Highly fluorescent Ag nanoclusters: Microwave-assisted green synthesis and Cr^{3+} sensing, Chem. Commun. **47**(9), 2661–2663 (2011)
9.576 M. Treguer, F. Rocco, G. Lelong, A. Le Nestour, T. Cardinal, A. Maali, B. Lounis: Fluorescent silver oligomeric clusters and colloidal particles, Solid State Sci. **7**(7), 812–818 (2005)
9.577 H. Xu, K.S. Suslick: Sonochemical synthesis of highly fluorescent Ag nanoclusters, Am. Chem. Soc. Nano **4**(6), 3209–3214 (2010)
9.578 H. Liu, X. Zhang, X. Wu, L. Jiang, C. Burda, J.-J. Zhu: Rapid sonochemical synthesis of highly luminescent non-toxic AuNCs and Au@AgNCs and Cu(II) sensing, Chem. Commun. **47**(14), 4237–4239 (2011)
9.579 T.U.B. Rao, B. Nataraju, T. Pradeep: Ag_9 quantum cluster through a solid-state route, J. Am. Chem. Soc. **132**(46), 16304–16307 (2010)
9.580 C. Shao, B. Yuan, H. Wang, Q. Zhou, Y. Li, Y. Guan, Z. Deng: Eggshell membrane as a multimodal solid state platform for generating fluorescent metal nanoclusters, J. Mater. Chem. **21**(9), 2863–2866 (2011)
9.581 Z. Huang, F. Pu, D. Hu, C. Wang, J. Ren, X. Qu: Site-specific DNA-programmed growth of fluorescent and functional silver nanoclusters, Chemistry **17**(13), 3774–3780 (2011)
9.582 W. Guo, J. Yuan, Q. Dong, E. Wang: Highly sequence-dependent formation of fluorescent silver nanoclusters in hybridized DNA duplexes for single nucleotide mutation identification, J. Am. Chem. Soc. **132**(3), 932–934 (2009)
9.583 A. Ledo-Suárez, J. Rivas, C.F. Rodríguez-Abreu, M.J. Rodríguez, E. Pastor, A. Hernández-Creus, S.B. Oseroff, M.A. López-Quintela: Facile synthesis of stable subnanosized silver clusters in microemulsions, Angew. Chem. Int. Ed. **46**(46), 8823–8827 (2007)
9.584 J. Zhang, S. Xu, E. Kumacheva: Photogeneration of fluorescent silver nanoclusters in polymer microgels, Adv. Mater. **17**(19), 2336–2340 (2005)
9.585 K.V. Mrudula, T.U. Bhaskara Rao, T. Pradeep: Interfacial synthesis of luminescent 7 kDa silver clusters, J. Mater. Chem. **19**(25), 4335–4342 (2009)
9.586 T.U. Bhaskara Rao, T. Pradeep: Luminescent Ag_7 and Ag_8 clusters by interfacial synthesis, Angew. Chem. Int. Ed. **49**(23), 3925–3929 (2010)
9.587 H. Xu, K.S. Suslick: Water-soluble fluorescent silver nanoclusters, Adv. Mater. **22**(10), 1078–1082 (2010)
9.588 J. Zheng, R.M. Dickson: Individual water-soluble dendrimer-encapsulated silver nanodot fluorescence, J. Am. Chem. Soc. **124**(47), 13982–13983 (2002)
9.589 B.G. Ershov, A. Henglein: Time-resolved investigation of early processes in the reduction of Ag^+ on polyacrylate in aqueous solution, J. Phys. Chem. B **102**(52), 10667–10671 (1998)
9.590 Z. Shen, H. Duan, H. Frey: Water-soluble fluorescent Ag nanoclusters obtained from multiarm

star poly(acrylic acid) as "molecular hydrogel" templates, Adv. Mater. **19**(3), 349–352 (2007)
9.591 N. Cathcart, V. Kitaev: Silver nanoclusters: Single-stage scaleable synthesis of monodisperse species and their chirooptical properties, J. Phys. Chem. C **114**(38), 16010–16017 (2010)
9.592 B. Adhikari, A. Banerjee: Facile synthesis of water-soluble fluorescent silver nanoclusters and Hg^{II} sensing, Chem. Mater. **22**(15), 4364–4371 (2010)
9.593 C.I. Richards, S. Choi, J.-C. Hsiang, Y. Antoku, T. Vosch, A. Bongiorno, Y.-L. Tzeng, R.M. Dickson: Oligonucleotide-stabilized Ag nanocluster fluorophores, J. Am. Chem. Soc. **130**(15), 5038–5039 (2008)
9.594 J.T. Petty, J. Zheng, N.V. Hud, R.M. Dickson: DNA-templated Ag nanocluster formation, J. Am. Chem. Soc. **126**(16), 5207–5212 (2004)
9.595 C.I. Richards, J.-C. Hsiang, D. Senapati, S. Patel, J. Yu, T. Vosch, R.M. Dickson: Optically modulated fluorophores for selective fluorescence signal recovery, J. Am. Chem. Soc. **131**(13), 4619–4621 (2009)
9.596 C.M. Ritchie, K.R. Johnsen, J.R. Kiser, Y. Antoku, R.M. Dickson, J.T. Petty: Ag nanocluster formation using a cytosine oligonucleotide template, J. Phys. Chem. C **111**(1), 175–181 (2006)
9.597 V. Soto-Verdugo, H. Metiu, E. Gwinn: The properties of small Ag clusters bound to DNA bases, J. Chem. Phys. **132**(19), 195102 (2010)
9.598 E.G. Gwinn, P. O'Neill, A.J. Guerrero, D. Bouwmeester, D.K. Fygenson: Sequence-dependent fluorescence of DNA-hosted silver nanoclusters, Adv. Mater. **20**(2), 279–283 (2008)
9.599 S.S. Narayanan, S.K. Pal: Structural and functional characterization of luminescent silver-protein nanobioconjugates, J. Phys. Chem. C **112**(13), 4874–4879 (2008)
9.600 N. Makarava, A. Parfenov, I.V. Baskakov: Water-soluble hybrid nanoclusters with extra bright and photostable emissions: A new tool for biological imaging, Biophys. J. **89**(1), 572–580 (2005)
9.601 J. Yu, S.A. Patel, R.M. Dickson: In vitro and intracellular production of peptide-encapsulated fluorescent silver nanoclusters, Angew. Chem. Int. Ed. **46**(12), 2028–2030 (2007)
9.602 L. Peyser-Capadona, J. Zheng, J.I. González, T.-H. Lee, S.A. Patel, R.M. Dickson: Nanoparticle-free single molecule anti-Stokes Raman spectroscopy, Phys. Rev. Lett. **94**(5), 058301 (2005)
9.603 B. Adhikari, A. Banerjee: Short-peptide-based hydrogel: A template for the in situ synthesis of fluorescent silver nanoclusters by using sunlight, Chemistry **16**(46), 13698–13705 (2010)
9.604 A. Mathew, P.R. Sajanlal, T. Pradeep: A fifteen atom silver cluster confined in bovine serum albumin, J. Mater. Chem. **21**(30), 11205–11212 (2011)
9.605 L. Dhanalakshmi, T.U.B. Rao, T. Pradeep: Conversion of double layer charge-stabilized Ag@citrate colloids to thiol passivated luminescent quantum clusters, Chem. Commun., 859–861 (2012)
9.606 T. Udayabhaskararao, Y. Sun, N. Goswami, S.K. Pal, K. Balasubramanian, T. Pradeep: Ag_7Au_6: A 13 atom alloy quantum cluster, Angew. Chem. Int. Ed. **51**, 2155–2159 (2012)
9.607 Y. Watanabe: Photosensitivity in phosphate glass doped with Ag^+ upon exposure to near-ultraviolet femtosecond laser pulses, Appl. Phys. Lett. **78**(15), 2125 (2001)
9.608 M. Bellec, A. Royon, K. Bourhis, J. Choi, B. Bousquet, M. Treguer, T. Cardinal, J.-J. Videau, M. Richardson, L. Canioni: 3-D patterning at the nanoscale of fluorescent emitters in glass, J. Phys. Chem. C **114**(37), 15584–15588 (2010)
9.609 E. Maik, R. Klaus, H. Armin, M.T. Dragomir, W. Wilfried, S.E. Reinhard, P. Gianfranco: Photoluminescence of atomic gold and silver particles in soda-lime silicate glasses, Nanotechnology **19**(13), 135701 (2008)
9.610 G.A. Ozin, F. Hugues, S.M. Mattar, D.F. McIntosh: Low nuclearity silver clusters in faujasite-type zeolites: Optical spectroscopy, photochemistry and relationship to the photodimerization of alkanes, J. Phys. Chem. **87**(18), 3445–3450 (1983)
9.611 G. De Cremer, Y. Antoku, M.B.J. Roeffaers, M. Sliwa, J. Van Noyen, S. Smout, J. Hofkens, D.E. De Vos, B.F. Sels, T. Vosch: Photoactivation of silver-exchanged zeolite A, Angew. Chem. Int. Ed. **47**(15), 2813–2816 (2008)
9.612 G. De Cremer, E. Coutiño-Gonzalez, M.B.J. Roeffaers, B. Moens, J. Ollevier, M. Van der Auweraer, R. Schoonheydt, P.A. Jacobs, F.C. De Schryver, J. Hofkens, D.E. De Vos, B.F. Sels, T. Vosch: Characterization of fluorescence in heat-treated silver-exchanged zeolites, J. Am. Chem. Soc. **131**(8), 3049–3056 (2009)
9.613 G. De Cremer, B.F. Sels, J.-I. Hotta, M.B.J. Roeffaers, E. Bartholomeeusen, E. Coutiño-Gonzalez, V. Valtchev, D.E. De Vos, T. Vosch, J. Hofkens: Optical encoding of silver zeolite microcarriers, Adv. Mater. **22**(9), 957–960 (2010)
9.614 C.-A.J. Lin, T.-Y. Yang, C.-H. Lee, S.H. Huang, R.A. Sperling, M. Zanella, J.K. Li, J.-L. Shen, H.-H. Wang, H.-I. Yeh, W.J. Parak, W.H. Chang: Synthesis, characterization, and bioconjugation of fluorescent gold nanoclusters toward biological labeling applications, Am. Chem. Soc. Nano **3**(2), 395–401 (2009)
9.615 R. Archana, S. Sonali, M. Deepthy, R. Prasanth, M. Habeeb, P. Thalappil, N. Shantikumar, K. Manzoor: Molecular-receptor-specific, non-toxic, near-infrared-emitting Au cluster-protein nanoconjugates for targeted cancer imaging, Nanotechnology **21**(5), 055103 (2010)
9.616 Y. Zhu, H. Qian, M. Zhu, R. Jin: Thiolate-protected Au_n nanoclusters as catalysts for selective oxidation

and hydrogenation processes, Adv. Mater. **22**(17), 1915–1920 (2010)

9.617 A. Leelavathi, T.U.B. Rao, T. Pradeep: Supported quantum clusters of silver as enhanced catalysts for reduction, Nanoscale Res. Lett. **6**, 123 (2011)

9.618 A. Mohanty, N. Garg, R. Jin: A universal approach to the synthesis of noble metal nanodendrites and their catalytic properties, Angew. Chem. Int. Ed. **49**(29), 4962–4966 (2010)

9.619 I. Chakraborty, T.U.B. Rao, T. Pradeep: Luminescent sub-nanometer clusters for metal ion sensing: A new direction in nanosensors, J. Hazard. Mater. **211/212**, 396–403 (2012)

9.620 T.S. Sreeprasad, M.S. Maliyekkal, K. Deepti, K. Chaudhari, P.L. Xavier, T. Pradeep: Transparent, luminescent, antibacterial and patternable film forming composites of graphene oxide/reduced graphene oxide, ACS Appl. Mater. Interfaces **3**(7), 2643–2654 (2011)

10. Nanostructures of Common Metals

Melinda Mohl, Krisztián Kordás

Since nanosized metals with magnetic features, and porous and noble metals, are discussed in other chapters of this handbook, here we present a complementary, comprehensive review on other metal nanostructures. Accordingly, this chapter is devoted to review the strategies of synthesis as well as properties of the most common transition- and post-transition-metal nanoparticles. Particular attention is paid to scalable production methods and enabled or foreseen applications of such metals, including low-melting-point lead, bismuth, tin, and indium, some of the refractories including tungsten, molybdenum, tantalum, and titanium, as well as a few more of the very commonly used metals such as copper, aluminum, and zinc. The review is expected to help the readers to get a glance at the state-of-the-art in the field and to foster new studies to overcome challenges associated typically with controlled bulk production and exploitation of this family of nanomaterials.

10.1 **Post-Transition Metals** 390
10.1.1 Lead, Bismuth, Tin, and Indium ... 390
10.1.2 Aluminum 392

10.2 **Transition Metals** 392
10.2.1 Titanium 393
10.2.2 Tungsten 394
10.2.3 Molybdenum 395
10.2.4 Tantalum 395
10.2.5 Zinc 396
10.2.6 Copper 397

10.3 **Concluding Remarks** 398

References 399

Looking at the Periodic Table of elements, we find about 80 natural/stable isotopes of metals that are nonmagnetic and nonprecious. Among these, the alkali and alkali-earth metals (s-group) are extremely reactive, and the lanthanoids and actinoids (f-group) and some of the d-group metals are of low abundance, leaving roughly 20 elements that can be considered as practical choices for large-scale industrial use in metallic form, especially when talking about nanoparticles. Though each metal has its peculiarities, the basic rules concerning their size-dependent physical properties follow the general trends observed when talking about nanosized structures of other metals. Small crystal size can result in: increased chemical reactivity due to the relatively large number of surface atoms and vacancies at specific crystal edges and apices, melting point depression because of the large surface energy, decreased electrical and thermal conductivity due to the more pronounced electron and phonon scattering at the crystal boundaries, the appearance of molecular-like electronic states instead of the ordinary overlapped valence and conduction bands giving rise to the onset of semiconducting/semimetallic behavior in very small clusters or very thin wires, the appearance of magnetic polarization, etc. [10.1–13].

Since the pioneering work of *Granqvist* and *Buhrman* [10.14], quite some efforts have been devoted to synthesize and study fine metal particles, and to determine how their properties, which may differ from those of their bulk counterparts, could be exploited for the benefit of various industries [10.15–23]. Synthesis methods may be divided into physical and chemical routes. Within these, we can further distinguish crystal growth with or without a template. The common feature in most of these methods is how the nanoparticles form:

1. Decomposition/reduction of precursor material or evaporation of metal atoms/clusters,
2. Formation of nuclei, and finally
3. Nanocrystal growth.

In this chapter, we select 11 metals – aluminum, bismuth, copper, indium, lead, molybdenum, tantalum, tin, titanium, tungsten, and zinc – which we consider as the most relevant ones, and present a review on their synthesis and applications reported in the open literature.

10.1 Post-Transition Metals

Metals of the p-block elements – and in some classifications also Zn, Cd, and Hg – belong to the category of post-transition metals. Though the chemical properties of p-block metals can be very different due to the rapid decrease of their metallic character with decreasing number of periods and increasing group number, common features of these metals are their low melting point, ductility, and moderate electrical as well as thermal conductivity (except for aluminum, which has superior electron and phonon transport behavior compared with most of the metals in the entire Periodic Table of elements). In Sect. 10.1, we consider lead, bismuth, tin, indium, and aluminum, as the most frequently applied metals of the p-block elements with reasonable potential in future nanodevices [10.24, 25].

10.1.1 Lead, Bismuth, Tin, and Indium

Lead, bismuth, tin, and indium, typically known for their low melting point, ductility, and good wetting by other metals, are all predestined to be excellent soldering materials. Owing to their low Young's moduli ($E_{Pb} = 14.0\,GPa$, $E_{Bi} = 31.7\,GPa$, $E_{Sn} = 41.4\,GPa$, and $E_{In} = 12.7\,GPa$) [10.26] compared with other ordinary metals (e.g., $E_{Cu} = 110\,GPa$, $E_{Al} = 68.0\,GPa$, and $E_{W} = 400\,GPa$), soft mechanical bonds are enabled and used in sealing, plumbing, as well as (solid-state) lubrication. The electrical properties, which depend also on the crystal size of these materials, also have some peculiarities. Lead has a relatively high superconductivity-transition temperature ($T_c \approx 6\,K$ [10.27, 28], one of the highest values among pure metals). Bismuth has a very high thermoelectric coefficient ($S \approx -30$ to $60\,\mu V/K$ [10.29, 30], depending on crystal size) and large mean free path of carriers [10.31–36], and shows semiconducting behavior on the nanoscale [10.37–39], suggesting applications in novel electronic devices. Although many studies deal with the superconducting behavior of nanowires of tin and indium, demonstrating shape- and size-dependent [10.40–42] properties [10.43,44], real applications of these nanostructured metals are mainly related to lead-free electronics packaging [10.45], catalysis [10.46], and batteries [10.47], although they are also used as a sacrificial template for galvanic exchange plating [10.48] or as a starting material of the widely used tin and indium oxides and other compounds. Accordingly, a large number of different methods have been developed to generate both Pb [10.49–64] and Bi [10.31–36, 65–76] nanostructures of various shapes and sizes [10.49–56].

Lee and coworkers recently demonstrated a vapor condensation method to synthesize zero-dimensional Pb nanoparticles by evaporating high-purity lead in Ar atmosphere at 0.1–2 Torr pressure [10.57]. The particles were collected by thermophoresis using a steel plate cooled with liquid nitrogen. The mean size of the nanoparticles could be varied from 4.5 to 86 nm. Another useful route leading to nanoparticles was developed by *Dang* et al., in which a surfactant-assisted solution-phase approach was applied to generate nanoparticles with average diameter of 40 nm [10.53]. First, Pb granules were dispersed in stearic acid containing paraffin oil at 330 °C. Small droplets of lead were generated by a stirring force, immediately reacting with stearic acid to form a lead stearate layer around the droplet. Tribological measurements of the nanoparticles dispersed in paraffin oil showed that, even at very low concentration, the antiwear performance was markedly improved.

In a set of publications [10.49, 50], *Xia* and coworkers demonstrated a bottom-up approach for chemical synthesis of Pb spherical colloids by thermal decomposition of lead acetate in the presence of tetra(ethylene glycol) (TEG) and poly(vinyl pyrrolidone) (PVP). Large quantities of single-crystal Pb nanowires [10.54, 58] (Fig. 10.1a) can be obtained under conditions similar to in the aforementioned approach; however, the reaction must be performed in ethylene glycol. In comparison with the evolution of face-centered cubic (fcc) metal nanowires, ethylene glycol here only serves as a high-boiling-point solvent to facilitate thermal decomposition of the precursor, while the major function of PVP is to prevent Pb nanoparticles from aggregating in the nucleation stage. The growth mechanism (Fig. 10.1c,d)

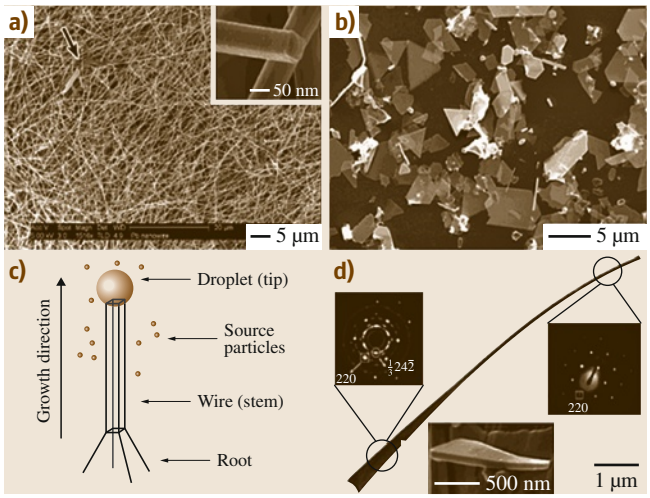


Fig. 10.1 **(a)** Scanning electron microscopy (SEM) image of Pb nanowires prepared in ethylene glycol in the presence of PVP. *Inset* shows the rectangular cross-section of the nanowires. **(b)** SEM image of hexagonal and triangular flakes of Pb synthesized by increasing the amount of PVP. **(c)** Schematic image of the presumed mechanism for nanowire growth. **(d)** Transmission electron microscopy (TEM) image of a growing nanowire; *insets* show selected-area electron diffraction (SAED) patterns of its root and stem. (After [10.58]) ▶

of these nanowires is believed to be a combination of the solution–liquid–solid (SLS) [10.59] method and the Ostwald ripening phenomenon. In addition to nanoparticles and nanowires, Pb hexagonal and triangular nanoprisms (Fig. 10.1b) have also been reported [10.55, 58]. The preparation of thin plates (thickness $< 100\,\mathrm{nm}$) is based on a kinetically controlled polyol process.

Another useful route to synthesize one-dimensional nanostructures is to load materials into the channels of porous membranes such as track-etched polycarbonate (PTCE), anodic aluminum oxide (AAO) or mesoporous silica membranes (e.g., MCM-41, SBA-15). Loading of these porous structures can be achieved by a wide variety of techniques, such as liquid-phase injection, vapor-phase sputtering, and chemical or electrochemical deposition. Besides porous mesoscopic membranes, crystal surfaces with specific steps and edges may also be used as templates for self-ordering nanoparticles [10.60–64]. One of the major problems associated with such template-directed methods is the difficulty in achieving single-crystalline nanowires in large quantities.

Among the physical methods, evaporation, liquid-phase injection into channels of alumina templates [10.32, 34], as well as breaking up of elongated molten filaments under shear force [10.51, 52] have been utilized to obtain nanostructures of bismuth.

Chemical growth of bismuth nanocrystals was demonstrated by a set of various chemical processes including hydrothermal reactions [10.35, 65], synthesis in reverse micelles [10.66], decomposition/reduction of organometallic precursors and inorganic bismuth salts [10.35, 65, 67, 70–72, 76], and PVP- and/or polyol-mediated syntheses [10.50, 51, 68]. Polyol-mediated methods are of great importance as they allow large-scale synthesis, and most importantly the shape and size of the particles are easy to control by adjusting the ratio of reactants [10.68]; For instance, *Wang* and coworkers [10.73] (Fig. 10.2d) showed that, depending on the Bi/PVP ratio, nanocubes, triangular nanoplates (Fig. 10.2c), and nanospheres of bismuth could be obtained. By adding a trace amount of Fe^{3+}, nanobelts may also be produced.

Sn and In nanostructures are mostly synthesized in a similar fashion to Pb and Bi (i. e., physical vapor deposition and chemical reduction in templates or in solution) [10.43, 47, 77–79]; however, due to the very low standard reduction potential of In ($E^\circ = -0.34\,\mathrm{V}$), stronger reduction conditions are usually needed than are applied for the other metals [10.43, 77–79].

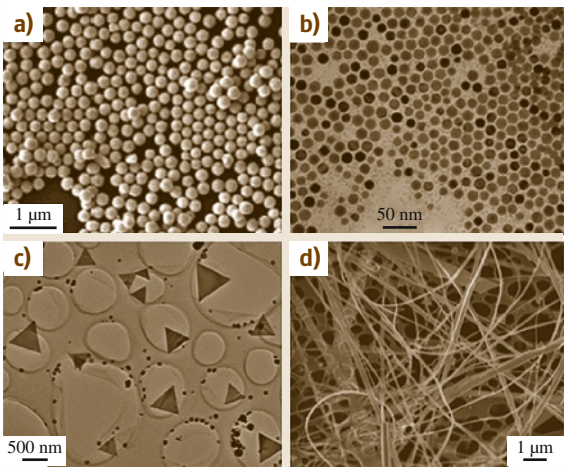


Fig. 10.2 **(a)** SEM image of Bi spherical colloids prepared by the top-down method. (After [10.51], 2012 ACS) **(b)** TEM image of Bi nanoparticles. (After [10.70], 2012, RSC) **(c,d)** TEM and SEM images of Bi triangular nanoplates and nanobelts. (After [10.73])

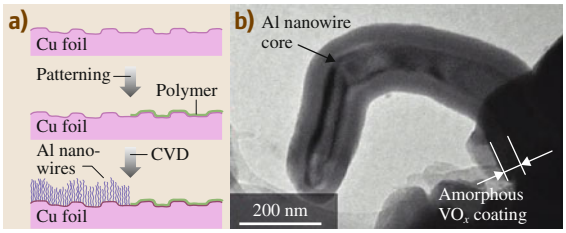


Fig. 10.3 (a) Schematic of CVD growth of Al nanowires. (b) TEM image of VO_x-coated Al nanowire. (After [10.80])

10.1.2 Aluminum

Owing to its wide variety of beneficial properties – such as low density, high strength-to-weight ratio, ductility, electrical conductivity, and corrosion resistance – bulk-phase metallic aluminum is widely used in the packaging, transport, and construction industries, in household appliances, in electronic devices, etc. It is worth pointing out that Al is one of the most abundant elements in the Earth's crust; however, it is almost always found combined with other elements due to its high reactivity. Because of the low standard reduction potential ($E^\circ = -1.66\,\mathrm{V}$), aluminum ions can be reduced almost only with alkali metals. In practice, electrolysis of a melt of Na_3AlF_3-Al_2O_3-CaF_2 (and alternatively other additives such as AlF_3, MgF_2, and KF) is applied for bulk production [10.81]. To date, two main types of methods have been developed for low-temperature electrochemical deposition of Al from nonaqueous solutions. For the first procedure, which was demonstrated in the 1950s [10.82], $AlCl_3$ together with $LiAlH_4$ or LiH is dissolved either in tetrahydrofuran or diethylether. In recent electrochemical deposition techniques, various ionic liquids [10.83–85] are used as solvents for aluminum chloride.

Aluminum nanostructures have been researched and used for several decades in optical coatings and in electrically conductive wiring in micro- and nanoelectronics, since Al thin films are quite easy to produce by thermal evaporation [10.86, 87] and sputtering of the pure metal or by chemical vapor deposition, e.g., from Al-alkyl precursors [10.88–90]. Nanosized patterns of thin Al films are routinely obtained by e-beam lithography [10.91, 92]. A further advantage of using aluminum is the thin, self-limiting native oxide layer, which grows rapidly on exposure of the surface to ambient air. This oxide may be directly used as electrically insulating passivation, or it can be etched easily if not needed. Apart from electrical and optical devices, Al nanoparticles (NPs) have also attracted interest as a future fuel or propellant material owing to the energetic bonds that form on oxidation of Al with oxygen or halogens [10.93, 94].

Various methods to produce aluminum nanostructures have been reported lately. *Mahendiran* and coworkers [10.95] demonstrated synthesis of NPs of ca. 25 nm diameter from a solution of $AlCl_3$ and $LiAlH_4$ in THF using a combined electro- and sonochemical route. *Foley* et al. reported a chemical route, in which triethylamine alane in heptane solution is decomposed at 70 °C in the presence of Ti-isopropoxide, yielding NPs with size from 50 to 500 nm [10.96]. Pulsed laser ablation of Al targets under ethanol or in vacuum – as a rather generic route to prepare various metal nanoparticles – has also been utilized to form Al NPs [10.97–99].

Template-directed techniques offer a plausible way to grow Al nanowires (NWs) too. Electrodeposition from ionic-liquid-based electrolytes [10.100, 101] and injection molding of molten Al metal [10.102] in porous templates have been reported. Aluminum nanowires can be synthesized, in a similar fashion as Zn or Sn, by employing physical vapor deposition (PVD) techniques based on vapor–solid (VS) growth mechanism [10.80, 103]. *Benson* and coworkers decomposed $H_3AlN(CH_3)_3$ precursor at temperatures of 125–300 °C to produce Al nanowires of 45–85 nm diameter on Ni, Cu, and steel surfaces and then used them as a large-specific-surface electrode material for supercapacitor application (Fig. 10.3) [10.80].

10.2 Transition Metals

The elements of the d-block are usually referred to as transition metals and have an incomplete outer d-shell of electrons. In a strict sense, Zn with its electron configuration $[Ar]3d^{10}4s^2$ is not a member of this group, and actually shows quite similar chemical properties to alkali-earth elements. Since most textbooks treat the elements of the Zn group together with the transition metals, here we also discuss it along with copper and some of the refractory metals [10.24, 25, 104]. Titanium, tungsten, molybdenum, and tantalum as hard, mechanically and thermally durable materials are listed after each other in this section. Not only their physical but

also their chemical properties – stemming from their relatively low standard reduction potentials – tie these elements together.

10.2.1 Titanium

Physical vapor deposition methods are among the plausible routes to form nanosized structures of titanium. Evaporated thin films and e-beam lithography-defined patterns represent the mainstream of fabrication, and are used in generating catalyst nanoparticles, thin coatings, as well as electrical components.

Electron-beam-deposited thin (< 1 nm) titanium films have been applied as a solid precursor on a Si surface for titanium silicide nanoparticle formation. When annealing the film in H_2 at 670–900 °C, the metal diffuses into the substrate and forms a silicide phase, which is catalytically active for subsequent chemical vapor deposition (CVD) of Si nanowires [10.106].

Lehtinen and coworkers fabricated Ti nanowires (tens of micrometers long, less than 50 nm in diameter) on a Si surface using e-beam lithography followed by evaporation in ultrahigh-vacuum conditions. Low-energy ion milling was applied to decrease the diameter of the nanowires, allowing size-dependent analysis of electrical transport behavior. Experiments carried out below 1 K showed that the critical temperature for superconductivity is reduced and that broadening of the transition temperature range occurs with decreasing wire diameter. This latter effect is due to quantum fluctuations of the order parameter, which may be utilized to construct new quantum devices such as qubits and standards of electric current [10.107, 108].

Titanium is known to form strong bonds with a number of different types of solid surfaces, and thus Ti (and also W and Ta) is frequently used as an adhesion-promoter sublayer for thin films of other metals (such as Au, Pt, Cu, and Ni) to be deposited on plastics or metal oxides/nitrides [10.109]. While most of the metals directly adhere to Ti, the reason for good sticking to oxides (and some polymers) is the −OH-terminated Ti surface, which may easily form when the surface is exposed to ambient air or to traces of oxygen and water vapor in the vacuum chamber. The interaction between the hydroxyl groups of a Ti surface and, e.g., the hydroxyl, carboxyl, and amine groups of the other surface can result in H-bonding or eventually in covalent Ti-O-Me (where Me is a metal) bonds if a condensation reaction takes place, similar to those exploited in nanotransfer printing [10.110]. Carbon also seems to have a reasonably strong interaction with titanium, as

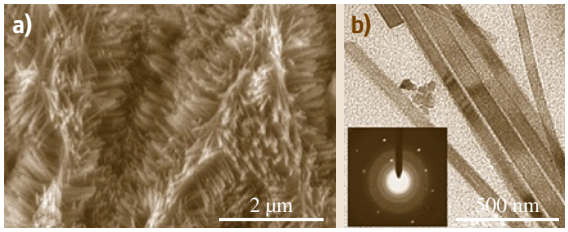


Fig. 10.4 (a) SEM and (b) TEM images of Ti nanowires synthesized on a Ti plate in 5% HCl solution at 180 °C. *Inset* shows a selected-area electron diffraction pattern. (After [10.105])

concluded by Zhang and Dai after studying e-beam-evaporated Ti films deposited on single-walled carbon nanotubes (SWCNT). Titanium films form thin continuous coatings, in contrast to other metals (such as Au, Pd, Fe, and Al), which tend to agglomerate to particles. The as-made Ti coating may be used as a metal nanotube with a coaxial carbon nanotube (CNT) interior, or alternatively can be applied as a buffer layer or adhesion promoter for other metals, thus enabling synthesis of multilayer structures having single-walled carbon nanotubes in their core, Ti in the mid-layer, and a tubular metal coating layer (Au, Pd, Fe, and Al) outside [10.111].

While pulsed laser ablation (PLA) of a Ti target in vacuum has been demonstrated as a potential tool for generating nanoparticles of Ti [10.112, 113], somehow PLA has not become a practical production method for metallic Ti NPs during the past years. Instead, TiO_2 nanoparticles have been synthesized by ablating a metal target submerged in water [10.114–116].

Chemical synthesis of Ti has also been demonstrated by a variety of methods. Though it was found impossible to reduce Ti^{4+} to Ti with $NaBH_4$ in ionic liquids [10.117], chemical vapor deposition from a $TiCl_4$ precursor at 640–670 °C followed by annealing in H_2 at 920 °C was sufficient to produce Ti-rich nanosized islands on Si wafers and to form $TiSi_2$ catalyst particles for subsequent Si nanowire synthesis [10.118]. *Corrias* and coworkers applied potassium intercalated multi-walled carbon nanotubes (MWCNTs) as templates with reducing behavior to generate α-Ti (hexagonal close-packed, hcp) nanoparticles of 2 nm size on the surfaces of CNTs from Ti isopropoxide [10.119].

A facile route to produce Ti nanowires on Ti plates was proposed by *Wu* and coworkers [10.105]. In their method, Ti surfaces were etched in dilute (5%) aqueous HCl solution at elevated temperature (150–200 °C) in an autoclave, resulting in the for-

mation of nanowire forests on the surface (Fig. 10.4). When decorated with Pt nanoparticles, the Ti nanowire-supported materials could be used as high specific surface area catalytic electrodes with low charge-transfer resistance ($85\,\Omega/cm^2$), e.g., for oxidation of methanol [10.105].

Another interesting route to produce Ti nanowires was proposed by *Huang* et al. [10.121]. They used electrochemical (anodic) etching of NiTi substrates in 20% H_2SO_4 and 80% methanol solution (at 18 V for 60 s), yielding single-crystal titanium nanowires along the ⟨110⟩ directions of the substrate.

While both chemical- and electrochemical etching techniques were suitable to form Ti nanostructures on Ti or Ti-containing surfaces, attempts to obtain metallic Ti on conductive surfaces by electrodeposition seemed to fail. In their work, *Endres* et al. showed that metallic titanium cannot be electrodeposited from titanium halides and isopropoxide when using ionic liquids (ILs) as solvents despite the wide electrochemical window offered by the solvents. They suppose that the underlying reason is the insolubility of partially reduced nonstoichiometric halide and oxide products in the ILs [10.122].

As synthesis of truly metallic Ti nanostructures is mainly limited to low-throughput methods, applications of such structures have not really spread into daily use in commercial devices. However, once large-scale production of Ti nanoparticles or nanowires and their packaging to prevent, e.g., their oxidation become possible, a series of novel and fascinating applications may be realized according to computational studies reported lately.

First-principles total-energy calculations revealed that Ti atoms adsorbed on the surface of SWCNTs are able to bond four H_2 molecules per Ti atom because of a unique hybridization of the Ti-d, H-σ*, and C-p orbitals. Though calculations for nanoparticles were not performed, the results suggest hydrogen storage and catalyst applications [10.3]. Molecular dynamics (MD) simulations showed that ultrathin ($d < 2$ nm) Ti NWs have helical structure with molecule-like electronic states for diameters below 1 nm and bulk-like behavior above that [10.5]. The melting temperature of similar ultrathin Ti NWs with multishell cylindrical structures was calculated (by MD simulations) to be lower than that of the bulk metal but higher than that of nanoparticles of similar size (i. e., less than 1.2 nm in diameter). The computed smooth heat capacity versus temperature curve and the sensitivity of bond length fluctuation to temperature suggest the coexistence of liquid and solid phases due to finite-size effects [10.4, 6]. Though bulk Ti is a paramagnetic material, deformed nanowires of Ti are predicted to show ferromagnetic ordering due to the polarization of the d-electron states [10.7, 8].

10.2.2 Tungsten

Large amounts of bulk-phase tungsten are used in hard materials such as tungsten carbide and in alloys that provide high mechanical strength and corrosion resistance. Owing to its good electrical conductivity and good wetting properties, tungsten is a component of under-metallization layers in integrated circuits (similar to titanium and molybdenum). Its high melting point and low vapor pressure at elevated temperatures allow high-temperature applications in vacuum tube filaments, heating elements, and incandescence lamps.

Interest in tungsten nanostructures has been growing steadily as they may find use in applications as pH-sensitive electrodes [10.123], atomic force microscopy probes [10.124], and field emitters [10.125, 126], and in components of nanoelectromechanical systems [10.127].

Metal nanoparticles can be obtained by reducing tungsten oxides at 500 °C in H_2 [10.128], in contrast to microparticles requiring 900 °C [10.129]. Nanoparticles of tungsten (with oxide shell) have also been prepared by reducing a metal complex by an organopolysilane oligomer at low temperature [10.130]. Further synthesis procedures include thermal decompo-

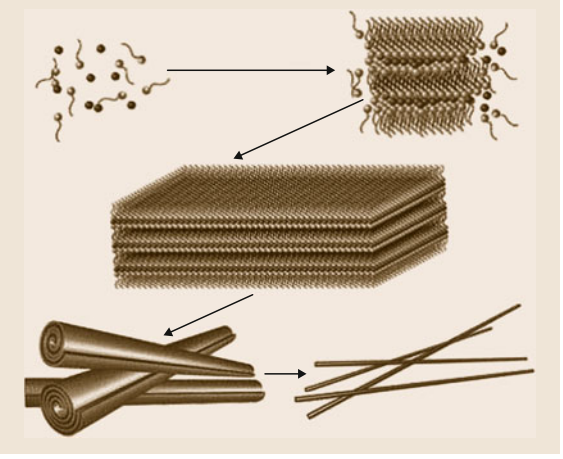


Fig. 10.5 Growth mechanism of tungsten nanowires by a vacuum pyrolysis carbothermal (VPC) process from a mesolamellar precursor. (After [10.120])



Fig. 10.6 Tungsten nanowires prepared by directional solidification and electrochemical processing of NiAl-W eutectic alloy. (After [10.140], courtesy of Wiley-VCH)

sition of $W(CO)_6$ [10.131, 132], sonoelectrochemical reduction from citrate complexes [10.133], e-beam-induced radiation damage of WO_3 [10.134], pulsed laser ablation of a W target in He atmosphere [10.135], ultraviolet (UV) laser-assisted chemical vapor deposition from $WF_6/H_2/Ar$ [10.136], and e-beam-induced decomposition of $W(CO)_6$ [10.137, 138]. Besides nanoparticles, only a few reports have been published on synthesis of one-dimensional tungsten nanostructures [10.120, 139–141].

In a novel method, metallic tungsten nanowires with diameters of 20–80 nm and lengths of several micrometers have been obtained in large quantities [10.120] by *Li* and coworkers. First, mesolamellar tungsten oxide-surfactant precursor (WO-L) was generated under mild hydrothermal conditions. Then, a vacuum pyrolysis/carbothermal (VPC) process was applied to remove the surfactant species from the lamellar inorganic-surfactant precursor. The authors proposed a new mechanism (Fig. 10.5) for the nanowire formation including four steps:

1. Evolution of cetyltrimethylammonium (CTA)–WO_4 ion pairs
2. Formation of highly ordered lamellar assemblies
3. Development of scrolls by rolling up of lamellar sheets owing to vacuum heating
4. Reduction of tungstate by pyrolytic carbon.

High-aspect-ratio single-crystalline NWs with a thin oxide layer were successfully synthesized by directional solidification and electrochemical processing of NiAl-W eutectic alloy (Fig. 10.6) [10.140] and by rapid thermal annealing of W films [10.126]. Catalytic synthesis based on a vapor–solid–solid (VSS) mechanism route was reported by Wang and coworkers. Tungsten powder mixed and then annealed together with $NiNO_3$ was used to prepare WO_3 and $NiWO_4$, which in turn was reduced with H_2 [10.142] to obtain W nanowires as the product with Ni nanoparticles at the tip of the wires.

10.2.3 Molybdenum

Bulk molybdenum is primarily utilized in metallurgy to prepare alloys with advanced wear- and corrosion-resistance behavior. When going to the nanoscale, direct applications of Mo are very rare and limited to catalysis mainly. Though nanoparticles or clusters of this metal are relatively easy to synthesize by both chemical [10.9, 143–148] and physical [10.149–151] methods, its practical/industrial relevance – other than in catalysis – seems to be negligible compared with molybdenum oxides and sulfides, and is mainly the focus of academic research today [10.10–13].

However, molybdenum sulfides and oxides are widely studied and used, e.g., in tribology (wear and friction of surfaces) [10.152, 153], in catalysis [10.154–161], and in catalytic electrodes for supercapacitors and fuel cells [10.162–165], as well as holding promise for use in novel electrical components [10.166–168]. So far, the petrol industry has been the major user of MoS_2 catalyst nanoparticles (and their different modified derivatives) on alumina support for hydrodesulfurization (HDS) of hydrocarbons [10.154–157]. Apart from HDS, sulfides are also considered to be useful in catalyzing methanation [10.158] and in H_2 generation reactions [10.159, 160].

10.2.4 Tantalum

While nanostructures of carbides, oxides, nitrides, oxynitrides, and sulfides of tantalum are routinely synthesized by, e.g., vapor–solid reaction, chemical vapor deposition, laser ablation, surface-assisted chemical vapor transport, anodization, and sputtering, and used in superconductor, photocatalyst, and other applications, research on metallic Ta nanoparticles is rather sparse [10.169–179]. The reason is similar to that of other transition metals: it is difficult to reduce from its oxidized state, and once reduced, it is prone to oxidation under common environmental conditions. There are, however, some interesting methods to produce and utilize Ta nanostructures.

Mativetsky and coworkers have grown nanoparticles (and self-aligned chains of those along surface

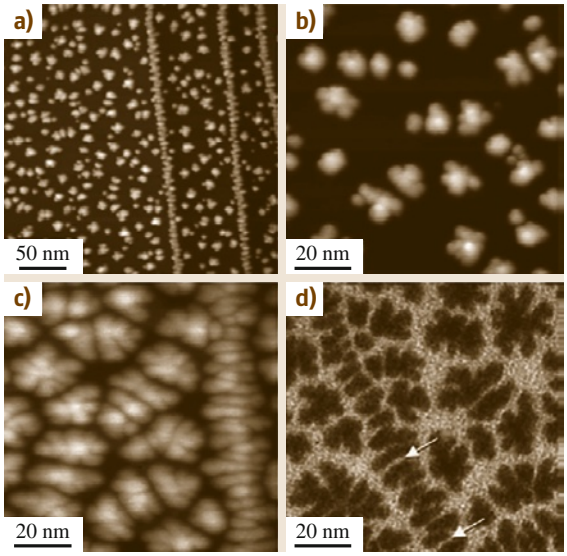


Fig. 10.7a–d Tantalum nanoparticles formed on KBr 001 surface after e-beam deposition of **(a,b)** 0.6 and **(c,d)** 1.8 molecular layers. Images in panels **(a–c)** were acquired using non-contact-mode atomic force microscopy, while the image in panel **(d)** was taken by transmission electron microscopy. *Arrows* indicate gaps between adjacent nanoparticles nucleated at a step. (After [10.180])

steps) on single-crystal KBr by e-beam deposition (Fig. 10.7). Despite the cubic lattice of the substrate, the Ta particles form as separate islands with fractal-like shape, suggesting poor interaction between the substrate and the nanoparticles [10.180].

Nanoparticles of Ta were shown to form in a H_2/Ar arc plasma when applying bulk Ta as both anode and cathode material. Because of the high temperature, the electrodes start to melt and evaporate, leading to a vapor of metal atoms and clusters, which thermalize and coalesce through collisions, thus forming nanoparticles [10.182].

Besides the aforementioned physical methods, chemical routes may also be possible under strongly reducing conditions. Metal-graphite multilayer (MGM) structures may be obtained by intercalating metal chlorides for instance with natural or highly oriented pyrolytic graphite (NG or HOPG, respectively) followed by chemical reduction of the chloride in H_2 flow at elevated temperatures [10.183, 184]. Using a two-step procedure reported by Walter et al., first, anhydrous $TaCl_5$ is mixed with HOPG and stored in Cl_2 atmosphere at 400 °C for 4 days, then exposed to H_2 gas at 1000 °C for 1 week to prepare Ta nanoparticles intercalated with the graphene layers in graphite. The as-obtained structures behave as superconductors similar to tantalum carbide. As suggested by *Suzuki* and coworkers, the Ta nanoparticles act as localized spins, which can couple with the adjacent layers separated by the graphitic layers [10.184].

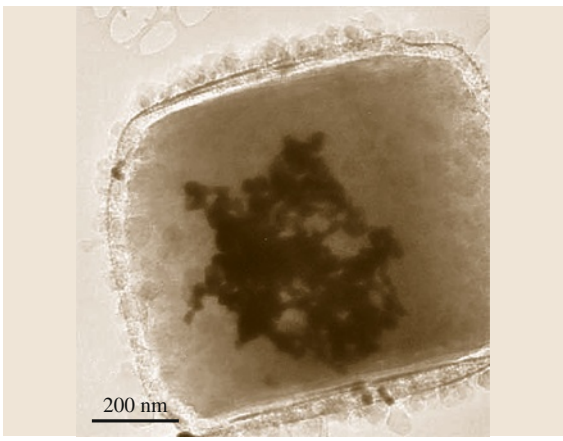


Fig. 10.8 TEM image of salt-encapsulated Ta nanoparticles synthesized by the sodium/halide gas-phase (flame) combustion process. (After [10.181])

Axelbaum and colleagues developed and patented a technology capable of producing large volumes of nanopowders of metals as well as their composites by reacting sodium vapor with gas-phase metal chlorides in a flame [10.181, 185] (Fig. 10.8). At high temperatures, Na vapor reduces metal (such as Ta, Ti, Al, Nb, Si, W, or Fe) chlorides (or other halides) and produces metal nanoparticles. By controlling the temperature and heat losses in the reactor, condensation of the byproduct NaCl vapor on the metal nanoparticles can be regulated. Increased temperature favors sublimation of the salt and consequently the formation of larger metal nanoparticle cores, while lower temperatures result in condensation of the salt vapor on the core. The as-formed shell acts as a barrier coating, protecting the metal core from moisture and air. The salt encapsulation can be removed, for instance, by vacuum sublimation, thus releasing the Ta nanoparticles for their end use.

10.2.5 Zinc

Zinc is an industrially important metal applied in large quantities in batteries, anticorrosion coatings, and various structural alloys today. Most of the studies related to elemental zinc are focused on the generation of zinc

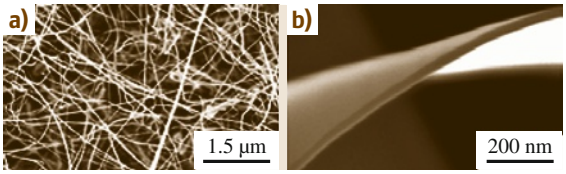


Fig. 10.9 Low- (a) and high-magnification (b) SEM images of Zn nanobelts. (After [10.190])

chalcogenide nanostructures due to their semiconducting and piezo- and pyroelectric properties, which find applications in pigments and (photo)catalytic processes, and thus are widely studied in the contemporary literature [10.186–189].

Vapor–solid (VS) growth of Zn nanowires has been reported by several groups. In this method, a vapor of Zn is generated first under protective gas, by either evaporating pure metal [10.191] or decomposing organic zinc compounds [10.192], or by reacting ZnO or ZnS with carbon, ammonia, H_2, etc. at elevated temperature [10.190, 193, 194]. When the vapor of Zn enters a colder zone of the reactor (typically a two-zone furnace is employed), condensation of the vapor starts and Zn nanowires are observed to grow. Since the process is not catalyzed by any separate nanoparticle or seed, it is referred to as VS growth [10.191]. To produce nanoparticles, PLA has been applied [10.195, 196]. Most of these studies, however, agree that Zn nanostructures are covered by a thin layer of ZnO [10.191, 193, 195] (Fig. 10.9a,b).

Solution-phase synthesis of Zn nanomaterials has not been widely explored, since the procedure has to be conducted under inert gas protection to avoid oxidation. Electrochemical deposition as one of the major synthesis tools for metallic zinc has been successfully utilized to prepare both single- and polycrystalline nanowires with diameter of 40–100 nm in porous AAO and PTCE membranes [10.197].

10.2.6 Copper

In everyday life, copper is used for several kinds of applications and devices. One major advantage of copper, compared with other metals, is its excellent electrical conductivity, which is greater than that of any other metal apart from silver. Most copper is used in electrical wires for motors, transformers, cars, integrated circuits, etc. to transfer electrical energy in an efficient manner with minimal environmental impact. Copper is also widely used in heat exchangers and heat sinks due to its high thermal conductivity. Other attractive properties of this metal are its durability, corrosion resistance, and antimicrobial effect, which enable a vast number of applications in the construction industry as a structural and alloying material, and as a functional surface coating.

Most probably, catalysis and electronics are the two main fields that could greatly benefit from the availability of copper nanostructures. In the last decades, copper nanostructures with various morphologies and oxidation states have been widely studied for applications in heterogeneous catalysis [10.198–200]. Furthermore, the surface chemistry on Cu has also been elaborated in detail by *Somorjai* et al. [10.201]. Copper, particularly in nanoparticle form [10.202], has found use as a catalyst in water–gas shift reactions [10.200,203,204], methanol synthesis [10.205–207], aryl homocoupling [10.208], growth of Si nanowires by chemical vapor deposition (CVD) [10.209], etc.

One of the very first methods for preparation of Cu nanowires (which were encapsulated in carbon nanotubes) was demonstrated by *Setlur* et al. in a hydrogen arc between a graphite cathode and a graphite–copper anode [10.210]. Evaporation and subsequent condensation of Cu, forming nanorods and nanowires at 10^{-4} Pa pressure in a transmission electron microscope (TEM) column, was reported by *Liu* and *Bando* [10.211]. Though several other physical methods such as laser ablation [10.212, 213], pulsed wire discharge [10.214], and evaporation [10.215] exist, because of their limited production volume and associated price, the aforementioned physical methods are surpassed by the chemical ones, since a number of different reaction routes enable the production of nanoparticles of different sizes and shapes, even in a simple beaker under mild conditions [10.216–228]. The key to obtaining various crystal shapes is the presence of surface-capping agents (to selectively adsorb onto and block specific crystal planes) [10.17, 229] or addition of ionic impurities [10.69, 225].

Hexagonal nanoplates of copper have been prepared by reduction of $Cu(CH_3CO_2)_2$ with hydrazine hydrate in acetonitrile [10.226]. Nanoparticles of cubic, tetrahedral, and rod shapes with size ranging from 5 to 25 nm were obtained by reduction of copper acetylacetonate with 1,2-hexadecanethiol in octyl ether in the presence of oleyl amine and oleic acid serving as capping molecules [10.227]. Cu nanowires with diameter of ca. 85 nm were prepared by a complex-surfactant-assisted hydrothermal route from Cu(II)–glycerol complexes reduced by phosphite in the presence of sodium dodecyl benzenesulfonate (SDBS) [10.221]. Recently,

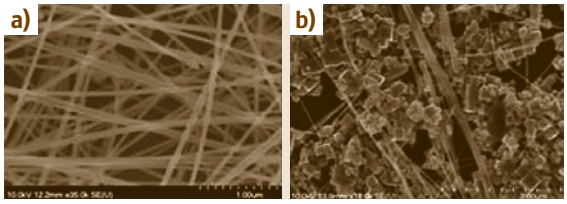


Fig. 10.10 (**a**) SEM image of Cu nanowires prepared by a hydrothermal process in the presence of hexadecylamine (HDA). (**b**) SEM image of Cu nanocubes. (After [10.220])



Fig. 10.11 CuPd bimetallic nanotubes prepared by galvanic exchange reaction on Cu nanowires. (After [10.232])

we reported a very rapid route to ultralong copper nanowires (Fig. 10.10a) and nanocubes (Fig. 10.10b) on a large scale with HDA as capping agent [10.220]. In a typical synthesis, $CuCl_2$ and glucose were dissolved in water, followed by addition of hexadecylamine (HDA). After stirring for several hours, the light-blue solution was placed in an autoclave that was heated to 120 °C. In a recent study, this method was slightly modified by *Jin* and coworkers to produce single-crystal Cu nanowires [10.230]. In a similar hydrothermal route, polycrystalline and single-crystalline Cu nanowires were generated in the presence of octadecylamine [10.231]. Though copper has a positive standard electrode potential ($E^\circ = 0.34\,\mathrm{V}$) it is still rather easy to oxidize its surface, or even the entire volume of the material if it is nanostructured. For instance, exposing Cu nanowires to solvated cations of nobel metals (Pt^{2+} or Pd^{2+}) can initiate galvanic replacement reactions, in which the nanowires undergo oxidation and dissolution while the precious metal is depositing on the surface of copper thus forming nanotubes of CuPt or CuPd alloys [10.232] (Fig. 10.11).

It is worth mentioning that Cu nanostructures are prone to oxidation. Even trace amounts of oxygen dissolved in the solution of reactants can cause partial oxidation, causing sometimes controversial results, thus it still remains a great challenge to synthesize pure copper particles by solution-phase methods [10.69, 233–235]. One way to protect Cu seeds from oxidation during production is to apply a N_2 atmosphere and to purge the reaction solution with inert gases.

10.3 Concluding Remarks

In this chapter, we have provided an overview on nanostructures of metals excluding ferromagnetic and precious ones, which are described in Chap. 9. As most of the metals belong to this category, we organized them based on the following criteria:

1. Reasonable chemical stability under ordinary conditions
2. Abundance of raw materials
3. Industrial importance in bulk form.

As it turns out from the literature review, this particular field of materials science has not yet been fully explored. Some potential applications of the metal nanostructures are discussed in the cited literature. However, despite numerous reports on laboratory-scale synthesis, controlled bulk production and utilization of such nanostructures are still in the early stage of technical development and should be improved. Since the majority of these elements are prone to oxidation, difficulties related to chemical stability need to be studied and should be solved by surface engineering; otherwise nanostructures made of compounds of these metals are expected as a result. Besides the existing knowledge, further peculiarities of these materials at the nanoscale remain to be revealed to enable their wide use in novel technologies and devices.

References

10.1 A.S. Edelstein, R.C. Cammarata: *Nanomaterials: Synthesis, Properties and Applications* (Institute of Physics, Bristol 2002)

10.2 G. Schmid: *Nanoparticles: From Theory to Application* (Wiley-VCH, Weinheim 2011)

10.3 T. Yildirim, S. Ciraci: Titanium-decorated carbon nanotubes as a potential high-capacity hydrogen storage medium, Phys. Rev. Lett. **94**, 175501 (2005)

10.4 B. Wang, G. Wang, X. Chen, J. Zhao: Melting behavior of ultrathin titanium nanowires, Phys. Rev. B **67**, 193403 (2003)

10.5 B. Wang, S. Yin, G. Wang, J. Zhao: Structures and electronic properties of ultrathin titanium nanowires, J. Phys. Condens. Matter **13**, L403 (2001)

10.6 Y. Imry, D.J. Scalapino: Pseudo - first - order phase transitions in one dimension, Phys. Rev. A **9**, 1672–1675 (1974)

10.7 Z. Zhu, J. Gu, Y. Jia: Emergence of magnetism in titanium nanowires, J. Phys. Condens. Matter **387**, 190–193 (2007)

10.8 H.R. Hajiyani, M. Jafari: Magneto optical properties of β [110] and ω [100] titanium nanowires, J. Magn. Magn. Mater. **324**, 418–423 (2012)

10.9 H.K. Kim, S.H. Huh, J.W. Park, J.W. Jeong, G.H. Lee: The cluster size dependence of thermal stabilities of both molybdenum and tungsten nanoclusters, Chem. Phys. Lett. **354**, 165–172 (2002)

10.10 Y. Shibuta, T. Suzuki: Phase transition in substrate-supported molybdenum nanoparticles: A molecular dynamics study, Phys. Chem. Chem. Phys. **12**, 731–739 (2010)

10.11 Y. Shibuta, T. Suzuki: A molecular dynamics study of the phase transition in bcc metal nanoparticles, J. Chem. Phys. **129**, 144102 (2008)

10.12 W. Zhang, X. Ran, H. Zhao, L. Wang: The nonmetallicity of molybdenum clusters, J. Chem. Phys. **121**, 7717–7724 (2004)

10.13 W.H. Qi: Comment on: The cluster size dependence of thermal stabilities of both molybdenum and tungsten nanoclusters, Chem. Phys. Lett. **402**, 279–281 (2005)

10.14 C.G. Granqvist, R.A. Buhrman: Ultrafine metal particles, J. Appl. Phys. **47**, 2200–2219 (1976)

10.15 K. Sattler, J. Muhlbach, E. Recknagel: Generation of metal clusters containing from 2 to 500 atoms, Phys. Rev. Lett. **45**, 821–824 (1980)

10.16 C.W. Won, H.H. Nersisyan, H.I. Won, J.H. Lee: Refractory metal nanopowders: Synthesis and characterization, Curr. Opin. Solid State Mater. Sci. **14**, 53–68 (2010)

10.17 M. Mohl: Egydimenziós fém nanoszerkezetek előállítása és vizsgálata/Preparation and Characterization of One-Dimensional Nanostructures, Dissertation (University of Szeged, Hungary 2011)

10.18 R.W. Murray: Nanoelectrochemistry: Metal nanoparticles, nanoelectrodes, and nanopores, Chem. Rev. **108**, 2688–2720 (2008)

10.19 B.R. Cuenya: Synthesis and catalytic properties of metal nanoparticles: Size, shape, support, composition, and oxidation state effects, Thin Solid Films **518**, 3127–3150 (2010)

10.20 C.N.R. Rao, G.U. Kulkarni, P.J. Thomas, P.P. Edwards: Metal nanoparticles and their assemblies, Chem. Soc. Rev. **29**, 27–35 (2000)

10.21 A. Tavakoli, M. Sohrabi, A. Kargari: A review of methods for synthesis of nanostructured metals with emphasis on iron compounds, Chem. Pap. **61**, 151–170 (2007)

10.22 K. Watanabe, D. Menzel, N. Nilius, H. Freund: Photochemistry on metal nanoparticles, Chem. Rev. **106**, 4301–4320 (2006)

10.23 H.M. Chen, R. Liu: Architecture of metallic nanostructures: Synthesis strategy and specific applications, J. Phys. Chem. C **115**, 3513–3527 (2011)

10.24 D.R. Lide: *Handbook of Chemistry and Physics*, 72nd edn. (CRC, Boca Raton 1991–1992)

10.25 P. Atkins, T. Overton, J. Rourke, M. Weller, F. Armstrong: *Shriver and Atkins Inorganic Chemistry* (Oxford University Press, New York 2006)

10.26 MatWeb: Material Property Data (MatWeb LLC, Blacksburg 2012) available at http://www.matweb.com/index.aspx

10.27 J. Wang, Y. Sun, M. Tian, B. Liu, M. Singh, M.H.W. Chan: Superconductivity in single crystalline Pb nanowires contacted by normal metal electrodes, Phys. Rev. B **86**, 035439 (2012)

10.28 J. Wang, X. Ma, S. Ji, Y. Qi, Y. Fu, A. Jin, L. Lu, C. Gu, X. Xie, M. Tian, J. Jia, Q. Xue: Magnetoresistance oscillations of ultrathin Pb bridges, Nano Res. **2**, 671–677 (2009)

10.29 V.D. Das, N. Soundararajan: Size and temperature effects on the Seebeck coefficient of thin bismuth films, Phys. Rev. B **35**, 5990–5996 (1987)

10.30 Y. Ishikawa, Y. Hasegawa, H. Morita, A. Kurokouchi, K. Wada, T. Komine, H. Nakamura: Resistivity and Seebeck coefficient measurements of a bismuth microwire array, Phys. Condens. Matter **368**, 163–167 (2005)

10.31 V. Kamaev, V. Kozhevnikov, Z.V. Vardeny, P.B. Landon, A.A. Zakhidov: Optical studies of metallodielectric photonic crystals: Bismuth and gallium infiltrated opals, J. Appl. Phys. **95**, 2947–2951 (2004)

10.32 Z. Zhang, D. Gekhtman, M.S. Dresselhaus, J.Y. Ying: Processing and characterization of single-crystalline ultrafine bismuth nanowires, Chem. Mater. **11**, 1659–1665 (1999)

10.33 M. Tian, J. Wang, Q. Zhang, N. Kumar, T.E. Mallouk, M.H.W. Chan: Superconductivity and quantum os-

cillations in crystalline Bi nanowire, Nano Lett. **9**, 3196–3202 (2009)
10.34 Z. Zhang, J.Y. Ying, M.S. Dresselhaus: Bismuth quantum-wire arrays fabricated by a vacuum melting and pressure injection process, J. Mater. Res. **13**, 1745 (1998)
10.35 Y. Gao, H. Niu, C. Zeng, Q. Chen: Preparation and characterization of single-crystalline bismuth nanowires by a low-temperature solvothermal process, Chem. Phys. Lett. **367**, 141–144 (2003)
10.36 D. Gekhtman, Z.B. Zhang, D. Adderton, M.S. Dresselhaus, G. Dresselhaus: Electrostatic force spectroscopy and imaging of Bi wires: Spatially resolved quantum confinement, Phys. Rev. Lett. **82**, 3887–3890 (1999)
10.37 Z. Zhang, X. Sun, M.S. Dresselhaus, J.Y. Ying, J. Heremans: Electronic transport properties of single-crystal bismuth nanowire arrays, Phys. Rev. B **61**, 4850–4861 (2000)
10.38 S.H. Choi, K.L. Wang, M.S. Leung, G.W. Stupian, N. Presser, B.A. Morgan, R.E. Robertson, M. Abraham, E.E. King, M.B. Tueling, S.W. Chung, J.R. Heath, S.L. Cho, J.B. Ketterson: Fabrication of bismuth nanowires with a silver nanocrystal shadowmask, J. Vac. Sci. Technol. A **18**, 1326–1328 (2000)
10.39 M.R. Black, G. Dresselhaus, M.S. Dresselhaus: Nanowires. In: *Springer Handbook of Nanotechnology*, ed. by B. Bhushan (Springer, Berlin, Heidelberg 2004) pp. 99–138, http://www.springerlink.com/Content/g52qg1542050x561/
10.40 A.A. Shanenko, M.D. Croitoru, M. Zgirski, F.M. Peeters, K. Arutyunov: Size-dependent enhancement of superconductivity in Al and Sn nanowires: Shape-resonance effect, Phys. Rev. B **74**, 052502 (2006)
10.41 S. Michotte, S. Matefi-Tempfli, L. Piraux: Current–voltage characteristics of Pb and Sn granular superconducting nanowires, Appl. Phys. Lett. **82**, 4119–4121 (2003)
10.42 M. Tian, J. Wang, J.S. Kurtz, Y. Liu, M.H.W. Chan, T.S. Mayer, T.E. Mallouk: Dissipation in quasi-one-dimensional superconducting single-crystal Sn nanowires, Phys. Rev. B **71**, 104521 (2005)
10.43 N.H. Chou, X. Ke, P. Schiffer, R.E. Schaak: Room-temperature chemical synthesis of shape-controlled indium nanoparticles, J. Am. Chem. Soc. **130**, 8140–8141 (2008)
10.44 Y. Hsu, S. Lu, Y. Lin: Nanostructures of Sn and their enhanced, shape-dependent superconducting properties, Small **2**, 268–273 (2006)
10.45 M. Amagai: A study of nanoparticles in Sn-Ag based lead free solders, Microelectron. Reliab. **48**, 1–16 (2008)
10.46 C.L. Monica, G.J. Siri, G.F. Santori, O.A. Ferretti, M.M. Ramirez-Corredores: Surface characterization of Li-modified platinum/tin catalysts for isobutane dehydrogenation, Langmuir **16**, 5639–5643 (2000)
10.47 M. Noh, Y. Kim, M.G. Kim, H. Lee, H. Kim, Y. Kwon, Y. Lee, J. Cho: Monomer-capped tin metal nanoparticles for anode materials in lithium secondary batteries, Chem. Mater. **17**, 3320–3324 (2005)
10.48 N.H. Chou, R.E. Schaak: Shape-controlled conversion of β-Sn nanocrystals into intermetallic M-Sn (M=Fe, Co, Ni, Pd) nanocrystals, J. Am. Chem. Soc. **129**, 7339–7345 (2007)
10.49 Y. Wang, L. Cai, Y. Xia: Monodisperse spherical colloids of Pb and their use as chemical templates to produce hollow particles, Adv. Mater. **17**, 473–477 (2005)
10.50 Y. Wang, M. Ibisate, Z.Y. Li, Y. Xia: Metallodielectric photonic crystals assembled from monodisperse spherical colloids of bismuth and lead, Adv. Mater. **18**, 471–476 (2006)
10.51 Y. Wang, Y. Xia: Bottom-up and top-down approaches to the synthesis of monodispersed spherical colloids of low melting-point metals, Nano Lett. **4**, 2047–2050 (2004)
10.52 U. Jeong, Y. Wang, M. Ibisate, Y. Xia: Some new developments in the synthesis, functionalization, and utilization of monodisperse colloidal spheres, Adv. Funct. Mater. **15**, 1907–1921 (2005)
10.53 Y. Zhao, Z. Zhang, H. Dang: Fabrication and tribological properties of Pb nanoparticles, J. Nanopart. Res. **6**, 47–51 (2004)
10.54 Y. Wang, T. Herricks, Y. Xia: Single crystalline nanowires of lead can be synthesized through thermal decomposition of lead acetate in ethylene glycol, Nano Lett. **3**, 1163–1166 (2003)
10.55 X. Lin, H. Claus, U. Welp, I.S. Beloborodov, W. Kwok, G.W. Crabtree, H.M. Jaeger: Growth and properties of superconducting anisotropic lead nanoprisms, J. Phys. Chem. C **111**, 3548–3550 (2007)
10.56 J.D. Joannopoulos, J.N. Winn, R.D. Meade: *Photonic Crystals* (Princeton Univ. Press, Princeton 1995)
10.57 W.H. Li, C.C. Yang, F.C. Tsao, K.C. Lee: Quantum size effects on the superconducting parameters of zero-dimensional Pb nanoparticles, Phys. Rev. B **68**, 184507 (2003)
10.58 Y. Wang, X. Jiang, T. Herricks, Y. Xia: Single crystalline nanowires of lead: Large-scale synthesis, mechanistic studies, and transport measurements, J. Phys. Chem. B **108**, 8631–8640 (2004)
10.59 T.J. Trentler, K.M. Hickman, S.C. Goel, A.M. Viano, P.C. Gibbons, W.E. Buhro: Solution-liquid-solid growth of crystalline III–V semiconductors: An analogy to vapor-liquid-solid growth, Science **270**, 1791–1794 (1995)
10.60 S. Dubois, A. Michel, J.P. Eymery, J.L. Duvail, L. Piraux: Fabrication and properties of arrays of superconducting nanowires, J. Mater. Res. **14**, 665–671 (1999)
10.61 Y.T. Pang, G.W. Meng, L.D. Zhang, Y. Qin, X.Y. Gao, A.W. Zhao, Q. Fang: Arrays of ordered Pb nanowires

and their optical properties for laminated polarizers, Adv. Funct. Mater. **12**, 719–722 (2002)
10.62 M. Jałochowski, E. Bauer: Growth of metallic nanowires on anisotropic Si substrates: Pb on vicinal Si(001), Si(755), Si(533), and Si(110), Surf. Sci. **480**, 109–117 (2001)
10.63 M. Jałochowski, E. Bauer: Self-assembled parallel mesoscopic Pb-wires on Au-modified Si(533) substrates, Prog. Surf. Sci. **67**, 79–97 (2001)
10.64 G. Yi, W. Schwarzacher: Single crystal superconductor nanowires by electrodeposition, Appl. Phys. Lett. **74**, 1746–1748 (1999)
10.65 J. Wang, Y. Li: Rational synthesis of metal nanotubes and nanowires from Lamellar structures, Adv. Mater. **15**, 445–447 (2003)
10.66 E.E. Foos, R.M. Stroud, A.D. Berry, A.W. Snow, J.P. Armistead: Synthesis of nanocrystalline bismuth in reverse micelles, J. Am. Chem. Soc. **122**, 7114–7115 (2000)
10.67 M. Gutierrez, A. Henglein: Nanometer-sized Bi particles in aqueous solution: Absorption spectrum and some chemical properties, J. Phys. Chem. **100**, 7656–7661 (1996)
10.68 J. Wang, X. Wang, Q. Peng, Y. Li: Synthesis and characterization of bismuth single-crystalline nanowires and nanospheres, Inorg. Chem. **43**, 7552–7556 (2004)
10.69 Y. Xia, Y. Xiong, B. Lim, S.E. Skrabalak: Shape-controlled synthesis of metal nanocrystals: Simple chemistry meets complex physics?, Angew. Chem. Int. Ed. **48**, 60–103 (2009)
10.70 J. Fang, K.L. Stokes, W.L. Zhou, W. Wang, J. Lin: Self-assembled bismuth nanocrystallites, Chem. Commun., 1872–1873 (2001)
10.71 J. Wang, G. Cao, Y. Li: Giant positive magnetoresistance in non-magnetic bismuth nanoparticles, Mater. Res. Bull. **38**, 1645–1651 (2003)
10.72 H. Yu, P.C. Gibbons, K.F. Kelton, W.E. Buhro: Heterogeneous seeded growth: A potentially general synthesis of monodisperse metallic nanoparticles, J. Am. Chem. Soc. **123**, 9198–9199 (2001)
10.73 W.Z. Wang, B. Poudel, Y. Ma, Z.F. Ren: Shape control of single crystalline bismuth nanostructures, J. Phys. Chem. B **110**, 25702–25706 (2006)
10.74 J. Heremans, C.M. Thrush, Y. Lin, S. Cronin, Z. Zhang, M.S. Dresselhaus, J.F. Mansfield: Bismuth nanowire arrays: Synthesis and galvanomagnetic properties, Phys. Rev. B **61**, 2921–2930 (2000)
10.75 K. Liu, C.L. Chien, P.C. Searson, K. Yu-Zhang: Structural and magneto-transport properties of electrodeposited bismuth nanowires, Appl. Phys. Lett. **73**, 1436–1438 (1998)
10.76 Y. Li, J. Wang, Z. Deng, Y. Wu, X. Sun, D. Yu, P. Yang: Bismuth nanotubes: A rational low-temperature synthetic route, J. Am. Chem. Soc. **123**, 9904–9905 (2001)
10.77 P.K. Khanna, K. Jun, K.B. Hong, J. Baeg, R.C. Chikate, B.K. Das: Colloidal synthesis of indium nanoparticles by sodium reduction method, Mater. Lett. **59**, 1032–1036 (2005)
10.78 K. Soulantica, A. Maisonnat, F. Senocq, M. Fromen, M. Casanove, B. Chaudret: Selective synthesis of novel In and In_3Sn nanowires by an organometallic route at room temperature, Angew. Chem. Int. Ed. **40**, 2983–2986 (2001)
10.79 K. Soulantica, A. Maisonnat, M. Fromen, M. Casanove, P. Lecante, B. Chaudret: Synthesis and self-assembly of monodisperse indium nanoparticles prepared from the organometallic precursor $[In(\eta^5\text{-}C_5H_5)]$, Angew. Chem. Int. Ed. **40**, 448–451 (2001)
10.80 J. Benson, S. Boukhalfa, A. Magasinski, A. Kvit, G. Yushin: Chemical vapor deposition of aluminum nanowires on metal substrates for electrical energy storage applications, ACS Nano **6**, 118–125 (2012)
10.81 L. Cassayre, P. Palau, P. Chamelot, L. Massot: Properties of low-temperature melting electrolytes for the aluminum electrolysis process: A review, J. Chem. Eng. Data **55**, 4549–4560 (2010)
10.82 D.E. Couch, A. Brenner: A hydride bath for the electrodeposition of aluminum, J. Electrochem. Soc. **99**, 234–244 (1952)
10.83 S. Zein El Abedin, E.M. Moustafa, R. Hempelmann, H. Natter, F. Endres: Electrodeposition of nano- and microcrystalline aluminium in three different air and water stable ionic liquids, Chem. Phys. Chem. **7**, 1535–1543 (2006)
10.84 N. Koura, H. Nagase, A. Sato, S. Kumakura, K. Takeuchi, K. Ui, T. Tsuda, C.K. Loong: Electroless plating of aluminum from a room-temperature ionic liquid electrolyte, J. Electrochem. Soc. **155**, D155–D157 (2008)
10.85 J. Chang, S. Chen, W. Tsai, M. Deng, I. Sun: Electrodeposition of aluminum on magnesium alloy in aluminum chloride ($AlCl_3$)-1-ethyl-3-methylimidazolium chloride (EMIC) ionic liquid and its corrosion behavior, Electrochem. Commun. **9**, 1602–1606 (2007)
10.86 F. Altomare, A.M. Chang, M.R. Melloch, Y. Hong, C.W. Tu: Ultranarrow AuPd and Al wires, Appl. Phys. Lett. **86**, 172501–172503 (2005)
10.87 F. Altomare, A.M. Chang, M.R. Melloch, Y. Hong, C.W. Tu: Evidence for macroscopic quantum tunneling of phase slips in long one-dimensional superconducting Al wires, Phys. Rev. Lett. **97**, 017001 (2006)
10.88 M. Zgirski, K. Riikonen, V. Touboltsev, K. Arutyunov: Size dependent breakdown of superconductivity in ultranarrow nanowires, Nano Lett. **5**, 1029–1033 (2005)
10.89 S. Franssila: *Introduction to Microfabrication* (John Wiley & Sons, West Sussex, UK 2004)
10.90 T.A. Fulton, G.J. Dolan: Observation of single-electron charging effects in small tunnel junctions, Phys. Rev. Lett. **59**, 109–112 (1987)

10.91 P. Santhanam, C.C. Chi, S.J. Wind, M.J. Brady, J.J. Bucchignano: Resistance anomaly near the superconducting transition temperature in short aluminum wires, Phys. Rev. Lett. **66**, 2254–2257 (1991)

10.92 H. Tamada, T. Doumuki, T. Yamaguchi, S. Matsumoto: Al wire-grid polarizer using the s-polarization resonance effect at the 0.8-μm-wavelength band, Opt. Lett. **22**, 419–421 (1997)

10.93 D.D. Dlott: Thinking big (and small) about energetic materials, Mater. Sci. Technol. **22**, 463–473 (2006)

10.94 M.A. Zamkov, R.W. Conner, D.D. Dlott: Ultrafast chemistry of nanoenergetic materials studied by time-resolved infrared spectroscopy: Aluminum nanoparticles in teflon, J. Phys. Chem. C **111**, 10278–10284 (2007)

10.95 C. Mahendiran, R. Ganesan, A. Gedanken: Sonoelectrochemical synthesis of metallic aluminum nanoparticles, Eur. J. Inorg. Chem. **2009**, 2050–2053 (2009)

10.96 T.J. Foley, C.E. Johnson, K.T. Higa: Inhibition of oxide formation on aluminum nanoparticles by transition metal coating, Chem. Mater. **17**, 4086–4091 (2005)

10.97 S. Eliezer, N. Eliaz, E. Grossman, D. Fisher, I. Gouzman, Z. Henis, S. Pecker, Y. Horovitz, M. Fraenkel, S. Maman, Y. Lereah: Synthesis of nanoparticles with femtosecond laser pulses, Phys. Rev. B **69**, 144119 (2004)

10.98 E. Stratakis, M. Barberoglou, C. Fotakis, G. Viau, C. Garcia, G.A. Shafeev: Generation of Al nanoparticles via ablation of bulk Al in liquids with short laser pulses, Opt. Express **17**, 12650–12659 (2009)

10.99 C.A. Crouse, E. Shin, P.T. Murray, J.E. Spowart: Solution assisted laser ablation synthesis of discrete aluminum nanoparticles, Mater. Lett. **64**, 271–274 (2010)

10.100 M. Singh, J. Wang, M. Tian, Q. Zhang, A. Pereira, N. Kumar, T.E. Mallouk, M.H.W. Chan: Synthesis and superconductivity of electrochemically grown single-crystal aluminum nanowires, Chem. Mater. **21**, 5557–5559 (2009)

10.101 G. Oltean, L. Nyholm, K. Edström: Galvanostatic electrodeposition of aluminium nano-rods for Li-ion three-dimensional micro-battery current collectors, Electrochim. Acta **56**, 3203–3208 (2011)

10.102 C.A. Huber, T.E. Huber, M. Sadoqi, J.A. Lubin, S. Manalis, C.B. Prater: Nanowire array composites, Science **263**, 800–802 (1994)

10.103 L. Li, X. Xu, H. Chew, X. Huang, X. Dou, S. Pan, G. Li, L. Zhang: Direct growth of Al nanowire arrays: Thermal expansion and field emission properties, J. Phys. Chem. C **112**, 5328–5332 (2008)

10.104 W.B. Jensen: The place of zinc, cadmium, and mercury in the periodic table, J. Chem. Educ. **80**, 952 (2003)

10.105 G. Wu, B. Adams, M. Tian, A. Chen: Synthesis and electrochemical study of novel Pt-decorated Ti nanowires, Electrochem. Commun. **11**, 736–739 (2009)

10.106 S. Sharma, T.I. Kamins, R.S. Williams: Diameter control of Ti-catalyzed silicon nanowires, J. Cryst. Growth **267**, 613–618 (2004)

10.107 J.S. Lehtinen: Experimental Study of Quantum Fluctuations in Titanium Nanowires in Highly Resistive Environment. M.Sc. Thesis (University of Jyväskylä, Finland 2009)

10.108 J.S. Lehtinen, T. Sajavaara, K.Y. Arutyunov, M.Y. Presnjakov, A.L. Vasiliev: Evidence of quantum phase slip effect in titanium nanowires, Phys. Rev. B **85**, 094508 (2012)

10.109 R. Spolenak, E. Zschech: *Interconnects for Microelectronics in Metal Based Thin Films for Electronics* (Wiley-VCH, Weinheim 2006)

10.110 J.A. Rogers: Stamping techniques for micro and nanofabrication: Methods and applications. In: *Springer Handbook of Nanotechnology*, ed. by B. Bhushan (Springer, Berlin, Heidelberg 2004) pp. 185–202, http://www.springerlink.com/content/ml1644666-tph405r/

10.111 Y. Zhang, H. Dai: Formation of metal nanowires on suspended single-walled carbon nanotubes, Appl. Phys. Lett. **77**, 3015–3017 (2000)

10.112 M. Ye, C.P. Grigoropoulos: Time-of-flight and emission spectroscopy study of femtosecond laser ablation of titanium, J. Appl. Phys. **89**, 5183–5190 (2001)

10.113 D. Scuderi, O. Albert, D. Moreau, P.P. Pronko, J. Etchepare: Interaction of a laser-produced plume with a second time delayed femtosecond pulse, Appl. Phys. Lett. **86**, 071502–071503 (2005)

10.114 B. Kumar, D. Yadav, R.K. Thareja: Growth dynamics of nanoparticles in laser produced plasma in liquid ambient, J. Appl. Phys. **110**, 074903–074908 (2011)

10.115 T. Sasaki, C. Liang, W.T. Nichols, Y. Shimizu, N. Koshizaki: Fabrication of oxide base nanostructures using pulsed laser ablation in aqueous solutions, Appl. Phys. A **79**, 1489–1492 (2004)

10.116 P. Jafarkhani, S. Dadras, M.J. Torkamany, J. Sabbaghzadeh: Synthesis of nanocrystalline titania in pure water by pulsed Nd:YAG Laser, Appl. Surf. Sci. **256**, 3817–3821 (2010)

10.117 A. Ayi, V. Khare, P. Strauch, J. Girard, K. Fromm, A. Taubert: On the chemical synthesis of titanium nanoparticles from ionic liquids, Monatsheft Chem. **141**, 1273–1278 (2010)

10.118 T.I. Kamins, R.S. Williams, D.P. Basile, T. Hesjedal, J.S. Harris: Ti-catalyzed Si nanowires by chemical vapor deposition: Microscopy and growth mechanisms, J. Appl. Phys. **89**, 1008–1016 (2001)

10.119 A. Corrias, G. Mountjoy, D. Gozzi, A. Latini: Multi-walled carbon nanotubes decorated with titanium nanoparticles: Synthesis and characterization, Nanotechnology **18**, 485610 (2007)

10.120 Y. Li, X. Li, Z. Deng, B. Zhou, S. Fan, J. Wang, X. Sun: From surfactant-inorganic mesostructures to tungsten nanowires, Angew. Chem. Int. Ed. **41**, 333–335 (2002)

10.121 X. Huang, Y.I. Chumlyakov, A.G. Ramirez: Defect-driven synthesis of self-assembled single crystal titanium nanowires via electrochemistry, Nanotechnology **23**, 125601 (2012)

10.122 F. Endres, Z.E. Abedin, A.Y. Saad, E.M. Moustafa, N. Borissenko, W.E. Price, G.G. Wallace, D.R. MacFarlane, P.J. Newman, A. Bund: On the electrodeposition of titanium in ionic liquids, Phys. Chem. Chem. Phys. **10**, 2189–2199 (2008)

10.123 C. Fenster, A.J. Smith, A. Abts, S. Milenkovic, A.W. Hassel: Single tungsten nanowires as pH sensitive electrodes, Electrochem. Commun. **10**, 1125–1128 (2008)

10.124 A.B.H. Tay, J.T.L. Thong: High-resolution nanowire atomic force microscope probe grown by a field-emission induced process, Appl. Phys. Lett. **84**, 5207–5209 (2004)

10.125 J.P. Singh, F. Tang, T. Karabacak, T.M. Lu, G.C. Wang: Enhanced cold field emission from ⟨100⟩ oriented β-W nanoemitters, J. Vac. Sci. Technol. B **22**, 1048–1051 (2004)

10.126 Y. Lee, C. Choi, Y. Jang, E. Kim, B. Ju, N. Min, J. Ahn: Tungsten nanowires and their field electron emission properties, Appl. Phys. Lett. **81**, 745–747 (2002)

10.127 V. Cimalla, C. Röhlig, J. Pezoldt, M. Niebelschütz, O. Ambacher, K. Brückner, M. Hein, J. Weber, S. Milenkovic, A.J. Smith, A.W. Hassel: Nanomechanics of single crystalline tungsten nanowires, J. Nanomater., 638947–638955 (2008)

10.128 L. Xiong, T. He: Synthesis and characterization of ultrafine tungsten and tungsten oxide nanoparticles by a reverse microemulsion-mediated method, Chem. Mater. **18**, 2211–2218 (2006)

10.129 V.K. Sarin: Morphological changes occurring during reduction of WO_3, J. Mater. Sci. **10**, 593–598 (1975)

10.130 Y. Chang, H. Wang, C. Chiu, D. Cheng, M. Yen, H. Chiu: Low-temperature synthesis of transition metal nanoparticles from metal complexes and organopolysilane oligomers, Chem. Mater. **14**, 4334–4338 (2002)

10.131 P.K. Sahoo, S.S. Kalyan Kamal, M. Premkumar, T. Jagadeesh Kumar, B. Sreedhar, A.K. Singh, S.K. Srivastava, K. Chandra Sekhar: Synthesis of tungsten nanoparticles by solvothermal decomposition of tungsten hexacarbonyl, Int. J. Refract. Met. Hard Mater. **27**, 784–791 (2009)

10.132 M.H. Magnusson, K. Deppert, J. Malm: Single-crystalline tungsten nanoparticles produced by thermal decomposition of tungsten hexacarbonyl, J. Mater. Res. **15**, 1564 (2000)

10.133 H. Lei, Y.J. Tang, J.J. Wei, J. Li, X.-B. Li, H.L. Shi: Synthesis of tungsten nanoparticles by sonoelectrochemistry, Ultrason. Sonochem. **14**, 81–83 (2007)

10.134 Y. Tamou, S. Tanaka: Formation and coalescence of tungsten nanoparticles under electron beam irradiation, Nanostruct. Mater. **12**, 123–126 (1999)

10.135 E. Ozawa, Y. Kawakami, T. Seto: Formation and size control of tungsten nano particles produced by Nd:YAG laser irradiation, Scr. Mater. **44**, 2279–2283 (2001)

10.136 L. Landstrom, J. Kokavecz, J. Lu, P. Heszler: Characterization and modeling of tungsten nanoparticles generated by laser-assisted chemical vapor deposition, J. Appl. Phys. **95**, 4408–4414 (2004)

10.137 Z.Q. Liu, K. Mitsuishi, K. Furuya: Features of self-supporting tungsten nanowire deposited with high-energy electrons, J. Appl. Phys. **96**, 619–623 (2004)

10.138 Z.Q. Liu, K. Mitsuishi, K. Furuya: The growth behavior of self-standing tungsten tips fabricated by electron-beam-induced deposition using 200 keV electrons, J. Appl. Phys. **96**, 3983–3986 (2004)

10.139 S. Vaddiraju, H. Chandrasekaran, M.K. Sunkara: Vapor phase synthesis of tungsten nanowires, J. Am. Chem. Soc. **125**, 10792–10793 (2003)

10.140 A.W. Hassel, S. Milenkovic, A.J. Smith: Large scale synthesis of single crystalline tungsten nanowires with extreme aspect ratios, Phys. Status Solidi (a) **207**, 858–863 (2010)

10.141 J.T.L. Thong, C.H. Oon, M. Yeadon, W.D. Zhang: Field-emission induced growth of nanowires, Appl. Phys. Lett. **81**, 4823–4825 (2002)

10.142 S. Wang, Y. He, J. Zou, Y. Jiang, J. Xu, B. Huang, C.T. Liu, P.K. Liaw: Synthesis of single-crystalline tungsten nanowires by nickel-catalyzed vapor-phase method at 850 °C, J. Cryst. Growth **306**, 433–436 (2007)

10.143 E. Redel, R. Thomann, C. Janiak: Use of ionic liquids (ILs) for the IL-anion size-dependent formation of Cr, Mo and W nanoparticles from metal carbonyl $M(CO)_6$ precursors, Chem. Commun., 1789–1791 (2008)

10.144 J.A. Rodriguez, J. Dvorak, T. Jirsak, J. Hrbek: Formation of Mo and MoS_x nanoparticles on Au(1 1 1) from $Mo(CO)_6$ and S_2 precursors: Electronic and chemical properties, Surf. Sci. **490**, 315–326 (2001)

10.145 C. Vollmer, E. Redel, K. Abu-Shandi, R. Thomann, H. Manyar, C. Hardacre, C. Janiak: Microwave irradiation for the facile synthesis of transition-metal nanoparticles (NPs) in ionic liquids (ILs) from metal-carbonyl precursors and Ru-, Rh-, and Ir-NP/IL dispersions as biphasic liquid-liquid hydrogenation nanocatalysts for cyclohexene, Chem. Eur. J. **16**, 3849–3858 (2010)

10.146 D.V. Potapenko, J.M. Horn, R.J. Beuhler, Z. Song, M.G. White: Reactivity studies with gold-supported molybdenum nanoparticles, Surf. Sci. **574**, 244–258 (2005)

10.147 P. Liu, J.A. Rodriguez, J.T. Muckerman, J. Hrbek: The deposition of Mo nanoparticles on Au(111) from

a $Mo(CO)_6$ precursor: Effects of CO on Mo–Au intermixing, Surf. Sci. **530**, L313–L321 (2003)
10.148 S. Mitra, K. Sridharan, J. Unnam, K. Ghosh: Synthesis of nanometal oxides and nanometals using hot-wire and thermal CVD, Thin Solid Films **516**, 798–802 (2008)
10.149 M. Komarneni, E. Kadossov, J. Justin, M. Lu, U. Burghaus: Adsorption of thiophene on silica-supported Mo clusters, Surf. Sci. **604**, 1221–1229 (2010)
10.150 Z. Jiang, W. Huang, Z. Zhang, H. Zhao, D. Tan, X. Bao: Multiple coordination of CO on molybdenum nanoparticles: Evidence for intermediate $Mo_x(CO)_y$ species by XPS and UPS, J. Phys. Chem. B **110**, 26105–26113 (2006)
10.151 L. Bugyi, R. Németh: Characterization of Rh, Mo and Rh–Mo particles formed on TiO_2(110) surface: A TDS, AES and RAIRS study, Surf. Sci. **605**, 808–817 (2011)
10.152 M. Chhowalla, G.A.J. Amaratunga: Thin films of fullerene-like MoS_2 nanoparticles with ultra-low friction and wear, Nature **407**, 164–167 (2000)
10.153 J.M. Martin, C. Donnet, T. Le Mogne, T. Epicier: Superlubricity of molybdenum disulphide, Phys. Rev. B **48**, 10583–10586 (1993)
10.154 L.W. Vernon, J.T. Richardson: Hydrogenolysis of thiophene, US Patent 19 (1961)
10.155 F.C. Riddick Jr., B. Peralta: Hydrodesulfurization of oil feedstock with presulfided catalyst, US Patent 22 (1980)
10.156 G.B. Brignac, J. Kociscin, C.A. McKnight: Catalyst activation method for selective cat naphtha hydrodesulfurization, US Patent 6 (2001)
10.157 A. Tuxen, J. Kibsgaard, H. Gobel, E. Laegsgaard, H. Topsoe, J.V. Lauritsen, F. Besenbacher: Size threshold in the dibenzothiophene adsorption on MoS_2 nanoclusters, ACS Nano **4**, 4677–4682 (2010)
10.158 J. Chen, S. Li, Q. Xu, K. Tanaka: Synthesis of open-ended MoS_2 nanotubes and the application as the catalyst of methanation, Chem. Commun., 1722–1723 (2002)
10.159 T.F. Jaramillo, K.P. Jørgensen, J. Bonde, J.H. Nielsen, S. Horch, I. Chorkendorff: Identification of active edge sites for electrochemical H_2 evolution from MoS_2 nanocatalysts, Science **317**, 100–102 (2007)
10.160 M.L. Tang, D.C. Grauer, B. Lassalle-Kaiser, V.K. Yachandra, L. Amirav, J.R. Long, J. Yano, A.P. Alivisatos: Structural and electronic study of an amorphous MoS_3 hydrogen-generation catalyst on a quantum-controlled photosensitizer, Angew. Chem. Int. Ed. **50**, 10203–10207 (2011)
10.161 L.X. Song, M. Wang, S.Z. Pan, J. Yang, J. Chen, J. Yang: Molybdenum oxide nanoparticles: Preparation, characterization, and application in heterogeneous catalysis, J. Mater. Chem. **21**, 7982–7989 (2011)
10.162 R. Liang, H. Cao, D. Qian: MoO_3 nanowires as electrochemical pseudocapacitor materials, Chem. Commun. **47**, 10305–10307 (2011)
10.163 S. Lee, Y. Kim, R. Deshpande, P.A. Parilla, E. Whitney, D.T. Gillaspie, K.M. Jones, A.H. Mahan, S. Zhang, A.C. Dillon: Reversible lithium-ion insertion in molybdenum oxide nanoparticles, Adv. Mater. **20**, 3627–3632 (2008)
10.164 R. Tenne, M. Remškar, A. Enyashin, G. Seifert: Inorganic nanotubes and fullerene-like structures (IF). In: *Carbon Nanotubes*, Topics in Applied Physics Ser., Vol. 111, ed. by J. Ado, G. Dresselhaus, M.S. Dresselhaus, S. Mildred (Springer, Berlin, Heidelberg 2008) pp. 631–671
10.165 T. Matsumoto, Y. Nagashima, T. Yamazaki, J. Nakamura: Fuel cell anode composed of Mo_2C catalyst and carbon nanotube electrodes, Electrochem. Solid-State Lett. **9**, A160–A162 (2006)
10.166 B. Radisavljevic, M.B. Whitwick, A. Kis: Integrated circuits and logic operations based on single-layer MoS_2, ACS Nano **5**, 9934–9938 (2011)
10.167 K. Lee, H. Kim, M. Lotya, J.N. Coleman, G. Kim, G.S. Duesberg: Electrical characteristics of molybdenum disulfide flakes produced by liquid exfoliation, Adv. Mater. **23**, 4178–4182 (2011)
10.168 S. Wu, Z. Zeng, Q. He, Z. Wang, S.J. Wang, Y. Du, Z. Yin, X. Sun, W. Chen, H. Zhang: Electrochemically reduced single-layer MoS_2 nanosheets: Characterization, properties, and sensing applications, Small **8**, 2264–2270 (2012)
10.169 A. Fukunaga, S. Chu, M.E. McHenry: Synthesis, structure, and superconducting properties of tantalum carbide nanorods and nanoparticles, J. Mater. Res. **13**, 2465–2471 (1998)
10.170 C.M. Lieber, E. Wong: Preparation of carbide nanorods, US Patent 7 (1999)
10.171 K.Y. Chick, M. Nath, B.A. Parkinson: TaS_2 nanoplatelets produced by laser ablation, J. Mater. Res. **21**, 1243–1247 (2006)
10.172 C.W. Dunnill, H.K. Edwards, P.D. Brown, D.H. Gregory: Single-step synthesis and surface-assisted growth of superconducting TaS_2 nanowires, Angew. Chem. Int. Ed. **45**, 7060–7063 (2006)
10.173 X. Wu, Y. Tao, Y. Hu, Y. Song, Z. Hu, J. Zhu, L. Dong: Tantalum disulfide nanobelts: Preparation, superconductivity and field emission, Nanotechnology **17**, 201 (2006)
10.174 H. El-Sayed, V.I. Birss: Controlled growth and monitoring of tantalum oxide nanostructures, Nanoscale **2**, 793–798 (2010)
10.175 X. Feng, T.J. LaTempa, J.I. Basham, G.K. Mor, O.K. Varghese, C.A. Grimes: Ta_3N_5 nanotube arrays for visible light water photoelectrolysis, Nano Lett. **10**, 948–952 (2010)
10.176 M. Tabata, K. Maeda, M. Higashi, D. Lu, T. Takata, R. Abe, K. Domen: Modified Ta_3N_5 powder as a photocatalyst for O_2 evolution in a two-step water splitting system with an iodate/iodide shuttle re-

dox mediator under visible light, Langmuir **26**, 9161–9165 (2010)
10.177 A. Engel, A. Aeschbacher, K. Inderbitzin, A. Schilling, K. Ilin, M. Hofherr, M. Siegel, A. Semenov, H.-W. Hubers: Tantalum nitride superconducting single-photon detectors with low cut-off energy, Appl. Phys. Lett. **100**, 062601–062603 (2012)
10.178 S. Sato, T. Morikawa, S. Saeki, T. Kajino, T. Motohiro: Visible-light-induced selective CO_2 reduction utilizing a ruthenium complex electrocatalyst linked to a p-type nitrogen-doped Ta_2O_5 semiconductor, Angew. Chem. Int. Ed. **49**, 5101–5105 (2010)
10.179 M. Higashi, K. Domen, R. Abe: Highly stable water splitting on oxynitride TaON photoanode system under visible light irradiation, J. Am. Chem. Soc. **134**, 6968–6971 (2012)
10.180 J.M. Mativetsky, S. Fostner, S.A. Burke, P. Grutter: High-resolution investigation of metal nanoparticle growth on an insulating surface, Phys. Rev. B **80**, 045430 (2009)
10.181 J. Barr, R. Axelbaum, M. Macias: Processing salt-encapsulated tantalum nanoparticles for high purity, ultra high surface area applications, J. Nanopart. Res. **8**, 11–22 (2006)
10.182 Y. Wang, Z. Cui, Z. Zhang: Synthesis and phase structure of tantalum nanoparticles, Mater. Lett. **58**, 3017–3020 (2004)
10.183 J. Walter, H. Shioyama, Y. Sawada: The generation of nanometer-size tantalum particles in a graphite host lattice, Carbon **37**, 41–45 (1999)
10.184 I.S. Suzuki, M. Suzuki, J. Walter: Superconductivity and magnetism in tantalum–graphite multilayers based on natural graphite, Solid State Commun. **118**, 523–527 (2001)
10.185 R.L. Axelbaum, D.P. DuFaux, L.J. Rosen: Method and apparatus for producing high purity and unagglomerated submicron particles, US Patent 30 (1995)
10.186 M. Law, L.E. Greene, J.C. Johnson, R. Saykally, P. Yang: Nanowire dye-sensitized solar cells, Nat. Mater. **4**, 455–459 (2005)
10.187 B. Liu, H.C. Zeng: Mesoscale organization of CuO nanoribbons: Formation of "Dandelions", J. Am. Chem. Soc. **126**, 8124–8125 (2004)
10.188 B.O. Dabbousi, J. Rodriguez-Viejo, F.V. Mikulec, J.R. Heine, H. Mattoussi, R. Ober, K.F. Jensen, M.G. Bawendi: (CdSe)ZnS core-shell quantum dots: Synthesis and characterization of a size series of highly luminescent nanocrystallites, J. Phys. Chem. B **101**, 9463–9475 (1997)
10.189 P.X. Gao, Z.L. Wang: Nanoarchitectures of semiconducting and piezoelectric zinc oxide, J. Appl. Phys. **97**, 044304–044307 (2005)
10.190 Y. Wang, L. Zhang, G. Meng, C. Liang, G. Wang, S. Sun: Zn nanobelts: A new quasi one-dimensional metal nanostructure, Chem. Commun., 2632–2633 (2001)
10.191 X.S. Peng, L.D. Zhang, G.W. Meng, X.Y. Yuan, Y. Lin, Y.T. Tian: Synthesis of Zn nanofibres through simple thermal vapour-phase deposition, J. Phys. D **36**, L35 (2003)
10.192 J. Wu, S. Liu, C. Wu, K. Chen, L. Chen: Heterostructures of ZnO–Zn coaxial nanocables and ZnO nanotubes, Appl. Phys. Lett. **81**, 1312–1314 (2002)
10.193 J.Q. Hu, Q. Li, X.M. Meng, C.S. Lee, S.T. Lee: Thermal reduction route to the fabrication of coaxial Zn/ZnO nanocables and ZnO nanotubes, Chem. Mater. **15**, 305–308 (2003)
10.194 Y. Yan, P. Liu, M.J. Romero, M. Al-Jassim: Formation of metallic zinc nanowires, J. Appl. Phys. **93**, 4807–4809 (2003)
10.195 S.C. Singh, R. Gopal: Zinc nanoparticles in solution by laser ablation technique, Bull. Mater. Sci. **30**, 291–293 (2007)
10.196 S.C. Singh, R.K. Swarnkar, R. Gopa: Zn/ZnO core/shell nanoparticles synthesized by laser ablation in aqueous environment: Optical and structural characterizations, Bull. Mater. Sci. **33**, 21–26 (2010)
10.197 J. Wang, M. Tian, N. Kumar, T.E. Mallouk: Controllable template synthesis of superconducting Zn nanowires with different microstructures by electrochemical deposition, Nano Lett. **5**, 1247–1253 (2005)
10.198 G.G. Jernigan, G.A. Somorjai: Carbon monoxide oxidation over three different oxidation states of copper: Metallic copper, copper (I) oxide, and copper (II) oxide – A surface science and kinetic study, J. Catal. **147**, 567–577 (1994)
10.199 Y. Zhang, W. Huang, S.E. Habas, J.N. Kuhn, M.E. Grass, Y. Yamada, P. Yang, G.A. Somorjai: Near-monodisperse NiCu bimetallic nanocrystals of variable composition: Controlled synthesis and catalytic activity for H_2 generation, J. Phys. Chem. C **112**, 12092–12095 (2008)
10.200 R.L. Keiski, O. Desponds, Y. Chang, G.A. Somorjai: Kinetics of the water-gas shift reaction over several alkane activation and water-gas shift catalysts, Appl. Catal. A **101**, 317–338 (1993)
10.201 G.A. Somorjai, R.L. York, D. Butcher, J.Y. Park: The evolution of model catalytic systems; studies of structure, bonding and dynamics from single crystal metal surfaces to nanoparticles, and from low pressure ($<10^{-3}$ Torr) to high pressure ($>10^{-3}$ Torr) to liquid interfaces, Phys. Chem. Chem. Phys. **9**, 3500 (2007)
10.202 J.A. Rodriguez, P. Liu, J. Hrbek, J. Evans, M. Pérez: Water gas shift reaction on Cu and Au nanoparticles supported on $CeO_2(111)$ and $ZnO(000\bar{1})$: Intrinsic activity and importance of support interactions, Angew. Chem. Int. Ed. **46**, 1329–1332 (2007)
10.203 A.A. Gokhale, J.A. Dumesic, M. Mavrikakis: On the mechanism of low-temperature water gas shift re-

action on copper, J. Am. Chem. Soc. **130**, 1402–1414 (2008)
10.204 T. Ressler, B.L. Kniep, I. Kasatkin, R. Schlögl: The microstructure of copper zinc oxide catalysts: Bridging the materials gap, Angew. Chem. Int. Ed. **44**, 4704–4707 (2005)
10.205 S. Vukojevic, O. Trapp, J. Grunwaldt, C. Kiener, F. Schüth: Quasi-homogeneous methanol synthesis over highly active copper nanoparticles, Angew. Chem. Int. Ed. **44**, 7978–7981 (2005)
10.206 P.L. Hansen, J.B. Wagner, S. Helveg, J. Rostrup-Nielsen, B.S. Clausen, H. Topse: Atom-resolved imaging of dynamic shape changes in supported copper nanocrystals, Science **295**, 2053–2055 (2002)
10.207 M.K. Schröter, L. Khodeir, M.W.E. van der Berg, T. Hikov, M. Cokoja, S. Miao, W. Grünert, M. Muhler, R.A. Fischer: A colloidal ZnO/Cu nanocatalyst for methanol synthesis, Chem. Commun., 2498–2500 (2006)
10.208 A.A. Ponce, K.J. Klabunde: Chemical and catalytic activity of copper nanoparticles prepared via metal vapor synthesis, J. Mol. Catal. A **225**, 1–6 (2005)
10.209 V.T. Renard, M. Jublot, P. Gergaud, P. Cherns, D. Rouchon, A. Chabli, V. Jousseaume: Catalyst preparation for CMOS-compatible silicon nanowire synthesis, Nat. Nano **4**, 654–657 (2009)
10.210 A.A. Setlur, J.M. Lauerhaas, J.Y. Dai, R.P.H. Chang: A method for synthesizing large quantities of carbon nanotubes and encapsulated copper nanowires, Appl. Phys. Lett. **69**, 345 (1996)
10.211 Z. Liu, Y. Bando: A novel method for preparing copper nanorods and nanowires, Adv. Mater. **15**, 303–305 (2003)
10.212 R.K. Swarnkar, S.C. Singh, R. Gopal: Effect of aging on copper nanoparticles synthesized by pulsed laserablation in water: Structural and optical characterizations, Bull. Mater. Sci. **34**, 1363–1369 (2011)
10.213 N. Bärsch, J. Jakobi, S. Weiler, S. Barcikowski: Pure colloidal metal and ceramic nanoparticles from high-power picosecond laser ablation in water and acetone, Nanotechnology **20**, 445603 (2009)
10.214 K. Murai, Y. Tokoi, H. Suematsu, W. Jiang, K. Yatsui, K. Niihara: Particle size controllability of ambient gas species for copper nanoparticles prepared by pulsed wire discharge, Jpn. J. Appl. Phys. **47**, 3726 (2008)
10.215 G. Vitulli, M. Bernini, S. Bertozzi, E. Pitzalis, P. Salvadori, S. Coluccia, G. Martra: Nanoscale copper particles derived from solvated Cu atoms in the activation of molecular oxygen, Chem. Mater. **14**, 1183–1186 (2002)
10.216 Y.H. Kim, D.K. Lee, B.G. Jo, J.H. Jeong, Y.S. Kang: Synthesis of oleate capped Cu nanoparticles by thermal decomposition, Colloids Surf. Physicochem. Eng. Asp. **284–285**, 364–368 (2006)
10.217 M.E. Toimil Molares, V. Buschmann, D. Dobrev, R. Neumann, R. Scholz, I.U. Schuchert, J. Vetter: Single-crystalline copper nanowires produced by electrochemical deposition in polymeric ion track membranes, Adv. Mater. **13**, 62 (2001)
10.218 M.E. Toimil Molares, E.M. Hohberger, C. Schaeflein, R. Blick, H.R. Neumann, C. Trautmann: Electrical characterization of electrochemically grown single copper nanowires, Appl. Phys. Lett. **82**, 2139 (2003)
10.219 H. Choi, S. Park: Seedless growth of free-standing copper nanowires by chemical vapor deposition, J. Am. Chem. Soc. **126**, 6248 (2004)
10.220 M. Mohl, P. Pusztai, A. Kukovecz, Z. Konya, J. Kukkola, K. Kordas, R. Vajtai, P.M. Ajayan: Low-temperature large-scale synthesis and electrical testing of ultralong copper nanowires, Langmuir **26**, 16496–16502 (2010)
10.221 Z. Liu, Y. Yang, J. Liang, Z. Hu, S. Li, S. Peng, Y. Qian: Synthesis of copper nanowires via a complex-surfactant-assisted hydrothermal reduction process, J. Phys. Chem. B **107**, 12658 (2003)
10.222 N.J. Gerein, J.A. Haber: Effect of AC electrodeposition conditions on the growth of high aspect ratio copper nanowires in porous aluminum oxide templates, J. Phys. Chem. B **109**, 17372 (2005)
10.223 M. Yen, C. Chiu, C. Hsia, F. Chen, J. Kai, C. Lee, H. Chiu: Synthesis of cable-like copper nanowires, Adv. Mater. **15**, 235 (2003)
10.224 M. Pileni: The role of soft colloidal templates in controlling the size and shape of inorganic nanocrystals, Nat. Mater. **2**, 145 (2003)
10.225 A. Filankembo, M.P. Pileni: Is the template of self-colloidal assemblies the only factor that controls nanocrystal shapes?, J. Phys. Chem. B **104**, 5865 (2000)
10.226 A.C. Curtis, D.G. Duff, P.P. Edwards, D.A. Jefferson, B.F.G. Johnson, A.I. Kirkland, A.S. Wallace: A morphology-selective copper organosol, Angew. Chem. Int. Ed. **27**, 1530–1533 (1988)
10.227 D. Mott, J. Galkowski, L. Wang, J. Luo, C. Zhong: Synthesis of size-controlled and shaped copper nanoparticles, Langmuir **23**, 5740–5745 (2007)
10.228 Y. Chang, M.L. Lye, H.C. Zeng: Large-scale synthesis of high-quality ultralong copper nanowires, Langmuir **21**, 3746–3748 (2005)
10.229 I. Lisiecki: Size, shape, and structural control of metallic nanocrystals, J. Phys. Chem. B **109**, 12231–12244 (2005)
10.230 M. Jin, G. He, H. Zhang, J. Zeng, Z. Xie, Y. Xia: Shape-controlled synthesis of copper nanocrystals in an aqueous solution with glucose as a reducing agent and hexadecylamine as a capping agent, Angew. Chem. Int. Ed. **50**, 10560–10564 (2011)
10.231 Y. Shi, H. Li, L. Chen, X. Huang: Obtaining ultralong copper nanowires via a hydrothermal process, Sci. Technol. Adv. Mater. **6**, 761 (2005)

10.232 M. Mohl, D. Dobo, A. Kukovecz, Z. Konya, K. Kordas, J. Wei, R. Vajtai, P.M. Ajayan: Formation of CuPd and CuPt bimetallic nanotubes by galvanic replacement reaction, J. Phys. Chem. C **115**, 9403–9409 (2011)
10.233 Y. Wang, P. Chen, M. Liu: Synthesis of well-defined copper nanocubes by a one-pot solution process, Nanotechnology **17**, 6000 (2006)
10.234 G. Zhou, M. Lu, Z. Yang: Aqueous synthesis of copper nanocubes and bimetallic copper/palladium core-shell nanostructures, Langmuir **22**, 5900–5903 (2006)
10.235 M.H. Kim, B. Lim, E.P. Lee, Y. Xia: Polyol synthesis of Cu_2O nanoparticles: Use of chloride to promote the formation of a cubic morphology, J. Mater. Chem. **18**, 4069–4073 (2008)

11. Alloys on the Nanoscale

Giovanni Barcaro, Alfredo Caro, Alessandro Fortunelli

An overview is provided of nanostructured alloy materials as both isolated particles with nanoscale diameter (nanoalloys) and bulk materials with nanoscale structure. The methods for preparing and characterizing these systems from both experimental and theoretical modeling points of view are presented, and the basic knowledge on their structural, catalytic, mechanical, optical, and magnetic properties is reviewed. It is shown that, due to the increased freedom associated with composition and chemical ordering, new physical phenomena appear in metal multicomponent nanosystems, as well as novel or profoundly modified properties: For example, new structural motifs can arise depending on the structural and energetic characteristics of the metal components, and the size of the system. Hence, the catalytic activity, mechanical strength, plasmonic and nonlinear optical, as well as magnetic responses exhibit features in multicomponent nanostructured systems which are different and can in principle be finely tuned with respect to their pure counterparts. The challenges associated with full exploitation of these possibilities are outlined.

The chapter starts by defining some concepts and principles specific to the field of nanoalloys which are then used in the next sections (Sect. 11.1). A brief overview of the methods for preparing (Sect. 11.2) and characterizing (Sect. 11.3) nanostructured alloys then follows. The core of the chapter (Sect. 11.4) presents a discussion of the properties of these materials, distinguished into: structural, catalytic, optical, and magnetic. Section 11.5 is devoted to nanostructured bulk alloys. A brief section on applications (Sect. 11.6) and an outlook (Sect. 11.7) conclude the chapter.

11.1 **Concepts and Principles** 411

11.2 **Preparation and Synthesis** 413
11.2.1 Solution-Phase Methods 413
11.2.2 Surface Deposition Methods 416

11.3 **Characterization of Nanoparticles and Nanoalloys** 417
11.3.1 Scanning Force Microscopy (SFM) 417
11.3.2 Grazing-Incidence Small-Angle X-ray Scattering (GISAXS) 418
11.3.3 X-ray Absorption Spectroscopy (XAS) 418
11.3.4 Scanning Tunneling Microscopy (STM) 419
11.3.5 X-ray Photoelectron Spectroscopy (XPS) 420
11.3.6 Surface X-ray Diffraction (SXRD) 421
11.3.7 Transmission Electron Microscopy (TEM) 421
11.3.8 Vibrational Sum-Frequency Generation (VSFG) 424

11.4 **Properties** 424
11.4.1 Structural Properties of Alloyed Nanoparticles 425
11.4.2 Catalytic Properties 437
11.4.3 Optical Properties 442
11.4.4 Magnetic Properties 448

11.5 **Nanostructured Bulk Alloys** 450
11.5.1 Bulk Materials Incorporating Nanoscale Precipitates of a Different Phase 450
11.5.2 Bulk Nanophase Materials 453

11.6 **Applications** 457

11.7 **Concluding Remarks** 458

References 459

Metal nanoclusters and nanoalloys (i. e., pure or mixed metallic aggregates of dimensions ranging between 1 and 100 nm) are a subject of great interest in basic science as well as in current technology, where they find many applications (and many more promising ones have been prospected in the literature) due to their unique properties: from chemical sensing (artificial noses) to heterogeneous catalysis [11.1, 2], from magnetic recording to optoelectronic devices, thermal treatment of cancer, and *cell imaging*, i. e., colorimetric probes for DNA detection [11.3–6].

In a wide historical perspective, all this may be thought to stem from metallurgy thousands of years ago, when humanity unknowingly discovered how to produce metal nanoparticles and to exploit their surface plasmonic resonance, i. e., the coherent and collective oscillation of electrons involved in metallic bonds in confined systems subjected to electromagnetic radiation of proper wavelength, for esthetic purposes (stained glass and fine glassware, with coloring durable till today) [11.7]. Materials containing metal nanoparticles were also proposed for curative use [11.7] in what can be considered as a forerunner of nanomedicine. A more conscious step forward was achieved in the mid-19th century by *Michael Faraday*, with the preparation of colloidal suspensions via chemical reduction of metal salts in the presence of stabilizing agents in solution [11.8] and the study of their optical properties. The physics of nanoscale metal clusters then strongly developed in the 20th century with the advent of nanocatalysis and dramatically in recent years, following the continuous advances in synthetic and characterization tools that allow manipulation of matter at the nanometer scale by preparing and measuring the properties of nanostructured systems with increasing precision [11.9–14] and the development of theoretical methods able to rationalize and predict experimental behavior and properties [11.15–18].

The fundamental reasons for the interest in metal nanosystems and their fascinating applications ultimately lie in the peculiar features of confined metallic bonds [11.19, 20]. The presence of conduction-band electrons whose mobility enhances transport and response properties [11.21] confined within a finite space, combined in transition metals with localized electrons in incomplete d-shells, assuring both easy formation and breaking of chemical bonds (and thus a rich and varied chemistry) and large magnetic moments, and the sensitivity of these properties to coupling with size, shape, composition, and external fields, make metal nanoparticles and nanoalloys truly unique materials, an ideal topic of research and investigation in many fields of science and technology.

In particular, combining nanostructured metal systems or metal nanodots with alloying results in a class of systems of great interest in terms of both basic and applied science: alloyed (multicomponent) metal nanoparticles or nanoalloys [11.22–25] (Fig. 11.1), which are the subject of the present chapter.

There are a number of reasons why a gain can be achieved by employing a multicomponent nanostructured system with respect to pure and/or extended systems and which justify the importance of nanostructured alloys in the field of metal nanoparticles and in the general field of nanomaterials. First, new structural motifs with respect to pure systems can be created by alloying, thus generating novel structure–property relationships. Second, the chemical and physical properties of a particle can be tuned by varying not only the size and shape but also the composition (i. e., the ratio between the different chemical species within the particle) and the degree of atomic mixing or chemical ordering or compositional structure (i. e., the distribution of the different atomic species in the structural framework): For example, the surface chemistry of a particle and its interaction with the environment can be modified by coating with an overlayer of a different material, or additional functionalities can be added to change its recognition capabilities. All this is very important as it allows one to finely modulate the physics of the metal–metal interactions and consequently to tune the properties of these systems nearly at will. This same freedom, however, especially that associated with chemical ordering, also represents a challenge in terms of both experimental realizations and theoretical predictions. In particular, a high degree of precision is required in the synthesis protocols to achieve control over chemical ordering in nanoalloys, and – once achieved – the corresponding link to properties must be clarified. This is not easy, as only recently have characterization techniques been developed that allow one to obtain accurate information on the structural properties of these materials; see [11.26–29] and Sect. 11.3. In the cases in which this has been possible it has been shown that chemical ordering can be crucial in determining the system properties. Ag-Pt particles, for example, exhibit a different optical response depending on whether they are core–shell or random solutions [11.30]. Mechanical properties are equally known to be strongly affected by surface segregation [11.31]. The precise arrangement of the species in the particle is also important in catalysis, being dominated by processes occurring at surface or

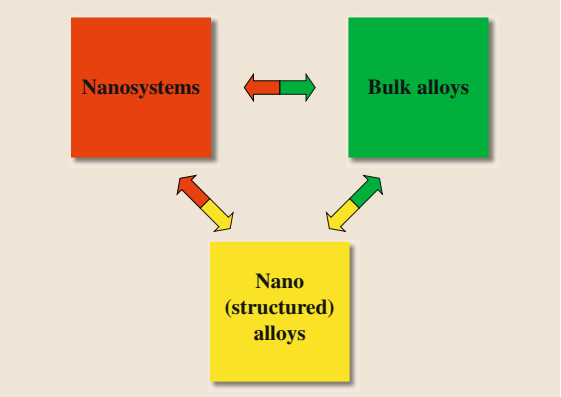


Fig. 11.1 Definition of nanoalloys

subsurface shells, and changes in the segregation pattern under operating conditions have been observed [11.32]. In short, novel phenomena or novel metamorphoses of old phenomena should be expected and are indeed encountered in this field, as the following sections attempt to show.

Moreover, by enlarging the perspective, one encounters other materials that are not usually classified as nanoalloys but that share with them most of the basic knowledge, namely nanostructured bulk alloys. In general, alloyed nanostructures can then be distinguished as: (a) isolated particles with nanoscale size, and (b) bulk materials with nanoscale structure. Section 11.5 is therefore devoted to these latter materials and their peculiar mechanical properties.

11.1 Concepts and Principles

In this section we briefly discuss some of the concepts and methods that are peculiar to the field of nanostructured alloys, especially at the theoretical level. An excellent introduction to the field of nanoalloys can be found in [11.25].

The first issue that one encounters in dealing with nanoalloys is how to compare the stability of nanoalloys of different chemical composition. In this context, a very useful concept is that of mixing energy. Suppose that one has alloy nanoparticles all of a given size (i. e., the same number of atoms) but different chemical composition and suppose that one knows the energy of each one of them; then, which quantity can one define to compare their energies and single out the most stable one? One possibility is the mixing energy, defined as

$$\Delta[N_\mathrm{A}, N_\mathrm{B}] = E_\mathrm{alloy}[N_\mathrm{A}, N_\mathrm{B}] - N_\mathrm{A} E_\mathrm{A}[N]/N - N_\mathrm{B} E_\mathrm{B}[N]/N \,,$$

where $E_\mathrm{alloy}[N_\mathrm{A}, N_\mathrm{B}]$ is the energy of a nanoalloy cluster composed of N_A atoms of species A and N_B atoms of species B, $N = N_\mathrm{A} + N_\mathrm{B}$ is the total number of atoms in the cluster, $E_\mathrm{A}[N]$ is the energy of a pure cluster of N atoms of species A, and $E_\mathrm{B}[N]$ is the corresponding quantity for species B (it is assumed that these are global minimum energies, i. e., the lowest energies among all possible isomers); $\Delta[N_\mathrm{A}, N_\mathrm{B}]$ is the mixing energy of the given nanoalloy at a specific composition, i. e., the energy released by mixing N_A A-type clusters and N_B B-type clusters all of size N to produce N alloyed clusters of size N with composition $(N_\mathrm{A}, N_\mathrm{B})$, divided by N. The quantity $\Delta[N_\mathrm{A}, N_\mathrm{B}]$ provides a measure of how thermodynamically favorable alloying is at the given size and composition. Its definition represents the natural generalization of the corresponding concept used for bulk alloys [11.24, 33].

Another complication connected with the theoretical computational description of nanoalloys is the *match* among the energy scales of the different elements composing the alloy and the crucial need to describe this accurately to achieve reliable predictions. This feature, i. e., the presence of multiple length and energy scales, is common to all multifunctional or composite systems. To provide a simple example, if a given approach calculates the ratios between the surface energies of a given element accurately, this is sufficient to correctly predict the shape of a pure nanoparticle of this element (see the Wulff construction in Sect. 11.4.1), but this is no longer true for mixed systems if the scaling factors differ for the different elements. In such a case, an absolute accuracy (or at least a homogeneous inaccuracy) should be aimed for, which is more difficult to achieve than simple relative accuracy.

The crux of theoretical and experimental research on nanoalloys is truly connected with the degree of atomic mixing or chemical ordering or compositional structure of the particles (i. e., the distribution of the different atomic species in the structural framework). The problem at the experimental level is that, while it is in principle not too difficult to control composition, it

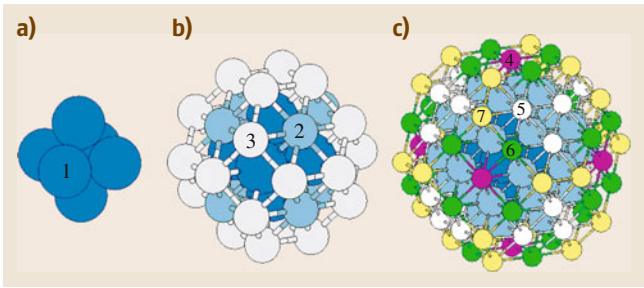


Fig. 11.2a–c Orbit structure of selected even-numbered truncated octahedra: **(a)** 6-atom TO(2,0); **(b)** 38-atom TO(4,1), obtained by adding 32 atoms to **(a)**; **(c)** 116-atom TO(6,2), obtained by adding 78 atoms to **(b)**. Different symmetry orbits are singled out by different *colors* and *numbers*. (After [11.36] with permission of ACS)

is instead much more awkward to precisely control the chemical ordering of a nanoparticle, and invasive post-preparation treatments are often necessary to equilibrate this variable. The point is that chemical ordering greatly increases the degrees of freedom of the system, for example, the number of different possible realizations of a nanoalloy of given size, structure, and composition. Just to give a rough idea, it can be observed that, neglecting the reduction due to point group symmetry, for a cluster with given structure and N atoms, of which N_A are of species A and N_B are of species B, one has $(N_{tot})!/((N_A)!(N_B)!)$ possible different *homotops*, i. e., isomers sharing the same skeletal structure and composition but differing in the mixing pattern [11.23]. This is a number which increases exponentially with the size of the system, rapidly becoming impossible to sample or explore even using computationally inexpensive theoretical approaches. Even the simple description of which phases of chemical ordering are realized is nontrivial. Order parameters associated with chemical order have been defined to distinguish the various ordered phases of bulk alloys [11.34] but have seldom been used so far for nanoalloys [11.35].

At the theoretical level, a viable procedure to search for the equilibrium configurations of the system is to start from a random arrangement and to consider moves based on an exchange of the coordinates of two atomic species, as realized in the exchange-only basin-hopping algorithm [11.37]. An alternative and more effective solution is to consider structurally magic clusters. In this approach [11.24] attention is focused on configurations exhibiting structural shell closure and thus as a norm a high point-group symmetry, which is exploited to partition the atoms into symmetry *orbits*, i. e., group of atoms equivalent by symmetry (transformed into one another by the operation of the symmetry group) (Fig. 11.2). As a consequence, the degrees of freedom of the system are reduced from the number of atoms N to the number of symmetry-nonequivalent orbits N_{orb}, and correspondingly the number of distinct homotops is exponentially decreased, making theoretical simulations feasible even at the first-principles level for medium-sized particles: For example, the segregation patterns of PdPt nanoparticles were recently studied [11.36], finding that the interplay of metal–metal homo- and heterointeractions produces an unusual Pt surface segregation in Pd-rich particles (in spite of the larger Pt bulk energy) and a novel patchy multishell pattern around the equimolar composition in which each shell is decorated by *patches* of like atoms; see the discussion in Sect. 11.4.1. The use of magic clusters is also very useful for studying properties (see, e.g., the Sects. 11.4.3 and 11.4.4 on optical and magnetic properties), both to reduce the computational effort associated with a single computation and to reduce the number of homotops to be considered (Sect. 11.4.1).

In this connection it can be added that another very efficient tool to drastically reduce the computational effort and to enlarge the scope of systems amenable to first-principles simulations is based on the use of periodic models [11.38]. Instead of studying a zero-dimensional (0-D) nanodot, in fact, one can consider a one-dimensional (1-D) or *wire* model, as depicted in Fig. 11.3. In this figure, the correspondence between a truncated octahedral 0-D cluster, supported on a square-symmetry oxide surface, to a 1-D wire in which the section of the cluster is replicated ad infinitum, is clearly shown. As in the case of magic clusters, in this approach one exploits symmetry (in this case, periodic symmetry) to strongly reduce the number of nonequivalent atoms (in this case, those contained in the unit cell). In Fig. 11.3, the indexes defining the level of truncation of the wire corners are also shown. The simplifications assured by the use of wire models in terms of reduction of the number of atoms in the unit cell and also of the degrees of freedom of the system are apparent. Through the use of such models, a 1-D system with a unit cell of 110–120 atoms can be constructed to resemble or mimic 0-D particles with 7–8 times this number of atoms, which would be otherwise extremely expensive or hardly affordable at the first-principles level with present computational facilities. This approach has been used in several instances; see, e.g., the discussion in Sect. 11.4.4 of magnetic properties later in connection with interface effects on the magnetism of CoPt particles supported on MgO(100) [11.39].

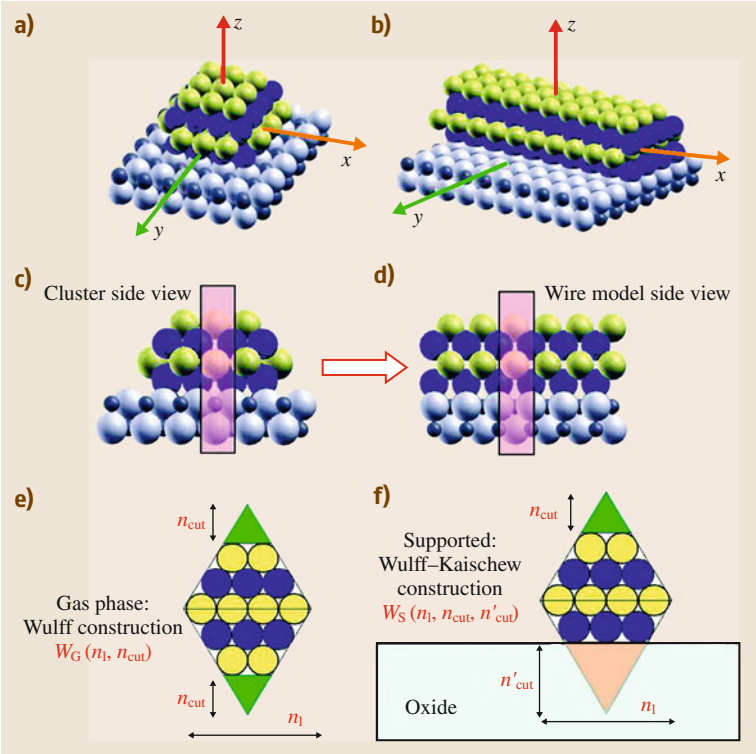


Fig. 11.3a–f One-dimensional (wire) modeling of supported binary particles. A 0-D particle **(a)** and a side view with its cross-section **(c)** are shown, together with a piece of the corresponding 1-D wire model **(b)** and a side view with its cross-section **(b)**. The Cartesian axes are also indicated in **(a,b)**. Side views are along y-axis. The truncations of a free **(e)** and supported **(f)** wire viewed along the x-axis are also shown, defining the quantities n_l, n_{cut}, and n'_{cut}, respectively. (After [11.39] with permission of ACS)

11.2 Preparation and Synthesis

In this section we discuss some of the main experimental procedures utilized in the synthesis of nanoalloy particles. Nanostructured bulk alloys are treated in Sect. 11.5.

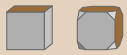
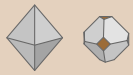
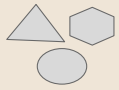
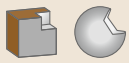
Roughly categorizing, the techniques used to produce alloy nanoparticles can be distinguished into two main groups: homogeneous (Sect. 11.2.1) and heterogeneous (Sect. 11.2.2). In the former class one typically finds approaches which pass through chemical synthesis in solution phase; in the latter, those relying on chemical and/or physical vapor deposition of precursors onto a support surface.

11.2.1 Solution-Phase Methods

The array of methods and techniques developed in the past to produce nanoalloys in the homogeneous phase is really endless. Limitations in both space and specific expertise hinder us from attempting a comprehensive treatment. Rather, we refer to recent excellent reviews for a discussion of the issues and opportunities in this field [11.4, 40–45], limiting the following presentation to some general ideas and information that can help orient the reader in the vast literature on this subject, with particular attention to *hybrid* or multicomponent nanostructures [11.44].

To start with, let us recall some very basic concepts of the chemical routes for preparing metallic nanoparticles in colloidal form [11.4]. As in the pioneering work by Michael Faraday, this is most often achieved via reduction of metal salts in solution by a reductant, e.g., sodium borohydride [11.46], or alternatively via thermal decomposition of an organometallic precursor. In these homogeneous-phase methods, one usually starts from a supersaturated solution obtained either by directly dissolving the solute at higher temperature and then cooling down to low temperatures or by adding an excess of reactants. The solution must be supersaturated to make the aggregated phase (the nanoparticles) thermodynamically favored. The precipitation process

Table 11.1 Summary of the shapes, LSPR absorption peaks, demonstrated applications, and methods for synthesis of Ag nanostructures discussed in [11.43]. (After [11.43] with permission of ACS)

Shape	Illustration	LSPR	Applications	Method of synthesis
Sphere and quasisphere		320–450	SERS; LSPR sensing; assembly	Polyol process (single-crystal); Citrate reduction (quasisphere)
Cube and truncated cube		400–480	SERS; LSPR sensing; assembly	Polyol process; seed-mediated growth
Tetrahedron and truncated tetrahedron		350–450	SERS	Polyol process. light-mediated growth
Octahedron and truncated octahedron		400–500	Assembly	Polyol process; seed-mediated growth; light-mediated growth
Bar		350–900	SERS	Polyol process
Spheroid		350–900	SERS	Polyol process
Right bipyramid		500–700	–	Polyol process
Beam		–	Electron transport	Polyol process
Decahedron		350–450	–	Seed-mediated growth; light-mediated growth; citrate reduction
Wire and rod		380–460	Waveguiding; electronics; SERS; assembly	Seed-mediated growth
Polygonal plates and disc		350–1000	SERS; LSPR sensing	Light-mediated growth; polyol process
Branched structures		400–1100	SERS	Seed-mediated growth
Hollow structures		380–800	SERS; LSPR sensing	Template-directed growth

then has to overcome a thermodynamic energy barrier and thus basically consists of a nucleation step followed by a particle growth stage. In this homogeneous nucleation mechanism, a critical size exists such that clusters smaller than this size will dissolve whereas larger clusters will grow [11.4, 42]. Achieving a small size dispersion (ideally monodispersity) is one important goal [11.42], usually sought by separating as much as possible the nucleation and growth stages [11.47]. In the heterogeneous nucleation mechanism, instead, an external seed is provided, around which aggregation of metal atoms is promoted [11.43, 48–52], which is a different, highly controllable way of separating the nucleation and growth stages. Through all these approaches, a huge variety of different morphologies have been obtained in practice, sometimes with exquisite

control over the shape and also the size of the resulting nanostructures. To show some examples, we report in Table 11.1 an overview of the different shapes in which Ag nanostructures have been modeled, taken from a recent review [11.43].

As underlined above, nanoparticles are metastable phases, tending toward the thermodynamically stable bulk phases if not hindered by, e.g., a surfactant layer which acts as a stabilizing barrier, and a large variety of different surfactant molecules and their effects on the growth have been studied in the literature [11.53]. Monodispersity can be also achieved via post facto treatments, i. e., by separating particles of specific sizes. This has been especially effective in producing very small metal particles at *magic* sizes by exploiting the higher chemical stability of metal clusters with specific numbers of atoms [11.6, 54–59]. Apart from operating on the kinetic parameters of the preparation conditions (which can lead to very effective results [11.60]), another way to orient the growth of colloidal particles is via the use of templates. This path has been thoroughly reviewed recently [11.45], so we do not discuss it in detail. One important example in this field is the use of reverse micelles as confined nanoreactors [11.12].

The problem becomes much more complicated when a multicomponent nanosystem is targeted.

Some synthetic methods are based on simultaneous growth of two (or more) components.

Coprecipitation is a common approach in this class, in which solution conditions are chosen in such a way that both elements can precipitate simultaneously and – ideally – on top of one another [11.61]. A problem in this approach is that the metal with lower redox potential is prone to be reduced before the other metal(s). This is usually avoided by using a very strong reductant to accelerate reaction so much that simultaneity is practically achieved. Still, care must be taken to avoid precipitation of the two elements as separate nanoparticles [11.62, 63]. The composition can be modulated by changing the molar ratio of the two precursors.

In other methods the growth of the two elements is separated in time.

One example is deposition precipitation or surface growth [11.45, 64, 65]. This is a two-step procedure in which nanoparticles composed of one element are first produced, ideally with a narrow particle size distribution [11.4, 41, 42], followed by a change in the reaction environment so that a second element is deposited onto the surface of the previously produced nanoparticles. In this approach the already existing surface favors heterogeneous nucleation on the particle surface with respect to homogeneous nucleation of the second element in the solution phase [11.66], while the mutated reaction conditions should disfavor homogeneous nucleation of the first element, thus producing a composite system. The size, morphology, and faceting of the nanoparticles used as seeds are important in determining the success and the features of the resulting systems [11.67]. Smaller seeds are more active than larger ones, and regions with higher radius of curvature will typically grow faster than smoother regions. This can be true also for some facets with respect to other ones, giving rise to preferential growth along specific directions. External influences such as light or heat can also be used to accelerate or control the process [11.45]. In particular, exploiting electromagnetic field enhancement at the surface of the underlying core facilitates the reduction of the second element, thus producing high yields and shape control [11.68] so that prisms, tetrahedra, decahedra, etc. can be obtained. The as-prepared alloy nanoparticles can naturally be in a metastable phase or configuration, in which case they will evolve in time depending on the kinetics of atomic or vacancy diffusion.

A second example is galvanic replacement [11.43, 69, 70]. Here, one starts from a given nanoparticle composed of an element A (A_s) and incorporates atoms of a second element B initially as a solvated ions (B_{aq}^{m+}) by reducing them into B_s at the expense of some A_s atoms, which are oxidized into A_{aq}^{n+}

$$m\mathrm{A_s} + n\mathrm{B_{aq}^{m+}} \rightarrow m\mathrm{A_{aq}^{n+}} + n\mathrm{B_s}. \qquad (11.1)$$

Clearly, a prerequisite for this reaction to proceed is that the standard reduction potential of the B_{aq}^{m+}/B_s pair must be higher than that of the A_{aq}^{n+}/A_s pair, which poses constraints on the application of this technique. Second, if $n \neq m$, the different stoichiometry of the two species will generate vacancies and porosity within the particle [11.71], which may then evolve with time. Third, by playing with the mobility and concentration of the different species, it has been shown that it is possible to precisely control the final morphology and in part the chemical ordering of the resulting particles [11.43, 69, 70, 72–77].

Note that we do not discuss explicitly polymer-protected composite nanoparticles, whose preparation is partly similar to what has been described so far [11.78, 79].

Moreover, so far we have mainly discussed the synthesis of individual nanoparticles, without hinting at

the possibility of supra-organizing the particles to obtain 1-D, two-dimensional (2-D), and three-dimensional (3-D) arrays [11.43, 80, 81], which are very important, e.g., in optical or microelectronic applications. In this context, an interesting concept is that of mixing two different types of colloidal nanoparticles to achieve a supra-organized ensemble in which both species coexist [11.82]. All this lies outside the scope of this presentation.

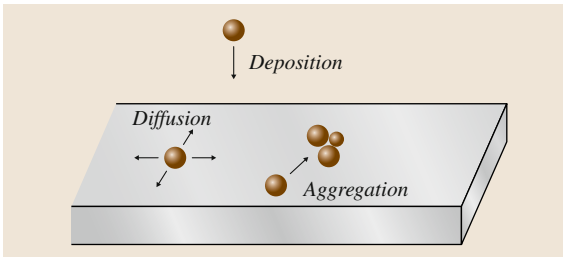


Fig. 11.4 Surface processes in physical vapor deposition of metal species and growth of nanoparticles

11.2.2 Surface Deposition Methods

Technical heterogeneous catalysts are usually produced by wet impregnation from solution [11.2, 83, 84]. In contrast, in basic or academic research, *cleaner* (more controllable) preparation methods are often employed, and chemical vapor deposition (CVD) or physical vapor deposition (PVD) are both processes which are used to grow metal particles on top of a surface. In the former, the precursor metal atoms or clusters are protected by ligands which are eliminated usually via pyrolysis (the vaporized precursors are introduced into a CVD reactor and adsorb onto a substance held at an elevated temperature, where they decompose to produce metal species), whereas the latter involves condensation from the vapor phase of the bare precursor in the form of atoms or clusters, which are deposited onto a surface where nucleation and growth take place (Fig. 11.4). Various techniques can be adopted in surface deposition methods to obtain alloyed rather than pure nanoparticles: For example, one can use a metal alloy as a vaporization source instead of a pure metal, or use two difference vaporization sources, either simultaneously or sequentially, the latter procedure being especially useful to produce core–shell or multishell particles. Among the possible supports, traditionally very relevant ones are oxide surfaces for their importance in the field of heterogeneous catalysis [11.2].

From the point of view of basic research, the interest in surface-deposited metal nanoclusters and nanoalloys has translated into a series of fundamental studies in surface science in which complicated real-world systems are replaced by model systems, ideally under the most well-controlled conditions [11.85]. Two model systems are possible and have been used in the literature. In the former, extended surfaces of pure or alloyed metals are used as models of nanoparticle facets [11.86–88]. In the latter, metal nanoparticles and nanoalloys rather than extended systems were grown, typically on oxide substrates [11.85, 86, 89–91]. Excellent introductions to the field of metal nanoparticles deposited on model oxide supports from the point of view of surface science are available in the literature [11.89, 90], to which we refer for more detailed discussion. In these latter surface science studies of metal nanoparticles on oxide substrates, two major simplifications are usually adopted: (a) the chosen support is a single-crystal surface – possibly with highly controlled defectivity – instead of a complicated, amorphous one as in many applications, and (b) vaporization, deposition, and growth are often achieved in ultrahigh-vacuum (UHV) conditions (i. e., at pressure below 10^{-10} mbar) instead of at atmospheric or even higher pressures. A single-crystal surface is chosen as it allows one to employ space-integrated surface science techniques (see the next section). UHV conditions ensure that each surface atom is hit by residual gas species with extremely low frequency (much less than once per hour). The aim of these studies is to derive rigorous knowledge on model systems that can shed light on the basic mechanisms underlying the complex phenomena occurring in real-world systems, and indeed a wealth of information has been derived from these efforts [11.89, 90]. Characterizing and orienting the structure of the particles and their epitaxy to the substrate are naturally fundamental steps to achieve this goal [11.91] (see Sect. 11.4.1 on structural properties). In this respect, it is worthwhile underlining that substrate preparation is crucial to achieve a thorough understanding of the phenomena at play [11.92]. An interesting analogy can also be drawn with the previous subsection, as the template-directed preparation methods discussed in the context of colloidal nanoparticles find here a counterpart in the surface-directed growth or surface nanopatterning [11.93, 94], i. e., the possibility of producing a substrate exhibiting a regular array of defects that act as (heterogeneous) nucleation centers for the metal nanoparticles or nanoalloys [11.95]. When such a templating substrate is adopted, the growing

species spontaneously self-assemble into long-range-ordered arrays of nanoparticles with reproducible size and structure over macroscopic sample areas, providing the opportunity to investigate at a fundamental level the collective functionalities originating from the ensemble behavior of the particles (Sect. 11.4.3).

Despite the importance of and the fundamental insight gained from these studies, the huge difference in experimental conditions poses the issue of the so-called *pressure and materials gaps* [11.96, 97], i. e., the thermodynamic and kinetic effects of reducing the pressure by orders of magnitude, e.g., on the system composition and mass transport phenomena, and the effect of considering extended surfaces instead of nanoparticles in the studies in which this further simplification is adopted. A line of current research is therefore aimed at developing characterization tools that can be used under environmental conditions, such as spectroscopic (see, e.g., [11.98, 99]) or microscopy techniques [11.100] (Sect. 11.3).

11.3 Characterization of Nanoparticles and Nanoalloys

The properties of an alloyed nanoparticle depend sensitively on the microscopic details of its structure and surroundings. To characterize these, one common way consists in adsorbing the particle on a proper support and using the tools of surface science. The major ones are described in this section. Note that a few techniques, such as high-resolution transmission electron microscopy (HR-TEM) and x-ray photoelectron spectroscopy (XPS), are also able to discriminate between the two elements forming the alloy.

11.3.1 Scanning Force Microscopy (SFM)

SFM is a suitable tool to study in situ the morphology of supported nanoparticles both under UHV and under not too large pressure [11.101]. Atomic resolution of both the nanoparticle and the insulating support can in principle be achieved. SFM is based on detection of the change in frequency (detuning) of an oscillating cantilever due to the interaction of the microscope tip at the end of the cantilever with the investigated system (Fig. 11.5).

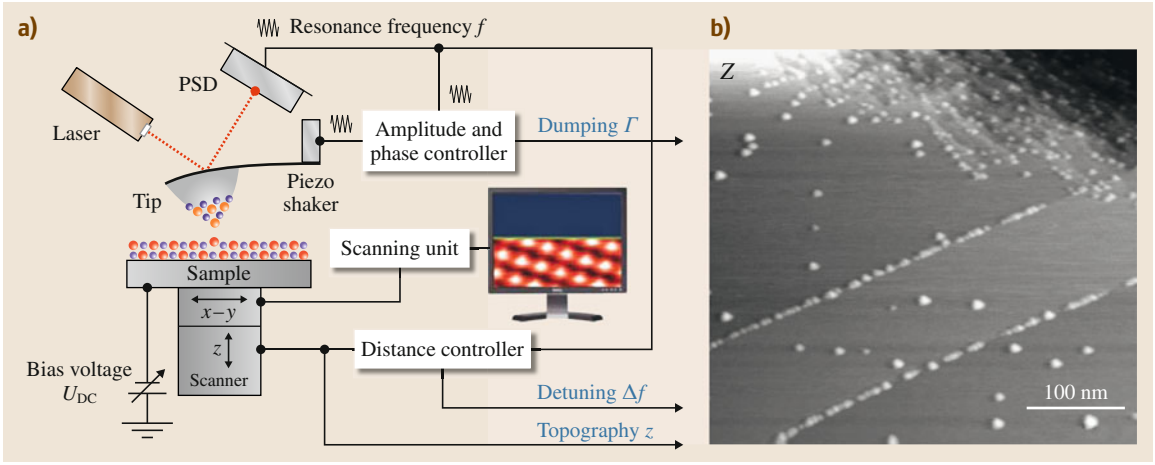


Fig. 11.5 **(a)** Schematic setup of a frequency-modulation noncontact AFM (nc-AFM), consisting of two independent regulation loops. The amplitude/phase controller keeps the amplitude of the cantilever oscillation constant, whereas the distance controller adjusts the tip–surface distance by keeping the detuning Δf at a constant value. The damping or dissipation output reflects the energy required to maintain a constant amplitude of the cantilever oscillation, and can also be used as an imaging signal. Note that the drawing is only a simplified diagram of the function principle (PSD: photo signal detector). (After [11.101]). **(b)** Topography image of the KBr(001) surface after deposition of 0.07 monolayers (ML) of gold. Note that the density of clusters directly scales with the density of steps, which is lower in the *lower part of the image* than in the region at the *top of the image* ($400\times400\,\mathrm{nm}^2$, 293.2 kHz tip, $\Delta f = -23.9\,\mathrm{Hz}$, $k = 48\,\mathrm{N/m}$, $A_{\mathrm{p-p}} = 13\,\mathrm{nm}$, $U_{\mathrm{DC}} = 5.0\,\mathrm{V}$, contrast in $z = 6\,\mathrm{nm}$). (After [11.102] with permission of APS)

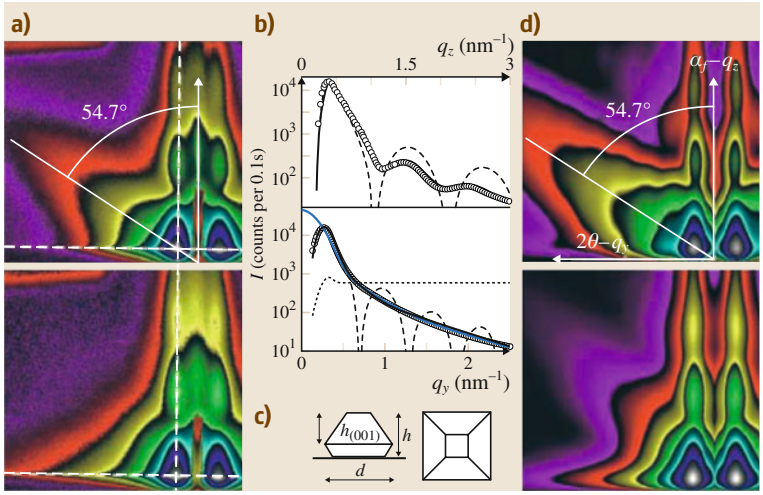


Fig. 11.6 **(a)** 1.5 nm-thick Pd deposit on MgO(001) at 650 K. GISAXS images recorded in 0.1 s with the incident beam along the MgO [110] (*top*) and [100] (*bottom*) directions. White dotted lines show the positions of the four cuts simultaneously used to fit the data, perpendicular and parallel to the surface. **(b)** Best fit of the cuts (continuous lines) perpendicular (*top*) and parallel (*bottom*) to the surface in (**(a)**, *bottom*), with (*circles*) and without (*dashed lines*) size distribution, for a truncated octahedron. In the parallel cut (**(b)**, *bottom*), the averages of the square of the structure factor appear as *blue diamonds*. The fitted interference function $S(\boldsymbol{q})$ (*dotted line*) is reported on an arbitrary scale; I intensity. **(c)** Schematic drawing of the fitted, truncated octahedron shape. **(d)** Simulated GISAXS images obtained after simultaneous fitting of the four experimental cuts. The specular reflectivity (close to $q_y = 0$) was not calculated. (After [11.27] with permission of HighWire Press)

High spatial resolution can be achieved if a constant bias is applied to the rear of the system in order to minimize electrostatic forces originating from residual surface charges. This technique is not able to discriminate between the two elements forming an alloyed particle. SFM can be used on insulating supports. In the example given in Fig. 11.5, SFM is applied to the observation of Au clusters supported on KBr(100) [11.102].

11.3.2 Grazing-Incidence Small-Angle X-ray Scattering (GISAXS)

In GISAXS, a narrow and well-collimated incident x-ray beam hits the system at a grazing angle close to the critical angle for total external reflection. This beam is scattered by the surface due to the nanometric inhomogeneities of the surface (such as steps, kinks, or adsorbed nanoparticles). As a first approximation, the intensity of the scattered light is proportional to the form factor $F(\boldsymbol{q})$ multiplied by the interference function $S(\boldsymbol{q})$, where $\boldsymbol{q}$ is the transferred momentum. $F(\boldsymbol{q})$ and $S(\boldsymbol{q})$ are the Fourier transforms of the particle shape and the island–island pair correlation function, respectively. From the appearance of the scattered light spectrum and from its evolution in time, it is possible to extract information on the particle shape as a function of time (for example, during nanoparticle growth or during a chemical reaction). When dealing with an alloyed particle, this technique is not able to provide information about the distribution of the two elements inside the particle. Like SFM, GISAXS can be used on insulating supports. In the example given in Fig. 11.6, GISAXS was successfully applied to the investigation of the growth of Pd particles on MgO(100) [11.27].

11.3.3 X-ray Absorption Spectroscopy (XAS)

XAS is another x-ray technique utilizing synchrotron radiation. This technique allows one to extract in situ structural information on materials which lack long-range order, including amorphous and nanometer-scale clusters [11.103]. One of its drawbacks concerns the difficulty in characterizing stacking faults in metallic particles [11.104].

When the system is irradiated, an adsorption edge is observed if the energy of the x-ray photons is high enough to excite a core electron to an empty energy state or to the continuum. The position of the adsorption edge

depends on the binding energy of the core electrons of each atom, making the technique element specific. The technique which analyzes the first part of the spectrum (about 50 eV above the edge) is called x-ray absorption near-edge spectroscopy (XANES), providing useful information about the electronic properties of the atoms involved in the edge adsorption. The features observed in the second part of the spectrum (starting from 50 eV above the edge) give rise to the higher-energy extended x-ray absorption fine structure (EXAFS) portion and give information about the local structure around the absorber atoms, that is, the number and type of neighbors. XAS is very useful when studying catalytic processes taking place at the surface of nanoparticles. As an example, XANES has been used to detect the formation of small metallic copper particles (not detectable via XRD) during the reduction of the methanol synthesis catalyst precursor CuO/ZnO and CuO/ZnO/Al_2O_3 [11.105] (Fig. 11.7). Although EXAFS can provide information about the neighborhood of the adsorbing atoms, it is not so useful to extract information about the chemical ordering of the alloyed nanoparticles.

11.3.4 Scanning Tunneling Microscopy (STM)

STM is a technique developed in the early 1980s to provide images of solid surfaces with unprecedented resolution. STM is based on the tunneling current which flows when a sharp tip gets close to a (semi)conducting surface at a distance of approximately 1 nm or less. The tip is mounted on a piezoelectric material, which allows accurate regulation of the tip movement by applying an external bias. The electronic setup of the STM system can control the tip position in two different ways: (i) by maintaining a constant current through the external circuit (constant-current mode), or (ii) by maintaining a constant height of the tip above the sample (constant-height mode). Under ideal conditions, atomistic resolution of the surface can be achieved. STM observation of a supported nanoparticle can give useful information on its structure, although direct information on the chemical ordering is difficult to achieve due to the small contrast of different metallic species and tip convolution effects. As an example, in Fig. 11.8, room-temperature STM images of 2 Å Pd (Fig. 11.8a), 2 Å Ag (Fig. 11.8b), and 2 Å Pd + 0.4 Å Ag (Fig. 11.8c) deposited on alumina film at 100 K are shown [11.106]. As conductive systems are characterized by a high density of both occupied and empty states around the Fermi level, metallic aggregates (such as those shown in the images) usually appear as very bright spots; in this case it results very difficult to achieve atomic resolution and to distinguish between pure and alloyed particles.

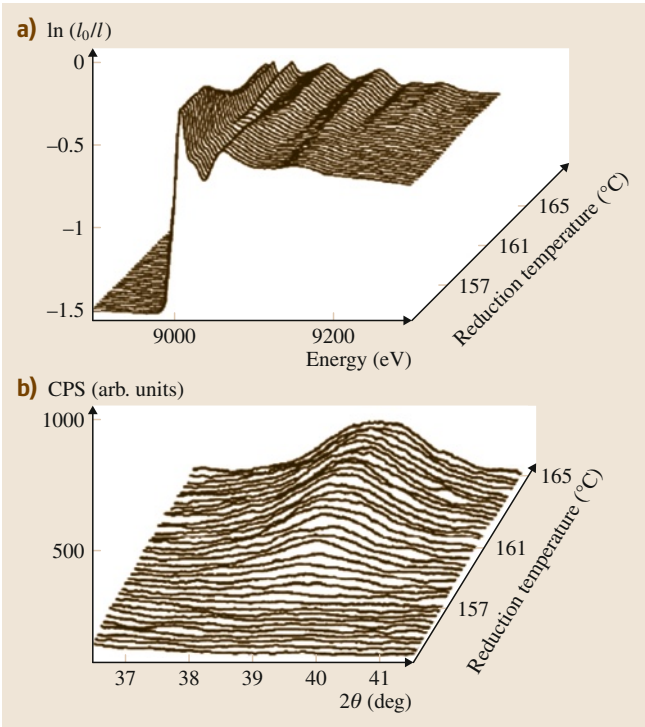


Fig. 11.7 (a) In situ quick EXAFS (QEXAFS) data around the Cu K-edge obtained online during the reduction of CuO/ZnO/Al_2O_3 catalyst with Cu : Zn = 30 : 70 (120 s/spectrum) and (b) corresponding XRD diffractograms of the Cu(111) reflection, recorded simultaneously (CPS: collected photo signal). (After [11.105] with permission of Springer)

STM is one of the few characterization techniques which can in principle provide direct access to structural and electronic information both in vacuum and at atmospheric pressure (and beyond). In fact, despite the necessity of operating with a small gap between the tip apex and the substrate, relatively high gas pressures can be tolerated simply by backfilling a UHV chamber [11.107]. Furthermore, a proper choice of low-expansion-coefficient materials reduces the thermal drift in the instrumentation, allowing meaningful observations at elevated temperatures. Despite these two favorable properties of STM, the combination of high pressure and high temperature presents a new challenge for the design of the instrumentation. The main limitation of STM is that the underlying substrate must be (semi)conductive.

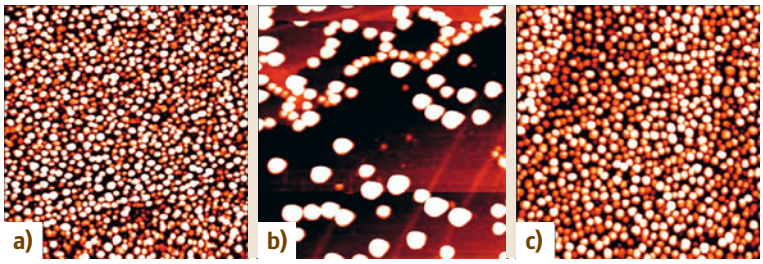


Fig. 11.8a–c Room-temperature STM images of 2 Å Pd **(a)**, 2 Å Ag **(b)**, and 2 Å Pd + 0.4 Å Ag **(c)** deposited on alumina film at 100 K (image size $100 \times 100\,\mathrm{nm}^2$). (After [11.106] with permission of Elsevier)

11.3.5 X-ray Photoelectron Spectroscopy (XPS)

XPS is one of the most useful analytical techniques for probing the electronic structure and chemical composition of a sample. In XPS, the system is irradiated with a monochromatic x-ray beam which promotes electronic transitions from the core and valence states of the surface atoms to the continuum.

The emitted photoelectrons are then collected and analyzed using an electron spectrometer. The binding energy (E_b) of the emitted photoelectrons can be calculated from the energy of the incident beam ($E = h\nu$, where ν is the frequency of the x-ray beam) and the measured kinetic energy (E_k) of the electrons via $E_\mathrm{b} = h\nu - E_\mathrm{k} - \Phi$, where Φ is the work function of the electron analyzer. The work function is the minimum energy necessary to bring an electron from the Fermi energy of the system to the vacuum level. XPS enables quantitative analysis of the surface composition and provides information about the chemical state of elements via measurement of *chemical shifts* in the binding energies of the photoelectrons, i. e., the differences in binding energy with respect to a reference system. The probing depth in XPS depends on the kinetic energy of the emitted photoelectrons, with a minimum of a few angstroms at kinetic energies of around 100 eV.

Because the incident photon energy is lower than 1500 eV in most cases, the kinetic energies of the detected electrons are smaller than this value (after interacting with the surface material). The short mean free path of the emitted electrons in a solid makes XPS a surface-sensitive method. Furthermore, the emitted electrons are also strongly scattered by gas molecules, and XPS is therefore conventionally performed under high-vacuum conditions.

As shown in Fig. 11.9, XPS can be used to quantitatively detect all the elements forming a nanoalloy, discriminating between the different oxidation states of each element; in the example reported here, XPS was used to estimate the fraction of cobalt atoms reduced from the Co^{2+} oxidation state to Co^0 due to reduction by H_2 [11.108].

XPS can be also used in the investigation of the catalytic properties of pure and alloyed nanoparticles at moderate pressures ($> 10^{-5}$ Torr) in so-called ambient

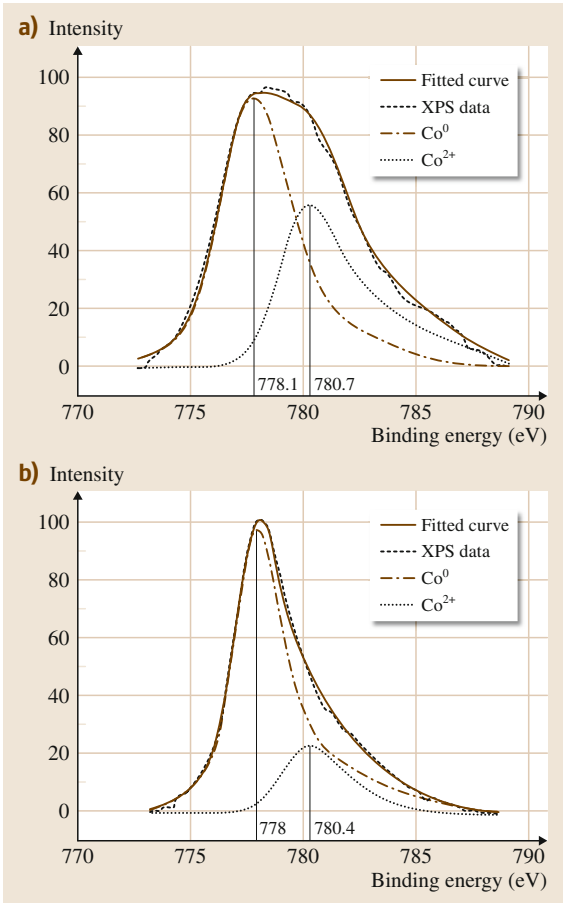


Fig. 11.9a,b X-ray photoelectron spectra for reduced **(a)** Pt-Co/Al_2O_3 and **(b)** Pt-Co/NaY measured at Co 2p lines. (After [11.108] with permission of Springer)

pressure photoelectron spectroscopy (APPES) [11.109], but the attenuation of the electrons due to scattering by gas molecules has to be reduced. The attenuation of the photoelectron signal is proportional to $\exp(-z\sigma p/(k_B T))$, where σ is the electron scattering cross-section, z is the electron's mean free path at pressure p, k_B is the Boltzmann constant, and T is the temperature. The electron attenuation can thus be reduced by placing the sample surface close to a differentially pumped aperture, behind which the pressure drops by several orders of magnitude. This technique can be applied, as an example, to follow the oxidation of the Pd(111) surface (Fig. 11.10) [11.109]. As another example, in the case of a SnPt alloy [11.110], a joint experimental/theoretical analysis of the XPS core-level shifts of the 4d states of the Sn atoms provided useful information for elucidating the surface chemical ordering of the alloy (Fig. 11.11).

11.3.6 Surface X-ray Diffraction (SXRD)

SXRD is another technique which can be used to determine structural parameters at surfaces both under UHV and under high-pressure operating conditions, due to the negligible attenuation of the x-ray beam (due to the low interaction between high-energy x-rays and gases). This, together with the fact that it can be used on insulating substrates, makes the SXRD technique particularly well suited to study the catalytic properties of supported nanoalloys.

In Fig. 11.12, an application of SXRD to the study of the catalytic activity of Pd clusters adsorbed on MgO(100) is shown. When exposed to O_2, the Pd clusters get oxidized (forming a PdO_x phase); when exposed to CO, the oxidation is reversed as CO_2 is formed. These changes can be followed by inspecting the evolution in time of the XRD pattern of the metal nanoaggregates [11.111]. SXRD is not suited to investigate the chemical composition of nanoalloys.

11.3.7 Transmission Electron Microscopy (TEM)

High-resolution TEM (HR-TEM) has made impressive advances in latest years and currently provides a versatile tool for studying the geometric, compositional, and electronic structure of a solid with real-space resolution down to the atomic scale [11.112]. Specifically, the ability of TEM to provide information on the local structure and composition of individual nanoclusters makes this technique an essential complement to the

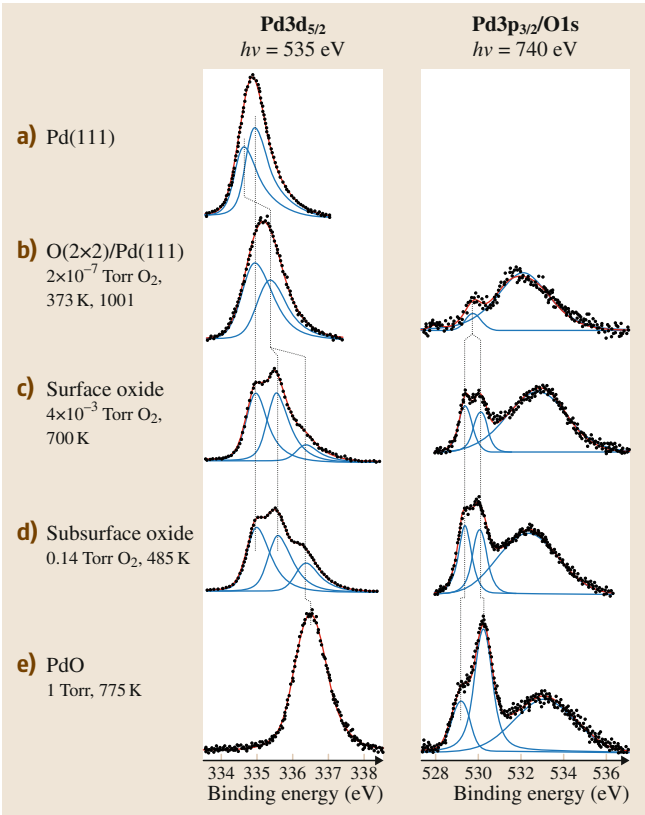


Fig. 11.10a–e Pd $3d_{5/2}$ and O 1s/Pd $3p_{3/2}$ XPS regions at different stages in the oxidation of Pd(111). **(a)** Clean Pd (bulk and surface peaks), **(b)** O (2×2) chemisorbed layer, **(c)** $\sqrt{6}\times\sqrt{6}$ surface oxide, **(d)** subsurface oxide, and **(e)** bulk PdO. Peaks are normalized to the total Pd $3d_{5/2}$ and Pd $3p_{3/2}$ area, respectively. (After [11.109] with permission of Elsevier)

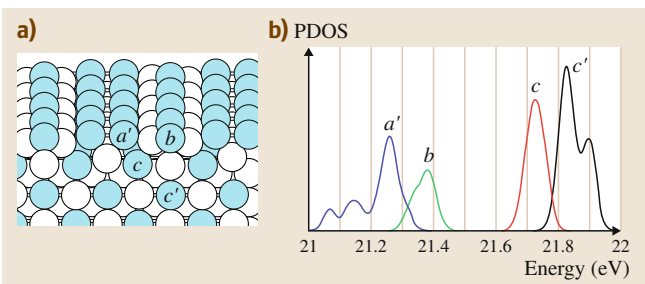


Fig. 11.11 **(a)** Optimized structure of the SnPt[110] alloyed surface; **(b)** simulated phonon density of states (PDOS) where the 4d peaks are attributed to the different Sn atoms of the alloy. (After [11.110] with permission of ACS) ▶

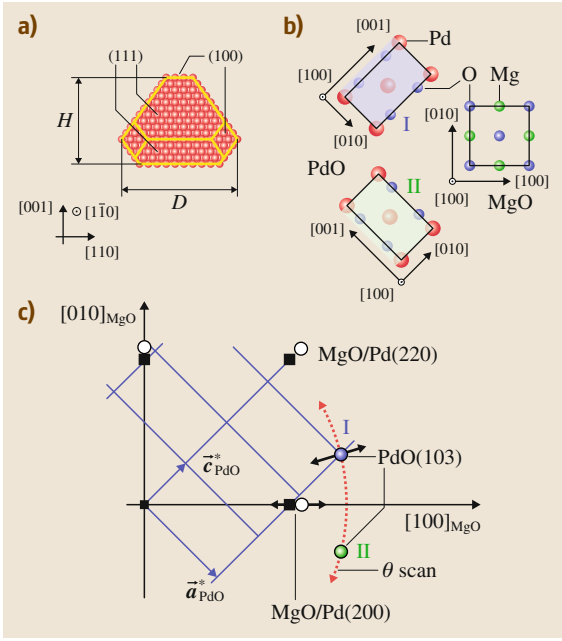


Fig. 11.12 **(a)** Truncated octahedral shape of Pd nanoparticles on MgO(001). In the present experiment the average particle height was $h = 6$ nm and the particle diameter $d = 9$ nm. **(b)** Two (out of five) epitaxial PdO domains observed on MgO(001) during Pd nanoparticle oxidation. **(c)** Sketch of the in-plane reciprocal space ($l = 0$) investigated during the in situ x-ray studies. *Squares* (*open circles*) denote positions of MgO (Pd) Bragg reflections. The PdO reciprocal lattice for oxide domain I is included. The PdO(103) reflection is monitored for both domains during the in situ x-ray experiment by θ scans. (After [11.111] with permission of Elsevier) ◀

variety of other microscopic and spectroscopic techniques that average information over considerably larger length scales. HR-TEM micrographs are often thought of as images of the atom columns in a sample. In fact, HR-TEM lattice images are obtained by illuminating the sample with a parallel electron beam, and to obtain atomic resolution, the sample must be oriented along a low-index zone axis. The transmitted electrons are collected by a high-angle annular dark-field (HAADF) detector.

To quantify HAADF-STEM intensity profiles, some simple models can be invoked: particles are assumed to possess spherical symmetry, and the HAADF intensities are assumed to depend exclusively on the height of the projected atomic column; the result of such a model is shown in Fig. 11.13; such a procedure allows one

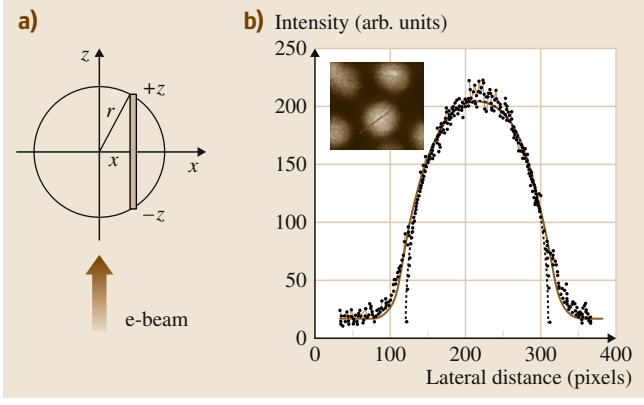


Fig. 11.13 **(a)** Schematic showing that a pure nanoparticle or a homogeneously alloyed nanoparticle is modeled by a sphere with radius of r. HAADF intensity is proportional to the projected atomic column depth along the electron beam. **(b)** Comparison of the experimental data from a pure Au nanoparticle with the simulated line profiles with and without taking into account the finite-size effect of the probe. The *inset* displays the STEM image from which the experimental line profile is taken. (After [11.113] with permission of RSC)

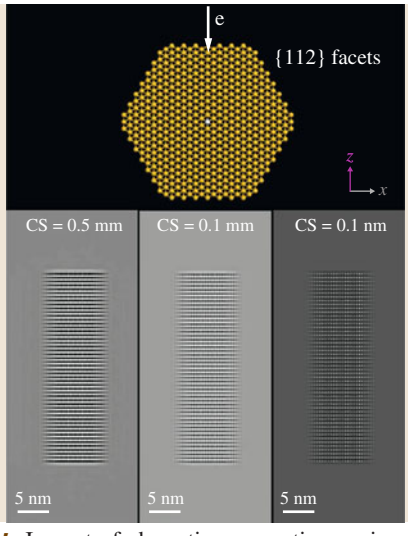


Fig. 11.14 Impact of aberration correction on imaging the side of a nanowire. Cross section (CS) is decreased from 0.5 mm to 0.1 nm, showing that aberration correction greatly improves imaging of the nanowire's edge. (After [11.114] with permission of IEEE)

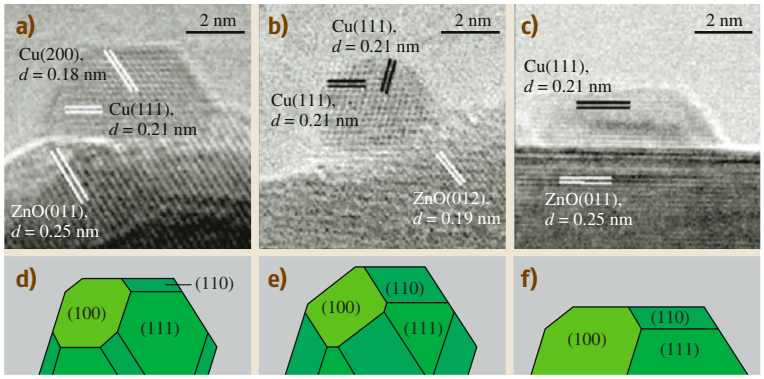


Fig. 11.15a–f In situ TEM images **(a,c,e)** of a Cu/ZnO catalyst in various gas environments together with the corresponding Wulff constructions of the Cu nanocrystals **(b,d,f)**. **(a)** The image was recorded at pressure of 1.5 mbar of H_2 at 220 °C. The electron beam is parallel to the [011] zone axis of copper. **(c)** Obtained in a gas mixture of H_2 and H_2O, $H_2 : H_2O = 3 : 1$, at total pressure of 1.5 mbar at 220 °C. **(e)** Obtained in a gas mixture of H_2 (95%) and CO (5%) at total pressure of 5 mbar at 220 °C. (After [11.116] with permission of Highwire Press)

to estimate the number of atoms in each column and accurately estimate the cluster size [11.113, 115].

Aberration-corrected HR-TEM has been developed to improve the resolution of TEM. The images can be aberration-corrected by hardware or by software, and it is reported that a combination of both procedures provides optimal results (Fig. 11.14, [11.114]). Essentially all the commercial or free available software packages for calculating HR-TEM images are capable of computing images from nanowires, nanotubes, and nanoparticles.

As the scattering section depends on the atomic numbers of the atoms (the contrast being roughly proportional to Z^3, where Z is the atomic number), this technique can be used to discriminate between the different elements forming an alloyed nanoparticle, if they differ significantly in atomic number. An example discussed in more detail in Sect. 11.4.1 is the observation of Ag-Au alloyed nanoclusters, where a sufficiently high contrast led to the identification of a Janus-like chemical order over a long time scale [11.118].

In the field of heterogeneous catalysis, a novel atomic-resolution environmental TEM (ETEM) has been recently developed [11.100] to investigate gas/solid reaction processes under controlled and realistic conditions of pressure and temperature. To this aim, the whole electron microscope was modified by the introduction of a fully integrated and permanently mounted environmental cell (ECELL) system based on a multistage differential pumping system. An application is reported in Fig. 11.15, which shows the evolution of the shape of Cu nanoparticles (supported on ZnO), under the action of a mixture of H_2 and CO at different values of temperature and total pressure [11.116].

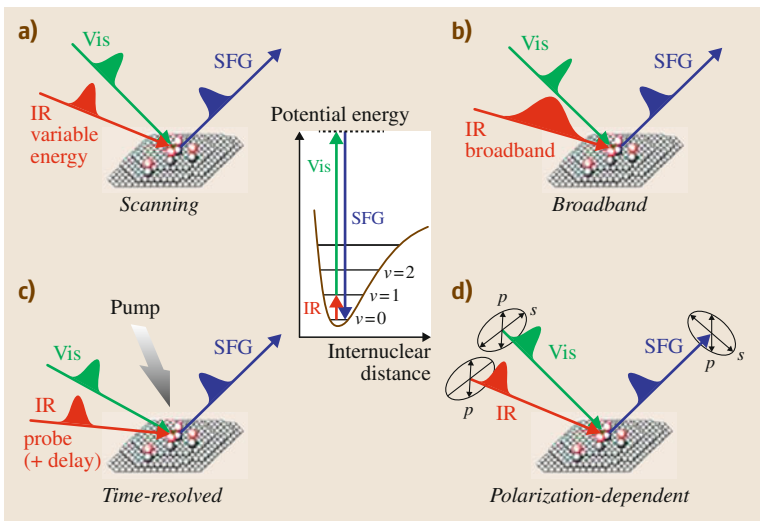


Fig. 11.16a–d Modes of operation and potential energy plot of vibrational IR-Vis sum-frequency generation (VSFG). In the case of a vibrational resonance of an adsorbed molecule (*center plot*, where v indicates vibrational levels), visible light is generated at a frequency that is the sum of the frequencies of the two incident optical fields ($\omega_{SFG} = \omega_{IR} + \omega_{vis}$). The different modes of operation include **(a)** scanning, **(b)** broadband, **(c)** pump–probe (time-resolved), and **(d)** polarization-dependent VSFG. (After [11.117] with permission of MRS)

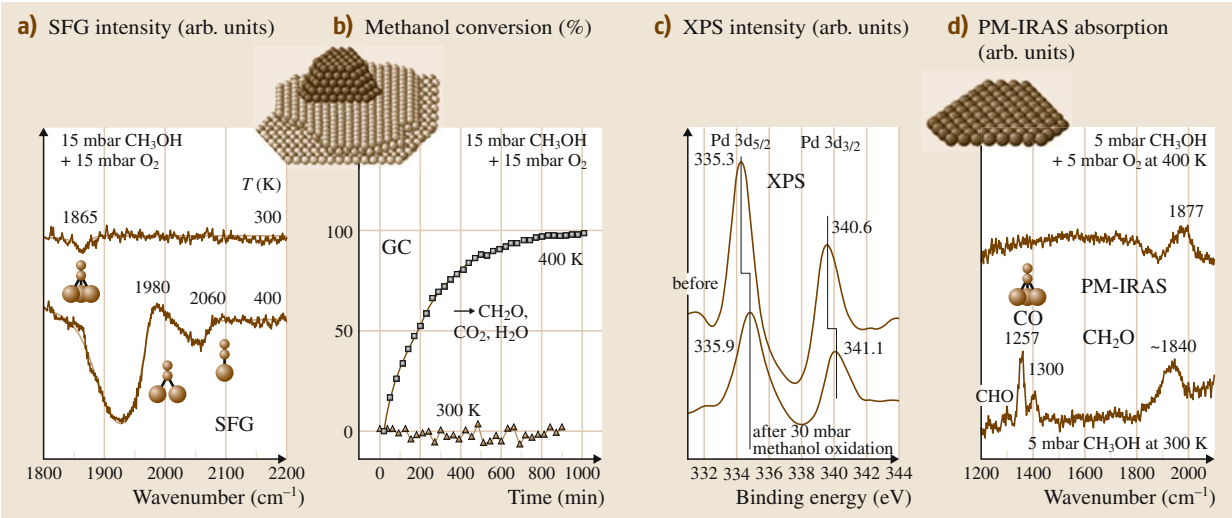


Fig. 11.17 SFG, XPS, and PM-IRAS (polarization-modulation infrared reflection absorption spectroscopy) measurements during CH_3OH oxidation on Al_2O_3-supported Pd nanoparticles and on Pd(111). (After [11.119] with permission of RSC)

11.3.8 Vibrational Sum-Frequency Generation (VSFG)

A technique which is particularly useful in the characterization of catalytic reactions taking place at the surface of metallic nanoparticles is laser spectroscopy based on the second-order nonlinear optical process of sum-frequency generation [11.98, 99] (Fig. 11.16). The system is irradiated by two (laser) light waves of different frequencies; they interact in a medium characterized by a nonlinear susceptibility tensor $\chi^{(2)}$ and generate a wave at the sum of their frequencies. To acquire an SFG vibrational spectrum during a chemical reaction, two picosecond laser pulses are spatially and temporally overlapped on the sample. One input beam is in the visible range at a fixed frequency (ω_{vis}), while the second is tunable in the mid-infrared (IR) region (ω_{IR}) to probe the vibrational modes of the surface species. When the high-energy virtual state relaxes, light is generated at a frequency that is the sum of the frequencies of the two incident optical fields ($\omega_{SFG} = \omega_{IR} + \omega_{vis}$), resulting in a signal in the visible region. By tuning the wavelength of the IR beam and monitoring the intensity of the SFG output, an adsorbate vibrational spectrum is obtained as a plot of the SFG intensity against the IR wavenumber. An example is shown in Fig. 11.17, where this technique has been applied to methanol oxidation on Pd-Al_2O_3 [11.119].

Other spectroscopic techniques can be used to characterize the surface of nanoparticles: For example, one can monitor the infrared (IR) spectrum of adsorbed CO species [11.120], extracting information on the status of the surface. More recently, advances in electron paramagnetic resonance (EPR) have been realized to allow identification of extremely low concentrations of unpaired spins, also located at the solid–vacuum interface [11.121]. Finally, before the advent of advanced microscopy and spectroscopic techniques, chemisorption data or in general reactivity data were widely used to characterize, at least semiquantitatively, the structure (e.g., the dispersion and surface composition) of alloy heterogeneous nanocatalysts [11.2, 22, 83, 84].

11.4 Properties

As recalled in the Introductory, the expansion of possibilities afforded by combining two different metal species is truly vast. Practically any interesting property of metal nanosystems can in principle be tuned and the associated difficulties solved by judicious mixing of different species. This section first describes some of the knowledge on the novel phenomena that are encountered at the structural level in this field (Sect. 11.4.1), pointing out the great freedom and also the unexpected findings that have emerged in recent

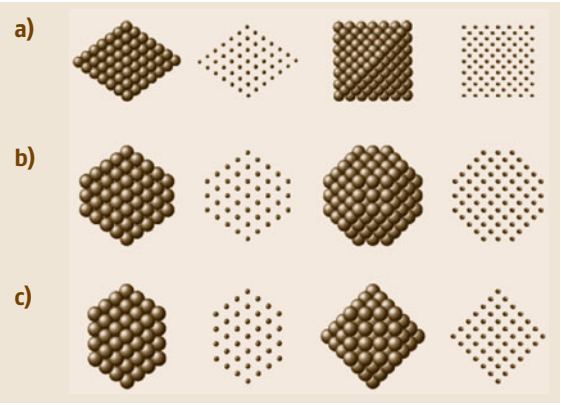


Fig. 11.18a–c Face-centered cubic (fcc) clusters: **(a)** octahedron, **(b)** truncated octahedron, and **(c)** cuboctahedron. Each cluster is shown in four views. An octahedron is made up of two square pyramids sharing a common basis. Its surface consists of eight triangular close-packed (111) facets, but the structure has a high surface-to-volume ratio. Polyhedra with a lower surface-to-volume ratio are obtained by symmetrically truncating the six vertices of an octahedron, thus obtaining square and hexagonal (or triangular, see later) facets. A truncated octahedron can be characterized by two indexes: n_1 is the length of the edges of the complete octahedron; n_{cut} is the number of layers cut at each vertex. In the figure, for the octahedron in **(a)** $(n_1, n_{cut}) = (7, 0)$, for the truncated octahedron in **(b)** $(n_1, n_{cut}) = (7, 2)$, and for the cuboctahedron in **(c)** $(n_1, n_{cut}) = (7, 3)$. A perfect truncated octahedron thus has a number of atoms, $N_{TO}(n_1, n_{cut}) = 1/3(2n_1^3 + n_1) - 2n_{cut}^3 - 3n_{cut}^2 - n_{cut}$. This equation defines the series of magic numbers for truncated octahedron structures. The square facets have (100) symmetry and edges of $n_{cut} + 1$ atoms. The (111) facets are not in general regular hexagons. In fact, three edges of the hexagons are in common with square facets, thus having $n_{cut} + 1$ atoms, while the remaining three edges have $n_1 - 2n_{cut}$ atoms. Regular hexagons are thus possible if $n_1 = 3n_{cut} + 1$; truncated octahedra with regular hexagonal facets are referred to as regular truncated octahedra. When $n_1 = 2n_{cut} + 1$, the hexagonal facets degenerate to triangles and the cuboctahedron is obtained, which is usually not energetically favored because of its large (100) facets. (After [11.122] with permission of APS)

years, with the discovery of novel structural motifs peculiar to multicomponent systems. The rest of the section is devoted to the fascinating properties of alloy nanoparticles, from the chemical ones that are exploited in the field of heterogeneous catalysis to the optical ones studied by Michael Faraday and the more recent interest on magnetism. The mechanical properties that are obtained by nanostructuring bulk alloys are treated in Sect. 11.5. Clearly, this represents only a subset of the recent developments, achievements, and realizations. Our aim is to give a flavor of what has been and is currently being pursued in this field and some basic understanding that should enable the reader to follow the relevant literature. Most subsections include a brief part on the theoretical methods as available or appropriate. Theoretical simulations have already made a very important contribution to the understanding and a priori prediction of the structural properties of nanostructured alloys (Sect. 11.4.1). Moreover, also in the field of the catalytic, optical, magnetic, and mechanical properties, computational methods are nowadays becoming able to treat realistic systems with sufficient accuracy and will make a decisive contribution to future advances in both basic and oriented research.

11.4.1 Structural Properties of Alloyed Nanoparticles

In this section, the morphologies and chemical order patterns of metallic nanoalloys are briefly described. Due to the *greedy* and *fluxional* character of the metal–metal interaction [11.19, 20], i. e., the fact that metal atoms can sustain a wide range of coordination numbers (up to 12–14) and that the energy barriers between various structures are not too high so that particles may transition among them in working conditions, metal nanoparticles and nanoalloys exhibit an impressive variety of different morphologies [11.91, 123] and mixing patterns [11.25]. The study of the structure of metal particles is thus at the forefront of current research, due to both unsolved fundamental challenges and its close links with particle functions and properties, and its relevance in technological applications [11.26]. We will discuss in particular particles either free or supported on a substrate, leaving aside for reasons of space the vast field of particles or clusters coated by a protective layer of surfactants [11.6, 54, 58].

Morphology in the Gas Phase

We start by describing the morphology, or structural motifs, of free nanoparticles [11.123], distinguished into crystalline, noncrystalline, and those peculiar to very small clusters.

Crystalline Structures. In this family the atoms of the clusters are positioned at the crystalline sites character-

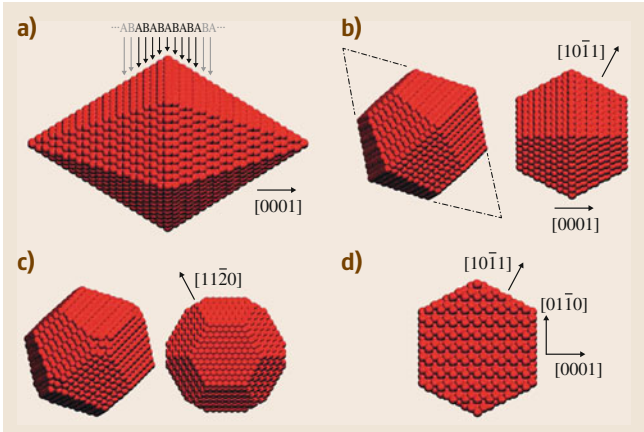


Fig. 11.19a–d Morphology of the hcp motif. The hcp motif is obtained by truncating hexagonal bipyramids **(a)**, whose axis is parallel to the *c*-axis of the hcp lattice of the metal. The first cut **(b)** eliminates top and bottom vertices of the pyramids, thus generating hexagonal (0001) faces. The second cut **(c)** eliminates lateral vertices, creating small (11$\bar{2}$0) facets, with their typical zigzag atomic arrangement. The final cut **(d)** is due to the contact with the substrate and generates a large (11$\bar{2}$0) face. Close-packed planes are perpendicular to the substrate. (After [11.125] with permission of ACS)

izing the metal in its bulk form. When cutting a particle from a bulk crystal, the driving force is to minimize the surface energy of the resulting cluster. One way is to make cuts by exposing only close-packed (111) facets: the resulting shape is the octahedron (Fig. 11.18a), that is, two opposite square pyramids sharing a basis. Even though all the octahedron faces are close packed, the particle shape does not optimize the surface energy because of its high surface-to-volume ratio. Clusters with more spherical shapes can be obtained by cutting the vertices of the octahedron, thus producing a truncated octahedron (TO) (Fig. 11.18b). The TO surface has eight hexagonal close-packed (111) facets and six square (100) facets. A more (or less) deep cut determines an increase (or decrease) of the square facets at the expense of the close-packed ones; when the shape of the (111) facets becomes a triangle, the resulting cluster structure is called a cuboctahedron (CO, Fig. 11.18c). In general, the CO is not favored with respect to other TO because of the too large (100) facets. For sufficiently large sizes, the optimal particle shape is given by the canonical Wulff construction [11.124], a model developed to determine the lowest-energy shape of macroscopic crystals via minimization of the surface energy. According to this construction, the best truncated octahedron structure should fulfil the condition

$$\frac{\gamma(100)}{g\gamma(111)} = \frac{d(100)}{d(111)} ,$$

where $\gamma(100)$ and $\gamma(111)$ are the surface energies of the (100) and (111) facets, respectively, while $d(100)$ and $d(111)$ are the distances of the facets from the center of the cluster. The higher the surface energy of a given facet, the greater its distance from the center of the cluster. The same relation also applies to any other surface plane.

Several metals possess a face-centered cubic (fcc) structure in the bulk form. Some metals (such as cobalt and titanium) are hexagonal close packed (hcp) in the bulk form; when cutting an hcp crystal, the solid which is obtained is shown in Fig. 11.19: the hcp nanodots are truncated hexagonal bipyramids whose axis coincides with the *c*-axis of the hcp lattice [11.125]. As in the case of the TO, also in this case it is possible to reduce the surface-to-volume ratio by cutting the vertices of the solid, as shown in Fig. 11.19. Analogous reasoning holds for body-centered cubic (bcc) clusters.

Noncrystalline Structures. Noncrystalline motifs, i. e., structures which cannot give rise to a periodic pattern because they contain, e.g., fivefold symmetry axes, are an alternative way to obtain low-energy structures [11.123].

The Mackay icosahedron (Fig. 11.20) was the first noncrystalline motif discussed, in 1962, and corresponds to one of the Platonic solids. This is a structure with fivefold rotational axes. Icosahedral clusters are limited by (111) close-packed facets only, thus minimizing the cluster surface energy. However, this is obtained at the expense of a volume contribution due to the fact that the atoms are not in their crystalline positions; radial intershell bonds are compressed, whereas intrashell bonds are expanded. Therefore Mackay icosahedra are highly strained structures, suggesting that icosahedra could be expected to be the most favorable structures only at small sizes.

Icosahedra are not the only possible noncrystalline structures. Another motif is represented by the Ino decahedron (Fig. 11.21a). This structure is formed by two pentagonal pyramids sharing a base; its surface has only (111) close-packed facets, but its shape is very far from being spherical.

Truncation of the five edges limiting the common basis of the pyramids to expose (100)-like facets is advantageous (Fig. 11.21b), but this cut does not usually produce the best possible decahedron. In 1984,

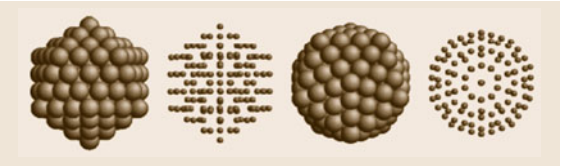


Fig. 11.20 Icosahedral clusters. The Mackay icosahedron is a noncrystalline structure organized in shells. An icosahedron with k shells has $N_{Ih}(k) = 10/3k^3 - 5k^2 + 1/3k - 1$ atoms (so that the series of magic numbers is 1, 13, 55, 147, ...). The icosahedron in the figure has $k = 4$ shells. An icosahedron with k shells has the same number of particles as a cuboctahedron with $n_{cut} = k - 1$. An icosahedron has 20 triangular facets of side k and 12 vertices. Each pair of opposite vertices lie along a fivefold symmetry axis. An icosahedron can be thought of as composed of 20 fcc tetrahedra sharing a common vertex in the central site. When 20 regular tetrahedra are packed around a common vertex, large interstices remain. To fill these spaces the tetrahedral must be distorted, thus generating a huge strain on the structure. Intershell distances are compressed, while intrashell distances are expanded. The facets of an icosahedron are of distorted (111) symmetry. Adatoms deposited on the facets of a Mackay icosahedron can be placed on sites of either fcc or hcp stacking. Islands of fcc stacking are part of the next Mackay shell, while islands of hcp stacking form a so-called anti-Mackay overlayer. (After [11.122] with permission of APS)

Marks proposed a different cut, with reentrances exposing further close-packed facets separating neighboring (100)-like facets (Fig. 11.21c). Marks decahedra achieve better optimization of the surface energy than truncated octahedron structures. Decahedra are also strained structures, although the strain is much smaller than for icosahedra. This means that the icosahedral motif should be the most favored motif at small sizes, and truncated octahedron clusters are expected for large sizes; truncated decahedra could be favored in an intermediate range [11.126].

The explosive surge of activity in recent years (see, e.g., the collection of data in the Cambridge crystallographic data base (CCDB [11.127]), has enriched the set of classical structural motifs (i. e., decahedral, icosahedral, and crystalline) with new additions.

Among these, a notable class is that of polyicosahedra (pIh) [11.128, 129]. pIh structures (Fig. 11.22) are built by packing elementary icosahedra (Ih) of 13 atoms in such a way that core (interior) atoms in the structure are surrounded by a complete Ih_{13} shell [11.128]. They have been predicted to be kinetically favored due to coalescence or rapid growth,

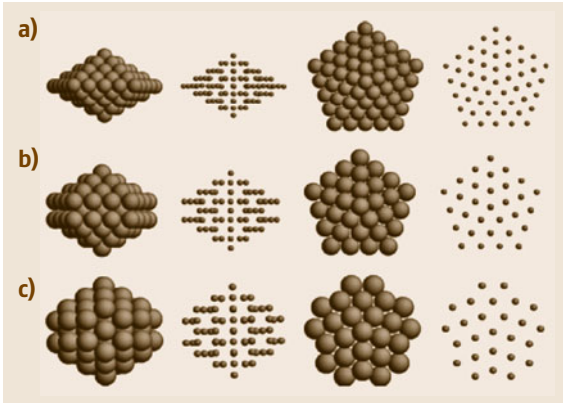


Fig. 11.21a–c Decahedral clusters: **(a)** regular decahedra, **(b)** Ino truncated decahedra, and **(c)** Marks truncated decahedra. A decahedron is made up of two pentagonal pyramids sharing a common basis. It has a single fivefold axis and is formed by five tetrahedra sharing a common edge along the fivefold axis. When five regular tetrahedra are packed, gaps remain, but they are smaller than in the case of the icosahedra. These gaps are filled by distorting the tetrahedra, thus introducing some strain. Regular decahedra (*first row*) are limited by ten close-packed (111)-like facets, but have a large surface-to-volume ratio, which can be lowered by truncating the edges around the common basis, thus obtaining the Ino decahedron with five (100)-like facets. An even better structure is the Marks decahedron, obtained by introducing reentrances that separate the (100)-like facets (*third row*). A decahedron is characterized by three integer indices (m, n, p), where m and n are the lengths of the sides of the (100) facets, perpendicular and parallel to the axis, respectively, and p is the depth of the Marks reentrance. A regular decahedron has indices of the form $(m, 1, 1)$ [the (5, 1, 1) decahedron is shown in the *top row*], Ino decahedra have indices $(m, n, 1)$ with $n > 1$ [the (4, 2, 1) Ino decahedron is shown in the *second row*], and Marks decahedra have (m, n, p) with $n, p > 1$ [the (2, 2, 2) Marks decahedron is shown in the *third row*]. A Marks decahedron has $h = m + n + 2p - 3$ atoms along its symmetry axis and a total number of atoms given by $N_{M\text{-}Dh} = (30p^3 - 135p^2 + 207p - 102)/6 + \{5m^3 + (30p - 45)m^2 + [60(p^2 - 3p) + 136]m\}/6 + \{n[15m^2 + (60p - 75)m + 3(10p^2 - 30p) + 66]\}/6 - 1$. From this formula it follows that a *Ino* decahedron has $N_{Ino} = [5m^3 - 15m^2 + 16m + n(15m^2 - 15m + 6)]/6 - 1$ atoms. For $n = m$ and $p = 1$ [square (100)-like facets] a decahedron thus has the same number of atoms as an icosahedron of m shells and as a cuboctahedron with $n_{cut} = m - 1$. Finally, a regular decahedron has $N_{Dh} = (5m^3 + m)/6$ atoms. (After [11.122] with permission of APS)

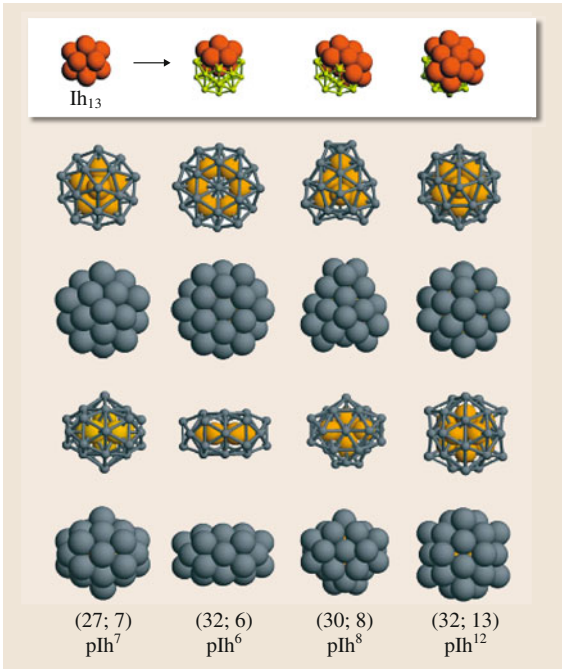


Fig. 11.22 Magic core–shell pIh clusters; pIh clusters are built by packing elementary Ih_{13} clusters, as shown in the *top row*, where three different fragments of the pIh^7 structure are given. From *left* to *right*, the fragments comprise one, two, and four interpenetrating Ih_{13}. Below, a selection of magic core–shell pIh is given. Each pIh is shown in four views; in two of them the Ag atoms (*grey color*) are represented by small points to show the arrangement of the core (Ni or Cu, *orange color*) atoms. The (27;7)pIh^7 has a decahedral Ni or Cu core of 7 atoms, and the 27 Ag atoms are placed in an anti-Mackay overlayer. The (32;6)pIh^6 is a pancake structure, with the six inner atoms placed on a regular hexagonal ring. The (30;8)pIh^8 is the perfect core–shell structure including the maximum number of core atoms at size 38. The (32;13)pIh^{12} is the complete anti-Mackay icosahedron of size 45, including a perfect Ih_{13} core. It is made of 12 interpenetrating Ih_{13} sharing the central atom as a common vertex. (After [11.128] with permission of APS) ◀

but also to be thermodynamically stable for given isolated particles [11.130], especially for binary metal nanoclusters (or nanoalloys) in proper combinations of the constituent metals [11.131, 132]. In fact, by mixing two metals of different atomic size and by adopting a core–shell chemical ordering, one can achieve great stabilization of an Ih-type structure if the smaller element segregates into the core and if the size mismatch is of the proper amount. pIh motifs are important also because they can be seen as the finite-size analogs of *Frank–Kasper* bulk phases [11.133] and thus, ultimately, quasicrystals [11.134, 135].

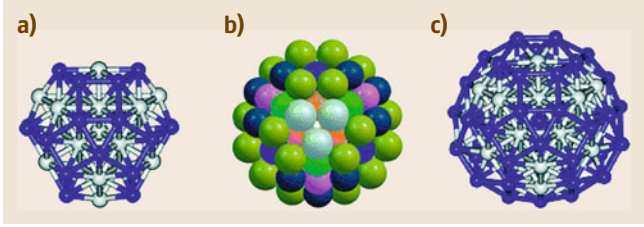


Fig. 11.23 **(a)** Leary tetrahedron fragment for the composition $Pd_{28}Pt_{28}$. **(b)** Leary tetrahedron structure with different shells indicated by *different colors*. **(c)** Leary tetrahedron structure for $Pd_{49}Pt_{49}$. Pd and Pt atoms are represented by *dark-* and *light-blue spheres*, respectively, in **(b)** and **(c)**. (After [11.37] with permission of RSC)

Another important novel family is represented by hybrid motifs, such as hybrid decahedral/close-packed structures, in which a close-packed core in the form of a trigonal pyramid or bipyramid is surrounded by atoms growing on the core faces in hcp(111) stacking plus further atoms arranged along edges between two faces, thus creating a local decahedral arrangement ([11.37, 136, 137], Fig. 11.23).

The reason why the occurrence of these hybrid structural motifs can be favored in nanoalloyed particles can be rationalized. Suppose that one mixes two species with very different cohesion in the bulk, and suppose also that the size mismatch between the two species is small or such that the more cohesive element also presents the smaller size. In these conditions, it is not unreasonable to expect a core–shell arrangement with a core segregation of the latter species. Moreover, once this species achieves full coordination in the core (i. e., coordination number = 12), it will tend to arrange in a close-packed (cp) configuration. The less cohesive species, instead, being surface-segregated and thus low-coordinated, will tend to adopt a noncrystalline, fivefold arrangement.

These are hybrid structures which combine a close-packed core with a decahedral or icosahedral surface. One such example is the Dh-cp (DT) structure described in [11.138] for $(Pd\text{-}Pt)_{34}$ (Fig. 11.24a). At $Pd_{14}Pt_{20}$ composition, the internal core made of Pt atoms is a double tetrahedron or trigonal bipyramid (i. e., two tetrahedra sharing a face), while the Pd shell grows in hcp stacking on the faces and at edges. The DT structure can be thought of belonging to the family of so-called

Leary tetrahedra [11.37, 136]. Note, however, that at these small sizes the interplay of bond count and bond strength is subtle, and it turns out that the Leary tetrahedron is not favored at its own magic number ($N = 44$) but in the size range immediately below it (around 34 atoms).

Another example of a hybrid structural motif is the Oh-Ih structure described in [11.137] for $(Ag\text{-}Pt)_{38}$ (Fig. 11.24b). This structure is similar to the TO_{38} structure as it has an internal octahedral core. However, the surface atoms do not grow exactly on top of the (111) faces of the internal octahedron (as would happen in a TO_{38} arrangement) but are placed according to a distorted arrangement, in such a way that only two square faces (instead of six as in TO_{38}) and no hexagonal faces are created. From an internal perspective, it resembles two double icosahedra joined by the central atoms, and in this sense it can be considered as an example of a mixed fivefold-symmetric/closed-packed arrangement.

To summarize, mixing two different metal species can give rise to novel structural motifs, such as pIh or hybrid ones, that are either unknown or not favorable for pure species. Core–shell or multishell configurations in general are ubiquitous. Among these, those realized, e.g., in fivefold pIh structures, represent an efficient way to express at the nanoscale the segregation or immiscibility tendency present in the bulk with additional energetic benefits. The idea that metals immiscible in the bulk could mix at the nanoscale, i. e., by forming core–shell segregated configurations, had been hypothesized for some time [11.22, 140], being spectacularly confirmed by the advent of improved microscopy, spectroscopic, and theoretical characterization techniques.

Very Small Clusters. To complete this general overview, the case of very small clusters (composed by, say, fewer than 20 atoms) deserves some consideration. When the size is very small, almost all the atoms are undercoordinated, resulting in stabilization of *exotic* structures. In the case of gold clusters, for example, the relativistic contraction of the Au 6s orbital concomitant with a significant shortening of the interatomic bond distances (typically by 0.25 Å) results in increased overlap between the 5d orbitals of neighboring atoms. The increased tendency towards strong directional chemical bonds explains the stabilization of planar structures [11.139] for very small nuclearities (fewer than 12 atoms) (Fig. 11.25); the transition to compact structures takes place above size 12–13, due to the lengthening of the bond distances at increased

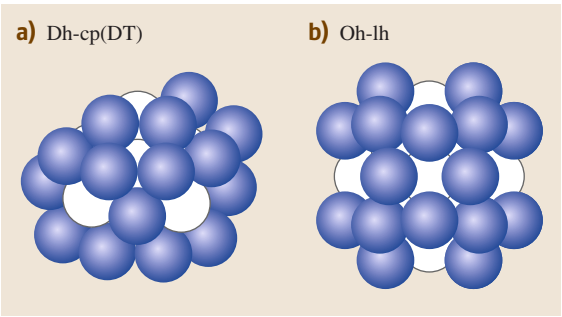


Fig. 11.24a,b Two hybrid fivefold-symmetry/close-packed structures. **(a)** Dh-cp (DT) at size $N = 34$, and **(b)** OhIh at size $N = 38$

coordination numbers. Moreover, in the size range between 16 and 18 atoms, hollow cages have been experimentally detected and theoretically studied. These hollow golden cages (*bucky gold*), which are shown in Fig. 11.26, have average diameter > 5.5 Å and can easily accommodate one guest atom inside [11.141, 142].

Morphology of Supported Particles

We now describe the morphology of nanoparticles supported on a regular substrate.

The Wulff–Kaischew Model. Metal nanoparticles can be stabilized or directly grown on a support, and a common choice of substrate is represented by oxide surfaces.

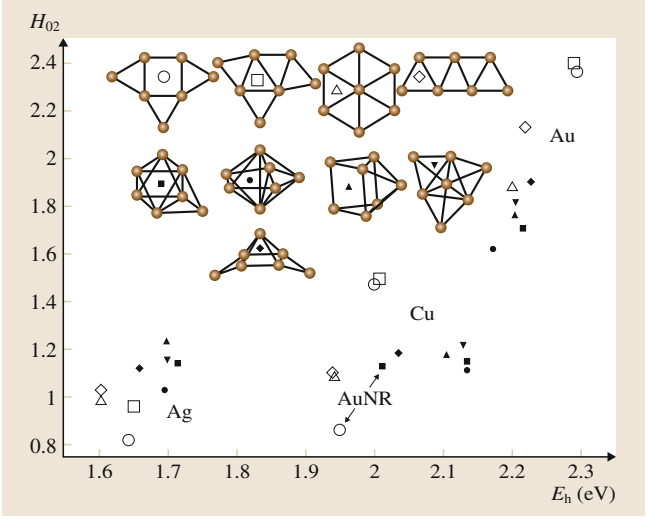


Fig. 11.25 Correlation between the sd hybridization index H_{02} and the binding energy per atom; a larger value of H_{02} indicates stronger sd hybridization. (After [11.139] with permission of APS)

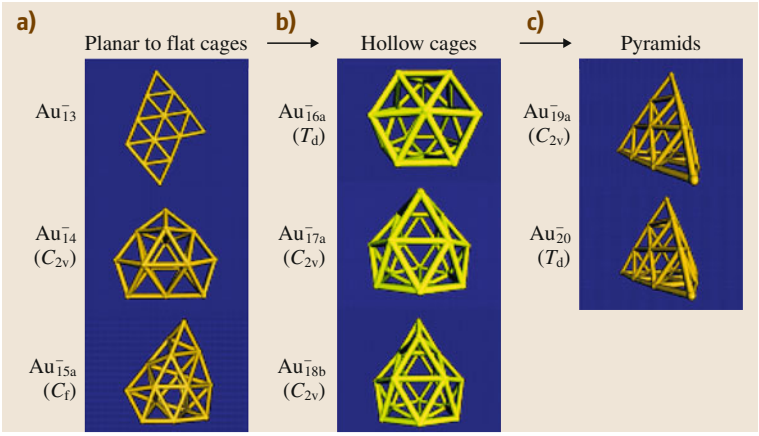


Fig. 11.26a–c Structural evolution of mid-sized gold anion clusters from Au_{13}^- to Au_{20}^-. **(a)** The 2-D planar to 3-D flat-cage structural transitions. **(b)** The hollow gold cages with diameters > 5.5 Å. **(c)** The pyramid-like clusters, which resemble bulk gold. (After [11.141] with permission of NAS)

The equilibrium shape of a supported nanoparticle can be different from that in the gas phase, and the problem of the equilibrium shape of supported nanoparticles was first solved by Kaischew via the Wulff–Kaischew construction, an extension of the Wulff criterion ruling the equilibrium shape of large clusters in the gas phase [11.91]. As can be observed in Fig. 11.27, due to the adhesion between the metal particle and the substrate, a larger portion of the cluster can be cut off, resulting in an asymmetric shape with respect to the central plane of the particle. In practice, the adhesion energy of the particle to the substrate plays the role of a surface energy in the Wulff construction. To elucidate how this criterion can be used to rationalize the structure of supported metal clusters, let us examine the results of global optimization searches carried out on four pure metals (Ag, Au, Pd, and Pt) adsorbed on MgO(100) [11.143, 144]. In general, the shape of the clusters is the result of the competition between metallic bond and metal–substrate interaction. Typically, within each structural motif, the clusters tend to grow according to a given shape which optimizes, for example, the metal–substrate interaction energy, until this requires too high an energetic price, at which point the competing quantity (the metal–metal interaction energy) sets in, overcoming the corresponding energy penalty and the structure *collapses*, or better realizes a transition into a different shape.

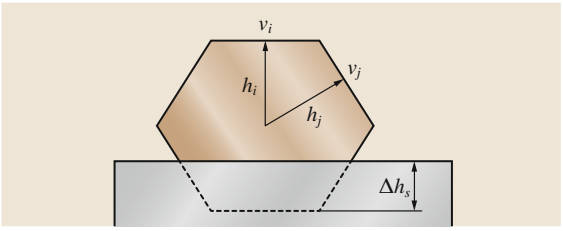


Fig. 11.27 Schematic representation of the equilibrium shape of a supported crystal. The Wulff shape of the free crystal is truncated at the interface by Δh_s, which is proportional to the adhesion energy. (After [11.91] with permission of Elsevier)

Simulations on Ag, Au, Pd, and Pt particles adsorbed on MgO(100) singled out three dominant motifs:

1. fcc clusters in (001) epitaxy (Fig. 11.28a,b)
2. fcc clusters in (111) epitaxy (Fig. 11.28c,d)
3. Decahedral clusters which adhere to the substrate with a pseudo-(001) facet.

Icosahedral clusters do not achieve good matching with the substrate, and are therefore not favorable for these metal/support combinations. Concerning fcc clusters, the competition between the (001) and the (111) epitaxy is due to the following reason: The (001) epitaxy has stronger adhesion energy per unit contact area, due to its better matching with the oxygen atoms of the square-symmetry substrate, especially when the lattice mismatch between metal and oxide is small. However, for (111) epitaxy, this can be compensated by a larger contact area, so that the total adhesion energy may become even larger than for (001) epitaxy.

In Ag/MgO(001), extensive calculations [11.143] predict that the fcc(001) motif is dominant in the size range up to 3000 atoms at least, followed by the decahedral and by the fcc(111) motifs. This compares well with the experimental data on this system [11.145, 146], which find the fcc(001) epitaxy dominant for all sizes. On the contrary, calculations on the Au/MgO(001) system [11.143] reveal close competition between the fcc epitaxies, with decahedral clusters being higher

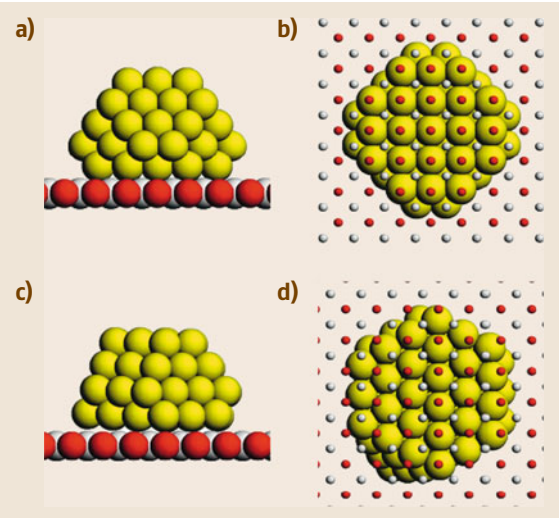


Fig. 11.28 **(a,b)** Side and bottom views of a fcc(001) cluster. **(c,d)** Side and bottom views of a fcc(111) cluster. In all panels, oxygen atoms are in *dark gray* (*red*) and magnesium atoms are in *white* (*light gray*). In the bottom views **(b,d)**, substrate atoms are represented by small spheres so that the contact epitaxy of the cluster is visible. (After [11.143] with permission of AIP)

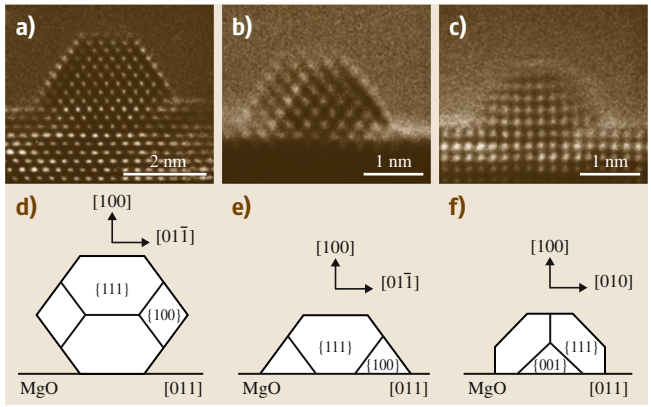


Fig. 11.29a–f Au clusters deposited on MgO. **(a)** HR-TEM image of a truncated octahedral cluster in a ⟨011⟩ zone axis orientation. **(b)** Half-octahedral cluster in a ⟨011⟩ orientation. **(c)** Half-octahedral cluster in a ⟨001⟩ orientation. **(d–f)** Profiles of the clusters shown in **(a–c)**, respectively, with indexation of the crystallographic directions and the faces. (After [11.29] with permission of APS)

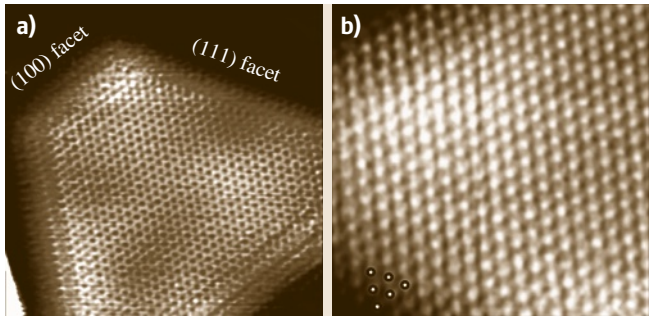


Fig. 11.30a,b Atomic-resolution images of crystalline nanosize Pd clusters. **(a)** 95×95 Å^2, $I_t = -0.8$ nA, $V_s = -5.0$ mV. **(b)** 45×45 Å^2. The resolution is kept a few layers down the sides, allowing identification of the side facets. The *dots* indicate atomic positions consistent with a (111) facet. $I_t = -1.8$ nA, $V_s = -1.5$ mV. (After [11.147] with permission of APS)

in energy. For sizes below around 1000 atoms, the fcc(001) epitaxy prevails. Then, a crossover range follows, in which both fcc epitaxies are very close in energy, and finally, for sizes above 1500 atoms, the fcc(111) epitaxy prevails. These results are again in agreement with the available experimental data. In fact, for sizes below 1000 atoms, only fcc(001) structures are observed [11.29] (Fig. 11.29), while for larger nanoparticles both epitaxies are produced [11.91].

The Pd and Pt cases are more controversial. The calculations [11.144] predict a crossover between (001) and (111) epitaxies at rather small sizes, well below 1000 atoms. This size-dependent crossover has not been observed experimentally. However, the experiments observe a temperature-dependent change of epitaxy in Pt/MgO(001) [11.148], which is still to be investigated theoretically. In Fig. 11.30, an STM image of Pd clusters growing in (111) epitaxy on amorphous alumina is shown [11.147]. It should be noted that for all these metals the Wulff–Kaischew construction predicts that the (111) epitaxy should prevail in the large size limit [11.144]. In the small size regime, to reconcile the results of the Wulff–Kaischew model with the experimental evidence, it is possible to define a size-dependent adhesion energy per unit contact area (in the framework of a size-dependent Wulff–Kaischew construction), so that the crossover to the (001) epitaxy with decreasing size can be recovered [11.144]. In fact, the adhesion energy per unit contact area of the fcc(001) epitaxy increases appreciably as the nanoparticle adheres with a smaller facet, because the contact atoms can more easily accommodate the lattice mismatch with the substrate. This is especially evident for Pd and Pt. On the contrary, the adhesion energy per unit contact area of the fcc(111) epitaxy is almost constant with size.

Interface-Stabilized Morphologies. In the case of an appreciable interaction between the support and the metal particles, exotic structures are possible which are stabilized by the substrate and that, in some cases, have no counterpart in the gas phase. A well-understood example is given by Ni particles on MgO(100) [11.125]; in this system, due to the large size mismatch between the nearest-neighbor distance in bulk Ni and the O−O distance in the MgO substrate, the preferred structural motif is made of hcp nanocrystals, whose close-packed planes, alternating in ... ABAB... stacking, are *perpendicular* to the oxide substrate and oriented along the [100] direction of the substrate (Fig. 11.31). Theoretical simulations show that, as the size of the clusters increases above $N = 40$, the lowest-energy structures are hcp for almost all sizes.

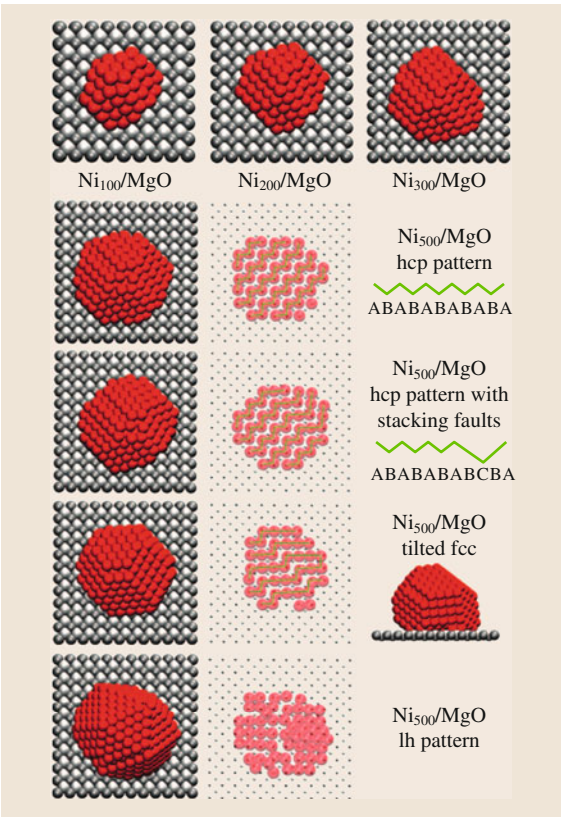


Fig. 11.31 Global minima of Ni/MgO nanodots (of hcp structure) shown for $N = 100$, 200, and 300 atoms. For $N = 500$ we show, *from top to bottom*, an unfaulted hcp structure, a hcp structure with a stacking fault (global minimum), a fcc structure, and an icosahedral (Ih) structure. (After [11.125] with permission of ACS)

The morphology of the hcp nanodots is easily understood: the hcp nanodots are the same truncated hexagonal bipyramids shown in Fig. 11.31, whose axis coincides with the *c*-axis of the hcp lattice. These bipyramids are cut to expose (0001), (1011), and small (1120) surfaces. A larger (1120) face is in contact with the substrate, where Ni atoms assume a typical configuration in zigzag rows. The driving forces leading to the stabilization of the hcp nanodots can be extended to other metal/oxide couples: Pd/CaO, Pt/CaO, Ni/CoO, and Co/MgO. It is to be noted that Ni, Pd, and Pt are fcc rather than hcp in the bulk, so that a transition to fcc configurations is expected to occur with increasing size of the particles. In fact, experiments on Ni particles on MgO(100) [11.149] observe the hcp morphology at small sizes and locate a transition to the usual fcc(001) structures for diameters larger than about 5 nm. At the theoretical level, the comparison of hcp and fcc(001) motifs as a function of size locates this transition between 2000 and 2500 atoms, corresponding to cluster diameters of about 4.5 nm, in excellent agreement with experimental data.

Another case of structures stabilized by the support is offered by Au/MgO: in the same size range between 25 and 40 atoms in which Pd clusters develop fcc epitaxial configurations [11.150], first-principles simulations predict that hollow gold cages are the most favorable structures on the MgO(001) surface. In particular, the interaction with the substrate stabilizes a novel class of hollow cage nanoparticles, namely open pyramidal hollow cages, which have no counterpart in free-space clusters [11.151].

Other *exotic* epitaxial relationships can be conceived, and have been actually found in more complex cases, such as in particular binary metal clusters. The case of CoPt particles adsorbed on MgO(100) [11.152] is briefly reviewed here, as this system in important in magnetism [11.153] and catalysis [11.154]. Pt clusters with $N \leq 100$ exhibit amorphous-like (or, better, reconstructed icosahedral) configurations [11.155], and become fcc-like when adsorbed on the MgO(100) surface [11.144]. Co clusters in the same size range are decahedral, and become hcp when adsorbed on the same surface [11.125]. Bulk solid CoPt at 50–50% composition presents an ordered phase of $L1_0$ structure, with tetragonal crystal lattice of alternating homogeneous Pt and Co planes along a (001) axis. However, for free nanoparticles smaller than about 3 nm, pIh structures are predicted [11.156, 157] and experimentally observed [11.153, 158]. The reason for this transition to noncrystalline structure at small sizes is that a certain

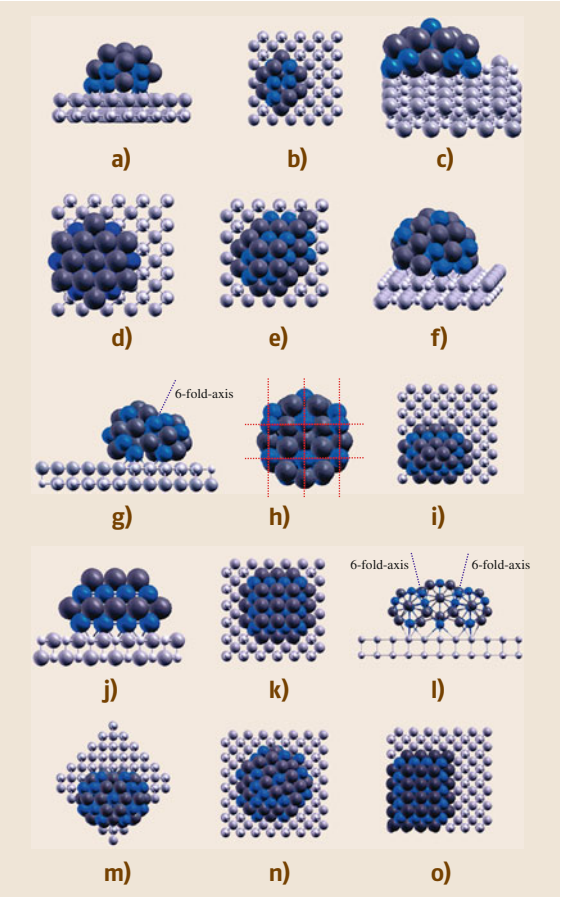


Fig. 11.32a–o Schematic pictures of various supported CoPt clusters: **(a)** $Co_{10}Pt_{10}$ double icosahedron ($N = 19$) plus a lateral Co atom lying on the surface; **(b)** $Co_{10}Pt_{10}$ $L1_0$-type structure; **(c)** $Co_{10}Pt_{10}$ incomplete pIh; **(d)** $Co_{20}Pt_{20}$ pIh6-based structure; **(e)** $Co_{20}Pt_{20}$ $L1_0$-type structure; **(f)** $Co_{20}Pt_{20}$ incomplete pIh; **(g)** $Co_{24}Pt_{24}$ pIh6-based structure with its disclination axis indicated; **(h)** bottom view of **(g)** to better show its epitaxial relationship to the substrate; **(i)** $Co_{20}Pt_{20}$ $L1_0$-type structure; **(j)** side view of a $Co_{32}Pt_{30}$ $L1_0$-type structure; **(k)** top view of **(j)**; **(l)** side view of a $Co_{32}Pt_{32}$ double-pIh6-based structure with its two disclination axes indicated; **(m)** top view of **(l)**; **(n)** $Co_{40}Pt_{40}$ structure based on the double pIh6 plus fcc-type surface growth; and **(o)** $Co_{40}Pt_{40}$ $L1_0$-type truncated pyramid. (After [11.152] with permission of ACS)

type of sixfold-symmetric pIh configuration maximizes the number of mixed bonds [11.152]. When adsorbed on the MgO(100) surface, it is found that pIh clusters can be satisfactorily accommodated on the substrate

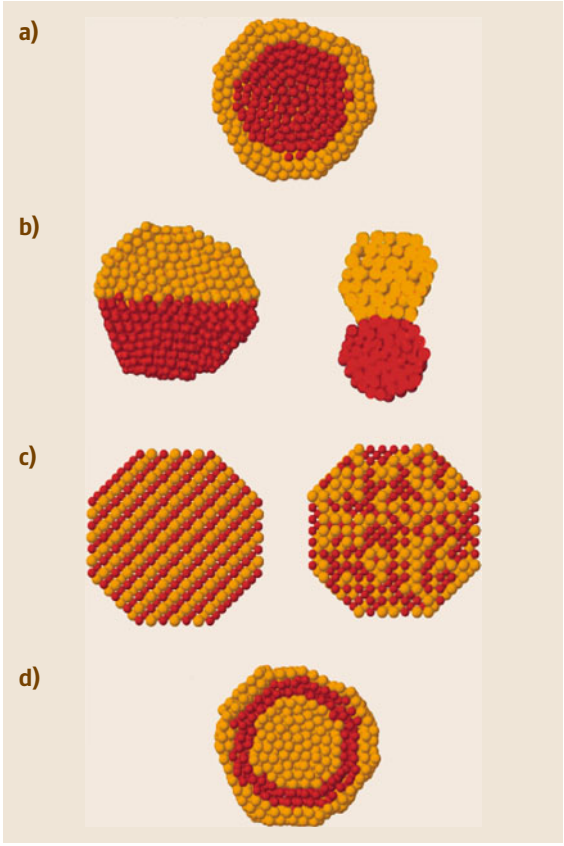


Fig. 11.33a–d Schematic representation of some possible mixing patterns: core–shell **(a)**, subcluster segregated **(b)**, mixed **(c)**, three shell **(d)**. The pictures show cross-sections of the clusters. (After [11.25] with permission of ACS)

while preserving their gas-phase shape by simply segregating cobalt at the interface. Some examples of supported CoPt clusters are shown in Fig. 11.32. From these examples, it can be seen that pIh structures can accommodate on the surface either by adding lateral Co atoms at the interface or by tilting their sixfold-symmetry axis and by inserting further Co atoms to fill up the void so created (Fig. 11.32). Moreover, a tilted pIh6 can match with another one tilted in the opposite way, creating a structure which achieves shell closure at $N = 64$.

Chemical Ordering

Once the morphology of an alloyed nanoparticle has been determined, its complete characterization requires the determination of the chemical ordering pattern. There exist four main types of mixing patterns [11.25].

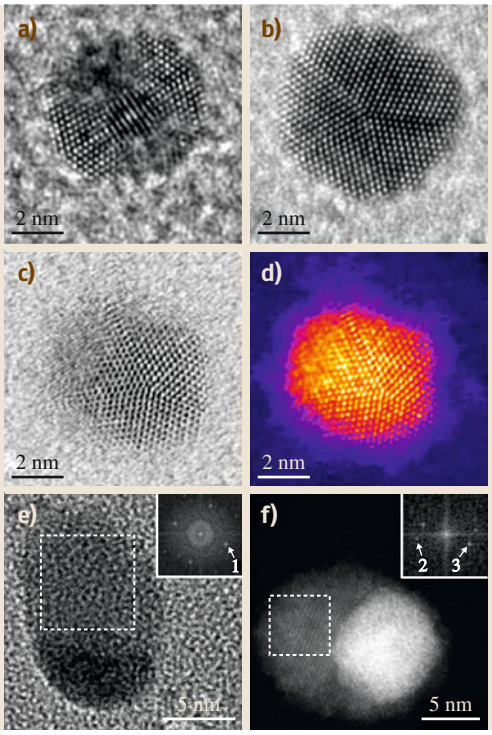


Fig. 11.34a–f Bright field (BF) HR-TEM images **(a)** and **(b)** showing typical structure of Ag-Au clusters from a fresh sample ($\theta = 3\%$ and $d6 \pm 0.5$ nm). **(a)** Icosahedron, **(b)** decahedron, **(c)** BF, and **(d)** HAADF. STEM images taken simultaneously showing a typical core–shell cluster from an aged sample. **(e)** BF TEM and **(f)** HAADF STEM images of two typical Janus particles in an aged sample. Fast Fourier transforms (FFTs) of selected areas on **(e)** and **(f)** are shown in the *insets*. (After [11.118] with permission of AIP)

Subcluster Segregated Nanoalloys. Subcluster segregated nanoalloys consist of two separated phases, which may share a mixed interface (Fig. 11.33b, *left*) or may only have a small number of mixed bonds (Fig. 11.33b, *right*). This structure has been observed in aged Ag-Au nanoparticles synthesized via the gas aggregation method [11.118], as shown in Fig. 11.34.

Mixed Nanoalloys. This pattern may be either ordered (Fig. 11.33c, *left*) or random (i. e., a solid solution, Fig. 11.33c, *right*). Still in the case of mixed Ag-Au nanoparticles synthesized via the gas aggregation method [11.118], it is apparent that freshly produced clusters are characterized by a solid solution (random mixing) of the two elements. On the other hand, an

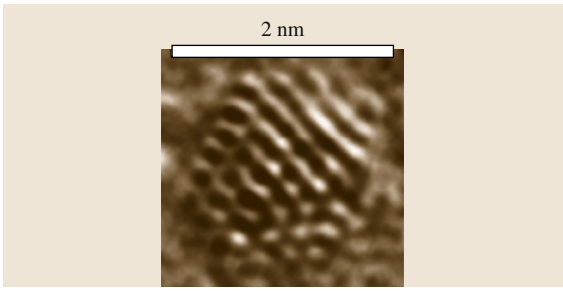


Fig. 11.35 HR-TEM micrograph of $Co_{58}Pt_{42}$ cluster. (After [11.153] with permission of APS)

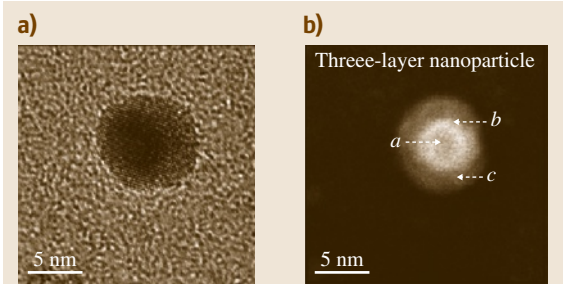


Fig. 11.36a,b Detailed structure of Au-Pd nanoparticles at high magnification. The high-resolution **(a)** and scanning TEM images **(b)** confirm the presence of three different layers in the domains of the core–shell structure for typical single nanoparticles. (After [11.159] with permission of ACS)

example of ordered alloy is given by PtCo nanoparticles grown on MgO(100) [11.153] and observed via HR-TEM (Fig. 11.35).

Multishell Nanoalloys. Multishell nanoalloys present an onion-like structure of alternating shells of the two elements (Fig. 11.33d). An example is given by Au-Pd nanoparticles synthesized via wet chemistry methods; TEM observation highlights the presence of an internal Pd core, an intermediate Au shell, and an external Pd shell [11.159] (Fig. 11.36).

Core–Shell Segregated Nanoalloys. This pattern is formed by a shell of one type of atom (B) surrounding a core of another (A), though there may be some mixing between the shells (Fig. 11.33a). This mixing pattern is common to a large variety of systems. This is a particular case of multishell nanoalloys with only two shells.

In addition to these main ordering patterns, novel ones have also been described. An example is shown for

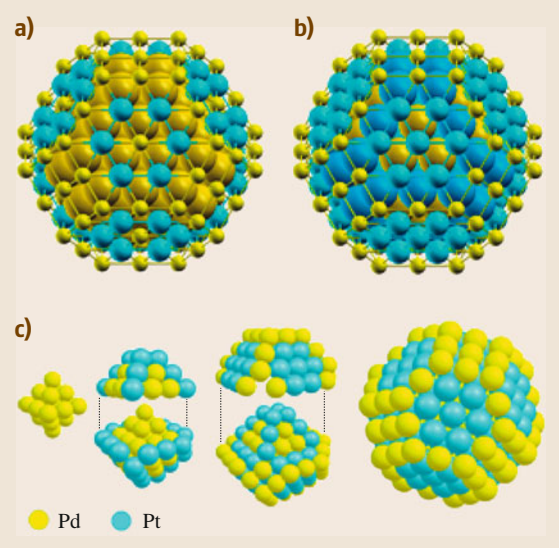


Fig. 11.37a–d Optimal chemical ordering in a PdPt nanoparticle of size $N_{tot} = 201$: **(a)** composition $Pd_{153}Pt_{48}$; **(b)** composition $Pd_{110}Pt_{91}$. The view represents atoms of different sizes to highlight the patchy multishell pattern in **(c)**. Atom coloring: *yellow* for Pd and *blue* for Pt, with *slightly darker shades* for the inner shells. **(d)** The inner compositional structure of the $Pd_{110}Pt_{91}$ particle. (After [11.36] with permission of ACS)

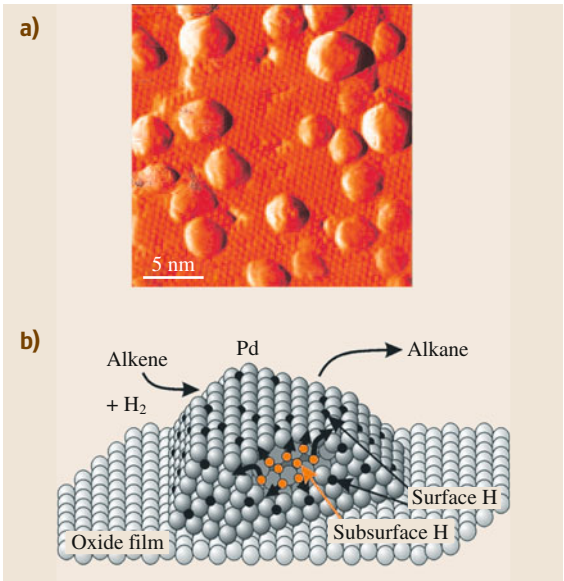


Fig. 11.38 (a) STM image of Pd nanoparticles on $Fe_3O_4(111)$. The crystallographic facets of the particles are clearly recognizable, as is the atomic corrugation of the support. **(b)** Schematic representation of a Pd nanoparticle indicating atomic hydrogen adsorbed on the surface and in the particle. (After [11.161] with permission of Wiley)

a $(Pd\text{-}Pt)_{201}$ nanoparticle in Fig. 11.37. For this system, first-principles results for a few Pt impurities within a Pd-rich cluster unexpectedly show a marked tendency of Pt to populate the (111) surface, in agreement with coordination-dependent bond-energy variations (CBEV) predictions [11.160], but opposite to what is found in extended systems (this is thus a feature peculiar to the nanoscale). This tendency is latent at very small sizes but increases with cluster size and is clearly realized when the (111) facets are of the right size. Furthermore, a new picture emerges around composition 1 : 1. The lowest-energy chemical ordering pattern, e.g., at composition 110 : 91, is reported in Fig. 11.37, and it is clearly a multishell arrangement, but of a different kind. As can be drawn from inspection of Fig. 11.37, the structure of the fourth shell is such that Pt atoms occupy the center of surface (111) facets, whereas Pd atoms occupy the (100) facets and the edges of the surface shell. However, for the subsurface shell the chemical order is *reversed* with respect to that of the surface shell: Pd atoms occupy the three central positions of the (111) facets, whereas Pt occupies the (100) facets and the edges. In other words, in correspondence with segregation of Pt at the center of surface facets, we find segregation of Pd at the center of the underlying facets, and so on. In this segregation pattern each shell is a *patchwork* of islands of atoms of the two elements, but the order of the patchwork is reversed in the alternating shells. Note that this arrangement is not bound to a precise number of atoms but is stable in a range of compositions around the equimolar one between at least 45–55% and 58–42% compositions.

Theoretical Methods for Structure Prediction

We conclude this subsection with a brief summary of the most important approaches to investigate the potential energy surface (PES) of a metallic system. Recent years have witnessed an explosive surge in the development and applications of computational science. The advances in computer science (in both software and hardware) have stimulated this surge, and a large community of computationally oriented researchers is now active in all fields of science, ranging from experimental and theoretical researchers to undergraduate and graduate students. The field of metal nanoclusters and nanoalloys is no exception to this trend: in recent years an increasing number of theoretical and computational

studies have appeared, especially dealing with predictions of the structural properties of these systems, but also extending to their magnetic, optical, and catalytic responses. Two types of approaches are traditionally distinguished: first-principles and empirical ones. In the former, one attempts to solve (at least in an approximate way) the Schrödinger equation of the system. This can be accurate and reliable, but it is computationally extremely demanding. In the latter, the system PES is expressed as an analytic function of the geometrical coordinates, depending on a set of empirical parameters that are usually fitted onto first-principles calculations or experimental data. These latter approaches are of course computationally much cheaper, and systems with thousands to millions of atoms can be easily described on nanosecond to microsecond time scales.

The problem with metal nanoparticles and nanoalloys is that they often present a fluxional character; i. e., they exhibit a rugged PES with a great number of local minima rather close in energy. They can be thus catalogued among complex systems, which are an active field of current research. To predict the structural properties of these systems, the first step consists in systematic sampling of their PES. This is usually achieved via global-optimization techniques [11.162], i. e., those computational techniques aimed at finding the absolute minimum (or global minimum) of a mathematical function. One thus selects a computational approach to evaluate the PES of the system, and then explores it via systematic searches.

The knowledge of the global minimum structure in the gas phase can obviously have limited importance when studying the behavior of metal particles in complex environments and/or undergoing dynamical processes: For example, it is recalled below that metal particles can undergo structure fluctuations and bistabilities during experiments reproducing, e.g., typical catalytic conditions. However, the output of a global optimization search is not simply the lowest-energy structure, but also a set of low-lying isomers, which are very important in determining the dynamic mechanical response of the system (e.g., during melting). Moreover, structure determination has great importance in view of *static* phenomena such as optical and magnetic properties, but even for chemical ones under mild conditions. In addition, the influence of the environment can be also introduced into the theoretical analysis. On the experimental side, recent advances allow one to characterize with a good degree of certainty the structure and morphology of metal nanoparticles and nanoalloys (see the previous section). On the theoretical side, effective tools are nowadays available to explore and predict the structural properties of metal nanoparticles, ranging from combined empirical potential/first principles global optimization algorithms to statistical-mechanics techniques with improved sampling.

The most successful computational algorithms to perform systematic sampling of the PES of nanoalloys [11.163] are based on a hierarchy of length scales; i. e., in these approaches, the choice of the theoretical modeling to be employed in performing simulations on a specific system is tuned according to its size. The idea behind these hierarchical approaches is to use for systems of different size the approach which is most efficient and also makes physical sense for each one of them.

This hierarchy is implemented in the following way. For small clusters (with number of atoms N less than a few tens, presently $N \leq 40$), it is computationally feasible to conduct global optimization using energy and forces derived from a first-principles method; see [11.164] for one of the first implementations for gas-phase metal nanoclusters (or [11.130] for a recent application), [11.165] for the first implementation for supported metal nanoclusters, and [11.166, 167] for the first implementations to (supported) alloy nanoclusters.

Aggregates with number of atoms between 40 and 200 are very interesting as they are still in the nonscalable regime in terms of electronic, magnetic, etc. properties [11.168] and at the same time novel structures are continuously being discovered in this size range, exhibiting, e.g., polytetrahedral character, hybrid combinations of close-packed and fivefold-symmetry motifs, or other exotic forms. For these aggregates it is still feasible to perform numerous first-principles calculations at various sizes using common computational resources. A full first-principles approach, however, becomes progressively less and less feasible in practice. More approximate methods such as empirical potentials must be employed. An efficient possibility is to use a combination of first-principles and empirical potential simulations [11.163].

For yet larger clusters (presently $200 \leq N \leq 1000$), even performing first-principles calculations becomes progressively infeasible, at least to conduct them in large numbers, and one has to rely entirely on global optimization searches based on empirical potential approaches. This makes sense also from a theoretical point of view, as these larger particles start to exhibit a clear metallic character and an average description of the metallic bond should be reasonable, and empirical po-

tential predictions are expected and usually found to become more and more accurate [11.169].

Finally, when a particle has more than 1000–2000 atoms, global optimization using empirical potentials becomes computationally very heavy. Moreover, empirical potentials are often overinformative. The size of the system itself in fact usually quenches structural diversity and simplifies the problem, orienting the system into a few low-energy competing motifs. It is thus meaningful and efficient to focus on these motifs and study their crossover as a function of the number of atoms, as in [11.126].

Nanoalloy Phase Diagrams

In the field of bulk metal alloys, the CALPHAD project (http://www.calphad.org) should be mentioned. This project, started in the early 1970s and substantiated in a scientific journal, aims at collecting and providing precise information on the thermodynamic properties of extended multicomponent systems, thus including metal alloys, in the form of accurate phase diagrams. CALPHAD in fact originally stood for *calculation of phase diagrams*. Translating this project into the field of nanostructured alloys, thus producing *size-dependent* phase diagrams, is not an easy task, but is currently being undertaken by a few groups in the scientific community, in the European context also in connection with the presently ongoing European Cooperation in Science and Technology (COST) action MP0903 (www.nanoalloy.eu).

11.4.2 Catalytic Properties

To achieve a more straightforward presentation, we focus in this subsection on heterogeneous catalysis by metal nanoparticles and nanoalloys. We thus exclude the vast field of homogeneous catalysis by coated alloy clusters, and in particular by polynuclear complexes composed of more than one metal element and by colloidal nanoalloys [11.170]. We also do not treat polymer-protected bimetallic or polymetallic nanoparticles, which are also known to be very effective and interesting systems [11.78, 79].

As recalled in Sect. 11.2, heterogeneous catalysis by metal nanoclusters and nanoalloys has been the subject of a wealth of model studies in surface science. Investigations initially focused on the reactivity of extended surfaces of pure or alloyed metals as models of nanoparticle facets [11.86–88]. In a second step, metal nanoparticles and nanoalloys rather than extended systems were grown, typically on oxide substrates [11.85, 86, 89–91]. In all cases the associated simplifications of single-crystal surfaces (either for the metal or for the oxide support) and UHV conditions were employed to allow use of the sophisticated and powerful analytical tools of surface science. The use of molecular beams [11.26, 171] was greatly beneficial in these studies as it allowed quantitative and detailed investigations of the kinetics and dynamics of surface reactions. Despite the limitations associated with the pressure and materials gaps recalled above, much fundamental knowledge has been produced through such studies that would have been hardly derivable otherwise, as we show presently.

We start from the concept of descriptors of the catalytic activity of a materials system. Screening a set of possible catalysts to find the optimal one via a trial-and-error approach is an extremely demanding task, at both the experimental and theoretical levels, even though combinatorial screening can be successfully applied [11.172, 173]. Think, e.g., of all the possible binary pairs of an alloyed catalyst and all the possible different compositions. Even using computational simulations which can be faster and cheaper than performing actual experiments, one needs thorough sampling of the kinetics of a catalytic reaction, singling out local minima, reaction paths, and kinetic prefactors connecting them, which can be extremely demanding if repeated thousands of times in the search for new technical catalysts (assuming of course that such calculations are sufficiently accurate to be reliable). Some general guiding principles are in order. A viable option is to single out some descriptors determining the catalytic activity or selectivity of a catalyst [11.174]. These descriptors could be the adsorption energies of intermediates, reactants, products, or the activation energies of the rate-determining elementary steps, decided on the basis of experimental and/or theoretical results. In this perspective, surface science studies on model systems in which experimental investigations were coupled with theoretical analysis have made an important contribution to shed light on the overall picture. First of all, it has been shown that the actual choice of the descriptor may not be crucial, as some linear energy correlations between adsorption energies and activation energies, such as the Brønsted–Evans–Polanyi (BEP) relations [11.175], do seem to exist, which effectively reduce the number of independent variables for a given catalytic process. Second, it has been shown that the position of the d-band of a transition metal often correlates nicely with its chemical activity and can thus be used as a useful descriptor [11.176], although exceptions and

refinements have been recently proposed. Finally, an old principle in heterogeneous catalysis, the *Sabatier* principle [11.177], has been entirely confirmed and put on quantitative grounds. This principle states that, when trying to optimize the performance of any given catalyst, one faces as a norm conflicting requirements, i. e., the fact that if the adsorption energy of the reactants on the catalyst is too strong (or they dissociate too easily) then the successive reaction energy barriers or desorption energies will also be large, whereas vice versa if the adsorption energy is too low, then the dissociation step necessary for the catalytic activity will be difficult, so that the best compromise lies in between strong and weak energetics, and the performance of a catalyst as a function of any given descriptor will go through a maximum, leading to a *volcano* relationship between reaction rate and the energy descriptor. Using this approach, the cost of either a computational or experimental search for new catalysts can be reduced by using only a limited number of descriptors in the computational or experimental screening and locating the maximum in the volcano curve [11.174]. Clearly, given the semiquantitative character of the knowledge derived from energy descriptors, thorough exploration of the kinetics pathway for the most promising candidates is necessary to confirm the indications derived from the preliminary analysis at the theoretical level, and eventually actual catalytic experiments are needed to validate descriptor predictions. To provide a concrete successful example, using this approach the Ni_3Fe system was proposed as an efficient methanation catalyst, and this proposal was fully confirmed by experimental tests [11.178]. Note in passing that what we have discussed so far concerns the so-called electronic structure factor in catalysis. Later we also discuss the structure factor.

To summarize this first conclusion: using descriptors taken from studies on extended surfaces, one can screen the activity of a catalyst. This is connected with the fact that in some cases extended surfaces can indeed be taken as good models of the facets of nanoparticles, and this can be used to predict, e.g., the dependence of the catalytic activity on the shape and morphology of the particles [11.179]. Another important result derived from model surface science studies is however that size effects can be very important in heterogeneous catalysis by metal nanoparticles and nanoalloys, as has been definitively proven by experiments in which carefully size-selected particles were employed [11.180, 181]. This is to be expected, as their finite size endows the nanostructures with low-coordinated sites that are absent in single-crystal surfaces of an extended (bulk) system, and that can be beneficial or detrimental (or in some cases noninfluential) to the catalytic activity depending on its mechanistic path. An in-depth discussion is given in [11.182], in which a rationale for the distinction between structure-sensitive and structure-insensitive catalytic reactions at surfaces is advanced. In detail, in this theory three types of behavior are distinguished. In the first class of reactions, in which a π-type bond is formed or dissociated, the reactants need to have multiple contacts with several atoms from the nanoparticle surface, which is not possible below a certain particle size, whence the decrease of the catalytic activity with size. In the second class of reactions, in which a σ-type bond is dissociated in the rate-determining step such as in methane activation, the catalytic activity correlates with the ability of the catalyst particle to break strong bonds, and thus to the number of coordinatively unsaturated edge and corner atoms, which is inversely proportional to the particle size. In the third class of reactions, in which a σ-type bond is formed in the rate-determining step such as in hydrocarbon hydrogenation reactions, the catalytic activity is roughly independent of the particle size.

The view proposed in [11.182] is clearly a general and necessarily approximate one, which can be and has actually been better articulated in other studies. Even in the event that interesting reactivity occurs on smooth facets rather than at edges or corners of the particles, in fact, the greater flexibility induced by their limited size can make a difference in terms of adsorption energies and reaction energy barriers. To exemplify matters, let us consider the hydrogenation of *cis*-2-butene on Pd nanoparticles (Fig. 11.38). In a series of studies [11.161, 183] it has been shown that:

- Pd nanoparticles of 4–5 nm size supported on a Fe_3O_4 support are good models of the corresponding technical hydrogenation catalysts, whereas this does not hold for extended Pd(111) single-crystal surfaces, which are catalytically much more inert.
- The catalytic activity of the Pd nanoparticles is strongly connected with the presence of subsurface hydrogen atoms.
- These subsurface atoms are much more abundant on a (111) facets of a supported nanoparticle than on an extended (111) surface, due to: (1) the greater structural freedom of the nanoparticle, which better accommodates subsurface hydrogen and carbonaceous species which promote H diffusivity, and (2) the finite size of the nanoparticles with the presence of an underlying support which confines

hydrogen closer to the surface. In short, in this case extended surfaces do not make a good modeling job. However, in this and similar cases, they may be used to model the catalytic process if properly mimicking finite-size effects by considering stepped surfaces, i. e., by bridging the so-called *structure gap*, that is, the greater structural flexibility of confined facets with respect to extended systems [11.184]. The importance of local defectivity and structural relaxation on the catalytic activity of metal nanosystems has been also proved in detailed investigations of the catalytic activity of Cu nanoparticles in methanol steam reforming [11.185, 186], in which it has been shown that the catalytic activity correlates not only with the decreasing particle size but also with the local microstrain and structural disorder. These investigations have brought about not only new knowledge, but also practical advantages, as they have led to improving by a factor of 2 the activity of technical catalysts. It should also be mentioned that, for full understanding of the kinetics of catalytic reactions on nanoscale particles, coverage fluctuations and microkinetic models also have a crucial influence according to recent contentions [11.187].

These results point to the importance of the status of the catalyst surface under reaction conditions, with the possibility, e.g., of forming surface alloys or ligand-induced reconstructions or intermetallic compounds [11.188], and some of the knowledge derived from model studies relevant for catalysis concerns this topic: For example, an important effect that can be drawn even from model studies at low pressures and that has been further confirmed by investigations at more realistic pressures is the possibility of particle restructuring and reshaping under reaction conditions. Adsorption of reactant molecules in fact modifies the relative energetics of the different facets of the nanoparticles, and thus – as a consequence of the Wulff construction – can give rise to substantial changes in the particle morphology, as observed experimentally [11.189] in fair agreement with theoretical predictions, e.g., the study in [11.181]. To summarize, one typically expects that more open facets, such as (100) with respect to (111), will be more reactive and therefore more stabilized by the interaction with, e.g., oxygen species, so that they will grow in oxidative conditions at the expense of the more inert ones; a simple example is given in Fig. 11.39, but more complicated ones with more extensive faceting can be also expected on general terms [11.190].

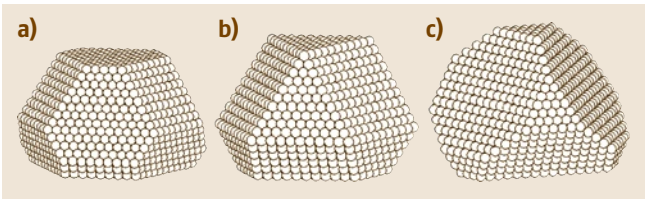


Fig. 11.39a–c Morphology of supported silver particles in case of **(a)** nonoxidized surfaces, and oxygen-covered surfaces at **(b)** $p(O_2) = 5 \times 10^{-3}$ atm and **(c)** $p(O_2) = 1$ atm. The lateral dimension of the clusters is about 6 nm. (After [11.181] with permission of Elsevier)

The precise chemical status of the surface of the nanoparticles is important also in view of the ongoing debate concerning whether the active catalysts in oxidation reactions are the metal nanoparticles themselves or rather the corresponding metal oxide particles generated by their preliminary oxidation under reaction conditions. Recent findings, e.g., on the CO oxidation reaction catalyzed by Pd nanoparticles of ≈ 5 nm diameter supported on γ-Al_2O_3 [11.191], seem to indicate that under oxygen pressure the surface of the particle is indeed covered by oxygen species as in analogous oxidation catalysts [11.181], but that substoichiometric $PdO_{x<1}$ species can be rapidly reduced by CO to Pd^0, so that they exhibit a comparable CO oxidation activity, whereas stoichiometric PdO nanoparticles show lower catalytic activity due to their greater stability and more difficult reduction by CO. In other words, the active phase present under the current reaction conditions seems to be oxygen-covered – and thus appreciably modified – metallic Pd particles.

Size effects and low-coordinated atoms, which have been mentioned above, are especially important for those metals that have been traditionally thought of as catalytically inert, but that acquire a rich, fascinating, and unexpected catalytic activity when forged at the nanoscale, as has been proved for gold [11.192–197]. Indeed, there is recent experimental evidence that the real actors of CO oxidation by Au nanoclusters are subnanometer species containing ≈ 10 Au atoms [11.198]. This leads us to the field of extremely small particles, a somewhat novel field, despite the fact that the possibility of the importance of very small metal clusters in catalysis was advanced long ago [11.22], as supported by EXAFS evidence [11.199].

At one extreme of size effects, one finds in fact the catalysis by extremely small or subnanometer clusters, i. e., pure or alloyed metal clusters containing fewer than, say, 20 atoms and thus with size of the order of

1 nm or less. Clearly, in such species the metallic bond is only partially developed, and they exhibit molecule-like rather than conductive behavior. Still, they belong to the class of metal nanoclusters and nanoalloys, are very interesting materials, and often possess catalytic properties which are very different and sometimes more interesting than their extended analogs [11.200]. Finite-size effects are here in the extremely nonscalable regime in which adding or removing a single atom from the cluster may lead to dramatic changes in catalytic performance. In addition, the effect of the support is here crucial, and it has been shown for example both experimentally and theoretically that even a simple ionic oxide support can transform inert species such as Ag_3 or Au_3 into efficient oxidation catalysts [11.200, 201]. Also, in such clusters it does not make much sense to talk about facets and the link to extended systems become questionable. Corners and edges dominate the morphology of these systems, and descriptors that have been developed for bulk surfaces may not be useful here and new descriptors may need to be developed (an interesting example in this direction is given in [11.202]). From the theoretical point of view, subnanometer metal heterogeneous catalysts are particularly interesting because they offer the chance to exploit recent methodological advances in the computational sampling of rugged potential energy surfaces, as recently proposed [11.201]. An especially interesting effects that can be simulated via these theoretical approaches and compared with experiment, and whose validity probably exceeds the field of subnanometer clusters, is disruption of catalyst particles induced by ligands and reactants and their reformation to achieve a dynamic equilibrium [11.203]. This is also connected with the phenomenon of Ostwald ripening or sintering [11.204], i. e., the disappearance of small metal clusters in favor of larger aggregates. Without entering into the details of this complex phenomenon, it can be observed that it is an experimental observation supported by theoretical simulations that the presence of CO but also especially the coadsorption of CO and O_2 can weaken metal–metal bonds and lead to cluster disgregation [11.201, 205]. To summarize, subnanometer metal cluster and alloy catalysts represent a field in vigorous expansion, in which further surprises can be expected in the near future.

Coming now to the field of nanoalloys (which is the topic of the present chapter), in addition to the concepts discussed above and valid for both pure and mixed nanoparticles, some new, specific features arise.

The first point concerns the structural properties discussed in the previous subsection. In general, when studying a bi- or multicomponent nanosystem, it must first be ascertained whether the two (or more) elements form some kind of alloys or remain as separated pure nanoparticles. Second, it should also be known whether the chemical composition is the same over all particles, i. e., the dispersion of the composition. Third, one should ascertain which structure is generated by alloying, as we have shown above that even minor amounts of a second element can completely change the dominant structural motifs of the particles. Fourth, once the structural framework is clear, it should be determined which kind of chemical ordering is realized on this framework. Regarding the latter issue, i. e., the crux of nanoalloys, namely chemical ordering, it must be recalled that, given a certain chemical ordering, e.g., with segregation of one component to the surface, the presence of ligands and reactants can entail reversal of such segregation under catalytic conditions [11.32]. This phenomenon, which is probably a ubiquitous one [11.206], is due to the fact that the surface energies of the metal can be strongly affected by the interaction with exogenous species [11.207], so much as to fully revert their relative ordering and thus produce a segregation inversion under reaction conditions (see the discussion on restructuring and reshaping above). Indeed, Ni reversed segregation at the surface of Au-Ni particles under oxygen and Pd reversed segregation at the surface of Ag-Pd particles under CO have long been suggested on the basis of chemisorption [11.22] or EXAFS [11.208] data.

The second point concerns the discussion of the effects of alloying on the activity of the nanocatalysts (or *bimetallic or polymetallic cluster catalysts*, as they were once called). These effects have been traditionally distinguished into two types: structural and electronic [11.22].

Electronic effects on the chemical properties of a binary metal system have long been proposed in the search for improved catalysts [11.22, 209], assuming intimate mixing of the two species: For example, charge transfer [11.210] was suggested to have an important influence on surface metal–metal bonds that involve dissimilar elements, so that the cohesive energy of a bimetallic bond correlates with the flow of electron density toward the element with the larger fraction of empty states in its valence band, and it was pointed out that this phenomenon is realized at a surface in a very different way from what occurs in bulk alloys, thus entailing a strong dependence on the structural geometry of the bimetallic system. Charge transfer effects have been investigated again at the

first-principles level, and their importance in determining structural properties confirmed on more realistic Ag-Au nanoparticles [11.137], also proposing a way to efficiently account for such effects within empirical potentials [11.211]. More recently, it can be noted that the descriptor approach discussed above to screen a set of possible catalysts in the search for the optimal one [11.174] is essentially based on the investigation of electronic effects due to alloying, and we have already recalled that this approach was successful in singling out an efficient novel methanation catalyst [11.178]. It should be added in this connection that an inverse correlation was observed concerning electronic effects due to alloying: in other words, if alloying element A with B increases the interaction energy with a ligand species, then one should expect that alloying B with A decreases the interaction energy of B with the same species [11.207].

As for structural effects due to alloying, still assuming intimate mixing of the two species, the hypothesis that the structure, through the surface composition, of *bimetallic cluster catalysts* can appreciably influence their selectivity dates back to several decades ago [11.22]. Cu segregation at the surface of both Cu-Ni and Cu-Ru particles were hypothesized on the basis of hydrogen chemisorption data, and used to explain the decreased activity of Cu-Ni particles in ethane hydrogenolysis [11.22, 140] via a mechanism similar to that in which a π-type bond is formed or dissociated discussed above [11.182]. Analogously, the much higher selectivity of Cu-Ru particles with respect to pure Ru ones in orienting the dehydrogenation of cyclohexane into benzene rather than its hydrogenolysis into methane was rationalized by invoking that hydrogenolysis needed a multiplet of Ru centers and was therefore hampered by Cu alloying and surface segregation, whereas dehydrogenation went through a mechanism similar to that in which a σ-type bond is formed in the rate-determining step discussed above [11.182], and was therefore structure and alloying insensitive (also being insensitive to electronic structure and the electronic structure due to alloying).

In more recent work the activity of Cr-Pt nanoalloys with respect to oxygen reduction reaction was studied [11.212], and it was shown that only when an ordered $CrPt_3$ alloy phase was formed throughout the particle (not only at the surface) was a substantial enhancement by 2–3.5 times of the catalytic activity achieved. In this case, such an enhancement was connected with a structural effect: the reduction in the Pt–Pt distances due to thorough mixing with Cr.

Other alloying effects on nanocatalysis are easier to explain and predict. Going to the nanoscale is known to be advantageous from an economic point of view even in the absence of other benefits as it increases the surface-to-bulk composition ratio, which – given that catalysis is dominated by processes occurring at surface atoms – increases the activity per atom of nanosystems. A merely economic gain can correspondingly be obtained in multicomponent systems even under the hypothesis that there is no structural or electronic effect due to alloying, supposing for example production of a core–shell particle in which a catalytically inert, inexpensive element fills the particle core, while the catalytically active precious one segregates at the surface; such systems are therefore called *atomically economical*. Other effects are simply due to the synergy of having a multifunctional catalyst, i. e., a system simultaneously containing two or more active species, each of which realizes a different and specific function, as for Pt and Ru sites in CO oxidation [11.213] or Cu and Pd sites in electrocatalytic reduction of NO_3^- [11.214]. In such cases the catalytic system could in principle work also in the presence of strong segregation or spatial separation of the two components. However, the proximity in space of the two catalytically active species can facilitate mass transport phenomena which are sometimes essential to achieve efficient catalysis.

An electronic effect has also been suggested for the promotional role of Au in Au-Pd nanoparticles with Au (core)–Pd (shell) chemical ordering [11.215, 216], even though theoretical analysis does not predict an important electronic effect for this binary pair [11.207]. Later investigations in fact showed that the core–shell ordering is not essential for the observation of high reaction rates and selectivity, which are also obtained when Au and Pd are homogeneously mixed [11.206]. The true origin of this synergic effect is thus still unknown. Another very interesting example is provided by Ag-Au nanoparticles, which have been recently shown to be both more stable and more active to promote CO oxidation than either Au or Ag pure particles [11.217], although it is not yet fully clear whether this improvement is due to electronic or structural effects. Many other examples exist in which one finds a substantial improvement of the activity and/or selectivity of a catalyst due to alloying, which have not yet been rationalized. As an interesting and most recent example, we mention the aerobic oxidation of allyl alcohol to 3-hydroxypropionic acid by carbon-supported Au nanoparticles when even a minor amount (≈ 1%) of Cu is added [11.218].

Now focusing attention briefly on the topic of heterogeneous catalysis by extremely small or subnanometer clusters, discussed above for pure systems, it should be noted that the related knowledge is scarce (the situation is different in the field of homogeneous catalysis, in which polynuclear multicomponent organometallic complexes have been studied). In one of the pioneering examples [11.219] Ru_5PtSn and Ru_4Sn_2 species grafted on mesoporous silica were shown to exhibit exceptional activities and selectivities in hydrogenation reactions at lower temperatures and pressures than those used in industrial processes. Very recently, a positive effect of alloying on the catalytic properties of subnanometer clusters has been proposed [11.201], in which $(Ag\text{-}Au)_3$ binary clusters were predicted via first-principles simulations to possess improved features with respect to Ag_3 or Au_3 pure clusters in partial oxidation reactions.

We conclude this subsection with a few considerations on theory and simulations of catalysis by nanoalloys. Due to the difficulties of in situ experimental characterization (despite the notable recent advances in this direction reviewed in Sect. 11.3), the possibility of realizing *thought experiments* or *computational experiments* and deriving with often sufficient accuracy quantities that are hardly measurable at the experimental level has made such theory and simulations play a very important role in this field. We have recalled the computational screening of novel catalysts [11.174], and in general the successes of theory in predicting novel catalysts [11.178] or in rationalizing reaction mechanisms [11.185, 186]. We have also underlined that, in order to be fully predictive, complete computational modeling needs thorough sampling of the kinetics of a catalytic reaction, singling out local minima, reaction paths, and kinetic prefactors connecting them, which is an extremely demanding task. Recent methodological advances in computational sampling of rugged potential energy surfaces [11.201] have made this task already achievable for subnanometer metal clusters. However, this is probably still not sufficient if one aims to describe at a computational level in a predictive way extremely complex systems such as fuel cells. These involve modeling of electrocatalysts, proton conducting membrane, reactants, and interfaces between them, something that probably will not be realizable at the first-principles level only for many years to come. A possible solution lies in multiscale algorithms [11.221] in which quantum-mechanical simulations are at some point replaced by classical ones employing empirical potentials or force fields, or even higher levels of length and time rescaling. In this context, reactive force fields [11.222] are necessary, given the chemical transformations with bond rupture and formation which are at the basis of catalysis. All this lies at the forefront of current research.

11.4.3 Optical Properties

The optical properties of metal nanoparticles and nanoalloys are a subject of great interest from the points of view of both basic science and technological applications [11.3]. The reasons for this interest lie first of all in the main feature of the optical response of simple or noble metal nanoclusters to excitation by light, which is a strong absorption band in the UV-Visible range related to the surface plasmonic resonance (SPR), i. e., a coherent and collective oscillation of the electrons involved in the metallic bonds in confined systems subjected to electromagnetic radiation of proper wavelength. Plasmons (Fig. 11.40) are thus collective oscillations of conduction electrons in metals. As recalled in previous sections, the use of metal nanoclusters as light absorbers has been unknowingly employed by humanity for thousands of years. The association of this effect with the presence of metal nanoparticles was however first recognized by *Faraday* only in 1857 [11.8], and theoretically explained by *Mie* in 1908 [11.223].

A second feature that makes metal nanoparticles attractive in optical studies is the fact that their electronic structure and consequently their optical response are sensitive to structural parameters such as size, shape, and – for multicomponent systems – composition and chemical ordering, in addition to the dielectric environment, so that they can be tuned with great freedom.

A third important point is that plasmonic resonances of nearby nanosystems can interact with each other via electromagnetic coupling, providing an effective way

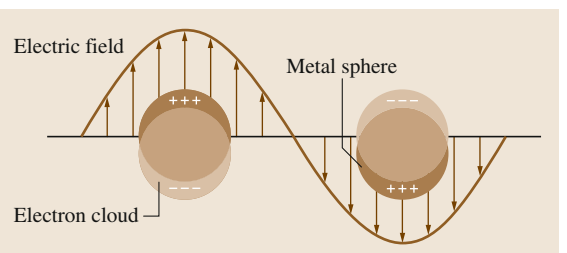


Fig. 11.40 Schematic diagrams illustrating a localized surface plasmon. (After [11.220] Annual Reviews)

of manipulating light at the nanoscale and giving rise to a wealth of phenomena going under the heading of *plasmonics*.

The coupling of the electromagnetic fields at the surface of the particles (possibly amplified by plasmonics effects) with optical excitation of other neighboring species can then be exploited in the so-called surface-enhanced spectroscopies [11.6], such as surface-enhanced Raman scattering (SERS) and surface-enhanced infrared absorption (SEIRA), which are very important and extremely promising, e.g., in biomedical applications.

Experimental studies in this area thus include synthetic techniques, spectroscopic studies of the particle properties and of molecules on the particles, and the development of applications, such as detection of single molecules and enhancing optical absorption in solar energy conversion devices. From the theoretical point of view, the efficient extension of electromagnetic calculations to the complex systems present in *plasmonic materials* and the inclusion of quantum effects especially when molecules at the surface of the particles are investigated should be mentioned.

It is important to mention that in 2011 an entire issue of *Chemical Reviews* [11.224] as well as virtual issues of the *Journal of Physical Chemistry* [11.225] and of *ACS Nano* [11.226] were dedicated to plasmonics. The optical properties of metal nanoparticles are also treated in Chap. 9 by Pradeep, while their application in nanomedicine are treated in Chap. 30 by Letfullin et al. in this handbook. Our presentation will therefore be necessarily contained to avoid excessive overlap with these excellent reference works.

We begin by briefly recalling Mie theory [11.3] to provide some basic knowledge as a starting point. This theory, based on the classical Maxwell equations, applies to a spherical particle interacting with a plane electromagnetic wave and solves these equations by imposing appropriate boundary conditions. The main result for a particle for which the dipolar approximation is valid (i. e., whose size is much smaller than the wavelength of the radiation) is that the extinction cross-section reads

$$\sigma(\omega) = \frac{9\left(\frac{\omega}{c}\right)(\varepsilon_\mathrm{m})^{\frac{3}{2}}\varepsilon_2(\omega)}{\left\{[\varepsilon_1(\omega)+2\varepsilon_\mathrm{m}]^2+\varepsilon_2(\omega)^2\right\}}V_0\,, \qquad (11.2)$$

where V_0 is the particle volume, ε_m the dielectric constant of the surrounding medium, and $\varepsilon_1(\omega)$ and $\varepsilon_2(\omega)$ are the real and imaginary part of the dielectric function of the particle, respectively. The maximum in $\sigma(\omega)$ occurs when the denominator of the fraction in (11.2)) is minimized, which – in the hypothesis of neglecting $\varepsilon_2(\omega)$ (justified for simple metals, less so for noble ones) – corresponds to the condition $\varepsilon_1(\omega) = -2\varepsilon_\mathrm{m}$. If one uses a model of a simple electron gas (Drude model) to estimate $\varepsilon_1(\omega)$ and $\varepsilon_2(\omega)$, one finds

$$\varepsilon_1(\omega) = 1 - \left(\frac{\omega_\mathrm{p}}{\omega}\right)^2\,,$$
$$\varepsilon_2(\omega) = \left(\frac{\Gamma}{\omega}\right)\left(\frac{\omega_\mathrm{p}}{\omega}\right)^2\,,$$

where ω_p is the frequency of the plasmon resonance in the bulk and Γ is a damping constant that takes into account electron–phonon and other intrinsic electron relaxation mechanism. This translates into an extinction cross-section with adsorption peak of Lorentzian shape centered at $\omega_1 = \omega_\mathrm{p}/(1+2\varepsilon_\mathrm{m})^{1/2}$ and of width equal to $\Gamma/2$.

Several points are worth mentioning: first, the proportionality of the cross-section to the particle volume, which entails a cubic dependence on its diameter; second, the weak dependence of the position of the peak (ω_1) on the particle size, entering only via the dependence of $\varepsilon_1(\omega)$ and $\varepsilon_2(\omega)$ such that a slight red-shift is observed for larger particles (Fig. 11.41); third, the fact that the damping constant is instead appreciably sensitive to the particle size: for small particles (less than, say, 20 nm in diameter) Γ increases with decreasing particle size as contributions from scattering of conduction electrons from the particle surface become important [11.63]; for larger particles, instead, higher-order terms than the dipole start contributing and the finite particle size produces depolarization and radiative contributions which broaden and eventually wash out plasmon resonance effects [11.227].

From the point of view of Mie's theory, all metal nanoparticles should in principle give rise to a plasmon peak, as all metals have mobile and polarizable conduction-band electrons. This is indeed experimentally verified for simple and noble metals. For transition metals, however, the plasmonic response of conduction (s-type) electrons is strongly damped by the coupling with d-band electrons, to such an extent that it has a minor importance in applications. Also, the smaller chemical activity and greater inertness of noble metals as compared with simple metals such as the alkali ones (even though at the nanoscale also noble metals can exhibit an important catalytic activity, see Sect. 11.4.2) entails that in practice only Cu, Ag, and Au are usually considered in plasmonics applications. With respect to Ag and Cu, Au presents s-orbitals which are more localized due to the so-called relativistic contraction [11.228]

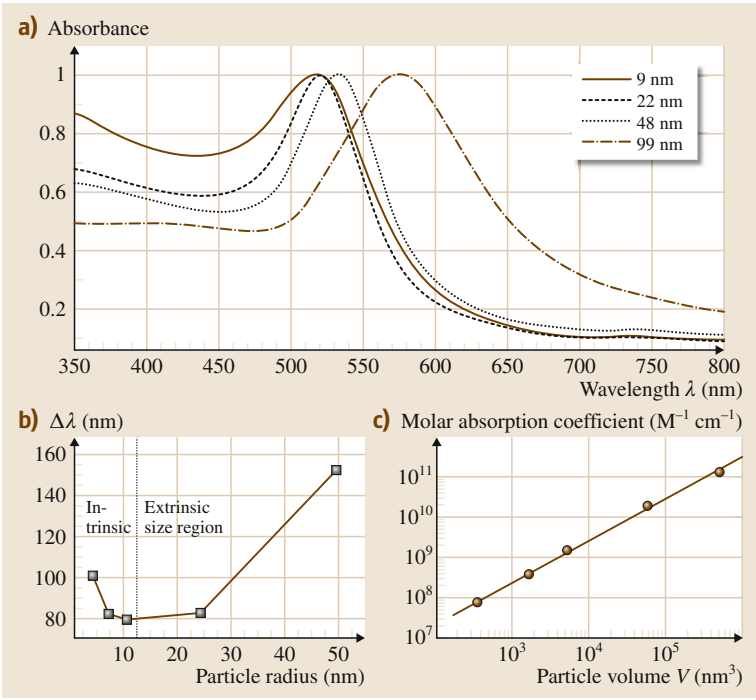


Fig. 11.41a–c Size effects on the surface plasmon absorption of spherical gold nanoparticles. The UV-Vis absorption spectra of colloidal solutions of gold nanoparticles with diameters varying between 9 and 99 nm show that the absorption maximum red-shifts with increasing particle size in **(a)**, while the plasmon bandwidth follows the behavior illustrated in **(b)**. The bandwidth increases with decreasing nanoparticle radius in the intrinsic size region and also with increasing radius in the extrinsic size region as predicted by theory. In **(c)** the extinction coefficients of these gold nanoparticles at their respective plasmon absorption maxima are plotted against their volume on a double logarithmic scale. The *solid line* is a linear fit of the data points, illustrating that a linear dependence is observed, in agreement with Mie theory. (After [11.63] with permission of ACS)

and interact appreciably with 5d electrons (despite the fact that the 5d band is formally full), and this relatively attenuates the plasmonic response of Au nanoparticles. In short, electrons in silver clusters behave more like a free electron gas, giving rise to well-defined, intense and sharp plasmonic features, while in gold clusters interband transitions somewhat decrease effects such as intensity and sensitivity to shape.

The Mie solution for a single spherical particle is analytic as shown above. For more complicated systems, a very common approach is the discrete dipole approximation (DDA) in which the metal system is described in terms of an array of polarizable elements whose polarizabilities are determined by the metal dielectric function [11.229] and the corresponding coupled equations are solved self-consistently. For systems up to a few hundred nanometers in size, these equations can be solved with reasonable computational effort, thus allowing one to predict the optical spectra of unusual shapes such as tetrahedra, disks, ensembles of particles, etc. using available software [11.230]. Alternative approaches solve the Maxwell equations via finite-difference or finite-element methods [11.229]. These studies have shown that a great variety of behavior can be obtained and that the plasmon peak can be freely manipulated by choosing the right geometrical configuration [11.231–234]. One major point to be recalled is that the optical spectrum of elongated systems, such as nanorods or nanowires, presents both transverse and longitudinal absorption peaks [11.63, 235], and that the latter are strongly red-shifted with respect to comparable spherical systems [11.236]. Shape manipulation is thus an effective way of modulating the position and the width of the SPR of a nanosystem with great freedom.

These electrodynamical models are thus appropriate and can be accurate for not so small, single-component structures [11.6, 237]. Rigorous data are however still partly lacking for small metal nanoparticles a few nanometers in size and for more complicated cases such as multicomponent metallic nanoparticles or nanoalloys. The finite size of the particles can be taken into account in electrodynamical models by introducing nonlocal effects into the particle dielectric function [11.238], but this extension presents some ambiguities and it is not yet clear whether it can provide a real advantage with respect to the original theory. First-principles approaches, in particular those based on time-dependent density-functional theory (TDDFT) [11.6, 239, 240], could give a rigorous answer for these more complicated cases, if the issue of the computational effort rapidly increasing with system

size is solved. A reasonable starting point along this line is to consider a so-called jellium model, i. e., a model in which the confining complicated potential due to the atoms is replaced by a constant potential background. In other words, attention is limited to conduction electrons moving in a simplified external potential with an idealized spatial behavior; for example, a nanoparticle can be modeled by a potential which is constant within a sphere of given radius and zero outside it. The number of electrons corresponds to the given density, while the value of the constant is a parameter which is adjusted to reproduce, e.g., the work function of the particle [11.241–244]. The simplifications in the jellium model allow one to conduct calculations on systems containing hundreds of thousands electrons, and have shown that classical electrodynamics normally does a good job in predicting the position of plasmon resonances for not so small nanostructures, but is obviously much less accurate in predicting their width and fine details such as field enhancements in close proximity to the particle surface. The next step is to consider a higher level in which a fully atomistic description of the nanosystems is used and TDDFT calculations are conducted in which in principle all the electrons of the particles, both conduction and valence, and a full description of the nuclei are employed. Such calculations have been performed in the literature on small metal clusters (see as one example [11.245]) but unfortunately rapidly become unfeasible for larger systems. The computational effort of atomistically detailed TDDFT calculations in fact increases so rapidly with the size of the system that one needs to push this approach to its present limits to produce results on clusters of experimentally and physically interesting size. As mentioned in a previous section, an effective tool to enlarge as much as possible the size of computationally affordable systems is then to consider high-symmetry magic clusters [11.24, 36, 246–251]. The exploitation of symmetry (with high-order point groups such as Oh or Ih) reduces by orders of magnitude the computational effort, as the electronic excitations which make up the optical response can be catalogued into appropriate irreducible representations of the symmetry group, and the interactions among excitations belonging to irreducible representations not coupled by the perturbation operator are automatically null by symmetry. As of now, the size range of around 200 atoms is about the maximum that can be confidently treated when studying linear optical response using current computational resources even with full exploitation of point group symmetry, but future developments can probably double this size limit in the near future. Anyway, clusters of 150–200 atoms are large enough to start observing a resonance peak that will lead to the SPR. Using this approach, the optical properties of Au nanoclusters in the size range around 150–170 atoms were studied as a function of the approximation used for the DFT exchange–correlation (xc) functional and the shape or morphology of the nanocluster [11.250]. From this study, it resulted that the position of the peak in the absorption spectrum was weakly dependent on the shape of the Au cluster but was essentially related to its size and to the DFT methodology (xc-functional) used in the calculations, and that the predictions of the van Leeuwen–Baerends (LB94) xc-functional compared better with the available experimental data with respect to those of the local density approximation (LDA) xc-functional, once corrections for the environment were properly accounted for. The main results of this work are shown in Fig. 11.42.

Clearly, for the reasons mentioned above, interband transitions damp the sensitivity of the optical response of Au nanoclusters to shape, especially for sphere-like configurations such as those considered in [11.250].

Let us now come to a topic more strictly connected with the subject of the present chapter and discuss the effects of alloying on the optical response of metal nanoparticles. Let us consider for example the most thoroughly investigated case, namely that of Ag-Au alloyed nanoparticles [11.63, 252–254]. At the experimental level [11.63, 254], what is observed when alloying Ag and Au in nanoparticles of essentially spherical shape is that the plasmonic peak shifts to higher energies, becomes relatively narrower, and gains in intensity on increasing the Ag concentration from pure Au to pure Ag cluster (Fig. 11.43a). In a classical electrodynamics calculation or even within the jellium model the atomistic details of the systems are basically lost, and one has to resort to some sort of averaged description; i. e., one needs to define an effective dielectric function or an effective potential which is constant throughout the particle in the case of homogeneously alloyed systems or stepwise constant in the case of segregated systems. The problem is that it is not clear how to define these quantities without reference to experimental results. In other words, the extent of the interplay between local and collective electronic states in interatomic metallic bonding as a function of composition and of the distribution of the atomic species within the particle is scarcely known. To answer the consequent need for rigorous information and respond to some basic questions still existing in this field (e.g., the exact dependence of the shape and peak

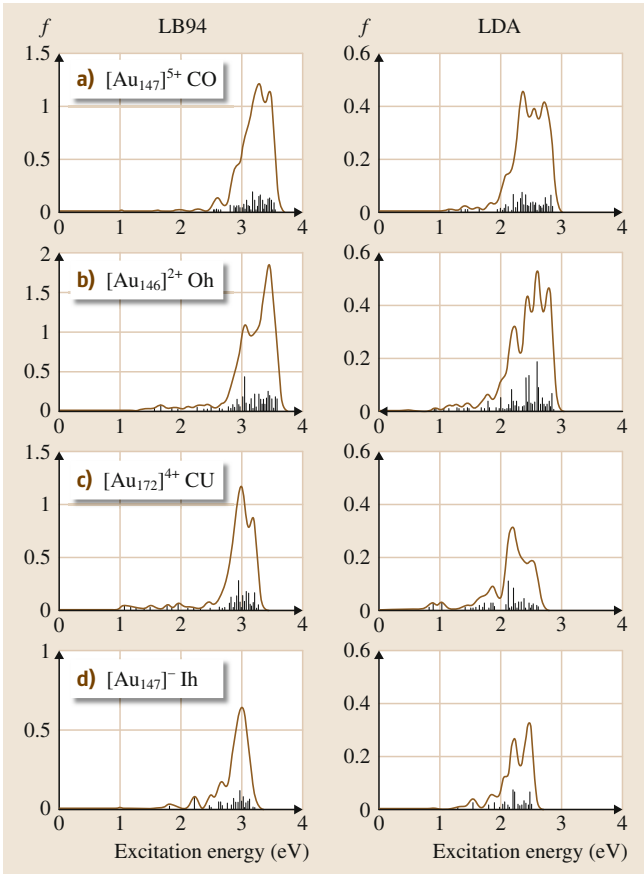


Fig. 11.42 Photoabsorption spectra simulated via a TDDFT approach at the LB94 and LDA level for Au nanoclusters at LDA-relaxed geometries: CO = cuboctahedron, Oh = octahedron, CU = cube, Ih = icosahedron. (After [11.250] with permission of ACS)

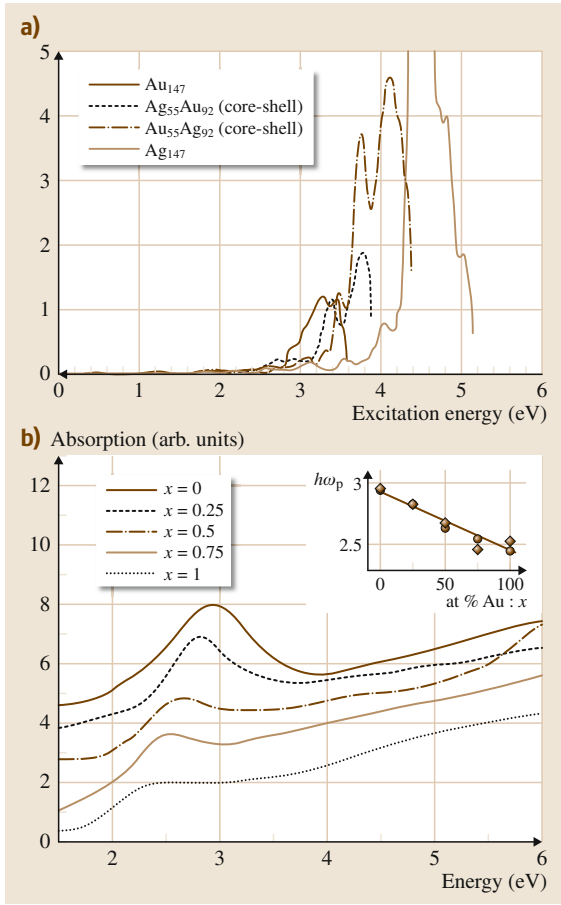


Fig. 11.43a,b Photoabsorption spectra of cuboctahedral bimetallic clusters with increasing silver concentration. **(a)** Calculated TDDFT LB94 spectra; **(b)** experimental spectra. (After [11.251] with permission of ACS)

of SPR upon nanoparticle composition and chemical ordering), TDDFT calculations with fully atomistic description can make a decisive contribution. Again, the use of magic clusters is crucial to decrease the computational effort of atomistic TDDFT to a manageable size. In the case of nanoalloys, exploitation of symmetry has another great advantage. In addition to structural morphology and chemical composition, in fact, chemical ordering can play a role in nanoalloys, but thorough sampling of the chemical ordering degrees of freedom is not feasible with present computational facilities, not even for particles of around 150 atoms. As mentioned earlier, the high symmetry assured by magic structures is particularly convenient for nanoalloys, as it can be exploited not only to reduce the computational effort but also to partition the atoms into symmetry shells or orbits, i. e., groups of symmetry-equivalent species (which are converted into one another by the operations of the symmetry group). This exponentially reduces the configurational degrees of freedom of the system, making sampling of the nanoalloy configurational phase space feasible via first-principles simulations even for medium-sized particles [11.24, 36]. This magic-cluster approach was applied in recent work to pure Ag and mixed Ag-Au nanoclusters of size around 150 atoms, focusing on the effect of alloying on the optical response of these systems [11.251]. It was found that the absorption spectrum of Ag clusters is more sensitive to the particle shape than that of Au clusters, as expected on the basis of a smaller damping due to interband

transitions, that configurations with rather different chemical ordering (such as core–shell versus intermixed ones) present spectra with similar position and intensity but different shape, and that the plasmonic peak shifts to higher energies, becomes relatively narrower, and gains in intensity on increasing the Ag concentration in the cluster. The behavior of the nanoalloy plasmon peak with composition can be understood by thinking that, after all, Ag and Au are quite similar, except in the extent of the coupling among s- and d-states which damps and broadens the plasmon peak for Au systems, so that when mixing the two metals a progressive transformation of one's spectral features into the other one's occurs. An example of the kind of agreement that can be obtained between theory and available experimental information is shown in Fig. 11.43 [11.251], where it should be taken into account for a proper comparison between theory and experiment that experimental spectra are shifted at lower energy with respect to gas-phase systems due to environmental (matrix) effects [11.255]. This good agreement opens promising perspectives for applications also in view of the possibility of investigating more complicated systems such as those presenting chiral [11.6, 256–258] and magnetooptical effects [11.15].

The minor dependence of the plasmon resonance upon chemical ordering found in [11.251], such that only a slight difference was observed between core–shell and fully mixed configurations, is possibly due to the limited size of the clusters which were considered in this work due to computational limitations. Let us take for example the case of Au-Pt particles. One should expect a significant difference in the optical response of these systems between core–shell and fully mixed configurations, as in the former one has a Au shell which should be optically active and somewhat decoupled from the optically inert Pt core, whereas in the latter the strong mixing of Au and Pt states might lead to the disappearance of the plasmon peak. Indeed, a similar scenario was hypothesized in the literature [11.259] and can be invoked to rationalize other experimental results [11.260] also on similar systems [11.253] (see also below), especially in connection with a slow dynamics of chemical ordering in specific nanoalloys. Further studies are needed to confirm and validate these expectations.

For future perspectives of a more detailed and thorough comparison between theory and experiment, it should be mentioned that one of the topics of current research is realization of measurements on a single nanoparticle [11.10, 236]. This allows one to disentangle all the convolution effects due to particle size dispersion and furnish much more detailed experimental information. It should also be mentioned that the data reported in the right-hand side of Fig. 11.43 were conducted on particles embedded in a matrix, but the general principles here outlined should also apply to particles coated by surfactants and organic or biological ligands. In this respect and focusing on the case of very small particles (containing up to 200 atoms), an interesting recent alternative proceeds via the preparation of size-selected coated clusters, specifically of gold. This has been achieved via synthetic routes which exploit the magic character and thus the increased chemical stability of some of these clusters at specific numbers: 25, 38, 144, ... [11.6,58,59]. Further developments have led to the synthesis of the same clusters but in which alloyed Ag-Au rather than pure Au systems were prepared, and to their accurate optical characterization [11.261]. It is interesting to observe that at these very small sizes one can find a fragmentation of the spectrum due to quantum size effects [11.262], which is predicted theoretically (Fig. 11.43b) and has been confirmed experimentally [11.261]. On the theoretical side, so far the optical spectra of these magic systems have been simulated via TDDFT only for the smallest sizes [11.263], revealing good agreement with experiment, but it is likely that the lack of simulations for the larger sizes will be filled in the near future.

One fascinating field of research is that of interacting plasmons, i. e., interactions between strongly coupled metallic nanostructures [11.5, 264]. By properly tailoring these interactions by playing with geometrical parameters it has been shown that it is possible to control electromagnetic radiation at the nanoscale, thus enabling a variety of possible applications: For example, if the coupling of two nearby oscillators is sufficiently strong, their resonant frequencies can be shifted, resulting in new red-shifted and blue-shifted resonances with respect to the original nanoparticle signals. Also, the junction between adjacent nanostructures can give rise to highly intense and localized electromagnetic fields when excited by incident light of the appropriate polarization (so-called *hot spots*) which can be effectively used to enhance the optical spectra of adsorbed or adjacent molecules by many orders of magnitude such as in surface-enhanced Raman scattering (SERS) and surface-enhanced infrared absorption (SEIRA). This is extremely important in order to achieve the single-molecule detection limit [11.265]. These effects can enhance not only absorption spectroscopies, but also fluorescence ones; an interesting

example can be found in [11.266, 267]. Plasmon systems that are strongly coupled because of their close proximity cannot be described by classical electrodynamics, as quantum-mechanical processes such as tunneling start dominating their optical properties. Moreover, complex systems of coupled plasmons can also exhibit coherence effects, such as Fano resonances, which can be used to modify the properties of plasmonic media [11.5, 268]. Clearly, all these fascinating developments will require significant advances in quantum modeling for their deep understanding.

Most of this research on interacting plasmons is not specific to nanoalloys. In this context, nanoalloys can be useful to tune the properties of the single plasmonic unit, as shown above. Other intriguing possibilities, such as hybrid core–shell nanostructures in which both the core and the shell exhibit a plasmonic response which can interact between themselves, have been less considered in the literature, even though they can be important, e.g., in Förster resonance energy transfer (FRTE) [11.269, 270]. Also, nonlinear optical properties represent a fascinating topic which is outside the scope of this chapter [11.271–273].

As a link to the next subsection, we can briefly introduce magnetooptical properties of metal nanoclusters [11.15]. This is an exciting field of research aimed at preparing and investigating multifunctional nanostructures exhibiting both magnetic and plasmonic properties [11.274–276]. To focus on a specific example, let us consider Au-Fe nanoparticles at roughly equimolar composition obtained as solid-solution (random) nanoalloys (with a somewhat broad distribution centered around 4–6 nm diameter) implanted in a SiO_2 matrix [11.260]. Experimentally, it was shown that in such Au-Fe nanoparticles, strong hybridization of Au and Fe electronic states occurs, producing a decrease in the magnetic moments on Fe atoms and a concomitant magnetic polarization of Au atoms, together with a strong damping of the particle SPR signal. These studies are only at their beginning, and much work will be needed to achieve proper control on the synthetic protocols and detailed comparison between theory and experiment, but they point to a promising evolution in a near future [11.277]: For example, one fascinating goal in this field is to produce photoswitchable nanomagnets that can be controlled and monitored by light [11.278].

11.4.4 Magnetic Properties

The magnetism of hybrid nanostructures is the subject of Chap. 12 in this handbook. We thus refer to this other chapter for basic information on concepts, theory, and experimental techniques used for synthesizing and characterizing magnetic nanoalloys, and in this subsection focus on only one example to illustrate a different (surface science) approach: the use of self-assembled Co-Pt (and Fe-Pt) nanoparticle arrays as potential candidates for high-density data storage.

We start by recalling that first-row transition metals from the middle of the row possess high magnetic moments due to the presence of partly occupied d-orbitals. A quantity which is crucial for applicative purposes is the magnetic anisotropy, i. e., the preferential orientation of magnetization in a particular crystal axis direction. The magnetic anisotropy consists of two major components: crystalline anisotropy and shape anisotropy. Here we consider only magnetocrystalline anisotropy, which is of atomic origin and stems from the interaction of spin–orbit (L–S) coupling with crystal field energy. If the thermal energy is much smaller than the magnetic anisotropy energy (MAE), i. e., the energy barrier to reorient the direction of the particle magnetic moment satisfies $KV > 25-40k_BT$, where K is the magnetocrystalline anisotropy energy density and V is the volume of the particle, then a particle with its spin oriented in a given direction will maintain it for a long time, and could be used as a magnetic bit. The magnitude of spin–orbit coupling (which scales as a power of the atomic number) is small for first-row transition metals and large for third-row ones, actually so large for the latter that it effectively quenches magnetism in extended structures. Alloying a first-row transition metal with a third-row one is a way to produce systems which exhibit at the same time high magnetic moments and high magnetocrystalline anisotropy energy. Indeed Co-Pt and Fe-Pt bulk alloys at 50–50% composition crystallize in the $L1_0$ phase, i. e., a phase with a tetragonal crystal lattice of alternating homogeneous Pt and Co planes along a (001) axis, and are the bulk materials with the highest MAE values: around 0.8–1.0 meV per magnetic atom. Such a high MAE value entails that – in principle – Co-Pt nanoparticles of ≈ 3000 atoms could be used as magnetic bits. Note also that, being so small, they are expected to be single-domain ferromagnetic particles. Due to their potential applications in future high-density magnetic recording in multiterabit data storage and high-energy-density permanent magnets, Co-Pt and Fe-Pt nanoparticles have thus received immense research interest. In an important work [11.61] it has been proved that assemblies of high-coercivity FePt particles of ≈ 4 nm in size can in principle support stable magnetization. In order to real-

ize this possibility, however, several constraints should be satisfied. First, the particles should be in the $L1_0$ face-centered tetragonal (fct) phase and not in the disordered fcc phase or other phases exhibiting small MAE. Second, one should achieve long-range-ordered two-dimensional arrays of such nanoparticles. Third, their easy magnetization axis should be perpendicular to the plane of the substrate on which they are deposited. Perpendicular magnetization in fact allows smaller bit size and increases data storage density. Moreover, Kerr rotation of polarized light is larger when the magnetization is perpendicular to the plane compared with the in-plane magnetization. Fourth, their MAE should be at least as high as in the bulk – the higher the better.

The first requirement immediately poses some problems. As recalled in Sect. 11.4.1, in fact it has been shown both theoretically for free particles [11.156, 279] and experimentally for particles embedded in weakly interacting substrates such as amorphous carbon [11.158] that noncrystalline structures, in particular polyicosahedral (pIh) ones [11.128], are favored for Co-Pt and Fe-Pt nanoalloys up to 3–4 nm diameter. The interaction with a substrate could reverse the situation and favor fct configuration. As the lattice parameter of the $L1_0$ fct phase is not too distant from that of pure Pt, and it is known that Pt clusters on MgO(100) adopt a fcc structure at very small sizes, contrary to what happens in the gas phase, one could think that the square-symmetry MgO(001) substrate should favor the $L1_0$ fct phase for Co-Pt nanoparticles. This expectation is only partly fulfilled: as recalled in the subsection on structural properties, for Co-Pt clusters smaller than 100–200 atoms, Frank–Kasper structures are favored also when deposited on MgO(100) [11.152], and interfacial adhesion actually enhances the stability of these structures, via a novel epitaxial adhesion mechanism. It is important to observe that one of the reasons for this phenomenon is that the lowest-energy structures of Co-Pt/MgO(100) particles are dominated by Co segregation at the interface with the substrate. For larger particles, the situation changes again. First, the pIh configurations become progressively less and less stable with respect to fct ones due to a less efficient interfacial matching, so that they are not favorable any more for particles with more than 200 atoms. Second, for fcc-like particles, one finds a strong tendency of Pt to form a segregated layer at the topmost (100) facet from both theoretical predictions and experimental observations [11.153, 280]. For these particles, then, one-layer Co surface segregation at the interface together with one-layer Pt surface segregation at the topmost facet translates into $L1_0$ chemical ordering, which is the first of the requirements quoted above (Fig. 11.3).

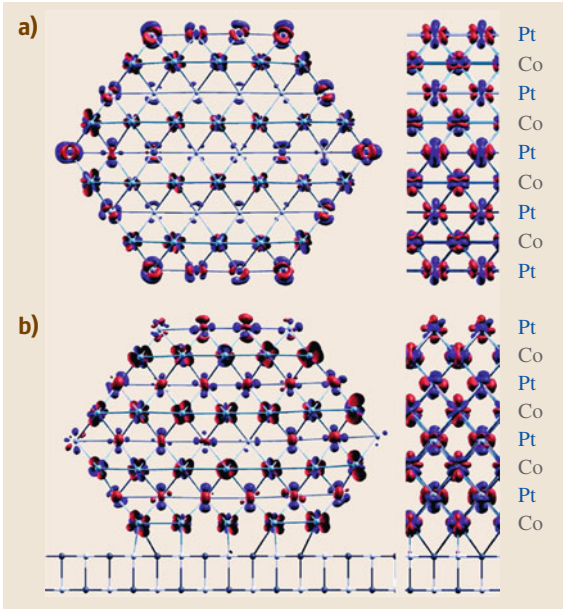


Fig. 11.44a,b Isocontours of differential electronic density $\Delta\rho = \rho(M_z) - \rho(M_y)$, obtained by subtracting the total electron density of the state in which the magnetization axis is parallel to the surface and perpendicular to the wire main axis (M_y) from the state in which the magnetization axis is perpendicular to the surface (M_z), for suspended **(a)** or supported **(b)** wires. In the larger images on the *left*, the view is taken along the main axis of the wire; on the *right*, side view of the wire is also shown. Contour value $= 0.004\,\mathrm{e/Å^3}$. Planes of cobalt atoms are displayed in *blue*; platinum atoms are displayed in *dark gray*. (After [11.39] with permission of ACS)

As for the second requirement, i. e., long-range 2-D order of possibly size-selected particles, we will not discuss this in detail, but we refer to the concept of surface nanopatterning in order to achieve it [11.93–95]. As the $L1_0$ chemical ordering is realized with Co planes in (100)/(100) epitaxy, one expects that the easy magnetization axis of the particles should be perpendicular to the plane of the substrate on which they are deposited, and this is indeed what is predicted by simulations exploiting 1-D modeling [11.39], thus satisfying the third requirement quoted above. Simulations however give a disappointing response in terms of the fourth requirement. Despite the fact that the particles have high magnetic moments, in fact, it is found that the mix-

ing of particle and oxide electronic wave functions at the interface dominates and results in a reduction of the MAE by a factor of at least $\approx 1/2$ [11.39]. The value of the MAE depends on which type of d-states are available at the Fermi energy. As shown in Fig. 11.44, tilting the magnetization axis of the wire from perpendicular to parallel to the (100) planes move electrons into orbitals occupying (100) planes. Furthermore, the increase of the regions where $\Delta\rho$ is large in Fig. 11.44b with respect to Fig. 11.44a indicates greater availability of d-states at the Fermi energy in the supported system, which reduces the energy cost associated with tilting the magnetization and thus the MAE. This finding in a highly controlled and regular interface points to an even larger effect when a rougher environment is present and rationalizes the experimental difficulties in achieving supported particles with a stable and non-fluctuating magnetization direction [11.281]. Supports other than MgO(100) can be however considered in the search for systems with a stable magnetization. This example – although negative for our purposes – shows how subtle the interplay of structural and electronic effects can be in determining the magnetic properties of alloy nanoparticles.

11.5 Nanostructured Bulk Alloys

The possibilities opened by nanotechnology over the last two decades in terms of manipulating composition and structure at the atomic level are hard to overemphasize, permeating into all major science and technology domains. While much has already been achieved, much more is expected, as can be inferred by the funding strategies of the major scientific organizations around the world.

While the previous part of this chapter has addressed nanoparticle alloys, we focus in this section on bulk materials whose internal structure has been designed at a nanometer scale to achieve desirable properties, not accessible at larger scales.

Alloying has been part of metallurgical practice since historic times, but it is only recently that nanoscale structured alloys have captured the attention of the scientific and technological audience.

Many amazing properties emerge as the scale of a structure is reduced to the nanometer range. The general reader is probably familiar with the continuous progress in miniaturization of electronic devices, which allows for impressively dense packing of our electronic tools and toys, but is probably less familiar with a similar revolution taking place in other domains of nanoscience/technology, including the mechanical properties of structural materials and radiation damage for new concepts in the field of nuclear energy.

We focus here on a few aspects of nanoscale alloying, namely the search for ultrastrong materials with capability to withstand extremes in temperature, stress, radiation doses, and/or plastic deformation.

Many avenues are explored in this quest; in fact, so many that here we choose only two, namely: (i) bulk materials that incorporate nanoscale precipitates of a different phase, generally oxides, and (ii) bulk nanophase materials that aim at reducing the grain size of a polycrystal to dimensions in the nanometer scale so as to incorporate a large amount of grain boundary interfaces.

11.5.1 Bulk Materials Incorporating Nanoscale Precipitates of a Different Phase

Usually the strength of a material is given by a combination of factors that are optimized by both the constituents of the material and the processing steps that produce the final microstructure.

Steels are basically iron-carbon alloys with additions of other elements such as Cr, V, Mn, Si, W, Ni, Ta, and Nb. Alloying elements in solid solution are used to produce solution hardening and also to react with C and produce fine-scale carbide precipitates that induce precipitation hardening. Also, alloying elements alter the kinetics of phase transformations, allowing easier handling of the thermal treatments that control the final hardening. Finally, some elements such as Cr enhance corrosion resistance.

Nanostructured ferritic alloys (NFA) are 12–20% Cr ferritic stainless steels that are dispersion strengthened by a very high density (up to several 10^{23} particles/m^3) of ultrafine Y-Ti-O-enriched nanofeatures. Their roots trace back to the pioneering work of *Fisher*, who patented a mechanical alloying (MA)/hot extrusion powder processing route to produce NFAs, which were marketed in the 1980s as International Nickel Company (INCO) MA956 and MA957 [11.282]. Extensive studies in the US breeder reactor program showed that MA957

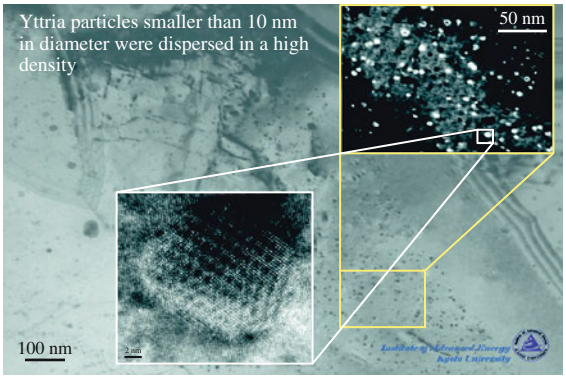


Fig. 11.45 Picture of the structure of a ODS steel showing the high density of nanometer-scale precipitates. (After [11.284] with permission of Taylor & Francis)

has high tensile and creep strengths as well as unusual resistance to radiation damage [11.283].

The oxide particles provide hard and stable dislocation pinning centers that improve the mechanical strength. They also provide sites acting as sinks for defects produced by irradiation. Figure 11.45 shows an example of the microstructure of an oxide dispersion strengthened (ODS) steel showing a very high density of nanoparticles [11.284].

These materials are currently under development at several places around the world, mainly for general high-temperature and for nuclear fission and fusion applications, in particular in the USA, Europe, and Japan. The main interest is fueled by the substantial increase in strength at high temperatures, creep resistance, and irradiation response that is obtained.

Given the significantly large composition–processing parameter space that define steels, and the fact that most of the knowledge is empirical, every laboratory/industry has its own composition and processing path, the goal being to obtain the finest particle size distribution and the highest number density.

Research in Japan led to the development of dual-phase 9Cr nanostructured transformable steels (NTS) for fast-reactor fuel cladding, as described in a recent review [11.290]. The Japanese program placed special emphasis on working–recrystallization sequences that are necessary for plate and tubing fabrication and that also produce more isotropic properties [11.284, 291–295].

In Europe, various processing and characterization studies were performed on MA957 and small experimental heats of NFAs [11.296–298]. More recently, European research programs aimed at developing

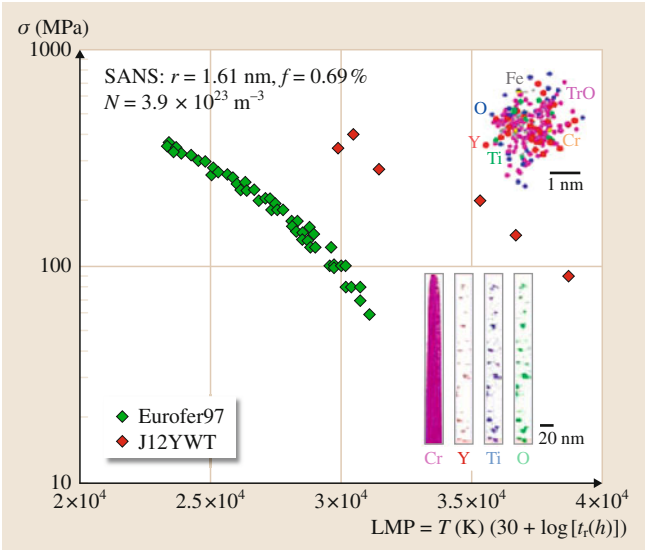


Fig. 11.46 A Larson–Miller plot (LMP) comparing the creep strength of nanostructured ferritic alloys J12YWT [11.285] with that of normalized and tempered martensitic steel Eurofer97 [11.286]. The *insets* show atom probe tomography maps of the nanofeatures (NF) in J12YWT [11.287]. SANS data on the NF size (r), number density (N), and volume fraction (f) are shown (*top left*). (After [11.288, 289])

the martensitic ODS Eurofer97 for fusion applications [11.299, 300].

In the USA, *Klueh* et al. [11.301, 302] have worked on NFA for possible use up to 700 °C, a substantial increase in maximum operation temperature of steels containing 9% Cr, such as T91, which is of the order of 590 °C. This is illustrated in Fig. 11.46, which shows a creep rupture time (t_r) Larson–Miller plot for a Japanese NFA, J12YWT [11.285], compared with a 9Cr TMS Eurofer97 [11.286]. (Note: the Larson–Miller plot shows the maximum stress a material can sustain at a given temperature before rupture at a given time.) The insets show an atom probe tomography (APT) map and Y-Ti-O cluster image for the NFs in J12YWT [11.287], along with the average radius (r), number density (N), and volume fraction (f), measured by small-angle neutron scattering (SANS) [11.288, 289, 303].

These ultrafine-scale features distinguish NFAs from conventional dispersion strengthened ODS alloys, which generally contain refined, but larger, equilibrium oxide phases.

Regarding strength at high temperature, the ODS alloys developed under the Japanese High Burnup

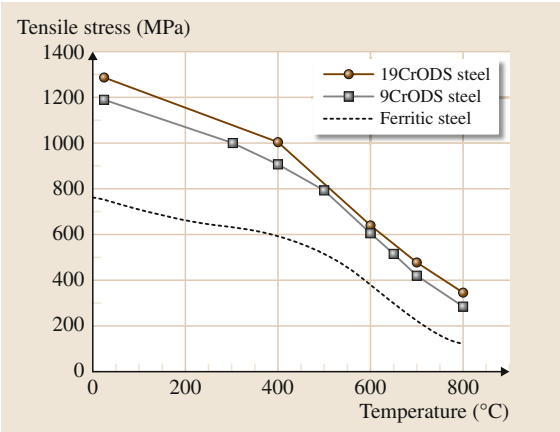


Fig. 11.47 Strength of two ODS steels developed by *Kimura* et al., compared with traditional ferritic steels. (After [11.284] with permission of Taylor & Francis)

Fuel Cladding Materials R&D program by *Kimura* et al. [11.284] show a significant increase in tensile stress compared with conventional ferritic steels (Fig. 11.47. These alloys are being irradiated in Japan and Russia to reach high displacements per atom (dpa) levels (in the range of ≈ 200 dpa), and the results will be available in a few more years.

Swelling Resistance

As already mentioned, besides the increase in strength/creep behavior at high temperature, one of the most interesting properties of NFAs is their ability to resist radiation damage. In a nutshell, radiation damage comprises a series of phenomena produced when energetic particles hit a solid. Among them the displacements of atoms, creating interstitials and vacancies, and the transmutation of the original species into new ones via nuclear reactions are the most important. For future nuclear fusion application, the requirements on materials are extreme due to the large damage produced by energetic 14 MeV neutrons in terms of both displacements (measured in displacements per atom, or dpa) and He generation via fusion of D and T and decay of heavy elements, measured in He/dpa. Vacancies and He atoms have a tendency to coalesce into voids and bubbles that induce swelling and promote intergranular or creep fracture via a fine dispersion of bubbles at grain boundaries.

The lifetime under creep conditions is determined by the kinetics of bubble growth. Nanofeatured alloys show excellent capacity to prevent He-induced embrittlement via the ability to capture He at fine bubbles at the interface between the oxide particles and the matrix. Intensive work is being pursued at present, trying to understand quantitatively this behavior in order to define the best type of interfaces for this purpose, also in materials other than steels [11.304].

The fabrication of ODS or NFA alloys at industrial scale remains a challenge; at present no commercial ODS steels are produced. At the laboratory level, an example of a synthesis route is as follows [11.305]: Starting from 70 μm-diameter, argon-atomized, prealloyed metal powders and 20 nm Y_2O_3 powder, the process involved milling in a high-energy attritor mill in an argon atmosphere. After the mechanical alloying step, the flakes are degassed and consolidated into a bar by hot extrusion at 1150 °C. Further processing by hot and cold rolling interspersed with annealing treatments is used to convert the extruded bar into sheet with final thickness of 2 mm. A schematic picture of the process is shown in Fig. 11.48.

One of the most detailed studies of the morphology and stoichiometry of these nanoparticles is that of *Hsiung* and collaborators, working on one Japanese ODS steel named K3, with a composition that includes Al: 16Cr-4Al-2W-0.3Ti-0.3Y_2O_3 [11.306–308]. Using high-resolution TEM and software to simulate diffraction patterns, they were able to resolve the chemical composition of these particles and to propose a possible path for the their formation from the original powder to the final precipitate. They found that the oxide nanoparticles (Fig. 11.49) are mainly $Y_4Al_2O_9$ (YAM), a complex oxide with monoclinic structure, mean particle size of 6 nm, and particle density of 1.33×10^{22} m^{-3}.

By comparing the $Y_4Al_2O_9$ nanoparticles formed in the ODS steel with the starting Y_2O_3 particles (space group *Ia*3, a cubic structure, with size between 15–30 nm) used to fabricate the ODS steel, these authors suggest that the formation of oxide nanoparticles in ODS steels does not take place solely through a fragmentation mechanism, but requires the decomposition of Y_2O_3 through $Y_2O_3 \rightarrow 2[Y] + 3[O]$ and the following internal oxidation reactions: $2[Al] + 3[O] \rightarrow Al_2O_3$ and $2Y_2O_3 + Al_2O_3 \rightarrow Y_4Al_2O_9$ during MA and consolidation, in which the internal oxidation reactions are governed by the oxygen affinity of alloying elements: That is, the formation of Y-Al complex oxides becomes predominant when both Al and Ti are present in ODS steels.

The small nanoparticles (< 10 nm) show facets and ledges at the oxide–matrix interfaces and tend to be coherent or semicoherent with the matrix. A structure of

crystalline oxide core in association with amorphous shell was observed in both large and small nanoparticles in as-fabricated K3 ODS steel. The core–shell structure vanishes after prolonged annealing at 900 °C for 168 h, suggesting that the core–shell structure is far from chemical equilibrium. A three-stage formation mechanism of ODS nanoparticles including fragmentation, amorphization, and crystallization is accordingly proposed to rationalize the observations.

Other recent studies also describe the evolution of these particles for different alloy compositions. The MA957 ODS alloy was studied by *Kaoumi* [11.310], with a composition that includes 1 Ti and 0.3 Mo, besides 0.25 Y_2O_3 (wt%). Titanium and molybdenum are added in small quantities to improve the ductility and the oxidation resistance of the material; they give solid-solution strengthening in iron. Also, they are believed to trap the carbon and nitrogen present in the matrix, thus preventing the formation of chromium carbides and nitrides, which are a cause for grain boundary embrittlement.

The ambient- and elevated-temperature strength of an alloy can be improved by plastic deformation (hot or cold working). However, in conventional alloys which do not contain a fine dispersion of a second phase, the strengthening provided by the cold and hot working quickly anneals out when exposed to high temperatures, due to migration of dislocations and recrystallization of the new grains. Mota explains that the presence of a uniformly distributed dispersoid can prevent recrystallization by blocking the dislocation migration.

The advantage of using yttria instead of other oxides, carbides, or nitrides is its relative stability at high temperatures. Other refractory oxides, carbides, and nitrides would be suitable as dispersoid materials provided that they have such high temperature stability; such suitable dispersoids are thoria, ceria, and rare-earth oxides, carbides or nitrides of zirconium, titanium, and hafnium. The less desirable materials are alumina, titania, and chromium carbides since it is expected that their size should increase at high temperatures, making them less efficient at retarding the recrystallization process.

The worldwide interest in this type of alloys is so large that moving the frontier forward, well above 200 dpa, is to be expected soon as basic science based on computational materials modeling in combination with careful experimental validation may accelerate the optimization of alloys in ways never foreseen before.

Finally, *Odette* and *Hoelzer* [11.311] believe that, while there are still unresolved challenges facing the successful development of nanostructured ferritic alloys, these challenges also represent opportunities for materials science to make critical contributions, akin to the superalloy single crystals that revolutionized the jet engine and gas turbine technologies.

In summary, we have presented here a small part of a huge international effort to develop ferritic alloys capable of preserving their strength at high temperatures, resisting creep and radiation damage, and managing He, an undesirable byproduct of radiation damage in fast/fusion reactor technology.

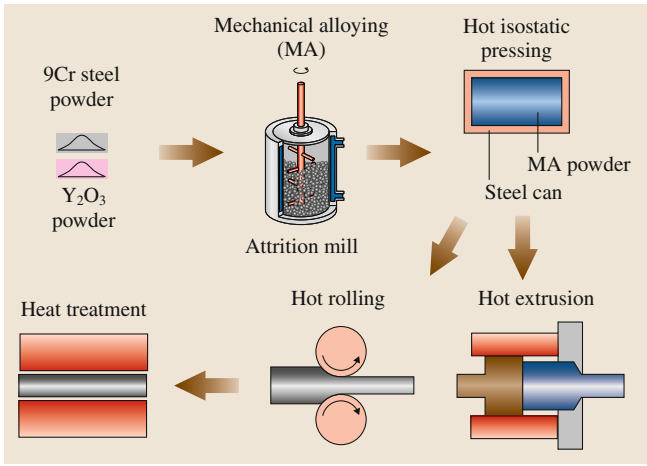


Fig. 11.48 Schematic view of the different steps to produced the ODS steel via powder alloying technique. (After [11.309] with permission of Elsevier)

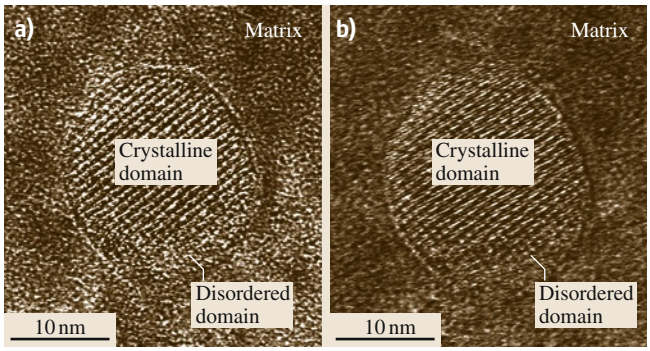


Fig. 11.49a,b HR-TEM images of a large $Y_4Al_2O_9$ (YAM) nanoparticle at two different defocus conditions **(a)** −75 nm, **(b)** −50 nm. (After [11.306] with permission of APS)

11.5.2 Bulk Nanophase Materials

We focus now on a field that has been growing quickly for the last two decades, namely the development of

nanophase materials, i. e., bulk materials with grain size below 100 nm. These materials have generated interest in terms of both basic science and technological applications due to their unusual mechanical [11.312–319], electrical [11.320–322], magnetic [11.323–328], and corrosion [11.329–331] properties.

From the perspective of mechanical response, nanophase materials present amazing properties since, as the grain size decreases, a well-known hardening law – the Hall–Petch relation [11.332] – predicting that the yield strength increases as $1/d^{1/2}$ (grain size strengthening) – anticipates an unprecedented increase in hardness [11.333]. *Chokshi* et al. [11.334] were among the first to report that pure nanocrystalline Pd materials become extremely hard with decreasing grain size. With progress in synthesis techniques leading to the nanometer grain size regime, exceedingly high strength has been obtained.

However, below a grain size limit of around 10–20 nm, the Hall–Petch relation ceases to be valid and a new world of nanomechanics appears, where plasticity generated at grain boundaries (GBs) becomes relevant [11.335–338]. Below 10–20 nm materials begin to soften, giving rise to a so-called inverse Hall–Petch (HP) regime. This general behavior occurs in a number of pure metals and intermetallic compounds [11.339, 340]. Since these early experiments till today, a great deal of effort has been focused on elucidating the physical mechanisms that control plasticity in nanocrystalline materials, both experimentally and through molecular dynamics (MD) computer simulations [11.312, 337], that has not yet succeeded in providing a conclusive picture.

Recent experimental investigations have suggested that the earlier measurements showing an inverse HP behavior may not represent an intrinsic nanocrystalline behavior but rather are a consequence of defects in the samples, such as porosity and grain boundary (GB) contamination [11.314, 338, 341, 342].

The molecular dynamics (MD) studies, on the other hand, reproduce an inverse HP behavior [11.336, 343], most notably the work of *Schiotz* et al. [11.318], which extended earlier observations [11.336] to grain sizes of 5–50 nm.

Nearly all such simulations conclude that the cause of the inverse HP behavior arises from a crossover in the mechanism of deformation from dislocation glide to GB sliding. However, none of these MD computer simulation studies had provided a quantitative account of these two mechanisms or how one mechanism switches to the other, until a recent work by *Lebensohn* et al. at the continuum model level [11.344] and *Vo* et al. [11.345] using MD. These works aimed at quantifying the contribution to total plasticity coming from intragrain dislocation activity and GB-mediated mechanisms. What was found is that, for all but the highest strain rates, plasticity comes from equal contributions from GB and from intragrain dislocation activity, suggesting that the two mechanisms are closely related.

Further studies by *Vo* on the limits of hardness at the nanoscale [11.333] bear a remarkable similarity to a recent experimental report by *Trelewicz* and *Schuh* [11.346], who succeeded in preparing a set of Ni-W alloy samples with grain size between 3 and 150 nm using pulsed electrodeposition. They observed that, as the grain size decreases, plasticity shifts from crystal-like behavior (Hall–Petch) to amorphous or glassy-like behavior, where hardness is independent of grain size.

In summary, what *Vo*'s work shows is that, by relaxing the grain boundaries by a brief high-temperature annealing treatment, the strength of nanocrystalline materials as simulated by MD in a computer can be greatly modified. In particular, plasticity in unrelaxed samples shows a transition from normal Hall–Petch behavior for grain sizes above 12 nm to inverse Hall–Petch; in partially relaxed samples, a regime below 12 nm is observed where the strength becomes independent of grain size, and in samples undergoing grain growth during relaxation, the Hall–Petch behavior extends to significantly smaller grain sizes. This analysis linking the relationship between GB sliding and GB relaxation offers a key to resolve the long-standing controversy concerning the inverse Hall–Petch relation, as it illustrates that grain size alone is not sufficient to characterize hardness in nanoscale systems but that a measure of GB relaxation is required as well.

Vo's observations bring about a connection to alloying effects. Nanocrystalline materials are generally unstable due to the large volume fraction of interface regions, representing high-energy far-from-equilibrium structures. Consequently their synthesis has proven challenging [11.347–349], and in many cases, they cannot be produced in bulk form. For potential applications, the problem of stability has to be addressed.

Pure metals such as Cu, Pd, Sn, Pb, Al, and Mg in nanocrystalline phases exhibit grain growth even at room temperature [11.350–352].

The standard procedure in metallurgy to lock in a desired microstructure is to explore alloying routes, which in this particular problem of nanophase materials led to significant advances in nanostructure stability at elevated temperature compared with their pure metal

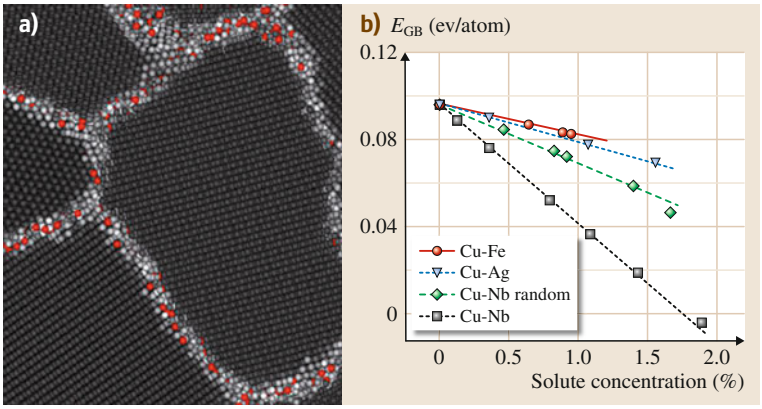


Fig. 11.50 **(a)** Atomic configuration of an MC/MD Nb-doped Cu nanocrystalline (nc) sample showing that the solute is fully segregated in GB. **(b)** Specific GB energy as a function of solute concentration in nc Cu. (After [11.365] with permission of Elsevier)

counterparts [11.353–358] and has enabled synthesis of materials with the finest possible length scales [11.359–364].

Thermal stability of a microstructure has traditionally been linked to kinetic phenomena [11.366]: by alloying the grain boundary, mobility is decreased. However, it has been suggested that the improved stability at the nanoscale may also derive from a thermodynamic reduction in grain boundary energy [11.365, 367–369]. With reduced grain boundary energy, the driving force for grain growth decreases, and in the extreme case of zero boundary energy, it becomes null. In this scenario, a high volume fraction of intergranular regions would represent no energy penalty to the system and nanocrystalline structures could therefore exist in equilibrium.

The idea of thermodynamically stabilizing nanocrystalline (nc) alloys by eliminating the energetic penalty of grain boundaries was first introduced by *Weissmuller* [11.370], who presented a simple model to illustrate that nanocrystalline structures might exist in a stable state. The basis for grain boundary energy reduction relies on a heterogeneous distribution of solutes, where alloying atoms preferentially occupy grain boundary sites (Fig. 11.50).

Schuh and collaborators have worked extensively on the Ni-W system, which exhibits significant solubility (≈ 12 at. % at room temperature) and consequently a weak tendency for grain boundary segregation [11.364]. Despite this weak tendency to segregate, they have shown that W can be used to control the grain size in nanocrystalline Ni as shown in Fig. 11.51, and that the materials also show negligible grain growth even above 500 °C [11.353, 364, 368, 371] despite not reaching the zero GB energy.

Analytical models for this phenomenon have been proposed [11.354, 367, 368, 372, 373]. An interesting conclusion from these works is that, as solutes prefer GB sites, an increase in global composition promotes an increase in GB area and thus a decrease in grain size, implying that nanocrystalline grain size might be tailored via the composition of the alloy [11.364].

Recently, computational work by *Vo* et al. [11.365] probed these ideas in nanocrystalline Cu alloyed with Fe, Ag, and Nb. Figure 11.52 shows stress–strain curves for several compositions of Nb-doped nc Cu and the yield stress versus composition for several alloying elements.

These authors summarize their results in terms of the lattice mismatch between solute and matrix

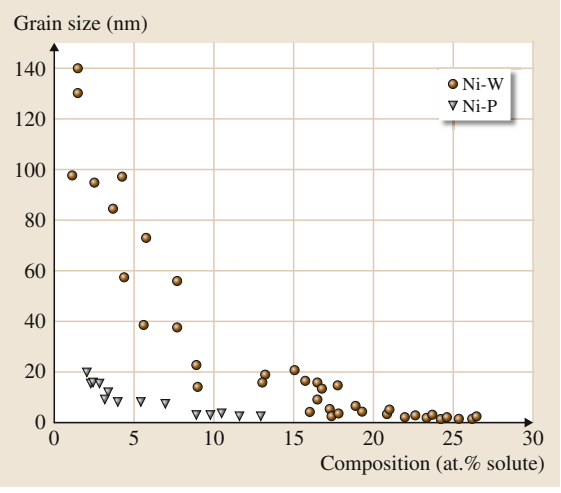


Fig. 11.51 Experimental grain size–composition relationship in electrodeposited Ni-W and Ni-P. Increasing the global solute content leads to a decrease in nanocrystalline grain size. (After [11.364] with permission of Elsevier)

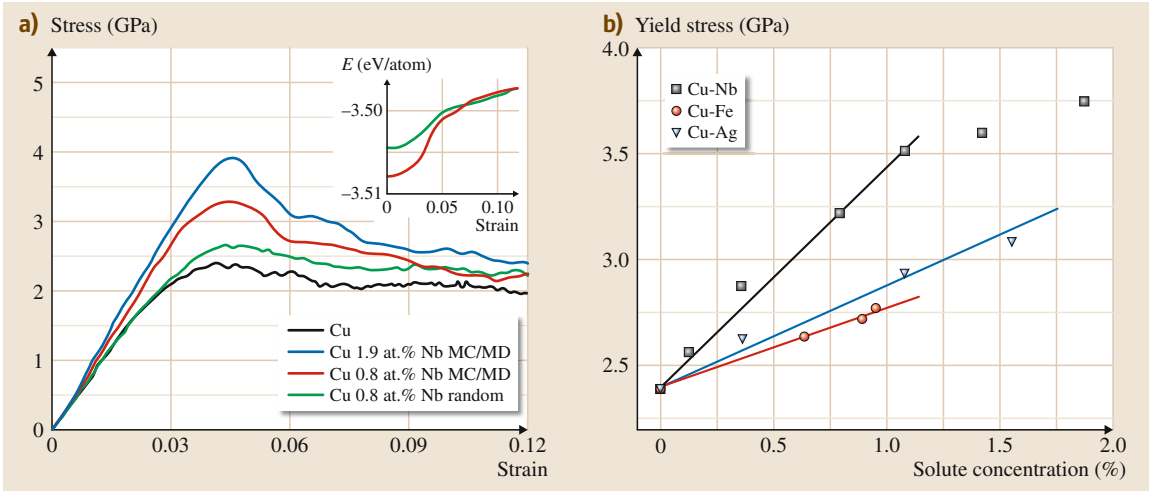


Fig. 11.52 **(a)** Stress–strain curve of pure and Nb-doped nc Cu at constant strain rate of $1 \times 10^9\ s^{-1}$. Potential energy as a function of strain of Cu 0.8 at. % Nb MC/MD and random–GB samples are shown in the *inset*. **(b)** Yield stress of MC/MD nc Cu alloys as a function of solute concentration at constant strain rate of $1 \times 10^9\ s^{-1}$. (After [11.365] with permission of Elsevier)

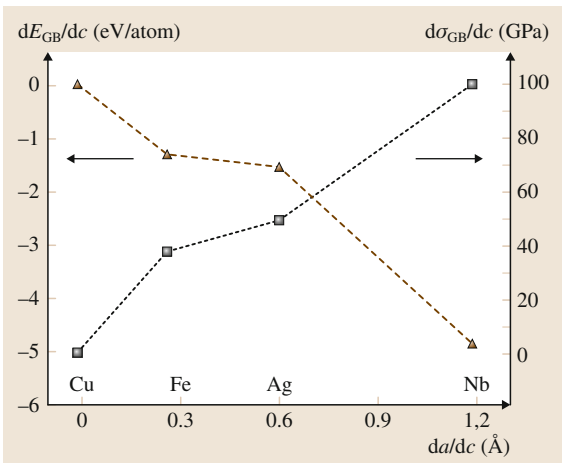


Fig. 11.53 dE/dc, da/dc, $d\sigma_y/dc$: Linear relationships between lattice mismatch of solute and matrix atoms versus GB energy and yield strength of nc samples. (After [11.365] with permission of Elsevier)

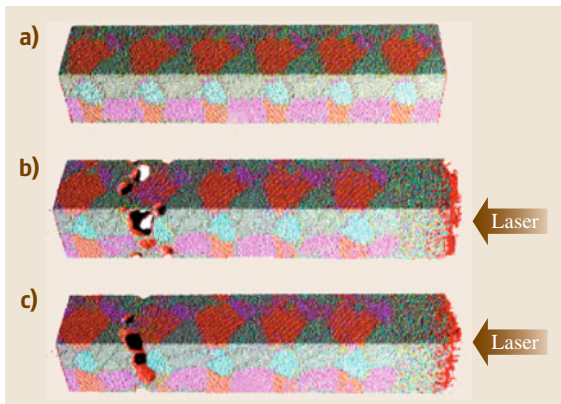


Fig. 11.54a–c Results of shock-wave simulation in pure and nanoalloyed samples: **(a)** as prepared, **(b)** pure Cu sample, and **(c)** sample containing 3% Fe. The *arrows* show the direction of the incoming laser shot. (After [11.358] with permission of Trans Tech Publications)

(Fig. 11.53). In terms of this variable, they find a linear relationship for the GB energy and the yield strength, with Nb being the best alloying element in Cu to increase both strength and thermal stability.

Solute addition to GBs in nanophase materials affects not only the GB energy but also its gliding and bonding characteristics [11.358]. Figure 11.54 shows how alloying nc Cu with 3% Fe changes the spalling behavior under shock loading, reflecting changes in GB cohesion.

In summary, we have reviewed a small number of papers in the abundant literature, addressing the alloying route to improve the stability and mechanical properties of nanophase materials. This field is still at a development stage, but its potential cannot be overstated, as it promises to deliver bulk ultra high-strength materials for a diversity of applications.

11.6 Applications

In this section we give a few examples of the applicative use of nanostructured alloys. Its aim is mostly to provide a very brief illustration of the capabilities of these materials, while we refer to the chapters on fuel cells and energy storage (Chap. 28), nanomedicine (Chap. 30), magnetic nanostructures (Chap. 12), and plasmonics (Chap. 9) in this handbook for more detailed and thorough discussion.

First of all, alloy nanoparticles are very relevant in heterogeneous catalysis. We have mentioned above as one of the first examples the much higher selectivity of Cu-Ru particles with respect to pure Ru ones in orienting dehydrogenation of cyclohexane into benzene rather than its hydrogenolysis into methane [11.22]. We have also mentioned that the Ni_3Fe system was proposed and indeed found to be an efficient methanation catalyst [11.178], and we show in Fig. 11.55 the data on which the theoretical prediction was grounded together with its experimental validation.

In this context, alloys seem very promising in the very important field of heterogeneous catalysis for carbon management [11.374], i. e., to achieve a carbon-neutral cycle in the world economy.

Another fundamental field is the practical application of the optical and magnetic properties of nanoalloys for chemical assays and nanoscale biological research. It is important to underline that in 2011 an entire issue of the *Accounts of Chemical Research* [11.375] was dedicated to theranostics, a term derived from thera(py) + (diag)nostics to link the fields of diagnostics and therapeutics in medicine. We have mentioned in the previous section how plasmonic nanostructures can enhance or enable the detection of molecular processes [11.376]. In this context, nanoalloys are useful for example in the synthesis and fabrication of new nanostructures with nanoparticle–surface interactions or chains of plasmonic nanostructures for the propagation of plasmons along confined geometries. Gold nanocages (nanostructures characterized by a hollow core and an ultrathin porous shell) exhibit tunable plasmonic peaks in the near-infrared region, being prepared by galvanic replacement from Ag nanocubes [11.71], but incomplete replacement could lead to hybrid structures with potentially improved features.

Metal nanoparticles are also already utilized and many more applications are prospected in therapeutic and diagnostic applications, after proper functionalization to improve or achieve biocompatibility [11.377].

A biomedical application which is currently under development but that holds great promise for the future and should not present great difficulties for full exploitation is the use of the attraction between magnetic nanoalloys and external fields to separate biomolecules such as proteins, bacteria, and cells. As an example, biofunctionalized Fe-Pt nanoparticles were shown to be able to capture and separate Gram-positive bacteria, as illustrated in Fig. 11.56 [11.378].

Another biomedical application currently under development is the use of magnetic nanoalloys as imaging probes for biological events via magnetic resonance imaging (MRI). The magnetic field generated by the nanoparticle in fact perturbs magnetic relaxation processes and thus alters the contrast in MRI response [11.379], as shown in Fig. 11.57. By using such MRI contrast effects of magnetic nanoparticles as probes, it will be possible to observe molecular events in biological systems.

In terms of magnetic properties, Fe-Co nanoparticles have the advantage of high magnetizations, but present the issue of being very reactive and undergoing fast oxidation in biological solutions. Once coated

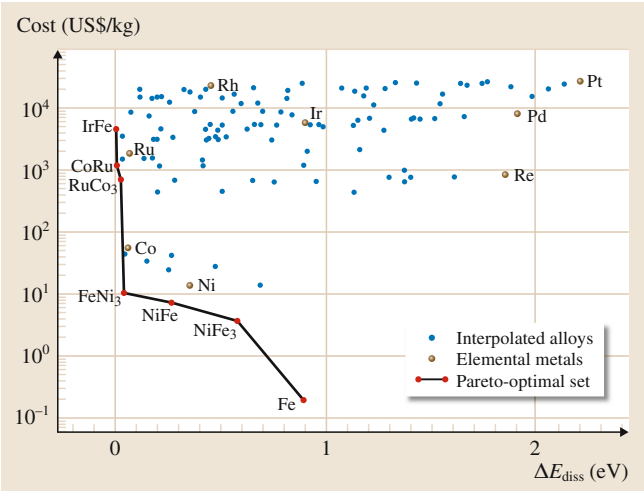


Fig. 11.55 Pareto plot of the activity measure $\Delta E_{diss}(M) = |E_{diss}(M) - E_{diss}(\text{optimal})|$ and the cost for 117 elemental metals and bimetallic alloys of the form $A_xB_{1-x}(x = 0, 0.25, 0.50, 1)$. Each *blue point* corresponds to a particular alloy. The elemental metals are shown (*black*), and the Pareto-optimal set is also indicated (*red*). The cost of the bimetallic alloys has been approximated by the current commodity price of the constituent elemental metals. (After [11.178] with permission of Elsevier)

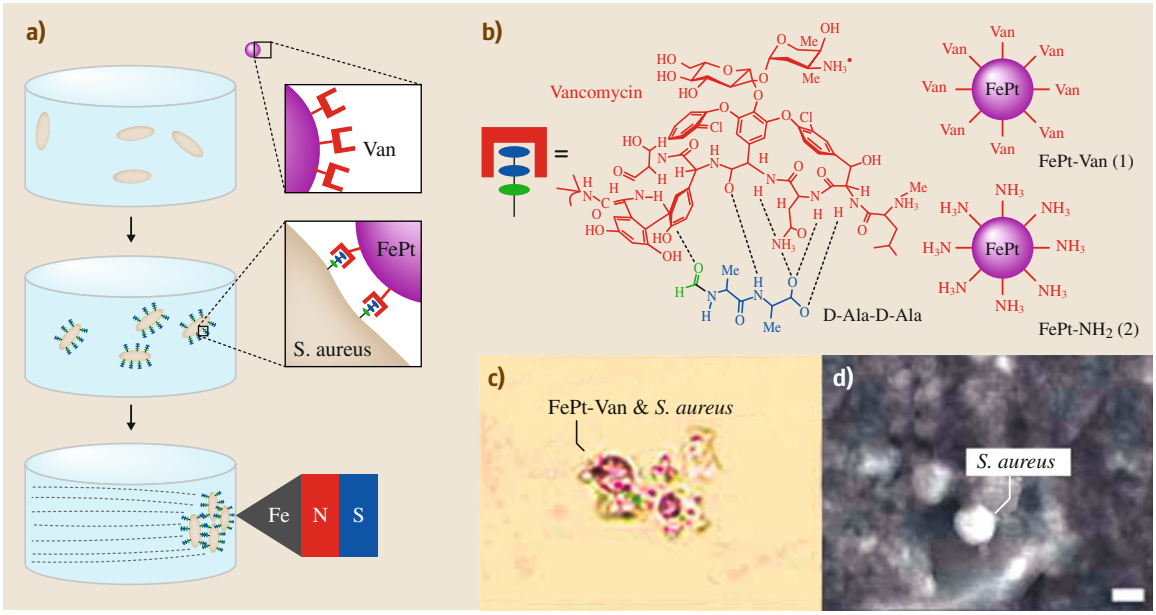


Fig. 11.56a,b Magnetic separation of bacteria (*Staphylococcus aureus*) using vancomycin (Van)-coated FePt nanoparticles. **(a)** Schematic of magnetic separation procedures. **(b)** Biorecognition of vancomycin and D-Ala-Ala terminal peptide. **(c,d)** Optical and scanning electron microscopy (SEM) images of magnetically separated bacteria. (After [11.379] with permission of RSC)

with a layer of Fe_3O_4 or other protective agents, they can provide better contrast for MRI and more effective heating for magnetic fluid hyperthermia. Fe-Pt nanoparticles are interesting for their chemical stability and have shown great potential as contrast agents for both MRI and x-ray computed tomography, and as robust probes for controlled heating in magnetic fluid hyperthermia [11.380]. Finally, the combination of optical and magnetic response is very promising: For example, Au-Fe nanoparticles could be useful in simultaneous diagnostic imaging and photothermal ablation therapy of cancer (multimodal imaging and therapeutics) [11.381].

11.7 Concluding Remarks

In this chapter, which is far from being exhaustive, especially in terms of literature citation (and we apologize to the authors of important contributions not cited for reasons of space or presentation), we have presented a brief overview of nanostructured alloy materials as both isolated particles with nanoscale diameter (nanoalloys) and bulk materials with nanoscale structure. We have discussed the methods for preparing and characterizing these systems from both the experimental and theoretical modeling points of view, and reviewed some basic knowledge on their structural, catalytic, mechanical, optical, and magnetic properties. Attention has been focused on concepts and methods which can help rationalize the available information and provide a general framework for future investigations. Even from this brief overview, the importance of nanostructured alloys in the field of nanoscience and nanotechnology should appear clear. By taking advantage of the degrees of freedom associated with composition and chemical ordering it is possible to expand the scope of physical phenomena exhibited by metal nanosystems and modulate or even dramatically change their corresponding properties. Catalytic activity, mechanical strength, plasmonic and nonlinear optical, as well as magnetic response, or the combination of these features, can all be tuned to meet the requirements of applications. This has already been achieved in some cases, such as in heterogeneous catalysis and nanomagnetism, but to an extent which is only a fraction of the actual potential. In order to better exploit these

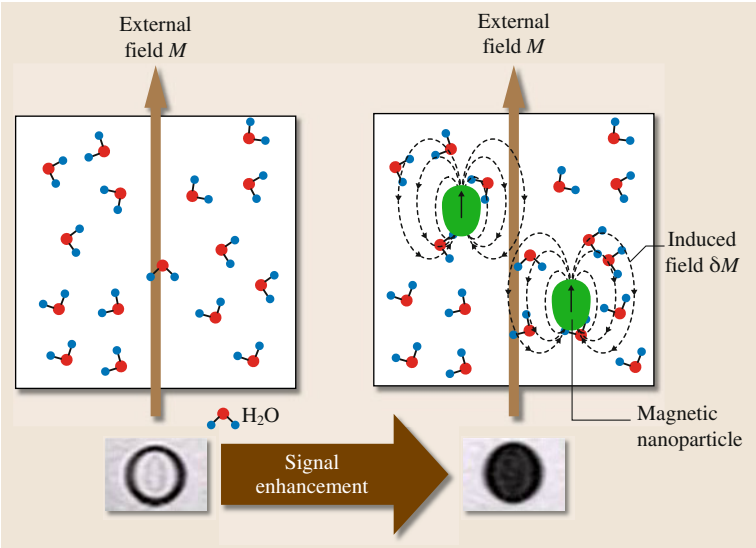


Fig. 11.57 Magnetic contrast effect of magnetic nanoparticles in water. Induced magnetic field by magnetic nanoparticles perturbs the magnetic relaxation processes of the protons in water molecules, which results in shortening of T_2 of the proton with dark MR contrast. (After 11.379 with permission of RSC)

opportunities, precise control of synthetic protocols, improved experimental and theoretical characterization techniques, and fundamental understanding still need to be further advanced, and this represents the major challenge of both basic and applied research in the years to come. Our hope is that the present overview will contribute to promote interdisciplinary research (especially as concerns the interaction between theory and experiment) and advance the general field of nanostructured alloys.

References

11.1 L.N. Lewis: Chemical catalysis by colloids and clusters, Chem. Rev. **93**, 2693–2730 (1993)

11.2 G. Ertl, H. Knotziger, F. Schuth, J. Weitkamp (Eds.): *Handbook of Heterogeneous Catalysis*, 2nd edn. (Wiley, New York 2008)

11.3 K. Kreibig, M. Vollmer: *Optical Properties of Metal Clusters* (Springer, New York 1995)

11.4 C. Burda, X. Chen, R. Narayanan, M.A. El-Sayed: Chemistry and properties of nanocrystals of different shake, Chem. Rev. **105**, 1025–1102 (2005)

11.5 N.J. Halas, S. Lal, W.-S. Chang, S. Link, P. Nordlander: Plasmons in strongly coupled metallic nanostructures, Chem. Rev. **111**, 3913–3961 (2011)

11.6 S.M. Morton, D.W. Silverstein, L. Jensen: Theoretical studies of plasmonics using electronic structure methods, Chem. Rev. **111**, 3962–3994 (2011)

11.7 M.-C. Daniel, D. Astruc: Gold nanoparticles: Assembly, supramolecular chemistry, quantum-size-related properties and applications toward biology, catalysis, and nanotechnology, Chem. Rev. **104**, 293–346 (2004)

11.8 M. Faraday: The Bakerian Lecture: Experimental relations of gold (and other metals) to light, Philos. Trans. R. Soc. Lond. **147**, 145–181 (1857)

11.9 Y. Ma, W.Y. Li, E.C. Cho, Z.Y. Li, T.K. Yu, J. Zeng, Z.X. Xie, Y.N. Xia: AuAg core-shell nanocubes with finely tuned and well-controlled sizes, shell thicknesses, and optical properties, ACS Nano **4**, 6725–6734 (2010)

11.10 N. Del Fatti, D. Christofilos, F. Vallée: Optical response of a single gold nanoparticle, Gold Bull. **41**, 147–158 (2008)

11.11 F.P. Netzer: Small and beautiful – The novel structures and phases of nano-oxides, Surf. Sci. **604**, 485–489 (2010)

11.12 M.P. Pileni: The role of soft colloidal templates in controlling the size and shape of inorganic nanocrystals, Nat. Mater. **2**, 145–150 (2003)

11.13 K. Judai, S. Abbet, A.S. Worz, U. Heiz, C.R. Henry: Low-temperature cluster catalysis, J. Am. Chem. Soc. **126**, 2732–2737 (2004)

11.14 P. Gambardella, S. Rusponi, M. Veronese, S.S. Dhesi, C. Grazioli, A. Dallmeyer, I. Cabria, R. Zeller, P.H. Dederichs, K. Kern, C. Carbone, H. Brune: Giant magnetic anisotropy of single cobalt atoms and nanoparticles, Science **300**, 1130–1133 (2003)

11.15 H. Ebert: Magneto-optical effects in transition metal systems, Rep. Prog. Phys. **59**, 1665–1735 (1996)

11.16 A. Caro: The computational modeling of alloys: From ab initio calculations and thermodynamics

to heterogeneous precipiation. In: *Materials Issues for Generation IV Systems*, ed. by V. Ghetta, D. Gorse, D. Mazière, V. Pontikis (Springer, Berlin 2008)
11.17 H. Chen, J.M. McMahon, M.A. Ratner, G.C. Schatz: Classical electrodynamics coupled to quantum mechanics for calculation of molecular optical properties: A RT-TDDFT/FDTD approach, J. Phys. Chem. C **114**, 14384–14392 (2010)
11.18 B.E. Zhu, Z.Y. Pan, M. Hou, D. Cheng, Y.X. Wang: Melting behaviour of gold nanowires in carbon nanotubes, Mol. Phys. **109**, 527–533 (2011)
11.19 R. McWeeny: *Coulson's Valence*, 3rd edn. (Oxford Univ., Oxford 1980)
11.20 L. Pauling: *The Nature of the Chemical Bond* (Cornell Univ., New York 1960)
11.21 G.L. Timp (Ed.): *Nanotechnology* (Springer, New York 1999)
11.22 J.H. Sinfelt: Catalysis by alloys and bimetallic clusters, Acc. Chem. Res. **10**, 15–20 (1977)
11.23 J. Jellinek, E.B. Krissinel: Ni_nAl_m alloy clusters: Analysis of structural forms and their energy ordering, Chem. Phys. Lett. **258**, 283–329 (1996)
11.24 A. Fortunelli, A.M. Velasco: Structural and electronic properties of Pt/Fe nanoclusters from EHT calculations, J. Mol. Struct. (Theochem) **487**, 251–266 (1999)
11.25 R. Ferrando, J. Jellinek, R.L. Johnston: Nanoalloys: From theory to applications of alloy clusters and nanoparticles, Chem. Rev. **108**, 845–910 (2008)
11.26 J. Libuda, H.-J. Freund: Molecular beam experiments on model catalysts, Surf. Sci. Rep. **57**, 157–298 (2005)
11.27 G. Renaud, R. Lazzari, C. Revenant, A. Barbier, M. Noblet, O. Ulrich, F. Leroy, J. Jupille, Y. Borensztein, C.R. Henry, J.P. Deville, F. Scheurer, J. Mane-Mane, O. Fruchart: Real-time monitoring of growing nanoparticles, Science **300**, 1416–1419 (2003)
11.28 J. Yacaman, J.A. Ascencio, S. Tehuacanero, M. Marin: Modem applications of electron microscopy to catalysis, Top. Catal. **18**, 167–173 (2002)
11.29 B. Pauwels, G.V. Tendeloo, W. Bouwen, L.T. Kuhn, P. Lievens, H. Lei, M. Hou: Low-energy-deposited Au clusters investigated by high-resolution electron microscopy and molecular dynamics simulations, Phys. Rev. B **62**, 10383–10393 (2000)
11.30 M. Broyer, E. Cottancin, J. Lermé, M. Pellarin, N. Del Fatti, F. Valle, J. Burgin, C. Guillon, P. Langot: Optical properties and relaxation processes at femtosecond scale of bimetallic clusters, Faraday Discuss. **138**, 137–145 (2008)
11.31 A. Biswas, D. Siegel, D.N. Seidman: Simultaneous segregation at coherent and semicoherent heterophase interfaces, Phys. Rev. Lett. **105**, 076102 (2010)
11.32 F. Tao, M.E. Grass, Y. Zhang, D.R. Butcher, J.R. Renzas, Z. Liu, J.Y. Chung, B.S. Mun, M. Salmeron, G.A. Somorjai: Reaction-driven restructuring of Rh-Pd and Pt-Pd core-shell nanoparticles, Science **322**, 932–934 (2008)
11.33 R. Ferrando, A. Fortunelli, G. Rossi: Quantum effects on the structure of pure and binary metallic nanoclusters, Phys. Rev. B **72**, 085449 (2005)
11.34 I.S. Atanasov, M. Hou: A multi-range order parameter for binary alloy bulk materials and nanoparticles, Eur. Phys. J. D **52**, 51–54 (2009)
11.35 I.S. Atanasov, M. Hou: Equilibrium ordering properties of Au-Pd alloys and nanoalloys, Surf. Sci. **603**, 2639–2651 (2009)
11.36 G. Barcaro, A. Fortunelli, M. Polak, L. Rubinovich: Patchy multishell segregation in Pd-Pt alloy nanoparticles, NanoLett. **11**, 1766–1769 (2011)
11.37 L.O. Paz-Borbon, T.V. Mortimer-Jones, R.L. Johnston, A. Posada-Amarillas, G. Barcaro, A. Fortunelli: Structures and energetics of 98 atom Pd-Pt nanoalloys: Potential stability of the Leary tetrahedron for bimetallic nanoparticles, Phys. Chem. Chem. Phys. **9**, 5202–5208 (2007)
11.38 L. Molina, B. Hammer: Theoretical study of CO oxidation on Au nanoparticles supported by MgO(100), Phys. Rev. B **69**, 155424 (2004)
11.39 G. Barcaro, L. Sementa, F.R. Negreiros, R. Ferrando, A. Fortunelli: Interface effects on the magnetism of CoPt-supported nanostructures, Nano Lett. **11**, 5542–5547 (2011)
11.40 Y. Yin, A.P. Alivisatos: Colloidal nanocrystal synthesis and the organic-inorganic interface, Nature **437**, 664–670 (2005)
11.41 P.D. Cozzoli, T. Pellegrino, L. Manna: Synthesis, properties and perspectives of hybrid nanocrystal structures, Chem. Soc. Rev. **35**, 1195–1208 (2006)
11.42 J. Park, J. Joo, S.G. Kwon, Y. Jang, T. Hyeon: Synthesis of monodisperse spherical nanocrystals, Angew. Chem. Int. Ed. **46**, 4630–4660 (2007)
11.43 M. Rycenga, C.M. Cobley, J. Zeng, W. Li, C.H. Moran, Q. Zhang, D. Qin, Y. Xia: Controlling the synthesis and assembly of silver nanostructures for plasmonic applications, Chem. Rev. **111**, 3669–3712 (2011)
11.44 M.B. Cortie, A.M. McDonagh: Synthesis and optical properties of hybrid and alloy plasmonic nanoparticles, Chem. Rev. **111**, 3713–3735 (2011)
11.45 M.R. Jones, K.D. Osberg, R.J. Macfarlane, M.R. Langille, C.A. Mirkin: Templated techniques for the synthesis and assembly of plasmonic nanostructures, Chem. Rev. **111**, 3736–3827 (2011)
11.46 M. Brust, J. Fink, D. Bethell, D.J. Schiffrin, C.J. Kiely: Synthesis and reactions of functionalised gold nanoparticles, J. Chem. Soc. Chem. Commun., 1655–1656 (1995)
11.47 X. Peng, J. Wickham, A.P. Alivisatos: Kinetics of II-VI and III-V colloidal semiconductor nanocrystal growth: "Focusing" of size distributions, J. Am. Chem. Soc. **120**, 5343–5344 (1998)

11.48 Y. Xia, Y. Xiong, B. Lim, S.E. Skrabalak: Shape-controlled synthesis of metal nanocrystals: Simple chemistry meets complex physics?, Angew. Chem. Int. Ed. **48**, 60–103 (2009)

11.49 Q. Zhang, W. Li, C. Moran, J. Chen, L.P. Wen, Y. Xia: Seed-mediated synthesis of Ag nanocubes with controllable edge lengths in the range of 30–200 nm and comparison of their optical properties, J. Am. Chem. Soc. **132**, 11372–11378 (2010)

11.50 N.R. Jana, L. Gearheart, C.J. Murphy: Seed-mediated growth approach for shape-controlled synthesis of spheroidal and rod-like gold nanoparticles using a surfactant template, Adv. Mater. **13**, 1389–1393 (2001)

11.51 B. Pietrobon, M. McEachran, V. Kitaev: Synthesis of size-controlled faceted pentagonal silver nanorrods with tunable plasmonic properties and self-assembly of these nanorods, ACS Nano **3**, 21–26 (2009)

11.52 Y. Sun, Y. Yin, B.T. Mayers, T. Herricks, Y. Xia: Uniform silver nanowires synthesis by reducing $AgNO_3$ with ethylene glycol in the presence of seeds and poly(vinyl pyrrolidone), Chem. Mater. **14**, 4736–4745 (2002)

11.53 B. Nikoobakht, M.A. El-Sayed: Preparation and growth mechanism of gold nanorods (NRs) using seed-mediated growth method, Chem. Mater. **15**, 1957–1962 (2003)

11.54 G. Schmid: Large clusters and colloids – Metals in the embryonic state, Chem. Rev. **92**, 1709–1727 (1992)

11.55 O. Lopez-Acevedo, J. Akola, R.L. Whetten, H. Grönbeck, H. Häkkinen: Structure and bonding in the ubiquitous icosahedral metallic gold cluster $Au_{144}(SR)_{60}$, J. Phys. Chem. C **113**, 5035–5038 (2009)

11.56 H. Qian, R. Jin: Controlling nanoparticles with atomic precision: The case of $Au_{144}(SCH_2CH_2Ph)_{60}$, Nano Lett. **9**, 4083–4087 (2009)

11.57 G. Periyasamy, F. Remacle: Ligand and solvation effects on the electronic properties of Au_55 clusters: A density functional theory study, Nano Lett. **9**, 3007–3011 (2009)

11.58 M. Walter, J. Akola, O. Lopez-Acevedo, P.D. Jadzinsky, G. Calero, C.J. Ackerson, R.L. Whetten, H. Grönbeck, H. Häkkinen: A unified view of ligand-protected gold clusters as superatom complexes, Proc. Natl. Acad. Sci. USA **105**, 9157–9162 (2008)

11.59 J. Akola, M. Walter, R.L. Whetten, H. Hakkinen, H. Grönbeck: On the structure of thiolate-protected Au-25, J. Am. Chem. Soc. **130**, 3756 (2008)

11.60 M.L. Personick, M.R. Langille, J. Zhang, C.A. Mirkin: Shape control of gold nanoparticles by silver underpotential deposition, Nano Lett. **11**, 3394–3398 (2011)

11.61 S. Sun, C.B. Murray, D. Weller, L. Folks, A. Moser: Monodisperse FePt nanoparticles and ferromagnetic FePt nanocrystal superlattices, Science **287**, 1989–1992 (2000)

11.62 M.P. Mallin, C.J. Murphy: Solution-phase synthesis of sub-10 nm Au-Ag alloy nanoparticles, Nano Lett. **2**, 1235–1237 (2002)

11.63 S. Link, Z.L. Wang, M.A. El-Sayed: Alloy formation of gold-silver nanoparticles and the dependence of the plasmon absorption on their composition, J. Phys. Chem. B **103**, 3529 (1999)

11.64 R. Costi, A.E. Saunders, U. Banin: Colloidal hybrid nanostructures: A new type of functional materials, Angew. Chem. Int. Ed. **49**, 4878–4897 (2010)

11.65 H. Zeng, S. Sun: Syntheses, properties and potential applications of multicomponent magnetic nanoparticles, Adv. Funct. Mater. **18**, 391–400 (2008)

11.66 R.P. Sear: Heterogeneous and homogeneous nucleation compared: Rapid nucleation on microscopic impurities, J. Phys. Chem. B **110**, 4985–4989 (2006)

11.67 S.E. Habas, J. Lee, V. Radmilovic, G.A. Somorjai, P. Yang: Shaping binary metal nanocrystals through epitaxial seeded growth, Nat. Mater. **6**, 692–697 (2007)

11.68 R. Jin, Y.W. Cao, C.A. Mirkin, K.L. Kelly, G.C. Schatz, J.G. Zheng: Photoinduced conversion of silver nanospheres to nanoprisms, Science **294**, 1901–1903 (2001)

11.69 Y. Sun, B.T. Mayers, Y. Xia: Template-engaged replacement reaction: A one-step approach to the large-scale synthesis of metal nanostructures with hollow interiors, Nano Lett. **2**, 481–485 (2002)

11.70 Y. Sun, Y. Xia: Mechanistic study on the replacement reaction between silver nanostructures and chloroauric acid in aqueous medium, J. Am. Chem. Soc. **126**, 3892–3901 (2004)

11.71 Y. Xia, W. Li, C.M. Cobley, J. Chen, X. Xia, Q. Zhang, M. Yang, E. Chul Cho, P.K. Brown: Gold nanocages: From synthesis to theranostic applications, Acc. Chem. Res. **44**, 914–924 (2011)

11.72 J. Chen, B. Wiley, J. McLellan, Y. Xiong, Z.Y. Li, Y. Xia: Optical properties of Pd-Ag and Pt-Ag nanoboxes synthesized via galvanic replacement reactions, Nano Lett. **5**, 2058–2062 (2005)

11.73 X. Lu, L. Au, J. McLellan, Z.Y. Li, M. Marquez, Y. Xia: Fabrication of cubic nanocages and nanoframes by dealloying Au/Ag alloy nanoboxes with an aqueous etchant based on $Fe(NO_3)_3$ or NH_4OH, Nano Lett. **7**, 1764–1769 (2007)

11.74 Y.S. Shon, G.B. Dawson, M. Porter, R.W. Murray: Monolayer-protected bimetal cluster synthesis by core metal galvanic exchange reaction, Langmuir **18**, 3880–3885 (2002)

11.75 T. Huang, R.W. Murray: Luminescence of tiopronin monolayer-protected silver clusters changes to that of gold clusters upon galvanic core metal exchange, J. Phys. Chem. B **107**, 7434–7440 (2003)

11.76 Q. Zhang, J. Xie, J. Liang, J.Y. Lee: Synthesis of Monodisperse Ag-Au Alloy Nanoparticles with Independently Tunable Morphology, Composition, Size, and Surface Chemistry and Their 3-D Superlattices, Adv. Funct. Mater. **19**, 1387–1398 (2009)

11.77 Y. Sun, B. Wiley, Z.Y. Li, Y. Xia: Synthesis and optical properties of nanorattles and multiple-walled nanoshells/nanotubes made of metal alloys, J. Am. Chem. Soc. **126**, 9399–9406 (2004)

11.78 M. Harada, K. Asakura, N. Toshima: Catalytic activity and structural-analysis of polymer-protected Au/Pd bimetallic clusters prepared by the successive reduction of $HAuCl_4$ and $PdCl_2$, J. Phys. Chem. **97**, 5103–5114 (1993)

11.79 N. Toshima, T. Yonezawa: Bimetallic nanoparticles – Novel materials for chemical and physical applications, N. J. Chem. **22**, 1179–1201 (1998)

11.80 C.J. Kiely, J. Fink, M. Brust, D. Bethell, D.J. Schiffrin: Spontaneous ordering of bimodal ensembles of nanoscopic gold clusters, Nature **396**, 444–446 (1998)

11.81 M.P. Pileni: 2D superlattices and 3D supracrystals of metal nanocrystals: A new scientific adventure, J. Mater. Chem. **21**, 16748–16758 (2011)

11.82 C.J. Kiely, J. Fink, J.G. Zheng, M. Brust, D. Bethell, D.J. Schiffrin: Ordered colloidal nanoalloys, Adv. Mater. **12**, 640–643 (2000)

11.83 G.C. Bond: *Heterogeneous Catalysis*, 3rd edn. (Oxford Univ., Oxford 1987)

11.84 J.M. Thomas, W.J. Thomas: *Principle and practice of heterogeneous catalysis* (VCH, Weinheim 1997)

11.85 G. Ertl, H.J. Freund: Catalysis and surface science, Phys. Today **52**, 32–38 (1999)

11.86 D.W. Goodman: Model studies in catalysis using surface science probes, Chem. Rev. **95**, 523–536 (1995)

11.87 P.L.J. Gunter, G. Somorjai: Surface science approach to modeling supported catalysts, Catal. Rev. **39**, 77–168 (1997)

11.88 R. Imbihl, G. Ertl: Oscillatory kinetics in heterogeneous catalysis, Chem. Rev. **95**, 697–733 (1995)

11.89 C.R. Henry: Surface studies of supported model catalysts, Surf. Sci. Rep. **31**, 235–325 (1998)

11.90 H.J. Freund: Clusters and islands on oxides: From catalysis via electronics and magnetism to optics, Surf. Sci. **500**, 271–299 (2002)

11.91 C.R. Henry: Morphology of supported nanoparticles, Prog. Surf. Sci. **80**, 92–116 (2005)

11.92 M. Sterrer, E. Fischbach, T. Risse, H.J. Freund: Geometric characterization of a singly charged oxygen vacancy on a single-crystalline MgO(001) film by electron paramagnetic resonance spectroscopy, Phys. Rev. Lett., **94**, 186101 (2005)

11.93 H. Brune, M. Giovannini, K. Bromann, K. Kern: Self-organized growth of nanostructure arrays on strain-relief patterns, Nature **394**, 451–453 (1998)

11.94 H. Brune: Microscopic view of epitaxial metal growth: Nucleation and aggregation, Surf. Sci. Rep. **31**, 121–229 (1998)

11.95 L. Gavioli, E. Cavaliere, S. Agnoli, G. Barcaro, A. Fortunelli, G. Granozzi: Template-assisted assembly of transition metal nanoparticles on oxide ultrathin films, Prog. Surf. Sci., **86**, 59–81 (2011)

11.96 R. Imbihl, R.J. Behm, R. Schlogl: Bridging the pressure and material gap in heterogeneous catalysis, Phys. Chem. Chem. Phys. **9**, 3459 (2007)

11.97 G.A. Somorjai, R.L. York, D. Butcher, J.Y. Park: The evolution of model catalytic systems; studies of structure, bonding and dynamics from single crystal metal surfaces to nanoparticles, and from low pressure ($< 10^{-3}$ Torr) to high pressure ($> 10^{-3}$ Torr) to liquid interfaces, Phys. Chem. Chem. Phys. **9**, 3500–3513 (2007)

11.98 G.A. Somorjai, G. Rupprechter: Molecular studies of catalytic reactions on crystal surfaces at high pressures and high temperatures by infrared-visible sum frequency generation (SFG) surface vibrational spectroscopy, J. Phys. Chem. B **103**, 1623–1638 (1999)

11.99 T. Dellwig, G. Rupprechter, H. Unterhalt, H. J. Freund: Bridging the pressure and materials gaps: High pressure sum frequency generation study on supported Pd nanoparticles, Phys. Rev. Lett. **85**, 776–779 (2000)

11.100 S. Giorgio, S.S. Joao, S. Nitsche, D. Chaudanson, G. Sitja, C.R. Henry: Environmental electron microscopy (ETEM) for catalysts with a closed E-cell with carbon windows, Ultramicroscopy **106**, 503–507 (2006)

11.101 C. Barth, A.S. Foster, C.R. Henry, A.L. Shluger: Recent trends in surface characterization and chemistry with high-resolution scanning force methods, Adv. Mater. **23**, 477–501 (2011)

11.102 O.H. Pakarinen, C. Barth, A.S. Foster, N.M. Nieminen, C.R. Henry: High-resolution scanning force microscopy of gold nanoclusters on the KBr(001) surface, Phys. Rev. B **73**, 235428 (2006)

11.103 J. Evans, A. Puig-Molina, M. Tromp: In situ EXAFS characterization of nanoparticulate catalysts, MRS Bull. **32**, 1038–1043 (2007)

11.104 O. Ducreux, B. Rebours, J. Lynch, M. Roy-Auberger, D. Bazin: Microstructure of supported cobalt Fischer–Tropsch Catalysts, Oil Gas Sci. Technol. **64**, 49–62 (2009)

11.105 J.D. Grunwaldt, B.S. Clausen: Combining XRD and EXAFS with on-line catalytic studies for in situ characterization of catalysts, Top. Catal. **18**, 37–43 (2002)

11.106 N.A. Khan, A. Uhl, S. Shaikhutdinov, H.J. Freund: Alumina supported model Pd–Ag catalysts: A combined STM, XPS, TPD and IRAS study, Surf. Sci. **600**, 1849–1853 (2006)

11.107 B.J. McIntyre, M. Salmeron, G.A. Somorjai: A variable pressure/temperature scanning tunneling

microscope for surface science and catalysis studies, Rev. Sci. Instrum. **64**, 687–691 (1993)
11.108 L. Guczi, D. Bazin, I. Kovacs, L. Borko, Z. Schay, J. Lynch, P. Parent, C. Lafon, G. Stefler, Z. Koppany, I. Sajo: Structure of Pt–Co/Al_2O_3 and Pt–Co/NaY bimetallic catalysts: Characterization by in situ EXAFS, TPR, XPS and by activity in Co (carbon monoxide) hydrogenation, Top. Catal. **20**, 129–139 (2002)
11.109 M. Salmeron, R. Schlögl: Ambient pressure photoelectron spectroscopy: A new tool for surface science and nanotechnology, Surf. Sci. Rep. **63**, 169–199 (2008)
11.110 S. Agnoli, G. Barcaro, A. Barolo, A. Fortunelli, M. Sambi, F. Sedona, M. Marino, T. Di Skala, G. Granozzi: Interplay between layer-resolved chemical composition and electronic structure in a Sn/Pt(110) surface alloy, J. Phys. Chem. C **115**, 14264–14269 (2011)
11.111 P. Nolte, A. Stierle, O. Balmes, V. Srot, P.A. van Aken, L.P.H. Jeurgens, H. Dosch: Carbon incorporation and deactivation of MgO(001) supported Pd nanoparticles during CO oxidation, Catal. Today **145**, 243–250 (2009)
11.112 P.L. Gai, E.D. Boyes, S. Helveg, P.L. Hansen, S. Giorgio, C.R. Henry: Atomic-resolution environmental transmission electron microscopy for probing gas–solid reactions in heterogeneous catalysis, MRS Bull. **32**, 1044–1050 (2007)
11.113 Z.Y. Li, J.P. Wilcoxon, F. Yin, Y. Chen, R.E. Palmer, R.L. Johnston: Structures and optical properties of 4–5 nm bimetallic AgAu nanoparticles, Faraday Discuss. **138**, 363–373 (2008)
11.114 B.A. Korgel, D.C. Lee, T. Hanrath, M. José-Yacaman, A. Thesen, M. Matijevic, R. Kilaas, C. Kisielowski, A.C. Diebold: Application of aberration-corrected TEM and image simulation to nanoelectronics and nanotechnology, IEEE Trans. Semicond. Manuf. **19**, 391–396 (2006)
11.115 Z.Y. Li, N.P. Young, M. Di Vece, S. Palomba, R.E. Palmer, A.L. Bleloch, B.C. Curley, R.L. Johnston, J. Jiang, J. Yuan: Three-dimensional atomic-scale structure of size-selected gold nanoclusters, Nature **451**, 46–48 (2008)
11.116 P.L.B. Hansen, J. Wagner, S. Helveg, J.R. Rostrup-Nielsen, B.S. Clausen, H. Topsoe: Atom-resolved imaging of dynamic shape changes in supported copper nanocrystals, Science **295**, 2053–2055 (2002)
11.117 G. Rupprechter: Sum frequency laser spectroscopy during chemical reactions on surfaces, MRS Bull. **32**, 1031–1037 (2007)
11.118 D. Belic, R.L. Chantry, Z.Y. Li, S.A. Brown: Ag-Au nanoclusters: Structure and phase segregation, App. Phys. Lett. **99**, 171914 (2011)
11.119 M. Baumer, J. Libuda, K.M. Neyman, N. Rosch, G. Rupprechter, H.J. Freund: Adsorption and reaction of methanol on supported palladium catalysts: Microscopic-level studies from ultrahigh vacuum to ambient pressure conditions, Phys. Chem. Chem. Phys. **9**, 3541–3548 (2007)
11.120 O. Seiferth, K. Wolter, B. Dillmann, G. Klivenyi, H.J. Freund, D. Scarano, A. Zecchina: IR investigations of CO_2 adsorption on chromia surfaces: Cr_2O_3 (0001)/Cr(110) versus polycrystalline α-Cr_2O_3, Surf. Sci. **421**, 176–190 (1999)
11.121 M. Yulikov, M. Sterrer, T. Risse, H.J. Freund: Gold atoms and clusters on MgO(100) films; an EPR and IRAS study, Surf. Sci. **603**, 1622–1628 (2009)
11.122 F. Baletto, R. Ferrando: Structural properties of nanoclusters: Energetic, thermodynamic, and kinetic effects, Rev. Mod. Phys. **77**, 371–423 (2005)
11.123 L.D. Marks: Experimental studies of small particle structures, Rep. Prog. Phys. **57**, 603–649 (1994)
11.124 G. Wulff: On the question of speed of growth and dissolution of crystal surfaces, Z. Krystallogr. **34**, 449–530 (1901)
11.125 R. Ferrando, G. Rossi, F. Nita, G. Barcaro, A. Fortunelli: Interface-stabilized phases of metal-on-oxide nanodots, ACS Nano **2**, 1849–1856 (2008)
11.126 F. Baletto, R. Ferrando, A. Fortunelli, F. Montalenti, C. Mottet: Crossover among structural motifs in transition and noble-metal clusters, J. Chem. Phys. **116**, 3856–3863 (2002)
11.127 D.J. Wales, J.P.K. Doye, A. Dullweber, M.P. Hodges, F.Y. Naumkin, F. Calvo, J. Hernandez-Rojas, T.F. Middleton: The Cambridge Cluster Database, http://www-wales.ch.cam.ac.uk/CCD.html
11.128 G. Rossi, A. Rapallo, C. Mottet, A. Fortunelli, F. Baletto, R. Ferrando: Magic polyicosahedral core-shell clusters, Phys. Rev. Lett. **93**, 105503 (2004)
11.129 J.P.K.L. Doye Meyer: Mapping the magic numbers in binary Lennard-Jones clusters, Phys. Rev. Lett. **95**, 063401 (2005)
11.130 S.M. Ghazi, S. Zorriasatein, D.G. Kanhere: Building clusters atom-by-Atom: From local order to global order, J. Phys. Chem. A **113**, 2659–2662 (2009)
11.131 A. Rapallo, G. Rossi, R. Ferrando, A. Fortunelli, B. Curley, L. Lloyd, G. Tarbuck, R. Johnston: Global optimization of bimetallic cluster structures. I. Size-mismatched Ag-Cu, Ag-Ni, and Au-Cu systems, J. Chem. Phys. **122**, 194308 (2005)
11.132 G. Rossi, R. Ferrando, A. Rapallo, A. Fortunelli, B. Curley, L. Lloyd, R. Johnston: Global optimization of bimetallic cluster structures. II. Size-matched Ag-Pd, Ag-Au, and Pd-Pt systems, J. Chem. Phys. **122**, 194309 (2005)
11.133 F.C. Frank, J.S. Kasper: Complex alloy structures regarded as sphere packing 1: Definitions and basic principles, Acta Cryst. **11**, 184–190 (1958)
11.134 D. Shechtman, I. Blech, D. Gratias, J.W. Cahn: Metallic phase with long-range orientational order and no translational symmetry, Phys. Rev. Lett. **53**, 1951–1953 (1984)

11.135 B. Dubost, J.M. Lang, M. Tanaka, P. Sainfort, M. Audier: Large AlCuLi single quasicrystals with triacontahedral solidification morphology, Nature **324**, 48–50 (1986)

11.136 R.H. Doye, J.P.K. Doye: Tetrahedral global minimum for the 98-atom Lennard-Jones cluster, Phys. Rev. E **60**, R6320–R6322 (1999)

11.137 L.O. Paz-Borbon, R.L. Johnston, G. Barcaro, A. Fortunelli: Structural motifs, mixing, and segregation effects in 38-atom binary clusters, J. Chem. Phys. **128**, 134517 (2008)

11.138 L.O. Paz-Borbon, R.L. Johnston, G. Barcaro, A. Fortunelli: A mixed structural motif in 34-atom Pd-Pt clusters, J. Phys. Chem. C **111**, 2936–2941 (2007)

11.139 H. Häkkinen, M. Moseler, U. Landman: Bonding in Cu, Ag, and Au clusters: Relativistic effects, trends, and surprises, Phys. Rev. Lett. **89**, 033401 (2002)

11.140 J.H. Sinfelt: Structure of metal catalysts, Rev. Mod. Phys. **51**, 569–589 (1979)

11.141 S. Bulusu, X. Li, L.S. Wang, X.C. Zeng: Evidence of hollow golden cages, Proc. Natl. Acad. Sci. USA **103**, 8326–8330 (2006)

11.142 N. Veldeman, E. Janssens, K. Hansen, J. De Haeck, R.E. Silverans, P. Lievens: Stability and dissociation pathways of doped Au_nX^+ clusters (X = Y, Er, Nb), Faraday Discuss. **138**, 147–162 (2008)

11.143 R. Ferrando, G. Rossi, A.C. Levi, Z. Kuntová, F. Nita, G. Barcaro, A. Fortunelli, A. Jelea, C. Mottet, J. Goniakowski: Structures of metal nanoparticles adsorbed on MgO(001). I. Ag and Au, J. Chem. Phys. **130**, 174702 (2009)

11.144 J. Goniakowski, A. Jelea, C. Mottet, G. Barcaro, A. Fortunelli, Z. Kuntová, F. Nita, A.C. Levi, G. Rossi, R. Ferrando: Structures of metal nanoparticles adsorbed on MgO(001). II. Pt and Pd, J. Chem. Phys. **130**, 174703 (2009)

11.145 O. Robach, G. Renaud, A. Barbier: Structure and morphology of the Ag/MgO(001) interface during in situ growth at room temperature, Phys. Rev. B **60**, 5858–5871 (1998)

11.146 C. Revenant, G. Renaud, R. Lazzari, J. Jupille: Growth of Ag on MgO(001) studied in situ by grazing incidence small angle X-ray scattering, Nucl. Instrum. Methods B **246**, 112–117 (2006)

11.147 K. Højrup Hansen, T. Worren, S. Stempel, E. Lægsgaard, M. Bäumer, H.J. Freund, F. Besenbacher, I. Stensgaard: Palladium nanocrystals on Al_2O_3: Structure and adhesion energy, Phys. Rev. Lett. **83**, 4120–4123 (1999)

11.148 J. Olander, R. Lazzari, J. Jupille, B. Mangili, J. Goniakowski, G. Renaud: Size- and temperature-dependent epitaxy for a strong film-substrate mismatch: The case of Pt/MgO(001), Phys. Rev. B **76**, 075409 (2007)

11.149 W. Tian, H.P. Sun, X.Q. Pan, J.H. Yu, M. Yeadon, C.B. Boothroyd, Y.P. Feng, R.A. Lukaszew, R. Clarke: Hexagonal close-packed Ni nanostructures grown on the (001) surface of MgO, Appl. Phys. Lett. **86**, 131915 (2005)

11.150 G. Barcaro, A. Fortunelli, G. Rossi, F. Nita, R. Ferrando: Epitaxy, truncations, and overhangs in palladium nanoclusters adsorbed on MgO(001), Phys. Rev. Lett. **98**, 156101 (2007)

11.151 R. Ferrando, G. Barcaro, A. Fortunelli: Surface-supported gold cages, Phys. Rev. Lett. **102**, 216102 (2009)

11.152 G. Barcaro, R. Ferrando, A. Fortunelli, G. Rossi: Exotic supported CoPt nanostructures: From clusters to wires, J. Phys. Chem. Lett. **1**, 111–115 (2010)

11.153 L. Favre, V. Dupuis, E. Bernstein, P. Melinon, A. Perez: Structural and magnetic properties of CoPt mixed clusters, Phys. Rev. B **74**, 014439 (2006)

11.154 Y. Gauthier, M. Schmid, S. Padovani, E. Lundgren, V. Bus, G. Kresse, J. Redinger, P. Varga: Adsorption sites and ligand effect for CO on an alloy surface: A direct view, Phys. Rev. Lett. **87**, 036103 (2001)

11.155 E. Aprà , F. Baletto, R. Ferrando, A. Fortunelli: Amorphization mechanism of icosahedral metal nanoclusters, Phys. Rev. Lett. **93**, 065502 (2004)

11.156 M.E. Gruner, G. Rollmann, P. Entel, M. Farle: Multiply twinned morphologies of FePt and CoPt nanoparticles, Phys. Rev. Lett. **100**, 087203 (2008)

11.157 G. Rossi, R. Ferrando, C. Mottet: Structure and chemical ordering in CoPt nanoalloys, Faraday Discuss. **138**, 193–210 (2008)

11.158 J. Penuelas, P. Andreazza, C. Andreazza-Vignolle, H.C.N. Tolentino, M. De Santis, C. Mottet: Controlling structure and morphology of CoPt nanoparticles through dynamical or static coalescence effects, Phys. Rev. Lett. **100**, 115502 (2008)

11.159 D. Ferrer, A. Torres-Castro, X. Gao, S. Sepúlveda-Guzmán, U. Ortiz-Méndez, M. José-Yacamán: Three-layer core/shell structure in Au-Pd bimetallic nanoparticles, Nano Lett. **7**, 1701–1705 (2007)

11.160 L. Rubinovich, M. Polak: Prediction of distinct surface segregation effects due to coordination-dependent bond-energy variations in alloy nanoclusters, Phys. Rev. B **80**, 045404 (2009)

11.161 H.J. Freund: Model studies in heterogeneous catalysis, Chem. Eur. J. **16**, 9384–9397 (2010)

11.162 M. Sahimi, H. Hamzehpour: Efficient computational strategies for solving global optimization problems, Comput. Sci. Eng. **12**, 74–82 (2010)

11.163 R. Ferrando, A. Fortunelli, R.L. Johnston: Searching for the optimum structures of alloy nanoclusters, Phys. Chem. Chem. Phys. **10**, 640–649 (2008)

11.164 E. Aprá, R. Ferrando, A. Fortunelli: Density-functional global optimization of gold nanoclusters, Phys. Rev. B **73**, 205414 (2006)

11.165 G. Barcaro, E. Aprà , A. Fortunelli: Structure of Ag clusters grown on F_s-defect sites of an MgO(100) surface, Chem. Eur. J. **13**, 6408–6418 (2007)

11.166 G. Barcaro, A. Fortunelli: A magic Pd-Ag binary cluster on the F_s-Defected MgO(100) surface, J. Phys. Chem. C **111**, 11384–11389 (2007)

11.167 G. Barcaro, A. Fortunelli: A study of bimetallic Cu–Ag, Au–Ag and Pd–Ag clusters adsorbed on a double-vacancy-defected MgO(100) terrace, Faraday Disc. **138**, 37–47 (2008)

11.168 I.V. Yudanov, R. Sahnoun, K.M. Neyman, N. Rösch: Metal nanoparticles as models of single crystal surfaces and supported catalysts: Density functional study of size effects for CO/Pd(111), J. Chem. Phys. **117**, 9887–9896 (2002)

11.169 F.R. Negreiros, Z. Kuntová, G. Barcaro, G. Rossi, R. Ferrando, A. Fortunelli: Structures of gas-phase Ag–Pd nanoclusters: A computational study, J. Chem. Phys. **132**, 234703 (2010)

11.170 N. Toshima, Y. Shiraishi, T. Teranishi, M. Miyake, T. Tominaga, H. Watanabe, W. Brijoux, H. Bönnemann, G. Schmid: Various ligand-stabilized metal nanoclusters as homogeneous and heterogeneous catalysts in the liquid phase, Appl. Organomet. Chem. **15**, 178–196 (2001)

11.171 L. Vattuone, L. Savio, F. Pirani, D. Cappelletti, M. Okada, M. Rocca: Interaction of rotationally aligned and of oriented molecules in gas phase and at surfaces, Prog. Surf. Sci. **85**, 92–160 (2010)

11.172 S. Guerin, B.E. Hayden, C.E. Lee, C. Mormiche, J.R. Owen, A.E. Russell: Combinatorial electrochemical screening of fuel cell electrocatalysts, J. Comb. Chem. **6**, 149–158 (2004)

11.173 S. Guerin, B.E. Hayden, C.E. Lee, C. Mormiche, A.E. Russell: High-throughput synthesis and screening of ternary metal alloys for electrocatalysis, J. Phys. Chem. B **110**, 14355–14362 (2006)

11.174 J.K. Nørskov, T. Bligaard, J. Rossmeisl, C.H. Christensen: Towards the computational design of solid catalysts, Nat. Chem. **1**, 37–46 (2009)

11.175 J.K. Nørskov, T. Bligaard, A. Logadottir, S. Bahn, L.B. Hansen, M. Bollinger, H. Bengaard, B. Hammer, Z. Sljivancanin, M. Mavrikakis, Y. Xu, S. Dahl, C.J.H. Jacobsen: Universality in heterogeneous catalysis, J. Catal. **209**, 275–278 (2002)

11.176 B. Hammer, J.K. Norskov: Theoretical surface science and catalysis – Calculations and concepts, Adv. Catal. **45**, 71–129 (2000)

11.177 P. Sabatier: Hydrogénations et déshydrogénations par catalyse, Ber. Deutsch. Chem. Gesellschaft **44**, 1984–2001 (1911)

11.178 M.P. Andersson, T. Bligaard, A. Kustov, K.E. Larsen, J. Greeley, T. Johannessen, C.H. Christensen, J.K. Nørskov: Toward computational screening in heterogeneous catalysis: Pareto-optimal methanation catalysts, J. Catal. **239**, 501–506 (2006)

11.179 K.M. Bratlie, H. Lee, K. Komvopoulos, P. Yang, G.A. Somorjai: Platinum nanoparticle shape effects on benzene hydrogenation selectivity, Nano Lett. **7**, 3097–3101 (2007)

11.180 U. Heiz, F. Vanolli, A. Sanchez, W.D. Schneider: Size-dependent molecular dissociation on mass-selected, supported metal clusters, J. Am. Chem. Soc. **120**, 9668–9671 (1998)

11.181 L.M. Molina, S. Lee, K. Sell, G. Barcaro, A. Fortunelli, B. Lee, S. Seifert, R.E. Winans, J.W. Elam, M.J. Pellin, I. Barke, V. von Oeynhausen, Y. Lei, R.J. Meyer, J.A. Alonso, A.F. Rodriguez, A. Kleibert, S. Giorgio, C.R. Henry, K.H. Meiwes-Broer, S. Vajda: Size-dependent selectivity and activity of silver nanoclusters in the partial oxidation of propylene to propylene oxide and acrolein: A joint experimental and theoretical study, Catal. Today **160**, 116–130 (2011)

11.182 R.A. Van Santen: Complementary structure sensitive and insensitive catalytic relationships, Acc. Chem. Res. **42**, 57–66 (2009)

11.183 N. Nilius, T. Risse, S. Schauermann, S. Shaikhutdinov, M. Sterrer, H.J. Freund: Model studies in catalysis, Top. Catal. **54**, 4–12 (2011)

11.184 L. Vattuone, L. Savio, M. Rocca: Bridging the structure gap: Chemistry of nanostructured surfaces at well-defined defects, Surf. Sci. Rep. **63**, 101–168 (2008)

11.185 B.L. Kniep, T. Ressler, A. Rabis, F. Girgsdies, M. Baenitz, F. Steglich, R. Schlögl: Rational design of nanostructured copper–zinc oxide catalysts for the steam reforming of methanol, Angew. Chem. Int. Ed. **43**, 112–115 (2004)

11.186 T. Ressler, B.L. Kniep, I. Kasatkin, R. Schlögl: The microstructure of copper zinc oxide catalysts: Bridging the materials gap, Angew. Chem. Int. Ed. **44**, 4704–4707 (2005)

11.187 V. Johanek, M. Laurin, A.W. Grant, B. Kasemo, C.R. Henry, J. Libuda: Fluctuations and bistabilities on catalyst nanoparticles, Science **304**, 1639–1644 (2004)

11.188 D. Teschner, J. Borsodi, A. Wootsch, Z. Révay, M. Hävecker, A. Knop-Gericke, S.D. Jackson, R. Schlögl: The roles of subsurface carbon and hydrogen in palladium-catalyzed alkyne hydrogenation, Science **320**, 86–89 (2008)

11.189 M. Cabie, S. Giorgio, C.R. Henry, M. Rosa Axet, K. Philippot, B. Chaudret: Direct observation of the reversible changes of the morphology of Pt nanoparticles under gas environment, J. Phys. Chem. C **114**, 2160–2163 (2010)

11.190 F. Mittendorfer, N. Seriani, O. Dubay, G. Kresse: Morphology of mesoscopic Rh and Pd nanoparticles under oxidizing conditions, Phys. Rev. B **76**, 233413 (2007)

11.191 K. Zorn, S. Giorgio, E. Halwax, C.R. Henry, H. Grönbeck, G. Rupprechter: CO oxidation on technological Pd-Al_2O_3 catalysts: Oxidation state and activity, J. Phys. Chem. C **115**, 1103–1111 (2011)

11.192 M. Haruta: Novel gold catalysts for the oxidation of carbon monoxide at a temperature far below 0 °C, Chem. Lett. **16**, 405–409 (1987)

11.193 M. Haruta, N. Yamada, T. Kobayashi, S. Iijima: Gold catalysts prepared by coprecipitation for low-temperature oxidation of hydrogen and of carbon monoxide, J. Catal. **115**, 301–309 (1989)

11.194 M. Valden, X. Lai, D.W. Goodman: Onset of catalytic activity of gold clusters on titania with the appearance of nonmetallic properties, Science **281**, 1647–1650 (1998)

11.195 A. Stephen, K. Hashmi, G.J. Hutchings: Gold catalysis, Angew. Chem. Int. Ed. **45**, 7896–7936 (2006)

11.196 G.J. Hutchings, M. Haruta: A golden age of catalysis: A perspective, Appl. Catal. A **291**, 2–5 (2005)

11.197 G.C. Bond, C. Louis, D.T. Thomson: *Catalysis by Gold* (Imperial College, London 2006)

11.198 A.A. Herzing, C.J. Kiely, A.F. Carley, P. Landon, G.J. Hutchings: Identification of active gold nanoclusters on iron oxide supports for CO oxidation, Science **321**, 1331–1335 (2008)

11.199 D. Bazin: Bridging nanoscience and surface science to understand heterogeneous catalysis, Macromol. Res. **14**, 230–234 (2006)

11.200 Y. Lei, F. Mehmood, S. Lee, J.P. Greeley, B. Lee, S. Seifert, R.E. Winans, J.W. Elam, R.J. Meyer, P.C. Redfern, D. Teschner, R. Schlögl, M.J. Pellin, L.A. Curtiss, S. Vajda: Increased silver activity for direct propylene epoxidation via sub-nanometer size effects, Science **328**, 224–228 (2010)

11.201 F.R. Negreiros, E. Aprà , G. Barcaro, L. Sementa, S. Vajda, A. Fortunelli: A first-principles theoretical approach to heterogeneous nanocatalysis, Nanoscale **4**, 1208–1219 (2012)

11.202 S. Chretien, S.K. Buratto, H. Metiu: Catalysis by very small Au clusters, Curr. Opin. Solid State Mater. Sci. **11**, 62–75 (2007)

11.203 A.J. Dent, J. Evans, S.G. Fiddy, B. Jyoti, M.A. Newton, M. Tromp: Structure–performance relationships of Rh and RhPd alloy supported catalysts using combined EDE/DRIFTS/MS, Faraday Discuss. **138**, 287–300 (2008)

11.204 S.C. Parker, C.T. Campbell: Reactivity and sintering kinetics of Au/TiO(2)(110) model catalysts: Particle size effects, Top. Catal. **44**, 3–13 (2007)

11.205 M.C. Saint-Lager, I. Laoufi, A. Bailly, O. Robach, S. Garaudee, P. Dolle: Catalytic properties of supported gold nanoparticles: New insights into the size-activity relationship gained from in operando measurements, Faraday Discuss. **152**, 253–265 (2011)

11.206 J.K. Edwards, A.F. Carley, A.A. Herzing, C.J. Kiely, G.J. Hutchings: Direct synthesis of hydrogen peroxide from H_2 and O_2 using supported Au–Pd catalysts, Faraday Discuss. **138**, 225–239 (2008)

11.207 P. West, R.L. Johnston, G. Barcaro, A. Fortunelli: The effect of CO and H chemisorption on the chemical ordering of bimetallic clusters, J. Phys. Chem. C **114**, 19678–19686 (2010)

11.208 J.H. Sinfelt: Structure of bimetallic clusters, Acc. Chem. Res. **20**, 134–139 (1987)

11.209 J.H. Sinfelt: Supported "Bimetallic Cluster" Catalysts, J. Catal. **29**, 308–315 (1973)

11.210 J.A. Rodriguez, D.W. Goodman: The nature of the metal-metal bond in bimetallic surfaces, Science **257**, 897–903 (1992)

11.211 M. Cerbelaud, R. Ferrando, G. Barcaro, A. Fortunelli: Optimization of chemical ordering in AgAu nanoalloys, Phys. Chem. Chem. Phys. **13**, 10232–10240 (2011)

11.212 P.P. Wells, Y. Qian, C.R. King, R.J.K. Wiltshire, E.M. Crabb, L.E. Smart, D. Thompsett, A.E. Russel: To alloy or not to alloy? Cr modified Pt/C cathode catalysts for PEM fuel cells, Faraday Discuss. **138**, 273–285 (2008)

11.213 M.T.M. Koper, T.E. Shubina, R.A. van Santen: Periodic density functional study of co and oh adsorption on Pt-Ru alloy surfaces: Implications for CO tolerant fuel cell catalysts, J. Phys. Chem. B **106**, 686–692 (2002)

11.214 A.C.A. de Vooys, R.A. van Santen, J.A.R. van Veen: Electrocatalytic reduction of NO_3^- on palladium/copper electrodes, J. Mol. Catal. A – Chem. **154**, 203–215 (2000)

11.215 M. Chen, D. Kumar, C.-W. Yi, D.W. Goodman: The promotional effect of gold in catalysis by palladium-gold, Science **310**, 291–293 (2005)

11.216 D.I. Enache, J.K. Edwards, P. Landon, B. Solsona-Espriu, A.F. Carley, A.A. Herzing, M. Watanabe, C.J. Kiely, D.W. Knight, G.J. Hutchings: Solvent-free oxidation of primary alcohols to aldehydes using Au-Pd/ TiO_2 catalysts, Science **311**, 362–365 (2006)

11.217 A. Sandoval, A. Aguilar, C. Louis, A. Traverse, R. Zanella: Bimetallic Au–Ag/TiO_2 catalyst prepared by deposition–precipitation: High activity and stability in CO oxidation, J. Catal. **281**, 40–49 (2011)

11.218 E. Falletta, C. Della Pina, M. Rossi, Q. He, C.J. Kiely, G.J. Hutchings: Enhanced performance of the catalytic conversion of allyl alcohol to 3-hydroxypropionic acid using bimetallic gold catalysts, Faraday Discuss. **152**, 367–379 (2011)

11.219 J.M. Thomas, R.D. Adams, E.M. Boswell, B. Captain, H. Gronbeck, R. Raja: Synthesis, characterization, electronic structure and catalytic performance of bimetallic and trimetallic nanoparticles containing tin, Faraday Discuss. **138**, 301–315 (2008)

11.220 K.A. Willets, R.P. Van Duyne: Localized surface plasmon resonance spectroscopy and sensing, Annu. Rev. Phys. Chem. **58**, 267–297 (2007)

11.221 W. Goddard III, B. Merinova, A. van Duina, T. Jacoba, M. Blancoa, V. Molineroa, S.S. Janga, Y.H. Janga: Multi-paradigm multi-scale simulations for fuel cell catalysts and membranes, Mol. Simulat. **32**, 251–268 (2006)

11.222 K.D. Nielson, A.C.T. van Duin, J. Oxgaard, W.-Q. Deng, W.A. Goddard III: Development of the ReaxFF Reactive Force Field for Describing Transition Metal Catalyzed Reactions, with Application to the Initial Stages of the Catalytic Formation of Carbon Nanotubes, J. Phys. Chem. A **109**, 493–499 (2005)

11.223 G. Mie: Contributions to the optics of turbid media, particularly solutions of colloidal metals, Ann. Phys. **25**, 377–445 (1908)

11.224 http://pubs.acs.org/toc/chreay/111/6 (last accessed November 2012)

11.225 http://pubs.acs.org/page/vi/2011/plasmon_resonances.html (last accessed November 2012)

11.226 http://pubs.acs.org/page/ancac3/vi/3 (last accessed November 2012)

11.227 G.V. Hartland: Optical studies of dynamics in noble metal nanostructures, Chem. Rev. **111**, 3858–3887 (2011)

11.228 J.P. Desclaux, P. Pyykkö: Dirac–Fock one-centre calculations. The molecules CuH, AgH and AuH including p-type symmetry functions, Chem. Phys. Letters **39**, 300–303 (1976)

11.229 J. Zhao, A.O. Pinchuk, J.M. McMahon, S. Li, L.K. Ausman, A.L. Atkinson, G.C. Schatz: Methods for describing the electromagnetic properties of silver and gold nanoparticles, Acc. Chem. Res. **41**, 1710–1720 (2008)

11.230 B. T. Draine, P. J. Flatau: User Guide to the Discrete Dipole Approximation Code Ddscat 6.1, http://Arxiv.Org/Abs/Astro-Ph/0409262v2 (2004)

11.231 K.L. Kelly, E. Coronado, L.L. Zhao, G.C. Schatz: The optical properties of metal nanoparticles: The influence of size, shape, and dielectric environment, J. Phys. Chem. B **107**, 668–677 (2003)

11.232 C. Noguez: Surface plasmons on metal nanoparticles: The influence of shape and physical environment, J. Phys. Chem. C **111**, 3806–3819 (2007)

11.233 E. Ringe, J.M. McMahon, K. Sohn, C. Cobley, Y. Xia, J. Huang, G.C. Schatz, L.D. Marks, R.P. Van Duyne: Unraveling the effects of size, composition, and substrate on the localized surface plasmon resonance frequencies of gold and silver nanocubes: A systematic single-particle approach, J. Phys. Chem. C **114**, 12511–12516 (2010)

11.234 C.J. Murphy, T.K. Sau, A.M. Gole, C.J. Orendorff, J. Gao, L. Gou, S.E. Hunyadi, T. Li: Anisotropic metal nanoparticles: Synthesis, assembly, and optical applications, J. Phys. Chem. B **109**, 13857–13870 (2005)

11.235 P.K. Jain, K. Seok Lee, I.H. El-Sayed, M.A. El-Sayed: Calculated absorption and scattering properties of gold nanoparticles of different size, shape, and composition: Applications in biological imaging and biomedicine, J. Phys. Chem. B **110**, 7238–7248 (2006)

11.236 H. Baida, P. Billaud, S. Marhaba, D. Christofilos, E. Cottancin, A. Crut, J. Lermeì, P. Maioli, M. Pellarin, M. Broyer, N. Del Fatti, F. Vallée: Quantitative determination of the size dependence of surface plasmon resonance damping in single Ag@SiO_2 nanoparticles, Nano Lett. **9**, 3463–3469 (2009)

11.237 A. Moores, F. Goettmann: The plasmon band in noble metal nanoparticles: An introduction to theory and applications, New J. Chem. **30**, 1121–1132 (2006)

11.238 R. Ruppin: Surface modes of two spheres, Phys. Rev. B **26**, 3440–3444 (1982)

11.239 A. Zangwill, P. Soven: Density-functional approach to local-field effects in finite systems: Photoabsorption in the rare gases, Phys. Rev. A **21**, 1561–1572 (1980)

11.240 M.E. Casida: All-electron local and gradient-corrected density-functional calculations of NA_n dipole plorarizabilities for $n = 1 - 6$. In: *Recent Advances in Density-Functional Methods*, ed. by D.P. Chong (World Scientific, Singapore 1995)

11.241 W. Jacak, J. Krasnyj, J. Jacak, A. Chepok, L. Jacak, W. Donderowicz, D.Z. Hu, D.M. Schaadt: Undamped collective surface plasmon oscillations along metallic nanosphere chains, J. App. Phys. **108**, 084304 (2010)

11.242 K. Frey, J.C. Idrobo, M.L. Tiago, F. Reboredo, S. Öğüt: Quasiparticle gaps and exciton Coulomb energies in Si nanoshells: First-principles calculations, Phys. Rev. B **80**, 153411 (2009)

11.243 M. Quijada, A.G. Borisov, R. Díez Muiño: Time-dependent density functional calculation of the energy loss of antiprotons colliding with metallic nanoshells, Phys. Status Solidi (a) **205**, 1312–1316 (2008)

11.244 V.V. Kulish, P.M. Tomchuk: Optical properties of metal nanotubes and metal nanoshells, Surf. Sci. **602**, 1045–1052 (2008)

11.245 M. Harb, F. Rabilloud, D. Simon, A. Rydlo, S. Lecoultre, F. Conus, V. Rodrigues, C. Félix: Optical absorption of small silver clusters: Ag_n ($n = 4–22$), J. Chem. Phys. **129**, 194108 (2008)

11.246 O.D. Haberlen, S.C. Chung, M. Stener, N. Rosch: From clusters to bulk: A relativistic density functional investigation on a series of gold clusters Au_n, $n = 6, \ldots, 147$, J. Chem. Phys. **106**, 5189–5201 (1997)

11.247 R. Ahlrichs, S.D. Elliott: Clusters of aluminium, a density functional study, Phys. Chem. Chem. Phys. **1**, 13–21 (1999)

11.248 C.M. Aikens, S.Z. Li, G.C. Schatz: From discrete electronic states to plasmons: TDDFT optical absorption properties of Ag_n ($n = 10, 20, 35, 56, 84, 120$) tetrahedral clusters, J. Phys. Chem. C **112**, 11272–11279 (2008)

11.249 H.E. Johnson, C.M. Aikens: Electronic structure and TDDFT optical absorption spectra of silver nanorods, J. Phys. Chem. A **113**, 4445–4450 (2009)

11.250 N. Durante, A. Fortunelli, M. Broyer, M. Stener: Optical properties of Au nanoclusters from TD-DFT calculations, J. Phys. Chem. C **115**, 6277–6282 (2011)

11.251 G. Barcaro, M. Broyer, N. Durante, A. Fortunelli, M. Stener: Alloying effects on the optical properties of Ag-Au nanoclusters from TDDFT

calculations, J. Phys. Chem. C **115**, 24085–24091 (2011)
11.252 E. Cottancin, J. Lermé, M. Gaudry, M. Pellarin, J.-L. Vialle, M. Broyer: Size effects in the optical properties of AunAgnembedded clusters, Phys. Rev. B **62**, 5179–5185 (2000)
11.253 M. Broyer, E. Cottancin, J. Lermé, M. Pellarin, N. Del Fatti, F. Vallée, J. Burgin, C. Guillon, P. Langot: Optical properties and relaxation processes at femtosecond scale of bimetallic clusters, Faraday Discuss. **138**, 137–145 (2008)
11.254 M. Gaudry, J. Lermé, E. Cottancin, M. Pellarin, J.-L. Vialle, M. Broyer, B. Prével, M. Treilleux, P. Mélinon: Optical properties of $(Au_xAg_{1-x})_n$ clusters embedded in alumina: Evolution with size and stoichiometry, Phys. Rev. B **64**, 085407 (2001)
11.255 E. Cottancin, G. Celep, J. Lermé, M. Pellarin, J.R. Huntzinger, J.L. Vialle, M. Broyer: Optical properties of noble metal clusters as a function of the size: Comparison between experiments and a semi-quantal theory, Theor. Chem. Acc. **116**, 514–523 (2006)
11.256 C. Noguez, I.L. Garzon: Optically active metal nanoparticles, Chem. Soc. Rev. **38**, 757–771 (2009)
11.257 A. Sanchez-Castillo, C. Noguez, I.L. Garzon: On the origin of the optical activity displayed by chiral-ligand-protected metallic nanoclusters, J. Am. Chem. Soc. **132**, 1504–1505 (2010)
11.258 S. Zhang, H. Wei, K. Bao, U. Hakanson, N.J. Halas, P. Nordlander, H. Xu: Chiral surface plasmon polaritons on metallic nanowires, Phys. Rev. Lett. **107**, 096801 (2011)
11.259 D.I. Garcia-Gutierrez, C.E. Gutierrez-Wing, L. Giovanetti, J.M. Ramallo-López, F.G. Requejo, M. José-Yacaman: Temperature effect on the synthesis of Au-Pt bimetallic nanoparticles, J. Phys. Chem. B **109**, 3813–3821 (2005)
11.260 C. de Julian Fernandez, G. Mattei, E. Paz, R.L. Novak, L. Cavigli, L. Bogani, F.J. Palomares, P. Mazzoldi, A. Caneschi: Coupling between magnetic and optical properties of stable Au–Fe solid solution nanoparticles, Nanotechnology **21**, 165701 (2010)
11.261 C. Kumara, A. Dass: $(AuAg)_{144}(SR)_{60}$ alloy nanomolecules, Nanoscale **3**, 3064–3067 (2011)
11.262 J. Lermé, H. Baida, C. Bonnet, M. Broyer, E. Cottancin, A. Crut, P. Maioli, N. Del Fatti, F. Vallée, M. Pellarin: Size dependence of the surface plasmon resonance damping in metal nanospheres, J. Phys. Chem. Lett. **1**, 2922 (2010)
11.263 C.M. Aikens: Effects of core distances, solvent, ligand, and level of theory on the TDDFT optical absorption spectrum of the thiolate-protected Au_25 nanoparticle, J. Phys. Chem. A **113**, 10811–10817 (2009)
11.264 P.K. Jain, M.A. El-Sayed: Plasmonic coupling in noble metal nanostructures, Chem. Phys. Lett. **487**, 153–164 (2010)
11.265 S.M. Nie, S.R. Emery: Probing single molecules and single nanoparticles by surface-enhanced Raman scattering, S. R. Science **275**, 1102–1106 (1997)
11.266 C. Maurizio, E. Trave, G. Perotto, V. Bello, D. Pasqualini, P. Mazzoldi, G. Battaglin, T. Cesca, C. Scian, G. Mattei: Enhancement of the Er^{3+} luminescence in Er-doped silica by few-atom metal aggregates, Phys. Rev. B **83**, 195430 (2011)
11.267 E. Trave, G. Mattei, P. Mazzoldi, G. Pellegrini, C. Scian, C. Maurizio, G. Battaglin: Sub-nanometric metallic Au clusters as efficient Er^{3+} sensitizers in silica, Appl. Phys. Lett. **89**, 151121 (2006)
11.268 V. Giannini, A.I. Fernandez-Domínguez, S.C. Heck, S.A. Maier: Plasmonic nanoantennas: Fundamentals and their use in controlling the radiative properties of nanoemitters, Chem. Rev. **111**, 3888–3912 (2011)
11.269 M. Lessard-Viger, M. Rioux, L. Rainville, D. Boudreau: FRET enhancement in multilayer core-shell nanoparticles, Nano Lett. **9**, 3066–3071 (2009)
11.270 M.A.H. Muhammed, A.K. Shaw, S.K. Pal, T. Pradeep: Quantum clusters of gold exhibiting FRET, J. Phys. Chem. C **112**, 14324–14330 (2008)
11.271 M.G. Papadopoulos (Ed.): *Non-Linear Optical Properties of Matter: From Molecules to Condensed Phases* (Springer, Berlin 2006)
11.272 G. Bachelier, I. Russier-Antoine, E. Benichou, C. Jonin, P.F. Brevet: Multipolar second-harmonic generation in noble metal nanoparticles, J. Opt. Soc. Am. B **25**, 955–960 (2008)
11.273 M.A. Noginov, G. Zhu, V.I. Gavrilenko: Sensitized nonlinear emission of gold Nanoparticles, Opt. Express **15**, 15648–15655 (2007)
11.274 B.H. Sohn, J.M. Choi, S.I. Yoo, S.H. Yun, W.C. Zin, J.C. Jung, M. Kanehara, T. Hirata, T. Teranishi: Directed self-assembly of two kinds of nanoparticles utilizing monolayer films of diblock copolymer micelles, J. Am. Chem. Soc. **125**, 6368–6369 (2003)
11.275 G. Armelles, A. Cebollada, A. García-Martín, J.M. García-Martín, M.U. Gonzalez, J.B. Gonzalez-Díaz, E. Ferreiro-Vila, J.F. Torrado: Magnetoplasmonic nanostructures: Systems supporting both plasmonic and magnetic properties, J. Opt. A: Pure Appl. Opt. **11**, 114023–114033 (2009)
11.276 C. Wang, C. Xu, H. Zheng, S. Sun: Recent progress in syntheses and applications of Dumbbell-like nanoparticles, Adv. Mater. **21**, 3045–3052 (2009)
11.277 V.V. Temnov, G. Armelles, U. Woggon, D. Guzatov, A. Cebollada, A. Garcia-Martin, J.-M. Garcia-Martin, T. Thomay, A. Leitenstorfer, R. Bratschitsch: Active magneto-plasmonics in hybrid metal-ferromagnet structures, Nat. Photonics **4**, 107–111 (2010)
11.278 L. Bogani, L. Cavigli, C. Julián Fernández, P. Mazzoldi, G. Mattei, M. Gurioli, M. Dressel, D. Gatteschi: Photocoercivity of nano-stabilized Au:Fe superparamagnetic nanoparticles, Adv. Mater. **22**, 4054–4058 (2010)

11.279 G. Rollmann, M.E. Gruner, A. Hucht, R. Meyer, P. Entel, M.L. Tiago, J.R. Chelikowsky: Shellwise mackay transformation in iron nanoclusters, Phys. Rev. Lett. **99**, 083402 (2007)

11.280 A.I. Shapiro, P. Rooney, M. Tran, F. Hellman, K. Ring, K. Kavanagh, B. Rellinghauss, D. Weller: Growth-induced magnetic anisotropy and clustering in vapor-deposited Co-Pt alloy films, Phys. Rev. B **60**, 12826–12836 (1999)

11.281 O. Ersen, V. Parasote, V. Pierron-Bohnes, N.C. Cadeville, C. Ulhaq-Bouillet: Growth conditions to optimize chemical order and magnetic properties in molecular-beam-epitaxy-grown CoPt/MgO(001) thin films, J. Appl. Phys. **93**, 2987–2995 (2003)

11.282 J.J. Fisher: Dispersion strengthened ferritic alloy for use in liquid-metal fast breeder reactors, US Patent 4075010 (1978)

11.283 M.L. Hamilton, D.S. Gelles, R.J. Lobsinger, G.D. Johnson, W.F. Brown, M.M. Paxton, R.J. Puigh, C.R. Eiholzer, C. Martinez, M.A. Blotter: *Fabrication technological development of the oxide dispersion strengthened alloy MA957 for fast reactor applications. PNL-13168* (Pac. Northwest Lab, Richland, 2000)

11.284 A. Kimura, H.S. Cho, N. Toda, R. Kasada, K. Yutani, H. Kishimoto, N. Iwata: High burnup fuel cladding materials R&D for advanced nuclear systems: Nano-sized oxide dispersion strengthening steels, J. Nucl. Sci. Technol. **44**, 323–328 (2007)

11.285 R.L. Klueh, J.P. Shingledecker, R.W. Swindeman, D.T. Hoelzer: Oxide dispersion-strengthened steels: A comparison of some commercial and experimental alloys, J. Nucl. Mater. **341**, 103 (2005)

11.286 M. Rieth, M. Schirra, A. Falkenstein, P. Graf, S. Heger, H. Kempe, R. Lindau, H. Zimmermann: Eurofer97 tensile, charpy, creep, and structural tests, Forsch. Karlsruhe FZKA6911 (2003)

11.287 M.K. Miller, E.A. Kenik, K.F. Russell, L. Heatherley, D.T. Hoelzer, P.J. Maziasz: Atom probe tomography of nanoscale particles in ODS ferritic alloys, Mater. Sci. Eng. **A353**, 140 (2003)

11.288 M.J. Alinger: On the formation and stability of nanometer scale precipitates in ferritic alloys during processing and high temperature service. Ph.D. Thesis (Univ. Calif., Santa Barbara 2004)

11.289 M.J. Alinger, G.R. Odette, D.T. Hoelzer: *On the role of alloy composition and processing variables in nanofeature formation and dispersion strengthening in nanostructured ferritic alloys. Fusion Mater. Semiannual Prog. Rep. DOE-ER-0313/43* (DOE, Oak Ridge, 2008)

11.290 S. Ukai, S. Ohtsuka: Nano-mesoscopic structure control in 9Cr-ODS ferritic steels, Energy Mater. **2**, 26 (2007)

11.291 N. Akasaka, S. Yamashita, T. Yoshitake, S. Ukai, A. Kimura: Microstructural changes of neutron irradiated ODS ferritic and martensitic steels, J. Nucl. Mater. **329–333**, 1053 (2004)

11.292 S. Yamashita, N. Akasaka, S. Ukai, S. Ohnuki: Microstructural development of a heavily neutron-irradiated ODS ferritic steel (MA957) at elevated temperature, J. Nucl. Mater. **367–370**, 202 (2007)

11.293 H. Kishimoto, K. Yutani, R. Kasada, O. Hashitomi, A. Kimura: Heavy-ion irradiation effects on the morphology of complex oxide particles in oxide dispersion strengthened ferritic steels, J. Nucl. Mater. **367–370**, 179 (2007)

11.294 H.S. Cho, R. Kasada, A. Kimura: Effects of neutron irradiation on the tensile properties of high-Cr oxide dispersion strengthened ferritic steels, J. Nucl. Mater. **367–370**, 239 (2007)

11.295 K. Yutani, H. Kishimoto, R. Kasada, A. Kimura: Evaluation of helium effects on swelling behavior of oxide dispersion strengthened ferritic steels under ion irradiation, J. Nucl. Mater. **367–370**, 423 (2007)

11.296 A. Alamo, V. Lambard, X. Averty, M.H. Mathon: Assessment of ODS-14%Cr ferritic alloy for high temperature applications, J. Nucl. Mater. **329–333**, 333 (2004)

11.297 A. Alamo, J.L. Bertin, V.K. Shamardin, P. Wident: Mechanical properties of 9Cr martensitic steels and ODS-FeCr alloys after neutron irradiation at 325 °C up to 42 dpa, J. Nucl. Mater. **367–370**, 54 (2007)

11.298 B. Wilshire, T.D. Lieu: Deformation and damage processes during creep of Incoloy MA957, Mater. Sci. Eng. **A386**, 81 (2004)

11.299 Z. Oksiuta, N. Baluc: Microstructure and Charpy impact properties of 12–14Cr oxide-dispersion strengthened steels, J. Nucl. Mater. **374**, 178 (2008)

11.300 M. Klimiankou, R. Lindau, A. Moslang: Direct correlation between morphology of $(Fe,Cr)_{23}C_6$ precipitates and impact behavior of ODS steels, J. Nucl. Mater. **367–370**, 173 (2007)

11.301 R.L. Klueh, A.T. Nelson: Ferritic/martensitic steels for next-generation reactors, J. Nucl. Mater. **371**, 37 (2007)

11.302 R.L. Klueh, N. Hashimoto, P.J. Maziasz: New nanoparticle strengthened ferritic/martensitic steels by conventional thermo-mechanical treatment, J. Nucl. Mater. **367–370**, 48 (2007)

11.303 M.J. Alinger, G.R. Odette, D.T. Hoezler: The development and stability of Y-Ti-O nanoclusters in mechanically alloyed Fe-Cr based ferritic alloys, J. Nucl. Mater. **329–333**, 382 (2004)

11.304 M.J. Demkowicz, A. Misra, A.J. Caro: The role of interface structure in controlling high helium concentrations, Curr. Opin. Solid State Mater. Sci. **16**, 101–108 (2012)

11.305 R.L. Klueh, P.J. Maziasz, I.S. Kim, L. Heatherley, D.T. Hoelzer, N. Hashimoto, E.A. Kenik, K. Miyahara: Tensile and creep properties of an oxide dispersion-strengthened ferritic steel, J. Nucl. Mater. **307–311**, 773 (2002)

11.306 L. Hsiung, M.J. Fluss, S.J. Tumey, B.W. Choi, Y. Serruys, F. Willaime, A. Kimura: Formation mechanism and the role of nanoparticles in Fe–Cr ODS steels developed for radiation tolerance, Phys. Rev. **B82**, 184103 (2010)

11.307 L. Hsiung, M.J. Fluss, A. Kimura: Structure of oxide nanoparticles in Fe–16Cr MA/ODS ferritic steel, Mater. Lett. **64**, 1782 (2010)

11.308 L. Hsiung, M. Fluss, S. Tumey, J. Kuntz, B. El-Dasher, M. Wall, B. Choi, A. Kimura, F. Willaime, Y. Serruys: HRTEM study of oxide nanoparticles in K3-ODS ferritic steel developed for radiation tolerance, J. Nucl. Mater. **409**, 72 (2011)

11.309 C. Fazio: Innovative materials for Gen IV systems and transmutation facilities: The crosscutting research project GETMAT, Nucl. Eng. and Des. **241**, 3514 (2011)

11.310 D. Kaoumi, A. Motta, M. Kirk: Characterization and in-situ ion-irradiation of MA957 ODS steel, Trans. Am. Nucl. Soc. **98**, 1113 (2008)

11.311 G.R. Odette, D.T. Hoelzer: Irradiation-tolerant nanostructured ferritic alloys: Transforming He from a liability to an asset, J. Met. **62**, 84–92 (2010)

11.312 K.S. Kumar, H. Van Swygenhoven, S. Suresh: Mechanical behavior of nanocrystalline metals and alloys, Acta Mater. **51**, 5743 (2003)

11.313 M.A. Meyers, A. Mishra, D.J. Benson: Mechanical properties of nanocrystalline materials, Prog. Mater. Sci. **51**, 427 (2006)

11.314 K.S. Kumar, S. Suresh, M.F. Chisholm, J.A. Horton, P. Wang: Deformation of electrodeposited nanocrystalline nickel, Acta Mater. **51**, 387 (2003)

11.315 R. Schwaiger, B. Moser, M. Dao, N. Chollacoop, S. Suresh: Some critical experiments on the strain-rate sensitivity of nanocrystalline nickel, Acta Mater. **51**, 5159 (2003)

11.316 V. Yamakov, D. Wolf, S.R. Phillpot, A.K. Mukherjee, H. Gleiter: Deformation mechanism crossover and mechanical behaviour in nanocrystalline materials, Philos. Mag. Lett. **83**, 385 (2003)

11.317 A.C. Lund, C.A. Schuh: Strength asymmetry in nanocrystalline metals under multiaxial loading, Acta Mater. **53**, 3193 (2005)

11.318 J. Schiotz, K.W. Jacobsen: A maximum in the strength of nanocrystalline copper, Science **301**, 1357 (2003)

11.319 H. Van Swygenhoven, P.M. Derlet: Grain-boundary sliding in nanocrystalline fcc metals, Phys. Rev. **B64**, 224105 (2001)

11.320 L. Lu, Y.F.H. Shen, X. Chen, L.H. Qian: Ultrahigh strength and high electrical conductivity in copper, Science **304**, 422 (2004)

11.321 C.W. Nan, A. Tschope, S. Holten, H. Kliem, R. Birringer: Grain size-dependent electrical properties of nanocrystalline ZnO, J. Appl. Phys. **85**, 7735 (1999)

11.322 T. Suzuki, I. Kosacki, H.U. Anderson: Microstructure-electrical conductivity relationships in nanocrystalline ceria thin films, Solid State Ion. **151**, 111 (2002)

11.323 G.J. Herzer: Anisotropies in soft magnetic nanocrystalline alloys, Magn. Magn. Mater. **294**, 99 (2005)

11.324 M.E. McHenry, M.A. Willard, D.E. Laughlin: Amorphous and nanocrystalline materials for applications as soft magnets, Prog. Mater. Sci. **44**, 291 (1999)

11.325 D.C. Jiles: Recent advances and future directions in magnetic materials, Acta Mater. **51**, 5907 (2003)

11.326 G. Herzer: Nanocrystalline soft-magnetic materials, Phys. Scr. **T49A**, 307 (1993)

11.327 M.J. Aus, B. Szpunar, A.M. El-Sherik, U. Erb, G. Palumbo, K.T. Aust: Magnetic properties of bulk nanocrystalline Ni, Scr. Mater. **27**, 1639 (1992)

11.328 R. Grossinger, R. Sato, D. Holzer, M. Dahlgren: Properties, benefits and application of nanocrystalline structures in magnetic materials, Adv. Eng. Mater. **5**, 285 (2003)

11.329 L. Wang, J. Zhang, Y. Gao, L. Hu, T. Xu: Grain size effect in corrosion behavior of electrodeposited nanocrystalline Ni coatings in alkaline solution, Scr. Mater. **55**, 657 (2006)

11.330 S.H. Kim, K.T. Aust, F. Gonzalez, G. Palumbo: The corrosion behavior of nanocrystalline electrodeposits, Plat. Surf. Fin. **91**, 68 (2004)

11.331 K.M.S. Youssef, C.C. Koch, P.S. Fedkiw: Improved corrosion behavior of nanocrystalline zinc produced by pulse-current electrodeposition, Corros. Sci. **46**, 51 (2004)

11.332 E.O. Hall: The deformation and ageing of mild steels 2. Characteristics of the Luder deformation, Proc. R. Soc. B **64**, 742 (1951)

11.333 N.Q. Vo, R.S. Averback, P. Bellon, A. Caro: Limits of hardness at the nanoscale: Molecular dynamics simulations, Phys. Rev. B **78**, 241402 (2008)

11.334 A.H. Chokshi, A. Rosen, J. Karch, H. Gleiter: On the validity of the Hall–Petch relationship in nanocrystalline materials, Scr. Metall. **23**, 1679 (1989)

11.335 H. Gleiter: Nanocrystalline materials, Prog. Mater. Sci. **33**, 223 (1989)

11.336 H. Van Swygenhoven, M. Spaczer, A. Caro: Microscopic description of plasticity in computer generated metallic nanophase samples: A comparison between Cu and Ni, Acta Mater. **47**, 3117 (1999)

11.337 M. Dao, L. Lu, R.J. Asaro, J.T.M. De Hosson, E. Ma: Toward a quantitative understanding of mechanical behavior of nanocrystalline metals, Acta Mater. **55**, 4041 (2007)

11.338 J. Chen, L. Lu, K. Lu: Hardness and strain rate sensitivity of nanocrystalline Cu, Scr. Mater. **54**, 1913 (2006)

11.339 G.W. Nieman, J.R. Weertman, R.W. Siegel: Microhardness of nanocrystalline Palladium and Copper

produced by inert-gas condensation, Scr. Metall. **23**, 2013 (1989)
11.340 H. Chang, C.J. Altsetter, R.S. Averback: Characteristics of nanophase TiAl produced by inert gas condensation, J. Mater. Res. **7**, 2962 (1992)
11.341 P.G. Sanders, J.A. Eastman, J.R. Weertman: Elastic and tensile behavior of nanocrystalline copper and palladium, Acta Mater. **45**, 4019 (1997)
11.342 C.C. Koch, J. Narayan: Structure and mechanical properties of nanophase materials-theory and computer simulations vs. experiment, MRS Symp. Proc. No. 634 (Materials Research Society, Pittsburgh 2000), B5.1.1
11.343 V. Yamakov, D. Wolf, M. Salazar, S.R. Phillpot, H. Gleiter: Length-scale effects in the nucleation of extended dislocations in nanocrystalline Al by molecular-dynamics simulation, Acta Mater. **49**, 2713 (2001)
11.344 R.A. Lebensohn, E.M. Bringa, A. Caro: A viscoplastic micromechanical model for the yield strength of nanocrystalline materials, Acta Mater. **55**, 261 (2007)
11.345 N.Q. Vo, R.S. Averback, P. Bellon, S. Odunuga, A. Caro: Quantitative description of plastic deformation in nanocrystalline Cu: Dislocation glide versus grain boundary sliding, Phys. Rev. B **77**, 134108 (2008)
11.346 J.R. Trelewicz, C.A. Schuh: The Hall–Petch breakdown in nanocrystalline metals: A crossover to glass-like deformation, Acta Mater. **55**, 5948 (2007)
11.347 R.Z. Valiev, R.K. Islamgaliev, I.V. Alexandrov: Bulk nanostructured materials from severe plastic deformation, Prog. Mater. Sci. **45**, 103 (2000)
11.348 G. Wilde, G.P. Dinda, H. Rosner: Synthesis of bulk nanocrystalline materials by repeated cold rolling, Adv. Eng. Mater. **7**, 11 (2005)
11.349 F.H. Froes, O.N. Senkov, E.G. Baburaj: Synthesis of nanocrystalline materials – An overview, Mater. Sci. Eng. **A301**, 44 (2001)
11.350 R. Birringer: Nanocrystalline materials, Mater. Sci. Eng. **117**, 33 (1998)
11.351 B. Gunther, A. Kumpmann, H.D. Kunze: Secondary recrystallization effects in nanostructured elemental metals, Scr. Mater. **27**, 833 (1992)
11.352 T.R. Malow, C.C. Koch: Thermal stability of nanocrystalline materials, Mater. Sci. Forum **225–227**, 595 (1996)
11.353 T. Yamasaki, P. Schlossmacher, K. Ehrlich, Y. Ogino: Formation of amorphous electrodeposited Ni-W alloys and their nanocrystallization, Nanostruct. Mater. **10**, 375 (1998)
11.354 C.E. Krill, H. Ehrhardt, R. Birringer: Thermodynamic stabilization of nanocrystallinity, Z. Metallkd. **96**, 1134 (2005)
11.355 F. Ebrahimi, H.Q. Li: Grain growth in electrodeposited nanocrystalline fcc Ni-Fe alloys, Scr. Mater. **55**, 263 (2006)
11.356 A.A. Talin, E.A. Marquis, S.H. Goods, J.J. Kelly, M.K. Miller: Thermal stability of Ni-Mn electrodeposits, Acta Mater. **54**, 1935 (2006)
11.357 K.W. Liu, F. Muecklich: Thermal stability of nano-RuAl produced by mechanical alloying, Acta Mater. **49**, 395 (2001)
11.358 A. Caro, D. Farkas, E.M. Bringa, G.H. Gilmer, L.A. Zepeda-Ruiz: Effects of microalloying on the mobility and mechanical response of interfaces in nanocrystalline Cu, Mater. Sci. Forum **633/634**, 21 (2010)
11.359 E. Chassaing, M.P. Roumegas, M.F. Trichet: Electrodeposition of NiMo alloys with pulse reverse potentials, J. Appl. Electrochem. **25**, 667 (1995)
11.360 A.O. Aning, A. Wang, T.H. Courtney: Tungsten solution kinetics and amorphization of Ni in mechanically alloyed Ni-W alloys, Acta Mater. **41**, 165 (1993)
11.361 B.Y.C. Wu, P.J. Ferreira, C.A. Schuh: Nanostructured Ni-Co alloys with tailorable grain size and twin density, Met. Mater. Trans. **36A**, 1927 (2005)
11.362 F. Ebrahimi, H.Q. Li: Structure and properties of electrodeposited nanocrystalline fcc Ni-Fe alloy, Rev. Adv. Mater. Sci. **5**, 134 (2003)
11.363 T. Yamasaki, R. Tomohira, Y. Ogino, P. Schlossmacher, K. Ehrlich: Formation of ductile amorphous and nanocrystalline Ni-W alloys by electrodeposition, Plat. Surf. Finish. **87**, 148 (2000)
11.364 A.J. Detor, C.A. Schuh: Tailoring and patterning the grain size of nanocrystalline alloys, Acta Mater. **55**, 371–379 (2007)
11.365 N.Q. Vo, J. Schafer, R.S. Averback, K. Albe, Y. Ashkenazya, P. Bellon: Reaching theoretical strengths in nanocrystalline Cu by grain boundary doping, Scr. Mater. **65**, 660 (2011)
11.366 F.J. Humphreys, M. Hatherly: *Recrystallization and Related Annealing Phenomena*, 1st edn. (Pergamon, Tarrytown 1995)
11.367 R. Kirchheim: Grain coarsening inhibited by solute segregation, Acta Mater. **50**, 413 (2002)
11.368 F. Liu, R. Kirchheim: Nano-scale grain growth inhibited by reducing grain boundary energy through solute segregation, J. Cryst. Growth **264**, 385 (2004)
11.369 D. Gupta: Influence of solute segregation on grain-boundary energy and selfdiffusion, Metall. Trans. **8A**, 1431 (1977)
11.370 J. Weissmuller: Alloy effects in nanostructures, Nanostruct. Mater. **3**, 261 (1993)
11.371 A.J. Detor, M.K. Miller, C.A. Schuh: Solute distribution in nanocrystalline Ni-W alloys examined through atom probe tomography, Philos. Mag. **86**, 4459 (2006)
11.372 C.E. Krill, R. Klein, S. Janes, R. Birringer: Thermodynamic stabilization of grain boundaries in nanocrystalline alloys, Mater. Sci. Forum **179–181**, 443 (1995)

11.373 D.L. Beke, C. Cserhati, I.A. Szabo: Segregation inhibited grain coarsening in nanocrystalline alloys, J. Appl. Phys. **95**, 4996 (2004)
11.374 H. Arakawa, M. Aresta, J.N. Armor, M.A. Barteau, E.J. Beckman, A.T. Bell, J.E. Bercaw, C. Creutz, E. Dinjus, D.A. Dixon, K. Domen, D.L. DuBois, J. Eckert, E. Fujita, D.H. Gibson, W.A. Goddard, D.W. Goodman, J. Keller, G.J. Kubas, H.H. Kung, J.E. Lyons, L.E. Manzer, T.J. Marks, K. Morokuma, K.M. Nicholas, R. Periana, L. Que, J. Rostrup-Nielson, W.M.H. Sachtler, L.D. Schmidt, A. Sen, G.A. Somorjai, P.C. Stair, B.R. Stults, W. Tumas: Catalysis research of relevance to carbon management: Progress, challenges, and opportunities, Chem. Rev. **101**, 953–996 (2001)
11.375 X. Chen, S.S. Gambhir, J. Cheon: Theranostic nanomedicine, Acc. Chem. Res. **44**, 841 (2011)
11.376 T.W. Odom, C.L. Nehl: How gold nanoparticles have stayed in the light: The 3M's principle, ACS Nano **2**, 612–616 (2008)
11.377 N. Erathodiyil, J.Y. Ying: Functionalization of inorganic nanoparticles for bioimaging applications, Acc. Chem. Res. **44**, 925–935 (2011)
11.378 H. Gu, P.-L. Ho, K.W.T. Tsang, L. Wang, B. Xu: Using biofunctional magnetic nanoparticles to capture vancomycin-resistant enterococci and other gram-positive bacteria at ultralow concentration, J. Am. Chem. Soc. **125**, 15702–15703 (2003)
11.379 Y. Jun, J. Choi, J. Cheon: Heterostructured magnetic nanoparticles: Their versatility and high performance capabilities, Chem. Commun., 1203–1214 (2007)
11.380 D. Ho, X. Sun, S. Sun: Monodisperse magnetic nanoparticles for theranostic applications, Acc. Chem. Res. **44**, 875–882 (2011)
11.381 M.P. Melancon, M. Zhou, C. Li: Cancer theranostics with near-infrared light-activatable multimodal nanoparticles, Acc. Chem. Res. **44**, 947–956 (2011)

12. Magnetic Nanostructures: Synthesis, Properties, and Applications

Shashwat Shukla, Pratap Kumar Deheri, Raju V. Ramanujan

Advances in magnetic nanostructures are rapid in the field of science and technology due to the unique magnetic properties observed at the nanoscale such as superparamagnetism, enhanced magnetic moment, high saturation field, shape anisotropy, etc. The common morphologies of magnetic nanostructures are dots, nanoparticles, nanocrystals, nanowires, nanotubes, and thin films. With the emergence of new synthesis and fabrication techniques, magnetic nanomaterials with diverse shapes and sizes have been fabricated and their structure–property relationships established. Characterization techniques such as magnetic force microscopy (MFM), Lorentz microscopy, magnetometry based on superconducting quantum interference device (SQUID), and small-angle neutron scattering (SANS) have been utilized to study magnetism in nanostructures.

In this chapter, the magnetism of atoms is discussed and the effect of nanostructuring on magnetic properties is reviewed. Characteristic magnetic length scales are presented. When the size of magnetic materials, in at least one dimension, becomes comparable to characteristic magnetic length scales, size-specific magnetic properties such as superparamagnetism, remanence enhancement, random anisotropy, and giant magnetoresistance (GMR) effects are observed. The change in magnetic moment and anisotropy with dimensionality is discussed; e.g., broken symmetry at surfaces and interfaces may increase magnetic moment compared with the bulk counterpart. In nanostructured materials, shape and surface anisotropy is induced and thickness dependence of anisotropy is observed in thin films.

Magnetization reversal mechanisms and the use of micromagnetic modeling in establishing microstructure–property relationships are discussed. Magnetic nanostructures such as particles, nanowires, nanorings, thin films, and molecular nanomagnets are reviewed. Current trends in synthesis by physical (melt spinning, ball milling, sputtering, and molecular beam epitaxy (MBE)) and chemical (reduction, self-assembly, and electrodeposition) processes are outlined. The use of atomic force microscopy, Mössbauer spectroscopy, electron holography, scanning electron microscopy, and transmission electron microscopy is discussed. The magnetic properties of hard and soft nanostructured magnets are reviewed. Exchange-coupled nanocomposites and the GMR effect are also discussed. Applications of magnetic nanostructures in data storage and biomedical applications are summarized.

12.1 **Background** 474
12.2 **Atomic Origin of Magnetism** 475
12.2.1 Quantum Mechanics of Ferromagnetism 475
12.2.2 Atomic-Scale Magnetism and Exchange Effect 476
12.3 **Magnetic Length Scales and Origin of Nanomagnetic Behavior** 478
12.3.1 Domains in Fine Particles 478
12.3.2 Nanomagnetism 479
12.4 **Magnetic Nanostructures** 483
12.4.1 Processing of Magnetic Nanostructures 483
12.4.2 Characterization of Magnetic Nanostructures 488
12.4.3 Hard Magnetic Nanostructures 492
12.4.4 Soft Magnetic Nanostructures 498
12.4.5 GMR and Spin Valves 502
12.4.6 Applications 503
12.5 **Conclusions** 505
References 506

12.1 Background

Magnetic nanostructures are attracting considerable interest due to their unique properties and potential applications in storage, sensing, spintronic, and optoelectronic technologies. The magnetic properties of nanostructures are governed by several factors such as composition, shape, size, surface morphology, anisotropy, layer thickness, and molecular interactions. There is a dramatic change in magnetic properties when the size reduces to a critical magnetic length scale, such as the exchange length or domain wall width; e.g., magnetization is induced in noble metals [12.1], electron interference patterns are observed [12.2], oscillatory exchange interactions between two magnetic layers separated by a nonmagnetic layer are observed [12.3], and magnetorestivity is enhanced (GMR) [12.4].

The main thrust behind the research in nanomagnetism is the production of novel magnetic nanostructures and understanding of structure–magnetic properties relationships. Technologically, this is challenging and requires the combined effort of chemists, physicists, and materials scientists. Prior development in nanostructured materials, their magnetic properties, and theoretical discussion have been presented in the literature [12.5–8]. Magnetic nanostructures can be fabricated or synthesized into nanoclusters, nanoparticles, nanoarrays, nanowires, self-assemblies, multilayers, and thin films. Magnetic nanostructures of both hard (Nd-Fe-B, FePt, and SmCo) and soft (Fe, Co, Ni, FeCo, Finemet, Nanoperm, and Hitperm) magnetic materials have been studied [12.9]. The wide range of chemical compositions as well as wide variety of nanostructures requires a variety of processing techniques, each technique being restricted to a relatively narrow class of magnetic materials; For example, nanostructured magnetic powders are produced by ball milling, anisotropic/isotropic magnetic ribbons are prepared by melt spinning, nanostructured thin films of both hard and soft magnetic materials are produced by sputtering, molecular beam epitaxy, and electrodeposition, magnetic nanowires are produced by electrodeposition in porous templates, and nanolithography is a versatile technique to fabricate magnetic dots, nanoparticle arrays, nanowires, and nanorings.

Nanostructured materials have large surface area to volume ratios, which can result in inhomogeneous magnetic properties. Due to the quenching of orbital moments in the bulk, there is no orbital contribution to total magnetic moment; hence, magnetic moment in the bulk is generally lower than that at the surface. Surface anisotropy also differs from bulk anisotropy, and exchange interactions can vary within the nanostructure. Several methods are used for characterization of structural and magnetic properties of nanostructured magnetic materials [12.10]. X-ray magnetic circular dichroism provides information about the local magnetic environment, small-angle neutron scattering (SANS) yields information about the magnetic environment around atoms, and spin-polarized scanning tunneling microscopy (SP-STM) also yields data on the local magnetism of atoms at surfaces or interfaces. Magnetic measurements are performed by the same techniques used for bulk magnetic materials, e.g., vibrating sample magnetometry (VSM), SQUID magnetometry, and magneto-optical Kerr effect (MOKE). Magnetic force microscopy (MFM) is used for study of magnetic domains and domain wall motion. Structural characterization is performed by techniques such as scanning electron microscopy (SEM) and transmission electron microscopy (TEM).

Understanding nanostructuring-induced phenomena in magnetic materials such as spin-polarized tunneling and GMR effects requires theoretical study of atomic-scale magnetism, in addition to experimental investigations. Theoretical studies, primarily based on density functional theory (DFT), have been conducted to understand the electronic structure, and methods have been developed to relate ab initio electronic structure calculations with large-scale molecular dynamics simulations to elucidate the magnetic behavior of nanostructured materials [12.11–13].

Magnetic nanostructures have found a wide range of applications in information storage [12.14], magnetic resonance imaging (MRI) [12.15], drug delivery [12.16–18], magnetic hyperthermia [12.19, 20], cell separation [12.21, 22], gene delivery [12.23], and magnetic refrigeration [12.24,25]. Hard magnetic nanostructures are used for bonded magnet preparation, recording media, and microelectromechanical system (MEMS) applications. Self-assembled FePt nanoparticle arrays are potential candidates for high-density data storage. Soft magnetic nanostructures are used in common-mode electrical chokes, high-frequency transformers, magnetic sensors, magnetic shielding sheets, and for flux guidance in permanent magnets. Nanostructuring is used to reduce magnetic losses by controlling anisotropy and eddy current losses. Magnetic nanoparticle-based magnetic relaxation switch

(MRSw) biosensors have been used for nucleic acid, protein, enzyme, and virus sensing [12.21]. When magnetic nanoparticles interact with molecular targets, they switch from dispersed state to clustered (or the reverse); this changes the magnetic resonance of the solvent. This change of magnetic relaxation can be detected to characterize the attached molecular targets.

12.2 Atomic Origin of Magnetism

Magnetism is a force of attraction or repulsion. The magnetic properties of matter are determined by the electronic configuration. The rotation of a free electron with negative charge around its own axis produces a magnetic moment parallel to the axis. In addition, moment due to revolution around the nucleus is perpendicular to the orbit. The magnetic moment associated with the electron is calculated from the angular momentum.

According to the Bohr model, the orbital angular momentum of the electron is equal to an integral multiple of $h/2\pi$ as

$$m\boldsymbol{vr} = \frac{nh}{2\pi} , \tag{12.1}$$

where m is the electron rest mass, $\boldsymbol{v}$ is the velocity of an orbiting electron, $\boldsymbol{r}$ is the radius of the orbit, and h is Planck's constant. The magnetic moment μ due to this revolution of the electron around the nucleus can be calculated from the current and area of the loop as

$$\mu = (\text{area of loop}) \times (\text{current in [emu]}) . \tag{12.2}$$

If e is the charge of an electron and c is the velocity of light, the current associated with an electron is $ev/(2\pi r)$ (SI units), so

$$\mu = \pi r^2 \times \frac{ev}{2\pi rc} = \frac{evr}{2c} . \tag{12.3}$$

Combining (12.1) and (12.3) yields

$$\mu = \frac{neh}{4\pi m} \text{ [SI units]} . \tag{12.4}$$

If $n = 1$, i. e., for the first Bohr orbit, the magnetic moment of an electron is 9.27×10^{-24} A m^2 (SI units). The moment due to spin, termed the Bohr magneton μ_B, is equal to the orbital moment of an electron for the first Bohr orbit, being used in magnetic moment calculations.

12.2.1 Quantum Mechanics of Ferromagnetism

According to Heisenberg's uncertainty principle, the position and momentum of an electron cannot be simultaneously calculated with precision. Quantum mechanics considers discrete space quantization of orbital and spin momenta through L–S coupling, being characterized by quantum numbers L, S, and J. Orbit–orbit coupling of an atom results in orbital angular moment L, spin–spin coupling results in spin moment S, and orbital and spin moment coupling gives the total angular moment J. These magnetic moments are expressed as

$$\mu_L = \sqrt{L(L+1)}\mu_B , \tag{12.5}$$

$$\mu_S = \sqrt{S(S+1)}\mu_B , \tag{12.6}$$

$$\mu_J = \sqrt{J(J+1)}\mu_B . \tag{12.7}$$

The net magnetic moment of an atom can be expressed in terms of μ_J and g (spectroscopic splitting factor) as

$$\mu_{\text{eff}} = g\sqrt{J(J+1)}\mu_B , \tag{12.8}$$

where μ_B is the Bohr magnetron, expressed as $eh/(4\pi m)$. The angular momentum J can be used to explain magnetic phenomena such as magnetocrystalline anisotropy, magnetostriction, the Kerr effect, and anisotropic magnetoresistance.

The energy levels of the angular momentum J are discrete in an isolated atom. However, when an external magnetic field is applied, the energy levels split into different energy states to a total number of $(2J+1)$ levels; this phenomenon is known as Zeeman splitting. The possible values of the moment for different levels are given by

$$\mu_J = gM_J\mu_B , \tag{12.9}$$

where $-J \le M_J \le +J$. For the simple case of $J = \frac{1}{2}$, M_J takes the values $\pm\frac{1}{2}$. The lower energy level corresponds to $J = -\frac{1}{2}$ where the magnetic moment is parallel to the applied field, while the upper value corresponds to moment antiparallel to the applied field. The Zeeman energy in the magnetic field is expressed

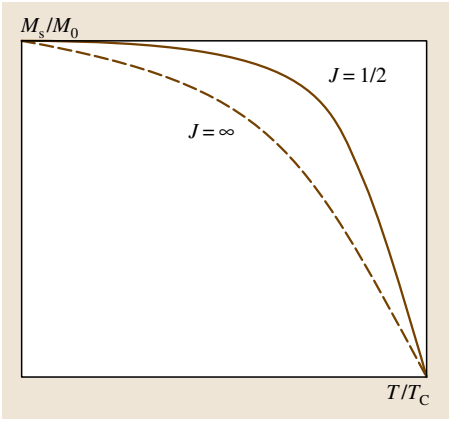


Fig. 12.1 Reduced magnetization versus reduced temperature plot for nickel (after [12.26])

as

$$E = -\mu_J \cdot \mu_0 H = gJ\mu_B \cdot \mu_0 H = \pm\tfrac{1}{2}\mu_0 g\mu_B H \,. \tag{12.10}$$

The energy difference between these two levels is

$$\Delta E \mu_0 g\mu_B H \,. \tag{12.11}$$

The magnetization M depends on the ratio of atoms (N_2/N_1) in these two energy levels and can be expressed by the Boltzmann distribution law as

$$M = g\mu_B(N_1 - N_2)\,,$$
$$\frac{N_2}{N_1} = e^{-\Delta E/(k_B T)}\,,$$
$$N = N_1 + N_2\,.$$

Using these expressions, the magnetization M can be expressed as

$$M = Ng\mu_B \tanh\left(\frac{\Delta E}{k_B T}\right)$$
$$= Ng\mu_B \tanh\left(\frac{g\mu_B\mu_0 H}{k_B T}\right)\,. \tag{12.12}$$

In the weak field approximation,

$$\tanh\left(\frac{g\mu_B\mu_0 H}{k_B T}\right) = \left(\frac{g\mu_B\mu_0 H}{k_B T}\right)\,,$$

which leads to

$$M = Ng\mu_B \times \frac{g\mu_B\mu_0 H}{k_B T}\,. \tag{12.13}$$

The magnetic susceptibility χ can be expressed as

$$\chi = \frac{M}{H} = N\mu_0 \times \frac{(g\mu_B)^2}{k_B T}\,, \tag{12.14}$$

which leads to the Curie law of paramagnetism as

$$\chi = \frac{C}{T}\,, \quad \text{where } C = \frac{N\mu_0(g\mu_B)^2}{k_B}\,. \tag{12.15}$$

The quantum theory of ferromagnetism is derived from the quantum theory of paramagnetism by introducing exchange interactions between electrons on neighboring atoms as

$$E = -\mu_J \cdot \mu_0(H + \alpha M)\,. \tag{12.16}$$

Now, if we consider the case of atoms with one electron for which the angular moment J is $\pm\frac{1}{2}$, the magnetization M can be expressed as

$$M = NgJ\mu_B \times \tanh\left(\frac{gJ\mu_B\mu_0(H + \alpha M)}{k_B T}\right)\,. \tag{12.17}$$

The solution of (12.17) is shown in Fig. 12.1 [12.26, 27]. For a multielectron atom, J takes values of $-J$ to $+J$ through 0 for a total of $(2J+1)$ states. The magnetization of a multielectron atom is given by an expression using the Brillouin function B_J,

$$B_J = \frac{2J+1}{2J}\coth\left(\frac{2J+1}{2J}x\right) - \frac{1}{2J}\coth\left(\frac{x}{2J}\right)\,,$$
$$\text{where} \quad x = \frac{gJ\mu_B H}{k_B T}\,,$$
$$M = NgJ\mu_B \times B_J\left(\frac{gJ\mu_B\mu_0(H + \alpha M)}{k_B T}\right)\,. \tag{12.18}$$

12.2.2 Atomic-Scale Magnetism and Exchange Effect

Intrinsic magnetic properties, such as magnetic moment and anisotropy, are of atomic origin and involve quantum phenomena such as spin–orbit coupling, crystal field interactions, and exchange phenomena. In transition metals (Fe, Co, and Ni), magnetic moment arises from partially filled 3d electrons, whereas in rare earths magnetic moment originates from the incomplete 4f

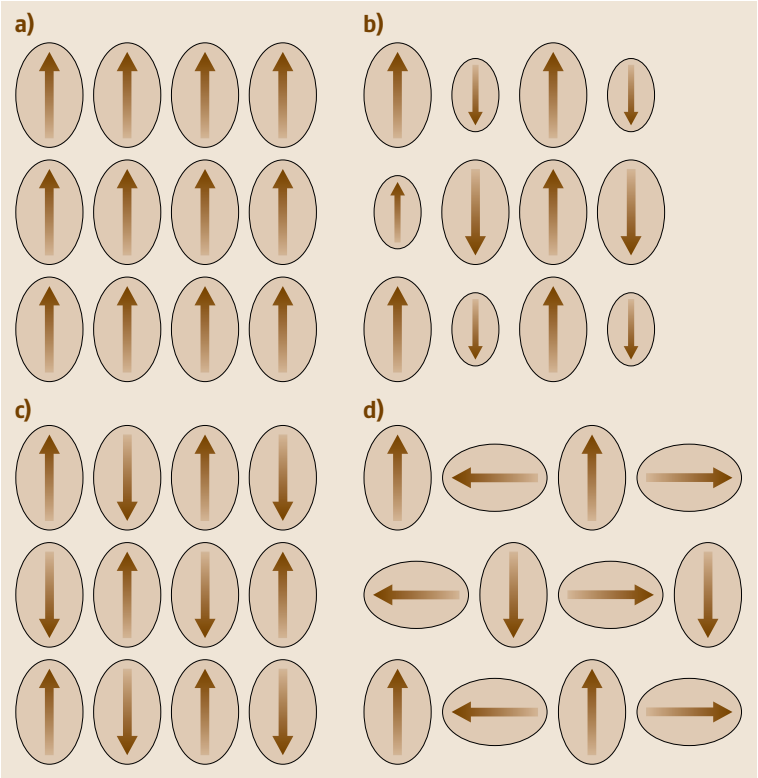


Fig. 12.2 (**a**) Ferromagnetic order, (**b**) ferrimagnetic order, (**c**) antiferromagnetic order, and (**d**) ferromagnet above T_C

shell. Magnetic moments of atoms are calculated in terms of spin and orbital magnetic moment.

In transition metals, the strength of the spin–orbital coupling ($\approx 10^2\,\mathrm{cm}^{-1}$) is much smaller than the crystal field energy ($\approx 10^4\,\mathrm{cm}^{-1}$), hence the orbital moment is quenched. Due to quenching of the orbital moment, typically $\approx 0.1\mu_B$, only the spin moment contributes to magnetic moment. The moment of transition metals is determined by μ_B and the total number of unpaired electrons. In contrast, in rare earths, the strength of spin–orbital coupling ($\approx 10^3\,\mathrm{cm}^{-1}$) is much greater than the crystal field energy ($\approx 10^2\,\mathrm{cm}^{-1}$); this is attributed to shielding of the crystal field by the outer fully filled 5p and partially filled 5d and 6s orbitals. The magnetic behavior in rare earths is like that of free atoms: spin and orbital moments are governed by *Hund*'s rule and are a function of the number of inner-shell electrons [12.28].

The value of intra-atomic exchange (1.0 eV) is much larger than that of interatomic exchange (0.1 eV) [12.28], hence the moment per atom is largely determined by intra-atomic exchange interactions [12.28]. Moreover, the origin of long-range ferromagnetic/antiferromagnetic order and magnetocrystalline anisotropy is also attributed to interatomic exchange interactions and can be explained on the basis of Heisenberg interactions between two neighboring atomic spins S_i and S_j. The exchange energy is expressed as

$$E_{ex} = -2J_{ex}S_iS_j\,. \tag{12.19}$$

Positive values of the exchange integral J_{ex} favor parallel spin alignment, and negative values favor antiparallel spin alignment. In ferromagnets, such as Fe, Co, Ni, FePt, and $Nd_2Fe_{14}B$ alloys, J_{ex} is positive and all atomic spins are parallel. Antiferromagnets and ferrimagnets such as MnF_2, CoO, and Fe_3O_4, however, comprise two sublattices having antiparallel moments. If the moments of the two sublattices cancel each other leaving no net moment, antiferromagnetism results, while in a ferrimagnet there is a lowering of net moments. Disorder in magnetic moment due to thermal effects competes with interatomic exchange forces. At a temperature, defined as the Curie temperature T_C, thermal disorder exceeds exchange forces and the ferromagnet behaves like a paramagnet (Fig. 12.2).

Another intrinsic magnetic property, the magnetocrystalline anisotropy, is also of atomic origin. The interaction of L–S coupling with the local crystal field energy determines the shape and orientation of the charge density and is the origin of magnetocrystalline anisotropy. Due to shielding effects, the rare-earth 4f orbital has strong spin–orbital coupling and hence high magnetocrystalline anisotropy compared with 3d transition metals. These atomic-scale phenomena (magnetization, exchange, and magnetic anisotropy) are significantly modified by nanostructuring [12.28].

12.3 Magnetic Length Scales and Origin of Nanomagnetic Behavior

Thefundamental length scales which govern the magnetic properties are the domain wall width δ_m, exchange length L_{ex}, and magnetostatic length L_s. These length scales are determined from the competition between internal magnetic forces [12.29]. Competition between exchange energy and magnetocrystalline anisotropy energy defines the domain wall width $\delta_m = \sqrt{A_{ex}/K}$. Competition between the exchange energy and magnetostatic energy defines the exchange length $L_{ex} = \sqrt{2A_{ex}/\mu_0 M_s^2}$. The magnetostatic length is $L_s = \sqrt{A_{ex}/2\pi M_s^2}$.

Here, K is the bulk magnetic anisotropy constant and A_{ex} is the exchange constant within a grain. The magnetic properties of a material are dominated by the shortest characteristic length. Some of these characteristic length scales are given in Table 12.1; it is evident that the dimensions of nanostructured magnetic materials lie in the range of relevant characteristic lengths; hence these materials are considerably influenced by nanoscale interactions such as exchange and Rudermann–Kittel–Kasuya–Yosida (RKKY) interactions.

12.3.1 Domains in Fine Particles

Due to the dramatic change in magnetic properties compared with their bulk counterparts, nanoparticles are of great research interest for engineering applications. Two important aspects of nanostructured magnetic materials are single-domain particles and superparamagnetism [12.30]. The key difference between bulk and single-domain particles is the magnetization reversal mechanism; in single domains, reversal takes place via coherent rotation and maximum coercivity is observed. In the single- to multidomain transformation there is magnetostatic energy minimization, hence the critical radius of a single-domain particle is determined by the balance of domain wall energy and magnetostatic energy as

$$R_c = \frac{36\sqrt{A_{ex}K_{eff}}}{\mu_0 M_s^2}\,, \tag{12.20}$$

where A_{ex} is the exchange constant, M_s is the saturation magnetization, and K_{eff} is the effective anisotropy. For many magnetic materials, the single domain size is ten to a few hundred nanometers [12.9, 30]. If single-domain particles become small enough that the thermal energy exceeds the anisotropy energy (e.g., $k_B T \ll KV$), the magnetic moment fluctuates from one easy direction to another. This phenomena is termed superparamagnetism. This thermal switching frequency is explained by the Arrhenius–Neel equation

$$\tau = \tau_0 e^{KV/(k_B T)}\,, \tag{12.21}$$

where τ is the magnetization switching frequency, τ_0 is a proportionality constant ($10^9\,s^{-1}$), k_B is the Boltzmann constant, and T is temperature. Superparamagnetism is characterized by zero remanence, zero coercivity, and a blocking temperature (T_B) below which ferromagnetic order reappears. For $k_B T \gg KV$, the system behaves like a paramagnet. Single-domain

Table 12.1 Magnetic characteristic lengths (after [12.29])

Domain size (nm)	10–10^4
Domain wall width (nm)	≈ 1–$\approx 10^2$
Exchange length (nm)	≈ 1–$\approx 10^2$
Exchange interaction range (nm)	$\approx 10^{-1}$–≈ 1
Superparamagnetic diameter (nm)	≈ 1–$\approx 10^2$
Ruderman–Kittel–Kasuya–Yosida (RKKY) interaction length (nm)	$\approx 10^{-1}$–≈ 10

particle magnetism plays an important role in magnetic recording. The thermal stability limit for magnetic recording is $KV > 25k_BT$ [12.31].

12.3.2 Nanomagnetism

The phenomena that cause nanomagnetic properties are:

- Dimensions of nanostructured materials are comparable to characteristic length scales such as domain size and exchange length;
- Nanostructured materials exhibit higher number of surface/interface atoms with broken symmetry and low coordination numbers.

Another factor that alters the magnetic behavior in nanostructured materials is contact with other physical systems such as for thin films and multilayers. Interactions with the substrate cause perpendicular or in-plane anisotropy depending on the nature of the substrate; For example, in thin films, the thermal response of a nanostructured magnetic material is changed due to its contact with the substrate, leading to a reduction in the Curie temperature [12.28]. Thermal effects become important in a single particle of volume V and effective anisotropy K_{eff}; superparamagnetism is observed when $K_{\text{eff}}V = 25k_BT$.

Magnetic Moment

The magnetic moment can be affected by several nanoscale mechanisms. Ferromagnetism may be observed in noble metals; in contrast to diamagnetism in gold, thiol-capped gold nanoparticles show ferromagnetism due to localization of 5d holes through Au–S bonds [12.1]. Observation of the magnetic moment of $1.0\,\mu_B$ in nitrogen atoms due to spin polarization by neighboring atoms is another example of the effect of nanomagnetism [12.33]. Similarly, DFT calculations of Cu-doped GaN predict spin polarization in Cu [12.34]. This spin polarization further magnetizes the p electrons of the four neighboring N atoms through p–d hybridization and causes ferromagnetic coupling in Cu dopants.

The value of magnetic moment also depends on the dimensionality of the structure [12.29, 35]. The magnetic moments of Fe and Ni are listed in Table 12.2. There is a large variation in magnetic moment from 0-D to 3-D bulk state; For example, the magnetic moment is calculated to be $3\,\mu_B$ for an isolated Fe atom, but the bulk value is found to be $2.2\,\mu_B$, and this decrease in moment is due to the increase in coordination number and partial delocalization of 3d electrons [12.32, 36]. However, the coordination number is still low at the surface. So, when the number of surface atoms is large, as in nanostructured materials, the moment becomes comparable to the atomic moment value. Moreover, the spin–orbit coupling in nanostructured magnetic materials is also comparable to the crystal field energy, and hence a large orbital contribution of magnetization results [12.35]. This results in increased magnetic moment in nanostructures compared with bulk magnetic materials. The enhancement of surface magnetization is explained in terms of itinerant exchange [12.32,36]. For clusters comprising a few tens to hundreds of atoms, most of the atoms are at the surface and hence are more magnetic compared with the bulk. It is observed that the average moment per atom decreases with cluster size, e.g., see the magnetic moment variation for Fe nanoclusters with cluster size in Fig. 12.3 [12.32].

Often, magnetic thin films are deposited on a nonmagnetic substrate. Due to different chemical or electronic environments, the interaction of the magnetic film with different substrates can vary and change the magnetic moment [12.37]; For example, the interface moment of Fe is enhanced when in contact with Cu, Pd, Ag, and Au, and the moment of Co is enhanced for Co/Cu monolayers but decreases for

Table 12.2 Variation of magnetic moment (in μ_B) with dimensionality (after [12.29])

Element	Dimensionality			
	0-D	1-D	2-D	3-D
Fe	4.0	3.3	2.96	2.27
Ni	2.0	1.1	0.68	0.56

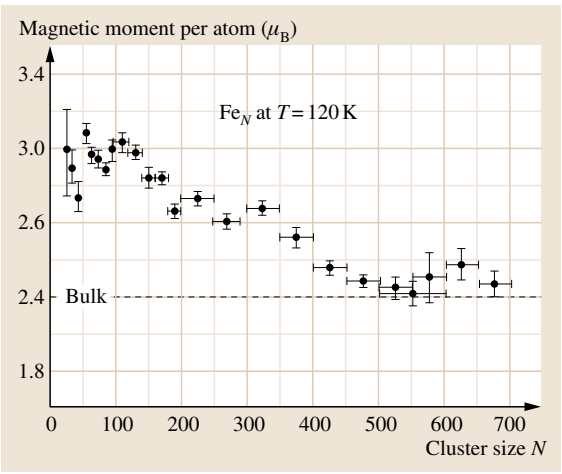


Fig. 12.3 Magnetic moment per atom as a function of cluster size at $T = 120$ K (after [12.32])

multilayers. The moment of a Ni monolayer is decreased for Cu and Au substrates but enhanced for Pd and Ag substrates [12.37]. The substrate–magnetic layer interactions affect the Curie temperature T_C; the Curie temperature of the Fe/W thin-film system is lower than that of the Fe/Ag system, and layers with identical thickness grown in different crystallographic planes exhibit different T_C values as the crystallographic orientation of the film changes from (100) to (110) to (111) [12.37]. Disordered two-phase nanostructures usually exhibit a single Curie temperature that is close to the Curie temperature of the phase having the strongest exchange coupling [12.28].

Magnetic Anisotropy

Preferential orientation of magnetization in a particular crystal axis direction is called magnetic anisotropy. Hard magnetic nanostructures are characterized by high magnetic anisotropy, while soft magnetic nanostructures possess low anisotropy. Magnetic anisotropy consists of two major components: crystalline anisotropy and shape anisotropy. Shape anisotropy is more important in polycrystalline nonspherical magnetic materials [12.9, 38–40]. Shape anisotropy is prominent in very small particles, but in large particles it is minimized by internal flux closure [12.9]. Magnetocrystalline anisotropy is of atomic origin and originates from interaction of spin–orbit coupling with crystal field energy. The lowest-order uniaxial anisotropy energy is given by [12.28]

$$E_a = K_1 V \sin^2\theta \,, \tag{12.22}$$

where K_1 is the first uniaxial anisotropy constant. For low symmetry (orthorhombic, monoclinic, triclinic), the lowest-order anisotropy energy is

$$E_a = K_1 V \sin^2\theta + K_1' V \sin^2\theta \cos(2\phi) \,, \tag{12.23}$$

where θ and ϕ are the magnetization angles. Breaking of symmetry at the surface or interface introduces lower-order anisotropy and is termed surface anisotropy [12.37], first pointed out by Neel and expressed as

$$E_s = K_s \cos^2\theta + K_{s,p} \sin^2\theta \cos^2\phi \,, \tag{12.24}$$

where the first term is out-of-plane anisotropy and the second term is in-plane surface anisotropy. Due to the large number of surface atoms in nanostructured materials, surface anisotropy dominates over bulk anisotropy. In thin films, normally surface anisotropy originates at the surface layer and extends to the first few monolayers. Therefore, the anisotropy energy of thin films is the sum of the anisotropy terms that scale with volume and surface area [12.38, 41], i. e.,

$$E_a = K_{\text{eff}} \sin^2\theta \,,\; K_{\text{eff}} = K_V + \frac{2K_s}{t} \,, \tag{12.25}$$

where t is film thickness, K_V is volume anisotropy and K_s is surface anisotropy. For uniaxial anisotropy perpendicular to the plane, $K_V = 2\pi D_m M_s^2 + K_1$, where K_1 is the bulk uniaxial anisotropy and D_m is the out-of-plane demagnetization factor ($D_m \approx 1$ for thin film). For in-plane anisotropy, another term ($B_{me}\varepsilon$) due to strain is added to the volume anisotropy term as

$$K_V = 2\pi M_s^2 + B_{me}\varepsilon + K_1 \,,$$

where B_{me} is the magneto-elastic coupling coefficient and ε is the strain. The critical thickness at which the in-plane and the out-of-plane anisotropy switch can be estimated from the ratio of the surface and volume terms of the anisotropy, expressed as [12.37]

$$t_{SRT} = -\frac{2K_s}{2\pi M_s^2 + K_1} \,. \tag{12.26}$$

The existence of surface anisotropy and its dependence on thickness have been studied [12.37]. Epitaxial Ni/Cu(001) shows interesting magnetic anisotropy behavior with thickness: below 1.5 nm, Ni shows in-plane anisotropy, but above, it changes to perpendicular anisotropy. Beyond the case of thin films, surface anisotropy applies to atoms located at the surface of any nanostructure, e.g., nanowires.

Coercivity/Magnetization Process of Nanostructured Materials

Magnetization changes due to applied field can be represented by an M versus H plot, known as the hysteresis loop (Fig. 12.4). The characteristic parameters are saturation magnetization M_s, remanent magnetization M_r,

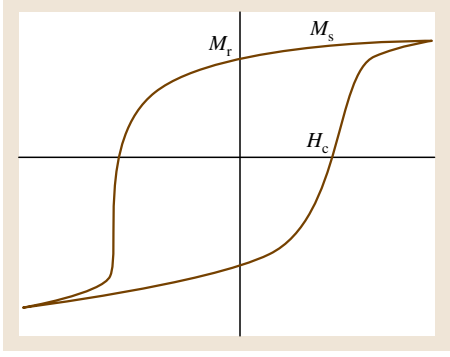


Fig. 12.4 Hysteresis loop of a ferromagnetic material

and coercivity H_c. Coercivity is the field needed to bring the magnetization back to a zero state from a previously saturated state, and remnant magnetization is the magnetization remaining at zero applied field.

The starting point for the study of hysteresis in magnetic materials is the Stoner–Wohlfarth (S–W) model, which assumes uniform rotation of magnetization. Considering the lowest-order twofold uniaxial anisotropy, the total energy is the sum of two competing energy terms, the anisotropy energy $K_1 \sin^2\theta$ and the Zeeman energy $-M \cdot H$ [12.42], i.e.,

$$E = K_1 \sin^2\theta - \mu_0 M_s H \cos(\phi - \theta) \ , \qquad (12.27)$$

where K_1 is the magnetocrystalline anisotropy constant that tends to align the moment in the easy axis direction, whereas the Zeeman energy due to the external field orients the moment in the field direction. ϕ is the angle between the easy axis and applied field, and θ is the angle between magnetic moment and applied field (Fig. 12.5a). Energy minimization with respect to θ of this total energy expression results in the following expression for the anisotropy field H_a [12.42]

$$H_a = \frac{2K_1}{\mu_0 M_s} \ . \qquad (12.28)$$

The anisotropy field H_a is the maximum field needed to align the magnetic moments in the field direction. When $\theta = 0$, the coercivity is equal to the anisotropy field, resulting in a perfect square (Fig. 12.5b); depending upon the value of ϕ, the switching field is either equal to (for $\phi < 45°$) or more than (for $\phi > 45°$) the coercive field [12.41].

Hysteresis of Magnetic Nanostructures. Magnetic properties derived from the hysteresis loop are extrinsic properties, because they describe the real structure of the magnet. In the absence of interactions, magnetization reversal in small magnetic particles is S–W like, though the coercivity tends to be lower than the S–W prediction. In real nanostructured ferromagnets, the switching units are not strictly independent. To predict the hysteresis of real magnetic nanostructures, exchange effects, dipolar effects, and local magnetization as a function of applied field need to be considered, and the derivation of the micromagnetic free energy by modeling nanostructures remains a key problem [12.9].

In nanostructured materials, exchange coupling tends to suppress inhomogeneous magnetization states, leading to coherent rotation of magnetization. If shape anisotropy is considered, the free energy of uniaxial ellipsoids of rotation having symmetry axis parallel to the

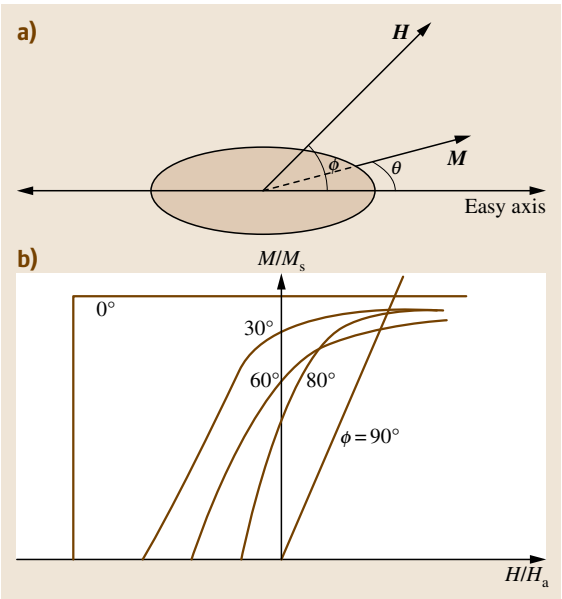


Fig. 12.5 **(a)** Coordinate system for magnetization reversal in SW particle. **(b)** M–H loop of Stoner–Wohlfarth particle for various angles ϕ (after [12.26])

external field is expressed as [12.9]

$$\frac{E}{V} = K_1 \sin^2\theta + \frac{\mu_0}{2}(1-3D)M_s^2 \sin^2\theta - \mu_0 M_s H \cos\theta \ , \qquad (12.29)$$

where D is the demagnetization factor. The solution to (12.29) is obtained by setting the free energy minimum at $\theta = 0$, which yields the S–W coercivity as [12.9]

$$H_c = \frac{2K_1}{\mu_0 M_s} + \frac{1}{2}(1-3D)M_s \ . \qquad (12.30)$$

For spherical S–W particles ($D = \frac{1}{3}$), $H_c = 2K_1/(\mu_0 M_s)$. As the radius of the particle increases, the magnetization process changes from coherent rotation to curling mode and the expression for coercivity becomes [12.9]

$$H_c = \frac{2K_1}{\mu_0 M_s} - DM_s + \frac{c(D)A}{\mu_0 M_s R^2} \ . \qquad (12.31)$$

Here, R is the mean radius of the ellipsoid, and $c = 8.666$ ($D = \frac{1}{3}$) for a sphere and $c = 6.678$ ($D = 0$) for a needle.

Although coherent rotation is one of the primary processes of magnetization reversal, other competing processes such as domain wall propagation and domain nucleation may dominate depending on the sample size

and shape. For most magnetic materials, coercivity does not reach the theoretical limit calculated using the nucleation mechanism developed by *Brown* and termed the Brown paradox [12.43]. *Kronmüller* [12.44] introduced the α factor into Brown's equation to obtain quantitative information on the influence of microstructure. The coercive field expression now becomes

$$\mu_0 H_c = \alpha \frac{2K_1}{M_s} - N_{\text{eff}} J_s \,. \tag{12.32}$$

Here, α is a microstructural parameter and depends on the dimensionality and easy axis orientation, N_{eff} is the demagnetization coefficient, and $J_s = \mu_0 M_s$ is the saturation polarization. The parameters α and N_{eff} can be determined experimentally. The value of α is 1 for aligned particles with easy axis in the direction of applied field. For 3-D and 2-D randomly oriented particles, α is 0.48 and 0.254, respectively [12.46]. In general, the parameter α consists of three subparameters: $\alpha = \alpha_K \alpha_\psi \alpha_{ex}$; α_K describes the anisotropy reduction at the grain surface, the grain boundary, and in the intergranular phases, α_ψ describes the coercive field reduction due to misaligned grains, and α_{ex} reflects exchange coupling between grains [12.47, 48]. For a complete understanding of coercivity, it is necessary to correlate it with microstructural parameters. From the temperature dependence of the coercivity H_c (12.24), and plotting the experimental data for $H_c(T)/M_s$ versus theoretical $2K/M_s^2\alpha$, the magnetization reversal mechanism can be identified as nucleation, pinning, or single-particle rotation; For example, the nucleation-controlled magnetization reversal mechanism was observed in Pr-Fe-B magnet by *Kronmüller* [12.49].

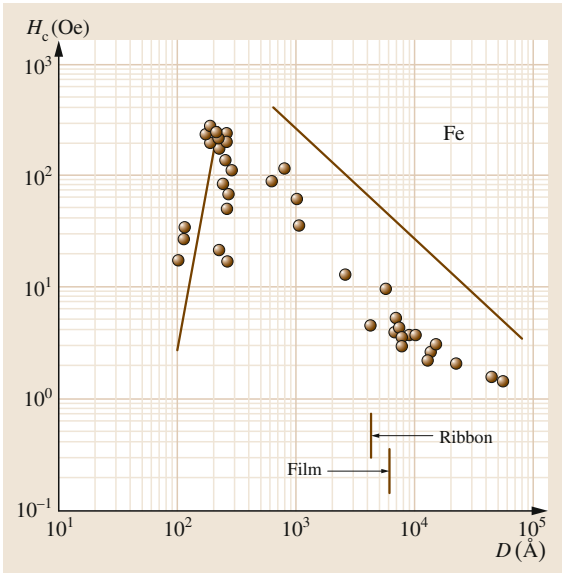


Fig. 12.6 Coercivity versus grain diameter plot for Fe (after [12.45])

Random Anisotropic Effect. Magnetic nanostructures exhibit a particularly rich extrinsic behavior, including effects such as random anisotropy scaling, remanence enhancement, and exchange coupling effects. The key to the extrinsic behavior is the magnetocrystalline anisotropy and its dependence on local atomic structure. In the actual microstructure, the magnetization cannot adapt the local anisotropy from grain to grain, due to exchange stiffness which favors homogeneous magnetization; this leads to variation in magnetization orientation over the structural correlation length. This local magnetization process can be modeled by the random anisotropy model. The anisotropy of grains averages out over several structural units and is reflected in the coercivity of nanomaterials [12.50, 51].

The length scale below which the random anisotropy effect is observed is given by the exchange length L_{ex}. The typical value of L_{ex} is 20–40 nm for Fe-based alloys and 5–10 nm for Co-based alloys. The anisotropy of the grains within the exchange coupled volume is averaged out and scales as

$$K_{\text{eff}} = \frac{K_1}{\sqrt{n}} = K_1 \left(\frac{D}{L_{ex}}\right)^{3/2} , \tag{12.33}$$

where N is the average number of grains within a volume of the exchange length L_{ex}, which is given by substituting

$$L_{ex} = \sqrt{\frac{A_{ex}}{K_{\text{eff}}}} ,$$

into (12.33) to give

$$K_{\text{eff}} = \frac{K_1}{A_{ex}^3} D^6 .$$

The coercivity for coherent rotation can be expressed as

$$H_c = P_c \frac{K_{\text{eff}}}{M_s} = P_c \frac{K_1 D^6}{M_s A_{ex}^3} , \tag{12.34}$$

where p_c is a dimensionless quantity related to crystal structure; $H_c \propto D^6$ when $D \le L_{ex}$.

However, for large D ($D \ge \pi L_{ex}$), $H_c \propto 1/D$ [12.32] and the coercivity is

$$H_c = p_c \frac{\sqrt{AK_1}}{M_s D} .$$

For magnetic thin films, where thickness is smaller, K_{eff} becomes [12.50]

$$K_{\text{eff}} = K_1 \left(\frac{D}{L_{\text{ex}}} \right) ,$$

and the coercivity is

$$H_{\text{c}} = P_{\text{c}} \frac{K_{\text{eff}}}{M_{\text{s}}} \approx P_{\text{c}} \frac{K_1 D^2}{M_{\text{s}} A_{\text{ex}}} . \qquad (12.35)$$

When the grain diameter D is less than the exchange length L_{ex}, the coercivity of magnetic nanoparticles follows the sixth power of D, while thin films follow the second power of grain diameter D. The variation of coercivity for Fe nanostructures is presented in Fig. 12.6 [12.45]. The transition of coercivity change with grain size defines the exchange length, which for Fe is 20 nm.

12.4 Magnetic Nanostructures

Magnetic nanostructures exhibit many interesting magnetic phenomena; For example, exchange coupling in hard–soft nanocomposite magnets leads to high remanence and high energy product (BH_{max}), disappearance of random anisotropy effects is observed in oriented magnetic nanostructures, e.g., nanorods, and multilayer thin films exhibit high saturation magnetization. More recently, it has been shown that single-domain superparamagnetic nanoparticles can play a significant role in novel biomedical applications such as drug targeting and gene delivery [12.17, 23].

Magnetic nanostructures can be produced in a wide range of geometries such as nanoparticles, nanoparticle arrays, nanowires, nanodots, nanorings, nanotubes, and thin films [12.28]. In nanoparticles, all three dimensions are in the nanoscale range, while nanorods and nanodots are examples of low-dimensional systems. Magnetic nanoparticles can be embedded in a medium to form a composite and then self-assembled onto a substrate surface to form a particle array. Future high-density magnetic recording may rely on two-dimensional arrays of nanoparticles. Magnetic nanoparticles can form stable colloidal suspensions in organic liquid or water to form a ferrofluid. Very small nanoparticles are known as clusters; the magnetic properties, e.g., magnetization and anisotropy, of such clusters exhibit strong size dependence due to their high surface to volume ratio [12.28].

Based on the correlation between structure and magnetic properties, magnetic nanostructures are broadly classified as [12.52]:

- Isolated particles with nanoscale diameters
- Bulk materials with nanoscale structure.

In isolated particles, the magnetic properties are due to reduced dimensions, with no contribution from interparticle interactions. In bulk nanostructures, the magnetic properties are dominated by interactions and critically dependent on the nature of the interfaces.

Thin-film or multilayer magnetic nanostructures have only one dimension in the nanoscale range. Magnetic and nonmagnetic layers are stacked to make heterostructured thin films, which have applications in spin valves, tunnel junctions, GMR, etc. Magnetic thin films show interesting magnetic phenomena such as perpendicular anisotropy, moment modifications at surfaces and interfaces, and thickness-dependent domain wall motion.

In a nanowire structure, two dimensions are nanoscale and exhibit interesting magnetic properties due to shape anisotropy, magnetostatic interactions, magnetic mode localization, spin waves, and current-induced magnetization reversal [12.28]. Magnetic nanowires can be obtained by deposition on a surface by exploiting surface anisotropy or by electrodeposition of magnetic materials into porous templates [12.28]. Magnetic nanowires have potential applications in patterned magnetic media and microwave applications.

Another class of magnetic nanostructures are molecular nanomagnets, sometimes termed single-molecule magnets. Magnetic molecular clusters are intermediate between classical and quantum magnets and show unusual properties [12.9]. Molecular nanomagnets are mainly organic molecules that are bonded to metals with unpaired electrons. Molecular nanomagnets are promising candidates for observations of quantum phenomena due to their well-defined structure and well-characterized spin state. Thermally activated quantum tunneling of magnetization was first observed in molecular nanomagnets [12.9].

12.4.1 Processing of Magnetic Nanostructures

Processing of magnetic nanostructures can be performed by a variety of physical methods, e.g., mechanical milling, melt spinning, lithography, and spark

erosion, as well as chemical synthesis methods such as self-assembly and coprecipitation. Conventional lithography allows fabrication on the micron scale; more recently, new techniques such as x-ray lithography, electron beam lithography, and nanoindentation have been developed to achieve nanoscale resolution. Bombardment by heavy ions of a matrix and the focused atom jet deposition technique have been successfully applied to synthesize low-dimensional systems such as nanowires. Due to the exciting magnetic properties of hard–soft multilayered structures and GMR, magnetic thin films are of considerable interest; sputtering, molecular beam epitaxy, and electrodeposition are some of the techniques used for thin-film magnetic nanostructure development.

Lithography

Lithography is a technique in which patterns are recorded onto a substrate using a resist. Depending on the radiation used to record the pattern, lithography is classified as optical, e-beam, x-ray or ion beam lithography [12.53–55]. The substrate to be patterned is coated with radiation-sensitive resist. The resist is then exposed to high-energy radiation with small spot size and subsequently developed in an appropriate solvent medium to leave the desired pattern on it. Finally, the pattern in resist is transformed to the substrate by etching, and the magnetic nanostructure is developed by deposition into the pattern. The small spot size of the electron beam in electron beam lithography enables fabrication of nanosized patterns in magnetic materials [12.53]. There are several other varieties of lithography techniques that can be applied to achieve nanopatterning (Fig. 12.7) [12.53, 54]: Interference lithography is useful for magnetic array development, while nanoimprint lithography is generally employed for nanowires. In interference lithography, an interference pattern of two standing laser beams is used to generate a pattern on the resist. In nanoimprint lithography, however, patterns are developed by physical deformation of the resist. *Chou* and *Krauss* recently fabricated quantum magnetic discs of nickel by lithography [12.56]. AFM nano-oxidation lithography is an effective technique for nanodevice fabrication on patterned NiFe thin film [12.57]. Nanosphere lithography, another modification of the lithography technique, has shown promise for metallic nanostructure preparation [12.58].

Sputtering

Direct current (DC) and radio frequency (RF) magnetron sputtering have become standard procedures in thin-film preparation of metals and ceramics. Magnetic films for recording (FeAlSi, FeNiMo, and FeSi) can be prepared by sputtering [12.59]. During sputtering, a target material is bombarded with high-energy argon plasma so that target material is removed and allowed to condense on the substrate, forming the thin film. In magnetron sputtering, a magnetic field is applied parallel to the target surface for electron trapping. This helps in producing high-density plasma near the cathode and accelerates the sputtering rate. Use of a magnetic bias substrate in magnetic film deposition induces uniaxial anisotropy [12.59]. There are a number of reports on controlling magnetic properties of sputtered films by applying a voltage bias on the substrate [12.60–63]. Reactive sputtering, which is carried out in a reactive gas or reactive gas-argon mixture, is used to prepare oxide and nitride films of a metal target. The sputtering rate of a metal oxide or nitride in conventional sputtering is usually low; the process of reactive sputtering can be used to resolve this issue [12.64]. The main advantage of sputtering is that it is a fairly easy technique for preparation of a large number of layers within a short period of time. The quality of the deposited films (roughness, thickness, stoichiometry, and grain size) depends on variables such as argon pressure, deposition pressure, etc. Sputtering can produce a large range of mean cluster size ranging from 200–15 000 atoms.

Molecular Beam Epitaxy

In molecular beam epitaxy (MBE), materials are evaporated by thermal energy or high-energy electrons and deposited on a substrate, forming the thin film. This technique is used for epitaxial growth via interaction of one or several atomic or molecular beams on a heated substrate. It provides a unique capability to study crystal growth in real time and on a subnanometer scale and to produce complex, artificially layered crystals with high degree of control and reproducibility. The characteristics of MBE are: low growth rate, low growth temperature, smooth growth surface, precise control of surface composition and morphology, and in situ control of crystal growth at atomic scale. A variety of magnetic thin films and nanoparticles arrays can be fabricated by this technique [12.65–68]. Control over microstructure and excellent magnetic properties are advantages of the MBE technique for patterned media applications [12.66, 68].

Electrodeposition

In contrast to sputtering and MBE, electrodeposition is a low-cost and simple technique to fabricate magnetic

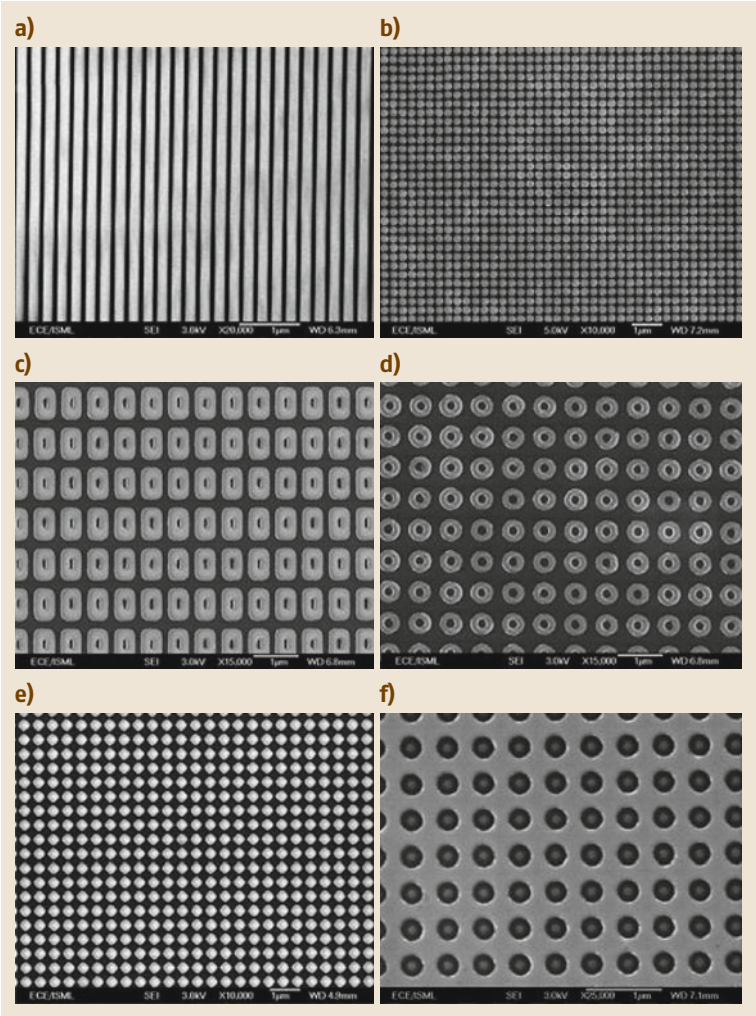


Fig. 12.7a–f Magnetic nanostructures developed by lithography (after [12.54]): **(a)** nanowires, **(b)** circular dots, **(c)** elongated rings, **(d)** circular rings, **(e)** magnetic nanodiamonds, and **(f)** circular dots encircled with antidots

nanostructures [12.69, 70]. Electrochemical processes have many advantages such as room-temperature operation, easy scale-up and maintenance, low-cost, relatively rapid deposition rate, and the capability to handle complex geometries. By applying a voltage between the substrate (working electrode/cathode) and counterelectrode (anode), the metal ions are reduced and become deposited at the substrate surface. The deposition potential is controlled by the reference electrode, and the layer thickness is controlled by the potential applied and time of deposition. Hard/soft magnetic thin films and template-supported nanowires have been synthesized by electrodeposition [12.71–74]. *Lee* et al. prepared Fe–FeO_x core–shell nanowires by anodized aluminum oxide template-supported electrode deposition of iron and subsequent annealing [12.75]. Soft magnetic film such as Fe, Co, Ni, or their alloys can be successfully fabricated by electrodeposition. However deposition of hard magnetic materials with good magnetic properties remains difficult, and reduction of rare-earth elements such as neodymium (Nd) and samarium (Sm) by electrodeposition is challenging due to their high reduction potential. Moreover, appropriate complexing species, such as glycine and other aminocarboxylates, are usually required to codeposit rare earths with high reduction potentials along with transition metals having relatively low reduction potentials.

Chemical Synthesis

The simplicity and high yield of chemical synthesis have drawn attention for wide applications in nanostructure material preparation. Chemical techniques have the advantage of particle size control by controlling nucleation and growth during synthesis. Chemical synthesis of magnetic nanostructured materials is presented in literature [12.52, 76–79]. The common chemical synthesis coprecipitation, microemulsion, sonochemistry, self-assembly, and surface modification of nanocrystals for biological application.

In the reduction process, several reducing agents are used, e.g., an alkali metal (Na) in a suitable solvent (liquid ammonia), $NaBH_4$, N_2H_4, polyol, etc.; there are several reports on Fe, Ni, and Co nanopowder synthesis by the reduction method using these reducing agent [12.80–83]. However, there is one issue associated with the $NaBH_4$ reduction method: the chemical reaction may produce borides instead of pure metal nanoparticles [12.78, 81]. The coprecipitation method is generally used to synthesize oxide-based nanostructures [12.84–86]. In this method, a metal salt is treated with a strong alkali to obtain the hydroxide, which is heated in air to produce the oxide. If these reactions are carried out inside a micelle, which acts as a microreactor, size can be controlled by confining the growth of reaction products [12.87, 88]. In a microemulsion, by varying the concentration of surfactant and solvent, different microstructures can be synthesized [12.88].

Magnetic nanostructures have also been prepared by high-temperature decomposition of organometallics such as $Fe(CO)_5$, $Co_2(CO)_8$, and $Ni(CO)_4$ in a nonaqueous medium in the presence of a stabilizing surfactant [12.88–90]. Size and morphology can be controlled by controlling the reaction temperature, time, and aging period [12.77, 91]. Another well-studied process for magnetic nanostructure preparation is the polyol process [12.77, 91, 92]. In this process, a polyol is used as a reducing agent to obtain Fe, Co, Ni, or FePt magnetic nanoparticles from their corresponding organometallic salts. In this process, a solvent having a relatively high boiling point is required, since reduction takes place at temperatures of 200–300 °C. Recently, another technique, solution-based synthesis followed by high-temperature reduction, has become popular to produce nanocrystalline powders. Rare earths, due to their high reduction potential, are difficult to reduce by high-temperature decomposition or polyol-based reduction processes; the technique of solution-based synthesis and subsequent reduction is a more effective method for synthesizing rare-earth-based nanopowders [12.93–95].

HDDR Process

The hydrogenation–decomposition–desorption–recombination (HDDR) process is mainly used for preparation of anisotropic $Nd_2Fe_{14}B$ nanocrystalline powders [12.9]. This process involves a series of heat treatments of bulk $Nd_2Fe_{14}B$ in hydrogen and in vacuum. The anisotropy is induced by the orientation relationship between newly formed and parent grains. This process involves four steps: hydrogenation of $Nd_2Fe_{14}B$ at low temperatures, decomposition of $Nd_2Fe_{14}BH_x$ into Nd_2H_x, Fe, and FeB, desorption of hydrogen gas from Nd_2H_x, and recombination of Nd, Fe, and FeB into $Nd_2Fe_{14}B$. This technique is also used to prepare SmFe-based alloys [12.96].

Melt Spinning

This technique is very useful to produce magnetically soft alloys as well as hard–soft exchange-coupled magnetic nanocomposites. Both amorphous and nanocrystalline precursors can be prepared by melt spinning by controlling the quenching rate [12.52, 97]. Heating of the amorphous precursor produces small crystallites in an amorphous matrix [12.52]. Tuning the annealing conditions permits control of the grain size. The resultant microstructure is a function of the processing parameters and alloy characteristics. The process parameters are the ejection and chamber pressure, diameter of crucible orifice, distance of crucible from the wheel, wheel speed, melting temperature of the alloy, thermal conductivity of the melt, and heat capacity of the alloy.

In melt spinning, the water-cooled rotating Cu wheel extracts heat from the ribbon. Upon leaving the Cu wheel, cooling is via convective heat transfer. At high wheel speeds, this allows a reduced solidification rate in unsolidified portions or reheating of the initial solidified region and suppresses nucleation of crystalline phase. This allows the melt to be transformed into an amorphous structure. At optimum wheel speeds during melt spinning, the nanocrystallites nucleate and coexist with an amorphous matrix. The melt-spinning technique is used in synthesis of rare-earth-based permanent magnetic materials, especially $Nd_2Fe_{14}B$, SmCo compounds, and their alloys. This technique has also been successfully utilized to prepare ribbons of FePt alloys. Nanocrystalline soft magnetic materials (Finemet, Nanoperm, and Hitperm) have been prepared by partial devitrification of a melt-spun amorphous precursor.

Mechanical Milling

Using this technique, nanostructured as well as amorphous magnetic powders can be produced in large quantities at room temperature by repeated mechanical deformation and alloying in a ball mill [12.52]. Amorphous precursors can be annealed to achieve nanostructured magnetic powders. The advantage of mechanical milling over other physical methods such as sputtering and melt spinning is that milling produces powders which can be readily consolidated to manufacture magnets of desired shapes. A surfactant can be used during milling to obtain better control over the shape and size of the powder particles.

High-energy ball milling is a promising and commercially viable method for large-scale fabrication of Nd-Fe-B, and SmCo magnetic nanostructured powders. Nanocrystalline soft magnetic materials (FeZr and CoFeZr) have also been prepared by this technique. A variation of mechanical milling is reactive milling (RM) or mechanochemical synthesis, which involves reduction/oxidation reactions, decomposition of compounds, and phase transformations. This process has been used to prepare nanoparticles of a number of ferrites such as Fe_3O_4, $NiFe_2O_4$, $CoFe_2O_4$, etc. Sm_2Co_{17} has also been produced by mechanochemical synthesis, by coreduction of Sm_2O_3 and CoO by Ca metal during milling [12.98]. However, wide size distribution and contamination are two barriers to the application of the mechanical milling process for fabricating nanostructured magnetic powders.

Self-Assembly

Self-assembly is a bottom-up fabrication approach to produce materials with highly uniform morphology for various advanced application. In self-assembly, atoms, molecules, or particles organize themselves into functional structures. 1-D, 2-D, and 3-D ordered nanostructured magnetic materials have been synthesized by self-assembly techniques [12.82, 99–101]. The physical forces which drive self-assembly are Coulomb interactions, van der Waals interaction, magnetostatic interactions among particles, hydrogen bonding, and steric repulsion of surfactant [12.88]. Self-assembled magnetic nanocrystals are formed by solvent evaporation, either using the reverse micelle technique or by applying a magnetic field during synthesis [12.52, 88, 102–104]. The product of solvent evaporation-induced self-assembly is dependent on the solvent composition, evaporation temperature, and evaporation rate. It also depends on the wettability of the substrate. Self-assembly by reverse micelle synthesis provides better size control and surface passivation to prevent oxidation. The interparticle spacing can be tuned by the surfactant chain length. Self-assembly on a patterned, textured, or structured template can control the diffusion of atoms and growth, resulting in control of the shape and size of the nanostructures [12.105]. For the growth of complex 3-D structures, nanostructures themselves can act as templates [12.79].

Magnetic nanoparticles coated with surfactants can form close-packed arrays on a substrate. As the solvent is allowed to evaporate, magnetic nanoparticles interact by van der Waals and dipolar interactions and self-assemble. In this process, three interactions need to be considered: between solvent and substrate, between particle and substrate, as well as between particle and particle. If the surfactant is hydrophobic, only nonpolar solvents can be used for dispersion; such dispersions spread on hydrophobic surfaces only, such as carbon or Si-H [12.9]. If the substrate is hydrophilic in nature, isolated islands of particles will form due to the dewetting nature of the hydrophobic surfactant.

FePt nanoparticles prepared by solution-phase synthesis and stabilized by oleic acid and oleylamine are ideal building blocks for FePt superlattice formation by self-assembly [12.92]. Self-assembly of iron dots with a narrow size distribution on the insulating surface of NaCl(001) was reported by *Gai* et al. [12.106]. Such dots can be used as model systems for micromagnetism. As they display simple flux-closure magnetic states, they can bridge the gap between nanomagnetism (single domain) and macroscopic materials (with a large number of domains and domain walls). Self-assembled Fe, Co, Ni, and Co-Pt nanowires have been synthesized by electrodeposition using a porous substrate [12.107]. A key challenge in self-assembled magnetic patterned media development is the placement and alignment of the magnetic dot arrays at the predetermined positions; this can be achieved by lithography.

A substrate functionalized with proper molecules can be used to anchor particles onto its surface via exchange reaction, known as polymer-mediated self-assembly [12.9]. Polyethylene amine-mediated self-assembly of FePt has been reported by *Sun* et al. [12.108]. Polyethylene amine is a NH-based polymer that can replace oleic acid/oleyl amine molecules around FePt nanoparticles and attached to a hydrophilic substrate. PEI/FePt assemblies have been prepared by dipping the substrate alternately in PEI and dispersed FePt particles. By manipulation of the protecting polymer, the interparticle distance can be readily manipulated.

Surface Modification for Biological Application

Magnetic nanostructures, e.g., superparamagnetic particles, are used in biomedical engineering for imaging and hyperthermia application. To make magnetic nanoparticles biocompatible, their surfaces are modified to be hydrophilic by surfactant addition [12.30]. For specific applications different molecules such as drugs, targeting agents, fluorescent molecules, etc. should be bonded to the magnetic nanostructure surfaces [12.109]. For these applications, the surface needs to be functionalized for biocompatibility and to facilitate interactions with molecules. The functionalizing molecule should have two functional groups: one to interact with the magnetic nanoparticles, and the other for molecule bonding. Besides the bonding interactions, surface functionalization ensures stabilization against agglomeration in an aqueous medium.

Organic surfactants are frequently used for stabilization and coating. One of the common approaches is to use fatty acid (oleic acid or stearic acid) to stabilize magnetic nanoparticles. Both dicarboxylic acid and tricarboxylic acid are used for surface functionalization and stabilization of iron oxide-based nanoparticles. Some functional groups are attached to the nanoparticles; the remaining functional groups provide charged surfaces and thus improve the hydrophilicity of the nanoparticles. Polymers with multifunctional groups are also used for surface modification. Due to their good solubility and biocompatibility, polysaccharides such as dextran and carboxydextran are used for stabilization of magnetic nanoparticles. Chitosan, polylactic acid, and polyethylene glycol (PEG) are biocompatible and biodegradable and are of particular interest to coat magnetic nanoparticles for use in MRI.

12.4.2 Characterization of Magnetic Nanostructures

To understand the structure–property relationships in magnetic materials, it is essential to know the distribution of magnetization at various length scales. A variety of instruments and techniques have been developed to achieve these objectives. These methods involve applications of electron optical techniques, including differential phase-contrast imaging and spin-polarized electron microscopy in a scanning transmission electron microscope [12.10, 110], electron holography, quantitative Lorentz microscopy in a transmission electron microscope [12.111], magnetic force microscopy [12.112], as well as x-ray and neutron-based techniques [12.113].

Nondestructive surface analysis of ferromagnetic materials is performed by spin-polarized scanning electron microscopy and magnetic force microscopy; however, for quantitative study of domains, differential phase-contrast microscopy is preferred [12.10]. In electron holography, the phase shift of electrons passing through a thin foil ferromagnetic specimen is analyzed, which provides contour maps corresponding to lines of force distribution and quantitative data on flux distribution [12.10]. Imaging of magnetic domain walls and thereby determination of their structure is usually performed by Lorentz microscopy in defocus mode. These techniques are used in conjunction with transmission electron microscopy (TEM), which provides nanoscale spatial resolution, making direct imaging of magnetic nanostructures possible.

Magnetic Structures Using Scanning Electron Microscopy

Scanning electron microscopy is applied to investigate the magnetization distribution near the surface [12.114]. The surface domains in the ferromagnetic sample interact with secondary electrons and deflect them. When the sample is oriented in an appropriate direction, it becomes possible to detect the Lorentz deflection of the scattered electrons. There are generally two geometrical arrangements for detecting Lorentz deflection (Fig. 12.8) [12.10]. Since it is easy to manipulate the sample in the chamber of a scanning electron microscope, in situ hysteresis or heating experiments, as well as direct real-time observation of domain wall dynamics under an applied field can be conducted.

Unlike Lorentz microscopy in a transmission electron microscope, the geometry of scanning electron microscopy permits alignment of the incident beam and the detection system along arbitrary angles to the surface normal, and thus investigation of the magnetization distribution at an angle to the surface normal becomes easier.

More recently, rather than observing the Lorentz deflection of secondary electrons in a scanning electron microscope, the idea of observing their polarization has attracted considerable attention [12.115]. The alignment of magnetization vectors in different domains on the surface of the ferromagnetic sample is different; hence, polarization of backscattered electrons occurs

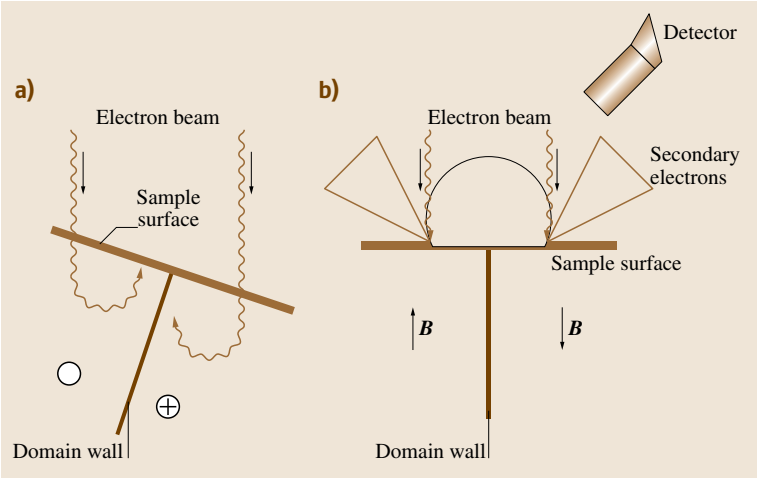


Fig. 12.8a,b Schematic showing geometrical configuration of a scanning electron microscope for detection of Lorentz deflection. **(a)** The field inside the domains gives rise to Lorentz deflection; magnetization is parallel to the surface. **(b)** The field outside the sample gives rise to Lorentz deflection; magnetization is normal to the surface (after [12.10])

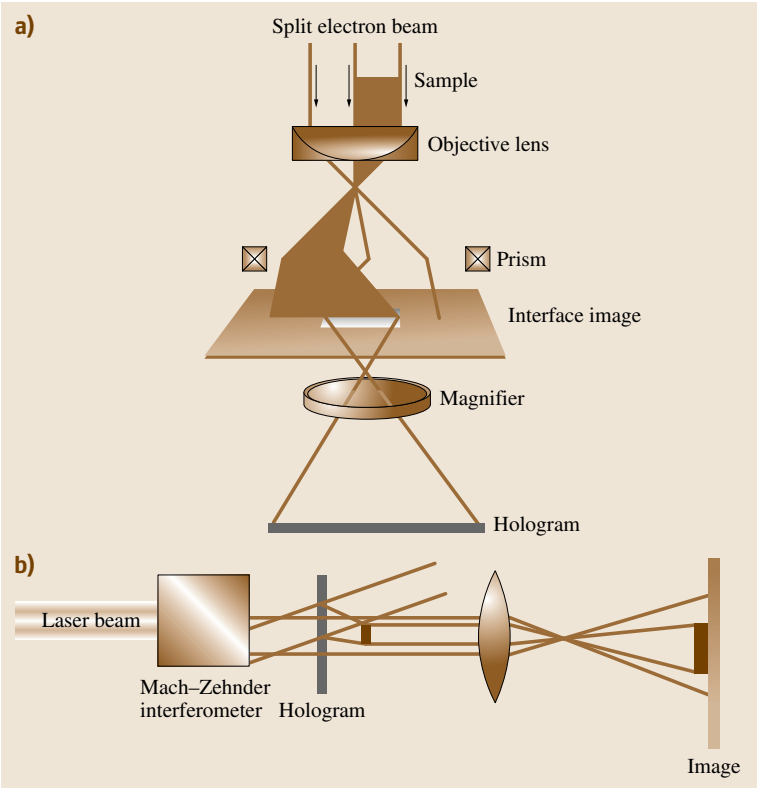


Fig. 12.9a,b Schematic showing **(a)** the formation of electron hologram and **(b)** the formation of contour maps and Lorentz images, using optical image reconstruction from the hologram (after [12.10])

in different directions. The difference in magnetization distributions between different surface domains contributes to the image contrast.

To form images of magnetic domains and domain walls, the instrumentation in a field-emission scanning electron microscope needs to be augmented. A Mott detector and a quadrant electron detector [12.10] are included for spin-polarization analysis and image reconstruction, respectively. This setup allows observation of surface domain configurations in thin-film recording heads and other applications where surface magnetism is important.

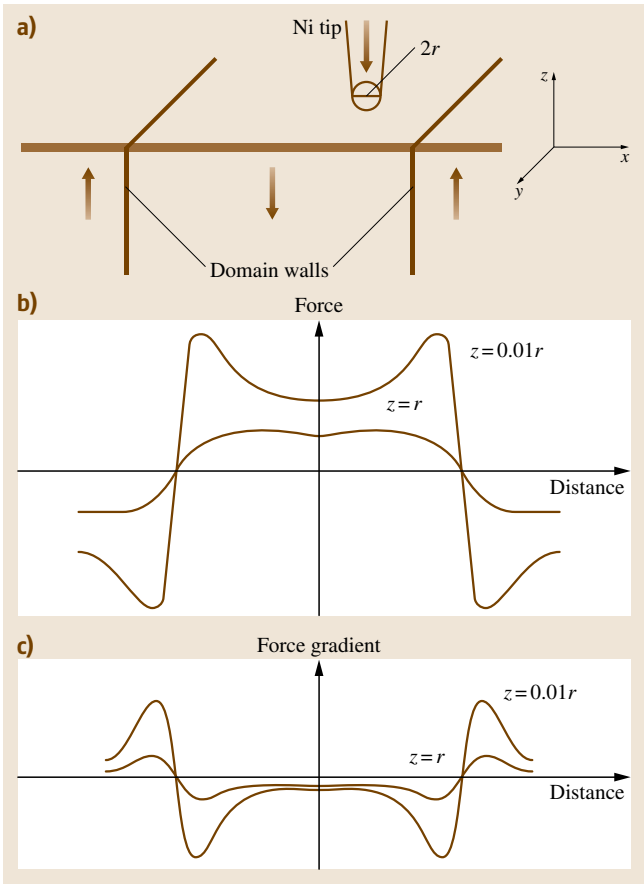


Fig. 12.10a–c Schematic showing **(a)** the magnetization distribution on surface domains and tip geometry in a magnetic force microscope, **(b)** the calculated magnetic dipolar force between the tip and the sample, and **(c)** the force gradient corresponding to **(b)** (after [12.10])

Interference Electron Microscopy and Electron Holography

In this technique an electron hologram is formed, which is subsequently optically reconstructed using a laser beam to create Lorentz images [12.10, 111, 116]. An electron biprism is employed to split the incident electron beam. One-half of the beam traverses the regions outside the specimen, while the other half passes through the specimen. Interference between these two beams gives rise to the formation of the electron hologram. Figure 12.9a,b schematically represent the processes of hologram formation and optical reconstruction, respectively [12.117]. Optically reconstructed images yield counter maps which provide quantitative information about the distribution of magnetic lines of force. This technique usually has the disadvantages [12.10] that it does not permit high holographic spatial resolution (≈ 5 nm) and the maximum thickness of the specimen that can be examined by this technique does not usually exceed several tens of nanometers.

Atomic Force Microscopy

In this technique a sharp ferromagnetic tip is scanned across the surface of the specimen, which contains domain walls [12.117–121]. The tip is usually made up of nickel and is attached to a small cantilever. When the tip scans different regions of the surface of the magnetic specimen, the force and the force gradient on the tip change, depending upon the local magnetization distribution. These changes directly correspond to the actual domain distribution on the surface; the relationship between the two [12.10] is shown in Fig. 12.10. A modification of the atomic force microscopy (AFM) technique is magnetic force microscopy (MFM) [12.112, 122–124], in which the tip is maintained at a constant distance from the sample surface and the change in the force on the cantilever spring required to maintain this constant distance is measured and plotted.

The instrumentation of scanning tunneling microscope has been improved, and it has been demonstrated that in the field-emission mode it can provide resolution of 2–3 nm [12.120]. The secondary electrons emitted from the surface of the ferromagnetic sample can subsequently be analyzed using a Mott detector, and images can be formed using spin-polarized electrons.

Magnetic Structures by Transmission Electron Microscopy

Lorentz images are formed in a transmission electron microscope, when the electron beam is deflected by in-plane magnetization vectors that change in direction as well as in magnitude [12.110]. In a cluster of crystals, deflection of the electron beam by the in-plane component of magnetization is usually dominated by those crystals which have nearly horizontally oriented magnetization vectors. Such clusters of crystals interact with the incident electron beam as though they were a single domain separated from the adjacent domains by a domain wall.

A drawback of this technique [12.10] is that it cannot provide quantitative information about domain wall thickness, since precise representation of magnetization vectors or anisotropy constants of individual crystals is not usually possible in Lorentz images. This issue,

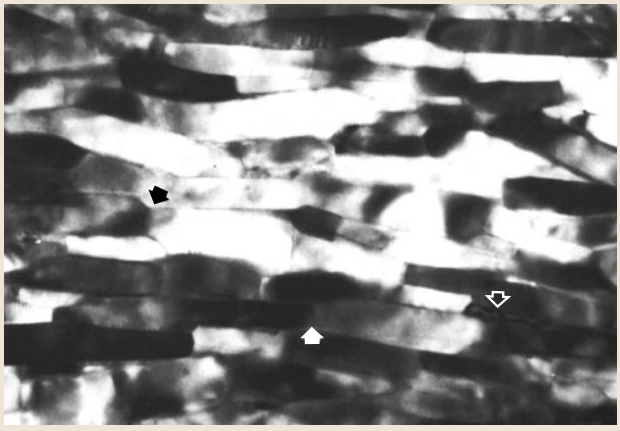


Fig. 12.11 Cross-sectional (parallel to the press axis) transmission electron micrograph of a die-upset Nd-Fe-B magnet showing a stack of platelet-shaped $Nd_2Fe_{14}B$ crystals; *arrows* indicate the Nd-rich phase surrounding these crystals (after [12.10]) ▶

however, can be resolved, and equilibrium domain wall thickness can be determined with good accuracy using specimens comprising large crystals, having preferred orientation in a given direction.

The cross-sectional transmission electron micrograph in Fig. 12.11 shows oriented platelet-shaped $Nd_2Fe_{14}B$ crystals [12.10]. The sample is an Nd-Fe-B magnet, consolidated by die-upsetting and sectioned parallel to the press axis. The Lorentz microscopy micrograph corresponding to this microstructure is shown in Fig. 12.12. By combining the information in Figs. 12.11 and 12.12, the hysteresis behavior of the ferromagnetic material during cyclic magnetization–demagnetization processes can be understood.

The alignment of the magnetization vectors in platelet-shaped $Nd_2Fe_{14}B$ crystals is parallel or antiparallel. The domain walls separating domains of opposite magnetizations pass through a number of grains. These walls have a zigzag shape owing to local pinning but otherwise cross from grain to grain easily. To obtain a quantitative measurement of domain wall width from the wall width measurements in Fig. 12.12, it is necessary to compute the wall image profile from saturation magnetization data and microscope operating parameters for the specific specimen thickness and orientation [12.10].

The advantage of Lorentz microscopy is that it can be combined with other imaging modes of TEM to obtain crystallographic and magnetic information simultaneously. This combined information is often essential to reveal the correlation between the magnetic domains and crystallographic microstructures, and it has led to significant progress, e.g., in the field of ferromagnetic shape-memory alloys (SMAs) [12.111, 125–127], which provide large magnetostriction under an applied magnetic field. Similarly, the combination of Lorentz microscopy with conductivity measurements provides an effective method for determination of physical properties of transition-metal oxides in which the magnetic structure can have considerable effect on conductivity. A new TEM-based system for conductivity measurements, which can be combined with Lorentz microscopy, has recently been developed [12.111] to undertake such investigations.

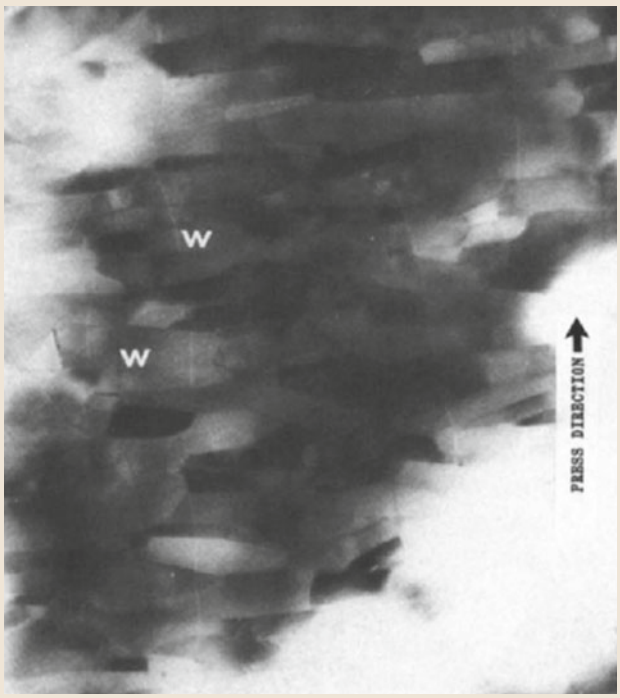


Fig. 12.12 Lorentz microscopy micrograph showing the magnetic structure of a die-upset Nd-Fe-B magnet. The micrograph was taken in Fresnel mode showing domain walls oriented at 180° and defocused crystals as in Fig. 12.11. The vertical domain walls, designated by "w", change their shape as they get pinned while passing near the crystal edges; other walls, however, move from one crystal to the next without interruption (after [12.10])

12.4.3 Hard Magnetic Nanostructures

The hard magnetic nanostructures discussed in this section are based on FePt and rare-earth transition metal-based NdFeB hard magnetic materials. In light of their important magnetic properties and applications, the following section focuses on synthesis processes of nanostructured FePt, FePt/FeCo, Nd-Fe-B, and Nd-Fe-B/FeCo hard magnetic materials. Their compositional, morphological, and magnetic properties are discussed. Magnetic properties of exchange-coupled–decoupled nanostructured materials are also discussed.

Nanoparticles and Nanowires

Due to their potential applications in multi-terabit data storage, ferrofluids, and high-energy-density permanent magnets, nanoparticles of ferromagnetic materials have received immense research interest. Magnetic nanoparticle synthesis of hard magnetic FePt, and $Nd_2Fe_{14}B$ (high magnetocrystalline anisotropy) alloys has been carried out by several methods [12.90, 94, 102, 103]; however, reports on Nd-Fe-B nanoparticles showed much lower room-temperature coercivity than expected for perfectly exchange-coupled nanoparticles due to their relatively large crystal size, structural inhomogeneity, and sometimes chemical instability [12.94].

There are a number of reports on chemical synthesis of FePt nanostructures [12.92, 102, 128–131].

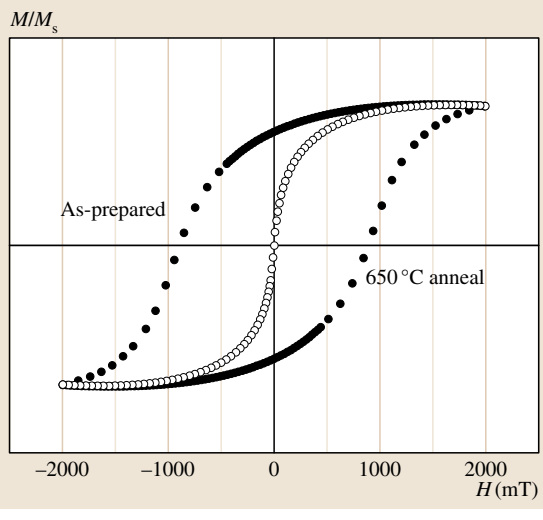


Fig. 12.13 Room-temperature hysteresis of FePt–SiO_2 core–shell (after [12.128])

As-synthesized FePt possesses the low-coercivity face-centered cubic (fcc) crystal structure. When heated to transform from fcc to face-centered tetragonal (fct) with high magnetocrystalline anisotropy, nanoparticle agglomeration occurs [12.129]. By controlling the synthesis parameters and using surfactant, *Sun* et al. [12.102] prepared FePt particles with tuneable size of 3–10 nm. Magnetic properties such as coercivity, which reflects the extrinsic and intrinsic properties of magnetic materials, are size dependent. The maximum coercivity is observed near the single-domain size (Stoner–Wohlfarth particle).

Measurements of magnetic properties show that coercivity increases after annealing and due to the phase transformation from fcc to high-anisotropy fct structure (Fig. 12.13) [12.102, 128, 129]. There have been efforts to reduce the phase transformation temperature and conduct annealing in a salt matrix to reduce particle agglomeration [12.130–132]. To retain the particle ordering, a capping material can be attached to the FePt nanoparticles [12.128].

FePt nanowires have also been synthesized by template-supported electrodeposition [12.132, 133]; however, the coercivity observed was lower than the expected value in spite of the fact that nanowires possessed shape anisotropy [12.134, 135]. Coercivity of 25 kOe was observed in randomly oriented nanocrystals, indicating high magnetocrystalline anisotropy [12.134], but this is much lower than the coercivity value of 100 kOe for randomly distributed Stoner–Wohlfarth FePt particles [12.135]. This large discrepancy in coercivity suggests incomplete atomic ordering of fcc to fct [12.135]. It could also be due to a large contribution from exchange interactions within nanowires and dipole–dipole interactions between two different nanowires [12.136].

The interparticle interactions (exchange/dipole–dipole), can be determined by calculating δM [12.137, 138], defined as

$$\delta M = \left(\frac{M_\mathrm{d}(H)}{M_\mathrm{r}(\infty)}\right) - \left(1 - 2\times\frac{M_\mathrm{r}(H)}{M_\mathrm{r}(\infty)}\right) . \qquad (12.36)$$

For noninteracting single-domain particles, δM is zero [12.137]. If δM is positive, the interparticle interaction is exchange coupling, while negative δM suggests that magnetostatic interaction is dominant. Annealing of assembled FePt nanoparticles leads to a decrease in interparticle spacing and formation of polycrystalline aggregates, due to which magnetic interactions switch from magnetostatic to exchange coupling and remanent magnetization is enhanced [12.139].

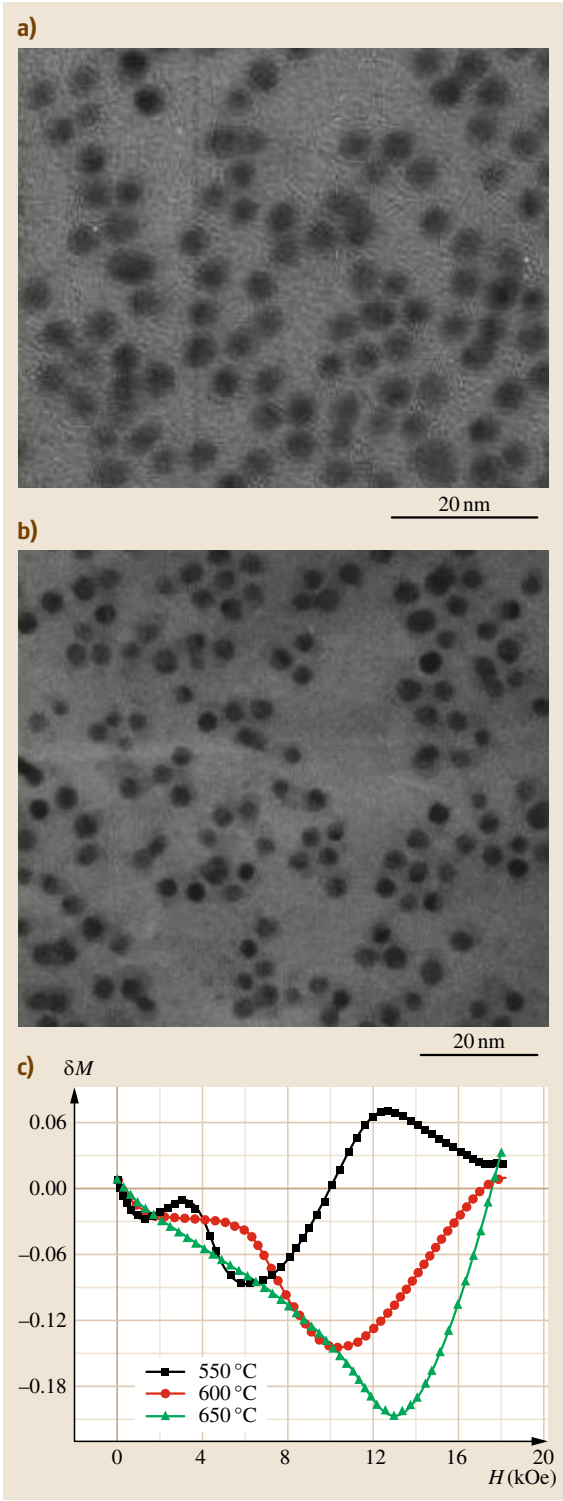


Fig. 12.14a–c TEM micrographs of $Fe_{46}Pt_{54}$ annealed at **(a)** 600 °C, **(b)** 650 °C, and **(c)** δM plot (after [12.140]) ▶

Ordered FePt nanocrystals, synthesized by *Lu* et al. and *Gao* et al. [12.140, 141], showed coercivity of 10 kOe. A negative value of δM (Fig. 12.14c) for annealed FePt suggests the absence of exchange coupling, indicating well-separated ordered nanoparticles; TEM micrographs (Fig. 12.14a,b) substantiated this fact [12.140]. As the separation between particles increases, the particles are less affected by interparticle interactions and approach the Stoner–Wohlfarth condition, resulting in high coercivity [12.135].

Nanowires. Shape control of nanoparticles such as nanowires and nanotubes provides an opportunity to tune shape anisotropy. Progress in experimental techniques has made it possible to synthesize nanowires with high aspect ratio. Among the methods used for fabrication of nanowire arrays, template-assisted electrodeposition is a low-cost and high-yield technique, and FePt nanowire preparation by electrodeposition and solvothermal synthesis has been reported [12.134, 142–146]; due to the high reduction potential of Nd, however, it is difficult to synthesize $Nd_2Fe_{14}B$ nanowires by electrodeposition.

In the solvothermal synthesis process, by controlling the surfactant concentration, different shapes and sizes of FePt nanoparticles can be synthesized (Fig. 12.15) [12.134]. Due to the high anisotropy of nanowires, high coercivity of FePt nanowires is expected. However, the coercivity observed is much smaller than the anisotropy field [12.134, 144], suggesting that magnetization rotation is not coherent but involves domain nucleation and domain wall motion.

The coercivity/magnetization reversal mechanism of nanowires is different from that of the bulk. The easy magnetization direction of nanowires is along the nanowire axes, and the overall magnetic anisotropy is dominated by the shape anisotropy [12.147]. Hysteresis loops exhibit greater squareness for fields applied parallel to the nanowire arrays compared with when the applied field is perpendicular. However, *Cagon* et al. [12.144] observed no significant difference between curves with the field applied parallel or perpendicular to the wires. The magnetization reversal and coercivity of the nanowires are sensitive to the nanowire diameter [12.136]. Magnetization reversal may occur by coherent rotation, magnetization curling, and buckling. The critical diameter below which coherent rotation oc-

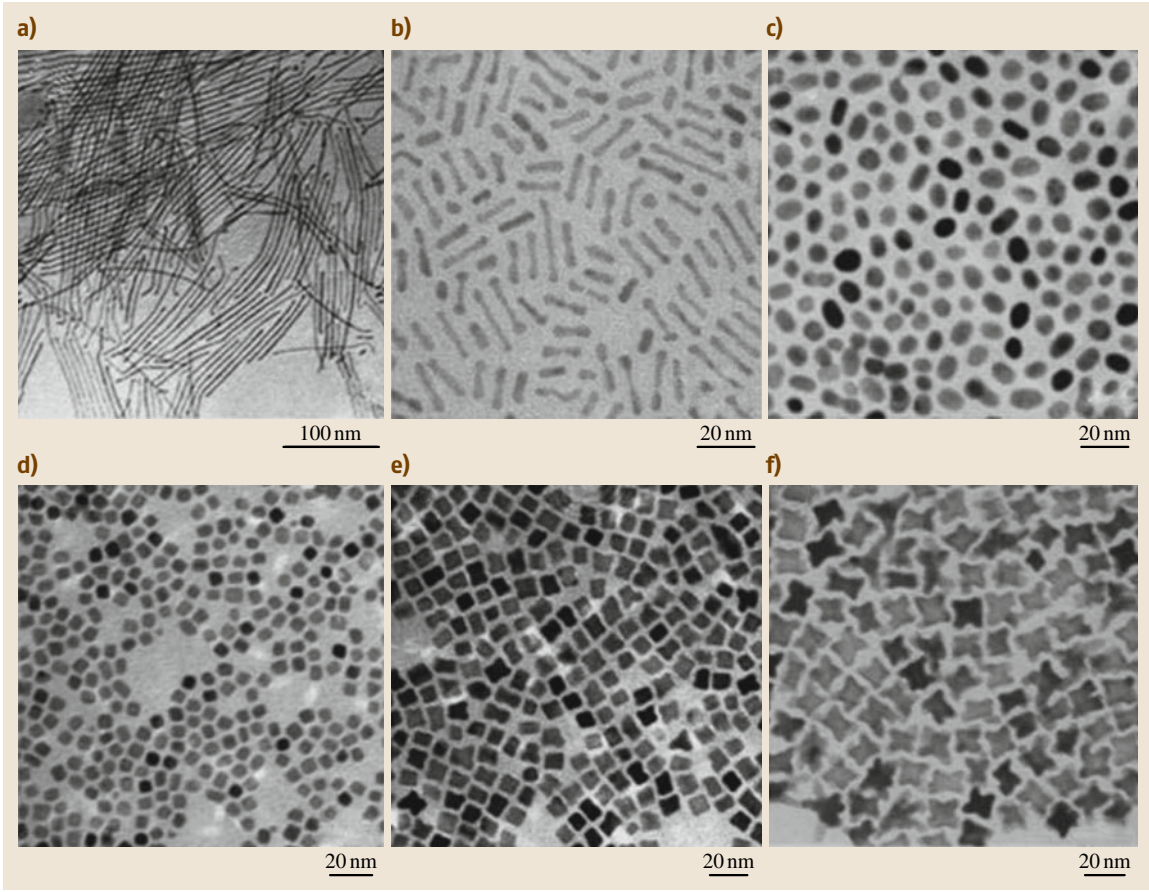


Fig. 12.15a–f FePt prepared by solvothermal synthesis (after [12.134]): **(a)** wires, **(b)** nanorods, **(c)** oval nanoparticles, **(d)** spherical, **(e)** nanocube, and **(f)** multipod

curs is given by [12.136]

$$d_{\mathrm{coh}} = \sqrt{\frac{24A}{\mu_0 M_\mathrm{s}^2}} \,. \tag{12.37}$$

In larger-diameter nanowires, the magnetization reversal process occurs by magnetization curling mode or buckling mode [12.136]. The dependence of coercive fields on diameter is expressed by (12.38) (for the curling mechanism) and (12.39) (for the buckling mechanism) [12.136]

$$H_{\mathrm{cc}} = \frac{2\pi kA}{\mu_0 M_\mathrm{s} d^2} + H_\mathrm{a} \,, \tag{12.38}$$

$$H_{\mathrm{cb}} = \frac{2\pi kA}{\mu_0 M_\mathrm{s} d^{2/3}} + H_\mathrm{a} \,, \tag{12.39}$$

where A is the exchange stiffness, k is the geometric parameter, and d is the diameter of the nanowires. The coercivity decreases with increasing wire diameter, irrespective of reversal mechanism (Fig. 12.16) [12.136].

Single-Domain Particles. The critical single-domain radius is an equilibrium property, involving comparison of single-domain state energy with multidomains. Whether the material will be in a single-domain state or a multi-domain state, is determined by the competition between the magnetostatic energy and domain wall energy. The critical radius below which single-domain state is favored is given by

$$R_\mathrm{c} = \frac{36\sqrt{A_{\mathrm{ex}} K}}{\mu_0 M_\mathrm{s}^2} \,.$$

Due to the high magnetocrystalline anisotropy K, the critical radius for hard magnetic nanostructures is large. For $Nd_2Fe_{14}B$ the critical radius is 107 nm, while for

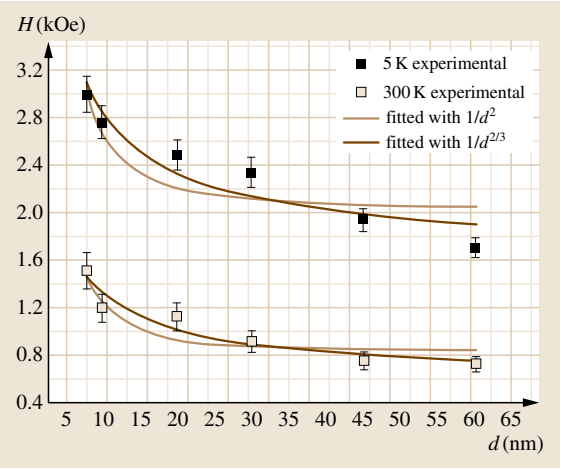


Fig. 12.16 Variation of coercivity parallel to *c*-axis with wire diameter (after [12.136])

FePt it is 340 nm; however, it should be noted that the critical domain size is geometry dependent. Magnetization reversal in single domains is favored by coherent rotation because reversal by nucleation propagation involves the formation of a nonuniform magnetic state similar to magnetic wall formation.

FePt nanoparticles of single-domain size or less, embedded in a carbon matrix, have been prepared by sputtering [12.9, 148]. Coercivity is found to be dependent on layer thickness and annealing temperature, which control the size and interparticle separation. Deposition of Fe and Pt on heated $MgO/Al_2O_3/NaCl$ substrate by electron beam epitaxy leads to FePt island formation [12.149]. Each island is a single-crystal FePt grain smaller than the single-domain size. By considering a random distribution of noninteracting single-domain particles with uniaxial anisotropy, the coercivity of the particles should follow the relationship $H_c = 2K/(\mu_0 M_s)$; these FePt islands showed extremely high coercivity (> 4 T).

Thin Films

Study of magnetic thin films provides understanding of magnetic properties of nanostructured materials in 2-D systems. The magnetic characteristic length is dependent on the dimensionality as well as on the surface/interface electronic structure, due to which interesting effects are observed. Examples are moment enhancement, surface anisotropy, change in Curie temperature, and thickness-dependent domain wall formation. The electrons are more localized at surfaces or interfaces as compared with the bulk, and moment is enhanced. The strength of spin–orbit coupling is changed at the surface, hence the surface anisotropy is altered. The interface chemistry controls the magnetic properties by controlling the coupling phenomena. At the interface, due to atomic orbital hybridization, magnetic moment is induced at nonmagnetic elements such as Pd, Pt, etc.

An ideal thin film is characterized by smooth layer-by-layer growth with high degree of epitaxial order and a smooth interface. The interlayer diffusion has to be minimized, and an overlayer of immiscible elements may have to be used to obtain a smooth interface. The technique of RF/magnetron sputtering is usually employed for Nd-Fe-B and FePt thin-film preparation [12.149–152]. Synthesis of FePt thin films with excellent magnetic properties has also been achieved by electrodeposition [12.153, 154].

For thin films with perpendicular magnetic anisotropy, the saturation magnetization in the perpendicular direction is higher than that in the parallel direction. The perpendicular magnetic anisotropy in thin films is thickness dependent and vanishes with increasing film thickness, due to multidomain particle formation at larger thickness [12.155]. At low thickness, Nd-Fe-B films are single domain and magnetization reversal is dominated by coherent rotation of magnetic domains, resulting in high coercivity. However, for larger thickness, the magnetization/demagnetization mechanism is different (domain wall motion) and results in low coercivity [12.155].

The anisotropy strength of film can be expressed by a quality factor Q as [12.156]

$$Q = \frac{K_1}{2\pi M_s^2} \,. \tag{12.40}$$

For Q smaller than 1, the demagnetizing energy exceeds the anisotropy energy and the magnetization vector lies in the film plane; for Q greater than 1, magnetization is out of plane. For soft magnetic materials, anisotropy is small resulting in $Q < 1$, and magnetic anisotropy lies within the plane. However, for hard magnetic materials such as Nd-Fe-B and FePt alloys, the anisotropy energy is high, hence $Q > 1$ and perpendicular anisotropy is observed in an extended thickness range (i. e., 35–1500 nm for Nd-Fe-B) [12.157]. However, *Leva* et al. [12.156] reported a critical thickness of 30 nm for FePt thin films; below this thickness, magnetization orientation is in plane, while above this thickness it is out of plane.

Liu et al. [12.158] observed that (001) planes of tetragonal $Nd_2Fe_{14}B$ grown on the (110) planes of *W* exhibit prominent perpendicular magnetic anisotropy

within 30 nm film thickness. Magnetization reversal is dominated by incoherent rotation, resulting in high coercivity. $Nd_2Fe_{14}B$ film deposited on a Mo buffer layer shows coercivity as high as 19.5 kOe when the film thickness is ≤ 8 nm [12.155]. In this thickness range the film consists of a mixture of single- and multiple-domain particles. Below this thickness, particles are single domain and hard to magnetize. The low coercivity at low thickness is attributed to crystal imperfections. The coercivity can be further enhanced by particle isolation [12.155]. *Wei* and *Yao* [12.159] reported coercivity enhancement in FePt films by reducing exchange coupling in the presence of a Cu top layer; Cu diffuses into grain boundaries during annealing, and the magnetization reversal mechanism shifts from the domain wall mechanism to coherent rotation. A similar phenomenon was observed by *Yan* et al. [12.160]. By increasing the silver content in FePt/Ag thin films, the coercivity increases due to exchange decoupling between FePt grains. Magnetic hardening may also arise due to the pinning mechanism caused by crystal imperfections [12.161] or due to nonmagnetic phase formation [12.162].

It is also observed that addition of some nonmagnetic additives to thin films can lead to enhancement of magnetic properties [12.163, 164]. Addition of Nb to Nd-Fe-B thin films resulted in grain refinement [12.163], giving rise to enhanced exchange coupling and remanent magnetization. However, in certain cases, addition of nonmagnetic elements can enhance dipolar interactions; For example, in FePt/C multilayers or in FePt/Cu bilayers [12.135, 164], the layer structure breaks down into a dispersion of FePt particles in the carbon/copper matrix during annealing. In the case of FePt/C multilayer, the particle separation makes dipolar interactions predominant and high coercivity results due to the more Stoner–Wohlfarth particle-like behavior. However, in FePt/Cu bilayers [12.164], Cu addition creates a high density of pinning centers, resulting in coercivity enhancement. Addition of a ferromagnetic layer (e.g., Fe or Co) to Nd-Fe-B or FePt thin films results in interesting magnetic properties due to exchange coupling between the hard and soft phases [12.150, 154, 165].

Exchange-Coupled Nanocomposites

Kneller and *Hawig* in 1991 put forward the theory of remanence enhancement and high energy product in exchange-coupled hard–soft nanocomposites [12.166]. Remanence enhancement compared with conventional magnet was first reported experimentally by *Coehoorn* et al. in melt-spun $Nd_4Fe_{78}B_{18}$ alloys [12.167]. The hard phase with high anisotropy provides high coercivity, and the soft phase provides high saturation magnetization resulting in high energy product. In exchange-coupled nanocomposites, the easy axis of the soft phase aligns with the magnetization direction of the hard phase through exchange interactions, leading to a considerable enhancement of remanent magnetization [12.168]. The remanence of a nanocomposite magnet is given by

$$M_r = f_h M_h + f_s M_s \,, \tag{12.41}$$

where f_s, f_h and M_s, M_h are the volume fraction and magnetization of the hard and soft phase, respectively. In exchange-coupled magnets, magnetization reversal originates at the soft phase center and propagates towards the hard phase. The magnetization rotation induced in the hard phase due to the soft phase by exchange coupling leads to a decrease in the nucleation field/coercivity. The effective nucleation field is expressed as [12.168]

$$\mu_0 H_n = 2\frac{f_s K_s + f_h K_h}{f_s M_s + f_h M_h} \,, \tag{12.42}$$

where f and K represent the volume fraction and anisotropy constant, respectively. When the soft phase size is small enough, the hard phase *stiffens* the magnetization direction of the soft phase and a high nucleation field is needed for demagnetization [12.168]. This results in high remanence and coercivity, and a high energy product.

For exchange coupling to be effective, the grain size of both the hard and soft phases should be of the order of the hard phase domain wall thickness. The ideal microstructure for enhanced exchange coupling is homogeneous precipitates of the hard phase in a soft matrix [12.166]. To obtain the optimum microstructure, melt spinning, mechanical milling, sputtering, electrodeposition, and chemical synthesis methods have been explored in $Nd_2Fe_{14}B/\alpha$-Fe, $Nd_2Fe_{14}B$/FeCo, FePt/α-Fe, and FePt/Co nanocomposites. In $Nd_2Fe_{14}B/\alpha$-Fe nanocomposites, the RE content generally has to be reduced compared with the stoichiometric composition (8–12 at.%).

The magnetization reversal process in nanocomposite RE-Fe-B alloys has been proposed to occur by nucleation of reverse domains [12.49]. In melt-spun Nd-Fe-B nanocomposites with nonideal microstructures, the coercive field can be described by a modification of Brown's equation [12.44]

$$\mu_0 H_c = \alpha\frac{2K}{\mu_0 M_s} - N_{eff} J_S \,, \tag{12.43}$$

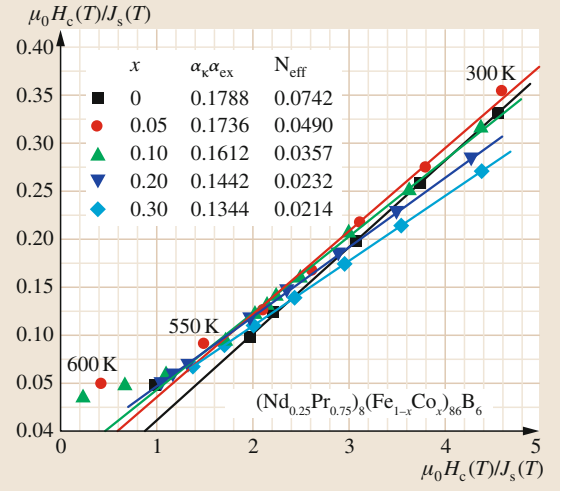


Fig. 12.17 Experimental versus theoretical nucleation field plot for $(Nd_{0.25}Pr_{0.75})_8(Fe_{1-x}Co_x)_{86}B_6$ alloys (after [12.169])

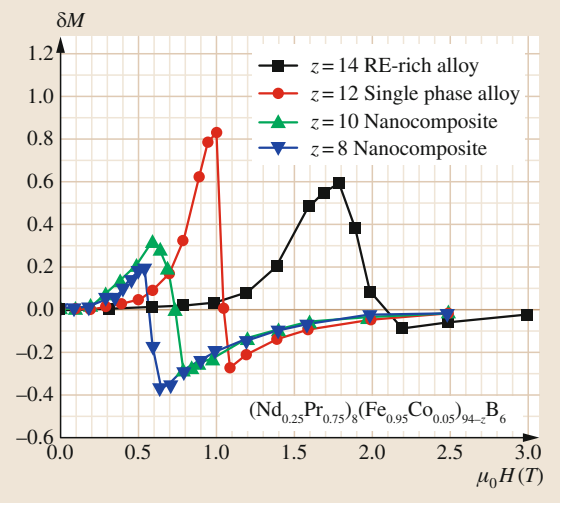


Fig. 12.18 Henkel plot of a (NdPr)(FeCo)B alloy (after [12.169])

where α is a combination of three factors and is given as $\alpha = \alpha_K\alpha_\psi\alpha_{ex}$. α_{ex} results from the influence of exchange coupling on magnetic properties. The value of α_{ex} for melt-spun ribbons can be calculated from the nucleation field plot (Fig. 12.17) [12.171]. It has been observed that the value of α_{ex} depends on the volume fraction of the soft phase, grain size, and grain size distribution [12.169, 171]. With Co addition the value of $\alpha_K\alpha_{ex}$ reduces, indicating enhanced exchange interactions [12.169]. The improved exchange coupling is attributed to decreased anisotropy constant and hence increased L_{ex} through $L_{ex} = \sqrt{A/K}$.

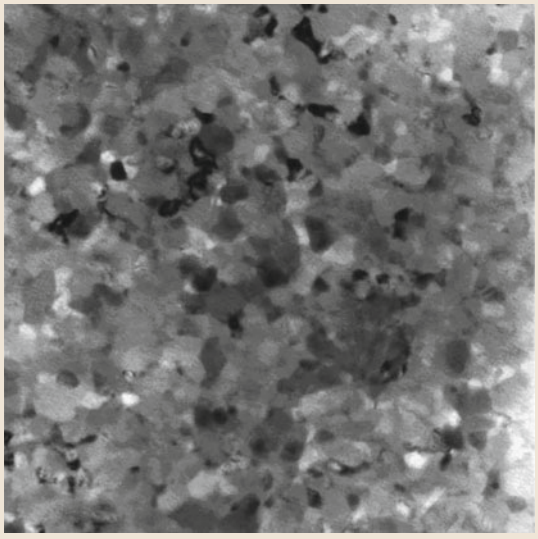


Fig. 12.19 TEM micrograph of a $Nd_9Fe_{84}Ta_2B_5$ alloy obtained by melt spinning (after [12.170])

The strength of coupling between the hard and soft phase can be quantified by using the Henkel plot (Fig. 12.18) [12.169]. The value of δM for the nanocomposite is positive, though much weaker than the single-phase magnet. In composite magnets, after reversal, δM becomes more negative with higher FeCo content; magnetostatic interactions increase with FeCo content. Optimum microstructure for Nd-Fe-B magnet with enhanced exchange coupling can be obtained in optimally quenched melt-spun ribbons (Fig. 12.19) [12.170]; both $Nd_2Fe_{14}B$ and α-Fe phases are almost equal in size (< 50 nm) and are homogeneously distributed. However, size control is difficult when these materials are synthesized by annealing the amorphous precursors; α-Fe grain growth is usually unavoidable due to the large difference in crystallization temperature of $Nd_2Fe_{14}B$ and α-Fe. However, small concentrations of elemental additions have been reported to be useful in grain refining [12.169, 170], resulting in enhanced magnetic properties.

The magnetic properties of exchange-coupled nanocomposite materials depend on microstructure as well as on composition [12.169, 170, 172, 173].

Appropriate choice of composition leads to higher $(BH)_{max}$, the value depending strongly on the volume fraction of the hard phase and intrinsic properties of the hard phase and the microstructure. Micromagnetic calculations using finite-element analysis can predict quantitative correlations between the microstructure and magnetic properties [12.174,175]. Exchange spring magnets are characterized by the high degree of reversibility in their demagnetization behavior. The *spring back* phenomenon is observed when the soft phase grain diameter is smaller than $2b_s$, where b_s is given by [12.166]

$$b_s = \pi \sqrt{\frac{A_s}{2K_h}} \,. \tag{12.44}$$

When the soft phase grain diameter is less than or equal to $2b_s$ (of the order of ≈ 10 nm), strong exchange coupling is observed. Another interesting property observed is the Curie temperature enhancement of the hard phase due to exchange coupling [12.176, 177]. For an ideal exchange-coupled composite (hard phase precipitation in soft phase matrix), the effective anisotropy is (for grain size smaller than 40 nm) [12.178]

$$\langle K \rangle = K_1 v \left(\frac{D}{L_0}\right)^6 \,, \tag{12.45}$$

where L_0 is the intrinsic exchange length, and D and v are the grain diameter and volume fraction of the hard phase. By decreasing the grain diameter D and volume fraction, $\langle K \rangle$ will decrease and in turn the exchange length ($L_{ex} = \sqrt{A/\langle K \rangle}$) will increase, enhancing the exchange coupling between the hard and soft phase. The amorphous phase at the grain boundaries decreases the effective anisotropy through the random anisotropy effect. Hence, an enhanced exchange coupling is observed [12.178]. This is true for small grain sizes (≤ 40 nm), but when the grain diameter is greater than 50 nm, dipolar interactions play a major role in the demagnetization of the exchange-coupled magnet. Due to its large size, the magnetization at the center of the soft phase is not aligned with the hard easy axis. In such a situation, the coercivity is decreased due to the low nucleation field of the soft phase and demagnetization pinning at hard–soft interfaces [12.175].

Nanocomposite Bulk Metallic Glasses. Bulk metallic ferromagnets are a novel group of engineering materials having unique mechanical, thermal, and magnetic properties. Devitrification of bulk metallic glass (BMG) precursors is another simple technique to prepare nanocomposite magnetic alloys [12.172,179–181]. This process is used to prepare high-density nanocomposites with unique magnetic properties, unlike other techniques where magnetic properties can degrade during consolidation [12.172]. To fabricate bulk metallic glass by this method a high glass formability has to be achieved. To the mother alloy system of Nd-Fe-B, different elements with large lattice parameter variation are added to increase the glass formability. However, in these systems due to low rare-earth content, the mass fraction of hard phase as well as the coercivity observed are low. The rare-earth content can be increased but at the cost of glass formability [12.179].

Thin-Film Nanocomposites. A simple approach to produce exchange-coupled nanocomposites in the FePt/α-Fe and FePt/Co systems is to use multilayers of the hard and soft phases [12.172, 182, 183]. In FePt thin films, the FePt/Fe multilayers, due to the higher degree of chemical homogeneity in their microstructure, produce better exchange coupling than the Fe/Pt multilayers [12.182]. Coercivity increases with decreasing thickness of the Fe layers. Theoretical calculations predict a high anisotropy, high coercivity, and thereby an enhanced energy product of $\approx 700\,\mathrm{kJ/m^3}$ for 8 nm α-Fe in an aligned FePt matrix [12.166, 172, 184].

During the last decade, considerable effort has been made to synthesize thin-film nanocomposites based on Nd-Fe-B and FePt alloys [12.150, 165, 172, 182–187]. The nature of interlayer coupling investigated by Henkel plots [12.150, 186] revealed that, in Nd-Fe-B and FePt thin films, as in bulk composites, the coupling is dominated by exchange interactions. *Sun* et al. observed that the degree of this exchange coupling depends on the thickness of the soft layer [12.188].

12.4.4 Soft Magnetic Nanostructures

Soft magnetic materials can be readily magnetized and demagnetized. Their applications fall in the areas where there is a requirement to enhance and/or channel the flux produced by an AC/DC current. In DC applications the material is magnetized, and as a result it performs an operation; when the operation is complete, it is demagnetized. In AC applications, however, the material is first magnetized in one direction and then in the other; this cycle is continued throughout the period of operation [12.189–192].

For such applications the material should have high saturation magnetization and the ability to respond promptly to an external applied magnetic field, being characterized by high permeability. Moreover, for

AC applications, the energy loss encountered while the material is continuously cycled around its hysteresis loop should also be minimized [12.193]. This energy loss, apart from hysteresis loss, stems from two more sources:

1. Eddy current loss, which is the result of flux-induced electric currents in the magnetic material and the concomitant resistive losses
2. Anomalous loss, which is attributed to energy loss arising from the motion of domain walls.

Eddy current losses can obviously be minimized by decreasing the electrical conductivity; however, to reduce hysteresis and anomalous losses, the intrinsic coercivity of the material and the hindrance to motion of domain walls should be reduced [12.194].

The performance of soft magnetic materials is therefore characterized by high combined permeability and magnetization and low values of coercivity and energy losses arising from hysteresis, eddy current, and anomalous effects [12.195]. For high permeability, the microstructure should facilitate easy domain wall motion as well as easy rotation of magnetic moments. These requirements result in the demand for low magnetocrystalline anisotropy energy and low magnetostriction in a soft magnetic material. Low magnetic anisotropy leads to easy saturation in magnetization, while low domain wall energy results in small pinning forces and thereby low coercivity [12.196–198].

Soft magnetic materials used in industrial settings should also have good mechanical properties and corrosion resistance, and may be required to retain these properties at high temperatures [12.199]. Most of these properties are a function of alloy composition, crystal structure, and microstructural features; hence, to fabricate soft magnetic materials with good properties, factors pertaining to alloy chemistry, atomic structure, and alloy microstructure must be optimized [12.200].

It is usually difficult to meet all the different requirements for soft magnetic materials described above; this limits the alloy selection, and there are only a few classes of materials which fulfill these criteria. Transition metals (TM) and alloys, such as body-centered cubic (bcc) Fe, face-centered cubic (fcc) α-Co, Fe-Si, and Fe-Co alloys, have received considerable attention due to their high magnetizations and high Curie temperatures [12.201–205]. However, the permeabilities of these alloys are smaller compared with those of corresponding nanocrystalline/nanocomposite (nanocrystalline–amorphous) alloys; hence, the choice of soft magnetic materials has been dictated by developments in the field of TM-based metallic glasses and nanostructured alloys. The overall soft magnetic properties of the Co- and Fe-based amorphous and nanocrystalline alloys developed during the past decade now exceed those of the counterpart bulk metals and alloys [12.189].

Nanocrystalline Soft Magnetic Alloys

The composition of soft magnetic nanocrystalline alloys is generally represented using the formula $TL_{1-x-y-z}TE_xM_yNM_z$, where TL, TE, M, and NM indicate a late ferromagnetic transition-metal element (TL = Co, Ni, or Fe), an early transition-metal element (TE = Zr, Nb, Hf, Ta, etc.), a metalloid (M = B, P, Si, etc.), and a noble metal (NM), respectively. The rationale for adding TE and M elements is to promote the glass-forming ability, while the NM elements are added to provide nucleation sites for the ferromagnetic nanocrystalline phase. TE elements are also known to act as growth inhibitors [12.189].

The soft magnetic nanocrystalline alloys are broadly classified into two types [12.189]. Type I corresponds to single-phase ferromagnetic nanocrystalline alloys. Type II alloys, on the other hand, comprise two phases; one phase is a nanocrystalline ferromagnet, while the second phase is the residual amorphous phase at the grain boundaries. Figure 12.20 compares the performance of some important soft magnetic materials on the basis of magnetic permeability and saturation magnetization. It is clear from this comparison that TM-based nanocrystalline alloys (both type I and type II alloys) are superior to other alloys such as Mn-Zn ferrites, as well as the counterpart bulk or amorphous alloys, since they simultaneously exhibit relatively large values of magnetic permeability and saturation magnetization. The enhanced soft magnetic properties of such alloys are usually attributed to the synergistic effect of refined grain size, the intergranular amorphous matrix phase, and the composition of each phase [12.206].

Yoshizawa and coworkers [12.207–210] and *Naitoh* et al. [12.211] developed nanocrystalline alloys having excellent soft magnetic properties with low coercivity ($< 2\,A/m$), near-zero magnetostriction coefficients, and saturation magnetization of more than 1.3 T. The magnetic properties of these novel Fe-Si-B-Nb-Cu alloys were comparable to those of commercial Co-based amorphous alloys which possessed excellent magnetic softness. Another great advantage of these alloys was that they had Fe-rich compositions leading to a huge reduction in costs compared with the expensive Co-based amorphous alloys.

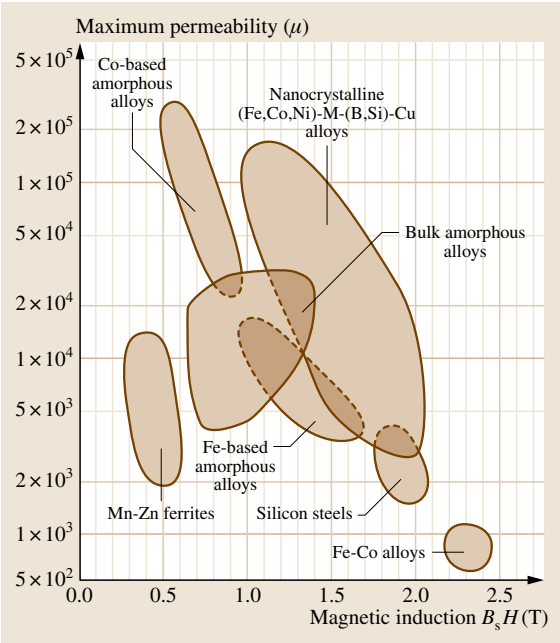


Fig. 12.20 Magnetic permeability plotted against saturation magnetization ($\mu_0 M_s$) for some important soft magnetic materials (after [12.189])

These alloys were patented under the trade name Finemet. The nominal composition of these alloys was optimized to obtain high glass formability and to control the nucleation and growth kinetics of the nanocrystalline phase, leading to lower Fe concentration and high B concentration, with addition of a different nonmagnetic element such as Nb and Cu, respectively, which resulted in a decrease in saturation magnetization [12.207–211].

Inoue and coworkers developed a different class of Fe-based nanocrystalline alloys based on the Fe-Zr-B system. These alloys, which were patented under the trade name Nanoperm, had larger concentrations of Fe (83–89 at.%) compared with the Finemet alloys ($\approx$ 74 at. % Fe), and as a result they exhibited much higher values of saturation magnetization ($\approx$ 1.6–1.7 T) [12.211,213,214]. Nanoperm alloys also showed low magnetostriction coefficient, high permeability, and very low energy losses at power frequencies (60 Hz), making them promising candidate soft magnets for use in electrical power distribution transformers. The synthesis of nanocrystalline Hitperm alloys was the next development in this field. These (Fe,Co)-TE-B-Cu (TE = Nb, Hf, or Zr) based alloys, showed relatively low permeability but high Curie temperatures combined with high saturation magnetization [12.211,213,214].

Alloy Chemistry and Microstructure of Nanocrystalline Soft Magnetic Alloys

The magnetic properties exhibited by these various nanocrystalline alloys depend on the phase composition and microstructural features. Both Finemet and Nanoperm alloys comprise a grain boundary amorphous phase along with nanocrystals: $\approx$ 15 nm α-FeSi nanocrystals with a DO_3 structure in Finemet alloy and $\approx$ 25 nm α-Fe nanocrystals with a bcc structure in Nanoperm alloy [12.215]. Table 12.3 presents the nanocrystalline phases as well as saturation induction and Curie temperature of Finemet, Nanoperm, and Hitperm alloys.

The grain boundary amorphous phase facilitates exchange interactions between the nanocrystals, resulting in high saturation magnetization. When this amorphous phase is not present to envelope the nanocrystals, they become magnetically decoupled, leading to deterioration in magnetic properties. Thus, an optimum grain size and the degree of encapsulation of nanocrystals by the amorphous phase play a key role in determining the efficiency of the spatial averaging of anisotropy, which in turn governs the soft magnetic behavior. Figure 12.21, which is a field ion image of an annealed Finemet alloy, shows the encapsulation of nanocrystals by the grain boundary amorphous phase [12.189, 215].

Thus, enhancement in soft ferromagnetic properties of nanocrystalline materials can be achieved by tailoring the alloy chemistry and optimizing the microstructure, which involves the creation of appropriate

Table 12.3 Typical composition, saturation induction, and Curie temperature of various nanocrystalline soft magnetic alloys (after [12.212])

Alloy name	Typical composition	Primary phase	Saturation induction (T)	Curie temperature (°C)
Finemet	$Fe_{73.5}Si_{13.5}B_9Nb_3Cu_1$	α-FeSi (DO_3)	1.0–1.2	< 770
Finemet2	$Fe_{76.9}Si_{11}B_9Nb_{2.5}Cu_{0.6}$	α-FeSi (DO_3)	1.45	< 770
Nanoperm	$Fe_{89}Zr_7B_4$	α-Fe	1.5–1.8	770
Hitperm	$Fe_{89}Zr_7B_4$	α-FeCo (B2)	1.6–2.1	> 965

interfaces and crystal size reduction. When the crystal size exceeds the domain wall thickness, grain boundaries cause hindrance in domain wall motion, resulting in high intrinsic coercivity. However, when the crystal size is smaller than the domain wall thickness, fluctuations in magnetic anisotropy on the crystal size length scale become irrelevant to domain wall pinning, and as a result intrinsic coercivity decreases rapidly with decreasing crystal size. This explains why nanocrystalline and amorphous alloys have significant potential as soft magnetic materials [12.189].

The degree of the intergrain exchange coupling, which determines the saturation magnetization of soft nanocrystalline materials, can be enhanced by creating a grain boundary amorphous phase, as well as by increasing the interaction volume by consolidating freestanding nanoparticles. *Kojima* et al. [12.217] were the first to report compaction of $Fe_{84}Nb_7B_9$ and $Fe_{90}Zr_7B_3$ alloys using the warm extrusion technique at high temperature (300–500 °C) and pressure (800–1200 MPa). To avoid coarsening of nanocrystals due to the high temperature, *Kojima* et al. in a subsequent report [12.218] employed spark plasma sintering and were able to consolidate the $Fe_{90}Zr_7B_3$ alloy at a much lower temperature of ≈ 600 °C. More recently, there have been several reports [12.219, 220] on consolidation of soft nanocrystalline materials employing rapid consolidation at ultrahigh pressure (≈ 5–6 GPa).

This method has been reported to achieve better size control of the nanocrystalline phase (10–16 nm), as well as high relative density (≈ 98.3%). Both conventional and novel consolidation methods take advantage of the flow behavior of amorphous alloys, which tend to soften in the vicinity of the crystallization temperature.

Thin-Film Nanocrystalline Soft Magnetic Alloys

Thin films and multilayer structures permit more flexibility in terms of alloy chemistry, and as a result considerable efforts have been made to synthesize such structures to explore a wider range of alloy compositions and magnetic properties [12.221]. These systems are particularly promising for magnetic storage devices and other micromagnetic device applications such as passive circuit elements, micromagnetic sensors, and read/write heads for magnetic disk memories. Along with high saturation magnetization and high permeability, another important property for high-frequency applications is high ferromagnetic resonance (FMR). FMR is defined as the maximum permissible frequency at which the film can be used in an inductive device [12.222].

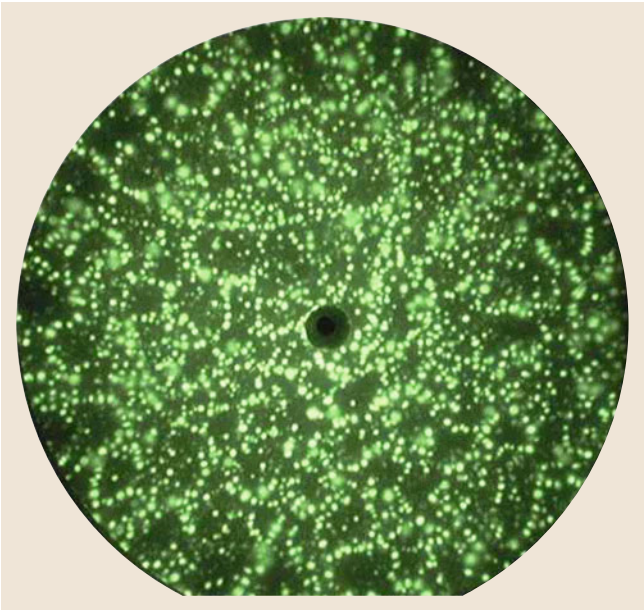


Fig. 12.21 Ne field ion image of $Fe_{73.5}Si_{13.5}B_9Nb_3Cu_1$ melt-spun alloy annealed at 500 °C for 60 min. *Dark* and *bright areas* correspond to the bcc-FeSi nanocrystalline particles and the residual/amorphous matrix phase, respectively (after [12.216])

Using sputtering, *Klemmer* et al. [12.223] synthesized magnetically soft amorphous FeCoB thin films, having low coercivity (1–2 Oe) and high saturation magnetization of 17.5 kG. Interestingly, the anisotropy field of the films was found to be a function of the target–substrate arrangement, and samples sputtered using an oblique incidence configuration were found to have an additional anisotropy component. While this additional anisotropy did not influence the coercivity and resulted in a decrease in permeability, it allowed the synthesis of thin films with FMR values lying beyond 1 GHz.

FeXN (X = Hf, Ta, Al, Rh) thin films with nanocrystalline structure have also been thoroughly investigated as promising soft materials for high-frequency applications [12.224–226]. Nitrogen diffuses into 3d metals and 3d–4f intermetallic compounds as an interstitial atom, leading to lattice expansion and concomitant enhancement in ferromagnetic properties. The as-deposited films are amorphous, and usually the desired magnetic properties are only obtained after annealing, which results in the formation of α-Fe nanocrystals. Transition-metal nitrides are also formed during annealing and act as nucleation sites and/or pinning sites which impede crystal growth.

Using magnetron sputtering, *Kim* et al. [12.226] synthesized a series of FeN and FeXN (X = Ti, Al, Hf, CoHf, CrHf) thin films having good soft magnetic properties with low coercivity (< 2 Oe) and high saturation magnetization (15–20 kG). *Shin* et al. [12.227] reported synthesis of Fe-Co-Ta-N soft magnetic thin films with thickness of 250 nm, which exhibited high saturation magnetization (21 kG), low coercivity (< 3 Oe), and good high-frequency characteristics. *Pan* and *Du* [12.228] fabricated nanocrystalline $(FeCo/CoNbZr)_n$ and $(FeCo/CoZr)_n$ multilayers by sputtering; magnetic annealing of these structures yielded excellent saturation magnetization (22.5 kG), low coercivity, and good high-frequency performance. On the basis of cross-sectional transmission electron microscopy, the authors suggested that the soft magnetic Co-M (M = Zr, Nb, etc.) amorphous layers play two roles:

1. They act as pinning sites, which helps to control crystal growth.
2. They encapsulate the FeCo layers, resulting in enhanced exchange coupling and thereby high saturation magnetization.

More recently, *Greve* et al. [12.229] explored the possibility of using hybrid materials, consisting of metal nanoparticles dispersed in a dielectric matrix, as soft ferromagnetic materials. They reported synthesis of thin multilayer films of sputtered polytetrafluoroethylene (Teflon) and $Fe_{54}Ni_{27}Co_{19}$ with different layer thicknesses using the vapor-phase tandem deposition technique. The films showed excellent FMR values ranging from 3.0 to 4.7 GHz, with almost negligible losses up to 700 MHz.

Synthesis of Nanocrystalline Soft Magnetic Alloys

Synthesis of amorphous and nanocrystalline soft magnetic alloys requires an appropriate processing method able to drive the initial polycrystalline material to an amorphous state without oxidation/contamination, preferably with minimum processing steps. A brief description of the synthesis routes that have been employed to produce such alloys is given below:

1. Powder synthesis techniques: These techniques, (e.g., carbon-arc synthesis, plasma torch synthesis, gas atomization, and mechanical milling) can be used to produce nanocrystalline soft magnetic alloys in the form of freestanding powders or nanoencapsulates. The as-synthesized materials, however, subsequently need to be consolidated to reduce porosity and increase relative density while retaining their nanocrystalline structure [12.221].
2. Rapid solidification processing: Rapid solidification techniques (e.g., splat quenching, melt spinning) involve fast quenching from the liquid melt and can be used to produce amorphous alloys in the form of ribbons. These ribbons are then pulverized and consolidated to manufacture magnets of desired shapes. The as-quenched ribbon is sometimes also used as a precursor; annealing of this ribbon yields the desired nanostructure [12.222].
3. Conventional solidification processing of bulk amorphous alloys: Metallic amorphous materials having larger dimensions (1–4 mm) than the thickness of rapidly solidified ribbon (10^{-6} μm) are termed bulk amorphous alloys. The chemistry of these alloys is optimized to provide them with very high glass-forming ability; hence, their solidification requires slower cooling rates, and they can be cast by the conventional solidification techniques (e.g., suction casting). The demand for high glass-forming ability results in the requirement for adding high concentration of metalloids such as B and Si, as well as heavy elements such as Zr and Nb, leading to a decrease in saturation magnetization [12.223].

12.4.5 GMR and Spin Valves

GMR is the change in electrical resistance in response to an applied magnetic field and was first discovered in an epitaxially grown Fe-Cr multilayer by *Fert* [12.230]. When two ferromagnetic layers separated by a nonmagnetic layer are coupled (ferromagnetic/antiferromagnetic coupling), the phenomenon of GMR is observed (Fig. 12.22a). The GMR effect is also observed in magnetic multilayers of varying co-

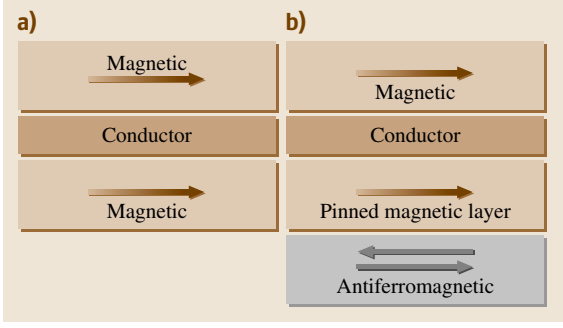


Fig. 12.22a,b Basic structure of (a) GMR and (b) spin valves

ercivities [12.230, 231]. In spin valves, an additional antiferromagnetic (pinning) layer is added to the top or bottom part of the structure (Fig. 12.22b). The magnetization direction of the pinned layer is fixed by the exchange-coupling field from the antiferromagnetic layer.

The electric current in a magnetic multilayer consisting of thin magnetic layers separated by a thin nonmagnetic metallic layer is strongly influenced by the relative orientation of the magnetization of the magnetic layers. When the two magnetic layers are ferromagnetically coupled, the electrical resistance will be lower than if they are coupled antiferromagnetically. When ferromagnetic films are separated by a metallic spacer layer, the magnetizations of the layers are coupled to each other by an exchange interaction through the electrons of the spacer layer. This coupling is known as the Rudermann–Kittel–Kasuya–Yosida (RKKY) interaction [12.28].

The cause of this giant variation of the resistance is the scattering of electrons at the layer interfaces. The change of electrical resistance ($\Delta R/R$) can be tailored by changing the layer thickness. In such multilayers, the resistance of current in the plane (CIP) is found to be much larger than current perpendicular to the plane (CPP). Current in-the-plane (CIP) GMR is most commonly used in magnetic read heads, whereas current perpendicular-to-the-plane (CPP) GMR is the basis of tunnel magnetoresistance (TMR). In spin valves, the free layer magnetization rotates depending on the input signal and changes the electrical resistance accordingly [12.232].

There are several potential applications of devices based on GMR or spin valves, such as magnetic field sensors, read heads, and random-access memories [12.232–237]. Spin valve-based read heads have shown much promise for achieving magnetic recording beyond 100 Gbit/inch^2 [12.233]. Magnetic field sensors based on GMR can also be used in position detection, e.g., distance, speed, angle, and angular speed [12.234]. GMR has also found several applications in biomedical engineering such as in magnetic switches [12.237] and biosensors [12.238].

12.4.6 Applications

Magnetic nanostructures have a number of potential applications in various diverse fields; for example, magnetic thin films with magnetization perpendicular to the plane are potential candidate recording media; perpendicular magnetization allows smaller domains and bit size and increases data storage density. Moreover, Kerr rotation of polarized light is larger when the magnetization is perpendicular to the plane compared with in-plane magnetization; this property is used in high-density magneto-optical recording. A new class of applications is magnetic random-access memory (MRAM), which consists of magnetic tunnel junctions; each tunnel junction is one bit. MRAM is faster than semiconductor RAM and is nonvolatile. Functionalized magnetic nanostructures also have important biological applications such as in drug targeting, gene delivery, hyperthermia, MRI, magnetic cell sorting, etc. Another interesting application is the magnetic tweezers used to manipulate molecules and thereby investigate intermolecular interactions.

Data Storage

Important applications in magnetic data storage are to write, store, and read magnetic information in recording media. With the advent of nanostructured magnetic materials, data storage has been advancing rapidly. Storage densities in hard disk drives continue to increase, aiming to reach 1 Tbit/inch^2. The write head aligns the spins of the grains into tiny patches; data are stored as the magnetic moment orientation of these patches, being termed a bit. Increasing the areal density requires the bit size to be as small as possible. The bit length a depends on the thickness δ, remanence magnetization M_r, and the coercivity H_c of the material and is expressed as $a = \delta M_r/(2\pi H_c)$.

For the bit size to be small, the coercivity H_c must be high and the product of remanence and thickness (δM_r) must be small. At the same time, high remanence is required to ensure a sufficient readout signal. With nanostructuring, it has become possible to optimize these parameters. The current research focus is in perpendicular recording media, patterned media, hybrid recording, and self-organized magnetic arrays [12.102, 239–242]. In perpendicular recording media the easy axis of magnetization is perpendicular to the film surface. Uniform easy axis orientation and high thermal stability would permit higher data densities [12.242]. The stability of magnetization orientation of each bit depends on the anisotropy constant K and volume V. The magnetization becomes unstable when the anisotropy energy of the bit becomes comparable to the thermal energy ($KV = k_B T$), i. e., at the superparamagnetic limit, resulting in loss of data. Single-domain particle magnetism plays an important role in the field of magnetic recording; the thermal stability limit for magnetic recording is $KV > 25 k_B T$ [12.9].

To bypass this superparamagnetic limit, use of discrete patterned media of highly anisotropic magnetic materials is required. Permanent magnets such as $Nd_2Fe_{14}B$, SmCo, and FePt can support data storage at grain size as low as 2.5 nm without thermal loss. However, the high coercivity of these materials can inhibit writing the data bits; GMR or spin valve is a potential solution to this problem.

Sun et al. [12.102] demonstrated that assemblies of high-coercivity FePt of ≈ 4 nm size can support stable magnetization, a future hope for multi-terabit data storage. The key requirement for technical applications of this approach is long-range order of self-assembly. For good signal-to-noise ratio (SNR), grains need to be small, isolated (to reduce exchange coupling), and uniformly distributed. To achieve high SNR, antiferromagnetically coupled (AFC) media have been developed. AFC media are composed of two magnetic layers antiferromagnetically coupled through a nonmagnetic layer to improve thermal stability and thereby increase storage density [12.242].

Environmental Applications

Functionalized magnetic nanomaterials have been developed for removal of pollutants such as heavy ions (Cd^{2+}, Cu^{2+}, and Hg^{2+}), radioactive pollutants, and organic pollutants such as organic dyes, pesticides, and drugs from the environment [12.21, 243, 244]. Extraction of environmental pollutants by magnetic nanomaterials involves capture of the pollutant and its subsequent manipulation by external magnetic fields. The bonding between pollutant and magnetic nanoparticles is based on hydrophobic interactions, electrostatic attraction, and/or covalent bond formation [12.243]. The pollutants adsorbed on the surface are released by ligand or H exchange or by adding organic solvent or acid. Magnetic nanoparticles containing thiol groups at the surface easily bind heavy-metal ions by coordination bonding, and the absorbed metal ions can be liberated by adding HCl. Naturally occurring magnetotactic bacteria remove organic pollutants from water by enzymatic reactions [12.244]. Pesticides, drugs, and organic pollutants get adsorbed onto magnetic nanoparticle surfaces by electrostatic interactions or hydrophobic/hydrophilic interactions depending on the nature of surfactant used [12.243].

Magnetic Biosensor

Magnetic nanoparticles such as superparamagnetic particles are used as biomolecular labels; because of their comparable size, they can be manipulated inside complex biological fluids to achieve the desired detection and sensitivity. For example, magnetic particles of size ≤ 20 nm can be used to detect DNA molecules [12.21].

The mechanism of detection involves binding of magnetic nanoparticles with molecular targets, thereby inducing a change in proton relaxation rate. This technique is analogous to magnetic resonance imaging (MRI) [12.245]. Another method is to use magnetic relaxation switching (MRSw) [12.21,245,246]. Magnetic nanoparticles react with molecular targets and assemble into clusters, thereby affecting the bulk magnetic relaxation rate. MRSw has been used to detect nucleic acids, proteins, enzymes, viruses, cells, etc. [12.21,245, 246].

MRI Contrast Agent

MRI, one of the most powerful imaging methods, is based on the relaxation of protons in tissues. Magnetic nanoparticles are being increasingly used to improve MRI contrast. Most imaging techniques offer a single contrast mechanism, but MRI contrast is generated from the local physicochemical environment [12.21, 247]. Magnetic nanoparticles enhance the image quality by altering the magnetic resonance of protons and hence enhance the signal intensity. Superparamagnetic iron oxides have been used for MRI of liver, spleen, bone marrow, kidney, etc. [12.21], because of their chemical stability, nontoxicity, and biodegradability. The success of such in vivo imaging techniques is highly dependent on the molecular imaging agents; e.g., T cells in mouse spinal cord labeled with iron oxide nanoparticles complexed to poly-L-lysine were detected by MRI [12.248]. Due to high saturation magnetization, cobalt may have a larger proton relaxation effect compared with iron oxide. However, due to toxicity effects it has less applicability [12.249]. Another advantage of MRI is the dynamic imaging modality in which magnetic nanoparticle-loaded cells can be monitored in vivo using MRI [12.21].

Tissue Engineering

Cells labeled with magnetic nanoparticles can be manipulated using magnets to create artificial tissue [12.21, 22]. Cell can be cultured to reconstitute human tissue. Magnetically labeled keratinocytes can be accumulated to form sheet-like 3-D constructs using a magnet [12.21]. Tubes of the cultured cells can be created by using a rotating cylindrical magnet to attract the 2-D cell layer and then rolling it into the desired configuration. This ability to manipulate cells and tissues has opened up a new field of regenerative medicine [12.21].

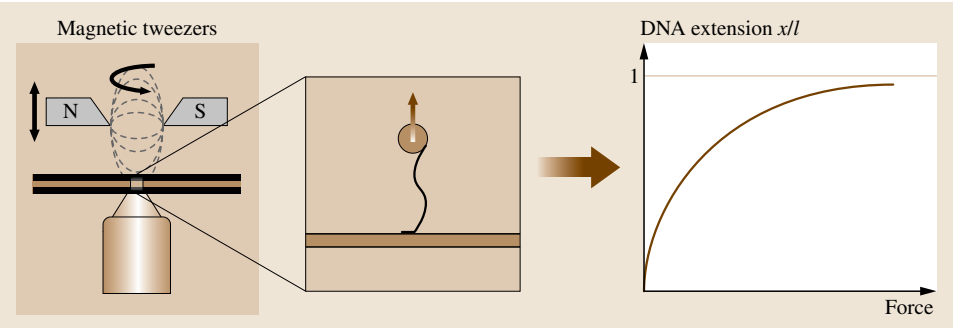


Fig. 12.23 Schematic diagram of the magnetic tweezers setup (after [12.250])

Drug and Gene Delivery

Targeted drug delivery by an external magnetic field can reduce the dosage by 50–80% [12.9, 18, 21, 23]. The ideal magnetic particles for drug targeting should be biocompatible, form a stable suspension, and incorporate high amount of the drug. The drug may be encapsulated or adsorbed onto the surface and must be released at the targeted site by degradation or by heating. In magnetofection or magnetic nanoparticle-assisted exogenous DNA incorporation into a cell, magnetic targeting helps to overcome the difficulty of diffusion through the cell membrane [12.9, 23], helping to enhance drug uptake in the targeted tissues.

Hyperthermia

Hyperthermia is a promising approach to cancer therapy and is based on heating of the target tissue to slightly above body temperature. Magnetic nanoparticles can be used as heat sources for magnetic hyperthermia. Magnetic nanoparticles in an external AC magnetic field generate heat through Neel and Brown relaxation processes. The main challenge lies in control heating to cancer cells in vivo without damaging normal cells and tissues. One approach is to use magnetic materials with Curie temperature in the range 42–47 °C [12.9]. Another approach in hyperthermia that has gained substantial attention in recent years is multimodal cancer therapy [12.20, 251, 252]. In this process, magnetic nanoparticles coated with a thermoresponsive polymer are used as drug targeting agents, followed by simultaneous hyperthermia and drug release.

Magnetic Tweezers

Magnetic tweezers are an advanced tool to manipulate single DNA or RNA molecules. In magnetic tweezers, DNA strands are attached to a glass surface on one end and to superparamagnetic beads on the other end (Fig. 12.23) [12.250, 253]. Magnetic beads can provide a *handle* that can be used to manipulate molecules and investigate intermolecular interactions [12.9].

Magnetic fields can be used to apply linear or torsional force to DNA, allowing investigation of the extension and elasticity of the molecule. The reliability of this measurement is influenced by the nature of the bonding of the magnetic bead to the DNA [12.9].

12.5 Conclusions

Much of the recent progress in magnetism and magnetic materials is due to nanostructuring and the interesting magnetic properties of magnetic nanostructures. Understanding the magnetic phenomena at nanoscale requires knowledge of physics, materials science, and chemistry, and the work reviewed here substantiates this point.

We have discussed some fundamental aspects of nanomagnetism such as the effect of nanostructuring on magnetic moment, anisotropy, coercivity, and Curie temperature. As an example, nanostructuring of magnetic materials induces surface anisotropy, and this in turn controls the demagnetization process and the hysteresis loop. Many interesting properties already demonstrated for magnetic nanostructures, such as superparamagnetism, GMR, shape anisotropy, and Curie temperature enhancement, hold immense promise for advanced technological applications. The energy product for a hard–soft nanocomposite is predicted to be much higher than for a single-phase magnet. Advanced fabrication techniques are needed to obtain optimal

microstructure with enhanced coercivity as well as magnetization.

The requirements for precise shapes and sizes of magnetic nanostructures have resulted in the development of new fabrication or synthesis techniques. We have presented various bottom-up and top-down approaches for fabrication of magnetic nanostructures. Bottom-up approaches such as mechanical milling, melt spinning, sputtering, MBE, and electrodeposition as well as various top-down chemical synthesis methods have been successful in producing nanostructured thin films, nanowires, nanorods, and nanopowders. Nanolithography has made it possible to fabricate various sophisticated nanostructures such as nanorings, circular dots, and nanodiamonds. In addition to synthesis/fabrication, structural and magnetic characterization is a basic step in establishing structure–property relationships. Therefore, characterization techniques such as electron optical techniques, including differential phase-contrast imaging and spin-polarized electron microscopy, electron holography, and quantitative Lorentz microscopy, AFM/MFM, and SEM/TEM have been reviewed. The wide range of applications of nanostructured magnets in the fields of data storage and biomedical engineering have also been illustrated.

References

12.1 P. Crespo, R. Litrán, T.C. Rojas, M. Multigner, J.M. de la Fuente, J.C. Sánchez-López, M.A. García, A. Hernando, S. Penadés, A. Fernández: Permanent magnetism, magnetic anisotropy, and hysteresis of thiol-capped gold nanoparticles, Phys. Rev. Lett. **93**, 087204-1–087204-4 (2004)

12.2 H. Oka, P.A. Ignatiev, S. Wedekind, G. Rodary, L. Niebergall, V.S. Stepanyuk, D. Sander, J. Kirschner: Spin-dependent quantum interference within a single magnetic nanostructure, Science **327**, 843–846 (2010)

12.3 M.D. Stiles: Interlayer exchange coupling, J. Magn. Magn. Mater. **200**, 322–337 (1999)

12.4 F. Giron, P. Boher, P. Houdy, F. Pierre, P. Beauvillain, C. Chappert, K. Le Dang, P. Veillet: Enhanced differential magnetoresistance of Cu/Co (100) multilayers, J. Magn. Magn. Mater. **104–107**, 1887–1888 (1992)

12.5 B. Heinrich, J.F. Cochran: Ultrathin metallic magnetic films: Magnetic anisotropies and exchange interactions, Adv. Phys. **42**, 523–639 (1993)

12.6 R. Allenspach: Ultrathin films: Magnetism on the microscopic scale, J. Magn. Magn. Mater. **129**, 160–185 (1994)

12.7 F.J. Himpsel, J.E. Ortega, G.J. Mankey, R.F. Willis: Magnetic nanostructures, Adv. Phys. **47**, 511–597 (1998)

12.8 J.F. Bobo, L. Gabillet, M. Bibes: Recent advances in nanomagnetism and spin electronics, J. Phys. Condens. Matter **16**, S471 (2004)

12.9 D. Sellmyer, R. Skomski: *Advanced Magnetic Nanostructures* (Springer, Berlin, Heidelberg 2006)

12.10 R.K. Mishra: Electron microscopy and the study of microstructure and domain structure of magnetic materials, Mater. Sci. Eng. B **7**, 297–306 (1991)

12.11 M. Giesen, H. Ibach: On the mechanism of rapid mound decay, Surf. Sci. **464**, L697–L702 (2000)

12.12 W. Kohn, L.J. Sham: Self-consistent equations including exchange and correlation effects, Phys. Rev. **140**, A1133–A1138 (1965)

12.13 N.A. Levanov, V.S. Stepanyuk, W. Hergert, D.I. Bazhanov, P.H. Dederichs, A. Katsnelson, C. Massobrio: Energetics of Co adatoms on the Cu(001) surface, Phys. Rev. B **61**, 2230 (2000)

12.14 X. Sun, Y. Huang, D.E. Nikles: FePt and CoPt magnetic nanoparticles film for future high density data storage media, Int. J. Nanotechnol. **1**, 328–346 (2004)

12.15 Y.X.J. Wang, S.M. Hussain, G.P. Krestin: Superparamagnetic iron oxide contrast agents: Physicochemical characteristics and applications in MR imaging, Eur. Radiol. **11**, 2319–2331 (2001)

12.16 U.O. Häfeli: Magnetically modulated therapeutic systems, Int. J. Pharm. **277**, 19–24 (2004)

12.17 S. Kayal, R.V. Ramanujan: Anti-cancer drug loaded irongold coreshell nanoparticles (FeAu) for magnetic drug targeting, J. Nanosci. Nanotechnol. **10**, 5527–5539 (2010)

12.18 S. Kayal, R.V. Ramanujan: Doxorubicin loaded PVA coated iron oxide nanoparticles for targeted drug delivery, Mater. Sci. Eng. C **30**, 484–490 (2010)

12.19 R. Hergt, S. Dutz, R. Müller, M. Zeisberger: Magnetic particle hyperthermia: Nanoparticle magnetism and materials development for cancer therapy, J. Phys. Condens. Matter **18**, S2919 (2006)

12.20 S. Purushotham, R.V. Ramanujan: Thermoresponsive magnetic composite nanomaterials for multimodal cancer therapy, Acta Biomater. **6**, 502–510 (2010)

12.21 C.S.S.R. Kumar: *Magnetic Nanomaterials* (Wiley, Weinheim 2009)

12.22 K. Ino, A. Ito, H. Honda: Cell patterning using magnetite nanoparticles and magnetic force, Biotechnol. Bioeng. **97**, 1309–1317 (2007)

12.23 D. Ang, Q.V. Nguyen, S. Kayal, P.R. Preiser, R.S. Rawat, R.V. Ramanujan: Insights into the mechanism of magnetic particle assisted gene delivery, Acta Biomater. **7**, 1319–1326 (2010)

12.24 R.D. Shull: Magnetocaloric effect of ferromagnetic particles, IEEE Trans. Magn. **29**, 2 (1993)

12.25 J.Y. Law, R.V. Ramanujan, V. Franco: Tunable Curie temperatures in Gd alloyed Fe-B-Cr magnetocaloric materials, J. Alloys Compd. **508**, 14–19 (2010)

12.26 R.C.O. Handley: *Modern Magnetic Materials: Principles and Applications* (Wiley, New York 1999)

12.27 P. Weiss, R. Forrer: The atomic moments of iron cobalt and nickel as determined from the magnetic saturation of the ferro-cobalts and nickel-cobalts, Ann. Phys. **5**, 413–417 (1926)

12.28 R. Skomski: Nanomagnetics, J. Phys. Condens. Matter **15**, R841 (2003)

12.29 A.P. Guimaraes: *Principles of Nanomagnetism* (Springer, London, New York 2009)

12.30 N.A. Frey, S. Peng, K. Cheng, S. Sun: Magnetic nanoparticles: Synthesis, functionalization, and applications in bioimaging and magnetic energy storage, Chem. Soc. Rev. **38**, 2532–2542 (2009)

12.31 B.D. Cullity: *Introduction to Magnetic Materials* (Addison-Wesley, Boston 1972)

12.32 I.M.L. Billas, A. Châtelain, W.A. De Heer: Magnetism of Fe, Co and Ni clusters in molecular beams, J. Magn. Magn. Mater. **168**, 64–84 (1997)

12.33 Q.Y. Wu, R. Wu, Z.G. Chen, Y.B. Lin, J.M. Zhang, Z.G. Huang: Ab initio study of ferromagnetism in N doped Zn0 and its stabilization by Li codoping, 2nd IEEE Int. Nanoelectron. Conf., INEC 2008, Shanghai (2008) pp. 700–703

12.34 R.Q. Wu, G.W. Peng, L. Liu, Y.P. Feng, Z.G. Huang, Q.Y. Wu: Cu-doped GaN: A dilute magnetic semiconductor from first-principles study, Appl. Phys. Lett. **89**, 062505 (2006)

12.35 D.L. Mills, J.A.C. Bland: *Nanomagnetism Ultrathin Films, Multilayers and Nanostructures* (Elsevier, Amsterdam 2006)

12.36 J.A. Alonso: Electronic and atomic structure, and magnetism of transition-metalclusters, Chem. Rev. **100**, 637–677 (2000)

12.37 C.A.F. Vaz, J.A.C. Bland, G. Lauhoff: Magnetism in ultrathin film structures, Rep. Prog. Phys. **71**, 056501 (2008)

12.38 H. Zeng, M. Zheng, R. Skomski, D.J. Sellmyer, Y. Liu, L. Menon, S. Bandyopadhyay: Magnetic properties of self-assembled Co nanowires of varying length and diameter, J. Appl. Phys. **87**, 4718–4720 (2000)

12.39 G.T.A. Huysmans, J.C. Lodder, J. Wakui: Magnetization curling in perpendicular iron particle arrays (alumite media), J. Appl. Phys. **64**, 2016–2021 (1988)

12.40 M. Zheng, R. Skomski, Y. Liu, D.J. Sellmyer: Magnetic hysteresis of Ni nanowires, J. Phys. Condens. Matter **12**, L497 (2000)

12.41 J.M.D. Coye: *Magnetism and Magnetic Materials* (Cambridge Univ. Press, Cambridge 2010)

12.42 E.C. Stoner, E.P. Wohlfarth: A mechanism of magnetic hysteresis in heterogeneous alloys, IEEE Trans. Magn. **27**, 3475–3518 (1991)

12.43 W.F. Brown Jr.: Virtues and weaknesses of the domain concept, Rev. Mod. Phys. **17**, 15–19 (1945)

12.44 H. Kronmüller: Theory of nucleation fields in inhomogeneous ferromagnets, Phys. Status Solidi (b) **144**, 385–396 (1987)

12.45 F. Sato, N. Tezuka, T. Sakurai, T. Miyazaki: Grain diameter and coercivity of Fe, Ni, and Co metals, IEEE Trans. Magn. Jpn. **9**, 100–106 (1994)

12.46 G.C. Hadjipanayis: *Magnetic Hysteresis in Novel Magnetic Materials* (Kluwer, New York 1996)

12.47 M.S.J. Bauer, A. Zern, H. Kronmüller: Nanocrystalline FeNdB permanent magnets with enhanced remanence, J. Appl. Phys. **80**, 6 (1996)

12.48 H. Kronmüller, K.D. Durst, M. Sagawa: Analysis of the magnetic hardening mechanism in RE-FeB permanent magnets, J. Magn. Magn. Mater. **74**, 291–302 (1988)

12.49 H. Kronmüller, D. Goll: Micromagnetic analysis of nucleation-hardened nanocrystalline PrFeB magnets, Scr. Mater. **47**, 551–556 (2002)

12.50 J.F. Löffler, H.B. Braun: Magnetization response in bulk nanostructured magnets, Mater. Sci. Eng. A **448–451**, 407–413 (2007)

12.51 S. Thomas, S.H. Al-Harthi, D. Sakthikumar, I.A. Al-Omari, R.V. Ramanujan, Y. Yoshida, M.R. Anantharaman: Microstructure and random magnetic anisotropy in Fe-Ni based nanocrystalline thin films, J. Phys. D **41**, 155009 (2008)

12.52 D.L. Leslie-Pelecky, R.D. Rieke: Magnetic properties of nanostructured materials, Chem. Mater. **8**, 1770–1783 (1996)

12.53 K.D. Sattler: *Handbook of Nanophysics: Nanotubes and Nanowires* (CRC, Boca Raton 2011)

12.54 A.O. Adeyeye, N. Singh: Large area patterned magnetic nanostructures, J. Phys. D **41**, 153001 (2008)

12.55 S.Y. Chou: Patterned magnetic nanostructures and quantized magnetic disks, Proc. IEEE **85**, 652–671 (1997)

12.56 S.Y. Chou, P.R. Krauss: Quantum magnetic disk, J. Magn. Magn. Mater. **155**, 151–153 (1996)

12.57 Y. Takemura, J.-I. Shirakashi: AFM lithography for fabrication of magnetic nanostructures and devices, J. Magn. Magn. Mater. **304**, 19–22 (2006)

12.58 X. Wei, X. Chen, K. Jiang: Fabrication of nickel nanostructure arrays via a modified nanosphere lithography, Nanoscale Res. Lett. **6**, 1–5 (2010)

12.59 H.S. Nalwa: *Handbook of Thin Film Materials: Nanomaterials and Magnetic Thin Films* (Academic, San Diego 2002)

12.60 S. Yoshino, S. Tsunashima, M. Masuda, S. Uchiyama: Magnetostriction and perpendicular magnetic anisotropy of amorphous GdFeCo thin films, Jpn. J. Appl. Phys. **27**, 1247–1249 (1988)

12.61 G. Choe, R.M. Walser: Structure and magnetic properties of compositionally modulated Tb–Fe thin films (abstract), J. Appl. Phys. **67**, 5686 (1990)

12.62 J.-F. Bobo, P. Delcroix, J.-C. Ousset, M.-F. Ravet, M. Piecuch: Magnetic properties of sputtered Fe/Al multilayers, J. Magn. Magn. Mater. **93**, 452–456 (1991)

12.63 H.S. Lee, J.A. Bain, D.E. Laughlin: Use of bias sputtering to enhance decoupling in oxide composite perpendicular recording media, Appl. Phys. Lett. **90**, 252511 (2007)

12.64 R.P. Howson: The reactive sputtering of oxides and nitrides, Pure Appl. Chem. **66**, 7 (1994)

12.65 M. Cantoni, D. Petti, C. Rinaldi, R. Bertacco: Epitaxial growth of Fe/MgO/Ge(001) heterostructures, Microelectron. Eng. **88**, 530–533 (2011)

12.66 J.Y. Ahn, N.J. Lee, T.H. Kim: Perpendicular magnetization of FePt alloy films epitaxially grown on Si(100), J. Magn. **14**, 144–146 (2009)

12.67 A.P. Mihai, J.P. Attané, L. Vila, C. Beigné, J.C. Pillet, A. Marty: Magnetization reversal dominated by domain wall pinning in FePt based spin valves, Appl. Phys. Lett. **94**, 122509 (2009)

12.68 D.H. Wei, F.T. Yuan, H.W. Chang, K.L. You, Y. Liou, T.S. Chin, C.C. Yu, Y.D. Yao: Self-organized magnetic assemblies of (001) oriented FePt nanoparticles with SiO_2 additive, Nanotechnology **18**, 335603 (2007)

12.69 W. Schwarzacher, K. Attenborough, A. Michel, G. Nabiyouni, J.P. Meier: Electrodeposited nanostructures, J. Magn. Magn. Mater. **165**, 23–29 (1997)

12.70 Y. Jyoko, S. Kashiwabara, Y. Hayashi, W. Schwarzacher: Characterization of electrodeposited magnetic nanostructures, J. Magn. Magn. Mater. **198/199**, 239–242 (1999)

12.71 H. Cao, Z. Xu, D. Sheng, J. Hong, H. Sang, Y. Du: An array of iron nanowires encapsulated in polyaniline nanotubules and its magnetic behavior, J. Mater. Chem. **11**, 958–960 (2001)

12.72 Q. Ri, L.Z. Xiao, Q. Ru, L. Yan, S.L. Myung, I.K. Yeong, S.K. Young: FePt magnetic material synthesis by electrochemical methods, IEEE Nanotechnol. Mater. Dev. Conf., NMDC, Gyeongju (2006) pp. 660–661

12.73 K. Rumpf, P. Granitzer, P. Poelt: Metal semiconductor hybrid system with two magnetic terms dependent on the field region, J. Phys. **200**, 072081(1)–072081(4) (2010)

12.74 X. Tang, H.-W. Zhang, H. Su, Y.-L. Jing, Z.-Y. Zhong: Polarized current changes the exchange bias in a current-in-plane spin valve, J. Magn. Magn. Mater. **321**, 1851–1855 (2009)

12.75 J.H. Lee, J.H. Wu, J.S. Lee, K.S. Jeon, H.R. Kim, J.H. Lee, Y.D. Suh, C.O. Kim: Synthesys and characterization of Fe–FeO_x core–shell nanowires, IEEE Trans. Magn. **44**, 4 (2008)

12.76 C.B. Murray, S. Sun, W. Gaschler, H. Doyle, T.A. Betley, C.R. Kagan: Colloidal synthesis of nanocrystals and nanocrystal superlattices, IBM J. Res. Dev. **45**, 47–56 (2001)

12.77 T. Hyeon: Chemical synthesis of magnetic nanoparticles, Chem. Commun. **9**, 927–934 (2003)

12.78 J.P. Wilcoxon, B.L. Abrams: Synthesis, structure and properties of metalnanoclusters, Chem. Soc. Rev. **35**, 1162–1194 (2006)

12.79 A. Enders, R. Skomski, J. Honolka: Magnetic surface nanostructures, J. Phys. Condens. Matter **22**, 433001 (2010)

12.80 V.P. Novikov, V.V. Pan'kov, L.I. Kunitskii: Preparation of nickel, iron, and cobalt nanopowders via reduction of salts with sodium dissolved in liquid ammonia, Inorg. Mater. **40**, 809–814 (2004)

12.81 G.N. Glavee, K.J. Klabunde, C.M. Sorensen, G.C. Hadjipanayis: Borohydride reduction of cobalt ions in water. Chemistry leading to nanoscale metal boride, or borate particles, Langmuir **9**, 162–169 (1993)

12.82 A.K. Srivastava, S. Madhavi, T.J. White, R.V. Ramanujan: Cobalt-ferrite nanobowl arrays: Curved magnetic nanostructures, J. Mater. Res. **22**, 1250–1254 (2007)

12.83 X. Hu, J.C. Yu: High-yield synthesis of nickel and nickel phosphide nanowires via microwave-assisted processes, Chem. Mater. **20**, 6743–6749 (2008)

12.84 N. Pérez, F. Bartolomé, L.M. García, J. Bartolomé, M.P. Morales, C.J. Serna, A. Labarta, X. Batlle: Nanostructural origin of the spin and orbital contribution to the magnetic moment in $Fe_{3-x}O_4$ magnetite nanoparticles, Appl. Phys. Lett. **94**, 093108(1)–093108(3) (2009)

12.85 R.Y. Hong, S.Z. Zhang, G.Q. Di, H.Z. Li, Y. Zheng, J. Ding, D.G. Wei: Preparation, characterization and application of Fe_3O_4/ZnO core/shell magnetic nanoparticles, Mater. Res. Bull. **43**, 2457–2468 (2008)

12.86 S.W. Ko, M.S. Yang, H.J. Choi: Adsorption of polymer coated magnetite composite particles onto carbon nanotubes and their magnetorheology, Mater. Lett. **63**, 861–863 (2009)

12.87 B.L. Cushing, V.L. Kolesnichenko, C.J. O'Connor: Recent advances in the liquid-phase syntheses of inorganic nanoparticles, Chem. Rev. **104**, 3893–3946 (2004)

12.88 X.-M. Lin, A.C.S. Samia: Synthesis, assembly and physical properties of magnetic nanoparticles, J. Magn. Magn. Mater. **305**, 100–109 (2006)

12.89 R. Che, S. Wang, B. Yu: Preparation of nano-Fe_xO_y by thermal decomposition method and morphology research, Adv. Mater. Res. **148**, 1124–1128 (2011)

12.90 C. Srivastava, D. Nikles, J. Harrell, G. Thompson: Composition distributions in FePt(Au) nanoparticles, J. Nanopart. Res. **12**, 2051–2056 (2010)

12.91 M. Vázqueza, C. Lunaa, M.P. Morales, R. Sanza, C.J. Serna, C. Mijangos: Magnetic nanoparticles:

Synthesis, ordering and properties, Physica B **354**, 71–79 (2004)
12.92 X. Sun, C.J. Thode, J.K. Mabry, J.W. Harrell, D.E. Nikles, K. Sun, L.M. Wang: Self-assembly of magnetic biofunctional nanoparticles, J. Appl. Phys. **97**, 1–3 (2005)
12.93 B.Y. Hou, Z. Xu, S. Peng, C. Rong, J.P. Liu, S. Sun: A facile synthesis of $SmCo_5$ magnets from core/shell Co/Sm_2O_3 nanoparticles, Adv. Mater. **19**, 3349–3352 (2007)
12.94 P.K. Deheri, V. Swaminathan, S.D. Bhame, Z. Liu, R.V. Ramanujan: Sol-gel based chemical synthesis of $Nd_2Fe_{14}B$ hard magnetic nanoparticles, Chem. Mater. **22**, 6509–6517 (2010)
12.95 S.D. Bhame, V. Swaminathan, P.K. Deheri, R.V. Ramanujan: Exchange coupled hard magnetic $Nd_2Fe_{14}B$ nanoparticles by novel autocombustion-reduction diffusion synthesis, Adv. Sci. Lett. **3**, 174–179 (2010)
12.96 J. McGuiness, K. Žužek, B. Podmiljšak, S. Kobe: Magnetic monitoring of the hydrogenation-decomposition-desorption-recombination process in SmFe-based alloys, J. Appl. Phys. **93**, 6918–6920 (2003)
12.97 S.P.H. Marashi, A. Abedi, S. Kaviani, S.H. Aboutalebi, M. Rainforth, H.A. Davies: Effect of melt-spinning roll speed on the nanostructure and magnetic properties of stoichiometric and near stoichiometric Nd-Fe-B alloy ribbons, J. Phys. D **42**, 115410 (2009)
12.98 W. Liu, P.G. McCormick: Synthesis of Sm_2Co_{17} alloy nanoparticles by mechanochemical processing, J. Magn. Magn. Mater. **195**, 279–283 (1999)
12.99 C. Petit, M.P. Pileni: Physical properties of self-assembled nanosized cobalt particles, Appl. Surf. Sci. **162**, 519–528 (2000)
12.100 H. Zhou, J. Narayan: Self-assembled magnetic nanostructures: Epitaxial Ni nanodots on TiN/Si (001) surface, J. Nanopart. Res. **8**, 595–600 (2006)
12.101 M. Albrecht, G. Hu, I.L. Guhr, T.C. Ulbrich, J. Boneberg, P. Leiderer, G. Schatz: Magnetic multilayers on nanospheres, Nat. Mater. **4**, 203–206 (2005)
12.102 S. Sun, C.B. Murray, D. Weller, L. Folks, A. Moser: Monodisperse FePt nanoparticles and ferromagnetic FePt nanocrystal, Superlattices Sci. **287**, 1989–1992 (2000)
12.103 T. Ichitsubo, K. Tanaka, M. Koujina, M. Kawashima, M. Hirao: Effects of external magnetic field on FePt films during heat treatment, Jpn. J. Appl. Phys. **43**, 273–276 (2004)
12.104 A.K. Srivastava, S. Madhavi, R.V. Ramanujan: Directed magnetic field induced assembly of high magnetic moment cobalt nanowires, Appl. Phys. A **98**, 821–830 (2010)
12.105 A.K. Srivastava, R.S. Singh, K.E. Sampson, V.P. Singh, R.V. Ramanujan: Templated assembly of magnetic cobalt nanowire arrays, Metall. Mater. Trans. A **38**, 717–724 (2007)
12.106 Z. Gai, B. Wu, J.P. Pierce, G.A. Farnan, D. Shu, M. Wang, Z. Zhang, J. Shen: Self-assembly of nanometer-scale magnetic dots with narrow size distributions on an insulating substrate, Phys. Rev. Lett. **89**, 235502 (2002)
12.107 H. Schlörb, V. Haehnel, M.S. Khatri, A. Srivastav, A. Kumar, L. Schultz, S. Fähler: Magnetic nanowires by electrodeposition within templates, Phys. Status Solidi (b) **247**, 2364–2379 (2010)
12.108 S. Sun, S. Anders, H.F. Hamann, J.U. Thiele, J.E.E. Baglin, T. Thomson, E.E. Fullerton, C.B. Murray, B.D. Terris: Polymer mediated self-assembly of magnetic nanoparticles, J. Am. Chem. Soc. **124**, 2884–2885 (2002)
12.109 S. Kralj, M. Drofenik, D. Makovec: Controlled surface functionalization of silica-coated magnetic nanoparticles with terminal amino and carboxyl groups, J. Nanopart. Res. **13**, 2829–2841 (2011)
12.110 K. Tsuno: Magnetic domain observation by means of Lorentz electron microscopy with scanning technique, Rev. Solid State Sci. **2**, 623–658 (1988)
12.111 Y. Murakami, T. Yano, D. Shindo, R. Kainuma, T. Arima: Transmission electron microscopy of magnetic phase transformations in functional materials, Metall. Mater. Trans. A **38**, 815–820 (2007)
12.112 S. Porthun, L. Abelmann, C. Lodder: Magnetic force microscopy of thin film media for high density magnetic recording, J. Magn. Magn. Mater. **182**, 238–273 (1998)
12.113 W. Szmaja, J. Grobelny, M. Cichomski, K. Makita, W. Kozlowski: Imaging domains of hard magnetic materials by SEM and MFM, Vacuum **81**, 1367–1370 (2007)
12.114 J.N. Chapman: The investigation of magnetic domain structures in thin foils by electron microscopy, J. Phys. D **17**, 623–647 (1984)
12.115 T. Kohashi, M. Konoto, K. Koike: High-resolution spin-polarized scanning electron microscopy (spin SEM), J. Electron Microsc. **59**, 43–52 (2010)
12.116 M.A. Schofield, M. Beleggia, Y. Zhu, G. Pozzi: Characterization of JEOL 2100F Lorentz-TEM for low-magnification electron holography and magnetic imaging, Ultramicroscopy **108**, 625–634 (2008)
12.117 F.J. Giessibl: Advances in atomic force microscopy, Rev. Mod. Phys. **75**, 949–983 (2003)
12.118 P. Hinterdorfer, Y. Dufrêne: Detection and localization of single molecular recognition events using atomic force microscopy, Nat. Methods **3**, 347–355 (2006)
12.119 R.V. Lapshin: Feature-oriented scanning methodology for probe microscopy and nanotechnology, Nanotechnology **15**, 1135–1151 (2004)
12.120 G. Schitter, M.J. Rost: Scanning probe microscopy at video-rate, Mater. Today **11**, 40–48 (2008)
12.121 H.J. Butt, B. Cappella, M. Kappl: Force measurements with the atomic force microscope:

Technique, interpretation and applications, Surf. Sci. Rep. **59**, 1–152 (2005)
12.122 C. Schönenberger, S.F. Alvarado: Observation of single charge carriers by force microscopy, Phys. Rev. Lett. **65**, 3162–3164 (1990)
12.123 L. Belliard, A. Thiaville, S. Lemerle, A. Lagrange, J. Ferré, J. Miltat: Investigation of the domain contrast in magnetic force microscopy, J. Appl. Phys. **81**, 3849–3851 (1997)
12.124 A. Winkler, T. Muhl, S. Menzel, R. Kozhuharova-Koseva, S. Hampel, A. Leonhardt, B. Buchner: Magnetic force microscopy sensors using iron-filled carbon nanotubes, J. Appl. Phys. **99**, 104905 (2006)
12.125 P. Müllner, V.A. Chernenko, G. Kostorz: Stress-induced twin rearrangement resulting in change of magnetization in a Ni-Mn-Ga ferromagnetic martensite, Scr. Mater. **49**, 129–133 (2003)
12.126 R.D. James, M. Wuttig: Magnetostriction of martensite, Philos. Mag. A **77**, 1273–1299 (1998)
12.127 T. Kakeshita, T. Takeuchi, T. Fukuda, M. Tsujiguchi, T. Saburi, R. Oshima, S. Muto: Giant magnetostriction in an ordered FePt nanoparticle Fe_3Pt single crystal exhibiting a martensitic transformation, Appl. Phys. Lett. **77**, 1502–1504 (2000)
12.128 Q. Yan, A. Purkayastha, T. Kim, R. Kröger, A. Base, G. Ramanath: Synthesis and assembly of monodisperse high-coercivity silica-capped FePt nanomagnets of tunable size, composition, and thermal stability from microemulsions, Adv. Mater. **18**, 2569–2573 (2006)
12.129 S. Foglia, A. Notargiacomo, A. Capobianchi, A.M. Testa, D. Fiorani, L. Arrizza, C. Veroli: Novel ultrasonic-assisted alignment of L_{10} FePt nanoparticles, Superlattices Microstruct. **46**, 121–124 (2009)
12.130 L.C. Varanda, M. Jafelicci Jr.: Self-assembled FePt nanocrystals with large coercivity: Reduction of the fcc-to- L_{10} ordering temperature, J. Am. Chem. Soc. **128**, 11062–11066 (2006)
12.131 C.B. Rong, N. Poudyal, G.S. Chaubey, V. Nandwana, R. Skomski, Y.Q. Wu, M.J. Kramer, J.P. Liu: Structural phase transition and ferromagnetism in monodisperse 3 nm FePt particles, J. Appl. Phys. **102**, 043913 (2007)
12.132 H. Wang, L. Zhang, L. Li, E. Jia, X. Zhao: Fabrication and magnetic properties of FePt/Ag multilayered nanowires, J. Magn. Magn. Mater. **322**, 3555–3557 (2010)
12.133 H. Wang, E. Jia, L. Zhang, L. Li, M. Li: On low-temperature ordering of FePt nanowires, Phys. Lett. A **372**, 5712–5715 (2008)
12.134 N. Poudyal, G.S. Chaubey, C.B. Rong, J.P. Liu: Shape control of FePt nanocrystals, J. Appl. Phys. **105**, 07A749–1–07A749–3 (2009)
12.135 J.A. Christodoulides, M.J. Bonder, Y. Huang, Y. Zhang, S. Stoyanov, G.C. Hadjipanayis, A. Simopoulos, D. Weller: Intrinsic and hysteresis properties of FePt nanoparticles, Phys. Rev. B **68**, 544281–544287 (2003)
12.136 J.H. Gao, D.L. Sun, Q.F. Zhan, W. He, Z.H. Cheng: Magnetization reversal process and magnetic relaxation of self-assembled Fe_3Pt nanowire arrays with different diameters: Experiment and micromagnetic simulations, Phys. Rev. B **75**, 064421–064427 (2007)
12.137 E.P. Wohlfarth: Relations between different modes of acquisition of the remanent magnetization of ferromagnetic particles, J. Appl. Phys. **29**, 595–596 (1958)
12.138 P.E. Kelly, K. O'Grady, P.I. Mayo, R.W. Chantrell: Switching mechanisms in cobalt-phosphorus thin films, IEEE Trans. Magn. **25**, 3881–3883 (1989)
12.139 H. Zeng, J. Li, Z.L. Wang, J.P. Liu, S. Sun: Interparticle interactions in annealed FePt nanoparticle assemblies, IEEE Trans. Magn. **38**, 2598–2600 (2002)
12.140 L.Y. Lu, D. Wang, X.G. Xu, Q. Zhan, Y. Jiang: Enhancement of magnetic properties for FePt nanoparticles by rapid annealing in a vacuum, J. Phys. Chem. C **113**, 19867–19870 (2009)
12.141 Y. Gao, X.W. Zhang, Z.G. Yin, S. Qu, J.B. You, N.F. Chen: Magnetic properties of FePt nanoparticles prepared by a micellar method, Nanoscale Res. Lett. **5**, 1–6 (2010)
12.142 H. Wang, Y.C. Wu, L. Zhang, X. Hu: Fabrication and magnetic properties of FePt multilayered nanowires, Appl. Phys. Lett. **89**, 232508 (2006)
12.143 Y.H. Huang, H. Okumura, G.C. Hadjipanayis, D. Weller: CoPt and FePt nanowires by electrodeposition, J. Appl. Phys. **91**, 6869 (2002)
12.144 L. Cagnon, Y. Dahmane, J. Voiron, S. Pairis, M. Bacia, L. Ortega, N. Benbrahim, A. Kadri: Electrodeposited CoPt and FePt alloys nanowires, J. Magn. Magn. Mater. **310**, 2428–2430 (2007)
12.145 Y. Hou, H. Kondoh, R. Che, M. Takeguchi, T. Ohta: Ferromagnetic FePt nanowires: Solvothermal reduction synthesis and characterization, Small **2**, 235–238 (2006)
12.146 C. Wang, Y. Hou, J. Kim, S. Sun: A general strategy for synthesizing FePt nanowires and nanorods, Angew. Chem. **46**, 6333–6335 (2007)
12.147 J.H. Gao, Q.F. Zhan, W. He, D.L. Sun, Z.H. Cheng: Synthesis and magnetic properties of Fe_3Pt nanowire arrays fabricated by electrodeposition, Appl. Phys. Lett. **86**, 1–3 (2005)
12.148 J. Wan, S. Stoyanov, Y. Huang, Y. Zhang, G. Hadjipanayis, V. Skumryev, D. Weller: Thickness dependence of coercivity in FePt/C multilayers, J. Magn. Magn. Mater. **272–276**, 1625–1627 (2004)
12.149 M.G. Kim, S.C. Shin, K. Kang: Ordering of island-like FePt L_{10} thin films, Appl. Phys. Lett. **80**, 3802 (2002)
12.150 B.Z. Cui, M.J. O'Shea: Exchange coupling and magnetic properties of $Nd_2Fe_{14}B$/Co nanocomposite thin films, J. Magn. Magn. Mater. **256**, 348–354 (2003)
12.151 N. Li, B.M. Lairson, O.-H. Kwon: Magnetic characterization of intermetallic compound FePt and

FePtX (X= B, Ni) thin films, J. Magn. Magn. Mater. **205**, 1–6 (1999)
12.152 N. Zotov, R. Hiergeist, A. Savan, A. Ludwig: Effects of annealing time on the structural and magnetic properties of L_{10} FePt thin films, Thin Solid Films **518**, 4977–4985 (2010)
12.153 K. Leistner, J. Thomas, S. Baunack, H. Schlörb, L. Schultz, S. Fähler: Influence of oxygen and copper in electrodeposited FePt films, J. Magn. Magn. Mater. **290/291**, 1270–1273 (2005)
12.154 S.H. Teh, I.I. Yaacob: The effect of cobalt addition on structural and magnetic properties of electrodeposited iron-platinum nanocrystalline thin films, Mater. Sci. Forum, Cairns, QLD (2010) pp. 1736–1739
12.155 T. Sato, H. Kato, T. Shima, Y.K. Takahashi, K. Hono: Effect of film morphology on the magnetic properties for NdFeB thin films, J. Magn. Magn. Mater. **323**, 163–166 (2011)
12.156 E. Sallica Leva, R.C. Valente, F. Martínez Tabares, M. Vásquez Mansilla, S. Roshdestwensky, A. Butera: Magnetic domain crossover in FePt thin films, Phys. Rev. B **82**, 144410–144418 (2010)
12.157 S.N. Piramanayagam, M. Matsumoto, A. Morisako: Perpendicular magnetic anisotropy in NdFeB thin films, J. Appl. Phys. **85**, 5898–5900 (1999)
12.158 X. Liu, T. Okumoto, M. Matsumoto, A. Morisako: Effect of W underlayer on the crystal orientation and microstructure of NdFeB thin films, J. Appl. Phys. **97**, 1–3 (2005)
12.159 D.H. Wei, Y.D. Yao: Enhanced magnetic properties in FePt (001) epitaxial thin films by Cu capping layer, INEC 2010 – 2010 3rd Int. Nanoelectron. Conf. Hongkong (2010) pp. 704–705
12.160 M.L. Yan, R. Skomski, A. Kashyap, L. Gao, S.H. Liou, D.J. Sellmyer: Hysteresis of granular FePt:Ag films with perpendicular anisotropy, IEEE Trans. Magn. **40**, 2495–2497 (2004)
12.161 C.M. Kuo, P.C. Kuo, H.C. Wu, Y.D. Yao, C.H. Lin: Magnetic hardening mechanism study in FePt thin films, J. Appl. Phys. **85**, 4886–4888 (1999)
12.162 Z.L. Zhao, J.P. Wang, J.S. Chen, J. Ding: Control of magnetization reversal process with pinning layer in FePt thin films, Appl. Phys. Lett. **81**, 3612 (2002)
12.163 J.-L. Tsai, T.-S. Chin, Y.-D. Yao, A. Melsheimer, S. Fisher, T. Drogen, M. Kelsch, H. Kronmüller: Preparation and properties of $[(NdFeB)_x/(Nb)_z]_n$ multi-layer films, Physica B **327**, 283–286 (2003)
12.164 S.K. Chen, F.T. Yuan, T.S. Chin: Effect of interfacial diffusion on microstructure and magnetic properties of CuFePt bilayer thin films, J. Appl. Phys. **97**, 1–6 (2005)
12.165 W. Liu, Z.D. Zhang, J.P. Liu, Z.R. Dai, Z.L. Wang, X.K. Sun, D.J. Sellmyer: Nanocomposite (Nd,Dy)(Fe,Co,Nb,B)$_{5.5}$/α-Fe multilayer magnets with high performance, J. Phys. D **36**, L63 (2003)
12.166 E.F. Kneller, R. Hawig: The exchange-spring magnet: A new material principle for permanent magnets, IEEE Trans. Magn. **27**, 3588–3600 (1991)
12.167 R. Coehoorn, D.B. de Mooij, C. de Waard: Meltspun permanent magnet materials containing Fe_3B as the main phase, J. Magn. Magn. Mater. **80**, 101–104 (1989)
12.168 R. Skomski, J.M.D. Coey: Giant energy product in nanostructured two-phase magnets, Phys. Rev. B **48**, 15812–15816 (1993)
12.169 Z.W. Liu, D.C. Zeng, R.V. Ramanujan, X.C. Zhong, H.A. Davies: Exchange interaction in rapidly solidified nanocrystalline RE-(Fe/Co)-B hard magnetic alloys, J. Appl. Phys. **105**, 07 (2009), A736
12.170 Z.W. Liu, Y. Liu, P.K. Deheri, R.V. Ramanujan, H.A. Davies: Improving permanent magnetic properties of rapidly solidified nanophase RE-TM-B alloys by compositional modification, J. Magn. Magn. Mater. **321**, 2290–2295 (2009)
12.171 O.V. Billoni, S.E. Urreta, L.M. Fabietti, H.R. Bertorello: Dependence of the coercivity on the grain size in a FeNdB+αFe nanocrystalline composite with enhanced remanence, J. Magn. Magn. Mater. **187**, 371–380 (1998)
12.172 I. Betancourt, H.A. Davies: Exchange coupled nanocomposite hard magnetic alloys, Mater. Sci. Technol. **26**, 5–19 (2010)
12.173 Z.W. Liu, R.V. Ramanujan, H.A. Davies: Improved thermal stability of hard magnetic properties in rapidly solidified RE-TM-B alloys, J. Mater. Res. **23**, 2733–2742 (2008)
12.174 T. Schrefl, J. Fidler: Modelling of exchange-spring permanent magnets, J. Magn. Magn. Mater. **177–181**, 970–975 (1998)
12.175 C.B. Rong, H.W. Zhang, R.J. Chen, S.I. He, B.G. Shen: The role of dipolar interaction in nanocomposite permanent magnets, J. Magn. Magn. Mater. **302**, 126–136 (2006)
12.176 L.H. Lewis, D.O. Welch, V. Panchanathan: Curie temperature enhancement of $Nd_2Fe_{14}B$ in nanocomposite exchange-spring alloys, J. Magn. Magn. Mater. **175**, 275–278 (1997)
12.177 M. Dahlgren, R. Grossinger, E. De Morals, S. Gama, G. Mendoza, J.F. Liu, H.A. Davies: Enhancement of the curie temperature for exchange coupled Nd-Fe-B and Pr-Fe-B magnets, IEEE Trans. Magn. **33**, 3895–3897 (1997)
12.178 S. Li, B. Gu, H. Bi, Z. Tian, G. Xie, Y. Zhu, Y. Du: Role of amorphous grain boundaries in nanocomposite NdFeB permanent magnets, J. Appl. Phys. **92**, 7514–7518 (2002)
12.179 W.Y. Zhang, M. Stoica, J. Eckert, P. Yu, J.Z. Jiang: Preparation of bulk $Nd_2Fe_{14}B/Fe_3B$ nanocomposite magnets with high rare earth content, Intermetallics **16**, 341–344 (2008)
12.180 S. Ishihara, W. Zhang, H. Kimura, M. Omori, A. Inoue: Consolidation of Fe-Co-Nd-Dy-B glassy powders by spark-plasma sintering and magnetic

properties of the consolidated alloys, Mater. Trans. **44**, 138–143 (2003)
12.181 X. Cui, Z.W. Liu, D.C. Zeng: Bulk metallic glass formation, crystallization, and magnetic properties of $RE_2Fe_{72}B_{22}M_2$ alloys, Mater. Sci. Forum, Cairns, QLD (2010) pp. 1062–1065
12.182 Y. Gu, D. Zhang, X. Zhan, Z. Ji, Y. Zhang: Structural and magnetic properties of RF sputtered FePt/Fe multilayers, J. Magn. Magn. Mater. **297**, 7–16 (2006)
12.183 Z. Zhang, B. Cui, G. Wang, B. Ma, Q.Y. Jin, Y. Liu: Ultrafast laser-induced magnetization precession dynamics in FePt/CoFe exchange-coupled films, Appl. Phys. Lett. **97**, 172508 (2010)
12.184 J.P. Liu, Y. Liu, R. Skomski, D.J. Sellmyer: High energy products in exchange-coupled nanocomposite films, IEEE Trans. Magn. **35**, 3241–3246 (1999)
12.185 T.V. Khoa, L.T. Tai, T.D. Hien, N.P. Duong, C.O. Kim: Enhancement of the Curie temperature and the remanence in NdFeB/Fe multilayer films, J. Korean Phys. Soc. **52**, 1677–1680 (2008)
12.186 N. Kaushik, P. Sharma, H. Kimura, A. Inoue, A. Makino: Exchange coupling in nanocomposite FePtB thin film magnets, J. Appl. Phys. **103**, 07E121–07E121–3 (2008)
12.187 X. Rui, J.E. Shield, Z. Sun, L. Yue, Y. Xu, D.J. Sellmyer, Z. Liu, D.J. Miller: High-energy product exchange-spring FePt/Fe cluster nanocomposite permanent magnets, J. Magn. Magn. Mater. **305**, 76–82 (2006)
12.188 A.C. Sun, F.T. Yuan, J.H. Hsu, Y.H. Lin, P.C. Kuo: Magnetic reversal behaviors of perpendicular exchange-coupled Fe/FePt bilayer films, IEEE Trans. Magn. **45**, 2709–2715 (2009)
12.189 M.E. McHenry, D.E. Laughlin: Nano-scale materials development for future magnetic applications, Acta Mater. **48**, 223–238 (2000)
12.190 D.C. Jiles: Recent advances and future directions in magnetic materials, Acta Mater. **51**, 5907–5939 (2003)
12.191 C. Suryanarayana, C.C. Koch: Nanocrystalline materials – Current research and future directions, Hyperfine Interact. **130**, 5–44 (2000)
12.192 M. Ohta, Y. Yoshizawa: Recent progress in high Bs Fe-based nanocrystalline soft magnetic alloys, J. Phys. D **44**, 064004 (2011)
12.193 V. Valchev, A. Van den Bossche, P. Sergeant: Core losses in nanocrystalline soft magnetic materials under square voltage waveforms, J. Magn. Magn. Mater. **320**, 53–57 (2008)
12.194 E. Ferrara, C. De Luigi, C. Beatrice, C. Appino, F. Fiorillo: Energy loss versus magnetizing frequency in field-annealed nanocrystalline alloys, J. Magn. Magn. Mater. **215**, 466–468 (2000)
12.195 M.A. Willard, T. Francavilla, V.G. Harris: Core-loss analysis of an (Fe,Co,Ni)-based nanocrystalline soft magnetic alloy, J. Appl. Phys. **97**, 1–3 (2005)
12.196 T.D. Shen, R.B. Schwarz, J.D. Thompson: Soft magnetism in mechanically alloyed nanocrystalline materials, Phys. Rev. B **72**, 1–8 (2005)
12.197 G. Herzer: Anisotropies in soft magnetic nanocrystalline alloys, J. Magn. Magn. Mater. **294**, 99–106 (2005)
12.198 C. Gómez-Polo, P. Marín, L. Pascual, A. Hernando, M. Vázquez: Structural and magnetic properties of nanocrystalline $Fe_{73.5-x}Co_xSi_{13.5}B_9CuNb_3$ alloys, Phys. Rev. B **65**, 244331–244336 (2002)
12.199 M.A. Willard, D.E. Laughlin, M.E. McHenry, D. Thoma, K. Sickafus, J.O. Cross, V.G. Harris: Structure and magnetic properties of $(Fe_{0.5}Co_{0.5})_{88}Zr_7B_4Cu_1$ nanocrystalline alloys, J. Appl. Phys. **84**, 6773–6777 (1998)
12.200 A. Inoue, A. Takeuchi: Recent progress in bulk glassy, nanoquasicrystalline and nanocrystalline alloys, Mater. Sci. Eng. A **375–377**, 16–30 (2004)
12.201 C. Kuhrt, L. Schultz: Formation and magnetic properties of nanocrystalline mechanically alloyed Fe-Co, J. Appl. Phys. **71**, 1896–1900 (1992)
12.202 Q. Li, H. Li, V.G. Pol, I. Bruckental, Y. Koltypin, J. Calderon-Moreno, I. Nowik, A. Gedanken: Sonochemical synthesis, structural and magnetic properties of air-stable Fe/Co alloy nanoparticles, New J. Chem. **27**, 1194–1199 (2003)
12.203 F. Johnson, P. Hughes, R. Gallagher, D.E. Laughlin, M.E. McHenry, M.A. Willard, V.G. Harris: Structure and thermomagnetic properties of new FeCo-based nanocrystalline ferromagnets, IEEE Trans. Magn. **37**, 2261–2263 (2001)
12.204 K.E. Mooney, M.J. Wagner: Nanocrystalline $Co_{30}Fe_{70}$ alloy synthesized by alkalide reduction, J. Mater. Chem. **19**, 611–616 (2009)
12.205 T. Kumakawa, T. Fukuzaki, K. Nishimoto, R. Tamura: Synthesis of Fe-based nanocrystalline soft magnets with high saturation magnetization, J. Phys. **232**, 012009 (2010)
12.206 Y. Zhang, K. Hono, A. Inoue, A. Makino, T. Sakurai: Nanocrystalline structural evolution in $Fe_{90}Zr_7B_3$ soft magnetic material, Acta Mater. **44**, 1497–1510 (1996)
12.207 Y. Yoshizawa, K. Yamauchi: Magnetic properties of FeCuMSiB (M = Cr, V, Mo, Nb, Ta, W) alloys, Mater. Sci. Eng. A **133**, 176–179 (1991)
12.208 Y. Yoshizawa, S. Oguma, K. Yamauchi: New Fe-based soft magnetic alloys composed of ultrafine grain structure, J. Appl. Phys. **64**, 6044–6046 (1988)
12.209 Y. Yoshizawa, K. Yamauchi: Effects of magnetic field annealing on magnetic properties in ultrafine crystalline Fe-Cu-Nb-Si-B alloys, IEEE Trans. Magn. **25**, 3324–3326 (1989)
12.210 Y. Yoshizawa, K. Yamauchi: Fe-based soft magnetic alloys composed of ultrafine grain structure, Mater. Trans. **31**, 307–314 (1990)
12.211 Y. Naitoh, T. Bitoh, T. Hatanai, A. Makino, A. Inoue, T. Masumoto: Development of common mode

choke coil made of new nanocrystalline soft magnetic alloy Nanoperm, Sci. Rep. Res. Inst. Tohoku Univ. Ser. A **43**, 161–165 (1997)
12.212 A summary of the projects undertaken by the National Institute of Materials Science, Tsukuba, Japan on nanocrystalline soft magnetic materials: http://www.nims.go.jp/apfim/project/finemet.html (last accessed June 19, 2012)
12.213 A. Makino, T. Hatanai, A. Inoue, T. Masumoto: Nanocrystalline soft magnetic Fe–M–B (M = Zr, Hf, Nb) alloys and their applications, Mater. Sci. Eng. A **226–228**, 594–602 (1997)
12.214 A. Makino, T. Hatanai, Y. Naitoh: Applications of nanocrystalline soft magnetic Fe–M–B (M = Zr, Nb) alloys Nanoperm, IEEE Trans. Magn. **33**, 3793–3798 (1997)
12.215 M.E. McHenry, F. Johnson, H. Okumura, T. Ohkubo, V.R.V. Ramanan, D.E. Laughlin: The kinetics of nanocrystallization and microstructural observations in Finemet, Nanoperm and Hitperm nanocomposite magnetic materials, Scr. Mater. **48**, 881–887 (2003)
12.216 K. Hono: Nanoscale microstructural analysis of metallic materials by atom probe field ion microscopy, Prog. Mater. Sci. **47**, 621–729 (2002)
12.217 A. Kojima, H. Horikiri, Y. Kawamura, A. Makino, A. Inoue, T. Masumoto: Production of nanocrystalline b.c.c. FeNbB bulk alloys by warm extrusion and their magnetic properties, Mater. Sci. Eng. A **179/180**, 511–515 (1994)
12.218 A. Kojima, T. Mizushima, A. Makino, A. Inoue, T. Masumoto: Soft magnetic properties of bulk nanocrystalline $Fe_{90}Zr_7B_3$ alloys consolidated by spark-plasma sintering, J. Jpn. Soc. Powder Powder Metall. **43**, 613–618 (1996)
12.219 W. Lu, L. Yang, B. Yan, B. Lu, W.H. Huang: Bulk amorphous and nanocrystalline $Fe_{86}Zr_{5.5}Nb_{5.5}B_3$ alloy by rapid consolidation at super-high pressure, J. Magn. Magn. Mater. **292**, 299–303 (2005)
12.220 W. Lu, B. Yan: Bulk amorphous and/or nanocrystalline finemet alloy prepared by super-high-pressure consolidation, Mater. Sci. Forum, 1297–1300 (2007)
12.221 O. Kohmoto: Recent development of thin film materials for magnetic heads, IEEE Trans. Magn. **27**, 3640–3647 (1991)
12.222 X. Liu, Y. Sasaki, J.K. Furdyna: Ferromagnetic resonance in $Ga_{1-x}Mn_xAs$: Effects of magnetic anisotropy, Phys. Rev. B **67**, 2052041–2052049 (2003)
12.223 T.J. Klemmer, K.A. Ellis, L.H. Chen, B. Van Dover, S. Jin: Ultrahigh frequency permeability of sputtered Fe–Co–B thin films, J. Appl. Phys. **87**, 830–833 (2000)
12.224 L. Varga, W.D. Doyle, T. Klemmer: Magnetostriction constants of sputtered FeTaN single crystal thin films, IEEE Trans. Magn. **32**, 3542–3544 (1996)
12.225 S.G. Wang, C.K. Ong, Z.W. Li: Thickness and angle dependence of the coercivity on highly uniaxial anisotropy FeTaN thin films, Physica B **349**, 129–135 (2004)
12.226 K.H. Kim, H.W. Choi, J. Kim, S.R. Kim, K.Y. Kim, S.H. Han, H.J. Kim: Magnetic properties and reliabilities of FeXN (X = Ti, Al, Hf, CoHf, CrHf) nanocrystalline thin film head materials, IEEE Trans. Magn. **36**, 2656–2659 (2000)
12.227 J.M. Shin, Y.M. Kim, J. Kim, S.H. Han, H.J. Kim: Fabrication of nanocrystalline Fe–Co–Ta–N magnetic films with high saturation magnetization and excellent high-frequency characteristics, J. Appl. Phys. **93**, 6677–6679 (2003)
12.228 G. Pan, H. Du: $(FeCo/Co–M)_n$ soft magnetic multilayers with uniaxial anisotropy and very high saturation magnetization, J. Appl. Phys. **93**, 5498–5502 (2003)
12.229 H. Greve, C. Pochstein, H. Takele, V. Zaporojtchenko, F. Faupel, A. Gerber, M. Frommberger, E. Quandt: Nanostructured magnetic Fe–Ni–Co/Teflon multilayers for high-frequency applications in the gigahertz range, Appl. Phys. Lett. **89**, 242501 (2006)
12.230 A. Fert: Origin, development, and future of spintronics (Nobel lecture), Angew. Chem. **47**, 5956–5967 (2008)
12.231 C. Dupas, P. Beauvillain, C. Chappert, J.P. Renard, F. Trigui, P. Veillet, E. Velu, D. Renard: Very large magnetoresistance effects induced by antiparallel magnetization in two ultrathin cobalt films, J. Appl. Phys. **67**, 5680–5682 (1990)
12.232 H. Kanai, K. Noma, J. Hong: Advanced spin-valve GMR head, Fujitsu Sci. Tech. J. **37**, 174–182 (2001)
12.233 J.M. Daughton: GMR applications, J. Magn. Magn. Mater. **192**, 334–342 (1999)
12.234 G. Rieger, K. Ludwig, J. Hauch, W. Clemens: GMR sensors for contactless position detection, Sens. Actuators A **91**, 7–11 (2001)
12.235 T. Uhrmann, L. Bär, T. Dimopoulos, N. Wiese, M. Rührig, A. Lechner: Magnetostrictive GMR sensor on flexible polyimide substrates, J. Magn. Magn. Mater. **307**, 209–211 (2006)
12.236 K.M. Goh, H.L. Chan, S.H. Ong, W.P. Moh, D. Töws, K.V. Ling: Wireless GMR sensor node for vibration monitoring, Proc. 2010 5th IEEE Conf. Ind. Electron. Appl., ICIEA 2010, Taichung (2010) pp. 23–28
12.237 H. Zhu, Z. Qian, X. Huang: Integrated GMR magnetic switch for implantable medical devices, PrimeAsia 2010 – 2nd Asia Pacific Conf. Postgrad. Res. Microelectron. Electron., Shanghai (2010) pp. 412–415
12.238 S.X. Wang, G. Li: Advances in giant magnetoresistance biosensors with magnetic nanpparticle tags: Review and outlook, IEEE Trans. Magn. **44**, 1687–1702 (2008)
12.239 J.C. Lodder: Methods for preparing patterned media for high-density recording, J. Magn. Magn. Mater. **272–276**, 1692–1697 (2004)

12.240 S.A.M. Tofail, I.Z. Rahman, M.A. Rahman: Patterned nanostructured arrays for high-density magnetic recording, Appl. Organomet. Chem. **15**, 373–382 (2001)
12.241 C.A. Ross: Patterned magnetic recording media, Annu. Rev. Mater. Sci. **31**, 203–235 (2001)
12.242 A. Moser, K. Takano, D.T. Margulies, M. Albrecht, Y. Sonobe, Y. Ikeda, S. Sun, E.E. Fullerton: Magnetic recording: Advancing into the future, J. Phys. D **35**, R157–R167 (2002)
12.243 J.H. Lin, Z.H. Wu, W.L. Tseng: Extraction of environmental pollutants using magnetic nanomaterials, Anal. Methods **2**, 1874–1879 (2010)
12.244 R.D. Ambashta, M. Sillanpää: Water purification using magnetic assistance: A review, J. Hazard. Mater. **180**, 38–49 (2010)
12.245 J.B. Haun, T.J. Yoon, H. Lee, R. Weissleder: Magnetic nanoparticle biosensors, Nanomed. Nanobiotechnol. **2**, 291–304 (2010)
12.246 I. Koh, L. Josephson: Magnetic nanoparticle sensors, Sensors **9**, 8130–8145 (2009)
12.247 A. Ito, M. Shinkai, H. Honda, T. Kobayashi: Medical application of functionalized magnetic nanoparticles, J. Biosci. Bioeng. **100**, 1–11 (2005)
12.248 S.A. Anderson, J. Shukaliak-Quandt, E.K. Jordan, A.S. Arbab, R. Martin, H. McFarland, J.A. Frank: Magnetic resonance imaging of labeled T-cells in a mouse model of multiple sclerosis, Ann. Neurol. **55**, 654–659 (2004)
12.249 Q.A. Pankhurst, N.K.T. Thanh, S.K. Jones, J. Dobson: Progress in applications of magnetic nanoparticles in biomedicine, J. Phys. D **42**, 224001 (2009)
12.250 P. Liebesny, S. Goyal, D. Dunlap, F. Family, L. Finzi: Determination of the number of proteins bound nonspecifically to DNA, J. Phys. Condens. Matter **22**, 414104 (2010)
12.251 S. Purushotham, P.E.J. Chang, H. Rumpel, I.H.C. Kee, R.T.H. Ng, P.K.H. Chow, C.K. Tan, R.V. Ramanujan: Thermoresponsive core-shell magnetic nanoparticles for combined modalities of cancer therapy, Nanotechnology **20**, 305101 (2009)
12.252 S. Purushotham, R.V. Ramanujan: Modeling the performance of magnetic nanoparticles in multimodal cancer therapy, J. Appl. Phys. **107**, 114701 (2010)
12.253 A. Celedon, D. Wirtz, S. Sun: Torsional mechanics of DNA are regulated by small-molecule intercalation, J. Phys. Chem. B **114**, 16929–16935 (2010)

Part C

NanoCera

Part C NanoCeramics

13 Nanocrystalline Functional Oxide Materials
Rakesh Shukla, Mumbai, India
Dimple P. Dutta, Mumbai, India
Jayshree Ramkumar, Mumbai, India
Balaji P. Mandal, Mumbai, India
Avesh K. Tyagi, Mumbai, India

14 Piezoelectric Nanoceramics
Xiaohui Wang, Beijing, China
Shaopeng Zhang, Beijing, China
Longtu Li, Beijing, China

15 Graphite Oxide
Wei Gao, Los Alamos, USA

16 Compound Crystals
Roi Levi, Rehovot, Israel
Maya Bar-Sadan, Be'er Sheba, Israel
Reshef Tenne, Rehovot, Israel

17 Growth of Nanomaterials by Screw Dislocation
Fei Meng, Madison, USA
Stephen A. Morin, Cambridge, USA
Song Jin, Madison, USA

18 Glasses on the Nanoscale
Hellmut Eckert, Sao Carlos, Brazil
Sidney J.L. Ribeiro, Araraquara, Brazil
Silvia H. Santagneli, Araraquara, Brazil
Marcelo Nalin, Sao Carlos, Brazil
Gael Poirier, Poços de Caldas, Brazil
Younès Messaddeq, Québec, Canada

13. Nanocrystalline Functional Oxide Materials

Rakesh Shukla, Dimple P. Dutta, Jayshree Ramkumar, Balaji P. Mandal, Avesh K. Tyagi

Nanoparticles are small clusters of atoms about 1–100 nm long. The term "nano" derives from the Greek word *nanos*, which means dwarf or extremely small. A nanometer is a billionth of a meter or 10^{-9} m. Nanostructured materials have attracted the attention of different types of people such as scientists, engineers, etc. Essentially, the reason is that nanocrystals in the 1–10 nm range make up a new realm of matter in which physical and chemical properties change as size changes. Metal oxide nanoparticles are an important class of materials for their optical, magnetic, and electronic properties and have a wide range of applications such as in catalysts, sensors, optical materials, electrical materials, and magnetic storage. Synthesis routes for nanoparticles can be broadly classified into solid-state and soft chemical routes such as gel combustion, coprecipitation, sol–gel, hydrothermal/solvothermal, sonochemical, template synthesis, etc. This chapter deals with the various properties of nanoparticles synthesized using different techniques. The application of nanooxides as sorbents for environmental remediation is also discussed in this chapter.

13.1 **Synthesis Methods** 518
13.1.1 Solid-State Route 518
13.1.2 Soft Chemical Routes 519
13.2 **Optical Properties of Oxide Nanomaterials** 524
13.3 **Sorbent Properties of Oxide Nanomaterials** 532
13.3.1 Sorbents for Environmental Remediation 533
13.4 **Catalytic Properties of Oxide Nanomaterials** 536
13.5 **Oxide Nanomaterials in Ionics** 538
13.6 **Conclusions** 541
References 542

Traditionally, materials can be classified based on their bonding, fundamental properties or structures, or origin. They can be either crystalline or amorphous depending on the long or short range of crystallographic ordering.

Furthermore, based on their surface finishing and dielectric properties, they are termed as opaque, transparent, semitransparent, or reflecting materials. They can also be classified based on the processing techniques, leading to thin films, single crystals, ingots, powders, slurries, aerosols, etc. Materials can also be classified based on size and shape. This conventional classification of materials fails miserably when different types of materials are used for the same function. The contemporary emphasis is on materials that simultaneously exhibit two or more properties. Sometimes, these properties can be antagonistic properties also; for example, multiferroics are a class of materials that are supposed to be ferromagnetic and ferroelectric at the same time. This greatly changed scenario calls for a more practical classification of materials. In view of this, a new scheme has been proposed wherein materials (more appropriately now termed *functional materials*) comprising representatives from different existing classes are categorized solely based on their functional properties and their prospective applications [13.1]. Functional materials have assumed a very prominent position in several high-technology areas. Such materials are not classified on the basis of their origin, nature of bonding, or processing techniques but rather on the basis of the functions they can perform. This is a significant deviation from the earlier

Table 13.1 Classification of materials

Material	Type	Sensing action for	Sensing mechanism	Reference
In_2O_3	Semiconductor	Toxic gases (H_2S)	Resistivity	[13.2]
Yttria-doped thoria (YDT)	Insulator	Water ingress in liquid Na coolant used in fast breeder reactors	Ionic conductivity	[13.3]
Calixarene	Organic	Cs-137 in nuclear waste	Electrochemical	[13.4]
Ag@R6G	Hybrid material	Pb^{2+} in potable water	Fluorescence	[13.5]
Conducting polymers (polyaniline (PANI))	Organic	Thyroid hormone	Radioimmuno-assay (RIA)	[13.6]

mentioned traditional classifications. According to this new scheme of classification, a material will be termed as a gas sensor irrespective of whether it is organic, inorganic, or hybrid in origin, and the sensing mechanism may be either resistive, luminescent, or by surface modification; for example, several altogether different materials have been clubbed together in Table 13.1 owing to the fact that they have the same functionality, i. e., sensing action. The probing mechanism is also different, but the end functionality classifies them according to their sensing action, irrespective of their origin and properties.

Nanoparticles are small clusters of atoms about 1–100 nm long. Nanostructured materials have attracted the attention of different types of people such as scientists, engineers, etc. Essentially, the reason is that nanocrystals in the 1–100 nm range make up a new realm of matter in which physical and chemical properties change as size changes. Although it is still difficult to understand such property changes theoretically, this phenomenon presents enormous opportunities for advances in science and technology. Contemplating that any nanostructured solid material can have variable properties based simply on size essentially makes the Periodic Table of elements *three dimensional*. Actually, the potential new materials based on nanostructure are even broader than the solid elements of the Periodic Table, since metal oxides, metal sulfides, tellurides, arsenides, bimetallics, and of course metals themselves need to be considered. The properties that change in the nanoregime include bandgaps (for semiconductors), magnetic moments (for ferro- and ferrimagnetism), specific heats, melting points, surface chemistry, and morphology/particle shape. For consolidated nanoparticles, metal pieces can be harder, and ceramic pieces can be more plastic than normal materials made from microcrystal–polycrystal consolidation.

Metal oxide nanoparticles are an important class of materials for their optical, magnetic, and electronic properties [13.7, 8]. These properties make nanostructured metal oxides useful for a wide range of applications such as in catalysts, sensors, optical materials, electrical materials, and magnetic storage [13.9–20]. Hence, over the past half-decade, research in functional oxide-based nanostructures has attracted considerable attention due to their unique and innovative applications in optics, optoelectronics, catalysis, and piezoelectricity. Metal oxides can act as semiconductors or insulators depending on their bandgap values. When the bandgap value is below 3.5 eV, they behave as semiconductors, whereas a bandgap value above 3.5 eV categorizes them as insulators. Oxides of iron are colored due to the small bandgap, whereas those of zinc have no color as the bandgap is large.

13.1 Synthesis Methods

Synthesis is an important part of any work. The preparatory routes for nanoparticles are broadly classified into two categories: the solid-state route and the soft chemical route.

13.1.1 Solid-State Route

The solid-state process is a conventional and widely used synthesis method to prepare polycrystalline ceramic materials. This method is not only common but also most promising for scaling up of compound production. Solid-state diffusion is an inherently sluggish process. It involves the mechanical mixing of the solid constituents (oxides/carbonates) with repeated grindings and annealing at elevated temperatures, generally over a long duration [13.21, 22]. Solid-state reaction is different from solution reaction, since in solution all ions and molecules are available for reaction. However,

Table 13.2 Comparison of solid-state reaction and solution reaction

Solid-state reactions	Solution reactions
Kinetically slow	Kinetically fast
Mostly need higher temperatures	Room temperature (RT) or slightly above RT
Diffusion controlled	Diffusion is not very important
No well-defined rate laws	Well-defined rate laws
Sample history influence	No sample history influence
Defects' role is important	No such concept exists
Progress of reaction is difficult to monitor	Progress of reaction easy to monitor
Larger particles are obtained	Fine particles are obtained

this is not the case in a solid-state reaction. Here, the reaction takes place only at that point where the reactants are in intimate contact with each other. Once the product layer is formed at the interface between the reactants, further progress of the reaction depends upon the diffusion of one or both reactants through this product layer. This depend on various factors such as the size of the diffusing ions, the structure of the product as well as of the reactants, the reaction temperature, and also the presence of defects and the history of the sample.

Before proceeding with an experimental solid-state reaction, a few important points have to be considered. The melting temperature, decomposition temperature, vapor pressure, etc. of the reactants need to be compiled. Heating should be done in pellet form preferably. A proper atmosphere needs to be selected, depending upon the requirement and the stability of the reactants. Crucible material selection is also important, as the material should be chemically inert even at high temperature, e.g., Al_2O_3 or platinum. Selection of the heating temperature is done by considering the compound with the lowest melting point or decomposition temperature.

In case of powder reactions, grinding of the reactants continuously peels off the product layer formed at the interface, hence providing fresh contact area for the reaction to take place. Grinding homogenizes the reaction mixture, reduces the particle size, and in turn increases the surface area and also reduces the diffusion path. Hence, thorough grinding plays an important role in case of powder reaction. However, mixing and grinding of the reactants may sometimes give rise to nonuniform composition and local stoichiometric variations.

Also, the purity of the product is limited by the impurities introduced during grinding. Powder products obtained by solid-state synthesis are larger in size, usually in the micrometer range. A brief comparison of solid-state versus solution reaction is tabulated in Table 13.2.

The shortcomings of the solid-state synthesis method can be overcome by employing solution chemistry techniques.

13.1.2 Soft Chemical Routes

Nanocrystalline ceramics are generally synthesized by soft chemical routes, wherein the homogeneity of the reacting constituents can be achieved at atomic level. These methods employ a solvent medium from which the required product can be obtained by precipitation, solvent evaporation, etc.

Gel–Combustion Synthesis

This is a facile synthesis technique that can be employed on a laboratory scale to prepare nanocrystalline ceramic powders with reproducible characteristics. Combustion is basically a redox reaction between the oxidant and fuel and is controlled by various factors such as the nature and amount of fuel. This preparative method consists of two steps, which are described as follows:

1. Preparation of fuel–oxidant precursor or gel formation. In this step, nitrate/oxynitrate salts of the metals, in the required molar ratio, are mixed together in an aqueous media to produce a transparent mixed metal nitrate solution. A suitable fuel (glycine, citric acid, urea, etc.) is then added in an appropriate amount to this solution. The aqueous solution of fuel and oxidants is then thermally dehydrated on a hot plate (at about 80–100 °C) to obtain a viscous liquid (hereafter termed as gel). This thermal dehydration and gel formation process is an important step, because any excess water left behind would lead to sluggish combustion, deteriorating the phase purity and powder quality. The nature of the fuel, its amount, and the pH of the starting solution are some of the important process parameters to obtain a transparent viscous gel without any phase separation or precipitation.
2. Combustion of the fuel–oxidant precursor or autoignition. The gel, as formed in the first step, is further heated at a higher temperature (200–250 °C) that initiates self-propagating combustion. The exothermic decomposition of the fuel–oxidant precursor is visible in the form of flame, which rapidly propagates throughout the gel, therefore this step is

also termed as *auto-ignition*. The auto-ignition is a very short-lived phenomenon as the flame persists for only a few (5–10) seconds. It is within this short duration that the product formation takes place.

The auto-ignition of the gel results in a large voluminous powder. However, the resultant product may be the desired phase, or semi-decomposed precursor having a considerable carbonaceous residue, depending on the nature and amount of fuel used in the process. During auto-ignition, gaseous products are evolved which dissipate the heat and fragment the solid residual product, resulting in ultrafine powders of oxide.

Fuel in Gel Combustion

A fuel can be defined as a substance that is consumed to produce energy in a reaction. In other words, any substance which on its consumption provides heat or energy is termed as a fuel. Thus, there are naturally occurring fuels such as coal, petroleum, natural gas, etc., which are prime source of energy in day-to-day life. These materials burn in the presence of oxygen, releasing energy in the form of heat and light. However, the basic characteristics of the fuel in the combustion process are that it should be able to maintain compositional homogeneity among constituents and should undergo combustion with an oxidizer (i. e., nitrates) at low ignition temperature. A large variety of organic materials can serve as fuel for the combustion process. These include carboxylic acids such as citric acid, tartaric acid, ascorbic acid, glycine, ethylenediaminetetraacetic acid (EDTA), etc., and materials such as urea, hydrazine, dimethyl urea ($C_3H_8N_2O$), hexamethylenetetramine (HMTA), etc.

Glycine (NH_2CH_2COOH). This is one of the cheapest α-amino acids and is known to act as a complexing agent for a number of metal ions, as it has a carboxylic acid group at one end and amino group at the other. This zwitterionic character of the glycine molecule enables it to effectively form complexes with metal ions of varying ionic sizes, helping to prevent their selective precipitation to maintain compositional homogeneity among the constituents.

Aspartic Acid ($C_4H_7NO_4$) and Glutamic Acid ($C_5H_9NO_4$). These are commonly available acidic α-amino acids with two carboxylic (−COOH) and one amino ($-NH_2$) group for coordinating metal ions to maintain compositional homogeneity through gel formation. These are low-cost materials and can be combusted with nitrates at low ignition temperatures (200–250 °C). In addition, the combustion reactions involving these acids are found to be of comparatively controlled nature, due to their somewhat sluggish combustion, which helps in scaling up of the process.

Arginine ($C_6H_{14}N_4O_2$) and Tryptophan ($C_{10}H_{10}N_2O_2$). Arginine is a strong basic α-amino acid, while tryptophan is a weakly basic α-amino acid. Arginine contains two amino ($-NH_2$) groups and one carboxyl (−COOH) group, whereas tryptophan contains one amino group and a heterocyclic moiety containing nitrogen as the heteroatom. The characteristic feature of α-amino acids is that they contain one amino group at the α-position to the carboxyl group. They are capable of complex formation with metal ions to give a homogeneous gel and undergo combustion at low ignition temperature.

Valine ($C_5H_{11}NO_2$) and Phenylalanine ($C_9H_{11}NO_2$). These two compounds are neutral α-amino acids like glycine, carrying one amino and one carboxyl group at α-position to each other. Therefore, they also behave in the same manner as glycine when used as a fuel. All these compounds are used as fuels.

Citric Acid ($C_6H_8O_7H_2O$). Citric acid is also a good complexing agent due to its multidenticity. The combustion reaction with this fuel gives mostly flameless combustion with lots of evolution of gases.

Concept of Fuel-to-Oxidant Ratio

The oxidant-to-fuel molar ratio has a significant bearing on the product phase as well as the product powder properties. This is because the extent of exothermicity associated with the combustion process is governed by the oxidant-to-fuel ratio used. Based on the so-called concept of propellant chemistry, the ratio of oxidizing and reducing valencies should be unity to achieve maximum exothermicity [13.23, 24]. The calculation of these valencies and the ratio satisfying this concept can be illustrated by means of a typical example of nanocrystalline lanthanum oxide (La_2O_3). The oxidizing valency calculated for the oxidant in this case, viz. $La(NO_3)_3 \cdot 6H_2O$, is 15−, whereas the reducing valency of the fuel, viz. glycine, is 9+. These oxidizing and reducing valencies can be calculated as:

1. $La(NO_3)_3 \cdot 6H_2O$:
   - Oxidizing valency of Ce = 3+, N = 0
   - Reducing valency of O = 2−.

   Thus, the net oxidizing valency = 15−.

2. NH_2CH_2COOH:
   - Oxidizing valency of $N = 0$, $H = 1+$, $C = 4+$
   - Reducing valency of $O = 2-$.

   Thus, the net reducing valency $= 9+$.

The valencies of C and N are taken as 4+ and 0, as these species are lost as CO_2 and N_2, respectively, during the combustion process [13.25]. The ratio of oxidizing to reducing valency then turns out to be 1 : 1.66, which is the propellant chemistry ratio. An oxidant-to-fuel ratio less than 1.66 is termed as fuel deficient, and any ratio greater than 1.66 is termed as fuel rich. For other fuels, the stoichiometric ratios can be calculated in a similar manner.

Powder properties such as crystallite size, nature and extent of agglomeration, surface area, sinterability, etc. are primarily dependent on the nature and amount of fuel used, which are the two main parameters responsible for controlling the exothermicity or flame temperature and gas evolution nature of the auto-ignition part of the combustion reaction.

Nature and Amount of Fuel

The selection should be based on the following points.

Fuels should be capable of forming multidentate complex with the metal ion. The fuel should be such that it binds to most of the metal ion. The bond formed should be stable enough to prevent precipitation. The gel formed should have lower auto-ignition temperature, so that the combustion process occurs at lower temperature.

A lower amount of fuel, i.e., use of a fuel-deficient ratio (with higher amounts of nitrates), helps in single-step decomposition of the precursors. A very high rate of combustion is observed in such cases, but at the same time, due to effective cooling of the powders by evolution of a large volume of gaseous molecules, the local temperature is reduced quickly. Thus, the crystallite size is not increased much, due to insufficient time for aggregate formation.

Using a higher amount of fuel (or lesser amount of nitrates), i.e., a fuel-excess ratio, leads to the formation of dense structure in the agglomerates as a result of poor heat dissipation and longer time of high local temperature in the sluggish combustion that takes place in such cases. The presence of large amounts of remaining carbonaceous residue can deteriorate the powder properties during calcination.

If the system under study has a high phase formation temperature and is also difficult to form, the stoichiometric oxidant-to-fuel (O/F) ratio gives the best result, due to its higher exothermicity along with single-step decomposition of the precursor to produce the desired phase with improved powder characteristics.

A few advantages of the aforementioned steps of gel combustion synthesis are listed here:

1. The possibility of local composition variations in combustion-synthesized powders is very low, as formation of the homogeneous gel prevents a random redox reaction between the fuel and oxidant.
2. Atomic-level blending of the constituent elements is achieved, which facilitates formation of the compound.
3. The gel precursor does not require any special processing such as washing as it undergoes exothermic decomposition.
4. Although the auto-ignition exists for a very short time, the heat of combustion is sufficiently high to produce the required phase in most cases. Hence, the combustion technique can be considered as time saving, low-temperature synthesis.

Thus, the combustion process is quite simple and can easily be carried out in a laboratory. However, a few precautionary measures are necessary while performing such experiments:

1. Combustion is a spontaneous and vigorous process wherein large amounts of heat and gases are released in a very short duration. Thus, it is necessary to carry out such reactions in a fume hood, which facilitates safe ventilation of the gaseous products.
2. It is advisable to use wide-mouthed and large-volume apparatus (beakers) to avoid poor heat dissipation and for easy liberation of the gaseous products. Also, a narrow-opening container might lead to an explosion, due to the large swelling of the viscous precursor.
3. Since combustion-synthesized powders are very reactive due to their high surface area, the right conditions for calcination (e.g., time and temperature) and their proper storage in desiccators are necessary to avoid any attack of atmospheric gases (e.g., formation of carbonates due to attack of atmospheric carbon dioxide) and moisture.

These combustion-synthesized powders are further calcined at $\approx 600\,^{\circ}C$ for 1 h to remove any carbonaceous residue and/or undecomposed precursor. Calcination involves heat-treating a powder at a temperature well below its melting point to effect decomposition, i. e., to liberate unwanted gases and/or chemically

bound waste, as well as structural transformations to produce the desired composition and phase product.

Coprecipitation Synthesis

Precipitation is a very simple preparative method employed to synthesize nanoparticles of a variety of inorganic compounds. Coprecipitation refers to simultaneous precipitation of more than one metal ion from the same solution. This gives more intimate mixing of cations as compared with that achieved by mixing oxides/salts of individual cations. Coprecipitation reactions tend to exhibit the following characteristics [13.20]:

1. The products of coprecipitation reactions are generally sparingly soluble species formed under conditions of high supersaturation.
2. Nucleation is a primary step in this process, wherein a large number of small particles are formed.
3. Secondary processes, such as Ostwald ripening and aggregation, dramatically affect the size, morphology, and properties of the products.

The key to any precipitation process is the degree of supersaturation (S) given by

$$S = \frac{a_A \times a_B}{K_{sp}} , \tag{13.1}$$

where a_A and a_B are the activities of solutes A and B, and K_{sp} is the solubility product constant. As nucleation begins in a supersaturated solution, there exists an equilibrium critical radius (R), which is given by

$$R = \frac{\alpha}{\Delta C} ; \tag{13.2}$$

where ΔC is the difference in solute concentration at saturation (C) and equilibrium (C_{eq}).

The term α is given by

$$\alpha = \left(\frac{2\sigma_{SL}}{kT \times \ln S} \right) \times vC_{\infty} , \tag{13.3}$$

where σ_{SL} is the surface tension at solid–liquid interface, k is the Boltzmann constant, T is temperature, v is the atomic volume of solute, and S is the supersaturation as given in (13.2). Nucleated particles with radius $> R$ will continue to grow, while those with radius $< R$ will dissolve. In the majority of precipitation reactions, the growth process of the precipitated particles is found to be diffusion limited. Concentration gradients and temperature become the predominant factors determining the growth rate as new material is supplied to the particle surface via long-distance mass transport. Ostwald ripening is the phenomenon by which smaller particles are essentially consumed by larger particles during the growth process. Agglomeration of the precipitated nanoparticles can be prevented by addition of a stabilizer or capping agent or a grain growth inhibitor.

Coprecipitation of various salts (nitrates, chlorides, and sulfates) using a suitable precipitating agent yields the corresponding oxides. However, the products of coprecipitation reactions performed at or near room temperature are usually amorphous, insoluble precursors. Thermal decomposition of such compounds results in chemically homogeneous fine oxide powders with high surface area.

The coprecipitation technique offers various advantages:

1. It is a facile synthesis technique facilitating easy control of overall homogeneity, particle size, composition, etc.
2. Coprecipitation reactions can be easily performed in a small laboratory.
3. Because of the intimate mixing produced by coprecipitation, the calcination temperature required to produce the desired crystalline phase in the powder is usually lower than that required for calcination of the individual oxide powders.
4. This preparative method can be employed for synthesis of advanced multication powders, multicomponent oxide systems, etc.

Coprecipitation of mixed salts from liquid solutions is a well-established method of ceramic powder synthesis. In this technique, a multicomponent liquid solution of soluble inorganic salts (metal nitrates, sulfates) is typically combined with a liquid solution of a precipitating compound. The precipitating agent is chosen in such a way that, when dissolved and combined with the metal solution, one of its radicals combines with the metal ions to form insoluble salts. These salts are precipitated in a very finely divided and intimately mixed state. Heating of the precipitate decomposes these salts, resulting in a chemically homogeneous and fine oxide powder.

In many coprecipitation procedures, the precipitated salts exhibit slight solubilities in the supernatant liquid, leading to incomplete precipitation. The coprecipitation process is governed by two competing factors, viz. nucleation and crystal growth. Thus, merely inducing precipitation of a compound does not ensure that the product will be nanoparticulate and/or monodispersed.

If nucleation is very fast and the subsequent growth rate is very slow, nanosized material can be obtained. Sometimes, soft templates are used as structure-directing agents in order to obtain nanoparticles with different morphologies such as nanorods, nanowires, etc. [13.26, 27]. The coprecipitation route is capable of producing powders with closely controlled stoichiometry, composition, and particle size on a large-scale commercial basis [13.28].

Sol–Gel Synthesis

The sol–gel process is a low-temperature approach for synthesizing solid-state oxide materials (usually polymeric). A sol is a colloidal suspension of solid particles in a liquid. The clusters in the sol are linked into frameworks. The gel is a solid whose pores contain liquid. A gel has been defined as a two-component system with a semisolid nature. Synthesis of SiO_2 from liquid silicon metalorganic precursors is probably the most investigated sol–gel process. It is generally a two-step process which involves hydrolysis of precursors followed by their condensation to form oxide frameworks. Product properties are affected by the rate of hydrolysis and condensation. Generally, slower and controlled hydrolysis leads to smaller particle sizes. Pore size, distribution, and interconnectivity are also affected by other processing parameters, such as the type and amount of solvent and/or catalyst, temperature, and in some cases the presence and arrangement of templating molecules. This low-temperature soft chemical method is safe and inexpensive, and can yield nanomaterials with complex shapes. In recent years, a variety of nanomaterials have been synthesized using the sol–gel process [13.29].

Hydrothermal/Solvothermal Synthesis

In a sealed vessel, it is possible to bring solvents to temperatures well above their boiling points by increase in their autogenous pressures resulting from heating. Performing a chemical reaction under such conditions is referred to as hydrothermal processing in case of water and as solvothermal processing in case of nonaqueous solvents. The process simply takes advantage of the increased solubility of metal salts and complexes at elevated temperatures and pressures (with or without bringing the solvent to its critical point). This type of processing allows many inorganic materials to be prepared at temperatures substantially below those required by traditional solid-state reactions. Unlike other low-temperature methods such as coprecipitation and sol–gel synthesis, the products of solvo/hydrothermal reactions are usually crystalline and do not require subsequent annealing treatment. The mechanism of hydrothermal reactions usually follows a liquid nucleation model. It differs from the solid-state reaction mechanism in the process of diffusion of atoms or ions between reactants. In the hydro/solvothermal technique new materials can be obtained in an inexpensive manner, but it is generally difficult to have absolute control over the morphology and size of the nanoparticles. A variety of metal oxide nanoparticles have been synthesized using this method [13.30].

Template Synthesis

The template method involves fabrication of the desired material within the pores or channels of a nanoporous template. In the broadest sense, a template may be defined as a central structure within which a network forms in such a way that removal of the template creates a filled cavity with morphological and/or stereochemical features related to those of the template. Track-etch membranes, porous alumina, and other nanoporous structures have been characterized as templates. Nearly any solid matter can in principle be synthesized within nanoporous templates, provided a suitable chemical pathway can be developed. There are essentially five representative strategies to carry out template synthesis of nanostructures: electrochemical deposition, electroless deposition, chemical polymerization, sol–gel deposition, and chemical vapor deposition.

Sonochemical Synthesis

Ultrasound has become an important tool for synthesis of nanoparticles. When liquids are subjected to ultrasonic irradiation, ultrasonic cavitation occurs, involving the formation, growth, and implosive collapse of bubbles. Cavitation bubbles are vacuum bubbles. The vacuum is created by a fast-moving surface on one side and an inert liquid on the other. The resulting pressure differences serve to overcome the cohesive and adhesive forces within the liquid. Ultrasonic cavitation produces a variety of physical and chemical effects, such as high temperature ($> 5000\,\mathrm{K}$), pressure ($> 20\,\mathrm{MPa}$), and cooling rate ($> 1010\,\mathrm{K\,s^{-1}}$), which could provide a unique environment for chemical reactions under extreme conditions. The sonochemical effects observed in chemical reactions and processes can involve increase in reaction speed, increase in reaction output, more efficient energy usage, sonochemical methods for switching of reaction pathway, activation of metals and solids, improvement of particle synthesis, and also coating of nanoparticles. The temperature

plays an important role in sonochemical reactions. The equation of an adiabatic implosion is

$$T_{\max} = T\frac{P_{\mathrm{ex}}(\gamma - 1)}{P_{\mathrm{bub}}}\,, \tag{13.4}$$

where $T_{\max}$ is the temperature reached after the collapse of the bubble, T is the temperature of the sonication bath, $\gamma = C_{\mathrm{p}}/C_{\mathrm{v}}$, P_{ex} is the external pressure equal to the sum of the hydrostatic and acoustic pressure, and P_{bub} is the pressure of the gas inside the cavity, at the radius at which it collapses. Lower P_{bub} (vapor pressure of the solute) results in higher temperatures and faster reaction rates. Thus, the temperature has a dual effect. Low temperatures increase the viscosity, making the process of bubble formation difficult, but at the same time also increases the rate of the sonochemical reaction. Over the last two decades, a variety of metal, metal oxide, and chalcogenide nanomaterials have been synthesized using the sonochemical technique [13.31].

13.2 Optical Properties of Oxide Nanomaterials

Among the various oxides, a lot of work has been done on TiO_2, which has many promising applications in areas ranging from photovoltaics and photocatalysis to photo/electrochromics and sensors. The structural, thermal, electronic, and optical properties of TiO_2 nanomaterials have been reviewed extensively over the past decade [13.32–40]. Similarly, ZnO is another important compound semiconductor having a wide bandgap (3.37 eV) that is suitable for short-wavelength optoelectronic applications. It is transparent to visible light and can be made highly conductive by doping. The potential applications and novel nanodevices demonstrated for ZnO have been studied comprehensively [13.41].

Indium oxide (In_2O_3) is an n-type semiconducting material, and its observed optical transparency arises from its relatively wide bandgap. In_2O_3 has a direct, wide bandgap of ≈ 3.6 eV and an indirect bandgap of ≈ 2.6 eV [13.42–44]. Undoped In_2O_3 shows resistivity of $\approx 10^4\,\Omega\,\mathrm{cm}$. However, it can be made highly conducting by doping with extrinsic impurities or by controlled stoichiometric deviation. Tin-doped indium oxide (ITO) corresponds to the former case, while the low resistivities observed in undoped, oxygen-deficient In_2O_3 are explained by the latter mechanism. Hence, it is a technologically important transparent conducting oxide, which is found to be an alternate choice for many interesting applications including for transparent electrodes in electroluminescence devices, solar cells, antireflection coatings, and optoelectronic devices and also in gas sensors [13.45–51]. Increasing interest has been shown in depositing transparent conductive oxide (TCO) materials on plastics substrates for light-emitting diode (LED), organic light-emitting diode (OLED), and flat-panel display applications. As an example, *Shin* et al. reported resistivities of $6\times10^4\,\Omega\,\mathrm{cm}$ and optical transparencies of 85% at 550 nm for direct-current (DC) magnetron-sputtered ITO films [13.52]. Doped conducting oxides also hold considerable potential from the physics and application points of view. Rare-earth-doped conducting oxides such as indium oxide may allow electrical excitation of rare-earth ions as well as optical excitation. Such materials have immense potential for application in the development of electrically driven light-emitting devices.

The technological utility of In_2O_3 has prompted considerable interest in the development of synthesis techniques that are capable of manufacturing nanoparticulate In_2O_3 powders with controlled particle size and low levels of agglomeration [13.53, 54]. High-quality nanoparticulate powders of In_2O_3 are characterized by enhanced physical properties and improved processing behavior compared with conventional coarse-grained powders; for example, nanoparticulate In_2O_3 powders exhibit heightened sinterability and show higher sensitivity in gas sensor applications [13.55–57]. It is also anticipated that low-dimensional In_2O_3 may exhibit some unique properties, including novel optical behaviors [13.58, 59]. Nanometer-sized In_2O_3 shows obvious differences in its optical properties (e.g., optical bandgap and luminescence properties) relative to bulk In_2O_3 [13.60, 61]. Consequently, In_2O_3 nanoparticles have been prepared by a variety of methods, including thermal hydrolysis, thermal decomposition, sol–gel technique, microemulsion, reactive magnetron sputtering, metalorganic laser photolysis, spray pyrolysis, template method, pulsed laser deposition technique, vapor-phase transport and condensation deposition process, carbothermal reduction, decomposition of the organometallic precursor, sonochemical method, etc. [13.62–73].

It is well known that bulk In_2O_3 cannot emit light at room temperature [13.74–77]. On moving down to the

nanoregime, a considerable change is observed in the optical properties.

However, the optical properties, such as the photoluminescence (PL), of In_2O_3 nanoparticles obtained by different synthesis techniques vary greatly. A consolidated account of the optical properties of these In_2O_3 nanoparticles of various size and shape is given here.

Bulk In_2O_3 exhibits a photoluminescence (PL) emission peak at 3.67 eV. Nanoparticles of indium oxide synthesized by pulsed laser ablation of a pure indium metal target show a strong PL emission peak at 3.78 eV. The weak size dependence revealed by this blue-shift of about 110 meV in the PL spectra is consistent with a particle size on the order of the Bohr exciton diameter [13.9]. The exciton Bohr diameter for In_2O_3 is reported to be in the range between 2.6 and 5 nm [13.78].

In_2O_3 nanoparticles synthesized by homogeneous precipitation using hexamethylenetetramine as ligand and indium nitrate or indium chloride as precursor exhibited photoluminescence emission at room temperature with peak onset at 315 nm as a consequence of the small size of the particles [13.79]. Thermal decomposition of $In(acac)_3$ precursor in the presence of stabilizing surfactant oleylamine yielded In_2O_3 nanoparticles of different sizes depending on the molar ratio of the latter. On excitation at 275 nm, the PL emission maximum appear at 3.81 eV (325 nm) for 4 nm In_2O_3, 3.76 eV (330 nm) for 6 nm In_2O_3, and 3.73 eV (332 nm) for 8 nm In_2O_3, thus being blue-shifted (60–140 meV) compared with the value of 3.67 eV (338 nm) for bulk In_2O_3 [13.80]. Thermal decomposition of $In(dipy)_3Cl_3 \cdot 2H_2O$ in oleylamine and oleic acid under inert atmosphere yielded In_2O_3 nanoparticles with tunable size from 10–15 nm to 40–50 nm, depending on the molar ratio of precursor to combined solvent in the reaction system. When 10–15 nm In_2O_3 nanoparticles redispersed in cyclohexane were excited at 275 nm at room temperature, strong PL emission was observed at 378 nm, which is in fact red-shifted compared with that of bulk In_2O_3 [13.81].

In_2O_3 nanocrystals with controllable phases and morphologies have been synthesized by decomposing $In(OH)_3$ under different reaction conditions. Well-defined cubic In_2O_3 nanocubes were fabricated by treating $In(OH)_3$ in methanol at 250 °C for 25 h, whereas replacement of the solvent by ethanol yielded nanorods. In_2O_3 nanocubes displayed two blue emission peaks centered at 428 and 433 nm, which was attributed to the formation of new energy levels induced by oxygen vacancies. During the solution-based synthesis method, a high density of oxygen vacancies will be induced because of incomplete crystallization. The In_2O_3 nanorods did not exhibit any luminescence, indicating that the luminescence properties of In_2O_3 nanocrystals are strongly dependent on their crystal phase, crystallinity, and morphology [13.82].

Synthesis of In_2O_3 nanostructures at different growth temperatures by using the thermal evaporation method has been reported [13.83]. The In_2O_3 nanostructures exhibited different luminescence peaks in the range of 400–600 nm with broad bands when using different growth temperatures. The optical transition energy of the In_2O_3 nanostructures becomes tunable owing to the different amount of oxygen vacancies provided by different growth conditions. This could render the material beneficial for possible applications in white-light illumination.

Since In_2O_3 has a high refractive index of 2, its one-dimensional (1-D) nanostructures are expected to function as waveguides for guiding and manipulating light on the micrometer scale. To utilize In_2O_3 nanowires in the field of nanoscale optoelectronic devices, different methods have been exploited to synthesize In_2O_3 nanowires and nanofibers [13.84–89]. In_2O_3 nanowires synthesized by the gas reaction method exhibit a wide ultraviolet (UV) emission and a blue emission at room temperature [13.76]. In_2O_3 nanowires synthesized by the template method exhibit a UV PL emission at room temperature [13.68]. Since short-wavelength ultraviolet laser plays an important role in the storage density of optical memory systems, a semiconductor material with a short-wavelength PL emission property is needed for optical memory systems. Very recently, In_2O_3 nanofibers have shown potential for application as a waveguide element for future photonic devices [13.90]. Thus, In_2O_3 nanowires may be one of the promising materials applicable for nanoscale optoelectronic devices, short-wavelength lasers, and nanosensors.

Liang et al. produced In_2O_3 nanofibers by heating an Au-coated InP substrate in an Ar-oxygen atmosphere at 1080 °C [13.90]. *Li* et al. produced In_2O_3 nanowires by an Au-assisted laser ablation technique using an InAs target [13.84]. In_2O_3 nanowires were also produced by evaporating In_2O_3 powder onto Ag nanoparticle-coated Si wafers in an N_2/H_2 mixed gas atmosphere [13.86]. The electrodeposition route has also been employed to fabricate In_2O_3 nanowire arrays [13.85]. *Kam* et al. produced various In_2O_3 nanostructures such as nanowires, nanotrees, and nanobouquets by carbon-assisted thermal evaporation of In and

In_2O_3 powder [13.88]. The optical properties of these 1-D and two-dimensional (2-D) nanostructures varied depending on the morphology of the product, the synthesis method, and the reactants used; For instance, *Liang* et al. used InP as the starting material to grow In_2O_3 nanofibers using a furnace, and their PL spectra exhibited emission at 470 nm [13.87]. *Zheng* et al. observed PL emission at 429 and 460 nm from their In_2O_3 nanowires using a three-probe DC method [13.85]. *Li* et al. measured the PL of In_2O_3 nanotubes, which exhibited emission at 593 nm [13.91]. The peculiar visible PL emissions in the blue to orange region from lotus-root In_2O_3 nanostructures have been explained on the basis of the novel hierarchical nanostructures [13.92]. In_2O_3 nanobelts synthesized without catalyst at low temperature using a simple physical vapor deposition, under excitation at 325 nm, showed a strong and broad emission at 570 nm with a shoulder at 630 nm [13.93].

The PL mechanisms of all these In_2O_3 nanomaterials were mainly attributed to the effect of oxygen vacancies or oxygen deficiencies, which are inevitable defects occurring in the crystallization process [13.76, 78, 86, 94]. Oxygen vacancies can induce the formation of new energy levels in the bandgap. Hence, the emission results from radiative recombination of a photoexcited hole with an electron occupying an oxygen vacancy [13.87, 95]. In general, emission spectra can be divided into near-band-edge (NBE) emissions and deep-level emissions [13.68, 96]. The emission peak position and strength depend upon the species of the oxygen vacancy and the intensities of PL. The near-band-edge UV emission is attributed to singly ionized oxygen vacancies in the In_2O_3 nanowires [13.68]. Hence, we can see that nanosized In_2O_3 materials exhibit tunability in the wavelength range from ultraviolet (UV) to visible blue-green, as well as yellow emission for optoelectronic devices [13.68, 78, 85, 92]. To achieve red emission from In_2O_3, appropriate dopants need to be added. Red emission is important, as it can also be used for many commercial, industrial, and medical applications. It is also a necessary source of red laser eyesights for military weapons. Interstitially N-doped In_2O_3 nano/microstructures including nanorods, nanoellipses, microspheres, and microbricks have been synthesized recently by annealing the corresponding $In(OH)_3$ precursors [13.97]. They show a unique and wide range of red light emission under 350 nm wavelength excitation, in addition to blue light emissions. These newly developed red light emission materials, N-doped In_2O_3 nano/microstructures, can be added to the red light emission semiconductor family and have significant application potential for optoelectronic devices such as red light-emitting diodes and lasers.

Nanocrystalline indium oxide doped with rare-earth (RE) and transition-metal ions also exhibits optical properties which are significantly different from those of bulk materials [13.42–44]. Such differences are expected due to the confinement effects on the vibrational spectra of nanocrystals, the increased role of the impurity ions at the surface whose optical properties are modified by the disorder at the surface, and the alteration of the electronic bands of the matrix. Cr-doped In_2O_3 nanostructures with diverse morphologies including nanotowers, nanowires, and octahedrons, synthesized by using a vapor transport method, exhibit broad orange-red emission peak at $\approx$ 640 nm [13.98].

Optical properties of In_2O_3:RE^{3+} microstructures and nanopowders have been reported recently [13.99–102]. Generally, rare-earth ions such as Eu^{3+}, Er^{3+}, etc. are incorporated into semiconductors to improve the luminescence efficiency by energy transfer processes. The optical properties of rare-earth ions trapped in host lattices have received much attention in terms of their fundamental and technological importance [13.103]. These matrices effectively reduce the quenching of surface rare-earth emission by shielding the rare-earth ions present on the surface of the nanoparticles from the external ligands. *Kim* et al. and *Choi* et al. observed Er^{3+} emission at around 1.54 μm in In_2O_3:Er^{3+} under direct excitation of Er^{3+} ions [13.99, 100, 102]. The Eu^{3+} luminescence was observed in In_2O_3:Eu^{3+} quantum dots (QDs) upon indirect excitation above 350 nm at room temperature, possibly due to host sensitization. However, the above luminescence lines of Eu^{3+} were broad [full-width at half-maximum (FWHM) of $\approx$ 9 nm for the 614 nm peak] and weak, indicating that the Eu^{3+} ions were probably located at (or near) the surface of In_2O_3 nanocrystals [13.101].

We have synthesized indium oxide and europium/dysprosium-doped indium oxide nanoparticles using a sonochemical technique where indium ethoxide was used as precursor [13.104]. Transmission electron microscopy (TEM) of the nanoparticles showed that they have mean diameter of 8.5 nm with standard deviation of 2.2 nm (Fig. 13.1). The emission spectrum of the In_2O_3 nanoparticles is shown in Fig. 13.2. On excitation at 235 nm, the pattern is characterized by a strong, broad asymmetric peak centered at 460 nm (blue) and two relatively lower-intensity peaks centered around 548 nm (yellow) and 618 nm (orange). The emission peaks in the visible region have been attributed to oxygen vacancies/defects present in the nanoparticles. The

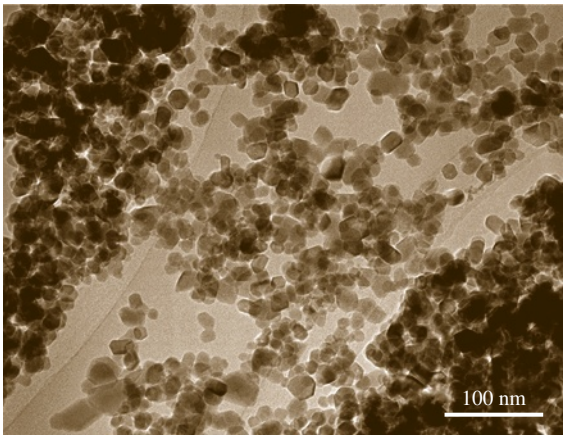


Fig. 13.1 TEM micrograph of In_2O_3 particles obtained from sonochemical synthesis

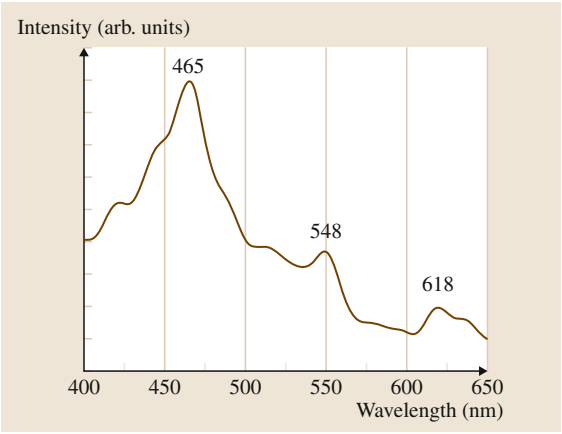


Fig. 13.2 Emission spectrum after excitation at 235 nm for In_2O_3 nanoparticles

PL spectrum of the In_2O_3:Eu particles, obtained after excitation at 235 nm, showed weak emission bands corresponding to $^5D \rightarrow {}^7F_0$ (≈ 575 nm), $^5D \rightarrow {}^7F_1$ (587 and 601 nm) and $^5D \rightarrow {}^7F_2$ (612 nm) transitions of Eu^{3+}. The excitation spectrum corresponding to the $^5D \rightarrow {}^7F$ transition of Eu^{3+} consisted of a broad peak centered at 265 nm, which was attributed to the charge transfer transition between Eu^{3+} and O^{2-} ions. The absence of a In_2O_3 host band in the excitation spectrum of Eu^{3+} indicated that there was almost no energy transfer from the In_2O_3 host to the doped Eu^{3+}. The relatively weak Eu^{3+} emission detected in In_2O_3:Eu^{3+} nanoparticles was possibly due to the highly strained and distorted environment around the lanthanide ions in the In_2O_3 lattice. In_2O_3:Dy^{3+} nanoparticles, however, did not show any luminescence, possibly due to the fact that Dy^{3+} ions exhibit poor absorption and emission cross-section characteristics compared with Eu^{3+}. However, very recently Eu^{3+} ion-doped In_2O_3 nanocrystals have been synthesized via a facile solvothermal method, which showed intense and well-resolved intra-4f emissions of Eu^{3+} upon bandgap excitation [13.105]. This highlights the fact that, by altering the method of synthesis, it is possible to manipulate the optical properties of undoped and doped indium oxide nanoparticles and thus tune them according to the final application.

Cerium oxide or ceria (CeO_2) is a rare-earth metal oxide with an energy gap of 3.2 eV and high dielectric constant ($\varepsilon = 26$) [13.106]. It well known for its optical properties and ability to filter UV radiation [13.107, 108]. Cerium oxides have also been investigated in processes related to the production of hydrogen for fuel cells and the abatement of organic pollutants from industrial wastewater [13.109–113]. Additionally, they have been used as polishing materials in optics, as components of oxygen sensors, and as efficient catalysts in fuel-cell technology, catalytic wet oxidation, engine exhaust catalysts, NO removal, and photocatalytic oxidation of water [13.114–121]. Due to their nontoxic nature and excellent biocompatibility, ceria nanoparticles have the potential to be used in many biomedical applications. They find applications as radical-scavenging antioxidants, can protect healthy cells from radiation-induced damage during radiation therapy, and also provide neuroprotection to spinal cord neurons [13.122–124]. These properties are dictated to a large extent by their crystal structure and morphology as well as grain size. The physical and chemical properties of ceria nanocrystalline material often differ from those of crystalline or amorphous materials. Bulk CeO_2 is not generally considered as a semiconductor since its bandgap is usually attributed to an $O_{2p} \rightarrow Ce_{4f}$ transition. Hence, it is not regarded as a photoactive material. However, CeO_2 nanoparticles exhibit a photovoltaic response derived directly from the nanometric structure of the constituent particles. Thus, an important field of research is the development of new synthetic processes to produce ultrafine CeO_2 particles with nanocrystalline structure that will heighten the performance of the material.

Consequently, CeO_2 nanoparticles have been prepared using various methods such as sol–gel processing [13.125, 126], hydrothermal synthesis [13.127–130], homogeneous precipitation with urea or hexamethylenetetramine [13.131, 132], flame spray pyrolysis [13.133], a reverse micelle route [13.134,

135], combustion synthesis [13.136], sonochemical and microwave-assisted heating routes [13.137], egg white solution route [13.138], a complex thermodecomposition method [13.139], a two-stage precipitation process [13.140], nonhydrolytic sol–gel synthesis [13.141, 142], solid-state reactions [13.143], mechanochemical reactions [13.144], etc. A semibatch reactor method was developed for synthesizing CeO_2 nanoparticles at room temperature [13.145]. Stable monodispersed cerium oxide nanoparticles have been synthesized in hydrocarbon solvents using oleic acid as surfactant [13.146]. The synthesis of some novel CeO_2 structures, including nanorods, nanowires, nanotubes, nanocubes, microplates, and other morphological structures, has also been reported by chemists [13.147–154, 154–166].

The estimated Bohr exciton radius for CeO_2 is about 78 nm [13.167]. Hence, for CeO_2 nanoparticles of sizes smaller that this, strong quantum confinement is expected. The optical properties of nanocrystalline CeO_2 vary widely depending on the size, shape, and morphology of the particles and also depend on the method of synthesis; For example, blue-shifts of the absorption peak and the absorption edges have been observed in the UV/Vis absorption spectra of sonochemically synthesized CeO_2 nanoparticles with mean particle size of 3.3 nm as a result of the quantum size effect [13.168]. However, the bandgap energy of reversed-micelle-synthesized CeO_2 nanoparticles changed little when the particle size was reduced from 4.1 to 2.6 nm [13.134]. The estimated bandgap of the CeO_2 nanoparticles (5–10 nm) prepared by a polymer complex method using cerium(III) acetate hydrate and polyvinyl pyrrolidone (PVP) was 3.44 eV. This value was within the range reported by *Yin* et al. ($E_g = 3.03–3.68$ eV for CeO_2 nanoparticles synthesized using sonochemical synthesis) [13.168]; *Ho* et al. ($E_g = 3.36–3.62$ eV for mesoporous CeO_2 nanostructures prepared using a polyol method) [13.169] and *Chen* and *Chang* ($E_g = 3.56–3.71$ eV for CeO_2 nanoparticles prepared using a precipitation method) [13.170]. However, the bandgap of CeO_2 nanoparticles (5 nm) synthesized using a self-assembly method was found to be 3.0 eV [13.171]. Ideally, quantum size effects arising from a reduction of the particle size predict a bandgap increase that is opposite to the effect observed here. However, simple quantum size effect calculations assume that no significant variation of the chemical structure of the metal oxide occurs during the particle size reduction. The discrepancy observed in this case is explained by the presence of oxygen vacancies and defects whose influence on the bandgap overcomes the expected influence of the regular quantum size effect [13.172, 173].

The room-temperature photoluminescence properties of CeO_2 nanoparticles also show a lot of variation. On excitation with continuous-wave (CW) 325 nm laser light, an emission peak was displayed at room temperature by bulk CeO_2 in the range 2.4–2.7 eV, whereas no emission was observed from commercially available CeO_2 nanoparticles with mean size of 25 nm [13.174]. Hydrothermally synthesized CeO_2 nanoparticles with average size of 1.8 nm exhibited a strong blue emission at 425 nm (2.92 eV) [13.175]. On dilution of these CeO_2 nanoparticles with double-distilled water, the emission peaks shifted their positions with the changing concentration. This kind of dependence of the PL peak blue-shift on the particle concentration has also been observed for CeO_2 nanoparticles synthesized by reverse micelle route [13.127]. This arises due to charge transitions from the 4f band to the valence band of the CeO_2 nanoparticles. Broadband PL emission from 325 to 550 nm with four emission bands at $\approx$ 406 nm (3.06 eV), 420 nm (2.95 eV), a blue-green band at $\approx$ 483 nm (2.57 eV), and a weak green band at 530 nm (2.34 eV) were observed in case of CeO_2 nanoparticles synthesized using a polymer route [13.176]. CeO_2 nanoparticles synthesized by a surfactant cetyltrimethylammonium bromide (CTAB)-assisted coprecipitation process showed a strong photoluminescence peak at 469 nm (2.64 eV) and three relative weak peaks at 452, 483, and 493 nm, respectively [13.177]. These were explained on the basis of surface defects and oxygen vacancies present in the nanoparticles synthesized using the different techniques. CeO_2 nanoparticles obtained from the decomposition of cerium-oleate complex emitted strong violet/blue emission at 400 nm in the photoluminescence (PL) spectrum. The PL emission was found to be sensitive to the particle size and shifted to shorter wavelengths with decreasing size. This has been explained by charge transitions from the 4f band to the valence band of CeO_2 [13.178]. The emission pattern also depends on the morphology of the nanoparticles. For CeO_2 nanorods, three emission peaks located at 370, 414, and 468 nm can be found [13.179], while two peaks at 415 and 435 nm have been reported for flower-like CeO_2 [13.180].

Due to their nontoxic nature and excellent biocompatibility, ceria nanoparticles have the potential to be used in many biomedical applications. However, ceria shows weak emission characteristics, and various approaches have been used to improve its luminescence properties. Attaching a tag, such as a fluorescent dye,

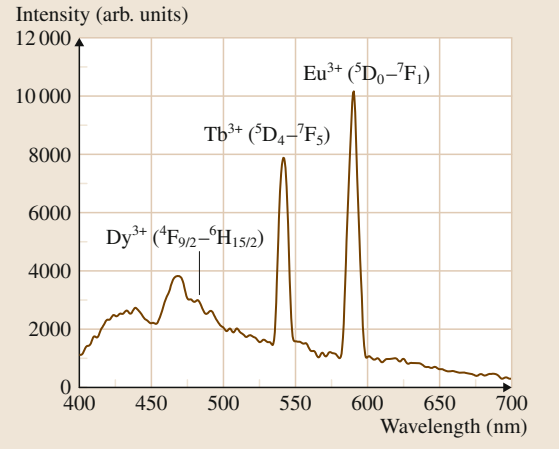


Fig. 13.3 Emission spectrum after excitation at 290 nm for CeO_2:Dy^{3+}(0.5%):Tb^{3+} (5.5%):Eu^{3+}(8%) nanoparticles

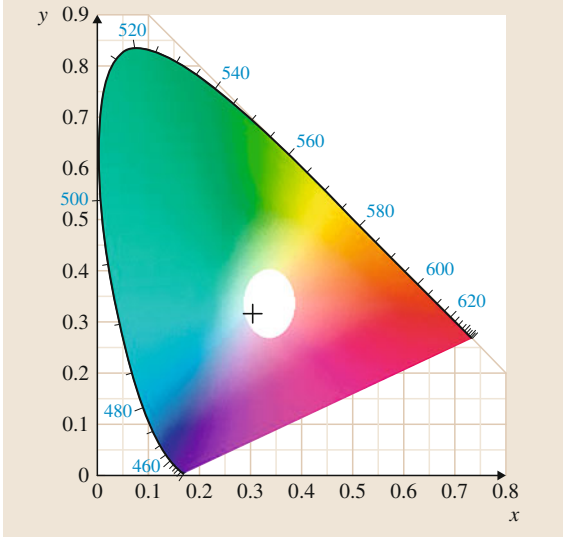


Fig. 13.4 CIE chromaticity diagram for CeO_2:Dy^{3+} (0.5%):Tb^{3+}(5.5%):Eu^{3+} (8%) nanoparticles

like a shell to the surface of the nanoparticles provides reliable and consistent emission from the fluorescent tag, but modification of the surface may lead to biological inactivity of the nanoparticle [13.181]. It also makes the material more bulky and thus limits the penetration of cells by the nanoparticles. A better alternative involves doping of the parent matrix with elements that can emit themselves upon excitation in the UV–visible range of the spectrum [13.182]. Also, recently there has been a lot of interest in rare-earth ion-doped CeO_2 as a potential phosphor material. The luminescent properties of CeO_2:RE^{3+} seem to depend on the preparation method. Europium (Eu) belongs to the rare-earth metal group and exhibits a strong red emission when doped in different matrices. The excitation spectrum of CeO_2:Eu^{3+} lies at 373 nm when using a solid-state reaction, while it occurs at 340 nm in CeO_2:Eu^{3+} prepared by the Pechini sol–gel process [13.183, 184]. Systematic investigation of nanocrystalline Eu^{3+}-doped CeO_2 prepared through a sol–gel process shows that the broad band in the excitation spectrum of CeO_2:Eu^{3+} (353 nm) comes from the charge transfer (CT) transition from O^2 to Ce^{4+}, not from the oxygen vacancy or from the CT of O^2 to Eu^{3+}. The emission spectra were dominated by the $^5D \rightarrow {}^7F_1$ transition located at 591 nm [13.185]. CeO_2:Eu^{3+} phosphor powders synthesized by the solid-state reaction method exhibited different behavior for direct excitation at 467 nm and indirect excitation of the CeO_2 host at 373 nm. Emission from Eu^{3+} was observed, but the intensity ratios of the various peaks were different in each case. The nature of this behavior is closely related to the defects and symmetry distortion generated by Eu^{3+} replacing Ce^{4+} [13.183]. Undoped CeO_2 nanocrystals, and those doped with other lanthanide ions (Eu^{3+}, Tb^{3+}, Sm^{3+}), synthesized via a high-boiling-point solvent process exhibited unusual optical properties. The undoped CeO_2 nanocrystals showed a very weak emission band peaking at 501 nm, which was remarkably enhanced by doping additional lanthanide ions (Eu^{3+}, Tb^{3+}, Sm^{3+}) in the CeO_2 nanocrystals. The greatly increased emission band of CeO_2:Eu^{3+} (Tb^{3+}, Sm^{3+}) nanocrystals (located at 500 nm) was not attributed to the characteristic emission of the lanthanide ions (Eu^{3+}, Tb^{3+}, Sm^{3+}) but to the presence of oxygen vacancies in the lattice of the CeO_2 nanocrystals [13.186].

We have synthesized a novel nanocrystalline CeO_2:RE^{3+} (RE = Dy, Tb, Eu) phosphor which simultaneously emits blue, green, yellow, and red light from its active region on excitation of the host and consequently is expected to have tremendous applications in white light-emitting UV LEDs. These phosphors were synthesized using a sonochemical technique based on acoustic cavitation resulting from continuous formation, growth, and implosive collapse of bubbles in a liquid. The emission spectra of CeO_2:Dy^{3+}(0.5%):Tb^{3+}(5.5%):Eu^{3+} (8%) on excitation at 290 nm is illustrated in Fig. 13.3, which shows the presence of characteristic yellow, blue, green, and red emissions due to Dy^{3+}, Tb^{3+}, and Eu^{3+} ions, respectively, along with the blue emission of the host. As

seen in this spectrum, on excitation at the main host site (290 nm), there is efficient energy transfer from the host to the various dopants. The corresponding chromaticity diagram is shown in Fig. 13.4. On excitation at 290 nm, the emission appeared predominantly white with CIE 1931 chromaticity coordinates of $x = 0.308$, $y = 0.308$. The correlated color temperature (CCT) was found to be 6967 K. The International Commission on Illumination (CIE) standard illuminant D_{65} has a CCT of 6500 K, representing standard daylight. For the present sample, excitation at 290 nm resulted in a CCT of 6967 K, near to that of D_{65}. Hence, this nanocrystalline CeO_2:Dy^{3+}(2%):Tb^{3+}(0.5%):Eu^{3+}(1.5%) sample has tremendous potential application as a white light-emitting phosphor for deep-UV LEDs. Recently, there have been reports on undoped and rare-earth-doped CeO_2 nanoparticles exhibiting a photovoltaic response derived directly from the nanometric structure of the constituent particles [13.171]. These nanoparticles did not need photosensitization to have photovoltaic activity in the visible region, and the excitation spectrum depended notably on the presence of dopants. Consequently, operational organic-dye-free solar cells using nanometric ceria particles (in mesostructured or amorphous form) as the active component have been constructed with efficiencies that depend on the illuminating power.

Gadolinium oxide (Gd_2O_3), a rare-earth sesquioxide, has unique properties which can be utilized in a wide range of technological applications. Its high chemical stability, wide bandgap with transmission coefficient in the visible region of the solar spectrum, high neutron absorption cross-section, and relaxivity along with its ability to provide effective emission of radiation make it a very suitable material for use in solar cells, as phosphors in display devices, in reactors, neutron detectors, and neutron capture cancer therapy, and as a good contrast agent for medical imaging [13.187]. Such materials are also promising for use as labels in biotechnology because of their optical properties such as large Stokes shift, lack of photobleaching, and long fluorescence lifetime (about 1 ms). Gadolinium oxide (Gd_2O_3) is an attractive host lattice for several lanthanide ions to produce efficient phosphors emitting a variety of colors. Recently, Gd_2O_3:Eu^{3+} phosphor has been considered as one of the better phosphor candidate for flat-panel displays (FPDs) owing to its good color purity [13.188–190]. The red-emitting Eu-doped Gd_2O_3 phosphor is gaining importance due to its favorable low thermal expansion, phase stability, and high melting point [13.191]. It has been widely used as an x-ray scintillator material and in high-definition projection televisions, flat-panel displays, and photoelectronic apparatus [13.192]. Over the past decade, Eu^{3+}- and Tb^{3+}-activated Gd_2O_3 phosphors have been investigated extensively [13.190, 193–195]. Tb^{3+}, Dy^{3+}, and Eu^{3+} ion-doped Gd_2O_3 particles have potential applications in immunoassays [13.196].

In view of this, a number of preparative methods have been explored for synthesis of doped Gd_2O_3 phosphors. Gd_2O_3:Eu nanoparticles have been prepared using a direct oxide precipitation method in high-boiling polyalcohol solutions, by a hydroxide precipitation method at 1073 K, and also by using soft chemical routes such as spray pyrolysis, sol–gel process, glycine–nitrate combustion, solid-state reactions, co-precipitation method, etc. [13.197–204]. The gas-phase condensation technique has been explored to individually dope Tb^{3+}, Dy^{3+}, and Eu^{3+} ions in Gd_2O_3 matrix. Nanocrystalline doped Gd_2O_3 phosphor films have also been prepared by the Pechini sol–gel soft lithography technique [13.205]. Gd_2O_3 exhibits a host absorption around 230–240 nm, and exciting the host might result in an energy transfer between the host and doped luminescent lanthanide ions. The rare-earth ions show abundant emission colors based on their 4f–4f or 5d–4f transitions. Eu^{3+} and Tb^{3+} show red/orange and green emission, respectively, at 611/590 nm and 544 nm. The characteristic emission of Dy^{3+} is dominated by two main groups of lines in the blue region (460–505 nm) and yellow region (570–600 nm). The optical properties exhibited by these nanoparticles differ slightly compared with their bulk counterparts. It is reported that the emission lifetime, luminescence quantum efficiency, and concentration quenching are strongly dependent on the particle size in the nanometer range [13.206, 207]. Gd_2O_3 nanocrystals of different sizes doped with 2.5 at. % Eu^{3+} synthesized by a sol lyophilization process exhibited a gap blue-shift with decrease in particle size [13.190]. Compared with the bulk material properties, some important changes in luminescence were observed. In particular, some lines were strengthened when the size of the nanoparticles diminished. A blue-shift in the $^5D_0 \rightarrow {}^7F$ transition in Gd_2O_3:Eu^{3+} nanoparticles synthesized by direct precipitation in high-boiling diethylene glycol (DEG) has been observed with decrease in particle size [13.197]. This has been attributed to the increasing Eu−O distance and associated decrease in the Eu−O bond strength.

Recently there have also been a few reports on synthesis of 1-D Gd_2O_3:Eu^{3+} nanomaterials, whose applications could be widely extended due to the shape-

specific and quantum confinement effects. Gd_2O_3:Eu^{3+} nanotubes have been prepared via a wet chemical route with subsequent heat treatment [13.208]. The nanotubes exhibited strong red emission corresponding to the $^5D_0 \rightarrow {}^7F_2$ transition of the Eu^{3+} ions under UV light or low-voltage electron beam excitation, which might find potential applications in fields such as light-emitting phosphors, advanced flat-panel displays, or biological labeling. *Li* et al. prepared Gd_2O_3:Eu^{3+} nanowires via the anodized aluminum oxide (AAO) template method [13.209]. The decay time constant of the $^5D_0 \rightarrow {}^7F_2$ transition became longer with increasing annealing temperature in Gd_2O_3:Eu/AAO. The lifetime of $^5D_0 \rightarrow {}^7F_J$ in Gd_2O_3:Eu/AAO composite films was more than that in the bulk powder. Gd_2O_3:Eu^{3+} nanotubes synthesized using multi-walled carbon nanotube (MWCNT) templates emit strong red luminescence peaking at 610 nm, implying their potential application in the field of luminescence devices [13.210]. Gd_2O_3:Eu^{3+} nanowires prepared by a simple solvothermal method in the presence of polyethylene glycol followed by a subsequent calcination process show a strong red emission corresponding to the $^5D_0 \rightarrow {}^7F_2$ transition (610 nm) of Eu^{3+} under ultraviolet excitation (250 nm), with potential applications in red-emitting phosphors and field-emission display devices [13.211].

The photoluminescent properties of Gd_2O_3:Tb^{3+} nanoparticles synthesized via the polyol method originate principally from the Tb^{3+} dopant, which exhibits a strong emission peak at ≈ 544 nm [13.212]. Similar emission spectra were observed for colloidal dispersions of the particles using fluorescent spectroscopy. These nanoparticles demonstrated the potential to be used both as fluorescent contrast agents in imaging fibroblast cells and macrophages and as magnetic resonance imaging (MRI) contrast agents. Nanostructured Tb^{3+}-doped Gd_2O_3 particles have also been synthesized from chloride precursors by NaOH addition in a polyol medium [13.213]. The typical emission spectrum on excitation at 275 nm showed four peaks from 470 to 640 nm, corresponding to the $^5D_4 \rightarrow {}^7F_{6,5,4,3}$ transition of Tb^{3+}. The most intense peak of $^5D_4 \rightarrow {}^7F_5$ was located at about 545 nm, and three other peaks were observed at 485 nm ($^5D_4 \rightarrow {}^7F_6$), 585 nm ($^5D_4 \rightarrow {}^7F_4$), and 620 nm ($^5D_4 \rightarrow {}^7F_3$). Gd_2O_3:Tb^{3+}/Eu^{3+} nanospheres and nanoplates have been synthesized using the hot solution nonhydrolytic procedure [13.214]. The shape was varied from nanospheres to nanoplates by changing the Gd precursor (acetates versus acetylacetonate), the major organic surfactant (1,2-hexadecanediol (HDD) versus trioctylphosphine oxide (TOPO)), and the concentration ratio of precursor to surfactant. Though the PL peak energies were the same for nanoplates and nanospheres, the luminescent intensity from nanospheres was about 2–3 times higher than that from nanoplates, which has been explained in terms of the doping efficiency, crystal structure, and ratio of surface to volume.

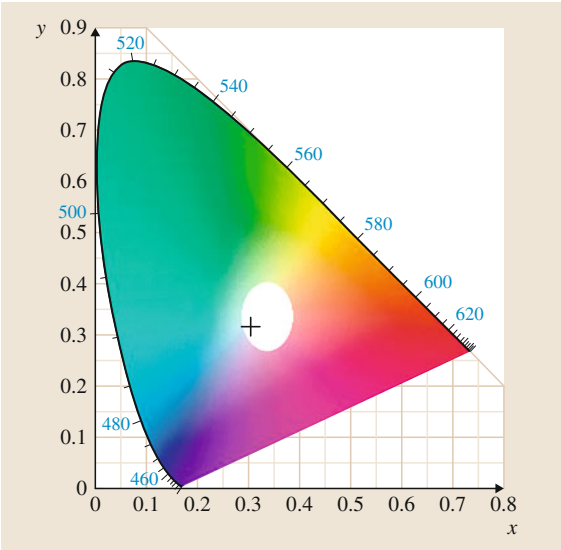


Fig. 13.5 CIE chromaticity diagram for Gd_2O_3:Dy^{3+} (1.95%):Tb^{3+}(0.05%) nanoparticles

Recently, we reported sonochemical synthesis of a novel nanocrystalline Gd_2O_3:RE (RE = Dy, Tb) phosphor which simultaneously emits blue and yellow light from its active region on excitation of the host and consequently is expected to have tremendous applications in white light-emitting deep-UV LEDs [13.215]. The CIE chromaticity coordinates calculated from the emission curve of Gd_2O_3:Dy^{3+}(1.95%):Tb^{3+}(0.05%) for 247 nm excitation were $x = 0.315$, $y = 0.316$ (Fig. 13.5). These values correspond almost exactly to the CIE coordinates of the balanced white-light region of the chromaticity diagram, where $x = 0.33$, $y = 0.33$. The corresponding CCT value was found to be 6508 K. The CIE standard illuminant D_{65} has CCT of 6500 K, which represents standard daylight. For this double-doped sample, excitation at 247 nm resulted in CCT of 6508 K, which is extremely close to that of D_{65}. Due to the nondispersibility of the sonochemically synthesized Gd_2O_3:Tb^{3+}:Dy^{3+} nanoparticles in aqueous/organic solvents, the polyol method of synthesis was explored [13.216]. The CIE chromaticity coordinates

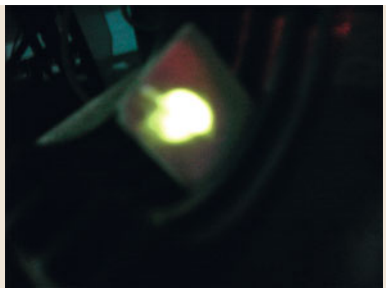


Fig. 13.6 Gd_2O_3:Dy^{3+}(2%) film on quartz under UV light with room lights switched off. Bright white emission is observed with the ultraviolet excitation

($x = 0.270$, $y = 0.328$) and the CCT value (9157 K) of the Gd_2O_3:Dy^{3+}(1.95%):Tb^{3+}(0.05%) phosphor synthesized by the polyol route was distant from that of the D_{65} point (6500 K). This proves that the method of synthesis plays a major role in the optical properties of nanomaterials. Dispersible Gd_2O_3:Dy^{3+}(2%) phosphor was then synthesized using the polyol technique. The phosphor showed white luminescence in solid form, as aqueous solution, and also when spin-coated onto quartz substrate. For the spin-coated sample, the CIE coordinates were $x = 0.313$, $y = 0.296$ and the correlated color temperature was 6815 K. Figure 13.6 shows a spin-coated Gd_2O_3:Dy^{3+}(2%) phosphor film on a quartz slide substrate and the bright white luminescence of this film observed under ultraviolet light with $\lambda_{exc} = 310$ nm. This demonstrates that Gd_2O_3:Dy^{3+}(2%) films are good candidate materials for new lighting devices.

13.3 Sorbent Properties of Oxide Nanomaterials

Residual surface hydroxides can also add to the rich surface chemistry exhibited by metal oxides such as MgO, CaO, SrO, BaO, Al_2O_3, TiO_2, Fe_2O_3, ZnO, etc., and this chemistry is generally attributable to Lewis acid, Lewis base, and Brønsted acid sites of varying coordination, i.e., metal cations, oxide anions, and surface −OH, which can be isolated or lattice bound. Study of their use as adsorbents and catalysts has led to two important discoveries: (i) surface reactivates are inherently higher per unit surface area for nanocrystals versus microcrystals, and (ii) compaction of nanocrystals into pellets does not significantly degrade their surface area or surface reactivity when moderate pressures are employed, enabling these nanostructured materials to be employed as very fine powders or as porous, reactive pellets.

Though the surface chemistry of crystals has been of interest for a long time [13.217–221], the recent availability of nanocrystalline samples has allowed the demonstration of vast differences due to crystal size and shape that had not been imagined before. Therefore, new and deeper understanding is required, which in turn suggests additional work. Another approach to investigating the differences in surface reactivity of nano- versus microcrystals is to look at pH changes in water as a function of time.

Generally, nanomaterials cause pH adjustments more rapidly than normal powders, and this is especially true for MgO and Al_2O_3. These results can be explained by surface area effects, and enhanced surface reactivity per m^2 is not indicated by these pH studies of powder samples. On the other hand, in destructive adsorption studies in which polar organic molecules are adsorbed, nanomaterials do exhibit inherently more active surfaces.

Hydroxyl groups may form by the redox reaction in which the OH group with its electron pair appears bound by a Lewis acid site (M) and a hydrogen atom reacts with either lattice oxygen (a Lewis base) or an adsorbed oxygen molecule. The hydroxyl groups may be formed in two ways:

1. OH group with an oxygen atom from lattice oxygen plays the role of the electron donor. The reaction involves hemolytic dissociation of water on the surface and the reaction of a neutral hydrogen atom with a lattice oxygen, which is usually in the 2− state. The OH group formed may be ionized and become an electron donor.
2. According to the second mechanism, there is a possibility of the reaction between a hydrogen atom and a lattice oxygen, and the hydroxyl group thus formed may bind to a metal atom. In this case, an oxygen vacancy is ionized by providing an additional electron.
3. The third mechanism takes place at low temperatures and is related to the competition between water and oxygen molecules for the same adsorption sites.

In equilibrium conditions, some of the active sites are occupied by water molecules and the concentration

of chemisorbed oxygen decreases, which leads to the lower surface charge.

13.3.1 Sorbents for Environmental Remediation

First, we deal with new discoveries in the field of sorbents. Activated high-surface-area carbon is the *gold standard* in sorbent technology. A wide variety of carbon sorbents made from coal, wood, coconut shells, fruit seeds, polymers, etc. have been used for centuries for purification of chemicals, water, and air. Chemical additives to carbon sorbents often enhance their abilities to be more selective for certain sorbates. Also, recent developments in the field of fullerenes, carbon nanotubes, graphene, and carbon fibers have added greatly to the usefulness of carbon as a whole. Carbon is certainly an intriguing and amazing material, especially in nanostructured solid form. Nonetheless, there are some drawbacks to carbon sorbents. Since it mainly operates by physisorption (rather than strong chemisorption), many volatile sorbates are not trapped very well by carbon. Also, sorbates are usually not destroyed or detoxified by carbon, and eventual leaching or bleeding-off of sorbates is a common problem. There are, of course, many other solids that serve as high-surface-area (high-capacity) sorbents. This has become especially the case in recent years as new synthetic methods have allowed nanoscale metal oxides such as magnesium oxide (MgO), calcium oxide (CaO), titanium oxide (TiO_2), aluminum oxide (Al_2O_3), iron oxide (Fe_2O_3), and zinc oxide (ZnO) to be prepared [13.222–224]. These oxides in high-surface-area form, and their physical mixtures and intimate (molecular or nanoscale) mixtures, have proven to be excellent sorbents for many applications. We have used metal oxides as *destructive adsorbents* of organophosphorus compounds (chemical warfare agent mimics and pesticides). The metal oxide (MgO) was contained in a fixed bed reactor tube, and heated to temperatures hot enough to very rapidly destroy a series of organophosphorus chemicals. As an example, triethylphosphate [$(CH_3CH_2O)_3P{=}O$] adsorbed strongly on a MgO surface, and about four surface MgO moieties adsorbed one phosphate molecule [13.225, 226]. A wide variety of toxic industrial chemicals (TICs) have been found to be susceptible to treatment by these destructive adsorbents. Remediation of chemical spills, contaminants in commercial gases, and odors in air are now commonplace with this class of safe-to-use nanoscale metal oxides.

Biological toxins, including bacteria, bacterial spores such as anthrax, and viruses, are probably the most serious threats. The need is growing for broad-spectrum biocides that can decontaminate tough-to-kill spores, as well as other biological threats [13.227–230]. Indeed, these high-surface-area solids were very effective for destroying *Escherichia coli*, *Bacillus cereus*, and *Bacillus subtilis* spores, with MgO, Al_2O_3, TiO_2, and CeO_2. There were four modes of action discerned:

1. Electrostatic attraction of the spores to the nanoparticles
2. High local pH weakening the spore's protective outer layer
3. Abrasive action
4. Oxidative reactions with the attached zero-valent halogens.

The high surface area of the nanooxides makes them efficient adsorbents for toxic inorganic cations and anions also. Treatment processes make use of one or a combination of processes such as precipitation, membrane filtration, ion exchange, and adsorption. However, adsorption using simple and cheap adsorbents is gaining a lot of importance due to its economic benefits as well as the easy availability of different kinds of adsorbents [13.227]. There is always ongoing research for the development of sorbents that are cheap and easily synthesized to avoid expensive regeneration processes after use. Hence, research in developing new adsorbents is focused on the development of simple and economic procedures for their synthesis or reuse.

Environmental fluoride has received much attention on account of its known beneficial and detrimental effects on health. Lower levels of fluoride in drinking water may lead to dental caries, whereas excess injection through drinking water causes dental and skeletal fluorosis. The World Health Organization has specified the tolerance limit for fluoride content in drinking water as 1.5 mg/l. Hence, defluoridation of water is important to provide safe water. The presence of heavy metals in the environment is a serious global, social, and environmental problem. Many industrial facilities, such as metal plating and mining operations, fertilizer industry, tanneries, and textile industries, discharge heavy metals via their waste effluents. Toxic metal ions are a serious health hazard, and every possible care should be taken to prevent their contact with and mixing into air, water, and soil. High levels of lead damage brain and kidney,

mercury vapors lead to permanent brain damage at high concentration levels, higher concentration of copper in water can cause eye irritation, headache, dizziness, and diarrhea, and inhaling too much chromium causes fragile bones and probably acts as a human carcinogen. Therefore, in an effort to reduce heavy-metal levels in wastewater, drinking water, and water used for agriculture to the maximum permissible concentration, several methods such as ion exchange, adsorption, precipitation, and membrane separation have been adopted. Based on its toxicity, the US Environmental Protection Agency (EPA) has set the maximum permissible limit for lead ions in drinking water as 0.05 mg/l, and the Bureau of Indian Standards as 0.1 mg/l. The upper limit for lead in drinking water recommended by the World Health Organization (WHO) and the American Water Works Association (AWWA) is 0.05 mg/l. These limits suggest more stringent requirement for removal of lead from the aqueous environment, which necessitates the development of innovative and cost-effective treatment methods for effluents containing lead before discharging into natural water bodies.

Among various techniques, the ion-exchange process is used exclusively in water treatment, and many studies have been carried out to find inexpensive and chemicophysically feasible adsorbents. Therefore, for an ion exchanger to be practical for removal of heavy metals from industrial wastewater containing other competing ions such as calcium and magnesium, it is essential that the chosen sorbent be sufficiently selective toward heavy metals against calcium and magnesium. Extensive studies on the adsorption and ion-exchange properties of hydrous oxides have been carried out from the point of view of analytical separation, as adsorbents for the recovery of trace metals present in natural waters, and as matrices for radioactive nuclear waste. The ion-exchange and adsorption properties of hydrous oxides arise from the pH-dependent protonation and deprotonation reactions of surface hydroxyl groups when in contact with solution.

The use of nanocrystalline compounds as simple adsorbents appeared as a good alternative. There is increasing interest in the field of nanoparticles as these are more efficient in processing as compared with thin films. Moreover, high-density pellets can be made from nanoparticles as compared with bulk. Thus, the sorption property could also be improved by using nanocompounds. In general, a decrease in particle size increases the surface area and hence increases the number of adsorption sites. There are a number of synthesis procedures that have been adopted for synthesis of nanoparticles [13.231–234]. Combustion synthesis using an oxidant and fuel is one of the simplest and fastest procedures adopted. In the synthesis of magnesia–alumina mixed oxide, magnesium nitrate ($Mg(NO_3)_2 \cdot 6H_2O$, 99.9% pure) and aluminum nitrate ($Al(NO_3)_3 \cdot 9H_2O$, 99.9% pure) were used as the oxidants along with glycine as the fuel (35%) in fuel-deficient ratio. The reactants were mixed in deionized water in the required molar ratios, which on thermal dehydration resulted in the formation of a viscous liquid (gel). The viscous liquid swelled and auto-ignited on increasing the temperature ($\approx 250\,^{\circ}C$). This was accompanied with the rapid evolution of a large volume of gases, to produce voluminous powders. Since the duration of auto-ignition is short ($< 10\,s$), the powders were calcined at 600 °C in air to remove traces of any carbon impurities that could be present. Three different ratios (0.8 : 0.2, 1 : 1, and 1 : 2) of Mg and Al were taken, respectively. The x-ray diffraction (XRD) pattern of the compound indicated that the initial compound is periclase-type MgO structure with 20% Al solubility. The observed XRD pattern showed a shift in the peak from the standard MgO pattern, thus confirming the solubility of Al in the MgO, forming the $Mg_{0.8}Al_{0.2}O_{1.1}$ compound. The oxide $Mg_{0.8}Al_{0.2}O_{1.1}$ was found to be single-phasic and nanocrystalline (with low amorphous content). The crystallite size was calculated using Scherrer's formula, and the average crystallite size of the nanopowders was found to be 8 nm. Nanosize pure and mixed ferrite composites were synthesized by combustion of aqueous solutions containing stoichiometric amounts of iron nitrate and glycine (analytical grade, E. Merck) as the oxidant and reductant, respectively. The stoichiometric composition of the redox mixture was calculated based on the total oxidizing and reducing valencies of the oxidizer and the fuel, keeping the O/F ratio at unity. For synthesis of cobalt ferrite, cobalt carbonate as the cobalt source was added along with the redox mixture of ferric nitrate and glycine taken in stoichiometric ratio. $CoCO_3$ was dissolved in a minimum quantity of $\approx 50\%$ HNO_3 (fuming), and $Fe(NO_3)_3 \cdot 9H_2O$ and glycine in deionized water. In the synthesis of both pure and mixed ferrites, the homogeneous aqueous mixture of the nitrates and glycine was heated on a hot plate till it became dehydrated to form a viscous gel. When the obtained gel was introduced into a muffle furnace preheated to 300 °C, the gel boils, foams, and undergoes smoldering (flameless) combustion to produce nanosized oxide particles. The synthesis was also carried out by using a fuel-deficient composition (1 : 0.5). The oxide pow-

ders obtained were calcined at 600 °C for 1 h to remove carbonaceous impurities. Structural elucidation studies showed that ferrite synthesized in the fuel-deficient condition (oxidant : fuel = 1 : 0.5) had a single phase of Fe_2O_3, whereas that synthesized in stoichiometric conditions (oxidant : fuel = 1 : 1.66) showed mixed phases containing Fe_2O_3 and Fe_3O_4 and the particle size was around 50 nm. The surface areas of α-Fe_2O_3 synthesized in fuel-deficient and stoichiometric conditions were 2.055 and 2.26 m^2/g, respectively, and that of $CoFe_2O_4$ was 2.02 m^2/g. Characterization of the oxide by zeta potential measurements was carried out at the pH at which sorption studies were carried out. For pure ferrite produced in the fuel-deficient and stoichiometric conditions, the zeta potential value was +34.6 and +32.4 mV, respectively, whereas for $CoFe_2O_4$, it was found to be −38.1 mV. α-Manganese oxide was prepared by hydrolysis of $KMnO_4$, and the particles were characterized using XRD and TEM. It was shown that the particles were spherical and the particle size was 6 nm. Sorption studies were carried out in batch mode wherein 10 ml of aqueous solution of the ion of interest or its mixture at a particular pH was equilibrated with a weighed amount of oxide sample for a known period of time, and the amount taken up was studied as a function of various experimental conditions. Nanocrystalline magnesia–alumina mixed oxide ($Mg_{0.80}Al_{0.20}O_{1.10}$) prepared by the combustion synthesis method was found to be an excellent adsorbent for uptake of fluoride anion of up to 120 mg/l concentration with uptake capacity of 10 mg F^-/g. A bioinorganic composite of nanohydroxyapatite/chitosan (n-HApC) showed a defluoridation capacity (DC) of 1560 mg F^-/kg in comparison with DC of 1296 mg F^-/kg for nanohydroxyapatite (n-HAp).

Nanocrystalline cobalt ferrite and MnO_2 showed good uptake capacity for lead ion. Titania–silica (TiO_2/SiO_2) binary mixed oxide with surface area of 405.3 m^2/g was found to be a good sorbent for lead ions. A novel hybrid adsorbent HMO-001 was fabricated by impregnating nanosized hydrous manganese dioxide (HMO) into a porous polystyrene cation-exchange resin (D-001) for enhanced removal of Cd(II) and Zn(II) ions from waters. The nanohydroxyapatite particles (nHAp) had sorption capacity of 1.17 mmol/g of Pb.

The sorption results were fitted using both kinetic and equilibrium modeling. For equilibrium modeling, Langmuir and Freundlich adsorption models were chosen, and the obtained experimental data were fitted to the equations of the two models. For this, the amount of inorganic ion taken up by the oxide was calculated by the simple concentration difference method. Batch-mode experiments were carried out with W g of oxide and V ml of the ion solution. If the initial and final concentrations of inorganic ion are C and C_1 (mg/l), the ion uptake q (mg/g) is calculated from the mass balance using (13.5)

$$q = \frac{(C_0 - C_1) \cdot V}{W \cdot 1000} \,. \tag{13.5}$$

The linearized form of the Freundlich equation [13.235] is given in (13.6), where q_e is the amount adsorbed at equilibrium (mg/g), C_e is the equilibrium concentration (mg/l), and K_f and n are constants indicative of adsorption capacity and adsorption intensity, respectively,

$$\ln q_e = \ln K_f + \frac{1}{n} C_e \,. \tag{13.6}$$

The Langmuir equation [13.236] assumes that:

1. The solid surface presents a finite number of identical sites which are energetically uniform.
2. There are no interactions between adsorbed species, meaning that the amount adsorbed has no influence on the rate of adsorption.
3. A monolayer is formed when the solid surface reaches saturation.

The linear form of the Langmuir equation is given in (13.7), where q_e is the amount adsorbed at equilibrium (mg/g), C_e is the equilibrium concentration (mg/l), b is a constant, and Q^0 is the mass of adsorbed solute required to saturate a unit mass of adsorbent (mg/g). Q^0 represents a practical limiting adsorption capacity when the surface is fully covered with lead ion. By plotting C_e/q_e versus C_e, Q and b can be determined if a straight line is obtained

$$\frac{C_e}{q_e} = \frac{1}{Q^0 \cdot b} + \frac{C_e}{Q^0} \,. \tag{13.7}$$

It is reported that, if the value of the Freundlich constant n lies between 1 and 10, it indicates favorable adsorption. The applicability of the Langmuir model indicates monolayer coverage, which indicates the possibility of an ion-exchange mechanism.

In the reaction-based modeling, the pseudo-first-order and pseudo-second-order models proposed by Lagergren and Ho and Mackay, respectively, were employed to explain the solid/liquid adsorption. To distinguish the kinetic equation based on the adsorption capacity of solid from the one that is based on the concentration of solution, the first-order and second-order

reactions in solution phase are termed pseudo first order and pseudo second order, respectively. It was Lagergren who first presented the first-order rate equation for adsorption [13.237], and thereafter it has been extensively used for the adsorption of an adsorbate from an aqueous solution. Lagergren's first-order rate equation has been called pseudo first order since 1998 [13.238] and is expressed as

$$\log(q_e - q_t) = \log q_e - \frac{k_{ad} \cdot t}{2.303}, \tag{13.8}$$

where q_e and q_t are the amount of inorganic ion on the surface of the sorbent beads (mg/g) at equilibrium and at time t, respectively, and k_{ad} is the equilibrium rate constant of pseudo-first-order sorption (h^{-1}). The slope of the straight-line plot of $\log(q_e - q_t)$ against t will give the values of the rate constants (k_{ad}).

Ho's second-order rate expression, known as pseudo second order [13.239], is expressed linearly as

$$\frac{t}{q_t} = \frac{1}{K_{2ads} q_e^2} + \frac{t}{q_e}, \tag{13.9}$$

where q_t is the amount of ion on the surface of the bead (mg/g) at any time t, K_{2ads} is the pseudo-second-order rate constant (g/mg min) and q_e is the amount of ion sorbed at equilibrium (mg/g) and the initial sorption rate. The data obtained are fitted on a plot of t/q_t against t, which should be a straight line, and the values of q_e and K_{2ads} can be calculated from the slope and intercept, respectively.

13.4 Catalytic Properties of Oxide Nanomaterials

Catalysis is the subject which deals with the change of rate of reaction due to the presence of any substance, called the catalyst. The catalyst does not participate in the chemical reaction like other substrates. Depending on the reaction, a catalyst may take part in multiple chemical transformations. Materials that improve the rate of reaction are called positive catalysts, whereas those that slow down the rate of reaction are called inhibitors or negative catalysts. In addition, materials which increase the activity of any catalyst are called promoters, whereas materials which deactivate catalysts are called catalytic poisons. Mostly, in heterogeneous catalysis, the reaction occurs on a solid surface and involves the reaction of gases or liquids [13.240–242]. Therefore, the specific surface area of the solid plays an important role in the reaction rate, and in this respect nanotechnology plays an important role. Nanomaterials have a few times more surface area than bulk samples.

Various nanocatalysts such as doped ceria, Au nanoparticles dispersed on TiO_2, Co_2O_3, Fe_2O_3, etc. have been developed to oxidize CO at lower temperatures [13.243–249]. Carbon monoxide is one of the toxic gases, and can disturb the normal functioning of hemoglobin by converting it into carboxyhemoglobin, if its level is more than 100 ppm in the atmosphere. This can be prevented by oxidation of the fatal CO into nontoxic CO_2 [13.250]. Rh, Au dispersed ceria nanoparticles also form an excellent catalyst for CO oxidation [13.251–253]. Ceria is also a vital component in three-way catalyst (TWC), which is used to remove pollutants other than CO from the environment. The possibility of the conversion $Ce^{3+} \leftrightarrow Ce^{4+}$ assists in accepting or removing oxygen from ceria. Moreover, the fluorite structure of ceria or doped ceria has superior chemical and physical stability. Pure CeO_2 alone as a catalyst is not of much interest due to its low textural stability under high-temperature conditions, as usually encountered in exhaust gases. At high temperatures, the surface area of CeO_2 reduces drastically and it loses its redox properties and oxygen storage capacity [13.254]. It has been observed that doped ceria has superior stability towards sintering as well as its catalytic activity [13.255]. The versatility of rare-earth-doped ceria depends on the availability of the 4f shell. On substitution of trivalent rare-earth oxide, the oxygen vacancies increase, which subsequently improves the oxygen mobility and also the oxygen storage capacity.

It has been observed that ceria in nanoform is more important since nanoceria exhibits superior catalytic properties compared with bulk ceria. The homogeneity of the sample can be controlled in nanocrystalline form, which in turn can improve the catalytic properties of sintered ceria [13.256]. Nanocrystalline ceria and doped ceria have been prepared by several methods such as sol–gel, gel combustion, sonochemical, ball milling, spray hydrolysis, homogeneous precipitation, etc. [13.126, 257–262]. In a few of these synthetic procedures, the precursor needs to be heated to obtain the final product, but such thermal treatment leads to agglomeration of the powders, which is not very encouraging since the powders become difficult to disperse.

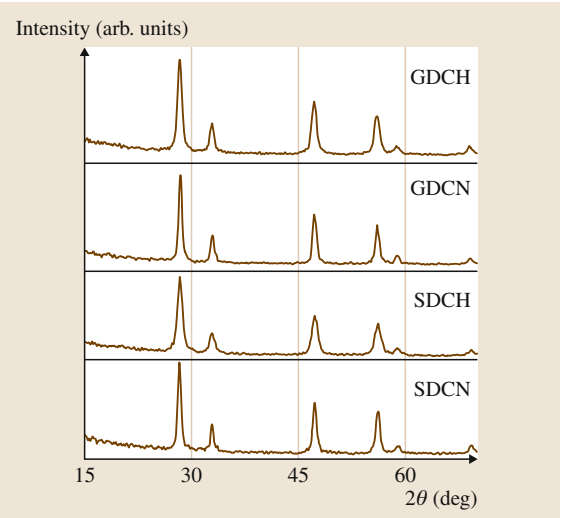


Fig. 13.7 XRD patterns of SDCN, SDCH, GDCN, and GDCH

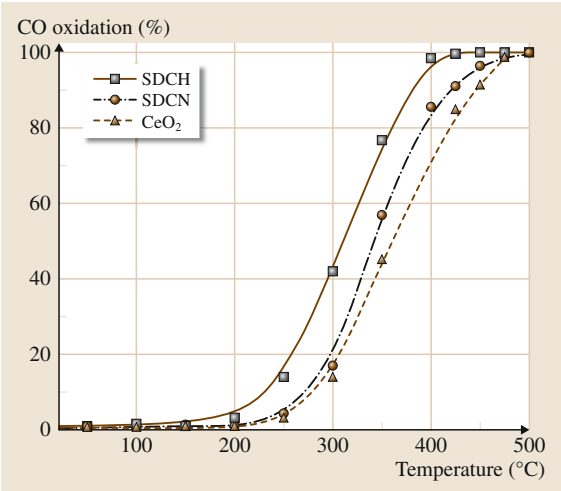


Fig. 13.8 Oxidation of CO in presence of different catalysts

Table 13.3 Physicochemical properties of doped ceria

	Surface area (m^2/g)	Particle size (nm)	Agglomerate size	
			Before sonication (μm)	After sonication (μm)
SDCH	135	10	19	4
GDCH	128	11	19	5
SDCN	102	16	26	9
GDCN	76	16	27	11

For catalytic purposes, it is necessary to synthesize monodisperse ceria or doped ceria nanopowders having high surface area. It has been demonstrated that addition of H_2O_2 before precipitation of cerium hydroxide leads to less agglomeration between the particles [13.263, 264].

We have demonstrated the effect of the presence of H_2O_2 on the synthesis and catalytic properties of doped ceria nanopowders. For this purpose, four sets of samples were prepared wherein two sets consisted of $Ce_{0.8}M_{0.2}O_{1.90}$ ($M = Gd^{3+}$, Sm^{3+}) without H_2O_2 and the other two sets consisted of $Ce_{0.8}M_{0.2}O_{1.90}$ ($M : Gd^{3+}$, Sm^{3+}) with H_2O_2 in molar ratio of 1 : 2 (metal ion : H_2O_2). The samples are referred to as GDCH for gadolinia-doped ceria and SDCH for samaria-doped ceria. The samples prepared in the absence of H_2O_2 are referred to as GDCN and SDCN, respectively. Pure ceria was also prepared by the same procedure without H_2O_2 to compare with the results. Calcination of all samples was done at 600 °C for 1 h before further characterization.

Careful analysis of the XRD patterns (Fig. 13.7) revealed that the doped samples were of fluorite type with structure similar to pure CeO_2. Also, it is clearly visible from Fig. 13.7 that the (111) diffraction peak of GDCH and SDCH were broader than that of GDCN and SDCN, which implies that the samples prepared in the presence of H_2O_2 had smaller particle size than the samples prepared without H_2O_2. Thus, H_2O_2 affects the particle size of the nanoparticles. The samples prepared in the absence of H_2O_2 form hydroxide precipitate upon addition of NaOH to the mixed nitrate solution. During the condensation process, H_2O is eliminated, thus forming a three-dimensional (3-D) network of M−O−M (M = metal ion) linkages. The samples prepared in the presence of H_2O_2 have peroxo linkages. These peroxo species would disrupt this 3-D network as it is a sideways linkage, thus reducing the number of adjacent −OH species. Upon calcination, these O−O linkages also break down, which ultimately leads to smaller crystallite size. The presence of peroxo linkages has been confirmed by Raman spectroscopy, which is described later. The crystallite size of all the as-prepared and calcined samples was determined using the Scherrer equation.

The crystallite sizes of the as-prepared material were found to be smaller than for the calcined samples, as expected (Table 13.3).

To study the efficiency of these nanopowders as catalyst as well as to investigate the effect of H_2O_2 on the

same, Sm-doped ceria powders were investigated for their catalytic activity. The catalytic property of pure CeO_2 prepared by the same route was also investigated under similar conditions for better comparison. Figure 13.8 presents the catalytic activity of CeO_2, SDCN, and SDCH nanopowders for the CO oxidation reaction as a function of temperature. Samarium-substituted samples were found to show better activity as compared with the unsubstituted sample. Even though the onset of conversion of CO to CO_2 could be observed in pure ceria at room temperature, 100% conversion was achieved only at $\approx 500\,^{\circ}C$, suggesting a sluggish rise in activity with increasing temperature. For the Sm-doped sample prepared in the absence of H_2O_2, 100% conversion took place at 475 °C, whereas for the same composition prepared in the presence of H_2O_2, the 100% conversion temperature dropped to 395 °C, which is a marked improvement from 500 °C. This observation reveals that substitution as well as particle size has profound effects on the conversion temperature and subsequently on the catalytic activity. The decreasing order of catalytic activity as evident from Fig. 13.10 is: SDCH > SDCN > CeO_2. The catalytic activity of ceria is attributed to factors such as ease of movement of lattice ions and the possibility of readily changing between Ce^{3+} and Ce^{4+}, together with the high oxidizing capability of the Ce^{4+} ion. The presence of a trivalent rare-earth ion introduces oxygen ion vacancies which further increases the mobility. The higher catalytic activity of SDCH as compared with SDCN could be due to the higher surface area and smaller particle size of the former as compared with the latter. In the sample having higher surface area and lower particle size, the activation barrier is easily overcome and subsequently higher conversions are observed at relatively lower temperature.

Thus, the samaria-doped nanoceria prepared in the presence of H_2O_2 showed marked improvement in catalytic properties compared with pure ceria.

13.5 Oxide Nanomaterials in Ionics

Nanocrystalline ceramics are expected to exhibit improved or unique characteristics as compared with conventional ceramic materials. Generally, ceramic nanopowders are functional materials as they have great potential for many advanced applications due to their unique characteristics, particularly related to their electrical, optical, mechanical, and thermal properties [13.265]. Among the technologically important ceramics, pyrochlores in general have received a lot of attention due to their potential for use in fuel cells as electrolytes [13.266]. In $A_2B_2O_7$ pyrochlores, the A^{3+} ions occupy the 16d sites (1/2, 1/2, 1/2), the B^{4+} ions are at the 16c sites (0, 0, 0), and the O ions occupy the 48f sites (x, 1/8, 1/8) and 8b sites (3/8, 3/8, 3/8). The 8a sites in pyrochlore remain unoccupied. Here, x is a positional parameter that indicates the extent to which the 48f oxygen ion is off-centered, and it is sensitive to the sizes of the A and B ions. Studies have shown that the ionic conduction is due to oxygen vacancy hopping along the 48f–48f pathway [13.267–269].

Riess et al. have demonstrated that the ionic conductivity strongly depends on the synthesis route used to produce the ceramics [13.270]. Soft chemical routes play an important role in the preparation of nanomaterials, on further manipulation giving rise to highly dense pellets. Among the solution chemistry routes, the combustion technique is capable of producing nanocrystalline powders of oxide ceramics at a lower calcination temperature in a short time with improved powder characteristics [13.271]. The success of this process is attributed to the intimate mixing among the constituents using suitable fuel or complexing agents in an aqueous medium followed by an exothermic redox reaction between the fuel and an oxidizer (i. e., nitrates) [13.272]. During gel combustion, the generated heat helps in crystallization and formation of the desired phase. The evolution of gaseous products during the combustion dissipates the heat of combustion and limits the rise of temperature, thus reducing the possibility of premature local partial sintering among the primary particles, which helps to form soft agglomerates. Dense pellets can be prepared from soft agglomerated powders. To rule out electronic conduction in the samples, measurement in H_2 atmosphere was also performed. Electrolyte material to be used in solid oxide fuel cells (SOFCs) has to survive in the presence of H_2 atmosphere. Therefore, it is important to ensure the stability of pyrochlores in reducing environment also.

As an example of an ionic conductor a series of samples, namely $Nd_{2-y}Gd_yZr_2O_7$, were investigated. These samples prepared by the solid-state route indicated that the composition near $y = 1.0$ showed the highest conductivity in the range of 350–423 °C in air only [13.273]. However, solid-state synthesized sam-

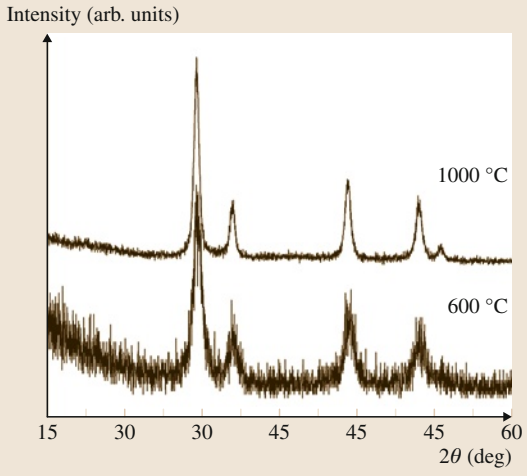


Fig. 13.9 XRD pattern of $NdGdZr_2O_7$ calcined at different temperature

ples in general do not have high sintered density. Hence, we also explored the ionic conductivity of samples (around $y = 1.0$) prepared by the rapid gel combustion route, which often results in sinter active powder.

The net oxidizing valency of gadolinium and neodymium nitrates and zirconium oxynitrate and the reducing valencies of fuel were estimated using the valencies of the individual elements [13.274]. Therefore, based on the stoichiometry concept, the ratio of oxidizing and reducing valencies should be unity, which implies that the ratio of valencies of metal nitrates/oxynitrates to citric acid should be 1 : 2.78.

Using this synthetic procedure, the obtained powders were found to be in pyrochlore structure only. The XRD pattern of the calcined powder of $NdGdZr_2O_7$ is shown as an example in Fig. 13.9 [13.275]. However, due to the presence of broad peaks and noisy background for the samples calcined at 600 °C, the superstructure peaks, characteristic of pyrochlore orderings, are difficult to visualize. The superstructure peaks start to become prominent upon further heating. The crystallite sizes were calculated using Scherrer's formula. The average crystallite size of all the samples was within the range 4–6 nm. The crystallinity improves with increase in calcination temperature, as inferred by the appearance of narrow and sharp XRD peaks (Fig. 13.9). The intensity of the superstructure peaks decreases with increase in Gd^{3+} content in the solid solution, suggesting that the disorder also increases.

The conductivity in these pyrochlore materials arises due to hopping of oxygen ions along the 48f–48f vacancy pathway [13.267–269]. The ionic conductivity of these samples was determined from measured impedance data. A typical impedance spectrum of a polycrystalline material consists of two semicircular arcs corresponding to grains and grain boundaries, in the high- and intermediate-frequency ranges, respectively. The electrode polarization is the third part of the impedance spectrum in the low-frequency region, which becomes significant as the measuring temperature increases. While considering the electrical properties of the material, each of the individual arcs due to grains and grain boundaries is represented by a parallel resistance–capacitance ($R-C$) circuit having a specific time constant for relaxation [13.275]. The real–imaginary impedance spectra show a grain boundary arc with capacitance value obtained from curve fitting in the range of 10^{-8}–10^{-9} F. As the capacitance value of the grain conductivity–relaxation process is very small, only one arc due to grain boundaries is visible in the spectrum. In this case, the high-frequency intercept with the axis of the real part of the impedance is considered as the grain resistance. The grain boundary resistance (R_{gb}) is obtained by subtracting the grain resistance (R_g) from the total resistance (R_t). It can be seen that, with increasing measuring temperature, both R_g and R_{gb} decrease significantly. At the same time, it is observed that the influence of electrode polarization processes starts to dominate the electrical conduction mechanism. With further increase in the measuring temperature, the arc due to grain boundaries disappears and the intercept with the real impedance axis represents the total resistance of the material. Thus, it is again found that, with increasing Gd doping concentration, the material becomes more resistive due to both grains and grain boundaries. One more important point is that the influence of the grain boundaries is not so significant in the measurement temperature range of 375–800 °C when the grain size is around 0.8–1.0 μm.

The activation energy and preexponential factors could be calculated based on the Arrhenius behavior. The activation energy ranges from 0.98 to 1.06 eV with increasing Gd^{3+} content in the series, which agrees with oxide ion migration [13.276]. The interesting observation is that the activation energy in air (E_a) and the preexponential factor (σ_0) increase with increasing Gd content in the solid solution (Fig. 13.10). It has been reported earlier that, with increase in the Nd content in the $Nd_{2-y}Gd_yZr_2O_7$ series, the degree of order increases [13.277]. On the other hand, with increase in Gd content in the same series, the degree of disorder in

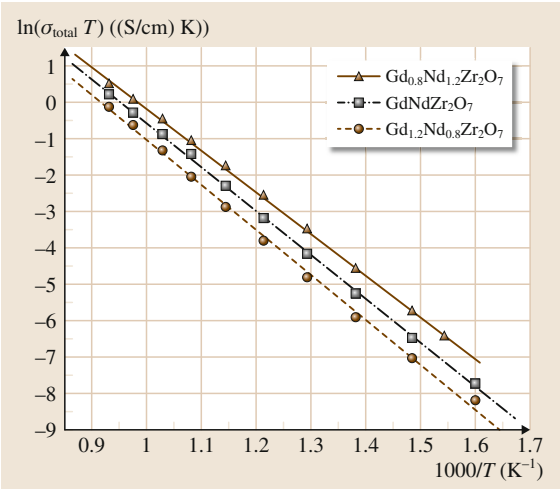


Fig. 13.10 Arrhenius plots of total electrical conductivity of $Gd_{0.8}Nd_{1.2}Zr_2O_7$, $GdNdZr_2O_7$, and $Gd_{1.2}Nd_{0.8}Zr_2O_7$ samples measured in air

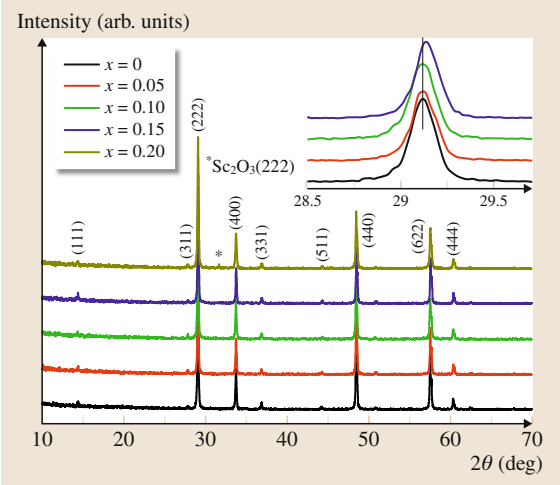


Fig. 13.11 Room-temperature x-ray diffraction patterns of $NdGdZr_{2-x}Sc_xO_{7-\delta}$ $(0 \le x \le 0.20)$ samples sintered at 1773 K for 12 h. Inset shows the systematic shift in the (222) peak for the $NdGdZr_{2-x}Sc_xO_{7-\delta}$ $(0 \le x \le 0.15)$ samples

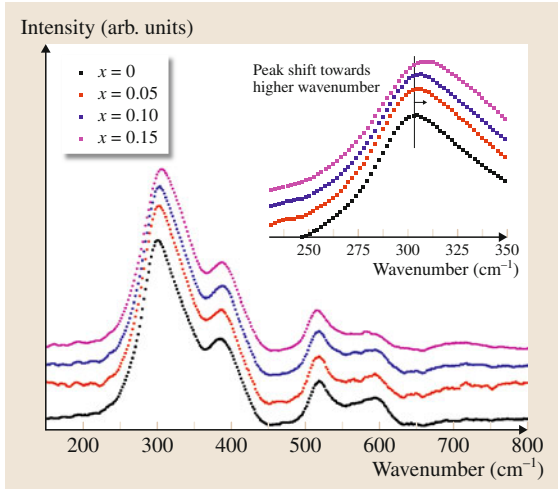


Fig. 13.12 Raman spectra recorded on the sintered samples (1773 K for 12 h) of $NdGdZr_{2-x}Sc_xO_{7-\delta}$ $(0 \le x \le 0.15)$. *Inset* shows the blue-shift of the band corresponding to E_g mode

the crystal increases, which results in an increase in the activation energy. The preexponential factor is proportional to the number of mobile species (concentration of oxygen ion vacancies), which increases with increasing disorder in the system.

Since only a single activation energy is observed in the measured temperature range for all the samples, the concentration of mobile species in the preexponential factor is temperature independent. The impedance measurement in hydrogen atmosphere reveals that the activation energy and preexponential factor do not deviate significantly from the values obtained in air. The Nd^{3+}, Gd^{3+}, and Zr^{4+} ions are very stable in reducing atmosphere. Therefore, it can be concluded that these materials possess only oxygen ionic conduction even at low pO_2 and no significant electronic conduction is introduced into the electrolyte, a criterion which is essential for an electrolyte material for application in electrochemical devices such as solid oxide fuel cells, oxygen sensors, etc.

Based on these results, we optimized the concentration of Nd^{3+} at the Gd^{3+} site, finding a result of 1 : 1, i. e., $NdGdZr_2O_7$. To further improve the conductivity we attempted to incorporate Sc^{3+} ions at the Zr^{4+} site in the composition with the highest ionic conductivity (i. e., $NdGdZr_2O_7$) to enhance the oxygen vacancy concentration. These would, in turn, increase the charge carrier mobility and thereby further improve the ionic conductivity of this composition. The samples were also prepared through the gel combustion route, as it resulted in very high-density products upon sintering as compared with the conventional solid-state prepared samples. The extent of Sc^{3+} solubility in $NdGdZr_2O_7$ along with the phase relation and subsequently the ionic conductivity of these compositions were studied.

Table 13.4 Corresponding activation energy and preexponential factor of $NdGdZr_{2-x}Sc_xO_{7-\delta}$ ($0 \le x \le 0.15$)

Sample composition	Activation energy E_a (eV)	Preexponential factor A ((S/cm)K)	σ at 923 K (S/cm)
$x = 0.00$	1.011	2.26×10^4	7.96939×10^{-5}
$x = 0.05$	1.052	9.34×10^4	1.89504×10^{-4}
$x = 0.10$	1.061	10.23×10^4	1.87601×10^{-4}
$x = 0.15$	1.126	21.70×10^4	1.72634×10^{-4}

From the XRD data (Fig. 13.11) it is clear that Sc^{3+} ions were successfully doped to substitute at Zr^{4+} sites in $NdGdZr_2O_7$ to form a homogeneous solid solution up to doping concentration of $x = 0.15$ Sc^{3+}. A local lattice distortion in the doped pyrochlores, arising due to Zr(Sc) site distribution and additional oxygen vacancy creation, can be explained in terms of shifting of Raman bands (Fig. 13.12) from their normal positions as a function of the Sc^{3+} content. Ionic conductivity measurements on the system indicate an increase in activation energy of ionic conduction as well as a significant increase in the charge carrier concentration, as given in Table 13.4. Among the whole series, the composition with $x = 0.05$ was found to have good conductivity.

13.6 Conclusions

Synthesis is an important part of any work. The preparatory routes for nanoparticles are broadly classified into two categories as mentioned below. The solid-state process is a conventional and widely used synthesis method to prepare polycrystalline ceramic materials. This method is not only common but is also most promising for scaling up of compound production. Solid-state diffusion is an inherently sluggish process. It involves the mechanical mixing of the solid constituents (oxides/carbonates) with repeated grindings and annealing at elevated temperatures, generally over a long duration. However, with solid-state routes, there are some disadvantages such as being kinetically slow, mostly needing higher temperatures, the influence of sample history and defects, that reaction progress monitoring is difficult, and that larger particles are obtained. The shortcomings of the solid-state synthesis method can be overcome by employing solution chemistry techniques which possess advantages such as fast kinetics at room or slightly elevated temperatures with no influence of sample history and defects, resulting in finer particles with the reaction being easy to monitor. Gel combustion synthesis is a facile synthesis technique used for laboratory-scale preparation of nanocrystalline ceramic powders with reproducible characteristics, being based on a redox reaction between the oxidant and fuel. Coprecipitation refers to simultaneous precipitation of more than one metal ion from the same solution, resulting in more intimate mixing of cations as compared with that achieved by mixing oxides/salts of individual cations. Thermal decomposition of such compounds results in chemically homogeneous fine oxide powders with high surface area. The sol–gel process is a low-temperature approach for synthesizing solid-state oxide materials (usually polymeric). The template method involves fabrication of the desired material within the pores or channels of a nanoporous template. Ultrasound has become an important tool for synthesis of nanoparticles. TiO_2 has many promising applications in areas ranging from photovoltaics and photocatalysis to photo/electrochromics and sensors. The structural, thermal, electronic, and optical properties of TiO_2 nanomaterials have been reviewed extensively in the past decade. Indium oxide (In_2O_3) is an n-type semiconducting material, and its observed optical transparency arises from the relatively wide bandgap. Cerium oxide or ceria (CeO_2) is a rare-earth metal oxide with optical properties and ability to filter ultraviolet radiation. Residual surface hydroxides can also add to the rich surface chemistry exhibited by metal oxides such as MgO, CaO, SrO, BaO, Al_2O_3, TiO_2, Fe_2O_3, ZnO, etc. and this chemistry is generally attributable to Lewis acid, Lewis base, and Brønsted acid sites of varying coordination. This forms the basis of the use of nanooxides as sorbents for removal of different species from aqueous streams.

References

13.1 S. Banerjee, A.K. Tyagi (Eds.): *Functional Materials: Preparation, Processing and Applications* (Elsevier, Amsterdam 2011)

13.2 M. Kaur, N. Jain, K. Sharma, S. Bhattacharya, M. Roy, A.K. Tyagi, S.K. Gupta, V. Yakhmi: Room temperature H_2S gas sensing at ppb level by single crystal In_2O_3 whiskers, Sens. Actuators B **133**, 456 (2008)

13.3 V. Jayaraman, D. Krishnamurthy, R. Ganesan, A. Thiruvengadasami, R. Sudha, M.V.R. Prasad, T. Gnanasekaran: Development of yttria doped thoria solid electrolyte for use in liquid sodium systems, Ionics **13**, 299 (2007)

13.4 P.S. Ramanjaneyulu, A.N. Kumar, Y.S. Sayi, K.L. Ramakumar, S.K. Nayak, S. Chattopadhyay: A new ion selective electrode for cesium(I) based on calix[4]arene-crown-6 compounds, J. Hazard. Mater. **205/206**, 81–88 (2012)

13.5 A.K. Tyagi, J. Ramkumar, O.D. Jayakumar: Inorganic-organic hybrid nanorod of Ag and rhodamine 6G: *Turn on* fluorescence sensors for highly selective detection of Pb(II) ions in aqueous solution, Analysts **137**, 760 (2012)

13.6 T. Karir, P.A. Hassan, S.K. Kulshreshtha, G. Samuel, N. Sivaprasad, V. Meera: Surface modification of polystyrene using polyaniline nanostructures for biomolecule adhesion in radioimmunoassay, Anal. Chem. **78**, 3577 (2006)

13.7 A. Khaleel: Nanostructured pure γ-Fe_2O_3 via forced precipitation in an organic solvent, Chem. Eur. J. **10**, 925 (2004)

13.8 Q. Tang, Q. Zhang, P. Wang, Y. Wang, H. Wan: Characterizations of cobalt oxide nanoparticles within faujasite zeolites and the formation of metallic cobalt, Chem. Mater. **16**, 1967 (2004)

13.9 H.R. Chen, J.L. Shi, Y.S. Li, J.N. Yan, Z.L. Hua, H.G. Chen, D.S. Yan: A new method for the synthesis of highly dispersive and catalytically active platinum nanoparticles confined in mesoporous zirconia, Adv. Mater. **15**, 1078 (2003)

13.10 G. Ertl, H. Knözinger, J. Weitkamp (Eds.): *Handbook of Heterogeneous Catalysis* (Wiley VCH, Weinheim 1997)

13.11 N. Perkas, Y. Koltypin, O. Palchik, A. Gedanken, S. Chandrasekaran: Oxidation of cyclohexane with nanostructured amorphous catalysts under mild conditions, Appl. Catal. A: Gen. **209**, 125 (2001)

13.12 V. Kesavan, D. Dhar, Y. Koltypin, N. Perkas, O. Palchik, A. Gedanken, S. Chandersekaran: Nanostructured amorphous metals, alloys, and metal oxides as new catalysts for oxidation, Pure Appl. Chem. **73**, 85 (2001)

13.13 N. Pinna, G. Neri, M. Antonietti, M. Niederberger: Nonaqueous synthesis of nanocrystalline semiconducting metal oxides for gas sensing, Angew. Chem. Int. Ed. **43**, 4345–4349 (2004)

13.14 S. Li, R. Guo, J. Li, Y. Chen, W. Liu: Synthesis of NiO–ZrO_2 powders for solid oxide fuel cells, Ceram. Int. **29**, 883 (2003)

13.15 A. Murali, A. Barve, V.J. Leppert, H. Risbud: Synthesis and characterization of indium oxide nanoparticles, Nano Lett. **1**, 287 (2001)

13.16 J. Liang, Z. Deng, X. Jiang, F. Li, Y. Li: Photoluminescence of tetragonal ZrO_2 nanoparticles synthesized by microwave irradiation, Inorg. Chem. **41**, 3602 (2002)

13.17 R. Viswanatha, S. Sapra, S.S. Gupta, B. Satpati, P.V. Satyam, B.N. Dev, D. Sarma: Synthesis and characterization of Mn-doped ZnO nanocrystals, J. Phys. Chem. B **108**, 6303–6310 (2004)

13.18 S.C. Pillai, J.M. Kelly, D.E. McCormack, R. Ramesh: Self-assembled arrays of ZnO nanoparticles and their application as varistor materials, J. Mater. Chem. **14**, 1572 (2004)

13.19 Z. Li, H. Chen, H. Bao, M. Gao: One-pot reaction to synthesize water-soluble magnetite nanocrystals, Chem. Mater. **16**, 1391 (2004)

13.20 W.S. Seo, H.H. Jo, K. Lee, B. Kim, S.J. Oh, T. Park: Size-dependent magnetic properties of colloidal Mn_3O_4 and MnO nanoparticles, Angew. Chem. Int. Ed. **43**, 1115 (2004)

13.21 R.J. Brook (Ed.): *Processing of Ceramics*, Materials Science and Technology, Vol. 17 (VCH, Weinheim 1996)

13.22 W.D. Kingery, K.H. Bowen, D.R. Uhlmann: *Introduction to Ceramics* (Wiley, New York 1976)

13.23 S.S. Manoharan, K.C. Patil: Convergent beam electron diffraction analysis of lattice shifts in aluminum nitride, J. Am. Ceram. Soc. **75**, 1012 (1992)

13.24 S.R. Jain, K.C. Adiga, V.R. Pai Verneker: A new approach to thermochemical calculations of condensed fuel-oxidizer mixtures, Combust. Flame. **40**, 71 (1981)

13.25 L.A. Chick, L.R. Pederson, G.D. Maupin, J.L. Bates, L.E. Thomas, J. Exarhos: Glycine-nitrate combustion synthesis of oxide ceramic powders, Mater. Lett. **10**, 6 (1990)

13.26 Y.R. Ma, L.M. Qi, J.M. Ma, H.M. Cheng, W. Shen: Synthesis of submicrometer-sized CdS hollow spheres in aqueous solutions of a triblock copolymer, Langmuir **19**, 9079 (2003)

13.27 Y. Liu, W.W. Zhao, G. Zhang: Soft template synthesis of mesoporous $Co_3O_4/RuO_2 \cdot xH_2O$ composites for electrochemical capacitors, Electrochim. Acta **53**, 3296 (2008)

13.28 A.J. Moulson, J.M. Herbert: *Electroceramics: Materials, Properties and Applications*, 2nd edn. (Wiley, Chichester 2003) p. 100

13.29 J.D. Mackenzie, E.P. Bescher: Chemical routes in the synthesis of nanomaterials using the sol–gel process, Acc. Chem. Res. **40**, 810–818 (2007)

13.30 H. Hayashi, Y. Hakuta: Hydrothermal synthesis of metal oxide nanoparticles in supercritical water, Materials **3**, 3794–3817 (2010)

13.31 A. Gedanken: Sonochemistry andits application to nanochemistry, Curr. Sci. **85**, 1720–1722 (2003)

13.32 A. Fujishima, T.N. Rao, D.A. Tryk: Titanium dioxide photocatalysis, Photochem. Photobiol. C **1**, 1–21 (2000)

13.33 D.A. Tryk, A. Fujishima, K. Honda: Recent topics in photoelectrochemistry: Achievements and future prospects, Electrochim. Acta **45**, 2363 (2000)

13.34 M. Grätzel: Photoelectrochemical cells, Nature **414**, 338 (2001)

13.35 A. Hagfeldt, M. Grätzel: Light-induced redox reactions in nanocrystalline systems, Chem. Rev. **95**, 49 (1995)

13.36 A.L. Linsebigler, G. Lu, J.T. Yates Jr.: Photocatalysis on TiO_2 surfaces: Principles, mechanisms, and selected results, Chem. Rev. **95**, 735 (1995)

13.37 A. Millis, S. Le Hunte: An overview of semiconductor photocatalysis, J. Photochem. Photobiol. A **108**, 1 (1997)

13.38 M.R. Hoffmann, S.T. Martin, W. Choi, D.W. Bahnemann: Environmental applications of semiconductor photocatalysis, Chem. Rev. **95**, 69 (1995)

13.39 M.A. Fox, M.T. Dulay: Heterogeneous photocatalysis, Chem. Rev. **93**, 341 (1993)

13.40 X. Chen, S.S. Mao: Titanium dioxide nanomaterials: Synthesis, properties, modifications, and applications, Chem. Rev. **107**, 2891–2959 (2007)

13.41 Z.L. Wang: Zinc oxide nanostructures: Growth, properties and applications, J. Phys.: Condens. Matter **16**, R829–R858 (2004)

13.42 S.P. Feofilov, A.A. Kaplyanskii, R.I. Zakharchenya: Optical generation of nonequilibrium terahertz resonant vibrational excitations in highly porous aluminium oxide, J. Lumin. **66/67**, 349 (1996)

13.43 S.P. Feofilov, A.A. Kaplyanskii, R.I. Zakcharchenya, Y. Sun, K.W. Jang, R.S. Meltzer: Spectral hole burning in Eu^{3+}-doped highly porous γ-aluminum oxide, Phys. Rev. B **54**, 3690 (1996)

13.44 K.S. Hong, R.S. Meltzer, B. Bihari, D.K. Williams, B.M. Tissue: Spectral hole burning in crystalline Eu_2O_3 and Y_2O_3:Eu^{3+} nanoparticle, J. Lumin. **76/77**, 234 (1998)

13.45 K. Kobayashi, T. Ishida, Y. Nakato, H. Tsbomura: Mechanism of carrier transport in highly efficient solar cells having indium tin oxide/Si junctions, J. Appl. Phys. **69**, 1736 (1991)

13.46 C. Cantalini, W. Wlodarski, H.T. Sun, M.Z. Atashbar, M. Passacantando, A.R. Phani, S. Santucci: Investigation of the cross sensitivity of NO_2 sensors based on In_2O_3 thin films prepared by sol gel and vacuum thermal evaporation, Thin Solid Films **350**, 276 (1999)

13.47 H. Steffes, C. Imawan, F. Solzbacher, E. Obermeier: Enhancement of NO_2 sensing properties of In_2O_3 based thin films using an Au or Ti surface modification, Sens. Actuators B **78**, 106 (2001)

13.48 J. Tamaki, C. Naruo, Y. Yamamoto, M. Matsuoka: Sensing properties to dilute chlorine gas of indium oxide based thin film sensors prepared by electron beam evaporation, Sens. Actuators B **83**, 190 (2002)

13.49 W.-Y. Chung, G. Sakai, K. Shimanoe, N. Miura, D.-D. Lee, N. Yamazoe: Spin coated indium oxide thin film on alumina and silicon substrate and their gas sensing properties, Sens. Actuators B **65**, 312 (2000)

13.50 K.L. Chopra, S. Major, K. Pandya: Transparent conductors – A status review, Thin Solid Films **102**, 1 (1983)

13.51 A. Gurlo, N. Barsan, M. Ivanovskaya, U. Weimar, W. Gopel: In_2O_3 and MoO_3–In_2O_3 thin film semiconductor sensors:interaction with NO_2 and O_3, Sens. Actuators, B **47**, 92 (1998)

13.52 J.H. Shin, S.H. Shin, I. Park: Properties of dc magnetron sputtered indium tin oxide films on polymeric substrates at room temperature, J. Appl. Phys. **89**, 5199 (2001)

13.53 L. Qingsheng, L. Weigang, A. Ma, T. Jinke, J. Lin, J. Fang: Study of quasi-monodisperse In_2O_3 nanocrystals: Synthesis and optical determination, J. Am. Chem. Soc. **127**, 5276–5279 (2005)

13.54 Y. Zhao, Z. Zhang, Z. Wu, H. Dang: Synthesis and characterization of single-crystalline In_2O_3 nanocrystals via solution dispersion, Langmuir **20**, 27–29 (2004)

13.55 H. Yamamura, Y. Takahashi, K. Kakinuma: Preparation of In_2O_3 fine powders and their two-step sintering, J. Ceram. Soc. Jpn. **109**, 1000–1003 (2001)

13.56 S. Kim, K. Seo, J. Lee, J. Kim, H. Lee, J. Lee: Preparation and sintering of nanocrystalline ITO powders with different SnO_2 content, J. Eur. Ceram. Soc. **26**, 73–80 (2006)

13.57 A. Gurlo, M. Ivanovskaya, N. Barsan, M. Schweizer-Berberich, U. Weimar, W. Gopel, A. Dieguez: Grain size control in nanocrystalline In_2O_3 semiconductor, Sens. Actuators B Chem. **44**, 327–333 (1997)

13.58 I.V. Kityk, J. Ebothé, A.E. Hichou, B.E. Idrissi, M. Addou, J. Krasowski: Nonlinear optical effects in In_2O_3:Sn-glass nano-interfaces, J. Opt. A. **5**, 61–65 (2003)

13.59 J. Ederth, A. Hultåker, P. Heszler, G.A. Niklasson, C.G. Granqvist, A. van Doorn, C. van Haag, M.J. Jongerius, D. Burgard: Electrical and optical properties of thin films prepared by spin coating a dispersion of nano-sized tin-doped indium oxide particles, Smart Mater. Struct. **11**, 675–678 (2002)

13.60 D.-B. Yu, S.-H. Yu, S.-Y. Zhang, J. Zuo, D.-B. Wang, Y.-T. Qian: Metastable hexagonal In_2O_3 nanofibers templated from InOOH nanofibers under ambient pressure, Adv. Funct. Mater. **13**, 497 (2003)

13.61 S.-C. Chang, M.H. Huang: Formation of short In_2O_3 nanorod arrays within mesoporous silica, J. Phys. Chem. C **112**, 2304–2307 (2008)

13.62 B. Yu: Nonlinear optical properties of In_2O_3 nanoparticles, Acta Phys. Sin. **48**(2), 320 (1999)

13.63 H. Zhou, W. Cai, L. Zhang: Synthesis and structure of indium oxide nanoparticles dispersed within pores of mesoporous silica, Mater. Res. Bull. **34**(6), 845 (1999)

13.64 T. Wang, Q. Pan, J. Zhang: In_2O_3 ultrafine powder synthesis by sol–gel method, J. Shanghai Univ. Engl. Ed. **5**(4), 331 (2001)

13.65 X. Wu: Synthesis, structure, and optical properties of nanometer-sized In_2O_3 capped by anionic surfactant, J. Vac. Sci. Technol. **15**(6), 1889 (1997)

13.66 A.S. Ryzhikov, R.B. Vasiliev, M.N. Rumyantseva: Microstructure and electrophysical properties of SnO_2, ZnO and In_2O_3 nanocrystalline films prepared by reactive magnetron sputtering, Mater. Sci. Eng. B **96**, 268 (2002)

13.67 T. Tsuchiya, T.A. Watanabe, H. Niino, A. Yabe, I. Yamaguchi, T. Manabe, T. Kumagai, S. Mizuta: Low temperature growth of metal oxide thin films by metallorganic laser photolysis, Appl. Surf. Sci. **186**, 173 (2002)

13.68 H. Cao, X. Qiu, Y. Liang, Q. Zhu: Room-temperature ultraviolet-emitting In_2O_3 nanowires, Appl. Phys. Lett. **83**, 761 (2003)

13.69 S.B. Qadri, H. Kim, M. Yousuf, H.R. Khan: Synthesis of In_2O_3–Sc_2O_3 transparent conducting oxide films, Appl. Surf. Sci. **208/209**, 611 (2003)

13.70 J.G. Wen, J.Y. Lao, D.Z. Wang, T.M. Kyaw, Y.L. Foo, Z.F. Ren: Self-assembly of semiconducting oxide nanowires, nanorods, and nanoribbons, Chem. Phys. Lett. **372**, 717 (2003)

13.71 X.C. Wu, J.M. Hong, Z.J. Han, Y.R. Tao: Fabrication and photoluminescence characteristics of single crystalline In_2O_3 nanowires, Chem. Phys. Lett. **373**, 28 (2003)

13.72 K. Soulantica, L. Erades, M. Sauvan, F. Senocq, A. Maisonnat, B. Chaudret: Synthesis of indium and indium oxide nanoparticles from indium cyclopentadienyl precursor and their application for gas sensing, Adv. Funct. Mater. **13**, 553 (2003)

13.73 S. Avivi, O. Palchik, V. Palchik, M.A. Slifkin, A.M. Weiss, A. Gedanken: Sonochemical synthesis of nanophase indium sulfide, Chem. Mater. **13**, 2195 (2001)

13.74 Y. Ohhata, F. Shinoki, S. Yoshida: Optical properties of r.f. reactive sputtered tin-doped In_2O_3 films, Thin Solid Films **59**, 255 (1979)

13.75 L. Dai, X.L. Chen, J.K. Jian, M. He, T. Zhou, B.Q. Hu: Fabrication and characterization of In_2O_3 nanowires, Appl. Phys. A **75**, 687 (2002)

13.76 Y.H. Ng, S. Ikeda, T. Harada, S. Higashida, T. Sakat, H. Mori, M. Matsumura: Fabrication of hollow carbon nanospheres encapsulating platinum nanoparticles using a photocatalytic reaction, Adv. Mater. **19**, 597 (2007)

13.77 I. Hamberg, C.G. Granqvist: Evaporated Sn-doped In_2O_3 films: Basic optical properties and applications to energy-efficient windows, J. Appl. Phys. **60**, R123 (1986)

13.78 H.J. Zhou, W.P. Cai, L.D. Zhang: Photoluminescence of indium–oxide nanoparticles dispersed within pores of mesoporous silica, Appl. Phys. Lett. **75**, 495 (1999)

13.79 E.C.C. Souza, E.N.S. Muccillo: Characterization of indium oxide nanoparticles prepared by soft chemistry route, Adv. Sci. Technol. **45**, 248 (2006)

13.80 W.S. Seo, H.H. Jo, K. Lee, J.T. Park: Direct printing of bioceramic implants with spatially localized angiogenic factors, Adv. Mater. **15**, 795 (2003)

13.81 P. Zhu, W. Wu, J. Zhou, W. Zhang: Preparation of size-controlled In_2O_3 nanoparticles, Appl. Organomet. Chem. **21**, 909 (2007)

13.82 D. Chu, Y.-P. Zeng, D. Jiang, J. Xu: Tuning the phase and morphology of In_2O_3 nanocrystals via simple solution routes, Nanotechnology **18**, 435605 (2007)

13.83 T.-S. Ko, C.-P. Chu, J.-R. Chen, T.-C. Lu, H.-C. Kuo, S.-C. Wang: Tunable light emissions from thermally evaporated In_2O_3 nanostructures grown at different growth temperatures, J. Cryst. Growth **310**, 2264–2267 (2008)

13.84 C. Li, D. Zhang, S. Han, X. Liu, T. Tang, C. Zhou: Diameter-controlled growth of single-crystalline In_2O_3 nanowires and their electronic properties, Adv. Mater. **15**, 143 (2003)

13.85 M.J. Zheng, L.D. Zhang, G.H. Li, X.Y. Zhang, F. Wang: Ordered indium-oxide nanowire arrays and their photoluminescence properties, Appl. Phys. Lett. **79**, 839 (2001)

13.86 J. Zhang, X. Qing, F. Jing, Z. Dai: A route to Ag-catalyzed growth of the semiconducting In_2O_3 nanowires, Chem. Phys. Lett. **371**, 311 (2003)

13.87 C. Liang, G. Meng, Y. Lei, F. Phillipp, L. Zhang: Catalytic growth of semiconducting In_2O_3 nanofibers, Adv. Mater. **13**, 1330 (2001)

13.88 K.C. Kam, F.L. Deepak, A.K. Cheetham, R. Rao: In_2O_3 nanowires, nanobouquets and nanotrees, Chem. Phys. Lett. **397**, 329 (2004)

13.89 X.Y. Kong, L. Wang: Structures of indium oxide nanobelts, Solid State Commun. **128**, 1 (2003)

13.90 T. Tsuruoka, C.H. Liang, K. Terabe, T. Hasegawa: Optical waveguide properties of single indium oxide nanofibers, J. Opt. A: Pure Appl. Opt. **10**, 055201 (2008)

13.91 Y. Li, Y. Bando, D. Golberg: Single-crystalline In_2O_3 nanotubes filled with In, Adv. Mater. **15**, 581 (2003)

13.92 C. Wang, D. Chen, X. Jiao, C. Chen: Lotus-root-like In_2O_3 nanostructures: Fabrication, characterization, and photoluminescence properties, J. Phys. Chem. C **111**, 13398–13403 (2007)

13.93 J.S. Jeong, J.Y. Lee, C.J. Lee, S.J. An, G.-C. Yi: Synthesis and characterization of high-quality In_2O_3 nanobelts via catalyst-free growth using a simple physical vapor deposition at low temperature, Chem. Phys. Lett. **384**, 246–250 (2004)

13.94 J.S. Lee, K. Park, S. Nahm, S.W. Kim, S. Kim: Ga_2O_3 nanomaterials synthesized from ball-milled GaN powders, J. Cryst. Growth **244**, 287 (2002)

13.95 K. Vanheusden, W.L. Warren, C.H. Seager, D.R. Tallant, J.A. Voigt, B.E. Gnade: Mechanisms behind green photoluminescence in ZnO phosphor powders, J. Appl. Phys. **79**, 7983 (1996)

13.96 D.M. Bagnall, Y.F. Chen, M.Y. Shen, Z. Zhu, T. Goto, T. Yao: Room temperature excitonic stimulated emission from zinc oxide epilayers grown by plasma-assisted MBE, J. Cryst. Growth **184/185**, 605 (1998)

13.97 W. Yin, D.V. Esposito, S. Yang, C. Ni, J.G. Chen, G. Zhao, Z. Zhang, C. Hu, M. Cao, B. Wei: Controlling novel red-light emissions by doping In_2O_3 nano/microstructures with interstitial nitrogen, J. Phys. Chem. C, **114**(31), 13234–13240 (2010)

13.98 G.Z. Xing, J.B. Yi, D.D. Wang, L. Liao, T. Yu, Z.X. Shen, C.H.A. Huan, T.C. Sum, J. Ding, T. Wu: Strong correlation between ferromagnetism and oxygen deficiency in Cr-doped $In_2O_{3-\delta}$ nanostructures, Phys. Rev. B **79**, 174406 (2009)

13.99 E. Antic-Fidancev, J. Aride, M. Lemaitre-Blaise, P. Porcher, M. Taibi: Emission spectra and crystal field calculation of europium-doped C-type In_2O_3 oxide, J. Alloys Compd. **188**, 242 (1992)

13.100 H.K. Kim, C.C. Li, P.J.J. Barrios: Erbium-doped indium oxide films prepared by radio frequency sputtering, Vac. Sci. Technol. A **12**, 3152 (1994)

13.101 J. Vela, B.S. Prall, P. Rastogi, D.J. Werder, J.L. Casson, D.J. Williams, V.I. Klimov, J.A. Hollingsworth: Sensitization and protection of lanthanide ion emission in In_2O_3:Eu nanocrystal quantum dots, J. Phys. Chem. C **112**, 20246 (2008)

13.102 Y.G. Choi, S.M. Yu, W.J. Chung: Local structural environment and photoluminescence of Er^{3+} ions doped in indium tin oxide nanopowder, Chem. Phys. Lett. **461**, 290 (2008)

13.103 R. Reisfeld, C.K. Jorgensen, K.A. Gschneider, L. Eyring (Eds.): *Handbook of the physics and chemistry of rare earths* (Elsevier, Amsterdam, 1987)

13.104 D.P. Dutta, V. Sudarsan, P. Srinivasu, A. Vinu, A.K. Tyagi: Indium oxide and europium/dysprosium doped indium oxide nanoparticles: Sonochemical synthesis, characterization and photoluminescence studies, J. Phys. Chem. C **112**, 6781 (2008)

13.105 Q. Xiao, Y. Liu, L. Liu, R. Li, W. Luo, X. Chen: Eu^{3+}-doped In_2O_3 nanophosphors: Electronic structure and optical characterization, J. Phys. Chem. C **114**(20), 9314–9321 (2010)

13.106 Z. Orel, B. Orel: Optical properties of pure CeO_2 and mixed CeO_2/SnO_2 thin film coatings, Phys. Status Solidi (b) **186**, K33–K36 (1994)

13.107 S. Tsunekawa, T. Fukuda, A. Kasuya: Blue shift in ultraviolet absorption spectra of monodisperse CeO_{2-x} nanoparticles, J. Appl. Phys. **87**, 1318 (2000)

13.108 M. Yamashita, K. Kameyama, S. Yabe, S. Yoshida, Y. Fujishiro, T. Kawai, T. Sato: Synthesis and microstructure of calcia doped ceria as UV filters, J. Mater. Sci. **37**, 683 (2002)

13.109 C.H. Kim, T. Thompson: On the importance of nanocrystalline gold for Au/CeO_2 water-gas shift catalysts, J. Catal. **244**, 248 (2006)

13.110 Q. Fu, W. Deng, H. Saltsburg: Activity and stability of low-content gold–cerium oxide catalysts for the water–gas shift reaction, Appl. Catal. B **56**, 57–68 (2006)

13.111 S. Imamura: Ceria-based wet-oxidation catalysts. In: *Catalysis by Ceria and Related Materials*, Vol. 14, ed. by A. Trovarelli (Imperial College, London 2002) p. 431

13.112 D. Goi, C. Leitenburg, G. Dolcetti, A. Trovarelli: Catalytic wet-oxidation of a mixed liquid waste: COD and AOX abatement, Environ. Technol. **25**, 1397 (2004)

13.113 G. Blanco, M.A. Cauqui, J.J. Delgado, A. Galtayries: Preparation and characterization of CeMnO composites with applications in catalytic wet oxidation processes, Surf. Interface Anal. **36**, 752 (2004)

13.114 V.D. Kosynkin, A.A. Arzgatkina, E.N. Ivanov, G. Chtoutsa: The study of process production of polishing powder based on cerium dioxide, J. Alloys Compd. **303/304**, 421 (2000)

13.115 T.S. Stefanik, L. Tuller: Ceria-based gas sensors, J. Eur. Ceram. Soc. **21**, 1967 (2001)

13.116 G.R. Leandro, S.A. Jose, H. Miguel: Single-step process to prepare CeO_2 nanotubes with improved catalytic activity, Nano Lett. **9**, 1395–1400 (2009)

13.117 S. Logothetidis, O. Patsalas, C. Charitidis: Enhanced catalytic activity of nanostructured cerium oxide films, Mater. Sci. Eng. C **23**, 803 (2003)

13.118 F. Larachi, J. Pierre, A. Adnot, A. Bernis: Ce 3d XPS study of composite $Ce_xMn_{1-x}O_{2-y}$ wet oxidation catalysts, Appl. Surf. Sci. **195**, 236 (2002)

13.119 M.T. Dario, A. Bachiorrini: Interaction of mullite with some polluting oxides in diesel vehicle filters, Ceram. Int. **25**, 511 (1999)

13.120 R. DiMonte, P. Fornasiero, M. Graziani, J. Kaspar: Oxygen storage and catalytic NO removal promoted by CeO_2-containing mixed oxides, J. Alloys Compd. **277**, 877 (1998)

13.121 G.R. Bamwenda, H. Arakawa: Cerium dioxide as a photocatalyst for water decomposition to O_2 in the presence of Ce_{aq}^{4+} and Fe_{aq}^{3+} species, J. Mol. Catal. A **161**, 105 (2000)

13.122 A.S. Karakoti, N.A. Monteiro-Riviere, R. Aggarwal, J.P. Davis, R.J. Narayan, W.T. Self, J. McGinnis,

S. Seal: Nanoceria as antioxidant: Synthesis and biomedical applications, JOM **60**, 33 (2008)
13.123 R.W. Tarnuzzer, J. Colon, S. Patil, S. Seal: Vacancy engineered ceria nanostructures for protection from radiation-induced cellular damage, Nano Lett. **5**, 2573 (2005)
13.124 M. Das, S. Patil, N. Bhargava, J.F. Kang, L.M. Riedel, S. Seal, J.J. Hickman: Auto-catalytic ceria nanoparticles offer neuroprotection to adult rat spinal cord neurons, Biomaterials **28**, 1918 (2007)
13.125 M. Alifanti, B. Baps, N. Blangenois, J. Naud, P. Grange, B. Delmon: Characterization of CeO_2–ZrO_2 mixed oxides. Comparison of the citrate and sol–gel preparation methods, Chem. Mater. **15**, 395 (2003)
13.126 C. Laberty-Robert, J.W. Long, E.M. Lucas, K.A. Pettigrew, R.M. Stroud, M.S. Doescher, R. Rolison: Sol–gel-derived ceria nanoarchitectures: Synthesis, characterization, and electrical properties, Chem. Mater. **18**, 50 (2006)
13.127 M. Hirano, M. Inagaki: Preparation of monodispersed cerium(IV) oxide particles by thermal hydrolysis: Influence of the presence of urea and Gd doping on their morphology and growth, J. Mater. Chem. **10**, 473 (2000)
13.128 M. Hirano, E. Kato: Hydrothermal synthesis of cerium(IV) oxide, J. Am. Ceram. Soc. **79**, 777 (1996)
13.129 M. Hirano, Y. Fukuda, H. Iwata, Y. Hotta, M. Inagaki: Preparation and spherical agglomeration of crystalline cerium(IV) oxide nanoparticles by thermal hydrolysis, J. Am. Ceram. Soc. **83**, 1287 (2000)
13.130 Y. Zhou, N. Rahaman: Effect of redox reaction on the sintering behavior of cerium oxide, Acta Mater. **45**, 3635 (1997)
13.131 X. Chu, W. Chung, D. Schmidt: Sintering of sol–gel-prepared submicrometer particles studied by transmission electron microscopy, J. Am. Ceram. Soc. **76**, 2115 (1993)
13.132 P.L. Chen, W. Chen: Reactive cerium(IV) oxide powders by the homogeneous precipitation method, J. Am. Ceram. Soc. **76**, 1577 (1993)
13.133 L. Mädler, J.W. Stark, E. Pratsinis: Flame-made ceria nanoparticles, J. Mater. Res. **17**, 1356 (2002)
13.134 T. Masui, K. Fujiwara, K. Machida, G. Adachi, T. Sakata, H. Mori: Characterization of cerium(IV) oxide ultrafine particles prepared using reversed micelles, Chem. Mater. **9**, 2197 (1997)
13.135 S. Sathyamurthy, K.J. Leonard, R.T. Dabestani, P. Paranthaman: Reverse micellar synthesis of cerium oxide nanoparticles, Nanotechnology **16**, 1960 (2005)
13.136 T. Mokkelbost, I. Kaus, T. Grande, M.-A. Einarsrud: Combustion synthesis and characterization of nanocrystalline CeO_2-based powders, Chem. Mater. **16**, 5489 (2004)
13.137 S. Maensiri, C. Masingboon, P. Laokul, W. Jareonboon, V. Promarak, P.L. Anderson, S. Seraphin: Egg white synthesis and photoluminescence of plate-like clusters of CeO_2 nanoparticles, Cryst. Growth Des. **7**, 950 (2007)
13.138 L. Li, Y. Chen: Preparation of nanometer-scale CeO_2 particles via a complex thermo-decomposition method, Mater. Sci. Eng. A **406**, 180 (2005)
13.139 X.H. Liao, J.M. Zhu, J.J. Zhu, J.Z. Xu, Y. Chen: Preparation of monodispersed nanocrystalline CeO_2 powders by microwave irradiation, Chem. Commun. (10), 937 (2001)
13.140 B. Djuričić, S. Pickering: Nanostructured cerium oxide: Preparation and properties of weakly-agglomerated powders, J. Eur. Ceram. Soc. **19**, 1925 (1999)
13.141 R. Si, Y.W. Zhang, L.P. You, C.H. Yan: Rare-earth oxide nanopolyhedra, nanoplates, and nanodisks, Angew. Chem. Int. Ed. **44**, 3256 (2005)
13.142 T. Yu, J. Joo, Y.I. Park, T. Hyeon: Large-scale nonhydrolytic sol–gel synthesis of uniform-sized ceria nanocrystals with spherical, wire, and tadpole shapes, Angew. Chem. Int. Ed. **44**, 7411 (2005)
13.143 F. Li, X.H. Yu, H.J. Pan, M.L. Wang, X.Q. Xin: Syntheses of MO_2 (M = Si, Ce, Sn) nanoparticles by solid-state reactions at ambient temperature, Solid State Sci. **2**, 767 (2000)
13.144 Y.X. Li, X.Z. Zhou, Y. Wang, X.Z. You: Preparation of nano-sized CeO_2 by mechanochemical reaction of cerium carbonate with sodium hydroxide, Mater. Lett. **58**, 245 (2003)
13.145 X.D. Zhou, W. Huebner, H.U. Anderson: Processing of nanometer-scale CeO_2 particles, Chem. Mater. **15**, 378 (2003)
13.146 H. Gu, M.D. Soucek: Preparation and characterization of monodisperse cerium oxide nanoparticles in hydrocarbon solvents, Chem. Mater. **19**, 1103–1110 (2007)
13.147 S.C. Kuiry, S.D. Patil, S. Deshpande, S. Seal: Spontaneous self-assembly of cerium oxide nanoparticles to nanorods through supraaggregate formation, J. Phys. Chem. B **109**, 6936–6939 (2005)
13.148 H.X. Mai, L.D. Sun, Y.W. Zhang: Shape-selective synthesis and oxygen storage behavior of ceria nanopolyhedra, nanorods, and nanocubes, J. Phys. Chem. B **109**, 24380–24385 (2005)
13.149 K.B. Zhou, X. Wang, X.M. Sun, Q. Peng, Y.D. Li: Enhanced catalytic activity of ceria nanorods from well-defined reactive crystal planes, J. Catal. **229**, 206–212 (2005)
13.150 D.E. Zhang, X.M. Ni, H.G. Zheng, X.J. Zhang, J.M. Song: Fabrication of rod-like CeO_2: Characterization, optical and electrochemical properties, Solid State Sci. **8**, 1290–1293 (2006)
13.151 G.S. Wu, T. Xie, X.Y. Yuan, B.C. Cheng, L.D. Zhang: An improved sol–gel template synthetic route to

large-scale CeO_2 nanowires, Mater. Res. Bull. **39**, 1023–1028 (2004)
13.152 M. Yada, S. Sakai, T. Torikai, T. Watari, S. Fyruta, H. Katsuki: Cerium compound nanowires and nanorings templated by mixed organic molecules, Adv. Mater. **16**, 1222–1225 (2004)
13.153 C.W. Sun, H. Li, Z.X. Wang, L.Q. Chen, X.J. Huang: Synthesis and characterization of polycrystalline CeO_2 nanowires, Chem. Lett. **133**, 662–663 (2004)
13.154 R. Yang, L. Guo: Synthesis of cubic fluorite CeO_2 nanowires, J. Mater. Sci. **40**, 1305–1309 (2005)
13.155 R.J. La, Z.A. Hu, H.L. Li, X.L. Shang, Y.Y. Yang: Template synthesis of CeO_2 ordered nanowire arrays, Mater. Sci. Eng. A **368**, 145–148 (2004)
13.156 W.Q. Han, L.J. Wu, Y.M. Zhu: Formation and oxidation state of CeO_{2-x} nanotubes, J. Am. Chem. Soc. **127**, 12814–12815 (2005)
13.157 R. Yang, L. Guo: Synthesis of the nanotublar cubic fluorite CeO_2, Chin. J. Inorg. Chem. **20**, 152–158 (2004)
13.158 S.W. Yang, L. Gao: Controlled synthesis and self-assembly of CeO_2 nanocubes, J. Am. Chem. Soc. **128**, 9330–9331 (2006)
13.159 J.J. Miao, H. Wang, Y.R. Li, J.M. Zhu, J.J. Zhu: Ultrasonic-induced synthesis of CeO_2 nanotubes, J. Crys. Growth **281**, 525–529 (2005)
13.160 Z.Y. Guo, F.L. Du, Z.L. Cui: Synthesis and characterization of single-crystal $Ce(OH)CO_3$ and CeO_2 triangular microplates, Inorg. Chem. **45**, 4167–4169 (2006)
13.161 A. Hadi, I.I. Yaacob: Novel synthesis of nanocrystalline CeO_2 by mechanochemical and water-in-oil microemulsion methods, Mater. Lett. **61**, 93–96 (2007)
13.162 J.Y. Bai, Z.D. Xu, Y.F. Zheng, H.Y. Yin: Shape control of CeO_2 nanostructure materials in microemulsion systems, Mater. Lett. **60**, 1287–1287 (2006)
13.163 Y.Q. Zhai, S.Y. Zhang, H. Pang: Preparation, characterization and photocatalytic activity of CeO_2 nanocrystalline using ammonium bicarbonate as precipitant, Mater. Lett. **61**, 1863–1867 (2007)
13.164 D.E. Zhang, X.J. Zhang, X.M. Ni, J.M. Song, H.G. Zheng: Optical and electrochemical properties of CeO_2 spindles, Chem. Phys. Chem. **7**, 2468–2470 (2006)
13.165 D.E. Zhang, X.J. Zhang, X.M. Ni, J.M. Song, H.G. Zheng: Fabrication of novel threefold shape CeO_2 dendrites: Optical and electrochemical properties, Chem. Phys. Lett. **430**, 326–329 (2006)
13.166 H.Y. Chang, H.I. Chen: Morphological evolution for CeO_2 nanoparticles synthesized by precipitation technique, J. Crys. Growth **283**, 457–461 (2005)
13.167 S. Tsunekawa, J.-T. Wang, Y. Kawazoe: Lattice constants and electron gap energies of nano- and subnano-sized cerium oxides from the experiments and first-principles calculations, J. Alloys Compd. **408–412**, 1145 (2006)
13.168 L. Yin, Y. Wang, G. Pang, Y. Koltypin, A. Gedanken: Sonochemical synthesis of cerium oxide nanoparticles – Effect of additives and quantum size effect, J. Colloid Interface Sci. **246**, 78–84 (2002)
13.169 C. Ho, J.C. Yu, T. Kwong, A.C. Mak, S. Lai: Morphology-controllable synthesis of mesoporous CeO_2 nano- and microstructures, Chem. Mater. **17**, 4514 (2005)
13.170 H.-I. Chen, H.-Y. Chang: Synthesis of nanocrystalline cerium oxide particles by the precipitation method, Ceram. Int. **31**, 795 (2005)
13.171 A. Corma, P. Atienzar, H. García, J.-Y. Chane-Ching: Hierarchically mesostructured doped CeO_2 with potential for solar-cell use, Nat. Mater. **3**, 394 (2004)
13.172 R.M. Bueno, J.M. Martinez-Duart, M. Hernandez-Velez, L. Vazquez: Optical and structural characterization of r.f. sputtered CeO_2 thin films, J. Mater. Sci. **32**, 1861–1865 (1997)
13.173 P. Patsalas, S. Logothetidis, L. Sygellou, S. Kennou: Structure-dependent electronic properties of nanocrystalline cerium oxide films, Phys. Rev. B **68**, 035104 (2003)
13.174 S. Mochizuki, F. Fujishiro: The photoluminescence properties and reversible photoinduced spectral change of CeO_2 bulk, film and nanocrystals, Phys. Status Solidi (b) **246**, 2320 (2009)
13.175 S.-H. Yu, H. Colfen, A. Fischer: High quality CeO_2 nanocrystals stabilized by a double hydrophilic block copolymer, Colloid Surf. A **243**, 49 (2004)
13.176 S. Phoka, P. Laokul, E. Swatsitang, V. Promarak, S. Seraphin, S. Maensiri: Synthesis, structural and optical properties of CeO_2 nanoparticles synthesized by a simple polyvinyl pyrrolidone (PVP) solution route, Mater. Chem. Phys. **115**, 423–428 (2009)
13.177 G. Wang, Q. Mu, T. Chen, Y. Wang: Synthesis, characterization and photoluminescence of CeO_2 nanoparticles by a facile method at room temperature, J. Alloys Compd. **493**, 202–207 (2010)
13.178 F. Gao, G.H. Li, J.H. Zhang, F.G. Qin, Z.Y. Yao, Z.K. Liu, Z.G. Wang, L.Y. Lin: Growth and photoluminescence of epitaxial CeO_2 film on Si(111) substrate, Chin. Phys. Lett. **18**, 443 (2001)
13.179 C.W. Sun, H. Li, H.R. Zhang, Z.X. Wang, Q. Chen: Controlled synthesis of CeO_2 nanorods by a solvothermal method, Nanotechnology **16**, 1454–1463 (2005)
13.180 C.W. Sun, H. Li, Q. Chen: Study of flowerlike CeO_2 microspheres used as catalyst supports for CO oxidation reaction, J. Phys. Chem. Solids **68**, 1785–1790 (2007)
13.181 S. Patil, S. Reshetnikov, M. Haldar, S. Seal: Surface-Derivatized Nanoceria with Human Carbonic Anhydrase II Inhibitors and Fluorophores: A Potential Drug Delivery Device, J. Phys. Chem. C **111**, 8437 (2007)

13.182 L. Li, J. Tao, H. Pan, H. Chen, X. Wu, F. Zhu, X. Xu, R. Tang: Colour tuning of core–shell fluorescent materials, J. Mater. Chem. **18**, 5363 (2008)

13.183 X. Liu, S. Chen, X. Wang: Synthesis and photoluminescence of CeO_2:Eu^{3+} phosphor powders, J. Lumin. **127**, 650 (2007)

13.184 H. Guo, Y. Qiao: Preparation, structural and photoluminescent properties of CeO_2:Eu^{3+} films derived by Pechini sol–gel process, Appl. Surf. Sci. **254**, 1961 (2008)

13.185 L. Li, H.K. Yang, B.K. Moon, Z. Fu, C. Guo, J.H. Jeong, S.S. Yi, K. Jang, H.S. Lee: Photoluminescence properties of CeO_2:Eu^{3+} nanoparticles synthesized by a sol–gel method, J. Phys. Chem. C **113**, 610 (2009)

13.186 Z. Wang, Z. Quen, J. Lin: Remarkable changes in the optical properties of CeO_2 nanocrystals induced by lanthanide ions doping, Inorg. Chem. **46**, 5237 (2007)

13.187 G. Adachi, N. Imanaka, Z.C. Kang: *Binary Rare Earth Oxides* (Springer, New York 2004)

13.188 J.C. Park, H.K. Moon, D.K. Kim, S.H. Byeon, B.C. Kim, K.S. Suh: Morphology and cathodoluminescence of Li-doped Gd_2O_3:Eu^{3+}, a red phosphor operating at low voltages, Appl. Phys. Lett. **77**, 2162 (2000)

13.189 Y.C. Kang, S.B. Park, I.W. Lenggoro, K. Okuyama: Gd_2O_3:Eu phosphor particles with sphericity, submicron size and non-aggregation characteristics, J. Phys. Chem. Solids **60**, 379 (1999)

13.190 B. Mercier, C. Dujardin, G. Ledoux, C. Louis, O. Tillement: Observation of the gap blueshift on Gd_2O_3:Eu^{3+} nanoparticles, J. Appl. Phys. **96**, 650 (2004)

13.191 H. Guo, N. Dong, M. Yin, W. Zhang, L. Lou, S. Xia: Visible upconversion in rare earth ion-doped Gd_2O_3 nanocrystals, J. Phys. Chem. B **108**, 19205–19209 (2004)

13.192 A. Bril, W.L. Wanmaker: Fluorescent properties of some europium-activated phosphors, J. Electrochem. Soc. **111**, 1363–1368 (1964)

13.193 S. Seo, H. Yang, P.H. Holloway: Controlled shape growth of Eu- or Tb-doped luminescent Gd_2O_3 colloidal nanocrystals, J. Colloid Interface Sci. **331**, 236–242 (2009)

13.194 S.Y. Seo, S. Lee, H.D. Park, N. Shin, K.-S. Sohn: Luminescence of pulsed laser deposited Gd_2O_3:Eu^{3+} thin film phosphors on quartz glass substrates, J. Appl. Phys. **92**, 5248 (2002)

13.195 J.S. Bae, S.S. Yi, J.H. Kim, K.S. Shim, B.K. Moon, J.H. Jeong, Y.S. Kim: Crystalline-phase-dependent red emission behaviors of Gd_2O_3:Eu^{3+} thin-film phosphors, Appl. Phys. A **82**, 369–372 (2006)

13.196 W.O. Gordon, J.A. Carter, B.M. Tissue: Long-lifetime luminescence of lanthanide-doped gadolinium oxide nanoparticles for immunoassays, J. Lumin. **108**, 339 (2004)

13.197 R. Bazzi, M.A. Flores, C. Louis, K. Lebbou, W. Zhang, C. Dujardin, S. Roux, B. Mercier, G. Ledoux, E. Bernstein, P. Perriat, O. Tillement: Synthesis and properties of europium-based phosphors on the nanometer scale: Eu_2O_3,Gd_2O_3:Eu, and Y_2O_3:Eu, J. Colloid Interface Sci. **273**, 191 (2004)

13.198 H. Chen, J. Zhang, X. Wang, S. Gao, M. Zhang, Y. Ma, Q. Dai, D. Li, S. Kan, G. Zou: The effect of the size of raw $Gd(OH)_3$ precipitation on the crystal structure and PL properties of Gd_2O_3:Eu, J. Colloid Interface Sci. **297**, 130 (2006)

13.199 Y.C. Kang, H.S. Roh, S.B. Park, H.D. Park: Use of LiCl flux in the preparation of Y_2O_3:Eu phosphor particles by spray pyrolysis, J. Eur. Ceram. Soc. **22**, 1661 (2002)

13.200 C. Lin, K. Lin, Y. Li: Sol–gel synthesis and photoluminescent characteristics of Eu^{3+} doped Gd_2O_3 nanophosphors, J. Lumin. **126**, 795 (2007)

13.201 Y. Tao, G. Zhao, S. Xia: Combustion synthesis and photoluminescence of nanocrystalline Y_2O_3:Eu phosphors, Mater. Res. Bull. **32**, 501 (1997)

13.202 L. Sun, J. Yao, C. Liu, C. Liao, C. Yan: Rare earth activated nanosized oxide phosphors: Synthesis and optical properties, J. Lumin. **87–89**, 447 (2000)

13.203 S. Neeraj, N. Kijima, A.K. Cheetham: Novel red phosphors for solid state lighting; the system $Bi_xLn_{1-x}VO_4$; Eu^{3+}/Sm^{3+} (Ln = Y, Gd), Solid State Commun. **131**, 65 (2004)

13.204 C. He, Y. Guan, L. Yao, W. Cai, X. Li, Z. Yao: Synthesis and photoluminescence of nano-Y_2O_3:Eu^{3+} phosphors, Mater. Res. Bull. **38**, 973 (2003)

13.205 M.L. Pang, J. Lin, J. Fu, R.B. Xing, C.X. Luo, Y.C. Han: Preparation, patterning and luminescent properties of nanocrystalline Gd_2O_3:A (A = Eu^{3+}, Dy^{3+}, Sm^{3+}, Er^{3+}) phosphor films via Pechini sol–gel soft lithography, Opt. Mater. **23**, 547 (2003)

13.206 S.C. Sun, B. Murray: Synthesis of monodisperse cobalt nanocrystals and their assembly into magnetic superlattices, J. Appl. Phys. **85**, 4325 (1999)

13.207 F.E. Kruis, H. Fissan, A. Peled: Synthesis of nanoparticles in the gas phase for electronic, optical and magnetic applications – a review, J. Aerosol Sci. **29**, 511 (1998)

13.208 G. Jia, K. Liu, Y. Zheng, Y. Song, M. Yang, H. You: Highly Uniform $Gd(OH)_3$ and Gd_2O_3:Eu^{3+} Nanotubes: Facile Synthesis and Luminescence Properties, J. Phys. Chem. C **113**(15), 6050–6055 (2009)

13.209 S. Li, H. Song, H. Yu, S. Lu, X. Bai, G. Pan, Y. Lei, L. Fan, T. Wang: Influence of annealing temperature on photoluminescence characteristics of Gd_2O_3:Eu/AAO nanowires, J. Lumin. **122/123**, 876–878 (2007)

13.210 G. Liu, G. Hong, X. Dong, J. Wang: Preparation and characterization of Gd_2O_3:Eu^{3+} luminescence nanotubes, J. Alloys Compd. **466**(1/2), 512–516 (2008)

13.211 G. Liu, S. Zhang, X. Dong, J. Wang: Solvothermal synthesis of Gd_2O_2:Eu^{3+} luminescent nanowires, J. Nanomater., 365079 (2010)

13.212 R.M. Petoral Jr., F. Söderlind, A. Klasson, A. Suska, M.A. Fortin, N. Abrikossova, L. Selegård, P. Käll, M. Engström, K. Uvdal: Synthesis and characterization of Tb^{3+}-doped Gd_2O_3 nanocrystals: A bifunctional material with combined fluorescent labeling and MRI contrast agent properties, J. Phys. Chem. C **113**, 6913–6920 (2009)

13.213 M. Ou, B. Muteleta, M. Martini, R. Bazzi, S. Roux, G. Ledoux, O. Tillement, P. Perriat: Optimization of the synthesis of nanostructured Tb^{3+}-doped Gd_2O_3 by in-situ luminescence following up, J. Colloid Interface Sci. **333**, 684–689 (2009)

13.214 S. Seo, H. Yang, P.H. Holloway: Controlled shape growth of Eu- or Tb-doped luminescent Gd_2O_3 colloidal nanocrystals, J. Colloid Interface Sci. **331**, 236–242 (2009)

13.215 V. Bedekar, D.P. Dutta, M. Mohapatra, S.V. Godbole, R. Ghildiyal, A.K. Tyagi: Rare earth doped gadolinia based phosphors for potential multicolor and white light emitting deep UV LEDs, Nanotechnology **20**, 125707 (2009)

13.216 V. Bedekar, D.P. Dutta, A.K. Tyagi: White light emission from spin coated Gd_2O_3:Dy nano phosphors synthesized using polyol technique, J. Nanosci. Nanotechnol. **10**, 8234–8238 (2010)

13.217 K.J. Klabunde, C. Mohs: Nanoparticles and nanostructural materials. In: *Chemistry of Advanced Materials: An Overview*, ed. by L. Interrante, M. Hampden-Smith (Wiley-VCH, New York 1998) p. 271

13.218 M.L. Steigerwald, L.E. Brus: Semiconductor crystallites: A class of large molecules, Acc. Chem. Res. **23**, 183 (1990)

13.219 A. Henglein: Small-particle research: Physicochemical properties of extremely small colloidal metal and semiconductor particles, Chem. Rev. **89**, 1861 (1989)

13.220 H.J. Fecht: Formation of nanostructures by mechanical attrition. In: *Nanomaterials: Synthesis, Properties, and Applications*, ed. by A.S. Edelstein, R.C. Cammarata (Institute of Physics, Philadelphia 1996) p. 89

13.221 T.P. Martin, U. Naher, H. Schaber, U. Zimmerman: Evidence for a size-dependent melting of sodium clusters, J. Chem. Phys. **100**, 2322 (1994)

13.222 K.J. Klabunde, J.V. Stark, O. Koper, C. Mohs, D.G. Park, S. Decker, Y. Jiang, I. Lagadic, D. Zhang: Nanocrystals as stoichiometric reagents with unique surface chemistry, J. Phys. Chem. **100**, 12142 (1996)

13.223 R. Richards, W. Li, S. Decker, C. Davidson, O. Koper, V. Zaikovski, A. Volodin, T. Rieker: Consolidation of metal oxide nanocrystals. Reactive pellets with controllable pore structure that represent a new family of porous, inorganic materials, J. Am. Chem. Soc. **122**, 4921 (2000)

13.224 J. Karch, R. Birringer, H. Gleiter: Ceramics ductile at low temperature, Nature **330**, 556 (1987)

13.225 R.P. Andres, R.S. Averback, W.L. Brown, L.E. Brus, W.A. Goddard III., A. Kalder, S.G. Louie, M. Moscovits, P.S. Peercy, S.J. Riley, R.W. Siegel, F. Spaepen, Y. Wang: Research opportunities on clusters and cluster-assembled materials – A Department of Energy, Council on Materials Science Panel Report, J. Mater. Res. **4**, 704 (1989)

13.226 A. Pelmenschikov, G. Morosi, A. Gamba, S. Coluccia: A check of quantum chemical molecular models of adsorption on oxides against experimental infrared data, J. Phys. Chem. **99**, 15018 (1995)

13.227 J. Ramkumar, R. Shukla, S. Chandramouleeswaran, T. Mukherjee, A.K. Tyagi: Transition metal oxide nanoparticles as potential room temperature sorbents, Nanosci. Nanotechnol. Lett. **4**, 693–700 (2012)

13.228 H.D. Gesser, P.C. Goswami: Aerogels and related porous materials, Chem. Rev. **89**, 765 (1989)

13.229 J.V. Stark, D.G. Park, I. Lagadic, K.J. Klabunde: Nanoscale metal oxide particles/clusters as chemical reagents. Unique surface chemistry on magnesium oxide as shown by enhanced adsorption of acid gases (sulfur dioxide and carbon dioxide) and pressure dependence, Chem. Mater. **8**, 1904 (1996)

13.230 L.V. Interrante, M.J. Hampden-Smith (Eds.): *Chemistry of Materials* (Wiley-VCH, New York 1998) pp. 1–18

13.231 K.J. Klabunde (Ed.): *Nanoscale Materials in Chemistry* (Wiley Interscience, New York 2001) pp. 1–14, 85–120, 223–262

13.232 K.J. Klabunde, R. Richards (Eds.): *Nanoscale Materials in Chemistry*, 2nd edn. (Wiley, New York 2009) pp. 629–768

13.233 C.J. Brinker, G.W. Scherer: *Sol-Gel Science* (Academic, San Diego 1990) pp. 1–403

13.234 V. Grassian (Ed.): *Environmental Catalysis* (CRC, Boca Raton 2005) pp. 1–3, 391–420

13.235 H. Freundlich: *Colloid and Capillary Chemistry* (Methuen, London 1926)

13.236 I. Langmuir: The adsorption of gases on plane surfaces of glass, mica and platinum, J. Am. Chem. Soc. **40**, 1361–1403 (1918)

13.237 S. Lagergren: About the theory of so-called adsorption of soluble substances, K. Sven. Vetensk. Handlingar **4**, 1–39 (1898)

13.238 Y.S. Ho., G. McKay: Kinetic models for the sorption of dye from aqueous solution by wood, Process Saf. Environ. Prot. **76B**, 183–191 (1998)

13.239 Y.S. Ho., G. McKay: The kinetics of sorption of divalent metal ions onto sphagnum moss peat, Water Res. **34**, 735–742 (2000)

13.240 G.K. Boreskev: *Heterogeneous Catalysis* (Nova Publishers, New York 2003) pp. 1–2

13.241 G. Ertl: *Reaction at Solid Surface* (Wiley, Hoboken 2009) pp. 1–3

13.242 G. Ertl: *Handbook of heterogeneous catalysis* (VCH, Weinheim 1997)

13.243 T. Murota, T. Hasegawa, S. Aozasa, H. Matsui, M. Motoyama: Production method of cerium oxide with high storage capacity of oxygen and its mechanism, J. Alloys Compd. **193**, 298 (1993)

13.244 P. Fornasiero, R. Di Monte, R.G. Rao, J. Kaspar, S. Meriani, A. Trovarelli, M. Graziani: Rh-loaded CeO_2–ZrO_2 solid-solutions as highly efficient oxygen exchangers: Dependence of the reduction behavior and the oxygen storage capacity on the structural-properties, J. Catal. **151**, 168 (1995)

13.245 M. Ozawa, M. Kimura, A. Isogai: The application of CeZr oxide solid solution to oxygen storage promoters in automotive catalysts, J. Alloys Compd. **193**, 73 (1993)

13.246 C. de Leitenburg, A. Trovarelli, J. Lloorca, F. Cavani, G. Bini: The effect of doping CeO_2 with zirconium in the oxidation of isobutene, Appl. Catal. A **139**, 161 (1996)

13.247 M. Haruta, S. Tsubota, T. Kobayashi, H. Kageyama, M.J. Genet, B. Delmon: Low-temperature oxidation of CO over gold supported on TiO_2, α-Fe_2O_3, and Co_3O_4, J. Catal. **144**, 175 (1993)

13.248 S. Tsubota, T. Nakamura, K. Tanaka, M. Haruta: Effect of calcination temperature on the catalytic activity of Au colloids mechanically mixed with TiO_2 powder for CO oxidation, Catal. Lett. **56**, 131 (1998)

13.249 O. Mitsutaka, N. Shyunichi, T. Susumu, N. Toshiko, A. Masashi, H. Masatake: Chemical vapor deposition of gold on Al_2O_3, SiO_2, and TiO_2 for the oxidation of CO and of H_2, Catal. Lett. **51**, 53 (1998)

13.250 Y. Chen, D. Wu, C. Yeh: Oxidation of carbon monoxide over nanoparticles of cobalt oxides, Rev. Adv. Mater. Sci. **5**, 41 (2003)

13.251 M.F. Camellone, S. Fabris: Reaction mechanisms for the CO. Oxidation on Au/CeO_2 catalysts: Activity of substitutional Au^{3+}/Au^{+} cations and deactivation of supported Au^{+} adatoms, J. Am. Chem. Soc. **131**, 10473 (2009)

13.252 F. Romero-Sarria, L.M.T. Martínez, M.A. Centeno, J.A. Odriozola: Surface dynamics of Au/CeO_2 catalysts during CO oxidation, J. Phys. Chem. C **111**, 14469 (2007)

13.253 J. Xua, D.R. Mullinsa, H. Overbury: CO desorption and oxidation on CeO_2-supported Rh: Evidence for two types of Rh sites, J. Catal. **243**, 158 (2006)

13.254 K. Krishna, A. Bueno-Lopez, M. Makkee, J.A. Moulijn: Potential rare earth modified CeO_2 catalysts for soot oxidation: I. Characterisation and catalytic activity with O_2, Appl. Catal. B **75**, 189 (2007)

13.255 U. Hennings, R. Reimert: Noble metal catalysts supported on gadolinium doped ceria used for natural gas reforming in fuel cell applications, Appl Cat B **70**, 498 (2007)

13.256 A. Tschope, D. Schaadt, R. Birringer, J.Y. Ying: Catalytic properties of nanostructured metal oxides synthesized by inert gas condensation, Nanostruct. Mater. **9**, 423 (1997)

13.257 F. Deganello, V. Esposito, M. Miyayama, E.J. Traversa: Cathode performance of nanostructured $La_{1-a}SraCo_{1-b}FebO_{3-x}$ on a $Ce_{0.8}Sm_{0.2}O_2$ electrolyte prepared by citrate-nitrate autocombustion, Electrochem. Soc. **154**, A89 (2007)

13.258 F. Deganello, L.F. Lotta, A. Longo, P. Casaletto, M. Scopelitti: Cerium effect on the phase structure, phase stability and redox properties of Ce-doped strontium ferrates, J. Solid State Chem. **179**, 3406 (2006)

13.259 J.C. Yu, L.Z. Zhang, J. Lin: Direct sonochemical preparation of high-surface-area nanoporous ceria and ceria-zirconia solid solutions, J. Colloid Interface Sci. **260**, 240 (2003)

13.260 T. Tsuzuki, P.G. McCormick: Synthesis of ultrafine ceria powders by mechanochemical processing, J. Am. Ceram. Soc. **84**, 1453 (2001)

13.261 H.R. Xu, L. Gao, H.C. Gu, J.K. Guo, D.S. Yan: Synthesis of solid, spherical CeO_2 particles prepared by the spray hydrolysis reaction method, J. Am. Ceram. Soc. **85**, 139 (2002)

13.262 P.L. Chen, I.W. Chen: Reactive cerium(IV) oxide powders by the homogeneous precipitation method, J. Am. Ceram. Soc. **76**, 1577 (1993)

13.263 J.L. Woodhead: Process for preparing aqueous dispersion of ceria and resulting product, US Patent 4231893 (1980)

13.264 B. Djuricic, S. Pickering: Nanostructured cerium oxide: Preparation and properties of weakly-agglomerated powders, J. Eur. Ceram. Soc. **19**, 1925 (1999)

13.265 Y.S. Cho, H.D. Glicksman, V.R.W. Amarakoon: Ceramic nanopowders. In: *Encylopedia of Nanoscience and Nanotechnology*, Vol. 1, ed. by H.S. Nalwa (American Scientific, Valencia 2004) p. 7

13.266 K.J. Moreno, G. Mendonza-Suarez, A.F. Fuentes, J. Garcia-Barriocanal, C. Leon, J. Santamaria: Cooperative oxygen ion dynamics in $Gd_2Ti_{2-y}Zr_yO_7$, Phys. Rev. B **71**, 132301 (2005)

13.267 M.T. Weller, R.W. Hughes, J. Rouke, C.S. Knee, J. Reading: The pyrochlore family – A potential panacea for the frustrated perovskite chemist, Dalton Trans., 3032 (2004)

13.268 P.K. Moon, R.H. Tuller: Ionic conduction in the $Gd_2Ti_2O_7$–$Gd_2Zr_2O_7$ system, Solid State Ionics **28**, 470 (1988)

13.269 M. Pirzada, R.W. Grimes, L. Minervini, J.F. Maguire, K.E. Sickafus: Oxygen migration in $A_2B_2O_7$ pyrochlores, Solid State Ionics **140**, 201 (2001)

13.270 I. Riess, D. Braunshtein, D.S. Tannhauser: Density and ionic conductivity of sintered $(CeO_2)_{0.82}(GdO_{1,5})_{0.18}$, J. Am. Ceram. Soc. **64**, 479 (1981)

13.271 J.J. Kingsley, K. Suresh, K.C. Patil: Combustion synthesis of fine-particle metal aluminates, J. Mater. Sci. **25**, 1305 (1990)

13.272 S. Bhaduri, S.B. Bhaduri, E. Zhou: Auto ignition synthesis and consolidation of Al_2O_3–ZrO_2 nano/nano composite powders, J. Mater. Res. **13**, 156 (1998)

13.273 B.P. Mandal, S.K. Deshpande, A.K. Tyagi: Ionic conductivity enhancement in $Gd_2Zr_2O_7$ pyrochlore by Nd doping, J. Mater. Res. **23**, 911 (2008)

13.274 L.R. Pederson, L.A. Chick, G.J. Exarhos: Method of making metal oxide ceramic powders by using a combustible amino acid compound, US Patent 5114702 (1992)

13.275 A. Hara, Y. Hirata, S. Sameshima, N. Matsunaga, T. Horita: Grain size dependence of electrical properties of Gd-doped ceria, J. Ceram. Soc. Jpn. **116**, 291 (2008)

13.276 A.G. Belous, K.V. Kravchyk, E.V. Pashkova, O. Bohnke, C. Galven: Influence of the chemical composition on structural properties and electrical conductivity of Y–Ce–ZrO_2, Chem. Mater. **19**(21), 5179–5184 (2007)

13.277 B.P. Mandal, A. Banerji, V. Sathe, S.K. Deb, K. Tyagi: Order–disorder transition in $Nd_{2-y}Gd_yZr_2O_7$ pyrochlore solid solution: An x-ray diffraction and Raman spectroscopic study, J. Solid State Chem. **180**, 2643 (2007)

14. Piezoelectric Nanoceramics

Xiaohui Wang, Shaopeng Zhang, Longtu Li

Understanding ferroelectricity in perovskite, bulk dense nanograin ceramics is a fundamental issue that has remained unsolved for decades. The novel development of an unconventional pressureless two-step sintering strategy featuring densification without grain growth is deemed particularly exciting because it is more desirable for commercial production. Using this technique, high-density pure barium titanate (BT) ceramic samples could be produced, which allowed for better understanding of the size effect in nanometer-scale BT ceramic systems and to address real industrial applications. In this chapter, we describe the methods for fabrication of highly dense piezoelectric nanoceramics followed by the systemic investigation of the size effect on the microstructures and piezoelectric behavior of $(1-x)BiScO_3$-$xPbTiO_3$ (BSPT) nanoceramics. BSPT ceramics with average grain size from the micrometer scale down to 10 nm have been prepared by a two-step sintering method. The microstructures and properties of these bulk dense nanocrystalline ceramics were characterized by means of x-ray diffraction (XRD), high-resolution transmission electron microscopy (HRTEM), atomic force microscopy (AFM), scanning probe microscopy (SPM), and hysteresis-loop and dielectric measurements.

14.1 **Introduction to BSPT** 554
14.1.1 Structures and Morphotropic Phase Boundary 554
14.1.2 Ceramic Properties and Grain Size Effects 554
14.2 **Synthesis of BSPT Nanopowders via Sol–Gel Method** 555
14.3 **Sintering of BSPT Nanoceramics** 556
14.3.1 Two-Step Sintering 556
14.3.2 Combination of Spark Plasma Sintering and Two-Step Sintering 558
14.3.3 Ultrahigh-Pressure (UHP) Forming and Two-Step Sintering 561
14.4 **Grain Size Effect on the Properties of BSPT Ceramics** 563
14.4.1 Dielectric Properties 563
14.4.2 Ferroelectric Property 564
14.4.3 Piezoelectric Property 564
14.5 **Summary** 567
References 568

Motivated by the market demand for small-grain-size ferroelectric ceramics and the promise of enhanced properties in fine-grained ceramics, investigation of the grain size effect on microstructures and properties of ferroelectric/piezoelectric ceramics becomes significantly important.

Piezoelectric material as one kind of ferroelectric can convert electrical energy into mechanical energy and vice versa. This electromechanical property arises due to the coupling of the spontaneous polarization with the lattice strain. Many devices such as ultrasonic transducers and piezoelectric actuators make use of this property. Since the synthesis of $(1-x)BiScO_3$-$xPbTiO_3$ (BSPT) by *Eitel* and coworkers in 2001 [14.1], this new perovskite solid solution has attracted considerable attention as a promising candidate for high-temperature actuator and transducer applications due to its high Curie temperature and robust thermal stability as well as excellent piezoelectric properties. Most of the work has focused on microstructure and properties (electrical, dielectric, and ferroelectric) as a function of composition and phase.

14.1 Introduction to BSPT

BSPT ($(1-x)BiScO_3$-$xPbTiO_3$) solid-solution ceramics were first reported by *Eitel* et al. [14.1] in 2001, as new high-temperature piezoelectric materials. They investigated a series of complex perovskites with general formula $Bi(Me^{3+})O_3$-$PbTiO_3$ (Me^{3+}=Sc^{3+}, Fe^{3+}, In^{3+}, Yb^{3+}, etc.), under the guidance of a tolerance factor t proposed by Goldschmidt [14.3]. Among these solid solutions, only $BiScO_3$-$PbTiO_3$ (BSPT) has a tolerance factor ($t = 0.907$) less than that for $Pb(Zr, Ti)O_3$ ($t = 0.96$) and can maintain stable perovskite structure under atmospheric conditions. It exhibits a significantly high T_c of 450 °C near the morphotropic phase boundary (MPB), and other piezoelectric properties such as electromechanical coupling factor of $K_p = 0.57$ and piezoelectric constant of $d_{33} = 450\,pC/N$. Since then, extensive studies have been carried out on BSPT ceramics [14.1,2,4–13], single crystals [14.14–18], and thin films [14.19–25], revealing its high Curie temperature, excellent ferroelectric/piezoelectric properties, and robust thermal stability. BSPT solid solution is considered as a promising candidate for high-temperature sensor and actuator applications.

14.1.1 Structures and Morphotropic Phase Boundary

Since the synthesis of Rochelle salt by Seignette in 1665 and the discovery of its dielectric properties by *Valasek* in 1921 [14.26], the number of ferroelectrics has grown rapidly. Among them, ferroelectrics with ABO_3-type perovskite structure are the most numerous, including $BaTiO_3$ and $Pb(Zr,Ti)O_3$ (PZT), being extremely important for the electronic and automobile industries. BSPT solid solution has a similar structure, with Bi^{3+}/Pb^{2+} ions occupying the A sites, Sc^{3+}/Ti^{4+} ions taking the B site, and O_2^- taking the face-center sites (Fig. 14.1).

Similar to the $Pb(Zr_{1-x}Ti_x)O_3$ system, the structure of $(1-x)BiScO_3$-$xPbTiO_3$ solid solution changes with the composition x, and in their composition phase diagram there exists a specific region called the morphotropic phase boundary (MPB). The MPB was initially defined in the PZT system as a near-vertical line separating compositions with rhombohedral and tetragonal symmetries. Actually, it represents a region with a certain composition range and commonly exists in other binary system including $PbTiO_3$ (PT), such as $PbMg_{1/3}Nb_{2/3}O_3$-$PbTiO_3$ (PMN-PT), $PbZn_{1/3}Nb_{2/3}O_3$-$PbTiO_3$ (PZN-PT), etc. In the vicinity of the MPB region, these materials show superior piezoelectric and dielectric properties. The phase diagram of the BSPT system given by *Chaigneau* et al. [14.2] in 2007 is shown in Fig. 14.2.

14.1.2 Ceramic Properties and Grain Size Effects

Since the discovery of BSPT solid solution, the properties of BSPT ceramics have attracted more attention due to their excellent piezoelectric properties and robust thermal stability. Like PZT, the best piezoelectric activity is found near the MPB between the tetragonal phase and the rhombohedral phase. In a previous study [14.8], the optimum piezoelectric properties were determined to occur at $x = 0.635$, with d_{33} value up to 700 pC/N

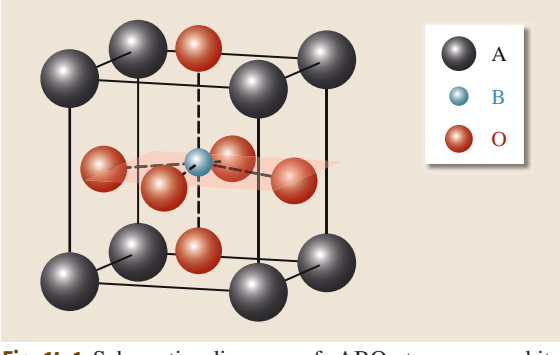


Fig. 14.1 Schematic diagram of ABO_3-type perovskite structure

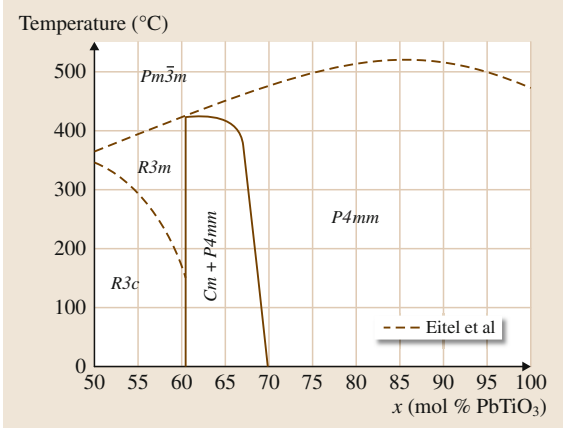


Fig. 14.2 Composition phase diagram of BSPT solid solution (after [14.2])

($K_p = 0.632$) and Curie temperature of 446 °C, both of which are much higher than commercial Pb(Zr, Ti)O_3 (PZT).

However, motivated by the market demand for small-grain-size ferroelectric ceramics and the promise of enhanced properties in fine-grained ceramics, investigation of the grain size effects on the properties of ferroelectric/piezoelectric ceramics becomes significantly important [14.27]. In recent years, studies of grain size effects in ferroelectric ceramics have been extended to the nanoscale, and the so-called *ferroelectric critical size* has attracted much interest [14.28–40]. As a promising candidate for high-temperature applications, research on the grain size effect in BSPT ceramics has also attracted more attention [14.7, 8, 41, 42]. However, owing to the difficulties of achieving high density while maintaining the nanograin nature, the size effect in sintered bulk ceramics has rarely been reported, and there is still no consistent conclusion regarding the grain size effect on the piezoelectric properties of BSPT ceramics, especially for grain sizes less than 100 nm. One of the obstacles lies in sintering. Normal sintering generally requires a high sintering temperature (1000 °C). This causes great difficulties in obtaining ceramics with both high density and fine grain size even when using nanocrystalline powder, thus limiting the grain size to the nanometer scale.

Highly dense BSPT ceramics with average grain size from a micrometer to as small as 10 nm have been prepared separately by a two-step sintering method. The size effects on the microstructures and piezoelectric behavior of BSPT nanoceramics were investigated. The microstructures and properties of the bulk dense nanocrystalline ceramics were characterized by means of x-ray diffraction (XRD), high-resolution transmission electron microscopy (HRTEM), atomic force microscopy (AFM), scanning probe microscopy (SPM), and hysteresis-loop and dielectric measurements. The existence of the ferroelectric phase in the nanocrystalline ceramics at room temperature has been proved by the polarization-reversal characteristics according to the measurement of hysteresis loops as well as the local ferroelectric switching behavior investigated by piezoresponse force microscopy. These results provide incontestable experimental evidence for ferroelectricity and piezoelectricity in bulk dense BSPT ceramic with grain size as fine as 10 nm with high T_c of 700 K.

14.2 Synthesis of BSPT Nanopowders via Sol–Gel Method

Nanopowder is a necessary prerequisite to fabricating bulk dense nanoceramics. When the particle size of the powders reduces to the nanoscale, agglomeration increases due to the high specific surface area and energy. Thus, it is the size of the agglomerates rather than the size of the nanoparticles that determines the sintering behavior of the powder and the final microstructure of the ceramic. Therefore, low-cost production of nanopowders without agglomeration and compaction of particles to achieve homogeneous, high green density are required to fabricate nanoceramics.

The citrate sol–gel method is extensively used for synthesis of metal oxide nanopowders due to its simple setup and relatively low processing temperature. For BSPT nanopowders, Sc_2O_3, $Bi(NO_3)_3 \cdot 5H_2O$, $Pb(NO_3)_2 \cdot 3H_2O$, and $C_{16}H_{16}O_4Ti$ are chosen as starting materials to provide Sc^{3+}, Bi^{3+}, Pb^{2+}, and Ti^{4+}. Besides, $C_6H_8O_7 \cdot H_2O$ (analytical reagent (AR)), HNO_3 (AR), $NH_3 \cdot H_2O$ (AR), and H_2O_2 (AR) are used as accessory materials [14.7]. The whole process is illustrated in the flowchart in Fig. 14.3.

The as-prepared BSPT nanopowders were observed under TEM (Fig. 14.4). The particles are well resolved with average size ≤ 10 nm. x-ray diffraction (XRD) patterns of BSPT nanopowders with different compositions and different calcination temperatures are depicted in Fig. 14.5.

It is known from the Scherrer equation that, if the particle size of the powder is very small, the XRD peaks will be significantly broadened. Consequently, the XRD patterns of BSPT nanopowders calcined at 600 °C do not show their characteristic splitting and, at first glance, are like those of the pseudocubic phase. On further increase of the calcination temperature to 800 °C, grain growth is induced and powders with larger particle sizes can be obtained. Then, the XRD patterns of BSPT powders exhibit peak-splitting behavior. For the rhombohedral phase ($x = 0.600$) the 111 peak splits, while for the tetragonal phase ($x = 0.680$) the 110 and 200 peaks split. However, for BSPT powders with MPB composition ($x = 0.635$), peak splitting is masked due to the coexistence of different phases.

14.3 Sintering of BSPT Nanoceramics

Due to their extremely large specific surface area, as-prepared BSPT nanopowders have very high sintering activity and are very sensitive to sintering temperature and holding time. Moreover, Pb and Bi tend to be volatile at high temperatures, making it easy for the grains to grow. Figure 14.6 displays the grain size change for different holding times at sintering temperature of 1000 °C using BSPT nanopowders prepared by the sol–gel method. When sintered at 1000 °C for 5 min, the grain size of BSPT ceramics reached ≈ 400 nm. Increasing the holding time to only 10 min, the grain size grows to ≈ 1 μm. On further prolonging the sintering time from 10 to 30 min, the rate of grain growth slows to an increase of 1 μm. So, it is obvious that the conventional sintering method cannot be used for fabricating fine-grained BSPT ceramics. Therefore, an innovative sintering method is required.

14.3.1 Two-Step Sintering

The two-step sintering method was first reported by *Chen* and *Wang* [14.43] in 2001 and has been proved to be an efficient method to prepare fully dense nanograin bulk ceramics of numerous kinds of oxides or even nonoxides [14.44–49]. This technique exploits the difference in kinetics between grain boundary diffusion and migration during sintering. As shown in Fig. 14.7, first a green ceramic sample is heated up to a higher temperature T_1 to obtain a starting density $\geq 75\%$. Then, the sintering temperature is rapidly reduced to a lower temperature T_2 and held at T_2 for a long time. This unique sintering schedule guarantees that all pores in the ceramic are subcritical and unstable against shrinkage after the first step and the ceramic can fulfill densification without grain growth in the second sintering step.

Determination of Sintering Parameters

Based on the discussion above, three essential parameters should be determined: the first-step temperature T_1, the second-step temperature T_2, and the holding time t. Among these, the first-step temperature T_1 defines the final grain size, because grain growth mainly occurs in this stage. It also provides the required starting density of $\geq 75\%$, as suggested in [14.43]. To determine the density of the ceramic after the first-step sintering, the green pellets are heated to different T_1 temperatures at heating rate of 4 °C/min. Then, the pellets are taken out of the furnace to be rapidly cooled down to room temperature in air. The relative densities of as-sintered pellets are measured using the Archimedes method. Figure 14.8 shows the relative density change of BSPT ($x = 0.64$) ceramics with T_1. According to Fig. 14.8, the first-step temperature T_1 should be at least 950 °C. Therefore, $T_1 = 930$, 960, 1000, 1020, and 1050 °C were chosen in this work.

Various sintering schedules with different values of T_1 and T_2 were used to explore the temperature region without grain growth while maintaining full density. Ex-

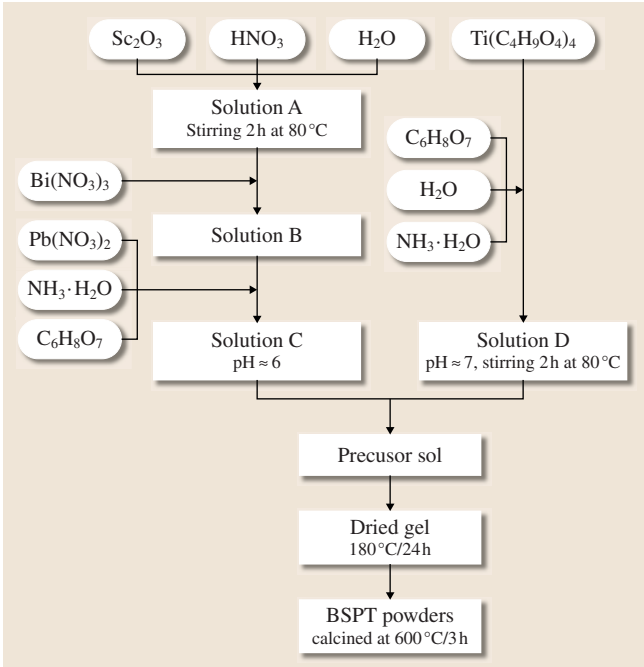


Fig. 14.3 BSPT powder process flowchart

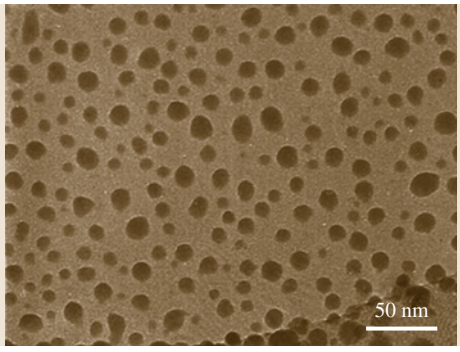


Fig. 14.4 TEM micrograph of BSPT powder

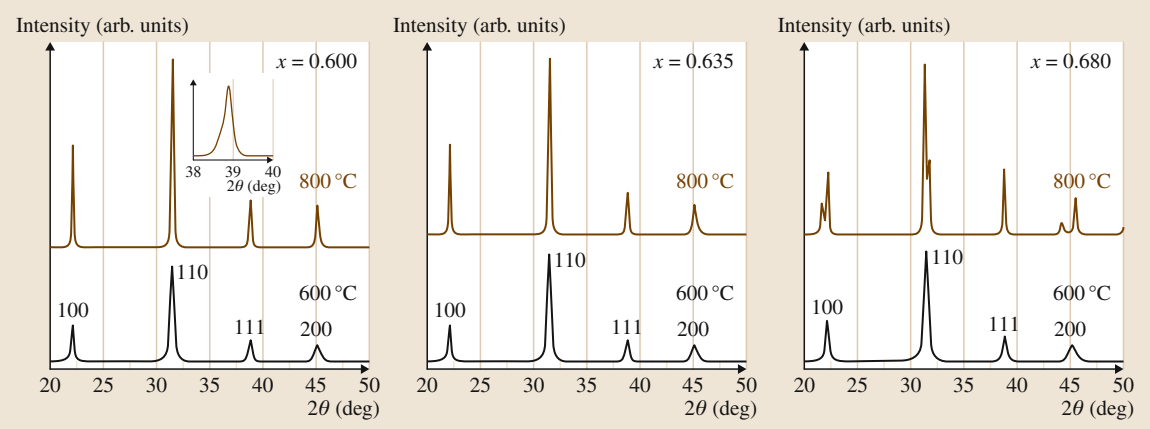


Fig. 14.5 x-Ray diffraction patterns of BSPT nanopowders with different compositions and calcination temperatures

amples of these experiments are presented in Table 14.1. The average grain size (GS_A) was calculated by measuring Feret's diameters of more than 150 grains for each sample. The changes of relative density and the average grain size of samples obtained under different sintering conditions are listed in Table 14.1.

Based on the data in Table 14.1, the relative density and grain size changes of the ceramic samples sintered at different T_1 and the same $T_2 = 800\,°C$ are also depicted in Fig. 14.9. Comparing the relative density curves in Figs. 14.8 and 14.9, there is a 10–20% increase of density due to the densification occurring in the second step. Moreover, the insufficient relative density of samples A and B indicates that the first-step temperature is not high enough and T_1 should be higher than 1000 °C to ensure a relative density ≥ 95%. Thus, $T_1 = 1000\,°C$ and 1050 °C were chosen to determine the effect of the second-step temperature T_2, and the results are shown in Fig. 14.10. Comparing the two curves in Fig. 14.10, an increase of 50 °C in T_1 leads to about 100 nm larger grain size of the samples, and an increase of T_2 from 850 to 900 °C causes grain growth of 200–250 nm. This phenomenon again proves that BSPT solid solution is extremely sensitive to sintering temperature. However, when the second-step temperature T_2 is lower than 850 °C, no grain growth is observed. This could be attributed to the suppression of grain boundary migration at such a low temperature.

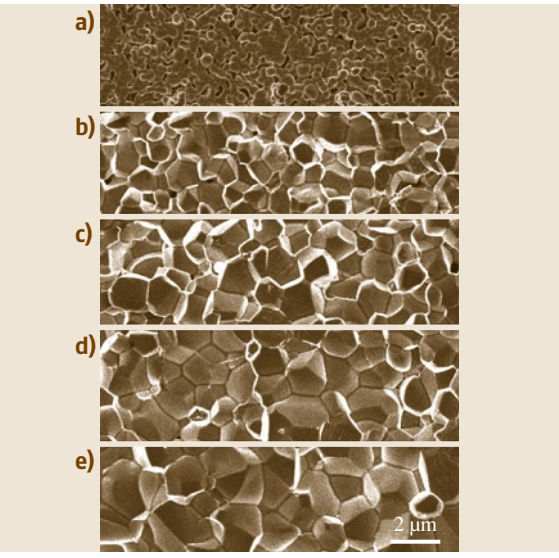


Fig. 14.6a–e The microstructure change with holding time during sintering at 1000 °C for BSPT ceramics: **(a)** 5 min, **(b)** 10 min, **(c)** 15 min, **(d)** 20 min, and **(e)** 30 min

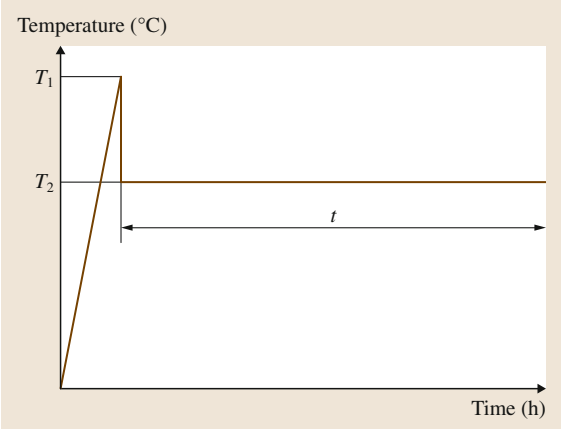


Fig. 14.7 Schematic diagram of two-step sintering

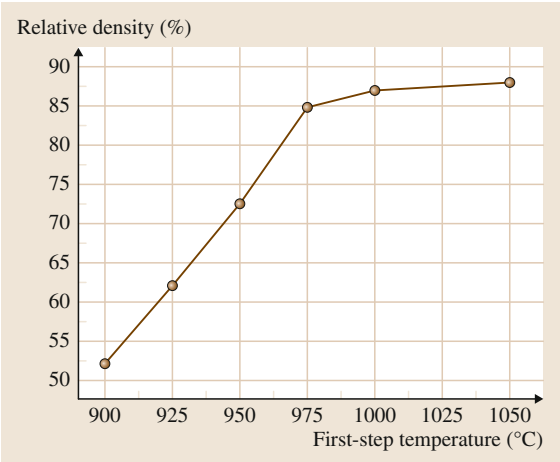


Fig. 14.8 Relative density change of BSPT ceramics with the first-step temperature T_1 (after [14.7])

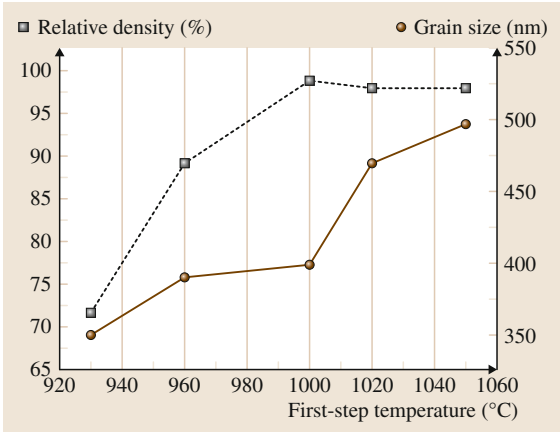


Fig. 14.9 Relative density and grain size change with T_1 for samples A, B, C2, D, and E1 in Table 14.1 (after [14.7])

Kinetic Window for BSPT Ceramic Sintering

Based on the above data and analysis, the kinetic window for BSPT ceramic sintering can be determined (Fig. 14.11). Solid symbols indicate sintering conditions that can obtain full densification without grain growth, while open symbols indicate those that cannot reach full density (below the lower boundary) or cause uncontrollable grain growth (above the upper boundary). Such behavior resembles that of Y_2O_3 [14.43] and $BaTiO_3$ [14.47, 48], providing a feasible approach of two-step sintering to produce high-density fine-grained MPB BSPT ceramic using the pressureless sintering method. Highly dense MPB BSPT ceramics with homogeneous fine grains could be achieved using pressureless sintering without any sintering aids at a low temperature of 800 °C with grain size as small as 200 nm [14.7]. Furthermore, the piezoelectric coefficient was found to reach 520 pC/N for the sample with grain size of 200 nm, higher than that of coarse-grained BSPT ceramics (450 pC/N), indicating a promising path for improvement of the piezoelectric coefficient.

14.3.2 Combination of Spark Plasma Sintering and Two-Step Sintering

Spark plasma sintering (SPS) has been proved as a very efficient method for fabrication of various nanomaterials [14.50]. Although the physical nature of the observed enhancement of the consolidation process is still under debate, the advantages of this sintering method, including the effect of the current, such as accelerated particle bonding, the high heating and cooling

Table 14.1 Parameters of two-step sintering for BSPT ceramics

Sample	Sintering methods		Holding time (h)	Relative density (%)	Average grain size (nm)
	T_1 (°C)	T_2 (°C)			
A	930	800	8	71.8	350
B	960		8	89.0	390
C1	1000	750	8	96.1	400
C2		800	8	98.8	400
C3		850	8	95.8	400
C4		900	8	98.0	600
D	1020	800	8	97.9	470
E1	1050	800	8	98.1	497
E2		850	8	98.5	497
E3		900	8	97.4	750
E4		950	8	95.5	795

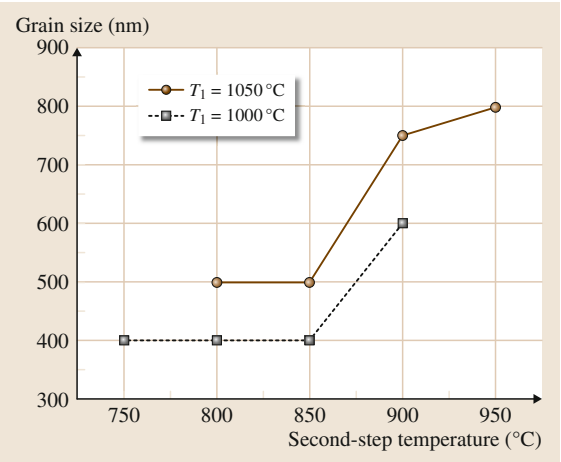


Fig. 14.10 Grain size change with T_2 for samples with $T_1 =$ 1000 °C (samples C1, C2, C3, and C4 in Table 14.1) and 1050 °C (samples E1, E2, E3, and E4 in Table 14.1)

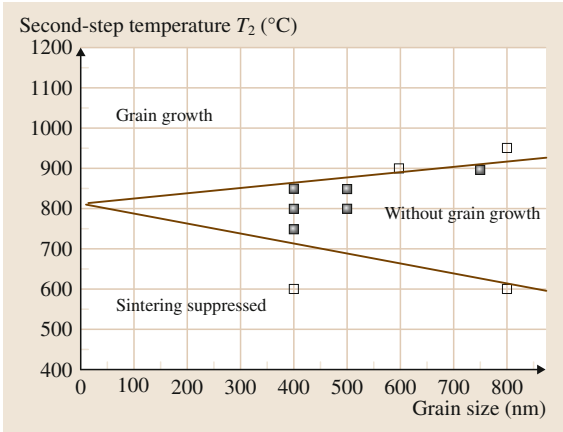


Fig. 14.11 Kinetic window for reaching full density without grain growth for BSPT ceramics (after [14.7])

rate, and the applied pressure during sintering [14.50–52], have already been proved for numerous materials. Extensive research has been carried out on sintering of piezoelectric ceramics, most of which include lead [14.53–57]. This method has also been used for BSPT ceramic sintering. In 2009 *Algueró* et al. [14.42] prepared BSPT ceramics with average grain size of 80 nm via SPS, and in 2010 *Amorín* et al. [14.41] reported that the average grain size could be decreased to 28 nm. However, possibly due to the activation of particle surface and the high ion mobility during the SPS process, the grain size of BSPT ceramic is very sensitive to the sintering temperature and mechanical pressure, thus being difficult to control. When the sintering temperature was increased from 650 °C to 800 °C, the grain size increased almost five times, from 80 to 375 nm [14.41].

A combination of SPS and the two-step sintering technique was explored to obtain BSPT nanoceramics with grain size ≤ 100 nm. Firstly, BSPT nanopowders with $x = 0.63$ prepared by the sol–gel method are filled in a cylindrical graphite die and heated up in a SPS equipment to a certain final temperature in 4–5 min with mechanical axial pressure of 50 MPa, holding at this temperature for 3 min. Subsequently, the as-prepared SPS sample is taken out from the graphite die and sintered in an ordinary furnace using the two-step sintering method.

Appropriate sintering schedules are chosen to vary the grain sizes of the ceramic samples, as presented in Table 14.2. Since the initial density of the SPS samples is much higher, the first-step temperature T_1 can be decreased significantly. As discussed previously, the grain growth mainly happens in the first step of the two-step sintering method, and the samples can achieve densification with less or no grain growth at a relatively low T_1 temperature. Finally, the samples are held at T_2 to eliminate the residual pores that reach the critical size and are unstable. All these factors ensure minimum grain growth during sintering and full densification of the ceramic.

Figure 14.12 shows a comparison of density of the SPS samples ($x = 0.63$ close to MPB) before and after two-step sintering. Before two-step sintering, the

Table 14.2 Sintering parameters for the combination of SPS and two-step sintering

	SPS				Two-step sintering			
BSPT sample ($x = 0.63$)	Heating rate (°C/min)	T_S (°C)	Holding time t (min)	Mechanical pressure (MPa)	T_1 (°C)	T_2 (°C)	Holding time t (h)	GS_A (nm)
ST1	150	650	3	50	800	750	6	70
ST2	175	700	3	50	800	750	6	33
ST3	150	600	3	50	900	750	6	23

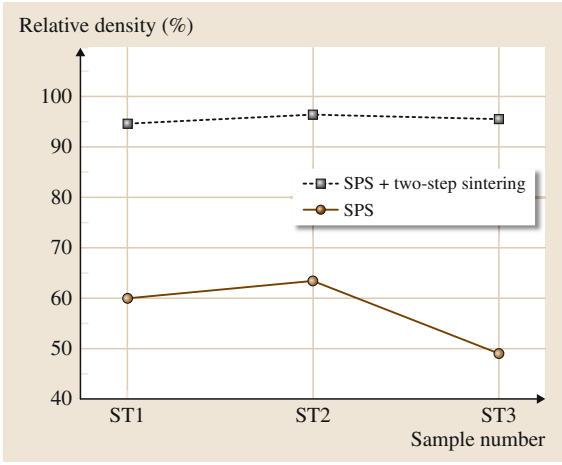


Fig. 14.12 Density change of SPS samples before and after two-step sintering

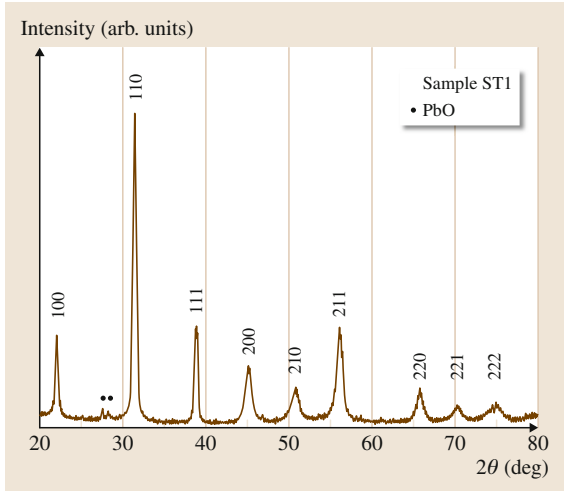


Fig. 14.13 XRD pattern of sample ST1 with grain size of 70 nm

BSPT samples can achieve relative density of 50–60%, about 15–25% higher than pellets ordinarily prepared under uniaxial mechanical pressure. There is an increase of about 35–45% in relative density for the SPS samples sintered by the two-step sintering method.

Since the first-step temperature T_1 is much lower than that for sintering of BSPT ceramics prepared by the ordinary method, grain growth can be suppressed further.

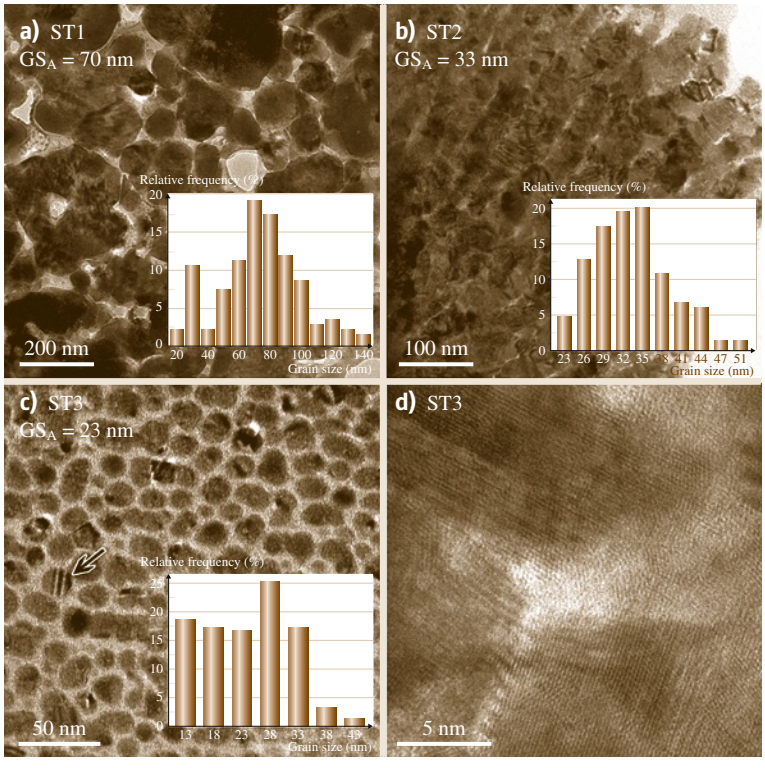


Fig. 14.14 TEM morphologies and grain size distributions of samples ST1, ST2, and ST3

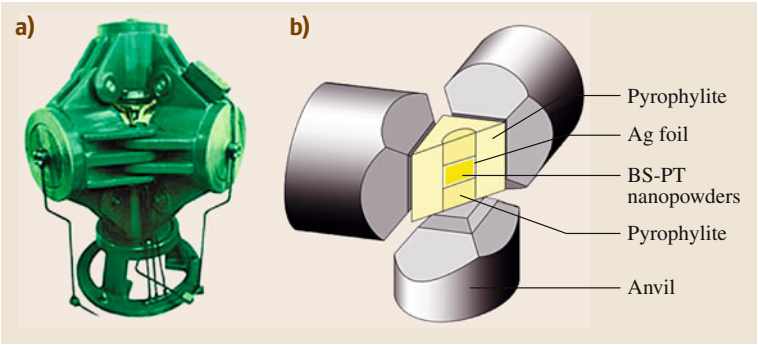


Fig. 14.15 **(a)** Photo of the UHP molding apparatus. **(b)** Schematic diagram of the internal setup of the apparatus

The XRD pattern of sample ST1 is shown in Fig. 14.13. The pattern can be well indexed according to the pseudocubic phase with a ≈ 4 Å unit cell, demonstrating the pure perovskite single phase of the sample. From the composition phase diagram of BSPT solution [14.13, 58, 59], the actual phase of the samples ($x = 0.63$) is rhombohedral. However, since the grain size is small, the XRD peaks are so significantly broadened that the characteristic peak splitting is masked and the pattern seems like that of the cubic phase.

The micromorphology of samples ST1, ST2, and ST3 was observed by TEM (Fig. 14.14). For TEM observation, samples were first prepared by polishing ceramics down to thickness of approximately 35 μm, followed by ion-beam thinning to electron transparency. The grain size distribution was obtained by measuring Feret's diameters of more than 150 grains for each sample. Based on these statistical data, the average grain size (GS_A) was calculated and is shown in Fig. 14.14a–c. It is noteworthy that the grain boundary region in Fig. 14.14c seems very *thick* and disordered. However, when observed under higher magnification, these *thick* regions show a clear lattice image and the grain boundaries are much *thinner* (Fig. 14.14d). It can be concluded that all three samples prepared by the combination of spark plasma sintering and two-step sintering are highly dense with homogeneous nanograin microstructures as fine as 23 nm.

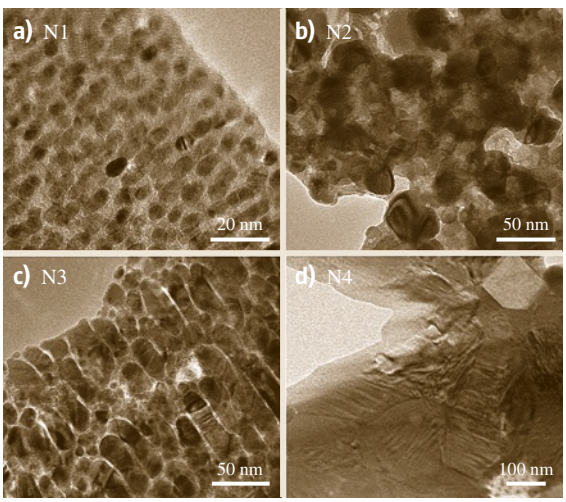


Fig. 14.16a–d TEM morphologies of sample **(a)** N1 (11 nm), **(b)** N2 (21 nm), **(c)** N3 (33 nm), and **(d)** N4 (114 nm)

14.3.3 Ultrahigh-Pressure (UHP) Forming and Two-Step Sintering

With the combination of the advantages of the SPS method and the two-step sintering method, BSPT samples with average grain size ranging from 23 to 70 nm have been obtained. However, to achieve the relative density of 50–60% needed for the subsequent two-step sintering, a certain sintering temperature $T_s \geq 600\,^{\circ}\mathrm{C}$ for SPS is required, and there is still considerable grain growth during the SPS process. Therefore, it is beyond the capability of this combined method to prepare BSPT nanoceramics with small grain size < 20 nm from starting powders of about 8–10 nm. Other strategies that can achieve higher initial green density with no grain growth are in great demand. The ultrahigh-pressure (UHP) molding method featuring extremely high pressures up to several GPa provides an opportunity.

These experiments were carried out using a cubic anvil-type apparatus. A picture and schematic diagram of the internal setup of the apparatus are shown in Fig. 14.15. BSPT nanopowders with MPB composition were encapsulated with Ag foil and then placed in the center of a solid cube made of pyrophyllite which acts as the pressure medium. The Ag foil is used to prevent

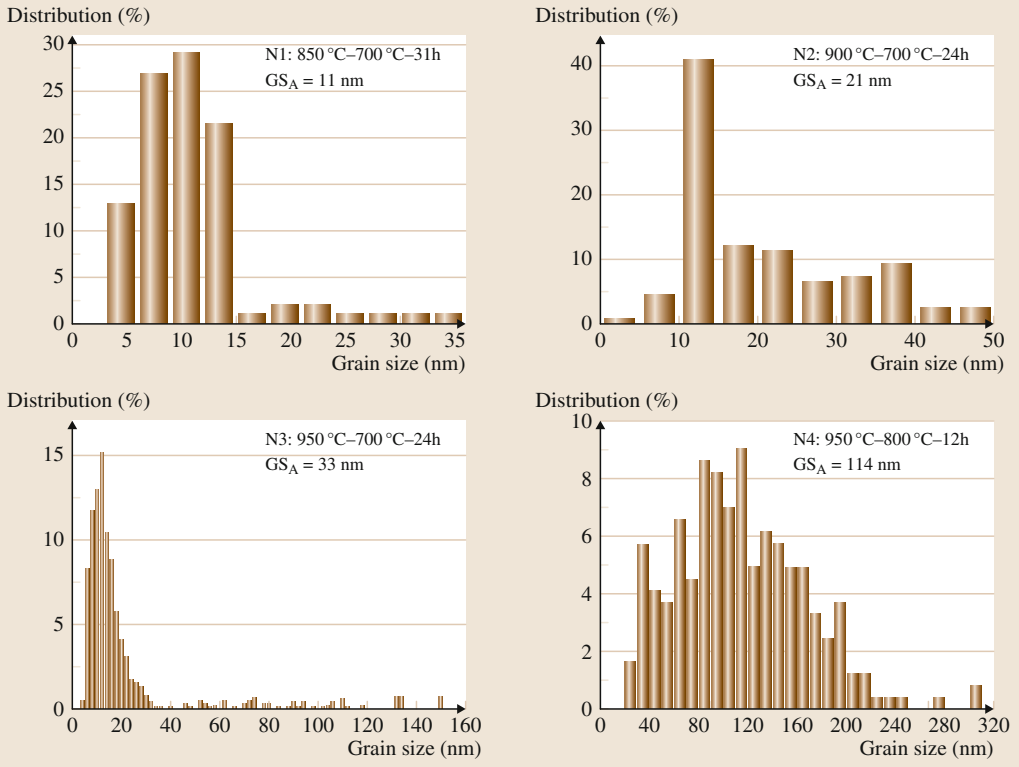


Fig. 14.17a–d Grain size distribution of sample **(a)** N1, **(b)** N2, **(c)** N3, and **(d)** N4

mixing of the pyrophyllite and BSPT powder. During the pressing process, six anvils squeeze the six faces of the solid cube with the same pressure in order to make BSPT nanopowders inside the solid cube experience the same pressure from six different directions. The BSPT nanopowders are held at the highest pressure of ≈ 5.5 GPa for 15 min at room temperature. Finally, BSPT green ceramics with high relative density of about 74% can be obtained.

The as-prepared green ceramic pellets are then sintered using the two-step sintering method. The parameters of the sintering schedule are presented in Table 14.3. The densities of the fired ceramic samples are measured by the Archimedes method using distilled water, and the relative densities calculated by dividing the measured densities by the theoretical density.

The TEM morphologies of the four samples are shown in Fig. 14.16. From the TEM images, it can be seen that the fired ceramics show very uniform microstructures. Sample N1 has the finest grain size, ranging from 6–10 nm, which is almost the same as the particle size of the starting nanopowder. It has been proved that the two-step sintering method without grain growth is powerful for fabricating 10 nm bulk dense ceramics. Similar to the micromorphologies of the samples prepared by the combination of SPS and the two-step sintering method in Fig. 14.14, samples N1, N2, and N3 seem to have *thick* grain boundaries, which

Table 14.3 Two-step sintering schedule for samples prepared by UHP molding

Sample	T_1 (°C)	T_2 (°C)	Holding time, t (h)	Relative density (%)	GS$_A$ (nm)
N1	850	700	31	90.0	11
N2	900	700	24	90.6	21
N3	950	700	24	92.6	33
N4	950	800	12	94.0	114

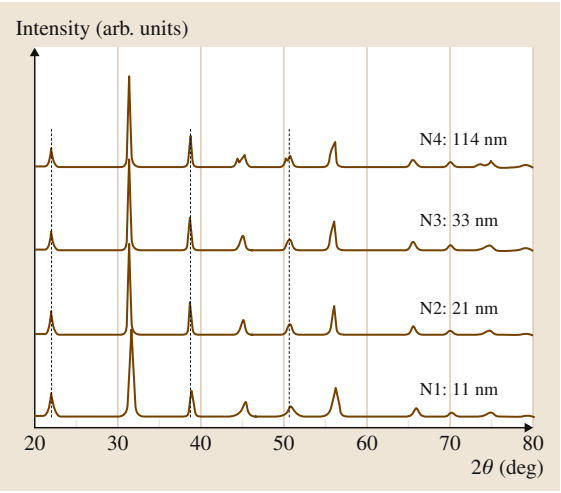


Fig. 14.18 XRD patterns of samples N1–N4

could be due to different types of TEM contrasts under different magnifications. In contrast, when the grain size reaches 114 nm as in sample N4, the grain boundary region seems much *thinner* and is *normal* compared with the morphology usually observed in BSPT ceramics with grain size on the microscale [14.12]. Another noticeable phenomenon is the elongated grains shown in Fig. 14.16c, which is caused by the ultrahigh axial pressure applied during the green ceramic molding process.

The grain size distribution was obtained by measuring Feret's diameters of more than 200 grains, and the average grain size calculated for each sample is shown in Fig. 14.17. The four samples N1–N4 have average grain size of 11, 21, 33, and 114 nm, respectively. Comparing the sintering parameters and grain sizes of samples N1–N4, the average grain size increases slightly with the first-step temperature T_1, but is very sensitive to the second-step temperature T_2 because of the long heating time in the second step, which is consistent with the trends shown in Fig. 14.10. So, the optimal parameter of two-step sintering is strict in the BSPT system due to the volatile elements Bi and Pb. With increasing sintering temperature, the distribution of grain sizes becomes wider.

XRD patterns of samples N1, N2, N3, and N4 are shown in Fig. 14.18. Similar to the XRD pattern of sample ST1 with grain size of 70 nm shown in Fig. 14.13, the XRD peaks of samples N1, N2, and N3 do not show the splitting characteristic which is commonly observed in BSPT ceramics with coarse grains [14.13]. This is because of the peak broadening due to the small grain size effect. When the grains grow up to 114 nm or more, the peak splitting appears. With decreasing grain size, the peak position moves towards higher angles. This might be caused by the decrease of lattice parameters and lattice spacing with the reduction of the grain size. According to Bragg's equation, $2d \sin\theta = n\lambda$, when the lattice spacing decreases, the Bragg angle θ will increase, which means that the peak position moves towards higher angle. Without considering the unique characteristics of the peak profiles and positions in the BSPT nanoceramics, the perovskite structure is confirmed for all the samples. The full-pattern XRD refinement results show that even the finest, 11 nm BSPT ceramic consists of two phases, tetragonal and monoclinic, with phase fractions of 23% and 77%.

14.4 Grain Size Effect on the Properties of BSPT Ceramics

Early studies already noted that, for coarse $BaTiO_3$ ceramics, the relative permittivity decreases with grain size and reaches a maximum at average grain size of approximately 1 μm [14.60]. Various assumptions and models have been used to explain the observed phenomenon, including the internal stress model [14.32, 61], distribution model [14.62], domain size effect [14.60], etc. However, the dielectric properties of the piezoelectric ceramic BSPT system have rarely been reported until now, especially the dependence of the dielectric properties on grain size at the nanoscale.

14.4.1 Dielectric Properties

Figure 14.19 shows dielectric–temperature curves of MPB BSPT ceramics with different grain sizes, ranging from 11 nm to 1.5 μm. The dielectric anomaly associated with the ferroelectric transition is clearly observed for all the samples, but is strongly flattened and broadened for the ceramics with smaller grain size (as shown in Fig. 14.19b). The dielectric constant peak at 100 kHz significantly decreases when the grain size reduces from 1.5 μm to 11 nm. The nanoceramics show lower di-

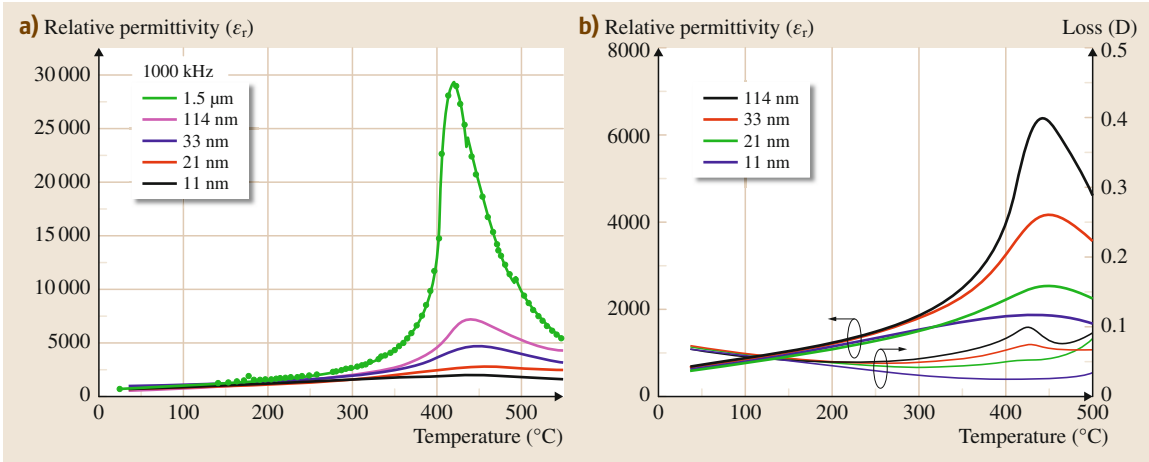


Fig. 14.19a,b Grain size effects on dielectric properties of BSPT ceramics. **(a)** Dielectric constant–temperature curves for grain size ranging from nano- to micrometer. **(b)** Dielectric constant–temperature curves for different nanoscale grain sizes

electric constant and a smeared transition as the grain size decreases. However, the Curie temperature (ferroelectric transition temperature) for the nanoceramics ($T_c = 437\,°C$) is less sensitive to the change of grain size, almost the same as for the coarse ceramics. As suggested by *Buscaglia* et al. [14.39], a wide distribution of grain sizes over the volume of nanoceramics leading to different local polarizations and Curie temperatures T_c might correspond to the broadening of the dielectric–temperature peaks of nanoceramics.

14.4.2 Ferroelectric Property

The ferroelectric property is the most important characteristic of piezoelectric ceramics. Figure 14.20 shows polarization–electric field hysteresis loops for MPB BSPT ceramics with different grain sizes. In Fig. 14.20a, square loops close to saturation are obtained for BSPT ceramics with grain size $\geq 114\,nm$. However, when the grain size is less than 100 nm, polarization switching is strongly suppressed and the loops become narrow. Both the remnant polarization and coercive field decrease with the reduction of grain size. Similar results were observed for MPB BSPT ceramics prepared by SPS sintering by *Amorin* et al. [14.8] (Fig. 14.20b). In addition, unlike the behavior of BSPT nanoceramics with average grain size of 114 nm in Fig. 14.20d, on increasing the electric field applied to the BSPT nanoceramics with grain size of 11 nm, no square loops can be achieved even at the maximum electric field of 60 kV/cm (Fig. 14.20c). This indicates incomplete polarization switching. Two factors should be considered in such macropolarization behavior in nanoceramic BSPT. As the grain size reduces to the nanoscale, the volume of grain boundary grows rapidly. During polarization switching, most of the electric field applied to the nanoceramics is shared by the grain boundaries because of their high resistivity. The electric field applied to the grains is insufficient to switch the domain walls [14.8]. On the other hand, the domain walls are pinned by the grain boundary and defects, thus like *frozen* [14.36]. The energy needed to switch the domain walls increases, and the electric field is now inadequate. Considering all these factors, polarization switching is difficult (or even impossible) under common electric fields used for coarse ceramics. However, the existence of a ferroelectric phase in the nanocrystalline BSPT ceramics with grain size as fine as 11 nm at room temperature has been proved by the polarization-reversal characteristics according to the measurement of hysteresis loops.

14.4.3 Piezoelectric Property

To investigate the size effect on the piezoelectric property, we prepared samples of BSPT ceramics with MPB composition using nanopowders and the two-step sintering method.

Macroscopic Piezoelectric Response

The variation of the macroscopic piezoelectric coefficient (d_{33}) as a function of grain size in MPB

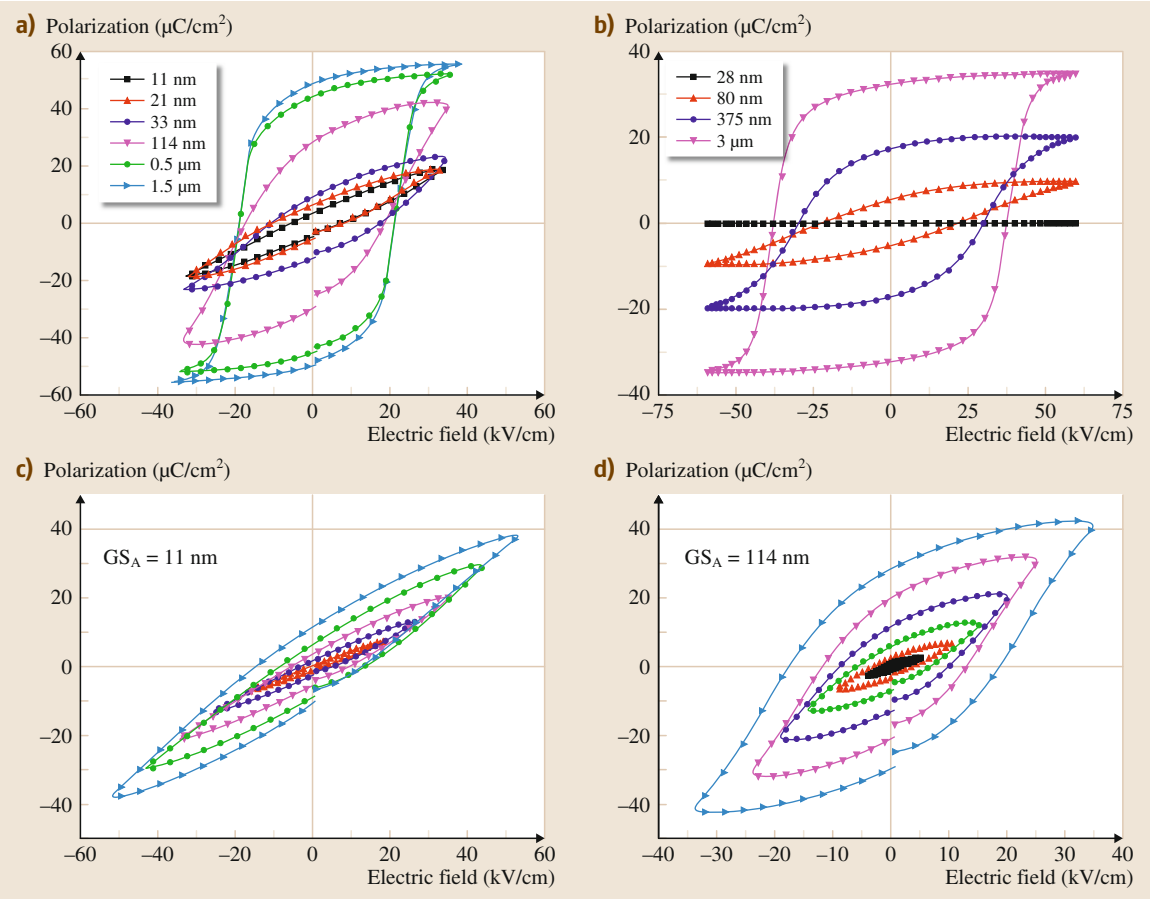


Fig. 14.20 **(a)** Grain size effects on the hysteresis loops for BSPT ceramics obtained by the two-step sintering method. **(b)** Grain size effects on the hysteresis loops for BSPT ceramics obtained by SPS (after [14.41]). **(c,d)** Hysteresis loops for BSPT ceramics produced by two-step sintering with grain size of 11 and 114 nm, respectively

BSPT ceramics is shown in Fig. 14.21. There is a maximum value of $d_{33} = 700\,\mathrm{pC/N}$ at grain size of around 1.5 μm [14.8], which is much higher than that (450 pC/N) of coarse-grained BSPT ceramics prepared by the conventional method, and d_{33} decreases with decreasing grain size. However, in the submicrometer range of 200–1000 nm, d_{33} can maintain a very high value, with a drastic increase of d_{33} (620 pC/N) for grain size decrease from 500 to 300 nm. The enhanced piezoelectric activity at the MPB is usually explained in terms of its intermediate structure between the rhombohedral and tetragonal phases. As a result, there may be more crystallographic directions suitable for polarization, facilitating piezoelectricity. On the other hand, nanosized domains have also been suggested to contribute to enhanced piezoelectricity [14.63–65]. In our study, the piezoelectric force microscopy (PFM) image reveals a fine domain structure, with probably 90° domains having width of 60–70 nm [14.8]. Using computer simulation, *Ahluwalia* et al. [14.63] investigated the domain-size dependence of the piezoelectric properties of a model ferroelectric, and their results showed that the piezoelectric coefficient is enhanced by reducing the domain size. Supporting experimental evidence was observed by *Wada* et al. [14.64] in barium titanate single crystals and *Takahashi* et al. [14.65] in microwave-sintered $BaTiO_3$ ceramics, correlating superior piezoelectric properties to small domain sizes. Therefore, the superior piezoelectric properties of the MPB ($x = 0.635$) ceramic could be a result of both the MPB composition and the small domain size, although further experiments

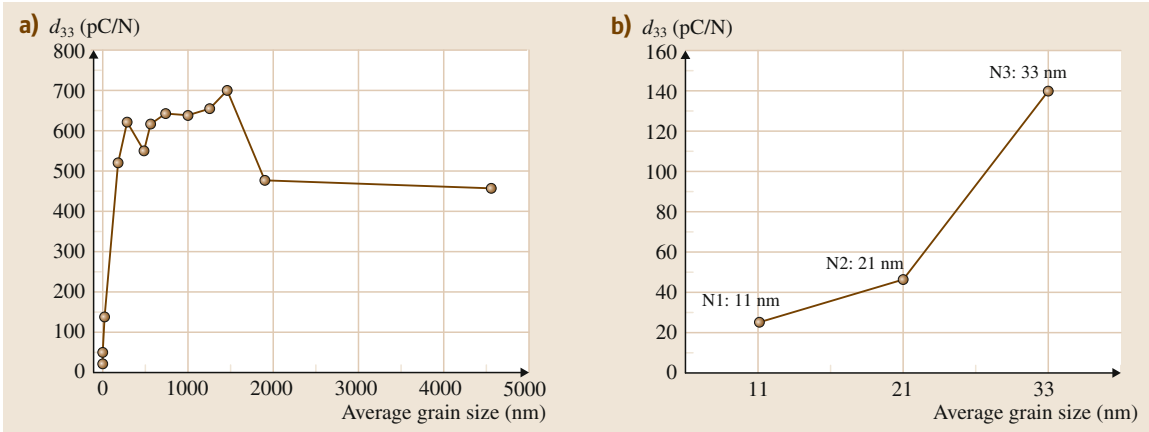


Fig. 14.21a,b Grain size effect on the macroscopic piezoelectric properties of BSPT ceramics: **(a)** from micro- to nanoscale; **(b)** nanoscale

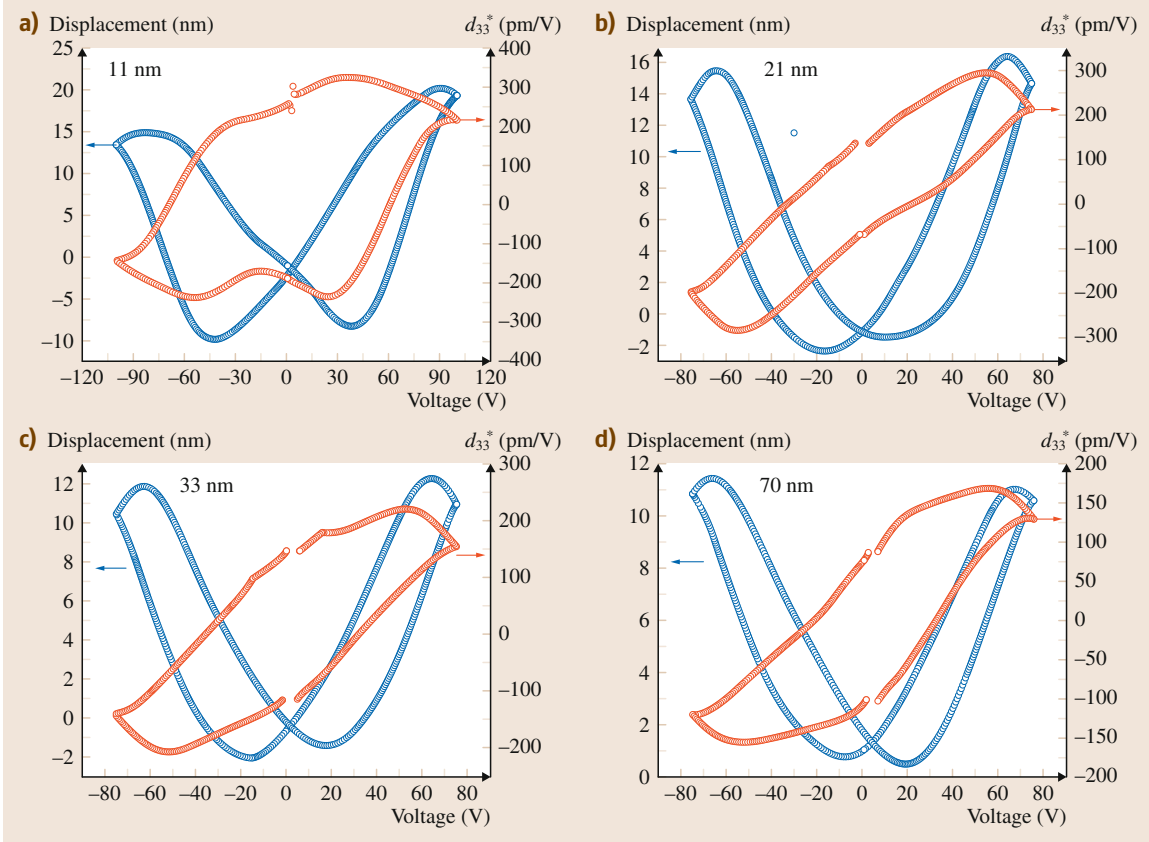


Fig. 14.22a–d Local piezoelectric response versus applied voltage for BSPT nanoceramics of various grain sizes: 11 nm **(a)**, 21 nm **(b)**, 33 nm **(c)**, and 70 nm **(d)**. Displacement–voltage ($Z-V$) loops (*blue curves*); piezoelectric hysteresis loops (*red curves*)

separating these two effects are required to verify this hypothesis.

Moreover, with the grain size reducing to the nanoscale (less than 100 nm), the fraction of the grain boundary and internal stress will increase rapidly, inhibiting realignment of the nanodomains. The grain boundary shares more voltage, leading to insufficient polarization of the grain *core*. Considering all these factors, polarization switching for nanoceramics is difficult under the same common electric field (40 kV/cm) used for coarse ceramics, so that the macroscopic piezoelectric property d_{33} measured by quasistatic piezoelectric coefficient testing shows a smaller value (Fig. 14.21b).

Local Piezoelectric Response

To investigate the local piezoelectric response for BSPT nanoceramics, scanning probe microscopy (SPM) was used in our study. Local nanoscale piezoresponse AFM and piezoelectric force microscopy (PFM) were carried out using a SPM system (AFM, SPI3800N&SPA400; Seiko, Tokyo) by inducing mechanical oscillations with an alternating-current (AC) voltage at 5.0 kHz applied to the tip of a microcantilever (SI-DF3-R, Rh coated) with spring constant of 1.9 N/m and free resonance frequency of 28 kHz. For this measurement, the sample was polished and glued to a conductive substrate serving as a bottom electrode connected to ground.

Measurements were carried out by keeping the SPM tip at fixed height above the surface of the samples and applying a bias voltage from -100 to $+100$ V over the small AC excitation voltage while recording the piezoresponse signal (displacement). Typical well-shaped *butterfly* displacement–voltage ($Z-V$) loops for BSPT nanoceramics were recorded (Fig. 14.22, blue curves). The effective piezoelectric coefficient d^*_{33} can be derived from the slope of the displacement versus voltage, exhibiting a piezoelectric hysteresis loop curve (Fig. 14.22, red curves). A ferroelectric state for BSPT nanoceramics with average grain size as small as 11 nm has been confirmed. Fifty different regions were chosen randomly on each sample, and $Z-V$ curves at these regions were measured, considering the variations

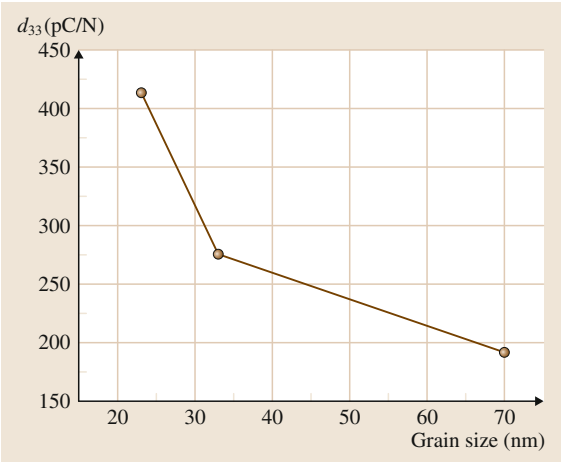


Fig. 14.23 Grain size effect on the microscopic piezoelectric properties of BSPT nanoceramics

in the local piezoelectric response among different regions which are common in $BaTiO_3$ [14.38]. The mean effective piezoelectric coefficient for each sample was calculated by averaging values obtained from the 50 curves.

The grain size effect on the mean values of the local effective piezoelectric coefficient d^*_{33} is shown in Fig. 14.23. In contrast to the trend of macroscopic d_{33} for nanoceramic BSPT shown in Fig. 14.21b, the local effective piezoelectric coefficient d^*_{33} was found to increase with reduction of grain size. This can be explained by the different polarization degrees caused by SPM measurement and the microscopic poling process, as suggested by *Buscaglia* et al. [14.39]. As discussed previously, in the macroscopic poling process, the voltage applied to the nanograin ceramic samples cannot reach the high value required for domain switching due to the pinning effect of grain boundaries and defects, or it may cause dielectric breakdown of the samples. However, during SPM measurement, the electric field could be very high in the microregion under the cantilever tip, leading to full switching of the nanodomains and resulting in the higher piezoelectric response.

14.5 Summary

Highly dense BSPT morphotropic phase boundary ceramics with average grain size from micrometer scale to 10 nm have been successfully prepared by the two-step sintering or modified two-step sintering method. Maximal piezoelectric constant d_{33} of 700 pC/N was achieved with grain size around 1.5 μm due to the high density and fine domain size. The size effect on the microstructures and piezoelectric behavior of BSPT

nanoceramics was investigated and characterized by means of XRD, HRTEM, AFM, SPM, and hysteresis-loop and dielectric measurements. The dielectric anomaly associated with the ferroelectric transition is clearly observed for all the samples, but is strongly flattened and broadened for ceramics with smaller grain size. The existence of ferroelectrics in nanocrystalline ceramics as fine as 10 nm has been proved by the polarization-reversal characteristics according to the measurement of hysteresis loops as well as the local ferroelectric switching behavior investigated by piezoresponse force microscopy. When the grain size reduces to less than 100 nm, polarization switching is strongly suppressed, leading to small macroscopic piezoelectric constants. However, BSPT nanoceramics present very strong local piezoelectricity as observed by SPM.

References

14.1 R.E. Eitel, C.A. Randall, T.R. Shrout, P.W. Rehrig, W. Hackenberger, S.E. Park: New high temperature morphotropic phase boundary piezoelectrics based on $Bi(Me)O_3$–$PbTiO_3$ ceramics, Jpn. J. Appl. Phys. **40**(10), 5999 (2001)

14.2 J. Chaigneau, J.M. Kiat, C. Malibert, C. Bogicevic: Morphotropic phase boundaries in $(BiScO_3)_{(1-x)}(PbTiO_3)_{(x)}$ $(0.60 < x < 0.75)$ and their relation to chemical composition and polar order, Phys. Rev. B **76**(9), 094111 (2007)

14.3 V. Goldschmidt: Skrifter Norske Videnskops-Akad. Oslo, Mat.-Naturv. Kl. **1**, 7 (1926)

14.4 G. Tutuncu, D. Damjanovic, J. Chen, J.L. Jones: Deaging and asymmetric energy landscapes in electrically biased ferroelectrics, Phys. Rev. Lett. **108**(17), 177601 (2012)

14.5 S.W. Gotmare, S.O. Leontsev, R.E. Eitel: Thermal degradation and aging of high-temperature piezoelectric ceramics, J. Am. Ceram. Soc. **93**(7), 1965 (2010)

14.6 A. Sehirlioglu, A. Sayir, F. Dynys: High temperature properties of $BiScO_3$–$PbTiO_3$ piezoelectric ceramics, J. Appl. Phys. **106**(1), 014102 (2009)

14.7 T.T. Zou, X.H. Wang, W. Zhao, L.T. Li: Preparation and properties of fine-grain $(1-x)BiScO_{3-x}PbTiO_3$ ceramics by two-step sintering, J. Am. Ceram. Soc. **91**(1), 121 (2008)

14.8 T.T. Zou, X.H. Wang, H. Wang, C.F. Zhong, L.T. Li, I.W. Chen: Bulk dense fine-grain $(1-x)BiScO_{3-x}PbTiO_3$ ceramics with high piezoelectric coefficient, Appl. Phys. Lett. **93**(19), 192913 (2008)

14.9 I. Grinberg, A.M. Rappe: Nonmonotonic T_C trends in Bi-based ferroelectric perovskite solid solutions, Phys. Rev. Lett. **98**(3), 037603 (2007)

14.10 S. Chen, X.L. Dong, C.L. Mao, F. Cao: Thermal stability of $(1-x)BiScO_{3-x}PbTiO_3$ piezoelectric ceramics for high-temperature sensor applications, J. Am. Ceram. Soc. **89**(10), 3270 (2006)

14.11 Y. Inaguma, A. Miyaguchi, M. Yoshida, T. Katsumata, Y. Shimojo, R.P. Wang, T. Sekiya: High-pressure synthesis and ferroelectric properties in perovskite-type $BiScO_3$–$PbTiO_3$ solid solution, J. Appl. Phys. **95**(1), 231 (2004)

14.12 C.A. Randall, R.E. Eitel, T.R. Shrout, D.I. Woodward, I.M. Reaney: Transmission electron microscopy investigation of the high temperature $BiScO_3$–$PbTiO_3$ piezoelectric ceramic system, J. Appl. Phys. **93**(11), 9271 (2003)

14.13 R.E. Eitel, C.A. Randall, T.R. Shrout, S.E. Park: Preparation and characterization of high temperature perovskite ferroelectrics in the solid-solution $(1-x)BiScO_{3-x}PbTiO_3$, Jpn. J. Appl. Phys. **41**, 2099 (2002)

14.14 S.J. Zhang, C.A. Randall, T.R. Shrout: Dielectric and piezoelectric properties of $BiScO_3$–$PbTiO_3$ crystals with morphotropic phase boundary composition, Jpn. J. Appl. Phys. **43**, 6199 (2004)

14.15 S.J. Zhang, C.A. Randall, T.R. Shrout: Dielectric, piezoelectric and elastic properties of tetragonal $BiScO_3$–$PbTiO_3$ single crystal with single domain, Solid State Commun. **131**(1), 41 (2004)

14.16 S.J. Zhang, C.A. Randall, T.R. Shrout: Electromechanical properties in rhombohedral $BiScO_3$–$PbTiO_3$ single crystals as a function of temperature, Jpn. J. Appl. Phys. **42**, 1152 (2003)

14.17 S.J. Zhang, C.A. Randall, T.R. Shrout: High curie temperature piezocrystals in the $BiScO_3$–$PbTiO_3$ perovskite system, Appl. Phys. Lett. **83**(15), 3150 (2003)

14.18 S.J. Zhang, L. Lebrun, S. Rhee, R.E. Eitel, C.A. Randall, T.R. Shrout: Crystal growth and characterization of new high Curie temperature $(1-x)BiScO_{3-x}PbTiO_3$ single crystals, J. Cryst. Growth **236**(1–3), 210 (2002)

14.19 C.F. Zhong, X.H. Wang, J.A. Fang, L.T. Li: Investigation of thickness dependence of structure and electric properties of sol-gel-derived $BiScO_3$–$PbTiO_3$ thin films, J. Am. Ceram. Soc. **93**(10), 3305 (2010)

14.20 C.F. Zhong, X.H. Wang, H. Wen, L.T. Li, C.W. Nan, Y.H. Lin: Fabrication and properties of epitaxial growth $BiScO_3$–$PbTiO_3$ thin film via a hydrothermal method, Appl. Phys. Lett. **92**(22), 222910 (2008)

14.21 H. Wen, X.H. Wang, C.F. Zhong, L.K. Shu, L.T. Li: Epitaxial growth of sol-gel derived $BiScO_3$–$PbTiO_3$ thin film on Nb-doped $SrTiO_3$ single crystal substrate, Appl. Phys. Lett. **90**(20), 202902 (2007)

14.22 H. Wen, X.H. Wang, C.F. Zhong, L. Shu, L.T. Li: Properties of compositionally graded $BiScO_3$–$PbTiO_3$ thin

films fabricated by a sol–gel process, J. Am. Ceram. Soc. **90**(8), 2441 (2007)
14.23 H. Wen, X.H. Wang, L.T. Li: Orientation control in sol–gel-derived $BiScO_3$–$PbTiO_3$ thin films, J. Am. Ceram. Soc. **90**, 3248 (2007)
14.24 H. Wen, X.H. Wang, X.Y. Deng, T.Y. Sun, L.T. Li: Effect of crystallization process on the ferroelectric properties of sol–gel derived $BiScO_3$–$PbTiO_3$ thin films, J. Appl. Phys. **101**(1), 016103 (2007)
14.25 T. Yoshimura, S. Trolier-McKinstry: Growth and properties of (001) $BiScO_3$–$PbTiO_3$ epitaxial films, Appl. Phys. Lett. **81**(11), 2065 (2002)
14.26 J. Valasek: Piezo-electric and allied phenomena in Rochelle salt, Phys. Rev. **17**(4), 475 (1921)
14.27 J.F. Scott: Applications of modern ferroelectrics, Science **315**(5814), 954 (2007)
14.28 T.Y. Sun, X.H. Wang, H. Wang, X.Q. Zhang, Z.D. Cheng, C.Q. Sun, L.T. Li: A phenomenological model on phase transitions in nanocrystalline barium titanate ceramic, J. Am. Ceram. Soc. **93**(9), 2571 (2010)
14.29 Z.Y. Shen, J.F. Li: Enhancement of piezoelectric constant d_{33} in $BaTiO_3$ ceramics due to nano-domain structure, J. Ceram. Soc. Jpn. **118**(1382), 940 (2010)
14.30 I. Fujii, M. Ugorek, S. Trolier-McKinstry: Grain size effect on the dielectric nonlinearity of $BaTiO_3$ ceramics, J. Appl. Phys. **107**(10), 104116 (2010)
14.31 X.H. Wang, X.Y. Deng, H. Wen, L.T. Li: Phase transition and high dielectric constant of bulk dense nanograin barium titanate ceramics, Appl. Phys. Lett. **89**(16), 162902 (2006)
14.32 S. Lin, T. Lu, C.Q. Jin, X.H. Wang: Size effect on the dielectric properties of $BaTiO_3$ nanoceramics in a modified Ginsburg–Landau–Devonshire thermodynamic theory, Phys. Rev. B **74**(13), 134115 (2006)
14.33 X.Y. Deng, X.H. Wang, H. Wen, L.L. Chen, L. Chen, L.T. Li: Ferroelectric properties of nanocrystalline barium titanate ceramics, Appl. Phys. Lett. **88**(25), 252905 (2006)
14.34 V. Buscaglia, M.T. Buscaglia, M. Viviani, L. Mitoseriu, P. Nanni, V. Trefiletti, P. Piaggio, I. Gregora, T. Ostapchuk, J. Pokorny, J. Petzelt: Grain size and grain boundary-related effects on the properties of nanocrystalline barium titanate ceramics, J. Eur. Ceram. Soc. **26**(14), 2889 (2006)
14.35 M.T. Buscaglia, M. Viviani, V. Buscaglia, L. Mitoseriu, A. Testino, P. Nanni, Z. Zhao, M. Nygren, C. Harnagea, D. Piazza, C. Galassi: High dielectric constant and frozen macroscopic polarization in dense nanocrystalline $BaTiO_3$ ceramics, Phys. Rev. B **73**(6), 064114 (2006)
14.36 V. Buscaglia, M.T. Buscaglia, M. Viviani, T. Ostapchuk, I. Gregora, J. Petzelt, L. Mitoseriu, P. Nanni, A. Testino, R. Calderone, C. Harnagea, Z. Zhao, M. Nygren: Raman and AFM piezoresponse study of dense $BaTiO_3$ nanocrystalline ceramics, J. Eur. Ceram. Soc. **25**(12), 3059 (2005)
14.37 Z. Zhao, V. Buscaglia, M. Viviani, M.T. Buscaglia, L. Mitoseriu, A. Testino, M. Nygren, M. Johnsson, P. Nanni: Grain-size effects on the ferroelectric behavior of dense nanocrystalline $BaTiO_3$ ceramics, Phys. Rev. B, **70**(2), 024107 (2004)
14.38 L. Mitoseriu, C. Harnagea, P. Nanni, A. Testino, M.T. Buscaglia, V. Buscaglia, M. Viviani, Z. Zhao, M. Nygren: Local switching properties of dense nanocrystalline $BaTiO_3$ ceramics, Appl. Phys. Lett. **84**(13), 2418 (2004)
14.39 M.T. Buscaglia, V. Buscaglia, M. Viviani, J. Petzelt, M. Savinov, L. Mitoseriu, A. Testino, P. Nanni, C. Harnagea, Z. Zhao, M. Nygren: Ferroelectric properties of dense nanocrystalline $BaTiO_3$ ceramics, Nanotechnology **15**(9), 1113 (2004)
14.40 X.H. Wang, R.Z. Chen, Z.L. Gui, L.T. Li: The grain size effect on dielectric properties of $BaTiO_3$ based ceramics, Mater. Sci. Eng. B **99**(1–3), 199 (2003)
14.41 H. Amorin, R. Jimenez, J. Ricote, T. Hungria, A. Castro, M. Alguero: Apparent vanishing of ferroelectricity in nanostructured $BiScO_3$–$PbTiO_3$, J. Phys. D **43**(28), 285401 (2010)
14.42 M. Alguero, H. Amorin, T. Hungria, J. Galy, A. Castro: Macroscopic ferroelectricity and piezoelectricity in nanostructured $BiScO_3$–$PbTiO_3$ ceramics, Appl. Phys. Lett. **94**(1), 012902 (2009)
14.43 I.W. Chen, X.H. Wang: Sintering dense nanocrystalline ceramics without final-stage grain growth, Nature **404**(6774), 168 (2000)
14.44 D.L. Wang, K.J. Zhu, H.L. Ji, J.H. Qiu: Two-step sintering of the pure $K_{0.5}Na_{0.5}NbO_3$ lead-free piezoceramics and its piezoelectric properties, Ferroelectrics **392**, 120 (2009)
14.45 M. Mazaheri, A. Simchi, F. Golestani-Fard: Densification and grain growth of nanocrystalline 3Y-TZP during two-step sintering, J. Eur. Ceram. Soc. **28**(15), 2933 (2008)
14.46 K. Maca, V. Pouchly, Z.J. Shen: Two-step sintering and spark plasma sintering of Al_2O_3, ZrO_2 and $SrTiO_3$ ceramics, Integr. Ferroelectr. **99**, 114 (2008)
14.47 X.H. Wang, X.Y. Deng, H.L. Bai, H. Zhou, W.G. Qu, L.T. Li, I.W. Chen: Two-step sintering of ceramics with constant grain-size, II: $BaTiO_3$ and Ni–Cu–Zn ferrite, J. Am. Ceram. Soc. **89**(2), 438 (2006)
14.48 X.H. Wang, I.W. Chen: Sintering of nanoceramics. In: *Nanomaterials Handbook*, ed. by Y. Gogotsi (Taylor Francis, New York 2006) pp. 359–382
14.49 H.D. Kim, B.D. Han, D.S. Park, B.T. Lee, P.F. Becher: Novel two-step sintering process to obtain a bimodal microstructure in silicon nitride, J. Am. Ceram. Soc. **85**(1), 245 (2002)
14.50 K. Lu: Sintering of nanoceramics, Int. Mater. Rev. **53**(1), 21 (2008)
14.51 R. Chaim, M. Levin, A. Shlayer, C. Estournes: Sintering and densification of nanocrystalline ceramic oxide powders: A review, Adv. Appl. Ceram. **107**(3), 159 (2008)

14.52 Z.A. Munir, U. Anselmi-Tamburini, M. Ohyanagi: The effect of electric field and pressure on the synthesis and consolidation of materials: A review of the spark plasma sintering method, J. Mater. Sci. **41**(3), 763 (2006)

14.53 T. Hungria, H. Amorin, J. Galy, J. Ricote, M. Alguero, A. Castro: Nanostructured ceramics of $0.92PbZn_{(1/3)}Nb_{(2/3)}O_3$-$0.08PbTiO_3$ processed by SPS of nanocrystalline powders obtained by mechanosynthesis, Nanotechnology **19**(15), 155609 (2008)

14.54 Y.J. Wu, J. Li, X.M. Chen, R. Kimura, K. Kakegawa: Effects of La_2O_3 addition and PbO excess on the transmittance of $PbZrO_3$-$PbTiO_3$-$Pb(Zn_{1/3}Nb_{2/3})O_3$ ceramics by spark plasma sintering, J. Am. Ceram. Soc. **91**(1), 13 (2007)

14.55 L. Zhou, Z. Zhao, A. Zimmermann, F. Aldinger, M. Nygren: Preparation and properties of lead zirconate stannate titanate sintered by spark plasma sintering, J. Am. Ceram. Soc. **87**(4), 606 (2004)

14.56 K. Kakegawa, Y. Kawai, Y.J. Wu, N. Uekawa, Y. Sasaki: Sintering of lead titanate using a spark-plasma-sintering technique, J. Am. Ceram. Soc. **87**(4), 541 (2004)

14.57 T. Takeuchi, M. Takahashi, K. Ado, N. Tamari, K. Ichikawa, S. Miyamoto, M. Kawahara, M. Tabuchi, H. Kageyama: Rapid preparation of lead titanate sputtering target using spark-plasma sintering, J. Am. Ceram. Soc. **84**(11), 2521 (2001)

14.58 R.E. Eitel, S.J. Zhang, T.R. Shrout, C.A. Randall, I. Levin: Phase diagram of the perovskite system $(1-x)BiScO_{3-x}PbTiO_3$, J. Appl. Phys. **96**(5), 2828 (2004)

14.59 Y. Shimojo, R. Wang, T. Sekiya, L.E. Cross, T. Nakamura: MPB phase diagram and ferroelectric properties in the $PbTiO_3$-$BiScO_3$ system, Ferroelectrics **284**(1), 121 (2003)

14.60 G. Arlt, D. Hennings, G. Dewith: Dielectric-properties of fine-grained barium-titanate ceramics, J. Appl. Phys. **58**(4), 1619 (1985)

14.61 W.R. Buessem, L.E. Cross, A.K. Goswami: Effect of 2-dimensional pressure on permittivity of fine- and coarse-grained barium titanate, J. Am. Ceram. Soc. **49**(1), 36 (1966)

14.62 H.T. Martirena, J.C. Burfoot: Grain-size effects on properties of some ferroelectric ceramics, J. Phys. C **7**(17), 3182 (1974)

14.63 R. Ahluwalia, T. Lookman, A. Saxena, W. Cao: Domain-size dependence of piezoelectric properties of ferroelectrics, Phys. Rev. B **72**, 014112 (2005)

14.64 S. Wada, K. Yako, H. Kakemoto, T. Tsurumi, T. Kiguchi: Enhanced piezoelectric properties of barium titanate single crystals with different engineered-domain sizes, J. Appl. Phys. **98**, 014109 (2005)

14.65 H. Takahashi, Y. Numamoto, J. Tani, S. Tsurekama: Lead-free barium titanate ceramics with large piezoelectric constant fabricated by microwave sintering, Jpn. J. Appl. Phys. (Part 1) **45**, 7405 (2006)

15. Graphite Oxide

Wei Gao

This chapter introduces a peculiar carbon compound previously named as graphitic acid, graphite oxide (GO), or more recently, graphene oxide (GO). It is basically a wrinkled two-dimensional carbon sheet with various oxygenated functional groups on its basal plane and peripheries, with thickness of around 1 nm and lateral dimensions varying from a few nanometers to several microns. It was first prepared by the British chemist B.C. Brodie in 1859, and became very popular in the scientific community during the last half decade, simply because it was believed to be an important precursor to graphene (a single atomic layer of graphite, the discovery of which won Andre Geim and Konstantin Novoselov the 2010 Nobel Prize in Physics). Several strategies have been introduced to reduce GO back to graphene; however, in this chapter we mainly focus on GO itself, and more relevantly, its synthesis, chemical structure, physical and chemical properties, and possible applications. We emphasize here that, despite its strong relevance to graphene, GO also has its own scientific significance as a basic form of oxidized carbon and technological importance as a platform for all kinds of derivatives and composites that have already demonstrated various interesting applications. The synthesis recipes include the Brodie and Staudenmaier methods (Sect. 15.1.1), the Hummers method and its modification (Sect. 15.1.2), and the Tour method (Sect. 15.1.3). Section 15.2 covers characterization methods together with chemical structure models as well as physical properties of graphite oxide. In the application section (Sect. 15.3) several examples are given, followed by concluding remarks in Sect. 15.4.

15.1 **Synthesis of Graphite Oxide** 572
15.1.1 Brodie and Staudenmaier Methods 573
15.1.2 Hummers Method and Its Modifications 573
15.1.3 Tour Method and Discussion 574
15.2 **Characterization, Chemical Structure and Properties** 576
15.2.1 Characterizations 576
15.2.2 Chemical Structure 581
15.2.3 Reactivity and Physical Properties 583
15.3 **Applications** 589
15.3.1 Platform for RGOs and GO Derivatives/Composites 589
15.3.2 An Anisotropic Proton Conductor .. 591
15.3.3 Catalyst and an Electron Transparent Window 591
15.4 **Concluding Remarks** 592
References 592

Two-dimensional nanomaterials typically refer to flat or slightly corrugated sheets with nanometer thickness and infinite lateral dimensions, such as graphene, single-layer boron nitride (BN), molybdenum disulfide (MoS_2), etc. The quantum confinement in the thickness direction results in exotic electronic properties and highlighted surface effects that can be useful in sensing, catalysis, and energy storage applications [15.1]. They have attracted tremendous attention recently, since they are one of the major categories in nanoscience that were predicted to be thermodynamically unstable in the free state and have not been well explored. In 2005, *Geim*'s group first reported the experimentally observed room-temperature quantum Hall effect on a real piece of graphene, which was obtained by mechanical exfoliation of highly oriented pyrolytic graphite (HOPG) [15.2, 3]; soon after that, a storm of graphene research dominated the world of carbon nanomaterials science. The term "graphene" then became a new superstar after carbon nanotubes (CNTs) in the carbon world. One of the

biggest challenges in graphene research at that time was large-scale production of graphene, since the first method that *Geim*'s group adapted was both time consuming and extremely low in yield. Different strategies have been introduced, including metal-ion intercalation [15.4], liquid-phase exfoliation of graphite [15.1, 5], chemical vapor deposition (CVD) growth [15.6], vacuum graphitization of silicon carbide (SiC) [15.7], bottom-up organic synthesis of large polycyclic aromatic hydrocarbons (PAHs) [15.8–10], and of course, chemical reduction of GO [15.11, 12]. Each strategy has its own advantages and disadvantages; nevertheless, GO was believed to be one of the most promising pathways to graphene, mainly due to its wet chemical processability and large-scale availability in monolayers.

GO is not a naturally occurring compound, and the history of GO research can be dated back to over 150 years ago. When it was first made by chemical treatments of graphite with potassium chlorate ($KClO_3$) and fuming nitric acid (HNO_3), British chemist *Brodie* named it graphitic acid or graphite oxide [15.13], and after graphene research emerged in 2004, people started calling it graphene oxide. From a chemistry point of view, there is barely any difference between the two. If there has to be, we would refer to a single atomic layer of graphite oxide as graphene oxide. Since most of the experiments on GO were done in wet chemical processes, and people are generally dealing with large amounts of GO flakes in solution, we believe that when GO is dispersed in certain solvents, it is at least partially exfoliated by the solvent molecules, and thus can be referred to as graphene oxide. Otherwise, in solid state, GO powder or GO film is basically graphite oxide. In the following content, we will generally abbreviate both graphite oxide and graphene oxide as GO, since there is really no big difference between them, even in the context of electronic structures and properties (the case is different for graphite and graphene).

In terms of chemistry, GO is a new type of nonstoichiometric macromolecule that is chemically labile and hygroscopic in ambient condition. However, synthesis of GO has evolved and been modified several times with different chemicals such as potassium permanganate, concentrated sulfuric acid [15.14], and even phosphoric acid [15.15], and the resulting compounds differ slightly in their chemical composition depending on the protocol used.

Over the past 150 years, research in GO has been quite limited. Without the recent popularity of graphene, researchers would still be confused about its detailed chemical structure. In the past few years, extensive research has been done to elucidate its chemical composition [15.16, 17], which turns out to be a corrugated carbon sheet with over half of the carbon atoms functionalized with hydroxyl and epoxy groups, and edges partially occupied by hydroxyl, carboxyl, ketone, ester, and even lactol structures. Even with those clarifications, the distribution of these groups and the spatial connectivity remain obscure even today. Chemical reduction of GO to graphene is one of the hottest topics in GO research, and the most commonly accepted reagent is hydrazine, as first introduced by *Ruoff* at UT Austin [15.12]. Pristine GO is an electrical insulator, and after reduction, it becomes electrically conductive. Several orders of magnitude increase in conductivity are usually observed during reduction processes; however, so far all graphene materials derived from GO have much poorer crystallinity [15.18] and carrier mobility than their mechanically cleaved counterparts [15.2, 3]. Thus, researchers would rather name them reduced GO (RGO), chemically modified graphene (CMG), or chemically converted graphene (CCG). For convenience, we will stick to the term RGO for these materials in the following discussion. The harsh chemical oxidation environment in GO synthesis processes actually creates lots of defects and vacancies within the sp^2 carbon lattice, which are almost impossible to recover by subsequent chemical treatments [15.18]. Taking this into account, GO researchers have switched their interest toward GO and RGO applications. Despite its poor crystallinity, GO, RGOs, and their derivatives have shown several promising applications in energy storage, sensing, water purification, electronics, etc. We note that, in literature, some researchers tend to ignore the differences between RGOs and high-quality graphene, and announce their results as graphene properties and applications, while we think it is necessary to put GO and RGOs into different categories and summarize RGO results into a separate chapter from the graphene chapter.

15.1 Synthesis of Graphite Oxide

In this section we introduce four different recipes for GO preparation in chronological order, and discuss and compare their chemical processes and product structures in detail.

Table 15.1 Comparison of chemical compositions of Staudenmaier and Hummers GO (after [15.14])

Method	Carbon (wt%)	Oxygen (wt%)	Water (wt%)	Ash (wt%)	C/O atomic ratio
Acid–permanganate–nitrate (Hummers)	47.06	27.92	22.99	1.98	2.25
Staudenmaier	52.11	23.99	22.22	1.90	2.89

15.1.1 Brodie and Staudenmaier Methods

Brodie prepared the first batch of GO when he was investigating the chemistry of graphite in 1859 [15.13]. When he added $KClO_3$ to a slurry of graphite in fuming HNO_3, he obtained a new batch of compound which later was determined to contain carbon, oxygen, and hydrogen. He washed the batch free from the salts produced in the reaction, dried it at 100 °C, and again put it under an oxidation environment. The appearance of the product changed in the following three repeated treatments, finally resulting in a substance with *light-yellow color* which would not change with any additional oxidation treatment. He emphasized that the product could not be produced by one prolonged treatment and that one had to promote the oxidation process with restoration of the original conditions each time.

According to his elemental analysis, the molecular formula for the final product was $C_{11}H_4O_5$. Weak acidity and mild dispersibility in basic solution were observed; however, reflective goniometric characterization failed due to the small size, limited thickness, and imperfect structure. He also reacted the final product with *protochloride of copper and protochloride of tin* to obtain GO salts, and followed up with detailed analysis of composition and thermal decomposition. Nonetheless, his observations and conclusions were limited by the theories and characterization techniques available at that time, leaving a huge space for work and improvement until today.

One of the earliest improvements on Brodie's work was carried out in 1898 by *Staudenmaier* [15.19, 20]. Two major changes were introduced:

1. Adding concentrated sulfuric acid to improve the acidity of the mixture.
2. Addition of multiple aliquots of potassium chlorate solution to the reaction mixture over the course of the reaction.

These changes led to a highly oxidized GO product (with the same composition as the final product obtained by Brodie) in a single reaction vessel, thus greatly simplifying the GO synthesis process.

However, Staudenmaier's method was both time consuming and hazardous. The addition of potassium chlorate typically lasted over 1 week, and the chlorine dioxide evolved needed to be removed by an inert gas, while explosion was a constant hazard. Therefore, further modification or development of this oxidation process was still worth investigation.

15.1.2 Hummers Method and Its Modifications

Almost 60 years after the introduction of Staudenmaier's strategy, chemists *Hummers* and *Offeman* at the Mellon Institution of Industrial Research developed a different recipe for making GO [15.14]. A water-free mixture of concentrated sulfuric acid, sodium nitrate, and potassium permanganate was prepared and maintained below 45 °C for graphite oxidation. According to their description, the whole oxidation process finished within 2 h, leading to a final product with higher degree of oxidation than Staudenmaier's product (Table 15.1).

However, it was found that Hummers' product usually has an incompletely oxidized graphite core with GO shells, and a preexpansion process is helpful to achieve a higher degree of oxidation. Firstly introduced by *Kovtyukhova* in 1999 [15.21], pretreatment of graphite with an 80 °C mixture of concentrated H_2SO_4, $K_2S_2O_8$, and P_2O_5 for several hours was widely adopted thereafter. The pretreated mixture was diluted, filtered, washed, and dried before the real Hummers oxidation step took place. Other reported modifications also include increase of the amount of potassium permanganate, etc. [15.11]. Nowadays, this modified Hummers method is the most common recipe used for GO preparation (Fig. 15.1). A typical GO product made by this method consists of thin flakes of GO with 1 nm thickness (corresponding to a single layer), and around 1 μm in lateral dimensions on average; meanwhile the chemical composition was determined to be C : O : H = 4 : 2.95 : 2.5 [15.21]. The oxidation degree and yield of GO have been extensively improved when compared with the very first product by Brodie. However, the separation and purification processes in the modified Hummers method are still quite complicated and time consuming.

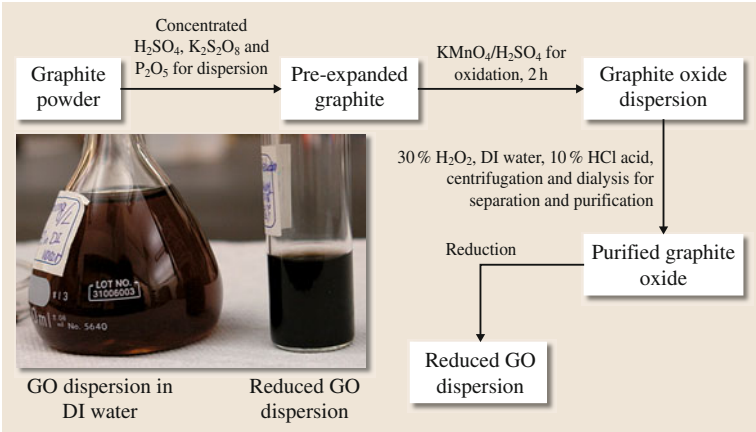


Fig. 15.1 Schematic of the recipe of the most commonly used modified Hummers method for GO preparation [15.11]. *Lower left*: Photograph of the final GO product in deionized (DI) water (*left*) and the dispersion after hydrazine reduction with ammonia (*right*)

15.1.3 Tour Method and Discussion

Tour Method

As the gold rush of graphene research started in 2004, GO jumped into the center of carbon nanomaterials research, and lots of publications have emerged talking about its structure, reduction, and applications. In 2010, a new recipe was introduced by *Tour*'s group at Rice University, which avoided use of sodium nitride and increased the amount of potassium permanganate, and also introduced a new acid into the reaction vessel: phosphoric acid [15.15]. They reported a GO product with higher degree of oxidation made by reacting graphite with six equivalents of $KMnO_4$ in a 9 : 1 mixture of H_2SO_4/H_3PO_4. One of the biggest advantages of this protocol is the absence of $NaNO_3$, thus avoiding generation of toxic gases such as NO_2, N_2O_4, or ClO_2 in the reaction, and making it more environmentally friendly. Furthermore, phosphoric acid is believed to offer more intact graphitic basal planes and the final yield is much higher than with the Hummers method. A comparison among these protocols is shown in Fig. 15.2.

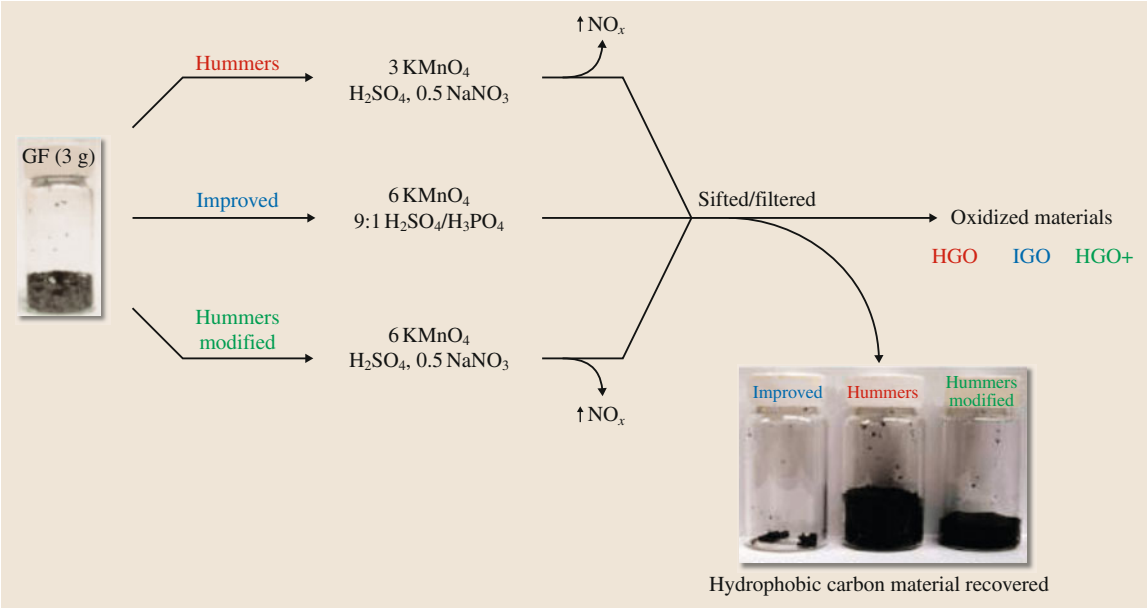


Fig. 15.2 A comparison of procedures and yields among different GO preparation recipes (after [15.15])

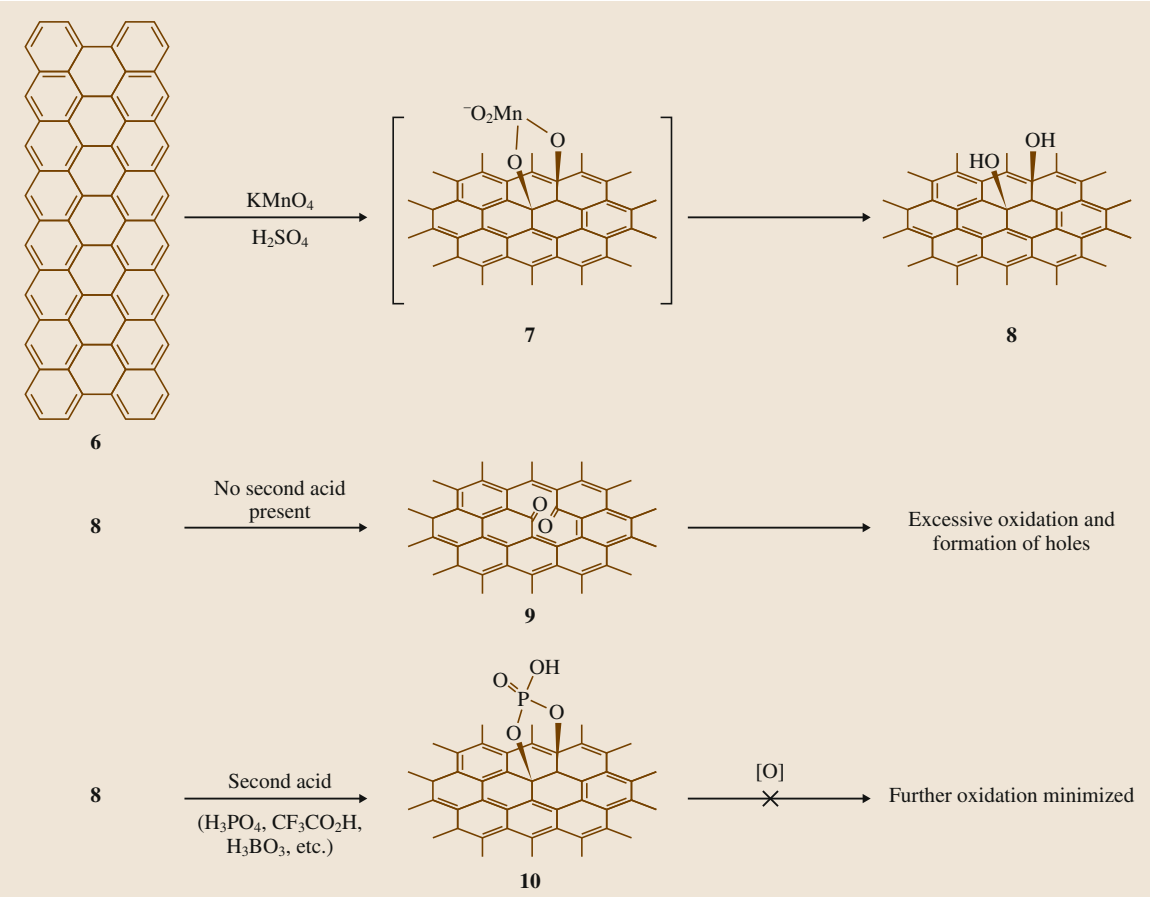


Fig. 15.3 Proposed mechanisms for the effect of the second acid in prevention of overoxidation of the sp^2 carbon network once they have formed the vicinal diols (after [15.22])

Discussion

The source of the graphite is also an important factor in GO fabrication. The most common source of graphite is a naturally occurring mineral which has been purified to remove heteroatomic contaminations such as sulfur and iron. As a result, there must be certain defects in the crystalline structure which could serve as starting sites for chemical oxidation. However, also due to the inherent defects and complexity of the structure, the precise oxidation mechanism in those reactions is hard to elucidate. Besides that, graphite nanofibers have also been used as starting material to make GO, and the resulting GO nanosheets are more uniform in size distribution. The coin-stacked graphene planes along the length of the fibers are believed to play an important role here, and tunability of the GO size by the oxidation time was also observed [15.23].

So far, two different combinations of oxidation reagents have been used to oxidize graphite to GO, including potassium chlorate with nitric acid, and potassium permanganate with sulfuric acid (both acids in the most concentrated state). In literature, nitric acid has been reported to react with aromatic carbon surfaces such as carbon nanotubes [15.24] and fullerenes [15.25], resulting in various oxygenated functional groups such as carboxyls, lactones, and ketones as well as release of toxic gases such as NO_2 and N_2O_4. Similarly, potassium chlorate provides its oxidation capability by in situ generation of dioxygen, which is very reactive [15.26]. When the Brodie and Staudenmaier methods were introduced for GO synthesis, these chemicals were believed to be the strongest oxidizers available. As for the second combination ($KMnO_4$ and H_2SO_4), the permanganate ion is also a typical oxi-

dation reagent. The reactivity of MnO_4^- can only be activated in acidic solution, mainly described by the formation of dimanganese heptoxide from $KMnO_4$ in the presence of strong acid as follows [15.27]:

$$KMnO_4 + 3H_2SO_4 \rightarrow K^+ + MnO_3^+ + H_3O^+ + 3HSO_4^-$$
$$MnO_3^+ + MnO_4^- \rightarrow Mn_2O_7$$

The transformation of MnO_4^- into the more reactive form Mn_2O_7 will certainly help oxidize graphite, but the bimetallic form of manganese oxide has been reported to detonate when heated to 55 °C or when reacted with organic compounds [15.27, 28].

The final acid introduced for GO synthesis is phosphoric acid, which is also believed to have the advantage of offering more intact benzene rings in the basal planes of the final product [15.22]. Figure 15.3 shows a possible explanation for this advantage [15.22]. The formation of the five-membered phosphor ring helps prevent further oxidation of the diols.

Purification is another important but tedious step in GO fabrication, since all of these protocols require long washing, filtration, centrifugation, and dialysis step. It has been reported that GO contaminated with potassium salts is highly flammable, which poses a fire hazard. The volume expansion and gelation observed during water washing of GO significantly slow down the purification process, and substitution with HCl acid and acetone was introduced by *Kim* et al. [15.29].

In summary, at least four different recipes have been introduced in the history of GO synthesis, and improvements in oxidation, simplicity, yield, and product qualities have been demonstrated. Today, making a batch of GO is no longer a problem, which thus has facilitated the rush of GO research; however, we still lack basic understanding of the oxidation processes and detailed mechanisms, which prevents chemically engineering and manipulation of the reaction to tackle critical technology issues, such as bandgap tuning, size distribution control, edge structure selection, etc.

15.2 Characterization, Chemical Structure and Properties

As a unique form of oxidized carbon, GO lies beyond the scope of organic compounds and large polycyclic aromatic hydrocarbons (PAHs), thus making it quite interesting and challenging to characterize the peculiar structure. In this section, we start with a variety of characterization results shown in literature on GO and then try to clarify its molecular structure, electronic states, and chemical reactivity.

15.2.1 Characterizations

Solid-State ^{13}C Nuclear Magnetic Resonance (SSNMR) Spectroscopy

GO sheets are gigantic molecules that fall into the category of colloids. GO dispersions in water are much too concentrated to be analyzed by liquid-phase NMR. In literature, the most powerful and precise technique to characterize GO is solid-state ^{13}C NMR [15.30]. Due to the low natural abundance of ^{13}C (1.1%), the signal-to-noise ratio in the measurement of regular samples is quite low, and long acquisition time is usually required for good-quality data. Therefore, in 2008, *Ruoff* and coworkers prepared a ^{13}C-enriched GO sample and clarified its chemical structure to a new level [15.16]. According to their analysis, cross polarization/magic angle spinning (CP/MAS) experiments displayed three broad resonances at 60, 70, and 130 ppm in the ^{13}C NMR spectrum of GO. Figure 15.4 shows typical one-dimensional (1-D) and two-dimensional (2-D) ^{13}C pulse spectra from a ^{13}C-labeled sample, clearly demonstrating both the chemical structure assignments of the major peaks and the spatial proximity between the sp^2 carbon, epoxy carbon, and hydroxyl carbon atoms (as indicated by the green, blue, and red circles in Fig. 15.4b).

Interestingly, although the isotopical labeling of GO greatly improved the SSNMR analysis resolution, there still remained some unassigned peaks in this work. Later on, further reports came out with more detailed assignments of those peaks, such as a new identification of the 101 ppm peak, which had long been ignored by previous researchers. The 101 ppm peak probably comes from the five- or six-membered-ring lactol structure as shown in Fig. 15.5. Figure 15.6 shows a typical comparison of a ^1H–^{13}C cross polarization spectrum and a direct ^{13}C pulse spectrum obtained from unlabeled GO, with quantitative data on the relative ratio of all these functionalities being 115 (hydroxyl and epoxy):3 (lactol O–C–O):63 (graphitic sp^2 carbon):10 (lactol + ester + acid carbonyl):9 (ketone carbonyl) [15.17].

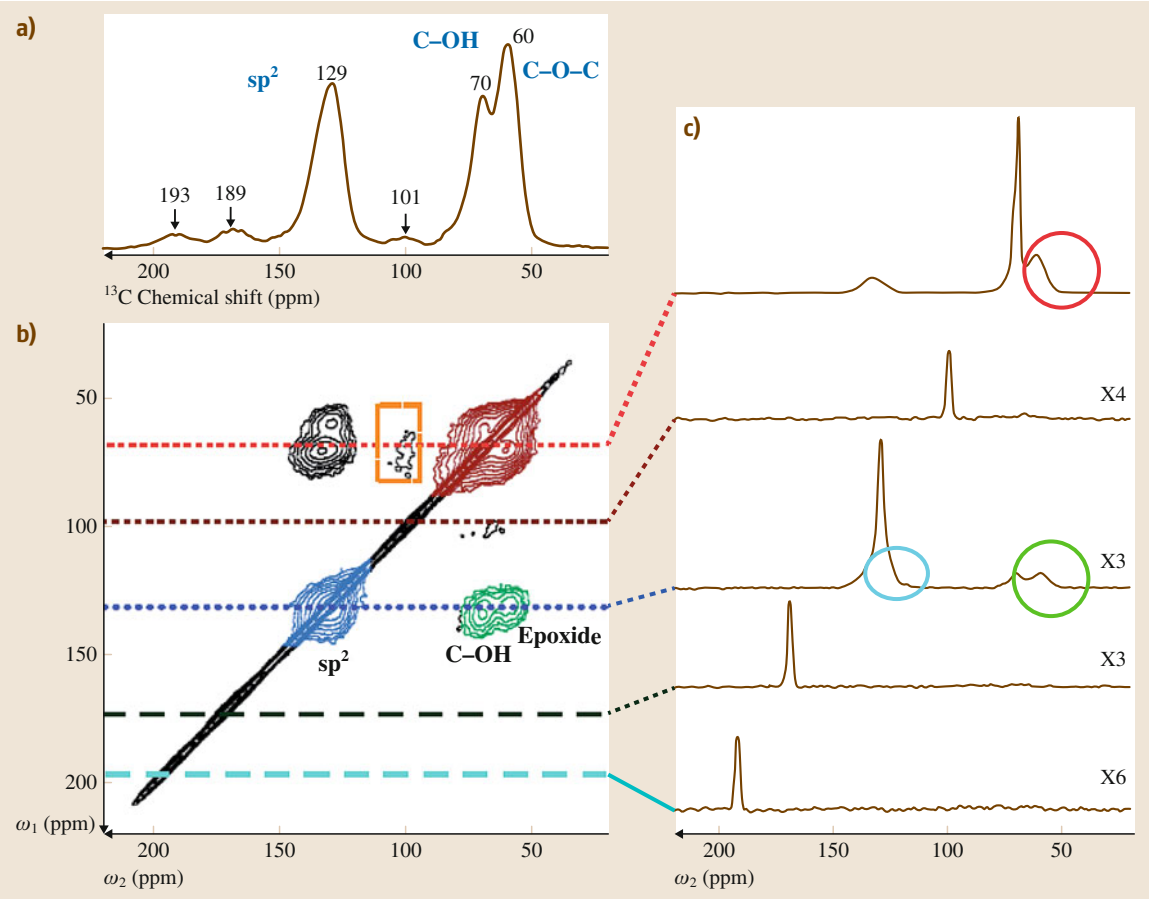


Fig. 15.4 **(a)** 1-D ^{13}C MAS and **(b)** 2-D ^{13}C/^{13}C chemical-shift correlation solid-state NMR (SSNMR) spectra of ^{13}C-labeled graphite oxide with **(c)** slices selected from the 2-D spectrum at the indicated positions (70, 101, 130, 169, and 193 ppm) in the ω_1 dimension. All the spectra were obtained at a ^{13}C NMR frequency of 100.643 MHz with 90 kHz ^{1}H decoupling and 20 kHz MAS for 12 mg of sample. In **(a)**, the ^{13}C MAS spectrum was obtained with direct ^{13}C excitation by a $\frac{\pi}{2}$ pulse. The recycle delay was 180 s, and the experimental time was 96 min for 32 scans. In **(b)**, the 2-D spectrum was obtained with cross polarization and finite-pulse radio frequency-driven dipolar recoupling (fpRFDR) ^{13}C−^{13}C dipolar recoupling sequence. The experimental time was 12.9 h with recycle delays of 1.5 s and 64 scans for each real or imaginary t_1 point. Gaussian broadening of 150 Hz was applied. The *green*, *red*, and *blue areas* in **(b)** and *circles* in **(c)** represent cross peaks between sp^2 and C−OH/epoxide (*green*), those between C−OH and epoxide (*red*), and those within sp^2 groups (*blue*), respectively (after [15.16])

More advanced SSNMR techniques were later used for GO characterization, including 2-D ^{13}C double-quantum/single-quantum (2Q/SQ) correlation SSNMR, 2-D ^{13}C chemical shift anisotropy (CSA)/isotropic shift correlation SSNMR, and 2-D triple-quantum/single-quantum (3Q/SQ) correlation SSNMR [15.31]. The 2Q/SQ spectrum eliminates diagonal signals in the 2-D spectrum, offering a clearer correlation signal between ^{13}C–OH carbon and ^{13}C−O−^{13}C carbon (Fig. 15.7). The 3Q/SQ spectrum offers coherence correlation between three different carbons, thus providing a large amount of information regarding the connectivity between differently functionalized carbon atoms as well as the distribution of those functional groups on GO surfaces. Interestingly, theoretical simulation was used simultaneously to fit these data with a simplified GO

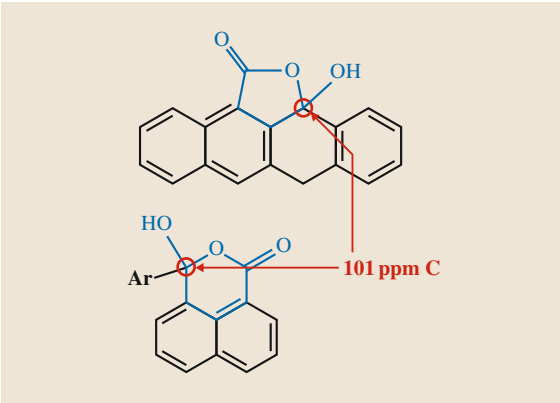


Fig. 15.5 Structure of the five- and six-membered lactol rings. The carbons *circled in red* are those that give ^{13}C NMR signals at 101 ppm (after [15.17])

structural model, and satisfactory fitting was obtained by ab initio calculations with structure model A (with only 1,2-ether) shown in Fig. 15.7d.

All these analyses significantly helped to identify GO's chemical structure, leading to improved clarity in its chemical composition. However, it is also noteworthy to point out here that all those SSNMR characterizations were done on GO samples made by the modified Hummers method, and GO products from other methods do differ in the relative ratio of these functionalities [15.15].

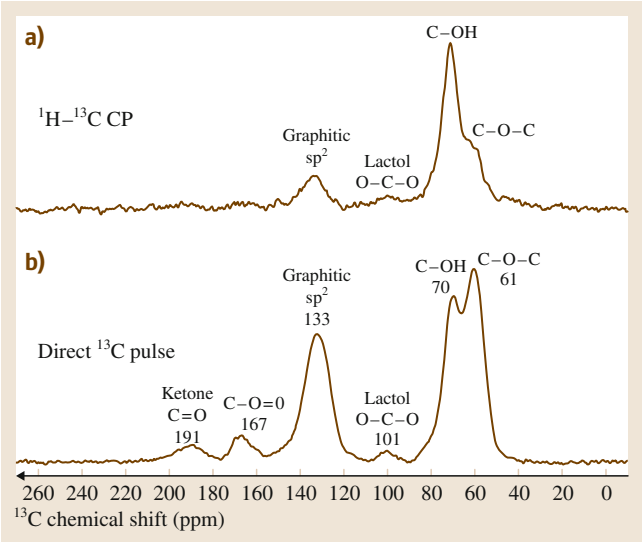


Fig. 15.6a,b $^{1}H–^{13}C$ cross polarization (CP) spectrum of GO obtained with 7.6 kHz MAS and contact time of 1 ms (67 000 scans, **(a)**), and a direct ^{13}C pulse spectrum obtained with 12 kHz MAS and a 90° ^{13}C pulse (10 000 scans, **(b)**). The peak at 101 ppm is caused by the carbons of five- and six-membered-ring lactols (after [15.17])

Diffuse Reflectance Infrared Fourier-Transform (DRIFT) Spectroscopy

Besides SSNMR, DRIFT is another powerful tool to detect chemical functionalities in oxidized carbons [15.32]. For samples of GO, since it is hygroscopic, the large amounts of water molecules adsorbed in the structure have become the biggest obstacle to FTIR analysis. Therefore, in 2005, Dekany and coworkers reported a detailed DRIFT analysis of deuterated GO samples prepared with the Brodie method, and they were able to assign most of the peaks observed in the spectra and distinguish the signals of hydroxyl groups from that of others, thus providing a strong clarification of all the previous debated assignments in GO FTIR spectrum (Fig. 15.8; Table 15.2). Deuterium exchange of GO imposes red-shifts of all hydroxyl-related bands, thus one can easily distinguish between C–OH and COOH stretching vibrations, and a new band was also uncovered around 1384 cm^{-1}, which was hidden in the spectrum of air-dry GO and was attributed to organic carbonates. The possible functional moieties in GO include carboxyl, lactone, phenol, lactol, chromene, ketone, etheric rings, and organic carbonate, but definitely no pyrones [15.32].

Other Characterizations

As a pseudo-ordered structure, the surface of GO is covered nonuniformly with oxygenated groups, leaving approximately 2–3 nm sp^2 carbon clusters isolated within the sp^3 carbon matrix, as can be easily verified by Raman spectroscopy [15.18, 33], scanning tunneling microscopy (STM) [15.34, 35], high-resolution transmission electron microscopy (HR-TEM) [15.36, 37], and transport studies [15.38, 39].

The Raman spectrum of GO basically consists of a broad D peak ($\approx$ 1350 cm^{-1}) and G peak ($\approx$ 1594 cm^{-1}), with a wide weak bump extending from 2681 to 3050 cm^{-1}. The D/G ratio is around 0.95, indicating a large amount of defects within the crystal lattice. However, upon chemical reduction, an increase in the D/G ratio is usually observed, the explanation for which remains ambiguous.

The UV-Vis spectrum of GO in water has two featured peaks around 233 nm due to $\pi-\pi^*$ transition of C=C bonds, and a broad shoulder between 290 and $\approx$ 300 nm assigned to n-to-π^* transition of C=O bonds [15.40]. Upon reduction, a red-shift of the first

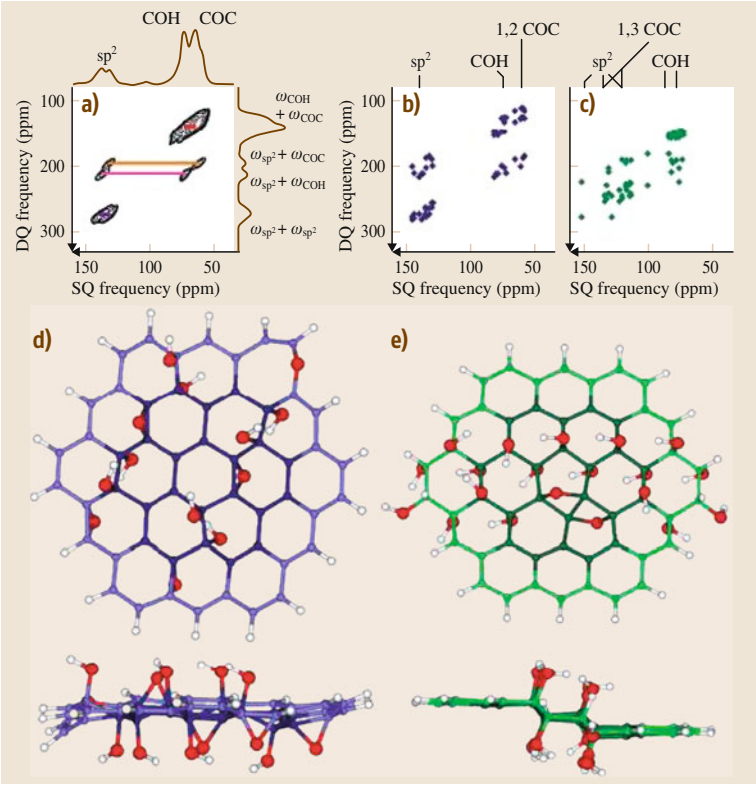


Fig. 15.7 **(a)** Experimental 2-D ^{13}C DQ/SQ correlation SSNMR spectrum of uniformly ^{13}C-labeled GO using ^{13}C–^{13}C J coherence transfer. Fast recycling with short recycle delays of 0.3 s and low-power (7 kHz) decoupling was used. Signal assignments in **(a)** are those made in [15.10] and confirmed here. The carrier frequency was set at 211.17 ppm. **(b,c)** Predicted DQ/SQ correlation spectra based on isotropic chemical shifts calculated for **(b)** model A and **(c)** model B. **(d,e)** Structural models for **(d)** model A and **(e)** model B from the (*top*) top and (*bottom*) side views. Carbons in **(d,e)** are color coded to match the spectra in **(b,c)**. *Red* and *white spheres* denote O and H, respectively. ^{13}C at the edge of the models (*light blue or green*) were not included in **(b,c)**. The calculated spectrum **(b)** based on model A well reproduced the experimental spectrum **(a)** (after [15.31])

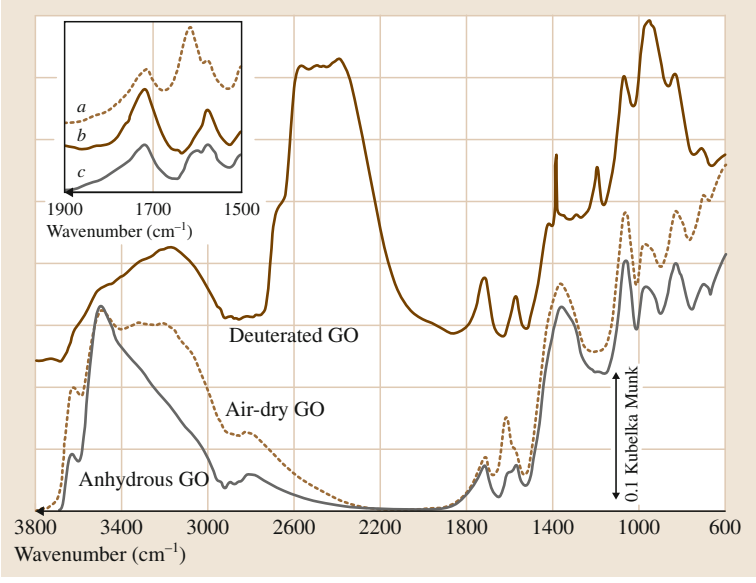


Fig. 15.8a–c DRIFT spectra of graphite oxide (GO) samples. Spectrum of deuterated GO is offset by 0.12 Kubelka–Munk units. The *inset* shows the enlarged 1900–1500 cm^{-1} region of **(a)** air-dry GO, **(b)** deuterated GO, and **(c)** anhydrous GO spectra (after [15.32])

Table 15.2 IR peak positions of air-dry GO (GO/H_2O) and deuterated GO (GO/D_2O) and their assignments. *Asterisks* (in the same row) designate isotopomer peak pairs. Band intensities and widths are classified as: w (weak), m (medium), s (strong), and vs (very strong) and sh (shoulder), vsp (very sharp), sp (sharp), and br (broad), respectively (after [15.32])

GO/H_2O (cm^{-1})	GO/D_2O (cm^{-1})	Assignment	D/H
–	3210 m, br	ν_{OH} in HDO	–
3630∗ m, sp	2680∗ m, sh	ν_{OH} in C−OH/ν_{OD} in C−OD	0.738
3490* s, sp	2568* vs, br	ν_{OH} in C−OH/ν_{OD} in C−OD	0.736
3210* s, br	2396* vs, br	ν_{OH} in H_2O/ν_{OD} in D_2O	0.746
2814 w, br	–	ν_{OH} in dimeric COOH	–
1714 m, sp	1716 m, sp	$\nu_{C=O}$	–
1616* m, sp	1196* m, sp	β_{OH} in H_2O/β_{OD} in D_2O	0.740
1574 w, sh	1574 m, sp	Aromatic $\nu_{C=C}$	–
1368* s, br	968* s, br	β_{OH} in C−OH/β_{OD} in D_2O	0.708
–	1384 m, vsp	Organic carbonate	–
1064	1064	Skeletal modes of ν_{C-C} and ν_{C-O} bonds (m, sp)	–
968	968		–
828	828		–
698	698		–

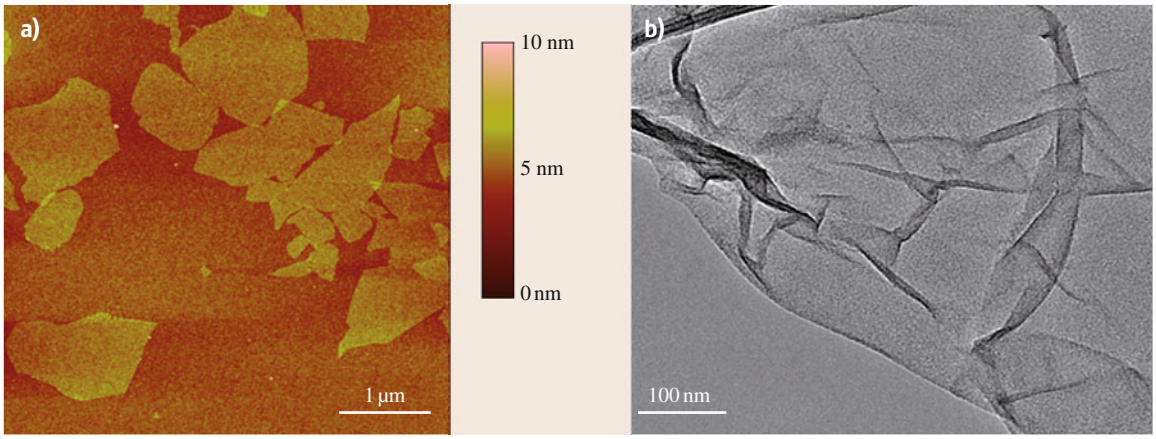


Fig. 15.9 (**a**) AFM and (**b**) TEM images of GO sheets

peak and the disappearance of the second one were usually observed.

x-Ray diffraction (XRD) analysis of GO powder shows a prominent but somewhat broad peak around 11°, the position of which can be easily influenced by the degree of oxidation and hydration of the GO sample, and of course, the humidity level of the atmosphere during the measurement. The reported interlayer distance of GO samples varies from 5.97 Å [15.32] to 9.5 Å [15.15].

x-Ray photoelectron spectroscopy (XPS) analysis of GO powder also offers two broadened and overlapped peaks centered around 284 and 286 eV, corresponding to sp^2 carbon and oxidized carbon, respectively. Some studies try to deconvolute these peaks into different oxidation functionalities, while we think XPS is at most a semiquantitative analysis technique, and this kind of analysis is going beyond the resolution limit of the instrument.

Atomic force microscopy (AFM) and TEM could easily confirm the 2-D nature of GO sheets when they are spin-coated onto a pretreated silicon wafer. The thickness of a GO sheet is typically around 1–2 nm, and the lateral dimensions vary between several hundred nanometers and micrometers. Based on AFM studies, it is believed that sonication results in near-complete

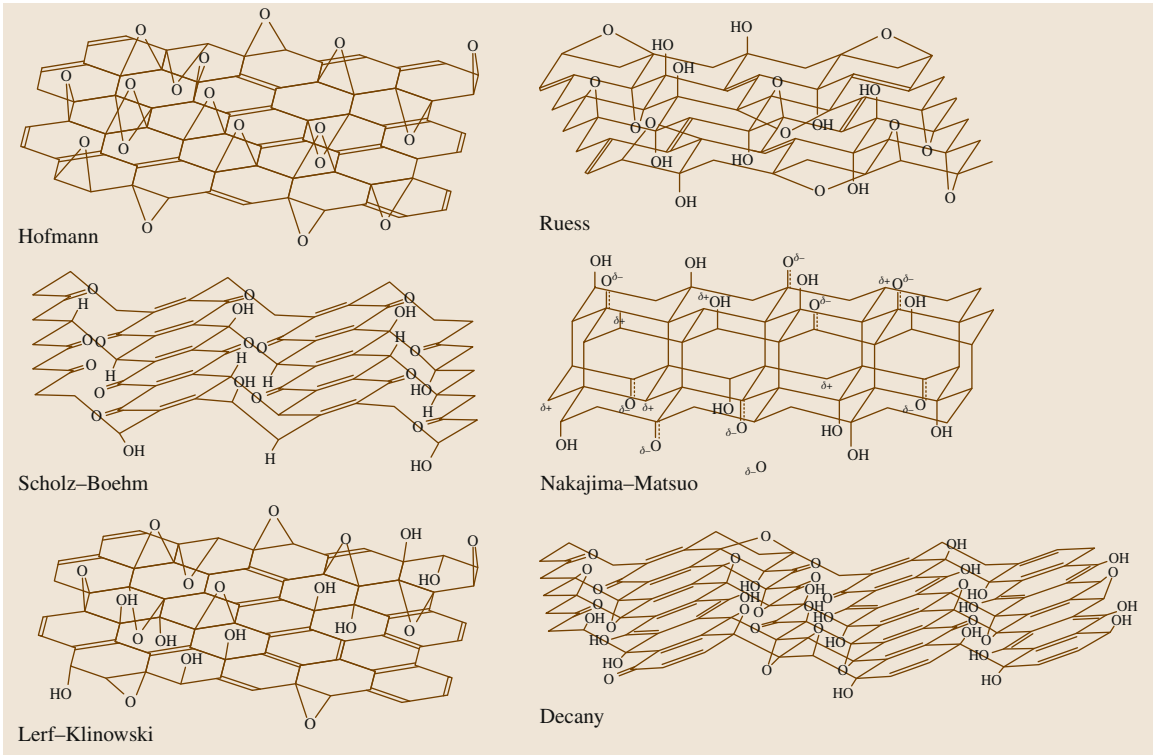


Fig. 15.10 Proposed structure models for GO

exfoliation of GO [15.41]. The wrinkled surface and occasionally holes can be observed in both AFM and TEM images of GO (Fig. 15.9).

Thermal gravimetric analysis (TGA) offers information on the thermal stability of GO. Unfortunately, GO is thermally unstable. When heated in Ar, GO starts decomposing slowly above 60–80 °C, and loses up to 60% of its total weight when heated up to 950 °C. The loss of adsorbed water will also occur during this process. It is important to mention that, for GO TGA analysis, the temperature ramping rate is usually set to be very low (around 1 K/min), in case the rapidly evolved gases explode and cause problems.

15.2.2 Chemical Structure

Based on the characterizations listed above (mainly SSNMR and DRIFT analysis data), at least six different structural models for GO have been suggested [15.42], and the precise chemical structure of GO remains controversial (Fig. 15.10).

The earliest model by *Hofmann* and *Holst* presented in 1939 consists of epoxy groups spreading across the basal planes of graphene, with C/O ratio of two [15.43]. The model was modified by *Ruess* in 1946 with the introduction of hydroxyl groups into the lattice and also the corrugation of the basal plane [15.44]. Different from the Hofmann model, the Ruess model prefers 1,3-ether on a cyclohexane ring with the 4-position hydroxylated, also being stoichiometrically regular. Ruess's suggestion was supported by the observed structure of poly(carbon monofluoride), $(CF)_n$ [15.45], later by *Mermoux* in 1991. The existence of hydroxyl groups in this model accounted for the hydrogen content in GO for the first time; in 1957, *Clauss* and *Boehm* supplemented this contribution with C=C bonds, ketone and enolic groups, as well as carboxylic groups around the edges [15.46]. More than a decade later, *Scholz* and *Boehm* reconsidered the stereochemistry of this model, and modified it into a corrugated carbon layer consisting of alternately linked ribbons of quinoidal structure and opened cyclohexane rings in chair conformation [15.47]. They completely removed epoxy and ether structures from this model, and put hydroxyl groups at the 4-position of 1,2-oxidized cyclohexane rings. On the other hand, the Ruess model

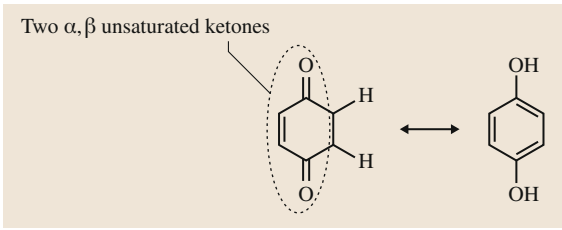


Fig. 15.11 Schematics of phenol–quinone exchange, favoring the forward direction due to the aromaticity of the phenol structure

was still a possibility; in 1988, *Nakajima* and *Matsuo* proposed a stage 2 type model $(C_2F)_n$ in fluorinated graphite product, and tried to make the oxide analog for GO [15.48].

Most of these models have now been supplanted by the two most recent models, named after *Lerf* and *Klinowski* [15.30, 49, 50] and *Dekany* [15.42], respectively. In the Lerf–Klinowski model, the periodicity in the structure was rejected, being substituted by a nonstoichiometric amorphous alternative. In their studies, the SSNMR technique was used for the first time for GO structural characterization, while all previous reports were simply based on elemental analysis, reactivity observations, and XRD data. Obviously this is an important milestone in the GO structure debate, and as discussed in the previous section, the assignments of all those CP/MAS signals in SSNMR spectra soon helped to clarify the basic structural information for GO.

Lerf and coworkers have presented many detailed discussions and analyses of the GO structure, based on not only SSNMR analysis, but also GO reactivity with a variety of compounds and infrared spectroscopic data. First of all, they attempted Diels–Alder-type cycloaddition reactions (4 + 2) on GO (conjugated double bonds should react) with maleic anhydride; however, no reaction was observed [15.49]. In the context of the distribution of the alkenes on the GO basal plane, this result is definitely inconclusive, since the lack of reactivity of GO with dienophile could be due to the complexity of the GO local environment such as the steric effect of epoxy and hydroxyl groups. Later, they suggested that alkenes (C=C) in GO are probably either aromatic or conjugated, based on the logic that isolated double bonds could not survive the harsh oxidation environment applied when making GO [15.30]. Secondly, in combination with the interpretation of FTIR data earlier, they proposed that keto groups are more favored at the periphery of GO than carboxylic acids [15.51]. The acidity of GO was further explained by them through a keto–enol tautomerization and proton exchange on the enol site. The keto form is supposed to be thermodynamically more favored; however, α,β-unsaturated ketones that are present in aromatic regions would favor phenoxide product and allow proton exchange (also known as phenol–quinone exchange, shown in Fig. 15.11). Thirdly, they observed strong hydrogen bonding between GO flakes themselves and water molecules, as indicated by the constant full-width at half-maximum of the water peak in the ^{1}H NMR spectrum [15.50].

The Dekany model was another well-recognized structure for GO, which adopted the logic of the Ruess and Scholz–Boehm models, and stuck to the corrugating nature of the carbon network. It followed the basic framework of the Scholz–Boehm model, while adding 1,3-ethers into the structure and extending the *trans*-linked cyclohexyl networks [15.42]. In 2008, *Cai* et al. prepared a ^{13}C-labeled GO sample, and conducted 1-D and 2-D SSNMR analysis on it. According to their conclusion, only the Lerf–Klinowski model and the Dekany model are possible [15.16].

Later on, ab initio chemical shift calculations were used to simulate the SSNMR signals in GO by *Ruoff*'s group [15.31], and an experimental 2-D ^{13}C double-quantum/single-quantum correlation SSNMR spectrum of ^{13}C-labeled GO was compared with spectra simulated for different structural models using ab initio geometry optimization and chemical shift calculations. According to their conclusion, only the Lerf–Klinowski model fits best with the experimental data; furthermore, all the previous proposed models were excluded. This is definitely another big step forward in the clarification of the GO structure; however, we need to point out that, due to the size limitation in the theoretical modeling, the Lerf–Klinowski model used to simulate the NMR spectrum in this paper is quite simplified, and thus trivial details of the structure on the edges as well as the precise distributions of those functional groups are still unclear.

Unfortunately, to date, the precise structure of GO remains elusive. Major reasons include sample-to-sample variability due to different synthesis methods and degrees of oxidation, the amorphous, nonstoichiometric nature of GO, and the limited resolution of the major characterization techniques such as SSNMR and FTIR. In this case, the term "graphite oxide" may refer to a family of different compounds with certain discrepancies in the functional group distribution and relative content.

15.2.3 Reactivity and Physical Properties

Dispersibility

The most common reaction medium for GO is water, and there are different ways to disperse GO into water, including sonication and mechanical stirring. Sonication has been reported to create defects and decrease the sheet size of GO from several microns to 100 nm, and also widen the size distributions, thus being less favorable than mechanical stirring in many applications [15.41, 52, 53]. The dispersibility of GO in water is typically on the order of 1–4 mg/ml [15.54]. On the other hand, GO can also be dispersed in organic solvents such as dimethylformamide (DMF), *N*-methylpyrrolidone (NMP), tetrahydrofuran (THF), etc. [15.55, 56], thus is also believed to be amphiphilic with the core more hydrophobic and edges more hydrophilic [15.55, 56], acting just like a surfactant [15.57]. As a giant molecule with amphiphilicity, GO can be assembled into continuous single-layer films by the Langmuir–Blodgett method [15.58–60].

Toxicity

GO and RGOs were reported to be toxic to *bacteria* (*Escherichia* and *Staphylococcus*) due to cell membrane damage to the bacteria in contact with the sharp edges of GO and RGO by *Akhaven* et al., and hydrazine-reduced GO was more toxic than pristine GO [15.61]; inhibition of bacterial growth with minimal toxicity to human alveolar epithelial A549 cells was also shown by *Hu* et al. [15.62]. *Wang* et al. demonstrated that GO has dose-dependent toxicity to human fibroblast cells, with obvious toxicity being observed at doses above 50 μg/ml [15.63]. GO toxicity and blood compatibility were also reported to be dependent on dose, extent of exfoliation, and sheet size [15.64–66]. RGO was demonstrated to be less toxic than carbon nanotubes to PC12 cells at high concentrations by *Zhang* et al. [15.67]. PEGylated nanosized GO only exhibited mild toxicity toward Raji cells at concentrations as high as 100 mg/l [15.68]. Paradoxically, other recent reports showed high biocompatibility of GO or RGO [15.69–73]. To address these discrepancies, *Ruiz* et al. reported the nonspecific enhancement of cellular growth by GO, thus verifying that GO is nontoxic to both bacteria and mammalian cells, and attributing the previous reported toxicity as effects from carry-on impurities in GO [15.74]. However, incorporating Ag nanoparticles onto the GO matrix significantly activated its antibacterial activity [15.75, 76].

Hygroscopicity

The hydroxyl, epoxy, and carboxyl groups on GO make it very hydrophilic, and adsorbed water molecules tend to present in the interlayer voids even after prolonged drying [15.77]. Therefore, GO turns out to be quite hygroscopic, with water content strongly depending on the humidity of the environment [15.78]. When a large amount of interlamellar water is present in stacked GO films, a network of hydrogen bonds (H-bonds) forms between water molecules and those oxygenated groups on GO, thus significantly influencing its structural, mechanical, and electronic properties [15.77–80]; For example, as the humidity level rises, GO film swells in volume [15.78, 80] and its tensile modulus decreases [15.77]. Some theoretical simulations have predicted that the interlayer distance between GO flakes rises from 5.1 to 9.0 Å when the water content increases from nearly 0 to 26 wt %, and that when the water content exceeds 15 wt %, the H-bond network is dominated by water–water H-bonds while the functional groups are connected indirectly via a chain of water molecules [15.81]. The dynamics of the interlamellar water has also been studied by neutron scattering, and a *two-site* jump motion mechanism has been proposed [15.78]. Interestingly, when water is replaced by D_2O, a lower interlayer distance was always observed, probably due to the lower solubility, lower reactivity, and stronger bonding of D_2O compared with H_2O [15.78]. The presence of water has also been used to account for the carbonyl formation and hole formation during GO reduction processes [15.78].

Reactivity

Independent of the dispersion medium, a stable colloidal dispersion of GO is readily reactive with a variety of chemicals, most of which have been reducing reagents. The first example would be the hydrogen sulfide reduction introduced by *Hofmann* in 1934 [15.82]. No report on lithium aluminium hydride ($LiAlH_4$) reduction has emerged, probably due to the strong reactivity of $LiAlH_4$ with the common dispersion medium of water. Although $NaBH_4$ is slowly reactive with water, the reaction is kinetically slow enough to allow GO reduction to occur. Meanwhile, the most popular reductant so far has been hydrazine [15.12]. The reduction mechanism has been proposed, at least for one of the major functional groups on GO, as shown in Fig. 15.12 [15.12]. Besides these, GO was believed to be one of the most important precursors to graphene; thus in literature, lots of chemical reduction protocols have been demonstrated, and to compare their effectiveness,

Table 15.3 Comparison in reduction protocols of GO (NA: not available)

	Electrical conductivity (S/cm)	C/O (elemental analysis)	XPS (eV)	Raman (cm^{-1})	XRD (nm)	FTIR (cm^{-1})	SS^{13}CNMR (ppm)	UV (nm)
GO	5.3×10^{-6}–4×10^{-3} [15.17, 83]	2.7 [15.12] 2.44 [15.17]	284.8 (C–C) 286.2 (C–O) 287.8 (C=O) 289.0 (C(O)–O) [15.12, 83]	1594 (G) 1363 (D) [15.12]	0.63–1.2 [15.12]	1060 (C–O) 1220 (phenolic) 1370 (OH bending) 1620 (H_2O bending) 1720 (C=O) [15.17]	57 (C–O–C) 68 (C–OH) 130 (sp^2) 188 (C=O) [15.12]	230 [15.84]
Hydrazine monohydrate [15.12] ($NH_2NH_2\cdot H_2O$)	2	10.3	284.5 with tails	1584 (G) 1352 (D)	NA	NA	117 (sp^2)	
Pure hydrazine [15.85]	10^8-fold higher than GO	NA	284.5 dominant 532 (O) 533 (O) after thermal annealing	1600 (G) 1350 (D) 2700 (2-D) 2950 (D + G) D/G increase	NA	NA	NA	NA
Vapor-phase hydrazine [15.11]	4 orders increase	NA	NA	Changes observed	NA	NA	NA	NA
Dimethylhydrazine [15.86]	1×10^{-3} with 1 vol % in polystyrene (PS)	NA	NA	NA	0.426 0.245	NA	NA	NA
p-Toluenesulfonyl hydrazide [15.87]	1.64	NA	285.89 C–N	NA	NA	1052, 1226, 1727, 3400 decreased	NA	268
Trioctylphosphine [15.88]	2.5	NA	C/O = 9.09 284.6 with tails	1608 (G) 1312 (D)	0.385	1574 (C=C)	NA	268
Hydriodic acid with acetic acid [15.89]	3.04×10^2 7.85×10^3 (vapor phase)	15.27	C/O = 6.67 284.6 with tails	1581 (G) 1350 (D) D/G = 1.10	0.362	Absence of obvious peaks	110.1 (sp^2)	Flat absorbance up to 900 nm
Hydrogen iodide (HI) [15.90]	NA	NA	NA	NA	NA	1710 (C=O) disappeared	NA	NA
Melatonin [15.91]	NA	NA	284.5 with tails	1583 (G) 2- D/G = 0.23 D/G = 1.07	NA	NA	NA	269
Aqueous only [15.92]	5 orders of magnitude decrease	6	284.4 with tails	NA	None	Reduction in C=C, C=O, and C–O–C	NA	NA
Hydrothermal steam etching [15.93]	Increase observed	NA	287 peak decrease					
SO_2 [15.94]	NA	NA	C/O = 4.49	1583 (G) 1349 (D) D/G = 1.01	0.395	NA	NA	272.5

Table 15.3 (continued)

	Electrical conductivity (S/cm)	C/O (elemental analysis)	XPS (eV)	Raman (cm^{-1})	XRD (nm)	FTIR (cm^{-1})	SS^{13}CNMR (ppm)	UV (nm)
Hydrazine with NH_3 (NH)/HI in acetic acid (HI); (HI/NH) [15.95]	4.88; 24.5	15.06; 16.58	67.9% (sp^2); 75.6% (sp^2)	NA	0.368; 0.368	NA	NA	NA
Microwave [15.96–98]	2	4.5	284.5 with tails, $\pi-\pi^*$ bump	1591 (G) 1348 (D) D/G = 0.96	0.355/no peak	1562/1577 appear 1724 decrease 1622 absent	NA	260
Sodium hydrosulfite ($Na_2S_2O_4$) [15.99]	13.77	NA	79% (C−C, C−H)	D/G = 1 1570.7 (G) 1347.3 (D)	0.377	NA	NA	NA
Polyphenol [15.100]	4.33×10^{1}	NA	284.6 with tails	D/G = 1.18	0.43	NA	NA	278
$NaBH_4$ [15.84]	1.5×10^{-6}–$\approx 4.5\times10^{1}$	2.6–8.6	284 with tails $\pi-\pi^*$ bump	D/G increase upon C_{NaBH_4} increase	0.380–0.373	NA	≈ 120 (sp^2)	260
Variable-valence metal-assisted $NaBH_4$ [15.101]	3×10^{2}	1.81–4.99	284.6 with lower tails	D/G: 1.39–1.48 1595 (G) 1360 (D)	0.356 ≈ 0.366	All disappear except for 1220 (C−OH)	NA	NA
Thermal reduction [15.102]	0.009 ≈ 2.75	NA	NA	D/G increase	NA	NA	NA	NA
Single large sheet thermal annealing [15.103]	760	NA	Decrease of oxygenated carbon peaks 89% C−C	D/G decrease 1586 (G)	NA	NA	NA	NA
Solvent thermal reduction [15.104–106]	2.3/52.30	NA	C/O = 4.70/ C/O = 6.8 ≈ 8.3	1586 (G) 1347 (D)	0.41/0.36	1573 exists/most peaks disappeared	NA	NA
Hydrothermal dehydration [15.107]	NA	NA	$sp^2/sp^3 = 5.6$	1593 (G) 1352 (D) D/G = 0.90	NA	NA	Broad 94–160	254
Sulfur-containing compounds ($NaHSO_3$, Na_2SO_3, $Na_2S_2O_3$, $Na_2S\cdot9H_2O$, $SOCl_2$, and SO_2) [15.108]	6.5×10^{1} ($NaHSO_3$)	6.48–7.89 ($NaHSO_3$) 2.32 (Na_2SO_3) 3.88 ($Na_2S_2O_3$) 5.61 (Na_2S) 6.49 (SO_2) 6.75–8.48 ($SOCl_2$)	284.7 (C=C) 285.5 (C−C)	1352 (D) D/G: 0.95–1.22	NA	NA	1577 (C=C, aromatic)	NA

Table 15.3 (continued)

	Electrical conductivity (S/cm)	C/O (elemental analysis)	XPS (eV)	Raman (cm^{-1})	XRD (nm)	FTIR (cm^{-1})	$SS^{13}CNMR$ (ppm)	UV (nm)
Vitamin C [15.109–113]	8/ 7.7×10^{1}/ 0.141/ 15	12.5	284.5 with tails/ 284.6 (C–C) FWHM 0.8–1.1/ N content observed/ 284.5 with tails	D/G increase/ D/G = 1.752	0.37	1726, 3395, 1410, 1226, 1025 decrease dramatically/ 1300–1350	NA	264/ 268
KOH/NaOH [15.114]	NA	NA	291.5 ($\pi-\pi^*$)	NA	NA	NA	90–150	NA
Reducing sugar [15.115]	NA	NA	Oxygen binding peaks decrease	1584 (G) 1354 (D) D/G increase	No peaks	Peaks from oxide groups decrease	NA	261
Bovine serum albumin [15.116]	NA	NA	284.6 with tails	NA	NA	NA	NA	268
H_3PO_4/H_2SO_4 [15.117]	69	NA	C/O = 8.5–11.7 291.5 ($\pi-\pi^*$)	D/G: 0.85	NA	C–H (2950) C=C (1600)	NA	270
$NaBH_4 + H_2SO_4 +$ thermal annealing [15.17]	2.02×10^{2}	> 246	284.5 with tails	1582 (G) 1346 (D)	0.337	No signal	119 (CCG2) 105 (CCG3)	
Electrochemical reduction [15.107, 118–124]	35 85 [15.124]	23.9 [15.124]	NA	1595 (G) 1360 (D) 2-D observed	0.335	C–O remains	NA	NA
Al powder [15.125]	2.1×10^{1}	18.6	284.6 with tails	D/G = 1.81	0.375	NA	NA	NA
Hydroquinone [15.126]	NA	NA	NA	1595 (G) 1350 (D)	NA	NA	NA	NA
Hydrogen (H_2) [15.127]	1×10^{3}	NA	284.3 with tails C/O: 10.8 ≈ 14.9	NA	NA	NA	NA	NA
UV irradiation [15.128, 129]	NA/one order decrease	NA	C/O = 10	D/G decrease	NA	NA	NA	Red-shift of adsorption peak
Flash light [15.130]	10	4.23	NA	NA	22.5°	Decrease of major peaks	NA	NA

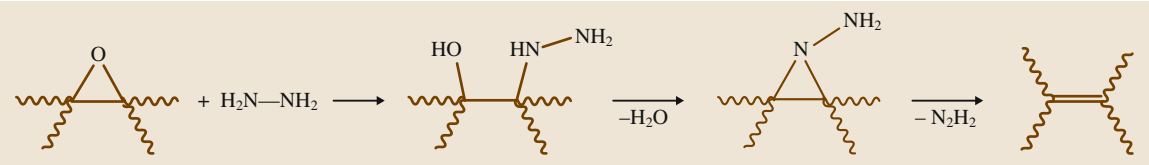


Fig. 15.12 A proposed reaction pathway for epoxide reduction by hydrazine (after [15.12])

characterizations of products with electrical measurement, elemental analysis, ^{13}C SSNMR, XPS, FTIR, Raman, XRD, TEM, near-edge x-ray absorption fine structure (NEXAFS) spectroscopy, etc. have been widely reported. These chemical or thermal treatments and their product characterizations are summarized in Table 15.3.

The restoration of π conjugation can be verified by changes between GO and RGO in UV-Vis spectra, XPS data, and electrical conductivities. The red-shifts of UV adsorption peaks suggested the extension of $\pi-\pi$ conjugation according to Hückel's rule. The appearance of the $\pi-\pi$ satellite peak in XPS was also a good indication. Electrical conductivity would be another good criterion to judge the degree of restoration. As shown in Table 15.3, more than 20 chemicals have been reported as reducing reagents for GO, and so far the product with highest electrical conductivity is produced by hydriodic acid with acetic acid treatment [15.89]. As mentioned above, it must be emphasized that all these chemical treatments worked as reduction protocols to GO, but their products were far from HOPG graphene in terms of crystallinity, since the carrier mobility in these products is at least three orders of magnitude lower than that of graphene. In this case, we conclude that GO as a chemically active compound is prone to be reduced very easily, but the defects and disorder structure in GO are very hard to remove. This can also be verified by the Raman data in Table 15.3. All of the Raman spectra reported on RGOs have prominent D peaks, and most of them have higher D/G ratio than that of GO, indicating highly defected structures.

On the other hand, the reduction processes are usually accompanied by heteroatom incorporation into the final product, further complicating the structure and pushing RGOs further from pristine graphene. As shown in Table 15.3, both elemental analysis and XPS data show the existence of heteroatoms in the final product, including oxygen, nitrogen, sulfur, boron, hydrogen, etc. Thus, researchers have also tried to compare the purity of their products by comparing the ratios of C/O, C/(O+N), etc. These heteroatoms influence the electrical conductivity as well, such as residual C−N groups that can act as n-type dopants [15.134].

To elucidate the reduction mechanism as far as possible, how the functional groups on GO react with various chemicals is summarized in Table 15.4. Most of these reactions are explained based on fundamental organic chemistry in terms of the reactivity of the individual functional groups. As one can see from this table, even the most popular reagent (hydrazine) would still

Table 15.4 Reactivity of functional groups on GO with different chemical reagents (NA: not available)

	NH_2NH_2	$NaBH_4$	$LiAlH_4$	KOH/NaOH [15.114]	H_2SO_4 (conc.) [15.17]	H_3PO_4 [15.117]	HI and AcOH [15.89]	Diazonium salts [15.131]
Epoxy (C−O−C) [15.132]	C=C/$C_2N_2H_2$	CH−COH (low)	CH−COH	COH−COH	NA	COH−CH_2PO_4	CI−COH	NA
Hydroxyl (C−OH)	$CNHNH_2$	NA	NA	NA	C=C	NA	C−I	NA
Ketone (C=O)	C=NNH_2	C−OH	CHOH	COH−COH	NA	COH−CH_2PO_4	CICOH	NA
Carboxyl (−COOH)	Inert [15.12, 133]	NA	−CHOH	−COONa	NA	NA	NA	NA
sp^2 carbon	NA	NA	NA	NA	NA	NA	NA	C(sp^3)−Ph−
Ester (−O−C=O)	O−C=NNH_2	NA	−O−CHOH	−COOH	NA	−COOH	NA	NA
Lactol (−O−C−OH)	O−C−$NHNH_2$	NA	−O−CHOH	NA	NA	NA	NA	NA

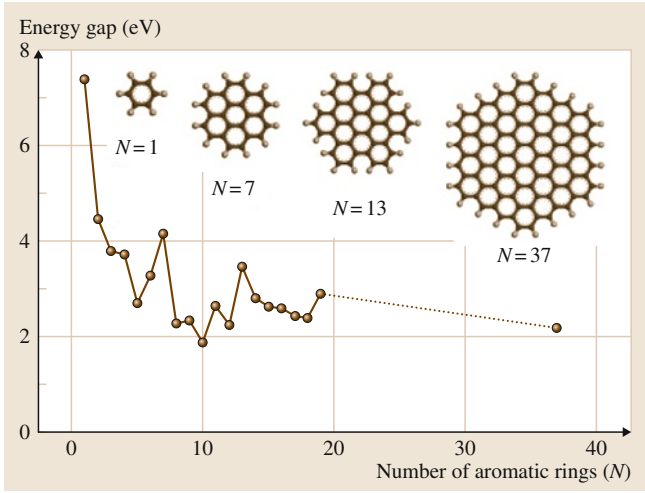


Fig. 15.13 Energy gap of $\pi-\pi^*$ transitions calculated based on density functional theory (DFT) as a function of the number of fused aromatic rings (N). The *inset* shows the structures of the graphene molecules used for calculation (after [15.135])

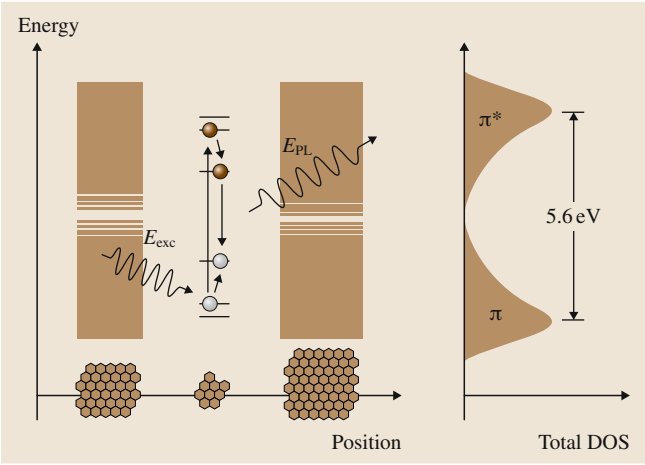


Fig. 15.14 Representative band structure of GO. The energy levels are quantized with large energy gaps for small fragments due to confinement. A photogenerated e–h pair recombining radiatively is depicted (after [15.135])

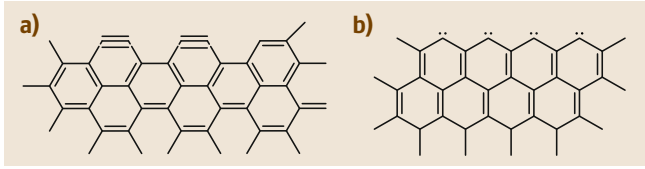


Fig. 15.15a,b Carbyne **(a)** and carbene **(b)** structures on graphene edges, corresponding to armchair and zigzag edges, respectively

leave some functional groups intact. Therefore, though the sp^2 carbon lattice structure is thermodynamically favorable over GO, complete restoration of π conjugation is very hard, let alone the carbon vacancies created in the oxidation process.

Electronic Structure and Fluorescence

If we recall the chemical structure of GO, it is basically composed of 2–3 nm sp^2 carbon clusters surrounded by a heterogeneous sp^3 carbon matrix. In a carbon material with a mixture of sp^2 and sp^3 carbon atoms, the photoluminescence behavior is determined by the π states of the sp^2 clusters [15.136]. This is simply because the π and π^* electronic levels lie within the bandgap of the σ and σ^* states (typically around 6 eV [15.136]) of the sp^3 domains [15.137, 138]. π-Electrons are highly localized in sp^2 domains, and radiative recombination of electron–hole pairs in those sp^2 clusters can give rise to fluorescence [15.138–140]. Therefore, the size, the shape, and even the interface structure of sp^2 carbon clusters can determine the local bandgap and thus the energy of the fluorescence.

Since the oxygenated functional groups are randomly distributed on the GO surface, the corresponding sp^2 carbon clusters have a wide size distribution; hence, no signature features can be assigned in the electronic structure. The size-dependent bandgap of sp^2 carbon clusters has been calculated, as shown in Fig. 15.13 [15.135]. Just as expected, larger clusters have lower-energy bandgaps, varying from ≈ 7 eV for a single benzene ring to ≈ 2 eV for about 40 fused rings, though it is necessary to point out that the structural model adapted in this simulation was quite simplified (with only zigzag edges and ordered hexagonal shapes) and that it did not take into account of the electronegativity effect of the nearby connected sp^3 carbons. When only cluster size is taken into account, the ensemble band diagram corollary is shown in Fig. 15.14 [15.135]. Interestingly, in Fig. 15.14, the authors also depicted a photoluminescence process from a finite-sized sp^2 cluster (composed of several conjugated repeating alkene units that were populated at the initial stage of the vapor hydrazine reduction), corresponding to the enhanced blue luminescence (≈ 390 nm, 3.18 eV) that they observed in the first 3 min of reduction.

On the other hand, some researchers have suggested that edge structures can also account for the optoelectronic properties of GO/RGO, or preferably GO/RGO quantum dots [15.141]. When the size of GO/RGO sheets decrease to the nanometer scale, the peripheries start to play a major role in the electronic structure.

As for GO, the periphery is partially occupied by oxygenated groups; however, these groups are excluded as the origin of observed luminescence, because the luminescence was reported to be enhanced with reduction [15.135]. As proposed earlier [15.142], instead of the commonly assumed H-termination or σ-type dangling bonds, the armchair edges are actually of carbyne (o-benzyne) type, whereas the zigzag edges are of carbene type (Fig. 15.15). This means that the nonbonding electron on the edge carbon is no longer in its free state, but couples with another electron on the adjacent carbon (the armchair case), or interacts with the π electron on the same carbon atom (the zigzag case). Therefore, the activity of an unsaturated valence has not been seen in this case, and stabilization is achieved by localization of the itinerant π electrons through $\sigma-\pi$ coupling in the zigzag case [15.143]. Based on both theoretical calculations and experimental data, Radovic et al. strongly suggested that this type of edge structure tends to be stable in ambient conditions, and the stability increases when the number of conjugated aromatic rings increases. Carbenes have two electronic configurations in the ground state, the triplet ($\sigma^1\pi^1$) and singlet (σ^2) state, with the triplet configuration typically lower in energy [15.142]. In the case of carbyne, the situation is exactly the opposite. Regardless of its detailed configurations, the strong blue luminescence observed in RGO quantum dots has been assigned to the highest occupied molecular orbital (HOMO)–lowest unoccupied molecular orbital (LUMO) transition in the triplet state of carbenes at zigzag edges [15.141].

Although the exact mechanism for the observed visible and ultraviolet fluorescence in GO remains to be reconciled, GO as a unique carbon platform, together with its chemical activity, tunability, and solution processability, has already shown its technological significance. The photoluminescence from GO derivatives varies from the near-infrared to the ultraviolet region [15.16, 117, 135, 141, 144–147], and further demonstrations of its application have been widely reported, such as in drug delivery, live cell imaging [15.16, 145], fluorescence quenching [15.148–153], biosensing [15.154, 155], and nonlinear optics [15.156–158].

15.3 Applications

At the beginning of this section, we distinguish the applications of RGOs from those of GO. There are numerous reports in literature suggesting possible applications for RGOs and their derivatives (such as metal oxide–RGO and polymer–RGO composites), as vital components in conductive polymer composites [15.86], transparent conductors [15.41, 159–162], molecular, electrochemical, or biochemical sensors [15.11, 93, 110, 155, 163–185], electrochemical or photocatalysts [15.63, 108, 171, 172, 186–206], lithium storage materials [15.5, 6, 64, 207–222], electron field-emission electrodes [15.223], supercapacitor electrodes [15.152, 174, 224–239], electronic transistors [15.240], artificial muscles [15.207], electroluminescence electrodes [15.109, 241], solid-phase microextraction materials [15.242], water purification adsorbents [15.239, 243–250], organic photovoltaic components [15.150, 251–255], electromechanical actuators [15.256], etc. RGO here acts as either major functioning components themselves or as matrix supports for active nanoparticles and/or metal oxides in the composites. However, as stated above, direct use of unreduced GO is relatively rare. The applications of GO can be summarized into three different categories:

1. As an important platform for RGO and GO derivatives/composites (Sect. 15.3.1)
2. As an anisotropic proton conductor (Sect. 15.3.2)
3. Others, such as a catalyst and an electron-transparent window (Sect. 15.3.3).

15.3.1 Platform for RGOs and GO Derivatives/Composites

RGOs

We have discussed and compared reduction of GO in previous sections (Table 15.3). RGOs derived from GO differ in their electrical conductivities, micromorphologies, Brunauer–Emmett–Teller (BET) surface areas, optical activities, etc., thus leading to a variety of applications as mentioned above. Despite being referred to as graphene or RGO applications, these results actually take advantage of the large scale, wet chemical processability, high surface area, and tunable conductivity [15.257] of GO. In order to focus on GO itself, we just skip this RGO part here.

GO Derivatives

The addition of other functional groups directly onto GO, to form either covalent or noncovalent attachments,

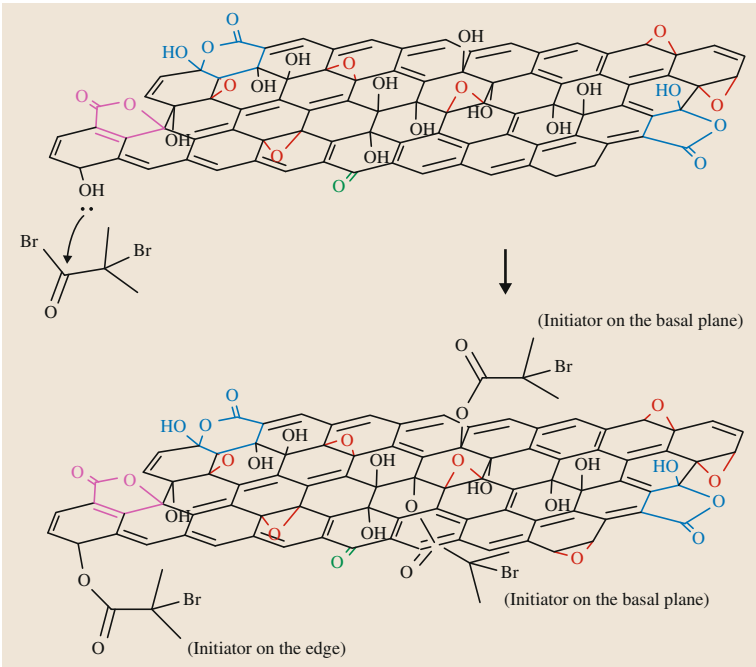


Fig. 15.16 Nucleophilic attack of hydroxyl groups on GO to 2-bromo-2-methylpropanoyl bromide, offering an initiator for ATRP

falls into another big category of GO chemistry. According to the widely accepted *Lerf–Klinowski* model, reactive functional groups on GO are epoxy, hydroxyl, carbonyl, carboxyl, and ester moieties. It would be useful if one could selectively react with one of these groups while keeping the others intact; however, so far such orthogonal reactions have not been demonstrated. Most functionalization occurs on more than one type of oxygenated group and results in very complicated products with separation and purification being almost impossible. Regardless of their vague chemical characterization, most of these products have shown interesting applications in various fields.

For instance, carboxyl acid groups, after being activated by thionyl chloride ($SOCl_2$) [15.258–260], 1-ethyl-3-(3-dimethylaminopropyl)-carbodiimide (EDC) [15.145], *N*,*N*′-dicyclohexylcarbodiimide (DCC) [15.261], or 2-(7-aza-1*H*-benzotriazole-l-yl)-1,1,3,3,-tetramethyluronium hexafluorophosphate (HATU) [15.262], are attacked by nucleophiles such as amines or hydroxyl groups, forming covalent attachments. The resulted amides have shown possible applications in optoelectronics [15.258, 260, 263], biodevices [15.262], drug-delivery vehicles [15.145], and polymer composites [15.261, 264]. A more complicated case involves the attachment of diamine, further covalent binding with bromide-terminated initiators, and subsequent polymerization on the GO surface [15.265, 266]. The resulting GO–polymer composites usually offer better dispersibility in many solvents. Besides that, isocyanate derivatives have also been shown to react with carboxyl and hydroxyl groups, leading to amide and carbamate esters [15.267]. These products can be well dispersed in polar aprotic organic solvents. Chitosan chains also reacted with the carboxyl groups on GO, forming amino bonds with only microwave assistance, offering possible biomedical applications [15.268].

Epoxy group is another major functionality on GO. The epoxy rings can be easily opened under acidic conditions or by nucleophilic attack; For example, octadecylamine was used to react with GO and offered a colloidal dispersion of functionalized GO (FGO) in organic solvents [15.269]. Hexylamine was also used to attack the epoxy rings on GO to form alkylated GO, which can further be reduced into alkylated conductive graphene paper [15.270]. Ethylenediamino-β-cyclodextrin was also introduced to attach cyclodextrin onto the GO surface via amine–epoxy reaction [15.145]. An ionic liquid [1-(3-aminopropyl)-3-methylmidazolium bromide, RNH_2] was attached to GO via the end amine group in a nucleophilic attack of the epoxy groups [15.271]. Another example involved 3-aminopropyltriethoxysilane (APTS) attachment onto

epoxy via a S_N2 reaction and of course ring-opening of epoxy groups, while reinforcement in the mechanical properties of the resulting silica composite was demonstrated [15.272]. Interestingly, inspired by the synthetic polymer chemistry or biochemical systems, cross-linking of GO with poly(allylamine) or sodium borate, via epoxy and hydroxyl groups, has also been investigated [15.118, 273], and mechanical enhancement of the resulting GO film was observed in both cases. Unfortunately, these cross-linking strategies cannot stabilize GO in solvents, especially in water; unlike the case for polymers, cross-linked GO paper still breaks down when in contact with water, hence other chemical methodologies to tackle this problem are of interest to GO chemists.

Hydroxyl groups on GO can act as nucleophiles to attack ketones; For instance, 2-bromo-2-methylpropanoyl bromide was used to react with hydroxyl groups on GO to form an initiator for atom-transfer radical polymerization (ATRP), offering GO-polymethyl methacrylate (GO-PMMA) as the final product (Fig. 15.16) [15.274].

It is also worthwhile to mention the covalent functionalization of RGOs with diazonium salts [15.54, 131, 275]. The aryl diazonium salt was believed to react with the sp^2 carbon domain in RGOs [15.276] to yield highly functionalized RGOs with superior dispersibility. Direct reaction of diazonium salts with GO was also reported by *Gao* [15.243], rendering thiophenol-functionalized GO with high mercuric ion adsorption capability. All the reactions mentioned above lead to strong covalent bonding between GO and the other chemical, and most of them happen with more than one functionality on GO, proving GO to be a very active compound.

Additionally, noncovalent functionalization of GO has also been demonstrated. Noncovalent interactions such as $\pi-\pi$ stacking, cation–π, or van der Waals interactions mainly happen on sp^2 carbon domains; For instance, a GO-based biosensor has been demonstrated utilizing GO–protein/DNA $\pi-\pi$ interactions [15.155]. Doxorubicin hydrochloride was also reported to form a hybrid with GO via noncovalent interactions [15.277].

15.3.2 An Anisotropic Proton Conductor

As we revisit the chemical structure of GO, we find that over half of the carbon atoms in GO are sp^3 hybridized, attached with oxygenated groups including hydroxyl, epoxy, and carboxyl moieties. These oxygen-containing functionalizations allow GO to be used as a unique substrate for a hydrogen-bonding network on its surface, and lead to its hygroscopicity, just as in the very first polymer electrolyte, Nafion.

Protons in the H-bond network can hop from one to another, thus ionic conductivity was observed in GO [15.225]. It is not hard to understand that this ionic conductivity observed in GO is humidity dependent: as the humidity goes down, the conductivity also decreases. Also, the two-dimensional structure renders it anisotropic, since the proton hopping should be facilitated in the lateral direction rather than the vertical direction. Around two orders of magnitude difference in vertical and in-plane conductivity was observed. Taking advantage of this attribute, both sandwich and in-plane supercapacitor devices, employing GO as the solid electrolyte and RGO as electrodes, have been reported to be important complementary devices to the existing thin-film ultracapacitors [15.225].

Such ionic (protonic) conductivity was also noticed by *Cao* et al., and by incorporating only 5 wt % GO into a poly(ethylene oxide) matrix, they were able to develop a solid electrolyte membrane for low-temperature polymer fuel cells [15.278]. The authors attributed the observed ionic conductivity mainly to the carboxyl acid groups on GO edges, whereas we suggest that other oxygenated groups also play important roles. The composite film offered temperature-dependent conductivity from 0.089 S/cm at 25 °C to 0.134 S/cm at 60 °C and 100% relative humidity, leading to a maximum powder density of 53 mW/cm^2 without optimizing the catalyst layer composition.

Interestingly, a relevant application of *unreduced* GO as a hole transport layer, substituting PEDOT:PSS (poly(3,4-ethylenedioxythiophene):poly(styrenesulfonate)) in polymer solar cells, has also been demonstrated [15.279, 280]. *Li* et al. claimed that the sp^2 domain hopping at the Fermi level does not contribute to the blocking of electron transport, and observed that the injection of holes into the valence band of GO is much more favorable [15.279]. *Murray* et al. also showed that GO is an effective replacement for PEDOT:PSS in organic photovoltaics, and that it enhances the device durability by 20 times in humid ambient condition [15.280].

15.3.3 Catalyst and an Electron Transparent Window

Due to its extraordinary hygroscopicity, GO has been demonstrated as a dehydrative polymerization catalyst [15.281]. During the polymerization process, GO

was substantially reduced by the thermal effect and further acted as a conductive carbon additive in the polymer matrix. The elastic modulus was increased from 40 to 320 MPa with only 0.1 wt % GO loading. GO has also been used as a catalyst in Friedel–Crafts addition of indoles to α,β-unsaturated ketones, with recyclable activity up to five cycles [15.282].

On the other hand, GO turns out to be transparent enough to photoelectrons (energy higher than 450 eV) that are captured and analyzed in XPS, Auger electron spectroscopy (AES), and electron energy-loss spectroscopy (EELS), but not permeable to molecules [15.283]. Kolmakov et al. demonstrated the application of 100–1000 μm^2 GO sheets as transparent windows for an in situ environmental cell in XPS analysis. They obtained good-quality XPS data from aqueous solutions and nanoparticles deposited on the back side of GO films [15.283]. *Krueger* et al. also applied self-assembled GO for SEM environmental cell membranes [15.284].

15.4 Concluding Remarks

GO, a group of gigantic organic molecules first discovered over one and a half centuries ago, has reemerged as an important precursor to graphene since the last decade, yet now has written its own history independent of its relationship with graphene.

In this chapter, we summarize and discuss its synthesis, characterizations, structures, chemical activities, and physical features based on the fundamental understanding in chemistry and material science. The applications of GO and its derivatives have also been introduced and categorized. Starting from natural graphitic material, GO can be prepared in a large amount by strong chemical oxidation. Various characterizations have proved GO to be an oxidized carbon compound with two-dimensional structure, in other words a sheet of fused hexagonal rings with lots of oxygenated groups attached on both sides. The mixture of sp^2 and sp^3 carbon atoms in GO makes it corrugated, amphiphilic, and fluorescent, while the oxygen-containing functionalization renders it hygroscopic, dispersible, and chemically reactive. Its two-dimensional nature leads to large-scale availability of atomically thin, transparent GO films, which can be further reduced to form transparent, conductive membranes. Wide applications extending into more than ten different categories have been demonstrated, and GO has become an important material in both fundamental science and contemporary technologies.

The salient features of GO have made it hard to identify its precise chemical structure. Although many researchers have tried to tailor its molecular structure using various chemicals, well-resolved control or manipulation of its sp^2/sp^3 domain, the location, density, and type of chemical functionalizations, and of course, the size, shape, and edge structure of GO itself remain far from realization. The development of better chemical processes to eliminate the oxygenated groups and to restore π conjugation is also of interest for technological applications. Water-stable cross-linking strategies would also be intriguing in terms of enhanced mechanical properties and wider technological applications.

References

15.1 J.N. Coleman, M. Lotya, A. O'Neill, S.D. Bergin, P.J. King, U. Khan, K. Young, A. Gaucher, S. De, R.J. Smith, I.V. Shvets, S.K. Arora, G. Stanton, H.-Y. Kim, K. Lee, G.T. Kim, G.S. Duesberg, T. Hallam, J.J. Boland, J.J. Wang, J.F. Donegan, J.C. Grunlan, G. Moriarty, A. Shmeliov, R.J. Nicholls, J.M. Perkins, E.M. Grieveson, K. Theuwissen, D.W. McComb, P.D. Nellist, V. Nicolosi: Two-dimensional nanosheets produced by liquid exfoliation of layered materials, Science **331**(6017), 568–571 (2011)

15.2 K.S. Novoselov, A.K. Geim, S.V. Morozov, D. Jiang, M.I. Katsnelson, I.V. Grigorieva, S.V. Dubonos, A.A. Firsov: Two-dimensional gas of massless Dirac fermions in graphene, Nature **438**(7065), 197–200 (2005)

15.3 K.S. Novoselov, A.K. Geim, S.V. Morozov, D. Jiang, Y. Zhang, S.V. Dubonos, I.V. Grigorieva, A.A. Firsov: Electric field effect in atomically thin carbon films, Science **306**(5696), 666–669 (2004)

15.4 L.M. Viculis, J.J. Mack, R.B. Kaner: A chemical route to carbon nanoscrolls, Science **299**(5611), 1361 (2003)

15.5 Y. Hernandez, V. Nicolosi, M. Lotya, F.M. Blighe, Z. Sun, S. De, I.T. McGovern, B. Holland, M. Byrne, Y.K. Gun'Ko, J.J. Boland, P. Niraj, G. Duesberg, S. Krishnamurthy, R. Goodhue, J. Hutchison,

V. Scardaci, A.C. Ferrari, J.N. Coleman: High-yield production of graphene by liquid-phase exfoliation of graphite, Nat. Nanotechnol. **3**(9), 563–568 (2008)

15.6 X. Li, W. Cai, J. An, S. Kim, J. Nah, D. Yang, R. Piner, A. Velamakanni, I. Jung, E. Tutuc, S.K. Banerjee, L. Colombo, R.S. Ruoff: Large-area synthesis of high-quality and uniform graphene films on copper foils, Science **324**(5932), 1312–1314 (2009)

15.7 C. Berger, Z. Song, X. Li, X. Wu, N. Brown, C. Naud, D. Mayou, T. Li, J. Hass, A.N. Marchenkov, E.H. Conrad, P.N. First, W.A. de Heer: Electronic confinement and coherence in patterned epitaxial graphene, Science **312**(5777), 1191–1196 (2006)

15.8 J. Cai, P. Ruffieux, R. Jaafar, M. Bieri, T. Braun, S. Blankenburg, M. Muoth, A.P. Seitsonen, M. Saleh, X. Feng, K. Mullen, R. Fasel: Atomically precise bottom-up fabrication of graphene nanoribbons, Nature **466**(7305), 470–473 (2010)

15.9 Ž. Tomović, M.D. Watson, K. Müllen: Superphenalene-based columnar liquid crystals, Angew. Chem. Int. Ed. **43**(6), 755–758 (2004)

15.10 M. Treier, C.A. Pignedoli, T. Laino, R. Rieger, K. Mullen, D. Passerone, R. Fasel: Surface-assisted cyclodehydrogenation provides a synthetic route towards easily processable and chemically tailored nanographenes, Nat. Chem. **3**(1), 61–67 (2011)

15.11 S. Gilje, S. Han, M. Wang, K.L. Wang, R.B. Kaner: A chemical route to graphene for device applications, Nano Lett. **7**(11), 3394–3398 (2007)

15.12 S. Stankovich, D.A. Dikin, R.D. Piner, K.A. Kohlhaas, A. Kleinhammes, Y. Jia, Y. Wu, S.T. Nguyen, R.S. Ruoff: Synthesis of graphene-based nanosheets via chemical reduction of exfoliated graphite oxide, Carbon **45**(7), 1558–1565 (2007)

15.13 B.C. Brodie: On the atomic weight of graphite, Philos. Trans. R. Soc. Lond. **149**, 249–259 (1859)

15.14 W.S. Hummers, R.E. Offeman: Preparation of graphitic oxide, J. Am. Chem. Soc. **80**(6), 1339–1339 (1958)

15.15 D.C. Marcano, D.V. Kosynkin, J.M. Berlin, A. Sinitskii, Z. Sun, A. Slesarev, L.B. Alemany, W. Lu, J.M. Tour: Improved synthesis of graphene oxide, ACS Nano **4**(8), 4806–4814 (2010)

15.16 W. Cai, R.D. Piner, F.J. Stadermann, S. Park, M.A. Shaibat, Y. Ishii, D. Yang, A. Velamakanni, S.J. An, M. Stoller, J. An, D. Chen, R.S. Ruoff: Synthesis and solid-state NMR structural characterization of ^{13}C-labeled graphite oxide, Science **321**(5897), 1815–1817 (2008)

15.17 W. Gao, L.B. Alemany, L. Ci, P.M. Ajayan: New insights into the structure and reduction of graphite oxide, Nat. Chem. **1**(5), 403–408 (2009)

15.18 C. Mattevi, G. Eda, S. Agnoli, S. Miller, K.A. Mkhoyan, O. Celik, D. Mostrogiovanni, G. Granozzi, E. Garfunkel, M. Chhowalla: Evolution of electrical, chemical, and structural properties of transparent and conducting chemically derived graphene thin films, Adv. Funct. Mater. **19**(16), 2577–2583 (2009)

15.19 L. Staudenmaier: Verfahren zur Darstellung der Graphitsäure, Ber. dtsch. chem. Ges. **31**(2), 1481–1487 (1898)

15.20 L. Staudenmaier: Verfahren zur Darstellung der Graphitsäure, Ber. dtsch. chem. Ges. **32**(2), 1394–1399 (1899)

15.21 N.I. Kovtyukhova, P.J. Ollivier, B.R. Martin, T.E. Mallouk, S.A. Chizhik, E.V. Buzaneva, A.D. Gorchinskiy: Layer-by-layer assembly of ultrathin composite films from µm-sized graphite oxide sheets and polycations, Chem. Mater. **11**(3), 771–778 (1999)

15.22 A.L. Higginbotham, D.V. Kosynkin, A. Sinitskii, Z. Sun, J.M. Tour: Lower-defect graphene oxide nanoribbons from multiwalled carbon nanotubes, ACS Nano **4**(4), 2059–2069 (2010)

15.23 J. Luo, L.J. Cote, V.C. Tung, A.T.L. Tan, P.E. Goins, J. Wu, J. Huang: Graphene oxide nanocolloids, J. Am. Chem. Soc. **132**(50), 17667–17669 (2010)

15.24 I.D. Rosca, F. Watari, M. Uo, T. Akasaka: Oxidation of multiwalled carbon nanotubes by nitric acid, Carbon **43**(15), 3124–3131 (2005)

15.25 L. Becker, R.J. Poreda, T.E. Bunch: Fullerenes: An extraterrestrial carbon carrier phase for noble gases, Proc. Natl. Acad. Sci. USA **97**(7), 2979–2983 (2000)

15.26 J.A. McCleverty: Making a meal, Nature **338**(6211), 182–182 (1989)

15.27 K.R. Koch: Oxidation by Mn207. An impressive demonstration of the powerful oxidizing property of dimanganeseheptoxide, J. Chem. Educ. **59**(11), 973 (1982)

15.28 A. Simon, R. Dronskowski, B. Krebs, B. Hettich: The crystal structure of Mn207, Angew. Chem. Int. Ed. **26**(2), 139–140 (1987)

15.29 F. Kim, J. Luo, R. Cruz-Silva, L.J. Cote, K. Sohn, J. Huang: Self-propagating domino-like reactions in oxidized graphite, Adv. Funct. Mater. **20**(17), 2867–2873 (2010)

15.30 A. Lerf, H.Y. He, M. Forster, J. Klinowski: Structure of graphite oxide revisited, J. Phys. Chem. B **102**(23), 4477–4482 (1998)

15.31 L.B. Casabianca, M.A. Shaibat, W.W. Cai, S. Park, R. Piner, R.S. Ruoff, Y. Ishii: NMR-based structural modeling of graphite oxide using multidimensional ^{13}C solid-state NMR and ab initio chemical shift calculations, J. Am. Chem. Soc. **132**(16), 5672–5676 (2010)

15.32 T. Szabo, O. Berkesi, I. Dekany: DRIFT study of deuterium-exchanged graphite oxide, Carbon **43**(15), 3186–3189 (2005)

15.33 K.N. Kudin, B. Ozbas, H.C. Schniepp, R.K. Prud'homme, I.A. Aksay, R. Car: Raman spectra of graphite oxide and functionalized graphene sheets, Nano Lett. **8**(1), 36–41 (2008)

15.34 M. Ishigami, J.H. Chen, W.G. Cullen, M.S. Fuhrer, E.D. Williams: Atomic structure of graphene on SiO2, Nano Lett. **7**(6), 1643–1648 (2007)

15.35 J.I. Paredes, S. Villar-Rodil, P. Solís-Fernández, A. Martínez-Alonso, J.M.D. Tascón: Atomic force and scanning tunneling microscopy imaging of graphene nanosheets derived from graphite oxide, Langmuir **25**(10), 5957–5968 (2009)

15.36 C. Gomez-Navarro, J.C. Meyer, R.S. Sundaram, A. Chuvilin, S. Kurasch, M. Burghard, K. Kern, U. Kaiser: Atomic structure of reduced graphene oxide, Nano Lett. **10**(4), 1144–1148 (2010)

15.37 N.R. Wilson, P.A. Pandey, R. Beanland, R.J. Young, I.A. Kinloch, L. Gong, Z. Liu, K. Suenaga, J.P. Rourke, S.J. York, J. Sloan: Graphene oxide: Structural analysis and application as a highly transparent support for electron microscopy, ACS Nano **3**(9), 2547–2556 (2009)

15.38 G. Eda, C. Mattevi, H. Yamaguchi, H. Kim, M. Chhowalla: Insulator to semimetal transition in graphene oxide, J. Phys. Chem. C **113**(35), 15768–15771 (2009)

15.39 A.B. Kaiser, C. Gomez-Navarro, R.S. Sundaram, M. Burghard, K. Kern: Electrical conduction mechanism in chemically derived graphene monolayers, Nano Lett. **9**(5), 1787–1792 (2009)

15.40 Z.T. Luo, Y. Lu, L.A. Somers, A.T.C. Johnson: High yield preparation of macroscopic graphene oxide membranes, J. Am. Chem. Soc. **131**(3), 898 (2009)

15.41 H.A. Becerril, J. Mao, Z. Liu, R.M. Stoltenberg, Z. Bao, Y. Chen: Evaluation of solution-processed reduced graphene oxide films as transparent conductors, ACS Nano **2**(3), 463–470 (2008)

15.42 T. Szabó, O. Berkesi, P. Forgo, K. Josepovits, Y. Sanakis, D. Petridis, I. Dékány: Evolution of surface functional groups in a series of progressively oxidized graphite oxides, Chem. Mater. **18**(11), 2740–2749 (2006)

15.43 U. Hofmann, R. Holst: The acidic nature and the methylation of graphitoxide, Ber. dtsch. chem. Ges. **72**, 754–771 (1939)

15.44 G. Ruess: Über das Graphitoxyhydroxyd (Graphitoxyd), Monatsh. Chem. **76**(3), 381–417 (1947)

15.45 M. Mermoux, Y. Chabre, A. Rousseau: FTIR and ^{13}C NMR-study of graphite oxide, Carbon **29**(3), 469–474 (1991)

15.46 H.P. Boehm, A. Clauss, U. Hofmann, G.O. Fischer: Dünnste Kohlenstoff-Folien, Z. Naturforsch. **17b**(3), 150 (1962)

15.47 W. Scholz, H.P. Boehm: Graphite oxide/structure of graphite oxide, Z. Anorg. Allg. Chem. **369**(3–6), 327 (1969)

15.48 T. Nakajima, A. Mabuchi, R. Hagiwara: A new structure model of graphite oxide, Carbon **26**(3), 357–361 (1988)

15.49 H.Y. He, T. Riedl, A. Lerf, J. Klinowski: Solid-state NMR studies of the structure of graphite oxide, J. Phys. Chem. **100**(51), 19954–19958 (1996)

15.50 A. Lerf, H.Y. He, T. Riedl, M. Forster, J. Klinowski: C-13 and ^{1}H MAS NMR studies of graphite oxide and its chemically modified derivatives, Solid State Ionics **101**, 857–862 (1997)

15.51 H. He, J. Klinowski, M. Forster, A. Lerf: A new structural model for graphite oxide, Chem. Phys. Lett. **287**(1/2), 53–56 (1998)

15.52 C. Gomez-Navarro, R.T. Weitz, A.M. Bittner, M. Scolari, A. Mews, M. Burghard, K. Kern: Electronic transport properties of individual chemically reduced graphene oxide sheets, Nano Lett. **7**(11), 3499–3503 (2007)

15.53 S. Stankovich, R.D. Piner, X.Q. Chen, N.Q. Wu, S.T. Nguyen, R.S. Ruoff: Stable aqueous dispersions of graphitic nanoplatelets via the reduction of exfoliated graphite oxide in the presence of poly(sodium 4-styrenesulfonate), J. Mater. Chem. **16**(2), 155–158 (2006)

15.54 Y. Si, E.T. Samulski: Synthesis of water soluble graphene, Nano Lett. **8**(6), 1679–1682 (2008)

15.55 J. Kim, L.J. Cote, F. Kim, W. Yuan, K.R. Shull, J. Huang: Graphene oxide sheets at interfaces, J. Am. Chem. Soc. **132**(23), 8180–8186 (2010)

15.56 J.I. Paredes, S. Villar-Rodil, A. Mártinez-Alonso, J.M.D. Tascón: Graphene oxide dispersions in organic solvents, Langmuir **24**(19), 10560–10564 (2008)

15.57 L.J. Cote, J. Kim, V.C. Tung, J.Y. Luo, F. Kim, J.X. Huang: Graphene oxide as surfactant sheets, Pure Appl. Chem. **83**(1), 95–110 (2011)

15.58 L.J. Cote, F. Kim, J. Huang: Langmuir-blodgett assembly of graphite oxide single layers, J. Am. Chem. Soc. **131**(3), 1043–1049 (2008)

15.59 L.J. Cote, J. Kim, Z. Zhang, C. Sun, J. Huang: Tunable assembly of graphene oxide surfactant sheets: Wrinkles, overlaps and impacts on thin film properties, Soft Matter **6**(24), 6015–6218 (2010)

15.60 F. Kim, L.J. Cote, J. Huang: Graphene oxide: Surface activity and two-dimensional assembly, Adv. Mater. **22**(17), 1954–1958 (2009)

15.61 O. Akhavan, E. Ghaderi: Toxicity of graphene and graphene oxide nanowalls against bacteria, ACS Nano **4**(10), 5731–5736 (2010)

15.62 W. Hu, C. Peng, M. Lv, X. Li, Y. Zhang, N. Chen, C. Fan, Q. Huang: Protein corona-mediated mitigation of cytotoxicity of graphene oxide, ACS Nano **5**(5), 3693–3700 (2011)

15.63 K. Wang, J. Ruan, H. Song, J.L. Zhang, Y. Wo, S.W. Guo, D.X. Cui: Biocompatibility of graphene oxide, Nanoscale Res. Lett. **6**, 8 (2011)

15.64 S.K. Behera: Enhanced rate performance and cyclic stability of $Fe_3O(4)$-graphene nanocomposites for Li ion battery anodes, Chem. Commun. **47**(37), 10371–10373 (2011)

15.65 K.H. Liao, Y.S. Lin, C.W. Macosko, C.L. Haynes: Cytotoxicity of graphene oxide and graphene in human erythrocytes and skin fibroblasts, ACS Appl. Mater. Interfaces **3**(7), 2607–2615 (2011)

15.66 M. Wojtoniszak, X. Chen, R.J. Kalenczuk, A. Wajda, J. Lapczuk, M. Kurzewski, M. Drozdzik, P.K. Chu, E. Borowiak-Palen: Synthesis, dispersion, and cytocompatibility of graphene oxide and reduced graphene oxide, Colloids Surf. B **89**, 79–85 (2012)

15.67 Y. Zhang, S.F. Ali, E. Dervishi, Y. Xu, Z. Li, D. Casciano, A.S. Biris: Cytotoxicity effects of graphene and single-wall carbon nanotubes in neural phaeochromocytoma-derived PC12 cells, ACS Nano **4**(6), 3181–3186 (2010)

15.68 X.M. Sun, Z. Liu, K. Welsher, J.T. Robinson, A. Goodwin, S. Zaric, H.J. Dai: Nano-graphene oxide for cellular imaging and drug delivery, Nano Res. **1**(3), 203–212 (2008)

15.69 Y.L. Chang, S.T. Yang, J.H. Liu, E. Dong, Y.W. Wang, A.N. Cao, Y.F. Liu, H.F. Wang: In vitro toxicity evaluation of graphene oxide on A549 cells, Toxicol. Lett. **200**(3), 201–210 (2011)

15.70 S.R. Ryoo, Y.K. Kim, M.H. Kim, D.H. Min: Behaviors of NIH-3T3 fibroblasts on graphene/carbon nanotubes: Proliferation, focal adhesion, and gene transfection studies, ACS Nano **4**(11), 6587–6598 (2010)

15.71 S. Agarwal, X.Z. Zhou, F. Ye, Q.Y. He, G.C.K. Chen, J. Soo, F. Boey, H. Zhang, P. Chen: Interfacing live cells with nanocarbon substrates, Langmuir **26**(4), 2244–2247 (2010)

15.72 H. Chen, M.B. Muller, K.J. Gilmore, G.G. Wallace, D. Li: Mechanically strong, electrically conductive, and biocompatible graphene paper, Adv. Mater. **20**(18), 3557 (2008)

15.73 S. Park, N. Mohanty, J.W. Suk, A. Nagaraja, J.H. An, R.D. Piner, W.W. Cai, D.R. Dreyer, V. Berry, R.S. Ruoff: Biocompatible, robust free-standing paper composed of a TWEEN/graphene composite, Adv. Mater. **22**(15), 1736 (2010)

15.74 O.N. Ruiz, K.A.S. Fernando, B.J. Wang, N.A. Brown, P.G. Luo, N.D. McNamara, M. Vangsness, Y.P. Sun, C.E. Bunker: Graphene oxide: A nonspecific enhancer of cellular growth, ACS Nano **5**(10), 8100–8107 (2011)

15.75 Q. Bao, D. Zhang, P. Qi: Synthesis and characterization of silver nanoparticle and graphene oxide nanosheet composites as a bactericidal agent for water disinfection, J. Colloid Interface Sci. **360**(2), 463–470 (2011)

15.76 M.R. Das, R.K. Sarma, R. Saikia, V.S. Kale, M.V. Shelke, P. Sengupta: Synthesis of silver nanoparticles in an aqueous suspension of graphene oxide sheets and its antimicrobial activity, Colloids Surf. B **83**(1), 16–22 (2011)

15.77 D.A. Dikin, S. Stankovich, E.J. Zimney, R.D. Piner, G.H.B. Dommett, G. Evmenenko, S.T. Nguyen, R.S. Ruoff: Preparation and characterization of graphene oxide paper, Nature **448**(7152), 457–460 (2007)

15.78 A. Buchsteiner, A. Lerf, J. Pieper: Water dynamics in graphite oxide investigated with neutron scattering, J. Phys. Chem. B **110**(45), 22328–22338 (2006)

15.79 I. Jung, D. Dikin, S. Park, W. Cai, S.L. Mielke, R.S. Ruoff: Effect of water vapor on electrical properties of individual reduced graphene oxide sheets, J. Phys. Chem. C **112**(51), 20264–20268 (2008)

15.80 A. Lerf, A. Buchsteiner, J. Pieper, S. Schöttl, I. Dekany, T. Szabo, H.P. Boehm: Hydration behavior and dynamics of water molecules in graphite oxide, J. Phys. Chem. Solids **67**, 1106–1110 (2006)

15.81 N.V. Medhekar, A. Ramasubramaniam, R.S. Ruoff, V.B. Shenoy: Hydrogen bond networks in graphene oxide composite paper. Structure and mechanical properties, ACS Nano **4**(4), 2300–2306 (2010)

15.82 U. Hofmann, A. Frenzel: The reduction of graphite oxide with hydrogen sulphide, Kolloid-Zeitschrift **68**(2), 149–151 (1934)

15.83 S. Park, J.H. An, R.D. Piner, I. Jung, D.X. Yang, A. Velamakanni, S.T. Nguyen, R.S. Ruoff: Aqueous suspension and characterization of chemically modified graphene sheets, Chem. Mater. **20**(21), 6592–6594 (2008)

15.84 H.J. Shin, K.K. Kim, A. Benayad, S.M. Yoon, H.K. Park, I.S. Jung, M.H. Jin, H.K. Jeong, J.M. Kim, J.Y. Choi, Y.H. Lee: Efficient reduction of graphite oxide by sodium borohydrilde and its effect on electrical conductance, Adv. Funct. Mater. **19**(12), 1987–1992 (2009)

15.85 V.C. Tung, M.J. Allen, Y. Yang, R.B. Kaner: High-throughput solution processing of large-scale graphene, Nat. Nanotechnol. **4**(1), 25–29 (2009)

15.86 S. Stankovich, D.A. Dikin, G.H.B. Dommett, K.M. Kohlhaas, E.J. Zimney, E.A. Stach, R.D. Piner, S.T. Nguyen, R.S. Ruoff: Graphene-based composite materials, Nature **442**(7100), 282–286 (2006)

15.87 J.M. Yun, J.S. Yeo, J. Kim, H.G. Jeong, D.Y. Kim, Y.J. Noh, S.S. Kim, B.C. Ku, S.I. Na: Solution-processable reduced graphene oxide as a novel alternative to PEDOT:PSS hole transport layers for highly efficient and stable polymer solar cells, Adv. Mater. **23**(42), 4923–4928 (2011)

15.88 J. Liu, H. Jeong, J. Liu, K. Lee, J.Y. Park, Y.H. Ahn, S. Lee: Reduction of functionalized graphite oxides by trioctylphosphine in nonpolar organic solvents, Carbon **48**(8), 2282–2289 (2010)

15.89 I.K. Moon, J. Lee, R.S. Ruoff, H. Lee: Reduced graphene oxide by chemical graphitization, Nat. Commun. **1**, 73 (2010)

15.90 F. Cataldo, O. Ursini, G. Angelini: Graphite oxide and graphene nanoribbons reduction with hydrogen iodide, Fuller. Nanotub. Carbon Nanostruct. **19**(5), 461–468 (2011)

15.91 A. Esfandiar, O. Akhavan, A. Irajizad: Melatonin as a powerful bio-antioxidant for reduction of graphene oxide, J. Mater. Chem. **21**(29), 10907–10914 (2011)

15.92 K.H. Liao, A. Mittal, S. Bose, C. Leighton, K.A. Mkhoyan, C.W. Macosko: Aqueous only route

toward graphene from graphite oxide, ACS Nano **5**(2), 1253–1258 (2011)
15.93 T.H. Han, Y.-K. Huang, A.T.L. Tan, V.P. Dravid, J. Huang: Steam etched porous graphene oxide network for chemical sensing, J. Am. Chem. Soc. **133**(39), 15264–15267 (2011)
15.94 Y. Long, C.C. Zhang, X.X. Wang, J.P. Gao, W. Wang, Y. Liu: Oxidation of SO_2 to SO_3 catalyzed by graphene oxide foams, J. Mater. Chem. **21**(36), 13934–13941 (2011)
15.95 I.K. Moon, J. Lee, H. Lee: Highly qualified reduced graphene oxides: The best chemical reduction, Chem. Commun. **47**(34), 9681–9683 (2011)
15.96 W.F. Chen, L.F. Yan, P.R. Bangal: Preparation of graphene by the rapid and mild thermal reduction of graphene oxide induced by microwaves, Carbon **48**(4), 1146–1152 (2010)
15.97 A.V. Murugan, T. Muraliganth, A. Manthiram: Rapid, facile microwave-solvothermal synthesis of graphene nanosheets and their polyaniline nanocomposites for energy strorage, Chem. Mater. **21**(21), 5004–5006 (2009)
15.98 K. Wang, T. Feng, M. Qian, H.I. Ding, Y.W. Chen, Z.O. Sun: The field emission of vacuum filtered graphene films reduced by microwave, Appl. Surf. Sci. **257**(13), 5808–5812 (2011)
15.99 T.N. Zhou, F. Chen, K. Liu, H. Deng, Q. Zhang, J.W. Feng, Q.A. Fu: A simple and efficient method to prepare graphene by reduction of graphite oxide with sodium hydrosulfite, Nanotechnology **22**(4), 045704–045710 (2011)
15.100 R.J. Liao, Z.H. Tang, Y.D. Lei, B.C. Guo: Polyphenol-reduced graphene oxide: Mechanism and derivatization, J. Phys. Chem. C **115**(42), 20740–20746 (2011)
15.101 C. Chen, T. Chen, H. Wang, G. Sun, X. Yang: A rapid, one-step, variable-valence metal ion assisted reduction method for graphene oxide, Nanotechnology **22**(40), 405602–405608 (2011)
15.102 I. Jung, D.A. Dikin, R.D. Piner, R.S. Ruoff: Tunable electrical conductivity of individual graphene oxide sheets reduced at *low* temperatures, Nano Lett. **8**(12), 4283–4287 (2008)
15.103 S. Wang, P.K. Ang, Z. Wang, A.L.L. Tang, J.T.L. Thong, K.P. Loh: High mobility, printable, and solution-processed graphene electronics, Nano Lett. **10**(1), 92–98 (2009)
15.104 W.F. Chen, L.F. Yan: Preparation of graphene by a low-temperature thermal reduction at atmosphere pressure, Nanoscale **2**(4), 559–563 (2010)
15.105 C. Nethravathi, M. Rajamathi: Chemically modified graphene sheets produced by the solvothermal reduction of colloidal dispersions of graphite oxide, Carbon **46**(14), 1994–1998 (2008)
15.106 Y.W. Zhu, M.D. Stoller, W.W. Cai, A. Velamakanni, R.D. Piner, D. Chen, R.S. Ruoff: Exfoliation of graphite oxide in propylene carbonate and thermal reduction of the resulting graphene oxide platelets, ACS Nano **4**(2), 1227–1233 (2010)
15.107 M. Zhou, Y.L. Wang, Y.M. Zhai, J.F. Zhai, W. Ren, F.A. Wang, S.J. Dong: Controlled synthesis of large-area and patterned electrochemically reduced graphene oxide films, Chemistry **15**(25), 6116–6120 (2009)
15.108 W.F. Chen, L.F. Yan, P.R. Bangal: Chemical reduction of graphene oxide to graphene by sulfur-containing compounds, J. Phys. Chem. C **114**(47), 19885–19890 (2010)
15.109 Y. Chen, Y. Shen, D. Sun, H. Zhang, D. Tian, J. Zhang, J.-J. Zhu: Fabrication of a dispersible graphene/gold nanoclusters hybrid and its potential application in electrogenerated chemiluminescence, Chem. Commun. **47**(42), 11733–11735 (2011)
15.110 V. Dua, S.P. Surwade, S. Ammu, S.R. Agnihotra, S. Jain, K.E. Roberts, S. Park, R.S. Ruoff, S.K. Manohar: All-organic vapor sensor using inkjet-printed reduced graphene oxide, Angew. Chem. Int. Ed. **49**(12), 2154–2157 (2010)
15.111 M.J. Fernández-Merino, L. Guardia, J.I. Paredes, S. Villar-Rodil, P. Solís-Fernández, A. Martínez-Alonso, J.M.D. Tascón: Vitamin C is an ideal substitute for hydrazine in the reduction of graphene oxide suspensions, J. Phys. Chem. C **114**(14), 6426–6432 (2010)
15.112 J. Gao, F. Liu, Y.L. Liu, N. Ma, Z.Q. Wang, X. Zhang: Environment-friendly method to produce graphene that employs vitamin C and amino acid, Chem. Mater. **22**(7), 2213–2218 (2010)
15.113 Z. Sui, X. Zhang, Y. Lei, Y. Luo: Easy and green synthesis of reduced graphite oxide-based hydrogels, Carbon **49**(13), 4314–4321 (2011)
15.114 X.B. Fan, W.C. Peng, Y. Li, X.Y. Li, S.L. Wang, G.L. Zhang, F.B. Zhang: Deoxygenation of exfoliated graphite oxide under alkaline conditions. A green route to graphene preparation, Adv. Mater. **20**(23), 4490–4493 (2008)
15.115 C.Z. Zhu, S.J. Guo, Y.X. Fang, S.J. Dong: Reducing sugar: New functional molecules for the green synthesis of graphene nanosheets, ACS Nano **4**(4), 2429–2437 (2010)
15.116 J.B. Liu, S.H. Fu, B. Yuan, Y.L. Li, Z.X. Deng: Toward a universal *adhesive nanosheet* for the assembly of multiple nanoparticles based on a protein-induced reduction/decoration of graphene oxide, J. Am. Chem. Soc. **132**(21), 7279 (2010)
15.117 J.L. Chen, X.P. Yan: A dehydration and stabilizer-free approach to production of stable water dispersions of graphene nanosheets, J. Mater. Chem. **20**(21), 4328–4332 (2010)
15.118 S.J. An, Y.W. Zhu, S.H. Lee, M.D. Stoller, T. Emilsson, S. Park, A. Velamakanni, J.H. An, R.S. Ruoff: Thin film fabrication and simultaneous anodic reduction of deposited graphene oxide platelets by

electrophoretic deposition, J. Phys. Chem. Lett. **1**(8), 1259–1263 (2010)
15.119 H.L. Guo, X.F. Wang, Q.Y. Qian, F.B. Wang, X.H. Xia: A green approach to the synthesis of graphene nanosheets, ACS Nano **3**(9), 2653–2659 (2009)
15.120 Y. Guo, B. Wu, H. Liu, Y. Ma, Y. Yang, J. Zheng, G. Yu, Y. Liu: Electrical assembly and reduction of graphene oxide in a single solution step for use in flexible sensors, Adv. Mater. **23**(40), 4626–4630 (2011)
15.121 J. Ping, Y. Wang, K. Fan, J. Wu, Y. Ying: Direct electrochemical reduction of graphene oxide on ionic liquid doped screen-printed electrode and its electrochemical biosensing application, Biosens. Bioelectron. **28**(1), 204–209 (2011)
15.122 G.K. Ramesha, S. Sampath: Electrochemical reduction of oriented graphene oxide films: An in situ raman spectroelectrochemical study, J. Phys. Chem. C **113**(19), 7985–7989 (2009)
15.123 Y.Y. Shao, J. Wang, M. Engelhard, C.M. Wang, Y.H. Lin: Facile and controllable electrochemical reduction of graphene oxide and its applications, J. Mater. Chem. **20**(4), 743–748 (2010)
15.124 R.S. Sundaram, C. Gómez-Navarro, K. Balasubramanian, M. Burghard, K. Kern: Electrochemical modification of graphene, Adv. Mater. **20**(16), 3050–3053 (2008)
15.125 Z. Fan, K. Wang, T. Wei, J. Yan, L. Song, B. Shao: An environmentally friendly and efficient route for the reduction of graphene oxide by aluminum powder, Carbon **48**(5), 1686–1689 (2010)
15.126 G. Wang, J. Yang, J. Park, X. Gou, B. Wang, H. Liu, J. Yao: Facile synthesis and characterization of graphene nanosheets, J. Phys. Chem. C **112**(22), 8192–8195 (2008)
15.127 Z.S. Wu, W.C. Ren, L.B. Gao, B.L. Liu, C.B. Jiang, H.M. Cheng: Synthesis of high-quality graphene with a predetermined number of layers, Carbon **47**(2), 493–499 (2009)
15.128 Y. Matsumoto, M. Koinuma, S. Ida, S. Hayami, T. Taniguchi, K. Hatakeyama, H. Tateishi, Y. Watanabe, S. Amano: Photoreaction of graphene oxide nanosheets in water, J. Phys. Chem. C **115**(39), 19280–19286 (2011)
15.129 G. Williams, B. Seger, P.V. Kamat: TiO2-graphene nanocomposites. UV-assisted photocatalytic reduction of graphene oxide, ACS Nano **2**(7), 1487–1491 (2008)
15.130 L.J. Cote, R. Cruz-Silva, J.X. Huang: Flash reduction and patterning of graphite oxide and its polymer composite, J. Am. Chem. Soc. **131**(31), 11027–11032 (2009)
15.131 J.R. Lomeda, C.D. Doyle, D.V. Kosynkin, W.F. Hwang, J.M. Tour: Diazonium functionalization of surfactant-wrapped chemically converted graphene sheets, J. Am. Chem. Soc. **130**(48), 16201–16206 (2008)
15.132 M.C. Kim, G.S. Hwang, R.S. Ruoff: Epoxide reduction with hydrazine on graphene: A first principles study, J. Chem. Phys. **131**(6), 064704–064709 (2009)
15.133 D. Li, M.B. Muller, S. Gilje, R.B. Kaner, G.G. Wallace: Processable aqueous dispersions of graphene nanosheets, Nat. Nanotechnol. **3**(2), 101–105 (2008)
15.134 S.J. Kang, C. Kocabas, T. Ozel, M. Shim, N. Pimparkar, M.A. Alam, S.V. Rotkin, J.A. Rogers: High-performance electronics using dense, perfectly aligned arrays of single-walled carbon nanotubes, Nat. Nanotechnol. **2**(4), 230–236 (2007)
15.135 G. Eda, Y.-Y. Lin, C. Mattevi, H. Yamaguchi, H.-A. Chen, I.S. Chen, C.-W. Chen, M. Chhowalla: Blue photoluminescence from chemically derived graphene oxide, Adv. Mater. **22**(4), 505 (2010)
15.136 J. Robertson, E.P. Oreilly: Electronic and atomic-structure of amorphous-carbon, Phys. Rev. B **35**(6), 2946–2957 (1987)
15.137 C.W. Chen, J. Robertson: Nature of disorder and localization in amorphous carbon, J. Noncryst. Solids **227**, 602–606 (1998)
15.138 M. Koos, M. Veres, M. Fule, I. Pocsik: Ultraviolet photoluminescence and its relation to atomic bonding properties of hydrogenated amorphous carbon, Diam. Relat. Mater. **11**(1), 53–58 (2002)
15.139 F. Demichelis, S. Schreiter, A. Tagliaferro: Photoluminescence in a-C:H films, Phys. Rev. B **51**(4), 2143–2147 (1995)
15.140 Rusli, J. Robertson, G.A.J. Amaratunga: Photoluminescence behavior of hydrogenated amorphous carbon, J. Appl. Phys. **80**(5), 2998–3003 (1996)
15.141 Y. He, Z.-G. Wang, H.-W. Tang, D.-W. Pang: Low background signal platform for the detection of ATP: When a molecular aptamer beacon meets graphene oxide, Biosens. Bioelectron. **29**(1), 76–81 (2011)
15.142 L.R. Radovic, B. Bockrath: On the chemical nature of graphene edges: Origin of stability and potential for magnetism in carbon materials, J. Am. Chem. Soc. **127**(16), 5917–5927 (2005)
15.143 S. Mrozowski: Semiconductivity and diamagnetism of polycrystalline graphite and condensed ring systems, Phys. Rev. **85**(4), 609–620 (1952)
15.144 T.V. Cuong, V.H. Pham, Q.T. Tran, S.H. Hahn, J.S. Chung, E.W. Shin, E.J. Kim: Photoluminescence and Raman studies of graphene thin films prepared by reduction of graphene oxide, Mater. Lett. **64**(3), 399–401 (2010)
15.145 Z. Liu, J.T. Robinson, X.M. Sun, H.J. Dai: PEGylated nanographene oxide for delivery of water-insoluble cancer drugs, J. Am. Chem. Soc. **130**(33), 10876 (2008)
15.146 Z. Luo, P.M. Vora, E.J. Mele, A.T.C. Johnson, J.M. Kikkawa: Photoluminescence and band gap modulation in graphene oxide, Appl. Phys. Lett. **94**(11), 3 (2009)

15.147 K.S. Subrahmanyam, P. Kumar, A. Nag, C.N.R. Rao: Blue light emitting graphene-based materials and their use in generating white light, Solid State Commun. **150**(37–38), 1774–1777 (2010)
15.148 H.F. Dong, W.C. Gao, F. Yan, H.X. Ji, H.X. Ju: Fluorescence resonance energy transfer between quantum dots and graphene oxide for sensing biomolecules, Anal. Chem. **82**(13), 5511–5517 (2010)
15.149 J. Kim, L.J. Cote, F. Kim, J.X. Huang: Visualizing graphene based sheets by fluorescence quenching microscopy, J. Am. Chem. Soc. **132**(1), 260–267 (2010)
15.150 Q. Liu, Z.F. Liu, X.Y. Zhang, N. Zhang, L.Y. Yang, S.G. Yin, Y.S. Chen: Organic photovoltaic cells based on an acceptor of soluble graphene, Appl. Phys. Lett. **92**(22), 3 (2008)
15.151 E. Treossi, M. Melucci, A. Liscio, M. Gazzano, P. Samori, V. Palermo: High-contrast visualization of graphene oxide on dye-sensitized glass, quartz, and silicon by fluorescence quenching, J. Am. Chem. Soc. **131**(43), 15576 (2009)
15.152 Y.B. Wang, D. Kurunthu, G.W. Scott, C.J. Bardeen: Fluorescence quenching in conjugated polymers blended with reduced graphitic oxide, J. Phys. Chem. C **114**(9), 4153–4159 (2010)
15.153 L.M. Xie, X. Ling, Y. Fang, J. Zhang, Z.F. Liu: Graphene as a substrate to suppress fluorescence in resonance raman spectroscopy, J. Am. Chem. Soc. **131**(29), 9890 (2009)
15.154 S.J. He, B. Song, D. Li, C.F. Zhu, W.P. Qi, Y.Q. Wen, L.H. Wang, S.P. Song, H.P. Fang, C.H. Fan: A graphene nanoprobe for rapid, sensitive, and multicolor fluorescent DNA analysis, Adv. Funct. Mater. **20**(3), 453–459 (2010)
15.155 C.H. Lu, H.H. Yang, C.L. Zhu, X. Chen, G.N. Chen: A graphene platform for sensing biomolecules, Angew. Chem. Int. Ed. **48**(26), 4785–4787 (2009)
15.156 S. Kumar, M. Anija, N. Kamaraju, K.S. Vasu, K.S. Subrahmanyam, A.K. Sood, C.N.R. Rao: Femtosecond carrier dynamics and saturable absorption in graphene suspensions, Appl. Phys. Lett. **95**(19), 3 (2009)
15.157 Z.B. Liu, Y. Wang, X.L. Zhang, Y.F. Xu, Y.S. Chen, J.G. Tian: Nonlinear optical properties of graphene oxide in nanosecond and picosecond regimes, Appl. Phys. Lett. **94**(2), 3 (2009)
15.158 J. Wang, Y. Hernandez, M. Lotya, J.N. Coleman, W.J. Blau: Broadband nonlinear optical response of graphene dispersions, Adv. Mater. **21**(23), 2430 (2009)
15.159 K.S. Choi, Y. Park, K.C. Kwon, J. Kim, C.K. Kim, S.Y. Kim, K. Hong, J.L. Lee: Reduced graphite oxide-indium tin oxide hybrid materials for use as a transparent electrode, J. Electrochem. Soc. **158**(8), J231–J235 (2011)
15.160 J.H. Kim, J.M. Jung, J.Y. Kwak, J.H. Jeong, B.C. Choi, K.T. Lim: Preparation of properties of SWNT/graphene oxide type flexible transparent conductive films, J. Nanosci. Nanotechnol. **11**(8), 7424–7427 (2011)
15.161 Y.Q. Liu, L. Gao, J. Sun, Y. Wang, J. Zhang: Stable Nafion-functionalized graphene dispersions for transparent conducting films, Nanotechnology **20**(46), 107002–107008 (2009)
15.162 Y. Matsuo, K. Iwasa, Y. Sugie, H. Usami, M. Kawaguchi: Effect of the perfluoroalkyl groups on the preparation of carbon-based transparent and conductive thin films from silylated graphite oxides, J. Fluor. Chem. **132**(10), 669–672 (2011)
15.163 S.K. Bhunia, N.R. Jana: Peptide-functionalized colloidal graphene via interdigited bilayer coating and fluorescence turn-on detection of enzyme, ACS Appl. Mater. Interfaces **3**(9), 3335–3341 (2011)
15.164 X. Dong, Q. Long, J. Wang, M.B. Chan-Park, Y. Huang, W. Huang, P. Chen: A graphene nanoribbon network and its biosensing application, Nanoscale **3**(12), 5156–5160 (2011)
15.165 T. Gan, S. Hu: Electrochemical sensors based on graphene materials, Microchim. Acta **175**(1–2), 1–19 (2011)
15.166 Y.P. He, Q.L. Sheng, J.B. Zheng, M.Z. Wang, B. Liu: Magnetite-graphene for the direct electrochemistry of hemoglobin and its biosensing application, Electrochim. Acta **56**(5), 2471–2476 (2011)
15.167 K.-J. Huang, Q.-S. Jing, Z.-W. Wu, L. Wang, C.-Y. Wei: Enhanced sensing of dopamine in the present of ascorbic acid based on graphene/poly(p-aminobenzoic acid) composite film, Colloids Surf. B **88**(1), 310–314 (2011)
15.168 F.-Y. Kong, M.-T. Xu, J.-J. Xu, H.-Y. Chen: A novel lable-free electrochemical immunosensor for carcinoembryonic antigen based on gold nanoparticles-thionine-reduced graphene oxide nanocomposite film modified glassy carbon electrode, Talanta **85**(5), 2620–2625 (2011)
15.169 N. Lei, P. Li, W. Xue, J. Xu: Simple graphene chemiresistors as pH sensors: Fabrication and characterization, Meas. Sci. Technol. **22**(10), 465605–465612 (2011)
15.170 W. Li, X. Geng, Y. Guo, J. Rong, Y. Gong, L. Wu, X. Zhang, P. Li, J. Xu, G. Cheng, M. Sun, L. Liu: Reduced graphene oxide electrically contacted graphene sensor for highly sensitive nitric oxide detection, ACS Nano **5**(9), 6955–6961 (2011)
15.171 H. Liu, J. Gao, M.Q. Xue, N. Zhu, M.N. Zhang, T.B. Cao: Processing of graphene for electrochemical application: Noncovalently functionalize graphene sheets with water-soluble electroactive methylene green, Langmuir **25**(20), 12006–12010 (2009)
15.172 S. Liu, L. Wang, J. Tian, Y. Luo, X. Zhang, X. Sun: Aniline as a dispersing and stabilizing agent for reduced graphene oxide and its subsequent decoration with Ag nanoparticles for enzymeless hydrogen peroxide detection, J. Colloid Interface Sci. **363**(2), 615–619 (2011)

15.173 L.M. Lu, H.B. Li, F.L. Qu, X.B. Zhang, G.L. Shen, R.Q. Yu: In situ synthesis of palladium nanoparticle-graphene nanohybrids and their application in nonenzymatic glucose biosensors, Biosens. Bioelectron. **26**(8), 3500–3504 (2011)
15.174 X.J. Lu, H. Dou, B. Gao, C.Z. Yuan, S.D. Yang, L. Hao, L.F. Shen, X.G. Zhang: A flexible graphene/multiwalled carbon nanotube film as a high performance electrode material for supercapacitors, Electrochim. Acta **56**(14), 5115–5121 (2011)
15.175 Y. Mao, Y. Bao, S. Gan, F. Li, L. Niu: Electrochemical sensor for dopamine based on a novel graphene-molecular imprinted polymers composite recognition element, Biosens. Bioelectron. **28**(1), 291–297 (2011)
15.176 Y. Pu, Z. Zhu, D. Han, H. Liu, J. Liu, J. Liao, K. Zhang, W. Tan: Insulin-binding aptamer-conjugated graphene oxide for insulin detection, Analyst **136**(20), 4138–4140 (2011)
15.177 J.T. Robinson, F.K. Perkins, E.S. Snow, Z.Q. Wei, P.E. Sheehan: Reduced graphene oxide molecular sensors, Nano Lett. **8**(10), 3137–3140 (2008)
15.178 T. Sun, L. Wang, N. Li, X. Gan: Label-free electrochemical aptasensor for thrombin detection based on the nafion@graphene as platform, Bioproc. Biosyst. Eng. **34**(9), 1081–1085 (2011)
15.179 H. Vedala, D.C. Sorescu, G.P. Kotchey, A. Star: Chemical sensitivity of graphene edges decorated with metal nanoparticles, Nano Lett. **11**(6), 2342–2347 (2011)
15.180 L. Wang, K.-Y. Pu, J. Li, X. Qi, H. Li, H. Zhang, C. Fan, B. Liu: A graphene-conjugated oligomer hybrid probe for light-up sensing of lectin and *Escherichia coli*, Adv. Mater. **23**(38), 4386–4391 (2011)
15.181 F. Xu, Y. Sun, Y. Zhang, Y. Shi, Z. Wen, Z. Li: Graphene-Pt nanocomposite for nonenzymatic detection of hydrogen peroxide with enhanced sensitivity, Electrochem. Commun. **13**(10), 1131–1134 (2011)
15.182 D. Ye, L. Luo, Y. Ding, Q. Chen, X. Liu: A novel nitrite sensor based on graphene/polypyrrole/chitosan nanocomposite modified glassy carbon electrode, Analyst **136**(21), 4563–4569 (2011)
15.183 J.W. Yi, J. Park, K.S. Kim, B.H. Kim: pH-responsive self-duplex of (Py)A-substituted oligodeoxyadenylate in graphene oxide solution as a molecular switch, Org. Biomol. Chem. **9**(21), 7434–7438 (2011)
15.184 B. Zhang, D. Tang, B. Liu, H. Chen, Y. Cui, G. Chen: GoldMag nanocomposite-functionalized graphene sensing platform for one-step electrochemical immunoassay of alpha-fetoprotein, Biosens. Bioelectron. **28**(1), 174–180 (2011)
15.185 W. Zhang, Z. Guo, D. Huang, Z. Liu, X. Guo, H. Zhong: Synergistic effect of chemo-photothermal therapy using PEGylated graphene oxide, Biomaterials **32**(33), 8555–8561 (2011)
15.186 H.R. Byon, J. Suntivich, Y. Shao-Horn: Graphene-based nonnoble-metal catalysts for oxygen reduction reaction in acid, Chem. Mater. **23**(15), 3421–3428 (2011)
15.187 W.Q. Fan, Q.H. Lai, Q.H. Zhang, Y. Wang: Nanocomposites of TiO_2 and reduced graphene oxide as efficient photocatalysts for hydrogen evolution, J. Phys. Chem. C **115**(21), 10694–10701 (2011)
15.188 L.L. Feng, G. Gao, P. Huang, X.S. Wang, C.L. Zhang, J.L. Zhang, S.W. Guo, D.X. Cui: Preparation of Pt Ag alloy nanoisland/graphene hybrid composites and its high stability and catalytic activity in methanol electrooxidation, Nanoscale Res. Lett. **6**, 551–556 (2011)
15.189 Y.J. Gao, D. Ma, C.L. Wang, J. Guan, X.H. Bao: Reduced graphene oxide as a catalyst for hydrogenation of nitrobenzene at room temperature, Chem. Commun. **47**(8), 2432–2434 (2011)
15.190 J.-S. Lee, T. Lee, H.-K. Song, J. Cho, B.-S. Kim: Ionic liquid modified graphene nanosheets anchoring manganese oxide nanoparticles as efficient electrocatalysts for Zn-air batteries, Energy Environ. Sci. **4**(10), 4148–4154 (2011)
15.191 S.H. Lee, N. Kakati, S.H. Jee, J. Maiti, Y.-S. Yoon: Hydrothermal synthesis of PtRu nanoparticles supported on graphene sheets for methanol oxidation in direct methanol fuel cell, Mater. Lett. **65**(21–22), 3281–3284 (2011)
15.192 Y.J. Li, W. Gao, L.J. Ci, C.M. Wang, P.M. Ajayan: Catalytic performance of Pt nanoparticles on reduced graphene oxide for methanol electrooxidation, Carbon **48**(4), 1124–1130 (2010)
15.193 Y. Liang, Y. Li, H. Wang, J. Zhou, J. Wang, T. Regier, H. Dai: Co_3O_4 nanocrystals on graphene as a synergistic catalyst for oxygen reduction reaction, Nat. Mater. **10**(10), 780–786 (2011)
15.194 C.-S. Liao, C.-T. Liao, C.-Y. Tso, H.-J. Shy: Microwave-polyol synthesis and electrocatalytic performance of Pt/graphene nanocomposites, Mater. Chem. Phys. **130**(1-2), 270–274 (2011)
15.195 B. Neppolian, A. Bruno, C.L. Bianchi, M. Ashokkumar: Graphene oxide based Pt-TiO_2 photocatalyst: Ultrasound assisted synthesis, characterization and catalytic efficiency, Ultrason. Sonochem. **19**(1), 9–15 (2012)
15.196 R.F. Nie, J.H. Wang, L.N. Wang, Y. Qin, P. Chen, Z.Y. Hou: Platinum supported on reduced graphene oxide as a catalyst for hydrogenation of nitroarenes, Carbon **50**(2), 586–596 (2012)
15.197 C. Peng, B.W. Jiang, Q. Liu, Z. Guo, Z.J. Xu, Q. Huang, H.J. Xu, R.Z. Tai, C.H. Fan: Graphene-templated formation of two-dimensional lepidocrocite nanostructures for high-efficiency catalytic degradation of phenols, Energy Environ. Sci. **4**(6), 2035–2040 (2011)
15.198 B. Seger, P.V. Kamat: Electrocatalytically active graphene-platinum nanocomposites. Role of 2-D carbon support in PEM fuel cells, J. Phys. Chem. C **113**(19), 7990–7995 (2009)

15.199 D.V. Stergiou, E.K. Diamanti, D. Gournis, M.I. Prodromidis: Comparative study of different types of graphenes as electrocatalysts for ascorbic acid, Electrochem. Commun. **12**(10), 1307–1309 (2010)
15.200 Y. Wen, H. Ding, Y. Shan: Preparation and visible light photocatalytic activity of Ag/TiO_2/graphene nanocomposite, Nanoscale **3**(10), 4411–4417 (2011)
15.201 Q.J. Xiang, J.G. Yu, M. Jaroniec: Preparation and enhanced visible-light photocatalytic H_2-production activity of graphene/C_3N_4 composites, J. Phys. Chem. C **115**(15), 7355–7363 (2011)
15.202 P. Zeng, Q.G. Zhang, T.Y. Peng, X.H. Zhang: One-pot synthesis of reduced graphene oxide-cadmium sulfide nanocomposite and its photocatalytic hydrogen production, Phys. Chem. Chem. Phys. **13**(48), 21496–21502 (2011)
15.203 Y. Zhang, Y.-E. Gu, S. Lin, J. Wei, Z. Wang, C. Wang, Y. Du, W. Ye: One-step synthesis of PtPdAu ternary alloy nanoparticles on graphene with superior methanol electrooxidation activity, Electrochim. Acta **56**(24), 8746–8751 (2011)
15.204 Y. Zhang, Z.-R. Tang, X. Fu, Y.-J. Xu: Engineering the unique 2-D mat of graphene to achieve graphene-TiO_2 nanocomposite for photocatalytic selective transformation: What advantage does graphene have over its forebear carbon nanotube?, ACS Nano **5**(9), 7426–7435 (2011)
15.205 C. Zhu, P. Wang, L. Wang, L. Han, S. Dong: Facile synthesis of two-dimensional graphene/SnO_2/Pt ternary hybrid nanomaterials and their catalytic properties, Nanoscale **3**(10), 4376–4382 (2011)
15.206 Y. Zu, J. Tang, W. Zhu, M. Zhang, G. Liu, Y. Liu, W. Zhang, M. Jia: Graphite oxide-supported CaO catalysts for transesterification of soybean oil with methanol, Bioresour. Technol. **102**(19), 8939–8944 (2011)
15.207 K. Min, J.Y. Jung, T.H. Han, Y. Park, C. Jung, S.M. Hong, C.M. Koo: Graphene electrodes for artificial muscles, Mol. Cryst. Liq. Cryst. **539**, 260–265 (2011)
15.208 S. Chen, P. Chen, Y. Wang: Carbon nanotubes grown in situ on graphene nanosheets as superior anodes for Li-ion batteries, Nanoscale **3**(10), 4323–4329 (2011)
15.209 P.A. Denis: Improving the chemical reactivity of single-wall carbon nanotubes with lithium doping, J. Phys. Chem. C **115**(41), 20282–20288 (2011)
15.210 S. Dong, X. Chen, K. Zhang, L. Gu, L. Zhang, X. Zhou, L. Li, Z. Liu, P. Han, H. Xu, J. Yao, C. Zhang, X. Zhang, C. Shang, G. Cui, L. Chen: Molybdenum nitride based hybrid cathode for rechargeable lithium-O_2 batteries, Chem. Commun. **47**(40), 11291–11293 (2011)
15.211 C.X. Guo, M. Wang, T. Chen, X.W. Lou, C.M. Li: A hierarchically nanostructured composite of MnO_2/conjugated polymer/graphene for high-performance lithium ion batteries, Adv. Energy Mater. **1**(5), 736–741 (2011)
15.212 C.-T. Hsieh, C.-Y. Lin, J.-Y. Lin: High reversibility of Li intercalation and de-intercalation in MnO-attached graphene anodes for Li-ion batteries, Electrochim. Acta **56**(24), 8861–8867 (2011)
15.213 H. Liu, W. Yang: Ultralong single crystalline V_2O_5 nanowire/graphene composite fabricated by a facile green approach and its lithium storage behavior, Energy Environ. Sci. **4**(10), 4000–4008 (2011)
15.214 Y.J. Mai, X.L. Wang, J.Y. Xiang, Y.Q. Qiao, D. Zhang, C.D. Gu, J.P. Tu: CuO/graphene composite as anode materials for lithium-ion batteries, Electrochim. Acta **56**(5), 2306–2311 (2011)
15.215 D.Y. Pan, S. Wang, B. Zhao, M.H. Wu, H.J. Zhang, Y. Wang, Z. Jiao: Li storage properties of disordered graphene nanosheets, Chem. Mater. **21**(14), 3136–3142 (2009)
15.216 Y. Shi, L. Wen, F. Li, H.-M. Cheng: Nanosized Li(4)Ti_5O_{12}/graphene hybrid materials with low polarization for high rate lithium ion batteries, J. Power Sources **196**(20), 8610–8617 (2011)
15.217 L. Su, Y. Jing, Z. Zhou: Li ion battery materials with core-shell nanostructures, Nanoscale **3**(10), 3967–3983 (2011)
15.218 Y. Sun, X. Hu, W. Luo, Y. Huang: Self-assembled hierarchical MoO_2/graphene nanoarchitectures and their application as a high-performance anode material for lithium-ion batteries, ACS Nano **5**(9), 7100–7107 (2011)
15.219 L. Tian, Q. Zhuang, J. Li, Y. Shi, J. Chen, F. Lu, S. Sun: Mechanism of intercalation and deintercalation of lithium ions in graphene nanosheets, Chin. Sci. Bull. **56**(30), 3204–3212 (2011)
15.220 J. Zhu, K. Sun, D. Sim, C. Xu, H. Zhang, H.H. Hng, Q. Yan: Nanohybridization of ferrocene clusters and reduced graphene oxides with enhanced lithium storage capability, Chem. Commun. **47**(37), 10383–10385 (2011)
15.221 J.X. Zhu, T. Zhu, X.Z. Zhou, Y.Y. Zhang, X.W. Lou, X.D. Chen, H. Zhang, H.H. Hng, Q.Y. Yan: Facile synthesis of metal oxide/reduced graphene oxide hybrids with high lithium storage capacity and stable cyclability, Nanoscale **3**(3), 1084–1089 (2011)
15.222 X.J. Zhu, Y.W. Zhu, S. Murali, M.D. Stollers, R.S. Ruoff: Nanostructured reduced graphene oxide/Fe_2O_3 composite as a high-performance anode material for lithium ion batteries, ACS Nano **5**(4), 3333–3338 (2011)
15.223 M. Qian, T. Feng, H. Ding, L.F. Lin, H.B. Li, Y.W. Chen, Z. Sun: Electron field emission from screen-printed graphene films, Nanotechnology **20**(42), 425702–425707 (2009)
15.224 B.G. Choi, J. Hong, W.H. Hong, P.T. Hammond, H. Park: Facilitated ion transport in all-solid-state flexible supercapacitors, ACS Nano **5**(9), 7205–7213 (2011)
15.225 W. Gao, N. Singh, L. Song, Z. Liu, A.L.M. Reddy, L.J. Ci, R. Vajtai, Q. Zhang, B.Q. Wei, P.M. Ajayan:

Direct laser writing of micro-supercapacitors on hydrated graphite oxide films, Nat. Nanotechnol. **6**(8), 496–500 (2011)
15.226 S. Konwer, R. Boruah, S.K. Dolui: Studies on conducting polypyrrole/graphene oxide composites as supercapacitor electrode, J. Electron. Mater. **40**(11), 2248–2255 (2011)
15.227 M.A. Pope, C. Punckt, I.A. Aksay: Intrinsic capacitance and redox activity of functionalized graphene sheets, J. Phys. Chem. C **115**(41), 20326–20334 (2011)
15.228 R.B. Rakhi, H.N. Alshareef: Enhancement of the energy storage properties of supercapacitors using graphene nanosheets dispersed with metal oxide-loaded carbon nanotubes, J. Power Sources **196**(20), 8858–8865 (2011)
15.229 Y. Sun, Q. Wu, G. Shi: Supercapacitors based on self-assembled graphene organogel, Phys. Chem. Chem. Phys. **13**(38), 17249–17254 (2011)
15.230 C.P. Tien, H.S. Teng: Polymer/graphite oxide composites as high-performance materials for electric double layer capacitors, J. Power Sources **195**(8), 2414–2418 (2010)
15.231 Y. Wang, Z.Q. Shi, Y. Huang, Y.F. Ma, C.Y. Wang, M.M. Chen, Y.S. Chen: Supercapacitor devices based on graphene materials, J. Phys. Chem. C **113**(30), 13103–13107 (2009)
15.232 Z. Weng, Y. Su, D.-W. Wang, F. Li, J. Du, H.-M. Cheng: Graphene-cellulose paper flexible supercapacitors, Adv. Energy Mater. **1**(5), 917–922 (2011)
15.233 G. Yu, L. Hu, N. Liu, H. Wang, M. Vosgueritchian, Y. Yang, Y. Cui, Z. Bao: Enhancing the supercapacitor performance of graphene/MnO_2 nanostructured electrodes by conductive wrapping, Nano Lett. **11**(10), 4438–4442 (2011)
15.234 J. Zhang, J. Jiang, H. Li, X.S. Zhao: A high-performance asymmetric supercapacitor fabricated with graphene-based electrodes, Energy Environ. Sci. **4**(10), 4009–4015 (2011)
15.235 K. Zhang, L. Mao, L.L. Zhang, H.S.O. Chan, X.S. Zhao, J.S. Wu: Surfactant-intercalated, chemically reduced graphene oxide for high performance supercapacitor electrodes, J. Mater. Chem. **21**(20), 7302–7307 (2011)
15.236 K. Zhang, L.L. Zhang, X.S. Zhao, J.S. Wu: Graphene/polyaniline nanoriber composites as supercapacitor electrodes, Chem. Mater. **22**(4), 1392–1401 (2010)
15.237 L. Zhang, G.Q. Shi: Preparation of highly conductive graphene hydrogels for fabricating supercapacitors with high rate capability, J. Phys. Chem. C **115**(34), 17206–17212 (2011)
15.238 Y.P. Zhang, H.B. Li, L.K. Pan, T. Lu, Z. Sun: Capacitive behavior of graphene-ZnO composite film for supercapacitors, J. Electroanal. Chem. **634**(1), 68–71 (2009)
15.239 G. Zhao, L. Jiang, Y. He, J. Li, H. Dong, X. Wang, W. Hu: Sulfonated graphene for persistent aromatic pollutant management, Adv. Mater. **23**(34), 3959 (2011)
15.240 B.J. Kim, M.S. Kang, V.H. Pham, T.V. Cuong, E.J. Kim, J.S. Chung, S.H. Hur, J.H. Cho: Low-voltage solution-processed graphene transistors based on chemically and solvothermally reduced graphene oxide, J. Mater. Chem. **21**(34), 13068–13073 (2011)
15.241 L. Zhou, W. Wang, J. Tang, J.-H. Zhou, H.-J. Jiang, J. Shen: Graphene oxide noncovalent photosensitizer and its anticancer activity in vitro, Chemistry **17**(43), 12084–12091 (2011)
15.242 S. Zhang, Z. Du, G. Li: Layer-by-layer fabrication of chemical-bonded graphene coating for solid-phase microextraction, Anal. Chem. **83**(19), 7531–7541 (2011)
15.243 W. Gao, M. Majumder, L.B. Alemany, T.N. Narayanan, M.A. Ibarra, B.K. Pradhan, P.M. Ajayan: Engineered graphite oxide materials for application in water purification, ACS Appl. Mater. Interfaces **3**(6), 1821–1826 (2011)
15.244 J. Kysilka, M. Rubes, L. Grajciar, P. Nachtigall, O. Bludsky: Accurate description of argon and water adsorption on surfaces of graphene-based carbon allotropes, J. Phys. Chem. A **115**(41), 11387–11393 (2011)
15.245 S. Liu, T.H. Zeng, M. Hofmann, E. Burcombe, J. Wei, R. Jiang, J. Kong, Y. Chen: Antibacterial activity of graphite, graphite oxide, graphene oxide, and reduced graphene oxide: Membrane and oxidative stress, ACS Nano **5**(9), 6971–6980 (2011)
15.246 Q. Min, X. Zhang, H. Zhang, F. Zhou, J.-J. Zhu: Synthesis of Fe_3O_4-graphene-TiO_2 ternary composite networks for enhanced capture of phosphopeptides, Chem. Commun. **47**(42), 11709–11711 (2011)
15.247 H. Pang, Q. Lu, F. Gao: Graphene oxide induced growth of one-dimensional fusiform zirconia nanostructures for highly selective capture of phosphopeptides, Chem. Commun. **47**(42), 11772–11774 (2011)
15.248 Q. Wu, G. Zhao, C. Feng, C. Wang, Z. Wang: Preparation of a graphene-based magnetic nanocomposite for the extraction of carbamate pesticides from environmental water samples, J. Chromatogr. A **1218**(44), 7936–7942 (2011)
15.249 S. Zhang, Y. Shao, J. Liu, I.A. Aksay, Y. Lin: Graphene-polypyrrole nanocomposite as a highly efficient and low cost electrically switched ion exchanger for removing ClO_4^- from wastewater, ACS Appl. Mater. Interfaces **3**(9), 3633–3637 (2011)
15.250 G. Zhao, X. Ren, X. Gao, X. Tan, J. Li, C. Chen, Y. Huang, X. Wang: Removal of Pb(II) ions from aqueous solutions on few-layered graphene oxide nanosheets, Dalton Trans. **40**(41), 10945–10952 (2011)

15.251 Q. Liu, Z.F. Liu, X.Y. Zhong, L.Y. Yang, N. Zhang, G.L. Pan, S.G. Yin, Y. Chen, J. Wei: Polymer photovoltaic cells based on solution-processable graphene and P3HT, Adv. Funct. Mater. **19**(6), 894–904 (2009)
15.252 Z. Liu, Q. Liu, Y. Huang, Y. Ma, S. Yin, X. Zhang, W. Sun, Y. Chen: Organic photovoltaic devices based on a novel acceptor material. Graphene, Adv. Mater. **20**(20), 3924–3930 (2008)
15.253 M.S. Ryu, J. Jang: Effect of solution processed graphene oxide/nickel oxide bi-layer on cell performance of bulk-heterojunction organic photovoltaic, Sol. Energy Mater. Sol. Cells **95**(10), 2893–2896 (2011)
15.254 K. Yang, C. Xu, L. Huang, L. Zou, H. Wang: Hybrid nanostructure heterojunction solar cells fabricated using vertically aligned Zn0 nanotubes grown on reduced graphene oxide, Nanotechnology **22**(40), 405401–405407 (2011)
15.255 Y. Zang, D. Xie, X. Wu, Y. Chen, Y. Lin, M. Li, H. Tian, X. Li, Z. Li, H. Zhu, T. Ren, D. Plant: Enhanced photovoltaic properties in graphene/polycrystalline $BiFeO_3$/Pt heterojunction structure, Appl. Phys. Lett. **99**(13), 32904–32904 (2011)
15.256 J. Liang, Y. Huang, J. Oh, M. Kozlov, D. Sui, S. Fang, R.H. Baughman, Y. Ma, Y. Chen: Electromechanical actuators based on graphene and graphene/Fe_3O_4 hybrid paper, Adv. Funct. Mater. **21**(19), 3778–3784 (2011)
15.257 K.P. Loh, Q. Bao, G. Eda, M. Chhowalla: Graphene oxide as a chemically tunable platform for optical applications, Nat. Chem. **2**(12), 1015–1024 (2010)
15.258 Z.B. Liu, Y.F. Xu, X.Y. Zhang, X.L. Zhang, Y.S. Chen, J.G. Tian: Porphyrin and fullerene covalently functionalized graphene hybrid materials with large nonlinear optical properties, J. Phys. Chem. B **113**(29), 9681–9686 (2009)
15.259 S. Niyogi, E. Bekyarova, M.E. Itkis, J.L. McWilliams, M.A. Hamon, R.C. Haddon: Solution properties of graphite and graphene, J. Am. Chem. Soc. **128**(24), 7720–7721 (2006)
15.260 Y.F. Xu, Z.B. Liu, X.L. Zhang, Y. Wang, J.G. Tian, Y. Huang, Y.F. Ma, X.Y. Zhang, Y.S. Chen: A graphene hybrid material covalently functionalized with porphyrin: Synthesis and optical limiting property, Adv. Mater. **21**(12), 1275 (2009)
15.261 L.M. Veca, F.S. Lu, M.J. Meziani, L. Cao, P.Y. Zhang, G. Qi, L.W. Qu, M. Shrestha, Y.P. Sun: Polymer functionalization and solubilization of carbon nanosheets, Chem. Commun. (18), 2565–2567 (2009)
15.262 N. Mohanty, V. Berry: Graphene-based single-bacterium resolution biodevice and DNA transistor: Interfacing graphene derivatives with nanoscale and microscale biocomponents, Nano Lett. **8**(12), 4469–4476 (2008)
15.263 Y.J. Zhang, W.B. Hu, B. Li, C. Peng, C.H. Fan, Q. Huang: Synthesis of polymer-protected graphene by solvent-assisted thermal reduction process, Nanotechnology **22**(34), 345601–345606 (2011)
15.264 Y.F. Yang, J. Wang, J. Zhang, J.C. Liu, X.L. Yang, H.Y. Zhao: Exfoliated graphite oxide decorated by PDMAEMA chains and polymer particles, Langmuir **25**(19), 11808–11814 (2009)
15.265 M. Fang, K.G. Wang, H.B. Lu, Y.L. Yang, S. Nutt: Covalent polymer functionalization of graphene nanosheets and mechanical properties of composites, J. Mater. Chem. **19**(38), 7098–7105 (2009)
15.266 S.H. Lee, D.R. Dreyer, J.H. An, A. Velamakanni, R.D. Piner, S. Park, Y.W. Zhu, S.O. Kim, C.W. Bielawski, R.S. Ruoff: Polymer brushes via controlled, surface-initiated atom transfer radical polymerization (ATRP) from graphene oxide, Macromol. Rapid Commun. **31**(3), 281–288 (2010)
15.267 S. Stankovich, R.D. Piner, S.T. Nguyen, R.S. Ruoff: Synthesis and exfoliation of isocyanate-treated graphene oxide nanoplatelets, Carbon **44**(15), 3342–3347 (2006)
15.268 H.T. Hu, X.B. Wang, J.C. Wang, F.M. Liu, M. Zhang, C.H. Xu: Microwave-assisted covalent modification of graphene nanosheets with chitosan and its electrorheological characteristics, Appl. Surf. Sci. **257**(7), 2637–2642 (2011)
15.269 S. Wang, P.J. Chia, L.L. Chua, L.H. Zhao, R.Q. Png, S. Sivaramakrishnan, M. Zhou, R.G.S. Goh, R.H. Friend, A.T.S. Wee, P.K.H. Ho: Band-like transport in surface-functionalized highly solution-processable graphene nanosheets, Adv. Mater. **20**(18), 3440 (2008)
15.270 O.C. Compton, D.A. Dikin, K.W. Putz, L.C. Brinson, S.T. Nguyen: Electrically conductive *alkylated* graphene paper via chemical reduction of amine-functionalized graphene oxide paper, Adv. Mater. **22**(8), 892 (2010)
15.271 H.F. Yang, C.S. Shan, F.H. Li, D.X. Han, Q.X. Zhang, L. Niu: Covalent functionalization of polydisperse chemically-converted graphene sheets with amine-terminated ionic liquid, Chem. Commun.(26), 3880–3882 (2009)
15.272 H.F. Yang, F.H. Li, C.S. Shan, D.X. Han, Q.X. Zhang, L. Niu, A. Ivaska: Covalent functionalization of chemically converted graphene sheets via silane and its reinforcement, J. Mater. Chem. **19**(26), 4632–4638 (2009)
15.273 S. Park, D.A. Dikin, S.T. Nguyen, R.S. Ruoff: Graphene oxide sheets chemically cross-linked by polyallylamine, J. Phys. Chem. C **113**(36), 15801–15804 (2009)
15.274 R.K. Layek, S. Samanta, D.P. Chatterjee, A.K. Nandi: Physical and mechanical properties of poly(methyl methacrylate)-functionalized graphene/poly(vinylidine fluoride) nanocomposites Piezoelectric beta polymorph formation, Polymer **51**(24), 5846–5856 (2010)
15.275 S. Kamada, H. Nomoto, K. Fukuda, T. Fukawa, H. Shirai, M. Kimura: Noncovalent wrapping of

chemically modified graphene with pi-conjugated disk-like molecules, Colloid Polym. Sci. **289**(8), 925–932 (2011)

15.276 X.Y. Chen, L. Yuan, P.Y. Yang, J.H. Hu, D. Yang: Covalent polymeric modification of graphene nanosheets via surface-initiated single-electron-transfer living radical polymerization, J. Polym. Sci. A **49**(23), 4977–4986 (2011)

15.277 X.Y. Yang, X.Y. Zhang, Z.F. Liu, Y.F. Ma, Y. Huang, Y. Chen: High-efficiency loading and controlled release of doxorubicin hydrochloride on graphene oxide, J. Phys. Chem. C **112**(45), 17554–17558 (2008)

15.278 Y.-C. Cao, C. Xu, X. Wu, X. Wang, L. Xing, K. Scott: A poly (ethylene oxide)/graphene oxide electrolyte membrane for low temperature polymer fuel cells, J. Power Sources **196**(20), 8377–8382 (2011)

15.279 S.-S. Li, K.-H. Tu, C.-C. Lin, C.-W. Chen, M. Chhowalla: Solution-processable graphene oxide as an efficient hole transport layer in polymer solar cells, ACS Nano **4**(6), 3169–3174 (2010)

15.280 I.P. Murray, S.J. Lou, L.J. Cote, S. Loser, C.J. Kadleck, T. Xu, J.M. Szarko, B.S. Rolczynski, J.E. Johns, J. Huang, L. Yu, L.X. Chen, T.J. Marks, M.C. Hersam: Graphene oxide interlayers for robust, high-efficiency organic photovoltaics, J. Phys. Chem. Lett. **2**(24), 3006–3012 (2011)

15.281 D.R. Dreyer, K.A. Jarvis, P.J. Ferreira, C.W. Bielawski: Graphite oxide as a dehydrative polymerization catalyst: A one-step synthesis of carbon-reinforced poly(phenylene methylene) composites, Macromolecules **44**(19), 7659–7667 (2011)

15.282 A.V. Kumar, K.R. Rao: Recyclable graphite oxide catalyzed Friedel-Crafts addition of indoles to alpha,beta-unsaturated ketones, Tetrahedron Lett. **52**(40), 5188–5191 (2011)

15.283 A. Kolmakov, D.A. Dikin, L.J. Cote, J. Huang, M.K. Abyaneh, M. Amati, L. Gregoratti, S. Guenther, M. Kiskinova: Graphene oxide windows for in situ environmental cell photoelectron spectroscopy, Nat. Nanotechnol. **6**(10), 651–657 (2011)

15.284 M. Krueger, S. Berg, D.A. Stone, E. Strelcov, D.A. Dikin, J. Kim, L.J. Cote, J. Huang, A. Kolmakov: Drop-casted self-assembling graphene oxide membranes for scanning electron microscopy on wet and dense gaseous samples, ACS Nano **5**(12), 10047–10054 (2011)

16. Compound Crystals

Roi Levi, Maya Bar-Sadan, Reshef Tenne

Graphite nanoparticles are known to be unstable due to the abundance of rim atoms with dangling bonds, closing into fullerenes and nanotubes under appropriate conditions. It was proposed in 1992 that this property is common also to nanoparticles of inorganic layered materials rather than being limited to carbon. Indeed, inorganic fullerene-like nanoparticles (IF) and inorganic nanotubes (INT) were produced initially from the layered materials WS_2 and MoS_2, and subsequently from numerous other layered compounds. The state of the art in this field is described briefly in this review.

This chapter reviews the main methods used for IF and INT synthesis and discusses the relations between the different mechanisms and the resulting morphologies. Emphasis is placed on methods reported recently. The main differences between the morphologies are presented using WS_2 and MoS_2 as representatives of the inorganic IF/INT family. The measured properties of W(Mo)S_2 IF and INT are further examined and compared with theoretical calculations.

Finally, current applications of WS_2 and MoS_2 IF and INT are reviewed, highlighting recent advances in the fields of tribology and nanocomposite materials.

16.1 **Nanostructures** 605
16.2 **Synthetic Methods** 608
16.2.1 IF Synthesis 608
16.2.2 INT Synthesis 614
16.3 **Physical Properties** 618
16.3.1 Synthesis and Structural Properties 618
16.3.2 Mechanical Properties 622
16.3.3 Electronic and Optical Properties 625
16.3.4 Calculations and Simulations 627
16.4 **Applications** 628
16.4.1 Tribological Applications 629
16.4.2 Composites 629
16.4.3 Hydrogen and Lithium Adsorption/Desorption in INT 630
16.4.4 Miscellaneous 630
16.5 **Conclusions** 630
References 631

16.1 Nanostructures

Zero- and one-dimensional nanostructures such as nanoparticles, fullerenes, nanorods, nanobelts, nanowires, and nanotubes often possess unique properties with respect to the single-crystal bulk material. Thus, intensive attention is focused on their various applications in materials sciences and nanoscale devices, where commercial applications are being explored [16.1, 2].

Nanostructures possess a relatively small number of atoms in their smallest dimension and exhibit an extremely high surface-to-volume ratio. Therefore, their properties may be significantly influenced by their shape, interfaces, and structure down to the level of a single atom [16.3]; for example, the electrical properties of a particle may depend strongly on the interfaces between different phases or compositions inside the particle as well as the atomic configurations of the different areas [16.2]. Moreover, these configurations may yield new insights into the growth mechanisms of these nanoparticles [16.2]. Thus, deep understanding of the composition and structure at the atomic level is key to understanding the relations between the unique properties of nanomaterials when compared with the bulk phase [16.3].

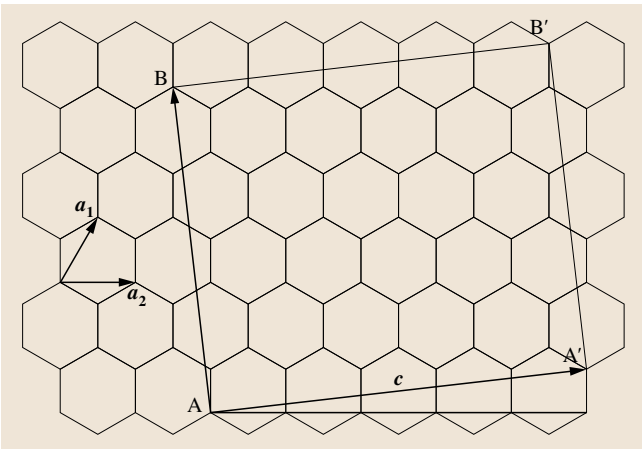


Fig. 16.1 Schematic drawing of a nanotube roll-up vector (n,m = 1,4)

Closed-cage structures, namely nanotubes and fullerenes, are an important subgroup of nanostructures. The discovery of carbon nanotubes [16.4] immediately brought to mind the question of whether nanotubular structures can be produced exclusively from carbon. The synthesis of noncarbon nanotubes based on molybdenum and tungsten disulfides in 1992 proved that hollow one-dimensional (1-D) nanostructures are not unique to carbon [16.5]. These hollow nanoparticles were termed inorganic nanotubes (INT) and inorganic fullerene-like (IF) nanoparticles. In contrast to carbon nanotubes (CNT) and fullerenes (e.g., C_{60}), these nanostructures are made of inorganic compounds with layered structure, and more recently from nonlayered compounds. Today, it is well established that numerous materials form closed-cage structures, and that carbon fullerenes and nanotubes are only a special case [16.6]. The last 20 years of research into nanomaterials have seen the discovery of nanotubulenes composed of dozens of inorganic compounds. Some of them were even found in rocks from Earth and space, as was the case with carbon nanostructures [16.7, 8].

Closed-cage structures are generally constructed from folded two-dimensional (2-D) layers. In analogy to graphite, nanoplatelets of many layered inorganic compounds are unstable towards folding and can form closed-cage structures, i. e., INT and IF [16.9]. The two most relevant interactions in 2-D (layered) compounds are the strong chemical (mostly covalent) bonds within the molecular sheet, and the weak van der Waals (vdW) interactions responsible for stacking the layers with the vdW gap between them.

A monolayer of a 2-D compound can be defined as a 2-D lattice which is constructed by the lengths of two translation vectors ($\boldsymbol{a}_1$ and $\boldsymbol{a}_2$) and the angle between them (φ); for example, the cylindrical surfaces of a CNT are composed of carbon atoms arranged in a hexagonal structure, which is essentially a rolled-up 2-D lattice of hexagonal graphene [16.10]. Similarly, many of the inorganic compounds which form tubular structures possess a hexagonal (trigonal) atomic arrangement within the layer. Furthermore, the structure of INT may be classified in the same manner as for CNT, i. e., as (n, m). Using the basis vectors of the 2-D lattice $(\boldsymbol{a}_1, \boldsymbol{a}_2)$, the *roll-up* vector is defined as $\boldsymbol{c} = n\boldsymbol{a}_1 + m\boldsymbol{a}_2$ (Fig. 16.1). For a 2-D hexagonal lattice ($|\boldsymbol{a}_1| = |\boldsymbol{a}_2| \equiv |\boldsymbol{a}|$), the radius R of the corresponding tube is then given by $R = c/2\pi = a/2\pi \cdot \sqrt{3(n^2 + m^2 + mn)}$.

INT and IF differ significantly from many of the other zero-dimensional (0-D) and 1-D nanostructures (e.g., quantum dots and nanowires, respectively). Here, the surface and bulk atoms of the former experience an almost identical chemical and physical environment. Thus, the properties of many known 0-D and 1-D nanostructures are negatively affected by surface oxidation and reconstruction. Various examples include the luminescence of quantum dots, the magnetic behavior of spintronic devices, and the superconducting behavior of 1-D nanowires, all of which are overshadowed by surface effects. INT and IF are therefore relatively immune to these effects, since in general the chemical bonding of the surface atoms is the same as those situated in the inner layers [16.1].

An additional subgroup of nanostructures with hollow structures are those obtained from compounds with a three-dimensional (3-D) crystal lattice such as GaN [16.11], MgO [16.12], and spinel ($ZnAl_2O_4$) [16.13]. Another recent example is polycrystalline arrays of nanotubes from TiO_2 and similar materials via electrochemical anodization of Ti foils in fluoride and other acidic solutions [16.14, 15]. As these topics will not be covered here, the reader is referred to [16.16] for further information.

There has been a significant increase of scientific interest in INT and IF over the last decade. The first INT and IF synthesized belong to the transition-metal dichalcogenides (MX_2, M = W, Mo). These were polyhedra and cylinders of WS_2 which were produced by heating thin tungsten (molybdenum) films in a reducing H_2S atmosphere [16.17]. Since then, multiple MX_2 chalcogenide nanostructures have been synthesized from a variety of materials such as M = Mo,

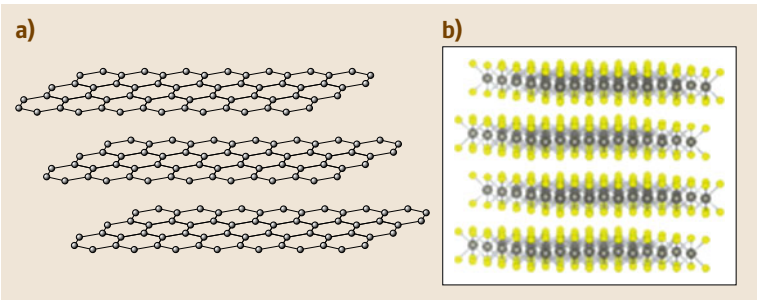


Fig. 16.2 **(a)** Schematic drawing of monoatomic graphite layers. **(b)** Schematic drawing of MoS_2 triatomic layers

Nb, Ta, Zr, Hf, and Re, and X = S, Se [16.18–24]. Various approaches to nanotubes of other materials, such as $NiCl_2$ [16.25], VS_2 [16.26], TiS_2 [16.27], and InS [16.28], have also been reported. Furthermore, INT of several materials such as binary oxides, nitrides, and halides, as well as metals and nonmetallic elemental materials, have been prepared and characterized [16.29–32]. In addition to the INT from binary compounds, INT of complex materials such as perovskite titanates have also been reported, as well as composites involving nanotubes, nanowires, and nanoparticles.

In contrast with INT, IF nanoparticles are known only for a few families of materials, such as WS_2 [16.5], MoS_2 [16.18, 33], TaS_2 [16.34], TiS_2 [16.35], BN [16.36, 37], TiO_x [16.38], Cs_2O [16.39], V_2O_5 [16.40], $CdCl_2$ [16.41], CdI_2 [16.42], and $NiBr_2$ [16.43]. All the above indicate that, under suitable conditions, many 2-D inorganic compounds may form INT or IF. Therefore, research in this area has focused on synthesis of new INT and IF materials and understanding their different properties. However, scaling up the synthetic process for semi-industrial applications has been achieved so far in a limited number of cases only.

Molybdenum and tungsten disulfides (MS_2, M = Mo, W) are typical representative compounds of the rather extensive family of layered binary and ternary metal chalcogenides. Typically, the lattice of metal disulfides consists of triple atomic layers (S–M–S) stacked in a hexagonal order. The metal atoms are sixfold coordinated and are hexagonally packed between two trigonal atomic layers of S atoms. Therefore, INT and IF possess a more complex structure when compared with CNT and C_{60} (Fig. 16.2). Furthermore, nanotubes with the same radius formed from thicker 2-D monolayers experience larger internal strains and are thus less stable [16.44]; for example, the strain energies of single-walled CNT (SW-CNT) are lower when compared with the those of TiS_2 and GaSe tubes formed with three and four atomic monolayers, respectively [16.45, 46]. To compensate for the larger strain, INT and IF accommodate a larger radius and also gain stability by forming multi-walled structures. Therefore, INT and IF are relatively more energetic than their organic counterparts, frequently resulting in a very challenging synthetic procedure to overcome these obstacles.

In recent years, INT and IF have been produced by various synthetic routes and experimental techniques, resulting in a large variety of nanostructured materials with different properties. Several routes to INT of Mo and W sulfides and selenides have been reported in the last decade [16.29, 30]. Among the synthetic routes used are electron beam irradiation in a transmission electron microscope (TEM) [16.47], electrical pulse in a scanning tunneling microscope (SEM) [16.48], sonoelectrochemical bath reaction [16.17], and electrochemical deposition from ethylene glycol solution [16.49]. However, to date, only in the case of INT and IF of $W(Mo)S_2$ could production be scaled up to the pilot stage of several kg per day in the case of the IF and a few hundred grams of INT-WS_2. Currently, the most efficient methods for producing $W(Mo)S_2$ INT and IF are based on sulfurization of $W(Mo)O_x$ nanoparticles (NP) in a fluidized bed reactor using a stream of H_2S gas [16.50, 51].

The present chapter reviews the main synthetic routes to obtain INT and IF with a focus on those of $W(Mo)S_2$ as model compounds for the layered chalcogenide family. The different mechanisms that affect the various morphologies of the final products will be discussed. Furthermore, these nanostructures will be examined in light of recent advances in calculations and theoretical modeling of the stability and properties of nanostructures. These well-studied materials allow for some generalizations relating the synthetic process with their emergent properties by ultimately understanding their structure.

16.2 Synthetic Methods

Following the first INT and IF nanostructures reported in 1992 by *Tenne* et al. [16.5], numerous synthetic routes have been utilized to produce these structures. The synthetic methodologies can be divided into two main categories: chemical and physical synthesis. The first includes synthetic routes in which a chemical reaction is applied. The second group consists of routes in which the starting material undergoes a structural change into a closed hollow nanostructure following an energy stroke.

16.2.1 IF Synthesis

The most common chemical synthetic methods rely on sulfurization of the appropriate metal oxide. Additional methods have been developed which rely on decomposition, rolling up of sheets, and crystallization of the appropriate amorphous metal sulfide. However, as the next sections will show, the morphology and exact composition of the precursor have a significant influence on the final shape, size, and structure of the products.

Formation of IF by chemical synthesis generally takes place by two different mechanisms: the first from the outside inwards, i. e., starting from the nanoparticle surface, and the second in the opposite direction, i. e., starting from a small nucleus and growing outwards to become a nanocrystal. The outside-in approach was the first method to be used in the production of large amounts of IF. Here, solid metal oxide nanoparticles are sulfurized to the appropriate metal sulfide nanoparticles with closed-cage structure (IF). Therefore, the rate of formation of the IF NP strongly depends on the diffusion rate of the sulfurizing agent within the nanoparticle lattice, while the initial diameter of the precursor NP dictates the final IF size.

The syntheses of IF-WS_2 and IF-MoS_2 differ in some important details, but the main features are common to both. Within the first few seconds of the reaction, the outer surface of the oxide NP precursor reacts with the H_2S gas and a completely closed MS_2 layer, or two, are formed. This sulfide layer is an inert surface and protects the NP against aggregation, which would otherwise lead to the formation of the bulk 2H-MS_2 phase. Fast hydrogen diffusion into the NP reduces the oxide core to MoO_{3-x} or $W_{18}O_{49}$ within 1–2 min [16.53]. The oxide core is then converted to the respective sulfide (IF) through a slow diffusion-controlled reaction ending after ca. 30 min. Deep understanding of the outside-in growth mechanism for this synthesis (Fig. 16.3) for both IF-WS_2 and IF-MoS_2 made it possible to control the resulting product.

The final IF size is determined by the size of the precursor oxide NP. The produced IF possesses a hollow core (5–10 vol. %). This is due to the density difference between the oxide precursor and the sulfide product (5%), and the fact that the initial volume of the oxide NP is preserved during the chemical transformation. This means that, prior to the IF-WS_2 synthesis, the precursor oxide NP of a desirable size and shape must be prepared.

The first two completely closed MS_2 layers serve a second purpose of protecting the metal oxide core from being completely reduced to the respective metal [16.18]. The driving forces for hydrogen propagation into the core of the oxide NP are the uniform hydrostatic pressure and the chemical reactivity of the

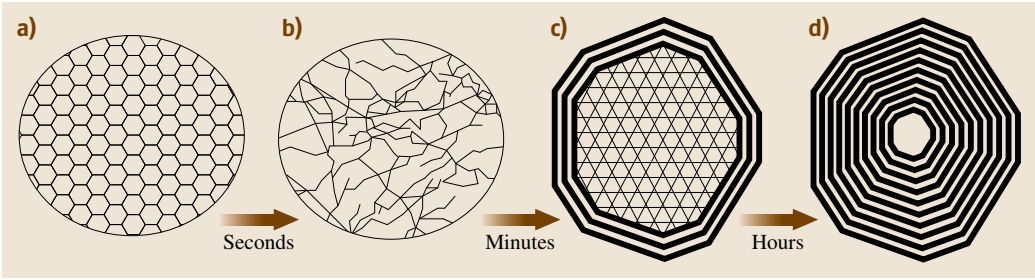


Fig. 16.3 Schematic depiction of the growth mechanism of IF-WS_2, using WO_3 NP as a precursor in a solid–phase reaction: **(a)** initial WO_3 NP; **(b)** partly reduced oxide ($W_{20}O_{58}$) NP, encapsulated with several (1–2) layers of tungsten disulfide; **(c)** the suboxide ($W_{18}O_{49}$) core within the envelope of a few (3–5) disulfide layers; **(d)** the final quasispherical closed-cage IF-WS_2 NP (after [16.52])

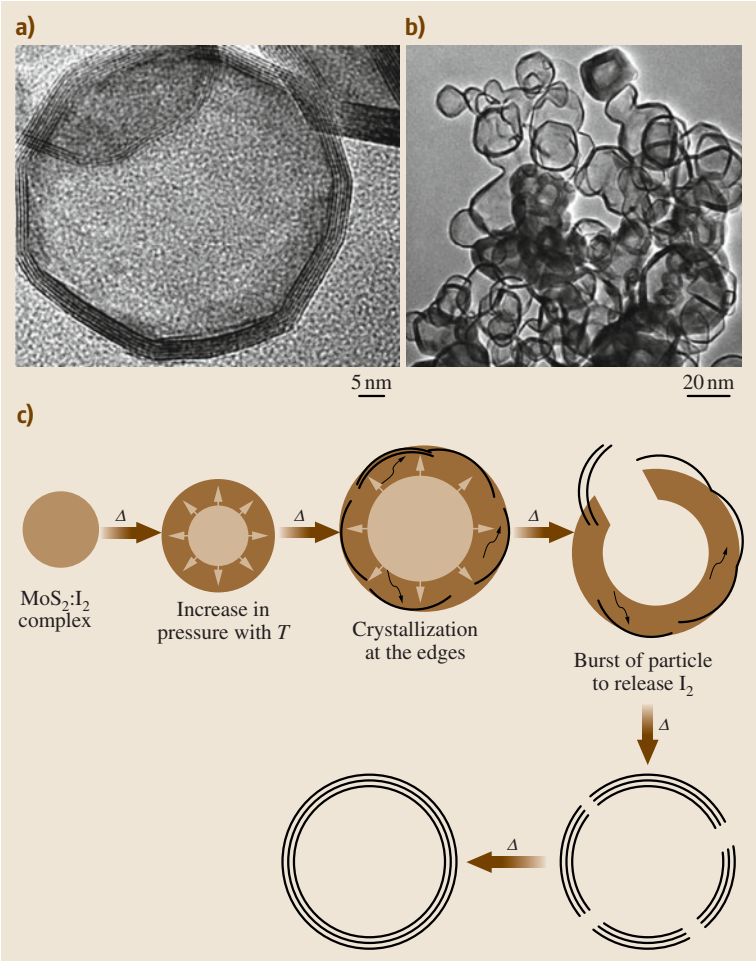


Fig. 16.4 **(a,b)** Giant IF-MoS_2 *bubbles*; **(c)** growth mechanism of a giant IF-MoS_2 fullerene (after [16.54])

oxide core towards hydrogen. Thus, the hydrogen radial diffusion into the core of the NP is also uniform. However, if H_2S is not provided in sufficient amounts, the oxide core is rapidly reduced. Since the metal is appreciably denser than its oxide, subsequent diffusion and reaction of the sulfur atoms in the core is blocked, as the H_2S is unable to penetrate the dense core. Therefore, in the case of complete reduction of the oxide NP into the respective metal, sulfurization of the metallic NP is truncated after only two closed layers of MS_2 enfolding the metallic core are formed [16.18].

The last stage of the reaction is controlled by the slow inward diffusion of sulfur or H_2S through the outer layers of MS_2 and outward diffusion of O or OH moieties from the core. The sulfurization of the reduced tungsten oxide core is a slow process, as the large sulfur atoms are unable to diffuse through the closed outer layers. However, sporadically occurring defects in the curved WS_2 layers allow diffusion of the sulfur atoms inwards. The probability of this event is rather low, providing an upper limit on the rate of this process. Once hopping into an inner layer has occurred, fast diffusion of the sulfur atom in the van der Waals (vdW) gap between the layers follows until the sulfur atom encounters another defect in the inner MS_2 layer and another hop to the next gap occurs, and so on. Eventually, the diffusing sulfur atom reaches the lateral growth front of the innermost layer as it forms, allowing it to rapidly react with the suboxide core. This process results in a single growth front, which progresses inwards in a quasi-epitaxial fashion. This stage is thus controlled by the diffusion of sulfur to the single growth front and may take several hours depending on the NP precursor size and reaction temperature.

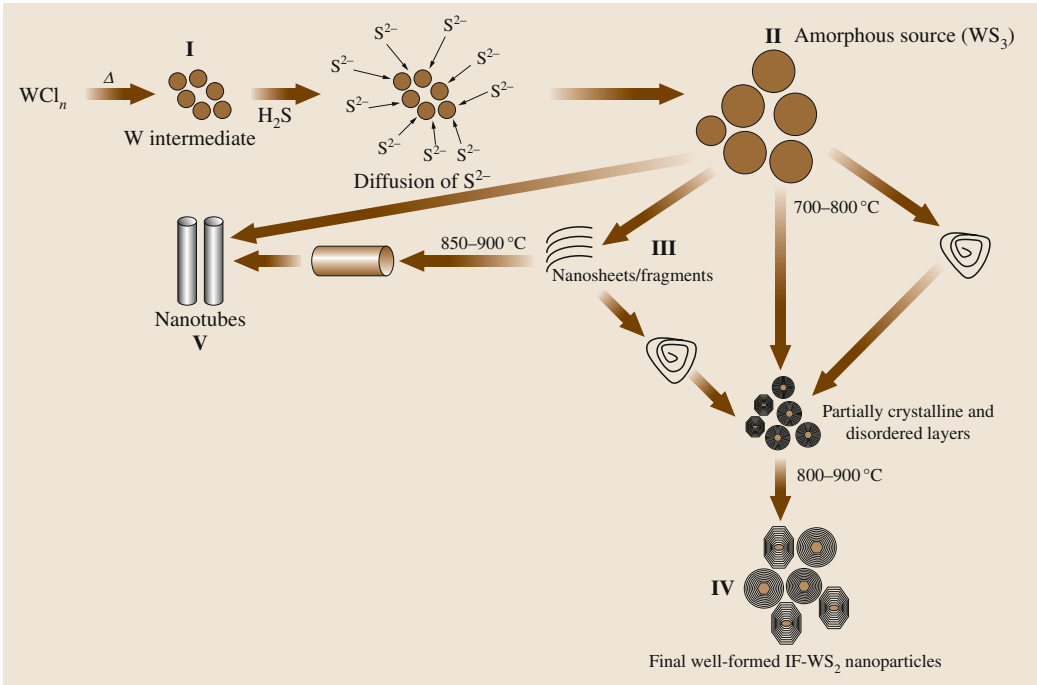


Fig. 16.5 Illustration of inside-out mechanism for the formation of INT and IF-WS_2 from WCl_n (after [16.57])

Prepreparedoxide precursors allow a degree of control over the final IF size but require an additional synthetic step. This prepreparation step may be performed in situ as reported for IF-MoS_2 [16.55]. Here, the synthetic process consists of two additional steps: evaporation of MoO_3 powder at $T \geq 700\,^{\circ}C$ and reduction and condensation of the oxide vapor to give MoO_{3-x} NP in the gas phase. The parameters influencing the formation of the IF are the temperature, flow rates, and concentrations of gases (H_2 and H_2S). Furthermore, the reactor design has a large influence on the reaction products [16.55]. The size of the IF-MoS_2 particles produced in this study varied between 10 and 250 nm. However, in situ production of the precursor NP by random agglomeration in the gas phase may result in a nonsymmetric size distribution with respect to the average final size of the product, shifting it towards smaller sizes (left-skewed) [16.56]. Also interestingly, the shape of the IF-MoS_2 nanoparticles is not fully spherical but somewhat squashed. This could be associated with the shape of the in situ formed molybdenum suboxide nanoparticles and requires further investigation.

The outside-in process for IF-WS_2 NP was also shown to occur in the case of crystallization of an amorphous metal sulfide precursor [16.58]. This process is initiated on the surface, resulting in the formation of WS_2 layers around the amorphous core and progressing inwards. Due to a larger density of crystalline WS_2, a hollow core is eventually formed. Here, the mass transfer is driven by a concentration gradient of WS_2 due to the compactization.

This mechanism was also shown to create giant IF-MoS_2 *bubbles* (Fig. 16.4) when an amorphous NP containing a mixture of $MoS_2 : I_2$ was used as the precursor [16.54]. The formation of the exceptionally large voids during the annealing was attributed to entrapment of iodine released by the thermal decomposition inside the NP. The simultaneous formation of patches of 2-D layers is enhanced by the isothermal chemical transport reaction of the iodine. Eventually, the increasing amounts of iodine being released *inflate* the NP due to rising internal vapor pressure until the NP ruptures. Subsequently, the IF-MoS_2 NP is formed by stitching the 2-D patches, thus *healing* the ruptured NP.

The sulfurizing reagent is commonly gaseous H_2S, which is hazardous, therefore complicating the process. Most of the alternatives to this problem involve in situ production of H_2S [16.59–61]. IF-WS_2 and MoS_2 have been synthesized using only solid precursors by reacting the metal oxide nanopowder, sulfur, and a hydrogen-releasing agent ($NaBH_4$ or $LiAlH_4$)

in a conventional furnace operated at 900 °C [16.59]. Another solid reagent used to release sulfur in situ is thiourea [16.60, 61].

In contrast to the outside-in mechanism, the opposite mechanism, i. e., inside-out growth, is usually initiated by the formation of a small fragment of layers which serve as a nucleus and template for growth of additional layers (Fig. 16.5). Therefore, this mechanism is controlled by gas-phase diffusion rather than by a solid-phase diffusion process. Indeed, outside-in synthesis of INT and IF from oxide NP is a slow, diffusion-controlled process. Furthermore, it is limited to reactive oxides such as WO_3 and cannot be readily applied to obtain IF-MS_2 NP from less reactive oxides such as TiO_x and NbO_x. To circumvent these inherent difficulties, a new strategy was developed using volatile metal halides or carbonyls as precursors [16.21]. These highly reactive compounds have high vapor pressure at low temperatures ($T < 300$ °C). Moreover, their vapor reacts promptly with H_2X (X = S, Se, Te) gas to produce IF nanoparticles.

The formation of IF NP from the reaction of volatile metal halides with H_2S is driven by nucleation and subsequent layer-by-layer growth of the small nucleus outwards [16.35, 57, 62, 63]. While the growth process is diffusion controlled here as well, it is the diffusion of the reagents through the gas phase that dictates the overall growth rate, thus making it a faster process when compared with solid-state diffusion. This mechanism also allows for in situ IF doping, where the dopant is present in the gas phase, as opposed to ex situ doping, which is harder to carry out [16.64, 65]. Furthermore, it has been indicated that the products of this reaction have the advantage of being much less agglomerated than those obtained from the oxide NP [16.57]. Interestingly, the growth of the IF is self-limiting (arrested growth) with the NP not growing beyond, say, 150 nm.

IF-NbS_2 [16.21] were the first IF NP to be synthesized via this mechanism, followed by a large number of nanostructures including INT-TiS_2 [16.27], IF-TiS_2 [16.35], IF-WS_2 [16.66], and IF-MoS_2 [16.63]. Unlike the outside-in mechanism, which influences the outer radius of the IF product, the small size of the incipient NP strongly influences the inner radius; for example, in the case of IF-TiS_2 synthesis [16.35], only tiny hollow cores were obtained in the center of the NP (Fig. 16.6a). Furthermore, this reaction pathway was shown to result in IF with many layers with an almost perfectly spherical contour and relatively smooth curvature (Fig. 16.6b). In a similar approach, IF-MoS_2 were produced using $Mo(CO)_6$ and elemental sulfur or selenium as precursors in a metalorganic chemical vapor deposition (MOCVD) approach [16.67]. In conclusion, therefore, the inside-out mechanism may be applied to produce different chemical species by choosing the correct vapor-phase precursor.

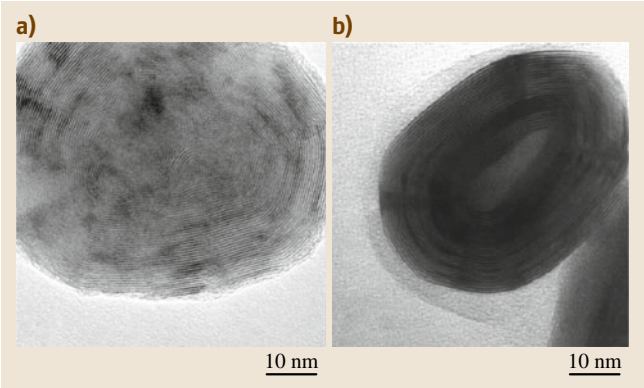


Fig. 16.6 **(a)** IF-TiS_2 and **(b)** IF-WS_2 (after [16.62] and [16.57], respectively)

Formation of IF-WS_2 nanobuds was also shown to take place in locally confined conditions as reported in [16.68], where longitudinal surface corrugations act as diffusion paths for tungsten atoms feeding the growth of WS_2 nanobuds on the INT surface (Fig. 16.7). The nanobuds are thought to nucleate in corrugations in the forming INT surface which create favorable regions for their growth. The nanobuds may then be described in the same terms used in the inside-out mechanism (Fig. 16.5). The main difference with IF is the asymmetric (planar) environment imposed on the incipient NP, which in the case of the nanobuds, are forced to

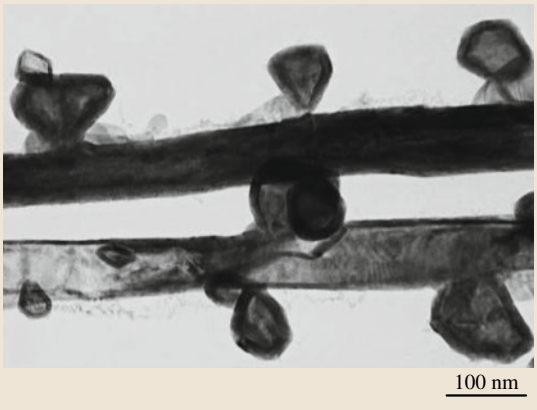


Fig. 16.7 IF-WS_2 nanobuds (after [16.9])

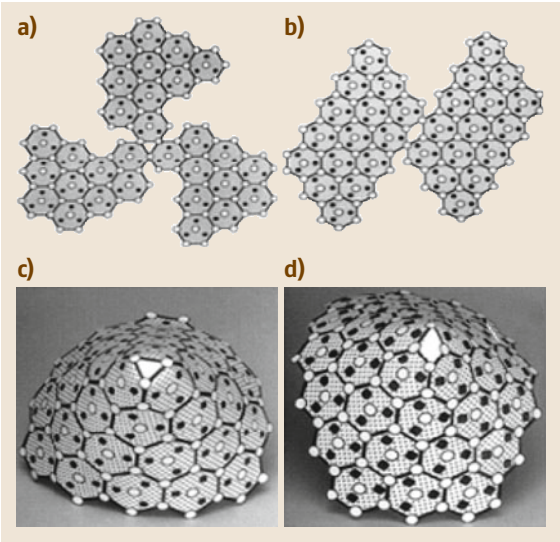


Fig. 16.8 (a,b) View of the elemental trigonal prism of the 2H-MoS_2 lattice. *Open circles*: sulfur, *closed circles*: molybdenum. (c) 3-D drawing of a conical apex around a triangle joining three hexagons. (d) 3-D drawing of a conical apex around a rhombus joining four hexagons (after [16.5])

grow only in one direction, i. e., outwards from the INT surface, resulting in the bud-like appearance.

An additional mechanism which usually results in INT but occasionally results in IF is that of rolling up of 2-D sheets [16.70]. This is the result of the fact that rolling up of a 2-D sheet into a 0-D sphere (IF) as opposed to a 1-D cylinder (INT) entails folding along two directions as opposed to one direction in the latter case. Folding along two axes necessitates the introduction of defects with symmetry lower than six; such defects are rhombi (four-membered rings), triangles, or simply point defects (dislocation) with ill-defined structure and chemical composition. In fact, scrolls and fullerene-like structures of 2-D materials were reported even before INT and IF were recognized as a universal phenomenon. Among the earliest cases were nanoscrolls of MoS_2 obtained by reacting $MoCl_4$ with LiS_2 in tetrahydrofurane (THF) solution which were annealed at 400 °C [16.71]. Additional reports include core–shell nanostructures of MoS_2 layers enfolding NiS NP [16.72, 73]. The roll-up process was also observed to occur during irradiation by a TEM electron beam [16.74].

This rolling-up mechanism was the first used by sulfurizing ultrathin WO_3 (MoO_3) films in a reducing atmosphere at $T = 850$ °C to produce INT and IF-WS_2 [16.5]. Various apex angles could be observed in these structures [16.5], some of which may be deduced by careful inspection of the structure of the MoS_2 layers. Figure 16.8 shows the original schematic visualization of an apex created by forming dislocations in the 2-D layer and subsequent folding and joining either three or four hexagons around a triangle or rhombus, respectively [16.5]. Surprisingly, this process was found to occur naturally. Samples containing substantial amount of amorphous W-S material (probably WS_3) kept in ambient conditions for several years gradually lost excess sulfur and spontaneously crystallized into small WS_2 hollow closed structures. Some of these nanostructures were shaped like a tetrahedron or octahedron [16.73, 75]. This indicated that IF-WS_2 are a genuine phase which is formed through a slow, diffusion-controlled process. It nucleates on the phase boundary between amorphous WS_3 and crystalline WS_2 in sulfur-deficient atmosphere.

Formation of IF-MoS_2 *nanopods* inside INT-MoS_2, i. e., so-called *Mama-tubes*, was reported during the sulfurization of $Mo_6S_2I_8$ nanowires (Fig. 16.9) [16.69]. They appear to originate from a rolling-up process of curved MoS_2 flakes. It was theorized that first a MoS_2

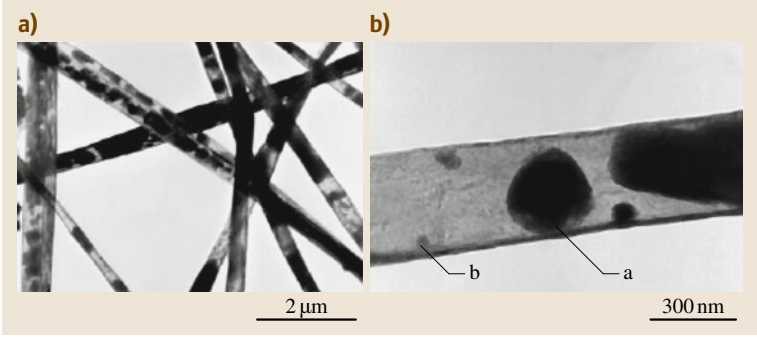


Fig. 16.9 (a) Overview of INT-MoS_2 *Mama tubes* with encapsulated IF-MoS_2; (b) single IF-MoS_2 inside a thin-walled INT-MoS_2 *Mama tube* (after [16.69])

envelope is formed on the surface of the $Mo_6S_2I_8$ and almost simultaneously the volume of the core is significantly decreased due to iodine release. The remaining material is then sulfurized further to form IF-MoS_2 by diffusion of molecules along the inner INT surface. The formation of these *flakes* may have been initiated by defects of the inner INT surface. The appearance of IF localizes the diffusion even more until the IF-MoS_2 nanopods are complete.

The physical synthesis methods rely on a rapid, high-energy stroke by means of a laser, arc discharge, etc. and in general do not involve a net chemical reaction. This drives the precursors and reaction medium very far from thermodynamic equilibrium, which enables sampling of local energetic minima which may be otherwise unattainable. These conditions may result in the formation of high-energy structures such as INT, IF, and even nanooctahedra, which will be elaborated upon later in this section. In fact, C_{60} was first produced by laser ablation of graphite [16.76], and arc discharge was the first method to be utilized in the production of large quantities of C_{60} and CNT [16.4]. Various physical methods have been used in the synthesis of nanostructures including laser ablation [16.25, 39, 77–80], arc discharge [16.81], resistive heating of graphite targets [16.82], and e-beam irradiation [16.37, 42, 83–85], as well as short electrical pulses from the tip of an STM [16.86]. Most of these methods entail the creation of a plasma or vapor phase in which the nanostructures are formed.

The main advantage of these high-energy experimental setups is their nonspecificity, i. e., their ability to accommodate many different precursor materials. Among them are BN [16.37], transition-metal sulfides (MoS_2 [16.87], SnS_2 [16.79], Hf_2S [16.88]), transition-metal halides ($NiCl_2$ [16.25, 80], $NiBr_2$ [16.43], CdI_2 [16.89], $CdCl_2$ [16.85]), transition-metal oxides (V_2O_5 [16.40]), and alkali-metal oxides (Cs_2O [16.39, 90]).

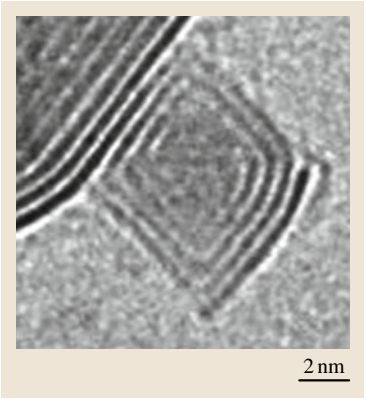


Fig. 16.10 TEM image of a MoS_2 nanooctahedron

Another important advantage of the physical routes is that the characteristic time and length scales are generally such that diffusion plays only a minor part. This situation leads to the formation of nanostructures which represent a local energetic minimum for a small number of atoms such as C_{60} and MoS_2 nanooctahedra. This is due to the local conditions consisting of a low concentration of atoms in a confined volume (a few nm wide) and large energy of the constituents, which allows adequate sampling of the energy landscape including the local minimum. The rapid nature of the physical routes confines the process in space and time as the energy is removed from the structure, preventing further coarsening of the nanoparticles. Thus, the physical techniques are unlike the chemical outside-in or inside-out mechanisms (Figs. 16.3 and 16.5, respectively) where the final IF dimensions are largely defined by the size of the precursor NP. Here, the formation of the small closed polyhedral structures by energetic techniques is distinctly different and is more conducive to the formation of nanooctahedra (Fig. 16.10) and smaller IF [16.39, 43, 55, 79, 80, 89, 91, 92].

The common characteristics of the physical mechanisms may be illustrated with the pulsed laser ablation

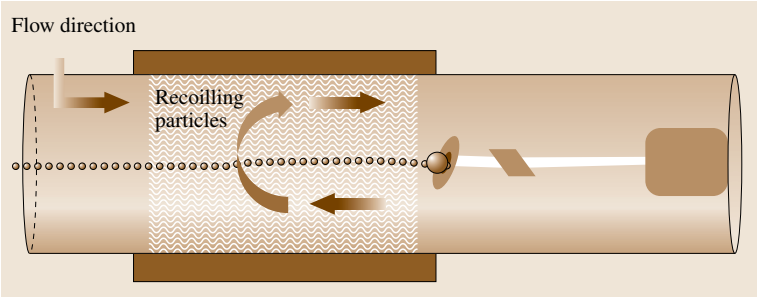


Fig. 16.11 Laser ablation setup

(PLA) process depicted in Fig. 16.11. Here, a pulsed laser beam hits a solid target, thereby ablating it. During the ablation process the incident light is absorbed by the electronic modes, leading to rupture of chemical bonds in the solid and surface evaporation of atomic and molecular moieties. Depending on the duration of the pulse and other parameters [16.92–94], this may be followed by a process of thermalization and conversion of the excess energy to vibrational excitations. Generally speaking, the thermalization process leads to evaporation of larger moieties from the solid surface than the short-lived electronic excitations. These processes can result in liquefaction, evaporation, ionization, and surface rupture due to pressure buildup of gases inside the solid.

An important phenomenon in PLA is the formation of a recoiling plume, which is largely attributed to the high pressure of the gases formed inside the cavities and subsequent surface rupture. The PLA processes generally occur on very short time scales of less than a few nanoseconds. The temperature of the plume may be in excess of 2000 °C [16.93, 95] in certain regions and consist of plasma, vapors, liquid droplets, and solid ejecta mixtures. This plume may also partially shield the target while being continuously irradiated by the incoming beam. This plume then undergoes rapid quenching ($> 10^9$ K/s) due to the large temperature gradient with respect to the plume environment. The temperature of this environment may be controlled by adding a furnace which anneals the products of the PLA process. The annealing process is intended to supply the gas-phase condensate with sufficient additional energy to form stable nanostructures.

The processes taking place in the physical synthesis techniques that result in the formation of IF and nanooctahedra are not yet well understood, as opposed to the chemical techniques. This is mainly due to the rapid nature of the processes, which do not allow for isolation of intermediates. In fact, despite the fact that C_{60} was discovered more than 25 years ago, current understanding of its formation mechanism by either laser ablation or arc-discharge techniques is still rather limited [16.96–98]. Some indications were given by arc-discharge experiments with targets made of a mixture of ^{12}C and ^{13}C, which resulted in complete mixing of the isotopes in the C_{60} fullerene product [16.99]. This indicates that the formation of C_{60} in physical techniques is unlikely to take place by initial formation of 2-D graphene sheets followed by their direct folding into closed-cage structures. In contrast to the relatively simple carbon nanoclusters, the inorganic systems are much more complex, with triatomic layers, the number of atoms in even the smallest inorganic nanostructure being orders of magnitude larger. Given this level of complexity, it is hardly surprising that the exact mechanisms of IF and INT formation in the physical techniques are still only partially understood at best [16.2].

A synthesis method which has been showing increasingly promising results in recent years is irradiation with concentrated sunlight, also known as solar ablation (SA) [16.90, 100, 101]. The solar ablation method incorporates aspects of both the chemical and the traditional physical synthesis approaches. Using this method, INT- and IF-MoS_2 have been produced, with some nanostructures achieving a fundamental minimum size as predicted by molecular structural theory [16.100]. These nanostructures are indicative of the high-temperature conditions inside the SA reactor, where small polyhedral shapes with a few layers imply hotter annealing that favors curling and closing due to defects.

The main advantage of solar ablation as opposed to laser ablation is that it encompasses a much larger active area [16.101]. However, the differences between PLA and SA are not clear cut. Relative to PLA systems, SA provides higher vapor pressure of reactants with peak reactor temperatures in excess of 2700 K [16.102]. Thermal radiation from the heated precursor powder provides a natural, extensive, and hot annealing environment. On the other hand, PLA systems drive the reaction volume much further from equilibrium due to the temporal confinement of the high-energy stroke. This suggests that a truly hybrid system incorporating laser/arc ablation and solar ablation on the same spot may reveal even more interesting structures.

16.2.2 INT Synthesis

Nanotubes are of great interest from both the scientific and application points of view, as manifested by the thousands of studies devoted to their synthesis, characterization, and applications. As mentioned previously, it was suggested [16.5] that the propensity of graphite to form polyhedral structures is not singular, and hence INT of WS_2 were indeed first observed [16.5]. Since then, a great variety of nanotubes of 2-D, and more recently 3-D, compounds have been reported. Among the 2-D compounds, transition-metal chalcogenide NT make up the largest group, including WS_2 [16.5] MoS_2 [16.33], NbS_2 [16.20], TaS_2 [16.20], HfS_2 [16.23], ZrS_2 [16.23], TiS_2 [16.23], and SnS_2 [16.79, 103]. BN nanotubes [16.104] were

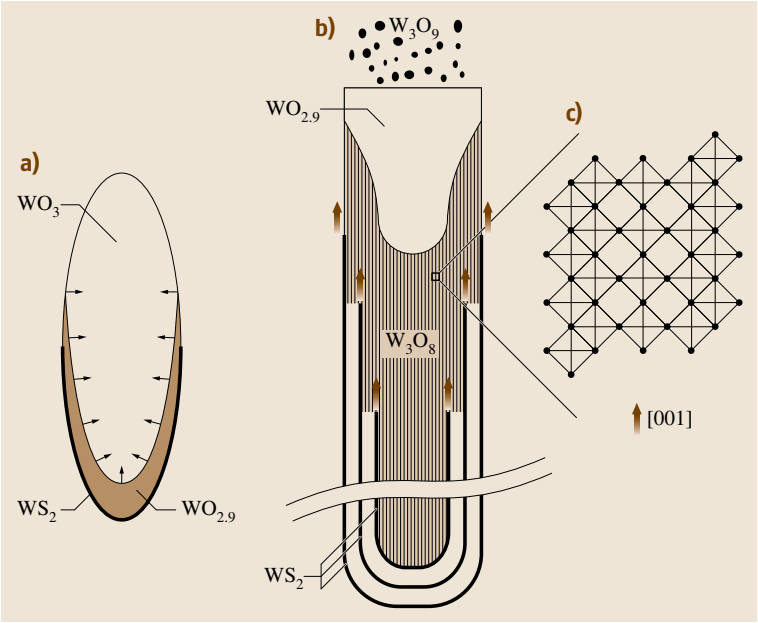


Fig. 16.12a–c Schematic illustration of the growth process of the encapsulated sulfide/oxide nanowhisker in a horizontal reactor: **(a)** initialization of the sulfurization process of the asymmetric oxide nanoparticle; **(b)** growth of a long sulfide/oxide encapsulated nanowhisker; and **(c)** enlargement of the {001}R crystallographic shear planes exhibiting within one crystallographic shear plane regions of edge sharing octahedra (after [16.106])

reported as well as $NiCl_2$ nanotubes [16.25], which belong to the metal halide group, and VO_x-alkylamine composite NT [16.105] of the metal oxide group.

As in the case of IF synthesis, it is possible to divide the synthetic methods into chemical and physical approaches. While physical methods are much less likely to produce INT, the chemical synthesis methods may also be divided into the same categories used for the IF. Furthermore, the influence of the synthetic technique on the nanotube morphology will be demonstrated by discussing the various synthetic approaches for the formation of INT-WS_2.

The growth of WS_2 nanotubes has advanced in four stages, and understanding of the growth mechanism has evolved accordingly. In the first stage [16.5], nanotubes were produced sporadically by reaction of H_2S gas with thin tungsten (or oxidized tungsten) film [16.5]. In the second stage, a methodological approach to nanotubes synthesis was undertaken [16.106–109]. Here, the asymmetric tungsten oxide rods (whiskers) were preprepared and fired in a horizontal oven in H_2S and forming gas atmosphere. The yield in this case approaches 100%, but the process is tedious and the typical amounts of the nanotubes were in the range of 50–200 mg. In the third stage, the small vertical fluidized bed reactor (FBR) was established [16.107]. Here, very thin (20–25 nm diameter) WS_2 nanotubes made of 4–10 layers were formed spontaneously and very rapidly. In this case, the previous growth model of outside-in became irrelevant and a new model had to be invoked. The major drawback of this reaction was that, although the overall quantities of the nanoparticles were in the range of 20 g, the production yield of nanotubes never exceeded 5–10%. The remaining content of the product in these reactions was mostly IF-WS_2 nanoparticles and a few percent of WS_2 platelets. In the fourth stage, the larger FBR was erected and used for the synthesis of the nanotubes [16.51]. Here, the nanotube synthesis followed the path described in the second step, but now in a single reaction. This progress has led to large-scale synthesis for a variety of applications.

The conceived growth mechanisms of the nanotubes can now be recounted in an orderly fashion. The following mechanism has been proposed for the nanotubes produced in the second stage [16.106–109]. Similar to IF, one of the most common methods for INT synthesis involves an outside-in reaction (Fig. 16.3). Here, WO_{3-x} nanoparticles elongate under the reducing atmosphere (1% H_2/99% N_2) to tungsten suboxide nanorods (nanowhiskers), which are subsequently converted to INT-WS_2 by sulfurizing the needle-like WO_{3-x} precursors [16.52, 106, 108, 109]. Thus, the reaction pathway involved a reduced tungsten oxide precursor with asymmetric unit cell. Depending on the synthesis conditions (total flow rate, flow rate of hydrogen, etc.), two kinds of morphologies were observed:

short nanotubes of approximately the same length as their precursors (50 nm) or long ones (several micrometers). Roughly 80–90% of the long nanotubes were *thin* (20–30 nm diameter), and the remainder were rather *thick* (ca. 100 nm diameter) [16.108].

While this conversion takes place in an outside-in mechanism similar to IF, an additional aspect is observed here for the *thin* INT, which are believed to grow in two steps (Fig. 16.12). In the rapid first step, three processes occur simultaneously: elongation of the needles' oxide tip, reduction, and sulfurization. As the sulfurization is unable to *catch up* with the elongation rate, the needles grow into whiskers similar to those formed by reducing tungsten oxide. During this step the tungsten oxide is amorphous and thus forms a cylinder in order to minimize the surface energy. When the whiskers reach a length of a few micrometers, the sulfurization closes the cap, thus forming the first few protective layers which serve a similar role to those in the IF formation. The process then proceeds to the second step in a similar manner to that of IF [16.92] and forms cylindrical INT.

On the other hand, when the oxide growth is sufficiently fast to prevent the sulfurization from transforming the nanowhisker into INT, the oxide characteristics dictate the final shape. Thus, the nanowhisker is reduced and crystallizes into a cuboid. The sulfurization may be sufficiently slow that the outer surface is not completely covered along the circumference, resulting in oxide thickening and subsequently forming nonregular cross-sections. Furthermore, it has been pointed out that the nanowhisker precursors may be fabricated in a separate step, although in this case the INT are far from perfectly cylindrical with their caps often open [16.109, 110]. This may be the mechanism responsible for the formation of rhombohedral INT-MoS_2 [16.61] obtained by the reaction of MoO_3 with thiourea, which serves as a sulfur source. This is supported by the presence of the oxide core observed in some of the INT.

A similar formation mechanism was used in a scaled-up production of INT-WS_2 (stage 4) reported by *Zak* et al. [16.51]. Here, however, the reaction was one pot; i. e., self-controlled temporal separation between the reduction/elongation step of the tungsten suboxide and the sulfurization step was achieved. The first step consisted of fast growth of long (tens of micrometers) suboxide ($W_{18}O_{49}$) nanowhiskers through oxide reduction, sublimation, and condensation, excluding the sulfurization process.

The starting material was shown to contain WO_3, $W_{25}O_{73}$ ($WO_{2.92}$), $W_{20}O_{58}$ ($WO_{2.9}$), and $W_{24}O_{68}$ ($WO_{2.83}$) nanoparticles. The elongated nanowhiskers were found to consist of the reduced nonvolatile $W_{18}O_{49}$ ($WO_{2.72}$) phase (Fig. 16.12). This phase consists of an ordered 2-D lattice of edge-sharing WO_6 octahedra forming a network of pentagonal columns (PC) interspersed with hexagonal channels (HC), which stabilize the highly asymmetric nanowhisker structure. qThis phase is known as the most stable reduced suboxide, indicating that a volatile oxide intermediate is likely involved in the rapid growth of the oxide nanowhisker. Thus, once the oxide is reduced to the nonvolatile phase, further growth of the nanowhiskers is inhibited and the sulfurization reaction is started.

In the second step, the sulfurization proceeds similarly to the reaction of IF [16.91, 109–111], where the oxide is gradually converted to the sulfide by an outside-in, diffusion-controlled reaction. The INT empty core is the result of the difference between the oxide and sulfide densities. The slower oxide to sulfide conversion in the case of the INT may be attributed to topological effects. The INT are folded along one axis, in contrast to IF, which fold along two axes and thus, in general, contain a higher defect density. As this density determines the rate of sulfur diffusion towards the core of the nanostructure, the rate of oxide to sulfide conversion is subsequently lower for the synthesis of INT.

An entirely different mechanism was invoked in the case of INT-WS_2 formed as a small fraction during the synthesis of IF-WS_2 from agglomerated tungsten oxide NP (step 3) [16.52] (Fig. 16.13). These INT were distinctly different from previously synthesized INT, being

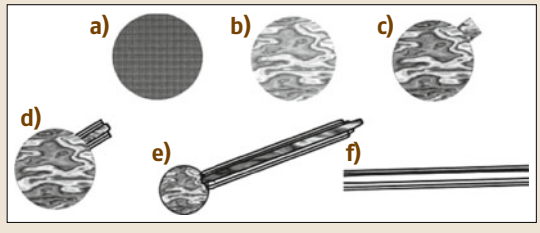


Fig. 16.13a–f Schematic INT-WS_2 vapor–solid (VS) growth mechanism (third stage). **(a)** Starting oxide NP. **(b)** The volatile oxide phase encapsulated in the NP. **(c)** Breakthrough (dimple) of the volatile phase through the encapsulating surface. **(d)** Formation of the root of the WS_2 nanotube on the top surface of the WO_{3-x} nanoparticle. **(e)** Further growth of the nanotube: the volatile oxide that is emitted from the nanotube's hollow core. Reacting with H_2S it forms WS_2 at the tip of the tube. **(f)** Completed WS_2 nanotube (after [16.52])



Fig. 16.14 Schematic illustration of an inside-out mechanism for fabricating INT-WS_2 by thermal decomposition of $(NH_4)_2WS_4$ (after [16.112]).

perfectly cylindrical, crystalline, open ended, and slender (length ≈ 2–500 μm, diameter ≈ 15–20 nm), with the most distinctive feature being the thin walls (5–8 layers) and the large hollow core (up to 70 vol. %). These INT were typically found on the surface of the large agglomerates (20–100 μm in size) of IF-WS_2 and generally constituted 10% of the product. It was concluded that the specific conditions in the reactor induced the formation of a volatile phase inside the oxide NP. The pressure of this phase results in a cylindrical protrusion, which is subsequently sulfurized, forming an incipient INT which serves as a conduit for the release of the volatile phase. At the tip of the INT, the volatile tungsten oxide phase is sulfurized and the WS_2 molecules land on the tip of the INT, resulting in a continuous growth process of the INT. Once the tube has grown to a few micrometers in size, the fast spinning of the agglomerate can lead to its detachment from the NP agglomerate.

The fact that the INT-WS_2 were helical with a helicity angle preserved along the entire length of the nanotube lent credence to this mechanism. The chiral growth mode is energetically and kinetically favorable, because it provides a continuous growth front. In the case of nonhelical nanotubes, the growth process is interrupted each time a ring is completed and another ring must start to form. Since the growth process is continuous, the helicity angle is preserved during the growth.

The mechanism described above which entails the continuous growth of INT may be defined as a vapor–solid (VS) mechanism. It is similar to the well-known vapor–solid–liquid (VLS) mechanism which has been used extensively in the growth of nanowires and carbon nanotubes. However, to date, the VLS mechanism has been invoked only in the case of INT-$NiCl_2$ [16.80] and INT-SnS_2 [16.103]. The limited variety of INT grown via the VLS mechanism is most likely due to the stringent requirements of this process. For the VLS mechanism to be applicable, a eutectic point in the phase diagram of the catalyst and INT material [16.80] and a congruent melting point for these compounds are required.

The inside-out (nucleation and growth) mechanism is not encountered often in INT synthesis. Synthesis of INT (in low yields) has been observed by reacting volatile metal halides with H_2S (or S vapors) [16.63]. Here, the incipient seed should roll up into a cylindrical morphology in order to serve as a template for incoming reactant molecules which end up in INT.

A similar mechanism is a hybrid between the inside-out mechanism and rolling up in which a single-walled INT-WS_2 rolls up and then serves as a seed for subsequent sheets rolling up around it. This mechanism is observed in the case of thermally decomposed $(NH_4)_2WS_2$. Here, the synthesis is based on a catalytic gas–solid mechanism [16.112]. The $(NH_4)_2WS_2$ particles were heated under a flow of H_2 and thiophene, which strongly catalyzes the transformation of $(NH_4)_2WS_2$ to WS_2 at low temperatures [16.113]. First, a single-walled INT-WS_2 is formed that serves as a template for subsequent WS_2 shells, which grow on top of the first one as shown schematically in Fig. 16.14. During the second step, the rolling up of the WS_2 sheets is induced by the escape of the NH_3 and H_2S vapors.

The rolling-up process is in fact common and may be induced by chemical methods such as heating up layered fragments [16.5] and asymmetric reduction [16.60] or physical methods such as electron beam irradiation [16.74]. As mentioned previously, rolling up forms INT more readily than it would IF, due to the nature of the defects that must be inserted in order to stabilize the structure.

A related mechanism is the solution-based use of structure-directing molecules, such as alkylamines. Here, hydrothermal reaction of the cationic (structure-directing) surfactant cetyl-triamine cation (CTA^+) with dissolved WS_4^- ions produces nanotubular structures. Upon further annealing the nanotubes lose the intercalated surfactant moieties and excess sulfur, converting into regular multi-walled WS_2 nanotubes [16.114]. This reduces the interlayer interactions at the edges during the heating process and supplies sufficient energy for the layers to start rolling up [16.92]. The rolling-up mechanism may also be responsible for the reduction of nanoribbons to nanotubes [16.60], where sulfidization of metal oxide sheets might result in compressive stress on the exposed side, thus inducing rolling of the nanoribbons into tubular structures or nanotubes.

INT-MoS_2 were also shown to be produced by physical methods such as solar ablation [16.100], albeit not in large quantities. Furthermore, some single-walled INT-MoS_2 with diameter of 7 nm and length of 60 nm were observed. The diameter of these INT conformed to the minimum diameter stability limit (6–7 nm) predicted for INT-MoS_2 [16.115,116]. These results may suggest that the formation mechanism here is that of rolling induced by heating as opposed to the previous mechanisms which included a chemical component as well.

While the synthetic methods mentioned above were among the first to be used, the field of INT synthesis has grown explosively in recent years, with a large variety of inorganic compounds being synthesized by various methods. Among these, chemical vapor transport [16.9,68,69,117–119] has been used for synthesis of nanotubes. This technique was used extensively in the past for growth of high-quality single crystals of layered metal dichalcogenide (MX_2) compounds.

Various methods of guided growth have been utilized, chief among them being the use of external templates such as anodized alumina membranes (AAM) and templates fabricated by soft chemistry (*chemie douche*) methods [16.105,120–123]; for example, synthesis of INT-MoS_2 nanotubes using a solid AAM template was reported [16.124]. Various metal oxide NT were synthesized via *chemie douche* processes, such as hydrothermal, sol–gel, intercalation-exfoliation, sonochemical reactions, etc. One extensively studied example, the composite VO_x-alkylamine NT, were used as a template for INT-VS_2 synthesis [16.26]. The outstanding feature of this study is that, so far, the layered bulk phase of VS_2 does not exist, thus showcasing the inherent stability of the nanotubular phases [16.26].

The examples above demonstrate that different synthetic routes may be employed to control the morphology of the various INT. Furthermore, the present discussion highlights the fact that understanding the mechanism and the reaction details during the synthesis is of utmost significance for controlling the morphology and properties of the resultant INT.

16.3 Physical Properties

Use of a synthetic method which allows placement of atoms at desired locations in the required morphology of the nanostructure is obviously intimately tied to the resulting properties. Thus, understanding the relationship between the synthetic method of choice and the characteristic structures produced is crucial to achieving the desirable functionality of the nanotubes. Although this is easier for the chemical methods than the physical ones, the current methods do not offer complete control over the resultant structures and, thus, their properties. Of further interest is the fact that INT can be synthesized free of defects, allowing quantitative comparisons with first-principle theoretical calculations.

This section will examine the known relationship between the different synthetic methods and the structural properties such as defect concentration and strain, and their effect on the physical properties of the IF/INT. This kind of study was lately made possible by the advent of a new generation of high-resolution/performance nanotools for the manipulation of single nanostructures. While a relatively large amount of work has been done lately on the mechanical properties of INT, the number of studies on the electronic, optical, and magnetic properties of such nanotubes is rather limited as yet. Moreover, there are only a small number of reports linking the different synthetic methods with the resulting structures.

16.3.1 Synthesis and Structural Properties

To discuss the effects of a given synthetic method, it is useful to consider the characteristics of the three different polytypes found for the layered bulk of W(Mo)S_2, whose structure will be detailed later on. The most common polytype (2H) is stable in ambient conditions, the second (3R) is usually stable only above pressure of 4 GPa [16.125], and the third (1T) is generally unstable as a pristine material.

These phases may be used to probe the differences between the different synthetic methods; for example, it is believed that IF (INT) nanostructures which are produced by chemical synthesis routes are more thermodynamically stable compared with those synthesized by physical methods, which are more energy intensive and hence far from equilibrium. This assumption is supported by a recent report showing that the generally unstable phase (1T-MoS_2), i. e., trigonal symmetry with one layer as a repeat unit [16.101], is produced to some minor extent by solar ablation [16.101].

There are a few reports which indicate that the INT/IF nanostructures formed by the outside-in mechanism suffer from high internal stress. Contrarily, similar nanostructures produced by reactions involving the inside-out (nucleation and growth) synthetic methods seem to be mechanically more relaxed. One example is provided by the work of *Remskar* et al. on IF-MoS_2 *peapods* and the IF-WS_2 *nanobuds* mentioned in the previous section [16.68, 69]. The structure of the IF-MoS_2 *peapods* was determined to be 3R (high-pressure phase) as opposed to the IF-WS_2 *nanobuds* that exhibited the 2H structure. It should be noted that the structure was inferred from the electron diffraction as well as the number of initial layers formed. IF-MoS_2 *peapods* are obtained by firing $Mo_6S_2I_8$ nanowires in forming gas atmosphere. Release of iodine and rearrangement of the Mo–S bonds produces IF-MoS_2 nanoparticles in the cavity of the MoS_2 nanotubes. The formation mechanism of the closed-cage (polyhedral) IF-MoS_2 NP is characterized by rolling up of 2-D layers [16.69]. This process occurs in a confined environment (the cavity of the INT), in analogy to the outside-in mechanism for IF NP. These IF-MoS_2 *peapod* nanostructures are highly strained as reflected by their tendency to adopt the 3R polytype of MoS_2. In contrast, the IF-WS_2 *nanobuds* grow in an unconfined inside-out mechanism and exhibit the low-pressure phase of 2H composition.

However, the situation is much more complex due to the large kinetic differences in the two reactions. The outside-in method is characterized by an overall slow diffusion of the reactants to and from the growth front. A typical time for the full conversion of tungsten oxide nanoparticle into IF-WS_2 is a few hours, in this growth mode. Also, the kinetics of the reaction is much faster at the leading edges of the layer, where atoms with unsaturated chemical bonds are present, relative to the formation of the next (inner) layer. Thus, complete single layers are formed and only then are the subsequent WS_2 layers initialized, resulting in a low number of defects in the layers. The inner layers have a smaller amount of freedom to shear with respect to each other and expand/contract according to the local stress. Furthermore, they are forced to accommodate curvature according to the contour of the top layer and are further limited by the inner oxide core [16.125]. The inside-out growth mode allows for more relaxed accretion of the layers in an unconfined environment. However, the very high growth rate leaves little time for relaxation of the nanostructures; for example, the reaction of $TiCl_4$ and H_2S to produce IF-TiS_2 nanoparticles may last a few seconds only [16.62]. Dislocations which are trapped in the structure during the growth can nevertheless be annealed out afterwards.

In the inside-out growth mechanism, the seed may exert some measure of guidance on the subsequent layers. In contrast, the rolling-up method for the synthesis of INT [16.114] enables the formation of subsequent shells whose chirality may be unrelated to the previous ones.

Knowledge of the structure at the atomic level may also lead to a better understanding of the synthetic process. A remarkable example, made possible by high-resolution TEM (HRTEM) and high-angle annular dark-field (HAADF) STEM in conjunction with imaging simulation, is the consistent observation of a single chiral shell [16.2] in INT-WS_2 produced by fast spontaneous reaction without WO_{3-x} nanowhiskers as an intermediate phase. Previous studies could only detect chiral WS_2 nanotubes with chiral angle of $7 \pm 3°$. With one exception, each of the measured tubes consisted of only one chiral shell while the other shells were achiral (zigzag or armchair) [16.107]. It was assumed that the growth of a chiral layer was energetically and kinetically favorable, because it provided a continuous growth front. Consequently, the chiral layer may serve as scaffolding for subsequent inner and outer armchair and/or zigzag layers to form [16.52, 107]. This insight also sheds light on the mechanical and electrical properties which will be detailed in the relevant sections.

When the chemical processes are close to equilibrium, the reaction time and temperature play an important role. In particular, longer annealing times and higher temperatures favor annealing of dislocations, resulting in more perfect structures. An additional role in the chemical processes is attributed to diffusion. The diffusion rates of reactants and reagents may play a decisive role in the final structure of the product; for example, the outward diffusion rate of the iodine used as a chemical transport agent from the interior of $Mo_xS_yI_z$ nanowires determines the amount of iodine interstitials in the final product [16.17].

The physical methods are typified by highly energetic structures, which grow very fast and generally at low yields. Not surprisingly, therefore, these nanostructures incorporate point defects and dislocations, which are much less likely to occur close to equilibrium conditions. Notable in this regard are the square-like point defects which decorate the apexes of MoS_2 nanooctahedra [16.2, 126, 127] (Fig. 16.15). Deeper investigation of the laser ablation products has shown that imperfect structures of nanooctahedra – distorted octahedra and

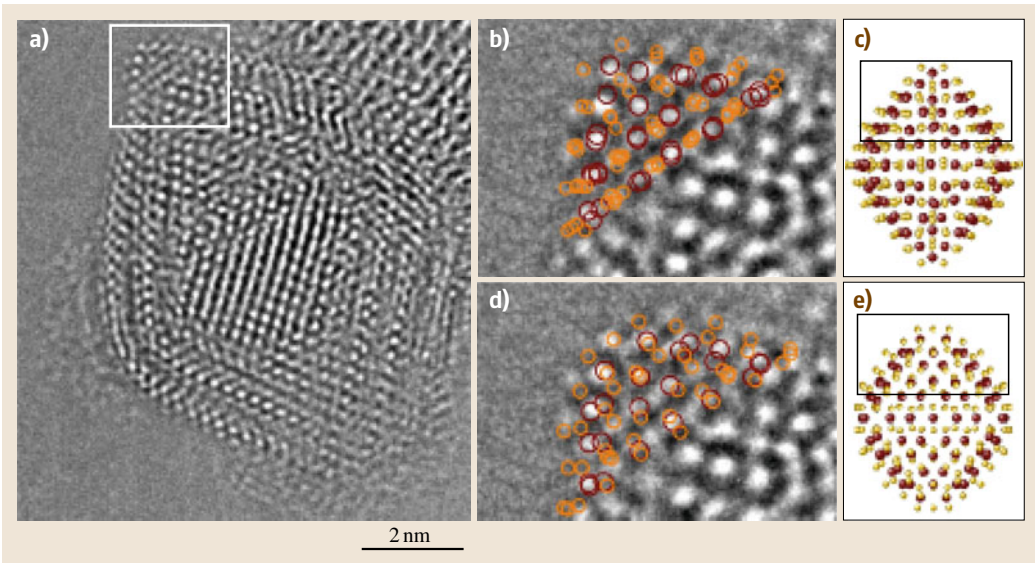


Fig. 16.15a–e Atomic-resolution image of a MoS_2 nanooctahedron taken in an image-side aberration-corrected FEI Titan 80 300 (under negative Cs imaging conditions). Full structure **(a)**. A magnified part of the tip of the octahedron revealing the sulfur atoms is shown in **(b)** and **(d)**, with a superposition of the models presented in **(c)** and **(e)**. The models in (c) and (e) correspond to 2 of the 15 hypothetical structures proposed for MoS_2 nanooctahedra in [16.127]. Mo atoms are displayed in *red*; S atoms are displayed in *yellow*. In **(b)**, one of the most stable structures [16.127] coincides with **(c)**, whereas the less stable structure depicted in **(e)** fails to match (in **(d)**) (after [16.2])

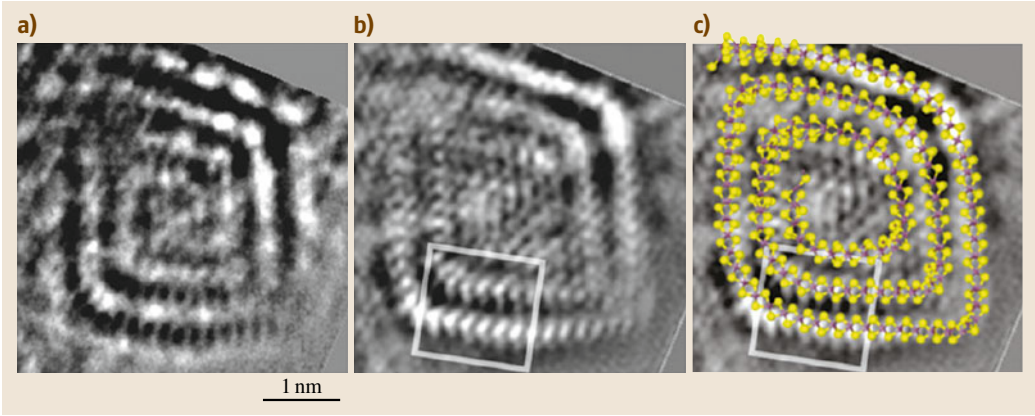


Fig. 16.16 **(a)** Conventional Scherzer defocus HRTEM image of a nanoseashell. **(b)** Reconstructed phase image produced from a focal series of images obtained from the same specimen. **(c)** Central plane of a matching model structure of a nanoseashell (after [16.128])

seashell structures with meander-like cross sections – are formed as well [16.128], as seen in Fig. 16.16. These structures appear to contain the square-like defects connecting two or more facets of different sizes. This may inhibit the facets from closing to form a perfect closed-cage structure, like nanooctahedra, and produce a scroll structure, resembling a spiral seashell. In contrast to the symmetric and closed-cage structure of the MoS_2 nanooctahedra, the external edge of the scroll structure is capable of continuous growth.

As was pointed out in the previous section, the physical techniques such as laser ablation and arc

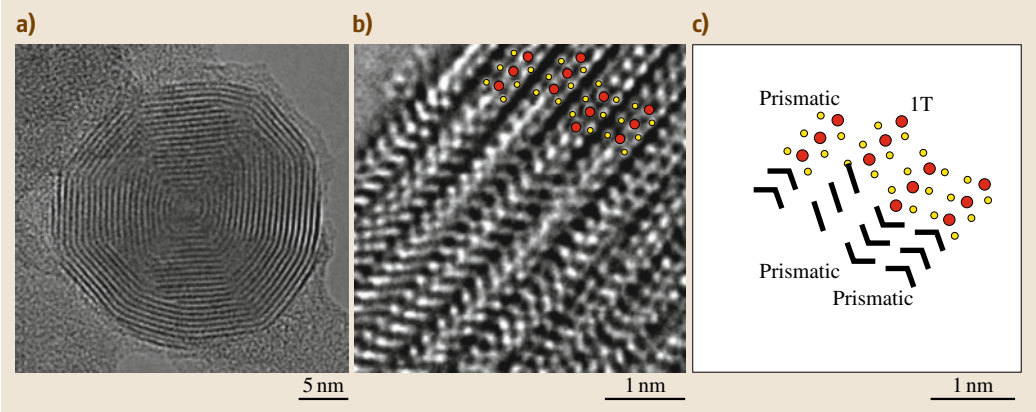


Fig. 16.17a–c Typical MoS_2 closed nanoparticles in which a nanooctahedral core undergoes morphology change to quasi-spherical outer shells, obtained by ablating MoS_2 powder in a solar furnace. **(a)** Hybrid nanocluster of 26 nm in diameter. **(b)** Atomic resolution of the MoS_2 layers. The atomic model is overlaid in *red* (Mo) and *yellow* (S), and detailed in **(c)** with *black lines* as visual guides to their appearance in the TEM image. The *chevron motif* (≫) correlates with a prismatically coordinated MoS_2 layer, which is a semiconductor. The pattern of *diagonal lines* indicates the 1T phase with MoS_6 octahedral coordination (after [16.101])

discharge are characterized by their operation in far-from-equilibrium conditions, i. e., high temperatures and short reaction times. Thus, it is often quite challenging to isolate the unstable intermediates and investigate the formation mechanisms of the products. Consequently, the exact reaction mechanism that leads to the formation of the nanooctahedra remains an open issue. While this aspect does pose problems in scaling up production using physical techniques, it is nevertheless useful in highlighting worthwhile goals for the chemical techniques. An example for this process is solar ablation [16.90], which allows production of larger amounts of nanostructures which are either scarce or totally absent otherwise.

As mentioned previously, the solar ablation technique is somewhat of a hybrid between the chemical and physical techniques. The relatively large diameter of the beam (1 mm^2) produces substantially denser vaporized atoms than most laser ablation setups used for this purpose. Furthermore, the large and continuous irradiation field creates an extensive hot zone with temperatures in the range of a few thousand degrees Celsius. This annealing zone allows for thermalization and stabilization of the incipient nanoclusters. This thermalization is not available in the pulsed laser ablation setup. Obviously, such nanoclusters cannot be obtained by the pure chemical method, which uses substantially lower temperatures. One such product observed in solar ablation is single-walled INT-MoS_2 [16.100]. The hybrid nature of the solar ablation process is exemplified in the recently reported hybrid nanooctahedra-IF-MoS_2 (NO-IF) shown in Fig. 16.17 [16.101]. These nanostructures likely start growing from the inside out in a growth mode typical for a nucleation and growth mechanism from the vapor phase. The size of the hollow core is determined by the maximum strain the nanooctahedra can accommodate, which correlates with their theoretical minimum size (≈ 3 nm) [16.126, 127]. Furthermore, the nanooctahedra may be formed initially and then serve as a nucleus for an outer IF shell formation in the extended annealing zone. Most importantly, aberration-corrected TEM revealed first-ever octahedral (1T) coordination of the MoS_2 layers embedded within nanoparticles (Fig. 16.17).

To understand the significance of this finding, it is necessary to study the structure of the three phases mentioned at the beginning of this section. The coordination of the sulfur atoms with respect to the tungsten atoms and the stacking of the layers give rise to three polytypes: a hexagonal polytype 2Hb with two molecular layers as a repeat unit (*P63/mmc*), a rhombohedral polytype 3R with three molecular layers per unit cell (*R3m*), which is stable in plane geometry at pressures above 4 GPa [16.125], and the less common trigonal polytype 1T with one molecular layer (Fig. 16.17c). It should be emphasized that full commensuration is not possible between the layers of the INT and/or IF. Therefore, the layers are slightly shifted with respect to each

other and the stacking cannot be accurately described as pure 2H, 3R, or 1T phase. As seen in Fig. 16.17, the S–M–S configurations produce a diagonal pattern for 1T and chevrons for 2H and 3R, being parallel and antiparallel, respectively. These alignments are observed in INT-WS_2 and IF-MoS_2. Due to the lack of complete commensuration between the layers, the stacking is better described as prismatic parallel, prismatic antiparallel, or octahedral diagonal. However, the terms 2H, 3R, and 1T will be used here in order to adhere to the terms used previously for bulk materials in the literature.

However, there is an ongoing debate in the literature on which phases are prevalent in INT and IF of MS_2. The techniques generally utilized in studying the structure, morphology, and defects of INT and IF are TEM, HRTEM, x-ray diffraction (XRD), and Raman spectroscopy. XRD line broadening is a standard technique to quantify the effective crystallite sizes by applying the Debye–Scherrer equation. Raman spectroscopy has been also applied to detect and quantify the morphological and structural properties as well as defects in IF and INT [16.49, 70, 129, 130].

As the 1T phase is metallic, incorporation of a single 1T layer might have dramatic effects on the mechanical and electronic properties of the whole particle due to inner metal–semiconductor junctions. Furthermore, the presence of the 1T phase in MoS_2 nanostructures was overlooked until recently. This fact could be attributed to the small number of layers arranged in this phase within the nanostructure. Another factor was the absence, until recent years, of a credible ultrahigh-resolution (aberration-corrected) TEM which could analyze such small domains in nanostructures. Obviously, the sensitivity of *bulk* techniques such as XRD and Raman was not sufficient to analyze such tiny domains. Another factor could be the unstable nature of the 1T phase, preventing the formation of multiple 1T shells.

Some generalities may also be drawn from recent reports on IF of 2-D materials with relatively high ionic character, such as $CdCl_2$, or $NiBr_2$. These allowed connections to be made between the properties of the layered bulk and the resulting nanostructures [16.40, 43, 90, 131]. It was suggested that highly ionic bonds, encountered in the 2-D metal dihalides, resulted in a faceted nanostructure and that the amount of commensuration between the layers is related to the shear modulus. Most importantly, it was suggested that the complexity of the unit cell influences the ability to seam facets and the overall stability of the nanostructure: if the lattice is not symmetric in both in-layer directions, there are more boundary conditions to satisfy in order to produce a stable and seamless closed-cage structure [16.40].

These insights all point to one conclusion: The benefits arising from thorough understanding of the structure down to the atomic level, intimate knowledge of the synthetic mechanism, and most importantly, the interrelations between them allow for better selection of the desired properties. This is most evident in the amount of structural defects of IF and INT and their nature, which directly influence their mechanical, electrical, and optical properties.

16.3.2 Mechanical Properties

In analogy to the case of CNT, the mechanical properties of individual INT and IF have been shown to be superior to those of the bulk material. Unlike CNT, INT-WS_2 or MoS_2 do not undergo a pressure-induced phase change. In fact, under high pressure they eventually collapse, making INT and IF nanoparticles very robust under compression. While the Young's and shear moduli of CNT are appreciably higher than those of most INT, their application in ultrahigh-strength nanocomposites suffers from the pressure-induced transformation of the C–C bond into the sp^3 (diamond) bond. The goal of these studies is to elucidate the structure–function relationship in INT and IF nanoparticles and eventually enhance the mechanical properties of various matrices.

While measurements of the mechanical properties of individual INT and IF nanostructures are very challenging, quite a few works have been reported on this subject in recent years. These studies will be reviewed briefly, and then the influence of the structure and defects on these properties will be examined too. It should be noted that this section focuses on the mechanical properties of single IF and INT. Nonetheless, the mechanical properties of composites will be briefly touched upon in the applications section.

The experimentally Young's modulus of INT-WS_2 agrees very well with the bulk WS_2 value [16.132]. However, in the case of the bulk material, the measurements were carried out in the $a-b$ (basal) plane. In contrast, the mechanical properties of the bulk material along the c-axis are substantially inferior. They are influenced by the weakness of the van der Waals interactions and are further exacerbated by intercalation of impurities in the van der Walls galleries. The mechanical properties of individual INT and more recently of individual IF nanoparticles were systematically studied using high-resolution SEM, scanning probe microscopy (SPM) [16.132–134], and lately also TEM [16.135]. For

INT-WS_2 the Young's modulus (E) was found to be 150 GPa; the elongation to failure was 12%, and the tensile strength was 16 GPa ($\approx$ 11% of E), as shown in Fig. 16.18. The latter value is significant, since it is much higher (for INT) than for bulk materials, whose values are commonly around 2–5% E [16.134].

These measurements are supported by first-principle calculations for zigzag (22,0) and armchair (14,14) single-walled INT-MoS_2, which are generally in agreement with the experimental findings [16.132]. The calculated Young's modulus was found to be in agreement with the bulk value (230 GPa) with elongation to failure and tensile strength of 17%, 40 GPa and 19%, 34 GPa, respectively. These values are equivalent to 17.4% and 14.7% of E. Both cases show good agreement between the experimentally observed and calculated values of the Young's modulus, as well as very high ratio of the tensile strength to the Young's modulus.

The anisotropic behavior of nanostructures under shear in different directions reflects the 2-D layered structure; i. e., the intralayer shear modulus is much higher than the interlayer shear (sliding) modulus. This was shown to be the case for INT-WS_2, where the interlayer shear modulus was measured by three-point bending as 2 GPa [16.133]. Recent measurements of the radial modulus gave similar results (3–6 GPa). This indicates that the interlayer shear may play a key role in the mechanical response to radial compression [16.136], similar to the importance of interlayer shear in the response of INT-WS_2 to torsion [16.137]. These values also concur relatively well with atomistic density-functional tight-binding calculations (DFTB) giving values of 4 and 12 GPa [16.133,136] for the shear and radial compression moduli, respectively. Considering MoS_2 as an example, similar values were found for the interlayer shear modulus of 2H-MoS_2 (15 GPa) by neutron and x-ray scattering of the linear compressibility [16.138]. These values are in contrast with the shear modulus obtained for a solid, filled beam which assumes an isotropic nature (57 GPa) [16.10]. They also contrast with the intralayer shear modulus calculated by DFTB for single-walled, armchair and zigzag INT-MoS_2 (53 and 82 GPa, respectively) [16.139]. This discussion once again highlights the anisotropy of INT properties.

It is significantly more challenging to measure the mechanical properties of single IF NP, sometimes simply due to technical issues. In addition, folding up the layers into the IF NP nested, closed-cage structure creates larger amounts of defects when compared to INT. The elastic behavior and compression failure strength of individual IF-WS_2 (IF-MoS_2) nanoparticles were measured in situ with an AFM tip fixed inside a high-resolution scanning electron microscope (HRSEM) [16.140] as shown in Fig. 16.19. It was found that the compression failure strength of these nanoparticles is as high as 1–2.5 GPa. IF-MoS_2 nanoparticles were found to collapse only under 2.5–3.5 GPa. A similar in situ experiment was carried out in the TEM and was used to characterize the exfoliation of IF NP under shearing force [16.135].

The mechanical properties are directly related to the crystal structure, but are also strongly affected by structural imperfections or defects, which are the weakest

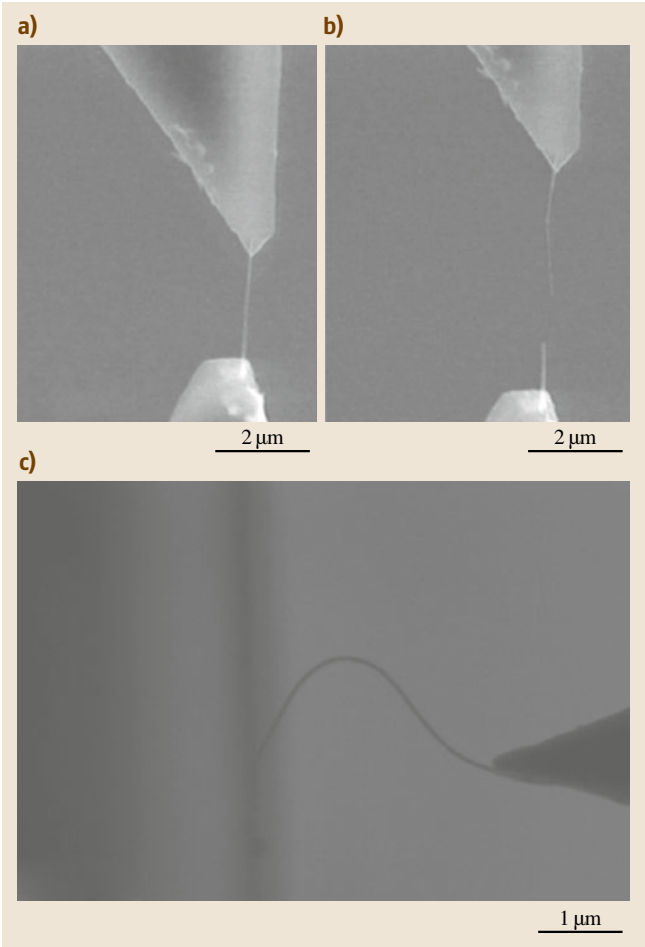


Fig. 16.18a–c Typical mechanical test of WS_2 nanotubes. Under tension before **(a)** and after **(b)** fracture. **(c)** Buckling under compression (after [16.134])

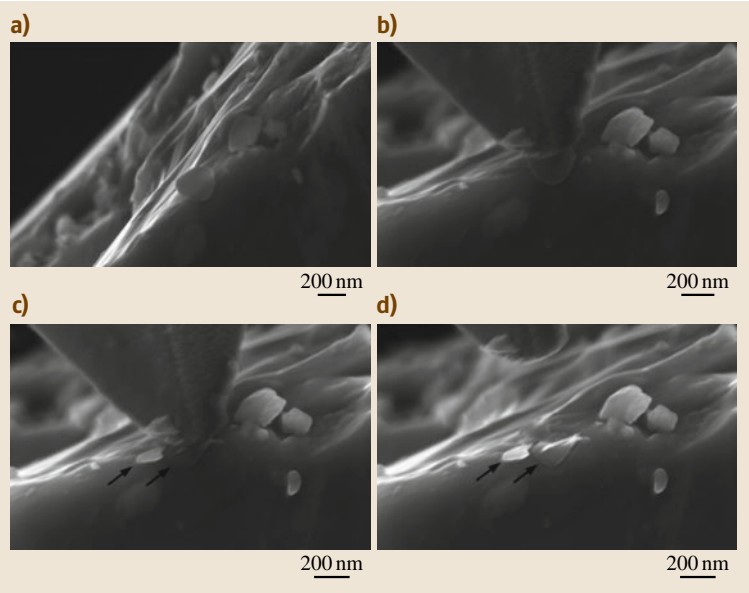


Fig. 16.19a–d Typical mechanical HRSEM images of the axial nanocompression test. **(a)** IF-WS_2; **(b)** AFM tip pressing the IF-WS_2; **(c)** compressive failure; **(d)** collapsed IF-WS_2. The *arrows* in **(c)** and **(d)** indicate the fragments (after [16.140])

link in the structure and first to fail. This is especially true in the case of INT-WS_2 and INT-MoS_2, which have been shown to have a very small amount of critical structural defects. This is evident from the narrow scattering of the experimental data [16.132, 134, 141]. It can therefore be concluded that the INT exhibit excellent mechanical characteristics that are commensurate with the calculated values [16.133, 134]. The lack of defects is further highlighted by the ratio of the tensile strength to the Young's modulus in INT-WS_2, which is 11%. This is an exceedingly high value in comparison with other high-strength materials [16.134]. This value is very close to the theoretical maximum emerging from the calculation for excessive distortion of a chemical bond [16.134].

As explained above, for a given diameter, INT and IF of layered materials are under higher strain compared with CNT due to the triple-layer structure [16.142]. It was also shown theoretically that line defects such as dislocations, and more extended defects such as grain boundaries and stacking faults, are intrinsic features of IF, once the thickness exceeds a certain number of layers [16.142]. The occasional formation of edges or apexes (Fig. 16.17) in IF releases some of the stress in a similar way to grain boundaries.

The effect of the morphology on the mechanical properties was observed in compression experiments of IF-MoS_2 [16.140]. It was found that the faceted nature of the IF-MoS_2 NP led to stress concentration under uniaxial compression. Therefore, faceted IF can withstand lower loads and lower stiffness when compared with spherical, nonfaceted IF.

While the failure mechanisms of macroscopic objects are often attributed to dislocation diffusion and propagation of cracks along grain boundaries, the failure of INT under stress is in general the result of the excessive distortion of the chemical bonds. The ultimate strength and elongation of INT is believed to be limited by the breaking of a single chemical bond in the middle of the INT. This causes stress transfer to the adjacent chemical bonds, which become overstrained and consequently fail, resulting in almost instantaneous tear of the INT [16.134]. Furthermore, tensile tests of multi-walled INT-WS_2 in the TEM revealed a telescopic failure mode, supporting the idea that the strain is taken by the outermost layer of the INT [16.143].

The crystalline perfection, which is dictated by the synthetic method, strongly affects the mechanical properties of INT and IF. The likely origin of the INT-WS_2 failure mode [16.2] is supported by the good agreement between the experimental and calculated data for such nanotubes [16.134]. The correspondence of experimental and theoretical data is explained by atomic-resolution TEM study showing the outer shells of the nanotubes to be mostly achiral (armchair or zigzag) [16.2]. Due to limited computation resources and complexity, calculations are generally carried out on achiral INT. The good correlation between the theo-

retical and experimental results may be attributed to the outermost shell taking up most of the strain, which is in most cases an achiral one and defect free.

In fact, the tensile failure mode of the INT can vary quite dramatically between chiral and achiral INT. In chiral tubes, the failure mode of the tube does not require the immediate failure of a chemical bond. Instead, it may involve a mechanism whereby the pitch is elongated under tensile strain with the collapse of the hollow core of the INT. This failure mode is analogous to the lengthening mode of a spring under tensile stress [16.2]. Indeed, the failure mode of INT-WS_2 strongly suggests that the chemical bonds are broken at once with seemingly little variation in the tube diameter [16.134], supporting the conclusion that the outermost layer of the nanotube is indeed achiral. This shows once more the intimate relationship between the structure and functionality of the nanotubes.

16.3.3 Electronic and Optical Properties

Controllable electronic properties are of great importance for fabrication of nanoscale devices and multifunctional materials. In comparison with the substantial work done on the mechanical properties of INT and IF, the number of experimental studies on the electronic, optical, and magnetic properties of such INT and IF is still very small. Moreover, many of the measurements were performed on large amounts of nanoparticles, with only a few studies dedicated to the study of individual nanotubes. The absence of such data does not reflect a lack of interest in this field, but rather the great difficulties in fabricating such devices in a reproducible fashion. One such problem that plagues electronic properties on the nanoscale in general is that of contacting the nanostructure in question. In particular, the issue of contacting CNT still involves a large amount of ongoing research with a focus on matching the contact material workfunction with that of the measured material [16.144], as well as matching the Fermi surface in order to reduce electron scattering at the interface [16.145].

The physical properties of inorganic nanostructures are variable and largely depend on the properties of the bulk compound from which they are derived; for example, INT-MoS_2 [16.116] are semiconductors, while INT-$NbSe_2$ [16.146] are low-temperature superconductors. However, in contrast to compact semiconductor nanoparticles and nanorods, which exhibit a blue-shift of the band gap due to the quantum size effect [16.109], the band gap of INT and IF undergoes a red-shift with decreasing size [16.147], probably due to strain.

This opposite effect is attributed to the more complex nature of 2-D layered compounds. Unlike CNT, the inorganic nanotube band structure cannot be estimated from a simple zone-folding scheme of the corresponding band structure of the bulk material. The rolled inorganic 2-D layer undergoes a significant structural relaxation. The innermost atomic layer of sulfur undergoes compression, while the outermost one is under tension. This results in a less than perfect hybridization of the atomic orbitals. Thus, the valence band of INT-$W(Mo)S_2$ is composed of three bands, i. e., quasi-core sulfur 3s-states, hybridized S3p-Mo4d(W5d)-states, and Mo4d(W5d)-states. The lower edge of the conduction band is composed of metal d-states [16.44].

The semiconducting character of INT and IF NP was also confirmed by optical measurements of the UV-Vis spectrum of IF-$W(Mo)S_2$, which are in agreement with the theoretical calculations [16.116,148]. The excitonic absorption agrees with the semiconducting nature of the material [16.149]. A clear red-shift in the exciton energy, which increased with the number of the closed layers in the IF nanoparticles, was observed. The fact that the temperature dependence of the exciton energy was similar to that of the exciton in the bulk indicated that the red-shift cannot be attributed to defects or dislocations in the IF material, and is a genuine property of INT and IF. Thus, the red-shift of the exciton energy in the absorption measurements was attributed to the strain in the bent layers [16.149].

Another aspect in which INT-$W(Mo)S_2$ nanostructure differs significantly from CNT is that the former were found to be semiconductors irrespective of their chirality as shown by DFTB calculations [16.116, 148]. However, while armchair INT-MoS_2 were found to exhibit an indirect ($\Delta-\Gamma$) electronic transition, the zigzag INT possess a direct ($\Gamma-\Gamma$) transition. This observation suggests a possible luminescence of zigzag INT-MoS_2 following optical or electrical excitation [16.150]. Furthermore, recent results for INT-MoS_2 indicate that a high density of defects in the nanostructure may result in a metallic behavior [16.9]. Thus, the band gap of semiconducting INT and IF may be tuned, using the whole spectrum all the way from the UV down to the infrared, by varying the diameter of the nanotubes and also the number of layers.

An important correlation between the Raman spectra and the structure of INT has recently been reported [16.130]. The optical properties of INT and IF-$W(Mo)S_2$ have been studied in detail by resonance

Raman spectroscopy in a number of studies over the last decade [16.49, 70, 129, 130, 151, 152]. The strongest peaks at 417 and 351 cm^{-1} of IF-MoS_2 correspond to the A_{1g} and E_{2g} modes, respectively. The intensity of the low-energy component of the A_{1g} mode range is enhanced in INT and IF, creating a mode labeled D-A_{1g}. It was found that the ratio of intensities between the D-A_{1g} mode and the A_{1g} mode correlates with the amount of disorder in the nanostructure. Thus, this ratio increases with decreasing diameter of the nanotube, most likely due to increased strain and larger amount of defects. Furthermore, this ratio is larger for IF than INT [16.130], which further illustrates the larger number of defects in a 2-D layer folded into a quasispherical structure as opposed to a cylinder.

The polarizability of INT-WS_2 further demonstrates the anisotropic character of the nanotube [16.151]. Raman spectroscopy measurements showed that the A_{1g} and E_{2g} modes have the same polarization behavior with a strong signal along the tube axis (ZZ) only and almost none for light polarized perpendicular to the tube axis (X-polarized light). Similar polarization effects were observed for incident and scattered light. The ratio of the perpendicular to parallel polarizabilities ($\alpha_{XX}/\alpha ZZ = 0.16$) is estimated from the orientation dependence of the INT resonant Raman intensity, demonstrating the strong polarization along the INT axis. It was concluded that this effect arises both from the anisotropy due to the 2-D layered structure, as well as from the antenna effect caused by the large aspect ratio of the tubular morphology.

The Raman spectra of agglomerated INT-WS_2 nanotubes were measured under hydrostatic pressure. The two main Raman modes shift linearly to higher energies with normalized pressure coefficients of $\omega_0^{-1}\, d\omega/dp \approx 4.5\,TPa^{-1}$. The two-dimensional (in-plane) Grüneisen parameter value of INT-WS_2 nanotubes is 0.45, as compared with the value of 2 for CNT, which shows the softness of the INT-WS_2.

In contrast to the semiconducting IF and INT, the calculated electronic properties of MoS_2 nanooctahedra were found to be radically different from those of the bulk solid [16.126]. These properties were elucidated theoretically by density-functional tight-binding calculations (DFTB) accompanied with molecular dynamics (MD) annealing. Irrespective of their size and exact stoichiometry, all hollow octahedral molybdenum sulfide fullerenes exhibit a practically vanishing band gap between the highest occupied molecular orbital (HOMO) and the lowest occupied molecular orbital (LUMO), which are mainly of Mo 4d character. Thus, these calculations suggest that the nanooctahedra should exhibit a metallic-like character. According to the DFTB-MD calculations, the occurrence of metallic-like d-band conductivity correlates sensitively with the square-like defects at the apexes and the seams between the triangular facets [16.2]. Experimental verification of these calculations is rather challenging due to the difficulties in isolation of the nanooctahedra and subsequent measurement of such small (3–7 nm) objects.

The influence of the nanooctahedra morphology on its electronic structure was studied by calculating the density of states (DOS) for particular cases of distorted nanooctahedron $(MoS_2)_{389}$, symmetric nanooctahedron $(MoS_2)_{400}$, and nanoseashell $(MoS_2)_{408}$, with roughly the same size [16.128] (see Figs. 16.15 and 16.16 for models of the nanooctahedra and nanoseashells). The calculations of all three nanostructures gave similar results and were characterized by a metal-like character of the DOS, independent of the exact morphology of the particles. The HOMO–LUMO gap did not exceed 0.01 eV, with the states around the HOMO–LUMO gap dominated by Mo 4d states. Thus, distorted nanooctahedra and nanoseashells demonstrate similar features of their electronic structure to the symmetric nanooctahedra, with the metallic character attributed to the square-like defects at the apexes and the seams.

The transport properties of WS_2 nanotubes are rather disappointing at this time. It is difficult to explain the dichotomy between the very good mechanical behavior of INT and their poor transport properties. Nonetheless, the low conductivity of INT with respect to the bulk material [16.153] may be attributed to the growth of achiral shells within and on top of the chiral shell [16.2], resulting in different electron mobility in each shell. This may further result in the formation of scattering centers that negatively affect the overall INT conductivity.

The electronic properties of INT and IF may be modified further by intercalation or doping, which is thus a subject of current interest. The large van der Waals gap typical of layered metal dichalcogenides renders them good host matrices for intercalation. Therefore, their electronic properties may also be modified not only by defects and substitutional dopant atoms, but also by the introduction of various impurities into the cavities between the layers [16.44, 65, 154].

Doping of INT and IF may pave the way for their application in semiconducting nanoelectronic devices or as a conductive phase in nanocomposites, thus offering numerous potential applications; for example, the INT-MoS_2 saturated surfaces are much more resistant

towards oxidation and humidity when compared with silicon or other semiconductors of groups IV, III–V, and II–VI while possessing a similar band gap to that of silicon (0.89–1.07 versus 1.17 eV, respectively) [16.155]. Therefore, there is great interest in n- or p-type doping of INT and IF by substitutional dopants such as Re and Nb, respectively [16.64, 155].

Another advantage that substitutional doping has over intercalations is that, unlike intercalated atoms, dopants are assumed to be less mobile under applied potential, pH, etc., and thus much effort has been put into synthesis of doped INT and IF. Doped INT have been reported for specific cases, such as Ti-doped INT-MoS_2, Nb-doped INT-WS_2, and Mo- and C-doped INT-WS_2 [16.156–159]. This is in addition to alloying in the case of INT-(W/Mo)S_2 [16.160]. Doping of IF has also been reported for Nb-doped IF-MoS_2 [16.21], Re-doped IF-MoS_2 [16.155], and recently for alloyed IF-(W/Mo)S_2 [16.161].

Incorporation of substitutional dopants in nanostructures is relatively easier in gas-phase synthesis, which allows for easy incorporation of dopant atoms in the lattice achieved by thorough mixing of the constituent atoms. This has been demonstrated for Nb- and Re-doped IF-MoS_2 [16.64, 155], which were synthesized by the inside-out (nucleation and growth) method from volatile metal chloride precursors. However, doping of the foreign atoms with 5% Re and 30% Nb resulted in segregation of secondary phases and nonuniformity of the sample. The driving force for this segregation is the large differences in crystal structure of MoS_2 (2H or 3R) as opposed to the ReS_2 structure (distorted C6) [16.162].

The electronic properties of Nb-doped INT-MoS_2 were investigated theoretically using the density-functional tight-binding method (DFTB) [16.163, 164]. The doping resulted in metallic behavior which correlates with the experimental results for Nb-doped IF-MoS_2 [16.64]. This work predicted that INT-$Mo_{1-x}Nb_xS_2$ should exhibit a metallic character, irrespective of their chirality, diameter, and ordering type of dopant atoms after a certain Nb threshold level is surpassed. Thus, the density of states close to the Fermi level of Nb-doped INT-MoS_2 may be tuned over a wide range by the degree of Nb doping.

Another area, where progress is slow and much further work is needed, is the coupling between the mechanical and electrical, thermal, or optical effects in a single nanotube or fullerene. In this respect, there is some promise in recent advancements in TEM, SEM, Raman, and optical in situ measurements of coupled properties such as the optoelectronic or electromechanical properties of nanostructures.

16.3.4 Calculations and Simulations

Quantum-chemical calculations using density-functional approaches in conjunction with molecular dynamics (MD) are extremely important for predicting the stable structures and their physiochemical characteristics. The unit cells of inorganic nanotubes contain considerably more atoms than carbon nanotubes. Moreover, the atoms involved are usually heavier and contain many more electrons, increasing the computational resources needed for calculations of inorganic nanotubes significantly. Thus, an accommodation widely utilized is simulations of smaller structures with subsequent use of semi-empirical models to extrapolate to larger structures. These extrapolations are then compared with the measured values, if available.

In addition to these general considerations, atomistic simulations of the structure and stability for a series of existing and hypothetical inorganic nanotubes have been carried out. An overview on theoretical investigations of INT and IF is presented in [16.44, 165], respectively. These calculations were performed with empirical force fields, semi-empirical quantum-mechanical methods, and particularly with density-functional-based methods (DF), mainly using pseudopotentials and plane-wave (PW) basis expansions or within a tight-binding approach (DFTB). The calculations for INT are usually more straightforward compared with IF as their structure is more perfect and allows for the use of periodic boundary conditions along the tube direction. Therefore, a narrow ring may represent the structure for the calculations of, e.g., zigzag nanotubes. This is opposed to IF, which invariably necessitate construction of full structures with thousands of atoms, containing edges and defects. These defects may vary greatly between individual IF and may even render the simulations inaccurate. In general INT with a simple roll-up vector, such as armchair or zigzag, are easier to handle with ab initio calculations. Chiral nanotubes with large pitch have larger unit cell and cannot be easily calculated using accurate quantum-chemical methods. Thus, a few studies which use line-group symmetries have also been published [16.166], allowing for analysis of rather large tubes of various chiralities.

The first quantum-mechanical calculations of metal sulfide nanotubes were performed by DFTB for INT-MoS_2 and WS_2 nanotubes [16.116,167]. As anticipated, the strain energy is clearly larger than that of CNT

due to the triple atomic layer structure of the former. Moreover, the strain energy of the INT is inversely proportional to the radius squared of the nanotube. Thus, the nanotube becomes less stable than the corresponding strip below diameter of 6 nm. This is consistent with the experimental finding that the smallest observed (inner) diameter of INT-W(Mo)S_2 is around 6–7 nm. Moreover, the interlayer van der Waals interactions in the strips and INT contribute to stabilization of nanotubes of larger inner diameters. This may account for the difficulties in the synthesis of single-walled INT-W(Mo)S_2 [16.115].

Recent simulations of INT-MoS_2 under radial mechanical compressive deformation revealed several remarkable trends [16.168]. As expected, the strain–stress correlation slope is steeper for smaller nanotubes, i. e., nanotubes with smaller diameter are stiffer, which nicely correlates with the reduced stability of INT with decreasing diameter [16.115, 116]. Furthermore, the strain–stress relation is essentially independent of the tube's chirality, as the slope (normalized by the INT diameter) is nearly identical for different chiralities [16.168]. Another trend is that, in contrast to tensile strain–stress curves, the radial compression deviates from linearity toward higher stress values; i. e., the more the system is deformed, the harder it is to deform them further.

The calculations show that nanotubes with small diameter possess lower strength. This implies that the innermost shell determines the failure point of the multi-walled INT as they break from the inside out. When loaded, the innermost tube wall is under the highest strain energy, and it bursts and unbends. Subsequently, the strain is transferred to the next largest tube, which collapses beyond a given strain as well, and so forth. These calculations indicate that it might be possible to tune the mechanical properties of INT-MoS_2 by controlling the structural properties of the innermost shell [16.168].

The quantum chemical calculations of nanooctahedra represent the upper limit of full DFTB exact calculations. This allowed a comparison between detailed investigations of synthesized nanooctahedra by electron microscopy and the calculated structures [16.126]. Full quantum-mechanical calculations for IF-MoS_2 NP consisting of several thousand atoms are beyond the limit of presently available technology. A phenomenological model for the energetics and stability of the nanoparticles was therefore developed. This model circumnavigated the computational obstacles in the full quantum-mechanical calculations of such large nanoclusters. Furthermore, by using several approximations, the calculations were extended to larger multi-walled IF-MoS_2. This development enabled a comparison between the calculated phase diagram of hollow MoS_2 nanoparticles with the experimentally observed structures. The validity of the model and the approximations was supported by the good agreement between the calculated results and the published experimental data [16.5, 18, 87]. Thus, the stability of nanooctahedra increases proportionally with the number of layers, while single-walled MoS_2 nanooctahedra were found to be less stable than nanoplatelets over the whole size range. Furthermore, the calculations show that multi-walled octahedral MoS_2 fullerenes with more than 10^4 atoms are more stable than the corresponding nanoplatelets. This exemplifies the general underlying principle of fullerene formation of forming the structure with the lowest energy possible.

Knowledge of the structure at the atomic level is also needed for interpreting high-resolution electron microscopy data. The calculated lattice is then used to calculate the exit wave for comparison with HRTEM results. Therefore, it is easily seen that modeling and simulation is crucial to thorough investigation of the structure. Ultimately, modeling and simulation is a very powerful tool for elucidation of the structure and properties at the nanolevel. Moreover, its predictive power has been illustrated in a number of important cases, such as the transition from nanooctahedra to quasispherical (IF) MoS_2 nanoparticles. Here, the theoretical calculations predicted that such transitions would occur when the size of the nanocluster exceeds about 10^5 atoms, which was confirmed experimentally [16.101].

16.4 Applications

The extensive advancements in the synthesis and structural elucidation of these nanostructures has been paralleled by the major progress achieved in scaling up the production and applications of W(Mo)S_2 IF and INT. One such example is the commercial engine oil *NanoLub* utilizing the superior tribological behavior of IF. The large number of potential applications in the fields of lubrication, high-performance nanocomposites, energy storage, as well as others is briefly reviewed in this section.

16.4.1 Tribological Applications

MoS_2 has been used as a solid lubricant or as an additive in oil or grease for more than 60 years. The weak interlayer interactions (van der Waals forces) between the 2-D layers results in a low interlayer shear modulus which allows for easy shearing in a vacuum environment. However, the application of MoS_2 platelets in tribological applications is limited to oxygen- or moisture-free atmosphere. In the presence of such vapors, tribologically induced reactions with the rim atoms of the platelets lead to fast deterioration of the solid lubricant. Therefore, it was assumed that the IF and INT stability in lubricating conditions would be enhanced with respect to platelets due to their closed-cage structure which exposes only the vdW surfaces and (almost) no dangling bonds. Moreover, it was hypothesized that spherical IF-MS_2 would behave like nano ball-bearings, giving rise to rolling and thus providing superior solid lubrication over the platelets. Further work suggested that, under mechanical stress, the IF would slowly deform and exfoliate, transferring MS_2 nanosheets onto the underlying surfaces (third-body effect). These sheet fragments coating the moving surfaces asperities provide effective lubrication until they are completely gone, or oxidize. Finally, the IF NP have been proposed as environmentally friendly lubricant additives as alternatives to the classical phosphorus- and/or sulfur-based lubricants due to their small sizes and morphology [16.161].

The beneficial tribological effects of IF powder additives in lubricants have been studied in quite some detail, as summarized in [16.169–171]. Work in progress indicates that this effect is particularly important when the clearance (gap) between the two mating surfaces and the surface roughness are approximately of the same order of magnitude as the nanoparticles themselves, i. e., 30–300 nm. Additionally, IF aggregation was found to be an important parameter in these applications [16.172]. Thus, there is great interest in preventing aggregation and mass production of nonagglomerated IF.

Recent years have seen an increase in the attention given to self-lubricating coatings, which have numerous potential applications in machining, aerospace, sport, medical, and various other industries. Unlike fluid lubricants, IF embedded in a coating cannot lubricate by acting as ball-bearings unless a gradual release from the coating is invoked. Thus, under heavy load/shear conditions, the IF NP are gradually exfoliated, transferring nanosheets onto the moving mating surfaces, which provide the lubrication and a reduction in the friction coefficient within a few run-in cycles. Another advantage of the IF is that they inhibit oxidation of the metal surface dramatically, thereby preventing decomposition of the brittle oxide and scratching of the metal surface. Recent work showed improved performance of orthodontic implements and endodontic files coated with such self-lubricating films [16.173, 174]. Moreover, toxicological tests indicated that the product is benign [16.175, 176], though further work is needed to confirm this important point. Finally, such coatings may be highly suitable for harsh environments such as outer space, where regular lubricants would either freeze or boil, or deep-sea thermal vents, where lubricants have to withstand high compressive pressures and high temperatures.

16.4.2 Composites

The mechanical properties of INT and IF indicate an abundance of applications in composite materials such as the shielding of vehicles or as additives in high-strength construction materials. Among these promising properties are the mechanical robustness of INT- and IF-W(Mo)S_2 [16.132–134], high-pressure resilience to degradation under hydrostatic pressures of up to 20 GPa [16.177], and the ability to withstand shockwaves of up to 30 GPa with local temperatures rising up to 1000 °C [16.178]. These works led to a surge of interest in fabricating nanocomposites with enhanced mechanical properties incorporating INT- and IF-W(Mo)S_2.

The aforementioned findings stimulated numerous studies which were devoted to the study of nanocomposites of INT and IF embedded in polymer matrices. Thus, *Naffakh* et al. [16.179] found that addition of small amounts of IF to isotactic polypropylene (iPP) increased the thermal stability of the polymer with a remarkable effect on the polymer's crystallization rate. The increased rate of crystallization of polymer matrices by IF nanoparticles was found to be common to a variety of other polymer matrices such as Nylon 6 [16.180]. Furthermore, the storage moduli of IF-iPP nanocomposites were appreciably higher than those of pristine iPP. Recent work on IF and INT embedded in epoxy resin demonstrated a substantial increase in their mechanical properties, including shear strength and moduli, as well as peel strength and fracture toughness [16.181, 182].

16.4.3 Hydrogen and Lithium Adsorption/Desorption in INT

As mentioned above, layered dichalcogenides are good host matrices for intercalation due to their large van der Waals gap. Thus, INT are attractive substrates for hydrogen and lithium intercalation storage in energy applications; for example, adsorption and desorption of hydrogen in INT-MoS_2 was investigated at room temperature [16.183] with adsorption kinetics that was nearly linear and with a saturation after ≈ 30 min allowing for fast and steady hydrogen buildup. Comparison of the gas adsorption (1.2 wt %) and electrochemical storage (0.97 wt %) indicates that the gas adsorption process is the result of physisorption of hydrogen in the INT-MoS_2 nanotubes. Similarly, Li insertion into INT-$MoS_2I_{0.3}$ bundles prepared by chemical vapor transport was investigated [16.184], with a significant increase in the amount of inserted lithium and a decrease of ≈ 0.7 V in the insertion potential for the electrodes when compared with bulk 2H-MoS_2 powder. Furthermore, electron paramagnetic resonance (EPR) measurements showed that the lithiated INT bundles were less sensitive to air than the bulk material.

16.4.4 Miscellaneous

As the preceding sections demonstrate, the applications of IF and INT are numerous and are steadily expanding. Recent work in the area of functionalization is promising to expand these areas even more [16.58]. This is especially promising in the context of catalysis, where nanostructured materials have long been heralded as the next leap in heterogeneous and homogeneous catalysis. Thus, one of the most important potential applications of INT-MoS_2 is their use as catalysts for hydrodesulfurization of thiophene and dibenzothiophene and desulfurization of petroleum and gasoline [16.64, 68, 69, 155, 185, 186].

The optical properties of INT and IF have also revealed potential for practical applications; for example, black metallic coatings containing IF showing less than 1.7% reflectivity over the range of 300–1100 nm were demonstrated with various applications ranging from solar-to-thermal converters to optical coatings [16.1]. Also promising are the optical-limiting (OL) properties of INT-MoS_2 in aqueous suspensions, which were shown to surpass those of CNT at 1064 and 532 nm [16.187].

16.5 Conclusions

The formation of inorganic nanotubes and fullerene-like nanostructures is now considered a generic phenomenon of inorganic compounds with layered (two-dimensional) compounds. The most prominent members of this family are WS_2 and MoS_2, which are currently produced in relatively large amounts. Therefore, the underlying principles governing the synthetic processes of these materials could be used as guidelines for a large variety of materials.

The superior qualities of INT and IF as well as their tunable properties elicit great interest due to both the fundamental questions that these nanostructures pose and the substantial breadth of potential applications. In particular, their inherent stability under harsh conditions is promising for numerous applications in various fields. Thus, study of these nanostructures has led to the observation of a number of interesting properties offering numerous potential applications in tribology, high-energy-density batteries, composites, and catalysis. Chemical modifications (surface functionalization) of the IF and INT surfaces could lead in the future to new strategies for drug delivery, contrast agents, and a variety of other medical applications.

The progress achieved on all these fronts is still dwarfed by the numerous challenges facing the field. Controllable and reproducible synthesis of inorganic nanotubes with predefined structural parameters is one such challenge, let alone the optical and electronic properties of the nanotubes. Thus, controlling the size, shape, and resultant properties is still in its infancy. This chapter highlights the fact that a real and deep understanding of the interplay between synthesis and structure is essential, as well as comprehension of how the structure relates to the resultant properties.

References

16.1 R. Tenne, G. Seifert: Recent progress in the study of inorganic nanotubes and fullerene-like structures, Annu. Rev. Mater. Res. **39**(1), 387–413 (2009)

16.2 M. Bar-Sadan, L. Houben, A.N. Enyashin, G. Seifert, R. Tenne: Atom by atom: HRTEM insights into inorganic nanotubes and fullerene-like structures, Proc. Natl. Acad. Sci. USA **105**(41), 15643–15648 (2008)

16.3 M. Sadan Bar, L. Houben, S.G. Wolf, A. Enyashin, G. Seifert, R. Tenne, K. Urban: Toward atomic-scale bright-field electron tomography for the study of fullerene-like nanostructures, Nano Lett. **8**(3), 891–896 (2008)

16.4 S. Iijima: Helical microtubules of graphitic carbon, Nature **354**(6348), 56–58 (1991)

16.5 R. Tenne, L. Margulis, M. Genut, G. Hodes: Polyhedral and cylindrical structures of tungsten disulphide, Nature **360**(6403), 444–446 (1992)

16.6 R. Tenne: Inorganic nanotubes and fullerene-like nanoparticles, Nat. Nanotechnol. **1**(2), 103–111 (2006)

16.7 S. Amelinckx, B. Devouard, A. Baronnet: Geometrical aspects of the diffraction space of serpentine rolled microstructures: Their study by means of electron diffraction and microscopy, Acta Crystall. **52**(6), 850–878 (1996)

16.8 T.J. Zega, L.A.J. Garvie, I. Dodony, P.R. Buseck: Serpentine Nanotubes in CM chondrites, Paper presented at the 35th Lunar and Planetary Science Conference (2004)

16.9 M. Remskar, A. Mrzel, M. Virsek, M. Godec, M. Krause, A. Kolitsch, A. Singh, A. Seabaugh: The MoS_2 nanotubes with defect-controlled electric properties, Nanoscale Res. Lett. **6**(1), 26 (2011)

16.10 R. Tenne, M. Remškar, A. Enyashin, G. Seifert: Inorganic nanotubes and fullerene-like structures (IF), Top. Appl. Phys. **111**, 631–671 (2008)

16.11 J. Goldberger, R.R. He, Y.F. Zhang, S.W. Lee, H.Q. Yan, H.J. Choi, P.D. Yang: Single-crystal gallium nitride nanotubes, Nature **422**(6932), 599–602 (2003)

16.12 J.H. Zhan, Y. Bando, J.P. Hu, D. Golberg: Bulk synthesis of single-crystalline magnesium oxide nanotubes, Inorg. Chem. **43**(8), 2462–2464 (2004)

16.13 H.J. Fan, U. Gosele, M. Zacharias: Formation of nanotubes and hollow nanoparticles based on Kirkendall and diffusion processes: A review, Small **3**(10), 1660–1671 (2007)

16.14 D. Gong, C.A. Grimes, O.K. Varghese, W.C. Hu, R.S. Singh, Z. Chen, E.C. Dickey: Titanium oxide nanotube arrays prepared by anodic oxidation, J. Mater. Res. **16**(12), 3331–3334 (2001)

16.15 R. Beranek, H. Hildebrand, P. Schmuki: Self-organized porous titanium oxide prepared in H_2SO_4/*HF* electrolytes, Electrochem. Solid State Lett. **6**(3), B12–B14 (2003)

16.16 C.N.R. Rao, A. Govindaraj: Synthesis of inorganic nanotubes, Adv. Mater. **21**(42), 4208–4233 (2009)

16.17 M. Viršek, M. Krause, A. Kolitsch, A. Mrzel, I. Iskra, S.D. Škapin, M. Remškar: The transformation pathways of $Mo_6S_2I_8$ nanowires into morphology-selective MoS_2 nanostructures, J. Phys. Chem. C **114**(14), 6458–6463 (2010)

16.18 L. Margulis, G. Salitra, R. Tenne, M. Talianker: Nested fullerene-like structures, Nature **365**(6442), 113–114 (1993)

16.19 M. Hershfinkel, L.A. Gheber, V. Volterra, J.L. Hutchison, L. Margulis, R. Tenne: Nested polyhedra of MX_2 (M = W, Mo; X = S, Se) probed by high-resolution electron microscopy and scanning tunneling microscopy, J. Am. Chem. Soc. **116**(5), 1914–1917 (1994)

16.20 M. Nath, C.N.R. Rao: New metal disulfide nanotubes, J. Am. Chem. Soc. **123**(20), 4841–4842 (2001)

16.21 C. Schuffenhauer, R. Popovitz-Biro, R. Tenne: Synthesis of NbS_2 nanoparticles with (nested) fullerene-like structure (IF), J. Mater. Chem. **12**(5), 1587–1591 (2002)

16.22 M. Nath, C. Rao: Nanotubes of group 4 metal disulfides, Angew. Chem. **114**(18), 3601–3604 (2002)

16.23 M. Nath, C.N.R. Rao: Nanotubes of group 4 metal disulfides, Angew. Chem. Int. Ed. **41**, 3451–3454 (2002)

16.24 K.S. Coleman, J. Sloan, N.A. Hanson, G. Brown, G.P. Clancy, M. Terrones, H. Terrones, M.L.H. Green: The formation of ReS_2 inorganic fullerene-like structures containing Re_4 parallelogram units and metal-metal bonds, J. Am. Chem. Soc. **124**(39), 11580–11581 (2002)

16.25 Y.R. Hacohen, E. Grunbaum, R. Tenne, J. Sloan, J.L. Hutchison: Cage structures and nanotubes of $NiCl_2$, Nature **395**(6700), 336–337 (1998)

16.26 H.A. Therese, F. Rocker, A. Reiber, J. Li, M. Stepputat, G. Glasser, U. Kolb, W. Tremel: VS_2 nanotubes containing organic-amine templates from the NT-VO_x precursors and reversible copper intercalation in NT-VS_2, Angew. Chem. Int. Ed. **44**(2), 262–265 (2005)

16.27 J. Chen, S.-L. Li, Z.-L. Tao, Y.-T. Shen, C.-X. Cui: Titanium disulfide nanotubes as hydrogen-storage materials, J. Am. Chem. Soc. **125**(18), 5284–5285 (2003)

16.28 J.A. Hollingsworth, D.M. Poojary, A. Clearfield, W.E. Buhro: Catalyzed growth of a metastable ins crystal structure as colloidal crystals, J. Am. Chem. Soc. **122**(14), 3562–3563 (2000)

16.29 S.R.C. Vivekchand, A. Govindaraj, C.N.R. Rao: Nanotubes and nanowires: Recent developments. In: *Nanomaterials Chemistry*, ed. by C.N.R. Rao,

A. Müller, A.K. Cheetham (Wiley-VCH, Weinheim 2007)
16.30 C. Rao, A. Govindaraj: *Nanotubes and Nanowires* (R. Soc. Chem., London, 2006)
16.31 C.N.R. Rao, M. Nath: Inorganic nanotubes, Dalton Trans. **1**, 1–24 (2003)
16.32 R. Tenne, C.N.R. Rao: Inorganic nanotubes, Philos. Trans. R. Soc. **362**(1823), 2099–2125 (2004)
16.33 Y. Feldman, E. Wasserman, D.J. Srolovitz, R. Tenne: High-rate, gas-phase growth of MoS_2 nested inorganic fullerenes and nanotubes, Science **267**(5195), 222–225 (1995)
16.34 C. Schuffenhauer, B.A. Parkinson, N.Y. Jin-Phillipp, L. Joly-Pottuz, J.-M. Martin, R. Popovitz-Biro, R. Tenne: Synthesis of fullerene-like tantalum disulfide nanoparticles by a gas-phase reaction and laser ablation, Small **1**(11), 1100–1109 (2005)
16.35 A. Margolin, R. Popovitz-Biro, A. Albu-Yaron, A. Moshkovich, L. Rapoport, R. Tenne: Fullerene-like nanoparticles of titanium disulfide, Curr. Nanosci. **1**(3), 253–262 (2005)
16.36 F. Jensen, H. Toftlund: Structure and stability of C_{24} and $B_{12}N_{12}$ isomers, Chem. Phys. Lett. **201**(1-4), 89–96 (1993)
16.37 O. Stéphan, Y. Bando, A. Loiseau, F. Willaime, N. Shramchenko, T. Tamiya, T. Sato: Formation of small single-layer and nested BN cages under electron irradiation of nanotubes and bulk material, Appl. Phys. **67**(1), 107–111 (1998)
16.38 C. Ducati, E. Barborini, G. Bongiorno, S. Vinati, P. Milani, P.A. Midgley: Titanium fullerenoid oxides, Appl. Phys. Lett. **87**(20), 201906 (2005)
16.39 A. Albu-Yaron, T. Arad, R. Popovitz-Biro, M. Bar-Sadan, Y. Prior, M. Jansen, R. Tenne: Preparation and structural characterization of stable Cs_20 closed-cage structures, Angew. Chem. Int. Ed. **44**(27), 4169–4172 (2005)
16.40 R. Levi, M. Bar-Sadan, A. Albu-Yaron, R. Popovitz-Biro, L. Houben, C. Shahar, A. Enyashin, G. Seifert, Y. Prior, R. Tenne: Hollow V_2O_5 nanoparticles (fullerene-like analogues) prepared by laser ablation, J. Am. Chem. Soc. **132**(32), 11214–11222 (2010)
16.41 R. Tenne, R. Popovitz-Biro, A. Twersky, Y. Rosenfeld Hacohen: Nanoparticles of $CdCl_2$ with closed cage structures, Isr. J. Chem. **41**(1), 7–14 (2001)
16.42 R. Popovitz-Biro, N. Sallacan, R. Tenne: CdI_2 nanoparticles with closed-cage (fullerene-like) structures, J. Mater. Chem. **13**(7), 1631–1634 (2003)
16.43 M. Bar-Sadan, R. Popovitz-Biro, Y. Prior, R. Tenne: Closed-cage (fullerene-like) structures of $NiBr_2$, Mat. Res. Bull. **41**(11), 2137–2146 (2006)
16.44 A.N. Enyashin, S. Gemming, G. Seifert: Simulation of inorganic nanotubes. In: *Materials for Tomorrow*, Springer Series in Materials Science, Vol. 93, ed. by S. Gemming, M. Schreiber, J.-B. Suck (Springer, Berlin Heidelberg 2007) pp. 33–57
16.45 V.V. Ivanovskaya, G. Seifert: Tubular structures of titanium disulfide TiS_2, Solid State Commun. **130**(3/4), 175–180 (2004)
16.46 T. Köhler, T. Frauenheim, Z. Hajnal, G. Seifert: Tubular structures of GaS, Phys. Rev. B **69**(19), 193403 (2004)
16.47 A. Meden, A. Kodre, J. Padežnik Gomilšek, I. Arčon, I. Vilfan, D. Vrbanic, A. Mrzel, D. Mihailovic: Atomic and electronic structure of $Mo_6S_{9-x}I_x$ nanowires, Nanotechnology **16**(9), 1578 (2005)
16.48 S. Jiménez Sandoval, D. Yang, R.F. Frindt, J.C. Irwin: Raman study and lattice dynamics of single molecular layers of MoS_2, Phys. Rev. B **44**(8), 3955 (1991)
16.49 G.L. Frey, R. Tenne, M.J. Matthews, M.S. Dresselhaus, G. Dresselhaus: Raman and resonance Raman investigation of MoS_2 nanoparticles, Phys. Rev. B **60**(4), 2883 (1999)
16.50 Y. Feldman, A. Zak, R. Popovitz-Biro, R. Tenne: New reactor for production of tungsten disulfide hollow onion-like (inorganic fullerene-like) nanoparticles, Solid State Sci. **2**(6), 663–672 (2000)
16.51 A. Zak, L. Sallacan-Ecker, A. Margolin, M. Genut, R. Tenne: Insight into the growth mechanism of WS_2 nanotubes in the scaled-up fluidized-bed reactor, Nano **4**, 91–98 (2009)
16.52 A. Margolin, R. Rosentsveig, A. Albu-Yaron, R. Popovitz-Biro, R. Tenne: Study of the growth mechanism of WS_2 nanotubes produced by a fluidized bed reactor, J. Mater. Chem. **14**(4), 617–624 (2004)
16.53 H.H. Kung: *Transition metal oxides: Surface chemistry and Catalysis*, Studies in Surface Science and Catalysis, Vol. 45 (Elsevier, Amsterdam 1989)
16.54 A. Yella, M. Panthöfer, M. Kappl, W. Tremel: Snapshots of the formation of inorganic MoS_2 onion-type fullerenes: A "shrinking giant bubble" pathway, Angew. Chem. Int. Ed. **49**(14), 2575–2580 (2010)
16.55 A. Zak, Y. Feldman, V. Alperovich, R. Rosentsveig, R. Tenne: Growth mechanism of MoS_2 fullerene-like nanoparticles by gas-phase synthesis, J. Am. Chem. Soc. **122**(45), 11108–11116 (2000)
16.56 D. Vollath (Ed.): *Nanomaterials* (Wiley, New York 2008)
16.57 A. Margolin, F.L. Deepak, R. Popovitz-Biro, M. Bar-Sadan, Y. Feldman, R. Tenne: Fullerene-like WS_2 nanoparticles and nanotubes by the vapor-phase synthesis of WCl_n and H_2S, Nanotechnology **19**(9), 095601 (2008)
16.58 M.N. Tahir, A. Yella, J.K. Sahoo, H. Annal-Therese, N. Zink, W. Tremel: Synthesis and functionalization of chalcogenide nanotubes, Phys. Status Solidi (b) **247**(10), 2338–2363 (2010)
16.59 I. Wiesel, H. Arbel, A. Albu-Yaron, R. Popovitz-Biro, J. Gordon, D. Feuermann, R. Tenne: Synthesis of WS_2 and MoS_2 fullerene-like nanoparticles from solid precursors, Nano Res. **2**(5), 416–424 (2009)

16.60 F. Deepak, A. Mayoral, M. Yacaman: Structural transformation of MoO_3 nanobelts into MoS_2 nanotubes, Appl. Phys. A: Mater. Sci. Process. **96**(4), 861–867 (2009)

16.61 F.L. Deepak, A. Mayoral, M.J. Yacaman: Faceted MoS_2 nanotubes and nanoflowers, Mater. Chem. Phys. **118**(2/3), 392–397 (2009)

16.62 A. Margolin, R. Popovitz-Biro, A. Albu-Yaron, L. Rapoport, R. Tenne: Inorganic fullerene-like nanoparticles of TiS_2, Chem. Phys. Lett. **411**(1-3), 162–166 (2005)

16.63 F. Deepak, A. Margolin, I. Wiesel, M. Bar-Sadan, R. Popovitz-Biro, S. Cohen, H. Cohen, R. Tenne, E.M. Unit: MoS_2 Fullerene-like nanoparticles and nanotubes using gas-phase reaction with $MoCl_5$, Nano **1**(2), 167–180 (2006)

16.64 F.L. Deepak, H. Cohen, S. Cohen, Y. Feldman, R. Popovitz-Biro, D. Azulay, O. Millo, R. Tenne: Fullerene-like (IF) $Nb_xMo_{1-x}S_2$ nanoparticles, J. Am. Chem. Soc. **129**(41), 12549–12562 (2007)

16.65 A. Zak, Y. Feldman, V. Lyakhovitskaya, G. Leitus, R. Popovitz-Biro, E. Wachtel, H. Cohen, S. Reich, R. Tenne: Alkali metal intercalated fullerene-like MS_2 (M = W, Mo) nanoparticles and their properties, J. Am. Chem. Soc. **124**(17), 4747–4758 (2002)

16.66 X.-L. Li, J.-P. Ge, Y.-D. Li: Atmospheric pressure chemical vapor deposition: An alternative route to large-scale MoS_2 and WS_2 inorganic fullerene-like nanostructures and nanoflowers, Chemistry **10**(23), 6163–6171 (2004)

16.67 J. Etzkorn, H.A. Therese, F. Rocker, N. Zink, U. Kolb, W. Tremel: Metal–organic chemical vapor depostion synthesis of hollow inorganic-fullerene-type MoS_2 and $MoSe_2$ nanoparticles, Adv. Mater. **17**(19), 2372–2375 (2005)

16.68 M. Remskar, M. Virsek, A. Jesih: WS_2 Nanobuds as a new hybrid nanomaterial, Nano Lett. **8**(1), 76–80 (2007)

16.69 M. Remškar, A. Mrzel, M. Viršek, A. Jesih: Inorganic nanotubes as nanoreactors: The first MoS_2 nanopods, Adv. Mater. **19**(23), 4276–4278 (2007)

16.70 M. Krause, M. Viršek, M. Remškar, N. Salacan, N. Fleischer, L. Chen, P. Hatto, A. Kolitsch, W. Möller: Diameter and morphology dependent Raman signatures of WS_2 nanostructures, ChemPhysChem **10**(13), 2221–2225 (2009)

16.71 R.R. Chianelli, E.B. Prestridge, T.A. Pecoraro, J.P. Deneufville: Molybdenum disulfide in the poorly crystalline "rag" structure, Science **203**(4385), 1105–1107 (1979)

16.72 J.V. Sanders: Structure of catalytic particles, Ultramicroscopy **20**(1/2), 33–37 (1986)

16.73 J.V. Sanders: Transmission electron microscopy of catalysts, J. Electron Micr. Tech. **3**(1), 67–93 (1986)

16.74 T. Tsirlina, Y. Feldman, M. Homyonfer, J. Sloan, J.L. Hutchison, R. Tenne: Synthesis and characterization of inorganic fullerene-like WSe_2 material, Fuller. Sci. Techn. **6**, 157–165 (1998)

16.75 L. Margulis, R. Tenne, S. Iijima: Nucleation of WS_2 fullerenes at room temperature, Microsc. Microanal. Microstruct. **7**(2), 87–89 (1996)

16.76 H.W. Kroto, J.R. Heath, S.C. Obrien, R.F. Curl, R.E. Smalley: C_{60}: Buckminsterfullerene, Nature **318**(6042), 162–163 (1985)

16.77 W. Krätschmer, L.D. Lamb, K. Fostiropoulos, D.R. Huffman: C_6O: A new form of carbon, Nature **347**(6291), 354–358 (1990)

16.78 P.A. Parilla, A.C. Dillon, B.A. Parkinson, K.M. Jones, J. Alleman, G. Riker, D.S. Ginley, M.J. Heben: Formation of nanooctahedra in molybdenum disulfide and molybdenum diselenide using pulsed laser vaporization, J. Phys. Chem. B **108**(20), 6197–6207 (2004)

16.79 S.Y. Hong, R. Popovitz-Biro, Y. Prior, R. Tenne: Synthesis of SnS_2/SnS fullerene-like nanoparticles: A superlattice with polyhedral shape, J. Am. Chem. Soc. **125**(34), 10470–10474 (2003)

16.80 Y.R. Hacohen, R. Popovitz-Biro, E. Grunbaum, Y. Prior, R. Tenne: Vapor-liquid-solid growth of $NiCl_2$ nanotubes via reactive gas laser ablation, Adv. Mater. **14**(15), 1075 (2002)

16.81 Y. Saito, T. Yoshikawa, M. Inagaki, M. Tomita, T. Hayashi: Growth and structure of graphitic tubules and polyhedral particles in arc-discharge, Chem. Phys. Lett. **204**(3/4), 277–282 (1993)

16.82 T. Guo, C.M. Jin, R.E. Smalley: Doping bucky – formation and properties of boron-doped buckminsterfullerene, J. Phys. Chem. **95**(13), 4948–4950 (1991)

16.83 M. Jose-Yacaman, H. Lopez, P. Santiago, D.H. Galvan, I.L. Garzon, A. Reyes: Studies of MoS_2 structures produced by electron irradiation, Appl. Phys. Lett. **69**(8), 1065–1067 (1996)

16.84 F. Banhart, M. Zwanger, H.J. Muhr: The formation of curled concentric-shell clusters in boron-nitride under electron-irradiation, Chem. Phys. Lett. **231**(1), 98–104 (1994)

16.85 R. Popovitz-Biro, A. Twersky, Y.R. Hacohen, R. Tenne: Nanoparticles of $CdCl_2$ with closed cage structures, Isr. J. Chem. **41**(1), 7–14 (2001)

16.86 M. Homyonfer, Y. Mastai, M. Hershfinkel, V. Volterra, J.L. Hutchison, R. Tenne: Scanning tunneling microscope induced crystallization of fullerene-like MoS_2, J. Am. Chem. Soc. **118**(33), 7804–7808 (1996)

16.87 P.A. Parilla, A.C. Dillon, K.M. Jones, G. Riker, D.L. Schulz, D.S. Ginley, M.J. Heben: The first true inorganic fullerenes?, Nature **397**(6715), 114–114 (1999)

16.88 M. Nath, C.N.R. Rao, R. Popovitz-Biro, A. Albu-Yaron, R. Tenne: Nanoparticles produced by laser ablation of HfS_3 in liquid medium: Inorganic fullerene-like structures of Hf_2S, Chem. Mater. **16**(11), 2238–2243 (2004)

16.89 N. Sallacan, R. Popovitz-Biro, R. Tenne: Nanoparticles of CdI_2 with closed cage structures obtained

via electron-beam irradiation, Solid State Sci. **5**(6), 905–908 (2003)
16.90 A. Albu-Yaron, T. Arad, M. Levy, R. Popovitz-Biro, R. Tenne, J.M. Gordon, D. Feuermann, E.A. Katz, M. Jansen, C. Muhle: Synthesis of fullerene-like Cs_20 nanoparticles by concentrated sunlight, Adv. Mater. **18**(22), 2993 (2006)
16.91 Y. Feldman, G.L. Frey, M. Homyonfer, V. Lyakhovitskaya, L. Margulis, H. Cohen, G. Hodes, J.L. Hutchison, R. Tenne: Bulk synthesis of inorganic fullerene-like MS_2 (M = Mo, W) from the respective trioxides and the reaction mechanism, J. Am. Chem. Soc. **118**(23), 5362–5367 (1996)
16.92 M. Bar-Sadan, I. Kaplan-Ashiri, R. Tenne: Inorganic fullerenes and nanotubes: Wealth of materials and morphologies, Eur. Phys. J. Spec. Top. **149**, 71–101 (2007)
16.93 R.E. Russo: Laser ablation, Appl. Spectrosc. **49**, 14A–28A (1995)
16.94 R.E. Russo, X. Mao, S.S. Mao: The physics of laser ablation in microchemical analysis, Anal. Chem. **74**(3), 70–77 (2002)
16.95 Y.R. Hacohen, R. Popovitz-Biro, Y. Prior, S. Gemming, G. Seifert, R. Tenne: Synthesis of $NiCl_2$ nanotubes and fullerene-like structures by laser ablation: Theoretical considerations and comparison with MoS_2 nanotubes, Phys. Chem. Chem. Phys. **5**(8), 1644–1651 (2003)
16.96 S. Irle, G. Zheng, Z. Wang, K. Morokuma: The C_{60} formation puzzle "solved": QM/MD simulations reveal the shrinking hot giant road of the dynamic fullerene self-assembly mechanism, J. Phys. Chem. B **110**(30), 14531–14545 (2006)
16.97 B. Saha, S. Shindo, S. Irle, K. Morokuma: Quantum chemical molecular dynamics simulations of dynamic fullerene self-assembly in benzene combustion, ACS Nano **3**(8), 2241–2257 (2009)
16.98 A.A. Shvartsburg, R.R. Hudgins, P. Dugourd, R. Gutierrez, T. Frauenheim, M.F. Jarrold: Observation of "stick" and "handle" intermediates along the fullerene road, Phys. Rev. Lett. **84**(11), 2421 (2000)
16.99 T.W. Ebbesen, J. Tabuchi, K. Tanigaki: The mechanistics of fullerene formation, Chem. Phys. Lett. **191**(3-4), 336–338 (1992)
16.100 J.M. Gordon, E.A. Katz, D. Feuermann, A. Albu-Yaron, M. Levy, R. Tenne: Singular MoS_2, SiO_2 and Si nanostructures-synthesis by solar ablation, J. Mater. Chem. **18**(4), 458–462 (2008)
16.101 A. Albu-Yaron, M. Levy, R. Tenne, R. Popovitz-Biro, M. Weidenbach, M. Bar-Sadan, L. Houben, A.N. Enyashin, G. Seifert, D. Feuermann, E.A. Katz, J.M. Gordon: MoS_2 hybrid nanostructures: From octahedral to quasi-spherical shells within individual nanoparticles, Angew. Chem. Int. Ed. **50**, 1810–1814 (2011)
16.102 J.M. Gordon, D. Feuermann, M. Huleihil, E.A. Katz: New optical systems for the solar generation of nanomaterials, Proc. SPIE **5185**, 99–108 (2004)
16.103 A. Yella, E. Mugnaioli, M. Panthöfer, H.A. Therese, U. Kolb, W. Tremel: Bismuth-catalyzed growth of SnS_2 nanotubes and their stability, Angew. Chem. Int. Ed. **48**(35), 6426–6430 (2009)
16.104 N.G. Chopra, A. Zettl: Measurement of the elastic modulus of a multi-wall boron nitride nanotube, Solid State Commun. **105**(5), 297–300 (1998)
16.105 F. Krumeich, H.J. Muhr, M. Niederberger, F. Bieri, B. Schnyder, R. Nesper: Morphology and topochemical reactions of novel vanadium oxide nanotubes, J. Am. Chem. Soc. **121**(36), 8324–8331 (1999)
16.106 A. Rothschild, G.L. Frey, M. Homyonfer, R. Tenne, M. Rappaport: Synthesis of bulk WS_2 nanotube phases, Mat. Res. Innov. **3**(3), 145–149 (1999)
16.107 R. Rosentsveig, A. Margolin, Y. Feldman, R. Popovitz-Biro, R. Tenne: WS_2 nanotube bundles and foils, Chem. Mater. **14**(2), 471–473 (2002)
16.108 A. Rothschild, R. Popovitz-Biro, O. Lourie, R. Tenne: Morphology of multiwall WS_2 nanotubes, J. Phys. Chem. B **104**(38), 8976–8981 (2000)
16.109 A. Rothschild, J. Sloan, R. Tenne: Growth of WS_2 Nanotubes Phases, J. Am. Chem. Soc. **122**(21), 5169–5179 (2000)
16.110 Y.Q. Zhu, W.K. Hsu, H. Terrones, N. Grobert, B.H. Chang, M. Terrones, B.Q. Wei, H.W. Kroto, D.R.M. Walton, C.B. Boothroyd, I. Kinloch, G.Z. Chen, A.H. Windle, D.J. Fray: Morphology, structure and growth of WS_2 nanotubes, J. Mater. Chem. **10**(11), 2570–2577 (2000)
16.111 G.L. Frey, A. Rothschild, J. Sloan, R. Rosentsveig, R. Popovitz-Biro, R. Tenne: Investigations of nonstoichiometric tungsten oxide nanoparticles, J. Solid State Chem. **162**(2), 300–314 (2001)
16.112 J. Chen, S.-L. Li, F. Gao, Z.-L. Tao: Synthesis and characterization of WS_2 nanotubes, Chem. Mater. **15**(4), 1012–1019 (2003)
16.113 R.L.D. Whitby, W.K. Hsu, P.K. Fearon, N.C. Billingham, I. Maurin, H.W. Kroto, D.R.M. Walton, C.B. Boothroyd, S. Firth, R.J.H. Clark, D. Collison: Multiwalled carbon nanotubes coated with tungsten disulfide, Chem. Mater. **14**(5), 2209–2217 (2002)
16.114 Y.D. Li, X.L. Li, R.R. He, J. Zhu, Z.X. Deng: Artificial lamellar mesostructures to WS_2 nanotubes, J. Am. Chem. Soc. **124**(7), 1411–1416 (2002)
16.115 G. Seifert, T. Köhler, R. Tenne: Stability of Metal Chalcogenide Nanotubes, J. Phys. Chem. B **106**(10), 2497–2501 (2002)
16.116 G. Seifert, H. Terrones, M. Terrones, G. Jungnickel, T. Frauenheim: Structure and electronic properties of MoS_2 nanotubes, Phys. Rev. Lett. **85**(1), 146 (2000)
16.117 M. Remskar, Z. Skraba, C. Ballif, R. Sanjinés, F. Lévy: Stabilization of the rhombohedral polytype in MoS_2 and WS_2 microtubes: TEM and AFM study, Surf. Sci. **433-435**, 637–641 (1999)

16.118 M. Remskar, Z. Skraba, F. Cleton, R. Sanjines, F. Levy: MoS_2 as microtubes, Appl. Phys. Lett. **69**(3), 351–353 (1996)
16.119 M. Remskar, A. Mrzel, Z. Skraba, A. Jesih, M. Ceh, J. Demšar, P. Stadelmann, F. Lévy, D. Mihailovic: Self-assembly of subnanometer-diameter single-wall MoS_2 nanotubes, Science **292**(5516), 479–481 (2001)
16.120 A.R. Armstrong, J. Canales, P.G. Bruce: WO_2Cl_2 nanotubes and nanowires, Angew. Chem. Int. Ed. **43**(37), 4899–4902 (2004)
16.121 P. Hoyer: Formation of a titanium dioxide nanotube array, Langmuir **12**(6), 1411–1413 (1996)
16.122 T. Kasuga, M. Hiramatsu, A. Hoson, T. Sekino, K. Niihara: Formation of titanium oxide nanotube, Langmuir **14**(12), 3160–3163 (1998)
16.123 G.H. Du, Q. Chen, R.C. Che, Z.Y. Yuan, L.M. Peng: Preparation and structure analysis of titanium oxide nanotubes, Appl. Phys. Lett. **79**(22), 3702–3704 (2001)
16.124 C.M. Zelenski, P.K. Dorhout: Template synthesis of near-monodisperse microscale nanofibers and nanotubules of MoS_2, J. Am. Chem. Soc. **120**(4), 734–742 (1998)
16.125 J.A. Wilson, A.D. Yoffe: The transition metal dichalcogenides discussion and interpretation of the observed optical, electrical and structural properties, Adv. Phys. **18**(73), 193–335 (1969)
16.126 A.N. Enyashin, S. Gemming, M. Bar-Sadan, R. Popovitz-Biro, S.Y. Hong, Y. Prior, R. Tenne, G. Seifert: Structure and stability of molybdenum sulfide fullerenes, Angew. Chem. Int. Ed. **46**(4), 623–627 (2007)
16.127 M. Bar-Sadan, A.N. Enyashin, S. Gemming, R. Popovitz-Biro, S.Y. Hong, Y. Prior, R. Tenne, G. Seifert: Structure and stability of molybdenum sulfide fullerenes, J. Phys. Chem. B **110**(50), 25399–25410 (2006)
16.128 A.N. Enyashin, M. Bar-Sadan, J. Sloan, L. Houben, G. Seifert: Nanoseashells and nanooctahedra of MoS_2: Routes to inorganic fullerenes, Chem. Mater. **21**(23), 5627–5636 (2009)
16.129 M. Virsek, A. Jesih, I. Milosevic, M. Damnjanovic, M. Remskar: Raman scattering of the MoS_2 and WS_2 single nanotubes, Surf. Sci. **601**(13), 2868–2872 (2007)
16.130 M. Krause, M. Virsek, M. Remškar, A. Kolitsch, W. Möller: Diameter dependent Raman scattering of WS_2 nanotubes, Phys. Status Solidi (b) **246**(11/12), 2786–2789 (2009)
16.131 R. Levi, M. Bar-Sadan, A. Albu-Yaron, R. Popovitz-Biro, L. Houben, Y. Prior, R. Tenne: Stability criteria of fullerene-like nanoparticles: Comparing V_2O_5 to layered metal dichalcogenides and dihalides, Materials **3**(8), 4428–4445 (2010)
16.132 I. Kaplan-Ashiri, S. Cohen, K. Gartsman, R. Rosentsveig, G. Seifert, R. Tenne: Mechanical behavior of individual WS_2 nanotubes, J. Mater. Res. **19**(2), 454–459 (2004)
16.133 I. Kaplan-Ashiri, S.R. Cohen, N. Apter, Y. Wang, G. Seifert, H.D. Wagner, R. Tenne: Microscopic investigation of shear in multiwalled nanotube deformation, J. Phys. Chem. C **111**(24), 8432–8436 (2007)
16.134 I. Kaplan-Ashiri, S.R. Cohen, K. Gartsman, V. Ivanovskaya, T. Heine, G. Seifert, I. Wiesel, H.D. Wagner, R. Tenne: On the mechanical behavior of WS_2 nanotubes under axial tension and compression, Proc. Natl. Acad. Sci. USA **103**(3), 523–528 (2006)
16.135 I. Lahouij, F. Dassenoy, L. de Knoop, J.-M. Martin, B. Vacher: In situ TEM observation of the behavior of an individual fullerene-like MoS_2 nanoparticle in a dynamic contact, Tribol. Lett. **42**(2), 133–140 (2011)
16.136 E. Kalfon-Cohen, O. Goldbart, R. Schreiber, S.R. Cohen, D. Barlam, T. Lorenz, A. Enyashin, G. Seifert: Radial compression studies of WS_2 nanotubes in the elastic regime, J. Vac. Sci. Technol. B **29**(2), 021009 (2011)
16.137 K.S. Nagapriya, O. Goldbart, I. Kaplan-Ashiri, G. Seifert, R. Tenne, E. Joselevich: Torsional stick-slip behavior in WS_2 nanotubes, Phys. Rev. Lett. **101**(19), 195501 (2008)
16.138 J.L. Feldman: Elastic constants of 2H-MoS_2 and 2H-$NbSe_2$ extracted from measured dispersion curves and linear compressibilities, J. Phys. Chem. Solids **37**(12), 1141–1144 (1976)
16.139 G. Seifert: Unpublished work
16.140 O. Tevet, O. Goldbart, S.R. Cohen, R. Rosentsveig, R. Popovitz-Biro, H.D. Wagner, R. Tenne: Nanocompression of individual multilayered polyhedral nanoparticles, Nanotechnology **21**(36), 365705 (2010)
16.141 A.H. Barber, I. Kaplan-Ashiri, S.R. Cohen, R. Tenne, H.D. Wagner: Stochastic strength of nanotubes: An appraisal of available data, Compos. Sci. Technol. **65**(15/16), 2380–2384 (2005)
16.142 D.J. Srolovitz, S.A. Safran, M. Homyonfer, R. Tenne: Morphology of nested fullerenes, Phys. Rev. Lett. **74**(10), 1779 (1995)
16.143 M. Wang, I. Kaplan-Ashiri, X. Wei, R. Rosentsveig, H. Wagner, R. Tenne, L. Peng: In situ TEM measurements of the mechanical properties and behavior of WS_2 nanotubes, Nano Res. **1**(1), 22–31 (2008)
16.144 A. Javey, J. Guo, Q. Wang, M. Lundstrom, H. Dai: Ballistic carbon nanotube field-effect transistors, Nature **424**(6949), 654–657 (2003)
16.145 J. Tersoff: Contact resistance of carbon nanotubes, Appl. Phys. Lett. **74**(15), 2122–2124 (1999)
16.146 M. Nath, S. Kar, A.K. Raychaudhuri, C.N.R. Rao: Superconducting $NbSe_2$ nanostructures, Chem. Phys. Lett. **368**(5-6), 690–695 (2003)
16.147 L. Scheffer, R. Rosentzveig, A. Margolin, R. Popovitz-Biro, G. Seifert, S.R. Cohen, R. Tenne: Scanning

tunneling microscopy study of WS_2 nanotubes, Phys. Chem. Chem. Phys. **4**(11), 2095–2098 (2002)
16.148 G. Seifert, H. Terrones, M. Terrones, G. Jungnickel, T. Frauenheim: On the electronic structure of WS_2 nanotubes, Solid State Commun. **114**(5), 245–248 (2000)
16.149 G.L. Frey, S. Elani, M. Homyonfer, Y. Feldman, R. Tenne: Optical-absorption spectra of inorganic fullerenelike MS_2 (M = Mo, W), Phys. Rev. B **57**(11), 6666 (1998)
16.150 S.-H. Jhi, D.J. Roundy, S.G. Louie, M.L. Cohen: Formation and electronic properties of double-walled boron nitride nanotubes, Solid State Commun. **134**(6), 397–402 (2005)
16.151 P.M. Rafailov, C. Thomsen, K. Gartsman, I. Kaplan-Ashiri, R. Tenne: Orientation dependence of the polarizability of an individual WS_2 nanotube by resonant Raman spectroscopy, Phys. Rev. B **72**(20), 205436 (2005)
16.152 G.L. Frey, R. Tenne, M.J. Matthews, M.S. Dresselhaus, G. Dresselhaus: Optical properties of MS_2 (M = Mo, W) inorganic fullerenelike and nanotube material optical absorption and resonance raman measurements, J. Mater. Res. **13**(09), 2412–2417 (1998)
16.153 A. Johansson, G. Sambandamurthy, D. Shahar, N. Jacobson, R. Tenne: Nanowire acting as a superconducting quantum interference device, Phys. Rev. Lett. **95**(11), 116805 (2005)
16.154 R.H. Friend, A.D. Yoffe: Electronic properties of intercalation complexes of the transition metal dichalcogenides, Adv. Phys. **36**(1), 1–94 (1987)
16.155 F.L. Deepak, R. Popovitz-Biro, Y. Feldman, H. Cohen, A. Enyashin, G. Seifert, R. Tenne: Fullerene-like $Mo(W)_{1-x}Re_xS_2$ nanoparticles, Chemistry **3**(8-9), 1568–1574 (2008)
16.156 Y.Q. Zhu, W.K. Hsu, M. Terrones, S. Firth, N. Grobert, R.J.H. Clark, H.W. Kroto, D.R.M. Walton: Tungsten-niobium-sulfur composite nanotubes, Chem. Commun. **1**, 121–122 (2001)
16.157 Y.Q. Zhu, W.K. Hsu, S. Firth, M. Terrones, R.J.H. Clark, H.W. Kroto, D.R.M. Walton: Nb-doped WS_2 nanotubes, Chem. Phys. Lett. **342**(1/2), 15–21 (2001)
16.158 W.K. Hsu, Y.Q. Zhu, N. Yao, S. Firth, R.J.H. Clark, H.W. Kroto, D.R.M. Walton: Titanium-doped molybdenum disulfide nanostructures, Adv. Funct. Mater. **11**(1), 69–74 (2001)
16.159 W.K. Hsu, Y.Q. Zhu, C.B. Boothroyd, I. Kinloch, S. Trasobares, H. Terrones, N. Grobert, M. Terrones, R. Escudero, G.Z. Chen, C. Colliex, A.H. Windle, D.J. Fray, H.W. Kroto, D.R.M. Walton: Mixed-phase $W_xMo_yC_zS_2$ nanotubes, Chem. Mater. **12**(12), 3541–3546 (2000)
16.160 M. Nath, K. Mukhopadhyay, C.N.R. Rao: $Mo_{1-x}W_xS_2$ nanotubes and related structures, Chem. Phys. Lett. **352**(3-4), 163–168 (2002)
16.161 J. Tannous, F. Dassenoy, A. Bruhács, W. Tremel: Synthesis and tribological performance of novel $Mo_xW_{1-x}S_2$ ($0 = x = 1$) inorganic fullerenes, Tribol. Lett. **37**(1), 83–92 (2010)
16.162 K.K. Tiong, P.C. Liao, C.H. Ho, Y.S. Huang: Growth and characterization of rhenium-doped MoS_2 single crystals, J. Cryst. Growth **205**(4), 543–547 (1999)
16.163 V.V. Ivanovskaya, T. Heine, S. Gemming, G. Seifert: Structure, stability and electronic properties of composite $Mo_{1-x}Nb_xS_2$ nanotubes, Phys. Status Solidi (b) **243**(8), 1757–1764 (2006)
16.164 V. Ivanovskaya, G. Seifert, A. Ivanovskii: Electronic structure of niobium-doped molybdenum disulfide nanotubes, Russ. J. Inorg. Chem. **51**(2), 320–324 (2006)
16.165 A.N. Enyashin: Theoretical studies of inorganic fullerenes and fullerene-like nanoparticles, Isr. J. Chem. **50**(4), 468–483 (2010)
16.166 I. Milošević, T. Vuković, M. Damnjanović, B. Nikolić: Symmetry based properties of the transition metal dichalcogenide nanotubes, Eur. Phys. J. B **17**(4), 707–712 (2000)
16.167 G. Seifert, T. Frauenheim: On the stability of non carbon nanotubes, J. Korean Phys. Soc. **37**, 89–92 (2000)
16.168 M. Stefanov, A.N. Enyashin, T. Heine, G. Seifert: Nanolubrication: How do MoS_2-based nanostructures lubricate?, J. Phys. Chem. C **112**(46), 17764–17767 (2008)
16.169 L. Rapoport, N. Fleischer, R. Tenne: Applications of $WS_2(MoS_2)$ inorganic nanotubes and fullerene-like nanoparticles for solid lubrication and for structural nanocomposites, J. Mater. Chem. **15**(18), 1782–1788 (2005)
16.170 L. Joly-Pottuz, F. Dassenoy, M. Belin, B. Vacher, J.M. Martin, N. Fleischer: Ultralow-friction and wear properties of IF-WS_2 under boundary lubrication, Tribol. Lett. **18**(4), 477–485 (2005)
16.171 J.J. Hu, J.S. Zabinski: Nanotribology and lubrication mechanisms of inorganic fullerene-like MoS_2 nanoparticles investigated using lateral force microscopy (LFM), Tribol. Lett. **18**(2), 173–180 (2005)
16.172 C. Shahar, D. Zbaida, L. Rapoport, H. Cohen, T. Bendikov, J. Tannous, F. Dassenoy, R. Tenne: Surface functionalization of WS_2 fullerene-like nanoparticles, Langmuir **26**(6), 4409–4414 (2009)
16.173 A.R. Adini, Y. Feldman, S.R. Cohen, L. Rapoport, A. Moshkovich, M. Redlich, J. Moshonov, B. Shay, R. Tenne: Alleviating fatigue and failure of NiTi endodontic files by a coating containing inorganic fullerene-like WS_2 nanoparticles, J. Mater. Res. **26**, 1234–1242 (2011)
16.174 G.R. Samorodnitzky-Naveh, M. Redlich, A. Katz, A.R. Adini, A. Gorodnev, L. Rapoport, A. Moshkovich, S.R. Cohen, R. Rosentsveig, J. Moshonov, B. Shay, R. Tenne: Towards medical applications of self-lubricating coatings with fullerene-like IF WS_2

nanoparticles, Int. J. Nano Biomater. **3**, 140–152 (2010)

16.175 H. Tsabari: *Inorganic Fullerene-like WS_2 nanospheres (IF-WS_2), (Batch No.HP6) acute oral toxicity, acute toxic class method in the rat (Final Report)* (Harlan Biotech, Rehovot 2005)

16.176 I. Haist: *Test for sensitization (local lymph node assay LLNA) with inorganic fullerene-like WS_2 nano-spheres. Technical Report* (BSL Bioservice, Planegg 2005)

16.177 L. Joly-Pottuz, J.M. Martin, F. Dassenoy, M. Belin, G. Montagnac, B. Reynard, N. Fleischer: Pressure-induced exfoliation of inorganic fullerene-like WS_2 particles in a Hertzian contact, J. Appl. Phys. **99**(2), 023524 (2006)

16.178 Y.Q. Zhu, T. Sekine, Y.H. Li, M.W. Fay, Y.M. Zhao, C.H. Patrick Poa, W.X. Wang, M.J. Roe, P.D. Brown, N. Fleischer, R. Tenne: Shock-absorbing and failure mechanisms of WS_2 and MoS_2 nanoparticles with fullerene-like structures under shock wave pressure, J. Am. Chem. Soc. **127**(46), 16263–16272 (2005)

16.179 M. Naffakh, Z. Martín, N. Fanegas, C. Marco, M.A. Gómez, I. Jiménez: Influence of inorganic fullerene-like WS_2 nanoparticles on the thermal behavior of isotactic polypropylene, J. Polym. Sci. B: Polym. Phys. **45**(16), 2309–2321 (2007)

16.180 M. Naffakh, C. Marco, M.A. Gómez, I. Jiménez: Novel melt-processable nylon-6/inorganic fullerene-like WS_2 nanocomposites: Complex isothermal crystallization kinetics and melting behaviour, Mater. Chem. Phys. **128**(1/2), 265–273 (2011)

16.181 M. Shneider, H. Dodiuk, S. Kenig, R. Tenne: The effect of tungsten sulfide fullerene-like nanoparticles on the toughness of epoxy adhesives, J. Adhes. Sci. Technol. **24**, 1083–1095 (2010)

16.182 E. Zohar, S. Baruch, M. Shneider, H. Dodiuk, S. Kenig, R. Tenne, H.D. Wagner: The Effect of WS_2 nanotubes on the properties of epoxy-based nanocomposites, J. Adhes. Sci. Technol. **25**, 1603–1617 (2011)

16.183 J. Chen, S.L. Li, Z.L. Tao: Novel hydrogen storage properties of MoS_2 nanotubes, J. Alloys Compd. **356/357**, 413–417 (2003)

16.184 R. Dominko, D. Arčon, A. Mrzel, A. Zorko, P. Cevc, P. Venturini, M. Gaberscek, M. Remskar, D. Mihailovic: Dichalcogenide nanotube electrodes for Li-ion batteries, Adv. Mater. **14**(21), 1531–1534 (2002)

16.185 S. Bastide, D. Duphil, J.P. Borra, C. Levy-Clement: WS_2 closed nanoboxes synthesized by spray pyrolysis, Adv. Mater. **18**(1), 106–109 (2006)

16.186 N. Zink, H.A. Therese, J. Pansiot, A. Yella, F. Banhart, W. Tremel: In situ heating TEM study of onion-like WS_2 and MoS_2 nanostructures obtained via MOCVD, Chem. Mater. **20**(1), 65–71 (2008)

16.187 K.P. Loh, H. Zhang, W.Z. Chen, W. Ji: Templated deposition of MoS_2 nanotubules using single source precursor and studies of their optical limiting properties, J. Phys. Chem. B **110**(3), 1235–1239 (2005)

17. Growth of Nanomaterials by Screw Dislocation

Fei Meng, Stephen A. Morin, Song Jin

Controlling the morphology of nanomaterials is important for their fundamental study and practical application. Especially one-dimensional nanowires, nanorods, and nanotubes and two-dimensional nanoplates possess interesting physical and chemical properties due to their structural anisotropy. The key to obtaining these morphologies is to break the symmetry of crystal growth to promote anisotropic growth. In this chapter we discuss the catalyst- and template-free screw-dislocation-driven nanomaterial growth mechanism, in which an axial screw dislocation creates self-perpetuating growth steps upon intersecting with the crystal surface and enables anisotropic crystal growth under low supersaturation conditions. The presence of screw dislocations not only alters the growth kinetics of nanomaterials, but also distorts the crystal lattice and generates a strain field, both of which lead to morphology variation of the nanomaterials. The structural characteristics associated with dislocation-driven growth can be readily detected using transmission electron microscopy techniques. A review is presented on a wide range of nanomaterials formed under various conditions whose growth has been confirmed to be driven by screw dislocations, demonstrating the generality of this mechanism. A framework for rationally synthesizing anisotropic nanomaterials via dislocation-driven growth is provided. This will enable large-scale, low-cost production of nanomaterials for various applications.

17.1 **Classical Crystal Growth Theories** 640
17.1.1 Layer-By-Layer Crystal Growth 640
17.1.2 Screw-Dislocation-Driven Crystal Growth 641

17.2 **Theories for Screw-Dislocation-Driven Growth of Nanomaterials** 642
17.2.1 Eshelby Twist 642
17.2.2 Dislocation-Driven Nanotube Formation 643
17.2.3 Dislocation-Driven Growth of 2-D Nanoplates 644

17.3 **Structural Characterization of these Nanomaterials** 645
17.3.1 Observation of Dislocation Contrast 645
17.3.2 Determination of Eshelby Twist 646
17.3.3 Lattice Tilt 648
17.3.4 Observation of Nanotubes or Voided NWs 649

17.4 **Generality of Dislocation-Driven Nanomaterial Growth** 649
17.4.1 Vapor-Phase Synthesis 650
17.4.2 Solution-Phase Synthesis 652
17.4.3 Solution Growth of 2-D Nanoplates 655

17.5 **Rational Growth of Dislocation-Driven Nanomaterials – General Strategies** 658

17.6 **Applications** 659

17.7 **Summary and Perspectives** 660

References 661

One of the major goals in nanoscience and nanotechnology is to synthesize nanoscale building blocks of arbitrary dimensions, morphologies, and materials with increasing complexity from the bottom up. Anisotropic nanomaterials have already found many applications and are therefore of great interest; For example, one-dimensional (1-D) nanowires (NWs), nanorods (NRs), and nanotubes (NTs) and two-dimensional

(2-D) nanoplates have shown new fundamental physical properties and demonstrated promising utility in nanoelectronics, nanophotonics, solar energy conversion, thermoelectricity, electrochemical energy storage, and chemical and biological sensing [17.1–9]. The fundamental understanding of the growth of anisotropic nanomaterials is critically important for developing rational and controllable synthesis to yield nanoscale morphologies suited for specific applications.

Several common mechanisms or methods have been established to explain bottom-up anisotropic NW growth or enable fabrication of 1-D nanomaterials. The vapor–liquid–solid (VLS) [17.10, 11] mechanism and other analogous catalyst-driven mechanisms, such as solution–liquid–solid (SLS) [17.12, 13] and vapor–solid–solid (VSS) [17.14] growth, have been the most commonly used methods for synthesis of NWs. In VLS (or SLS) growth, a nanoscale liquid droplet is formed between a nanoparticle metal catalyst and the desired precursor species due to eutectic phase behavior, and further supersaturation of the precursor leads to precipitation and growth of crystalline NW material from the catalyst. Use of 1-D templates such as anodic aluminum oxide (AAO) is another common way to confine the growth of nanomaterials to achieve 1-D growth [17.15]. The *oriented attachment* mechanism can also result in the formation of thin 1-D NWs in solution via the assembly of zero-dimensional (0-D) nanocrystals, as recently confirmed using the in situ transmission electron microscopy (TEM) technique [17.16, 17]. From the perspective of crystal growth, the challenge of growing anisotropic nanomaterials, including 1-D NW materials, is to break the symmetry of crystal growth to ensure that crystals grow in a highly anisotropic fashion instead of forming bulk crystals with polyhedral shapes.

In this chapter, we discuss the screw-dislocation-driven mechanism for growth of anisotropic nanomaterials, in which axial screw dislocations provide self-perpetuating steps and break the symmetry of crystal growth. The key is to manipulate the kinetics of crystal growth and enable the formation of anisotropic crystals instead of polyhedral-shaped crystals or thin films [17.18–20]. The presence of the axial screw dislocations and the consequent strain field introduces unique characteristics to the dislocation-driven nanomaterial, including macroscopic growth kinetics and variations in nanostructure morphologies, which are explained next. We then introduce the technique to characterize these features in nanoobjects to confirm the growth mechanism. The generality of this mechanism is demonstrated by a survey of a wide range of different nanomaterials whose growth has been confirmed to be driven by screw dislocations. The general rule of design is then summarized to provide a framework for rationally synthesizing anisotropic nanomaterials via dislocation-driven growth, which may eventually enable large-scale, low-cost production of nanomaterials for various practical applications.

17.1 Classical Crystal Growth Theories

Since the key to successful anisotropic growth is controlling the kinetics of crystal growth and breaking the symmetry of crystal growth, we first review the fundamental kinetics of crystal growth processes [17.21].

17.1.1 Layer-By-Layer Crystal Growth

Layer-by-layer (LBL) crystal growth is the most intuitive mechanism for the formation of the extended periodic crystal structure of solids. However, due to the high energy barriers required to nucleate new layers of atoms which create step edges that facilitate the addition of more atoms (Fig. 17.1), LBL crystal growth theory predicts that much higher concentrations of gas-phase or liquid-phase precursors than the equilibrium concentration are necessary to enable a reasonable crystal growth rate. In other words, LBL growth requires high supersaturation. The supersaturation σ of the system is defined by (17.1) [17.21]

$$\sigma = \ln(c/c') \,, \tag{17.1}$$

where c is the precursor concentration and c' is the equilibrium concentration.

Study on the kinetics of LBL growth reveals that it has an *exponential* growth rate (R_{LBL}),

$$\mathrm{R_{LBL}} = J_0 l^2 \beta \propto \mathrm{e}^{(-g_n/kT)} l^2 \beta \,, \tag{17.2}$$

where J_0 is the rate of 2-D nucleation, l is the length of the facet (assuming a square growth facet), β is

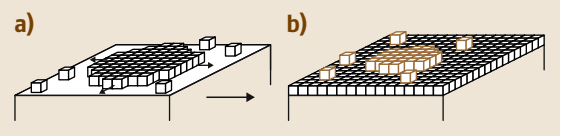


Fig. 17.1a,b Schematic illustration of the layer-by-layer crystal growth mechanism. **(a)** A 2-D island is nucleated and spreads to cover the active growth facet. **(b)** Once the first layer is completed, a new island (cluster of *brown cubes*) is nucleated on the first layer and the growth of a new layer begins

the step height, k is the Boltzmann constant, T is the temperature, and g_n is the energy barrier to 2-D nucleation, which is inversely proportional to supersaturation [17.21]. These expressions illustrate that LBL growth requires the formation of 2-D nuclei by overcoming the energy barrier g_n.

The prevailing catalyst-driven mechanisms, such as VLS [17.10, 11], SLS [17.12, 13], and VSS [17.14], that explain the 1-D anisotropic growth of NWs are fundamentally still LBL growth, but mediated by the catalyst droplets at the catalyst–solid interface [17.22, 23]. The nucleation barrier for LBL growth is lowered by the presence of the catalyst relative to the respective interface on the side-wall; therefore, the crystal growth is much faster at this interface. In this way, the symmetry of the crystal growth is broken and 1-D anisotropic crystal growth can proceed.

17.1.2 Screw-Dislocation-Driven Crystal Growth

Experimental observations reveal that crystal growth can actually happen under moderate supersaturation, contradicting the prediction of LBL growth theory. *Frank* [17.24, 25] solved this conflict by pointing out that crystals often have imperfections such as screw dislocation line defects [17.26, 27], which upon intersection with a crystal surface would make steps that propagate as spirals and thus become an endless source of crystal steps (Fig. 17.2). This theoretical model, known as the *Burton–Cabrera–Frank* (BCF) theory [17.24], successfully explains the observed growth rates of crystals under moderate and low supersaturation. Such surface dislocation spirals have been observed in many materials [17.28], and the dislocation-driven growth mechanism has become a cornerstone of crystal growth theory.

BCF theory predicts a dislocation growth rate ($R_{\text{dislocation}}$) that is *linearly* dependent on supersaturation

$$R_{\text{dislocation}} = C\sigma \,, \tag{17.3}$$

where C is a rate constant that depends on the maximum possible flux of monomers to the crystal surface via diffusion through the stagnant layer. This growth kinetics of the dislocation-driven mechanism is a characteristic feature that can distinguish it from other growth modes.

According to classical crystal growth theory, the growth mechanism of a crystal depends on the supersaturation. As schematically illustrated in Fig. 17.3, at low supersaturation the dislocation-driven spiral growth mechanism is followed; at intermediate supersaturation the LBL growth mechanism is followed; at high supersaturation the dendritic growth mechanism is followed.

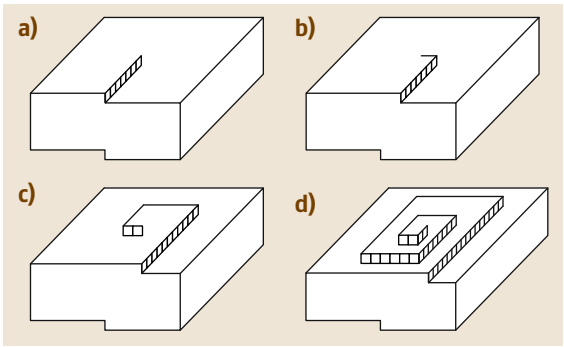


Fig. 17.2a–d Illustration of screw dislocation growth spirals. **(a–d)** Schematic illustration of a screw dislocation spiral propagating new step edges as the crystal grows (after [17.21])

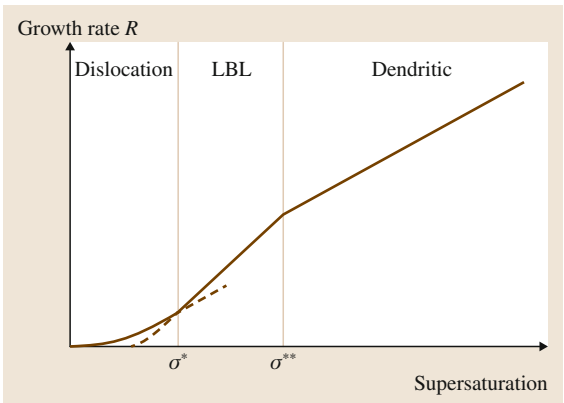


Fig. 17.3 Schematic illustration of crystal growth mechanism as a function of supersaturation. As the supersaturation increases, the dislocation, LBL, and dendritic growth mechanisms progressively dominate (after [17.20])

These different growth regimes are separated by two characteristic supersaturations, namely σ^* and σ^{**}, at which the growth rate of the next mechanism overtakes the previous one (Fig. 17.3). In the context of current studies which focus on well-faceted single-crystalline nanomaterials, the dislocation growth and LBL growth mechanisms are the most relevant and are the topics of the following discussion.

These crystal growth theories are applicable to growth of any crystals, whether formed from the vapor phase, solution phase, or even the melt, and forming bulk single crystals, thin films, or nanoscale solids. Therefore, understanding how to manipulate the crystal growth kinetics to differentiate the growth rates along different directions is the key for enabling anisotropic nanomaterial growth.

17.2 Theories for Screw-Dislocation-Driven Growth of Nanomaterials

Screw dislocation has been proven to be responsible for both 1-D and 2-D crystal growth. The essence of screw-dislocation-driven nanomaterial growth, especially nanowire growth, is that, under appropriate low supersaturation conditions that favor dislocation-driven growth over LBL growth, crystal growth occurs more rapidly at the dislocation spirals along the axial direction whereas radial dimension expansion via the LBL mode is prohibited (Fig. 17.4a). In this way, the symmetry of the crystal growth is broken and highly anisotropic crystal growth is enabled by the self-perpetuating steps of screw dislocations.

The basic idea that screw dislocations can drive anisotropic growth of 1-D crystals was in fact proposed and discussed in the 1950s by *Sears* [17.29–32]. Indirect evidence such as lattice twist within whiskers was observed, suggesting the presence of axial screw dislocations [17.33, 34]. Decoration of axial dislocations in whiskers of alkali halides was first observed in 1958 [17.35]. Direct observation and identification of screw dislocations in whiskers using electron microscopy was not reported until 1965, in single-crystal whiskers of aluminum nitride [17.36, 37], and later chalcotrichite (Cu_2O) [17.38]. In the modern literature, observation and confirmation of dislocation-driven NW growth was first reported in NW trees of PbS [17.18,39] and PbSe [17.40]. In these fascinating tree-like structures, growth of the trunk is driven by screw dislocations whereas the branches are grown by the more traditional VLS NW growth mechanism.

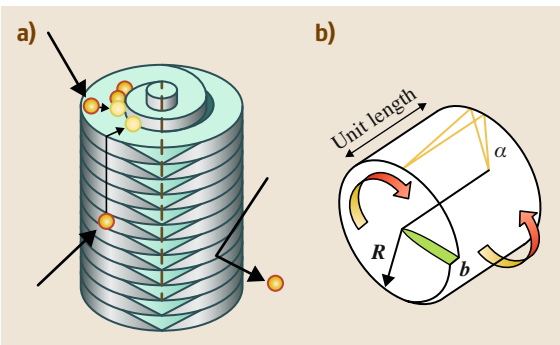


Fig. 17.4a,b Illustrations of screw-dislocation-driven NW growth and the associated Eshelby twist. **(a)** A screw dislocation drives 1-D growth at low supersaturation, where LBL growth is prohibited (after [17.19]); **(b)** Eshelby twist (after [17.18])

17.2.1 Eshelby Twist

A screw dislocation disrupts the perfect periodicity within the crystal lattice and thereby causes a strain energy per unit length E that is quadratically dependent on the magnitude of the dislocation Burgers vector $\boldsymbol{b}$, i. e.,

$$E = \frac{b^2\mu}{4\pi}\int_{r_0}^{R}\frac{\mathrm{d}r}{r} = \frac{b^2\mu}{4\pi}\ln\left(\frac{R}{r_0}\right), \tag{17.4}$$

where μ is the shear modulus, R is the radius of the cylinder containing the dislocation, and r is the core radius of the dislocation. This stress field exerts a torque at the free ends of the rod, resulting in a twist of the rod along the axial direction (Fig. 17.4b) [17.26,41], known as the Eshelby twist, which in turn serves as evidence of the dislocation-driven growth mechanism. This Eshelby twist is mathematically expressed as

$$\alpha = \frac{b}{\pi R^2}, \tag{17.5}$$

where α is the twist of the lattice in radians per unit length. Attempts to observe the Eshelby twist in micrometer-scale whiskers were made in the late 1950s, but the results were often inconclusive [17.34, 42]. Because of the $1/R^2$ dependence, the Eshelby twist is

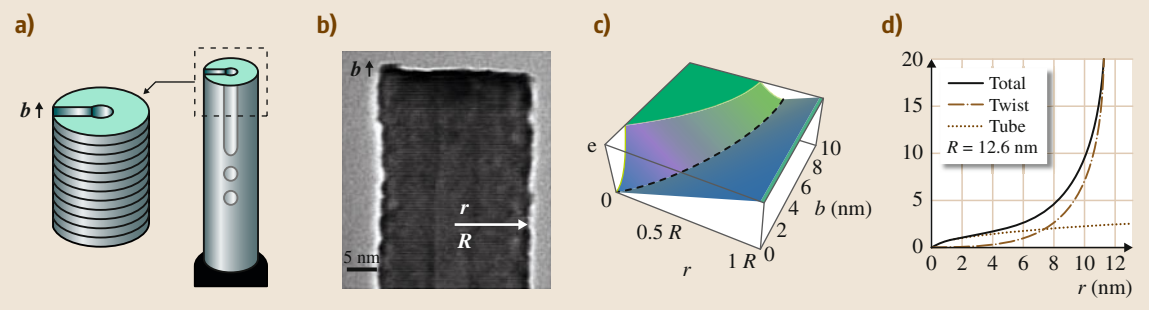


Fig. 17.5a–d Two pathways to relieve the strain energy and the estimation of $\boldsymbol{b}$ in ZnO NTs: **(a)** Schematic illustration of screw-dislocation-driven formation of a hollow NT. **(b)** High-resolution transmission electron microscopy (HRTEM) image of the tip of a ZnO NT in which the critical parameters R, r, and b can be directly measured. **(c)** Calculated three-dimensional (3-D) energy plot using (17.8) for the ZnO NT shown in **(b)**; the *dashed line* represents the energy minimum. **(d)** Energy-minimized relation for b versus r/R by explicitly solving (17.8) along this energy valley for the specific ZnO NT in **(b)**; the total contribution to b has components due to the hollow inner tube surface energy (*red dash-dotted line*) and to the Eshelby twist (*blue dotted line*) (after [17.20])

more pronounced at the nanoscale compared with in micrometer-sized whiskers, making it readily observable in NWs and NTs. Particularly in the case of hyperbranched nanostructures such as PbS and PbSe nanotrees, overgrowth of epitaxial branching nanowires allows easy visualization of the twist [17.18, 39, 40]. This allows direct measurement of the Eshelby twist and a simple estimate of the Burgers vector's screw component magnitude. In recent years, more accurate theoretical calculations of Eshelby twists based on molecular dynamics have been carried out for thin NW and NT materials [17.43, 44].

17.2.2 Dislocation-Driven Nanotube Formation

The formation of single-crystal NTs is a signature of nanomaterial growth driven by dislocations with large Burgers vector $\boldsymbol{b}$ (Fig. 17.5a). In the case of a hollow tube, the elastic energy caused by the dislocation can be expressed by modifying (17.4) as

$$E = \frac{b^2\mu}{4\pi}\ln\left(\frac{R}{r}\right), \tag{17.6}$$

where R and r are the outer and inner tube radii, respectively [17.27]. As b increases, eventually the crystal contains enough strain energy that it exceeds the energy cost of creating a new inner surface and the dislocation core becomes hollow. This causes the formation of micropipes, which are often observed in dislocation-prone materials such as SiC or GaN and sometimes termed *open-core dislocations* [17.45, 46]. In the classical open-core dislocation model, an energy balance between the surface energy ($2\pi\gamma r$, where γ is the surface energy) and the strain energy from (17.6) (both per unit length) results in a relationship between r and b [17.45]

$$b_{\text{tube}} = \sqrt{\frac{8\pi^2\gamma r}{\mu}}\,. \tag{17.7}$$

For NWs reaching this energy threshold, the solid NW becomes a hollow NT. In other words, the equilibrium morphology of 1-D nanomaterials whose growth is driven by screw dislocations should be hollow NTs when the Burgers vector is sufficiently large [17.47]. The commonly observed voided NWs [17.47, 48] might be an intermediate stage lying on the threshold, oscillating between the solid and hollow conditions due to small fluctuations in growth environment and NW thickness that subtly change the energy balance, or tubes initially formed could partially close up after synthesis.

Furthermore, forming a hollow core and producing a torque around the NW axis via the Eshelby twist mechanism are two competing pathways to alleviate the strain caused by the screw dislocations. Once the nanostructure becomes hollow, the overall energy per unit length E contains three terms: the surface energy of the hollow inner tube, the lattice strain due to the dislocation, and the reduction in lattice strain due to the Eshelby twist

$$E = 2\pi\gamma r + \frac{\mu b^2}{4\pi}\ln\left(\frac{R}{r}\right) - \frac{\mu b^2}{4\pi}\frac{(R^2-r^2)}{(R^2+r^2)}\,. \tag{17.8}$$

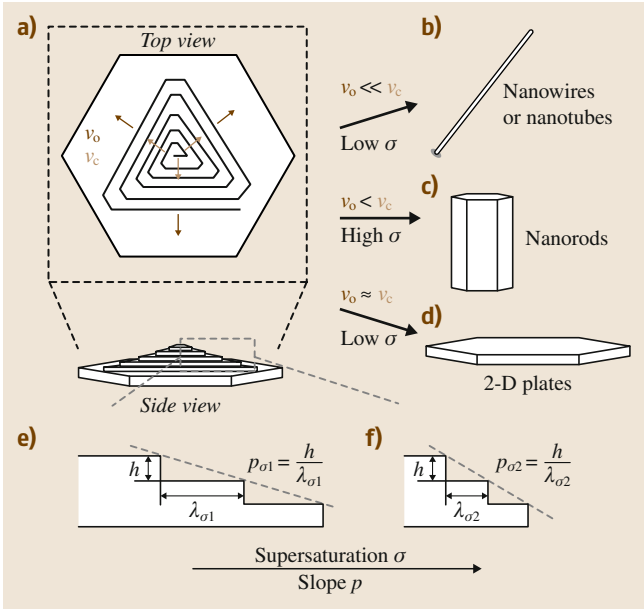


Fig. 17.6a–f A unified scheme illustrating dislocation-driven growth of various nanomaterial morphologies. **(a)** Top view and dramatized side view of an idealized nanoplate with one screw dislocation with various step velocities at the dislocation core (v_c) and the outer edges (v_o). Nanowires or nanotubes **(b)**, nanorods **(c)**, or nanoplates **(d)** are achieved when specific step velocity and supersaturation conditions are met. **(e,f)** Side views reveal the relationship between the nanoplate slope p, step height h, terrace width d, and supersaturation σ (after [17.50]) ◀

When ZnO nanotubes are used as a model system to evaluate (17.8), with the specific values of surface energy of $0.31\,\mathrm{J/m^2}$ and shear modulus of 44.3 GPa [17.49], and the radii of the NT shown in Fig. 17.5b, a three-dimensional surface plot of (17.8) constructed for E versus b and r/R (Fig. 17.5b) shows that there is an energy valley (minimum) associated with certain optimized r and b values (marked with a dashed line). The energy-minimized relation between r and b can be solved by setting the energy derivative with respect to r to zero,

$$\frac{\mathrm{d}E}{\mathrm{d}r} = 0 \rightarrow b_{\mathrm{total}} = \sqrt{\frac{8\pi^2\gamma r}{\mu}}\left(\frac{R^2+r^2}{R^2-r^2}\right) . \quad (17.9)$$

The first factor in (17.9) represents the effect from *Frank's* open-core dislocation model in (17.7) [17.45], while the second factor is the modification due to the Eshelby twist pathway. The Eshelby twist component can also be expressed explicitly as the difference between (17.7) and (17.9),

$$b_{\mathrm{twist}} = b_{\mathrm{total}} - b_{\mathrm{tube}} = \sqrt{\frac{8\pi^2\gamma r}{\mu}}\left(\frac{R^2+r^2}{R^2-r^2} - 1\right) . \quad (17.10)$$

This direct relation between the r and b variables along the energy valley (17.9; dashed line in Fig. 17.5c) contains the contributions to the total energy from the Eshelby twist and hollow tube components and can be alternately displayed as a plot of b versus r/R (Fig. 17.5d). It is clear from Fig. 17.5d that, when r/R is small, representing the scenario of a thick-walled NT, the total energy minimization approximates the *Frank's* open-core dislocation model, and most energy is relieved by making the tube hollow; however, at much larger r/R values, the total energy minimization begins to follow the Eshelby twist line, indicating that a thin-walled NT has more significant twist, as creating more surface becomes energetically unfavorable.

17.2.3 Dislocation-Driven Growth of 2-D Nanoplates

Screw dislocations can also drive 2-D anisotropic crystal growth. The key herein is to control the crystal growth step velocities at different positions from the dislocation core (Fig. 17.6a) [17.51]. In general, the velocity of steps at the core v_c should be the same as those at the outer edges of the dislocation hillocks v_o due to their crystallographic equivalence. However, the velocity of steps can be affected by environmental factors such as impurities or mass transport, such that steps created earlier in growth (thus at the outer edge v_o) develop more slowly than newly generated steps closer to the core of the dislocation (v_c), which leads to two scenarios. When v_o is slightly less than v_c, newly generated steps from the dislocation core would very slowly catch up with those at the outer edge to create a step pile-up and thus a step-free facet, which will lead to low-aspect-ratio NRs or bulk polyhedral crystals (Fig. 17.6c), particularly when under higher supersaturation and if there is significant LBL growth. Furthermore, if v_o is much less than v_c, possibly because the steps at the outer edge have more impurity pinning sites, more adsorbed surfactants [17.52], or slower mass transport kinetics [17.7], newly generated steps quickly catch up with those further out, rapidly producing a step-free facet and thus leading to almost pure 1-D growth under low supersaturation conditions

(Fig. 17.6b). Finally, if v_o is equal to v_c, which is more common in general crystal growth, all steps, regardless of whether they are newly generated steps at the dislocation core or earlier steps at the outer edge of the growth spiral, propagate at the same velocity and a step pile-up is never created; thus, the steps spread in 2-D (Fig. 17.6d).

According to BCF theory [17.51, 53], the terrace width d is inversely proportional to the supersaturation σ of the system, and thus, for the same step height h, the slope of the nanoplate hillocks ($p = h/d$) increases as the supersaturation increases (Fig. 17.6e,f). Therefore, the thickness-to-diameter ratio of 2-D nanoplates depends on the supersaturation of the growth solutions; i. e., low-supersaturation growth favors generation of very thin nanoplates with small slopes, while higher supersaturation leads to thicker plates of increasing slope. This relationship between terrace width (and thus the slope of dislocation hillocks) and supersaturation has been well documented in crystal growth studies, such as those shown by *De Yoreo* et al. [17.52].

Despite the drastic difference between the morphologies of NWs, NTs, and nanoplates, their growth can be unified using the dislocation-driven mechanism. Understanding how to control the nanomaterial anisotropy is of great importance to design dislocation-driven growth for specific applications.

17.3 Structural Characterization of these Nanomaterials

Dislocation-driven growth is a general mechanism, and therefore the principles described above are applicable to many crystalline materials grown from solution or vapor phase. However, dislocations are mobile and especially not stable in small volumes [17.26, 27], so that postgrowth mechanical perturbation could work the dislocations out of nanomaterials. As a result, dislocations themselves might not always be directly visualized, and the operation of the dislocation-driven mechanism might have been overlooked in many anisotropic nanomaterials (especially 1-D nanomaterials) whose growth is not completely or correctly understood. Nevertheless, there is other evidence closely associated with the dislocation-driven growth mechanism that can support this mechanism, including the lattice twist, lattice tilt, and formation of hollow tubes. In this section we discuss the common techniques that can be used to characterize dislocation-driven nanomaterials.

17.3.1 Observation of Dislocation Contrast

Transmission electron microscopy (TEM) has been the most common and powerful tool used to analyze the microstructures of materials. Screw dislocations can be readily detected and their associated Burgers vectors identified using the diffraction-contrast TEM technique, which relies on additional electron diffraction due to the bending of atomic planes near the dislocation core. If an image is reconstructed from specific reciprocal-space diffraction spots $\boldsymbol{g}$ that are selected by a physical aperture, these additional diffracted electrons create a visible contrast around the dislocation. However, diffraction spots $\boldsymbol{g}$ that are normal to the Burgers vector of the dislocation $\boldsymbol{b}$ ($\boldsymbol{g} \times \boldsymbol{b} = 0$) produce no dislocation contrast – the *invisibility criterion* [17.54]. Therefore, the direction of a Burgers vector can be identified by taking the cross-product of two non-collinear $\boldsymbol{g}$ vectors that make the dislocation contrast disappear. A general procedure for identifying the Burgers vector's direction is detailed in the following:

- First step: Tilt the sample onto an appropriate zone axis which contains the diffraction spots that are perpendicular to the potential Burgers vector's direction. Most crystal lattice types have their own habitual Burgers vectors, for example, [110] in the face-centered cubic (fcc) structure or [001] in the hexagonal closed-packed (hcp) structure [17.26]. Otherwise, the growth direction of NWs can be well used as a guide to screen the $\boldsymbol{g}$ vectors and the corresponding zone axes, because the axial growth direction by definition has to be parallel to the screw component of the dislocation Burgers vector that is responsible for driving the NW growth.
- Second step: Approach the two-beam condition by further tilting the sample until almost all other reflections disappear with the exception of the transmitted beam (the zero beam) and the selected $\boldsymbol{g}$ beam. Repeat these two steps to find another non-collinear $\boldsymbol{g}$ beam that satisfies the invisibility criterion.
- Third step: Determine the Burgers vector direction by taking the cross-product of the $\boldsymbol{g}$ vectors. Ap-

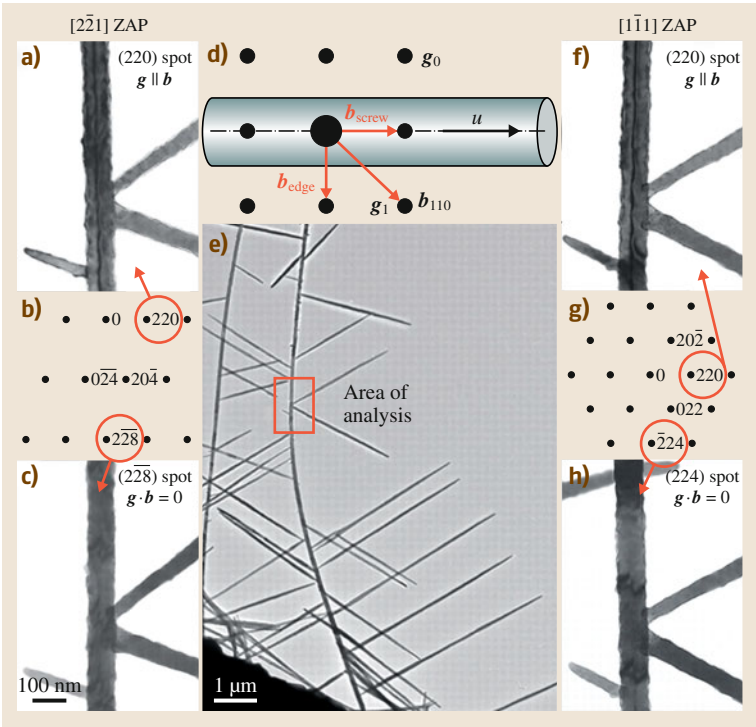


Fig. 17.7a–h Diffraction-contrast TEM imaging of the dislocation in the tree trunk: **(a–c)** TEM images along the [2$\bar{2}$1] zone axis under strong two-beam conditions; **(a)** $\boldsymbol{g}\|\boldsymbol{b}$ conditions showing strong diffraction contrast; **(c)** invisibility conditions as *highlighted* (*red circles*) in the zone axis diagram **(b)**. **(a)** Schematic superposition of real and reciprocal space of a dislocation-containing NW along the [001] zone axis is shown to illustrate the Burgers vector relationship. **(b)** Low-magnification TEM image showing the tree and area analyzed. **(c–e)** [1$\bar{1}$1] zone axis TEM under strong two-beam conditions. **(f)** $\boldsymbol{g}\|\boldsymbol{b}$ conditions and **(h)** invisibility conditions as *highlighted* (*red circles*) in the zone axis diagram **(g)** (ZAP: zone axis pattern; after [17.18])

proach the two-beam condition composed of the zero beam and the determined Burgers vector beam to verify the presence of strong dislocation contrast (the $\boldsymbol{g}\|\boldsymbol{b}$ condition that exhibits the highest contrast of dislocations).

The determination of the Burgers vector in the PbS tree-like structure can be used as an example to illustrate the entire process [17.18]. The same segment of a tree structure was tilted to the [2$\bar{2}$1] zone axis (Fig. 17.7a–c) and the [1$\bar{1}$1] zone axis (Fig. 17.7f–h), respectively. The dislocation meets the invisibility criterion under the perpendicular (2$\bar{2}$ $\bar{8}$) two-beam condition near the [2$\bar{2}$1] zone axis and the perpendicular ($\bar{2}$24) two-beam condition near the [1$\bar{1}$1] zone axis. Therefore, taking the cross-product of the (2$\bar{2}$ $\bar{8}$) and ($\bar{2}$24) vectors shows that the Burgers vector is along the [110] direction, which is confirmed by the images under two-beam conditions of the parallel [220] spots showing high contrast of the dislocation line. It is known that the Burgers vector of the most stable dislocations in rock-salt crystals is along ⟨110⟩, and this has been previously observed in bulk PbS crystals [17.26, 55]. Since the dislocation line direction (u) is along the [100] NW growth direction, the [110] Burgers vector represents a mixed dislocation: a screw dislocation component along the [100] (or [$\bar{1}$00]) direction mostly responsible for driving the NW growth, and an edge dislocation component along the [010] (or [0$\bar{1}$0]) direction. The role of edge dislocations in promoting crystal growth [17.56] is not clear but cannot be ruled out completely at present.

Using such methods, dislocation contrast has been conclusively observed for NWs of PbS [17.18, 39], PbSe [17.40], CdS, CdSe [17.57], AlN [17.37], ZnO [17.20, 47], α-FeOOH [17.58], $Co(OH)_2$ [17.59], Cu [17.60], and Cu_2O [17.38, 48]. However, complete two-beam analysis of the dislocation and invisibility criterion has only been carried out for a smaller set of materials including PbS, CdSe, and Cu. The stability of the nanomaterials under high-vacuum and high-energy electron beam conditions inside the TEM, and the tilting angle range of the TEM goniometer are two main limiting factors to achieve a complete two-beam analysis.

17.3.2 Determination of Eshelby Twist

Various techniques based on TEM and electron diffraction have been established to identify and quantify the Eshelby twist. The most intuitive method relies on the

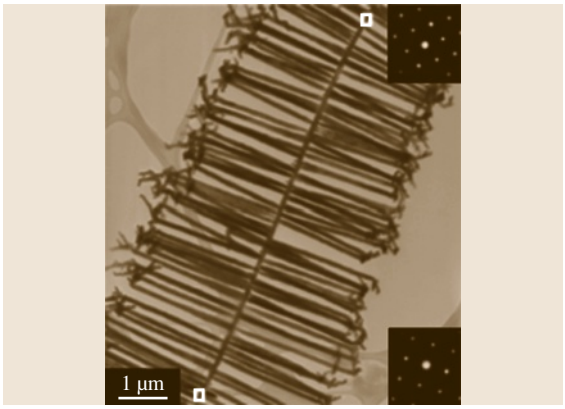


Fig. 17.8 TEM image of a single chiral branched NW. *White boxes* indicate the positions at which the CBED patterns were acquired. *Upper inset*: CBED pattern obtained at the top box showing [110] zone axis. *Lower inset*: CBED pattern obtained at the bottom box showing [100] zone axis (after [17.40])

variation of the electron diffraction on different regions of a NW caused by the rotation in the crystal lattice. Convergent-beam electron diffraction (CBED) is often chosen to acquire diffraction patterns due to its small probe area, which can minimize the interference caused by lattice rotation. In brief, the electron probe is moved along the NW's axial direction to find two distinct zone axes. The twist angle can be calculated by dividing the angular separation between the two identified zone axes by the spatial separation between the two probed areas; For example, starting with the end of the PbSe NW on the [100] zone axis (bottom of Fig. 17.8), the diffraction pattern continuously rotates about the (001) reflection as the probe moves along the wire, reaching the [110] zone axis (top of Fig. 17.8) [17.40]. These two spots are separated by 9.1 μm along the NW axis, while the [100] and [110] directions are 45° apart in the cubic structure, which gives approximately 5°/μm twist of the lattice. The NW has a diameter of 96 nm, which leads to a calculated value of $b = 0.624$ nm. This method, however, requires the NW to have a relatively large twist angle and/or length so that both zone axes are observable. In addition, this measurement is inaccurate in the presence of other geometrical distortion of the lattice, e.g., bending, because this also affects the orientation of the lattice planes and the consequent electron diffraction.

The twist contour analysis reported by *Drum* in 1965 provides an alternative and more accurate method to determine the sense and magnitude of the twist in crystals [17.37]. Unlike the previously discussed method based on CBED, twist contour analysis is essentially a diffraction-contrast TEM technique. First, twist contours must be differentiated from the bend contours commonly observed in TEM of nanomaterials. Bend contours, as the name suggests, occur when a NW is bent about its axis. This distorts many atomic planes locally at the bend, causing the diffraction of electrons from this region of the crystal to be different from everywhere else. Therefore, when a zero-beam bright-field TEM image is taken of a bent object, because electrons are diffracted in such a way that virtually none of them remain in the zero beam, the bend contour appears very dark compared with everywhere else. In contrast, when real-space crystal lattice twists along the growth axis cause the reciprocal-space lattice to twist simultaneously, the various reciprocal $\boldsymbol{g}$ vectors that are orthogonal to the NW growth axis come on and off the Laue condition at different angles, creating several twist contour bands. If we generically choose $-\theta$ for $-\boldsymbol{g}$ and $+\theta$ for $+\boldsymbol{g}$, which we will call θ_-, $\boldsymbol{g}_-$ and θ_+, $\boldsymbol{g}_+$, respectively, the difference between the two angles $\Delta\theta$ can be calculated geometrically using the relation

$$\Delta\theta = (\theta_+ - \theta_-) = \left(\frac{\lambda}{2}\right) |g_+ - g_-| \ , \tag{17.11}$$

where λ is the electron wavelength (the inverse of k). Note that the approximation $\theta \approx \lambda g/2$ is made because of the large radius of the Ewald sphere for electron diffraction. For a twisting NW, the upper and lower conditions in Fig. 17.9b can be simultaneously met at different points along the NW, and the resulting twist contours can be imaged using zero-beam bright-field TEM and indexed directly using displaced-aperture dark-field TEM. Unlike bend contours, each of these twist contours is associated with one set of planes and can be easily differentiated. The measured real-space distance L between two indexed twist contours can be used to calculate the real-space twist α, effectively the Eshelby twist, of the NW using the following relation:

$$\alpha = \left(\frac{\Delta\theta}{L}\right) = \left(\frac{\lambda}{2L}\right) |g_+ - g_-| \ . \tag{17.12}$$

In practice, any $\boldsymbol{g}$ vectors that are not parallel to the NW growth axis (which contains the orthogonal component) can be selected for the twist contour analysis. An angle correction is needed in this case, and (17.12) needs to be modified to

$$\alpha = \frac{\lambda}{2L} \left| \frac{g_+ - g_-}{\sin\beta} \right| \ , \tag{17.13}$$

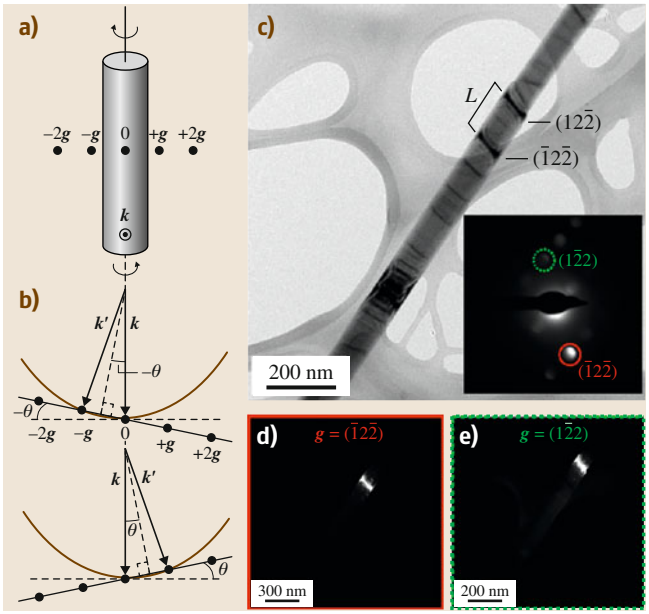


Fig. 17.9a–e Observation and determination of Eshelby twist using twist contours. **(a)** Schematic illustration of a NW showing $\boldsymbol{g}$ vectors orthogonal to the growth axis and the $\boldsymbol{k}$ vector of the electron beam. **(b)** Conditions where $-\boldsymbol{g}$ and $+\boldsymbol{g}$ vectors (*top* and *bottom diagrams*, respectively) meet the Laue condition. **(c)** Zero-beam bright-field TEM image of a representative NW showing two indexed twist contours and the physical separation L. *Inset* convergent-beam electron diffraction pattern. **(d,e)** Displaced-aperture dark-field TEM used to index the two labeled contours as $(\bar{1}2\bar{2})$ and $(1\bar{2}2)$ (after [17.47])

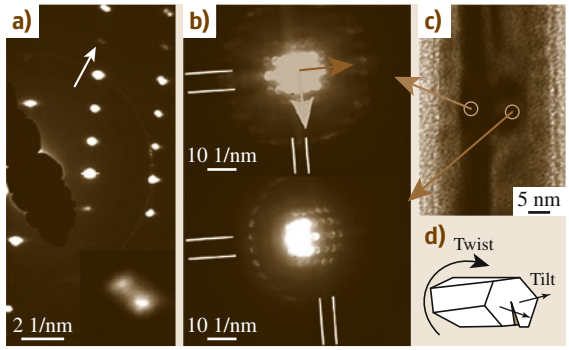


Fig. 17.10a–d Quantification of the lattice tilt using TEM and electron diffraction. **(a)** SAED showing the splitting of the diffraction spots (*inset* shows the split spot indicated by the *arrow*, scale 0.21 nm^{-1}). **(b)** CBED patterns showing the tilt of the structure from the *left* (*above*) to the *right part* (*below*) of the section of the NW. **(c)** Bright-field (BF) image showing the positions of measurement (*brown circles*) for each CBED pattern. The *dark-brown arrow* indicates the twist axis, while the *light-brown arrow* indicates the tilt axis in **(b)**. This is shown schematically in **(d)**. The Kikuchi bands observed have been used to measure the tilt angle (after [17.61])

where β is the angle between $\pm\boldsymbol{g}$ and the NW growth direction; For example, the ZnO NW shown in Fig. 17.9 was firstly oriented so that a pair of $\pm\boldsymbol{g}$ vectors $[\pm(1\bar{2}2)]$ were selectively illuminated [17.47]. A zero-beam bright-field image (Fig. 17.9c) was then taken to record the locations of the contour bands so that the separations between them could be measured. Next, each twist contour was uniquely indexed to a specific $\boldsymbol{g}$ vector using displaced-aperture dark-field imaging (Fig. 17.9d,e). A pair of twist contour bands are clearly present in the bright-field image (Fig. 17.9c), and they are indexed to $\pm(1\bar{2}2)$ $\boldsymbol{g}$ vectors, respectively. The calculated twist for the NW shown in Fig. 17.9c is approximately 9°/μm using (17.13), which is in agreement with the Eshelby twist predicted for a NW with radius of 46 nm and Burgers vector's magnitude of approximately 1.0 nm.

In practice, using twist contours to quantify Eshelby twist is much more easily implemented on NW samples than the other techniques discussed above, and twist contour analysis can quantify twist of ≈ 1°/μm or less, which is a much higher resolution than the other techniques [17.18, 40, 41]. Eshelby twist has been conclusively observed for NWs or NTs of PbS [17.18, 39], PbSe [17.40], CdS, CdSe [17.57], AlN [17.37], ZnO [17.20, 47], Fe : ZnO [17.62], Er : ZnO [17.63], α-FeOOH [17.58], Cu [17.60], and Cu_2O [17.48].

17.3.3 Lattice Tilt

The screw dislocation not only causes the atomic planes to form a helicoid but also splits the crystal lattice at its core. As a consequence, the normal to the basal planes of a dislocated NW is slightly tilted in relation to the growth axis. The degree of tilt ϕ between planes on opposite sides of the screw dislocation is a function of the pitch of the helicoid, which is essentially equal to the magnitude of the Burgers vector $\boldsymbol{b}$, and the radial position R of the measurement point

$$\cos(\phi) = \frac{1-(b/(2\pi R))^2}{1+(b/(2\pi R))^2} \,. \qquad (17.14)$$

Therefore, the magnitude of the Burgers vector can be derived from the tilt ϕ and R values [17.61].

Electron diffraction techniques including selected-area electron diffraction (SAED) and convergent-beam

electron diffraction (CBED) are convenient ways to determine the tilt angle ϕ. SAED usually illuminates a large area on the NW sample (hundreds of nanometers) and averages the tilt over all radial positions. The resulting pattern exhibits splitting of diffraction spots because the atomic plane normal is slightly tilted away from the NW axis. The angle of splitting in the diffraction spots is the same as that of the tilt ϕ. The average radial position R can be approximately estimated using one-half of the radius of the NW; For example, the InP NW shown in Fig. 17.10c has a radius of 12.0 nm, and its corresponding diffraction pattern (Fig. 17.10a) shows 2.0° splitting; thus the Burgers vector is calculated to be 0.69 nm, which is approximately one unit cell length of InP [17.61].

CBED, in contrast, measures the local lattice distortion due to its small probe size. The CBED pattern changes abruptly on different sides of the screw dislocation, which is visualized as a shift (Δk, in nm^{-1}) of the Kikuchi bands in reciprocal space (Fig. 17.10b). Therefore, the tilt angle ϕ can be derived from

$$\phi \approx \tan(\phi) = \frac{\Delta k}{\boldsymbol{k}} , \qquad (17.15)$$

where $\boldsymbol{k}$ is the wavevector of the incident electron beam. The radial position R is determined from the area being analyzed. Because NWs are thin objects, lower practical electron beam energy is preferred to make the Kikuchi bands visible. Using this CBED technique to determine the Burgers vector of the same NW shown in Fig. 17.10 returns a similar value (0.7 nm) to that obtained by the SAED technique. This measurement of lattice tilt is a newly developed technique, and has only been implemented for InP NWs [17.61].

17.3.4 Observation of Nanotubes or Voided NWs

As discussed earlier, the template-free, spontaneous formation of single-crystal inorganic NTs is a consequence of growth driven by screw dislocations with large Burgers vectors. The NT can be conveniently visualized under TEM, as the core of the NT appears brighter than the wall due to the greater electron transmission.

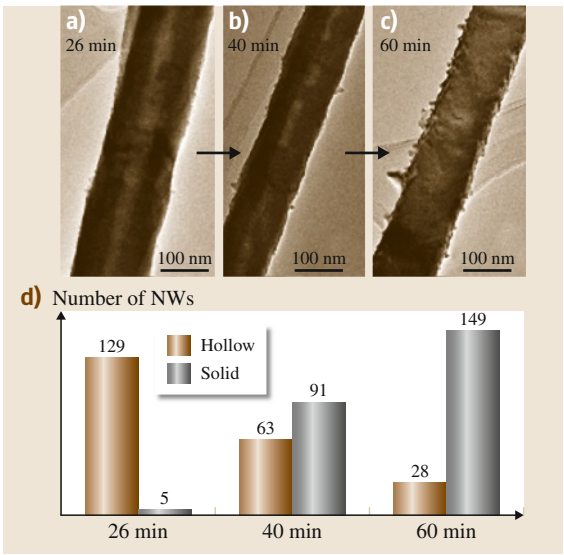


Fig. 17.11a–d Growth history of Cu_2O NTs and NWs revealed by TEM examination of the products with different growth times. **(a)** The completely hollow NT product from a 26 min reaction, **(b)** the partially hollow product from a 40 min reaction, and **(c)** the solid NW product from a 60 min reaction; **(d)** statistics of the observed Cu_2O NTs and NWs at different reaction times (after [17.48])

In addition to NT structures whose interior is completely hollow, partially filled tubes and NWs with voids also imply the operation of the dislocation-driven mechanism; For example, investigating the growth time effect on Cu_2O NW growth revealed that the 1-D structures are almost exclusively hollow NTs at the beginning, and then were gradually filled up to become voided NWs and eventually solid NWs (Fig. 17.11) [17.48]. Hollow or voided structures have been observed in NWs/NTs of GaN [17.64], ZnO [17.20], α-FeOOH [17.58], Cu [17.60], Cu_2O [17.48], AlN [17.65], and In_2O_3 (doped or undoped) [17.66–68].

17.4 Generality of Dislocation-Driven Nanomaterial Growth

In this section we review a variety of different anisotropic nanomaterials whose growth has been proven to be driven by screw dislocations in contemporary nanomaterial literature and thus demonstrate the generality of the dislocation-driven mechanism. The material classes of the nanomaterials known to form via the dislocation-driven mechanism vary from metal, metal oxide/hydroxide, metal chalcogenide, to

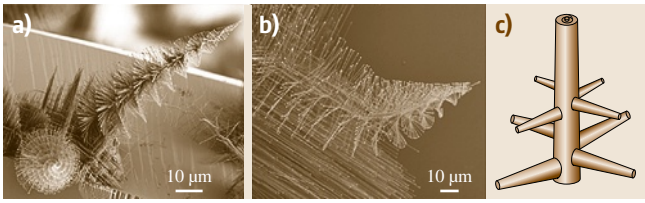


Fig. 17.12a–c Screw-dislocation-driven growth of PbS tree-like NWs. **(a,b)** SEM images of pinetree-like PbS NWs. **(a)** Schematic illustration to explain the growth of the pinetree structure: the trunk's growth is driven by axial screw dislocation and that of the branches by VLS (after [17.19])

metal nitride; the chemistry involved in forming the dislocation-driven nanomaterials can be distinctly different, ranging from simple hydrolysis reaction to reduction–oxidation (redox) reaction, and dislocation-driven growth can be accomplished in both vapor phase and solution phase. Despite the diversity in the physical and chemical properties of these nanomaterials, the rule of thumb in pursuit of rational synthesis of anisotropic nanomaterials is to maintain low supersaturation of the precursor to favor the dislocation-driven mechanism. We also present evidence of the dislocation-driven mechanism for each material using methods reviewed in the previous section.

17.4.1 Vapor–Phase Synthesis

The growth of NWs in vapor phase has been almost exclusively explained by the VLS and other analogous catalyst-driven mechanisms. The dislocation-driven crystal growth mechanism has long been underappreciated because of the easy visualization of a catalyst particle decorating the tip of the NW, whereas the TEM techniques to detect dislocations are not straightforward. Even in cases where catalyst particles were absent yet NW growth still occurred, researchers used to claim that the 1-D anisotropic growth was driven by self-catalyzed VLS. It should be cautioned that the role of dislocation-driven growth needs to be reexamined in these cases. Even in the presence of catalyst particles, there is still the possibility of the cooperation of both mechanisms. It is likely that, without the presence of catalyst nanoparticles, there is a higher energy barrier to nucleation of NW growth, therefore causing the low yield and slow growth rate of NWs that are commonly observed. Addition of catalyst nanoparticles promotes nanostructure growth with high yield by creating numerous nucleation sites, and thus facile and fast 1-D crystal growth is initiated. Furthermore, addition of catalyst impurities and the fast and disordered crystal growth could potentially lead to the generation of dislocation sites that further facilitate the crystal growth process, which might become more responsible for the subsequent NW growth under the low supersaturation level.

PbS

PbS pinetree-like NWs were the first reported case of dislocation-driven growth among the modern NWs (Fig. 17.12a,b). Nanostructures of PbS are synthesized via chemical vapor deposition using $PbCl_2$ and elemental sulfur as precursors under argon flow with a co-flow of H_2 at atmospheric pressure and with temperatures of 600–650 °C [17.18, 39]. A piece of freshly exposed Si substrate is used to collect the NW product. The formation of the tree structure is indeed a combined effect of the operation of both the dislocation-driven NW growth mechanism and the VLS mechanism: the growth of the trunks is driven by axial dislocations, whereas the branches are formed via in situ VLS growth, as illustrated in Fig. 17.12c. The hydrogen flow plays an important role in triggering the dislocation-driven growth of the tree trunks. The chemical reactions involved are

$$PbCl_2(s) + 1/2S_2(g) = PbS(s) + Cl_2(g)\,, \quad (17.16)$$

$$H_2 + S(s) = H_2S(g)\,, \quad (17.17)$$

$$PbCl_2(s) + H_2S(g) = PbS(s) + 2HCl(g)\,, \quad (17.18)$$

$$2H_2S(g) + Si(s) = SiS_2(s) + 2H_2(g)\,. \quad (17.19)$$

The onset of hydrogen flow likely creates a spike in H_2S supersaturation and initiates dislocations with screw components that then propagate anisotropically to form the NW trunks. Maintaining an optimum hydrogen flow can provide a favorable supersaturation that promotes dislocation-driven trunk NW growth and enable the simultaneous growth of the VLS-driven NW branches.

PbSe

PbSe tree-like NWs (Fig. 17.8) have also been reported [17.40]. The synthesis of PbSe NWs was analogous to that of PbS due to their structural similarity, though some minor details of the chemical vapor deposition (CVD) precursors vary. Again, screw dislocation is responsible for the trunk growth, and VLS for the branch growth. One different aspect in the PbSe synthesis is that an intentional metal catalyst, bismuth in this case, was used, yet no obvious catalyst cap on the NW trunk was observed. This agrees with the hy-

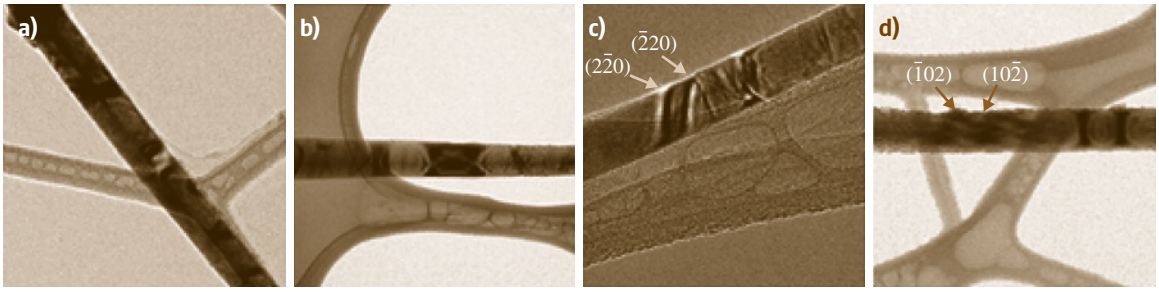


Fig. 17.13a–d Evidence of dislocation-driven growth of CdS and CdSe NWs. Dislocation contrast of a CdS NW **(a)** and a CdSe NW **(b)**, and twist contours on a CdS NW **(c)** and a CdSe NW **(d)** (after [17.57])

pothesis that metal particles might serve to facilitate dislocation-driven growth rather than acting as a VLS catalyst.

CdS/CdSe

CdS and CdSe share the wurtzite crystal structure, which is considered to be dislocation prone. There have been early reports on the dislocation structures in CdS/CdSe whiskers and ribbons [17.69–71]. Recently, CdS or CdSe NWs were grown via the chemical vapor deposition (CVD) process using $CdCl_2$ and elemental sulfur/selenium as precursors under argon flow with a co-flow of H_2 at relatively low system pressure of 40 Torr at temperatures of 600–650 °C [17.57]. Si substrates, either covered with gold nanoparticles or not, were used to collect the products. With the presence of gold nanoparticles, NWs with high yield and uniformity were obtained. Interestingly, even when the gold nanoparticle catalyst was absent, short NWs could still be grown. The vapor pressure was low in this reaction compared with most of the other reported CVD synthesis conditions [17.72–74], thus favoring dislocation-driven crystal growth.

Evidence for dislocation-driven growth was indeed detected in the NWs synthesized with the presence of gold nanoparticles. Dislocation contrast was observed in both as-synthesized CdS (Fig. 17.13a) and CdSe (Fig. 17.13b) NWs, and the Burgers vectors of the dislocation were determined to be [120] for CdSe under strong two-beam conditions. Moreover, twist contour analysis revealed the presence of Eshelby twist associated with the dislocation in both CdS (Fig. 17.13c) and CdSe (Fig. 17.13d) NWs.

These results clearly showed that dislocation-driven NW growth had occurred during the CVD growth of CdS and CdSe NWs, even when gold nanoparticle catalysts were employed for the synthesis, suggesting that both VLS growth and the dislocation-driven growth mechanism can coexist in the growth of 1-D CdS and CdSe NWs.

AlN

AlN whiskers were one of the earliest examples whose growth was demonstrated to be driven by screw dislocation. Back in 1965, *Drum* et al. observed the dislocation contrast running through AlN whiskers and developed the twist contour analysis to verify the presence of Eshelby twist in these whiskers (Fig. 17.14a) [17.37]. More recently, hollow AlN NTs (Fig. 17.14b) were synthesized by nitridization of Al metal powder in the presence of Co(III) salts [17.65]. The spontaneous formation of the NT structure is highly suggestive of screw-dislocation-driven growth.

GaN

GaN NWs were synthesized by catalyst-free direct reaction of gallium vapor and ammonia at 1000 °C [17.64]. Cross-sectional investigation (Fig. 17.15) of these NWs revealed the presence of nanopipes. Particularly cross-

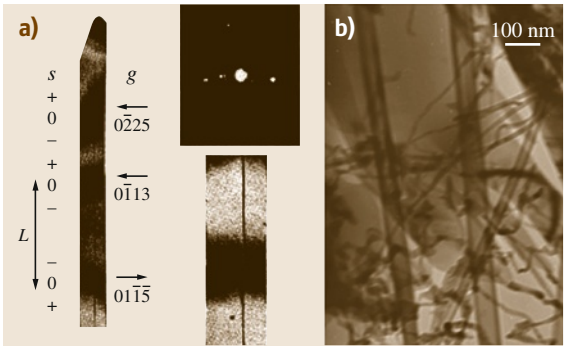


Fig. 17.14a,b Screw-dislocation-driven growth of AlN NWs. **(a)** Twist contour analysis of AlN whiskers; the dislocation contrast was also clearly observed (after [17.37]); **(b)** TEM image of AlN NTs (after [17.65])

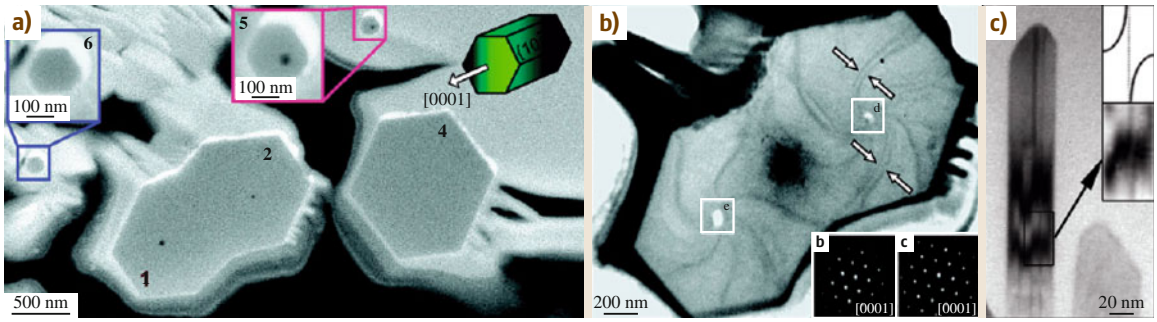


Fig. 17.15a–c Screw-dislocation-driven growth of GaN NWs and NRs. **(a,b)** Cross-sectional SEM **(a)** and TEM **(b)** images of GaN NWs with nanopipes in the middle (after [17.64]). **(c)** TEM image of a GaN NR displaying dislocation contrast (after [17.75])

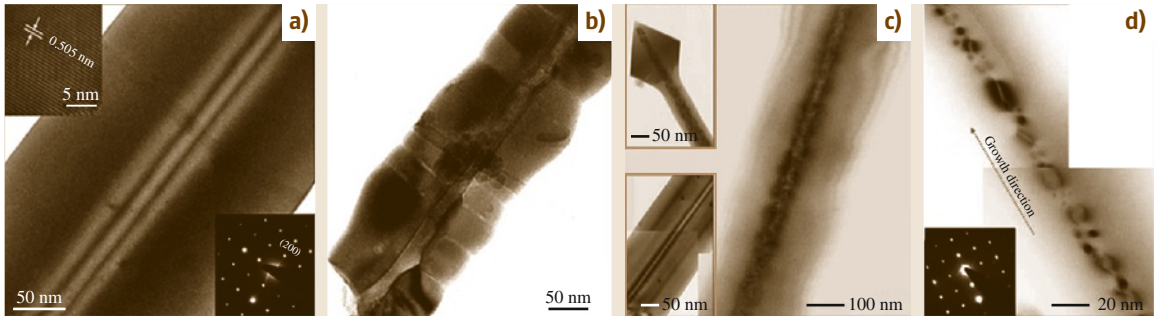


Fig. 17.16a–d Screw-dislocation-driven growth of undoped and doped In_2O_3 NTs. **(a,b)** TEM images of undoped In_2O_3 NTs; **(c,d)** TEM images of Sn-doped In_2O_3 NWs that display voids and dislocation loops (after [17.68, 68])

sectional TEM imaging (Fig. 17.15b) shows interesting spiral bend contours, which were believed to be associated with screw dislocations with large Burgers vectors. This is consistent with the mechanism of NT formation that was discussed previously.

GaN NRs grown by molecular-beam epitaxy were also reported to display dislocation contrast (Fig. 17.15c) [17.75].

In_2O_3/Sn:In_2O_3/Zn:In_2O_3

In_2O_3 NWs were synthesized using simple thermal evaporation of InN powder at ambient condition [17.66]. Sn/Zn doping was introduced by mixing InN and SnO_2/ZnO powder followed by a similar evaporation process [17.67, 68]. The resulting undoped 1-D In_2O_3 nanostructures were indeed hollow nanopipes (Fig. 17.16a,b), which is one of the characteristics of dislocation-driven growth. More intriguingly, the doped NWs exhibited curious features such as nanoprecipitates, voids, and dislocation loops (Fig. 17.16c,d). It is likely that the formation of the nanopipe to relieve the dislocation strain energy can be locally affected by the presence of dopants around the dislocation and the formation of nanoprecipitates and loops, leading to the observed discontinuous nanopipe.

Fe:ZnO/Er:ZnO

Fe-doped ZnO NWs were synthesized by thermal evaporation of a mixture of ZnS and Fe_2O_3 powder [17.62]. Eshelby twist was detected using twist contour analysis (Fig. 17.17a), which supports the dislocation-driven growth of these NWs.

Er-doped ZnO tree-like NWs were synthesized using a similar thermal evaporation method except that the precursors were ZnO and Er_2O_3 [17.63]. The twist of the NW trunk was evidenced by the rotation of the branches, which is indicative of the dislocation-driven growth of the trunk (Fig. 17.17b,c).

17.4.2 Solution-Phase Synthesis

Direct Hydrolysis

The hydrolysis reaction is probably one of the simplest types of chemical reactions, yet it is a versatile

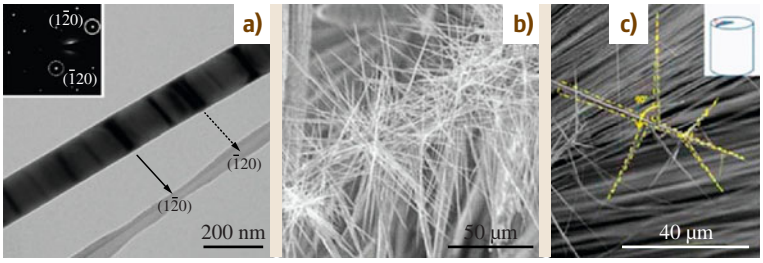


Fig. 17.17a–c Screw-dislocation-driven growth of undoped and doped ZnO NWs. **(a)** Twist contour analysis of an Fe : ZnO NW (after [17.62]) and **(b,c)** SEM images of tree-like Er : ZnO NWs (after [17.63])

route to produce many important metal oxides at large scale in low-temperature aqueous solutions. ZnO, the first solution-grown dislocation-driven nanomaterial to be demonstrated, was synthesized via direct hydrolysis of Zn^{2+} in the presence of hexamethylenetetramine (HMT) as the precipitation reagent and pH buffer [17.20]. The details of the synthesis and characterization of ZnO have been discussed in previous sections. This example provides the general framework for designing the rational synthesis of anisotropic nanomaterials driven by screw dislocations. The understanding on how to control the concentration of the precursor metal ions and therefore the supersaturation level for hydrolysis in order to favor dislocation-driven crystal growth kinetics may enable rationally designed low-cost NW/NT production for practical applications. In many cases, the direct products of the hydrolysis reactions are metal oxyhydroxides and hydroxides, depending on their surface energetics, size, and environment [17.76], so that a secondary, thermal annealing treatment might be needed to form the desired metal oxides.

Iron Oxyhydroxide. Iron oxyhydroxide (FeOOH) NWs were synthesized using a continuous flow reactor (CFR) with flow of low-concentration $FeCl_2$ aqueous solution and co-flow of iron microparticles [17.58]. The CFR allows a *constant* low supersaturation level and enables indefinite growth time for the NWs. The contrast between the product morphologies seen for a CFR reaction and a static hydrothermal reaction with comparable conditions is drastic: there are copious amounts of fairly uniform NWs (Fig. 17.18a) for the CFR reactions, while the static hydrothermal reaction yields mainly microparticles with sparse NW growth (Fig. 17.18b). Defective particles were still produced at the initial stage of the growth where a spike of precursor supersaturation occurred, likely providing the source of dislocations, as evidenced by the observation of the seed particles at the end of the NWs (Fig. 17.18b, inset). Dislocation contrast (Fig. 17.18c), Eshelby twist (Fig. 17.18d), and hollow structures were readily observed using TEM, confirming the dislocation-driven growth of these NWs.

The hydrolysis reaction to form FeOOH is

$$Fe^{3+} + 2H_2O \rightarrow FeOOH + 3H^+ . \qquad (17.20)$$

Direct hydrolysis of low-concentration Fe^{3+} solution seems to be the most intuitive way to gain good control of the supersaturation. However, the problem is that the hydrolysis of Fe^{3+} is so favorable (K_{sp} for $Fe(OH)_3 = 4\times10^{-38}$) and fast that preventing such favorable hydrolysis (high supersaturation) requires an

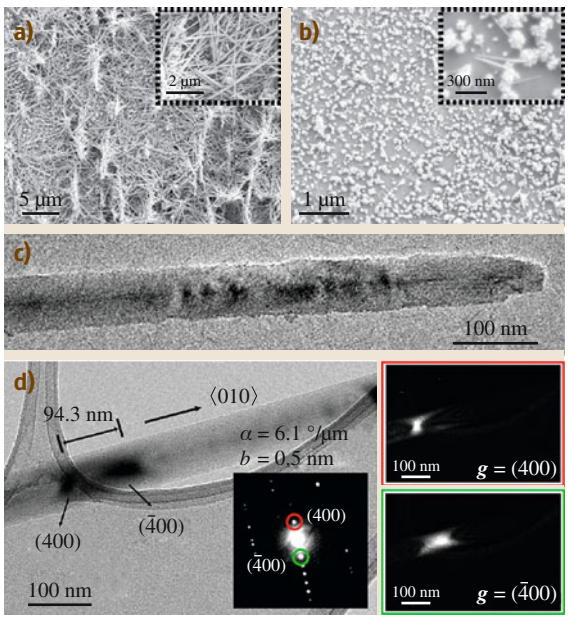


Fig. 17.18a–d Screw-dislocation-driven growth of α-FeOOH NWs. **(a)** SEM images of α-FeOOH NWs yielded from a CFR reaction. **(b)** SEM images of α-FeOOH NWs yielded from a static hydrothermal reaction. **(c,d)** TEM characterization of α-FeOOH NWs. **(a)** Zero-beam bright-field image showing the dislocation contrast. **(d)** Twist contour analysis of an α-FeOOH NW

extreme low pH. In contrast, Fe^{2+} ions do not hydrolyze and precipitate significantly even at near-neutral pH because the K_{sp} for $Fe(OH)_2$ is 8×10^{-16}, but they can be readily oxidized to Fe^{3+} by dissolved oxygen in the aqueous solution,

$$4Fe^{2+} + O_2 + 4H^+ \rightarrow 4Fe^{3+} + 2H_2O\,. \qquad (17.21)$$

Secondly, the presence of Fe metal can reduce Fe^{3+} back to Fe^{2+} ions and therefore guarantee a low concentration (supersaturation) of Fe^{3+} as dictated by the Fe^{3+}/Fe^{2+} redox equilibrium,

$$2Fe^{3+} + Fe \rightarrow 3Fe^{2+}\,. \qquad (17.22)$$

By coupling these two *protection* schemes (low-concentration flow and redox equilibrium) to the original hydrolysis reaction, a low supersaturation of Fe^{3+} ions can be maintained to guarantee slow and controlled hydrolysis, which favors dislocation-driven 1-D crystal growth. Unlike other reports of iron oxide/oxyhyrdoxide nanomaterial syntheses where either surfactants or organic ligands were used and argued to be important in the NW synthesis [17.77–80], this method merely requires the simple inorganic precursors Fe^{2+} and Fe.

$Co(OH)_2$. $Co(OH)_2$ NWs are an intermediate product during the synthesis of Co_3O_4 NWs, where cobalt nitrate is hydrolyzed in the presence of concentrated ammonia ($NH_3\cdot H_2O$) [17.59]. The $Co(OH)_2$ NWs started to grow 2 h after initiation of the reaction. NH_3 can form a series of complex compounds with Co^{2+} ions, and thus a concentrated NH_3 environment effectively reduces the concentration/supersaturation of the free Co^{2+} ions to favor dislocation-driven growth. Dislocation contrast was clearly observed in the as-synthesized $Co(OH)_2$ NWs under TEM (Fig. 17.19). Unfortunately rigorous two-beam and twist contour analysis were not available, likely due to instability of the hydroxide species under vacuum and the high-energy electron beam.

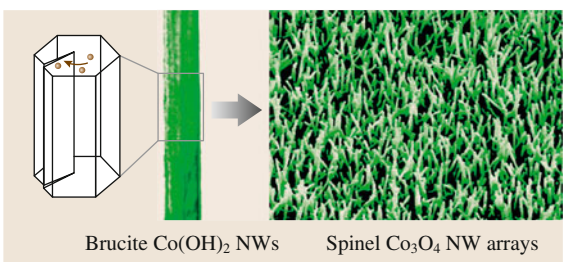


Fig. 17.19 Schematic illustration of dislocation-driven growth of $Co(OH)_2$ NWs and their conversion into Co_3O_4 NWs (after [17.59])

Redox Reaction

In contrast to hydrolysis reactions where single precursor ions account for the supersaturation level of the system, in a redox reaction the supersaturation is necessarily determined by both the reducing reagent(s) and the oxidizing reagent(s). Thus, using the concentration of the precursors to describe the supersaturation level in a redox system becomes ambiguous. Indeed, in this case, the best way to represent the equilibrium position of the chemical reaction (and crystal growth) is the electrochemical potential: chemical equilibrium is reached when the electrochemical potential of the reaction is zero. The supersaturation of the redox reaction system is simply the electrochemical overpotential. By tuning the electrochemical potential to be slightly over zero, the low-supersaturation condition is achieved, which favors the dislocation crystal growthregime. The necessity for multiple reactant species increases the complexity of controlling the supersaturation; nevertheless, by understanding this complexity, we can achieve better control of the supersaturation of such redox reactions to promote dislocation-driven NW growth.

Copper (Cu) NWs. Cu represents an entirely different class of materials, metals, which again demonstrates the generality of the dislocation-driven growth mechanism. Cu NWs were initially synthesized by reducing Cu^{2+} ions using hydrazine (N_2H_4) in the presence of ethylenediamine (EDA) and concentrated sodium hydroxide (7 M NaOH) in a closed vial [17.60]. The main reaction taking place to form Cu NWs is

$$2Cu^{2+} + 4OH^- + N_2H_4 \rightarrow 2Cu + N_2 + 4H_2O\,. \qquad (17.23)$$

The OH^- ion plays dual roles in the reaction: firstly, it provides a suitable pH condition that allows the redox reaction to occur (the electrochemical potential is dependent on the solution pH); and secondly, it is intrinsically a ligand that can complex with Cu^{2+} to form $Cu(OH)_4^{2-}$. This complexation lowers the activity (supersaturation) of the Cu^{2+} ions, which promotes the dislocation-driven growth mechanism. Moreover, EDA is a strong complexing ligand (rather than a surfactant) capable of binding with Cu^{2+}, thus further lowering the supersaturation of the system.

Dislocation contrast was observed in many as-synthesized Cu NWs. Rigorous TEM analysis under

strong two-beam conditions characterized the Burgers vector direction of the dislocation to be [110], which is a pure screw dislocation (Fig. 17.20). Twist contour analysis confirmed the presence of an Eshelby twist structure and quantified the magnitude of the Burgers vector to be 1/2 [110], which is the most common Burgers vector in the face-centered cubic (fcc) structure [17.27]. Furthermore, hollow NTs of Cu were present occasionally.

Understanding of the dislocation-driven growth of Cu NWs allows improved synthesis under a much milder chemical environment. The static reaction (17.23) has two drawbacks: firstly, an extremely high concentration of NaOH (7 M) is required; and secondly, NW lengths are limited due to precursor depletion. Understanding and controlling the supersaturation of the crystal growth is the key to promote dislocation-driven growth. For the redox reaction between Cu^{2+} and N_2H_4, the change in the free Cu^{2+} ion concentration only affects one half-cell reaction for supersaturation control. Tuning the concentration of N_2H_4 also influences the supersaturation of the reaction system. One of the roles of NaOH is complexing Cu^{2+} and reducing the concentration of free Cu^{2+} ions; thus, by compensating the reduction in NaOH concentration with an increase in the other complexing ligand, EDA, low supersaturation can be maintained and successful dislocation-driven NW growth can still be achieved. Indeed, a modified static reaction with a much lower concentration of NaOH (pH $\approx$ 12) still led to the formation of Cu NWs. Since EDA is a much stronger ligand ($\beta[Cu(EDA)_2] = 10^{20}$) than OH^- ($\beta[Cu(OH)_4^{2-}] = 10^{16}$), a modest increase in EDA concentration can sufficiently compensate for a two order of magnitude drop in NaOH concentration. Furthermore, according to reaction (17.23), OH^- ions participate in the redox reaction that forms Cu, thus reducing the NaOH concentration also lowers the redox overpotential and crystal growth supersaturation, thus favoring dislocation-driven growth. NWs yielded from this protocol are typically $\approx$5 μm in length and 200–300 nm in diameter with slight tapering (Fig. 17.21a,b), indicating that precursor depletion occurs as the reaction proceeds. The precursor depletion problem could be solved using a CFR, which yielded much longer Cu NWs (about 30 μm on average, up to 50 μm, Fig. 17.21c,d) with uniform diameter distribution.

Cuprous Oxide (Cu_2O) NWs. Natural Cu_2O (cuprite) mineral whiskers were among the earlier examples where axial screw-dislocation contrast was clearly observed in

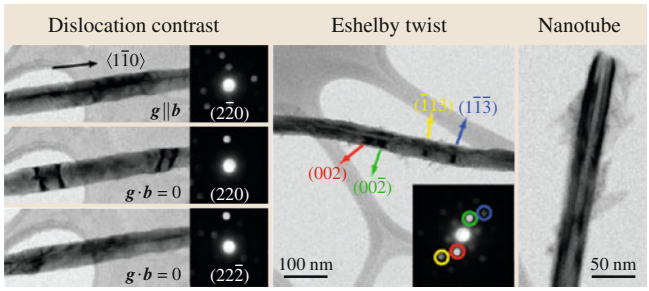


Fig. 17.20 TEM evidence proving the dislocation-driven growth of Cu NWs/NTs (after [17.60])

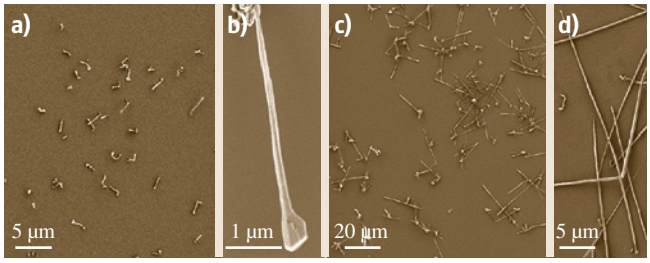


Fig. 17.21a–d Improved synthesis of Cu NWs. SEM images of Cu NWs synthesized under modified conditions via static reaction **(a,b)** or CFR reaction **(c,d)** (after [17.60])

TEM [17.38]. Recently, Cu_2O NWs were synthesized using a low-concentration Fehling's reaction where Cu^{2+} ions were reduced by glucose in the presence of sodium hydroxide and sodium tartrate [17.48]. The formation of the Cu_2O in solution is similar to that of Cu in terms of the redox chemistry. However, glucose is a much weaker reducing reagent, so Cu(II) can only be reduced to Cu(I) species. Tartrate forms a Cu^{2+}–tartrate coordination complex ($K_f \approx 10^7$) that both prevents $Cu(OH)_2$ precipitation and serves to reduce the concentration of free Cu^{2+} ions, lowering the supersaturation to promote dislocation-driven NW growth.

TEM characterization of these NWs only detected a few of them with dislocation contrast, since most of the NWs were actually formed by filling up the initially formed Cu_2O NTs (Fig. 17.22). Besides the dislocation contrast and spontaneous formation of NTs, the observation of the Eshelby twist in these NTs/NWs also confirms that their growth is driven by screw dislocations.

17.4.3 Solution Growth of 2-D Nanoplates

As discussed earlier, the spiral step edges generated by screw dislocations can be chemically modified, re-

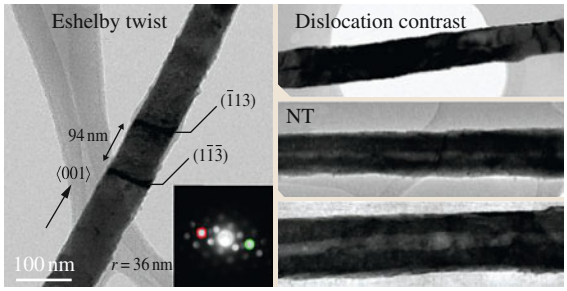


Fig. 17.22 TEM evidence proving the dislocation-driven growth of Cu_2O NWs/NTs (after [17.48])

sulting in disparate step velocities. This is the key to achieve desirable anisotropic growth driven by screw dislocations. Despite the drastic differences in morphologies between 1-D NWs/NTs and 2-D nanoplates, dislocation-driven crystal growth is common to both and the subtle kinetics of spiral step propagation associated with dislocation growth can be used to explain each. The characterization of dislocation-driven 2-D nanomaterial is more straightforward as the spiral step edges lying on the basal plane of the nanoplates can be directly observed using both scanning electron microscopy (SEM) and atomic force microscopy (AFM). Dislocation-driven 2-D growth has already been proven to be responsible for the growth of a variety of materials including zinc hydroxysulfate (ZHS), $Co(OH)_2$, $Ni(OH)_2$, and gold nanoplates. Here, their synthesis and characterization are discussed.

Zinc Hydroxysulfate (ZHS)

In a typical synthesis of ZHS nanoplates, aqueous solutions containing $ZnSO_4$, $Zn(NO_3)_2$, and hexamethylenetetramine (HMT) are heated in sealed glass vials [17.50]. A piece of Si substrate is placed in the solution to collect the nanoplate products. SEM re-

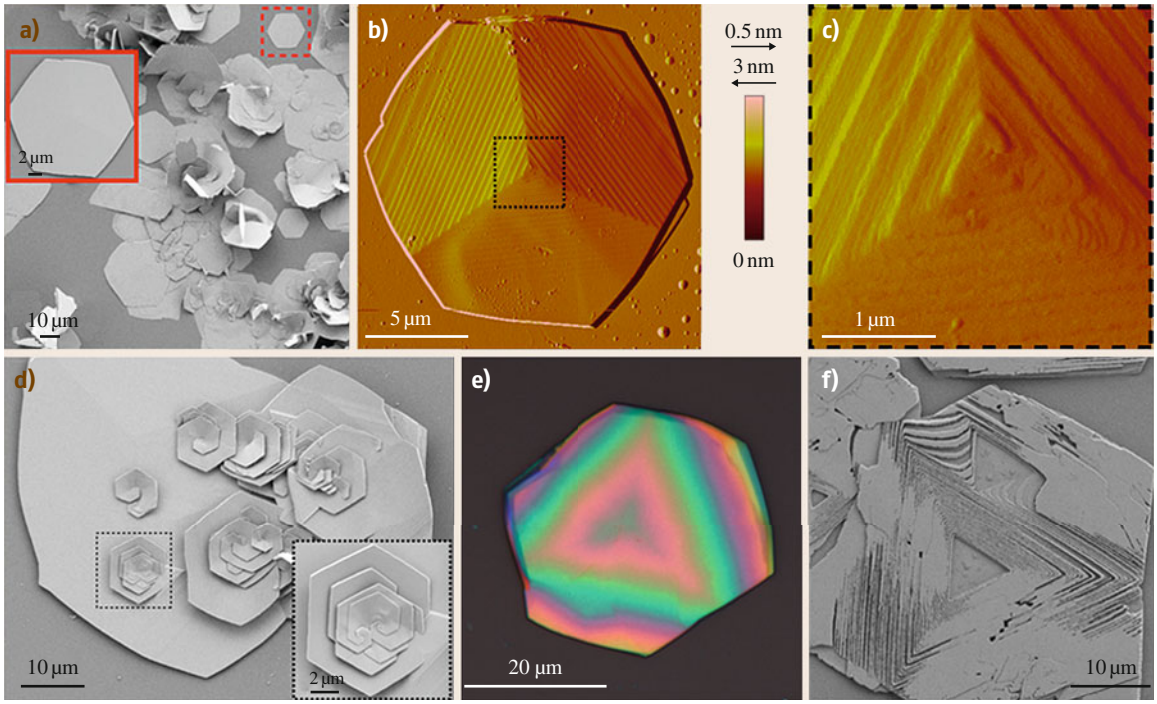


Fig. 17.23a–f Overview of nanoplate morphology and screw dislocation step edges of ZHS. **(a)** Low-magnification scanning electron microscopy (SEM) image of as-synthesized ZHS nanoplates; *inset* is a representative *hexagonal* nanoplate. **(b)** Low-magnification contact-mode AFM image of a representative nanoplate (deflection signal shown). **(c)** Higher-magnification image of the dislocation core. **(d)** Large nanoplate containing several screw dislocations of different handedness. **(e)** Bright-field optical image showing the thin-film interference pattern generated between the nanoplate and the reflective silicon substrate, revealing the radial thickness variations within the nanoplate. **(f)** SEM image of a nanoplate grown on a silicon substrate with native oxide (after [17.50])

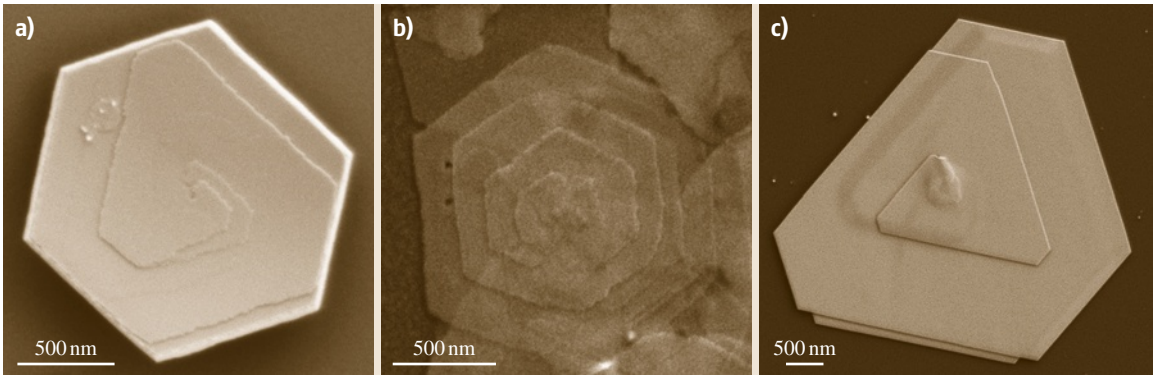


Fig. 17.24a–c Other examples of dislocation-driven nano-plates. SEM images of representative nanoplates of **(a)** α-$Co(OH)_2$, **(b)** $Ni(OH)_2$, and **(c)** gold, highlighting the screw dislocation spirals (after [17.50])

vealed that the substrates are densely coated with many nanoplates (Fig. 17.23a) after this reaction procedure. In contrast, in the absence of $ZnSO_4$, ZnO nanorods are the exclusive reaction product [17.81, 82]. All of these nanoplates were found to contain screw dislocations using contact-mode AFM. For the representative hexagonal morphology, these dislocations were single-source dislocations and the core was located at the very center of the nanoplate (Fig. 17.23b,c). Interestingly, simple bright-field optical microscopy revealed the thin-film interference pattern generated between the surface of a nanoplate and the reflective silicon substrate surface, which demonstrated the geometry and thickness variation of the nanoplate and the location of the dislocation cores (Fig. 17.23e). Due to the dislocation hillocks, these nanoplates are in fact *pyramids* with extremely high width-to-thickness ratios. Multiple dislocation centers with different chirality were observed in larger and more complex nanoplate morphologies (Fig. 17.23d). Moreover, when nanoplates are grown on silicon surfaces with native oxides, the dislocation spirals are heavily etched, clearly revealing their morphology under standard SEM (Fig. 17.23f). Similar zinc hydroxydodecylsulfate (ZHDS) nanoplates were also reported to grow via the dislocation-driven mechanism [17.83].

$Co(OH)_2$

$Co(OH)_2$ nanoplates (Fig. 17.24a) were synthesized via direct hydrolysis of cobalt(II) chloride in the presence of HMT as the pH buffer [17.50]. The α-$Co(OH)_2$ samples had high densities of nanoplates that all showed dislocations. However, due to their smaller diameter and wider terrace widths, they did not display the same dramatic thin-film interference under optical microscopy.

$Ni(OH)_2$

$Ni(OH)_2$ nanoplates (Fig. 17.24b) were synthesized similarly via direct hydrolysis of nickel(II) acetate in the presence of HMT [17.50]. The $Ni(OH)_2$ nanoplates were equally dense but thinner than ZHS and exhibited a propensity to form flower-like structures [17.84] similar to the off-shooting nanoplates seen in ZHS (Fig. 17.23a).

Gold

Gold nanoplates (Fig. 17.24c) were synthesized by reducing chloroauric acid ($HAuCl_4$) in aqueous solution using salicylic acid [17.50]. Consistent with literature [17.85], gold nanoplates form as triangles and hexagons as well as truncated triangles; however, only a small percentage of these plates clearly show dislocation spirals. Moreover, the step heights, previously estimated to be ≈ 100 Å [17.85], and thus the Burgers vectors of the dislocations observed in gold plates, are very large in comparison with the (111) spacing of 2.35 Å for gold. The surface of gold nanoplates is the (111) plane, and this should be the elementary Burgers vector.

17.5 Rational Growth of Dislocation-Driven Nanomaterials – General Strategies

The empirical understanding gained from the examples discussed above provides general guidelines for dislocation-driven nanomaterial growth, which requires two basic ingredients:

1. The presence of dislocation sources (*seeds*) to propagate the growth
2. A suitable low supersaturation condition for promoting dislocation-driven growth over LBL and other crystal growth modes [17.19].

We discuss these two aspects separately.

Manipulation of the supersaturation level to favor dislocation-driven growth of nanomaterials needs to be specific depending on the chemistry of the materials. In general, an overall low concentration (in solution) or vapor pressure of reactants is preferred. Particularly in solution growth, introduced ligand compounds can complex with free ions of the precursor and thereby effectively reduce the activity (supersaturation) of the reactants. The versatile nature of coordination chemistry can be exploited to rationally tune the supersaturation level to promote dislocation-driven growth. The role of the *surfactants* commonly employed in many solution syntheses might need to be reexamined from the perspective of controlling the supersaturation in the solution system, since many of them are multidendate ligands. Redox chemical equilibrium or other chemical equilibrium systems can also result in a buffering effect and allow the supersaturation level to be effectively controlled. Furthermore, the employment of a continuous flow reactor (CFR) (Fig. 17.25a) can allow better control over the supersaturation than the commonly practiced closed-system growth (referred to as *static growth* later) does. Static growth, where precursors are introduced at the beginning and allowed to react to completion, suffers from a significant decline in precursor concentration (supersaturation) during the course of the reaction (Fig. 17.25b), which leads to irregular growth kinetics that are difficult to deconvolute and control. CFR can maintain a constant low supersaturation targeting the dislocation-driven regime and enable indefinite growth times.

On the other hand, to date, there are few rational routes to engineer the dislocation source. To create dislocation sources, the most common and straightforward approach is to generate defective seed crystals [17.86] under high-supersaturation reaction conditions. Ideally, the seeds are prepared separately from the growth system [17.20]; nevertheless, oftentimes an initial spike of high supersaturation of precursors in the growth system can achieve a similar objective [17.18, 39, 48, 58, 60]. Screw dislocations can also come from other crystalline substrate surfaces, since they are always present in crystals. Screw dislocations in defect-rich substrates, such as GaN thin film grown on sapphire, have been utilized to *seed* dislocation-driven growth of vertically epitaxial ZnO NWs (Fig. 17.26) from solution [17.47]. The density of the ZnO NWs is comparable to the densities of screw dislocations found in such GaN thin films, and NWs are found to grow only from the disloca-

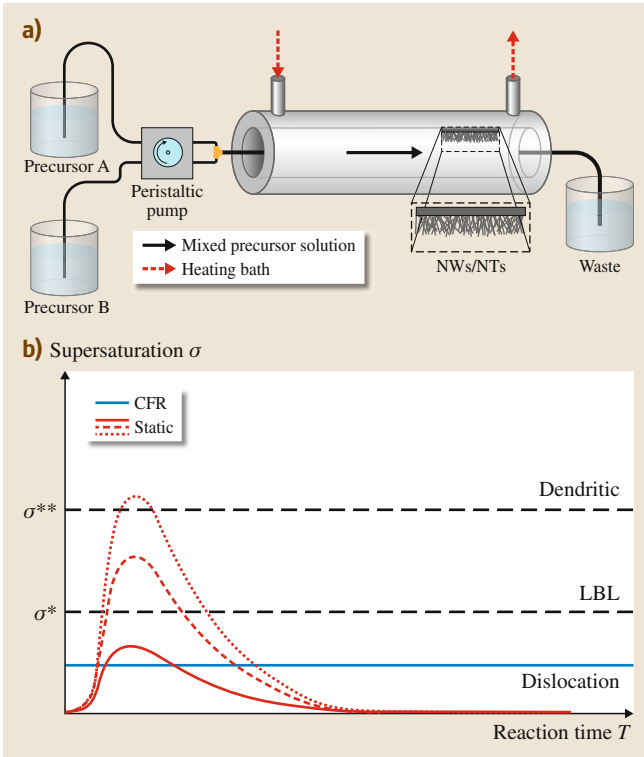


Fig. 17.25a,b Schematic of continuous flow reactor (CFR) and supersaturation profiles. **(a)** Consisting of a jacketed chromatographic column, a heated circulating water bath, and a dual-head peristaltic pump, the CFR enables precise control over reaction temperature, precursor solution composition/flow rate, substrate location, and reaction time (heated circulating water bath not shown). **(b)** Comparison of schematic supersaturation profiles for closed-system reactions and the CFR reaction (after [17.20])

tion etch pits formed on the surface of GaN substrates that have been cleaned aggressively. It is possible that the *seeding layers* of ZnO film or other materials initially formed on various substrates that are crucial for successful growth of NWs of ZnO or other materials could play similar roles; i. e., such *seeding layers* could in fact be the highly defective substrates that contain numerous screw dislocations that then initiate dislocation-driven growth of NWs. Furthermore, this *threading* dislocation growth that propagates from substrate to NW of another material lays the foundation for the creation of NW heterostructures driven by dislocations.

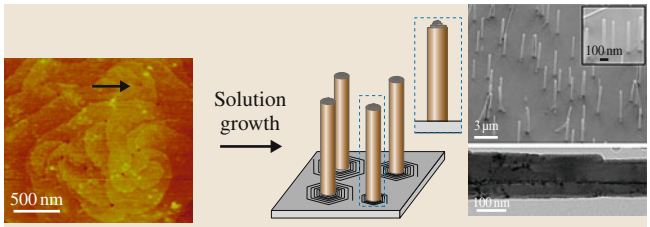


Fig. 17.26 Schematic illustration of dislocation-driven growth of ZnO NWs *seeded* by screw dislocations in GaN substrates (after [17.47])

17.6 Applications

The dislocation-driven nanomaterial growth mechanism is a general mechanism that can apply to any material. It does not require catalysts that form eutectics with the targeted nanomaterials and does not depend on the same material compatibility; therefore, more materials can be grown in the anisotropic fashion dictated by the dislocation. Another significant advantage of dislocation-driven growth is that it can be conveniently implemented in low-temperature aqueous solutions, which can lead to less expensive and energy-intensive production of anisotropic nanostructures of many useful materials. Furthermore, dislocation-driven growth operates at low supersaturation, which is essentially the near-equilibrium state. In this sense, the consumption of the precursors is low, so that the synthesis can be more cost-efficient.

Particularly for the significant applications of NWs and NTs in renewable energy, such as solar energy conversion, battery electrodes, and thermoelectrics, large amounts of ecologically sustainable nanomaterials made at low cost are demanded to address the large-scale energy challenges. Some Earth-abundant semiconductor materials that are promising for solar energy and other renewable energy applications suffer from poor mobility, carrier density, or minority carrier diffusion length. For many of these unconventional abundant materials, new design concepts based on nanoscale materials such as NWs may enhance their utility, because the nanoscale dimensions may circumvent their shortcomings or make them much more tolerable for applications [17.6, 87–90].

A good example are the nanomaterials of various iron-based compounds such as α-Fe_2O_3 (hematite, bandgap 2.1 eV) [17.89, 91], β-FeS_2 (pyrite, bandgap 0.95 eV) [17.92, 93], and FeF_3 [17.94, 95]. Because iron (Fe) is the fourth most abundant element in the Earth's crust, these compounds have the potential to meet or exceed the annual worldwide energy demand at a significantly lower material production cost over traditional or leading solar materials that are based on rare elements such as indium, gallium, and selenium [17.96]; For example, hematite has been intensively studied because it is a promising photoanode material for catalyzing photoelectrochemical (PEC) water splitting, yet the performance of hematite electrodes still suffers from its poor semiconducting properties [17.89, 91]. NWs of hematite could circumvent its shortcomings, and they can be conveniently converted from screw-dislocation-driven α-FeOOH NWs via thermal annealing [17.58].

Iron fluoride (FeF_3), on the other hand, is a promising high-capacity Li-ion battery cathode material that is much cheaper than the current lithium cobalt oxide ($LiCoO_2$) cathode material [17.94]. However, such promise has been held back by the slow ionic diffusion and low conductivity of FeF_3. $FeF_3 \cdot 3H_2O$ NWs have been synthesized following the guideline of dislocation-driven NW growth at gram scale in solution using low-concentration iron(III) nitrate and hydrofluoric acid as precursors (Fig. 17.27a) [17.95]. Due to the high solubility of $FeF_3 \cdot 3H_2O$ in water (5.92 g/100 g H_2O at 25 °C), ethanol was chosen as the solvent, in which $FeF_3 \cdot 3H_2O$ dissolves very little [17.97]. F^- is a good complexing ligand for Fe^{3+} to make the stable FeF_6^{3-} complex ($K_f = 10^{15.04}$) [17.98], which effectively maintains the low supersaturation environment

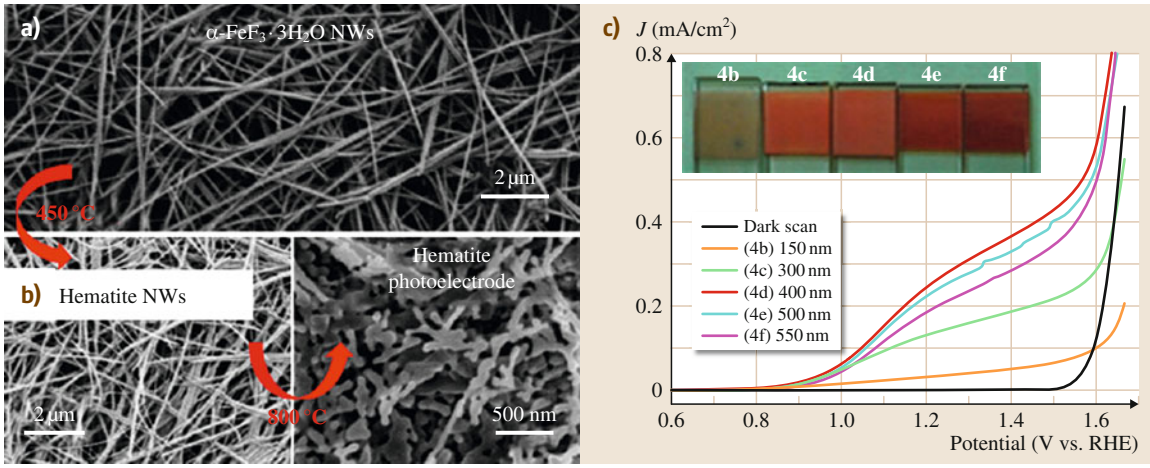


Fig. 17.27a,b Application of screw-dislocation-driven nanomaterials in solar energy conversion. SEM images of as-synthesized α-$FeF_3 \cdot 3H_2O$ NWs **(a)** and converted hematite NW photoelectrode **(b)**; photocurrent densities J versus bias voltage (V versus RHE) under AM1.5 G simulated solar light at 100 mW/cm^2 for hematite NW photoelectrodes of various thicknesses (after [17.16])

to favor NW growth. The following two reactions are responsible for NW growth:

$$Fe^{3+} + 6F^- \rightarrow FeF_6^{3-} , \qquad (17.24)$$

$$FeF_6^{3-} + 3H_2O \rightleftarrows FeF_3(H_2O)_3 + 3F^- . \qquad (17.25)$$

The H_2O in the second equation comes from the hydrated Fe(III) salt and HF solution. F^- and H_2O should be considered as both reactants and ligands to the Fe^{3+} ions. This equilibrium likely helps maintain a constant and low supersaturation of $FeF_3(H_2O)_3$, which is considered to be the precursor of crystal growth for α-$FeF_3 \cdot 3H_2O$ [17.99, 100]. The growth of α-$FeF_3 \cdot 3H_2O$ NWs is likely driven by screw dislocations given the low supersaturation conditions applied in the synthesis [17.18–20], but the as-grown NW samples are not electron-beam stable due to the easy loss of lattice water, and thus it is impossible to either confirm or disprove this hypothesis. These α-$FeF_3 \cdot 3H_2O$ NWs can be readily converted to semiconducting α-Fe_2O_3 (hematite) NWs (Fig. 17.27b), which exhibited respectable PEC performance of 0.54 mA/cm^2 photocurrent density at 1.23 V versus reversible hydrogen electrode potential (Fig. 17.27c).

17.7 Summary and Perspectives

This chapter has illustrated that the screw-dislocation-driven growth mechanism is applicable to many nanomaterials grown in solution or vapor phase, with the families of materials involved ranging from oxides and hydroxides, nitrides, chalcogenides, to metals. As the understanding of dislocation-driven growth deepens, this list of examples will continue to expand in the future. The procedures for microstructural characterization and confirmation of dislocation-driven growth discussed above can guide future work on searching for dislocation-driven growth. Moreover, the dislocation mechanism and elasticity theory could be used to explain other intriguing crystal growth phenomena that are commonly observed but often unconvincingly explained.

Fundamental studies on dislocation-driven nanomaterial growth not only enhance the understanding of anisotropic crystal growth but also open up the exploitation of large-scale, low-cost solution growth for rational catalyst-free synthesis of anisotropic nanomaterials for diverse applications, such as those for renewable energy. The discussion in Sect. 17.5 established a general framework for rational design of dislocation-driven growth of nanomaterials.

It can also be expected that by utilizing dislocations one can fabricate more complex structures, such as het-

erojunctions with abrupt crystal interface, which could be of more interest than simple NWs/NTs for many applications, including solar energy conversion [17.101]. Engineering the locations and density of dislocations in substrates can enable control over the location and morphology of dislocation-driven NWs. Furthermore, it is interesting to investigate how a single axial screw dislocation affects the physical properties of a single NW, including its electrical and mechanical properties. Deeper understanding of the screw-dislocation-driven growth of nanomaterials and their properties, and better control over such growth, will lead to a new stage of nanomaterial design and production for various applications.

References

17.1 M.J. Bierman, S. Jin: Potential applications of hierarchical branching nanowires in solar energy conversion, Energy Environ. Sci. **2**, 1050–1059 (2009)

17.2 J.R. Szczech, J.M. Higgins, S. Jin: Enhancement of the thermoelectric properties in nanoscale and nanostructured materials, J. Mater. Chem. **21**, 4037–4055 (2011)

17.3 Y. Xia, P. Yang, Y. Sun, Y. Wu, B. Mayers, B. Gates, Y. Yin, F. Kim, H. Yan: One-dimensional nanostructures: Synthesis, characterization, and applications, Adv. Mater. **15**, 353–389 (2003)

17.4 C.M. Lieber, Z.L. Wang: Functional nanowires, MRS Bulletin **32**, 99–108 (2007)

17.5 R.X. Yan, D. Gargas, P.D. Yang: Nanowire photonics, Nat. Photonics **3**, 569–576 (2009)

17.6 A.I. Hochbaum, P.D. Yang: Semiconductor nanowires for energy conversion, Chem. Rev. **110**, 527–546 (2010)

17.7 B. Tian, T.J. Kempa, C.M. Lieber: Single nanowire photovoltaics, Chem. Soc. Rev. **38**, 16–24 (2009)

17.8 X. Huang, S. Tang, X. Mu, Y. Dai, G. Chen, Z. Zhou, F. Ruan, Z. Yang, N. Zheng: Freestanding palladium nanosheets with plasmonic and catalysic properties, Nat. Nanotechnol. **6**, 28–32 (2011)

17.9 D.S. Kong, W.H. Dang, J.J. Cha, H. Li, S. Meister, H.L. Peng, Z.F. Liu, Y. Cui: Few-layer nanoplates of Bi_2Se_3 and Bi_2Te_3 with highly tunable chemical potential, Nano Lett. **10**, 2245–2250 (2010)

17.10 R.S. Wagner, W.C. Ellis: Vapor-liquid-solid mechanism of single crystal growth, Appl. Phys. Lett. **4**, 89–90 (1964)

17.11 A.M. Morales, C.M. Lieber: A laser ablation method for the synthesis of crystalline semiconductor nanowires, Science **279**, 208–211 (1998)

17.12 T.J. Trentler, K.M. Hickman, S.C. Goel, A.M. Viano, P.C. Gibbons, W.E. Buhro: Solution-liquid-solid growth of crystalline III–V semiconductors – An analogy to vapor-liquid-solid growth, Science **270**, 1791–1794 (1995)

17.13 F.D. Wang, A.G. Dong, J.W. Sun, R. Tang, H. Yu, W.E. Buhro: Solution-liquid-solid growth of semiconductor nanowires, Inorg. Chem. **45**, 7511–7521 (2006)

17.14 A.I. Persson, M.W. Larsson, S. Stenstrom, B.J. Ohlsson, L. Samuelson, L.R. Wallenberg: Solid-phase diffusion mechanism for GaAs nanowire growth, Nat. Mater. **3**, 677–681 (2004)

17.15 H.J. Fan, P. Werner, M. Zacharias: Semiconductor nanowires: From self-organization to patterned growth, Small **2**, 700–717 (2006)

17.16 D.S. Li, M.H. Nielsen, J.R.I. Lee, C. Frandsen, J.F. Banfield, J.J. De Yoreo: Direction-specific interactions control crystal growth by oriented attachment, Science **336**, 1014–1018 (2012)

17.17 H.G. Liao, L.K. Cui, S. Whitelam, H.M. Zheng: Real-time imaging of Pt_3Fe nanorod growth in solution, Science **336**, 1011–1014 (2012)

17.18 M.J. Bierman, Y.K.A. Lau, A.V. Kvit, A.L. Schmitt, S. Jin: Dislocation-driven nanowire growth and Eshelby twist, Science **320**, 1060–1063 (2008)

17.19 S. Jin, M.J. Bierman, S.A. Morin: A new twist on nanowire formation: Screw-dislocation-driven growth of nanowires and nanotubes, J. Phys. Chem. Lett. **1**, 1472–1480 (2010)

17.20 S.A. Morin, M.J. Bierman, J. Tong, S. Jin: Mechanism and kinetics of spontaneous nanotube growth driven by screw dislocations, Science **328**, 476–480 (2010)

17.21 I.V. Markov: *Crystal Growth for Beginners: Fundamentals of Nucleation, Crystal Growth, and Epitaxy* (World Scientific, Singapore 1995)

17.22 S.H. Oh, M.F. Chisholm, Y. Kauffmann, W.D. Kaplan, W. Luo, M. Ruhle, C. Scheu: Oscillatory mass transport in vapor-liquid-solid growth of sapphire nanowires, Science **330**, 489–493 (2010)

17.23 S. Hofmann, R. Sharma, C.T. Wirth, F. Cervantes-Sodi, C. Ducati, T. Kasama, R.E. Dunin-Borkowski, J. Drucker, P. Bennett, J.J. Robertson: Ledge-flow-controlled catalyst interface dynamics during Si nanowire growth, Nat. Mater. **7**, 372–375 (2008)

17.24 W.K. Burton, N. Cabrera, C. Frank: The growth of crystals and the equilibrium structure of their surfaces, Philos. Trans. R. Soc. A **243**, 299–358 (1951)

17.25 F.C. Frank: The influence of dislocations on crystal growth, Discuss. Farady Soc. **23**, 48–54 (1949)

17.26 J.R. Hirth, J. Lothe: *Theory of Dislocations* (McGraw-Hill, New York 1968)

17.27 F.R.N. Nabarro: *Theory of Crystal Dislocations* (Oxford Univ. Press, London 1967)

17.28 F.C. Frank: Crystal growth and dislocations, Adv. Phys. **1**, 91–109 (1952)

17.29 G.W. Sears: A mechanism of whisker growth, Acta Metall. **3**, 367–369 (1955)
17.30 G.W. Sears: A growth mechanism for mercury whiskers, Acta Metall. **3**, 361–366 (1955)
17.31 G.W. Sears: Mercury whiskers, Acta Metall. **1**, 457–459 (1953)
17.32 S.S. Brenner, G.W. Sears: Mechanism of whisker growth – III nature of growth sites, Acta Metall. **4**, 268–270 (1956)
17.33 W.W. Webb, R.D. Dragsdorf, W.D. Forgeng: Dislocations in whiskers, Phys. Rev. **108**, 498–499 (1957)
17.34 R.D. Dragsdorf, W.W. Webb: Detection of screw dislocations in a-alumina whiskers, J. Appl. Phys. **29**, 817–819 (1958)
17.35 S. Amelinckx: Decoration of dislocations in alkali halide whiskers, J. Appl. Phys. **29**, 1610–1611 (1958)
17.36 C.M. Drum: Axial imperfections in filamentary crystals of aluminum nitride. I, J. Appl. Phys. **36**, 816 (1965)
17.37 C.M. Drum: Twist and axial imperfections in filamentary crystals of aluminum nitride. II, J. Appl. Phys. **36**, 824–829 (1965)
17.38 D.R. Veblen, J.E. Post: A TEM study of fibrous cuprite (chalcotrichite): Microstructures and growth mechanisms, Am. Miner. **68**, 790–803 (1983)
17.39 Y.K.A. Lau, D.J. Chernak, M.J. Bierman, S. Jin: Formation of PbS nanowire pine trees driven by screw dislocations, J. Am. Chem. Soc. **131**, 16461–16471 (2009)
17.40 J. Zhu, H.L. Peng, A.F. Marshall, D.M. Barnett, W.D. Nix, Y. Cui: Formation of chiral branched nanowires by the Eshelby Twist, Nat. Nanotechnol. **3**, 477–481 (2008)
17.41 J.D. Eshelby: Screw dislocations in thin rods, J. Appl. Phys. **24**, 176–179 (1953)
17.42 G.W. Sears: Twist in lithium fluoride Whiskers, J. Chem. Phys. **31**, 53–54 (1959)
17.43 I. Nikiforov, D.B. Zhang, T. Dumitrica: Screw dislocations in ⟨100⟩ silicon nanowires: An objective molecular dynamics study, J. Phys. Chem. Lett. **2**, 2544–2548 (2011)
17.44 D.B. Zhang, T. Dumitrica, G. Seifert: Helical nanotube structures of MoS_2 with intrinsic twisting: An objective molecular dynamics study, Phys. Rev. Lett. **104**, 065502 (2010)
17.45 F.C. Frank: Capillary equilibria of dislocated crystals, Acta Crystallogr. **4**, 497–501 (1951)
17.46 J. Heindl, H.P. Strunk, V.D. Heydemann, G. Pensl: Micropipes: Hollow tubes in silicon carbide, Phys. Status Solidi (a) **162**, 251–262 (1997)
17.47 S.A. Morin, S. Jin: Screw dislocation-driven epitaxial solution growth of ZnO nanowires seeded by dislocations in GaN substrates, Nano Lett. **10**, 3459–3463 (2010)
17.48 S. Hacialioglu, F. Meng, S. Jin: Facile and mild solution synthesis of Cu_2O nanowires and nanotubes driven by screw dislocations, Chem. Commun. **48**, 1174–1176 (2012)
17.49 T.B. Bateman: Elastic moduli of single-crystal zinc oxide, J. Appl. Phys. **33**, 3309–3312 (1962)
17.50 S.A. Morin, A. Forticaux, M.J. Bierman, S. Jin: Screw dislocation-driven growth of two-dimensional nanoplates, Nano Lett. **11**, 4449–4455 (2011)
17.51 H.H. Teng, P.M. Dove, J.J. De Yoreo: Kinetics of calcite growth: Surface processes and relationships to macroscopic rate laws, Geochim. Cosmochim. Acta **64**, 2255–2266 (2000)
17.52 H.H. Teng, P.M. Dove, C.A. Orme, J.J. De Yoreo: Thermodynamics of calcite growth: Baseline for understanding biomineral formation, Science **282**, 724–727 (1998)
17.53 I.V. Markov: *Crystal Growth for Beginners: Fundamentals of Nucleation, Crystal Growth, and Epitaxy* (World Scientific, Singapore 1995) p. 422
17.54 D.B. Williams, C.B. Carter: *Transmission Electron Microscopy* (Plenum, New York 1996)
17.55 A. Foitzik, W. Skrotzki, P. Haasen: Dislocation microstructure on {100} and {110} slip planes in lead sulphide, Phys. Status Solidi (a) **121**, 81–94 (1990)
17.56 E. Bauser, H. Strunk: Analysis of dislocations creating mono-molecular growth steps, J. Cryst. Growth **51**, 362–366 (1981)
17.57 H.Y. Wu, F. Meng, L.S. Li, S. Jin, G.F. Zheng: Dislocation-driven CdS and CdSe nanowire growth, ACS Nano **6**, 4461–4468 (2012)
17.58 F. Meng, S.A. Morin, S. Jin: Rational solution growth of alpha-FeOOH nanowires driven by screw dislocations and their conversion to alpha-Fe_2O_3 nanowires, J. Am. Chem. Soc. **133**, 8408–8411 (2011)
17.59 Y. Li, Y. Wu: Critical role of screw dislocation in the growth of $Co(OH)_2$ nanowires as intermediates for Co_3O_4 nanowire growth, Chem. Mater. **22**, 5537–5542 (2010)
17.60 F. Meng, S. Jin: The solution growth of copper nanowires and nanotubes is driven by screw dislocations, Nano Lett. **12**, 234–239 (2012)
17.61 L.H.G. Tizei, A.J. Craven, L.F. Zagonel, M. Tencé, O. Stéphan, T. Chiaramonte, M.A. Cotta, D. Ugarte: Enhanced eshelby twist on thin wurtzite InP nanowires and measurement of local crystal rotation, Phys. Rev. Lett. **107**, 195503 (2011)
17.62 B. Aleman, Y. Ortega, J.A. Garcia, P. Fernandez, J. Piqueras: Fe solubility, growth mechanism, and luminescence of Fe doped ZnO nanowires and nanorods grown by evaporation-deposition, J. Appl. Phys. **110**, 014317 (2011)
17.63 Y.K. Ryu, P. Fernandez, J. Piqueras: Growth and characterization of Er-doped ZnO elongated nanostructures, Phys. Status Solidi (a) **208**, 868–873 (2011)
17.64 B.W. Jacobs, M.A. Crimp, K. McElroy, V.M. Ayres: Nanopipes in gallium nitride nanowires and rods, Nano Lett. **8**, 4353–4358 (2008)

17.65 Q. Wu, Z. Hu, X.Z. Wang, Y.N. Lu, X. Chen, H. Xu, Y. Chen: Synthesis and characterization of faceted hexagonal aluminum nitride nanotubes, J. Am. Chem. Soc. **125**, 10176–10177 (2003)

17.66 D. Maestre, D. Haeussler, A. Cremades, W. Jaeger, J. Piqueras: Nanopipes in In_2O_3 nanorods grown by a thermal treatment, Cryst. Growth Des. **11**, 1117–1121 (2011)

17.67 J. Bartolome, D. Maestre, M. Amati, A. Cremades, J. Piqueras: Indium zinc oxide pyramids with pinholes and nanopipes, J. Phys. Chem. C **115**, 8354–8360 (2011)

17.68 D. Maestre, D. Haussler, A. Cremades, W. Jager, J. Piqueras: Complex defect structure in the core of Sn-doped In_2O_3 nanorods and its relationship with a dislocation-driven growth mechanism, J. Phys. Chem. C **115**, 18083–18087 (2011)

17.69 J. Chikawa, T. Nakayama: Dislocation structure and growth mechanism of cadmium sulfide crystals, J. Appl. Phys. **35**, 2493–2501 (1964)

17.70 B.M. Bulakh: The real conditions of CdS single crystal growth from the vapour phase, J. Cryst. Growth **5**, 243–250 (1969)

17.71 G.H. Dierssen, T. Gabor: Growth mechanism of CdS platelets, J. Cryst. Growth **16**, 99–109 (1972)

17.72 C. Ma, Y. Ding, D. Moore, X.D. Wang, Z.L. Wang: Single-crystal CdSe nanosaws, J. Am. Chem. Soc. **126**, 708–709 (2004)

17.73 J.P. Ge, Y.D. Li: Selective atmospheric pressure chemical vapor deposition route to CdS arrays, nanowires, and nanocombs, Adv. Funct. Mater. **14**, 157–162 (2004)

17.74 J. Zheng, X.B. Song, N. Chen, X.G. Li: Highly symmetrical CdS tetrahedral nanocrystals prepared by low-temperature chemical vapor deposition using polysulfide as the sulfur source, Cryst. Growth Des. **8**, 1760–1765 (2008)

17.75 D. Cherns, L. Meshi, I. Griffiths, S. Khongphetsak, S.V. Novikov, N.R.S. Farley, R.P. Campion, C.T. Foxon: Defect-controlled growth of GaN nanorods on (0001) sapphire by molecular beam epitaxy, Appl. Phys. Lett. **93**, 111911 (2008)

17.76 A. Navrotsky, L. Mazeina, J. Majzlan: Size-driven structural and thermodynamic complexity in iron oxides, Science **319**, 1635–1638 (2008)

17.77 N. Beermann, L. Vayssieres, S.E. Lindquist, A. Hagfeldt: Photoelectrochemical studies of oriented nanorod thin films of hematite, J. Electrochem. Soc. **147**, 2456–2461 (2000)

17.78 B. Tang, G.L. Wang, L.H. Zhuo, J.C. Ge, L.J. Cui: Facile route to alpha-FeOOH and alpha-Fe_2O_3 nanorods and magnetic property of alpha-Fe_2O_3 nanorods, Inorg. Chem. **45**, 5196–5200 (2006)

17.79 A. Saric, S. Music, K. Nomura, S. Popovic: Microstructural properties of Fe-oxide powders obtained by precipitation from $FeCl_3$ solutions, Mater. Sci. Eng. B **56**, 43–52 (1998)

17.80 M. Ozaki, S. Kratohvil, E. Matijevic: Formation of monondispersed spindle-type hematite particles, J. Colloid Interface Sci. **102**, 146–151 (1984)

17.81 K. Govender, D.S. Boyle, P.B. Kenway, P. O'Brien: Understanding the factors that govern the deposition and morphology of thin films of ZnO from aqueous solution, J. Mater. Chem. **14**, 2575–2591 (2004)

17.82 S.A. Morin, F.F. Amos, S. Jin: Biomimetic assembly of zinc oxide nanorods onto flexible polymers, J. Am. Chem. Soc. **129**, 13776–13777 (2007)

17.83 F. Wang, J.H. Seo, Z.Q. Ma, X.D. Wang: Substrate-free self-assembly approach toward large-area nanomembranes, ACS Nano **6**, 2602–2609 (2012)

17.84 H. Jiang, T. Zhao, C.Z. Li, J. Ma: Hierarchical self-assembly of ultrathin nickel hydroxide nanoflakes for high-performance supercapacitors, J. Mater. Chem. **21**, 3818–3823 (2011)

17.85 E. Suito, N. Uyeda: Electron microscopy and diffraction studies on the growth and structure of laminar single crystals of colloidal gold (Special Issue on Electron Microscopy), Bull. Inst. Chem. Res. Kyoto Univ. **42**, 511–541 (1965)

17.86 R.L. Penn, J.F. Banfield: Imperfect oriented attachment: Dislocation generation in defect-free nanocrystals, Science **281**, 969–971 (1998)

17.87 J. Baxter, Z. Bian, G. Chen, D. Danielson, M.S. Dresselhaus, A.G. Fedorov, T.S. Fisher, C.W. Jones, E. Maginn, U. Kortshagen, A. Manthiram, A. Nozik, D.R. Rolison, T. Sands, L. Shi, D. Sholl, Y. Wu: Nanoscale design to enable the revolution in renewable energy, Energy Environ. Sci. **2**, 559–588 (2009)

17.88 A.J. Nozik: Nanoscience and nanostructures for photovoltaics and solar fuels, Nano Lett. **10**, 2735–2741 (2010)

17.89 K. Sivula, F. Le Formal, M. Grätzel: Solar water splitting: Progress using hematite (α-Fe_2O_3) photoelectrodes, Chem. Sus. Chem. **4**, 432–449 (2011)

17.90 J.R. Szczech, S. Jin: Nanostructured silicon for high capacity lithium battery anodes, Energy Environ. Sci. **4**, 56–72 (2011)

17.91 Y. Lin, G. Yuan, S. Sheehan, S. Zhou, D. Wang: Hematite-based solar water splitting: Challenges and opportunities, Energy Environ. Sci. **4**, 4862–4869 (2011)

17.92 A. Ennaoui, S. Fiechter, C. Pettenkofer, N. Alonso-Vante, K. Büker, M. Bronold, C. Höpfner, H. Tributsch: Iron disulfide for solar energy conversion, Sol. Energy Mater. Sol. Cells **29**, 289–370 (1993)

17.93 M. Caban-Acevedo, M.S. Faber, Y.Z. Tan, R.J. Hamers, S. Jin: Synthesis and properties of semiconducting iron pyrite (FeS_2) nanowires, Nano Lett. **12**, 1977–1982 (2012)

17.94 F. Badway, N. Pereira, F. Cosandey, G.G. Amatucci: Carbon–metal fluoride nanocomposites. Structure and electrochemistry of FeF_3:C, J. Electrochem. Soc. **150**, A1209–A1218 (2003)

17.95 L.S. Li, Y.H. Yu, F. Meng, Y.Z. Tan, R.J. Hamers, S. Jin: Facile solution synthesis of α-$FeF_3 \cdot 3H_2O$ nanowires and their conversion to α-Fe_2O_3 nanowires for photoelectrochemical application, Nano Lett. **12**, 724–731 (2012)
17.96 C. Wadia, A.P. Alivisatos, D.M. Kammen: Materials availability expands the opportunity for large-scale photovoltaics deployment, Environ. Sci. Technol. **43**, 2072–2077 (2009)
17.97 W.M. Haynes: Physcial constants of inorganic compounds. In: *Handbook of Chemistry and Physics*, Vol. 91, ed. by D.R. Lide (CRC, Boca Raton 2010)
17.98 R.K. Hocking, S. DeBeer George, K.N. Raymond, K.O. Hodgson, B. Hedman, E.I. Solomon: Fe L-Edge X-ray absorption spectroscopy determination of differential orbital covalency of siderophore model compounds: Electronic structure contributions to high stability constants, J. Am. Chem. Soc. **132**, 4006–4015 (2010)
17.99 K.M. Forsberg, A.C. Rasmuson: Crystallization of metal fluoride hydrates from mixed hydrofluoric and nitric acid solutions, Part I, Iron (III) and Chromium (III), J. Cryst. Growth **312**, 2351–2357 (2010)
17.100 K.M. Forsberg, A.C. Rasmuson: Crystal growth kinetics of iron fluoride trihydrate, J. Cryst. Growth **296**, 213–220 (2006)
17.101 G. Dhanaraj, K. Byrappa, V. Prasad, M. Dudley (Eds.): *Springer Handbook of Crystal Growth* (Springer, Berlin, Heidelberg 2010)

18. Glasses on the Nanoscale

Hellmut Eckert, Sidney J.L. Ribeiro, Silvia H. Santagneli, Marcelo Nalin, Gael Poirier, Younès Messaddeq

Homogeneity is supposed to be a particular feature of glasses leading to the well-known isotropic optical properties and mechanical behavior. However, in some cases heterogeneity can be detected at the molecular scale. Amorphous phase separation, incipient crystallization, and concentration gradients are representative of heterogeneities that can be exploited in the preparation of nanostructured glass-derived materials.

Nuclear magnetic resonance (NMR) is one of the spectroscopic methods widely used for characterization of the structure of glassy materials, and the basis of new NMR techniques for study on the medium range is first presented in Sect. 18.1. Afterwards, nanoceramics with small crystal volume fractions and crystal dimensions of some nanometers are described, displaying new emerging properties (Sect. 18.2). Metal nanoparticles, quantum dots, and lanthanide-containing nanocrystals are some of the structures that can be grown in glasses (Sect. 18.2). Glasses are unique in the sense that they can be obtained in any morphology, and a final perspective is presented for glass waveguides containing these nanoscale heterogeneities (Sect. 18.3).

18.1 **Studying Medium-Range Order in Glasses and Nanoceramics** 666
18.1.1 Static Dipolar NMR Spectroscopy ... 668
18.1.2 Spin-Echo Decay Spectroscopy 669
18.1.3 Spin-Echo Double Resonance 670
18.1.4 High-Resolution Dipolar NMR Spectroscopy 671
18.1.5 Homonuclear *J*-Resolved Spectroscopy 675

18.2 **Nanoceramics** 676
18.2.1 Lanthanide-Containing Transparent Glass Ceramics 676
18.2.2 Metal Nanoparticles in Glasses 680
18.2.3 Quantum Dots in Glasses 682

18.3 **Perspectives and Concluding Remarks** 684

References 685

Three of the most widely accepted definitions of *glasses* in classic textbooks [18.1–3] are as follows:

1. *Glasses are amorphous solids.*
2. *Glasses are amorphous materials displaying* T_g (*glass-transition temperature*).
3. *Any state, thermodynamically metastable, with frozen-in properties can be considered a glass.*

All these definitions take into account the out-of-equilibrium situation characterizing these materials, whose preparation and main properties have been known for centuries.

The first definition indeed highlights the noncrystalline or amorphous nature of glass, i. e., the absence of translational symmetry. In this case it is imperative to add to the glass definition the technique used in order to check for crystallinity. In fact, powder x-ray diffraction (XRD) and electron diffraction (ED) would check for the presence of crystal domains at different volume scales. A well-defined diffraction profile could be obtained from a single nanocrystal if one uses ED. However, if the nanocrystals represent a small volume fraction of a glass sample (typically up to around 3%), they would be invisible in a diffraction pattern obtained under standard experimental conditions in commercial diffractometers.

The second definition leads one to discard amorphous materials not presenting enough internal stability as seen in *real glasses* to allow the observation of

a second-order-like phase transition (the so-called glass transition) [18.2].

The third definition, more general than the previous ones, includes all metastable phases that can be obtained for a given system. Nonequilibrium thermodynamics provides the basis for their study [18.3].

In any case, homogeneity is supposed to be a particular feature of glasses. Homogeneity leads to isotropic optical properties and mechanical behavior, which are characteristics of glasses. However, in some cases, several sophisticated characterization techniques have suggested heterogeneity at the molecular scale. Amorphous phase separation, incipient crystallization nuclei, and concentration gradients would be representative of such heterogeneities. In fact the common practice among glass producers is to avoid compositions displaying such not well-behaved properties in order to obtain good-quality glasses. As pointed out by *Roy* [18.4], theoretical approaches to glass theory and formation all confirm the ubiquity of nanoheterogeneity.

The important point to be stressed is that these heterogeneities can be exploited in the preparation of nanostructured glass-derived materials. In the preparation of so-called *glass ceramics*, amorphous phase separation or formation of nuclei with subsequent growth can both be perfectly controlled. Glass ceramics or nanoceramics displaying small crystal volume fractions and crystal dimensions of some nanometers can be obtained with new emerging properties. Metal nanoparticles, quantum dots, and lanthanide-containing nanocrystals are some of the interesting structures that can be grown in glasses, in most cases by selected thermal treatment or focused ultrafast ($<$ ps) laser pulses.

As also stated by *Roy* in [18.4], glass provides one of the earliest examples of controlled use of science at the nanolevel in a well-established gigatechnology. The manipulation of matter at the nano- and subnanoscale has been the basis of the development of glasses and glass ceramics for centuries [18.4]. Therefore, nanoscale characterization plays a fundamental role in the almost endless list of potential applications that can be foreseen.

This chapter focuses on some interesting materials obtained from nanoscale control of glass systems. Firstly, the potential of new nuclear magnetic resonance (NMR) techniques in the study of medium-range order is presented.

Secondly, transparent glass ceramics are presented. Oxyfluoride glasses present heterogeneities at the molecular scale. These heterogeneities may be used to explain the unusual ionic conductivities observed experimentally. Moreover, by well-controlled heat treatments, fluoride nanocrystals may be obtained, while transparency levels remain the same as for the mother glass. It is shown that glass systems with lanthanide-containing nanocrystals well dispersed in the glass bulk present new emerging optical properties due to the synergy between the crystal and glass components.

Finally, the possibility of obtaining metal nanoparticles and quantum dots in bulk glasses is also reviewed. The exploration of quantum confinement effects in the case of semiconductor systems and the entirely new emerging area of plasmonics related to metal nanoparticles take advantage of the optical properties of these nanoscale systems.

The chapter ends with a brief section presenting concluding remarks and potential future applications and tendencies.

18.1 Studying Medium-Range Order in Glasses and Nanoceramics

Compared with crystalline solids, glasses present a formidable challenge in terms of structure elucidation. Owing to the lack of long-range periodicity in the glassy state, diffraction techniques are fairly powerless, and structural concepts typically emerge from joint interpretation of numerous, complementary spectroscopic experiments. For a comprehensive view, glass structure must be discussed on different length scales, namely:

1. *Short-range order* involving only the first atomic coordination spheres (distance region 0.15–0.3 nm)
2. *Second-nearest-neighbor environments* (0.3–0.5 nm)
3. *Nanostructure* (0.5–3 nm)
4. *Mesostructure* (3–500 nm) and, finally
5. *Microstructure* ($>$ 500 nm).

Spectroscopic methods such as NMR, Raman, photoelectron (PE), and extended x-ray absorption fine structure (EXAFS) provide primarily local information about the first coordination sphere. Thus, EXAFS offers accurate bond distances and coordination numbers,

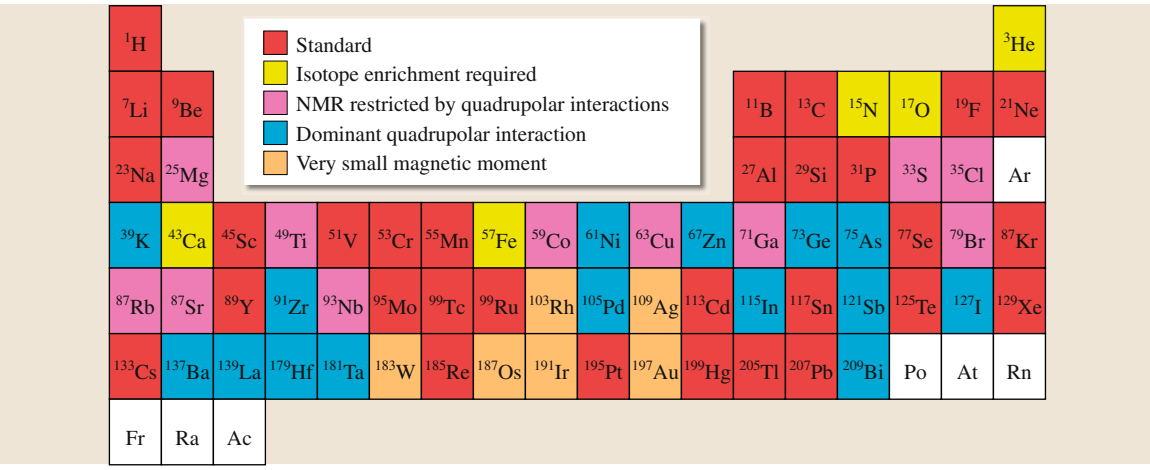


Fig. 18.1 Some characteristics of the nuclear isotopes for the main-group and transition-metal elements in the Periodic Table

while NMR spectra contain complementary information about bonding and site geometries, allowing quantitative identification of nearest-neighbor atomic species and specific types of coordination polyhedra [18.5, 6]. While the utility of solid-state NMR for characterizing the short-range order of glasses was reviewed nearly 20 years ago [18.6], the present contribution concerns the study of structural issues on the 0.3–3 nm length scale (domains 2 and 3), particularly in the subnanometer region commonly denoted as *medium-range structure*. The structural issues addressed include:

1. The *connectivity* between different network former species
2. *Distance correlations* involving network former and network modifier species
3. The overall *spatial distribution* of the network modifier ions.

The most powerful NMR approach to such questions is the measurement of internuclear magnetic dipole–dipole couplings, which have a straightforward relationship to internuclear distances and their distributions. Information beyond the second coordination sphere includes nanoclustering and/or segregation phenomena, up to macroscopic phase-separation effects and crystallization mechanisms.

Solid-state NMR is based on the magnetic moment of nuclei carrying spin angular momentum I. The latter is subject to the fundamental laws of orientational quantization, according to

$$|\hat{I}_z| = m\hbar \,, \tag{18.1}$$

where m, the orientational quantum number, can adopt values within the range $(+I, I-1, \ldots, -I+1, -I)$, and I is the nuclear spin quantum number. To detect nuclear magnetic moments, an external magnetic field is applied, represented by the magnetic flux density B_0. The resulting *Zeeman interaction*, represented by the Zeeman Hamiltonian,

$$H_z = -\mu_z B_0 \,, \tag{18.2}$$

lifts the energetic equivalence of these orientational states and causes a splitting into $2I+1$ individual levels with energies

$$E_m = -m\gamma\hbar B_0 \,. \tag{18.3}$$

By application of electromagnetic waves satisfying the Bohr condition $\Delta E = \hbar\omega$, allowed transitions between adjacent orientational states can be stimulated and observed spectroscopically. To a first approximation, the angular resonance frequency is given by

$$\omega = \gamma B_0 \,. \tag{18.4}$$

This resonance frequency is identical to the angular frequency, the so-called *Larmor frequency* ω_L, with which the nuclei precess in the applied magnetic field. Since the values of γ differ greatly for different kinds of nuclei, NMR spectroscopy is intrinsically element selective as, at a given magnetic field strength, different kinds of nuclei have different resonance and precession frequency ranges.

Figure 18.1 gives an overview of the elements amenable to solid-state NMR and summarizes some

of their isotopes' general features. About 50% of the elements lend themselves to solid-state NMR investigation in a rather facile manner. Limitations arise in the case of low natural abundances of the relevant NMR isotope, low values of magnetic moments, and – in particular – nuclear electric quadrupole interactions, which compete with the Zeeman interaction for nuclear spin alignment. If the quadrupole interaction is of similar strength to the Zeeman interaction or even dominant, obtaining an interpretable NMR signal will be difficult if not impossible. Likewise, if the atom under investigation shows paramagnetism originating from unpaired electron spins, no NMR signal can be obtained from its nucleus by standard measurement techniques, because the nuclear Zeeman levels are strongly affected by paramagnetic interactions and relaxation broadening effects. Consequently, the opportunities for measuring NMR of transition and rare-earth elements are severely limited.

With typical values of applied magnetic flux densities of the order of magnitude of 1 T, the frequencies lie in the radiowave region (10^7–10^9 MHz). The precession frequencies are measured using pulsed excitation, followed by Fourier transformation of the time-domain response signal, the so-called free induction decay.

While the nuclear precession frequencies are usually dominated by the Zeeman interaction, they are additionally influenced by a number of internal interactions, whose parameters reflect the details of the local structural environment and whose effect on the energy levels can be calculated using standard perturbation theory. The total spin Hamiltonian relevant in solid-state NMR can be written as

$$H_{\text{total}} = H_z + H_{\text{rf}} + H_{\text{cs}} + H_{\text{D}} + H_{\text{J}} + H_{\text{Q}} \,, \qquad (18.5)$$

where $H_z + H_{\text{rf}}$ describe the interactions of the nuclear magnetic moments with the applied magnetic field and the oscillating magnetic field component associated with the externally applied radiofrequency waves. In contrast, $H_{\text{cs}} + H_{\text{D}} + H_{\text{J}} + H_{\text{Q}}$ define the relevant Hamiltonians of distinct types of internal interactions, namely:

1. The magnetic interactions of the nuclei with the surrounding electrons (*magnetic or chemical shielding*), described by H_{cs}
2. The internuclear *direct and indirect magnetic dipole–dipole interactions*, described by H_{D} and H_{J}, respectively
3. Interactions between the electric quadrupole moments of spin $> 1/2$ nuclei and the electrostatic field gradients surrounding these nuclei (*quadrupole interaction*), described by H_{Q}.

In the solid state, all of these interactions are anisotropic and hence cause line broadening in powdered samples. A particular strength of solid-state NMR lies in the fact that the Hamiltonian of (18.5) can be simplified, using special *selective averaging* techniques. One particularly effective technique is the *magic angle sample spinning* (MAS) method which removes all of the anisotropic interactions, producing high-resolution spectra. By combining MAS with special dipolar recoupling techniques, one can look selectively at individual parts of the spin Hamiltonian under the high-resolution conditions afforded by MAS. Using the potential of *multidimensional spectroscopy*, it is further possible to separate different spin interactions into two (or more) different time (and frequency) domains and to correlate them with each other. The design of new pulse sequences is greatly aided by the availability of program packages that calculate the behavior of the spins under the influence of the external and internal interaction Hamiltonians using standard time-dependent perturbation theory [18.5–7]. Especially noteworthy is the program package *SIMPSON*, which enables the simulation of complex NMR experiments under the precise experimental conditions used at the spectrometer [18.8]. This freeware has proven invaluable in the analysis of complex experiments and profoundly influenced NMR research in many laboratories. The following sections describe a number of useful dipolar NMR experiments as well as some theoretical and practical aspects of their application to glassy materials.

18.1.1 Static Dipolar NMR Spectroscopy

Magnetic dipole–dipole couplings between the observed nuclei and those in their vicinity result in a modification of the measured precession frequencies. The effect is distance dependent and anisotropic, depending on the orientation of the internuclear distance vector relative to B_0, contributing to the NMR line-broadening effects observed in powdered solid samples. There are homonuclear and heteronuclear contributions, whose respective Hamiltonians – within the limit of first-order perturbation theory – are given by the expressions

$$H_{\text{D,homo}} = -\left(\frac{\mu_0}{4\pi}\right)\frac{\gamma^2\hbar^2}{r_{ij}^3}\left(\frac{3\cos^2\theta - 1}{2}\right) \times \left(3\hat{I}_z^2 - \hat{I}^2\right) \,, \qquad (18.6)$$

$$H_{\mathrm{D,hetero}} = -\left(\frac{\mu_0}{4\pi}\right)\frac{\gamma_I\gamma_S\hbar^2}{r_{IS}^3}\left(\frac{3\cos^2\theta-1}{2}\right)\left(\hat{I}_z\hat{S}_z\right) . \quad (18.7)$$

Most importantly, both Hamiltonians are proportional to the inverse cube of the internuclear distance, providing a straightforward connection to geometric structure. The orientational dependence is governed by the term $3\cos^2\theta - 1$, where θ is the angle between the internuclear distance vector and the magnetic field direction. In systems characterized by multiple-spin interactions, the dipolar couplings are characterized by the average mean square of the local field (the second moment), which can be related to internuclear distance distributions by the *van Vleck* formulae [18.9]

$$M_{2,\mathrm{homo}} = \frac{3}{5}\left(\frac{\mu_o}{4\pi}\right)^2 I(I+1)\gamma^4\hbar^2\sum_{i\neq j} r_{ij}^{-6} , \quad (18.8)$$

$$M_{2,\mathrm{hetero}} = \frac{4}{15}\left(\frac{\mu_o}{4\pi}\right)^2 S(S+1)\gamma_I^2\gamma_S^2\hbar^2\sum_{S} r_{IS}^{-6} . \quad (18.9)$$

Thus, homo- or heteronuclear dipolar second moments represent quantitative criteria against which structural models (derived, e.g., from molecular dynamics simulations) can be tested in a rigorous fashion. In the following sections, various experimental techniques for obtaining such dipolar second moments are described and their significance for the structural analysis of glasses is highlighted.

18.1.2 Spin-Echo Decay Spectroscopy

Homonuclear dipolar interactions can be measured selectively by Hahn spin-echo decay spectroscopy, using the pulse sequence shown in Fig. 18.2 [18.10]. For a spin-1/2 system, a plot of normalized echo intensity I/I_0 as a function of evolution time $2t_1$ is only affected by these homonuclear dipole–dipole interactions, while all the other above-mentioned types of interactions affecting solid-state NMR spectra (including heteronuclear dipole–dipole couplings) are refocused. For a multispin system, a Gaussian decay is expected (and observed),

$$\frac{I\,(2t_1)}{I_0} = \exp\left[-\frac{M_{2\mathrm{hom}}}{2}\,(2t_1)^2\right] , \quad (18.10)$$

affording a reliable measurement of the homonuclear van Vleck second moment M_2^{hom}.

The method has been widely and successfully applied for examining the spatial distribution of ^{31}P and ^{19}F spins ($I = 1/2$) in a variety of nonoxide glasses [18.6, 11–15].

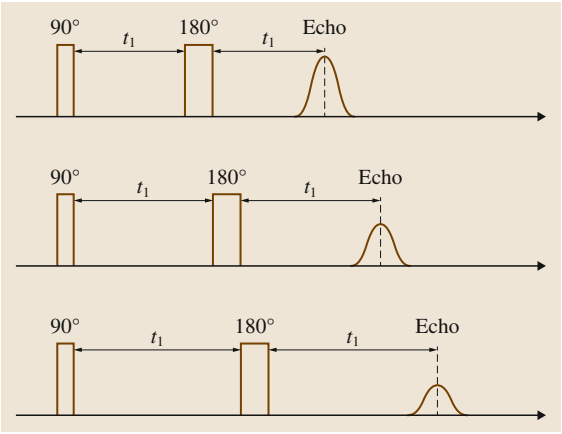


Fig. 18.2 Timing diagram of the spin-echo decay method. The spin-echo amplitude is measured as a function of the total dipolar evolution time $2t_1$

The glass systems $(1-x)As_2S_3$-xP_2S_5, $(1-x)As_2P_2S_8$-xGa_2S_3, and $(1-x)GeS_2$-xP_2S_5 can be cited here as examples of the chalcogenide glasses families. The $(1-x)As_2S_3$-xP_2S_5 glass system was studied in [18.12]. ^{31}P NMR together with vibrational spectroscopy results were decisive in reaching the conclusion that P atoms were incorporated into the structure through the formation of molecular-like units dispersed in an As_2S_3 matrix. For low P_2S_5 relative contents, $As_2P_2S_8$ units could be identified, which become progressively interconnected as the P concentration approaches $x = 0.5$. For glasses with $x > 0.5$, there is a coexistence of $As_2P_2S_8$ groups with molecular units connecting more P atoms via P–S–P bridges such as P_4S_{10} or P_4S_9 units. The same techniques were used in [18.13] for the study of the $(1-x)As_2P_2S_8$-xGa_2S_3 glasses. In this case, for $x < 0.2$, GaS_4E^- groups (E = nonbonding electron) were identified. For higher x values, depolymerization of the $As_2P_2S_8$ units was observed, with the formation of $GaPS_4$ units with each $PS_{4/2}$ unit (Q^4) species carrying a single positive formal charge.

In [18.14], neutron diffraction was used together with NMR and Raman spectroscopies in the study of $(1-x)GeS_2$-xP_2S_5 glasses. P_2S_5 addition was observed not to be in a random, homogeneous fashion. The distribution of P atoms, as reasoned from the ^{31}P M_2 values, was observed to be much more clustered than a random distribution would predict. Moreover, a significant fraction of P atoms were found in strained environ-

ments such as those found in P_4S_{10} and P_4S_9 molecular clusters.

In the next topic of this chapter, transparent glass ceramics obtained in mixed oxyfluoride glasses are described. Nanometric crystals of the β-PbF_2 phase are obtained by heat treatments at selected temperatures, with crystal-like spectroscopic properties emerging from the nanocomposite structure in $PbGeO_3$-PbF_2-CdF_2 glasses. Interestingly enough, the M_2 values obtained from ^{19}F NMR measurements show that F–F distances are shorter than those found if homogeneous dispersion of fluoride ions in the glass host is supposed. Fluorine-rich regions at the nanometric scale would explain the interesting properties of these mixed glasses, such as high ionic conductivity and the particular crystallization behavior [18.15].

The spin-echo decay method could be extended to the study of quadrupolar nuclei such as ^{23}Na, using a modified formula that takes into account the peculiar spin dynamics present in dipolar-coupled quadrupolar nuclei [18.17, 18].

$$M_2 = 0.9562 \left(\frac{\mu_0}{4\pi}\right)^2 \gamma^4 \hbar^2 \sum_j r_{ij}^{-6} \qquad (18.11)$$

The validity of (18.11) was confirmed experimentally for homonuclear ^{23}Na–^{23}Na dipole–dipole interactions in crystalline solids, for which the M_2 values are readily calculable from the known crystal structures [18.18].

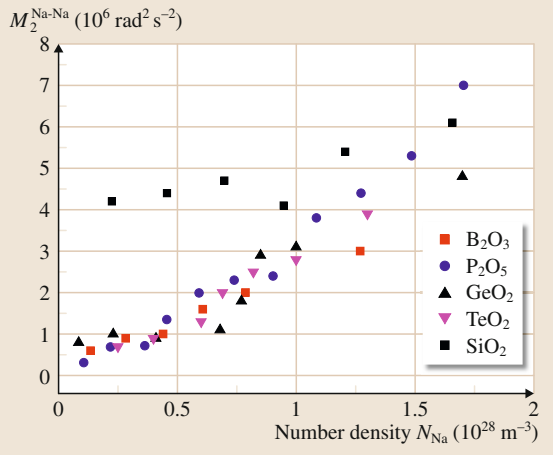


Fig. 18.3 Dipolar second moment values $M_2(^{23}Na$–$^{23}Na)$ measured via the ^{23}Na spin-echo decay method, for sodium borate, phosphate, silicate, tellurite, and germanate glasses as a function of cation number density (after [18.16])

Application of this technique to a wide range of oxide glasses provided detailed quantitative information about the spatial distribution of sodium ions in different kinds of oxide glasses [18.16]. Figure 18.3 summarizes these results, plotting the $M_2(^{23}Na$–$^{23}Na)$ values as a function of number density. The rather different behavior of sodium silicate glasses as opposed to all the other glass-forming systems studied so far is evident from this figure: A more or less constant value of $M_2 = 4.5 \times 10^6$ rad^2/s^2 is observed at Na concentrations below 1.5×10^{28} m^{-3}, indicating significant clustering of the sodium ions. In contrast, M_2 values are much smaller in sodium borate, phosphate, tellurite, and germanate-based glass systems, and scale linearly with the sodium number density, consistent with a spatial distribution that is more or less random in space. At Na concentrations higher than 1.5×10^{28} m^{-3}, the M_2 values for the silicate glasses converge with this line, indicating that the sodium distribution can also be considered as random in this composition range. The inhomogeneous distributions of alkaline ions in silicate glasses are consistent with the proposal of *ion-conducting channels*, maintaining the possibility of long-range ion transport even at relatively low cation contents [18.19]. In contrast, this possibility does not exist if the mobile ion distribution is statistical, as this would result in very large average jump distances at low cation contents. On this basis, it is now possible to understand why at a given number density the ionic conductivities of alkali silicate glasses are significantly larger than those of the corresponding alkali borate glasses, as reported in [18.20].

18.1.3 Spin-Echo Double Resonance

It is further possible to use the principle of spin-echo decay spectroscopy for selective measurement of heteronuclear dipole–dipole interactions between an observed spin species I and a different spin species S. In this case, a 180° recoupling pulse is applied to the S spins during the dipolar evolution period [18.21]. The corresponding pulse sequence, termed spin-echo double resonance (SEDOR), compares the spin-echo intensity of the observed nuclei as a function of dipolar evolution time (a) in the absence and (b) in the presence of these recoupling pulses. Experiment (a) produces a decay $F(2t_1)/F_0$, which is largely governed by homonuclear dipole–dipole interactions, while experiment (b) results in an accelerated decay reflecting the contribution from the heteronuclear dipole–dipole

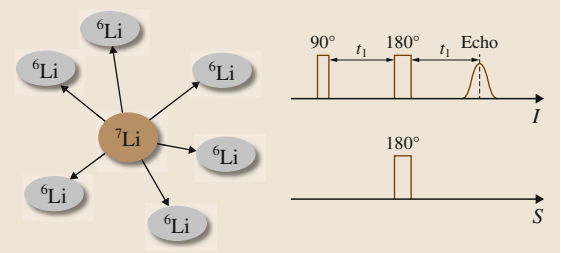


Fig. 18.4 Illustration of the SEDOR method, applied to the measurement of lithium–lithium interactions on glasses having ^{6}Li isotopic content of 95%

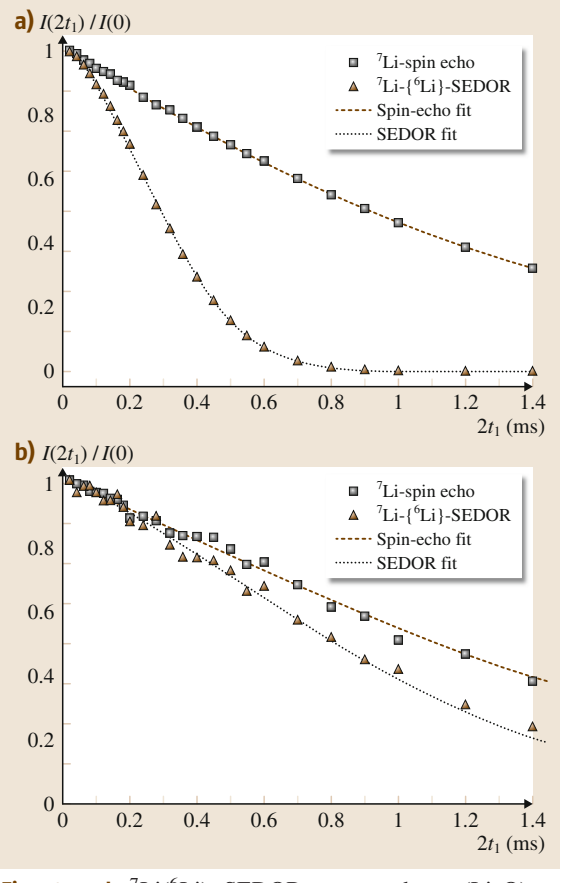


Fig. 18.5a,b ^{7}Li(^{6}Li) SEDOR measured on $(Li_2O)_{0.1}$-$(SiO_2)_{0.9}$ glass **(a)** and $(Li_2O)_{0.1}$-$(B_2O_3)_{0.9}$ glass **(b)**. Both glasses have ^{6}Li/^{7}Li isotope ratio of 9 : 1. The Hahn spin-echo amplitude of the residual ^{7}Li nuclei is measured as a function of the dipolar evolution time $2t_1$ in the absence (*squares*) and the presence (*triangles*) of the ^{6}Li recoupling pulses. The *dotted curves* are fits to the experimental data using (18.2) (after [18.22])

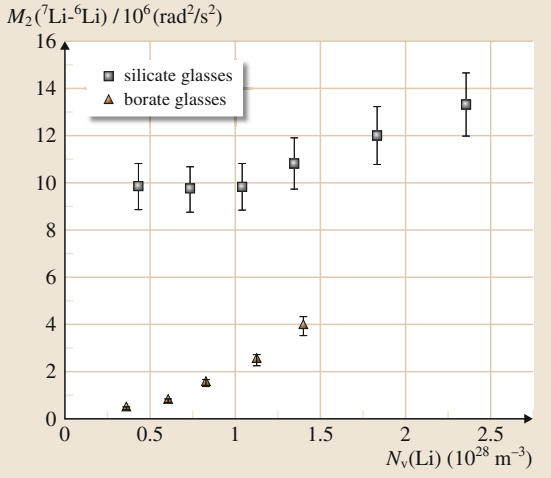


Fig. 18.6 Dipolar second moment $M_2(^6\text{Li}–^7\text{Li})$ measured via ^{7}Li(^{6}Li) SEDOR in lithium silicate and lithium borate glasses as a function of cation number density (after [18.22])

interaction. For multispin systems, a Gaussian decay is expected,

$$\frac{I(2t_1)}{I_0} = \frac{F(2t_1)}{F_0} \cdot \exp - \left(2t_1^2 M_2^{\text{hetero}}\right), \qquad (18.12)$$

the rate of which is given by the heteronuclear second moment M_2^{hetero} [18.23]. Using the SEDOR method, the spatial distribution of the lithium ions and the extent of their clustering have been studied in lithium-oxide-containing glasses, having an isotopic enrichment level of 95% ^{6}Li (Fig. 18.4). Figure 18.5 compares the experimental results for a lithium silicate and a lithium borate glass with comparable lithium oxide contents (10 mol%). Clearly, the ^{7}Li spins in the silicate glass dephase much more rapidly in the dipolar field of the surrounding ^{6}Li spins, indicating much stronger dipolar interactions than in the borate glass. Figure 18.6 summarizes the dependence of M_2 on the lithium content in these glasses [18.22]. The results are found to be completely analogous to the situation in Fig. 18.3, consistent with lithium clustering in the silicate but not in the borate glass systems.

18.1.4 High-Resolution Dipolar NMR Spectroscopy

Rotational Echo Double Resonance

An even more powerful experiment, termed *rotational echo double resonance* (REDOR), is able to provide

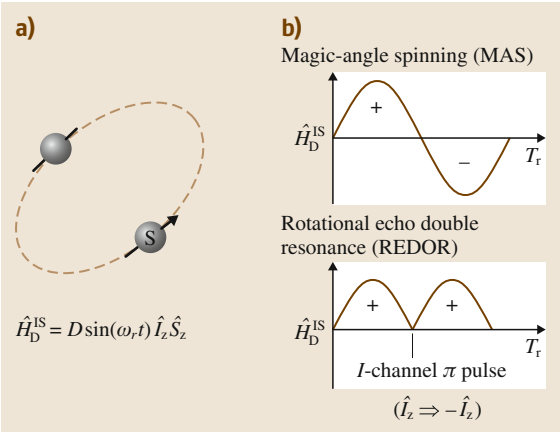


Fig. 18.7 (**a**) Principle of the REDOR experiment. Under MAS conditions the heteronuclear dipolar Hamiltonian oscillates sinusoidally with rotor orientation, leading to cancelation of H_D upon completion of the rotor cycle ((**b**), *top*). Sign inversion created by a π-pulse applied to the nonobserved I spins interferes with this cancelation ((**b**) *bottom*)

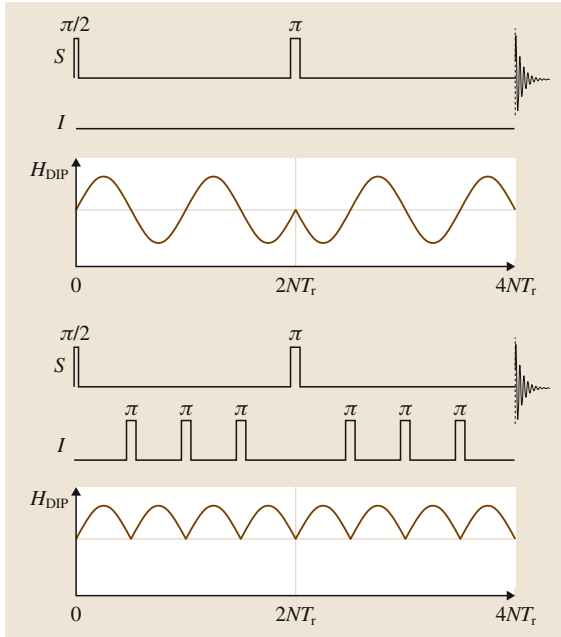


Fig. 18.8 Timing of a REDOR pulse sequence, showing the evolution of the dipolar coupling Hamiltonian during the rotor cycle (after [18.24])

site-selective dipolar coupling information under the high-resolution conditions afforded by magic angle spinning [18.24]. In general, the dipolar coupling constant oscillates according to the term $\sin\omega_r t$ and is averaged out over the rotor cycle. However, if we invert the sign of the dipolar Hamiltonian by applying a π-pulse to the nonobserved I spins somewhere during the rotor cycle, this average is nonzero; the interaction is recoupled and now interferes with the ability of MAS to provide signal refocusing (Fig. 18.7).

Figure 18.8 shows a typical pulse sequence used for such purposes [18.24]. Recoupling is accomplished by 180° pulse trains applied to the I spins, while the S spin signal is detected by a rotor-synchronized Hahn spin-echo sequence. One measures the normalized difference signal $\Delta S/S_0 = (S_0 - S)/S_0$ in the absence (intensity S_0) and the presence (intensity S) of the recoupling pulses. A REDOR curve is then generated by plotting $\Delta S/S_0$ as a function of the dipolar evolution time NT_r, i. e., the duration of one rotor period multiplied by the number of rotor cycles.

For isolated two spin-1/2 pairs, the REDOR curve has universal character and can be directly used to extract the internuclear distance. In contrast, for larger spin clusters the REDOR curve depends on the detailed shape and distance geometry of the spin system [18.25, 26]. In glasses, one generally expects a distribution of spin geometries and magnetic dipole coupling strengths which is a priori unknown. As previously shown, this problem can be circumvented by limiting the REDOR data analysis to the initial curvature, where $\Delta S/S_0 < 0.2$ [18.26, 27]. In this limit of short dipolar evolution times, the REDOR curve is found to be geometry independent and can be approximated by

$$\frac{\Delta S}{S_0} = \frac{S_0 - S}{S_0} = \frac{4}{3\pi^2}(NT_r)^2 M_2 \,, \qquad (18.13)$$

where the average van Vleck second moment (18.9) can be extracted from a simple parabolic fit to the experimental data. For the case when dipolar coupling to $I > 1/2$ spins are studied, the results are strongly affected by the nuclear electric quadrupole couplings of the I spins. Using modified pulse sequences and data reduction routines, a dipolar analysis is still possible in such cases if the quadrupolar coupling is taken into account appropriately [18.28].

^{29}Si(^{7}Li) REDOR experiments have been used to study interactions between the network former and network modifier species, supplementing further evidence for lithium clustering in silicate glasses [18.29]. In sodium borate and sodium phosphate glasses, closest internuclear ^{23}Na–^{11}B and ^{23}Na–^{31}P distances have been derived from the corresponding REDOR

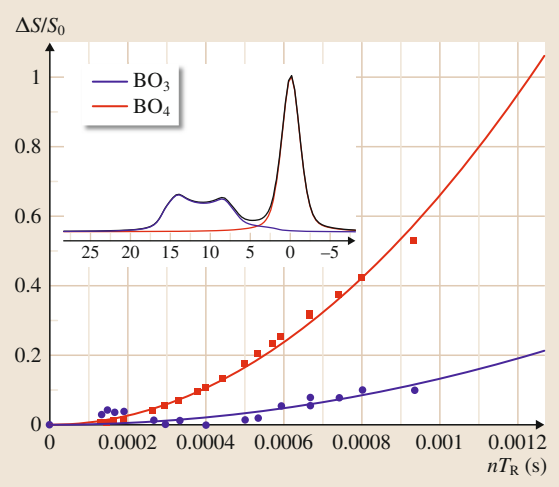


Fig. 18.9 $^{11}B(^{31}P)$ REDOR results on a silver borophosphate glass of composition $0.5(Ag_2O)\text{-}0.5(B_2O_3)_{0.5}(P_2O_5)_{0.5}$. *Red* and *blue curves* show the data for three- and four-coordinated boron atoms (after [18.32])

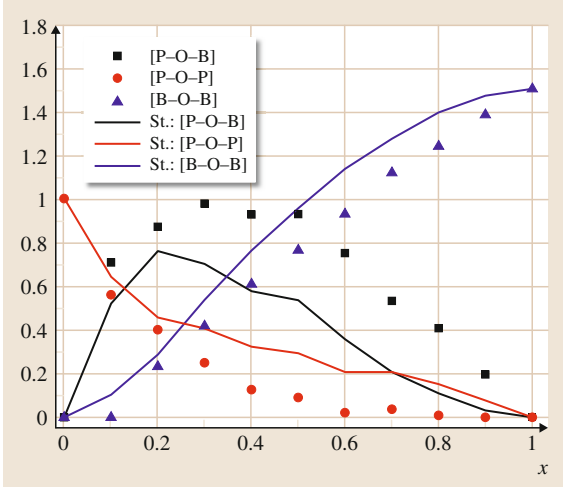


Fig. 18.10 Comparison of measured values of the fraction of different bridging oxygen species of $(B_2O_3)_x(NaPO_3)_{1-x}$ glasses with calculations based on a statistical (St.) linkage model

curves [18.30, 31]. Furthermore, REDOR has been widely implemented for quantifying network former connectivities in mixed-network former systems. As an example, Fig. 18.9 shows a $^{11}B(^{31}P)$ REDOR curve obtained on a silver borophosphate glass [18.32]. In this glass, both three- and fourfold boron atoms are found in the network, and can be well differentiated by ^{11}B MAS-NMR. However, only the four-coordinated boron atoms show a sizeable REDOR effect indicating a next-nearest-neighbor relationship. In contrast, no ^{11}B–O–^{31}P connectivities are present for the trigonal boron species, suggesting that the latter are located rather remote from the boron atoms. As subsequent REDOR studies of other glass compositions have shown, this seems to be a rather general structural feature of borophosphate glasses [18.33–36]. Figure 18.10 summarizes the concentrations of the B–O–B, B–O–P, and P–O–P connectivities in the glass system $(NaPO_3)_{1-x}(B_2O_3)_x$, extracted from such REDOR measurements. The data are compared with the predicted concentrations of these connectivities based on a random linkage model. The large preference for heteroatomic over homoatomic linkage formation in this glass system is clearly evident, and has been quantified on the basis of such REDOR data in different borophosphate glass systems [18.33–36]. Analogously, heteroatomic bonding preferences have been observed in aluminophosphate [18.37, 38] and aluminoborate glass systems [18.39, 40].

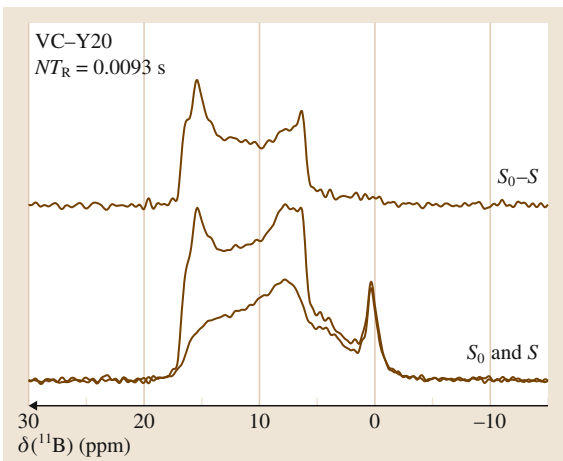


Fig. 18.11 Spectral editing via $^{11}B(^{27}Al)$ REDOR, demonstrated for a $(Y_2O_3)_y(Al_2O_3)_{0.4-y}(B_2O_3)_{0.6}$ glass ceramic ($y = 0.2$) for dipolar evolution time of 0.0093 s. *Top*: REDOR difference signal ($S_0 - S$), emphasizing the YAB contribution. *Bottom*: Regular rotor synchronized spin echo (S_0) and dipolar dephased signal (S), the latter emphasizing the glassy B_2O_3 contribution (after [18.41])

Figure 18.11 shows another application of REDOR to the structural analysis of a luminescent yttrium aluminoborate glass ceramic system studied along the composition line $(Y_2O_3)_y(Al_2O_3)_{0.4-y}(B_2O_3)_{0.6}$. Based on detailed NMR analysis, a quantitative crys-

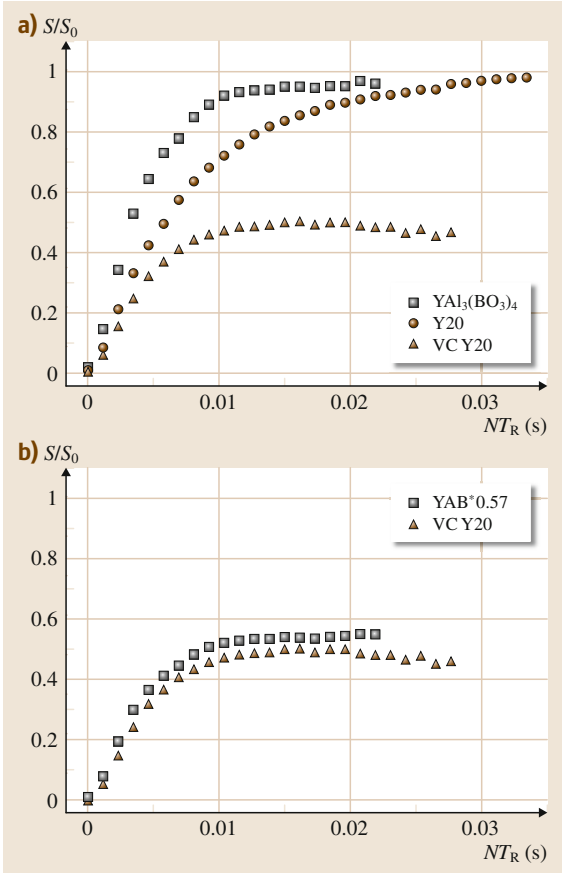


Fig. 18.12a,b $^{11}B(^{27}Al)$ REDOR curves for the B(3) units of $(Y_2O_3)_{0.2}(Al_2O_3)_{0.2}(B_2O_3)_{0.6}$ glass (*blue*), glass ceramic (*red*), and the model compound $YAl_3(BO_3)_4$ **(a)** and comparison of the data obtained from the glass ceramics with the crystallization model of (18.14) **(b)** (after [18.41])

tallization model expressed by

$$(B_2O_3)_{0.6}(Al_2O_3)_{0.4-y}(Y_2O_3)_y \rightarrow [(0.8/3)-(2y/3)]YAl_3(BO_3)_4 + [(8y/3)-0.8/3]YBO_3 + 0.2B_2O_3 \qquad (18.14)$$

was formulated, allowing the phase composition to be predicted directly from the glass composition y [18.41]. Equation (18.14) predicts the formation of two types of trigonal boron species: those associated with the crystalline compound $YAl_3(BO_3)_4$ (YAB), and those associated with glassy B_2O_3 (in the second crystallized phase, YBO_3, the boron atoms are four-coordinated). While the ^{11}B MAS-NMR line shapes of these two trigonal boron units indeed overlap strongly, they are

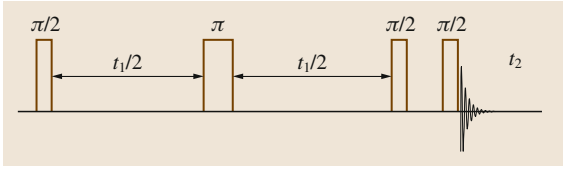


Fig. 18.13 Two-dimensional homonuclear J-resolved spectroscopy. Following preparation by a $\pi/2$ pulse, evolution takes place under the influence of homonuclear J-coupling during the evolution time t_1. Chemical shift and heteronuclear J-coupling evolution are refocused by the central π-pulse, and direct dipolar couplings are averaged out by MAS. The evolution is stopped by the second $\pi/2$-pulse, while the third $\pi/2$-pulse is used for detection. During the acquisition period t_2, the regular MAS Hamiltonian is effective

unambiguously differentiated on the basis of the heteronuclear ^{11}B–^{27}Al magnetic dipole–dipole coupling, which can be probed by using $^{11}B(^{27}Al)$ REDOR experiments. Figure 18.11 illustrates for a glass ceramic with $y = 0.2$ that the two spectral components can be completely separated by a REDOR experiment executed with a sufficiently long dipolar evolution time. The REDOR difference signal is identical to that of crystalline YAB, while the nondephased spin-echo signal closely resembles that of glassy B_2O_3. To test the quantitative aspects of the aforementioned crystallization scenario, we can determine the fraction of trigonal boron atoms that interact with aluminum atoms from these REDOR experiments; For example, for the composition $y = 0.2$, (18.14) predicts that 57% of the three-coordinated boron atoms arise from YAB. These are expected to show a REDOR effect, whereas 43% of the three-coordinated boron atoms belong to glassy B_2O_3, which do not interact with aluminum. Figure 18.12a shows the experimental REDOR curves obtained for the three-coordinated boron atoms on the $y = 0.20$ glass, on the glass ceramic, and on YAB. In the glass, the normalized difference signal approaches 1.0 at long dipolar evolution times, indicating that all of the threefold boron atoms interact with aluminum to some extent. This REDOR curve is consistent with a homogeneous elemental distribution in the glass [18.42]. In contrast, the glass-to-glass ceramic transition produces a pronounced change in the REDOR curve, indicating a dramatic rearrangement in the medium-range environment. The REDOR difference signal approaches 0.51, which is close to the value of 0.57 predicted from (18.14). Figure 18.12b juxtaposes the experimental REDOR

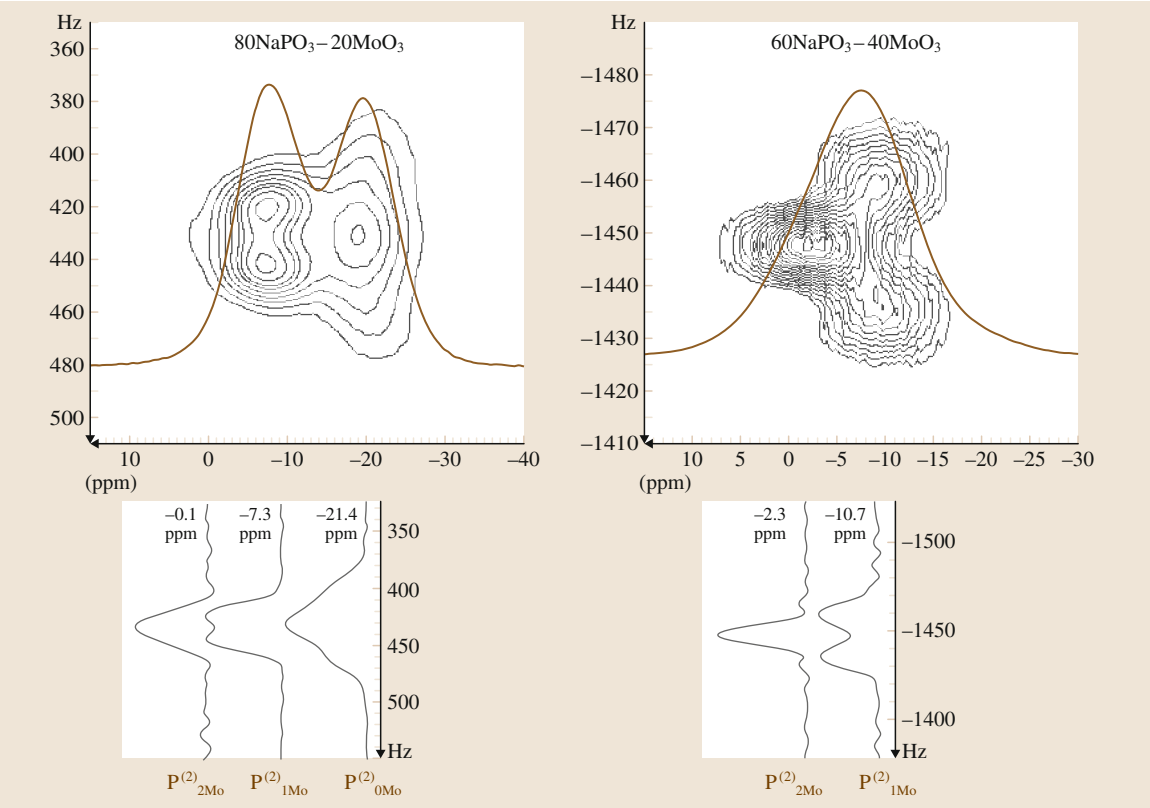


Fig. 18.14 ^{31}P J-resolved spectra of two representative $(NaPO_3)_{1-x}(MoO_3)_x$ glasses. The individual J-coupling multiplets are resolved in the second dimension (after [18.43])

data with a simulation in which the experimental data obtained on YAB are scaled by the factor 0.57, suggesting close agreement with the crystallization model.

18.1.5 Homonuclear *J*-Resolved Spectroscopy

The technique of homonuclear J-resolved spectroscopy exploits the presence of indirect magnetic dipole–dipole interactions between species that are connected via chemical bonds to specify homonuclear connectivity. The pulse sequence (Fig. 18.13) combines the two types of selective averaging afforded by MAS and the Hahn spin echo, in a two-dimensional experiment [18.44,45]. In glassy solids, the MAS-NMR peak width is often dominated by distributions of isotropic chemical shifts, which makes it generally impossible to resolve peak splitting produced by indirect spin–spin interactions in directly acquired spectra. This problem is solved by conducting a Hahn spin echo in the indirect (t_1) dimension of a two-dimensional NMR experiment: At the end of each evolution period t_1 the inhomogeneous broadening is refocused, so that the amplitude and phase of the signal are exclusively governed by the strength of the isotropic J-coupling. Thus, the corresponding signal observed after Fourier-transforming the data acquired along the time domain t_1 allows selective measurement of the homonuclear J-interaction.

Figure 18.14 shows an application to $(NaPO_3)_{1-x}(MoO_3)_x$ glasses [18.43]. The standard solid-state ^{31}P MAS-NMR spectra of these glasses reveal that addition of MoO_3 to $NaPO_3$ glass successively replaces the regular metaphosphate ($P^{(2)}$) site near -20 ppm by a new well-defined resonance near -8 ppm, which dominates the spectrum at $x = 0.30$; at higher MoO_3 contents the spectra are rather poorly resolved. The structural interpretation of these data is greatly facilitated by J-resolved spectra. For the -20 ppm signal, these spectra show the expected triplet consistent with the two

P−O−P linkages present in the $P^{(2)}$ sites. Furthermore, both a doublet component (one P–O–P linkage, signal near −8 ppm), and a singlet component (no P–O–P linkage, signal near −3 ppm) can be identified. The relative signal areas lead to the conclusion that, for each MoO_3 unit added to the glass, approximately two $P^{(2)}_{0Mo}$ units are transformed into $P^{(2)}_{1Mo}$ groups. In principle, the process of P–O–Mo interlinking operative in this composition region could produce both $P^{(2)}_{1Mo}$ and $P^{(2)}_{2Mo}$ units. However, the *J*-resolved spectra actually give no evidence for the formation of $P^{(2)}_{2Mo}$ units for $x < 0.30$. This result is consistent with a simple *binary* structural transformation model, in which the MoO_3 component first converts all the $P^{(2)}_{0Mo}$ polyphosphate chains into $P^{(2)}_{1Mo}$ units before the latter are converted to $P^{(2)}_{2Mo}$ units (or other structures without P–O–P linkages) at higher MoO_3 contents.

Recoupling of the homonuclear magnetic dipole–dipole interactions can also be exploited to prove homonuclear network connectivity on the basis of two-dimensional zero- or double-quantum NMR methods. Such information is derived from the presence (or absence) of cross-peaks linking resolved resonances attributable to distinct chemical species via spin diffusion or coherence transfer. To date, this type of analysis has been predominantly applied to spin-1/2 nuclei, specifically ^{29}Si and ^{31}P in binary silicate [18.46] and phosphate glasses [18.47]; For example, the observation of cross-peaks in two-dimensional (2-D) exchange, radiofrequency-driven recoupling (RFDR), as well as double-quantum (DQ) experiments unambiguously reveals the occurrence of $Q^{(1)}$–$Q^{(2)}$ and $Q^{(2)}$–$Q^{(3)}$ linkages in binary alkali phosphate glasses. The intensities of these cross-peaks strongly suggest that in binary lithium, sodium, silver, and lead phosphate glasses the phosphorus $Q^{(n)}$ units are linked in a more or less random fashion.

18.2 Nanoceramics

18.2.1 Lanthanide-Containing Transparent Glass Ceramics

Glass ceramics are polycrystalline materials obtained from controlled crystallization of glasses. This is the textbook definition [18.48], and the important aspect differentiating these materials from classic ceramics relies on the fact that the crystal phase is produced from the glass phase, by a well-controlled nucleation and growth mechanism. It is therefore possible to obtain highly homogeneous materials, with uniform grain size distributions and no porosity. It is out of the scope of this chapter to discuss the large field of glass ceramics. The interested reader is referred to the huge literature on that subject [18.49–51].

One of the interesting points concerning glass ceramics is related to the fact that it is possible to obtain transparent materials. Basically, it is necessary that both the crystals' optical anisotropy and the refractive index difference between the crystal and glass phases be small [18.52].

Historically, systematic research on transparent glass ceramics started with *Stookey*'s works in the 1950s using colloidal metal particles in the nucleation of glasses [18.53]. Nuclei should promote an amorphous phase separation, and the crystal phase would be obtained from one of the amorphous phases [18.48–51].

In parallel, *Hummel* discovered that negative expansion coefficients were obtained from crystal aggregates of β-eucryptite (Li_2O-Al_2O_3-$2SiO_2$) [18.54]. Stookey's and Hummel's ideas were then combined to prepare materials with expansion coefficient values close to zero. Thermal shock-resistant materials stable in dimension could be prepared. Kitchenware based on these materials has been available now for more than two decades [18.55].

When optically active ions are present in the glass phase, the controlled crystallization can give rise to nanocomposites displaying unique properties due to the synergy between the nanocrystalline and parent glass phases. From the spectroscopic point of view, several interesting applications may be foreseen when the optically active ion concentrates in the crystalline phase. Among the first materials produced with that aim were Cr^{3+}-doped glasses and glass ceramics studies in the 1980s by *Reisfeld* and *Jorgensen* [18.56, 57]. The Cr^{3+} emission quantum efficiency was observed to increase on going from the base glass to the glass ceramic, with the optical quality of the materials being preserved due to the crystal size, volume fraction, and matching of refractive index between the crystalline phase and the mother glass. These materials were therefore proposed as laser hosts or concentrators for photovoltaic Si solar cells [18.56–58].

Lanthanide ions have also been explored due to their characteristic spectroscopic properties allowing many different applications [18.59–61]. Lanthanide-doped glasses have been studied for more than 60 years. Phos-

Table 18.1 Some of the oxyfluoride mixed glass systems that have been observed to lead to transparent glass ceramics displaying a fluoride crystal phase dispersed in an amorphous oxide host

Glass precursors	Crystal phase	References
SiO_2-Al_2O_3-PbF_2-CdF_2-YbF_3-ErF_3	$Pb_xCd_{1-x}F_2$:Yb^{3+},Er^{3+}	[18.67]
GeO_2-PbO-PbF_2-CdF_2	PbF_2:Tm^{3+}	[18.68]
SiO_2-Al_2O_3-AlF_3-Na_2CO_3-$NaNO_3$-$BaCO_3$-$Ba(NO_3)_2$,La_2O_3-LaF_3	LaF_3:Y^{3+},Tb^{3+},Gd^{3+},Eu^{3+}	[18.67]
$PbGeO_3$-PbF_2-CdF_2	β-PbF_2:Eu^{3+},Er^{3+}	[18.15, 69–71]
SiO_2-PbF_2-CdF_2	PbF_2:Er^{3+}	[18.72]
B_2O_3-PbF_2-CdF_2	PbF_2:Er^{3+}	[18.72]
GeO_2-PbO-PbF_2-ErF_3	PbF_2:Er^{3+}	[18.73]
SiO_2-Al_2O_3-CaO-NaF-CaF_2-ErF_3	CaF_2:Er^{3+}	[18.69]
SiO_2-GeO_2-Al_2O_3-TiO_2-PbF_2-TmF_3-GdF_3-YF_3	PbF_2:Tm^{3+}	[18.74]
SiO_2-Al_2O_3-CdF_2-PbF_2-ZnF_2-ErF_3	PbF_2:Er^{3+}	[18.75]
SiO_2-Al_2O_3-CdF_2-PbF_2-ZnF_2-PrF_3-YF_3	PbF_2:Pr^{3+}	[18.76]
SiO_2-Al_2O_3-CdF_2-PbF_2-YF_3-EuF_3	EuF_3-$Pb_xCd_{1-x}F_2$	[18.77]
SiO_2-Al_2O_3-CdF_2-PbF_2-ErF_3-YbF_3-TmF_3	PbF_2:Er^{3+}:Yb^{3+}:Tm^{3+}	[18.78, 79]
SiO_2-Al_2O_3-CdF_2-PbF_2-ZnF_2-ErF_3	PbF_2	[18.80]
GeO_2-PbO-PbF_2-CdF_2-Er_2O_3	PbF_2:Er^{3+}	[18.81]
TeO_2-GeO_2-PbO-PbF_2-CdF_2-Er_2O_3	PbF_2:Er^{3+}	[18.81]

phors, laser hosts, and optical amplifiers are some of the potential applications [18.62–64]. Concerning spectroscopic properties, the inhomogeneous broadening of the spectral lines, due to the multisite distribution, is one of the particular characteristics observed. The line broadening can be either an interesting feature to be exploited or a problem to be solved, depending on the specific application. If one looks for a broad spectral profile within which induced emission will be used for optical amplification for example, glasses appear to be the ideal host material. In optical telecommunications, the larger the bandwidth, the larger the number of optical channels that can be used. Glasses and fibers displaying the largest bandwidths for the Er^{3+} emission band at 1.5 μm are the *holy grail* in modern telecommunications optics [18.65]. However, if one looks for a laser host with enhanced emission cross-section at a given wavelength, glasses will not be the best option. Crystals with well-defined coordination sites would be better [18.66].

Transparent glass ceramics can combine in fact the best of both worlds: that of glass materials and that of crystals. Glass preparation is no doubt much simpler than the preparation of crystals. Flexibility of chemical compositions, sizes, and forms are some of the important glass characteristics. Crystal properties on the other hand may be optimized depending on the chemical nature and structure. Spectroscopic properties of active metal ion centers have been well explored for the many different well-known applications of crystals.

For lanthanide ions, fluoride crystals are especially attractive host matrices. They present compelling advantages for optical applications due to their unique combination of low phonon energy, high ultraviolet (UV) absorption edge energy, and relatively weak crystal field [18.65, 82]. Interestingly enough, some fluoride crystals may be obtained from controlled crystallization of mixed oxyfluoride glasses. In the 1970s, interesting ceramic materials were obtained from composites of glass-forming oxides such as SiO_2, GeO_2, and P_2O_5 and lead fluoride and lanthanide ion precursors. Efficient infrared to visible conversion was observed for those materials [18.83, 84]. Some years later, *Wang* and *Ohwaki* showed that crystallization of related glasses could be controlled, leading to lanthanide-containing $Pb_xCd_{1-x}F_2$ crystals of nanometric dimensions. Infrared (IR) to visible up-conversion involving Yb^{3+} and Er^{3+} ions was observed to be more efficient in the transparent glass ceramic than in the parent glass [18.67].

Those early observations triggered intense activity from different research groups, and somewhat different oxyfluoride glass compositions have been exploited in the last two decades. Table 18.1 presents a not exhaustive list of glass systems being studied. The main precursors used in the glass preparation and the main crystal phases obtained by heat treatment of the mother glass are indicated, together with the respective references. For a systematic review on transparent glass ceramics also dealing with other individual oxide

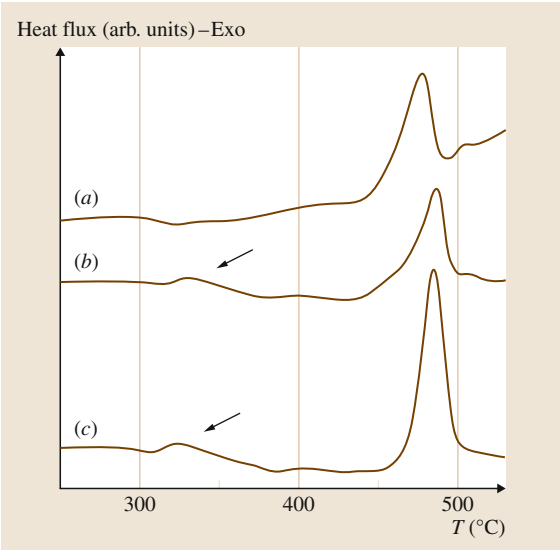


Fig. 18.15 DSC scans obtained for glasses with compositions (mol%): (*a*) $60PbGeO_3$-$10PbF_2$-$30CdF_2$, (*b*) the same glass as (*a*) doped with 0.5% Eu^{3+}, and (*c*) the same glass as (*a*) doped with 0.5% Er^{3+} (after [18.69])

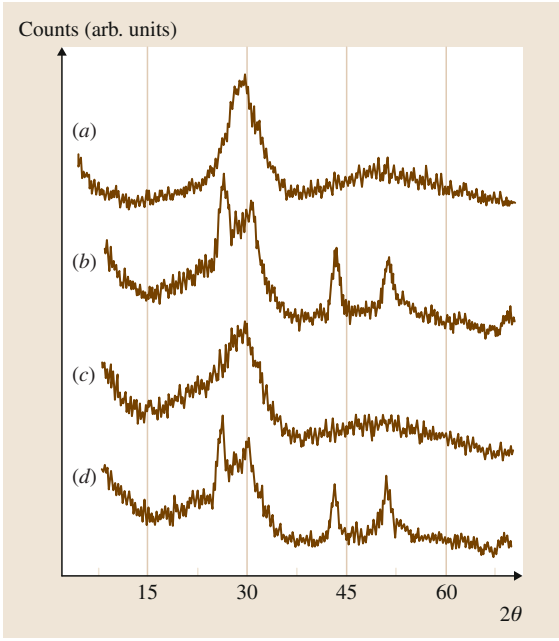


Fig. 18.16 x-Ray diffraction patterns. (*a*) Glass with composition $60PbGeO_3$-$10PbF_2$-$30CdF_2$ containing 0.5% Eu^{3+}, (*b*) transparent glass ceramic obtained after 60 h heat treatment at 331 °C of the (*a*) glass, (*c*) glass with composition $60PbGeO_3$-$10PbF_2$-$30CdF_2$ containing 0.5% Er^{3+}, and (*d*) transparent glass ceramic obtained after 60 h heat treatment at 324 °C of the (*c*) glass (after [18.69])

and/or fluoride systems, the interested reader is referred to [18.85].

The common characteristic of all glass systems mentioned in Table 18.1 is that heat treatments at selected temperatures lead to transparent glass ceramics displaying a fluoride crystal phase dispersed in an oxide glass host.

Figure 18.15 shows differential scanning calorimetry (DSC) scans obtained for glasses with composition (mol%) $60PbGeO_3$-$10PbF_2$-$30CdF_2$. Characteristic temperatures (T_g glass-transition temperature, T_x onset of glass crystallization, and T_p glass crystallization peak) obtained for the undoped glass (Fig. 18.15(*a*)) are $T_g = 302\,°C$, $T_x = 449\,°C$, and $T_p = 476\,°C$. With the addition of 0.5% Eu^{3+} these temperature values are observed to shift to $T_g = 300\,°C$, $T_x = 458\,°C$, and $T_p = 486\,°C$. An additional exothermic effect (marked with an arrow in the figure) is observed near T_g, at 331 °C. For the Er^{3+}-doped sample, these temperature values are $T_g = 292\,°C$, $T_x = 470\,°C$, and $T_p = 484\,°C$. The peak near T_g is also observed at 324 °C (also marked with an arrow). These general features are also common to all oxyfluoride glass systems listed in Table 18.1; that is, the addition of lanthanide ions leads to the observation of a *ceramization* peak at temperatures near T_g. Heat treatments around those temperatures lead to homogeneous precipitation of PbF_2 nanocrystals clearly identified from x-ray diffraction patterns and transmission electron microscopy (TEM) images, as presented in [18.69] and also reproduced in Figs. 18.16 and 18.17.

The glass ceramics thus obtained are transparent. Moreover, the lanthanide ions concentrate in the crystal phase, as observed from photoexcitation and photoemission spectra. In particular, Eu^{3+} ions are known for their sensitivity to the crystal field, with the spectroscopic properties being used to probe the metal ion environments [18.86–89]. In oxyfluoride glasses the transition from the mother glass to the final transparent glass ceramics can be indeed well followed by monitoring Eu^{3+} spectra.

Figure 18.18 [18.86] shows Eu^{3+} emission spectra obtained for the mother glass and the transparent glass ceramic, with the peaks being assigned to transitions between levels of the $4f^6$ electronic configuration. Following the excitation to the $Eu^{3+5}L_6$ energy level, at around 394 nm, nonradiative decays populate the $^5D_{0,1,2}$ levels, from which emission is observed. The

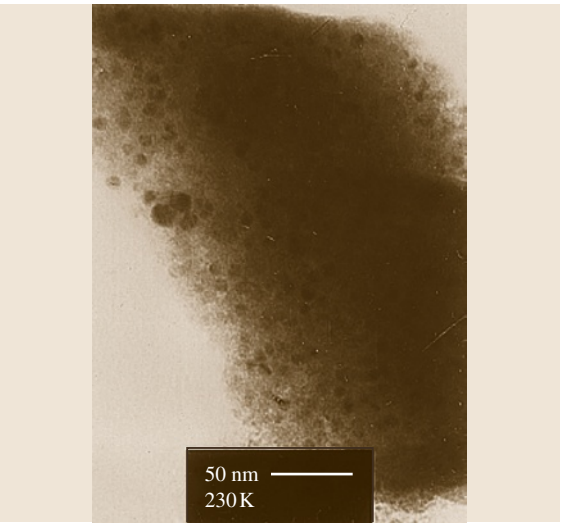


Fig. 18.17 TEM micrograph obtained for a transparent Er^{3+}-doped sample submitted to 60 h heat treatment at 324 °C (after [18.69])

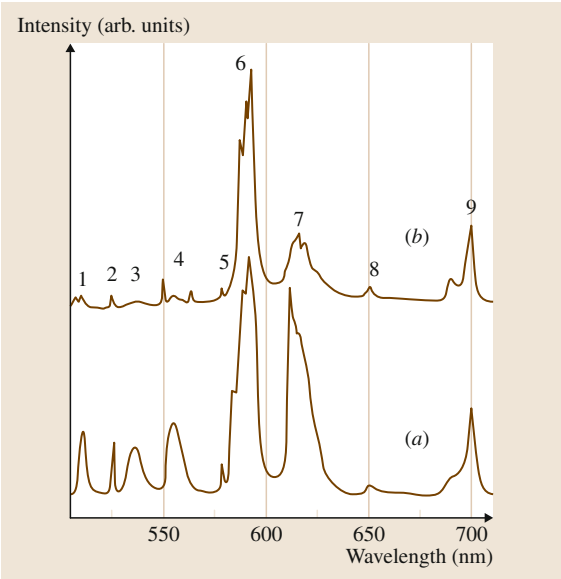


Fig. 18.18 Room-temperature Eu^{3+} emission spectra ($\lambda_{exc} = 394$ nm). (*a*) Glass with composition $60PbGeO_3$-$10PbF_2$-$30CdF_2$ containing 0.5% Eu^{3+}, (*b*) transparent glass ceramic obtained after 60 h heat treatment at 331 °C of the (*a*) glass. Assignments (Eu^{3+} electronic levels) $1 - {}^5D_2 \rightarrow {}^7F_3$; $2 - {}^5D_1 \rightarrow {}^7F_0$; $3 - {}^5D_1 \rightarrow {}^7F_1$; $4 - {}^5D_1 \rightarrow {}^7F_2$; $5 - {}^5D_0 \rightarrow {}^7F_0$; $6 - {}^5D_0 \rightarrow {}^7F_1$; $7 - {}^5D_0 \rightarrow {}^7F_2$; $8 - {}^5D_0 \rightarrow {}^7F_3$; $9 - {}^5D_0 \rightarrow {}^7F_4$ (after [18.86])

proximity in energy of these levels makes emission from the upper levels (${}^5D_{1,2}$) highly sensitive to the host phonon energies and also to so-called concentration quenching.

Figure 18.18 clearly shows the changes observed for relative intensities with the transition from the glass to the crystalline environment. Also, a decrease is observed for the relative intensity of the bands assigned to transitions from excited states ${}^5D_{1,2}$ and ${}^5D_0$. With the crystallization and the consequent concentration of lanthanide ions in the crystal phases, the volume concentration of the active ions increases relative to the mother glass. Energy transfer processes that depend on the ion–ion distance will therefore be affected by the ceramization. It is in fact observed that concentration quenching and IR-to-visible up-conversion efficiencies all increase [18.67–81, 83–91]. This effect is clearly observed in Fig. 18.18 with the decrease in the relative intensity for transition arising from the upper ${}^5D_{1,2}$ levels compared with those arising from the lower ${}^5D_0$ level.

Figure 18.19 [18.86] shows vibronic spectra appearing together with the excitation band assigned to the ${}^7F_0 \rightarrow {}^5D_2$ Eu^{3+} transition at 21 560 cm^{-1} (463.8 nm). Spectra obtained for the mother glass, the transparent glass ceramic, and also a Eu^{3+}-containing lead germanate glass ($PbGeO_3$:Eu^{3+} (0.5 mol%)) are presented. Numbers in the figure refer to relative positions of the bands taking the electronic line as a reference. These sidebands can be attributed to vibrational modes coupled to the Eu^{3+} electronic state. Considering the germanate glass, the vibronic bands at 653 and 750 cm^{-1} are related to Q^2 structures of the germanate chain, where Q^n is the usual nomenclature identifying the number n of bridging oxygen atoms connecting GeO_4 tetrahedra. In the spectrum obtained for the fluorogermanate glass, bands at 562, 689, and 786 cm^{-1} correspond to Q^2 structures with some substitution of fluoride ions for oxide ions in the glass network in the vicinity of Eu^{3+} ions. The vibrational mode at 219 cm^{-1} is attributed to Eu^{3+} ions strongly interacting with metal fluoride-rich regions. With the glass-to-glass ceramic transition vibrational modes of 94 and 201 cm^{-1} could be identified, related to the PbF_2:Eu^{3+} crystal phase. The vibronic spectrum obtained for the glass ceramic still shows the interaction of Eu^{3+} ions with the fluorogermanate network, since bands are observed at 556, 676, and 778 cm^{-1}. Therefore the partition of Eu^{3+} ions between the crystalline fluoride and amorphous germanate phases can be well monitored by Eu^{3+} vibronic spectroscopy, which highlights the role of Eu^{3+} as probes of the structure.

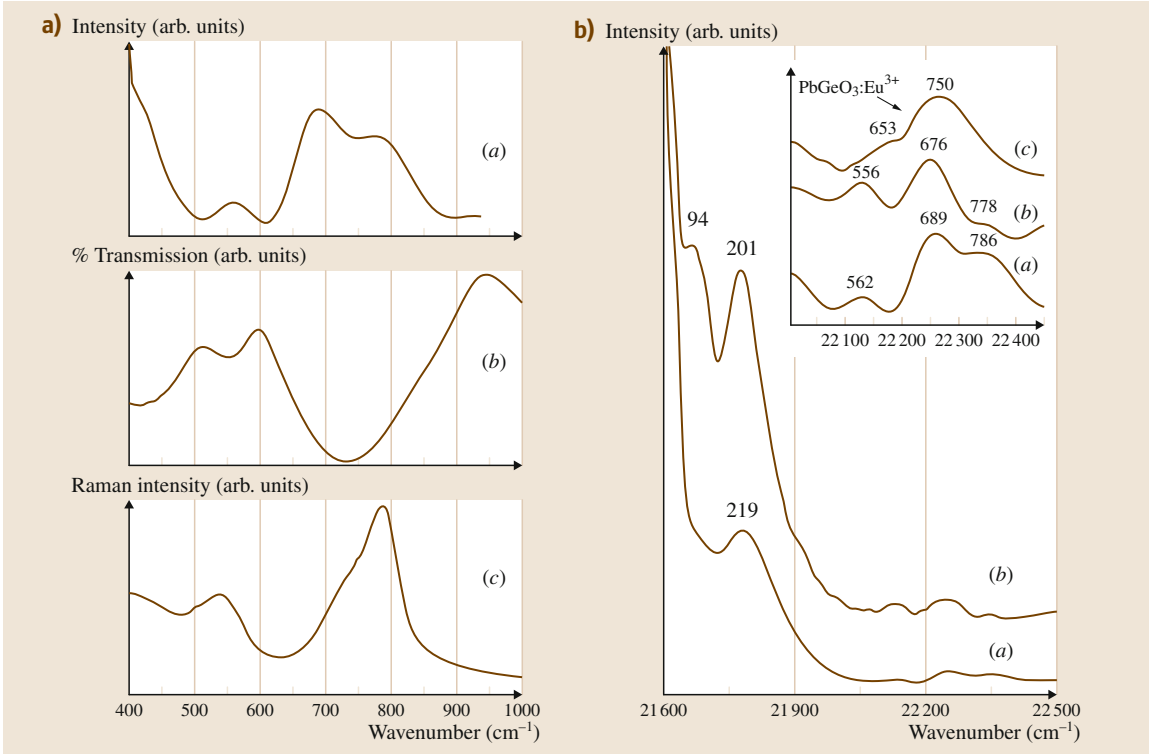


Fig. 18.19 **(b)** Eu^{3+} vibronic spectra. (*a*) Glass with composition $60PbGeO_3$-$10PbF_2$-$30CdF_2$ containing 0.5% Eu^{3+}, (*b*) transparent glass ceramic obtained after 60 h heat treatment at 331 °C of the (*a*) glass. *Inset*: Detail for the germanate spectral regions with the additional vibronic spectrum observed in $PbGeO_3$:Eu^{3+} (*c*). **(a)** Eu^{3+} vibronic spectrum for the $60PbGeO_3$-$10PbF_2$-$30CdF_2$ (0.5% Eu^{3+}) glass with the electronic line at 21 560 cm^{-1} taken as a reference (zero) (*a*); (*b*) infrared transmission spectrum and (*c*) Raman scattering spectrum obtained from the same sample (after [18.86])

Figure 18.19 also shows the relationship between the vibronic spectrum, the infrared transmission, and Raman scattering spectra obtained for the fluorogermanate glass. The same vibrational modes seem to be operative in the three spectra.

The exact mechanism occurring in the crystallization of oxyfluoride glasses is still a matter of discussion. It is clear from ^{19}F NMR measurements that heterogeneities, in this case associated with clustering of fluoride ions, occur in the mother glasses, which can no longer be considered homogeneous at the molecular scale [18.15, 86]. Fluoride-rich regions would lead to the ionic conduction pathways claimed to explain the unusual ionic conduction properties displayed by oxyfluoride glasses and also their particular crystallization behavior [18.15, 86].

The addition of lanthanide ions clearly influences the crystallization process. However, this nucleating action is not well understood. Indeed, EXAFS measurements lead to the suggestion that the antecedent formation of ErF_3 phase is followed by the crystallization of the PbF_2, $Pb_xCd_{1-x}F_2$, LaF_3, and other phases [18.72]. Eu^{3+} spectroscopic data also point to the existence of heterogeneities characterized by fluoride-rich regions [18.81, 86–88], corroborating the model proposed in [18.15, 86].

18.2.2 Metal Nanoparticles in Glasses

One of the earliest examples highlighting the important role played by nanoscale heterogeneities in glasses is the well-known Roman Lycurgus Cup from the 4th century AD [18.92]. It looks green under reflected light and red under transmitted light. Other masterpieces of the glass world, the red Venetian glasses from the 13th century, do not display the green reflected color. Both glasses are known to contain colloidal metal particles: Au-Ag in Roman glass and Au in Venetian glass. Per-

haps neither the Romans nor Venetians were aware that surface plasmon resonances (SPR) due to metallic heterogeneities could be claimed, together with scattering due to the sizes of the particles in the case of the Roman glass, to explain the amazing color effects they achieved.

Beyond the subject of glass art, potential technological applications of such nanoscale heterogeneous systems have emerged in the last decades. In fact, the study of metallic nanostructures and their applications has expanded in the past years into a major field called *plasmonics* [18.94]. SPR localized near the boundary between the metal nanostructure and the surrounding dielectric also produces an enhanced electromagnetic field at the interface. This enhanced field is the basis of two important applications related to metallic nanoparticles, namely:

1. The enhancement of intensities of intra-4f electronic transitions of lanthanide ions close to the particles [18.95]
2. The enhancement of Raman lines attributed to some vibrational modes of molecules close to the particles [18.96, 97].

Several families of oxide glasses containing metallic nanoparticles have been reported in the literature, including silica [18.98–113], borates [18.114, 115], phosphates [18.116–129], and heavy metal oxide glasses (HMOG) [18.118–135]. Nanoparticles being studied include silver (Ag), gold (Au), platinum (Pt) and copper (Cu), nickel (Ni), cobalt (Co), iron (Fe), and bismuth (Bi).

SPR in glasses is the phenomenon responsible for the colors observed. In fact, the absorption band may be localized from the near-infrared to the limit between the visible and ultraviolet regions. The metal–dielectric boundary on the nanoscale leads to changes in the optical properties, making them size and shape dependent. The SPR also depends on the dielectric refractive index, as shown below.

To take advantage of the unique properties of the metallic nanoparticles, it is interesting to prepare samples with size distributions below an average of 25 nm. This scenario allows use of the quantum confinement effect while light scattering can be neglected. The increase in size (considering, for example, the spherical shape) leads to a red-shift in the SPR band [18.136]. Such an effect is usually observed when glasses are annealed during different periods of time or at distinct temperatures, or even when exposed to different doses of laser light. Figure 18.20 shows the evolution of the SPR band due to silver nanoparticles with heat treatments performed for different periods of time in glasses with composition $(0.6KPO_3\text{-}0.4WO_3)_{0.85}\text{-}AgCl_{0.15}$ [18.93]. Figure 18.20 also shows a TEM image of the nanoparticles thus obtained. A red-shift (535–550 nm) is observed for longer treatments, related to increasing sizes of the nanoparticles. The intensity of the band is mostly related to the number of particles, which also increase with the increasing duration of heat treatment. Increasing the size of the nanoparticles, by either heat treatment or laser irradiation, can be explained using the Ostwald ripening approach [18.137] where atoms or very small particles join together to form larger clusters. For most glass compositions, the crystal growth takes place at temperatures above the glass-transition temperature because, in such conditions, the glass viscosity decreases and atomic diffusion starts to become more important, allowing Ostwald ripening.

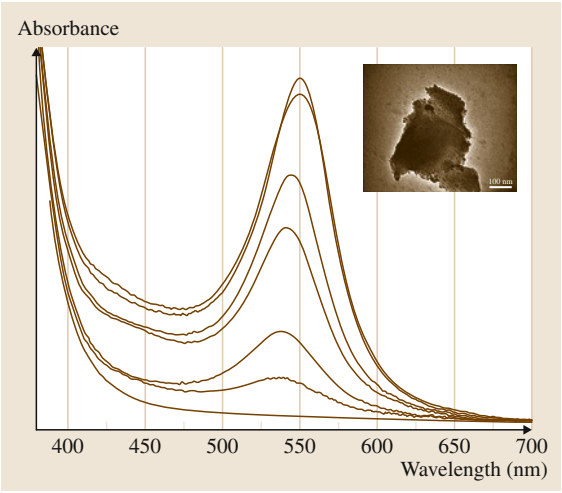


Fig. 18.20 Absorption spectra obtained for a glass sample of composition $(0.6KPO_3\text{-}0.4WO_3)_{0.85}\text{-}AgCl_{0.15}$. The evolution of the SPR band with the duration of heat treatment is shown. From the lower spectrum obtained for the base glass, spectra are shown with increasing absorption for the same sample treated for 10, 65, 75, 85, 110, and 130 min at 450 °C. The *inset* shows a TEM image for the sample treated for 250 min. *Black dots* are silver particles (4–10 nm) distributed in the glass bulk (*scale bar* = 100 nm, after [18.93])

The dependence of the SPR on the refractive index (at 632 nm) n of the medium is shown in Fig. 18.21. Values are obtained from the literature (indicated in the figure) for silver particles in different glasses. Al-

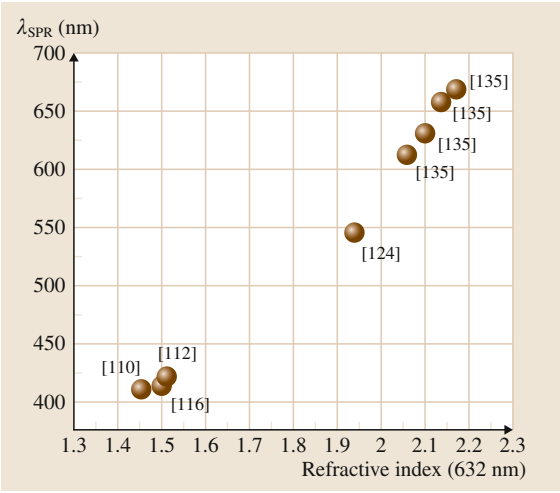


Fig. 18.21 Maximum observed for Ag SPR bands (λ_{SPR}) as a function of the refractive index of the glass host. References are cited in the figure

though the particle sizes were observed to vary from 1.6 to 28 nm among the glass systems, the almost 300 nm shift cannot be attributed only to size effects. Refractive index plays an important role here.

Three main techniques have been used in the preparation of glasses containing metallic nanoparticles: ion implantation, ionic exchange, and melt quenching. Ion implantation has been successfully used to introduce ionic transition metals, such as Ag^{+}, Au^{2+}, Cu^{+} [18.138], Ni^{2+} [18.100], and Co^{2+} [18.139]. However, in all cases, annealing processes are necessary to promote the reduction from ion to metal and the consequent formation of nanoparticles. One of the drawbacks of this technique is the intrinsic heterogeneous distribution of the nanoparticles, since ions are implanted only within a few microns from the glass surface.

Ionic exchange methods have been largely used due to their simplicity. Basically, a Na^{+}-rich glass composition is submitted to ionic exchange in a molten salt bath. Subsequently, the ion-exchanged glass must be submitted to UV irradiation or thermal annealing to effect nanoparticle formation. This method is widely employed to introduce Ag atoms into the glass composition.

The most employed method to prepare metallic nanoparticles embedded in oxide glasses is the melt-quenching technique. It consists in introducing the metal atom of interest together with the other components of the glass which will be later melted at high temperatures and, subsequently, quenched to temperatures below T_g. The metal-containing starting materials include chlorides, nitrates, oxalates, among other salts that will decompose during the melting process, forming ions. Alternatively, metal atoms can be directly introduced into the glass structure. In both cases, nanoparticles are hardly observed in the quenched glass. Nanoparticle clustering and growth occur by subsequent annealing of the glasses at temperatures close to or higher than T_g, Thermal treatment above T_g is efficient because the glass viscosity decreases above this temperature and the diffusion of the atoms is facilitated.

Melt-quenching may be used in conjunction with laser and x-ray irradiation of the glasses. Usually, glass samples are previously irradiated and later submitted to a fast annealing step inducing crystallization only in the irradiated region. Three-dimensional (3-D) nanostructures can be fabricated by using focused femtosecond laser beams [18.140].

18.2.3 Quantum Dots in Glasses

As shown in the previous section, metallic nanoparticles exhibit major changes in the optical spectra derived from effects that can be explained using a classical dielectric picture.

Glass nanoheterogeneities may also be composed of semiconductor nanoparticles, leading to amazing optical properties as well. In this case the quantum confinement produces quantization of the electron and hole energy states that lead to major modification in the optical spectra. Therefore, *quantum dots* (QD) are nanoparticles of semiconductors representing the case of an electron trapped in a three-dimensional box.

QD generally range from 2–10 nm in diameter, but the maximum size of a semiconductor to be considered a QD depends on several parameters. A classical semiconductor is a material that has a small bandgap between the valence and conduction band, allowing electrons to be excited to the conduction band, leaving behind a hole in the valence band. In this model, the exciton Bohr radius is the average separation of the electron–hole pair.

For a semiconductor nanocrystal to exhibit quantum confinement or quantum size effects and be considered a QD, the size of the crystal must be smaller than the exciton Bohr radius [18.141]. This quantum confinement causes the energy bands observed in the bulk material to turn into discrete energy levels, resulting in intermediate properties between the bulk material and discrete molecules and new optical and electronic behaviors [18.142–145].

QD were first discovered by *Ekimov* [18.146] in a glass matrix and by *Brus* in colloidal solutions, and are often composed of binary alloys such as cadmium chalcogenides (CdS, CdSe, CdTe) [18.147–150] or lead chalcogenides (PbS, PbSe, PbTe) [18.151–157], even if several works have reported ternary QDs (CdSSe) [18.158] or oxide compounds [18.159–162]. These binary chemical compositions, labeled II–VI and IV–VI QD, have been largely investigated because of their relatively large exciton Bohr radii compared with other compounds. In this sense, lead chalcogenide QD exhibit the largest exciton Bohr radii of about 18 nm for PbS and 46 nm for PbSe, resulting in a quantum confinement effect for a large diameter range and thus tunable absorption and emission wavelengths [18.152, 162].

Among the wide diversity of methods available for preparation of semiconductor nanocrystals, colloidal chemistry appears as a powerful method for high-quality QD with emission efficiencies as large as 20% of commercial dyes [18.153, 154, 163]. However, QD suspensions or powders are unstable, mainly due to agglomeration and coalescence processes. For these reasons, attempts have been made to incorporate QD into robust solids which can allow QD stability and easier device manufacture for technological applications. In this way QD have been obtained in polymers [18.164] and zeolites [18.165], both in the form of thin films [18.166] and inside bulk glasses prepared by both sol–gel and melt-quenching methods [18.167–169]. Incorporation of QD in glasses has been so far the most promising and investigated choice, since the final materials present both mechanical and chemical stability as well as simple manufacture into fibers or bulk devices with specific shapes. Many works in the literature have reported preparation and optical characterizations of QD in silicate- and phosphate-based glasses as well as a few works on QD-containing chalcogenide glasses [18.157,170–176]. The most promising quantum-dot compositions for nanostructured glasses are II–VI semiconductors such as cadmium chalcogenides (CdS, CdSe, CdTe) and IV–VI semiconductors such as lead chalcogenides (PbS, PbSe, PbTe) because of their quantum confinement properties in a large diameter range. However, some works have described the preparation and optical properties of oxide quantum dots such as ZnO, In_2O_3 or SnO_2 embedded in glasses [18.159–161, 177].

Several methodologies such as radiofrequency (RF) sputtering [18.178], ion implantation [18.179], and melt quenching of starting materials [18.170–175] are available for the incorporation of quantum dots, the latter being the most simple, versatile, and employed method for nanostructured semiconductor glasses. The semiconductor compound is generally added to the other starting materials of the glass composition, and the mixture is melted and quenched at around T_g as in classical glass preparation. QD generally do not form at this stage, and the semiconductor compound is dispersed homogeneously in the final glass, resulting in a sample with the same optical characteristics (color and transparency) as the undoped composition. As in the case of metallic particles, QD will nucleate and grow under heat treatments at selected temperature, usually above T_g.

Depending on the glass melting temperature, important chemical losses can occur by thermal decomposition or sublimation, since these chalcogenide compounds are unstable at high temperatures [18.174]. As a result, the final semiconductor concentration is in general lower than the desired one and is hard to control in the final sample. Such behavior is particularly well known in silicate glasses containing PbS and PbSe quantum dots because of the high melting temperatures (around 1300 °C) and high tendency of lead chalcogenides to decompose above their melting temperature (1118 °C for PbS and 1080 °C for PbSe). In these cases, several methodologies can be adopted to maintain a desired semiconductor concentration. Many authors describe the use of a large excess of the compound (about tenfold) in the starting materials to obtain a relatively high final concentration [18.180]. Other researchers bring each element from distinct compounds with higher melting temperatures T_m. As an example, ZnSe ($T_m = 1520$ °C) and PbO can be introduced in the starting materials of a silicate glass for final PbSe-containing glasses [18.157]. As mentioned above, after the glass preparation, one- or two-stage heat treatments at temperatures between the glass transition and the onset of crystallization must be applied to induce quantum dot nucleation from amorphous phase separation and further growth of the nanometric particles [18.181,182]. The main difficulty in multicomponent glasses is to ensure the single precipitation of the desired semiconductor phase without crystallization of the other glass components. Specific compounds such as ZnO can be added to the starting materials in multicomponent glasses to act as nucleating agents for selective crystallization of the semiconductor phase [18.162].

The appearance of discrete energetic levels associated with quantum size effects with energy gaps tuned by the quantum dot size leads to several new exciting properties and applications related to absorption and

emission processes in the visible and near-infrared regions [18.152]. Such materials are used as commercial optical cutoff filters in the visible [18.183, 184] and optical devices for near-infrared luminescence useful in telecommunications; For example, PbS luminescence in silicate glasses can be tuned in the range of 1.2–1.7 μm depending on the particle diameter below the exciton Bohr radius, and these materials are used as broadband optical amplifiers [18.185]. Other optical applications are related to their highly nonlinear optical properties and fast response times, which make them suitable for Raman amplifiers [18.186], active optical emitters [18.187], saturable absorbers for mode-locking and Q-switching of near-infrared lasers, and ultrafast signal switches [18.188, 189]. Some works have also reported more efficient luminescence properties of rare-earth ions when embedded inside quantum dots [18.161, 190–192].

18.3 Perspectives and Concluding Remarks

Glasses may present heterogeneities at the nanoscale that have been avoided by traditional glassmakers, to whom homogeneity is a fundamental glass property. However, the presence of heterogeneities may lead to amazing properties that may turn simple objects into icons of a given civilization, such as the already mentioned beautiful Lycurgus Cup fabricated by the Romans. From there, an entirely new area, plasmonics, is being explored today [18.94, 193].

Nanoscale heterogeneities may be characterized by sophisticated spectroscopic techniques. This chapter presents a special focus on modern NMR techniques. The results presented in Sect. 18.1 document the great power and potential of modern solid-state NMR spectroscopy to provide detailed information on the structural organization of disordered materials at the subnanometer distance scale. Figure 18.22 summarizes the key features of the technique in relation to other methods.

Local selectivity:	Disorder/Lack of periodicity
Element selectivity:	Compositional complexity Low scattering contrast (H; Si/Al)
Interaction selectivity:	Distance measurements Connectivity information Electron density information
Uniform sensitivity:	Quantitative applications
Dynamic sensitivity:	Motional processes on continuous timescale (10^{2} to 10^{-9} s)
Low detection sensitivity:	10^{17} to 10^{18} spins required
Bulk method:	Poor spatial resolution Surfaces/interfaces difficult to study
Magnetic interference:	Transition metals, rare earths limited

Fig. 18.22 Key features of solid-state NMR as a technique in the solid-state sciences. Strengths are shown on a *yellow background*, weaknesses on a *purple background*

During the past decade a substantial amount of information has been accumulated, much of which remains at the conceptual and qualitative level at the present time. Still there are numerous experimental and theoretical difficulties to overcome that relate directly to the measurement; For example, reliable quantification of *homonuclear* dipole–dipole interactions under high-resolution conditions (with MAS) is still an unsolved problem, in particular when quadrupolar nuclei are involved. Likewise, no rigorous strategy seems to be available at present for quantitative measurement of heteronuclear dipolar coupling between two quadrupolar nuclear species. Nevertheless, the systematic composition-dependent exploration of chemical systems offers a lot of fundamental insight into the structure–property relation of disordered materials. In this connection it is of utmost importance that NMR spectroscopy remains a vital and attractive research area in its own right. Assuredly, the continued influx of new solid-state NMR technology into this research area will provide an active stimulus for the study of increasingly sophisticated structural issues on increasingly complex materials. In the future, we expect that this research area will also greatly benefit from the continuing improvement and refinement of the calculational and modeling approaches used to *translate* spectroscopic observables into structural information.

This chapter also described the amazing properties that emerge due to the presence of specific heterogeneities in glasses, that is, lanthanide-containing nanocrystals, metallic nanoparticles, and quantum dots. Glasses themselves are unique materials considering the wide range of optical applications available by intelligent choice of glass compositions [18.194].

Control of the composition and dimensions of nanoscale structures, and therefore their structural study, is of utmost importance in order to explore the almost endless list of possible applications.

NMR together with vibrational spectroscopy, extended x-ray absorption fine structure (EXAFS), and the spectroscopic properties of lanthanide probe ions allow fundamental characterization of the glass structure at the nanoscale. Indeed, mixed oxyfluoride glasses may present emerging ionic conductivity properties that are distinct from the properties of the individual oxide and fluoride components. Heterogeneities (fluorine-rich regions) proposed from the analysis of data from all the spectroscopic techniques cited above may be used to explain the new properties. The presence of such heterogeneities at the molecular scale also explains the particular crystallization mechanism observed for these mixed glasses, allowing one to obtain transparent glass ceramics displaying crystal-like spectroscopic properties [18.15]. The multifunctionality of such systems may be useful in new applications, as in the enhancement of the photovoltaic efficiency of silicon cells proposed in [18.195]. Transparent glass ceramics presenting lanthanide ions well concentrated in the crystal phase may present optimized efficiency in converting energy ranging from regions for which silicon photovoltaic cells are not sensitive to those where light can be efficiently converted to electric current, near the silicon energy bandgap.

Optical properties due to the presence of metallic nanoparticles may also be tuned through control of sizes and shapes together with the dielectric host properties. The new area of plasmonics mainly hinges on such control [18.94, 193]. The possibility of using femtosecond lasers to build 3-D metallic nanostructures in the glass bulk opens a wide range of new applications [18.140].

Concerning glass containing QD, applications based on the quantum confinement properties are only at the infancy stage. Emission properties may, for example, be exploited to obtain completely new luminescent materials and laser systems that may find applications in photonics as well as in biology [18.196, 197]. Glass coating on QD is also feasible, preventing quenching and leaching effects in optical applications [18.197]. New nanocomposites of QD–metallic nanoparticles have also been proposed for innovative light-emitting diodes [18.198].

One of the amazing properties giving glasses utmost importance is without doubt their processability. Glasses may be obtained in any form, and waveguides, in the form of either optical fibers or thin films, are some of the best examples of the functionality that can be added to the glass world. In this way, optical fibers and planar waveguides containing quantum dots and metal nanoparticles constitute important materials to be cited in these concluding remarks concerning future applications. Real-time remote detection, miniaturization, immunity to electromagnetic interference, and multiplexing ability are some of the important characteristics of optical fibers. Photostability and multiplexing capability are unique features of QD that can provide new and interesting solutions for fiber sensing. Several examples of such applications may be found in [18.199, 200], where the optical sensing properties of QD heterogeneities present in the glass host allow unique sensing characteristics. The relatively recent advent of photonic crystal fibers (PCF) enlarges the field of applications of these QD-containing waveguides [18.201].

Optical fibers containing metal nanoparticles also find interesting applications in different areas. By incorporating optical fiber-based devices into woven and nonwoven fabrics, one can distribute these devices across large areas. By incorporating metallic nanoparticles (and also QDs) inside optical fibers, continuous fibers are obtained that can be woven, or placed into nonwoven textiles. Interesting new sensors are obtained in this way [18.202].

PCFs containing metal nanoparticles can also be prepared, constituting integrated next-generation plasmonic devices. Proof-of-principle experiments have been demonstrated with liquids of different refractive indices where the dependence of the localized surface plasmon resonance (LSPR) on the surroundings was confirmed [18.203].

In conclusion, the study of glasses at the nanoscale paves the way for innovative applications of glasses and nanocomposites that can be prepared from the base glass. The synergy existing between guest heterogeneity and glass host leads to the emergence of entirely new properties that are impossible to obtain from other materials.

References

18.1 R.H. Doremus: *Glass Science* (Wiley, New York 1994)

18.2 J. Zarzycki: *Les verres et l'État Vitreaux* (Masson, Paris 1982)

18.3 I. Gutzov, J. Schmelzer: *The Vitreous State: Thermodynamic, Structure, Rheology and Crystallization* (Springer, Berlin, Heidelberg 1995)

18.4 R. Roy: Glass science and glassmaking: A personal perspective, Int. J. Appl. Glass Sci. **1**(1), 3 (2010)

18.5 M.J. Duer: *Introduction into Solid-State NMR Spectroscopy* (Blackwell, Oxford 2004)

18.6 H. Eckert: Structural characterization of noncrystalline solids and glasses by solid-state NMR, Prog. NMR Spectrosc. **24**, 159 (1992)

18.7 K. Schmidt-Rohr, H.W. Spiess: *Solid-state NMR and Polymers* (Academic, London 1996)

18.8 M. Bak, J.T. Rasmussen, N.C. Nielsen: SIMPSON: A general simulation program for solid-state NMR spectroscopy, J. Magn. Reson. **147**, 296 (2000)

18.9 J.H. van Vleck: The dipolar broadening of magnetic resonance lines in crystals, Phys. Rev. **54**, 1168 (1948)

18.10 D. Lathrop, D. Franke, R. Maxwell, T. Tepe, R. Flesher, Z. Zhang, H. Eckert: Dipolar ^{31}P NMR spectroscopy of crystalline inorganic phosphorus compounds, Solid State Nucl. Magn. Reson. **1**, 73 (1992)

18.11 H. Eckert: Structural characterization of nonoxide chalcogenide glasses using solid-state NMR, Angew. Chem. Adv. Mater. **101**, 1763 (1989)

18.12 S.H. Santagneli, I. Skripatchev, S.J.L. Ribeiro, Y. Messaddeq, J. Schneider: NMR: Structural study on the As-P-S glassy system, Chem. Mater. **19**(23), 5493 (2007)

18.13 S.H. Santagneli, J. Schneider, I. Skripachev, S.J.L. Ribeiro, Y. Messaddeq: Preparation and characterization of new glassy system $As_2P_2S_8$-Ga_2S_3, J. Phys. Chem. B **112**(16), 4943 (2008)

18.14 B. Cherry, J.W. Zwanziger, B.G. Aitken: The structure of GeS_2-P_2S_5 Glasses, J. Phys. Chem. B **106**, 11093 (2002)

18.15 C.C. Tambelli, J.P. Donoso, C.J. Magon, L.A. Bueno, Y. Messaddeq, S.J.L. Ribeiro, L.F.C. Oliveira, I. Kosacki: Glass structure and ion dynamics of lead-cadmium fluorgermanate glasses, J. Chem. Phys. **120**(20), 6938 (2004)

18.16 H. Eckert: Short and medium range order in ion conducting glasses studied by modern solid-state NMR techniques, Z. Phys. Chem. **224**, 1591 (2010)

18.17 J. Haase: Quadrupolar nuclei in inorganic solids, J. Magn. Reson. A **101**, 30 (1993)

18.18 B. Gee, H. Eckert: ^{23}Na nuclear magnetic resonance spin echo decay spectroscopy of sodium silicate glasses and crystalline model compounds, Solid State Nucl. Magn. Reson. **5**, 113 (1995)

18.19 G.N. Greaves, S.J. Gurman, C.R.A. Catlow, A.V. Chadwick, S. Houde-Walter, B. Dobson, C.M.B. Henderson, B.R. Dobson: A structural basis for ionic diffusion in oxide glasses, Philos. Mag. A **64**, 1059 (1991)

18.20 A. Bunde, K. Funke, M.D. Ingram: Ionic glasses: History and challenges, Solid State Ionics **105**, 1 (1998)

18.21 D.E. Kaplan, E. Hahn: Experiences de double irradiation en resonance magneticque par la methode d'impulsions, J. Phys. Radium **19**, 821 (1958)

18.22 S. Puls, H. Eckert: Spatial distribution of lithium ions in glasses studied by ^{7}Li{^{6}Li} spin echo double resonance, Phys. Chem. Chem. Phys. **9**, 3992 (2007)

18.23 B. Gee, H. Eckert: Cation distribution in mixed alkali silicate glasses. NMR studies by ^{23}Na-{^{7}Li} and ^{23}Na-{^{6}Li} spin echo double resonance, J. Phys. Chem. **100**, 3705 (1996)

18.24 T. Gullion, J. Schaefer: Rotational echo double resonance NMR, J. Magn. Reson. **81**, 196 (1989)

18.25 A. Naito, K. Nishimura, S. Tuzi, H. Saito: Inter- and intra-molecular contributions of neighboring dipolar pairs to the precise determination of interatomic distances in a Simple [^{13}C, ^{15}N]-peptide by ^{13}C,^{15}N-REDOR NMR Spectroscopy, Chem. Phys. Lett. **229**, 506 (1994)

18.26 M. Bertmer, H. Eckert: Dephasing of spin echoes by multiple dipolar interactions in rotational echo double resonance NMR experiments, Solid State Nucl. Magn. Reson. **15**, 139 (1999)

18.27 J.C.C. Chan, H. Eckert: Dipolar coupling information in multi-spin systems: Application of a compensated REDOR NMR approach to inorganic phosphates, J. Magn. Reson. **147**, 170 (2000)

18.28 W. Strojek, M. Kalwei, H. Eckert: Dipolar NMR strategies for multi-spin systems involving quadrupolar nuclei: ^{31}P ^{23}Na rotational echo double resonance (REDOR) of crystalline sodium phosphates and phosphate glasses, J. Phys. Chem. B **108**, 7061 (2004)

18.29 U. Voigt, H. Eckert, H. Lammert, A. Heuer: Cation clustering in lithium silicate glasses: Quantitative description by solid-state NMR and molecular dynamics simulations, Phys. Rev. B **72**, 064207 (2005)

18.30 J.D. Epping, W. Strojek, H. Eckert: Cation environments and spatial distribution in Na_2O-B_2O_3 glasses: New results from solid-state NMR, Phys. Chem. Chem. Phys. **7**, 2384 (2005)

18.31 W. Strojek, H. Eckert: Medium-range order in sodium phosphate glasses: A quantitative rotational echo double resonance solid-state NMR study, Phys. Chem. Chem. Phys. **8**, 2276 (2006)

18.32 S. Elbers, W. Strojek, H. Eckert, L. Koudelka: Site connectivities in silver borophosphate glasses: New results from ^{11}B{^{31}P} and ^{31}P{^{11}B} rotational echo double resonance nmr spectroscopy, Solid State Nucl. Magn. Reson. **27**, 65 (2005)

18.33 D. Zielniok, H. Eckert, C. Cramer: Direct correlation between nonrandom ion hopping and network structure in ion-conducting borophosphate glasses, Phys. Rev. Lett. **100**, 035901 (2008)

18.34 D. Zielniok, C. Cramer, H. Eckert: Structure/property correlations in ion-conducting mixed-network former glasses: Solid-state NMR studies of the system Na_2O-B_2O_3-P_2O_5, Chem. Mater. **19**, 3162 (2007)

18.35 D. Raskar, M. Rinke, H. Eckert: The mixed-network former effect in phosphate glasses: XPS and NMR studies of the connectivity distribution in the glass system $(NaPO_3)_{1-x}(B_2O_3)_x$, J. Phys. Chem. C **112**, 12530 (2008)

18.36 M.T. Rinke, H. Eckert: The mixed network former effect in glasses: Solid-state NMR and XPS structural studies of the glass system $(Na_2O)_x(BPO_4)_{1-x}$, Phys. Chem. Chem. Phys. **13**, 6552 (2011)

18.37 B.G. Aitken, R.E. Youngman, R.R. Deshpande, H. Eckert: Structure-property relations in mixed-network glasses: Multinuclear solid-state NMR investigations of the system $xAl_2O_3:(30-x)P_2O_5:70SiO_2$, J. Phys. Chem. C **113**, 332 (2009)

18.38 L. Zhang, H. Eckert: Short- and medium-range order in sodium aluminophosphate glasses: New insights from high-resolution dipolar solid-state NMR spectroscopy, J. Phys. Chem. B **110**, 8946 (2006)

18.39 M. Bertmer, L. Züchner, J.C.C. Chan, H. Eckert: Short and medium range order in sodium aluminoborate glasses: II. Site connectivities and cation distributions studied by rotational echo double resonance NMR spectroscopy, J Phys. Chem. B **104**, 6541 (2000)

18.40 J.C.C. Chan, M. Bertmer, H. Eckert: Site connectivities in amorphous materials studied by double resonance NMR of quadrupolar nuclei: High resolution $^{11}B \leftrightarrow {}^{27}Al$ spectroscopy of aluminoborate glasses, J. Am. Chem. Soc. **121**, 5238 (1999)

18.41 H. Deters, A.S.S. de Camargo, C.N. Santos, H. Eckert: Glass-to-vitroceramic transition in the yttrium aluminoborate system: Structural studies by solid-state NMR, J. Phys. Chem. C **114**, 14618 (2010)

18.42 H. Deters, A.S.S. de Camargo, C.N. Santos, C.R. Ferrari, A.C. Hernandes, A. Ibanez, M.T. Rinke, H. Eckert: Structural characterization of rare-earth doped yttrium aluminoborate laser glasses using solid-state NMR, J. Phys. Chem. C **113**, 16216 (2009)

18.43 S. Santagneli, C.C. de Araujo, W. Strojek, H. Eckert, G. Poirier, S.J.L. Ribeiro, Y. Messaddeq: Structural studies of $NaPO_3$-MoO_3 glasses by solid-state NMR and raman spectroscopy, J. Phys. Chem. B **111**, 10109 (2007)

18.44 L. Duma, W.C. Lai, M. Caravetta, L. Emsley, S.P. Brown, M.H. Levitt: Principles of spin-echo modulation by *J*-couplings in magic-angle-spinning solid-state NMR, Chem. Phys. Chem. **5**, 815 (2004)

18.45 F. Fayon, I.J. King, R.K. Harris, J.S.O. Evans, D. Massiot: Application of the through-bond correlation NMR experiment to the characterization of crystalline and disordered phosphates, C. R. Chim. **7**, 351 (2004)

18.46 L. Olivier, X. Yuan, A.N. Cormack, C. Jäger: Combined ^{29}Si double quantum NMR and MD simulation studies of network connectivities of binary $Na_2O \cdot SiO_2$ glasses: New prospects and problems, J. Non-Cryst. Solids **293–295**, 53 (2001)

18.47 M. Feike, C. Jäger, H.W. Spiess: Connectivities of coordination polyhedra in phosphate glasses from ^{31}P double-quantum NMR spectroscopy, J. Non-Cryst. Solids **223**, 200 (1998)

18.48 M.H. Lewis (Ed.): *Glasses and Glass Ceramics* (Chapman Hall, New York 1989)

18.49 P.W. McMillan: *Glass Ceramics* (Academic, New York 1979)

18.50 Z. Strnad: *Glass Ceramic Materials-Liquid Phase Separation, Nucleation and Crystallization in Glasses*, Glass Sci. Technol., Vol. 8 (Elsevier, Amsterdam 1986)

18.51 E.D. Zanotto: A bright future for glass ceramics, Am. Ceram. Soc. Bull. **89**(8), 19 (2010)

18.52 G.H. Beall, D. Duke: Transparent glass ceramics, J. Mater. Sci. **4**, 340 (1969)

18.53 S.D. Stookey: Method of Making Ceramics and Product Thereof, US Patent 2920971 (1960)

18.54 F.A. Hummel: Thermal expansion properties of some synthetic lithia minerals, J. Am. Ceram. Soc. **34**, 235 (1951)

18.55 G.J. Fine: Glass and glassmaking, J. Chem. Ed. **68**(1), 765 (1991)

18.56 R. Reisfeld, C.K. Jorgensen: Luminescent solar concentrators for energy conversion, Struct. Bonding **49**, 1 (1982)

18.57 R. Reisfeld: Potential uses of chromium(III)-doped transparent glass ceramics in tunable lasers and luminescent solar concentrators, Mater. Sci. Eng. **71**, 375 (1985)

18.58 B.C. Rowan, L.R. Wilson, B.S. Richards: Advanced material concepts for luminescent solar concentrators, IEEE J. Sel. Top. Quantum Electron. **14**(5), 1312 (2008)

18.59 L.D. Carlos, R.A.S. Ferreira, V. de Zéa Bermudez, S.J.L. Ribeiro: Lanthanide-containing light-emitting organic-inorganic hybrids: A bet on the future, Adv. Mater. **21**, 509 (2009)

18.60 K. Binnemans: Lanthanide-based luminescent hybrid materials, Chem. Rev. **109**, 4283 (2009)

18.61 S.V. Eliseeva, J.C.G. Bunzli: Lanthanide luminescence for functional materials and bio-sciences, Chem. Soc. Rev. **39**, 189 (2010)

18.62 M.J. Weber: Science and technology of laser glass, J. Non-Cryst. Solids **123**(1–3), 208 (1990)

18.63 R. Reisfeld, C.K. Jorgensen: *Lasers and Excited States of Rare Earths* (Springer, Berlin, Heidelberg 1977)

18.64 J.E. Marion, M.J. Weber: Phosphate laser glasses, Eur. J. Solid State Inorg. Chem. **28**, 271 (1991)

18.65 P.C. Becker, N.A. Olsson, J.R. Simpson: *Erbium-doped Fiber Amplifiers. Fundamentals and Technology* (Academic, San Diego 1999)

18.66 A.A. Kaminski: *Laser Crystals*, 2nd edn. (Springer, Berlin, Heidelberg 1990)

18.67 Y. Wang, J. Ohwaki: New transparent vitroceramics codoped with Er^{3+} and Yb^{3+} for efficient fre-

quency upconversion, Appl. Phys. Lett. **63**(24), 3268 (1993)
18.68 K. Hirao, K. Tanaka, M. Makita, N. Soga: Preparation and optical-properties of transparent glass ceramics containing β-PbF2-Tm^{3+}, J. Appl. Phys. **78**(5), 3445 (1995)
18.69 L.A. Bueno, P. Melnikov, Y. Messaddeq, S.J.L. Ribeiro: Er^{3+} and Eu^{3+} containing transparent glass ceramics in the system $PbGeO_3$-PbF_2-CdF_2, J. Non-Cryst. Solids **247**, 87 (1999)
18.70 A.S. Gouveia-Neto, L.A. Bueno, R.F. Nascimento, M.L. Sundheimer, E.B. Costa, S.J.L. Ribeiro, Y. Messaddeq: Upconversion luminescence and thermal effects in terbium-ytterbium codoped fluorogermanate glass-ceramic, Phys. Chem. Glasses – Eur. J. Glass Sci. Technol. B **50**(1), 34 (2009)
18.71 A.S. Gouveia-Neto, L.A. Bueno, R.F. Nascimento, E.B. Costa, S.J.L. Ribeiro, Y. Messaddeq: Multiwavelength visible and white light generation by upconversion emission in Ho/Tm/Yb triply doped fluorogermanate glass-ceramic, Phys. Chem. of Glasses – Eur. J. Glass Sci. Technol. B **50**(1), 37 (2009)
18.72 M.A.P. Silva, G. Dantelle, M. Mortier, A. Monteil, S.J.L. Ribeiro, Y. Messaddeq, V. Briois, M. Poulain: Local order around rare earth ions during the devitrification of oxyfluoride glasses, J. Chem. Phys. **128**, 244516 (2008)
18.73 M. Mortier, F. Auzel: Rare-earth doped transparent glass ceramics with high cross-sections, J. Non-Cryst. Solids **256**, 361 (1999)
18.74 H. Hayashi, S. Tanabe, T. Hanada: 1.4 μm band emission properties of Tm^{3+} ions in transparent glass ceramics containing PbF_2 nanocrystals for S-band amplifier, J. Appl. Phys. **89**, 1041 (2001)
18.75 V.K. Tikhomirov, D. Furniss, A.B. Seddon, I.M. Reaney, M. Beggiora, M. Ferrari, M. Montagna, R. Rolli: Fabrication and characterization of nanoscale, Er^{3+}-doped, ultratransparent oxy-fluoride glass ceramics, Appl. Phys. Lett. **81**, 1937 (2002)
18.76 P.A. Tick, N.F. Borrelli, L.K. Cornelius, M.A. Newhouse: Transparent glass ceramics for 1300 nm amplifier applications, J. Appl. Phys. **78**, 6367 (1995)
18.77 J. Mendez-Ramos, V. Lavin, I.R. Martin, U.R. Rodriguez-Mendoza, V.D. Rodriguez, A.D. Lozano-Gorrin, P. Nunez: Role of the Eu^{3+} ions in the formation of transparent oxyfluoride glass ceramics, J. Appl. Phys. **89**(10), 5307 (2001)
18.78 S.F. León-Luis, J. Abreu-Afonso, J. Pena-Martinez, J. Méndez-Ramos, A.C. Yanes, J. del-Castillo, V.D. Rodriguez: Up-conversion and colour tuneability in Yb^{3+}-Er^{3+}-Tm^{3+} Co-doped transparent nano-glass ceramics, J. Alloys Compd. **479**, 557 (2009)
18.79 J. Méndez-Ramos, V.D. Rodrigues, V.K. Tikhomirov, J. del-Castillo, A.C. Yanes: Yb^{3+}-Er^{3+}-Tm^{3+} Co-doped nano-glass ceramics tuneable up-conversion phosphor, Eur. Phys. J. Appl. Phys. **43**, 149 (2008)
18.80 V.K. Tikhomirov, A.B. Seddon, M. Ferrari, M. Montagna, L.F. Santos, R.M. Almeida: On a qualitative model for the incorporation of fluoride nanocrystals within an oxide glass network in oxyfluoride glass ceramics, J. Non-Cryst. Solids **337**, 191 (2004)
18.81 Z. Pan, A. Ueda, R. Um, S.H. Morgan: Upconversion luminescence in Er^{3+}-doped germanate-oxyfluoride and tellurium-germanate-oxyfluoride transparent glass ceramics, J. Lumin. **126**, 251 (2007)
18.82 A.J. Stevenson, H. Serier-Brault, P. Gredin, M. Mortier: Fluoride materials for optical applications: Single crystals, ceramics, glasses, and glass ceramics, J. Fluor. Chem. **132**, 1165 (2011)
18.83 F. Auzel: Materials and devices using double-pumped phosphors with energy transfer, Proc. IEEE **61**, 758 (1973)
18.84 F. Auzel, D. Pecile, D. Morin: Rare-earth doped vitroceramics – New, efficient, blue and green emitting materials for infrared up-conversion, J. Electrochem. Soc. **122**, 101 (1975)
18.85 M. Clara Gonçalves, L.F. Santos, R.M. Almeida: Rare-earth-doped transparent glass ceramics, C.R. Chim. **5**, 845 (2002)
18.86 S.J.L. Ribeiro, Y. Messaddeq, L.A. Bueno, J. Dexpert-ghys, A.S. Gouveia-Neto, C.C. Tambelli, J.P. Donoso, C. Magon: Lead-cadmium fluorogermanate glasses and transparent glass ceramics. Spectroscopy and structure, Mater. Sci. Forum **514–516**, 1299 (2006)
18.87 L.A. Bueno, A.S. Gouveia-Neto, E.B. Costa, Y. Messaddeq, S.J.L. Ribeiro: Structural and spectroscopic study of oxyfluoride glasses and glass ceramics using europium ion as a structural probe, J. Phys. D **20**, 145201 (2008)
18.88 C. Bensalem, M. Mortier, D. Vivien, M. Dial: Thermal and optical investigation of EuF_3-doped lead fluorogermanate glasses, J. Non-Cryst. Solids **356**, 56 (2010)
18.89 C. Bensalem, M. Mortier, D. Vivien, M. Dial: Optical investigation of Eu^{3+}:PbF_2 ceramics and transparent glass ceramics, Opt. Mater. **33**, 791 (2011)
18.90 M.J. Dejneka: The luminescence and structure of novel transparent oxyfluoride glass ceramics, J. Non-Cryst. Solids **239**, 149 (1998)
18.91 D. Chen, Y. Wang, Y. Yu, E. Ma: Improvement of Er^{3+} emissions in oxyfluoride glass ceramic nanocomposite by thermal treatment, J. Solid State Chem. **179**, 1445 (2006)
18.92 U. Leonhardt: Optical metamaterials – Invisibility cup, Nat. Photon. **1**, 207 (2007)
18.93 S.H. Santagneli, S.J.L. Ribeiro, Y. Messaddeq, L. Misoguti, M. Nalin: Unpublished data
18.94 P. Prasad: *Nanophotonics* (Wiley, Hoboken 2004)
18.95 O.L. Malta, P.A. Santa-Cruz, G.F. de Sá, F. Auzel: Fluorescence enhancement induced by the pres-

ence of small silver particles in Eu^{3+} doped materials, J. Lumin. **33**(2), 261 (1985)
18.96 K. Kneipp, M. Moskovits, H. Kneipp (Eds.): *Surface Enhanced Raman Scattering – Physics and Applications* (Springer, Berlin, Heidelberg 2006)
18.97 A. Simo, U. Joseph, R. Fonger, J. Keipp, K. Rademann: Long-term stable silver subsurface ion-exchanged glasses for SERS applications, Chem. Phys. Chem. **12**(1), 1683 (2011)
18.98 J. Qiu, X. Jiang, C. Zhu, M. Shirai, J. Si, N. Jiang, K. Hirao: Manipulation of gold nanoparticles inside transparent materials, Angew. Chem. Int. Ed. **43**, 2230 (2004)
18.99 A.V. Podlipensky, V. Grebenev, G. Seifert, H. Graener: Ionization and photomodification of Ag nanoparticles in soda–lime glass by 150 fs laser irradiation: A luminescence study, J. Lumin. **109**, 135 (2004)
18.100 H. Amekura, Y. Takeda, N. Kishimoto: Criteria for surface plasmon resonance energy of metal nanoparticles in silica glass, Nucl. Instrum. Met. Phys. Res. B **222**, 96 (2004)
18.101 A.P. Nacharov, N.V. Kikonorov, A.I. Sodorov, V.A. Tsekhomskii: Influence of ultraviolet irradiation and heat treatment on the morphology of silver nanoparticles in photothermorefractive glasses, Glass Phys. Chem. **34**, 693 (2008)
18.102 X. Yang, W. Li, Z. Li, Y. Wei, W. Huang: Depth profiles of Ag nanoparticles in silicate glass, Appl. Phys. A **90**, 465 (2008)
18.103 S. Bahniwal, A. Sharma, S. Aggarwal, S.K. Deshpande: Dielectric spectroscopy of silver nanoparticle embedded soda glass, J. Appl. Phys. **104**, 064318 (2008)
18.104 J. Zhang, W. Dong, J. Sheng, J. Zheng, J. Li, L. Qiao, L. Jiang: Silver nanoclusters formation in ion-exchanged glasses by thermal annealing, UV-laser and x-ray irradiation, J. Cryst. Growth **310**, 234 (2008)
18.105 B. Karthikeyan, M. Anija, C.S.S. Sandeep, T.M.M. Nadeer, R. Philip: Optical and nonlinear optical properties of copper nanocomposite glasses annealed near the glass softening temperature, Opt. Commun. **281**, 2933 (2008)
18.106 J. Feng, X. Zhao, B. Liu, X. Zhou: Microstructural characterization and optical polarization of glass with needle-like micro-nano silver oriented arrangement, Opt. Commun. **281**, 5041 (2008)
18.107 A. Lin, X. Liu, P.R. Watekar, W. Zhao, B. Feng, C. Sun, Y. Wang, W. Han: All-optical switching application of germanium-silicate optical fiber incorporated with Ag nanocrystals, Opt. Lett. **34**, 791 (2009)
18.108 M. Eichelbaum, K. Rademann: Plasmonic enhancement or energy transfer? On the luminescence of gold-, silver-, and lanthanide-doped silicate glasses and its potential for light-emitting devices, Adv. Funct. Mater. **19**, 2045 (2009)
18.109 O.A. Podsvirov, A.I. Sidorov, V.A. Tsekhomskii, A.V. Vostokov: Formation of copper nanocrystals in photochromic glasses under electron irradiation and heat treatment, Phys. Solid State **52**, 1776 (2010)
18.110 P.K. Kuiri: Size saturation in low energy ion beam synthesized nanoparticles in silica glass: 50 keV Ag-ions implantation, a case study, J. Appl. Phys. **108**, 054301 (2010)
18.111 Y. Ma, J. Lin, L.F. Zhu, H.Y. Wey, D.W. Li, S. Qin: Optical properties of Ag nanoparticles embedded silicate glass prepared by field-assisted diffusion, Appl. Phys. A **102**, 521 (2011)
18.112 E. Cattaruzza, M. Mardegan, E. Trave, G. Battaglin, P. Calvelli, F. Enrichi, F. Gonella: Modifications in silver-doped silicate glasses induced by ns laser beams, Appl. Surf. Sci. **257**, 5435 (2011)
18.113 M.G. Ventura, A.J. Parola, A.P. de Matos: Influence of heat treatment on the colour of Au and Ag glasses produced by the sol-gel pathway, J. Non-Cryst. Solids **357**, 1342 (2011)
18.114 J. Shin, K. Jang, K. Lim, I. Sohn, Y. Noh: Formation and control of Au and Ag nanoparticles inside borate glasses using femtosecond laser and heat treatment, J. Appl. Phys. A **93**, 923 (2008)
18.115 H. Masai, Y. Takahashi, T. Fujiwara, Y. Tokuda, T. Yoko: Precipitation of heterogeneous nanostructures: Metal nanoparticles and dielectric nanocrystallites, J. Appl. Phys. **108**, 023503 (2010)
18.116 J.A. Jimenez, S. Lysenko, G. Zhang, H. Liu: Optical properties of silver-doped aluminophosphate glasses, J. Mater. Sci. **42**, 1856 (2007)
18.117 S. Lysenko, J. Jimenez, V. Vikhnin, H. Liu: Excited state dynamics in silver nanoparticles embedded in phosphate glass, J. Lumin. **128**, 821 (2008)
18.118 J.A. Jimenez, H. Liu, E. Fachini: X-ray photoelectron spectroscopy of silver nanoparticles in phosphate glass, Mater. Lett. **64**, 2046 (2010)
18.119 L.R.P. Kassab, C.B. De Araújo, R.A. Kobayashi, R.A. Pinto, D.M. Silva: Influence of silver nanoparticles in the luminescence efficiency of Pr^{3+}-doped tellurite glasses, J. Appl. Phys. **102**, 103517 (2007)
18.120 R. Almeida, D.M. Silva, L.R.P. Kassab, C.B. de Araújo: Eu^{3+} luminescence in tellurite glasses with gold nanostructures, Opt. Commun. **281**, 108 (2008)
18.121 V.K. Raí, L.S. Menezes, C.B. de Araújo, L.R.P. Kassab, D.M. Silva, R.A. Kobayashi: Surface-plasmon-enhanced frequency upconversion in Pr^{3+} doped tellurium-oxide glasses containing silver nanoparticles, J. Appl. Phys. **103**, 093526 (2008)
18.122 L.R.P. Kassab, R. Almeida, D.M. Silva, C.B. de Araújo: Luminescence of Tb^{3+} doped TeO_2–ZnO–Na_2O–PbO glasses containing silver nanoparticles, J. Appl. Phys. **104**, 093531 (2008)
18.123 L.R.P. Kassab, F.A. Bomfim, J.R. Martinelli, N.U. Wetter, J.J. Neto, C.B. de Araújo: Energy transfer and frequency upconvertion in Yb^{3+}–Er^{3+}

doped PbO–GeO_2 glass containing silver nanoparticles, Appl. Phys. B **94**, 239 (2009)
18.124 S. Tirtha, B. Karmakar: Nano Au enhanced upconversion in dichroic Nd^{3+}:Au–antimony glass, Solid State Sci. **11**, 100 (2009)
18.125 L.A. Gomes, F.E.P. Santos, A.S.L. Gomes, C.B. de Araújo, L.R.P. Kassab, W.G. Hora: Near infrared third-order nonlinearity of PbO–GeO_2 films containing Cu and Cu_2O nanoparticles, Appl. Phys. Lett. **9**, 141916 (2008)
18.126 L.R.P. Kassab, D.S. Silva, R. Almeida, C.B. de Araújo: Photoluminescence enhancement by gold nanoparticles in Eu^{3+} doped GeO_2–Bi_2O_3 glasses, Appl. Phys. Lett. **94**, 101912 (2009)
18.127 T. Som, B. Karmakar: Plasmon tuning of nano-Au in dichroic devitrified antimony glass nanocomposites by refractive index control, Chem. Phys. Lett. **479**, 100 (2009)
18.128 T. Som, B. Karmakar: Nanosilver enhancement upconversion fluorescence of erbium ions in Er^{3+}:Ag–antimony glass nanocomposites, J. Appl. Phys. **105**, 013102 (2009)
18.129 L.R.P. Kassab, D.S. Silva, C.B. de Araújo: Influence of metallic nanoparticles on electric-dipole and magnetic-dipole transitions of Eu^{3+} doped germinate glasses, J. Appl. Phys. **107**, 113506 (2010)
18.130 T. Som, B. Karmakar: Enhanced frequency upconversion of Sm^{3+} ions by elliptical Au nanoparticles in dichroic Sm^{3+}:Au–antimony glass nanocomposites, Spectroc. Acta Part A: Mol. Biomol. Spectrosc. **75**, 640 (2011)
18.131 T. Xu, F. Chen, X. Shen, S. Dai, Q. Nie, X. Wang: Observation of surface plasmon resonance of silver particles and enhanced third-order optical nonlinearities in AgCl doped Bi_2O_3–B_2O_3–SiO_2 ternary glasses, Mater. Res. Bull. **45**, 1501 (2011)
18.132 T. Som, B. Karmakar: Nano silver: Antimony glass hybrid nanocomposites and their enhanced fluorescence application, Solid State Sci. **13**, 887 (2011)
18.133 N. Zhavoronkov, R. Driben, B.A. Bregadiolli, M. Nalin, B.A. Malomed: Observation of asymmetrical spectrum broadening induced by silver nanoparticles in a heavy-metal oxide glass, Eur. Phys. Lett. **94**, 37011 (2011)
18.134 H. Masai, Y. Takahashi, T. Fujiwara, Y. Tokuda, T. Yoko: Precipitation of heterogeneous nanostructures: Metal nanoparticles and dielectric nanocrystallites, J. Appl. Phys. **108**, 023503 (2011)
18.135 F. Chen, S. Dai, T. Xu, X. Shen, B. Song, C. Lin, X. Wang, C. Liu, K. Xu, J. Heo: Redshifted surface plasma resonance-induced enhancement of third-order optical nonlinearities in silver nanoclusters embedded in Bi_2O_3–B_2O_3–TiO_2 pseudoternaty glasses, J. Opt. Soc. Am. B **28**, 1283 (2011)
18.136 K. Lance, E. Coronado, L.L. Zhao, G.C. Schatz: The influence of size, shape and dielectric environment, J. Phys. Chem. B **107**, 668 (2003)
18.137 K. Yata, T. Yamaguchi: Ostwald ripening of silver in glass, J. Mater. Sci. **27**, 101 (1992)
18.138 A. Oliver, J.C. Chenang-Wong, J. Roiz, L. Rodriguez-Fernandez, J.M. Hernandez, A. Crespo-Sosa, E. Muñoz: Metallic nanoparticle formation in ion-implanted silica after annealing in reducing or oxidizing atmospheres, Nucl. Instrum. Met. Phys. Res. B **191**, 333 (2002)
18.139 L.G. Jacobson, M.E. Hawley, D.W. Cooke, M. F. Hundley, J.D. Thompson, R.K. Shulze, M. Nastasi: Synthesis of cobalt nanoparticles by ion implantation and effects of postimplantation annealing, J. Appl. Phys. **96**, 4444 (2004)
18.140 A. Podlipensky, A. Abdolvand, G. Seifert, H. Graener: Femtosecond laser assisted production of dichroic 3D structures in composite glass containing Ag nanoparticles, Appl. Phys. Lett. A **80**, 1647 (2005)
18.141 V.L. Colvin, M.C. Schlamp, A.P. Alivisatos: Ligth-emitting-diodes made from cadmium selenide nanocrystals and a semiconducting polimer, Nature **370**, 354 (1994)
18.142 M. Bruchez Jr., M. Moronne, P. Gin, S. Weiss, A.P. Alivisatos: Semiconductor nanocrystals as fluorescent biological labels, Science **281**, 2013 (1998)
18.143 V.I. Klimov, A.A. Milhailovsky, S. Xu, A. Malko, J.A. Hollings-Worth, C.A. Leatherdale, H.J. Eisler, M.G. Bawendi: Optical gain and stimulated emission in nanocrystal quantum dots, Science **290**, 314 (2000)
18.144 N. Peyghambarian, B. Fluegel, D. Hull, A. Migus: Fentosecond optical nonlinearities of CdSe quantum dots, IEEE J. Quantum Electron. **QE25**(12), 2516 (1989)
18.145 V.C. Dneprovskii, V.I. Klimov, D.K. Okorokov, Y.V. Vandyshev: Ultrafast light-induced transmission changes and laser-emission of semiconductor quantum dots, Phys. Status Solidi (b) **173**(6), 405 (1992)
18.146 A.I. Ekimov, A.A. Onushchenko: Quantum size effect in 3-dimensional microscopic semiconductor crystals, JETP Lett. **34**, 345 (1981)
18.147 J. Allegre, G. Arnaud, P. Lefebre: Absorption properties of CdS nanocrystals in glasses – Evidence of both weak and strong confinement regimes, J. Cryst. Growth, **138**(1–4), 998 (1994)
18.148 M. Nogami, S. Suzuki, K. Nogasaka: Sol-gel processing of small-sized CdSe crystal-doped silica glasses, J. Non-Cryst. Solids **135**, 182 (1992)
18.149 Y. Lui, C.S. Reynoso, L.C. Barbosa: Improvement of size-dispersion in CdTe quantum dots in glass by using double annealing process, J. Mater. Sci. Lett. **15**(2), 423 (1996)
18.150 A.A. Onushchenko, E.L. Raaben: Optical properties of phosphate glasses activated with cadmium selenide, Glass Phys. Chem. **23**(1), 84 (1997)

18.151 I. Kang, F.W. Wise: Electronic structure and optical properties of PbS and PbSe quantum dots, J. Opt. Soc. Am. B **14**(7), 1632 (1997)

18.152 S.W. Chen, L.A. Truax, J.M. Sommer: Alkanethiolate-protected PbS nanoclusters: Synthesis, spectroscopic and electrochemical studies, Chem. Mater. **12**, 3864 (2000)

18.153 A. Eychmüller, A. Hässelbarth, L. Katsikas, H. Weller: Fluorescence investigations on the nature of electron and hole traps in Q-sized colloidal particles, Phys. Chem. **95**, 79 (1991)

18.154 Y. Wang, N. Herron: Nanometer-sized semiconductor clusters – Materials synthesis, quantum effects and photophysical properties, J. Phys. Chem. **95**, 525 (1991)

18.155 J. Heo, C. Liu: PbS quantum dots in glass matrix for universal fiber-optic amplifier, J. Mater. Sci. **18**, S135 (2007)

18.156 F.W. Wise: Salt quantum dots: The limit of strong quantum confinement, Acc. Chem. Res. **33**, 773 (2000)

18.157 E.V. Kolobkova, A.A. Lipovskii, V.D. Petrikov: Fluorophosphate glasses with quantum dots based on lead sulfide, Glass. Phys. Chem. **28**, 246 (2002)

18.158 P.D. Persans, L.B. Lurio, J. Pant, G.D. Lian, T.M. Hayes: Zn incorporation in CdS nanoparticles in glass, Phys. Rev. B **63**, 5320 (2001)

18.159 G. Chen, M. Nikl, N. Solovieva, A. Beitlerova, J. Rao, Y. Yang, Y. Zhang, X. Jiang, C. Zhu: Photoluminescent properties of nanocrystallized zinc borosilicate glasses, Radiat. Meas. **38**, 771 (2004)

18.160 J. Del-Castillo, A.C. Yanes, J. Mendes-Ramos: Undoped and Eu^{3+} doped In_2O_3 quantum-dots in transparent glass ceramics, J. Nanosci. Nanotechnol. **9**(8), 4834 (2009)

18.161 A.C. Yanes, J.J. Velázquez, J. del-Castillo, J. Méndez-Ramos, V.D. Rodríguez: Site-selective spectroscopy in Sm^{3+} doped sol-gel derived nano-glass ceramics containing SnO_2 quantum dots, Nanotechnology **19**(29), 295707 (2008)

18.162 C. Liu, J. Heo, X. Zhang, J.L. Adam: Photoluminescence of PbS quantum dots embedded in glasses, J. Non-Cryst. Solids **354**, 618 (2008)

18.163 M.A. Hines, G.D. Scholes: Colloidal PbS nanocrystals with size-tunable near infrared emission: Observation of post-synthesis self-narrowing of the particle size distribution, Adv. Mater. **15**, 1844 (2003)

18.164 R.S. Kane, R.E. Cohen, R. Silbey: Synthesis of PbS nanoclusters within copolymer nanoreactors, Chem. Mater. **8**, 1919 (1996)

18.165 Y. Chen, Z. Wang, Z. Lin, J. Qian, L. Lin: New observation on the formation of PbS clusters in zeolite-Y, Appl. Phys. Lett. **68**, 1990 (1996)

18.166 J. Yang, J.H. Fendler: Epitaxial-growth of size-quantized cadmium-sulfide crystals under arachidic acid monolayers, J. Phys. Chem. **99**, 5505 (1995)

18.167 M. Mukherjee, A. Datta, D. Chakravorty: Growth of nanocrystalline PbS within a glass, J. Mater. Res. **12**, 2507 (1997)

18.168 T. Takada, Y. Nihei, T. Yano, A. Yasumori: Preparation of quantum size CdS-doped Na_2O-B_2O_3-SiO_2 glasses with high nonlinearity, Proc. Int. Conf. Sci. Technol. New Glasses (1991) pp. 418–423

18.169 M. Nogami: Microcrystalline PbS doped silica glasses prepared by the sol-gel process, J. Non-Cryst. Solids **126**, 87 (1990)

18.170 R.S. Sonawane, S.D. Naik, S.K. Apte, M.V. Kulkarni, B.B. Kale: CdS/CdSSe quantum dots in glass matrix, Bull. Mater. Sci. **31**(3), 495 (2008)

18.171 J. Chang, C. Liu, J. Heo: Optical properties of PbSe quantum dots doped in borosilicate glass, J. Non-Cryst. Solids **355**, 1897 (2009)

18.172 K. Xu, C. Liu, W.J. Chung, J. Heo: Optical properties of CdSe quantum dots in silicate glasses, J. Non-Cryst. Solids **356**, 2299 (2010)

18.173 P. Watekar, S. Ju, A. Lin, M.J. Kim, B.H. Lee, W.T. Han: Linear and Non-linear Optical Properties of the PbSe Quantum Dots Doped Germano-Silica Glass Optical Fiber, J. Non-Cryst. Solids **356**, 2384 (2010)

18.174 N.F. Borelli, D.W. Smith: Quantum confinement of PbS microcrystals in glass, J. Non-Cryst. Solids **180**, 25 (1994)

18.175 A.A. Lipovskii, E.V. Kolobkova, V.D. Petrikov: PbSe quantum dot doped phosphate glass, Electron. Lett. **33**, 101 (1997)

18.176 B. Mashford, J. Baldauf, N. Tich-Lam: Synthesis of quantum dot doped chalcogenide glasses via sol-gel processing, J. Appl. Phys. **109**(9), 094305 (2011)

18.177 L.R. Pinckney: Transparent glass ceramics based on ZnO crystals, Phys. Chem. Glasses – Eur. J. Glass Sci. Technol. B **47**, 127 (2006)

18.178 O.R. Ochoa, C. Colajacomo, E.J. Witkowaski, J.H. Simmons, B.G. Potter: Quantum confinement effects on the photoluminescence spectra of CdTe nanocrystallites, Solid State Commun. **98**, 717 (1996)

18.179 A. Meldrum, E. Sonder, R.A. Zuhr, I.M. Anderson, J.D. Budai, C.W. White, L.A. Boatner, D.O. Henderson: A transmission electron microscopy investigation of sulfide nanocrystals formed by ion implantation, J. Mater. Res. **14**, 4489 (1999)

18.180 V.C.S. Reynoso, K. Yukimitu, T. Nogami: Synthesis and growth of PbS semiconductor nanocrystallites, J. Mater. Sci. Lett. **20**(12), 3450 (2001)

18.181 L.C. Liu, S.H. Risbud: Quantum dot size distribution analysis and precipitation stages in semiconductor doped glasses, J. Appl. Phys. **68**, 28 (1990)

18.182 L.C. Barbosa, V.C.S. Reynoso, A.M. de Paula, C.R.M. de Oliveira, O.L. Alves, A.F. Craievich, R.E. Marotti, C.H. Brito Cruz, C.L. Cesar: CdTe quantum dots by melt heat treatment in borosilicate glasses, J. Non-Cryst. Solids **219**, 205 (1997)

18.183 N.F. Borrelli, D.W. Hall, H.J. Holland, D.W. Smith: Quantum confinement effects of semiconducting microcrystallites in glass, J. Appl. Phys. **61**, 5399 (1987)
18.184 J.B.G. Potter, J.H. Simmons: Quantum size effects in optical properties of CdS glass composites, Phys. Rev. B **37**, 10838 (1988)
18.185 L. Bakueva, S. Musikhin, M.A. Hines: Size tunable infrared (1000–1600 nm) electroluminescence from PbS quantum dot nanocrystals in a semiconducting polymer, Appl. Phys. Lett. **82**, 2895 (2003)
18.186 A. Cereyon, A.M. Jurdyc, V. Martinez, E. Burov, A. Pastouret, B. Champagnon: Raman amplification in nanoparticles doped glasses, J. Non-Cryst. Solids **354**, 3458 (2008)
18.187 R. Jia, D.S. Jiang, P.H. Tan, B.Q. Sun: Quantum dots in glass spherical microcavity, Appl. Phys. Lett. **79**, 153 (2001)
18.188 P.T. Guerreiro, S. Ten, N.F. Borrelli, J. Butty: PbS quantum-dot doped glasses as saturable absorbers for mode locking of a Cr:forsterite laser, Appl. Phys. Lett. **71**, 1595 (1997)
18.189 P.R. Watekar, S. Moon, A. Lin, S. Ju: Linear and non-linear optical properties of Si nanoparticles/Er-ions doped optical fiber, J. Lightwave. Technol. **27**, 568 (2009)
18.190 Y. Yu, Y. Wang, D. Chen, P. Huang, E. Ma, F. Bao: Enhanced emissions of Eu^{3+} by energy transfer from ZnO quantum dots embedded in SiO_2 glass, Nanotechnology **19**(5), 055711 (2008)
18.191 I.A. Denisov, N.A. Skoptsov, M.S. Gaponenko: Passive mode locking of 2,09 µm Cr,Tm,Ho:$Y_3Sc_2Al_3O_{12}$ laser using PbS quantum-dot doped glass, Opt. Lett. **34**(21), 3403 (2009)
18.192 M.S. Gaponenko, V.E. Kisel, N.V. Kuleshov: Passive mode locking of diode pumped Tm:KYW laser with PbS quantum-dot doped glass, Laser Phys. Lett. **7**(4), 286 (2010)
18.193 J.R. Lakowicz: Plasmonics in biology and plasmon-controlled fluorescence, Plasmonics **1**, 5 (2006)
18.194 K. Richardson, D. Krol, K. Hirao: Glasses for photonic applications, Int. J. Appl. Glass Sci. **1**(1), 74 (2010)
18.195 V.D. Rodriguez, V.K. Tikhomirov, J. Méndez-Ramos, A.C. Yanes, V.V. Moshchalkov: Towards broad range and highly efficient down-conversion of solar spectrum by Er^{3+}-Yb^{3+} co-doped nano-structured glass ceramics, Sol. Energy Mater. Sol. Cells **94**, 1612 (2010)
18.196 R.P. Panmand, G. Kumar, S.M. Mahajan, N. Shroff, B.B. Kale, S.W. Gosavi: Growth of Bi_2Te_3 quantum dots/rods in glass: A unique highly stable nanosystem with novel functionality for high performance magneto optical devices, Phys. Chem. Chem. Phys. **14**, 47 (2012), published online, DOI: 10.1039/c2cp43169f
18.197 P. Yang, M. Ando, N. Murase: Hybrid SiO_2-coated nanocrystal-based heterostructures: Assembly, morphology transition, and photoluminescence at room temperature, Colloids Interfaces A **384**, 289 (2011)
18.198 K. Xu, J. Heo, W.J. Chung: CdS quantum dots in glass: Modification of photoluminescence by silver doping, Int. J. Appl. Glass Sci. **2**(3), 157 (2011)
18.199 P. Jorge, M.A. Martins, T. Andrade, J.L. Santos, F. Farahi: Optical fiber sensing using quantum dots, Sensors **7**, 3489 (2007)
18.200 J.E. Kesner, R.M. Gavalis, P.Y. Wong, C.G.L. Cao: Multifiber optical bend sensor to aid colonoscope navigation, Opt. Eng. **50**(12), 124402 (2011)
18.201 B. Larrión, M. Hernáez, F.J. Arregui, J. Goicoechea, J. Bravo, I.R. Matias: Photonic crystal fiber temperature sensor based on quantum dot nanocoatings, J. Sens. **2009**, 932471 (2009)
18.202 A. Dhawan, J.F. Muth, D.J. Kekas, T.K. Ghosh: Optical nano-textile sensors based on the incorporation of semiconducting and metallic nanoparticles into optical fibers, MRS Proc. **920**, 0920–S05–06 (2006)
18.203 K. Schroder, A. Csaki, A. Schwuchow, F. Jahn, K. Strelau, I. Latka, T. Henkel, D. Malsch, K. Schuster, K. Weber, T. Schneider, R. moller, W. Fritzsche: Functionalization of microstructured optical fibers by internal nanoparticle mono-layers for plasmonic biosensor applications, IEEE Sens. J. **12**(1), 218 (2012)

Part D NanoComposites

19 Carbon in Polymer

Robert J. Young, Manchester, UK
Libo Deng, Manchester, UK
Lei Gong, Manchester, UK
Ian A. Kinloch, Manchester, UK

20 Nanoparticle Dispersions

Krisztián Kordás, Oulu, Finland
Jarmo Kukkola, Oulu, Finland
Géza Tóth, Oulu, Finland
Heli Jantunen, Oulu, Finland
Mária Szabó, Szeged, Hungary
András Sápi, Szeged, Hungary
Ákos Kukovecz, Szeged, Hungary
Zoltán Kónya, Szeged, Hungary
Jyri-Pekka Mikkola, Åbo-Turku, Finland

19. Carbon in Polymer

Robert J. Young, Libo Deng, Lei Gong, Ian A. Kinloch

This chapter provides insight into the composition, preparation, properties, and applications of composites based on polymer matrix and different forms of nanosized carbon filler. Carbon nanotube and graphene filler materials are discussed in greater detail. The dispersion and orientation of these fillers and the interfacial adhesion between the filler and the matrix material play important roles in determining the mechanical, electrical, and other properties of the composites created. Accordingly, this chapter describes the role as well as the characterization techniques of these properties.

In particular, it will be shown how Raman spectroscopy is becoming an important noninvasive technique both to characterize the electronic structure and to follow the deformation behavior of carbon-based nanomaterials. Such spectroscopic knowledge reveals the intrinsic properties of these nanomaterials, the interaction of the reinforcement with the surrounding environment, and hence the efficiency of the mechanical reinforcement in these composites.

19.1 **Materials Basics** 695
19.1.1 Carbon Nanotubes 696
19.1.2 Graphene 698
19.1.3 Raman Spectroscopy and the Deformation of Carbon Nanomaterials 701

19.2 **Carbon Nanotube Composites** 702
19.2.1 Preparation and Properties of Bulk Composites 702
19.2.2 Preparation and Properties of Composite Fibers 703
19.2.3 Reinforcement Mechanisms and Modelling 703
19.2.4 Fundamental Aspects of CNT Composites 705
19.2.5 Characterization of CNT Composites 709
19.2.6 Characterization of CNT Composites Using Raman Spectroscopy 712

19.3 **Graphene Composites** 716
19.3.1 Preparation Methods 716
19.3.2 Mechanical Properties 716
19.3.3 Functional Properties 719
19.3.4 Nanomechanics 720
19.3.5 Model Graphene Monolayer Composites 720

19.4 **Conclusions** 722

References 722

19.1 Materials Basics

The past 25 years has seen a massive growth of interest in the different forms of carbon-based nanomaterials shown in Fig. 19.1. The discovery of C_{60} buckyballs in 1985 [19.1] spurred an upsurge of research activity leading to the identification of carbon nanotubes in 1991 [19.2] and graphene in 2004 [19.3]. The importance of these findings has been recognized in the awards of Nobel Prizes for both Chemistry (for C_{60} in 1996) and Physics (for graphene in 2010). Much of the original interest in these carbon-based nanomaterials was because of their electronic properties but direct measurements of the mechanical properties of both nanotubes and graphene led to it becoming increasingly clear that the materials have considerable potential as mechanical reinforcements in nanocomposites. Such excellent mechanical properties of nanotubes

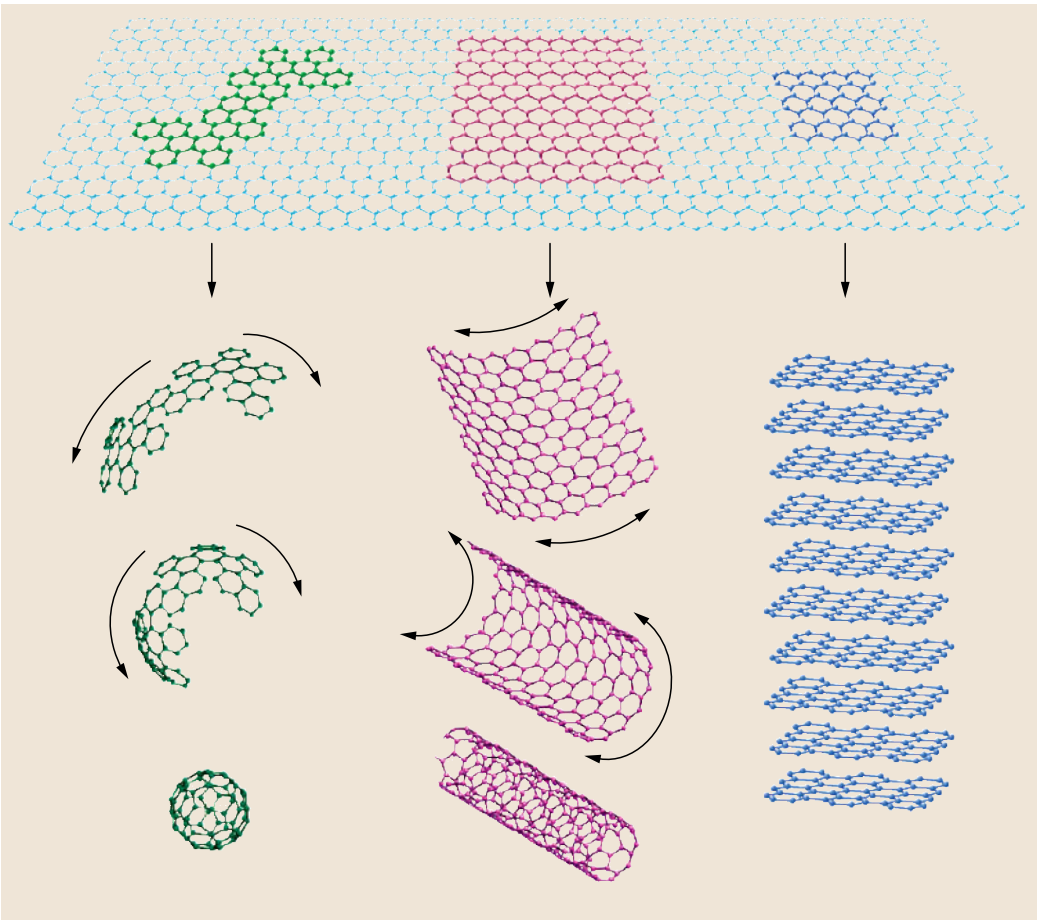


Fig. 19.1 Family of all graphitic forms. Graphene is the 2-D building material for carbon materials of all other dimensionalities. It can be wrapped up into 0-D C_{60} buckyballs, rolled into 1-D nanotubes or stacked into 3-D graphite (after [19.4])

and graphene are related to the strong sp^2 hybridized carbon–carbon bonds and the perfect hexagonal structures from which they are built.

Most of the interest in the use of carbon-based nanomaterials as a composite reinforcement has been concerned with carbon nanotubes and graphene rather than C_{60} as it is well-known that reinforcement by particles is generally less efficient than reinforcement by fibers or platelets [19.5]. Other forms of carbon-based nanomaterials such as carbon black have been used as reinforcements for polymers for over 100 years. For example, a large increase in the Young's modulus and improvements in wear resistance are found when carbon black is incorporated into natural rubber [19.5]. Although carbon black is basically a particulate filler the material has *structure* whereby the particles form networks that lead to better reinforcement than would be encountered with individual particles.

19.1.1 Carbon Nanotubes

Carbon nanotubes (CNTs) are long cylinders of covalently bonded carbon atoms. The carbon atoms are arranged on a hexagonal network and each of them has three neighbours with which they form strong sp^2 hybridized carbon–carbon bonds. There are basically two main types of carbon nanotubes as shown in Fig. 19.2, according to the numbers of graphene cylinder in their structure: single-wall nanotubes (SWNTs) and multi-walled nanotubes (MWNTs); double-wall nanotubes (DWNTs) are a special case of MWNTs [19.6].

An SWNT can be considered as a seamless roll of a single graphene sheet. The nanotube is one atom in thickness (which is 0.34 nm), tens of atoms in circumference, and up to a few millimeters in length. The different ways of rolling graphene into tubes are described by the chirality as defined by the circumferential

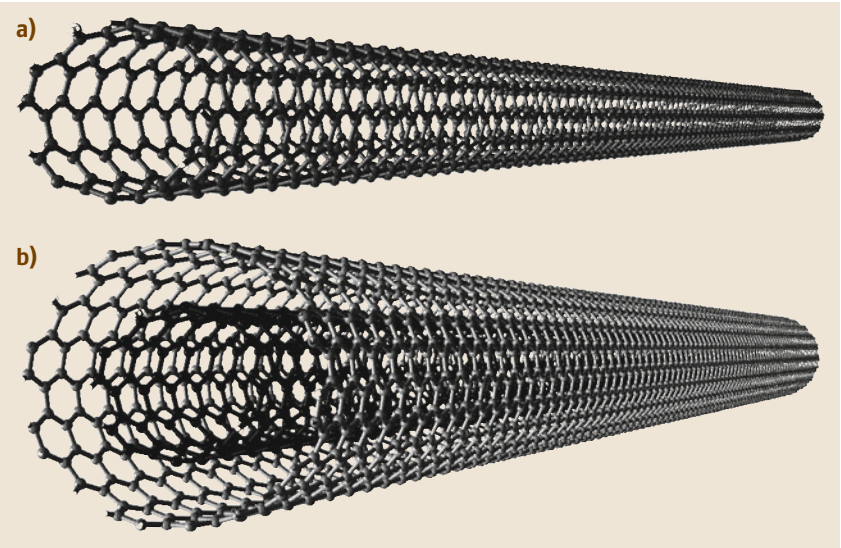


Fig. 19.2a,b Schematic representations of **(a)** single- and **(b)** double-walled carbon nanotubes. Multi-walled nanotubes can have up to 20 layers of nested tubes. (courtesy Dr. F. Ding, Hong Kong Polytechnic University)

vector [19.6]

$$\boldsymbol{C}_h = n\boldsymbol{a}_1 + m\boldsymbol{a}_2 \,, \tag{19.1}$$

where n and m is the length along the unit vectors of the two lattice vectors. MWNTs are made of many coaxial single-wall nanotubes with an interlayer separation of 0.34 nm, and each of the walls may possess different chiralities.

Preparation

Three methods are employed widely to prepare nanotubes: arc-discharge, laser ablation, and chemical vapor deposition (CVD) [19.7]. The first two methods involve the condensation of hot gaseous carbon atoms generated from the evaporation of solid carbon while in the CVD process, a gaseous carbon source is decomposed catalytically and the nanotubes are deposited on a substrate or grown from a substrate. Catalytic-grown nanotubes have fewer impurities but have more defects than the arc-grown nanotubes. The arc-grown CNTs are therefore mechanically stronger than the CVD-CNTs, but the latter will almost certainly find more applications. This is because the length and structure are more controllable in a CVD process than in other methods, and this process is also more amenable to being scaled-up for industrial production [19.7].

Properties

The high aspect ratio, the strong sp^2 carbon–carbon bonds, and the one-dimensional confinement of electronic states, confer CNTs with a range of interesting physical properties such as unique electronic properties, excellent mechanical properties, and good thermal conductivity and electrical conductivity.

SWNTs behave as either semiconductors or metals, depending on the remainder of $(n-m)$ divided by 3: those with $n-m=3k$ are metallic nanotubes while those with $n-m=3k\pm1$ are semiconducting nanotubes (where k is integer) [19.7]. Therefore, approximately one third of SWNTs are metallic and the rest are semiconducting. For semiconducting nanotubes, the band gap decreases as the diameter increases [19.8].

Deformation has a significant effect on the electronic structure of nanotubes. The effect of strain on the electronic structure depends on the deformation mode (i. e. uniaxial strain, torsional strain or radial deformation) and the nanotube chirality. For example, uniaxial strain opens the band gap of nonarmchair metallic nanotubes but has no effect on armchair nanotubes. Torsional strain can change the electronic structure of armchair nanotubes but does not affect zigzag nanotubes [19.8].

Nanotubes and graphite share the same hexagonal network of sp^2 carbons in their structure. Mechanical properties of nanotubes are therefore expected to be comparable with graphite which has in-plane Young's modulus of 1.06 and strength of 130 GPa [19.9, 10]. In fact, some computer simulation work soon after the discovery of nanotubes did predict similar mechanical properties to those of graphite [19.11]. The first actual mechanical measurement on nanotubes was performed using transmission electron microscopy (TEM) in 1996 [19.12]. Since then, bending tests using an

Table 19.1 Physical properties of CNTs and other engineering materials (after [19.14])

Material	Mechanical properties		Thermal conductivity (W/(m K))	Electrical conductivity (S/m)
	Young's modulus (GPa)	Strength (GPa)		
Carbon nanotubes	100	30–100	> 3000	10^6–10^7
Carbon fiber (pitch-based)	300–700	5–7	1000	2–8.5×10^6
Copper	110–128		400	6×10^7

atomic force microscopy (AFM) tip have been developed and used widely [19.13]. A modulus for SWNTs of 1.0 TPa and 0.3–0.9 TPa for MWNTs, and tensile strength of 50–150 GPa for SWNTs and 10–50 GPa for MWNTs are generally quoted by the scientific community. The actual values vary from nanotube to nanotube, cover a wide range, and depend on many factors such as the nanotube type, preparation method, purity and diameter.

Theoretical work has predicted a very high thermal conductivity for CNTs, of approximately 6000 W/(m K), while experimental work has recorded a value of 3000 W/(m K). MWNTs have been found to also exhibit good electrical conductivity, which is in the range of 10^6–10^7 S/m (as a comparison, the copper has a thermal conductivity of 400 W/(m K) and electrical conductivity of 6×10^7 S/m) [19.14]. The physical properties of CNTs and a comparison with typical engineering materials are summarized in Table 19.1.

19.1.2 Graphene

Graphene is the basic building block of all graphitic forms of carbon and consists of a single atomic layer of sp^2 hybridized carbon atoms arranged in a honeycomb structure as shown in Fig. 19.1. There has been an explosion of interest in the study of the structure and properties of graphene following the first report in 2004 of the preparation and isolation of single graphene layers by *Novoselov* and coworkers [19.3] in Manchester, UK, for which they were awarded the 2010 Nobel Prize in Physics. It had long been thought that the isolation and study of single layer graphene would not be feasible since such 2-D crystals would be unstable thermodynamically [19.15] and/or might roll up into scrolls if prepared as single atomic layers [19.16]. Subsequent studies have shown that this is certainly not the case.

Preparation

Considerable effort has been put into the development of methods of preparing high quality graphene in large quantities for both research purposes and with a view to eventual applications [19.17]. Since the first isolation of graphene in 2004 two general approaches have been developed to prepare the material. One is to take graphite and break it down into graphene by techniques such as a mechanical cleavage or exfoliation (sometimes termed *top-down*). The other method is to synthesize graphene using techniques such as *chemical vapour deposition* CVD (often known as *bottom-up*).

Expanded graphite was developed more than 100 years as a filler for the newly-developed polymer resins and it has been investigated continually over the intervening period [19.18, 19]. In more recent times there have been other developments in the preparation of thinner forms of graphite, known as graphite nanoplatelets (GNPs) [19.20] which can be produced by a number of techniques that include the exposure of acid-intercalated graphite to microwave radiation, ball-milling and ultrasonication. The addition of GNPs has been found to lead to substantial improvements in the mechanical and electrical properties of polymers at lower loadings than would be needed with expanded graphite [19.21, 22]. Although the definition of GNPs strictly covers all types of graphitic material from 100 nm thick platelets down to single layers [19.20], it is the availability of single- or few-layer graphene that has caused by far the most excitement in recent times.

The simplest, and probably the most celebrated, way of preparing small samples of single- or few-layer graphene is by the mechanical cleavage (repeated peeling of graphene layers with adhesive tape) from either highly-oriented pyrolytic graphite or good-quality natural graphite [19.3]. An optical micrograph of a sample prepared by mechanical cleavage and deposited upon a polymer substrate is shown in Fig. 19.3. This method typically produces a mixture of one-, two- and many-layer graphene flakes with dimensions of the order of tens of micrometers.

As soon as the interest in graphene for use in applications that required high volumes of material, such as in composites, people tried to develop methods of undertaking large-scale exfoliation. One of the first successful methods was the exfoliation and dispersion of graphite in organic solvents such as *N*-methylpyrrolidone [19.23, 24]. The method yields about

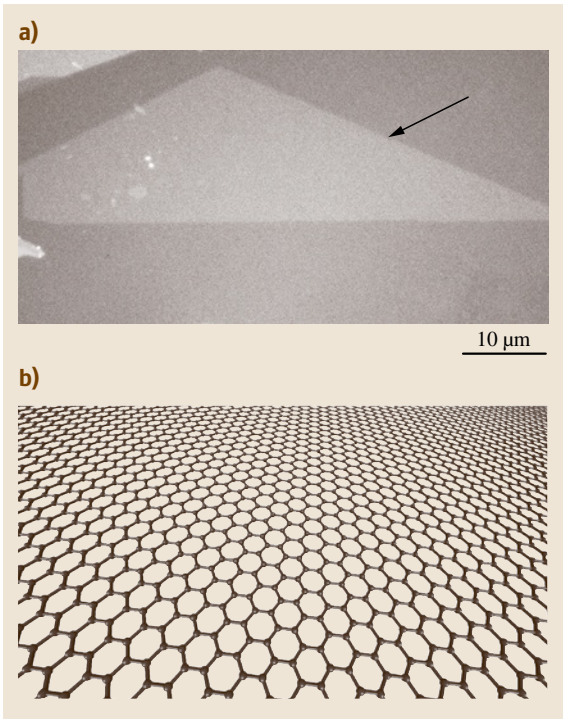


Fig. 19.3 (a) Optical micrograph of a graphene monolayer (indicated by an *arrow*) prepared by mechanical cleavage and deposited on a polymer substrate. (courtesy K.S. Novoselov, Univ. Manchester) (b) Schematic representation of a graphene monolayer on the atomic level (courtesy F. Ding, Hong Kong Polytechnic Univ.)

1% of graphene monolayers along with bi-layer and multilayer material. Although the graphene produced by this method is relatively defect-free and not oxidized the lateral dimensions of the monolayers are typically only of the order of a few micrometers.

Graphite oxide was first prepared over 150 years ago by *Brodie* in his attempt to determine the *atomic weight* of graphite [19.25] through oxidation using potassium chlorate and fuming nitric acid. Two methods used these days are based upon the development of the Brodie method by *Staudenmaier* [19.26] which was then refined by *Hummers* and *Offeman* [19.27] who employed a water-free mixture of concentrated sulfuric acid, sodium nitrate and potassium permanganate to treat the graphite more quickly and safely. The Brodie material was found to be highly-oxidized with a C/O/H ratio of around 2.2/1/0.8 [19.25] which is typical of graphite oxide produced by these chemical routes. The current state-of-the-art in the preparation of graphite oxide has been summarized and reviewed by *Ruoff* and coworkers [19.28, 29].

Graphite oxide is made up of stacks of *graphene oxide* sheets, with an interlayer spacing of between 0.6 and 1.0 nm depending upon the relative humidity [19.28], in a similar way to which graphite is made up of stacks of more closely spaced graphene sheets. An important difference, however, is that graphite oxide can be readily exfoliated by simple sonication to produce colloidal suspensions of graphene oxide sheets using a range of solvents [19.28,29] which has led to the present upsurge of interest in the material with the view to scaling up production to produce material in large quantities for applications such as in composites. The graphene oxide that is produced directly from graphite oxide is not particularly useful in that it is thermally unstable and does not conduct electricity. Its properties are greatly improved through reduction, either chemical or thermal, although it has not yet proven to be possible to reduce the material fully back to graphene.

Properties

The original excitement in graphene was because of its electronic properties, with its charge carriers exhibiting very high intrinsic mobility, having zero effective mass and being able to travel distances of micrometers at room temperature without being scattered [19.4,30]. The majority of the initial research upon graphene concentrated upon these electronic properties and was aimed at applications such as in electronic devices [19.31, 32].

Interest in the material has now broadened considerably as it was soon realized that graphene might have other interesting physical properties such as high levels of thermal conductivity, stiffness and strength, coupled with impermeability to gases. One obvious application was in the field of nanocomposites [19.33] and researchers working upon nanocomposites using other forms of nanocarbon such nanotubes, and nanoclays were soon able to refocus their efforts towards graphene nanocomposites. In addition there was preexisting expertise in exfoliating graphite (e.g. expanded graphite) and in the preparation of graphene oxide (originally termed *graphite oxide*). The latter was shown to be relevant to the study of graphene, in that it can be reduced chemically towards a material that is closely related to graphene.

The direct determination of the mechanical properties of monolayer graphene was first undertaken by *Lee* et al. [19.34] by the nanoindentation of graphene membranes, suspended over holes of around 1.0 and

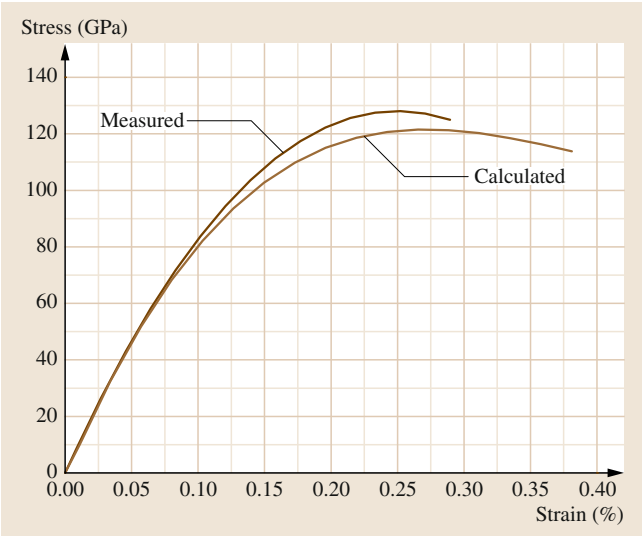


Fig. 19.4 Measured [19.34] and calculated [19.35] stress–strain curve for the deformation of a graphene monolayer

1.5 μm in diameter on a silicon substrate, in an AFM. The monolayers were found using optical microscopy and identified using Raman spectroscopy. The variation of force with indentation depth was determined and the stress–strain curve was derived assuming the graphene behaves mechanically as a 2-D membrane with a thickness of 0.335 nm. The graphene was found to break at large displacements with fracture starting at the indentation point. Figure 19.4 shows the stress–strain curve for the graphene derived from the analysis of the indentation experiments and it can be seen that it becomes nonlinear as the strain increases with fracture occurring at a strain in excess of 20%.

Earlier, in 2007, *Liu* et al. [19.35] undertook an ab initio calculation, using density functional theory, of the stress–strain curve of a single layer graphene and this is also plotted in Fig. 19.4. It can be seen that there is remarkably good agreement between the experimentally-derived curve and the theoretical analysis. The experimentally-determined value of Young's modulus [19.34] is 1000 ± 100 GPa which compares very well with the theoretical estimate [19.35] of 1050 GPa and the value of 1020 GPa determined many years ago for bulk graphite [19.36]. The strength of the graphene monolayer was found experimentally to be 130 ± 10 GPa which is of the order of $E/8$, where E is the Young's modulus, and close to the generally-accepted value of the theoretical strength of a defect-free material [19.37]. The failure stress can also be determined from the peak stress in the stress–strain curve calculated using density functional theory in Fig. 19.4. The high-strain behavior is found to differ slightly depending upon the crystallographic direction in which the graphene is deformed [19.35] and the strength is predicted to be in the range 107–121 GPa, again in very good agreement with the experimental measurements.

It is to be expected that the mechanical properties of graphene oxide are inferior to those of graphene due to the disruption of the structure through oxidation and the presence of sp^3 rather than sp^2 bonding. The elastic deformation of chemically-reduced graphene oxide has been investigated by *Gomez-Navarro* et al. [19.38], again using an AFM indentation technique on a suspended film of material. In this case they suspended single layers of graphene oxide up to 1 μm^2 in size over a trench in a SiO_2/Si wafer and monitored force-displacement curves when the AFM tip was pushed into the film. They determined a Young's modulus of 250 ± 150 GPa, although there was considerable scatter in their data. In addition they noted that graphene oxide sheets consisting of 3 or more layers had a Young's modulus an order of magnitude lower than this value.

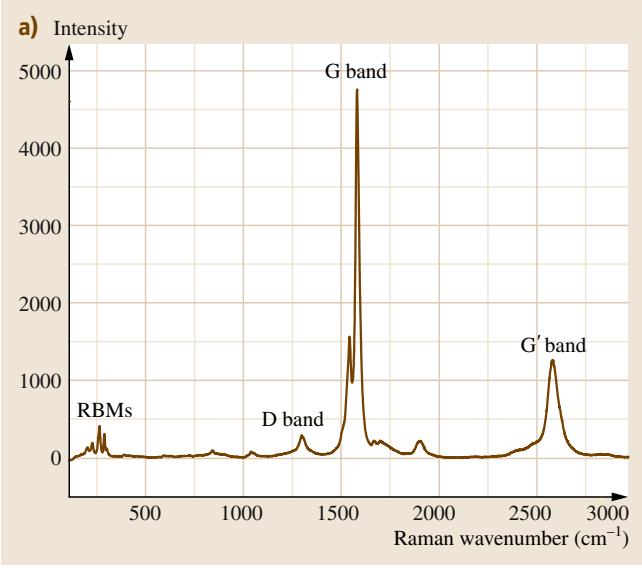


Fig. 19.5a A typical Raman spectrum of SWNTs showing the four characteristic bands

19.1.3 Raman Spectroscopy and the Deformation of Carbon Nanomaterials

The Raman spectroscopy of different carbon nanomaterials has become an important research topic since the first work on CNTs was published in 1997. This technique is particularly useful for investigation of the properties of SWNTs due to the resonance effects. Four characteristic Raman bands are found for SWNTs, namely the radial breathing modes (RBMs), G-band, D-band and G′-band (also called the 2-D band) carry a large amount of structural information and have been studied in most detail, although several other weaker and broader features have also been observed in the nanotube spectra [19.39]. A typical Raman spectrum of SWNTs is shown in Fig. 19.5a.

Raman spectroscopy can also be used to characterize and identify different forms of graphene as shown in Fig. 19.5b and, in addition, the Young's modulus of graphene can also be determined indirectly from stress-induced Raman band shifts. Stress-induced Raman band shifts have been found to occur for a number of high-performance materials such as high-modulus polymer fibers [19.40], carbon fibers [19.41] and CNTs [19.42]. It is found that in general the rate of band shift per unit strain scales with the Young's modulus of the material [19.40]. When carbon fibers are subjected to tension there is an approximately linear shift of the G and G′ (or 2-D) band positions to lower wavenumber with strain [19.41, 43]. *Cooper* et al. [19.43] showed that for the G′ band, the rate of shift increased with the carbon fiber modulus. They went on to show that there was in fact a linear dependence of the shift rate upon modulus which implied that there is a universal dependence of band shift upon stress for the G′ band of $-5\,\mathrm{cm}^{-1}/\mathrm{GPa}$ [19.43]. Both CNTs and graphene have well-defined G′ bands and assuming that the universal calibration for carbon fibers can be used for the same band in other forms of carbon, then the Young's modulus of these other material can be estimated.

Large stress-induced shifts of both the G and G′ bands are found when graphene is subjected to stress [19.44–49] and this phenomenon has recently been reviewed by *Ferralis* [19.50]. The simplest way of deforming the material is to deposit exfoliated material on a substrate which is then stretched or flexed in a Raman spectrometer. The behavior is shown in Fig. 19.6 for the deformation of monolayer graphene on a poly(methyl methacrylate) beam [19.47]. It can be seen that there is a large shift in the position of the G′ band with strain and the slope of the line is of the order of $-60 \pm 5\,\mathrm{cm}^{-1}/\%$ strain. Using the universal calibration of $-5\,\mathrm{cm}^{-1}/\mathrm{GPa}$ for carbon fibers, this slope corresponds to a Young's modulus for a graphene monolayer of $(-60 \times 100)/(-5)$ GPa, equivalent to 1200 ± 100 GPa and similar to the values measured both directly and calculated theoretically.

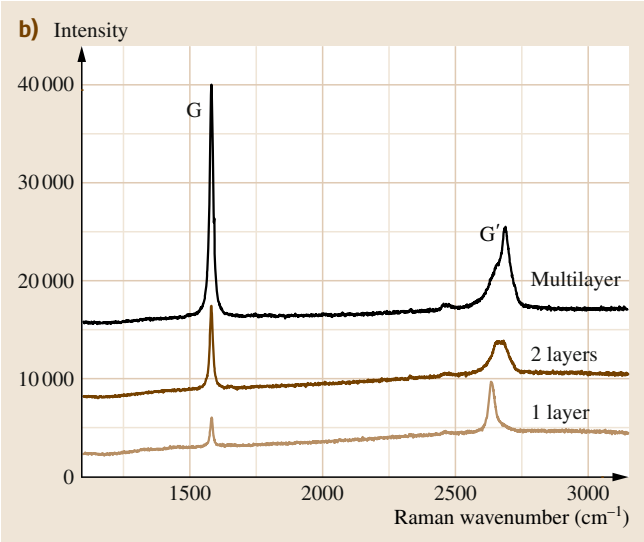


Fig. 19.5b Typical Raman spectra of mechanically cleaved graphene with different numbers of layers

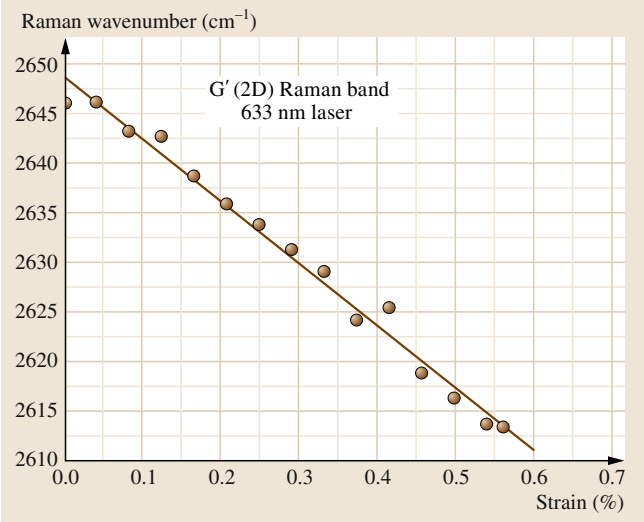


Fig. 19.6 Shift of the G′ Raman band with strain for single-layer graphene

19.2 Carbon Nanotube Composites

One of the best ways to fulfil the enormous potential of CNTs is to incorporate them into polymers. It has been demonstrated CNTs can significantly improve the mechanical properties, electrical conductivity, thermal conductivity, thermal stability and fire-retardant ability of polymers [19.7]. There has been impressive progress and interests are still growing in this area since the first polymer/CNT composite was prepared by *Ajayan* et al. in 1994 (their initial purpose, though, was not to make a composite but to prepare a TEM sample) [19.52].

Mechanical reinforcement on polymers is probably one of the most promising applications of nanotubes. In fact, CNTs have shown reinforcement in Young's modulus, tensile strength and toughness for a variety of polymers and the amount of nanotubes required to achieve significant improvement is much lower than the conventional fillers such as high performance fibers and clay. The extraordinary mechanical properties, high specific surface area, and high aspect ratio make nanotubes ideal candidates for polymer reinforcement [19.53–55].

This section reviews the preparation methods, mechanical properties, the factors that determine the mechanical properties of polymer/CNT composites and the techniques to characterize these factors. The preparation and properties of polymer/CNT bulk composites and composite fibers are considered separately. While there are numerous articles dealing with mechanical reinforcement of polymers by nanotubes, only a few typical examples are summarized.

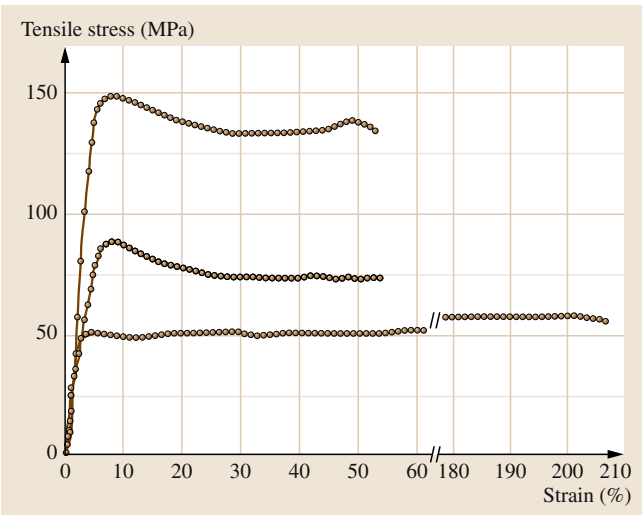


Fig. 19.7 Typical stress–strain curves for PVA and PVA/SWNT films (after [19.51])

19.2.1 Preparation and Properties of Bulk Composites

Most studies on CNT composites have been carried out with bulk composites due to their ease of preparation. The basic methods to produce CNT composites are solution processing and melt processing, and other methods have been developed, by firstly dispersing and integrating nanotubes with polymers and then by using solution or melt processing to prepare the final composites.

Solution processing is probably the most common method for the preparation of polymer/CNT composites. In a typical process [19.7, 9, 53], the nanotubes are firstly dispersed in a solvent, the nanotube dispersion is then mixed with the polymer solution by energetic agitation and finally the composite is obtained by either controlled evaporation or coagulation. Any polymers that are soluble can be processed using this method in theory and small amount of nanotubes leads to significant improvement in mechanical properties of the polymer in most cases. For example, *Ryan* et al. incorporated different types of nanotubes into poly(vinyl alcohol) (PVA) matrix and prepared thin films by solution processing [19.56]. They observed a threefold increase in Young's modulus and twofold increase in tensile strength for the composite containing only 0.1% of Elicarb SWNTs. The exceptional high efficiency of reinforcement is thought to be related to crystallization of polymers nucleated by the nanotubes. *Zhang* et al. also observed a 60% increase in Young's modulus and a 200% increase in tensile strength of PVA by adding 5% of HiPco SWNTs [19.51]. Figure 19.7 shows typical stress–strain curves of the neat PVA and PVA/SWNT composite films.

Melt processing is a common alternative technique to prepare polymer nanocomposites for polymers that are insoluble in solvent but melt when heated and it is most suitable for industrial production [19.9]. This method includes three steps [19.7, 9, 53]: the polymers are firstly melted to form a viscous liquid, nanotubes are then added into the melt and dispersed by a high shear force and finally composites are obtained by compression molding or extrusion. Good mechanical reinforcing efficiency has been found in a range of com-

posites that are fabricated using melt processing. *Liu* et al. prepared a nylon-6 (PA 6)/MWNTs composite using a melt-compounding approach [19.57]. The elastic modulus and yield strength were improved by 214 and 162%, respectively for composites with 2% MWNTs loading and the reinforcement was explained as a consequence of strong interfacial adhesion in the composite *Díez-Pascual* et al. produced poly(ether ether ketone). (PEEK)/SWNT composites using a similar method and observed a 27% increase in storage modulus at room temperature at 1% loading of arc-SWNTs [19.58]. Nanotubes have been incorporated into other polymers such as polypropylene (PP), poly(methyl methacrylate) (PMMA), polycarbonate (PC), and polystyrene (PS) using this process.

Other methods such as in-situ polymerization and solid-state pulverization have also been employed to prepare CNT composites. In an in-situ polymerization process, polymerization of the monomers occur on nanotube surface such that the polymers are grafted onto the nanotubes, the polymer-modified nanotubes are then processed by solution or melt processing. The main advantage of this method lies in that it provides a better dispersion of nanotube and stronger interface between the nanotubes and the polymer matrix. *Velasco-Santos* et al. introduced chemically functionalized MWNTs into PMMA matrix by in-situ polymerization. With 1% of MWNTs, the storage modulus and tensile strength of the matrix were improved by 66% and 40%, respectively [19.59].

19.2.2 Preparation and Properties of Composite Fibers

Fibers such as polyacrylonitrile (PAN) and poly(*p*-phenylene benzobisoxazole) (PBO) fibers are favoured over bulk polymers for many applications [19.9]. Generally, CNTs show more promising reinforcement in fibers than in bulk composites due to the possibility of improved alignment. The most important methods to fabricate polymer/CNT composite fibers include melt spinning, coagulation spinning and electrospinning.

The process for melt spinning of fibers is similar to the melt processing of bulk composite except that the dopes are extruded through a smaller nozzle and fibers are drawn further. *Kearns* and *Shambaugh* prepared PP/SWNT composite fibers by melt spinning [19.60]. The modulus and tensile strength were increased by 56 and 45% respectively by adding 1% of SWNTs. They also observed an increase of the elongation at break from 19 to 27%, which is of particular significance for the composite fibers.

Coagulation spinning is a new method which was first reported by *Vigolo* et al. in 2000 [19.61]. This method disperses SWNTs using a surfactant solution and coagulates the nanotubes into a mesh by spinning it into an aqueous PVA solution. *Dalton* et al. optimized this method and prepared super tough PVA/SWNT composite fibers containing 60% of SWNTs, which had a tensile strength of 1.8 GPa, comparable to that of spider silk [19.62]. What leads to this simple method attracting much attention is the extraordinary toughness of the fiber, of 570 J/g, which is much higher than that of any existing high-performance fiber.

Electrospinning is the only method that can prepare fibers as small as several nanometers in diameter to date and it is the most effective technique to orient nanotubes in composites [19.63, 64]. In the electrospinning process, a high electric voltage is applied to a polymer solution (or melt) such that the solution is charged. When the electrostatic force overcomes the surface tension, a charged jet emanates from the nozzle, the solvent evaporates and fibers are deposited on the collector (Fig. 19.8 for a schematic diagram of the process). The nanotubes in the fibers are aligned by the strong drawing force exerted by the electric field. *Young* et al. demonstrated recently that the nanotube orientation has a dominant effect on the fiber strength [19.65]. The good orientation achieved in electrospun fibers is thus expected to enhance the strength of the fiber significantly. *Almecija* et al. measured the mechanical properties of individual PVA/SWNT electrospun nanofibers and observed an effective modulus of 27 TPa and effective strength of 600 GPa for the nanotubes, suggesting a superb reinforcing efficiency that has never been achieved in less-aligned CNT composites [19.66]. These values are much higher than the theoretical mechanical properties of nanotubes. Nanotube-nucleated polymer ordering and crystallization might be responsible for this extraordinary reinforcement.

19.2.3 Reinforcement Mechanisms and Modelling

For composites for which the properties of the polymer matrix are unaffected by the nanotubes, mechanical reinforcement originates from stress transfer to the nanotubes. In an ideal case where long and highly aligned nanotubes are embedded in polymers, the mechanical properties of the composite can be described

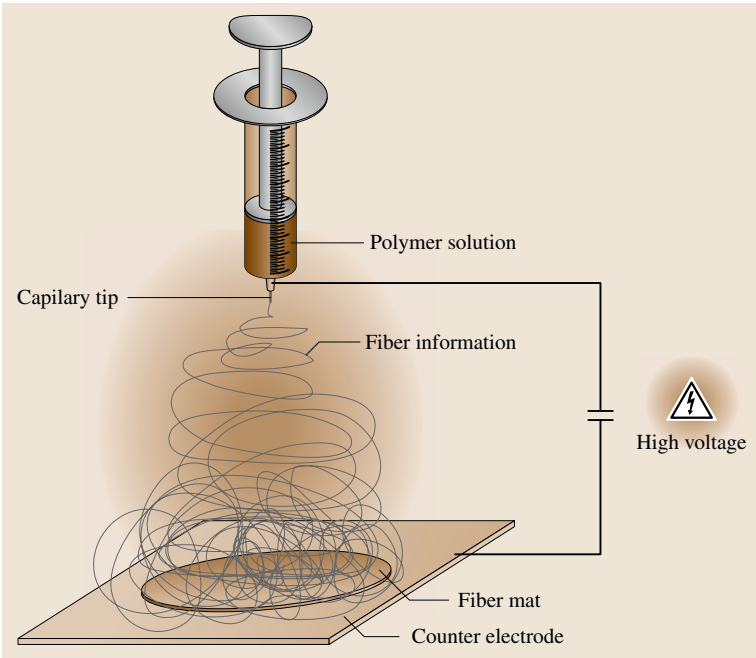


Fig. 19.8 A laboratory setup for an electrospinning experiment (after [19.63])

by the simple rule of mixtures [19.67]

$$E_c = V_{NT}E_{NT} + (1 - V_{NT})E_m \,, \tag{19.2}$$

$$\sigma_c = V_{NT}\sigma_{NT} + (1 - V_{NT})\sigma_m \,, \tag{19.3}$$

where E_c, E_{NT}, and E_m are the modulus of the composite, nanotubes, and the polymer matrix, respectively; σ_c, σ_{NT}, and σ_m are the strength of the composite, nanotubes, and the polymer matrix, respectively; and V_{NT} is the volume fraction of nanotubes.

When all nanotubes are not aligned in the same direction and the length is too short such that the stress is nonuniform in the majority part of the nanotube, the mechanical properties of the composite are given by [19.9]

$$E_c = \eta_o \eta_L V_{NT}E_{NT} + (1 - V_{NT})E_m \,, \tag{19.4}$$

$$\sigma_c = \eta_s V_{NT}\sigma_{NT} + (1 - V_{NT})\sigma_m \,, \tag{19.5}$$

where η_o is the orientation efficiency factor, η_L is the length efficiency factor, and η_s is the strength efficiency factor. The effective modulus E_{eff} of nanotubes which is defined as $E_{eff} = \eta_L E_{NT}$ (similarly, σ_{eff} is defined as $\sigma_{eff} = \eta_s \sigma_{NT}$), accounts for the length and bundling effect on nanotube modulus. The effective modulus and strength allow the efficiency of mechanical reinforcement in different composite systems to be compared.

The important results for the mechanical properties of bulk composites and composite fibers reported in the literature are summarized in Tables 19.2, 19.3, respectively. The effective modulus (E_{eff}) and strength (σ_{eff}) of nanotubes which characterize the efficiency of reinforcement are back-calculated using the rule of mixtures and assuming the matrices were unaffected by nanotubes in all these cases. It is noted although nanotubes

Table 19.2 Mechanical properties of CNT-reinforced bulk composites

CNT type	Polymer	CNT (vol.%)	E_c (GPa)	E_m (GPa)	E_{eff} (GPa)	σ_{eff} (GPa)	Reference
SWNT	PVA	5	4	2.5	33	2	[19.51]
DWNT	Epoxy	10	10.9	3	82	0.3	[19.68]
MWNT	PP	0.5	1.12	0.77	70	2.8	[19.69]
MWNT	PC	2	2.6	2	32	0.46	[19.70]
MWNT	PA6	1	1.24	0.4	84	3	[19.57]
MWNT	PS	0.5	1.69	1.19	100	0.64	[19.71]
MWNT	PMMA	0.5	2.6	1.6	200	2.4	[19.72]

Table 19.3 Mechanical properties of CNT-reinforced polymer fibers

CNT type	Polymer	CNT (vol.%)	E_c (GPa)	E_m (GPa)	E_{NT} (GPa)	σ_{NT} (GPa)	Reference
SWNT	PVA	3	35.8	25.6	366	7.6	[19.73]
SWNT	PA 6	0.1	0.54	0.44	100	45	[19.74]
SWNT	PP	0.7	1	0.4	86	–	[19.75]
SWNT	PBO	12	167	138	380	16	[19.76]
SWNT	PAN	0.9	1.07	0.9	730	19	[19.77]

display reinforcing effect on a range of polymers, only few of them have values of E_{eff} and σ_{eff} approaching the theoretical values for individual nanotubes (i. e. 1000 GPa for modulus and 30–100 GPa for strength). Moreover, the degree of strength improvement is less than that of the modulus improvement in most cases, which is believed to be due to the shortened length and bundling effect of nanotubes in composites. This suggests the mechanical performance of composites can be further improved. A better understanding of the structure/property relationship is needed and this requires powerful techniques to characterize the composites, which will be reviewed in the following sections.

Nanotubes can nucleate some polymers such as PVA to crystallize on their surface and the crystalline layer is much stiffer than the surrounding amorphous polymers. In this case the modulus and strength of the composites are higher than those predicted by the simple rule of mixtures, which is due to the contribution of the stiffer crystalline phase. *Coleman* et al. modified the rule of mixtures to calculate the composite modulus considering the contribution of the three phases [19.54]

$$E_c = \eta_o E_{eff} V_{NT} + E_a \left(1 - V_{NT}\right) + \left(E_\chi - E_a\right)\left(\frac{b^2 + 2r_t b}{r_t^2}\right) V_{NT}\,, \qquad (19.6)$$

where E_a is the modulus of the amorphous polymer, E_χ is the modulus of the crystalline phase, b is the average thickness of the nanotube-nucleated crystalline layer and r_t is the nanotube radius.

When the nanotube induced crystallization occurs, the fracture of the composite occurs at the interface between the bulk polymer and the crystalline layer. The composite strength can be described as a sum of the strength of the bulk polymer and the interface. *Coleman* et al. developed another form of rule of mixtures to calculate the composite strength which is given by [19.78]

$$\sigma_c = \tau \frac{(r_t + b)\, l_p}{r_t^2} V_{NT} + \sigma_m \left[1 - \frac{(r_t + b)\, V_{NT}}{r_t^2}\right], \qquad (19.7)$$

where τ is the interfacial shear strength, σ_m is the tensile strength of the polymer, and l_p is the pull out length of nanotubes. Equations (19.6) and (19.7) suggest that the crystalline layer has a significant effect on mechanical properties of the composites when b is large, and the simple rule of mixtures is not valid when the properties of polymer matrix are affected upon addition of nanotubes.

19.2.4 Fundamental Aspects of CNT Composites

Although nanotubes have exhibited their promising reinforcing effect in composites, there is still a gap between the measured and the theoretical values of modulus and strength. It is recognized that the dispersion, orientation and the interfacial adhesion have significant effect on mechanical properties of composites [19.79]. This section discusses how these factors influence the properties and how to optimize them in the composite structure.

Dispersion

The state of dispersion is probably the most important factor that determines the mechanical properties of composites and good dispersion of nanotubes is crucial for any composite. The state of dispersion of nanotubes can influence the mechanical properties of composites through the following aspects [19.79]:

1. The surface area decreases when individual nanotubes tend to aggregate into ropes (or bundles). The surface area is important for mechanical reinforcement because:
   a) It acts as an interface for stress transfer, and larger surface area leads to higher efficiency of stress transfer.
   b) When the nanotubes are in ropes, the load is carried mainly by the nanotube on the perimeter of each rope which is evidenced by the inter-tube sliding when subjected to external stress [19.80]. Hence, larger nanotube ropes re-

sult in smaller effective volume fraction for reinforcing fillers.

2. Nanotubes can induce polymers to crystalline on their surface. The crystalline layer, which is related to the nanotube surface area, can determine the mechanical performance for some semi-crystalline polymer composites [19.54, 78].
3. Good dispersion gives rise to a uniform distribution of stress and minimizes the stress concentration centres in the composites. Poor dispersion which results in stress concentrations consequently leads to a smaller degree of strength improvement than that of modulus improvement.
4. The mechanical properties of nanotubes bundles are much poorer than those of individual nanotubes. *Salvetat* et al. measured the modulus of nanotube ropes by bending the nanotubes with an AFM tip [19.81]. They found the modulus decreased from over 1 TPa for the nanotube rope with a diameter of 3 nm to 149 GPa for the rope with a diameter of 13.5 nm.

The aforementioned theoretical analysis of the effect of dispersion has been supported by a range of experimental works. For example, *Song* and *Youn* observed a greater improvement in tensile strength and elongation at break for epoxy composites with good MWNTs dispersion compared to a poorly dispersed system [19.82]. *Zhu* et al. compared the mechanical properties of epoxy composites containing untreated SWNTs (poor dispersion) and functionalized SWNTs (good dispersion), and found that the tensile strength is worse for a poorly dispersed system than the neat epoxy, whereas the modulus and strength are increased by 18 and 30% respectively for composite with good dispersion of nanotubes [19.83]. Although they claimed that the relatively better reinforcement was a consequence of the improvement of dispersion, the effect of a stronger interface, however, could not be excluded as improvements in dispersion are usually coupled with an increase of interfacial adhesion with the matrix.

Nanotube exfoliation can be accomplished by stirring, shear mixing and/or ultrasonication [19.9]. Stable and uniform dispersions of pristine nanotubes are however difficult to achieve using these techniques alone. Compared to MWNTs, SWNTs are even more difficult to disperse because they possess larger specific surface area and have a stronger tendency for aggregation. In addition, intensive mechanical agitation can induce defects and damage the sidewall structure, which consequently degrades the mechanical properties of nanotubes. Two main methods have thus been developed to facilitate the dispersion of nanotubes in polymers:

1. Dispersing nanotubes with the aid of surfactants or other dispersants. The dispersant molecule wrapping around the nanotubes can induce strong noncovalent bonding with the matrix, giving rise to stable dispersion. *Gong* et al. [19.84] prepared epoxy/CNT composites using a nonionic surfactant to assist dispersion of nanotubes. They found the elastic modulus is increased by 30% by adding 1% of nanotubes, while the incorporation of nanotubes without the surfactant has only a moderate effect on mechanical properties.
2. Introducing covalent bonding between nanotubes and the matrix by chemically functionalizing the nanotubes. This can be achieved by introducing functional groups (such as carboxyl group) or by grafting matrix polymer onto the nanotube surface through in-situ polymerization. Improving the dispersion via chemical functionalization confers extra benefit, i. e. better interfacial adhesion in the composites.

It should be pointed out however, there is a maximum volume fraction for isolated nanotubes in the polymer matrix, assuming the minimum separation between the nanotubes is the radius of a polymer molecule. For nanotubes arranged in hexagonal arrays, the separation S_{hex} between the nanotubes is given by [19.37]

$$S_{\text{hex}} = d_{\text{t}}\left(\sqrt{\frac{\pi}{2\sqrt{3}V_{\text{NT}}}} - 1\right), \tag{19.8}$$

where d_{t} is the nanotube diameter. The typical radius for a polymer is of the order of 5 nm [19.85]. For SWNTs with an average diameter of 1 nm, more than 2.5% of nanotubes in the polymer will naturally lead to nanotube aggregation, and in the case of MWNTs with a diameter of $\approx$ 10 nm, the maximum volume fraction for individual nanotubes is 40%.

Orientation

Carbon nanotubes show highly anisotropic mechanical properties, e.g. the longitudinal modulus is $\approx$ 1000 GPa while the transverse modulus is only $\approx$ 15 GPa [19.86, 87]. The mechanical properties of composites are thus strongly dependent on the orientation of nanotubes and the mechanical reinforcing efficiency is lower when all nanotubes are not aligned in the same direction. A Cox

orientation efficiency factor η_o can be introduced to the rule of mixtures to take into account the effect of orientation distribution of the reinforcing fillers on properties of the composites [19.43, 88]. The parameter η_o can be considered as a summation of contribution of all fillers (nanotubes) lying at any angle Ψ with respect to the longitudinal direction of the composite

$$\eta_o = \sum_n a_n \cos^4 \Psi \,, \tag{19.9}$$

where a_n is the proportion of fillers lying at the angle Ψ_n and is given by $\sum_n a_n = 1$. For fillers randomly distributed in a plane (2-D distribution), η_o is an integration over the range $-\pi/2 - \pi/2$ and is given by

$$\eta_o = \frac{1}{\pi} \int_{-\pi/2}^{\pi/2} \cos^4 \Psi \mathrm{d}\Psi = \frac{3}{8} \,, \tag{19.10}$$

while for fillers randomly distributed in three dimensions, η_o can be determined by

$$\eta_o = \frac{1}{\pi} \int_{0}^{\pi/2} \sin \Psi \cos^4 \Psi d\Psi = \frac{1}{5} \,. \tag{19.11}$$

This indicates the modulus and strength of nanotubes is 3/8 (for 2-D distribution) or 1/5 (for 3-D distribution) of those of the uniaxially-aligned nanotubes. Some reports are consistent with these theoretical values. For example, *Thostenson* and *Chou* prepared PS/SWNT composites and observed an increase of 49% in storage modulus for an aligned composite, whereas for a randomly oriented composite the modulus was increased by only 10% compared to the bulk polymer [19.89]. This means a fivefold relative increase for the aligned system over the randomly oriented system.

There are a variety of methods to align nanotubes in composites. These techniques can be generally classified into two categories:

1. Aligning nanotubes using fiber spinning techniques such as melt spinning, coagulation spinning and most efficiently, electrospinning. In the electrospinning process, there are tremendous drawing forces acting on tiny jets of the polymer solution, which leads to the rigid-rod like nanotubes rotating around their centre of gravity and orienting along the drawing direction to minimize the torque applied to them. Similarly, the shear force in a melt spinning process and the drawing force in a mechanical stretching process can also orient the nanotubes in the composites. Fiber spinning processes together with the mechanical stretching are the most common methods to align nanotubes in composites.
2. Aligning nanotubes using magnetic or electric fields. A high magnetic field is efficient to align nanotubes along the magnetic field axis when the diamagnetic susceptibilities parallel to the nanotube axis is larger than that perpendicular to the nanotube axis. In 2002, *Kimura* et al. [19.90] firstly demonstrated the magnetic field-induced orientation of MWNTs in a PS matrix. In this process, MWNTs were dispersed in a monomer solution of unsaturated polyester, and then a constant magnetic field of 10 T was applied to align nanotubes. Polymerization under the strong magnetic filed yielded good alignment of nanotubes, and this was revealed by the anisotropic properties of the composites. This procedure has been followed and modified by a number of groups to achieve good orientation.

It should be pointed out that good orientation can only be achieved when nanotubes are well separated because nanotubes bundles are often entangled during growth. Aligned nanotube arrays can be grown directly on substrates, but few examples that transfer the arrays and preserve their alignment in composites have been reported [19.91].

Interfacial Adhesion

The interfacial adhesion between the polymer matrix and nanotubes is a key factor for the properties of nanocomposites because it determines the efficiency of stress transfer from the matrix to the reinforcing filler [19.9, 10]. Adequate interfacial stress transfer from the matrix to the nanotubes is only possible when the interface has not failed during composite loading [19.92–94].

The interfacial shear strength (IFSS) is defined as the maximum shear stress before the interface fails. It governs the maximum stress transferred to the nanotube and is quite sensitive to the nanotube and matrix type, as well as the bonding type, i. e. whether it is covalent bonding or noncovalent bonding [19.9, 55]. *Liao* and *Li* found that in the absence of covalent bonding between the nanotubes and the matrix, the nanotube/matrix adhesion comes from a) electrostatic and van der Waals interactions and b) stress/deformation arising from the mismatch in the coefficients of thermal expansion between nanotubes and the polymer matrix [19.95].

There are four mechanisms for composite fracture, namely fiber fracture, fiber pull out, fiber/matrix debonding, and matrix cracking (Fig. 19.9) [19.55].

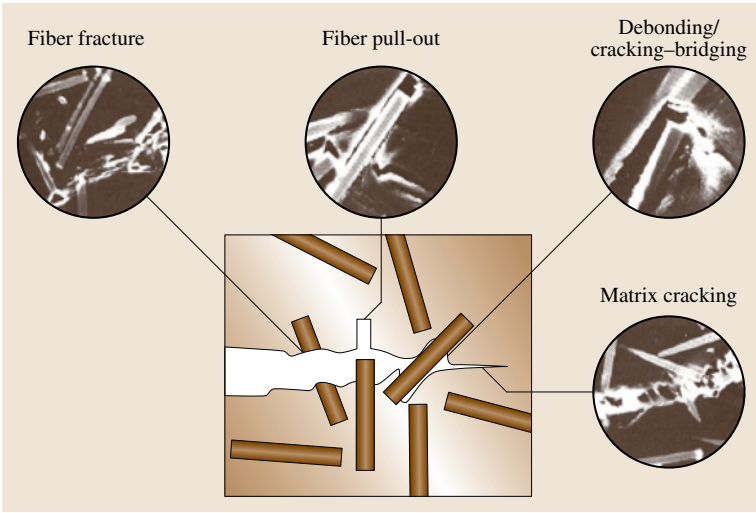


Fig. 19.9 Schematic diagram showing the fracture mechanisms of nanocomposites (after [19.55])

Which kind of fracture occurs depends on the relative strength among the polymer matrix, the interface between the bulk polymer and interfacial polymer, and the nanotube–matrix interface.

For noncovalently bonded systems, the nanotube-polymer interfacial strength is around 50 MPa, and for covalently bonded systems this value is typically of a few hundred MPa although large variation has been found in the literature [19.93]. *Barber* et al. found the average stress to pull out a single MWNT from a polyethylene-butene/MWNT composite is 47 MPa, which is about ten times higher than the system made up of the same polymer and carbon fibers [19.93]. They inferred that covalent bonding existed between the polymer matrix and the defects of MWNTs. *Cooper* et al. determined that the interfacial strength for epoxy/CNT composites ranges from 42 MPa to $\approx$ 300 MPa and concluded that substantial adhesion between nanotubes and the epoxy resin exists in some cases, probably related to the defects on the nanotubes [19.94]. *Coleman* et al. found an exceptional high IFSS of 95 MPa for their PVA/MWNT films [19.78]. They ascribed this to the nucleation effect of nanotubes which induced the polymer to form a crystalline coating around the nanotubes.

The interface can be tailored, according to the matrix type, by introducing different functional groups onto nanotube surface. *Barber* et al. functionalized MWNTs with carboxylic groups and found that the IFSS increased significantly from 30 MPa for epoxy/pristine-MWNT interface to 150 MPa for the chemically functionalized system [19.96]. *Duncan* et al. modified the MWNTs with epoxide terminated groups which can further react with the matrix polycarbonate through thermal trans-esterification reaction [19.97]. They found the IFSS almost triples upon chemical functionalization, from the range of 5–14 MPa for untreated MWNTs to the range of 11–38 MPa for the functionalized system.

In addition to the effect of dispersion, orientation and interfacial adhesion, other factors such as the nanotube type and the preparation method of nanotubes can also influence the mechanical properties of the composites. Essentially, these factors influence the mechanical reinforcing through the more fundamental aspects, namely the dispersion, orientation and the interfacial stress transfer. For example, *Chae* et al. compared the reinforcing efficiency of different types of nanotubes on PAN and found a general trend of SWNT $\approx$ MWNT $>$ DWNT [19.98]. They explained this as a result of a better dispersion and orientation of SWNTs (or MWNTs) than those of DWNTs (because the DWNTs they used were highly entangled and were difficult to align) in the composites.

The nanotube aspect ratio, however, has a more profound effect on the reinforcing efficiency. When the composite is deformed, the stress is transferred to the nanotubes through a shear mechanism and the stress in the nanotubes builds up from the ends to the midsection. The length required for the stress to build up until the nanotube has a strain equal to that of the matrix is called the stress transfer length. At a critical nanotube length l_c, the stress transferred to the nanotube is large enough to break the nanotube. If the interfacial shear stress along the nanotube is assumed to be constant (the

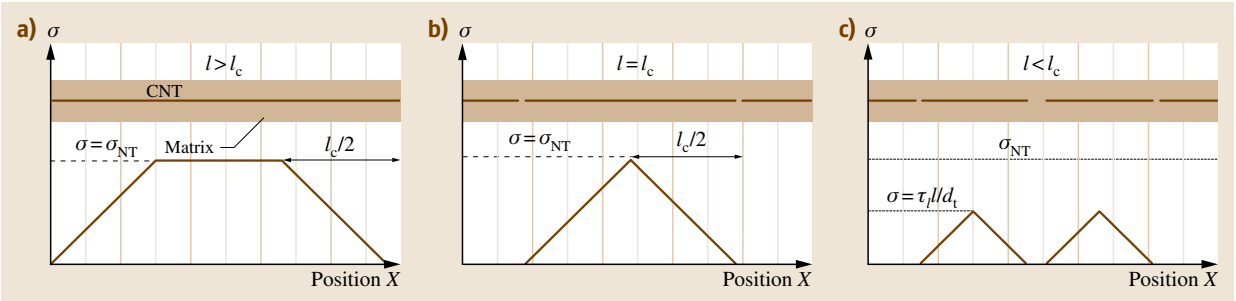


Fig. 19.10a–c The idealized profile of stress in nanotube composites that contain nanotubes with different lengths: **(a)** Nanotubes longer than the critical length; **(b)** nanotubes equal to the critical length; **(c)** nanotubes shorter than the critical length (after [19.97])

Kelly–Tyson model [19.37]), the critical length can be determined by [19.97]

$$l_c = \frac{d_t \sigma_{NT}}{\tau_{ave}} , \qquad (19.12)$$

where σ_{NT} is the nanotube tensile strength and τ_{ave} is the average interfacial shear stress. The profiles of stress along nanotubes that possess different lengths l are shown in Fig. 19.10 and it can be seen the regions of nanotubes near the ends are less heavily stressed and nanotubes do not carry the maximum load when they are too short ($l < l_c$). Hence, the reinforcing efficiency decreases as the fiber length (or the aspect ratio) is reduced [19.67].

19.2.5 Characterization of CNT Composites

Dispersion

Despite the importance recognized unanimously of nanotube dispersion on mechanical properties of the composites, the assessment of dispersion state relies largely on qualitative and subjective interpretation of TEM and SEM images. Efforts have been made to quantify the dispersion by analysing the images. *Lillehei* et al. established a quantitative approach by analysing the frequency of spatial features in SEM images to evaluating the dispersion quality [19.99]. Their approach allowed the estimation of diameter of nanotube bundle, the segment length and bundle spacing. *Luo* et al. employed ImageJ software to measure the free-path spacing between nanotubes in TEM images and used a parameter $D_{0.1}$ to quantify the dispersion quality. This parameter is defined as the probability of the free-path distance distribution in the range of $0.9-1.1\mu$, where μ is the mean spacing [19.100]. Figure 19.11 shows an example of the process of quantitative assessment based on TEM images.

Fluorescence spectroscopy is another useful technique for the assessment of dispersion. When a semiconducting nanotube absorbs excitation light via an E_{22} transition, it emits the light through a $c_1 \rightarrow v_1$ transition (c_1 and v_1 are the first conduction and valence bands, respectively). The emission is quenched when the nanotubes are in bundles. Only truly debundled nanotubes can therefore be detected by fluorescence spectroscopy and this can be obtained only for an extremely low loading of nanotubes in composites. Such composites are not of particular interest for mechanical reinforcement, but are of great importance for studying the intrinsic properties and the interaction with the environment at the single nanotube level.

Other techniques such as optical microscope, UV-Vis spectroscopy, small angle neutron scattering (SANS), size exclusion chromatography (SEC) [19.101] and differential scanning calorimetry (DSC) [19.102] have also been employed to examine the dispersion quality. *Fagan* et al. compared the reliability of four techniques, i. e. SANS, fluorescence spectroscopy, optical absorption spectroscopy and Raman spectroscopy for evaluating the dispersion [19.103]. They demonstrated that the first two techniques both offer reliable measures due to their sensitivity to bundling or clustering of nanotubes and are more definitive than the latter two techniques. While the SANS technique is powerful in evaluating the local dispersion quality on the nanoscale (i. e. the size of individual nanotubes or nanotube bundles), it does not give information as to the distribution of bundle spacing which is a measure of the uniformity of the dispersion.

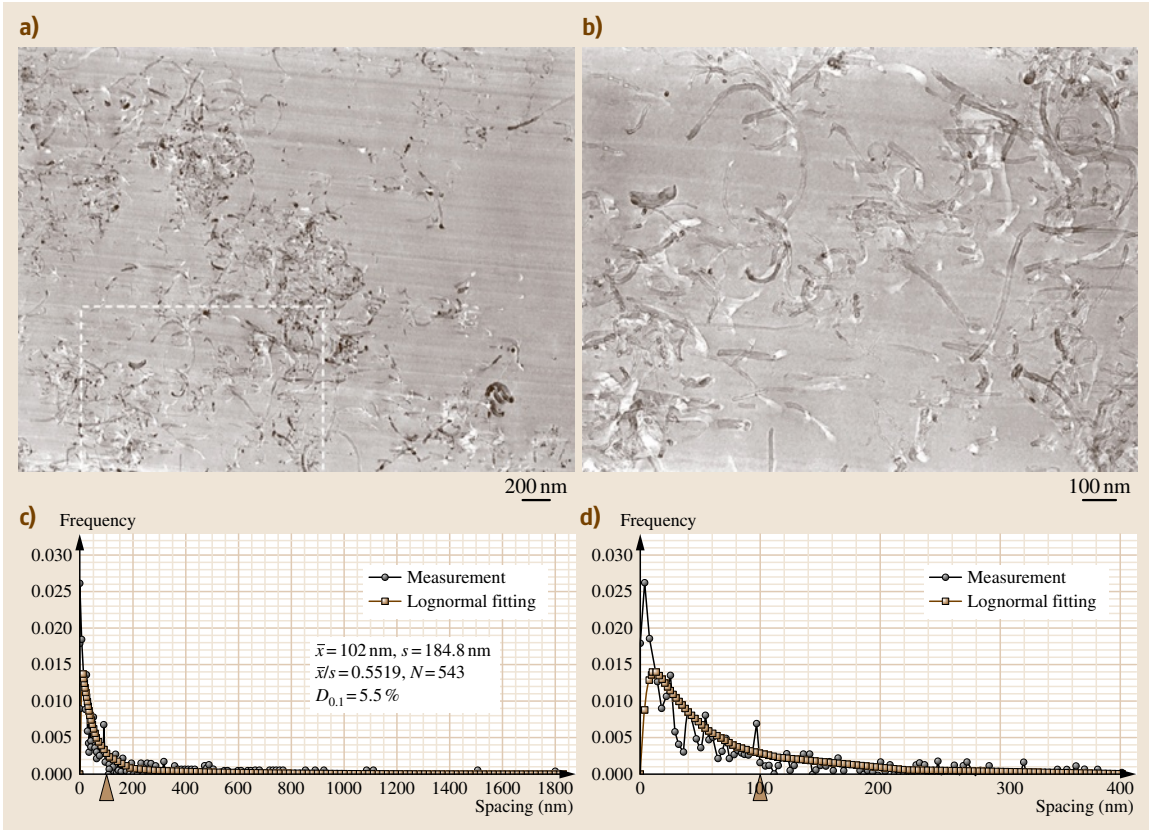


Fig. 19.11 **(a)** A TEM image of a thermoset polymer/MWNT composite; **(b)** enlargement from the framed area in **(a)**; **(c)** histogram of the filler free-path spacing measured from **(a)**; **(d)** enlarged histogram from **(c)** showing the short spacing range (after [19.100])

Orientation

TEM is the most common characterization technique which provides a direct view of the arrangement of nanotubes in composites. It is however difficult to image SWNTs with TEM due to the low contrast between polymers and SWNTs. This is made even more difficult when SWNTs are well separated. *Salalha* et al. used a reactive ion etching process to etch the polymer matrix so that SWNTs are exposed (Fig. 19.12) [19.104]. The processing time needs to be carefully controlled to reduce the matrix thickness without damaging the SWNTs. Characterizing the orientation using TEM requires tedious and careful sample preparation and it should be noted cutting the composites into slices using a diamond knife (a common method for TEM sample preparation) may lead to the nanotubes orient along the cutting direction, as has been demonstrated by *Ajayan* et al. in an early example [19.52].

Orientation of the nanotubes (particularly MWNTs) can also be characterized using x-ray diffraction. Figure 19.13 shows the wide angle x-ray diffraction (WAXD) pattern of PAN/MWNT composite nanofibers. The arc at $2\Phi = 26.5°$ is identified as the diffraction of (002) crystal plane of MWNTs. By azimuthal scanning of the (002) diffraction arc, the average value of the angle β between the molecular axis and the fiber axis can be determined. A quantitative parameter, i. e. Herman's orientation factor f, can then be determined by

$$f = \frac{\left(3\left\langle\cos^2\beta\right\rangle - 1\right)}{2} \,. \qquad (19.13)$$

Using this method, *Ge* et al. determined the orientation factor of both polymer molecules and nanotubes in PAN/MWNT nanofibers and found the nanotubes are better oriented than the polymer molecules [19.105].

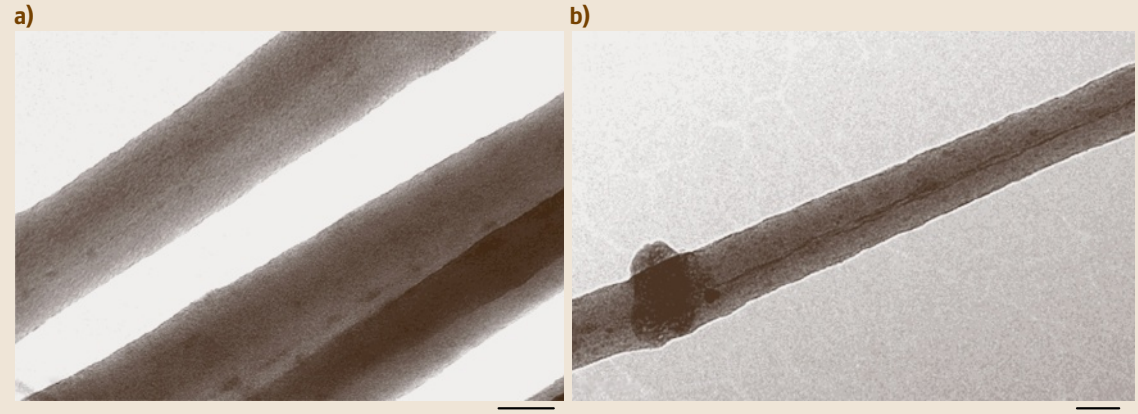


Fig. 19.12a,b TEM images of poly(ethylene oxide) (PEO)/SWNT electrospun fibers before etching **(a)** and after etching showing the good orientation of SWNTs **(b)**, bar = 50 nm (after [19.104])

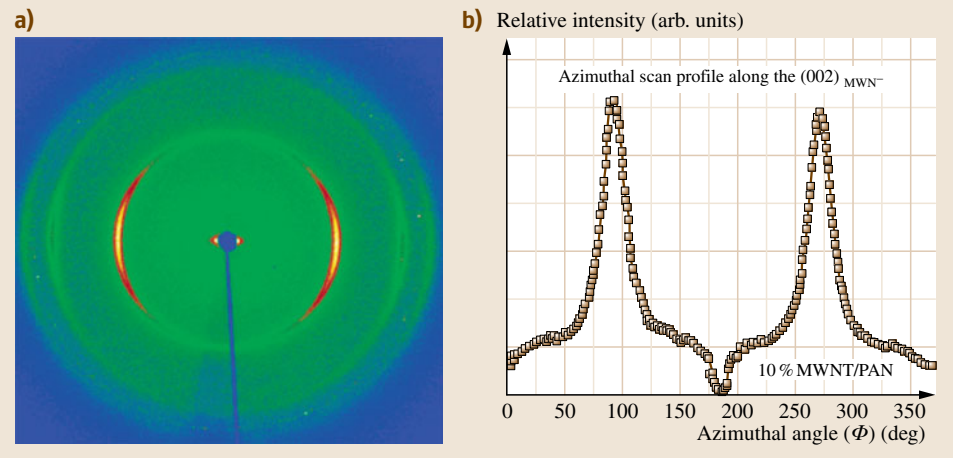


Fig. 19.13 **(a)** Two-dimensional WAXD pattern of PAN/MWNT composite fibers. **(b)** The azimuthal scan of (002) diffraction ring from **(a)** (after [19.105])

However, to acquire appreciable intensity requires a relatively high loading of nanotubes in the composites, and for some type of SWNTs, there is no Bragg peak at all.

Interfacial Adhesion

The interfacial adhesion and strength can be examined qualitatively by SEM observation of the fracture surface which gives the information on the failure mechanism (i. e. whether the composite fails due to nanotube pull out, nanotube fracture or matrix failure). TEM has been used to investigate the wetting of nanotubes in polymer and crystallization of polymer on the nanotube surface. These all produce indirect information on interfacial adhesion, however.

AFM and scanning probe microscopy (SPM) tips can be utilized to apply small and accurate force to nanotubes. Combining these tips with electron microscopy, the IFSS in nanotube composites can be determined quantitatively. Barber et al. carried out a nanopullout experiment on nanotube composites. For a typical measurement, an individual nanotube is attached to the end of an AFM tip and is then pushed into a liquid epoxy polymer. After curing of the epoxy, the nanotube is pulled away from the matrix by the tip which is driven by a cantilever (Fig. 19.14). The embedded length l_{emb} (or equivalently the pull out length l_p) can be measured using SEM (by measuring the free length of nanotube before and after pull out), TEM (by measuring the empty cylinder in the matrix upon pull out) and AFM (by measuring the depth of the hole). The pull out force applied by the cantilever can be calculated by $F_{pull} = KD$, where K is the spring constant

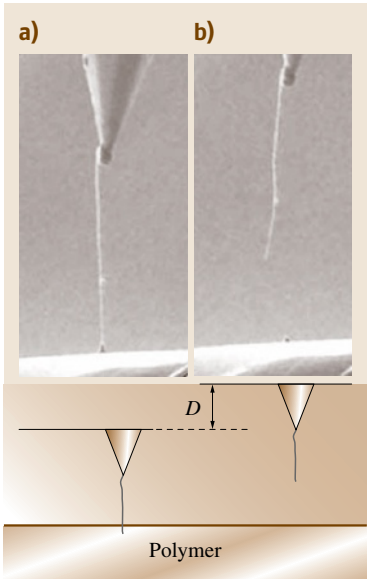


Fig. 19.14a,b SEM images of a MWNT before **(a)** and after **(b)** pulling out from an epoxy by an AFM tip. *Bottom* schematic movement of the AFM tip (after [19.96])

and D is the bending deflection of the cantilever. The average interfacial shear stress τ_{ave} is given by

$$\tau_{ave} = \frac{F_{pull}}{\pi d_t l_{emb}} . \qquad (19.14)$$

Using this method, *Barber* et al. measured the IFSS for polyethylene-butene/MWNT to be 47 MPa [19.93], for epoxy/MWNT to be 30 MPa and a much higher IFSS for epoxy/MWNT-COOH to be 150 MPa [19.96]. *Cooper* et al. used a SPM tip to pull nanotubes out from the epoxy matrix and found that IFSS for epoxy/MWNT ranges from 35 to 380 MPa [19.94].

19.2.6 Characterization of CNT Composites Using Raman Spectroscopy

Raman qspectroscopy has becoming an important technique to characterize polymer/CNT composites. This technique shows the advantages over the other techniques in the rich information it can provide, the capability of studying the composites structure on the molecular scale and simple sample preparation. In fact, Raman spectroscopy has been employed to study almost all aspects that influence the mechanical properties of nanocomposites.

Dispersion

Raman spectroscopy provides a qualitative but convenient way to assess the dispersion of nanotubes in composites. For composites containing a single type of nanotube (i. e. SWNTs or MWNTs), the Raman intensity is proportional to the amount of nanotubes in the laser spot for a given laser. The dispersion of nanotubes can therefore be monitored by mapping out the Raman band intensity across the composite. The spatial resolution depends on the laser spot size, which is mostly on the order of a few micrometers.

Rasheed et al. prepared poly(styrene-*co*-vinyl phenol) (PSVPh)/SWNT composites and examined the dispersion of nanotubes using Raman spectroscopy combined with optical microscopy. They mapped out the nanotube G-band intensity and found the oxidized nanotubes are more evenly distributed than the pristine nanotubes in the composite [19.106].

Assessment of the dispersion on the nanoscale (i. e. individual nanotubes) is a more complicated issue. When SWNTs are separated into individual ones, the Raman features including the band frequency, intensity and lineshape are different from those of nanotube bundles. For example, the RBM peaks shift to higher frequencies by 1–9 cm^{-1} upon debundling, and some RBM peaks (e.g. the 267 cm^{-1} peak when excited with a 785 nm laser) seen in nanotube bundles are absent when the SWNTs are individualized [19.80].

Orientation

Raman spectroscopy is an important technique in characterising the orientation of nanotubes. It is particularly powerful in determining the orientation of individual SWNTs which is difficult to achieve using other techniques such as TEM or XRD.

The degree of alignment of SWNTs can be determined quantitatively using polarized Raman spectroscopy. This is based on the orientation dependent Raman band intensity of nanotubes: the Raman band intensity is a maximum when the nanotube axis is parallel to both the incident and scattered laser and is a minimum when the nanotube is perpendicular to the axis of laser polarization [19.107]. This orientation dependence of the Raman scattering is ascribed to the polarization behavior of nanotubes, where the absorption of the light polarized parallel to the nanotube axis is up to ≈ 20 times stronger than for perpendicularly polarized light, which in turn influences the resonance enhancement in the Raman spectra of nanotubes [19.108].

Characterization of the orientation is usually performed using a polarized Raman spectroscopy with the VV configuration where the incident light and scattered light are both parallel to the principal axis of the spectrometer, the VH configuration where the incident light is parallel and the scattered light is perpendicular to the

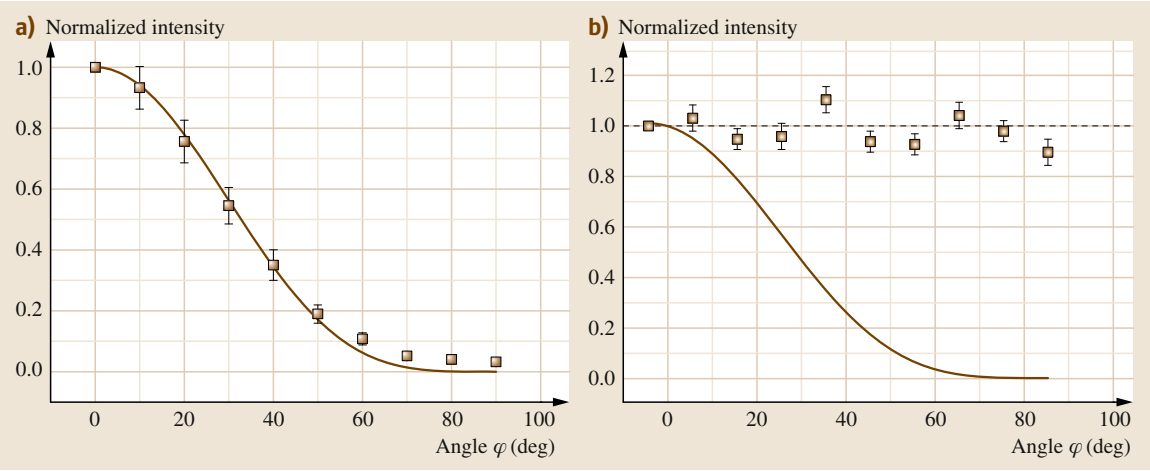


Fig. 19.15 **(a)** Variation of nanotube G-band intensity recorded using the VV configuration, as a function of the angle ϕ between the fiber axis and the laser polarization direction for an electrospun PVA/SWNT fiber. **(b)** G-band intensity obtained for the PVA/SWNT film rotated at different angles ϕ and using the VV configuration The solid lines are generated for $I \propto \cos^4 \phi$ expected for perfect orientation (19.15) (after [19.109])

principal axis of the spectrometer and the HH configuration where the incident light and scattered light are both perpendicular to the principal axis of the spectrometer. An example of this is shown in Fig. 19.15 for a PVA/SWNT nanocomposite [19.109]. In the case of an electrospun fiber the intensity of the G-band decreases as the fiber is rotated relative to the axis of laser polarization. In contrast, for a nanocomposite film of the same composition the intensity of the G-band does not change as the film is rotated.

Several models describing the dependence of Raman band intensity upon the nanotube orientation have been proposed. A typical model based on the resonance theory is briefed as follows: for perfectly aligned nanotubes using a VV configuration, the dependence of scattering intensity upon the angle α between the nanotube axis and the axis of laser polarization is found to be [19.107]

$$I_{VV} \propto \cos^4 \alpha \,. \tag{19.15}$$

For a composite comprising nanotubes over a range of angles the total Raman band intensity can be integrated to sum the contribution from nanotubes at each angle. The Raman band intensity $I(\phi)$ at a sample angle ϕ is given by [19.107]

$$I(\phi) \propto \int_{\phi-\pi/2}^{\phi+\pi/2} F(\alpha-\phi, \Delta) \cos^4 \alpha \mathrm{d}\alpha \,, \tag{19.16}$$

where ϕ is the composite angle with respect to the axis of laser polarization, $F(\alpha-\varphi, \Delta)$ is an orientation distribution function (ODF). The degree of alignment is characterized by the parameter Δ which indicates the average orientation angle. *Hwang* et al. found a special Lorentzian function fitted their data well [19.107]

$$\mathrm{F}(\alpha-\phi, \Delta) = \frac{\Delta/2\pi}{(\alpha-\phi)^2 - (\Delta/2)^2} \,. \tag{19.17}$$

Anglaret et al. used both Lorentzian and Gaussian functions as the ODF [19.110] and obtained slightly different results for the orientation distribution. More recently, *Pérez* et al. derived a Wigner function as the ODF and simplified to Legendre polynomials after symmetry considerations [19.111] The method based on (19.16) can give the orientation factor as well as the fraction of nanotubes that make an angle Δ with respect to the sample axis. It has been used by a number of groups with a variety of samples.

Liu and *Kumar* proposed another model to calculate the orientation factor of nanotubes [19.112]. Considering that the Raman band intensity of SWNTs is determined by its polarizability tensor rather than the derivative of the polarizability tensor, and assuming a uniaxial orientation of the sample, the dependence of Raman band intensity on the angle is given by

$$I_{VV}(\phi) \propto \left(\cos^4 \phi - \tfrac{6}{7}\cos^2 \phi + \tfrac{3}{35}\right) \langle P_4(\cos\beta)\rangle + \left(\tfrac{6}{7}\cos^2 \phi - \tfrac{2}{7}\right) \langle P_2(\cos\beta)\rangle + \tfrac{1}{5} \,, \tag{19.18}$$

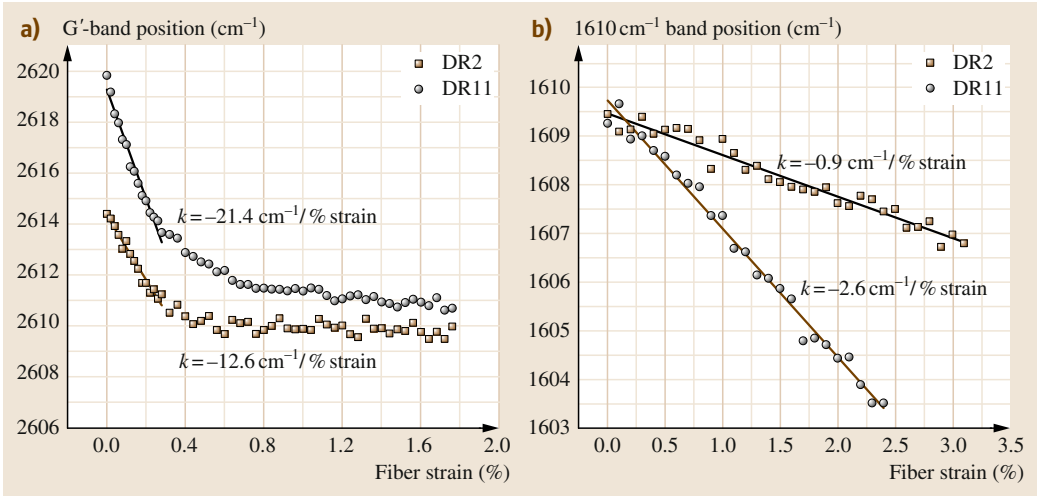


Fig. 19.16a,b Variation of Raman band peak position for composite fiber with different DRs under tensile deformation: **(a)** nanotube G′-band and **(b)** PPTA 1610 cm^{-1} peak (after [19.113])

$$I_{VH}(\phi) \propto \left(-\cos^4\phi + \cos^2\phi - \tfrac{4}{35}\right)\langle P_4(\cos\beta)\rangle + \tfrac{1}{21}\langle P_2(\cos\beta)\rangle + \tfrac{1}{15}\,, \qquad (19.19)$$

where $\langle P_2(\cos\beta)\rangle$ and $\langle P_4(\cos\beta)\rangle$ are the second-order and fourth-order orientation parameters, respectively. Specifically, $\langle P_2(\cos\beta)\rangle$ is the Herman's orientation factor, which has a value of 1 for perfect orientation, 0 for random distribution and -0.5 for the vibration perpendicular to the main axis. The orientation factors can be determined by recording the Raman intensity at different angles and then fitting the data using (19.18) and/or (19.19). For uniaxially-oriented samples, only the VV and VH intensities at 0 and 90° are needed to determine the orientation factor accurately. This provides a simple and straightforward method for orientation determination.

Zamora-Ledezma et al. also developed a method to assess the orientation assuming that: a) the system is uniaxial and b) only the zz component (z is the coordinate along the nanotube axis) of the SWNT Raman polarization tensor is nonzero. For a 3-D orientation of the nanotubes which has a uniaxial symmetry, the orientation factor is given by [19.114]

$$f = \frac{3I_{VV} + 3I_{VH} - 4I_{HH}}{3I_{VV} + 12I_{VH} + 8I_{HH}}\,, \qquad (19.20)$$

while for a 2-D orientation, the orientation factor is given by

$$f = \frac{I_{VV} - I_{HH}}{I_{VV} + I_{VH} + 2I_{HH}}\,. \qquad (19.21)$$

To determine the orientation factor using Zamora-Ledezma's method does not require rotating the sample relative to the laser polarization, as only the intensities obtained using VV, VH and HH configurations at 0° are needed. The errors brought by heterogeneities in the sample can therefore be eliminated.

It should be noted the orientation factors determined using these methods are not identical to each other due to the different assumptions made in different models. Generally, the intensity ratio $I_{VV}^{0°}/I_{VV}^{90°}$ can be used for a quick and qualitative assessment of the orientation. A higher intensity ratio corresponds to a better orientation.

Interfacial Adhesion

Raman spectroscopy can be used to probe the load transfer from the matrix to nanotubes and the interfacial slippage in the composites. This is based on the well known stress dependent Raman G-band and G′-band frequencies, where both bands shift to lower wavenumber under tensile stress and to higher wavenumber under compression.

An example of this is shown in Fig. 19.16 for the deformation of SWNT/aramid PPTA fibers of different draw ratios (DR) [19.113]. There is a large shift of the G′ SWNT band with strain up until around 0.3% above which the shift rate (with respect to strain) decreases, indicating failure of the aramid-SWNT interface. In contrast the 1610 cm^{-1} aramid (matrix) band shifts linearly with strain up to over 2% strain. The nanotube Raman band shift during deformation is an indication of stress transfer and larger shift rate (the shift rate is defined as the slope of the linear region in the Raman band frequency–strain curve) indicates higher efficiency of stress transfer and consequently higher efficiency of

Table 19.4 Factors that influence the Raman band shift rate of nanotubes in composites

Factor	Influence on the G′-band shift rate	Reference
Nanotube type	SWNTs > MWNTs	[19.43]
Preparation method	CVD CNTs > arc-discharge CNTs	[19.43]
Bonding type	Covalent bonding > noncovalent bonding	[19.115]
Dispersion state	Good dispersion > poor dispersion	[19.109]
Polymer type	Stiff polymers > elastomers	[19.113]
Nanotube orientation	Aligned > random	[19.109]

mechanical reinforcement. The Raman band shift rate depends on many factors such as the nanotube type, preparation method, state of dispersion and orientation. The factors studied in the literature that influence the shift rate are listed in Table 19.4. This is certainly not a full list, e.g. the G′ shift rate for individual SWNTs is believed to be dependent on the nanotube chirality, and the aspect ratio of nanotube should also influence the Raman band shift rate during deformation, but how these factors influence the shift rate is still unclear. A systematic investigation of the effect of these factors is needed if the shift rate is to be used properly in assessing the interfacial adhesion and the efficiency of reinforcement.

While it is difficult to compare the Raman band shift rate in different composite systems, the strain at which nanotube Raman bands cease to shift during deformation is a measure of the interfacial shear strength. *Roy* et al. [19.115] incorporated both collagen-modified SWNTs and pristine SWNTs into PVA and observed a strain-induced shift of the nanotube G′-band in the collagen-modified system while no stress transfer was observed in the unmodified system during deformation. They determined the onset of interfacial slippage for the PVA/collagen-SWNT film is at 3.5% strain. This strain value was then used to calculate the IFSS which turned out to be 187.5 MPa [19.115]. *Kannan* et al. also observed a transition in the G′ frequency–strain plot for the PVA/SWNT electrospun fibers, where the interface failed at 0.6% strain [19.116]. *Kao* and *Young* investigated the deformation behavior of an epoxy/SWNT composite under cyclic loading by following the nanotube G′-band [19.117]. They found the deformation is completely reversible over a low strain range (< 0.4%). When a larger strain (e.g. 1%) was released, residual compression was observed, due to friction at the damaged interface in the composite.

The stress transfer between nanotubes inside nanotube bundles and between the layers in an individual MWNT is also important because intertube sliding in nanotube ropes or interlayer sliding in individual MWNTs are detrimental to mechanical performance of the composites. *Kumar* and *Cronin* [19.80] deformed nanotube bundles by stretching a poly(dimethyl siloxane) (PDMS) substrate on which nanotube are sitting and observed intertube slippage, based on the response of the Raman bands such as:

1. A discrete jump in the G-band frequency at certain strains.
2. The relative intensity I_D/I_G remained constant during deformation.
3. The strain-induced G-band shift rate for bundles was significantly lower than those of individual nanotubes.
4. The RBM frequency of metallic nanotubes shifted to higher-wavenumber by $4\,cm^{-1}$. These phenomena suggested only a fraction of the strain applied to the bundle was transferred to the individual nanotubes within the bundles and the main effect of deformation was to debundle the nanotubes [19.80].

Cui et al. studied the interlayer stress transfer in MWNTs using an epoxy/DWNT composite as a model material [19.118]. By deforming the composite using a four-point bending rig, the higher-frequency component of the G′-band which corresponds to the outer wall, shifted at a rate of $-9.2\,cm^{-1}/\%$ strain, whereas the lower-frequency component which corresponds to the inner wall shifted at a much lower rate, of $-1.1\,cm^{-1}/\%$ strain. This indicates the efficiency of stress transfer from the outer wall to the inner wall is rather low such that the inner wall does not carry load, which is consistent with the theoretical predictions [19.119, 120] and previous experimental findings [19.121]. They demonstrated the effective modulus of MWNTs in composites decreases as the number of walls increases, and cross-linking the walls may possibly increase the resistance of the walls to the shear process.

19.3 Graphene Composites

The preparation and properties of bulk graphene composites has been recently reviewed in detail by *Kim* et al. [19.33]. The vast majority of research in this area has been undertaken using graphene oxide, often in the reduced form, although this is often difficult to tell from the title of a paper, where the word *graphene* is often used to describe work upon graphene oxide. Some research has also been undertaken upon composites containing graphite nanoplatelets (GNP).

There are some attractions in employing graphene oxide rather than graphene since it is readily obtainable in large quantities, much easier to exfoliate and disperse in a polymer matrix, and has built-in functional groups that are available for bonding to a polymer matrix. The individual nanoplatelets of graphene oxide are, however, often wrinkled and graphene oxide has significantly inferior mechanical properties to graphene. In the following sections care will be taken to distinguish between research upon the different forms of graphene.

There are a number of reasons for producing graphene based composites. The addition of a filler with such impressive mechanical properties is expected to lead to a significant improvement in the mechanical properties of the host polymer matrix. It is also found, however, that changes to the mechanical properties are also accompanied by modification of functional properties such as electrical conductivity, thermal conductivity and barrier behavior. This presentation will be concerned principally with mechanical properties but a brief discussion of the effect of graphene on functional properties is also included.

19.3.1 Preparation Methods

One of the greatest challenges in the preparation of polymer-based nanocomposites is to be able to obtain a good distribution of the nano-reinforcement [19.7] and it will be demonstrated that the properties of the nanocomposites can be compromized by a poor dispersion. For example, carbon nanotubes have a tendency to form bundles which can be difficult to break down and so much of the effort in the area of nanotube-based composites has focussed upon developing methods of obtaining good distributions of nanotubes using techniques such as chemical functionalization of the nanotubes [19.122]. In the case of graphene or graphene oxide the formation of bundles is not an issue but there can still be a tendency for incomplete exfoliation to be obtained and restacking to occur.

One of the advantages of using graphite oxide is that it can be exfoliated in water and nanocomposites can readily be prepared with the use of water-soluble polymers such as poly(vinyl alcohol) [19.123] and poly(ethylene oxide) [19.124]. It is possible also to prepare nanocomposites using solution-based methods with nonwater-soluble polymers such as poly(methyl methacrylate) [19.125] and polyurethanes [19.126] by chemically modifying the graphene oxide.

In situ polymerization of the polymer matrix offers an attractive method of preparing graphene-based composites although solvents are often employed to reduce the viscosity of the dispersions. For example, intercalative polymerization of methyl methacrylate [19.127] and epoxy resins [19.128, 129] has been achieved with graphite oxide to produce nanocomposites with enhanced properties.

Melt blending offers a simple and attractive method of dispersing nanoparticles in a polymer matrix and has been used to disperse thermally-reduced graphite oxide in a number of polymers including polycarbonate [19.130] and poly(ethylene-2,6-naphthalate) [19.131]. It is possible to obtain a reasonable dispersion in these systems but the addition of the nanoparticles increases the viscosity of the polymer melt significantly and makes processing more difficult. Solid-state shear dispersion, using a modified twin-screw extruder, has been employed to produce nanocomposites of unmodified, as-received graphite dispersed in polypropylene [19.132]. Although significant property improvements were reported it was found by x-ray diffraction and electron microscopy that the composites contained graphite nanoplatelets ranging from a few to 10 nm thick and so containing up to 30 graphene layers, rather than individual graphene platelets.

19.3.2 Mechanical Properties

The effect of particulate reinforcement upon the mechanical properties of polymers has been discussed in detail in the textbook of *Young* and *Lovell* [19.5]. It is relatively easy to predict the Young's modulus of particulate-reinforced polymers, although in practice only upper and lower bounds can be determined rather than exact values. It is necessary to determine the Young's modulus for the situations where the particles and matrix (and hence the composite) are subjected to either *uniform strain* or *uniform stress*.

Mechanics of Reinforcement

In the case of uniform strain it is found that the Young's modulus E_c of the composites is given by the rule of mixtures as

$$E_c = V_p E_p + V_m E_m \,, \tag{19.22}$$

or

$$\frac{E_c}{E_m} = V_p \frac{E_p}{E_m} + V_m \,, \tag{19.23}$$

where E_p is the Young's modulus of the particles, E_m is the Young's modulus of the matrix and V_p and V_m are the volume fraction of particles and matrix respectively, within the composite (where $V_p + V_m = 1$).

In the case of uniform stress the Young's modulus of the composites is given by

$$\frac{1}{E_c} = \frac{V_p}{E_p} + \frac{V_m}{E_m} \tag{19.24}$$

which can be rearranged to give

$$\frac{E_c}{E_m} = \frac{E_p}{V_m E_p + V_p E_m} \,. \tag{19.25}$$

It is found that these equations give very large differences in the prediction of the Young's modulus of particulate composites, especially when $E_p \gg E_m$, and are normally taken as upper and lower bounds of the behavior. There is normally a distribution of stress in the reinforcement such that the particles are subjected to neither uniform stress nor uniform strain and the Young's modulus normally lies between the two predictions which can be considered to be upper (uniform strain) and lower (uniform stress) bounds of composite Young's modulus.

There have been a number of attempts to produce more appropriate predictions of the Young's modulus of particulate reinforced composites without having to have widely-separated bounds [19.133–136]. *Halpin* and *Kardos* developed an approach based upon the self-consistent micromechanics method of Hill which enabled them to predict the elastic behavior of a variety of both fiber and particulate geometries [19.133]. This approach was employed by *Halpin* and *Thomas* [19.136] to predict the behavior of ribbon-shaped reinforcements which is clearly relevant to graphene-based composites. The theory predicts that in the case of aligned reinforcement, the ratio of the Young's modulus of the composite to that of the matrix is given by

$$\frac{E_c}{E_m} = \frac{1 + \xi\eta V_p}{1 - \eta V_p} \,, \tag{19.26}$$

where

$$\eta = \frac{E_p/E_m - 1}{E_p/E_m + \xi} \,. \tag{19.27}$$

The parameter ξ is a measure of reinforcement geometry which depends upon the loading conditions and is essentially a parameter controlled by the aspect ratio of the reinforcement. The limiting values of ξ are $\xi = 0$ and $\xi = \infty$ and for the prediction of the longitudinal modulus of reinforcement by a ribbon of length l and thickness t, the value of ξ can be taken as $2l/t$ [19.133]. Equation (19.26) tends to the lower, uniform stress, bound (19.25) as $\xi \to 0$ and to the upper, uniform strain, bound (19.23) as the aspect ratio of the reinforcement increases and $\xi \to \infty$. There are a number of other approaches that can be employed to model the reinforcement by nanoparticles [19.134,135], but the Halpin–Tsai approach for aligned reinforcement [19.133] produces relatively-simple equations that will be used next to account for the measured levels of reinforcement found in graphene-based nanocomposites.

Measured Levels of Reinforcement

The simplest way of assessing the level of reinforcement imparted upon a polymer matrix by a filler is to plot the ratio of the Young's modulus of the composites to that of the matrix E_c/E_m against the volume fraction of filler particles, V_p as shown in Fig. 19.17. The widely-spaced upper and lower bounds, given by (19.25) and (19.23) for uniform strain and uniform stress respectively, are indicated. The expected behavior for a ribbon-shaped reinforcement is given by (19.26) but the form of this relationship depends upon both the aspect ratio ξ and the ratio of the Young's modulus of the filler to that of the matrix, (E_p/E_m) through the parameter η. In order to compare the behavior of different systems it is necessary therefore to make different plots for families of materials with different ratios of E_p/E_m and values of ξ.

Most of the published research upon the mechanical properties of graphene-reinforced polymers is concerned with either rigid polymers (both glassy and semi-crystalline) for which $E_p/E_m \approx 10^3$, taking the Young's modulus of graphene as around 1 TPa or elastomers for which $E_p/E_m \approx 10^6$, since most elastomers have a Young's modulus of the order of 1 MPa. It is therefore possible to produce general plots for the two types of matrix materials with a series of lines for different values of ξ. Experimentally-determined values of E_p/E_m as a function of V_p for nanocomposites with

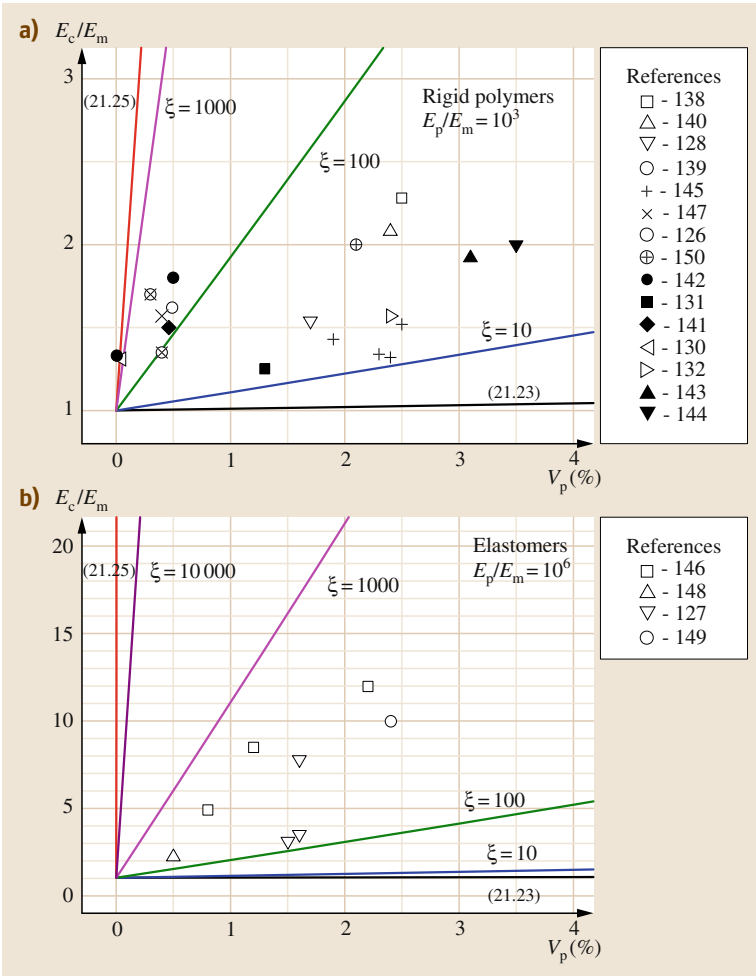


Fig. 19.17a,b Predicted and measured variation of E_c/E_m with volume fraction of graphene filler particles for **(a)** rigid polymers and **(b)** glassy polymers

either rigid [19.125, 127, 129–131, 137–146] or elastomeric [19.126, 147–149] matrices are also plotted. Since some of the data in the literature are given in terms of the weight fraction of filler, it is necessary to convert this to volume fraction using the density of the filler and matrix. Where this has not been given, a filler density of 2280 kg/m^3 has been assumed for the data in Fig. 19.17.

It is instructive to examine the relationship between the experimental data and theoretical predictions. It would be expected that in the case of fully-exfoliated graphene or graphene oxide the parameter ξ $(= 2l/t)$ would be of the order of at least 1000 and that if the particles were providing good reinforcement, the experimental data should lie above the line for $\xi = 1000$. It can be seen that in the case of the rigid reinforcement (Fig. 19.17a) the data lie close to the line for $\xi = 1000$ only at very low volume fractions ($< 0.1\%$) and then fall in the range $1000 < \xi < 100$ for volume fractions up to around 0.5%. Above volume fractions of 1% the data points lie in the region in which $100 < \xi < 10$. In the case of the limited data available for elastomeric matrices, it can be seen in Fig. 19.17b that the data all fall in the range $1000 < \xi < 100$.

It appears therefore that the level of reinforcement measured experimentally is less than the theoretical value for graphene except at very low volume fractions. There are a number of possible reasons why this might be the case:

1. Equations (19.25) and (19.26) are strictly valid only for aligned platelets and the values of E_p/E_m

will be lower in the case of randomly oriented platelets [19.129, 150, 151]. Waviness of the reinforcing flakes that is found particularly in the case of thermally-reduced graphite oxide will contribute further to the reduction of modulus [19.129, 144].
2. The majority of the reports are concerned with graphene oxide rather than pristine graphene and it is known that defects and holes in the material reduce the modulus of the reinforcement to around 250 GPa [19.38].
3. In many cases the length of the flakes is relatively short and reinforcing material is not completely exfoliated [19.131] making the appropriate value of ξ significantly less than 1000.
4. There may be a poor dispersion of the reinforcement, especially at higher volume fractions, leading to clustering – a similar problem to that encountered with nanotubes [19.7].
5. The interface between the platelets and the matrix may not be particularly strong leading to poor stress transfer. The presence of the functional groups on the surface of graphene oxide may help to provide a stronger interface with a polymer matrix than in the case of graphene or graphite nanoplatelets. Recent work has also shown that an improvement in Young's modulus of the nanocomposites can be obtained through the use of coupling agents [19.152].

Overall it can be concluded that the levels of reinforcement achieved so far in graphene-based composites have been disappointing but there is considerable scope to overcome some of the problems listed above and produce nanocomposites with greatly improved properties.

Although the discussion outlined above has been concerned solely with enhancement of Young's modulus there are other important mechanical properties that need to be considered. The increase in modulus encountered in graphene-based nanocomposites is often accompanied by a reduction in elongation to failure and sometimes lower failure strength. There are reports, however, of ductility being maintained along with an increase in modulus and strength for poly(vinyl alcohol)/graphene oxide nanocomposites [19.137]. Other mechanical property improvements of note on the addition of graphite oxide to polymers include increases in hardness [19.125, 149], fracture toughness and fatigue crack growth resistance [19.129].

19.3.3 Functional Properties

It is possible to make polymers *electrically conductive* by the addition of graphene in a similar way to what is done using other nanofillers [19.153] such as carbon black [19.154, 155] and carbon nanotubes [19.7, 156]. The presence of the graphene can lead to percolation pathways through which the electrical charge can pass and this will occur if there is a good distribution of the graphene. It is possible, in fact, to use the conductivity of the nanocomposite to monitor the quality of the filler distribution. It has been found that it is possible to make a number of different polymers conductive by the addition of graphite nanoplatelets [19.21, 22] and different forms of graphene [19.126, 127, 131, 132, 144, 147, 157, 158]. An important factor is the amount of filler needed to render the polymer conductive – the percolation threshold – which depends strongly upon the shape and distribution of the filler particles. This has been found to be of the order of 0.1% by volume of chemically-reduced graphene oxide in polystyrene [19.159] which is approaching the best values obtained for carbon nanotubes [19.156]. The thresholds for percolation of graphene in a number of different polymers have been reviewed by *Kim* et al. and they are found to vary from 0.1 to over 2% depending upon the matrix polymer, form of graphene and processing method [19.33].

Since it was found that a monolayer graphene membrane is impermeable to common gases including helium [19.160] it was anticipated that graphene-based polymer nanocomposites should have good *gas barrier properties*. *Kalaitzidou* et al. [19.161] showed that the incorporation of appropriately-aligned graphite nanoplatelets into polypropylene could increase the oxygen barrier of the material more efficiently than other nanofiller particles. The gas permeation data for a series of different polymer nanocomposites has been reviewed and summarized by *Kim* et al. [19.33]. Reductions of diffusion rate for a variety of common gases for loadings of around 1.5–2.2% graphite oxide or reduced graphite oxide in a number of different polymers are found to be in the range 30–90% [19.126, 131, 132, 147].

The addition of graphene to polymers can have a significant effect upon their thermal properties. It has been found that the addition of graphene nanoplatelets to polymers can improve the *thermal conductivity* of polymer by over 3000% when particles with a high aspect ratio (≈ 200) are used [19.162]. This enhancement is found to be superior to that found with nanotubes although a synergistic effect has been reported with

a mixture of single-walled nanotubes and graphene nanoplatelets out-performing composites made using the pure nanofillers [19.163]. Polymers generally have high *thermal expansion coefficients* and the addition of aligned graphene nanoplatelets to polypropylene has been shown to reduce the thermal expansion coefficient in two directions rather than one in the case of aligned fibers [19.161]. A similar reduction in the thermal expansion coefficient of an epoxy resin has been found with the use of graphene oxide [19.128]. Finally, it is found that the addition of graphene-based nanofillers to a polymer can increase *thermal stability* [19.164, 165]. This effect has been attributed to the suppression of the mobility of polymer segments at the filler–polymer interface [19.164]. Based upon experience with nanotube-based nanocomposites [19.166] it has been suggested that graphene-based polymer nanocomposites may also have good *flame-retardant* properties [19.33].

19.3.4 Nanomechanics

The mechanical behavior of a graphene monolayer in a matrix can be modeled using shear lag theory in which it is assumed that the graphene is a mechanical continuum and surrounded by a layer of elastic resin as shown in Fig. 19.18. It is predicted [19.47] from shear-lag analysis that for a given level of matrix strain e_m the variation of strain in the graphene monolayer e_f with position x across the monolayer will be of the form

$$e_f = e_m \left(1 - \frac{\cosh\left(ns\frac{x}{l}\right)}{\cosh\left(\frac{ns}{2}\right)}\right), \tag{19.28}$$

where

$$n = \sqrt{\frac{2G_m}{E_p}\left(\frac{t}{T}\right)} \tag{19.29}$$

and G_m is the matrix shear modulus, E_p is the Young's modulus of the graphene monolayer, l is the length of the graphene monolayer in the x direction, t is the thickness of the graphene, T is the total resin thickness and s is the aspect ratio of the graphene (l/t) in the x direction. In composite micromechanics [19.5] the parameter n is accepted widely as an effective measure of the interfacial stress transfer efficiency, so ns depends on both the morphology of the graphene monolayer and the degree of interaction it has with the matrix.

Moreover, the variation of shear stress τ_i at the polymer–graphene interface is given by [19.47]

$$\tau_i = nE_p e_m \frac{\sinh\left(ns\frac{x}{l}\right)}{\cosh\left(\frac{ns}{2}\right)} . \tag{19.30}$$

It can be seen that the graphene monolayer is most highly stressed, i. e. the most efficient platelet reinforcement is obtained, when the product ns is high. This implies that a high aspect ratio s is desirable along with a high value of n. This analysis relies on the assumption that both the graphene monolayer and polymer behave as linear elastic continua.

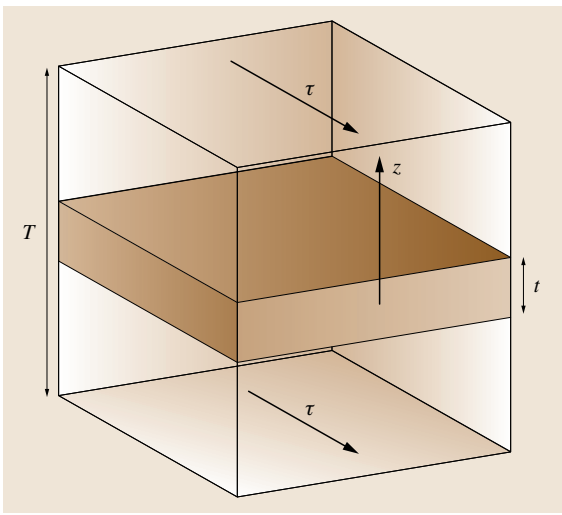


Fig. 19.18 Model of a graphene monolayer within a resin used in shear-lag theory. The shear stress τ acts at a distance z from the center of the monolayer

19.3.5 Model Graphene Monolayer Composites

Gong et al. [19.47] used Raman spectroscopy to monitor stress transfer in a model graphene composite consisting of a thin polymer matrix layer and a mechanically-cleaved single graphene monolayer using the stress-sensitivity of the graphene G′ band [19.44–50]. A schematic diagram of their specimen is shown in Fig. 19.19 where an approximately diamond-shaped graphene monolayer is sandwiched between thin layers of transparent polymer.

Mapping the local strain along a carbon fiber in a polymer matrix allows the level of adhesion between the fiber and matrix to be evaluated [19.167, 168]. In a similar way mapping the strain across the graphene monolayer enables stress transfer from the polymer to the graphene to be followed. Figure 19.20 shows the local variation of strain across the graphene monolayer

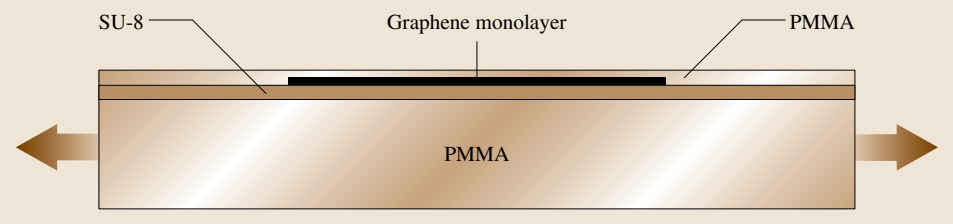


Fig. 19.19 Schematic diagram (not to scale) of a section through a single monolayer graphene composite

determined from the stress-induced Raman band shifts at 0.4% matrix strain. The laser beam in the spectrometer was focused to a spot around 2 μm which allows a spatial resolution of the order of 1 μm on the monolayer by taking overlapping measurements.

Figure 19.20 shows the variation of axial strain across the monolayer in the direction, x, parallel to the strain axis. It can be seen that the strain builds up from the edges and is constant across the middle of the monolayer where the strain in the monolayer equals the applied matrix strain (0.4%). This is completely analogous to the situation of a single discontinuous fiber in a model composite when there is good bonding between the fiber and matrix [19.167, 168] which has been analyzed using the well-established shear-lag theory [19.5, 37, 169]. The experimental data are fitted to (19.28) in Fig. 19.20 and it can be seen that the fits of the theoretical shear-lag curves to the strain distribution are sensitive to the value of ns chosen with the best fit being for $ns = 20$.

Deformation of the graphene monolayer composite to higher axial strain led to breakdown of the graphene polymer interface at an interfacial shear stress of the order of around 1 MPa and a different shape of strain distribution [19.47]. The quality of fiber reinforcement is often described in terms of the *critical length* l_c – the parameter is small for strong interfaces and is defined as 2 × the distance over which the strain rises from the fiber ends to the plateau level [19.5, 37]. It can be seen from Fig. 19.20 that the strain rises to about 90% of the plateau value over about 1.5 μm from the edge of the flake making the critical length of this graphene reinforcement of the order of 3 μm. It is generally thought that in order to obtain good fiber reinforcement the fiber length should be $\approx 10 l_c$. Hence, relatively large graphene flakes (> 30 μm) will be needed before efficient reinforcement can take place. Processes for exfoliating graphene to single layers efficiently reported recently produce monolayers of no larger than a few micrometers across [19.23, 170]. The relatively poor

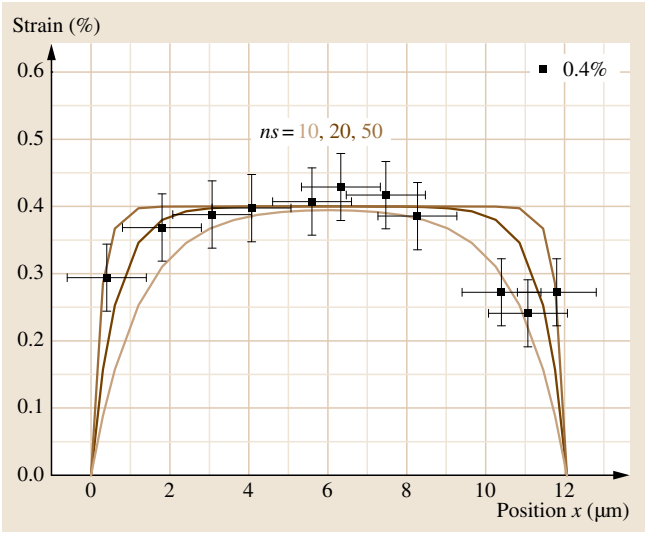


Fig. 19.20 Distribution of strain in the graphene in the direction of the tensile axis across a single monolayer at 0.4% strain. The *curves* were calculated from (19.28) using different values of ns

level of adhesion between the graphene and polymer matrix is also reflected in the low level of interfacial shear stress, τ_i, determined – carbon fibers composites have values of $\tau_i \approx 20$–40 MPa, an order of magnitude higher [19.167, 168]. The efficiency of reinforcement is also reflected in the value of the parameter ns (= 20) in the shear lag analysis used to fit the experimental data. Since the graphene is so thin, the aspect ratio s will be large (in this case, 12 μm/0.35 nm = 3.5×10^4) making n small ($\approx 6 \times 10^{-4}$) compared to carbon fibers.

This study of *Gong* et al. [19.47] has important significance for the use of graphene as reinforcement in composites. It appears that the continuum mechanics approach is also valid at the atomic level – a question widely asked in the field of nanocomposites – and that the composite micromechanics developed for the case of fiber reinforcement is also valid at the atomic level for graphene monolayers.

19.4 Conclusions

It is clear that there is a great deal of interest in preparing composites reinforced with different forms of nanocarbons, although a number of major challenges still exist. As yet the full potential of these high-modulus fillers is yet to be realized in the mechanical behavior of the nanocomposites. One of the main reasons for this is that it is difficult to obtain good distributions of the nano-reinforcement at levels of loading that would be expected to lead to significant improvements in mechanical behavior. Fibrous reinforcements such as nanotubes are difficult to disperse and lead to a rise in the viscosity of the polymer system, making processing very much more difficult. In the case of graphene, it is found that procedures that are needed to produce good exfoliation of the nanoplatelets tend to either oxidize or damage the material.

It has been shown clearly that the use of Raman spectroscopy enables stress transfer from the matrix to the nano-reinforcement to be followed in these systems with a great deal of precision and it is likely that this technique will find increasing use in the characterization of polymer nanocomposites reinforced with carbon nanotubes and graphene in the future.

References

19.1 H.W. Kroto, J.R. Heath, S.C. O'Brien, R.F. Curl, R.E. Smalley: C–60 – Buckminsterfullerene, Nature **318**, 162–163 (1985)

19.2 S. Iijima: Helical microtubules of graphitic carbon, Nature **354**, 56–58 (1991)

19.3 K.S. Novoselov, A.K. Geim, S.V. Morozov, D. Jiang, Y. Zhang, S.V. Dubonos, I.V. Grigorieva, A.A. Firsov: Electric field effect in atomically thin carbon films, Science **306**, 666–669 (2004)

19.4 A.K. Geim, K.S. Novoselov: The rise of graphene, Nat. Mater. **6**, 183–190 (2007)

19.5 R.J. Young, P.A. Lovell: *Introduction to Polymers*, 3rd edn. (CRC Press, London 2011), Chapter 24

19.6 R. Satio, G. Dresselhaus, M.S. Dresselhaus: *Physical Properties of Carbon Nanotubes* (Imperial College Press, London 1998)

19.7 M. Moniruzzaman, K. Winey: Polymer nanocomposites containing carbon nanotubes, Macromolecules **39**, 5194–5205 (2006)

19.8 M. Lucas: Effect of Deformation upon the Intensity of the Raman Radial Breathing Modes of Single-Wall Carbon Nanotubes in Epoxy/SWNT Composites. Ph.D. Thesis (Univ. Manchester, Manchester 2005)

19.9 J. Coleman, U. Khan, W. Blau, Y. Gun'Ko: Small but strong: A review of the mechanical properties of carbon nanotube–polymer composites, Carbon **44**, 1624–1652 (2006)

19.10 J. Coleman, U. Khan, Y. Gun'Ko: Mechanical reinforcement of polymers using carbon nanotubes, Adv. Mater. **18**, 689–706 (2006)

19.11 J.P. Lu: Elastic properties of single and multilayered nanotubes, J. Phys. Chem. Solids **58**, 1649–1652 (1997)

19.12 M.M. Treacy, T.W. Ebbesen, T.M. Gibson: Exceptionally high Young's modulus observed for individual carbon nanotubes, Nature **381**, 680–687 (1996)

19.13 E.W. Wong, P.E. Sheehan, C.M. Lieber: Nanobeam mechanics: Elasticity, strength, and toughness of nanorods and nanotubes, Science **277**, 1971–1975 (1997)

19.14 Z. Wang: Reinforcing Efficiency of Carbon Nanotubes in Poly(Vinyl Alcohol) Composites. Ph.D. Thesis (Univ. London, London 2007)

19.15 R.E. Peierls: Quelques propriétés typiques des corps solides, Ann. Inst. Henri Poincaré **5**, 177–222 (1935), in French

19.16 H. Shioyama: Cleavage of graphite to graphene, J. Mater. Sci. Lett. **20**, 499–500 (2001)

19.17 C.N.R. Rao, K. Biswas, K.S. Subrahmanyam, A. Govindaraj: Graphene, the new carbon, J. Mater. Chem. **19**, 2457–2469 (2009)

19.18 A. Celzard, J.F. Marêché, G. Furdin: Surface area of compressed expanded graphite, Carbon **40**, 2713–2718 (2002)

19.19 G.H. Chen, D. Wu, W.G. Weng, C.L. Wu: Exfoliation of graphite flake and its nanocomposites, Carbon **41**, 619–621 (2003)

19.20 B.Z. Jang, A. Zhamu: Processing of nanographene platelets (NGPs) and NGP nanocomposites: A review, J. Mater. Sci. **43**, 5092–5101 (2008)

19.21 K. Kalaitzidou, H. Fukushima, L.T. Drzal: A new compounding method for exfoliated graphite–polypropylene nanocomposites with enhanced flexural properties and lower percolation threshold, Compos. Sci. Technol. **67**, 2045–2051 (2007)

19.22 K. Kalaitzidou, H. Fukushima, P. Askeland, L.T. Drzal: The nucleating effect of exfoliated graphite nanoplatelets and their influence on the crystal structure and electrical conductivity of polypropylene nanocomposites, J. Mater. Sci. **43**, 2895–2907 (2008)

19.23 Y. Hernandez, V. Nicolosi, M. Lotya, F.M. Blighe, Z.Y. Sun, S. De, I.T. McGovern, B. Holland, M. Byrne, Y.K. Gun'ko, J.J. Boland, P. Niraj, G. Duesberg, S. Krishnamurthy, R. Goodhue, J. Hutchison,

V. Scardaci, A.C. Ferrari, J.N. Coleman: High-yield production of graphene by liquid-phase exfoliation of graphite, Nat. Nanotechnol. **3**, 563–568 (2008)

19.24 C. Vallés, C. Drummond, H. Saadaoui, C.A. Furtado, M.S. He, O. Roubeau, L. Ortolani, M. Monthioux, A. Pénicaud: Solutions of negatively charged graphene sheets and ribbons, J. Am. Chem. Soc. **130**, 15802–15804 (2008)

19.25 B.C. Brodie: On the atomic weight of graphite, Philos. Trans. R. Soc. Lond. **149**, 249–259 (1859)

19.26 L. Staudenmaier: Verfahren zur Darstellung der Graphitsäure, Ber. Dtsch. Chem. Ges. **31**, 1481–1487 (1898), in German

19.27 W.S. Hummers, R.E. Offeman: Preparation of graphitic oxide, J. Am. Chem. Soc. **80**, 1339 (1958)

19.28 S.J. Park, R.S. Ruoff: Chemical methods for the production of graphenes, Nat. Nanotechnol. **4**, 217–224 (2009)

19.29 D.R. Dreyer, S.J. Park, C.W. Bielawski, R.S. Ruoff: The chemistry of graphene oxide, Chem. Soc. Rev. **39**, 228–240 (2010)

19.30 A.K. Geim: Graphene: Status and prospects, Science **324**, 1530–1534 (2009)

19.31 K.S. Novoselov, A.K. Geim, S.V. Morozov, D. Jiang, M.I. Katsnelson, I.V. Grigorieva, S.V. Dubonos, A.A. Firsov: Two-dimensional gas of massless Dirac fermions in graphene, Nature **438**, 197–200 (2005)

19.32 Y.B. Zhang, Y.W. Tan, H.L. Stormer, P. Kim: Experimental observation of the quantum Hall effect and Berry's phase in graphene, Nature **438**, 201–204 (2005)

19.33 H. Kim, A.A. Abdala, C.W. Macosko: Graphene/polymer nanocomposites, Macromolecules **43**, 6515–6530 (2010)

19.34 C. Lee, X.D. Wei, J.W. Kysar, J. Hone: Measurement of the elastic properties and intrinsic strength of monolayer graphene, Science **321**, 385–388 (2008)

19.35 F. Liu, P.B. Ming, J. Li: Ab initio calculation of ideal strength and phonon instability of graphene under tension, Phys. Rev. B **76**, 064120 (2007)

19.36 O.L. Blakslee, D.G. Proctor, E.J. Seldin, G.B. Spence, T. Weng: Elastic constants of compression-annealed pyrolytic graphite, J. Appl. Phys. **41**, 3373–3382 (1970)

19.37 A. Kelly, N.H. Macmillan: *Strong Solids*, 3rd edn. (Clarendon, Oxford 1986)

19.38 C. Gomez-Navarro, M. Burghard, K. Kern: Elastic properties of chemically derived single graphene sheets, Nano Lett. **8**, 2045–2049 (2008)

19.39 M. Dresselhaus, G. Dresselhaus, R. Saito, A. Jorio: Raman spectroscopy of carbon nanotubes, Phys. Rep. **409**, 47–99 (2005)

19.40 R.J. Young: Monitoring deformation processes in high-performance fibres using Raman spectroscopy, J. Text. Inst. **86**, 360–381 (1995)

19.41 Y. Huang, R.J. Young: Effect of fibre microstructure upon the mechanical properties of PAN- and pitch-based carbon fibres, Carbon **33**, 97–107 (1995)

19.42 P. Kannan, S.J. Eichhorn, R.J. Young: Deformation of isolated single-wall carbon nanotubes in electrospun polymer nanofibres, Nanotechnology **18**, 235707 (2007)

19.43 C.A. Cooper, R.J. Young, M. Halsall: Investigation into the deformation of carbon nanotubes and their composites through the use of Raman spectroscopy, Compos. A: Appl. Sci. Manuf. **32**, 401–411 (2001)

19.44 Z.H. Ni, T. Yu, Y.H. Lu, Y.Y. Wang, Y.P. Feng, Z.X. Shen: Uniaxial strain on graphene: Raman spectroscopy study and band-gap opening, ACS Nano **2**, 2301–2305 (2008)

19.45 T.M.G. Mohiuddin, A. Lombardo, R.R. Nair, A. Bonetti, G. Savini, R. Jalil, N. Bonini, D.M. Basko, C. Galiotis, N. Marzari, K.S. Novoselov, A.K. Geim, A.C. Ferrari: Uniaxial strain in graphene by Raman spectroscopy: G peak splitting, Grüneisen parameters, and sample orientation, Phys. Rev. B **79**, 205433 (2009)

19.46 M.Y. Huang, H. Yan, C.Y. Chen, D.H. Song, T.F. Heinz, J. Hone: Phonon softening and crystallographic orientation of strained graphene studied by Raman spectroscopy, Proc. Natl. Acad. Sci. USA **106**, 7304–7308 (2009)

19.47 L. Gong, I.A. Kinloch, R.J. Young, I. Riaz, R. Jalil, K.S. Novoselov: Interfacial stress transfer in a graphene monolayer nanocomposite, Adv. Mater. **22**, 2694–2697 (2010)

19.48 M.Y. Huang, H. Yan, T.F. Heinz, J. Hone: Probing strain-induced electronic structure change in graphene by Raman spectroscopy, Nano Lett. **10**, 4074–4079 (2010)

19.49 F. Ding, H.X. Ji, Y.H. Chen, A. Herklotz, K. Dörr, Y.F. Mei, A. Rastelli, O.G. Schmidt: Stretchable graphene: A close look at fundamental parameters through biaxial straining, Nano Lett. **10**, 3453–34580 (2010)

19.50 N. Ferralis: Probing mechanical properties of graphene with Raman spectroscopy, J. Mater. Sci. **45**, 5135–5149 (2010)

19.51 X. Zhang, T. Liu, S. Kumar, R. Hauge, R.E. Smalley: Poly(vinyl alcohol)/SWNT composite film, Nano Lett. **3**, 1285–1288 (2003)

19.52 P.M. Ajayan, O. Stephan, C. Colliex, D. Trauth: Aligned carbon nanotube arrays formed by cutting a polymer resin-nanotube composite, Science **265**, 1212–1214 (1994)

19.53 J. Coleman, U. Khan, Y. Gun'Ko: Mechanical reinforcement of polymers using carbon nanotubes, Adv. Mater. **18**, 689–706 (2006)

19.54 J.N. Coleman, M. Cadek, K.P. Ryan, A. Fonseca, J.B. Nagy, W.J. Blau, M.S. Ferreira: Reinforcement of polymers with carbon nanotubes, the role of an ordered polymer interfacial region: Experiment and modeling, Polymer **47**, 8556–8561 (2006)

19.55 E.T. Thostenson, C. Li, T.W. Chou: Nanocomposites in context, Compos. Sci. Technol. **65**, 491–516 (2005)

19.56 K.P. Ryan, M. Cadek, V. Nicolosi, J.N. Coleman: Carbon nanotubes for reinforcement of plastics? A case study with poly(vinyl alcohol), Compos. Sci. Technol. **67**, 1640–1649 (2007)

19.57 T. Liu, I.Y. Phang, L. Shen, S.Y. Chow, W. Zhang: Morphology and mechanical properties of multiwalled carbon nanotubes reinforced nylon-6 composites, Macromolecules **37**, 7214–7222 (2004)

19.58 A.M. Díez-Pascual, M. Naffakha, M.A. Gómez, Y. Martínez-Rubic, B. Simard: Development and characterization of PEEK/carbon nanotube composites, Carbon **47**, 3079–3090 (2009)

19.59 C. Velasco-Santos, A.L. Martínez-Hernández, F.T. Fisher, R. Ruoff, V.M. Castaño: Improvement of thermal and mechanical properties of carbon nanotube composites through chemical functionalization, Chem. Mater. **15**, 447–4475 (2003)

19.60 J. Kearns, R. Shambaugh: Polypropylene fibers reinforced with carbon nanotubes, J. Appl. Polym. Sci. **86**, 2079–2084 (2002)

19.61 B. Vigolo, A. Penicaud, C. Coulon, C. Sauder, R. Pailler, C. Journet, P. Bernier, P. Poulin: Macroscopic fibers and ribbons of oriented carbon nanotubes, Science **290**, 1331–1334 (2000)

19.62 A. Dalton, S. Collins, E. Munoz, J. Razal, V. Ebron, J. Ferraris, J. Coleman, B. Kim, R. Baughman: Super-tough carbon-nanotube fibres – These extraordinary composite fibres can be woven into electronic textiles, Nature **423**, 703–703 (2003)

19.63 A. Greiner, J. Wendorff: Electrospinning: A fascinating method for the preparation of ultrathin fibres, Angew. Chem. Int. Ed. **46**, 5670–5703 (2007)

19.64 Z. Huang, Y. Zhang, M. Kotaki, S. Ramakrishna: A review on polymer nanofibers by electrospinning and their applications in nanocomposites, Compos. Sci. Technol. **63**, 2223–2253 (2003)

19.65 K. Young, F.M. Blighe, J.J. Vilatela, A.H. Windle, I.A. Kinloch, L. Deng, R.J. Young, J.N. Coleman: Strong dependence of mechanical properties on fibre diameter for polymer-nanotube composite fibres: Differentiating defect from orientation effects, ACS Nano **4**, 6989–6997 (2010)

19.66 D. Almecija, D. Blond, J.E. Sader, J.N. Coleman, J.J. Boland: Mechanical properties of individual electrospun polymer-nanotube composite nanofibers, Carbon **47**, 2253–2258 (2009)

19.67 D. Hull, T.W. Clyne: *An Introduction to Composite Materials*, 2nd edn. (Cambridge Univ. Press, Cambridge 1996)

19.68 S.R. Brownlow, A.P. Moravsky, N.G. Kalugin, B.S. Majumdar: Probing deformation of double-walled carbon nanotube (DWNT)/epoxy composites using FTIR and Raman techniques, Compos. Sci. Technol. **70**, 1460–1468 (2010)

19.69 B. Yang, J. Shi, K.P. Pramoda, S.H. Goh: Enhancement of the mechanical properties of polypropylene using polypropylene-grafted multiwalled carbon nanotubes, Compos. Sci. Technol. **68**, 2490–2497 (2008)

19.70 A. Eitan, F.T. Fisher, R. Andrews, L.C. Brinson, L.S. Schadler: Reinforcement mechanisms in MWCNT-filled polycarbonate, Compos. Sci. Technol. **66**, 1162–1173 (2006)

19.71 D. Qian, E.C. Dickey, R. Andrews, T. Rantell: Load transfer and deformation mechanisms in carbon nanotube-polystyrene composites, Appl. Phys. Lett. **76**, 2868–2870 (2000)

19.72 C. Velasco-Santos, A.L. Martinez-Hernandez, F.T. Fisher, R. Ruoff, V.M. Castano: Improvement of thermal and mechanical properties of carbon nanotube composites through chemical functionalization, Chem. Mater. **15**, 4470–4475 (2003)

19.73 X. Zhang, T. Liu, T. Screekumar, S. Kumar, X. Hu, K. Smith: Gel spinning of PVA/SWNT composite fibre, Polymer **45**, 8801–8807 (2004)

19.74 J. Gao, M. Itkis, A. Yu, E. Bekyarova, B. Zhao, R. Haddon: Continuous spinning of a single-walled carbon nanotube-nylon composite fiber, J. Am. Chem. Soc. **127**, 3847–3854 (2005)

19.75 T.E. Chang, L.R. Jensen, A. Kisliuk, R.B. Pipes, R. Pyrz, A.P. Sokolov: Microscopic mechanism of reinforcement in single-wall carbon nanotube/polypropylene nanocomposite, Polymer **46**, 439–444 (2005)

19.76 S. Kumar, T. Dang, F. Arnold, A. Bhattacharyya, B. Min, X. Zhang, R. Vaia, C. Park, W. Adams, R. Hauge, R. Smalley, S. Ramesh, P. Willis: Synthesis, structure, and properties of PBO/SWNT composites, Macromolecules **35**, 9039–9043 (2002)

19.77 H.G. Chae, M.L. Minus, S. Kumar: Oriented and exfoliated single wall carbon nanotubes in polyacrylonitrile, Polymer **47**, 3494–3504 (2006)

19.78 J. Coleman, M. Cadek, R. Blake, V. Nicolosi, K. Ryan, C. Belton, A. Fonseca, J. Nagy, Y. Gun'ko, W. Blau: High-performance nanotube-reinforced plastics: Understanding the mechanism of strength increase, Adv. Funct. Mater. **14**, 791–798 (2004)

19.79 X.L. Xie, Y.W. Mai, X.P. Zhou: Dispersion and alignment of carbon nanotubes in polymer matrix: A review, Mater. Sci. Eng. Rep. **49**, 89–112 (2005)

19.80 R. Kumar, S.B. Cronin: Raman scattering of carbon nanotube bundles under axial strain and strain-induced debundling, Phys. Rev. B **75**, 155421 (2007), 1–4

19.81 J.P. Salvetat, G.A.D. Briggs, J.M. Bonard, R.R. Bacsa, A.J. Kulik, T. Stöckli, N.A. Burnham, L. Forró, Y.S. Song, J.R. Youn: Elastic and shear moduli of single-walled carbon nanotube ropes, Phys. Rev. Lett. **82**, 944–947 (1999)

19.82 Y.S. Song, J.R. Youn: Influence of dispersion states of carbon nanotubes on physical properties

of epoxy nanocomposites, Carbon **43**, 1378–1385 (2005)
19.83 J. Zhu, J.D. Kim, H.Q. Peng, J.L. Margrave, V.N. Khabashesku, E.V. Barrera: Improving the dispersion and integration of single-walled carbon nanotubes in epoxy composites through functionalization, Nano Lett. **3**, 1107–1113 (2003)
19.84 X. Gong, J. Liu, S. Baskaran, R.D. Voise, J.S. Young: Surfactant-assisted processing of carbon nanotube/polymer composites, Chem. Mater. **12**, 1049–1052 (2000)
19.85 B. Fiedler, F. Gojny, M. Wichmann, M. Nolte, K. Schulte: Fundamental aspects of nano-reinforced composites, Compos. Sci. Technol. **66**, 3115–3125 (2006)
19.86 T. Liu, S. Kumar: Effect of orientation on the modulus of SWNT films and fibers, Nano Lett. **3**, 647–650 (2003)
19.87 V.N. Popov, V.E.V. Doren, M. Balkanski: Elastic properties of crystals of single-walled carbon nanotubes, Solid State Commun. **114**, 395–399 (2000)
19.88 C. Cooper: Structure/property relationships in particulate composites. Ph.D. Thesis (Univ. Manchester, Manchester 2000)
19.89 E.T. Thostenson, T.W. Chou: Aligned multi-walled carbon nanotube-reinforced composites: Processing and mechanical characterization, J. Phys. D **35**, L77–L80 (2002)
19.90 T. Kimura, H. Ago, M. Tobita, S. Ohshima, M. Kyotani, M. Yamura: Polymer composites of carbon nanotubes aligned by a magnetic field, Adv. Mater. **14**, 1380–1383 (2002)
19.91 W. Feng, X.D. Bai, Y.Q. Lian, J. Liang, X.G. Wang, K. Yoshino: Well-aligned polyaniline/carbon-nanotube composite films grown by in-situ aniline polymerization, Carbon **41**, 1551–1557 (2003)
19.92 A. Barber, S. Cohen, S. Kenig, H. Wagner: Interfacial fracture energy measurements for multi-walled carbon nanotubes pulled from a polymer matrix, Compos. Sci. Technol. **64**, 2283–2289 (2004)
19.93 A. Barber, S. Cohen, H. Wagner: Measurement of carbon nanotube-polymer interfacial strength, Appl. Phys. Lett. **82**, 4140–4142 (2003)
19.94 C. Cooper, S. Cohen, A. Barber, H. Wagner: Detachment of nanotubes from a polymer matrix, Appl. Phy. Lett. **81**, 3873–3875 (2002)
19.95 K. Liao, S. Li: Interfacial characteristics of a carbon nanotube-polystyrene composite system, Appl. Phy. Lett. **79**, 4225–4227 (2001)
19.96 A.H. Barber, S.R. Cohen, A. Eitan, L.S. Schadler, D.H. Wagner: Fracture transitions at a carbon-nanotube/polymer interface, Adv. Mater. **18**, 83–87 (2006)
19.97 R.K. Duncan, X.G. Chen, J.B. Bult, L.C. Brinson, L.S. Schadler: Measurement of the critical aspect ratio and interfacial shear strength in MWNT/polymer composites, Compos. Sci. Technol. **70**, 599–605 (2010)
19.98 H.G. Chae, T.V. Sreekumar, T. Uchida, S. Kumar: A comparison of reinforcement efficiency of various types of carbon nanotubes in poly acrylonitrile fiber, Polymer **46**, 10925–10935 (2005)
19.99 P.T. Lillehei, J. Kim, L.J. Gibbons, C. Park: A quantitative assessment of carbon nanotube dispersion in polymer matrices, Nanotechnology **20**, 325708 (2009)
19.100 Z.P. Luo, J.H. Koo: Quantitative study of the dispersion degree in carbon nanofiber/polymer and carbon nanotube/polymer nanocomposites, Mater. Lett. **62**, 3493–3496 (2008)
19.101 B.J. Bauer, M.L. Becker, V. Bajpai, J.A. Fagan, W.R. Blair: Measurement of single-wall nanotube dispersion by size exclusion chromatography, J. Phys. Chem. C **111**, 17914–17918 (2007)
19.102 S.H. Kim, W.I. Lee, J.M. Park: Assessment of dispersion in carbon nanotube reinforced composites using differential scanning calorimetry, Carbon **47**, 2699–2703 (2009)
19.103 J.A. Fagan, B.J. Landi, B.J. Bauer, R. Raffaelle, E.K. Hobbie: Comparative measures of single-wall carbon nanotube dispersion, J. Phys. Chem. B **110**, 23801–23805 (2006)
19.104 W. Salalha, Y. Dror, R.L. Khalfin, Y. Cohen, A.L. Yarin, E. Zussman: Single-walled carbon nanotubes embedded in oriented polymeric nanofibers by electrospinning, Langmuir **20**, 9852–9855 (2004)
19.105 J. Ge, H. Hou, Q. Li, M. Graham, A. Greiner, D. Reneker, F. Harris, S. Cheng: Assembly of well-aligned multiwalled carbon nanotubes in confined polyacrylonitrile environments: Electrospun composite nanofiber sheets, J. Am. Chem. Soc. **126**, 15754–15761 (2004)
19.106 A. Rasheed, M.D. Dadmun, I. Ivanov, P.F. Britt, D.B. Geohegan: Improving dispersion of single-walled carbon nanotubes in a polymer matrix using specific interactions, Chem. Mater. **15**, 3513–3522 (2006)
19.107 J. Hwang, H. Gommans, A. Ugawa, H. Tashiro, R. Haggenmueller, K. Winey, J. Fischer, D. Tanner, A. Rinzler: Polarized spectroscopy of aligned single-wall carbon nanotubes, Phys. Rev. B **62**, R13310–R13313 (2000)
19.108 W.C. Ren, F. Li, H.M. Cheng: Polarized Raman analysis of aligned double-walled carbon nanotubes, Phys. Rev. B **71**, 115428 (2005)
19.109 L. Deng, S.J. Eichhorn, C.-C. Kao, R.J. Young: The effective Young's modulus of carbon nanotubes in composites, Am. Chem. Soc. Appl. Mater. Inter. **3**, 433–440 (2011)
19.110 E. Anglaret, A. Righi, J. Sauvajol, P. Bernier, B. Vigolo, P. Poulin: Raman resonance and orientational order in fibers of single-wall carbon nanotubes, Phys. Rev. B **65**, 165426 (2002)

19.111 R. Pérez, S. Banda, Z. Ounaiesa: Determination of the orientation distribution function in aligned single wall nanotube polymer nanocomposites by polarized Raman spectroscopy, J. Appl. Phys. **103**, 074302 (2008), 1–9

19.112 T. Liu, S. Kumar: Quantitative characterization of SWNT orientation by polarized Raman spectroscopy, Chem. Phys. Lett. **378**, 257–262 (2003)

19.113 L. Deng, R.J. Young, S. van der Zwaag, S. Picken: Characterisation of the adhesion of single-walled carbon nanotubes in poly(p-phenylene terephthalamide) composite fibres, Polymer **51**, 2033–2039 (2010)

19.114 C. Zamora-Ledezma, C. Blanc, M. Maugey, C. Zakri, P. Poulin, E. Anglaret: Anisotropic thin films of single-wall carbon nanotubes from aligned lyotropic nematic suspensions, Nano Lett. **12**, 4103–4107 (2008)

19.115 D. Roy, S. Bhattacharyya, A. Rachamim, A. Plati, M. Saboungi: Measurement of interfacial shear strength in single wall carbon nanotubes reinforced composite using Raman spectroscopy, J. Appl. Phys. **107**, 043501 (2010), 1–6

19.116 P. Kannan, S.J. Eichhorn, R.J. Young: Deformation of isolated single-wall carbon nanotubes in electrospun polymer nanofibres, Nanotechnology **18**, 235707 (2007)

19.117 C. Kao, R.J. Young: Assessment of interface damage during the deformation of carbon nanotube composites, J. Mater. Sci. **45**, 1425–1431 (2010)

19.118 S. Cui, I.A. Kinloch, R.J. Young, L. Noé, M. Monthioux: The effect of stress transfer within double-walled carbon nanotubes upon their ability to reinforce composites, Adv. Mater. **21**, 3591–3595 (2009)

19.119 A.F. Fonseca, T. Borders, R.H. Baughman, K. Cho: Load transfer between cross-linked walls of a carbon nanotube, Phys. Rev. B **81**, 045429 (2010), 1–7

19.120 L. Zalamea, H. Kim, R.B. Pipes: Stress transfer in multi-walled carbon nanotubes, Compos. Sci. Technol. **67**, 3425–3433 (2007)

19.121 L.S. Schadler, S.C. Giannaris, P.M. Ajayan: Load transfer in carbon nanotube epoxy composites, Appl. Phys. Lett. **73**, 3842–3844 (1998)

19.122 J.L. Bahr, J.P. Yang, D.V. Kosynkin, M.J. Bronikowski, R.E. Smalley, J.M. Tour: Functionalization of carbon nanotubes by electrochemical reduction of aryl diazonium salts: A bucky paper electrode, J. Am. Chem. Soc. **123**, 6536–6542 (2001)

19.123 M. Hirata, T. Gotou, S. Horiuchi, M. Fujiwara, M. Ohba: Thin-film particles of graphite oxide 1: High-yield synthesis and flexibility of the particles, Carbon **42**, 2929–2937 (2004)

19.124 Y. Matsuo, K. Tahara, Y. Sugie: Structure and thermal properties of poly(ethylene oxide)-intercalated graphite oxide, Carbon **35**, 113–120 (1997)

19.125 B. Das, K.E. Prasad, U. Ramamurty, C.N.R. Rao: Nano-indentation studies on polymer matrix composites reinforced by few-layer graphene, Nanotechnology **20**, 125705 (2009)

19.126 H.W. Kim, Y. Miura, C.W. Macosko: Graphene/polyurethane nanocomposites for improved gas barrier and electrical conductivity, Chem. Mater. **22**, 3441–3450 (2010)

19.127 J.Y. Jang, M.S. Kim, H.M. Jeong, C.M. Shin: Graphite oxide/poly(methyl methacrylate) nanocomposites prepared by a novel method utilizing macroazoinitiator, Compos. Sci. Technol. **69**, 186–191 (2009)

19.128 S.R. Wang, M. Tambraparni, J.J. Qiu, J. Tipton, D. Dean: Thermal Expansion of Graphene Composites, Macromolecules **42**, 5251–5255 (2009)

19.129 M.A. Rafiee, J. Rafiee, Z. Wang, H.H. Song, Z.-Z. Yu, N. Koratkar: Enhanced mechanical properties of nanocomposites at low graphene content, ACS Nano **3**, 3884–3890 (2009)

19.130 H.W. Kim, C.W. Macosko: Processing-property relationships of polycarbonate/graphene composites, Polymer **50**, 3797–3809 (2009)

19.131 H.W. Kim, C.W. Macosko: Morphology and properties of polyester/exfoliated graphite nanocomposites, Macromolecules **41**, 3317–3327 (2008)

19.132 K. Wakabayashi, C. Pierre, D.A. Dikin, R.S. Ruoff, T. Ramanathan, L.C. Brinson, J.M. Torkelson: Polymer-graphite nanocomposites: Effective dispersion and major property enhancement via solid-state shear pulverization, Macromolecules **41**, 1905–1908 (2008)

19.133 J.C. Halpin, J.L. Kardos: Halpin-Tsai equations – Review, Polym. Eng. Sci. **16**, 344–352 (1976)

19.134 T. Mori, K. Tanaka: Average stress in matrix and average elastic energy of materials with misfitting inclusions, Acta Met. **21**, 571–574 (1973)

19.135 G.P. Tandon, G.J. Weng: The effect of aspect ratio of inclusions on the elastic properties of unidirectionally aligned composites, Polym. Compos. **5**, 327–333 (1984)

19.136 J.C. Halpin, R.L. Thomas: Ribbon reinforcement of composites, J. Compos. Mater. **2**, 488–497 (1968)

19.137 Y.X. Xu, W.J. Hong, H. Bai, C. Li, G.Q. Shi: Strong and ductile poly(vinyl alcohol)/graphene oxide composite films with a layered structure, Carbon **47**, 3538–3543 (2009)

19.138 J.J. Liang, Y. Huang, L. Zhang, Y. Wang, Y.F. Ma, T.Y. Guo, Y.S. Chen: Molecular-level dispersion of graphene into poly(vinyl alcohol) and effective reinforcement of their nanocomposites, Adv. Funct. Mater. **19**, 2297–2302 (2009)

19.139 W.H. Kai, Y. Hirota, L. Hua, Y. Inoue: Thermal and mechanical properties of a poly(epsilon-caprolactone)/graphite oxide composite, J. Appl. Polym. Sci. **107**, 1395–1400 (2008)

19.140 D.Y. Cai, M. Song: A simple route to enhance the interface between graphite oxide nanoplatelets

and a semi-crystalline polymer for stress transfer, Nanotechnology **20**, 315708 (2009)
19.141 T. Ramanathan, A.A. Abdala, S. Stankovich, D.A. Dikin, M. Herrera-Alonso, R.D. Piner, D.H. Adamson, H.C. Schniepp, X. Chen, R.S. Ruoff, S.T. Nguyen, I.A. Aksay, R.K. Prud'homme, L.C. Brinson: Functionalized graphene sheets for polymer nanocomposites, Nat. Nanotechnol. **3**, 327–331 (2008)
19.142 S. Ansari, E.P. Giannelis: Functionalized graphene sheet-poly(vinylidene fluoride) conductive nanocomposites, J. Polym. Sci. B **47**, 888–897 (2009)
19.143 S. Ansari, A. Kelarakis, L. Estevez, E.P. Giannelis: Oriented arrays of graphene in a polymer matrix by in situ reduction of graphite oxide nanosheets, Small **6**, 205–209 (2010)
19.144 P. Steurer, R. Wissert, R. Thomann, R. Mülhaupt: Functionalized graphenes and thermoplastic nanocomposites based upon expanded graphite oxide, Macromol. Rapid Commun. **30**, 316–327 (2009)
19.145 M. Fang, K.G. Wang, H.B. Lu, Y.L. Yang, S. Nutt: Single-layer graphene nanosheets with controlled grafting of polymer chains, J. Mater. Chem. **19**, 7098–7105 (2009)
19.146 J.J. Mack, L.M. Viculis, A. Ali, R. Luoh, G.L. Yang, H.T. Hahn, F.K. Ko, R.B. Kaner: Graphite nanoplatelet reinforcement of electrospun polyacrylonitrile nanofibers, Adv. Mater. **17**, 77–80 (2005)
19.147 R.K. Prud'homme, B. Ozbas, I.A. Aksay, R.A. Register, D.H. Adamson: Polymer composition used for functional graphene sheet, contains polymer matrix which comprises elastomer, and functional graphene which displays no signature of graphite and/or its oxide, as determined by X-ray diffraction, WO Patent, 2008/045778 A1 (2008)
19.148 J.J. Liang, Y.F. Xu, Y. Huang, L. Zhang, Y. Wang, Y.F. Ma, F.F. Li, T.Y. Guo, Y.S. Chen: Infrared-triggered actuators from graphene-based nanocomposites, J. Phys. Chem. C **113**, 9921–9927 (2009)
19.149 D.Y. Cai, K. Yusoh, M. Song: The mechanical properties and morphology of a graphite oxide nanoplatelet/polyurethane composite, Nanotechnology **20**, 085712 (2009)
19.150 D.D. Kulkarni, I.J. Choi, S.S. Singamaneni, V.V. Tsukruk: Graphene oxide-polyelectrolyte nanomembranes, ACS Nano **4**, 4667–4676 (2010)
19.151 I.-H. Kim, Y.G. Jeong: Polylactide/exfoliated graphite nanocomposites with enhanced thermal stability, mechanical modulus, and electrical conductivity, J. Polym. Sci. B **48**, 850–858 (2010)
19.152 S.G. Miller, J.L. Bauer, M.J. Maryanski, P.J. Heimann, J.P. Barlow, J.-M. Gosau, R.E. Allred: Characterization of epoxy functionalized graphite nanoparticles and the physical properties of epoxy matrix nanocomposites, Compos. Sci. Technol. **70**, 1120–1125 (2010)
19.153 R. Gangopadhyay, A. De: Conducting polymer nanocomposites: A brief overview, Chem. Mater. **12**, 608–622 (2000)
19.154 M. Hindermann-Bischoff, F. Ehrburger-Dolle: Electrical conductivity of carbon black-polyethylene composites – Experimental evidence of the change of cluster connectivity in the PTC effect, Carbon **39**, 375–382 (2001)
19.155 J.-C. Huang: Carbon black filled conducting polymers and polymer blends, Adv. Polym. Technol. **21**, 299–313 (2002)
19.156 J.K.W. Sandler, J.E. Kirk, I.A. Kinloch, M.S.P. Shaffer, A.H. Windle: Ultra-low electrical percolation threshold in carbon-nanotube-epoxy composites, Polymer **44**, 5893–5899 (2003)
19.157 D.A. Nguyen, Y.R. Lee, A.V. Raghu, H.M. Jeong, C.M. Shin, B.K. Kim: Morphological and physical properties of a thermoplastic polyurethane reinforced with functionalized graphene sheet, Polym. Int. **58**, 412–417 (2009)
19.158 H.B. Lee, A.V. Raghu, K.S. Yoon, H.M. Jeong: Preparation and characterization of poly(ethylene oxide)/graphene nanocomposites from an aqueous medium, J. Macromol. Sci. B **49**, 802–809 (2010)
19.159 S. Stankovich, D.A. Dikin, R.D. Piner, K.A. Kohlhaas, A. Kleinhammes, Y.Y. Jia, Y. Wu, S.-B.T. Nguyen, R.S. Ruoff: Synthesis of graphene-based nanosheets via chemical reduction of exfoliated graphite oxide, Carbon **45**, 1558–1565 (2007)
19.160 J.S. Bunch, S.S. Verbridge, J.S. Alden, A.M. van der Zande, J.M. Parpia, H.G. Craighead, P.L. McEuen: Impermeable atomic membranes from graphene sheets, Nano Lett. **8**, 2458–2462 (2008)
19.161 K. Kalaitzidou, H. Fukushima, L.T. Drzal: Multifunctional polypropylene composites produced by incorporation of exfoliated graphite nanoplatelets, Carbon **45**, 1446–1452 (2007)
19.162 A.P. Yu, P. Ramesh, M.E. Itkis, E. Bekyarova, R.C. Haddon: Functionalized single-walled carbon nanotubes for carbon fiber-epoxy composites, J. Phys. Chem. C **111**, 7565–7569 (2007)
19.163 A.P. Yu, P. Ramesh, X.B. Sun, E. Bekyarova, M.E. Itkis, R.C. Haddon: Enhanced thermal conductivity in a hybrid graphite nanoplatelet – Carbon nanotube filler for epoxy composites, Adv. Mater. **20**, 4740–4744 (2008)
19.164 N. Liu, F. Luo, H.X. Wu, Y.H. Liu, C. Zhang, J. Chen: One-step ionic-liquid-assisted electrochemical synthesis of ionic-liquid-functionalized graphene sheets directly from graphite, Adv. Funct. Mater. **18**, 1518–1525 (2008)
19.165 H.J. Salavagione, M.A. Gómez, G. Martínez: Polymeric modification of graphene through esterification of graphite oxide and poly(vinyl alcohol), Macromolecules **42**, 6331–6334 (2009)

19.166 T. Kashiwagi, F.M. Du, J.F. Douglas, K.I. Winey, R.H. Harris Jr., J.R. Shields: Nanoparticle networks reduce the flammability of polymer nanocomposites, Nat. Mater. **4**, 928–933 (2005)
19.167 Y.L. Huang, R.J. Young: Analysis of the fragmentation test for carbon-fiber epoxy model composites by means of Raman-spectroscopy, Compos. Sci. Technol. **52**, 505–517 (1994)
19.168 P.W.J. van den Heuvel, T. Peijs, R.J. Young: Failure phenomena in two-dimensional multi-fibre microcomposites. 2. A Raman spectroscopic study of the influence of inter-fibre spacing on stress concentrations, Compos. Sci. Technol. **57**, 899–911 (1997)
19.169 H.L. Cox: The elasticity and strength of paper and other fibrous materials, Br. J. Appl. Phys. **3**, 72–79 (1952)
19.170 P. Blake, P.D. Brimicombe, R.R. Nair, T.J. Booth, D. Jiang, F. Schedin, L.A. Ponomarenko, S.V. Morozov, H.F. Gleeson, E.W. Hill, A.K. Geim, K.S. Novoselov: Graphene-based liquid crystal device, Nano Lett. **8**, 1704–1708 (2008)

20. Nanoparticle Dispersions

Krisztián Kordás, Jarmo Kukkola, Géza Tóth, Heli Jantunen, Mária Szabó, András Sápi, Ákos Kukovecz, Zoltán Kónya, Jyri-Pekka Mikkola

This chapter aims to provide an insight into the physics and chemistry of nanoparticle–liquid systems. The first part of the chapter discusses parameters and effects that influence dispersion stability (Sect. 20.1), including particle size and shape as well as the interactions at the interface between the solid and liquid phases. Section 20.2 summarizes the practical aspects of making a dispersion, collecting and listing hundreds of examples from contemporary literature. Because of the broad spectrum of materials in question, the survey is limited to dispersions of inorganic nanoparticles including metals, their oxides/sulfides, some (compound) semiconductors, as well as nanostructured carbon particles such as fullerenes, nanotubes, and graphene/graphite (Sect. 20.3). Dispersions of polymers of either synthetic or biological origin lie beyond the scope of this work. Since a very large fraction of applications are related to various surface coatings using dispersions as the source of nanoparticles, Sect. 20.4 is devoted to drying phenomena and particle self-ordering.

20.1 **Stabilization of Nanoparticle Dispersions** 730
20.1.1 Shape of Nanoparticles 730
20.1.2 Sedimentation, Ordering, and Coarsening of Nanoparticles in Liquid Dispersions 730
20.1.3 Electrolytes and the DLVO Theory .. 732
20.1.4 Steric (Nonelectric) Stabilization ... 734
20.2 **Nanoparticle Dispersion in Practice** 734
20.3 **Dispersions of Carbon Nanomaterials** 745
20.4 **Drying Dispersions on Surfaces** 752
20.4.1 Ring-Stain Effect 752
20.4.2 Self-Organized Structures 756
20.4.3 Inkjet Printing of Nanoparticle Dispersions 757
20.5 **Concluding Remarks** 758
References 758

Dispersions of various particles have been made since prehistoric times, at that time applied mainly as paints and inks. The oldest cave paintings, made of various kinds of dyestuff such as hematite, charcoal, manganese oxide, and red and yellow ochre, are more than 30 000 years old [20.1]. These paints (i. e., dispersions) were made by grinding the solid followed by mixing in water, grease, and sometimes with blood. Later, many ancient cultures discovered their own inks for writing and drawing. The basic recipes were quite similar. Soot collected from the smoke of burning wood or lamp oil was mixed with oils or grease. To change the smell, color, and probably drying and sticking behavior of the inks, usually some additives such as gelatin extracted from animal skin, honey, powdered minerals, and natural dyes of plants were applied as well [20.2–5]. Milled particles of a number of different minerals such as calcite, gypsum, lime, hematite, goethite, cuprorivaite, azurite, cinnabar, red lead, etc. were utilized to tune color [20.6–8]. Water-based inks of lampblack or charcoal were made with the help of added gum and sugar. For coloration, natural dyes but also powders of silver and gold were applied [20.9]. In 1450, Gutenberg developed oil-based inks of carbon black and metal particles (Cu, Pb, Ti) that properly wetted the lead-based alloy types in his printing press [20.10, 11]. Paints similar to those used in prehistoric times still have practical importance today. Ochre mixed with seal oil (North America) or linseed oil (Scandinavia) has been the traditional paint of wooden houses [20.12].

Conscious synthesis and use of micro- and nanoparticle dispersions other than for inks and paints probably started with the advent of colloid chemistry in the middle of the 19th century. Recognizing that the surface properties of particles are of key importance in preparing and storing dispersions shifted the trial-and-error experimental work towards more scientific approaches. The previously accumulated empirical knowledge combined with understanding of particulate–solvent interactions finally resulted in the birth of the fascinating world of colloid chemistry – the science of multiphase systems with large interfacial surface areas. Today, several industries utilize and are still developing further knowhow of making dispersions tailored for particular applications. Apart from paints and coatings, sub-micrometer-size particles suspended in liquids are employed in medicine, biotechnologies, electronics, optoelectronics, materials processing, and mechanical and civil engineering, just to mention a few. Though a large selection of various nanoparticle dispersions are commercially available from several vendors, the continuously increasing number of novel nanomaterials and the need for engineered nanoparticle–liquid systems for a particular end-use sustain and inspire research in the field.

20.1 Stabilization of Nanoparticle Dispersions

The suspension and then stabilization of nanoparticles in a liquid is a function of a number of different variables. The shape, size, material, concentration, and surface chemistry of the nanoparticles, the nature of the solvent, the mixing technique applied, and external parameters such as the temperature and directing fields are all important to consider when designing and synthesizing nanoparticle dispersions. Both theoretical and practical aspects of nanoparticle stabilization are discussed in this section.

20.1.1 Shape of Nanoparticles

Nanoparticles differ from their bulk counterparts – amongst many other aspects – in their shape. When using the prefix *nano* it is assumed that the size along at least one direction is small (by convention, shorter than 100 nm). If the structure is confined to planar geometry, we refer to a two-dimensional (2-D) structure such as nanoflakes, nanosheets, or thin plates. Having small extension in two perpendicular dimensions, we obtain one-dimensional (1-D) structures called nanowires, nanorods, nanofibers, and (with a hollow interior) nanotubes. Continuing this train of thought, small dimensions along all three coordinates results in zero-dimensional (0-D) objects such as spherical and polygon-shaped nanoparticles – often called quantum dots in the case of semiconducting materials. The shape of nanoparticles has some effects on the properties of their dispersions. The viscosity, stability, and even the optical behavior are all influenced depending on whether nanoparticles, nanowires/tubes/rods, or particles of lamellar/sheet-like shape are present in the liquid. The nanoparticles are in continuous movement in the dispersion (Brownian motion), thus drag forces, which depend on the shape of the moving particles, are different, causing for instance higher viscosity and slower sedimentation for elongated and lamellar nanoparticle dispersions than for those consisting of spherical nanoparticles of similar volume. On the other hand, the shape of the primary particles also determines how these particles agglomerate to form secondary particles, thus indirectly influencing the rheological properties of the dispersion (0-D particles usually form clusters, chains, and branches thereof, 1-D particles form elongated bundles but also may tangle into bigger clumps, while 2-D particles often agglomerate as lamellar stacks) [20.13].

20.1.2 Sedimentation, Ordering, and Coarsening of Nanoparticles in Liquid Dispersions

In dispersions, the spatial distribution and – in certain applications – also the orientation of the nanoparticles are probably the most important measures. The system is homogeneous if the concentration of particles is the same throughout the whole volume. The medium is heterogeneous when the solid phase is separated from the solvent. Between these two extremes, we talk about diffuse dispersions; i. e., slight concentration gradients may be present. From a practical point of view, homogeneous nanoparticle inks are preferred; however, diffuse dispersions may be useful as well, provided the concentration gradients in the inks are minimized by stirring, shaking, or ultrasonic agitation immediately before application of the medium [20.13].

External fields exerting forces on dispersed nanoparticles may result in sedimentation, separation, as well as orientation/ordering of the nanoparticles in reference to the liquid. The efficiency of particle migration and rotation depends on whether the driving forces can overcome the disorder caused by Brownian motion.

In a gravitational field, the drift of particles (i. e., velocity with respect to the liquid phase, or terminal velocity) is determined by the buoyancy and drag forces and can be expressed as

$$v_\mathrm{d} = \frac{2r^2(\rho - \rho_0)g}{9\eta} ,$$

where r is the radius and ρ is the density of the particle, ρ_0 is the density of the liquid, g is the acceleration, and η is the viscosity of the liquid. It is important to note that the equation is only valid for spherical particles that are not interacting with each other. In the case of 1-D or 2-D particles, a sphere with equivalent radius may be calculated to enable reasonable approximations. Furthermore, the particles are assumed to be wetted by the surrounding medium (viz. the momentum transfer is taking place at the interface of the adsorption layer and liquid) [20.14]. When the terminal velocity becomes higher than the rms speed along to gravitational axis of particles due to thermal motion

$$v_\mathrm{t} = \left(\frac{k_\mathrm{B}T}{m}\right)^{1/2} ,$$

sedimentation of the particles occurs (k_B is Boltzmann's constant, T is the thermodynamic temperature, and m is the mass of the particle). The rms displacement of a particle within a time interval t due to thermal diffusion is

$$\Delta = (2Dt)^{1/2} ,$$

where $D = k_\mathrm{B}T/(6\pi\eta r)$ is the diffusivity at temperature T of a spherical particle having r radius, in a fluid with viscosity η. To demonstrate the importance of the role played by diffusion when talking about nanoparticle–liquid systems, let us consider a dispersion of nanoparticles with diameter 20 nm and density $4\,\mathrm{g/cm^3}$ in water ($\eta = 10^{-3}\,\mathrm{N\,s/m^2}$) and estimate the diffusion length within 1 s period of time and compare it with the sedimentation height within the same time. Substituting the materials parameters into the above equations, we get $\Delta \approx 6.6\,\mu\mathrm{m}$ and $v_\mathrm{d} \cdot 1\,\mathrm{s} \approx 0.7\,\mathrm{nm}$, suggesting that such a colloidal system is supposed to remain homogeneously dispersed for several years. On the other hand, when the nanoparticles are agglomerated in larger clusters, with diameter of say 500 nm, the corresponding length values become comparable (≈ 1.3 and $\approx 0.4\,\mu\mathrm{m}$), indicating very rapid sedimentation of the large agglomerates.

Since v_d is a quadratic function of the particle radius, decreasing the size of the particles to be dispersed helps to avoid their sedimentation. In the case of polydisperse systems, separation of the solid particles having the largest size takes place first. This effect is frequently utilized in practice when separating nanoparticles that are chemically similar but with different sizes simply by speeding up the sedimentation process using high acceleration in centrifuges (up to several tens of thousands of g) and ultracentrifuges (up to $10^6 g$). Besides the application of smaller particles, a good strategy for disabling sedimentation can be the use of liquids having density close to that of the nanoparticles, since then $\rho - \rho_0 \approx 0$, leading to $v_\mathrm{d} \approx 0$. Increasing the viscosity may also help in maintaining the homogeneity of the dispersions, as $v_\mathrm{d} \propto \eta^{-1}$.

Charged particles can be separated in electrostatic fields (electrophoresis). The process is very similar to the previously discussed sedimentation, but besides gravity, also Coulomb forces proportional to the electrical field and the charge of the particles are exerted on the particles. Particles with a dipole moment can only be rotated and oriented in a uniform electric field (liquid-crystal displays); however, when applying a field gradient, movement of dipole particles is enabled in dispersions (as in optical tweezers).

Nanoparticles having a magnetic momentum can be manipulated in magnetic fields. In a uniform field, only rotation occurs, while in the presence of field gradients a magnetic force is exerted and moves the particles. This latter effect is frequently applied in separating ferromagnetic nanoparticles from dia- and paramagnetic phases. As the viscosity of aligned nanoparticles in a dispersion is higher than in a random (or disordered) system, such magnetic colloids (ferrofluids) are very often used in mechanical vibration damping. In practice, ferromagnetic or antiferromagnetic materials are applied in various inks and pastes to enable use of low magnetic fields below 1 T, e.g., with ferrites and rare-earth magnets or with ordinary electromagnets. In the case of paramagnetic nanomaterials, magnetic fields above 10 T are required for efficient manipulation, thus the applicability of such nanomaterials is mainly limited to laboratory experiments.

Until this point, only individual nanoparticles have been considered; i. e., any interaction between the

nanoparticles has been neglected. Though this enabled a very simple discussion of the spatial distribution and orientation of nanoparticles in dispersions, in reality, the picture is much more complex than this, since the particles interact with the liquids as well as with each other.

The surface energies of solid nanoparticles (in J/m^2) are usually very different from the surface tension of solvents. From the point of view of thermodynamics, such dispersions cannot be assumed to be stable and thus will undergo coagulation to minimize the Gibbs energy of the system. Coagulation takes place as the particles in (thermal) motion collide and then adhere together, resulting in agglomeration of the primary nanoparticles into larger, secondary particles. In some cases, also irreversible merging (recrystallization) of the particles that are in intimate contact may occur [20.13, 15].

The particle-size- or surface-curvature-dependent solubility of materials known as Ostwald ripening is another reason for coarsening of nanoparticles in dispersions. As derived by Ostwald, the solubility of particles L_r increases exponentially with decreasing radius r as

$$L_r = L\,\mathrm{e}^{\frac{2\gamma M}{rRT\rho}} ,$$

where L is the solubility of a particle with infinite radius (i. e., the conventional solubility of a macroscopic bulk material), γ is the surface tension, ρ is the density, and M is the molecular weight of the solute. Accordingly, polydisperse systems cannot be in equilibrium, since the smaller particles dissolve and the dissolved moieties then deposit on the larger particles, thus continuously increasing the average particle size (a process also called isotherm distillation) [20.13, 16–18].

20.1.3 Electrolytes and the DLVO Theory

It was observed long ago that some particles form stable dispersions in certain solvents while others require additional substances to achieve stability. As we will see, the structure of the solid–liquid interface and the interactions between the particles and the medium strongly determine the stability of the corresponding dispersions. Accordingly, we have to take a look at various scenarios of how a nanoparticle is actually situated in liquids and what sort of solid–liquid interfaces may form in dispersions [20.13, 15].

Very often, stable sols are obtained when dispersing nanoparticles in electrolytes. In such cases, an electric double layer forms at the solid–liquid interface, which helps in the separation of the nanoparticles due to the repulsive electrostatic forces exerted among them. This phenomenon is described by the Derjaguin–Landau–Verwey–Overbeek (DLVO) theory, named after the scientists who developed its fundamentals. The surface of solid particles in a liquid may dissociate and/or adsorb ions, resulting in a surface charge buildup, which then attracts ions of the opposite charge (counterions) from the surrounding solution and repels ions with charge of the same sign (co-ions). The region of ions and balancing counterions is called the electrical double layer (EDL). According to the DLVO theory, the interaction between two particles is described by a potential function V (Fig. 20.1), which is a sum of the attractive and repulsive potentials (V_a and V_r, respectively), both being dependent on the interparticle distance d. Note that Born repulsion is typically neglected; however, at distances below 0.2 nm, this interaction is to be considered, as it becomes the dominant force that prevents the electron clouds of atoms from approaching each other arbitrarily closely [20.19, 20].

The attractive potential (van der Waals attraction) [20.15] between two spheres of the same radius r is

$$V_a = -\frac{rA}{12d} ,$$

where A denotes the Hamaker constant (accounting for the energy of interactions among the atoms of adjacent nanoparticles). The Hamaker constants for various materials of different size and shape can be measured with good accuracy using, e.g., atomic force microscopy and electrophoresis, or can be calculated, e.g., by the Lifshitz theory or the Tabor–Winterton approximation [20.13, 15]. The typical Hamaker constants for ceramic materials in water are in the range $\approx 10^{-21}$–10^{-19} J, while in vacuum the values are somewhat higher, in the range $\approx 5\times10^{-20}$–5×10^{-19} J [20.21, 22]. For common metals (such as Au, Ag, and Cu), $A \approx 5\times10^{-20}$–$3\times10^{-19}$ J in both water and vacuum [20.14, 23, 24]. For TiO_2 nanoparticles of 20 nm diameter at spacing of 1 nm in water, considering $A \approx 6\times10^{-20}$ J, the energy of van der Waals attraction is $V_a \approx -5\times10^{-20}$ J, which is about an order of magnitude higher than the thermal energy of particles at room temperature, meaning that thermal motion without other repulsive interactions would not be enough to separate such particles. The force exerted on such particles due to van der Waals attraction is

$$F_a = -\frac{rA}{12d^2} \approx -5\times10^{-11}\,\mathrm{N} .$$

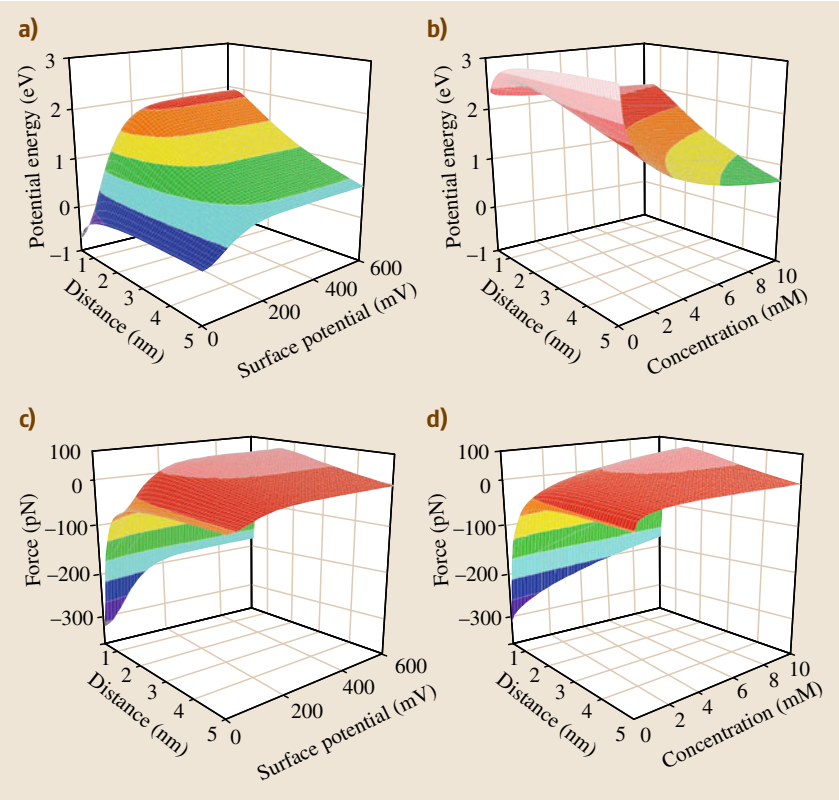


Fig. 20.1a–d Calculated attractive and repulsive potentials considering interparticle distance, electrolyte concentration, and surface charge. Interparticle-distance-dependent potential energy between two TiO_2 nanoparticles as a function of **(a)** surface potential at 10 mM electrolyte concentration and as a function of **(b)** electrolyte concentration at constant 500 mV surface potential. Panels **(c)** and **(d)** show the respective force between the nanoparticles

The repulsive potential [20.15], assuming that $r \gg d$, is

$$V_\mathrm{r} = \frac{r}{2} Z \mathrm{e}^{-\kappa d} \,,$$

where

$$\kappa^{-1} = \left(\frac{\varepsilon \varepsilon_0 k_\mathrm{B} T}{e^2 N_\mathrm{A} \sum_i z_i^2 M_i} \right)^{1/2}$$

is the Debye length and

$$Z = 64\pi\varepsilon\varepsilon_0 \left(\frac{k_\mathrm{B} T}{e} \right)^2 \tanh^2 \left[\frac{ze\psi_0}{4k_\mathrm{B} T} \right] \,,$$

where ε is the dielectric permittivity of the electrolyte, ε_0 is the vacuum permittivity, ψ_0 is the surface potential, N_A is the Avogadro number, e is the elementary charge, z_i is the valency, and M_i is the concentration of ions ($\frac{1}{2}\sum_i z_i^2 M_i$ representing the ionic strength of the electrolyte). While the Debye length depends on the electrolyte and indicates the thickness of the diffuse ionic layer, Z is determined by the surface charge. In aqueous electrolytes, the Debye length is below 1 µm (pure water) and decreases with the square root of the ionic strength (e.g., $\kappa^{-1} \approx 30$ nm for 10^{-4} M and ≈ 3 nm for 10^{-2} M KCl solution but ≈ 15 nm for 10^{-4} M and ≈ 1.5 nm for 10^{-2} M $MgSO_4$ solutions). As we see, the repulsive potential decays exponentially with the distance between particles and with the ionic strength of the electrolyte. An example value for the repulsive potential, assuming similar nanoparticles as previously when calculating the van der Waals potential (particles of radius 10 nm each with separation of 1 nm) but having 500 mV surface potential in 10^{-2} M KCl solution, is $V_\mathrm{r} \approx 3 \times 10^{-19}$ J with a corresponding force of $F_\mathrm{r} = \kappa \frac{r}{2} Z \mathrm{e}^{-\kappa d} \approx 11 \times 10^{-11}$ N. The obtained repulsive force F_r is thus larger than the van der Waals attraction calculated earlier ($F_\mathrm{a} \approx -5 \times 10^{-11}$ N), meaning that the particles have not crossed the energy barrier to emerge as one cluster. Allowing d to vary, one gets $|F_\mathrm{a}| = |F_\mathrm{r}|$ at $d \approx 0.6$ nm particle spacing. Accordingly, if the nanoparticles reach separation below 0.6 nm, the attractive van der Waals force binds the nanoparticles together, leading to agglomeration.

Nanoparticles of silicates and clays form stable dispersions in pure water without addition of any elec-

trolytes to the system. In such cases, partial surface dissociation results in the appearance of ionic species both on the solid surface and in the liquid phase, leading to the formation of an electric double layer similar to that found in ordinary electrolyte-stabilized dispersions [20.25–31].

20.1.4 Steric (Nonelectric) Stabilization

Although the DLVO theory gives a quite reliable account of the interactions between nanoparticles in electrolytes, it cannot explain the stability of dispersions without electric double layers. In a number of different dispersions, a thin adsorbed layer of the solvent forms on the surface of nanoparticles. A good example is dispersion of carbonaceous particles with apolar behavior in organic solvents. Their stabilization is based on the entropy production (and thus decreased overall Gibbs energy) as the particles separate from each other in the solvent. Earlier, soot and other carbonaceous particles were stabilized in oils. In contemporary scientific works – due to their potential in future electronics – pristine (nonfunctionalized) carbon nanotubes and graphenes have been studied and found to be dispersable reasonably well in *N*-methyl-pyrrolidone (NMP), dimethylformamide (DMF), γ-butyrolactone (GBL), dimethylacetamide (DMA), or benzene. In the case of graphene in DMF, the interaction is so strong that, under ultrasonic agitation, the graphene layers of graphite could be separated (exfoliation) [20.32–35].

Dispersion stabilization with surfactants and macromolecules is another approach to establish a gradual transition between particles and solvents of dissimilar nature [20.13, 36, 37]. As we all well know from daily experiences (e.g., when cleaning surfaces or washing clothes), hydrophobic surfaces are immiscible in polar solvents. The reason is the strong interaction between the polar solvent molecules (van der Waals forces and hydrogen bonding), which cannot be disrupted by a hydrophobic surface, thus such systems remain phase-separated. Although the dipoles of the solvent might induce a weak dipole moment on the surface of particles, such interactions are weak and the overall Gibbs energy of the mixture will be higher than the phase-separated one, thus considerable mixing cannot occur. The picture is very similar for hydrophilic surfaces in nonpolar solvents, but here the strong attraction between particles is responsible for the immiscibility. To mix hydrophobic and hydrophilic materials, a very convenient approach is to apply amphiphiles (surfactants, i. e., molecules having both hydrophilic and hydrophobic parts) which can mediate the dissimilarities of the two different phases. The hydrophilic part of the molecule (an anionic, cationic, zwitterionic or a noncharged but polar group) is solvated by the polar solvent or adsorbed on the hydrophilic nanoparticle surface, while the hydrophobic part (hydrocarbon chain or ring) is attracted to the molecules of apolar solvents or to the apolar surface of nanoparticles (for a comprehensive set of various types of surfactants, see [20.38]). Since the surfactant molecules typically form an oriented interface between the two phases, the separation between two nanoparticles in such a dispersion is at least twice the length of the apolaric hydrocarbon group of the surfactant molecule (the size of the polar part being negligible). Accordingly, nanoparticles stabilized, for instance, with oleyl alcohol ($C_{18}H_{36}O$) or with stearyl alcohol ($C_{18}H_{38}O$) will be separated (sterically) by a distance of at least ≈ 2 or ≈ 4 nm, respectively. In this case, it is assumed that the surfactant molecules adsorbed on the two adjacent nanoparticles cannot be pushed into each other. Within such a distance, the van der Waals potential drops considerably, resulting in small attractive forces, thus avoiding the particles sticking together. For TiO_2 nanoparticles, similar to those discussed above, the van der Waals potential energies at 2 and 4 nm are −0.16 and −0.08 eV, respectively.

20.2 Nanoparticle Dispersion in Practice

Direct dispersion of nanoparticles in ordinary solvents is possible only very seldom. As we have seen in Sect. 20.1.3, the attractive van der Waals forces between nanoparticles is to be compensated for by electrostatic stabilization or to be reduced by steric hindrance through addition of molecules that can adsorb onto the nanoparticles, forming spacer units between the primary particles.

Metals and metal oxides are often stabilized in electrolytes of NaCl, Na_2SO_4, $HClO_4$, ascorbic acid, and citrates [20.38, 39].

Application of surfactants and various capping agents is probably the most widespread method used to disperse virtually any type of nanoparticle in a large selection of different solvents. Surfactants and capping

agents adhere to the particles by van der Waals forces (dipole–dipole, induced dipole) or electrostatic attraction (e.g., ions on a partially dissolved surface with ionic surfactants of opposite charge). Because of the large variety of polar and ionic groups linked to the apolar part of the molecules, it is relatively easy to find the optimal one for a particular type of nanoparticle–solvent system [20.40].

The application of either ionic or nonionic conventional surfactants (such as sodium dodecyl sulfate (SDS), oleic acid, cetyltrimethylammonium bromide (CTAB) or polyethylene ethers, Triton X) offers a quite generic route to suspend nanoparticles [20.40, 46, 57–62]. The disadvantage of this method is the difficulty in getting rid of the excess surfactant molecules, which might be disadvantageous in several applications (e.g., in electrical devices or in catalysis).

Capping agents (alkyl thiols, polyvinyl pyrrolidone (PVP), trioctylphosphine oxide (TOPO), amines or dendrimers) have a reactive head group that can strongly coordinate to the surface of the particle, while the hydrophobic tails (for example, an alkane chain) help to keep the particle suspended. Because of the crystal facet-dependent chemisorption of capping agents, both the particle size and shape of the forming particles can be tuned when they are applied during growth [20.63–77].

Thiol-containing molecules are an especially attractive choice, as the sulfur of the thiol can form a strong coordinative covalent bond with several metals (e.g., Au, Ag, Cu, and Pt). With proper choice or further modification of the hydrophobic tail, again many solvents can be applied to stabilize thiol-functionalized nanoparticles [20.68, 71–73, 75, 77–89].

Steric stabilization by coating the particles is also a popular approach. Some parts of the polymer chain bond to the surface of the particle, while the other parts are solvated by the solvent, forming a spacing layer around the nanoparticles [20.90–96].

Table 20.1 presents details of various nanoparticle dispersions. The *Preparation* column contains information about the synthesis of the nanoparticles. Details about the solvents, and the stabilization or surface modification of the particles are also collected.

Table 20.1 Dispersions and applications of inorganic nanoparticles

NP	Preparation	Solvent	Stabilization/ functionalization	Application	References
2-D					
Ag	Chemical reduction (from $AgNO_3$ as metal precursor using hydrazine in DMF as reducing agent)	Ethanol Ethanol, water	PVP PVP		[20.41, 42] [20.43, 44]
Au	Wet chemical method (using $HAuCl_4$ in a replacement reaction of Ag nanoparticles) Reduction of $HAuCl_4$	Water Ethanol	Sodium citrate CTAB	Surface-enhanced Raman spectroscopy applications	[20.45] [20.46]
MnO_2	Wet chemical method (calcination of the mixture of KOH and Mn_2O_3; or hydrothermal treatment of the precipitate of $Mn(NO_3)_2$, NaOH, and H_2O_2)	Water	Tetramethylammonium for making stable suspensions, chitosan coating for biological application	Energy storage, solar cell application, H_2O_2 sensor	[20.47–50]
1-D					
Ag	Polyol process ($AgNO_3$ as precursor) Template-assisted method (the nanorods were deposited in the pores of a polycarbonate filtering membrane)	Water Hexafluoro-2-propanol or $CHCl_3$	PVP PVP	Transparent electrodes, ink	[20.51–54] [20.55]
Ag/Au core/ shell	Wet chemical method (Ag from aqueous solution of $AgNO_3$ was deposited on the surface of Au nanorods)	Water	PVP		[20.56]

Table 20.1 (continued)

NP	Preparation	Solvent	Stabilization/ functionalization	Application	References
Au	Electrochemical method (in a two-electrode type cell, Au plate as anode)	Water	C_{16}TAB		[20.97, 98]
	Template-assisted method (the nanorods were deposited in the pores of a polycarbonate filtering membrane)	Hexafluoro-2-propanol or $CHCl_3$	PVP		[20.55]
	Electrodeposition in nanoporous alumina	NaOH solution	PVP		[20.99]
	Chemical reduction (of $HAuCl_4$)	Hexane	Oleic acid and oleylamine	Nanoelectronic applications	[20.57, 100]
	Photochemical synthesis ($HAuCl_4$ solution was irradiated with 254 nm UV light)	Water	CTAB, tetradodecyl-ammonium bromide (TDABr)		[20.58]
	Seed-mediated growth method (seeds from $HAuCl_4$ and $NaBH_4$, then in the second step ascorbic acid was used)	Water	CTAB, benzyldimethyl-ammoniumchloride (BDAC)		[20.101]
Ni	Decomposition of bis(cycloocta-diene)nickel(0) ($Ni(cod)_2$) with hexadecylamine (HDA)	Pentane	TOPO		[20.66]
Si	One-dimensional growth via a vapor–liquid–solid (VLS) bis(cyclooctadiene)nickel(0)	Ethanol		Nanoelectronic devices	[20.102, 103]
CdS	Microwave-assisted method (from cadmium ethylxanthate)	Toluene	HDA, octadecylamine (ODA)		[20.104]
CdSe	Microwave-assisted method (from cadmium acetate and selenourea)	Toluene	HDA, ODA		[20.104]
	Precipitation method (from dimethylcadmium and tri-*n*-butylphosphine in a glovebox)	Chloroform, toluene	TOPO, hexylphosphonic acid (HPA)		[20.105, 106]
CdSe/CdS core/shell	Seed growth approach	Toluene	–	Lasers	[20.107, 108]
CoP	Thermal decomposition of cobalt acetylacetonate ($Co(acac)_2$) and tetradecylphosphonic acid (TDPA)	Organic solvents	TOPO, HDA	Anodes, catalyst, magnetic sensing	[20.109]
TiO_2	Hydrolysis of titanium tetraisopropoxide (TTIP)	$CHCl_3$, hexane	Oleic acid stabilizes the particles, but the ligands can be easily replaced by adding alkyl phosphonic acids	Cancer treatment, antimicrobial applications	[20.110–112]
ZnS	Microwave-assisted method (from zinc ethylxanthate)	Toluene	HDA, ODA		[20.104]
ZnSe	Microwave-assisted method (from zinc acetate and selenourea)	Toluene	HDA, ODA		[20.104]
Al_2O_3	Carbothermal procedure (from Al powder)	DMF			[20.113, 114]

Table 20.1 (continued)

NP	Preparation	Solvent	Stabilization/ functionalization	Application	References
0-D					
Ag	Solvothermal method from $AgNO_3$	Toluene	Dodecylamine	Printing, fabrication of silver wires	[20.67]
	Polyol process from $AgNO_3$	Ethylene glycol	PVP	Photonics, catalysis, and surface enhanced raman spectroscopy (SERS)-based sensing	[20.115, 116]
	solvated metal atom dispersion (SMAD) followed by digestive ripening	*t*-Butyl toluene	Synthesis with 2-butanone as stabilizing agent followed by funcionalization with dodecane thiol and trioctyl phosphine		[20.79]
	γ-Irradiation from $AgNO_3$	Water/ ethanol	SDS		[20.117]
	Chemical reduction (of usually $AgNO_3$)	Aceton/ chloroform	Polydimethylsiloxane (PDMS)	Microwire fabrication	[20.118]
		Hexane	Oleic acid		[20.59]
		Water	Mercaptoacetic acid	SERS-active substrate	[20.119]
		Water	Dodecanethiol		[20.68, 75, 76]
		Water	Bis(11-trimethyl-ammonio-undecanoyl-aminoethyl) disulfide dibromide		[20.120]
		Water	Na-citrate as reducing and stabilizing agent		[20.121]
		DMF	3-Aminopropyltri-methoxysilane		[20.122]
		Methanol, ethanol, acetone	Dodecanethiol		[20.69]
		Water	Polyvinyl alcohol (PVA)		[20.80]
		Diethylene glycol/ water	PVP	Inkjet printing for electronic devices	
		Water	PVP	SERS-active substrate, microinterconnects antimicrobial application	[20.123–125]
		Formamide	PVP, colloidal silica		[20.126]
		Water	Dendrimers, amphilic block copolymers, citrate quaternary ammonium disulfide	Water-based inkjet ink	[20.70, 127–130]
$Ag/CaCO_3$ composite	Flame spray synthesis (Ag-octanoate and Ca-2-ethyl-hexanoate as precursors)	Water	Disperbyk 190	Fabrication of membranes for filtering	[20.131]

Table 20.1 (continued)

NP	Preparation	Solvent	Stabilization/ functionalization	Application	References
Au	Chemical reduction (usually from $HAuCl_4$)	Water	Thiocyanuric acid		[20.132]
		Water	PVA		[20.80]
		Water	Place exchange and amide-forming coupling modification of tiopronin-protected particles		[20.133]
		Dichloromethane and methanol solution	Surface modification of alkylthiolate-protected particles by coupling reactions		[20.133, 134]
		Ethanol	Thiol-capped nanoparticles		[20.71, 72]
		Water	Thiol-capped nanoparticles	Chemiresistor sensors	[20.81, 82]
		Organic solvents	Capping with alkyl thiols and further functionalization of the alkyl chain		[20.78, 83–87]
		Organic solvents	Place exchange reactions of monolayer-protected nanoparticles		[20.135–139]
		Organic solvents	Modification of the surface of dodecanethiol-protected particles by atom transfer radical (ATR) polymerization		[20.88]
		Organic solvents	didecyldimethylammonium bromide (DDAB)		[20.140]
		Organic solvents	*p*-Mercaptophenol		[20.141]
		Formamide	PVP		[20.74]
		TOPO	TOPO/ODA		[20.142]
		Toluene/ water	Linear alkylamine, triphenyl phosphine, dendrimers		[20.143–146]
		Water	Na_2SO_4, NaCl, SDS, amino acid, PVP, tiopronin and coenzyme A, poly(methacrylic) acid, polystyrene		[20.147–151]
		Water/ toluene	Dodecanethiol		[20.75, 152–154]
	Citrate reduction	Butyl acetate, water	Citrate ions, *comb* stabilizer, sodium 3-mercaptopropionate, sulfur ligands, lysine, amine, thiols, dendrimer, amphilic block copolymers	Coatings, electronic devices, catalytic surfaces, sugar sensors, biodiagnostics, biological application	[20.130, 155–173]
	Brust–Schiffrin method	Toluene	Thiols, poly(methyl methacrylate), 5-(*N*-pyrrolyl)pentanethiol		[20.174–178]

Table 20.1 (continued)

NP	Preparation	Solvent	Stabilization/ functionalization	Application	References
	Reduction with ascorbic acid	Water			[20.179]
	Reduction with tetrakis(hydroxy-methyl)phosphonium chloride (THPC)	Water			[20.76, 180–182]
	γ-Irradiation	Water	PVP/PVA, sodium citrate	Laser	[20.183–185]
	Seed growth method	Water/ toluene	Dodecanethiol		[20.77]
	SMAD and digestive ripening	Toluene	Dodecanethiol, dodecylamine, octadecyl silane, trioctyl phosphine, dodecyl bromide, dodecyl iodide, dodecanol, and decane		[20.186, 187]
	Displacement reaction	Water	Dendrimers		[20.188]
Au-Pd alloy	Sonochemical method (from aqueous solution of $NaAuCl_4 \cdot 2H_2O$ and $PdCl_2 \cdot 2NaCl \cdot 3H_2O$)	Water	SDS		[20.60]
Au-coated magnetite	Wet chemical method (gold coating from the reduction of $HAuCl_4$)	Ethanol	Surface modification by carboxylation	DNA sensor	[20.189]
Co	Wet chemical method (reduction of $CoCl_2$ or decomposition of dicobalt octacarbonyl)	Organic solvents, toluene	Oleic acid, methylmethacrylate-ethylacrylate-vinyl pyrrolidone terpolymer $Al(C_8H_{17})_3$		[20.190–196]
	Sonochemical method (ultrasonic decomposition of $Co(NO)(CO)_3$)	Decane	Oleic acid		[20.197]
	Reduction of cobalt acetate tetrahydrate	Water	SDS	Catalyst	[20.61]
	γ-Irradiation of $Co(ClO_4)_2$ solution in the presence of Na-formiate	Water	Polyacrylate, poly(vinylsulfate)		[20.198]
	Microemulsion method [reduction of $CoCl_2$ or cobalt bis(2 ethyl-hexyl) sulfosuccinate in the micelles]	Toluene	DDAB		[20.199–201]
Co-ferrite	Wet chemical method (coprecipitation from cobalt and iron dodecylsulfate solutions)	Water	Dodecyl sulfate	Magnetic fluid	[20.202, 203]
	Microemulsion method (from $CoCl_2$ and $FeCl_2$)	Water/ toluene	SDS		[20.204, 205]

Table 20.1 (continued)

NP	Preparation	Solvent	Stabilization/ functionalization	Application	References
Cu	Polyol process ($CuSO_4 \cdot 5H_2O$ as precursor)	Ethyleneglycol/2-methoxyethanol	PVP	Conductive ink	[20.206]
	Polyol process ($CuSO_4 \cdot 5H_2O$ as precursor)	Water/ diethyleneglycol	PVP		[20.207]
	Reduction (of copper salts or the product after the decomposition of organometallic precursors)	Water	Dendrimers, PVP		[20.188, 208]
Fe	Sonochemical method (decomposition of $Fe(CO)_5$)	Hexadecane/ octanol	Oleic acid/PVP stabilization		[20.209]
	Thermal decomposition of $Fe(CO)_5$	Organic solvents	Vinyl polymers		[20.210–212]
	Chemical reduction of $FeCl_2$	THF	Poly(methyl metacrylate) (PMMA)		[20.213]
	Hydrothermal method from $Fe(CO)_5$	Organic solvents	Oleic acid		[20.214]
Fe/Fe_3O_4	Commercial	Water	Poly(styrene sulfonate), carboxymethylcellulose, polyaspartate		[20.90]
Ni	Reduction of $NiCl_2$, $Ni(acac)_2$ or $Ni(cod)_2$	Ethylene glycol			[20.215]
		DMF	DMF		[20.216]
		Dichloromethane	PVP		[20.217]
Pd	Reduction (K_2PdCl_4, H_2PdCl_4, organometallic compounds, $PdCl_2$ as precursors)	Water	Dendrimers	Catalyst	[20.218–223]
		THF	Carbonyl and phosphine ligands		[20.224]
		Polar and apolar solvent	*n*-Hexanethiol		[20.89]
		Water/ ethanol	PVP		[20.225]
	Displacement of Cu nanoparticles by Pd in K_2PdCl_4 solution	Water	Dendrimers		[20.188]
Pt	Chemical reduction (H_2PtCl_4, H_2PtCl_6, $Pt(acac)_2$, and organometallic precursors)	Water/ toluene	Dendrimer, amphilic block copolymers nitrocellulose or cellulose acetate as capping agents	Catalyst	[20.174, 226–230]
		Water, methanol	PVA, citrate		[20.231]

Table 20.1 (continued)

NP	Preparation	Solvent	Stabilization/ functionalization	Application	References
	Microwave-assisted method (H_2PtCl_6 as precursor)	Ethylene glycol	PVP		[20.232]
	Displacement reaction of Cu nanoparticles	Water	Dendrimer		[20.188]
Pt coated Fe	Polyol process (reduction of $Pt(acac)_2$ followed by decompostion of $Fe(CO)_5$)	Dioctylether	Oleic acid and oleic amine		[20.62]
Si	Laser-induced pyrolysis	Ethanol, toluene	Stabilization with mercapto-propyl triethoxysilane, functionalization with silanization	Photodetectors, solar energy converters, and chemical sensors	[20.233, 234]
	High-current-density galvanostatic etching (from boron-doped p-Si)	Toluene, di-chlorometh-ane or tri-chlorometh-ane	Functionalization with alkyl groups		[20.235]
	Laser-induced dissociation (silane as precursor)	Toluene and ethanol	Stabilization with octadecene and undecylenic acid, func-tionalization with alkyl groups	Displays, bio-imaging, semi-conductor devi-ces	[20.236–238]
	Commercial	Toluene, 1-butanol	Stabilized with DAPRAL (copolymer of maleic anhydride and α-olefin), fish oil, styrenyl functionalization		[20.239–241]
	Reduction (reaction of $SiCl_4$ and sodium naphthalide)	Hexane	Functionalization with alco-hols, alkyl groups		[20.242, 243]
	Wet chemical method (an-nealing SiO_2 and etched with HF; reaction of $SiCl_4$ and Mg_2Si; thermal de-gradation of the precursor; using Mg_2Si or tetraethyl orthosilicate as precursor)	Organic solvents	Octanethiol functionalized		[20.244–246]
		Water	Functionalization with poly-aniline, alkyl groups, ferro-cenyl, and alcohols	Magnetic resonance (MR) imaging agent	[20.247–251]
Ge	Wet chemical method (Mg_2Ge, $Ge[N(SiMe_3)_2]_2$ or NaGe as precursor; ther-mal degradation of tetra-ethylgermane)	Organic solvents, water	Functionalization with alkyl groups, acetals, alcohols, esters, polymers		[20.252–257]
	Reduction ($Ge(NR_2)_2$, $Ge(OR)_2$, GeI_2, $Ge[N(SiMe_3)_2]_2$ and and $GeCl_4$ as precursors)	Chloroform, toluene, hexane	Trioctylphosphine (TOP) and oleylamine stabilization; functionalization with polyethylene glycol (PEG) and alkyl groups	Cell imaging, biological appli-cation, optoelec-tronics, nanopho-tonics, and elec-tronics	[20.258–263]

Table 20.1 (continued)

NP	Preparation	Solvent	Stabilization/ functionalization	Application	References
	Ultrasonic-mediated reduction ($GeCl_4$ as precursor)	Polar and nonpolar solvents			[20.264]
CdS	Solvothermal method (CdO as precursor)	Organic solvents	TOP/TOPO, stabilization with oleic acid and functionalization with pyridine, thioglycerol or polyphosphate	Biological detection and imaging, biomedical application	[20.265–271]
	Precipitation (from the reaction of Na_2S and $Cd(OAc)_2$)	Organic solvents	Thiophenol		[20.272]
CdSe	Solvothermal (reaction of selenium and $CdCO_3$, Cd-stearate and H_2Se, dimethyl cadmium and bis-(trimethylsilyl)selenium, Se and $Cd(CH_3)_2$ or CdO)	Organic solvents, water	TOP/TOPO, HPA/TDPA, citrate; functionalization with thioglycerol or polyphosphate, dendrimers, thiols and mercaptoacetic acid; surface modification by silica and ZnS coating or ligand exchange	In vivo targeted imaging, biomedical applications, multiplexed coding technology, molecular sensing, biological detection and imaging	[20.267, 26964, 273–290]
CdTe	Wet chemical method (from the reaction of CdO or $Cd(Me)_2$ and Te)	Toluene, chloroform, or hexane	Stabilization with oleic acid/octadecylphosphonic acid (ODPA)/TDPA		[20.291]
		Water	Functionalization with mercaptopropionic acid or the mixture of amino-ethanethiol and HCl		[20.292]
Co_3O_4	Thermal decomposition of cobalt cupferronate	Toluene	Octylamine		[20.293]
CuO	Alcothermal method from $Cu(CH_3COO)_2$	Ethanol		Thin-film fabrication, gas sensors, and photovoltaic cells	[20.294]
	Commercial	Ethylene glycol		Heat transfer liquid	[20.294, 295]
	Precipitation followed by microwave irradiation from $CuSO_4$	Water	Ammonium citrate	Heat transfer liquid	[20.296]
	Submerged arc nanoparticle synthesis system (pure Cu rod as metal source)	Water			[20.297, 298]
	Co-precipitation (reaction of $Cu(NO_3)_2$ and NaOH)	Organic solvents	Oleic acid and sodium oleate		[20.299]
ITO	Commercial	Water	Ammonium polyacrylate	Conductive coating, cathode ray tubes	[20.91, 300, 301]
		Ethanol	2-[2-(2-Methoxyethoxy)-ethoxy]acetic acid		[20.302]

Table 20.1 (continued)

NP	Preparation	Solvent	Stabilization/ functionalization	Application	References
	Solvothermal (from $In(Ac)_3$ and $Sn(Ac)_2$; $InCl_3$ and $SnCl_4$)	Organic solvents	ODA, octadecene (ODE)	Conductive coating, ink for inkjet printing	[20.303–305]
		Ethylene glycol and water or ethanol	β-Alanine		[20.306, 307]
γ-Fe_2O_3	Decomposition (precursors are iron cupferron complex, $Fe(CO)_5$)	Octane/ toluene	Lauric acid		[20.214]
		Organic solvents	Trioctylamine		[20.308]
			Functionalization by functional group interchange		[20.309]
	Coprecipitation (reaction of $FeCl_2$ and $FeCl_3$ and NH_3)	Water	Stabilization with dextran, surface modification by aminopropylsilane groups, and coupling of partially oxidized dextran via Schiff's bases and secondary amine bonds	Molecular MR imaging, cell tracking, targeted intracellular hyperthermia, heat-triggered drug delivery platform	[20.310]
			PVA		[20.39]
			Tetramethylammonium hydroxide, perchloric acid		[20.311]
			Poly(acrylamide)		[20.92]
			$HClO_4$	Drug delivery	[20.312]
	Commercial	Paraffin	Oleic acid		[20.313]
Ferrite (Fe_3O_4)	Wet grinding of Fe_3O_4	Organic solvents	Oleic and linoleic acid	Ferromagnetic liquids	[20.314, 315]
Magnetite (Fe_3O_4)	Coprecipitation (reaction of $FeCl_2$ and $FeCl_3$ and NH_3)	Water	Surface modification by polyaspartate coating and HCl solution was used to make the suspensions stable	Biomedical applications	[20.316]
			Surface modification with proteins	Biomedical applications	[20.317]
			Dextran-modified surface	Cancer treatment	[20.318]
			Oleic acid and dichloromethane	Drug delivery	[20.319]
			Decanoic acid for stabilizing the particles and hematoporphyrin coating for further application	Tumor treatment	[20.320]
			PEG		[20.321]

Table 20.1 (continued)

NP	Preparation	Solvent	Stabilization/ functionalization	Application	References
				Biomedical applications, cancer treatment, magnetic nanodevices, MRI contrast agent, sealing, damping, heat transfer, bearing, sensing/ detection	[20.322–327]
		Toluene/ methanol	Functionalization with (3-aminopropyl)-trimethoxysilane and L-aspartic acid		[20.189]
		Water and kerosene or dodecane	Oleic acid		[20.328]
		Water and kerosene or dodecane	Oleic acid		[20.328]
		Acetone and low-boiling-point solvents	Capped by polyoxyethylene alkyl ether acetates		[20.329]
		Hexane	Oleic acid and oleylamine		[20.330]
		Octane	Oleic acid		[20.331]
	Solvothermal method (reaction of magnetite and ammonia at 40–50 °C)	Water	β-Cyclodextrin		[20.332]
		Hexane	Oleic acid and oleylamine		[20.333]
PbS	Wet chemical method (reaction of hexanethiol and $Pb(ac)_2$)	Organic solvents	1-Hexanethiol		[20.334]
Silica-coated magnetite	Coprecipitation of $FeCl_2$ and $FeCl_3$ followed by depositing silica from silicic acid solution or tetraethyl orthosilicate (TEOS)	Toluene or ethanol	CTAB-stabilized and β-lactamase-functionalized nanoparticles	Biocatalysis, biomolecular separations	[20.335, 336]
TiO_2	High-temperature nonhydrolytic method (titanium alkoxide as precursor) hexoic acid	Water	Functionalization with Dimercaptosuccinic acid (DMSA) and 2-ethyl	Photocatalytic applications	[20.337–339]
	Laser pyrolysis	Water	Ammonium polyacrylate		[20.93]
	Sol–gel method (titanium(IV) isopropoxide or $TiCl_4$ as precursor)	Organic solvents	Stearate	Gas sensors, antimicrobial applications	[20.340–342]

Table 20.1 (continued)

NP	Preparation	Solvent	Stabilization/ functionalization	Application	References
	Commercial	Acetylacetonate		Cancer treatment	[20.343, 344]
		Water	Stabilization with p(MAA/nBA) (copolymer of metacrylic acid and *n*-butyl acrylate), lactic acid, and stearate	Ceramics patterning by inkjet printing, antimicrobial applications	[20.94, 345, 346]
		Organic solvents Span 60	Functionalization with	Photovoltaic cells	[20.347, 348]
		Water	Sodium polyacrylates as stabilizing agent		[20.95]
	Hydrolysis of $TiCl_4$, titanium *n*-butoxide or titanium(IV) isopropoxide	Water or organic solvents	Surface modification with *n*-aliphatic carboxylic acids and acetylacetone	Photocatalytic applications	[20.349–355]
	Microwave-assisted precipitation method (from $TiCl_4$)	Water	Glycolic acid, citric acid, glycine, L-alanine, β-alanine as capping agents		[20.356]
	Precipitation method from $TiCl_4$	Water			[20.356]
WO_3	Wet chemical method (from WCl_6, Na_2WO_4, phosphotungstic acid hydrate)	Toluene	Dispersing polymer		[20.357]
		Water	PVA	Oxygen generation, gas sensing	[20.358, 359]
	Thermal decomposition of $W(CO)_6$	Hexane	Oleic acid and TOPO		[20.360]
ZnO	Commercial	Ethyl acetate	Silquat J15	For fabricating superhydrophobic surface	[20.361]
		Water	Ammonium polymethacrylate	Coolant application	[20.96]
	Hydrothermal method from $Zn(NO_3)_2$	Water	Oleic acid		[20.362]
ZnS	Wet chemical method (reaction of $ZnSO_4$ and Na_2S)	Water	Surface modification with cystein		[20.363]
Alumina	Commercial	DMF, ethylene glycol monomethyl ether (MCS) : dipropylene glycol monomethylether, (PM) = 3 : 1 water, ethylene glycol	HCl	Fabrication of alumina-resin hybrid films by inkjet printing, heat transfer applications	[20.364–372]

20.3 Dispersions of Carbon Nanomaterials

As shown in the previous sections, apart from their size, mainly the surface chemistry of nanoparticles plays the most decisive role in their stabilization in liquids. The surfaces of pristine carbon nanomaterials such as

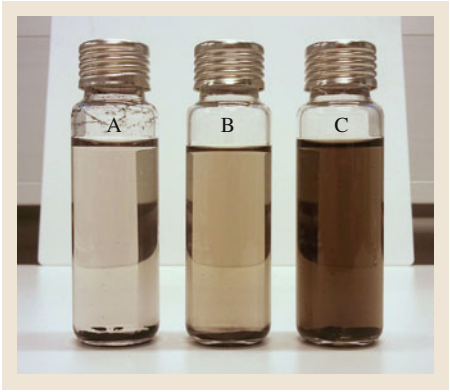


Fig. 20.2 Photograph of single-walled carbon nanotube dispersions each ultrasonicated for 1 h then centrifuged for 10 min at 3000 rpm. *Vial A*: 0.5 mg SWCNTs in 15 ml water; *vial B*: 0.5 mg SWCNT in 15 ml 1% Triton X-100 in water; *vial C*: 0.5 mg SWCNT-COOH in 15 ml water

fullerenes, nanotubes, and graphene/graphite are composed of sp^2-hybridized C atoms, which are chemically quite unreactive. The equivalent chemical bonds between adjacent C atoms make these materials apolar, thus direct dispersion or – in the cases of fullerenes – dissolution in liquids is limited to a few organic solvents only. To enable preparation of dispersions in a large variety of solvents, the surfaces must be modified, i. e., chemically functionalized, in order to stick various *easy-to-disperse* groups onto the surface (Fig. 20.2). Functionalization of carbon surfaces may be accomplished by a large variety of methods including covalent chemical bond formation as well as noncovalent adsorption/wrapping of molecules.

Creating strong first-order covalent bonds is typically achieved under harsh conditions. Using strong oxidizing acids to create defects and form hydroxyl, carbonyl, and carboxylic moieties on the surface is one approach to generate the starting points for subsequent synthetic construction of virtually any side-groups via, e.g., esterification or amidation. Since carboxyl-functionalized nanotubes and graphite/graphene can be simply dispersed in water, these products are often sufficient for applications without further modification. It is worth pointing out that various halogenation, cycloaddition, and radical-addition reactions are also often used to enable side-wall functionalization and dispersion in a large variety of solvents [20.373–376].

Noncovalent adsorption of molecules having delocalized electrons may take place on sp^2-hybridized carbon surfaces due to the overlapping of π-electrons between the two molecules. Such interaction can be very useful and attractive in practice. If the adsorbing moiety has some polar groups, the nanocomposite structure becomes dispersable in various polar solvents without altering the original structure of the host material [20.377–379].

Surfactants adsorbed on the surface as well as polymers wrapping nanoparticles offer further options for exfoliating and stabilizing nanotubes and graphene flakes in solvents. In practice, sodium dodecyl sulfate (SDS), sodium dodecylbenzene sulfonate (NaDDBS), and Triton X-100 are the most frequently applied amphiphiles enabling reasonably high carbon concentrations in aqueous dispersions ($> 0.1\,mg/cm^3$) (Fig. 20.2). Both synthetic and biopolymers have been demonstrated to establish strong molecular interactions by wrapping carbon nanotubes. The process is widely utilized to synthesize polymer-nanotube composites with added electrical and/or mechanical features [20.380, 381] and lately has been shown to be a powerful tool for separating carbon nanotubes according to their chirality. Selective wrapping of nanotubes has been demonstrated by several groups using DNA [20.382] and also various synthetic polymers [20.383]. Highly selective separation of near-armchair chiralities has been shown in toluene suspensions with poly(9,9-di-*n*-octylfluorenyl-2,7-diyl). In the separated suspensions, 90% of the carbon nanotubes (CNTs) had (9,7) chirality when applying laser-grown nanotubes, while for the HiPCo nanotubes the dispersions were composed of mainly (7,5), (7,6), and (8,6) chiralities (50, 25, and 20%, respectively) [20.384, 385].

Tables 20.2–20.4 collect some of the most frequently used nanostructured carbon materials and their derivatives, which are applied in forms of solutions and dispersions. Fullerenes dissolve quite well in organic solvents such as toluene, xylene, benzene, 1-methylnaphthalene, and *N*-methyl-2-pyrrolidinone. However, direct dispersion in polar solvents is very limited; when a solution of fullerenes with apolar solvents is mixed with polar organic solvents (acetonitrile, ethanol, acetone), precipitates of stable colloidal fullerene clusters appear in the polar phase. Similar phenomena also occur when saturated solutions of fullerenes in tetrahydrofuran (THF) are injected into water. The stability of the colloidal particles has been explained by the negatively charged surface [20.386–391]. Dispersions in water by complexing fullerenes with cyclodextrin or by anchoring carboxyl groups on the surface offer direct applications in biology

Table 20.2 Fullerene solutions/dispersions and their applications

Fullerene/funtionalization	Solvent/dispergant	Application	Notes	References
C_{60}, C_{70}	Toluene, xylene, benzene, 1-methyl-naphthalene, *N*-methyl-2-pyrrolidinone	Preparation of colloidal agglomerates of fullerenes	The fullerenes dissolved in apolar solvents, then mixed with polar organic solvents (acetonitrile, ethanol, or acetone) to get precipitates	[20.386]
C_{60}, C_{70}	1,2-Dichloro-benzene, 1,2-dimethyl-benzene, bromo-benzene iodo-benzene, and toluene			[20.387]
C_{60}, C_{70}	Toluene, water	Because of water as solvent, biochemical-biophysical studies are suggested	200 mg/dm^3 fullerenes dissolved in toluene. Water added then sonicated and toluene evaporated resulting in ≈ 5 mg/dm^3 aqueous dispersion of fullerene nanocrystals	[20.388]
C_{60}, C_{70}	THF, water	Because of water as solvent, biological uses or medical applications would be enabled as suggested by the authors	1.3×10^{-5} and 2.7×10^{-5} mol/dm^3 negatively charged stable fullerene clathrates form after injecting the THF solution into water	[20.389]
C_{60}	Toluene, water, THF	Studying bacterial response to nano-C_{60} under both aerobic and anaerobic conditions in various media	Nanocrystals of C_{60} remain stable in solution at or below ionic strengths of 0.05*I* for months	[20.390]
C_{60}	Toluene, acetonitrile	Nanostructured SnO_2 films for enhanced photocurrent generation	Nanoparticles of fullerene clusters are made by precipitating a toluene solution in acetonitrile	[20.391]
C_{60} complexed in γ-cyclodextrin	Water		8×10^{-5} mol/dm^3	[20.392]
$C_{63}((COOH)_2)_3$	Water	Neuroprotective agent		[20.393]
Carboxylic acid derivatives of C_{60}, C_3C_{60}, and D_3C_{60}	Water	Use as antioxidants preventing lipids from radical-initiated peroxidation of membrane		[20.394]
$Gd@C_{60}[C(COOH)_2]_{10}$ and $Gd@C_{60}[C(COOCH_2CH_3)_2]_{10}$	Water	MRI contrast agent		[20.395]
Fluorinated derivatives of C_{60}, $C_{60}F_{30}$, $C_{60}F_{36}$, $C_{60}F_{52}$	Benzene, toluene, THF, acetone	Contact angle measurements with water hold promise of lubricating applications	Thin films may be prepared by sublimation or spin-coating from solution	[20.396]
Amphiphilic C_{60} derivatives	Water	Langmuir–Blodgett films		[20.397]

Table 20.2 (continued)

Fullerene/funtionalization	Solvent/dispergant	Application	Notes	References
[6,6]-Phenyl-C_{61} butyric acid methyl ester	Chlorobenzene	Polymer solar cells, components of charge separating layers		[20.398, 399]
[6,6]-Phenyl-C_{71} butyric acid methyl ester	Chloroform, dichlorobenzene	Polymer solar cells, components of charge separating layers		[20.398, 400]

Table 20.3 Carbon nanotube (CNT) solutions/dispersions and their applications

CNT/ funtionalization	Solvent/dispergant	Application	Notes	References
SWCNTs (single-walled CNTs)	Cyclohexylpyrrolidone (CHP) and 1-benzyl-2-pyrrolidinone (NBenP)		Concentrations up to 3.5 and 0.2 mg/cm^3 for CHP and NBenP, respectively	[20.401]
SWCNTs	*N*-Methyl-pyrrolidone		Concentrations up to 0.03 mg/cm^3	[20.402]
SWCNTs	Toluene	Chirality- and diameter-selective dispersion of nanotubes (i. e., separation) using polymers such as poly[9,9-dioctylfluorenyl-2,7-diyl] (PFO), poly[9,9-dihexyl-fluorenyl-2,7-diyl], (PFH), poly[(9,9-dioctylfluorenyl-2,7-diyl)-*co*-(1,4-phenylene)] (PFO-P), poly[(9,9-dioctyl-fluorenyl-2,7-diyl)-*alt-co*-(1,4-benzo-2,10,3-thiadiazole)] (PFO-BT)	5 mg SWNT, 6 mg polymer, and 10 cm^3 solvent homogenized in a sonic bath then centrifuged	[20.383]
SWCNTs	Dimethylformamide (DMF), dimethylacetamide (DMA)	Polymer composite reinforcement		[20.403]
SWCNTs	*N*,*N*-Dimethylformamide (DMF), *N*-methylpyrrolidone (NMP), hexamethylphosphoramide, cyclopentanone, tetramethylene sulfoxide, and ε-caprolactone			[20.404]
SWCNTs	*N*-Methyl-2-pyrrolidone (NMP)	Inkjet printing of field-effect transistors	Ink concentrations after ultrasonic treatment and centrifuging are $\approx$ 0.012 mg/cm^3	[20.405]
MWCNTs (multiwalled CNTs)	Epoxy polymer	Electrically conductive polymer composites	Studied up to 0.15 wt % nanotube loading	[20.406]
SWCNTs	Gum arabic (0.5–15 wt %) dissolved in water	Authors suggest applications of the gum arabic–nanotube composites in adhesion promoters at interfaces between individual tubes and polymeric matrix	CNT powder (0.2–3 wt %) sonicated (50 W, 43 kHz) for 15–20 min in the polymeric solutions	[20.407]

Table 20.3 (continued)

CNT/ funtionalization	Solvent/dispergant	Application	Notes	References
SWCNTs	1 wt % SDS in water	Wrapping the dispersed nanotubes with polymers such as polyvinyl pyrrolidone (PVP), polystyrene sulfonate (PSS), poly(1-vinyl pyrrolidone-*co*-vinyl acetate), poly(1-vinyl pyrrolidone-*co*-acrylic acid), poly(1-vinyl pyrrolidone-*co*-dimethylaminoethyl methacrylate), polyvinyl sulfate, poly-(sodium styrenesulfonic acid-*co*-maleic acid), dextran, dextran sulfate, and bovine serum albumin	Concentration of PVP-wrapped CNTs is 1.4 g/dm^3. Wrapping with poly(methyl methacrylate-*co*-ethyl acrylate), polyvinyl alcohol, polyethylene glycol, or polyallyl amine was unsuccessful	[20.408]
SWCNTs	Sodium dodecylbenzene sulfonate (NaDDBS), sodium octylbenzene sulfonate (NaOBS), sodiumbutylbenzene sulfonate (NaBBS), sodium benzoate, sodium dodecyl sulfate (SDS), Triton X-100, dodecyl-trimethylammonium bromide (DTAB), dextrin, poly(styrene)-poly-(ethylene oxide) (PS-PEO) diblock copolymer	Highest dispersion concentrations are: NaDDBS (20 mg/cm^3); NaOBS (8 mg/cm^3); SDS (0.1 mg/cm^3); Triton X-100 (0.5 mg/cm^3); sodium benzoate (0.01 mg/cm^3); NaBBS (0.1 mg/cm^3); dextrin (0.05 mg/cm^3); DTAB (0.1 mg/cm^3); PS-PEO diblocks (0.1 mg/cm^3)		[20.409]
SWCNTs	1 wt % aqueous SDS in deionized water	Inkjet printing of supercapacitors	Ink concentration of 0.2 mg/cm^3	[20.410]
Octadodecylamine-functionalized SWCNTs (ODA-SWCNTs)	Chloroform, dichloro-methane, benzene, toluene, chlorobenzene, 1,2-dichlorobenzene, CS_2	Authors suggest applications related to polymer composite with mechanical reinforcement and new electrical properties as well as metal complexation	Solubility in 1,2-dichlorobenzene and CS_2 is > 1 g/dm^3	[20.411]
DWCNTs and amino-functionalized DWCNTs	Epoxy resin with an amine curing agent	Mechanical reinforcing of epoxy polymer	Up to 1 wt % CNT load was tested	[20.412]
Pyrene carboxylic acid (PCA) functionalized SWCNTs	Water or tetrahydrofuran (THF)	Improvement of dispersion and adhesion of SWCNTs in poly-carbonate matrix	Up to 1 wt % CNT load was tested	[20.413]
Carboxylic-functionalized MWCNTs (MWCNT-COOH)	Water	Printing inks, electrically conductive pattern and gas sensor printing, optical polarizer	Stable dispersions with concentration up to ≈ 0.26 mg/cm^3	[20.414, 415]

Table 20.3 (continued)

CNT/ funtionalization	Solvent/dispergant	Application	Notes	References
Carboxylic-functionalized CNTs (SWCNT-COOH and MWCNT-COOH)	Water	Dispersions for drop casting, electrically conductive film, and gas sensor applications		[20.416]
SWCNT-COOH	Water	Printing inks, electrically conductive pattern, and field-effect transistor printing	Stable dispersions with concentration up to $\approx 0.1\,mg/cm^3$	[20.417–419]
Amide-, polyethylene glycol (PEG)-, and polyaminobenzene sulfonic acid (PABS)-functionalized SWCNTs	Water	Printing inks, electrically conductive pattern, and field-effect transistor printing	Stable dispersions with concentrations up to $\approx 0.046\,mg/cm^3$ (amide), $0.035\,mg/cm^3$ (PEG), and $0.038\,mg/cm^3$ (PABS)	[20.419]
Acid-treated MWCNTs	Water with added surfactant (S27000)	Inkjet printing of conductive patterns	Ink concentration up 0.4 wt %	[20.420]

Table 20.4 Graphene–graphite solutions/dispersions and their applications

Graphene–graphite and funtionalization	Solvent/dispergant	Application	Notes	References
Graphene	*N*-Methylpyrrolidone (NMP), *N*,*N*-dimethylacetamide (DMA), γ-butyrolactone (GBL), 1,3-dimethyl-2-imidazolidinone (DMEU)	The authors suggest spray coating, vacuum filtration or drop casting to deposit graphene flakes on surfaces and potential applications in sensors, transparent electrodes, and conductive composites	Concentrations up to $0.01\,mg/cm^3$	[20.32]
Graphite platelets	THF	Mechanical reinforcing of PMMA		[20.421]
Graphene (4–5 layers)	DMF	Transparent conductive coatings	Concentration: $0.7\,mg/cm^3$	[20.422]
Graphite	Sodium cholate (SC) 2% w/v in water	Dispersions for density gradient ultracentrifugation (for separating graphene fractions of various thicknesses). Fabrication of transparent conductive films	After sonication, the exfoliated graphene layers are surrounded with the amphiphilic SC with solid contents up to $0.09\,mg/cm^3$	[20.423]
Graphite oxide	Water	Solar cell electrode fabrication by spin coating deposition of graphene oxide followed by reduction in hydrazine	$\approx 15\,mg/cm^3$ exfoliated graphite oxide in water	[20.424]
Graphite oxide	Water	Self-assembled multilayer thin films of graphite oxide with poly(diallyldimethylammoniumchloride)	$1\,mg/cm^3$ dispersion is applied	[20.425]

Table 20.4 (continued)

Graphene–graphite and funtionalization	Solvent/dispergant	Application	Notes	References
Graphite oxide	Water films	Production of large-area graphene	0.05 wt % GO is exfoliated by ultrasonic treatment to obtain graphene oxide dispersions	[20.426]
Graphite oxide	Water	Graphene film production for thin-film transistor manufacturing	Graphite oxide slurry with a concentration of 49 mg/cm^3 is diluted with water, then sonicated to exfoliate graphene oxide	[20.427]
Graphite oxide	Hydrazine	Thin-film transistors after spin coating and annealing hydrazinium graphene	Stable dispersions of hydrazinium graphene (HG) shown with a concentration of 1.5 mg/cm^3	[20.428]
Graphite oxide	DMF	Electrically conductive composites with polystyrene	1 mg/cm^3 dispersion for further processing	[20.429]
Graphene functionalized with Congo Red ($\pi-\pi$ stacking)	DMF, methanol, Dimethyl sulfoxide (DMSO), ethanol, water	Synthesis of Au nanoparticle composites with graphene	The functionalized graphene was also partially dispersed in other organic solvents such as NMP and 1,4-dioxane	[20.430]
Graphene oxide – MWCNT composite ($\pi-\pi$ stacking)	Water			[20.431]

and medicine [20.392–395]. Other derivatives suitable for both polar and apolar solvents hold promise in thin-film applications in tribology as well as in electronics [20.396–400].

Pristine carbon nanotubes can be dispersed reasonably well in various organic solvents such as *N*,*N*-dimethylformamide (DMF), *N*-methylpyrrolidone (NMP), cyclohexylpyrrolidone (CHP) [20.383, 401–405], in polymers [20.406, 407], and also in water when using surfactants [20.408–410]. CNTs with functional side-groups may be suspended in various solvents determined by the nature of the functional groups [20.32, 411–420].

Dispersions of graphene sheets and thin graphite flakes can be made by vigorous ultrasonic treatment of microscopic graphitic particles in NMP, DMA, DMF,

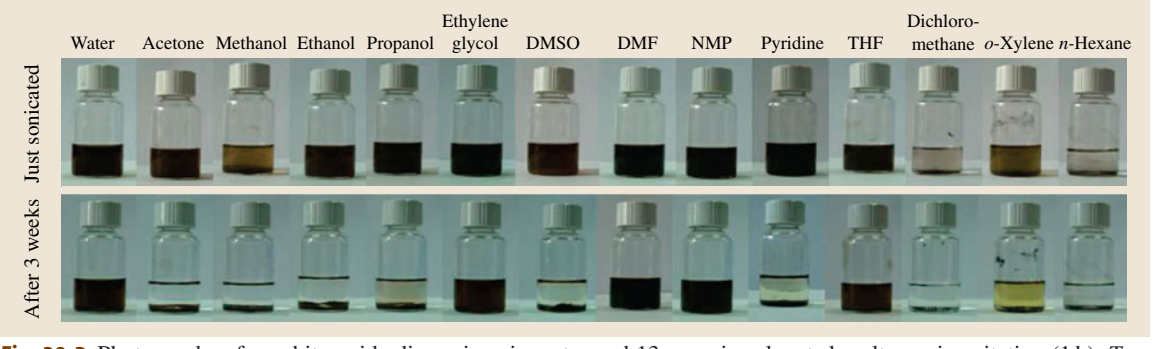


Fig. 20.3 Photographs of graphite oxide dispersions in water and 13 organic solvents by ultrasonic agitation (1 h). *Top*: freshly prepared dispersions. *Bottom*: after 3 weeks of storage (after [20.432])

GBL, 1,3-dimethyl-2-imidazolidinone (DMEU), and THF [20.32, 326, 421, 422], but also in water if surfactants are added [20.423]. Anyhow, the most common method of graphene dispersion preparation is based on graphite oxide, which is obtained by partial oxidation of graphite particles in strong oxidizing acids. Graphite oxide is suspended and exfoliated in water or DMF by ultrasonic agitation to yield graphene oxide (Fig. 20.3) and annealed or reduced in hydrazine to get graphene [20.424–428]. Exfoliation directly in hydrazine has been also reported [20.429]. Noncovalent functionalization of pristine graphene by $\pi-\pi$ stacking of Congo Red molecules on the surface has been proven to be efficient to disperse the hybrid nanoparticles in a large variety of solvents [20.430]. In a similar vein, nanocomposites of carbon nanotubes with graphene oxide adsorbed on their surface could be suspended in aqueous media [20.431].

20.4 Drying Dispersions on Surfaces

A considerably large fraction of nanoparticle dispersion applications aim at deposition of the particles on solid as well as soft surfaces for use as decorative, electrical, or optical functional coatings and patterns and so forth. The surface morphology of the deposits is important in all cases, thus understanding the transformation of the dispersion to solid nanoparticles – i. e., the drying process – is of key importance. When a dispersion is brought into contact with a surface, new interfaces appear at the substrate–dispersion and substrate–dispersion–air contact regions, breaking the continuity of the bulk of the liquid. As long as the surface is chemically inert, not electrostatically charged, and not magnetized, and temperature differences are not introduced, the new system remains stable until considerable evaporation of the solvent. When that happens, the dispersion stability conditions may change but also various fluxes can start in the bulk of the liquid, giving rise to the formation of a large variety of surface structures/morphologies during the drying process. This section discusses the formation of various surface deposit morphologies upon drying associated with solvent evaporation, contact-line pinning, particle–solvent flow fluxes, and self-ordering phenomena.

20.4.1 Ring-Stain Effect

As we often see in our daily life, drying droplets of liquids in which solid particles are present leave stains on surfaces along the perimeter of the droplet. A similar effect is observed when depositing and drying nanoparticle inks on surfaces. For most solute–solvent–surface systems, the deposited nanoparticles do not form a film with ideal flat-top surface profile, but rather a thick pattern at the perimeter of the droplet and a thin inner area with smaller amounts of solid particles. Such an effect might seem to be disturbing when applying nanoparticle dispersions on various surfaces; however, under optimized conditions, good spatial homogeneity of solid nanoparticle deposits has been demonstrated for a large variety of materials and solvents. On the other hand, ring-shaped stains or other narrow patterns forming at the contact lines enable the generation of self-assembled narrow features made of nanoparticles.

Based on a simplified model constructed by *Deegan* and coworkers [20.433], the primary reasons for such ring-stain formation (often referred to as the coffee-ring effect) are the pinned contact line, i. e., the perimeter of droplet at the substrate, and the surface-curvature-dependent solvent evaporation rate [20.433]. Because of the smaller curvature radius at the contact-line region, evaporation of solvent takes place faster there than on the top of the droplet. To ensure pinning of the contact line (and avoid shrinking of the droplet), a radial flow of fluid starts, which compensates for the amount of evaporated solvent. The dispersed solid particles are carried outwards by the radial flow, and they sediment at the sharp apex of the contact line. Although the model gives a reasonable explanation for the formation of solid particle deposits at the contact line, it lacks a number of different effects which may contribute to other solute–solvent fluxes in the drying droplet. The previously mentioned curvature-dependent evaporation rate of the solvent inherently generates concentration gradients in the droplet and results in solute diffusion [20.434] from the zone of the contact line towards the center of the droplet. Temperature gradients may form as well due to the different solvent evaporation rates to induce Marangoni flows [20.435, 436]. Electrostatic (DLVO) interactions and van der Waals forces may also modify the particle deposition process [20.435]. High solvent viscosity can influence the deposition by decreasing the diffusivity of nanoparticles and limiting the flow of the solvent itself [20.433].

Applying surfactants to change the contact angle may change the surface pinning conditions of the contact line and consequently the overall spatial particle distribution of the nanoparticles in the deposits after solvent evaporation [20.437].

Shen et al. proposed that ring-shaped stains can be avoided by applying small enough droplets (typically $D_c \approx 5-50\,\mu m$), since in small droplets, the solvent can evaporate before the solid particles can diffuse to form the ring-shaped deposits [20.438]. Thus, the maximum (or critical) droplet diameter D_c is a function of the liquid evaporation rate, the diffusive particle transport within the droplet, and the contact angle as

$$D_c = L_m \left[\frac{32 D_v (c_0 - c_\infty)}{\rho_L \pi \left(\theta_{initial} - \theta_{receding}\right) D_p} \right]^{1/2},$$

where L_m is the mean distance between two particles within the liquid droplet, D_v is the molecular diffusion coefficient of the vapor in air, c_0 and c_∞ are the densities of the saturated vapor at the liquid–air interface and the ambient vapor, respectively, ρ_L is the liquid density, $\theta_{initial}$ and $\theta_{receding}$ are the initial and receding contact angles of the colloidal droplet, and D_p is the particle diffusivity in the solvent (Fig. 20.4).

Heating of the substrate – frequently utilized in inkjet printing applications – to induce efficient evaporation of the solvent makes the deposits uniform as well [20.440–444]. Applying solvents with different boiling points (or different vapor pressure at a given temperature) allows tuning of the surface morphology of the deposits [20.439]. The concentration of solute in dispersions gives another degree freedom to alter the deposit morphology. With increasing solute concentration the width of the dried pattern increases and eventually may form fairly uniform disks as well as hill-shaped dots (Fig. 20.5) [20.445].

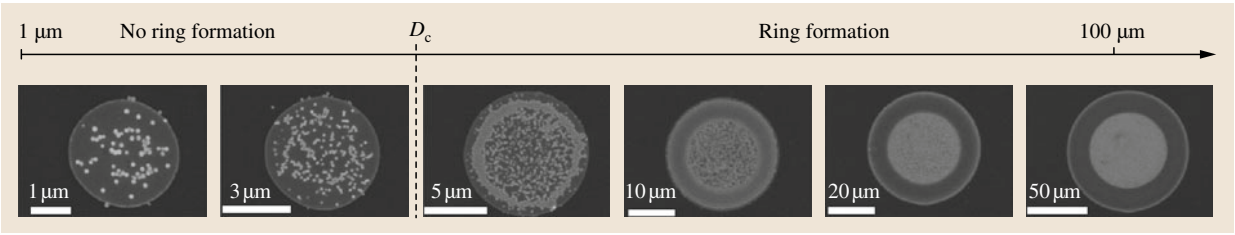


Fig. 20.4 Scanning electron microscopy (SEM) images of nanoparticle deposits on hydrophilic Pt structures of differing size (3–100 µm). Two different size regimes of the deposit patterns – either avoiding or causing ring formation – can be distinguished (after [20.438])

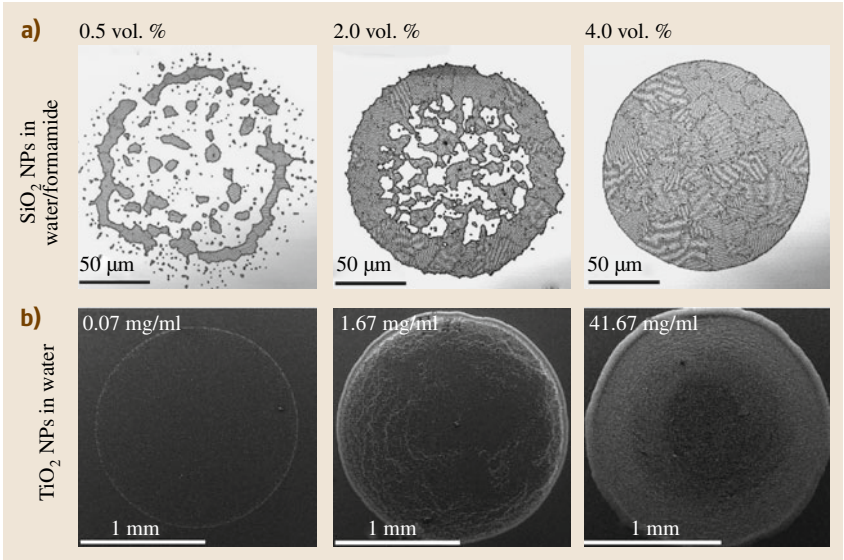


Fig. 20.5 **(a)** Sub-millimeter-size ring stains of SiO_2 nanoparticles deposited on a hydrophilic Si surface by a drop-on-demand inkjet printer from water/formamide-based inks of different solid concentration (images after [20.439]). **(b)** Macroscopic ring-shape stains of TiO_2 nanoparticles deposited on a gold surface from aqueous dispersions of different concentrations (each droplet is $\approx 0.5\,\mu l$)

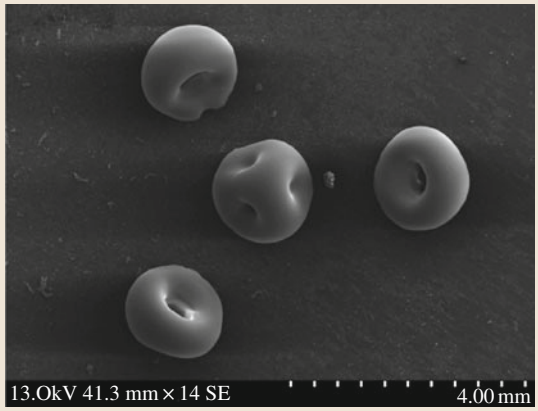


Fig. 20.6 Drops (2.4 µl) of alumina powder dispersion [20 vol. %, average particle size of 480 nm dispersed in water with the help of 0.75 wt % ammonium poly(methacrylic acid)] on silicone release paper (after [20.446])

Under extremely high nanoparticle concentrations, complex three-dimensional surface features have been demonstrated [20.446]. As an interesting feature, the morphology of the three-dimensional stains could be altered by depositing droplets of alumina suspension close to each other (Fig. 20.6). Since the evaporation of solvent is less favored in the volume between two droplets (viz. because the ambient in such regions becomes easily saturated with solvent vapor), concentration gradients of the solvent vapor occur, influencing the evaporation rates at different surface locations and giving rise to Marangoni flows in the droplets.

Having nonuniform pattern morphologies of the nanoparticles is usually undesirable in applications for optics and electronics, therefore special attention is paid to avoid ring-stain formation by optimizing solvent viscosities, vapor pressure, processing temperature, droplet size, nanoparticle concentration, and substrate wetting behavior [20.447–453]. On the other hand, having narrow rings, lines, or other patterns caused by the coffee-ring effect can indeed be very advantageous when the goal is to generate narrow and thin patterns of various types of nanoparticles. Normally, lithographic methods are applied to make such patterns; however, taking advantage of the self-ordering and alignment of nanoparticles at the contact line [20.454, 455], one may avoid the tedious multistep lithography process to prepare narrow patterns of nanoparticles on a large variety of surfaces (Fig. 20.7).

One particularly interesting and practically relevant application of ring-shaped stains has been identified in the fabrication of transparent conductive coatings with metal nanoparticle dispersions (Fig. 20.8) [20.456,457]. In such coatings, the substrate is covered with a two-dimensional network of metal rings composed of metal nanoparticles. Since only a minor fraction of the surface area is coated with optically nontransparent thick metal, the overall optical transmittance of the deposited layer can be high. As demonstrated lately by *Magdassi* and coworkers [20.457], sheet resistivity down to $\rho = 4.0 \pm 0.5\,\Omega/\square$ could be achieved while having optical transparency of 95% when inkjet printing silver nanoparticle rings onto transparent surfaces from a dispersion of 0.5 wt % Ag nanoparticles stabilized in water with poly(acrylic acid). Such two-dimensional networks of metallic rings might eventually be competitors of other transparent conductive coatings such as indium-tin oxide (ITO) [20.458] ($\rho_{\mathrm{ITO}} \approx 0.1\,\mathrm{k}\Omega/\square$ at 90% transmittance) and emerging solution-processed carbon nanotube [20.459, 460] as well as graphene [20.461, 462] films ($\rho_{\mathrm{SWCNT}} \approx 0.3\,\mathrm{k}\Omega/\square$ and $\rho_{\mathrm{graphene}} \approx 10\,\mathrm{k}\Omega/\square$ at $T = 90\%$).

In analogy with the ring-shaped stains at the contact line of a drying droplet, deposition of nanoparticles may also occur at the meniscus formed between a solid surface and a (partially) wetting dispersion as the solvent evaporates [20.463–465]. For planar substrates, the geometry of the deposits is a line (which is curved at the proximity of the substrate edge). Furthermore, parallel lines can be deposited by pulling the surface out from the liquid, ensuring that the pinned contact line is detaching, sliding, and then pinning again parallel in a location under the previous line (stick–slip phenomenon). To be able to detach the contact line, a threshold force $F_{\mathrm{c}} = \gamma\left(\cos\theta_{\mathrm{r}} - \cos\theta_{\mathrm{eq}}\right)$ has to be exceeded, where γ is the surface tension of the liquid, and θ_{r} and θ_{eq} are the contact angles for the receding and equilibrium contact lines [20.463]. Applying the stick–slip process, Huang and coworkers deposited electrically conductive parallel line patterns of Ag nanowires on oxygen-plasma-treated SiO_2 as well as on glass surfaces from methylene chloride suspensions [20.466]. The thickness of the deposits could be controlled well by the duration of contact-line sticking, while the spacing of adjacent lines was adjusted by the pulling velocity. Using a similar process – but with drying-induced slip of the contact line – microscopic parallel lines of single-walled carbon nanotubes (SWCNT) were deposited on Si/SiO_2 chips from aqueous dispersions (1% SDS), and used as channels of field-effect transistors [20.467]. It is worth pointing out that, in both experiments, the nanowires as well as the

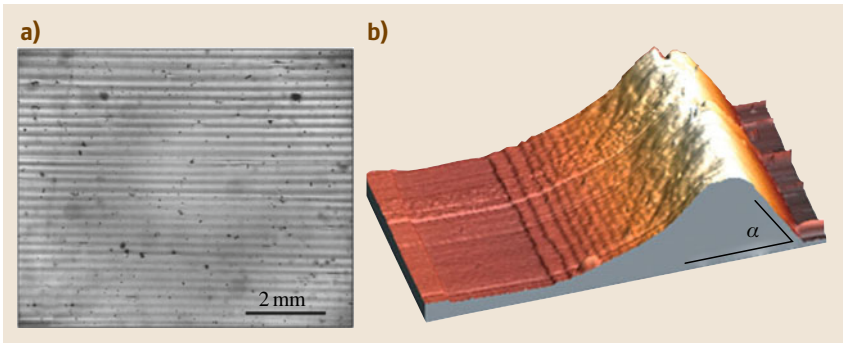


Fig. 20.7 **(a)** Optical image of periodic parallel line-shaped deposits of SiO_2 nanoparticles (10 wt % in water) on glass surface based on the contact-line stick–slip mechanism (contact-line velocity of 6.2 µm/s). **(b)** Atomic force microscopy (AFM) image of a contact-line deposit (contact-line velocity of 1 µm/s). The AFM scan area is 100 µm × 50 µm, and the height of the deposit is 1.45 µm (after [20.464])

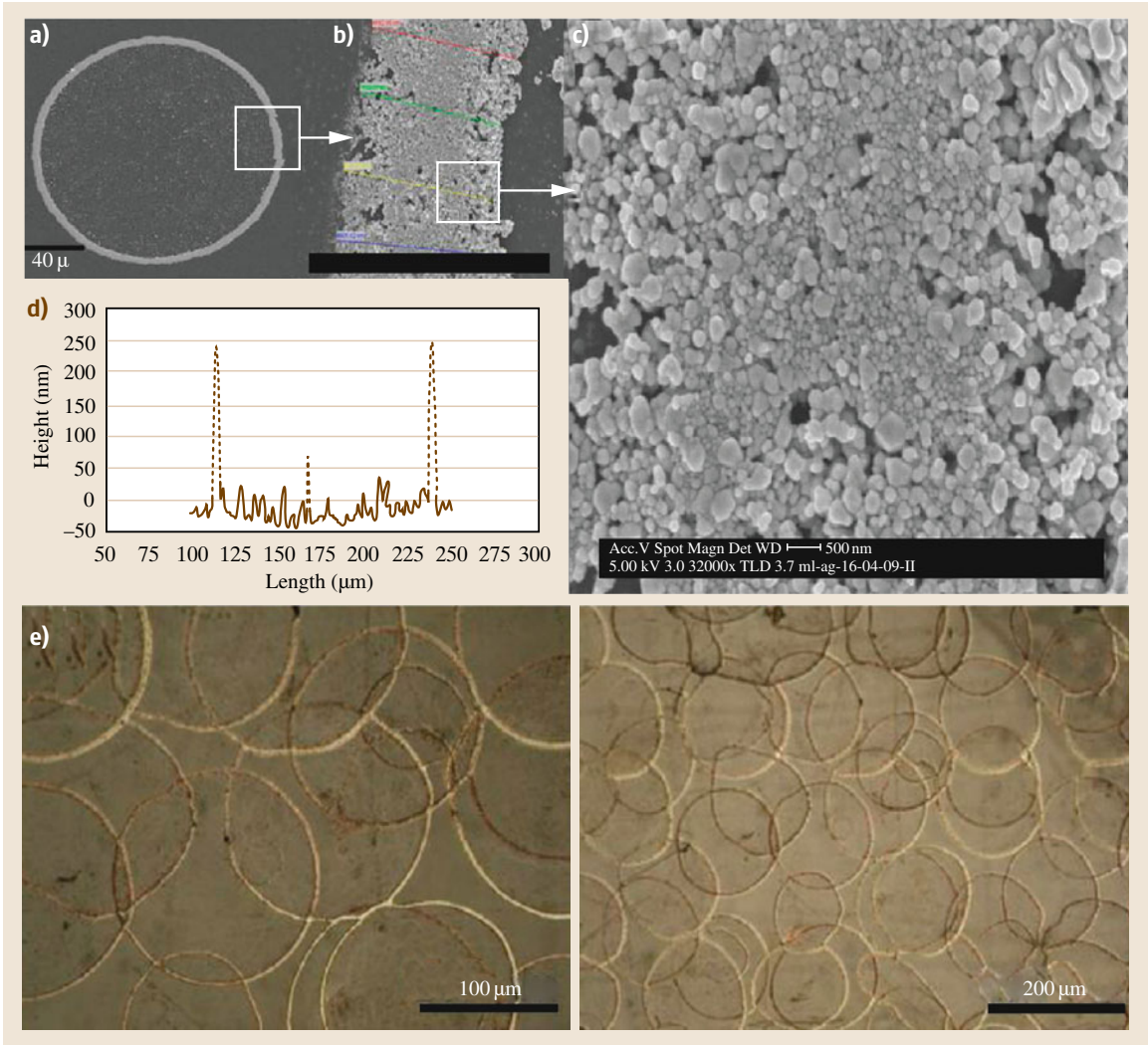


Fig. 20.8 **(a–c)** Scanning electron microscopy images taken from of ring-shaped deposit of silver nanoparticles. **(d)** Plot of height profile across a ring stain. **(e)** Ring-shaped stains of Ag nanoparticles forming an electrically conductive, two-dimensional network (after [20.457])

nanotubes were also aligned parallel within each microscopic line along the axis of the pattern.

20.4.2 Self-Organized Structures

After drying, particles of similar shape and size tend to be organized in a periodic uniform fashion just like atoms in a crystal lattice, but instead of atoms the nanoparticles now form superlattices. The common name for this process is self-assembly; however, the term "directed self-assembly" is also frequently used when the assembly is perturbed/modulated by external fields (electrical, magnetic, flow), capillary forces, or by surface topology inducing spatial confinement of the particles to certain surface areas or enabled volumes [20.469].

The symmetry of the superlattice depends on the particle–particle and substrate–particle interactions, and particle confinement within surface structures, while the range of ordering is a function of the particle size uniformity [20.470]. The simplest structures are composed of uniform spherical particles which typically form two-dimensional layers with hexagonal symmetry (Fig. 20.9) and close-packed (face-centered cubic (fcc), body-centered cubic (bcc), and hexagonal close-packed (hcp)) structures in three dimensions [20.471–474].

During the past few years, template-assisted self-assembly (TASA) has received much attention because of its direct applications in photonics [20.475–479] and nanoelectronics [20.480, 481]. Surfaces having three-dimensional topology features (cavities, channels, or tiny capillaries) can spatially confine the nanoparticles, which – after evaporation of the solvent – form microscopic patterns that are self-similar to the geometry of the three-dimensional surface features [20.482–487]. Another approach to accomplish constrained geometries on chemically functionalized surfaces that are patterned, e.g., by means of photolithography, is to generate surface areas with different wetting/electrostatic behavior, thus forcing the deposited dispersions to cover only the desired locations of the surface [20.488, 489]. TASA has been recognized as a powerful technology for creating patterned assemblies of micro- and nanoparticles. Lines but also micropatterns of arbitrary shape composed of ordered micro- and nanoparticles have been demonstrated. What makes the process even more fascinating is that the confinement itself enables the symmetry of the superlattices to be tuned simply by adjusting the particle size and the template feature geometry (diameter/shape of cavities, channels, width/spacing of functionalized surface patterns).

Further complexity may be brought into the deposited structures by applying nanoparticles of bimodal size distribution – provided that the diameters of the smaller as well as the larger nanoparticles are uniform (Fig. 20.10). Spontaneous assembly of bimodal decanethiol-functionalized Au nanoparticles into hexagonal and pseudohexagonal lattices, and binary mixtures of nanoparticles – such as Fe_2O_3, PbSe, PbS,

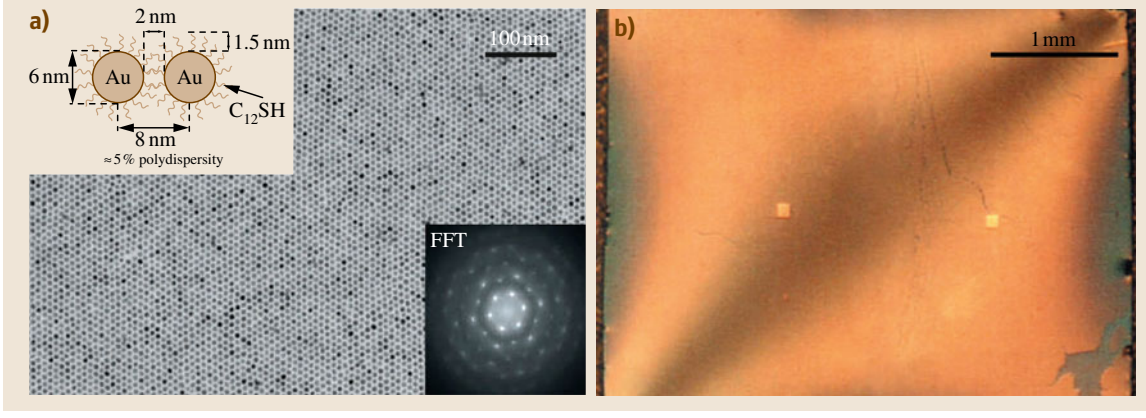


Fig. 20.9 (a) Micrograph of a gold nanoparticle monolayer (dodecanethiol-ligated nanocrystals of 6 nm diameter) and its fast Fourier-transformed (FFT) pattern in the *lower right inset*. A schematic arrangement of two adjacent nanoparticles of the monolayer is shown in the *upper left inset*. (b) Image of a compact nanocrystal monolayer on the top surface of a thin liquid droplet extending completely across a $3 \times 4\,mm^2$ Si_3N_4 substrate (after [20.468])

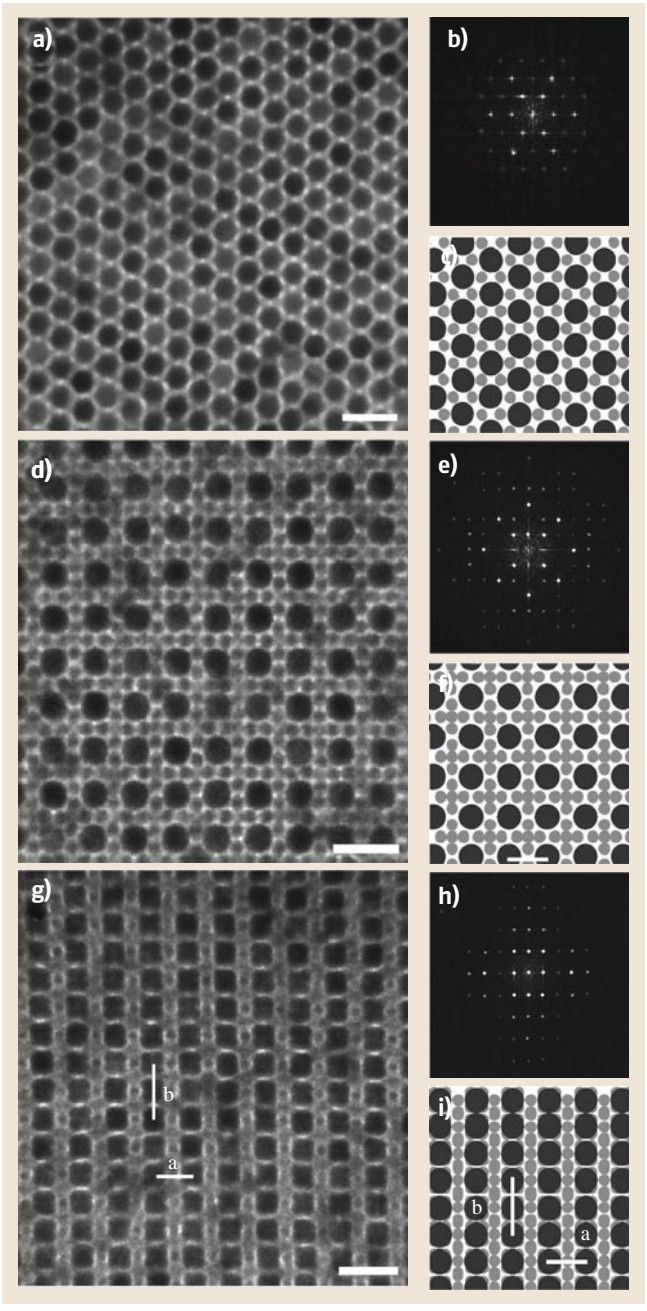


Fig. 20.10a–i Transmission electron microscopy (TEM) images of binary structures made of CdSe and PbSe nanoparticles (each *scale bar* denotes 20 nm). Panels **(a)**–**(c)** show an AB_2 structure (0001) plane, the corresponding FFT pattern, and model structure, respectively; **(d)** cub-AB_{13} (100) plane with the corresponding FFT image **(e)** and schematic structure **(f)**; **(g)** cub-AB_{13} with the (110)PbSe terminated with the corresponding FFT image **(h)** and schematic structure **(i)** (after [20.494]) ▶

CdSe, Pd, Ag, Au – into various types of superlattices have been reported [20.490–494].

20.4.3 Inkjet Printing of Nanoparticle Dispersions

Inkjet printing as a cost-effective, rapid, and – for many applications – reasonably precise technology for depositing films and patterns of various materials on virtually any substrate has emerged and found use in diverse fields. With the rapid development of silicon microelectromechanical systems (Si-MEMS) technology, very accurate but still robust piezoelectric printing heads became possible to fabricate at low cost and very high throughput, offering a feasible platform for printing head production. Today's printers enable adjustment of printing parameters (piezo voltage, waveform, frequency), and if needed the process may be run by applying individual nozzles (drop-on-demand). These features may be extremely useful in process optimization and in laboratory-scale experiments to explore new ink formulations designed for a specific nanoparticle, substrate, or end-use application. State-of-the-art printers can eject droplets as small as of 1 pl in volume, corresponding to lateral print resolution of $\approx 10\,\mu m$/pixel on smooth unstructured surfaces. Surface confinement of the deposited droplets in microscopic or even sub-micrometer-size topographic and/or chemically modulated features – similar to that in directed self-assembly – can help in further enhancing the resolution. Apart from press/printing industry, inkjet deposition of nanoparticles is clearly becoming an important enabling technology in electronics and optoelectronics sectors. Electrodes and electrical interconnects deposited from metal, carbon nanotube, and graphene dispersions have been demonstrated by several research groups. Inkjet-printed patterns of semiconducting nanomaterials are of great importance too, due to their potential in cost-effective large-scale fabrication of field-effect transistor channels as well as emitting layers in light-emitting diodes [20.405, 414, 416–420, 439, 442–444, 447–453, 495–501].

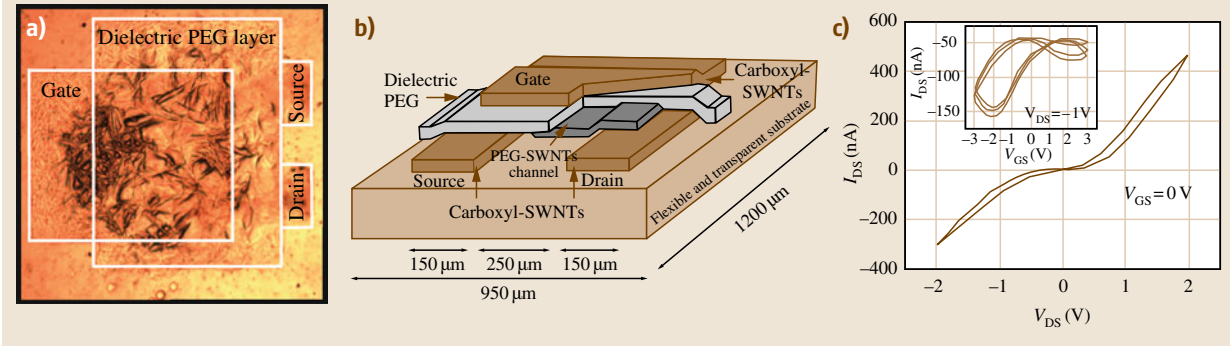


Fig. 20.11 **(a)** Optical micrograph of an entire inkjet-printed carbon nanotube-based field-effect transistor. **(b)** Schematic drawing of the structure and **(c)** source–drain current–voltage and gate-transfer curves of a transistor with p-channel behavior (after [20.419])

20.5 Concluding Remarks

The long history of making dispersions is not over. In fact, the continuously evolving new nanoparticles of various functionalities synthesized today necessitate well-engineered dispersion formulations, thus giving rise to a renaissance of the discipline. Considering the shape, size, composition, and surface chemistry of the solid particles along with the composition of the liquid-phase dispersion medium, the number of possible variations of dispersions is enormous, offering a rich pool of materials for applications in diverse fields. To be able to exploit nanoparticles in wet chemical/physical processes fully, some basic principles of dispersion-making need to be followed. In this chapter, we have discussed the parameters influencing dispersion stability and summarized the practical aspects of dispersion-making by compiling hundreds of examples from contemporary literature for nanoparticles of semiconductors, metals, their oxides/sulfides, as well as nanostructured carbon particles such as fullerenes, nanotubes, and graphene/graphite. As a considerable fraction of the applications are related to surface coatings, drying phenomena and self-ordering of the particles have also been discussed.

References

20.1 J. Clottes: *Chauvet Cave: The Art of Earliest Times* (Univ. Utah Press, Salt Lake City 2003)

20.2 A. Schopen: *Tinten und Tuschen des arabisch islamischen Mittelalters* (Vandenhoeck Ruprecht, Göttingen 2006), in German

20.3 D. Carvalho: *Forty Centuries of Ink* (BiblioBazaar LLC, Charleston 2008)

20.4 C.C. Pines: The story of ink, Am. J. Police Sci. **2**, 290–301 (1931)

20.5 C.-P. Li: *The Chemical Arts of Old China* (Journal of Chemical Education, Easton 1948)

20.6 A. Brysbaert: Painted plaster from Bronze Age Thebes, Boeotia (Greece): A technological study, J. Archaeol. Sci. **35**, 2761–2769 (2008)

20.7 P. Pallecchi, G. Giachi, M.P. Colombini, F. Modugno, E. Ribechini: The painting of the Etruscan "Tomba della Quadriga Infernale" (4th century BC), in Sarteano (Siena, Italy): Technical features, J. Archaeol. Sci. **36**, 2635–2642 (2009)

20.8 S. Sotiropoulou, S. Daniilia, C. Miliani, F. Rosi, L. Cartechini, D. Papanikola-Bakirtzis: Microanalytical investigation of degradation issues in Byzantine wall paintings, Appl. Phys. A **92**, 143–150 (2008)

20.9 D.C. Sircan: *Indian Epigraphy* (Motilal Banarsidass, Delhi 1996)

20.10 R.H. Leach, P.J. Pierce: *The Printing Ink Manual* (Kluwer, Dordrecht 1999)

20.11 R.N. Schwab, T.A. Cahill, B.H. Kuslco, D.L. Wick: Cyclotron analysis of the ink in the 42-line Bible, Pap. Bibliograph. Soc. Am. **77**, 285–315 (1983)

20.12 Red Ochre. Wikipedia. http://en.wikipedia.org/wiki/Red_ochre (last accessed 29 June 2012)

20.13 F. Szántó: *A kolloidkémia alapjai* (Gondolat, Budapest 1987)

20.14 G.L. Klimchitskaya, U. Mohideen, V.M. Mostepanenko: Casimir and van der Waals forces between two plates or a sphere (lens) above a plate made of real metals, Phys. Rev. A **61**, 062107 (2000)

20.15 B. Bhushan (Ed.): *Springer Handbook of Nanotechnology*, 3rd edn. (Springer, Berlin, Heidelberg 2010)

20.16 L.M. Skinner, J.R. Sambles: The Kelvin equation – A review, J. Aerosol Sci. **3**, 199–210 (1972)

20.17 Y. Liu, K. Kathan, W. Saad, R.K. Prud'homme: Ostwald ripening of β-carotene nanoparticles, Phys. Rev. Lett. **98**, 036102 (2007)

20.18 A.V. Volkov, M.A. Moskvina, F.M. Spiridonov, I.A. Volkov, A.E. Varfolomeev, A.L. Volynskii, N.F. Bakeev: Mechanism of formation and structure of polymer nanocomposites based on poly(vinyl alcohol) and magnetite, Polym. Sci. Ser. A **50**, 977–984 (2008)

20.19 P. Christian, F. von der Kammer, M. Baalousha, T. Hofmann: Nanoparticles: Structure, properties, preparation and behaviour in environmental media, Ecotoxicology **17**, 326–343 (2008)

20.20 A. Reindl: *Dispersing and Stabilizing Semiconducting Nanoparticles for Application in Printable Electronics*, Dissertation (University of Erlangen-Nuremberg, Erlangen 2009)

20.21 H.D. Ackler, R.H. French, Y.-M. Chiang: Comparisons of Hamaker constants for ceramic systems with intervening vacuum or water: From force laws and physical properties, J. Colloid Interface Sci. **179**, 460–469 (1996)

20.22 P. Sarkar, P.S. Nicholson: Electrophoretic deposition (EPD): Mechanisms, kinetics, and application to ceramics, J. Am. Ceram. Soc. **79**, 1987–2002 (1996)

20.23 H.J. Butt, B. Cappella, M. Kappl: Force measurements with the atomic force microscope: Technique, interpretation and applications, Surf. Sci. Rep. **59**, 1–152 (2005)

20.24 K.D. Sattler: *Handbook of Nanophysics: Nanoparticles and Quantum Dots* (CRC, Boca Raton 2011)

20.25 K. Itami, H. Fujitani: Charge characteristics and related dispersion/flocculation behavior of soil colloids as the cause of turbidity, Colloids Surf. A **265**, 55–63 (2005)

20.26 G. Lagaly, S. Ziesmer: Colloid chemistry of clay minerals: The coagulation of montmorillonite dispersions, Adv. Colloid Interface Sci. **100–102**, 105–128 (2003)

20.27 A. Nosrati, J. Addai-Mensah, W. Skinner: Rheology of aging aqueous muscovite clay dispersions, Chem. Eng. Sci. **66**(2), 119–127 (2011)

20.28 A. Szücs, F. Berger, I. Dékány: Preparation and structural properties of Pd nanoparticles in layered silicate, Colloids Surf. A **174**, 387–402 (2000)

20.29 R.E. Grim: *Clay Minerology* (McGraw-Hill, New York 1953)

20.30 I. Dékány, T. Haraszti: Layered solid particles as self-assembled films, Colloids Surf. A **123/124**, 391–401 (1997)

20.31 H.E. Bergna, W.O. Roberts (Eds.): *Colloidal Silica: Fundamentals and Applications* (CRC, Boca Raton 2006)

20.32 Y. Hernandez, V. Nicolosi, M. Lotya, F.M. Blighe, Z. Sun, S. De, I.T. McGovern, B. Holland, M. Byrne, Y.K. Gun'ko, J.J. Boland, P. Niraj, G. Duesberg, S. Krishnamurti, R. Goodhue, J. Hutchinson, V. Scardaci, A.C. Ferrari, J. Coleman: High-yield production of graphene by liquid-phase exfoliation of graphite, Nat. Nanotechnol. **3**, 563–568 (2008)

20.33 C. Soldano, A. Mahmood, E. Dujardin: Production, properties and potential of graphene, Carbon **48**, 2127–2150 (2010)

20.34 P. Blake, P.D. Brimicombe, R.R. Nair, T.J. Booth, D. Jiang, F. Schedin, L.A. Ponomarenko, S.V. Morozov, H.F. Gleeson, E.W. Hill, A.K. Geim, K.S. Novoselov: Graphene-based liquid crystal device, Nano Lett. **8**, 1704–1708 (2008)

20.35 Z. Osváth, A. Darabont, P. Nemes-Incze, E. Horváth, Z.E. Horváth, L.P. Biro: Graphene layers from thermal oxidation of exfoliated graphite plates, Carbon **45**, 3022–3026 (2007)

20.36 F.A. Greco: Polar, aprotic solvents and the hydrophobic effect, J. Phys. Chem. **88**, 3132–3133 (1984)

20.37 D. Chandler: Interfaces and the driving force of hydrophobic assembly, Nature **437**, 640–647 (2005)

20.38 R. Nagarajan, T. Alan Hatton: Chap. 2. In: *Nanoparticles: Synthesis, Stabilization, Passivation and Functionalization*, Vol. 996 (Oxford Univ. Press, Oxford 2008)

20.39 C. Albornoz, S.E. Jacobo: Preparation of a biocompatible magnetic film from an aqueous ferrofluid, J. Magn. Magn. Mater. **305**, 12–15 (2006)

20.40 B.L. Cushing, V.L. Kolesnichenko, C.J. O'Connor: Recent advances in the liquid-phase syntheses of inorganic nanoparticles, Chem. Rev. **104**, 3893–3946 (2004)

20.41 D.O. Yener, J. Sindel, C.A. Randall, J.H. Adair: Synthesis of nanosized silver platelets in octylamine-water bilayer systems, Langmuir **18**, 8692–8699 (2002)

20.42 Y. Xiong, I. Washio, J. Chen, H. Cai, Z.-Y. Li, Y. Xia: Poly(vinyl pyrrolidone): A dual functional reductant and stabilizer for the facile synthesis of noble metal nanoplates in aqueous solutions, Langmuir **22**, 8563–8570 (2006)

20.43 I. Pastoriza-Santos, L.M. Liz-Marzán: Synthesis of silver nanoprisms in DMF, Nano Lett. **2**, 903–905 (2002)

20.44 I. Pastoriza-Santos, L.M. Liz-Marzán: Colloidal silver nanoplates. State of the art and future challenges, J. Mater. Chem. **18**, 1724–1737 (2008)

20.45 E. Hao, S. Li, R.C. Bailey, S. Zou, G.C. Schatz, J.T. Hupp: Optical properties of metal nanoshells, J. Phys. Chem. B **108**, 1224–1229 (2004)

20.46 Z. Wang, J. Yuan, M. Zhou, L. Niu, A. Ivaska: Synthesis, characterization and mechanism of cetyltrimethylammonium bromide bilayer-encapsulated gold nanosheets and nanocrystals, Appl. Surf. Sci. **254**, 6289–6293 (2008)

20.47 Y. Omomo, T. Sasaki, L. Wang, M. Watanabe: Redoxable nanosheet crystallites of MnO_2 derived via delamination of a layered manganese oxide, J. Am. Chem. Soc. **125**, 3568–3575 (2003)

20.48 R. Ma, Y. Bando, T. Sasaki: Directly rolling nanosheets into nanotubes, J. Phys. Chem. B **108**, 2115–2119 (2004)

20.49 Z.-H. Liu, K. Ooi, H. Kanoh, W.-P. Tang, T. Tomida: Swelling and delamination behaviors of birnessite-type manganese oxide by intercalation of tetraalkylammonium ions, Langmuir **16**, 4154–4164 (2000)

20.50 X. Chen, X. Zhang, W. Yang, D.G. Evans: Biopolymer-manganese oxide nanoflake nanocomposite films fabricated by electrostatic layer-by-layer assembly, Mater. Sci. Eng. C **29**, 284–287 (2009)

20.51 Y. Sun, B. Mayers, T. Herricks, Y. Xia: Polyol synthesis of uniform silver nanowires: A plausible growth mechanism and the supporting evidence, Nano Lett. **3**, 955–960 (2003)

20.52 Y. Sun, B. Gates, B. Mayers, Y. Xia: Crystalline silver nanowires by soft solution processing, Nano Lett. **2**, 165–168 (2002)

20.53 L. Hu, H.S. Kim, J.-Y. Lee, P. Peumans, Y. Cui: Scalable coating and properties of transparent, flexible, silver nanowire electrodes, ACS Nano **4**, 2955–2963 (2010)

20.54 J.-Y. Lee, S.T. Connor, Y. Cui, P. Peumans: Solution-processed metal nanowire mesh transparent electrodes, Nano Lett. **8**, 689–692 (2008)

20.55 V.M. Cepak, C.R. Martin: Preparation and stability of template-synthesized metal nanorod sols in organic solvents, J. Phys. Chem. B **102**, 9985–9990 (1998)

20.56 M. Liu, P. Guyot-Sionnest: Synthesis and optical characterization of Au/Ag core/shell nanorods, J. Phys. Chem. B **108**, 5882 (2008)

20.57 C. Wang, Y. Hu, C.M. Lieber, S. Sun: Ultrathin Au nanowires and their transport properties, J. Am. Chem. Soc. **130**, 8902–8903 (2008)

20.58 F. Kim, J.H. Song, P. Yang: Photochemical synthesis of gold nanorods, J. Am. Chem. Soc. **124**, 14316–14317 (2002)

20.59 Y. Wang, H. Yang: Oleic acid as the capping agent in the synthesis of noble metal nanoparticles in imidazolium-based ionic liquids, Chem. Commun. **24**, 2545–2547 (2006)

20.60 Y. Mizukoshi, K. Okitsu, Y. Maeda, T.A. Yamamoto, R. Oshima, Y. Nagata: Sonochemical preparation of bimetallic nanoparticles of gold/palladium in aqueous solution, J. Phys. Chem. B **101**, 7033–7037 (1997)

20.61 S.U. Son, S.I. Lee, Y.K. Chung, S.-W. Kim, T. Hyeon: The first intramolecular Pauson–Khand reaction in water using aqueous colloidal cobalt nanoparticles as catalysts, Org. Lett. **4**, 277–279 (2002)

20.62 S. Sun, C.B. Murray, D. Weller, L. Folks, A. Moser: Monodisperse FePt nanoparticles and ferromagnetic FeP nanocrystal superlattices, Science **287**, 1989–1992 (2000)

20.63 B. Pignataro: *Tomorrow's Chemistry Today* (Wiley, Weinheim 2008)

20.64 C.B. Murray, D.J. Noms, M.G. Bawendi: Synthesis and characterization of nearly monodisperse CdE (E = S, Se, Te) semiconductor nanocrystallites, J. Am. Chem. Soc. **115**, 8706–8715 (1993)

20.65 M. Green, N. Allsop, G. Wakefield, P.J. Dobson, J.L. Hutchison: Trialkylphosphine oxide/amine stabilised silver nanocrystals – The importance of steric factors and Lewis basicity in capping agents, J. Mater. Chem. **12**, 2671–2674 (2002)

20.66 N. Cordente, M. Respaud, F. Senocq, M.-J. Casanove, C. Amiens, B. Chaudre: Synthesis and magnetic properties of nickel nanorods, Nano Lett. **1**, 565–568 (2001)

20.67 D. Wakuda, M. Hatamura, K. Suganuma: Novel method for room temperature sintering of Ag nanoparticle paste in air, Chem. Phys. Lett. **441**, 305–308 (2007)

20.68 S.Y. Kang, K. Kim: Comparative study of dodecanethiol-derivatized silver nanoparticles prepared in one-phase and two-phase systems, Langmuir **14**, 226–230 (1998)

20.69 J.R. Heath, C.M. Knobler, D.V. Leff: Pressure/temperature phase diagrams and superlattices of organically functionalized metal nanocrystal monolayers: The influence of particle size, size distribution, and surface passivant, J. Phys. Chem. B **101**, 189–197 (1997)

20.70 T. Yonezawa, S.-Y. Onoue, N. Kimizuka: Preparation of highly positively charged silver nanoballs and their stability, Langmuir **16**, 5218–5220 (2000)

20.71 R. Nagarajan, T.A. Hatton: Chap. 5. In: *Nanoparticles: Synthesis, Stabilization, Passivation, and Functionalization* (American Chemical Society, Washington 2008)

20.72 L.O. Brown, J.E. Hutchison: Convenient preparation of stable, narrow-dispersity, gold nanocrystals by ligand exchange reactions, J. Am. Chem. Soc. **119**, 12384–12385 (1997)

20.73 R. Nagarajan, T.A. Hatton: Chap. 4. In: *Nanoparticles: Synthesis, Stabilization, Passivation, and Functionalization* (American Chemical Society, Washington 2008)

20.74 M.Y. Han, C.H. Quek, W. Huang, C.H. Chew, L.M. Gan: A simple and effective chemical route

for the preparation of uniform nonaqueous gold colloids, Chem. Mater. **11**, 1144–1147 (1999)
20.75 K.V. Sarathy, G. Raina, R.T. Yadav, G.U. Kulkarni, C.N.R. Rao: Thiol-derivatized nanocrystalline arrays of gold, silver, and platinum, J. Phys. Chem. B **101**, 9876–9880 (1997)
20.76 K.V. Sarathy, G.U. Kulkarni, C.N.R. Rao: A novel method of preparing thiol-derivatised nanoparticles of gold, platinum and silver forming superstructures, Chem. Commun. **6**, 537–538 (1997)
20.77 N.R. Jana, L. Gearheart, C.J. Murphy: Seeding growth for size control of 5-40 nm diameter gold nanoparticles, Langmuir **17**, 6782–6786 (2001)
20.78 A.C. Templeton, M.J. Hostetler, E.K. Warmoth, S. Chen, C.M. Hartshorn, V.M. Krishnamurthy, M.D.E. Forbes, R.W. Murray: Gateway reactions to diverse, polyfunctional monolayer-protected gold clusters, J. Am. Chem. Soc. **120**, 4845–4849 (1998)
20.79 A.B. Smetana, K.J. Klabunde, C.M. Sorensen: Synthesis of spherical silver nanoparticles by digestive ripening, stabilization with various agents, and their 3-D and 2-D superlattice formation, J. Colloid Interface Sci. **284**, 521–526 (2005)
20.80 P.C. Lee, D. Meisel: Adsorption and surface-enhanced Raman of dyes on silver and gold sols, J. Phys. Chem. **86**, 3391–3395 (1982)
20.81 B. Raguse, C.S. Barton, K.-H. Müller, E. Chow, L. Wieczorek: Gold nanoparticle chemiresistor sensors in aqueous solution: Comparison of hydrophobic and hydrophilic nanoparticle films, J. Phys. Chem. C **113**, 15390–15397 (2009)
20.82 B. Raguse, E. Chow, C.S. Barton, L. Wieczorek: Gold nanoparticle chemiresistor sensors: Direct sensing of organics in aqueous electrolyte solution, Anal. Chem. **79**, 7333–7339 (2007)
20.83 X. Zhou, J.M.E. Khoury, L. Qu, L. Dai, Q. Li: A facile synthesis of aliphatic thiol surfactant with tunable length as a stabilizer of gold nanoparticles in organic solvents, J. Colloid Interface Sci. **308**, 381–384 (2007)
20.84 M.J. Hostetler, A.C. Templeton, R.W. Murray: Dynamics of place-exchange reactions on monolayer-protected gold cluster molecules, Langmuir **15**, 3782–3789 (1999)
20.85 B.L.V. Prasad, S.I. Stoeva, C.M. Sorensen, K.J. Klabunde: Digestive ripening of thiolated gold nanoparticles: The effect of alkyl chain length, Langmuir **18**, 7515–7520 (2002)
20.86 M.J. Hostetler, S.J. Green, J.J. Stokes, R.W. Murray: Monolayers in three dimensions: Synthesis and electrochemistry of ω-functionalized alkanethiolate-stabilized gold cluster compounds, J. Am. Chem. Soc. **118**, 4212–4213 (1996)
20.87 R.S. Ingram, M.J. Hostetler, R.W. Murray: Polyhetero-ω-functionalized alkanethiolate-stabilized gold cluster compounds, J. Am. Chem. Soc. **119**, 9175–9178 (1997)
20.88 S. Nuß, H. Böttcher, H. Wurm, M.L. Hallensleben: Gold nanoparticles with covalently attached polymer chains, Angew. Chem. Int. Ed. **40**, 4016–4018 (2001)
20.89 C. Amiens, D. de Caro, B. Chaudret: Selective synthesis, characterization, and spectroscopic studies on a novel class of reduced platinum and palladium particles stabilized by carbonyl and phosphine ligands, J. Am. Chem. Soc. **115**, 11638–11639 (1993)
20.90 T. Phenrat, N. Saleh, K. Sirk, H.-J. Kim, R.D. Tilton, G.V. Lowry: Stabilization of aqueous nanoscale zerovalent iron dispersions by anionic polyelectrolytes: Adsorbed anionic polyelectrolyte layer properties and their effect on aggregation and sedimentation, J. Nanopart. Res. **10**, 795–814 (2008)
20.91 W.J. Tseng, F. Tzeng: Effect of ammonium polyacrylate on dispersion and rheology of aqueous ITO nanoparticle colloids, Colloids Surf. A **276**, 34–39 (2006)
20.92 N. Jain, Y. Wang, S.K. Jones, B.S. Hawkett, G.G. Warr: Optimized steric stabilization of aqueous ferrofluids and magnetic nanoparticles, Langmuir **26**, 4465–4472 (2010)
20.93 C. Sentein, B. Guizard, S. Giraud, C. Yé, F. Ténégal: Dispersion and stability of TiO_2 nanoparticles synthesized by laser pyrolysis in aqueous suspensions, J. Phys. Conf. Ser. **170**, 012013 (2009)
20.94 M. Cho, H. Chung, W. Choi, J. Yoon: Linear correlation between inactivation of *E. coli* and OH radical concentration in TiO_2 photocatalytic disinfection, Water Res. **38**, 1069–1077 (2004)
20.95 K. Sato, J.-G. Li, H. Kamiya, T. Ishigaki: Ultrasonic dispersion of TiO_2 nanoparticles in aqueous suspension, J. Am. Ceram. Soc. **91**, 2481–2487 (2008)
20.96 S.J. Chung, J.P. Leonard, I. Nettleship, J.K. Lee, Y. Soong, D.V. Martello, M.K. Chyu: Characterization of ZnO nanoparticle suspension in water: Effectiveness of ultrasonic dispersion, Powder Technol. **194**, 75–80 (2009)
20.97 Y.-Y. Yu, S.-S. Chang, C.-L. Lee, C.R.C. Wang: Gold nanorods: Electrochemical synthesis and optical properties, J. Phys. Chem. B **101**, 6661–6664 (1997)
20.98 S. Link, C. Burda, B. Nikoobakht, M.A. El-Sayed: Laser-induced shape changes of colloidal gold nanorods using femtosecond and nanosecond laser pulses, J. Phys. Chem. B **104**, 6152–6163 (2000)
20.99 B.M.I. van der Zande, M.R. Böhmer, L.G.J. Fokkink, C. Schönenberger: Aqueous gold sols of rod-shaped particles, J. Phys. Chem. B **101**, 852–854 (1997)
20.100 V. Sharma, K. Park, M. Srinivasarao: Colloidal dispersion of gold nanorods: Historical background, optical properties, seed-mediated synthesis, shape separation and self-assembly, Mater. Sci. Eng. R **65**, 1–38 (2009)
20.101 B. Nikoobakht, M.A. El-Sayed: Preparation and growth mechanism of gold nanorods (NRs) using

seed-mediated growth method, Chem. Mater. **15**, 1957–1962 (2003)
20.102 Y. Huang, X. Duan, Y. Cui, L.J. Lauhon, K.-H. Kim, C.M. Lieber: Logic gates and computation from assembled nanowire building blocks, Science **294**, 1313–1317 (2001)
20.103 Y. Cui, L.J. Lauhon, M.S. Gudiksen, J. Wang, C.M. Lieber: Diameter-controlled synthesis of single-crystal silicon nanowires, Appl. Phys. Lett. **78**, 2214–2216 (2001)
20.104 A.B. Panda, G. Glaspell, M.S. El-Shall: Microwave synthesis of highly aligned ultra narrow semiconductor rods and wires, J. Am. Chem. Soc. **128**, 2790–2791 (2006)
20.105 L. Manna, E.C. Scher, A.P. Alivisatos: Synthesis of soluble and processable rod-, arrow-, teardrop-, and tetrapod-shaped CdSe nanocrystals, J. Am. Chem. Soc. **122**, 12700–12706 (2000)
20.106 Z.A. Peng, X. Peng: Mechanisms of the shape evolution of CdSe nanocrystals, J. Am. Chem. Soc. **123**, 1389–1395 (2001)
20.107 M. Zavelani-Rossi, M.G. Lupo, R. Krahne, L. Manna, G. Lanzani: Lasing in self-assembled microcavities of CdSe/CdS core/shell colloidal quantum rods, Nanoscale **2**, 931–935 (2010)
20.108 L. Carbone, C. Nobile, M. De Giorgi, F. Della Sala, G. Morello, P. Pompa, M. Hytch, E. Snoeck, A. Fiore, I.R. Franchini, M. Nadasan, A.F. Silvestre, L. Chiodo, S. Kudera, R. Cingolani, R. Krahne, L. Manna: Synthesis and micrometer-scale assembly of colloidal CdSe/CdS nanorods prepared by a seeded growth approach, Nano Lett. **7**, 2942–2950 (2007)
20.109 Y. Li, M.A. Malik, P. O'Brien: Synthesis of single-crystalline CoP nanowires by a one-pot metal-organic route, J. Am. Chem. Soc. **127**, 16020–16021 (2005)
20.110 P.D. Cozzoli, A. Kornowski, H. Weller: Low-temperature synthesis of soluble and processable organic-capped anatase TiO_2 nanorods, J. Am. Chem. Soc. **125**, 14539–14548 (2003)
20.111 M. Kalbacova, J.M. Macak, F. Schmidt-Stein, C.T. Mierke, P. Schmuki: TiO_2 nanotubes: Photocatalyst for cancer cell killing, Phys. Status Solidi – Rapid Res. Lett. **2**, 194–196 (2008)
20.112 J. Joo, S.G. Kwon, T. Yu, M. Cho, J. Lee, J. Yoon, T. Hyeon: Large-scale synthesis of TiO_2 nanorods via nonhydrolytic sol–gel ester elimination reaction and their application to photocatalytic inactivation of *E. coli*, J. Phys. Chem. B **109**, 15297–15302 (2005)
20.113 G. Gundiah, F.L. Deepak, A. Govindaraj, C.N.R. Rao: Carbothermal synthesis of the nanostructures of Al_2O_3 and ZnO, Top. Catal. **24**, 137–146 (2003)
20.114 F.L. Deepak, P. Saldanha, S.R.C. Vivekchand, A. Govindaraj: A study of the dispersions of metal oxide nanowires in polar solvents, Chem. Phys. Lett. **417**, 535–539 (2006)
20.115 Y. Sun, Y. Xia: Shape-controlled synthesis of gold and silver nanoparticles, Science **298**, 2176–2179 (2002)
20.116 M. Popa, T. Pradell, D. Crespo, J.M. Calderón-Moreno: Stable silver colloidal dispersions using short chain polyethylene glycol, Colloids Surf. A **303**, 184–190 (2007)
20.117 S. Wang, H. Xin: Fractal and dendritic growth of metallic Ag aggregated from different kinds of γ-irradiated solutions, J. Phys. Chem. B **104**, 5681–5685 (2000)
20.118 U. Olgun: Rapid microwave-assisted deposition of microwire patterns of nanoaluminum and nanosilver from colloids, ACS Appl. Mater. Interface **2**, 28–34 (2010)
20.119 X. Li, J. Zhang, W. Xu, H. Jia, X. Wang, B. Yang, B. Zhao, B. Li, Y. Ozaki: Mercaptoacetic acid-capped silver nanoparticles colloid: Formation, morphology, and SERS activity, Langmuir **19**, 4285–4290 (2003)
20.120 D.M. Ledwith, A.M.W. Kelly, J.M. Kelly: A rapid, straight-forward method for controlling the morphology of stable silver nanoparticles, J. Mater. Chem. **17**, 2459–2464 (2008)
20.121 Z.S. Pillai, P.V. Kamat: What factors control the size and shape of silver nanoparticles in the citrate ion reduction method?, J. Phys. Chem. B **108**, 945–951 (2004)
20.122 I. Pastoriza-Santos, L.M. Liz-Marzán: Formation and stabilization of silver nanoparticles through reduction by *N*,*N*-dimethylformamide, Langmuir **15**, 948–951 (1999)
20.123 S. Fullam, S.N. Rao, D. Fitzmaurice: Noncovalent self-assembly of silver nanocrystal aggregates in solution, J. Phys. Chem. B **104**, 6164–6173 (2000)
20.124 S.L.-C. Hsu, R.-T. Wu: Synthesis of contamination-free silver nanoparticle suspensions for micro-interconnects, Mater. Lett. **61**, 3719–3722 (2007)
20.125 V.K. Sharma, R.A. Yngard, Y. Lin: Silver nanoparticles: Green synthesis and their antimicrobial activities, Adv. Colloid Interface Sci. **145**, 83–96 (2009)
20.126 A. Sarkar, S. Kapoor, T. Mukherjee: Preparation, characterization, and surface modification of silver nanoparticles in formamide, J. Phys. Chem. B **109**, 7698–7704 (2005)
20.127 A. Henglein, M. Giersig: Formation of colloidal silver nanoparticles: Capping action of citrate, J. Phys. Chem. B **103**, 9533–9539 (1999)
20.128 R.W.J. Scott, O.M. Wilson, R.M. Crooks: Synthesis, characterization, and applications of dendrimer encapsulated nanoparticles, J. Phys. Chem. B **109**, 692–704 (2005)
20.129 S. Magdassi, A. Bassa, Y. Vinetsky, A. Kamyshny: Silver nanoparticles as pigments for water-based ink-jet inks, Chem. Mater. **15**, 2208–2217 (2003)
20.130 R.M. Crooks, M. Zhao, L. Sun, V. Chechik, L.K. Yeung: Dedrimer-encapsulated metal nanoparticles:

Synthesis, characterization, and applications to catalysis, Acc. Chem. Res. **34**, 181–190 (2001)
20.131 N.A. Luechinger, S.G. Walt, W.J. Stark: Printable nanoporous silver membranes, Chem. Mater. **22**(17), 4980–4986 (2010)
20.132 Y. Tan, Y. Li, D. Zhu: Fabrication of gold nanoparticles using a trithiol (thiocyanuric acid) as the capping agent, Langmuir **18**, 3392–3395 (2002)
20.133 A.C. Templeton, D.E. Cliffel, R.W. Murray: Redox and fluorophore functionalization of water-soluble, tiopronin-protected gold clusters, J. Am. Chem. Soc. **121**, 7081–7089 (1999)
20.134 S. Chen, K. Kimura: Synthesis and characterization of carboxylate-modified gold nanoparticle powders dispersible in water, Langmuir **15**, 1075–1082 (1999)
20.135 A.W. Shaffer, J.G. Worden, Q. Huo: Comparison study of the solution phase versus solid phase place exchange reactions in the controlled functionalization of gold nanoparticles, Langmuir **20**, 8343–8351 (2004)
20.136 J.G. Worden, A.W. Shaffer, Q. Huo: Controlled functionalization of gold nanoparticles through a solid phase synthesis approach, Chem. Commun. **5**, 518–519 (2004)
20.137 J.G. Worden, Q. Dai, A.W. Shaffer, Q. Huo: Monofunctional group-modified gold nanoparticles from solid phase synthesis approach: Solid support and experimental condition effect, Chem. Mater. **16**, 3746–3755 (2004)
20.138 X. Liu, J.G. Worden, Q. Dai, J. Zou, J. Wang, Q. Huo: Monofunctional gold nanoparticles prepared via a noncovalent-interaction-based solid-phase modification approach, Small **2**, 1126–1129 (2006)
20.139 K.-M. Sung, D.W. Mosley, B.R. Peelle, S. Zhang, J.M. Jacobson: Synthesis of monofunctionalized gold nanoparticles by Fmoc solid-phase reactions, J. Am. Chem. Soc. **126**, 5064–5065 (2004)
20.140 K.J. Klabunde: Ligand-induced gold nanocrystal superlattice formation in colloidal solution, Chem. Mater. **11**, 198–202 (1999)
20.141 M. Brust, J. Fink, D. Bethell, D.J. Schiffrin, C. Kiely: Synthesis and reactions of functionalised gold nanoparticles, J. Chem. Soc. Chem. Commun. **16**, 1655–1656 (1995)
20.142 M. Green, P. O'Brien: A simple one phase preparation of organically capped gold nanocrystals, Chem. Commun. **3**, 183–184 (2000)
20.143 M.E. Garcia, L.A. Baker, R.M. Crooks: Preparation and characterization of dendrimer-gold colloid nanocomposites, Anal. Chem. **71**, 256–258 (1999)
20.144 J.G. Worden, Q. Dai, Q. Huo: A nanoparticle–dendrimer conjugate prepared from a one-step chemical coupling of monofunctional nanoparticles with a dendrimer, Chem. Commun. **14**, 1536–1538 (2006)
20.145 D.V. Leff, L. Brandt, J.R. Heath: Synthesis and characterization of hydrophobic, organically-soluble gold nanocrystals functionalized with primary amines, Langmuir **12**, 4723–4730 (1996)
20.146 W.W. Weare, S.M. Reed, M.G. Warner, J.E. Hutchison: Improved synthesis of small (d_{CORE} = 1.5 nm) phosphine-stabilized gold nanoparticles, J. Am. Chem. Soc. **122**, 12890–12891 (2000)
20.147 F. Porta, L. Prati, M. Rossi, S. Coluccia, G. Martra: Metal sols as a useful tool for heterogeneous gold catalyst preparation: Reinvestigation of a liquid phase oxidation, Catal. Today **61**, 165–172 (2000)
20.148 I. Hussain, S. Graham, Z. Wang, B. Tan, D.C. Sherrington, S.P. Rannard, A.I. Cooper, M. Brust: Size-controlled synthesis of near-monodisperse gold nanoparticles in the 1–4 nm range using polymeric stabilizers, J. Am. Chem. Soc. **127**, 16398–16399 (2005)
20.149 Y. Tan, X. Dai, Y. Li, D. Zhu: Preparation of gold, platinum, palladium and silver nanoparticles by the reduction of their salts with a weak reductant–potassium bitartrate, J. Mater. Chem. **13**, 1069–1075 (2003)
20.150 A.C. Templeton, S. Chen, S.M. Gross, R.W. Murray: Water-soluble, isolable gold clusters protected by tiopronin and coenzyme A monolayers, Langmuir **15**, 66–76 (1999)
20.151 M.K. Corbierre, N.S. Cameron, M. Sutton, S.G.J. Mochrie, L.B. Lurio, A. Rühm, R.B. Lennox: Polymer-stabilized gold nanoparticles and their incorporation into polymer matrices, J. Am. Chem. Soc. **123**, 10411–10412 (2001)
20.152 M.J. Hostetler, J.E. Wingate, C.-J. Zhong, J.E. Harris, R.W. Vachet, M.R. Clark, J.D. Londono, S.J. Green, J.J. Stokes, G.D. Wignall, G.L. Glish, M.D. Porter: Alkanethiolate gold cluster molecules with core diameters from 1.5 to 5.2 nm: Core and monolayer properties as a function of core size, Langmuir **14**, 17–30 (1998)
20.153 A.C. Templeton, W.P. Wuelfing, R.W. Murray: Monolayer-protected cluster molecules, Acc. Chem. Res. **33**, 27–36 (2000)
20.154 C.A. Waters, A.J. Mills, K.A. Johnson, D.J. Schiffrin: Purification of dodecanethiol derivatised gold nanoparticles, Chem. Commun. **4**, 540–541 (2003)
20.155 B.G. Prevo, O.D. Velev: Controlled, rapid deposition of structured coatings from micro- and nanoparticle suspensions, Langmuir **20**, 2099–2107 (2004)
20.156 B.G. Prevo, J.C. Fuller, O.D. Velev: Rapid deposition of gold nanoparticle films with controlled thickness and structure by convective assembly, Chem. Mater. **17**, 28–35 (2005)
20.157 D.C. Hone, A.H. Haines, D.A. Russell: Rapid, quantitative colorimetric detection of a lectin using mannose-stabilized gold nanoparticles, Langmuir **19**, 7141–7144 (2003)
20.158 N.L. Rosi, C.A. Mirkin: Nanostructures in biodiagnostics, Chem. Rev. **105**, 1547–1562 (2005)

20.159 C.M. Niemeyer: Nanoparticles, proteins, and nucleic acids: Biotechnology meets materials science, Angew. Chem. Int. Ed. **40**, 4128–4158 (2001)

20.160 J. Turkevich, P.C. Stevenson, J. Hillier: A study of the nucleation and growth progress in the synthesis of colloidal gold, J. Discuss. Faraday Soc. **11**, 55–75 (1951)

20.161 T. Yonezawa, T. Kunitake: Practical preparation of anionic mercapto ligand-stabilized gold nanoparticles and their immobilization, Colloids Surf. A **149**, 193–199 (1999)

20.162 J.W. Slot, H.J. Geuze: A new method of preparing gold probes for multiple-labeling cytochemistry, Eur. J. Cell Biol. **38**, 87–93 (1985)

20.163 K.C. Grabar, K.J. Allison, B.E. Baker, R.M. Bright, K.R. Brown, R.G. Freeman, A.P. Fox, C.D. Keating, M.D. Musick, M.J. Natan: Two-dimensional arrays of colloidal gold particles: A flexible approach to macroscopic metal surfaces, Langmuir **12**, 2353–2361 (1996)

20.164 N.R. Jana, L. Gearheart, C.J. Murphy: Wet chemical synthesis of high aspect ratio cylindrical gold nanorods, J. Phys. Chem. B **105**, 4065–4067 (2001)

20.165 K. Torigoe, K. Esumi: Preparation and catalytic effect of gold nanoparticles in water dissolving carbon disulfide, J. Phys. Chem. B **103**, 2862–2866 (1999)

20.166 A. Manna, P.-L. Chen, H. Akiyama, T.-X. Wei, K. Tamada, W. Knoll: Optimized photoisomerization on gold nanoparticles capped by unsymmetrical azobenzene disulfides, Chem. Mater. **15**, 20–28 (2003)

20.167 T. Yonezawa, K. Yasui, N. Kimizuka: Controlled formation of smaller gold nanoparticles by the use of four-chained disulfide stabilizer, Langmuir **17**, 271–273 (2003)

20.168 L.A. Porter, D. Ji, S.L. Westcott, M. Graupe, R.S. Czernuszewicz, N.J. Halas, T.R. Lee: Gold and silver nanoparticles functionalized by the adsorption of dialkyl disulfides, Langmuir **14**, 7378–7386 (1998)

20.169 P.R. Selvakannan, S. Mandal, S. Phadtare, R. Pasricha, M. Sastry: Capping of gold nanoparticles by the amino acid lysine renders them water-dispersible, Langmuir **19**, 3545–3549 (2003)

20.170 S. Gomez, K. Philippot, V. Colliére, B. Chaudret, F. Senocq, P. Lecante: Gold nanoparticles from self-assembled gold(I) amine precursors, Chem. Commun. **19**, 1945–1945 (2000)

20.171 C.S. Weisbecker, M.V. Merritt, G.M. Whitesides: Molecular self-assembly of aliphatic thiols on gold colloids, Langmuir **12**, 3763–3772 (1996)

20.172 S. Förster, M. Antonietti: Amphiphilic block copolymers in structure-controlled nanomaterial hybrids, Adv. Mater. **10**, 195–217 (1998)

20.173 C.M. Niemeyer: Nanoparticles, proteins, and nucleic acids: Biotechnology meets materials science, Angew. Chem. Int. Ed. **40**, 4128–4158 (2001)

20.174 M. Brust, M. Walker, D. Bethell, D.J. Schiffrin, R. Whyman: Synthesis of thiol-derivatised gold nanoparticles in a two-phase liquid–liquid system, J. Chem. Soc., Chem. Commun. **7**, 801–802 (1994)

20.175 R. Shenenhar, V.M. Rotello: Nanoparticles: Scaffolds and building blocks, Acc. Chem. Res. **36**, 549–561 (2003)

20.176 I. Hussain, Z. Wang, A.I. Cooper, M. Brust: Formation of spherical nanostructures by the controlled aggregation of gold colloids, Langmuir **22**, 2938–2941 (2006)

20.177 T.K. Mandal, M.S. Fleming, D.R. Walt: Preparation of polymer coated gold nanoparticles by surface-confined living radical polymerization at ambient temperature, Nano Lett. **2**, 3–7 (2002)

20.178 W. Xu, W. Liu, D. Zhang, Y. Xu, T. Wang, D. Zhu: Synthesis, characterization and chemical oxidation of 5-(*N*-pyrrolyl)pentanethiol protected gold nanoparticles, Colloids Surf. A **204**, 201–209 (2002)

20.179 D. Andreescu, T.K. Sau, D.V. Goia: Stabilizer-free nanosized gold sols, J. Colloid Interface Sci. **298**, 742–751 (2006)

20.180 D.G. Duff, A. Baikeraand, P.P. Edwards: A new hydrosol of gold clusters, J. Chem. Soc., Chem. Commun. **1**, 96–98 (1993)

20.181 R. Seshadri, G.N. Subbanna, V. Vijayakrishnan, G.U. Kulkami, G. Ananthakrishna, C.N.R. Rao: Growth of nanometric gold particles in solution phase, J. Phys. Chem. **99**, 5639–5644 (1995)

20.182 D.G. Duff, A. Baiker: A new hydrosol of gold clusters 1. formation and particle size variation, Langmuir **9**, 2301–2309 (1993)

20.183 L. Francois, M. Mostafavi, J. Belloni, J.-F. Delouis, J. Delaire, P. Feneyrou: Optical limitation induced by gold clusters. 1. Size effect, J. Phys. Chem. B **104**, 6133–6137 (2000)

20.184 A. Henglein: Radiolytic preparation of ultrafine colloidal gold particles in aqueous solution: Optical spectrum, controlled growth, and some chemical reactions, Langmuir **15**, 6738–6744 (1999)

20.185 A. Henglein, D. Meisel: Radiolytic control of the size of colloidal gold nanoparticles, Langmuir **14**, 7392–7396 (1998)

20.186 B.L.V. Prasad, S.I. Stoeva, C.M. Sorensen, K.J. Klabunde: Digestive-ripening agents for gold nanoparticles: Alternatives to thiols, Chem. Mater. **15**, 935–942 (2003)

20.187 S. Stoeva, K.J. Klabunde, C.M. Sorensen, I. Dragieva: Gram-scale synthesis of monodisperse gold colloids by the solvated metal atom dispersion method and digestive ripening and their organization into two- and three-dimensional structures, J. Am. Chem. Soc. **124**, 2305–2311 (2002)

20.188 M. Zhao, R.M. Crooks: Intradendrimer exchange of metal nanoparticles, Chem. Mater. **11**, 3379–3385 (1999)

20.189 G.K. Kouassi, J. Irudayaraj: Magnetic and gold-coated magnetic nanoparticles as a DNA sensor, Anal. Chem. **78**, 3234–3241 (2006)

20.190 S. Sun, C.B. Murray: Synthesis of monodisperse cobalt nanocrystals and their assembly into magnetic superlattices (invited), J. Appl. Phys. **85**, 4325–4330 (1999)

20.191 J.R. Thomas: Preparation and magnetic properties of colloidal cobalt particles, J. Appl. Phys. **37**, 2914–2915 (1966)

20.192 O.A. Platonova, L.M. Bronstein, S.P. Solodovnikov, I.M. Yanovskaya, E.S. Obolonkova, P.M. Valetsky, E. Wenz, M. Antonietti: Cobalt nanoparticles in block copolymer micelles: Preparation and properties, Colloid Polym. Sci. **275**, 426–431 (1997)

20.193 V.F. Puntes, D. Zanchet, C.K. Erdonmez, A.P. Alivisatos: Synthesis of hcp-Co nanodisks, J. Am. Chem. Soc. **124**, 12874–12880 (2002)

20.194 V.V. Baranauskas III, M.A. Zalich, M. Saunders, T.G. St. Pierre, J.S. Riffle: Poly(styrene-*b*-4-vinylphenoxyphthalonitrile)-cobalt complexes and their conversion to oxidatively stable cobalt nanoparticles, Chem. Mater. **17**, 5246–5254 (2005)

20.195 H. Bönnemann, W. Brijoux, R. Brinkmann, N. Matoussevitch, N. Waldöfner, N. Palina, H. Modrow: A size-selective synthesis of air stable colloidal magnetic cobalt nanoparticles, Inorg. Chim. Acta **350**, 617–624 (2003)

20.196 Z.L. Wang, Z. Dai, S. Sun: Polyhedral shapes of cobalt nanocrystals and their effect on ordered nanocrystal assembly, Adv. Mater. **12**, 1944–1946 (2002)

20.197 K.V.P.M. Shafi, A. Gedanken, R. Prozorov: Surfactant-assisted self-organization of cobalt nanoparticles in a magnetic fluid, Adv. Mater. **10**, 590–593 (1998)

20.198 B.G. Ershov, N.L. Sukhov, E. Janata: Formation, absorption spectrum, and chemical reactions of nanosized colloidal cobalt in aqueous solution, J. Phys. Chem. B **104**, 6138–6142 (2000)

20.199 J.P. Chen, C.M. Sorensen, K.J. Klabunde, G.C. Hadjipanayis: Magnetic properties of nanophase cobalt particles synthesized in inversed micelles, J. Appl. Phys. **76**, 6316–6318 (1994)

20.200 C. Petit, A. Taleb, M.-P. Pileni: Self-organization of magnetic nanosized cobalt particles, Adv. Mater. **10**, 259–261 (1998)

20.201 V. Russier, C. Petit, J. Legrand, M.P. Pileni: Collective magnetic properties of cobalt nanocrystals self-assembled in a hexagonal network: Theoretical model supported by experiments, Phys. Rev. B **62**, 3910–3916 (2000)

20.202 N. Moumen, M.P. Pileni: New syntheses of cobalt ferrite particles in the range 2–5 nm: Comparison of the magnetic properties of the nanosized particles in dispersed fluid or in powder form, Chem. Mater. **8**, 1128–1134 (1996)

20.203 N. Moumen, M.P. Pileni: Control of the size of cobalt ferrite magnetic fluid, J. Phys. Chem. **100**, 1867–1873 (1996)

20.204 A.J. Rondinone, A.C.S. Samia, Z.J. Zhang: Superparamagnetic relaxation and magnetic anisotropy energy distribution in $CoFe_2O_4$ spinel ferrite nanocrystallites, J. Phys. Chem. B **103**, 6876–6880 (1999)

20.205 C. Liu, B. Zou, A.J. Rondinone, Z.J. Zhang: Chemical control of superparamagnetic properties of magnesium and cobalt spinel ferrite nanoparticles through atomic level magnetic couplings, J. Am. Chem. Soc. **122**, 6263–6267 (2000)

20.206 B.K. Park, D. Kim, S. Jeong, J. Moon, J.S. Kim: Direct writing of copper conductive patterns by ink-jet printing, Thin Solid Films **515**, 7706–7711 (2007)

20.207 B.K. Park, S. Jeong, D. Kim, J. Moon, S. Lim, J. Sub Kim: Synthesis and size control of monodisperse copper nanoparticles by polyol method, J. Colloid Interface Sci. **311**, 417–424 (2007)

20.208 J. Osuna, D. de Caro, C. Amiens, B. Chaudret, E. Snoeck, M. Respaud, J.-M. Broto, A. Fert: Synthesis, characterization, and magnetic properties of cobalt nanoparticles from an organometallic precursor, J. Phys. Chem. **100**, 14571–14574 (1996)

20.209 K.S. Suslick, M. Fang, T. Hyeon: Sonochemical synthesis of iron colloids, J. Am. Chem. Soc. **118**, 11960–11961 (1996)

20.210 C.H. Griffiths, M.P. O'Horo, T.W. Smith: The structure, magnetic characterization, and oxidation of colloidal iron dispersions, J. Appl. Phys. **37**, 7108–7115 (1979)

20.211 T.W. Smith, D. Wychlck: Colloidal iron dispersions prepared via the polymer-catalyzed decomposition of iron pentacarbonyl, J. Phys. Chem. **84**, 1621–1629 (1960)

20.212 J. van Wonterghem, S. Morup, S.W. Charles, S. Wells, J. Villadsen: Formation and chemical stability of metallic glass particles prepared by termolysis of $Fe(CO)_5$, Hyperfine Interact. **27**, 333–336 (1986)

20.213 Z. Guo, L.L. Henry, V. Palshin, E.J. Podlaha: Synthesis of poly(methyl methacrylate) stabilized colloidal zero-valence metallic nanoparticles, J. Mater. Chem. **16**, 1772–1777 (2006)

20.214 T. Hyeon, S.S. Lee, J. Park, Y. Chung, H.B. Na: Synthesis of highly crystalline and monodisperse maghemite nanocrystallites without a size-selection process, J. Am. Chem. Soc. **123**, 12798–12801 (2001)

20.215 S.-H. Wu, D.-H. Chen: Synthesis and characterization of nickel nanoparticles by hydrazine reduction in ethylene glycol, J. Colloid Interface Sci. **259**, 282–286 (2003)

20.216 Y. Hou, S. Gao: Monodisperse nickel nanoparticles prepared from a monosurfactant system and their magnetic properties, J. Mater. Chem. **13**, 1510–1512 (2003)

20.217 T.O. Ely, C. Amiens, B. Chaudret: Synthesis of nickel nanoparticles: influence of aggregation induced by modification of poly(vinylpyrrolidone) chain length on their magnetic properties, Chem. Mater. **11**, 526–529 (1999)

20.218 H. Ye, R.W.J. Scott, R.M. Crooks: Synthesis, characterization, and surface immobilization of platinum and palladium nanoparticles encapsulated within amine-terminated poly(amidoamine) dendrimers, Langmuir **20**, 2915–2920 (2004)

20.219 R.W.J. Scott, H. Ye, R.R. Henriquez, R.M. Crooks: Synthesis, characterization, and stability of dendrimer-encapsulated palladium nanoparticles, Chem. Mater. **15**, 3873–3878 (2003)

20.220 T. Teranishi, H. Hori, M. Miyake: ESR study on palladium nanoparticles, J. Phys. Chem. B **101**, 5774–5776 (1997)

20.221 M. Zhao, R.M. Crooks: Homogeneous hydrogenation catalysis with monodisperse, dendrimer-encapsulated Pd and Pt nanoparticles, Angew. Chem. Int. Ed. **38**, 364–366 (1999)

20.222 Y. Niu, L.K. Yeung, R.M. Crooks: Size-selective hydrogenation of olefins by dendrimer-encapsulated palladium nanoparticles, J. Am. Chem. Soc. **123**, 6840–6846 (2001)

20.223 L.K. Yeung, C.T. Lee Jr., K.P. Johnston, R.M. Crooks: Catalysis in supercritical CO_2 using dendrimer-encapsulated palladium nanoparticles, Chem. Commun. **7**, 2290–2291 (2001)

20.224 J.-L. Pellegatta, C. Blandy, R. Choukroun, C. Lorber, B. Chaudret, P. Lecante, E. Snoeck: Palladium colloids from an organometallic route: Redox reaction between $[VCp_2]$ and $[Pd(\eta^3\text{-allyl})_2Cl]_2$. Catalytic application to the hydrogenation of aromatic nitro compounds, New J. Chem. **27**, 1528–1532 (2003)

20.225 S. Chen, K. Huang, J.A. Stearns: Alkanethiolate-protected palladium nanoparticles, Chem. Mater. **12**, 540–547 (2000)

20.226 M. Zhao, R.M. Crooks: Dendrimer-encapsulated Pt nanoparticles: Synthesis, characterization, and applications to catalysis, Adv. Mater. **11**, 217–220 (1999)

20.227 K. Angermund, M. Bühl, E. Dinjus, U. Endruschat, F. Gassner, H.-G. Haubold, J. Hormes, G. Köhl, F.T. Mauschick, H. Modrow, R. Mörtel, R. Mynott, B. Tesche, T. Vad, N. Waldöfner, H. Bönnemann: Nanoscopic Pt colloids in the "embryonic state", Angew. Chem. Int. Ed. **41**, 4041–4044 (2002)

20.228 K. Angermund, M. Bühl, U. Endruschat, F.T. Mauschick, R. Mörtel, R. Mynott, B. Tesche, N. Waldöfner, H. Bönnemann, G. Köhl, H. Modrow, J. Hormes, E. Dinjus, F. Gassner, H.-G. Haubold, T. Vad, M. Kaupp: In situ study on the wet chemical synthesis of nanoscopic Pt colloids by "reductive stabilization", J. Phys. Chem. B **107**, 7507–7515 (2003)

20.229 P. Shah, Y. Kevrekidis, J. Benziger: Ink-jet printing of catalyst patterns for electroless metal deposition, Langmuir **15**, 1584–1587 (1999)

20.230 H. Ihm, J.M. White: Stepwise dissociation of thermally activated phenol on Pt(111), J. Phys. Chem. B **104**, 6202–6211 (2000)

20.231 A. Rodriguez, C. Amiens, B. Chaudret, M.-J. Casanove, P. Lecante, J.S. Bradley: Synthesis and isolation of cuboctahedral and icosahedral platinum nanoparticles. Ligand-dependent structures, Chem. Mater. **8**, 1978–1986 (1996)

20.232 W. Tu, H. Liu: Continuous synthesis of colloidal metal nanoclusters by microwave irradiation, Chem. Mater. **12**, 564–567 (2000)

20.233 X. Li, Y. He, M.T. Swihart: Surface functionalization of silicon nanoparticles produced by laser-driven pyrolysis of silane followed by HF-HNO_3 etching, Langmuir **20**, 4720–4727 (2004)

20.234 A.E. Harrak, G. Carrot, J. Oberdisse, C. Eychenne-Baron, F. Boue: Surface-atom transfer radical polymerization from silica nanoparticles with controlled colloidal stability, Macromolecules **37**, 6376–6384 (2004)

20.235 L.H. Lie, M. Duerdin, E.M. Tuite, A. Houlton, B.R. Horrocks: Preparation and characterisation of luminescent alkylated-silicon quantum dots, J. Electroanal. Chem. **538/539**, 183–190 (2002)

20.236 W.D. Kirkey, Y. Sahoo, X. Li, Y. He, M.T. Swihart, A.N. Cartwright, S. Bruckenstein, P.N. Prasad: Quasi-reversible photoluminescence quenching of stable dispersions of silicon nanoparticles, J. Mater. Chem. **15**, 2028–2034 (2005)

20.237 F. Hua, M.T. Swihart, E. Ruckenstein: Efficient surface grafting of luminescent silicon quantum dots by photoinitiated hydrosilylation, Langmuir **21**, 6054–6062 (2005)

20.238 Z.F. Li, M.T. Swihart, E. Ruckenstein: Luminescent silicon nanoparticles capped by conductive polyaniline through the self-assembly method, Langmuir **20**, 1963–1971 (2004)

20.239 A. Reindl, A. Voronov, P.K. Gorle, M. Rauscher, A. Roosen, W. Peukert: Dispersing and stabilizing silicon nanoparticles in a low-epsilon medium, Colloids Surf. A **320**, 183–188 (2008)

20.240 A. Reindl, S. Aldabergenova, E. Altin, G. Frank, W. Peukert: Dispersing silicon nanoparticles in a stirred media mill – Investigating the evolution of morphology, structure and oxide formation, Phys. Status Solidi (a) **204**, 2329–2338 (2007)

20.241 A. Reindl, C. Cimpean, W. Bauer, R. Comanici, A. Ebbers, W. Peukert, C. Kryschi: Dispersing silicon nanoparticles with a stirred media mill and subsequent functionalization with phenyl acetylene, Colloids Surf. A **301**, 382–387 (2007)

20.242 R.K. Baldwin, K.A. Pettigrew, E. Ratai, M.P. Augustine, S.M. Kauzlarich: Solution reduction synthesis of surface stabilized silicon nanoparticles, Chem. Commun. **17**, 1822–1823 (2002)

20.243 R.K. Baldwin, K.A. Pettigrew, J.C. Garno, P.P. Power, G.-Y. Liu, S.M. Kauzlarich: Room temperature solution synthesis of alkyl-capped tetrahedral shaped silicon nanocrystals, J. Am. Chem. Soc. **124**, 1150–1151 (2002)

20.244 S.-M. Liu, Y. Yang, S. Sato, K. Kimura: Enhanced photoluminescence from Si nano-organosols by functionalization with alkenes and their size evolution, Chem. Mater. **18**, 637–642 (2006)

20.245 C.-S. Yang, R.A. Bley, S.M. Kauzlarich, H.W.H. Lee, G.R. Delgado: Synthesis of alkyl-terminated silicon nanoclusters by a solution route, J. Am. Chem. Soc. **121**, 5191–5195 (1999)

20.246 D.S. English, L.E. Pell, Z. Yu, P.F. Barbara, B.A. Korgel: Size tunable visible luminescence from individual organic monolayer stabilized silicon nanocrystal quantum dots, Nano Lett. **2**, 681–685 (2002)

20.247 B. Sweryda-Krawiec, T. Cassagneau, J.H. Fendler: Surface modification of silicon nanocrystallites by alcohols, J. Phys. Chem. B **103**, 9524–9529 (1999)

20.248 K.A. Pettigrew, Q. Liu, P.P. Power, S.M. Kauzlarich: Solution synthesis of alkyl- and alkyl/alkoxy-capped silicon nanoparticles via oxidation of Mg_2Si, Chem. Mater. **15**, 4005–4011 (2003)

20.249 X.Y. Ling, D.N. Reinhoudt, J. Huskens: Ferrocenyl-functionalized silica nanoparticles: Preparation, characterization, and molecular recognition at interfaces, Langmuir **22**, 8777–8783 (2006)

20.250 R.J. Clark, M.K.M. Dang, J.G.C. Veinot: Exploration of organic acid chain length on water-soluble silicon quantum dot surfaces, Langmuir **26**(19), 15657–15664 (2010)

20.251 J.W. Aptekar, M.C. Cassidy, A.C. Johnson, R.A. Barton, M. Lee, A.C. Ogier, C. Vo, M.N. Anahtar, Y. Ren, S.N. Bhatia, C. Ramanathan, D.G. Cory, A.L. Hill, W. Mair, M.S. Rosen, R.L. Walsworth, C.M. Marcus: Silicon nanoparticles as hyperpolarized magnetic resonance imaging agents, ACS Nano **3**, 4003–4008 (2009)

20.252 B.R. Taylor, S.M. Kauzlarich: Solution synthesis of germanium nanocrystals demonstrating quantumconfinement, Chem. Mater. **10**, 22–24 (1998)

20.253 B.R. Taylor, S.M. Kauzlarich, G.R. Delgado, H.W.H. Lee: Solution synthesis and characterization of quantum confined Ge nanoparticles, Chem. Mater. **11**, 2493–2500 (1999)

20.254 X. Lu, K.J. Ziegler, A. Ghezelbash, K.P. Johnston, B.A. Korgel: Synthesis of germanium nanocrystals in high temperature supercritical fluid solvents, Nano Lett. **4**, 969–974 (2004)

20.255 X. Ma, F. Wu, S.M. Kauzlarich: Alkyl-terminated crystalline Ge nanoparticles prepared from NaGe: Synthesis, functionalization and optical properties, J. Solid State Chem. **181**, 1628–1633 (2008)

20.256 R.S. Tanke, S.M. Kauzlarich, T.E. Patten, K.A. Pettigrew, D.L. Murphy, M.E. Thompson, H.W.H. Lee: Synthesis of germanium nanoclusters with irreversibly attached functional groups: Acetals, alcohols, esters, and polymers, Chem. Mater. **15**, 1682–1689 (2003)

20.257 T.N. Lambert, N.L. Andrews, H. Gerung, T.J. Boyle, J.M. Oliver, B.S. Wilson, S.M. Han: Water-soluble germanium(0) nanocrystals: Cell recognition and near-infrared photothermal conversion properties, Small **3**, 691–699 (2007)

20.258 B.A. Hernandez-Sanchez, T.J. Boyle, T.N. Lambert, S.D. Daniel-Taylor, J.M. Oliver, B.S. Wilson, D.S. Lidke, N.L. Andrews: Synthesizing biofunctionalized nanoparticles to image cell signaling pathways, IEEE Trans. Nanobiosci. **5**, 222–230 (2006)

20.259 X. Lu, B.A. Korgel, K.P. Johnston: High yield of germanium nanocrystals synthesized from germanium diiodide in solution, Chem. Mater. **17**, 6479–6485 (2005)

20.260 H.W. Chiu, C.N. Chervin, S.M. Kauzlarich: Phase changes in Ge nanoparticles, Chem. Mater. **17**, 4858–4864 (2005)

20.261 H. Gerung, S.D. Bunge, T.J. Boyle, C.J. Brinker, S.M. Han: Anhydrous solution synthesis of germanium nanocrystals from the germanium(II) precursor $Ge[N(SiMe_3)_2]_2$, Chem. Commun. **14**, 1914–1916 (2005)

20.262 S. Prabakar, A. Shiohara, S. Hanada, K. Fujioka, K. Yamamoto, R.D. Tilley: Size controlled synthesis of germanium nanocrystals by hydride reducing agents and their biological applications, Chem. Mater. **22**, 482–486 (2010)

20.263 E. Fok, M. Shih, A. Meldrum, J.G.C. Veinot: Preparation of alkyl-surface functionalized germanium quantum dots via thermally initiated hydrogermylation, Chem. Commun. **7**, 386–387 (2004)

20.264 J.R. Heath, J.J. Shiang, A.P. Alivisatos: Germanium quantum dots: Optical properties and synthesis, J. Chem. Phys. **101**, 1607–1615 (1994)

20.265 W.W. Yu, X. Peng: Formation of high-quality CdS and other II–VI semiconductor nanocrystals in noncoordinating solvents: Tunable reactivity of monomers, Angew. Chem. Int. Ed. **41**, 2368–2371 (2002)

20.266 K. Sill, T. Emrick: Nitroxide-mediated radical polymerization from CdSe nanoparticles, Chem. Mater. **16**, 1240–1243 (2004)

20.267 W.C.W. Chan, D.J. Maxwell, X. Gao, R.E. Bailey, M. Han, S. Nie: Luminescent quantum dots for multiplexed biological detection and imaging, Curr. Opin. Biotechnol. **13**, 40–46 (2002)

20.268 H. Noglik, W.J. Pietro: Surface functionalization of cadmium sulfide quantum confined semiconductor nanoclusters. 2. Formation of a "quantum dot" condensation polymer, Chem. Mater. **7**, 1333–1336 (1996)

20.269 L. Qu, Z.A. Peng, X. Peng: Alternative routes toward high quality CdSe nanocrystals, Nano Lett. **1**, 333–337 (2001)

20.270 X. Michalet, F.F. Pinaud, L.A. Bentolila, J.M. Tsay, S. Doose, J.J. Li, G. Sundaresan, A.M. Wu, S.S. Gambhir, S. Weiss: Quantum dots for live cells, in vivo imaging, and diagnostics, Science **307**, 538–544 (2005)

20.271 J.O. Winter, T.Y. Liu, B.A. Korgel, C.E. Schmidt: Recognition molecule directed interfacing between semiconductor quantum dots and nerve cells, Adv. Mater. **13**, 1673–1677 (2001)

20.272 H. Noglik, W.J. Pietro: Chemical functionalization of cadmium sulfide quantum-confined microclusters, Chem. Mater. **6**, 1593–1595 (1994)

20.273 U.K. Gautam, M. Rajamathi, F. Meldrum, P. Morgan, R. Seshadri: A solvothermal route to capped CdSe nanoparticles, Chem. Commun. **7**, 629 (2001)

20.274 X. Peng, J. Wickham, A.P. Alivisatos: Kinetics of II–VI and III–V colloidal semiconductor nanocrystal growth: "Focusing" of size distributions, J. Am. Chem. Soc. **120**, 5343–5344 (1998)

20.275 H. Skaff, M.F. Ilker, E.B. Coughlin, T. Emrick: Preparation of cadmium selenide-polyolefin composites from functional phosphine oxides and ruthenium-based metathesis, J. Am. Chem. Soc. **124**, 5729–5733 (2002)

20.276 Z.A. Peng, X. Peng: Formation of high-quality CdTe, CdSe, and CdS nanocrystals using Cd0 as precursor, J. Am. Chem. Soc. **123**, 183–184 (2001)

20.277 Y. Wang, Z. Tang, M.A. Correa-Duarte, I. Pastoriza-Santos, M. Giersig, N.A. Kotov, L.M. Liz-Marzán: Mechanism of strong luminescence photoactivation of citrate-stabilized water-soluble nanoparticles with CdSe cores, J. Phys. Chem. B **108**, 15461–15469 (2004)

20.278 W. Liu, H.S. Choi, J.P. Zimmer, E. Tanaka, J.V. Frangioni, M. Bawendi: Compact cysteine-coated CdSe(ZnCdS) quantum dots for in vivo applications, J. Am. Chem. Soc. **129**, 14530–14531 (2007)

20.279 W. Guo, J.J. Li, Y.A. Wang, X. Peng: Conjugation chemistry and bioapplications of semiconductor box nanocrystals prepared via dendrimer bridging, Chem. Mater. **15**, 3125–3133 (2003)

20.280 M. Han, X. Gao, J.Z. Su, S. Nie: Quantum-dot-tagged microbeads for multiplexed optical coding of biomolecules, Nat. Biotechnol. **193**, 631–635 (2001)

20.281 X. Gao, W.C.W. Chan, S. Nie: Quantum-dot nanocrystals for ultrasensitive biological labeling and multicolor optical encoding, J. Biomed. Opt. **7**, 532–537 (2002)

20.282 H. Skaff, T. Emrick: Reversible addition fragmentation chain transfer (RAFT) polymerization from unprotected cadmium selenide nanoparticles, Angew. Chem. Int. Ed. **43**, 5383–5386 (2004)

20.283 W.W. Yu, L. Qu, W. Guo, X. Peng: Experimental determination of the extinction coefficient of CdTe, CdSe and CdS nanocrystals, Chem. Mater. **15**, 2854–2860 (2003)

20.284 X. Wu, H. Liu, J. Liu, K.N. Haley, J.A. Treadway, J.P. Larson, N. Ge, F. Peale, M.P. Bruchez: Immunofluorescent labeling of cancer marker Her2 and other cellular targets with semiconductor quantum dots, Nat. Biotechnol. **21**, 41–46 (2003)

20.285 P.S. Eastman, W. Ruan, M. Doctolero, R. Nuttall, G.D. Feo, J.S. Park, J.S.F. Chu, P. Cooke, J.W. Gray, S. Li, F.F. Chen: Qdot nanobarcodes for multiplexed gene expression analysis, Nano Lett. **6**, 1059–1064 (2006)

20.286 D. Gerion, F. Pinaud, S.C. Williams, W.J. Parak, D. Zanchet, S. Weiss, A.P. Alivisatos: Synthesis and properties of biocompatible water-soluble silica-coated CdSe/ZnS semiconductor quantum dots, J. Phys. Chem. B **105**, 8861–8871 (2001)

20.287 S.T. Selvan, T.T. Tan, J.Y. Ying: Robust, non-cytotoxic, silica-coated CdSe quantum dots with efficient photoluminescence, Adv. Mater. **17**, 1620–1625 (2005)

20.288 I.L. Medintz, H.T. Uyeda, E.R. Goldman, H. Mattousi: Quantum dot bioconjugates for imaging, labelling and sensing, Nat. Mater. **4**, 435–446 (2005)

20.289 W.C.W. Chan, S. Nie: Quantum dot bioconjugates for ultrasensitive nonisotopic detection, Science **281**, 2016–2018 (1998)

20.290 J. Aldana, Y.A. Wang, X. Peng: Photochemical instability of CdSe nanocrystals coated by hydrophilic thiols, J. Am. Chem. Soc. **123**, 8844–8850 (2001)

20.291 W.W. Yu, Y.A. Wang, X. Peng: Formation and stability of size-, shape-, and structure-controlled CdTe nanocrystals: Ligand effects on monomers and nanocrystals, Chem. Mater. **15**, 4300–4308 (2003)

20.292 S.F. Wuister, I. Swart, F. van Driel, S.G. Hickey, C. de Mello Donega: Highly luminescent water-soluble CdTe quantum dots, Nano Lett. **3**, 503–507 (2003)

20.293 P.J. Thomas, P. Saravanan, G.U. Kulkarni, C.N.R. Rao: Arrays of magnetic nanoparticles capped with alkylamines, Pramana – J. Phys. **58**, 371–383 (2002)

20.294 T. Kida, T. Oka, M. Nagano: Synthesis and application of stable copper oxide nanoparticle suspensions for nanoparticulate film fabrication, J. Am. Ceram. Soc. **90**, 107–110 (2007)

20.295 M.-S. Liu, M.C.-C. Lin, I.-T. Huang, C.-C. Wang: Enhancement of thermal conductivity with Cu0 for nanofluids, Chem. Eng. Technol. **29**, 72–77 (2006)

20.296 H.T. Zhu, C.Y. Zhang, Y.M. Tang, J.X. Wang: Novel synthesis and thermal conductivity of Cu0 nanofluid, J. Phys. Chem. C **111**, 1646–1650 (2007)

20.297 C.-H. Lo, T.-T. Tsung, L.-C. Chen, C.-H. Su, H.-M. Lin: Fabrication of copper oxide nanofluid using submerged arc nanoparticle synthesis system (SANSS), J. Nanopart. Res. **7**, 313–320 (2005)

20.298 H. Chang, C.S. Jwo, C.H. Lo, T.T. Tsung, M.J. Kao, H.M. Lin: Rheology of Cu0 nanoparticle suspension prepared by ASNSS, Rev. Adv. Mater. Sci. **10**, 128–132 (2005)

20.299 C.-C. Lia, M.-H. Chang: Colloidal stability of CuO nanoparticles in alkanes via oleate modifications, Mater. Lett. **58**, 3903–3907 (2004)

20.300 Y. Ishihara, T. Hirai, C. Sakurai, T. Koyanagi, H. Nishida, M. Komatsu: Applications of the particle ordering technique for conductive antireflection films, Thin Solid Films **411**, 50–55 (2002)

20.301 K. Abe, Y. Sanada, T. Morimoto: Anti-reflective coatings for CRTs by sol-gel process, J. Sol-Gel Sci. Technol. **26**, 709–713 (2003)

20.302 A. Reindl, M. Mahajeri, J. Hanft, W. Peukert: The influence of dispersing and stabilizing of indium tin oxide nanoparticles upon the characteristic properties of thin films, Thin Solid Films **517**, 1624–1629 (2009)

20.303 R.A. Gilstrap Jr., C.J. Capozzi, C.G. Carson, R.A. Gerhardt, C.J. Summers: Synthesis of a nonagglomerated indium tin oxide nanoparticle dispersion, Adv. Mater. **20**, 4163–4166 (2008)

20.304 G. Bühler, D. Thölmann, C. Feldmann: One-pot synthesis of highly conductive indium tin oxide nanocrystals, Adv. Mater. **19**, 2224–2227 (2007)

20.305 R.A. Gilstrap Jr., C.J. Summers: Synthesis and analysis of an indium tin oxide nanoparticle dispersion, Thin Solid Films **518**, 1136–1139 (2009)

20.306 C. Goebbert, R. Nonninger, M.A. Aegerter, H. Schmidt: Wet chemical deposition of ATO and ITO coatings using crystalline nanoparticles redispersable in solutions, Thin Solid Films **351**, 79–84 (1999)

20.307 N. Al-Dahoudi, M.A. Aegerter: Comparative study of transparent conductive In_2O_3:Sn (ITO) coatings made using a sol and a nanoparticle suspension, Thin Solid Films **502**, 193–197 (2006)

20.308 J. Rockenberger, E.C. Scher, A.P. Alivisatos: A new nonhydrolytic single-precursor approach to surfactant-capped nanocrystals of transition metal oxides, J. Am. Chem. Soc. **121**, 11595–11596 (1999)

20.309 S.M. Gravano, R. Dumas, K. Liu, T.E. Patten: Methods for the surface functionalization of γ-Fe_2O_3 nanoparticles with initiators for atom transfer radical polymerization and the formation of core–shell inorganic–polymer structures, J. Polym. Chem. A **43**, 3675–3688 (2005)

20.310 S. Mornet, J. Portier, E. Duguet: A method for synthesis and functionalization of ultrasmall superparamagnetic covalent carriers based on maghemite and dextran, J. Magn. Magn. Mater. **293**, 127–134 (2005)

20.311 R. Massart: Preparation of aqueous magnetic liquids in alkaline and acidic media, IEEE Trans. Magn. **17**, 1247–1248 (1981)

20.312 C. Albornoz, S.E. Jacobo: Preparation of a biocompatible magnetic film from an aqueous ferrofluid, J. Magn. Magn. Mater. **305**, 12–15 (2006)

20.313 S.M. Hosseini, A. Fazlali, E. Ghasemi, H.A. Moghaddam, M. Salehi: Rheological properties of a γ-Fe_2O_3 paraffin-based ferrofluid, J. Magn. Magn. Mater. **322**, 3792–3796 (2010)

20.314 E.P. Wohlfarth: *Handbook of Magnetic Materials*, Vol. 2 (Rowe, Eastbourne 1980)

20.315 S.W. Charles, J. Popplewell: Properties and application of magnetic liquids, Endeavour **6**, 153–161 (1982)

20.316 K. Aurich, M. Schwalbe, J.H. Clement, W. Weitschies, N. Buske: Polyaspartate coated magnetite nanoparticles for biomedical applications, J. Magn. Magn. Mater. **311**, 1–5 (2007)

20.317 T.-H. Wang, W.-C. Lee: Immobilization of proteins on magnetic nanoparticles, Biotechnol. Bioprocess Eng. **8**, 263–267 (2003)

20.318 I. Hilger, R. Hergt, W.A. Kaiser: Use of magnetic nanoparticle heating in the treatment of breast cancer, Nanobiotechnology **152**, 33–39 (2005)

20.319 R. Asmatulu, M.A. Zalich, R.O. Claus, J.S. Riffle: Synthesis, characterization and targeting of biodegradable magnetic nanocomposite particles by external magnetic fields, J. Magn. Magn. Mater. **292**, 108–119 (2005)

20.320 S.I. Park, J.H. Kim, C.O. Kim: Preparation of photosensitizer-coated magnetic fluid for treatment of tumor, J. Magn. Magn. Mater. **272–276**, 2340–2342 (2004)

20.321 M. Kim, J. Jung, J. Lee, K. Na, S. Park, J. Hyun: Amphiphilic comblike polymers enhance the colloidal stability of Fe_3O_4 nanoparticles, Colloids Surf. B **76**, 236–240 (2010)

20.322 S.W. Charles: Alignment of biological assemblies using magnetic fluids – A review, J. Magn. Magn. Mater. **85**, 277–284 (1990)

20.323 M. Lauva, E. Auzans, V. Levickis, J. Plavins: Selective HGMS of colloidal magnetit-binding cells from whole blood, J. Magn. Magn. Mater. **85**, 295–298 (1990)

20.324 P. Pradhan, J. Giri, R. Banerjee, J. Bellare, D. Bahadur: Preparation and characterization of manganese ferrite-based magnetic liposomes for hyperthermia treatment of cancer, J. Magn. Magn. Mater. **311**, 208–215 (2007)

20.325 D. Patel, J.Y. Moon, Y. Chang, T.J. Kim, G.H. Lee: Poly(d,l-lactide-co-glycolide) coated superparamagnetic iron oxide nanoparticles: Synthesis, characterization and in vivo study as MRI contrast agent, Colloids Surf. A **313/314**, 91–94 (2008)

20.326 K. Raj, R. Moskowitz: Commercial applications of ferrofluids, J. Magn. Magn. Mater. **85**, 233–245 (1990)

20.327 Y.-W. Jun, Y.-M. Huh, J.-S. Choi, J.-H. Lee, H.-T. Song, S. Kim, S. Yoon, K.-S. Kim, J.-S. Shin, J.-S. Suh, J. Cheon: Nanoscale size effect of magnetic nanocrystals and their utilization for cancer diagnosis via magnetic resonance imaging, J. Am. Chem. Soc. **127**, 5732–5733 (2005)

20.328 D. Maity, D.C. Agrawal: Synthesis of iron oxide nanoparticles under oxidizing environment and

their stabilization in aqueous and non-aqueous media, J. Magn. Magn. Mater. **308**, 46–55 (2007)
20.329 T. Fujita, T. Miyazaki, H. Nishiyama, B. Jeyadevan: Preparation and properties of low boiling point of alcohol and acetone-based magnetic fluid, J. Magn. Magn. Mater. **201**, 14–17 (1999)
20.330 S. Sun, H. Zeng, D.B. Robinson, S. Raoux, P.M. Rice, S.X. Wang, G. Li: Monodisperse MFe_2O_4 (M = Fe, Co, Mn) nanoparticles, J. Am. Chem. Soc. **126**, 273–279 (2004)
20.331 F. Montagne, O. Mondain-Monval, C. Pichot, H. Mozzanega, A. Elaissari: Preparation and characterization of narrow sized (o/w) magnetic emulsion, J. Magn. Magn. Mater. **250**, 302–312 (2002)
20.332 A. Bocanegra-Diaz, N.D.S. Mohallem, M.A. Novak, R.D. Sinisterra: Preparation of ferrofluid from cyclodextrin and magnetite, J. Magn. Magn. Mater. **272–276**, 2395–2397 (2004)
20.333 S. Sun, H. Zeng: Size-controlled synthesis of magnetite nanoparticles, J. Am. Chem. Soc. **124**, 8204–8205 (2002)
20.334 S. Chen, L.A. Truax, J.M. Sommers: Alkanethiolate-protected PbS nanoclusters: Synthesis, spectroscopic and electrochemical studies, Chem. Mater. **12**, 3864–3870 (2000)
20.335 I.J. Bruce, J. Taylor, M. Todd, M.J. Davies, E. Borioni, C. Sangregorio, T. Sen: Synthesis, characterisation and application of silica-magnetite nanocomposites, J. Magn. Magn. Mater. **284**, 145–160 (2004)
20.336 X. Gao, K.M.K. Yu, K.Y. Tam, S.C. Tsang: Colloidal stable silica encapsulated nano-magnetic composite as a novel bio-catalyst carrier, Chem. Commun. **24**, 2998–2999 (2003)
20.337 J.-W. Seo, H. Chung, M.Y. Kim, J. Lee, I.-H. Choi, J. Cheon: Development of water-soluble single-crystalline TiO_2 nanoparticles for photocatalytic cancer-cell treatment, Small **3**, 850–853 (2007)
20.338 Q. Xue, W. Liu, Z. Zhang: Friction and wear properties of a surface-modified TiO_2 nanoparticle as an additive in liquid paraffin, Wear **213**, 29–32 (1997)
20.339 A. Fujishima, T.N. Rao, D.A. Tryk: Titanium dioxide photocatalysis, J. Photochem. Photobiol. C Photochem. Rev. **1**, 1–21 (2000)
20.340 X. Wu, D. Wang, S. Yang: Preparation and characterization of stearate-capped titanium dioxide nanoparticles, J. Colloid Interface Sci. **222**, 37–40 (2000)
20.341 Y. Zhu, J. Shi, Z. Zhang, C. Zhang, X. Zhang: Development of a gas sensor utilizing chemiluminescence on nanosized titanium dioxide, Anal. Chem. **74**, 120–124 (2002)
20.342 G. Fu, P.S. Vary, C.-T. Lin: Anatase TiO_2 nanocomposites for antimicrobial coatings, J. Phys. Chem. B **109**, 8889–8898 (2005)
20.343 S.-J. Kim, D.E. McKean: Aqueous TiO_2 suspension preparation and novel application of ink-jet printing technique for ceramics patterning, J. Mater. Sci. Lett. **17**, 141–144 (1998)
20.344 Y. Kubota, T. Shuin, C. Kawasaki, M. Hosaka, H. Kitamura, R. Cail, H. Sakai, K. Hashimoto, A. Fujishima: Photokilling of T-24 human bladder cancer cells with titanium dioxide, Br. J. Cancer **70**, 1107–1111 (1994)
20.345 G. Fu, B.J.M. Monk, R. McIntyre: Transparent, stable, titanium dioxide sols, Patent 7763565 (2010)
20.346 H.A. Capelle, L.G. Britcher, G.E. Morris: Sodium stearate adsorption onto titania pigment, J. Colloid Interface Sci. **268**, 293–300 (2003)
20.347 F.-T. Li, D.-S. Zhao, Q.-Z. Luo, R.-H. Liu, R. Yin: Research on surface-modification of nano-TiO_2 by span 60, J. Ceram. Proc. Res. **9**, 398–400 (2008)
20.348 R. Vaßen, Z. Yi, H. Kaßner, D. Stöver: Suspension plasma spraying of TiO_2 for the manufacture of photovoltaic cells, Surf. Coat. Technol. **203**, 2146–2149 (2009)
20.349 P.T. Dawson, D.A. Haydon: The stabilization of titanium dioxide in dry benzene by *n*-aliphatic carboxylic acids, Colloid Polym. Sci. **203**, 133–138 (1965)
20.350 E. Scolan, C. Sanchez: Synthesis and characterization of surface-protected nanocrystalline titania particles, Chem. Mater. **10**, 3217–3223 (1998)
20.351 A.-P. Zhang, Y.-P. Sun: Photocatalytic killing effect of TiO_2 nanoparticles on Ls-174-t human colon carcinoma cells, World J. Gastroenterol. **10**, 3191–3193 (2004)
20.352 C. Kormann, D.W. Bahnemann, M.R. Hoffmann: Preparation and characterization of quantum-size titanium dioxide, J. Phys. Chem. **92**, 5196–5201 (1988)
20.353 B. O'Regan, J. Moser, M. Anderson, M. Gratzel: Vectorial electron injection into transparent semiconductor membranes and electric field effects on the dynamics of light-induced charge separation, J. Phys. Chem. **94**, 8720–8726 (1990)
20.354 M. Tripathi, K. Pandey, S.D. Kumar: Surface modification of semiconductor photoelectrode for improved solar cell performance, Solar Energy Mater. Solar Cell. **91**, 1663–1668 (2007)
20.355 S. Han, S.-H. Choi, S.-S. Kim, M. Cho, B. Jang, D.-Y. Kim, J. Yoon, T. Hyeon: Low-temperature synthesis of highly crystalline TiO_2 nanocrystals and their application to photocatalysis, Small **1**, 812–816 (2005)
20.356 B. Zhou, S. Parasher, Z. Wu, Z. Zhou: Stabilized suspension of titanium dioxide nanoparticles and methods of manufacture, US Patent 18 (2008)
20.357 H. Takeda, K. Adachi: Near infrared absorption of tungsten oxide nanoparticle dispersions, J. Am. Ceram. Soc. **90**, 4059–4061 (2007)
20.358 M.T. Nenadovic, T. Rajh, O.I. Micic, A.J. Nozik: Electron transfer reactions and flat-band potentials of WO_3 colloids, J. Phys. Chem. **88**, 5827–5830 (1984)

20.359 E.K. Heidari, E. Marzbanrad, C. Zamani, B. Raissi: Nanocasting synthesis of ultrafine WO_3 nanoparticles for gas sensing applications, Nanoscale Res. Lett. **5**, 370–373 (2010)

20.360 P.K. Sahoo, S.S.K. Kamal, M. Premkumar, T.J. Kumar, B. Sreedhar, A.K. Singh, S.K. Srivastava, K.C. Sekhar: Synthesis of tungsten nanoparticles by solvothermal decomposition of tungsten hexacarbonyl, Int. J. Refract. Met. Hard Mater. **27**, 784–791 (2009)

20.361 A. Steele, I. Bayer, S. Moran, A. Cannon, W.P. King, E. Loth: Conformal ZnO nanocomposite coatings on micro-patterned surfaces for superhydrophobicity, Thin Solid Films **518**, 5426–5431 (2010)

20.362 Y.-S. Fu, X.-W. Du, S.A. Kulinich, J.-S. Qiu, W.-J. Qin, R. Li, J. Sun, J. Liu: Stable aqueous dispersion of ZnO quantum dots with strong blue emission via simple solution route, J. Am. Chem. Soc. **129**, 16029–16033 (2007)

20.363 R. Kho, C.L. Torres-Martinez, R.K. Mehra: A simple colloidal synthesis for gram-quantity production of water-soluble ZnS nanocrystal powders, J. Colloid Interface Sci. **227**, 561–566 (2000)

20.364 H.W. Jang, J. Kim, H.-T. Kim, Y. Yoon, S.-N. Lee, H. Hwang, J. Kim: Fabrication of nonsintered alumina–resin hybrid films by inkjet-printing technology, Jpn. J. Appl. Phys. **49**, 071501 (2010)

20.365 C.J. Ho, W.K. Liu, Y.S. Chang, C.C. Lin: Natural convection heat transfer of alumina-water nanofluid in vertical square enclosures: An experimental study, Int. J. Thermal Sci. **49**, 1345–1353 (2010)

20.366 M.P. Beck, T. Sun, A.S. Teja: The thermal conductivity of alumina nanoparticles dispersed in ethylene glycol, Fluid Phase Equilib. **260**, 275–278 (2007)

20.367 D. Zhu, X. Li, N. Wang, X. Wang, J. Gao, H. Li: Dispersion behavior and thermal conductivity characteristics of Al_2O_3–H_2O nanofluids, Curr. Appl. Phys. **9**, 131–139 (2009)

20.368 M.P. Beck, Y. Yuan, P. Warrier, A.S. Teja: The effect of particle size on the thermal conductivity of alumina nanofluids, J. Nanopart. Res. **11**, 1129–1136 (2009)

20.369 M.P. Beck, Y. Yuan, P. Warrier, A.S. Teja: The thermal conductivity of alumina nanofluids in water, ethylene glycol, and ethylene glycol + water mixtures, J. Nanopart. Res. **12**, 1469–1477 (2010)

20.370 E.V. Timofeeva, A.N. Gavrilov, J.M. McCloskey, Y.V. Tolmachev, S. Sprunt, L.M. Lopatina, J.V. Selinger: Thermal conductivity and particle agglomeration in alumina nanofluids: Experiment and theory, Phys. Rev. E **76**, 061203 (2007)

20.371 W.Y. Lai, P.E. Phelan, S. Vinod: Convective heat transfer for water-based alumina nanofluids in a single 1.02 mm tube, J. Heat Transf. **131**, 112401 (2009)

20.372 R. Hegde, S.S. Rao, R.P. Reddy: Critical heat flux enhancement in pool boiling using alumina nanofluids, Heat Transf. Asian Res. **39**, 323–331 (2010)

20.373 J.L. Bahr, J.M. Tour: Covalent chemistry of single-wall carbon nanotubes, J. Mater. Chem. **12**, 1952–1958 (2002)

20.374 S. Niyogi, M.A. Hamon, H. Hu, B. Zhao, P. Bhowmik, R. Sen, M.E. Itkis, R.C. Haddon: Chemistry of single-walled carbon nanotubes, Acc. Chem. Res. **35**, 1105–1113 (2002)

20.375 Y.-P. Sun, K. Fu, Y. Lin, W. Huang: Functionalized carbon nanotubes: Properties and applications, Acc. Chem. Res. **35**, 1096–1104 (2002)

20.376 S. Banerjee, T. Hemraj-Benny, S.S. Wong: Covalent surface chemistry of single-walled carbon nanotubes, Adv. Mater. **17**, 17–29 (2005)

20.377 D. Tasis, N. Tagmatarchis, A. Bianco, M. Prato: Chemistry of carbon nanotubes, Chem. Rev. **106**, 1105–1136 (2006)

20.378 R.J. Chen, Y. Zhang, D. Wang, H. Dai: Noncovalent sidewall functionalization of single-walled carbon nanotubes for protein immobilization, J. Am. Chem. Soc. **123**, 3838–3839 (2001)

20.379 A. Hirsch: Functionalization of single-walled carbon nanotubes, Angew. Chem. Int. Ed. **41**, 1853–1859 (2002)

20.380 P.M. Ajayan, L.S. Schadler, P.V. Braun: *Nanocomposite Science and Technology* (Wiley-VCH, Weinheim 2003)

20.381 P.M. Ajayan, J.M. Tour: Nanotube composites, Nature **447**, 1066–1068 (2007)

20.382 M. Zheng, A. Jagota, E.D. Semke, B.A. Diner, R.S. McLean, S.R. Lustig, R.E. Richardson, N.G. Tassi: DNA-assisted dispersion and separation of carbon nanotubes, Nat. Mater. **2**, 338–342 (2003)

20.383 A. Nish, J.-Y. Hwang, J. Doig, R.J. Nicholas: Highly selective dispersion of single walled carbon nanotubes using aromatic polymers, Nat. Nanotechnol. **2**, 640–646 (2007)

20.384 F. Hennrich, S. Lebedkin, M.M. Kappes: Improving separation techniques for single-walled carbon nanotubes: Towards monodisperse samples, Phys. Status Solidi (b) **245**, 1951–1953 (2008)

20.385 A. Vijayaraghavan, F. Hennrich, N. Sturzl, M. Engel, M. Ganzhorn, M. Oron-Carl, C.W. Marquardt, S. Dehm, S. Lebedkin, M.M. Kappes, R. Krupke: Toward single-chirality carbon nanotube device arrays, ACS Nano **4**, 2748–2754 (2010)

20.386 R.G. Alargova, S. Deguchi, K. Tsujii: Stable colloidal dispersions of fullerenes in polar organic solvents, J. Am. Chem. Soc. **123**, 10460–10467 (2001)

20.387 M.V. Korobov, A.L. Mirakyan, N.V. Avramenko, G. Olofsson, A.L. Smith, R.S. Ruoff: Calorimetric studies of solvates of C_{60} and C_{70} with aromatic solvents, J. Phys. Chem. B **103**, 1339–1346 (1999)

20.388 G.V. Andrievsky, M.V. Kosevich, O.M. Vovk, V.S. Shelkovsky, L.A. Vashchenko: On the production of an aqueous colloidal solution of fullerenes, J. Chem. Soc. Chem. Commun. **12**, 1281–1282 (1995)

20.389 S. Deguchi, R.G. Alargova, K. Tsujii: Stable dispersions of fullerenes, C_{60} and C_{70}, in water. Preparation and characterization, Langmuir **17**, 6013–6017 (2001)

20.390 T. Anderson, K. Nilsson, M. Sundahl, G. Westman, O. Wennerstrom: C_{60} embedded in γ-cyclodextrin: A water-soluble fullerene, J. Chem. Soc. Chem. Commun. **8**, 604–606 (1992)

20.391 P.V. Kamat, S. Barazzouk, K.G. Thomas, S. Hotchandani: Electrodeposition of C_{60} cluster aggregates on nanostructured SnO_2 films for enhanced photocurrent generation, J. Phys. Chem. B **104**, 4014–4017 (2000)

20.392 J.D. Fortner, D.Y. Lyon, C.M. Sayes, A.M. Boyd, J.C. Falkner, E.M. Hotze, L.B. Alemany, Y.J. Tao, W. Guo, K.D. Ausman, V.L. Colvin, J.B. Hughes: C_{60} in water: Nanocrystal formation and microbial response, Environ. Sci. Technol. **39**, 4307–4316 (2005)

20.393 L.L. Dugan, D.M. Turetsky, C. Du, D. Lobner, M. Wheeler, C.R. Almli, C.K.-F. Shen, T.-Y. Luh, D.W. Choi, T.-S. Lin: Carboxyfullerenes as neuroprotective agents, Proc. Natl. Acad. Sci. USA **94**, 9434–9439 (1997)

20.394 I.C. Wang, L.A. Tai, D.D. Lee, P.P. Kanakamma, C.K.-F. Shen, T.-Y. Luh, C.H. Cheng, K.C. Hwang: C_{60} and water-soluble fullerene derivatives as antioxidants against radical-initiated lipid peroxidation, J. Med. Chem. **42**, 4614–4620 (1999)

20.395 R.D. Bolskar, A.F. Benedetto, L.O. Husebo, R.E. Price, E.F. Jackson, S. Wallace, L.J. Wilson, J.M. Alford: First soluble M@C_{60} derivatives provide enhanced access to metallofullerenes and permit in vivo evaluation of Gd@$C_{60}[C(COOH)_2]_{10}$ as a MRI contrast agent, J. Am. Chem. Soc. **125**, 5471–5478 (2003)

20.396 K. Kniaz, J.E. Fischer, H. Selig, G.B.M. Vaughan, W.J. Romanow, D.M. Cox, S.K. Chowdhury, J.P. McCauley, R.M. Strongin, A.B. Smith III: Fluorinated fullerenes: Synthesis, structure, and properties, J. Am. Chem. Soc. **115**, 6060–6064 (1993)

20.397 J.-F. Nierengarten: Chemical modification of C_{60} for materials science applications, New J. Chem. **28**, 1177–1191 (2004)

20.398 J.Y. Kim, K. Lee, N.E. Coates, D. Moses, T.-Q. Nguyen, M. Dante, A.J. Heeger: Efficient tandem polymer solar cells fabricated by all-solution processing, Science **317**, 222–225 (2007)

20.399 S. Lee, S. Nam, H. Kim, Y. Kim: Organic solar cells with submicron-thick polymer:fullerene bulk heterojunction films, Appl. Phys. Lett. **97**, 103503 (2010)

20.400 S.H. Park, A. Roy, S. Beaupre, S. Cho, N. Coates, J.S. Moon, D. Moses, M. Leclerc, K. Lee, A.J. Heeger: Bulk heterojunction solar cells with internal quantum efficiency approaching 100%, Nat. Photonics **3**, 297–303 (2009)

20.401 S.D. Bergin, Z. Sun, P. Streich, J. Hamilton, J.N. Coleman: New solvents for nanotubes: Approaching the dispersibility of surfactants, J. Phys. Chem. C **114**, 231–237 (2010)

20.402 S. Giordani, S.D. Bergin, V. Nicolosi, S. Lebedkin, M.M. Kappes, W.J. Blau, J.N. Coleman: Debundling of single-walled nanotubes by dilution: Observation of large populations of individual nanotubes in amide solvent dispersions, J. Phys. Chem. B **110**, 15708 (2006)

20.403 T.V. Sreekumar, T. Liu, B.G. Min, H. Guo, S. Kumar, R.H. Hauge, R.E. Smalley: Polyacrylonitrile single-walled carbon nanotube composite fibers, Adv. Mater. **16**, 58–61 (2004)

20.404 K.D. Ausman, R. Piner, O. Lourie, R.S. Ruoff, M. Korobov: Organic solvent dispersions of single-walled carbon nanotubes: Toward solutions of pristine nanotubes, J. Phys. Chem. B **104**, 8911–8915 (2000)

20.405 P. Beecher, P. Servati, A. Rozhin, A. Colli, V. Scardaci, S. Pisana, T. Hasan, A.J. Flewitt, F.M. Li, A. Nathan, A.C. Ferrari, W.I. Milne: Ink-jet printing of carbon nanotube thin film transistors, J. Appl. Phys. **102**, 043710 (2007)

20.406 J. Sandler, M.S.P. Shaffer, T. Prasse, W. Bauhofer, K. Schulte, A.H. Windle: Development of a dispersion process for carbon nanotubes in an epoxy matrix and the resulting electrical properties, Polymer **40**, 5967–5971 (1999)

20.407 R. Bandyopadhyaya, E. Nativ-Roth, O. Regev, R. Yerushalmi-Rozen: Stabilization of individual carbon nanotubes in aqueous solutions, Nano Lett. **2**, 25–28 (2002)

20.408 M.J. O'Connell, P. Boul, L.M. Ericson, C. Huffman, Y. Wang, E. Haroz, C. Kuper, J. Tour, K.D. Ausman, R.E. Smalley: Reversible water-solubilization of single-walled carbon nanotubes by polymer wrapping, Chem. Phys. Lett. **342**, 265–271 (2001)

20.409 M.F. Islam, E. Rojas, D.M. Bergey, A.T. Johnson, A.G. Yodh: High weight fraction surfactant solubilization of single-wall carbon nanotubes in water, Nano Lett. **3**, 269–273 (2003)

20.410 P. Chen, H. Chen, J. Qiu, C. Zhou: Inkjet printing of single-walled carbon nanotube/RuO_2 nanowire supercapacitors on cloth fabrics and flexible substrates, Nano Res. **3**, 594–603 (2010)

20.411 J. Chen, M.A. Hamon, H. Hu, Y. Chen, A.M. Rao, P.C. Eklund, R.C. Haddon: Solution properties of single-walled carbon nanotubes, Science **282**, 95–98 (1998)

20.412 F.H. Gojny, M.H.G. Wichmann, U. Köpke, B. Fiedler, K. Schulte: Carbon nanotube-reinforced epoxy-composites: Enhanced, stiffness and fracture toughness at low nanotube content, Compos. Sci. Technol. **64**, 2363–2371 (2004)

20.413 T.J. Simmons, J. Bult, D.P. Hashim, R.J. Linhardt, P.M. Ajayan: Noncovalent functionalization as an alternative to oxidative acid treatment of single wall carbon nanotubes with applications for polymer composites, ACS Nano **3**, 865–870 (2009)

20.414 K. Kordás, T. Mustonen, G. Tóth, H. Jantunen, M. Lajunen, C. Soldano, R. Vajtai, P.M. Ajayan: Inkjet printing of electrically conductive patterns of carbon nanotubes, Small **2**, 1021–1025 (2006)

20.415 K. Kordás, T. Mustonen, G. Tóth, J. Vähäkangas, A. Uusimäki, H. Jantunen, A. Gupta, K.V. Rao, R. Vajtai, P.M. Ajayan: Magnetic-field induced efficient alignment of carbon nanotubes in aqueous solutions, Chem. Mater. **19**, 787–791 (2007)

20.416 J. Mäklin, T. Mustonen, K. Kordás, G. Tóth, S. Saukko, J. Vähäkangas: Nitric oxide gas sensors with functionalized carbon nanotubes, Phys. Status Solidi (b) **244**, 4298 (2007)

20.417 T. Mustonen, J. Mäklin, K. Kordás, N. Halonen, G. Tóth, J. Vähäkangas, H. Jantunen, S. Kar, P.M. Ajayan, R. Vajtai, P. Helistö, H. Seppä: Controlled Ohmic and nonlinear electrical transport in inkjet printed single-wall carbon nanotube films, Phys. Rev. B **77**, 125430 (2008)

20.418 J. Kukkola, A. Rautio, G. Sala, F. Pino, G. Tóth, A.-R. Leino, J. Mäklin, H. Jantunen, A. Uusimäki, K. Kordás, E. Gracia, M. Terrones, A. Shchukarev, J.-P. Mikkola: Electrical transport through single-wall carbon nanotube–anodic aluminum oxide–aluminum heterostructures, Nanotechnology **21**, 035707 (2010)

20.419 E. Gracia-Espino, G. Sala, F. Pino, N. Halonen, J. Luomahaara, J. Mäklin, G. Tóth, K. Kordás, H. Jantunen, M. Terrones, P. Helistö, H. Seppä, P.M. Ajayan, R. Vajtai: Electrical transport and field effect transistors using inkjet printed SWCNTs films having different functional side groups, ACS Nano **4**, 3318 (2010)

20.420 Z. Fan, T. Wei, G. Luo, F. Wei: Fabrication and characterization of multi-walled carbon nanotubes-based ink, J. Mater. Sci. **40**, 5075–5077 (2005)

20.421 T. Ramanathan, A.A. Abdala, S. Stankovich, D.A. Dikin, M. Herrera-Alonso, R.D. Piner, D.H. Adamson, H.C. Schniepp, X. Chen, R.S. Ruoff, S.T. Nguyen, I.A. Aksay, R.K. Proud'homme, L.C. Brinson: Functionalized graphene sheets for polymer nanocomposites, Nat. Nanotechnol. **3**, 327–331 (2008)

20.422 Y. Wu, B. Wang, Y. Ma, Y. Huang, N. Li, F. Zhang, Y. Chen: Efficient and large-scale synthesis of few-layered graphene using an arc-discharge method and conductivity studies of the resulting films, Nano Res. **3**, 661–669 (2010)

20.423 A.A. Green, M.C. Hersam: Solution phase production of graphene with controlled thickness via density differentiation, Nano Lett. **9**, 4031–4036 (2009)

20.424 J. Wu, H.A. Becerril, Z. Bao, Z. Liu, Y. Chen, P. Peumans: Organic solar cells with solution-processed graphene transparent electrodes, Appl. Phys. Lett. **92**, 263302 (2008)

20.425 T. Szabó, A. Szeri, I. Dékány: Composite graphitic nanolayers prepared by self-assembly between finely dispersed graphite oxide and a cationic polymer, Carbon **43**, 87–94 (2005)

20.426 D. Li, M.B. Muller, S. Gilje, R.B. Kaner, G.G. Wallace: Processable aqueous dispersions of graphene nanosheets, Nat. Nanotechnol. **3**, 101–105 (2008)

20.427 G. Eda, G. Fanchini, M. Chhowalla: Large-area ultrathin films of reduced graphene oxide as a transparent and flexible electronic material, Nat. Nanotechnol. **3**, 270–274 (2008)

20.428 V.C. Tung, M.J. Allen, Y. Yang, R.B. Kaner: High-throughput solution processing of large-scale graphene, Nat. Nanotechnol. **4**, 25–29 (2009)

20.429 S. Stankovich, D.A. Dikin, G.H.B. Dommett, K.M. Kohlhaas, E.J. Zimney, E.A. Stach, R.D. Piner, S.T. Nguyen, R.S. Ruoff: Graphene-based composite materials, Nature **442**, 282–286 (2006)

20.430 F. Li, Y. Bao, J. Chai, Q. Zhang, D. Han, L. Niu: Synthesis and application of widely soluble graphene sheets, Langmuir **26**, 12314–12320 (2010)

20.431 C. Zhang, L. Ren, X. Wang, T. Liu: Graphene oxide-assisted dispersion of pristine multiwalled carbon nanotubes in aqueous media, J. Phys. Chem. C **114**, 11435–11440 (2010)

20.432 J.I. Paredes, S. Villar-Rodil, A. Martínez-Alonso, J.M.D. Tascón: Graphene oxide dispersions in organic solvents, Langmuir **24**(19), 10560–10564 (2008)

20.433 R.D. Deegan, O. Bakajin, T.F. Dupont, G. Huber, S.R. Nagel, T.A. Witten: Capillary flow as the cause of ring stains from dried liquid drops, Nature **389**, 827–829 (1997)

20.434 P.W. Atkins: *Physical Chemistry* (Oxford Univ. Press, Oxford 2006)

20.435 R. Bhardwaj, X. Fang, P. Somasundaran, D. Attinger: Self-assembly of colloidal particles from evaporating droplets: Role of DLVO interactions and proposition of a phase diagram, Langmuir **26**, 7833–7842 (2010)

20.436 P.J. Jaijus, A. Singh: Flow visualization and solute transport in evaporating droplets, AIChE J. **56**, 1674–1683 (2010)

20.437 W.R. Small, C.D. Walton, J. Loos, M. in het Panhuis: Carbon nanotube network formation from evaporating sessile drops, J. Phys. Chem. B **110**, 13029–13036 (2006)

20.438 X. Shen, C.-M. Ho, T.-S. Wong: Minimal size of coffee ring structure, J. Phys. Chem. B **114**, 5269–5274 (2010)

20.439 J. Park, J. Moon: Control of colloidal particle deposit patterns within picoliter droplets ejected by ink-jet printing, Langmuir **22**, 3506–3513 (2006)

20.440 K. Lee, M. Duchamp, G. Kulik, A. Magrez, J.W. Seo, S. Jeney, A.J. Kulik, L. Forró, R.S. Sundaram, J. Brugger: Uniformly dispersed deposition of colloidal nanoparticles and nanowires by boiling, Appl. Phys. Lett. **91**, 173112 (2007)

20.441 D. Soltman, V. Subramanian: Inkjet-printed line morphologies and temperature control of the coffee ring effect, Langmuir **24**, 2224–2231 (2008)

20.442 J. Perelaer, C.E. Hendriks, A.W.M. de Laat, U.S. Schubert: One-step inkjet printing of conductive silver tracks on polymer substrates, Nanotechnology **20**, 165303 (2009)

20.443 E. Tekin, P.J. Smith, U.S. Schubert: Inkjet printing as a deposition and patterning tool for polymers and inorganic particles, Soft Matter **4**, 703–713 (2008)

20.444 D. Kim, Y. Jeong, K. Song, S.-K. Park, G. Cao, J. Moon: Inkjet-printed zinc tin oxide thin-film transistor, Langmuir **25**, 11149–11154 (2009)

20.445 D.J. Harris, J.A. Lewis: Marangoni effects on evaporative lithographic patterning of colloidal films, Langmuir **24**, 3681–3685 (2008)

20.446 L. Chen, J.R.G. Evans: Arched structures created by colloidal droplets as they dry, Langmuir **25**, 11299–11301 (2009)

20.447 A. Kamyshny, M. Ben-Moshe, S. Aviezer, S. Magdassi: Ink-jet printing of metallic, nanoparticles and microemulsions, Macromol. Rapid Commun. **26**, 281–288 (2005)

20.448 J. Perelaer, P.J. Smith, C.E. Hendriks, A.M.J. van den Berg, U.S. Schubert: The preferential deposition of silica microparticles at the boundary of inkjet printed droplets, Soft Matter **4**, 1072–1078 (2008)

20.449 Y. Wu: *Functional Metal Oxide Materials deposited by Inkjet Printing Technique*, Dissertation (The Royal Institute of Technology, Stockholm 2010)

20.450 Y. Wu, T. Tamaki, W. Voit, L. Belova, K.V. Rao: Ultraviolet photoconductivity of pure and Al doped ZnO thin films by inkjet printing, Mater. Res. Soc. Symp. Proc. **1161**, 103–122 (2009)

20.451 H. Haverinen: *Inkjet-Printed Quantum Dot Hybrid Light-Emitting Devices – Towards Display Applications*, Dissertation (University of Oulu, Oulu 2009), Acta Universitatis Ouluensis C 351

20.452 M. Singh, H.M. Haverinen, P. Dhagat, G.E. Jabbour: Inkjet-printing – Process and its applications, Adv. Mater. **21**, 1–13 (2009)

20.453 H.M. Haverinen, R.A. Myllylä, G.E. Jabbour: Inkjet printing of light emitting quantum dots, Appl. Phys. Lett. **94**, 073108 (2009)

20.454 T. Ming, X. Kou, H. Chen, T. Wang, H.-L. Tam, K.-W. Cheah, J.-W. Chen, J. Wang: Ordered gold nanostructure assemblies formed by droplet evaporation, Angew. Chem. Int. Ed. **47**, 9685–9690 (2008)

20.455 S. Zhang, Q. Li, I.A. Kinloch, A.H. Windle: Ordering in a droplet of an aqueous suspension of single-wall carbon nanotubes on a solid substrate, Langmuir **26**, 2107–2112 (2010)

20.456 S. Magdassi, M. Grouchko, D. Toker, A. Kamyshny, I. Balberg, O. Millo: Ring stain effect at room temperature in silver nanoparticles yields high electrical conductivity, Langmuir **21**, 10264–10267 (2005)

20.457 M. Layani, M. Gruchko, O. Milo, I. Balberg, D. Azulay, S. Magdassi: Transparent conductive coatings by printing coffee ring arrays obtained at room temperature, ACS Nano **3**, 3537–3542 (2009)

20.458 T. Minami: Transparent conducting oxide semiconductors for transparent electrodes, Semicond. Sci. Technol. **20**, S35–S44 (2005)

20.459 M. Kaempgen, G.S. Duesberg, S. Roth: Transparent carbon nanotube coatings, Appl. Surf. Sci. **252**, 425–429 (2005)

20.460 B. Dan, G.C. Irvin, M. Pasquali: Continuous and scalable, fabrication of transparent conducting carbon nanotube films, ACS Nano **3**, 835–843 (2009)

20.461 H.A. Becerril, J. Mao, Z. Liu, R.M. Stoltenberg, Z. Bao, Y. Chen: Evaluation of solution-processed reduced graphene oxide films as transparent conductors, ACS Nano **2**, 463–470 (2008)

20.462 J.B. Wu, M. Agrawal, H.A. Becerril, Z.N. Bao, Z.F. Liu, Y.S. Chen, P. Peumans: Organic light-emitting diodes on solution-processed graphene transparent electrodes, ACS Nano **4**, 43–48 (2009)

20.463 D. Bonn, J. Eggers, J. Indekeu, J. Meunier, E. Rolley: Wetting and spreading, Rev. Mod. Phys. **81**, 739–805 (2009)

20.464 H. Bodiguel, F. Doumenc, B. Guerrier: Pattern formation during the drying of a colloidal suspension, Eur. Phys. J. Special Top. **166**, 29–32 (2009)

20.465 J.R. Moffat, K. Sefiane, M.E.R. Shanahan: Effect of TiO_2 nanoparticles on contact-line stick-slip behavior of volatile drops, J. Phys. Chem. B **113**, 8860–8866 (2009)

20.466 J. Huang, R. Fan, S. Connor, P. Yang: One-step patterning of aligned nanowires arrays by programmed dip coating, Angew. Chem. Int. Ed. **46**, 2414–2417 (2007)

20.467 M. Engel, J.P. Small, M. Steiner, M. Freitag, A.A. Green, M.C. Hersam, P. Avouris: Thin film nanotube transistors based on self-assembled, aligned, semiconducting carbon nanotube, ACS Nano **2**, 2445–2452 (2008)

20.468 T.P. Bigioni, X.-M. Lin, T.T. Nguyen, E.I. Corwin, T.A. Witten, H.M. Jaeger: Kinetically driven self assembly of highly ordered nanoparticle monolayers, Nat. Mater. **5**, 265–270 (2006)

20.469 M. Grzelczak, J. Vermant, E.M. Furst, L.M. Liz-Marzán: Directed Self-assembly of nanoparticles, ACS Nano **4**, 3591–3605 (2010)

20.470 C.P. Collier, T. Vossmeyer, J.R. Heath: Nanocrystal superlattices, Ann. Rev. Phys. Chem. **49**, 371–404 (1998)

20.471 L. Motte, F. Billoudet, E. Lacaze, J. Douin, M.P. Pileni: Self-organization into 2D and 3D superlattices of nanosized particles differing by their size, J. Phys. Chem. B **101**, 138–144 (1997)

20.472 H. Weller: Synthesis and self-assembly of colloidal nanoparticles, Philos. Trans. R. Soc. **361**, 229–240 (2003)

20.473 C.B. Murray, C.R. Kagan, M.G. Bawendi: Self-organisation of CdSe nanocrystallites into 3-dimensional quantum dot superlattices, Science **270**, 1335–1338 (1995)

20.474 R.L. Whetten, J.T. Khoury, M.M. Alvarez, S. Murthy, I. Vezmar, Z.L. Wang, P.W. Stephens, C.L. Cleveland, W.D. Luedtke, U. Landman: Nanocrystal gold molecules, Adv. Mater. **8**, 428–433 (1996)

20.475 M.D. Bentzon, J. van Wonterghem, S. Morup, A. Thölén, C.J.W. Koch: Ordered aggregates of ultrafine iron oxide particles: 'Super crystals', Philos. Mag. B **60**, 169–178 (1989)

20.476 A. Taleb, C. Petit, M.P. Pileni: Optical properties of self-assembled 2D and 3D superlattices of silver nanoparticles, J. Phys. Chem. B **102**, 2214–2220 (1998)

20.477 A.R. Tao, D.P. Ceperley, P. Sinsermsuksakul, A.R. Neureuther, P. Yang: Self-organized silver nanoparticles for three-dimensional plasmonic crystals, Nano Lett. **8**, 4033–4038 (2008)

20.478 J. Song, H. Sun, Y. Xu, Y. Fu, S. Matsuo, H. Misawa, G. Du: Three-dimensional photonic crystal structures achieved with self-organization of colloidal particles, Opt. Quantum Electron. **32**, 1295–1300 (2000)

20.479 Y. Xia, B. Gates, Y. Yin, Y. Lu: Monodispersed colloidal spheres: Old materials with new applications, Adv. Mater. **12**, 693–713 (2000)

20.480 S.M. Yang, H. Míguez, G.A. Ozin: Opal circuits of light – Planarized microphotonic crystal chips, Adv. Funct. Mater. **12**, 425–431 (2002)

20.481 G. Yang, L. Tan, Y. Yang, S. Chen, G.-Y. Liu: Single electron tunneling and manipulation of nanoparticles on surfaces at room temperature, Surf. Sci. **589**, 129–138 (2005)

20.482 A.N. Shipway, E. Katz, I. Willner: Nanoparticle arrays on surfaces for electronic, optical and sensor applications, Chem. Phys. Chem. **1**, 18–52 (2000)

20.483 A. Mathur, A.-D. Brown, J. Erlebacher: Self-ordering of colloidal particles in shallow nanoscale surface corrugations, Langmuir **22**, 582–589 (2006)

20.484 S. Choi, S. Stassi, A.P. Pisano, T.I. Zohdi: Coffee-ring effect-based three dimensional patterning of micro/nanoparticle assembly with a single droplet, Langmuir **26**, 11690–11698 (2010)

20.485 Y. Yin, Y. Lu, B. Gates, Y. Xia: Template-assisted self-assembly: A practical route to complex aggregates of monodispersed colloids with well-defined sizes, shapes and structures, J. Am. Chem. Soc. **123**, 8718–8729 (2001)

20.486 R.K. Golding, P.C. Lewis, E. Kumacheva: In situ study of colloid crystallization in constrained geometry, Langmuir **20**, 1414–1419 (2004)

20.487 G. Su, Q. Guo, R.E. Palmer: Colloidal lines and strings, Langmuir **19**, 9669–9671 (2003)

20.488 D.K. Yi, E.-M. Seo, D.-Y. Kim: Surface-modulation-controlled three-dimensional colloidal crystals, Appl. Phys. Lett. **80**, 225–227 (2002)

20.489 J. Tien, A. Terfort, G.M. Whitesides: Microfabrication through electrostatic self-assembly, Langmuir **13**, 5349–5355 (1997)

20.490 K.M. Chen, X. Jiang, L.C. Kimerling, P.T. Hammond: Selective self-organization of colloids on patterned polyelectrolyte templates, Langmuir **16**, 7825–7834 (2000)

20.491 C.J. Kiely, J. Fink, M. Brust, D. Bethell, D.J. Schiffrin: Spontaneous ordering of bimodal ensembles of nanoscopic gold clusters, Nature **396**, 444–446 (1998)

20.492 F.X. Redl, K.-S. Cho, C.B. Murray, S. O'Brien: Three-dimensional binary superlattices of magnetic nanocrystals and semiconductor quantum dots, Nature **423**, 968–971 (2003)

20.493 E.V. Shevchenko, D.V. Talapin, N.A. Kotov, S. O'Brien, C.B. Murray: Structural diversity in binary nanoparticle superlattices, Nature **439**, 55–59 (2006)

20.494 K. Overgaag, W. Evers, B. de Nijs, R. Koole, J. Meeldijk, D. Vanmaekelbergh: Binary superlattices of PbSe and CdSe nanocrystals, J. Am. Chem. Soc. **130**, 7833–7835 (2008)

20.495 T. Mustonen: *Inkjet Printing of Carbon Nanotubes for Electronic Applications*, Dissertation (University of Oulu, Oulu 2009)

20.496 Y.-Y. Noh, N. Zhao, M. Caironi, H. Sirringhaus: Downscaling of self-aligned, all-printed polymer thin-film transistors, Nat. Nanotechnol. **2**, 784–789 (2007)

20.497 J. Perelaer, M. Klokkenburg, C.E. Hendriks, U.S. Schubert: Microwave flash sintering of inkjet-printed silver tracks on polymer substrates, Adv. Mater. **21**, 4830–4834 (2009)

20.498 J. Perelaer, B.-J. de Gans, U.S. Schubert: Ink-jet printing and microwave sintering of conductive silver tracks, Adv. Mater. **18**, 2101–2104 (2006)

20.499 T.H.J. van Osch, J. Perelaer, A.W.M. de Laat, U.S. Schubert: Inkjet printing of narrow conductive tracks on untreated polymeric substrates, Adv. Mater. **20**, 343–345 (2008)

20.500 H. Sirringhaus, T. Kawase, R.H. Friend, T. Shimoda, M. Inbasekaran, W. Wu, E.P. Woo: High-resolution inkjet printing of all-polymer transistor circuits, Science **290**, 2123–2126 (2000)

20.501 N. Zhao, M. Chiesa, H. Sirringhaus, Y. Li, Y. Wu, B. Ong: Self-aligned inkjet printing of highly conducting gold electrodes with submicron resolution, J. Appl. Phys. **101**, 064513 (2007)

Nanopore

Part E

Part E Nanoporous Materials

21 Nanoporous Metals
Yi Ding, Jinan, China
Zhonghua Zhang, Shandong, China

22 Zeolites
István Pálinkó, Szeged, Hungary
Zoltán Kónya, Szeged, Hungary
Ákos Kukovecz, Szeged, Hungary
Imre Kiricsi

23 Porous Anodic Aluminum Oxide
Qiaoling Xu, Anhui, China
Guowen Meng, Hefei, China

24 Porous Silicon
Paolo Bettotti, Povo, Italy

21. Nanoporous Metals

Yi Ding, Zhonghua Zhang

In this chapter, we mainly describe the fabrication, properties, and potential applications of nanoporous metals (NPMs) with random porous structure. Nanoporous metals represent an interesting type of nanostructured material with nanosized porosity and ultrahigh specific surface area, and thus possess unique mechanical, physical, and chemical properties associated with their nanoporous structure. Based upon the porosity distribution, nanoporous metals can be classified into two categories: one has a random porous structure, and the other has a regular pore distribution. Nanoporous metals with random porous structure can be synthesized by the dealloying strategy, whereas template methods are normally used to fabricate nanoporous metals with more regular pore distribution. Nanoporous metals date back to the days of Raney (1920s) when high specific surface metal catalysts were prepared by dealloying Al-based alloys in alkaline solutions. In the new century, monolithic nanoporous metals received renewed attention due to the observation of a series of very intriguing structural properties. Nanoporous metals made by dealloying exhibit a three-dimensional bicontinuous interpenetrating ligament (metal)–channel (void) structure with a length scale of several nanometers to hundreds of nanometers, and the characteristic size can be modulated to as large as several microns by treatments such as thermal annealing. In contrast, the template technique can precisely control the pore size and microstructure of nanoporous metals, but dynamic modulation of the dominant length scale is virtually impossible. In addition, nanoporous metals are different from metallic foams, which have a length scale of several microns to more than 1 cm, and are normally used as damping and acoustic materials. Here, we mainly focus on dealloyed nanoporous metals. Firstly, the dealloying method and formation mechanism of nanoporous metals are reviewed based upon previous experimental observations and computer simulation. Secondly, we summarize recent knowledge on microstructures of nanoporous metals and their unique properties (catalytic, electrocatalytic, mechanical, sensing, optical, etc.). Finally, potential applications of nanoporous metals are discussed in the fields of fuel cells, catalysis, sensors, actuators, etc.

21.1 **Preparation of Nanoporous Metals** 779
21.1.1 Alloy Design of Precursors Suitable for Dealloying 780
21.1.2 Formation Mechanisms of Nanoporous Metals by Dealloying 781
21.1.3 Control over Structures of Nanoporous Metals 784
21.2 **Properties of Nanoporous Metals** 789
21.2.1 Structure and Morphology 789
21.2.2 Catalytic Properties 794
21.2.3 Electrocatalytic Properties 796
21.2.4 Mechanical Properties 799
21.2.5 Optical Properties 802
21.2.6 Sensing and Actuation Properties 805
21.2.7 Electrical, Thermal, and Magnetic Properties 807
21.3 **Applications** 808
21.4 **Concluding Remarks and Prospects** 810
References 811

21.1 Preparation of Nanoporous Metals

Many routes have been reported to prepare nanoporous metals, including transmetallation (galvanic replacement) reaction [21.1–3], the combination of block-copolymer template with deposition [21.4], chem-

ical reduction of metal ions [21.5, 6], hydrothermal synthesis method [21.7–11], ballistic deposition [21.12], powder metallurgy [21.13], filter casting [21.14], potential-controlled anodization [21.15, 16], electroplating [21.17], electrodeposition [21.18–20], potential-controlled displacement [21.21], surfactant emulsion template [21.22], catalytic chemical deposition method [21.23], one-step square-wave potential pulse treatment [21.24], inkjet printing–sintering technique [21.25], template-printing method [21.26], and wet-chemical strategy [21.27]. However, the dealloying strategy is at present the most popular method to prepare nanoporous metals with random porous structure. Dealloying refers to selective dissolution of one or more components out of an alloy. In fact, dealloying is an ancient process and has a long history. Indians of pre-Columbian Central America had invented such a technique (also named depletion gilding) for coloration of castings prepared from copper–gold alloys. A very closely related process for coloration of silver–gold alloys, known as cementation, is known to have been used by European and Near Eastern goldsmiths before the early Middle Ages [21.28]. At that time, however, people did not know about the formation of nanoporous structures during the dealloying or depletion gilding process.

Historically, dealloying has received significant attention in the context of corrosion, including stress corrosion cracking (SCC) and corrosion fatigue, such as dezincification of brass [21.29–40]; for example, dealloying was found to be a common feature of both intergranular and transgranular cracking during stress corrosion of Cu-Zn and Cu-Zn-Ni alloys [21.29]. Raney catalysts, named after their inventor Murray Raney, were well known throughout most of the last century [21.41]. They are formed by selective dissolution (usually by alkali) of an active metal (usually aluminum) from an alloy, leaving a noble metal residue which is an active hydrogenation catalyst [21.42]. Recently, dealloying has received renewed attention due to the fact that certain systems exhibit nanoporosity evolution upon dealloying. As early as the 1960s, *Pickering* and *Swann* [21.43, 44] used gold alloys as model systems to study their electrochemical behavior, and were also the first to use transmission electron microscopy (TEM) to characterize the resulting structures, which confirmed a nanoporous structure with feature size of ≈ 10 nm. In 1979, *Forty* [21.28] presented electron micrographs for a free-standing nanoporous gold (NPG) membrane material, which had pore size of approximately 20 nm and was made by etching an Ag-Au alloy film in HNO_3. Since the 1980s, *Sieradzki* and *Newman* and others have systematically investigated the corrosion process of Ag-Au alloys [21.45–47]. With advanced electrochemical techniques, such as electrochemical scanning tunneling microscopy, they discussed in great detail two key parameters associated with dealloying: the parting limit and the critical potential, where the parting limit defines the concentration of noble metal in an alloy above which dealloying does not occur, while the critical potential is empirically defined as a voltage threshold above which the dissolution current rises dramatically, resulting in substantial dealloying. At the very beginning of this century, *Erlebacher* et al. [21.48] further clarified the underlying physical mechanism of dealloying of Ag-Au alloys using experiments and computer simulation. After that, *Ding* and *Erlebacher* [21.49–52] continued to pay more attention to the microstructural morphology of NPG by dealloying commercial Ag-Au leaves. In the past 10 years, increasing interest has been paid to nanoporous metals made by dealloying, as well as their microstructures, unique properties, and potential applications.

21.1.1 Alloy Design of Precursors Suitable for Dealloying

Alloy systems that form porosity upon dealloying share a number of characteristics, and there are four basic common characteristics that an alloy typically possesses if it has a chance of becoming nanoporous during dealloying:

1. The difference in potential required to dissolve the alloy component in its pure form must be a few hundred millivolts, with one element being more noble (MN) and the other less noble (LN).
2. The composition is usually rich in the less noble component (the content of the more noble element is below its parting limit).
3. The alloy must be homogeneous with no phase separation prior to dissolution. Porosity evolution thus forms dynamically during dissolution and is not due to one phase simply being excavated from a two-phase material.
4. Diffusion of more noble atoms at the alloy/electrolyte interface must be sufficiently fast [21.53].

The prototypical alloy system for dealloying is Ag-Au, which has single-phase solid solubility across all compositions. Until now, dealloying has been observed in many binary alloy systems including Cu-based alloys (Cu-Au, Ag, Pt, Mn, Zr, Ni, etc.) [21.54–59],

Al-based alloys (Al-Au, Ag, Pt, Pd, Cu, etc.) [21.60,61], Mg-based alloys (Mg-Ag, Cu, etc.) [21.62, 63], Zn-based alloys (Zn-Pt, Au, Ag, Cu, etc.) [21.64–67], etc. These binary systems are composed of a single-phase solid solution, or a single-phase intermetallic compound or a combination of solid solution and/or intermetallic phase [21.68–70]. Accordingly, nanoporous metals such as Au, Ag, Pd, Pt, Cu, etc. can be fabricated through chemical or electrochemical dealloying of these binary precursors. Figure 21.1 shows typical scanning electron microscopy (SEM) micrographs of NPG obtained by dealloying Ag-Au leaf in nitric acid [21.51], and optical images before and after dealloying are also included.

Besides binary systems, dealloying can also be realized in ternary or multicomponent precursors [21.71, 72]. Dealloying of ternary or multicomponent precursors is more complicated than that of binary systems, but they also provide the opportunity to tune the microstructure of the as-obtained nanoporous metals and to fabricate nanoporous alloy materials. Other than crystalline precursors, some amorphous alloys (metallic glasses) can also be dealloyed to form corresponding nanoporous metals [21.73, 74]. In comparison with crystalline alloys, multicomponent metallic glasses are monolithic in phase with homogeneous composition and structure down to subnanoscale. In addition, the shapes of precursors are also diverse, and films, ribbons, powders, nanoparticles, nanowires, and even bulk form have been reported.

It is well established that the composition, structure, and phase constitution of precursors have a significant influence on the dealloying process and the formation of nanoporous metals. It has been reported that electrochemical dealloying of nanocrystalline 62Cu-38Zr films results in formation of porous copper with uniform diameter of approximately 500 nm. In contrast, no porous copper could be obtained from coarse-grained 62Cu-38Zr alloys under the same conditions [21.70]. The following routes are normally used to prepare precursors: melt casting, rapid solidification, rolling, surface alloying, template-assisted electrodeposition, vapor deposition, sputtering deposition, etc. It is obvious that one can control the dealloying process by adopting a proper processing method of precursors.

21.1.2 Formation Mechanisms of Nanoporous Metals by Dealloying

In 1967, *Pickering* and *Wagner* [21.75] argued that, when one metal is preferentially dissolved, it may be assumed that one or more of the following three mechanisms operate:

1. Both metals ionize followed by redeposition of the more noble metal.
2. Only the less noble metal ionizes and enters the solution, while the atoms of the more noble metal aggregate by surface diffusion.
3. Only the less noble metal ionizes and enters the solution, and atoms of both metals move in the solid phase by volume diffusion.

Later, *Forty* et al. [21.28, 76, 77] thought that the formation of the island–channel structure during dealloying of Ag-Au alloys can be explained in terms of a corrosion disordering/diffusion reordering model in which corrosion proceeds by selective dissolution of the less noble component, thereby creating a disordered surface layer which subsequently reorders by surface diffusion of gold adatoms. In 1989, *Sieradzki* et al. [21.78] developed a new model to account for all the known features of dealloying based upon percolation theory. Their Monte Carlo simulation results could reproduce many of the features usually associated with dealloying in real binary noble–metal alloy sys-

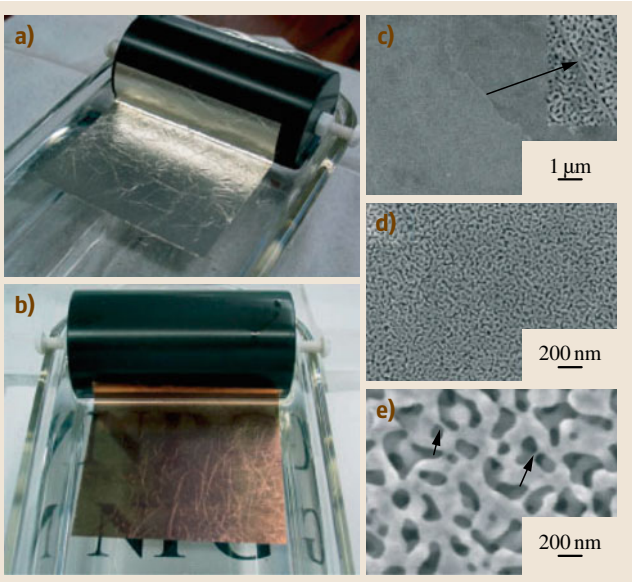


Fig. 21.1 (a–b) Optical and (c–e) SEM images of white gold leaf before and after dealloying in nitric acid for 15 min. The *inset image* in (c) shows a region where a slid grain boundary is located. Very thin gold ligaments with diameter smaller than 2 nm are often observed. Examples are marked with *arrows* in (e) (after [21.51])

tems, including the porous morphology of the dealloyed residue, coarsening of this porosity, sharp dealloying thresholds or parting limits, and the development of intermediate compositions.

In 2001, *Erlebacher* et al. [21.48] proposed a continuum model that is fully consistent with experiments and theoretical simulations of alloy dissolution, and demonstrated that nanoporosity in metals is due to an intrinsic dynamical pattern formation process; that is, pores form because the more noble atoms are chemically driven to aggregate into two-dimensional clusters by a phase separation process (spinodal decomposition) at the solid/electrolyte interface, and the surface area continuously increases owing to etching. Figure 21.2 clearly shows the simulated nanoporosity evolution during dealloying. Moreover, the nanoporous structure of NPG can be well modeled by their simulations. In 2004, *Erlebacher* [21.53] further described the microscopic details of porosity formation during dealloying as illuminated by a kinetic Monte Carlo model incorporating site coordination-dependent surface diffusion of all alloy components, and site coordination-dependent dissolution of the less noble atoms. Their simulation model can reproduce many of the characteristics of dealloying, particularly the observation of porosity evolution and reproduction of the classical phenomenology of a parting limit and a composition-dependent critical potential.

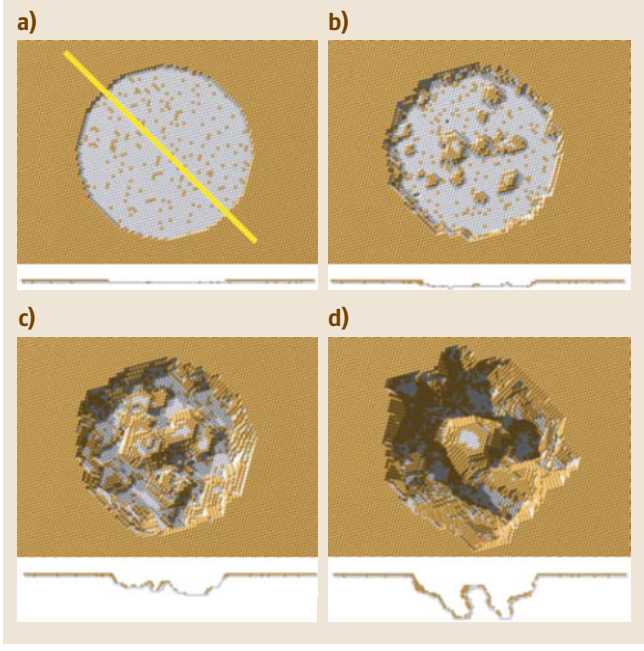


Fig. 21.2a–d Simulated evolution of an artificial pit in $Au_{10\%}$–$Ag_{90\%}$ (at.%), $f = 1.8$ eV. Cross-sections along the $(11\bar{1})$ plane defined by the *yellow line* in **(a)** are shown below each plan view. **(a)** The initial condition is a surface fully passivated with gold except within a circular region (the *artificial pit*). **(b)** After 1 s, the pit has penetrated a few monolayers into the bulk. We note how there are fewer gold clusters near the side wall than at the center of the pit. **(c)** After 10 s, a gold cluster has nucleated in the center of the pit. **(d)** At 100 s, the pit has split into multiple pits; each will continue to propagate into the bulk to form a porous structure (after [21.48])

Below the dealloying critical potential, passivation normally occurs, but its origin is still unclear. Recently, *Renner* et al. [21.79] revealed the microscopic structural changes associated with a general passivation phenomenon on the atomic scale by in situ x-ray diffraction with picometer-scale resolution. They observed the formation of a gold-enriched single-crystal layer that is two to three monolayers thick and has an unexpected inverted (CBA-) stacking sequence. At higher potentials, the protective passivation layer dewets and pure gold islands are formed; such structures form the templates for the growth of nanoporous metals.

It is known that, for most systems, the critical dealloying potential E_c is determined by a balance between dissolution-induced surface roughening and surface-diffusion-induced smoothing. Below the critical potential, the current density is surface diffusion limited and is typically less than $1\,\mu A/cm^2$. The conventional view of morphology evolution in the region below the critical potential is that the alloy surface maintains a stable planar interface while enriching in the more noble constituent. The current decay is believed to be correlated with the B (MN element) enrichment, but the current never drops identically to zero. *Wagner* et al. [21.80] studied in detail the dealloying behavior below the critical potential, and found the existence of different regimes of power-law current decay behavior at potentials below the critical potential. The initial current decay displays t^{-1} behavior, which their modeling has shown to be consistent with the exhaustion of sites available for dissolution. When the current from this process falls to a low enough level, the power law adopts an exponent indicative of one of three mechanisms dominating in the surface-vacancy diffusion process. The current resulting from the surface-diffusion-controlled process can follow $t^{-5/8}$, $t^{-1/2}$, and $t^{-1/4}$ behaviors, respectively, for surface-vacancy-controlled periphery diffusion, terrace diffusion, and evaporation–condensation.

It is well recognized that the formation of nanoporous metals by dealloying involves selective

dissolution of the less noble element coupled with coarsening of the more noble element by surface diffusion. However, minor dissolution of the more noble element is also possible during dealloying, especially when the electrolyte contains Cl^-. During dealloying of brass in aqueous sodium chloride, Cu dissolves into the solution to form Cu(I) and Cu(II) complex ions [21.31]. At appropriately high dealloying potentials, relatively steady chloride compound or chloride complexes can form between chloride ions and the more noble metals included, such as soluble $[AuCl_4]^-$, $PdCl_2$, $[AgCl_2]^-$, $[CuCl_2]^-$, and insoluble AgCl and CuCl during the electrochemical dealloying of Al-based alloys [21.61]. Eventually, the dissolution of Cu to form soluble $[CuCl_2]^-$ complex plays a key role in the dealloying of $MgCu_2$ and the formation of nanoporous copper [21.81]. Moreover, inductively coupled plasma (ICP) measurements also verify the existence of minor Ag ions in the electrolyte after chemical dealloying of Mg-Ag-Pd alloys [21.71]. In addition, the electrochemical dealloying mechanism of Al_2Au in neutral NaCl solution can be explained based upon the Pourbaix diagram and chloride ion effect [21.82]. During the dealloying process, a self-acidifying effect is triggered due to the dissolution and instant hydrolysis of Al^{3+}/Al, which is assisted by chloride ions in the electrolyte (Fig. 21.3). The self-acidifying effect accelerates the dealloying process of the Al-Au alloys and thus the formation of NPG.

If multiple phases exist in the alloy, *Pugh* et al. [21.55] argued that porosity formation of any individual phase would follow the same requirement for a single phase, and hence typically only the A-rich phase would dealloy (here A is the less noble element). In this case, dealloying would be isolated to only surface grains unless a mechanism existed for penetration of the electrolyte throughout the alloy; for example, the A-rich grains form a percolating path through the alloy. As for a two-phase alloy, we have found that the dealloying process depends upon the composition, activity, and electrochemical properties of each phase in the alloy. According to the reactions (being excavated, dealloyed, or retained) of the constitutive phases in a biphasic alloy during dealloying, six types of dealloying are classified, and four typical dealloying scenarios can be identified from the viewpoint of nanoporosity evolution during dealloying [21.61]. Moreover, it is interesting to note that dealloying of the less noble phase has a promoting effect on dealloying of the more noble phase (for example, Al-Ag alloys containing Al and Ag_2Al) [21.83]. In addition, the promoting effect in eutectic structures is stronger than that in peritectic structures, the effect of a solid solution as the less noble phase is stronger than that of an intermetallic phase, and the higher the diffusivity and the lower the equilibrium potential of the more noble element in the electrolyte, the more substantial the promoting effect is.

Most recently, the chemical dealloying mechanism of bimetallic Pt-Co nanoparticles (NPs) has been investigated on a fundamental level by the combination of x-ray absorption spectroscopy (XAS) and aberration-corrected scanning transmission electron microscopy (STEM) [21.84]. Structural parameters, such as coordination numbers, alloy extent, and the unfilled d states of Pt atoms, are derived from the XAS spectra, together with the compositional variation analyzed by line-scanning energy-dispersive x-ray spectroscopy (EDX) on an atomic scale, to gain new insights into the dealloying process of bimetallic Pt-Co NPs. The XAS results on acid-treated Pt-Co/C NPs reveal that the Co–Co bonding in the bimetallic NPs dissolves first, and the remaining morphology gradually transforms to a Pt skin structure. Furthermore, it is observed that such an imperfect Pt skin surface feature will collapse due to penetration of electrolyte into layers underneath and cause further dissolution of Co and the loss of Pt. The electrocatalytic activity decreases accordingly, if the dealloying process lasts for 4 h.

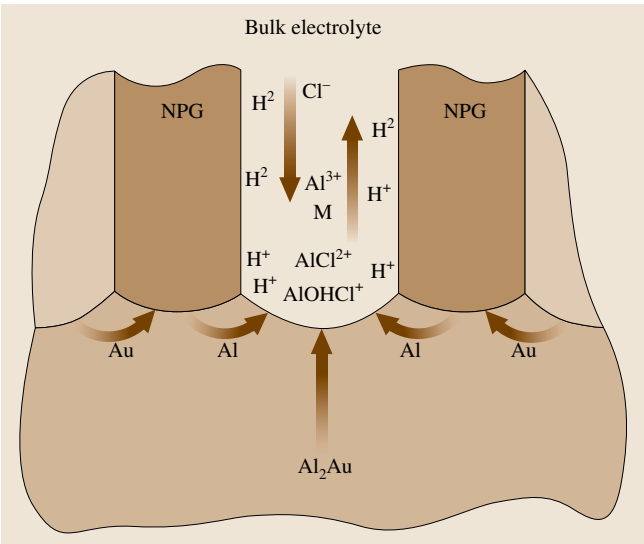


Fig. 21.3 Schematic illustration of pore evolution and hydrogen bubble emergence during electrochemical dealloying of Al_2Au in 10 wt % NaCl aqueous solution (after [21.82])

Normally, a minor residue of the less noble element is inevitable in the resultant nanoporous metals formed by dealloying, but less attention has been paid to the retention of the less noble element during dealloying. Recently, *Liu* et al. [21.85] investigated factors controlling retention of the less noble metal in nanoporous structures processed by electrochemical dealloying, taking Ag-Au as an example. It has been found that, while the dealloying critical potential is generally independent of pH, the dissolution rate is strongly affected by the solution acidity. pH substantially affects Ag retention in both the oxide and alloy forms. To discriminate between the retention forms, two different approaches employed for removing the Ag oxide from freshly dealloyed samples are: (i) oxide dissolution in 1 M $HClO_4$, and (ii) oxide reduction to elemental Ag followed by subsequent electrochemical oxidation to Ag^+ ions. Critical analysis of the experimental results suggests that the pH and dissolution rate affect more significantly the amount of Ag retained in the form of oxide, while the dealloying potential has a stronger impact on Ag trapping. In addition, the Ag retained as oxide is determined to be predominantly AgO. Their findings could enable the development of strategies for structural and compositional control in electrochemically processed metallic nanoporous materials.

21.1.3 Control over Structures of Nanoporous Metals

It is known that the properties of nanoporous metals are closely related to their microstructure and especially the characteristic length scale of ligaments/channels. It is of great importance to control the microstructures of nanoporous metals. Some factors including the microstructure of precursors, the kind and type of electrolytes, the applied dealloying potential, and the dealloying temperature and time will affect the dealloying process and thus the formation/structure of nanoporous metals. At the same time, formation of nanoporous metals by dealloying is a self-organization process by surface diffusion of the more noble element along the alloy/solution interface, and the surface diffusivity of the more noble element has a significant influence on the length scale of the ligaments/channels of nanoporous metals. We can tune the microstructure of nanoporous metals by adjusting the dealloying parameters, especially by control of the surface diffusivity of the more noble element.

Pt has a value of surface diffusivity ($< 10^{-19}\,cm^2/s$) that is at least 3–4 orders of magnitude lower than that ($< 10^{-15}$–$10^{-16}\,cm^2/s$) of Au under their respective electrochemical environment. Therefore, nanoporous Pt normally shows a ligament–channel structure with a length scale of only a few nanometers through dealloying of Cu-Pt and Al-Pt alloys [21.55, 60, 86]. Figure 21.4 shows TEM and high-resolution TEM (HRTEM) images of nanoporous Pt obtained by chemical dealloying of $Al_{88}Pt_{12}$ alloy in 20 wt % NaOH solution [21.60]. The corresponding selected-area electron diffraction (SAED) pattern and the HRTEM image confirm that the as-obtained nanoporous Pt is composed of randomly oriented face-centered cubic (fcc) nanocrystals. For a given dealloying solution, the length scale of the ligaments/channels in the resulting nanoporous metal is associated with surface diffusion of more noble atoms, and increases with increasing diffusion coefficients in the sequence: Pt/Pd < Au < Ag < Cu [21.60].

Antoniou et al. [21.87] reported synthesis of nanoporous platinum (np-Pt) through electrochemical dealloying in aqueous HF from cosputtered Pt_xSi_{1-x}

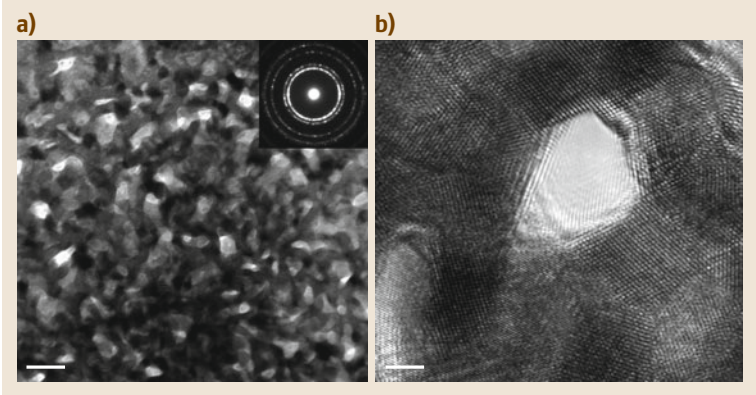


Fig. 21.4 **(a)** TEM image of nanoporous Pt obtained by chemical dealloying of $Al_{88}Pt_{12}$ alloy in 20 wt % NaOH solution. (*Inset*) Corresponding SAED pattern. *Scale bar*, 20 nm. **(b)** HRTEM image of nanoporous Pt. *Scale bar*, 2 nm (after [21.60])

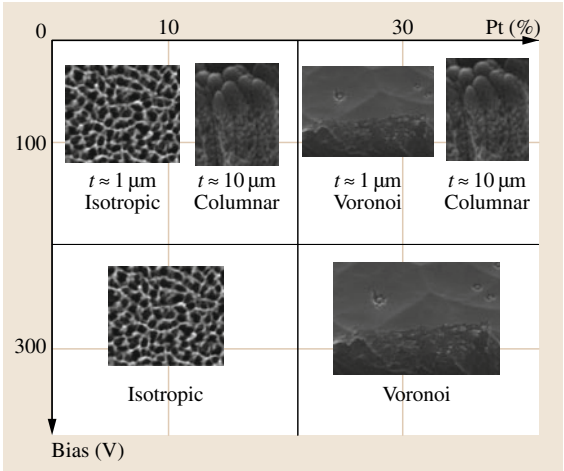


Fig. 21.5 Schematic of the possible np-Pt foam morphologies as a function of cosputtering parameters, initial alloy composition, and thickness (after [21.87])

amorphous films for different initial compositions and sputter bias conditions. They found that, in addition to the expected isotropic open-cell np-Pt foam, anisotropic columnar and Voronoi np-Pt is obtained. There are two levels of anisotropy: On the micron scale, 100 nm columns or 1 µm Voronoi polygons form, whereas inside the columnar and Voronoi hyperstructures, the ligaments and pores are anisotropic, ranging from 5 to 25 nm. The ligament diameter and grain size were 5 nm for all reported structures. A processing–structure map was developed to correlate np-Pt structure to the processing conditions (Fig. 21.5).

Monolithic nanoporous copper can be synthesized by dealloying $Mn_{0.7}Cu_{0.3}$ by two distinct methods: potentiostatically driven dealloying and free corrosion [21.57]. Both the ligament size and morphology were found to be highly dependent on the dealloying methods and conditions; for example, ligaments of 16 or 125 nm were obtained by dealloying either electrochemically or by free corrosion, respectively. Optimization of the starting Mn-Cu alloy microstructure allowed generation of uniform porous structures. *Seker* et al. [21.88] reported that thermal treatment of Ag-Au films can reduce microscale void formation in blanket nanoporous gold films. *Okman* et al. [21.89] found that the ramped potential increase gave better NPG film uniformity than stepped potential increase during potentiostatic dealloying of Ag-Au films. *Li* and *Balk* [21.90] reported effects of substrate curvature on dealloying of cosputtered Au-Pd-Ag alloy films. They found that ligament morphology, film cracking, and composition were significantly different for np-AuPd in concave versus convex film regions. Convex substrate curvature led to extensive film cracking, wide and high-aspect-ratio ligaments, and low residual Ag content. A more tensile stress state is believed to enhance the dissolution rate of Ag. *Li* et al. [21.91] reported that the microstructure of precursors has a significant influence on the dealloying of ternary amorphous Si-Pt-Ni precursors, and the ligament patterns and mechanical properties of the resulting nanoporous Pt-Ni alloys.

Snyder et al. [21.92] investigated dealloying behaviors of Ag-Au alloys in neutral silver nitrate solution. A small-pore (5 nm) NPG can be formed over a potential range of 1.3–2.0 V versus normal hydrogen electrode. They explained the observations in terms of residual surface oxides passivating the pores behind the dissolution front, which is itself acidified and thus corrosive due to accumulation of protons associated with oxide formation and water dissociation. Their method of fabricating NPG has the advantages of simplicity and safety. Linear relationships have been observed between the dealloying potential and the size of ligaments and pores [21.93]. Moreover, at low dealloying potential the pore size is larger than the ligament diameter, whereas at high dealloying potential they are comparable. *Li* and *Balk* [21.94] found that the pore and ligament dimensions of nanoporous palladium nickel (np-PdNi) were reduced by 50% when surfactants were added to the sulfuric acid etching solution. Ultrasonic agitation was also used to enhance dealloying and shortened the time required from 5 to 1 h, while retaining pore/ligament size of 5 nm.

During dealloying, adsorption of anions (such as Cl^-) from the electrolyte can accelerate surface diffusion of the more noble element. *Dursun* et al. [21.95] studied dealloying of $Ag_{0.7}Au_{0.3}$ and $Ag_{0.65}Au_{0.35}$ alloys in 0.1 M $HClO_4$ with addition of either 0.1 M KCl, 0.1 M KBr, or 0.1 M KI. They found that the critical overpotential decreases with addition of halides, with KI having the largest potential reduction of almost 50%. This decrease can be rationalized according to competition between the rates of increase of Au surface diffusivity and Ag exchange current density with halide addition. The size scale of porosity produced during dealloying of $Ag_{0.65}Au_{0.35}$ was found to increase with addition of halides. Also, it has been found that the length scale of ligaments/channels of nanoporous metals can be modulated by simply changing the dealloying solution (from HCl to NaOH) [21.60].

Low-temperature dealloying treatment is an effective method to tailor the characteristic length scale of

nanoporous gold. By systematically investigating the kinetics of nanopore formation during free corrosion, *Qian* and *Chen* [21.96] experimentally demonstrated that the dealloying process is controlled by diffusion of gold atoms at alloy/electrolyte interfaces, which strongly relies on the reaction temperatures. Low dealloying temperatures significantly reduce the interfacial diffusivity of gold atoms and result in ultrafine nanoporous structure. NPG with ultrafine ligaments/channels (less than 10 nm) can be obtained by dealloying of Al_2Au in alkaline solution at low temperature. The surface diffusivity of Au adatoms was evaluated as 2.1×10^{-23}, 2.3×10^{-21}, and $1.6\times10^{-19}\,m^2/s$ for dealloying at 253, 298, and 368 K, respectively. Measurement of the activation energy demonstrates that formation and coarsening of NPG are governed by Au diffusion at alloy/solution interfaces, regardless of the dealloying medium [21.97].

Addition of elements with low surface diffusivity into precursors can effectively refine the ligaments and channels of nanoporous metals (or alloys). In addition, as is well known, the noble metals Pt and Pd are widely used in the field of fuel cells as electrocatalysts and exhibit excellent catalytic activities for oxidation of small organic molecules. Introduction of Pt or/and Pd into nanoporous metals (such as NPG) can also generate a kind of novel bi-/trimetallic nanoporous functionalized alloys. Addition of Pt to precursor Ag/Au alloys was, upon dealloying, found to stabilize the morphology of the porous metal formed, to refine its pore size to nearly atomic dimensions, and to stabilize its morphology even in harsh chemical and thermal environments [21.99]. As Pt possesses much slower surface diffusion rates than Au, during dissolution, Pt embedded in exposed terraces should segregate to the edges of the growing vacancy island step edges,

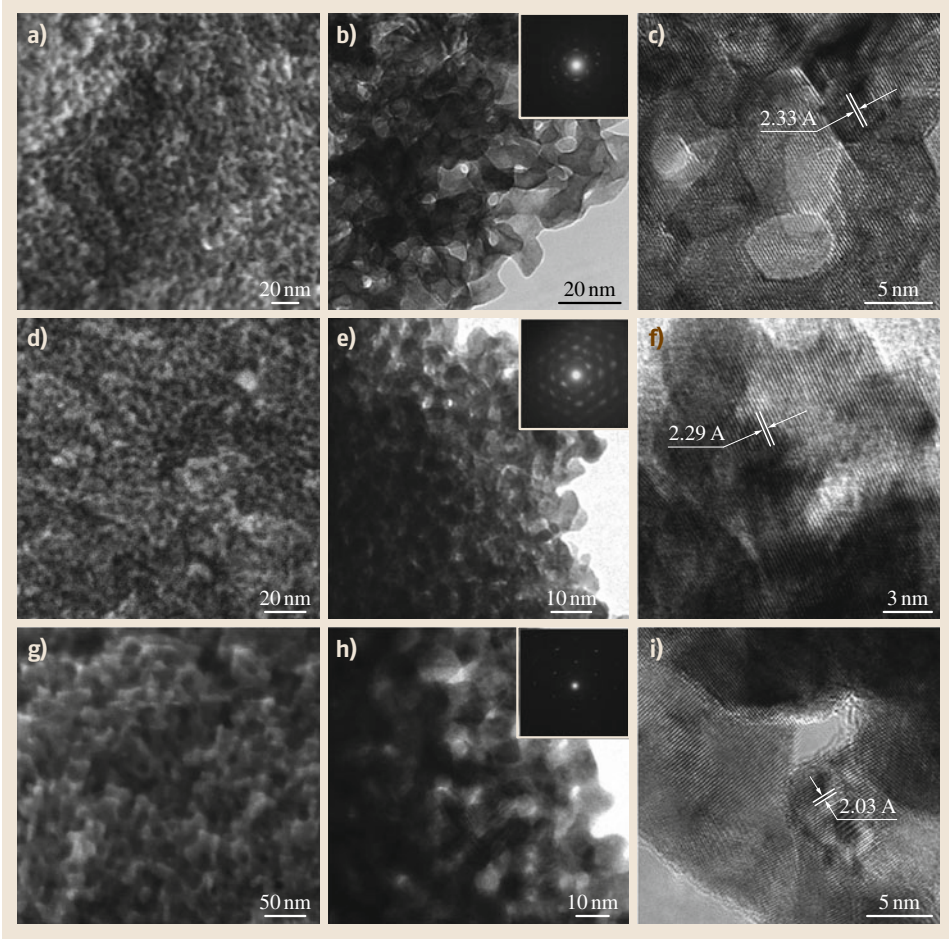


Fig. 21.6 SEM, TEM, and HRTEM images of nanoporous Au/Pt alloys obtained by dealloying **(a–c)** $Au_{10}Pt_{10}Cu_{80}$, **(d–f)** $Au_4Pt_{16}Cu_{80}$, and **(g–i)** $Au_{16}Pt_4Cu_{80}$ alloys, respectively (after [21.98])

stabilizing them and ultimately reducing the scale of porosity as well as leading to a Pt-rich shell. Selective etching of Cu from Au/Pt/Cu alloy precursors results in the formation of three-dimensional bicontinuous porous network structures with uniform pores and ligaments less than 10 nm (Fig. 21.6) [21.98]. Moreover, nanoporous Au/Pt alloys have a single-phase cubic structure with relatively uniform composition across the samples. The addition of the third element Pd into Mg-Ag results in the formation of an ultrafine nanoporous $Ag_{80}Pd_{20}$ alloy which exhibits superior catalytic activity towards electrooxidation of ethanol [21.71]. It has been found that elemental doping has no influence on the phase constitution of rapidly solidified Al-Au-Pt, Al-Au-Pd, and Al-Au-Pt-Pd alloys, and all these precursor alloys are composed of a single Al_2Au-type intermetallic compound (Al_2(Au,Pt), Al_2(Au,Pd), and Al_2(Au,Pt,Pd)). Ultrafine nanoporous gold alloys with ligaments/channels less than 10 nm can be facilely fabricated through dealloying these rapidly solidified Al_2Au-based precursors under free corrosion conditions. When performing dealloying in 20 wt % NaOH solution, a certain amount of Pt or/and Pd addition exhibits a superior refining effect, and the length scale of the ligaments/channels in the as-obtained np-Au alloys can reach $\approx$ 3 nm for Pt doping or Pt/Pd codoping. When performing dealloying in 5 wt % HCl solution, the anticoarsening capacity of Pt doping is more remarkable than that of Pd doping. In addition, the amount of doping can significantly affect the anticoarsening ability of ligaments/channels in thus-obtained np-Au alloys [21.72].

Generally, the structure of nanoporous metals can be coarsened to larger length scales (up to micrometers) at elevated temperatures and has been shown to coarsen at room temperature as a function of the applied voltage and electrolyte composition; for example, fast surface diffusion of gold in electrolyte gives NPG leaf the unique ability to have its porosity adjusted using simple room-temperature acid-induced postprocessing (Fig. 21.7) [21.51]. *Hakamada* and *Mabuchi* [21.100] reported a simple and spontaneous synthesis of a nanoporous gold prism microassembly with highly dense skins, which was achieved just by immersing nanoporous gold into concentrated hydrochloric acid. Coarsening of the porous structure can be attributed to the rapid surface diffusion of gold accelerated by Cl^-. Moreover, the morphology of the nanoporous gold prism microassembly was significantly different from that of annealed nanoporous gold.

Through combination with other routes such as template methods, galvanic replacement reactions, and underpotential deposition electroless plating, dealloying can be used to further tailor the morphology, microstructure, and properties of nanoporous metals. *Ji* and *Searson* [21.101] reported fabrication of nanoporous nanowires with high surface area and well-defined pore morphology (Fig. 21.8). The nanoporous nanowires were formed in a two-step process involving electrochemical deposition of a single-phase, two-component A_xB_{1-x} alloy into a nanoporous template (AAO), with subsequent chemical etching of one component from the alloy after removal from the template. Moreover, nonporous segments can be incorporated into

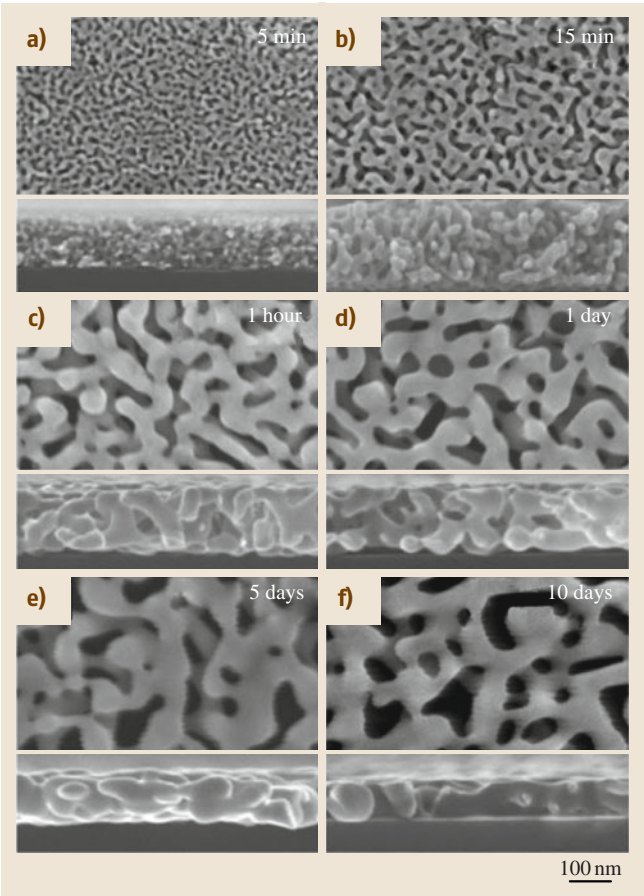


Fig. 21.7a–f Plan-view and cross-sectional SEM images of NPG leaf samples showing significant structure coarsening upon continued immersion in acid for extended times after the leaf is completely dealloyed (dealloying is usually complete after 5 min) (after [21.51])

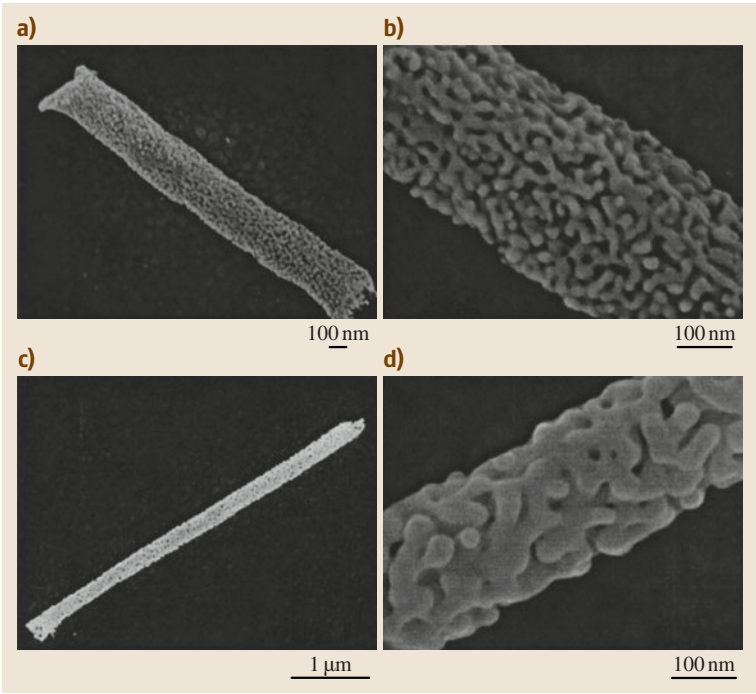


Fig. 21.8a–d SEM images of NPG nanowires (after [21.101])

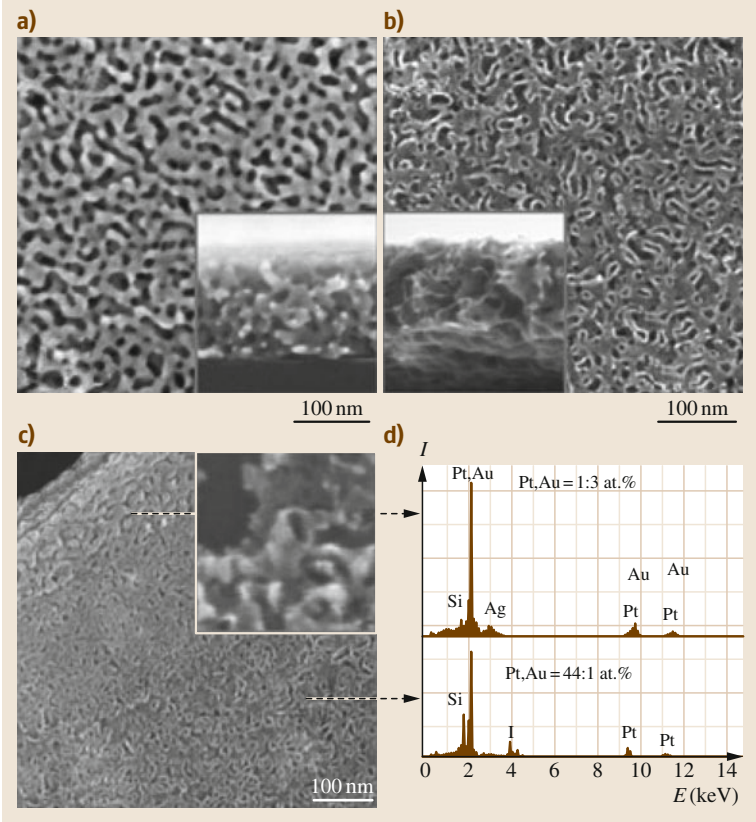


Fig. 21.9 **(a)** Plan-view and cross-section (*inset*) SEM images of NPG. **(b)** Plan-view and cross-section (*inset*) SEM images of NMP. **(c)** SEM image of a Pt-coated NPG sample within which gold has been only partially removed; the *inset* shows a tube opening of NMP. **(d)** EDS analysis indicates a gradual structure transition from Pt/NPG to NMP (after [21.52])

multisegment nanowires. *Chen* et al. [21.102] reported synthesis of a novel gold-decorated nanoporous copper (Au at NPC) core–shell composite. Thin gold shells with controllable thickness are homogeneously deposited onto the internal surfaces of three-dimensional (3-D) nanoporous copper via a spontaneous displacement reaction, while nanoporous copper is utilized as a reduction agent as well as 3-D template and substrate. *Ding* et al. reported the design and fabrication of nanotubular mesoporous platinum (NMP), a new material that can be described as a network of platinum nanotubes with diameter of about 15 nm and walls 1 nm thick that interconnect to form an open, doubly bicontinuous structure that may possess the highest surface-area to-volume ratio known for a macroscopic sample of metal (Fig. 21.9) [21.52]. Nanotubular mesoporous platinum can be synthesized by epitaxial casting using nanoporous gold membrane molds (dealloying–plating–dealloying). They further investigated the structure evolution of a novel electrocatalyst, Pt-decorated nanoporous gold (Pt-NPG), during thermal annealing at relatively low temperatures [21.103]. Pt-NPG was made by plating a thin layer of Pt over NPG substrate during an electroless plating process that generated epitaxial Pt nanoislands loaded on the NPG surface. In comparison with Pt's very high melting point, thermal annealing at temperatures as low as 100 °C was found to significantly change the structure and surface chemistry of these nanomaterials. While Pt-NPG preserved very well its initial porous morphology, the deposited Pt islands collapsed to form a thin Au-Pt alloy layer coating on the NPG surface upon heating. This structure change results in severe modulation of the electronic structure and surface reactivity of Pt, as proved by the markedly different behaviors in electrocatalytic reactions such as formic acid electrooxidation and CO stripping.

21.2 Properties of Nanoporous Metals

The phase constitution, microstructure, and composition of nanoporous metals can be characterized using XRD, SEM, TEM, HRTEM, x-ray photoelectron spectroscopy (XPS), energy-dispersive x-ray (EDX) analysis, atomic force microscopy (AFM), scanning tunneling microscopy (STM), small-angle neutron scattering (SANS), x-ray absorption spectroscopy (XAS), high-angle annular dark-field scanning transmission electron microscopy (HAADF-STEM), and many other techniques.

21.2.1 Structure and Morphology

Characterization Methods

Corcoran [21.104] explored the use of small-angle neutron scattering and scanning tunneling microscopy as potential tools for determining the mechanisms involved in porosity formation. The average pore size and distribution were found to depend upon the electrolyte composition, dealloying rate, applied potential, and time. Figure 21.10 shows in situ scattering data for spontaneous corrosion of $Ag_{0.7}Au_{0.3}$ in concentrated HNO_3. The length scale of nanopores can be evaluated from the characteristic peak position. *Fujita* and *Chen* [21.105] proposed a method derived from the fast Fourier transform (FFT) process to measure the characteristic length scale of bicontinuous nanoporous structures. By rotationally averaging the FFT power spectrum of a nanoporous micrograph from SEM or TEM, a significant peak in the power spectrum can be obtained, which reflects the characteristic length scale

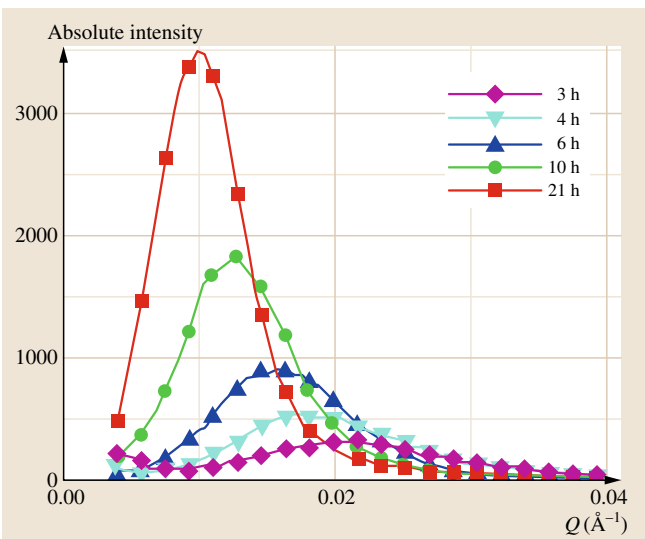


Fig. 21.10 In situ scattering data for spontaneous corrosion of $Ag_{0.7}Au_{0.3}$ in concentrated HNO_3. The *dealloying time* associated with each curve is indicated (after [21.104])

of the quasiperiodic structure. This method is valid for the bicontinuous morphology that is frequently observed in nanoporous metals prepared by chemical or electrochemical dealloying.

Renner et al. [21.107] presented an in situ x-ray diffraction study of the initial steps of potential-controlled, selective dissolution of Cu from a Cu_3Au (111) single-crystal surface immersed in 0.1 M H_2SO_4. They found structural evolution of an ultrathin Au-rich metallic passivation layer at low overpotentials toward thicker, pure Au islands at elevated overpotentials below the critical potential. The thickness of the ultrathin layer grows from two hexagonal close-packed (hcp) monolayers to several fcc-stacked monolayers. The epitaxial Au-rich layer, which exhibits a reversed stacking with regard to the single-crystal substrate, passivates the Cu_3Au (111) surface. Complementary ex situ AFM images showed at elevated overpotentials a surface completely covered with islands of a homogeneous size distribution, which agrees well with the findings from the x-ray experiments. The Au islands are found to be weakly hexagonally correlated.

Rösner et al. [21.108] developed a method to reconstruct a nanoporous metal (taking NPG as an example) in three dimensions from TEM images. Normally, the small feature sizes of NPG prevent characterization using many established techniques such as optical microscopy serial sectioning or x-ray tomography. The most important observations obtained using TEM tomography are:

1. The structure represents a contiguous network of branched ligaments.
2. The structure is quite inhomogeneous, with a broad distribution of ligament and pore diameters and shapes.
3. As a consequence, the specific surface area is larger than what would be estimated based on the characteristic ligament size.
4. In spite of the many saddle-point-like features, the average mean curvature is positive and close to what would be expected for convex objects of a size corresponding to the ligament diameter.
5. Encased voids are observed within the ligaments; there is no obvious explanation for the formation of these features.

This information contributes to establishing a basic description of the topology and local structure of nanoporous metals prepared by dealloying, which may form the basis for future models leading to predictive understanding of their properties, such as strength, surface induced strain, or transport properties.

Fujita et al. [21.106] reported transmission electron tomography of nanoporous gold fabricated by chemically dealloying $Au_{35}Ag_{65}$ films. A number of algorithms were employed to quantitatively characterize the complex three-dimensional nanoporous structure. It was found that gold ligaments and nanopore channels are topologically and morphologically equivalent; i. e., they are inverses of each other in three-dimensional space. Statistical analysis reveals that this bicontinuous nanostructured material is actually quasiperiodic and has, on average, near-zero surface curvature. Figure 21.11 shows corresponding 3-D tomographic reconstruction of nanoporous gold. These quantitative measurements will help in understanding the structural stability of nanoporous gold and in modeling its physical and chemical performance.

Petegem et al. [21.109] studied the evolution of the grain structure, internal strain, and lattice misori-

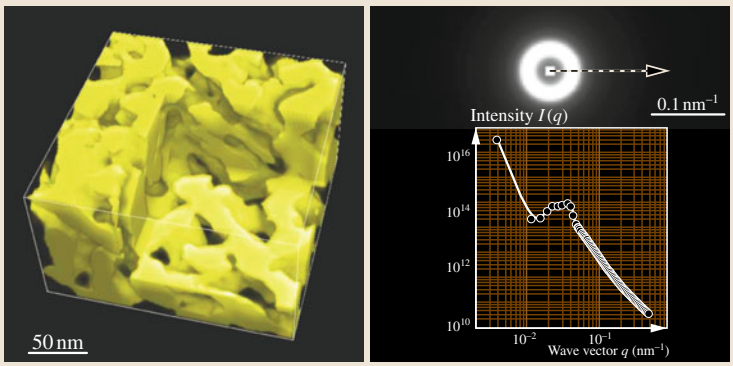


Fig. 21.11a,b 3-D tomographic reconstruction of nanoporous gold. **(a)** Magnified 3-D image revealing the internal bicontinuous structure of nanoporous gold. **(b)** Fourier-transformed pattern showing the quasiperiodic feature of nanoporous gold. The *inserted intensity profile* was taken along the *dashed arrow* in the Fourier-transform pattern (after [21.106])

entation of nanoporous gold during dealloying of bulk (3-D) Ag-Au alloy samples by various in situ and ex situ x-ray diffraction techniques including powder and Laue diffraction (Fig. 21.12a). Their experiments revealed that the dealloying process preserves the original crystallographic structure but leads to a small spread in orientations within individual grains. Initially, most grains develop in-plane tensile stresses, which are partly released during further dealloying. Simultaneously, the feature size of the developing nanoporous structure increases with increasing dealloying time. Finally, microdiffraction experiments on dealloyed micron-sized nanoporous pillars revealed significant surface damage introduced by focused ion beam milling. Figure 21.12b shows a two-dimensional (2-D) x-ray microdiffraction image of a nanoporous gold pillar. The inset displays a 3-D image of a part of the (111) ring.

Thin films of nanoporous gold, with ligaments and pores of the order of 10-nm diameter, offer a highly constrained geometry for deformation and thus provide an opportunity to study the role of defects such as dislocations in the plasticity of nanomaterials. *Sun* et al. [21.110] studied the mechanical behavior of nanoporous gold by using in situ nanoindentation in a transmission electron microscope. They found that dislocations were generated and moved along ligament axes, after which they interacted with other dislocations at the nodes of the porous network. For thicker films, the load–displacement curves exhibited load drops at regular intervals. Additionally, they also investigated the effect of the indenter displacement rate on the mechanical response of these gold films with nanoscale porosity. There appears to be a kinetic factor related to dislocation nucleation, where slower displacement rates cause load drops to occur at shorter distance intervals and over longer time intervals.

Liu et al. [21.111] developed an inexpensive, fast, selective, and sensitive technique for surface area measurement of metallic nanoporous materials (MNPM). Their approach is based on underpotential deposition (UPD) of metals on foreign substrates. In their work, Pb UPD on Au was chosen to illustrate the applicability, and revealed the advantages and limitations, of the proposed method. They measured the surface area of NPG electrodes with pore sizes in the range of 5–15 nm, prepared by electrochemical dealloying of single-phase AuAg. A critical comparison with Brunauer–Emmett–Teller (BET) analysis reveals important advantages of the method developed for surface area measurement in MNPM specimens.

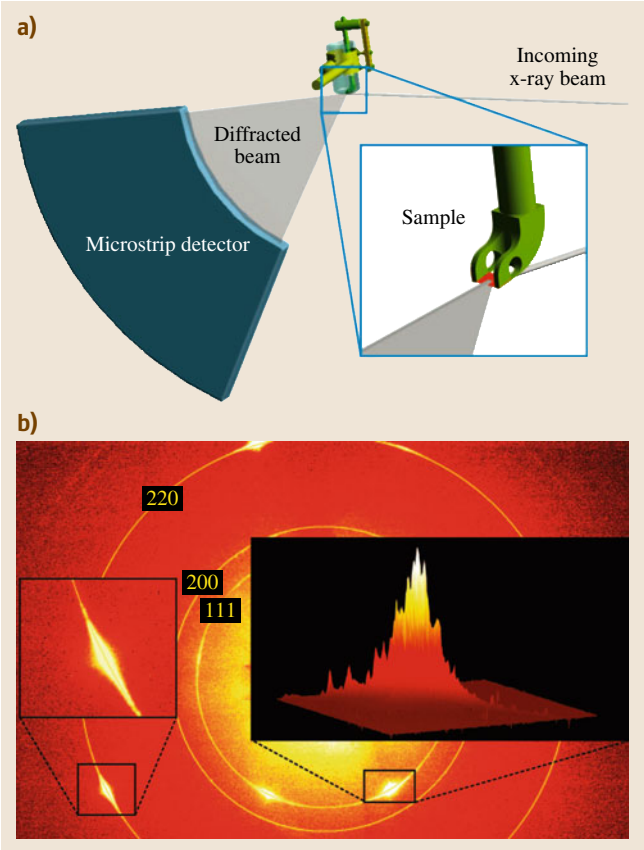


Fig. 21.12 **(a)** Schematic view of the in situ setup. **(b)** 2-D x-ray microdiffraction image of a nanoporous gold pillar. The *inset* displays a 3-D image of a part of the (111) ring (after [21.109])

Microstructure and Morphology

Through design of precursors and control over the dealloying process, nanoporous metals with diverse structures and morphologies can be fabricated, such as homogeneous structure, bimodal pore distribution, composite structure, ultrafine porous structure, etc. Moreover, both nanostructures (nanowires, nanotubes) and monolithic forms (films, ribbons, bulk samples) can be obtained. In addition, as well as pure metals, nanoporous alloys can also be produced.

Normally, larger-sized pores (hundreds of nm) are useful in microfluidic flow control, whereas very small pores (tens of nm) are useful for increasing device surface area as required for sensor applications. For microfluidic-based sensors, a bimodal pore size distribution composed of large porosity channels with highly porous channel walls is desirable to

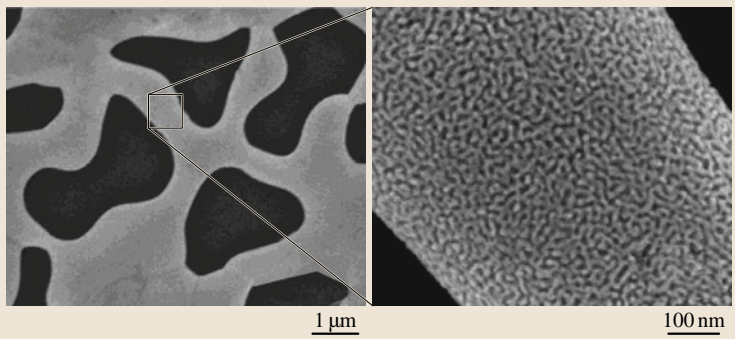


Fig. 21.13a,b A 2-D/3-D hybrid NPG structure, where the dimension of the unit structure in 2-D (1–2 μm) is two orders of magnitude larger than that in 3-D substructure (≈ 8 nm). Here, 100 nm-thick gold leaf was used, and the second-stage annealing was carried out at 500 °C for 8 h (after [21.49])

achieve fast response time and high sensitivity. *Ding* and *Erlebacher* [21.49] reported a two-step dealloying (dealloying–plating–annealing–dealloying) strategy to create nanoporous gold with multimodal pore size distributions. Figure 21.13 shows a 2-D/3-D hybrid NPG structure. In addition, NPG ribbons with bimodal channel size distributions can also be fabricated by chemical dealloying of Al-Au alloys composed of Al and Al_2Au phases [21.68]. The as-obtained NPG ribbons are composed of large-sized channels (hundreds of nanometers) with highly porous channel walls (tens of nanometers). Both large- and small-sized channels are 3-D, open, and bicontinuous. Moreover, the length scales of the large-sized channels can be modulated by changing the alloy composition, while those of the small ligaments/channels in the channel walls can be tuned by changing the dealloying solution.

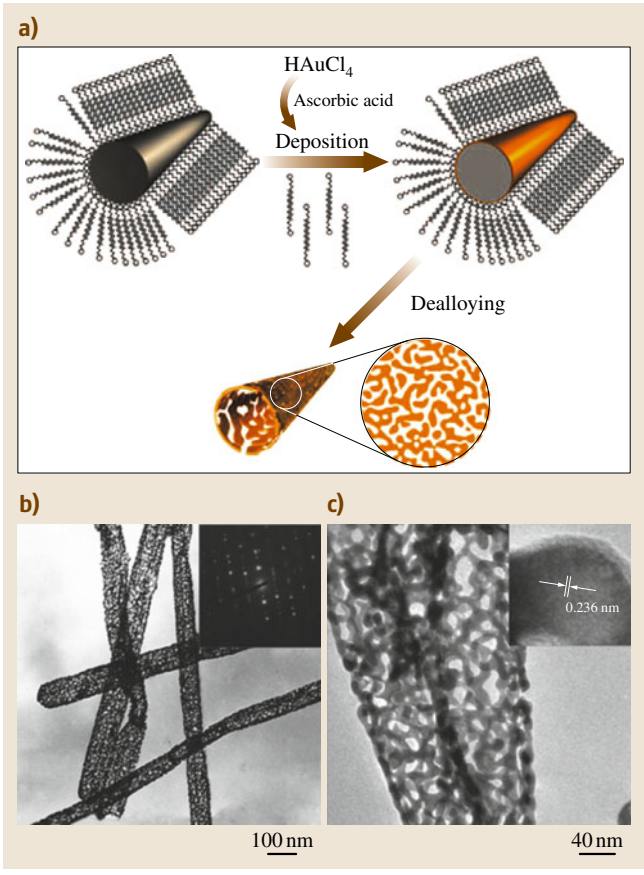


Fig. 21.14 (a) Schematic illustration of the synthesis process of Au-Ag alloy NPNTs. **(b–c)** TEM images of Au-Ag alloy NPNTs (after [21.112])

Yoo and *Park* [21.113] reported that ultrathin, platinum-coated, nanoporous nanorod arrays can be synthesized by electrodepositing gold and silver ions into porous alumina membranes, followed by selective dealloying and copper-UPD redox exchange reactions. Using a similar strategy, *Shin* et al. [21.114] synthesized hollow nanotubes (pore $d > 100$ nm) with nanoporous walls (pore $d < 10$ nm).

Metallic nanostructures with hollow interiors or tailored porosity represent a special class of attractive materials with intriguing chemicophysical properties. *Gu* et al. [21.112] recently reported the fabrication of a new type of metallic nanoporous nanotube structure based on a facile and effective combination of nanocrystal growth and surface modification. By controlling the individual steps involved in this process, such as nanowire growth, surface modification, thermal diffusion, and dealloying, one-dimensional (1-D) Ag-Au alloy nanoporous nanotubes (NPNTs) could be prepared with tailored structural features and predesigned functionalities. Figure 21.14a schematically shows the

synthesis process of Au-Ag alloy NPNTs, and the corresponding microstructures are presented in Fig. 21.14b,c.

We have found that high-surface-area Ag nanostructures can be used as novel effective template materials for construction of nanotubular mesoporous Pt/Ag and Pd/Ag alloy structures (Fig. 21.15), which are realized via room-temperature galvanic replacement reactions with H_2PtCl_6 and K_2PdCl_4 solutions by adding a high concentration of Cl^- ions as a coordinating agent [21.115]. Moreover, electrochemical measurements indicate that the resulting hollow and porous bimetallic nanostructures show enhanced electrocatalytic activities and CO tolerance with better durability toward methanol and formic acid oxidation due to alloying with Ag.

Due to the difference in dealloying between individual phases, a two-phase alloy can be dealloyed to form nanoporous metal composites. Nanoporous gold composites (NPGCs) can be produced through chemical dealloying of two-phase Al-Au alloys comprising Al_2Au and AlAu intermetallic compounds under free corrosion conditions [21.69]. The dealloying of Al_2Au and AlAu proceeds separately, resulting in the formation of the NPGCs. The microstructures of the NPGCs are composed of intracellular and intercellular areas which exhibit two kinds of nanoporous structures with different length scales of ligaments/channels. The nanoporous structure of the intracellular areas forms due to the dealloying of Al_2Au, while that of the intercellular areas forms owing to the dealloying of AlAu. Moreover, the proportion of the intercellular areas in the NPGCs increases with increasing Au content in the starting Al-Au alloys. Nanoporous palladium composites with second-phase embeddings can be fabricated through chemical dealloying of a rapidly solidified $Al_{70}Pd_{30}$ alloy in alkaline or acidic solutions under free corrosion conditions [21.116]. The experimental results show that the precursor alloy is composed of Al_3Pd and Al_3Pd_2 intermetallic compounds, and the resultant composites comprise the nanoporous palladium matrix dealloyed from Al_3Pd and the undealloyed Al_3Pd_2 embeddings.

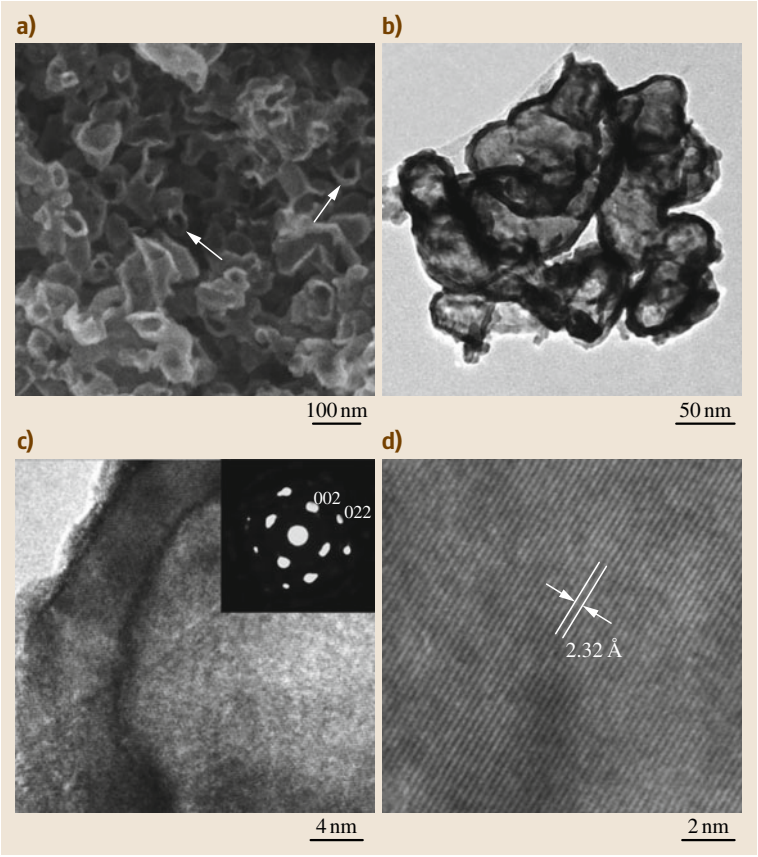


Fig. 21.15 **(a)** SEM, **(b–c)** TEM, and **(d)** HRTEM images of the sample resulting from reacting nanoporous silver (NPS) with $[PtCl_6]^{-2}$ solution. The *inset* in **(c)** is the corresponding SAED pattern (after [21.115])

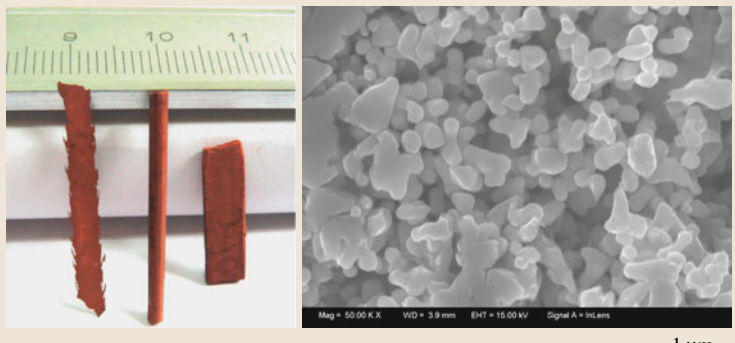


Fig. 21.16 (a) Macrograph showing nanoporous Cu ribbon, rod, and slice obtained by two-step dealloying of Al-40 at % Cu (*from left to right*). (b) SEM image of nanoporous Cu rod (after [21.117])

In addition, bulk nanoporous Cu ribbons, rods, and slices (of centimeter scale) can be fabricated by dealloying of Al-Cu alloys under free corrosion conditions (Fig. 21.16) [21.117]. These nanoporous Cu ribbons and bulk rods/slices can serve as model materials to investigate the mechanical, physical (for example, electrical resistivity), and chemical properties associated with the random porous structure of nanoporous solids.

21.2.2 Catalytic Properties

Due to their very high specific surface area and nanosized ligaments, nanoporous metals show excellent catalytic properties for a series of important heterogeneous reactions.

Despite the general inertness of gold, finely dispersed gold nanoparticles on suitable oxide supports can demonstrate remarkable catalytic activity for propene epoxidation or CO oxidation. Gold-based catalysts have potential applications in automotive emission control, because unlike platinum or palladium catalysts, they remain active at low temperatures (room temperature). *Zielasek* et al. [21.119] first pointed out that nanoporous gold is a promising material for catalytic applications, because it is self-supporting, thermally and mechanically stable, and shapeable; as a thin foil it could possibly find use as a membrane catalyst. Almost at the same time, *Xu* et al. reported that unsupported nanoporous gold could show extraordinary properties in low-temperature CO oxidation (−30 °C) [21.118]. Figure 21.17 shows the catalytic performance of a-NPG at different temperatures. It was believed that the curved shape of the ligaments could accommodate a high density of low-coordinated surface sites, such as step and kink atoms, which are responsible for the observed catalytic activity. More detailed studies have been carried out on this new catalytic system, including discussion of the active sites of catalysts, the reaction kinetics, and the dependence of the activity on space velocity and temperature [21.120]. The results show strong evidence that metallic gold atoms on NPG are the intrinsic active sites at which the reaction of CO with O_2 occurs. The kinetic study found that the reaction rate of CO oxidation on unsupported NPG depends significantly on the

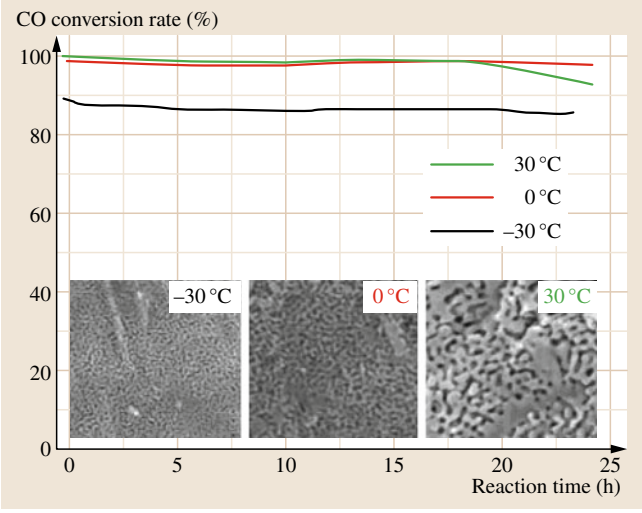


Fig. 21.17 Catalytic performance of a-NPG at different temperatures. In each experiment, 50 mg NPG catalyst and a gas mixture of 1% CO, 10% O_2, and 89% N_2 were used with flow rate of 66.7 ml/min, corresponding to space velocity of 80 040 ml/h gcat. The turnover frequency (TOF) was measured to be about 0.034 s^{-1}. *Insets* are SEM images of NPG samples after catalytic reactions. *Scale bars*: 100 nm (after [21.118]) ◀

CO concentration but only slightly on the O_2 concentration, suggesting that CO adsorption plays a decisive role in CO oxidation on NPG as the rate-limiting step.

Wittstock et al. [21.122] recently reported that nanoporous Au can catalyze selective oxidative coupling of methanol to methyl formate with selectivity above 97% and high turnover frequencies at temperatures below 80 °C. Because the overall catalytic characteristics of nanoporous Au are in agreement with studies on Au single crystals, they deduced that the selective surface chemistry of Au is unaltered but that O_2 can be readily activated with this material. Residual silver is shown to regulate the availability of reactive oxygen.

Recently, *Han* et al. found that nanoporous gold catalysts made by dealloying could be applied in gas-phase selective oxidation of benzyl alcohol to benzaldehyde, delivering good catalytic activity with high selectivity under ambient reaction conditions (Fig. 21.18) [21.121]. By increasing the concentration of oxygen in the gas mixture, the conversion increased greatly, accompanied by a slight decline in selectivity. By using pure oxygen, over 61% conversion with 95% selectivity was achieved at 240 °C. Interestingly, after the catalysts were pretreated with NaOH, the catalytic activity was promoted considerably. The dependence on residual Ag of the performance of NPG catalysts was tested, and in general, higher Ag content did not seem improve the activity and selectivity of NPG for benzyl alcohol oxidation. However, this study cannot rule out the possibility that low levels of Ag may contribute as a promoter to improve the selectivity.

As to the unsupported nature of NPG, however, there is still controversy. *Haruta* [21.123] classified the hypotheses for the active states of gold proposed so far as follows, in order of decreasing size of the gold catalyst:

1. Unsupported gold
2. Junction perimeter between gold and the metal-oxide supports
3. Specific size or thickness of gold clusters or thin layers
4. Cationic gold

He argued that gold nanoporous foams, the surfaces of which might be substantially contaminated by Ag_2O fine particles or patches, are highly active at temperatures even below 0 °C without water and OH^- ions. Actually, the catalysts can be regarded as inversely supported gold catalysts, and the junction perimeters between gold and Ag_2O can account for the high catalytic activity, as in the cases of TiO_2, Fe_2O_3, Co_3O_4, NiO, and CeO_2 supports (hypothesis 2). *Wittstock* et al. [21.124] investigated NPG with respect to its morphology, surface composition, and catalytic properties. In particular, they studied the reaction kinetics for low-temperature CO oxidation in detail, taking the mass transport limitation due to the porous structure of the material into account. Their results revealed that Ag, even if removed almost completely from the bulk, would segregate to the surface, resulting in surface concentrations of up to 10 at. %. While no Ag_2O was observed, they believed that Ag plays a significant role in activating molecular oxygen. Therefore, they thought that NPG should be more appropriately considered as an unsupported bimetallic catalyst rather than a pure Au catalyst.



Fig. 21.18 NPG shows high selectivity and conversion for gas-phase selective oxidation of benzyl alcohol to benzaldehyde (after [21.121])

Most recently, *Moskaleva* et al. [21.125] investigated the catalytic properties of nanoporous gold foams via CO and oxygen adsorption/coadsorption. They analyzed experimental results using theoretical models representing flat Au(111) and kinked Au(321) slabs with Ag impurities. Their results show that Ag atoms incorporated into gold surfaces can facilitate the adsorption and dissociation of molecular oxygen on them. CO adsorbed on top of six-fold-coordinated Au atoms can in turn be stabilized by coadsorbed atomic oxygen by up to 0.2 eV with respect to the clean, unsubstituted gold surface. These experiments suggest a link between the most strongly bound CO adsorption state and the catalytic activity of np-Au. Thus, they believed that their results shed light on the role of silver admixtures in the striking catalytic activity of unsupported gold nanostructures.

NPG catalysts made by dealloying Ag/Au alloys were found to be novel unsupported Au nanocatalysts that exhibited effective catalytic activity and high selectivity ($\approx$ 99%) for aerobic oxidation of D-glucose to D-gluconic acid under mild conditions [21.126]. The activity dependence as functions of pH value, temperature, NPG ligament size, reaction active sites, and reaction kinetics was discussed in great detail. The pos-

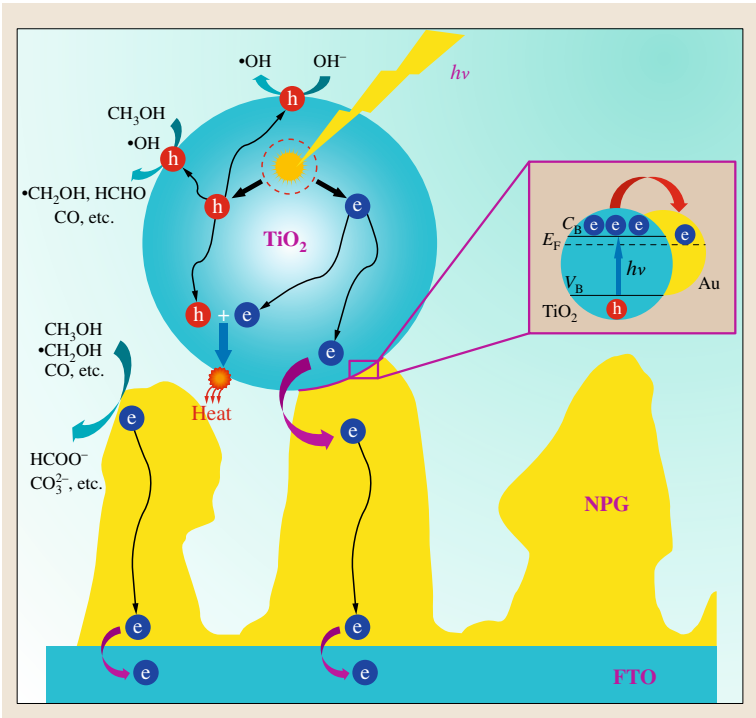


Fig. 21.19 Schematic illustration of a possible mechanism for methanol photoelectrocatalysis on the TiO_2/NPG electrode under UV illumination (after [21.127])

sible contribution from the residual Ag atoms trapped in the NPG ligaments was also discussed, which turned out to be unfavorable for glucose oxidation. The unexpected observation of catalytic activity of NPG with ligament size as large as 60 nm indicated that low-coordinated surface Au atoms should be the reaction active sites for glucose oxidation.

Recently, *Jia* et al. found that commercial TiO_2 nanoparticles can be assembled on the surface of NPG to fabricate novel TiO_2/NPG nanocomposite electrodes [21.127]. Large photocurrent and nearly reversible voltammetric responses were observed for methanol photoelectrocatalysis under ultraviolet (UV) radiation, indicating effective elimination of gold surface passivation due to a pronounced synergistic effect between TiO_2 and NPG. A possible mechanism was proposed to elucidate such a synergistic effect, based on the reaction of photogenerated reactive intermediates on the surface of NPG (Fig. 21.19). Kinetic studies showed that the coupling of TiO_2 with NPG in the system could lead to about a 30% decrease of apparent activation energy for methanol electrooxidation. In addition, porous AgCl/Ag nanocomposites show enhanced visible-light photocatalytic properties for degradation of methyl orange (MO) dye [21.128].

Asao et al. [21.129] recently discovered that nanoporous gold exhibited remarkable catalytic activity for oxidation of organosilane compounds with water. The catalyst was easily recoverable and could be used at least five times without leaching or loss of activity. The observed excellent durability of the catalyst was also confirmed by SEM images. Indeed, the nanoporous structure of the catalyst did not change, even after five uses for oxidation of dimethylphenylsilane.

21.2.3 Electrocatalytic Properties

Nanoporous metals represent a new class of high-surface-area nanostructures, where the interconnected interstices and channels extending in all three dimensions allow unblocked transport of medium molecules and electrons, which is particularly desirable for catalysis. In addition, made by dealloying in aqueous solutions, nanoporous metals have extremely clean surfaces, readily available for surface electrode reactions. Being support free and particle free, nanoporous metals completely eliminate the support corrosion problem and particle aggregation/sintering problem. It is thus interesting to explore their electrocatalytic performance by evaluating their potential in important energy con-

version applications, such as as anode catalysts in fuel cell technology.

NPG made by dealloying Au-Ag has been investigated as a novel electrode material for methanol electrooxidation [21.130]. Compared with bulk Au electrode, oxidation and subsequent reduction of NPG occur at significantly negative potentials in both acid and alkaline solutions. NPG shows great catalytic activity for methanol electrooxidation, but the structure quickly coarsens upon long-time potential cycling. Interestingly, after surface modification with only a tiny amount of platinum, NPG exhibits greatly enhanced electrocatalytic activity toward methanol oxidation in alkaline solution, which is exemplified by a broad and high anodic peak during the positive scan and two secondary oxidation peaks in the subsequent reverse scan. At the same time, SEM observation and long-time potential cycling both prove that Pt-NPG has greatly enhanced structure stability as compared with bare NPG. *Yu* et al. [21.131] also reported that self-supported nanoporous gold film electrodes show high catalytic activity and stability in direct electrooxidation of methanol.

Ge et al. investigated an ultralow-platinum-loading electrocatalyst based on a novel nanoporous membrane metal (NPG leaf), and its excellent performance toward methanol and CO electrooxidation [21.132]. Although it is widely accepted that the highest Pt utilization can be achieved only on monolayer (or submonolayer) type structures, to which these NPG-based nanostructures are close, the most important characteristic of Pt-NPG-type structures is the easy accessibility to almost all surface precious atoms by target molecules, which the current fabrication protocol based on physical mixing of nanoparticles can hardly achieve. This can explain why 0.5 min Pt-NPG samples exhibit much better performance than commercial Pt/C, although they have similar platinum utilization values. Considering the structure flexibility of NPG and the strong synergistic effect between Pt and Au, Pt-NPG may represent an alternative ultralow precious-metal loading catalyst to traditional ones with promising performance in important green energy technologies, such as direct methanol fuel cells (DMFC). Furthermore, by effectively enhancing the Pt utilization and providing a unique surface structure, electrooxidation of formic acid on Pt-NPG was found to be highly sensitive to its surface structure [21.133]. An unparalleled increase by nearly two orders of magnitude in catalytic activity was achieved on NPG electrodes decorated with submonolayer Pt atoms, as compared with commercial Pt/C catalyst under the same testing conditions. Figure 21.20 shows the catalytic activity of Pt-NPG membrane catalysts towards electrooxidation of small organic molecules. Through a simple immersion–electrodeposition (IE) method, a tiny amount of Pt can be deposited in quasi-two-dimensional form onto the NPG substrate, forming nanostructured bimetallic Pt-Au catalysts [21.134]. Such Pt-Au nanostructures have much higher structural stability than the bare NPG. Moreover, they exhibit better catalytic activity and stronger poison resistance than commercial Pt-Ru catalysts because of the synergistic effect of the bimetallic composition.

Ultrathin Pt films from one to several atomic layers can be decorated onto NPG membranes by utilizing UPD of Cu onto Au or Pt surfaces, followed by in situ redox replacement reaction (RRR) of UPD Cu by Pt [21.135]. The thickness of Pt layers can be controlled precisely by repeating the Cu-UPD-RRR cycles. TEM observations coupled with electrochemical testing suggest that the morphology of the Pt overlayers changes from an ultrathin epitaxial film in the case of one or two atomic layers to well-dispersed nanoislands in the case of four and more atomic layers. Moreover, the as-prepared NPG-Pt membranes maintain a single-crystalline structure, even though the thickness of the Pt films reaches six atomic layers, indicating that the decorated Pt films retain the same crystallographic relationship to the NPG substrate during the entire fabrication process. Due to the regular modulation of Pt utilization, the electrocatalytic activity of NPG-Pt exhibits interesting surface structure dependence in methanol, ethanol, and CO electrooxidation reactions (Fig. 21.21). These novel bimetallic nanocatalysts show excellent electrocatalytic activity and greatly enhanced poison tolerance as compared with commercial Pt/C catalysts.

Recently, *Wang* et al. successfully fabricated a new type of sandwich-type nanostructured electrocatalyst, NPG-Pt-Au, that simultaneously fulfills three key requirements as a good practical formic acid electrooxidation catalyst: ultralow Pt loading, great tolerance to poisoning, and high stability (Fig. 21.22) [21.136]. Time-resolved surface-enhanced infrared absorption (SEIRA) spectroscopy demonstrated that the greatly enhanced catalytic activity was achieved by changing the reaction pathways by using Au surface clusters, which also contribute to the stabilization of the catalyst. Considering that it is possible to tailor the respective structures and compositions within each structure unit, this work represents a general design strategy to

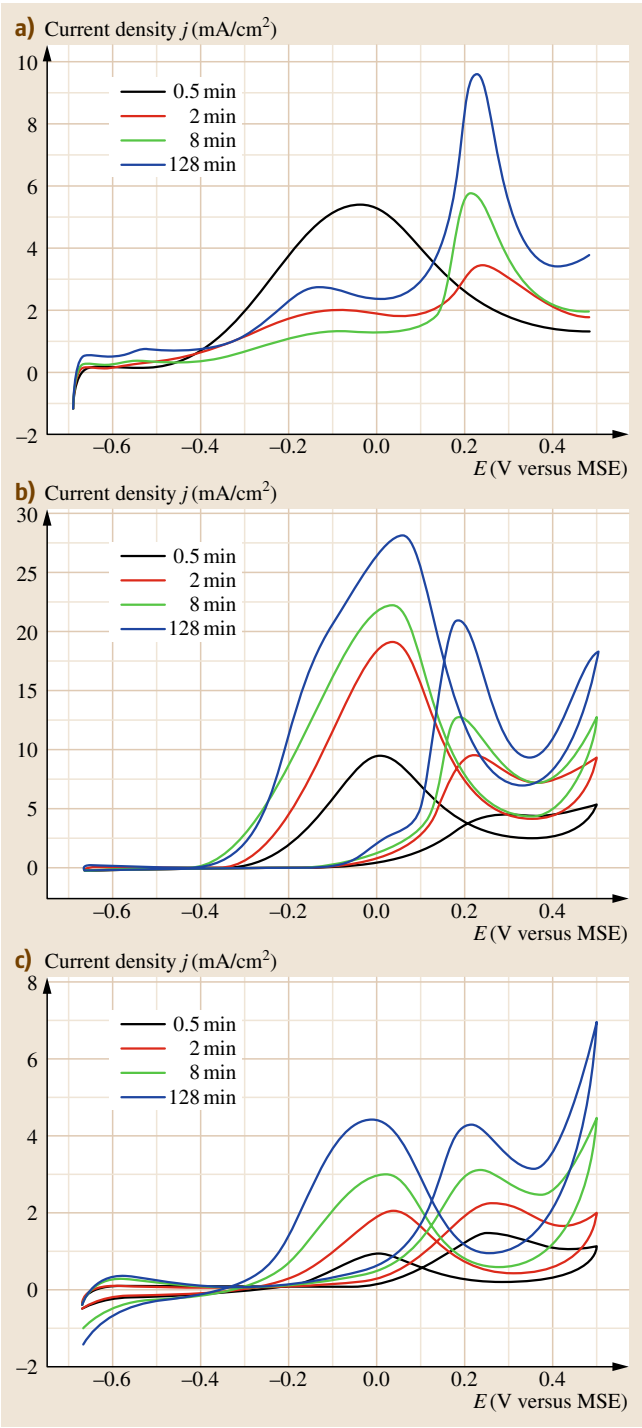


Fig. 21.20a–c Cyclic voltammetry (CV) curves for Pt-NPG samples in **(a)** 0.1 M $HClO_4$ + 0.1 M HCOOH, **(b)** 0.1 M $HClO_4$ + 0.1 M HCHO, and **(c)** 0.1 M $HClO_4$ + 0.1 M CH_3CH_2OH (MSE = mercury/mercurous sulfate electrode) (after [21.133]) ◀

functional nanocatalysts that shows great potential for various energy and environmental applications.

It is known that monometallic Pt is susceptible to deactivation or poisoning during catalytic and electrocatalytic processes; for example, Pt catalysts can be deactivated due to carbon deposition or coking in many heterogeneous catalytic reactions, and can also be poisoned by CO adsorption due to the strong bonding of CO on the Pt surface. Adding a second metallic component can enhance the activity, selectivity, and stability of pure metal catalysts. It has been reported that formation of bimetallic alloy nanostructures with other metals, such as Ru, Ag, and Au, can reduce CO poisoning. Nanoporous Au-Pt and Pt-Ru alloys with predetermined compositions can be fabricated through selective etching of Cu and Al from CuAuPt and PtRuAl precursors [21.98, 137]. Moreover, these high-surface-area alloy nanostructures show greatly enhanced specific activity and distinct surface reactivity toward electrooxidation of some small organic molecules, such as methanol and formic acid. The interaction between constituent metal elements may lead to special surface ensembles with unique structural properties, which can exhibit strong synergistic effects with greatly enhanced catalytic activities under appropriate conditions.

In addition, dealloying has been found to be an effective route to enhance the electrocatalytic properties of some other nanostructures, such as core–shell nanoparticles, nanowires, etc. *Shao* et al. [21.138] reported synthesis of a core–shell catalyst consisting of a Pt monolayer as the shell and porous/hollow Pd-Cu alloy nanoparticles as the core. The porous/hollow Pd-Cu nanoparticles were fabricated by selectively dissolving a less noble metal, Cu, using an electrochemical dealloying process. The Pt mass activity for the oxygen reduction reaction (ORR) of a Pt monolayer deposited on such a porous core is 3.5 times higher than that of a Pt monolayer deposited on bulk Pd nanoparticles and 14 times higher than that of state-of-the-art Pt/C electrocatalysts. *Strasser*'s group found that voltammetric dealloying of bimetallic platinum–copper (Pt-Cu) alloys is an effective strategy to modify the surface electrocatalytic reactivity of Pt bimetallic nanoparticles [21.139–

141]. The dealloyed active catalyst phase consists of a core–shell structure in which a multilayer Pt-rich shell surrounds a Pt-poor alloy particle core. The electrocatalytic Pt mass activity of the dealloyed core–shell particles for the ORR exceeds that of state-of-the-art Pt electrocatalyst by more than a factor of 4 and thus meets performance targets for fuel cell cathodes [21.142]. *Liu* et al. [21.143–145] fabricated nanoporous Pt-Co, Pt-Ni, and Pt-based multimetallic alloy nanowires through the combination of electrodeposition into AAO templates with dealloying. These nanoporous alloy nanowires exhibit distinctly enhanced electrocatalytic activities toward methanol oxidation as compared with current state-of-the-art Pt/C and PtCo/C catalysts.

The improvement of catalysts for the four-electron ORR ($O_2 + 4H^+ + 4e^- \rightarrow 2H_2O$) remains a critical challenge for fuel cells and other electrochemical energy technologies. Recently, *Snyder* et al. [21.146] showed that a tailored geometric and chemical materials architecture can further improve ORR catalysis by demonstrating that a composite nanoporous Ni-Pt alloy impregnated with a hydrophobic, high-oxygen-solubility, protic ionic liquid has extremely high mass activity (Fig. 21.23). They stated that the results are consistent with an engineered chemical bias within a catalytically active nanoporous framework that pushes the ORR towards completion.

21.2.4 Mechanical Properties

Mechanical breakdown or fracture in random porous media has been the subject of considerable computational and theoretical research [21.147]. Nanoporous metals should serve as a new model system for studying various physical properties and mechanical properties associated with three-dimensional random porous structures.

It should be noted that in network systems the terms "ductile" and "brittle" refer to the nature of the damage introduced into the sample during the fracture process. If many separated or distributed microcracks develop in the sample during fracture, the behavior of the system is termed *ductile*, and if only a few cracks form in the sample prior to failure, it is characterized as *brittle*. *Li* and *Sieradzki* [21.148] first observed a microstructural length scale-controlled ductile–brittle transition in NPG, similar to previous results for a network system described by *Kahng* et al. [21.149]. The sample-size-driven ductile–brittle transition may be quite universal with respect to the exact nature of the constitutive behavior of the individual ligaments in the random

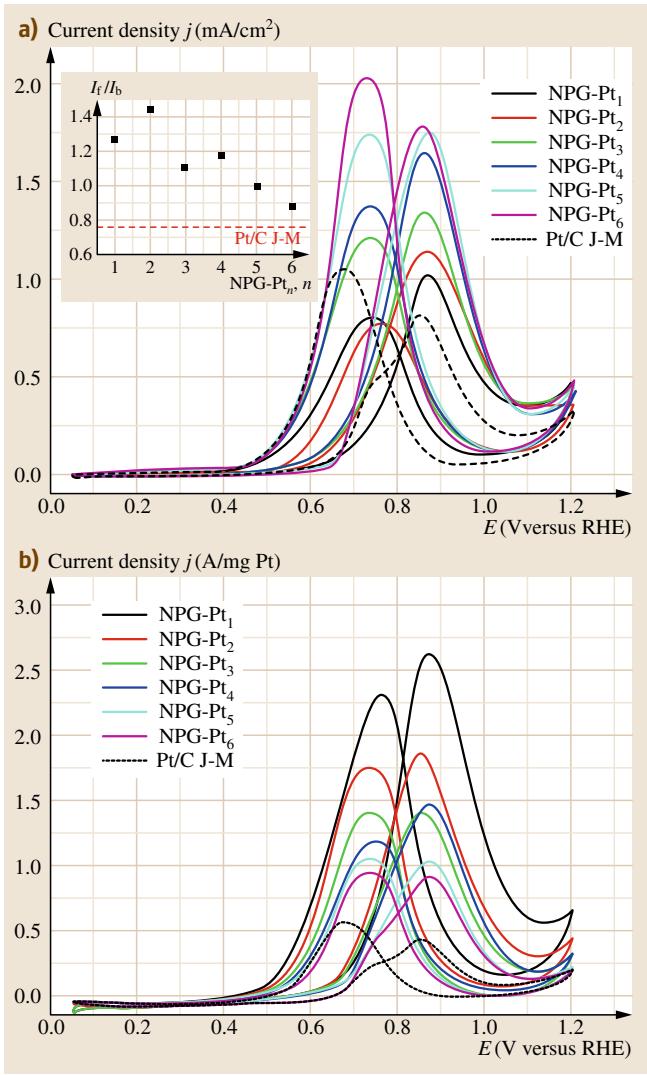


Fig. 21.21a,b ECSA (**a**) and mass (**b**) normalized CVs of NPG-Pt_n for methanol electrooxidation in 0.5 M H_2SO_4 + 1.0 M CH_3OH. CV curve (*dotted black line*) for a commercial Pt/C catalyst (Johnson Matthey, 20 wt %) is also included for comparison. The *inset* in part (**a**) shows the I_f/I_b values of NPG-Pt_n along with that for the commercial Pt/C catalyst (*red line*). Scan rate: 20 mV/s (RHE = reversible hydrogen electrode) (after [21.135])

structure. Thus, the strong length scale dependence of the mechanical behavior of NPG makes it a particularly useful material to study nanoscale mechanics.

The question still remains whether the brittle nature of nanoporous Au is caused by intrinsic brittleness of Au ligaments on the nanometer length scale or is

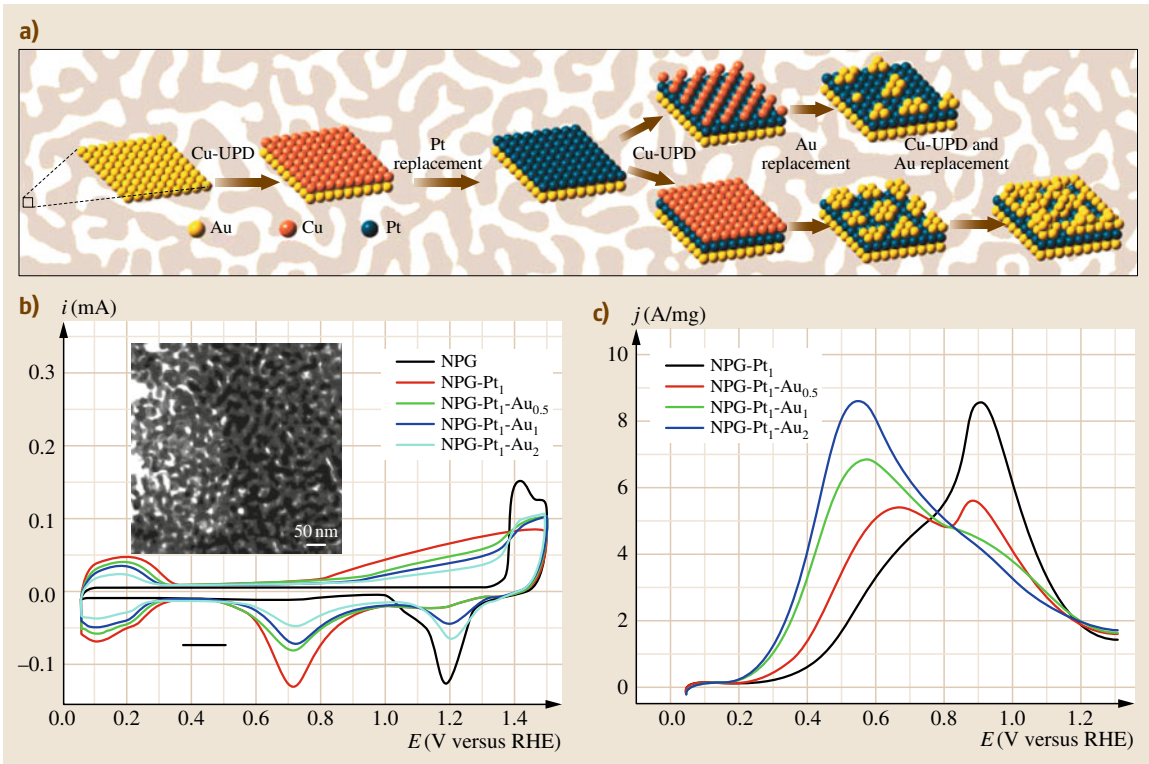
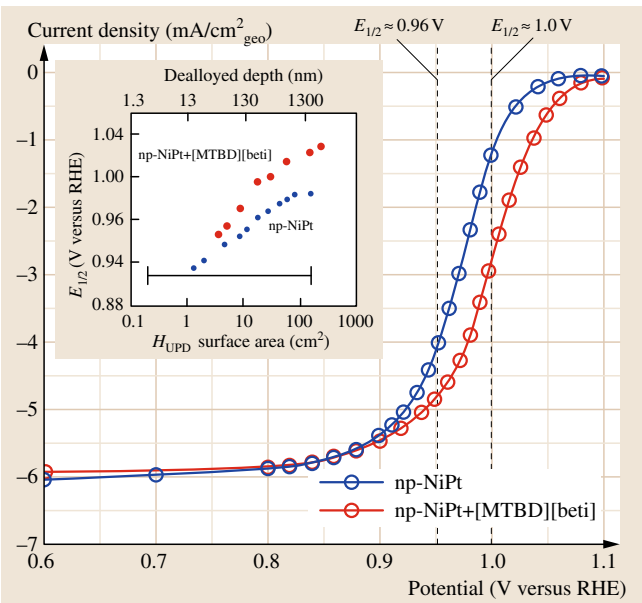


Fig. 21.22 **(a)** Schematic illustration of the fabrication procedure of NPG-Pt_1-Au_x catalysts. **(b)** Electrochemical CV for NPG-Pt_1-Au_x catalysts in 0.5 M H_2SO_4 (RHE, reversible hydrogen electrode). *Inset*: TEM image of NPG. **(c)** Mass-specific forward CV segments of NPG-Pt_1-Au_x catalysts in 0.1 M $HClO_4$ and 0.05 M HCOOH (after [21.136])



a consequence of the macroscopic structure. *Biener* et al. [21.150] reported on the fracture behavior of NPG with an open sponge-like morphology of interconnecting ligaments on the nanometer length scale. Despite its macroscopic brittleness, NPG is microscopically a very ductile material, as ligaments strained by as much as

Fig. 21.23 Potentiostatic ORR curves and half-wave as a function of roughness factor. np-NiPt (*red*) and np-NiPt+ [MTBD][beti] (*blue*) electrodes in O_2-saturated 0.1 M $HClO_4$ at 25 °C ($R_f = 143$ for all electrodes) with disc electrode rotation rate of 1600 rpm. Potentiostatic current measures were made at the indicated potential values (*circles*). *Inset*: Half-wave potential for both np-NiPt and composite np-NiPt + [MTBD][beti] as a function of H_{UPD} surface area, dealloyed depth, and roughness factor (R_f) (RHE = reversible hydrogen electrode; [MTBD][beti] = [7-methyl-1,5,7-triazabicyclo[4.4.0]dec-5-ene][bis(perfluoroethylsulfonyl)imide]) (after [21.146])
◀

200% can be observed in the vicinity of crack tips. Cell-size effects on the microscopic failure mechanism were studied by annealing treatments that increased the typical pore size/ligament diameter from 100 nm to 1 μm. Ligaments with diameter of 100 nm fail by plastic flow and necking, whereas failure by slip was observed for larger ligaments with diameter of 1 μm. The absence of slip marks in 100 nm-sized ligaments suggests strongly suppressed dislocation activity, consistent with the high yield strength of NPG. They also investigated the plastic deformation of NPG under compressive stress by depth-sensing *nanoindentation* [21.151]. Mean hardness of 145 ± 11 MPa was reported for the investigated NPG with a length scale of 100 nm, which is 10 times higher than the hardness predicted by scaling laws of open-cell foams. *Volkert* et al. [21.152] investigated the mechanical properties of NPG by uniaxial compression. Micrometer-sized columns were machined in the surface of NPG using a focused Ga^+ beam and compressed with a flat punch in a nanoindenter. Using scaling laws for foams, the yield strength of the 15 nm-diameter ligaments was estimated to be 1.5 GPa, close to the theoretical strength of Au. This value agrees well with extrapolations of the yield strength of submicron, fully dense gold columns and shows that, in addition to foam density and structure, the absolute size of ligaments and cell walls can be used to tailor foam properties. *Hodge* et al. [21.153] systematically investigated the mechanical properties of NPG with a wide range of ligament sizes and densities, and concluded that (a) NPG has a fracture behavior dictated by the ligament size, and (b) NPG is a high-yield-strength material.

Biener et al. [21.155] further demonstrated that nanoporous metals can be envisioned as a three-dimensional network of ultrahigh-strength nanowires, thus bringing together two seemingly conflicting properties: high strength and high porosity. They characterized the size-dependent mechanical properties of NPG using a combination of nanoindentation, column microcompression, and molecular dynamics simulations. They found that NPG can be as strong as bulk Au, despite being a highly porous material, and that the ligaments in NPG approach the theoretical yield strength of Au. *Mathur* and *Erlebacher* [21.156] determined the Young's modulus of NPG with controlled porosity variation between 3 and 40 nm by mechanical testing of ≈ 100 nm-thick, free-standing, large-grained, stress-free films of NPG using a buckling-based method. Their results show a dramatic rise in the effective Young's modulus of NPG with decreasing ligament size, especially below 10 nm. *Hodge* et al. [21.154] performed depth-sensing nanoindentation tests on NPG ranging from 20% to 42% relative density with ligament sizes ranging from 10 to 900 nm. The Gibson and Ashby yield strength equation for open-cell macrocellular foams was modified to incorporate ligament size effects. Their study demonstrated that, at the nanoscale, foam strength is governed by ligament size, in addition to relative density (Fig. 21.24). Furthermore, the ligament length scale was presented as a new parameter to tailor foam properties and achieve high strength at low densities. Later, *Hodge* et al. [21.157] studied the effect of Ag and the relative density on the elastic properties of NPG by depth-sensing nanoindentation. It was observed that the effect of the relative density on the elastic properties of NPG seems to be much stronger than predicted by the Gibson and Ashby relationship. Even Ag contents as low as 1 at. % can significantly change the modulus values. On the other hand, the elastic modulus of NPG seems to be independent of the ligament size.

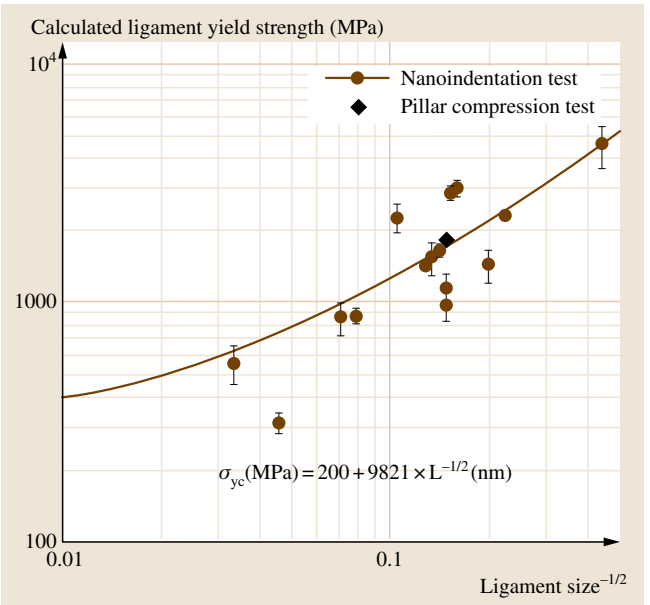


Fig. 21.24 Relationship of ligament size to ligament yield stress for nanoporous gold obtained by nanoindentation and by column microcompression testing (after [21.154])

Lee et al. [21.158] fabricated a free-standing dog-bone-shaped specimen with a gage section 7 μm long, 300 nm wide, and 100 nm thick, from NPG by dealloying *white gold* leaf ($Au_{37.4}Ag_{62.6}$ in [at.] %). The elastic modulus, residual stress, and yield stress were measured by deflective tensile testing and nanoindentation to be about 9 GPa, 65 MPa, and 110 MPa, respectively.

According to scaling laws, they further determined the yield stress within an individual ligament to be as high as 1.45 GPa, which approaches the theoretical shear strength of the material at which adjacent atomic planes slide past one another without the mediating influence of dislocations [21.159].

Seker et al. [21.160] investigated the effects of postfabrication annealing on the mechanical properties of free-standing nanoporous gold structures. Mechanical properties were measured using combinations of free-standing beam deflection, wafer curvature, and nanoindentation. The relative density of all sample geometries increased as the annealing temperature was increased. However, the evolution of the average pore size (with annealing) depended on the geometry, and hence on the boundary conditions, of the specimen. Differences in porosity evolution were reflected in the mechanical property measurements: while the elastic modulus and residual stress generally increased with increasing annealing temperature (due to densification), pore coalescence in films on substrates led to the most dramatic changes. Later, *Seker* et al. [21.161] studied the effects of annealing prior to dealloying on the mechanical properties of nanoporous gold microbeams. Normally, free-standing nanoporous gold beams fracture during dealloying owing to volume shrinkage. They found that annealing after release, yet prior to dealloying, prevents failure during the selective dissolution step. Experiments in which annealing was performed at temperatures $< 400\,^{\circ}\mathrm{C}$ illustrate that permanent buckling of the free-standing solid alloy beams is required to prevent failure of the nanoporous beams during dealloying. In contrast, annealing of beams prior to release, or annealing temperatures $< 200\,^{\circ}\mathrm{C}$ (which do not cause permanent buckling deformation), do not mitigate dealloying failures.

Jin et al. [21.162] recently reported on the fabrication and mechanical behavior of macroscopic, crack-free nanoporous gold samples which exhibit excellent ductility in compression tests. Their yield stress is significantly lower than that expected based on scaling laws or on previous nanoindentation experiments. Electron backscatter diffraction imaging reveals a polycrystalline microstructure with grains larger than 10 μm, which acquire a subdomain structure during plastic flow but remain otherwise intact. They highlighted the action of lattice dislocations which can travel over distances much larger than the ligament size. This results in collective deformation of the many ligaments in each grain. Remarkably, the dislocation cores are partly located in the pore channels. Their results suggest a critical view of the conversion between indentation hardness and yield stress in previous work.

The selection of a structural material requires a compromise between strength and ductility. Materials design strategies that allow for recoverable tuning of the mechanical properties would thus be desirable, either in response to external control signals or in the form of spontaneous adaptation, for instance, in self-healing. Most recently, *Jin* and *Weissmüller* [21.163] designed a material that has a hybrid nanostructure consisting of a strong metal backbone that is interpenetrated by an electrolyte as the second component. By polarizing the internal interface via an applied electric potential, they accomplished fast and repeatable tuning of yield strength, flow stress, and ductility (Fig. 21.25). Their results thus allow the user to select, for instance, a soft and ductile state for processing and a high-strength state for service as a structural material.

21.2.5 Optical Properties

Maaroof et al. [21.164] used ellipsometry and spectrophotometry to study the optical properties of mesoporous gold films obtained by dealloying of Al_2Au precursor. The complex refractive indices of the optically equivalent uniform smooth layer satisfy Kramers–Kronig (KK) self-consistency but have unusual dispersion relations and magnitudes for a film containing the amount of noble metal present. Mesoporous gold films exhibit unique dispersion in their optical response across all near-infrared (NIR) wavelengths. The effective optical constants as a function of wavelength, which are physically acceptable from a dispersion viewpoint, are neither metal nor insulator like. This is in effect a quite new class of optical material.

Later, *Maaroof* et al. [21.165] investigated and modeled the far-field plasmonic behavior of nanoporous gold films with void densities ranging from 60% to 90%. These layers have good direct-current (DC) conductivity and quite different nanostructure from traditional porous layers in which the metal percolates. Gold films with void density f above 70% have high thermal emittance for a conductor of their thicknesses, and their flat spectral response at visible and near-infrared wavelengths is not metal like. They derived effective optical constants which become plasmonic at wavelengths between 1.8 and 4 μm for f from 72% to 87%. This onset is much longer than that in bulk gold. For void densities below 70%, the onset of plasmonic behavior is much closer to the dense material. A test was implemented for surface plasmon polaritons (SPPs)

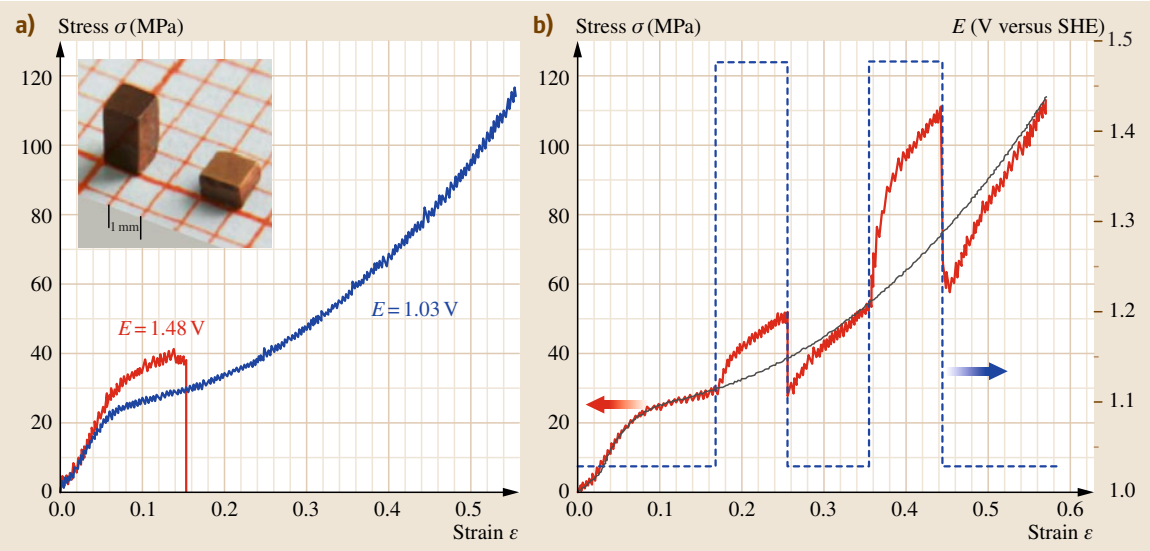


Fig. 21.25a,b Potential dependence of strength and flow stress of NPG. **(a)** Compressive stress–strain curves of engineering stress σ, versus engineering strain ε, measured in situ at constant potentials. Ligament surface is covered with submonolayer-thick oxygen when $E = 1.48$ V and is clean when potential is held at 1.03 V. The *inset* is a photograph of NPG samples with clean surface before and after compression. **(b)** Responses of plastic flow (*red*) to potential jumps. Data obtained at constant potential of 1.03 V (*gray*) were plotted for comparison (SHE = standard hydrogen electrode) (after [21.163])

under illumination. The more porous films show no evidence of SPP, while the less porous films display weak evidence. Thus, by tailoring the void content in these nanostructures, one can tailor the onset of effective plasmonic response across a wide range from 0.8 to 4 μm and emittance from around 0.9 down to low values. An effective uniform metal response was thus found in the presence of surface nanostructure without the interface absorption found in dense gold layers with structured surfaces.

Materials multifunctionality for optical sensing of adsorbates has obvious advantages: in addition to the potential for greater sensitivity, the different length scales associated with a variety of optical phenomena allow a greater variety of adsorption characteristics to be examined. *Yu* et al. [21.166] demonstrated that ultrathin (100 nm) nanoporous gold membranes possess features of both planar metal films that exhibit propagating surface plasmon resonance (SPR) excitations and nanofeatured metals that exhibit localized SPR excitations. They gave illustrative examples of using this material to probe biorecognition reactions and to probe the structure evolution of layer-by-layer deposition of charged dendrimers. Their results are consistent with the very different lengths of the tail of the evanescent field decays associated with each of these plasmon excitation modes. Later, they quantified the plasmonic properties of NPG through direct comparison with thermally evaporated gold (EG) films [21.167]. Cyclic voltammetry and electrochemical impedance spectroscopy experiments reveal that the NPG films have 4–8.5 times more accessible surface area than EG films. Assemblies of streptavidin–latex beads generate p-SPR responses on both NPG and EG films that correlate well with the bead density obtained from SEM images. A layer-by-layer assembly experiment on NPG involving biotinylated anti-avidin IgG and avidin, studied by l-SPR and SEM, showed that the l-SPR signal is directly linked to the accessibility of the interior of the NPG porosity.

Tuning of the localized surface plasmon resonance (l-SPR) of nanoporous metals lies at the heart of manipulating light within extremely small volumes for the implementation of optical devices at the nanoscale. *Qian* et al. [21.168] deposited amorphous alumina on chemically etched nanoporous gold films using atomic layer deposition at room temperature. Nanoporous gold with ultrafine pores of 7 nm diameter was uniformly coated with alumina film as thin as 1.4 nm. l-SPR of the gold skeleton exhibits a detectable red-shift

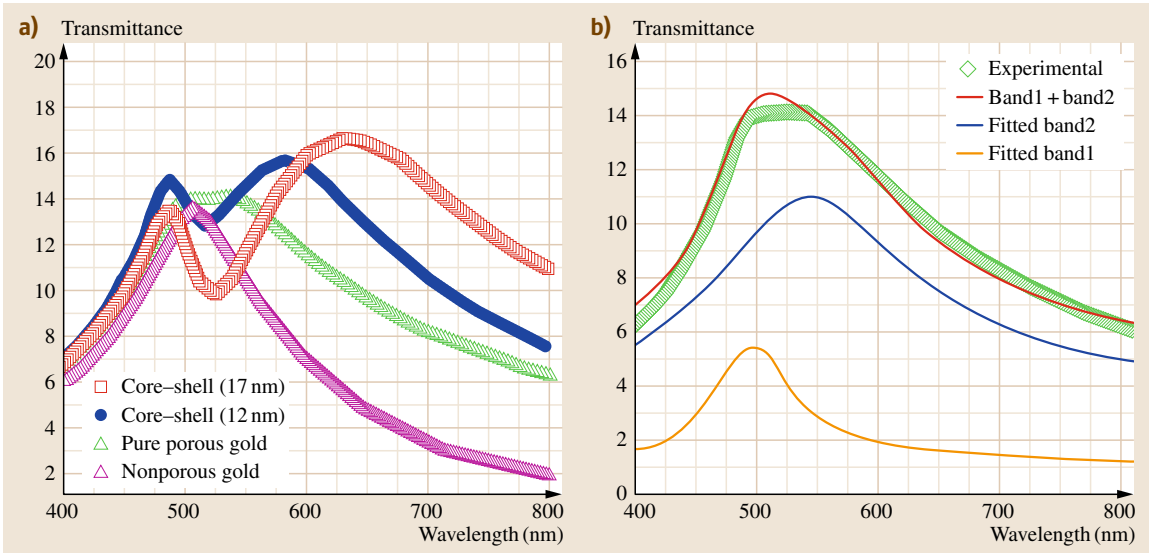


Fig. 21.26 **(a)** Transmittance spectra of nanoporous gold and nanoporous gold–alumina film with different shell thicknesses. The transmittance spectrum of 100 nm-thick gold film without pores is plotted for comparison. **(b)** Fitted spectrum of nanoporous gold indicates two isolated bands at 492 and 537 nm (after [21.169])

in the optical transmittance spectra, the magnitude of which depends on the thickness of the alumina layer. They further investigated the optical properties of nanoporous gold–alumina core–shell films with fixed gold skeletons and different thicknesses of alumina shells [21.169]. Optical transmission of the nanoporous composite films can be tailored through l-SPR excitations of the three-dimensional gold skeleton and the alterable alumina shells as the covering dielectric. A 92 nm red-shift of the l-SPR band is attained via its dielectric medium dependence and the comparable decay length with pore size (Fig. 21.26). The widely tunable optical transmission and significantly improved stability thus suggest incorporating nanoporous gold–alumina into promising nanodevices with reliable performance. Low-temperature surface decoration ($< 100\,^{\circ}\mathrm{C}$) provides a universal route to tune the optical properties while retaining the spatial geometry of the metallic nanostructures.

Surface-enhanced Raman scattering (SERS) originates from the improved inelastic scattering of molecules adsorbed on nanostructured metals and alloys. The SERS enhancements generally depend on the nanoscale characteristics of the metallic substrates, such as surface morphology, size, and aggregation state of nanoparticles. Nanoporous gold with excellent thermal stability and chemical inactivity has recently been exploited as an attractive substrate for SERS applications because of its large surface area and bicontinuous porous structure in three dimensions. *Kucheyev* et al. [21.170] reported that NPG with average pore widths of 250 nm exhibits the largest SERS signal for 632.8 nm excitation. They attributed this to the electromagnetic SERS enhancement mechanism with additional field localization within pores. *Dixon* et al. [21.171] prepared thin nanoporous gold films, ranging in thickness from 40 to 1600 nm, by selective chemical etching of Ag from Ag/Au alloy films supported on planar substrates. Raman scattering measurements for films functionalized with a self-assembled monolayer formed from 4-fluorobenzenethiol show significant enhancements which vary sharply with film thickness and etching times. The maximum enhancement factors reach $\approx 10^4$ for 632.8 nm excitation, peak sharply in the 200 nm thickness range for films prepared at optimum etching times, and show high spot-to-spot reproducibility with $\approx 1\,\mu\mathrm{m}$ laser spot sizes.

Chen's group at the Tohoku University carried out very systematic studies of the SERS behaviors of nanoporous metals. They found that the high SERS of nanoporous gold actually results from smaller microstructure features, either smaller pore sizes or the rough gold ligament surfaces, which are believed to promote electromagnetic field enhancements and provide more active sites for molecule adsorption. Moreover, the strongest SERS enhancement of nanoporous gold

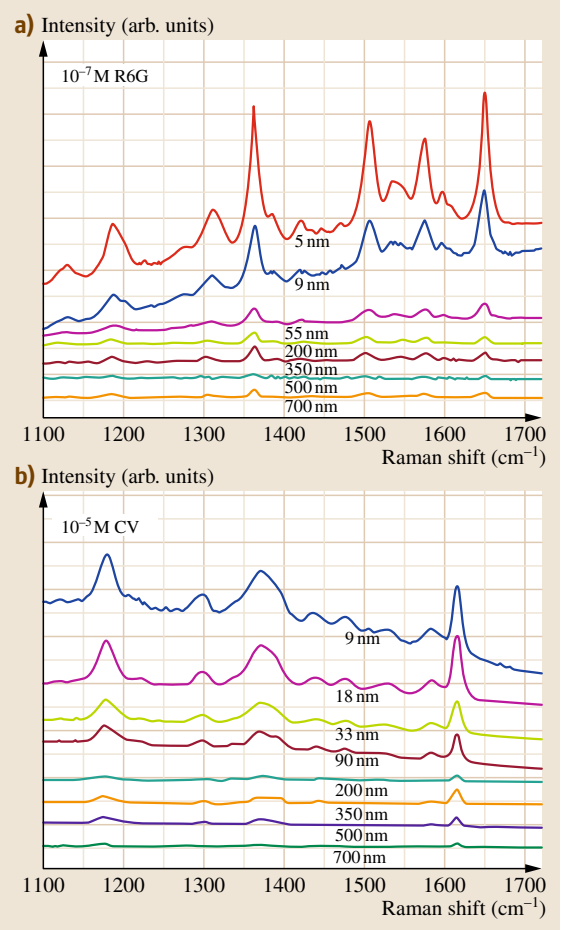


Fig. 21.27a,b SERS spectra of nanoporous gold with different pore sizes for **(a)** 10^{-7} mol/l R6G aqueous solution and **(b)** 10^{-5} mol/l CV methanol solution. Laser excitation: 514.5 nm for R6G and 632.8 nm for CV (CV = crystal violet 10B, R6G = rhodamine 6G) (after [21.172])

takes place for samples with ultrafine nanopore size of 5–10 nm (Fig. 21.27) [21.172]. The SERS intensities from the fracture surfaces of nanoporous gold are about one order of magnitude higher than those from the as-prepared samples [21.173]. Microstructural characterization reveals that the fracture surfaces contain numerous sharp protrusions with 5–10 nm apexes, produced by localized plastic deformation of gold ligaments during failure. They also reported a geometric effect on surface-enhanced Raman scattering of nanoporous gold and found that Raman scattering can be improved by tailoring ligament and nanopore ratios [21.174]. They studied SERS of NPG with various nanopore sizes at temperatures ranging from 80 to 300 K using rhodamine 6G (R6G) as probe molecule. It was found that the SERS intensity dramatically increases as temperature and nanopore size decrease. The improved SERS enhancements result from the combined effects of electron–phonon scattering, the finite ligament size effect, and the electromagnetic coupling between neighboring gold ligaments [21.175]. Moreover, the tunable nanoporosity leads to significant improvements in SERS of nanoporous copper, and peak values of SERS enhancements for both rhodamine 6G and crystal violet 10B (CV) molecules are observed at pore size of 30–50 nm [21.176]. In addition, silver on nanoporous copper core–shell composites also exhibit a dramatically improved SERS effect compared with that of the as-prepared nanoporous copper, and the enhancement factor strongly depends on the reaction time and Ag shell thickness [21.177]. Recently, *Qian* et al. [21.178] reported giant Raman enhancement on nanoporous gold film by conjugating with nanoparticles for single-molecule detection.

Lang et al. [21.179] reported molecular fluorescence enhancement of free-standing nanoporous gold with tunable nanopore size. They found that the fluorescence intensity of indocyanine green adsorbed on human-serum-albumin-coated nanoporous gold films significantly increases with decreasing nanopore size. The large fluorescence enhancement results from the near-field enhanced excitation and radioactive decay rate of fluorophore due to the strong electromagnetic fields produced by nanosized curvatures as well as the coupling between neighboring gold ligaments. By the combination of dealloying and electroless gold plating, they further tailored molecular fluorescence enhancement of free-standing nanoporous gold [21.180]. The nanoporous gold fabricated by this facile method possesses unique porous structures with large gold ligaments and very small pores, and exhibits significant improvements in surface-enhanced fluorescence as well as structure rigidity.

21.2.6 Sensing and Actuation Properties

Chou et al. [21.181] reported a nonenzymatic sensor using a nanoporous platinum electrode to detect glucose directly. The electrode was fabricated by electrochemical deposition and dissolution of Pt-Zn alloy in zinc chloride-1-ethyl-3-methylimidazolium chloride ($ZnCl_2$-EMIC) ionic liquid. Amperometric measurements allowed observation of the electrochemical oxidation of glucose at 0.4 V (versus Ag/AgCl) in pH 7.4

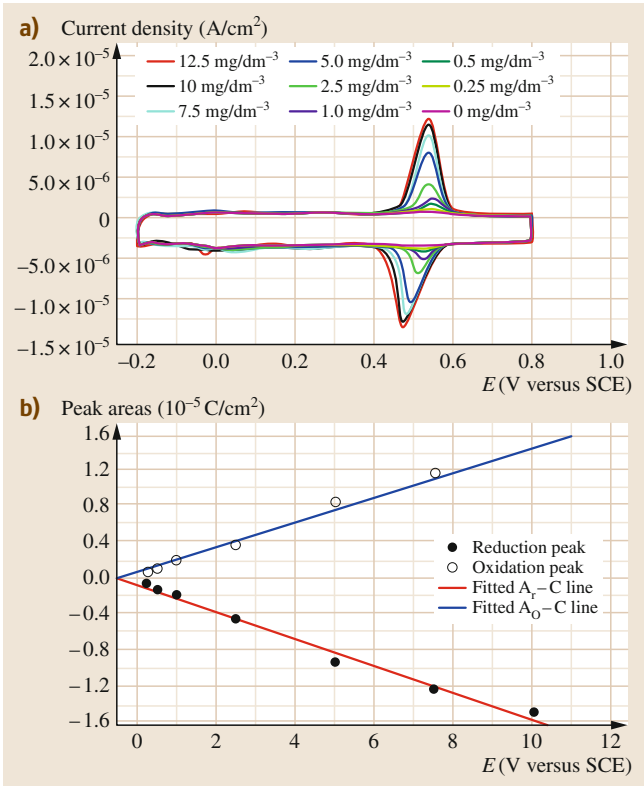


Fig. 21.28 **(a)** CVs for NPG electrode in 0.1 mol/dm^3 H_2SO_4 containing various concentrations of *p*-NP at 50 mV/s. **(b)** The linear dependence of redox peak areas on *p*-NP concentrations (after [21.182])

phosphate buffer solution. The sensor also demonstrates significant reproducibility in glucose detection; the higher the roughness factor of the Pt electrode, the lower the detection limit of glucose. Interfering species such as ascorbic acid and *p*-acetamidophenol can be avoided by using a Pt electrode with a high roughness factor of 151. Overall, the nanoporous Pt electrode is promising for enzymeless detection of glucose at physiological condition.

Qiu et al. [21.183, 184] have shown that nanoporous metals would be very good supports for immobilization of enzymes such as laccase, horseradish peroxidase (HRP), etc. Laccase was immobilized on the surface of NPG by physical adsorption. Laccase immobilized on NPG (100 nm in thickness) was used for enzyme electrode construction. Direct electrochemistry of laccase on NPG supported by glassy carbon electrode (NPG/GC) was achieved with high efficiency due to the outstanding physicochemical characteristics of the NPG. HRP can be immobilized on nanoporous copper by adsorption. Compared with free enzyme, the thermal stability of the immobilized enzyme was greatly improved due to the multiple attachments between the enzyme molecule and the nanoporous copper surface. Moreover, the HRP immobilized nanoporous electrode shows excellent sensing properties for electrochemical detection of *O*-phenylenediamine (OPD).

Liu et al. [21.182] used NPG samples as the working electrode to investigate the redox behavior of *p*-nitrophenol (*p*-NP) by cyclic voltammetry (CV). Quite different from the voltammetric behavior of polycrystalline gold electrode, the CV profiles of NPG display a pair of nearly symmetric redox waves which are ascribed to the reaction of the 4-(hydroxyamino)phenol/4-nitrosophenol couple. They also found that this pair of redox waves are hardly affected by the isomers of *p*-NP; and moreover, their peak areas are linear with the concentration of *p*-NP in the range from 0.25 to 10 mg/dm^3 (Fig. 21.28). Because of high sensitivity and good selectivity, NPG is expected to act as a promising electrochemical sensor material for detecting trace *p*-NP in wastewaters.

Most recently, *Ge* et al. reported that ultrathin freestanding nanoporous gold leaf made by dealloying exhibits excellent electrocatalytic activities toward nitrite oxidation [21.185]. The electrochemical response of nitrite ions on this novel nanoelectrode is found to be independent of pH over a wide range from 4.5 to 8.0, which is markedly different from that of gold oxidation, a process known to be highly pH sensitive. Amperometric study shows a linear relationship for nitrite determination in a concentration range from 1 μM to 1 mM. This nanostructured gold electrode displays good stability, repeatability, and selectivity, suggesting its potential for the development of new electrochemical sensors.

Although actuation in biological systems is exclusively powered by chemical energy, this concept has not been realized in manmade actuator technologies, as these rely on generating heat or electricity first. *Biener* et al. [21.186] have recently demonstrated that surface-chemistry-driven actuation can be realized in high-surface-area materials such as nanoporous gold. They achieved reversible strain amplitudes of the order of a few tenths of a percent by alternating exposure of nanoporous Au to ozone and carbon monoxide. The effect has been explained by adsorbate-induced changes of the surface stress, and can be used to convert chemical energy directly into a mechanical response, thus opening the door to surface-chemistry-driven actuator and sensor technologies. *Jin* et al. [21.187] fabricated

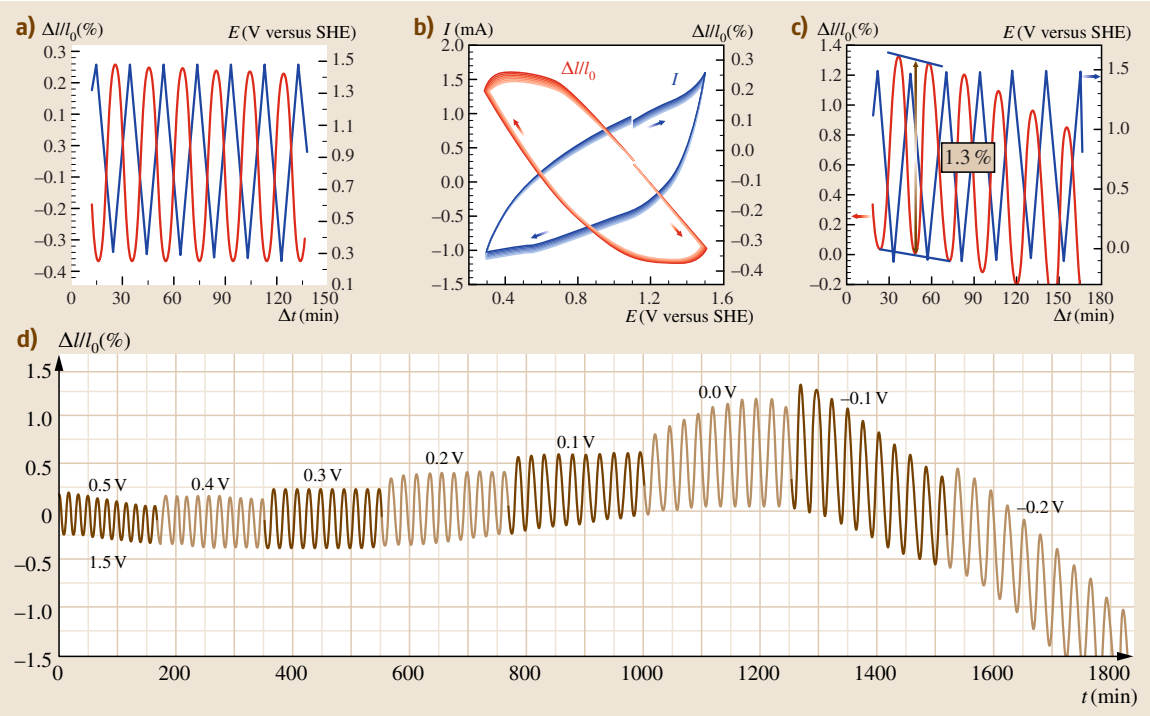


Fig. 21.29a–d Dilatometry experiments on an as-dealloyed nanoporous $Au_{0.8}Pt_{0.2}$ sample (with oxygen covered surface), in 0.7 M NaF solution. **(a)** Cyclic length change along with the potential sweep (10 successive scans) between 0.3 and 1.5 V. **(b)** The voltammogram and the reversible strain. **(c)** Cyclic length change along with the potential sweep between −0.1 and 1.5 V, showing largest strain up to 1.3%. **(d)** Cyclic length change during potential sweep. The upper vertex potential was fixed at 1.5 V. The lower vertex potential decreased by 100 mV after each 10 scans. The scan rate is 2 mV/s (after [21.187])

nanoporous Au-Pt alloys with pore and ligament size down to a few nanometers by dealloying Ag-Au-Pt. Owing to the small structure size and large specific surface area, the surface stress and its variation give rise to significant stress and strain in the bulk of these materials. Dilatometry experiments find electrochemical actuation with large reversible strain amplitude (Fig. 21.29). The linear strain reaches $\approx 1.3\%$, and the strain energy density is up to $6.0\,MJ/m^3$. The associated stresses may approach the elastic limit of the alloy. Their results show that nanoporous Au-Pt alloys are potential materials for use in large-strain electrochemical actuators.

21.2.7 Electrical, Thermal, and Magnetic Properties

Mishra et al. [21.188] measured the electrical conductivity of nanoporous gold in situ during charging and decharging of the surface of the metal. Charge was induced on the surface by making the sample a working electrode in an electrochemical cell. The conductivity was observed to vary reversibly with the induced surface charge. We have shown that the electrical resistivity of the nanoporous metals (Au, Ag, Cu) is one to two orders of magnitude higher than that of their bulk counterparts [21.60]. *Fujita* et al. [21.189] reported the electric conductivity of three-dimensional (3-D) nanoporous gold at low temperatures and in strong magnetic fields. It was found that topologically disordered 3-D nanoporosity leads to extremely low magnetoresistance and anomalous temperature dependence as the characteristic length of nanoporous gold is tuned to be 14 nm. Their study underscores the importance of the 3-D topology of a nanostructure on the electronic transport properties and has implications for manipulating electron transport by tailoring 3-D nanostructures.

Xia et al. [21.190] measured the thermal and electrical conductivities of nanoporous Au thin foils in the temperature range 93–300 K. Resulting from the nanoscale microstructure, the two types of conductivities are both temperature dependent and significantly lower than those of bulk Au. However, the corresponding Lorenz number is strikingly similar to that of bulk Au, indicating that the Wiedemann–Franz law holds perfectly well for nanoporous metals in this temperature range. Compared with the bulk value, the Debye temperature of nanoporous Au is decreased. The theoretical Debye temperature of nanoporous Au can be predicted by its relation to the elastic constants. The results indicate that the nanoporous Au foils should be comprised of macroscopic, single-crystalline porous grains rather than nanocrystals.

Wahl et al. [21.191] reported that the electrical resistance of nanoporous gold prepared by dealloying can be tuned by charging the surfaces of the porous structure in an electrolyte. Reversible variations in the resistance up to approximately 4% and 43% occur due to charging in the regimes of double-layer charging and specific adsorption, respectively. Charging-induced variations in the electron density or of the volume cannot account for the resistance variation, indicating that this variation is primarily caused by charge-induced modifications of the charge carrier scattering at the solid–electrolyte interface. The relative resistance variation in nanoporous Au with surface charging is found to be much higher than reported for porous nanocrystalline Pt. This is due to the lesser resistance contribution from internal grain boundaries. The resistance variation in nanoporous Au is also higher than that found in thin films owing to the stronger surface scattering in the ligament structure compared with plane surfaces. They argued that the strong resistance variation of up to 43% in the regime of specific adsorption is due to reversible formation of a chemisorbed surface layer acting as scattering centers for the charge carriers.

Sun et al. [21.59] reported that nanoporous nickel obtained by dealloying electrodeposited Ni_xCu_{1-x} alloys exhibits enhanced coercivity and reduced magnetic anisotropy. *Hakamada* et al. [21.192] reported that the coercivity of nanoporous Ni decreased with decreasing ligament length in a range below the critical size of about 50 nm. This trend for the nanoporous Ni is the same as those for nanoparticles and nanocrystals. However, the size dependence of coercivity for the nanoporous Ni is lower than those for the other materials. It is suggested that the dimension of the exchange length in the ligament is 1–2 for the nanoporous Ni, resulting in the low size dependence of coercivity. They also fabricated nanoporous Ni specimens with ligament lengths of 10–210 nm and specific surface areas of 0.03–0.58 nm^{-1} by dealloying of $Ni_{0.25}Mn_{0.75}$ alloy and annealing at 473–873 K, and investigated the saturation magnetization in terms of their size dependence [21.193]. Saturation magnetization decreased with decreasing ligament length or increasing specific surface area. This trend is the same as that for Ni nanoparticles. However, the saturation magnetization of nanoporous Ni tends to be lower than that of the Ni nanoparticles when their specific surface areas are the same. It is suggested, therefore, that the surface effect due to a noncollinear arrangement is enhanced by the surface defects in the nanoporous Ni.

21.3 Applications

Due to their unique mechanical, physical, and chemical properties associated with the 3-D bicontinuous interpenetrating ligament–channel structure, nanoporous metals show potential applications in the fields of fuel cells, sensors, actuators, supercapacitors, etc. Here, some examples are briefly summarized.

Increasingly stringent regulations on energy use and environmental protection lead to greater demands to commercialize clean energy-conversion technologies such as polymer electrolyte membrane fuel cells (PEMFCs). Considering that major obstacles remain for hydrogen mass production, storage, and transportation, direct methanol or formic acid fuel cells (DMFCs, DFAFCs) are gaining increasing attention. Therefore, there is growing interest in fabrication of effective electrocatalysts for formic acid and methanol electrooxidation, which is of great significance for commercialization of PEMFCs. One of the main obstacles to the commercialization of PEMFCs is the high cost of catalyst, which involves excess use of precious Pt. In comparison with nanoparticle catalysts supported on carbon black, platinum-coated NPG membranes simultaneously provide superior catalyst/substrate binding as well as high volume dispersion of catalyst, uniformly distributed through a very thin porous electrode with high in-plane conductivity [21.50]. Because the Pt load-

ing in platinum-plated nanoporous gold leaf (Pt-NPGL) can be controlled down to 0.01 mg/cm^2 using only simple benchtop chemistry, the material holds promise as a low-Pt-loading, carbon-free electrocatalyst [21.194]. Stable and high-performance Pt-NPGL/Nafion membrane electrode assemblies (MEAs) were made using a stamping technique by Zeis and coworkers. The performance of Pt-NPGL MEAs is comparable to conventional carbon-supported nanoparticle-based MEAs with much higher loading, generating output power density of up to 4.5 kW/g Pt in a nonoptimized test configuration. Through the construction of a novel NPG-Pt-Au nanostructure, superior performance of high activity and durability in electrocatalytic oxidation of formic acid was achieved at ultralow Pt loading down to microgram per unit-area scale [21.136]. Obviously, creating precious metal skins over nanoporous metal supports is a viable strategy for designing new catalysts for PEM fuel cells.

Chemisorption from the gas or liquid phase can result in a measurable resistance change in a metallic material when at least one dimension is smaller than the mean free path for electrons. *Liu* and *Searson* [21.196] reported on the fabrication of single nanoporous gold nanowires and demonstrated that adsorption of an alkanethiol can be monitored in real time. Single nanowire devices were fabricated by in situ etching of $Au_{0.18}Ag_{0.82}$ alloy nanowires in dilute nitric acid. The evolution of the porous structure was characterized by monitoring the resistance change and comparing with cross-sectional images. The feature size of about 10 nm is less than the mean free path for

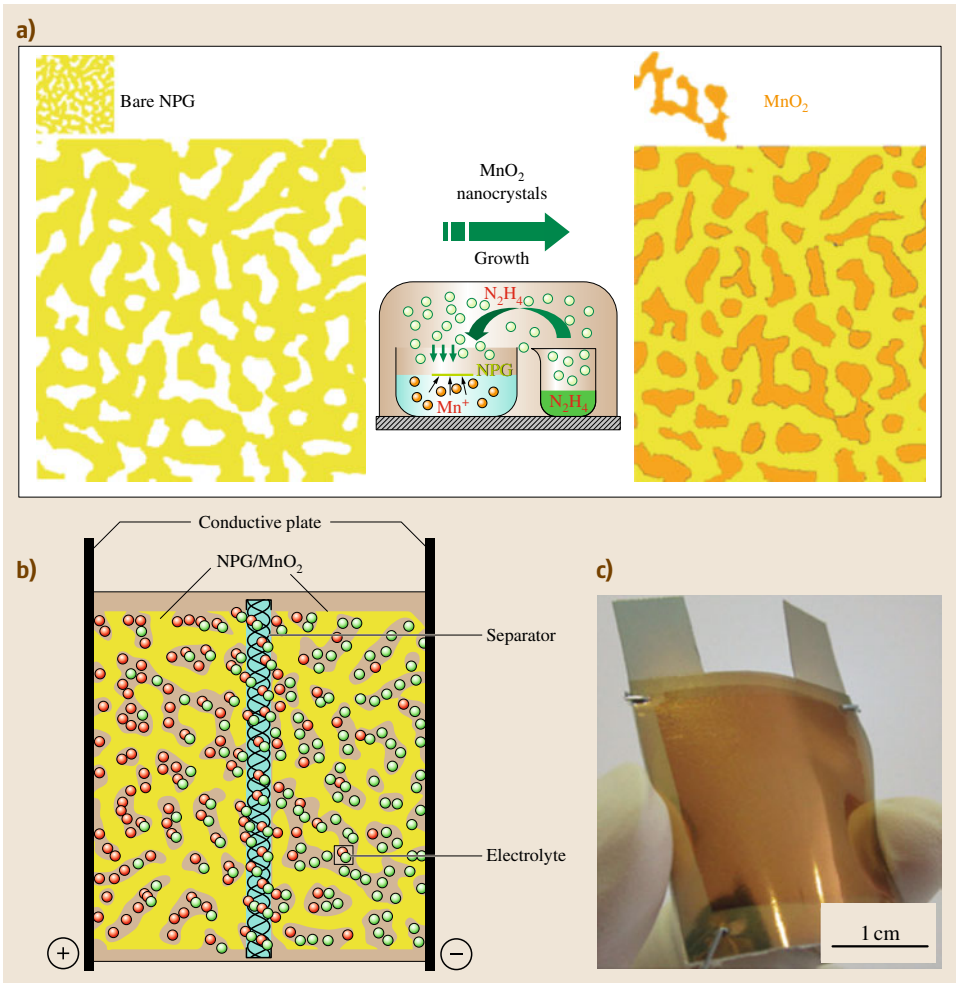


Fig. 21.30a–c Nanoporous gold/MnO_2-based supercapacitors. **(a)** Schematic showing the fabrication process for nanoporous gold/MnO_2 hybrid materials by directly growing MnO_2 (*orange*) onto nanoporous gold. **(b)** Supercapacitor device constructed with nanoporous gold/MnO_2 films as electrodes, aqueous Li_2SO_4 as electrolyte, and tissue paper as separator. **(c)** Photograph of a nanoporous gold/MnO_2-based supercapacitor (after [21.195])

electrons in bulk gold, and hence the resistance is dominated by surface scattering. Adsorption of a monolayer of octadecanethiol onto the nanoporous gold nanowire results in a resistance change of about 3%. The sensitivity factor of $1.0\times10^{-16}\,\mathrm{cm}^2$ is comparable to values reported for adsorption on ultrathin films.

Electrochemical supercapacitors can deliver high levels of electrical power and offer long operating lifetimes, but their energy storage density is too low for many important applications. Pseudocapacitive transition-metal oxides such as MnO_2 or SnO_2 could be used to make composite electrodes for such purposes, because they are predicted to have high capacitance for storing electrical charges while also being inexpensive and not harmful to the environment. However, the poor conductivity of MnO_2 (10^{-5}–$10^{-6}\,\mathrm{S/cm}$) limits the charge/discharge rate for high-power applications. Most recently, *Lang* et al. [21.195] showed that hybrid structures made of nanoporous gold and nanocrystalline MnO_2 have enhanced conductivity, resulting in a specific capacitance of the constituent MnO_2 ($\approx 1.145\,\mathrm{F/g}$) that is close to the theoretical value. The nanoporous gold allows electron transport through the MnO_2, and facilitates fast ion diffusion between the MnO_2 and the electrolytes while also acting as a double-layer capacitor (Fig. 21.30). The high specific capacitances and charge/discharge rates offered by such hybrid structures make them promising candidates as electrodes in supercapacitors, combining high energy storage densities with high levels of power delivery.

21.4 Concluding Remarks and Prospects

Nanoporous metals with three-dimensional bicontinuous ligament–channel structure can be fabricated by chemical or electrochemical dealloying, which involves selective dissolution of the less noble element and surface diffusion/agglomeration of the more noble element. The length scale of the ligaments and channels in nanoporous metals ranges from a few nanometers to several microns, and can be tuned by changing parameters such as the composition and microstructure of precursors, the applied potential, the kind and strength of the electrolyte, and the dealloying temperature and time, or by adopting post-dealloying treatments such as thermal annealing. By alloy design of precursors (addition of elements with lower surface diffusivity) and control over the applied dealloying potential or temperature, ultrafine pores of well below 10 nm can be achieved in nanoporous metals, which show enhanced SERS effects, superior catalytic activity towards CO oxidation, improved effective Young's modulus, etc. Both monoliths (films, ribbons, bulk) and nanostructures (nanoparticles, nanowires, nanotubes) can be obtained for nanoporous metals. Besides pure metals (containing a minor residue of the less noble element), nanoporous alloys can be produced by dealloying ternary or multicomponent precursors. Moreover, one can continuously modulate the compositions of these nanoporous alloys. Through combination with other routes such as the template method, UPD deposition, etc., dealloying provides more space to tailor the microstructure of nanoporous metal materials. Due to the bicontinuous porous structure and ultrahigh specific surface area, nanoporous metals show unique mechanical, catalytic, electrocatalytic, optical, electrical, sensing, and actuation properties, compared with their dense bulk counterparts or nonporous nanostructures; for example, the tunable length scale of ligaments and channels allows for investigation of the size-dependent mechanical behavior of nanoporous metals. The ultrahigh specific surface area is desirable for high sensitivity, and the 3-D channels contribute to fast transfer of adsorption species and shorter response time for applications of sensors. This point is also desirable for electrocatalysis in fuel cell applications. On the one hand, nanoporous metals can serve as model materials for investigations of mechanical, physical, and chemical properties of random porous solids, from the viewpoint of fundamental science; On the other hand, from the technological viewpoint, nanoporous metals show potential applications in many fields such as catalysis, electrocatalysis, sensors, actuators, fuel cells, supercapacitors, etc. It is expected that more and more fascinating properties of dealloyed nanoporous metals will soon be uncovered, as well as their tremendous potential for actual applications.

References

21.1 V. Bansal, H. Jani, J.D. Plessis, P.J. Coloe, S.K. Bhargava: Galvanic replacement reaction on metal films: A one-step approach to create nanoporous surfaces for catalysis, Adv. Mater. **20**, 717–723 (2008)

21.2 A. Kiani, E. Nekooiy Fard: Fabrication of palladium coated nanoporous gold film electrode via underpotential deposition and spontaneous metal replacement: A low palladium loading electrode with electrocatalytic activity, Electrochim. Acta **54**, 7254–7259 (2009)

21.3 J.F. Huang: Facile preparation of an ultrathin nickel film coated nanoporous gold electrode with the unique catalytic activity to oxidation of glucose, Chem. Commun. **10**, 1270–1272 (2009)

21.4 Y. Wang, C.C. He, W.H. Xing, F.B. Li, L. Tong, Z.Q. Chen, X.Z. Liao, M. Steinhart: Nanoporous metal membranes with bicontinuous morphology from recyclable block-copolymer templates, Adv. Mater. **22**, 2068–2072 (2010)

21.5 H. Ataee-Esfahani, N. Fukata, Y. Yamauchi: Templateless synthesis of nanoporous gold sponge with surface-enhanced Raman scattering activity, Chem. Lett. **39**, 372–373 (2010)

21.6 D.B. Robinson, S.J. Fares, M.D. Ong, I. Arslan, M.E. Langham, K.L. Tran, W.M. Clift: Scalable synthesis of nanoporous palladium powders, Int. J. Hydrogen Energy **34**, 5585–5591 (2009)

21.7 X.S. Peng, K. Koczkur, S. Nigro, A.C. Chen: Fabrication and electrochemical properties of novel nanoporous platinum network electrodes, Chem. Commun. **24**, 2872–2873 (2004)

21.8 X.S. Peng, K. Koczkur, A.C. Chen: Synthesis and characterization of ruthenium-decorated nanoporous platinum materials, Nanotechnology **18**, 305605 (2007)

21.9 Q.F. Yi, W. Huang, X.P. Liu, G.R. Xu, Z.H. Zhou, A.C. Chen: Electroactivity of titanium-supported nanoporous Pd-Pt catalysts towards formic acid oxidation, J. Electroanal. Chem. **619/620**, 197–205 (2008)

21.10 A.K.M. Kafi, A. Ahmadalinezhad, J.P. Wang, D.F. Thomas, A.C. Chen: Direct growth of nanoporous Au and its application in electrochemical biosensing, Biosens. Bioelectron. **25**, 2458–2463 (2010)

21.11 Q.F. Yi, W.Q. Yu, F.J. Niu: Novel nanoporous binary Au_Ru electrocatalysts for glucose oxidation, Electroanalyst **22**, 556–563 (2010)

21.12 J. Kim, Z. Dohnálek, B.D. Kay: Structural characterization of nanoporous Pd films grown via ballistic deposition, Surf. Sci. **586**, 137–145 (2005)

21.13 C. Bansal, S. Sarkar, A.K. Mishra, T. Abraham, C. Lemier, H. Hahn: Electronically tunable conductivity of a nanoporous Au–Fe alloy, Scr. Mater. **56**, 705–708 (2007)

21.14 J.R. Hayes, G.W. Nyce, J.D. Kuntz, J.H. Satcher, A.V. Hamza: Synthesis of bi-modal nanoporous Cu, CuO and Cu_2O monoliths with tailored porosity, Nanotechnology **18**, 275602 (2007)

21.15 Y.P. Deng, W. Huang, X. Chen, Z.L. Li: Facile fabrication of nanoporous gold film electrodes, Electrochem. Commun. **10**, 810–813 (2008)

21.16 K. Nishio, H. Masuda: Anodization of gold in oxalate solution to form a nanoporous black film, Angew. Chem. **123**, 1641–1645 (2011)

21.17 Y.J. Lee, D.J. Park, J.Y. Park: Fully packaged nonenzymatic glucose microsensors with nanoporous platinum electrodes for anti-fouling, IEEE Sens. J. **8**, 1922–1927 (2008)

21.18 J.B. Jia, L.Y. Cao, Z.H. Wang: Platinum-coated gold nanoporous film surface: Electrodeposition and enhanced electrocatalytic activity for methanol oxidation, Langmuir **24**, 5932–5936 (2008)

21.19 O.V. Shulga, D. Zhou, A.V. Demchenko, K.J. Stine: Detection of free prostate specific antigen (fPSA) on a nanoporous gold platform, Analyst **133**, 319–322 (2008)

21.20 B. Seo, J. Kim: Electrooxidation of glucose at nanoporous gold surfaces: Structure dependent electrocatalysis and its application to amperometric detection, Electroanalysis **22**, 939–945 (2010)

21.21 L.T. Viyannalage, Y. Liu, N. Dimitrov: Processing of nanoporous Ag layers by potential-controlled displacement (PCD) of Cu, Langmuir **24**, 8332–8337 (2008)

21.22 X.Y. Bu, J.H. Yuan, J.X. Song, D.X. Han, L. Niu: Controlled synthesis of nanoporous Au microsheet via surfactant emulsion template, Mater. Chem. Phys. **116**, 153–157 (2009)

21.23 Y. Du, J.J. Xu, H.Y. Chen: Ultrathin platinum film covered high-surface-area nanoporous gold (by anodization and subsequent reduction) for methanol electro-oxidation, Electrochem. Commun. **11**, 1717–1720 (2009)

21.24 H.J. Qiu, X.R. Huang: Effects of Pt decoration on the electrocatalytic activity of nanoporous gold electrode toward glucose and its potential application for constructing a nonenzymatic glucose sensor, J. Electroanal. Chem. **643**, 39–45 (2010)

21.25 R. Dou, B.J. Xu, B. Derby: High-strength nanoporous silver produced by inkjet printing, Scr. Mater. **63**, 308–311 (2010)

21.26 N.A. Luechinger, S.G. Walt, W.J. Stark: Printable nanoporous silver membranes, Chem. Mater. **22**, 4980–4986 (2010)

21.27 S.J. Guo, S.J. Dong, E. Wang: Ultralong Pt-on-Pd bimetallic nanowires with nanoporous surface: Nanodendritic structure for enhanced electrocatalytic activity, Chem. Commun. **46**, 1869–1871 (2010)

21.28 A.J. Forty: Corrosion micromorphology of noble metal alloys and depletion gilding, Nature **282**, 597–598 (1979)

21.29 A. Parthasarathi, N.W. Polan: Stress corrosion of Cu-Zn and Cu-Zn-Ni alloys: The role of dealloying, Metall. Trans. A **13**, 2027–2033 (1982)

21.30 K. Sieradzki, R.C. Newman: Stress-corrosion cracking, J. Phys. Chem. Solids **48**, 1101–1113 (1987)

21.31 H. Martín, P. Carro, A.H. Creus, J. Morales, G. Fernández, P. Esparza, S. González, R.C. Salvarezza, A.J. Arvia: Interplay of surface diffusion and surface tension in the evolution of solid/liquid interfaces. Dealloying of α-brass in aqueous sodium chloride, J. Phys. Chem. B **104**, 8229–8237 (2000)

21.32 F.M. Al-Kharafi, B.G. Ateya, R.M. Abd Allah: Selective dissolution of brass in salt water, J. Appl. Electrochem. **34**, 47–53 (2004)

21.33 M.B. Vukmirovic, N. Dimitrov, K. Sieradzki: Dealloying and corrosion of Al alloy 2024-T3, J. Electrochem. Soc. **149**, B428–B439 (2002)

21.34 Z. Han, Y.F. He, H.C. Lin, H. Zhao: Dealloying characterizations of Cu-Al alloy in marine environment, J. Mater. Sci. Lett. **19**, 393–395 (2000)

21.35 C.K. Lee, H.C. Shih: Effect of halide ions on electrochemical behavior and stress corrosion cracking of 67/33 α-brass in aqueous environments, Corrosion **52**, 690–696 (1996)

21.36 F. Mazza, S. Torchio: Factors influencing the susceptibility to intergranular attack, stress corrosion cracking and de-alloying attack of aluminium brass, Corros. Sci. **23**, 1053–1072 (1983)

21.37 J.S. Chen, M. Salmeron, T.M. Devine: Intergranular vs transgranular stress corrosion cracking of Cu 30-Au, Scri. Metall. Mater. **26**, 739–742 (1992)

21.38 J.G. Kim, S.B. Jung, O.H. Kwon: Dealloying behavior of unleaded brasses containing bismuth in potable water, Corrosion **57**, 291–294 (2001)

21.39 M.J. Pryor: The dealloying of a Cu-8.9% Al solid solution, J. Electrochem. Soc. **130**, 1625–1627 (1983)

21.40 K. Sieradzki, J.S. Kim, A.T. Cole, R.C. Newman: The relationship between dealloying and transgranular stress-corrosion cracking of Cu-Zn and Cu-Al alloys, J. Electrochem. Soc. **134**, 1635–1639 (1987)

21.41 M. Raney: US Patent 1563587 (1 Dec. 1925)

21.42 M. Raney: Catalysts from alloys, Ind. Eng. Chem. **32**, 1199–1203 (1940)

21.43 H.W. Pickering, P.R. Swann: Electron metallography of chemical attack upon some alloys susceptible to stress corrosion cracking, Corrosion **19**, 373–389 (1963)

21.44 P.R. Swann: Mechanism of corrosion tunnelling with special reference to Cu_3Au, Corrosion **25**, 147–150 (1969)

21.45 K. Sieradzki, R.C. Newman: Micro- and nanoporous metallic structures, US Patent 4977038 (11 Dec. 1990)

21.46 I.C. Oppenheim, D.J. Trevor, C.E.D. Chidsey, P.L. Trevor, K. Sieradzki: In situ scanning tunneling microscopy of corrosion of silver-gold alloys, Science **254**, 687–689 (1991)

21.47 R.C. Newman, K. Sieradzki: Corrosion science, MRS Bulletin **24**, 12–13 (1999)

21.48 J. Erlebacher, M.J. Aziz, A. Karma, N. Dimitrov, K. Sieradzki: Evolution of nanoporosity in dealloying, Nature **410**, 450–453 (2001)

21.49 Y. Ding, J. Erlebacher: Nanoporous metals with controlled multimodal pore size distribution, J. Am. Chem. Soc. **125**, 7772–7773 (2003)

21.50 Y. Ding, M.W. Chen, J. Erlebacher: Metallic mesoporous nanocomposites for electrocatalysis, J. Am. Chem. Soc. **126**, 6876–6877 (2004)

21.51 Y. Ding, Y.J. Kim, J. Erlebacher: Nanoporous gold leaf: "ancient technology"/advanced material, Adv. Mater. **16**, 1897–1900 (2004)

21.52 Y. Ding, A. Mathur, M.W. Chen, J. Erlebacher: Epitaxial casting of nanotubular mesoporous platinum, Angew. Chem. Int. Ed. **44**, 4002–4006 (2005)

21.53 J. Erlebacher: An atomistic description of dealloying: Porosity evolution, the critical potential, and rate-limiting behavior, J. Electrochem. Soc. **151**, C614–C626 (2004)

21.54 U.S. Min, J.C.M. Li: The microstructure and dealloying kinetics of a Cu-Mn alloy, J. Mater. Res. **9**, 2878–2883 (1994)

21.55 D.V. Pugh, A. Dursun, S.G. Corcoran: Formation of nanoporous platinum by selective dissolution of Cu from $Cu_{0.75}Pt_{0.25}$, J. Mater. Res. **18**, 216–221 (2003)

21.56 H.B. Lu, Y. Li, F.H. Wang: Dealloying behaviour of Cu–20Zr alloy in hydrochloric acid solution, Corros. Sci. **48**, 2106–2119 (2006)

21.57 J.R. Hayes, A.M. Hodge, J. Biener, A.V. Hamza: Monolithic nanoporous copper by dealloying Mn–Cu, J. Mater. Res. **21**, 2611–2616 (2006)

21.58 F.U. Renner, Y. Gründer, P.F. Lyman, J. Zegenhagen: In-situ X-ray diffraction study of the initial dealloying of $Cu_3Au(001)$ and $Cu_{0.83}Pd_{0.17}(001)$, Thin Solid Films **515**, 5574–5580 (2007)

21.59 L. Sun, C.L. Chien, P.C. Searson: Fabrication of nanoporous nickel by electrochemical dealloying, Chem. Mater. **16**, 3125–3129 (2004)

21.60 Z.H. Zhang, Y. Wang, Z. Qi, W.H. Zhang, J.Y. Qin, J. Frenzel: Generalized fabrication of nanoporous metals (Au, Pd, Pt, Ag, and Cu) through chemical dealloying, J. Phys. Chem. C **113**, 12629–12636 (2009)

21.61 Q. Zhang, Z.H. Zhang: On the electrochemical dealloying of Al-based alloys in a NaCl aqueous solution, Phys. Chem. Chem. Phys. **12**, 1453–1472 (2010)

21.62 C.C. Zhao, Z. Qi, X.G. Wang, Z.H. Zhang: Fabrication and characterization of monolithic nanoporous copper through chemical ealloying of Mg–Cu alloys, Corros. Sci. **51**, 2120–2125 (2009)

21.63 H. Ji, X.G. Wang, C.C. Zhao, C. Zhang, J.L. Xu, Z.H. Zhang: Formation, control and functionalization of nanoporous silver through changing

dealloying media and elemental doping, CrystEngComm. **13**, 2617–2628 (2011)
21.64 J.F. Huang, I.W. Sun: Fabrication and surface functionalization of nanoporous gold by electrochemcial alloying/dealloying of Au-Zn in an ionic liquid, and the self-assembly of L-Cysteine monolayers, Adv. Funct. Mater. **15**, 989–994 (2005)
21.65 F.H. Yeh, C.C. Tai, J.F. Huang, I.W. Sun: Formation of porous silver by electrochemical alloying/dealloying in a water-insensitive zinc chloride-1-ethyl-3-methyl imidazolium chloride ionic liquid, J. Phys. Chem. B **110**, 5215–5222 (2006)
21.66 Y.W. Lin, C.C. Tai, I.W. Sun: Electrochemical preparation of porous copper surfaces in zinc chloride-1-ethyl-3-methyl imidazolium chloride ionic liquid, J. Electrochem. Soc. **154**, D316–D321 (2007)
21.67 F. Jia, C.F. Yu, K.J. Deng, L.Z. Zhang: Nanoporous metal (Cu, Ag, Au) films with high surface area: General fabrication and preliminary electrochemical performance, J. Phys. Chem. C **111**, 8424–8431 (2007)
21.68 Z.H. Zhang, Y. Wang, Z. Qi, J.K. Lin, X.F. Bian: Nanoporous gold ribbons with bimodal channel size distributions by chemical dealloying of Al–Au alloys, J. Phys. Chem. C **113**, 1308–1314 (2009)
21.69 Z.H. Zhang, Y. Wang, Z. Qi, C. Somsen, X.G. Wang, C.C. Zhao: Fabrication and characterization of nanoporous gold composites through chemical dealloying of two phase Al-Au alloys, J. Mater. Chem. **19**, 6042–6050 (2009)
21.70 H.B. Lu, Y. Li, F.H. Wang: Synthesis of porous copper from nanocrystalline two-phase Cu–Zr film by dealloying, Scr. Mater. **56**, 165–168 (2007)
21.71 H. Ji, J. Frenzel, Z. Qi, X.G. Wang, C.C. Zhao, Z.H. Zhang, G. Eggeler: An ultrafine nanoporous bimetallic Ag–Pd alloy with superior catalytic activity, CrystEngComm. **12**, 4059–4062 (2010)
21.72 X.G. Wang, J. Frenzel, W.M. Wang, H. Ji, Z. Qi, Z.H. Zhang, G. Eggeler: Length – scale modulated and electrocatalytic activity enhanced nanoporous gold by doping, J. Phys. Chem. C **115**, 4456–4465 (2011)
21.73 J.S. Yu, Y. Ding, C.X. Xu, A. Inoue, T. Sakurai, M.W. Chen: Nanoporous metals by dealloying multicomponent metallic glasses, Chem. Mater. **20**, 4548–4550 (2008)
21.74 J.C. Thorp, K. Sieradzki, L. Tang, P.A. Crozier, A. Misra, M. Nastasi, D. Mitlin, S.T. Picraux: Formation of nanoporous noble metal thin films by electrochemical dealloying of Pt_xSi_{1-x}, Appl. Phys. Lett. **88**, 033110 (2006)
21.75 H.W. Pickering, C. Wagner: Electrolytic dissolution of binary alloys containing a noble metal, J. Electrochem. Soc. **114**, 698–706 (1967)
21.76 A.J. Forty, P. Durkin: A micromorphological study of the dissolution of silver – gold alloys in nitric acid, Philos. Mag. A **42**, 295–318 (1980)
21.77 A.J. Forty, G. Rowlands: A possible model for corrosion pitting and tunneling in noble – metal alloys, Philos. Mag. A **43**, 171–188 (1981)
21.78 K. Sieradzki, R. Corderman, K. Shukla, R.C. Newman: Computer simulations of corrosion: Selective dissolution of binary alloys, Philos. Mag. A **59**, 713–746 (1989)
21.79 F.U. Renner, A. Stierle, H. Dosch, D.M. Kolb, T.L. Lee, J. Zegenhagen: Initial corrosion observed on the atomic scale, Nature **439**, 707–710 (2006)
21.80 K. Wagner, S.R. Brankovic, N. Dimitrov, K. Sieradzki: Dealloying below the Critical Potential, J. Electrochem. Soc. **144**, 3545–3555 (1997)
21.81 C.C. Zhao, X.G. Wang, Z. Qi, H. Ji, Z.H. Zhang: On the electrochemical dealloying of Mg–Cu alloys in a NaCl aqueous solution, Corros. Sci. **52**, 3962–3972 (2010)
21.82 Q. Zhang, X.G. Wang, Z. Qi, Y. Wang, Z.H. Zhang: A benign route to fabricate nanoporous gold through electrochemical dealloying of Al–Au alloys in a neutral solution, Electrochim. Acta, **54**, 6190–6198 (2009)
21.83 X.G. Wang, Z. Qi, C.C. Zhao, W.M. Wang, Z.H. Zhang: Influence of alloy composition and dealloying solution on the formation and microstructure of monolithic nanoporous silver through chemical dealloying of Al-Ag alloys, J. Phys. Chem. C **113**, 13139–13150 (2009)
21.84 F.J. Lai, W.N. Su, L.S. Sarma, D.G. Liu, C.A. Hsieh, J.F. Lee, B.J. Hwang: Chemical dealloying mechanism of bimetallic Pt–Co nanoparticles and enhancement of catalytic activity toward oxygen reduction, Chem. Eur. J. **16**, 4602–4611 (2010)
21.85 Y. Liu, S. Bliznakov, N. Dimitrov: Factors controlling the less noble metal retention in nanoporous structures processed by electrochemical dealloying, J. Electrochem. Soc. **157**, K168–K176 (2010)
21.86 D.V. Pugh, A. Dursun, S.G. Corcoran: Electrochemical and morphological characterization of Pt-Cu dealloying, J. Electrochem. Soc. **152**, B455–B459 (2005)
21.87 A. Antoniou, D. Bhattacharrya, J.K. Baldwin, P. Goodwin, M. Nastasi, S.T. Picraux, A. Misra: Controlled nanoporous Pt morphologies by varying deposition parameters, Appl. Phys. Lett. **95**, 073116 (2009)
21.88 E. Seker, M.L. Reed, M.R. Begley: A thermal treatment approach to reduce microscale void formation in blanket nanoporous gold films, Scr. Mater. **60**, 435–438 (2009)
21.89 O. Okman, D. Lee, J.W. Kysar: Fabrication of crack – free nanoporous gold blanket thin films by potentiostatic dealloying, Scr. Mater. **63**, 1005–1008 (2010)
21.90 W.C. Li, T.J. Balk: Effects of substrate curvature on dealloying of nanoporous thin films, Scr. Mater. **61**, 1125–1128 (2009)

21.91 H.Q. Li, A. Misra, J.K. Baldwin, S.T. Picraux: Synthesis and characterization of nanoporous Pt–Ni alloys, Appl. Phys. Lett. **95**, 201902 (2009)

21.92 J. Snyder, K. Livi, J. Erlebacher: Dealloying silver/gold alloys in neutral silver nitrate solution: Porosity evolution, surface composition, and surface oxides, J. Electrochem. Soc. **155**, C464–C473 (2008)

21.93 E. Detsi, M. van de Schootbrugge, S. Punzhin, P.R. Onck, J.T.M. De Hosson: On tuning the morphology of nanoporous gold, Scr. Mater. **64**, 319–322 (2011)

21.94 W.C. Li, T.J. Balk: Achieving finer pores and ligaments in nanoporous palladium–nickel thin films, Scr. Mater. **62**, 167–169 (2010)

21.95 A. Dursun, D.V. Pugh, S.G. Corcoran: Dealloying of Ag–Au alloys in halide-containing electrolytes, affect on critical potential and pore size, J. Electrochem. Soc. **150**, B355–B360 (2003)

21.96 L.H. Qian, M.W. Chen: Ultrafine nanoporous gold by low-temperature dealloying and kinetics of nanopore formation, Appl. Phys. Lett. **91**, 083105 (2007)

21.97 Z.H. Zhang, Y. Wang, Y.Z. Wang, X.G. Wang, Z. Qi, H. Ji, C.C. Zhao: Formation of ultrafine nanoporous gold related to surface diffusion of gold adatoms during dealloying of Al_2Au in an alkaline solution, Scr. Mater. **62**, 137–140 (2010)

21.98 C.X. Xu, R.Y. Wang, M.W. Chen, Y. Zhang, Y. Ding: Dealloying to nanoporous Au/Pt alloys and their structure sensitive electrocatalytic properties, Phys. Chem. Chem. Phys. **12**, 239–246 (2010)

21.99 J. Snyder, P. Asanithi, A.B. Dalton, J. Erlebacher: Stabilized nanoporous metals by dealloying ternary alloy precursors, Adv. Mater. **20**, 4883–4886 (2008)

21.100 M. Hakamada, M. Mabuchi: Nanoporous gold prism microassembly through a self – organizing route, Nano Lett. **6**, 882–885 (2006)

21.101 C.X. Ji, P.C. Searson: Fabrication of nanoporous gold nanowires, Appl. Phys. Lett. **81**, 4437–4439 (2002)

21.102 L.Y. Chen, T. Fujita, Y. Ding, M.W. Chen: A three-dimensional gold-decorated nanoporous copper core-shell composite for electrocatalysis and nonenzymatic biosensing, Adv. Funct. Mater. **20**, 2279–2285 (2010)

21.103 X.B. Ge, X.L. Yan, R.Y. Wang, F. Tian, Y. Ding: Tailoring the structure and property of Pt-decorated nanoporous gold by thermal annealing, J. Phys. Chem. C **113**, 7379–7384 (2009)

21.104 S.G. Corcoran: The morphology of alloy corrosion, Proc. Electrochem. Soc. **3**, 1–8 (1998)

21.105 T. Fujita, M.W. Chen: Characteristic length scale of bicontinuous nanoporous structure by fast fourier transform, Jpn. J. Appl. Phys. **47**, 1161–1163 (2008)

21.106 T. Fujita, L.H. Qian, K. Inoke, J. Erlebacher, M.W. Chen: Three-dimensional morphology of nanoporous gold, Appl. Phys. Lett. **92**, 251902 (2008)

21.107 F.U. Renner, A. Stierle, H. Dosch, D.M. Kolb, T.L. Lee, J. Zegenhagen: In situ x-ray diffraction study of the initial dealloying and passivation of $Cu_3Au(111)$ during anodic dissolution, Phys. Rev. B **77**, 235433 (2008)

21.108 H. Rösner, S. Parida, D. Kramer, C.A. Volkert, J. Weissmüller: Reconstructing a nanoporous metal in three dimensions: An electron tomography study of dealloyed gold leaf, Adv. Eng. Mater. **9**, 535–541 (2007)

21.109 S.V. Petegem, S. Brandstetter, R. Maass, A.M. Hodge, B.S.E. Dasher, J. Biener, B. Schmitt, C. Borca, H. Van Swygenhoven: On the microstructure of nanoporous gold: An x-ray diffraction study, Nano Lett. **9**, 1158–1163 (2009)

21.110 Y. Sun, J. Ye, A.M. Minor, T.J. Balk: In situ indentation of nanoporous gold thin films in the transmission electron microscope, Microsc. Res. Technol. **72**, 232–241 (2009)

21.111 Y. Liu, S. Bliznakov, N. Dimitrov: Comprehensive study of the application of a Pb underpotential deposition-assisted method for surface area measurement of metallic nanoporous materials, J. Phys. Chem. C **113**, 12362–12372 (2009)

21.112 X.H. Gu, L.Q. Xu, F. Tian, Y. Ding: Au-Ag alloy nanoporous nanotubes, Nano Res. **2**, 386–393 (2009)

21.113 S.H. Yoo, S. Park: Platinum-coated, nanoporous gold nanorod arrays: Synthesis and characterization, Adv. Mater. **19**, 1612–1615 (2007)

21.114 T.Y. Shin, S.H. Yoo, S. Park: Gold nanotubes with a nanoporous wall: Their ultrathin platinum coating and superior electrocatalytic activity toward methanol oxidation, Chem. Mater. **20**, 5682–5686 (2008)

21.115 C.X. Xu, Y.Y. Li, F. Tian, Y. Ding: Dealloying to nanoporous silver and its implementation as a template material for construction of nanotubular mesoporous bimetallic nanostructures, ChemPhysChem **11**, 3320–3328 (2010)

21.116 X.G. Wang, W.M. Wang, Z. Qi, C.C. Zhao, H. Ji, Z.H. Zhang: Fabrication, microstructure and electrocatalytic property of novel nanoporous palladium composites, J. Alloy. Compd. **508**, 463–470 (2010)

21.117 Z. Qi, C.C. Zhao, X.G. Wang, J.K. Lin, W. Shao, Z.H. Zhang, X.F. Bian: Formation and characterization of monolithic nanoporous copper by chemical dealloying of Al-Cu alloys, J. Phys. Chem. C **113**, 6694–6698 (2009)

21.118 C.X. Xu, J.X. Su, X.H. Xu, P.P. Liu, H.J. Zhao, F. Tian, Y. Ding: Low temperature CO oxidation over unsupported nanoporous gold, J. Am. Chem. Soc. **129**, 42–43 (2007)

21.119 V. Zielasek, B. Jürgens, C. Schulz, J. Biener, M.M. Biener, A.V. Hamza, M. Bäumer: Gold catalysts:

Nanoporous gold foams, Angew. Chem. Int. Ed. **45**, 8241–8244 (2006)
21.120 C.X. Xu, X.H. Xu, J.X. Su, Y. Ding: Research on unsupported nanoporous gold catalyst for CO oxidation, J. Catal. **252**, 243–248 (2007)
21.121 D.Q. Han, T.T. Xu, J.X. Su, X.H. Xu, Y. Ding: Gas-phase selective oxidation of benzyl alcohol to benzaldehyde with molecular oxygen over unsupported nanoporous gold, ChemCatChem **2**, 383–386 (2010)
21.122 A. Wittstock, V. Zielasek, J. Biener, C.M. Friend, M. Bäumer: Nanoporous gold catalysts for selective gas-phase oxidative coupling of methanol at low temperature, Science **327**, 319–322 (2010)
21.123 M. Haruta: New generation of gold catalysts: Nanoporous foams and tubes – Is unsupported gold catalytically active?, ChemPhysChem **8**, 1911–1913 (2007)
21.124 A. Wittstock, B. Neumann, A. Schaefer, K. Dumbuya, C. Kübel, M.M. Biener, V. Zielasek, H.P. Steinrück, J.M. Gottfried, J. Biener, A. Hamza, M. Bäumer: Nanoporous Au: An unsupported pure gold catalyst?, J. Phys. Chem. C **113**, 5593–5600 (2009)
21.125 L.V. Moskaleva, S. Röhe, A. Wittstock, V. Zielasek, T. Klüner, K.M. Neyman, M. Bäumer: Silver residues as a possible key to a remarkable oxidative catalytic activity of nanoporous gold, Phys. Chem. Chem. Phys. **13**, 4529–4539 (2011)
21.126 H.M. Yin, C.Q. Zhou, C.X. Xu, P.P. Liu, X.H. Xu, Y. Ding: Aerobic oxidation of D-glucose on support-free nanoporous gold, J. Phys. Chem. C **112**, 9673–9678 (2008)
21.127 C.C. Jia, H.M. Yin, H.Y. Ma, R.Y. Wang, X.B. Ge, A.Q. Zhou, X.H. Xu, Y. Ding: Enhanced photoelectrocatalytic activity of methanol oxidation on TiO_2-decorated nanoporous gold, J. Phys. Chem. C **113**, 16138–16143 (2009)
21.128 Y.Y. Li, Y. Ding: Porous AgCl/Ag nanocomposites with enhanced visible light photocatalytic properties, J. Phys. Chem. C **114**, 3175–3179 (2010)
21.129 N. Asao, Y. Ishikawa, N. Hatakeyama, M. Menggenbateer, Y. Yamamoto, M.W. Chen, W. Zhang, A. Inoue: Nanostructured materials as catalysts: Nanoporous-gold-catalyzed oxidation of organosilanes with water, Angew. Chem. Int. Ed. **49**, 10093–10095 (2010)
21.130 J.T. Zhang, P.P. Liu, H.Y. Ma, Y. Ding: Nanostructured porous gold for methanol electrooxidation, J. Phys. Chem. C **111**, 10382–10388 (2007)
21.131 C. Yu, F. Jia, Z. Ai, L. Zhang: Direct oxidation of methanol on self-supported nanoporous gold film electrodes with high catalytic activity and stability, Chem. Mater. **19**, 6065–6067 (2007)
21.132 X. Ge, R. Wang, P. Liu, Y. Ding: Platinum-decorated nanoporous gold leaf for methanol electrooxidation, Chem. Mater. **19**, 5827–5829 (2007)
21.133 X. Ge, R. Wang, S. Cui, F. Tian, L. Xu, Y. Ding: Structure dependent electrooxidation of small organic molecules on Pt-decorated nanoporous gold membrane catalysts, Electrochem. Commun. **10**, 1494–1497 (2008)
21.134 J. Zhang, H. Ma, D. Zhang, P. Liu, F. Tian, Y. Ding: Electrocatalytic activity of bimetallic platinum–gold catalysts fabricated based on nanoporous gold, Phys. Chem. Chem. Phys. **10**, 3250–3255 (2008)
21.135 P. Liu, X. Ge, R. Wang, H. Ma, Y. Ding: Facile fabrication of ultrathin Pt overlayers onto nanoporous metal membranes via repeated Cu UPD and in situ redox replacement reaction, Langmuir **25**, 561–567 (2009)
21.136 R. Wang, C. Wang, W. Cai, Y. Ding: Ultralow-platinum-loading high-performance nanoporous electrocatalysts with nanoengineered surface structures, Adv. Mater. **22**, 1845–1848 (2010)
21.137 C.X. Xu, L. Wang, X.L. Mu, Y. Ding: Nanoporous PtRu alloys for electrocatalysis, Langmuir **26**, 7437 (2010)
21.138 M. Shao, K. Shoemaker, A. Peles, K. Kaneko, L. Protsailo: Pt monolayer on porous Pd-Cu alloys as oxygen reduction electrocatalysts, J. Am. Chem. Soc. **132**, 9253–9255 (2010)
21.139 S. Koh, P. Strasser: Electrocatalysis on bimetallic surfaces: Modifying catalytic reactivity for oxygen reduction by voltammetric surface dealloying, J. Am. Chem. Soc. **129**, 12624 (2007)
21.140 P. Mani, R. Srivastava, P. Strasser: Dealloyed Pt-Cu core-shell nanoparticle electrocatalysts for use in PEM fuel cell cathodes, J. Phys. Chem. C **112**, 2770–2778 (2008)
21.141 P. Strasser, S. Koha, J. Greeley: Voltammetric surface dealloying of Pt bimetallic nanoparticles: An experimental and DFT computational analysis, Phys. Chem. Chem. Phys. **10**, 3670–3683 (2008)
21.142 H.A. Gasteiger, S.S. Kocha, B. Sompalli, F.T. Wagner: Activity benchmarks and requirements for Pt, Pt-alloy, and non-Pt oxygen reduction catalysts for PEMFCs, Appl. Catal. B **56**, 9–35 (2005)
21.143 L. Liu, E. Pippel, R. Scholz, U. Gösele: Nanoporous Pt-Co alloy nanowires: Fabrication, characterization, and electrocatalytic properties, Nano Lett. **9**, 4352–4358 (2009)
21.144 L. Liu, R. Scholz, E. Pippel, U. Gösele: Microstructure, electrocatalytic and sensing properties of nanoporous $Pt_{46}Ni_{54}$ alloy nanowires fabricated by mild dealloying, J. Mater. Chem. **20**, 5621–5627 (2010)
21.145 L. Liu, Z. Huang, D. Wang, R. Scholz, E. Pippel: The fabrication of nanoporous Pt-based multimetallic alloy nanowires and their improved electrochemical durability, Nanotechnology **22**, 105604 (2011)
21.146 J. Snyder, T. Fujita, M.W. Chen, J. Erlebacher: Oxygen reduction in nanoporous metal–ionic liquid composite electrocatalysts, Nat. Mater. **9**, 904–907 (2010)

21.147 H.J. Herrmann, S. Roux: *Statistical Models for the Fracture of Disordered Media* (North-Holland, Amsterdam 1990)

21.148 R. Li, K. Sieradzki: Ductile-brittle transition in random porous Au, Phys. Rev. Lett. **68**, 1168–1171 (1992)

21.149 B. Kahng, G.G. Barttrouni, S. Redner, L. de Archangelis, H.J. Herrmann: Electrical breakdown in a fuse network with random, continuously distributed breakdown strengths, Phys. Rev. B **37**, 7625–7637 (1988)

21.150 J. Biener, A.M. Hodge, A.V. Hamza: Microscopic failure behavior of nanoporous gold, Appl. Phys. Lett. **87**, 121908 (2005)

21.151 J. Biener, A.M. Hodge, A.V. Hamza, L.M. Hsiung, J.H. Satcher: Nanoporous Au: A high yield strength material, J. Appl. Phys. **97**, 024301 (2005)

21.152 C.A. Volkert, E.T. Lilleodden, D. Kramer, J. Weissmüller: Approaching the theoretical strength in nanoporous Au, Appl. Phys. Lett. **89**, 061920 (2006)

21.153 A.M. Hodge, J.R. Hayes, J.A. Caro, J. Biener, A.V. Hamza: Characterization and mechanical behavior of nanoporous gold, Adv. Eng. Mater. **8**, 853–857 (2006)

21.154 A.M. Hodge, J. Biener, J.R. Hayes, P.M. Bythrow, C.A. Volkert, A.V. Hamza: Scaling equation for yield strength of nanoporous open-cell foams, Acta Mater. **55**, 1343–1349 (2007)

21.155 J. Biener, A.M. Hodge, J.R. Hayes, C.A. Volkert, L.A. Zepeda-Ruiz, A.V. Hamza, F.F. Abraham: Size effects on the mechanical behavior of nanoporous Au, Nano Lett. **6**, 2379–2382 (2006)

21.156 A. Mathur, J. Erlebacher: Size dependence of effective Young's modulus of nanoporous gold, Appl. Phys. Lett. **90**, 061910 (2007)

21.157 A.M. Hodge, R.T. Doucette, M.M. Biener, J. Biener, O. Cervantes, A.V. Hamza: Ag effects on the elastic modulus values of nanoporous Au foams, J. Mater. Res. **24**, 1600–1606 (2009)

21.158 D. Lee, X. Wei, X. Chen, M. Zhao, S.C. Jun, J. Hone, E.G. Herbert, W.C. Oliverd, J.W. Kysar: Microfabrication and mechanical properties of nanoporous gold at the nanoscale, Scr. Mater. **56**, 437–440 (2007)

21.159 D. Lee, X. Wei, M. Zhao, X. Chen, S.C. Jun, J. Hone, J.W. Kysar: Plastic deformation in nanoscale gold single crystals and open-celled nanoporous gold, Model. Simul. Mater. Sci. Eng. **15**, S181–S192 (2007)

21.160 E. Seker, J.T. Gaskins, H. Bart-Smith, J. Zhu, M.L. Reed, G. Zangari, R. Kelly, M.R. Begley: The effects of post-fabrication annealing on the mechanical properties of freestanding nanoporous gold structures, Acta Mater. **55**, 4593–4602 (2007)

21.161 E. Seker, J.T. Gaskins, H. Bart-Smith, J. Zhu, M.L. Reed, G. Zangari, R. Kelly, M.R. Begley: The effects of annealing prior to dealloying on the mechanical properties of nanoporous gold microbeams, Acta Mater. **56**, 324–332 (2008)

21.162 H. Jin, L. Kurmanaeva, J. Schmauch, H. Rösner, Y. Ivanisenko, J. Weissmüller: Deforming nanoporous metal: Role of lattice coherency, Acta Mater. **57**, 2665–2672 (2009)

21.163 H. Jin, J. Weissmüller: A material with electrically tunable strength and flow stress, Science **332**, 1179–1182 (2011)

21.164 A.I. Maaroof, M.B. Cortie, G.B. Smith: Optical properties of mesoporous gold films, J. Opt. A **7**, 303–309 (2005)

21.165 A.I. Maaroof, A. Gentle, G.B. Smith, M.B. Cortie: Bulk and surface plasmons in highly nanoporous gold films, J. Phys. D **40**, 5675–5682 (2007)

21.166 F. Yu, S. Ahl, A.-M. Caminade, J.-P. Majoral, W. Knoll, J. Erlebacher: Simultaneous excitation of propagating and localized surface plasmon resonance in nanoporous gold membranes, Anal. Chem. **78**, 7346–7350 (2006)

21.167 S. Ahl, P.J. Cameron, J. Liu, W. Knoll, J. Erlebacher, F. Yu: A comparative plasmonic study of nanoporous and evaporated gold films, Plasmonics **3**, 13–20 (2008)

21.168 L. Qian, W. Shen, B. Das, B. Shen, G.W. Qin: Alumina coating of ultrafine nanoporous gold at room temperature and their optical properties, Chem. Phys. Lett. **479**, 259–263 (2009)

21.169 L. Qian, W. Shen, B. Shen, G.W. Qin, B. Das: Nanoporous gold–alumina core–shell films with tunable optical properties, Nanotechnology **21**, 305705 (2010)

21.170 S.O. Kucheyev, J.R. Hayes, J. Biener, T. Huser, C.E. Talley, A.V. Hamza: Surface-enhanced Raman scattering on nanoporous Au, Appl. Phys. Lett. **89**, 053102 (2006)

21.171 M.C. Dixon, T.A. Daniel, M. Hieda, D.M. Smilgies, M.H.W. Chan, D.L. Allara: Preparation, structure, and optical properties of nanoporous gold thin films, Langmuir **23**, 2414–2422 (2007)

21.172 L.H. Qian, X.Q. Yan, T. Fujita, A. Inoue, M.W. Chen: Surface enhanced Raman scattering of nanoporous gold: Smaller pore sizes stronger enhancements, Appl. Phys. Lett. **90**, 153120 (2007)

21.173 L.H. Qian, A. Inoue, M.W. Chen: Large surface enhanced Raman scattering enhancements from fracture surfaces of nanoporous gold, Appl. Phys. Lett. **92**, 093113 (2008)

21.174 X.Y. Lang, L.Y. Chen, P.F. Guan, T. Fujita, M.W. Chen: Geometric effect on surface enhanced Raman scattering of nanoporous gold: Improving Raman scattering by tailoring ligament and nanopore ratios, Appl. Phys. Lett. **94**, 213109 (2009)

21.175 X.Y. Lang, P.F. Guan, L. Zhang, T. Fujita, M.W. Chen: Characteristic length and temperature dependence of surface enhanced Raman scattering of nanoporous gold, J. Phys. Chem. C **113**, 10956–10961 (2009)

21.176 L.-Y. Chen, J.-S. Yu, T. Fujita, M.-W. Chen: Nanoporous copper with tunable nanoporosity for SERS applications, Adv. Funct. Mater. **19**, 1221–1226 (2009)

21.177 L.Y. Chen, L. Zhang, T. Fujita, M.W. Chen: Surface-enhanced Raman scattering of silver@nanoporous copper core-shell composites synthesized by an in situ sacrificial template approach, J. Phys. Chem. C **113**, 14195–14199 (2009)

21.178 L.H. Qian, B. Das, Y. Li, Z. Yang: Giant Raman enhancement on nanoporous gold film by conjugating with nanoparticles for single-molecule detection, J. Mater. Chem. **20**, 6891–6895 (2010)

21.179 X.Y. Lang, P.F. Guan, L. Zhang, T. Fujita, M.W. Chen: Size dependence of molecular fluorescence enhancement of nanoporous gold, Appl. Phys. Lett. **96**, 073701 (2010)

21.180 X.Y. Lang, P.F. Guan, T. Fujita, M.W. Chen: Tailored nanoporous gold for ultrahigh fluorescence enhancement, Phys. Chem. Chem. Phys. **13**, 3795–3799 (2011)

21.181 C.-H. Chou, J.-C. Chen, C.-C. Tai, I.-W. Sun, J.-M. Zen: A nonenzymatic glucose sensor using nanoporous platinum electrodes prepared by electrochemical alloying/dealloying in a water-insensitive zinc chloride-1-ethyl-3-methylimidazolium chloride ionic liquid, Electroanalysis **20**, 771–775 (2008)

21.182 Z. Liu, J. Du, C. Qiu, L. Huang, H. Ma, D. Shen, Y. Ding: Electrochemical sensor for detection of p-nitrophenol based on nanoporous gold, Electrochem. Commun. **11**, 1365–1368 (2009)

21.183 H. Qiu, C. Xu, X. Huang, Y. Ding, Y. Qu, P. Gao: Adsorption of laccase on the surface of nanoporous gold and the direct electron transfer between them, J. Phys. Chem. C **112**, 14781–14785 (2008)

21.184 H. Qiu, L. Lu, X. Huang, Z. Zhang, Y. Qu: Immobilization of horseradish peroxidase on nanoporous copper and its potential applications, Bioresource Technol. **10**, 19415–19420 (2010)

21.185 X. Ge, L. Wang, Z. Liu, Y. Ding: Nanoporous gold Leaf for amperometric determination of nitrite, Electroanalysis **23**, 381–386 (2011)

21.186 J. Biener, A. Wittstock, L.A. Zepeda-Ruiz, M.M. Biener, V. Zielasek, D. Kramer, R.N. Viswanath, J. Weissmüller, M. Bäumer, A.V. Hamza: Surface-chemistry-driven actuation in nanoporous gold, Nat. Mater. **8**, 47–51 (2009)

21.187 H.-J. Jin, X.-L. Wang, S. Parida, K. Wang, M. Seo, J. Weissmüller: Nanoporous Au-Pt alloys as large strain electrochemical actuators, Nano Lett. **10**, 187–194 (2010)

21.188 A.K. Mishra, C. Bansal, H. Hahn: Surface charge induced variation in the electrical conductivity of nanoporous gold, J. Appl. Phys. **103**, 094308 (2008)

21.189 T. Fujita, H. Okada, K. Koyama, K. Watanabe, S. Maekawa, M.W. Chen: Unusually small electrical resistance of three-dimensional nanoporous gold in external magnetic fields, Phys. Rev. Lett. **101**, 166601 (2008)

21.190 R. Xia, J.L. Wang, R. Wang, X. Li, X. Zhang, X.-Q. Feng, Y. Ding: Correlation of the thermal and electrical conductivities of nanoporous gold, Nanotechnology **21**, 085703 (2010)

21.191 P. Wahl, T. Traußnig, S. Landgraf, H.-J. Jin, J. Weissmüller, R. Würschum: Adsorption-driven tuning of the electrical resistance of nanoporous gold, J. Appl. Phys. **108**, 073706 (2010)

21.192 M. Hakamada, M. Takahashi, T. Furukawa, M. Mabuchi: Coercivity of nanoporous Ni produced by dealloying, Appl. Phys. Lett. **94**, 153105 (2009)

21.193 M. Hakamada, M. Takahashi, T. Furukawa, M. Mabuchi: Surface effects on saturation magnetization in nanoporous Ni, Philos. Mag. **90**, 1915–1924 (2010)

21.194 R. Zeis, A. Mathur, G. Fritz, J. Lee, J. Erlebacher: Platinum-plated nanoporous gold: An efficient, low Pt loading electrocatalyst for PEM fuel cells, J. Power Sources **165**, 65–72 (2007)

21.195 X. Lang, A. Hirata, T. Fujita, M. Chen: Nanoporous metal/oxide hybrid electrodes for electrochemical supercapacitors, Nat. Nanotechnol. **6**, 232–236 (2011)

21.196 Z. Liu, P.C. Searson: Single nanoporous gold nanowire sensors, J. Phys. Chem. B **110**, 4318–4322 (2006)

Zeolites

22. Zeolites

István Pálinkó, Zoltán Kónya, Ákos Kukovecz, Imre Kiricsi

Zeolites are natural materials that have surrounded us since the beginnings of the history of mankind. They may have been used by ancient man instinctively; however, their use is only documented from about the middle of the 18th century. They became the wonder materials of the 20th century, and remain so in our time as well. Their secret lies in their porous structure, the wide variety of their three-dimensional channel system, and the diversity of their pore size, reaching nanometer dimensions. Their synthesized varieties have many applications, as described in this chapter, but perhaps the most important is their use as catalysts. Indeed, their use in acid-catalyzed isomerization of straight-chain hydrocarbons to produce high-octane gasoline has shaped our world and generated much wealth. However, this is not their only catalytic application; their tunable structural features and the constrained environment they provide allow their use in catalysis of many types of reactions, tremendously influencing the selectivities of transformations.

22.1 **Common Zeolite Frameworks** 822
22.1.1 Zeolites A, X, Y 822
22.1.2 Mordenite 822
22.1.3 Zeolites of Intermediate Pore Size 822
22.1.4 Other Zeolites of Commercial Interest 823

22.2 **Zeolite and Zeolite-Related Molecular Sieves** 823
22.2.1 Isomorphous Substitution of Si and/or Al Atoms in Zeolite Frameworks 823
22.2.2 New Large-Pore Zeolites 824

22.3 **Natural Zeolites: Occurrence and Formation** 825
22.3.1 Formation and Occurrence of Natural Zeolites 826

22.4 **Methods of Identification and Characterization** 828
22.4.1 Determining the Chemical Composition 828
22.4.2 Thermal Analysis Methods 828
22.4.3 Diffraction and Microscopic Techniques 828
22.4.4 Nuclear Magnetic Resonance (NMR) Spectroscopy 828
22.4.5 EPR Spectroscopy 829
22.4.6 Vibrational Spectroscopies 829
22.4.7 UV-Vis Spectroscopy 830
22.4.8 Mössbauer Spectroscopy 830
22.4.9 X-Ray Photoelectron Spectroscopy 830

22.5 **Synthesis of Zeolitic Materials** 830
22.5.1 Effects of Major Chemical Components and Further Additives 831
22.5.2 Influence of Various Physical Parameters on Zeolite Synthesis ... 834
22.5.3 Mechanisms of Zeolite Crystallization 835
22.5.4 Alternative Synthesis Procedures .. 835

22.6 **Ion Exchange, Sorption, and Diffusion in Microporous Materials** 836
22.6.1 Ion-Exchange Properties 836
22.6.2 Molecular Sieving Properties 837
22.6.3 Diffusion Properties 838

22.7 **Acid–Base Properties of Zeolites** 841
22.7.1 Acidity of Zeolites 841
22.7.2 Basicity of Zeolites 842

22.8 **Stability and Modification of Zeolite Structures** 843
22.8.1 Thermal Stability 843
22.8.2 Dealumination of Zeolites 843
22.8.3 Formation of Secondary Pore Structure 843
22.8.4 Isomorphous Substitution 844
22.8.5 Transition-Metal Ions and Metal Particles in Zeolites 845
22.8.6 Coke Formation in Zeolites 845

22.9 **Zeolites as Catalysts** 846
22.9.1 Zeolites in the Refining and Petrochemical Industry 847
22.9.2 Zeolites in the Fine Chemical Industry 847
22.10 **Some Special Applications of Zeolites** 848
22.11 **Conclusions** 850
References 850

Zeolites are crystalline aluminosilicates of group IA and group IIA elements such as sodium, potassium, magnesium, and calcium. Chemically, they are represented by the empirical formula

$$M_{2/n}O\text{-}Al_2O_3\text{-}ySiO_2\text{-}wH_2O\,, \qquad (22.1)$$

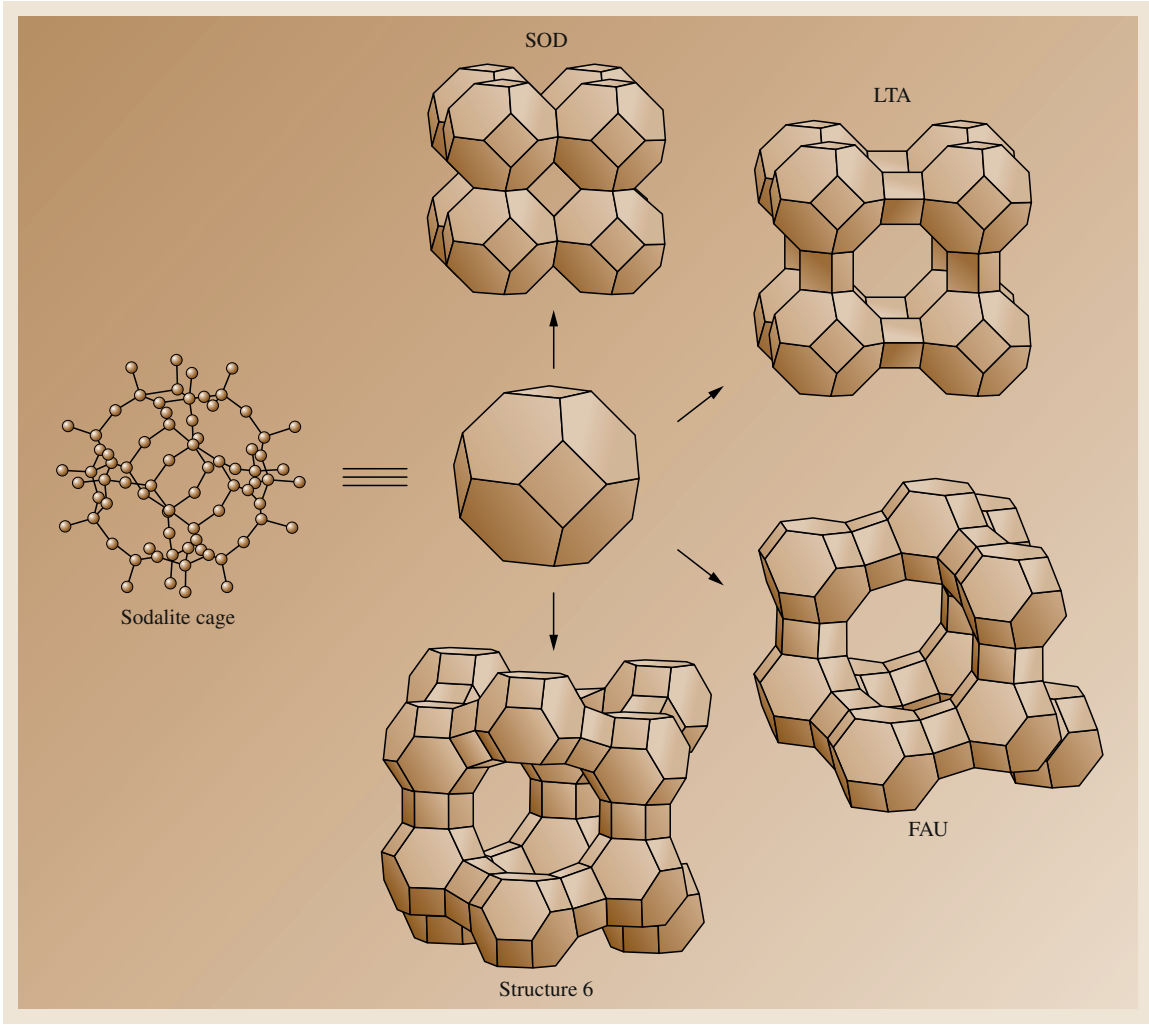


Fig. 22.1 Construction of zeolite frameworks

Table 22.1 Pore size dimensions of various zeolites and molecular sieves. (After [22.1])

Pore size (Å)	Definition	Typical material	Ring size	Pore diameter (Å)
> 500	Macroporous			
20–500	Mesoporous	MCM-41		15–100
< 20	Microporous			
	Ultralarge pore	Cloverite	20	6.0×3.2
		VPI-5	18	12.1
		$AlPO_4$-8	14	7.9×8.7
	Large pore	Faujasite	12	7.4
		$AlPO_4$-5	12	7.3
		ZSM-12	12	5.5×5.9
	Medium pore	ZSM-48	10	5.3×5.6
		ZSM-5	10	5.3×5.6
				5.1×5.5
	Small pore	CaA	8	4.2
		SAPO-34	8	4.3

where n is the charge of the cation, y varies from 2 to infinity, and w represents the water contained in the voids of the zeolite.

All zeolite framework structures are a three-dimensional arrangement of TO_4 tetrahedra (T = tetrahedrally coordinated atom, usually Si^{4+}, Al^{3+}), assembled together through sharing of oxygen atoms to form subunits, and finally infinite lattices by the repeat of identical building blocks (unit cells) (Fig. 22.1) [22.2–4].

The presence of trivalent T-atoms (Al^{3+}) generates negative charges in the framework. These charges can be compensated either by pentavalent T-atoms in the neighborhood (e.g., P^{5+} in aluminophosphates, AlPOs) or by the presence of cationic species in the voids of the framework, generating cation-exchange properties. In addition, the voids of the crystal structure (cages or channels) usually contain water or organic molecules (or salts) in addition to the cation. Removal of water or organics, by heating for instance, gives rise to a regular porous structure of molecular dimensions, which is responsible for the unique adsorption properties of zeotype materials [22.4–6].

Zeolite structures are not static systems. Indeed, various parameters will lead to modification of the zeolite symmetry, usually by bond angle and bond length modification. Such parameters include temperature, pressure, adsorbed molecules, or the cation species occluded in the crystal structure. The zeolite structure will always relax to the most favorable configuration upon variation of the circumstances [22.7–9].

In addition to their chemical composition, which can vary considerably, zeolites and zeolite-related materials are often classified according to their framework structure. Most of the known zeolitic framework topologies have been designated by an identification code of three letters by the International Zeolite Association (IZA) [22.3, 10]. Each framework type can be described by its secondary building units, framework density [number of tetrahedral atoms (T-sites) of the lattice/1000 Å], channel system, crystal symmetry, and unit cell content (number and configuration of T-sites).

The arrangement of the structural unit in zeolite frameworks results in the generation of pores and cavities of various dimensions (Table 22.1), responsible for the molecular sieving and confinement effects during adsorption of molecules. Generally, zeolites are classified as small-pore materials, with pore apertures consisting of six, eight, or nine tetrahedra (6-, 8-, and 9-membered rings), as medium-pore materials (10-membered rings), or as large-pore materials (12-membered rings). A new large-pore material, VPI-5, has been prepared by the team of the Virginia Polytechnic Institute. This material has 18-membered ring pores and thus is able to adsorb large molecules [22.11]. Other large-pore materials are AlPO-8 [22.10, 12] with 14-membered rings and cloverite [22.13] with 20-membered ring pores. Not too long ago a new family of mesoporous molecular sieves, MCM-41, was discovered [22.14].

22.1 Common Zeolite Frameworks

Many different structure types are known, and new structural varieties are constantly synthesized; thus, this area is diverse. Nevertheless, certain zeolites or zeolite-like materials occur more frequently in applications, as described below.

22.1.1 Zeolites A, X, Y

Linde type A (LTA) zeolite (Fig. 22.1) is one of the most frequently used zeolites. It can be considered as either a combination of double 4-ring (4–4) units, or truncated octahedra linked together through double 4-rings. Its pore structure consists of truncated octahedra linked to other cavities through 6-membered rings and of truncated cuboctahedra linked together through 8-membered rings. The most important uses of zeolite A include in ion exchange (water softening) and as adsorbents.

Synthetic faujasite materials are mainly zeolite X (high Al content, Si/Al ratio close to 1) and zeolite Y (higher Si/Al ratio). The structure of faujasite is presented in Fig. 22.1. It can be constructed from sodalite (truncated octahedra) cages in a diamond-like array, the sodalite cages being interconnected through 6–6 secondary building units (SBUs). In addition to the sodalite cages, the main cavities of faujasite material are about 11 Å in diameter, and they are interconnected through 12-membered rings with apertures about 7.4 Å in diameter, allowing large molecules such as trimethylbenzene to enter the supercage.

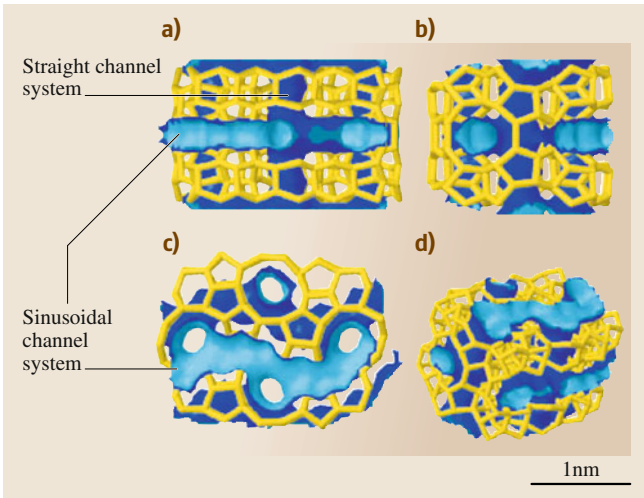


Fig. 22.2a–d Schematic representation of the ZSM-5 structure: **(a)** front [001], **(b)** left [100], **(c)** top [010], and **(d)** isometric projection [111]. (After [22.15], courtesy of Elsevier)

22.1.2 Mordenite

Mordenite, originally known as a natural mineral, was first synthesized by *Barrer* [22.16]. Its structure is composed of 4- and 5-membered rings, generating a porous system delimited by 8- and 12-membered rings. The porous system consists of linear channels, oriented along the crystallographic *c*-axis, with apertures consisting of 8- and 12-membered rings (6.7 Å × 7.0 Å). These channels are linked together through a secondary pore system consisting of 8-membered rings. Although first reported as a small-pore zeolite (8-membered rings), a fault-free structure exhibiting adsorption properties consistent with a 12-membered ring pore system was later synthesized [22.17].

Compared with zeolite A, X or Y, mordenite is characterized by higher silica content, resulting in higher thermal stability. In addition to a higher Si/Al ratio, the mordenite structure contains 5-membered rings, which is thought to enhance the acid site strength of the material.

22.1.3 Zeolites of Intermediate Pore Size

These materials are characterized by 10-membered or distorted 12-membered ring pore openings, being related to the mordenite/ferrierite family of materials [22.18].

The unusual properties of these materials are due to their intermediate pore size (lying between previously known small-pore and large-pore materials), their high Si/Al ratio, and the presence of 5-membered rings in the lattice. Consequently, these materials exhibit high intrinsic acidic strength, high thermal stability, and shape-selective properties.

Of these medium pore size materials, the pentasil materials (ZSM-5, ZSM-11, ZSM-8, etc.) are the most interesting, due to their three-dimensional pore system. This leads to better resistance of pentasil-based catalysts to pore blocking, e.g., through coke deposition, compared with materials with a monodimensional channel system. During the last 20 years, numerous processes have been developed using ZSM-5 or related materials [22.18] (zeolite sieve of molecular porosity, ZSM). The straight and sinusoidal channel system of ZSM-5 is displayed in Fig. 22.2 [22.15].

22.1.4 Other Zeolites of Commercial Interest

Zeolite L is characterized by a monodimensional pore system composed of parallel 12-membered ring linear channels and quite a low Si/Al atomic ratio. When doped with Pt metal, it is the basis of the new AROMAX process for production of aromatics by dehydrocyclization of linear paraffins [22.19].

Zeolite mazzite (omega) and offretite are also molecular sieves of 12-membered rings. Zeolite omega is only characterized by one parallel 12-membered ring linear channel system, while in offretite, the main 12-membered ring channels are interconnected through another set of channels with 8-membered rings [22.3].

Erionite has a structure very similar to offretite. As for offretite, the erionite structure consists of an arrangement of 6-membered rings connected to each other through 4-membered rings, but with a different stacking system, i. e., with cavities interconnected through 8-membered rings instead of 12-membered ring channels. While offretite or mazzite can accommodate large molecules, erionite can only adsorb linear paraffinic molecules [22.20].

22.2 Zeolite and Zeolite-Related Molecular Sieves

Perhaps the most important property of zeolite and related materials is their structural tunability. There are many ways of influencing the framework, and new frameworks are continuously being constructed.

22.2.1 Isomorphous Substitution of Si and/or Al Atoms in Zeolite Frameworks

Isomorphous substitution of Al by Si by either direct synthesis or modification of the framework to influence secondary pore structure, concentration and strength of acid sites, or enhance thermal stability is well known.

The first breakthrough in the synthesis of very high-silica zeolite was made by *Barrer* through the use of tetraalkylammonium cations for zeolite synthesis [22.22]. This led to the discovery of numerous new structures and, e.g., to the development of the ZSM family [22.18, 23].

Another breakthrough was the use of elements other than Si or Al. This first led to the preparation of metallosilicates containing boron, beryllium, titanium, and vanadium [22.24–26] and later to the discovery of aluminophosphates (AlPOs), silicoaluminophosphates (SAPOs), metalaluminophosphates (MAPOs), metalaluminophosphosilicates (MAPSOs), and finally element aluminophosphosilicates (ElAP(S)Os) [22.27–29]. Table 22.2 lists the sizes of the atoms that can be incorporated in the tetrahedral sites of zeolite materials [22.21].

The incorporation of various elements allowed synthesis of materials with already known framework for silicoaluminate materials, but also the preparation of new structures [22.27–29] such as the $AlPO_4$-5 framework, lovdarite (in which the three-membered ring units have been thought to be linked to the presence of beryllium), etc.

Finally, sodalite or sodalite-related materials have been prepared in the complete compositional range, in-

Table 22.2 Crystal ionic radii of various elements incorporated in tetrahedral position of zeolite lattices. (After [22.21])

Element	Valence	Crystal ionic radius (Å)
Be	+2	0.35
B	+3	0.23
Mg	+2	0.66
Al	+3	0.51
Si	+4	0.42
P	+5	0.35
Ti	+3	0.76
Ti	+4	0.68
V	+3	0.74
V	+4	0.63
V	+5	0.59
Cr	+3	0.63
Mn	+2	0.80
Fe	+2	0.74
Fe	+3	0.64
Ca	+2	0.72
Cu	+2	0.72
Zn	+2	0.74
Ga	+3	0.62
Ge	+4	0.53
As	+5	0.46

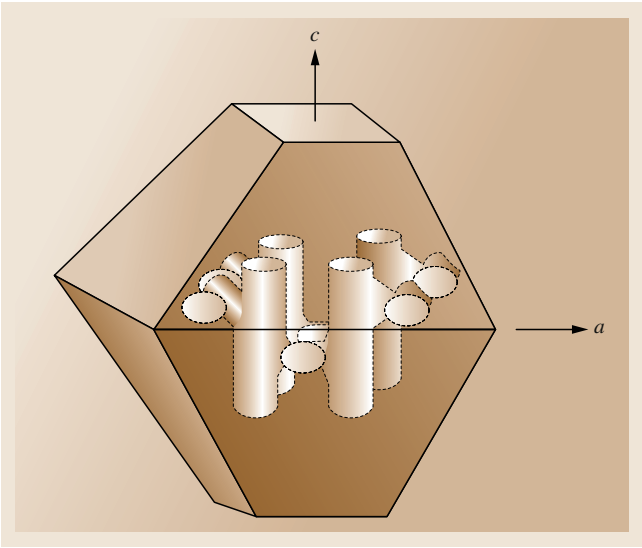


Fig. 22.3 Schematic representation of the bipyramidal morphology of zeolite β with the channel system oriented within a crystal. (After [22.31], courtesy of Elsevier)

cluding the classical silicoaluminate, an all-aluminate form [22.24, 30], an all-silica form [22.24], and the AlPO [22.28] material.

22.2.2 New Large-Pore Zeolites

Different new zeolitic phases with large pore diameters have been recently synthesized or identified; they include faujasite-related materials, new high-silica large-pore zeolites, and new AlPO or AlPO-related materials including the very large-pore molecular sieves. These new materials include the hexagonal varieties of faujasite, with higher Si/Al atomic ratio: zeolite ZSM-20 [22.33, 34] a *faujasite polytype* [22.35], and possibly CSZ-1, which could be an intergrowth of hexagonal and cubic phases [22.36]. SAPO-37 is the silicoaluminophosphate counterpart of faujasite [22.27–29, 37]. Finally, CSZ-3 is a rhombohedral analog of zeolite Y, synthesized in the presence of Cs^+, Na^+ (and Rb^+) [22.38].

Zeolite β is a high-silica material first reported in a US patent issued to Mobil Oil Corporation in 1967 [22.39]. This zeolite exhibits an open pore structure with large 12-membered ring openings and has been extensively used as a catalyst [22.40]. Due to the high degree of faulting, its structure could only be determined using the combination of various techniques [22.40–43]. The structure was found to be an intergrowth of two polymorphs: polymorph A forming an enantiomeric pair, and a chiral polymorph B. The poly-

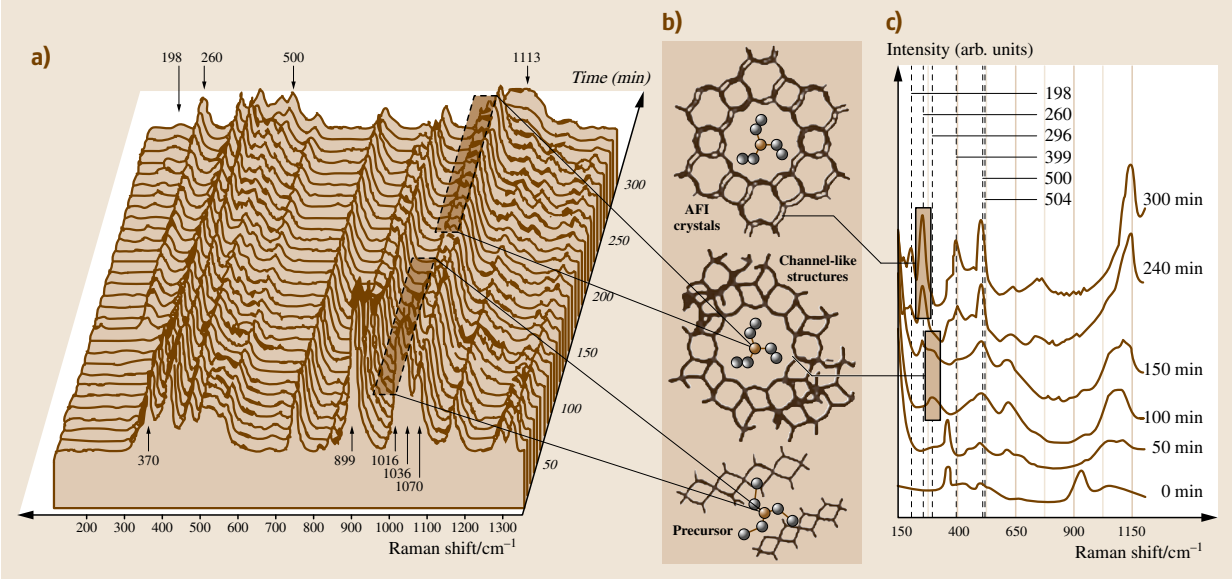


Fig. 22.4 **(a)** UV-Raman spectra recorded in situ during crystallization of AlPO-5. The synthesis temperature was 453 K. **(b)** A proposed scheme for the formation mechanism of AlPO-5 (AFI). **(c)** UV Raman spectra excited with 266 nm of AlPO-5 for different crystallization stages at various times of synthesis. (After [22.32], courtesy of Royal Society of Chemistry)

morphs are randomly distributed in the zeolite crystal, thus giving rise to large amounts of interplanar stacking faults. This generates a three-dimensional porous system with 12-membered ring apertures, the framework itself containing a large number of 5-membered rings. Zeolite β is the first high-silica zeolite containing 5-membered rings and having three-dimensional 12-membered rings channels. A schematic representation of the morphology and pore structure of zeolite β is shown in Fig. 22.3 [22.31]. Previously prepared or identified high-silica large-pore zeolites (ZSM-12, mordenite, mazzite) had only a one-dimensional large channel system that was not interconnected, or interconnected only through small apertures.

Another zeolite with high silica ratio and large pore system has also been identified; ECR-1 [22.44–46] is composed of an intimate twin of the mordenite and mazzite structures, constructed by interposing layers of mordenite-like sheets between layers of mazzite-like cages.

The development of the AlPO family and of related SAPO, MAPO, and MAPSO materials has produced numerous new materials with small, intermediate ($AlPO_4$-11), or large pore structure (AlPO-5) [22.27–29]. The formation of the ALPO-5 structure could be followed by in situ spectroscopic methods such as ultraviolet (UV) Raman spectroscopy [22.32] (Fig. 22.4).

In addition to large-pore materials with 12-membered ring openings, the AlPO family has also produced very large-pore molecular sieves. VPI-5, the first zeotype with pore openings larger than 12-membered rings, has very open structure containing linear parallel channels with 18-membered ring apertures [22.11, 47, 48]. This material is similar to MCM-9 [22.49, 50], but different from AlPO-8 [22.50]. Indeed, AlPO-8 porous structure has apertures consisting of 14-membered rings, instead of the 18-membered rings of VPI-5 [22.10, 12, 51].

Another kind of large-pore molecular sieve has also been identified: cacoxenite, with a one-dimensional pore system of 14.2 Å diameter, consisting of an arrangement of octahedrally coordinated Al atoms with tetrahedrally coordinated phosphorus [22.52, 53].

Finally, synthesis of a novel microporous aluminoborate with pore size of about 5–6 Å has also been reported. The structure was found to contain triangular BO_3 and tetrahedral BO_4 units [22.54].

22.3 Natural Zeolites: Occurrence and Formation

Zeolites were first recognized as a new group of minerals consisting of hydrated silicoaluminates of the alkali and alkaline earths by *Cronsted*, a Swedish mineralogist, as early as 1756 [22.55], with the discovery of stilbite. Because of the intumescence of these minerals when heated in a flame, they were named *zeolites*, from the Greek words *zeos* and *lithos*, meaning *boiling stones* [22.56].

Early zeolite discoveries were found in small cavities of rocks of volcanic origin, being indeed a classical zeolite occurrence, where zeolites form large crystals (Fig. 22.5).

Actually, zeolites occur in many types of rocks, but they are most common in volcanic sediments, and the largest (and also purest) zeolitic deposits are altered vitric tuffs.

Indeed, the major geologic settings of zeolites are saline, alkaline lakes; saline, alkaline soils; deep-sea sediments; low-temperature open hydrologic systems; burial diagenesis; and geothermal–hydrothermal systems [22.57].

The ion-exchange properties were already demonstrated by *Eichhorn* in 1858 (by studying the reversible ion-exchange properties of chabazite and natrolite) [22.58]. Hydration and dehydration were studied by *Damor* as early as 1840 [22.59]. *Friedel*, while studying the adsorption of various liquid organic compounds, suggested in 1896 that zeolites should consist of open spongy frameworks [22.60], and *Grandjean* studied adsorption of various gases after 1909 [22.61]. However, the main use of zeolites remained in jewelry for nearly 200 years.

The study of gas adsorption by *McBain*, with the development of the molecular sieve concept [22.62] in 1932 and the introduction of the physicochemical bases of zeolite science by *Barrer* [22.63] in 1938, marked the real start of zeolite technology development. This resulted in the development of synthesis procedures, first under high temperatures and autogenous pressure to simulate the formation of zeolites of volcanic origin, and later under milder conditions, producing synthetic materials either with a known naturally occurring counterpart or with a new structure [22.56, 64, 65].

Geological studies have shown that, although previously considered rare minerals, zeolites should be recognized as some of the most abundant mineral

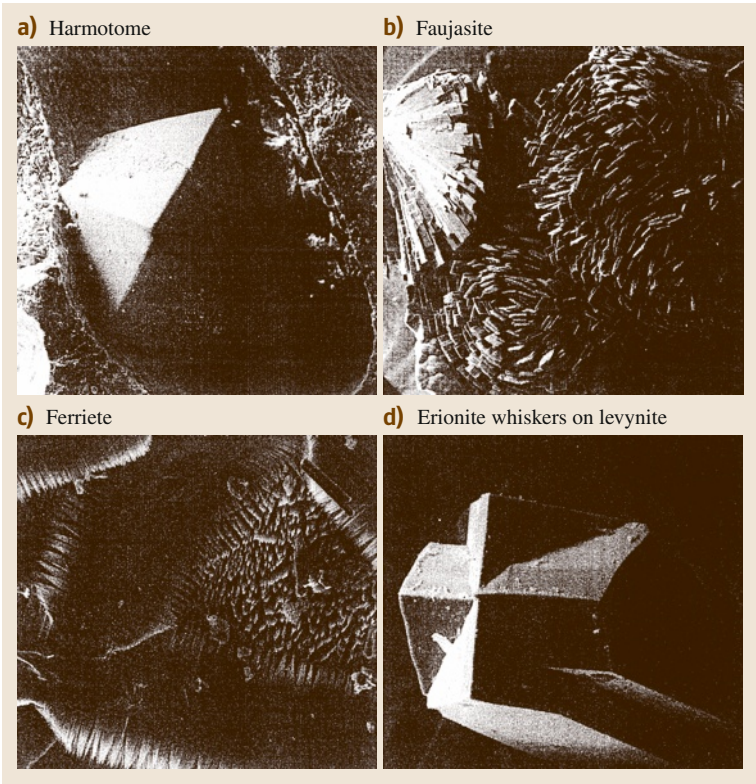


Fig. 22.5 Photos of some natural zeolites

species on Earth. Indeed, zeolite deposits are dispersed worldwide and often occur in megaton quantities and high purity (up to more than 90%), for instance in the USA, former USSR (Russia, Ukraine, Georgia), Japan, Cuba, South Africa, Mexico, south and central Europe (Hungary), and Korea. This has recently led to the development of uses for natural zeolites, e.g., as sorbents or in ion exchange, in sewage treatment plants.

22.3.1 Formation and Occurrence of Natural Zeolites

The geological occurrence of zeolite minerals has been extensively studied over the past 50 years, and the distribution and origins of zeolites are generally well established.

Although the most beautiful zeolite crystals have usually been found in altered basalt matrices, zeolites are not restricted to this origin. Indeed, since 1950, more than 1000 occurrences of zeolite minerals of various sedimentary origins have been reported in more than 40 countries [22.66], sometimes in near-monomineral deposits.

As a result of the many geological studies, the different origins of the zeolite minerals can be included in one of the following genetic types [22.24, 56, 57, 67]:

1. Geothermal, hydrothermal systems, where zeolite crystals result from hydrothermal or hot-spring activity involving reaction between solutions and basaltic lava flow
2. Closed alkaline, saline lakes, where deposits result from alteration of volcanic sediments
3. Similar formations resulting from the action of open freshwater lakes or groundwater on volcanic sediments
4. Transformation of volcanic rock in saline, alkaline soils
5. Deep-sea deposits resulting from low-temperature or hydrothermal alteration of marine sediments
6. Burial diagenesis (low-grade metamorphism).

Features common to the different geological occurrences are [22.24, 56, 57, 67]:

1. Available SiO_2 and Al_2O_3
2. Ca + Na + K/H activity ratio higher than in systems favoring phyllosilicates

The nature of the zeolites in a deposit depends on: (i) the SiO_2 and Al_2O_3 sources, (ii) the physicochemical characteristics of the pore fluids, (iii) the temperature of the deposit, and (iv) the age of the deposit.

Minerals associated with zeolites are clays, alkali feldspars, silica minerals, and other phyllosilicates. Zeolite deposits are usually zoned due to differences in water chemistry, temperature, or deposit age.

Hydrothermal–Geothermal Deposits [22.24, 56, 57, 67, 68]

Zeolites formed by hydrothermal–geothermal (e.g., geyser) alteration of basaltic lava or of hyaloclastic rock sequences in geothermal regions are found in many parts of the world. Classical occurrences are in areas such as Wairakei (New Zealand), Yellowstone National Park (USA), or Iceland.

These deposits are commonly zoned, depending on the temperature [22.69]. At low temperature, the nonzeolitic materials opal, kaolin, cristobalite, tridymite, and montmorillonite are already formed. Zeolites are formed in the 50–300 °C temperature range, while at higher temperatures, nonzeolitic materials such as albite appeared.

Saline, Alkaline Lake-Type Deposits [22.24, 56, 57]

In contrast to hydrothermal deposits, zeolite minerals formed from sediments usually consist of cemented agglomerates of very small crystallites with poorly developed crystal faces. However, these zeolites form the largest deposits, being those of economical interest.

The formation of zeolites in a saline alkaline lacustrine environment takes place in closed basins, in arid or semiarid regions, in which lake waters have gathered to produce high-pH (8–10) saline solutions containing high concentration of alkali or alkaline-earth carbonates/bicarbonates. In this environment, zeolites are readily formed by alteration of reactive materials deposited in the lake, e.g., vitric tuffs, biogenic silica, clays, etc. Zeolites found in these deposits usually include phillipsite, clinoptilolite, and erionite, and sometimes chabazite and mordenite. The deposits usually consist of different ring zones in a horizontal layer [22.24].

Deposits from Open Hydrologic Systems

Zeolites can be formed when water of high pH and salt content flows through vitric volcanic ash, causing rapid crystal growth. The high pH and salt contents of these systems are due to hydrolysis of volcanic ash.

Saline, Alkaline Soil Deposits

Zeolites can be formed at land surface, in saline alkaline soils (pH $\geq$ 9.5) with high sodium carbonate content, resulting from vapotranspiration in arid or semiarid regions [22.57]. In such deposits, the unconverted parent material is at the bottom, separated at the water table from the zeolitized layer on top [22.69]. The parent materials in these soils are either volcanic tuffs or montmorillonite, claystones, etc. Zeolites frequently formed in these areas are analcime, phillipsite, chabazite, and natrolite [22.57, 69–71].

Zeolites in Marine Deposits

The largest volumes of natural zeolites are found in seabed sediments [22.72]. They result from alteration of volcanic or nonvolcanic material: basaltic rocks, nontuffaceous material such as carbonates, vitroclastic sediments or glass, glass being very slowly altered to analcime and feldspars [22.57]. The most abundant species are clinoptilolite, phillipsite, and analcime, with the amount of analcime increasing with age.

Burial Diagenesis [22.24, 57, 73]

In deposits with active diagenesis process, temperatures may range from 50–60 °C at the top to 125–130 °C at the bottom of the zeolitization zones. Reaction occurs following either the so-called alkali zeolite reaction series: silicic volcanic glass + H_2O → clinoptilolite + mordenite + low cristobalite → analcime + quartz + H_2O → albite + H_2O, or the so-called calcic zeolite reaction series: clinoptilolite + Ca^{2+} → heulandite → laumontite + quartz + H_2O. The reaction pathways may of course be influenced by the circulation of groundwater through transportation of reactants. However, a temperature gradient resulting in very slow alteration is the main factor governing formation of zeolites in burial diagenesis.

22.4 Methods of Identification and Characterization

For efficient use of zeolites, their chemical compositions have to be known, whether they are of natural origin or synthetic and/or modified varieties. Their structures and properties also have to be characterized accurately and by as many means as possible.

22.4.1 Determining the Chemical Composition

To characterize these materials well, the chemical composition has to be accurately determined. In as-synthesized microporous materials, the concentration distribution of different framework constituents is generally not uniform; rather, a concentration gradient is frequently found. Hence, both bulk and surface analysis techniques are necessary to characterize samples.

Atomic absorption spectroscopy (AAS) and inductively coupled plasma (ICP) are considered among the best techniques for analysis of zeolites with high Si/Al ratios. However, proton-induced γ-ray emission offers the supplementary advantage of simultaneous multielement analysis. For low-Si/Al samples, a variety of other techniques are available [22.74–77].

For determining concentration gradients, microprobe techniques are recommended, combining both bulk and surface concentration measurements. Secondary-ion mass spectrometry (SIMS) or fast atom bombardment mass spectroscopy (FABMS) is the recommended technique [22.77].

22.4.2 Thermal Analysis Methods

Thermal analysis gives information on the water content and the organic molecules occluded in the cavities and/or channels during synthesis. Combined thermal analysis methods (thermal gravimetry–differential thermal analysis and differential thermal gravimetry) have been extensively used to characterize natural and synthetic microporous materials [22.78].

22.4.3 Diffraction and Microscopic Techniques

Since the development of zeolite science, determination of zeolite structure has involved an increasing number of techniques.

The crystal structure of zeolites (i. e., the TO_2 skeleton and the occluded species: cations, salts, water or organic molecules) can be resolved using modern x-ray single-crystal techniques [22.79, 80]. Some special synthesis techniques have been developed to obtain large crystals; however, synthetic zeolites are often obtained as powder, not suited for single-crystal refinement [22.2]. Nevertheless, recent use of synchrotron radiation sources has allowed use of smaller crystals for structure determination [22.81].

X-ray powder diffraction can be performed on a powder sample, producing a diffraction pattern from the regular arrays of atoms or ions within the crystal structure. This pattern reflects the symmetry of the constituents of the zeolite framework, and the diffraction angles represent a fingerprint characteristic of the structure. The pattern can thus be used for identification of known structures, by comparison with *standard patterns* obtained from known phases or published in the literature.

Other diffraction techniques can be used in conjunction with or to complement x-ray diffraction. Neutron diffraction, for instance, enables one to distinguish between Si and Al ordering in the zeolite framework, since Si and Al have different neutron scattering properties (but similar x-ray scattering properties) [22.82, 83]. Electron diffraction, coupled with scanning electron microscopy (SEM), allows identification of structural defects and intergrowths of superlattices [22.84, 85].

High-resolution electron microscopy (HREM) gives direct insight into zeolite symmetries, and, at very high resolution, one can even see zeolite pore structures. HREM is the most suitable technique to study defect or mixed zeolite phases [22.86, 87].

22.4.4 Nuclear Magnetic Resonance (NMR) Spectroscopy

NMR spectroscopy is particularly well suited for study of the surroundings of T-atoms or extraframework species. ^{29}Si magic-angle spinning (MAS) NMR in the solid state enables us to distinguish between Si surrounded by 0–4 Al atoms [22.88, 89]. In addition, chemical shifts of ^{29}Si NMR spectra (for silica-rich materials) are related to structural parameters such as T–O bond length or T–O–T angle, thus distinguishing between different T-sites [22.90–92]. Developments in two-dimensional (2-D) NMR techniques have enabled direct determination of connectivities [22.93]; as an example, the 2-D correlation spectroscopy (COSY) spectrum of ZSM-39 zeolite is displayed in Fig. 22.6. This zeolite has three different crystallographic sites:

T_1, T_2, and T_3. The connectivities between T_1 and T_2, and T_2 and T_3 are clearly observed, while, as expected, that between T_1 and T_3 is not seen [22.94].

^{27}Al MAS NMR measurements allow determination of the Al coordination in the material (tetrahedral Al in the lattice, extraframework octahedral, or pentavalent Al) [22.95, 96]. The combination of ^{29}Si and ^{27}Al measurements permits, to some extent, the determination of Si, Al orderings in aluminosilicate materials [22.97–99].

Among the different constituents of zeolite or zeotype materials, oxygen is one of the most important and abundant elements. However, due to the low isotopic abundance of ^{17}O, the NMR-sensitive nucleus, and its low magnetic susceptibility, study of the insertion of oxygen into the framework by O^{17} NMR requires the use of isotopically enriched materials [22.95, 100].

Other atoms (^{11}B, ^{31}P, ^{71}Ga, etc.) that can be incorporated into the tetrahedral sites of zeolite (or zeotypes) can also be studied by solid-state NMR [22.101–103].

Finally, analysis of probe molecules by ^{129}Xe, ^{31}P or ^{13}C NMR can allow determination of the cavity dimensions in zeolitic materials.

22.4.5 EPR Spectroscopy

Electron paramagnetic resonance (EPR) spectroscopy is typically used to characterize the environment of paramagnetic ions introduced into either the zeolitic framework or cation-exchange sites of zeolites. Schoonheydt and coworkers pioneered the use of EPR methods to investigate zeolites [22.104, 105]. Experimental and simulated spectra of zeolites containing Cu^{2+} and Ni^{+} ions and different Ag clusters were reported in their works.

The behavior of different transition-metal oxide–zeolite mixtures was systematically studied by *Kucherov* and *Slinkin* by applying EPR spectroscopy [22.106–109]. Modification of HZSM-5 zeolite with Mn^{2+} ions via solid-state ion-exchange method was monitored using EPR spectroscopy by *Wichterlova* et al. [22.110].

The EPR parameters of metal particles generated upon alkaline metal vapor treatment of FAU-X and -Y zeolites have been published and summarized by the groups of *Kevan* [22.111,112] and *Simon* et al. [22.113].

22.4.6 Vibrational Spectroscopies

Raman spectroscopic measurements are particularly useful for studying zeolites with similar structures [22.114].

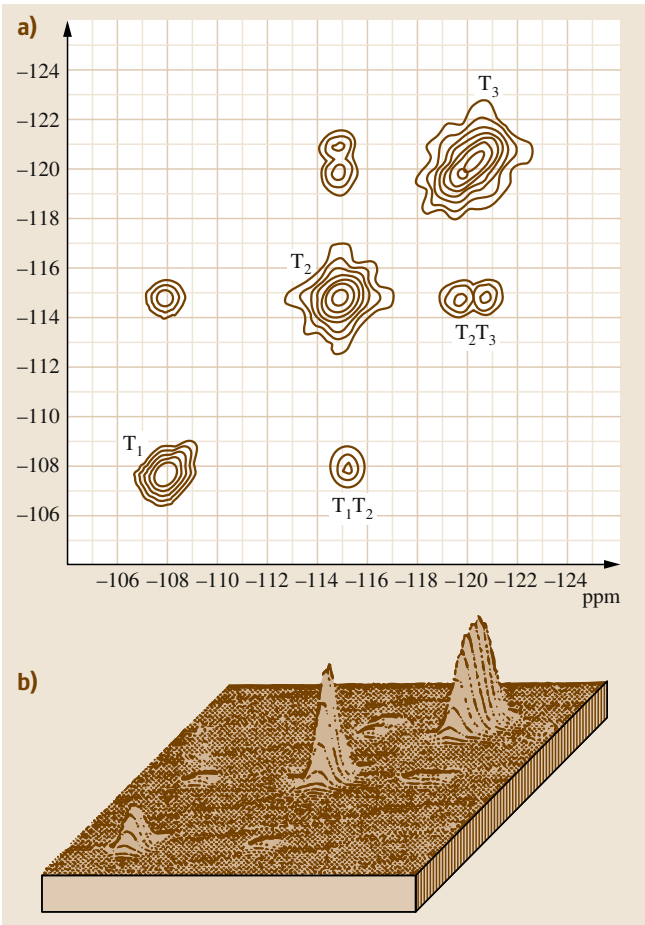


Fig. 22.6 Contour and stacked plots of a 2-D COSY experiment on ZSM-39 at 373 K. (After [22.94], courtesy of Elsevier)

Infrared (IR) spectroscopy is well suited to distinguish between different building units as well as to characterize acid sites.

Mid-IR spectra of zeolites in the 1400 to 200 cm^{-1} range are generally used for investigation of framework properties. The spectrum of FAU-Y zeolite is given as an example in Fig. 22.7 [22.115].

The observed bands were classified into two groups: (i) internal vibrations of the TO^4 tetrahedra, representing structure-insensitive modes, and (ii) external vibrations of the zeolite skeleton, being sensitive to the structure. Some of the structure-sensitive bands are shifted to lower frequencies with increasing Al content. This provides a fast and easy method to determine the fraction of Al in the zeolitic framework. *Miessner* and coworkers established the correlation

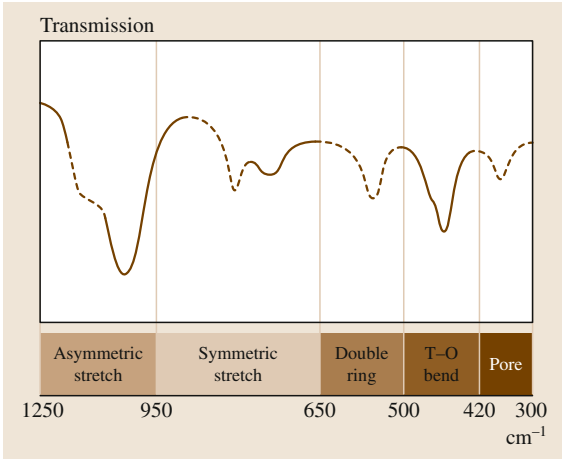


Fig. 22.7 Infrared assignments of the framework vibrations of Na-faujasite. (After [22.115], courtesy of ACS)

between unit cell parameters, skeletal stretching vibrations, and the molar fraction of faujasite-type zeolites for Si/Al = 1.1–1000 [22.116].

The far-IR region (400 to 10 cm^{-1}) is routinely accessible by modern spectrometers. In this range, low-frequency framework vibrations and vibrations of exchangeable cations can be observed. This field of zeolite characterization was developed and has been exhaustively discussed by *Ozin* and coworkers [22.117, 118].

22.4.7 UV-Vis Spectroscopy

In some special cases, UV-Vis spectroscopy has also been used to characterize transition-metal and/or complex ions and radicals present in zeolites [22.119].

22.4.8 Mössbauer Spectroscopy

Mössbauer spectroscopy can only be applied for zeolite characterization if the framework or the pores contain one of the few Mössbauer-active species. The method is very important in characterizing iron- and tin-containing materials. Mössbauer measurements reveal the coordination modes and oxidation states of these ions [22.120].

22.4.9 X-Ray Photoelectron Spectroscopy

X-ray photoelectron spectroscopy (XPS) is a powerful tool to analyze near-surface regions of zeolite crystals. Using the combination of classical elemental analysis and XPS measurements, information can be gathered on the distribution of framework constituents in the bulk phase as well as in the near-surface region [22.121].

22.5 Synthesis of Zeolitic Materials

Although the first zeolite synthesis was claimed as early as the 19th century, the first zeolite synthesis with reliable characterization by chemical analysis, optical properties, and x-ray diffraction was reported by Barrer in the early 1940s [22.2,4,24,122]. This work led to production of synthetic counterparts of naturally occurring species as well as the preparation of new phases. This resulted in the synthesis of zeolite A in the Union Carbide laboratories by *Milton* and *Breck* and collaborators, under mild conditions (< 100 °C and atmospheric pressure) [22.64, 65]. Zeolite A is regarded as the first fully characterized zeolite structure without corresponding natural minerals [22.2, 4, 24].

Since these early works, numerous systematic studies of zeolite syntheses have been carried out and have resulted in the preparation of many species with different structures, chemical compositions, or crystal habits. In addition, these works have helped increase understanding of mechanisms of zeolite crystallization as well as their formation under natural conditions.

Classically, zeolite synthesis involves preparation of an inhomogeneous gel, obtained by combining a silica source and an alumina source in water, under basic pH. Various additives can be added to the gel: alkali or alkaline-earth cations introduced as their oxides, hydroxides, or salts; ammonia in the form of ammonium salts, alkylamines, and alkylammonium compounds; etc. These compounds act in the synthesis as OH^- ion source, as electrolyte (salting-in or salting-out effects), as counterions of the formed anionic framework, or as structure-directing agents.

In addition to the composition of the reaction mixtures, two other major variables direct the formation of zeolites: temperature and time.

The effect of parameter variations can be studied, e.g., through crystallization curves (amount of zeolite produced against time). The crystallization curve is usually obtained using x-ray powder diffraction patterns of the sample taken at preselected times from the reaction mixture [22.123] (Fig. 22.8), often presented as %crys-

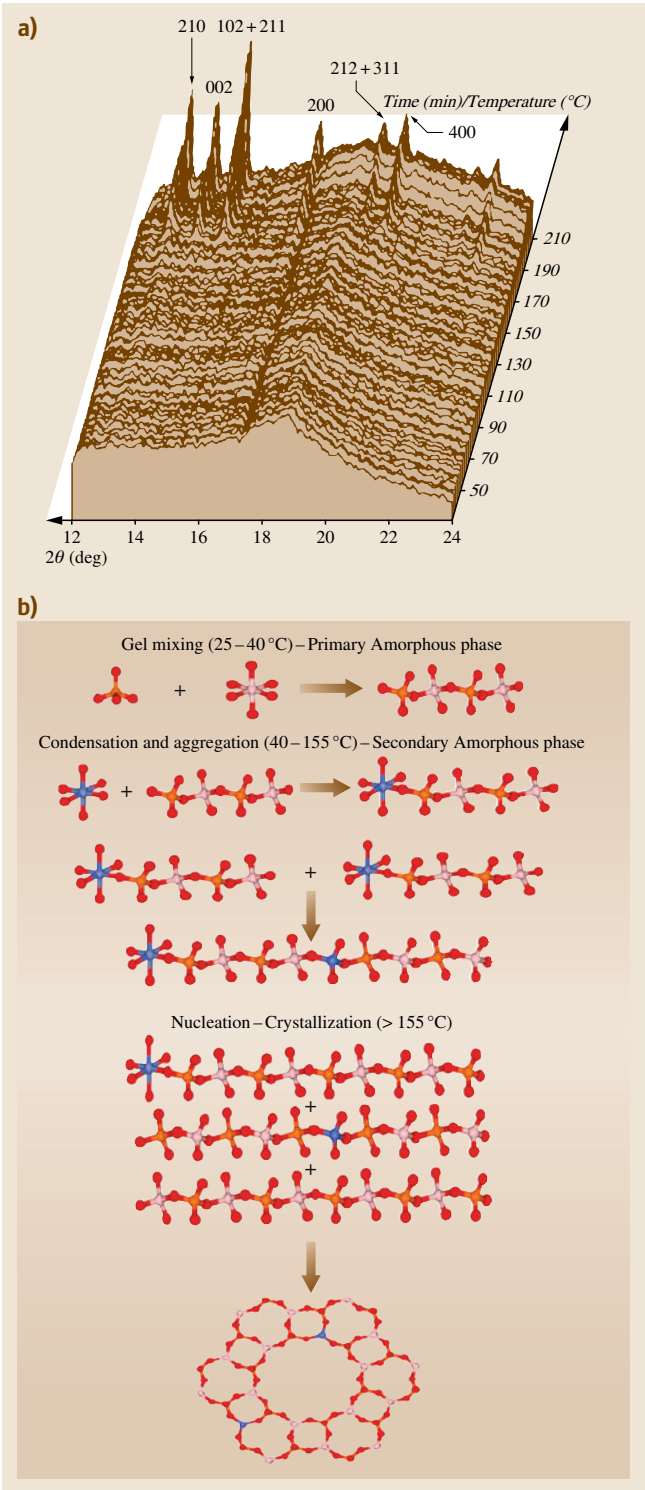


Fig. 22.8 **(a)** XRD patterns recorded during crystallization of CoAPO-5. **(b)** Schematic of the three-stage crystallization model. *Color code*: Co^{2+} – blue, Al^{3+} – pink, P^{5+} – orange, O^{2-} – red. (After [22.123], courtesy of ACS) ▶

tallinity (determined using a standard sample) against crystallization time. This method can be used to monitor crystallization of different species.

22.5.1 Effects of Major Chemical Components and Further Additives

The silica/alumina ratio of the synthesis mixture used to crystallize a zeolite is of paramount importance, since it directly governs both the silica/alumina ratio of the zeolite product and also the framework structure. Some zeolites only crystallize in a very narrow range of Si/Al atomic ratio (zeolite A, FAU-X, and FAU-Y). Other materials such as the pentasil-type zeolites crystallize in a very broad composition range: Si/Al atomic ratio of about 7.5 to infinity. Sodalite is the only material known to crystallize over the full compositional range: Si/Al = 1 to infinity [22.24, 122, 124]. Attempts to change the Si/Al ratio of a zeolite by changing the Si/Al ratio of the synthesis mixture often lead either to the formation of the desired structure with crystalline impurities or amorphous phase, or to the formation of completely different products.

Changing the nature of the silica or alumina sources can also lead either to changes in the final composition of the crystalline products or even to changes of the structure formed. This is exemplified in Table 22.3 for the synthesis of zeolite Y, zeolite ZSM-20, faujasite polytype, and zeolite β.

The hydroxide content of the system strongly influences the nature of the species (*monomeric* or *polymeric*) present in the reaction mixture, the concentration of dissolved silicoaluminate fragments, the charge of these species, and also the rate of hydrolysis or exchange between solid and liquid phases or between different species in solution. The hydroxide content of a reaction mixture is conventionally calculated by summing the moles of OH^- added as ROH, R = Na^+, K^+, quaternary ammonium ion, etc. as sodium silicate (defined as NaOH + SiO_2), and as sodium aluminate (defined as NaOH + Al_2O_3) and subtracting any moles of acid that has been added, as either free acid (HCl, H_2SO_4) or salt [$Al_2(SO_4)_3$ = Al_2O_3+ $3H_2SO_4$]. Al_2O_3 is considered as two moles of acid, as it will be converted to aluminate framework ions, and thus it must be considered in the hydrox-

Table 22.3 Crystalline phases formed from the reference gel $1.25Na_2O$-Al_2O_3-$30.2SiO_2$ × TEAOH-$243H_2O$ involving different TEAOH concentrations (TEA = triethylamine)

Sample no.	TEA^+/Al_2O_3	Si source	Synthesis time (days)	Final product (% crystallinity)
1	26.0	$Si(OEt)_4$	11	ZSM-20 [22.125]
2	17.5	$Si(OEt)_4$	11	Zeolite β
		$Si(OEt)_4$	15	Zeolite β [22.126, 127]
	2.5	$Si(OEt)_4$	13	Amorphous
		$Si(OEt)_4$	26	Amorphous
3	25	Aerosil	21	FAU polytype [22.128]
4	17.5	Aerosil	12	Zeolite β
		Aerosil	18	Zeolite β [22.129]
5	12.5	Aerosil	4	Zeolite β
		Aerosil	10	Zeolite β [22.129]
	2.5	Aerosil	10	Amorphous
		Aerosil	26	Amorphous

ide content calculation [22.122]. Hydroxide content can alter the crystallization rate of a particular structure or alter the type of framework formed or their composition. Indeed, silica species are more soluble than alumina species; i. e., when the hydroxide content is increased, this will encourage the formation of lower-silica/alumina zeolites. In addition, to maximize the solid yield of a synthesis, it is important to minimize the hydroxide content to avoid too high a level of unreacted silicate ions in solution. Finally, when different phases can be formed successively in a synthesis mixture, by optimizing the hydroxide content of the synthesis mixture, we can favor one or other species, or we are even able to prepare a pure metastable structure.

The pH of the reaction mixture does not relate directly to the total hydroxide ion concentration, since it will be greatly influenced by the nature of the dissolved species (degree of depolymerization), and also by the presence of organic species (such as amines) that can act as buffer, maintaining the alkaline pH. In many systems, crystallization of a zeolite is accompanied by a marked pH change, which can be used to monitor the crystallization process. However, this change is usually negligible in very alkaline media (too high pH), and it also depends on the crystallization mechanism to a large extent.

One of the primary roles of inorganic cations is to balance the zeolite framework charge created by the incorporation of Al(III) in the lattice. Since the space available for cations in a zeolite can be limited, exchanging a divalent cation by a monovalent cation, or replacing a cation by another one with larger dimensions, will tend to reduce the Al content of the framework [22.24]. On the other hand, replacing a monovalent cation by a divalent one will allow a larger charge density in the framework. One of the most spectacular examples of the latter case is sodalite. Na-sodalite has Si/Al atomic ratio of 1. However, replacing Na^+ by Ca^{2+} allowed the formation of an all-aluminate framework of the sodalite structure [22.24]. In addition to balancing the zeolite framework charge, inorganic cations often play a dominant role in determining the structure formed. The presence of inorganic cations can also alter the morphology of zeolite crystals, either by favoring nucleation of new crystals, or by selectively enhancing the crystal growth along a given direction. This has been extensively studied for numerous systems, but more particularly for ZSM-5 [22.130–132]. In addition, inorganic cations can decrease the induction time needed before the start of crystal growth [22.130, 131]. Finally, since one structure can often be favored by different cations, addition of a cation to the synthesis mixture can result in an increase of the crystallinity of the product. Such an effect has been observed by changing the Na/K ratio in the starting gel used to synthesize offretite [22.133]. The atomic force microscopy (AFM) method allows visualization of crystallization at near-molecular level [22.134] (Figs. 22.9, 22.10).

Use of organic amines or quaternary ammonium ions in zeolite synthesis was first developed by Barrer in the early 1960s [22.24], and has resulted in the discovery of numerous new zeolitic structures. In addition, use of organics during zeolite synthesis has often resulted in wider ranges of Si/Al atomic ratio than in conventional synthesis. In a synthesis mixture, the organic compounds can behave in different ways; they can (i) act

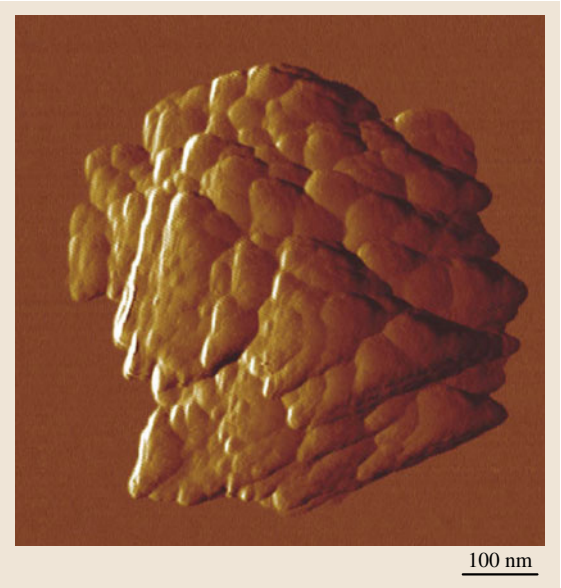


Fig. 22.9 AFM image of the solid phase separated from the reaction mixture after its hydrothermal treatment at 170 °C for $t_{cryst} = 2$ h. Image scan size: 700 nm × 700 nm, maximum particle height 200 nm. (After [22.134], courtesy of Elsevier)

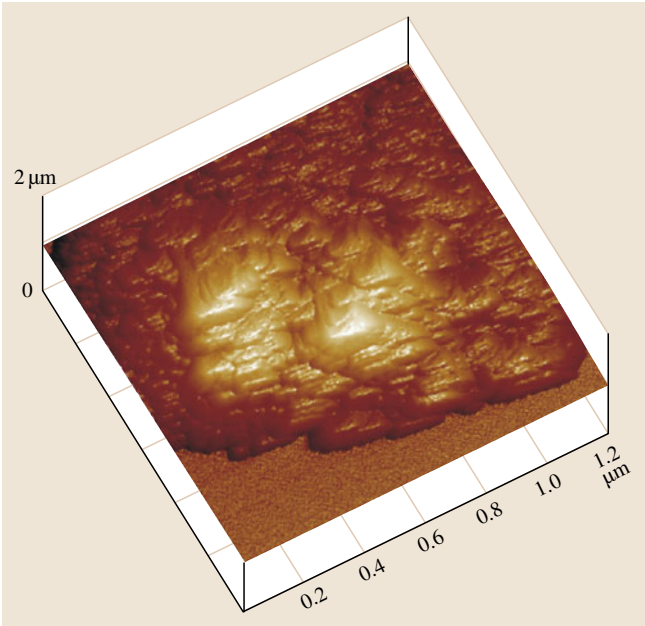


Fig. 22.10 AFM image showing a detail of characteristic silicalite-1 growing terraces. The solid phase was separated from the reaction mixture after its hydrothermal treatment at 170 °C for $t_{cryst} = 3$ h. Surface plot of height data, scan size: 1.2 µm × 1.2 µm with vertical scale of 1 µm. (After [22.134], courtesy of Elsevier)

as structure-directing or templating molecule, (ii) act as a gel modifier, which would allow the formation of structure with higher Si/Al ratio than could be obtained without organic additives, (iii) interact chemically with other component of the gel, altering the character of that gel, for instance, the alkalinity, (iv) interact physically with the gel, modifying the gelling process, the solubility of various species, the ageing process, the transport properties, and the mono- or multiphase behavior, and (v) act as a void filler, as water has been postulated to partake in the synthesis of higher aluminium-containing (hydrophilic) zeolites, being adsorbed into the structure during crystal formation.

The role of inorganic or organic species as *templating* or *structure-directing* agent has been thoroughly investigated in numerous zeolitic systems. Indeed, an ionic or neutral species is usually recognized as a structure-directing agent when its addition to the synthesis mixture results in the formation of a zeolite that would not have been formed without the agent. The way in which a species can direct the formation of a specific structure is not fully understood, yet. However, it is believed that (i) the structure-directing agent can favor a specific species in the gel, e.g., the double four ring (D4R) unit, and (ii) the zeolite structure grows around the template, thus tending to stabilize certain pore structures or subunits [22.135, 136].

Using tetraalkylammonium ions for zeolite synthesis has allowed synthesis of high-Si/Al materials. Indeed, due to the large size of the organic species, they can counterbalance only a limited number of negative centers of the lattice. This led, for instance, to the preparation of zeolite ZK-4, which is isostructural to zeolite A but with higher Si/Al ratio [22.137]. However, in materials with very high Si/Al ratio, the amount of organic (or inorganic) cations included does not match the amount of Al incorporated into the lattice. Indeed, the pentasil zeolite family with various Si/Al ratios has been extensively studied. Solid-state NMR measurements as well as thermal analysis data have shown the presence of structural defects, such as ≡Si–OR (R = tetrapropylammonium, or an inorganic cation) groups. Removal of excess cations by successive calcinations (in air) and ion exchanges with NH_4^+ led to the formation of ≡Si–OH group and successive condensation to ≡Si–O–Si≡ [22.138, 139].

Organic additives used for zeolite synthesis are frequently alkylamines or polyamines. Thus, these

species can behave as pH buffer, maintaining the pH at a constant level during the crystallization process and modifying the solubility and the polymerization degree of the silicate (or silicoaluminate) species of the aqueous gel. Moreover, addition of large amounts of organics can also change the solubility of the silicate species, by modifying the surface charge of the gel particles or the viscosity or dielectric constant of the media, selectively complexing with some compounds, or producing biphasic or micellar systems. Indeed, some syntheses have been carried out without water or with very limited amounts of water [22.124]. Other procedures using biphasic (micellar) systems have been described for preparation of aluminophosphate materials and their derivatives [22.140]. It has been shown that water plays an active role as a void-filler, stabilizing the zeolite porous framework during the crystallization process. It is possible that incorporation of organics into the pores can play a similar role. This is well illustrated for the synthesis of clathrasils (silica with a structure analogous to clathrate hydrates) [22.139], or for preparation of molecular sieves in nonaqueous environment [22.124]. This has also been proposed for the synthesis of ZSM-5, where the organics act as structure-directing agent and a pore-filling moiety [22.135].

Other nonionic or anionic compounds have also been used to modify the zeolite crystallization process. Inert simple gases were applied in the synthesis of clathrasils, including CH_4, N_2, and Ar molecules [22.142]. Organic dyestuffs have also been used to control the shape of zeolite microcrystals (e.g., mordenite [22.143]); these compounds are thought to adsorb on the surface of certain crystal faces, inhibiting their growth rate [22.24]. In addition to amines, alcohols are often present in the synthesis medium. They are produced by hydrolysis of alumina or silica sources (e.g., tetraethylorthosilicate), or are added intentionally either to act as template/pore-filling agents or to partially or fully replace water in the synthesis mixture [22.140]. Not long ago, a novel synthesis procedure applying fluoride ions has been developed, which allows operation at low pH and preparation of more fault-free material (Sect. 22.5.4) [22.144].

22.5.2 Influence of Various Physical Parameters on Zeolite Synthesis

Time is a very important parameter for control of zeolite synthesis. Indeed, crystallization of a zeolite is usually followed using a crystallization curve (crystallinity as defined by powder x-ray diffraction), as exemplified in Fig. 22.11 [22.141]. Since a desired zeolitic species is often a metastable product that can undergo further dissolution, while a more stable *parasite* species can be formed, it is very important to know the crystallization kinetics in order to prepare pure crystalline phases.

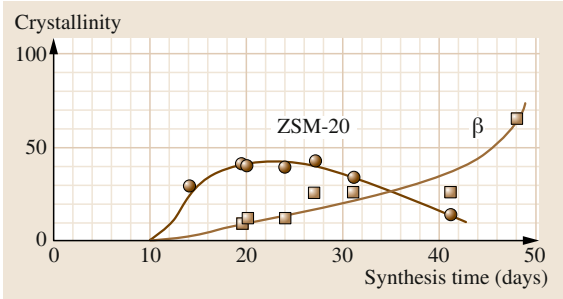


Fig. 22.11 Crystallization curves of ZSM-20 and zeolite β. Crystallinity was determined by powder XRD measurements. (After [22.141], courtesy of Elsevier)

Originally, zeolite synthesis was usually performed under high temperature and pressure to mimic the synthesis conditions in nature [22.4]. Syntheses at low temperature were first proposed by Union Carbide in the 1950s and led to preparation of zeolites A, X, and Y [22.145]. Temperature can alter several factors in zeolite synthesis such as (i) the nature of the zeolite phase (higher temperature usually produces more dense phases), and (ii) the crystallization kinetics (the induction period is usually shorter at high temperature, and the metastable species are decomposed faster) [22.4, 122]. Pressure is often a minor parameter in the synthesis of zeolites, since crystallization is usually performed under autogenous pressure. However, pressure can play an important role when the synthesis is performed in the presence of a volatile reagent (e.g., NH_3, N_2, or CH_4) and may thus affect both the pH and the concentration of dissolved species.

Stirring of the synthesis mixture during preparation of a zeolite can have different effects. It can modify the local concentration of the reagents, tending to produce a more uniform concentration of the reagents throughout the mixture, and may thus result in a lower gradient from a solid particle under dissolution to the surrounding media. It can change the transport properties of the different species and can break the *structure* of the gel, for example, by decreasing the viscosity.

22.5.3 Mechanisms of Zeolite Crystallization

Since the first successful syntheses of zeolites, numerous researchers have been attempting to understand how these microporous materials form from complex mixtures. In addition to the investigation of different parameters governing zeolite synthesis already described, two directions of experimental work have also been investigated:

- Identification of the different species present in liquid, gel, or solid phases during the crystallization process
- Studying the crystallization kinetics that characterize zeolite synthesis.

Major events taking place in the crystallizing mixture are (i) precipitation of an initial gel phase, (ii) dissolution of the gel, (iii) nucleation from the gel or the solution phase, (iv) crystallization and crystal growth of these structures, (v) dissolution/recrystallization of metastable phase, (vi) successive nucleation, crystallization, and dissolution of further nucleation phases, and (vii) formation of the equilibrium phase [22.146]. Corresponding processes occurring at the atomic level are the formation of simple or polynuclear species, formation of larger units (zeolite-like substructure) and nucleation of the zeolite by aggregation of various species, crystal growth through transportation, and rearrangement of species present in the gel or in the solution [22.122].

For identifying the species present in the synthesis mixture, numerous techniques are used [22.122, 139], such as chemical analysis of the phases, powder x-ray diffraction (to follow the crystallization process and to identify the crystal structure), IR and Raman spectroscopies (to obtain information on the presence of substructural species in solution and in the solid phase, even prior to x-ray-identifiable crystallization), thermal analysis (giving information on the dehydration and/or the decomposition processes of organic molecules in the solid product), transmission electron microscopy (TEM), scanning electron microscopy (SEM), microanalysis (providing information on crystal domains not yet identified by x-ray diffraction, crystal size distribution and shape, and concentration gradients possibly present in the solid particles), ^{129}Xe NMR (to investigate early porous domains [22.147]), XPS (to determine surface composition [22.148]), and gas chromatography (GC)-NMR analysis (to identify silicate species [22.24, 122]).

On the basis of the many systems studied, two processes, called A and B, have been proposed for the crystallization mechanism.

The type A mechanism essentially occurs in highly alkaline medium. In this case, depolymerization of the active silica to yield ultimately monomeric silicate anions was shown to be the essential rate-limiting step. As a result, a small number of negatively charged monomers are formed. They can either condense aluminate species to form aluminosilicate complexes or interact directly with Pr_4N^+ ions, known to order around the preferably Si-richer aluminosilicate units to form stable nuclei. It has also been shown that growing ZSM-5 crystallites accommodate silica in preference to aluminum. Consequently, the nuclei will grow with a relatively fast rate at the expense of the dissolved species in solution, resulting in further dissolution of the gel phase. As silicate species are exhausted, aluminum will be incorporated at the end of the process, resulting in inhomogeneous radial Al distribution through the particles. Condensation processes from low-molecular-weight species in solution was further confirmed by studying silicate species in solution. These species were found to be present in very high concentrations.

In the type B mechanism, a hydrogel is formed from solutions already containing mono- or oligomeric silica (aqueous sodium silicate) or alumina species. Its composition corresponds to that calculated from the ratio of reagents (no rate-limiting depolymerization step). Structure-directing Pr_4N^+ cations are present throughout the gel and can readily interact intimately with the gel species. This, associated with higher Si/Al and Na/Si ratios, leads to fast nucleation and recrystallization of the gel (direct hydrogel transformation or surface nucleation). Indeed, the final product consists of small crystallites (or aggregates of small crystallites) with either homogeneous Al distribution, or even enriched Si outer shell, the dissolved silicate species reacting later [22.139].

22.5.4 Alternative Synthesis Procedures

First pentasil materials, and later other zeolites such as ferrierite, Θ-1, ZSM-39, and ZSM-23, were synthesized from a mixture where the hydroxide ions were replaced by fluoride ions [22.137]. In this mixture the pH was decreased to the acidic region. This new route is particularly favorable for preparation of high-silica materials. Partial substitution of silicon with B(III), Al(III), Ga(III), Fe(III), Ge(IV), or Ti(IV) was also possible.

The degree of substitution decreases with increasing stability of the corresponding fluorocomplexes in the solution. The supersaturation of crystallizing species is lower in the presence of fluoride, resulting in fewer metastable phases and a more regular crystallization rate (formation of large crystals with fewer defects). The new medium enables incorporation of elements that are sparingly soluble in alkaline solution, for instance, Fe(III) or cations such as Ca^{2+} and NH_4^+.

Use of a mixture of an organic solvent (for instance hexanol), water, template, and an emulsifier [22.140, 149] led to the production of the MCM-type silicoaluminophosphate materials, some of which correspond to previously reported AlPO or SAPO materials. Among the most interesting materials, MCM-9 was later found to be related to the very large-pore VPI-5 material (18-membered ring pores).

The first reported synthesis of a zeolite in nonaqueous media was the preparation of silica sodalite in the SiO_2–Na_2O–ethylene glycol and SiO_2–Na_2CO_3–ethylene glycol systems [22.9, 150]. Systematic studies in the presence of ethylene glycol, but also of glycerol, dimethylsulfoxide, sulfolane, hexanol or heptanol, and ethanol in the presence of various inorganic cations, led to the formation of hydroxysodalites with various Si/Al atomic ratios, of zeolite BaT, and of kaliophilite [22.122]. Studying the formation of sodalite in the presence of ethylene glycol showed its incorporation in sodalite cavities, suggesting a templating role for this solvent. Attempts to prepare other zeolites without any water in the system, for example, in the presence of organic bases, failed [22.122]. However, synthesis of ZSM-5 and ferrierite has been reported in the presence of small amounts of water.

22.6 Ion Exchange, Sorption, and Diffusion in Microporous Materials

Ion exchange, sorption, and diffusion are among the most important properties of microporous materials. Indeed, zeolitic materials contain cations to compensate the negative charges of the framework, and these cations can be exchanged partially or fully. Since the cages and channels are of molecular dimensions, the microporous materials show the so-called molecular sieving effect [22.62], allowing certain molecules to enter while excluding others due to their too large size. Once the molecules or ions are adsorbed in the inner pores of these materials, they have to diffuse through the channels and cavities to reach a specific adsorption site or catalytic site, where they can be transformed. In this respect, zeolites can be compared to the active sites of enzymes [22.150].

22.6.1 Ion-Exchange Properties

Zeolites can be considered as solid electrolytes. The ion-exchange properties are well studied, and zeolites are classified following their specificities [22.4, 151].

The ion exchange can be presented as

$$aB_Z^b + bA_S^a - aB_S^b + bA_Z^a \,, \tag{22.2}$$

where cations A and B have charges a and b, respectively, and subscripts "Z" and "S" indicate zeolite and solution, respectively.

The equivalent fractions of the exchanging cations in the zeolite (A_Z) are defined as the ratio of the number of equivalents of exchanging cation A to the total equivalents of cations in the zeolite, with $A_Z + B_Z = 1$. A similar definition holds for the equivalent fractions in solution.

The selectivity of the zeolite for cation A is expressed by the separation factor α_A

$$\alpha_A = \frac{A_Z B_S}{B_Z A_S} \,. \tag{22.3}$$

If cation A is specifically preferred by the zeolite, $\alpha_A > 1$.

When the exchange process can be described as a true reversible equilibrium, a thermodynamic equilibrium constant K_a can be defined, and hence the free enthalpy change (ΔG^0), the enthalpy (ΔH^0), and entropy changes (ΔS^0) can be determined.

The ion sieving selectivity does not only depend on the size of the pore apertures but also on the hydrophilic or hydrophobic character of the zeolite; for example, the highly negatively charged framework of zeolite X (with Si/Al varying from 1 to 1.5) prefers smaller cations in the order

$$Na^+ > K^+ > Rb^+ > Cs^+ > Li^+ \,, \tag{22.4}$$

while zeolite Y with lower anionic charge (Si/Al = 1.5–3) preferentially takes up larger cations, following the order

$$Cs^+ > Rb^+ > K^+ > Na^+ > Li^+ \,. \tag{22.5}$$

Li^+ represents an exception for both zeolites, as this small cation essentially migrates with its first hydration shell.

In order to explain the above-mentioned selectivities, not only the Coulomb interaction between the cations and the framework has to be taken into account, but also the general van der Waals interactions between the ions and the walls of the cavities or channels. In addition, complication arises from the fact that the adsorbed cations do not occupy the same adsorption sites in the zeolite. Indeed, Fig. 22.12 shows the cation sites in the faujasite structure. Cations occupying sites I in the hexagonal prisms and those sites in the sodalite cages (sites I, II′, and U) are more hindered for exchange, while those found in the supercages (sites II, III, and IV) are more readily accessible.

The first series for specific exchange in zeolite X seems to follow a relationship with the potential energy (Z/r) of the bare nuclei, a relationship similar to that obtained for the energy of hydration [22.152]. Since the framework negative charge decreases in zeolite Y with respect to zeolite X, larger cations having better interaction with the surroundings are better exchanged. The unexpected role of Li cations can be explained if it is assumed that Li generally migrates with its hydration shell, increasing the effective radius of the cation and decreasing the interaction with the surrounding wall of the cavities.

For exchange of organic cations in hydrophilic zeolites A and X, the following selectivity sequence was obtained [22.153, 154]:

$$CH_3NH_2 > CH_3CH_2NH_2 > CH_3CH_2CH_2NH_2 \,, \tag{22.6}$$

while in the more hydrophobic dealuminated Y or ZSM-5, the sequence is reversed [22.155]. It seems to be clear that Coulomb stabilization prevails in the hydrophilic zeolites, whereas the van der Waals interaction predominates in the hydrophobic–hydrophobic adsorption.

Finally, it has to be emphasized that hysteresis occurs in several exchange processes; i. e., the reverse isotherm does not follow the same profile as the forward process [22.2]. This can be due, for example, to a phase transformation occurring during the ion exchange.

Ion exchange may occur from nonaqueous solutions or in the solid state [22.2, 4, 151, 156, 157].

Solid-state ion exchange may be described by the following equations, depending on whether the starting material is a cation-containing form, such as the sodium form of a zeolite, or the hydrogen (ammonium) form.

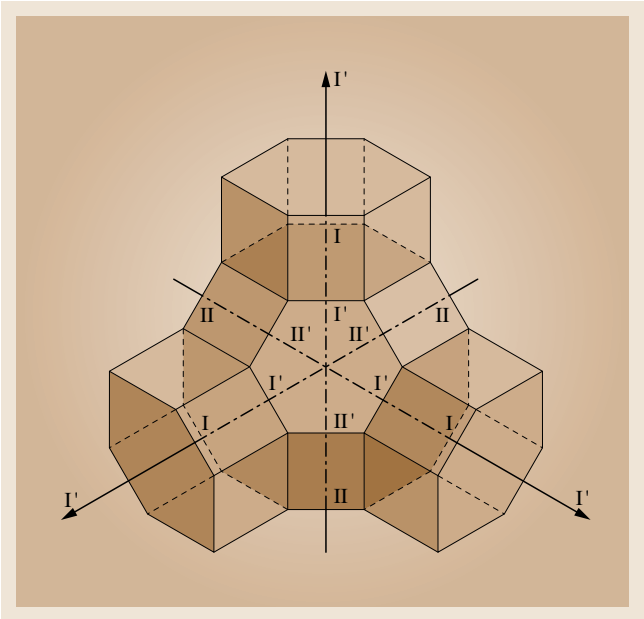


Fig. 22.12 The cationic sites of the faujasite framework

The solid-state reaction takes place between a chloride of the cation M and a Na- or H-form of the zeolite:

$$aMCl_n + bNaZ_xMZ_n + (a-x)MCl_n + (b-nx)NaZ + nxNaCl \,, \tag{22.7}$$

$$aMCl_n + bHZ \rightarrow xMZ_n + (a-x)MCl_n + (b-nx)HZ + nxHCl \uparrow \tag{22.8}$$

In a stoichiometric mixture, one may reach complete exchange without residual salt

$$aMCl_n + naHZ \rightarrow aMZ_n + naHCl \uparrow \,. \tag{22.9}$$

For Na-zeolite, equilibrium will be obtained similar to in conventional ion exchange. If one starts with the hydrogen (or ammonium) form and continuously removes the hydrogen halide (HCl) in an inert gas stream or high vacuum, the equilibrium may completely shift to the right, resulting in complete exchange [22.156, 157].

22.6.2 Molecular Sieving Properties

The adsorption of gases is characterized by an isotherm (volume of sorbed gas as a function of equilibrium pressure) at constant temperature, an isobar (quantity of gas adsorbed as a function of temperature at constant pressure), and an isostere (identical to a Clausius–Clapeyron relationship (plot of $\log p$ as a function of $1/T$) for

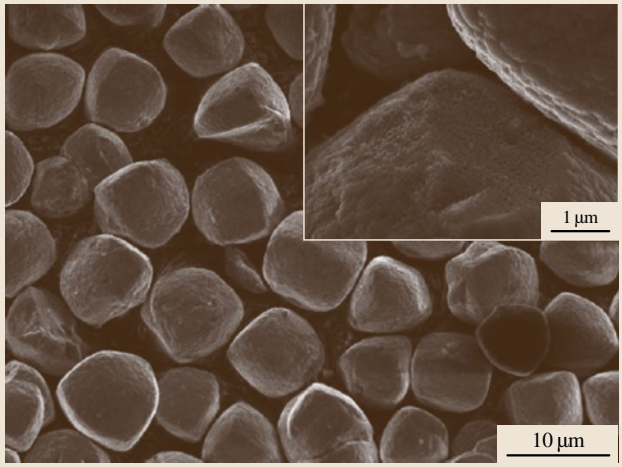


Fig. 22.13 SEM image of calcined rho zeolite (*insert*: high-resolution SEM image for the same sample). (After [22.160], courtesy of Elsevier)

a constant amount of sorbate on the zeolite). The latter provides valuable equilibrium data for design and optimization of gas sorption separation processes [22.158, 159] and for estimation of the differential heat of sorption, which can be used to define more precise contributions to zeolite–sorbate interactions [22.2].

The molecular sieving effect is based on exclusion of molecules larger than the pore apertures. Once the molecule is adsorbed into the channels or cavities, it is *solvated* by the solid framework and a mutual interaction is established between the adsorbate (or adsorbed molecule) and the adsorbent (or the microporous material). The confinement model based on the general van der Waals interaction explains quite adequately the chemical shift variation of ^{129}Xe of adsorbed Xe atoms and of ^{13}C of tetramethylammonium in various zeolites [22.161].

The presence of paramagnetic ions or metal particles greatly influences the ^{129}Xe NMR chemical shift [22.162]. Xe atoms are able to discriminate Pt particles where hydrogen is adsorbed from those covered with water and/or oxygen [22.163, 164]. Moreover, the chemical shift is also sensitive to the number of hydrogen atoms adsorbed per Pt particle [22.162].

Just as in the probe molecule–enzyme interaction, feedback also exists between the adsorbed molecule and the zeolitic framework. In this mutual interaction, both partners are perturbed electronically and sterically. The first report on the change of a zeolitic structure due to adsorption was based on crystallographic results. It was observed that as-synthesized ZSM-5 zeolite with occluded tetrapropylammonium (TPA) ions had orthorhombic symmetry, while the calcined zeolite became monoclinic [22.165]. This transformation involves only minor changes in atomic position and bond angles and is highly reversible [22.62, 166]. Neutron diffraction data showed a significant change in the pore volume of Ca-exchanged zeolite rho during dehydration, and the lattice volume decreased to ca. 80% of the initial volume [22.167]. An SEM image of a calcined rho zeolite sample is shown in Fig. 22.13 [22.160].

22.6.3 Diffusion Properties

Migration or diffusion of adsorbed molecules through the pores, cages, and channels within the crystals plays an important role in catalysis and selective adsorption/separation; for a review, see [22.168].

Various types of diffusion may be distinguished, such as as molecular diffusion (pore sizes 800–10 000 Å), Knudsen diffusion (10–800 Å), and intracrystalline or configurational diffusion (3–10 Å) [22.169]. The region of configurational diffusion, which characterizes molecular sieves, spans more than ten orders of magnitudes; intracrystalline diffusivities range from 10^{-8} to 10^{-20} m^2 s^{-1}. Such restricted molecular diffusion can have a beneficial effect in catalysis. So-called *shape-selective catalysis* is based on the special selectivity obtained by restriction in molecular diffusion [22.169].

As a first approximation, diffusion can be described by Fick's first law, which relates the molar flux J (mol m^{-2} s^{-1}) and the concentration gradient $\delta c/\delta x$:

$$J = -D_c \frac{\delta c}{\delta x} , \qquad (22.10)$$

where D_c is the diffusion constant.

If one is referring to the true driving force, which is the gradient of the chemical potential $\delta\mu/\delta x$, the molar flux becomes [22.151, 168, 170]

$$J = -B_c C \frac{\delta \mu}{\delta x} , \qquad (22.11)$$

where B_c stands for mobility. In general, both D_c and B_c are concentration dependent. The relationship between B_c and D_c is computed by assuming equilibrium between the adsorbed phase (concentration c) and an ideal vapor phase (pressure p and temperature T) as

$$D_c = B_c RT \frac{\mathrm{d}\ln p}{\mathrm{d}\ln c} , \qquad (22.12)$$

with $D_0 = B_c RT$ being the intrinsic diffusivity. D_c approaches the value of D_0 if Henry's law is obeyed, i. e., $\mathrm{d}\ln p/\mathrm{d}\ln c = 1$.

The intracrystalline transport diffusivities D_c and D_0 are in general different from the self-diffusivity D, which is defined under equilibrium conditions in a system with no concentration gradient.

From the experimental point of view, the change of concentration as a function of time is measured, instead of the concentration gradient. In that case, Fick's second law is applied

$$\frac{\delta c}{\delta t} = D_c \left(\frac{\delta^2 c}{\delta x^2}\right) . \qquad (22.13)$$

Overall migration of molecules requires their diffusion within the zeolitic crystal (intracrystalline diffusion $\approx r_c^2/D_c$), through the outer layer of the crystallites (surface barrier resistance $\approx r/k_{sb}$), and through the meso- and macropores ($\approx R_p^2/D_p$), where r_c and R_p are the radii of the crystals and the pores, respectively.

Many techniques are devoted to accurate measurement of the various diffusion coefficients. They can be divided into macroscopic and microscopic methods [22.171].

The uptake rate is measured either volumetrically or gravimetrically in the more widely used and experimentally straightforward macroscopic techniques. The change in weight is recorded using a microbalance, and the sorbate pressure is kept constant in the gravimetric method. The volumetric method uses a constant initial amount of sorbate, and the change in pressure is recorded by a sensitive differential pressure transducer as a function of time [22.168].

Another uptake-rate measurement method is the step frequency response method [22.172]. At sorption equilibrium, a zeolite sample is subjected to small (less than 1%) pressure changes brought about by very rapid, square-wave volume perturbations. From the gas pressure response on compression/expansion of the system, intracrystalline diffusion coefficients of small hydrocarbons are determined. The lower limit for the characteristic time is about 1 s.

The chromatographic method and the zero-length-column (ZLC) method are both macroscopic flow methods [22.168, 171]. In the ZLC method, fast desorption of the sorbate with an inert gas occurs from a small amount of zeolitic sample previously equilibrated with the sorbate at known concentration. The intracrystalline diffusion coefficient is obtained from the slope of $\ln(c/c_0)$ plotted as a function of t. The lower limit of the characteristic time is about 7 s.

If large zeolitic crystals of a few hundred microns can be prepared, the macroscopic steady-state membrane technique yields straightforward results for D_c/L^2, where L is the thickness of the zeolite used. The zeolitic membrane is mounted on a metal plate and sealed with an epoxy resin. On one side of the membrane, a constant sorbate pressure is applied, while the pressure change in the constant-volume cell situated on the other side of the membrane is measured as a function of time.

The microscopic methods are essentially based on NMR [22.173] and neutron diffraction measurements [22.174, 175]. These techniques all measure the self-diffusivity, either indirectly by determining the average time between molecular jumps (NMR relaxation or neutron scattering) or directly as in the NMR pulsed-field-gradient (PFG) method [22.168, 171, 173, 176]. In the indirect methods, the estimated diffusivity depends on the assumed jump length. The PFG method is illustrated in Fig. 22.14 [22.177].

In this experiment, in addition to the strong time- and space-independent magnetic field B_0, a pulsed field is also applied, increasing linearly with the space coordinate $\Delta B_0 = Gr$. The field gradient G is only applied during two short time intervals of identical duration δ, separated by a time Δ. In the normal spin-echo experiment, using the sequence of a $\pi/2$ and a refocusing π pulse, the attenuation is only due to transverse relaxation effects. If, however, τ is kept constant and either δ, Δ, or G is varied, molecular migration also leads to loss of phase coherence between the individual spins, and hence the intensity of the echo signal decreases. The ratio of the intensity of the echo signal in the presence $I(G)$ and in the absence $I(0)$ of the gradient field is given by

$$-\ln \frac{I(G)}{I(0)} = \gamma^2 G^2 \delta^2 \Delta D , \qquad (22.14)$$

where γ is the magnetogyric ratio. The self-diffusivity coefficient D is obtained from the slope of $-\ln I(G)/I(0)$ as a function of G. From D, the molecular mean-square displacement $\langle r^2(t)\rangle$ is easily obtained from the Einstein equation

$$\langle r^2(t-\Delta)\rangle = 6D\Delta . \qquad (22.15)$$

Depending on the ratio between the root-mean-square displacement $\langle r^2(t)\rangle^{1/2}$ and the mean crystal radius R, either the coefficient of intracrystalline diffusion D_{intra} or the coefficient of long-range (extracrystalline) diffusion may be determined [22.168, 171, 173]. The lower limit of intracrystalline self-diffusivity is on the order of 10^{-12}–$10^{-13}\,\mathrm{m^2\,s^{-1}}$.

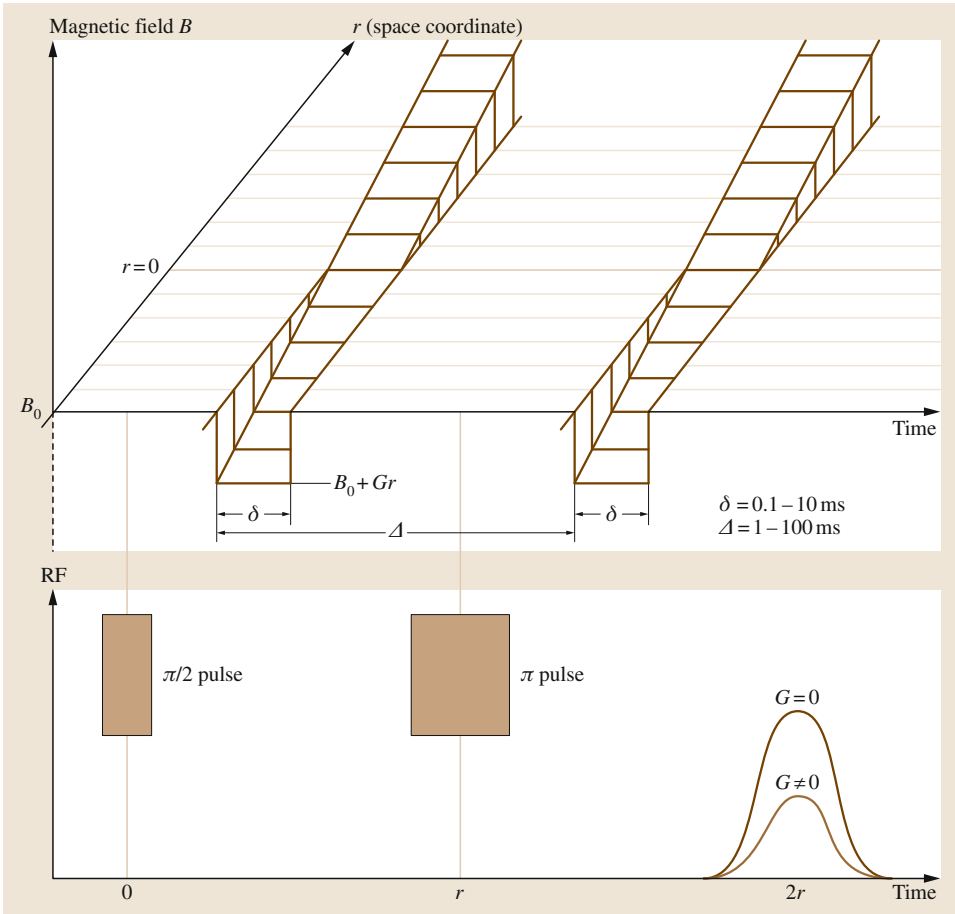


Fig. 22.14 Sequence of radiofrequency (RF) and field gradient pulses used in the NMR PFG method. (After [22.177], courtesy of AIP)

Extra- and intracrystalline diffusion can be readily distinguished by comparing a macroscopic (e.g., the apparent transport diffusivities obtained by volumetric method) and a microscopic (e.g., NMR) method. Indeed, extracrystalline diffusion of methane in natural chabazite depends on the crystal size, while intracrystalline diffusion is constant across the whole range of crystal sizes. Note that, for very large crystal sizes, both methods yield similar values, emphasizing the intracrystalline nature of the determined diffusion coefficients.

NMR tracer desorption measures the exchange rate of the molecules between crystal and surroundings [22.173]. If the measured desorption rate is equal to the intracrystalline diffusivity, no surface energy barrier limits desorption. In some cases, however, desorption rates are substantially reduced, showing the existence of a surface barrier.

Two specific examples are worth mentioning to illustrate molecular diffusion in pores of molecular sizes.

The first one deals with the transport diffusivity of linear alkanes in the potassium form of zeolite T. The mobility of C_4–C_8 *n*-paraffins decreases with chain length, but for larger chain lengths, the mobility increases from C_9 to C_{12} and reaches a rather high value close to that of C_2 and C_3 molecules [22.168, 178]. For molecules larger than C_{12} the mobility decreases again with chain length. This effect was called the *window effect*: the length of *n*-octane molecule just fits the length of the erionite cage, resulting in entrapment of the molecule leading to low mobility. Molecules that are smaller or larger than C_8 do not fit the erionite cage and preserve their higher mobility. For molecules larger than C_{12}, however, the mobility decreases, as expected, due to the normal chain length effect.

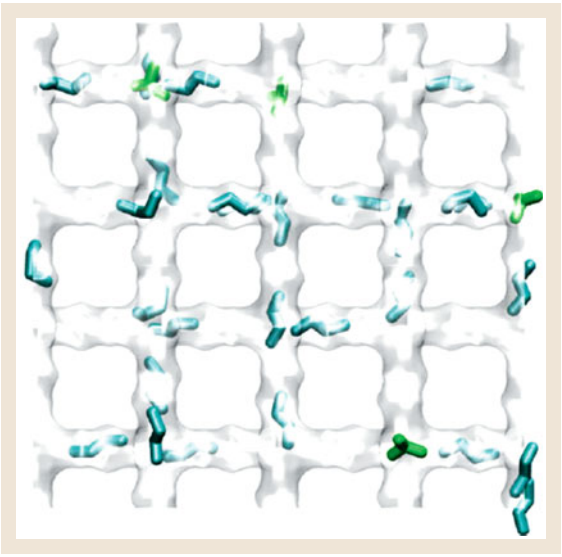


Fig. 22.15 Snapshots of the location of nC_4 (n-butane) and iC_4 (isobutene) within the straight and zigzag channels of ZSM-5. (After [22.179], courtesy of Elsevier) ▶

The second example concerns liquid-phase counterdiffusion of aromatic molecules into cyclohexane-saturated NaY. Here, the logarithm of the effective diffusion coefficient is linearly related to the critical molecular diameter, showing that the latter is the predominant parameter in the interaction. The diffusion coefficients vary within five orders of magnitude. This great variation is also the basis of the so-called shape-selective diffusion of molecules.

Molecular modeling methods are also used to study the diffusion of various molecules in the zeolitic channel system. A snapshot of a configurational bias Monte Carlo simulation is shown in Fig. 22.15, concerning diffusion of n-butane and isobutene in the channel network of a ZSM-5 model [22.179].

22.7 Acid–Base Properties of Zeolites

The acid–base properties of zeolites are of paramount importance in catalysis. It is also known that solid acid catalysts involved in the oil and chemical industries assure large economical yield. From the scientific point of view, the development of zeolite-based acid catalysts is also important, since a huge number of acid-catalyzed reactions are known. However, the catalysts used in these processes are very rarely solids that would fit with environmental requirements.

22.7.1 Acidity of Zeolites

A solid acid is able to convert an adsorbed basic molecule into its conjugated acid form. Therefore, the acid site is able to transfer either a proton from the solid to the adsorbed molecule (this type of acid center is called a Brønsted site) or an electron pair from the adsorbed molecule to the solid surface (this type of acidity is called Lewis acidity). Generally, both types of acid sites are present simultaneously in zeolites.

Brønsted acidic sites in zeolites, such as OH groups, should be formed on the surface, and should be able to transfer protons to the molecules adsorbed. For this purpose, OH groups containing mobile protons are required. Surface hydroxyl groups having the above-mentioned properties can be generated in various ways, e.g., direct ion exchange of zeolites with mineral acids such as diluted HCl, HNO_3, acetic acid, etc. Using this method, only zeolites with high Si/Al ratio may be transformed to protonic forms. Brønsted acidity can be generated by exchanging the counterions with ammonium or alkylammonium ions followed by calcination [22.2, 180]. Dissociation of water molecules under the influence of the strong electrostatic field of the multivalent cations, as well as reduction of transition- and noble-metal ion-containing zeolites with hydrogen, also provide protic sites.

The simplest way to generate Lewis acid sites is to prepare the metal ionic forms of zeolites, since the metal ions act as Lewis sites. High-temperature heat treatment results in completely dehydrated zeolite (presuming the zeolite itself survives).

Generally, heat treatment influences the state and the location of aluminum in zeolites. Upon heat treatment, Brønsted acid centers are converted to Lewis acid sites, while water is released. When the temperature of treatment is lower or equal to 573 K, essentially Brønsted acid sites are generated by calcinating the ammonium forms of the zeolites. At higher temperatures, however, e.g., at 773 K, dehydroxylation takes place, resulting in the formation of one Lewis site from two Brønsted ones. In so doing, the structure reorganizes and an aluminum ion leaves the framework to compensate the negative charge on the adjacent alu-

minum as AlO^+. *Jacobs* and *Beyer* suggested this extra framework AlO^+ species to be the true Lewis acid site [22.181].

Acids with $-H_0 > 12$, the value referring to 100% sulfuric acid, are regarded as superacids in solution. The strength of Brønsted acids can be increased by chemical modification, for instance, replacing hydroxyl groups for fluoride, e.g., OH in H_2SO_4 resulting in HSO_3F ($-H_0 = 15$). The second method is mixing a strong Lewis acid to a weaker Brønsted one such as SbF_5 with HF, where the Hammett constant depends on the ratio of the components. This latter method can be easily applied for zeolites. The acidity of Brønsted centers can be enhanced by modification of their local environment by introducing Lewis acid centers at adjacent positions. Superacidity can arise from a synergetic interaction between Brønsted and Lewis acid sites.

The main techniques characterizing the acidity of zeolites comprise temperature programmed desorption (TPD) of preadsorbed bases, particularly ammonia, the indicator method, IR spectroscopy of adsorbed probe molecules such as pyridine or CO, and multinuclear NMR spectroscopy [22.182].

From the TPD pattern the concentration of acid sites can be determined, and the temperature maximum of the desorption peaks characterizes their strength. However, interferences may occur, with nonacidic adsorption sites leading to molecules strongly adsorbed by van der Waals forces.

The disadvantage of the titration method is the restricted accessibility of the acidic sites for basic probe molecules. If bases of suitable size are used, this method resembles the one generally used in solution; i. e., the indicator shows the equivalence in the acid–base couple.

IR spectroscopy examines the variation of the OH stretching frequency in different zeolites or the influence of adsorbed bases on the same stretching frequency. Two major hydroxyl species signals can be identified in zeolites: one with absorption band at $3740\,cm^{-1}$ characterizing terminal defect hydroxyl groups (≡Si-OH), and another for the above-mentioned Brønsted acid site (≡Si–OHAl≡) with absorption band in the $3600–3650\,cm^{-1}$ region.

IR spectroscopy is also able to distinguish between Lewis and Brønsted acid sites using pyridine as probe molecule. Pyridine associated with Lewis acid sites shows a band around $1450\,cm^{-1}$, while the pyridinium ion vibrates around $1545\,cm^{-1}$.

Although IR spectroscopy is a valuable technique for identification of different acid sites, it is unable to yield quantitative results, because the relationship between the integrated intensity of the band and the amount of the species is not firmly established.

Multinuclear NMR identifies either directly the different OH groups by ^1H NMR spectroscopy, or indirectly using ^{13}C, ^{15}N, and/or ^{31}P NMR of adsorbed bases such as pyridine, ammonia, acetonitrile, carbon monoxide, nitrous oxide, and trimethyl phosphine [22.182–186]. In addition, the NMR method yields quantitative data for determination of the concentration of the different species present in the zeolites. ^{15}N NMR of adsorbed pyridine is of particular interest. Large upfield shift is observed upon protonation, and its variation is much larger than the ^{13}C NMR shift for the same molecule. Lewis acidity can also be probed by ^{15}N NMR of pyridine, provided that conditions of slow exchange prevail. For γ-alumina, silica–alumina, and acid-leached calcined mordenite, the chemical shift of the pyridine–Lewis acid pair complex (δ_L) could be estimated between -50 and -80 ppm [22.187, 188]. N_2O was also proposed as a base to probe surface Lewis acid sites [22.189]. Indeed, the terminal nitrogen atom is very sensitive to Lewis acidity, while it is only very slightly influenced by Brønsted acid sites. Moreover, this method is able to differentiate between the higher acidity of ZSM-5 and the lower acidity of zeolite HY. In these cases, because of the fast exchange between physisorbed and base–acid pair molecules, only an average ^{15}N NMR line is detected. ^{13}C NMR of carbon monoxide also predominantly probes Lewis acid sites. The NMR line is influenced by the strength and concentration of Lewis acid sites [22.186] to a large extent.

22.7.2 Basicity of Zeolites

The basicity of zeolites is much less well documented. In principle, one can distinguish between Lewis base sites linked to framework oxygen atoms and Brønsted base sites linked to basic hydroxyl groups. The former depends on the negative charge of the oxygen, while the latter depends on the extraframework cation present in the zeolite.

The basicity of zeolites is generally probed by IR of the NH stretching frequency of adsorbed pyrrole [22.190]. The NH stretching frequency decreases with increasing basicity of the sites in the order: Li-, Na-, K-, Rb-, and Cs-zeolite. In addition, it increases with increasing Al content [22.191], i. e., ZSM-5 (MFI) < mordenite (MOR) < L < Y < X.

22.8 Stability and Modification of Zeolite Structures

Since zeolites are widely used in chemical industry, how long a catalyst can remain in steam and how it can be modified to obtain better catalytic properties are relevant issues. Therefore, a great deal of work has been devoted to both the stability and modification of zeolites [22.2, 192–195].

As already discussed, zeolites are metastable solids; therefore, it is quite easy to modify the external surface, or the internal pore volume by pore blocking, create secondary pores, or vary the chemical composition, including isomorphous substitution of Al or Si.

22.8.1 Thermal Stability

The metastable nature of zeolites implies that conversion from one structure to another is possible, in certain cases even at room temperature [22.2]. Loss of intracrystalline water may result in structure collapse to an amorphous phase. Table 22.4 gives the temperature range of stability for various types of synthetic and natural zeolites [22.2].

The different countercations retain different amounts of water. The water content is quasiconstant for Li^+, Na^+, and K^+ in chabazite, while it decreases rapidly as a function of ionic radius for NH_4^+ and Rb^+. No satisfactory explanation exists at present to justify quantitatively the degree of hydration of the different zeolites. The two categories introduced distinguishing between hydrophilic and hydrophobic zeolites only indicate a tendency for water uptake.

22.8.2 Dealumination of Zeolites

Extraction of Al may lead both to changes in the acidic properties and to the formation of secondary structures. Selective aluminum removal without structure collapse was first described for clinoptilolite using strong mineral acid [22.196]. Presently, hydrothermal treatment is used in most cases, with or without chemical treatment. The latter may include reaction with mineral acids (HCl, NHO_3, HF), bases (NaOH), chelating agents ethylediaminetetraacetic acid (EDTA), acetylacetone (Acac), $(NH_4)_2SiF_6$, $SiCl_4$ vapor [22.197] or CCl_4 vapor [22.198], gaseous $COCl_2$ [22.199], etc.

Dealuminated zeolite Y (or ultrastable zeolite Y) is widely used as a cracking catalyst, and hence its dealumination is more widely commented. In hydrothermal or steam treatment, the degree of dealumination increases as a function of the steam partial pressure [22.200]. Dealumination leads to zeolites being ultrastable to heat treatment. Note that dealumination is accompanied by significant contraction of the unit cell, and the number of Al atoms remaining can be estimated from the unit cell dimension [22.201]. The process can be followed in detail by, e.g., advanced NMR methods [22.202] (Fig. 22.16).

22.8.3 Formation of Secondary Pore Structure

During dealumination and acid leaching, larger pores (or mesopores) may be found, with diameters ranging from 20 to ca. 250 Å [22.203]. The secondary pores are generally formed during dealumination, while acid leaching is necessary for elimination of the amorphous material deposited in the channels and/or cavities [22.204, 205]. For high-temperature treatments, the pore volume decreases due to partial amorphization of the structure [22.203].

It has been shown not too long ago that the distinction between *small*- and *large*-pore mordenite (SPM and LPM) is essentially due to the presence of structural

Table 22.4 Approximate classification of some zeolites by their temperature stability as defined by thermal analysis

Temperature range of stability	Zeolite
Ambient to 250 °C	Harmotome, phillipsite, paulingite, heulandite[a]
250–400 °C	Gismondine, yugawaralite, stilbite, brewsterite, stellerite
400–600 °C	Laumonite, faujasite, natrolite, scolecite, mesolite, thomsonite, gonnardite, edingtonite, P, ZK-4
Over 600 °C	Analcime, erionite, offretite, chabazite, mordenite, clinoptilolite, bikitaite, wairakite, dachiardite, merlionite, mazzite omega, A, X, Y, L, ZSM-5

[a] changes to heulandite B at 250 °C

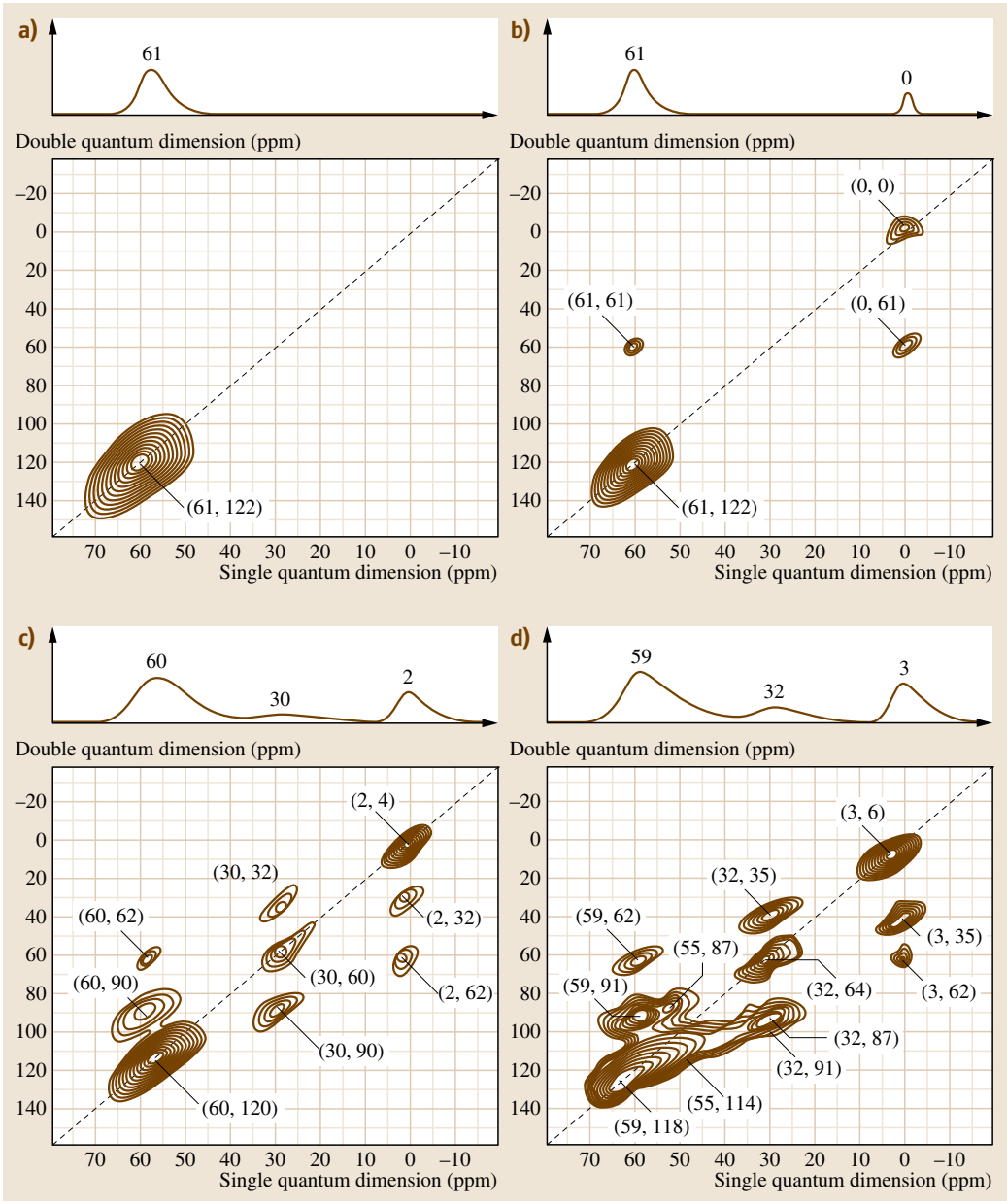


Fig. 22.16a–d ^{27}Al MAS and DQ-MAS (double quantum) NMR spectra of **(a)** parent HY, **(b)** HY-500, **(c)** HY-600, and **(d)** HY-700 zeolites. One-dimensional ^{27}Al MAS spectra are plotted on top of the two-dimensional ^{27}Al DQ-MAS spectra (calcination temperatures are 500 °C, 600 °C, and 700 °C). All spectra were recorded on hydrated samples at 18.8 T with a 3.2 mm probe at sample rotation rate of 21.5 kHz. (After [22.202], courtesy of Wiley-VCH)

defects along the channel axis c [22.206] in SP mordenite. The blocking of the unidimensional channels is caused by a glide plane resulting in successive LPM blocks shifted from each other by $c/2$. Dealumination eliminates the blocking tetrahedral sites, and LPM may be obtained from SPM [22.207].

22.8.4 Isomorphous Substitution

Isomorphous substitution refers to the replacement of silicon or aluminum atoms of the structure by elements with ionic radii and coordination requirements which are compatible with the tetrahedral sites in the

zeolite structure [22.23]. The probability of isomorphous substitution has been discussed on the basis of the simplified version of Pauling's minimum radius ratio [22.208]. Be, B, Cr, Fe, Ga, Ge, etc. have been successfully incorporated in the zeolite structure [22.192]. Indeed, for these cations the ratio between the cation radius (r_c) and the radius of oxygen ion (r_o) satisfies the condition for tetrahedral surroundings, i. e., $0.414 > \rho_s > 0.225$. However, any cation can be occluded in isomorphous positions provided its concentration is low [22.209]. Substitution can be made directly during hydrothermal synthesis or by postsynthetic modifications.

For low Si/Al-ratio zeolites (X, Y, MOR, etc.), framework exchange methods using fluorides and nonaqueous solvents at low temperatures can be used [22.210]. For high-Si/Al zeolites, generally, steam, acid, and/or base treatment is required to create internal OH groups or hydroxyl nests. These hydroxyl groups readily react with metal salts, and the metal ions are incorporated during calcination [22.211, 212].

Incorporation of Al into zeolites from alumina [22.213] has potentially important practical implications, since commercial zeolite catalysts are composed of zeolite crystals embedded in binder matrices that are assumed not to contribute to the catalytic performance.

To control the pore-opening size without affecting the internal pore system of the zeolite, modifying agents with molecular size larger than that of the zeolite pores have to be used, so they cannot enter the pores and interact only with the external surface [22.214]. $Si(OCH_3)_4$ is deposited irreversibly on a H-zeolite. The alkoxide groups react with surface hydroxyl groups, and calcination with oxygen removes the residual hydrocarbon, producing silica-coated zeolites [22.194, 214, 215]. The adsorption behavior can be influenced by the degree of SiO_2 deposition on the external surface.

22.8.5 Transition-Metal Ions and Metal Particles in Zeolites

It is well known that transition-metal ions and metal particles are very important catalytic centers. Introduction of these ions and/or particles into zeolites modifies their properties as follows: they (i) can exhibit physical and chemical properties often not found in known complexes, (ii) are often low-coordinated and bind molecules specifically, (iii) can be moved from one stable position to another when bonded with molecules, and (iv) can induce specific chemical reactions in the sorbed molecules [22.216].

Na^+ and NH_4^+ cations can be exchanged by cations such as Rh^{3+}, Pt^{2+}, Ni^{2+}, Co^{2+}, Cu^{2+}, Re^{3+} (rare earth), etc. Ions of rare-earth elements incorporated into X or Y zeolites produce the widely used cracking catalysts [22.217].

Preparation of active organometallic catalysts within the intracrystalline volume of the zeolite structures is a challenge that is relevant to homogeneous and heterogeneous catalysis as well as to enzyme modeling [22.218].

Size-quantized CdS is easily prepared inside zeolite Y sodalite cages. First, ca. 90% of the Na^+ ions are replaced by Cd^{2+} ions. After calcination, the dry zeolite is treated with H_2S, generating Cd_4S_4 clusters in the sodalite cages [22.148]. The larger supercages remain empty and available for absorption of substrate molecules. The obtained catalyst can be used for photooxidation reactions.

The preparation of metal particles in zeolites involves ion exchange followed by calcination and reduction. Alternative methods may involve the decomposition of complexes, such as metal carbonyls [22.219, 220]. Pt^{2+} or Pd^{2+} ions are introduced by ion exchange by $Pt(NH)_4{}^{2+}$ complexes. Calcination, in addition to destroying amine ligands and removing physisorbed water from the zeolite, affects the locations of the metal ions [22.219].

22.8.6 Coke Formation in Zeolites

Carbonaceous residues are inevitable byproducts of most heterogeneously catalyzed organic reactions [22.221]. The term "coke" designates deposits ranging from bulky molecules to heavy polynuclear aromatics. The formation of coke is usually acid-catalyzed, and it can become important on zeolite catalysts. The presence of coke generally leads to deactivation of the catalyst. It is hence of paramount importance to try to avoid coke formation, or if not possible, find a good way of catalyst regeneration.

Coke formed by secondary reaction products either blocks the pores of the zeolite or stays on the outer surface of the crystallites, or both [22.222, 223].

At very low coke content, coke molecules are smaller than the channel intersections, limiting but not blocking access to acid sites. At average coke content, coke blocks access to acid sites. At high coke content,

some it is deposited on the outer surface as well. The mode of deactivation very much depends on the zeolite pore structure, the nature of active sites, and the operating conditions [22.221, 222].

Coke deposits have been characterized by in situ spectroscopic techniques such as IR, UV-Vis, ^{13}C NMR, and electron paramagnetic resonance (EPR) spectroscopy [22.223, 224]. However, the precise composition of the coke can only be obtained when the carbonaceous compounds are recovered from the zeolite and analyzed via GC, ^{1}H NMR, mass spectrometry, etc.

It seems that coke molecules are formed inside the pores; coke on the outer surface results from its overflow onto the surface of zeolite crystallites [22.222].

At low temperature the retention of coke molecules is essentially due to their low volatility, while at high temperature it is due to trapping [22.222]. On H-ZSM-5 and H-MOR, aliphatic (10−60 ppm) as well as aromatic (120−150 ppm) compounds could be detected on both zeolites during methanol to hydrocarbon conversion [22.221, 224]. While only C-3 and C-4 compounds were identified on H-MOR, a variety of alkanes were entrapped on H-ZSM-5.

Regeneration of zeolites is carried out through coke combustion under air or oxygen flow [22.222]. Coke oxidation, like deactivation by coking, is a shape-selective process. The main difficulty is to limit the detrimental effects of water at high temperature on the active sites of the zeolite.

22.9 Zeolites as Catalysts

The intrinsic catalytic activity of zeolites was first related to the presence of acid sites in their channels. They are either Brønsted or Lewis sites. Acid sites in zeolites are responsible for their activity in cracking, olefin isomerization (both double-bond migration and skeletal rearrangement), oligomerization, alkylation of aromatics, etc. Use of zeolites as basic catalyst is much less common; indeed, base-catalyzed reactions that have been studied included mainly dehydrogenation of isopropanol to acetone, isomerization of allyl cyanide, and side-chain alkylation of alkylaromatics with olefins or alcohols. In addition to their acid sites, zeolitic catalysts often require another type of active site, a hydrogenation/dehydrogenation component. In order to introduce this function, various methods can be used, such as physical admixture with the hydrogenation/dehydrogenation component, impregnation, ion exchange/adsorption, or vapor deposition. The hydrogenation/dehydrogenation component can be certain noble and transition metals (Pt, Pd, Ni, Co, etc.), metal oxides (ZnO, CuO, Ga_2O_3, NiO, etc.), metal sulfides (NiS, Co/MoS, etc.), and metal complexes. Zeolites can be made capable to catalyze redox transformation as well. This functionality can be introduced by (i) direct incorporation of elements with changing oxidation states (e.g., titanium ions) during hydrothermal synthesis, or (ii) incorporation by postsynthetic treatments such as impregnation, ion exchange, isomorphous substitution, etc.

As previously described, zeolites are characterized by their unique, uniform pore/channel systems. Separation between molecules of different sizes or polarities can be achieved by selecting the proper zeolite structure, with the proper chemical properties. Indeed, chemical composition affects the polarity of the inner pore surface of the zeolite, making it more hydrophilic (low SiO_2/Al_2O_3) or hydrophobic (low Al_2O_3 content, for instance). Consequently, this can affect the adsorption/desorption properties of molecules on the outer surface, but more importantly inside the pores. However, the main parameters influencing feed or product selectivity are the size of the molecules and of the zeolite channels. If a feedstock contains different types of molecules, some being too large to enter the zeolite pores, only the ones with smaller dimensions or correct shape will be allowed to enter the crystal to react. On the other hand, if a reaction can produce different products, only the product that can diffuse out of the zeolite crystal will be detected. Sometimes, both reactant and product molecules are able to diffuse rapidly in or out of the zeolite crystal. Nevertheless, some selectivity is observed for given products. The reaction intermediates leading to a given molecule can be larger than the space available near the catalytic site, and thus, they may be spatially constrained by the size and geometry of the zeolite cavities. This has been termed transition-state selectivity. Some zeolites of interest have intersecting channels of different size. This is the case for ZSM-5, mordenite, offretite, and ferrierite. Since the smaller channels will adsorb only the smaller molecules while both large and small molecules will enter the larger pores, a new type of shape selectivity can be achieved. This concept is known as the molecular traffic control effect [22.225].

Table 22.5 Commercial refining and petrochemical processes using zeolite catalysts. (After [22.2, 226, 227])

Processes	Catalysts	Remarks
Catalytic cracking	REY, REX, REMY, REMgY, HY high-silica medium-pore zeolites	Selectivity and high conversion (high-octane gasoline)
Hydrocracking	Faujasite (X, Y), mordenite, erionite loaded with Co, Mo, W, Ni, also HY, USY, CaMgY, and HZSM-5	High conversion
Selectoforming	Ni-erionite, Ni-erionite/clinoptilolite	Increase in octane number via LPG production
Hydroisomerization	Pt-mordenite	Converts low-octane pentanes and hexanes to higher-octane products
Dewaxing	Pt-mordenite, ZSM-5, silicalite, other high-silica, medium-pore zeolites (ferrierite)	Low pore and cloud points
Aromatization	Pt, K-L, Ba-L, silicalite, (Pt)Ga,Zn-ZSM-5	Aromatization of C_6–C_8 cuts, aromatization of LPG
Benzene alkylation	ZSM-5	Ethylbenzene (and styrene) production with low by-product yield
Xylene isomerization	ZSM-5	Increase in *para*-xylene yield
Toluene disproportionation	ZSM-5, mordenite	Production of xylenes and benzene
Methanol to gasoline	ZSM-5, erionite	High gasoline yield with high olefin conversion rate to high-octane rating products
Fischer-Tropsch	Co- or Fe-ZSM-5	Natural gas to gasoline via CO/H_2
deNO_x	Cu-ZSM-5 (H-mordenite)	Effluents clean-up

In addition to their molecular sieving properties that induce shape-selective effects in catalysis, zeolites can also be considered as small reactors, favoring for instance bimolecular reactions, as ionizing solid solvents or as solid electrolytes.

22.9.1 Zeolites in the Refining and Petrochemical Industry

Zeolites were introduced as catalysts in the late 1950s and early 1960s, in fluid catalytic cracking. This is their largest scale application even today. Numerous other applications in the refining and petrochemical industries have also been developed, including hydrocracking, dewaxing, reforming or dehydrocyclodimerization, deNO_x processes, oligomerization, alkylation, isomerization, methanol transformation to gasoline, and the Fischer–Tropsch process (Table 22.5).

22.9.2 Zeolites in the Fine Chemical Industry

Although the main uses of zeolites as catalysts or catalyst supports remain in the refining and petrochemical industries, more and more applications are being developed in the intermediate and fine chemicals area. Actually, experiences gained in the refining and petrochemical areas with zeolite catalysts are being applied to other organic reactions involving fine chemicals. The accumulated knowledge allows enhancement of activity and selectivity and stabilization of the active catalytic sites in zeolite cavities. Replacement of homogeneous catalysts by heterogeneous materials often operated in fixed bed avoids problems due to corrosion of equipment, or separation of the catalyst from the products.

The major applications in this new field are proton or Lewis-acid-catalyzed reactions, using acidic zeolite materials, taking advantage of their shape-selective properties. Other functionalities can also be introduced, and acid–base properties can be modulated either during the hydrothermal synthesis, for instance, by introduction elements other than Si and Al in the zeolite framework, or by postsynthetic modifications, such as dealumination, ion exchange, impregnation, etc. This allows preparation of tailor-made catalysts by modulating the zeolite properties or by combining the zeolite with other catalyst sites, to achieve the best performance.

Reactions performed on zeolite catalysts involve double-bond isomerization, skeletal isomerization, dehydration, dehydrogenation, aromatic ring substitution

(halogenation, acylation, alkylation), isomerization of aromatics, selective hydrogenation, and selective oxidation. This area has been reviewed several times [22.228–232].

22.10 Some Special Applications of Zeolites

Although the ion-exchange properties of zeolites have been well documented in relation to catalysis and molecular sieving, very few practical uses as ion exchangers have emerged [22.2]. A major technical barrier to zeolite use as ion exchanger is in their apparent lack of compatibility with column use. Synthetic zeolites have sizes which are too small (0.1−10 μm) to allow reasonable liquid transport through a bed of particles [22.2]. Therefore, granulated synthetic or ground natural zeolite rocks such as clinoptilolite or mordenite are preferred for column use. Another major reason preventing wide use of zeolites as ion exchangers is their inherent instability at low pH. The limit of acid resistance of low Si/Al-ratio zeolites is at pH 3−4. The growing awareness of the environmental damage created by the use of polyphosphate-containing detergents caused detergent manufacturers to seek less hazardous replacements [22.2]. The function of polyphosphate is to enhance the cleaning efficiency of detergents by removing Ca^{2+} and Mg^{2+} ions from washing water to prevent their precipitation by surfactants. Zeolite A has proved to be a suitable substitute, and its current application as a detergent builder represents a major success in direct use of zeolites as ion exchangers [22.233].

When spent nuclear fuel elements are removed from a nuclear reactor they are stored under water in *ponds* [22.2]. The pH of the water is 11.4 with respect to NaOH and Na_2CO_3. Pond storage allows thermal and radiation cooling to take place prior to reprocessing. During the storage period a build-up of fission products – essentially $^{137}Cs^{+}$ and $^{90}Sr^{2+}$ – occurs in the pond water. Zeolites, such as mordenite and clinoptilolite, are used to decontaminate the effluent.

There is a constant need to remove heavy metals and ammonia from waste waters. Release of heavy metals into waste water is one of the most worrying pollution problems, since its effects on life may be particularly serious in plants and animals (mainly fish), and humans are also affected through the food chain [22.234]. Nitrogen pollution stems from municipal and industrial waste waters via washout of natural and artificial fertilizers, and seepage and runoff of liquid livestock wastes, effluents from aquaculture systems, and from food processing plants [22.235]. Natural zeolites, clinoptilolite, phillipsite, and chabazite, are particularly useful to selectively eliminate ammonia [22.2, 236, 237] and heavy metals, such as Cd^{2+}, Pb^{2+}, Zn^{2+}, Cu^{2+} [22.2, 235], and partially Cr^{3+} [22.234].

In agriculture, natural zeolites such as clinoptilolite, phillipsite, and chabazite act as neutralizers of low pH of soils, traps for harmful heavy metals, and effective carriers of herbicides, fungicides, and insecticides [22.2, 235]. In husbandry, pigs consuming clinoptilolite show beneficial weight gain and are less subject to disease [22.2]. Moreover, natural zeolites such as clinoptilolite, chabazite, mordenite, erionite, and phillipsite actively adsorb volatiles (ammonia, carbon dioxide, hydrogen sulfide, and mercaptans) and have a strong deodorizing effect. In the diets of calves and poultry, zeolites act, in addition to the above-mentioned benefits, as veterinary hygiene agents by inhibiting embryonation of worm eggs and protozoa.

Every chemical laboratory in the world has a bottle of 4A beads for use as a general-purpose drying agent [22.2]. The organic liquids are generally dried on Linde 3A or 4A [22.2, 238]. For drying of gases, zeolites A, X, and Y are also used. $CoCl_2$ plays the role of an indicator: it is blue at low water content (tetrahedral Co^{2+}), while it is pink at high water content (octahedral Co^{2+}). Natural gas is dried on Linde 4A, 5A, and natural zeolites. Larger crystallites have longer lifetime. In order to dry gases containing polymerizable monomers, Linde 4A is used first to adsorb the monomers and then Linde 3A for dehydration.

Elimination of sulfur-containing gaseous species such as H_2S/COS or CH_3SH from natural gas and biogas is of paramount importance [22.238]. General use is made of Linde 5A, X, natural zeolites, or zeolites impregnated with Fe_2O_3 [22.238]. Liquid hydrocarbons are desulfurized by zeolite impregnated with $CuSO_4$. Silanes are cleaned of PH_3 and AsH_3 on AgA zeolite, of ethylene on Linde 4A, $POCl_3$ on high-silica zeolite, and of HCl, HF, and SO_2 on H-mordenite [22.238]. Hydrogen is purified of nitrogen on Ca-mordenite, and the residual amount of nitrogen can be as low as 1 ppm [22.238]. Nitrogen is purified by eliminating oxy-

gen, methane, carbon monoxide, and carbon dioxide with the help of zeolites. For air purification, charcoal is used in combination with zeolites, impregnated or not with bactericides (Ag, $KMnO_4$, etc.). Natural zeolites are used for air refreshing in freezers of airplanes or in cars. Various zeolites are used for deodorizing sewers, toilets, freezers, etc. Zeolites are also used to adsorb methane (firedamp) in coal mines or carbon monoxide in sealing equipment.

The dangerous isotopes of Cs^+ and Sr^{2+} are eliminated by ion exchange with zeolites. The adsorption properties of zeolites help to extract tritium from waters used in this process. Tritium is adsorbed in the form THO on zeolites Linde 5A and X or zeolite exchanged with Ag^+ [22.233, 238]. Heavy water D_2O is adsorbed on zeolite X. Radioactive iodine is eliminated using faujasite in its hydrogen- or Ag^+-exchanged form, or using Ag-mordenite. The radioactive noble gases (Ar, Kr, Xe) are adsorbed on zeolite A or mordenite, which can then be vitrified under pressure or fixed by silicate cement [22.238].

The mobile cations in zeolites are apt to contribute to the ionic conductivity in batteries. The conductivity is dependent on the nature of the cation and the degree of hydration [22.238]. The anode is generally composed of a zeolite containing Li^+, Na^+, or K^+. The cathode is a CrO_3-, P-, $FeCl_3$-, Cl-, or S-containing zeolite [22.239]. In the presence of organic electrodes, the zeolite is used for its dehydration properties. In dry battery, zeolite eliminates impurities (peroxides) and impedes passivation of the anodes.

Various applications are already in use in the food industry. Zeolite saturated with CO_2 gives instantaneous carbonation of aqueous preparations. Beer is stabilized with NaA and LiX, which adsorb proteins responsible for further degradation [22.238]. Dealcoholization of beer is achieved using silicates. Decaffeination is also performed with the help of dealuminated zeolite Y [22.240]. Fatty acids of comestible oil are eliminated on zeolite X. Also, everyday use of toothpaste reminds us of the utility of zeolites, as they are included as polishing and anticorrosion agents [22.241].

Zeolites are also used as supports for enzymes or antibodies [22.238]. Glucose oxidase is fixed on zeolite 4A and zeolite X. Coenzymes have been stabilized on 4A. The thermal stability of trypsin is greatly enhanced when adsorbed on zeolite 4A. Zeolite treatment is, however, not beneficial for all enzymes, as, e.g., β-galactosidase is deactivated in presence of zeolites.

The best known procedure for separation of *n*-paraffins from isoparaffins involves adsorption on zeolite 5A, from which the latter are excluded by virtue of their larger effective kinetic diameter [22.2]. Another large-scale molecular sieving separation is that of enriching gases from air (oxygen, nitrogen, and inert gases) [22.2, 238]. This can be carried out cryogenically, but new pressure sieving processes at near-ambient temperature are progressively being used to generate oxygen and nitrogen. Natural clinoptilolites and mordenites are used with success in portable pressure sieving oxygen generators for use in hospitals or as home oxygen supplies for patients with respiratory problems [22.2]. Separation of inositol and sorbitol has recently been realized on Ca-zeolite X. First sorbitol and second inositol are adsorbed from a mixture [22.242]. Release with the help of a desorbing agent yields firstly inositol and secondly sorbitol. Use of zeolites in chromatographic separation and quantitative determination is also beneficial [22.2, 238]. The amount of N_2O in blood has been determined using zeolite 5A. Capillary columns impregnated with zeolite 5A or X have high performance.

Conjugated polymers, such as doped polyacetylene, polyaniline, and polypyrrole, have potential applications based on their conducting properties, ranging from lightweight batteries, antistatic equipment, and microelectronics to speculative concepts such as *molecular electronic* devices [22.243]. Pyrrole can be polymerized within the cavities of faujasite and the unidimensional channels of mordenite. Polymerization required the presence of intrazeolite oxidants, such as ferric or cupric ions. Intrazeolite heteroaromatic polymer chains represent host-stabilized one-dimensional molecular conductors or molecular wires [22.243]. Zeolites are also used as polymers protecting against degradation by ultraviolet radiation [22.238, 244].

The textile industry also uses zeolites as additives to synthetic fibres (polyesters, polyamides, polyacrylonitriles, etc.). They protect them from degradation (Cu-zeolite), have a bactericidal effect (Ag, Cu-A, X or Y), an antistatic effect (with Fe_2O_3), or a deodorizing function, and help fixation of dyes [22.238].

The paper industry uses zeolites as fillers to give more density to paper [22.238].

Zeolites also favor adhesion of polymers onto steel; for example, polyethylene coated with Ba-mordenite and Ag, Zn, or Sn-A zeolite has better adhesion to steel [22.245].

22.11 Conclusions

We hope that this chapter has convinced the reader that zeolites and related substances are very versatile materials. Many varieties can be found in nature, and these as well as structures not found in our environment can be synthesized with relative ease. Their framework can be modified without great difficulty, which means they can be tuned for particular applications. Applications are numerous, ranging from molecular sieving to catalytic applications. The latter are of outmost importance from oil refining to fine chemical industries. Active sites that can be generated in/on the framework are coupled with shape-selective effects, which is very useful in high atom-efficiency processes, which is one of the driving forces for constructing new frameworks with pore dimensions in the mesoporous range. This requirement keeps this area active today and will continue to do so in the foreseeable future.

References

22.1 X.S. Zhao, G.Q.M. Lu, G.J. Millar: Advances in mesoporous molecular sieve MCM-41, Ind. Eng. Chem. Res. **35**, 2075–2090 (1996)

22.2 A. Dyer: *An Introduction to Zeolite Molecular Sieves* (Wiley, Chichester 1988)

22.3 W.M. Meier, D.H. Olson: *Atlas of Zeolite Structure Types*, 4th edn., ed. by Structure Commission of the International Zeolite Association (Elsevier, London 1996) p. 5

22.4 D.W. Breck: *Zeolite Molecular Sieves, Structure, Chemistry, Use* (Wiley, New York 1974)

22.5 D. Barthomeuf: Vers la maîtrise des zéolithes en adsorption et en catalyse (Towards the improvement of performance of zeolites as adsorbents and catalysts), Inform. Chim. **295**, 227–230 (1988)

22.6 D.M. Ruthven: Zeolites as selective sorbents, Chem. Eng. Prog. **84**, 42–50 (1988)

22.7 H. Nakamoto, H. Takahashi: Crystal symmetry change of ZSM-5 by various treatments, Chem. Lett., 1013–1016 (1981)

22.8 G. Debras, A. Gourgue, J.B. Nagy, G. de Clippelier: Physico-chemical characterization of pentasil type materials. IV. Thermal and steam stability, dealumination and aluminum exchange, Zeolites **6**, 241–248 (1986)

22.9 J.M. Newsam: The structural chemistry of zeolites as viewed by powder neutron-diffraction, Physica B/C **136**, 213–217 (1986)

22.10 W.M. Meier, FNRS Contact Group on Catalysis, Clays and Zeolites: Molecular sieves and clays: Materials by design, Katholieke Universiteit Leuven, Belgium (1990), oral presentation

22.11 M.E. Davis, C. Saldarriaga, C. Montes, J. Garces, C. Crowder: A molecular sieve with 18-membered rings, Nature **331**, 698–699 (1988)

22.12 R.M. Dessau, J.L. Schlenker, J.B. Higgins: Framework topology of $AlPO_4$-8: The first 14-ring molecular sieve, Zeolites **10**, 522–524 (1990)

22.13 M. Estermann, L.B. Mccusker, C. Baerlocher, A. Merrouche, H. Kessler: A synthetic gallophosphate molecular-sieve with a 20-tetrahedral-atom pore opening, Nature **352**, 320–323 (1991)

22.14 J.S. Beck, C. Vartuli, W.J. Roth, M.E. Leonowicz, C.T. Kresge, K.D. Schmitt, C.T.-W. Chu, D.H. Olson, E.W. Sheppard, S.B. McCullen, J.B. Higgins, J.L. Schlenker: A new family of mesoporous molecular-sieves prepared with liquid-crystal templates, J. Am. Chem. Soc. **114**, 10834–10843 (1992)

22.15 O.C. Gobin, S.J. Reitmeier, A. Jentys, J.A. Lercher: Diffusion pathways of benzene, toluene and p-xylene in MFI, Micropor. Mesopor. Mater. **125**, 3–10 (2009)

22.16 R.M. Barrer: Syntheses and reactions of mordenite, J. Chem. Soc., 2158–2163 (1948)

22.17 L.B. Sand: *Molecular Sieves* (Society of Chemical Industry, London 1967) p. 71

22.18 N.Y. Chen, W.E. Garwood, F.G. Dwyer: *Shape Selective Catalysis in Industrial Applications* (Marcel Dekker Inc., New York 1989)

22.19 P.W. Tamm, D.H. Mohr, C.R. Wilson: Octane enhancement by selective reforming of light paraffins, Stud. Surf. Sci. Catal. **38**, 335–353 (1988)

22.20 C.D. Chang: Hydrocarbons from methanol, Catal. Rev. Sci. Eng. **25**, 1–118 (1983)

22.21 D.R. Lide (Ed.): *CRC Handbook of Chemistry and Physics*, 67th edn. (CRC Press, Boca Raton 1986)

22.22 R.M. Barrer, P.J. Denny: Hydrothermal chemistry of silicates. 9. Nitrogenous aluminosilicates, J. Chem. Soc., 971–982 (1961)

22.23 R.J. Argauer, G.R. Landolt: US Patent 3702886 (1972)

22.24 R.M. Barrer: *Hydrothermal Chemistry of Zeolites* (Academic Press, London 1982)

22.25 Z. Gabelica, J.B. Nagy, P. Bodart, G. Debras: High-resolution solid-state mas B-11-NMR evidence of boron incorporation in tetrahedral sites of zeolites, Chem. Lett., 1059–1062 (1984)

22.26 G. Perego, G. Belussi, C. Corno, M. Taramasso, F. Buonomo, A. Esposito: Titanium-silicalite: A novel derivative in the pentasil family, Stud. Surf. Sci. Catal. **28**, 129–136 (1986)

22.27 B.M. Lok, C.A. Messina, R.L. Patton, R.T. Gajek, T.R. Cannan, E.M. Flanigen: Silicoaluminophosphate molecular-sieves – Another new class of

microporous crystalline inorganic solids, J. Am. Chem. Soc. **106**, 6092–6093 (1984)
22.28 E.M. Flanigen, B.M. Lok, R.L. Patton, S.T. Wilson: Aluminophosphate molecular sieves and the periodic table, Stud. Surf. Sci. Catal. **28**, 103–112 (1986)
22.29 E.M. Flanigen, R.L. Patton, S.T. Wilson: Structural, synthetic and physicochemical concepts in aluminophosphate-based molecular sieves, Stud. Surf. Sci. Catal. **37**, 13–27 (1988)
22.30 W. Depmeier: Revised crystal data for the aluminate sodalite $Ca_8[Al_{12}O_{24}](WO_4)_2$, J. Appl. Cryst. **12**, 623–626 (1979)
22.31 Y. Chen, G. Zhu, Y. Peng, X. Yao, S. Qiu: Synthesis and characterization of (*h0l*) oriented high-silica zeolite beta membrane, Micropor. Mesopor. Mater. **124**, 8–14 (2009)
22.32 F. Fan, Z. Feng, C. Li: UV-Raman spectroscopic study on the synthesis mechanism and assembly of molecular sieves, Chem. Soc. Rev. **39**, 4794–4801 (2010)
22.33 E.G. Derouane, N. Dewaele, Z. Gabelica, J.B. Nagy: Physicochemical characterization of zeolite ZSM-20, Appl. Catal. **28**, 285–293 (1986)
22.34 V. Fülöp, G. Borbely, H.K. Beyer, S. Ernst, J. Weitkamp: Physicochemical characterization and framework topology of zeolite ZSM-20, J. Chem. Soc. Faraday Trans. I **85**, 2127–2139 (1989)
22.35 Z. Gabelica, N. Dewaele, L. Maistriau, J.B. Nagy, E.G. Derouane: Directing parameters in the synthesis of zeolites ZSM-20 and beta, ACS Symp. Ser. **398**, 518–543 (1989)
22.36 J.A. Martens, P.A. Jacobs, S. Cartlidge: Investigation of the pore architecture of CSZ-1 zeolites with the decane test reaction, Zeolites **9**, 423–427 (1989)
22.37 L. Maistriau, N. Dumont, J.B. Nagy, Z. Gabelica, E.G. Derouane: Single- and two-liquid-phase synthetic routes to sapo-37, Zeolites **10**, 243–250 (1990)
22.38 D.E.W. Vaughan, M.G. Barrett: US Patent 4333859 (1982)
22.39 R.L. Wadlinger, G.T. Kerr, E.J. Rosinski: US Patent 3308069 (1967)
22.40 J.M. Newsam, M.M.J. Treacy, W.T. Koetsier, C.B. de Gruyter: Structural characterization of zeolite beta, Proc. Roy. Soc. Lond A **420**, 375 (1988)
22.41 M.M.J. Treacy, J.M. Newsam: 2 new 3-dimensional 12-ring zeolite frameworks of which zeolite beta is a disordered intergrowth, Nature **332**, 249–251 (1988)
22.42 J.B. Higgins, R.B. LaPierre, J.L. Schlenker, A.C. Rohrman, J.D. Wood, G.T. Kerr, W.J. Rohrbaugh: The framework topology of zeolite beta, Zeolites **8**, 446–452 (1988)
22.43 J.B. Higgins, R.B. LaPierre, J.L. Schlenker, A.C. Rohrman, J.D. Wood, G.T. Kerr, W.J. Rohrbaugh: The framework topology of zeolite beta – a correction, Zeolites **9**, 358 (1989)
22.44 D.E.W. Vaughan, K.G. Strohmaier: The influence of template size and geometry on faujasite crystallization, Stud. Surf. Sci. Catal. **28**, 207–213 (1986)
22.45 M.E. Leonowicz, D.E.W. Vaughan: Proposed synthetic zeolite ECR-1 structure gives a new zeolite framework topology, Nature **329**, 819–821 (1987)
22.46 D.E.W. Vaughan, M.E. Leonowicz, K.G. Strohmaier: Characterization of the new zeolite ECR-1, ACS Symp. Ser. **411**, 303–318 (1989)
22.47 M.E. Davis, C. Saldarriaga, C. Montes, J. Garces, C. Crowder: VPI-5: The first molecular sieve with pores larger than 10 Å, Zeolites **8**, 362–366 (1988)
22.48 M.E. Davis, C. Montes, P.E. Hathaway, J.M. Garces: Synthesis of aluminophosphate and element-substituted aluminophosphate VPI-5, Stud. Surf. Sci. Catal. **49**, 199–214 (1989)
22.49 E.G. Derouane, R. von Ballmoos: US Patent 4673559 (1987)
22.50 M.E. Davis, P.E. Hathaway, C. Montes: VPI-5, $AlPO_4$-8, and MCM-9: Similarities and differences, Zeolites **9**, 436–439 (1989)
22.51 S.T. Wilson, B.M. Lok, E.M. Flanigen: US Patent 4310440 (1982)
22.52 J.B. Parise: Preparation and structure of the aluminum ammonium phosphate dihydrate $Al_2[NH_4](OH)(PO_4)_2{\cdot}2H_2O$ – A tunnel structure with ammonium-ions in the channels, Acta Cryst. C **40**, 1641–1643 (1984)
22.53 R. Szostak, R. Kuvadia, J. Brown, T.L. Thomas: Ultralarge pore molecular sieves: Characterization of the 14 Å pore mineral, Cacoxenite, Stud. Surf. Sci. Catal. **49**, 439–446 (1989)
22.54 J. Wang, S. Feng, R. Xu: Synthesis and characterization of a novel microporous aluminoborate, J. Chem. Soc. Chem. Commun., 265–266 (1989)
22.55 A. Cronstedt: Akad. Handl. Stockholm, 120 (1756)
22.56 D.W. Breck: *Zeolite Molecular Sieves, Structure, Chemistry and Use* (Wiley, New York 1974)
22.57 R.L. Hay: Geologic occurrence of zeolites and some associated minerals, Stud. Surf. Sci. Catal. **28**, 35–40 (1986)
22.58 H. Eichhorn: über die Einwirkung verdünnter Salzlösungen auf Silicate, Pogg. Ann. Phys. Chem. **105**, 126 (1858)
22.59 A. Damour: über das Bleigummi und thonerdhaltiges phosphorsaures Bleioxyd von Huelgoat, Ann. Mines **17**, 191 (1840)
22.60 G. Friedel: Sur un nouveau silicate artificial, Bull. Soc. Franc. Mineral. Crystallogr. **19**, 5–14 (1896)
22.61 F. Grandjean: An optic study of absorption of heavy vapours by certain zeolites, C. r. **149**, 866–868 (1909)
22.62 J.W. McBain: *The Sorption of Gases and Vapors by Solids* (Routledge, London 1932)
22.63 R.M. Barrer: The sorption of polar and non-polar gases by zeolites, Proc. R. Soc. A **167**, 392–420 (1938)
22.64 R.M. Milton: Molecular sieve adsorbents, US Patent 2882243 (1959)
22.65 D.W. Breck, W.G. Eversole, R.M. Milton, T.B. Reed, T.L. Thomas: Crystalline zeolites 1. The properties of

a new synthetic zeolite, type-A, J. Am. Chem. Soc. **78**, 5963–5971 (1956)
22.66 F.A. Mumpton: In: *Natural Zeolites, Occurrence, Properties, Use*, ed. by L.B. Sand, F.A. Mumpton (Pergamon, Oxford 1978) p. 3
22.67 H. Kristmannsdottir, J. Tomasson: In: *Natural Zeolites, Occurrence, Properties, Use*, ed. by L.B. Sand, F.A. Mumpton (Pergamon, Oxford 1978) p. 227
22.68 R.L. Hay: Zeolitic weathering of tuffs in Olduvai Gorge, Tanzania, Proc. 5th Int. Conf. Zeol. (1980) p. 155
22.69 A. Dyer: *An Introduction to Zeolite Molecular Sieve* (Wiley, Chichester 1988) p. 4
22.70 R.L. Hay: Silicate reaction in three lithofacies of a semiarid basin, Olduvai Gorge, Tanzania, Min. Soc. Am. Spec. Paper **3**, 237–255 (1970)
22.71 M. Kastner: In: *The Oceanic Lithosphere*, ed. by C. Emiliani (Wiley, New York 1981) p. 915
22.72 M. Utada: Zeolitic zoning of the Neogene pyroclastic rocks in Japan, Sci. Pap. Coll. Gen. Educ. Univ. Tokyo **21**, 189–221 (1971)
22.73 A. Jijima: In: *Occurrence, Properties and Utilization of Natural Zeolites*, ed. by D. Kalló, H.S. Sherry (Akadémiai Kiadó, Budapest 1988) p. 29
22.74 D.R. Corbin, B.F. Burgess, A.J. Vega Jr., R.D. Farlee: Comparison of analytical techniques for the determination of silicon and aluminum content in zeolites, Anal. Chem. **59**, 2722–2728 (1987)
22.75 K.J. Chao, S.H. Chen, M.H. Yang: Simultaneous multielement analysis of zeolite catalysts by inductively-coupled plasma atomic emission-spectrometry, Fresen. Z. Anal. Chem. **331**, 418–422 (1988)
22.76 G. Debras, E.G. Derouane, J.-P. Gilson, Z. Gabelica, G. Demortier: Prompt nuclear and atomic reactions for elemental analysis of zeolites I. A discussion of the experimental methods, Zeolites **3**, 37–42 (1983)
22.77 J. Dwyer, F.R. Fitch, G. Quin, J.C. Vickerman: Study of the surface-composition of zeolites by fast atom bombardment mass-spectrometry, J. Phys. Chem. **86**, 4574–4578 (1982)
22.78 Z. Gabelica, J.B. Nagy, E.G. Derouane, J.-P. Gilson: The use of combined thermal analysis to study crystallization, pore structure, catalytic activity and deactivation of synthetic zeolites, Clay Miner. **19**, 803–824 (1984)
22.79 J.M. Bennett, R.M. Kirchner, S.T. Wilson: Synthesis and idealized topology of $AlPO_4$-52, a new member of the ABC six-ring family, Stud. Surf. Sci. Catal. **49**, 731–739 (1988)
22.80 J.M. Bennett: Determining the structure of molecular-sieve materials using high-resolution powder data, ACS Symp. Ser. **368**, 162–176 (1988)
22.81 Z. Paiz, S.J. Andrews: Structure of the zeolite θ-1 – redetermination using single-crystal synchrotron-radiation data, Acta Cryst. C **46**, 172–173 (1990)
22.82 N.A. Briscoe, D.W. Johnson, M.D. Shannon, G.T. Kokotailo, L.B. McCusker: The framework topology of zeolite EU-1, Zeolites **8**, 74–76 (1988)
22.83 J.M. Newsam: Aluminum partitioning in zeolite-L, J. Chem. Soc. Chem. Commun., 123–124 (1987)
22.84 J.M. Thomas: Advances in the structural analysis of zeolites, zeolitic precursors and their analogues, Stud. Surf. Sci. Catal. **49**, 3–28 (1989)
22.85 A.C. Rohrman, R.B. LaPierre Jr., J.L. Schlenker, J.D. Wood, E.W. Valyocsik, M.K. Rubin, J.B. Higgins, W.J. Rohrbaugh: The framework topology of ZSM-23: A high silica zeolite, Zeolites **5**, 352–354 (1985)
22.86 O. Terasaki, J.M. Thomas, G.R. Millward, D. Watanabe: Role of high-resolution electron microscopy in the identification and characterization of new crystalline, microporous materials: "reading off" the structure and symmetry elements of pentasil molecular sieves, Chem. Mater. **1**, 158–162 (1989)
22.87 M.M.J. Treacy, J.M. Newsam: 2 new 3-dimensional 12-ring zeolite frameworks of which zeolite beta is a disordered intergrowth, Nature **332**, 249–251 (1988)
22.88 J.B. Nagy, E.G. Derouane: NMR spectroscopy and zeolite chemistry, ACS Symp. Ser. **368**, 2–32 (1988)
22.89 J. Klinowski: Solid-state NMR studies of zeolite catalysts, Colloid. Surface. **36**, 133–154 (1989)
22.90 S. Ramdas, J. Klinowski: A simple correlation between isotropic Si-29-NMR chemical shifts and T-O-T angles in zeolite frameworks, Nature **308**, 521–523 (1984)
22.91 G. Engelhardt, R. Radeglia: A semiempirical quantumchemical rationalization of the correlation between Si–O–Si angles and Si-29 NMR chemical shifts of silica polymorphs and framework aluminosilicates (zeolites), Chem. Phys. Lett. **108**, 271–274 (1984)
22.92 G. Engelhardt, S. Luger, J.C. Buhl, J. Felsche: Si-29 MAS NMR of aluminosilicate sodalites – correlations between chemical shifts and structure parameters, Zeolites **9**, 182–186 (1989)
22.93 C.A. Fyfe, H. Gies, Y. Feng, G.T. Kokotailo: Determination of 3-dimensional lattice connectivities in zeolites using natural-abundance Si-29 two-dimensional NMR and the direct observation of Si-29-O-Si-29 couplings, Nature **341**, 223–225 (1989)
22.94 C.A. Fyfe, H. Gies, G.T. Kokotailo, Y. Feng, H. Strobl, B. Marler, D.E. Cox: Multitechnique analysis of the lattice structures of highly siliceous zeolites, Stud. Surf. Sci. Catal. **49**, 545–557 (1989)
22.95 J. Klinowski: Nuclear magnetic-resonance studies of zeolites, Prog. NMR Spectrosc. **16**, 237–309 (1984)
22.96 J.W. Akitt: Multinuclear studies of aluminum compounds, Prog. NMR Spectrosc. **21**, 1–149 (1989)
22.97 P. Bodart, J.B. Nagy, G. Debras, Z. Gabelica, P.A. Jacobs: Aluminum siting in mordenite and dealumination mechanism, J. Phys. Chem. **90**, 5183–5190 (1986)

22.98 J.H. Raeder: Computer-aided interpretation of high-resolution ^{29}Si NMR spectra of offretites, Zeolites **4**, 311–314 (1984)

22.99 P. Bodart, J.B. Nagy, Z. Gabelica, E.G. Derouane: In: *Occurrence, Properties and Utilization of Natural Zeolites*, ed. by D. Kalló, H.S. Sherry (Akadémiai Kiadó, Budapest 1988) p. 245

22.100 H.K.C. Timken, N. Janes, G.L. Turner, S.L. Lambert, L.B. Welsh, E. Oldfield: Solid-state O-17 nuclear magnetic resonance spectroscopic studies of zeolites and related systems 2, J. Am. Chem. Soc. **108**, 7236–7241 (1986)

22.101 Z. Gabelica, J.B. Nagy, P. Bodart, G. Debras: High-resolution solid-state mas B-11-NMR evidence of boron incorporation in tetrahedral sites of zeolites, Chem. Lett., 1059–1062 (1984)

22.102 C.S. Blackwell, R.L. Patton: Solid-state NMR of silicoaluminophosphate molecular-sieves and aluminophosphate materials, J. Phys. Chem. **92**, 3965–3970 (1988)

22.103 C.R. Bayense, J.H.C. van Hooff, A.P.M. Kentgens, J.W. de Haan, L.J.M. van de Ven: The removal of gallium from the lattice of MFI-galosilicates as studied by ^{71}Ga MAS NMR spectroscopy, J. Chem. Soc. Chem. Commun. **17**, 1292–1293 (1989)

22.104 R.A. Schoonheydt: Combined ESR-DRS spectroscopies of transition-metal ions and metal-ion clusters in zeolites, J. Phys. Chem. Solids **50**, 523–539 (1989)

22.105 R.A. Schoonheydt, I. Vaesen, H. Leeman: Electron spin resonance and diffuse reflectance spectroscopy of the reduction of Ni^{2+} with H-2 in zeolite X and zeolite Y, exchanged with La^{3+} and NH^{4+}, J. Phys. Chem. **93**, 1515–1521 (1989)

22.106 A.V. Kucherov, A.A. Slinkin: Introduction of transition metal ions in cationic positions of high-silica zeolites by a solid state reaction, Interaction of copper compounds with H-mordenite or H-ZSM-5, Zeolites **6**, 175–180 (1986)

22.107 A.V. Kucherov, A.A. Slinkin: Introduction of Cr(V), Mo(V) and V(IV) ions in cationic positions of high-silica zeolites by a solid-state reaction, Zeolites **7**, 38–42 (1987)

22.108 A.V. Kucherov, A.A. Slinkin: Co-introduction of transition metal ions into cationic positions of H-ZSM-5 by a solid-state reaction, Zeolites **7**, 43–46 (1987)

22.109 A.V. Kucherov, A.A. Slinkin: Introduction Fe(III) ions in cationic positions of HZSM-5 by a solid-state reaction, Fe(III) cations in HZSM-5, and Fe(III) lattice ions in ferrisilicate, Zeolites **8**, 110–116 (1988)

22.110 B. Wichterlova, S. Beran, S. Bednarova, K. Nedomova, L. Dudiova, P. Jiru: Solid state interactions of Mn or Fe cations with ZSM-5 zeolites, Stud. Surf. Sci. Catal. **37**, 199–206 (1988)

22.111 B. Xu, L. Kevan: Formation of alkali metal particles in alkali metal cation exchanged X zeolite exposed to alkali metal vapor, control of metal particle identity, J. Phys. Chem. **96**, 2642–2645 (1992)

22.112 B. Xu, L. Kevan: Formation of metal clusters in alkaline-earth cation-exchanged X zeolites, J. Phys. Chem. **96**, 3647–3652 (1992)

22.113 M.W. Simon, J.C. Edwards, S.L. Suib: Characterization and catalytic studies on defect sites formed upon the thermal decomposition of sodium ionic clusters in NaX zeolite, J. Phys. Chem. **99**, 4698–4709 (1995)

22.114 P.K. Dutta, K.M. Rao, J.Y. Park: Correlation of Raman spectra of zeolites with framework architecture, J. Phys. Chem. **95**, 6654–6656 (1991)

22.115 E.M. Flanigen, H. Khatami, H.A. Szymanski: Infrared structural studies of zeolite frameworks, Adv. Chem. Ser. **101**, 201 (1971)

22.116 H. Fichtner-Schmittler, U. Lohse, H. Miessner, H.-E. Maneck: Correlation between unit-cell parameter, skeletal stretching vibrations and molar fraction of aluminum of faujasite type zeolites for Si-Aal = 1.1–1,000, Z. Phys. Chem. Leipzig **271**, 69–79 (1990)

22.117 M.D. Baker, G.A. Ozin, J. Godber: Direct probe Fourier-transform far infrared spectroscopy of metal atoms, metal ions, and metalclusters in zeolites, Catal. Rev. Sci. Eng. **27**, 591–651 (1985)

22.118 G.A. Ozin, M.D. Baker, J. Godber, C.J. Gil: Intrazeolite site-selective far-IR cation probe, J. Phys. Chem. **93**, 2899–2908 (1989)

22.119 R.A. Schoonheydt, H. van Brabant, J. Pelgrims: Chemistry of $Rh(NH_3)_5Cl^{2+}$ on mordenite, Zeolites **4**, 67–72 (1984)

22.120 G. Calis, P. Frenken, E. de Boer, A. Swolfs, M.A. Hefni: Synthesis and spectroscopic studies of Fe^{3+} substituted ZSM-5 zeolite, Zeolites **7**, 319–326 (1987)

22.121 J.A. Rossin, C. Saldarriaga, M.E. Davis: Synthesis of cobalt containing ZSM-5, Zeolites **7**, 295–300 (1987)

22.122 R. Szostak: *Molecular Sieves, Principles of Synthesis and Identification* (Van Nostrand Reinhold, New York 1989)

22.123 D. Grandjean, A.M. Beale, A.V. Petukhov, B.M. Weckhuysen: Unraveling the crystallization mechanism of CoAPO-5 molecular sieves under hydrothermal conditions, J. Am. Chem. Soc. **127**, 14454–14465 (2005)

22.124 D.M. Bibby, M.P. Dale: Synthesis of silica-sodalite from non-aqueous systems, Nature **317**, 157–158 (1985)

22.125 Mobil Oil Corporation: A porous crystalline material and a method of preparing same, Eur. Patent 0226674 (1985), US Patent 4568654 (1984)

22.126 Mobil Oil Corporation: A process for isomerizing xylenes, Eur. Patent 0102716 (1984)

22.127 Mobil Oil Corporation: Synthesis of zeolite ZSM-22 with a heterocyclic organic compound, Eur. Patent 0116203 (1987)

22.128 Mobil Oil Corporation: Crystalline zeolite and method of preparing same, US Patent 4016245 (1977)

22.129 Socony Mobil Oil Corporation: Synthetic zeolite and method for preparing the same, US Patent 3247195 (1966)

22.130 A. Nastro, L.B. Sand: Growth of larger crystals of ZSM-5 in the system $4(TPA)_2O$-$38(NH_4)_2O$-$x(Li,Na,K)_2$ O-Al_2O_3-$59SiO_2$-$750H_2O$, Zeolites **3**, 57–62 (1985)

22.131 A. Araya, B.M. Lowe: Synthesis and characterization of zeolite Nu-10, Zeolites **4**, 280–286 (1984)

22.132 Z. Gabelica, N. Blom, E.G. Derouane: Synthesis and characterization of ZSM-5 type zeolites 3, A critical-evaluation of the role of alkali and ammonium cations, Appl. Catal. **5**, 227–248 (1983)

22.133 K.P. Lillerud, J.H. Prader: On the synthesis of erionite – offretite intergrowth zeolites, Zeolites **6**, 474–483 (1986)

22.134 C. Kosanović, K. Havancsák, B. Subotić, V. Svetličić, T. Mišić, Á. Cziráki, G. Huhn: A contribution to understanding the mechanism of crystallization of silicalite-1 in heterogeneous systems (hydrogels), Micropor. Mesopor. Mater. **123**, 150–159 (2009)

22.135 Z. Gabelica, E.G. Derouane, N. Blom: Factors affecting the synthesis of pentasil zeolites, ACS Symp. Ser. **248**, 219–251 (1984)

22.136 J.B. Nagy, Z. Gabelica, E.G. Derouane: Position and configuration of the guest organic molecules within the framework of the ZSM-5 and ZSM-11 zeolites, Zeolites **3**, 43–49 (1983)

22.137 R.M. Barrer, J.A.W. Baynham, F.W. Bultitude, W.M. Meire: Hydrothermal chemistry of the silicates 8, Low-temperature crystal growth of aluminosilicates, and of some gallium and germainium analogues, J. Chem. Soc., 195–208 (1959)

22.138 J.B. Nagy, Z. Gabelica, E.G. Derouane, P.A. Jacobs: Molecular shape selectivity of ZSM-5, modified ZSM-5 and ZSM-11 type zeolites, Chem. Lett., 1105–1108 (1982)

22.139 P. Bodart, J.B. Nagy, Z. Gabelica, E.G. Derouane: Factors governing the synthesis of zeolites from silicoaluminate hydrogels – a comparative-study of the crystallization mechanisms of zeolitesY, mordenite and ZSM-5, J. Chim. Phys. Phys. Biol. **83**, 777–790 (1986)

22.140 E.G. Derouane, E.W. Valyocsik, R.P. von Ballmoos: Eur. Patent 146384 (1984)

22.141 N. Dewaele, L. Maistriau, J.B. Nagy, Z. Gabelica, E.G. Derouane: Parameters affecting the optimal synthesis of zeolite ZSM-20, Appl. Catal. **37**, 273–290 (1988)

22.142 H. Gerke, H. Gies: Studies on clathrasils 4, Crystal-structure of dodecasil-1H, a synthetic clathrate compound of silica, Z. Kristallogr. **166**, 11–22 (1984)

22.143 L.D. Rollmann, E.W. Valyocsik: Manufacture of synthetic mordenite, US Patent 4205052 (1980)

22.144 J.L. Guth, H. Kessler, J.M. Hiegel, J.M. Lamblin, J. Patarin, A. Seive, J.M. Chezeau, R. Wey: Zeolite synthesis in the presence of fluoride ions – a comparison with conventional synthesis methods, ACS Symp. Ser. **398**, 176–195 (1989)

22.145 Research Association for Petroleum Alternatives Development (RAPAD): Process for producing a crystalline silicate, Eur. Patent 0087017 (1983)

22.146 L.B. Sand: Zeolite synthesis and crystallization, Pure Appl. Chem. **52**, 2105–2113 (1980)

22.147 T. Ito, J. Fraissard, J.B. Nagy, N. Dewaele, Z. Gabelica, A. Nastro, E.G. Derouane: ^{129}Xe-NMR studies of type NaY, ZSM-5 and ZSM-20 zeolite crystallization, Stud. Surf. Sci. Catal. **49**, 579–588 (1989)

22.148 E.G. Derouane, J.P. Gilson, Z. Gabelica, C. Mousty-Desbuquoit, J. Verbist: Concerning the aluminum distribution gradient in ZSM-5 zeolites, J. Catal. **71**, 447–448 (1981)

22.149 W.A. van Erp, H.W. Kouwenhoven, J.M. Nanne: Zeolite synthesis in non-aqueous solvents, Zeolites **7**, 286–288 (1987)

22.150 N. Herron: Zeolite catalysts as enzyme mimics, ACS Symp. Ser. **392**, 141–154 (1989)

22.151 R.M. Barrer: *Zeolites and Clay Minerals as Sorbents and Molecular Sieves* (Academic, London 1978)

22.152 J. Burgess: *Metal Ions in Solution* (Ellis Horwood, Chichester 1978)

22.153 R.M. Barrer, W.M. Meier: Exchange equilibria in a synthetic crystalline exchanger, Trans. Faraday Soc. **55**, 130–141 (1959)

22.154 B.K.G. Theng, E.F. Vansant, J.B. Uytterhoeven: Ion exchange in synthetic zeolites I, Ammonium and some of its alkyl derivatives in Linde sieves X and Y, Trans. Faraday Soc. **64**, 3370 (1968)

22.155 P. Chu, F.G. Dwyer: Organic ion exchange of ZSM-5 zeolite, Zeolites **8**, 423–426 (1988)

22.156 H.K. Beyer, H.G. Karge, G. Borbély: Solid-state ion exchange in zeolites 1. Alkaline chlorides/ZSM-5, Zeolites **8**, 79–82 (1988)

22.157 H.G. Karge: Post-synthesis modification of microporous materials by solid-state reactions, Stud. Surf. Sci. Catal. **105**, 1901–1948 (1997)

22.158 M. Bülow, P. Lorenz: In: *Fundamentals of Adsorption II*, ed. by A. Liapus (Engineering Foundation, New York 1987) pp. 119–128

22.159 P. Graham, A.D. Hughes, L.V.C. Rees: In: *Gas Separation Technology*, ed. by E.F. Vansant, R. Dewolfs (Elsevier, Amsterdam 1990) p. 215

22.160 S. Liu, P. Zhang, X. Meng, D. Liang, N. Xiao, F.-S. Xiao: Cesium-free synthesis of aluminosilicate RHO zeolite in the presence of cationic polymer, Micropor. Mesopor. Mater. **132**, 352–356 (2010)

22.161 E.G. Derouane, J.B. Nagy: Surface curvature effects on the NMR chemical shift for molecules trapped in microporous solids, Chem. Phys. Lett. **137**, 341–344 (1987)

22.162 J. Fraissard, T. Ito: Xe-129 NMR study of adsorbed xenon – A new method for studying zeolites and metal-zeolites, Zeolites **8**, 350–361 (1988)

22.163 M. Boudart, L.-C. de Ménorval, J. Fraissard, G.P. Valença: Study by xenon NMR of platinum particles supported on alumina, J. Phys. Chem. **92**, 4033–4035 (1988)

22.164 J.B. Nagy: Multinuclear magnetic resonance in liquids and solids – Chemical applications, NATO ASI Ser. C **322**, 371 (1990)

22.165 E.L. Wu, S.L. Lawton, D.H. Olson, A.C. Rohrman, G.T. Kokotailo: ZSM-5-type materials – factors affecting crystal symmetry, J. Phys. Chem. **83**, 2777–2781 (1979)

22.166 C.A. Fyfe, H. Strobl, G.T. Kokotailo, G.J. Kennedy, G.E. Barlow: Ultra-high-resolution Si-29 solid-state MAS NMR investigation of sorbate and temperature-induced changes in the lattice structure of zeolite ZSM-5, J. Am. Chem. Soc. **110**, 3373–3380 (1988)

22.167 D.R. Korbin, L. Abrams, G.A. Jones, M.M. Eddy, G.D. Stucky, D.E. Cox: Flexibility of the zeolite-RHO framework – neutron powder structural characterization of Ca-exchanged zeolite-rho, J. Chem. Soc. Chem. Commun., 42–43 (1989)

22.168 M.F.M. Post: *Introduction to Zeolite Science and Practice* (Elsevier, Amsterdam 1991) p. 392

22.169 P.B. Weisz: Zeolites – New horizons in catalysis, Chemtech. **3**, 498–505 (1973)

22.170 D.M. Ruthven: *Principles of Adsorption and Adsorption Processes* (John Wiley, New York 1984)

22.171 J. Kärger, D.M. Ruthven: On the comparison between macroscopic and NMR measurements of intracrystalline diffusion in zeolites, Zeolites **9**, 267–281 (1989)

22.172 N. Van-Den-Begin, L.V.C. Rees, J. Caro, M. Bülow: Fast adsorption-desorption kinetics of hydrocarbons in silicalite-1 by the single-step frequency response method, Zeolites **9**, 287–292 (1989)

22.173 J. Kärger, H. Pfeifer: NMR self-diffusion studies in zeolite science and technology, Zeolites **7**, 90–107 (1987)

22.174 E.C. de Lara, R. Kahn, F. Mezei: Determination of the intracrystalline diffusion-coefficient of methane in A-zeolites by means of neutron spin-echo experiments, J. Chem. Soc. Faraday Trans. I, **79**, 1911–1920 (1983)

22.175 E.C. de Lara, R. Kahn: Physicochemical properties of zeolitic systems and their low dimensionality, NATO ASI Ser. B **221**, 169 (1990)

22.176 P. Stilbs: Fourier transform pulsed-gradient spin-echo studies of molecular diffusion, Prog. NMR Spectrosc. **19**, 1–45 (1987)

22.177 E.O. Stejskal, J.E. Tanner: Spin diffusion measurements: Spin echoes in the presence of a time-dependent field gradient, J. Chem. Phys. **42**, 288 (1965)

22.178 R.L. Gorring: Diffusion of normal paraffins in zeolite T: Occurrence of window effect, J. Catal. **31**, 13–26 (1973)

22.179 C. Chmelik, L. Heinke, J.M. van Baten, R. Krishna: Diffusion of *n*-butane/*iso*-butane mixtures in silicalite-1 investigated using infrared (IR) microscopy, Micropor. Mesopor. Mater. **125**, 11–16 (2009)

22.180 P.A. Jacobs: *Carboniogenic Activity of Zeolites* (Elsevier, Amsterdam 1977)

22.181 P.A. Jacobs, H.K. Beyer: Evidence for the nature of true Lewis sites in faujasite-type zeolites, J. Phys. Chem. **83**, 1174–1177 (1979)

22.182 H. Pfeifer, D. Freude, M. Hunger: Nuclear magnetic resonance studies on the acidity of zeolites and related catalysts, Zeolites **5**, 274–286 (1985)

22.183 H. Ernst: Highly resolved proton magnetic resonance studies on the acidity of zeolites and related catalysts, Z. Phys. Chem. Leipzig **269**, 1073–1094 (1988)

22.184 G. Engelhardt, D. Michel: *High-Resolution Solid-State NMR of Silicates and Zeolites* (Wiley, Chichester 1987)

22.185 J.B. Nagy, G. Engelhardt, D. Michel: High-resolution NMR on adsorbate-adsorbent systems, Adv. Colloid. Interface Sci. **23**, 67–128 (1985)

22.186 J.N. Lunsford, W.P. Rothwell, W. Shen: Acid sites in zeolite Y – A solid-state NMR and infrared study using trimethylphosphine as a probe molecule, J. Am. Chem. Soc. **107**, 1540–1547 (1985)

22.187 G. Engelhardt, H.-G. Jerschkewitz, U. Lohse, P. Saw, A. Samoson, E. Lippmaa: 500 MHz ^{1}H-*MAS* NMR studies of dealuminated HZSM-5 zeolites, Zeolites **7**, 289–292 (1987)

22.188 F. Haw, I.S. Chuang, B.L. Hawkins, G.E. Maciel: Surface titration of silica-alumina monitored by N-15 NMR with cross polarization and magic angle spinning, J. Am. Chem. Soc. **105**, 7206–7207 (1983)

22.189 J.A. Ripmeester: Surface acid site characterization by means of CP/MAS N-15 NMR, J. Am. Chem. Soc. **105**, 2925–2927 (1983)

22.190 V.M. Mastikhin, I.L. Mudrakovsky, S.V. Filimonova: Probing the Lewis acidity of heterogeneous catalysts by N-15 NMR of adsorbed N_2O, Chem. Phys. Lett. **149**, 175–179 (1988)

22.191 D. Barthomeuf: Conjugate acid-base pairs in zeolites, J. Phys. Chem. **88**, 42–45 (1984)

22.192 S. Kaliaguine, J.B. Nagy, Z. Gabelica: Chemically modified ZSM-5 zeolites: Structure and catalytic properties, Stud. Surf. Sci. Catal. **35**, 381–429 (1988)

22.193 R. Szostak: Modified zeolites, Stud. Surf. Sci. Catal. **58**, 153–199 (1991)

22.194 J.C. Vedrine: Physicochemical properties of zeolitic systems and their low dimensionality, NATO ASI Ser. B **221**, 121 (1990)

22.195 P.A. Jacobs (Ed.): *Structure and Reactivity of Modified Zeolites* (Elsevier, Amsterdam 1984)

22.196 R.M. Barrer, B. Coughlan: *Molecular Sieves* (Society Chemical Industry, London 1968) p. 141

22.197 J. Scherzer: The preparation and characterization of aluminum-deficient zeolites, ACS Symp. Ser. **248**, 157–200 (1984)

22.198 I. Hannnus, I.I. Ivanova, G. Tasi, I. Kiricsi, J.B. Nagy: Investigation of the surface-reactions of CCl_4 on zeolites studied by IR and MAS NMR spectroscopy, Colloid. Surf. A Physicochem. Eng. Asp. **101**, 199–206 (1995)

22.199 I. Hannus, A. Fonseca, I. Kiricsi, J.B. Nagy, P. Fejes: ^{29}Si and ^{27}Al MAS NMR investigation of H-mordenite dealuminated with phosgene, Stud. Surf. Sci. Catal. **94**, 155–162 (1995)

22.200 G. Engelhardt, V. Lohse, V. Patzelova, M. Magi, E. Lippmaa: High-resolution ^{29}Si NMR of dealuminated Y-zeolites 1, The dependence of the extent of dealumination on the degree of ammonium exchange and the temperature and water vapour pressure of the thermochemical treatment, Zeolites **3**, 233–238 (1983)

22.201 D.W. Breck, E.M. Flanigen: *Molecular Sieves* (Society Chemical Industry, London 1968) p. 47

22.202 Z. Yu, A. Zheng, Q. Wang, L. Chen, J. Xu, J.-P. Amoureux: Insights into the dealumination of zeolite HY revealed by sensitivity-enhanced Al-27 DQ-MAS NMR spectroscopy at high field, Angew. Chem. Int. Edit. **49**, 8657–8661 (2010)

22.203 E. Jacquinot, F. Raatz, A. Macedo, C. Marcilly: Evaluation of non-commercial modified large pore zeolites in FCC, Stud. Surf. Sci. Catal. **46**, 115–125 (1988)

22.204 J. Lynch, F. Raatz, C. Delalande: Characterization of the secondary pore system in dealuminated HY zeolites comparison between isomorphous substitution and hydrothermal treatment, Stud. Surf. Sci. Catal. **39**, 547–557 (1988)

22.205 J. Lynch, F. Raatz, P. Dufresne: Characterization of the textural properties of dealuminated HY forms, Zeolites **7**, 333–340 (1987)

22.206 F. Raatz, C. Marcilly, E. Freund: Comparison between small pore and large pore mordenites, Zeolites **5**, 329–333 (1985)

22.207 F. Raatz, E. Freund, C. Marcilly: Study of small-pore and large-pore mordenite modifications 1, Preparation of the HM forms, J. Chem. Soc. Faraday Trans. I **79**, 2299–2309 (1983)

22.208 M. Tielen, M. Geelen, P.A. Jacobs: Proc. Int. Symp. Zeol. Catal., Siófok, Hungary (1985) p. 1

22.209 K.G. Ione, L.A. Vostrikova, V.M. Mastikhin: Synthesis of crystalline metal silicates having zeolite structure and study of their catalytic properties, J. Mol. Catal. **31**, 355–370 (1985)

22.210 D.E.W. Vaughan: Zeolites and other microporous materials, Stud. Surf. Sci. Catal. **49**, 95–116 (1989)

22.211 P. Fejes, I. Kiricsi, I. Hannus, A. Kiss, G. Schöbel: Novel method for the dealumination of zeolites, React. Kinet. Catal. Lett. **14**, 481–488 (1980)

22.212 H.K. Beyer, I. Belenykaja: A new method for the dealumination of faujasite-type zeolites, Stud. Surf. Sci. Catal. **5**, 203–210 (1980)

22.213 D.S. Shihabi, W.E. Garwood, P. Chu, J.N. Miale, R.M. Lago, C.T.W. Chu, C.D. Chang: Aluminum insertion into high-silica zeolite frameworks 2, Binder activation of high-silica ZSM-5, J. Catal. **93**, 471–474 (1985)

22.214 E.F. Vansant: Pore size engineering in zeolites, Stud. Surf. Sci. Catal. **37**, 143–153 (1988)

22.215 M. Niwa, S. Kato, T. Hattori, Y. Marakami: Fine control of the pore-opening size of the zeolite mordenite by chemical vapor-deposition of silicon alkoxide, J. Chem. Soc. Faraday Trans. I **80**, 3135–3145 (1984)

22.216 K. Klier: Transition metal ions in zeolites – the perfect surface sites, Langmuir **4**, 13–25 (1988)

22.217 T.-Y. Yan: Zeolite-based catalysts for hydrocracking, I & EC Prod. Des. Devel. **22**, 154–160 (1983)

22.218 E.G. Derouane: Reactions of organometallics with the surfaces of zeolites, NATO ASI Ser. C **231**, 299 (1988)

22.219 S.T. Homeyer, W.M.H. Sachtler: Design of metal clusters in NaY zeolite, Stud. Surf. Sci. Catal. **49**, 975–984 (1989)

22.220 J.B. Nagy, M. van Eenoo, E.G. Derouane: Highly dispersed supported iron particles from the decomposition of iron carbonyl on HY zeolite, J. Catal. **58**, 230–237 (1979)

22.221 E.G. Derouane: Factors affecting the deactivation of zeolites by coking, Stud. Surf. Sci. Catal. **20**, 221–240 (1985)

22.222 M. Guisnet, P. Magnoux: Zeolite microporous solids, NATO ASI Ser. C **352**, 437 (1992)

22.223 J.W. Beeckman, G.F. Froment: Catalyst deactivation by active-site coverage and pore blockage, Ind. Eng. Chem. Fundam. **18**, 245–256 (1979)

22.224 H.G. Karge: Coke formation on zeolites. In: *Introduction to Zeolite Science and Practice*, ed. by H. van Bekkum, E.M. Flanigen, J.C. Jansen (Elsevier, Amsterdam 1991) p. 531

22.225 E.G. Derouane, Z. Gabelica: A novel effect of shape selectivity – Molecular traffic control in zeolite ZSM-5, J. Catal. **65**, 486–489 (1980)

22.226 N.Y. Chen, W.E. Yarwood, F.Y. Dwyer: Shape selective catalysis in industrial applications, Chem. Ind. **36** (1989)

22.227 D.E.W. Vaughan: The synthesis and manufacture of zeolites, Chem. Eng. Prog. **82**, 25–31 (1988)

22.228 W.F. Hölderich: New horizons in catalysis using modified and unmodified pentasil zeolites, Pure Appl. Chem. **58**, 1383–1388 (1986)

22.229 H. van Bekkum, H.W. Kauwenhoven: Zeolites and fine chemicals, Stud. Surf. Sci. Catal. **41**, 45–59 (1988)

22.230 W.F. Hölderich: New aspects in the performance of heterogeneous catalysts for intermediates and fine chemicals, Stud. Surf. Sci. Catal. **41**, 83–90 (1988)

22.231 W.F. Hölderich, M. Hesse, F. Naumann: Zeolites – Catalysts for organic syntheses, Angew. Chem. Int. Edit. **27**, 226–246 (1988)
22.232 A. Corma, M.J. Climent, H. Garcia, J. Primo: Design of synthetic zeolites as catalysts in organic reactions, acylation of anisole by acyl chlorides or carboxylic acids over acid zeolites, Appl. Catal. **49**, 109–123 (1989)
22.233 R.P. Townsend: *Introduction to Zeolite Science and Practice* (Elsevier, Amsterdam 1991) p. 359
22.234 M. Pansini, C. Colella, M. de Gennaro: Chromium removal from water by ion exchange using zeolite, Desalination **83**, 145–157 (1991)
22.235 E. Passaglia, G. Vezzalini: Crystal-chemistry of diagenetic zeolites in volcanoclastic deposits of Italy, Contrib. Mineral. Petrol. **90**, 190–198 (1985)
22.236 A. Nastro, C. Colella: Column ion-exchange data for ammonium removal from water by phillipsite tuff, Ing. Chim. Ital. **19**, 41–45 (1983)
22.237 C. Colella, R. Aiello: *Natural Zeolites, Occurrence, Properties and Utilization*, ed. by D. Kallo, H.S. Sherry (Akadémiai Kiadó, Budapest 1988) p. 491
22.238 J.L. Reymonent: A bibliographic study, 4th Meeting of French Zeolite Group, Evreux, France (1988)
22.239 Eli Lilly Co: Process for the Preparation of Tricyclazole, Ger. Offen. DE 2928867 (1980)
22.240 Union Carbide Corp.: *Removal of Caffeine by Selective Adsorption Using Zeolite Adsorbents*, Eur. Pat. Appl., Vol. EP0013451 (1980)
22.241 Blendax Werke Schneider Co.: *Tooth Paste*, JP, Vol. 55-105611 (1980)
22.242 Union Carbide Corp.: *Bulk Separation of Inositol and Sorbitol by Selective Adsorption on Zeolitic Sieves*, JP, Vol. 118409 (1988)
22.243 T. Bein, P. Enzel, F. Bauer, L. Zuppiroli: Stabilization of conducting heteroaromatic polymers in large-pore zeolite channels, Adv. Chem. Ser. **226**, 433–449 (1989)
22.244 T. Yamanaka, K. Honaga, K. Ichihashi, T. Murata, S. Nohara: *Light-Resistant Polyamide Moldings*, JP, Vol. 61009457A 19860117 (1986)
22.245 J. Karger-Kocsis, M. Sipos, M. Moser, K. Senyei, B. Lengyel: *Powder Coating Compositions, Hung. Teljes*, HU, Vol. 34228 A2 19850228 (1986)

23. Porous Anodic Aluminum Oxide

Qiaoling Xu, Guowen Meng

Porous anodic aluminum oxide (AAO) is one of the typical self-organized fine structures with cylindrical pores of uniform diameter arranged in a hexagonal array. AAO has been commonly used as a template for synthesis of nanostructures with a variety of materials. In this chapter, we first describe the preparation of AAO templates with various pore structures, such as straight, branched, and step-shaped pores. Then, we focus on the use of AAO with different pore structures as templates for construction of nanostructures with various architectures, including one-dimensional (1-D) nanostructures and nanoheterostructures with linear and complex shapes.

23.1 **Background** 859
23.2 **Preparation of AAO Templates** 860
23.2.1 AAO Templates with Straight Pores 860
23.2.2 AAO Templates with Branched Pores 860
23.2.3 AAO Templates with Step-Shaped Pores 862
23.3 **Nanostructures Constructed in AAO Templates** 862
23.3.1 One-Dimensional Nanostructures. 862
23.3.2 Complex-Shaped 1-D Nanostructures 863
23.3.3 Nanoheterostructures 869
23.3.4 Complex-Shaped Nanoheterostructures 878
23.4 **Conclusions and Outlook** 879
References 879

23.1 Background

Anodic aluminum oxide (AAO) template, which is prepared by electrochemical anodization of aluminum in an acidic electrolyte, is one of the typical self-organized fine structures with a nanohole array. AAO templates contain cylindrical pores of uniform diameter arranged in a hexagonal array with pore densities as high as 10^{11} pores/cm^2. AAO templates are sold commercially, but only a limited number of pore diameters are available. However, *Masuda* and coworkers [23.1] established a two-step anodization process for fabrication of AAO templates with a broad range of pore diameter (5–267 nm). The dimensions of AAO templates can be easily tailored during the two-step anodization process. The pore diameters of AAO templates can be adjusted by varying the composition and concentration of the acidic electrolyte solution as well as the temperature and voltage of the anodization. The template thickness is dependent on the anodization time, with longer anodization resulting in thicker templates.

Compared with ion-track-etched membranes (e.g., polycarbonate membrane), inorganic AAO templates show advantages of high stability at high temperature and homogeneous pore distribution. AAO has been commonly used as a template for synthesis of one-dimensional (1-D) nanostructures with a variety of materials. In the early 1990s, *Martin* and coworkers [23.2, 3] pioneered use of AAO templates in synthesis of metal and polymer tubules, rods, and wires by electrochemical or electroless deposition. From then on, AAO templates were typically used for fabrication of a series of 1-D nanostructures of metals [23.4, 5], semiconductors [23.6, 7], polymers [23.8–10], carbons [23.11, 12], and other materials by different techniques including electrochemical deposition, the sol–gel technique, electroless deposition, and chemical vapor deposition (CVD). As well as for synthesis of 1-D nanostructures with single-component materials in AAO templates, progress has been made towards

the synthesis and design of more complex, multicomponent 1-D nanostructures, i. e., nanoheterostructures, in such templates. These nanoheterostructures contain heterojunctions between various combinations of metals, semiconductors, carbon, and polymers, having nanoscale 1-D morphology. The formation of 1-D heterojunctions has led to materials with unique properties and multiple functionalities not realizable in single-component structures that are useful for a wide range of applications [23.13–16].

Fabrication inside AAO templates is an ideal way to produce nanostructures with predesigned diameters and lengths, because the diameters and lengths of the nanostructures formed inside the nanochannels of AAO templates can be tuned by adjusting the pore diameter and the thickness of the templates, respectively. Nanostructures filled in the nanochannels of AAO templates can also replicate the morphologies of the nanochannels. Previously reported architectures created inside AAO templates were all linear shape, until *Xu* et al. [23.17] reported the construction of Y-shaped carbon nanotubes (CNTs) in AAO templates with Y-branched pores. Later, *Meng* and coworkers [23.18] developed a rational approach for creating AAO templates with complex-shaped pores and fabricated a series of complex-shaped nanowires (NWs) and nanotubes (NTs) inside these templates. The complexity of such nanostructures may facilitate applications of these structures as complex nanoelectronics circuits and nanoelectromechanical systems.

In this chapter, we focus on the use of AAO templates with different pore structures for construction of nanostructures with various architectures. In Sect. 23.2, preparation of AAO templates with a variety of pore structures, including straight, branched, and step-shaped pores, is discussed in detail. In Sect. 23.3, we summarize the creation of 1-D nanostructures and nanoheterostructures with linear and complex shapes in AAO templates with various pore structures.

23.2 Preparation of AAO Templates

AAO templates are usually achieved by two-step anodic oxidation of aluminum in acidic electrolytes, as follows. High-purity Al foils (≈ 99.999%) are degreased in acetone and then ultrasonically cleaned in ethanol and deionized water for several minutes. Then, the aluminum foils are annealed in vacuum at 450–550 °C for 4–5 h to enhance the grain size of the metal and to obtain homogeneous conditions for pore growth over large areas. Subsequently, the aluminum foils are mounted on a copper plate that servers as the anode and exposed to an acidic solution in an electrochemical cell. Anodization is conducted under constant potential in the acidic electrolyte. Oxalic acid solution is commonly used. The first-step anodization of the aluminum foil in oxalic acid solution is performed in 0.3 M solution at 8–10 °C under constant voltage in the range of 40–72 V_{DC} for 8 h. Then, the resulting anodic aluminum layer is removed in a mixed solution of phosphoric acid (6 wt %) and chromic acid (1.8 wt %) at 60 °C. Different processes for the second-step anodization are carried out to construct AAO templates with different pore architectures (see below). After anodization, the remaining alumina is removed in saturated $SnCl_4$ solution. Subsequently, the pore bottoms are opened by chemical etching in 5 wt % aqueous phosphoric acid solution.

23.2.1 AAO Templates with Straight Pores

The second-step anodization for producing AAO templates with straight pores is carried out under the same conditions as in the first step. The thickness of the AAO template can be tuned by controlling the duration of the second-step anodization. The arrangement of the alumina pores is determined by the applied voltage, temperature, and electrolyte type and concentration. If special self-ordering conditions are used to anodize the

Table 23.1 AAO templates with different pore arrangements achieved under different self-ordering conditions (with permission from [23.19], © American Chemical Society (2002))

Electrolyte	Interpore distance (nm)	Inner-wall thickness (nm)	Pore diameter (nm)
H_2SO_4 (25 V, 0.3 M)	66.3	7.2	24
$(COOH)_2$ (40 V, 0.3 M)	105	9.1	31
H_3PO_4 (195 V, 0.1 M)	501	54	158.4

aluminum, AAO templates with different pore arrangements can be achieved (Table 23.1).

23.2.2 AAO Templates with Branched Pores

Not only the thickness and pore arrangement of the AAO templates can be varied; also, the shape of the channels of the AAO template can be controlled. By reducing the anodization voltage in the second-step anodization, AAO templates with complex-shaped pores can be achieved; for example, Y-branched and multiple-branched pores can be achieved by reducing the anodization voltage once, while multiple generations of branched pores can be achieved by reducing the anodization voltage more than once. Second-step anodization processes for constructing branched pores are described below.

AAO Templates with Y-Branched Pores

For fabrication of AAO templates with the simplest branched pores of Y-branched pores, where one stem of the pore is divided into two branches, the second-step anodization is firstly performed to create primary stem pores under the same conditions as those in the first step. Then, the anodization voltage is reduced by a factor of $1/\sqrt{2}$ to form Y-branched pores. Figure 23.1 shows a scanning electron microscopy (SEM) image of the cross section of an AAO template with Y-branched pores. The stems and branches of the nanochannels can be clearly observed in the inset.

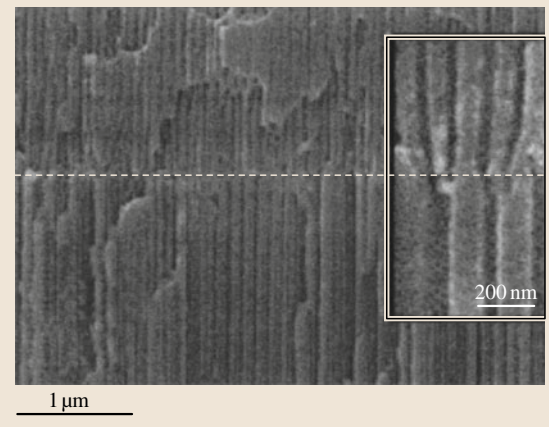


Fig. 23.1 SEM image of an AAO template with Y-branched nanochannels; the *inset* shows a close-up of the Y-branched nanochannels. The *dashed line* indicates the interface of the stems and branches (with permission from [23.20], © American Institute of Physics (2004))

AAO Templates with Multiple-Branched Pores

In the second-step anodization for creating nanochannels with a predetermined number of branches inside the AAO template, an anodizing voltage (denoted as V_s) is applied to form stem channels with large diameter (denoted as D_s), and then the anodizing voltage is reduced to a small value V_b to create the desired number (n) of branched channels of smaller diameter (denoted as D_b).

Based on the fact that the original total top-view area of the AAO template will not change during the whole anodization process, the original area of every stem channel $(\pi/4)D_s^2$ equals the total sum of the areas of the n branched channels that divide from the same stem channel: $n(\pi/4)D_b^2$. Thus, the relationship between D_s and D_b can be expressed as

$$D_s^2 = nD_b^2 \,. \tag{23.1}$$

The pore cell diameter (D) is proportional to the anodizing voltage (V) [23.18, 21],

$$D = kV \,, \tag{23.2}$$

where k is a constant. Combining (23.1) with (23.2), V_b for creating a predetermined number (n) of branched channels from a single stem channel can be calculated,

$$V_b = \frac{1}{\sqrt{n}} V_s \,. \tag{23.3}$$

After the initial anodization for the stem pores of an AAO template with multiple-branched pores, the template is cleaned in deionized water to remove oxalic acid solution remaining in the pores and the barrier layer at the pore bottom is thinned by immersing the samples in 5 wt % phosphoric acid solution at 31 °C for 30–70 min. Then, the anodizing voltage is reduced by a factor of $1/\sqrt{n}$ to create multiply branched (n branches) pores based on (23.3). If the voltage is reduced slowly, the stem pores are divided into branched pores gradually. On the contrary, the stem pores will be divided abruptly with sharp interfaces. It should be noted that, if the anodizing voltage for branched pores is lower than 25 V, sulfuric acid solution should be used as the electrolyte.

AAO Templates with Multiple Generations of Branched Pores

After the initial anodization for primary stem pores, the anodizing voltage is reduced by a factor of $1/\sqrt{n}$ ($n \geq 2$) to create the first-generation multiple-branched

pores, and subsequently by a factor of $1/\sqrt{m}$ ($m \geq 2$) to generate the second-generation multiple-branched pores from each of the first-generation multiple-branched pores. Further generation of branched pores can be created by sequentially reducing the anodizing voltage by a factor of $1/\sqrt{l}$ ($l \geq 2$). After any prior anodization, the samples should be washed in deionized water to clean acidic solution remaining in the pores. It is noted that, if the subsequent anodizing voltage is lower than 25 V, the anodization should be conducted in sulfuric acid solution at the same temperature as used previously.

23.2.3 AAO Templates with Step-Shaped Pores

The second-step anodization for AAO templates with step-shaped pores is performed under the same conditions as for the first step to create partial nanochannels. Then, the anodized sample is immersed in phosphoric acid solution to widen the existing pores. Subsequently, another anodization is carried out under the same conditions as in the previous step to create smaller-diameter channels of step-shaped nanochannels. Figure 23.2 presents a SEM image of the cross section of an AAO template with step-shaped nanochannels, clearly showing the large-diameter channels connected with the smaller-diameter channels.

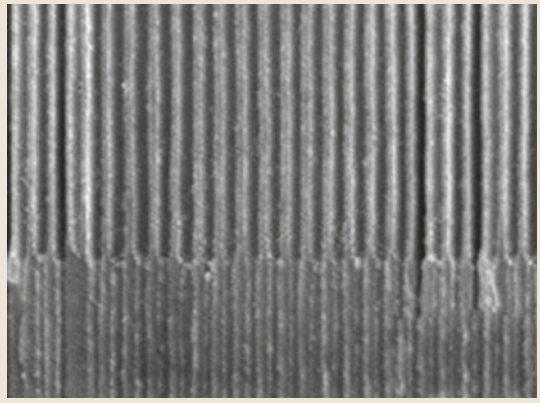


Fig. 23.2 SEM image of the cross section of step-shaped nanochannels of an AAO template (with permission from [23.22], © Institute of Physics (2006))

23.3 Nanostructures Constructed in AAO Templates

AAO with uniform cylindrical pores can serve as an ideal mold for construction of nanostructures, such as 1-D nanostructures and nanoheterostructures. By adjusting the pore diameter and the thickness of the AAO template, the resulting nanostructures can have controllable diameters and lengths. More importantly, these nanostructures actually conform to the shape of the AAO template. Thus, nanostructures with linear and even more complex shapes (e.g., branched and step shapes) can be achieved by appropriately designing the shape of the nanochannels of the AAO template.

23.3.1 One-Dimensional Nanostructures

AAO with uniform and dense pores is commonly used as a template for synthesis of 1-D nanostructures, including NWs and NTs. 1-D nanostructures of various materials, such as metals, semiconductors, and nonconducting and conducting polymers, can be constructed in the nanochannels of AAO templates. The diameters of the 1-D nanostructures are determined by the pore size of the template.

Nanowires (NWs)

NWs of various materials can be constructed inside the nanochannels of AAO templates by various approaches, such as electrodeposition, electroless deposition, chemical vapor deposition (CVD), and the sol–gel process.

Electrochemical deposition is commonly used for synthesis of NWs in AAO templates. It is accomplished by coating one face of the template with a metal film for use as a cathode for electroplating. Electrochemical deposition offers marked advantages over other methods for synthesis of 1-D nanostructures because it does not require expensive instrumentation, high temperatures, or low vacuum pressures. This method is also not time-consuming, since nanomaterials grown via this approach have a high growth rate. Using this method, NWs of magnetic Fe, Co, and Ni [23.23, 24], metallic Zn [23.25], Ag [23.26], and Cu [23.27], as well as semiconducting CdS [23.28] have been deposited inside AAO templates.

The drawback of electrochemical deposition methods is that the material to be deposited must be both easily reduced and conductive. Meanwhile, modification of the metal layer on the templates makes the

experiment complicated. Thus, other techniques, such as electroless deposition, CVD, and the sol–gel process, have been developed for fabrication of materials that are poor conductors and not easily reduced to be deposited into the nanochannels of AAO templates. *Xu* et al. [23.29] reported an electroless deposition approach for fabrication of metallic NWs of pure metals (e.g., Au, Pt, Pd, Cu, Ni, and Co) and their alloys, by infiltrating aqueous solutions of metal chloride salts into Au-coated AAO template with Al foil on its outside edge. The formation of the metallic NWs is ascribed to the redox reactions of two galvanic cells where the Al foil acts as the anode. CVD methods have been used for synthesis of semiconducting NWs of SiGe alloy [23.30], Si [23.6, 31], and Ge [23.32] in AAO templates, where a metal catalyst (e.g., Au) is firstly electrochemically deposited in the nanochannels of the AAO template, then semiconducting NWs are grown by pyrolysis of source gas (e.g., silane and germane) under metal catalysis in the nanochannels. In addition, *Miao* et al. [23.33] reported fabrication of single-crystalline TiO_2 NWs inside the straight pores of an AAO template by a cathodically induced sol–gel method.

Nanotubes (NTs)

CNTs were one of the first reported 1-D nanoscale materials to be successfully synthesized using a variety of methods. Typically, the AAO-template-assisted approach provides an effective route for synthesis of ordered CNT arrays. It has been reported that uniform CNT arrays can be formed in nanochannels of AAO templates by CVD [23.34, 35].

Electrodeposition is also an important method for fabrication of NTs. Metal [23.36, 37], metal alloy [23.38], semimetal [23.39], semiconductor [23.40], and oxide [23.41] NTs have been reported to be prepared by electrodeposition in nanochannels of AAO templates. *Yang* et al. [23.39] reported fabrication of BiNTs by electrodeposition inside the nanochannels of an AAO template coated with a thin mesh-like Au layer onto one planar surface side. They demonstrated that the wall thickness of the BiNTs could be tuned by adjusting the thickness of the Au layer and the current density during electrodeposition. Resistance–temperature measurements revealed that BiNTs showed semiconducting electronic transport behavior, and the resistance of BiNTs with thinner walls showed greater temperature dependence than that of BiNTs with thicker walls.

The conventional sol–gel template process involves immersing an AAO template into a precursor sol, followed by gelation inside the pores. The driving force in this technique is capillary action. This approach has been commonly used for synthesis of NTs made from oxides such as TiO_2, WO_3, ZnO, and SiO_2 in AAO templates [23.42, 43]. The internal diameters of the NTs can be adjusted by varying the concentration and viscosity of the initial sol as well as the immersion time. *Kovtyukhova* et al. [23.44] reported a *surface sol–gel* method for fabrication of SiO_2 NTs in AAO templates. This method involves repeats of a two-step deposition cycle in which adsorption of a molecular precursor and the hydrolysis step are separated by a post-adsorption wash. The *surface sol–gel* method allows fine control over the thickness of the NTs. Wu and coworkers [23.45] reported an improved sol–gel method for fabrication of Eu_2O_3 NTs in AAO templates. This method involves immersing the AAO template in a precursor sol, after which the template is taken out of the sol and sintered in a tube furnace. During the sintering process, the sol inside the nanochannels of the AAO template is changed into gel by condensation reactions, and the gel is further turned into Eu_2O_3 nanocrystallites. Via this approach, the same group also prepared Y_2O_3:Eu NTs by using AAO as template [23.46].

Atomic layer deposition (ALD) has been developed for synthesis of NTs in AAO templates. This method is based on successive, surface-controlled reactions from the gas phase to produce thin films and overlayers in the nanometer range with perfect conformality and process controllability. For synthesis of inorganic NTs, ALD is superior to the other approaches in terms of versatility and wall thickness control. *Lee* et al. [23.47] reported fabrication of Ru NTs in an AAO template by ALD. The NTs had diameter of 50 nm and aspect ratio of 10. The wall thickness of the Ru NTs could be precisely controlled from 13 to 23 nm by adjusting the number of ALD cycles. *Farhangfar* et al. [23.48] reported growth of high-aspect-ratio (≈ 300) ZnS NTs inside the pores of AAO templates by ALD at low temperature. The diameter (30–200 nm), wall thickness (10–60 nm), and length (up to several tens of micrometers) of the NTs could be precisely tailored by a combination of electrochemical and ALD techniques. *Pitzschel* et al. [23.49] first utilized ALD to coat the internal pore walls of the AAO template with conformal layers of an oxide, then ferromagnetic Fe_3O_4 NTs of 10 nm wall thickness and 10–30 μm length were prepared.

23.3.2 Complex-Shaped 1-D Nanostructures

The 1-D nanostructures formed in AAO templates discussed above are all linear in shape. By predesigning

the morphology of the nanochannels of the AAO templates, nanostructures with more complex shapes can be achieved. In the following, we focus on the synthesis of branched and step-shaped nanostructures by using AAO templates with correspondingly shaped nanochannels.

Y-Branched and Multiple-Branched Nanostructures

Among the branched nanostructures constructed inside branched nanochannels of AAO templates, Y-branched ones are the simplest. *Xu* et al. [23.17] first reported construction of Y-branched CNTs inside an AAO template with Y-branched nanochannels using CVD. The fabrication process of the Y-branched CNTs is as follows. Firstly, a Y-branched nanochannel AAO template is synthesized via a two-step anodization process. Then, a small amount of cobalt catalyst is electrochemically deposited in the bottom of the template channels and the catalyst is reduced at 600 °C for 4–5 h under carbon monoxide flow. Finally, Y-branched NTs are grown by pyrolysis of acetylene at 650 °C. They considered that the resulting well-aligned Y-branched CNTs with controllable length and diameter of the stem and branches have potential in nanoelectronics. Further research revealed that the Y-branched CNTs show intrinsic nonlinear transport and reproducible rectifying behavior at room temperature [23.50], further confirming that these Y-junction NTs represent new heterojunctions for use in nanoelectronics.

By using AAO templates with Y-branched nanochannels, Y-branched semimetallic and metallic NWs can also be created via electrochemical deposition. *Tian* et al. [23.20] reported fabrication of Y-branched BiNWs embedded in AAO templates by electrochemical deposition, with stems 80 nm in diameter and branches 50 nm in diameter. Current–voltage measurements revealed that the parallel Y-branched BiNWs exhibited characteristics of conventional metal–semiconductor junctions. *Mahima* et al. [23.51] reported construction of Y-branched Pt NWs in AAO templates, which showed unique electrocatalytic activity for formic acid and ethanol oxidation (two important reactions for microfuel cells). *Yang* et al. [23.52] reported synthesis of Y-branched CuNWs and NTs by using AAO with Y-branched nanochannels via electrodeposition, with an Au layer sputtered onto the planar surface of the stem-channel side of the Y-branched AAO template. For synthesis of Y-branched CuNTs, the Au layer must be thin enough to leave the pores open and cover only the top-view surface of the pore walls, while for fabrication of Y-branched Cu NWs, the Au layer must be thick enough to cover the pores completely. Figure 23.3a shows an SEM image of the stem roots of Y-branched CuNTs with stem-tube outer diameter of about 70 nm. Figure 23.3b shows a side-view SEM image of a bundle of Y-branched CuNTs, clearly showing the Y-shaped topology of the NTs. Figure 23.3c,d shows transmission electron microscopy (TEM) images of Y-branched CuNTs with tube-wall thicknesses of about 10 and 20 nm obtained inside the Y-branched nanochannels of an AAO template, with the stem surface side coated with Au layers of about 20 and 30 nm thickness, respectively. In situ x-ray diffraction investigation demonstrated that the thermal expansion of the Y-branched CuNTs and NWs was temperature dependent and that the thermal expansion coefficient of the stem of the CuNTs and NWs was higher than that of the branches.

By using AAO with Y-branched nanochannels as a template, *Xu* et al. [23.53] demonstrated fabrication of not only Y-branched metallic NWs but also Y-branched conducting polymer NWs by electrochemical deposition. Figure 23.4a shows an SEM image of electrodeposited Y-branched Au NWs after removing the AAO template. The diameters of the stems and the branches of the NWs are 80 and 50 nm, respectively, being consistent with those of the stem and the branches of the template channels. By an electrochemical polymerization process, Y-branched polypyrrole (PPy) NWs can be formed inside the channels of an AAO template. This process is accomplished in an electrolyte solution containing pyrrole under a positive potential. Figure 23.4b shows an SEM image of the resultant Y-branched PPy NWs after template removal.

It is known that a metal layer can be coated on either side surface of AAO templates with straight or Y-branched nanochannels prior to electrodeposition of NWs and NTs. However, for branched templates having nanochannels with more than two branches, the metal layer has to be sputtered onto the stem channel side of the templates to make the stem and the branches well connected, because the NWs or NTs electrodeposited inside the AAO nanochannels usually have different lengths. By using a three-branched AAO template with its stem channel side coated with a gold layer, three-branched Au NWs have been achieved by electrodeposition, as shown in Fig. 23.4c.

By using AAO templates with branched nanochannels, *Meng* and coworkers [23.54] constructed metallic NWs with predesigned branched architectures by electrodeposition. Firstly, they created AAO templates with nanochannels having a predetermined number of

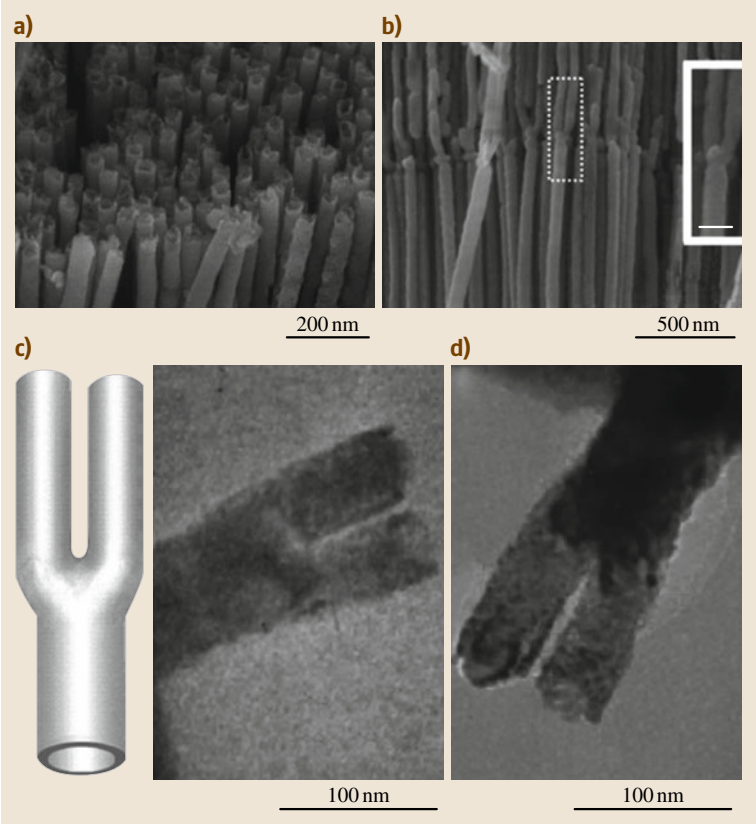


Fig. 23.3 **(a)** Bottom-view SEM image of the stem segments of Y-branched CuNTs. **(b)** Side-view SEM image of a bundle of Y-branched CuNTs. The *inset* shows a close-up view of the *dashed rectangular region* (*scale bar*: 100 nm). **(c)** Schematic of a Y-branched NT and TEM image of a Y-branched CuNT with tube-wall thickness of about 10 nm achieved under a 20 nm-thick sputtered Au layer with current density of 1.5 mA/cm^2. **(d)** TEM image of a Y-branched CuNT with tube-wall thickness of 20 nm achieved under a 30 nm-thick sputtered Au layer with current density of 1.5 mA/cm^2 (with permission from [23.52], © Wiley-VCH (2010))

branches, such as two- (or upside-down Y-), three-, and four-branched nanochannels by reducing the applied anodizing voltage multiple times during the second-step anodization of the aluminum (Fig. 23.5a). Then, metal NWs were electrodeposited in the branched nanochannels of the AAO template with the stem side coated

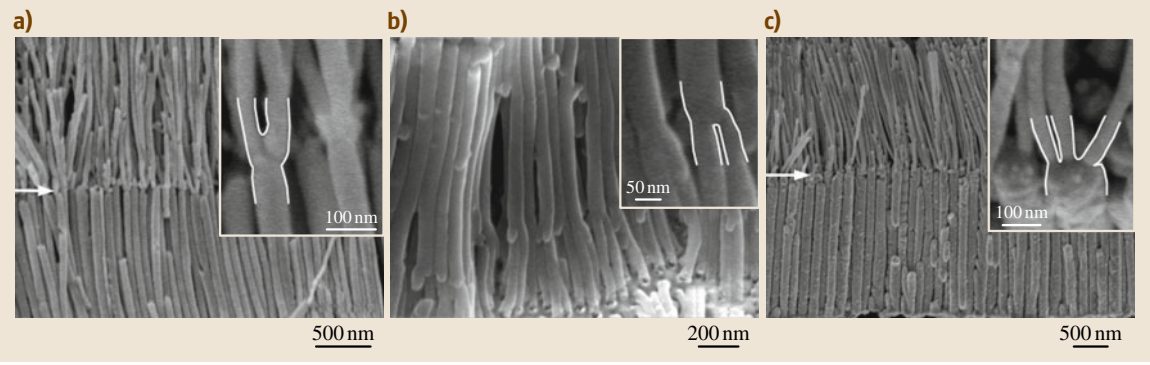


Fig. 23.4a–c SEM images of **(a)** Y-branched Au NWs, **(b)** Y-branched PPy NWs, and **(c)** three-branched Au NWs after removal of the AAO template. The *insets* show high-magnification images of the junctions, highlighted with *white line contours* for clarity. *White arrows* on the interface indicate where the branchings take place (with permission from [23.53], © Elsevier (2009))

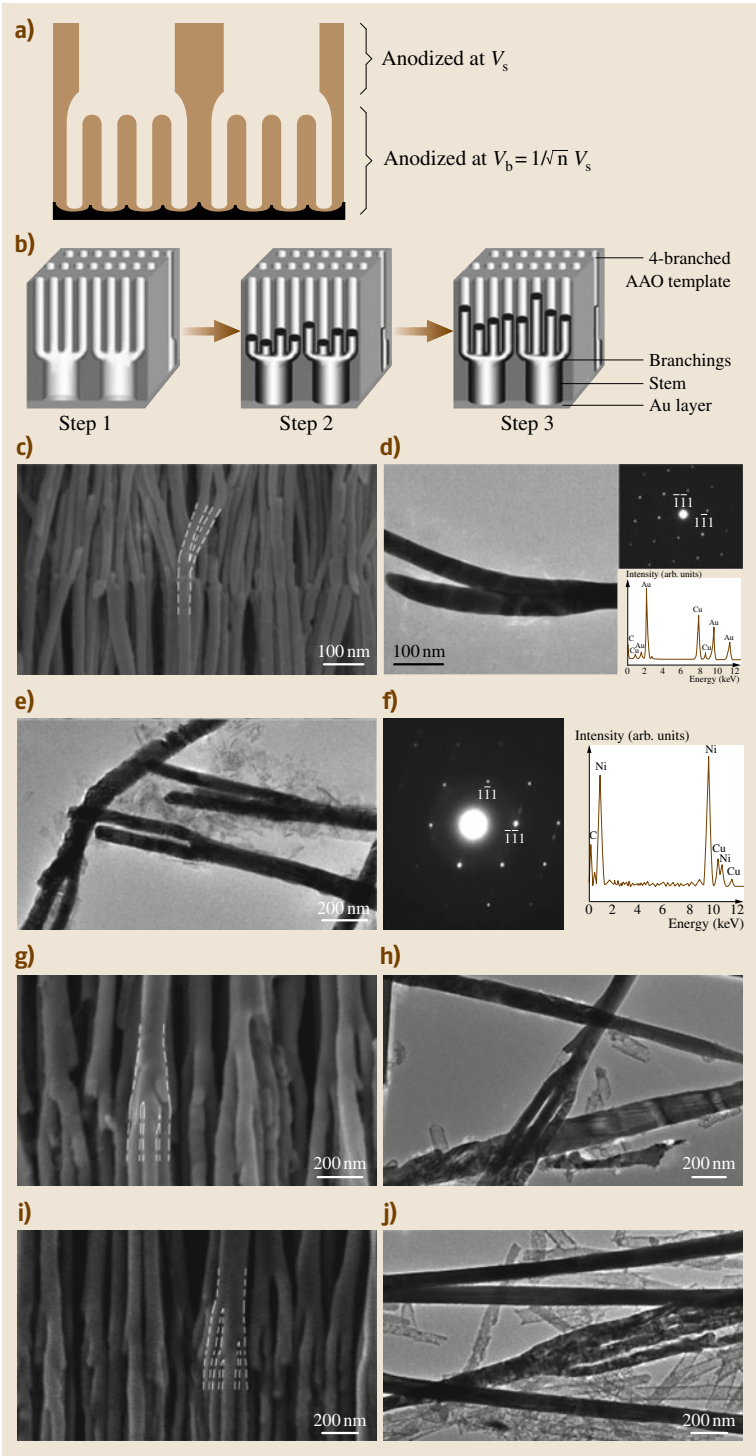


Fig. 23.5 **(a)** Schematic cross-sectional view of two representative stem nanochannels with multiple branches inside an AAO template with corresponding anodizing voltages (V_s). **(b)** Schematic electrodeposition process of four-branched NWs. **(c)** SEM image of a bundle of Y-branched Au NWs after template removal. **(d)** TEM image of a typical single Y-branched Au NW; *upper-right* and *lower-right insets* show the selected-area electron diffraction (SAED) pattern and energy-dispersive spectroscopy (EDS) results, respectively. **(e)** TEM image of Y-branched Ni NWs. **(f)** *Left*: SAED pattern taken from Ni NWs in **(e)**; *right*: EDS spectrum of the Ni NW. **(g)** SEM image of a bundle of three-branched Ni NWs. **(h)** TEM image showing one of the three-branched Ni NWs. **(i)** SEM image of a bundle of four-branched Ni NWs. **(j)** TEM image revealing one of the four-branched Ni NWs. One junction is contoured by *white dotted lines* in **(c,g)** and **(i)** for clarity (with permission from [23.54], © Wiley-VCH (2010))

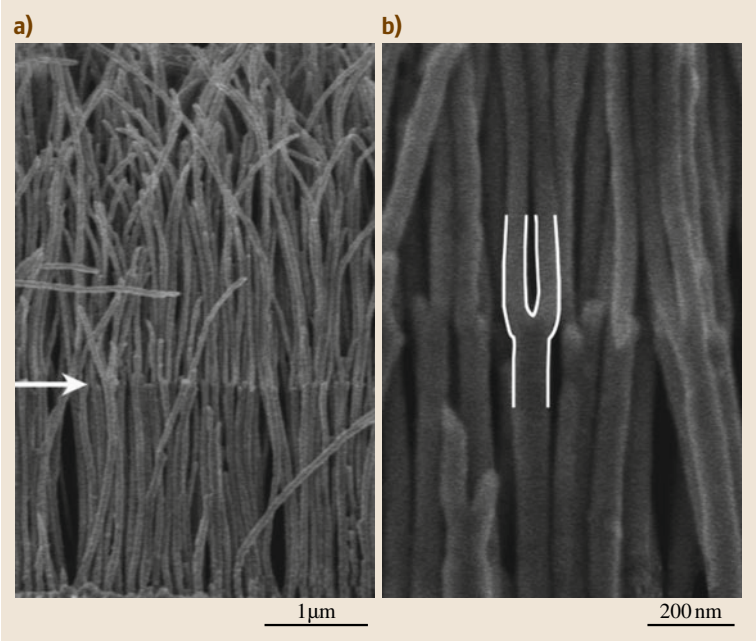


Fig. 23.6 **(a)** Low-magnification SEM image of a bundle of Y-branched Au NWs after template removal; a *white arrow* on the interface indicates where the Y-branchings take place. **(b)** High-magnification image of the NWs near the Y-junction region. One of the Y-junctions is contoured by *white lines* for clarity (with permission from [23.29], © American Chemical Society (2009))

with a metal layer as electrode (Fig. 23.5b). Using such nanochannel-confined electrochemical deposition, Y-branched Au NWs were constructed, as shown in Fig. 23.5c,d. The diameter of the stem segment and the branches of the Y-branched Au NWs were about 50 and 35 nm, respectively. By using similar approaches, two-, three-, and four-branched Ni NWs were also created, as shown in Fig. 23.5e–j. The stem and branch diameters of the two-, three-, and four-branched Ni NWs were 90 and 55 nm, 120 and 50 nm, and 125 and 50 nm, respectively.

Xu et al. [23.29] recently developed a porous AAO-template-assisted galvanic deposition approach for fabrication of branched metallic NWs, by infiltrating aqueous solutions of metal chloride salts into an Au-coated native AAO template with Al foil on its outside edge. The formation of the metallic NWs can be ascribed to the redox reactions of two galvanic cells where the Al foil acts as the anode. Y-branched Au NWs have been constructed by infiltrating aqueous $HAuCl_4$ solution into an AAO template with Y-branched nanochannels. Figure 23.6a shows a low-magnification SEM image of a bundle of Y-branched Au NWs after template removal. The interface between the larger-diameter stems and the smaller-diameter branches can be clearly observed. The Y-branched junctions are obvious in the high-magnification image shown in Fig. 23.6b. The diameters of the stems and branches are about 80 and 50 nm, respectively.

Multiple Generations of Branched Nanostructures

By using AAO templates with tree-like multigeneration branched nanochannels, *Meng* et al. [23.18] constructed multigeneration branched nanostructures. AAO templates with the simplest multigeneration branched nanochannels, in which each generation divides into two branches, were fabricated. Typically, four generations of two-branched complex channels were obtained by sequentially reducing the applied anodizing voltage four times during the anodization, each time by the same factor of $1/\sqrt{2}$. Four-generation Y-branched CNTs could be achieved by depositing CNTs in the four-generation Y-branched channels via CVD. Figure 23.7a (left) shows an SEM image of a large bundle of four-generation Y-branched CNTs obtained after template removal, with four parallel interfaces showing where each of the four generations of Y-branching takes place. Figure 23.7a (right) shows a schematic of the architecture formed inside the template. High-magnification images of each of the interfaces (Fig. 23.7b–e) clearly reveal the corresponding Y-branches. The diameters of the primary stems and the branches depend on the corresponding anodizing voltages, while the length of each branch is controlled

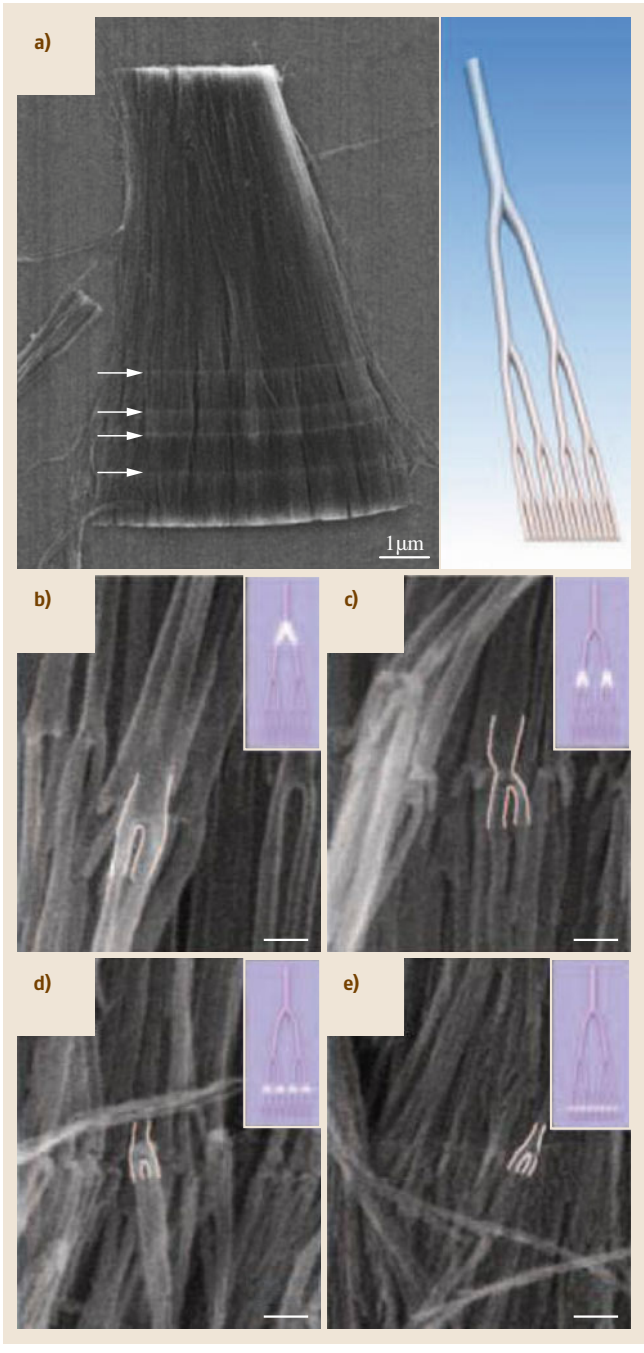


Fig. 23.7 **(a)** *Left*: Low-magnification SEM image of four-generation Y-branched CNTs, with the four parallel interfaces indicate by *white arrows*. *Right*: Structure of typical four-generation Y-branched CNTs. **(b–e)** High-magnification images from each interface clearly revealing the corresponding Y-branches and the decreasing diameter of the branched nanotube segments, showing the first **(b)**, second **(c)**, third **(d)**, and fourth **(e)** Y generations. The Y-junction is contoured by *white lines* for clarity. *Insets at top right* show schematics of the whole architecture with the specific junction highlighted in *white*. (*Scale bars*: 100 nm) (with permission from [23.18], © National Academy of Sciences USA (2005)) ◀

independently by the anodization time for each corresponding pore segment generation.

A combination of Y-shapes and multiple branches can lead to a wealth of new nanoscale architectures. This goal can be achieved by reducing the anodizing voltage in steps, by factors of $1/\sqrt{2}$ and $1/\sqrt{n}$ sequentially, consecutively generating Y-shapes and n-branched pores in the template. Continuing this approach, more complicated architectures, such as a single stem dividing into multiple branches each of which further subdivides into multiple branches, can be created. *Meng* et al. [23.18] reported the construction of two-generation branched CNTs, with each generation having three branches. AAO templates with three-branch-three-subbranch tree-like channels were created by sequentially reducing the applied anodizing voltage by a factor of $1/\sqrt{3}$. Using AAO with such tree-like branched channels as templates, CNTs with three-branch-three-subbranch morphology have been constructed via CVD. Figure 23.8a shows an SEM image of CNTs with three-branch-three-subbranch morphology, where two levels of multiple branching are shown. The primary stem first splits into three branches, each of which further splits into three subbranches. The high-magnification SEM images of the two interfaces (Fig. 23.8b,c) reveal the junctions, showing the branching and the diameter reduction as the branching occurs. These branched NTs could be used to build large supramolecular constructs for applications such as drug delivery, nanoscale separation, and fundamental diffusion studies, and also as complex nanoelectronics circuits and nanoelectromechanical systems.

Step-Shaped Nanostructures

Using AAO templates with other complex-shaped nanochannels, such as step shape, step-shaped nanostructures can be constructed. *Tian* et al. [23.22] reported fabrication of step-shaped BiNWs inside step-shaped nanochannels of AAO templates by electrodeposition. The current–voltage characteristics of the parallel uniform BiNWs showed conventional metal–semiconductor junction behavior.

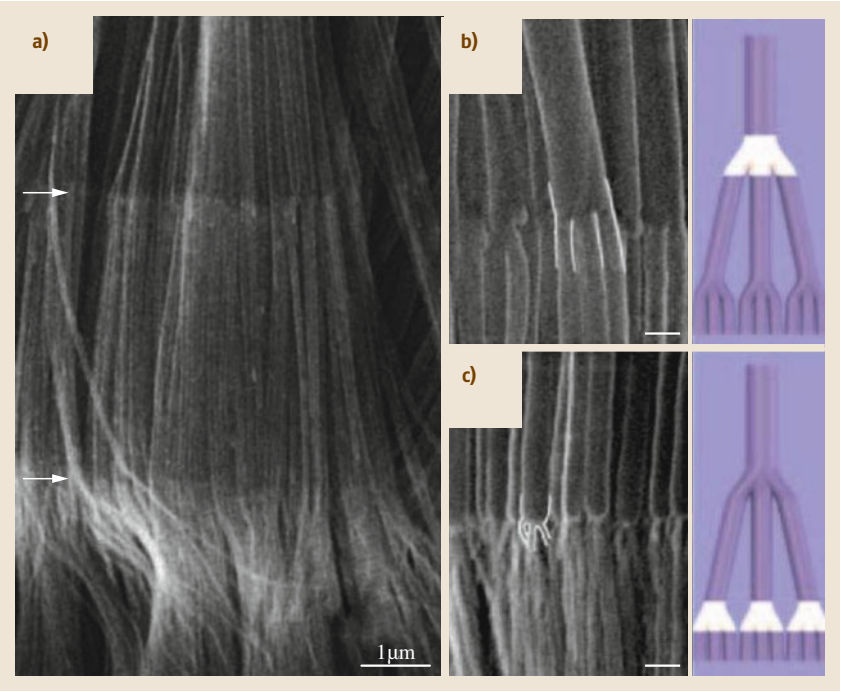


Fig. 23.8 **(a)** SEM image of CNTs with three-branch-three-subbranch morphology, showing two generations of branching (at the locations of the *white arrows*). **(b,c)** *Left*: close-up views of the junctions; *right*: schematic of each of the representative individual nanotube structures. Junctions are highlighted with *white line contours* for clarity. (*Scale bars*: 100 nm) (with permission from [23.18], © National Academy of Sciences USA (2005))

Yang et al. [23.52] reported synthesis of step-shaped CuNWs and NTs using AAO templates with correspondingly shaped nanochannels via electrodeposition (Fig. 23.9). To obtain NWs, the coated Au layer must be thick enough to fully cover the nanopores of the step-shaped AAO templates. Figure 23.9 shows a schematic and a TEM image of the step-shaped CuNWs, clearly showing that the large-diameter segments of the NWs are well connected to the small-diameter segments. In situ x-ray diffraction investigation demonstrated that the thermal expansion of the step-shaped CuNTs and NWs was temperature dependent and that the thermal expansion coefficients of the large-diameter segments of the CuNTs and NWs were greater than that of the small-diameter segments.

23.3.3 Nanoheterostructures

Nanoheterostructures can be synthesized inside nanochannels of AAO templates by various synthetic approaches, such as sequential electrodeposition, some combined techniques, etc. In the following, the fabrication of two kinds of nanoheterostructures (i. e., segmented and core/shell nanoheterostructures) in AAO templates is demonstrated in detail.

Segmented Nanoheterostructures

Sequential electrodeposition is commonly used for synthesis of segmented nanoheterostructures. This method has been used to fabricate metal–polymer heterostructures in AAO templates. *Park* and coworkers [23.55] reported synthesis of segmented nanorods made of Au hydrophilic blocks and PPy hydrophobic blocks that behave as mesoscopic amphiphiles in the AAO template by sequential electrodeposition. In a typical experiment, Au–PPy nanorods were prepared by electrodeposition of gold into the AAO templates, followed by electrochemical polymerization of pyrrole, then removal of the AAO template. The amphiphilic structures had pseudoconical shape because of a difference in diameter between the Au (large) and polymer (small) sections. They could assemble into three-dimensional bundle- and tubular-shaped microscale architectures.

Sequential electrodeposition also can be applied for synthesis of segmented metal–semimetal nanoheterostructures in AAO templates. *Yang* and coworkers [23.56] reported fabrication of heterostructures of NTs and NWs of metal Cu and semimetal Bi by sequential electrodeposition of the two materials inside nanochannels of an AAO template with an Au layer thin enough to leave the pores open. Segmented het-

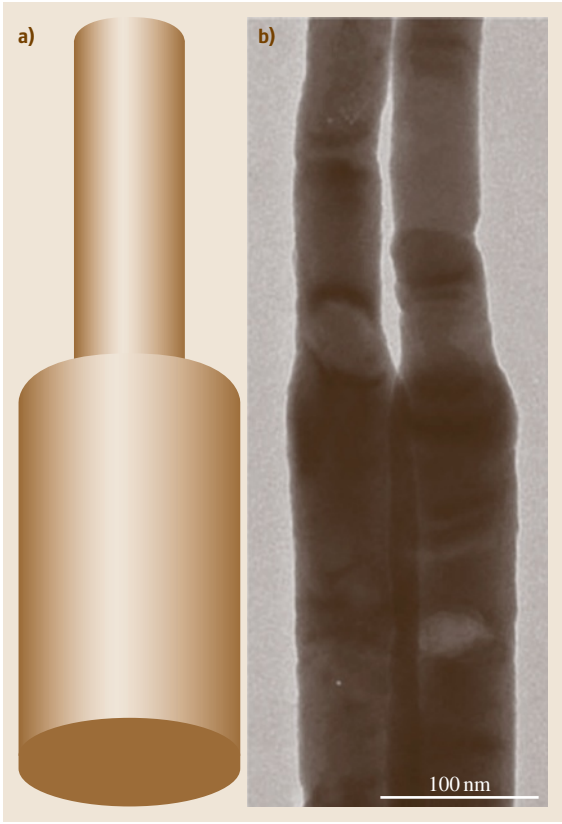


Fig. 23.9 **(a)** Schematic of a step-shaped NW. **(b)** TEM image of step-shaped CuNWs (with permission from [23.52], © Wiley-VCH 2010)

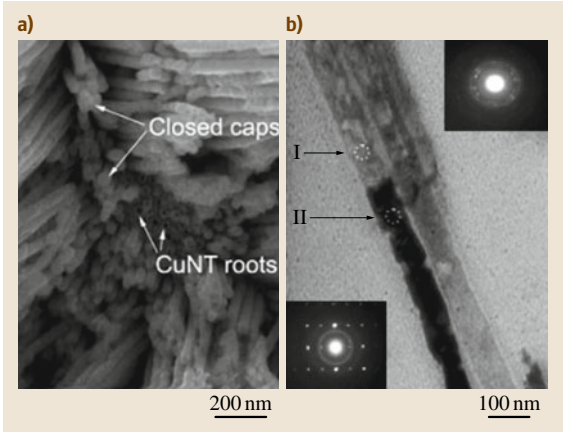


Fig. 23.10 **(a)** SEM image of electrodeposited CuNTs with closed caps, broken CuNTs, and CuNT roots. **(b)** TEM image of segmented CuNT–BiNW heterostructures. The *inset* SAED patterns at the *upper-right* and *lower-left* corners are taken from areas marked I and II, respectively (with permission from [23.56], © Royal Society of Chemistry (2007))

erostructures of CuNTs and BiNWs (CuNT–BiNW) were achieved by electrochemical deposition of Cu first, then Bi in the nanochannels of the AAO template with one side coated with an Au layer which was thin enough to leave the pores open and cover only the top surface of the pore walls. Similarly, if the electrodeposition sequence was changed to Bi first, then Cu, segmented heterostructures of BiNTs and CuNWs (BiNT–CuNW)

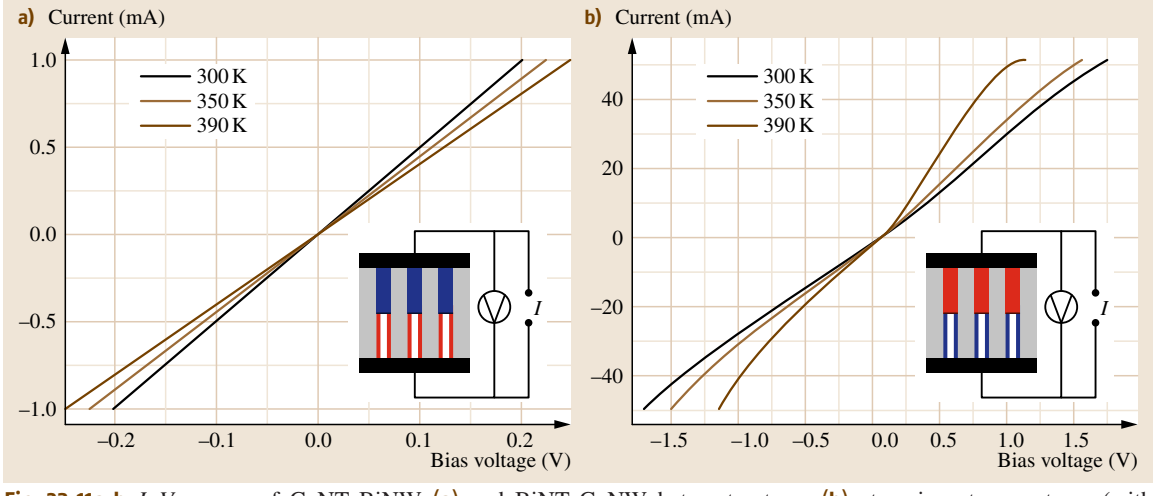


Fig. 23.11a,b *I–V* curves of CuNT–BiNW **(a)** and BiNT–CuNW heterostructures **(b)** at various temperatures (with permission from [23.56], © Royal Society of Chemistry (2007))

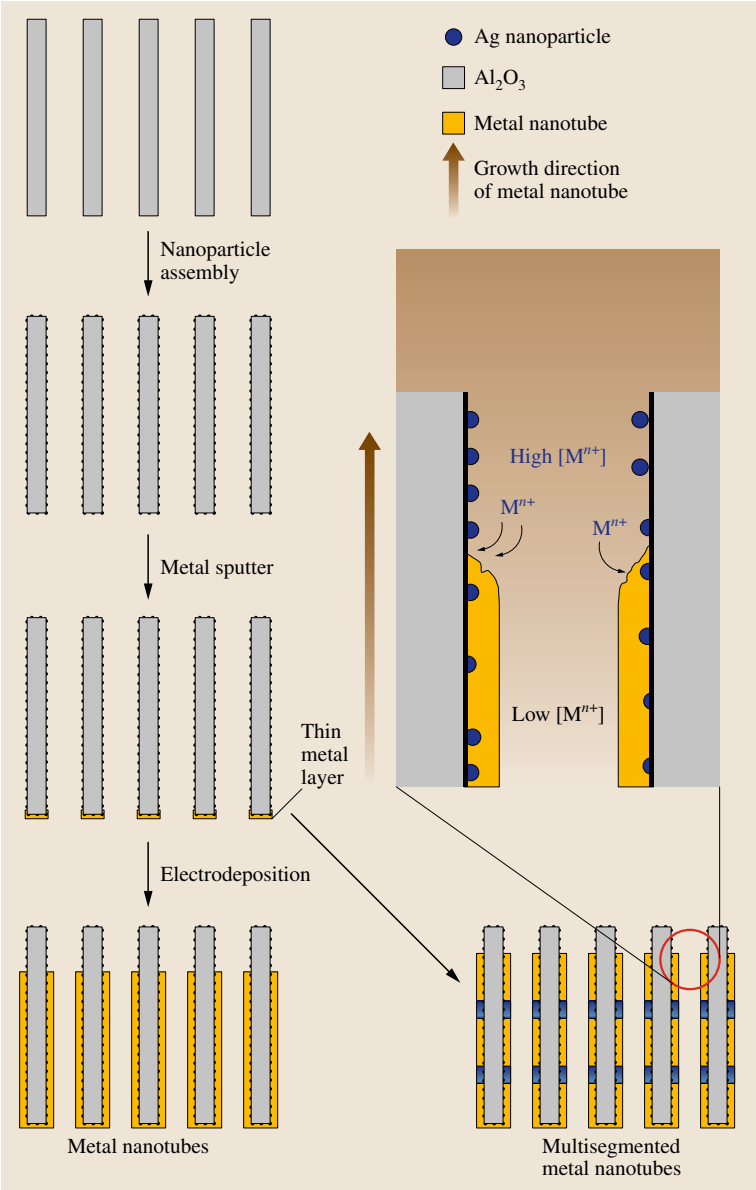


Fig. 23.12 Procedure for preparation of metal NTs and the proposed mechanism of metal NT growth (with permission from [23.57], © Wiley-VCH (2005))

could be achieved. Figure 23.10a shows SEM images of the electrodeposited CuNT segments. It can be clearly observed that the CuNTs have closed caps on the top. BiNW segments were subsequently deposited on the CuNTs to form CuNT–BiNW heterostructures, as shown in Fig. 23.10b. The junctions between Cu and Bi can be clearly observed. The light-contrast segment and the dark-contrast segment are CuNT and BiNW, respectively. The SAED patterns (insets in Fig. 23.10b) indicate that the CuNT is polycrystalline, while the BiNW is single crystalline. *I–V* curve measurements on these two kinds of heterostructures (Fig. 23.11) revealed that the CuNT–BiNW heterojunction arrays are metal–metal junctions, while the BiNT–CuNW heterojunction arrays showed metal–semiconductor electronic transport behavior.

Electrodeposition can be used for fabrication of segmented nanoheterostructures of other materials in

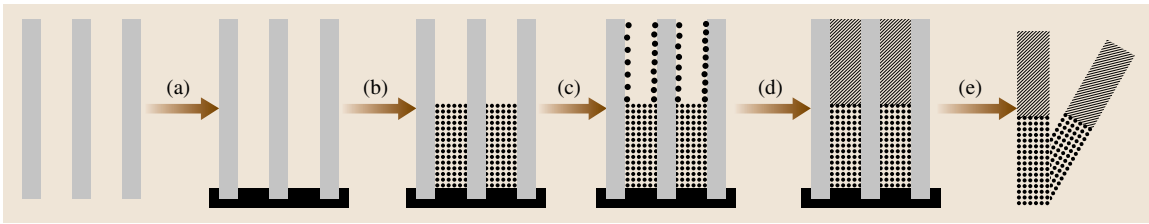


Fig. 23.13 Schematic illustration of synthesis of segmented CdS–BiNWs: (a) sputtering a thick gold layer, (b) electrodeposition of BiNWs, (c) sensitization of channel wall, (d) chemical bath deposition of CdSNWs, (e) removal of the Au layer (with permission from [23.61], © Elsevier (2008))

AAO templates; For example, *Liu* et al. [23.13] prepared segmented Pt–Ru, Pt–Ni, and Pt–RuNi nanorods by sequential electrodeposition of the metals into the nanochannels of AAO templates. They found that the segmented nanorods were catalytically active for room-temperature electrooxidation of methanol in acidic solution. *Zhang* et al. [23.58] synthesized segmented Sb–BiNWs inside nanochannels of AAO templates by sequential electrodeposition using two different electrolytes. The segmented Sb–BiNW arrays showed resistive switching behavior that may find applications in metal–semiconductor field-effect transistors. Using a single bath, Sb–Bi [23.59] and Bi–BiSb [23.60] superlattice NWs have been prepared in AAO templates by pulse electrodeposition.

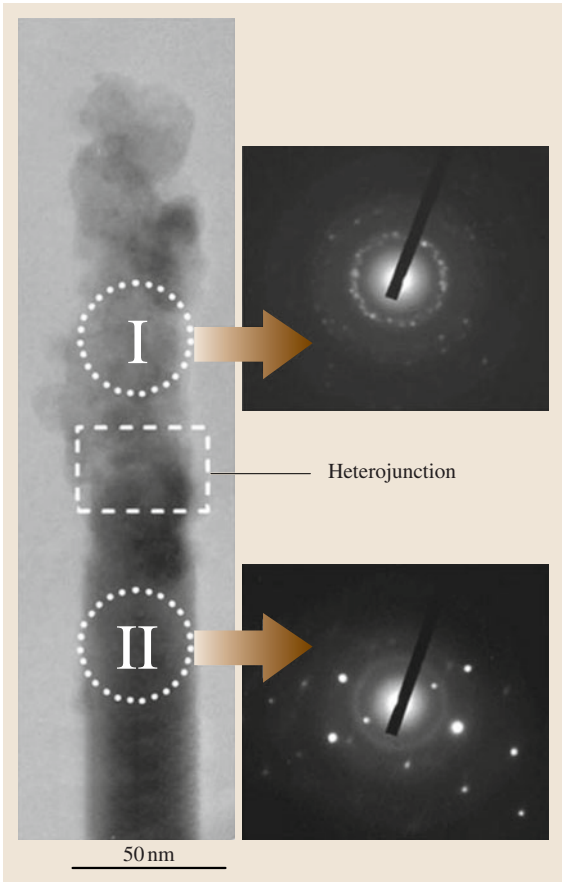


Fig. 23.14 A TEM image with SAED patterns of segmented CdS–BiNWs (with permission from [23.61], © Elsevier (2008))

Using a modified electrochemical deposition technique, *Lee* et al. [23.57] fabricated multisegment Au–Ni NTs in AAO templates. A typical fabrication process is shown in Fig. 23.12. Ag nanoparticles were first immobilized on the pore walls of the AAO template by spontaneous reduction of Ag^{I} by Sn^{II}, which is a modification of the previously established sensitization–preactivation process of AAO prior to electroless deposition of metals. Then, sequential electrodeposition of Au and Ni in the AAO template resulted in multisegment Au–Ni NTs. It is believed that the Ag nanoparticles immobilized on the nanochannel surfaces play a key role in the growth of the metallic NTs, enabling preferential electrodeposition of metal along the nanochannel surfaces.

Segmented heterostructures can also be achieved by methods combining electrodeposition with other techniques. *Yang* et al. [23.61] reported fabrication of segmented CdS–BiNWs in AAO templates via a method combining electrodeposition with electroless deposition. In a typical process (Fig. 23.13), BiNWs are first electrodeposited inside the nanochannels of the AAO template with a thick Au layer sputtered on one side surface. Then, the nanochannels of the AAO template are activated by Sn^{2+} and Pd^{2+}. The Pd^{2+} is deoxidized by Sn^{2+} via the reaction $Sn^{2+} + Pd^{2+} = Pd + Sn^{4+}$, leading to Pd nanoparticles attached to the channel walls of the AAO template. The Pd nanoparticles serve as seeds for subsequent heterogeneous nucleation and

growth of CdSNWs. When the AAO template is immersed in a mixed solution of CH_3CSNH_2 and $CdCl_2$, CdSNWs are deposited in the AAO template via the reactions $CH_3CSNH_2 \rightarrow CH_3CN + H_2S$ and $CdCl_2 + H_2S \rightarrow CdS + 2HCl$. Figure 23.14 shows a TEM image of the resulting segmented CdS–BiNWs. SAED patterns taken from the segmented NWs reveal that the CdSNW segment is polycrystalline whereas the BiNW segment is single crystalline. Measurements of the resistance–temperature relationship (Fig. 23.15) reveal that the CdS–BiNW heterojunctions display semiconductor–semiconductor behavior.

Han et al. [23.62] reported synthesis of two-segment CdSNW–CNT and three-segment CNT–CdSNW–CNT heterostructures inside nanochannels of AAO templates by a method combining electrodeposition with CVD. Figure 23.16 shows the fabrication procedure for the segmented nanoheterostructures. Two-segment CdSNW–CNT heterostructures were achieved by first electrodepositing CdSNWs in the nanochannels of an AAO template with one side coated with a silver layer as electrode, and then growing CNTs in the remaining empty channels via CVD. Three-segment CNT–CdSNW–CNT heterostructures were obtained by adding a procedure to selectively etch part of the deposited CdSNWs before chemical vapor deposition of the CNTs. Figure 23.17a shows a top view of the CNTs. Figure 23.17b and c show SEM images of a bundle of CdSNW–CNT and CNT–CdSNW–CNT heterostructures, respectively. The close-up view of the CdSNW–CNT heterojunctions in Fig. 23.17d clearly shows that the CNT and CdSNW are well connected.

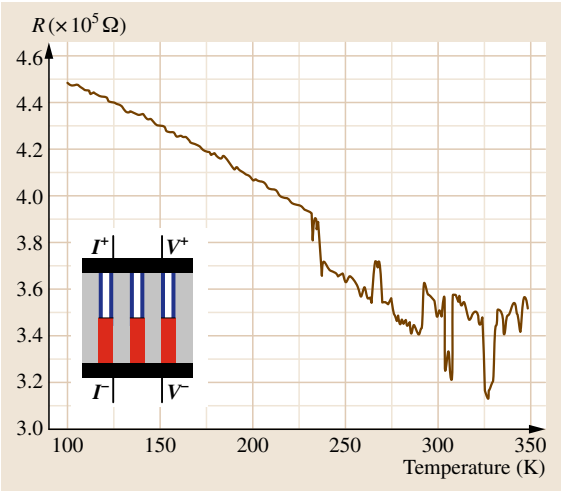


Fig. 23.15 Temperature dependence of the resistance of a segmented CdS–BiNW array (with permission from [23.61], © Elsevier (2008))

EDS spectra (Fig. 23.17e,f) reveal that the light- and dark-contrast parts in Fig. 23.17b,c are CdSNW and CNT segments, respectively. The TEM image of a single CdSNW–CNT junction in Fig. 23.17g shows good connection between the CdSNW and CNT. The SAED pattern (inset in Fig. 23.17g) indicates that the NW is single-crystal CdS with hexagonal structure. The high-resolution TEM image of the CdSNW–CNT junction in Fig. 23.17h shows that the CNT is closely ended at the CdSNW tip and that good adherence is achieved between the CdSNW and CNT. Electronic transport

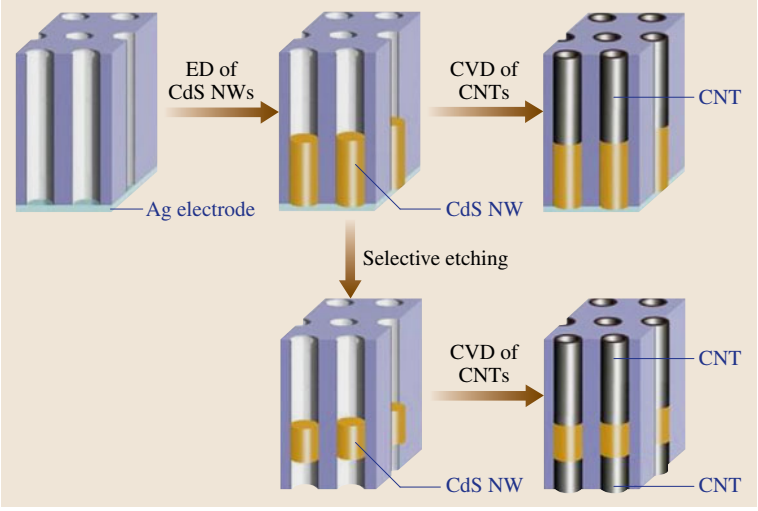


Fig. 23.16 Schematic of the fabrication procedure for two-segment CdSNW–CNT and three-segment CNT–CdSNW–CNT nanoheterostructures (with permission from [23.62], © Elsevier (2009))

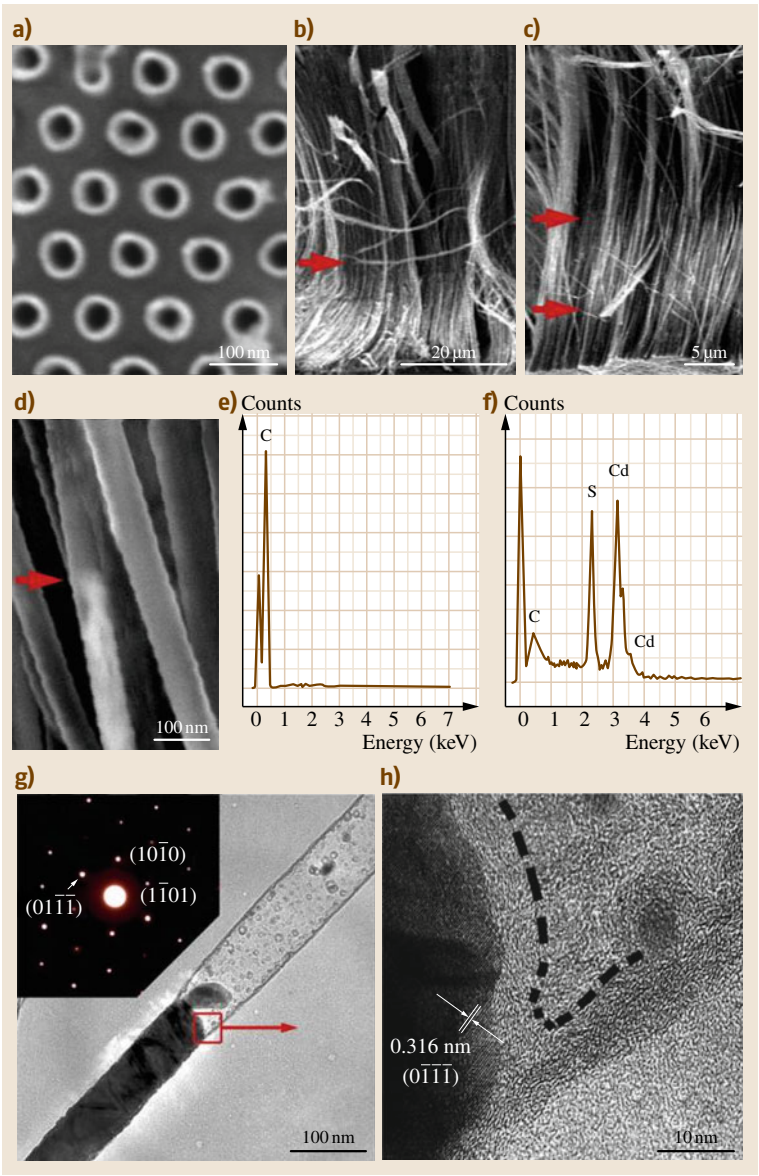


Fig. 23.17a–d Characterization of the nanoheterostructures. **(a)** Top view of the NT tip arrays. **(b–d)** SEM images of a bundle of CdSNW–CNT **(b)** and CNT–CdSNW–CNT **(c)** heterostructures, and an individual CdSNW–CNT nanoheterojunction **(d)**; the interface of the heterojunctions is marked with *red arrows*. **(e,f)** EDS spectra taken on the dark- and light-contrast parts in CdSNW–CNT and CNT–CdSNW–CNT heterostructures, respectively. **(g)** TEM image of an individual CdSNW–CNT heterojunction, with SAED pattern taken from the CdSNW segment (*inset*). **(h)** High-resolution TEM image showing the junction of a CdSNW–CNT taken from the *red rectangle* in **(g)**; the edge of the wall and the tip of the CNT are contoured by *dashed black lines* for clarity (with permission from [23.62], © Elsevier (2009))

measurements reveal that the CdSNW–CNT heterojunctions show ohm-like behavior.

Xu et al. [23.29] used the porous AAO-template-assisted galvanic deposition approach for fabrication of segmented metallic NWs consisting of different metals or alloys with distinct properties, by sequentially infiltrating corresponding aqueous solutions of metal chloride salts into the same piece of Au-coated native AAO template with Al foil on its outside edge. After sequential infiltration of $HAuCl_4$ and $NiCl_2$ aqueous solution into the nanochannels of the AAO template, two-segment Au–Ni NWs were obtained. Figure 23.18a shows an SEM image of the resulting two-segment Au–Ni NWs, clearly showing an interface between the two segments with different contrast. Figure 23.18b shows a TEM image of an individual two-segment Au–Ni NW. The dark-contrast segment is single-crystalline Au NW, whereas the light-contrast segment is polycrystalline Ni NW (Fig. 23.18c,e). The lattice-resolved image taken at the junction interface of the Au and Ni segments in

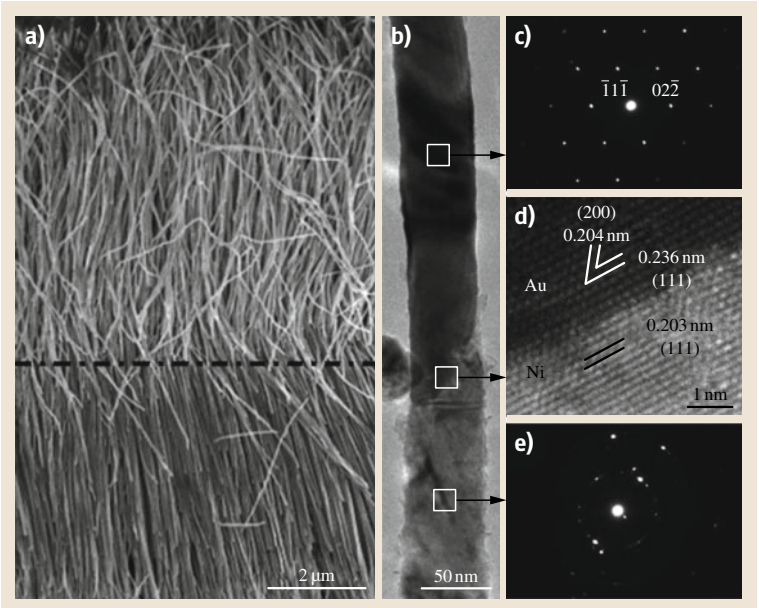


Fig. 23.18 **(a)** Side-view SEM image of two-segment Au-Ni NWs, with a *black dashed line* showing the interface of the two segments having different contrasts. **(b)** TEM image of part of the segmented NW near the junction area, along with SAED patterns taken from **(c)** the Au segment and **(e)** the Ni segment; **(d)** lattice-resolved image of the Au–Ni interface (with permission from [23.29], © American Chemical Society (2009))

Fig. 23.18d reveals that Au(111) plane is nearly parallel to Ni(111) plane. Using such an approach, multisegment metallic NWs with individual segments having distinct properties also could be achieved via multiple sequential infiltrations; for example, three-segment Au–Ni–Au NWs could be synthesized by sequentially infiltrating $HAuCl_4$, $NiCl_2$, and $HAuCl_4$ aqueous solutions into the nanochannels of the AAO template.

Core/Shell Nanoheterostructures

Sequential electrodeposition is a common approach to create core/shell nanoheterostructures in AAO templates. This method was used to produce core/shell conducting polymer NT/metal NT heterostructures in AAO templates. Conducting polymer NTs were firstly synthesized inside the nanochannels of the AAO template by an electrochemical polymerization method from an electrolyte containing the corresponding monomer. Then, metal NTs were electrodeposited inside the nanochannels as shells around the preformed conducting polymer NTs. Core/shell polyaniline (PANI) NT/Au NT [23.63] and PPy NT/Ni NT [23.64] nanoheterostructures have been synthesized by such an approach. Figure 23.19 shows a typical fabrication process for core/shell PPy NT/Ni NT heterostructures. Electrochemical polymerization was performed to deposit PPy NTs inside the AAO template (Fig. 23.19a). The Ni NTs were synthesized outside the PPy NTs by electrodeposition (Fig. 23.19b). After removal of the AAO template, core/shell PPy NT/Ni NT heterostructures were obtained (Fig. 23.19c). It was demonstrated that the Ni shells of the resultant core/shell nanoheterostructures had an anisotropic ferromagnetic nature with maximum coercivity and remanent-saturation magnetization when applying a magnetic field along the direction parallel to the tubes.

By the sequential electrodeposition method, *Yang* and coworkers [23.65] synthesized semimetal/metal coaxial nanocables in AAO templates. Figure 23.20 shows the fabrication process for the nanocables. Cable shells were first electrodeposited on the interior walls of the nanochannels of an AAO template coated with a mesh-like Au layer covering the top-view surface of the pore walls but still leaving the pores open; then, the cavities of the shells were filled by a second electrodeposition to obtain cable cores. This fabrication process has been used to demonstrate fabrication of Cu shell/Bi core (Fig. 23.21) and Bi shell/Cu core (Fig. 23.22) nanocables. Figure 23.21b shows a TEM image of a single Cu shell/Bi core nanocable with the core and shell clearly identified. The core and shell of the nanocable can be clearly distinguished from the cable end, where the core sticks out of the shell (Fig. 23.21c). The lattice-resolved image and SAED pattern (Fig. 23.21a) reveal that the preferred growth direction of the BiNW core is along the [003] orientation. Figure 23.22 shows SEM images of Bi shell/Cu core nanocables with the same outer diameter but differ-

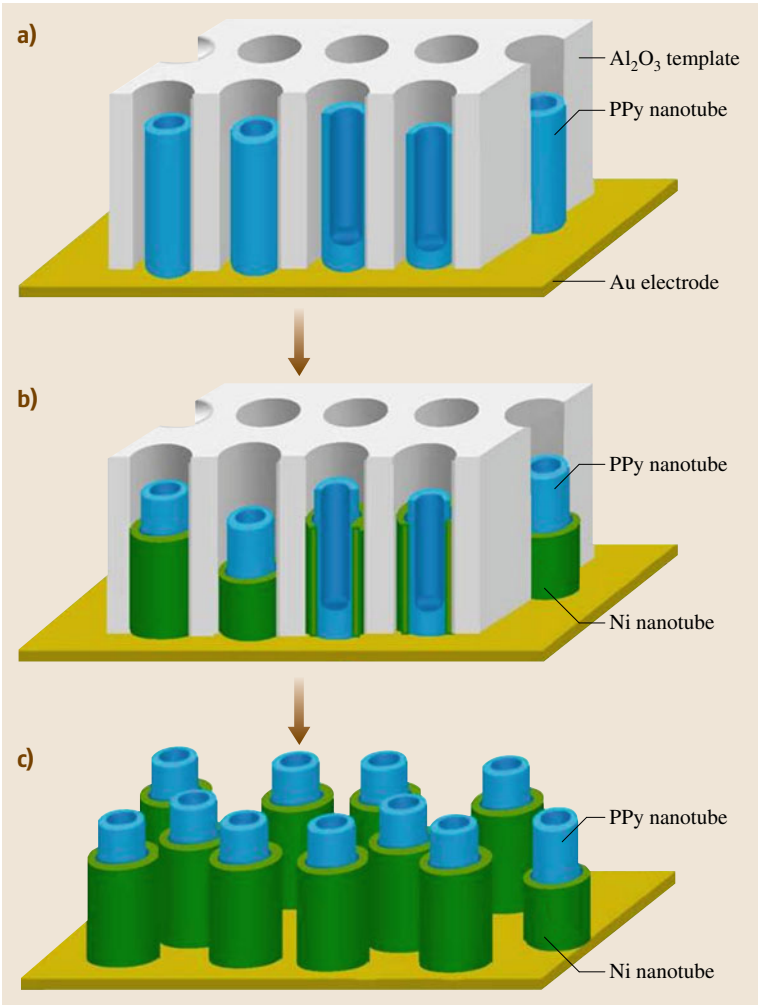


Fig. 23.19 Schematic of the synthesis of the core/shell PPy NT/Ni NT nanoheterostructures (with permission from [23.64], © American Institute of Physics (2007))

ent shell thicknesses and core diameters. The diameter of the cable core and the thickness of the cable shell can be tuned by modulating the thickness of the sputtered Au layer. As shown in Fig. 23.22, Bi shell/Cu core nanocables with thinner shells and thicker cores could be achieved when a thinner Au layer was coated on one planar surface side of the AAO template.

Except for preparation of core/shell conducting polymer/metal and semimetal/metal nanoheterostructures, sequential electrodeposition has been used to fabricate core/shell metal/metal nanoheterostructures; for example, ordered core/shell Cu/Ni nanocables were synthesized in an AAO template by sequential electrodeposition [23.66]. However, the two-step electrodeposition using two different electrolytes for deposition of corresponding materials in the AAO templates makes the experiments complicated. Thus, a one-step electrodeposition method, using only one electrolyte, has been developed for construction of core/shell nanoheterostructures in AAO templates. Synthesis of core/shell Cu/Ni [23.67] and Ni/TiO_2 [23.68] nanocables has been reported using this technique.

By combining electrodeposition with other synthetic approaches, core/shell nanoheterostructures of metal or semiconductor/oxide have been achieved; for instance, core/shell Co/TiO_2 nanocables were fabricated by deposition of TiO_2 NTs inside nanochannels of AAO templates via a sol–gel technique followed by electrodeposition of Co NWs into TiO_2 NTs [23.69]. By a combination of atomic layer deposition (ALD) and

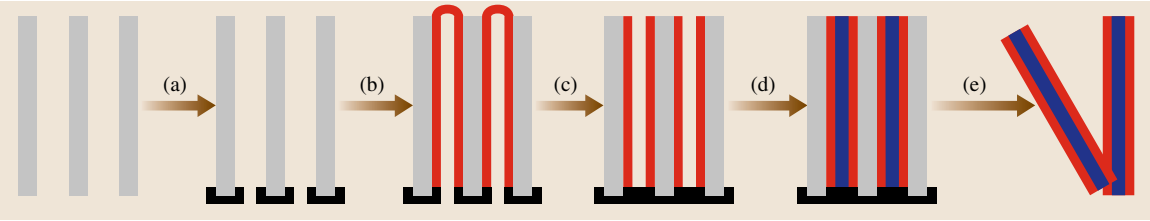


Fig. 23.20 Schematic for synthesis of nanocables consisting of two materials via electrodeposition: (a) sputtering a mesh-like Au layer on one planar surface side of the AAO template, (b) electrodepositing one material as the shells (*marked in red*) of the cables, (c) etching the caps on top of the deposited shells and sputtering a thick Au layer at the bottom of the shells, (d) electrodepositing another material as cores (*marked in blue*) of the cables inside the earlier deposited shells, (e) removal of the AAO template (with permission from [23.65], © American Institute of Physics (2008))

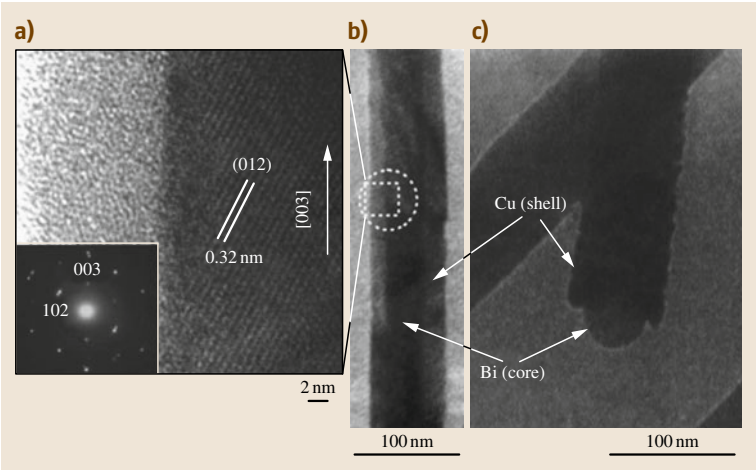


Fig. 23.21 **(a)** High-resolution TEM image of Cu shell/Bi core nanocable, taken from the *dashed circle* and *rectangle* marked in **(b)**, the *inset* is the SAED pattern. **(b,c)** TEM images of the middle **(b)** and end **(c)** segment of one nanocable (with permission from [23.65], © American Institute of Physics (2008))

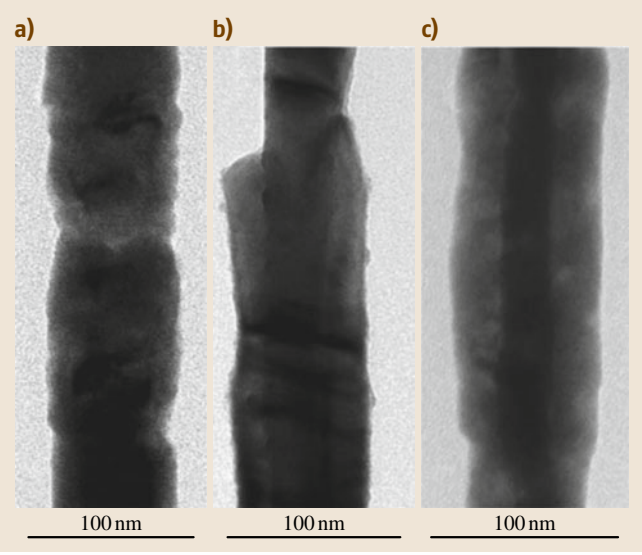


Fig. 23.22a–c Bi shell/Cu core nanocables with the same outer diameter of 75 nm but different shell thicknesses and core diameters. The Bi shell thicknesses and Cu core diameters are **(a)** 15 and 45 nm, **(b)** 20 and 35 nm, and **(c)** 25 and 25 nm, respectively (with permission from [23.65], © American Institute of Physics (2008))

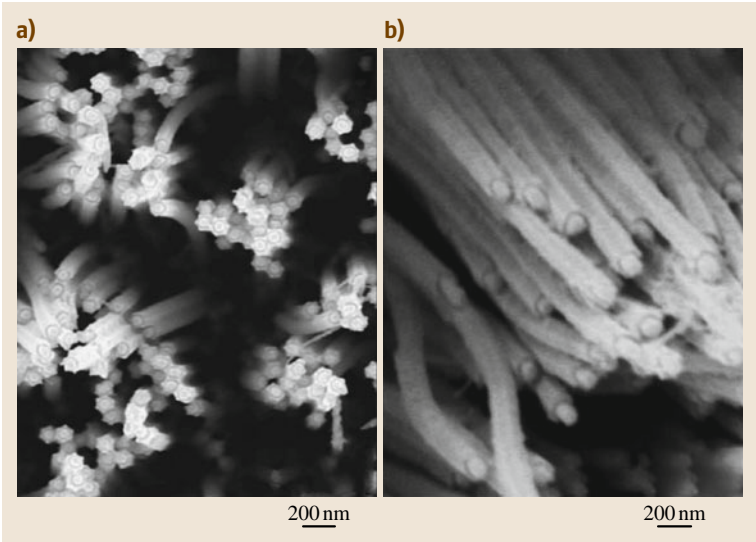


Fig. 23.23a,b SEM images of core/shell InSb/Al_2O_3 nanocables after chemically etching for **(a)** 3 min and **(b)** 5 min (with permission from [23.71], © Elsevier (2006))

electrodeposition, nanocables consisting of a Ni core and a Fe_3O_4 shell separated by a silica spacer layer have been synthesized in AAO templates [23.70]. ALD is used to conformally deposit the shells (including the inert layers), whereas electrodeposition furnishes the core. *Yang* et al. [23.71] reported a combinatorial method of electrodeposition and chemical etching for fabrication of core/shell InSb/Al_2O_3 nanocables. InSb NWs were first electrodeposited in the nanochannels of an AAO template. Then, the AAO template embedded with InSb NWs were immersed in aqueous NaOH solution for different periods of time to partially remove the AAO template. Finally, core/shell InSb/Al_2O_3 nanocables were obtained. The obtained InSb NW core was single crystalline along the [100] direction, whereas the Al_2O_3 sheath was amorphous. Figure 23.23 shows SEM images of core/shell InSb/Al_2O_3 nanocables after chemically etching for different times, revealing that the Al_2O_3 shell becomes thinner and shorter with increasing etching time.

In addition, a supercritical fluid inclusion process has been developed for synthesis of core/shell heterostructures in AAO templates, where the NT is first deposited onto the channel walls of the AAO templates and subsequently filled with core material to form core/shell heterostructures. Using the supercritical fluid inclusion processes, magnetic core/shell Ge/Co [23.72], Fe_3O_4/Co, and Co/Fe_3O_4 [23.73] nanocables have been achieved in nanochannels of AAO templates.

23.3.4 Complex-Shaped Nanoheterostructures

By using AAO templates with complex-shaped nanochannels, heterostructures with corresponding complex shapes can be constructed. *Meng* et al. [23.74] recently demonstrated fabrication of various branched two-segment NW/NT and three-segment NT/NW/NT heterojunctions in AAO templates with branched nanochannels. These heterostructures were achieved by a combinatorial process of electrodepositing NWs within the branched channels of AAO templates, selectively etching part of the electrodeposited NWs, and growing NTs on the ends of the NWs. The NW segment can either be made of a single material or consist of several subsegments of different materials (metals, alloys, or compound semiconductors), while the NT segment can be made from carbon, silicon, or silica; the two end NT segments in the NT/NW/NT architecture can comprise the same or different materials. These branched hybrid nanoarchitectures suggest the potential for fabrication of large-scale three-dimensionally interconnected multifunctional nanocircuits, nanodevices, and nanosystems.

23.4 Conclusions and Outlook

Preparation of AAO templates with a variety of pore structures, including straight, branched, and step-shaped pores, has been discussed in detail. We then focused on construction of a number of nanostructures including NTs, NWs, and nanoheterostructures in AAO templates with different pores. These nanostructures replicate the morphologies of the nanochannels of the AAO template, resulting in nanostructures of various shapes.

More recently, several AAO templates with novel pore structures have been achieved; for example, *Lee* et al. [23.75] delaminated a single as-prepared anodic film into a stack of well-defined nanoporous AAO sheets by pulse anodization. *Lim* et al. [23.76] reported fabrication of two-layer mild-hard AAO templates with different pore sizes and the same pore distance by a three-step anodization process. Future developments will continue to rely on engineering of the pore structures of the AAO template. The most important area is use of these AAO templates with novel pores for synthesis of novel architectures. Assembling the nanostructures in AAO templates into multifunctional nanodevices and nanosystems may have fascinating applications in future nanotechnology.

References

23.1 H. Masuda, K. Fukuda: Ordered metal nanohole arrays made by a two-step replication of honeycomb structures of anodic alumina, Science **268**, 1466–1468 (1995)

23.2 C.R. Martin: Membrane-based synthesis of nanomaterials, Chem. Mater. **8**(8), 1739–1746 (1996)

23.3 J.C. Hulteen, C.R. Martin: A general template-based method for the preparation of nanomaterials, J. Mater. Chem. **7**(7), 1075–1087 (1997)

23.4 X.Y. Zhang, G.H. Wen, Y.F. Chan, R.K. Zheng, X.X. Zhang, N. Wang: Fabrication and magnetic properties of ultrathin Fe nanowire arrays, Appl. Phys. Lett. **83**(16), 3341–3343 (2003)

23.5 R.-L. Zong, J. Zhou, Q. Li, B. Du, B. Li, M. Fu, X.-W. Qi, L.-T. Li, S. Buddhudu: Synthesis and optical properties of silver nanowire arrays embedded in anodic alumina membrane, J. Phys. Chem. B **108**(43), 16713–16716 (2004)

23.6 X. Zhang, L. Zhang, G. Meng, H. Guang, Y. Neng, P. Jin, P. Fritz: Synthesis of ordered single crystal silicon, Adv. Mater. **13**(16), 1238–1241 (2001)

23.7 J. Jie, G. Wang, Q. Wang, Y. Chen, X. Han, X. Wang, J.G. Hou: Synthesis and characterization of aligned ZnO nanorods on porous aluminum oxide template, J. Phys. Chem. B **108**, 11976–11980 (2004)

23.8 H. Cao, Y. Xu, J. Hong, H. Liu, G. Yin, B. Li, C. Tie, Z. Xu: Sol-gel template synthesis of an array of aingle crystal CdS nanowires on a porous alumina template, Adv. Mater. **13**(18), 1393–1394 (2001)

23.9 B.H. Kim, M.S. Kim, K.T. Park, J.K. Lee, D.H. Park, J. Joo, S.G. Yu, S.H. Lee: Characteristics and field emission of conducting poly(3,4-ethylenedioxythiophene) nanowires, Appl. Phys. Lett. **83**(3), 539–541 (2003)

23.10 J. Shen, Z. Chen, N. Wang, H. Yan, G. Shi, A. Jin, C. Gu: Electrical properties of a single electrochemically template-synthesized polypyrrole nanowire, Appl. Phys. Lett. **88**, 253106 (2006)

23.11 E.J. Bae, W.B. Choi, K.S. Jeong, J.U. Chu, G.-S. Park, S. Song, I.K. Yoo: Selective growth of carbon nanotubes on prepatterned porous anodic aluminum oxide, Adv. Mater. **14**(4), 277–279 (2002)

23.12 H. Gao, C. Mu, F. Wang, D. Xu, K. Wu, Y. Xie, S. Liu, E. Wang, J. Xu, D. Yu: Field emission of large-area and graphitized carbon nanotube array on anodic aluminum oxide template, J. Appl. Phys. **93**(9), 5602–5605 (2003)

23.13 F. Liu, J.Y. Lee, W.J. Zhou: Segmented Pt/Ru , Pt/Ni, and Pt/RuNi nanorods as model bifunctional catalysts for methanol oxidation, Small **2**(1), 121–128 (2006)

23.14 M. Chen, C.-L. Chien, P.C. Searson: Potential modulated multilayer deposition of multisegment Cu/Ni nanowires with tunable magnetic properties, Chem. Mater. **18**, 1595–1601 (2006)

23.15 K.-B. Lee, S. Park, C.A. Mirkin: Multicomponent magnetic nanorods for biomolecular separations, Angew. Chem. Int. Ed. **43**, 3048–3050 (2004)

23.16 F.S. Ou, M.M. Shaijumon, P.M. Ajayan: Controlled manipulation of giant hybrid inorganic nanowire assemblies, Nano Lett. **8**(7), 1853–1857 (2008)

23.17 J. Li, C. Papadopoulos, J. Xu: Growing Y-junction carbon nanotubes, Nature **402**, 253–254 (1999)

23.18 G. Meng, Y.J. Jung, A. Cao, R. Vajtai, P.M. Ajayan: Controlled fabrication of hierarchically branched nanopores, nanotubes, and nanowires, Proc. Natl. Acad. Sci. USA **102**(20), 7074–7078 (2005)

23.19 K. Nielsch, J. Choi, K. Schwirn, R.B. Wehrspohn, U. Gösele: Self-ordering regimes of porous alumina: The 10% porosity rule, Nano Lett. **2**, 677–680 (2002)

23.20 Y. Tian, G. Meng, U.K. Biswas, P.M. Ajayan, S. Sun, L. Zhang: Y-branched Bi nanowires with metal-semiconductor junction behavior, Appl. Phys. Lett. **85**(6), 967–969 (2004)

23.21 J. Choi, G. Sauer, K. Nielsch, R.B. Wehrspohn, U. Gösele: Hexagonally arranged monodisperse silver nanowires with adjustable diameter and high aspect ratio, Chem. Mater. **15**(3), 776–779 (2003)

23.22 Y.T. Tian, G.M. Meng, G.Z. Wang, F. Phillipp, S.H. Sun, L.D. Zhang: Step-shaped bismuth nanowires with metal–semiconductor junction characteristics, Nanotechnology **17**, 1041–1045 (2006)

23.23 G. Schmid: Materials in nanoporous alumina, J. Mater. Chem. **12**, 1231–1238 (2002)

23.24 H. Pan, B. Liu, J. Yi, C. Poh, S. Lim, J. Ding, Y. Feng, C.H.A. Huan, J. Lin: Growth of single-crystalline Ni and Co nanowires via electrochemical deposition and their magnetic properties, J. Phys. Chem. B **109**(8), 3094–3098 (2005)

23.25 J.G. Wang, M.L. Tian, N. Kumar, T.E. Mallouk: Controllable template synthesis of superconducting Zn nanowires with different microstructures by electrochemical deposition, Nano Lett. **5**(7), 1247–1253 (2005)

23.26 X.J. Xu, G.T. Fei, H. Yu, L. Chen, L.D. Zhang: In situ x-ray diffraction study of the thermal expansion of the ordered arrays of silver nanowires embedded in anodic alumina membranes, Appl. Phys. Lett. **88**, 211902 (2006)

23.27 W.F. Zhou, G.T. Fei, X.F. Li, S.H. Xu, L. Chen, B. Wu: In situ x-ray diffraction study on the orientation-dependent thermal expansion of Cu nanowires, J. Phys. Chem. C **113**(22), 9568–9572 (2009)

23.28 M. Biçer, A.O. Aydin, I. Sisman: Electrochemical synthesis of CdS nanowires by underpotential deposition in anodic alumina membrane templates, Electrochim. Acta **55**, 3749–3755 (2010)

23.29 Q. Xu, G. Meng, X. Wu, Q. Wei, M. Kong, X. Zhu: A generic approach to desired metallic nanowires inside native porous alumina template via redox reaction, Chem. Mater. **21**(12), 2397–2402 (2009)

23.30 K.-K. Lew, L. Pan, E.C. Dickey, J.M. Redwing: Vapor-liquid-solid growth of silicon-germanium nanowires, Adv. Mater. **15**(24), 2073–2076 (2003)

23.31 Z. Su, J. Sha, G. Pan, J. Liu, D. Yang, C. Dickinson, W. Zhou: Temperature-dependent Raman scattering of silicon nanowires, J. Phys. Chem. B **110**(3), 1229–1234 (2006)

23.32 L.T. Ngo, D. Almecija, J.E. Sader, B. Daly, N. Petkov, J.D. Holmes, D. Erts, J.J. Boland: Ultimate-strength germanium nanowires, Nano Lett. **6**(12), 2964–2968 (2006)

23.33 Z. Miao, D. Xu, J. Ouyang, G. Guo, X. Zhao: Electrochemically induced sol-gel preparation of single-crystalline TiO_2 nanowires, Nano Lett. **2**(7), 717–720 (2002)

23.34 J.S. Lee, G.H. Gu, H. Kim, K.S. Jeong, J. Bae, J.S. Suh: Growth of carbon nanotubes on anodic aluminum oxide templates: Fabrication of a tube-in-tube and linearly joined tube, Chem. Mater. **13**, 2387–2391 (2001)

23.35 A.D. Franklin, J.T. Smith, T. Sands, T.S. Fisher, K.-S. Choi, D.B. Janes: Controlled decoration of single-walled carbon nanotubes with Pd nanocubes, J. Phys. Chem. C **111**(37), 13756–13762 (2007)

23.36 T.-Y. Shin, S.-H. Yoo, S. Park: Gold nanotubes with a nanoporous wall: Their ultrathin platinum coating and superior electrocatalytic activity toward methanol oxidation, Chem. Mater. **20**(17), 5682–5686 (2008)

23.37 X.J. Xu, S.F. Yu, S.P. Lau, L. Li, B.C. Zhao: Magnetic and thermal expansion properties of vertically aligned Fe nanotubes fabricated by electrochemical method, J. Phys. Chem. C **113**(11), 4168–4171 (2008)

23.38 L. Liu, W. Zhou, S. Xie, L. Song, S. Luo, D. Liu, J. Shen, Z. Zhang, Y. Xiang, W. Ma, Y. Ren, C. Wang, G. Wang: Highly efficient direct electrodeposition of Co-Cu alloy nanotubes in an anodic alumina template, J. Phys. Chem. C **112**(7), 2256–2261 (2008)

23.39 D. Yang, G. Meng, Q. Xu, F. Han, M. Kong, L. Zhang: Electronic transport behavior of bismuth nanotubes with a predesigned wall thickness, J. Phys. Chem. C **112**(23), 8614–8616 (2008)

23.40 S.-M. Zhou, Y.-S. Feng, L.-D. Zhang: A two-step route to self-assembly of CdS nanotubes via electrodeposition, Eur. J. Inorg. Chem., 1794–1797 (2003)

23.41 R. Inguanta, S. Piazza, C. Sunseri: Template electrosynthesis of CeO_2 nanotubes, Nanotechnology **18**, 485605 (2007)

23.42 B.B. Lakshmi, P.K. Dorhout, C.R. Martin: Sol-gel template synthesis of semiconductor nanostructures, Chem. Mater. **9**(3), 857–862 (1997)

23.43 D.T. Mitchell, S.B. Lee, L. Trofin, N. Li, T.K. Nevanen, H. Soderlund, C.R. Martin: Smart nanotubes for bioseparations and biocatalysis, J. Am. Chem. Soc. **124**(40), 11864–11865 (2002)

23.44 N.I. Kovtyukhova, T.E. Mallouk, T.S. Mayer: Templated surface sol-gel synthesis of SiO_2, Adv. Mater. **15**(10), 780–785 (2003)

23.45 G. Wu, L. Zhang, B. Cheng, T. Xie, X. Yuan: Synthesis of Eu_2O_3 nanotube arrays through a facile sol-gel template approach, J. Am. Chem. Soc. **126**, 5976–5977 (2004)

23.46 G.S. Wu, Y. Lin, X.Y. Yuan, T. Xie, B.C. Cheng, L.D. Zhang: A novel synthesis route to Y_2O_3:Eu nanotubes, Nanotechnology **15**, 568–571 (2004)

23.47 D.-J. Lee, S.-S. Yim, K.-S. Kim, S.-H. Kim, K.-B. Kim: Formation of Ru nanotubes by atomic layer deposition onto an anodized aluminum oxide template, Electrochem. Solid-State Lett. **11**(6), K61–K64 (2008)

23.48 S. Farhangfar, R.B. Yang, M. Pelletier, K. Nielsch: Atomic layer deposition of ZnS nanotubes, Nanotechnology **20**, 325602 (2009)

23.49 K. Pitzschel, J.M.M. Moreno, J. Escrig, O. Albrecht, K. Nielsch, J. Bachmann: Controlled introduction

of diameter modulations in arrayed magnetic iron oxide nanotubes, ACS Nano **3**(11), 3463–3468 (2009)
23.50 C. Papadopoulos, A. Rakitin, J. Li, A.S. Vedeneev, J.M. Xu: Electronic transport in Y-junction carbon nanotubes, Phys. Rev. Lett. **85**, 3476–3479 (2000)
23.51 S. Mahima, R. Kannan, I. Komath, M. Aslam, V.K. Pillai: Synthesis of platinum Y-junction nanostructures using hierarchically designed alumina templates and their enhanced electrocatalytic activity for fuel-cell applications, Chem. Mater. **20**(3), 601–603 (2008)
23.52 D. Yang, G. Meng, C. Zhu, F. Han, L. Chen: Synthesis and thermal expansion of copper nanotubes and nanowires with Y- and step-shaped topologies, Small **6**(3), 381–385 (2010)
23.53 Q. Xu, G. Meng, F. Han, X. Zhao, M. Kong, X. Zhu: Controlled fabrication of gold and polypyrrole nanowires with straight and branched morphologies via porous alumina template-assisted approach, Mater. Lett. **63**, 1431–1434 (2009)
23.54 B. Chen, Q. Xu, X. Zhao, X. Zhu, M. Kong, G. Meng: Branched silicon nanotubes and metal nanowires via AAO-template-assistant approach, Adv. Funct. Mater. **20**, 3791–3796 (2010)
23.55 S. Park, J.-H. Lim, S.-W. Chung, C.A. Mirkin: Self-assembly of mesoscopic metal-polymer amphiphiles, Science **303**, 348–351 (2004)
23.56 D. Yang, G. Meng, S. Zhang, Y. Hao, X. An, Q. Wei, M. Ye, L. Zhang: Electrochemical synthesis of metal and semimetal nanotube–nanowire heterojunctions and their electronic transport properties, Chem. Commun., 1733–1735 (2007)
23.57 W. Lee, R. Scholz, K. Nielsch, U. Gösele: A template-based electrochemical method for the synthesis of multisegmented metallic nanotubes, Angew. Chem. Int. Ed. **44**, 6050–6054 (2005)
23.58 Y. Zhang, L. Li, G.H. Li: Fabrication and anomalous transport properties of an Sb/Bi segment nanowire nanojunction array, Nanotechnology **16**, 2096–2099 (2005)
23.59 F.H. Xue, G.T. Fei, B. Wu, P. Cui, L.D. Zhang: Direct electrodeposition of highly dense Bi/Sb superlattice nanowire arrays, J. Am. Chem. Soc. **127**(44), 15348–15349 (2005)
23.60 X. Dou, G. Li, H. Lei: Kinetic versus thermodynamic control over growth process of electrodeposited Bi/BiSb superlattice nanowires, Nano Lett. **8**(5), 1286–1290 (2008)
23.61 D. Yang, G. Meng, F. Han, L. Zhang: Two-segment CdS/Bi nanowire heterojunctions arrays and their electronic transport properties, Mater. Lett. **62**, 3213–3216 (2008)
23.62 F. Han, G. Meng, X. Zhao, Q. Xu, J. Liu, B. Chen, X. Zhu, M. Kong: Building desired heterojunctions of semiconductor CdS nanowire and carbon nanotube via AAO template-based approach, Mater. Lett. **63**(26), 2249–2252 (2009)
23.63 M. Lahav, E.A. Weiss, Q. Xu, G.M. Whitesides: Core-shell and segmented polymer-metal composite nanostructures, Nano Lett. **6**(9), 2166–2171 (2006)
23.64 D.H. Park, Y.B. Lee, M.Y. Cho, B.H. Kim, S.H. Lee, Y.K. Hong, J. Joo, H.C. Cheong, S.R. Lee: Fabrication and magnetic characteristics of hybrid double walled nanotube of ferromagnetic nickel encapsulated conducting polypyrrole, Appl. Phys. Lett. **90**, 093122 (2007)
23.65 D. Yang, G. Meng, Q. Xu, X. Zhao, J. Liu, M. Kong, Z. Chu, X. Zhu, L. Zhang: A generic approach to nanocables via nanochannel-confined sequential electrodeposition, Appl. Phys. Lett. **92**, 083109 (2008)
23.66 X. Li, Y. Wang, G. Song, Z. Peng, Y. Yu, X. She, J. Sun, J. Li, P. Li, Z. Wang, X. Duan: Fabrication and magnetic properties of Ni/Cu shell/core nanocable arrays, J. Phys. Chem. C **114**(15), 6914–6916 (2010)
23.67 Q. Wang, G. Wang, X. Han, X. Wang, J.G. Hou: Controllable template synthesis of Ni/Cu nanocable and Ni nanotube arrays: A one-step co-electrodeposition and electrochemical etching method, J. Phys. Chem. B **109**(49), 23326–23329 (2005)
23.68 W. Zhu, G. Wang, X. Hong, X. Shen: One-step fabrication of Ni/TiO_2 core/shell nanorod arrays in anodic aluminum oxide membranes, J. Phys. Chem. C **113**(14), 5450–5454 (2009)
23.69 Z. Ye, H. Liu, I. Schultz, W. Wu, D.G. Naugle, I. Lyuksyutov: Template-based fabrication of nanowire-nanotube hybrid arrays, Nanotechnology **19**, 325303 (2008)
23.70 S. Martens, M. Yan, E. Yau, S. Allende, J. Bachmann, K. Nielsch: Multilayered core/shell nanowires displaying two distinct magnetic switching events, Adv. Mater. **22**, 2435–2439 (2010)
23.71 Y.W. Yang, L. Li, X.H. Huang, M. Ye, Y.C. Wu, G.H. Li: Fabrication of InSb-core/alumina-sheath nanocables, Mater. Lett. **60**(4), 569–571 (2006)
23.72 T.A. Crowley, B. Daly, M.A. Morris, D. Erts, O. Kazakova, J.J. Boland, B. Wu, J.D. Holmes: Probing the magnetic properties of cobalt–germanium nanocable arrays, J. Mater. Chem. **15**, 2408–2413 (2005)
23.73 B. Daly, D.C. Arnold, J.S. Kulkarni, O. Kazakova, M.T. Shaw, S. Nikitenko, D. Erts, M.A. Morris, J.D. Holmes: Synthesis and characterization of highly ordered cobalt–magnetite nanocable arrays, Small **2**(11), 1299–1307 (2006)
23.74 G. Meng, F. Han, X. Zhao, B. Chen, D. Yang, J. Liu, Q. Xu, M. Kong, X. Zhu, Y.J. Jung, Y. Yang, Z. Chu, M. Ye, S. Kar, R. Vajtai, P.M. Ajayan: A general synthetic approach to interconnected nanowire/nanotube and nanotube/nanowire/nanotube heterojunctions with branched topology, Angew. Chem. Int. Ed. **48**, 7166–7170 (2009)

23.75 W.O.O. Lee, K. Schwirn, M. Steinhart, E. Pippel, R. Scholz: Structural engineering of nanoporous anodic aluminium oxide by pulse anodization of aluminium, Nat. Nanotechnol. **3**, 234–239 (2008)

23.76 J. Lim, W. Chae, H. Lee, L. Malkinski, S. Min, J.B. Wiley, J. Jun, S. Lee, J. Jung: Fabrication and magnetic properties of Fe nanostructures in anodic alumina membrane, J. Appl. Phys. **107**, 09A334 (2010)

24. Porous Silicon

Paolo Bettotti

Porous silicon (PS) is a nanoporous material obtained by electrochemical etching of crystalline silicon. Since its discovery in the mid 1950s it has been investigated as an active material in a number of research fields. The complexity of silicon electrochemistry, which is not yet completely understood, enables fine-tuning of etched nanoporous structures from the scale of a few nanometers up to tens of microns in a nearly continuous way (Sects. 24.1, 24.2). Historically, porous silicon was investigated for its bright visible luminescence and the possibility of realizing efficient silicon-based light emitters. Later, the shaping of complex photonic crystal (PC) structures led to porous silicon returning to the limelight in the form of silicon-based photonics. In fact, compared with other fabrication technologies (such as physical or chemical deposition methods), electrochemical etching has some fundamental advantages: it is a cheap and fast method that does not require complex facilities; it allows fabrication of complex structures with extremely high optical quality, composed by hundreds of layers; and moreover it enables etching of huge-aspect-ratio (>100) structures in a short time (Sects. 24.3–24.6). Lastly, applications of porous silicon in optical sensing and drug delivery have maintained interest in porous silicon as an extremely lively field.

24.1 **Basics of Porous Silicon Electrochemistry and Formation Models** 884
24.1.1 Chemical Dissolution Model 884
24.1.2 *I–V* Curves 885
24.1.3 Porous Silicon Formation Mechanisms 885
24.2 **Other Etching Methods** 886
24.3 **Porous Silicon Structural Properties** 887
24.4 **Light Emission from Porous Silicon** 890
24.5 **Thermal and Electrical Properties** 891
24.6 **The Role of the Surface** 891
24.7 **Applications of Porous Silicon** 892
24.7.1 Porous Silicon Light-Emitting Diodes 892
24.7.2 Porous Silicon-Based Photonic Crystals 893
24.7.3 Optical Sensing 896
24.7.4 Drug Delivery Systems 896
24.7.5 Oxidized Porous Silicon 897
24.8 **Conclusions** 897
References 898

Porous silicon (PS) is a porous material obtained by electrochemical etching of silicon. It was discovered during the 1950s [24.1], but it was not considered a material of interest until the early 1970s, when researchers underlined its porous nature [24.2]. Since then, the number of publications has steadily increased to the present day. Porous silicon has attracted a great deal of interest because of its many applications. In 1971, the discovery of the porous structure of electrochemically etched silicon opened the way to applications of this layer as an insulator in so-called *full isolation by porous oxidized silicon* (FIPOS) technology [24.3]. A strong effort was focused on the general electrochemical behavior of silicon and to find a model to describe the enormous variety of porous structures attainable with the electrochemical fabrication method [24.4–9]. Nearly 20 years later, *Canham* discovered that PS shows strong visible luminescence if illuminated with a blue or ultraviolet light source [24.10]. Since then, interest in PS has grown exponentially because of the intriguing possibilities of fabricating efficient silicon-based light-emitting devices.

24.1 Basics of Porous Silicon Electrochemistry and Formation Models

Semiconductor electrochemistry is a complex topic, and, concerning Si, some fundamentals are not yet fully understood. In this chapter we try to introduce the reader to the basic processes behind silicon dissolution in HF-containing media. In this chapter, we simply review the basics of Si electrochemistry. More in-depth treatises can be found in the literature [24.11, 12].

Different formation models have been proposed since the discovery of PS, but an exhaustive model able to correlate all possible etching conditions and PS morphologies is still lacking.

PS is generally etched in aqueous hydrofluoric acid (HF) solutions. Often, solutions have surfactants added or are mixed with another solvent (such as alcohols, dimethylsulfoxide (DMSO) or dimethylformamide (DMF)). Such additions reduce surface energies and improve wettability, so that pores are readily filled by solvent. Moreover, hydrogen that evolves during etching can be efficiently extracted without the formation of bubbles that would otherwise induce pore inhomogeneities and surface roughness.

24.1.1 Chemical Dissolution Model

A general mechanism for the chemical dissolution of silicon in dilute HF has been proposed by various authors [24.13–15]. The main step is the weakening of Si-hydride-terminated surface bonds by holes injected from the bulk silicon. This favors nucleophilic attack of fluorine anions on Si–Si bonds and dissolution of the semiconductor. The reaction steps are reproduced in Fig. 24.1. Holes are required at the silicon surface to bias the Si–H bond. This allows the fluorine ion to substitute a hydrogen atom (Fig. 24.1a). The substituted Si atom becomes more reactive and undergoes other substitutions (Fig. 24.1b–d) up to complete silicon dissolution (Fig. 24.1e).

In the case of an oxidized surface, it is believed that fluorine anions firstly remove the oxide, leaving a Si–H-terminated surface, followed by dissolution proceeding as described above.

This is a very general mechanism that does not account for many of the reactions actually encountered. Moreover, at large current densities, it has been proved that a nonnegligible contribution to the dissolution is due to anodic oxidation [24.16].

It is important to note that, during the reaction, hydrogen evolves (Fig. 24.1c) [24.17]. This process can strongly influence the final result of the etching. In fact, if hydrogen is not readily removed from the pores, it can form bubbles that stick onto the pore walls. The etch rate and pore structures are thus modified, and the properties of the resulting PS samples can differ from the expected ones.

PS is composed by a columnar array of silicon nanowires aligned along preferred crystalline directions

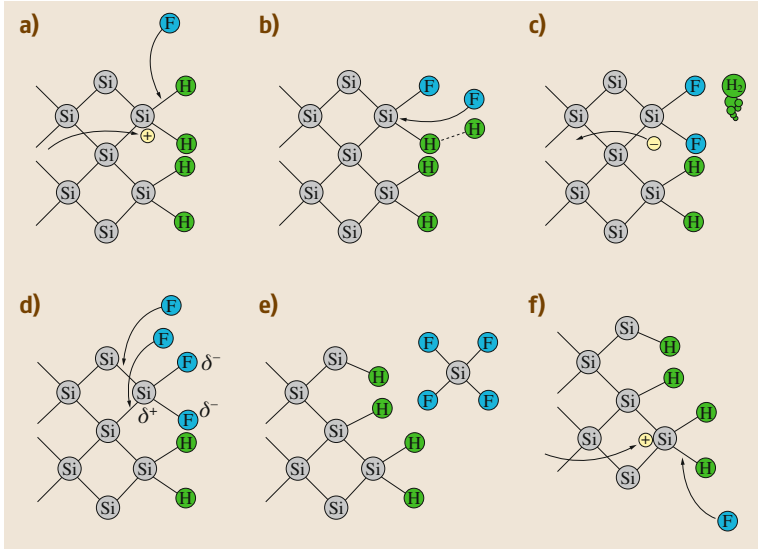


Fig. 24.1a–f Steps of a generalized chemical dissolution model. Silicon surface is assumed to be passivated by hydrogen. **(a)** Under proper bias holes diffuse from the bulk to the surface weakining the Si–H bonds, **(b)** fluoride ions substitute hydrogen atoms, **(c)** subsequent nucleophilic attacks produce hydrogen evolution and bring to the complete dissolution of Si superficial atoms **(d,e)**. **(f)** Similar reactions on different Si atoms gives rise to a complete dissolution

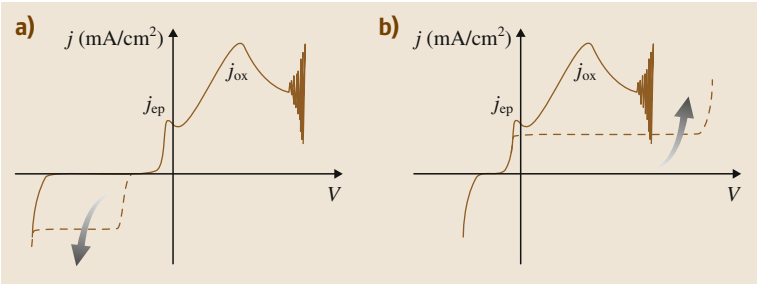


Fig. 24.2 **(a)** I–V curve for p-type silicon. The junction is forward biased. *Solid line* indicates the behavior in the dark. If the sample is illuminated the reverse current increases (*dashed line*). **(b)** n-Type silicon shows the behavior of a reverse biased junction. In the dark (*dashed curve*) the anodic current is determined by the doping level. If minority carriers are generated by illumination, the behavior is similar to the p-type case. *Black arrows* indicate the effect of increasing illumination

(generally ⟨100⟩, but also ⟨113⟩). Pore sizes from a few nanometers to tens of micrometers can be realized. Pore size varies in a complex way, depending on both the silicon doping content and etching conditions.

24.1.2 *I–V* Curves

Figure 24.2 shows the I–V curves for both p-type (Fig. 24.2a) and n-type (Fig. 24.2b) silicon substrates. The point where the current passes through zero is the open-circuit potential (OCP). The left side of the graphs shows the cathodic behavior, while at potential higher than the OCP, the curve indicates the anodic behavior, where the silicon can be oxidized and dissolved. Clearly these behaviors deviate from that of an ideal Schottky diode and are dominated by two current peaks (j_{ep} and j_{ox}). j_{ep} is called the electropolishing limit and indicates the maximum current that permits production of a porous structure. The exact position of this peak – in terms of both current and potential – strongly depends on the solvent composition and substrate type. Above j_{ep} the process proceeds in two steps: initially the electrode is oxidized, then the oxide is dissolved directly by HF (in this range, the dissolution valence changes from 2 to 4 [24.18]). This is the maximum current density that allows the formation of PS structures; in fact, etching performed using currents larger than j_{ep} produces complete dissolution of the Si. PS samples fabricated using currents near j_{ep} have extremely high porosity, and are extremely difficult to handle because of their fragility. Usually, such high-porosity PS samples require carefully controlled drying processes that minimize the stress induced in the porous sponge by solvent evaporation. In fact, the capillary pressure that develops during solvent evaporation is strong enough to collapse PS walls. The easiest way to achieve this result is to wash the sample in solvents with low surface tension (such as pentane or isopropyl alcohol), but in the case of extremely high-porosity layers, more complex approaches (such as supercritical drying) are sometimes required. Thus, fabrication of complex devices composed by multilayers requires currents well below this limit.

While in p-type substrates holes are the majority carriers, being readily available at the semiconductor–electrolyte interface, for n-type substrates they are the minority carriers and a surplus of carriers has to be generated by illuminating the backside of a biased sample. Absorbed photons generate electron–hole pairs that are separated by the sample bias and driven towards the interfaces.

24.1.3 Porous Silicon Formation Mechanisms

The formation of nanoporous silicon (with length scales in the range of a few nanometers) is considered a quantum phenomenon and does not depend on the type (i. e., doping or crystal orientation) of the substrate [24.19]. Meso- and macroporous structures show much richer behavior, and both silicon type and etching conditions determine the final porous structure. Here, we review the most important models that try to describe PS formation.

In all cases the growth of a stable PS layer requires that the dissolution takes place at the interface between PS and bulk silicon. In other words, the process is self-limiting, and the already formed PS layer is inert to HF etching (or, at least, must dissolve at a much slower rate). This assumption is experimentally confirmed and is supported by the fact that Si nanostruc-

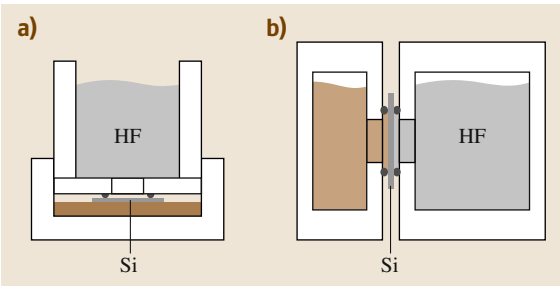


Fig. 24.3a,b Common geometries for PS electrochemical cells. **(a)** The most common case. The sample backside is in contact with a metallic electrode, while a platinum working electrode immersed in HF solution closes the circuit. **(b)** Double liquid contact. The sample is sealed between two cells: one filled with HF, and the other with a conductive liquid solution

tures are depleted of carriers and thus cannot contribute to electrochemical etching.

The first model to try to describe such porous structures postulated the presence of a space-charge region (SCR) parallel to the silicon–electrolyte interface [24.20, 21]. This SCR layer prevents anodic dissolution of the already formed porous layer, because the walls in between adjacent holes are completely depleted of carriers. Due to the reduced radius of curvature and the enhanced electric field, the SCR thickness is strongly reduced at the pore tip. The resultant field distribution induces strong anisotropy in the etching, and pores with extremely high aspect ratio can be realized [24.22]. The main difference between *p*- and *n*-type substrates lies in the fact that, in *p*-type Si, the holes are the majority carriers, while in *n*-type Si, they either have to be generated by suitable illumination or forced to flow by exploiting breakdown mechanisms that permit hole tunneling through the SCR. This model describes the types of structures realized in low-doped substrates, but fails to describes many other cases where the SCR model does not apply; For example, the SCR model cannot explain why pores grow along well-defined crystal directions, nor the complex dependence on I–V conditions required to obtain the same pore modulation at different length scales (which is not linear, as would be predicted by the SCR model) [24.23].

More recently, the so-called current burst model was presented [24.24, 25]. In this scheme, the silicon dissolution proceeds through a stochastic mechanism that includes various concurrent processes: spatially localized oxide formation and oxide etching together with oscillating current bursts that start on these oxide bumps depending on the etching conditions [24.26, 27]. This model is able to semiquantitatively describe all the possible PS structures and can be used to recover simplified models such as the SCR and the *Lehmann formula* [24.18]. More in-depth reviews about PS formation models can be found in [24.28, 29].

The PS growth rate is heavily dependent on both silicon properties and etching conditions. Etch rates can range from a few Å/s [24.30] to hundreds of nm/s [24.31]. *p*-Type Si shows an etch rate that is linearly dependent on both HF concentration and current density, whereas *n*-type Si is linear only under proper illumination. Sublinear conditions are found if etched in the dark and for high current density, because the reaction is limited by hole diffusion. More data can be found in [24.32].

It is worth underlining that there is not a simple model able to comprehensively describe PS etching, thus each PS study and application has to be carefully optimized by checking the existing literature and, eventually, optimizing the method to achieve the desired results.

PS is usually etched in electrochemical cells made of plastic materials (such as Teflon or polyvinylchloride (PVC)). Two main geometries are encountered, as sketched in Fig. 24.3. In the simplest case, the backside of the sample is in contact with a metallic electrode, while a platinum working electrode immersed in HF solution closes the circuit. The other cell type is composed by a double liquid contact. Here the sample is sealed between two cells: one filled with HF, and the other with a conductive liquid solution.

24.2 Other Etching Methods

PS can also be obtained under nonanodic conditions. In particular, three methods have been explored so far and are briefly described here. The first method is called *stain etching* and was developed during the mid 1980s. Stain etching is based on the OCP and addition of oxidant species to produce an autocatalytic effect. Typical etching solutions are composed by a HF/H_2O/HNO_3 mixture (although other oxidants

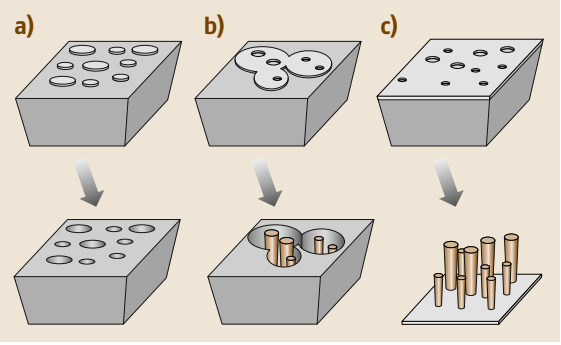


Fig. 24.4a–c Schematic of typical structures achievable by metal-assisted Si etching. **(a)** Isolated metal dots produce a porous structure similar to that obtained by using anodic etching. **(b)** By increasing the metal coverage on the Si surface, both pores and Si pillars can be obtained. **(c)** Under proper values of metal coverage, columnar structures can be etched

have also been proposed in the literature). PS dissolution proceeds following the formation of both localized anodic and cathodic regions on the surface of PS. Some reaction mechanisms have been proposed, based on HNO_3 reduction [24.33]. This reaction requires an incubation time that depends on both the solution composition and Si doping concentration [24.34]. Because of the random nucleation of surface-active sites, porous structures produced by this method are neither spatially homogeneous nor applicable for fabrication of complex structures (e.g., no pore modulation is possible). Nevertheless, considering its simplicity, stain etching can be used in niche research applications to study effects related to patterned surfaces [24.35].

A second nonanodic method to fabricate PS relies on the use of a metal catalyst. A noncontinuous metal film deposited on the Si surface acts as a cathode and promotes strongly enhanced Si dissolution in the regions covered by the metal itself [24.36, 37]. Thus, the pore size, shape, and density can be defined by the deposition of an appropriately structured metal layer, as shown in Fig. 24.4. A comprehensive review of this method can be found in [24.38].

Finally, the third nonelectrochemical method to obtain PS is based on reactive-ion etching (RIE) to form so-called *black silicon* (BS). BS was discovered in the mid 1980s as an unwanted side-effect of Si RIE processes [24.39]. Essentially, if RIE conditions are properly controlled, the competitive reactions of Si etching and passivation can be promoted or inhibited to give rise to either perfect Si etching (the so-called vertical-walls regime) or the creation of Si needles that resemble a porous structure. Recently, an interesting application of PS etched in the BS regime was proposed for photovoltaic applications [24.40]. In fact, a PS multilayer etched to form BS was found to have a very low reflection coefficient over a wide spectral range (3000–300 nm) and could be of interest for enhancing the efficiency of Si-based photovoltaic devices.

24.3 Porous Silicon Structural Properties

PS can have characteristic length scales ranging from a few nanometers to tens of micrometers in a nearly continuous way [24.41]. As a rule of thumb, larger macropores are obtained in low-doped substrates and concentrated HF solutions [24.42, 43], although many exceptions can be found in the literature.

While etching in alkaline solutions is highly anisotropic and strongly dependent on crystal orientation, HF shows very weak dependence of etch rate on silicon orientation and is considered to be an isotropic etchant. The strong etching anisotropy found in meso- and macropore formation is due to the different rates at which holes reach the solid–liquid interface along different crystalline directions. In fact, after nucleation of a pore site, the establishment of a SCR produces an increase of the etch rate along the ⟨100⟩ direction. If side-pores nucleate along a direction different from ⟨100⟩, they grow at a rate

$$v_{sp} \propto i_{sp} \cos\delta \,, \tag{24.1}$$

where v_{sp} is the speed of growth, i_{sp} is the current at the side-pore tip ($i_{sp} \ll i_{MP}$, where i_{MP} is the flux of holes that reach the bottom of the main pore), and δ is the angle between the [100] direction and the side-pore growth direction (Fig. 24.5). This means that the growth rate of side-pores is lower, because a small current of holes reaches their surface and because their growth direction is not parallel to the carrier flux. The main pore grows faster and efficiently collects the majority of the carriers. The net effect is increased spacing between the tips of pores growing along [100] and termination of lateral ones.

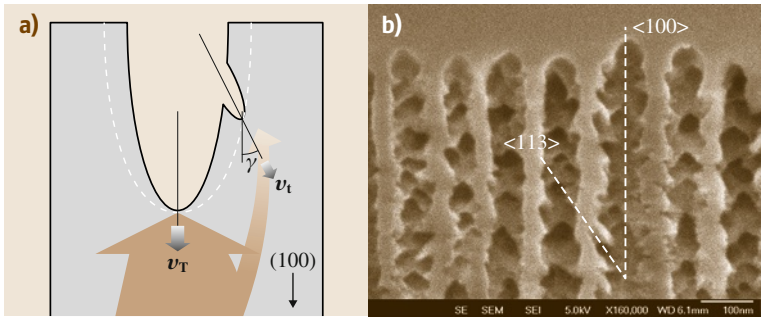


Fig. 24.5a,b The anisotropic PS formation mechanism is due to the different hole currents that reach the pore tips. **(a)** Pores parallel to the (100) direction collect carriers more efficiently. Side-pores are etched at slower speed because of this shielding effect. Moreover, their oblique growing direction moves these side-pores away from the bottom interface, meaning that they collect even fewer holes. Finally, they cease to grow. **(b)** SEM image showing an example of side-pore growth. The angle between the pore growth directions is 54°, corresponding to the angle between the ⟨100⟩ and ⟨113⟩ crystalline directions

This simplified model works well with large (> μm) macropores, which grow only perpendicular to the sample surface. Instead, submicrometer pores can be forced to grow preferentially along oblique directions. However, under such conditions, branching occurs and three-dimensional PS structures are realized. The final PS structure is heavily dependent on the details of the etching conditions. Nevertheless, oblique pores preferentially grow along [100], [113], and [110] directions [24.44, 45], whereas the interface between the PS layer and the bulk silicon is always parallel to the contact electrode.

During the initial etching time, a thin transition layer develops. In this layer, pores do not grow in a steady-state regime and with a regular structure, rather trying to arrange themselves to form a porous structure compatible with the etching conditions. The very first layer is homogeneously etched away, leaving a rough surface. Here pores start to grow. Generally, there are more nucleation sites than allowed by the etching conditions, and most of these initial pores stop growing after some tens of nanometers. Holes are thus collected by neighboring pores, which increase their size and define the correct PS structure (Fig. 24.6).

For this reason the size of the pores at the surface is generally smaller than that of the bulk pores, and estimates of pore size and density obtained by electron microscopy surface images can give incorrect results.

One of the main differences between *p*- and *n*-type silicon is the reduced anisotropy of the etching process in *p*-type substrates. In fact, the high concentration of holes in *p*-doped semiconductor favors chemical etching (corrosion process) and induces substantial lateral enlargement of pore size during etching. Experimentally it was found that this problem can be greatly reduced by using an aprotic solvent (such as DMF and DMSO) [24.46]. By using such a solvent, it is possible to obtain high-aspect-ratio porous samples also in *p*-type substrates.

Macroporous silicon usually has pore shapes from round to square-like with rounded edges. On *n*-type substrates, the pores are generally more rounded, while on *p*-type, due to the reduced anisotropy of the etching mechanism, complex-shaped structures can be realized starting from a simple geometrical pattern [24.47].

Etching of an unstructured silicon sample produces a random pore size distribution. Given a certain resistivity of the sample, pore sizes can be tuned within

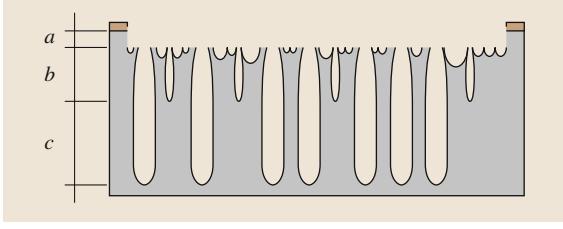


Fig. 24.6 The first superficial layer of a PS sample has a pore distribution that markedly differs from that representing the steady growth condition. This thin layer reflects the high density of nucleation sites. Most of these pores stop growing after a few tens of nanometers, and the carriers are collected by neighboring pores that increase in size. (a) A thin superficial layer is completely etched away during the PS formation, (b) transition layer, (c) steady-state pore growth region

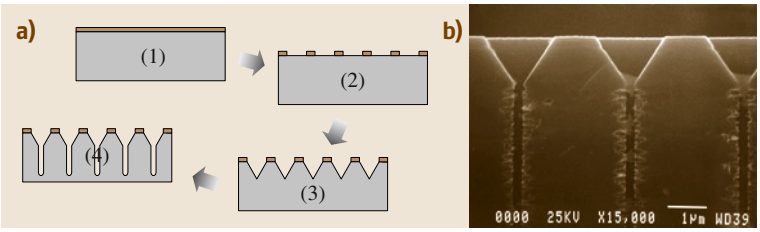


Fig. 24.7 (a) Flowchart of the process steps required to induce a predetermined pore array geometry: (1) deposition of a dielectric mask resistant to HF etching, (2) lithographic step to open the mask and expose the required silicon area, (3) etch pit definition, usually achieved by wet anisotropic chemical etching of the underlying silicon (using KOH or TMAH), (4) the lithographed pattern is finally transferred into the silicon substrate by electrochemical etching. (b) SEM image demonstrating the efficiency of the etch pits in the definition of the pore nucleation sites. With proper etching conditions, high-aspect-ratio submicrometer pore sizes can be obtained even in lattices with much larger periods

a certain range to obtain growth of regular pores but with different sizes. There are no rules to predict the size of this tunable range, because it is strongly dependent on the interplay of required pore sizes, etching conditions, and sample resistivity.

Porous samples with ordered pore geometry are obtained by inducing a surface structure that defines the pore site nucleation. Figure 24.7 illustrates this process:

1. A dielectric mask (usually SiO_2 or Si_3N_4) is deposited on top of the silicon sample.
2. A lithographic step is used to define the required geometrical lattice that has to be transferred into the silicon.
3. After the opening of the mask, alkaline silicon etching (generally using KOH or tetramethylammonium hydroxide (TMAH)) is used to form etch pits.
4. The tips of these inverted pyramids act as pore nucleation sites because the SCR at these tips is greatly reduced and the etching proceeds much faster at the bottom of the etch pits, starting an anisotropic etching mechanism.

Other processes can be used to determine the area to be porosified; For example, different etching properties resulting from silicon illumination can be used to spatially localize the area where PS is to growth. Also, localized ion implantation can be used to change the substrate resistivity and exploit the different etching properties of those localized areas.

It is important to remember that the final PS structure depends in a nontrivial way on all the etching parameters used during its formation. Only a few general rules are generally verified; in particular, the pore size and growth rate increase with both current density and HF concentration. However, fine-tuning of many critical parameters (pore density, PS porosity, pore separation, surface pore roughness, etc.) has to be determined based on the actual etching conditions and cannot be easily extrapolated from literature data.

Nevertheless, the two general trends underlined above make PS a very interesting material because of the possibility to etch high-quality nanoporous multilayered structures using a fast and easy method. In fact, as described in more detail in Sect. 24.7.2, if the current is modulated during etching, highly complex porosity profiles can be achieved, while maintaining optical-quality interfaces between each layer. Thus, Si electrochemistry is a unique method for fabrication of high-quality multilayers, and no other deposition method can compete with it for the fabrication of complex porous structures. One of the most striking features of Si electrochemical etching is its self-limiting property: once a PS layer is formed, electrochemical etching proceeds only at the interface between PS and the underlying, unetched bulk Si. The already porosified layers are not affected by the electrochemical etching. This is because the porous layer is depleted of carriers and electrochemical etching cannot proceed further (although, during the fabrication of complex samples composed by hundreds of layers, the slow, direct chemical etching of silicon by HF has to be taken into account and compensated for).

Crystallographic analysis has shown that Si preserves its crystalline nature even in nanoPS, where the solid scaffold is composed by an interconnected network of Si wires [24.48, 49]. After anodization, PS retains its crystalline structure with a small lattice expansion (of the order of 10^{-3}–10^{-4}). The PS surface achieves values from a few tens of m^2/cm^3 for macroporous samples up to nearly $600\,m^2/cm^3$ [24.50].

24.4 Light Emission from Porous Silicon

Nanoporous Si attracted much attention after the discovery of its efficient light emission under ultraviolet (UV) illumination. Since this discovery, a huge number of works tried to describe the origin of the luminescence, and different models were proposed (e.g., the hydrogenated amorphous silicon model [24.51], surface states model [24.52], surface hydrides model [24.53], defect models [24.54], and siloxene model [24.55]).

Spectroscopic analysis shows that both the valence-band maximum and the conduction-band minimum shift with respect to bulk crystalline Si, enlarging the material bandgap [24.56, 57]. Different models have been proposed to try to describe the origin of the luminescence. The quantum confinement model was the first proposed to describe the origin of the luminescence and is today well accepted as the most probable mechanism. Light emission originates from the extremely small nanocrystals (a few nanometers in size), where quantum effects enlarge the bandgap of the silicon nanocrystals (Si-nc), shifting the optical transitions towards the visible part of the spectrum. The reliability of the quantum confinement model is supported by its ability to describe a number of experimental facts, such as the relaxation of the momentum-conservation rules and the photoluminescence (PL) shift depending on the size of the PS nanostructures [24.58–61].

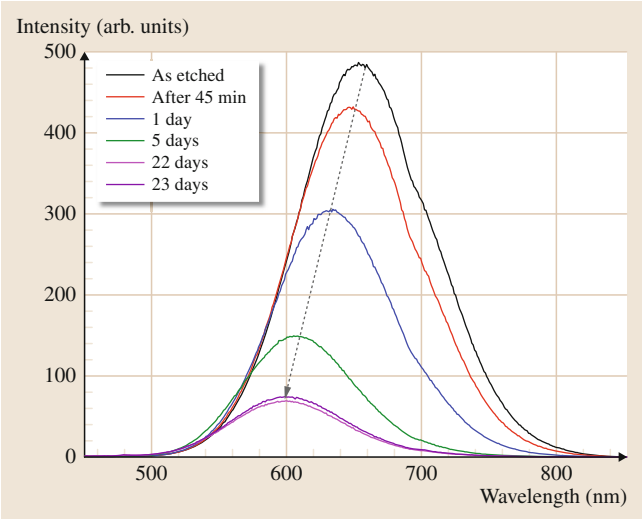


Fig. 24.8 PL spectra of Si nanocrystals obtained by sonication of PS. The typical PS PL red band shows a marked intensity decrease together with a blue-shift (emphasized by the *gray dotted arrow*). Both processes can be ascribed to surface oxidation of Si nanoparticles (data courtesy of Dr. E. Froner)

One of the most interesting features of PS is the tunability of its light emission [24.62]. The current density used for sample preparation directly affects the size of the silicon nanostructures and, consequently, their optical properties. Higher currents produce layers with greater porosity, smaller Si nanostructures, and thus blue-shifted PL emission. The energy of the emitted photons is directly linked to the Si-nc size and clearly shows a spectral shift of the emission that can be modeled by quantum confinement (blue-shift for smaller Si crystallites). Figure 24.8 shows a typical PL band of a PS sample. In this case, the PL sponge was sonicated in an ultrasonic bath, and the obtained nanocrystals were dispersed in liquid. The PL properties were monitored over time for many days. Sample aging produces a strong reduction of the emission intensity and a blue-shift of the PL peak. Both of these facts can be ascribed to surface oxidation of Si nanoparticles. Thus, light emitted from nanoPS can be tuned from the near-infrared (corresponding to the bulk Si bandgap of 1.1 eV) to the green and, in some cases, the blue part of the visible spectrum. These emissions are found to be generated by different mechanisms [24.63–66], as demonstrated also by the fact that the lifetimes of excited states differ by orders of magnitude [24.67]. The most interesting emission band is the so-called S-band, which covers roughly all the visible spectrum and is the only one that can be excited in electroluminescence experiments. This emission has a rather large bandwidth due to inhomogeneous broadening that arises from the wide size distribution of the Si-nc composing the nanoPS. Its center of mass depends on the porosity, while its intensity shows a threshold-like behavior, and it is recognized that a minimum porosity has to be achieved for efficient light emission to appear [24.68]. External quantum efficiency (EQE) values up to a few percent have been reported in the literature in as-etched samples [24.69, 70]. Spectroscopic analysis suggests that the light emission mechanism in nanoPS is the same as for bulk semiconductor, apart from an energy shift of the optical transitions due to quantum confinement effects [24.67].

It is worth remembering that PS is an extremely complex system, and its light emission depends on

the details of the fabrication process and sample history. The optical properties of PS show dependence on sample aging and sample posttreatment (e.g., surface stabilization process, controlled surface oxidation, etc.); For example, in properly stabilized samples, EQE greater than 20% has been reported [24.71].

24.5 Thermal and Electrical Properties

Electrical transport in PS was a matter of intense investigation during the 1990s, but its deep nature remains unclear. A number of models have been proposed, differing in both transport path and mechanism [24.72–75].

Because of carrier depletion, the resistivity of PS is nearly five orders of magnitude higher than that of intrinsic silicon. This high resistivity can be due either to bandgap enlargement and consequently to a reduced probability of thermal activation of carriers or to a high concentration of trap states (with activation energy on the order of 0.5 eV [24.76]). The deep origin of the transport mechanisms remains unclear, and both PS preparation conditions and temperature determine which model better describes the carrier transport [24.77]. Characterization of PS–metal diodes demonstrated the existence of two junctions: one at the metal–PS interface, and a second one at the PS–bulk Si interface. Moreover, the I–V curves mainly depend on the Si bulk properties and not on the type of metal [24.78, 79].

A number of works have tried to elucidate the electrical conduction mechanisms by analyzing PS conduction in alternating-current (AC) conditions. A more in-depth review of these arguments can be found in [24.80].

Because of its structure, PS possesses very low thermal conductivity (two to three orders of magnitude smaller than that of bulk Si) that is inversely proportional to the PS porosity (from $\approx 1\,\mathrm{W(m\,K)^{-1}}$ for 40–60% down to $\approx 0.04\,\mathrm{W(m\,K)^{-1}}$ for 90% porosity [24.81]), thus opening new perspectives in the field of thermal insulation of microsystems; For example, a PS layer was used in the fabrication of a complementary metal–oxide-semiconductor (CMOS)-compatible thermopile with high sensitivity [24.82].

It is of interest to note that the possibility of controlling the PS structure from nanometer up to micrometer scale enables the use of PS in the fabrication of phononic crystals, i. e., periodic structures able to control phonon propagation and thus the flow of thermal energy [24.83, 84]. Phononic crystals are a rather new research field, and advanced PS applications in thermal insulation and thermoelectrics should be expected in the coming years.

24.6 The Role of the Surface

The (chemical, optical, mechanical, and electronic) properties of porous silicon depend strongly on the state of its surface. The surface of as-etched PS is covered by Si−H bonds. Silicon hydrides are not stable under environmental conditions and are gradually substituted by other types of bonds; in particular, the PS surface is oxidized when exposed to air, and a thin layer of silicon oxide grows over time and stabilizes the PS surface [24.80].

Aging of PS luminescent samples is a well-known effect: after etching, the Si surface is passivated by Si−H bonds, which tend to be substituted by more stable Si−O bonds in ambient air at room temperature. As shown in Fig. 24.8, the photoluminescence band blueshifts, due to a decrease of the Si-nc size because of their conversion into a silicon oxide layer that passivates the PS surface [24.85].

Stabilization methods are of great importance, not only for the electrooptical properties of PS, but also for its application in (bio)sensing and even in passive optical devices. Many attempts have been made to stabilize the PS surface to either improve its optical properties or stabilize them.

Three main surface stabilization techniques have been developed and can be classified as follows: oxidation, hydrosilylation, and thermal carbonization.

Native oxide takes a long time to form, and it is difficult to control the extent of the reaction. Rather, faster and highly controlled oxidation can be induced either electrochemically [24.67] or thermally [24.86].

The thermal method is the most common, because of its better control over the oxide properties and extent of oxidation. Moreover, thermal oxide generally has better electrical properties than anodic oxide [24.15]. PS oxidizes even at 300 °C (backbone oxidation [24.87]). The degree of oxidation depends on the initial PS conditions (porosity) and oxidation conditions (process duration, temperature, and atmosphere composition). At higher temperatures, oxidation proceeds faster and to a more complete extent. The volume expansion subsequent to oxide formation reduces the PS porosity: too strong an oxidation process, performed at high temperature or for a long time, could lead to PS sintering and the formation of nonporous glass.

Recently, an extremely efficient method was proposed to achieve very good control over surface stabilization, being based on high-pressure water vapor annealing [24.88, 89]: the PS is placed in a pressure-resistant container and heated to 150–300 °C. Using this method, the luminescence properties of PS are strongly enhanced and stabilized. In fact, samples stabilized using this method show the highest external quantum efficiency ever reported for PS samples [24.71].

It is of importance to note that PS oxidation greatly modifies the surface wettability from hydrophobic to hydrophilic. Control over surface wetting properties is of fundamental importance for many PS applications.

Apart from pure oxidation methods, other thermal treatments have been investigated. In particular, we briefly describe two recently proposed methods to modify PS and increase its stability. The first process is based on thermal carbonization of PS surface by thermal treatment in acetylene atmosphere [24.90]. Thermally carbonized PS shows increased chemical resistance in hazardous environments (such as KOH and even HF/ethanol solutions) [24.91]. Two main drawbacks of thermal carbonization are: the complete quenching of the PS luminescence properties, and its CMOS incompatibility.

The second method relies on PS surface nitridation performed by a rapid thermal annealing process [24.92, 93]: PS samples are annealed for a few minutes at 600 °C in N_2 atmosphere. A great advantage of this method compared with the other thermal treatment is the fact that the refractive index of the PS is left unchanged, so that the optical properties of multilayer structures are preserved.

Other methods of PS surface passivation use pure chemical reactions that either substitute the hydride surface terminations with Si−C bonds (hydrosilylation reaction) or directly functionalize the oxidized PS surface. A number of research groups are working on this topic to develop different reaction mechanisms. The most common are based on hydrosilylation mediated by either light or Lewis acid [24.94, 95]; recent bibliography on this topic can be found in [24.96].

These methods enable the attachment of a number of organic substituents that endow the PS surface with specific functional reactivity. Moreover, while a PS surface oxide layer induces strong modification of the optoelectronic properties, a thin monolayer of organic molecules has a much lesser effect, while retaining a good surface passivation function. For these reasons, chemical methods are very attractive if PS is to be used as a sensing medium or in biorelated experiments.

24.7 Applications of Porous Silicon

24.7.1 Porous Silicon Light-Emitting Diodes

It is known that a Si *p–n* junction emits light under both forward- and reverse-bias conditions. The first and most encouraging results on PS-based light-emitting diodes (LEDs) were obtained using liquid electrodes to contact the device [24.97,98]. Luminescence originates from an electrochemical reaction at the surface of PS: free carriers are injected either from the PS to the electrolyte or in the opposite direction, depending on whether oxidation or reduction processes are involved. In the former case, the electroluminescence (EL) decreases with time because of the increasing thickness of the oxide layer on the Si surface [24.99], while if reduction is considered, no PS oxidation take place and the EL does not degrade with time [24.97]. The use of a liquid junction poses strong limitations on real applications, and alternative solutions have been investigated.

The simplest solid contacts were deposited on PS using thin metal layers [24.100] or transparent semiconductor materials [24.101]. Because of the poor contact between PS and conductor materials, high turn-on voltages (≈ 10 V) and low efficiency ($\approx 10^{-5}$) were found. Improved EL was achieved in metal-implanted PS samples [24.102, 103] and in devices that make use of conductive polymer electrodes [24.104–106]. In

fact, polymers deposited by spinning or electrochemical growth on PS permeate through the pores and produce a better electrical contact.

A different approach relies on the use of heterojunctions composed by a crystalline semiconductor and PS [24.107, 108]. High-efficiency devices have also been fabricated using amorphous silicon ($\eta \simeq 0.1\%$ and voltage-tunable spectra also obtained) [24.109] and silicon carbide [24.110].

Improved light emission efficiency from PS-based LEDs was also achieved by fabrication of optical cavities (see Sect. 24.7.2 for more details) [24.111]. To be appealing in real applications, PS LEDs must be realized by a fully CMOS-compatible fabrication process. This is a complex task, because the fragile porous structures have to be preserved during all the fabrication steps that lead to the realization of the final device. A lot of effort has been invested to try to optimize the process flowchart, and some applications have been demonstrated [24.112, 113].

24.7.2 Porous Silicon–Based Photonic Crystals

The most widely exploited use of PS is in the fabrication of photonic crystals (PCs). PCs are a broad class of passive optical devices based on interferometric or diffractive filters. The properties of Si electrochemical etching (strong anisotropy and self-limitation) together with the physical properties of bulk Si (high refractive index, and transparency in the range 1500–1600 nm, the so-called third telecommunication window) make PS an ideal material to develop high-quality photonic structures. Moreover, Si is the leading material in electronics, thus the development of PS optical devices compatible with CMOS technology will boost their implementation in the development of next-generation optoelectronic integrated devices.

PCs are composed by dielectrics structured over a length scale comparable to the wavelength with which they have to interact. Often, they are composed by periodic patterns, and their optical properties can be described by a band structure model, very similar to the one used to describe electrons in an atomic potential [24.114]: in a semiconductor, the periodic potential is defined by the atomic lattice, whereas in a PC it is the periodicity of the material dielectric function that defines an *effective* potential for photons. Here, we review only the fundamental characteristics that make PCs of interest for optical applications and that are of interest to describe PCs fabricated in PS.

Light propagation into structured material is heavily modified by diffraction phenomena, and photons impinging on the material are allowed to propagate only if their energy falls within permitted bands. In some cases, two bands are separated by a forbidden energy range where photons cannot propagate (so-called bandgaps).

The bandgap can be of different dimensionality depending on the number of directions in which the material is structured: periodicity along one dimension (a multilayer filter) forbids photon propagation only along the direction perpendicular to the periodicity itself. Bandgaps in two-dimensional (2-D) periodical systems can extend over a plane, while three-dimensional (3-D) periodicity (e.g., in opals) can forbid light propagation in all directions (light trapping).

The analogy with the semiconductor band diagram can be extended to the description of defect states: a defect in a semiconductor lattice is formed when an impurity breaks the atomic lattice periodicity. In PCs, a defect is an element that breaks the dielectric lattice periodicity. Defect states are highly localized in space and show a flat band, highly delocalized in k-space.

Photonic band dispersion is used to exploit another interesting phenomenon: the speed of light in a homogeneous dielectric medium scales with the material refractive index ($v = c/n$, where v and c are, respectively, the speed of light in the medium and in vacuum and n is the material refractive index). On a band diagram, the speed (group velocity) of light propagating through the material is represented by the first derivative of the band dispersion ($v_g = \partial\omega/\partial\boldsymbol{k}$, where ω is the frequency of the photonic mode and $\boldsymbol{k}$ is the wave vector). Thus, the minimum and maximum points are regions of slow light propagation. Also, defects with flat-band dispersion describe a narrow energy range of slow propagation speed. This slow-light regime is of extreme interest because of the prolonged interaction time between photons and matter (e.g., being used to enhance optical nonlinearity).

One-Dimensional Photonic Crystals

One-dimensional (1-D) PCs (1-DPCs) are filters composed by multilayered structures (also called a distributed Bragg mirror, DBR). Their use as antireflection coatings was discovered well before the development of PC theory [24.115]. The simplest multilayer filter is composed by two alternating materials with optimized refractive indexes and physical thicknesses. Without entering into details that can be found elsewhere [24.116], we describe here the basic equations that rule the optical response of the most common configuration. In fact, the

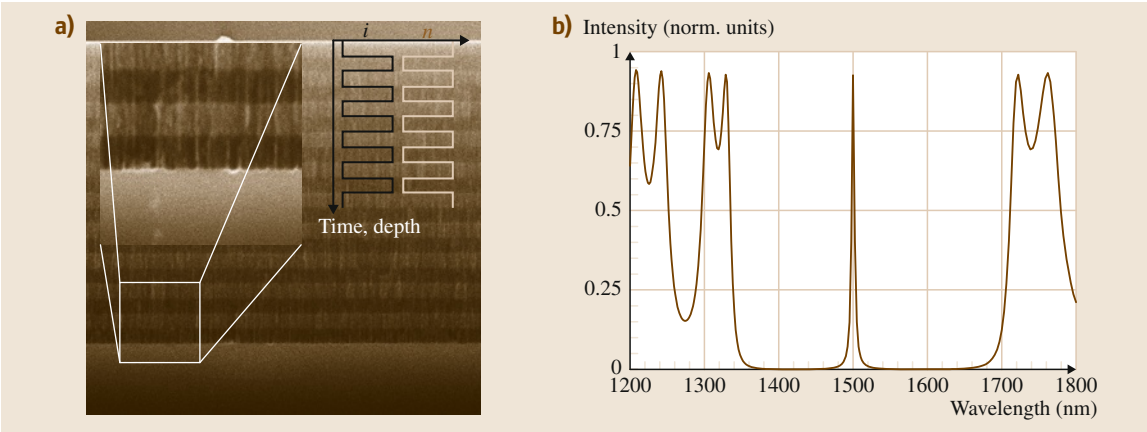


Fig. 24.9 (a) SEM cross-section of a PS multilayer. *Bright* and *dark layers* indicate low- and high-porosity layers, respectively. The *inset* is a zoomed view of the bottom layers that outlines single pores. The *superimposed graph* is a pictorial view of the modulated current profile used to etch the sample (*black line*) and of the corresponding refractive index profile (*white line*). (b) Transmission spectra of a similar structure simulated using a transfer-matrix code. The narrow peak at the *center* of the spectra is due to the insertion of a defect that breaks the periodicity of the porous lattice

width of the high-reflectivity stop band is maximized if the layer thicknesses satisfy the $\lambda/4n$ condition. The reflectivity (R) response will be centered at λ and depends on the number of periods

$$R = \left(\frac{1 - (n_H/n_L)^{2m} \left(n_H^2/n_s\right)}{1 + \leq (n_H/n_L)^{2m} \left(n_H^2/n_s\right)} \right), \qquad (24.2)$$

where n is the refractive index of the layer, m is the number of layer and subscripts H, L and s refer, respectively, to the high, low and substrate surrounding the filter and $2N$ is the number of periods. The stop-band width ($\Delta\omega$) is proportional to the refractive index contrast between the layers and is equal to

$$\Delta\omega = \omega \frac{4}{\pi} \arcsin\left(\frac{n_H - n_L}{n_H + n_L} \right) . \qquad (24.3)$$

These 1-D PCs can be fabricated using deposition processes (such as chemical vapor deposition (CVD), physical vapor deposition (PVD)-like, or coating techniques). However, these methods require complex facilities and long deposition times to obtain a few tens of layers. In PS, such filters can be fabricated in a few minutes, obtaining samples with extremely high optical quality. In fact, the proportionality between the etching current and the refractive index exhibited by nanoPS is used to transfer a periodical current profile into a periodic refractive index variation of the PS. After characterization of the etching rates (which are usually on the order of μm/min) and of the layer porosity, it is possible to design a DBR with the required optical response.

High-quality PCs require each layer to be modeled as a homogeneous material, thus the pore size should be much smaller than the wavelength. Considering a realistic case of a PS DBR with a stop band centered between 800 and 1500 nm, a single DBR layer has a thickness of less than 200 nm. Only nanoPS satisfies these requirements and can be used to realize high-quality 1-D PCs for the visible/near-infrared (NIR) range.

The electrochemical etching method allows the possibility to continuously tune the refractive index of the layer from that of bulk silicon down to the value of 1.3 of an extremely high-porosity layer. Nevertheless, this wide range cannot be used for fabrication of complex multilayer structures composed by tens of layers. In fact, a layer of extremely low porosity acts as a diffusion barrier for the HF solution, so that the concentration of HF changes with sample depth, as does the porosity. Moreover, extremely high-porosity layers have poor mechanical stability and have to be handled with great care: even the solvent drying and the capillary pressure developed can collapse the porous sponge. As a rule of thumb, indexes between 1.5 and 2.5 permit etching of complex filters made up of some tens of layers.

A critical parameter that determines the optical quality of a PC is the flatness of the interfaces. To minimize the roughness of these regions, good ohmic contact between the wafer and the backside electrode has to be established. The back of the wafer is usually im-

planted at high doses (on the order of 10^{19} atoms/cm^3) followed by deposition of a thick aluminum layer.

Scanning electron microscopy (SEM) cross-section imaging of a multilayered PS sample is shown in Fig. 24.9a, while Fig. 24.9b shows a simulation obtained by a transfer-matrix code for a similar structure but with a defect layer (cavity) added. As also described below, by breaking the periodicity of an otherwise perfect lattice, photonic states are allowed inside the bandgap.

PS 1-D PCs with extremely complex structures have been fabricated, permitting analysis of complex optical phenomena; For example, PS DBRs have demonstrated the optical analog of Bloch oscillations [24.117], light localization, and necklace states [24.118].

Higher-Dimensional Photonic Crystals

2-D PCs can be realized in macroPS. The lattice geometry is defined prior to the etching by a lithographic step as previously described. MacroPS is an ideal system to study the optical properties of PCs; in fact, it can exploit both the high Si refractive index and the very high aspect ratio of the macroPS pores that permits the fabrication of nearly ideal 2-D PCs [24.119]. Figure 24.10 shows two examples of macroPS. Both samples initially had the same filling factor. In the triangular sample, the pore size was enlarged after etching by applying a few cycles of thermal oxidation and oxide removal. Lattice parameters from micrometers [24.120] down to the submicrometer range [24.121] have been demonstrated in the literature. In general, large and smooth pores are easily etched in low-doped substrates, and for fixed lattice constant, a certain flexibility in pore size can be achieved by modifying the etching parameters. Reduction of the lattice parameter to the (sub)micrometer scale is required to obtain a bandgap of 1.55 μm, which is of great interest for integrated photonics.

The fabrication of high-quality PCs becomes extremely difficult with the shrinkage of the pore size. This is because some effects occur to reduce the quality of the etched structures. A first important parameter to control is the surface pore roughness, to avoid unwanted scattering effects. While on large macropores the effect of roughness can be neglected (a smooth pore has a surface roughness on the order of a few nanometers), it becomes of greater importance for small, submicrometer-size pores. Moreover, etching parameters that allow etching of smooth, submicrometer pores have to be carefully controlled and show strong dependence on substrate type and doping concentration. Thus, great control over the substrate used is also required [24.121]. Only a few experimental results demonstrating the achievement of the control over etching required to fabricate silicon-based PCs for applications in the 1.55 μm range have been published [24.122, 123].

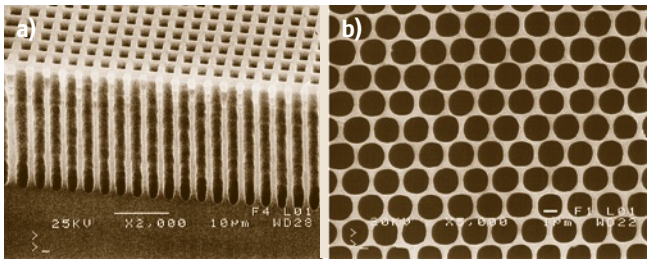


Fig. 24.10 **(a)** Bird's-eye view of a macroPS sample with square symmetry (*scale bar*: 10 μm). **(b)** SEM top view of a triangular lattice of pores (*scale bar*: 1 μm)

Larger macropores with a bandgap in the mid- to far-IR range (pore diameter > μm) do not require such highly controlled etching conditions. Moreover, once the lattice geometry is fixed, the pore diameter can be adjusted by modifying the solvent concentration or etching current. One-dimensional PCs made of nanoPS do not suffer from those limitations, because the nanopores are much smaller than the wavelength and behave as an effective medium. The intermediate regime, which is the most interesting for applied integrated photonics, requires good knowledge of silicon electrochemistry and long optimization processes.

Three-dimensional PCs are the most intriguing structures: ideally they are able to localize a photon inside a tiny volume and keep it for a long time. Their realization is a formidable task, and, excluding opals, only a few other examples have been proposed in the literature. Generally, all of them are fabricated using state-of-the-art nanofabrication technologies. The first Si-based 3-D PC was the so-called *yablonovite* and did not rely on an electrochemical process. Instead, it was realized using a focused ion beam technique to etch holes with the proper orientation into bulk silicon. Yablonovite was the first structure to demonstrate the realization of a high-quality 3-D PC with a bandgap in a wavelength range compatible with integrated optics applications. Some years later, the so-called *woodpile* structure was proposed and fabricated. This PC is composed by alternate layers of silicon sticks, each rotated by 90° with respect to the previous one [24.124]. While yablonovite shows a complete three-dimensional bandgap (no photonic states are allowed along any direction), the woodpile bandgap is limited to some spatial directions, and it is thus not able to confine photons completely in 3-D space.

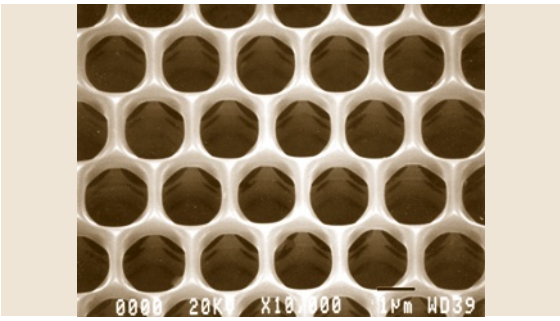


Fig. 24.11 SEM image of a 3-D macroPS sample: holes interconnecting adjacent pores can be seen on the *vertical pore walls* (*scale bar*: 1 μm)

The fabrication of a 3-D PC by an electrochemical method is a formidable task. As already noted, under certain conditions, a variation of the etching current is reflected by a pore size variation [24.125]. This is true at the nanoscale but can also be transferred to macropores. Thus, a 2-D lattice etched with proper modulation of the current forms a 3-D porous medium. Unfortunately, the pore size cannot be varied too much, and only a slight index variation can be achieved along the vertical profile. Moreover, the effect is highly nonlinear with etching conditions, and a suitable current profile has to be found with a trial-and-error approach [24.23]. Nevertheless, it was demonstrated that, after proper thermal treatment and subsequent oxide removal, an interconnected 3-D PC could be fabricated in macroPS [24.126]. An SEM image of such a sample is shown in Fig. 24.11.

24.7.3 Optical Sensing

PS is an excellent material to fabricate optical sensors. In fact, it possesses important characteristics such as:

1. Very high-quality optical structures can be etched in PS.
2. It offers high specific surface area, which can be tuned over a wide range.
3. It enables the achievement of rather high refractive index contrast (much higher than 1) even in 1-D PCs.
4. PS fabrication is based on a simple and fast etching method.
5. It can be chemically functionalized in a number of ways to make it stable and give it chemical specificity to particular analytes.

All of these are key requirements for a sensor device and are seldom found together in materials other than PS.

The great majority of the works that exploit PS in optical sensors rely on the use of PC structures. The presence of unknown analyte is detected by changes in optical properties induced by binding events.

Porous silicon microcavities have been investigated since the late 1990s [24.127, 128]. Generally, these works rely on spectral shifts of resonances induced by changes in refractive index. Extremely high sensitivity has been achieved (a limit of detection for refractive index change down to 10^{-6} has been demonstrated [24.129]).

Apart from the optical response, other physical parameters can be monitored using PS-based sensors. Here, we briefly discuss some of these alternative approaches.

As discussed in Sect. 24.7.1, PS shows bright visible PL if irradiated with UV light. PL quenching can be correlated to the presence of bound molecules that, by activating energy-transfer mechanisms, reduce the PL efficiency [24.130]. Unfortunately, PL quenching is generally an irreversible process, thus only disposable devices can be obtained from PS.

Electrical conductivity is another parameter subject to changes due to interaction with the environment. Sub-ppm sensitivity to NO_2 has been demonstrated [24.131]. The main limitations of PS-based sensors are their limited reversibility and hysteresis in the sensor optical response due to degradation processes (due to either aging or irreversible contamination), although improved reversibility was found in oxidized PS samples [24.132].

24.7.4 Drug Delivery Systems

PS possess many properties that make it an interesting material for biological applications. Following the pioneering work of *Canham* [24.133, 134] that demonstrated the biocompatibility of PS, many other groups have investigated the use of PS as a material in biosensing, drug delivery, and tissue engineering.

The pore size tunability provided by electrochemical etching allows the realization of optical structures with optimized sensitivity to particular molecule sizes. Thus, while nanoPS can be used to detect complementary DNA strands [24.135], macroPS structures can detect immunoglobulin G (IgG) or other, larger molecules [24.136].

Recently, PS has received great attention due to the possibility of its use as a drug delivery system or as a biodegradable marker. There is growing interest in the development of biodegradable smart materials that are

able to transport and deliver a drug payload in a well-controlled manner in vivo [24.137].

24.7.5 Oxidized Porous Silicon

PS is easily oxidized at low temperature. Sample porosity (pore wall thickness) and oxidation conditions (such as temperature, time, and atmosphere composition) determine the degree of the oxidation process. The same can be controlled to a very high level; in fact, high-porosity layers can be fully oxidized at temperature of 500 °C, while at higher temperatures the PS layer is sintered and porosity is reduced to low values.

Oxidized PS (OPS) has found applications as a sacrificial layer [24.138–140]. An OPS layer is easily removed by HF and can, thus, be used to fabricate free-standing structures, as sketched in Fig. 24.12. The process exploits the electrochemical etching selectivity of silicon areas with different doping concentrations. Initially, the layer to be rendered free-standing is subject to lithography to define the structures of interest (Fig. 24.12a). A subsequent etching process is used to expose the underlying substrate that will be rendered porous (Fig. 24.12b). The PS is then etched and finally removed, leaving suspended structures (Fig. 24.12c,d). The PS underetching shown in Fig. 24.12c can be used to obtain a silicon-on-insulator (SOI)-like structure, if the PS regions merge and no bulk silicon remains in between.

The dielectric properties of PS make it an ideal electrical insulating material. Since the early 1970s, NTT and Sony have developed methods that make use of PS as an insulating layer in integrated circuits (ICs) [24.141]. OPS has found application as an electrical insulator in bipolar ICs and was used in commercial products developed in the first half of the 1980s [24.142]. Here, a silicon chip is implanted with different dopants and concentrations to form *p*–*n* junctions. After electrochemical etching, they are laterally isolated by OPS regions.

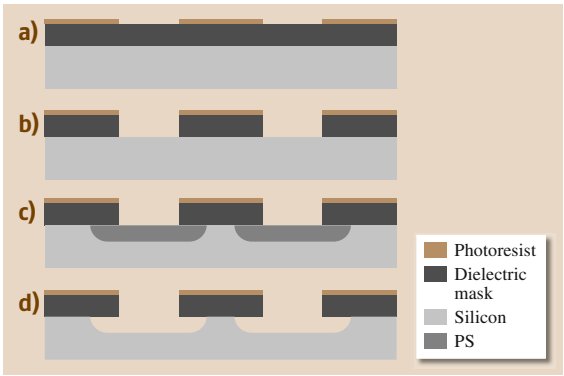


Fig. 24.12a–d Flowchart illustrating the process steps required to obtain free-standing structures using OPS as a sacrificial layer. **(a)** lithograhic step to define the area to be porosified, **(b)** etching of the dielectric mask, **(c)** etching of PS area, **(d)** removal of the porous layers

The extremely low refractive index achievable in OPS, together with the high material homogeneity and reproducibility, raised interest in its use as low-index cladding in waveguide (WG) structures. OPS can be fabricated with index as low as 1.1, and values around 1.2 are routinely achieved. Thus, use of OPS as low-index cladding in WG-based structures has been proposed and demonstrated [24.143, 144].

24.8 Conclusions

PS is an intriguing material that finds applications in a number of research fields.

Si electrochemistry offers a fast, simple, and fully CMOS-compatible fabrication method. The etching process allows the realization of porous structures with extremely complex profiles, with typical length scales that span from nanometers to hundreds of micrometers. Moreover, etched structures have very high quality, thus enabling detailed characterization of the properties of samples. NanoPS has been used to deeply understand the physical properties of Si-based nanostructures: both light emission and transport properties have been analyzed in depth using PS. Later, the development of the photonic crystal field further drove use of PS in nanophotonic applications, leading to great achievements concerning the demonstration of optical analogs of electronic phenomena and the realization of complex PC elements. At the same time, PS has also found applications in the development of high-sensitivity, multiparametric sensors. During recent years, use of PS in biological applications has become a lively research area thanks to its optical properties and biocompatibility.

The great flexibility of PS suggests that further developments can be expected in the coming years and that PS will remain in the limelight of nanostructured materials for a long time to come.

References

24.1 A. Uhlir Jr.: Electrolytic shaping of germanium and silicon, Bell Syst. Tech. J. **35**, 333–347 (1956)

24.2 Y. Watanabe, T. Sakai: Application of a thick anode film to semiconductor devices, Rev. Electron. Commun. Lab. **19**, 899 (1971)

24.3 K. Imai, H. Unno: FIPOS (full isolation by porous oxidized silicon) technology and its application to LSI's, IEEE T. Electron Devices **31**, 297–302 (1984)

24.4 T. Unagami: Formation mechanism of porous silicon layer by anodization in HF solution, J. Electrochem. Soc. **127**, 476–483 (1980)

24.5 G. Bomchil, R. Herino, K. Barla, J.C. Pfister: Pore-size distribution in porous silicon studied by absorption isotherm, J. Electrochem. Soc. **130**, 1611–1614 (1983)

24.6 C. Pickering, M.I.J. Beale, D.J. Robbins, P.J. Pearson, R. Greef: Optical studies of the structure of porous silicon films formed in p-type degenerate and non-degenerate silicon, J. Phys. C: Solid State Phys. **17**, 6535–6552 (1984)

24.7 K. Barla, R. Herino, G. Bomchil, J.C. Pfister, A. Freund: Determination of lattice-parameter and elastic properties of porous silicon by x-ray-diffraction, J. Cryst. Growth **68**, 727–732 (1984)

24.8 M.I.J. Beale, N.G. Chew, M.J. Uren, A.G. Cullis, J.D. Benjamin: Microstructure and formation mechanism of porous silicon, Appl. Phys. Lett. **46**, 86–88 (1985)

24.9 M.I.J. Beale, J.D. Benjamin, M.J. Uren, N.G. Chew, A.G. Cullis: An experimental and theoretical-study of the formation and microstructure of porous silicon, J. Cryst. Growth **73**, 622–636 (1985)

24.10 L.T. Canham: Silicon quantum wire array fabrication by electrochemical and chemical dissolution of wafers, Appl. Phys. Lett. **57**, 1046–1048 (1990)

24.11 N. Sato: *Electrochemistry at Metal and Semiconductor Electrodes* (Elsevier, Amsterdam 1998)

24.12 R. Memming: *Semiconductor Electrochemistry* (Wiley-VCH, Weinheim 2001)

24.13 D.R. Turner: Electropolishing silicon in hydrofluoric acid solutions, J. Electrochem. Soc. **105**, 402–408 (1958)

24.14 R. Memming, G. Schwandt: Potential distribution and formation of surface states at the silicon–electrolyte interface, Surf. Sci. **5**, 97–110 (1966)

24.15 V. Lehmann: *Electrochemistry of Silicon* (Wiley-VCH, Weinheim 2002)

24.16 J.N. Chazalviel: Ionic processes through the interfacial oxide in the anodic-dissolution of silicon, Electrochim. Acta **37**, 865–875 (1992)

24.17 R. Memming, G. Schwandt: Anodic dissolution of silicon in hydrofluoric acid solutions, Surf. Sci. **4**, 109–124 (1966)

24.18 V. Lehmann: The physics of macropore formation in low doped n-type silicon, J. Electrochem. Soc. **140**, 2836–2843 (1993)

24.19 V. Lehmann, U. Gösele: Porous silicon formation: A quantum wire effect, Appl. Phys. Lett. **58**, 856–858 (1991)

24.20 M.I.J. Beale, J.D. Benjamin, M.J. Uren, N.G. Chew, A.G. Cullis: An experimental and theoretical study of the formation and microstructure of porous silicon, J. Cryst. Growth **73**, 622–636 (1985)

24.21 V. Lehmann, H. Föll: Formation mechanism and properties of electrochemically etched trenches in n-type silicon, J. Electrochem. Soc. **137**, 653–659 (1990)

24.22 J.E.A.M. van den Meerakker, R.J.G. Elfrink, F. Roozeboom, J.F.C.M. Verhoeven: Etching of deep macropores in 6 in. Si wafers, J. Electrochem. Soc. **147**, 2757–2761 (2000)

24.23 A. Langner: Fabrication and Characterization of Macroporous Silicon. Ph.D. Thesis (Martin-Luther Universität Halle-Wittenberg, Halle 2008)

24.24 J. Carstensen, R. Prange, G.S. Popkirov, H. Föll: A model for current oscillations in the Si-HF system based on a quantitative analysis of current transients, Appl. Phys. A **67**, 459–467 (1998)

24.25 J. Carstensen, R. Prange, H. Föll: A model for current-voltage oscillations at the silicon electrode and comparison with experimental results, J. Electrochem. Soc. **146**, 1134–1140 (1999)

24.26 H. Föll, S. Langa, J. Carstensen, S. Lölkes, M. Christophersen, I.M. Tiginyanu: Pores in III–V semiconductors, Adv. Mater. **15**, 183–198 (2003)

24.27 H. Föll, J. Carstensen, M. Christophersen, G. Hasse: A new view of silicon electrochemistry, Phys. Status Solidi (a) **182**, 7–16 (2000)

24.28 V. Kochergin, H. Föll: *Porous Semiconductors* (Springer, London 2009)

24.29 H. Föll, M. Christophersen, J. Carstensen, G. Hasse: Formation and application of porous silicon, Mater. Sci. Eng. R **280**, 1–49 (2002)

24.30 Y. Arita, Y. Sunahama: Formation and properties of porous silicon film, J. Electrochem. Soc. **124**, 285–295 (1977)

24.31 X.Q. Bao, J.W. Jiao, J. Zhou, Y.L. Wang: Fast speed pore formation via strong oxidizers, Electrochem. Acta **52**, 6728–6733 (2007)

24.32 X.G. Zhang: *Electrochemistry of Silicon and its Oxide* (Kluwer, New York 2004)

24.33 D. Dimova-Malinovska, M. Sendova-Vassileva, N. Tzenov, M. Kamenova: Preparation of porous silicon layer by stain etching, Thin Solid Films **297**, 9–12 (1997)

24.34 A.J. Steckl, J. Xu, H.C. Mogul, S. Mogren: Doping-induced selective area photoluminescence in

porous silicon, Appl. Phys. Lett. **62**, 1982–1984 (1993)
24.35 A.V. Sapelkin, S.C. Bayliss, B. Unal, A. Charalambou: Interaction of B50 rat hippocampal cells with stain-etched porous silicon, Biomaterials **27**, 842–846 (2006)
24.36 X. Li, P.W. Bohn: Metal-assisted chemical etching in HF/H_2O_2 produces porous silicon, Appl. Phys. Lett. **77**, 2572–2574 (2000)
24.37 Z. Huang, H. Fang, J. Zhu: Fabrication of silicon annowire arrays with controlled diameter, length and density, Adv. Mater. **19**, 744–748 (2007)
24.38 Z. Huang, N. Geyer, P. Werner, J. de Boor, U. Gösele: Metal-assisted chemical etching of silicon: A review, Adv. Mater. **23**, 285–308 (2011)
24.39 M. Jansen, M. de Boer, R. Legtenberg, M. Elwenspoek: The black silicon method: A universal method for determining the parameter setting of a fluorine-based reactive ion etcher in deep silicon trench etching with profile control, J. Micromech. Microeng. **5**, 115–120 (1995)
24.40 L.L. Ma, Y.C. Zhou, N. Jiang, X. Lu, J. Shao, W. Lu, J. Ge, X.M. Ding, X.Y. Hou: Wide-band *black silicon* based on porous silicon, Appl. Phys. Lett. **88**, 171907 (2006)
24.41 V. Lehmann, R. Stengl, A. Luigart: On the morphology and the electrochemical formation mechanism of mesoporous silicon, Mater. Sci. Eng. B **69**, 11–22 (2000)
24.42 V. Lehmann, U. Grüning: The limits of macropore array fabrication, Thin Solid Films **297**, 13–17 (1997)
24.43 C.L. Clement, A. Lagoubi, M. Tomkiewicz: Morphology of porous n-type silicon obtained by photoelectrochemical etching, J. Electrochem. Soc. **141**, 958–967 (1994)
24.44 S. Ronnebeck, J. Carstensen, S. Ottow, H. Föll: Crystal orientation dependence of macropore growth in n-type silicon, Electrochem. Solid-State Lett. **2**, 126–128 (2000)
24.45 M. Christophersen, J. Carstensen, S. Ronnebeck, C. Jäger, W. Jäger, H. Föll: Crystal orientation dependence and anisotropic properties of macropore formation of p- and n-type silicon, J. Electrochem. Soc. **148**, E267–E275 (2001)
24.46 S. Lust, C. Levy-Clement: Macropore formation on medium doped p-type silicon, Phys. Status Solidi (a) **182**, 17–21 (2000)
24.47 P. Bettotti, L. Dal Negro, Z. Gaburro, A.L. Pavesi, A. Lui, M. Galli, M. Patrini, F. Marabelli: p-Type macroporous silicon for two-dimensional photonic crystals, J. Appl. Phys. **92**, 6966–6972 (2000)
24.48 Z. Yamani, O. Gurdal, A. Alqal, M.H. Nayfeh: Correlation of diffuse scattering with nanocrystallite size in porous silicon using transmission microscopy, J. Appl. Phys. **85**, 8050–8053 (1999)
24.49 T.K. Sham, D.T. Jang, I. Coulthard, J.W. Lorimer, X.H. Feng, K.H. Tang, S.P. Frigo, R.A. Rosenberg, D.C. Houghton, B. Bryskiewicz: Origin of luminescence from porous silicon deduced by synchrotron-light-induced optical luminescence, Nature **363**, 331–334 (1993)
24.50 M. Schoisswohl, H.J. von Bardeleben, V. Morazzani, A. Grosman, C. Ortega, S. Frohnhoff, M.G. Berger, H. Münder: Analysis of the surfaces structure in porous Si, Thin Solid Films **255**, 123–127 (1995)
24.51 M.J. Estes, G. Moddel: A model of size-dependent photoluminescence in amorphous silicon nanostructures: Comparison with observations of porous silicon, Appl. Phys. Lett. **68**, 1814–1816 (1996)
24.52 P.M. Fauchet, C.C. Tsai, L.T. Canham, I. Shimizu, Y. Aoyagi (Eds.): *Microcrystalline Semiconductors: Materials Science and Devices* (Materials Research Society, Pittsburgh 1993)
24.53 C. Tsai, K.H. Li, J. Sarathy, S. Shih, J.C. Campbell, B.K. Hance, J.M. White: Thermal treatment studies of the photoluminescence intensity of porous silicon, Appl. Phys. Lett. **59**, 2814–2816 (1991)
24.54 S.M. Prokes: Light emission in thermally oxidized porous silicon: Evidence for oxide-related luminescence, Appl. Phys. Lett. **62**, 3244–3246 (1993)
24.55 Z.Y. Xu, M. Gal, M. Gross: Photoluminescence studies on porous silicon, Appl. Phys. Lett. **60**, 1375–1377 (1992)
24.56 Y. Suda, T. Ban, T. Koizumi, H. Koyama, Y. Tezuka, S. Shin, N. Koshida: Surface structures and photoluminescence mechanisms of porous Si, Jpn. J. Appl. Phys. **33**, 581–585 (1994)
24.57 M. Wolkin, J. Jorne, P.M. Fauchet, G. Allan, C. Delerue: Electronic states and luminescence in porous silicon quantum dots: The role of oxygen, Phys. Rev. Lett. **82**, 197–200 (1999)
24.58 M.S. Hybertsen: Absorption and emission of light in nanoscale silicon structures, Phys. Rev. Lett. **72**, 1514–1517 (1994)
24.59 S. Ossicini, C.M. Bertoni, M. Biagini, A. Lugli, G. Roma, O. Bisi: Optical properties of isolated and interacting silicon quantum wires, Thin Solid Films **297**, 154–162 (1997)
24.60 P.D.J. Calcott, K.J. Nash, L.T. Canham, M.J. Kane, D. Brumhead: Spectroscopic identification of the luminescence mechanism of highly porous silicon, J. Lumin. **57**, 257–269 (1993)
24.61 G. Amato, C. Delerue, H.-J. von Bardeleben (Eds.): *Structural and Optical Properties of Porous Silicon Nanostructures* (Gordon and Breach, Amsterdam 1997)
24.62 H. Mizuno, H. Koyama, N. Koshida: Oxide-free blue photoluminescence from photochemically etched porous silicon, Appl. Phys. Lett. **69**, 3779–3881 (1996)
24.63 L. Tsybeskov, Y.V. Vandyshev, P.M. Fauchet: Blue emission in porous silicon: Oxygen-related photoluminescence, Phys. Rev. B **49**, 7821–7824 (1994)
24.64 P.M. Fauchet, E. Ettedgui, A. Raisanen, L.J. Brillson, F. Seiferth, S.K. Kurinec, Y. Gao, C. Peng, L. Tsybeskov: Can oxidation and other treatments

help us understand the nature of light-emitting porous silicaon?, Mater. Res. Soc. Symp. Proc. **298**, 271–276 (1993)
24.65 F. Koch: Models and mechanisms for the luminescence of porous Si, Mater. Res. Soc. Symp. Proc. **298**, 319 (1993)
24.66 S. Ossicini: Optical properties of confined Si structures, Phys. Status Solidi (a) **170**, 377–390 (1998)
24.67 A.G. Cullis, L.T. Canham, P.D.J. Calcott: The structural and luminescence properties of porous silicon, J. Appl. Phys. **82**, 909–965 (1997)
24.68 P.M. Fauchet, J. von Behren: The strong visible luminescence in porous silicon: Quantum confinement, not oxide-related defects, Phys. Status Solidi (b) **204**, R7–R8 (1997)
24.69 J.C. Vial, A. Bsiesy, F. Gaspard, R. Herino, M. Ligeon, F. Muller, R. Romestain, R.M. Macfarlane: Mechanisms of visible-light emission from electro-oxidized porous silicon, Phys. Rev. B **45**, 14171–14176 (1992)
24.70 V.A. Skryshevsky, A. Laugier, V.I. Strikha, V.A. Vikulov: Evaluation of quantum efficiency of porous silicon photoluminescence, Mater. Sci. Eng. B **40**, 54–57 (1996)
24.71 B. Gelloz, A. Kojima, N. Koshida: Highly efficient and stable luminescence of nanocrystalline porous silicon treated by high-pressure water vapor annealing, Appl. Phys. Lett. **87**, 031107 (2005)
24.72 A. Diligenti, A. Nannini, G. Pennelli, F. Pieri: Current transport in free-standing porous silicon, Appl. Phys. Lett. **68**, 687–689 (1996)
24.73 R. Tsu, D. Babić: Doping of a quantum dot, Appl. Phys. Lett. **64**, 1806–1808 (1994)
24.74 J. Kočka, J. Oswald, A. Fejfar, R. Sedlačík, V. Železný, H. The-Ha, K. Luterová, I. Pelant: Charge transport in porous silicon: Considerations for achievement of efficient electroluminescence, Thin Solid Films **276**, 187–190 (1996)
24.75 J.J. Mareš, J. Krištofík, J. Pangrác, A. Hospodková: On the transport mechanism in porous silicon, Appl. Phys. Lett. **63**, 180–182 (1993)
24.76 M. Ben-Chorin, F. Moller, F. Koch: Nonlinear electrical transport in porous silicon, Phys. Rev. B **49**, 2981–2984 (1994)
24.77 I. Balberg: Transport in porous silicon: The tea-pod model, Philos. Mag. B **80**, 691–703 (2000)
24.78 G. Giebel, L. Pavesi: About the *I–V* characteristic of metal-porous silicon diodes, Phys. Status Solidi (a) **151**, 355–361 (1995)
24.79 M. Ben-Chorin, F. Moller, F. Koch: Band alignment and carrier injection at the porous-silicon–crystalline-silicon interface, J. Appl. Phys. **77**, 4482–4488 (1995)
24.80 O. Bisi, S. Ossicini, L. Pavesi: Porous silicon: A quantum sponge structure for silicon based optoelectronics, Surf. Sci. Rep. **38**, 1–126 (2000)
24.81 F.X. Alvarez, D. Jou, A. Sellitto: Pore-size dependence of the thermal conductivity of porous silicon: A phonon hydrodynamic approach, Appl. Phys. Lett. **97**, 033103 (2010)
24.82 K. Ziouche, P. Godts, Z. Bougrioua, C. Sion, T. Lasri, D. Leclercq: Quasi-monolithic heat flux microsensor based on porous silicon boxes, Sens. Actuators A **164**, 35–40 (2010)
24.83 P.E. Hopkins, L.M. Phinney, P.T. Rakich, R.H. Olsson III, I. El-Kady: Phonon considerations in the reduction of thermal conductivity in phononic crystals, Appl. Phys. A **103**, 575–579 (2011)
24.84 L.C. Parsons, G.T. Andrews: Observation of hypersonic phononic crystal effects in porous silicon superlattices, Appl. Phys. Lett **95**, 241909 (2011)
24.85 L. Pavesi, R. Turan (Eds.): *Silicon Nanocrystals* (Wiley-VCH, Weinheim 2010)
24.86 B. Gelloz: Possible explanation of the contradictory results on the porous silicon photoluminescence evolution after low temperature treatments, Appl. Surf. Sci. **108**, 449–454 (1997)
24.87 J. Salonen, V.P. Lehto, E. Laine: Thermal oxidation of free-standing porous silicon films, Appl. Phys. Lett. **70**, 637–639 (1997)
24.88 B. Gelloz, T. Shibata, N. Koshida: Stable electroluminescence of nanocrystalline silicon device activated by high pressure water vapor annealing, Appl. Phys. Lett. **89**, 191103 (2006)
24.89 B. Gelloz, N. Koshida: Mechanism of a remarkable enhancement in the light emission from nanocrystalline porous silicon annealed in high-pressure water vapor, J. Appl. Phys. **98**, 123509 (2005)
24.90 V. Torres-Costa, R.J. Martín-Palma, J.M. Martínez-Duart, J. Salonen, V.-P. Lehto: Effective passivation of porous silicon optical devices by thermal carbonization, J. Appl. Phys **103**, 083124 (2008)
24.91 J. Salonena, E. Laine, L. Niinistö: Thermal carbonization of porous silicon surface by acetylene, J. Appl. Phys. **91**, 456–461 (2002)
24.92 T.D. James, A. Keating, G. Parish, C.A. Musca: Low temperature N_2-based passivation technique for porous silicon thin films, Solid State Commun. **149**, 1322–1325 (2009)
24.93 T.D. James, G. Parish, C.A. Musca, A.J. Keating: N_2-based thermal passivation of porous silicon to achieve long-term optical stability, Electrochem. Solid State **13**, H428–H431 (2010)
24.94 M.P. Stewart, E.G. Robins, T.W. Geders, M.J. Allen, H. Cheul Choi, J.M. Buriak.: Three methods for stabilization and functionalization of porous silicon surfaces via hydrosilylation and electrografting reactions, Phys. Status Solidi (a) **182**, 109–115 (2000)
24.95 S.D. Alvarez, A.M. Derfus, M.P. Schwartz, S.N. Bhatia, M.J. Sailor: The compatibility of hepatocytes with chemically modified porous silicon with reference to in vitro biosensors, Biomaterials **30**, 26–34 (2009)
24.96 J. Salonen, A.M. Kaukonen, J. Hirvonen, V.-P. Lehto: Mesoporous silicon in drug delivery applications, J. Pharma. Sci. **97**, 632–653 (2008)

24.97 L.T. Canham, W.Y. Leong, M.I.J. Beale, T.I. Cox, L. Taylor: Efficient visible electroluminescence from highly porous silicon under cathodic bias, Appl. Phys. Lett. **61**, 2563–2565 (1992)

24.98 A. Bsiesy, F. Muller, M. Ligeon, F. Gaspard, R. Herino, R. Romestain, J.C. Vial: Voltage-controlled spectral shift of porous silicon electroluminescence, Phys. Rev. Lett. **71**, 637–640 (1993)

24.99 A. Halimaoui, C. Oules, G. Bomchil, A. Bsiesy, F. Gaspard, R. Herino, M. Ligeon, F. Muller: Electroluminescence in the visible range during anodic oxidation of porous silicon films, Appl. Phys. Lett. **59**, 304–306 (1991)

24.100 N. Koshida, H. Koyama: Visible electroluminescence from porous silicon, Appl. Phys. Lett. **60**, 347–349 (1992)

24.101 F. Namavar, H.P. Maruska, N.M. Kalkhoran: Visible electroluminescence from porous silicon np heterojunction diodes, Appl. Phys. Lett. **60**, 2514–2516 (1992)

24.102 K. Nishimura, Y. Nagao, N. Ikeda: Effects of antimony diffusion into porous silicon light emitting diodes, Jpn. J. Appl. Phys. **36**, L643–L646 (1997)

24.103 S. Sen, J. Siejka, A. Savtchouk, J. Lagowski: Spin-on doping of porous silicon and its effect on photoluminescence and transport characteristics, Appl. Phys. Lett. **70**, 2253–2254 (1997)

24.104 N. Koshida, H. Koyama, Y. Yamamoto, G.J. Collins: Visible electroluminescence from porous silicon diodes with an electropolymerized contact, Appl. Phys. Lett. **63**, 2655–2657 (1993)

24.105 K. Li, D.C. Diaz, Y. He, J.C. Campbell, C. Tsai: Electroluminescence from porous silicon with conducting polymer film contacts, Appl. Phys. Lett. **64**, 2394–2396 (1994)

24.106 G. Wakefield, P.J. Dobson, Y.Y. Foo, A. Loni, A. Simons, J.L. Hutchison: The fabrication and characterization of nickel oxide films and their application as contacts to polymer/porous silicon electroluminescent devices, Semicond. Sci. Technol. **12**, 1304–1309 (1997)

24.107 L. Tsybeskov, S.P. Duttagupta, K.D. Hirschman, P.M. Fauchet: Stable and efficient electroluminescence from a porous silicon-based bipolar device, Appl. Phys. Lett. **68**, 2058–2060 (1996)

24.108 L. Pavesi, R. Guardini, P. Bellutti: Porous silicon n–p light emitting diode, Thin Solid Films **297**, 272–276 (1997)

24.109 Y.-A. Chen, N.-Y. Liang, L.-H. Laih, W.-C. Tsay, M.-N. Chang, J.-W. Hong: Improvement of current injection of porous silicon, Jpn. J. Appl. Phys. **31**, 1574–1577 (1997)

24.110 H. Mimura, T. Matsumoto, Y. Kanemitsu: Si-based optical devices using porous materials, Appl. Surf. Sci. **92**, 598–605 (1996)

24.111 L. Pavesi, R. Guardini, C. Mazzoleni: Porous silicon resonant cavity light emitting diodes, Solid State Commun. **97**, 1051–1053 (1996)

24.112 M.-K. Lee, C.-C. Hu, Y.-H. Wang: Utilization of GaAs masking layers for formation of patterned porous silicon, Jpn. J. Appl. Phys. **35**, L865–L868 (1996)

24.113 K.D. Hirschman, L. Tsybeskov, S.P. Duttagupta, P.M. Fauchet: Silicon-based visible light-emitting devices integrated into microelectronic circuits, Nature **384**, 338–341 (1996)

24.114 J.D. Joannopoulos, S.G. Johnson, J.N. Winn, R.D. Meade: *Photonic Crystals: Molding the flow of light*, 2nd edn. (Princeton Univ., Princeton 2008), available online at http://ab-initio.mit. edu/book/

24.115 L. Rayleigh: On the propagation of waves through a stratified medium, with special reference to the question of reflection, Proc. R. Soc. A **86**, 207–226 (1912)

24.116 M. Borm, E. Wolf: *Principles of Optics*, 6th edn. (Cambridge Univ., Cambridge 1997)

24.117 R. Sapienza, P. Costantino, D. Wiersma, M. Ghulinyan, C.J. Oton, L. Pavesi: Optical analogue of electronic Bloch oscillations, Phys. Rev. Lett. **91**, 263902 (2003)

24.118 J. Bertolotti, S. Gottardo, D.S. Wiersma, M. Ghulinyan, L. Pavesi: Optical necklace states in Anderson localized 1D systems, Phys. Rev. Lett. **94**, 113903 (2005)

24.119 M. Galli, M. Agio, L.C. Andreani, M. Belotti, G. Guizzetti, F. Marabelli, M. Patrini, P. Bettotti, L. Dal Negro, Z. Gaburro, L. Pavesi, A. Lui, P. Bellutti: Spectroscopy of photonic bands in two-dimensional macroporous silicon photonic crystals, Phys. Rev. B **65**, 113111 (2002)

24.120 V. Lehmann, U. Grüning: The limits of macropore array fabrication, Thin Solid Films **297**, 13–17 (1997)

24.121 H. Ouyang, M. Christophersen, P.M. Fauchet: Enhanced control of porous silicon morphology from macropore to mesopore formation, Phys. Status Solidi (a) **202**, 1396–1401 (2005)

24.122 S.W. Leonard, H.M. van Driel, A. Birner, U. Gösele, P.R. Villeneuve: Single-mode transmission in two-dimensional macroporous silicon photonic crystal waveguides, Opt. Lett. **25**, 1550–1552 (2000)

24.123 A. Birner, R.B. Wehrspohn, U.M. Gösele, K. Busch: Silicon-based photonic crystals, Adv. Mater. **13**, 377–388 (2001)

24.124 S.P. Ogawa, M. Imada, S. Yoshimoto, M. Okano, S. Noda: Control of light emission by 3D photonic crystals, Science **305**, 227–229 (2004)

24.125 S.W. Leonard: Complete three-dimensional band gap in macroporous silicon photonic crystals, Appl. Phys. Lett. **81**, 2917–2919 (2002)

24.126 S. Matthias, F. Müller, C. Jamois, R.B. Wehrspohn, U. Gösele: Large-area three-dimensional structuring by electrochemical etching and lithography, Adv. Mater. **16**, 2166–2170 (2004)

24.127 V.S.-Y. Lin, K. Motesharei, K.-P.S. Dancil, M.J. Sailor, M. Reza Ghadiri: A porous silicon-based optical interferometric biosensor, Science **278**, 840–843 (1997)

24.128 V. Mulloni, L. Pavesi: Porous silicon microcavities as optical chemical sensors, Appl. Phys. Lett. **76**, 2523–2525 (2000)
24.129 L.N. Acquaroli, R. Urteaga, R.R. Koropecki: Innovative design for optical porous silicon gas sensor, Sens. Actuators B **149**, 189–193 (2010)
24.130 M.J. Sailor, E.C. Wu: Photoluminescence-based sensing with porous silicon films, microparticles, and nanoparticles, Adv. Funct. Mater. **19**, 3195–3208 (2009)
24.131 Z. Gaburro, P. Bettotti, M. Saiani, L. Pavesi, L. Pancheri, C.J. Oton, N. Capuj: Role of microstructure in porous silicon gas sensors for NO_2, Appl. Phys. Lett. **85**, 555–557 (2004)
24.132 L. Pancheri, C.J. Oton, Z. Gaburro, G. Soncini, L. Pavesi: Improved reversibility in aged porous silicon NO_2 sensors, Sens. Actuators B **97**, 45–48 (2004)
24.133 L.T. Canham: Bioactive silicon structure fabrication through nanoetching techniques, Adv. Mater. **7**, 1033–1037 (1995)
24.134 L.T. Canham (Ed.): *Properties of Porous Silicon*, EMIS Datareview Series, Vol. 18 (EMIS, London 1997)
24.135 S. Chan, P.M. Fauchet, Y. Li, L.J. Rothberg, B.L. Miller: Porous silicon microcavities for biosensing applications, Phys. Status Solidi (a) **182**, 541–546 (2000)
24.136 H. Ouyang, M. Christophersen, R. Viard, B.L. Miller, P.M. Fauchet: Macroporous Silicon Microcavities for Macromolecule Detection, Adv. Mater. **15**, 1851–1859 (2005)
24.137 E.J. Anglin, L. Cheng, W.R. Freeman, M.J. Sailor: Porous silicon in drug delivery devices and materials, Adv. Drug. Deliv. Rev. **60**, 1266–1277 (2008)
24.138 C.J.M. Eijkel, J. Branebjerg, M. Elwenspoek, F.C.M. van de Pol: A new technology for micromachining of silicon: Dopant selective HF anodic etching for the realization of low-doped monocrystalline silicon structures, IEEE Electron Device Lett. **11**, 588–589 (1990)
24.139 P. Steiner, W. Lang: Micromachining applications of porous silicon, Thin Solid Films **255**, 52–58 (1995)
24.140 T.E. Bell, P.T.J. Gennissen, D. DeMunter, M. Kuhl: Porous silicon as a sacrificial material, J. Micromech. Microeng. **6**, 361–369 (1996)
24.141 Japan Patent 49-19090 (1974), USA Patent 3640806 (1972)
24.142 V. Yakovtseva, L. Dolgyi, N. Vorozov, N. Kazuchits, V. Bondarenko, M. Balucani, G. Lamedica, L. Franchina, A. Ferrari: Oxidized porous silicon: From dielectric isolation to integrated optical waveguides, J. Porous Mat. **7**, 215–222 (2000)
24.143 P. Bettotti, A. Pitanti, E. Rigo, F. De Leonardis, V. Passaro, L. Pavesi: Modeling of slot waveguide sensors based on polymeric materials, Sensors **11**, 7327 (2011)
24.144 D. Navarro-Urrios, M. Ghulinyan, P. Bettotti, E. Rigo, C.J. Oton, N.E. Capuj, F. Lahoz, I.R. Martin, L. Pavesi: Polymeric waveguides using oxidized porous silicon cladding for optical amplification, Opt. Mater. **31**, 1488–1491 (2009)

Part F

Organic a

Part F Organic and Bionanomaterials

25 Organic Nanomaterials
Huanli Dong, Beijing, China
Wenping Hu, Beijing, China

26 Nanocomposites as Bone Implant Material
Vinod Kumar, Lanka, Varanasi, India
Bipul Tripathi, Lanka, Varanasi, India
Anchal Srivastava, Lanka, Varanasi, India
Preeti S. Saxena, Lanka, Varanasi, India

27 Nanofiber Biomaterials
Rachelle N. Palchesko, Pittsburgh, USA
Yan Sun, Beijing, China
Ling Zhang, Pittsburgh, USA
John M. Szymanski, Pittsburgh, USA
Quentin Jallerat, Pittsburgh, USA
Adam W. Feinberg, Pittsburgh, USA

25. Organic Nanomaterials

Huanli Dong, Wenping Hu

Nanomaterials, notable for their extremely small feature size, have the potential for wide-ranging industrial, biomedical, and electronic applications. Organic nanomaterials, with the utility of weak noncovalent interactions for the design and self-assembly of molecules one by one into desired structures, give the potential advantages of constructing building blocks using synthetic chemistry at multiple levels, and open the *bottom-up* route for synthesis of organic and polymeric nanostructures; for example, self-assembly of organic molecules with the assistance of noncovalent interactions, such as hydrogen bonding, electrostatic interactions, and pi-stacking, provides a powerful strategy for synthesis of molecular nanostructures, which have been attracting particular attention since the 1990s as a *bottom-up* paradigm of nanosciences, and discrete nanoparticles with controlled chemical composition and size distribution are readily synthesized. However, the assembly of well-defined nanostructures in large areas, the tuning of noncovalent interactions for efficient assembly, and the dynamics and model of the self-assembly process remain challenging and demanding tasks. There is still a long way to go to achieve true mastery of the art. It will be attractive to find a simple, efficient, and controllable way to produce organic nanomaterials in large areas (mass production) as well as to bridge their applications in organic optoelectronics. In fact, organic nanomaterials have been projected as active components in optoelectronic devices recently, not to mention the great efforts invested in manipulating their morphologies and tailoring their functions. The overall aim of this chapter is to bring together science and applications on organic nanomaterials with emphasis on synthesis and preparation, processing, characterization, and applications of organic nanomaterials that enable novel or enhanced properties or functions, including experiments and applications.

25.1 **Preparation/Synthesis of Organic Nanomaterials** 905
25.1.1 Solution Processes 906
25.1.2 Vapor Processes 909
25.2 **Properties of Organic Nanomaterials** 910
25.2.1 Structure and Morphology 910
25.2.2 Absorption and Emission Properties 912
25.2.3 Optoelectronic Properties 916
25.2.4 Mechanical Properties 923
25.3 **Applications** 925
25.3.1 Sensors and/or Detectors 925
25.3.2 Surface Wettability Control 927
25.3.3 Optical Waveguides and Lasers 928
25.3.4 Nanocircuits 928
25.4 **Concluding Remarks** 930
References 932

25.1 Preparation/Synthesis of Organic Nanomaterials

The development of facile, mild, and universal construction strategies is a prerequisite to further investigation of organic nanomaterials. Most of the present approaches to inorganic nanomaterials are not applicable for organic ones due to the lower melting and sublimation points of organic and polymeric materials. However, some fruitful attempts have been developed during the past couple of years based on the characteristics of organic and polymeric materials. Judging from the phase state for the preparation/synthesis of organic

nanomaterials, the various methods can be divided into solution processes, vapor processes, and other special techniques such as supercritical and/or ionic liquid methods. Certainly, the methods also can be divided into template and template-free processes depending on whether they use a template or not during the preparation process. Here, we divide the methods into solution processes, vapor processes, and other methods.

25.1.1 Solution Processes

Solution processing is an effective method for growth of organic nanomaterials, mainly including templating, electrochemistry, recrystallization, solvent-exchange, dip-coating, and drop-casting methods, surface-assisted solvent–vapor annealing, etc., which usually require materials with good solubility.

Template Method

The template method represents a straightforward route to fabricate organic nanomaterials by forcing the target molecules into the template to grow desired nanomaterials according to the patterns of the templates, e.g., anodized aluminum oxide (AAO) templates. Probably, *Possin* was the first to use this technique to prepare semiconductor nanowires in the 1970s [25.2], and *Martin* extended this technique and first put forward the term *template synthesis* in the 1990s [25.3, 4]. Now the commonly used templates include but are not limited to ordered porous membranes prepared with AAO, but also silica and nanochannel glass, etc. [25.5]. Li and coworkers fabricated C_{60} nanotubes with this method by an easy dip-and-dry procedure, in which they dipped the AAO templates repeatedly into a C_{60} solution, and evaporated the solvent during the intervals between dipping. Owing to its versatility, this approach should be a promising route toward a variety of nanotubes (i. e., polymer and inorganic and organic compounds) and should be applicable to any compound that can be dissolved in a membrane-compatible solvent. Especially, this method could be a general technique for thermopolymerization and in situ polymerization under shape and size control, as shown in Fig. 25.1 [25.1].

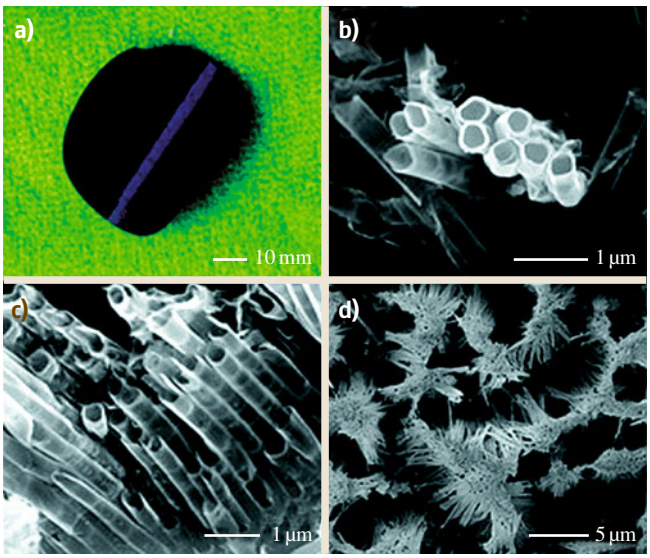


Fig. 25.1 (**a**) Photograph of the alumina template, and SEM images of C_{60} nanotubes: (**b**) top of C_{60} nanotubes after removal of the alumina templates, (**c**) ordered array of C_{60} nanotubes after complete removal of the template, and (**d**) large area of aligned C_{60} nanotubes. (After [25.1], courtesy of American Chemical Society (2002))

Zhao et al. reported the preparation of perylene nanotubes [25.6] by repeatedly immersing a porous alumina template (Whatman Ltd., Anodisc 13, quoted diameter 200 nm) into a saturated perylene solution for 2 min for every cycle and allowing the solvent to evaporate in air during the intervals. After 20 cycles, the templates were perylene-laden and heated to 240 °C for 10 h under a nitrogen atmosphere and then cooled to room temperature. The surface layer of the membrane was removed by polishing with 1500-grit sandpaper, and then the sample was fixed to a piece of copper tape. Field-emission scanning electron microscopy (FESEM, JEOL JSM-6700F) images of the as-prepared template-synthesized perylene nanotubes after complete removal of the alumina template by etching it away with 6 M aqueous sodium hydroxide are given in Fig. 25.2. It can be clearly seen that the nanotubes are arranged in a continuous, parallel, and well-ordered way with monodispersed diameters (ca. 200 nm), lengths (ca. 60 µm), and wall thicknesses (ca. 25 nm) at quite high density (about $2.6 \times 10^9\,\mathrm{cm}^{-2}$). The diameters and lengths of the nanotubes correspond well to the diameter of the pores of the membrane and the thickness of the template used (60 µm). After application of alkaline corrosion to the aluminum oxide membrane, the nanostructures in the pores of the membrane remained, which makes this method more suitable for fabricating nanotubes from small organic molecules that are not sensitive to the inorganic alkali.

It is well known that polymers and small organic molecules are attractive materials for (opto)electronics due to their chemically tunable optical and electronic properties as well as their potential for low-cost fab-

rication of flexible or large-area devices. In particular, pentacene has shown tremendous promise for thin-film transistor (TFT) applications, with reports of hole mobilities approaching $1\,cm^2/(V\,s)$ for TFTs fabricated on flexible substrates. *Barrett* et al. [25.7] reported on convenient synthesis of pentacene nanotubes by the method of melt-assisted template wetting and on electrical contacting of single tubes. Briefly, pentacene powder is placed on an alumina pore array and heated above its melting point under an inert atmosphere. As a result of the high surface energy of the alumina membrane, a thin surface film will rapidly cover the pore walls in the initial stages of wetting, forming nanotubes with well-defined wall thicknesses. Figure 25.3a shows a scanning electron microscopy (SEM) image of an array of pentacene nanotubes following partial dissolution of the alumina template in aqueous NaOH. The density of nanotubes (109 per template) demonstrates the efficiency of the melt-assisted wetting process for high-yield preparation of these novel one-dimensional (1-D) nanostructures. Figure 25.3b shows a high-magnification image of the back side of part of the membrane shown in Fig. 25.1a. The large number of protruding nanotubes indicates almost complete filling of the template during melt injection, confirming formation of 60 µm-long tubes. Histogram analysis of tube diameters and wall thicknesses measured using SEM yielded mean values for the tube outer diameter ($d \approx 350\,nm$) and wall thickness ($w \approx 40\,nm$).

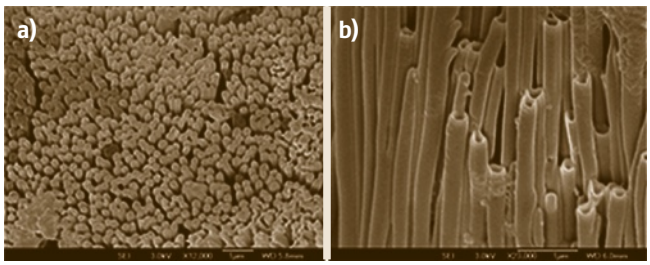


Fig. 25.2a,b FESEM images of an as-prepared ordered array of perylene nanotubes after complete removal of the template by applying an alkaline corrosion process with 6 M aqueous sodium hydroxide: **(a)** typical top view; **(b)** cross-sectional view. (After [25.6], courtesy of R. Society Chemistry (2003))

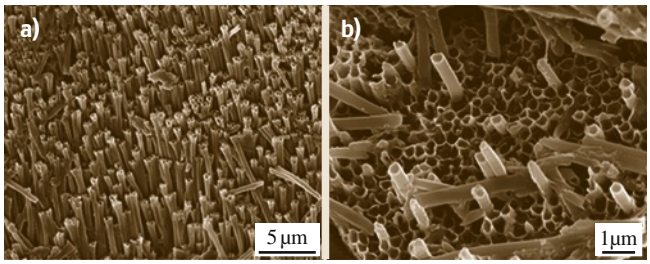


Fig. 25.3 **(a)** SEM image of a pentacene nanotube array following template removal. **(b)** Higher-magnification image of part of the back side of the membrane used in **(a)** following partial template removal. (After [25.7], courtesy of American Chemical Society (2002))

Template-Free Method

The template-free method is usually called self-assembly, which is the fundamental principle which generates structural organization on all scales from molecules to galaxies. Self-assembly can occur spontaneously in nature, for example, in cells (such as the self-assembly of the lipid bilayer membrane) and other biological systems, as well as in human-engineered systems. It usually results in the increase in internal organization of the system. Molecular self-assembly is the assembly of molecules without guidance or management from an outside source. There are two types of self-assembly, intramolecular self-assembly and intermolecular self-assembly, although in some books and articles the term self-assembly refers only to intermolecular self-assembly. Intramolecular self-assembling molecules are often complex polymers with the ability to assemble from the random coil conformation into a well-defined stable structure (secondary and tertiary structure). An example of intramolecular self-assembly is protein folding. Intermolecular self-assembly is the ability of molecules to form supramolecular assemblies (quaternary structure). A simple example is the formation of a micelle by surfactant molecules in solution. Certainly, self-assembly can be also classified as either static or dynamic. Static self-assembly is when the ordered state occurs when the system is in equilibrium and does not dissipate energy. Dynamic self-assembly is when the ordered state requires dissipation of energy.

Almost everything has the inclination for self-assembly. Molecular self-assembly in liquid solutions is a strategy for nanofabrication that involves designing molecules and supramolecular entities. The assembly of organic molecules into nanostructures with defined morphologies needs driving forces from the molecules themselves, including hydrogen bond, $\pi-\pi$ stacking van der Waals contact, etc. Sometimes, the self-assembly process also requires induction from the surroundings, such as interactions between the organic molecules and the solvents or auxiliaries. The use of noncovalent interactions for self-assembly is widely ap-

plied for preparation of organic nanomaterials. Usually, covalent interactions (bonds) hold the atoms together with large bond energies of the order of $\approx 10^2$ kcal/mol. Compared with covalent interactions, noncovalent interactions are much weaker. However, the cumulative energies of noncovalent interactions can be huge; For example, huge numbers of small noncovalent forces drive the spontaneous folding or unfolding of proteins and nucleic acids. Moreover, the weak noncovalent interactions (hydrogen bonding, π-stacking, electrostatic interactions, van der Waals forces, etc.) can be tuned with the design of molecules so that molecules can self-assemble one by one into desired architectures. This gives the potential advantages of constructing building blocks using synthetic chemistry at multiple levels, and opens the *bottom-up* route for synthesis of organic nanomaterials; For example, *Jiang* et al. [25.8] used anthracene and its series derivatives (Fig. 25.4) to demonstrate a simple way to cast-assemble nanowires of organic semiconductors through tuning of the intermolecular noncovalent interactions by molecular design. The tuning of intermolecular interactions could be achieved by:

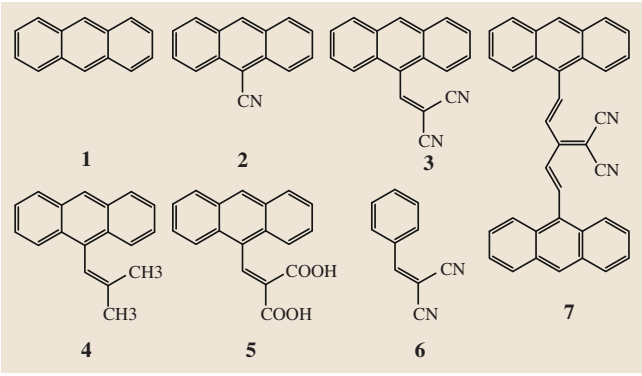


Fig. 25.4 Molecular structures of anthracene and its derivatives. (After [25.8], courtesy of R. Society Chemistry (2010))

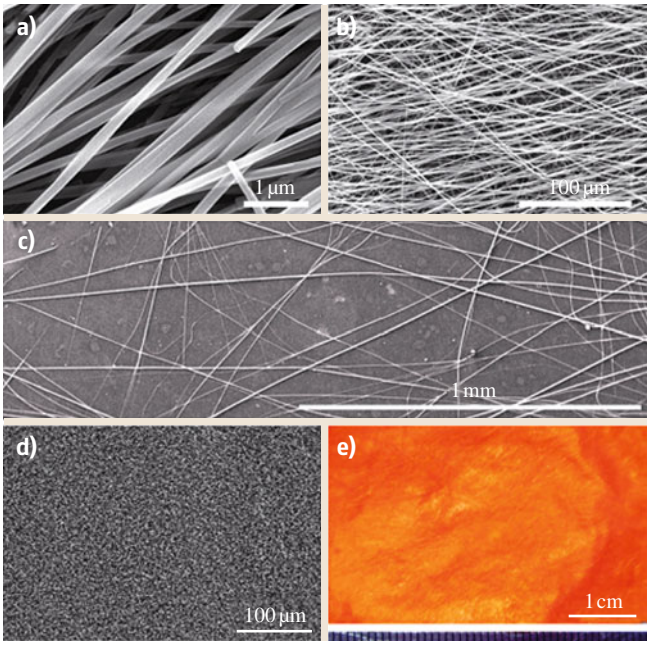


Fig. 25.5a–e Morphology of cast products of organic semiconductor (**1**) on glass substrate. **(a–d)** SEM images of cast products: **(a)** nanowires; **(b)** microwires; **(c)** ultralong microwires; **(d)** nanowires in large area. **(e)** Optical image of microwires in large area. (After [25.9], courtesy of American Chemical Society (2008))

1. Decreasing intermolecular hydrophobic interactions by linking hydrophilic side-chains to anthracene rings
2. Increasing intermolecular interaction for self-assembly with the assistance of hydrogen bonds
3. Enhancing molecular $\pi-\pi$ interaction by increasing the conjugated dimension of the compounds.

Attractively, nanowires and microwires of organic semiconductor (**3**) could be prepared by cast assembly efficiently and simply [25.9]. Due to the merits of cast assembly, these nanowires/microwires could be synthesized in large quantity and large scale at low cost. Transmission electron microscopy (TEM) images of individual nanowire/microwires and their corresponding selected-area electron diffraction pattern indicated that the whole nanowires/microwires are single crystals. Precise size-controlled nanowires and ultralong microwires with length reaching several millimeters were obtained by carefully adjusting the concentrations of (**1**) in cast solutions (Fig. 25.4). Control experiments and the growing process of microwires in solution monitored in situ by optical microscopy suggested that the formation mechanism of nanowires/microwires was a crystallization process. Moreover, the nanowires/microwires showed no substrate or solvent dependence and were orientation controllable. Highly reproducible and sensitive photoresponse characteristics were observed in these nanowires/microwires. Fast and reversible photoswitches based on multiple or individual nanowires/microwires were fabricated via the *multi times gold wire mask moving* technique with switch ratio of over 100.

25.1.2 Vapor Processes

Vapor deposition is a facile and feasible method for preparing nanomaterials and has achieved great success in fabricating inorganic 1-D nanostructures, polymeric thin films, and inorganic–polymer nanocomposites; For example, the physical vapor transport technique is a general method to produce high-quality nanocrystals. It is usually carried out in a quartz tube by sublimating high-purity compounds at a high-temperature zone, carrying the vapor with an inert gas, and then recrystallizing the compounds at a low-temperature zone of the tube [25.10]. This approach is widely used for oligomers and small-molecular-weight organic semiconductors; For example, *Tang* et al. [25.12] synthesized nanocrystals of copper phthalocyanine (CuPc) by the physical vapor transport technique (Fig. 25.6). A quartz tube was inserted in a two-zone horizontal tube furnace. CuPc powder was placed at the high-temperature zone and vaporized at 425 °C. Vapor of CuPc was then carried by high-purity Ar gas flowing from the high-temperature zone to the low-temperature zone at a rate of 200 sccm. Purple fuzz-like products, which were found to be CuPc nanoribbon crystals later (Fig. 25.6), were obtained on a substrate at the low-temperature zone (150 °C).

For vapor deposition, the degree of saturation is the predominant factor in controlling the morphology and dispersity of the products, and it should be possible to process most solid materials into 1-D nanostructures by maintaining the vapor saturation at a low level [25.11]. Several techniques have been adopted to control the local supersaturation in the preparation of organic 1-D nanomaterials by vapor deposition; For example, *Yao* and coworkers reported an adsorbent-assisted physical vapor deposition (PVD) method. Adsorbents such as neutral aluminum oxide or silica gel, used widely in column chromatography, were introduced into the PVD method to control the degree of saturation, considering that there should exist an adsorption–desorption equilibrium between the adsorbents and the organic sources. A series of single-crystalline 1-D organic nanostructures were prepared with this method [25.11, 13]. Figure 25.7a,b shows typical SEM and TEM images of tris(8-hydroxyquinoline)aluminum (Alq3) nanowires. The selected-area electron diffraction (SAED) pattern shown in Fig. 25.7c reveals that the Alq_3 nanowires are single-crystalline structures with preferential growth along the $[10\bar{1}]$ direction, which is also testified by the x-ray diffraction (XRD) patterns. The length and diameter of the nanowires prepared with this method

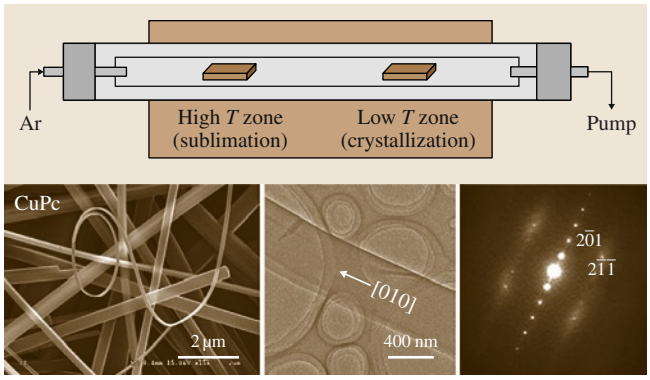


Fig. 25.6 Vapor process for synthesis of organic nanometer-sized single crystals. (After [25.10], courtesy of Wiley-VCH (2008))

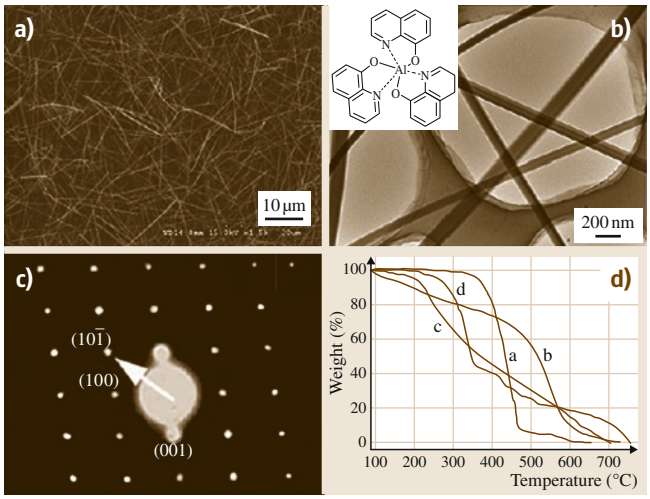


Fig. 25.7a–d FESEM images of Alq3 nanowires with **(a)** diameters of 150 nm and lengths of 1.5 μm and **(b)** diameters of 300 nm and lengths of 20 μm. **(c)** TEM images of some typical Alq3 nanowires. **(d)** SAED pattern of the Alq3 nanowire; the *arrow* indicates the direction of the wire. (After [25.11], courtesy of Wiley-VCH (2006))

can be well controlled by varying the deposition conditions, such as time and temperature. The results of analogous experiments and thermogravimetric analysis (TGA) measurements displayed in Fig. 25.7d indicate that the addition of adsorbents is indispensable in improving the uniformity of the nanowires. It can be observed that the adsorbents decreased the sublimation temperature and slowed the weight loss of Alq3 remarkably, through which the degree of saturation and the uniformity can be readily controlled. In contrast, the introduction of sodium chloride, which does not adsorb, hardly affects the slope of the TGA plot. No

catalyst was used and no droplet was found at the top, so the growth of the 1-D materials prepared with this method should be controlled by the vapor–solid (VS) process [25.14].

25.2 Properties of Organic Nanomaterials

Great attention has been drawn to nanomaterials due to their size, confinement, surface, and quantum tunneling effects, etc.. These effects result in unique properties of nanomaterials superior to those of their bulk counterparts; For example, owing to the phenomena of charge transfer and Frenkel excitons, their optoelectronic properties are more complicated than those of inorganic nanomaterials, which results in many difficulties in research of organic nanomaterials. Fortunately, rapid development in the understanding of organic nanomaterials is underway due to researchers' great efforts.

25.2.1 Structure and Morphology

Controllable synthesis is a key task for nanoscale science, and the morphologies of inorganic nanostructures have been successfully controlled by choosing appropriate materials and changing the synthesis methods. However, the morphology control of organic nanomaterials has met with limited success. The commonly used strategy to modulate the organic nanostructures is to slightly alter the molecular structures in a series of derivatives; For example, *Zang* and coworkers have prepared either nanobelts or nanospheres by using two different derivatives of perylene diimide [25.14, 15]. Nanobelt structures have been fabricated for an n-type semiconductor molecule (Fig. 25.8), *N*,*N*′-di(propoxyethyl)perylene-3,4,9,10-tetracarboxylic diimide (PTCDI) [25.14]. The short alkyloxy side-chain not only affords effective $\pi-\pi$ stacking in polar solvents for self-assembly but also provides sufficient solubility in nonpolar solvents for solution processing. As revealed by both atomic force microscopy (AFM) and electron microscopies, the nanobelts have an approximately rectangular cross-section, with typical thickness of about 100 nm and width in the range of 300–500 nm. The length of the nanobelts ranges from 10 to a few tens of micrometers. The highly organized molecular packing (uniaxial crystalline phase) has been deduced from the measurement of electron diffraction and polarized microscopy imaging. The detected optical axis is consistent with the one-dimensional stacking of the molecules.

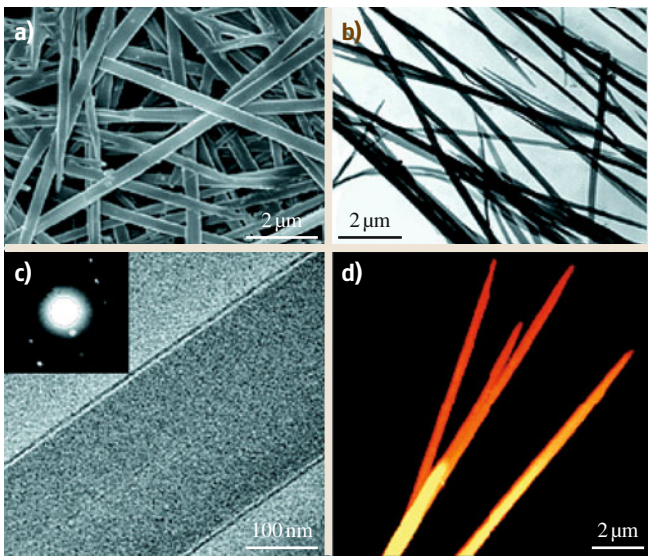


Fig. 25.8 (**a**) SEM image of propoxyethyl-PTCDI nanobelts (gold-stained) cast on glass; (**b**) TEM image of nanobelts cast on SiO_2 film; (**c**) zoom-in TEM image of a nanobelt cast on SiO_2 film (*inset*). Electron diffraction over a nanobelt cast on carbon film; (**d**) AFM image of nanobelts cast on mica (*z*-scale: 0–140 nm); average thickness, 100 nm. (After [25.14], courtesy of American Chemical Society (2005))

An obvious effect of side-chain substitutions on the morphology of self-assembly of perylene diimide molecules was also found with two derivatives modified with distinctly different side-chains: *N*,*N*′-di(dodecyl)-perylene-3,4,9,10-tetracarboxylic diimide (DD-PTCDI) and *N*,*N*′-di(nonyldecyl)-perylene-3,4,9,10-tetracarboxylic diimide (ND-PTCDI). Due to the different side-chain interference, the self-assembly of the two molecules results in totally different morphologies in aggregates: one-dimensional (1-D) nanobelts versus zero-dimensional (0-D) nanoparticles (Fig. 25.9). The distinct morphologies of self-assembly have been obtained from both solution-based processing and surface-supported solvent–vapor annealing. The nanobelts of DD-PTCDI fabricated in solution can feasibly be transferred to both polar (e.g., glass) and nonpolar (e.g., carbon) surfaces, implying high stability of the molecular assembly (due to the strong $\pi-\pi$ stacking). Compared with the emission of ND-PTCDI aggregate, the emission of DD-PTCDI aggregate was significantly red-shifted (ca. 30 nm) and the emission

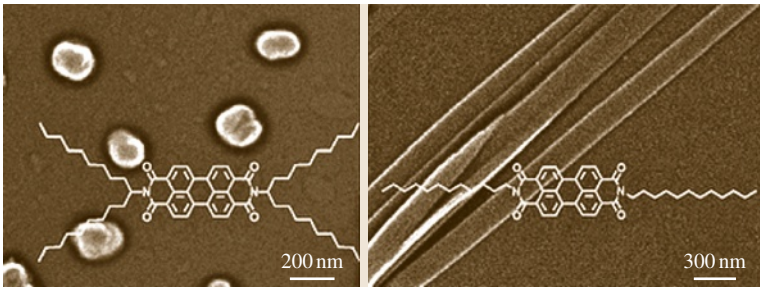


Fig. 25.9 Molecular structures of DD-PTCDI and ND-PTCDI and SEM images of their self-assembled structures. (After [25.15], courtesy of American Chemical Society (2006))

quantum yield decreased about three times, primarily due to the more favorable molecular stacking of DD-PTCID. Moreover, the aggregate of DD-PTCDI shows a pronounced absorption band at longer wavelength, whereas the absorption of ND-PTCDI aggregate is not significant in the same wavelength region.

The facile fabrication of nanostructures with well-defined shapes and uniform sizes from stilbazolium-like dyes was reported [25.16]. Stilbazolium-like dyes (**1**) and (**2**) (Fig. 25.10) with different substituents were synthesized with the intention of exploring the possible influence of the substituent on the shape and therefore the optical properties of the resulting nanostructures. The self-assembly of the target molecules was induced by solvent exchange. Figures 25.10a and 25.10b display SEM images of compounds (**1**) and (**2**), respectively, assembled in nonsolvents. It can be seen that changing the substituents influenced the morphology of the aggregates significantly. As shown in Fig. 25.10c, molecule (**1**) consists of a strong electron-withdrawing moiety *N*-methylpyridinium (Nmpd) and a strong electron-releasing group *N*-methylpyrrole (Nmpr) connected by a conjugated system. For molecule (**2**), two weaker electron-releasing groups, 4-hexadecyloxyphenyl (4Hop), are connected to the Nmpd moiety. In addition, (**1**) is a planar molecule, so strong donor–acceptor interactions are the main driving force for the aggregation of (**1**) and induce the formation of 1-D nanostructures. In comparison, (**2**) is a nonplanar molecule with weak donor–acceptor interactions. There are two long flexible alkyl side-chains on the ionized pyridine ring, and therefore (**2**) is a typical amphiphilic molecule bearing a hydrophilic head (ionized pyridine ring) and two long and flexible hydrophobic arms (alkyl chains), which will drive the molecules to form H-aggregates with monodisperse spherical morphologies as shown in Fig. 25.10c.

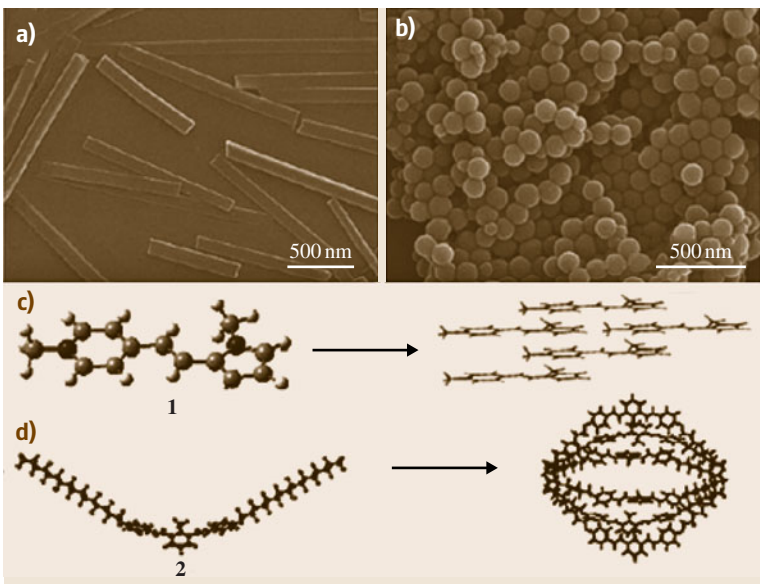


Fig. 25.10a–d SEM images of the nanorods formed from **(a)**: (**1**), nanospheres prepared with **(b)**: (**2**), and the simulated **(c)** 1-D and **(d)** 0-D aggregation of (**1**) and (**2**), respectively. (After [25.16], courtesy of Wiley-VCH (2004))

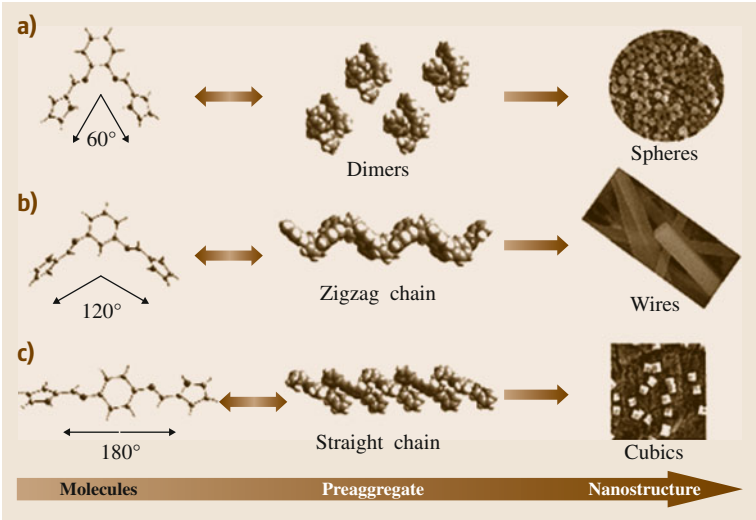


Fig. 25.11 Schematic representation of the formation processes of nanoscale materials of compounds *o*-, *m*- and *p*-bis(iminopyrrole)benzene, respectively. (After [25.17], courtesy of R. Society Chemistry (2010))

Besides those from derivatives with different substituents, nanostructures were also tuned between spheres, wires, and cubes via the self-assembly of three isomeric molecules of bis(iminopyrrole)benzene with the same substituents on different positions [25.17]. Although all three isomeric precursors, *o*-, *m*-, and *p*-bis(iminopyrrole) benzene, present similar strong multiple hydrogen-bonding interactions for molecular aggregation, distinctly shaped nanostructures were obtained. As shown in Fig. 25.11a, the two iminopyrrole (IP) groups in the *o*-isomer are 60° open-armed. Therefore, two monomers can embed into each other to form a dimer via quadruple hydrogen bonds, which act as the basic units for the formation of spherical structures. In contrast, the configurations of *m*- and *p*-isomers, with two IP groups open-armed at an angle of 120° and 180°, respectively, determine that each molecule connects with two others via hydrogen bonds, forming chain-like structures. Also determined by molecular configuration, the chain of the *m*-isomer is zigzag shape (Fig. 25.11b), while that of the *p*-isomer is almost linear (Fig. 25.11c). These chains are the actual building blocks for the solid states of the two isomers to form square wires and cubes, respectively. It is the different interactions for aggregate stacking at the supramolecular level caused by the isomeric molecular structures that are responsible for the different morphological evolution.

25.2.2 Absorption and Emission Properties

During the past several years, the unique optoelectronic properties have also sparked widespread investigation of hierarchical self-assembly of organic building blocks achieved by the induction of noncovalent intermolecular interactions. Besides exploration of synthetic strategies, much effort has also been made to investigate the unique properties of the organic nanomaterials obtained by molecular aggregation in the nanostructures. As mentioned above, it was found that the optical and electronic properties of organic nanomaterials are fundamentally different from those of their inorganic counterparts, because the intermolecular interactions in organic materials are basically of weak types, such as hydrogen bonds, $\pi-\pi$ stacking, van der Waals contacts, and charge-transfer (CT) interactions; For example, the size-dependent optical properties of organic nanoparticles, which are similar to but cannot be explained by the so-called quantum confinement effect observed in inorganic semiconductor quantum dots, were first observed in perylene nanocrystals and reported by *Nakanishi* and coworkers [25.18]. They prepared perylene microcrystals with different sizes from about 50 to about 200 nm using the reprecipitation method. Their excitonic absorption peaks were found to shift to the high-energy side with decreasing crystal size; that is to say, the shifts from that of the bulk crystal were about 500 and 1420 cm^{-1} for 200 and 50 nm microcrystals, respectively. Moreover, strong fluorescence from the free-exciton energy level in the microcrystals was observed even at room temperature, which is not usually observed in bulk crystals. Fu and Yao synthesized nanoparticles of 1-phenyl-3-((dimethylamino)styryl)-5-((dimethylamino)phenyl)-2-pyrazoline (PDDP) ranging from tens to hundreds of nanometers using the reprecip-

itation method. Their excitonic transitions responsible for absorption and emission, as compared with those of dilute solution, have been investigated as a function of nanoparticle size. They found that PDDP nanoparticles possess a special size dependence in their optical properties (Fig. 25.12). They identified an extended CT state stemming from PDDP molecules closely stacking in nanoparticles and observed its shift to the high-energy side with decreasing nanoparticle size due to exciton confinement. At the same time, the molecular $\pi-\pi^*$ absorption of the nanoparticles was also blue-shifted, accompanied by an almost unchanging $n-\pi^*$ absorption as a result of the reduced overlap of the pyrazoline ring π orbital and decreased intermolecular interactions. Moreover, S1 and CT states were in equilibrium in the nanoparticles, and the probability of fluorescence from S1 increased with decreasing nanoparticle size.

As mentioned above, an adsorbent-assisted PVD method was developed by Yao and coworkers for the preparation of crystalline 1-D organic nanomaterials. In very recent work, they extended this method to binary doped systems. 1,3,5-Triphenyl-2-pyrazoline (TPP) and rubrene were chosen as the model compounds, which were fabricated into uniformly doped crystalline nanorods and nanowires by adsorbent-assisted PVD; For example, binary doped organic nanowires were prepared with the above-mentioned adsorbent-assisted PVD method. A blue light emitter, 1,3,5-triphenyl-2-pyrazoline (TPP), and rubrene, a good orange dye used as the dopant in host–guest organic light-emitting diodes (OLEDs) with good transport property, were chosen as the model compounds, which were fabricated into uniformly doped crystalline nanorods and nanowires using the adsorbent-assisted PVD method [25.20]. The doping content was tuned by changing the molar ratio of the two sources.

Figure 25.13a–c shows fluorescence microscopy images of the binary nanostructures with various doping contents. The homogeneous emission color from all of the nanorods/wires in each sample testified that rubrene crystal grains were dispersed uniformly into the TPP matrices. The binary nanowires also show waveguide properties, which is proven by the microarea fluorescence microscopy of a single nanorod in Fig. 25.13c. It is revealed by the fluorescence microscopy images that the emission color evolves from blue to orange with the increase of rubrene content, and more importantly, white emission can be achieved when a proper TPP-to-rubrene molar ratio (100 : 1) is adopted. The tunable emission can also be observed from the evolution of the fluorescence spectra of the nanostructures with the

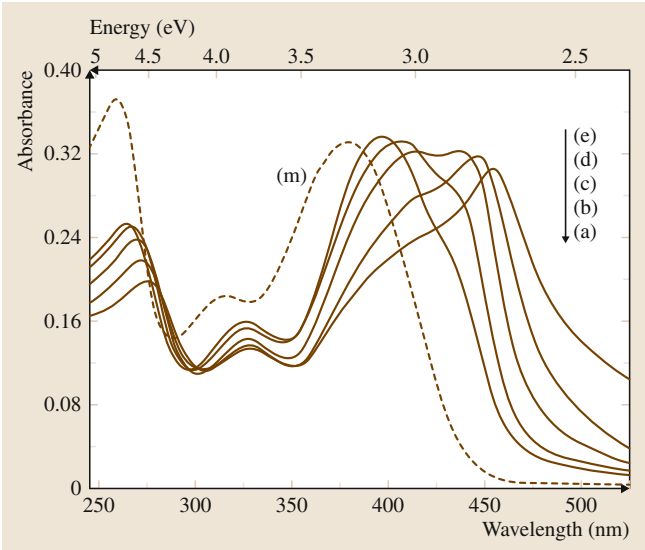


Fig. 25.12 Ultraviolet (UV)-visible absorption spectra of PDDP nanoparticle dispersions in water with different sizes: 20 nm, (b) 50 nm, (c) 105 nm, (d) 190 nm, and (e) 310 nm. (m) The spectrum of the PDDP/ethanol solution (1.0×10^{-5} mol/l). (After [25.19], courtesy of American Chemical Society (2001))

change of rubrene content shown in Fig. 25.13d. For comparison, doped amorphous thin films were also prepared using the coevaporation technique. The colors of the doped films are not stable because of the oxidation of rubrene. In contrast, the emission colors of the binary nanowires are very stable, which was ascribed to the crystallinity of rubrene. In the amorphous films, the emission of TPP can be quenched almost completely at 4% rubrene doping content, which is caused by the higher energy-transfer efficiency. In contrast, the emission of TPP cannot be quenched completely even when the dopant content was as high as 20% in the doped nanowires. Both the color stability and the incomplete quenching are essential to the realization of white-light emission.

In general, the fluorescence efficiency of organic chromophores decreases in the solid state, as a result of concentration quenching, even though they show high fluorescence efficiency in solution. However, a phenomenon named aggregation-induced enhanced emission (AIEE) was reported in recent years, in which enhanced emission instead of fluorescence quenching was observed in the solid state for some fluorophores [25.21–23]. As we know, solution investigations have made great contributions to the fundamental understanding of luminescence processes at molecu-

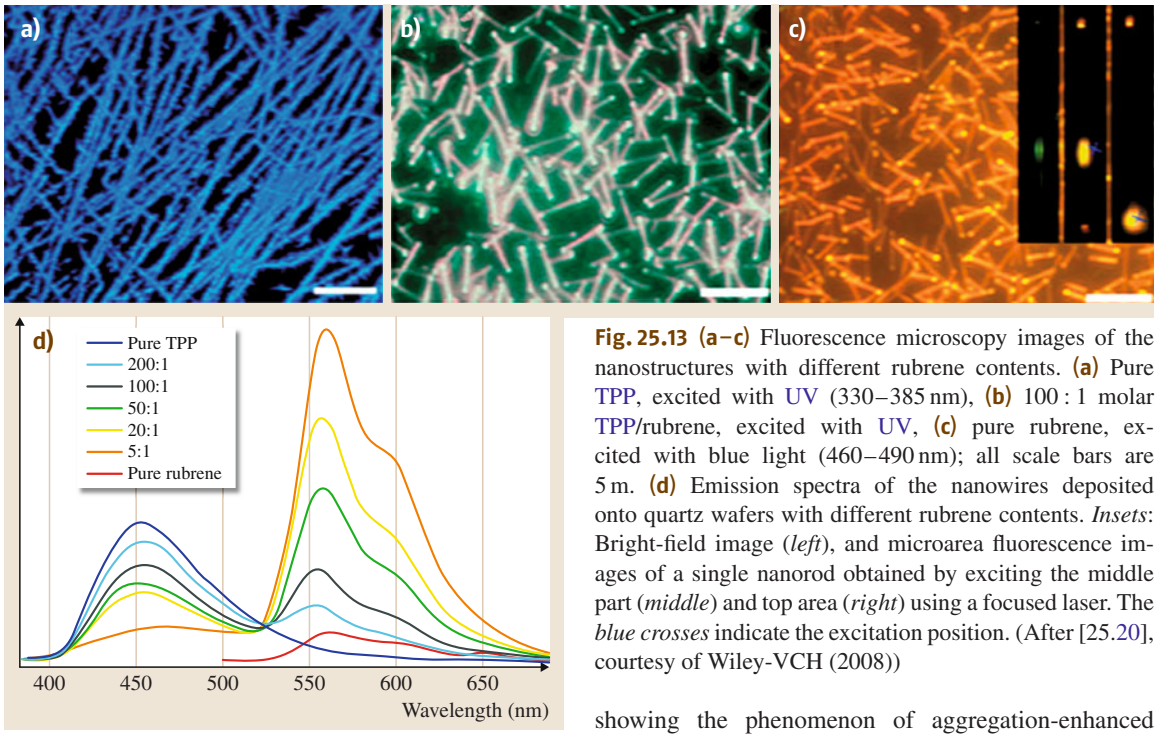


Fig. 25.13 (**a**–**c**) Fluorescence microscopy images of the nanostructures with different rubrene contents. (**a**) Pure TPP, excited with UV (330–385 nm), (**b**) 100 : 1 molar TPP/rubrene, excited with UV, (**c**) pure rubrene, excited with blue light (460–490 nm); all scale bars are 5 m. (**d**) Emission spectra of the nanowires deposited onto quartz wafers with different rubrene contents. *Insets*: Bright-field image (*left*), and microarea fluorescence images of a single nanorod obtained by exciting the middle part (*middle*) and top area (*right*) using a focused laser. The *blue crosses* indicate the excitation position. (After [25.20], courtesy of Wiley-VCH (2008))

lar level. The conclusions drawn from dilute-solution data, however, cannot commonly be extended to concentrated solutions; For example, luminescence is often weakened or quenched at high concentrations, a phenomenon widely known as *concentration quenching*. A main cause for the quenching process is mechanistically associated with the *formation of aggregates*, which is probably why the concentration quenching effect has frequently been referred to as *aggregation-caused quenching* (ACQ). However, in 2001, *Tang* et al. discovered an uncommon luminogen system in which aggregation worked constructively rather than destructively as in conventional systems [25.21, 22]. They found that a series of silole derivatives were nonemissive in dilute solutions but became highly luminescent when their molecules were aggregated in concentrated solutions or cast into solid films. Since the light emission was induced by aggregate formation, they termed the process as *aggregation-induced emission* (AIE).

A series of conjugated polymers that show enhanced light emissions in the solid state have been developed in recent years, examples of which include poly(1-phenyl-1-alkyne)s and poly(diphenylacetylene)s (Fig. 25.14) [25.24,25]. These polymers fluoresce when dissolved and emit more intensely when aggregated, showing the phenomenon of aggregation-enhanced emission (AEE). A common structural feature for these polymers is that each of their repeat units contains phenyl rotor(s) and an olefin stator. This is similar to tetraphenylethene (TPE), a well-known AIE luminogen [25.26]. In TPE, the olefin stator is surrounded by phenyl rotors and the restriction of intramolecular rotation (RIR) process is known to account for its AIE effect. In the polymer systems, the intramolecular rotations of the phenyl rotors are already partly restricted at molecular level due to the steric effect of the polymer chains. The polymers are thus fluorescent in the solution state, which explains why they are not AIE but AEE active.

Park et al. used AIE luminogens to fabricate nanowires, whose emission colors could be blue, green, yellow or red, readily tuneable by varying the luminogen structures [25.27]. It was found that the cyano group on the backbone of 1-cyano-trans-1,2-bis(3′,5′-bis-trifluoromethyl-biphenyl)ethylene (CN-TFMBE) serves to increase the polarity of the molecule and to give rise to an anisotropic electronic distribution, leading to stronger intermolecular Coulombic interactions. The $\pi-\pi$ interaction between nearest-neighbor molecules seems to be strengthened by coplanarization of the phenyl rings when the molecules are in close proximity. The bulky CF_3 groups attached to the phenyl

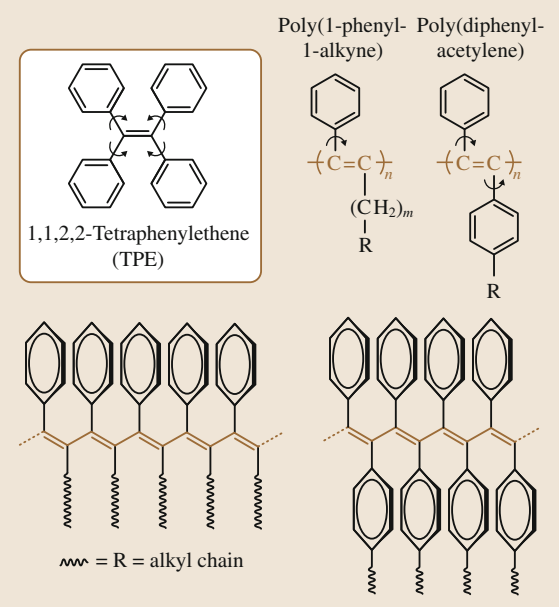


Fig. 25.14 AIE-active TPE and AEE-active disubstituted polyacetylenes. (After [25.23], courtesy of R. Society of Chemistry (2011))

rings at each end of CN-TFMBE give rise to sliding of the molecules along the molecular axis direction and the formation of hydrogen bonding of the type C–FH–C. The formation of 1-D nanowires of CN-TFMBE molecules was found to result from the relative contributions of these three major interactions to the intermolecular distances, arising intrinsically from the aforementioned structural factors. On the basis of these structural guidelines, they successfully prepared highly fluorescent color-tuned 1-D nanowires and two-dimensional (2-D) nanofabrics. These new nanomaterials exhibited well-defined optical properties and excellent mechanical stability. In addition, the compounds readily formed 1-D nanowires and 2-D nanofabrics, irrespective of the processing method and conditions used. *Tang* et al. achieved multicolor emissions from the same microfibers by changing the excitation wavelength but not the luminogen structure (Fig. 25.15) [25.28]. Generally, multicolor emissions are realized with blends of dyes or polymers emitting red, green, and blue light. They synthesized a group of silole derivatives with systematically varying 1,1- and 2,5-substituents. The solid-state emissions of the luminogens were found to be tunable by changing the molecular structure, especially the steric effects, of the substituents. Bulkier substituents help weaken the intermolecular interactions and restrict the intramolecular rotation IMR process, thereby blue-shifting the emission color and dramatically boosting the emission efficiency (Φ_F up to 99.9%). Polarized and multicolor emissions are realized in silole crystals and fibers, respectively. The information gained in this work on the structure–property relationships in the AIE system is of great value in terms of guiding future molecular engineering endeavors in designing molecular structures for new luminogenic materials with desired light-emitting properties in the solid state.

Regardless of the AIE materials, multicolor emission from the same nanostructures by changing the excitation wavelength was also found by *Zhao* et al. [25.29]. They demonstrated that it is also possible to obtain multicolor emission from crystalline 1-D nanomaterials and their hierarchical assemblies based on a single low-molecular-weight organic compound [25.29]. The selected model compound, 1,2,3,4,5-pentaphenyl-1,3-cyclopentadiene (PPCP, inset of Fig. 25.16), is a well-known blue-light-emitting dye used as the emitting layer material in electroluminescence devices. After being fabricated to crystalline nanoribbon assemblies, PPCP displayed a multicolor emission property; that is, blue, green, and red emission was achieved by exciting the same sample with appropriate wavelengths. Figure 25.16 displays the RGB emission obtained by exciting the PPCP nanoribbon arrays with UV, blue, and green light. Spectral measurements in-

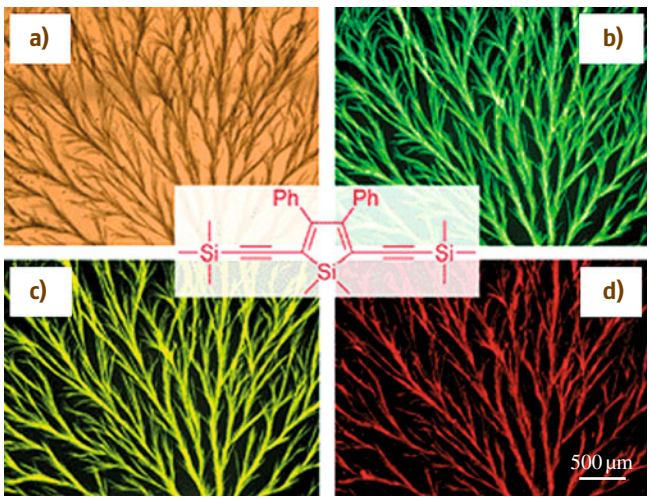


Fig. 25.15 **(a)** Photograph and **(b–d)** fluorescence images of microfibers of silole taken **(b)** under normal lighting and upon excitation by **(c)** UV, **(d)** blue, and **(e)** green light. (After [25.23], courtesy of R. Society of Chemistry (2011))

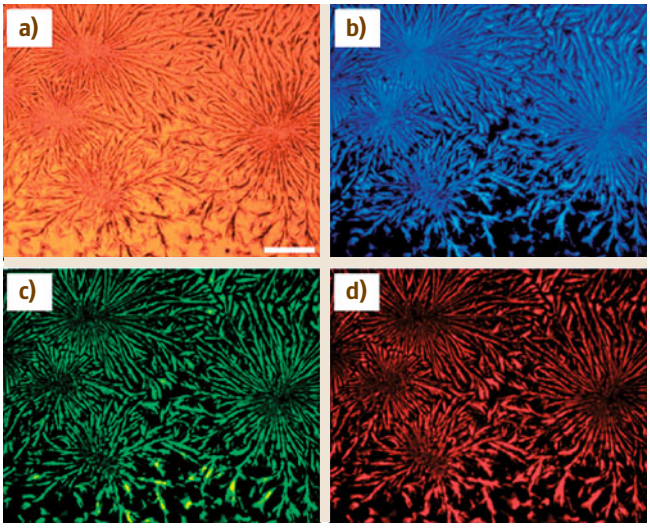


Fig. 25.16a–d Fluorescence microscopy images of PPCP nanoribbon assemblies. **(a)** Bright-field image, **(b)** excited with UV light (330–380 nm), **(c)** excited with blue light (460–490 nm), and **(d)** excited with green light (520–550 nm). The *scale bar* is 10 μm. (After [25.29], courtesy of Wiley-VCH (2007))

dicated that three kinds of emitting centers (blue, green, and red) coexist in the PPCP nanostructures, in which the blue-light-emitting centers came from single PPCP molecules in the nanostructures. Comparison of emissions from crystalline nanoribbons with different amounts of defects and the contrast between the emissions from crystalline and amorphous films proved that the green- and red-light-emitting centers in the PPCP nanoribbons were induced by their crystallinity and the structural defect energy levels therein. Meanwhile, the emission from each center can be further enhanced by the 1-D structure of the nanomaterials by self-convergence along specific directions.

25.2.3 Optoelectronic Properties

The optoelectronic properties of organic nanomaterials are fundamentally different from their inorganic counterparts due to the weak intermolecular interactions in organic nanomaterials. Moreover, owing to their unique nanoscale size, the optoelectronic properties of organic nanomaterials are also different from those of their monomer and bulk solid counterparts. Therefore, there is great interest in understanding the optoelectronic properties of organic nanomaterials for their practical application in optoelectronic devices. In this section, we focus on the field-emission, charge-transport, and photovoltaic properties of organic nanomaterials.

Field-Emission Property

The unique electrical and optical properties of organic nanomaterials are the focus of study in this field, for example, the field-emission property of organic nanomaterials. Liu et al. synthesized single-crystalline nanocone arrays of a charge-transfer complex, copper tetracyanoquinodimethane (CuTCNQ) in large area by controlling the reaction velocity of copper and tetracyanoquinodimethane (TCNQ). This was achieved by applying a constant current on the copper source (Cu film) and using a physical and chemical vapor combined deposition technique without catalyst or template [25.30]. It was attractive that, when the used Cu films were brushed with plow grooves but other growth conditions were kept constant, CuTCNQ nanocones grew along the grooves as shown in Fig. 25.17a–c. Regardless of the detailed mechanism, these large-area, homogeneous nanocones indicate their potential appli-

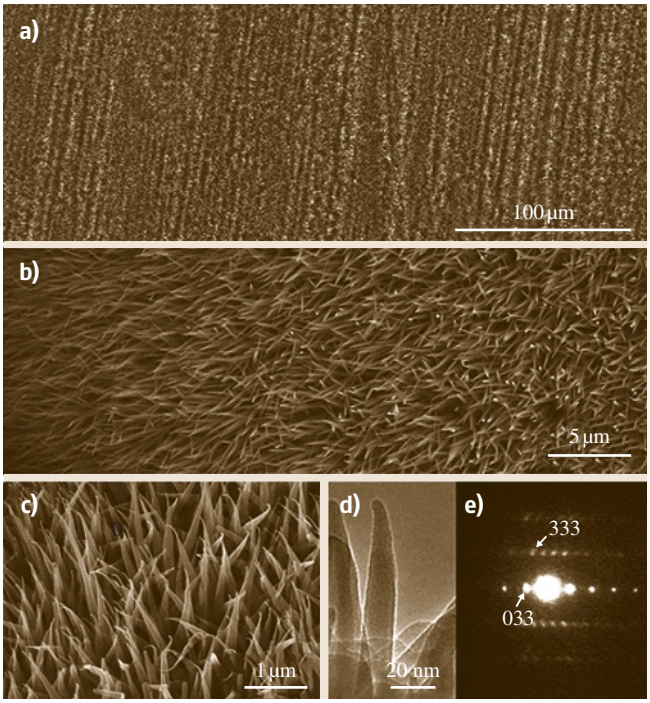


Fig. 25.17 **(a–c)** SEM images of CuTCNQ nanocone arrays grown at brushed grooves. **(d)** TEM image of CuTCNQ nanocones; **(e)** SAED pattern of one CuTCNQ nanocone. (After [25.30], courtesy of Wiley-VCH Verlag (2011)) ◀

cations. A TEM image of an individual nanocone is shown in Fig. 25.17d, and its corresponding selected-area electron diffraction (SAED) pattern is shown in Fig. 25.17e. It is obvious that the nanocones were rather sharp, and the tip diameter could reach down to several nanometers. Moreover, the SAED pattern exhibited no change in different parts of the same nanocone, indicating that the whole nanocone was a single crystal. The nanocones could be very sharp (e.g., with diameter less than several nanometers), and all the nanocones are single crystals, which indicated possibly excellent field-emission property.

The sharp nanocone arrays suggested their potential applications in field-emission devices. As preliminary experiments, the field-emission characteristic of the nanocone arrays were investigated in a vacuum chamber of $\approx 10^{-7}$ Pa at room temperature under a two-parallel-plate configuration. The sample was stuck onto a stainless-steel sample stage using conducting glue as the cathode. Another parallel stainless-steel plate served as the anode. The samples' areas were about 0.064 cm^2 (0.32 cm × 0.20 cm). The distance between the anode and cathode was 300 μm. A typical plot of the field-emission current density (J) versus the applied field (E) and the corresponding Fowler–Nordheim (F-N) plot are presented in Fig. 25.18a,b. The turn-on field of the sample is about 9.43 V/μm, defined as the field giving an emission current density of 10 mA/cm^2. The maximal current density of the sample reaches about 2.7 mA/cm^2 at 17.7 V/μm. This was better than the property of CuTCNQ nanowires [25.31], indicating the potential applications of these nanocone arrays in nanoelectronics. Moreover, it was found that the surface of CuTCNQ nanocones (Fig. 25.18c) exhibited superhydrophobicity with contact angles of around 155° (Fig. 25.18d), significantly larger than for other nanostructures of CuTCNQ (125−130°) [25.32], indicating the enhanced hydrophobicity of the nanocones.

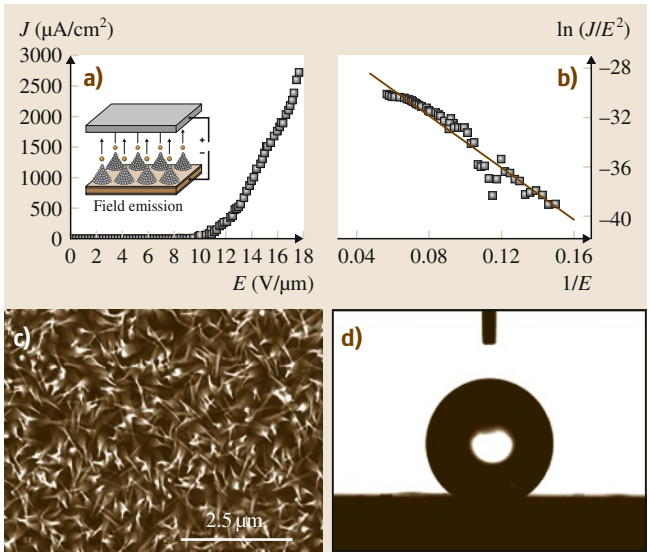


Fig. 25.18 (**a**) Field-emission J–E curve (*inset*: field-emission devices), (**b**) corresponding F–N plot, (**c**) SEM image, and (**d**) corresponding water contact angle (≈ 155°) of single-crystalline CuTCNQ nanocone layers. (After [25.30], courtesy of Wiley-VCH (2011))

Charge-Transport Property

The transport properties of organic nanomaterials are the subject of fundamental investigation of molecular nanoelectronics for the orientation of high-performance molecular nanomaterials and devices. Transport properties of the same materials will be different at different dimensionality or size scale; For example, in organic thin-film field-effect transistors, the two-dimensional (2-D) electron gas transports through the molecular/nanometer-thick film between the gate insulator and organic semiconductor, and depends strongly on the thickness and width of the conducting channel of the transistor. With reducing channel width, e.g., in organic nanowires or nanoribbons, the transport will be confined in the 1-D structure. The transport changing from 2-D to 1-D will result in some new phenomena due to the confinement effect of the nanomaterials. With further reduction in size, when the organic nanomaterials become zero-dimensional (0-D), many effects of quantum dots will appear. All the low-dimensional organic nanomaterials (1-D, 0-D) have received great scientific and technological interest due to their promising potential applications in electronics and optoelectronics, and are also attractive for fundamental investigation.

Organic field-effect transistors (OFETs), a kind of device with three terminals (drain, source, and gate electrodes), gate insulator, and active semiconductor layer, provide the ability to offer insight into the charge transport of π-conjugated systems, and are acting as a strong tool for exploration of the structure–property relationship of π-conjugated systems, such as field-effect mobility (μ, the drift velocity of carriers under unit electric field), current on/off ratio (the ratio of the maximum on-state current to the minimum off-state current), and threshold voltage (the minimum gate voltage required to turn on the transistor). More importantly, OFETs are essential building blocks for the next generation of cheap and flexible organic cir-

cuits. Therefore, since the discovery of OFETs in 1980s [25.33] they have attracted the world's attention over 20 years, including the discovery, design, and synthesis of π-conjugated systems for OFETs, extending their potential applications to radiofrequency identification (RFID) tags, flexible displays, electronic papers, sensors, etc. [25.34]. Indeed, electrical characterization of OFETs provides a wealth of information on π-conjugated systems [25.35]. The semiconductor layer of OFETs usually consists of organic thin films. Inevitably, the existence of disorder and grain boundaries in thin films masks the intrinsic properties of the organic semiconductors and restricts the mobility of such devices. It is expected that high-quality single crystals of organic semiconductors will reveal intrinsic charge transport in materials and give high mobility in OFETs. The first organic OFET devices based on an individual single-crystalline nanoribbon can be traced back to 2006 [25.36]. *Tang* et al. fabricated OFETs based on an individual CuPc nanoribbon. The activity of OFETs based on organic nanoribbons was highly sensitive to electron beam irradiation; For example, OFETs based on organic nanoribbons lost their field-effect activity after being scanned by SEM. Therefore, it was unsuitable to use electron beam deposition or focused ion beam deposition to fabricate devices based on organic nanoribbons. A series of new methods were developed to fabricate OFETs [25.37]. The bottom-contact configuration (Fig. 25.19a) is always adopted when organic crystals are unstable in vacuum (e.g., tetrathiafulvalene, TTF) or the deposition of a top electrode on them is difficult. It is also noticed that the bottom-contact configuration sometimes causes contact problems due to the weak van der Waals force between electrode and crystal. In contrast, top-contact devices could work effectively to avoid this problem, e.g., by using a copper grid or a Au microwire as a mask to deposit electrodes on a *small* organic crystal (Fig. 25.19b). But during the vacuum deposition of electrodes on organic crystal the thermal irradiation may also do harm to organic crystal. To avoid thermal radiation damage and filling of pinholes in the dielectric layer by metal atoms

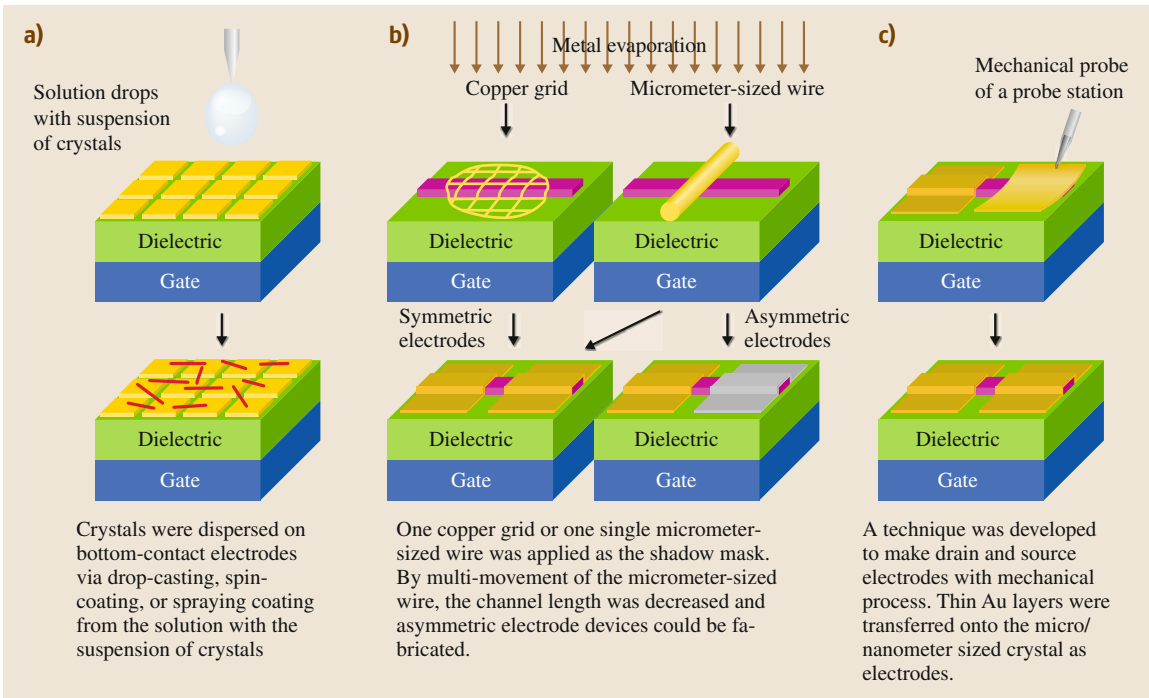


Fig. 25.19a–c Techniques for fabrication of devices based on organic micro- and nanocrystals. **(a)** Bottom-contact configuration with predeposited electrode arrays on substrate, dropping solution on the electrodes for crystallization, **(b)** shadow mask technique employing a copper grid or a Au microwire as the mask for deposition to make symmetrical and asymmetrical electrodes, **(c)** Au-layer stamping technique, thin Au layers are mechanically transferred and pasted on an individual crystal as the electrodes. (After [25.37], courtesy of Wiley-VCH (2008))

during electrode vacuum deposition, a mechanical technique was recently developed to paste electrodes onto crystals directly (Fig. 25.19c). Au thin film deposited on a Si wafer is cut into small pieces (approximately $30\,\mu m \times 150\,\mu m$) by a sharp probe, then a piece of the film is peeled off from the substrate by the probe and pasted onto the organic crystal as a source or drain electrodes. This *cold* electrode circumvents the disadvantages of thermal evaporation and thus ensures high device performance.

Based on OFETs with organic and polymer nanostructures, the transport properties of the nanostructures can be analyzed. Structure–property studies are a prerequisite to understand the fundamental properties of organic materials and their corresponding molecular structure and device properties. High mobility is expected when conjugated molecules have strong interactions with neighboring molecules to maximize the overlap between molecular orbits, e.g., cofacial $\pi-\pi$ stacking structure. However, so far, lots of organic semiconductors which exhibit high mobility (e.g., pentacene) adopt the edge-to-face herringbone structure with reduced intermolecular electronic couplings. It is imperative to establish the structure–property relationship of organic semiconductors explicitly. TTF and its derivatives have become one of the most studied heterocyclic systems since its discovery [25.39]. It is well known that TTF crystals have two phases: α-TTF, which belongs to space group $P21/c$ with two molecules at centrosymmetric sites of the unit cell, and β-TTF, which belongs to space group P1 with four symmetry-inequivalent molecules at the centrosymmetric sites of the unit cell (Fig. 25.20) [25.38]. Crystals of α-TTF can be grown from *n*-heptane solution, while β-TTF can be obtained by using chlorobenzene as solvent. Single-crystal transistors based on α- and β-TTF (Fig. 25.20) suggest that the maximum field-effect mobility of the α-phase is as high as $1.20\,cm^2/V\,s$ while that of the β-phase is only about $0.23\,cm^2/V\,s$, which is assigned to the strong $\pi-\pi$ stacking and the S···S intermolecular interactions of α-TTF. The results provide direct proof of the structure–property relationships of TTF crystals.

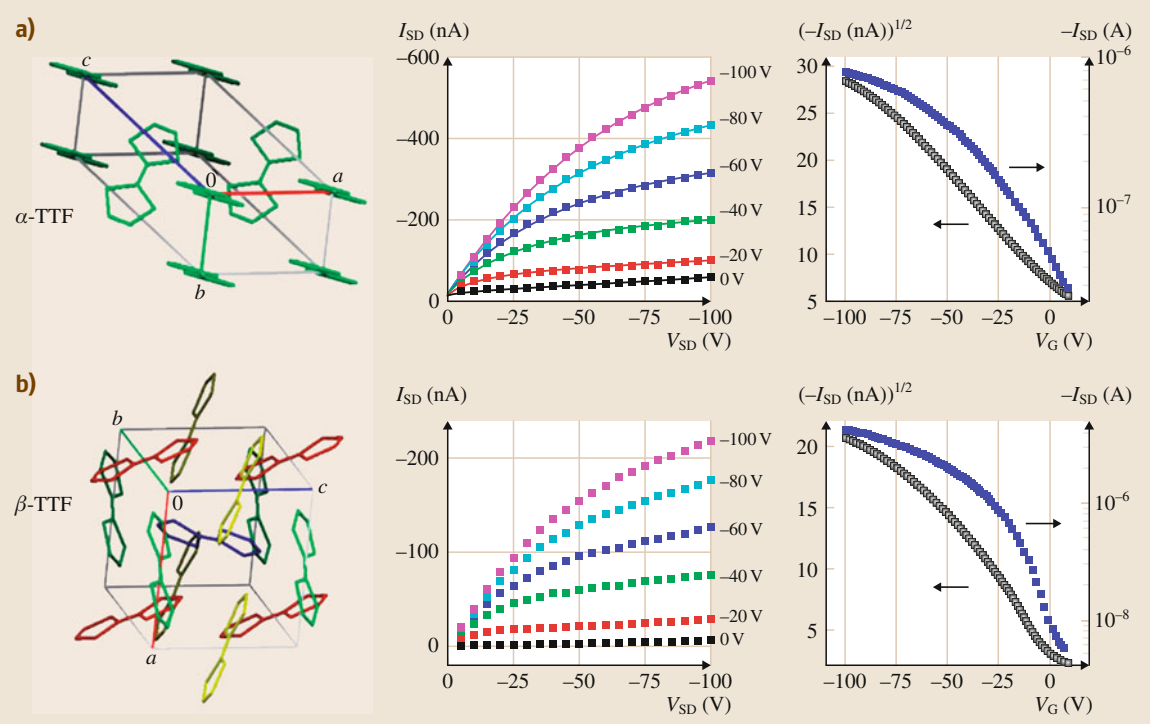


Fig. 25.20a,b Crystal structures of α- and β-TTF, and typical output and transfer characteristics of the transistors based on **(a)** α- and **(b)** β-TTF crystals. The maximum field-effect mobility of the α-TTF is as high as $1.20\,cm^2/V\,s$, while that of β-TTF is only about $0.23\,cm^2/V\,s$. The different charge-transport property indicates the importance of phase control for high-performance devices. (After [25.38], courtesy of American Institute of Physics (2007))

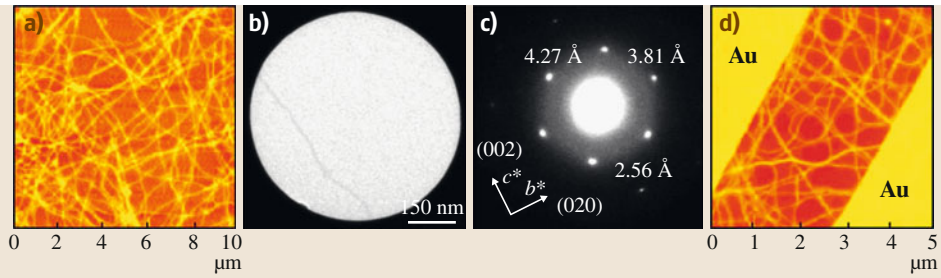


Fig. 25.21a–d Well-defined, highly crystalline nanowires of a derivative of PPE, TA-PPE, are obtained by self-assembly. **(a)** AFM image, **(b)** TEM image, **(c)** SAED pattern, and **(d)** devices. (After [25.40], courtesy of American Chemical Society (2009))

Certainly, the study of transport properties is not only confined to small molecules, but also extends to conjugated polymers. Well-defined, highly crystalline nanowires of a derivative of PPE, TA-PPE, were obtained by self-assembly [25.40]. Structure analyses demonstrated that the nanowires probably have an orthorhombic crystal unit cell with lattice parameters of $a \approx 13.63$ Å, $b \approx 7.62$ Å, and $c \approx 5.12$ Å. In the nanowires, the backbones of the TA-PPE chains are parallel to the nanowire long axis, with their side-chains standing on the substrate. The transport properties of the nanowires examined using OFETs suggest that the mobility of the polymer crystalline nanowire is $\approx 10^{-2}\,\mathrm{cm}^2/\mathrm{V\,s}$, with the highest mobility approaching $0.1\,\mathrm{cm}^2/\mathrm{V\,s}$, which is 3–4 orders higher than that of thin-film transistors of the same polymer, indicating the high performance and efficient charge transport of the 1-D polymer nanowire crystals (Fig. 25.21).

Photovoltaic Properties

The nanowire geometry provides potential advantages over planar wafer-based or thin-film solar cells in every step of the photoconversion process [25.41]. These advantages include reduced reflection, extreme light trapping, improved bandgap tuning, facile strain relaxation, and increased defect tolerance. These benefits are not expected to increase the maximum efficiency above standard limits; instead, they reduce the quantity and quality of material necessary to approach those limits, allowing for substantial cost reductions. Additionally, nanowires provide opportunities to fabricate complex single-crystalline semiconductor devices directly on low-cost substrates and electrodes such as aluminum foil, stainless steel, and conductive glass, addressing another major cost in current photovoltaic technology [25.42]:

Eindhoven University of Technology (TU) researchers want to develop solar cells with an efficiency of over 65% *by means of nanotechnology. In Southern Europe and North Africa these new solar cells can generate a substantial portion of the European demand for electricity. The Dutch government reserves EUR* 1.2 *million for the research. Stacking nanowires make it possible to stack a number of subcells (junctions). In this process each subcell converts one color of sunlight optimally to electricity. The highest yield reported until now in a nanowire solar cell is* 8.4%. *Haverkort:* We expect that a protective shell around the nanowires is the critical step towards attaining the same efficiency with nanowire solar cells as with thin-film cells. *Haverkort thinks that at* 5–10 *junctions he will arrive at an efficiency of* 65%. *In addition, the researchers expect considerable savings can be made on production costs, because nanowires grow on a cheap silicon substrate and also grow faster, which results in a lower cost of ownership of the growth equipment. What is more, the combination of the mirror systems with nanotechnology will imply an acceptable use of the scarce and hence expensive metals gallium and indium.*

Solar cells and photodetectors operate under the same basic process: converting light into current. Miniature versions of these devices will rely on nanostructured materials with good photoconducting properties. Although the figures of merit for inorganic photoconducting nanowires, such as those made from ZnO or Si, have been measured, relatively little is known about the properties of organic nanowires [25.43]. Given that organic nanowires could be both chemically tunable and relatively inexpensive to integrate into electronic

circuits, *Redmond*'s group at the Tyndall National Institute in Cork, Ireland has measured photoconductivity in a single polymer nanowire [25.44]. The authors fabricated the 200 nm-wide, 15 m-long polymer wires using a simple template wetting technique. Metal contacts were made on either end of a single wire to measure the photoinduced current over several on–off cycles of a near-ultraviolet laser. The wire's quantum efficiency – the number of current-carrying electrons produced per photon hitting the wire – is about 0.1%, which is competitive with several inorganic nanowires. As in many polymer-based electronic devices, the limiting factors may be the noncrystalline structure and poor electrical contact with the metal leads.

With the demands for new materials with enhanced properties, such as narrow bandgap and high carrier mobility, control over the interface and morphology of the active layer are key issues for achieving high-efficiency organic photovoltaics (OPVs). In particular, control over the nanoscale phase separation between the donor and acceptor, molecular ordering enhancement of the donor polymers, and an increase in the percolation of acceptor molecules are critical factors that determine bulk heterojunction (BHJ) device properties. Device efficiency is mainly determined by control over the nanostructure of the donor–acceptor blended active layer. A large interface between the donor and acceptor layers is needed for the dissociation of excitons, and efficient charge extraction requires a nanostructure that allows efficient charge transport to the electrodes. Bulk heterojunction solar cells based on blends of poly(3-hexylthiophene) (P3HT) and phenyl-C_{61}-butyric acid methyl ester ($PC_{61}BM$) were fabricated using self-assembled P3HT nanowires in a marginal solvent without posttreatments by *Cho* et al. [25.45]. The interconnected network structures of self-organized P3HT nanowires create continuous percolation pathways through the active layer and contribute to enhanced carrier mobility (Fig. 25.22). The morphology and photovoltaic properties are studied as a function of aging time of the P3HT precursor solution. Optimal photovoltaic properties are found at 60 h ageing time, which increases both light absorption and charge balance. Multilayered solar cells with a compositionally graded structure are fabricated using preformed P3HT nanowires by inserting a pure P3HT donor phase into the hole-collecting electrode. Applying optimized annealing conditions to the P3HT buffer layer achieves an enhanced hole mobility and a power conversion efficiency of 3.94%. The introduction of a compositionally graded device structure, which contains a P3HT-only region, reduces charge recombination and electron injection to the indium tin oxide (ITO) electrode and enhances the device properties. These results demonstrate that preformed semiconductor nanowires and compositionally graded structures constitute a promising approach to the control of bulk heterojunction morphology and charge-carrier mobility.

Jenekhe et al. [25.46] prepared P3BT nanowires by solution-phase self-assembly and used them to construct highly efficient P3BT/fullerene nanocomposite solar cells. The fullerene/P3BT nanocomposite films showed an electrically bicontinuous nanoscale morphology with average field-effect hole mobilities as high as $8.0\times10^{-3}\,cm^2/V\,s$ due to the interconnected P3BT nanowire network. The power conversion efficiency of fullerene/P3BT nanowire devices was 3.0% (at $100\,mW/cm^2$, AM1.5) in air.

p–n junctions are of great importance in optoelectronic devices. Organic/inorganic p–n junction nanowires composed of functional organic molecules and inorganic molecules may be able to realize new or improved chemical and physical properties that were not observed in the individual component on nanosize and their bulk materials. *Li* et al. [25.47] reported fabrication of an organic/inorganic semicon-

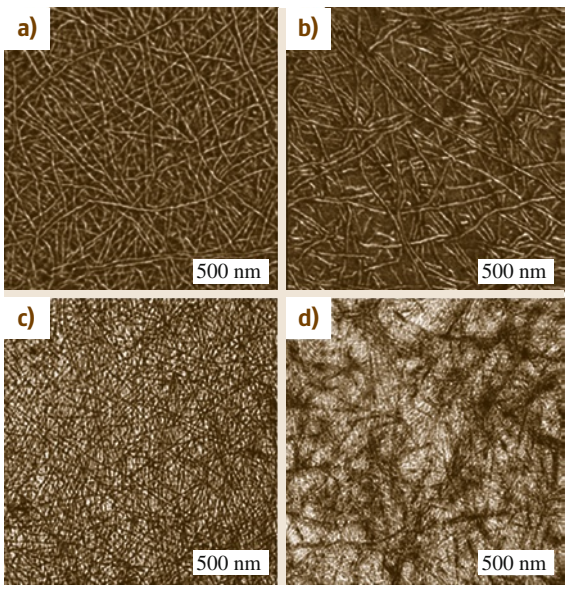


Fig. 25.22a–d AFM and TEM images, respectively, of (**a**,**c**) homo-P3HT nanowires and (**b**,**d**) P3HT nanowires/PCBM blend film. (After [25.45], courtesy of Wiley-VCH (2011))

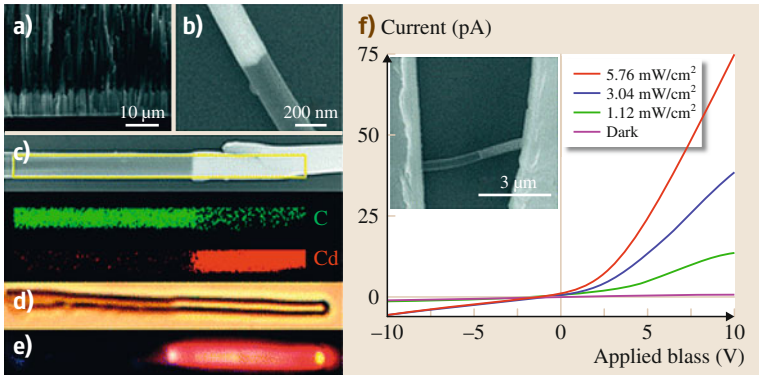


Fig. 25.23 **(a)** Side view of CdS–PPY nanowires inside the AAO template, **(b)** typical image of a single CdS–PPY nanowire, **(c)** element mapping of a single CdS–PPY nanowire, **(d)** optical image of a single CdS–PPY nanowire, **(e)** fluorescent image of a single CdS–PPY nanowire excited by a 405 nm laser, **(f)** typical current–voltage (I–V) curves for a single CdS–PPY heterojunction nanowire under light illumination with different intensities at room temperature. *Inset*: SEM image of the measured nanodevice. (After [25.47], courtesy of American Chemical Society (2008))

ductor p–n junction nanowire (Fig. 25.23). They used ordered porous AAO templates and chose the p-type organic semiconductor polypyrrole (PPY) and n-type inorganic semiconductor CdS to prepare heterojunction nanowires, finding remarkable performance of the light-controlled diode within a single hybrid p–n junction nanowire. The CdS–PPY heterojunction nanowire exhibited rectifying property at room temperature. Interestingly, with increasing illumination intensity, the conductivity of the CdS–PPY heterojunction nanowire increased. The rectification ratio of the diode increased from 8.0 to 13 with enhancement of the light intensity from 1.12 to 5.76 mW/cm^2. Controlling the conductivity of the p–n junction nanowire by the light irradiation simply to achieve diode action indicates a new way to realize photoelectric integration in a single nanowire device.

Hu et al. synthesized organic single-crystalline p–n junction nanoribbons of CuPc and F_{16}CuPc at large scale through crystallization of F_{16}CuPc on CuPc nanoribbon templates [25.48]. The selective crystallization strongly depended on the similar molecular structures, lattice parameters, and similar attachment energies at the interfacial basal planes of the (001) facets of F_{16}CuPc and CuPc. An attractive feature of this system is the ability to generate p–n heterojunction nanoribbons easily over large areas. An individual p–n heterojunction nanoribbon is shown in Fig. 25.24.

The length of the active p–n junction could reach about ≈ 25 μm, as unambiguously identified by optical microscopy and SEM (Fig. 25.24c). The lengths of the p–n junction will depend on the length of the CuPc template and the crystallization time of the F_{16}CuPc on CuPc templates. Such long p–n junctions encouraged us to utilize these structures in nanodevices and circuits. An example SEM image of an individual nanoribbon of several micrometers length is shown in Fig. 25.24c, and the corresponding composition distribution along the nanoribbon was identified by local elemental mapping by energy-dispersive x-ray spectroscopy as shown

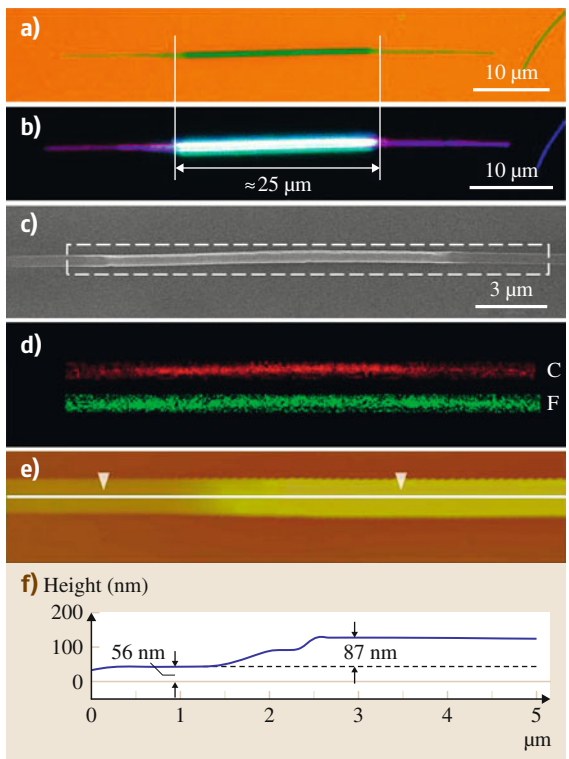


Fig. 25.24 **(a,b)** Optical images of an individual p–n heterojunction nanoribbon, **(c,d)** SEM image and corresponding local elemental mapping of an individual nanoribbon, **(e,f)** AFM image and height curve of the nanoribbon. (After [25.48], courtesy of American Chemical Society (2010))

in Fig. 25.24d. Along the nanoribbon the fluorine (F) was uniformly distributed, while the proportion of carbon (C) was higher at the middle region of the p–n junction than elsewhere because of the integration of C element from both CuPc and F_{16}CuPc. The thickness of the p–n junction was about 1418 nm, consisting of 87 nm of CuPc and 56 nm of F_{16}CuPc as determine by AFM experiments (Fig. 25.24e,f). Well-defined ambipolar transport characteristics were demonstrated on discrete devices. A discrete p–n heterojunction nanoribbon photovoltaic solar cell was fabricated. Figure 25.25a shows a schematic configuration of a p–n device, while Fig. 25.25b shows the current–voltage (I–V) characteristics for the SEM device shown in Fig. 25.20d. The plot for a CuPc–F_{16}CuPc nanoribbon device yielded a J_{SC} of $\approx 0.054\,\mathrm{mA/cm^2}$, V_{OC} of $\approx 0.35\,\mathrm{V}$, and fill factor (FF) of ≈ 0.36 under 1 sun ($100\,\mathrm{mW/cm^2}$). Furthermore, these individual test structures will enable detailed analysis to be carried out in areas that have been difficult to study in bulk heterojunction devices. The p–n nanoribbons will also serve as ideal systems to understand the fundamental charge-transport and photovoltaic behaviors at nanoscale organic–organic interfaces. This work opens the opportunity to explore synthesis of high-quality organic single-crystalline p–n junction nanoribbons and their application in fundamental science and new device technologies.

25.2.4 Mechanical Properties

Nanomaterials are an attractive group of modern engineering materials with properties superior to those of their coarse-structured counterparts. In particular, this applies to the mechanical properties, such as tensile strength, ductility, fatigue, and wear resistance. The novel mechanical properties of nanomaterials are a subject of nanomechanics research. Nanomechanics is a branch of nanoscience studying fundamental mechanical (elastic, thermal, and kinetic) properties of physical systems at the nanometer scale. It has emerged on the crossroads of classical mechanics, solid-state physics, statistical mechanics, materials science, and quantum chemistry. As an area of nanoscience, nanomechanics provides a scientific foundation for nanotechnology. However, despite the progress made in technology of such materials including nanocrystalline metals and nanocomposites, their application is still restricted by insufficient experimental data and interpretation; For example, organic nanocrystals are usually delicate and

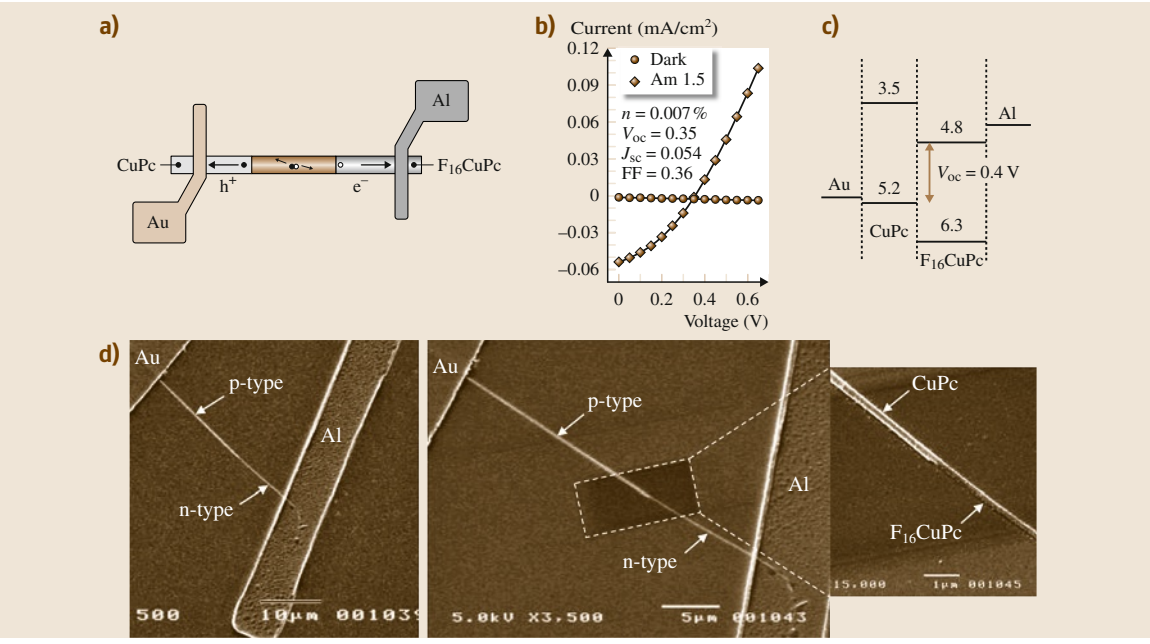


Fig. 25.25 **(a)** Schematic configuration of a discrete p–n heterojunction solar cell, and **(b)** the current–voltage characteristics, **(c)** band diagram, and **(d)** SEM image of a discrete CuPc-F_{16}CuPc nanoribbon photovoltaic solar cell. The devices were measured under AM 1.5 irradiation ($100\,\mathrm{mW/cm^2}$) (After [25.48], courtesy of American Chemical Society (2010))

easily broken. However, at micro- and nanometer sizes, some new phenomena are emerging, indicating great promise for organic and polymeric nanomaterials in the study of nanomechanics.

Flexible devices and circuits of organic thin films have been demonstrated successfully [25.50]. A remaining challenge at present is how to integrate flexibility and high carrier mobility together, because flexibility typically originates from microscopically disordered materials, while high mobility originates from highly ordered structures typically with crystalline order; For example, it is well know that organic single crystals exhibit high mobility compared with their amorphous and polycrystalline film counterparts, being some of the best candidates for fabrication of high-performance devices. However, organic bulk crystals are very fragile and delicate, so that they are challenging to use in flexible devices. It has been discovered that organic single crystals of nanometer size exhibit good flexibility [25.51], which provides a chance to obtain high-performance flexible electronic devices based on organic crystals. However, up till now, the mechanical and transport properties of organic nanocrystals at bent status have rarely been studied. One reason is probably due to the difficulty in performing such experiments, e.g., fabricating and investigating flexible devices based on individual organic nanocrystals.

Tang et al. [25.49] found that nanowire crystals with diameter smaller than 150 nm would not break even when bent to very small radius of curvature (Fig. 25.26), and could be twisted (Fig. 25.26a) or bent over 180° without breaking (Fig. 25.26b–d). The nanowire crystals had the unique ability to be bent, forming a perfect circular shape (Fig. 25.26b,c), or a ring adhered to the substrate surface (Fig. 25.26d). The maximum local strain of the wires shown in Fig. 25.26 could be estimated from $\varepsilon = d/2r_c = 3.1–5.4\%$, where r_c is the bending radius of curvature and d is the width of nanowire in the r_c direction [25.52]. These nanowire crystals could be bent to even smaller radius of curvature than shown in Fig. 25.26 and to endure larger local strains without fracture.

In situ manipulation of individual crystal in a SEM system as shown in Fig. 25.27 provided direct evidence of reversible bending of organic nanowire crystals. In order to reduce the damage of crystals caused by electron beam radiation, the lowest available voltage of 4 kV was used. An individual nanowire with diameter of ≈ 400 nm was transferred and pinned by the van der Waals force to the edge of a silicon wafer. Without ex-

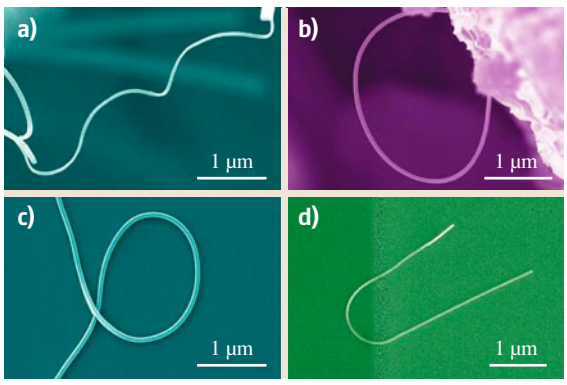


Fig. 25.26a–d SEM images of CuPc nanowire crystals with width smaller than 150 nm, which can be twisted and bent exhibiting excellent flexibility. (After [25.49], courtesy of Wiley-VCH (2011))

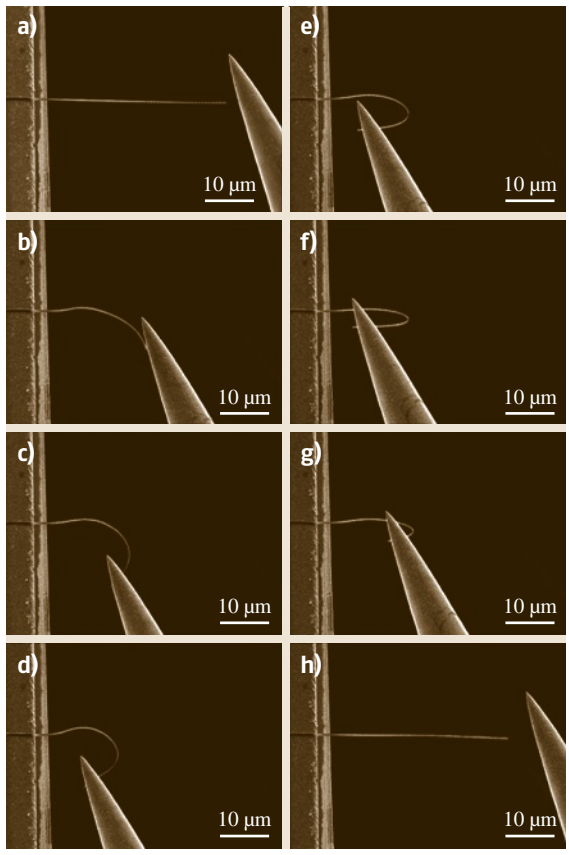


Fig. 25.27a–h SEM images for the typical bending configurations of a CuPc nanowire with width of ≈ 400 nm by a series of transverse manipulations with a mechanical probe. (After [25.49], courtesy of Wiley-VCH (2011))

ternal force, the nanowire was straight (Fig. 25.27a). Subsequently, the nanowire was taken through a series of distinct compression manipulations using the tip of a probe on a three-dimensional probe stage. When a pushing force towards the wafer was applied by the tip of the probe, the wire bent slightly (Fig. 25.27b). Driven by a larger force, the wire was bent further, and the bending radius of curvature decreased gradually (the curvature increased, Fig. 25.27b–d). The radius of curvature reached $\approx 3\,\mu m$ in Fig. 25.22d, and could be reduced further (Fig. 25.27e,f). The maximum local strain in the wires bent by the probe was estimated at over 10% without breaking. These data of local strain can be used as the reference for the design of flexible devices and circuits. Besides such flexibility, this experiment also showed the elasticity characteristic of the nanowire crystals, which is also important for flexible electronics. When the probe was moved far from the wire, the curvature decreased due to the elasticity of the wire (Fig. 25.27g). Finally, the wire recovered its original straight shape after the mechanical probe was removed (Fig. 25.27h). The bend and recovery could be carried out multiple times reversibly without fracture of the crystal. These results are relevant for the charge-transport theory of organic semiconductors as well as for flexible devices and circuits design. Moreover, our study suggested that small-size nanowire crystals (150–500 nm) showed good flexibility and elasticity. They could be bent over 180° with local strain over 10% without fracture. The Young's modulus of the single-crystalline wires was about 3.8–4.5 GPa, one order of magnitude smaller than that of inorganic nanostructures, indicating that organic nanowire crystals are much more appropriate for use in flexible devices.

25.3 Applications

Since the 1990s, great advancements have been made in the preparation/synthesis of organic nanomaterials and methodologies for characterization of their properties. Simultaneously, applications of organic nanomaterials in various fields have been developed rapidly, such as in sensors and actuators, photodetectors, surface wettability control devices, optical waveguides and lasers, and even organic nanocircuits. It is anticipated that, with the development of organic nanomaterials, many other new applications for these novel materials will be found.

25.3.1 Sensors and/or Detectors

Nanosensors are any biological, chemical, or surgical sensory points used to convey information about nanoparticles to the macroscopic world. Their uses mainly include various medical purposes and gateways to build other nanoproducts, such as computer chips that work at the nanoscale and nanorobots. One of the first working examples of a synthetic nanosensor was built by researchers at the Georgia Institute of Technology in 1999 [25.53]. It involved attaching a single particle onto the end of a carbon nanotube and measuring the vibrational frequency of the nanotube both with and without the particle. The discrepancy between the two frequencies allowed the researchers to measure the mass of the attached particle. Chemical sensors have been built using nanotubes to detect various properties of gaseous molecules. Carbon nanotubes have been used to sense ionization of gaseous molecules, while nanotubes made out of titanium have been employed to detect atmospheric concentrations of hydrogen at the molecular level [25.54, 55].

Organic nanomaterials are widely used as chemical sensors, e.g., to detect different gases, due to the functions of the nanomaterials achieved by molecular design. Certainly, chemical sensors can also detect the speed, wavelength, and level of molecules in strong light; For example, vertical organic nanowire arrays of 1,5-diaminoanthraquinone (DAAQ) on solid substrates were prepared by *Huang* et al. [25.56] by a facile physical vapor transport method. The color and fluorescence of the DAAQ nanowires could be bleached and quenched by acid vapor and rapidly regenerated by base vapor, making them useful as optical sensor materials (Fig. 25.28). The ease of oriented vertical growth makes them promising nanophotonic elements that may be directly integrated into photonic devices during growth. Similarly, *Li* et al. [25.57] prepared polyaniline nanofibers through the in situ oxidative polymerization method and used them for detection of aromatic organic compounds (AOCs). The sensor showed an increase in conductivity, and the maximum response measured at 1000 ppm was several tens of percent.

Photodetectors/photoswitches are a major kind of detectors based on organic nanomaterials. It is believed that photodetectors based on organic semiconductors

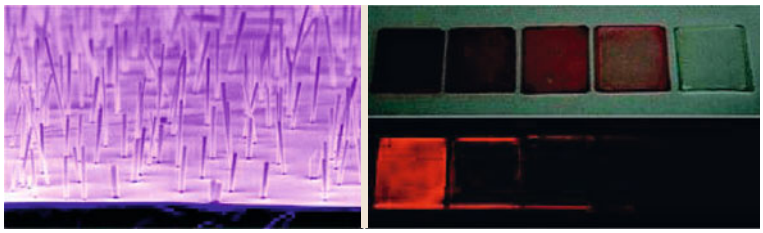


Fig. 25.28 Vertically aligned DAAQ nanowire arrays and photographs of changes after exposure to HCl for 0, 5, 10, 30, and 60 s, respectively. (After [25.56], courtesy of American Chemical Society (2009))

will afford devices with low cost, light weight, high efficiency, and good environmental benignity, which are important features for organic optoelectronic devices and circuits. Not only low dark current but also high photocurrents are required for fabrication of high-performance photodetectors. *Tang* et al. [25.58] have fabricated high-quality photoswitches based on F_{16}CuPc single crystals, an air-stable, n-type organic semiconductor. The response and recovery velocities were estimated to be near 100 and 50 Hz, respectively. More significantly, the devices also showed high reproducibility and retention ability. After several tens of cycles and nearly 1 h of continuous work, no degradation in the current was observed. *Zhou* et al. [25.59] also fabricated excellent photoswitches using organic single-crystal submicrometer ribbons on flexible poly(ethylene terephthalate) (PET) substrates by using low-cost solution methods. The photoswitch exhibited high performance with gain of about 1.3×10^3, responsivity of about 420 A/W, and highest on/off ratio of more than 1000. More interestingly, the highly reproducible on/off switching property was exhibited either with the planar geometry or in the bending state. No significant current changes under the same illumination level were observed in the bending state. It is worth noting that the photocurrent even increased a little in the bending state. The *Hu* group [25.9] also reported a high-performance photoswitch based on ordered single-crystal microwire arrays of anthracene derivatives, prepared via a solution process. Very recently, *Wang* et al. [25.60] reported that the performance of photoswitches based on 9,10-bis(phenylethynyl)anthracene (BPEA) single crystals showed strong phase dependence, as shown in Fig. 25.29. Devices of β-phase single crystals exhibited higher photoswitching performance than that of α-phase due to the supramolecular assembling motif governing the properties of organic photoswitches.

Phototransistors, a kind of three-terminal device with light as the *fourth terminal*, can reach especially high gains through the transistor action since the applied gate bias of the transistor provides an efficient way for dissociation of photogenerated excitons into free carriers, being beneficial for subsequent carrier transport and collection; i. e., phototransistors provide high efficiency for the mentioned processes and result in effective photodetection [25.61]. Moreover, phototransistors take advantage of the combined light detection and signal magnification properties to realize both functionalities in a single device. *Hu* et al. [25.62] first self-assembled nanojunction phototransistors based on

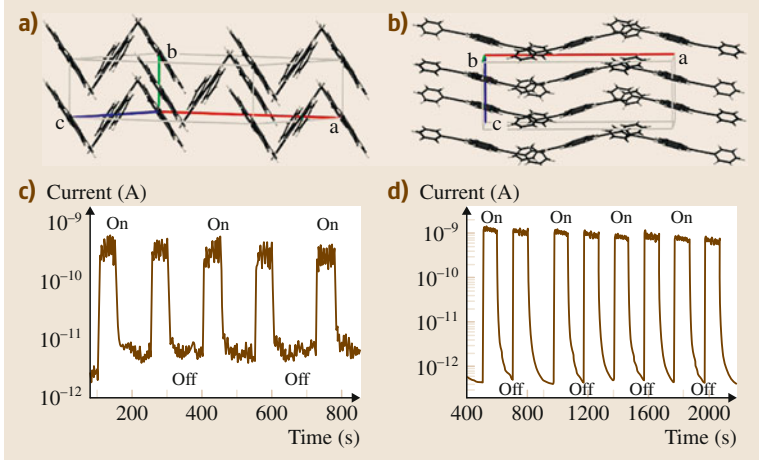


Fig. 25.29a–d The single-crystal structures of **(a)** α- and **(b)** β-phase BPEA photoswitching characteristics of **(c)** α- and **(d)** β-phase BPEA single crystals. (After [25.60], courtesy of American Institute Physics (2010))

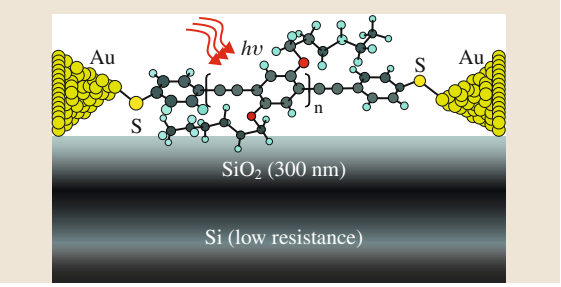


Fig. 25.30 Schematic of TA-PPE-based self-assembled phototransistors. (After [25.62], courtesy of American Chemical Society (2005))

TA-PPE and Au nanogap electrodes (Fig. 25.30), which worked well as nanometer-scale phototransistors. With increasing gate bias, strong conductance oscillation was observed in this self-assembled transistor (at low temperature, 147 K), which was assigned to single-electron charging oscillations arising from electron tunneling through the nanometer-scale transistor.

25.3.2 Surface Wettability Control

Wettability is a fundamental property of a solid surface, playing important roles in daily life, industry, and agriculture. Functional surfaces with special wettability have aroused much interest because of their great advantages in applications [25.64]. The chemical compositions determine the surface free energy and thus have great influence on wettability. However, this has certain limitations; For example, the CF_3-terminated surface was reported to possess the lowest free energy and the best hydrophobicity, while on flat surfaces, the maximum contact angle (CA) could only reach about 120°. The surface topographic structure is also an important factor that influences the wettability. Lotus is well known for the self-cleaning effect observed on its leaves, which show a water CA as large as $161.0 \pm 2.7°$ and a sliding angle (SA) as small as only about 2°. Such superhydrophobicity and the excellent anti-adhesion capability are the origin of the self-cleaning effect.

Jiang et al. [25.65] revealed the novel finding of micro- and nanoscale hierarchical structures on the leaf. The randomly distributed papillae with diameters ranging from 5 to 9 μm were found to consist of further branch-like nanostructures with average diameter of 124.3 ± 3.2 nm, which could also be observed on the lower part of the leaf. Theoretical simulation [25.65] indicates that the CA may increase to about 160° after considering the contribution of the nanostructures, which is well consistent with the experimental result, i. e., the role of the hierarchical micro- and nanostructures giving this property. To confirm this, a comparison between aligned carbon nanotube (ACNT) films with and without hierarchical structures was made. The results indicate that the hierarchical structures would not only further improve the hydrophobicity of the films but also result in small sliding angles. This opens the way to tune surface wettability by using organic nanomaterials; For example, by using molecular interactions such as hydrogen bonds and $\pi-\pi$ interactions, micro- and nanometer sized, single-crystalline nanowires of an anthracene derivative (Fig. 25.31a) could be cast efficiently into different morphologies by controlled the experimental conditions [25.63]. Attractively, large-area (4×4 cm^2) film consisting of assembled micro- and nanowires was obtained, which showed contact angles over 150° independent of whether composed of network or firework micro- and nanowires; i. e., the films exhibited excellent superhydrophobicity. For example,

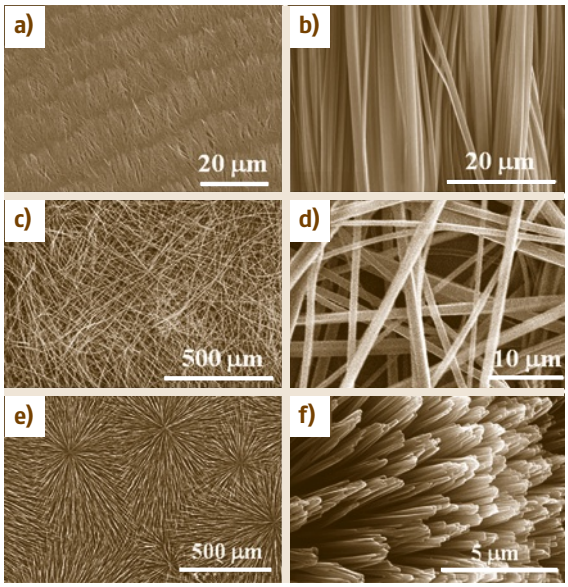


Fig. 25.31a–f SEM images of cast products **(a)** layer-like structures, **(b)** ordered microwires, **(c)** networks composed of micro- and nanowires, **(d)** enlarged SEM image of Fig. 25.25c microwires and nanowires networks, **(e)** self-assembled fireworks structures of the micro- and nanowires, the self-assembly was performed by heating the substrates under 100 °C for 30 min, **(f)** enlarged SEM image of Fig. 25.25e micro- and nanowires. (After [25.63], courtesy of Wiley-VCH (2010))

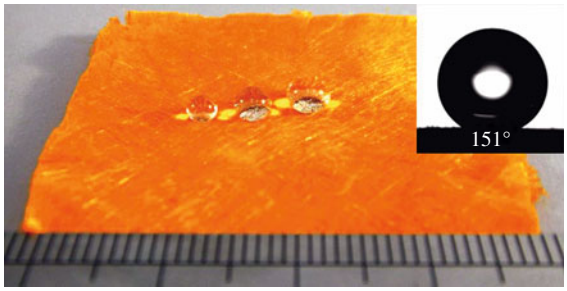


Fig. 25.32 The superhydrophobicity of a film consisting of self-assembled micro- and nanometer-sized wires; the water drops floated on the film with contact angle around 151°. (After [25.63], courtesy of Wiley-VCH (2010))

films with network structure exhibited contact angles of around 151°, as shown in Fig. 25.32.

25.3.3 Optical Waveguides and Lasers

In the last couple of years, nanowires have also gradually been adopted as optically driven lasers [25.67] because the significant difference in refractive index between the nanostructure and its surroundings defines a subwavelength-sized optical cavity. Moreover, semiconducting nanowires and nanoribbons have also been used as optical waveguides [25.68]. which propagate and manipulate light on the subwavelength scale. However, most of the research in this field is focused on inorganic materials, while fewer attempts are made to construct 1-D structured low-molecular-weight compounds [25.69] even though it is well known that the optical and optoelectronic properties of organic nanomaterials are fundamentally different from those of their inorganic counterparts [25.70]. Due to their optical tunability, high luminescence efficiency, and self-assembly property, organic compounds can serve as effective building blocks in future miniaturized optoelectronics that generate and propagate light [25.71]. Therefore, the fabrication of 1-D organic nanomaterials is of great scientific interest and technological significance. This is particularly the case for single-crystalline organic nanomaterials, because their high crystallinity effectively enhances the performance of corresponding devices [25.72].

Zhao et al. [25.73] prepared single-crystalline nanowires from a small organic functional compound, 2,4,5-triphenylimidazole (TPI), via adsorbent-assisted PVD. As-prepared TPI nanowires can serve as single-wire active optical waveguides and ultraviolet lasers, which may be used as building blocks for nanoscale

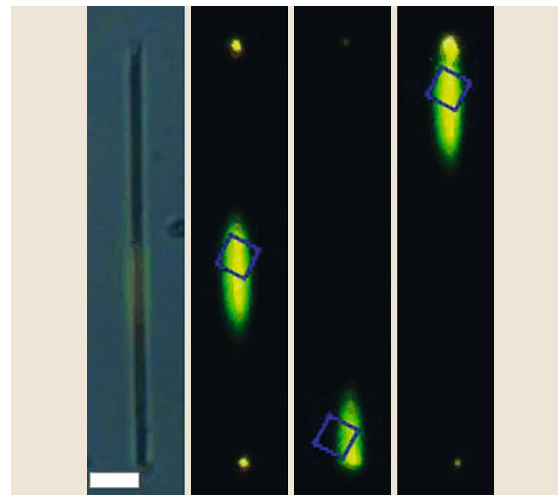


Fig. 25.33 PL microscopy images of isolated BPEA tubes excited with light between 460 and 490 nm. *Scale bars*: 20 μm. (After [25.66], courtesy of Wiley-VCH (2008))

photonic devices. The microcavity behavior of as-prepared wires is influenced significantly by their dimensions. The results presented in [25.73] provide useful information for the construction of nanoscaled photonic devices from molecular materials. After that, they further examined 9,10-bis(phenylethynyl)anthracene (BPEA) [25.66]. Two kinds of 1-D microstructures, tubes and rods, were prepared from BPEA. While both types of 1-D microstructures can absorb excitation light and propagate the photoluminescence (PL) emission towards the tips, the air inside the hollow tubes changes the waveguide behavior and helps to reduce the optical loss (Fig. 25.33).

25.3.4 Nanocircuits

Nanocircuits are electrical circuits operating on the nanometer scale. A variety of proposals have been made to implement nanocircuitry in different forms. These include single-electron transistors, quantum dot cellular automata, and nanoscale crossbar latches. In producing these nanocircuits, there are many aspects involved. Transistors are an integral part of circuits, as they control the flow of electricity and transform weak electrical signals into strong ones. They also control electric current as they can turn it on/off, or even amplify signals. Circuits currently use silicon as a transistor because it can easily be switched between conducting and nonconducting states. However, in nanoelectronics, transistors might be organic

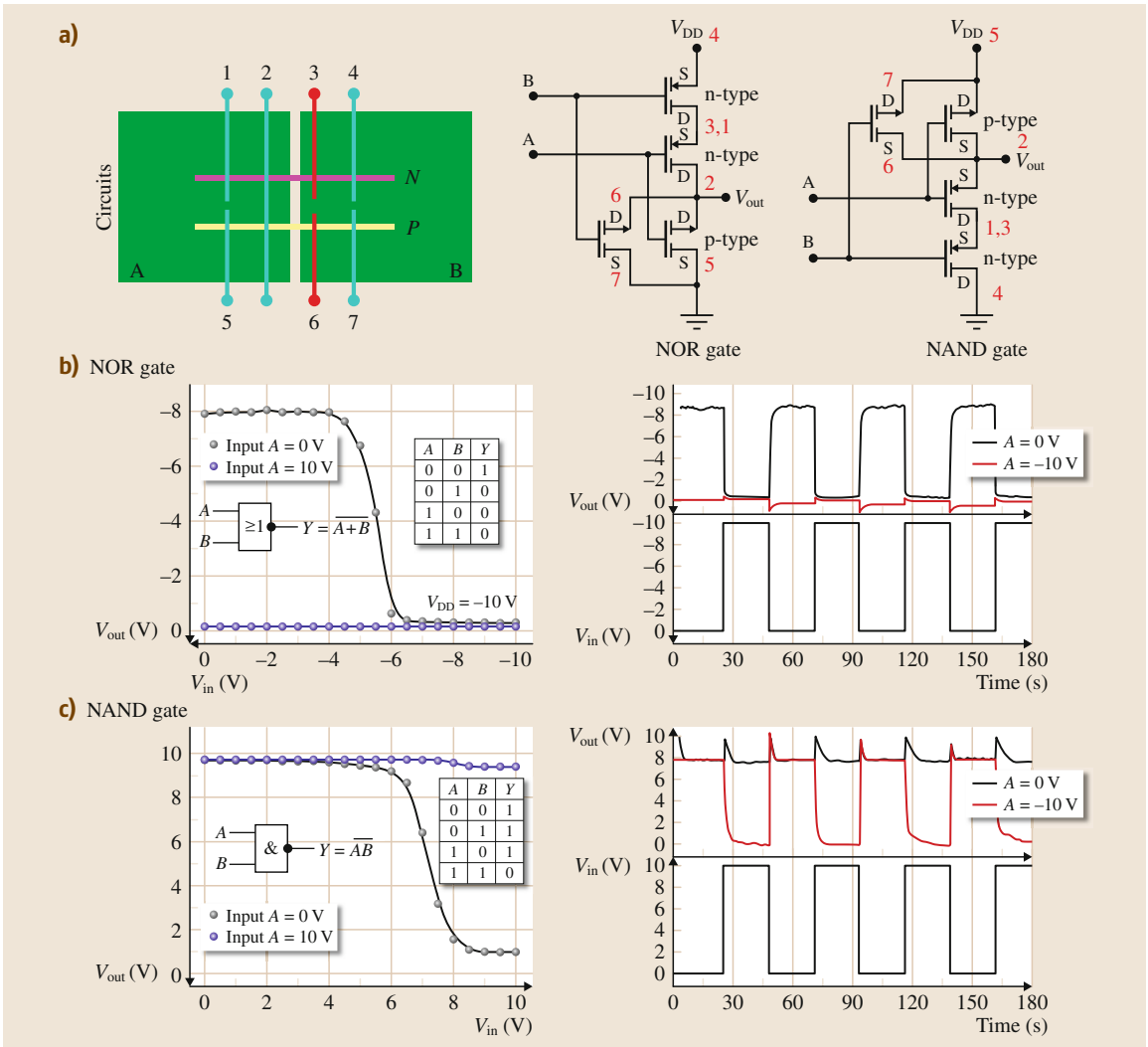


Fig. 25.34a–c Organic single-crystal NOR and NAND logic circuits using nanowires of CuPc, F_{16}CuPc, and SnO_2:Sb as building blocks. **(a)** Circuit and schematic of logic circuits of NOR and NAND, **(b)** transfer and dynamic switching characteristics of a NOR gate at $V_{DD} = -10$ V, **(c)** transfer and dynamic switching characteristics of a NAND gate at $V_{DD} = 10$ V. (After [25.74], courtesy of Wiley-VCH (2009))

molecules or organic and polymeric nanostructures. The second aspect of nanocircuit organization is interconnection. This involves logical and mathematical operations and the wires linking the transistors together that make this possible. The last part of nanocircuit organization is architecture. This has been explained as the overall way the transistors are interconnected, so that the circuit can plug into a computer or other system and operate, independently of the lower-level details.

Tang et al. [25.74] fabricated organic single-crystal transistors and circuits (Fig. 25.34) by mechanically assembling nanowires of CuPc, F_{16}CuPc, and SnO_2:Sb. The devices exhibited low operational voltage, high mobility, and excellent air stability. The complementary circuits of the nanowires demonstrate versatile functions such as inverters, NOR and NAND gates, wherein the inverters exhibit sharp switching and high gain, and the logic circuits of NOR and NAND demonstrate ultralow power consumption (< 40 pW). In combination

with generic *bottom-up* assembly methods developed for nanowires, this opens up important new opportunities based on tailor-made organic nanowires. The power consumption of the single-crystal logic circuits is even one order of magnitude lower than that of organic thin-film circuits (1 nW), of great interest for possible applications [25.75]. Logic circuits, such as NOR and NAND, are basic elements of large and superlarge integrated circuits, offering the advantages of low power consumption, high stability, and anti-interference ability. Several pioneering studies have addressed logic NOR and NAND gates based on carbon nanotubes, inorganic nanowires, polymer fibers, and organic thin films.

25.4 Concluding Remarks

Nanostructured materials represent a fascinating class of materials whose structural elements such as atomic clusters, crystallites or molecules have dimensions in the nanometer scale range, where intriguing phenomena are observed. Unique electrical, optical, and sensing properties that are readily tunable through controlling their size enable novel applications that are impossible to realize using their bulk counterparts. Organic nanomaterials play an important role in this field. Because organic nanomaterials are composed of molecular units with weaker intermolecular interactions, they allow for higher structural tunability, reactivity, and processability. Synthesis and processing of organic nanomaterials have come a long way. Methods have now been established to obtain organic nanomaterials with desired morphologies and properties, in particular advances in synthetic chemistry and in methods for the investigation and manipulation of individual

Table 25.1 Nanomaterials of some small molecules

Items	Materials	Properties/methods	References
1	Macrotricyclic complexes	^{1}H NMR	[25.76]
2	Triblocked heptadecathiophene	Absorption	[25.77]
3	Sexithiophene derivatives	Transport properties	[25.78, 79]
4	OPV derivatives	Absorption and emission	[25.80]
5	Thiophene derivatives	*I-V* characteristics	[25.81–84]
6	Naphthalenebisimides	Absorption	[25.85, 86]
7	Perylene bisimide derivatives	Absorption and fluorescence	[25.87–89]
8	Triphenylenes	Transport properties	[25.90–94]
9	Hexabenzocoronenes	Absorption	[25.95–97]
10	Azaaromatic compounds	DSC, XRD, and absorption	[25.98–101]
11	C_{60} derivatives	Small-angle x-ray diffraction	[25.102–105]
12	Phthalocyanines	Absorption and TEM	[25.106, 107]
13	Porphyrins	Matrix-assisted laser desorption/ionization-time of flight (MALDI-TOF), light-harvesting	[25.108–110]
14	Amphiphilic molecules	Microstructure control	[25.111]
15	Fullerenes	Adsorption on surfaces	[25.112]
16	Vanadyl phthalocyanine	Laser ablation	[25.113]
17	Tetraphenyl-1,3-butadiene	Microwaves/optical property	[25.114]
18	Rhovanil and Rhodiarome	Microemulsion	[25.115]
19	Polyaluminum chloride	Membrane reactor/Fourier transform infrared spectroscopy (FTIR)	[25.116]
20	Perylene	Emission properties	[25.117, 118]
21	β-Carotene	Absorption	[25.119]
22	Cyclohexane	Circular dichroism	[25.120]
23	Cholesterol derivatives	Organic gel fibers as template	[25.121]
24	Azo chelate compound	Nonlinear optical properties	[25.122]
25	Molecular materials	Field-emission properties etc.	[25.123]

molecules and small ensembles of molecules. Novel organic nanomaterials based on small molecules and polymers are being actively developed (beyond the examples in the text, some other examples are given in Tables 25.1–25.3). One key step towards novel applications of organic nanomaterials concerns their surface functionalization, assembly, patterning, orientation, and alignment into functional networks without mutual aggregation. Among the bottom-up strategies, self-assembly provides a promising route to build up complex systems with immense flexibility in terms of nanoscale building blocks and resulting functionalities and properties. As the name suggests, self-assembly is a process in which organization of organic molecules into the desired system occurs through naturally occurring phenomena, either mediated by physicochemical pathways or assisted by biomolecules to promote molecular selectivity and specificity. Methods have also been sought to exploit the properties of these materials in optoelectronic devices, and prototypes for new nanoscale devices have been demonstrated.

Though great progress has been made in research of organic nanomaterials, development of this area is still in its infancy. At present, the development of organic low-dimensional materials still lags far behind that of their inorganic counterparts. In the near future, further work on the molecular design of organic nanomaterials will continue to be crucial. On the one hand, developing multiple kinds of materials with various nanostructures is a primary task; in particular, considering the needs of practical applications, we should put emphasis on those materials with optimum optoelectronic properties and low-dimensional nanostructures, to further improve their optoelectronic properties. For those targets, none of the following elements is dispensable: design and synthesis of novel optofunctional molecules, successful construction of nanomaterials with desired structures from the synthesized molecules, and then powerful characterization of the constructed materials. More importantly, to realize the full potential of applications, the 1-D building blocks should be more efficiently integrated into devices with various optoelectronic functions; For example, one of the major challenge to maximize the competitiveness of organic solar/photovoltaic (PV) cells in terms of efficiency/cost ratio is to develop new

Table 25.2 Nanomaterials of some polymers

Items	Materials	Properties	References
1	Polyacetylene	Electrical properties	[25.124, 125]
2	Polypyrrole	Absorption, electrical properties	[25.126–133]
3	poly(3,4-ethylenedioxythiophene) (PEDOT)	I–V characteristics	[25.134, 135]
4	Polyaniline	Chemiresistive properties	[25.136–140]
5	Poly-*p*-phenylene	Optical measurement	[25.141]
6	Poly-*p*-phenylenevinylene (PPV)	Absorption and emission properties	[25.142]
7	Poly-*p*-phenyleneethynylene (PPE)	Emission and transport properties	[25.143–146]
8	Polythiophene derivatives (PATS)	Absorption and transport properties	[25.147–153]
9	Polythienylenevinylene	No	[25.154, 155]
10	PFO[a]	Emission and waveguide properties	[25.156, 157]
11	MEH-PPV[b]	I_2 sensitivity, I–V characteristics	[25.158–160]
12	PQT12[c]	Emission properties	[25.161, 162]
13	BBL[d]	Field-effect property	[25.159, 163]
14	F8T2[e]	Optical and electrical properties	[25.164]
15	P3HT-b-P3RT diblock copolymer	Absorption property	[25.165]
16	Perylenebisimide-OPV copolymer	Hydrogen-bonding effects	[25.166]
17	F8BT[f]	Chemiluminescence	[25.167]

[a] Poly(9,9-dioctylfluorene)
[b] Poly[2-methoxy-5-(2-ethylhexyloxy)-1,4-phenylenevinylene], end-capped with dimethyl phenyl
[c] Poly(3,3″-didodecylquarterthiophene)
[d] Poly-(benzimidazobenzophenanthroline ladder)
[e] Poly[(9,9-dioctylfluorenyl-2,7-diyl)-co-(bithiophene)]
[f] Poly(9,9-dioctylfluorene-co-benzothiadiazole)

Table 25.3 Nanomaterials of some hybrid structures

Items	Materials	Properties/methods	References
1	Organic–inorganic hybrids	Optoelectronic applications	25.169
2	Hybrid plasmonic nanoparticles	Optical properties	25.170
3	Host–guest nanomaterials	Enhanced guest behavior	25.171
4	Oxalate-based hybrid	Magnetic properties	25.172
5	Metal–organic frameworks	Metal-organic framework (MOF) functionalization	25.173
6	Block copolymers	Solar cells, batteries, fuel cells	25.174
7	Lanthanide-based hybrids	Lighting, optics, and solar cells	25.175
8	Organic–inorganic hybrids	Structure and functionalization	25.176
9	Cluster	Polymer-like properties etc.	25.177
10	Sol–gel nanoreactors	Optical sensors	25.178
11	Magnetic hybrids	Magnetic properties	25.179
12	Photochromic hybrid materials	Photochromic properties	25.180
13	Organic–inorganic hybrids	Various applications	25.181
14	Hybrid sol–gel materials	Optics and photonics	25.182

functional complex nanoarchitectures made of semiconductive organic electron-acceptor and electron-donor materials, in particular, to combine two molecular materials, one electron acceptor with one electron donor, and to try to achieve nanoscale control of the materials morphology, since whether an exciton can reach the interface and dissociate or not is critical, considering the exciton diffusion length (about 20 nm). Finally, it should be mentioned that the development of hybrid nanomaterials is also a key point of this field [25.168]. Hybrid materials with organic–inorganic or bio–inorganic character represent not only a new field of basic research but also, via their remarkable new properties and multifunctional nature, offer prospects for many new applications in extremely diverse fields.

References

25.1 H. Liu, Y. Li, L. Jiang, H. Luo, S. Xiao, H. Fang, H. Li, D. Zhu, D. Yu, J. Xu, B. Xiang: Imaging as-grown [60] fullerene nanotubes by template technique, J. Am. Chem. Soc. **124**, 13370–13371 (2002)

25.2 G.E. Possin: A method for forming very small diameter wires, Rev. Sci. Instrum. **41**, 772–774 (1970)

25.3 C.R. Martin: Template synthesis of electronically conductive polymer nanostructures, Acc. Chem. Res. **28**, 61–68 (1995)

25.4 C.R. Martin: Nanomaterials: A membrane-based synthetic approach, Science **266**, 1961–1966 (1994)

25.5 T. Kim, I. Park, R. Ryoo: A synthetic route to ordered mesoporous carbon materials with graphitic pore walls, Angew. Chem. Int. Ed. **42**, 4511–4515 (2003)

25.6 L. Zhao, W. Yang, Y. Ma, J. Yao, Y. Li, H. Liu: Perylene nanotubes fabricated by the template method, Chem. Commun. **19**, 2442–2443 (2003)

25.7 C. Barrett, D. Iacopino, D. O'Carroll, G. De Marzi, D.A. Tanner, A.J. Quinn, G. Redmond: Synthesis of pentacene nanotubes by melt-assisted template wetting, Chem. Mater. **19**, 338–340 (2007)

25.8 L. Jiang, J. Gao, Y. Fu, H. Dong, H. Zhao, H. Li, Q. Tang, K. Chen, W. Hu: Tuning intermolecular noncovalent interactions for nanowires of organic semiconductors, Nanoscale **2**, 2652–2656 (2010)

25.9 L. Jiang, Y. Fu, H. Li, W. Hu: Single crystalline size and orientation controllable nanowires and ultralong microwires of organic semiconductor with strong photo switching property, J. Am. Chem. Soc. **130**, 3937–3941 (2008)

25.10 C. Kloc, P.G. Simpkins, T. Siegrist, R.A. Laudise: Physical vapor growth of centimeter-sized crystals α-hexathiophene, J. Cryst. Growth **182**, 416–427 (1997)

25.11 Y. Zhao, C. Di, W. Yang, G. Yu, Y. Liu, J. Yao: Photoluminescence and electroluminescence from Tris(8-hydroxyquinoline)aluminum nanowires prepared by adsorbent-assisted physical vapor deposition, Adv. Funct. Mater. **16**, 1985–1991 (2006)

25.12 Q. Tang, H. Li, M. He, W. Hu, C. Liu, K. Chen, C. Wang, Y. Liu, D. Zhu: Low threshold voltage transistors based on individual single-crystalline

submicrometer-sized ribbons of copper phthalocyanine, Adv. Mater. **18**, 65–68 (2006)
25.13 Y. Zhao, H. Fu, A. Peng, Y. Ma, D. Xiao, J. Yao: Low-dimensional nanomaterials based on small organic molecules: Preparation and optoelectronic properties, Adv. Mater. **20**, 2859–2876 (2008)
25.14 K. Balakrishnan, A. Datar, R. Oitker, H. Chen, J. Zuo, L. Zang: Nanobelt self-assembly from an organic n-type semiconductor: Propoxyethyl-PTCDI, J. Am. Chem. Soc. **127**, 10496–10497 (2005)
25.15 K. Balakrishnan, A. Datar, T. Naddo, J. Huang, R. Oitker, M. Yen, J. Zhao, L. Zang: Effect of side-chain substituents on self-assembly of perylene diimide molecules: Morphology control, J. Am. Chem. Soc. **128**, 7390–7398 (2006)
25.16 Z. Tian, Y. Chen, W. Yang, J. Yao, L. Zhu, Z. Shuai: Low-dimensional aggregates from stilbazolium-like dyes, Angew. Chem. Int. Ed. **43**, 4060–4063 (2004)
25.17 Y. Wang, H. Fu, A. Peng, Y. Zhao, J. Ma, Y. Ma, J. Yao: Distinct nanostructures from isomeric molecules of bis(iminopyrrole) benzenes: effects of molecular structures on nanostructural morphologies, Chem. Commun.(16), 1623–1625 (2007)
25.18 H. Kasai, H. Kamatani, S. Okada, H. Oikawa, H. Matsuda, H. Nakanishi: Size-dependent colors and luminescences of organic microcrystals, Jpn. J. Appl. Phys. **35**, L221–L223 (1996)
25.19 H. Fu, J. Yao: Size effects on the optical properties of organic nanoparticles, J. Am. Chem. Soc. **123**, 1434–1439 (2001)
25.20 Y. Zhao, H. Fu, F. Hu, A. Peng, W. Yang, J. Yao: Tunable emission from binary organic one-dimensional nanomaterials: an alternative approach to white-light emission, Adv. Mater. **20**, 79–83 (2008)
25.21 J. Luo, Z. Xie, J.W. Lam, L. Cheng, H. Chen, C. Qiu, H.S. Kwok, X. Zhan, Y. Liu, D. Zhu, B. Tang: Aggregation-induced emission of 1-methyl-1,2,3,4,5-pentaphenylsilole, Chem. Commun.(18), 1740–1741 (2001)
25.22 B. Tang, X. Zhan, G. Yu, P.P.S. Lee, Y. Liu, D. Zhu: Efficient blue emission from siloles, J. Mater. Chem. **11**, 2974–2978 (2001)
25.23 Y. Hong, J.W.Y. Lam, B. Tang: Aggregation-induced emission, Chem. Soc. Rev. **40**, 5361–5388 (2011)
25.24 J. Liu, J.W.Y. Lam, B. Tang: Acetylenic polymers: Syntheses, structures, and functions, Chem. Rev. **109**, 5799–5867 (2009)
25.25 A. Qin, C.K.W. Jim, Y. Tang, J.W.Y. Lam, J. Liu, F. Mahtab, P. Gao, B. Tang: Aggregation-enhanced emissions of intramolecular excimers in disubstituted polyacetylenes, J. Phys. Chem. B **112**, 9281–9288 (2008)
25.26 Y. Hong, J.W.Y. Lam, B. Tang: Aggregation-induced emission: phenomenon, mechanism and applications, Chem. Commun.(29), 4332–4353 (2009)
25.27 B.K. An, S.H. Gihm, J.W. Chung, C.R. Park, S.K. Kwon, S.Y. Park: Color-tuned highly fluorescent organic nanowires/nanofabrics: easy massive fabrication and molecular structural origin, J. Am. Chem. Soc. **131**, 3950–3957 (2009)
25.28 Z. Zhao, Z. Wang, P. Lu, C.Y.K. Chan, D. Liu, J.W.Y. Lam, H.H.Y. Sung, I.D. Williams, Y. Ma, B. Tang: Structural modulation of solid-state emission of 2,5-Bis(trialkylsilylethynyl)-3,4-diphenylsiloles, Angew. Chem. Int. Ed. **48**, 7608–7611 (2009)
25.29 Y.S. Zhao, H. Fu, F. Hu, A. Peng, J. Yao: Multicolor emission from ordered assemblies of organic 1-D nanomaterials, Adv.Mater. **19**, 3554–3558 (2007)
25.30 Y. Liu, L. Jiang, H. Dong, Z. Tang, W. Hu: Large area single crystalline nanocone arrays of an organic charge-transfer complex: controlling growth, characterization and applications, Small **7**, 1412–1415 (2011)
25.31 H. Liu, Q. Zhao, Y. Li, Y. Liu: FS. Lu, J. Zhuang, S. Wang, L. Jiang, D. Zhu, D. Yu, L. Chi: Field emission properties of large-area nanowires of organic charge-transfer complexes, J. Am. Chem. Soc. **127**, 1120–1121 (2005)
25.32 Y. Liu, Z. Ji, Q. Tang, L. Jiang, H. Li, M. He, W. Hu, D. Zhang, L. Jiang, X. Wang, C. Wang, Y. Liu, D. Zhu: Particle-size control and patterning of a charge-transfer complex for nanoelectronics, Adv. Mater. **17**, 2953–2957 (2005)
25.33 A. Tsumura, H. Koezuka, T. Ando: Macromolecular electronic device: Field-effect transistor with a polythiophene thin film, Appl. Phys. Lett. **49**, 1210–1212 (1986)
25.34 C. Wang, H. Dong, W. Hu, Y. Liu, D. Zhu: Semiconducting π-conjugated systems in field-effect transistors: A material odyssey of organic electronics, Chem. Rev. **112**, 2208–2267 (2012)
25.35 Y. Wen, Y. Liu, Y. Guo, G. Yu, W. Hu: Experimental techniques for the fabrication and characterization of organic thin films for field-effect transistors, Chem. Rev. **111**, 3358–3406 (2011)
25.36 Q. Tang, H. Li, M. He, W. Hu, C. Liu, K. Chen, C. Wang, Y. Liu, D. Zhu: Low voltage single crystal transistors of individual sub-micro ribbons of copper phthalocyanine, Adv. Mater. **18**, 65–68 (2006)
25.37 Q. Tang, L. Jiang, Y. Tong, H. Li, Y. Liu, Z. Wang, W. Hu, Y. Liu, D. Zhu: Micro and nanometer sized organic single crystalline transistors, Adv.Mater. **20**, 2947–2951 (2008)
25.38 H. Jiang, X. Yang, Z. Cui, Y. Liu, H. Li, W. Hu, Y. Liu, D. Zhu: Phase dependence of single crystalline transistors of tetrathiafulvalene, Appl. Phys. Lett. **91**, 123505 (2007)
25.39 M. Mas-Torrent, P. Hadley, S.T. Bromley, X. Ribas, J. Tarrés, M. Mas, E. Molins, J. Veciana, C. Rovira: Correlation between crystal structure and mobility in organic field-effect transistors based on sin-

gle crystals of tetrathiafulvalene derivatives, J. Am. Chem. Soc. **126**, 8546–8553 (2004)
25.40 H. Dong, S. Jiang, L. Jiang, Y. Liu, H. Li, W. Hu, E. Wang, S. Yan, Z. Wei, W. Xu, X. Gong: Nanowire crystals of a rigid rod conjugated polymer, J. Am. Chem. Soc. **131**, 17315–17320 (2009)
25.41 E.C. Garnett, M.L. Brongersma, Y. Cui, M.D. McGehee: Nanowire solar cells, Annu. Rev. Mater. Res. **41**, 269–295 (2011)
25.42 Science Daily (2010)
25.43 J. Thomas: Polymer nanowires: Taking it lightly, Nat. Nanotechnol. (2006), doi:10.1038/nnano.2006.89
25.44 G.A. O'Brien, A.J. Quinn, D.A. Tanner, G. Redmond: A single polymer nanowire photodetector, Adv. Mater. **18**, 2379–2383 (2006)
25.45 J.S. Kim, J.H. Lee, J.H. Park, C. Shim, M. Sim, K. Cho: High-efficiency organic solar cells based on preformed poly(3-hexylthiophene) nanowires, Adv. Mater. **21**, 480–486 (2011)
25.46 H. Xin, F. Kim, S.A. Jenekhe: Highly efficient solar cells based on poly(3-butylthiophene) nanowires, J. Am. Chem. Soc. **130**, 5424–5425 (2008)
25.47 Y. Guo, Q. Tang, H. Liu, Y. Zhang, Y. Li, W. Hu, S. Wang, D. Zhu: Light controlled organic/inorganic p–n junction nanowires, J. Am. Chem. Soc. **130**, 9198–9199 (2008)
25.48 Y. Zhang, H. Dong, Q. Tang, S. Ferdous, F. Liu, W. Hu, A.L. Briseno: Organic single-crystalline p–n junction nanoribbons, J. Am. Chem. Soc. **132**, 11580–11584 (2010)
25.49 Q. Tang, Y. Tong, Y. Zheng, Y. Zhang, H. Dong, W. Hu, T. Hassenkam, T. Bjørnholm: Flexible organic nanowire crystals device performance and mechanical properties, Small **7**, 189–193 (2011)
25.50 G. Gustafsson, Y. Cao, G.M. Treacy, F. Klavetter, N. Colaneri, A.J. Heeger: Flexible light-emitting diodes made from soluble conducting polymers, Nature **357**, 477–479 (1992)
25.51 Q. Tang, H. Li, M. He, W. Hu, C. Liu, K. Chen, C. Wang, Y. Liu, D. Zhu: Low voltage single crystal transistors of individual sub-micro ribbons of copper phthalocyanine, Adv. Mater. **18**, 65–68 (2006)
25.52 J. Lewis: Material challenge for flexible organic devices, Mater. Today **9**, 38–45 (2006)
25.53 P. Poncharal, Z. Wang, D. Ugarte, W.A. de Heer: Electrostatic deflections and electromechanical resonances of carbon nanotubes, Science **283**, 1513–1516 (1999)
25.54 A. Modi, N. Koratkar, E. Lass, B. Wei, P.M. Ajayan: Miniaturized gas ionization sensors using carbon nanotubes, Nature **424**, 171–174 (2003)
25.55 J. Kong, N. Franklin, C. Zhou, M. Chapline, S. Peng, K. Cho, H. Dai: Nanotubes molecular wires as chemical sensors, Science **287**, 622–625 (2000)
25.56 Y. Zhao, J. Wu, J. Huang: Vertical organic nanowire arrays: Controlled synthesis and chemical sensors, J. Am. Chem. Soc. **131**, 3158–3159 (2009)
25.57 W. Li, N.D. Hoa, Y. Cho, D. Kim, J. Kim: Nanofibers of conducting polyaniline for aromatic organic compound sensor, Sens. Actuators B **143**, 132–138 (2009)
25.58 Q. Tang, L. Li, Y. Song, Y. Liu, H. Li, W. Xu, Y. Liu, W. Hu, D. Zhu: Photo switches and phototransistors of organic single crystalline sub-micro/nanometer ribbons, Adv. Mater. **19**, 2624–2628 (2007)
25.59 Y. Zhou, L. Wang, J. Wang, J. Pei, Y. Cao: Highly sensitive, air-stable photodetectors based on single organic sub-micrometer ribbons self-assembled through solution processing, Adv. Mater. **20**, 3745–3749 (2008)
25.60 C. Wang, Y. Liu, Z. Wei, H. Li, W. Xu, W. Hu: Biphase micro/nanometer sized single crystals of organic semiconductors: Control synthesis and their strong phase dependent optoelectronic properties, Appl. Phys. Lett. **96**, 143302 (2010)
25.61 H. Dong, H. Zhu, Q. Meng, X. Gong, W. Hu: Organic photoresponse materials and devices, Chem. Soc. Rev. **41**, 1754–1808 (2012)
25.62 W. Hu, H. Nakashima, K. Furukawa, Y. Kashimura, K. Ajito, Y. Liu, D. Zhu, K. Torimitsu: A self-assembled nano optical switcher and transistor based on a rigid conjugated polymer thioacetyl-end-functionalized poly(para- phenylene ethynylene, J. Am. Chem. Soc. **127**, 2804–2805 (2005)
25.63 L. Jiang, X. Yao, H. Li, Y. Fu, L. Chen, Q. Meng, W. Hu, L. Jiang: Self-assembling *water strider* legs with single crystalline nanowires of an organic semiconductor, Adv. Mater. **22**, 376–379 (2010)
25.64 T. Sun, L. Feng, X. Gao, L. Jiang: Bioinspired surfaces with special wettability, Acc. Chem. Res. **38**, 644–652 (2005)
25.65 L. Feng, S. Li, Y. Li, H. Li, L. Zhang, J. Zhai, Y. Song, B. Liu, L. Jiang, D. Zhu: Super-hydrophobic surfaces: From natural to artificial, Adv. Mater. **14**, 1857–1860 (2002)
25.66 Y. Zhao, J. Xu, A. Peng, H. Fu, Y. Ma, L. Jiang, J. Yao: Optical waveguide based on crystalline organic microtubes and microrods, Angew. Chem. Int. Ed. **47**, 7301–7305 (2008)
25.67 X. Duan, Y. Huang, Y. Cui, J. Wang, C.M. Lieber: Indium phosphide nanowires as building blocks for nanoscale electronic and optoelectronic devices, Nature **409**, 66–69 (2001)
25.68 M. Law, D.J. Sirbuly, J.C. Jonhson, J. Goldberger, R.G. Saykally, P. Yang: Nanoribbon waveguides for subwavelength photonics integration, Science **305**, 1269–1273 (2004)
25.69 Y.S. Zhao, W. Yang, D. Xiao, X. Sheng, X. Yang, Z. Shuai, Y. Luo, J. Yao: Single crystalline submicrotubes from small organic molecules, Chem. Mater. **17**, 6430–6435 (2005)
25.70 B.K. An, S.K. Kwon, S.D. Jung, S.Y. Park: Enhanced emission and its switching in fluorescent organic nanoparticles, J. Am. Chem. Soc. **124**, 14410–14415 (2002)

25.71 K. Takazawa, Y. Kitahama, Y. Kimura, G. Kido: Optical waveguide self-assembled from organic dye molecules in solution, Nano Lett. **5**, 1293–1296 (2005)

25.72 L. Qu, G. Shi: Crystalline oligopyrene nanowires with multicolored emission, Chem. Commun.(24), 2800–2801 (2004)

25.73 Y. Zhao, A. Peng, H. Fu, Y. Ma, J. Yao: Nanowire waveguides and ultraviolet lasers based on small organic molecules, Adv. Mater. **20**, 1661–1665 (2008)

25.74 Q. Tang, Y. Tong, W. Hu, Q. Wan, T. Bjørnholm: Assembly of nanoscale organic single-crystal crosswire circuits, Adv. Mater. **21**, 4234–4237 (2009)

25.75 H. Klauk, U. Zschieschang, J. Pflaum, M. Halik: Ultralow-power organic complementary circuits, Nature **445**, 745–748 (2007)

25.76 M. Fujita, S. Yu, T. Kusukawa, H. Funaki, K. Ogura, K. Yamaguchi: Self-assembly of nanometer-sized macrotricyclic complexes from ten small component molecules, Angew. Chem. Int. Ed. **37**, 2082–2085 (1998)

25.77 J.J. Apperloo, R.A.J. Janssen, P.R.L. Malenfant, J.M.J. Frechet: Concentration-dependent thermochromism and supramolecular aggregation in solution of triblock copolymers based on lengthy oligothiophene cores and poly(benzyl ether) dendrons, Macromolecules **33**, 7038–7043 (2000)

25.78 H. Sandberg, O. Henze, A.F.M. Kilbinger, H. Sirringhaus, W.J. Feast, R.H. Friend: Oligoethyleneoxide functionalised sexithiophene organic field effect transistors, Synth. Met. **137**, 885–886 (2003)

25.79 A.P.H.J. Schenning, A.F.M. Kilbinger, F. Biscarini, M. Cavallini, H.J. Cooper, P.J. Derrick, W.J. Feast, R. Lazzaroni, P. Leclére, L.A. McDonell, E.W. Meijer, S.C.J. Meskers: Supramolecular organization of α,α'-disubstituted sexithiophenes, J. Am. Chem. Soc. **124**, 1269–1275 (2002)

25.80 A. Ajayaghosh, S.J. George: First phenylenevinylene based organogels: Self-assembled nanostructures via cooperative hydrogen bonding and π-stacking, J. Am. Chem. Soc. **123**, 5148–5149 (2001)

25.81 S.F. Schoonbeek, J.H. van Esch, B. Wegewijs, D.B.A. Rep, M.P. De Haas, T.M. Klapwijk, R.M. Kellogg, B.L. Feringa: Efficient intermolecular charge transport in self-assembled fibers of mono- and bithiophene bisurea compounds, Angew. Chem. Int. Ed. **38**, 1393–1397 (1999)

25.82 D.B.A. Rep, R. Roelfsema, J.H. Van Esch, F.S. Schoonbeek, R.M. Kellogg, B.L. Feringa, T.T.M. Palstra, T.M. Klapwijk: Self-assembly of low-dimensional arrays of thiophene oligomers from solution on solid substrates, Adv. Mater. **12**, 563–566 (2000)

25.83 A. Gesquiére, M.M.S. Abdel-Mottaleb, S. De Feyter, F.C. De Schryver, F. Schoonbeek, J. van Esch, R.M. Kellogg, B.L. Feringa, A. Calderone, R. Lazzaroni, J.-L. Brédas: Molecular organization of bis-urea substituted thiophene derivatives at the liquid/solid interface studied by scanning tunneling microscopy, Langmuir **16**, 10385–10391 (2000)

25.84 A. Gesquiére, S. De Feyter, F.C. De Schryver, F. Schoonbeek, J. van Esch, R.M. Kellogg, B.L. Feringa: Supramolecular π-stacked assemblies of bis(urea)-substituted thiophene derivatives and their electronic properties probed with scanning tunneling microscopy and scanning tunneling spectroscopy, Nano Lett. **1**, 201–206 (2001)

25.85 N. Kimizuka, T. Kunitake: Specific assemblies of the naphthalene unit in monolayers and the consequent control of energy transfer, J. Am. Chem. Soc. **111**, 3758–3759 (1989)

25.86 N. Kimizuka, T. Kawasaki, K. Hirata, T. Kunitake: Tube-like nanostructures composed of networks of complementary hydrogen bonds, J. Am. Chem. Soc. **117**, 6360–6361 (1995)

25.87 F. Würthner, C. Thalacker, A. Sautter: Hierarchical organization of functional perylene chromophores to mesoscopic superstructures by hydrogen bonding and π-π interactions, Adv. Mater. **11**, 754–758 (1999)

25.88 F. Würthner, C. Thalacker, A. Sautter, W. Schartl, W. Ibach, O. Hollricher: Hierarchical self-organization of perylene bisimide-melamine assemblies to fluorescent mesoscopic superstructures, Chem. Eur. J. **6**, 3871–3886 (2000)

25.89 C. Thalacker, F. Würthner: Chiral perylene bisimide–melamine assemblies: hydrogen bond-directed growth of helically stacked dyes with chiroptical properties, Adv. Funct. Mater. **12**, 209–218 (2002)

25.90 N. Boden, R.J. Bushby, G. Cooke, O.R. Lozman, Z. Lu: CPI: A recipe for improving applicable properties of discotic liquid crystals, J. Am. Chem. Soc. **123**, 7915–7916 (2001)

25.91 A. Pecchia, O.R. Lozman, B. Movaghar, N. Boden, R.J. Bushby, K.J. Donovan, T. Kreouzis: Photoconductive transients and one-dimensional charge carrier dynamics in discotic liquid crystals, Phys. Rev. B **65**, 104204–1–104204–10 (2002)

25.92 B.R. Wegewijs, L.D.A. Siebbeles, N. Boden, R.J. Bushby, B. Movaghar, O.R. Lozman, Q. Liu, A. Pecchia, L.A. Mason: Charge-carrier mobilities in binary mixtures of discotic triphenylene derivatives as a function of temperature, Phys. Rev. B **65**, 245112–1–245112–8 (2002)

25.93 E.O. Arikainen, N. Boden, R.J. Bushby, J. Clements, B. Movaghar, A. Wood: Effects of side-chain length on the charge transport properties of discotic liquid crystals and their implications for the transport mechanism, J. Mater. Chem. **5**, 2161–2165 (1995)

25.94 B.Y. Tang, J.J. Ge, A. Zhang, B. Calhoun, P. Chu, H. Wang, Z. Shen, F.W. Harris, S.Z.D. Cheng: Liquid crystalline and monotropic phase behaviors of 2,3,6,7,10,11-hexa(4'-octyloxybenzoyloxy)triphen-

ylene discotic molecules, Chem. Mater. **13**, 78–86 (2001)
25.95 A. Tracz, J.K. Jeszka, M.D. Watson, W. Pisula, K. Müllen, T. Pakula: Uniaxial alignment of the columnar super-structure of a hexa (alkyl) hexa-peri-hexabenzocoronene on untreated glass by simple solution processing, J. Am. Chem. Soc. **125**, 1682–1683 (2003)
25.96 A.J. Fleming, J.N. Coleman, A.B. Dalton, A. Fechtenkoetter, M.D. Watson, K. Müllen, H.J. Byrne, W.J. Blau: Optical spectroscopy of isolated and aggregate hexabenzocoronene derivatives: A study of self-assembling molecular nanowires, J. Phys. Chem. B **107**, 37–43 (2003)
25.97 J. Wu, M.D. Watson, L. Zhang, Z. Wang, K. Müllen: Hexakis(4-iodophenyl)-peri-hexabenzocoronene – A versatile building block for highly ordered discotic liquid crystalline materials, J. Am. Chem. Soc. **126**, 177–186 (2004)
25.98 G. Wiosna-Satiga, Y. Nosenko, M. Kijak, R.P. Thummel, B. Brutschy, J. Waluk: Structure and hydrogen-bond vibrations of water complexes of aza-aromatic compounds: 7-(3′-pyridyl)indole, J. Phys. Chem. A **114**, 3270–3279 (2010)
25.99 C.H. Lee, T. Yamamoto: Synthesis and characterization of a new class of liquid-crystalline, highly luminescent molecules containing a 2,4,6-triphenyl-1,3,5-triazine unit, Tetrahedron Lett. **42**, 3993–3996 (2001)
25.100 A.-J. Attias, C. Cavalli, B. Donnio, D. Guillon, P. Hapiot, J. Malthete: Columnar mesophase from a new disclike mesogen based on a 3,5-dicyano-2,4,6-tristyrylpyridine core, Chem. Mater. **14**, 375–384 (2002)
25.101 K. Pieterse, A. Lauritsen, A.P.H.J. Schenning, J.A.J.M. Vekemans, E.W. Meijer: Symmetrical electron-deficient materials incorporating aza-heterocycles, Chem. Eur. J. **9**, 5597–5604 (2003)
25.102 T. Chuard, R. Deschenaux, A. Hirsch, H. Schönberger: A liquid-crystalline hexa-adduct of [60]fullerene, Chem. Commun. **20**, 2103–2104 (1999)
25.103 S. Dardel, D. Guillon, B. Heinrich, R. Deschenaux: Fullerene-containing liquid-crystalline dendrimers, J. Mater. Chem. **11**, 2814–2831 (2001)
25.104 T. Chuard, R. Deschenaux: Design, mesomorphic properties, and supramolecular organization of [60]fullerene-containing thermotropic liquid crystals, J. Mater. Chem. **12**, 1944–1951 (2002)
25.105 M. Sawamura, K. Kawai, Y. Matsuo, K. Kanie, T. Kato, E. Nakamura: Stacking of conical molecules with a fullerene apex into polar columns in crystals and liquid crystals, Nature **419**, 702–705 (2002)
25.106 A. de la Escosura, M.V. Martínez-Díaz, P. Thordarson, E. Rowan Alan, J.M. Nolte Roeland, T. Torres: Donor-acceptor phthalocyanine nanoaggregates, J. Am. Chem. Soc. **125**, 12300–12308 (2003)
25.107 M. Kimura, H. Narikawa, K. Ohta, K. Hanabusa, H. Shirai, N. Kobayashi: Star-shaped stilbenoid phthalocyanines, Chem. Mater. **14**, 2711–2717 (2002)
25.108 T. van der Boom, R.T. Hayes, Y. Zhao, P.J. Bushard, E.A. Weiss, M.R. Wasielewski: Charge transport in photofunctional nanoparticles self-assembled from zinc 5,10,15,20-tetrakis(perylenediimide)porphyrin building blocks, J. Am. Chem. Soc. **124**, 9582–9590 (2002)
25.109 H. Tamiaki, T. Miyatake, R. Tanikaga, A.R. Holzwarth, K. Schaffner: Self-assembly of an artificial light-harvesting antenna: Energy transfer from a zinc chlorin to a bacteriochlorin in a supramolecular aggregate, Angew. Chem, Int. Ed. Engl. **35**, 772–774 (1996)
25.110 T. Miyatake, H. Tamiaki, A.R. Holzwarth, K. Schaffner: Artificial light-harvesting antennae: Singlet excitation energy transfer from zinc chlorin aggregate to bacteriochlorin in homogeneous hexane solution, Photochem. Photobiol. **69**, 448–456 (1999)
25.111 T. Shimizu, M. Masuda, H. Minamikawa: Supramolecular nanotube architectures based on amphiphilic molecules, Chem. Rev. **105**, 1401–1443 (2005)
25.112 L. Sénchez, R. Otero, J.M. Gallego, R. Miranda, N. Martín: Ordering fullerenes at the nanometer scale on solid surfaces, Chem. Rev. **109**, 2081–2091 (2009)
25.113 Y. Tamaki, T. Asahi, H. Masuhara: Nanoparticle formation of vanadyl phthalocyanine by laser ablation of its crystalline powder in a poor solvent, J. Phys. Chem. A **106**, 2135–2139 (2002)
25.114 K. Baba, H. Kasai, S. Okada, H. Oikawa, H. Nakanishi: Fabrication of organic nanocrystals using microwave irradiation and their optical properties, Opt. Mater. **21**, 591–594 (2002)
25.115 F. Debuigne, L. Jeunieau, M. Wiame, J.B. Nagy: Synthesis of organic nanoparticles in different W/O microemulsions, Langmuir **16**, 7605–7611 (2000)
25.116 Z. Liu, G. Zhang, Y. Peng, S. Ji: The hollow fiber ultrafiltration membrane with inner skin and its application, Desalination **233**, 55–63 (2008)
25.117 H. Kasai, H. Kamatani, Y. Yoshikawa, S. Okada, H. Oikawa, A. Watanabe, O. Itoh, H. Nakanishi: Crystal size dependence of emission from perylene microcrystals, Chem. Lett. **26**, 1181–1182 (1997)
25.118 H. Oikawa, T. Mitsui, T. Onodera, H. Kasai, H. Nakanishi, T. Sekiguchi: Crystal size dependence of fluorescence spectra from perylene nanocrystals evaluated by scanning near-field optical microspectroscopy, Jpn. J. Appl. Phys. **42**, L111–L113 (2003)
25.119 H. Auweter, H. Haberkorn, W. Heckmann, D. Horn, E. Lüddecke, J. Rieger, H. Weiss: Supramolecular structure of precipitated nanosize beta-carotene particles, Angew. Chem. Int. Ed. **38**, 2188–2191 (1999)

25.120 K. Hanabusa, M. Yamada, M. Kimura, H. Shirai: Prominent gelation and chiral aggregation of alkylamides derived from trans-1,2-diaminocyclohexane, Angew. Chem. Int. Ed. **35**, 1949–1951 (1996)

25.121 Y. Ono, K. Nakashima, M. Sano, K. Kanekiyo, K. Inoue, J. Hojo, S. Shinkai: Organic gels are useful as a template for the preparation of hollow fiber silica, Chem. Commun.(14), 1477–1478 (1998)

25.122 Z.Y. Tian, W.T. Huang, D.B. Xiao, S.Q. Wang, Y.S. Wu, Q.H. Gong, W.S. Yang, J.N. Yao: Enhanced and size-tunable third-order nonlinearity of nanoparticles from an azo metal chelate, Chem. Phys. Lett. **391**, 283–287 (2004)

25.123 H. Liu, J. Xu, Y. Li, Y. Li: Aggregate nanostructures of organic molecular materials, Acc. Chem. Res. **43**, 1496–1508 (2010)

25.124 H.J. Lee, Z.X. Jin, A.N. Aleshin, J.Y. Lee, M.J. Goh, K. Akagi, Y.S. Kim, D.W. Kim, W. Park: Dispersion and current voltage characteristics of helical polyacetylene single fibers, J. Am. Chem. Soc. **126**, 16722–16723 (2004)

25.125 Y. Okawa, M. Aono: Materials science: Nanoscale control of chain polymerization, Nature **409**, 683–684 (2004)

25.126 Z. Niu, J. Liu, L.A. Lee, M.A. Bruckman, D. Zhao, G. Koley, Q. Wang: Biological templated synthesis of water-soluble conductive polymeric nanowires, Nano Lett. **7**, 3729–3733 (2007)

25.127 J. Huang, S. Virji, B.H. Weiller, R.B. Kaner: Polyaniline nanofibers: Facile synthesis and chemical sensors, J. Am. Chem. Soc. **125**, 314–315 (2003)

25.128 Y. Chen, Y. Luo: Precisely defined heterogeneous conducting polymer nanowire arrays – fabrication and chemical sensing applications, Adv. Mater. **21**, 2040–2044 (2009)

25.129 A. Rahman, M.K. Sanyal: Novel switching transition of resistance observed in conducting polymer nanowires, Adv. Mater. **19**, 3956–3960 (2007)

25.130 M. Liu, X. Liu, C. Ding, Z. Wei, Y. Zhu, L. Jiang: Reversible underwater switching between superoleophobicity and superoleophilicity on conducting polymer nanotube arrays, Soft Matter **7**, 4163–4165 (2011)

25.131 J. Janata, M. Josowicz: Conducting polymers in electronic chemical sensors, Nature Mater. **2**, 19–24 (2002)

25.132 E.W.H. Jager, E. Smela, O. Inganäs: Microfabricating conjugated polymer actuators, Science **290**, 1540–1545 (2000)

25.133 M.A. Bangar, D.J. Shirale, W. Chen, N.V. Myung, A. Mulchandani: Single conducting polymer nanowire chemiresistive label-free immunosensor for cancer biomarker, Anal. Chem. **81**, 2168–2175 (2009)

25.134 Y. Cao, A.E. Kovalev, R. Xiao, J. Kim, T.S. Mayer, T.E. Mallouk: Electrical transport and chemica sensing properties of individual conducting polymer nanowires, Nano Lett. **8**, 4653–4658 (2008)

25.135 K. Su, N. Nuraje, L. Zhang, I. Chu, R.M. Peetz, H. Matsui, N. Yang: Fast conductance switching in single-crystal organic nanoneedles prepared from an interfacial polymerization-crystallization of 3,4-ethylenedioxythiophene, Adv. Mater. **19**, 669–672 (2007)

25.136 F. Gu, L. Zhang, X. Yin, L. Tong: Polymer single-nanowire optical sensors, Nano Lett. **8**, 2757–2761 (2008)

25.137 M.D. Shirsat, M.A. Bangar, M.A. Deshusses, N.V. Myung, A. Mulchandani: Polyaniline nanowires-gold nanoparticles hybrid network based chemiresistive hydrogen sulfide sensor, Appl. Phys. Lett. **94**, 083502 (2009)

25.138 Y. Yan, Y. Zhang, W. Hu, Z. Wei: Hierarchical crystalline superstructures of conducting polymers with homohelicity, Chem. Eur. J. **16**, 8626–8630 (2010)

25.139 R.J. Tseng, J. Huang, J. Ouyang, R.B. Kaner, Y. Yang: Polyaniline nanofiber/gold nanoparticle nonvolatile memory, Nano Lett. **5**, 1077–1080 (2005)

25.140 K. Wang, P. Zhao, X. Zhou, H. Wu, Z. Wei: Flexible supercapacitors based on cloth-supported electrodes of conducting polymer nanowire array/SWCNT composites, J. Mater. Chem. **21**, 16373–16378 (2011)

25.141 P. Leclère, E. Hennebicq, A. Calderone, P. Brocorens, A.C. Grimsdale, K. Müllen, J.L. Brédas, R. Lazzaroni: Supramolecular organization in block copolymers containing a conjugated segment: A joint AFM/molecular modeling study, Prog. Poly. Sci. **28**, 55–81 (2003)

25.142 Y. Luo, H. Liu, F. Xi, L. Li, X. Jin, C.C. Han, C. Chan: Supramolecular assembly of poly(phenylene vinylene) with crown ether substituents to form nanoribbons, J. Am. Chem. Soc. **125**, 6447–6451 (2003)

25.143 H. Dong, S. Jiang, L. Jiang, Y. Liu, H. Li, W. Hu, E. Wang, S. Yan, Z. Wei, W. Xu, X. Gong: Nanowire crystals of a rigid rod conjugated polymer, J. Am. Chem. Soc. **131**, 17315–17320 (2009)

25.144 P. Samori, V. Francke, K. Mullen, J.P. Rabe: Self-assembly of a conjugated polymer: from molecular rods to a nanoribbon architecture with molecular dimensions, Chem. Eur. J. **5**, 2312–2317 (1999)

25.145 P. Samori, V. Francke, K. Mullen, J.P. Rabe: Growth of solution cast macromolecular pi-conjugated nanoribbons on mica, Thin Solid Films **336**, 13–15 (1998)

25.146 E. Hittinger, A. Kokil, C. Weder: Synthesis and characterization of cross-linked conjugated polymer milli-, micro-, and nanoparticles, Angew. Chem, Int. Ed. **43**, 1808–1811 (2004)

25.147 B.K. Sarker, J. Liu, L. Zhai, S.I. Khondaker: Fabrication of organic field effect transistor by directly grown poly(3 hexylthiophene) crystalline nanowires on carbon nanotube aligned array electrode, ACS Appl. Mater. Interfaces **3**, 1180–1185 (2011)

25.148 J. Chen, C. Kuo, C. Lai, W. Chen, H. Chen: Manipulation on the morphology and electrical properties of aligned electrospun nanofibers of poly(3-hexylthiophene) for field-effect transistor applications, Macromolecules **44**, 2883–2892 (2011)

25.149 J.A. Merlo, C.D. Frisbie: Field effect transport and trapping in regioregular polythiophene nanofibers, J. Phys. Chem. B **108**, 19169–19179 (2004)

25.150 H. Liu, C.H. Reccius, H.G. Craighead: Single electrospun regioregular poly(3-hexylthiophene) nanofiber field-effect transistor, Appl. Phys. Lett. **87**, 253106 (2005)

25.151 H. Xin, F.S. Kim, S.A. Jenekhe: Highly efficient solar cells based on poly(3-butylthiophene) nanowires, J. Am. Chem. Soc. **130**, 5424–5425 (2008)

25.152 S. Berson, R. De?Bettignies, S. Bailly, S. Guillerez: Poly(3-hexylthiophene) fibers for photovoltaic applications, Adv. Funct. Mater. **17**, 1377–1384 (2007)

25.153 D.H. Kim, J.T. Han, Y.D. Park, Y. Jang, J.H. Cho, M. Hwang, K. Cho: Single-crystal polythiophene microwires grown by self-assembly, Adv. Mater. **18**, 719–723 (2006)

25.154 F.J.M. Hoeben, P. Jonkheijm, E.W. Meijer, A.P.H.J. Schenning: About supramolecular assemblies of π-conjugated systems, Chem. Rev. **105**, 1491–1546 (2005)

25.155 Y. Fu, H. Cheng, R.L. Elsenbaumer: Electron-rich thienylene-vinylene low bandgap polymers, Chem. Mater. **9**, 1720–1724 (1997)

25.156 D. O'Carroll, D. Iacopino, A. O'Riordan, P. Lovera, É. O'Connor, G.A. O'Brien, G. Redmond: Poly(9,9-dioctylfluorene) nanowires with pronounced β-phase morphology: synthesis, characterization, and optical properties, Adv. Mater. **20**, 42–48 (2008)

25.157 D. O'Carroll, I. Lieberwirth, G. Redmond: Microcavity effects and optically pumped lasing in single conjugated polymer nanowires, Nat. Nanotechnol. **2**, 180–184 (2007)

25.158 Z. Lin, S. Granick: Patterns formed by droplet evaporation from a restricted geometry, J. Am. Chem. Soc. **127**, 2816–2817 (2005)

25.159 D.J. Lipomi, R.C. Chiechi, M.D. Dickey, G.M. Whitesides: Fabrication of conjugated polymer nanowires by edge lithography, Nano Lett. **8**, 2100–2105 (2008)

25.160 C. Wu, C. Szymanski, J. McNeill: Preparation and encapsulation of highly fluorescent conjugated polymer nanoparticles, Langmuir **22**, 2956–2960 (2006)

25.161 S. Samitsu, Y. Takanishi, J. Yamamoto: Self-assembly and one-dimensional alignment of a conducting polymer nanofiber in a nematic liquid crystal, Macromolecules **42**, 4366–4368 (2009)

25.162 Z. Hu, B. Muls, L. Gence, D.A. Serban, J. Hofkens, S. Melinte, B. Nysten, S. Demoustier-Champagne, A.M. Jonas: High-throughput fabrication of organic nanowire devices with preferential internal alignment and improved performance, Nano Lett. **7**, 3639–3644 (2007)

25.163 A.L. Briseno, S.C.B. Mannsfeld, P.J. Shamberger, F.S. Ohuchi, Z. Bao, S.A. Jenekhe, Y. Xia: Self-assembly, molecular packing, and electron transport in n-type polymer semiconductor nanobelts, Chem. Mater. **20**, 4712–4719 (2008)

25.164 G.A. O'Brien, A.J. Quinn, D.A. Tanner, G. Redmond: A single polymer nanowire photodetector, Adv. Mater. **18**, 2379–2383 (2006)

25.165 Y. Kim, R.F. Jordan: Synthesis, structures, and ethylene dimerization reactivity of palladium alkyl complexes that contain a chelating phosphine–trifluoroborate ligand, Chem. Mater. **23**, 4250–4256 (2011)

25.166 A.P.H.J. Schenning, J. v. Herrikhuyzen, P. Jonkheijm, Z. Chen, F. Würthner, E.W. Meijer: Photoinduced electron transfer in hydrogen-bonded oligo(p-phenylene vinylene)-perylene bisimide chiral assemblies, J. Am. Chem. Soc. **124**, 10252–10253 (2002)

25.167 Y. Chang, R.E. Palacios, F.F. Fan, A.J. Bard, P.F. Barbara: Electrogenerated chemiluminescence of single conjugated polymer nanoparticles, J. Am. Chem. Soc. **130**, 8906–8907 (2008)

25.168 C. Sanchez, K.J. Shea, S. Kitagawa: Recent progress in hybrid materials science, Chem. Soc. Rev. **40**, 471–472 (2011)

25.169 V.M. Agranovich, Y.N. Gartstein, M. Litinskaya: Hybrid resonant organic inorganic nanostructures for optoelectronic applications, Chem. Rev. **111**, 5179–5214 (2011)

25.170 M.B. Cortie, A.M. McDonagh: Synthesis and optical properties of hybrid and alloy plasmonic nanoparticles, Chem. Rev. **111**, 3713–3735 (2011)

25.171 S. Nishikiori, H. Yoshikawa, Y. Sano, T. Iwamoto: Inorganic-organic hybrid molecular architectures of cyanometalate host and organic guest systems: Specific behavior of the guests, Acc. Chem. Res. **38**, 227–234 (2005)

25.172 M. Clemente-León, E. Coronado, C. Martí-Gastaldo, F.M. Romero: Multifunctionality in hybrid magnetic materials based on bimetallic oxalate complexes, Chem. Soc. Rev. **40**, 473–497 (2011)

25.173 K.K. Tanabe, S.M. Cohen: Postsynthetic modification of metal–organic frameworks—a progress report, Chem. Soc. Rev. **40**, 498–519 (2011)

25.174 M.C. Orilall, U. Wiesner: Block copolymer based composition and morphology control in nanostructured hybrid materials for energy conversion and storage: solar cells, batteries, and fuel cells, Chem. Soc. Rev. **40**, 520–535 (2011)

25.175 L.D. Carlos, R.A.S. Ferreira, V. de Zea Bermudez, B. Julián-López, P. Escribano: Progress on lanthan-

ide-based organic–inorganic hybrid phosphors, Chem. Soc. Rev. **40**, 536–549 (2011)
25.176 A. Mehdi, C. Reye, R. Corriu: From molecular chemistry to hybrid nanomaterials. Design and functionalization, Chem. Soc. Rev. **40**, 563–574 (2011)
25.177 U. Schubert: Cluster-based inorganic–organic hybrid materials, Chem. Soc. Rev. **40**, 575–582 (2011)
25.178 T. Tran-Thi, R. Dagnelie, S. Crunaire, L. Nicole: Optical chemical sensors based on hybrid organic–inorganic sol–gel nanoreactors, Chem. Soc. Rev. **40**, 621–639 (2011)
25.179 J. Yuan, Y. Xu, A.H.E. Müller: One-dimensional magnetic inorganic–organic hybrid nanomaterials, Chem. Soc. Rev. **40**, 640–655 (2011)
25.180 R. Pardo, M. Zayat, D. Levy: Photochromic organic–inorganic hybrid materials, Chem. Soc. Rev. **40**, 672–687 (2011)
25.181 C. Sanchez, P. Belleville, M. Popall, L. Nicole: Applications of advanced hybrid organic–inorganic nanomaterials: from laboratory to market, Chem. Soc. Rev. **40**, 696–753 (2011)
25.182 B. Lebeau, P. Innocenzi: Hybrid materials for optics and photonics, Chem. Soc. Rev. **40**, 886–906 (2011)

26. Nanocomposites as Bone Implant Material

Vinod Kumar, Bipul Tripathi, Anchal Srivastava, Preeti S. Saxena

The increasing demand for a suitable bone implant material has been forcing researchers to work on various man-made materials that may be used as a suitable replacement for natural bone and are affordable and easy to fabricate. In the past years, although significant efforts have been made in tissue engineering and regenerative medicine to put forward an ideal bone implant, they are far from meeting the real objective. Recent advances in nanobiotechnology in the field of therapeutics hold great promise to achieve the objective of an ideal implant in proper synchronization with tissue engineering. Nanocomposites, a product of synergistic efforts in nanobiotechnology and tissue engineering towards an ideal orthopedic implant, possess enormous potential for use as suitable bone implant material. Along with discussing the existing/conventional bone implant materials and their shortcomings, the main focus of this chapter is to elucidate nanocomposite as a potential next generation bone implant material. In this review, attempts have been made to deliver concise and relevant information about various nanofabrication technologies, characterization of nanocomposites, and their in vitro and in vivo biocompatibility study. Primary investigations support that nanocomposites are an ideal implant material for orthopedic applications; however, substantial developments are still highly needed to put nanocomposites into real practice, where current leanings in nanobiotechnology foreshadow a bright future through the use of nanocomposites in orthopedics. After defining the quest for bone implants, Sect. 26.2 gives a brief introduction to bone, and its structure and composition will be discussed. Section 26.3 gives a description and highlights shortcomings of conventional implant materials, followed by Sect. 26.4 describing the challenges posed by conventional and existing implants. In Sect. 26.5 a detailed study of the possible role of nanotechnology for suitable orthopedic implants are presented. Future perspectives in Sect. 26.6 close the chapter.

26.1 **The Quest for a Suitable Bone Implant** 942
26.2 **Bone** 942
26.2.1 Structure and Composition of Bone 942
26.2.2 Limitations of Natural Bone 944
26.3 **Existing/Conventional Bone Implant Materials and Their Shortcomings** 944
26.3.1 Metallic Implants 945
26.3.2 Polymeric Implants 945
26.3.3 Ceramic Implant 945
26.3.4 Ceramic Polymer Composites as Implants 946
26.4 **Major Challenges with Existing/ Conventional Implant Materials** 949
26.4.1 Mechanical Integrity 949
26.4.2 Incorporation of Biomolecules 949
26.4.3 Long-Term Characterization of Porous Composite Scaffolds 949
26.4.4 Biocompatibility Study 949
26.5 **Nanotechnology and Tissue Engineering** 949
26.5.1 Unique Properties of Nanomaterials 950
26.5.2 Nanoscaffold Fabrication Techniques 951
26.5.3 Nanomaterial Scaffold for Orthopedic Purposes 954
26.6 **Future Perspectives** 965
References 965

26.1 The Quest for a Suitable Bone Implant

The human body is always prone to several kinds of diseases, injuries, and trauma, which leads to damage and degeneration of cells and tissues. To overcome this unavoidable problem, treatment should be personalized in such way that facilitates the repair, replacement, or regeneration at an early stage. Bone is a vital and versatile part of the human body, which provides the framework of the whole body. A healthy skeletal system keeps us active and working throughout life, but with the passing of time several kinds of bone disease development take place; the most common being osteoarthritis, osteoporosis, and bone cancer which affects billions of peoples worldwide. Apart from bone diseases, accidents are the leading cause of bone fracture. In fact, annually an estimated 1.5 million individuals in the United States suffer from bone fractures. Progression of bone diseases takes some time to completely inactivate the bone function but accidents or trauma immediately have an impact on the functioning of bone. Bone diseases like osteoarthritis and osteoporosis need continuous and long-term medications, but bone fracture due to accidents necessitate an accelerated treatment. Bone scaffolds or bone implants are the class of materials that have the potential to meet the early need for accelerated treatment during bone accidents or trauma along with possible therapeutic contribution to other bone diseases. A suitable bone scaffold has enormous potential for recruiting bone cells (osteoblast) at the site of trauma and helps in their proliferation and growth to mature bone cells (osteocytes), thus healing the site of trauma in a short period of time and relieving the patient from physical and mental stress.

Although the journey of finding and developing suitable bone implants started several decades ago under the brand name of bone tissue engineering, the development of an ideal bone scaffold that can support the growth and proliferation of osteoblast and thereby increment the replacement the bone tissues still remains a major challenge for biomedical engineers. The incredible pace and advancement of nanobiotechnology has created tremendous enthusiasm and opportunity in academia and industries to assimilate nanotechnology for tissue engineering applications. It is strongly believed that the new discoveries in nanotechnology and the new abilities of engineering will enable material scientists and engineers to design and fabricate novel scaffolds by incorporating nanoscale features, thus imitating the characteristics of the natural extracellular matrix.

By considering the potential of nanotechnology to improve the bone scaffold, this review is aimed at providing the best possible facts related to the application of nanotechnology in tissue engineering.

26.2 Bone

Bone is the dynamic and main vascularized component of the human skeletal system and plays a vital role in physiology, protection, and in mechanical functions in daily life. Hematopoiesis (formation of red blood cells) and homeostasis (storage of Ca and P ions and regulation of the concentration of key electrolytes in the blood) are the chief physiological functions of bone. The rigidity and hardness of bone enable the skeleton to maintain the shape of the body, to protect vital delicate organs, such as lungs, heart, etc., and bone marrow filled with nutrients. It is the primary site of muscle attachment for movement and provides mechanical support for soft tissue during adequate load-bearing capacity. Structure and properties of bone differ significantly on the basis of anatomical location, even though there are some common features among all bones.

26.2.1 Structure and Composition of Bone

Bone is a natural nanostructured composite and a perfect example of hierarchial structure [26.1]. Non-stoichiometric nanocrystalline hydroxyapatite HAP, ($Ca_{10}(PO_4)_6(OH)_2$) with 20–40 nm in length are the main inorganic components of bone, and type-I collagen molecules approximately 300 nm in length are the main organic counterpart.

Deep microscopic structural investigation into bone revealed that collagen molecules are covered with HAP nanocrystals and they form nanocomposites fibers, in which HAP C-axes are approximately aligned along with collagen molecules [26.2, 3]. From a mechanical point of view, bone is a non-homogeneous and anisotropic material.

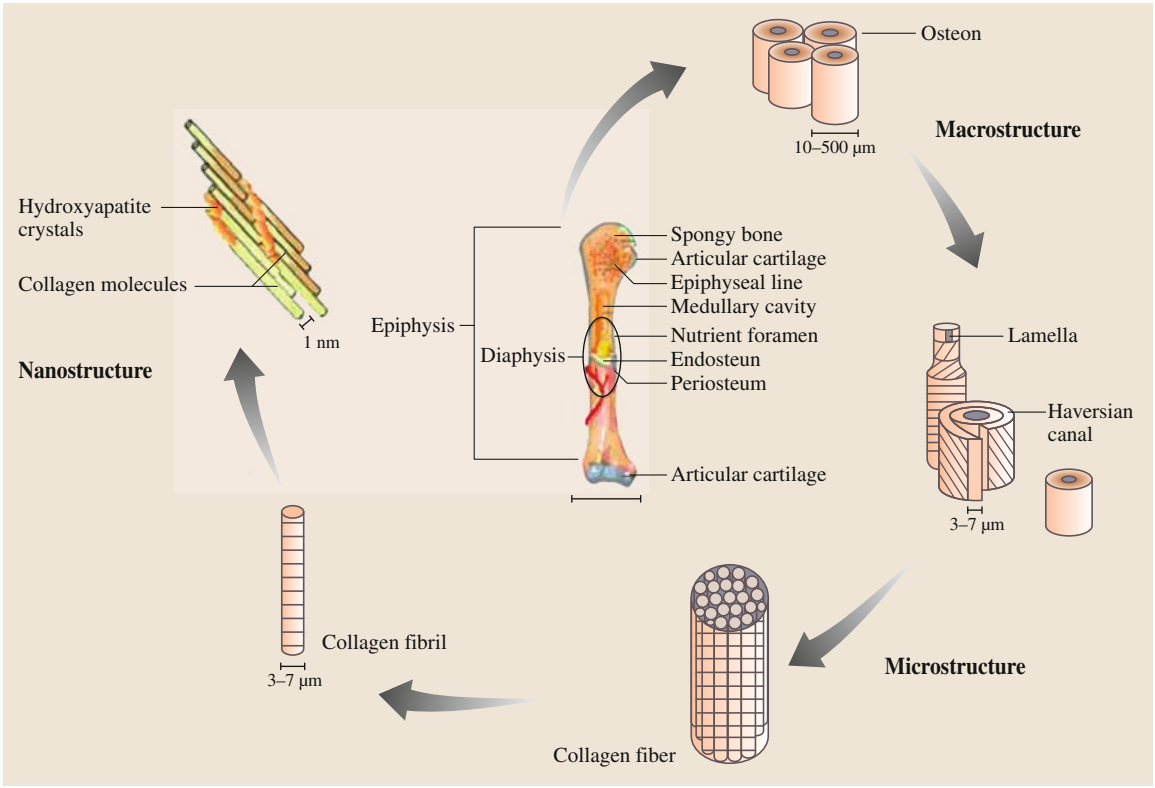


Fig. 26.1 Schematic diagram showing the hierarchical organization of bone

As mentioned before, bone consists of different hierarchical levels. At the macrostructure level, bone is distinguished into the cortical (or compact) and cancellous (spongy or trabecular) types. From its cross-section, it is revealed that the end of a long bone such as the femur has a dense cortical shell with a porous, cancellous interior [26.4]. Cancellous bone is primarily found at epiphysis and metaphysis of both long and cuboidal bones, while cortical bone is present at the diaphysis of long bones. Cancellous bone is characterized by a three-dimensional sponge-like structure with 50–90% porosity with a pore size up to several mm, while cortical bone porosity is less than 30% and the pore size is up to 1 mm.

Cancellous bone is a lattice of narrow rods and plates (70–200 μm in thickness) of calcified bone tissue called trabeculae, with an average thickness of 100–150 μm.

Osteon is the main structural unit of cortical bone, which is a hollow cylinder with 200 and 50 nm of outer and inner diameter, respectively. An osteon is composed up of 20–30 concentric lamellae and the outer border is lined by a 1–2 μm thick layer of mineralized matrix deficient in collagen fibers which act as crack stoppers [26.5]. There are no blood vessels in the cancellous bone but it is surrounded by bone marrow which is vascular and provides nutrients and waste disposal for bone cells. Cancellous bone is less mineralized than cortical bone and it is more active in bone remodeling than the cortical bone [26.6]. The main role of the cancellous bone is to receive compression under physiological loading conditions.

At the microstructure level, cancellous bone is composed of woven bone and lamellar bone. Woven bone is sometimes referred as primary bone or immature bone. Woven bone is isotropic, composed of relatively disoriented coarse collagen. Woven bone is normally present in the metaphysical region of growing bone, as well as in fracture callus and diseased bone such as pagetic bone. In contrast, lamellae bone is mature bone which is formed by the remodeling of woven bone or previous existing bone. Lemellae bone shows anisotropic characteristics and it is due to parallel orientation of collagen fibers to the lamellae; this imparts great strength

parallel to the longitudinal axis of collagen fibers. The thickness of lemallae bone is 3–7 μm and it is formed into concentric rings of (4–20 rings) as osteons. Each osteon has a central blood supply called a haversian system.

The nanolevel of bone is characterized by the presence of hydroxyapatite crystals and collagen fibers. In composition, 90% is type-I collagen protein while 10% is non-collagenous protein and other ground substances. The molecular weight of collagen protein is 139 kDa and it is composed of two identical $\alpha 1$ chains and one unique $\alpha 2$ chain. This configuration imparts collagen, a fairly rigid molecule that is 300 nm long [26.7]. Type-1 collagen molecules in bone are self-assembled to form a triple helix bundle having a periodicity of 67 nm with 40 nm of gap (hole zones) between the end of the collagen molecules and pores between the sides of parallel molecules. The chief role of collagen fibers is to provide the framework and architecture of bone. Inter-molecular and intramolecular cross-links between collagen fibrils stabilize the network and provide high levels of tensile strength and stiffness that are advantageous for tensile loading. Non-collagenous proteins are growth factors for, e.g., insulin-like growth factors, osteogenic proteins, and bone inductive protein like osteonectin, osteopontin, and osteocalcin are present. In extracellular matrix bone sialoprotein, bone proteoglycans, phosphoproteins, as well as proteolipids are found. The major role of these proteins is to regulate the size and orientations of the minerals and serve as reservoir for Ca^{2+} and PO_4^{2-}.

The hydroxyapatite or mineral component of bone is plate-like nanocrystals and is located in the hole zones with in collagen fibers. The dimension of HAP crystals are length × width × thickness and are 50 × 20 × 2–3 nm^3 [26.8]. The growth of HAP crystals is in a specific orientation, that is the C-axis of the HAP crystals is parallel to the long axis of the collagen fibrils [26.9].

HAP crystals improve the properties of bone by offering high strength and stiffness to resist compressive stresses.

Regeneration and remodeling is a peculiar property of bone Fig. 26.1. Bone can regenerate when damaged or remodeled during the change of loading conditions for, e.g., the mass of bone increases with exercise and thus prevents the bone from fracturing [26.10]. The remodeling and regeneration process of bone is governed by the cellular components of bone in a coordinated way. The major cellular components of bone are, osteoclasts, which are also known as bone resorbing cells, osteoblasts, known as bone making cells, osteocytes, known as mechano-sensors [26.10], and bone lining cells (inactive cells on the resting surfaces of bone) perform the coordinated process of bone regeneration and remodeling. The fate of bone implant material is determined by the remodeling process.

26.2.2 Limitations of Natural Bone

Bone plays an important role as the structural material maintaining the structure of the body of vertebrates and guarding the delicate internal organs. In fact, all material experiences fatigue by long use. To keep a material in working condition, periodic renewal of bone material is necessary to maintain sufficient toughness to work a whole life. In fact, annually, an estimated 1.5 million individuals in the United States suffer from bone fractures [26.11].

Although bone has its own capability to regenerate and remodel, during disease, its efficiency is greatly reduced. With the onset of bone disease like osteoarthritis and osteoporosis, bone gradually becomes weak and spongy and this time its own regeneration and remodeling machinery do are not efficiency enough to help cope with these diseases.

Therefore, bone implant is the one and only alternative that can help to improve the quality of bone.

26.3 Existing/Conventional Bone Implant Materials and Their Shortcomings

Implantation is the only possible way to treat bone fracture. Traditionally, autograft, allograft, and xenograft implants have been used to repair fractures and other bone defects. However, these substitutes are far from being ideal implants, as each has its own specific problems and limitations [26.12]. Autografts have been considered as the gold standards for bone replacement for many years, but they have some severe concerns like donor shortage and donor site morbidity with infection, pain, and hematoma, which further limit their suitability, thus their applications [26.13–19]. Allografts and xenografts always have the risk of disease transmis-

sion and immune response, and may cause loosening or complete loss of bone inductive factors [26.17, 20, 21].

As an alternative to autografts, allografts, and xenografts several materials like metal, ceramics, and polymers have been introduced as artificial bone implants. Out of these metallic implants have gained maximum popularity and have been able to reach real practice.

26.3.1 Metallic Implants

The most used artificial implant materials are metallic in nature, such as stainless steel, titanium alloys, and cobalt-chromium alloys [26.22–24]. Metallic implants provide the necessary strength and toughness that are required in load-bearing parts of the body, and due to these advantageous metals continue to play an important role as orthopedic biomaterials in the current era.

Metallic implants are strong enough to meet the requirements for the desired mechanical strength for an ideal implant; however, these traditional implant materials exhibit several problems, such as a short average lifetime 10–15 years, failure of implants due to implant loosening, inflammation, infection, osteolysis, and the release of certain ions and corrosion products (debris) at the site of implantation. Metallic implants may lead to mechanical mismatch problems (stress shielding) between the implant and the adjacent bone tissue where the integrity of bone/implant interface may be compromised due to the resorption of bone tissue. The short average lifetime (10–15 years) of traditional implants leads to much painful and expensive surgery to replace such failed implants.

26.3.2 Polymeric Implants

In addition to metal as an implant, polymers are a class of material that has shown enormous potential for use as a bone implant. There are number of biocompatible polymers that have been found suitable for different biomedical applications including orthopedics. Polyanhydride has been found to be useful as bone augmentation or replacement due to its photopolymerization property [26.25–27].

Polyphosphazenes are a suitable candidate for skeletal tissue regeneration [26.27], while polycarbonate-modified tyrosine derived amino acids have been the choice as suitable materials as scaffolds for bone replacement [26.25]. Polymethylmethacrylate (PMMA) is widely used in orthopedics as a bone cement for implant fixation, as well as to repair certain fractures and bone defects [26.28]. PMMA is not biodegradable and does not bind covalently to bones and is immunogenic [26.26, 29]. Polyethylene (PE) has been used as an implant for hip replacement [26.30, 31], while polyethylene terephthalate, polypropylene, and *polytetrafluoroethylene* (PTFE) have been used for knee ligaments [26.32].

Nonetheless, the most popular synthetic polymers used in medicine are the linear aliphatic poly(α-hydroxyesters), such as polylactic acid (PLA), polyglycolic acid (PGA) and their copolymers poly(lactic-co-glycolic) acid (PLGA), these are biodegradable polymers and have been approved by the FDA [26.27, 33–38]. Wide application of these polymers for orthopedic purposes is due to their good biocompatibility, nonimmunogenicity, and biodegradability [26.17, 25, 27, 36, 39–43].

Poly(α-hydroxyesters) have been investigated as scaffolds for replacement and regeneration of a variety of tissues, cell carriers, controlled delivery devices for drugs or proteins (e.g., growth factors), membranes or films, screws, pins, and plates for orthopedic applications [26.25, 27, 36, 44–46]. The degradation rate of PLGA can be adjusted by varying the amount of the two component monomers, which can be exploited to create an orthopedic material that degrades in concert with bone ingrowth [26.17, 47]. The suitability of PLGA as a scaffold material in tissue engineering is due to its unique physicochemical properties that support osteoblast migration and proliferation [26.27, 40, 48, 49]. Unfortunately, despite the potential as a scaffold material for orthopedic purposes, the poor mechanical strength of these polymers, further limits their applications and they are only recommended for certain clinical applications such as ankle and elbow fractures [26.36, 43]. Another major issue with these polymers is their bulk degradation when used as implants. This leads to a lowering of pH, and at this reduced pH further degradation of polymers occurs autocatalytically. This results in an increased number of monomer units in the body, which might lead to an inflammatory response [26.27].

26.3.3 Ceramic Implant

Next to the metal and polymeric implant materials, ceramic materials have been used extensively in orthopedics due to their well-known biocompatible properties with bone cells and tissues [26.50–53].

Metal oxides (e.g., alumina, zirconia, titania), calcium phosphates e.g., HAP, tricalcium phosphate (TCP), calcium tetraphosphate ($Ca_4P_2O_9$) [26.54], and

glass ceramics (e.g., Bioglass and Ceravital) [26.55] are commonly used as orthopedic implants. Ceramic materials are considered bioactive materials because they can bind with bone without intervening fibrous tissue. The surface property of bioactive ceramics support bone cell adhesion, proliferation, and differentiation. Ceramics such as HAP and TCP have similar chemical composition to the mineral phase of natural bone. Consequently, their reaction with physiological fluids creates strong bonds to hard and soft tissues, thereby increasing osseointegration between implant and bone. Moreover, these ceramics are degradable, and their dissolution rate depends on crystallinity. By virtue of this, degradation of many ceramic materials can be controlled to match the rate of new bone growth. Amorphous calcium degrades much faster than crystalline HAP [26.56]. Conventional ceramic materials, like alumina, titania, and HAP (grain size > 100 nm) possess good biocompatibility [26.50–53, 57–64].

However, similar to metallic implants, the clinical application of ceramic materials is still limited due to insufficient prolonged bonding of these materials to the just exposed bone and brittleness (this restrict its application to large bone defects).

26.3.4 Ceramic Polymer Composites as Implants

Although both ceramic and polymeric materials have shown much potential as bone implant material, their clinical application is still a challenging issue. Ceramic scaffolds alone can be suitable as an implant material because it is easy to engineer the macro and microporosity within the structure, but their poor degradability and poor mechanical properties like tensile strength and brittleness limit their further application. It is believed that the incorporation of biodegradable polymers to ceramic materials will help to improve their degradability and will also improve their mechanical (physical) properties.

Polylactic/Polyglycolic Acid–Based Polymer–Ceramic Composites

Polylactic/polyglycolic acid derived polymers are polylactic acid (PLA, PLLA), polyglycolic acid (PGA), poly-(D/L-lactic-co-glycolic) acid (PLGA), and polycaprolactone (PCL) have been investigated as bone material, due their good properties. Due to the good biocompatibility and ideal degradation properties of these polymers, they have been employed to make a composite bone implant material with ceramics. Most polylactic/ceramic composite materials, therefore, exploit these degradation properties by using the polymer as the scaffold material. Ceramic particles are added to the polymer to make it (more) osteoconductive and/or to increase mechanical properties. These scaffolds can be of either porous or dense structure using bioactive glass, HAP, amorphous calcium phosphate (ACP), and biphasic calcium phosphate (BCP) as ceramic component in a PLLA, PLGA or PCL matrix. *Navarro* et al. reported the fabrication of a glass-ceramic particle/PLA scaffold by homogeneous mixing of the glass ceramic into a PLA solution, and its macroporosity was controlled by the addition of H_2O solvable NaCl particles [26.65]. Furthermore, they found that the mechanical strength of PLA increased after the addition of 40% glass ceramic, which is far away from the desired compressive strength.

On the contrary, *Niemelä* et al. observed the decrease in bending strength/modulus as well as in compression and shear strength on the addition of glass ceramic to poly-L, DL-lactide by twin-screw extrusion [26.66]. *Yao* et al. observed that despite the unfavorable mechanical properties bioactivity of the polymer was increased by addition of bioactive glass [26.67].

Synthesis of a highly porous composite of HAP and PLLA/PLGA was reported by *Zhang* and *Ma* [26.68]. *Shikinami* and *Okuno* have shown that HAP and PLLA/PLGA composite show reinforcement of PLLA [26.69]. However, the degradation of these composite materials is very slow [26.70]. *Mondrinos* et al. synthesized a 3-D porous composite of PCL with 10–20% CaP and found that the compressive strength of the composite is increased dramatically with increased cell proliferation at 20% of CaP [26.71]. *Ambrosio* et al. prepared a macroporous scaffold by sintering composite CaP/PLGA microspheres, where the CaP-phase was trapped inside the microspheres [26.72]. It was found that the composites of slowly degrading polymers like PCL and PLLA do not show any toxicity and promote cell growth, while faster degrading polymers show signs of toxicity due to the presence of a vast number of acid degradation products both in in vitro and in vivo studies. *Ignatius* et al. observed a strong inflammatory response of composites of PLA and α-TCP or a glass ceramic in sheep, 24 months after implantation [26.73].

Polylactic/glycolic acid and CaP cement composites can be formulated by the introduction of PLA/PGA microspheres. *Simon Jr.* et al. were the first to introduce the PLGA microspheres inside the calcium phosphate [26.74]. In a further study, they introduced

180–360 μm of microspheres to tetracalcium phosphate cement and evaluated their cell response. As a result they found that this scaffold material promotes cell proliferation with improved biocompatibility.

Ruhe et al. [26.75] and *Habraken* et al. [26.76] synthesized the macroporous scaffold by placing 20–40 μm of PLGA microsphere and reported that the incorporation of 20% PLGA microsphere in the CaP scaffold decreased the compression strength, injectability, and increased cement setting time, but within manageable ranges. Bulk erosion of the microspheres in the scaffolds was also observed, corresponding to a sudden decrease in mechanical strength.

In comparison to microporous cement PLGA degradation causes a decrease in pH; in turn, resorption of cement is increased around the microsphere. This decreased pH does not cause considerable harm in in vivo applications because it has been found that subcutaneous implantation of these scaffolds showed no adverse tissue reaction during microsphere degradation [26.77]; in cranial defects even bone ingrowth was observed [26.78, 79].

Protein-Based Polymer-Ceramic Composites

Biocomposites of CaP ceramics and cements with protein-based polymers are being extensively investigated. It is believed that organic-inorganic biocomposites will be similar to bone composites with improved mechanical/physical and biological characteristics. Well-known examples of such biopolymers are collagen and gelatin.

Collagen is one of the most abundant protein components inside the human body and has been employed in numerous research as a tissue-engineered construct. Gelatin is a cheap and commercially available biomaterial. Gelatin is either a processed form of collagen that is usually derived from pig-skin with an acidic process (type A) or of bovine origin with a basic (lime cured) process (type B). Gelatin and collagen are biodegradable polymers which are solely degraded by proteolysis (collagenase, gelatinase). The tailored degradation rate of these biopolymers provides a better opportunity to make a biocomposite with ceramics, with a better control over degradation along with improved biological and physical properties of both materials.

Synthesis of biocomposites of a porous gelatin/collagen scaffold with CaP ceramic material has been reported in several works [26.80–82]. As a material of high interest, unfortunately some studies revealed that these biocomposites suffer from poor mechanical strength and biocompatibility (due to glutaldehyde as a cross-linker) [26.83]. To overcome the problem of the cross-linker, fabrication of a B-TCP/collagen biocomposite without use of any extra material was reported by *Shibata* et al. [26.82]. *Duo* et al. synthesized the collagen-CaP biocomposite with high tensile strength by using collagen-I as matrix for mineralization of CaP, exploiting the biomimetic property of collagen (with 60–70% of CaP) [26.84].

Tampieri et al. prepared a ceramic/gelatin scaffold by soaking macroporous HAP in a gelatin solution by using a cross-linker to slow down the diffusion rate of gelatin [26.85]. They further reported that at low concentration of the cross-linker, the scaffold shows good biocompatibility.

For the evaluation of the release characteristics of growth factors through these CaP-biopolymer composites, *Takahashi* et al. investigated gelatin sponges containing β-TCP particles that were loaded with BMP-2 [26.80]. A biocomposite of CaP cement (α-TCP) with 18% gelatin was synthesized by *Bigi* et al. in a further study, which showed improved osteoblast activity along with increased mechanical strength [26.86–88]. The synthesis of porous (20–100 μm) biocomposites of gelatin and α-TCP, at varying concentrations of gelatin 5–20% was reported by *Fujishiro* et al., and results showed an increase in mechanical properties with 5% gelatin content (with time), although with 20% gelatin the compressive strength was lowered [26.89]. The improved biological response and increased mechanical strength is mostly attributed by the biomimetic abilities of gelatin that function as a nucleation point of CaP-crystal growth [26.90].

Biocomposites of collagen with CaP cement were also investigated. *Rammelt* et al. added 3% of collagen-I to a nanocrystalline hydroxyapatite cements, which led to an increased bone remodeling in rat tibia defects [26.91]. *Knepper-Nicolai* et al. added 1–2.5% collagen-I to a commercial apatite cement and observed mechanical and physical changes of the cement especially when osteocalcin was added [26.92]. Extending the work of *Kneppes-Nicolai* et al., *Hempel* et al. studied the behavior of osteoblast on the same 2.5% collagen containing cement and found that proliferation and differentiation of cells was greatly influenced by a local microenvironment like pH [26.93].

Apart from gelatin and collagen, some other proteins like fibrin were used in biocomposite formation with CaP ceramics [26.94, 95] and cement [26.96], soybean and casein protein were used with Al_2O_3 and TCP [26.97], and polypeptide with CaP [26.98].

Carbohydrate-Based Polymer-Ceramic Composites

In addition to the protein-based polymer-ceramic composites, carbohydrate-based biopolymers are of great interest for biocomposites with ceramics. Chitin, chitosan, alginate hyaluronic acid, and cellulose are well-known carbohydrate polymers. Among these polymers, chitosan is often applied together with CaP-cement or CaP-particles because it is biodegradable by lytic enzymes and gives a good match to natural bone with respect to mechanical properties. Chitosan can improve the mechanical/physical properties of CaP cement in biocomposites, as well as influence the cement setting, although the compression strength of the ceramic is superior to chitosan.

Leroux et al. reported that chitosan can be added as adjuvant to CaP cement to make it more injectable without considerable modification in the setting reaction [26.99]. *Takagi* et al. also reported that the CPC-chitosan composite exhibits a better cohesion in water than TTCP [26.100]. Reinforcement of tetracalcium phosphate (TTCP) cement by chitosan lactate was investigated by *Xu* et al. [26.101]. Mannitol crystal introduces macroporosity to these biocomposites, which in turn reduces the flexural strength and elastic modulus [26.102]. *Lee* et al. introduced TCP particles to chitosan sponges, by freeze-drying and cross-linking a mixture of a chitosan solution and TCP [26.103]. *Zhang* and *Zhang* added HAP and calcium phosphate invert glass to a chitosan sponge using a similar procedure and reported that the osteogenicity of the scaffold is increased manyfold [26.104]. An improved elastic modulus and yield strength have been obtained in biocomposites of chitosan with invert glass and β-tricalcium phosphate (BTCP) [26.105].

Hydroxypropylmethyl cellulose (HPMC), a cellulose derivative) is another carbohydrate which has been used in combination with ceramic particles or as an addition to calcium phosphate cement for fabrication of biocomposites. By combining BCP and HMPC, *Daculsi* et al. developed an injectable bone substitute and reported its poor mechanical strength [26.106]. Cross-linking the HPMC by silanol groups (si-HPMC) renders a more stable scaffold with a comparable in vivo performance [26.107]. On addition of HMPC to the DCPD, a dramatic increase in the injectability of dicalcium phosphate dehydrate (DCPD) was observed by *Burguera* et al. [26.108]. Injectable paste of amylopectin with BTCP was prepared by *Ongpipattanakul* et al. and a better release profile (about 80%) of growth factor rhTGF-β was reported as a result of in vitro studies after 24 h [26.109]. Further, a positive sign towards the bone growth was reported when it was implanted in rabbit unilateral segmental defect model, after 56 days.

Biocomposites of bioactive glass and starch/cellulose acetate and a mixture of methylmethacrylate/acrylic acid have been reported by *Boesel* et al. [26.110]. Different amounts of bioactive glass were added (up to 30%), which resulted in a significant improvement in the elastic modulus and yield strength of the material. In general, no bioactivity was observed due to the inhibiting effect of the acrylic acid because only with the highly reactive bioglass, calcium phosphate precipitation occurred.

Hyaluronan is another attractive carbohydrate-based polymer for tissue engineering that is present in the human body and proteolytically degradable by hyaluronidases. *Liljensten* et al. investigated the biocomposite of HAP granules in a hyaluronan carrier and found better bone growth [26.111]. Application of alginate in inorganic–organic scaffolds is limited due to its poor biodegradability; recently attempts have been made to improve the biodegradation of alginates [26.112]. Alginates have been used as cohesion promoters in biocomposites with calcium phosphate which in turn decreases the rate of disintegration in biological fluids like blood/serum. Chitosan also possesses a cohesion property similar to alginates.

A thorough investigation of the cohesion property of commercially available carbohydrates after the addition of a wide range of these polymers, i. e. hydroxyethyl starch, starch, sodium dextran sulphate, $\alpha/\beta/\lambda$-cyclodextrine, alginic acid, hyaluronic acid, and chondroitin sulfate, has been done by *Khairoun* et al. [26.113].

Other Polymer-Ceramic Composites

Composites of ceramics with different types of polymers have also shown potential as bone implants. Especially synthetic polyesters, other than polylactic/glycolic acid discussed previously, can be suitable carrier materials for ceramic particles. In this paragraph the characteristics of these and other polymer composites, as well as their use for tissue engineering have been discussed briefly. *Peter* et al. formulated a biocomposite of 25% BTCP in a propylene fumarate (PPF) carrier, with increased mechanical strength, along with good osteoinductive properties [26.114]. *Charvet* et al. synthesized and reported a composite of a poly(desaminotyrosyl-tyrosine ethyl ester carbonate) (poly(DTE carbonate)) and CaP-glass fibers ($CaO\text{-}P_2O_5\text{-}Fe_2O_3$) with improved mechanical

strength [26.115]. Ceramic particles of β-TCP, HA and bioglass were added to polymers of poly (3HB) and poly(3HB-co-3HV) [26.116], which led to an increase in mechanical properties and bioactivity.

Qiu et al. reported the synthesis of poly(diol citrate)-HAP microparticles with better mechanical properties, a slower rate of degradation, along with improved mineralization in vitro [26.117]. *Mickiewicz* et al. added a range of water-soluble polymers comprising different polyelectrolytes, poly(ethylene-oxide), and bovine serum albumin (BSA) during cement setting of a brushite and reported an improvement in mechanical strength [26.118]. *Dos Santos* et al. reported the synthesis of a composite of a α-TCP-based apatite cement, reinforced with polypropylene nylon and carbon fibers, which showed a decrease in compressive strength and an increase in toughness and tensile strength [26.119].

Biocomposites consisting of fibers of aramide, carbon, epoxy-glass, or polyglactin with calcium phosphate cement was investigated by *Xu* et al., and an increase in tensile strength, work-of-fracture, and elastic modulus were found [26.120].

26.4 Major Challenges with Existing/Conventional Implant Materials

26.4.1 Mechanical Integrity

The mechanical properties of artificial scaffolds made up of porous bioactive ceramics and biodegradable polymers foams are insufficient to meet the real mechanical strength of bone [26.121–123]. The stiffness achieved by fabricated bioactive ceramics is less than the stiffness of the porous biodegradable polymer scaffolds. A slight increase in the stiffness and in the mechanical strength was found in polymer scaffolds but it was certainly below expectations.

26.4.2 Incorporation of Biomolecules

Surface modification of implants by protein adsorption or by plasma treatment generates significant scope and provides more clues to cells' attachment and response [26.124, 125]. The possibility of incorporating growth factors into composites formed by biodegradable polymers and bioactive glasses or HAP inclusions has started to be explored [26.126–136]. However, the immobilization of these proteins and growth factors on the scaffold surface results in the shortening of bone healing and reduction of patient recovery time. The incorporation of biomolecules does not allow extreme temperature ranges ($> 70\,^{\circ}\mathrm{C}$) or extremely aggressive chemical conditions during processing, this being a challenge to the scaffold fabrication process. The other challenge is the elucidation of the local impact of growth factors on the cell and tissue systems, including long-term effects.

26.4.3 Long-Term Characterization of Porous Composite Scaffolds

There is no sufficient proof in the literature which provides the long-term behavior of the existing scaffold material (in vivo and in vitro studies).

26.4.4 Biocompatibility Study

There are adequate reports about the biocompatibility of biodegradable polymers and bioactive ceramics [26.14, 19, 83, 131, 133, 134, 137–139] while for composite materials only a few are available.

26.5 Nanotechnology and Tissue Engineering

During the last several decades, a huge amount of research has been made in the field of tissue engineering and regenerative medicine to improve the design and performance of existing orthopedic implants. Tissue engineering proved its significant role in orthopedics in the form of various scaffolds of polymers, ceramics, and their composites, as discussed in the paragraphs above. Even though a positive sign towards the suitable implant materials is visualized, some considerable challenges still remain.

With the advent of nanotechnology and its accelerated progress in recent years, better opportunities have been created to tune material as needed. During the last few years, nanomaterials were developed with basic structural units, grains, particles, fibers, or other constituent components smaller than 100 nm in

at least one dimension [26.140]. They have received much attention for improving disease prevention, diagnosis, and treatment. Nanomaterials can be of different in sizes and different morphologies such as nanoparticles, nanoclusters, nanotubes, nanofibers, nanowires, nanorods, and nanofilms. The enormous therapeutic potential of nanomaterials has drawn the attention of tissue engineers towards nanomaterials to meet their requirements. To exploit the unique physicochemical properties which arise in nano dimensions, conventional micrometer-size implant materials like metal, ceramics, polymers, and composites can be tailored to materials with nano dimension. There are numerous nanofabrication technologies like electrospinning, phase separation, self-assembly, thin films deposition, chemical vapor deposition, chemical etching, nanoimpriting, photolithography, electron-beam lithography, and nanosphere lithographies [26.141] for the synthesis of ordered or random nanotopographies [26.142–145].

The biomimetic features and excellent physiochemical properties of nanomaterial play a key role in stimulating cell growth as well as in guiding tissue regeneration. Natural tissue or organs, which are themselves of nanometer size, can directly interact with nanostructure extracellular matrices (ECM) without any hindrance.

Of relevance to the merging of nanotechnology and tissue engineering is the realization that bone is a natural nanostructured composite material composed of intertwined inorganic (bone apatite) and organic compounds (mainly collagen) [26.146]. Natural bone formation, is itself a kind of nanofabrication that occurs inside the body and we have become familiar with this fact very recently. The material of natural choice in nanotechnology will be those occurring at the nano hierarchy level of bone.

Bone is a natural nanocomposite (as discussed in the preceding paragraphs) and its constituents contribute unique properties to create a structure optimized not only for high loading and bending moments, but also for fracture and fatigue resistance [26.8, 137]. The mechanical property of bone is highly dependent on the percentage of both mineral and protein matrix and their interaction, porosity, and degree of cross-linking [26.147, 148]. The viscoelastic property of bone is contributed by collagen molecules, comparable to rope, where it offers mechanical advantage for tensile loading but has poor compression or shear properties. While the role of apatite crystals in bone is to improve the compression or shear properties.

It is firmly believed that nanotechnology will help to overcome the challenges of tissue engineering in a synergistic way. *Nanocomposites*, the implant material created after the fusion of two novel technologies, i. e., tissue engineering and nanotechnology, will definitely solve the most awaited problem of an ideal implant. The principle of nanocomposite design is based on the creation of nanocomposite materials with superior properties by the fusion of two materials which individually possess inadequate properties.

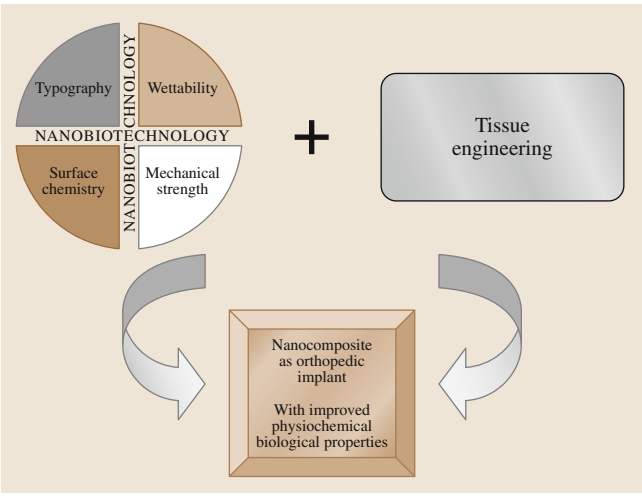


Fig. 26.2 Schematic diagram showing synergistic effect of nanotechnology and tissue engineering for orthopedic implants

26.5.1 Unique Properties of Nanomaterials

Features like pores, ridges, grooves, nodes, and their combination in scaffold material is known as nanotypographical features which improve the cellular function.

Nanotypography

Nanotypography created in Ti, Ti_6Al_4V and CoCrMo alloys resulted in increased osteoblast adhesion due to the presence of more particle boundaries in comparison to conventional metals [26.57]. Strong alignment and orientation of osteoblasts in the direction of patterned grooves was found in nanopatterned polystyrene grooves (with two different depths of 50 and 150 nm, with a periodicity of 500 ± 100 nm) [26.149]. Migration of primary human osteoblasts, away from the Ti oxide surface patterned with 110 nm hemispherical protrusion with varying topography has been reported [26.150].

Cell behavior on nanotopographic surfaces is dependent on the cell type [26.151]. At this stage, it

is not fully understood how cells detect and respond to nanofeatured surfaces. Thus, it is important to understand cell-nanotopography interactions and that variability in results may exist among varying cell types.

Surface Chemistry

Besides the nanotopography, the property of nanomaterials that plays an important role in deciding the fate of success and performance of implant is the surface chemistry. Protein and other biomolecules adsorbed over the implant surface can trigger the nonspecific inflammatory response characterized by foreign body reaction and fiber capsule formation, which in turn limit the integration of the scaffold and its in vivo performance. The self-assembled monolayer with different terminal functionalities like $-CH_3$, $-OH$, $-COOH$, and $-NH_2$ possesses a different affinity for fibronection adsorption, thus differentially influences the integration, binding, and cell adhesion [26.152, 153]. Differences in integrin binding differentially regulate local adhesion assembly and signaling, which, in turn, modulate cellular functions in biomaterial and implant surfaces.

Wettability

Apart from surface functionalization the hydrophilicity and hydrophobicity of the implant surface significantly influence the cell behavior for a particular implant. The wettability of a material allows the characterization of nanomaterials with regards to their, hydrophobic/hydrophilic categories. The surface wettability that affects the cell behavior depends on the surface composition, surface treatment, surface roughness, surface functionalization, and the presence of nanofeatures on the surface. Surface wettability of Al_2O_3 can be improved by reducing the size of grain from 167 to 24 nm [26.154]. An enhanced adhesion rate of preosteoblasts was observed on a titanium surface with a high degree of wettability created by high pressure torsion [26.155]. Enhancement of the adsorption of vitronection and fibronection due to improved surface wettability stimulated the adhesion of osteoblasts over the surface of the implant.

26.5.2 Nanoscaffold Fabrication Techniques

An ideal scaffold should have the property to augment or completely replace damaged, missing, or compromised tissue, or organs without creating any further complexities. The scaffold should be bioresorbable or should be permanently attached to the applied part and must be capable of mimicking the condition and characteristics of the local micro-environments.

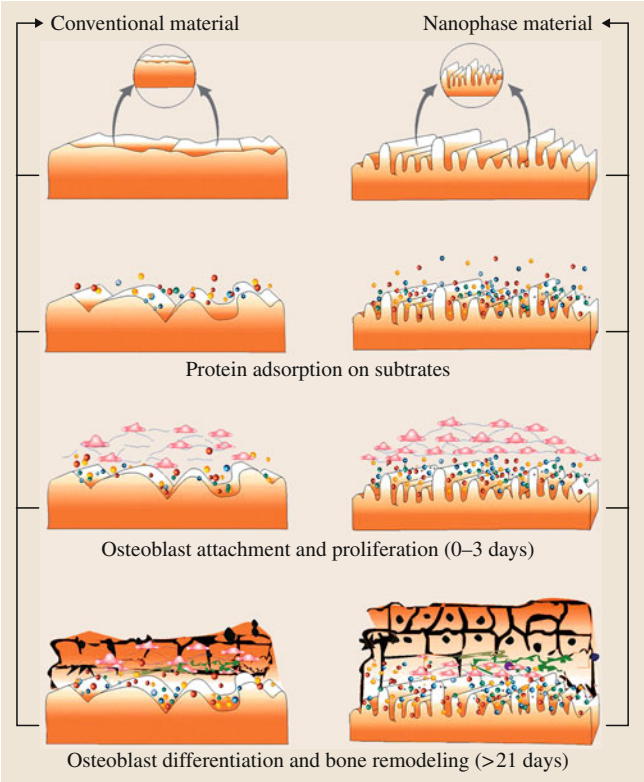


Fig. 26.3 Schematic diagram showing the comparison of conventional and nanophase scaffolds for bone cell function

Nanofabrication technology has shown great promise for the development of clinically relevant scaffolds specifically in the field of nanofiber fabrication. Nanofibers composed of natural or synthetic material, can be fabricated by self-assembly, phase separation, or by electrospinning methods.

Self-Assembly

This is a technique where the organization of disordered molecules into a structured pattern without external intervention takes place. It is a very good approach for the fabrication of supra-molecular structures [26.156].

Self-assembly takes place by non-covalent bonds such as hydrogen bonds, van der Waals bonds, and electrostatic and hydrophobic interactions. Self-assembly is ubiquitous in nature; biomolecules like proteins and peptides achieve a special configuration by self-

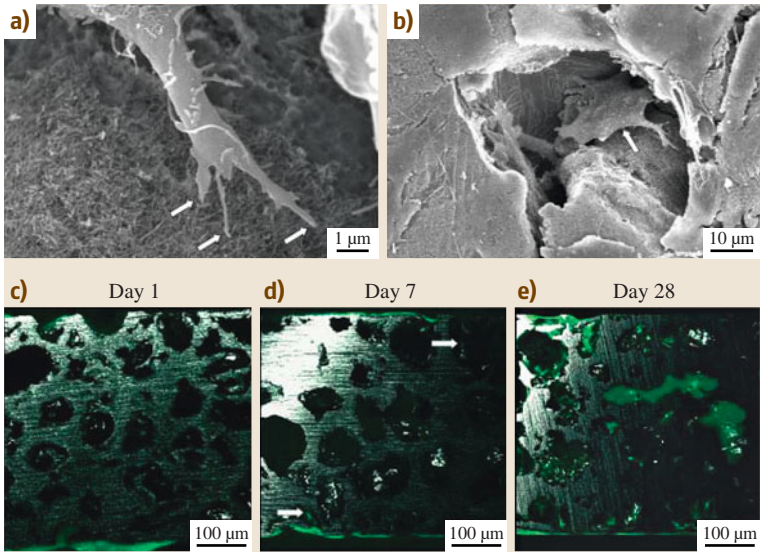


Fig. 26.4a–e SEM images of MC3T3-E1 pre-osteoblastic cells cultured for 7 days on 15% RGDS PA-Ti hybrids in a rotating bioreactor. **(a)** Cell stretched across a gap and adhering to the PA matrix (indicated by *arrows*). **(b)** Cell migrating into the PA matrix-filled porosity of the PA-Ti hybrid (*arrow*). **(c–e)** Confocal fluorescent images of cross-sectioned 15% RGDS PA-Ti hybrids at days 1, 7, and 28, showing GFP-transfected MC3T3-E1 pre-osteoblastic cellular ingrowths and proliferation. (After [26.159])

assembly, which is very important for their functional aspect. Nanostructured fibers can be formed by self-assembly [26.157, 158] under certain conditions.

The most commonly self-assembled nanofibers, peptide amphiphiles (PA), were initially developed by *Berndt* et al. for their application in investigating the interaction between peptide structures and ligands [26.160]. PA systems are ligand–receptor pairs that are integrated into separate lipid molecules and fixed by means of self-assembly onto a surface [26.160]. PA systems are made up of a head, N-alpha amino group which is hydrophilic in nature and is attached to dialkyl moiety of tail; both these moieties were developed from the peptide sequences from collagen fragments [26.161, 162]. Self-assembly takes place in both mono-alkyl and dialkyl PA to form a stable triple helix conformation [26.161]. Self-assembled PA nanofibers can have fiber diameters as small as 10 nm and pore sizes of 5–200 nm (well within the range of the native ECM and significantly smaller than those produced through electrospinning) [26.158, 162].

PA nanofiber scaffolds have been found to be good material for use as bioactive implant surfaces. PA fibers have been used to generate the bioactivity into inert Ti foam by filling foam with PA nanofibers. Bioactive Ti foam was used as a bone plug model in rat femurs to help implant fixation; bone formation was found inside and outside of the implant [26.159] after 4 weeks (Fig. 26.4a,b). Development of self-assembled bioactive hydrogels has also been reported [26.163–165]. PEG hydrogels have been synthesized containing arginine, glycine and aspartate peptides, and matrix metalloprotein as a substrate [26.163, 164].

The cells are shown in green, with the top surface of the metal reflecting white, and the PA matrix not visible. At day 1, cells adhere to the exterior of the implant and proceed to migrate and proliferate into the core of the PA-Ti hybrid up to 28 days (Fig. 26.4c–e). At 28 days cells are observed both adjacent to the pore wall and in the PA matrix in the center of the pores [26.159].

Although the self-assembly technique produces fibers that are very close to the approximate size-scale of the native ECM, issues regarding mechanical properties of the scaffold and high complexity limits the use of this technique.

Phase Separation

To produce highly porous scaffolds, a phase separation technique is used. With this technique porous polymer membranes can also be fabricated for purification and separation purposes [26.166].

The process of phase separation can be achieved either by thermal induction or by using a non-solvent technique. The result of non-solvent induced phase separation is heterogeneous pore formation, which is not suitable for scaffold fabrication where uniform pores are desired. A thermally induced phase separation (TIPS) technique can be employed to fabricate nanofibers to mimic natural collagen fibers [26.167]. The TIPS process for nanofiber formation follows the five steps: polymer dissolution, phase separation and gelation, solvent extraction, and freezing and freeze

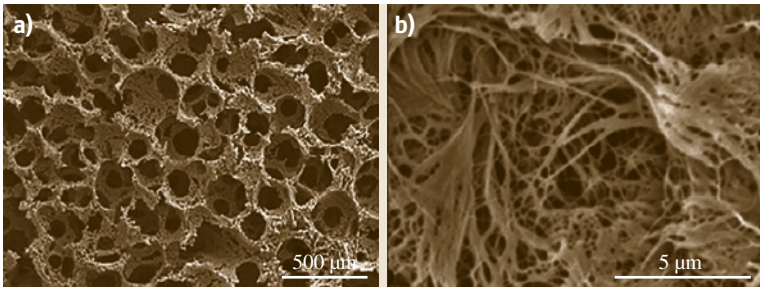


Fig. 26.5a,b SEM micrograph of PLLA nanofibrous matrix prepared from a 7.5 wt/v % PLLA/dioxane/pyridine (dioxane/pyridine = 1/1) solution and paraffin spheres showing increasing interconnectivity with increasing time of heat treatment up to 40 min. Sphere size range was $d = 250–420\,\mu m$: **(a)** original magnification × so; and **(b)** oringinal magnfication × 8000

drying under vacuum. The fiber network formation depends on the solvent of the polymer solution and the gelation temperature. During the process of TIPS, a homogenous polymer solution becomes thermodynamically unstable under certain temperature conditions and tends to separate into a multiphase system for, e.g., a polymer-rich phase and a polymer-lean phase, and thus lower the free energy. The polymer-rich phase is solidified to form the structure of the scaffold and the polymer-lean phase forms the pores. Numerous 3-D polymeric scaffolds have been fabricated by the phase separation technique [26.12, 68]. Fibers of PLA, PLLA, and PLGA with a size range of 50–500 nm and with 95% porosity (which is close to natural collagen fiber size) were fabricated using TIPS [26.161, 167, 168] (Fig. 26.5).

During the scaffold fabrication, the polymer gelation time and its temperature are the critical parameters that control the porosity and size of fibers [26.161]. The major loop hole in the nanofiber scaffolds, generated by TIPS, is the lack of interconnected pores, which is very critical for cell seeding and recruiting, mass transfer, vascularization, and tissue organization. To overcome this problem, the phase separation technique was combined with a progen leaching technique and a solid freedom fabrication (SFF) technique which results in better control over the porous architecture from macro, micro to nano [26.142, 169, 170]. A number of progens such as sugar, inorganic salt, and paraffin spheres [26.142, 168, 171] have been incorporated into the phase separation technique to provide better control over the size of the scaffold and have the potential to work well in bone tissue engineering [26.172, 173].

Layered phase separation scaffolds have been reported with various biomolecule coatings (such as matrigel, collagen type I and III, and elastin) for small diameter tube scaffolds or with multiple polymers (such as polyurethane (PU) and collagen) for nerve conduits [26.174, 175]. Although the phase separation technique is simple and consistent, the practical use of this method for scaffold production [26.161, 168] is limited due some issues, like progen extraction, the restricted number of usable polymers, and its amenability to large-scale production.

Electrospinning

Electrospinning is an established non-mechanical process that has been used for the fabrication of ultrafine fibers including microfibers (> 1 mm) or nanofibers (< 1000 nm) from a variety of synthetic polymers and natural proteins [26.176, 177]. In this technique, a high voltage is applied to a polymer solution or melt, which overcomes the surface tension to form a charged jet. Ejection of the charged polymer solution or melt takes place on a grounded substrate, which is subsequently dried, and solidified. Repulsion occurs among the ejected polymer solutions during their travel to the grounded collector, and formation of thin fibers after evaporation of the solvent takes place. Fibers ranging from 0.02 to 20 µm can be produced by controlling the spinning conditions. The orientation of fibers is random when a stationary collector is use, but preferential orientation can be obtained by using an electrically grounded rotating drum as the collector [26.176]. Electrospinning techniques have been applied for the fabrication of numbers of biomaterial scaffolds [26.178, 179]. Biodegradable polymers PGA, PLGA, PLLA, PCL, and several natural macromolecules like collagen and silk fibroin have been used in the electrospinning technique for scaffold fabrication (Fig. 26.6a,b) [26.138, 139, 176, 180–182]. Proteins, the growth factor, and HAP can be incorporated into nanofibrous material during electrospinning [26.139, 183].

The diameter of fiber and porosity can be regulated by controlling the composition of the electrospinning solvent and the identity, the concentration, and the degree of chain entanglements (viscosity) present in the starting polymer(s) [26.176, 177, 184].

The main advantage of the electrospinning process is the relative quick and simple way to fabricate a va-

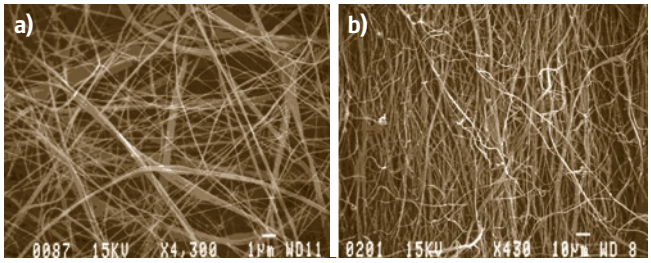


Fig. 26.6 **(a)** SEM of electrospun type-III collagen (human placenta). The isotype (type-I versus type-III) collagen used in electrospinning also determines the structural properties of the deposited filaments. Under conditions optimized for calfskin type-I collagen an electrospun matrix of type-III collagen is composed of fibers that average 250 ± 150 nm in diameter (magnification 4300 ×). **(b)** SEM of collagen type-I calfskin electrospun onto a rotating mandrel (magnification 4300 ×). (After [26.176])

riety of materials into nanofibrous structures but the fabrication of a 3-D scaffold is still a challenge for this technique. Thus although it is an easy fabrication technology, its inability to fabricate 3-D scaffolds or to generate the designed internal pore structure, limits its potential for many tissue engineering applications.

26.5.3 Nanomaterial Scaffold for Orthopedic Purposes

Metallic Nanoparticle Scaffold

Numerous studies have reported the increased adhesion of osteoblasts to the surface of metallic nanoscale implants [26.57, 185–187] and this gives a clear picture that there is strong potential for long-standing osseointegration of nanostructured metals to replace bone.

Osteoblast functions like adhesion, proliferation, and deposition of calcium containing minerals have increased in the nanophase compared to conventional metals like Ti, Ti_6Al_4V, and CoCrMo [26.185]. In a comparative study of nano and micro-powder of Ti, Ti_6Al_4V, and CoCrMo for osteoblast adhesion, a significantly higher osteoblast adhesion of nano-powder was found than of micro-powder of the same elements (Fig. 26.7) [26.7]. The osteoblast adhesion occurred primarily at metal particle boundaries. Increased osteoblast adhesion might be due to the greater number of defect boundaries at the surface of nanophase materials, creating unique surface energy, attracting the adsorption of certain proteins.

Anodization is another possible way to create nanostructure of metals. *Yao* et al. reported that performance of the metallic implant could be increased by anodization process [26.62]. In his study, *Yao* et al. created the nanotubes like pores over the surface of the Ti implant by an anodization process and increased osteoblast function was found over nanoscale Ti implants (Fig. 26.8) [26.62]. *Sirivisoot* et al. grew carbon nanotubes on the surface of anodized Ti and tried to create in situ orthopedic biosensors to detect the control of bone growth (Fig. 26.9) [26.64]. Carbon nanotubes (CNT) grown out of anodized nanotubular Ti show significantly higher alkaline phosphatase activity and calcium deposition by osteoblasts in comparison to micro Ti implants. Many other recent studies have reported an improvement of bone cell functions by nanophase materials [26.185, 186]. Ambiguities concerning the contribution of nanostructure surfaces have been found in some of the results, since the nanophase materials simultaneously changed surface roughness and chemistry [26.58–60, 188].

Khang et al. studied the role of nanosurface alone without changing the chemistry of the surface for tissue growth enhancement, by taking three types of Ti implant which differ in their surface structure (flat, nanometer, and submicrometer) [26.61]. They found that the cell densities were higher on the nanometer and sub-micron surfaces compared to flat Ti surfaces. This study further provides a support that nanometer roughness had the highest efficiency for increasing both surface energy and osteoblast adhesion compared to the altered pattern width of surface features, and therefore suggested an important role of nanometer and submicrometer surface features on the future design of improved Ti-based implants.

Ceramic Nanomaterial Scaffolds

Nanostructured metal has presented great potential for osteoblast function. Next to the metal nanostructure, nanostructured ceramics promote the bone cell functions compared to traditional, nano-smooth ceramics [26.185, 186]. The influence of nanometer-size ceramics was first studied in the year 1999 [26.185] and it was found that osteoblast adhesion was significantly higher on nanophase alumina and titania substrates when compared to micrometer-size conventional substrates. The study further adds that the increased osteoblast growth is due to surface topography of the nanophase implant only and independently to the surface chemistry in the same way as the nanostructured metal. An increase in osteoblast function like proliferation, alkaline phosphate activity, and calcium deposition on nanoceramics was further evidenced in [26.186]. Nanophase titania, alumina, and HAP show

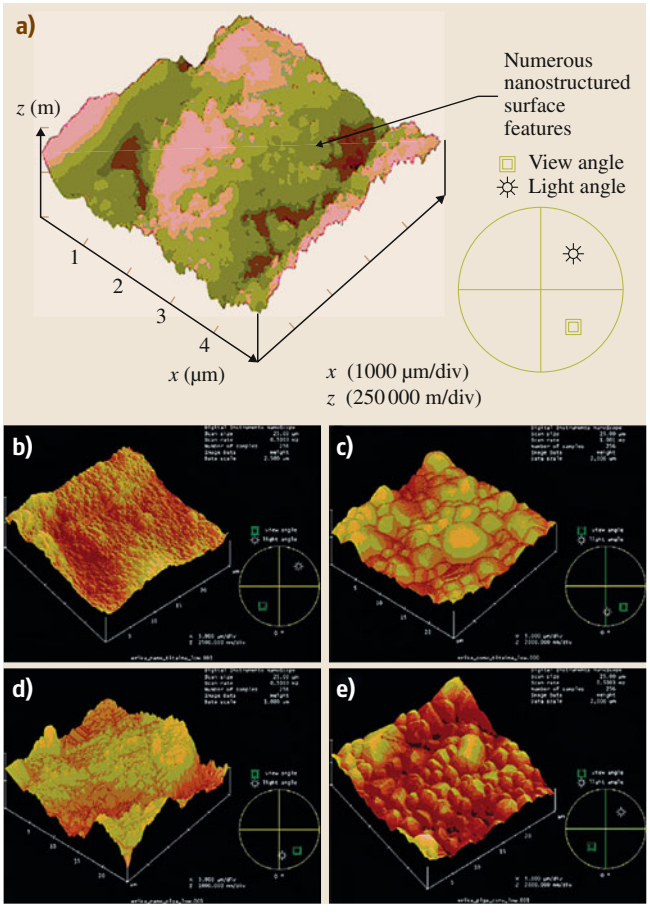


Fig. 26.7 **(a)** Representative AFM image of cortical bovine bone. Numerous nanostructured features on the surface are visible. Root-mean-square values from AFM for 5 μm × 5 μm and 25 μm × 25 μm scans were 32 and 25 nm, respectively (Digital Instruments NanoScope, scan size 5000 μm, scan rate 1.001 Hz, number of samples 256, data scale 250.0 m). **(b–e)** AFM images of nanophase titania and the PLGA mold of nanophase titania, conventional titania and the PLGA mold of conventional titania. Images provide evidence of the successful transfer of the surface roughness of nanophase titania to PLGA molds of nanophase titania, and conventional titania to PLGA molds of conventional titania. Root-mean-square values from AFM for nanophase titania at 5 μm × 5 μm and 25 μm × 25 μm scans were 29 and 22 nm, respectively. Root-mean-square values from AFM for the PLGA mold of nanophase titania at 5 μm × 5 μm and 25 μm × 25 μm scans were 35 and 27 nm, respectively. Root-mean-square values from AFM for conventional titania at 5 μm × 5 μm and 25 μm × 25 μm scans were 12 and 11 nm, respectively. Root-mean-square values from AFM for the PLGA mold of conventional titania at 5 μm × 5 μm and 25 μm × 25 μm scans were 13 and 12 nm, respectively. **(b)** Nanophase titania; **(c)** PLGA mold of nanophase titania; **(d)** conventional titania; **(e)** PLGA mold of conventional titania. (After [26.7])

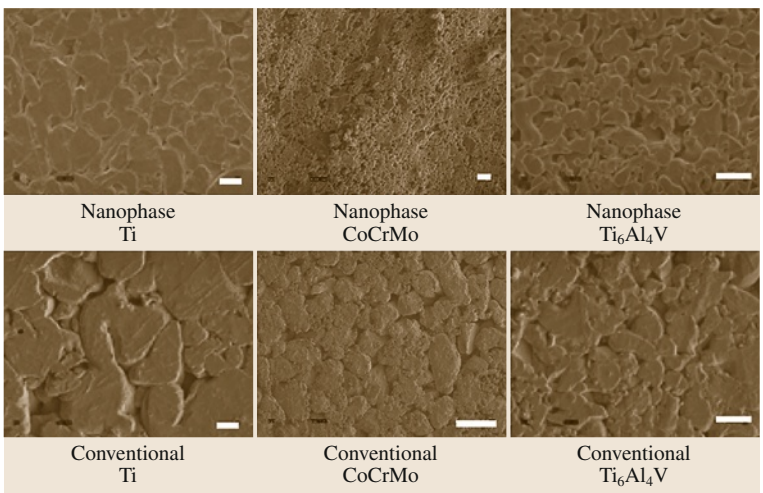


Fig. 26.8 Scanning electron microscopy images of Ti, CoCrMo, and Ti_6Al_4V compacts. Increased nanostructured surface roughness was observed in the nanophase compared to conventional Ti, CoCrMo, and Ti_6Al_4V (*bar* = 1 μm for nanophase, 10 μm for conventional ones). (After [26.62])

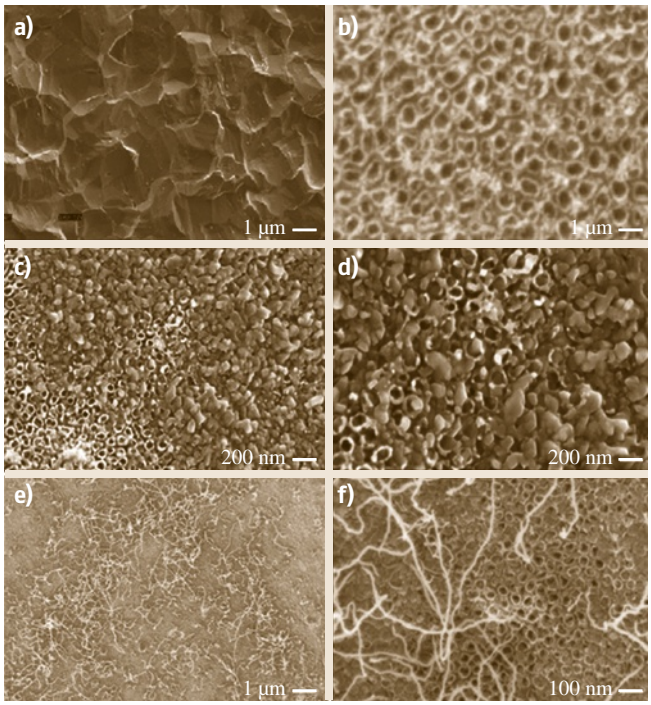


Fig. 26.9a–f SEM micrographs of (**a**) unanodized Ti, (**b**) anodized Ti without CNTs, (**c**) lower and (**d**) higher magnification of CNTs grown from the nanotubes of anodized Ti without a Co catalyst, and (**e**) lower and (**f**) higher magnification of CNTs grown from the nanotubes of anodized Ti surface with a Co catalyst. (After [26.64])

higher cell densities (after 5 days) as a result of osteoblast proliferation in comparison to conventional micron-sized ceramics of these materials. The calcium content in the extracellular matrix of osteoblasts cultured on nanophase alumina, titania, and HAP was 4, 6, and 2 times greater than, on the respective conventional ceramics. This study provides important information regarding the unique properties of nanophase ceramics which enhance the bonding of orthopedic/dental implants to juxtaposed bone and therefore, possibly improve bone implant efficacy. The increased osteoblast function on nanophase ceramics is due to the increased adsorption of vitronectin over the surface of nanophase ceramics [26.189]. The increased wettability of nanostructured ceramics enhances the adsorption of vitronectin in comparison to their conventional micro implant. Increased adsorption of vitronectin on nanophase ceramics induces increased oseteoblast adhesion and proliferation. Decreased adsorption of apolipoprotein A-I and/or increased adsorption of calcium on nanophase alumina were additional possible causes of the observed enhanced adsorption of vitronectin on nanophase alumina [26.189]. Moreover, this study provides evidences related to different conformations of vitronectin adsorbed on nanophase materials compared to conventional alumina, which in turn result into an increased unfolding of the cell-adhesive macromolecule to exposed epitopes (such as arginine-glycine-aspartic acid or RGD) recognized by specific cell membrane receptors.

Polymeric Nanomaterials Scaffold

Among other bone implant materials, polymers have also shown great promise as implant material. Synthetic polymers have presented enormous potential in tissue engineering applications [26.25]. Synthetic polymers can be fabricated and tailored to give a wide range of properties and are often free from concerns of immunogenicity [26.190]. Recently, it was reported that the nanophase polymer enhances the adsorption and conformation of proteins (such as fibronectin and vitronectin), which regulate osteoblast adhesion and other functions, in comparison to conventional polymers [26.7, 154, 189]. Selective adsorption of proteins, including fibronectin and vitronectin, on 3-D nanofibrous polymer scaffolds was reported by *Wei* and *Ma* (Fig. 26.10) [26.12]. Synthesis of nanoparticulate hydroxyapatite/poly(L-lactic acid) (NHAP/PLLA) composite scaffolds was achieved by the phase separation technique and the protein adsorption study was compared to micron particulate hydroxyapatite/poly(L-lactic acid) (MHAP/PLLA) scaffolds. Higher protein adsorption was found on NHAP/PLLA for higher HAP content and this further enhances osteoblast functions like adhesion, proliferation, and Ca deposition. In another study, the nano-rough surface of PLGA was prepared by treating nano-smooth PLGA with 0.1 N NaOH for several periods to transform it, into a nano-rough surface. The nano-rough surface improves the osteoblast function [26.191]. Bone cell promotion by polymers can be obtained by combining the features of nanophase ceramics and metals to the polymers (Fig. 26.11) [26.192–194]. *Price* et al. conducted an experimental study of osteoblast cell function over polymer PLGA cast over carbon nanofiber-based material and noticed an improved osteoblast function in comparison to conventional carbon fiber materials [26.192]. In the same manner, polymer casts on composites of polycarbonate urethane-CNTs also promoted osteoblast functions compared to casts of polycarbonate urethane/conventional carbon tubes [26.194]. The mechanism behind the increased bone cell function

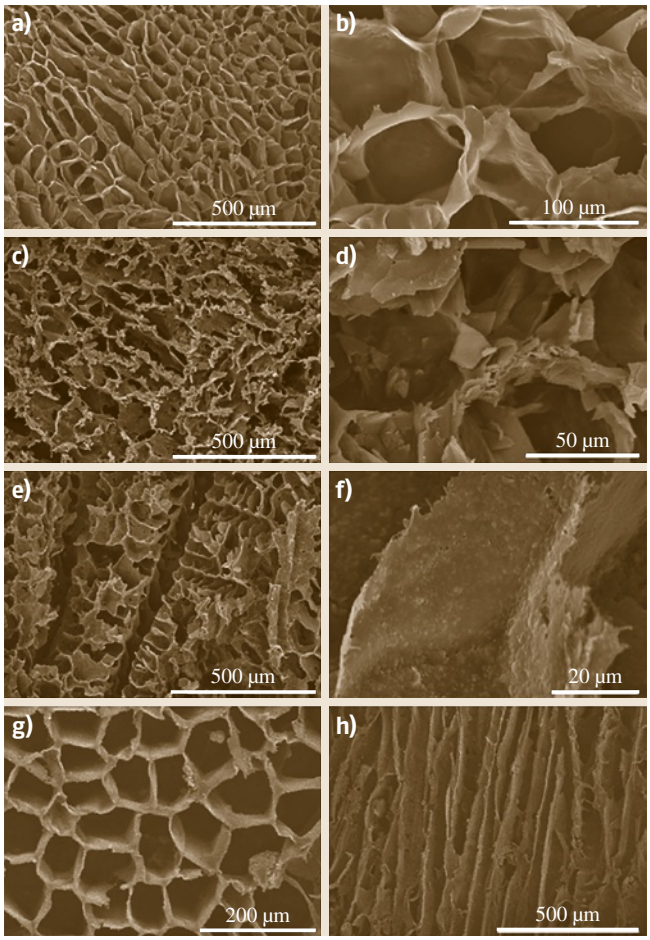


Fig. 26.10a–h SEM micrographs of plain PLLA, NHAP/PLLA, and MHAP/PLLA scaffolds fabricated from 5% dioxane **(a–e)** and benzene **(f,g)** solution. **(a,b)** Pure PLLA scaffold, ×50, ×400; **(c,d)** MHAP/PLLA 50 : 50 scaffold, ×100, ×500; **(e,f)** NHAP/PLLA 50 : 50 scaffold, ×100, ×1000; **(g)** tubular NHAP/PLLA scaffold, cross-section, ×200; **(h)** tubular NHAP/PLLA scaffold, longitudinal section, ×100. (After [26.12]) ▶

over nanophase polymers in comparison to conventional polymers is same as presented by nanophase metals and ceramics and is mediated by fibronectin and vitronectin [26.154, 189].

Nanostructured polymers have been used for vascular, cartilage, and bladder applications where unique nanometer surface features are needed for each type of tissue engineering application [26.190].

Nanocomposites as Smart Orthopedic Implants

The independent promising results shown by nanophase ceramic and polymeric material, led to the foundation of thinking about even better bone scaffold material by combining the advantages of both types of materials [26.39, 195, 196]. The composite material created by the combination of nanophase of both constituents is termed nanocomposite scaffold. An important feature of the nanocomposite is that it can mimic the constituents of natural bone to some extent better than individual counterparts [26.197]. Nanocomposite material can improve the osteoconductivity several folds in comparison to their individual counterparts [26.198, 199]. For, example, the nanoscaffold of nanohydroxyapatite (NHAP) and calcium phosphate can give greater strength to the scaffold as well as improved cell function than conventional material can. However, both calcium phosphate and NHAP suffers a slow rate of biodegradation, which limits their further usefulness.

Nanocomposites with biodegradable polymer can remove such drawbacks and will provide a more favorable material for orthopedic purposes. Nanocomposites of nanophase ceramics and nanostructured polymers offer improved bone cell function over their individual constituents [26.17, 200–203]. NHAP, a most promising nanoceramic, is a popular bone substitute due to its documented ability to promote mineralization, has also been used as filler and coating material in several applications. Due to the presence of the high surface fraction of grain boundaries in nanoceramics, osteoblast functions such as adhesion, proliferation, and Ca deposition is greatly enhanced. In some in vitro studies it was found that nanophase HAP with 79 nm grain

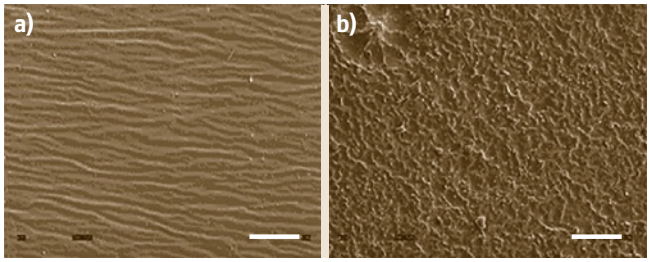


Fig. 26.11a,b Scanning electron micrographs of chemically treated PLGA surfaces. Representative scanning electron micrograph images of **(a)** chemically untreated (conventional) PLGA (feature dimensions 10 000–15 000 nm). **(b)** Chemically treated nanostructured PLGA (feature dimensions 50–100 nm). *Scale bar* = 100 000 nm. (After [26.193]) ▶

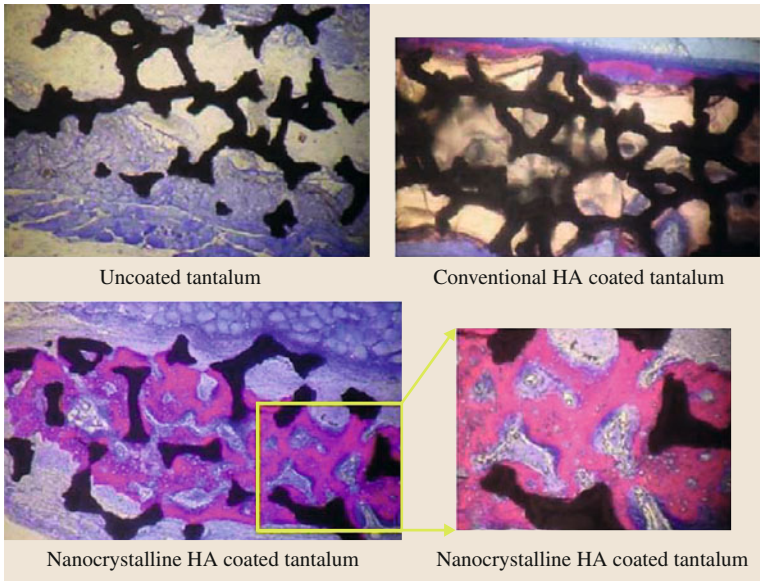


Fig. 26.12 Histology of rat calvaria after 6 weeks of implantation of uncoated tantalum, conventional HA-coated tantalum and nanocrystalline HA-coated tantalum. Greater amounts of new bone formation occur in the rat calvaria when implanting nanocrystalline HA-coated tantalum than uncoated and conventional HA-coated tantalum. *Red* represents new bone and *blue* represents collagen. (After [26.204])

size, significantly enhances the fibroblast adhesion and strikingly inhibiting competitive fibroblast adhesion compared to the conventional 179 nm grain size of HAP, just within 4 h [26.154].

Nukavarapu et al. fabricated a biodegradable NHAP/polyphosphazene microsphere 3-D scaffold with suitable mechanical properties (compressive moduli of 46–81 MPa) and cytocompatible properties for bone tissue engineering applications [26.205]. It should not be surprising that nanostructured composites have similar mechanical properties to bone since bone itself is a nanostructured composite. Importantly, such results have not been limited to in vitro studies. In in vivo studies it was demonstrated that nanocrystalline HAP accelerates new bone formation on tantalum scaffolds, when used as an osteocinductive coating in comparison to uncoated or conventional micron-sized HAP coated tantalum (Fig. 26.12) [26.204].

Nanophase ceramics like alumina, zinc oxide, and titania have shown increased bone cell functions, which are highly dependent on their surface features and independent of the surface chemistry. For example, osteoblast adhesion increased by 146 and 200% on nanophase zinc oxide (23 nm) and titania (32 nm) compared to microphase zinc oxide (4.9 μm) and titania (4.1 μm), respectively [26.206]. Furthermore, nanophase zinc oxide, nanophase titania and nanofiber alumina enhanced collagen synthesis, alkaline phosphatase activity and calcium mineral deposition compared to conventional equivalents [26.206, 207].

In bone and cartilage, collagen is present in triple helical structure self-assembled into nanofibers 300 nm in length and 1.5 nm diameter. Numerous of efforts have been made to understand the inductive effect of novel biomimetic nanofibrous or nanotubular scaffolds on regenerative medicine by following a bottom-up self-assembly approach. *Hartgerink* et al. reported a peptide-amphiphile (PA) with the cell-adhesive ligand RGD (Arg-Gly-Asp) self-assembled into supramolecular nanofibers [26.208]. A new nanofiber composite was designed by directly nucleating and aligning HAP on the long axis of a nanofiber with the same self-assembly pattern as collagen and HAP crystals in bone. Promise has also been validated for other novel nanostructured self-assembled chemistries. For example, bone tissue engineering applications of osteogenic helical rosette nanotubes obtained through the self-assembly of DNA base pairs (guanine, cytosine) in aqueous solutions have been reported (Fig. 26.13c). The presence of tailorable amino acid and peptide side chains such as lysine, RGD, and KRSR (Lys-Arg-Ser-Arg) over rosette nanotubes help in osteoblast adhesion and inhibits fibroblast adhesion and further works as excellent mineralization templates to assemble a biomimetic nanotube/HAP structure (Fig. 26.13d). Improved osteoblast adhesion has been noticed over helical rosette nanotubes irrespective of their incorporation into hydrogels or their coating over titanium in comparison to untreated control (Fig. 26.13) [26.208, 209]. A fibrous nanocomposite of PCL/HAP/gelatin at a ratio

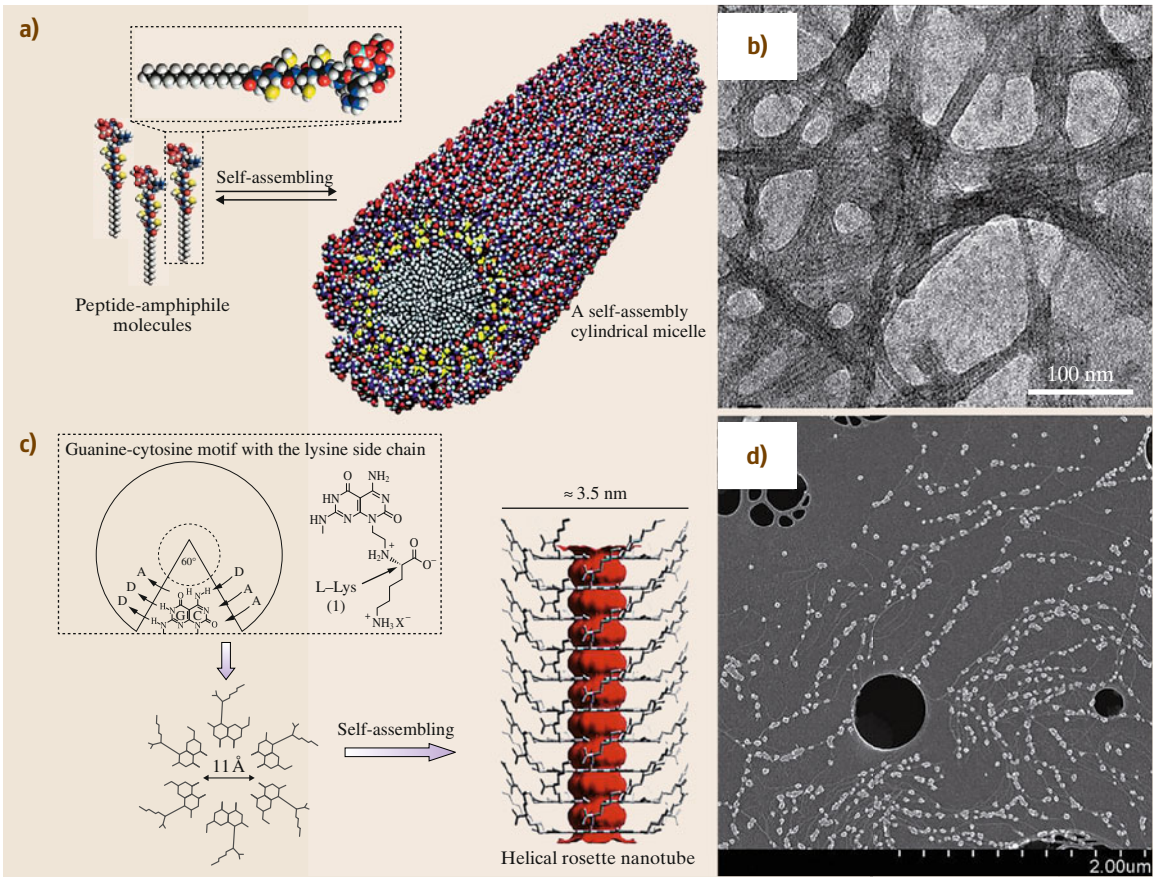


Fig. 26.13a–d Self-assembled nanofibers and nanotubes for bone/cartilage tissue engineering applications. **(a)** Schematic illustration of the self-assembly process of peptide-amphiphiles functionalized with RGD to form a nanofiber 7.6±1 nm in diameter. **(b)** TEM image of the self-assembled nanofibers. **(c)** Schematic illustration of the self-assembly process of the guanine-cytosine DNA base pairs forming helical rosette nanotubes (HRN). **(d)** SEM images of biomimetic nano-HA aligned with HRNs on a porous carbon TEM grid. (After [26.204])

of 1 : 1 : 2 was synthesized (by electrospinning) by *Venugopal* et al., and increased osteoblast proliferation, alkaline phosphatase activity and Ca deposition was reported in comparison to other PCL nanofibrous scaffolds [26.143]. In a recent study, *Osathanon* et al. reported the synthesis of polymer/calcium phosphate nanocomposites, which further promotes the osteoblast alkaline phosphatase activity and osteoblast marker gene (mRNA) expression thus supports the bone maturation in vitro and in vivo (mouse calvarial defect model) [26.210]. Nanocomposites of Ti/PLGA were also prepared with different ultrasonic power to ensure dispersion of nanoceramic particles into the polymer because agglomeration of ceramic nanoparticles in polymers is a major problem [26.197, 211]. In a further study, improved osteoblast adhesion and long-term functions were reported in comparison to the scaffold made of pure PLGA. Adherence of osteoblasts was found to be increased threefold on nanophase titania/PLGA over the conventional titania/PLGA composite with same weight ratio and porosity (Fig. 26.14a,b) [26.211].

Nanocomposites offer great advantages in mechanical properties in comparison with conventional materials. *McManus* et al. reported superior mechanical properties of polymer-ceramics with nanometer grain size over micron sized ones [26.212].

Nanocomposites of PLA with 40 and 50 wt % nanophase (< 100 nm) alumina, titania, and HAP showed significant increase in bending modulii that is

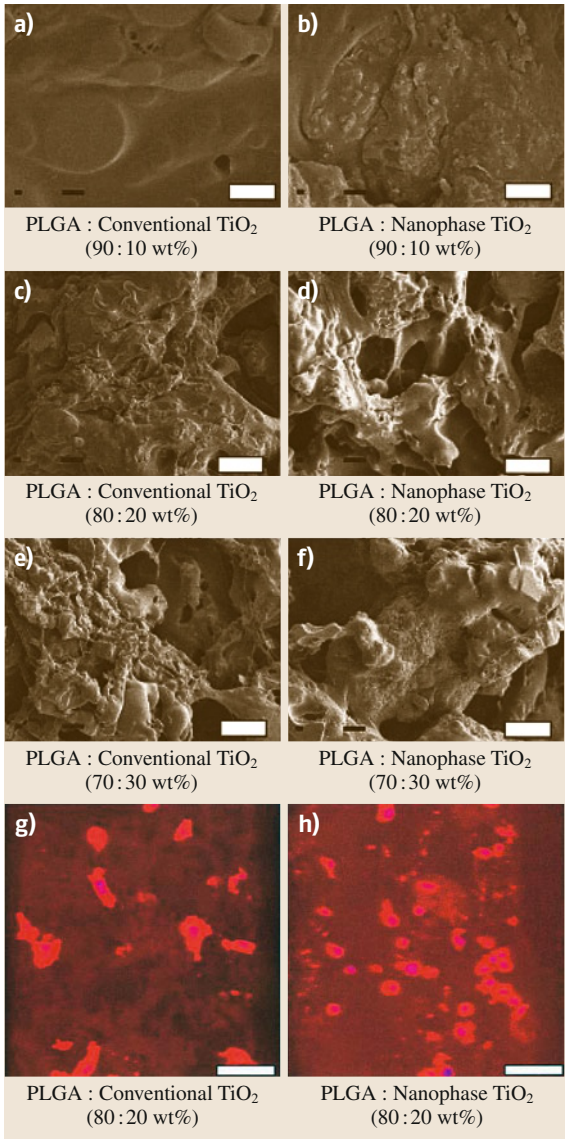


Fig. 26.14 **(a–f)** SEM micrographs of PLGA: TiO_2 scaffolds. Original magnification: 1500. The *scale bar* 10 μm. **(g,h)** Confocal microscopy still images of osteoblast adhesion on **(e)** PLGA: conventional TiO_2 (80 : 20 wt%) and **(f)** PLGA: nanophase TiO_2 (80 : 20 wt%). *Scale bar* = 50 μm. (After [26.211])

very close to bone, than composite of coarse grained ceramics. The bending modulus of nanophase titania/PLA composites with a weight ratio 50 : 50 was 1960 ± 250 MPa (close to the magnitude of the trabecular bone), which is much higher than the bending moduli of plain PLA, i. e., 60 ± 3 MPa and conventional titania/PLA composites, i. e., 870 ± 30 MPa, respectively.

Apart from the metallic, polymeric, ceramic nanoscaffolds along with their nanocomposites as scaffold materials, nanotechnology has introduced a class of carbon-based nanomaterial for orthopedic applications. Nanocomposites of carbon nanomaterials possess enormous potential for orthopedic application due to their outstanding physiochemical properties.

Since their discovery by Ijima, 1993, carbon nanotubes have gained tremendous popularity among all other allotropes of carbon. Carbon nanotubes are of tubular structure which is formed by a single cylindrical graphene sheet (single-walled carbon nanotubes) or several graphene sheets arranged concentrically (multi-walled carbon nanotubes (MWNT) or MWCNT). Due to the presence of sp^2 bonding, carbon nanotubes have excellent mechanical and electrical properties. Single-walled carbon nanotubes possess a tensile strength about one hundred times higher than that of steel at a specific weight which is six times lower than steel [26.213, 214].

The excellent mechanical properties of carbon nanotubes made them a suitable candidate for hard tissue engineering purposes to reinforce artificial implants that have poor mechanical strength.

Among the carbon-based nanomaterials, carbon nanotubes and carbon nanofibers (CNT/CNF) are the ideal scaffold candidates for bone tissue engineering applications [26.215]. Recently, *Price* et al. reported that 60 nm CNFs increases the osteoblast adhesion significantly and concurrently decreases competitive cell adhesion in order to stimulate sufficient osseointegration [26.216]. CNTs are suitable for osteoblast functions [26.217]. In a recent study, *Sitharaman* et al. demonstrated that SWCNT polymer nanocomposites exhibit favorable hard and soft tissue response after 4 and 12 weeks of implantation (femoral condyle and subcutaneously) in rabbits [26.218]. Further, they also reported that the SWCNT-polymer induces 300% greater bone volume after 4 weeks and 200% larger bone growth at defect sites than control polymers without CNT after 12 weeks. Excellent electrical conductivity has been demonstrated by the CNT/CNF polymer nanocomposite for tissue regeneration. PLA is an electrical insulator and not suitable for electrical stimulation for bone growth but PLA/CNTs nanocomposites (at 80/20 wt %) exhibit ideal electrical conductivity for bone growth. A 46% increase in osteoblast proliferation and 307% increase in Ca content was reported after electrical stimulation for 2 and 21 days

by the PLA/CNT composite, respectively, in comparison to PLA alone [26.219]. These studies indicate that CNT/CNF and their composites can serve as osteogenic scaffolds with good cytocompatibility properties, reinforced mechanical properties, and improved electrical conductivity to effectively enhance bone tissue growth. Carbon nanotubes have been widely used in combination with a variety of polymers [26.220, 221]. *Khang* et al. synthesized and reported a nanocomposite of carbon nanotubes with poly(carbonate)urethane [26.220, 221]. Supronowicz et al. demonstrated the synthesis of a nanocomposite of CNTs with PLA a biodegradable polymer. *Shi* et al. [26.222] synthesized the nanocomposite of carbon nanotubes and propylene fumarate. *Misra* et al. [26.223] reported a nanocomposite with poly(3-hydroxybutyrate). *Lahiri* et al. [26.224] and *Pelto* et al. [26.225] reported a nanocomposite with polylactide-caprolactone and polypyrrole-hyaluronic acid, respectively. *Balani* et al. [26.226], *Hahn* et al. [26.227], and *Yadav* et al. reported the reinforcement of HAP by carbon nanotubes [26.228]. They also reported the reinforcement of HAP-gel nanocomposites by different weight % of MWCNTs and found that the flexural strength of the composites without any reinforcement is 5.05 ± 1.18 MPa, which gradually improved with the increment in MWCNT concentration up to 3.5–4%. Further, they thoroughly investigated the biocompatibility of nanocomposites in a mouse model through the histopathological investigation of tissues from skin, kidney, and liver, and reported that that there is mild reversible change in the liver and tubular damage in the kidney for higher concentrations of MWCNTs (4 wt% of MWCNTs) (Fig. 26.15).

The usefulness of carbon nanotubes is not only limited as a reinforcement material that improves the mechanical properties like tensile strength, compressive and flexural moduli in polymeric material, and fracture toughness, hardness, elastic modulus and adhesion to the HAP, which was described before, but also increased the attractiveness of these materials in nanocomposites with improved bone cell functions (osteoblast adhesion, proliferation, and Ca-deposition). The mechanism of improved cell function by these composites is due to the increased adsorption of fibronectin, i. e., an important cell-adhesion mediating ECM protein which is a prerequisite for bone cell function [26.220, 221]. *Khang* et al. explained that the increased adsorption of fibronectin on this nanocomposite is due to surface properties such as the nanoscale surface roughness of the material by the addition of carbon nanotubes and an increased material surface hydrophilicity due to the presence of the polymeric component [26.217]. *Supronowicz* et al. [26.219], *Zanello* et al. [26.220], *Khang* et al. [26.220], and *Pelto* et al. have demonstrated that the excellent electrochemical property of carbon nanotubes can favor the electrical stimulation of cells [26.219]. *Supronowicz* et al. reported increased proliferation activity, concentration of extracellular Ca and mRNA expression for collagen type I by osteoblast cells cultured with a nanocomposite of PLA and carbon nanotubes and exposed to electrical stimulation (current 10 μA, frequency 10 Hz) [26.219]. *Khang* et al. reported that a similar response is presented by the human chondrocytes cell, when they are cultured with a nanocomposite of MWCNT/poly(carbonate) urethane (weight ratio 1 : 2) [26.220]. *Bacakova* et al. [26.229, 230] reported the synthesis of nanocomposites of carbon nanotubes with polymers like terpolymer of polytetrafluoroethylene, polyvinyldifluoride, and polypropylene (PTFE/PVDF/PP) or polysulfone (PSU) (the most promising material for the construction of bone implants). *Zhang* et al. [26.231] and *Orefice* et al. [26.232] synthesized the composite of PSU with bioactive glass and reported its potential bone and cartilage tissue engineering. *Jan* and *Grzegorz* [26.233] reported the application of the same composite for the fabrication of bone joint screws. Carbon nanotubes have also been used for the formation of prominences in nanoscale on the material surface, which could promote the colonization with bone cells. *Bacakova* et al. [26.229] reported the synthesis of nanocomposites of carbon nanoutubes and carbon nanohorns with PTFE/PVDF/PP. Further they reported that the addition of SWCNT or MWCNT to the PTFE/PVDF/PP terpolymer markedly improved several parameters like adhesion and growth of human osteoblast-like MG 63 cells. They further performed an ELISA study and found that the cells on the material with 4 wt% of SWCNT contained a higher concentration of vinculin, i. e., by 64 and 69%, a component of focal adhesion plaques, in comparison with the values in cells on pure terpolymer and tissue culture polystyrene, respectively. The higher concentration of talin (an important integrin-associated focal adhesion protein) was also found in cells grown on terploymer samples with 4 and 8 wt% of SWCNT (by 35 and 28%, respectively). MWCNT-terpolymer nanocomposites have shown a dramatically increased cell proliferation and it is was most apparent on samples with 4 wt% of MWCNT. On the 7th day, cell density, i. e., $228\,000 \pm 1050$ cell/cm^2 on the nanocomposite was found to be 4.5 times

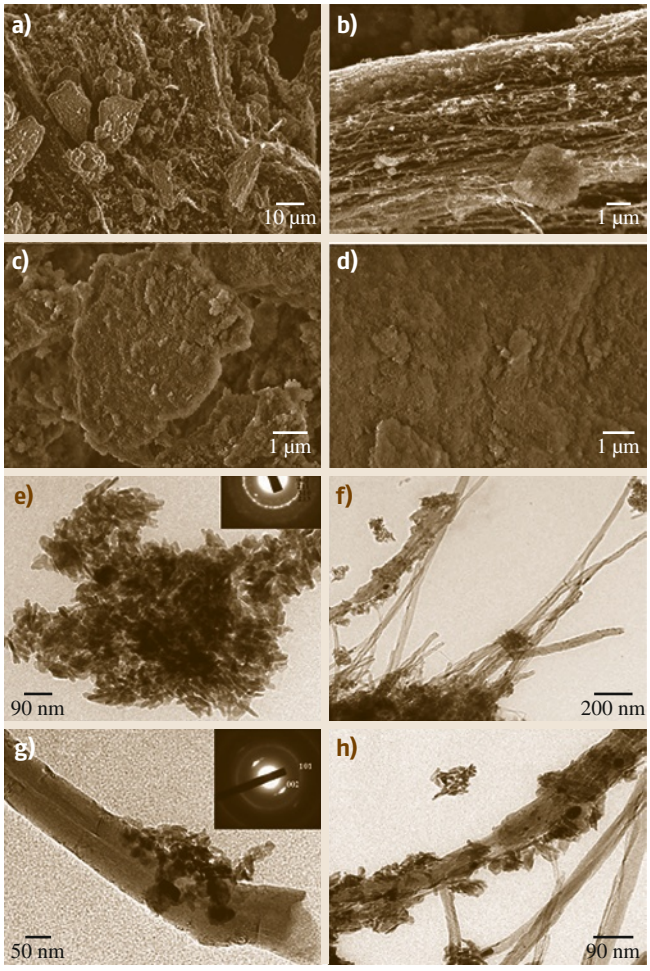


Fig. 26.15 **(a–d)** SEM micrograph of the composite with **(a)** 4% MWCNT at lower magnification showing overall morphology; **(b)** same at higher magnification showing an HAP particle adhered to a bundle of MWCNTs; and that of composites having **(c)** 1% and **(d)** 0% MWCNT provides a means to compare the presence MWCNTs as reinforcements. **(e–h)** TEM microphotographs of the composite **(e)** 0% MWCNT showing the rod-like HAP crystals distributed in the gel mesh work; the inset shows the indexed diffraction pattern; **(f)** 4% MWCNT showing the former is well entangled in the HAP-gel composite; **(g)** 1% MWCNT showing the nucleation of the HAP on MWCNT preferentially at the sites of defects; **(h)** 4% MWCNT showing the latter well coated with HAP crystals. **(i–p)** Histological photomicrographs of control tissues from **(i)** liver, **(j)** kidney, and **(k)** skin showing normal cytomorphology. Tissues from **(l)** liver, **(m)** kidney exposed to composites having 1% reinforcements showing no significant change due to toxicity. The tissues exposed to composites with 4% MWCNT **(n)** liver showing hydropic changes and ballooning of hepatocytes; **(o)** kidney exhibiting glomerular ablation and tubules showing cloudy swelling **(p)** skin exhibiting no significant alteration. (After [26.228])

higher than unmodified PTFE/PVDF/PP, i. e., $50\,300 \pm 5400$ cells/cm^2.

The addition of SWCNT or MWCNTs also lowers the wettability of the composite material (sessile water drop contact angle from $99 \pm 7°$ to $105 \pm 2°$) compared to the non-modified terpolymer (contact angle $100 \pm 4°$). The surface roughness of the composite material is also increased significantly on addition of MWCNTs and SWCNT. An increase in the microscale surface roughness in polymer-CNT composites has been considered as a factor decreasing the colonization of the composites with cells. *Misra* et al. [26.223] reported the synthesis of poly(3-hydroxybutyrate)/bioactive glass composites with MWCNTs and in a further study they found that the cell population density and growth rate of MG 63 cells decreased proportionally to the increasing concentrations of MWCNT (2, 4, 7 wt%) and increasing microscale surface roughness (RMS from 6 ± 2 to 10 ± 2 µm) of the material. On the contrary, *Bacakova* et al. reported that the cell adhesion and growth of MG 63 cells (evaluated by the concentration of integrin-associated proteins talin and vinculin and the cell population density) was, in most cases, the highest on composites with 4 wt% of SWCNT or MWCNT and then decreased [26.230].

Bacakova et al. also reported the synthesis of polysulfone-nanotube composites (Fig. 26.16) [26.230]. In a further study they found that the addition of carbon nanotubes to polysulfonate (PSU) did not significantly influence the adhesion, spreading, morphology, and growth of MG 63 cells in cultures on these materials from 5 days after seeding, the cell numbers on these composites were usually similar to the values found on the pure PSU. The cell adhesion area measured after

3 days was found to be significantly higher in the case of PSU with 2 wt% of MWCNT ($1770 \pm 90\,\mu m^2$) in comparison to pristine PSU ($1330 \pm 70\,\mu m^2$) and cell culture polystyrene dishes ($1400 \pm 110\,\mu m^2$). The possible explanation of such a finding is that a relatively higher surface hydrophilicity of the pure PSU (water drop contact angle $85 \pm 5°$) compared to the terpolymer PTFE/PVDF/PP (contact angle $100 \pm 4°$), which might mask the supportive effects of the surface nanoroughness (created by the addition of carbon nanotubes) (Ra from 11 ± 4 nm to 27 ± 8 nm versus 4 ± 2 nm on the pure PSU) as well as cell colonization. The addition of carbon nanotubes causes a slight decrease in the surface hydrophilicity of the materials (i. e., the water drop contact angle increased from $85.0 \pm 5°$ to $93 \pm 4°$), but these differences were not statistically significant [26.230].

In addition to nanocomposites, carbon nanotubes, in the form of film deposited on various substrates such as polycarbonate membranes [26.234] glass coverslips [26.235], titanium [26.236], silicone rubber [26.237], or pressed in compacts [26.238] have shown significant improvement in bone cell functions in comparison to non-coated substrates. *Hirata* et al. reported that films of carbon nanotubes on 3-D matrices like on the walls of pores inside sponge-like collagenous scaffolds improved the ingrowth of mouse osteoblast MC3T3-E1 cells and human osteosarcoma SaOs-2 cells inside the scaffolds, increased the strength of the cell adhesion and cell number (measured by DNA content), when compared to the scaffolds without nanotubes [26.239]. *Aoki* et al. [26.234], *Li* et al. [26.238], and *Zanello* et al. [26.217] synthesized composites of carbon nanotubes with polymers and ceramics, reports that composites promote the growth of bone cells in similar way as reported above, in brief, an increased adsorption of specific proteins (such as cell adhesion-mediating proteins from the serum of the culture medium and bone morphogenetic protein-2) promotes cell adhesion, growth and differentiation.

Among carbon materials, carbon nanofibers have also been shown to exhibit excellent conductivity and exceptional mechanical and cytocompatible properties, thereby giving a strong rationale to investigating them for application in orthopedic or dental tissue engineering [26.240]. Carbon nanofiber-based nanocomposite implants can be a better alternative to conventional metal alloys [26.193, 216]. *Price* et al.. showed that carbon nanofibers show greater osteoblast adhesion than conventional carbon fibers [26.216]. They further reported that PLGA coated carbon nanofibers enhanced the osteoblast function in comparison to conventional carbon fibers. Enhanced osteoblast function on carbon nanofiber composites is due to surface area of the nanofibers, nanometer topography, and surface chemistry of fibers.

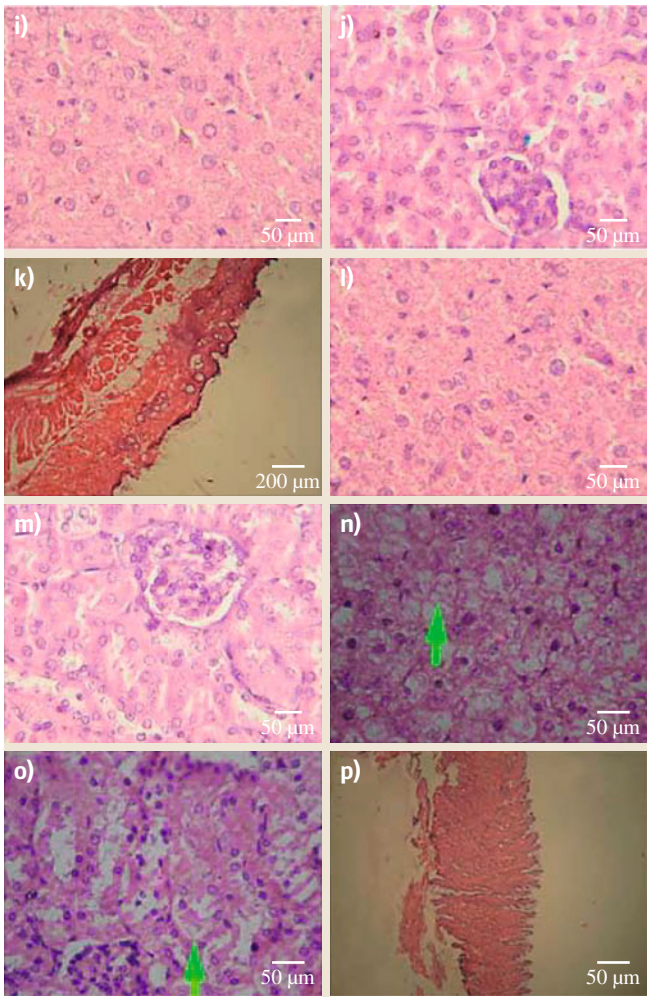


Fig. 26.15 (continued)

Graphite has been used in three-dimensional systems as a component of various composite materials used for construction of bone implants. *Ekstrand* and *Hirsch* [26.241] reported the reinforcement of poly(methylacrylate) implant by carbon/graphite designed for reconstruction of the maxilla damaged by malignant tumors. *Yildiz* et al. [26.242] reported the synthesis of graphite fiber reinforced composites of polyetheretherketone (PEEK) for hip joint prostheses [26.243].

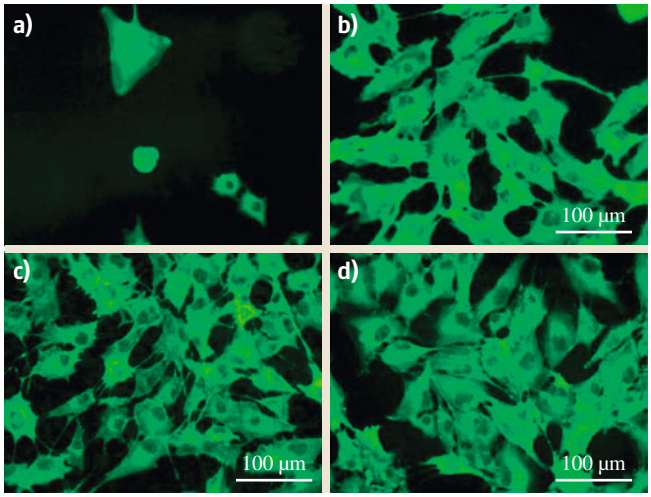


Fig. 26.16a–d Immunofluorescence staining of β-actin in osteoblast-like MG 63 cells on day 3 after seeding on a terpolymer of polytetrafluoroethylene, polyvinyldifluoride, and polypropylene **(a)**, terpolymer mixed with 4% of single-walled carbon nanohorns **(b)** or high crystalline electric arc multi-walled nanotubes **(c)** and tissue culture polystyrene dish **(d)**. Microscope Olympus IX 50, digital camera DP 70, obj. 20. *Bar* = 100 µm. (After [26.229]) ◀

Graphene is the mother of all forms of carbon-based nanomaterial and a material of wonder, due to novel properties such as the quantum Hall effect at room temperature [26.244], tunable bandgap [26.245], and high elasticity [26.246–249], etc. After its discovery and realization in the year 2004, graphene has become the center of attraction in scientific community. The excellent mechanical strength and good biocompatibility of graphene and graphene oxide [26.250–253] make them ideal candidates for tissue engineering purposes. Polymer composites containing graphene possess good electric and thermal conductivity along with improved mechanical stiffness [26.254–256]. Recently, *Rao* et al. [26.247] reported a significant increase in mechanical properties of polyvinyl alcohol (PVA) by the addition of functionalized few-layer graphene [26.257]. *Rafiee* et al. compared the mechanical properties of graphene/epoxy and carbon nanotube/epoxy nanocomposites at a low filler content of 0.1 wt% and found that graphene platelets significantly out-performed carbon nanotubes as a reinforced additive [26.258]. Fan et al. reported first a study on the reinforcement of biomacro-

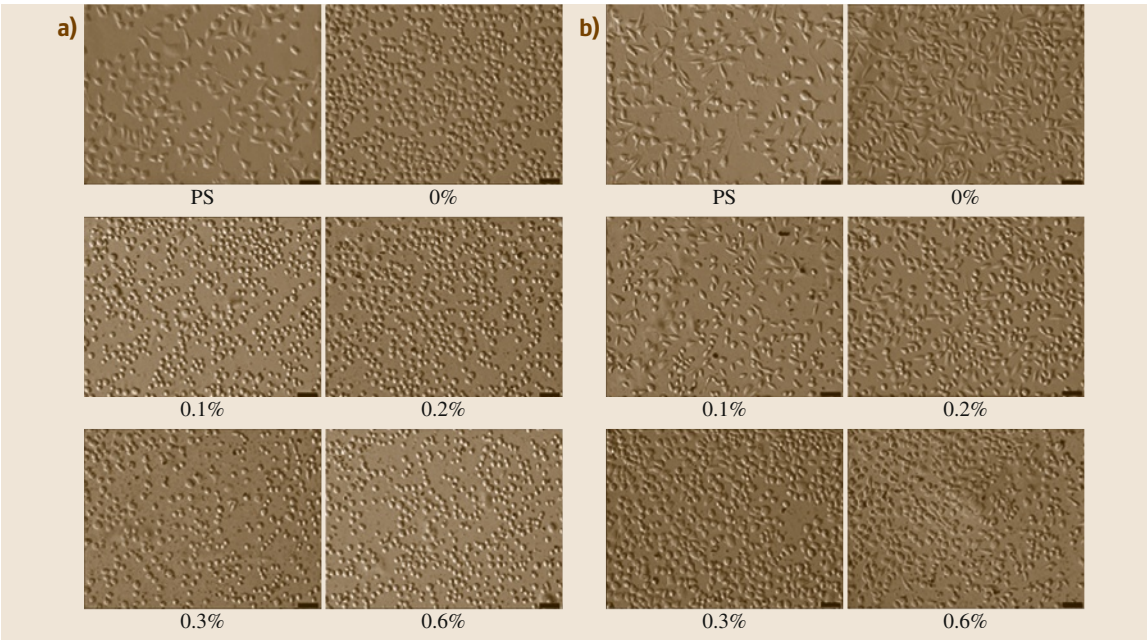


Fig. 26.17 **(a)** Cell phase contrast micrographs at 12 h. The *scale bar* represents 50 µm. **(b)** Cell phase contrast micrographs at 24 h. As time increases, cells extend gradually. Cells with the lower concentration graphene/chitosan composite materials performed better. (After [26.259])

molecules like chitosan by graphene [26.259]. In their study, they found that the addition of graphene significantly increased the modulus of chitosan at a very low content (between 0.1 and 0.3 wt%) and in addition these composites showed good biocompatibility for L929 cells (Fig. 26.17).

26.6 Future Perspectives

Nanotechnology has shown great potential to solve the ever challenging issues in tissue engineering, i. e., the search for suitable artificial implants. Advancement and integration of nanotechnology to tissue engineering has made it possible to fabricate advanced materials, i. e., nanocomposites with more favorable properties for orthopedic purposes.

Nanocomposites have shown a better response as artificial scaffold material than conventional scaffold materials. The commercialization of nanomaterials in the form of nanoproducts has already begun. Nanoceramic products such as nano-HA-paste-ostim from Obernburg, Germany, nano-beta-tricalcium phosphate-Vitoss from Orthovita, USA, are commercially available and have started their impact on society [26.260]. The inclination of nanotechnology towards bone tissue engineering is in its early age and at this stage commercialization of nanoproducts raises some serious concerns.

Before pledging the complete reliability of the technology and products there are still some challenges that need to be addressed. The first concern related to the fabrication processes of nanocomposites is the need to develop facile and inexpensive techniques for the fabrication of nanomaterials with the desired size, shape, and topography. The currently used fabrication techniques are very costly and complicated, and often a lot of time and attention is needed to complete the fabrication (for instance e-beam lithography).

The second and most important concern is the biocompatibility of nanocomposite materials. Although some reports indicate that nanocomposite materials are safe, others tell about the toxic responses to nanoparticles generated from the degradation of implanted nanomaterials; the conflict about the toxicity of nanomaterials is a debatable issue. Accurate assessment of nanoparticle toxicity is very difficult because it depends on several factors like dose, chemical composition, method of administration, size, biodegradability, solubility, pharmacokinetics, bio distribution, surface chemistry, shape, and structure, etc. [26.261, 262] Most biocompatibility reports on nanocomposites are a result of in vitro evaluation and there are only few reports which are based on in vivo investigations. In vitro studies are enough for primary screening, but to obtain complete knowledge about the biological behavior of nanocomposites, sound in vivo studies are highly needed. In vivo research will help to establish the safety of nanocomposites and their applications in the near future. Therefore, to exploit the full potential of nanotechnology for tissue engineering purposes, safety evaluation is the first and utmost requirement at the time of synthesis and the time implantation.

Apart from carbon nanotubes, graphene, a class of material having superior mechanical and electrical properties, has a great potential to be used in nanocomposites for orthopedic implants. Good biocompatibility and the absence of metallic impurities on graphene sheets makes them potential candidates for tissue engineering applications.

References

26.1 R. Lakes, S. Saha: Cement line motion in bone, Science **204**(4392), 501–503 (1979)

26.2 G.E. Bacon, P.J. Bacon, R.K. Griffiths: Neutron diffraction studies of lumbar vertebrae, J. Anat. **128**, 277–283 (1979)

26.3 N. Sasaki, Y. Sudoh: X-ray pole figure analysis of apatite crystals and collagen molecules in bone, Calcif. Tissue Int. **60**(4), 361–367 (1997)

26.4 J.D. Bronzino: *The Biomedical Engineering Handbook*, 2nd edn. (CRC, Boca Raton 2000) pp. 274–706

26.5 M.C.H. van der Meulen, P.J. Prendergast: Mechanics in skeletal development, adaptation and disease, Philos. Trans. R. Soc. Lond. **358**(6), 565–578 (2000)

26.6 X.E. Guo, S.A. Goldstein: Is trabecular bone tissue different from cortical bone?, Forma **12**, 3–4 (1997)

26.7 T.J. Webster: *Nanophase Ceramics: The Future Orthopedic and Dental Implant Material, Adv. Chem. Eng* (Academic, New York 2001) pp. 125–166

26.8 J.Y. Rho, L. Kuhn-Spearing, P. Zioupos: Mechanical properties and the hierarchical structure of bone, Med. Eng. Phys. **20**(2), 92–102 (1998)

26.9 L. Kuhn-Spearing, C. Rey, H.M. Kim, M.J. Glimcher: Carbonated apatite nanocrystals of bone. In: *Synthesis and Processing of Nanocrystalline Powder*, ed. by D.L. Bourell (The Minerals, Metals and Materials Society, Warrendale, PA 1996)

26.10 E.H. Burger, J. Klein-Nulend: Mechanotransduction in bone–role of the lacuno-canalicular network, FASEB J. **13**(Suppl), S101–112 (1999)

26.11 R. Smith: *Bone Health and Osteoporosis: A Report of the Surgeon General* (US Department of Health and Human Services, Rockville 2004) pp. 68–70

26.12 G. Wei, P.X. Ma: Structure and properties of nano-hydroxyapatite/polymer composite scaffolds for bone tissue engineering, Biomaterials **25**(19), 4749–4757 (2004)

26.13 J.J. Tiedeman, K.L. Garvin, T.A. Kile, J.F. Connolly: The role of a composite, demineralized bone matrix and bone marrow in the treatment of osseous defects, Orthopedics **18**(12), 1153–1158 (1995)

26.14 R. Gepstein, R.E. Weiss, T. Hallel: Bridging large defects in bone by demineralized bone matrix in the form of a powder. A radiographic, histological, and radioisotope-uptake study in rats, J. Bone Joint Surg. Am. **69**(7), 984–992 (1987)

26.15 B.N. Summers, S.M. Eisenstein: Donor site pain from the ilium. A complication of lumbar spine fusion, J. Bone Joint Surg. Br. **71**(4), 677–680 (1989)

26.16 M.B. Coventry, E.M. Tapper: Pelvic instability: A consequence of removing iliac bone for grafting, J. Bone Joint Surg. Am. **54**(1), 83–101 (1972)

26.17 K.G. Marra, J.W. Szem, P.N. Kumta, P.A. DiMilla, L.E. Weiss: In vitro analysis of biodegradable polymer blend/hydroxyapatite composites for bone tissue engineering, J. Biomed. Mater. Res. **47**(3), 324–335 (1999)

26.18 E.M. Younger, M.W. Chapman: Morbidity at bone graft donor site, J. Orthop. Trauma **3**, 192–195 (1989)

26.19 W.M. Saltzman: *Engineering Principles for the Design of Replacement Organs and Tissues* (Oxford Univ Press, New York 2004) pp. 6–7

26.20 A. Nather: Biology of healing of large deep-frozen cortical bone allografts, Bone Biol. Heal. **1**, 50–65 (2003)

26.21 R.D. Bostrom, A.G. Mikos: Tissue engineering of bone. In: *Synthetic Biodegradable Polymers Scaffolds*, ed. by A. Atala, A.J. Mooney (Birkhäuser, Boston 1997) pp. 215–234

26.22 K.E. Healy, P. Ducheyne.: Passive dissolution of titanium in biological environments (review). In: *Medical Applications of Titanium and Its Alloys: The Material And Biological Issues*, ed. by S.A. Brown, J.E. Lemons (ASTM STP, Philadelphia 1996)

26.23 R. Van Noort: Titanium: The implant material of today, J. Mater. Sci. **22**(11), 3801–3811 (1987)

26.24 L.Z. Zhuang, E.W. Langer: Determination of cyclic strain-hardening behaviour produced during fatigue crack growth in cast cocrmo alloy used for surgical implants, Mater. Sci. Eng. A **108**(0), 247–252 (1989)

26.25 C.M. Agrawal, R.B. Ray: Biodegradable polymeric scaffolds for musculoskeletal tissue engineering, J. Biomed. Mater. Res. **55**(2), 141–150 (2001)

26.26 J.S. Temenoff, A.G. Mikos: Injectable biodegradable materials for orthopedic tissue engineering, Biomaterials **21**(23), 2405–2412 (2000)

26.27 E. Behravesh, A.W. Yasko, P.S. Engel, A.G. Mikos: Synthetic biodegradable polymers for orthopaedic applications, Clin. Orthop. Relat. Res. **367**, S118–129 (1999)

26.28 K.H.J. Buschow, R.W. Cahn, M.C. Flemings, B. Ilschner, E.J. Kramer, S. Mahajan, P. Veyssière (Eds.): *Encyclopedia of Materials* (Elsevier, Amsterdam 2001) p. 11

26.29 Y.W. Li, J.C. Leong, W.W. Lu, K.D. Luk, K.M. Cheung, K.Y. Chiu, S.P. Chow: A novel injectable bioactive bone cement for spinal surgery: A developmental and preclinical study, J. Biomed. Mater. Res. **52**(1), 164–170 (2000)

26.30 H. McKellop, F.W. Shen, B. Lu, P. Campbell, R. Salovey: Development of an extremely wear-resistant ultra high molecular weight polyethylene for total hip replacements, J. Orthop. Res. **17**(2), 157–167 (1999)

26.31 S.M. Kurtz, O.K. Muratoglu, M. Evans, A.A. Edidin: Advances in the processing, sterilization, and crosslinking of ultra-high molecular weight polyethylene for total joint arthroplasty, Biomaterials **20**(18), 1659–1688 (1999)

26.32 C.T. Laurencin, A.M. Ambrosio, M.D. Borden, J.A. Cooper Jr.: Tissue engineering: Orthopedic applications, Annu. Rev. Biomed. Eng. **1**, 19–46 (1999)

26.33 A.R. Boccaccini, J.J. Blaker: Bioactive composite materials for tissue engineering scaffolds, Expert Rev. Med. Devices **2**(3), 303–317 (2005)

26.34 A.U. Daniels, K.P. Andriano, W.P. Smutz, M.K. Chang, J. Heller: Evaluation of absorbable poly(ortho esters) for use in surgical implants, J. Appl. Biomater. **5**(1), 51–64 (1994)

26.35 K.P. Andriano, T. Pohjonen, P. Tormala: Processing and characterization of absorbable polylactide polymers for use in surgical implants, J. Appl. Biomater. **5**(2), 133–140 (1994)

26.36 K.A. Athanasiou, G.G. Niederauer, C.M. Agrawal: Sterilization, toxicity, biocompatibility and clinical applications of polylactic acid/polyglycolic acid copolymers, Biomaterials **17**(2), 93–102 (1996)

26.37 V. Thomas, D.R. Dean, Y.K. Vohra: Nanostructured biomaterials for regenerative medicine, Curr. Nanosci. **2**(3), 155–177 (2006)

26.38 S.M. Li, H. Garreau, M. Vert: Structure-property relationships in the case of the degradation of massive aliphatic poly-(α-hydroxy acids) in aque-

ous media, J. Mater. Sci. Mater. Med. **1**(3), 123–130 (1990)
26.39 R.C. Thomson, M.J. Yaszemski, J.M. Powers, A.G. Mikos: Hydroxyapatite fiber reinforced poly(α-hydroxy ester) foams for bone regeneration, Biomaterials **19**(21), 1935–1943 (1998)
26.40 K.C. Dee, R. Bizios: Mini-review: Proactive biomaterials and bone tissue engineering, Biotechnol. Bioeng. **50**(4), 438–442 (1996)
26.41 N. Ignjatović, S. Tomić, M. Dakić, M. Miljković, M. Plavsić, D. Uskoković: Synthesis and properties of hydroxyapatite/poly-l-lactide composite biomaterials, Biomaterials **20**(9), 809–816 (1999)
26.42 N. Ignjatović, V. Savić, S. Najman, M. Plavšić, D. Uskoković: A study of HAp/PLLA composite as a substitute for bone powder, using FT-IR spectroscopy, Biomaterials **22**(6), 571–575 (2001)
26.43 N. Ashammakhi, P. Rokkanen: Absorbable polyglycolide devices in trauma and bone surgery, Biomaterials **18**(1), 3–9 (1997)
26.44 G.O. Hofmann: Biodegradable implants in traumatology: A review on the state-of-the-art, Arch. Orthop. Trauma Surg. **114**(3), 123–132 (1995)
26.45 J.O. Hollinger, K. Leong: Poly(α-hydroxy acids): Carriers for bone morphogenetic proteins, Biomaterials **17**(2), 187–194 (1996)
26.46 L.G. Griffith: Polymeric biomaterials, Acta Mater. **48**(1), 263–277 (2000)
26.47 S.J. Peter, M.J. Miller, A.W. Yasko, M.J. Yaszemski, A.G. Mikos: Polymer concepts in tissue engineering, J. Biomed. Mater. Res. **43**(4), 422–427 (1998)
26.48 S.L. Ishaug, R.G. Payne, M.J. Yaszemski, T.B. Aufdemorte, R. Bizios, A.G. Mikos: Osteoblast migration on poly(α-hydroxy esters), Biotechnol. Bioeng. **50**(4), 443–451 (1996)
26.49 G.M. Crane, S.L. Ishaug, A.G. Mikos: Bone tissue engineering, Nat. Med. **1**(12), 1322–1324 (1995)
26.50 T. Matsuda, J.E. Davies: The in vitro response of osteoblasts to bioactive glass, Biomaterials **8**(4), 275–284 (1987)
26.51 H. Hayashi, A. Uchida, H. Hamada, H. Yoshikawa, Y. Shinto, K. Ono: Alumina ceramic prostheses for bone reactions to alumina oxide dental implants in man: A case report, Arch. Orthop. Trauma Surg. **112**, 1–4 (1992)
26.52 J.E. Davies, T. Matsuda: Extracellular matrix production by osteoblasts on bioactive substrate in vitro, Scanning Microsc. **2**(1445), 52 (1988)
26.53 J.M. Sautier, J.R. Nefussi, N. Forest: Ultrasonic study of bone formation on synthetic hydroxyapatite in osteoblasts cultures, Cell Mater. **1**, 209–217 (1991)
26.54 R.Z. LeGeros: Calcium phosphates in oral biology and medicine, Monogr. Oral Sci. **15**, 1–201 (1991)
26.55 T. Kokubo, S. Ito, Z.T. Huang, T. Hayashi, S. Sakka, T. Kitsugi, T. Yamamuro: Ca,P-rich layer formed on high-strength bioactive glass-ceramic A-W, J. Biomed. Mater. Res. **24**(3), 331–343 (1990)
26.56 M. Nagano, T. Nakamura, T. Kokubo, M. Tanahashi, M. Ogawa: Differences of bone bonding ability and degradation behaviour in vivo between amorphous calcium phosphate and highly crystalline hydroxyapatite coating, Biomaterials **17**(18), 1771–1777 (1996)
26.57 T.J. Webster, J.U. Ejiofor: Increased osteoblast adhesion on nanophase metals: Ti, Ti_6AL_4V, and CoCrMo, Biomaterials **25**(19), 4731–4739 (2004)
26.58 G. Zhao, A.L. Raines, M. Wieland, Z. Schwartz, B.D. Boyan: Requirement for both micron- and submicron scale structure for synergistic responses of osteoblasts to substrate surface energy and topography, Biomaterials **28**(18), 2821–2829 (2007)
26.59 T.P. Kunzler, T. Drobek, M. Schuler, N.D. Spencer: Systematic study of osteoblast and fibroblast response to roughness by means of surface-morphology gradients, Biomaterials **28**(13), 2175–2182 (2007)
26.60 M.A. Dyer, K.M. Ainslie, M.V. Pishko: Protein adhesion on silicon-supported hyperbranched poly(ethylene glycol) and poly(allylamine) thin films, Langmuir **23**(13), 7018–7023 (2007)
26.61 D. Khang, J. Lu, C. Yao, K.M. Haberstroh, T.J. Webster: The role of nanometer and sub-micron surface features on vascular and bone cell adhesion on titanium, Biomaterials **29**(8), 970–983 (2008)
26.62 C. Yao, V. Perla, J.L. McKenzie, E.B. Slamovich, T.J. Webster: Anodized Ti and Ti_6AL_4V possessing nanometer surface features enhances osteoblast adhesion, J. Biomed. Nanotechnol. **1**(1), 68–73 (2005)
26.63 T.-W. Chung, D.-Z. Liu, S.-Y. Wang, S.-S. Wang: Enhancement of the growth of human endothelial cells by surface roughness at nanometer scale, Biomaterials **24**(25), 4655–4661 (2003)
26.64 S. Sirivisoot, C. Yao, X. Xiao, B.W. Sheldon, T.J. Webster: Greater osteoblast functions on multiwalled carbon nanotubes grown from anodized nanotubular titanium for orthopedic applications, Nanotechnology **18**(36), 365102 (2007)
26.65 M. Navarro, M.P. Ginebra, J.A. Planell, S. Zeppetelli, L. Ambrosio: Development and cell response of a new biodegradable composite scaffold for guided bone regeneration, J. Mater. Sci. Mater. Med. **15**(4), 419–422 (2004)
26.66 T. Niemelä, H. Niiranen, M. Kellomäki, P. Törmälä: Self-reinforced composites of bioabsorbable polymer and bioactive glass with different bioactive glass contents. Part I: Initial mechanical properties and bioactivity, Acta Biomater. **1**(2), 235–242 (2005)
26.67 J. Yao, S. Radin, G. Reilly, P.S. Leboy, P. Ducheyne: Solution-mediated effect of bioactive glass in poly (lactic-co-glycolic acid)-bioactive glass composites on osteogenesis of marrow stromal cells, J. Biomed. Mater. Res. A **75**(4), 794–801 (2005)

26.68 R. Zhang, P.X. Ma: Poly(α-hydroxyl acids)/hydroxy apatite porous composites for bone-tissue engineering. I. Preparation and morphology, J. Biomed. Mater. Res. **44**(4), 446–455 (1999)

26.69 Y. Shikinami, M. Okuno: Bioresorbable devices made of forged composites of hydroxyapatite (HA) particles and poly-l-lactide (plla): Part i. Basic characteristics, Biomaterials **20**(9), 859–877 (1999)

26.70 Y. Shikinami, Y. Matsusue, T. Nakamura: The complete process of bioresorption and bone replacement using devices made of forged composites of raw hydroxyapatite particles/poly l-lactide (f-u-ha/plla), Biomaterials **26**(27), 5542–5551 (2005)

26.71 M.J. Mondrinos, R. Dembzynski, L. Lu, V.K. Byrapogu, D.M. Wootton, P.I. Lelkes, J. Zhou: Porogen-based solid freeform fabrication of polycaprolactone-calcium phosphate scaffolds for tissue engineering, Biomaterials **27**(25), 4399–4408 (2006)

26.72 A.M. Ambrosio, J.S. Sahota, Y. Khan, C.T. Laurencin: A novel amorphous calcium phosphate polymer ceramic for bone repair: I. Synthesis and characterization, J. Biomed. Mater. Res. **58**(3), 295–301 (2001)

26.73 A.A. Ignatius, O. Betz, P. Augat, L.E. Claes: In vivo investigations on composites made of resorbable ceramics and poly(lactide) used as bone graft substitutes, J. Biomed. Mater. Res. **58**(6), 701–709 (2001)

26.74 C.G. Simon Jr., C.A. Khatri, S.A. Wight, F.W. Wang: Preliminary report on the biocompatibility of a moldable, resorbable, composite bone graft consisting of calcium phosphate cement and poly(lactide-co-glycolide) microspheres, J. Orthop. Res. **20**(3), 473–482 (2002)

26.75 P.Q. Ruhe, E.L. Hedberg, N.T. Padron, P.H. Spauwen, J.A. Jansen, A.G. Mikos: rhBMP-2 release from injectable poly(dl-lactic-co-glycolic acid)/calcium-phosphate cement composites, J. Bone Joint Surg. Am. **85**(Suppl 3), 75–81 (2003)

26.76 W.J. Habraken, J.G. Wolke, A.G. Mikos, J.A. Jansen: Injectable PLGA microsphere/calcium phosphate cements: Physical properties and degradation characteristics, J. Biomater. Sci. Polym. Ed. **17**(9), 1057–1074 (2006)

26.77 P.Q. Ruhe, E.L. Hedberg, N.T. Padron, P.H. Spauwen, J.A. Jansen, A.G. Mikos: Biocompatibility and degradation of poly(dl-lactic-co-glycolic acid)/calcium phosphate cement composites, J. Biomed. Mater. Res. A **74**(4), 533–544 (2005)

26.78 D.P. Link, J. van den Dolder, W.J. Jurgens, J.G. Wolke, J.A. Jansen: Mechanical evaluation of implanted calcium phosphate cement incorporated with PLGA microparticles, Biomaterials **27**(28), 4941–4947 (2006)

26.79 P.Q. Ruhe, E.L. Hedberg-Dirk, N.T. Padron, P.H. Spauwen, J.A. Jansen, A.G. Mikos: Porous poly(dl-lactic-co-glycolic acid)/calcium phosphate cement composite for reconstruction of bone defects, Tissue Eng. **12**(4), 789–800 (2006)

26.80 Y. Takahashi, M. Yamamoto, Y. Tabata: Enhanced osteoinduction by controlled release of bone morphogenetic protein-2 from biodegradable sponge composed of gelatin and β-tricalcium phosphate, Biomaterials **26**(23), 4856–4865 (2005)

26.81 H.W. Kim, J.C. Knowles, H.E. Kim: Hydroxyapatite and gelatin composite foams processed via novel freeze-drying and crosslinking for use as temporary hard tissue scaffolds, J. Biomed. Mater. Res. A **72**(2), 136–145 (2005)

26.82 Y. Shibata, H. Yamamoto, T. Miyazaki: Colloidal β-tricalcium phosphate prepared by discharge in a modified body fluid facilitates synthesis of collagen composites, J. Dent. Res. **84**(9), 827–831 (2005)

26.83 F.H. Lin, C.H. Yao, J.S. Sun, H.C. Liu, C.W. Huang: Biological effects and cytotoxicity of the composite composed by tricalcium phosphate and glutaraldehyde cross-linked gelatin, Biomaterials **19**(10), 905–917 (1998)

26.84 C. Du, F.Z. Cui, W. Zhang, Q.L. Feng, X.D. Zhu, K. de Groot: Formation of calcium phosphate/collagen composites through mineralization of collagen matrix, J. Biomed. Mater. Res. **50**(4), 518–527 (2000)

26.85 A. Tampieri, G. Celotti, E. Landi, M. Montevecchi, N. Roveri, A. Bigi, S. Panzavolta, M.C. Sidoti: Porous phosphate-gelatine composite as bone graft with drug delivery function, J. Mater. Sci. Mater. Med. **14**(7), 623–627 (2003)

26.86 A. Bigi, B. Bracci, S. Panzavolta: Effect of added gelatin on the properties of calcium phosphate cement, Biomaterials **25**(14), 2893–2899 (2004)

26.87 A. Bigi, P. Torricelli, M. Fini, B. Bracci, S. Panzavolta, L. Sturba, R. Giardino: A biomimetic gelatin-calcium phosphate bone cement, Int. J. Artif. Organs **27**(8), 664–673 (2004)

26.88 A. Bigi, S. Panzavolta, L. Sturba, P. Torricelli, M. Fini, R. Giardino: Normal and osteopenic bone-derived osteoblast response to a biomimetic gelatin-calcium phosphate bone cement, J. Biomed. Mater. Res. A **78**(4), 739–745 (2006)

26.89 Y. Fujishiro, K. Takahashi, T. Sato: Preparation and compressive strength of α-tricalcium phosphate/gelatin gel composite cement, J. Biomed. Mater. Res. **54**(4), 525–530 (2001)

26.90 A. Bigi, E. Boanini, S. Panzavolta, N. Roveri: Biomimetic growth of hydroxyapatite on gelatin films doped with sodium polyacrylate, Biomacromolecules **1**(4), 752–756 (2000)

26.91 S. Rammelt, E. Schulze, M. Witt, E. Petsch, A. Biewener, W. Pompe, H. Zwipp: Collagen type I increases bone remodelling around hydroxyapatite implants in the rat tibia, Cells Tissues Organs **178**(3), 146–157 (2004)

26.92 B. Knepper-Nicolai, A. Reinstorf, I. Hofinger, K. Flade, R. Wenz, W. Pompe: Influence of osteocalcin and collagen I on the mechanical and biological properties of biocement D, Biomol. Eng. **19**(2–6), 227–231 (2002)

26.93 U. Hempel, A. Reinstorf, M. Poppe, U. Fischer, M. Gelinsky, W. Pompe, K.W. Wenzel: Proliferation and differentiation of osteoblasts on biocement D modified with collagen type I and citric acid, J. Biomed. Mater. Res. B **71**(1), 130–143 (2004)

26.94 D. Le Nihouannen, L.L. Guehennec, T. Rouillon, P. Pilet, M. Bilban, P. Layrolle, G. Daculsi: Microarchitecture of calcium phosphate granules and fibrin glue composites for bone tissue engineering, Biomaterials **27**(13), 2716–2722 (2006)

26.95 F. Jegoux, E. Goyenvalle, M. Bagot D'arc, E. Aguado, G. Daculsi: In vivo biological performance of composites combining micro-macroporous biphasic calcium phosphate granules and fibrin sealant, Arch. Orthop. Trauma Surg. **125**(3), 153–159 (2005)

26.96 U. Kneser, A. Voogd, J. Ohnolz, O. Buettner, L. Stangenberg, Y.H. Zhang, G.B. Stark, D.J. Schaefer: Fibrin gel-immobilized primary osteoblasts in calcium phosphate bone cement: In vivo evaluation with regard to application as injectable biological bone substitute, Cells Tissues Organs **179**(4), 158–169 (2005)

26.97 C.M. Vaz, M. Fossen, R.F. van Tuil, L.A. de Graaf, R.L. Reis, A.M. Cunha: Casein and soybean protein-based thermoplastics and composites as alternative biodegradable polymers for biomedical applications, J. Biomed. Mater. Res. A **65**(1), 60–70 (2003)

26.98 J. Lin, S. Zhang, T. Chen, C. Liu, S. Lin, X. Tian: Calcium phosphate cement reinforced by polypeptide copolymers, J. Biomed. Mater. Res. B **76**(2), 432–439 (2006)

26.99 L. Leroux, Z. Hatim, M. Freche, J.L. Lacout: Effects of various adjuvants (lactic acid, glycerol, and chitosan) on the injectability of a calcium phosphate cement, Bone **25**(2 Suppl), 31S–34S (1999)

26.100 S. Takagi, L.C. Chow, S. Hirayama, F.C. Eichmiller: Properties of elastomeric calcium phosphate cement-chitosan composites, Dent. Mater. **19**(8), 797–804 (2003)

26.101 H.H. Xu, J.B. Quinn, S. Takagi, L.C. Chow: Processing and properties of strong and non-rigid calcium phosphate cement, J. Dent. Res. **81**(3), 219–224 (2002)

26.102 H.H. Xu, C.G. Simon Jr.: Fast setting calcium phosphate-chitosan scaffold: Mechanical properties and biocompatibility, Biomaterials **26**(12), 1337–1348 (2005)

26.103 Y.M. Lee, Y.J. Park, S.J. Lee, Y. Ku, S.B. Han, S.M. Choi, P.R. Klokkevold, C.P. Chung: Tissue engineered bone formation using chitosan/tricalcium phosphate sponges, J. Periodontol. **71**(3), 410–417 (2000)

26.104 Y. Zhang, M. Zhang: Cell growth and function on calcium phosphate reinforced chitosan scaffolds, J. Mater. Sci. Mater. Med. **15**(3), 255–260 (2004)

26.105 Y. Zhang, M. Zhang: Calcium phosphate/chitosan composite scaffolds for controlled in vitro antibiotic drug release, J. Biomed. Mater. Res. **62**(3), 378–386 (2002)

26.106 G. Daculsi, P. Weiss, J.M. Bouler, O. Gauthier, F. Millot, E. Aguado: Biphasic calcium phosphate/hydrosoluble polymer composites: A new concept for bone and dental substitution biomaterials, Bone **25**(2 Suppl), 59S–61S (1999)

26.107 B.H. Fellah, P. Weiss, O. Gauthier, T. Rouillon, P. Pilet, G. Daculsi, P. Layrolle: Bone repair using a new injectable self-crosslinkable bone substitute, J. Orthop. Res. **24**(4), 628–635 (2006)

26.108 E.F. Burguera, H.H. Xu, M.D. Weir: Injectable and rapid-setting calcium phosphate bone cement with dicalcium phosphate dihydrate, J. Biomed. Mater. Res. B **77**(1), 126–134 (2006)

26.109 B. Ongpipattanakul, T. Nguyen, T.F. Zioncheck, R. Wong, G. Osaka, L. DeGuzman, W.P. Lee, L.S. Beck: Development of tricalcium phosphate/amylopectin paste combined with recombinant human transforming growth factor beta 1 as a bone defect filler, J. Biomed. Mater. Res. **36**(3), 295–305 (1997)

26.110 L.F. Boesel, M.H. Fernandes, R.L. Reis: The behavior of novel hydrophilic composite bone cements in simulated body fluids, J. Biomed. Mater. Res. B **70**(2), 368–377 (2004)

26.111 E.L. Liljensten, A.G. Attaelmanan, C. Larsson, H. Ljusberg-Wahren, N. Danielsen, J.M. Hirsch, P. Thomsen: Hydroxyapatite granule/carrier composites promote new bone formation in cortical defects, Clin. Implant. Dent. Relat. Res. **2**(1), 50–59 (2000)

26.112 A.D. Augst, H.J. Kong, D.J. Mooney: Alginate hydrogels as biomaterials, Macromol. Biosci. **6**(8), 623–633 (2006)

26.113 I. Khairoun, F.C. Driessens, M.G. Boltong, J.A. Planell, R. Wenz: Addition of cohesion promotors to calcium phosphate cements, Biomaterials **20**(4), 393–398 (1999)

26.114 S.J. Peter, P. Kim, A.W. Yasko, M.J. Yaszemski, A.G. Mikos: Crosslinking characteristics of an injectable poly(propylene fumarate)/β-tricalcium phosphate paste and mechanical properties of the crosslinked composite for use as a biodegradable bone cement, J. Biomed. Mater. Res. **44**(3), 314–321 (1999)

26.115 J.L. Charvet, J.A. Cordes, H. Alexander: Mechanical and fracture behavior of a fiber-reinforced bioabsorbable material for orthopaedic applications, J. Mater. Sci. Mater. Med. **11**(2), 101–109 (2000)

26.116 S.K. Misra, S.P. Valappil, I. Roy, A.R. Boccaccini: Polyhydroxyalkanoate (PHA)/inorganic phase

composites for tissue engineering applications, Biomacromolecules **7**(8), 2249–2258 (2006)
26.117 H. Qiu, J. Yang, P. Kodali, J. Koh, G.A. Ameer: A citric acid–based hydroxyapatite composite for orthopedic implants, Biomaterials **27**(34), 5845–5854 (2006)
26.118 R.A. Mickiewicz, A.M. Mayes, D. Knaack: Polymer–calcium phosphate cement composites for bone substitutes, J. Biomed. Mater. Res. **61**(4), 581–592 (2002)
26.119 L.A. dos Santos, R.G. Carrodeguas, A.O. Boschi, A.C. Fonseca de Arruda: Fiber-enriched double-setting calcium phosphate bone cement, J. Biomed. Mater. Res. A **65**(2), 244–250 (2003)
26.120 H.H. Xu, F.C. Eichmiller, A.A. Giuseppetti: Reinforcement of a self-setting calcium phosphate cement with different fibers, J. Biomed. Mater. Res. **52**(1), 107–114 (2000)
26.121 J.R. Jones, L.M. Ehrenfried, L.L. Hench: Optimising bioactive glass scaffolds for bone tissue engineering, Biomaterials **27**(7), 964–973 (2006)
26.122 H.W. Kim, J.C. Knowles, H.E. Kim: Hydroxyapatite porous scaffold engineered with biological polymer hybrid coating for antibiotic vancomycin release, J. Mater. Sci. Mater. Med. **16**(3), 189–195 (2005)
26.123 E.B. Giesen, M. Ding, M. Dalstra, T.M. van Eijden: Mechanical properties of cancellous bone in the human mandibular condyle are anisotropic, J. Biomech. **34**(6), 799–803 (2001)
26.124 H. Shin, S. Jo, A.G. Mikos: Biomimetic materials for tissue engineering, Biomaterials **24**(24), 4353–4364 (2003)
26.125 W.S. Koegler, L.G. Griffith: Osteoblast response to PLGA tissue engineering scaffolds with peo modified surface chemistries and demonstration of patterned cell response, Biomaterials **25**(14), 2819–2830 (2004)
26.126 S. Ladron de Guevara-Fernandez, C.V. Ragel, M. Vallet-Regi: Bioactive glass-polymer materials for controlled release of ibuprofen, Biomaterials **24**(22), 4037–4043 (2003)
26.127 W.L. Murphy, M.C. Peters, D.H. Kohn, D.J. Mooney: Sustained release of vascular endothelial growth factor from mineralized poly(lactide-co-glycolide) scaffolds for tissue engineering, Biomaterials **21**(24), 2521–2527 (2000)
26.128 C.T. Laurencin, M.A. Attawia, L.Q. Lu, M.D. Borden, H.H. Lu, W.J. Gorum, J.R. Lieberman: Poly(lactide-co-glycolide)/hydroxyapatite delivery of BMP-2-producing cells: A regional gene therapy approach to bone regeneration, Biomaterials **22**(11), 1271–1277 (2001)
26.129 G.A. Silva, F.J. Costa, O.P. Coutinho, S. Radin, P. Ducheyne, R.L. Reis: Synthesis and evaluation of novel bioactive composite starch/bioactive glass microparticles, J. Biomed. Mater. Res. A **70**(3), 442–449 (2004)
26.130 K. Anselme: Osteoblast adhesion on biomaterials, Biomaterials **21**(7), 667–681 (2000)
26.131 M. Mrksich: What can surface chemistry do for cell biology?, Curr. Opin. Chem. Biol. **6**(6), 794–797 (2002)
26.132 A. Ito, K. Ino, T. Kobayashi, H. Honda: The effect of RGD peptide-conjugated magnetite cationic liposomes on cell growth and cell sheet harvesting, Biomaterials **26**(31), 6185–6193 (2005)
26.133 F. Yang, C.G. Williams, D.-A. Wang, H. Lee, P.N. Manson, J. Elisseeff: The effect of incorporating rgd adhesive peptide in polyethylene glycol diacrylate hydrogel on osteogenesis of bone marrow stromal cells, Biomaterials **26**(30), 5991–5998 (2005)
26.134 T.A. Linkhart, S. Mohan, D.J. Baylink: Growth factors for bone growth and repair: IGF, TGFβ and BMP, Bone **19**(1 Suppl.), 1S–12S (1996)
26.135 J.A. Jansen, J.W. Vehof, P.Q. Ruhe, H. Kroeze-Deutman, Y. Kuboki, H. Takita, E.L. Hedberg, A.G. Mikos: Growth factor-loaded scaffolds for bone engineering, J. Control Release **101**(1–3), 127–136 (2005)
26.136 J.E. Babensee, L.V. McIntire, A.G. Mikos: Growth factor delivery for tissue engineering, Pharm. Res. **17**(5), 497–504 (2000)
26.137 J.D. Currey: Strength of bone, Nature **195**(4840), 513–514 (1962)
26.138 X. Zong, S. Ran, K.S. Kim, D. Fang, B.S. Hsiao, B. Chu: Structure and morphology changes during in vitro degradation of electrospun poly(glycolide-co-lactide) nanofiber membrane, Biomacromolecules **4**(2), 416–423 (2003)
26.139 Y.K. Luu, K. Kim, B.S. Hsiao, B. Chu, M. Hadjiargyrou: Development of a nanostructured DNA delivery scaffold via electrospinning of plga and pla-peg block copolymers, J. Control Release **89**(2), 341–353 (2003)
26.140 R.W. Siegel, G.E. Fougere: Mechanical properties of nanophase metals, Nanostruct. Mater. **6**(1–4), 205–216 (1995)
26.141 J.W. Freeman, L.D. Wright, C.T. Laurencin, S. Bhattacharyya: Nanofabrication techniques. In: *Biomedical Nanostructures* (Wiley, Hoboken 2008) pp. 3–24
26.142 V.J. Chen, P.X. Ma: Nano-fibrous poly(l-lactic acid) scaffolds with interconnected spherical macropores, Biomaterials **25**(11), 2065–2073 (2004)
26.143 J.R. Venugopal, S. Low, A.T. Choon, A.B. Kumar, S. Ramakrishna: Nanobioengineered electrospun composite nanofibers and osteoblasts for bone regeneration, Artif. Organs **32**(5), 388–397 (2008)
26.144 K. Hata, D.N. Futaba, K. Mizuno, T. Namai, M. Yumura, S. Iijima: Water-assisted highly efficient synthesis of impurity-free single-walled carbon nanotubes, Science **306**(5700), 1362–1364 (2004)
26.145 S. Sun, H. Zeng, D.B. Robinson, S. Raoux, P.M. Rice, S.X. Wang, G. Li: Monodisperse MFe_2O_4

(M = Fe,Co,Mn) nanoparticles, J. Am. Chem. Soc. **126**(1), 273–279 (2004)
26.146 M. Wang: Developing bioactive composite materials for tissue replacement, Biomaterials **24**(13), 2133–2151 (2003)
26.147 J.D. Currey: Tensile yield in compact bone is determined by strain, post-yield behaviour by mineral content, J. Biomech. **37**(4), 549–556 (2004)
26.148 J.S. Nyman, A. Roy, X. Shen, R.L. Acuna, J.H. Tyler, X. Wang: The influence of water removal on the strength and toughness of cortical bone, J. Biomech. **39**(5), 931–938 (2006)
26.149 S. Lenhert, M.B. Meier, U. Meyer, L. Chi, H.P. Wiesmann: Osteoblast alignment, elongation and migration on grooved polystyrene surfaces patterned by Langmuir–Blodgett lithography, Biomaterials **26**(5), 563–570 (2005)
26.150 J.M. Rice, J.A. Hunt, J.A. Gallagher, P. Hanarp, D.S. Sutherland, J. Gold: Quantitative assessment of the response of primary derived human osteoblasts and macrophages to a range of nanotopography surfaces in a single culture model in vitro, Biomaterials **24**(26), 4799–4818 (2003)
26.151 K.M. Woo, V.J. Chen, P.X. Ma: Nano-fibrous scaffolding architecture selectively enhances protein adsorption contributing to cell attachment, J. Biomed. Mater. Res. A **67**(2), 531–537 (2003)
26.152 B.G. Keselowsky, D.M. Collard, A.J. Garcia: Surface chemistry modulates fibronectin conformation and directs integrin binding and specificity to control cell adhesion, J. Biomed. Mater. Res. A **66**(2), 247–259 (2003)
26.153 C. Dahmen, J. Auernheimer, A. Meyer, A. Enderle, S.L. Goodman, H. Kessler: Improving implant materials by coating with nonpeptidic, highly specific integrin ligands, Angew. Chem. Int. Engl. Ed. **43**(48), 6649–6652 (2004)
26.154 T.J. Webster, C. Ergun, R.H. Doremus, R.W. Siegel, R. Bizios: Specific proteins mediate enhanced osteoblast adhesion on nanophase ceramics, J. Biomed. Mater. Res. **51**(3), 475–483 (2000)
26.155 S. Faghihi, F. Azari, A.P. Zhilyaev, J.A. Szpunar, H. Vali, M. Tabrizian: Cellular and molecular interactions between MC3T3-E1 pre-osteoblasts and nanostructured titanium produced by high-pressure torsion, Biomaterials **28**(27), 3887–3895 (2007)
26.156 G.M. Whitesides, J.P. Mathias, C.T. Seto: Molecular self-assembly and nanochemistry: A chemical strategy for the synthesis of nanostructures, Science **254**(5036), 1312–1319 (1991)
26.157 G.A. Silva, C. Czeisler, K.L. Niece, E. Beniash, D.A. Harrington, J.A. Kessler, S.I. Stupp: Selective differentiation of neural progenitor cells by high-epitope density nanofibers, Science **303**(5662), 1352–1355 (2004)
26.158 S. Zhang: Fabrication of novel biomaterials through molecular self-assembly, Nat. Biotechnol. **21**(10), 1171–1178 (2003)
26.159 T.D. Sargeant, M.O. Guler, S.M. Oppenheimer, A. Mata, R.L. Satcher, D.C. Dunand, S.I. Stupp: Hybrid bone implants: Self-assembly of peptide amphiphile nanofibers within porous titanium, Biomaterials **29**(2), 161–171 (2008)
26.160 P. Berndt, G.B. Fields, M. Tirrell: Synthetic lipidation of peptides and amino acids: Monolayer structure and properties, J. Am. Chem. Soc. **117**(37), 9515–9522 (1995)
26.161 R. Vasita, D.S. Katti: Nanofibers and their applications in tissue engineering, Int. J. Nanomed. **1**(1), 15–30 (2006)
26.162 Z. Ma, M. Kotaki, R. Inai, S. Ramakrishna: Potential of nanofiber matrix as tissue-engineering scaffolds, Tissue Eng. **11**(1–2), 101–109 (2005)
26.163 M. Zhou, A.M. Smith, A.K. Das, N.W. Hodson, R.F. Collins, R.V. Ulijn, J.E. Gough: Self-assembled peptide-based hydrogels as scaffolds for anchorage-dependent cells, Biomaterials **30**(13), 2523–2530 (2009)
26.164 T.P. Kraehenbuehl, P. Zammaretti, A.J. Van der Vlies, R.G. Schoenmakers, M.P. Lutolf, M.E. Jaconi, J.A. Hubbell: Three-dimensional extracellular matrix-directed cardioprogenitor differentiation: Systematic modulation of a synthetic cell-responsive PEG-hydrogel, Biomaterials **29**(18), 2757–2766 (2008)
26.165 Y. Park, M.P. Lutolf, J.A. Hubbell, E.B. Hunziker, M. Wong: Bovine primary chondrocyte culture in synthetic matrix metalloproteinase-sensitive poly(ethylene glycol)-based hydrogels as a scaffold for cartilage repair, Tissue Eng. **10**(3/4), 515–522 (2004)
26.166 R.W. Baker: *Membrane Technology and Applications* (Wiley, New York 2004)
26.167 P.X. Ma, R. Zhang: Synthetic nano-scale fibrous extracellular matrix, J. Biomed. Mater. Res. **46**(1), 60–72 (1999)
26.168 C.P. Barnes, S.A. Sell, E.D. Boland, D.G. Simpson, G.L. Bowlin: Nanofiber technology: Designing the next generation of tissue engineering scaffolds, Adv. Drug Deliv. Rev. **59**(14), 1413–1433 (2007)
26.169 V.J. Chen, L.A. Smith, P.X. Ma: Bone regeneration on computer-designed nano-fibrous scaffolds, Biomaterials **27**(21), 3973–3979 (2006)
26.170 G. Wei, P.X. Ma: Macroporous and nanofibrous polymer scaffolds and polymer/bone-like apatite composite scaffolds generated by sugar spheres, J. Biomed. Mater. Res. A **78**(2), 306–315 (2006)
26.171 R. Zhang, P.X. Ma: Synthetic nano-fibrillar extracellular matrices with predesigned macroporous architectures, J. Biomed. Mater. Res. **52**(2), 430–438 (2000)
26.172 Y.X. Huang, J. Ren, C. Chen, T.B. Ren, X.Y. Zhou: Preparation and properties of poly(lactide-co-

glycolide) (PLGA)/nano-hydroxyapatite (NHA) scaffolds by thermally induced phase separation and rabbit MSCS culture on scaffolds, J. Biomater. Appl. **22**(5), 409–432 (2008)

26.173 J.D. Fromstein, P.W. Zandstra, C. Alperin, D. Rockwood, J.F. Rabolt, K.A. Woodhouse: Seeding bioreactor-produced embryonic stem cell-derived cardiomyocytes on different porous, degradable, polyurethane scaffolds reveals the effect of scaffold architecture on cell morphology, Tissue Eng. A **14**(3), 369–378 (2008)

26.174 T. Cui, Y. Yan, R. Zhang, L. Liu, W. Xu, X. Wang: Rapid prototyping of a double-layer polyurethane-collagen conduit for peripheral nerve regeneration, Tissue Eng. C **15**(1), 1–9 (2009)

26.175 Y. Cao, B. Zhang, T. Croll, B.E. Rolfe, J.H. Campbell, G.R. Campbell, D. Martin, J.J. Cooper-White: Engineering tissue tubes using novel multilayered scaffolds in the rat peritoneal cavity, J. Biomed. Mater. Res. A **87**(3), 719–727 (2008)

26.176 J.A. Matthews, G.E. Wnek, D.G. Simpson, G.L. Bowlin: Electrospinning of collagen nanofibers, Biomacromolecules **3**(2), 232–238 (2002)

26.177 E.D. Boland, J.A. Matthews, K.J. Pawlowski, D.G. Simpson, G.E. Wnek, G.L. Bowlin: Electrospinning collagen and elastin: Preliminary vascular tissue engineering, Front. Biosci. **9**, 1422–1432 (2004)

26.178 C.Y. Xu, R. Inai, M. Kotaki, S. Ramakrishna: Aligned biodegradable nanofibrous structure: A potential scaffold for blood vessel engineering, Biomaterials **25**(5), 877–886 (2004)

26.179 L.S. Nair, S. Bhattacharyya, C.T. Laurencin: Development of novel tissue engineering scaffolds via electrospinning, Expert Opin. Biol. Ther. **4**(5), 659–668 (2004)

26.180 H. Yoshimoto, Y.M. Shin, H. Terai, J.P. Vacanti: A biodegradable nanofiber scaffold by electrospinning and its potential for bone tissue engineering, Biomaterials **24**(12), 2077–2082 (2003)

26.181 F. Yang, R. Murugan, S. Wang, S. Ramakrishna: Electrospinning of nano/micro scale poly(l-lactic acid) aligned fibers and their potential in neural tissue engineering, Biomaterials **26**(15), 2603–2610 (2005)

26.182 E.D. Boland, G.E. Wnek, D.G. Simpson, K.J. Pawlowski, G.L. Bowlin: Tailoring tissue engineering scaffolds using electrostatic processing techniques: A study of poly(glycolic acid) electrospinning, J. Macromol. Sci. A **38**(12), 1231–1243 (2001)

26.183 C. Li, C. Vepari, H.J. Jin, H.J. Kim, D.L. Kaplan: Electrospun silk-BMP-2 scaffolds for bone tissue engineering, Biomaterials **27**(16), 3115–3124 (2006)

26.184 C. Ayres, G.L. Bowlin, S.C. Henderson, L. Taylor, J. Shultz, J. Alexander, T.A. Telemeco, D.G. Simpson: Modulation of anisotropy in electrospun tissue-engineering scaffolds: Analysis of fiber alignment by the fast fourier transform, Biomaterials **27**(32), 5524–5534 (2006)

26.185 T.J. Webster, R.W. Siegel, R. Bizios: Osteoblast adhesion on nanophase ceramics, Biomaterials **20**(13), 1221–1227 (1999)

26.186 T.J. Webster, C. Ergun, R.H. Doremus, R.W. Siegel, R. Bizios: Enhanced functions of osteoblasts on nanophase ceramics, Biomaterials **21**(17), 1803–1810 (2000)

26.187 P.T. de Oliveira, A. Nanci: Nanotexturing of titanium-based surfaces upregulates expression of bone sialoprotein and osteopontin by cultured osteogenic cells, Biomaterials **25**(3), 403–413 (2004)

26.188 T.W. Chung, D.Z. Liu, S.Y. Wang, S.S. Wang: Enhancement of the growth of human endothelial cells by surface roughness at nanometer scale, Biomaterials **24**(25), 4655–4661 (2003)

26.189 T.J. Webster, L.S. Schadler, R.W. Siegel, R. Bizios: Mechanisms of enhanced osteoblast adhesion on nanophase alumina involve vitronectin, Tissue Eng. **7**(3), 291–301 (2001)

26.190 G. Balasundaram, T.J. Webster: An overview of nano-polymers for orthopedic applications, Macromol. Biosci. **7**(5), 635–642 (2007)

26.191 A. Thapa, D.C. Miller, T.J. Webster, K.M. Haberstroh: Nano-structured polymers enhance bladder smooth muscle cell function, Biomaterials **24**(17), 2915–2926 (2003)

26.192 R.L. Price, L.G. Gutwein, L. Kaledin, F. Tepper, T.J. Webster: Osteoblast function on nanophase alumina materials: Influence of chemistry, phase, and topography, J. Biomed. Mater. Res. A **67**(4), 1284–1293 (2003)

26.193 R.L. Price, K. Ellison, K.M. Haberstroh, T.J. Webster: Nanometer surface roughness increases select osteoblast adhesion on carbon nanofiber compacts, J. Biomed. Mater. Res. A **70**(1), 129–138 (2004)

26.194 T.J. Webster, M.C. Waid, J.L. McKenzie, R.L. Price, J.U. Ejiofor: Nano-biotechnology: Carbon nanofibers as improved neural and orthopaedic implants, Nanotechnology **15**, 48 (2004)

26.195 D.W. Hutmacher: Scaffolds in tissue engineering bone and cartilage, Biomaterials **21**(24), 2529–2543 (2000)

26.196 A.R. Boccaccini, V. Maquet: Bioresorbable and bioactive polymer/bioglass® composites with tailored pore structure for tissue engineering applications, Compos. Sci. Technol. **63**(16), 2417–2429 (2003)

26.197 H. Liu, E.B. Slamovich, T.J. Webster: Increased osteoblast functions on nanophase titania dispersed in poly-lactic-co-glycolic acid composites, Nanotechnology **16**(7), S601–S608 (2005)

26.198 C. Du, F.Z. Cui, Q.L. Feng, X.D. Zhu, K. de Groot: Tissue response to nano-hydroxyapatite/collagen

composite implants in marrow cavity, J. Biomed. Mater. Res. **42**(4), 540–548 (1998)
26.199 C. Du, F.Z. Cui, X.D. Zhu, K. de Groot: Three-dimensional nano-hap/collagen matrix loading with osteogenic cells in organ culture, J. Biomed. Mater. Res. **44**(4), 407–415 (1999)
26.200 P.X. Ma, R. Zhang, G. Xiao, R. Franceschi: Engineering new bone tissue in vitro on highly porous poly(α-hydroxyl acids)/hydroxyapatite composite scaffolds, J. Biomed. Mater. Res. **54**(2), 284–293 (2001)
26.201 J.J. Blaker, J.E. Gough, V. Maquet, I. Notingher, A.R. Boccaccini: In vitro evaluation of novel bioactive composites based on bioglass-filled polylactide foams for bone tissue engineering scaffolds, J. Biomed. Mater. Res. A **67**(4), 1401–1411 (2003)
26.202 S. Kalita, J. Finley, S. Bose, H. Hosick, A. Bandyopadhyay: Development of porous polymer-ceramic composites as bone grafts, MRS Online Proc. Libr. **726**, 91–96 (2002)
26.203 A.R. Boccaccini, J.A. Roelher, L.L. Hench, V. Maquet, R. Jérome: A composites approach to tissue engineering, Proc. 26th Annu Conf. on Compos., Adv. Ceram. Mater. Struct. B (Wiley, New York 2008) pp. 805–816
26.204 L. Zhang, T.J. Webster: Nanotechnology and nanomaterials: Promises for improved tissue regeneration, Nano Today **4**(1), 66–80 (2009)
26.205 S.P. Nukavarapu, S.G. Kumbar, J.L. Brown, N.R. Krogman, A.L. Weikel, M.D. Hindenlang, L.S. Nair, H.R. Allcock, C.T. Laurencin: Polyphosphazene/nano-hydroxyapatite composite microsphere scaffolds for bone tissue engineering, Biomacromolecules **9**(7), 1818–1825 (2008)
26.206 G. Colon, B.C. Ward, T.J. Webster: Increased osteoblast and decreased staphylococcus epidermidis functions on nanophase ZnO and TiO_2, J. Biomed. Mater. Res. A **78**(3), 595–604 (2006)
26.207 T.J. Webster, E.L. Hellenmeyer, R.L. Price: Increased osteoblast functions on theta + delta nanofiber alumina, Biomaterials **26**(9), 953–960 (2005)
26.208 J.D. Hartgerink, E. Beniash, S.I. Stupp: Self-assembly and mineralization of peptide-amphiphile nanofibers, Science **294**(5547), 1684–1688 (2001)
26.209 L. Zhang, S. Ramsaywack, H. Fenniri, T.J. Webster: Enhanced osteoblast adhesion on self-assembled nanostructured hydrogel scaffolds, Tissue Eng. **14**(8), 1353–1364 (2008)
26.210 T. Osathanon, M.L. Linnes, R.M. Rajachar, B.D. Ratner, M.J. Somerman, C.M. Giachelli: Microporous nanofibrous fibrin-based scaffolds for bone tissue engineering, Biomaterials **29**(30), 4091–4099 (2008)
26.211 T.J. Webster, T.A. Smith: Increased osteoblast function on PLGA composites containing nanophase titania, J. Biomed. Mater. Res. A **74**(4), 677–686 (2005)
26.212 A.J. McManus, R.H. Doremus, R.W. Siegel, R. Bizios: Evaluation of cytocompatibility and bending modulus of nanoceramic/polymer composites, J. Biomed. Mater. Res. A **72**(1), 98–106 (2005)
26.213 S. Iijima: Carbon nanotubes: Past, present, and future, Physica B **323**(1–4), 1–5 (2002)
26.214 D.S. Bethune, C.H. Klang, M.S. de Vries, G. Gorman, R. Savoy, J. Vazquez, R. Beyers: Cobalt-catalysed growth of carbon nanotubes with single-atomic-layer walls, Nature **363**(6430), 605–607 (1993)
26.215 L. Zhang, B. Ercan, T.J. Webster (Eds.): *Carbon Nanotubes and Nanofibers for Tissue Engineering Applications* (Research Signpost, Trivandrum 2009)
26.216 R.L. Price, M.C. Waid, K.M. Haberstroh, T.J. Webster: Selective bone cell adhesion on formulations containing carbon nanofibers, Biomaterials **24**(11), 1877–1887 (2003)
26.217 L.P. Zanello, B. Zhao, H. Hu, R.C. Haddon: Bone cell proliferation on carbon nanotubes, Nano Lett. **6**(3), 562–567 (2006)
26.218 B. Sitharaman, X. Shi, X.F. Walboomers, H. Liao, V. Cuijpers, L.J. Wilson, A.G. Mikos, J.A. Jansen: In vivo biocompatibility of ultra-short single-walled carbon nanotube/biodegradable polymer nanocomposites for bone tissue engineering, Bone **43**(2), 362–370 (2008)
26.219 P.R. Supronowicz, P.M. Ajayan, K.R. Ullmann, B.P. Arulanandam, D.W. Metzger, R. Bizios: Novel current-conducting composite substrates for exposing osteoblasts to alternating current stimulation, J. Biomed. Mater. Res. **59**(3), 499–506 (2002)
26.220 D. Khang, G.E. Park, T.J. Webster: Enhanced chondrocyte densities on carbon nanotube composites: The combined role of nanosurface roughness and electrical stimulation, J. Biomed. Mater. Res. A **86**(1), 253–260 (2008)
26.221 D. Khang, S.Y. Kim, P. Liu-Snyder, G.T. Palmore, S.M. Durbin, T.J. Webster: Enhanced fibronectin adsorption on carbon nanotube/poly(carbonate) urethane: Independent role of surface nanoroughness and associated surface energy, Biomaterials **28**(32), 4756–4768 (2007)
26.222 X. Shi, J.L. Hudson, P.P. Spicer, J.M. Tour, R. Krishnamoorti, A.G. Mikos: Injectable nanocomposites of single-walled carbon nanotubes and biodegradable polymers for bone tissue engineering, Biomacromolecules **7**(7), 2237–2242 (2006)
26.223 S.K. Misra, F. Ohashi, S.P. Valappil, J.C. Knowles, I. Roy, S.R. Silva, V. Salih, A.R. Boccaccini: Characterization of carbon nanotube (MWCNT) containing P(3HB)/bioactive glass composites for tissue engineering applications, Acta Biomater. **6**(3), 735–742 (2010)
26.224 D. Lahiri, F. Rouzaud, S. Namin, A.K. Keshri, J.J. Valdes, L. Kos, N. Tsoukias, A. Agarwal: Carbon nanotube reinforced polylactide-caprolactone copolymer: Mechanical strengthening and inter-

action with human osteoblasts in vitro, ACS Appl. Mater. Interfaces **1**(11), 2470–2476 (2009)
26.225 J. Pelto, S. Haimi, E. Puukilainen, P.G. Whitten, G.M. Spinks, M. Bahrami-Samani, M. Ritala, T. Vuorinen: Electroactivity and biocompatibility of polypyrrole-hyaluronic acid multi-walled carbon nanotube composite, J. Biomed. Mater. Res. A **93**(3), 1056–1067 (2010)
26.226 K. Balani, R. Anderson, T. Laha, M. Andara, J. Tercero, E. Crumpler, A. Agarwal: Plasma-sprayed carbon nanotube reinforced hydroxyapatite coatings and their interaction with human osteoblasts in vitro, Biomaterials **28**(4), 618–624 (2007)
26.227 B.D. Hahn, J.M. Lee, D.S. Park, J.J. Choi, J. Ryu, W.H. Yoon, B.K. Lee, D.S. Shin, H.E. Kim: Mechanical and in vitro biological performances of hydroxyapatite-carbon nanotube composite coatings deposited on ti by aerosol deposition, Acta Biomater. **5**(8), 3205–3214 (2009)
26.228 S.K. Yadav, T. Bera, P.S. Saxena, A.K. Maurya, R.S. Garbyal, R. Vajtai, P. Ramachandrarao, A. Srivastava: Mwcnts as reinforcing agent to the hap–gel nanocomposite for artificial bone grafting, J. Biomed. Mater. Res. **93**(3), 886–896 (2010)
26.229 L. Bacakova, L. Grausova, J. Vacik, A. Fraczek, S. Blazewicz, A. Kromka, M. Vanecek, V. Svorcik: Improved adhesion and growth of human osteoblast-like MG 63 cells on biomaterials modified with carbon nanoparticles, Diam. Relat. Mater. **16**(12), 2133–2140 (2007)
26.230 L. Bacakova, L. Grausova, M. Vandrovcova, J. Vacik, A. Frazcek, S. Blazewicz, A. Kromka, M. Vanecek, M. Nesladek, V. Svorcik, M. Kopecek: Carbon nanoparticles as substrates for cell adhesion and growth. In: *Nanoparticles: New Research*, ed. by S.L. Lombardi (Nova Science, Hauppauge 2008) pp. 39–107
26.231 K. Zhang, Y. Ma, L.F. Francis: Porous polymer/bioactive glass composites for soft-to-hard tissue interfaces, J. Biomed. Mater. Res. **61**(4), 551–563 (2002)
26.232 R. Orefice, A. Clark, J. West, A. Brennan, L. Hench: Processing, properties, and in vitro bioactivity of polysulfone–bioactive glass composites, J. Biomed. Mater. Res. A **80**(3), 565–580 (2007)
26.233 C. Jan, K. Grzegorz: The study of lifetime of polymer and composite bone joint screws under cyclical loads and in vitro conditions, J. Mater. Sci. Mater. Med. **16**(11), 1051–1060 (2005)
26.234 N. Aoki, T. Akasaka, F. Watari, A. Yokoyama: Carbon nanotubes as scaffolds for cell culture and effect on cellular functions, Dent. Mater. J. **26**(2), 178–185 (2007)
26.235 J. Holy, E. Perkins, X. Yu: Differentiation of pluripotent stem cells on multiwalled carbon nanotubes, Conf. Proc. IEEE Eng. Med. Biol. Soc. **2009**, 6022–6025 (2009)
26.236 M. Terada, S. Abe, T. Akasaka, M. Uo, Y. Kitagawa, F. Watari: Multiwalled carbon nanotube coating on titanium, Biomed. Mater. Eng. **19**(1), 45–52 (2009)
26.237 M. Matsuoka, T. Akasaka, T. Hashimoto, Y. Totsuka, F. Watari: Improvement in cell proliferation on silicone rubber by carbon nanotube coating, Biomed. Mater. Eng. **19**(2–3), 155–162 (2009)
26.238 X. Li, H. Gao, M. Uo, Y. Sato, T. Akasaka, Q. Feng, F. Cui, X. Liu, F. Watari: Effect of carbon nanotubes on cellular functions in vitro, J. Biomed. Mater. Res. A **91**(1), 132–139 (2009)
26.239 E. Hirata, M. Uo, H. Takita, T. Akasaka, F. Watari, A. Yokoyama: Development of a 3D collagen scaffold coated with multiwalled carbon nanotubes, J. Biomed. Mater. Res. B **90**(2), 629–634 (2009)
26.240 K.L. Elias, R.L. Price, T.J. Webster: Enhanced functions of osteoblasts on nanometer diameter carbon fibers, Biomaterials **23**(15), 3279–3287 (2002)
26.241 K. Ekstrand, J.M. Hirsch: Malignant tumors of the maxilla: Virtual planning and real-time rehabilitation with custom-made R-zygoma fixtures and carbon-graphite fiber-reinforced polymer prosthesis, Clin. Implant. Dent. Relat. Res. **10**(1), 23–29 (2008)
26.242 H. Yildiz, S.K. Ha, F.K. Chang: Composite hip prosthesis design. I. Analysis, J. Biomed. Mater. Res. **39**(1), 92–101 (1998)
26.243 H. Yildiz, F.K. Chang, S. Goodman: Composite hip prosthesis design. II. Simulation, J. Biomed. Mater. Res. **39**(1), 102–119 (1998)
26.244 K.S. Novoselov, Z. Jiang, Y. Zhang, S.V. Morozov, H.L. Stormer, U. Zeitler, J.C. Maan, G.S. Boebinger, P. Kim, A.K. Geim: Room-temperature quantum hall effect in graphene, Science **315**(5817), 1379 (2007)
26.245 E.V. Castro, K.S. Novoselov, S.V. Morozov, N.M. Peres, J.M. dos Santos, J. Nilsson, F. Guinea, A.K. Geim, A.H. Neto: Biased bilayer graphene: Semiconductor with a gap tunable by the electric field effect, Phys. Rev. Lett. **99**(21), 216802 (2007)
26.246 F. Scarpa, S. Adhikari, A. Srikantha Phani: Effective elastic mechanical properties of single layer graphene sheets, Nanotechnology **20**(6), 065709 (2009)
26.247 C.N. Rao, A.K. Sood, K.S. Subrahmanyam, A. Govindaraj: Graphene: The new two-dimensional nanomaterial, Angew. Chem. Int. Engl. Ed. **48**(42), 7752–7777 (2009)
26.248 K.S. Novoselov, D. Jiang, F. Schedin, T.J. Booth, V.V. Khotkevich, S.V. Morozov, A.K. Geim: Two-dimensional atomic crystals, Proc. Natl. Acad. Sci. USA **102**(30), 10451–10453 (2005)
26.249 K.S. Novoselov, A.K. Geim, S.V. Morozov, D. Jiang, Y. Zhang, S.V. Dubonos, I.V. Grigorieva, A.A. Firsov: Electric field effect in atomically thin carbon films, Science **306**(5696), 666–669 (2004)

26.250 W. Hu, C. Peng, W. Luo, M. Lv, X. Li, D. Li, Q. Huang, C. Fan: Graphene-based antibacterial paper, ACS Nano **4**(7), 4317–4323 (2010)
26.251 S. Park, N. Mohanty, J.W. Suk, A. Nagaraja, J. An, R.D. Piner, W. Cai, D.R. Dreyer, V. Berry, R.S. Ruoff: Biocompatible, robust free-standing paper composed of a tween/graphene composite, Adv. Mater. **22**(15), 1736–1740 (2010)
26.252 S. Agarwal, X. Zhou, F. Ye, Q. He, G.C. Chen, J. Soo, F. Boey, H. Zhang, P. Chen: Interfacing live cells with nanocarbon substrates, Langmuir **26**(4), 2244–2247 (2010)
26.253 H. Chen, M.B. Müller, K.J. Gilmore, G.G. Wallace, D. Li: Mechanically strong, electrically conductive, and biocompatible graphene paper, Adv. Mater. **20**(18), 3557–3561 (2008)
26.254 G. Eda, M. Chhowalla: Graphene-based composite thin films for electronics, Nano Lett. **9**(2), 814–818 (2009)
26.255 D.W. Wang, F. Li, J. Zhao, W. Ren, Z.G. Chen, J. Tan, Z.S. Wu, I. Gentle, G.Q. Lu, H.M. Cheng: Fabrication of graphene/polyaniline composite paper via in situ anodic electropolymerization for high-performance flexible electrode, ACS Nano **3**(7), 1745–1752 (2009)
26.256 S. Stankovich, D.A. Dikin, G.H. Dommett, K.M. Kohlhaas, E.J. Zimney, E.A. Stach, R.D. Piner, S.T. Nguyen, R.S. Ruoff: Graphene-based composite materials, Nature **442**(7100), 282–286 (2006)
26.257 B. Das, K. Eswar Prasad, U. Ramamurty, C.N. Rao: Nano-indentation studies on polymer matrix composites reinforced by few-layer graphene, Nanotechnology **20**(12), 125705 (2009)
26.258 M.A. Rafiee, J. Rafiee, Z. Wang, H. Song, Z.Z. Yu, N. Koratkar: Enhanced mechanical properties of nanocomposites at low graphene content, ACS Nano **3**(12), 3884–3890 (2009)
26.259 H. Fan, L. Wang, K. Zhao, N. Li, Z. Shi, Z. Ge, Z. Jin: Fabrication, mechanical properties, and biocompatibility of graphene-reinforced chitosan composites, Biomacromolecules **11**(9), 2345–2351 (2010)
26.260 V. Wagner, A. Dullaart, A.K. Bock, A. Zweck: The emerging nanomedicine landscape, Nat. Biotechnol. **24**(10), 1211–1217 (2006)
26.261 M. Arruebo, R. Fernández-Pacheco, M.R. Ibarra, J. Santamaría: Magnetic nanoparticles for drug delivery, Nano Today **2**(3), 22–32 (2007)
26.262 P.P. Macaroff, A.R. Simioni, Z.G.M. Lacava, E.C.D. Lima, P.C. Morais, A.C. Tedesco: Studies of cell toxicity and binding of magnetic nanoparticles with blood stream macromolecules, J. Appl. Phys. **99**(8), 08S102–08S102–3 (2006)

27. Nanofiber Biomaterials

Rachelle N. Palchesko, Yan Sun, Ling Zhang, John M. Szymanski, Quentin Jallerat, Adam W. Feinberg

Since its inception, the field of tissue engineering has sought to rebuild the complexity of normal tissues by seeding cells onto scaffolds to support the formation of new tissue. Recently, nanofibers have gained increasing attention because these biomaterials have unique properties and are able to interface with cells at the same scale as native extracellular matrix fibrils. New fabrication technologies provide novel ways to control the nanoscale structure and properties of biomaterials, which is advantageous in the engineering of tissues for in vitro study and in vivo applications in regenerative medicine. This chapter explores the properties of nanofiber biomaterials (diameters < 500 nm) and examines the specific advantages relative to other scaffold materials. This includes nanofibers from biopolymers as well as synthetic polymers, with consideration of relative advantages and disadvantages. A range of fabrication strategies is discussed that span from fiber spinning techniques, to phase separation in bulk, to directed and self-assembly. Insight is provided as to how synthetic polymers and biopolymers are used to make these nanofibers and the specific molecular structures that impart the unique mechanical, electrical, chemical, and biological properties. Analysis of these nanofiber biomaterials requires characterization techniques that are able to probe at the nanometer, micrometer, and macroscales. Examples are provided using optical microscopy, electron microscopy, scanning probe microscopy, mechanical characterization, and assessment of biocompatibility and biodegradation. Finally, nanofiber biomaterials have wide applications in tissue engineering; here we focus on representative examples in cardiac, musculoskeletal, ophthalmic, and neural tissue engineering.

27.1 **Methods of Production** 980
27.1.1 Fiber Spinning 980
27.1.2 Phase Separation 982
27.1.3 Directed and Self-Assembly 983
27.2 **Properties of Nanofiber Biomaterials** 986
27.2.1 Structure and Physical Properties 986
27.2.2 Mechanical Properties 988
27.2.3 Electrical Properties 988
27.2.4 Chemical Properties 989
27.2.5 Biological Properties and Cell Response 990
27.3 **Characterization of Nanofiber Biomaterials** 993
27.3.1 Optical Characterization 993
27.3.2 Electron Microscopy 995
27.3.3 Atomic Force Microscopy (AFM) 995
27.3.4 Mechanical Characterization 996
27.4 **Applications** 999
27.4.1 Cardiac Tissue Engineering 999
27.4.2 Skeletal Muscle Tissue Engineering 1001
27.4.3 Ophthalmic Tissue Engineering 1002
27.4.4 Neural Tissue Engineering 1004
27.5 **Conclusions and Outlook** 1005
References 1006

Nanofiber biomaterials provide a number of advantages over existing micro- and macroscale biomaterials. The small size (diameter < 500 nm) results in very high surface area such that surface properties often dominate over bulk material properties. When formed into tissue engineering scaffolds, nanofiber biomaterials possess low density and high porosity, which can facilitate cell attachment and infiltration. To leverage these and other unique properties, it is necessary to understand how cells and tissues are constructed and how nanoscale ma-

terials interact with biological systems. Every tissue in the body is composed of an extracellular matrix (ECM) consisting of biopolymer fibrils and fibers that structurally hold cells together and serve as an insoluble signaling network for biochemical and biomechanical communication. These biopolymers include ECM proteins, proteoglycans (PGs), and glycosaminoglycans (GAGs), each of which serves multiple roles in normal ECM structure and function. In fact, any tissue can be thought of as a complex network of different types of ECM nanofibers interconnected with each other and with the constituent cells (Fig. 27.1). Understanding the basic role of the ECM is necessary in order to design and utilize nanofiber biomaterials in tissue engineering and medical device applications. The focus here is on the basic structure and properties of the ECM as it relates to cell interactions with nanofibers; in-depth review articles are available on ECM proteins [27.1–6], PGs [27.7,8], and GAGs [27.9,10] as further reading. Collagens are ECM proteins that make up ≈ 25% of the protein mass in mammals, have at least 25 known isoforms, and are found in nearly all tissues. Collagen type I, with an elastic modulus of ≈ 1 GPa, is the most prevalent and is organized into fibers that are hierarchically assembled from a basic unit of three coiled polypeptide α-chains into larger and larger fibrils, fibers, and bundles with diameters from nanometers to micrometers [27.4]. Elastin is another ECM protein that is responsible for much of the elasticity of tissues such as arteries, lung, and skin [27.11, 12]. It is thought to be assembled in a random, cross-linked network and mechanically behave like an entropic spring, providing an elastic modulus of ≈ 0.1 MPa. Collagens and elastins are primarily considered structural ECM proteins, however they do have some role in biochemical interactions, and may be important in the mechanobiology of the ECM [27.13]. Adhesive ECM proteins include fibronectin and laminin, which contain binding

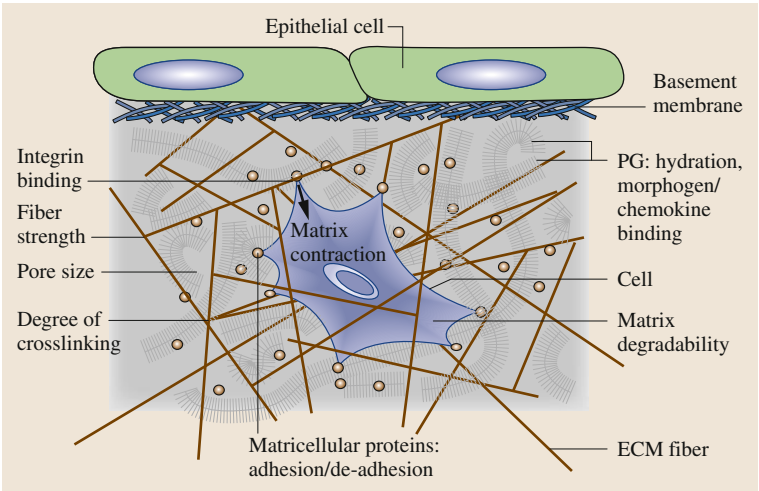


Fig. 27.1 The importance of the 3-D environment for engineering cell function. The composition, architecture, and degree of cross-linking dictate the mechanical properties of the extracellular matrix (ECM) and control how mechanical forces are transmitted to cells. Whereas collagen fibers resist tensional forces and compaction by cells, proteoglycans (PGs) control hydration, which, in turn, determines the resistance to compressive forces, and hinders protein transport by their high, fixed charge density. Basement membrane, which is secreted basally by epithelial and endothelial cells, further hinders protein transport and increases mechanical stiffness. The matrix composition also controls cell adhesion and migration, and its sensitivity to proteolytic enzymes will determine the ability of the cell to remodel the matrix and migrate through it. Other nonstructural ECM proteins are important for cell function in vivo, such as matrix proteins that support various intermediate states of cell adhesion and de-adhesion to help regulate cell migration, proliferation, apoptosis, and differentiation. Because many growth factors, chemokines, and other morphogenetic and signaling proteins are secreted in matrix-binding forms, particularly sulfated PGs, the presence of heparin sulfate in the matrix will allow better cellular control of local gradients of such molecules, which can be stored in the matrix and later released proteolytically. Perfusion of the tissue culture will promote nutrient transport and can also impart mechanical stresses on the cells, as well as alter local biochemical gradients (after [27.17])

domains for cells, other ECM proteins, growth factors, and signaling molecules as well as self-binding domains in order to form fibrils. Laminins are found in basement membranes in combination with collagen type IV to form ECM mats that underlie epithelial cells, fat, and muscle [27.14, 15]. Fibronectin is the first ECM protein assembled during embryogenesis and wound healing [27.16], and among many roles it forms a template upon which collagen fibrils are assembled [27.4]. There are also a number of other ECM proteins in various tissues, including fibrinogen, fibrin, and fibrillin. GAGs are nonprotein biopolymers consisting of unbranched polysaccharide chains, such as hyaluronan, that adsorb large amounts of water and occupy space in the ECM. PGs consist of GAGs attached to a protein core, such as decorin and aggrecan, and regulate the movement of water, cells, and molecules through the ECM. This is a very brief description of ECM proteins, PGs, and GAGs and is still only a subset of the biopolymers that make up the natural nanofibers in the ECM of tissues. It is important to realize that the chemical composition, two-dimensional (2-D) and three-dimensional (3-D) architecture, and synthesis/repair are all tightly regulated by the constituent cells and that as cells interact with nanofibers they secrete and assembly a new ECM.

Nanofiber biomaterials are engineered to mimic one, or multiple, structural and functional roles of the ECM. A large variety of synthetic and biologically derived polymers are processed into nanofibers using fiber spinning, phase separation, and directed or self-assembly techniques. Typical synthetic polymers include poly(lactic acid) (PLLA), poly(glycolic acid) (PGA), copolymers of PGA and PLLA (PGLA), poly(acrylic acid) (PAA), and poly(ε-caprolactone) (PCL). Typical biopolymers include collagen type I, fibrin, gelatin, and fibronectin. The fabrication method used depends on the specific polymers and the processing conditions necessary to achieve the final nanofiber structure. Also, the organization of the nanofibers in the context of the macroscale scaffolds varies greatly with fabrication methods; For example, electrospinning is commonly used to create biodegradable nanofibers from medical-grade polymers such as PLLA or natural polymers such as collagen type I. However, control over the architecture of the scaffold is limited, with minimal influence over the individual placement of nanofibers. Alternative techniques such as surface-initiated assembly provide submicrometer control of nanofiber placement, but are limited to a small set of ECM proteins such as fibronectin and are difficult to build into macroscale scaffolds. Thus, the choice of fabrication strategy and polymer type depends on the desired nanofiber properties for the specific application.

Biological systems that interface with nanofiber biomaterials are sensitive to a wide range of properties that must be controlled. Thus, characterizing the nano-, micro-, and macroscale properties is necessary in order to understand how molecules, cells, and tissues interact with these materials across spatial scales and dynamically over time. This requires analytical techniques that can probe at these dimensions, with nanoscale characterization being one of the more challenging aspects. The structure of nanofiber biomaterials is typically assessed using scanning electron microscopy (SEM), transmission electron microscopy (TEM), and/or atomic force microscopy (AFM), which are capable of resolving features from < 10 to > 100 nm. However, these techniques are typically not sensitive to chemical differences, requiring complementary techniques that can detect specific chemical bonds, such as Raman and infrared spectroscopy, or that can detect specific biological ligands such as fluorescently conjugated antibodies. At the micro- to macroscales, optical microscopy is an integral analytical technique, able to probe basic structure in bright field and specific biological structure/function using antibodies, transgenic fluorescent proteins, and voltage/ion-sensitive dyes. A number of advanced optical techniques such as confocal and multiphoton microscopy enable true 3-D imaging of cells and nanofibers, and a number of new superresolution techniques are able to image below the diffraction limit of light with true nanometer spatial resolution. Cells respond to the mechanical properties of their environment, making mechanical characterization an important part of determining how nanofibers will interact with biological systems. A number of techniques are used to probe the nano- and micromechanics of individual nanofibers as well as the macroscale mechanics of scaffolds, where the 3-D organization of the nanofibers is an important factor. Similarly, electrical properties are important for conductive nanofibers, which need to be analyzed at both the nanofiber and scaffold scales. These structural, chemical, mechanical, and electrical properties are all important in terms of biological interaction and determine the biocompatibility, bioactivity, and biostability/biodegradation of nanofiber biomaterials. These properties are tuned for the specific tissue engineering application, which can vary greatly depending on the tissue or organ system of interest.

Nanofiber biomaterials for tissue engineering have applications in nearly every tissue type in the body.

Presented here are representative examples where the organization of cells at the nano- and microscales relates directly to tissue function. This includes cardiac, muscle, ophthalmic, and neural tissue engineering. In each case, there are tissue-scale readouts of function that relate back to nanoscale interactions between cells and nanofibers: specifically, force generation in skeletal muscle, action potential propagation in nerve, force generation and action potential propagation in cardiac muscle, and optical transparency in cornea. Nanofiber biomaterials offer unique advantages in each of these areas, but achieving good results requires a detailed understanding of how the nanofibers interface with the biology.

27.1 Methods of Production

Nanofiber biomaterials require specialized methods that are able to fabricate structures that are truly at the nanometer scale. There are a limited number of techniques that can do this, which can be organized into three main categories:

1. Fiber spinning
2. Phase separation
3. Directed or self-assembly of polypeptides and amphiphiles.

Spinning is a standard approach to fiber production; however there are only a few techniques that can achieve nanometer dimensions. Electrospinning is the most common nanofiber fabrication method, and has been used with a wide variety of synthetic polymers and biopolymers. Not all polymers are compatible with the large electric field required for electrospinning, which has spurred the development of centrifugal force-based spinning techniques such as rotary jet spinning (RJS) and related methods. Phase separation involves the mixing of components that under the proper conditions separate into relatively pure fractions. This can be used to generate a bulk material composed of interconnected nanofibers, although it cannot be used to generate individual nanofibers as done with spinning techniques. Directed and self-assembly are done with biopolymers that naturally undergo assembly into fibrils and fibers or with engineered molecules that assemble due to their amphiphilic structure. These techniques can be used to create individual fibers and complex networks, and are the most recent development in nanofiber fabrication.

27.1.1 Fiber Spinning

Electrospinning

Electrospinning is a technique that is able to produce nanofibers out of a wide range of polymers. In this process, a polymer solution is loaded into a reservoir, where surface tension prevents it from flowing out of the tip (Fig. 27.2). A high-voltage source is connected between the tip and a metal collector, commonly a plate, but other setups are used including rotating drums. The electric potential overcomes the surface tension, and a jet of liquid is pulled toward the collector. In its most common form, a mat of randomly aligned fibers are collected, which can be used for many applications including tissue engineering.

A wide variety of polymers and copolymers have been successfully electrospun to produce fibers ranging in diameter from 3 nm up to 10 μm [27.18]; For example, *Li* et al. electrospun copolymers of gelatin and polyaniline (PANI) to form mats of 200 nm-diameter fibers [27.19], while *Riboldi* et al. electrospun much larger, 10 μm-diameter fibers of DegraPol (for skeletal muscle engineering) [27.20]. This versatility, as well as the straightforward setup and low cost, make electrospinning a popular technology to produce nanofibers. Properties can be optimized by controlling parameters such as flow rate, polymer viscosity, voltage, distance to the collector, tip and collector shape, and collector movement.

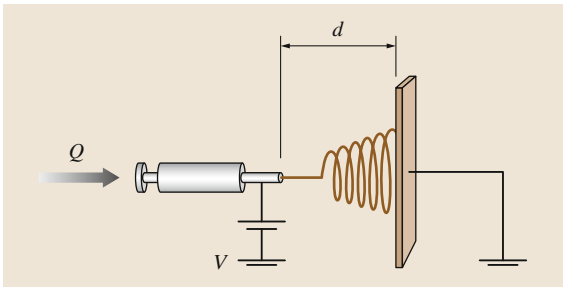


Fig. 27.2 Typical electrospinning setup: a polymer solution is spun from the syringe by high voltage and forms a mat of nanofibers on the collector. Important parameters include: V voltage, Q flow rate, and d distance between tip and collector (after [27.18])

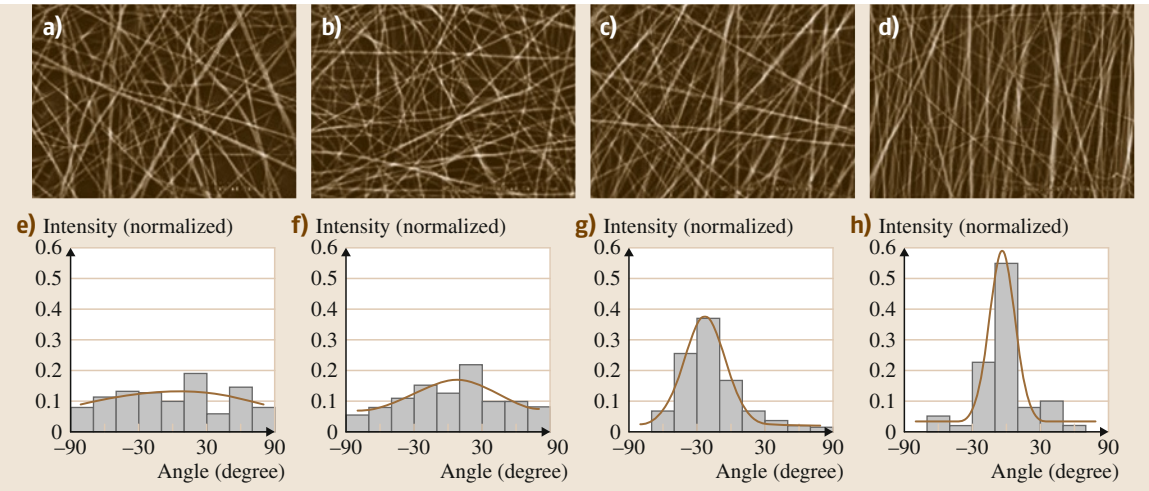


Fig. 27.3 Fiber angles for different rates of rotation: **(a–d)** SEM images of electrospun PCL/collagen nanofibers (4000× magnification) and **(e–h)** normalized histograms of fiber angle, **(a,e)** static, **(b,f)** 800 rpm, **(c,g)** 1500 rpm, and **(d,h)** 2350 rpm (after [27.21])

Scaffolds are often fabricated with a degree of anisotropy in order to align cells, for example, in nerve and muscle tissue engineering. Electrospinning using a static collector (Fig. 27.2) creates a random, isotropic architecture with nanofibers oriented in all directions (Fig. 27.3a,e). To align nanofibers, a rotating collector is used to create a degree of anisotropy; For example, *Li* et al. collected nanofibers on a rotating cylinder where a PCL solution was drawn on a 2.54 cm-diameter aluminum rod placed in the path of the polymer jet (Fig. 27.4) [27.21]. Increasing the speed of the rotating cylinder onto which the fibers are deposited increases alignment. *Choi* et al. produced PCL-collagen nanofiber meshes with progressive increases in fiber alignment by increasing the rotation rate of the cylindrical collector (Fig. 27.3) [27.22]. Their results also demonstrated that the rotation speed did not affect the nanofiber diameter. Other collectors, such as rotating drums, can also be used to align nanofibers [27.23]. Anisotropy can also be achieved by modifying electrospun scaffolds after spinning [27.24, 25]; For example, *Huang* et al. uniaxially stretched electrospun PLLA scaffolds 200% at 60 °C to obtain alignment of nanofibers [27.24].

Thermal, electrical, and mechanical properties of the fibers can also be modified by changing the parameters of the electrospinning process. Some examples are discussed in Sect. 27.4 for different applications in tissue engineering.

While electrospinning is widely used to produce nanofibers, there are two main drawbacks: (i) the high-voltage electric field to create the polymer jet, and (ii) the need for the polymers to be dissolved in a dielectric solution [27.26, 27]. The high electric fields can degrade certain polymers and cause interference between the nozzles in multinozzle systems. It is also difficult to

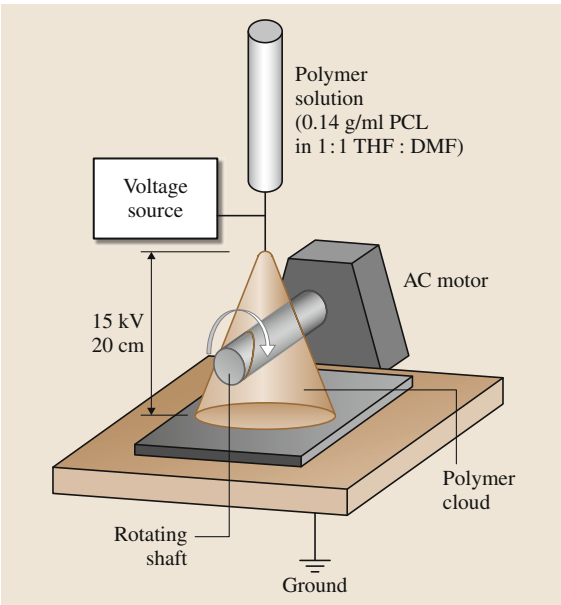


Fig. 27.4 Schematic of electrospinning device used to generate fiber-aligned scaffolds on a rotating shaft (THF: tetrahydrofuran, DMF: dimethylformamide) (after [27.21])

Table 27.1 Comparison of nanofiber techniques that can be used to synthesize tissue-engineered implants (after [27.27])

Fabrication technique	Advantages	Disadvantages
Temperature-induced phase separation	• Simple equipment • Convenient fabrication process • Mechanical properties of the fiber matrices can be varied by changing polymer compositions	• Discontinous process • Not scalable • No control on fiber dimensions
Molecular self-assembly	• Only smaller nanofibers of a few nanometers in diameter and few micrometers in length can be fabricated • Complex functional structures	• Complex process involving intermolecular forces • Not scalable • Weak nanofiber strength
Electrospinning	• Simple instrument • Continuous process • Cost effective compared with other existing methods • Scalable • Ability to fabricate fibers with diameter from a few nanometers to several micrometers	• Jet instability • Toxic solvents • Packaging, shipping, and handling

maintain a constant jet of polymer due to the need for frequent nozzle cleaning, the lack of uniformity in the feed rate, and the lack of consistent solution viscosity due to evaporation of the often toxic solvents [27.27]. Table 27.1 presents a few of the advantages and disadvantages of electrospinning versus the other nanofiber fabrication methods discussed below.

Rotary Jet Spinning

Two recently developed nanofiber fabrication techniques that are very closely related are rotary jet spinning (RJS) and ForceSpinning. RJS was developed in the Parker laboratory at Harvard University, and ForceSpinning was developed in the Lozano and Sarker laboratories at the University of Texas-Pan American. In these techniques, a high-speed rotating nozzle and centrifugal force are used to form a stream of polymer that is deposited onto a stationary collector [27.26, 28]. A schematic diagram of the RJS system is shown in Fig. 27.5. Briefly, a reservoir with two orifices is attached to a high-speed motor, and polymer in the reservoir is propelled by the rotation onto a stationary collector. Once the solvent evaporates the polymer solidifies into a fiber, with nanometer to micrometer diameters readily achievable. The morphology, diameter, and porosity of the resulting nanofibers and scaffold can be controlled through nozzle geometry, motor rotation speed, temperature, and the type of polymer solution; For example, using more volatile solvents and/or a slower rotational speed will result in fibers with larger diameter. RJS has been successfully used to form nanofibers with natural and synthetic polymers including PAA and gelatin [27.26]. The resulting fibrous scaffolds are three-dimensional, and the nanofibers are well aligned. ForceSpinning is commercially available from FibeRio Technology Corporation and has been used to form nanofibers of poly-ethylene oxide, PLA, polypropylene, acrylonitrile butadiene styrene, polyvinyl pyrrolidone, and polystyrene [27.28]. ForceSpinning and RJS have advantages over electrospinning in that a high electric field and dielectric solution are not needed, expanding the types of materials from which nanofibers can be produced.

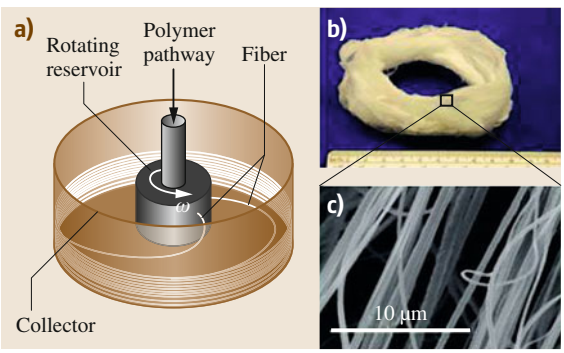


Fig. 27.5 **(a)** A diagram of the rotary jet spinner. **(b)** The resulting *spun* nanofibers. **(c)** The nanofibers viewed at 10 μm scale (after [27.26])

27.1.2 Phase Separation

Phase separation is a well-established method for creating porous polymer membranes or scaffolds by separating a polymer solution into two phases, typically a polymer-poor phase and a polymer-rich phase [27.29]; For example, *Ma* and *Zhang* first utilized phase separation to create a nanofibrous scaffold from

PLLA [27.30]. PLLA was dissolved in tetrahydrofuran (THF) and quenched to a lower temperature to allow gelation (phase separation) for a few hours. The THF was exchanged by water, and the scaffold was freeze-dried. This process led to a nanofibrous scaffold with porosity of 98.5% and fiber diameter ranging from 50 to 500 nm, which is similar to the range of natural collagen fibers. Fiber diameter was controlled by the gelling temperature, with high temperature resulting in only macroscale fibers. Below the nanofiber forming temperature, fiber diameter will not be affected by gelling temperature, while the scaffold architecture will be affected (i. e., the interfiber spacing becomes more uniform) (Fig. 27.6). Similarly, polymer concentration does not change the fiber diameter but affects the architecture of the scaffold, with higher concentration resulting in a more uniform fibrous structure. The type of solvent used determines the gelling temperature of the polymer solution. The *Ma* group has produced a scaffold with 3-D macrostructure by building a structured porogen (sugar or salt) into the scaffold solution before phase separation to further facilitate cell migration into the scaffold, mass transport of nutrient in and out of the scaffold, and tissue organization [27.31]. More recently, this phase separation has been applied to other polymers such as poly-hydroxyalkanoate, PCL, PLGA, chitosan, and gelatin [27.32–35].

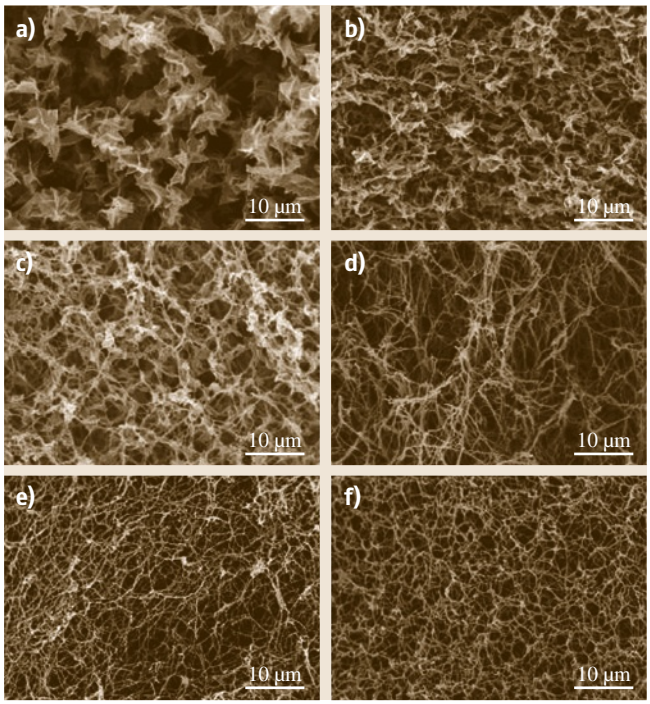


Fig. 27.6a–f SEM micrographs of PLLA matrices prepared from 5.0% (wt/v) PLLA/THF solution at different gelation temperatures: **(a)** 23 °C, 2000× magnification; **(b)** 19 °C, 2000× magnification; **(c)** 17 °C, 2000×; **(d)** 15 °C, 2000× magnification; **(e)** −18 °C, 2000× magnification; **(f)** liquid nitrogen, 2000× (after [27.30])

27.1.3 Directed and Self-Assembly

Directed Assembly – Surface-Initiated Assembly

Surface-initiated assembly is a directed assembly technique that mimics the way cells build ECM proteins into fibers. In vivo, the assembly of ECM protein fibers relies on the use of cell-derived mechanical forces to unfold protein subunits and expose their cryptic self-binding domains [27.36]. Mimicking this process in vitro has proven to be difficult, typically requiring denaturants or reducing agents to chemically denature proteins and expose their cryptic self-binding domains [27.37]. This results in a matrix of protein fibers that has no structural organization. Improved organizational control has been demonstrated by drawing fibrils out of a concentrated protein droplet, but this method is limited to creating planar geometries of fibers permanently bound to the substrate [27.38]. It is also necessary to point out that these fibers have diameters of the order of micrometers, well above the diameters of cell-derived fibers, which are of the order of nanometers.

Surface-initiated assembly is able to overcome the deficiencies of the prior methods to create free-standing protein fibers that are < 10 nm thick. This process utilizes protein–surface interactions instead of denaturants or force to form nanofibers (Fig. 27.7a). Briefly, ECM proteins are first adsorbed onto a patterned, hydrophobic poly(dimethylsiloxane) (PDMS) surface, causing them to partially unfold into an extended conformation. The unfolded proteins are then transferred to a thermally responsive poly(*N*-isopropylacrylamide) (PIPAAm) surface through microcontact printing. Subsequent hydration and reduction of temperature triggers the expansion followed by the dissolution of PIPAAm, resulting in the formation and nondestructive release of the protein nanofibers [27.39]. This technique has been demonstrated for a number of fiber-forming ECM proteins including fibronectin, laminin, collagen type I, collagen type IV, and fibrinogen (Fig. 27.7b–p). Microcontact printing is a soft lithography technique that enables the microscale patterning and formation of protein matrices in a variety

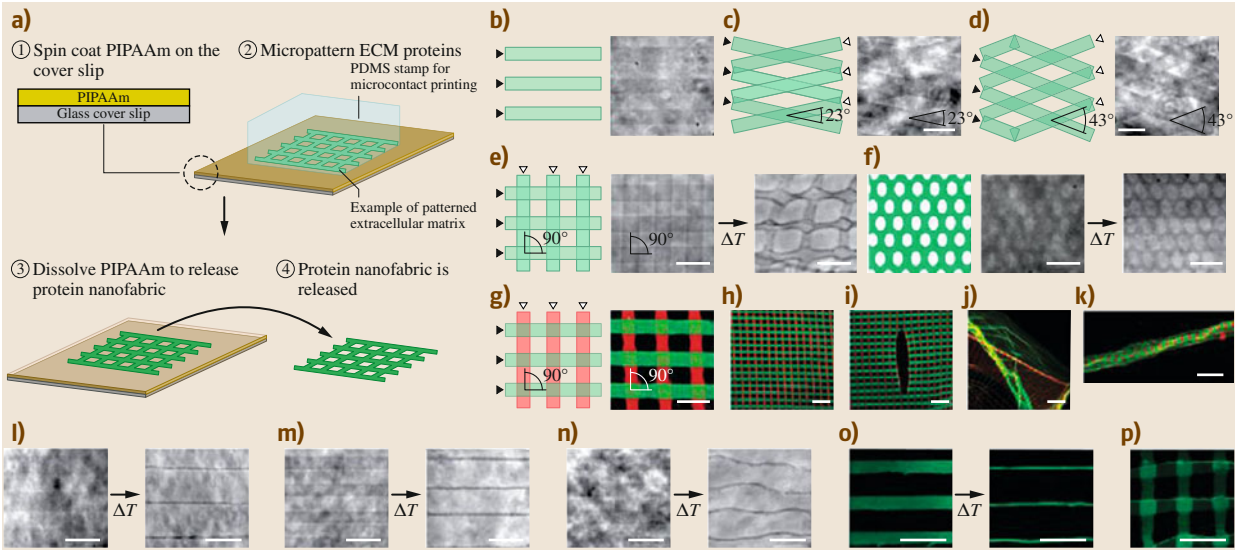


Fig. 27.7a–p Fabrication of protein nanofabrics and example architectures and compositions. **(a)** Schematic of the nanofabric fabrication process. **(b)** Schematic and example optical phase image of 20×20 fibronectin (FN) lines microcontact printed (μCP) onto PIPAAm. **(c–e)** The 20×20 FN lines were serially microcontact printed onto PIPAAm at angles of 23, 43, and 90° (**(c–e)**, respectively). **(e)** The 20×20 FN lines, crossed at 90°, maintain the patterned microstructure following thermal release. **(f)** A single stamping may have a more complex structure than lines, as demonstrated by this *fishnet* pattern with ≈ 20 μm-wide elliptical holes. **(g)** The 20×20 lines of laminin (LAM) (*red*, *vertical lines*) and FN (*green*, *horizontal lines*) were serially printed onto PIPAAm, demonstrating that an integrated protein nanofabric can consist of multiple ECM proteins. **(h)** The bicomponent FN and LAM nanofabric maintains its microstructure upon thermal release, **(i)** can support small tears without failing, **(j)** can be formed as continuous protein films, or **(k)** can be rolled into fibers. **(l)** The 20×20 LAM lines μCP onto PIPAAm and after thermal release. **(m)** The 15×15 fibrinogen (FIB) lines μCP onto PIPAAm and after thermal release. **(n)** The 15×15 collagen IV (COLIV) lines μCP onto PIPAAm and after thermal release. **(o)** The 20×20 collagen I (COLI) lines μP onto PIPAAm and after thermal release. **(p)** The 20×20 COLI lines crossed at 90° and μCP onto PIPAAm. *Scale bars* are 40 μm for **(b–g)** and **(l–p)** and 100 μm for **(h–k)** (after [27.4]) ▲

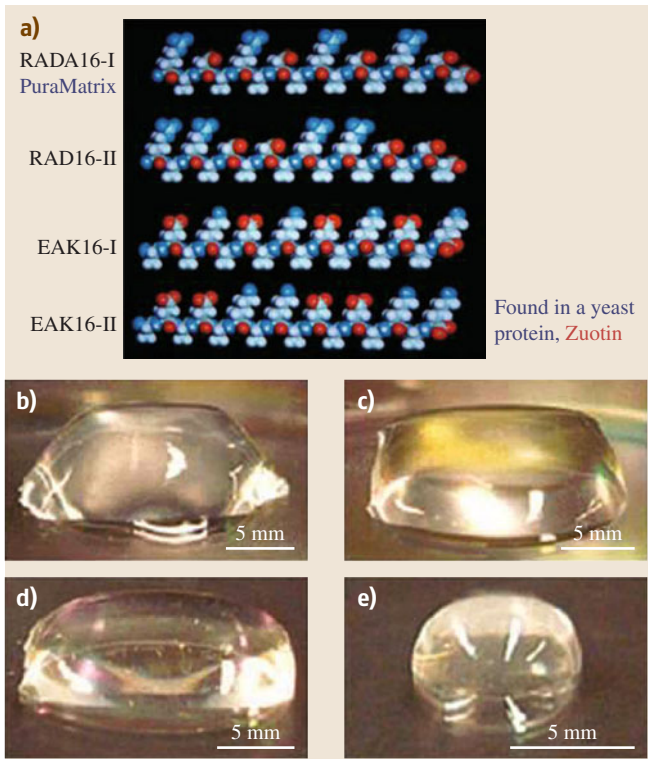


Fig. 27.8 **(a)** Models of amphiphilic self-assembling peptides that form well-ordered nanofibers. **(b–e)** Hydrogels formed from the RADA16-I peptide at various conditions. **(b)** 0.5 wt % (pH 7.5), **(c)** 0.1 wt %, (Tris-HCl pH 7.5), **(d)** 0.1 wt % (pH 7.5, PBS (phosphate buffered saline)) before sonication, **(e)** reassembled RADA16-I hydrogel after sonication four times (after [27.40])

of geometries and compositions. However, surface-initiated assembly is limited to ECM proteins that have self-binding domains in order to undergo fibrillogenesis.

Self-Assembly

Self-assembling nanofibers are molecular systems engineered to spontaneously undergo organization into nanofibers under specific conditions. The first self-assembling peptide (sapeptide), EAK16, was discovered in the Rich laboratory at MIT while researcher's were investing yeast genetics and Z-DNA [27.40, 42]. It was found to spontaneously assemble in an aqueous environment, first into nanofibers and then further into a hydrogel-like scaffold [27.40,43]. The three main factors that drive self-assembly for these peptides are the hydrophobic interaction, ionic interactions, and peptide backbone hydrogen bonds [27.40]. These peptides are ionic and self-complementary because both the positive and negative sides-chains are located on one side of the β-sheet and the hydrophobic side-chains are on the other, resulting in one hydrophobic and one hydrophilic side [27.40, 41]. The hydrophobic sides interact with one another and form double sheets inside the nanofiber, while the outside ionic/hydrophilic side interacts with the water to form a high-water-content hydrogel with around 99.5–99.9% water content [27.40] (Fig. 27.8).

The properties of all self-assembled peptide nanofibers are dependent upon the amino acid sequence chosen, the stereochemistry of the peptide, the molecular size, and the environmental conditions during and after formation of the nanofibers.

There are three different types of peptides that self-assemble into β-sheet nanofibers (Fig. 27.9). Type I, e.g., EAK16, are peptides with alternating hydrophobic and polar amino acids that self-assemble in the presence of Li^+ and Na^+ ions [27.41]. Type II are peptide amphiphiles, which have a hydrophobic alkyl tail coupled to a peptide block with β-sheet-forming segments and charged residues [27.41, 44–50]. The driving force behind peptide amphiphile nanofiber self-assembly is the tendency of the alkyl chains to aggregate together in water, with the main stabilizing forces being hydrogen bonding and hydrophobic and electrostatic interactions [27.41,51]. Peptide amphiphile self-assembly can be triggered by changing the pH or ion concentration in solution and results in well-defined fibers that are micrometers in length and usually about 5–10 nm in diameter [27.41]. The final type is type III, the peptidomimetics, which are amphiphilic oligopeptides combined with synthetic compounds, such as the dibenzofuran peptidomimetic [27.41, 52]. Peptidomimetics first self-assemble into quaternal structures, which (mediated by hydrophobic interactions) dimerize face to face [27.41]. These dimers then further elongate to form filaments that then interact to form ribbons or fibrils [27.41].

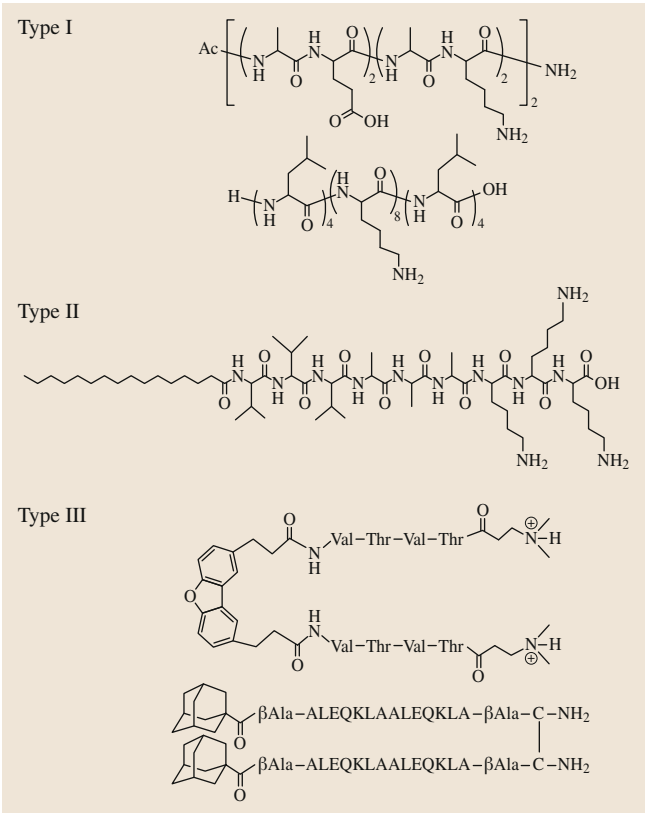


Fig. 27.9 Chemical structures of various types of artificial peptides and peptidomimetics (type I–III) that assemble into β-sheet-based nanofibers (after [27.41])

Self-assembly is usually spontaneous, but it can be tuned with *switches* that respond to light or enzymatic reactions; For example, a polyethylene glycol (PEG) sequence can be added to the end of the peptide sequence so that, as the polymer is digested using thrombin, the peptides are released and can interact with one another and begin to self-assemble [27.41]. The formation of self-assembled nanofibers and scaffolds can be dynamic, such that when the structure is disrupted, the fibers can spontaneously reassemble. This was shown by sonication of self-assembled nanofibers and analysis of the reformation of the nanofibers by AFM [27.40].

Although β-sheet-forming self-assembling nanofibers are the most common, there are a few reports on α-helix-forming self-assembling peptides. These structures are modeled after the collagens and keratins. One example is the switch from α-helix to β-sheet and

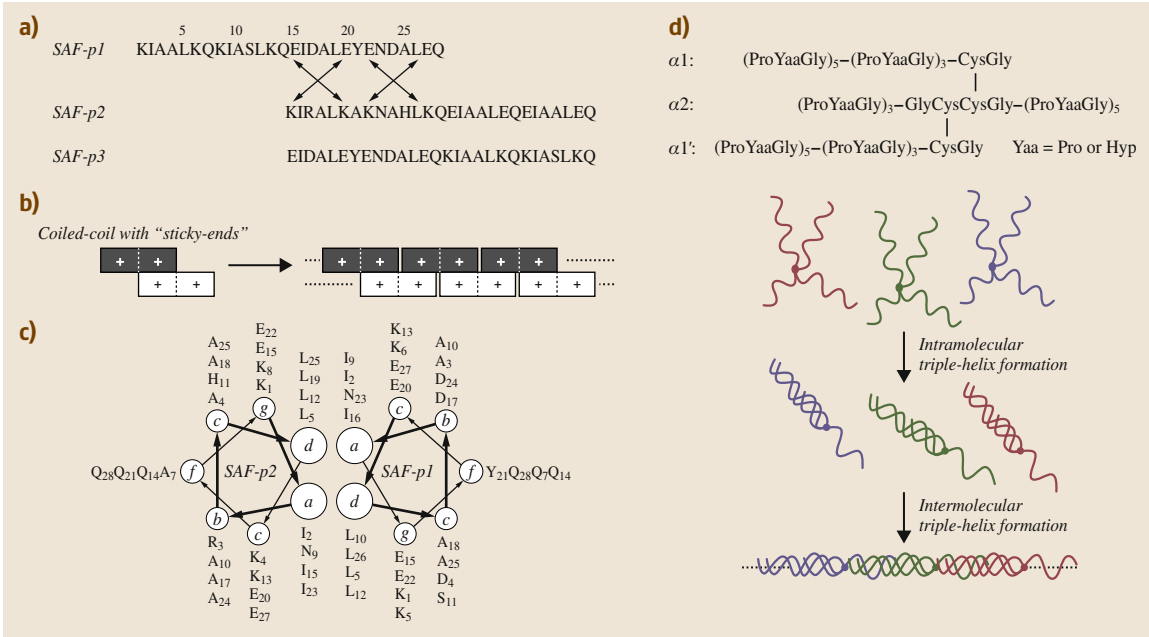


Fig. 27.10a–d Coiled-coil-based self-assembling peptide system designed by Woolfsen's group. **(a)** Amino acid sequences of self-assembling fiber peptides. **(b)** Concept for sticky-end assembly process. **(c)** Helical wheel representation of coiled-coil conformation. **(d)** Molecular structures of multibranched self-assembling collagen models and representation of the self-assembly process of the collagen models through triple helix formation (after [27.41])

vice versa of the LKL16 peptides, which can be controlled with pH [27.41]. Most commonly they feature the sequence *abcdefg* repeated, with *a* and *d* being hydrophobic residues and the rest being polar. The hydrophobic interaction between *a* and *d*, as with the β-sheet-forming peptides, stabilizes a core, but in this case the rest of the residues create a side-by-side packing of two α-helices, which the *e* and *g* residues stabilize (Fig. 27.10) [27.41]. These types of nanofibers can also be formed using collagen mimetics with *sticky ends*.

The properties of nanofibers made by self-assembly are determined by the environmental conditions, which is a limitation of this approach. The nanofibers are sensitive to changes in environment including pH, electrolyte addition, and electrostatic interactions [27.51]. The formation of self-assembled peptide nanofibers requires careful design of the starting peptide or peptide amphiphile, which is also important to tune properties for a given tissue engineering application.

27.2 Properties of Nanofiber Biomaterials

27.2.1 Structure and Physical Properties

Understanding the structural and physical properties of nanofibers is critically important because these factors influence how biomolecules and cells interact with the nanofibers. For tissue engineering, either single nanofibers or multiple nanofibers integrated into a scaffold should mimic some aspect of the natural ECM environment of the tissue. From a structural standpoint, the important properties include fiber diameter, spacing, orientation, entanglement, and interconnectedness.

Common Properties of Nanofiber Biomaterials

Regardless of the manufacturing technique applied, nanofiber biomaterials share a range of structural and physical properties due to the small size of the materials. The nanofibers considered here have diameters < 500 nm, making them distinct in size from microscale

and larger fibers. Relative to the diameter, nanofibers are typically quite long, from tens of micrometers up to centimeters or even meters in length. This high surface area means that surface properties can dominate over bulk properties, which become quite important in terms of chemical and biological properties. The small size also results in mechanically weak fibers that fail under very low stresses. However, when integrated into scaffolds the mechanical properties can be on par with solid bulk materials.

Fabrication-Dependent Properties of Nanofiber Biomaterials

While these nanofibers share many similar characteristics, there are structural differences that depend on the fabrication conditions and polymers used; For example, self-assembled peptide nanofibers are unique in that the hydrophobic interactions, electrostatic interactions, and hydrogen bonding drive the assembly of the amphiphilic peptides. The overarching structure of self-assembled peptide nanofibers is predominantly β-sheet, with similar structure to silk fibroin from silkworms or spiders with similar nanostructures to Matrigel [27.42]; however, there are some cases in which self-assembled peptide nanofibers are used to model collagen or keratin. In this case, the nanofibers have mostly α-helix structural character [27.41]. When formed into scaffolds, self-assembled peptide nanofibers have extremely high water content, above 99.5%, which is favorable for some tissue engineering applications. Ultimately, the most important determinants of the final structure of self-assembled peptide nanofibers are their specific amino acid sequence and the environmental conditions.

Directed self-assembly, in the form of surface-initiated assembly, is capable of producing protein nanofiber matrices in a variety of planar geometries. The scope of the geometries possible is limited by the soft lithography techniques used to pattern the PDMS substrates involved in the fabrication of the nanofibers [27.39].

Electrospinning enables the formation of nanofibers using either synthetic materials such as PLGA [27.55] and PCL [27.56] or natural ones such as collagen [27.57] and chitosan [27.58]. Altering the structure of scaffolds to include multiple types of nanofibers enables one to capitalize on the favorable qualities of each type of nanofiber. This is illustrated in the case of using electrospun scaffolds consisting of PANI and gelatin nanofibers [27.19]. PANI nanofibers are electrically conducting, whereas gelatin nanofibers provide biocompatibility and promote cell adhesion. Together,

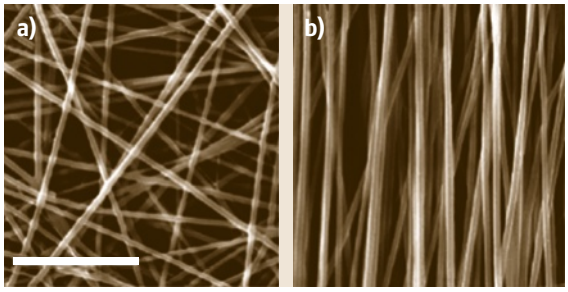


Fig. 27.11a,b Using electrospinning methods to create matrices of randomly oriented **(a)** or highly aligned nanofibers **(b)**. *Scale bar* is 10 μm (after [27.53])

they create a tissue-engineered scaffold capable of providing electrical stimulation to promote the desired cell response. In addition to forming random, porous networks of nanofibers, it is also possible to control the orientation of these fibrous matrices to promote a favorable cell response (Fig. 27.11). Although there is limited control over the exact size of the nanofibers and the uniformity of the pores, in both size and shape, electrospinning allows users to finely tune the composition and the general orientation of the nanofiber scaffolds.

Phase separation techniques have been used to create nanofibrous scaffolds that are extremely porous, in excess of 98%. From a physical standpoint, scaffolds containing such high percent porosity resemble more a nanofibrous foam than a scaffold [27.30]. This is evidenced by comparing the structure of scaffolds using phase separation (Fig. 27.12) with scaffolds fabricated from electrospinning (Figs. 27.10, 27.11). Similar to the previous methods, the structure and morphology of these scaffolds are dependent on the fabrication conditions such as the solvent used, type of polymer, and the polymer concentration. Phase separation methods easily enable the formation of complex three-dimensional scaffolds. Phase separation is a mold-based process; therefore, fabrication of the appropriate mold is the only

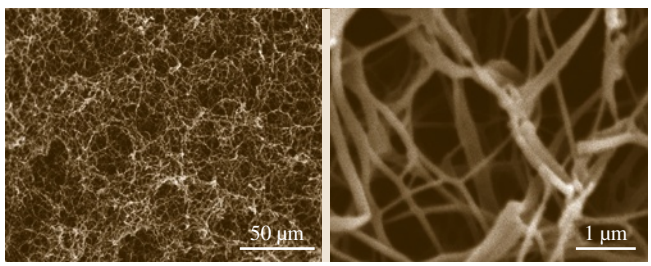


Fig. 27.12 Scanning electron micrographs of a PLLA fibrous matrix formed through phase separation methods (after [27.54])

limitation to the architecture of scaffolds formed using this method [27.54].

All of these methods are used to create nanofibers or nanofibrous networks/scaffolds that try to mimic the structural properties of the natural extracellular environment to promote cell adhesion, proliferation, and differentiation into desired tissues. However, obtaining the appropriate cell response is more complicated than simply recapitulating the diameter of fibers in the native ECM. There needs to be a distinct balance between the structural, mechanical, and biological properties of nanofiber matrices.

27.2.2 Mechanical Properties

Cells can sense and respond to their mechanical environment, affecting tissue form and function, which makes the mechanical properties of an engineered scaffold extremely important. The mechanical properties of nanofibers vary greatly depending on the starting polymers and the fabrication method used. Further, the mechanical properties of nanofiber scaffolds at the macroscale depend on the diameter, porosity, and physical arrangement of the fibers. The strength of a nanofiber scaffolds needs to be sufficient to withstand handling of the scaffold for transplantation purposes as well as to support the ingrowth of cells and tissue. It is also important to match the mechanical properties of the surrounding tissue to minimize mechanical mismatch and maximize host integration.

The mechanical properties of self-assembled peptide nanofibers are dependent on the hydrophobic interactions that occur between the peptide residues present at the core of the nanofiber. This makes the specific peptide sequence a primary factor in determining the resulting mechanical properties [27.40]. More efficient nanofiber formation and better mechanical properties result when more hydrophobic residues are present in the peptide sequence [27.40]. The mechanical properties of the macroscale scaffolds are determined by the interfiber interactions and the mechanical properties of the individual self-assembled nanofibers [27.51]. Although the peptide sequence can be controlled, it is difficult to control the pore size and shape inside of the macroscale scaffolds formed through self-assembly. This results in poor direct control of mechanical properties [27.43]. It is also difficult to predict the mechanical properties of the resulting scaffolds, because there is not a direct correlation between the starting concentration of peptide and the resulting mechanical properties, as there usually is with polymeric materials [27.51]. Due to the aqueous formation of the nanofibers and high water content of the scaffolds, both have an inherent lack of mechanical strength and cannot be used in structural tissues [27.43].

Electrospinning is a method capable of producing nanofiber scaffolds with a wide range of mechanical properties. This makes it an attractive fabrication method for a wide variety of tissue engineering applications. One way of controlling the mechanical properties, specifically the tensile strength, is use of appropriate starting materials; For example, electrospun nanofiber poly(3-hydroxybutyrate-*co*-3-hydroxyvalerate) matrices were found to have a Young's modulus of about 350 MPa [27.59], whereas PLGA and chitosan nanofibrous matrices were observed to have a Young's modulus of 2.5 and 40 MPa, respectively [27.60]. Controlling the alignment of the nanofibers within the scaffold is another method to optimize the mechanical properties. In the case of composite nanofiber scaffolds consisting of chitosan and PCL nanofibers, the tensile strength in scaffolds with randomly oriented fibers was 3.53 MPa whereas it was 13.21 MPa when the fibers were uniaxially aligned [27.61].

There are similar variables controlling the mechanical properties of nanofibers formed by phase separation. Like electrospinning, the orientation of the fibers is critical to the overall mechanical properties of the scaffold; For example, it was found that the compressive modulus is about 3 times higher if the load is parallel to the fibers ($\approx$ 9.5 MPa) than if the load is acting on randomly oriented fibers ($\approx$ 3 MPa) [27.43]. The polymers used and also the starting concentrations of the polymers have large effects on the mechanical properties; For example, for nanofiber PLLA scaffolds, if the starting polymer concentration is less than 1%, the Young's modulus is $\approx$ 1 kPa, whereas when the PLLA concentration is around 10%, the Young's modulus is $\approx$ 20 MPa. A similar trend was observed for the tensile strength, which is likely due to the increase in the fiber network density [27.30]. Phase separation techniques can therefore allow the creation of nanofibrous constructs with tunable mechanical properties.

27.2.3 Electrical Properties

The electrical properties of scaffolds are important in nerve and muscle tissue engineering, where propagation of an action potential is integral to the function of the tissue or organ. For nanofiber biomaterials, the materials used must be conductive and the processing of the material must preserve this conductivity or enhance

it. Nanofibers may be composed of either a conducting polymer with a conjugated backbone and/or doped with conductive nanoparticles such as gold or carbon nanotubes. The diameter of nanofibers means that the resistance of a single fiber may be high, but scaffolds can contain large numbers of fibers, which can mitigate this problem. In typical biological applications, the range of voltages will span from $> 10\,\mathrm{mV}$ to $< 10\,\mathrm{V}$.

Electroactive polymers such as polyacetylene, polypyrrole (PPY), polythiophene, and PANI, first developed for applications in applied physics and chemistry, are now widely investigated for tissue engineering. These polymers are often used in conjunction with another more biocompatible polymer to ensure good cell viability and function. Additionally, conductive nanostructured materials such as carbon nanotubes are used as additives to enhance the conductivity of both electroactive and nonconductive polymers; For example, *Stout* et al. added carbon nanofibers to electrospun PLGA meshes which showed good compatibility and raised the conductivity from $0\,\mathrm{S/m}$ for 100% PLGA to $\approx 0.001\,\mathrm{S/m}$ after adding 50% carbon nanofibers [27.63]. Conductive and nonconductive polymers can also be combined, as shown by *Lee* et al. in their study on PPY-coated PLGA nanofibers. It was found that the surface resistance was dependent on the fiber orientation, decreasing from $1.7 \pm 0.6 \times 10^4\,\Omega/\square$ for randomly aligned nanofibers to $17.4 \pm 3.2 \times 10^3\,\Omega/\square$ along the length of uniaxially aligned nanofibers [27.64].

27.2.4 Chemical Properties

The chemical and biochemical properties of nanofiber biomaterials are dependent on the natural and synthetic polymers and the fiber fabrication method used. Because of the high surface area to volume ratio, the surface chemistry of the nanofiber dominates the chemical properties. To work in a biological environment, the material chemistry must not be cytotoxic or mutagenic or otherwise damage cells. All the polymeric biomaterials discussed in this article fall into this category.

Nanofiber biomaterials interact with cells, but it is actually the surface interaction with biomolecules that are of utmost importance. Proteins and other biomolecules attach to the surface via nonspecific interactions (e.g., hydrophobic, hydrophilic, ionic, hydrogen bonding) or specific interactions (e.g., receptor–ligand bonding, covalent bonding). Controlling the first biomolecules that attach to a nanofiber surface is a key factor in controlling the subsequent attachment of other biomolecules and cells. There are a number of ways to do this by controlling the chemistry of the polymers used, applying surface treatments to the nanofibers, and/or incorporating biomolecules into the nanofibers.

Biomolecules such as proteins, DNA, viruses, and small molecules (such as pharmaceuticals) have been incorporated into or used to modify the surface of nanofibers by a number of techniques (Fig. 27.13). Direct incorporation has been achieved by solution blending during electrospinning and core–shell electrospinning techniques. Surface modification has been achieved through adsorption or covalent attachment using solu-

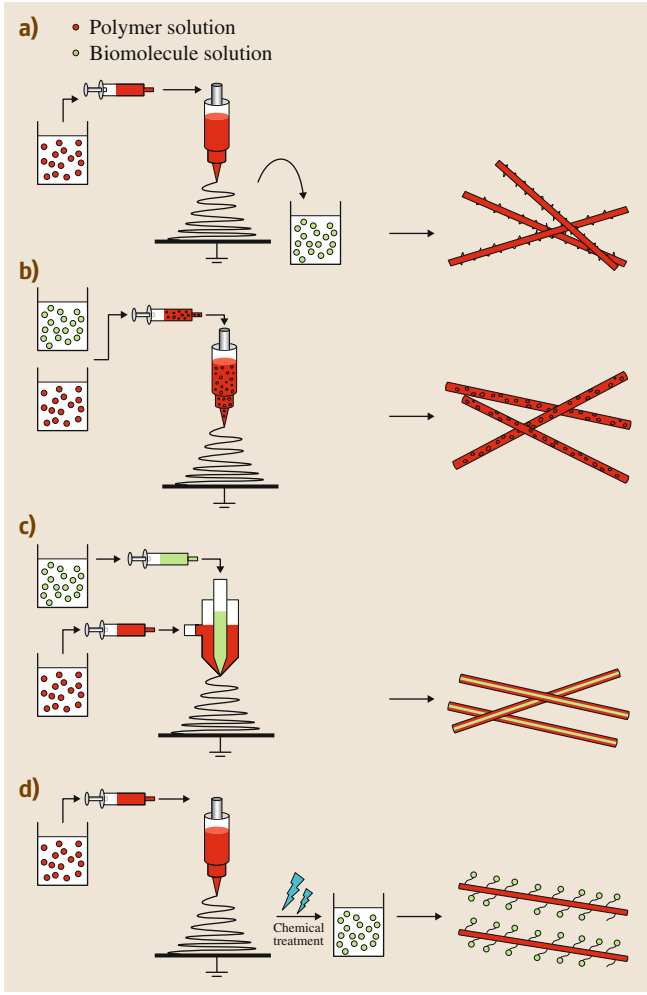


Fig. 27.13a–d Fabrication techniques for bioactive electrospun scaffolds. **(a)** Physical adsorption, **(b)** blend electrospinning, **(c)** coaxial electrospinning, **(d)** covalent immobilization (after [27.62])

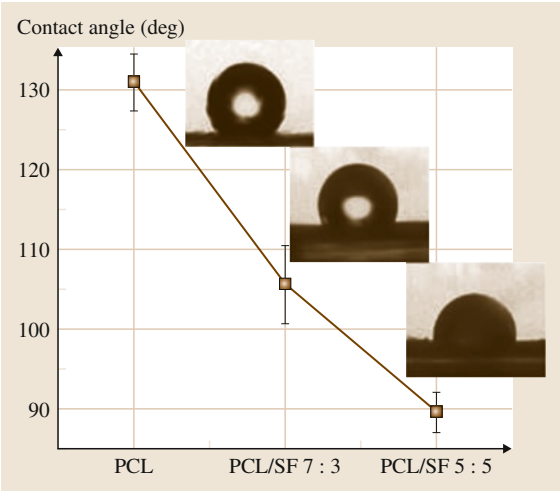


Fig. 27.14 Water contact angle of PCL/SF nanofibrous scaffolds. *Inset figures* show the variation in the contact angle shape on different scaffolds. Data are mean ± standard deviation (SD) ($n = 6$) (after [27.65])

tion deposition methods and plasma treatment [27.23, 62]. A common approach is the attachment of ECM proteins such as collagen, fibronectin or laminin to the surface of synthetic polymer nanofibers to enhance cell attachment. However, nanofibers composed of biopolymers, such as collagen, have intrinsic bioactivity and can bind cells directly or can be further modified. The chemical properties of the polymers used and the desired, final surface biochemistry will dictate the processing and any chemical modifications that need to be made.

The biochemical properties of self-assembling peptide nanofibers are dependent on the molecular structure of the polypeptides. This includes the amino acid sequence, the stereochemistry of the amino acids, and the molecular size of the polypeptide [27.41]. Further, the environmental conditions to which the nanofibers are exposed are important because they influence how the polypeptides interact with each other. Because of the protein content, these nanofibers are typically hydrophilic with specific hydrophobic amino acid residues that can associate in aqueous environments. Thus, self-assembled peptide nanofibers are extremely stable in water and typically remain stable at high temperatures, across a wide pH range and in high concentrations of urea and guanidine hydrochloride [27.40].

Many synthetic polymer nanofibers are hydrophobic and need to be modified in order to control protein attachment and/or increase hydrophilicity; For example, PCL nanofibers electrospun into a mat are very hydrophobic. *Li* et al. developed PCL–silk fibroin (SF) core–sheath nanofibers and found that increasing the ratio of silk fibroin to PCL increased hydrophilicity (as seen in Fig. 27.14) [27.65]. Pure PCL nanofibers have a very high water contact angle, whereas the PCL/SF 5 : 5 nanofibers have a much lower contact angle, yet the nanofibers are still hydrophobic relative to most materials. For comparison, the water contact angle of electrospun chitosan-graft-PCL/PCL nanofibers (CS-PCL/PCL) with as little as 20% CS-PCL decreases to $\approx 0°$, completely wetting the material [27.66]. Other polymers such as pure PLLA have contact angles ($\approx 73°$) in between that of PCL and self-assembling peptide nanofibers [27.67]. Blending PLLA with poly(aniline-*co*-3-aminobenzoic acid), increases the water contact angle as the ratio of PLLA decreases [27.67]. These experiments demonstrate that the surface chemistry of the nanofibers can be modified by combining synthetic polymers with natural biopolymers.

The chemical properties of nanofiber biomaterials are also dependent on the environment in which they are used; For example, *p*-carboxyphenoxy propane/sebacic acid nanofibers incubated at 37 °C in phosphate-buffered saline caused a drop in the pH of the solution from ≈ 7.4 to ≈ 6.7 [27.68]. This indicates that degradation of the nanofibers resulted in increased acid concentration of the solution, but also a possible decrease in the acid concentration at the nanofiber surface. Thus, the chemical composition and surface properties of nanofiber biomaterials may be environment dependent and change dynamically over time.

27.2.5 Biological Properties and Cell Response

The biological properties and cell response to nanofibers and nanofiber scaffolds is a primary issue for tissue engineering applications. The biological properties are closely related to the chemical properties, as many of the proteins and other biomolecules on the surface of nanofibers have specific biological functionality. An optimal scaffold should promote cell migration into the scaffold, cell adhesion to the nanofibers, and cell proliferation. Both synthetic and natural polymer nanofibers are considered biocompatible and used for tissue engineering applications. In this context, biocompatible means that the materials are not cytotoxic or mutagenic, nor are there any other abnormal metabolic responses; For example, synthetic nanofibers fabricated

from PLLA [27.69], PGA [27.70], PLGA [27.71], and PCL [27.56] and natural nanofibers fabricated from gelatin [27.72], silk [27.73], and collagen [27.57] have been widely used. Researchers have also coated synthetic nanofibers with ECM proteins such as fibronectin, laminin, and collagens, which contain many cell binding sites [27.74]. Also common is attaching short polypeptide fragments that contain the RGD amino acid sequence or other cell binding moieties.

Cell Response

The cell response to nanofiber scaffolds depends on multiple factors, including the mechanics, physical dimensions, and chemistry. A desirable response is typified by cell adhesion, proliferation, and the formation of a functional tissue. A representative example is shown in Fig. 27.15, where mesenchymal stem cells (MSCs) were seeded onto PCL electrospun scaffolds in vitro [27.56]. In this case, the PCL nanofiber scaffold is isotropic with a pore size that limits cell infiltration. Upon seeding, cells adhere to the nanofibers and begin to spread and proliferate (Fig. 27.15b). As the cells grow they modify their environment, which in the case of MSCs is secretion and assembly of collagen fibrils on top of the nanofibers (Fig. 27.15c). After extended culture, the cells have formed a continuous monolayer and continued to modify their environment with collagen fibrils and mineral calcifications (Fig. 27.15d,e). This illustrates a couple of points: (i) cells will remain on the surface of nanofiber scaffolds unless the pore size is large enough to enable cell infiltration, and (ii) cells modify their environment when seeded onto scaffolds by secreting and assembling ECM of their own. The choice of nanofiber materials and scaffold architecture are always tailored to the cell type involved and the desired cellular response.

Changing the properties of the nanofibers can change the cell response. In contrast to PCL and many similar hydrophobic synthetic polymers, scaffolds formed from self-assembled peptide nanofibers have an extremely high water content (usually above 99.5%) which allows cells to migrate easily throughout the scaffold [27.40]; For example, chondrocytes cultured on these nanofibers retain their shape and produce collagen type II, which does not usually occur in vitro as chondrocytes dedifferentiate into fibroblasts [27.40].

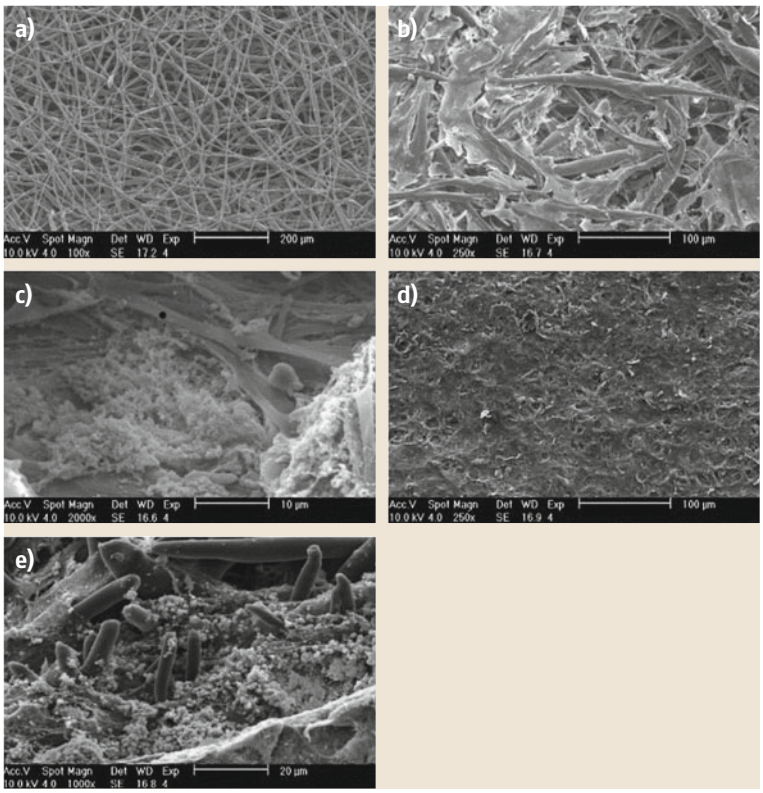


Fig. 27.15a–e SEM micrographs of MSCs seeded on electrospun PCL scaffolds. **(a)** Scaffold prior to seeding. The scaffold has a three-dimensional, interconnected pore structure and consists of randomly oriented fibers. The average fiber diameter is 400 nm (±200 nm). The standard deviation is denoted in parentheses. Occasional outliers with diameters of up to 5 μm are sometimes observed. The fibers have irregular surfaces. **(b)** Low-magnification view of the cell–polymer constructs after 1 week of culture. The surface is partially covered with multilayers of cells. **(c)** High-magnification view of the cell–polymer constructs after 1 week of culture. Osteoblast-like cells are present, and globular accretions together with collagen bundles are also observed. **(d)** Low-magnification view of the cell–polymer constructs after 4 weeks of culture. The surface is completely covered with cell multilayers. **(e)** High-magnification view of the cell–polymer constructs after 4 weeks of culture. The globular accretions have increased in size. Abundant calcification and collagen bundles are also seen (after [27.56])

The integration of bioactive motifs can further enhance cell attachment and migration [27.40].

Immune Response

The biological response occurs at the cell/material level, but this is important beyond just the cells seeded on the scaffold. For scaffolds implanted in vivo, the immune response is critically important and will dictate in part overall success/failure. Traditionally, implanted materials have undergone a foreign-body response where the body seeks to wall off the implant. This is characterized by inflammation and fibrosis, and needs to be avoided because it impedes tissue growth and regeneration. This has resulted in materials designed to prevent a foreign-body response and to be *invisible* to the body. One problem with nanofiber and nanostructured materials is that their interaction with cells is still being studied; it remains unclear how the many types of nanoscale materials enter cells and what their effect is once inside. Recently, it has become clear that there are different types of immune response, and that materials can modulate the immune response and actually improve regeneration, as illustrated in Fig. 27.16 [27.75]; For example, materials can be functionalized with or designed to release growth factors or cytokines to reduce or enhance inflammation and the behavior of dendritic cells. Using this process, it is possible to switch macrophages from an M1 phenotype, which is associated with phagocytic behavior and destruction of tissue-engineered scaffolds, to an M2 phenotype, which is associated with normal wound healing and tissue repair. The full complexity of the immune response to nanofiber biomaterials and scaffolds is beyond the scope of this chapter, and readers are encouraged to search the current literature for the latest developments. However, at a basic level, it should be understood that

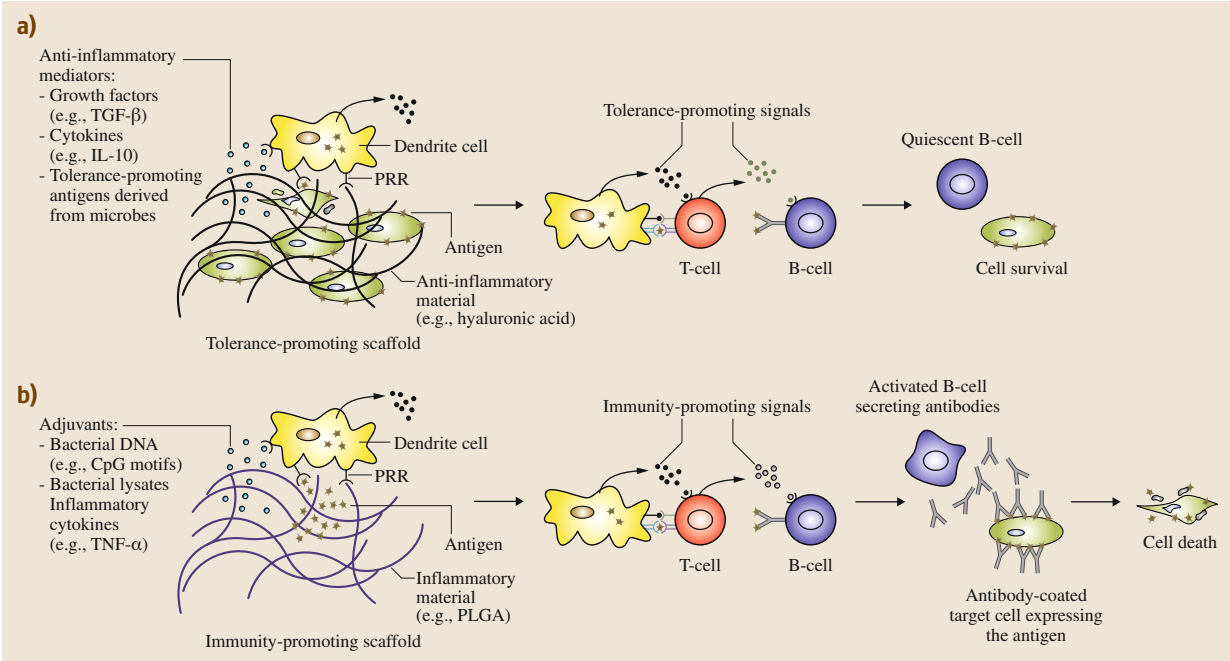


Fig. 27.16a,b Potential of materials to control the immune response. **(a)** Materials can promote tolerance to specific antigens and cells by directly signaling antigen-presenting cells (APCs), such as dendritic cells (DCs), or by releasing growth factors or cytokines that promote tolerance. After antigen internalization, DCs can activate effector cells, such as T and B cells, to promote tolerant responses to the associated antigen. This approach could potentially be used to promote the survival of transplanted cells. *Abbreviation*: PRR, pattern recognition receptor. **(b)** Alternatively, materials might promote a destructive immune response by directly providing immunity-promoting signals or by releasing soluble factors. Activated APCs can then induce destructive immune responses, for example, through B cells secreting antibodies specific for the antigen, which subsequently lead to the antigen's targeting and removal. This approach could be used to combat infectious diseases and cancer (TGF-β: transforming growth factor; IL: interleukin; TNF-α: tumor necrosis factor) (after [27.75])

in vitro assays that evaluate the biological response to nanofiber biomaterials may not be predictive of the biological response in vivo in the presence of the immune system.

Biodegradation

The biodegradative properties of a scaffold are extremely important in tissue engineering. Typically, the nanofiber scaffold is meant to be a temporary construct, with the goal for the tissue to regenerate and the scaffold to disappear. For this to occur, the scaffold needs to biodegrade into nonharmful products that can be metabolized or cleared by the body. Additionally, the degradation of the scaffold must be chosen carefully to match the rate of new tissue formation to avoid a mechanical property mismatch or large void formation [27.23]. Biodegradation is highly dependent on the polymer or protein of which the nanofibers are composed, as the molecular weight and concentration of polymer [27.23]. The size of nanofibers complicates this because the large surface area results in rapid degradation for surface-based processes such as hydrolysis. The degradation can be tuned by changing the polymer chemistry or by changing the ratio of the polymers in blended or core–shell nanofibers; For example, it was found that 70 : 30 PCL/gelatin nanofibers degrade more slowly than 50 : 50 fibers, and were therefore better for nerve regeneration applications where a slow degradation rate is desired [27.23]. In another study, pure PCL nanofibers exhibited no noticeable weight loss after 17 days, whereas the PCL/collagen composite nanofibers lost 20% of their weight in the 17-day period [27.76]. *Meng* et al. showed the impact of surface area on degradation, as bulk PCL degraded slower than electrospun PCL nanofibers. Incorporation of multiwalled carbon nanotubes in the nanofibers increased the degradation rate, showing that nonpolymer additives can also be used to tune degradation [27.77]. Changing the percent composition of blended polymer nanofibers can also change the degradation from surface to bulk erosion. For self-assembled peptide nanofibers, the degradation products are amino acids that can be reused by the body, and enzymatically cleavable peptides can be incorporated. Typically, the scaffolds cause minimal immune response and there is limited inflammatory reaction [27.42].

27.3 Characterization of Nanofiber Biomaterials

27.3.1 Optical Characterization

Optical Microscopy

Bright-field optical microscopy is a standard imaging technique, but is not effective for viewing most types of nanofibers because the submicrometer dimensions limit optical contrast. Thus, nanofibers need an optical contrast-enhancement technique in order to be visualized, typically either phase contrast or differential interference contrast (DIC) microscopy. Both techniques are able to image nanofibers and are based on modulation of phase or polarization of light to render contrast. These techniques enhance the edges of specimens being observed due to small difference in optical properties associated with cell membranes, organelles, and nanofibers. The contrast created makes observation of otherwise transparent specimens possible. It can also reveal very thin constructs such as nanofibers (Fig. 27.17a) [27.39, 78]. However, when the nanofiber dimensions are below the resolving power of the microscope objective, it is not possible to make accurate measurements, such as nanofiber diameter.

Fluorescence microscopy enables the characterization of nanofibers when conjugated with a wide variety of fluorophores. This is particularly useful when investigating the interaction between nanofibers and cells, as the nanofibers and many of the intracellular components can be fluorescently labeled (Fig. 27.17b). Fluorophores have traditionally been small molecules such as fluorescein isothiocyanate (FITC) and its derivatives, directly conjugated to the biomolecule of interest or conjugated to an antibody that targets the biomolecule of interest. However, more recently fluorophores have been genetically encoded, such as green fluorescent protein (GFP) and its derivatives, to create transgenes for the proteins of interest. This has enabled imaging of cells without application of chemical stains and enabled advances in imaging of live cells. Quantum dots are also another option for fluorophores, with the advantage of not photobleaching under typical imaging conditions. In the fluorescence technique, the fluorophore is illuminated with excitation light at a specific wavelength that causes emission of light at a longer wavelength (lower energy). When using samples with multiple fluorophores, it is necessary to prevent spectral bleedthrough, which is the measurement of the emission spectrum of one fluorophore in the emission spectrum of another. This can be largely overcome through the

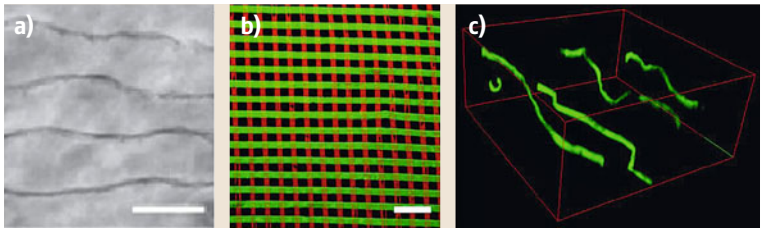


Fig. 27.17a–c Examples of nanofibers imaged using different types of optical microscopy. **(a)** Phase contrast image of collagen type IV nanofibers (*scale bar* is 40 μm). **(b)** Fluorescent image of a nanofabric consisting of fibronectin nanofibers labeled with antibodies conjugated to a green fluorescent dye and laminin nanofibers labeled with antibodies conjugated to a red fluorescent protein (*scale bar* is 100 μm). **(c)** 3-D image of collagen type I nanofibers conjugated with FITC green fluorescent dye and suspended in saline solution. Image was captured using a laser scanning confocal microscope and reconstructed in 3-D using image processing software. Panels **(a)** and **(c)** (after [27.39])

use of proper filtering of light such that a specific range of wavelengths are passed through to the imaging device [27.79]. Alternatively, a spectral image that records the emission intensity as a function of wavelength, followed by spectral unmixing, can be used to identify multiple fluorophores that have distinct emission wavelength maxima.

A number of advanced fluorescent imaging techniques have been developed to remove out-of-plane light and enhance the signal-to-noise ratio. Confocal microscopy eliminates out-of-focus light emitted from the sample by using a pinhole aperture placed in front of the detector (photomultiplier tube or digital camera). Only light from the focal plane of the sample is able to pass through the pinhole, which provides enhanced resolution. The confocal microscope captures a thin optical slice of the sample, enabling a 3-D image of the sample to be digitally reconstructed by imaging *xy* slices of the sample through subsequent *z*-axis focal planes (Fig. 27.17c) [27.80, 81]. Multiphoton microscopy is another technique that eliminates out-of-focus light, but instead of an aperture to block light, only a small volume at the focal plane of the objective is illuminated. An infrared laser with twice the wavelength (half the energy) of the excitation wavelength of a fluorophore is focused into a small volume using a high-numerical-aperture objective. This enables two lower-energy photons to simultaneously excite a higher energy state in the fluorophore. The result is an image similar to confocal microscopy, but with the advantage of being able to image deep into a tissue (up to ≈ 1 mm). Both confocal and multiphoton microscopy are widely used for imaging nanofibers and the interaction with cells in 3-D, but other new techniques are becoming available that can image nanofibers as well. Optical microscopy has traditionally been limited to resolutions of approximately one-half the wavelength of light (≈ 225 nm). However, a new generation of techniques are able to image at resolutions of ≈ 100 nm using structured illumination microscopy (SIM) and ≈ 25 nm using stochastic optical reconstruction microscopy (STORM).

Optical Spectroscopy

Optical spectroscopy techniques are able to provide information on the chemical composition of nanofiber biomaterials. Chemical bonds interact with light at specific frequencies, which can be used to identify the types and relative number of these bonds in a material. Raman spectroscopy, based on the inelastic scattering of photons, provides a molecular fingerprint of the chemical bonds in the nanofibers of interest. Raman scattering has been frequently used for characterization of carbon nanofibers and carbon nanotubes through monitoring of carbon's intrinsic D and G peaks in the Raman spectra [27.82]. Raman spectroscopy has also been applied to biological material, such as studying the unfolding of proteins [27.83]. Raman scattering methods could potentially be used in conjunction with protein nanofibers to observe processes such as fibrillogenesis or binding to a specific motif within a nanofiber. Fourier-transform infrared spectroscopy (FTIR) is used to identify the presence of specific chemical groups in a sample based on the energy absorption of the chemical bonds. FTIR quantifies the absorption of a wide range of IR wavelengths by the sample. The spectrum shows known patterns associated with specific chemical groups; For example, *Nirmala* et al. used FTIR to identify hydroxyl and phosphates groups in electrospun polyurethane nanofibers containing $CaCl_2$ at different concentration, before and after treatment with a simulated body fluid solution (Fig. 27.18) [27.84].

27.3.2 Electron Microscopy

Scanning Electron Microscopy (SEM)

SEM is frequently used to investigate the morphology and structure of nanofibers. SEM is capable of producing detailed images of nanofibers with a maximum resolution of ≈ 1 nm under ideal imaging condition. Images are formed by accelerating an electron beam onto the sample, which causes lower-energy secondary electrons to be emitted and detected. SEM is a useful technique to determine the diameter of nanofibers [27.73, 74, 85], nanofiber alignment, as well as cell–fiber interactions [27.73]. Traditionally, SEM required that the specimen be electrically conductive, so most nanofibers, either polymer or protein based, had to be coated with a conducting material such as gold, palladium or platinum. However, environmental SEMs now enable many nanofiber samples to be imaged without coating and in a hydrated state, better preserving the structure. In addition to imaging the surface, many SEMs are equipped with energy-dispersive x-ray spectroscopy (EDS) to identify the chemical composition of the material. This chapter includes multiple examples of SEM images used to characterize a wide range of nanofiber biomaterials, nanofiber scaffolds, and cell interactions with nanofibers (Figs. 27.3, 27.5, 27.6, 27.11, 27.12, 27.15, 27.20, 27.29, 27.32, and 27.33).

Transmission Electron Microscopy (TEM)

TEM is another powerful method that provides structural analysis with resolution < 1 nm. Unlike SEM, TEM detects electrons from an electron beam after they have passed through the sample. While TEM is limited to producing 2-D images, TEM images can yield structural information based on image contrast generated from differences in electron density, which is particularly useful when synthesizing nanofibers of different components. Regions of nanofibers that contain heavier atoms or are thicker tend to scatter electrons more than regions with lighter atoms and/or thinner regions [27.86]. Recent research has investigated the effects of coating synthetic nanofibers with natural bioactive agents to enhance cell–fiber interactions. Effective coating is most easily characterized using TEM because the different layers have different contrasts in the TEM image. This is illustrated in Fig. 27.19, where the authors coated PCL nanofibers with collagen [27.56]. TEM is also the best technique for looking at high-resolution interactions between cell membranes and nanofibers; For example, with TEM it is possible image the contact between cell membranes and nanofibers, and also to image nanofibers inside cells to determine subcellular localization.

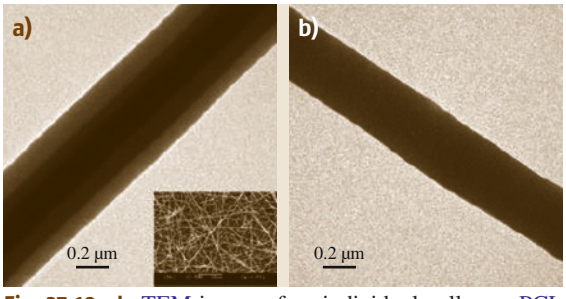


Fig. 27.19a,b TEM image of an individual collagen–PCL composite nanofiber with collagen as the shell material and PCL as the support **(a)**. **(b)** TEM image of a pure PCL nanofiber (after [27.56])

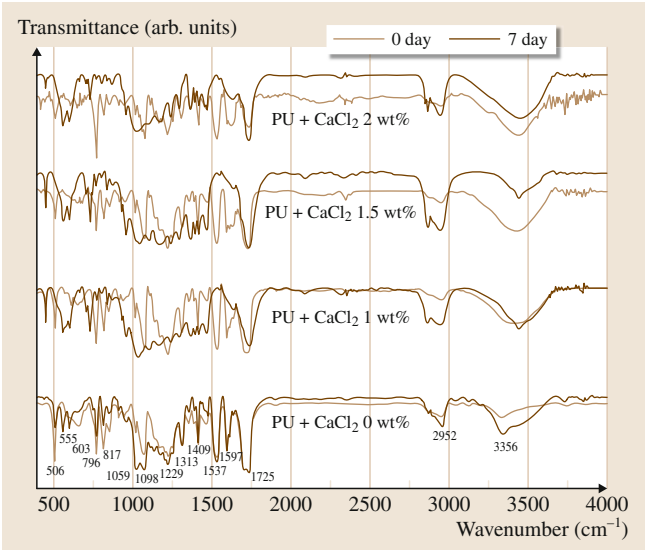


Fig. 27.18 FTIR spectra of different electrospun polyurethane nanofibers (after [27.84])

27.3.3 Atomic Force Microscopy (AFM)

AFM is a scanning probe technique used to determine the topography of a surface and as well as analyze its mechanical and adhesive properties. This is achieved using a physical probe that is brought into contact with the sample during imaging. A unique capability of AFM is that it can be operated in ambient conditions as well as under water, including in solutions that simulate physiologic conditions. In topographical analysis, AFM images can be used to determine whether a nanofiber

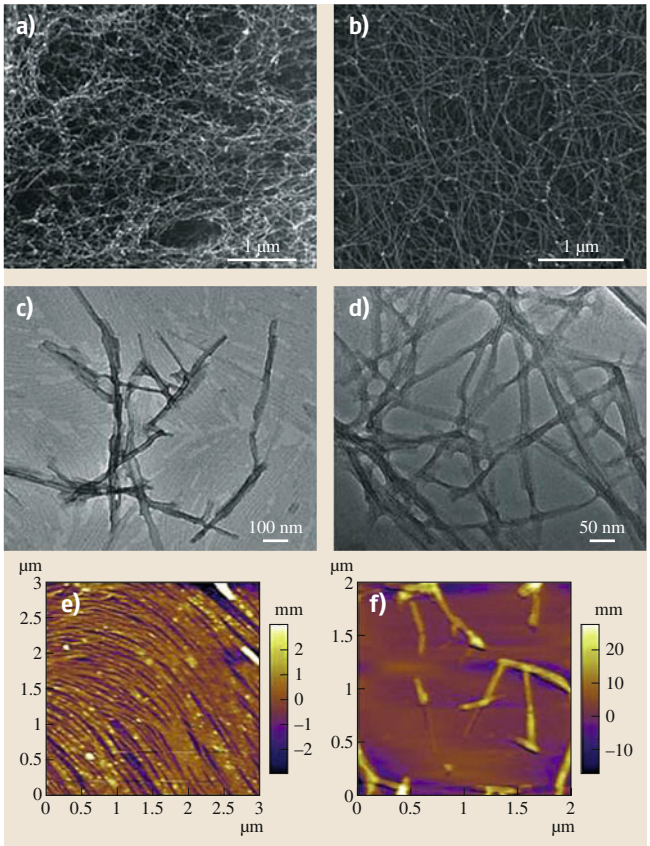


Fig. 27.20a–f Scanning electron micrographs of **(a)** PA with $CaCl_2$ gel, **(b)** PA with HCl gel (*scale bars* 1 µm). Transmission electron micrographs of **(c)** PA with $CaCl_2$ gel, **(d)** PA with HCl gel. AFM topography micrographs of **(e)** PA with $CaCl_2$ gel, **(f)** PA with HCl gel (after [27.51])

sample has globular or fibrillar structure as well as give information on the fiber diameter, length, and cross-section [27.40, 41, 87]. This can be used to evaluate the size of single nanofibers and to determine how many layers of nanofibers are present in a scaffold [27.40]. AFM can obtain detailed information about nanofibers that may not be visible using SEM (Fig. 27.20). When analyzed by SEM, two different gels formed from self-assembled peptide amphiphile nanofibers (one formed with $CaCl_2$ and the other with HCl) exhibited similar characteristics [27.87]. AFM images revealed that gels formed with $CaCl_2$ were composed of longer fibers whereas gels formed with HCl were made of shorter, more bundled fibers [27.51].

The unique environmental capability of AFM enables it to image dynamic nanofiber processes; For example, AFM is often used to monitor self-assembling peptide nanofiber formation, organization of those nanofibers into a scaffold, and refolding of β-sheet structure after sonication [27.40, 41]. As seen in Fig. 27.21b, after 3 min a solution of LKL16 peptide contained only globular species with a height of approximately 0.8 nm, indicating that the peptide was in the monomer state [27.41]. After incubation for 24 h, the presence of nanofibers can clearly be seen in the AFM image. Similarly, AFM images of RADA16 nanofibers over time show the progression of fiber/scaffold reassembly after sonication [27.40]. AFM topographic images of the self-assembling peptide nanofibers formed from the L- and D-LKL16 peptide clearly show the difference between the left-handed and right-handed twists formed during the self-assembly process (Figure 27.21a) [27.41].

An important AFM capability for tissue engineering applications is the measurement of force between the AFM tip and the nanofibers. Mechanical properties can be determined from the force versus cantilever deflection curve obtained when indenting the nanofibers. Details of this analysis are discussed in Sect. 27.3.4. Adhesive properties can be determined from the force versus cantilever deflection curve obtained when retracting the AFM tip from the nanofiber surface. The dynamics of adhesion can be determined with repeated indentation and retractions at various rates, and when the AFM tip has been functionalized with a ligand, the dynamics of specific binding interactions [27.88].

27.3.4 Mechanical Characterization

Nanofibers are mechanically characterized either as single fibers or as a collection of fibers organized into micro- to macroscale structures. For most applications, the properties of interest for macroscale structures are the tensile stress and strain, i. e., the stiffness, which can be determined using ASTM protocols for tensile testing. Characterizing the mechanical properties of single nanofibers is more challenging and requires the use of more advanced techniques. Further, in macroscale measurements the interactions between nanofibers (e.g., entanglement, adhesion, slippage, and abrasion) can greatly affect the measured mechanical properties. Here we focus on methods specific to nanofiber mechanical characterization at the nano- and microscales.

AFM nanoindentation is used to characterize the mechanical properties of individual nanofibers and nanofiber films, where the interfiber bonding has less of an effect than in macroscale measurements and the

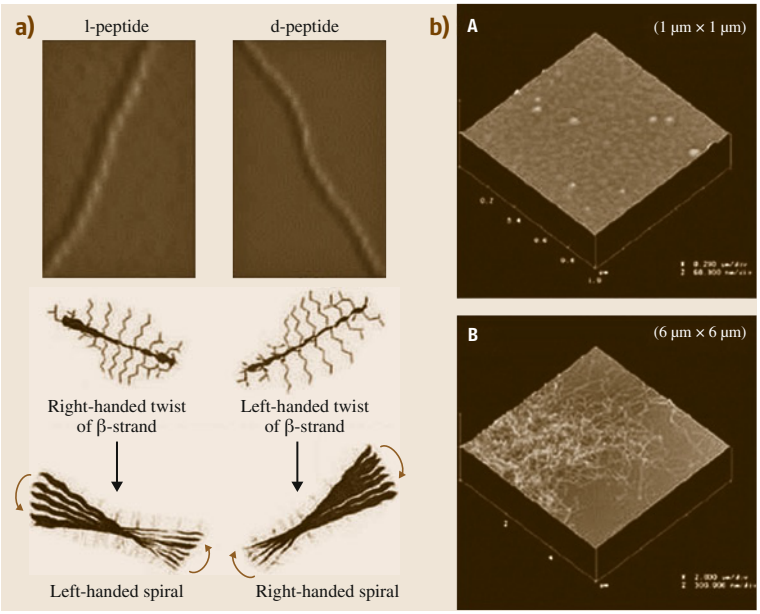


Fig. 27.21 **(a)** Amplitude AFM images of LKL16–nanofiber, LKL16-(D)–nanofiber and their plausible models. **(b)** Tapping-mode AFM images of LKL16 obtained after incubation for (A) 3 min and (B) 24 h at pH 9.2 [LKL16] = 40 μm; *z*-scales (A) 60 nm, (B) 300 nm (after [27.41])

slippage of fibers is minimal. AFM is one of the best options for measuring the mechanical properties of soft nanofibers and their scaffolds (Fig. 27.22) [27.51, 89]. There are still many factors to consider in the evaluation of nanoindentation data on nanofibers such as:

1. The effect of the underlying substrate
2. The use of ambiguous tip shape and cantilever spring constant
3. Fiber surface roughness
4. Curvature of the fiber surface
5. Nonperpendicular loading
6. The adhesion force.

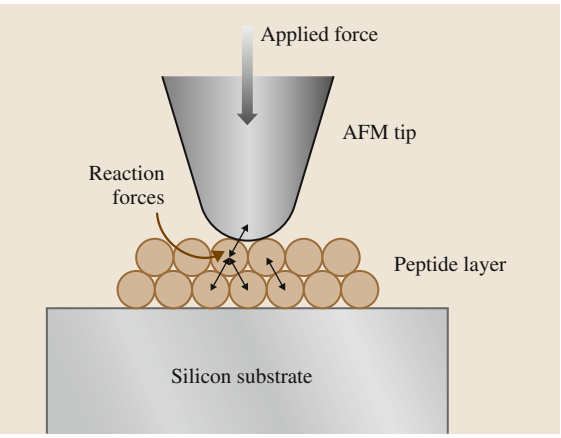


Fig. 27.22 In an indentation measurement on films of nanofibers, interfiber forces are mostly normal to the fiber surface and interfiber cross-linking has less effect on apparent material stiffness (after [27.51])

However, the effect of some of these factors can be limited; For example, the error can be reduced by choosing large enough nanofibers for analysis so that the effect of the underlying substrate can be limited and by calculating the spring constant and shape of the individual AFM tip [27.89].

Tensile testing is standard for macroscale samples, but is one of the most difficult mechanical tests to perform on single nanofibers due to the difficulty involved in trying to grip and pull a nanofiber. Typically, custom-designed systems are used to properly hold nanofibers and a highly sensitive force sensor and micropositioner are used to measure the stress versus strain; For example, to perform tensile tests single poly(ethylene oxide) (PEO) nanofibers were suspended across a wooden frame with an open center. One end of the frame was connected to a moveable optical stage and the other to a piezoresistive AFM cantilever (Fig. 27.23) [27.89]. The deflection of the cantilever was recorded as the stage was moved, and the Young's modulus was calculated to be approximately 45 MPa. Another tensile testing approach uses the AFM nanoindentation system in a different manner. In this case a nanofiber is attached to the nanoindenter tip and also to the substrate; it is then

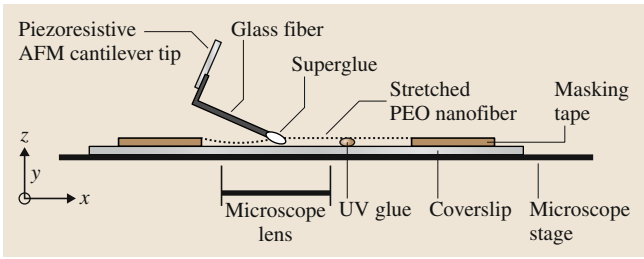


Fig. 27.23 Schematic representation of the tensile test of a nanofiber using a piezoresistive AFM tip (after [27.89])

stretched using the stepper motor of the AFM, and the force applied and the fiber elongation can be measured.

The AFM is also the best device to perform bending tests on nanofibers because of its ability to apply small forces and measure small deformations; For example, nanofibers are suspended across ridges and grooves on a surface [27.91]. The AFM cantilever is then used to stretch the fiber laterally by putting it next to the fiber and pulling it along the groove [27.91]. This technique determined that the three-point bend strength of collagen type I fibers is approximately 2.8 GPa and the strain is 12%.

Micropipettes have traditionally been used to characterize the mechanical properties of soft biological materials and can be adapted to characterize nanofibers. Glass microneedle-based mechanical characterization is similar to AFM in that bending of a calibrated cantilever is used to apply force (Fig. 27.24e). However, for the microneedles, the force applied to the nanofibers is measured by the deflection of an optical fiber, which can be quantified by the deviation of light transmitted through the optical fiber onto a photodetector [27.90, 92]. Force can also be applied through biomembrane force probe techniques (Fig. 27.24f). Essentially, nano-

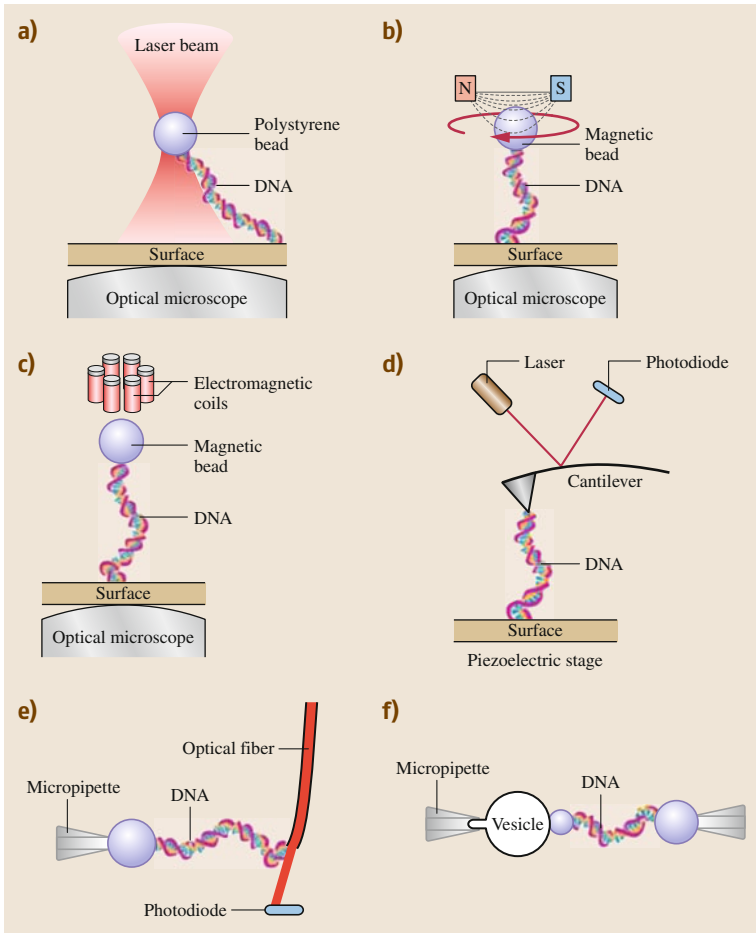


Fig. 27.24a–f Schematics of several micromanipulation techniques used to measure the pN to nN forces needed to strain nanofibers. While DNA is used in these examples, nanofibers could also be manipulated using these methods. **(a)** Optical tweezers, **(b)** magnetic tweezers, **(c)** magnetic tweezers with an electromagnet configuration, **(d)** AFM, **(e)** glass microneedle, and **(f)** biomembrane force probe; all represent techniques to characterize single nanofibers (after [27.90])

fibers of interest are bound to lipid vesicles. The force on the nanofiber is the result of moving a bead attached to the other end of the fiber and can be quantified by determining the movement of that bead and the stiffness of the membrane, which can be controlled through the pressure in the suction pipette attached to the vesicle [27.93].

Another method for determining the mechanical properties of nanofibers is based on optical and magnetic tweezers. Optical tweezers (Fig. 27.24a) (i. e., optical trapping) enables the measurement of forces applied on particles trapped within a laser beam. This technique is sensitive to the measurement of forces of the order of pN and nN. Particles ranging in size from tens of nanometers up to several micrometers in diameter can be trapped and manipulated [27.94]. Nanofibers can be attached to the trapped particles which are used to pull on the nanofibers to create stress versus strain data. Similarly, magnetic tweezers (Fig. 27.24b,c) are able to exert up to nN of force by using magnetic particles instead of optically trapped particles to apply force. The force experienced by the magnetic particle is proportional to the magnetic field gradient and the diameter of the particle [27.95].

27.4 Applications

Nanofiber biomaterials are a growing area of tissue engineering research and are being pursued for application in a wide range of tissues and organ systems. There are many advantages to using nanofibers, and how these are exploited depends largely on the nanofiber materials used, the tissue engineering application, and the desired outcome of the study. Here we focus on representative examples in cardiac, skeletal muscle, ophthalmic, and neural tissue engineering. In addition to these examples, there are multiple review articles that focus on nanofibers used in other applications including orthopedic [27.96–98], cartilage [27.99], and vascular [27.100] tissue engineering.

27.4.1 Cardiac Tissue Engineering

Heart failure remains the number one cause of death in the developed world, and because the heart cannot regenerate, transplantation remains the only viable therapy [27.101]. Scaffolds for cardiac repair need to restore electromechanical function of the heart muscle, which is a unique challenge not found anywhere else in the body. The most challenging criteria are specific to the nature of the myocardium (Fig. 27.25):

- Anisotropic structure
- Mechanical strength and elasticity to resist systemic blood pressure and contraction
- Electrical conductivity
- Dense vascularization.

Advances in nanotechnology and the availability of nanofibers offer new possibilities in cardiac tissue engineering. This section describes how nanofibers can be used to address some of the challenges of cardiac tissue engineering and what is expected as research progresses.

Heart function relies on the orientation of the cardiomyocytes, which form highly aligned myofibers in the heart wall. Several techniques have been used to create anisotropic nanofiber scaffolds. Electrospinning can be customized to produce aligned fibers by using rotating collectors, such as discs [27.102], mandrels, and drums, or by using several aligned electrodes [27.103]. *Orlova* et al. described a simple way to collect aligned nanofibers of polymethylglutaramide through a rectangular hole in the collector, which were then used to grow an anisotropic sheet of cardiomyocytes [27.78]. Electrospun PLGA membranes were uniaxially stretched by *Zong* et al. and showed significant alignment of cardiomyocytes (Fig. 27.26) [27.25]. Rotary jet spinning [27.26] produces naturally aligned gelatin nanofibers that direct the anisotropic organization of cardiac tissue. Nanofiber sheets created by surface-initiated assembly of fibronectin can follow any pattern made from a microfabricated stamp, and thus can be used to engineer cardiac muscle with specific degrees of cell alignment and tissue anisotropy [27.39].

The cardiac mechanical environment is demanding because the heart beats more than two billion times over an average human lifetime. Any construct meant for cardiac tissue engineering will need to withstand mechanical strains of $\approx 20\%$ and millions of contraction–relaxation cycles, which requires fatigue resistance. At the same time, scaffolds must remain extensible and flexible and not hinder the contraction of cardiomyocytes. Natural cardiac ECM composed primarily of collagen type I has anisotropic mechanical properties with Young's modulus of 157 ± 84 kPa parallel and 84 ± 8 kPa perpendicular to the myofibers in

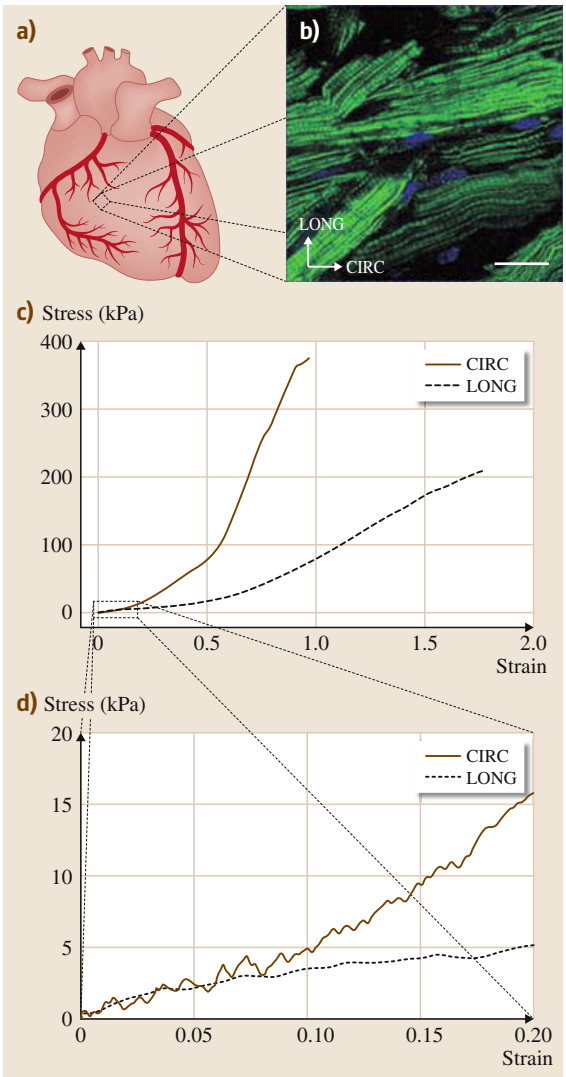


Fig. 27.25a,b Structural and mechanical aspects of cardiac anisotropy. **(a)** A schematic diagram illustrating the gross macroscopic appearance of a four-chamber mammalian heart. **(b)** A full-thickness specimen of adult rat right ventricular myocardium showing preferentially oriented cardiac muscle fibers, fluorescently labeled for F-actin and cell nuclei and imaged from the epicardial surface by confocal microscopy. (*Scale bar*: 50 µm; anatomically defined *circumferential* (CIRC) and *longitudinal* (LONG) axes are indicated.) **(c,d)** Representative uniaxial tensile stress–strain plots for circumferential and longitudinal specimens of full-thickness right ventricular myocardium demonstrated anisotropic mechanical properties consistent with observed cell orientations. **(c)** Full range to demonstrate failure properties; **(d)** physiologic regime. Collectively, these structural, mechanical, and associated electrical properties comprise the interrelated aspects of cardiac anisotropy (after [27.104]) ▶

the left ventricle of the heart [27.104]. PANI-containing gelatin fibers developed by *Li* et al. [27.19] showed moduli above 500 MPa, while *Kai* et al. [27.102] created PCL–gelatin composites with anisotropic properties of 5.41 ± 0.61 MPa parallel and 1.15 ± 0.09 MPa perpendicular to the nanofibers, closer to the values of natural cardiac ECM. Cardiac tissue engineering requires consideration of the mechanical properties of the constructs so they effectively mimic in vivo conditions.

The electrical environment of the heart is also demanding because cardiac function requires synchronized beating from the cardiomyocytes, organized in fibers and sheets [27.105]. Action potential propagation in the heart follows cardiomyocytes that are coupled together via gap junctions [27.106]. The electrical properties of a scaffold are critically important because abnormal electrical function can induce arrhythmia and lead to sudden cardiac death. Polyacetylene, polypyr-

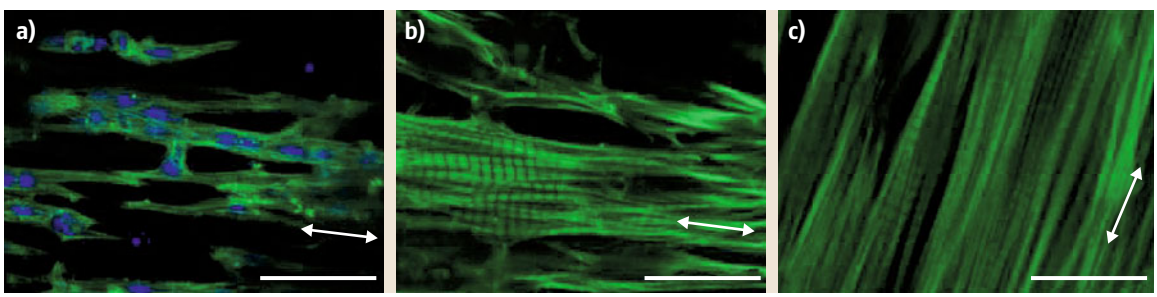


Fig. 27.26a–c Confocal laser scanning microscopy images of cardiomyocytes on stretched fibers with different compositions: **(a)** PLGA + PEG-PLA, **(b)** PLA10GA90 : PLLA (75 : 25), and **(c)** PLLA. *Scale bar* is 20 µm. *Arrows* indicate fiber direction. Nuclei stained with 4′,6-diamidino-2-phenylindole, dihydrochloride (DAPI) (*blue*), actin stained with phalloidin (*green*) (after [27.25])



Fig. 27.27 **(a)** Cross-sectional view of a single graft of electrospun PCL mesh. Hematoxylin and eosin (H&E) staining shows that cardiomyocytes have attached to the scaffold and proliferate (400 × magnification). **(b)** Cross-sectional view of a five-layer graft, with H&E staining (400 × magnification). **(c)** Cross-section of a single graft. Masson trichrome staining reveals the presence of muscle and collagen through the entire specimen (400 × magnification). **(d)** Cross-section of a five-layer graft. A stratified cardiac muscle-like structure can be seen (400 × magnification) (after [27.111])

role, polythiophene, and PANI belong to a category of electroactive polymers that can enhance electrical stimulation to the tissue in vitro; For example, electrospun PANI–gelatin [27.19], PANI and hyperbranched poly-L-lysine [27.107], and PANI/PCL [27.108] showed good biocompatibility of these electroactive scaffolds with cardiomyocytes. Li et al. also showed that electrospun nanofibers with PANI induced differentiation of mesenchymal stem cells into cardiomyocytes. It has been challenging to engineer aligned cardiac muscle in 3-D, but new techniques have been developed to fabricate nanofiber scaffolds for this application. The self-assembling nanopeptide RADA16 was modified with a cell adhesion sequence (RGDSP) and seeded in vitro with marrow-derived cardiomyocytes. The nanopeptides naturally assemble into a 3-D matrix that improves cell survival in vitro and cardiac function after transplantation, but the structure of the scaffold cannot be easily customized [27.109]. Researchers have also encapsulated an electrospun mesh of PGA within a collagen gel [27.110]. The composite sponges were seeded with cardiac stem cells after freeze-drying and dehydrothermal cross-linking. The constructs exhibited better cell attachment and proliferation, as well as a stronger compression modulus compared with collagen alone. As an alternative to making a bulk scaffold directly, it is also possible to take planar scaffolds produced by electrospinning or surface-initiated assembly and stack them to form thicker 3-D constructs; For example, *Ishii* et al. seeded rat cardiomyocytes onto electrospun PCL meshes and stacked up to five meshes to form a multilayered construct (Fig. 27.27). These engineered cardiac tissues maintained cell viability and exhibited synchronized beating [27.111].

Cardiac muscle needs to be perfused to support the high metabolic demand of contracting cells, yet it is currently not possible to engineer a microvascular network in tissue-engineered cardiac muscle. To address this, a number of studies have considered the effect of different nanofibers on the proliferation and function of smooth muscle cells and endothelial cells [27.112,113], which are required for the growth of a vascular network. The presence of endothelial cells in particular is required to improve cardiomyocyte survival and organization [27.114]. Methods to induce angiogenesis in vitro rely on growth factors, chemical cues in the constructs, and other cell–scaffold interactions in order to trigger the formation of endothelial networks. Progress in tissue engineering is dependent on the discovery of new cellular pathways and a better understanding of the angiogenesis process so that these triggers can be included in the design of scaffolds for cardiac regeneration.

27.4.2 Skeletal Muscle Tissue Engineering

Skeletal muscle tissue engineering shares many similarities with cardiac tissue engineering because both are highly vascularized striated muscle. Applications include repair of skeletal muscle loss from traumatic injury, tumor ablation, and other diseases [27.115]. Developing scaffolds that mimic muscle tissue mechanical properties and that support myotube alignment and contraction is a major challenge. The development of nanofiber techniques to fabricate scaffolds structurally and functionally similar to native ECM can potentially meet this need [27.44].

Myoblasts, the precursors of myotubes, can sense microscale and nanoscale topographic features in the extracellular space. A comparative study of myoblasts cultivated on biodegradable PLLA electrospun nanofibers with microgrooved surfaces indicated that both microscale and nanoscale topographic features could cause myoblast alignment and promote myotube assembly, but nanoscale features promoted the assembly of longer myotubes (Fig. 27.28) [27.22]. Further, electrospun collagen type I nanofibers were better than collagen type I sponges in supporting myoblast growth,

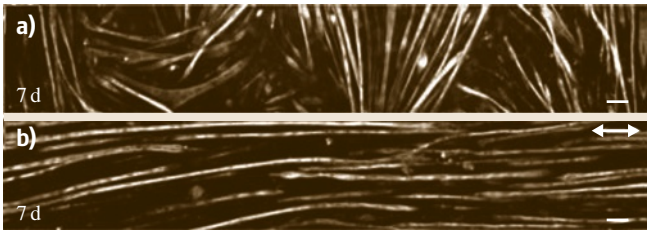


Fig. 27.28a,b Myotube alignment and myotube assembly on PLLA nanofibrous scaffold. Low-magnification merged images of skeletal MHC staining on **(a)** randomly oriented substrates after 7 days and **(b)** aligned substrates after 7 days showing the global alignment and length of myotubes. *Arrows* indicate direction of nanofibers. *Scale bars* are 100 μm (after [27.24])

with the nanofibers able to support aligned myoblasts and maintenance of myogenic phenotype [27.100].

Electrospinning is the most common method used to fabricate nanofibers for skeletal muscle tissue engineering, although other methods are used including self-assembly and phase separation [27.44]. Synthetic and natural polymers that are commonly used include PCL, PLLA, and ECM proteins (Fig. 27.29) [27.22, 24, 100]. Electrospun PCL–collagen nanofiber meshes supported cell adhesion, proliferation, and differentiation. The unidirectional alignment of the PCL–collagen nanofibers enhanced human skeletal muscle cell (hSKMC) alignment and myotube formation as compared with randomly oriented nanofibers [27.22]. *Copper* et al. electrospun aligned and randomly oriented polyblend chitosan–PCL nanofiber scaffolds and demonstrated that aligned nanofibers enhance muscle cell differentiation by upregulation of myogenic differentiation-specific genes, such as troponin T and myosin heavy chain [27.116]. The mechanical properties of these PCL blend nanofiber scaffolds were significantly different, with the tensile strength greater for unidirectional than randomly oriented nanofibers (Table 27.2).

27.4.3 Ophthalmic Tissue Engineering

Nanofibers have been used in ophthalmic tissue engineering for repair of the corneal stroma, ocular surface, and retina. The stroma is naturally composed of collagen type I nanofibers, ≈ 30 nm in diameter, which are bundled together into 200–2500 nm-thick sheets called lamellae [27.117, 118]. The collagen type I nanofibers are highly aligned, have a small diameter, and are regularly spaced, all of which allows for optimal cell alignment and corneal transparency [27.119]. When

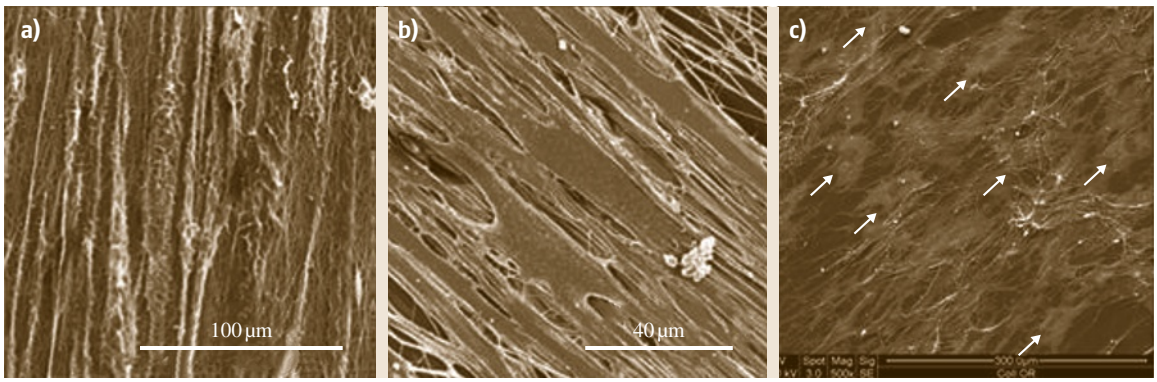


Fig. 27.29a–c SEM images showing morphology of muscle cells grown on different nanofibers. **(a)** hSKMCs on PCL–collagen aligned nanofibers for 7 days after differentiation (after [27.22]). **(b)** C_2C_{12} cells grow on chitosan–PCL nanofiber after 5 days of culture in fusion media. *Scale bars* represent 40 μm (after [27.116]); **(c)** Primary rat myoblasts parallel aligned on collagen-I nanofibers (after [27.100])

Table 27.2 Mechanical properties of electrospun PCL blend nanofibers

Nanofibers		Tensile strength (MPa)	Ref.
PCL–collagen	Parallel	4.88 ± 0.27	[27.22]
	Perpendicular	3.06 ± 0.18	
Chitosan–PCL	Aligned	13.21 ± 3.88	[27.116]
	Random	3.53 ± 0.48	

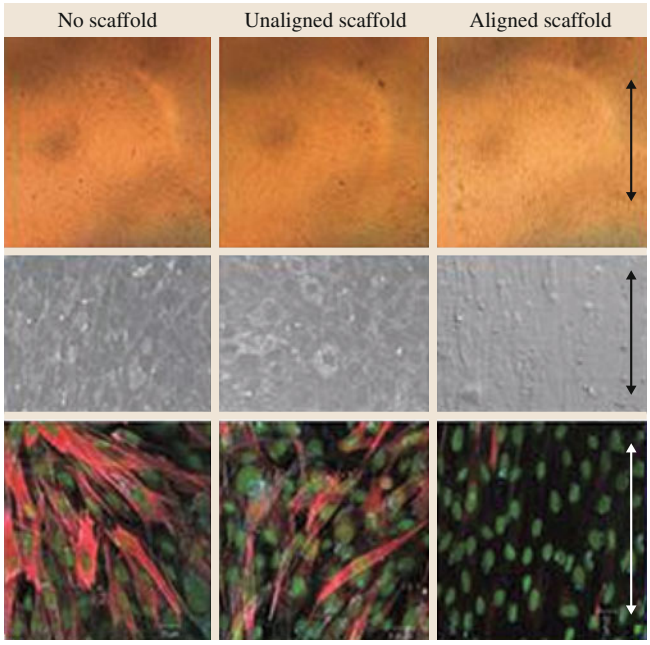


Fig. 27.30 Rabbit corneal fibroblasts (RCF) grown on aligned fibers expressed different amounts of α-SMA than RCFs grown on unaligned fibers and tissue culture dishes. *Top row*: Light-microscopy images of RCFs cultured on tissue culture plates, and on unaligned and aligned electrospun fibrous scaffolds. *Middle Row*: SEM images revealing the morphology of the RCFs grown on the various substrates. *Bottom row*: Immunofluorescence (IF) images of RCFs on the various substrates. Cell nuclei are *green*; α-SMA is stained *red*. *Arrows* indicate direction of fiber alignment (after [27.117]) ▶

an injury occurs to the stroma, this ordered structure is disrupted, leading to myofibroblast infiltration and corneal haze [27.120]. Nanofibers are the natural choice for tissue engineering a corneal stroma equivalent due to its inherent nanofiber composition. Aligned, collagen type I nanofibers, ≈ 30 nm in diameter, have been successfully electrospun using a dual plate glass substrate for collection [27.117]. Corneal fibroblasts uniaxially organized on the aligned collagen type I nanofiber scaffolds and expressed less α-smooth muscle actin (α-SMA, a myofibroblast marker) than those cultured on low-density nanofiber scaffolds, tissue culture plastic, and collagen type I gel (Fig. 27.30) [27.117, 121]. These types of constructs are being explored as an alternative to cornea transplantation.

Synthetic corneal prosthetics are clinically available but experience problems with integration into the eye. One approach to solving this problem is to replace the nonporous outer *skirts* of the synthetic corneas with nanofiber meshes that structurally mimic ECM proteins and allow for a larger surface area for cellular integration [27.123]; For example, a plasma-treated PCL nanofiber skirt for a polyvinyl alcohol (PVA) artificial cornea was able to promote limbal stem cell adhesion and proliferation for up to 10 days, indicating that the host cells on the periphery of the epithelium of the cornea could in fact penetrate and integrate [27.123].

Nanofiber biomaterials offer an alternative scaffold option for culturing limbal stem cells (LSCs) and to use as a transplant device to help LSCs survival; For example, copolymer PA 6/12 nanofibers were electrospun into scaffolds that had no significant effect on LSC growth, proliferation, and metabolic activity when compared with tissue culture plastic [27.122]. However, PKH26-labeled LSCs were able to migrate from the nanofiber scaffold onto the damaged ocular surface in an ocular injury mouse model and restore epithelial function (Fig. 27.31) [27.122]. Further, after transplantation, real-time polymerase chain reaction (RT-PCR) for interleukin-2, interferon-γ, and inducible nitric oxide synthase (inflammatory markers) of the ocular surface indicated that cell-free nanofiber scaffolds were able to reduce the inflammatory response after in-

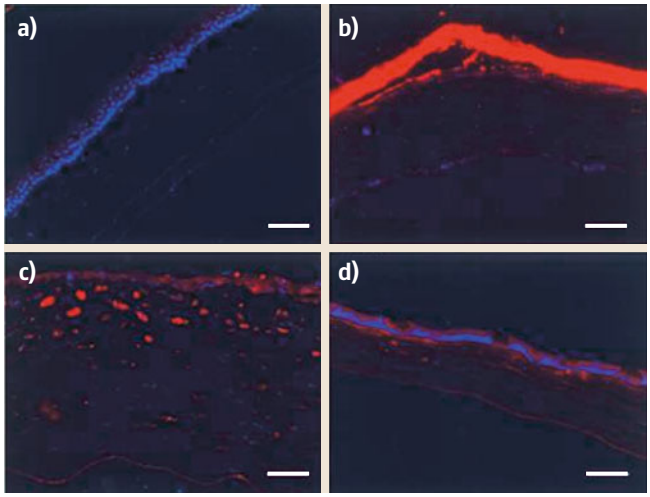


Fig. 27.31a–d Detection of PKH26-labeled LSCs on the damaged ocular surface after their transfer on a PA 6/12 nanofiber scaffold. **(a)** Control undamaged eye without labeled cells, **(b)** from the eye 2 days after operation, **(c)** 7 days and **(d)** 14 days after transfer. *Red stained* cells are still present, and the corneal epithelium is regenerated. *Scale bars*: 50 μm (after [27.122])

jury [27.122]. This demonstrates how proper design of nanofiber biomaterials can be used to modulate cell and immune response.

The retina is another ocular tissue where nanofibers have potential applications in the treatment of vision disorders. Retinitis pigmentosa and age-related macular degeneration cause progressive deterioration of the retina and photoreceptors resulting in loss of vision [27.66]. Delivery of retinal progenitor cells (RPCs) is one of the most promising therapies; however, direct injection of RPCs is ineffective due to a high rate of cell death postinjection [27.66]. Nanofiber scaffolds are a possible delivery vehicle for RPCs to increase cell survival; For example, RPCs were cultured on electrospun PCL (100%), chitosan-graft-PCL at 20 and 40% chitosan, and tissue culture polystyrene. RPCs proliferated faster on 20% CS-PCL nanofibers compared with 100% PCL scaffolds and differentiated more readily towards retinal neurons [27.66]. This was confirmed through quantitative PCR for the retinal developmental markers β type III tubulin, map2, recoverin, rhodopsin, and protein kinase C-α. As these scaffolds are further developed, new therapies to treat retinal disease may be possible.

27.4.4 Neural Tissue Engineering

Neural tissue engineering is a research area where nanofiber biomaterials have been widely used to direct or promote differentiation of stem cells into neuronal cells, guide neuron growth and axon extension, and inhibit glial scar formation by astrocytes. Multiple studies have investigated the relationship between fiber diameter and orientation with the proliferation, differentiation, and elongation of neural stem cells and neurons (NSCs); For example, *Yang* et al. found that the alignment of mouse C17.2 neural stem cells on aligned PLLA nano- and micro-electrospun scaffolds caused cells to extend neurites that were aligned with the nanofibers [27.124].

Neural cell adhesion is a critical step toward nerve regeneration, and physicochemical modification of the surface of nanofibers is often required; For example, *Koh* et al. successfully modified PLLA nanofibers with laminin using covalent binding, physical adsorption, and blended electrospinning methods, which enhanced neurite extension of PC12 cells [27.125]. Nanofibers have also been modified with growth factors or neurotrophic factors to facilitate nerve regeneration. *Horne* et al. modified PCL nanofibers with brain-derived neurotrophic factor (BDNF), which promoted NSC proliferation and survival and directed cell fate towards neuronal and oligodendrocyte specification [27.126]. Similarly, PLLA nanofiber scaffolds surface-modified with ECM proteins and basic fibroblast growth factor (bFGF) significantly induced neurite outgrowth compared with unmodified nanofibers [27.53]. The laminin-derived self-assembling peptide IKVAV, has also been shown to promote neurite sprouting and direct neurite outgrowth. The IKVAV polyacrylamide (IKVAV-PA) gel induced very rapid differentiation of cells into neurons, while suppressing the development of astrocytes [27.42].

Nanofiber scaffolds have also been developed and evaluated for long-term in vivo application; For example, *Zhu* et al. engineered nanofibrous conduits and implanted them into 1 cm lesion of rat sciatic nerve [27.127]. Electrophysiology, histological evaluation, and behavioral analysis showed that aligned nanofiber scaffolds promoted sciatic nerve regeneration after 2 and 12 months and had comparable therapeutic effect to nerve autografts. These scaffolds also showed that NSCs derived from human induced pluripotent stem cells (iPSCs) and embryonic stem cells (ESCs) and implanted in combination with these scaffold promoted axonal myelination and nerve regeneration [27.87].

Electroactive polymers have been used widely in nanofiber scaffolds due to the ability to apply electrical stimulation to engineered neural tissues. Polypyrrole (PPY) has been studied due to its biocompatibility, conductivity, and ease of synthesis; For example, *Lee* et al. cultured PC12 and embryonic hippocampal neurons on conductive nanofibers fabricated by growing PPY on electrospun PLGA nanofibers [27.64]. Electrical stimulation significantly enhanced the differentiation of PC12 cells on the PPY by increasing the number of neurite-bearing cells and the length of the neurites. Electrospun nanofibers of PCL and PLLA have been used as a template for polymerization of PPY for culture of dorsal root ganglion (DRG) neurons (Fig. 27.32) [27.128]. The PPY/PCL nanofibers had a smoother surface than the PPY/PLA nanofibers, and the maximum neurite length on aligned nanofibers ($1723 \pm 339\,\mu m$) was greater than on randomly oriented fibers ($946 \pm 164\,\mu m$). After electrical stimulation was applied for 6 days, the maximum neurite length increased to $2542 \pm 171\,\mu m$ on aligned fibers, demonstrating the effect that electrical stimulation can have on neurite extension. Similarly, *Ghasemi-Mobarakeh* et al. fabricated PCL-gelatin (PCL-G) and PANI/PCL-G nanofibers and applied electrical stimulation through the conductive nanofibrous scaffold on cultured neurons. Cell proliferation and neurite outgrowth were significantly enhanced by electrical stimulation compared with nonstimulated controls [27.129].

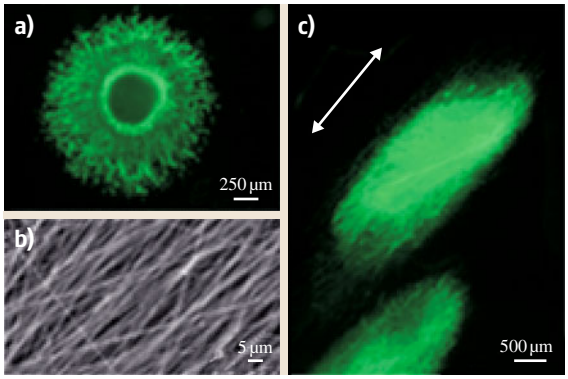


Fig. 27.32 **(a)** Fluorescence micrograph of NF200 showing the DRG neurite field on random PCL–PPY core–sheath nanofibers. **(b)** Aligned PCL–PPY core–sheath nanofibers. **(c)** Fluorescence micrograph showing the DRG neurite field on aligned PCL–PPY core–sheath nanofibers. (The *arrow* indicates the alignment direction for the underlying nanofibers) (after [27.128])

To overcome the difficulties in electrospinning conductive polymers, blended nanofibers of conductive camphorsulfonic acid-doped emeraldine PANI (C-PANI) and gelatin were electrospun and resulted in homogeneous electrospun fibers [27.130]. The biocompatibility of PANI films on PC12 cells was significantly enhanced by grafting adhesive peptides, such as Tyr-Ile-Gly-Ser-Arg.

Conductive polymer nanofibers can enhance neurite formation in the absence of electrical stimulation; For example, *Guo* et al. synthesized and purified a novel electroactive silsesquioxane precursor, *N*-(4-aminophenyl)-*N*′-(4′-(3-triethoxysilyl-propyl-ureido)phenyl-1,4-quinonenediimine) (ATQD), from the emeraldine form of amino-capped aniline trimmers [27.131]. An adhesive oligopeptide, cyclic Arg-Gly-Asp (RGD), was covalently immobilized to the aromatic amine terminals of self-assembled monolayers (SAMs) of ATQD on glass substrates (ATQD-RGD). Similar to tissue-culture-treated polystyrene surfaces, ATQD-RGD supported adhesion and proliferation of PC12 cells, and stimulated spontaneous neurite outgrowth, in the absence of neurotrophic growth factors, such as nerve growth factor (NGF). Ghasemi-Mobarakeh et al. fabricated PCL–gelatin (PG) and PANI/PG nanofibers and applied electrical stimulation through the conductive nanofibrous scaffold of PANI/PG on the cultured nerve cells (Fig. 27.33). Cell proliferation and neurite outgrowth were significantly enhanced by electrical stimulation compared with nonstimulated scaffold [27.129].

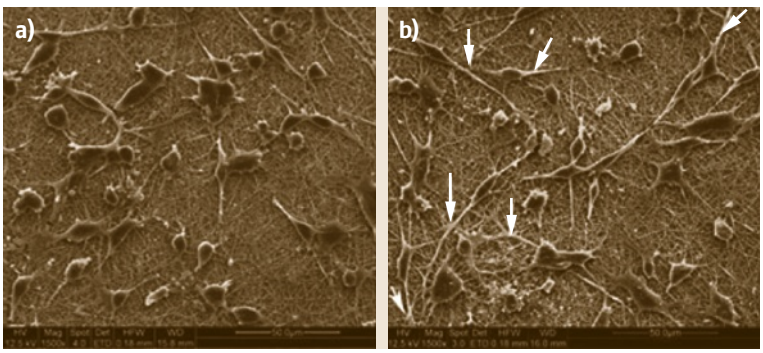


Fig. 27.33a,b Morphology of nerve cells (1500× magnification) on PANI/PG nanofibrous scaffolds: **(a)** without electrical stimulation; **(b)** with electrical stimulation. *Arrows* show neurite extension of neurons (after [27.129])

27.5 Conclusions and Outlook

The field of tissue engineering is rapidly evolving, and nanofiber biomaterials look to have a promising future in this research area. Normal tissues consist of an ECM nanofiber network of proteins and other biopolymers that dynamically interact with cells. Nanofiber biomaterials enable the engineering of biomimetic scaffolds that recapitulate many of these structural, mechanical, and chemical characteristics. A major difference between nanofiber biomaterials and protein fibrils in the ECM is the way they are fabricated. As described, most synthetic and biopolymer nanofibers are created by electrospinning, rotary spinning or phase separation. In contrast, cells build ECM nanofibers by directed and self-assembly processes. Thus, it is likely that the newer processing techniques using self-assembling polypeptides and amphiphiles and surface-initiated assembly

of ECM proteins will lead to improved nanofiber scaffolds for tissue engineering. There is the opportunity to further innovate in the area of nanofiber fabrication with the need for better control of fiber chemistry, size, and surface chemistry. There is also the opportunity to innovate in scaffold fabrication and control of nanofiber alignment in 3-D to better mimic the organization of ECM fibrils in tissue. As these types of fabrication techniques are developed and cell interactions are better understood, new tissue engineering applications will become possible. Current progress in cardiac, skeletal muscle, ophthalmic, and neural tissue engineering demonstrates the breadth of research being conducted and the many advances that have been achieved. However, the absence of Food and Drug Administration (FDA)-approved nanofiber biomaterials indicates that further improvements are needed before this technology reaches the clinic. Fortunately, the tremendous potential of nanofiber biomaterials means progress will continue as this technology is advanced towards the clinic as a viable therapeutic approach in regenerative medicine.

References

27.1 A. Alovskaya, T. Alekseeva, J.B. Phillips, V. King, R. Brown: Fibronectin, collagen, fibrin – Components of extracellular matrix for nerve regeneration, Top. Tissue Eng. **3**, 1–26 (2007), Chap. 12, available online from http://www.oulu.fi/spareparts/ebook_topics_in_t_e_vol3/abstracts/alovskaya_chapter_01.pdf

27.2 P. Bruckner, M. van der Rest: Structure and function of cartilage collagens, Microsc. Res. Tech. **28**(5), 378–384 (1994)

27.3 J.S. Janicki, G.L. Brower: The role of myocardial fibrillar collagen in ventricular remodeling and function, J. Card. Fail. **8**(6), S319–S325 (2002)

27.4 K.E. Kadler, A. Hill, E.G. Canty-Laird: Collagen fibrillogenesis: Fibronectin, integrins, and minor collagens as organizers and nucleators, Curr. Opin. Cell Biol. **20**(5), 495–501 (2008)

27.5 K.E. Kadler, D.F. Holmes, J.A. Trotter, J.A. Chapman: Collagen fibril formation, Biochem. J. **316**(1), 1–11 (1996)

27.6 A.J. Pope, G.B. Sands, B.H. Smaill, I.J. LeGrice: Three-dimensional transmural organization of perimysial collagen in the heart, Am. J. Physiol. Heart Circ. Physiol. **295**(3), H1243–H1252 (2008)

27.7 M. Bernfield, R. Kokenyesi, M. Kato, M.T. Hinkes, J. Spring, R.L. Gallo, E.J. Lose: Biology of the syndecans: A family of transmembrane heparan sulfate proteoglycans, Annu. Rev. Cell Biol. **8**, 365–393 (1992)

27.8 A. Woods, E.S. Oh, J.R. Couchman: Syndecan proteoglycans and cell adhesion, Matrix Biol. **17**, 477–483 (1998)

27.9 X. Lin: Functions of heparan sulfate proteoglycans in cell signaling during development, Development **131**(24), 6009–6021 (2004)

27.10 R. Raman, V. Sasisekharan, R. Sasisekharan: Structural insights into biological roles of protein-glycosaminoglycan interactions, Chem. Biol. **12**(3), 267–277 (2005)

27.11 L. Debelle, A.M. Tamburro: Elastin: Molecular description and function, Int. J. Biochem. Cell Biol. **31**(2), 261–272 (1999)

27.12 D.W. Urry, T. Hugel, M. Seitz, H.E. Gaub, L. Sheiba, J. Dea, J. Xu, T. Parker: Elastin: A representative ideal protein elastomer, Philos. Trans. R. Soc. B **357**(1418), 169–184 (2002)

27.13 J. Pedersen, M. Swartz: Mechanobiology in the third dimension, Ann. Biomed. Eng. **33**(11), 1469–1490 (2005)

27.14 H. Colognato, P.D. Yurchenco: Form and function: The laminin family of heterotrimers, Dev. Dynam. **218**(2), 213–234 (2000)

27.15 K.M. Malinda, H.K. Kleinman: The laminins, Int. J. Biochem. Cell Biol. **28**(9), 957–959 (1996)

27.16 Y. Mao, J.E. Schwarzbauer: Fibronectin fibrillogenesis, a cell-mediated matrix assembly process, Matrix Biol. **24**(6), 389–399 (2005)

27.17 L.G. Griffith, M.A. Swartz: Capturing complex 3D tissue physiology in vitro, Nat. Rev. Mol. Cell Biol. **7**(3), 211–224 (2006)

27.18 Q.P. Pham, U. Sharma, A.G. Mikos: Electrospinning of polymeric nanofibers for tissue engineering applications: A review, Tissue Eng. **12**, 1197–1211 (2006)

27.19 M. Li, Y. Guo, Y. Wei, A.G. MacDiarmid, P.I. Lelkes: Electrospinning polyaniline-contained gelatin nanofibers for tissue engineering applications, Biomaterials **27**, 2705–2715 (2006)

27.20 S.A. Riboldi, M. Sampaolesi, P. Neuenschwander, G. Cossu, S. Mantero: Electrospun degradable polyesterurethane membranes: Potential scaffolds for skeletal muscle tissue engineering, Biomaterials **26**(22), 4606–4615 (2005)

27.21 W.J. Li, R.L. Mauck, J.A. Cooper, X. Yuan, R.S. Tuan: Engineering controllable anisotropy in electrospun biodegradable nanofibrous scaffolds for musculoskeletal tissue engineering, J. Biomech. **40**(8), 1686–1693 (2007)

27.22 J.S. Choi, S.J. Lee, G.J. Christ, A. Atala, J.J. Yoo: The influence of electrospun aligned poly(ε-caprolactone)/collagen nanofiber meshes on the formation of self-aligned skeletal muscle myotubes, Biomaterials **29**(19), 2899–2906 (2008)

27.23 M.P. Prabhakaran, L. Ghasemi-Mobarakeh, S. Ramakrishna: Electrospun composite nanofibers for

tissue regeneration, J. Nanosci. Nanotechnol. **11**(4), 3039–3057 (2011)
27.24 N.F. Huang, S. Patel, R.G. Thakar, J. Wu, B.S. Hsiao, B. Chu, R.J. Lee, S. Li: Myotube assembly on nanofibrous and micropatterned polymers, Nano Lett. **6**(3), 537–542 (2006)
27.25 X. Zong, H. Bien, C.Y. Chung, L. Yin, D. Fang, B.S. Hsiao, B. Chu, E. Entcheva: Electrospun fine-textured scaffolds for heart tissue constructs, Biomaterials **26**, 5330–5338 (2005)
27.26 M.R. Badrossamay, H.A. McIlwee, J.A. Goss, K.K. Parker: Nanofiber assembly by rotary jet-spinning, Nano Lett. **10**, 2257–2261 (2010)
27.27 W.E. Teo, R. Inai, S. Ramakrishna: Technological advances in electrospinning of nanofibers, Sci. Technol. Adv. Mater. **12**(1), 013002–013021 (2011)
27.28 K. Sarkar, C. Gomez, S. Zambrano, M. Ramirez, E. de Hoyos, H. Vasquez, K. Lozano: Electrospinning to forcespinning (TM), Mater. Today **13**(11), 12–14 (2010)
27.29 R.L. Dahlin, F.K. Kasper, A.G. Mikos: Polymeric nanofibers in tissue engineering, Tissue Eng. B **17**(5), 349–364 (2011)
27.30 P.X. Ma, R. Zhang: Synthetic nano-scale fibrous extracellular matrix, J. Biomed. Mater. Res. **46**(1), 60–72 (1999)
27.31 R. Zhang, P.X. Ma: Synthetic nano-fibrillar extracellular matrices with predesigned macroporous architectures, J. Biomed. Mater. Res. **52**(2), 430–438 (2000)
27.32 L. He, B. Liu, G. Xipeng, G. Xie, S. Liao, D. Quan, D. Cai, J. Lu, S. Ramakrishna: Microstructure and properties of nano-fibrous PCL-*b*-PLLA scaffolds for cartilage tissue engineering, Eur. Cell Mater. **18**, 63–74 (2009)
27.33 X.T. Li, Y. Zhang, G.Q. Chen: Nanofibrous polyhydroxyalkanoate matrices as cell growth supporting materials, Biomaterials **29**(27), 3720–3728 (2008)
27.34 X.H. Liu, P.X. Ma: Phase separation, pore structure, and properties of nanofibrous gelatin scaffolds, Biomaterials **30**(25), 4094–4103 (2009)
27.35 J. Zhaoa, W. Hana, H. Chena, M. Tua, R. Zenga, Y. Shic, Z. Chab, C. Zhou: Preparation, structure and crystallinity of chitosan nano-fibers by a solid-liquid phase separation technique, Carbohydr. Polym. **83**(4), 1541–1546 (2011)
27.36 D.F. Mosher, R.B. Johnson: In vitro formation of disulfide-bonded fibronectin multimers, J. Biol. Chem. **258**(10), 6595–6601 (1983)
27.37 K. Sakai, T. Fujii, T. Hayashi: Cell-free formation of disulfide-bonded multimer from isolated plasma fibronectin in the presence of a low concentration of SH reagent under a physiological condition, J. Biochem. **115**(3), 415–421 (1994)
27.38 W.C. Little, M.L. Smith, U. Ebneter, V. Vogel: Assay to mechanically tune and optically probe fibrillar fibronectin conformations from fully relaxed to breakage, Matrix Biol. **25**(7), 451–461 (2008)
27.39 A.W. Feinberg, K.K. Parker: Surface-initiated assembly of protein nanofabrics, Nano Lett. **6**, 2184–2191 (2010)
27.40 C.A. Hauser, S. Zhang: Designer self-assembling peptide nanofiber biological materials, Chem. Soc. Rev. **39**(8), 2780–2790 (2010)
27.41 N. Higashi, T. Koga: Self-assembled peptide nanofibers, Adv. Polym. Sci. **219**, 27–68 (2008)
27.42 F. Gelain: Novel opportunities and challenges offered by nanobiomaterials in tissue engineering, Int. J. Nanomed. **3**(4), 415–424 (2008)
27.43 J.M. Holzwarth, P.X. Ma: 3D nanofibrous scaffolds for tissue engineering, J. Mater. Chem. **21**(28), 10243–10251 (2011)
27.44 R. Vasita, D.S. Katti: Nanofibers and their applications in tissue engineering, Int. J. Nanomed. **1**(1), 15–30 (2006)
27.45 H.A. Behanna, J.J. Donners, A.C. Gordon, S.I. Stupp: Coassembly of amphiphiles with opposite peptide polarities into nanofibers, J. Am. Chem. Soc. **127**(4), 1193–2000 (2005)
27.46 G.A. Silva, C. Czeisler, K.L. Niece, E. Beniash, D.A. Harrington, J.A. Kessler, S.I. Stupp: Selective differentiation of neural progenitor cells by high-epitope density nanofibers, Science **303**(5662), 1352–1355 (2004)
27.47 S.E. Paramonov, H.W. Jun, J.D. Hartgerink: Self-assembly of peptide-amphiphile nanofibers: The roles of hydrogen bonding and amphiphilic packing, J. Am. Chem. Soc. **128**(22), 7291–7298 (2006)
27.48 K.L. Niece, J.D. Hartgerink, J.J. Donners, S.I. Stupp: Self-assembly combining two bioactive peptide-amphiphile molecules into nanofibers by electrostatic attraction, J. Am. Chem. Soc. **125**(24), 7146–7147 (2003)
27.49 J.D. Hartgerink, E. Beniash, S.I. Stupp: Peptide-amphiphile nanofibers: A versatile scaffold for the preparation of self-assembling materials, Proc. Natl. Acad. Sci. USA **99**(8), 5133–5138 (2002)
27.50 P. Hartgerink, D.P. Fessell, J.A. Jacobson, M.T. van Holsbeeck: Full- versus partial-thickness Achilles tendon tears: Sonographic accuracy and characterization in 26 cases with surgical correlation, Radiology **220**(2), 406–412 (2001)
27.51 Y.S. Dagdas, A. Tombuloglu, A.B. Tekinay, A. Dana, M.O. Guler: Interfiber interactions alter the stiffness of gels formed by supramolecular self-assembled nanofibers, Soft Matter **7**, 3524–3532 (2011)
27.52 H.A. Lashuel, S.R. LaBrenz, L. Woo, L.C. Serpell, J.W. Kelly: Protofilaments, filaments, ribbons, and fibrils from peptidomimetic self-assembly: Implications for amyloid fibril formation and materials science, J. Am. Chem. Soc. **122**(22), 5262–5277 (2000)
27.53 S. Patel, K. Kurpinski, R. Quigley, H. Gao, B.S. Hsiao, M.M. Poo, S. Li: Bioactive nanofibers: Synergistic effects of nanotopography and chemical signaling on cell guidance, Nano Lett. **7**(7), 2122–2128 (2007)

27.54 L.A. Smith, P.X. Ma: Nano-fibrous scaffolds for tissue engineering, Colloids Surf. B **39**(3), 125–131 (2004)

27.55 W.J. Li, C.T. Laurencin, E.J. Caterson, R.S. Tuan, F.K. Ko: Electrospun nanofibrous structure: A novel scaffold for tissue engineering, J. Biomed. Mater. Res. A **60**(4), 613–621 (2002)

27.56 H. Yoshimoto, Y.M. Shin, H. Terai, J.P. Vacanti: A biodegradable nanofiber scaffold by electrospinning and its potential for bone tissue engineering, Biomaterials **24**(12), 2077–2082 (2003)

27.57 J.A. Matthews, G.E. Wnek, D.G. Simpson, G.L. Bowlin: Electrospinning of collagen nanofibers, Biomacromolecules **3**(2), 232–238 (2002)

27.58 A. Di Martino, M. Sittinger, M.V. Risbud: Chitosan: A versatile biopolymer for orthopaedic tissue-engineering, Biomaterials **26**(30), 5983–5990 (2005)

27.59 O.H. Kwon, I.S. Lee, Y.G. Ko, W. Meng, K.H. Jung, I.K. Kang, Y. Ito: Electrospinning of microbial polyester for cell culture, Biomed. Mater. **2**(1), S52–S58 (2007)

27.60 B. Duan, L. Wu, X. Yuan, Z. Hu, X. Li, Y. Zhang, K. Yao, M. Wang: Hybrid nanofibrous membranes of PLGA/chitosan fabricated via an electrospinning array, J. Biomed. Mater. Res. A **83A**(3), 868–878 (2007)

27.61 A. Cooper, S. Jana, N. Bhattarai, M. Zhang: Aligned chitosan-based nanofibers for enhanced myogenesis, J. Mater. Chem. **20**(40), 8904–8911 (2010)

27.62 W. Ji, Y. Sun, F. Yang, J.J. van den Beucken, M. Fan, Z. Chen, J.A. Jansen: Bioactive electrospun scaffolds delivering growth factors and genes for tissue engineering applications, Pharm. Res. **28**(6), 1259–1272 (2011)

27.63 D.A. Stout, B. Basu, T.J. Webster: Poly(lactic-co-glycolic acid): Carbon nanofiber composites for myocardial tissue engineering applications, Acta Biomater. **7**(8), 3101–3112 (2011)

27.64 J.Y. Lee, C.A. Bashur, A.S. Goldstein, C.E. Schmidt: Polypyrrole-coated electrospun PLGA nanofibers for neural tissue applications, Biomaterials **30**(26), 4325–4335 (2009)

27.65 L. Li, H. Li, Y. Qian, X. Li, G.K. Singh, L. Zhong, W. Liu, Y. Lv, K. Cai, L. Yang: Electrospun poly (ε-caprolactone)/silk fibroin core-sheath nanofibers and their potential applications in tissue engineering and drug release, Int. J. Biol. Macromol. **49**(2), 223–232 (2011)

27.66 H. Chen, X. Fan, J. Xia, P. Chen, X. Zhou, J. Huang, J. Yu, P. Gu: Electrospun chitosan-graft-poly (ε-caprolactone)/poly (ε-caprolactone) nanofibrous scaffolds for retinal tissue engineering, Int. J. Nanomed. **6**, 453–461 (2011)

27.67 M. Gizdavic-Nikolaidis, S. Ray, J.R. Bennett, A.J. Easteal, R.P. Cooney: Electrospun functionalized polyaniline copolymer-based nanofibers with potential application in tissue engineering, Macromol. Biosci. **10**(12), 1424–1431 (2010)

27.68 Q. Su, A. Zhao, H. Peng, S. Zhou: Preparation and characterization of biodegradable electrospun polyanhydride nano/microfibers, J. Nanosci. Nanotechnol. **10**(10), 6369–6375 (2010)

27.69 K. Kim, M. Yu, X. Zong, J. Chiu, D. Fang, Y.S. Seo, B.S. Hsiao, B. Chu, M. Hadjiargyrou: Control of degradation rate and hydrophilicity in electrospun non-woven poly(d,l-lactide) nanofiber scaffolds for biomedical applications, Biomaterials **24**(27), 4977–4985 (2003)

27.70 E.D. Boland, G.E. Wnek, D.G. Simpson, K.J. Pawlowski, G.L. Bowlin: Tailoring tissue engineering scaffolds using electrostatic processing techniques: A study of poly(glycolic acid) electrospinning, J. Macromolec. Sci. A **38**(12), 1231–1243 (2001)

27.71 D.S. Katti, K.W. Robinson, F.K. Ko, C.T. Laurencin: Bioresorbable nanofiber-based systems for wound healing and drug delivery: Optimization of fabrication parameters, J. Biomed. Mater. Res. B **70**(2), 286–296 (2004)

27.72 Y. Zhang, H. Ouyang, C.T. Lim, S. Ramakrishna, Z.M. Huang: Electrospinning of gelatin fibers and gelatin/PCL composite fibrous scaffolds, J. Biomed. Mater. Res. B **72**(1), 156–165 (2005)

27.73 B.M. Min, G. Lee, S.H. Kim, Y.S. Nam, T.S. Lee, W.H. Park: Electrospinning of silk fibroin nanofibers and its effect on the adhesion and spreading of normal human keratinocytes and fibroblasts in vitro, Biomaterials **25**(7/8), 1289–1297 (2004)

27.74 Y.Z. Zhang, J. Venugopal, Z.M. Huang, C.T. Lim, S. Ramakrishna: Characterization of the surface biocompatibility of the electrospun PCL-collagen nanofibers using fibroblasts, Biomacromolecules **6**(5), 2583–2589 (2005)

27.75 G. Chan, D.J. Mooney: New materials for tissue engineering: Towards greater control over the biological response, Trends Biotechnol. **26**(7), 382–392 (2008)

27.76 M. Gümüşderelioğlu, S. Dalkıranoğlu, R.S. Aydın, S. Cakmak: A novel dermal substitute based on biofunctionalized electrospun PCL nanofibrous matrix, J. Biomed. Mater. Res. A **98A**(3), 461–472 (2011)

27.77 Z.X. Meng, W. Zheng, L. Li, Y.F. Zheng: Fabrication and characterization of three-dimensional nanofiber membrane of PCL-MWCNTs by electrospinning, Mater. Sci. Eng. C **30**(7), 1014–1021 (2010)

27.78 Y. Orlova, N. Magome, L. Liu, Y. Chen, K. Agladze: Electrospun nanofibers as a tool for architecture control in engineered cardiac tissue, Biomaterials **32**, 5615–5624 (2011)

27.79 J.W. Lichtman, J.A. Conchello: Fluorescence microscopy, Nat. Methods **2**(12), 910–919 (2005)

27.80 S.W. Paddock: Principles and practices of laser scanning confocal microscopy, Mol. Biotechnol. **16**(2), 127–149 (2000)

27.81 C. Cremer: Optics far beyond the diffraction limit. In: *Springer Handbook of Lasers and Optics*, 2nd edn., ed. by F. Träger (Springer, Berlin, Heidelberg 2012) pp. 1359–1397, Chap. 20

27.82 C.D. Keating, S.P. Mulvaney: Raman spectroscopy, Anal. Chem. **72**(12), 145r–157r (2000)

27.83 J.J. Santiago-Aviles, Y. Wang, S. Serrano: Raman characterization of carbon nanofibers prepared using electrospinning, Synth. Met. **138**(3), 423–427 (2003)

27.84 R. Nirmala, K.T. Nam, R. Navamathavan, S.J. Park, H.Y. Kim: Hydroxyapatite mineralization on the calcium chloride blended polyurethane nanofiber via biomimetic method, Nanoscale Res. Lett. **6**(1), 2 (2010)

27.85 X. Zong, K. Kim, D. Fang, S. Ran, B.S. Hsiao, B. Chu: Structure and process relationship of electrospun bioabsorbable nanofiber membranes, Polymer **43**(16), 4403–4412 (2002)

27.86 Z.L. Wang: Transmission electron microscopy of shape-controlled nanocrystals and their assemblies, J. Phys. Chem. B **104**(6), 1153–1175 (2000)

27.87 R. Chen, C. Huang, Q. Ke, C. He, H. Wang, X. Mo: Preparation and characterization of coaxial electrospun thermoplastic polyurethane/collagen compound nanofibers for tissue engineering applications, Colloids Surf. B **79**(2), 315–325 (2010)

27.88 M. Xing, W. Zhong, X. Xu, D. Thomson: Adhesion force studies of nanofibers and nanoparticles, Langmuir **26**(14), 11809–11814 (2010)

27.89 E.P.S. Tan, C.T. Lim: Mechanical characterization of nanofibers- A review, Composit. Sci. Technol. **66**, 1102–1111 (2005)

27.90 K.C. Neuman, T. Lionnet, J.-F. Alleman: Single-molecule micromanipulation techniques, Annu. Rev. Mater. Res. **37**, 33–67 (2007)

27.91 C.R. Carlisle, C. Coulais, M. Guthold: The mechanical stress–strain properties of single electrospun collagen type I nanofibers, Acta Biomater. **6**(8), 2997–3003 (2010)

27.92 A. Ishijima, H. Kojima, H. Higuchi, Y. Harada, T. Funatsu, T. Yanagida: Multiple- and single-molecule analysis of the actomyosin motor by nanometer piconewton manipulation with a microneedle: Unitary steps and forces, Biophys. J. **70**(1), 383–400 (1996)

27.93 R. Merkel, P. Nassoy, A. Leung, K. Ritchie, E. Evans: Energy landscapes of receptor-ligand bonds explored with dynamic force spectroscopy, Nature **397**(6714), 50–53 (1999)

27.94 C. Veigel, C.F. Schmidt: Moving into the cell: Single-molecule studies of molecular motors in complex environments, Nat. Rev. Mol. Cell Biol. **12**(3), 163–176 (2011)

27.95 K.C. Neuman, A. Nagy: Single-molecule force spectroscopy: Optical tweezers, magnetic tweezers and atomic force microscopy, Nat. Meth. **5**(6), 491–505 (2008)

27.96 G.E. Park, T.J. Webster: A review of nanotechnology for the development of better orthopedic implants, J. Biomed. Nanotechnol. **1**(1), 18–29 (2005)

27.97 Z.G. Zhang, Z.H. Li, X.Z. Mao, W.C. Wang: Advances in bone repair with nanobiomaterials: Mini-review, Cytotechnology **63**(5), 437–443 (2011)

27.98 R. James, M. Deng, C.T. Laurencin, S.G. Kumbar: Nanocomposites and bone regeneration, Frontiers Mater. Sci. **5**(4), 342–357 (2011)

27.99 M. Keeney, J.H. Lai, F. Yang: Recent progress in cartilage tissue engineering, Curr. Opin. Biotechnol. **22**(5), 734–740 (2011)

27.100 J.P. Beier, D. Klumpp, M. Rudisile, R. Dersch, J.H. Wendorff, O. Bleiziffer, A. Arkudas, E. Polykandriotis, R.E. Horch, U. Kneser: Collagen matrices from sponge to nano: New perspectives for tissue engineering of skeletal muscle, BMC Biotechnol. **9**, 34 (2009)

27.101 V.L. Roger, A.S. Go, D.M. Lloyd-Jones, R.J. Adams, J.D. Berry, T.M. Brown, M.R. Carnethon, S. Dai, G. de Simone, E.S. Ford, C.S. Fox, H.J. Fullerton, C. Gillespie, K.J. Greenlund, S.M. Hailpern, J.A. Heit, P.M. Ho, V.J. Howard, B.M. Kissela, S.J. Kittner, D.T. Lackland, J.H. Lichtman, L.D. Lisabeth, D.M. Makuc, G.M. Marcus, A. Marelli, D.B. Matchar, M.M. McDermott, J.B. Meigs, C.S. Moy, D. Mozaffarian, M.E. Mussolino, G. Nichol, N.P. Paynter, W.D. Rosamond, P.D. Sorlie, R.S. Stafford, T.N. Turan, M.B. Turner, N.D. Wong, J. Wylie-Rosett, American Heart Association Statistics Committee, Stroke Statistics Subcommittee: Heart disease and stroke statistics-2011 update, Circulation **123**, e18–e209 (2011)

27.102 D. Kai, M.P. Prabhakaran, G. Jin, S. Ramakrishna: Guided orientation of cardiomyocytes on electrospun aligned nanofibers for cardiac tissue engineering. Journal of biomedical materials research, Appl. Biomater. B **98**, 379–386 (2011)

27.103 D. Li, Y. Wang, Y. Xia: Electrospinning of polymeric and ceramic nanofibers as uniaxially aligned arrays, Nano Lett. **3**, 1167–1171 (2003)

27.104 G.C. Engelmayr Jr., M. Cheng, C.J. Bettinger, J.T. Borenstein, R. Langer, L.E. Freed: Accordion-like honeycombs for tissue engineering of cardiac anisotropy, Nat. Mater. **7**, 1003–1010 (2008)

27.105 I.J. Legrice, P.J. Hunter, B.H. Smaill: Laminar structure of the heart: A mathematical model, Am. J. Physiol. **272**, H2466–H2476 (1997)

27.106 R.J. Young, A.V. Panfilov: Anisotropy of wave propagation in the heart can be modeled by a Riemannian electrophysiological metric, Proc. Natl. Acad. Sci. **107**, 15063–15068 (2010)

27.107 E. Fernandes, V. Zucolotto, A. De Queiroz: Electrospinning of hyperbranched poly-L-lysine/polyaniline nanofibers for application in cardiac tissue engineering, J. Macromolec. Sci. A **47**, 1203–1207 (2010)

27.108 A. Borriello, V. Guarino, L. Schiavo, M.A. Alvarez-Perez, L. Ambrosio: Optimizing PANi doped electroactive substrates as patches for the regeneration of cardiac muscle, J. Mater. Sci. Mater. Med. **22**, 1053–1062 (2011)
27.109 H.D. Guo, G.H. Cui, H.J. Wang, Y.Z. Tan: Transplantation of marrow-derived cardiac stem cells carried in designer self-assembling peptide nanofibers improves cardiac function after myocardial infarction, Biochem. Biophys. Res. Commun. **399**, 42–48 (2010)
27.110 H. Hosseinkhani, M. Hosseinkhani, S. Hattori, R. Matsuoka, N. Kawaguchi: Micro and nano-scale in vitro 3D culture system for cardiac stem cells, J. Biomed. Mater. Res. A **94**, 1–8 (2010)
27.111 O. Ishii, M. Shin, T. Sueda, J.P. Vacanti: In vitro tissue engineering of a cardiac graft using a degradable scaffold with an extracellular matrix-like topography, J. Thorac. Cardiovasc. Surg. **130**, 1358–1363 (2005)
27.112 N. Ashammakhi, A. Ndreu, Y. Yang, H. Ylikauppila, L. Nikkola: Nanofiber-based scaffolds for tissue engineering, Eur. J. Plast. Surg. **35**, 135–149 (2012)
27.113 X.M. Mo, C.Y. Xu, M. Kotaki, S. Ramakrishna: Electrospun P(LLA-CL) nanofiber: A biomimetic extracellular matrix for smooth muscle cell and endothelial cell proliferation, Biomaterials **25**, 1883–1890 (2004)
27.114 D.A. Narmoneva, R. Vukmirovic, M.E. Davis, R.D. Kamm, R.T. Lee: Endothelial cells promote cardiac myocyte survival and spatial reorganization: Implications for cardiac regeneration, Circulation **110**, 962–968 (2004)
27.115 C.A. Edwardo, P. Petrosko, T.O. Acarturk, P.A. DiMilla, W.A. LaFramboise, P.C. Johnson: Muscle tissue engineering, Clin. Plast. Surg. **26**(4), 647–656 (1999)
27.116 A. Cooper, S. Jana, N. Bhattarai, M.Q. Zhang: Aligned chitosan-based nanofibers for enhanced myogenesis, J. Mater. Chem. **20**(40), 8904–8911 (2010)
27.117 L.S. Wray, E.J. Orwin: Recreating the microenvironment of the native cornea for tissue engineering applications, Tissue Eng. A **15**(7), 1463–1472 (2009)
27.118 Y. Komai, T. Ushiki: The three-dimensional organization of collagen fibrils in the human cornea and sclera, Invest. Ophthalmol. Vis. Sci. **32**(8), 2244–2258 (1991)
27.119 K.M. Meek, C. Boote: The organization of collagen in the corneal stroma, Exp. Eye Res. **78**(3), 503–512 (2004)
27.120 J.V. Jester, W.M. Petroll, P.A. Barry, H.D. Cavanagh: Expression of alpha-smooth muscle (alpha-SM) actin during corneal stromal wound healing, Invest. Ophthalmol. Vis. Sci. **36**(5), 809–819 (1995)
27.121 D. Phu, L.S. Wray, R.V. Warren, R.C. Haskell, E.J. Orwin: Effect of substrate composition and alignment on corneal cell phenotype, Tissue Eng. A **17**(5/6), 799–807 (2011)
27.122 A. Zajicova, K. Pokorna, A. Lencova, M. Krulova, E. Svobodova, S. Kubinova, E. Sykova, M. Pradny, J. Michalek, J. Svobodova, M. Munzarova, V. Holan: Treatment of ocular surface injuries by limbal and mesenchymal stem cells growing on nanofiber scaffolds, Cell Transplant. **19**(10), 1281–1290 (2010)
27.123 H. Bakhshandeh, M. Soleimani, S.S. Hosseini, H. Hashemi, I. Shabani, A. Shafiee, A.H. Nejad, M. Erfan, R. Dinarvand, F. Atyabi: Poly (varepsilon-caprolactone) nanofibrous ring surrounding a polyvinyl alcohol hydrogel for the development of a biocompatible two-part artificial cornea, Int. J. Nanomed. **6**, 1509–1515 (2011)
27.124 F. Yang, R. Murugan, S. Wang, S. Ramakrishna: Electrospinning of nano/micro scale poly(L-lactic acid) aligned fibers and their potential in neural tissue engineering, Biomaterials **26**(15), 2603–2610 (2005)
27.125 H.S. Koh, T. Yong, C.K. Chan, S. Ramakrishna: Enhancement of neurite outgrowth using nanostructured scaffolds coupled with laminin, Biomaterials **29**(26), 3574–3582 (2008)
27.126 M.K. Horne, D.R. Nisbet, J.S. Forsythe, C.L. Parish: Three-dimensional nanofibrous scaffolds incorporating immobilized BDNF promote proliferation and differentiation of cortical neural stem cells, Stem Cell. Dev. **19**(6), 843–852 (2010)
27.127 Y. Zhu, A. Wang, S. Patel, K. Kurpinski, E. Diao, X. Bao, G. Kwong, W.L. Young, S. Li: Engineering bi-layer nanofibrous conduits for peripheral nerve regeneration, Tissue Eng. C **17**(7), 705–715 (2011)
27.128 J. Xie, M.R. Macewan, S.M. Willerth, X. Li, D.W. Moran, S.E. Sakiyama-Elbert, Y. Xia: Conductive core-sheath nanofibers and their potential application in neural tissue engineering, Adv. Funct. Mater. **19**(14), 2312–2318 (2009)
27.129 L. Ghasemi-Mobarakeh, M.P. Prabhakaran, M. Morshed, M.H. Nasr-Esfahani, H. Baharvand, S. Kiani, S.S. Al-Deyab, S. Ramakrishna: Application of conductive polymers, scaffolds and electrical stimulation for nerve tissue engineering, J. Tissue Eng. Regen. Med. **5**(4), e17–e35 (2011)
27.130 M. Li, Y. Guo, Y. Wei, A.G. MacDiarmid, P.I. Lelkes: Electrospinning polyaniline-contained gelatin nanofibers for tissue engineering applications, Biomaterials **27**(13), 2705–2715 (2006)
27.131 Y. Guo, M. Li, A. Mylonakis, J. Han, A.G. MacDiarmid, X. Chen, P.I. Lelkes, Y. Wei: Electroactive oligoaniline-containing self-assembled monolayers for tissue engineering applications, Biomacromolecules **8**(10), 3025–3034 (2007)

Part G Applications

Part G Applications and Impact

28 Nanostructured Materials for Energy-Related Applications

Arava L.M. Reddy, Houston, USA
Sundara Ramaprabhu, Chennai, India

29 Nanomaterials in Civil Engineering

Jaesang Lee, Seoul, Korea
Seunghak Lee, Seoul, Korea
Eunhyea Chung, Seoul, Korea
Vincent C. Reyes, Los Angeles, USA
Shaily Mahendra, Los Angeles, USA

30 Plasmonic Nanomaterials for Nanomedicine

Renat R. Letfullin, Terre Haute, USA
Thomas F. George, St. Louis, USA

31 Carbon Nanotube Membrane Filters

Anchal Srivastava, Lanka, Varanasi, India
Saurabh Srivastava, New Rajender Nagar, India
Kaushik Kalaga, Houston, USA

32 Nanomaterial Toxicity, Hazards, and Safety

Zuzanna A. Lewicka, Houston, USA
Vicki L. Colvin, Houston, USA

28. Nanostructured Materials for Energy-Related Applications

Arava L.M. Reddy, Sundara Ramaprabhu

Materials play a key role especially in the field of energy storage and conversion. Design of efficient and cost-effective materials for energy applications is of prime research focus. This chapter presents the recent trends in the energy-related applications of various carbon nanotubes (CNT) and their hybrid nanostructures. Development of CNT-based electrocatalysts for proton exchange membrane fuel cells and CNT-based electrodes for supercapacitors and Li-ion batteries are discussed.

28.1 **Energy-Related Carbon Nanotubes** 1013
28.1.1 Catalytic Support in Proton Exchange Membrane Fuel Cells (PEMFC) 1013
28.1.2 Electrochemical Supercapacitors... 1015
28.1.3 Lithium-Ion Batteries 1015

28.2 **CNTs as Support Material for Electrocatalysts in PEMFC** 1016
28.2.1 Nonnoble Metal Based Electrocatalysts for Fuel Cells 1020

28.3 **CNTs as Supercapacitor Electrode Materials** 1023
28.3.1 Cyclic Voltammetry 1025
28.3.2 Galvanostatic Charge–Discharge... 1027
28.3.3 Electrochemical Impedance Spectroscopy 1027
28.3.4 Lithium-Ion Batteries 1029

References 1032

Nanostructured materials have attracted great interest in recent years because of their unusual chemical, mechanical, electrical, and optical properties. The discovery of fullerenes [28.1] has significantly raised the general interest in carbon research activity. CNTs are currently the focus of intense research worldwide because of their unique properties that could impact various areas of science and technology. Various carbon-based materials have been used in fuel cells, batteries, and other electrochemical applications for decades [28.2–4]. Several studies have shown the superiority of carbon nanotubes over other carbon-based electrodes for applications in fuel cells, supercapacitors, and batteries [28.4, 5] due to their superior physical and chemical properties. Some of the energy-related applications of CNTs are reviewed in the following sections.

28.1 Energy-Related Carbon Nanotubes

28.1.1 Catalytic Support in Proton Exchange Membrane Fuel Cells (PEMFC)

Fuel cells, which are energy-converting devices with high efficiency and low/zero emissions, have attracted increasing attention in recent decades due to high energy demands, fossil-fuel depletion, and environmental pollution. A fuel cell is an electrochemical device which converts chemical energy to electrical energy. It uses hydrogen (hydrogen-rich fuel) and oxygen to create electricity. A single fuel cell consists of an electrolyte sandwiched between two thin electrodes (anode and cathode). Depending on the operation temperature and kind of electrolyte they employ, fuel cells are classified as follows:

1. Proton exchange membrane fuel cells (PEMFC)
2. Direct alcohol fuel cells (DAFC)
3. Alkaline fuel cells (AFC)
4. Phosphoric acid fuel cells (PAFC)

5. Molten carbonate fuel cells (MCFC)
6. Solid oxide fuel cells (SOFC)
7. Microbial fuel cells (MFC).

The primary components of a PEMFC are an ion-conducting electrolyte, a cathode, and an anode, as shown schematically in Fig. 28.1. Together, these are often referred to as the membrane electrode assembly (MEA). PEMFCs have attracted enormous research interest as power sources for vehicles and portable electronic devices [28.6]. They use a solid ion-exchange polymer as an electrolyte and porous carbon-containing platinum catalyst as electrodes, with hydrated protons as the charge carriers. The operating temperatures are below 120 °C, limited by the polymer properties. The most widely implemented electrolyte in PEMFC is Nafion (poly-perfluorosulfonic acid polymer), manufactured by DuPont, USA. Pt nanoparticles supported on carbon are used as electrocatalysts for both anode and cathode. PEMFC are typically fueled with pure hydrogen supplied from storage tanks or onboard reformers. Hydrogen fuel is channeled to the anode, where it catalytically splits into protons and electrons. The electrolyte membrane allows the protons to pass through to the cathode, while the electrons are forced to follow an external circuit, forming an electric current. At the cathode, the electrons and protons combine with oxygen to form water and heat. Highly porous carbon paper or carbon fabric treated with a hydrophobic polymer (e.g., polytetrafluoroethylene (PTFE)) is typically used as the current collector, which also serves as a gas diffusion layer. To fabricate a fuel cell stack, graphite bipolar plates are placed between individual MEAs. The Pt content (Pt loading) in PEMFCs has been reduced dramatically over the past decade from ≈ 4 to $\approx 0.6\,\mathrm{mg/cm^2}$, as a result of optimal dispersion of the Pt nanoparticles in the electrocatalyst layer of the fuel cell [28.7]. Due to Pt supply limitations, a further reduction in Pt loading by about fivefold needs to be achieved, for cost-effective large-scale automotive applications [28.8]. The various Pt, Pt-alloy, and non-Pt oxygen reduction catalysts for PEMFCs, together with the activity benchmark, have been extensively reviewed by *Gasteiger* et al. [28.8]. Recently, nanostructured Pt-M/C (M = Fe and Co) electrocatalysts have been synthesized by various routes and used for the oxygen reduction in PEMFCs [28.9–11]. The electrocatalytic activity of Pt depends on many factors such as high surface area and good electronic activity of the conductive catalyst support [28.12, 13].

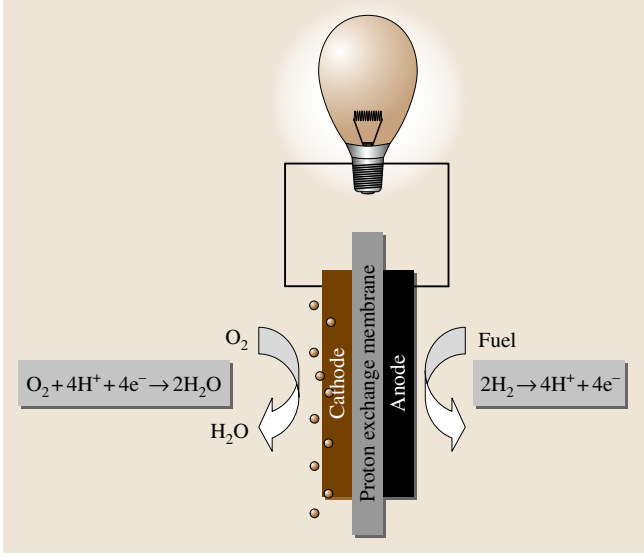


Fig. 28.1 Schematic illustration of a PEMFC, comprising an electrolyte, an anode, and a cathode

At present, Pt dispersed on carbon is used as electrocatalyst in PEMFC. The morphology and size of CNTs make them very significant in catalytic applications due to their ability to disperse catalytically active metal particles [28.14]. The high accessible surface area, interesting electronic properties, and high stability suggest that CNTs are suitable materials for electrodes and catalyst support in PEMFCs [28.15], effectively reducing the Pt catalyst loading and improving fuel cell performance. Functionalization and oxidation of CNTs have been shown to be effective for better loading and dispersion of the metal particles [28.16–18]. Various methods have been followed in the literature to prepare metal-loaded CNTs [28.19, 20]. The various chemical and electrochemical depositions of platinum group metals (PGMs) and their applications in fuel cell technologies have been reviewed [28.21–23]. Pt nanoparticles have been electrodeposited on multi-walled carbon nanotubes (MWNTs) by the potentiostatic method, and the electrocatalytic activity for oxygen reduction has been studied [28.13, 24]. Pt- and Pt-Ru-loaded MWNTs have been used for the methanol oxidation in direct methanol fuel cells (DMFC) [28.25, 26]. In recent years, there has been considerable interest in the design and development of micro fuel cells based on various technologies for their application in portable devices [28.27–30]. Microfabrication technology has been applied in the design of small fuel cells [28.31]. Planar micro fuel cells have been developed using micropatterning technology [28.32].

28.1.2 Electrochemical Supercapacitors

In response to the changing global landscape, energy has become a primary focus of the major world powers and scientific community. There has been great interest in developing and refining more efficient energy storage devices. One such device, the supercapacitor, has matured significantly over the last decade and emerged with the potential to facilitate major advances in energy storage. Supercapacitors are electrochemical capacitors with high capacitance and power density, typically comprising two electrodes separated by an insulating material that is ionically conducting in electrochemical devices [28.33]. They store electric energy in an electrochemical double layer formed at the solid–electrolyte interface. A schematic diagram showing the principle of a supercapacitor is shown in Fig. 28.2. Positive and negative charges from the electrolyte accumulate at the surface of the electrodes and compensate for the electronic charges at the electrode surface. The resulting charge distribution is called an electric double layer or electrochemical double layer (ECDL). The capacity of an electrochemical supercapacitor inversely depends on the separation between the charge on the electrode and the countercharge in the electrolyte. To achieve high capacitance, porous electrode materials with large accessible surface area are used. Based on the electrode materials, electrochemical capacitors are classified into three main categories, being based on carbon, metal oxides, and polymeric materials [28.34]. Due to their high specific surface area, relatively low cost, availability, and established production technology, use of activated carbon materials as the electrode materials in supercapacitors has been intensively investigated during the last decades [28.33–37]. The experimentally measured capacitance of activated carbons is not in good agreement with the theoretical values, since a significant part of the surface area remains in micropores which are not accessible to the electrolyte ions [28.33]. Therefore, pore size distribution together with surface area is important for the determination of electric double layer capacitance [28.38]. CNTs with their narrow distribution of mesopore sizes, highly accessible surface area, low resistivity, and high stability have attracted great interest worldwide as electrode materials for supercapacitors [28.38–41]. Supercapacitors fabricated using CNT-nanocomposite electrodes have shown enhanced performance due to the high usage efficiency of specific surface area following from the disintegrated bundle structure of CNTs. *Frackowiak* et al. [28.40] reported improved supercapacitance of composite electrodes

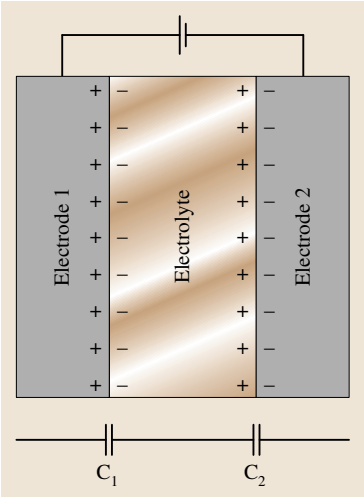


Fig. 28.2 Schematic illustration of an electrochemical double layer (ECDL) supercapacitor and its equivalent circuit in a two-electrode system

based on MWNTs deposited with polypyrrole (PPY). Nanocomposites of electronically conducting polymers (ECPs) and MWNTs have been used as electrode materials for supercapacitors, and the specific capacitance of these composite electrodes has been determined using different cell configurations [28.42]. Recently, supercapacitor electrodes fabricated using metal oxide/MWNT nanocomposite materials have shown increased specific capacitance with an improvement in cycle life and power density [28.43, 44]. In recent years, supercapacitors coupled with batteries have been considered as promising hybrid devices to combine the best features of each [28.45].

28.1.3 Lithium-Ion Batteries

A battery is an electrochemical device that has the ability to convert chemical energy to useful electrical energy. The basic battery consists of an anode, a cathode, an electrolyte, separators, and the external case. Among various batteries, rechargeable lithium batteries have revolutionized portable electronic devices due to their superior energy density [28.46–55]. They have become the dominant power source for cellphones, digital cameras, laptops, etc. The rechargeable lithium battery does not contain lithium metal. The basic principle of rechargeable lithium batteries is electrochemical intercalation and de-intercalation of lithium in both electrodes. The cathode materials are transition-metal oxides (Li_xMO_2, where M is the transition metal), while carbon materials are used as anodes. On charging, lithium ions are de-intercalated from the layered cathodes, pass across the electrolyte, and are intercalated

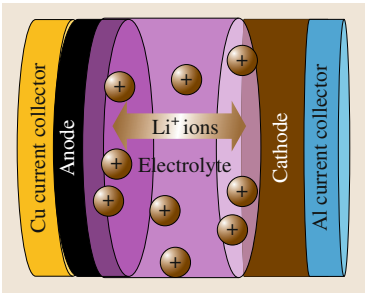


Fig. 28.3 Scheme of a common lithium ion battery

between the graphite layers in the anode (Fig. 28.3). The reverse process takes place during discharge.

Starting from microsized graphite powder or coke, various carbon structures including carbon nanowires, nanotubes, few layers of graphene, and fullerenes have been tried as negative electrodes for rechargeable lithium batteries due to their low cost and low operational voltage [28.56–64]. Highly reversible and irreversible capacities have been obtained for single-walled carbon nanotubes (SWNTs) [28.64]. Although carbon nanotubes exhibit twice the lithium storage compared with graphite, problems of surface-layer formation and safety limit their application. Carbon nanotubes do not seem to offer a major route to improved electrodes for lithium-ion batteries. In the search for alternatives to graphite/carbon nanotubes that will combine inherent protection against lithium deposition with low cost, low toxicity, and the ability to be fabricated as a nanomaterial delivering fast lithium insertion/removal, attention has focused on insertion metal alloys, e.g., Li_yM (M = Sn, Pb, Si, In, etc.) [28.65–74]. Such alloys have specific capacities which exceed that of the conventional graphite anode, for example, $Li_{4.4}Sn$ (993 mAh/g versus 372 mAh/g). However, the severe volume change which accompanies the alloy forming–decomposition process ($\approx 300\%$) causes progressive cracking and leads to pulverization of the metal particles, thereby inducing losses of contact between them [28.65–70]. Therefore, although greatly appealing in terms of storage capacity, lithium alloy electrodes are difficult to use in practice. Thus, processes based on intercalation/de-intercalation are inevitably limited in capacity, and the process based on insertion alloys is limited by cycle life. In the search for other options using lithium in the solid state that are not constrained by the requirements of intercalation/insertion, it has been shown that lithium can react with a range of transition-metal oxides by a process termed conversion. Various transition-metal oxides have been widely studied as electrode materials for rechargeable lithium-ion batteries because of their high theoretical capacity, safety, environmental benignity, and low cost [28.75–82]. However, the poor electronic conductivity of metal oxides limits their use in high-performance lithium ion batteries. One of the other challenging issues is to tackle their capacity decay with cycling, resulting from large volume expansion during the lithium uptake/release process. Extensive research efforts are presently being devoted to overcome these problems by using electronically conductive additives and carbon coatings [28.83–86].

28.2 CNTs as Support Material for Electrocatalysts in PEMFC

Wide application of PEMFCs is hindered by their high cost. It is generally believed that the large amount of depleting platinum required as a catalyst in PEMFCs is one of the main reasons why fuel cells are excluded from commercialization. In the past two decades, continuous efforts have been devoted to increase the utilization of Pt and reduce the amount of Pt used in PEMFCs. Electrocatalysts with small size and high dispersion result in high electrocatalytic activity [28.87]. This suggests that it is highly desirable to have good Pt supporting materials with high surface area, which will enhance the Pt dispersion and hence reduce the catalyst loading, thereby improving fuel cell performance [28.88–91]. CNTs are attractive materials for catalyst support in PEMFCs due to their morphology and interesting properties such as nanometer size, high accessible surface area, corrosion resistance, good electronic conductivity, and high stability [28.92]. Several methods have been developed to decorate CNTs with catalytic metal nanoparticles [28.15,93,94]. However, it is important to develop techniques to improve adhesion through surface modification such as functionalization of CNTs before the decoration of metal nanoparticles [28.95, 96]. CNT-supported Pt (Pt/MWNTs, Pt/SWNTs, and Pt/MWNCs (multi-walled carbon nanocoils)) electrocatalysts have been extensively prepared by the chemical reduction method using a Pt salt and prefunctionalized CNTs, synthesized by pyrolysis of acetylene/methane over hydrogen-decrepitated $MmNi_3$ hydride catalysts [28.95–97]. The pretreated

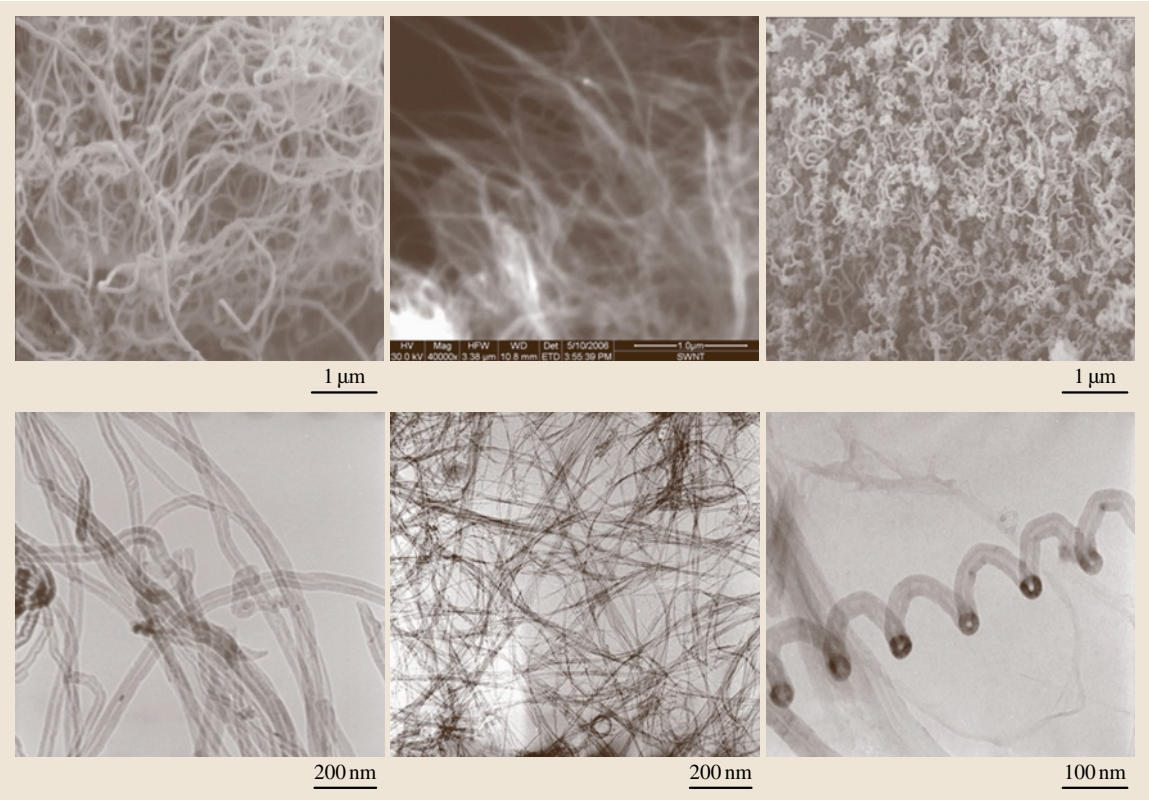


Fig. 28.4 SEM and TEM images of MWNT, SWNT, and MWNC synthesized by catalytic decomposition of acetylene/methane over alloy hydride catalyst (after [28.97])

CNTs were functionalized with carboxylic acid groups attached to act as anchoring sites for better adherence of Pt nanoparticles onto the CNT surface, thereby giving better performance at higher current densities.

Morphological characteristics of CNTs were obtained using scanning electron microscopy (SEM) and transmission electron microscopy (TEM). Figure 28.4 shows SEM and TEM images of different types of CNTs synthesized by pyrolysis of acetylene/methane over hydrogen-decrepitated $MmNi_3$ hydride catalysts. The crystallinity of the samples was obtained by x-ray powder diffraction (XRD) analysis, performed with monochromatic $Cu-K_\alpha$ radiation. Figure 28.5 shows the XRD pattern of as-prepared MWNTs using alloy hydrides as catalysts. The peaks are indexed to the reflections of hexagonal graphite. A few peaks corresponding to the catalytic impurities are also seen. The removal of metallic impurities by acid treatment is observed from the XRD patterns of purified MWNTs (Fig. 28.5b). The broader diffraction peaks of Pt along with hexagonal graphitic reflections for Pt/MWNTs are shown in Fig. 28.5c. Figure 28.6 shows SEM, TEM, and high-resolution TEM (HRTEM) images of Pt/MWNTs, Pt/SWNT, and Pt/MWNC. TEM images of Pt/CNTs show a more or less uniform distribution of noble-metal particles ($\approx 3-5$ nm) on the CNTs. The HRTEM image clearly shows lattice planes of Pt particles, indicating the crystalline nature of the catalytic Pt. The amount of Pt loaded on the CNT support was qualitatively evaluated to be 20% from energy-dispersive analysis (EDAX).

Half-cell reactions were carried out in three-arm electrochemical cell using PSGSTAT-30 (AUTOLAB). In the preparation of the working electrode, about 5 mg Pt/CNTs and 5 µL diluted Nafion (0.05 wt % Nafion) in ethanol were mixed using an ultrasonic bath. A measured volume of this mixture was then pipetted onto a glassy carbon electrode (0.03 cm^2) substrate and dried at room temperature for 24 h. The thickness of the film was estimated to be less than 0.1 µm, with platinum

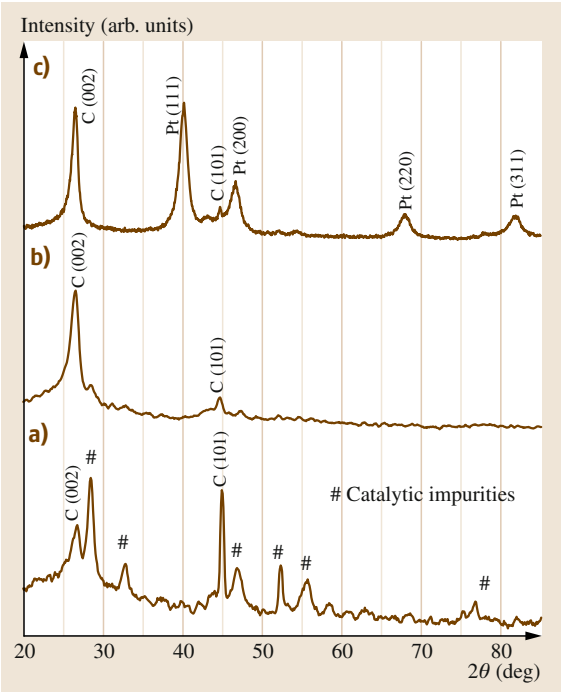


Fig. 28.5a–c Powder x-ray diffractograms of **(a)** as-grown MWNTs, **(b)** purified MWNTs prepared by pyrolysis of acetylene over $MmNi_3$ alloy hydride catalyst, and **(c)** Pt/MWNTs (after [28.95])

loading of 15 μg Pt/cm^2. A thin film is necessary to minimize diffusion resistance in the Nafion film. For comparison, x wt% Pt/MWNTs and y wt% Pt/C, with $x + y = 100$, where $x = 0$, 25, 50, 75, and 100 electrodes were prepared under the same conditions. Pt foil and saturated calomel electrode (SCE) were used as counter and reference electrodes, respectively. Initially, the electrode was operated by applying potential between -0.2 and $+1.2$ V at 0.05 V/s for 20 min in 0.1 M $HClO_4$ solution to eliminate any contamination in the Nafion membrane. Hydrodynamic voltammograms of different electrodes were recorded by scanning its potential from -0.25 to $+1.0$ V at 0.02 V/s in oxygen-saturated 0.1 M $HClO_4$. The electrolyte and reference electrode were refreshed every 4–6 h to avoid contamination such as chloride during the test. Desorption of underpotentially deposited hydrogen in a stationary voltammogram was used to evaluate the electrochemically active surface area (ECSA) of the Pt catalyst on the electrode. The ECSA of an electrocatalyst is a measure of the number of electrochemically active sites per gram of catalyst. The ECSA is an important parameter to compare different electrocatalytic supports of electrode materials, being determined by integrating the area under the potential window for H^+ adsorption/desorption peaks after subtracting the charge from the double layer region. Figure 28.7 shows cyclic voltammograms for H adsorption on different composites of Pt/C and Pt/MWNTs. Characteristic peaks in the negative region (0–0.1 V) are attributed to atomic hydrogen adsorption on the Pt surface and reflect the ECSA of Pt. The integrated area of the cyclic voltammogram represents Q_H (the charge arising from hydrogen evolution reactions) and can be used to determine the ECSA by employing the expression [28.98, 99]

$$\text{ESCA}\left(\frac{\text{cm}^2}{\text{g}}\text{ of Pt}\right) = \frac{Q_H\left(\frac{\mu\text{C}}{\text{cm}^2}\right)}{\left[210\left(\frac{\mu\text{C}}{\text{cm}^2}\right)\times\text{Electrode loading}\left(\frac{\text{g of Pt}}{\text{cm}^2}\right)\right]} . \quad (28.1)$$

Initially, the characteristic peaks increase with increase of Pt/MWNT content in the composite electrodes, reaching a maximum for the 50 wt % Pt/C + 50 wt % Pt/MWNTs composite electrode, which shows a remarkably larger peak reflecting a high surface area. With further increase of the Pt/MWNTs concentration in the composite electrode, a decrease in the characteristic peak is observed. The ECSA of Pt/C, Pt/SWNTs, and 50 wt % Pt/C + 50 wt % Pt/SWNTs composites have been found to be 56 m^2/g$_{Pt}$, 102 m^2/g$_{Pt}$, and 118 m^2/g$_{Pt}$, respectively [28.95, 96].

A full PEMFC has been constructed using the above-described electrocatalysts, and the performance of the fuel cell voltage output as a function of electrical current density drawn, or the polarization curve studied. The current–voltage characteristics of a PEMFC fabricated with different types of CNT-supported Pt electrocatalysts as cathode catalysts were studied using a PEMFC test station comprising a single stack fuel cell. A commercial 20 wt %. Pt on carbon (Pt/C) obtained from E-TEK Inc. was used as the anode with Pt loading of 0.25 mg/cm^2. To study the effect of the electrocatalytic activity of the Pt/CNTs on the performance of PEMFC, active material with composition 50 wt % Pt/CNTs and 50 wt % Pt/C was taken as the cathode catalyst. The membrane electrode assembly (MEA) was obtained by pressing the cathode and anode on either side of pretreated Nafion 1135 membrane at pressure of 50 kg/cm^2 and 130 °C for 2 min [28.95, 96]. Polarization curves were obtained from the single-cell PEMFC using these MEAs at dif-

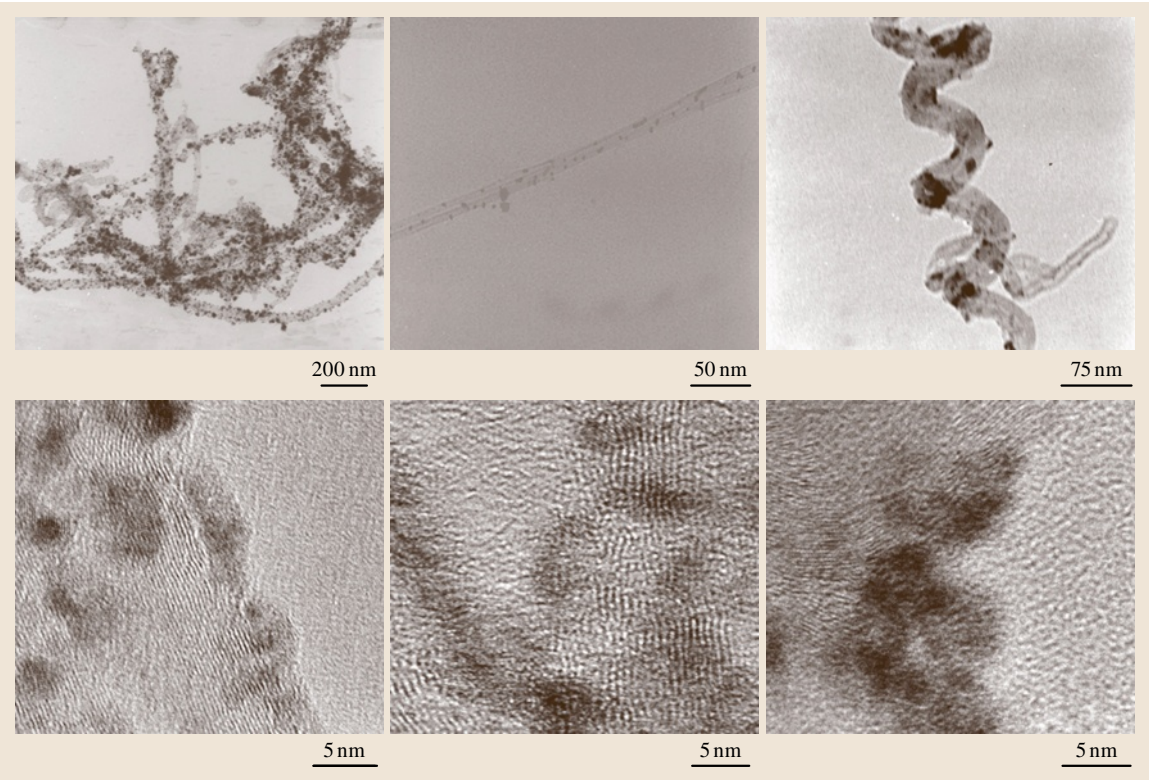


Fig. 28.6 TEM and HRTEM images of Pt-dispersed MWNT, SWNT, and MWNC (after [28.95, 96])

ferent temperatures under operating pressure of 1 bar (Fig. 28.8). Prior to polarization studies, the electrodes were activated between open-circuit potential and high current densities. This activation cycle is necessary to activate the catalyst for the oxygen reduction reaction. In the low-current-density region, the rapid voltage drop in the potential–current curve, generally known as activation polarization, reflects the sluggish kinetics intrinsic to the oxygen reduction reaction at the cathode surface. As the current density increases, a mild drop in voltage is observed because of the cell resistance. Mass transport limitations account for the rapid drop seen at higher current densities. Under the same operating conditions, the PEMFC with the cathode catalyst containing 50 wt % Pt/MWNCs shows the maximum performance. A maximum power density of $\approx 480\,\mathrm{mW/cm^2}$ at working temperature of 60 °C was observed when using the Pt/MWNC electrocatalyst, whereas the maximum power densities when using

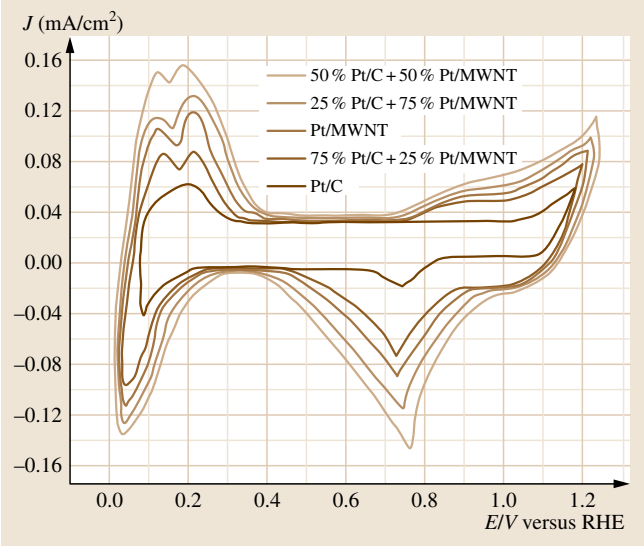


Fig. 28.7 Cyclic voltammograms for Pt/C-Pt/MWNTs composite electrodes recorded in 0.1 M $HClO_4$ at scan rate of 0.02 V/s (Pt loading 15 µm/cm²; RHE, reversible hydrogen electrode) (after [28.95]) ▶

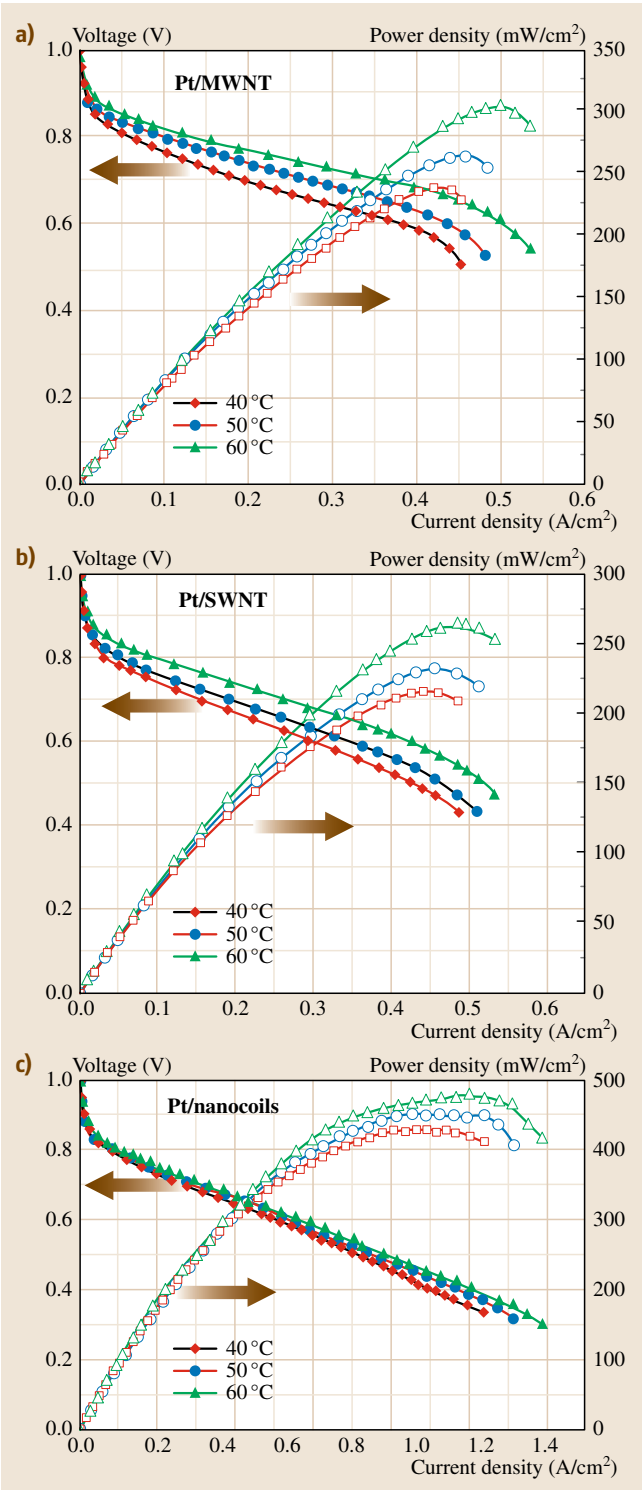


Fig. 28.8a–c Polarization curves of PEMFC with Pt/C anode catalyst and **(a)** 50 wt % Pt/MWNT and 50 wt % Pt/C, **(b)** 50 wt % Pt/SWNT and 50 wt % Pt/C, **(c)** 50 wt % Pt/MWNC and 50 wt % Pt/C cathode catalyst (after [28.95, 96]) ◀

Pt/MWNT, Pt/SWNT, and Pt/C electrocatalysts were only ≈ 310, ≈ 260, and ≈ 140 mW/cm^2, respectively.

28.2.1 Nonnoble Metal Based Electrocatalysts for Fuel Cells

Apart from the issue of high cost of catalyst and other fuel-cell system components (polymer electrolyte membrane, bipolar plates, power system), fuel cells suffer from insufficient performance durability, arising mainly from cathode catalyst agglomeration, oxidation, catalyst migration, loss of electrode active surface area, corrosion of the carbon support, etc. In the case of DMFC, in addition to all the above issues, Pt at the cathode also endures a performance loss resulting from the mixed potential due to methanol diffusion through the membrane from the anode side of the cell [28.100, 101]. Further, in fuel cells, the hydrogen produced via steam or partial oxidation reforming of hydrocarbons or renewable fuels typically contains 0.5–2.0 vol.% CO. However, Pt electrodes in PEMFC are extremely sensitive to even low levels of CO (50 ppm) [28.102, 103]. Hence, the search for efficient, durable, and most importantly, inexpensive catalysts as alternatives to Pt and Pt-based materials and as a support material is always in the limelight [28.104–106]. Recently, cobalt was confirmed as an effective promoter for improving the catalytic activity of mixed oxide catalysts [28.107]. Additionally, cobalt-based catalysts showed a very high activity promoting CO oxidation at low temperature [28.108–110]. Furthermore, catalytic performance depends on the nature of the support, active site, and preparation techniques. Although ideally the Pt catalyst should be replaced at both fuel-cell electrodes, the substitution of the cathode catalyst for the oxygen reduction reaction (ORR) with a nonprecious material is likely to result in significantly greater reduction of the Pt needed for fuel cells [28.111]. Recently, *Bashyam* and *Zelenay* demonstrated a new class of low-cost polypyrrole (PPY)-Co-carbon (Co loading 0.06 mg/cm^2) nanocomposite catalysts for the PEMFC cathode by using PPY as a matrix for entrapping cobalt and generating active ORR sites, and Pt-Ru-carbon (Pt-Ru loading 6 mg/cm^2) at the anode for hydrogen oxidation using a 2.0 atm back-pressured cell [28.112].

The performance with the novel MWNT-supported PPY-Co electrocatalyst for the oxygen reduction reaction along with Pt-Ru/MWNTs electrocatalyst for oxidation of hydrogen and methanol at the anode and Pt-Sn/MWNTs electrocatalyst for oxidation of ethanol at the anode in a PEMFC, direct methanol fuel cell (DMFC), and direct ethanol fuel cell (DEFC) were studied [28.113].

Figure 28.9 shows SEM, TEM, and HRTEM images of PPY-Co-dispersed MWNTs ORR catalysts. Uniform dispersion of PPY over MWNTs has been achieved by in situ polymerization technique by oxidizing monomer,

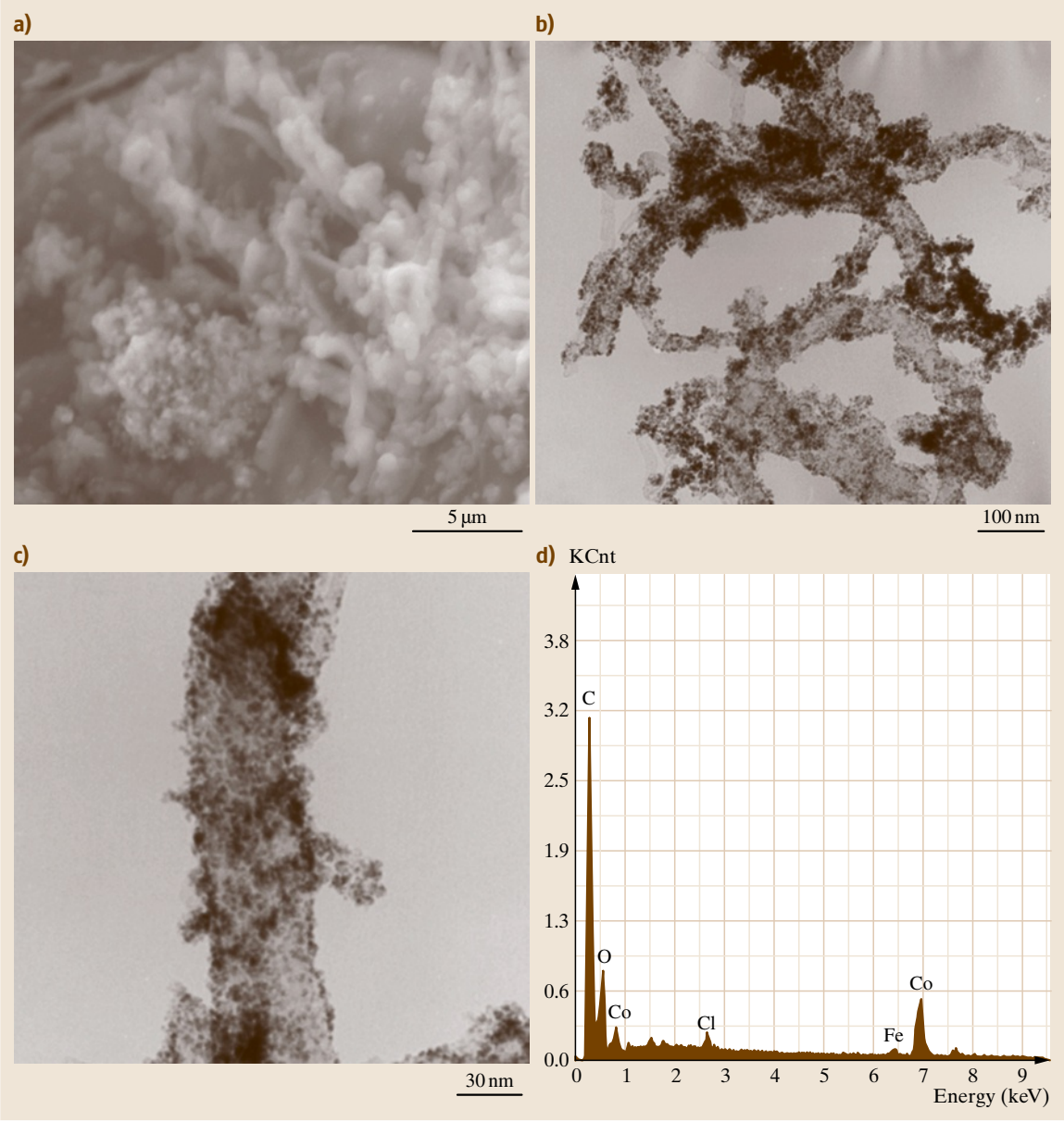


Fig. 28.9 **(a)** SEM image of Co-PPY/MWNTs. **(b)**, **(c)** TEM images of CoPPY/MWNTs and **(d)** EDX analysis of Co-PPY/MWNT (after [28.113])

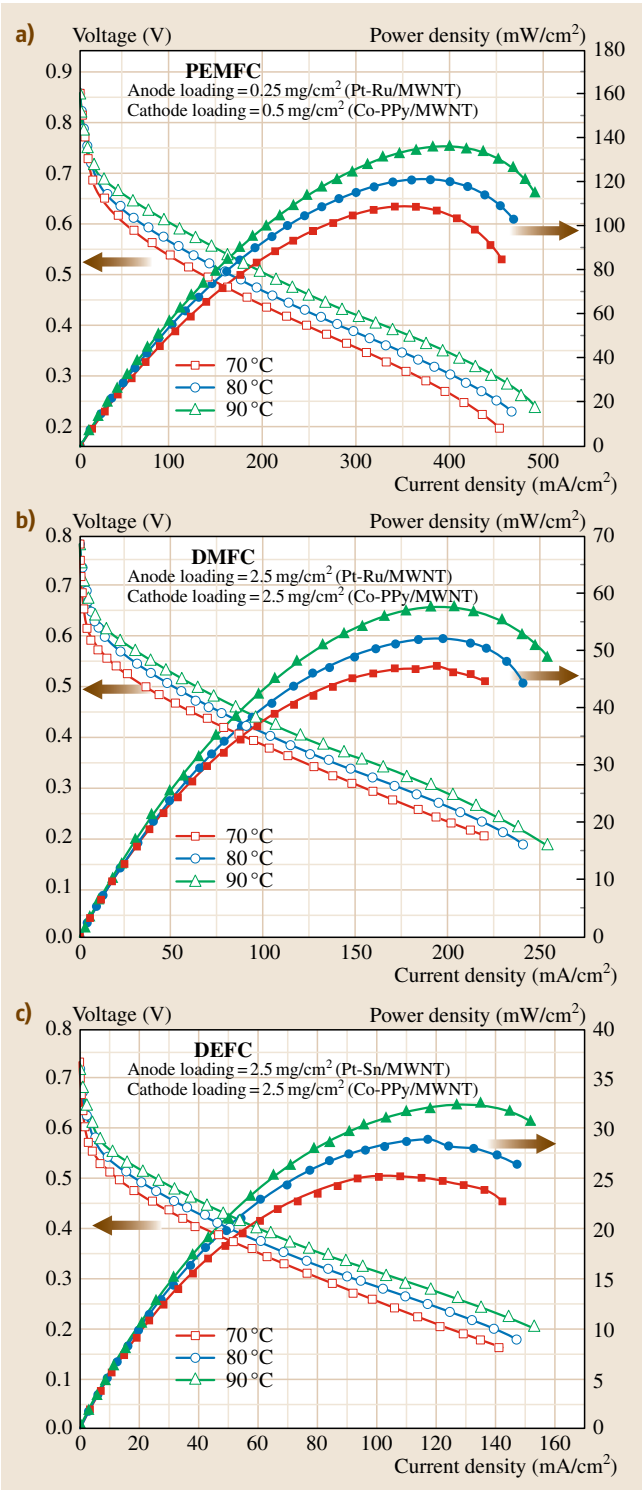


Fig. 28.10 (a) PEMFC, (b) DMFC, and (c) DEFC performance at 70–90 °C with cathode catalyst containing Co-PPY/MWNT (loading 0.5 mg/cm^2) and anode catalyst containing Pt-Ru/MWNT (loading 0.25 mg/cm^2) at ambient pressure (after [28.113]) ◀

and nanoparticles of Co could be dispersed on PPY-MWNTs composite. Uniform dispersion of PPY on MWNTs and nanoparticles of cobalt over PPY-MWNTs composites have been achieved for the first time. The amount of Co loaded on the PPY-MWNT support with reference to carbon was measured to be about 10% by EDX analysis (Fig. 28.9). Figure 28.10 shows the polarization curves of PEMFC, DMFC, and DEFC, respectively, at 70 °C, 80 °C, and 90 °C. After activation cycles, PEMFC generates 0.15 A/cm^2 at 0.5 V and maximum power density of 120 mW/cm^2 with catalyst loadings of 0.25 mg/cm^2 of Pt-Ru and 0.5 mg/cm^2 of Co on the anode and cathode, respectively. *Bashyam* and *Zelenay* [28.112] have reported a maximum power density of 140 mW/cm^2 for carbon-supported Co-PPY with catalyst loading of 6.0 mg/cm^2 of Pt-Ru (anode) and 0.06 mg/cm^2 of Co (cathode) at operating pressure of 2.8 atm. Although the present current density is about 7% less than the previous reported value [28.112], the present results were obtained with low platinum loading (about 24 times lower) at the anode, and at ambient pressure. The suitability of PPY-Co-dispersed MWNT ORR catalyst for use in alcohol-based fuel cells with appropriate anode electrodes was also tested (Fig. 28.10b). DMFC with Pt-Ru/MWNT (1.5 mg Pt/cm^2) at the anode and Co-PPY/MWNT (2.5 mg Co/cm^2) at the cathode resulted in a maximum power density of 52 mW/cm^2 at operating temperature of 90 °C with oxygen pressure at 1 atm, which is better than the value of 32 mW/cm^2 at 70 °C reported by *Prabhuram* et al. for Pt/C with 2 mg Pt/cm^2 at the cathode and Pt-Ru loading of 2.1 mg/cm^2 at the anode [28.114]. This better performance is attributed mainly due to the high oxygen reduction activity of the nonprecious Co-PPY-MWNT at the cathode electrode compared with Pt/C. Further, Pt-Sn/C has been proved to be a good candidate for oxidation of ethanol among other electrocatalysts such as Pt-Ru/C, PtW/C, PtPd/C, and Pt/C [28.115]. The performance values of DEFC are quite encouraging even with less loadings of Pt-Sn at the anode apart from complete elimination of precious metals at the cathode. DEFC could generate a maximum power density of 33 mW/cm^2 at 90 °C (Fig. 28.10c). Although the power density is less than the value of 55.8 mW/cm^2

recently reported with Pt-Sn/C catalyst [28.115], the present result was obtained at significantly lower absolute pressure of oxygen (1 atm versus 2.0 atm) with nonprecious Co-PPY-MWNTs at the cathode electrode rather than Pt/C.

The results obtained from the systematic studies of PEMFC using Pt/CNTs electrocatalysts for the oxygen reduction reaction show significant improvement in performance due to the good accessibility and dispersibility of the Pt nanoelectrocatalysts on the CNT support, resulting in more efficient Pt usage for the oxygen reduction reaction. The excellent catalytic activity of the novel MWNT-supported Co-PPY composites as electrode material for the oxygen reduction reaction has been attributed to the uniform dispersion of Co nanoparticles over the PPY-MWNT architecture.

28.3 CNTs as Supercapacitor Electrode Materials

Depending on the charge-storage mechanism, supercapacitors are basically classified into two types: electric double layer capacitors (EDLCs) based on carbon electrodes [28.116–120] and pseudocapacitors with certain metal oxides [28.121–126] or conducting polymers as electrode materials [28.127–134]. While the storage mechanism in carbon-based EDLCs is through electrostatic forces, fast Faradaic redox reactions are responsible for the charge-storage mechanism in pseudocapacitors. Carbon-based supercapacitor electrodes have been attractive due to their high surface area and porous nature [28.116–120]. Recently, both single-walled and multi-walled carbon nanotubes (SWNTs, MWNTs) have been recognized as potential electrode materials for electrochemical supercapacitors, owing to their special properties such as high chemical stability, low mass density, low resistivity, narrow distribution of mesopore sizes, and large surface area [28.135, 136]. However, due to the microtexture, defects, micropore volume, and catalyst contamination of carbon nanotubes (CNTs), their specific capacitance is restricted to low values. Hence, there have been considerable efforts to improve the capacitance of CNT-based supercapacitor electrodes by various techniques such as activating CNTs with heat/acid treatment [28.137] to improve the micropore volume of CNTs, and modification of CNTs with conducting polymers [28.138] or with certain transition-metal oxides [28.139, 140]. Thus, the hybrid of an electric double layer system and a Faradaic pseudocapacitive system could be a good candidate for a supercapacitor with high specific capacitance and energy density. Transition-metal oxides attached to CNTs have been studied recently and are expected to show improved capacitive behavior due to their enhanced stability and high conductivity. Among the transition-metal oxides, hydrous ruthenium dioxide has been recognized as one of the most promising candidates for electrodes in electrochemical capacitors as it can store charges reversibly by redox reaction [28.140, 141]. However, the high cost of RuO_2 has prompted the research community to focus on other transition-metal oxides such as MnO_2, NiO, etc., mainly for reasons of cost-effectiveness. Of the various nonnoble metals or transition-metal oxides studied, TiO_2 and SnO_2 enjoy a special place because of their lower cost and environmentally benign nature. On the other hand, among the conducting polymers, polyaniline (PANI) and polypyrrole (PPY) have been considered as the most promising materials for this application due to their excellent capacity for energy storage, easy synthesis, higher conductivity, and lower cost than many other conducting polymers. However, long-term stability during cycling is a major demand for industrial application of electrically conducting polymers (ECPs). Swelling and shrinkage of ECPs is well known and may lead to degradation of the electrode during cycling. This occurs because the doping of the polymers requires insertion/de-insertion of counterions, which cause a volume change. Thus, the mechanical stress in the polymer film is directly related to the cycle life of polymer-based capacitors. Various metal oxides (RuO_2, TiO_2, and SnO_2) dispersed MWNTs and polymer (PPY and PANI) dispersed MWNTs composites have been synthesized, and the supercapacitive performance of these composite electrodes has been studied systematically [28.142, 143]. MWNTs have been functionalized with nanocrystalline RuO_2, TiO_2, and SnO_2 by a simple chemical reduction method, and PPY and PANI dispersion on MWNTs was done by in situ polymerization technique. The supercapacitive behavior of these nanocrystalline composite electrodes has been studied using cyclic voltammetry, galvanostatic charge–discharge, and electrochemical impedance spectroscopy measurements.

RuO_2-supported MWNTs (RuO_2/MWNTs) nanocomposites were prepared by the chemical reduction

method using a Ru salt and pretreated MWNTs. Functionalized MWNTs were dispersed in a solution of 1 : 1 volume ratio of isopropanol and water by ultrasonic agitation. $RuCl_{3.3}H_2O$ (2 : 1 MWNTs to Ru wt. ratio) was added to the above mixture and ultrasonication continued for 1 h. The blank product of the reaction was filtered and washed repeatedly with distilled water to remove excess chloride ions. The RuO_2/MWNTs was dried in a vacuum oven at 100 °C for 12 h. Part of the final product was calcined at 350 °C for 2 h. TiO_2/MWNT composites were prepared using the sol–gel method as follows: Functionalized MWNTs were dispersed in dilute nitric acid (pH 0.5) by ultrasonic agitation. This solution was then transferred to a round-bottomed flask, and titanium tetraisopropoxide (Aldrich, 97%) was added dropwise, maintaining the volume ratio of titanium tetraisopropoxide to water at 1:4. The sol obtained was stirred for 2 days in air at room temperature (RT). The obtained turbid suspension was centrifuged at 6000 rpm, and the resultant residue was washed twice with distilled water. As-synthesized TiO_2/MWNTs composites were heat treated at temperatures of 350 °C for 2 h in air. SnO_2/MWNTs nanocomposites were synthesized by dissolving 1 g tin(II) chloride ($SnCl_2$) in 40 ml distilled H_2O followed by addition of 1.0 ml HCl (38%). Subsequently, 10 mg of the functionalized MWNTs was dispersed in the above solution. This mixture was sonicated for 5–10 min and then stirred for 60 min at RT. The precipitate was then separated from the mother liquor by centrifugation and was washed with distilled H_2O for several times, then dried at 70 °C under vacuum for 6 h. Part of the final product was calcined at 350 °C for 2 h.

PPY/MWNTs composites were first prepared by chemical oxidative polymerization of a monomer (pyrrole) on the surface of MWNTs in order to overcome the problems encountered with the electrochemical method. The electrochemical method is limited in terms of mass production of the materials, and also it is not suitable for preparing composites with a large proportion of polymer. Composites were prepared by immersion of the MWNTs (0.1 g) into an aqueous solution of monomer and addition of an oxidant to this solution. PPY was deposited on MWNTs by chemical polymerization of 0.5 ml pyrrole with 1.2 g $FeCl_3$ in 50 ml 0.1 mol/l HCl. The PANI/MWNTs nanocomposite was synthesized by polycondensation of 0.4 ml aniline by 0.4 g $K_2Cr_2O_7$ in 50 ml 1 mol/l HCl. The nanocomposite materials were then filtered and washed with large amount of water and subsequently with ethanol to remove the residual oxidant. Finally, all composites were washed with acetone and dried at 60 °C. The content of MWNTs in the composites was determined gravimetrically. All the above-prepared composites were characterized by powder XRD SEM, EDAX, and TEM measurements.

Figure 28.11 shows the XRD pattern of as-prepared MWNTs using alloy hydrides as catalysts. The peaks are indexed to the reflections of hexagonal graphite. A few peaks corresponding to the catalytic impurities are also seen. The XRD of purified MWNTs (Fig. 28.11b) shows the removal of metallic impurities by acid treatment. The XRD pattern of RuO_2/MWNTs nanocomposite material (Fig. 28.11c) shows the reflections of RuO_2 along with that for graphitic carbon, whereas Fig. 28.11d,e presents the XRD patterns of TiO_2/MWNTs and SnO_2/MWNTs composites showing the reflections of corresponding oxides along with

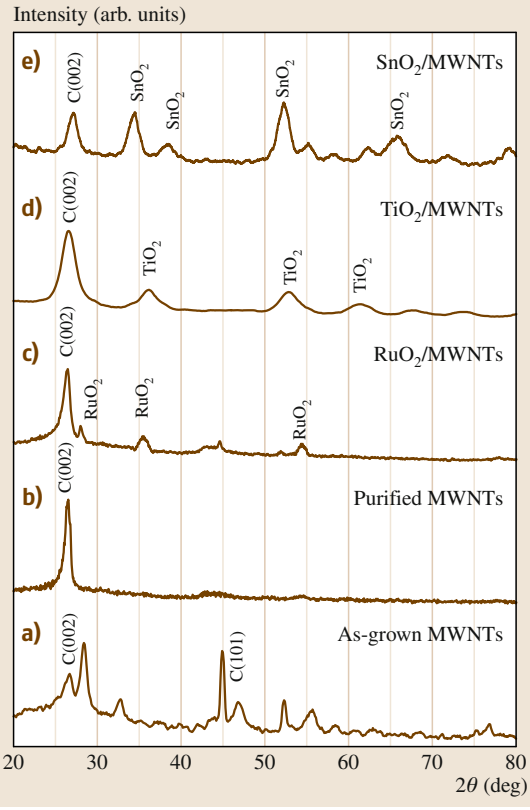


Fig. 28.11a–e Powder XRD patterns of **(a)** as-grown MWNTs, **(b)** purified MWNT, **(c)** RuO_2/MWNTs nanocomposite, **(d)** TiO_2/MWNTs, and **(e)** SnO_2/MWNTs nanocomposite (after [28.142])

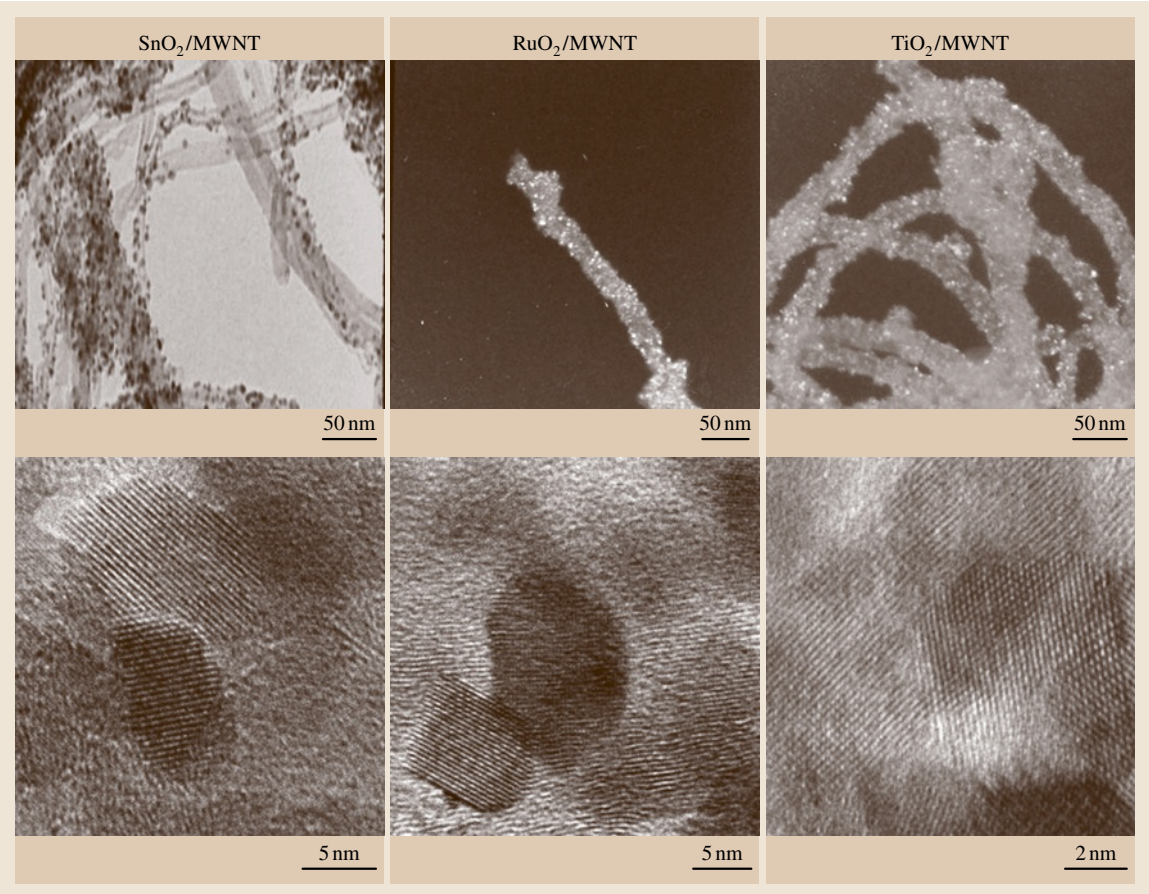


Fig. 28.12 SEM and TEM images of SnO_2/MWNTs, RuO_2/MWNTs, and TiO_2/MWNTs nanocomposite (after [28.142])

that of graphitic carbon. The broad peaks reveal the presence of nanostructured metal oxide crystals.

Figure 28.12 shows SEM, TEM, and HRTEM images of SnO_2/MWNTs, RuO_2/MWNTs, and TiO_2/MWNTs nanocomposites, respectively. TEM images of SnO_2/MWNTs, RuO_2/MWNTs, and TiO_2/MWNTs nanocomposites indicate the uniform distribution of nanocrystalline metal oxide particles with size of about 3–5 nm on the MWNTs. The lattice planes of SnO_2, RuO_2, and TiO_2 nanoparticles are seen clearly in the respective HRTEM images, indicating the crystalline nature of the catalytic particles. SEM and TEM images of PPY/MWNTs and PANI/MWNTs clearly show uniform dispersion of polymer over MWNTs (Fig. 28.13).

A supercapacitor test cell was fabricated with two MWNT composite electrodes separated by a thin polymer in 1 M H_2SO_4 solution. The electrodes, which were pellets of 12 mm diameter, were separated by a thin polymer (15 mm diameter) and were sandwiched in a Swagelok-type stainless steel (SS) cell with SS current collectors. The electrochemical properties and capacitance measurements of MWNT composite electrodes were studied in a two-electrode system by cyclic voltammetry, galvanostatic charge–discharge, and electrochemical impedance spectroscopy in an electrochemical workstation (CHI 660B).

28.3.1 Cyclic Voltammetry

The cyclic voltammetry (CV) responses of the different electrode materials at scan rate of 2 mV/s are shown in Figs. 28.14 and 28.15. Voltammetry testing was carried out at potentials between -1.0 and 1.0 V using 1 M H_2SO_4 aqueous electrolyte solution. The MWNTs present the typical box-like curve expected for an ideal

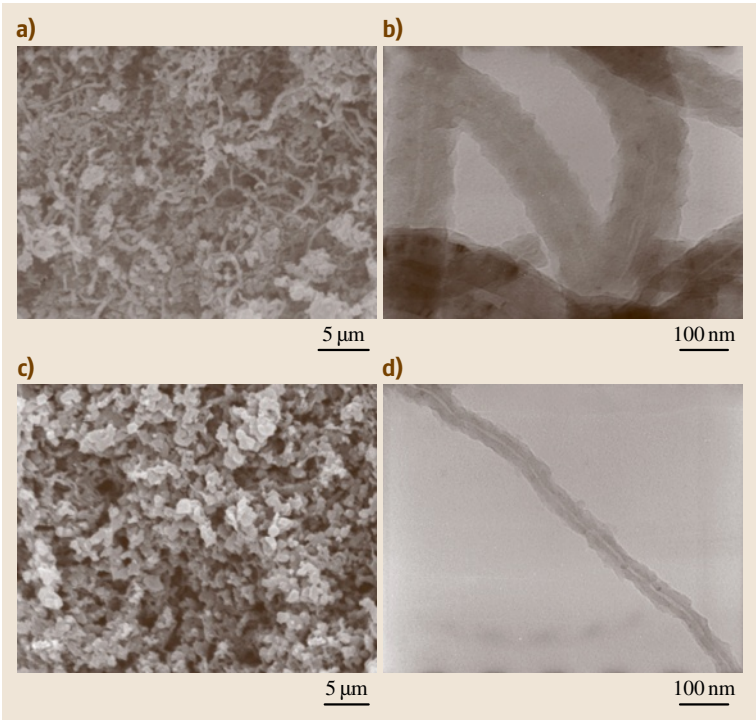


Fig. 28.13 **(a)** SEM and **(b)** TEM images of PANI/MWNTs. **(c)** SEM and **(d)** TEM images of PPY/MWNTs (after [28.143])

capacitor. However, there are oxidation peaks observed in the CV for metal oxide-dispersed MWNTs electrodes, which are attributed to redox reactions due to the functional groups on the nanotubes [28.40]. There is a reasonable symmetry to the curves for MWNTs electrodes, which may be due to the capacitance arising solely due to the double layer. However, in metal oxide/MWNTs and polymer/MWNTs electrodes, the lack of symmetry to the curves is probably due to a combination of double layer and pseudocapacitances contributing to the total capacitance. The area of the curve also increased with supercapacitor electrodes using RuO_2, TiO_2, SnO_2, PANI- and PPY-dispersed MWNTs, indicating enhancement of the specific capacitance for these electrodes. Since the measurements were made on symmetric assemblies of materials, by the basic circuit relationship for series capacitors, what is measured is actually $\frac{1}{2}$ of the capacitance of the free-standing electrode. The specific capacitance has been obtained from the CV curve according to

$$C_{\mathrm{sp}} = \frac{i}{s\,m}\,, \tag{28.2}$$

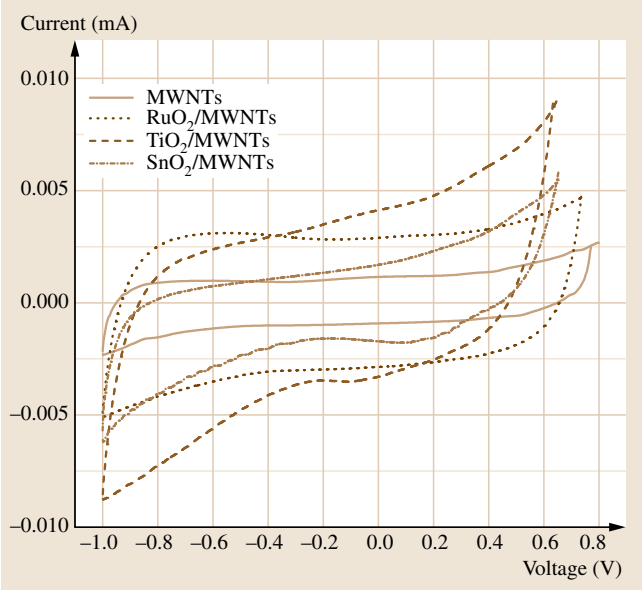


Fig. 28.14 Cyclic voltammograms of pure MWNTs, RuO_2/MWNTs, TiO_2/MWNTs, and SnO_2/MWNTs nanocomposite electrodes, at scan rate of 2 mV/s in 1 M H_2SO_4 aqueous electrolyte; mass of each electrode was 10 mg (after [28.142]) ◀

where i is the average cathodic current, s is the potential sweep rate, and m is the mass of each electrode.

28.3.2 Galvanostatic Charge–Discharge

The specific capacitance of the MWNT electrodes was also determined by galvanostatic charge–discharge technique. Galvanostatic cycling of supercapacitor cells was performed at constant current of 2 mA/10 mA between 0 and 1 V. Figures 28.16 and 28.17 show the galvanostatic charge–discharge behavior of the pure MWNTs, RuO_2/MWNTs, TiO_2/MWNTs, SnO_2/MWNNTs, PANI/MWNTs, PPY/MWNTs nanocomposite and aligned MWNT electrodes, respectively. The discharge curves are almost linear in the total range of potential with constant slope, showing perfect capacitive behavior. The capacitance of the cell was deduced from the slope of the $V-t$ curves using the equation

$$C = \frac{I}{(\mathrm{d}V/\mathrm{d}t)} \,. \tag{28.3}$$

The specific capacitance (F/g) of the MWNTs electrode was calculated according to

$$C_{\mathrm{sp}} = 2\frac{C}{m} \,, \tag{28.4}$$

where C is the experimentally measured capacitance of the supercapacitor (28.3) and m is the amount of each electrode material.

28.3.3 Electrochemical Impedance Spectroscopy

Electrochemical impedance spectroscopy (EIS) measurements were carried out at direct-current (DC) bias of 0 V with sinusoidal signal of 10 mV over the frequency range from 40 kHz and 10 MHz. Figures 28.18 and 28.19 present complex-plane impedance plots for purified MWNTs, RuO_2/MWNTs, TiO_2/MWNTs, SnO_2/MWNNTs, PANI/MWNTs, PPY/MWNTs nanocomposite and aligned MWNT electrodes, respectively. At lower frequency, the imaginary part of impedance sharply increases, which is typical of the capacitive behavior of the electrode. The impedance plot should theoretically be a vertical line parallel to the imaginary axis. In fact, a difference between this theoretical behavior and the experimental result can be observed. The impedance behavior of undoped MWNTs comes close to that of an ideal capacitor. A slight variation from the ideal capacitive behavior could be attributed to the pore size distribution of MWNTs [28.144].

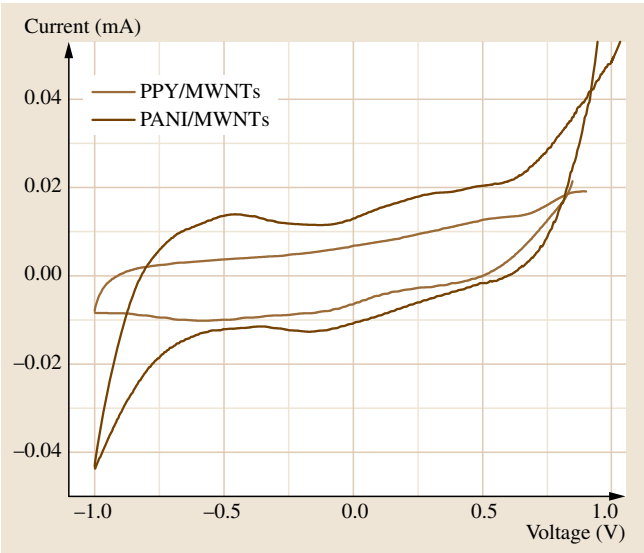


Fig. 28.15 Cyclic voltammograms of PANI/MWNTs and PPY/MWNTs nanocomposite electrodes at scan rate of 2 mV/s in 1 M H_2SO_4 aqueous electrolyte; mass of each electrode was 10 m (after [28.143])

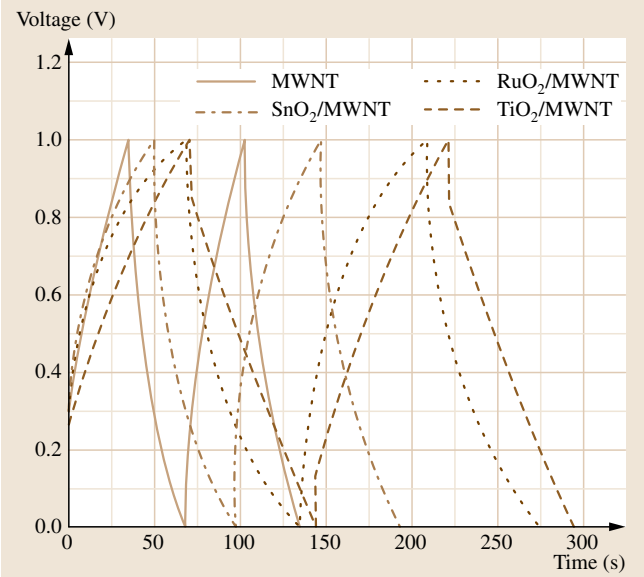


Fig. 28.16 Galvanostatic charge–discharge of pure MWNTs, RuO_2/MWNTs, TiO_2/MWNTs, and SnO_2/MWNTs nanocomposite electrodes at applied constant current of 10 mA in 1 M H_2SO_4 aqueous electrolyte; mass of each electrode was 10 mg (after [28.142])

However, the impedance behavior of RuO_2/MWNTs, TiO_2/MWNTs, SnO_2/MWNTs, PANI/MWNTs, and

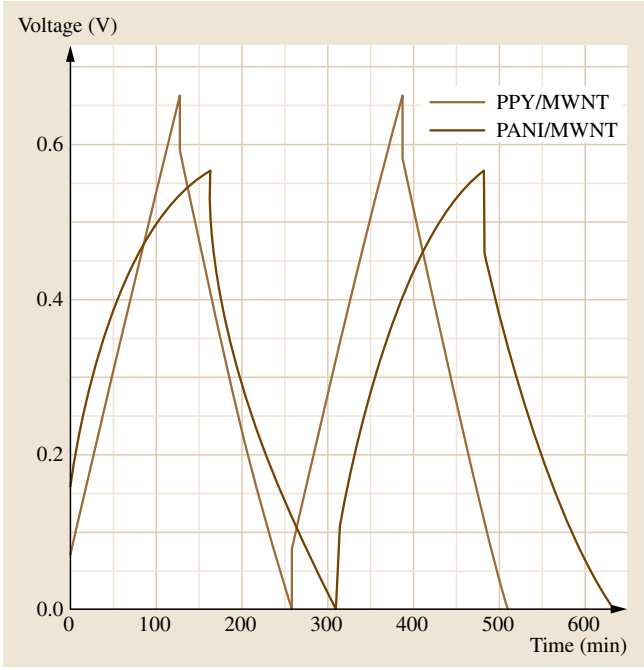


Fig. 28.17 Galvanostatic charge–discharge of PANI/MWNTs and PPY/MWNTs nanocomposite electrodes at applied constant current of 10 mA in 1 M H_2SO_4 aqueous electrolyte; mass of each electrode was 10 mg (after [28.143]) ◀

PPY/MWNTs nanocrystalline composite electrodes shows a deviation from the ideal capacitor response, with much lower impedance than pure MWNTs electrodes. The presence of a small semicircular loop for MWNT electrodes at higher frequencies is due to charge-transfer resistance of the electrode [28.35].

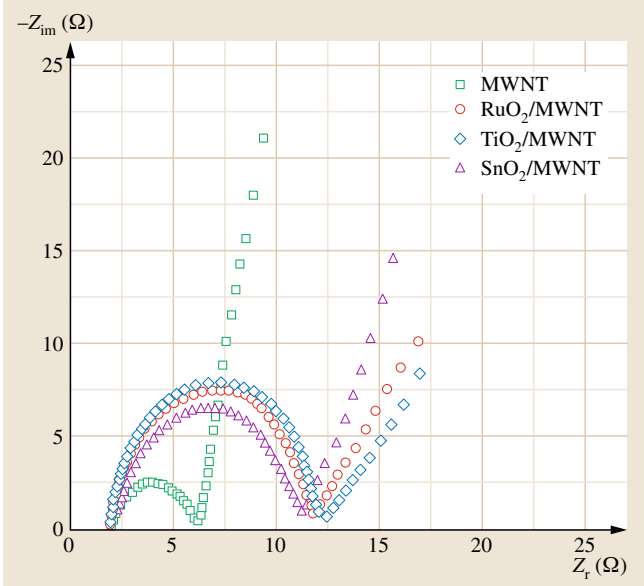


Fig. 28.18 Complex-plane impedance spectra of pure MWNTs, RuO_2/MWNTs, TiO_2/MWNTs, and SnO_2/MWNTs nanocomposite electrodes in 1 M H_2SO_4 aqueous electrolyte/mass of each electrode, 10 mg [28.142] ◀

Equivalent series resistance (ESR) of 7, 4, 3, and 5.5 Ω are measured for pure MWNTs, RuO_2/MWNTs, TiO_2/MWNTs, and SnO_2/MWNTs nanocomposites, respectively. The alternating-current (AC) impedance method has also been used to measure the specific capacitance of the electrodes, which is influenced by the frequency especially for porous electrodes where almost no current flows down the pore at higher frequencies.

The energy density (E) of the supercapacitor can be calculated by using

$$
\begin{aligned}
E &= \int V\,\mathrm{d}q\,,\\
C &= \frac{q}{V}\,,\\
q &= CV\,,\\
\mathrm{d}q &= C\,\mathrm{d}V + V\,\mathrm{d}C = C\,\mathrm{d}\,, \quad \text{if} \quad \mathrm{d}C = 0\,,\\
E &= C\int V\,\mathrm{d}V = \frac{1}{2}C(\Delta V)^2\,, \qquad (28.5)
\end{aligned}
$$

where C is the capacitance, V is the operating potential window (1.0 V), and m is the amount of active material in the supercapacitor (including positive and negative electrodes).

The specific power density (P) of the supercapacitor can be calculated according to

$$P = \frac{I\Delta V}{m}\,, \qquad (28.6)$$

where I is the constant current for charge–discharge, V is the potential range of a supercapacitor, and m is the mass of active material in the symmetric supercapacitor (including positive and negative electrodes).

The average specific capacitances measured using the three electrochemical techniques of the pure MWNTs, RuO_2/MWNTs, TiO_2/MWNTs, SnO_2/MWNTs, PANI/MWNTs, and PPY/MWNTs nanocomposite electrodes are 67, 138, 160, 93, 321, and 236 F/g, respectively (Table 28.1). The increase in the

capacitance of MWNTs is mainly due to the functionalization of MWNTs with carboxyl groups, and for RuO_2/MWNTs, the increase is due to uniform dispersion of metal oxide particles over functionalized MWNTs. Since the specific double layer capacitance arises from the ionic double layer at the electrode–electrolyte interface, the accessibility of the active layer depends on the diffusion of solvated ions and more precisely on the pore size distribution. The central hollow core of the CNTs is also accessible for double layer charging, and thus the purified MWNTs with opened tips along with the unique network of mesopores formed by the entanglement of CNTs would have acted as sites for accumulation of charges. The enhancement of the specific capacitance can be attributed to the presence of RuO_2, TiO_2, and SnO_2 nanoparticles attached to the surface of MWNTs, which in turn modify the microstructure and morphology of MWNTs, allowing the metal oxides to be available for the electrochemical reactions and improve the efficiency of the composites. The progressive redox reactions occurring at the surface and bulk of transition-metal oxides through Faradaic charge transfer between electrolyte and electrode result in the enhancement of the specific capacitance of metal oxide-dispersed MWNT electrodes compared with pure MWNT electrodes. Of the various nonnoble metals or transition-metal oxides studied, TiO_2 enjoys a special place because of its cost-effectiveness and environmental friendliness.

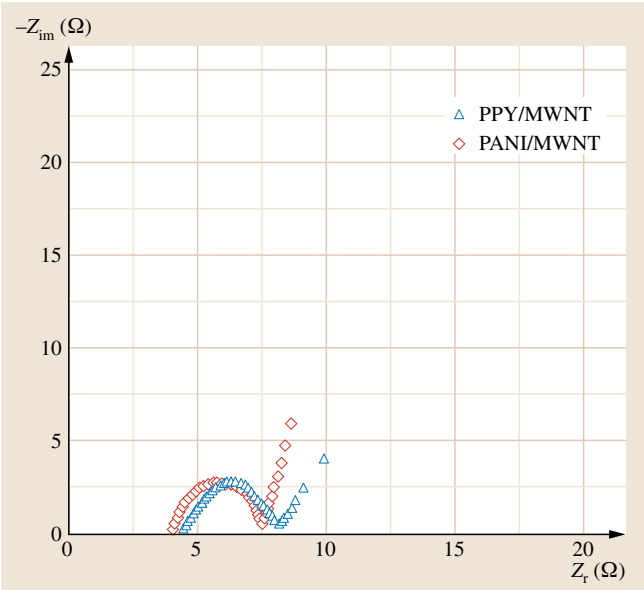


Fig. 28.19 Complex-plane impedance spectra of PANI/MWNTs and PPY/MWNTs nanocomposite electrodes in 1 M H_2SO_4 aqueous electrolyte; mass of each was 10 mg (after [28.143])

28.3.4 Lithium-Ion Batteries

The nanoscale approach to electrochemical energy storage applications such as in lithium batteries has been of great interest because of their unique properties leading to improved performance [28.50, 145]. Innovative material chemistry has been the key to various advancements in lithium rechargeable batteries [28.47, 146]. Among various transition-metal oxide electrode materials, manganese oxide (MnO_2) has been studied as an electrode for lithium batteries with high storage capacity, in addition to its low cost, environmental friendliness, and natural abundance [28.147–150]. However, its potential applications in practical Li-ion batteries are limited due to its poor electrical conductivity and large volume expansion during repeated lithium cycling process. One-dimensional (1-D) nanostructured morphologies of these electrodes with controlled size, crystallinity, and chemical composition have been designed to overcome some of these challenges [28.151,152]. However, the conductivity of these 1-D nanowires remains an issue. Coaxial 1-D nanowires with tin oxide core and indium oxide shell nanostruc-

Table 28.1 Comparison of specific capacitance of supercapacitors obtained by different techniques

Electrode material	Cyclic voltammetry (F/g)	Galvanostatic charge–discharge (F/g)	Electrochemical impedance spectroscopy (F/g)	Average specific capacitance (F/g)
MWNTs	68	69	64	67
RuO_2/MWNTs	147	133	134	138
TiO_2/MWNTs	166	148	166	160
SnO_2/MWNTs	95	91	93	93
PANI/MWNTs	300	325	338	321
PPY/MWNTs	248	236	224	236

tures have been shown to be promising Li-ion battery electrodes [28.153]. Coaxial nanowires/nanotubes will lead to multiple functionalities by combining the physical properties of different materials. To build Li batteries with improved capacity and power capabilities, coaxial nanowires/nanotubes of multiple materials with specific electrochemical and physiochemical properties need to be fabricated. Careful engineering of hybrid coaxial electrode material having high storage capacity metal oxide and highly conducting CNT will lead to enhanced Li storage properties. The tubular morphology offers a unique combination of high porosity and low internal resistance. Such a coaxial electrode configuration will have:

1. Improved electronic conductivity due to the presence of CNT
2. Homogeneous electrochemical accessibility and high ionic conductivity by avoiding agglomerative binder and other conductive additives
3. Well-directed 1-D conductive paths due to perfect coaxial alignment
4. A dual lithium storage mechanism (insertion/deinsertion in case of CNTs and formation and decomposition of Li_2O in case of MnO_2 nanotubes) [28.154].

Figure 28.20 presents SEM images of MnO_2/CNT hybrid nanostructures, clearly showing the uniform coaxial nanostructure prepared by a combination of simple vacuum infiltration and chemical vapor deposition technique through a template approach. MnO_2 nanotube walls were found to be ≈ 10 nm thick with good crystallinity and smooth surface. The structure

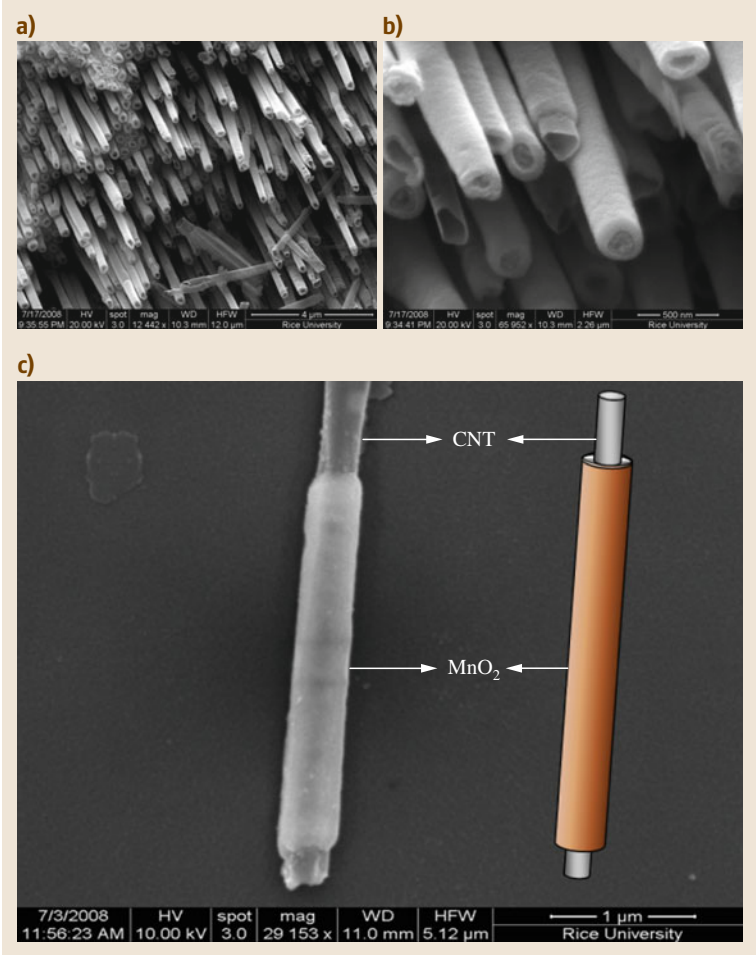


Fig. 28.20a–c Textural characterization of MnO_2/CNT hybrid coaxial nanotubes. **(a)** Low- and **(b)** high-resolution SEM images showing the coaxial nature of the nanotube. **(c)** SEM image and schematic representation of a single coaxial nanotube; the MnO_2 shell and carbon nanotube core are clearly seen (after [28.154])

of the coaxial nanotubes, such as the MnO_2 shell thickness and nanotube length, could be easily controlled by varying the infiltration time, enabling the electrochemical properties of the coaxial nanotubes to be tuned. CNTs protrude from both ends of the nanotubes, enabling effective contact with the gold thin-film current collector. Recently, coaxial nanowires of MnO_2/PEDOT have been synthesized by the co-electrodeposition method [28.155]. However, in case of the MnO_2/CNT structure, the presence of the CNT core has superior advantages in terms of electrical conductivity, mechanical stability, and electrochemical performance. Also, high-temperature annealing results in high crystallinity of the coaxial nanostructure. The growth process for the coaxial nanotubes follows a typical template synthesis, wherein a manganese precursor initially combines with the template by impregnation and results in nucleation and growth following an annealing treatment. This forms the MnO_2 shell. The chemical vapor deposition (CVD) process allows CNTs to grow in the inner cores left by the MnO_2 shells. Upon template removal, coaxial nanotubes with CNT core and MnO_2 shell are obtained.

Apart from fast Li insertion/de-insertion, high electronic conductivity of the electrode materials is necessary to develop high-performance lithium batteries. The electrochemical performance of MnO_2/CNT coaxial nanotubes as cathodes in Li batteries has been evaluated using galvanostatic charge–discharge measurements. Voltage versus specific capacity curves were obtained by cycling the cell at constant rate of 50 mA/g between 3.2 and 0.02 V versus Li/Li^+ (Fig. 28.21). A first discharge capacity of 2170 mAh/g and a reversible capacity of $\approx$ 500 mAh/g after 15 cycles were observed for MnO_2/CNT hybrid coaxial nanotubes. A large irreversible capacity is observed, which could be due to drastic, lithium-driven, and structural or textural modifications, as observed for transition-metal oxide electrodes. The large irreversible capacity occurring only in the first cycle may be caused by decomposition reactions of the electrolyte and the formation of a solid–electrolyte interphase (SEI) film on the surface of the manganese oxide electrode [28.156]. A high reversible capacity observed for MnO_2/CNT hybrid coaxial nanotubes compared with MnO_2 nanotubes indicates reduced structural changes. The reaction mechanism of different materials with lithium varies from classical Li insertion/de-insertion in the case of carbon-based materials to Li-alloying processes in the case of metal/alloy. With reference to transition-metal oxides, the reaction mechanism of manganese oxide with lithium has been proposed to be [28.154]

$$MnO_2 + 4Li^+ + 4e^- \leftrightarrow 2Li_2O + Mn\,, \tag{28.7}$$

$$4Li \leftrightarrow 4Li^+ + 4e\,, \tag{28.8}$$

$$MnO_2 + 4Li \leftrightarrow 2Li_2O + Mn\,. \tag{28.9}$$

Hence, the process involves the formation and decomposition of Li_2O, accompanying the reduction and oxidation of metal nanoparticles. Extraction of lithium from Li_2O is extremely difficult but has been shown

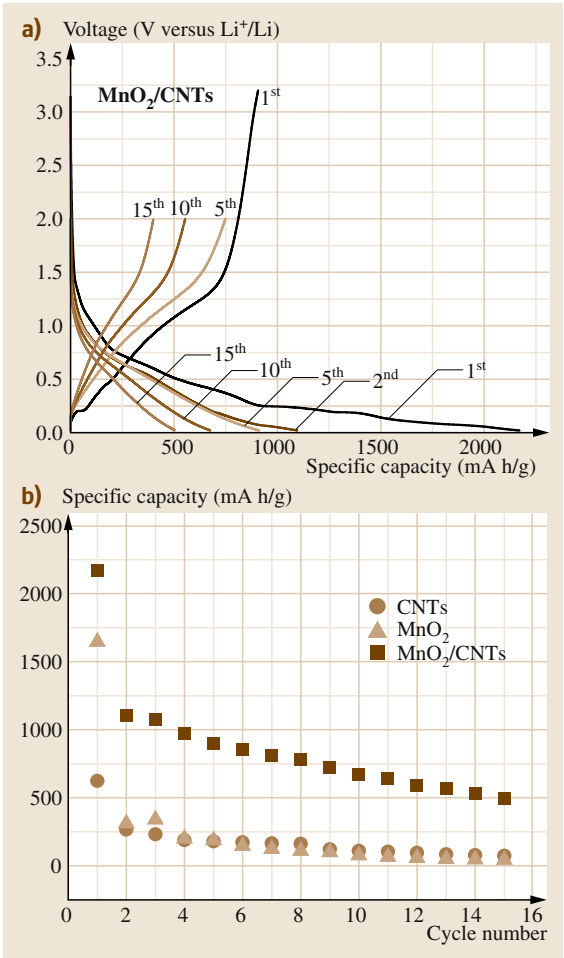


Fig. 28.21a,b Electrochemical properties of MnO_2/CNT hybrid coaxial nanotubes as positive electrodes in Li battery. **(a)** Charge–discharge voltage profiles for MnO_2/CNT nanotube electrodes cycled at rate of 50 mA/g between 3.2 V and 0.02 V versus Li/Li^+. **(b)** Variation in discharge capacity versus cycle number for MnO_2/CNT nanotubes, MnO_2 nanotubes, and carbon nanotubes (after [28.154])

to be possible with the use of nanosized materials. Bulk MnO_2 typically exhibited capacity no more than 120 mAh/g. Higher capacity values of nanofibers compared with their bulk counterparts were proposed to be derived from the large surface areas of the nanosized materials. However, there has been an inconsistency in the electrochemical behavior of MnO_2 nanotubes, presumably due to the different mechanisms of lithium insertion versus conversion reactions.

Thus, the coaxial hybrid structure formed by the highly conductive CNT core offers enhanced electronic transport to the MnO_2 shell and acts as a buffer to alleviate the volume expansion. CNTs provide additional sites for lithium storage, resulting in a dual mechanism of lithium storage, leading to enhanced reversible capacity for MnO_2/CNT hybrid coaxial nanotubes by an order compared with template-grown MnO_2 nanotubes.

An overview of synthesis methods for various carbon nanostructure has been presented. It is shown that CVD methods are promising for producing large quantities of CNTs. MWNTs, SWNTs and MWNCs have been synthesized by catalytic decomposition of appropriate hydrocarbons over alloy hydride catalysts obtained through hydrogen decrepitation route. The enormous potential of CNTs in Science and Technology has been illustrated by giving a short review of the several possible applications of CNTs with emphasis on their energy-related applications such as catalyst support material in PEMFC, supercapacitor electrode materials and Li-ion battery electrodes.

References

28.1 H.W. Kroto, J.R. Heath, S.C. O'Brien, R.F. Curl, R.E. Smalley: C_{60}: Buckminsterfullerene, Nature **318**, 162–163 (1985)

28.2 R. Kötz, M. Carlen: Principles and applications of electrochemical capacitors, Electrochim. Acta **45**, 2483–2498 (2000)

28.3 P.M. Ajayan: Carbon nanotubes. In: *Handbook of Nanostructured Materials and Nanotechnology*, Vol. 5, ed. by H.S. Nalwa (Academic, San Diego 2000) pp. 329–360

28.4 J.M. Planeix, N. Coustel, B. Coq, V. Brotons, P.S. Kumbhar, R. Dutartre, P. Geneste, P. Bernier, P.M. Ajayan: Application of carbon nanotubes as supports in heterogeneous catalysis, J. Am. Chem. Soc. **116**, 7935–7936 (1994)

28.5 P.J. Britto, K.S.V. Santhanam, A. Rubio, A. Alonso, P.M. Ajayan: Improved charge transfer on carbon nanotube electrodes, Adv. Mater. **11**, 154–157 (1999)

28.6 P. Costamagna, S. Srinivasan: Quantum jumps in the PEMFC science and technology from the 1960s to the year 2000. Part II. Engineering, technology development and application aspects, J. Power Source **102**, 253–269 (2001)

28.7 S.M. Haile: Fuel cell materials and components, Acta Mater. **51**, 5981–6000 (2003)

28.8 H.A. Gasteiger, S.S. Kocha, B. Sompalli, F.T. Wagner: Activity benchmarks and requirements for Pt, Pt-alloy, and non-Pt oxygen reduction catalysts for PEMFCs, Appl. Catal. **56**, 9–35 (2005)

28.9 L. Xiong, A. Manthiram: Nanostructured Pt–M/C (M = Fe and Co) catalysts prepared by a microemulsion method for oxygen reduction in proton exchange membrane fuel cells, Electrochim. Acta **50**, 2323–2329 (2005)

28.10 J.R.C. Salgado, E. Antolini, E.R. Gonzalez: Carbon supported $Pt_{70}Co_{30}$ electrocatalyst prepared by the formic acid method for the oxygen reduction reaction in polymer electrolyte fuel cells, J. Power Source **141**, 13–18 (2005)

28.11 P. Yu, M. Pemberton, P. Plasse: PtCo/C cathode catalyst for improved durability in PEMFCs, J. Power Source **144**, 11–20 (2005)

28.12 A. Kabbabi, F. Gloaguen, F. Andolfatto, R. Durand: Particle size effect for oxygen reduction and methanol oxidation on Pt/C inside a proton exchange membrane, J. Electroanal. Chem. **373**, 251–254 (1994)

28.13 J.S. Yu, S. Kang, S.B. Yoon, G. Chai: Fabrication of ordered uniform porous carbon networks and their application to a catalyst supporter, J. Am. Chem. Soc. **124**, 9382–9383 (2002)

28.14 J.M. Planeix, N. Coustel, B. Coq, V. Brotons, P.S. Kumbhar, R. Dutartre, P. Geneste, P. Bernier, P.M. Ajayan: Application of carbon nanotubes as supports in heterogeneous catalysis, J. Am. Chem. Soc. **116**, 7935–7936 (1994)

28.15 Z. Liu, X. Lin, J.Y. Lee, W. Zhang, M. Han, L.M. Gan: Preparation and characterization of platinum-based electrocatalysts on multiwalled carbon nanotubes for proton exchange membrane fuel cells, Langmuir **18**, 4054–4060 (2002)

28.16 E.T. Michelson, I.W. Chiang, J.L. Zimmermann, P.J. Boul, J. Lozano, J. Liu, R.E. Smalley, R.H. Hauge, J.L. Margrave: Solvation of Fluorinated Single-Wall Carbon Nanotubes in Alcohol Solvents, J. Phys. Chem. B **103**, 4318–4322 (1999)

28.17 V. Georgakilas, K. Kordatos, M. Prato, D.M. Guldi, M. Holzinger, A. Hirsch: Organic functionalization of carbon nanotubes, J. Am. Chem. Soc. **124**, 760–761 (2002)

28.18 B.C. Satishkumar, E.M. Vogl, A. Govindaraj, C.N.R. Rao: The decoration of carbon nanotubes by metal nanoparticles, J. Phys. D **29**, 3173 (1996)

28.19 V. Lordi, N. Yao, J. Wei: Method for supporting platinum on single-walled carbon nanotubes for a selective hydrogenation catalyst, Chem. Mater. **13**, 733–737 (2001)

28.20 H.C. Choi, M. Shim, S. Bangsaruntip, H. Dai: Spontaneous reduction of metal ions on the sidewalls of carbon nanotubes, J. Am. Chem. Soc. **124**, 9058–9059 (2002)

28.21 C.R.K. Rao, D.C. Trivedi: Chemical and electrochemical depositions of platinum group metals and their applications, Coord. Chem. Rev. **249**, 613–631 (2005)

28.22 A. Freund, J. Lang, T. Lehman, K.A. Starz: Improved Pt alloy catalysts for fuel cells, Catal. Today **27**, 279–283 (1996)

28.23 H.F. Cui, J.S. Ye, W.D. Zhang, J. Wang, F.S. Sheu: Electrocatalytic reduction of oxygen by a platinum nanoparticle/carbon nanotube composite electrode, J. Electroanal. Chem. **577**, 295–302 (2005)

28.24 H. Tang, J.H. Chen, Z.P. Huang, D.Z. Wang, Z.F. Ren, L.H. Nie, Y.F. Kuang, S.Z. Yao: High dispersion and electrocatalytic properties of platinum on well aligned carbon nanotube arrays, Carbon **42**, 191–197 (2004)

28.25 W. Li, C. Liang, W. Zhao, J. Qiu, Z. Zhou, G. Sun, Q. Xin: Preparation and characterization of multiwalled carbon nanotube-supported platinum for cathode catalysts of direct methanol fuel cells, J. Phys. Chem. B **107**, 6292–6299 (2003)

28.26 Z. He, J. Chen, D. Liu, H. Zhou, Y. Kuang: Electrodeposition of Pt-Ru nanoparticles on carbon nanotubes and their electrocatalytic properties for methanol oxidation, Diamond Relat. Mater. **13**, 1764–1770 (2004)

28.27 S.J. Lee, A.C. Chien, S.W. Cha, R. O'Hayre, Y.I. Park, Y. Saito, F.B. Prinz: Design and fabrication of a micro fuel cell array with "flip-flop" interconnection, J. Power Source **112**, 410–418 (2002)

28.28 K. Cowey, K.J. Green, G.O. Mepsted, R. Reeve: Portable and military fuel cells, Curr. Opin. Solid State Mater. Sci. **8**, 367–371 (2004)

28.29 D.J. Seo, W.L. Yoon, Y.G. Yoon, S.H. Park, G.G. Park, G.S. Kim: Development of a micro fuel processor for PEMFCs, Electrochim. Acta **50**, 719–723 (2004)

28.30 A.L.M. Reddy, S. Ramaprabhu: Design, fabrication and testing of carbon nanotube based fuel cell stack and micro fuel cell coupled with hydrogen storage device, Int. J. Hydrogen Energy **32**, 4272 (2007)

28.31 Y. Yamazaki: Application of MEMS technology to micro fuel cells, Electrochim. Acta **50**, 663–666 (2004)

28.32 R. Hahn, S. Wagner, A. Schmitz, H. Reichl: Development of a planar micro fuel cell with thin film and micro patterning technologies, J. Power Source **131**, 73–78 (2004)

28.33 R. Kötz, M. Carlen: Principles and applications of electrochemical capacitors, Electrochim. Acta **45**, 2483–2498 (2000)

28.34 S. Sarangapani, B.V. Tilak, C.P. Chen: Review – materials for electrochemical capacitors, J. Electrochem. Soc. **143**, 3791–3799 (1996)

28.35 J. Gamby, P.L. Taberna, P. Simon, J.F. Fauvarque, M. Chesneau: Studies and characterisations of various activated carbons used for carbon/carbon supercapacitors, J. Power Source **101**, 109–116 (2001)

28.36 E. Frackowiak, F. Beguin: Carbon materials for the electrochemical storage of energy in capacitors, Carbon **39**, 937–950 (2001)

28.37 Y. Kibi, T. Saito, M. Kurata, J. Tabuchi, A. Ochi: Fabrication of high-power electric double-layer capacitors, J. Power Source **60**, 219–224 (1996)

28.38 Y.H. Lee, K.H. An, J.Y. Lee, S.C. Lim: Carbon nanotube-based supercapacitors. In: *Encyclopedia of Nanoscience and Nanotechnology*, Vol. 1, ed. by H.S. Nalwa (American Scientific, Valencia 2004) p. 625

28.39 C. Niu, E.K. Sichel, R. Hoch, D. Moy, H. Tennet: High power electrochemical capacitors based on carbon nanotube electrodes, Appl. Phys. Lett. **70**, 1480–1482 (1997)

28.40 E. Frackowiak, K. Metenier, V. Bertagna, F. Beguin: Supercapacitor electrodes from multiwalled carbon nanotubes, Appl. Phys. Lett. **77**, 2421–2423 (2000)

28.41 K.H. An, W.S. Kim, Y.S. Park, J.M. Moon, D.J. Bae, S.C. Lim, Y.S. Lee, Y.H. Lee: Electrochemical properties of high-power supercapacitors using single-walled carbon nanotube electrodes, Adv. Funct. Mater. **11**, 387–392 (2001)

28.42 V. Khomenko, E. Frackowiak, F. Beguin: Determination of the specific capacitance of conducting polymer/nanotubes composite electrodes using different cell configurations, Electrochim. Acta **50**, 2499–2506 (2005)

28.43 J.Y. Lee, K. Liang, K.H. An, Y.H. Lee: Nickel oxide/carbon nanotubes nanocomposite for electrochemical capacitance, Synth. Met. **150**, 153–157 (2005)

28.44 G.X. Wang, B.L. Zhang, Z.L. Yu, M.Z. Qu: Manganese oxide/MWNTs composite electrodes for supercapacitors, Solid State Ion. **176**, 1169–1174 (2005)

28.45 A. Du Pasquier, A. Laforgue, P. Simon, G.G. Amatucci, J.-F. Fauvarque: A nonaqueous asymmetric hybrid $Li_4Ti_5O_{12}$/poly(fluorophenylthiophene) energy storage device, J. Electrochem. Soc. **149**, A302 (2002)

28.46 M. Armand, J.M. Tarascon: Building better batteries, Nature **451**, 652–657 (2008)

28.47 M.S. Whittingham: Lithium Batteries and Cathode Materials, Chem. Rev. **104**, 4271–4302 (2004)

28.48 W. Van Schalkwijk, B. Scrosati: *Advances in Lithium-Ion Batteries* (Kluwer Academic/Plenum, New York 2002)

28.49 P.L. Taberna, S. Mitra, P. Poizot, P. Simon, J.M. Tarascon: High rate capabilities Fe_3O_4-based Cu nano-architectured electrodes for lithium-ion battery applications, Nat. Mater. **5**, 567–573 (2006)

28.50 S.Y. Chung, J.T. Bloking, Y.M. Chiang: Electronically conductive phospho-olivines as lithium storage electrodes, Nat. Mater. **1**, 123–128 (2002)

28.51 N. Li, C.R. Martin, B. Scrosati: A high-rate, high-capacity, nanostructured tin oxide electrode, Electrochem. Solid-State Lett. **3**, 316–318 (2000)

28.52 A.S. Aricò, P. Bruce, B. Scrosati, J.M. Tarascon, W. Van Schalkwijk: Nanostructured materials for advanced energy conversion and storage devices, Nat. Mater. **4**, 366–377 (2005)

28.53 A.L.M. Reddy, M.M. Shaijumon, S.R. Gowda, P.M. Ajayan: Coaxial MnO_2/carbon nanotube array electrodes for high-performance lithium batteries, Nano Lett. **9**, 1002–1006 (2009)

28.54 M. Endo, C. Kim, K. Nishimura, T. Fujino, K. Miyashita: Recent development of carbon materials for Li ion batteries, Carbon **38**, 183–197 (1999)

28.55 S.H. Lee, Y.H. Kim, R. Deshpande, P.A. Parilla, E. Whitney, D.T. Gillaspie, K.M. Jones, A.H. Mahan, S. Zhang, A.C. Dillon: Reversible lithium-ion insertion in molybdenum oxide nanoparticles, Adv. Mater. **20**, 3627–3632 (2008)

28.56 E. Peled: The electrochemical behavior of alkali and alkaline earth metals in nonaqueous battery systems – the solid electrolyte interphase mode, J. Electrochem. Soc. **126**, 2047–2051 (1979)

28.57 R. Fong, V. von Schen, J.R. Aohn: Studies of lithium intercalation into carbons using nonaqueous electrochemical cells, J. Electrochem. Soc. **137**, 2009–2013 (1990)

28.58 R. Hanno, Y. Kawamdo: Carbon fiber as a negative electrode in lithium secondary cells, J. Electrochem. Soc. **139**, 3397–3404 (1992)

28.59 R.S. Morris, B.G. Dixon, T. Gennett, R. Raffaelle, M.J. Heben: Rechargeable Li-ion battery based on carbon nanotube technology, J. Power Source **138**, 277–280 (2004)

28.60 Z. Zhou, J.J. Zhao, X.P. Gao, Z.F. Chen, J. Yan, P.V. Schiever, M. Morinaga: Do composite single-walled nanotubes have enhanced capability for lithium storage?, Chem. Mater. **17**, 992–1000 (2005)

28.61 M. Wakihara, O. Yamamoto (Eds.): *Lithium Ion Batteries-Fundamentals and Performance*, Vol. 3 (Wiely-VCH, Weinheim 1998), No. 4

28.62 E. Frackowiak, S. Gautier, H. Gaucher, S. Bonnamy, F. Beguin: Electrochemical storage of lithium in multiwalled carbon nanotubes, Carbon **37**, 61–69 (1999)

28.63 F. Beguin, K. Metenier, R. Pellenq, S. Bonnamy, E. Frackowiak: Lithium insertion in carbon nanotubes, J. Mol. Cryst. Liq. Cryst. **340**, 547–552 (2000)

28.64 J.F. Snyder, E.L. Wong, C.W. Hubbard: Evaluation of commercially available carbon fibers, fabrics, and papers for potential use in multifunctional energy storage applications, J. Electrochem. Soc. **156**, A215–A224 (2009)

28.65 J.O. Bosenhard (Ed.): *Handbook of Battery Materials* (VCH, Weinheim 1998)

28.66 R.A. Huggins: Lithium alloy negative electrodes formed from convertible oxides, Solid State Ion. **57**, 113–115 (1998)

28.67 J.O. Besenhard, J. Yang, M. Winter: Will advanced lithium-alloy anodes have a chance in lithium-ion batteries?, J. Power Source **68**, 87–90 (1997)

28.68 M. Winter, J.O. Besenhard: Electrochemical lithiation of tin and tin-based intermetallics and composites, Electrochim. Acta **45**, 31–50 (1999)

28.69 H. Mukaibo, T. Osaka, P. Reale, S. Panero, B. Scrosati, M. Wachtler: Optimized Sn/SnSb lithium storage materials, J. Power Source **132**, 225–228 (2004)

28.70 I. Amadei, S. Panero, B. Scrosati, G. Cocco, L. Schiffini: The Ni_3Sn_4 intermetallic as a novel electrode in lithium cells, J. Power Source **143**, 227–230 (2005)

28.71 H. Mukaibo, T. Sumi, T. Yokoshima, T. Momma, T. Osaka: Electrodeposited Sn-Ni alloy film as a high capacity anode material for lithium-ion secondary batteries, Electrochem. Solid-State Lett. **6**, A218–A220 (2003)

28.72 J. Hassoun, S. Panero, B. Scrosati: Electrodeposited Ni–Sn intermetallic electrodes for advanced lithium ion batteries, J. Power Source **160**, 1336–1341 (2006)

28.73 M. Green, E. Fielder, B. Scrosati, M. Wachtler, J. Serra Moreno: Structured silicon anodes for lithium battery applications, Electrochem. Solid-State Lett. **6**, A75–A79 (2003)

28.74 P.L. Taberna, S. Mitra, P. Piozot, P. Simon, J.M. Tarascon: High rate capabilities Fe_3O_4-based Cu nano-architectured electrodes for lithium-ion battery applications, Nat. Mater. **5**, 567–573 (2006)

28.75 M.M. Thackeray: Manganese oxides for lithium batteries, Prog. Solid State Chem. **25**, 1–71 (1997)

28.76 F. Jiao, P.G. Bruce: Mesoporous Crystalline β-MnO_2 – a reversible positive electrode for rechargeable lithium batteries, Adv. Mater. **19**, 657–660 (2007)

28.77 P. Poizot, S. Laruelle, S. Grugeon, L. Dupont, J.M. Tarascon: Nano-sized transition-metal oxides as negative-electrode materials for lithium-ion batteries, Nature **407**, 496–499 (2000)

28.78 F. Badway, I. Plitz, S. Grugeon, S. Laruelle, M. Dolle, A.S. Gozdz, J.M. Tarascon: Metal oxides as negative electrode materials in li-ion cells, Electrochem. Solid-State Lett. **5**(6), A115–A118 (2002)

28.79 K.T. Nam, D.W. Kim, P.J. Yoo, C.Y. Chiang, N. Meethong, P.T. Hammond, Y.M. Chiang, A.M. Belcher: Virus-enabled synthesis and assembly of nanowires for lithium ion battery electrodes, Science **312**, 885–888 (2006)

28.80 C.K. Chan, H. Peng, R.D. Twesten, K. Jarausch, X.F. Zhang, Y. Cui: Fast, completely reversible Li in-

sertion in vanadium pentoxide nanoribbons, Nano Lett. **7**, 490–495 (2007)

28.81 A.C. Dillon, A.H. Mahan, R. Deshpande, P.A. Parilla, K.M. Jones, S.H. Lee: Metal oxide nano-particles for improved electrochromic and lithium-ion battery technologies, Thin Solid Films **516**, 794–797 (2008)

28.82 V. Subramanian, W.W. Burke, H. Zhu, B. Wei: Novel microwave synthesis of nanocrystalline SnO_2 and its electrochemical properties, J. Phys. Chem. C **112**, 4550–4556 (2008)

28.83 L. Kavan, I. Exnar, J. Cech, M. Graetzel: Enhancement of electrochemical activity of $LiFePO_4$ (olivine) by amphiphilic ru-bipyridine complex anchored to a carbon nanotube, Chem. Mater. **19**(19), 4716–4721 (2007)

28.84 F. Badway, A.N. Mansour, N. Pereira, J.F. Al-Sharab, F. Cosandey, I. Plitz, G.G. Amatucci: Structure and electrochemistry of copper fluoride nanocomposites utilizing mixed conducting matrices, Chem. Mater. **19**(17), 4129–4141 (2007)

28.85 G. Derrien, J. Hassoun, S. Panero, B. Scrosati: Nanostructured Sn–C composite as an advanced anode material in high-performance lithium-ion batteries, Adv. Mater. **19**, 2336–2340 (2007)

28.86 S.H. Ng, J. Wang, D. Wexler, K. Konstantinov, Z.P. Guo, H.K. Liu: Highly reversible lithium storage in spheroidal carbon-coated silicon nanocomposites as anodes for lithium-ion batteries, Angew. Chem. Int. Ed. **45**, 6896–6899 (2006)

28.87 T.S. Ahmadi, Z.L. Wang, T.C. Green, A. Henglein, M.A. El-Sayed: Shape-controlled synthesis of colloidal platinum nanoparticles, Science **272**, 1924–1925 (1996)

28.88 P. Serp, M. Corrias, P. Kalck: Carbon nanotubes and nanofibers in catalysis, Appl. Catal. A **253**, 337–358 (2003)

28.89 G.L. Che, B.B. Lakshmi, E.R. Fisher, C.R. Martin: Carbon nanotubule membranes for electrochemical energy storage and production, Nature **393**, 346–349 (1998)

28.90 B. Rajesh, K.R. Thampi, J.M. Bonard, N. Xanthopoulos, H.J. Mathieu, B. Viswanathan: Carbon nanotubes generated from template carbonization of polyphenyl acetylene as the support for electrooxidation of methanol, J. Phys. Chem. B **107**, 2701–2708 (2003)

28.91 M. Mastragostino, A. Missiroli, F. Soavi: Carbon supports for electrodeposited Pt-Ru catalysts for DMFCs, J. Electrochem. Soc. **151**, A1919–A1924 (2004)

28.92 Y. Shao, G. Yin, Y. Gao, P. Shi: Durability study of Pt/C and Pt/CNTs catalysts under simulated PEM fuel cell conditions, J. Electrochem. Soc. **153**, A1093–A1097 (2006)

28.93 H.C. Choi, M. Shim, S. Bangsaruntip, H. Dai: Spontaneous reduction of metal ions on the sidewalls of carbon nanotubes, J. Am. Chem. Soc. **124**, 9058–9059 (2002)

28.94 G. Che, B.B. Lakshmi, C.R. Martin, E.R. Fisher: Metal-nanocluster- filled carbon nanotubes: Catalytic properties and possible applications in electrochemical energy storage and production, Langmuir **15**(3), 750–758 (1999)

28.95 A.L.M. Reddy, M.M. Shaijumon, N. Rajalakshmi, S. Ramaprabhu: Performance of PEMFC using Pt/MWNT-Pt/C composites as electrocatalysts for oxygen reduction reaction in PEMFC, J. Fuel Cell Sci. Technol. **7**, 021001 (2010)

28.96 A.L.M. Reddy, S. Ramaprabhu: Pt/SWNT-Pt/C nanocomposites as electrocatalysts for proton exchange membrane fuel cell, J. Phys. Chem. C **111**(21), 16138 (2007)

28.97 A.L.M. Reddy, M.M. Shaijumon, S. Ramaprabhu: Alloy hydride catalyst route of synthesis of singlewalled carbon nanotubes, multiwalled carbon nanotubes and magnetic metal nanowire encapsulated multi walled carbon nanotubes, Nanotechnology **17**, 5299 (2006)

28.98 G. Girishkumar, M. Rettker, R. Underhile, D. Binz, K. Vinodgopal, P. McGinn, P.V. Kamat: Single-wall carbon nanotube-based proton exchange membrane assembly for hydrogen fuel cells, Langmuir **21**, 8487 (2005)

28.99 M. Sogaard, M. Odgaard, E.M. Skou: An improved method for the determination of the electrochemical active area of porous composite platinum electrodes, Solid State Ion. **145**, 31 (2001)

28.100 S.C. Thomas, X.M. Ren, S. Gottesfeld, P. Zelenay: Direct methanol fuel cells: Progress in cell performance and cathode research, Electrochim. Acta. **47**, 3741–3748 (2002)

28.101 J. Zhang, F.H.B. Lima, M.H. Shao, K. Sasaki, J.X. Wang, J. Hanson, R.R. Adzic: Platinum monolayer on non-noble metal-noble metal core-shell nanoparticle electrocatalysts for O_2 reduction, J. Phys. Chem. B **109**, 22701–22704 (2005)

28.102 G. Avgouropoulos, T. Loannides, C. Papadopoulou, J. Batista, S. Hocevar, H.K. Matralis: A comparative study of Pt/γ-Al_2O_3, Au/α-Fe_2O_3 and CuO–CeO_2 catalysts for the selective oxidation of carbon monoxide in excess hydrogen, Catal. Today **75**, 157 (2002)

28.103 H. Igarashi, H. Uchida, M. Suzuki, Y. Sasaki, M. Watanabe: Removal of carbon monoxide from hydrogen-rich fuels by selective oxidation over platinum catalyst supported on zeolite, Appl. Catal. A. **159**, 159 (1997)

28.104 X. Zhang, L.P. Filho, C. Torras, R. Garcia-Valls: Experimental and computational study of proton and methanol permeabilities through composite membranes, J. Power Source **145**, 223 (2005)

28.105 J. Zhang, F.H.B. Lima, M.H. Shao, K. Sasaki, J.X. Wang, J. Hanson, R.R. Adzic: Platinum monolayer on non-noble metal-noble metal core-shell nanoparticle electrocatalysts for O_2 reduction, J. Phys. Chem. B **109**, 22701 (2005)

28.106 J. Zhang, Y. Mo, M.B. Vukmirovic, R. Klie, K. Sasaki, R.R. Adzic: Platinum monolayer electrocatalysts for O_2 reduction: Pt monolayer on Pd (111) and on carbon-supported Pd nanoparticles, J. Phys. Chem. B **108**, 10955 (2004)

28.107 M. Wojciechowska, M. Zielinski, A. Malczewska, W. Przystajko, M. Pietrowski: Copper–cobalt oxide catalysts supported on MgF_2 or Al_2O_3 – their structure and catalytic performance, Appl. Catal. A **298**, 225 (2006)

28.108 P. Thormahlen, M. Skoglundh, E. Fridell, B. Andersson: Low-temperature CO oxidation over platinum and cobalt oxide catalysts, J. Catal. **188**, 300 (1999)

28.109 P. Konova, M. Stoyanova, A. Naydenov, S. Christoskova, D. Mehandjiev: Catalytic oxidation of VOCs and CO by ozone over alumina supported cobalt oxide, Appl. Catal. A **298**, 109 (2006)

28.110 S.G. Christoskova, M. Stoyanova, M. Georgieva: Low-temperature iron-modified cobalt oxide system: Part I. Preparation and characterization, Appl. Catal. A **208**, 235 (2001)

28.111 A.J. Appleby: Electrocatalysis of aqueous dioxygen reduction, J. Electroanal. Chem. **357**, 117–179 (1993)

28.112 R. Bashyam, P. Zelenay: A class of non-precious metal composite catalysts for fuel cells, Nature **443**, 63 (2006)

28.113 A.L.M. Reddy, N. Rajalakshmi, S. Ramaprabhu: Cobalt-polypyrrole-multiwalled carbon nanotube catalysts for hydrogen and alcohol fuel cells, Carbon **46**, 2 (2008)

28.114 J. Prabhuram, T.S. Zhao, Z.K. Tang, R. Chen, Z.X. Liang: Multiwalled carbon nanotube supported PtRu for the anode of direct methanol fuel cells, J. Phys. Chem. B. **110**, 5245–5252 (2006)

28.115 W.J. Zhou, W.Z. Li, S.Q. Song, Z.H. Zhou, L.H. Jiang, G.Q. Sun, Q. Xin, K. Poulianitis, S. Kontou, P. Tsiakaras: Bi- and tri-metallic Pt based anode catalysts for direct ethanol fuel cells, J. Power Source **131**, 217 (2004)

28.116 J. Lee, S. Yoon, T. Hyeon, S.M. Oh, K.B. Kim: Synthesis of a new mesoporous carbon and its application to electrochemical double-layer capacitors, Chem. Commun **21**, 2177–2178 (1999)

28.117 E. Frackowiak, F. Beguin: Carbon materials for the electrochemical storage of energy in capacitors, Carbon **39**, 937–950 (2001)

28.118 D. Qu, H. Shi: Studies of activated carbons used in double-layer capacitors, J. Power Source **74**, 99–107 (1998)

28.119 T. Momma, X. Liu, T. Osaka, Y. Ushio, Y. Sawada: Electrochemical modification of active carbon fiber electrode and its application to double-layer capacitor, J. Power Source **60**, 249–253 (1996)

28.120 Y.H. Lee, K.H. An, J. Lee, L. Young, C. Seong: Encycl. Nanosci. Nanotechnol. **1**(1), 625–634 (2010)

28.121 J.P. Zheng, P.J. Cygan, T.R. Jow: Hydrous ruthenium oxide as an electrode material for electrochemical capacitors, J. Electrochem. Soc. **142**, 2699–2703 (1995)

28.122 N.L. Wu: Nanocrystalline oxide supercapacitors, Mater. Chem. Phys. **75**, 6–11 (2002)

28.123 T.C. Liu, W.G. Pell, B.E. Conway: Stages in the development of thick cobalt oxide films exhibiting reversible redox behavior and pseudocapacitance, Electrochim. Acta **44**, 2829–2842 (1999)

28.124 V. Srinivasan, J.W. Weidner: Studies on the capacitance of nickel oxide films: effect of heating temperature and electrolyte concentration, J. Electrochem. Soc. **147**, 880–885 (2000)

28.125 T. Cottineau, M. Toupin, T. Delahaye, T. Brousse, D. Bélanger: Nanostructured transition metal oxides for aqueous hybrid electrochemical supercapacitors, Appl. Phys. A **82**, 599–606 (2006)

28.126 B.E. Conway, V. Birss, J. Wojtowicz: The role and utilization of pseudocapacitance for energy storage by supercapacitors, J. Power Source **66**, 1–14 (1997)

28.127 A. Laforgue, P. Simon, C. Sarrazin, J.F. Fauvarque: Polythiophene-based supercapacitors, J. Power Source **88**, 142–148 (1999)

28.128 M. Mastragostino, C. Arbizzani, F. Soavi: Polymer-based supercapacitors, J. Power Source **97–98**, 812–815 (2001)

28.129 D. Bélanger, X. Ren, J. Davey, F. Uribe, S. Gottesfeld: Characterization and long-term performance of polyaniline-based electrochemical capacitors, J. Electrochem. Soc. **147**, 2923–2929 (2000)

28.130 C. Arbizzani, M. Mastragostino, F. Soavi: New trends in electrochemical supercapacitors, J. Power Source **100**, 164–170 (2001)

28.131 J.C. Carlberg, O. Inganas: Poly(3,4-ethylenedioxythiophene) as electrode material in electrochemical capacitors, J. Electrochem. Soc. **144**, L61–L64 (1997)

28.132 Q. Xiao, X. Zhou: The study of multiwalled carbon nanotube deposited with conducting polymer for supercapacitor, Electrochim. Acta **48**, 575–580 (2003)

28.133 L. Li, D.C. Loveday, D.S.K. Mudigonda, J.P. Ferraris: Effect of electrolytes on performance of electrochemical capacitors based on poly[3-(3,4-difluorophenyl)thiophene], J. Electrochem. Soc. **149**, A1201–A1207 (2002)

28.134 K.S. Ryu, K.M. Kim, N.G. Park, S.H. Chang: Symmetric redox supercapacitor with conducting polyaniline electrodes, J. Power Source **103**, 305–309 (2002)

28.135 C. Portet, P.L. Taberna, P. Simon, E. Flahaut: Influence of carbon nanotubes addition on carbon–carbon supercapacitor performances in organic electrolyte, J. Power Source **139**, 371–378 (2005)

28.136 F. Beguin, K. Szostak, G. Lota, E. Frackowiak: A self-supporting electrode for supercapacitors

prepared by one-step pyrolysis of carbon nanotube/polyacrylonitrile blends, Adv. Mater. **17**, 2380–2384 (2005)

28.137 Y. Kim, T. Mitani: Competitive effect of carbon nanotubes oxidation on aqueous EDLC performance: Balancing hydrophilicity and conductivity, J. Power Source **158**, 1517–1522 (2006)

28.138 K.H. An, W.S. Kim, Y.S. Park, J.M. Moon, D.J. Bae, S.C. Lim, Y.S. Lee, Y.H. Lee: Electrochemical properties of high-power supercapacitors using single-walled carbon nanotube electrodes, Adv. Funct. Mater. **11**, 387–392 (2001)

28.139 G.X. Wang, B.L. Zhang, Z.L. Yu, M.Z. Qu: Manganese oxide/MWNTs composite electrodes for supercapacitors, Solid State Ion. **176**, 1169–1174 (2005)

28.140 G. Arabale, D. Wagh, M. Kulkarni, I.S. Mulla, S.P. Vernekar, K. Vijayamohanan, A.M. Rao: Enhanced supercapacitance of multiwalled carbon nanotubes functionalized with ruthenium oxide, Chem. Phys. Lett. **376**, 207–213 (2003)

28.141 W. Sugimoto, H. Iwata, K. Yokoshima, K.Y. Murakami, Y. Takasu: Proton and electron conductivity in hydrous ruthenium oxides evaluated by electrochemical impedance spectroscopy: The origin of large capacitance, J. Phys. Chem. B **109**, 7330 (2005)

28.142 A.L.M. Reddy, S. Ramaprabhu: Nanocrystalline metal oxides dispersed multiwalled carbon nanotubes as supercapacitor electrodes, J. Phys. Chem. C **111**(44), 16138–16146 (2007)

28.143 F.E. Amitha, A.L.M. Reddy, S. Ramaprabhu: A non-aqueous electrolyte based asymmetric supercapacitor with polymer and metal oxide/multiwalled nanotube electrodes, J. Nanopart. Res. **11**(3), 725 (2009)

28.144 H.K. Song, H.Y. Hwang, K.H. Lee, L.H. Dao: The effect of pore size distribution on the frequency dispersion of porous electrodes, Electrochim. Acta. **45**, 2241–2257 (2000)

28.145 A.S. Arico, P. Bruce, B. Scrosati, J.M. Tarascon, W. Van Schalkwijk: Nanostructured materials for advanced energy conversion and storage devices, Nat. Mater. **4**, 366–377 (2005)

28.146 F. Croce, G.B. Appetecchi, L. Persi, B. Scrosati: Nanocomposite polymer electrolytes for lithium batteries, Nature **394**, 456–458 (1998)

28.147 M.M. Thackeray, M.H. Rossouw, A. de Kock, A.P. de la Harpe, R.J. Gummow, K. Pearce, D.C. Liles: The versatility of MnO_2 for lithium battery applications, J. Power Source **434**, 289–300 (1993)

28.148 J. Desilvestro, O. Haas: Metal oxide cathode materials for electrochemical energy storage: A review, J. Electrochem. Soc. **137**, C5–C22 (1990)

28.149 M. Sugantha, P.A. Ramakrishnan, A.M. Hermann, C.P. Warmsingh, D.S. Ginley: Nanostructured MnO_2 for Li batteries, Int. J. Hydrogen Energy **28**, 597–600 (2003)

28.150 D.K. Kim, P. Muralidharan, H.W. Lee, R. Ruffo, Y. Yang, C.K. Chan, H. Peng, R.A. Huggins, Y. Cui: Spinel $LiMn_2O_4$ nanorods as lithium ion battery cathodes, Nano Lett. **8**(11), 3948–3952 (2008)

28.151 M.S. Wu, P.C.J. Chiang, J.T. Lee, J.C. Lin: Synthesis of manganese oxide electrodes with interconnected nanowire structure as an anode material for rechargeable lithium ion batteries, J. Phys. Chem. B **109**, 23279–23284 (2005)

28.152 F. Cheng, Z. Tao, J. Liang, J. Chen: Template-directed materials for rechargeable lithium-ion batteries, J. Chem. Mater. **20**, 667–681 (2008)

28.153 D.W. Kim, I.S. Hwang, S.J. Kwon, H.Y. Kang, K.S. Park, Y.J. Choi, K.J. Choi, J.G. Park: $LiMn_2O_4$ nanorods as lithium ion battery cathodes, Nano Lett. **7**(10), 3041–3045 (2007)

28.154 A.L.M. Reddy, S.M. Manikoth, S.R. Gowda, P.M. Ajayan: Co-axial MnO_2/carbon nanotube array electrodes for high performance lithium batteries, Nano Lett. **9**, 1002 (2009)

28.155 R. Liu, S.B. Lee: MnO_2/Poly(3,4-ethylenedioxythiophene) coaxial nanowires by one-step coelectrodeposition for electrochemical energy storage, J. Am. Chem. Soc. **130**(10), 2942–2943 (2008)

28.156 R. Dedryvere, S. Laruelle, S. Grugeon, P. Poizot, D. Gonbeau, J.M. Tarascon: Contribution of x-ray photoelectron spectroscopy to the study of the electrochemical reactivity of Co0 toward lithium, Chem. Mater. **16**(6), 1056–1061 (2004)

29. Nanomaterials in Civil Engineering

Jaesang Lee, Seunghak Lee, Eunhyea Chung, Vincent C. Reyes, Shaily Mahendra

Manufactured nanomaterials (MNMs) with unique physical and chemical properties have attracted a great deal of attention as key materials to underpin future scientific and technological advancements. Applications of MNMs can also provide breakthroughs in the construction industry by reinforcing mechanical properties, decreasing vulnerability to chemical corrosion and accidental damage, and providing supplementary functions such as anti-biofouling and hydrophilicity. With the enhancement of material performance and functionality, use of MNMs enables (partial) nonutility generation, low carbon emission, and self-assessment of structural health to increase the sustainability of buildings and infrastructures. On the other hand, recent research into the safety of MNMs has raised concerns about their adverse biological and environmental effects. There is a high probability that MNMs used in construction will have hazardous effects on human and ecological receptors, considering that MNMs incorporated into construction materials would be released via multiple exposure routes during their entire lifecycle (manufacturing, construction, demolition, and recycling/disposal). Consequently, to responsibly utilize the potential benefits of nanotechnology in construction, multidisciplinary efforts are required to develop proactive strategies to mitigate the environmental release of MNMs and guidelines to manage their environmental risks throughout construction-related activities.

29.1 **Applications of MNMs in Construction** 1041
29.1.1 Concrete and Cement 1041
29.1.2 Steel 1044
29.1.3 Plastic 1044
29.1.4 Window Glass 1044
29.1.5 Coatings 1045
29.1.6 Lighting 1046
29.1.7 Sensors 1046

29.2 **Environmental Release of MNMs Used in Construction** 1047
29.2.1 Construction Material Manufacturing 1047
29.2.2 Structural Applications 1048
29.2.3 Structural Demolition 1048
29.2.4 Construction Waste Disposal 1048

29.3 **Potential Adverse Biological Impacts and Toxicity Mechanisms** 1049
29.3.1 TiO_2 1050
29.3.2 Quantum Dots 1050
29.3.3 Carbon Nanotubes 1050
29.3.4 C_{60} Fullerene 1050
29.3.5 SiO_2 1052
29.3.6 Copper/Copper Oxide 1052

29.4 **Mitigation of Environmental and Health Impacts** 1052
29.4.1 Manufacturing 1052
29.4.2 Application 1053
29.4.3 Recycling/Disposal 1053

29.5 **Conclusions** 1054

References 1055

Nanotechnology, as a new industrial revolution, has brought myriad opportunities to a variety of scientific, engineering, and technology sectors. The *bottom-up* synthetic strategy in the transitional zone between atom and molecule creates nanodimensional materials with novel physical and chemical properties, offering great potential for diverse applications including (photo)catalysts, electronic and electrochemical materials, energy conversion and storage devices, mechanical composites, and optical instruments [29.1–5].

The incorporation of various manufactured nanomaterials (MNMs) into the matrices of conventional

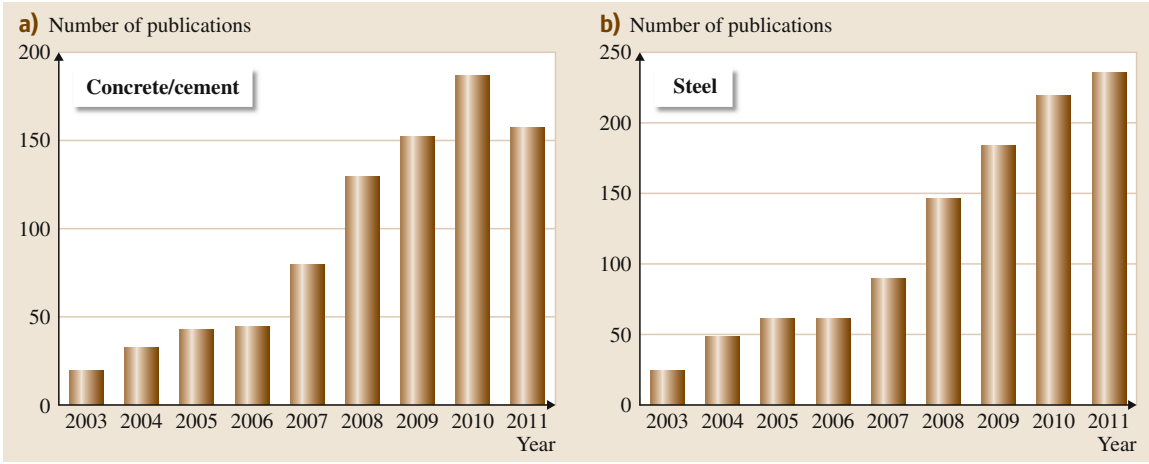


Fig. 29.1a,b Annual number of research articles published in the subject areas of **(a)** MNM-containing concrete/cement and **(b)** MNM-containing steel. The literature search was performed at the Scopus website using the keywords "Nano" and "Cement" or "Concrete" **(a)** and "Nano" and "Steel" and "Strength" or "Corrosion" **(b)**

construction materials leads to drastic advancement in vital characteristics including mechanical strength, fatigue and damage resistance, durability, and lightness [29.6–9]. MNMs as additives improve cohesive and tensile strength, flexibility, forgability, and weldability to enable facile construction and processing operations [29.8, 10]. MNMs incorporated into construction materials add new auxiliary functions such as photo-induced pollution control, antimicrobial activity, and heat- and sound-absorbing capacity [29.11–13]. Use of MNMs contributes to increased energy efficiency in commercial and residential buildings (e.g., highly insulating materials and energy-generating coatings) [29.14, 15]. Coatings of MNMs provide corrosion resistance, fire retardation, and water repulsion to protect construction materials from weathering, aging, and contamination, eventually promoting their long-term serviceability [29.8, 16, 17]. MNMs embedded in construction materials are also applied in sensing and monitoring functions to assess construction safety and structural health [29.18, 19].

Contrary to the general perspective on the promising applications of nanotechnology, technical viability has been relatively less explored in the construction industry, which is attributed to:

1. Lack of informative research to ensure the potential benefits and identify the functionalities,
2. Uncertainties associated with nanoscale materials' longevity and environmental health and safety,
3. Conservative nature of construction industry, leading to limited adoption of new technology, and
4. Economical feasibility.

Nevertheless, use of MNMs in the construction industry is expected to increase rapidly, as shown by the increasing number of research articles published on the subject of *nanoconstruction* in Fig. 29.1 because of:

1. Recent advancement in harnessing unique nanoscale properties,
2. Rapid expansion of commercial interest in nanoenabled products,
3. Several research projects underway to assess and control potential hazards associated with engineered nanomaterials (NMs),
4. High performance and versatility of MNMs imparted at low additive ratios, and
5. Decreasing cost of base NMs due to their mass production.

In particular, despite the benefits of incorporating MNMs into construction materials, it is highly probable that concerns about their potential to become harmful environmental contaminants after their unwanted discharge limit their utility [29.20–22]. This underscores the need for assessment, standard protocols, and regulatory guidelines to address the environmental health and safety issues associated with manufacturing, transportation, use, and disposal of construction materials and products containing MNMs.

29.1 Applications of MNMs in Construction

The unique properties of MNMs can be exploited in construction for a variety of applications that encompass reinforced structural materials, low-maintenance and ecofriendly materials, multifunctional paints and coatings, renewable energy generation systems, and intelligent sensor/actuator devices (Table 29.1). The current and potential applications of MNMs in construction are described below, and some selected examples for MNMs used in construction and related MNM-containing products are illustrated in Figs. 29.2 and 29.3.

29.1.1 Concrete and Cement

Concrete is one of the most common manmade materials in the world. Conventional concrete is relatively strong in compression because fine and coarse aggregates such as sand and natural gravel in concrete efficiently carry the compressive load. However, traditional concrete has heterogeneous micro- and mesoporous structures through the random packing of concrete mixture of aggregates, cement, and water. Thus, it is weak in tension and flexure due to the complex internal pore

Table 29.1 MNM applications in the construction industry

Construction materials	Manufactured nanomaterials	Expected functions	References
Concrete/cement	Carbon nanotubes SiO_2 nanoparticles Fe_2O_3 nanoparticles TiO_2 nanoparticles Ni nanoparticles $CaCO_3$ nanoparticles	Crack prevention Abrasion resistance Stress level monitoring Self-cleaning Whitening Reinforcement Cement hydration improvement	[29.7–9, 23–26]
Steel	Cu nanoparticles Mg nanoparticles V nanoparticles Mo nanoparticles	Weldability Corrosion resistance Strength improvement Ductility Fracture toughness	[29.8, 10]
Plastic	Carbon nanotubes Nanoclays	Electric/thermal conductivity Flame retardancy High compressive strength Rot resistance	[29.27–31]
Window	WO_3 nanoparticles LaB_6 nanoparticles SnO_2 nanoparticles Ag/TiO_2 nanocomposites TiO_2 nanoparticles SiO_2 nanoparticles Al nanoparticles	Infrared-absorbing UV and heat blocking Light transmittance control Antireflectivity Photo-induced depolluting Stain-proofing Antifogging Scratch and wear resistance Fire-protective	[29.11, 14, 32–38]
Coatings	SiO_2 nanoaerogols Carbon nanoparticles Ag nanoparticles TiO_2 nanoparticles ZnO nanoparticles Fe_2O_3 nanoparticles Zn nanoparticles	Thermal insulation UV and heat blocking Antimicrobial activity Dirt-proofing Corrosion inhibition Fire resistance	[29.14, 16, 20, 39–45]
Solar cells	TiO_2 nanoparticles CdSe quantum dots C_{60} fullerene Carbon nanotubes	Nonutility electricity generation	[29.15, 46, 47]
Lighting	GaN nanoparticles GaAsP nanoparticles	LED phosphors	[29.48, 49]
Sensors	$BaTiO_3$ nanoparticles Carbon nanotubes	Real-time monitoring of concrete strength and structural health	[29.18, 19, 50]

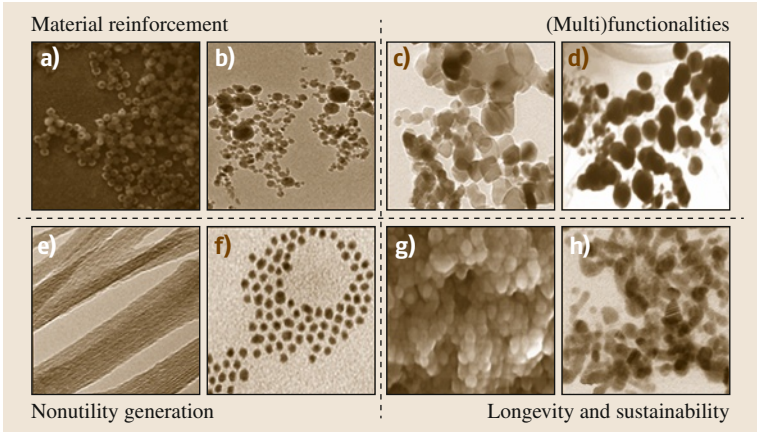


Fig. 29.2a–h Examples of MNMs used in the construction industry. **(a)** SiO_2 nanoparticles (source: Los Alamos National Laboratory); **(b)** Fe_2O_3 nanoparticles (courtesy of Dr. Changha Lee, Ulsan National Institute of Science and Technology); **(c)** TiO_2 nanoparticles; **(d)** Ag nanoparticles (source: US Environmental Protection Agency); **(e)** carbon nanotubes (source: National Cancer Institute); **(f)** CdSe quantum dots (source: Lawrence Berkeley National Laboratory); **(g)** $BaTiO_3$ nanoparticles (source: The National Academy of Sciences of Ukraine); **(h)** Cu nanoparticles (courtesy of Dr. Changha Lee, Ulsan National Institute of Science and Technology)

structure of the concrete. There are several possible explanations for the improvement of mechanical properties by MNMs [29.7]. Firstly, nanosized materials fill the cement pores and serve as packing materials in concrete. Secondly, nanoparticles (NPs) promote cement hydration through tight binding with the cement hydrate. Finally, NMs efficiently inhibit the growth of large crystals (e.g., $Ca(OH)_2$).

NPs have been applied to improve compressive strength during the past decade. Research into SiO_2, TiO_2 or Fe_2O_3 NPs used as a concrete additive material has shown that these nanosized particles serve as a filling agent to increase the strength of the concrete and improve its abrasion resistance [29.23–25]. Addition of silica NPs as a part of the mixture also enhances the durability of the concrete by blocking water penetration. SiO_2 NPs can control the degradation of $(CaO)\cdot(SiO_2)\cdot(H_2O)$, which is the product of the cement hydration process, by blocking water entry into the pores [29.8]. In addition, the weight of concrete would be reduced by using silica fume. Hematite (Fe_2O_3) NPs can be used as a monitoring material to quantify the stress levels by measuring section electrical resistance as well as a packing material [29.8]. Research into

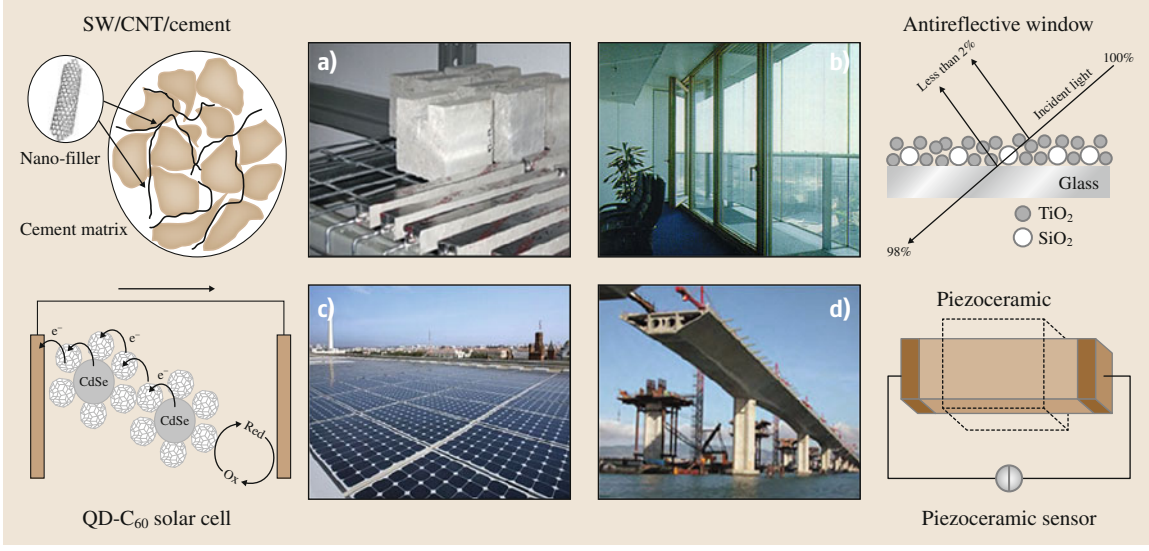


Fig. 29.3a–d MNM-containing construction products and their applications. **(a)** Concrete (source: US Department of Transportation Federal Highway Administration); **(b)** window glass (source: NBNL); **(c)** rooftop solar panel (source: US Department of Energy); **(d)** bridge (source: MCEER, the State University of New York Buffalo)

carbon-encapsulated nickel NPs incorporated into concrete also demonstrated an increase in the compressive strength of the cement due to the intense antiparallel ordering caused by a magnetic dipole interaction [29.7].

TiO_2 NPs have other supplementary functions when applied to cement/concrete, such as sterilizing and self-cleaning, as well as filling the pores [29.26]. TiO_2 as an ultraviolet (UV)-responsive photocatalyst yields reactive oxygen species (ROS) under light irradiation, resulting in destruction of volatile organic compounds, NO_x, and bacterial membranes. Due to the UV-activated hydrophilic conversion, rain droplets attracted to an outdoor surface containing nano-TiO_2 particles form a water layer which can wash away airborne pollutants, as airborne pollutants trapped in a TiO_2 particle matrix undergo further oxidative degradation under sunlight illumination. Since TiO_2 particles form a white pigment, nano-TiO_2-added concrete has the additional advantage that it can retain whiteness during the lifetime of the concrete. Incorporation of nano-TiO_2 into concrete has already been commercialized in the construction industry. The Jubilee Church in Rome was constructed from precast nano-TiO_2-integrated concrete panels, which is sometimes called *white concrete* [29.8]. Prior to the Jubilee Church, nano-TiO_2 was incorporated into road surfaces, and it was found that the NO_x concentration was significantly decreased near the constructed road [29.8].

$CaCO_3$ NPs have also been suggested as supplementary materials for addition to cement. Strength development during the initial period of cement hydration is significantly improved when nano-$CaCO_3$ is added [29.9]. The mechanism behind the improved cement hydration rate by nano-$CaCO_3$ needs to be further investigated, but the difference in the impact on hydration between micro-$CaCO_3$ and nano-$CaCO_3$ provides evidence that the size of the calcium carbonate particles plays a significant role in the hydration process. Another possible use of calcium carbonate as a biosealant in concrete is being studied [29.8]. Anaerobic microorganisms are incorporated into concrete mixing water, and subsequently excrete calcium carbonate, which fills the cement pores and results in improved compressive strength. Similarly, self-healing concrete in which microcapsules containing healing agents and catalysts are embedded is being investigated to solve crack problems of concrete [29.51]. When cracks form in the concrete, the capsules would be ruptured. The released healing agent then contacts the catalyst, and the crack will be filled through polymerization.

Traditionally, steel has been incorporated in conventional concrete as a *reinforcement bar* (rebar) in order to strengthen the concrete in tension and flexure, but the process of placing steel bars and introducing wet concrete is time consuming and expensive. Cracking due to rebar corrosion or freeze–thaw cycles is also an issue for steel-reinforced concrete. Glass, plastic, or steel fibers have sometimes been added to produce reinforced concrete. These materials can either replace the steel rebars entirely or be added to concrete already reinforced by steel bars. Concrete reinforced with fibers, for example, carbon graphite fiber, which is a corrosion-proof and very high strength-to-weight material, is less expensive and has still higher tensile strength. Nanosized fibers were recently studied as an alternative reinforcing material for concrete. Reinforced concrete was produced by introducing nano- and microsized carbon fibers [carbon nanotubes (CNTs)] and centimeter-sized carbon graphite fibers, exhibiting improved mechanical properties [29.6, 52]. Incorporation of CNTs is expected to show advantages over traditional fibers in reinforced concrete due to their distinct structural properties. CNTs are known as the strongest and stiffest materials in terms of tensile strength and elastic modulus, respectively. Therefore, they would improve the mechanical properties of the concrete. Also, the small size of CNTs should make them fill the cement pores and interrupt crack formation and growth at very early stages. On the other hand, the high aspect ratio of CNTs would play a role in preventing crack propagation, because higher energy would be required to propagate the crack around the nanotubes. In addition, CNTs can be chemically functionalized to interact with adjacent cement component. A recent study demonstrated that CNTs in concrete act as a nucleus to bind tightly with cement hydrate (C-S-H) around functionalized nanotubes [29.53].

In spite of their many advantages, there are economic and technical limitations to the use of CNTs in reinforced concrete. The cost of CNTs is still high and not competitive with other fiber materials. Furthermore, CNTs tend to form aggregates due to van der Waals forces, thus additional processes are required to achieve uniform distribution of individual tubes. Another issue with CNTs is weak bonding between the nanotubes and the cement matrix. Several research studies have been conducted to tackle these problems by functionalizing the nanotubes or through the use of surfactants and sonication to achieve uniform dispersion [29.27].

29.1.2 Steel

Steel has served as a reinforcement material in concrete or as a structural component in bridges, highways, or buildings by itself. In addition to its corrosion resistance, steel is also selected based on properties such as strength or weldability. Welding is one of the steel fabrication processes and creates a sector called the *heat-affected zone* (HAZ) adjacent to welds. The material properties of the HAZ are altered by heat-intensive cutting or welding processes, thus the HAZ and welds are brittle and can fail easily when a sudden dynamic load (e.g., seismic load) is applied. Addition of nanosized particles such as magnesium and calcium improves the weld toughness of steel as well as decreasing the size of the HAZ to 1/5 of that of conventional welded steel [29.8]. Not only improvement of toughness at welded joints, but also cost-saving due to the decreased material requirement to meet allowable limits is also expected when research currently underway is completed.

High-strength steel experiences delayed fracture problems, in which the steel material becomes brittle and fractures following exposure to hydrogen when strong tension is applied. Vanadium and molybdenum NPs have been incorporated to reduce the effects of hydrogen embrittlement and, therefore, to improve the delayed fracture problem of high-strength steel materials, especially high-strength bolts [29.8].

Many efforts have been made to improve the corrosion resistance of steel using nanotechnology, but very few products are available in the construction market. One of them is MMFX2 steel, which has a distinct nanostructure. A laminated lath structure resembling plywood in MMFX2 makes the steel corrosion resistant by hindering microgalvanic cell formation. In addition, according to the manufacturer, the unique features of the product provide improved strength, ductility, and toughness compared with conventional steel products. MMFX2 steel is currently used in many construction sites including bridges, parking structures, buildings, and highways. The Federal Highway Administration, the US Navy, and the American Iron and Steel Institute developed high-performance steel for bridges in 1990s. This new steel has higher fracture toughness, improved weldability, and better corrosion resistance than conventional steel by incorporating copper NPs, which are known to reduce the surface roughness of steel [29.10]. Another steel product available in the commercial market, but not for construction applications, is Sandvik Nanoflex. Although the manufacturer does not provide detailed information about the product, it is reported that very hard NPs are incorporated in the Sandvik Nanoflex steel matrix. Therefore, Sandvik Nanoflex has good corrosion and wear resistance and high modulus of elasticity.

Several ongoing research efforts focus on production of nanoscale fabricated metals, which are stronger than conventional steel or titanium. Such metals would be fabricated by weaving the material to produce ultrafine lattice structures or refining the cementite phase of steel to nanosize to produce cables [29.8]. The expected properties of such products are improved strength and reduced weight, and one of their applications could be as a structural component of suspension bridges.

29.1.3 Plastic

Multi-walled CNTs as a proxy for carbon black show improved performance as a filler material, drastically increasing the mechanical strength and electric and thermal conductivity of plastic composites [29.27, 28]. CNTs incorporated into plastics also function as a flame retardant to enable rapid heat dissipation, preventing the possible release of hazardous gasses under fire [29.29]. Addition of nanoscale ceramic materials (e.g., nanoclays) to the polymer matrices creates lightweight nanocomposite plastics with high compressive strength [29.30]. Wood–plastic composites produced by manipulating fiber-to-fiber bonding at the nanoscale, which require much less maintenance and have a long service life because of their high rot resistance, gain improved mechanical properties through modifications using carbon nanofibers and nanoclays [29.31].

29.1.4 Window Glass

Incorporation of MNMs into glass matrices allows the production of windows to control the passage of light and heat through the walls of buildings. Such applications can increase energy efficiency by reducing heat loss to conserve building heating energy (e.g., low-emissivity glass) and by blocking solar heat to curtail energy consumption for air-conditioning and ventilation (e.g., heat absorbing and solar control glass). Due to its strong visible and infrared absorption, nanosized tungsten oxide (WO_3) improves the heat reflectivity of a window to simultaneously reflect in-room heat back inside and mitigate solar heat gain through the window, and further enables variable light transmission [29.32]. Window glass containing lanthanum hexaboride (LaB_6)

NPs that selectively capture the heating wavelengths from 750 to 1300 nm secures sufficient natural daylight while maintaining uniform room temperature in hot weather seasons by transmitting visible light and blocking unwanted infrared light from the solar spectrum [29.11]. Nanostructured indium tin oxide (ITO) (or indium antimony oxide) film also creates highly transparent infrared-absorbing coatings on window glass, being commercialized under the product name AdNano ITO [29.11, 54]. Ultrafine TiO_2, ZnO, and TiO_2/CeO_2 uniformly cast on glass surfaces produce UV-reflecting windows by filtering out the UV fraction of sunlight without significantly decreasing visible light transmittance [29.8, 14, 33, 34]. In this case, rutile TiO_2 NPs with low photoactivity are in common use to avoid unwanted photocatalyzed destruction of surrounding matrices, as ZnO NPs are surface-modified with silica to facilitate homogeneous dispersion on the surface [29.14].

Light transmittance through the window can be controlled by photochromic coatings or layers that reversibly change their inherent color in response to incident light [29.55]. Photochromic films formed of MNMs including metal NPs, hybrid metal/metal oxide NPs, and quantum dots (QDs) can produce *smart windows* that react to light conditions, controlling the intensity of incident light, being translucent in the visible region to brighten interior spaces, or being reflective in the infrared region to retard thermal transfer [29.35, 36, 56–58]. Photochromic films containing platinum, palladium, or gold NPs exhibit coloration/color fading characteristics under light irradiation [29.57]. Dark-blue color rapidly develops on TiO_2 films in combination with phosphotungstic acid ($H_3PW_{12}O_{40}$) under UV irradiation and disappears in the presence of oxygen as an electron acceptor in the dark condition, as MoO_3 or WO_3 films coated with gold or platinum also undergo reversible UV-induced coloration on the window [29.35, 36]. In particular, TiO_2 film loaded with silver NPs on the window enables repeatable multicolor photochromism in which the initial brownish-grey color rapidly changes to the color of the excitation wavelength under irradiation by monochromatic visible light [29.58]. In addition to the photosensitive smart window, thermochromic glass that includes polymeric layers doped with various transition metals (e.g., Fe, Co) or metal/metal oxide nanocomposites (e.g., Au/VO_2) also modifies the transmission and reflection properties, adapting to the surrounding temperature to create a nonelectrically activated window to regulate daylight depending on the background thermal conditions [29.59, 60].

Antireflective coating of silica NPs causes micro- and nanoroughness on the glass surface, reducing the magnitude of visible light reflected and offering a clear view from inside to outside [29.14]. Vertically oriented pure rutile TiO_2 nanorods on glass substrate also form an antireflective coating [29.61]. Note that 20% of the incident light is reflected at the TiO_2–air interface, while the reflection at the uncoated glass–air interface is as low as 4%. Alternating layers of SiO_2 and TiO_2 NPs that exhibit a large refractive index contrast significantly improve light transmission through the window [29.14, 62].

Deposition of nano-TiO_2 on window glass offers a self-cleaning function under irradiation by sunlight or indoor light, because TiO_2 can photosensitize production of ROS such as OH radicals, valence-band holes, and relevant efficient oxidation of organic substrates [29.2, 63]. The photocatalyzed reactions initiating on nanosized TiO_2-coated glass lead to photooxidation of hydrocarbons and photokilling of pathogenic microorganisms attached to the window and from the surrounding atmosphere [29.37, 64]. In particular, metal or nonmetal doping allows TiO_2 NPs to utilize visible light for photocatalytic ROS generation. Photoinduced hydrophilic conversion occurring on a TiO_2 surface, which makes water spread out over the surface rather than remain as droplets, mitigates accumulation of hydrophobic dirt, as the increased density of surface hydroxyl groups under exposure to UV light enables antifogging and stain-proofing actions of the TiO_2-modified window [29.65, 66]. Such a photo-driven process for surface hydrophilization can be kinetically accelerated on TiO_2-based composite layers (e.g., TiO_2/WO_3 or TiO_2/SiO_2) [29.67, 68].

Inclusion of metal-oxide NPs can improve the mechanical strength, thermal stability, and chemical durability of window glass. Incorporation of aluminum nanopowders enhances the mechanical strength, microhardness, and chemical resistance of glass without significantly changing its optical properties [29.38], as silica NPs make windows highly scratch and wear resistant [29.14]. Nanoscale silica layers sandwiched between two glass panels form fire-protective window glass in which silica NPs swell, converting to mechanically reinforced and opaque forms in the event of a fire [29.8].

29.1.5 Coatings

Coatings utilizing MNMs are expected to impart diverse supplementary functionalities to construction-related

surfaces and produce the desired protective and resistant surfaces on existing construction materials. Use of MNMs for thermal insulation leads to energy conservation and carbon emission reduction through efficient heat management. Due to the large surface-to-volume ratio and high porosity, nanoporous silica as an insulator enables significant air entrapment within a layer of minimal thickness, thereby effectively hindering heat transfer across the layer [29.14, 20]. Aerogels or nanofoams of metal oxides (e.g., silica and alumina) that contain nanoscale pores primarily filled with air (> 90%) can be employed for ultrathin and lightweight insulating coatings (relative to conventional insulating layers of polystyrene or cellulose) [29.14, 20]. Three-dimensional and highly branched networks of SiO_2, TiO_2, or carbon NPs show exceptional insulative performance because nanosized cells, pores, and particles within the unique nanostructures produce substantially limited pathways for thermal conduction (through the interconnected NPs) and thermal energy transport (through the enclosed air molecules) [29.8, 14, 20].

Metallic NPs (e.g., silver and gold) produce antimicrobial coatings on diverse construction materials including cement/concrete, steel, plastic, and glass [29.14, 39–41]. The antimicrobial activity of silver NPs embedded in paint leads to efficient inactivation and sterilization of pathogenic microbes on the substrate surface [29.12]. Silver or gold NPs dispersed in polymer matrices form antibacterial metal/polymer nanocomposite coatings, hindering microbial adhesion on the substrate material [29.40, 41]. Thin films of metal-oxide-based semiconductor NPs (e.g., TiO_2 and ZnO) on pavements, walls, and roofs function as antifouling and self-cleaning coatings under solar irradiation to depollute airborne contaminants, protect construction products from stains and dirt, and inhibit growth of bacteria and mold on the surface [29.42, 69]. Micro- and nanopatterning reduce the surface energy and associated adhesion [29.70], offering water-repellant surfaces for construction products and making them less susceptible to dirt accumulation.

Thin films of ceramic NPs (e.g., SiO_2), which are highly resistant to oxidation, can function as physical barrier layers to protect metallic construction materials against corrosion [29.16]. TiO_2 NPs surface-modified with fluoroalkylsilane form hydrophobic coatings on the surface of stainless steel to prevent moisture-induced corrosion [29.17], as photogenerated conduction-band electrons are transferred from TiO_2 coatings to the corroding metals, providing corrosion resistance properties under solar irradiation [29.71]. Ultrafine metal-oxide particles (e.g., SiO_2, ZnO, and Al_2O_3 NPs) can serve as nanofillers for polymer-based coatings, thereby preventing infiltration of oxygen, water, and corrosive chemicals through the voids and cracks present in the polymer matrices [29.43]. Polymer encapsulation of nanosized Zn or Fe_2O_3 as anodic-type corrosion inhibitors leads to prolonged anticorrosion performance on the coated steel [29.43]. In particular, composite materials having metal-oxide core (e.g., CeO_2, SiO_2, TiO_2, and ZrO_2 NPs) with polymer shell responsive to an electric or mechanical trigger can produce *smart* corrosion-proof coatings by acting as nanoreservoirs to store organic corrosion inhibitors and release the entrapped reagents when external signals are applied [29.16]. In addition to corrosion resistance, nanosized SiO_2, TiO_2, and Sb_2O_3 as nonflammable fillers or additives reduce the thermal transfer rate, and improve the existing fire-resistant properties of polymer coatings or decorative paints [29.44, 45].

Flexible solar panels that utilize silicon-based photovoltaic or dye-sensitized TiO_2 solar cells are being integrated into roofing membranes and mounted on windows, converting solar energy to generate electric power available for homes and buildings. The solar energy coating as a partial nonutility power producer achieves improved efficiency of renewable energy generation through the incorporation of semiconductor QDs (e.g., CdSe and InAs) [29.15] and carbon-based NMs (e.g., C_{60} and CNTs) [29.46].

29.1.6 Lighting

A light-emitting diode (LED) employs inorganic semiconductor NPs (e.g., GaN, ZeSe, and GaAsP) with different band-gaps and produces various colors of light as a result of electroluminescence [29.48, 49]. LED devices are rapidly replacing conventional fluorescent and incandescent light bulbs because LEDs require low electric energy for lighting, provide long service life, and guarantee safe end-of-life management (i. e., no release of toxic metals).

29.1.7 Sensors

Nano- and microelectromechanical systems (NEMS and MEMS) can be applied as miniaturized implantable devices to allow real-time in situ monitoring and accurate assessment of the health status of construction materials/structures (e.g., cracking and stress) and environmental conditions (e.g., temperature, humidity, and pressure) [29.72]. In addition to nondestructive evalu-

ation, NEMS and MEMS can also enable an effective strategy for quality management in cement/concrete construction by in situ observation of the cement hydration process, cement/concrete hardening, and strength development [29.73]. Piezoelectric materials such as $BaTiO_3$ and $PbTiO_3$ that can convert mechanical force and stress to an electric charge create *intelligent aggregates* or *smart aggregates* that can be embedded into concrete blocks to monitor initial concrete strength and structural health [29.18]. Uniform dispersion of piezoelectric ceramic NPs into the polymer matrices forms sensor coatings to detect crack initiation and development and track the structural response to impact damage [29.74]. CNT/polyelectrolyte thin films fabricated by the layer-by-layer (LBL) method cause a change in electrical resistance in response to mechanical stress (i. e., piezoresistive characteristics), suggesting potential application as a high-resolution strain-sensing system in concrete structures [29.50].

29.2 Environmental Release of MNMs Used in Construction

With the projected rapid increase in MNM use for construction materials, the possible release into the environment and associated human exposure have become areas of growing concern [29.75–80] (Fig. 29.4). Although numerous studies have reported toxicological impacts of NMs, a knowledge gap still remains with respect to the environmental risk of NMs associated with their exposure pathways for the potential receptors (ecosystems and human beings). In particular, while a limited body of literature has focused on the environmental fate, behavior, exposure, and toxic effects of MNMs as raw materials prior to further processes toward an end-product [29.76, 77, 80–82], there are few safety and health considerations and lifecycle studies regarding MNMs incorporated into construction products and the resultant MNM wastes generated during construction activities. The identification of possible sources, environmental release scenarios, and exposure routes of MNMs used in construction is critical in assessment of their overall environmental hazard and risk, and development of countermeasures. Therefore, the possible exposure scenarios via multiple routes for environmental discharge of MNMs used in construction are considered herein based on previous published studies and typical construction practices.

29.2.1 Construction Material Manufacturing

It is highly probable that the manufacturing stage will be the major source for environmental release of MNMs during the whole lifecycle of NM-containing construction products. MNMs that are not properly bound or incorporated into the basic materials such as concrete, steel, glass, etc. can directly disperse into the surrounding environment. During specific manufacturing processes including coating, molding, compounding, and incorporation, unintentional emission of MNMs into the atmosphere can occur as the primary pathway for environmental discharge, resulting in possible exposure of manufacturing workers via inhalation; For

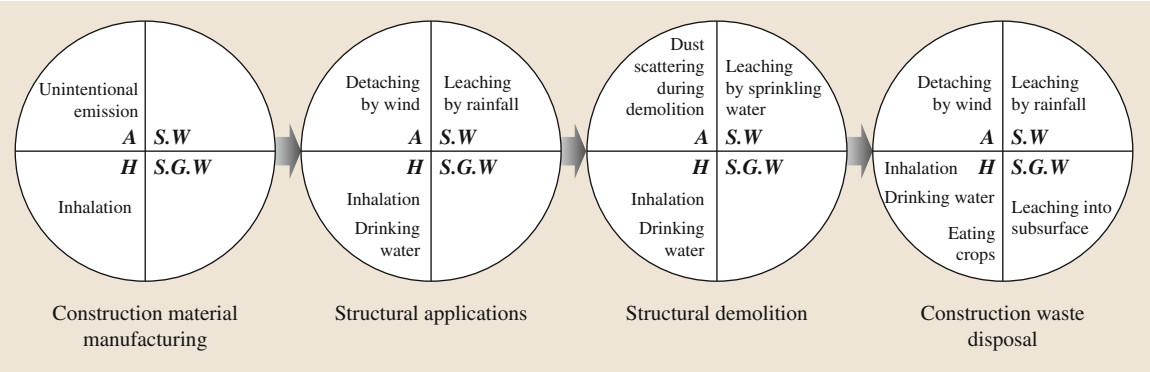


Fig. 29.4 Primary pathways into the environment and corresponding exposure routes to humans expected during the lifecycle of MNMs used in construction (*A* for air; *S.W* for surface water; *S.G.W* for soil and groundwater; *H* for human)

example, airborne NPs could be blown away during weighing of raw materials, and the aerosol type of fullerenes and CNTs could be emitted while treating carbon NMs in a sonicator for better dispersion in liquid media [29.83]. The risk assessment worksheet on the DuPont Light Stabilizer reported that nano-TiO_2 particles could be released during the packaging process over the acceptable level [29.84]. Sepiolite nanoclay used as a filler material in construction nanocomposites would be likely released into the air during early manufacturing processes of mining and transporting [29.85]. In closed manufacturing facilities, indoor air control using ventilation systems, dust collectors, and personal protective equipment such as masks, coveralls, and gloves locally mitigate exposure of workers to MNMs released from manufacturing and related processes.

29.2.2 Structural Applications

MNMs could be released into the environment from buildings and associated infrastructures constructed with nanorelated materials. Use of NM-containing construction products makes individuals and communities in commercial and residential buildings more susceptible to exposure to MNMs [29.31]; For instance, they could be exposed to MNMs incorporated into wallpapers, glasses, paints, etc. through inhalation, dermal contact, or accidental digestion. Wear and abrasion of such structures by accidents (e.g., fire, car crash or earthquake) or weather (e.g., rainfall, snow, and wind) can cause immediate or gradual weathering of MNMs from basic construction materials, increasing the potential for adverse effects on environment and human health. TiO_2 NPs used in exterior paints of building facades as a whitening pigment have been found in building runoff after rainfall [29.79]. MNMs suspended in runoff could be deposited on the topsoil in the surrounding area, and could be delivered to ecological receptors including plants, soil invertebrates, and soil microbes. MNMs released from structures could be transported through sewerage systems to enter adjacent surface waters, posing an immediate threat to aquatic habitats and deteriorating drinking-water quality. Also, MNMs could possibly infiltrate into the subsurface in significant quantities to reach and contaminate groundwater.

29.2.3 Structural Demolition

Partial or complete demolition of structures containing MNMs would also result in personal exposure to and environmental discharge of MNMs. Pulling down buildings and infrastructures proceeds in a relatively less controlled way, whether it is achieved by nonexplosive (using bulldozers, cranes, or hydraulic excavators) or explosive (or implosive) demolition practices. Consequently, it would be difficult to protect workers from the possible uptake of nano- and ultrafine particles and control their emission to the atmosphere during demolition activities. In addition to particulate emissions, water sprinkled on demolition waste to reduce dust levels could cause dissolution and suspension of MNMs and their subsequent transport to the aquatic environment. Demolition debris could emit hazardous wastes when NM-related components are not separated or eliminated beforehand. Proactive steps by trained specialists should be taken to preferentially dispose of NM-containing products such as windows, coatings/paintings, and sensor devices prior to the overall demolition operation.

29.2.4 Construction Waste Disposal

In general, construction (and demolition) wastes are transported to designated landfills equipped with engineered liner systems and leachate treatment facilities. However, environmental exposure to MNMs and associated adverse health effects would potentially arise if construction wastes containing MNMs are not properly treated and disposed of, e.g., dumped in shallow unlined pits or piled up in the open air. Furthermore, there is a high likelihood that construction debris, if disposed of with MNMs not encapsulated within sound structures, would discharge MNMs in the presence of prolonged exposure to rainfall or wind; For example, concrete debris exhibits high vulnerability to wind- or rainfall-induced erosion on the cleaved surfaces, which could lead to detachment of MNMs from NM-concrete debris in construction wastes and associated environmental release of free MNMs. Once MNMs in free particulate form are leached out from construction wastes, they would enter environmental media through various pathways. While MNMs initially undergo dispersion in air or in solution or suspension in runoff, it is highly probable that most MNMs released into the environment would penetrate into the subsurface and eventually reach groundwater aquifers. Despite limited mobility in soil (relative to air and aqueous media), CNTs and TiO_2 NPs could migrate significant distances through porous media (soil and groundwater) in the presence of dissolved organic matter in the pore water [29.81, 86].

For the overall risk assessment, further research should focus on the fate, behavior, and transport of MNMs in multiple environmental media [e.g., air, groundwater, sediment, (surface and subsurface) soil, or surface water] and environmental transformation processes for MNMs and associated modifications of their chemical structures, reactivity, mobility, bioavailability, and toxicity.

29.3 Potential Adverse Biological Impacts and Toxicity Mechanisms

The development of MNMs for the construction industry may produce unintentional environmental and human health impacts as a result of their unique chemical, biological, catalytic, and photoactive properties. Toxicological studies of these materials have shown that MNMs display a wide variety of toxicity mechanisms to organisms at every trophic level [29.87] (Fig. 29.5). Therefore, release from nanoenabled construction materials and structures could pose a risk to microorganisms (which provide valuable ecosystem services including primary productivity, nutrient cycling, and waste degradation) and higher organisms. These toxic responses include cell wall disruption (e.g., single-walled nanotubes, SWNTs), DNA/RNA damage

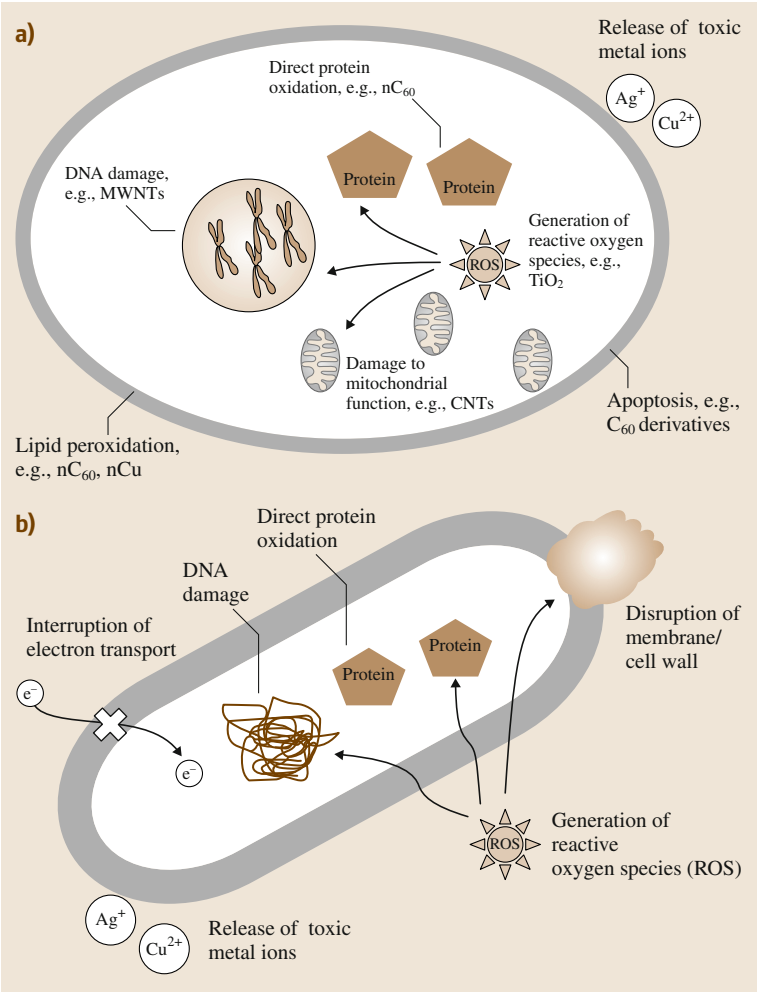


Fig. 29.5a,b Possible toxicity mechanisms of nanomaterials in **(a)** mammalian and **(b)** bacterial cells

(e.g., multi-walled nanotubes MWNT), direct cell membrane oxidation (e.g., nC_{60}), dissolution of toxic metal components (e.g., QDs), and ROS-induced oxidative stress (e.g., TiO_2) (Table 29.2).

29.3.1 TiO_2

TiO_2 NPs possess unique photocatalytic properties as UV light or sunlight irradiation of particles produces ROS, which can cause inflammation, cytotoxicity, and DNA damage in mammalian cells [29.88–98]. In addition, slight variations in TiO_2 morphology affect their uptake through cell membranes by stimulation of phagocytosis, and encourage endogenous ROS generation as an immune response within the cell matrix [29.94, 99]. Compared with their bulk counterparts, they exhibit differential toxicity [29.100]; for example, in one study, nano-TiO_2 displayed greater induction of apoptosis and white blood cell generation [29.101].

TiO_2 elicits similar ROS-derived toxicity in unicellular microorganisms. Solar irradiation enables the antimicrobial activity of TiO_2 towards various bacteria, including *Escherichia coli*, *Micrococcus luteus*, and *Bacillus subtilis*, and fungi, such as *Aspergillus niger* [29.13, 102, 103]. Membrane damage and particle adhesion are implicated as other mechanisms of toxicity [29.104]. Additionally, nano-TiO_2 appears to have a synergistic effect with other co-contaminants; For example, nano-TiO_2 toxicity and metal bioaccumulation were increased in the marine invertebrate *Daphnia magna* after simultaneous exposure with copper [29.105], and in carp species after simultaneously exposure with cadmium [29.106].

29.3.2 Quantum Dots

QDs contain toxic heavy metals such as cadmium, lead, and zinc in core/shell configurations [29.107] and have been recognized as among the most toxic materials [29.108]. The release of core metals has been accepted as the predominant mechanism of QDs' toxicity towards mammalian cells [29.109–114] and bacteria [29.115, 116]. In human cells, toxicity can manifest as ROS damage to organelles and release of inflammation signaling proteins [29.117, 118]. In whole-organism toxicity trials, mice displayed particle accumulation in the spleen, liver, and kidneys [29.119], while microorganisms, such as bacteria and algae, experience growth inhibition, cytotoxicity via lipid peroxidation, oxidative stress, and cellular particle uptake [29.115, 116, 120].

Toxicity, however, is not solely the result of metal ion release; some coating materials themselves may also be toxic [29.95, 117, 121]; For example, intact QDs can impair calcium influx and exocytotic mechanisms in murine brain cells [29.122]. It was also observed that eukaryotic cells experience oxidative stress, nucleic acid damage, and cytotoxicity resulting from internalization or membrane association with QDs [29.118, 119, 123]. Furthermore, gene expression studies in algae show that QDs elicit different responses compared with exposure to their respective ions [29.124].

29.3.3 Carbon Nanotubes

CNTs (SWNTs and MWNTs) pose a potential hazard [29.125] because they exert acute toxicity through ROS generation, inflammation, cell cycle arrest, and increased apoptosis in human and mammalian cells [29.126–128]. Trails of human cells exposed to chronically low doses show accumulation within cells and no adaptive protective mechanism development [29.129]. Extensive testing of whole organisms has been performed for CNTs. In rodent toxicity experiments, exposure through inhalation resulted in pulmonary toxicity such as inflammation, fibrosis, and epithelioid granulomas [29.125, 130]. In contrast, exposure through oral dosing resulted in increased weight gain, morphological changes to the liver, and increases in lipid hydroperoxide [29.131].

Both SWNTs and MWNTs can also exhibit antimicrobial properties. Recent studies have shown CNTs to inhibit bacterial processes in river water, activated sludge, and wastewater effluent, which are likely sinks for CNTs released into the environment [29.132, 133]. The mechanism of microbial toxicity of SWNTs appears to be direct damage to cell walls [29.133, 134], while MWNTs cause toxicity via oxidative stress [29.135, 136]. The antimicrobial properties appear to also be related to aggregate size [29.137] and interactions with bacterial extracellular polymeric substances (EPS) [29.132].

29.3.4 C_{60} Fullerene

C_{60} water-stable aggregates (referred to as nC_{60} [29.138]) display toxicity to human and mammalian cells ranging from lipid peroxidation to necrosis and inflammatory responses [29.138–152]. Meta-analysis of rodent lung exposure data suggests that levels as low as the mg/m^3 range can elicit a toxic response in mammalian cells [29.153, 154]. nC_{60} aggregates dis-

Table 29.2 MNM toxicity to microorganisms, laboratory test mammals, and human cell lines

Manufactured nanomaterials	Toxicological impacts		References
TiO_2 nanoparticles	Microorganisms	Bactericidal for Gram-positive bacteria Suppression of photosynthetic activity Acute lethality Growth inhibition Oxidative damage due to ROS	[29.13, 103, 105, 154, 160–162]
	Mammalian cells	Cell damage directly or indirectly via ion release Cellular uptake DNA damage Reduction in metabolic and mitochondrial activities	[29.88–98]
Quantum dots	Microorganisms	Bactericidal toxicity from metal release Lipid peroxidation and oxidative stress Transmembrane activity and proteolysis involving protea-some activation and ubiquitin-mediated processes	[29.115, 116, 120, 124]
	Mammalian cells	Particle uptake Oxidative damage to DNA Cytotoxic due to oxidative damage to multiple organelles Accumulation of metals in kidneys	[29.109, 113, 117–119, 121–123]
Carbon nanotubes	Microorganisms	Antibacterial Toxicity related to mechanical piercing ROS generation	[29.132–137, 160]
	Mammalian cells	Apoptosis/necrosis Inhibit respiratory functions in mitochondria ROS damage to DNA and cell membranes Induce granulomas and athereoschlerotic lesions Morphological damage to liver	[29.125, 128, 130, 131, 134, 160]
C_{60} fullerene (aqueous colloid)	Microorganisms	Antibacterial ROS-independent oxidative stress	[29.137, 138, 145–147]
	Mammalian cells	Cell death and oxidative damage Lipid peroxidation Cytotoxic to human cell lines Taken up by human keratinocytes Stabilizes protein oxidative damage due to ROS	[29.138–146, 148–153]
C_{60} derivatives	Microorganisms	Bactericidal for Gram-positive bacteria Cell wall/membrane damage	[29.158]
	Mammalian cells	Oxidative cytotoxicity Apoptosis/necrosis Accumulation in liver Induce gliomas, sarcomas in mice and human cells	[29.143, 149, 150, 152, 159]
SiO_2 nanoparticles	Microorganisms	Antibacterial activity to Gram-negative and Gram-positive bacteria Mild ROS toxicity Enlargement of cells due to cell division Reduction in photosynthetic pigment content	[29.154, 163–165]
	Mammalian cells	Inflammatory and immune responses Mild toxicity due to ROS production Apoptosis Upregulation of tumor necrosis factor-alpha genes	[29.62, 154, 163, 166–170]
Cu/CuO nanoparticles	Microorganisms	Toxic to freshwater algae Toxic to yeast Lipid peroxidation Inhibition of methane and biogas production	[29.105, 120, 160–162, 171, 172]
	Mammalian cells	DNA damage (single-strand breaks) Acute toxicity to liver, kidney, and spleen Necrosis of hepatocytes	[29.171, 173–175]

play broad antimicrobial activity independent of the preparation method, i. e., solvent mediated, sonication, or prolonged stirring in water [29.145, 147, 155]. Recent studies confirmed that nC_{60} toxicity to bacteria was due to direct oxidation of the cell upon direct contact rather than by ROS-dependent oxidative stress [29.146, 156]. Oxidative stress exerted by nC_{60} leads to lipid peroxidation, which is also responsible for cytotoxicity in eukaryotic organisms [29.141, 151, 157]. C_{60} derivatives such as fullerol and carboxyfullerene, designed to enhance their aqueous availability, are capable of puncturing the cell membrane [29.158] and behaving as oxidizing agents in biological systems [29.159].

29.3.5 SiO_2

The effect of silica NPs on human and mammalian cells has been studied extensively because of their extensive use in biomedical and industrial applications [29.154, 163, 166–170, 176, 177]. Exposure to nanosized SiO_2 triggers lipid peroxidation and membrane damage to human lung cancer cells [29.178], induces tumor necrosis genes in rats [29.170], and exerts carcinogenic activity [29.179]. While microbial toxicity occurs at higher doses as compared with mammalian cells [29.154, 180], nanosized silica causes toxicity via ROS generation [29.154] and impedes cell division in unicellular algae [29.163]. While the exact mechanism of toxicity is unclear, it has been related to size and relative surface area, where particles with greater surface area were more toxic to both mammalian [29.181, 182] and algal cells [29.183]. Regarding toxicity to microorganisms, studies suggest that toxicity is related to direct attachment and interaction of the particles [29.164, 165, 183].

29.3.6 Copper/Copper Oxide

Cu and CuO NPs induce oxidative stress, which can result in membrane, protein, and DNA damage in bacteria, algae, yeasts, mice, and human cells [29.91, 97, 160, 171, 184]. Oxidative toxicity results from ROS generation by copper ions via Fenton or Haber–Weiss reactions [29.185]. Furthermore, Cu NPs can exert toxicity over a range of lethal and nonlethal doses; For example, studies in mice showed that low, subtoxic doses of Cu NPs elicited the same cell stresses characteristic of higher doses [29.173]. While Cu NP toxicity is primarily linked to the bioavailability of free ions in the exposure media [29.161, 172], recent studies have found that ions cannot explain the total toxicity, and unique nanoproperties may also contribute to toxicity [29.162].

29.4 Mitigation of Environmental and Health Impacts

The most pressing challenges facing the construction industry community in using nanoenabled construction materials include manufacturing of safe materials without significant modifications of their unique desired properties, applications of NM-containing materials with minimal hazard during their service life, and recycling and disposal to reduce waste materials and prevent soil and groundwater contamination. Thus, it is important to discern the chemical compositions, structures, and associated properties of NMs that are essential for their characteristic toxicological activities and environmental behaviors. Such investigation provides basic information for the design of safer products under consideration of exposure control (e.g., protective coatings and magnetic composites) and adoption of greener substitutes for toxic MNMs. The assessment of exposure routes, environmental fate, and transport for MNMs used in construction, with development of analytical methodologies to trace MNMs in multimedia, should be critical in controlling environmental pollution related to construction activities and establishing the strategy for waste management (e.g., separation/collection, recycle/reuse, and disposal).

29.4.1 Manufacturing

Chemical structure–activity relationships that elucidate which specific properties of MNMs are critically associated with their environmental behavior and toxicological activity are urgently required. In the absence of empirical data on various MNMs, these will provide a foundation to develop strategies to mitigate hazards and assess exposure scenarios and pathways. Physicochemical and structural properties associated with MNMs affect their fate, behavior, and transformation in environmental matrices (e.g., adsorption/desorption, aggregation, chemical redox reaction, deposition, or dissolution), which will directly bear on bioavailability, bioaccumulation, and toxicity [29.186].

Structure–activity relationships, with research into the toxicity mechanisms of MNMs, can offer basic design concepts for environmentally safe nanocomposites;

For instance, encapsulation in polymer resins or surface functionalization hinders direct contact of carbon-based NMs (e.g., fullerene and SWNTs) as a key step in damage to bacterial cells, significantly diminishing their antimicrobial activity. Durable coating with inorganic film renders metal oxides (e.g., CuO and Fe_3O_4) and QDs resistant to weathering. Also, the predictive relationships may suggest the urgent need to remove potential toxic components from MNMs and switch to alternative materials.

Development of MNMs with easy degradation or recovery in response to specific environmental conditions may minimize environmental hazards in the event of accidental release during transportation, construction, or demolition. Incorporation of MNMs in pH- or temperature-responsive polymers can cause rapid hydrophobic conversion and resultant precipitation after their release into an aquatic environment, as encapsulation by nanomagnetite enables facile magnetic separation. Versatile MNMs can cover multiple functions to replace several MNMs without significant loss of functionalities (e.g., TiO_2 NPs as white pigment and TiO_2 coatings for light-transmittance control, self-cleaning, and superhydrophilicity), eventually decreasing the quantity of MNMs used in construction. Efforts to improve manufacturing processes should be initiated to increase production yields of NM-based construction products and highly promote their desirable properties with minimal generation of nanoscale wastes.

29.4.2 Application

In-depth studies should be carried out on the vulnerability of MNMs to redox reactions, corrosion and passivation, and photochemical and biological transformations encountered during the lifetime of nanoenabled products. The physical, chemical, and/or biological conversions may lead to modifications of MNMs' properties associated with their adverse biological effects and environmental mobility. Thus, it is important to identify the effects of physicochemical environmental parameters such as pH, salinity, and natural organic matter, and biological media compositions/metabolisms on the reactivity, distribution, bioavailability, and toxicity of MNMs.

Off-site fabrication, preassembly, and modularization of construction components containing MNMs in well-controlled conditions can minimize unwanted personal and environmental exposure. The effective longevity and projected life expectancy of MNM-containing construction products under conditions encountered should be considered for sustainable applications, based on laboratory and field studies to predict their resistance to aging, abrasion, chemical corrosion, cracking, and weathering. Leaching tests should be done to assess the possibility that MNMs incorporated into construction materials (e.g., TiO_2 in self-cleaning exterior and pavements, QDs in photovoltaic cells, and CNTs in concrete) may undergo separation from the matrices in some damaging conditions (e.g., fire, water, wind, and flood), dispersing into the surrounding atmosphere or entering stormwater runoff.

29.4.3 Recycling/Disposal

Recycling of MNM-containing construction materials, which aims to reduce the consumption of raw MNMs and minimize MNM-containing wastes, requires various prerequisite steps, including the development of efficient strategies to extract and collect MNMs from complex matrices (with minimal modification of the pristine properties), characterization of spent MNMs and evaluation of their capacity for reactivation, and assessment of the applicability of the reclaimed MNMs in terms of their original functionalities.

Since collective efforts are still underway to establish regulatory frameworks to specifically address MNM disposal, there should be special considerations for safe MNM waste disposal and recycling procedures. In an effort to prevent potential secondary contamination through landfill clay liners to the underlying aquifer, barrier reinforcement will be recommended to prevent infiltration of NM leachate and resultant groundwater pollution. Product labeling to identify and trace MNMs and relevant guidelines are needed to ecoresponsibly dispose of and recycle waste products that include MNMs and waste MNMs themselves. Following disposal, appropriate interception and remediation approaches may need to be developed depending on the MNM source, release dynamics, and disposal scenario.

29.5 Conclusions

Due to the potential for enhancement in material properties and functionalities, application of nanotechnology in construction is expected to create intelligent materials and systems, present opportunities for energy savings, and enable environmentally responsible products, buildings, and construction activities. Smart, nanoenabled products can detect and respond to changes in indoor environmental conditions, providing user-adapted control of key environmental parameters, e.g., dimming light and altering temperature and humidity. Nanosensor assemblies embedded in buildings and infrastructures can remotely monitor and assess their structural health and vulnerability. Self-healing materials, which are still in early stages of development, are capable of autonomous crack management to recover original mechanical properties (e.g., preventing crack development through slow release of a bonding agent from polymer capillaries embedded in the concrete matrices).

Use of MNMs for thermal insulation (e.g., SiO_2 NPs and aerogel) and light transmittance control (e.g., WO_3 NPs) can significantly contribute to energy conservation, considering that energy consumption by commercial buildings and residential houses (including heating, lighting, and air ventilation) accounts for approximately 40% of all energy used in the USA. Incorporation of MNMs such as fullerenes, CNTs, and graphenes [29.46, 47] advances energy conversion and storage systems including hydrocarbon-based fuel cells, thermo- and photovoltaic cells, batteries, and capacitors. Solar light activation of TiO_2 to generate ROS enables pollution-controlling and self-cleaning coatings, reducing energy associated with maintenance for surface-treated pavements, windows, and walls [29.26, 61, 64]. Due to the improved resistance to abrasion, corrosion, fire, and fatigue, MNM-containing construction materials could possibly outperform conventional materials in terms of durability and longevity, indirectly reducing energy consumed to repair, restore, and replace damaged materials.

Applications of MNMs as alternatives to toxic components prevent environmental hazards through the potential discharge and exposure during manufacturing, transporting, construction and renovation, and disposal. The opportunities for material replacement include silver and iron oxide NPs for cadmium, cobalt, and lead as pigment in paint [29.12], silica NPs for polychlorinated biphenyl (PCB) insulators [29.14], TiO_2 NPs for perfluorochemicals as stain repellents [29.17], and CNTs for halogenated flame retardants [29.29]. QD-based light-emitting diodes (LEDs) [29.48, 49] and CNT- or ZnO nanowire-based sensors and actuators [29.187, 188] possibly mitigate hazards associated with accidental release of mercury used in fluorescent lamp bulbs, pressure gages, thermometers, and switches. MNM-containing products enable buildings and infrastructures to capture or exploit natural heat and light (e.g., heat-absorbing windows, solar panels, and energy coatings) [29.11, 32], eventually reducing carbon emissions associated with heating and ventilation. Use of MNMs allows structural materials to be lighter and thinner without a significant loss of the desirable properties, mitigating wasteful use of raw materials and enabling resource-efficient production in construction.

As there are growing concerns that use of MNMs for the development of new construction products could increase possible environmental risk, it is critical to understand their potential mobility, properties, and impacts in and across air, water, soil, and biota. Analytical methodologies to detect and monitor MNMs (separate from or incorporated into construction materials) at environmentally relevant concentrations within complex environmental media and characterize their chemical and morphological features remain underdeveloped. Assessment of long-term global exposure to MNMs used in construction needs to be conducted, as the current focus of the potential adverse health effects is confined to manufacturing and construction workers. Considering that constructed infrastructure coexists with the natural environment, ecodesign strategies to enhance the environmental compatibility of materials and environmentally responsible lifecycle management of MNMs to minimize their unwanted environmental impacts also need to be prioritized. Overall, despite the current expectations regarding the promising opportunities of MNMs in construction, there are immediate concerns among the academic and industrial communities about the negative environmental implications. This highlights the need to encourage proactive research including green design and manufacturing, use and disposal practices, and recycling and reclamation strategies to ensure the ecoresponsibility and sustainability of both the nanotechnology and construction industries.

References

29.1 S.J. Tans, A.R.M. Verschueren, C. Dekker: Room-temperature transistor based on a single carbon nanotube, Nature **393**, 49–52 (1998)

29.2 M.R. Hoffmann, S.T. Martin, W.Y. Choi, D.W. Bahnemann: Environmental applications of semiconductor photocatalysis, Chem. Rev. **95**, 69–96 (1995)

29.3 M.C. Daniel, D. Astruc: Gold nanoparticles: Assembly, supramolecular chemistry, quantum-size-related properties, and applications toward biology, catalysis, and nanotechnology, Chem. Rev. **104**, 293–346 (2004)

29.4 W.C.W. Chan, D.J. Maxwell, X.H. Gao, R.E. Bailey, M.Y. Han, S.M. Nie: Luminescent quantum dots for multiplexed biological detection and imaging, Curr. Opin. Biotechnol. **13**, 40–46 (2002)

29.5 A.S. Arico, P. Bruce, B. Scrosati, J.M. Tarascon, W. Van Schalkwijk: Nanostructured materials for advanced energy conversion and storage devices, Nat. Mater. **4**, 366–377 (2005)

29.6 Y.S. de Ibarra, J.J. Gaitero, E. Erkizia, I. Campillo: Atomic force microscopy and nanoindentation of cement pastes with nanotube dispersions, Phys. Status Solidi (a) **203**, 1076–1081 (2006)

29.7 N. Guskos, G. Zolnierkiewicz, J. Typek, J. Blyszko, W. Kiernozycki, U. Narkiewicz: Ferromagnetic resonance and compressive strength study of cement mortars containing carbon encapsulated nickel and iron nanoparticles, Rev. Adv. Mater. Sci. **23**, 113–117 (2010)

29.8 S. Mann: Nanotechnology and construction, Nanoforum Report (2006) pp. 1–55

29.9 T. Sato, J.J. Beaudoin: The effect of nanosized $CaCO_3$ addition on the hydration of cement paste containing high volumes of fly ash, 12th Int. Congr. Chem. Cem., Montreal (2007) pp. 1–12

29.10 Z. Ge, Z. Gao: Applications of nanotechnology and nanomaterials in construction, 1st Int. Conf. Constr. Dev. Ctries., Karachi (2008) pp. 235–240

29.11 K. Adachi, M. Miratsu, T. Asahi: Absorption and scattering of near-infrared light by dispersed lanthanum hexaboride nanoparticles for solar control filters, J. Mater. Res. **25**, 510–521 (2010)

29.12 A. Kumar, P.K. Vemula, P.M. Ajayan, G. John: Silver-nanoparticle-embedded antimicrobial paints based on vegetable oil, Nat. Mater. **7**, 236–241 (2008)

29.13 E.J. Wolfrum, J. Huang, D.M. Blake, P.C. Maness, Z. Huang, J. Fiest, W.A. Jacoby: Photocatalytic oxidation of bacteria, bacterial and fungal spores, and model biofilm components to carbon dioxide on titanium dioxide-coated surfaces, Environ. Sci. Technol. **36**, 3412–3419 (2002)

29.14 M. Gleiche, H. Hoffschulz, S. Lenhert: Nanotechnology in consumer products, Nanoforum Report (2006) pp. 1–30

29.15 P.V. Kamat: Quantum dot solar cells. Semiconductor nanocrystals as light harvesters, J. Phys. Chem. C **112**, 18737–18753 (2008)

29.16 V.S. Saji, J. Thomas: Nanomaterials for corrosion control, Curr. Sci. **92**, 51–55 (2007)

29.17 G.X. Shen, Y.C. Chen, L. Lin, C.J. Lin, D. Scantlebury: Study on a hydrophobic nano-TiO_2 coating and its properties for corrosion protection of metals, Electrochim. Acta **50**, 5083–5089 (2005)

29.18 G.B. Song, H.C. Gu, Y.L. Mo: Smart aggregates: Multifunctional sensors for concrete structures – A tutorial and a review, Smart Mater. Struct. **17**, 1–17 (2008)

29.19 W. Zhang, J. Suhr, N. Koratkar: Carbon nanotube/polycarbonate composites as multifunctional strain sensors, J. Nanosci. Nanotechnol. **6**, 960–964 (2006)

29.20 P. van Broekhuizen, F. van Broekhuizen, R. Cornelissen, L. Reijnders: Use of nanomaterials in the European construction industry and some occupational health aspects thereof, J. Nanopart. Res. **13**, 447–462 (2011)

29.21 J. Lee, S. Mahendra, P.J.J. Alvarez: Nanomaterials in the construction industry: A review of their applications and environmental health and safety considerations, ACS Nano **4**, 3580–3590 (2010)

29.22 J. Lee, S. Mahendra, P.J.J. Alvarez: *Potential Environmental Impacts of Nanomaterials Used in the Construction Industry* (Springer, Berlin, Heidelberg 2009)

29.23 H. Li, M.H. Zhang, J.P. Ou: Abrasion resistance of concrete containing nanoparticles for pavement, Wear **260**, 1262–1266 (2006)

29.24 L. Raki, J. Beaudoin, R. Alizadeh, J. Makar, T. Sato: Cement and concrete nanoscience and nanotechnology, Materials **3**, 918–942 (2010)

29.25 K. Sobolev, M.F. Gutierrez: How nanotechnology can change the concrete world, Am. Ceram. Soc. Bull. **84**, 16–19 (2005)

29.26 H. Irie, K. Sunada, K. Hashimoto: Recent developments in TiO_2 photocatalysis: Novel applications to interior ecology materials and energy saving systems, Electrochemistry **72**, 807–812 (2004)

29.27 J.M. Makar, J.J. Beaudoin: Carbon nanotubes and their application in the construction industry, 1st Int. Symp. Nanotechnol. Constr., Paisley (2003) pp. 331–341

29.28 R.H. Baughman, A.A. Zakhidov, W.A. de Heer: Carbon nanotubes – The route toward applications, Science **297**, 787–792 (2002)

29.29 M. Moniruzzaman, K.I. Winey: Polymer nanocomposites containing carbon nanotubes, Macromolecules **39**, 5194–5205 (2006)

29.30 P. Podsiadlo, A.K. Kaushik, E.M. Arruda, A.M. Waas, B.S. Shim, J.D. Xu, H. Nandivada, B.G. Pumplin,

J. Lahann, A. Ramamoorthy, N.A. Kotov: Ultrastrong and stiff layered polymer nanocomposites, Science **318**, 80–83 (2007)
29.31 G. Elvin: Nanotechnology for green building, Green Technol. Forum (2007) pp. 1–96
29.32 H. Takeda, K. Adachi: Near infrared absorption of tungsten oxide nanoparticle dispersions, J. Am. Ceram. Soc. **90**, 4059–4061 (2007)
29.33 T. Morimoto, H. Tomonaga, A. Mitani: Ultraviolet ray absorbing coatings on glass for automobiles, Thin Solid Films **351**, 61–65 (1999)
29.34 B. Mahltig, H. Bottcher, K. Rauch, U. Dieckmann, R. Nitsche, T. Fritz: Optimized UV protecting coatings by combination of organic and inorganic UV absorbers, Thin Solid Films **485**, 108–114 (2005)
29.35 T. He, J.N. Yao: Photochromism in composite and hybrid materials based on transition-metal oxides and polyoxometalates, Prog. Mater. Sci. **51**, 810–879 (2006)
29.36 T. He, Y. Ma, Y.A. Cao, P. Jiang, X.T. Zhang, W.S. Yang, J.N. Yao: Enhancement effect of gold nanoparticles on the UV-light photochromism of molybdenum trioxide thin films, Langmuir **17**, 8024–8027 (2001)
29.37 Y. Paz, Z. Luo, L. Rabenberg, A. Heller: Photooxidative self-cleaning transparent titanium-dioxide films on glass, J. Mater. Res. **10**, 2842–2848 (1995)
29.38 M. Drajewicz, J. Wasylak: Properties of glass surface with nanoparticles aluminum compounds refined, Adv. Mater. Res. **39/40**, 567–570 (2008)
29.39 Y.H. Lv, H. Liu, Z. Wang, L.J. Hao, J. Liu, Y.M. Wang, G.J. Du, D. Liu, J. Zhan, J.Y. Wang: Antibiotic glass slide coated with silver nanoparticles and its antimicrobial capabilities, Polym. Adv. Technol. **19**, 1455–1460 (2008)
29.40 J. Niskanen, J. Shan, H. Tenhu, H. Jiang, E. Kauppinen, V. Barranco, F. Pico, K. Yliniemi, K. Kontturi: Synthesis of copolymer-stabilized silver nanoparticles for coating materials, Colloid Polym. Sci. **288**, 543–553 (2010)
29.41 V. Sambhy, M.M. MacBride, B.R. Peterson, A. Sen: Silver bromide nanoparticle/polymer composites: Dual action tunable antimicrobial materials, J. Am. Chem. Soc. **128**, 9798–9808 (2006)
29.42 K. Page, R.G. Palgrave, I.P. Parkin, M. Wilson, S.L.P. Savin, A.V. Chadwick: Titania and silver-titania composite films on glass-potent antimicrobial coatings, J. Mater. Chem. **17**, 95–104 (2007)
29.43 X.M. Shi, T.A. Nguyen, Z.Y. Suo, Y.J. Liu, R. Avci: Effect of nanoparticles on the anticorrosion and mechanical properties of epoxy coating, Surf. Coat. Technol. **204**, 237–245 (2009)
29.44 Z.Y. Wang, E.H. Han, F.C. Liu, W. Ke: Fire and corrosion resistances of intumescent nanocoating containing nano-SiO_2 in salt spray condition, J. Mater. Sci. Technol. **26**, 75–81 (2010)
29.45 Z.Y. Wang, E.H. Han, F.C. Liu, L. Ke: Thermal behavior of nano-TiO_2 in fire-resistant coating, J. Mater. Sci. Technol. **23**, 547–550 (2007)
29.46 P. Brown, K. Takechi, P.V. Kamat: Single-walled carbon nanotube scaffolds for dye-sensitized solar cells, J. Phys. Chem. C **112**, 4776–4782 (2008)
29.47 P.V. Kamat, M. Haria, S. Hotchandani: C_{60} cluster as an electron shuttle in a Ru(II)-polypyridyl sensitizer-based photochemical solar cell, J. Phys. Chem. B **108**, 5166–5170 (2004)
29.48 J.L. Zhao, J.A. Bardecker, A.M. Munro, M.S. Liu, Y.H. Niu, I.K. Ding, J.D. Luo, B.Q. Chen, A.K.Y. Jen, D.S. Ginger: Efficient CdSe/CdS quantum dot light-emitting diodes using a thermally polymerized hole transport layer, Nano Lett. **6**, 463–467 (2006)
29.49 H.S. Chen, S.J.J. Wang, C.J. Lo, J.Y. Chi: White-light emission from organics-capped ZnSe quantum dots and application in white-light-emitting diodes, Appl. Phys. Lett. **86**, 131905–131907 (2005)
29.50 K.J. Loh, J. Kim, J.P. Lynch, N.W.S. Kam, N.A. Kotov: Multifunctional layer-by-layer carbon nanotube-polyelectrolyte thin films for strain and corrosion sensing, Smart Mater. Struct. **16**, 429–438 (2007)
29.51 J. E. Kloeppel: Mimicking biological systems, composite material heals itself, http://www.news.uiuc.edu/scitips/01/0214selfheal.html
29.52 A. Cwirzen, K. Habermehl-Cwirzen, V. Penttala: Surface decoration of carbon nanotubes and mechanical properties of cement/carbon nanotube composites, Adv. Cem. Res. **20**, 65–73 (2008)
29.53 J.M. Makar, G.W. Chan: Growth of cement hydration products on single walled carbon nanotubes, J. Am. Ceram. Soc. **92**, 1303–1310 (2009)
29.54 T. Muromachi, T. Tsujino, K. Kamitani, K. Maeda: Application of functional coatings by sol-gel method, J. Sol-Gel Sci. Technol. **40**, 267–272 (2006)
29.55 S.S. Kanu, R. Binions: Thin films for solar control applications, Proc. R. Soc. A **466**, 19–44 (2010)
29.56 Z.G. Zhao, Z.F. Liu, M. Miyauchi: Tailored remote photochromic coloration of in situ synthesized CdS quantum dot loaded WO_3 films, Adv. Funct. Mater. **20**, 4162–4167 (2010)
29.57 G. Walters, I.P. Parkin: The incorporation of noble metal nanoparticles into host matrix thin films: Synthesis, characterisation and applications, J. Mater. Chem. **19**, 574–590 (2009)
29.58 Y. Ohko, T. Tatsuma, T. Fujii, K. Naoi, C. Niwa, Y. Kubota, A. Fujishima: Multicolour photochromism of TiO_2 films loaded with silver nanoparticles, Nat. Mater. **2**, 29–31 (2003)
29.59 M. Saeli, C. Piccirillo, I.P. Parkin, I. Ridley, R. Binions: Nanocomposite thermochromic thin films and their application in energy-efficient glazing, Sol. Energy Mater. Sol. Cells **94**, 141–151 (2010)
29.60 R. Arutjunjan, T. Markova, I. Halopenen, I. Maksimov, A. Tutunnikov, O. Yanush: Smart thermochromic glazing for energy saving window applications, Proc. SPIE **5946**, 94618 (2005)

29.61 Q.H. Mu, Y.G. Li, H.Z. Wang, Q.H. Zhang: Self-organized TiO_2 nanorod arrays on glass substrate for self-cleaning antireflection coatings, J. Colloid Interface Sci. **365**, 308–313 (2012)

29.62 X.D. Wang, J. Shen: Sol-gel derived durable antireflective coating for solar glass, J. Sol-Gel Sci. Technol. **53**, 322–327 (2010)

29.63 A. Mills, S. LeHunte: An overview of semiconductor photocatalysis, J. Photochem. Photobiol. A **108**, 1–35 (1997)

29.64 X.T. Zhang, O. Sato, M. Taguchi, Y. Einaga, T. Murakami, A. Fujishima: Self-cleaning particle coating with antireflection properties, Chem. Mater. **17**, 696–700 (2005)

29.65 M. Takeuchi, K. Sakamoto, G. Martra, S. Coluccia, M. Anpo: Mechanism of photoinduced superhydrophilicity on the TiO_2 photocatalyst surface, J. Phys. Chem. B **109**, 15422–15428 (2005)

29.66 A.I. Kontos, A.G. Kontos, D.S. Tsoukleris, G.D. Vlachos, P. Falaras: Superhydrophilicity and photocatalytic property of nanocrystalline titania sol-gel films, Thin Solid Films **515**, 7370–7375 (2007)

29.67 M. Miyauchi: Visible light induced superhydrophilicity on single crystalline TiO_2 nanoparticles and WO_3 layered thin films, J. Mater. Chem. **18**, 1858–1864 (2008)

29.68 K.S. Guan, B.J. Lu, Y.S. Yin: Enhanced effect and mechanism of SiO_2 addition in super-hydrophilic property of TiO_2 films, Surf. Coat. Technol. **173**, 219–223 (2003)

29.69 S.A. Ruffolo, M.F. Russa, M. Malagodi, C.O. Rossi, A.M. Palermo, G.M. Crisci: ZnO and $ZnTiO_3$ nanopowders for antimicrobial stone coating, Appl. Phys. A **100**, 829–834 (2010)

29.70 E. Martines, K. Seunarine, H. Morgan, N. Gadegaard, C.D.W. Wilkinson, M.O. Riehle: Superhydrophobicity and superhydrophilicity of regular nanopatterns, Nano Lett. **5**, 2097–2103 (2005)

29.71 H. Park, K.Y. Kim, W. Choi: Photoelectrochemical approach for metal corrosion prevention using a semiconductor photoanode, J. Phys. Chem. B **106**, 4775–4781 (2002)

29.72 M. Saafi, P. Romine: Nano- and microtechnology, Concr. Int. **27**, 28–34 (2005)

29.73 M. Saafi, P. Romine: Preliminary evaluation of MEMS devices for early age concrete property monitoring, Cem. Concr. Res. **35**, 2158–2164 (2005)

29.74 Y.F. Zhang: Piezoelectric paint sensor for real-time structural health monitoring, Smart Mater. Struct. **5765**, 1095–1103 (2005)

29.75 M.R. Wiesner, G.V. Lowry, P. Alvarez, D. Dionysiou, P. Biswas: Assessing the risks of manufactured nanomaterials, Environ. Sci. Technol. **40**, 4336–4345 (2006)

29.76 N. Solovitch, J. Labille, J. Rose, P. Chaurand, D. Borschneck, M.R. Wiesner, J.Y. Bottero: Concurrent aggregation and deposition of TiO_2 nanoparticles in a sandy porous media, Environ. Sci. Technol. **44**, 4897–4902 (2010)

29.77 A.R. Petosa, D.P. Jaisi, I.R. Quevedo, M. Elimelech, N. Tufenkji: Aggregation and deposition of engineered nanomaterials in aquatic environments: Role of physicochemical interactions, Environ. Sci. Technol. **44**, 6532–6549 (2010)

29.78 B. Nowack, T.D. Bucheli: Occurrence, behavior and effects of nanoparticles in the environment, Environ. Pollut. **150**, 5–22 (2007)

29.79 R. Kaegi, A. Ulrich, B. Sinnet, R. Vonbank, A. Wichser, S. Zuleeg, H. Simmler, S. Brunner, H. Vonmont, M. Burkhardt, M. Boller: Synthetic TiO_2 nanoparticle emission from exterior facades into the aquatic environment, Environ. Pollut. **156**, 233–239 (2008)

29.80 K.A.D. Guzman, M.P. Finnegan, J.F. Banfield: Influence of surface potential on aggregation and transport of titania nanoparticles, Environ. Sci. Technol. **40**, 7688–7693 (2006)

29.81 B.J.R. Thio, D.X. Zhou, A.A. Keller: Influence of natural organic matter on the aggregation and deposition of titanium dioxide nanoparticles, J. Hazard. Mater. **189**, 556–563 (2011)

29.82 J. Fang, X.Q. Shan, B. Wen, J.M. Lin, G. Owens: Stability of titania nanoparticles in soil suspensions and transport in saturated homogeneous soil columns, Environ. Pollut. **157**, 1101–1109 (2009)

29.83 D.R. Johnson, M.M. Methner, A.J. Kennedy, J.A. Steevens: Potential for occupational exposure to engineered carbon-based nanomaterials in environmental laboratory studies, Environ. Health Perspect. **118**, 49–54 (2010)

29.84 DuPont: DuPont Nanomaterial risk assessment worksheet – DuPont light stabilizer (2007) pp. 1–52

29.85 DuPont: DuPont crystar 6920 PET poly-(ethylene terephthalate) resin with sepiolite clay, Pangel S-9 as an encapsulated nanodispersed filler (2008) pp. 1–35

29.86 G.R. Aiken, H. Hsu-Kim, J.N. Ryan: Influence of dissolved organic matter on the environmental fate of metals, nanoparticles, and colloids, Environ. Sci. Technol. **45**, 3196–3201 (2011)

29.87 S.J. Klaine, P.J.J. Alvarez, G.E. Batley, T.F. Fernandes, R.D. Handy, D.Y. Lyon, S. Mahendra, M.J. McLaughlin, J.R. Lead: Nanomaterials in the environment: Behavior, fate, bioavailability, and effects, Environ. Toxicol. Chem. **27**, 1825–1851 (2008)

29.88 X.S. Zhu, L. Zhu, Z.H. Duan, R.Q. Qi, Y. Li, Y.P. Lang: Comparative toxicity of several metal oxide nanoparticle aqueous suspensions to zebrafish (*Danio rerio*) early developmental stage, J. Environ. Sci. Health A **43**, 278–284 (2008)

29.89 Q.W. Zhang, Y. Kusaka, K. Sato, K. Nakakuki, N. Kohyama, K. Donaldson: Differences in the extent of inflammation caused by intratracheal exposure to

three ultrafine metals: Role of free radicals, J. Toxicol. Environ. Health A **53**, 423–438 (1998)
29.90 L.L. Zhang, R. Bai, B. Li, C. Ge, J.F. Du, Y. Liu, L. Le Guyader, Y.L. Zhao, Y.C. Wu, S.D. He, Y.M. Ma, C.Y. Chen: Rutile TiO_2 particles exert size and surface coating dependent retention and lesions on the murine brain, Toxicol. Lett. **207**, 78–81 (2011)
29.91 Y.G. Wang, W.G. Aker, H.M. Hwang, C.G. Yedjou, H.T. Yu, P.B. Tchounwou: A study of the mechanism of in vitro cytotoxicity of metal oxide nanoparticles using catfish primary hepatocytes and human HepG2 cells, Sci. Total Environ. **409**, 4753–4762 (2011)
29.92 R. Tedja, C. Marquis, M. Lim, R. Amal: Biological impacts of TiO_2 on human lung cell lines A549 and H1299: Particle size distribution effects, J. Nanopart. Res. **13**, 3801–3813 (2011)
29.93 C.M. Sayes, R. Wahi, P.A. Kurian, Y.P. Liu, J.L. West, K.D. Ausman, D.B. Warheit, V.L. Colvin: Correlating nanoscale titania structure with toxicity: A cytotoxicity and inflammatory response study with human dermal fibroblasts and human lung epithelial cells, Toxicol. Sci. **92**, 174–185 (2006)
29.94 J.F. Reeves, S.J. Davies, N.J.F. Dodd, A.N. Jha: Hydroxyl radicals are associated with titanium dioxide (TiO_2) nanoparticle-induced cytotoxicity and oxidative DNA damage in fish cells, Mutat. Res. **640**, 113–122 (2008)
29.95 S. Park, Y.K. Lee, M. Jung, K.H. Kim, N. Chung, E.K. Ahn, Y. Lim, K.H. Lee: Cellular toxicity of various inhalable metal nanoparticles on human alveolar epithelial cells, Inhal. Toxicol. **19**, 59–65 (2007)
29.96 G. Oberdorster, R.M. Gelein, J. Ferin, B. Weiss: Association of particulate air-pollution and acute mortality – Involvement of ultrafine particles, Inhal. Toxicol. **7**, 111–124 (1995)
29.97 H.L. Karlsson, P. Cronholm, J. Gustafsson, L. Moller: Copper oxide nanoparticles are highly toxic: A comparison between metal oxide nanoparticles and carbon nanotubes, Chem. Res. Toxicol. **21**, 1726–1732 (2008)
29.98 R.D. Handy, T.B. Henry, T.M. Scown, B.D. Johnston, C.R. Tyler: Manufactured nanoparticles: Their uptake and effects on fish – A mechanistic analysis, Ecotoxicology **17**, 396–409 (2008)
29.99 T.C. Long, N. Saleh, R.D. Tilton, G.V. Lowry, B. Veronesi: Titanium dioxide (P25) produces reactive oxygen species in immortalized brain microglia (BV2): Implications for nanoparticle neurotoxicity, Environ. Sci. Technol. **40**, 4346–4352 (2006)
29.100 A. Nel, T. Xia, L. Madler, N. Li: Toxic potential of materials at the nanolevel, Science **311**, 622–627 (2006)
29.101 Y. Zhang, W. Yu, X. Jiang, K. Lv, S. Sun, F. Zhang: Analysis of the cytotoxicity of differentially sized titanium dioxide nanoparticles in murine MC3T3-E1 preosteoblasts, J. Mater. Sci. **22**, 1933–1945 (2011)
29.102 A. Rincon, C. Pulgarin: Effect of pH, inorganic ions, organic matter and H_2O_2 on *E. coli* K12 photocatalytic inactivation by TiO_2-implications in solar water disinfection, Appl. Catal. B **51**, 283–302 (2004)
29.103 A. Rincon, C. Pulgarin: Bactericidal action of illuminated TiO_2 on pure *Escherichia coli* and natural bacterial consortia: Post-irradiation events in the dark and assessment of the effective disinfection time, Appl. Catal. B **49**, 99–112 (2004)
29.104 N.B. Hartmann, F. Von der Kammer, T. Hofmann, M. Baalousha, S. Ottofuelling, A. Baun: Algal testing of titanium dioxide nanoparticles-Testing considerations, inhibitory effects and modification of cadmium bioavailability, Toxicology **269**, 190–197 (2010)
29.105 W. Fan, M. Cui, H. Liu, C. Wang, Z. Shi, C. Tan, X. Yang: Nano-TiO_2 enhances the toxicity of copper in natural water to *Daphnia magna*, Environ. Pollut. **159**, 729–734 (2011)
29.106 X. Zhang, H. Sun, Z. Zhang, Q. Niu, Y. Chen, J.C. Crittenden: Enhanced bioaccumulation of cadmium in carp in the presence of titanium dioxide nanoparticles, Chemosphere **67**, 160–166 (2007)
29.107 W.W. Yu, E. Chang, J.C. Falkner, J.Y. Zhang, A.M. Al-Somali, C.M. Sayes, J. Johns, R. Drezek, V.L. Colvin: Forming biocompatible and nonaggregated nanocrystals in water using amphiphilic polymers, J. Am. Chem. Soc. **129**, 2871–2879 (2007)
29.108 S. Zuin, C. Micheletti, A. Critto, G. Pojana, H. Johnston, V. Stone, L. Tran, A. Marcomini: Weight of evidence approach for the relative hazard ranking of nanomaterials, Nanotoxicology **5**, 445–458 (2011)
29.109 A. Shiohara, A. Hoshino, K. Hanaki, K. Suzuki, K. Yamamoto: On the cyto-toxicity caused by quantum dots, Microbiol. Immunol. **48**, 669–675 (2004)
29.110 Z.S. Lu, C.M. Li, H.F. Bao, Y. Qiao, Y.H. Toh, X. Yang: Mechanism of antimicrobial activity of CdTe quantum dots, Langmuir **24**, 5445–5452 (2008)
29.111 C. Kirchner, T. Liedl, S. Kudera, T. Pellegrino, A.M. Javier, H.E. Gaub, S. Stolzle, N. Fertig, W.J. Parak: Cytotoxicity of colloidal CdSe and CdSe/ZnS nanoparticles, Nano Lett. **5**, 331–338 (2005)
29.112 R. Hardman: A toxicologic review of quantum dots: Toxicity depends on physicochemical and environmental factors, Environ. Health Perspect. **114**, 165–172 (2006)
29.113 A.M. Derfus, W.C.W. Chan, S.N. Bhatia: Probing the cytotoxicity of semiconductor quantum dots, Nano Lett. **4**, 11–18 (2004)
29.114 K.E. Cha, H. Myung: Cytotoxic effects of nanoparticles assessed in vitro and in vivo, J. Microbiol. Biotechnol. **17**, 1573–1578 (2007)
29.115 J.A. Kloepfer, R.E. Mielke, J.L. Nadeau: Uptake of CdSe and CdSe/ZnS quantum dots into bacteria

via purine-dependent mechanisms, Appl. Environ. Microbiol. **71**, 2548–2557 (2005)
29.116 S. Mahendra, H.G. Zhu, V.L. Colvin, P.J. Alvarez: Quantum dot weathering results in microbial toxicity, Environ. Sci. Technol. **42**, 9424–9430 (2008)
29.117 J.P. Ryman-Rasmussen, J.E. Riviere, N.A. Monteiro-Riviere: Surface coatings determine cytotoxicity and irritation potential of quantum dot nanoparticles in epidermal keratinocytes, J. Investig. Dermatol. **127**, 143–153 (2007)
29.118 E. Chang, N. Thekkek, W.W. Yu, V.L. Colvin, R. Drezek: Evaluation of quantum dot cytotoxicity based on intracellular uptake, Small **2**, 1412–1417 (2006)
29.119 P. Lin, J.-W. Chen, L.W. Chang, J.-P. Wu, L. Redding, H. Chang, T.-K. Yeh, C.-S. Yang, M.-H. Tsai, H.-J. Wang, Y.-C. Kuo, R.S.H. Yang: Computational and ultrastructural toxicology of a nanoparticle, quantum dot 705, in mice, Environ. Sci. Technol. **42**, 6264–6270 (2008)
29.120 J.X. Wang, X.Z. Zhang, Y.S. Chen, M. Sommerfeld, Q. Hu: Toxicity assessment of manufactured nanomaterials using the unicellular green alga *Chlamydomonas reinhardtii*, Chemosphere **73**, 1121–1128 (2008)
29.121 A. Hoshino, K. Fujioka, T. Oku, M. Suga, Y.F. Sasaki, T. Ohta, M. Yasuhara, K. Suzuki, K. Yamamoto: Physicochemical properties and cellular toxicity of nanocrystal quantum dots depend on their surface modification, Nano Lett. **4**, 2163–2169 (2004)
29.122 S. Gosso, D. Gavello, C.N.G. Giachello, C. Franchino, E. Carbone, V. Carabelli: The effect of CdSe-ZnS quantum dots on calcium currents and catecholamine secretion in mouse chromaffin cells, Biomaterials **32**, 9040–9050 (2011)
29.123 J. Lovric, S.J. Cho, F.M. Winnik, D. Maysinger: Unmodified cadmium telluride quantum dots induce reactive oxygen species formation leading to multiple organelle damage and cell death, Chem. Biol. **12**, 1227–1234 (2005)
29.124 R.F. Domingos, D.F. Simon, C. Hauser, K.J. Wilkinson: Bioaccumulation and effects of CdTe/CdS quantum dots on *Chlamydomonas reinhardtii* – Nanoparticles or the free ions?, Environ. Sci. Technol. **45**, 7664–7669 (2011)
29.125 C.W. Lam, J.T. James, R. McCluskey, S. Arepalli, R.L. Hunter: A review of carbon nanotube toxicity and assessment of potential occupational and environmental health risks, Crit. Rev. Toxicol. **36**, 189–217 (2006)
29.126 W. Wei, A. Sethuraman, C. Jin, N.A. Monteiro-Riviere, R.J. Narayan: Biological properties of carbon nanotubes, J. Nanosci. Nanotechnol. **7**, 1284–1297 (2007)
29.127 G. Jia, H.F. Wang, L. Yan, X. Wang, R.J. Pei, T. Yan, Y.L. Zhao, X.B. Guo: Cytotoxicity of carbon nanomaterials: Single wall nanotube, multi wall nanotube, and fullerene, Environ. Sci. Technol. **39**, 1378–1383 (2005)
29.128 L.H. Ding, J. Stilwell, T.T. Zhang, O. Elboudwarej, H.J. Jiang, J.P. Selegue, P.A. Cooke, J.W. Gray, F.Q.F. Chen: Molecular characterization of the cytotoxic mechanism of multiwall carbon nanotubes and nanoonions on human skin fibroblast, Nano Lett. **5**, 2448–2464 (2005)
29.129 T. Thurnherr, C. Brandenberger, K. Fischer, L. Diener, P. Manser, X. Maeder-Althaus, J.P. Kaiser, H.F. Krug, B. Rothen-Rutishauser, P. Wick: A comparison of acute and long-term effects of industrial multiwalled carbon nanotubes on human lung and immune cells in vitro, Toxicol. Lett. **200**, 176–186 (2011)
29.130 T. Oyabu, T. Myojo, Y. Morimoto, A. Ogami, M. Hirohashi, M. Yamamoto, M. Todoroki, Y. Mizuguchi, M. Hashiba, B.W. Lee, M. Shimada, W.N. Wang, K. Uchida, S. Endoh, N. Kobayashi, K. Yamamoto, K. Fujita, K. Mizuno, M. Inada, T. Nakazato, J. Nakanishi, I. Tanaka: Biopersistence of inhaled MWCNT in rat lungs in a 4-week well-characterized exposure, Inhal. Toxicol. **23**, 784–791 (2011)
29.131 A.K. Patlolla, A. Berry, P.B. Tchounwou: Study of hepatotoxicity and oxidative stress in male Swiss-Webster mice exposed to functionalized multiwalled carbon nanotubes, Mol. Cell. Biochem. **358**, 189–199 (2011)
29.132 L.A. Luongo, X.Q. Zhang: Toxicity of carbon nanotubes to the activated sludge process, J. Hazard. Mater. **178**, 356–362 (2010)
29.133 S. Kang, M.S. Mauter, M. Elimelech: Microbial cytotoxicity of carbon-based nanomaterials: Implications for river water and wastewater effluent, Environ. Sci. Technol. **43**, 2648–2653 (2009)
29.134 S. Kang, M. Pinault, L.D. Pfefferle, M. Elimelech: Single-walled carbon nanotubes exhibit strong antimicrobial activity, Langmuir **23**, 8670–8673 (2007)
29.135 S. Kang, M.S. Mauter, M. Elimelech: Physicochemical determinants of multiwalled carbon nanotube bacterial cytotoxicity, Environ. Sci. Technol. **42**, 7528–7534 (2008)
29.136 S. Kang, M. Herzberg, D.F. Rodrigues, M. Elimelech: Antibacterial effects of carbon nanotubes: Size does matter, Langmuir **24**, 6409–6413 (2008)
29.137 S.R. Chae, M. Therezien, J.F. Budarz, L. Wessel, S.H. Lin, Y. Xiao, M.R. Wiesner: Comparison of the photosensitivity and bacterial toxicity of spherical and tubular fullerenes of variable aggregate size, J. Nanopart. Res. **13**, 5121–5127 (2011)
29.138 J.D. Fortner, D.Y. Lyon, C.M. Sayes, A.M. Boyd, J.C. Falkner, E.M. Hotze, L.B. Alemany, Y.J. Tao, W. Guo, K.D. Ausman, V.L. Colvin, J.B. Hughes: C_{60} in water: Nanocrystal formation and microbial response, Environ. Sci. Technol. **39**, 4307–4316 (2005)

29.139 W.A. Scrivens, J.M. Tour, K.E. Creek, L. Pirisi: Synthesis of ^{14}C-labeled C_{60}, its suspension in water, and its uptake by human keratinocytes, J. Am. Chem. Soc. **116**, 4517–4518 (1994)

29.140 C.M. Sayes, A.A. Marchione, K.L. Reed, D.B. Warheit: Comparative pulmonary toxicity assessments of C_{60} water suspensions in rats: Few differences in fullerene toxicity in vivo in contrast to in vitro profiles, Nano Lett. **7**, 2399–2406 (2007)

29.141 C.M. Sayes, A.M. Gobin, K.D. Ausman, J. Mendeza, J.L. West, V.L. Colvin: Nano-C_{60} cytotoxicity is due to lipid peroxidation, Biomaterials **26**, 7587–7595 (2005)

29.142 C.M. Sayes, J.D. Fortner, W. Guo, D. Lyon, A.M. Boyd, K.C. Ausman, Y.J. Tao, B. Sitharaman, L.J. Wilson, J.B. Hughes, J.L. West, V.L. Colvin: The differential cytotoxicity of water-soluble fullerenes, Nano Lett. **4**, 1881–1887 (2004)

29.143 S.P. Rozhkov, A.S. Goryunov, G.A. Sukhanova, A.G. Borisova, N.N. Rozhkova, G.V. Andrievsky: Protein interaction with hydrated C_{60} fullerene in aqueous solutions, Biochem. Biophys. Res. Commun. **303**, 562–566 (2003)

29.144 E.J. Park, H. Kim, Y. Kim, J. Yi, K. Choi, K. Park: Carbon fullerenes (C_{60}s) can induce inflammatory responses in the lung of mice, Toxicol. Appl. Pharmacol. **244**, 226–233 (2010)

29.145 D.Y. Lyon, J.D. Fortner, C.M. Sayes, V.L. Colvin, J.B. Hughes: Bacterial cell association and antimicrobial activity of a C_{60} water suspension, Environ. Toxicol. Chem. **24**, 2757–2762 (2005)

29.146 D.Y. Lyon, L. Brunet, G.W. Hinkal, M.R. Wiesner, P.J.J. Alvarez: Antibacterial activity of fullerene water suspensions (nC_{60}) is not due to ROS-mediated damage, Nano Lett. **8**, 1539–1543 (2008)

29.147 D.Y. Lyon, P.J. Alvarez: How a fullerene water suspension kills bacteria: Exploring three possible mechanisms, Chem. Res. Toxicol. **20**, 1991–1991 (2007)

29.148 M. Kovochich, B. Espinasse, M. Auffan, E.M. Hotze, L. Wessel, T. Xia, A.E. Nel, M.R. Wiesner: Comparative toxicity of C_{60} aggregates toward mammalian cells: Role of tetrahydrofuran (THF) decomposition, Environ. Sci. Technol. **43**, 6378–6384 (2009)

29.149 S. Kato, H. Aoshima, Y. Saitoh, N. Miwa: Biological safety of lipofullerene composed of squalane and fullerene-C_{60} upon mutagenesis, photocytotoxicity, and permeability into the human skin tissue, Basic Clin. Pharmacol. Toxicol. **104**, 483–487 (2009)

29.150 S. Kato, H. Aoshima, Y. Saitoh, N. Miwa: Biological safety of liposome-fullerene consisting of hydrogenated lecithin, glycine soja sterols, and fullerene-C_{60} upon photocytotoxicity and bacterial reverse mutagenicity, Toxicol. Ind. Health **25**, 197–203 (2009)

29.151 A. Isakovic, Z. Markovic, B. Todorovic-Markovic, N. Nikolic, S. Vranjes-Djuric, M. Mirkovic, M. Dramicanin, L. Harhaji, N. Raicevic, Z. Nikolic, V. Trajkovic: Distinct cytotoxic mechanisms of pristine versus hydroxylated fullerene, Toxicol. Sci. **91**, 173–183 (2006)

29.152 R. Bullard-Dillard, K.E. Creek, W.A. Scrivens, J.M. Tour: Tissue sites of uptake of ^{14}C-labeled C_{60}, Bioorg. Chem. **24**, 376–385 (1996)

29.153 N. Shinohara, M. Gamo, J. Nakanishi: Fullerene C_{60}: Inhalation hazard assessment and derivation of a period-limited acceptable exposure level, Toxicol. Sci. **123**, 576–589 (2011)

29.154 L.K. Adams, D.Y. Lyon, P.J.J. Alvarez: Comparative eco-toxicity of nanoscale TiO_2, SiO_2, and ZnO water suspensions, Water Res. **40**, 3527–3532 (2006)

29.155 D.Y. Lyon, L.K. Adams, J.C. Falkner, P.J.J. Alvarez: Antibacterial activity of fullerene water suspensions: Effects of preparation method and particle size, Environ. Sci. Technol. **40**, 4360–4366 (2006)

29.156 J. Fang, D.Y. Lyon, M.R. Wiesner, J. Dong, P.J.J. Alvarez: Effect of a fullerene water suspension on bacterial phospholipids and membrane phase behavior, Environ. Sci. Technol. **41**, 2636–2642 (2007)

29.157 E. Oberdörster: Manufactured nanomaterials (fullerenes, C_{60}) induce oxidative stress in the brain of juvenile largemouth bass, Environ. Health Perspect. **112**, 1058–1062 (2004)

29.158 N. Tsao, T. Luh, C. Chou, T. Chang, J. Wu, C. Liu, H. Lei: In vitro action of carboxyfullerene, J. Antimicrob. Chemother. **49**, 641–649 (2002)

29.159 J.P. Kamat, T.P.A. Devasagayam, K.I. Priyadarsini, H. Mohan: Reactive oxygen species mediated membrane damage induced by fullerene derivatives and its possible biological implications, Toxicology **155**, 55–61 (2000)

29.160 C. Blaise, F. Gagne, J.F. Ferard, P. Eullaffroy: Ecotoxicity of selected nanomaterials to aquatic organisms, Environ. Toxicol. Chem. **23**, 591–598 (2008)

29.161 V. Aruoja, H.C. Dubourguier, K. Kasemets, A. Kahru: Toxicity of nanoparticles of CuO, ZnO and TiO_2 to microalgae Pseudokirchneriella subcapitata, Sci. Total Environ. **407**, 1461–1468 (2009)

29.162 K. Kasemets, A. Ivask, H.C. Dubourguier, A. Kahru: Toxicity of nanoparticles of ZnO, CuO and TiO_2 to yeast *Saccharomyces cerevisiae*, Toxicol. in Vitro **23**, 1116–1122 (2009)

29.163 K. Fujiwara, H. Suematsu, E. Kiyomiya, M. Aoki, M. Sato, N. Moritoki: Size-dependent toxicity of silica nanoparticles to *Chlorella kessleri*, J. Environ. Sci. Health A **43**, 1167–1173 (2008)

29.164 C. Wei, Y. Zhang, J. Guo, B. Han, X. Yang, J. Yuan: Effects of silica nanoparticles on growth and photosynthetic pigment contents of *Scenedesmus obliquus*, J. Environ. Sci. **22**, 155–160 (2010)

29.165 W. Jiang, H. Mashayekhi, B. Xing: Bacterial toxicity comparison between nano- and micro-scaled oxide particles, Environ. Pollut. **157**, 1619–1625 (2009)

29.166 M. Lucarelli, A.M. Gatti, G. Savarino, P. Quattroni, L. Martinelli, E. Monari, D. Boraschi: Innate defence functions of macrophages can be biased by nano-sized ceramic and metallic particles, Eur. Cytokine Netw. **15**, 339–346 (2004)

29.167 Y. Li, L. Sun, M.H. Jin, Z.J. Du, X.M. Liu, C.X. Guo, Y.B. Li, P.L. Huang, Z.W. Sun: Size-dependent cytotoxicity of amorphous silica nanoparticles in human hepatoma HepG2 cells, Toxicol. in Vitro **25**, 1343–1352 (2011)

29.168 D. Dutta, S.K. Sundaram, J.G. Teeguarden, B.J. Riley, L.S. Fifield, J.M. Jacobs, S.R. Addleman, G.A. Kaysen, B.M. Moudgil, T.J. Weber: Adsorbed proteins influence the biological activity and molecular targeting of nanomaterials, Toxicol. Sci. **100**, 303–315 (2007)

29.169 H.-S. Choi, Y.-J. Kim, M. Song, M.-K. Song, J.-C. Ryu: Genotoxicity of nanosilica in mammalian cell lines, Toxicol. Environ. Health Sci. **3**, 7–13 (2011)

29.170 G. Attik, R. Brown, P. Jackson, O. Creutzenberg, I. Aboukhamis, B.H. Rihn: Internalization, cytotoxicity, apoptosis, and tumor necrosis factor-alpha expression in rat alveolar macrophages exposed to various dusts occurring in the ceramics industry, Inhal. Toxicol. **20**, 1101–1112 (2008)

29.171 Z. Chen, H.A. Meng, G.M. Xing, C.Y. Chen, Y.L. Zhao, G.A. Jia, T.C. Wang, H. Yuan, C. Ye, F. Zhao, Z.F. Chai, C.F. Zhu, X.H. Fang, B.C. Ma, L.J. Wan: Acute toxicological effects of copper nanoparticles in vivo, Toxicol. Lett. **163**, 109–120 (2006)

29.172 M. Heinlaan, A. Ivask, I. Blinova, H.-C. Dubourguier, A. Kahru: Toxicity of nanosized and bulk ZnO, CuO and TiO_2 to bacteria *Vibrio fischeri* and *crustaceans*, *Daphnia magna* and *Thamnocephalus platyurus*, Chemosphere **71**, 1308–1316 (2008)

29.173 B.H. Yang, Q.J. Wang, R.H. Lei, C.Q. Wu, C. Shi, Q.X. Wang, Y. Yuan, Y. Wang, Y.W. Luo, Z.H. Hu, H.Z. Ma, M.Y. Liao: Systems toxicology used in nanotoxicology: Mechanistic insights into the hepatotoxicity of nanocopper particles from toxicogenomics, J. Nanosci. Nanotechnol. **10**, 8527–8537 (2010)

29.174 H. Meng, Z. Chen, G.M. Xing, H. Yuan, C.Y. Chen, F. Zhao, C.C. Zhang, Y.L. Zhao: Ultrahigh reactivity provokes nanotoxicity: Explanation of oral toxicity of nanocopper particles, Toxicol. Lett. **175**, 102–110 (2007)

29.175 M. Midander, P. Cronholm, H.L. Karlsson, K. Elihn, L. Moller, C. Leygraf, I.O. Wallinder: Surface characteristics, copper release, and toxicity of nano- and micrometer-sized copper and copper(II) oxide particles: A cross-disciplinary study, Small **5**, 389–399 (2009)

29.176 Z.Y. Wang, K. Zhang, J. Zhao, X.Y. Liu, B.S. Xing: Adsorption and inhibition of butyrylcholinesterase by different engineered nanoparticles, Chemosphere **79**, 86–92 (2010)

29.177 A.T. Bauer, E.A. Strozyk, C. Gorzelanny, C. Westerhausen, A. Desch, M.F. Schneider, S.W. Schneider: Cytotoxicity of silica nanoparticles through exocytosis of von Willebrand factor and necrotic cell death in primary human endothelial cells, Biomaterials **32**, 8385–8393 (2011)

29.178 W.S. Lin, Y.W. Huang, X.D. Zhou, Y.F. Ma: Toxicity of cerium oxide nanoparticles in human lung cancer cells, Int. J. Toxicol. **25**, 451–457 (2006)

29.179 IARC: *Silica, Some Silicates, Coal Dust and Para-Aramid Fibrils*, IARC Monographs on the Evaluation of Carcinogenic Risks to Humans, Vol. 68 (International Agency for Research on Cancer World Health Organization, Lyon 1997) p. 41

29.180 N. Kumar, V. Shah, V.K. Walker: Perturbation of an arctic soil microbial community by metal nanoparticles, J. Hazard. Mater. **190**, 816–822 (2011)

29.181 V. Rabolli, L.C.J. Thomassen, F. Uwambayinema, J.A. Martens, D. Lison: The cytotoxic activity of amorphous silica nanoparticles is mainly influenced by surface area and not by aggregation, Toxicol. Lett. **206**, 197–203 (2011)

29.182 V. Rabolli, L.C.J. Thomassen, C. Princen, D. Napierska, L. Gonzalez, M. Kirsch-Volders, P.H. Hoet, F. Huaux, C.E.A. Kirschhock, J.A. Martens, D. Lison: Influence of size, surface area and microporosity on the in vitro cytotoxic activity of amorphous silica nanoparticles in different cell types, Nanotoxicology **4**, 307–318 (2010)

29.183 K. Van Hoecke, K.A.C. De Schamphelaere, P. Van der Meeren, S. Lcucas, C.R. Janssen: Ecotoxicity of silica nanoparticles to the green alga *pseudokirchneriella subcapitata*: Importance of surface area, Environ. Toxicol. Chem. **27**, 1948–1957 (2008)

29.184 W.M. Lee, Y.J. An, H. Yoon, H.S. Kweon: Toxicity and bioavailability of copper nanoparticles to the terrestrial plants mung bean (*Phaseolus radiatus*) and wheat (*Triticum aestivum*): Plant agar test for water-insoluble nanoparticles, Environ. Toxicol. Chem. **27**, 1915–1921 (2008)

29.185 M.E. Letelier, A.M. Lepe, M. Faundez, J. Salazar, R. Marin, P. Aracena, H. Speisky: Possible mechanisms underlying copper-induced damage in biological membranes leading to cellular toxicity, Chem. Biol. Interact. **151**, 71–82 (2005)

29.186 P.J.J. Alvarez, V. Colvin, J. Lead, V. Stone: Research priorities to advance eco-responsible nanotechnology, ACS Nano **3**, 1616–1619 (2009)

29.187 S. Ghosh, A.K. Sood, N. Kumar: Carbon nanotube flow sensors, Science **299**, 1042–1044 (2003)

29.188 Z.L. Wang, J. Song: Piezoelectric nanogenerators based on zinc oxide nanowire arrays, Science **312**, 242–246 (2006)

30. Plasmonic Nanomaterials for Nanomedicine

Renat R. Letfullin, Thomas F. George

Plasmonic nanoparticles are being researched as a noninvasive tool for ultrasensitive diagnostic, spectroscopic, and, recently, therapeutic technologies. With particular antibody coatings on nanoparticles, they attach to abnormal cells of interest (cancer or otherwise). Once attached, nanoparticles can be activated/heated with ultraviolet (UV)/visible/infrared (IR), radiofrequency (RF) or x-ray pulses, damaging the surrounding area of the abnormal cell to the point of death. Here, we describe an integrated approach to improved plasmonic therapy composed of nanomaterial optimization and the development of a theory for selective radiation nanophototermolysis of abnormal biological cells with gold nanoparticles and self-assembled nanoclusters. The theory takes into account radiation-induced linear and nonlinear synergistic effects in biological cells containing nanostructures, with focus on optical, thermal, bubble formation, and nanoparticle explosion phenomena. On the basis of the developed models, we discuss new ideas and new dynamic modes for cancer treatment by radiation-activated nanoheaters, which involve nanocluster aggregation in living cells, microbubbles overlapping around laser-heated intracellular nanoparticles/clusters, and the laser thermal explosion mode of single nanoparticles (*nanobombs*) delivered to cells.

30.1 **Introduction** 1063

30.2 **Nanooptics – Lorenz–Mie Formalism** 1064

30.3 **Optical Properties of Gold Nanoparticles in Biological Media** 1065

30.4 **Kinetics of Heating and Cooling of Nanoparticles** 1067
30.4.1 Time Dynamics of the Nanoparticle Temperature .. 1067
30.4.2 Comparison of Single-Pulse and Multipulse Modes of Heating . 1067

30.5 **Spatial Distribution of Temperature Fields Around the Nanoparticle** 1076
30.5.1 Theoretical Model 1076
30.5.2 Laser Heating of a Single Nanoparticle in Biomedia 1077
30.5.3 Bone Tissue Ablation by Plasmonic Nanoparticles 1079
30.5.4 Temperature Simulations for Many Heat Sources 1082

30.6 **New Dynamic Modes in Selective Plasmonic Nanotherapy** 1083
30.6.1 Nanocluster Aggregation Mode 1083
30.6.2 Microbubble Overlapping Mode 1086
30.6.3 Laser-Induced Thermal Explosion Mode – Nanobombs 1091

References 1095

30.1 Introduction

In recent years, there has been a tremendous increase in research at the nanoscale for materials (see, for example, [30.1], and references in this handbook). One particular area is the application of plasmonic nanoparticles to enhance the diagnostic and treatment methods available for cancer [30.2–8]. The application of nanotechnology for laser thermal-based killing of abnormal cells (e.g., cancer cells) targeted with absorbing nanoparticles (e.g., gold solid nanospheres, nanoshells or nanorods) is becoming an extensive area of research. Studies have shown that, by coating the surface of nanoparticles with a specific protein (a *targeting agent*, normally an antibody), the nanoparticles will bind to a complementary protein such as found on a cancer cell [30.3, 7–12], as

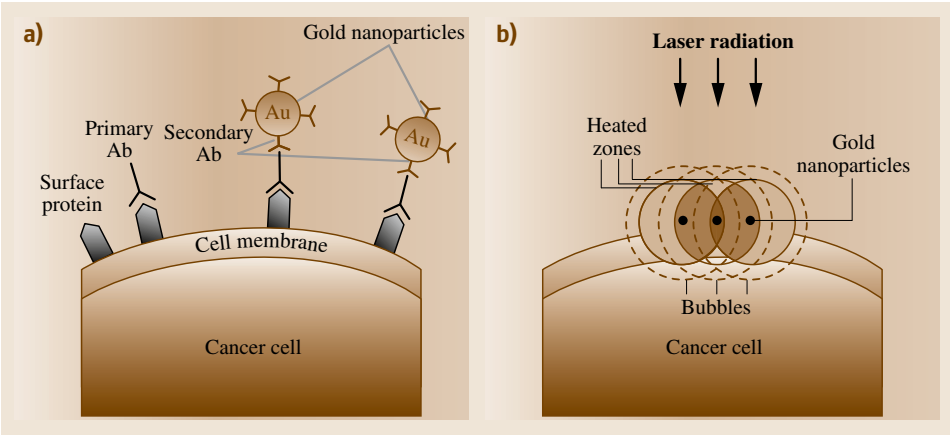


Fig. 30.1a,b Principle of selective nanophotothermolysis of cancer cell. **(a)** Cancer cell targeted with primary antibodies (Ab) which are selectively attached to secondary antibodies conjugated with gold nanoparticles. **(b)** Schematic of laser-induced heating effects around the particles

shown in Fig. 30.1a. After the nanoparticles are bound to the cancerous cells, they can be heated with electromagnetic radiation (UV/visible/IR, RF or x-ray pulses), inducing a variety of effects around the particles [30.7, 9, 11, 12], as shown in Fig. 30.1b. The heated particle can cause the cell to experience hyperthermia, resulting in surface-protein denaturing [30.13] and changing membrane permeability [30.14]. Alternatively, the nanoparticle itself can heat to the point of melting, evaporation or explosion [30.5, 6], causing further damage to cells. These effects can be used to increase the sensitivity of photoacoustic diagnosis or aid in therapy, such as selective photothermolysis, by selective thermal killing of tumor cells into which absorbing nanoparticles have been incorporated. The potential advantages of these new photothermal sensitizers heated with short laser pulses may include:

- Selective cancer-cell targeting by means of conjugation of absorbing particles (e.g., gold nanospheres, nanoshells or nanorods) with specific antibodies
- Localized tumor damage without harmful effects on surrounding healthy tissue
- Absorption at longer wavelengths in the transparency window of most biotissues
- No undesired side-effects (e.g., cytotoxicity or cutaneous photosensitivity)
- Relatively fast treatment involving potentially just one or several laser pulses.

Progress towards the development of selective nanophotothermolysis technology requires the investigation of new physical concepts and new approaches to the study of short/ultrashort laser pulse interactions with biological systems containing nanostructures. In this chapter, we develop a theory for laser-induced linear and nonlinear synergistic effects in biological cells containing nanostructures with focus on cluster aggregation, bubble formation, and nanoparticle explosion phenomena. The theory is based on our experience in theoretical studies relevant to nanoparticles [30.1, 5, 6, 12, 15–24].

30.2 Nanooptics – Lorenz–Mie Formalism

The optimal wavelength of laser radiation and optimal size range of nanoparticles for effective laser killing of cancer cells can be found by using an extended Lorenz–Mie diffraction theory, taking into account the plasmon-resonance absorption effect in metal nanoparticles. In the most general case, calculations based on the Mie theory are reduced to searching for the scattering matrix of j particles, $S^j(\theta, \phi)$, consisting of four complex functions, $S_i^j\ (\theta, \phi)$ $(i = 1, \ldots, 4)$, describing the amplitude and phase of a scattered scalar wave in any direction. Forward scattering $(\theta = 0°)$ contains the attenuation process of an electromagnetic wave, and for the case of spherical particles, $S_3^j = S_4^j = 0$. We can limit the description to a single scattering amplitude function

$$S^j(0) = S_1^j(0) = S_2^j(0) = \frac{1}{2}\sum_{l=1}^{\infty}(2l+1)\left(a_l^j + b_l^j\right) . \tag{30.1}$$

The Mie coefficients a_l and b_l contain the characteristics of the dispersal medium and are calculated through the cylindrical Bessel function of the first kind $\psi_l(y)$ and the Hankel function of the second kind $\xi_l(\rho)$, both with half-integral indices

$$a_l = \frac{\psi_l'(y)\psi_l(\rho) - \tilde{m}\psi_l(y)\psi_l'(\rho)}{\psi_l'(y)\xi_l(\rho) - \tilde{m}\psi_l(y)\xi_l'(\rho)} ,$$
$$b_l = \frac{\tilde{m}\psi_l'(y)\psi_l(\rho) - \psi_l(y)\psi_l'(\rho)}{\tilde{m}\psi_l'(y)\xi_l(\rho) - \psi_l(y)\xi_l'(\rho)} . \qquad (30.2)$$

Here, $\tilde{m} = m_0/m_1$ is the relative value of the refractive index of the medium; $m_0 = n_0 - \mathrm{i}\chi_0$ and $m_1 = n_1 - \mathrm{i}\chi_1$ are the complex refractive indices of the particle material and the aqueous suspension, respectively; $\rho = 2\pi r_0/\lambda$ is the Mie parameter; and $y = 2\pi r_0 n_0/\lambda$, $\psi_l(u) = (\pi u/2)^{1/2} J^{(1)}_{l+1/2}$, $\xi_l(u) = (\pi u/2)^{1/2} H^{(2)}_{l+1/2}$, and $\psi_l' = \mathrm{d}\psi_l(u)/\mathrm{d}u$. With knowledge of $S^j(0)$, it is possible to calculate the integrated optical performance of the particles (i. e., the dimensionless efficiency coefficients of scattering, $K^j_{\mathrm{sca}}(\rho,\tilde{m}) = \sigma^j_{\mathrm{sca}}(\rho,\tilde{m})/\sigma_0$, absorption, $K^j_{\mathrm{abs}}(\rho,\tilde{m}) = \sigma^j_{\mathrm{abs}}(\rho,\tilde{m})/\sigma_0$, and attenuation, $K^j_{\mathrm{att}}(\rho,\tilde{m}) = \sigma^j_{\mathrm{att}}(\rho,\tilde{m})/\sigma_0$, of the radiation at a given wavelength) as

$$K^j_{\mathrm{att}}(\rho,\tilde{m}) = \frac{4\pi}{k^2}\,\mathrm{Re}\left[S^j(0)\right] ,$$
$$K^j_{\mathrm{sca}}(\rho,\tilde{m}) = \frac{2}{\rho^2}\sum_{l=1}^{\infty}(2l+1)\left\{\left|a_l^j\right|^2 + \left|b_l^j\right|^2\right\} ,$$
$$K^j_{\mathrm{abs}}(\rho,\tilde{m}) = K_{\mathrm{ext}}(\rho,\tilde{m}) - K_{\mathrm{sca}}(\rho,\tilde{m}) , \qquad (30.3)$$

where $k = 2\pi/\lambda$ is the wavenumber, and $\sigma^j_{\mathrm{sca}}(\rho,\tilde{m})$, $\sigma^j_{\mathrm{abs}}(\rho,\tilde{m})$, $\sigma^j_{\mathrm{att}}(\rho,\tilde{m})$, and σ_0 are the scattering, absorption, attenuation, and geometric cross-sections of j particles, respectively.

In a simulation of electromagnetic wave propagation in a dispersed medium, our previously developed effective algorithm [30.25] was used. Here, the cylindrical functions of real or imaginary arguments and their derivatives, which occur in the expressions for the Mie coefficients a_l and b_l (30.2), are calculated as the ratio of the function and its derivative by using the recurrence relationships for direct and inverse recursions. Such an approach allows us to make an effective and accurate determination of the optical properties of a dispersal medium over a broad range of Mie parameters, $\rho = 2\pi r_0/\lambda = 0.001-1500$, below the diffraction limit simultaneously with small and large values of the real n_0 and the imaginary χ_0 parts of the refractive index of the particle's and surrounding medium substance.

30.3 Optical Properties of Gold Nanoparticles in Biological Media

The Lorenz–Mie formalism (30.1–30.3) requires the use of two dimensionless input parameters, $\rho = 2\pi r_0/\lambda$ and $\delta = \rho\tilde{m}$, where $\tilde{m}$ is the relative value of the complex refractive index of the nanoparticles in the surrounding medium at the wavelength λ. We examine the effects of the medium refractive index on the light-absorbing properties of gold particles in suspension as well as attached to a surface. Four media are used, namely water, cytoplasm, cell membrane, and collagen. The refractive indices of the media at the different wavelengths and the results of the Mie theory calculations of the maximum light-absorption factor (K_{abs}), wavelength ($\lambda_{\max}$), and radius ($r_{\max}$) for gold particles in media of different refractive indices are listed in Table 30.1. Results of computer simulations of the absorption coefficient K_{abs} as a function of the wavelength and radius of gold nanoparticles in various biological media are plotted in Fig. 30.2. Figure 30.2a shows the absorption spectrum of the gold particle over the visible range $\lambda = 400-700$ nm, and Fig. 30.2b illustrates the dependences of K_{abs} on particle size for different surrounding biomedia.

As follows from calculations, the optical properties of the gold nanosphere in low-absorbing biological media are substantially different from the case of the surrounding water medium. The maximal peak of the absorption factor increases continuously with increase in the refractive index of the surrounding media, and the color of the incident light changes from green to red; i. e., there is a red-shift effect of the absorption maximum with refractive index (Fig. 30.2a). Maximum absorption by gold nanoparticles is observed for the surrounding collagen medium, where the absorption cross-section of the gold nanoparticle exceeds its geometric cross-section by a factor of 5 for the optimal wavelength 549 nm. The presence of the low-absorbing biological surroundings also shifts the optimal radius of the gold nanoparticle for effective absorption to a smaller size region from 35 nm for the water medium to 26 nm for the collagen case (Table 30.1).

Table 30.1 Mie theory optima for the absorption factor (K_{abs}), wavelength (λ_{max}), and radius (r_{max}) for gold particles in biomedia of different refractive indices used in the simulations

Surrounding medium	λ (nm)	Refractive index n_1	K_{abs} (max)	λ_{max} (nm)	r_{max} (nm)	Surrounding medium	λ (nm)	Refractive index n_1	K_{abs} (max)	λ_{max} (nm)	r_{max} (nm)
Cytoplasm	400	1.35	4.145	540	33	Cell membrane	400	1.54	4.743	547	28
	500	1.36					500	1.5			
	600	1.365					600	1.46			
	700	1.367					700	1.4			
Blood	400	1.354	4.376	542	30	Collagen	400	1.6	4.954	549	26
	500	1.4					500	1.55			
	600	1.39					600	1.5			
	700	1.383					700	1.45			

Table 30.2 Example of absorption efficiency values for different nanoparticle shapes and structures at various wavelengths

Nanoparticle type	Effective radius (nm)	Wavelength (nm)	Absorption efficiency	References
Gold	35	532	3.50	
nanospheres	40	550	4.02	
Silica–gold	120	1100	3.5	[30.26]
nanoshells	120	750	3.75	
Gold nanorods	11.4	800	14.0	[30.26]
	17.9	825	14.5	

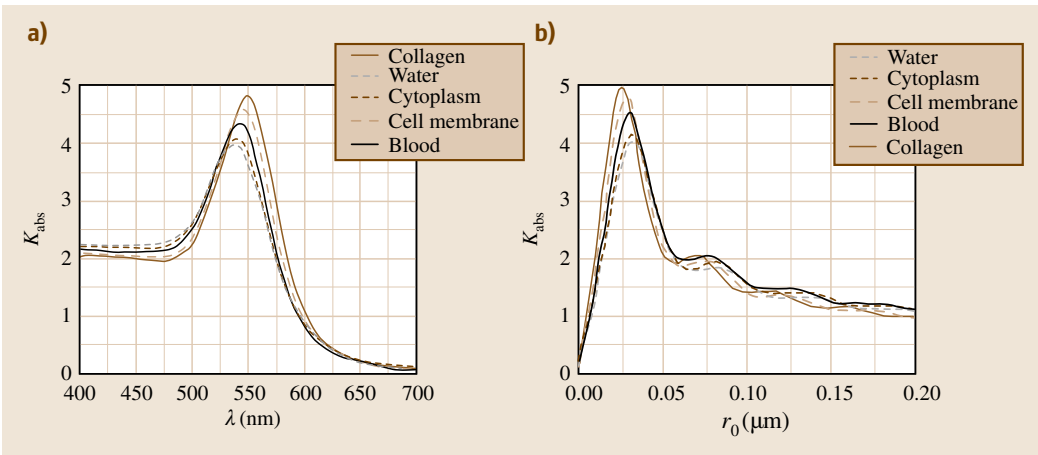


Fig. 30.2 **(a)** Absorption spectrum of the gold nanoparticle over the visible range $\lambda = 400–700$ nm. **(b)** Absorption efficiency K_{abs}, as a function of particle size for different surrounding biomedia

Thus, the absorption efficiency of gold nanoparticles is considerably higher in the low-absorbing biological media in comparison with the surrounding water medium.

The optical properties of the nanoparticles depend on the shape and internal structure of the particle as well. Table 30.2 contains results of calculations for the absorption efficiency of gold nanospheres, silica–gold nanoshells, and gold nanorods. For gold nanoparticles, the highest absorption efficiency is observed for nanorods; however, silica–gold nanoshells are tunable over the longer wavelengths in the transparency window of most biotissues. We should note that other materials can exhibit strong absorption efficiency, e.g., silver nanospheres, which show strong absorption around 394 nm in the UV range of spectrum.

30.4 Kinetics of Heating and Cooling of Nanoparticles

30.4.1 Time Dynamics of the Nanoparticle Temperature

In this section, we use the heat transfer equation with several simplifying assumptions to calculate the nanoparticle temperature as a function of time. It has been shown by *Letfullin* et al. [30.20] that a one-temperature model (OTM) is appropriate for plasmonic nanoparticle heating for lasers of pulse durations in the femto-, pico-, and nanosecond ranges. The first approximation used in this model is that the electron and lattice temperatures are equal (due to fast transfer of electron heat to the phonon subsystem). This provides the following heat–mass transfer rate equation for a single lattice temperature $T_s(t, r)$ that describes the laser interaction with the particle and surrounding medium

$$\frac{\mathrm{d}}{\mathrm{d}t}T_s(t,r) = \frac{\mu_s(T_s)}{\rho_s C_s(T_s)}\Delta T_s(t,r) + \frac{Q(t,r)}{\rho_s C_s(T_s)} - j_D(T_s)S_0 + \frac{3L}{r_0 C_s(T_s)}\frac{\mathrm{d}r_0}{\mathrm{d}t}\,. \tag{30.4}$$

Here, $\Delta = \partial^2/\partial x^2 + \partial^2/\partial y^2 + \partial^2/\partial z^2$ is the Laplace operator; $\mu_s(T_s)$, $C(T_s)$, L, ρ_s, and r_0 are, respectively, the heat conductivity of the surrounding medium and the specific heat, evaporation heat, density, and radius of the nanoparticle. The second assumption is that the particle is heated uniformly across the volume of the particle, i. e., $\Delta T_s(t, r) = 0$, provided that each point inside the particle volume has the same temperature $T_s(t)$. This homogeneous heating approximation can be applied if the heat diffusion time τ_D is less than the duration of the laser pulse: $\tau_D = r_0^2/4\chi < \tau_L$, where r_0 is a particle radius, χ is the thermal diffusivity of the particle material, and τ_L is the laser pulse duration. For gold nanoparticles with $r_0 = 20\,\mathrm{nm}$ and $\chi = 1.18\times10^{-4}\,\mathrm{m^2/s}$, τ_D is about $10^{-12}\,\mathrm{s}$. This is appropriate for heating of metal nanoparticles by pico- and nanosecond laser pulses and allows the use of a simplified relationship for the power density of the energy generated $Q(t, r_0)$ in the particle

$$Q(t, r_0) = \frac{3K_{abs}(r_0, \lambda)I_0 f(t)}{4r_0}\,. \tag{30.5}$$

Here, $K_{abs}(r_0, \lambda)$ is the absorption efficiency of the nanoparticle, $f(t)$ is the time profile of the laser pulse, and I_0 is the incident intensity of the laser pulse. The experiments analyzed utilize Gaussian beam profiles in the form $f(t) = \mathrm{e}^{-(at-b)^2}$; the coefficients are adjusted to create a pulse profile with the pulse duration of the laser used in the experiments. Another approximation limits heat loss to diffusion from the particle surface into the surrounding medium, defining the energy flux density $j_D(T_s)$ as

$$j_D(T_s) = \frac{\mu_\infty T_s}{(\alpha+1)r_0^2 C_s(T_s)\rho_s}\left[\left(\frac{T_s}{T_\infty}\right)^{\alpha+1} - 1\right], \tag{30.6}$$

where μ_∞ and T_∞ are, respectively, the heat conductivity and temperature of the surrounding medium at equilibrium; α is an exponent set to make the dynamics between the particle and medium more realistic; $\alpha > 1$ relates to high thermophysical characteristics of the surrounding medium, while $\alpha < 1$ relates to low thermophysical characteristics such as insulators; $\alpha = 1$ is a good approximation for biological media, which are of interest in the present chapter. The last assumption is that the particle temperature remains below the temperature of evaporation, which sets the last term in (30.4) to zero. The result (30.7) determines the particle temperature in terms of the energy accumulation from the incident laser radiation in the first term and energy loss due to heat diffusion into the medium in the second term

$$\frac{\mathrm{d}}{\mathrm{d}t}T_s = \frac{3K_{abs}(r_0, \lambda)I_0 f(t)}{4r_0\rho_s C_s(T_s)} - \frac{\mu_\infty T_s}{(\alpha+1)r_0^2 C_s(T_s)\rho_s}\left[\left(\frac{T_s}{T_\infty}\right)^{\alpha+1} - 1\right]. \tag{30.7}$$

30.4.2 Comparison of Single-Pulse and Multipulse Modes of Heating

The extent of the particle heating by radiation depends on many factors, divided primarily into three categories: (1) particle material, size, and shape; (2) laser pulse wavelength, energy density, duration, pulse shape, and generation frequency; and (3) properties of the surrounding medium. Even with the many factors involved in an experimental setup that contribute to the individual heating characteristics of a nanoparticle, several factors stay relatively constant across many experimental situations. Specifically, spherical gold nanoparticles are commonly used because they are relatively easy to fabricate, nontoxic, easily conjugated to antibodies, and strong absorbers [30.27]. Nanosecond pulse-width lasers with pulse firing frequencies of 10 Hz are often used because they are widely available and cheaper than pico- and femtosecond lasers or lasers with higher firing

Table 30.3 Experimental data for multipulse laser nanoparticle heating

Reference	[30.7]	[30.9]	[30.12]	[30.28]	[30.29]	[30.30]	[30.31]
Laser	**Nd:YAG**	**Nd:YAG**	**Nd:YAG**	**Nd:YAG**	**Nd:YAG**	**Ti:sapphire**	**Nd:YAG**
Wavelength (nm)	532	565	532	532	532	750	1064
Pulse energy (J/cm^2)	0.5	0.5	0.5	0.13	0.03	0.95	0.002
Pulse duration (ns)	12	20	12	6	7	10	7
Frequency of generation (Hz)	10[1]	10[1]	10[1]	10	20	11.8 MHz/ 50 MHz	10
Particle							
Material	Gold	Gold	Gold	Gold	Iron oxide	Gold	Gold
Structure	Sphere	Sphere	Sphere	Sphere	Sphere	Rod	Rod
Diameter (nm)	40	30	40	21/4.9	10	23.6[2]	22.76[2]
Aspect ratio	–	–	–	–	–	3.2	5.9
Other							
Number of pulses	100	100	30	3000	600	2	10
Surrounding medium	PBS	PBS	Water	Water	Water	Water	Water

[1] HOYA ConBio MedLite C Series and IV Series Nd:YAG lasers have a maximum generating frequency of 10 Hz, so the generation frequency for lasers when not provided was assumed as 10 Hz.
[2] It is common to use an effective radius (r_{eff}) when the particle is of nonstandard shape; this is the radius of a sphere that provides the equivalent volume as an arbitrary shape.

frequencies. Additionally, water or phosphate-buffered saline (PBS) solution is used as a surrounding medium due to strong similarities with a biological cell. Several experiments that use these factors are studied in our analysis [30.7, 8, 12, 28–31].

In experiments, *Zharov* et al. [30.7] used nanoparticle heating for bacterial killing. Spherical gold nanoparticles of diameter 10, 20, and 40 nm were heated with laser light, and it was determined that, at 3–5 J/cm^2, only 1–3 pulses are required for harmful effects on bacteria, while at 0.5–1 J/cm^2, at least 100 pulses are required to produce harmful effects. *Pitsillides* et al. [30.9] explored micro- and nanoparticles for selective cell therapy, finding that, for 20 nm-diameter gold nanospheres irradiated by 20 ns, 532 nm pulses at 0.5 J/cm^2, there is a much greater correlation of the number of particles attached to the cell than of the number of pulses when considering cellular damage. *Zharov* et al. [30.12] investigated bubble formation from nanoparticles. Using a smooth distribution of 40 nm-diameter gold nanospheres on a cell, they found that that 30 pulses of 0.5 J/cm^2 or one pulse of ≈ 2 J/cm^2 results in complete cell death. Alternatively, with cluster formation, cell damage occurs after 100 laser pulses at 80 mJ/cm^2. *Peng* et al. [30.28] focused on the effects of laser irradiation on particle size and peak absorption wavelength. They showed, using a Nd:YAG laser and 21 nm spherical gold nanoparticles, that irradiation causes the particles to fragment to an average diameter of 4.9 nm, changing the peak absorption wavelengths. *Kalambur* et al. [30.29] used iron oxide nanoparticles to compare RF heating with multipulse laser heating and determined that multipulse lasers produce a higher cellular uptake of particles, enabling greater cellular damage. *Hleb* and *Lapotko* [30.30] used gold nanorods to determine high-energy effects of lasers on nanorods and nanospheres, such as how long the particles maintain photothermal properties (before deterioration) and the effects of multiple pulses in the form of a *pulse train*, determining that very rapid pulse repetition leads to increased bubble effects. Lastly, *Takahashi* et al. [30.31] used gold nanorods irradiated with multipulse near-IR lasers to find that selective cell damage is achievable.

One of the greatest potential benefits from multipulse lasers is accumulative heating in the target. If multipulse lasers could be used to quickly accumulate heat in nanoparticles with many consecutive low-energy pulses, then the laser energy density would not be a prohibitive aspect of the treatment. Multiple low-energy-density pulses could be used rather than a single high-energy-density pulse to achieve the same nanoparticle temperature, sparing healthy cells from excessive heating as well as ensuring that the energy density required for treatment is below the medical standard of 100 mJ/cm^2 [30.12].

The focus of this section is to compare and contrast the effects of multipulse (set of short pulses) versus single-pulse laser heating of nanoparticles. The laser

Table 30.4 Additional input parameters for the theoretical calculations

Reference	[30.7]	[30.9]	[30.12]	[30.28]	[30.29]	[30.30]	[30.31]
Particle							
Calculated absorption efficiency	2.7225[1] ($\lambda = 532$ nm)	0.72[1] ($\lambda = 565$ nm)	2.72250 ($\lambda = 532$ nm)	1.29367 ($\lambda = 532$ nm)	1.68663 ($\lambda = 532$ nm)	11.5[2] ($\lambda = 725$ nm)	15.75[2] ($\lambda = 860$ nm)
Specific heat (J/(kg K))	129	129	129	129	937	129	129
Density (kg/cm^3)	0.0193	0.019	0.0193	0.0193	0.00524	0.0193	0.0193
Initial temperature (K)	300	300	300	300	300	300	300
Laser							
Energy density (J/cm^2) (original/revised)	0.5/0.01	0.5/0.1	0.5/0.01	0.13/0.0325	0.03	0.95/0.01	0.002
Medium							
Thermal conductivity (W/(cm K))	0.0075	0.0075	0.0060	0.0060	0.0060	0.0060	0.00604

[1] Absorption efficiency values calculated for nanoparticles in water due to difficulty in obtaining refractive index data for PBS solution
[2] Estimated absorption efficiency from *Jain* et al. [30.26] based on the effective radius and aspect ratio of the nanorods, using the closest values given based on wavelength r_{eff} and aspect ratio

heating of nanoparticles is very sensitive to the time structure of the incident pulsed laser radiation, i.e., the pulse shape and duration, and the number of pulses per unit time. We limit the maximum temperature of the theoretical calculations to the melting point of the material ($T_M \approx 1336$ K for bulk gold material and remaining above 1100 K for gold particles larger than 5 nm in diameter [30.32]) so that the particles will not undergo advanced phenomena of heating (evaporation, melting or explosion), but require that the nanoparticles surpass 433 K as required for protein denaturing [30.27].

The summary data obtained from experimental papers [30.7, 8, 12, 28–31] can be found in Table 30.3, while the additional input data we use for our calculations are listed in Table 30.4. We modified the energy density when the particle temperature exceeds the melting point of the material to reduce the particle temperature into our range of interest.

Peng et al. [30.28] used an incident energy density (0.13 J/cm^2) at a wavelength of 532 nm that causes particles to exceed the melting point, resulting in fragmentation. To make a case for reducing the incident energy density, we performed calculations to determine how changing the energy density would change the time–temperature profile of the nanoparticle heating and cooling. Our calculations show that changing the energy density has no effect on the time it takes for the particle to heat to the maximum temperature. Figure 30.3 demonstrates this with three different time–temperature profiles for: a 21 nm-diameter gold sphere irradiated by a 0.13 J/cm^2 pulse (solid line) and 0.0325 J/cm^2 pulse (dashed line), and a 4.9 nm-diameter gold sphere irradiated by a 0.13 J/cm^2 pulse (dotted line). Changing the energy density from a 0.13 pulse to a 0.0325 J/cm^2 pulse has no effect on the time required for the particle

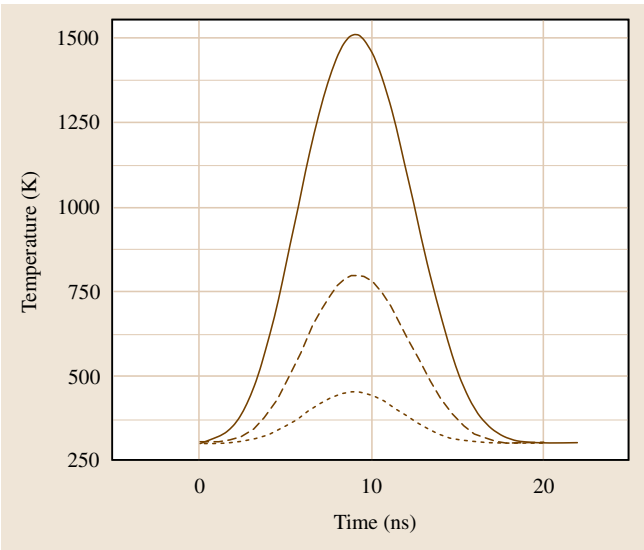


Fig. 30.3 Time–temperature profiles for 21 nm-diameter (*solid*) and 4.9 nm-diameter (*dotted*) gold particles in water irradiated by a 6 ns, 0.13 J/cm^2 pulse at 532 nm and a 21 nm-diameter gold particle irradiated by the same pulse at 0.0325 J/cm^2 (*dashed*)

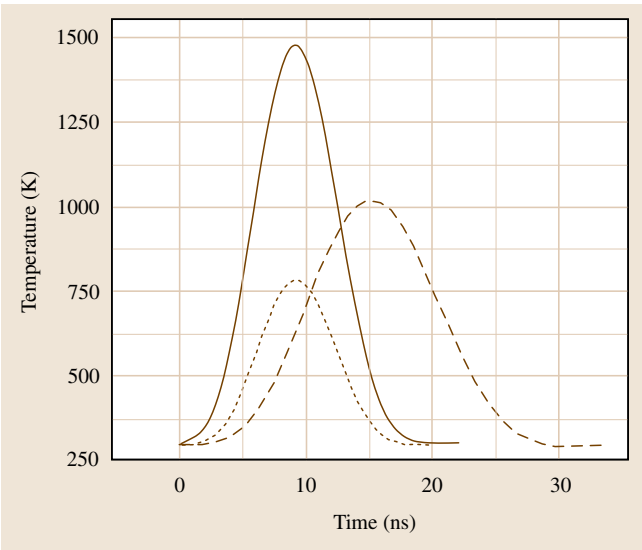


Fig. 30.4 Time–temperature profiles for 21 nm-diameter nanospheres with incident laser pulse duration of 6 ns at energy density of 0.13 J/cm^2 (*solid*) and 0.0325 J/cm^2 (*dotted*) and nanorods with effective diameter of 23.6 nm irradiated by a 10 ns, 0.01 J/cm^2 pulse (*dashed*)

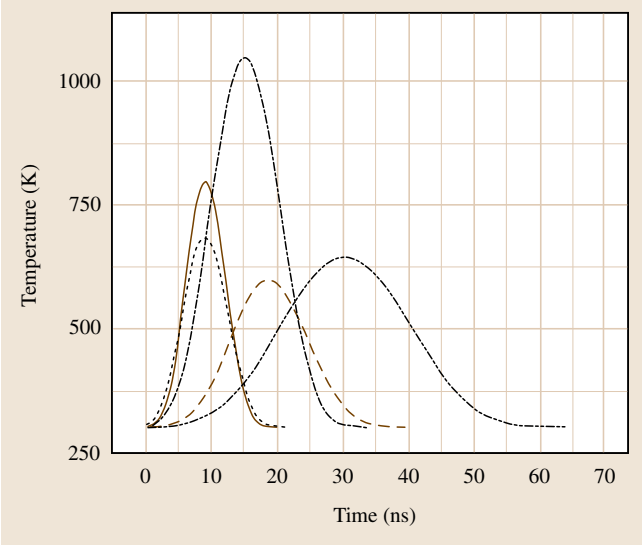


Fig. 30.5 Calculated time–temperature profiles for five different pulse durations used in single-pulse mode heating. Three gold nanosphere cases: [30.7] – 12 ns pulse (*dashed*); [30.9] – 20 ns (*dash-dot-dotted*); and [30.28] – 6 ns (*solid*). Two gold nanorod cases: [30.30] – 10 ns (*dash-dotted*); and [30.31] – 7 ns (*dotted*)

to reach its maximum temperature, which occurs 9 ns after the incident pulse in both cases.

The cooling time for the particle is slightly affected by the magnitude of the maximum temperature and is thus linked to the energy density. Heating the particles to 1500 and 800 K, respectively, for 0.13 and 0.0325 J/cm^2 pulses, we find that the cooling time is only slightly longer for the higher-energy-density pulse. For the 0.13 J/cm^2 pulse, the particle cools back to ambient temperature 11.4 ns after the peak, while for the 0.0325 J/cm^2 pulse the particle takes 10.6 ns after the maximum to cool.

Single-Pulse Mode

To analyze the effects due to varying characteristics of the experiments, in this section we compare theoretical calculations for those experiments that have contrasting characteristics, such as pulse duration, particle size and shape, and medium in the single-pulse mode of heating. Considering particle shape – between gold nanorods and gold nanospheres – we extrapolate from *Jain* et al. [30.26] that changing the particle shape significantly alters the peak absorption wavelengths and the respective coefficients of absorption, but these can be equated to spherical particles with an effective radius and aspect ratio, AR = length/diameter. In [30.30], the gold nanorods with $r_{\text{eff}} = 11.8$ nm and AR = 3.2 have an absorption efficiency around 11.5 when irradiated with 725 nm light [30.26]. Contrasted with the gold nanospheres in [30.28] ($r_0 = 11.5$ nm, $K_{\text{abs}} = 1.29$ at $\lambda = 532$ nm), a much lower energy density can be used to reach the same ablation temperature for the nanorods due to the extremely high absorption efficiency. Figure 30.4 shows the time–temperature profiles from [30.28] for nanospheres ($d = 21$ nm) under 0.13 and 0.0325 J/cm^2 pulses at 532 nm, as well as the temperature profile for the nanorods ($r_{\text{eff}} = 11.8$ nm, AR = 3.2) from [30.30] irradiated by 0.01 J/cm^2. This figure demonstrates how a much lower energy density can result in higher nanorod temperatures when compared with nanospheres of equivalent radius. The tunable characteristics of nanorods allow greater adjustment of the wavelength that will result in maximum absorption efficiency and how high the absorption efficiency will be, thus making nanorods potentially more effective for ablative treatments than nanospheres. As we will show in the next section, in terms of accumulative heating with a multipulse mode of irradiation, the difference between nanorods and nanospheres is not significant.

Another characteristic of the experimental setups [30.7, 9, 12, 28–31] is a laser pulse duration of roughly 10 ns. Figure 30.5 shows time–temperature pro-

files for five different pulse durations ranging from 6 to 20 ns. It follows from our calculations that, during the laser pulse, the transfer of heat from the nanoparticle into the surrounding media is slight, and the particle rapidly reaches its maximum temperature. The heating rate is about 10^2 K/s, depending on the pulse duration and incident energy density. The temperature of the particle continues to rise even after the end of the laser pulse. Using [30.30] as an example, the highest temperature of 1048.6 K for a 10 ns pulse is observed at a heating time of 15.2 ns, when the laser pulse has already degraded. After then, the transfer of heat from the particle to the surrounding medium becomes critical, since the energy source is no longer present in the system. The temperature of the particle and surrounding medium remains high (above 425 K) up to 24.6 ns after the pulse is fired, exceeding the laser pulse duration by 2.5 times. The total time for one cycle (heating from the initial temperature of 300 K to a maximum temperature and then cooling back to the initial temperature) is 32.8 ns, over thrice the pulse duration. Varying the pulse duration changes the maximum temperature of the particle as well as the time span of heating and cooling.

Due to the nature of the experiments and the intended application of the method for treatment of cancer inside the human body, the medium characteristics cannot be changed. Furthermore, the ability to change the material of the nanoparticle is also limited due to toxicity, but in the case of metal nanoparticles, they should all exhibit similar heating and cooling kinetics to those seen in gold and iron(III) oxide (Fe_3O_4). As we have shown above, the particle size, particle shape, and laser energy density do not significantly change the temporal behavior of nanoparticle heating and cooling, but just the magnitude of the maximum temperature reached. The laser pulse duration changes the maximum particle temperature as well as the temporal span of heating and cooling, following relatively predictable multiplicative values with respect to the pulse duration: the maximum temperature is at 1.46 times the pulse duration; the temperature remains above 425 K until 2.2 times the pulse duration; and the entire heating and cooling cycle takes about 3.23 times the pulse duration. These aspects could be useful for further single-pulse investigations, but they do not come into play when considering the multipulse heating of nanoparticles discussed below.

Multipulse Mode

Using the scaled-down energy density values determined in previous sections and a function to simulate multiple pulses, we have calculated the time profile of the nanoparticle temperature in a multipulse heating mode to determine what would enable accumulative heating of nanoparticles. To simulate multiple pulses, we use the same function as in the single-pulse simulations, but with the addition of several values of b to shift each consecutive pulse

$$f(t) = e^{-(at-b_1)^2} + e^{-(at-b_2)^2} + e^{-(at-b_3)^2} .$$

Three multipulse cases are shown in Fig. 30.6, demonstrating particle heating and cooling over time for the conditions of [30.7, 12, 29] as listed in Table 30.3. These simulations utilize a 37 and 62.5 MHz generation frequency due to the large time gap (relative to the pulse width) between each incident pulse when using the 10 Hz generation frequency specified in the references. These profiles demonstrate visually that, even at relatively high generation frequencies, multiple pulses do not produce any accumulative heating effect over time. The particle reaches the peak temperature and falls to equilibrium (300 K) in roughly three times the pulse duration, but the time delay between the pulses in experiments exceeds the pulse duration by five to ten million times.

Several of the experimental papers show effects from multipulse laser heating that are not present in the single-pulse laser mode, even though the pulse generation frequency for the multipulse mode is well below the MHz generation frequency. *Zharov* et al. [30.7] dis-

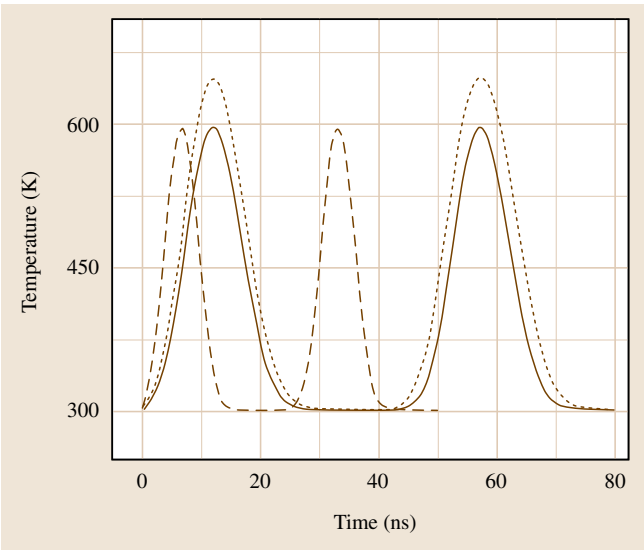


Fig. 30.6 Multipulse time–temperature profiles for [30.7] (*solid*), [30.12] (*dotted*), and [30.29] (*dashed*) with modified pulse generation frequencies

Table 30.5 Experimental data for healthy and tumor cells

Source	Cancer	Organelle	Healthy diameter (μm)	Well differentiated diameter (μm)	Moderately differentiated diameter (μm)	Poorly differentiated diameter (μm)
[30.33]	Hepatocellular carcinoma	Nucleus	7.5	8.5	8.8	10.3
[30.33]	Hepatocellular carcinoma	Mitochondria	1.1	0.9	0.9	0.66
[30.34]	Colorectal adenocarcinoma	Nucleus	5.2	7.2	–	–

Source	Cancer	Organelle	Benign diameter (μm)	In situ diameter (μm)	Invasive diameter (μm)
[30.35]	Ductal breast carcinoma	Nucleus	7	11.6	8.33
[30.36]	Intraductal breast cancer	Nucleus	8.58	–	8.97
[30.37]	Breast cancer	Nucleus	5.6	–	5.8

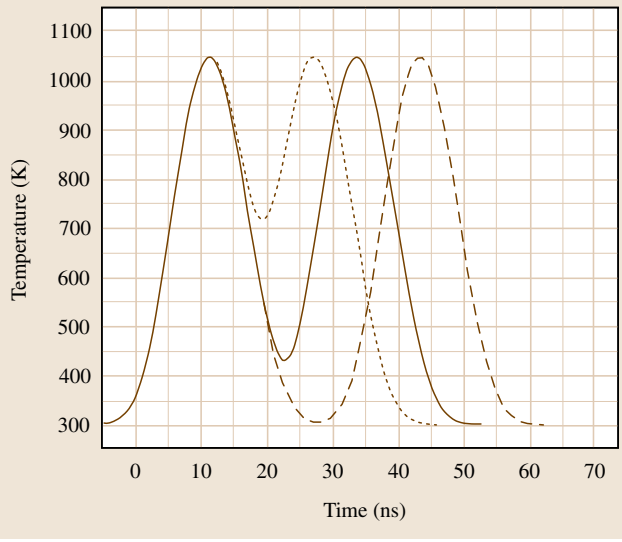


Fig. 30.7 Time–temperature profile for multipulse laser heating of gold nanorods ($r_{\text{eff}} = 11.8$ nm, AR = 3.2, $K_{\text{abs}} = 11.5$ at 725 nm) irradiated by 0.01 J/cm^2/10 ns pulses at repetition rate of 50 MHz (*dashed*), 66.6 MHz (*solid*), and 80 MHz (*dotted*)

cussed bacterial killing and find that, at 3–5 J/cm^2, only 1–3 pulses are required for bacterial damage, while at 0.5–1 J/cm^2 more than 100 pulses are required. We feel the reason for these effects are that at 3–5 J/cm^2 the particles undergo phenomena beyond simple heating and ablation of the surrounding cell due to the extremely high temperature of the nanoparticle, and thus have a large area of effect. In the case of 0.5–1 J/cm^2 pulses, the nanoparticles can still surpass the melting threshold, but without extreme particle phenomena (such as explosion) being observed. In either case, each pulse is incident on ambient-temperature particles, raising their temperature to the critical temperature for cell death. Additionally, the energy densities involved are well above the medical standard of 100 mJ/cm^2, so such results are helpful to show the high-energy phenomena and potential treatment options. However, the methods of implementing treatment require refinement before direct medical applications can be developed. Our current investigation to determine the potential of accumulative heating effects in metal nanoparticles is an attempt at localizing damage to cancer cells by using low-energy density lasers while still killing the cancer cells.

After determining that most other experimental characteristics (such as pulse duration, particle size, etc.) have no ability to create an accumulative heating phenomenon of interest in metal nanoparticles, the pulse generation frequency used in multipulse scenarios was tested with a high-pulse generation frequency experiment by *Hleb* and *Lapotko* [30.30]. This experiment uses two pulses of 10 ns duration that are separated by 20 and 150 ns time intervals (50 and 6.67 MHz, respectively). Figure 30.7 shows three different multipulse calculations based on the experimental setup used in [30.30] for gold nanorods ($r_{\text{eff}} = 11.8$ nm,

Table 30.6 Computational input data for OTM calculations

Source	Cancer	Organelle	Organelle state	Diameter (μm)	Absorption efficiency (at λ = 700 nm)[1]
[30.33]	Hepatocellular carcinoma	Nucleus	Healthy	7.5	0.944183362
			Well differentiated	8.5	0.964865712
			Moderately differentiated	8.8	0.969903343
			Poorly differentiated	10.3	0.989209877
[30.33]	Hepatocellular carcinoma	Mitochondria	Healthy	1.1	0.134234082
			Well differentiated	0.9	0.110949860
			Moderately differentiated	0.9	0.110949860
			Poorly differentiated	0.66	0.082130836
[30.35]	Ductal breast carcinoma	Nucleus	Benign	7.0	0.930908259
			In situ	11.6	1.000194442
			Invasive	8.33	0.961677234
[30.36]	Intraductal breast cancer	Nucleus	Benign	8.58	0.966255375
			Invasive	8.97	0.972557278
[30.37]	Breast cancer	Nucleus	Benign	5.6	0.880181004
			Invasive	5.8	0.889019082

[1] 700 nm was chosen because it is the wavelength with the greatest absorption efficiency difference between cancerous and healthy organelles at a wavelength in the range of 400–1000 nm

Table 30.7 Organelle and cytoplasm properties

Organelle	Diameter d (μm)	Specific heat c (J/(kg K))	Thermal conductivity μ (W/(m K))	Density ρ (kg/m^3)
Nucleus	5 [30.38], 5–10 [30.39], 7.5–10 [30.40], 5–10 [30.42]	3000 [30.41]	0.3 [30.41]	1050 [30.41], 1400 [30.42]
Mitochondria	0.85–1.15 [30.38], 1–3.57 [30.39], 0.87–3.57 [30.40], 1–2 [30.42]	3000 [30.41]	0.3 [30.41]	1050 [30.41], 1100 [30.42]
Ribosome	0.025 [30.4], 0.025 [30.40], 0.02 [30.42]	3000 [30.41]	0.3 [30.41]	1050 [30.41], 1600 [30.42]
Microtubules	0.025 [30.38], 0.028 [30.39], 0.02 [30.40], 1–2 [30.42]	3000 [30.41]	0.3 [30.41]	1050 [30.41], 1100 [30.42]
Cytoplasm	–	4180 [30.41]	0.59 [30.41]	

AR = 3.2, $K_{abs} = 11.5$ at 725 nm) in water irradiated by 0.01 J/cm^2 using 10 ns pulses with generation frequency of 50, 66.6, and 80 MHz. We exclude the case with pulse separation of 150 ns due to the previously shown rapid cooling of metal nanoparticles (32.8 ns for a 10 ns pulse in [30.30]) as well as the experimental result by *Hleb* and *Lapotko* [30.30] that there are no additional effects from two pulses separated by 150 ns over a single pulse. Even at the high pulse generation frequencies shown, the 10 ns pulse does not create an accumulative heating effect in the metal nanoparticles. Furthermore, changing the pulse duration concurrently with high-frequency pulse generation simulations only changes the magnitude of the maximum particle temperature but does not enable the accumulative heating effect in the metal nanoparticles of interest to our investigation.

Multipulse Heating of Healthy and Cancerous Cell Organelles

Using the multipulse form described above, we also tested the heating and cooling kinetics of biological cell organelles to determine the ability to selectively destroy cancer cells. Acquiring data for organelles (nucleus, mitochondrion, and ribosome) is difficult due to the wide variety of situations under which they must act; the added complexity of the large number of cancers makes finding very specific data difficult. Using a variety of

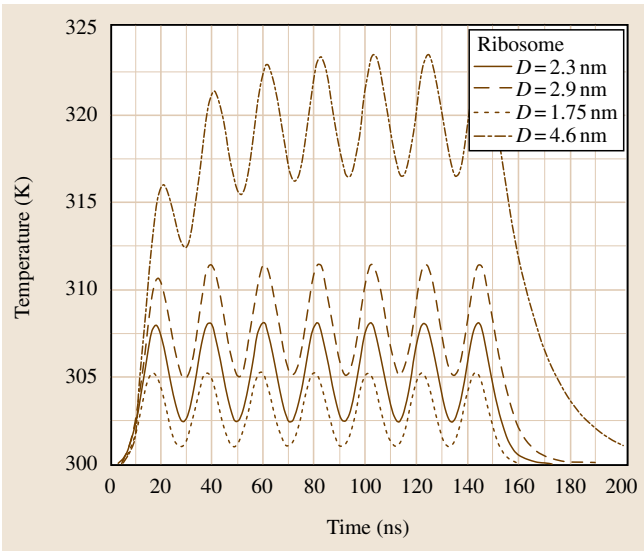


Fig. 30.8 Ribosomal time–temperature profiles at various diameter values. Multipulse laser parameters: 12 ns duration, 0.1 J/cm^2 at $\lambda = 700$ nm; $b_1 = 2.5$, $b_2 = 6$, $b_3 = 9.5$, $b_4 = 13$, $b_5 = 16.5$, $b_6 = 20$, and $b_7 = 23.5$

cited dimensions and organelle properties (Tables 30.5–30.7), we have calculated the *average* organelle size to determine the theoretical effects of the multipulse mode of laser irradiation on the organelle temperature with the same procedure as detailed above.

The cell organelles demonstrate the heat accumulation effect due to the multipulse mode of heating as shown in Figs. 30.8 and 30.9. The ribosomal heating in Fig. 30.8 contrasts with heating for the nuclei and mitochondria in Fig. 30.9; the ribosomes do not experience accumulative heating to the extent that nuclei or mitochondria do, based primarily on the much smaller size. Even with the small size, within the first few pulses the accumulative heating effect is apparent, which contrasts with any nanoparticle simulations previously discussed. The much higher values of specific heat in the organelles and the thermal conductivity of the medium is what causes the organelles to undergo accumulative heating, whereas metal nanoparticles do not experience accumulative heating, even at high-frequency pulse generation rates. This gives an advantage for organelles in using the multipulse versus single-pulse mode, since

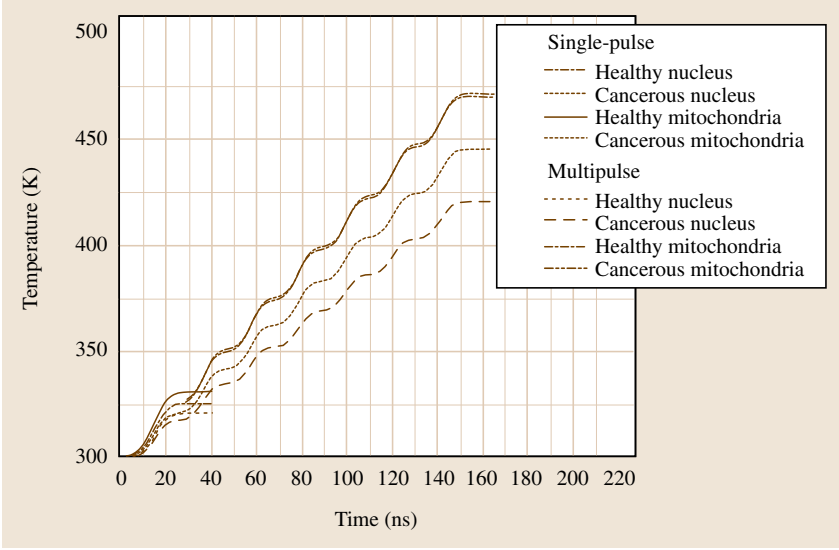


Fig. 30.9 Both single- and multipulse laser heating for *average* organelles. Average values: healthy nucleus (7.17 μm), cancerous nucleus (8.97 μm), healthy mitochondria (1.1 μm), and cancerous mitochondria (0.82 μm). Single-pulse laser parameters include a 0.1 J/cm^2 pulse at 700 nm wavelength

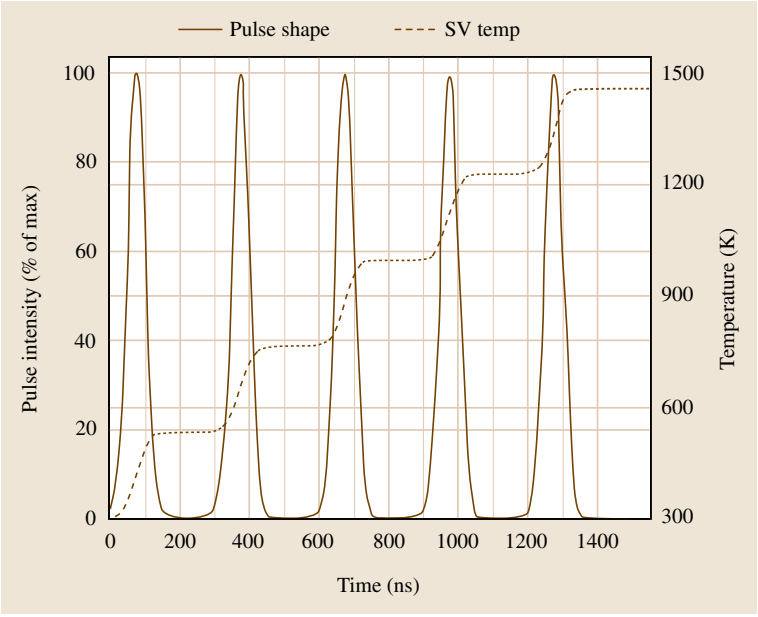


Fig. 30.10 Multipulse mode of heating of bone tissue. A representative multipulse function is drawn with a *solid line*, and the heating kinetics with a *dashed line*, showing five 30 mJ pulses of 60 ns pulse width repeating every 300 ns

the laser energy density per pulse can be reduced dramatically below the safety standard for medical usage of lasers. In this case, any desired final temperature of the organelle can be reached easily by adjusting the number of pulses at low-energy density per pulse.

While the organelles demonstrate a similarity in the heat accumulation effect, both the mitochondria and nuclei respond differently to the pulsed mode of heating. As shown in Fig. 30.9, healthy and cancerous mitochondria do not respond differently in a significant way to laser heating, while the healthy nucleus is heated 40 K higher than the cancerous nucleus. The difference in heating characteristics is due to several behavioral properties: the size of the nucleus is much larger than mitochondrion, mitochondrion has been shown to shrink when in cancerous cells, and the nucleus of cancerous cells is known to grow relative to their healthy cell size. The dynamics of size on temperature results in the mitochondria being heated to a higher temperature, but with very little specificity. Alternatively, nuclei are heated to a lower temperature at a higher specificity level, though the healthy nuclei are the first to get damaged. The potential method of selectively heating cancerous organelles to kill cancer cells is shown to be ineffective with our calculations due to the higher heating temperatures of mitochondria and the lower heating of cancerous nuclei. With that in mind, the effects of accumulative heating are very apparent.

The results of the simulation using cell organelles demonstrate the slow rate of the cooling kinetics of the biological particles. This allows for accumulation of heat by a multipulse heating mode for hard tissue, such as bone and teeth as well, as shown in [30.22, 23]. Here, the bone hydroxyapatite particles were heated by single- and multipulse laser pulses of 2.12 μm wavelength. Figure 30.10 shows the results for bone tissue temperature increase by five 0.03 J pulses. To reach the same maximum temperature in the bone tissue ($T_{max} = 1460$ K) using a single pulse requires a much higher energy per pulse of about 0.15 J. Thus, the multipulse mode could be utilized to attain the higher temperatures required for tissue ablation using many pulses with low individual energies. This gives a large amount of control over the individual pulse energies, which is especially important in medical and dental laser applications where regulations may limit the maximum pulse energies for different procedures.

Summary of the Heating Kinetics

We have performed time-dependent simulations and detailed analyses of different nonstationary laser–nanoparticle interaction modes to determine the accumulative heating potential of metal nanoparticles irradiated by multipulse lasers. Our analysis of the single-pulse mode of heating of metal nanoparticles in a biological cell environment has shown that alterations to the particle size, shape, and material (metal) all have

effects on the magnitude of the maximum particle temperature. Additionally, modifications to the laser energy density or wavelength can be used to change the maximum particle temperature. The most substantial change within single-pulse heating is the effect of pulse duration on the time dynamics of particle heating and cooling. By increasing the pulse duration, the maximum nanoparticle temperature decreases, but heating and cooling both take longer and allow for a longer time period when the nanoparticles are above the denaturing temperature of 433 K. This increased duration of high particle temperature could prove beneficial to ensure cellular damage. Alternatively, decreasing the pulse duration increases the maximum temperature reached by the nanoparticles while decreasing the time for heating and cooling. Such laser parameter modifications could allow for easier and more refined treatment than modification of particle size or shape, while still having dramatic implications for the effectiveness of the treatment.

Our simulations have shown that, at the instant when the laser pulse stops, the cooling rate reaches almost the same values as a heating rate due to the large surface area of the nanoparticle and high thermal conductivity of the surrounding aqueous medium. This becomes crucial for the multipulse mode of heating the metal nanoparticles. From our analysis of multipulse metal nanoparticle heating, we have determined that the multipulse mode of heating does not create accumulative heating effects in metal nanospheres or nanorods (diameters of 5–40 nm) due to the rapid cooling kinetics of metal nanoparticles in an aqueous environment.

However, changing the target material to biological particles, such as cell organelles or hard tissue particles with much higher values of specific heat, causes the biological particles to undergo accumulative heating, whereas metal nanoparticles do not experience accumulative heating, even at high frequency generation rates. The accumulative heating effect provides an advantage for organelles and biological tissue in using the multipulse versus single-pulse mode, since the laser energy density per pulse can be reduced dramatically below the safety standard for medical usage of lasers. In this case, any desired final temperature of the biotissue can be reached easily by adjusting the number of pulses at low energy density per pulse.

30.5 Spatial Distribution of Temperature Fields Around the Nanoparticle

30.5.1 Theoretical Model

For simulations of the spatial distribution of temperature in and outside the nanoparticle, we solve the heat–mass transfer equation (30.4) in a quasistationary heating approximation, namely $\mathrm{d}T_\mathrm{s}(r,t)/\mathrm{d}t = 0$. In this approximation, we neglect the time required to reach the maximum temperature (extremum of the $T_\mathrm{s}(t)$ curve) of the nanoparticle and solve the heat diffusion equation for the spatial distribution for that particular temperature. We use here the heat transfer model developed by *Goldenberg* and *Tranter* [30.43] for a uniformly heated, homogeneous sphere embedded in an infinite homogeneous medium. Consider a homogeneous sphere of radius r_0 surrounded by an infinite homogeneous medium, with heat produced in the sphere for time $t > 0$ at the constant rate A per unit time per unit volume. Since the surrounding medium is transparent to the chosen wavelength, we can neglect thermally induced changes in the cellular refractive index during the action of a nanosecond laser pulse. Both the sphere and medium are initially at zero temperature. Let the subscript "1" refer to the sphere and "2" to the medium, and T, μ, and χ denote the temperature, thermal conductivity, and diffusivity, respectively. Then, the heat transfer equations with boundary conditions are

$$\left.\begin{aligned} \frac{1}{\chi_1}\frac{\partial T_1}{\partial t} &= \frac{1}{r^2}\frac{\partial}{\partial r}\left(r^2\frac{\partial T_1}{\partial r}\right) + \frac{A}{\mu_1}\,, \\ &\quad 0 \le r < r_0\,, \\ \frac{1}{\chi_2}\frac{\partial T_2}{\partial t} &= \frac{1}{r^2}\frac{\partial}{\partial r}\left(r^2\frac{\partial T_2}{\partial r}\right)\,, \\ &\quad r > r_0\,, \end{aligned}\right\} \quad t > 0\,, \tag{30.8}$$

$$T_1 = T_2 = 0\,, \quad \text{when } t = 0\,, \tag{30.9}$$

$$\left.\begin{aligned} T_1 &= T_2 \\ \mu_1\frac{\partial T_1}{\partial r} &= \mu_2\frac{\partial T_2}{\partial r} \end{aligned}\right\} \quad \text{for } r = r_0\,, \tag{30.10}$$

$$T_1 \text{ finite as } r \to 0 \text{ and } T_2 \text{ finite as } r \to \infty\,. \tag{30.11}$$

Using the Laplace transformation for T, defined by

$$\overline{T} = \int_0^\infty \mathrm{e}^{-pt}T(t)\,\mathrm{d}t = L[T(t)]\,,$$

Eqs. (30.8–30.11) can be reduced to the stationary heat transfer equations

$$\left.\begin{aligned} \tfrac{\partial^2}{\partial r^2}\left(r\overline{T_1}\right) - rq_1^2\overline{T_1} &= -\tfrac{rA}{\mu_1 p}\,, 0 \le r < r_0\,, \\ \tfrac{\partial^2}{\partial r^2}\left(r\overline{T_2}\right) - rq_{21}^2\overline{T_2} &= 0\,, \quad r > r_0\,, \end{aligned}\right\}\,, \tag{30.12}$$

$$\left.\begin{aligned} \overline{T_1} &= \overline{T_2} \\ \mu_1\tfrac{\partial\overline{T_1}}{\partial r} &= \mu_2\tfrac{\partial\overline{T_2}}{\partial r} \end{aligned}\right\} \text{ for } r = r_0\,, \tag{30.13}$$

$$\overline{T_1} \text{ finite as } r \to 0 \text{ and } \overline{T_2} \text{ finite as } r \to \infty\,, \tag{30.14}$$

where $q_1^2 = p/\chi_1$ and $q_2^2 = p/\chi_2$.

The solution of (30.5–30.7) for the temperature distribution inside the heated sphere is [30.43]

$$\overline{T_1} = \frac{r_0^2 A}{\mu_1}\left\{\tfrac{1}{3}\tfrac{\mu_1}{\mu_2} + \tfrac{1}{6}\left(1 - \tfrac{r^2}{r_0^2}\right) - \tfrac{2r_0 b}{\pi r}\int_0^\infty \times \frac{\exp(-y^2 t/\gamma_1)}{y^2}\,\frac{(\sin y - y\cos y)\sin(ry/r_0)}{(c\sin y - y\cos y)^2 + b^2 y^2 \sin^2 y}\,\mathrm{d}y\right\}\,, \tag{30.15}$$

where

$$b = \frac{\mu_2}{\mu_1}\sqrt{\frac{\chi_1}{\chi_2}}\,, \quad c = 1 - \frac{\mu_2}{\mu_1} \quad \text{and} \quad \gamma_1 = \frac{r_0^2}{\chi_1}\,. \tag{30.16}$$

The temperature at the center of the sphere is

$$(\overline{T_1})_{r=0} = \frac{r_0^2 A}{\mu_1}\left\{\tfrac{1}{3}\tfrac{\mu_1}{\mu_2} + \tfrac{1}{6} - \tfrac{2b}{\pi}\int_0^\infty \frac{\exp(-y^2 t/\gamma_1)}{y} \times \frac{(\sin y - y\cos y)\sin(ry/r_0)}{(c\sin y - y\cos y)^2 + b^2 y^2 \sin^2 y}\,\mathrm{d}y\right\}\,, \tag{30.17}$$

and the temperature outside the sphere is

$$\overline{T_2} = \frac{r_0^3 A}{r\mu_1}\times \left\{\tfrac{1}{3}\tfrac{\mu_1}{\mu_2} - \tfrac{2}{\pi}\int_0^\infty \frac{\exp(-y^2 t/\gamma_1)}{y^3}\times \frac{(\sin y - y\cos y)[by\sin y\cos\sigma y - (c\sin y - y\cos y)\sin\sigma y]}{(c\sin y - y\cos y)^2 + b^2 y^2\sin^2 y}\,\mathrm{d}y\right\}\,, \tag{30.18}$$

with b, c, and γ_1 as in (30.16) and

$$\sigma = \left(\frac{r}{r_0} - 1\right)\sqrt{\frac{\chi_1}{\chi_2}}\,. \tag{30.19}$$

The heat source is characterized here by a constant rate A per unit time per unit volume as

$$A = \frac{E_{\mathrm{abs}}}{\tau_{\mathrm{rel}} V} = \frac{K_{\mathrm{abs}}\varepsilon_{\mathrm{L}} S}{\tau_{\mathrm{rel}} V}\,, \tag{30.20}$$

where E_{abs} is the energy absorbed by the nanoparticle, ε_{L} is the laser pulse energy density, K_{abs} is the absorption efficiency of the nanoparticle at the given wavelength of laser radiation, S and V are the area and volume of the absorbing center, and τ_{rel} is the thermal relaxation time in the biological medium. By using spherical symmetry for the absorbing center of radius r_0, we can reduce (30.20) to

$$A = \frac{3K_{\mathrm{abs}}\varepsilon_{\mathrm{L}}}{\tau_{\mathrm{rel}} r_0}\,. \tag{30.21}$$

The model described above can be used for simulating the spatial distribution of the temperature for a single or many heat sources in a cell volume.

30.5.2 Laser Heating of a Single Nanoparticle in Biomedia

Let us first calculate the laser heating of single gold nanoparticles with radii $r_0 = 30$–$35\,\mathrm{nm}$ in water and surrounding blood biomedia when the incident laser pulse has an energy density of $E = 5\,\mathrm{J/cm^2}$ and pulse duration of $\tau_{\mathrm{L}} = 8\,\mathrm{ns}$. The laser flux is chosen at the level of $5\,\mathrm{J/cm^2}$ to provide cell lethality during a single laser pulse shot, being comparable to the laser fluence currently used in clinical treatments of pigmented skin lesions. The results of these simulations are presented in Figs. 30.11 and 30.12. Figure 30.11 illustrates the spatial behavior of the temperature inside 30 and 35 nm gold particles heated and cooled in the surrounding water and blood media. Figure 30.12 shows the spatial distribution of the temperature outside these nanoparticles.

The events that take place after absorption of the laser pulse energy by small particles depend on the size of the locally heated region and duration of laser exposure. Long pulses that exceed the thermal relaxation time in biological tissue, $\tau_{\mathrm{r}} = l^2/4\chi_{\mathrm{t}}$ (where χ_{t} is the thermal diffusivity of the biological tissue, and l is the minimum size of the locally heated region), cause heating of both the particle and the surrounding media. If the size of the locally heated region l is chosen to be equal to the size of the laser focal spot, which is about $1\,\mu\mathrm{m}$, the thermal relaxation time for water is $1.75\,\mu\mathrm{s}$ and for blood is $1.56\,\mu\mathrm{s}$, which is much longer than the laser pulse duration ($\approx 10\,\mathrm{ns}$) used in our research. For ultrashort laser pulses when $\tau_{\mathrm{L}} \ll \tau_{\mathrm{r}}$, the absorbed energy can be thermally confined within the target, causing rapid heating of the absorber itself. The extreme temperature rise in the absorber can induce ex-

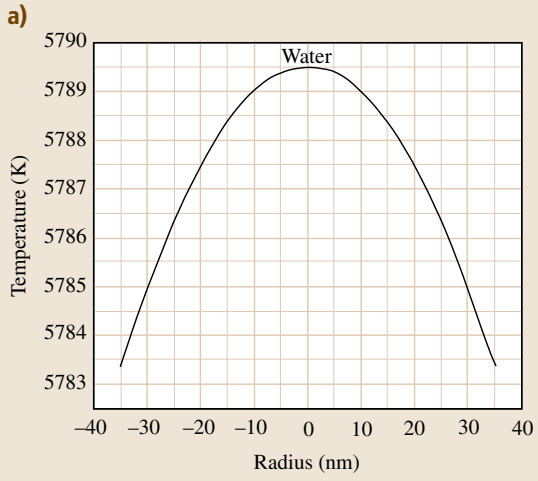


Fig. 30.11a,b One-dimensional distribution of the temperature inside a gold nanoparticle in surrounding water and blood media irradiated by a single laser pulse of energy density 5 J/cm^2 and duration 8 ns

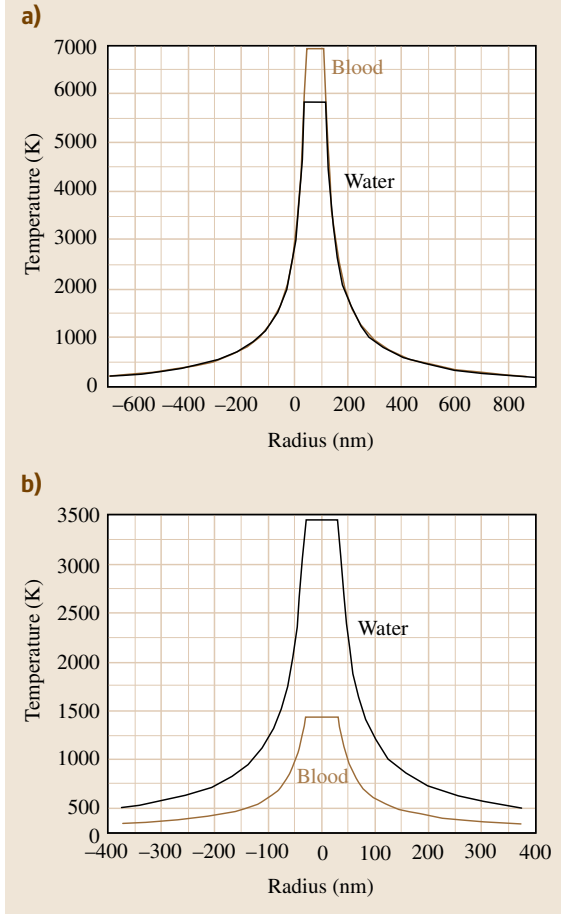


Fig. 30.12a,b Spatial distribution of the temperature outside the 30 nm gold particle **(a)** in surrounding water and blood media irradiated by a single laser pulse of energy density 5 J/cm^2 and duration 8 ns and **(b)** in a blood medium irradiated by a single laser pulse of energy density 2.5 J/cm^2 (*upper curve*) and 1 J/cm^2 (*lower curve*)

plosive vaporization of the nanoparticle, as described in the final section of this chapter.

Internal Temperature Distribution in a Single Nanoparticle

The integration of (30.15–30.17) gives the temperature distribution inside the heated nanoparticle surrounded by the biomedia. Our numerical simulations of the internal 30 nm gold particle's temperature distribution heated by a 5 J/cm^2 laser pulse of 8 ns width in the surrounding water and blood media show that the particle reaches its maximum temperature $T_{max} \approx 5789.5$ K in water and $T_{max} = 6870$ K in blood at the center of the sphere. Then we observe a small decrease of the inside temperature by 6 K to the particle's boundaries, establishing the stationary surface temperature of 5783.3 K in water and 6863.6 K in blood (Fig. 30.11). Since the temperature variation inside the nanoparticle occurs over a small range of 6 K, the internal particle's temperature can be assumed to be constant (Fig. 30.11b). Thus, the quasistationary and homogeneous approach can be applied to modeling the laser heating and evaporation of the nanoparticles in the biological media.

Table 30.8 Material properties of bone

Symbol	Property	Value	Reference
μ	Thermal conductivity	5.60×10^{-1} W/(m K)	[30.44]
ρ	Density	$1.85\times10^{+3}$ kg/m^3	[30.45]
c	Specific heat	$1.33\times10^{+3}$ J/(kg K)	[30.46]
χ	Thermal diffusivity	2.276×10^{-7} m^2/s	

Table 30.9 Material properties of gold

Symbol	Property	Value
μ	Thermal conductivity	$3.18\times10^{+2}$ W/(m K)
ρ	Density	$1.93\times10^{+4}$ kg/m^3
c	Specific heat	$1.29\times10^{+2}$ J/(kg K)
χ	Thermal diffusivity	1.276×10^{-4} m^2/s

Table 30.10 Material properties of silver

Symbol	Property	Value
μ	Thermal conductivity	$4.29\times10^{+2}$ W/(m K)
ρ	Density	$1.05\times10^{+4}$ kg/m^3
c	Specific heat	$2.35\times10^{+2}$ J/(kg K)
χ	Thermal diffusivity	1.74×10^{-4} m^2/s

Outside Temperature Distribution Around a Single Nanoparticle

As follows from Fig. 30.12, there is a significant heat loss from the surface of a nanoparticle to the surrounding medium, suggesting that even lower-energy pulses are enough to achieve true and large thermal damage of the biological surroundings. If the temperature of the surrounding medium exceeds some thermal thresholds, secondary phenomena of cell killing effects may develop, such as photothermal ablation, sound generation, bubble formation, and so on. For most cancer cell killing effects, the threshold temperature is about 150 °C (423 K). Calculations show that, at this level of the threshold temperature, the damage area produced by a heated 30 nm gold particle in blood has a size of ≈ 1 μm in diameter, which exceeds by 16 times the size of the nanoparticle (Fig. 30.12a). Thus, under chosen conditions, the damage area produced by one 30 nm particle heated by a single laser pulse of 5 J/cm^2 is comparable to the size of the laser focal spot.

To find the lowest energy level of the laser pulse required to achieve thermal thresholds for cell death, we have conducted calculations of the temperature spatial distribution of gold nanoparticles irradiated by different laser fluxes. The results of these simulations are illustrated in Fig. 30.12b. As follows from these calculations, a single 8 ns laser pulse of energy density 2.5 J/cm^2 provides heating of the 30 nm gold particle in the surrounding blood up to the boiling point of gold, ≈ 3400 K. The melting point of gold ≈ 1400 K is reached for a lower energy pulse density of 1 J/cm^2 for 8 ns laser pulse duration. Decreasing the energy density of the incident single laser pulse leads to a smaller damage volume around the nanoparticle. Using the threshold temperature of 423 K for cell death, we can determine the size of cell damage produced by the heated 30 nm gold particle. For the 8 ns single laser pulse with energy density of 2.5 J/cm^2, the damage volume around the nanoparticle has 0.5 μm diameter, which is smaller than but still comparable to the focal spot of the incident laser pulse. In the case of a 1 J/cm^2 single laser pulse, the damage area is 180 nm in diameter, which is only thrice the diameter of the nanoparticle. Thus, for experimental realization of selective nanophotothermolysis of cancer cells by a single 30 nm gold particle, we recommend use of a laser pulse with energy density 2.5 J/cm^2 for 8 ns width.

30.5.3 Bone Tissue Ablation by Plasmonic Nanoparticles

Both thermal and optical properties affect the behavior of the thermal field. The thermal properties of the material govern how easily a material can dissipate heat to the surrounding medium, while the optical properties govern how much heat is generated when exposed to an energy source. In these simulations we wish to examine the photothermal effect of a strongly absorbing nanoparticle in hard tissue for applications to medical procedures. For this reason, the material properties of bone and various nanoparticles are listed in Tables 30.8–30.10.

The optical properties of nanoparticles can be much more varied, however, as the absorption efficiency of the particles is affected by the material, size, and geometry of the nanoparticle. To achieve sufficient heating with pulses of lower energy densities, it is important to find absorption efficiency peaks. These peaks occur due to the plasmon resonance of the nanoparticle at that particular wavelength. To determine the ab-

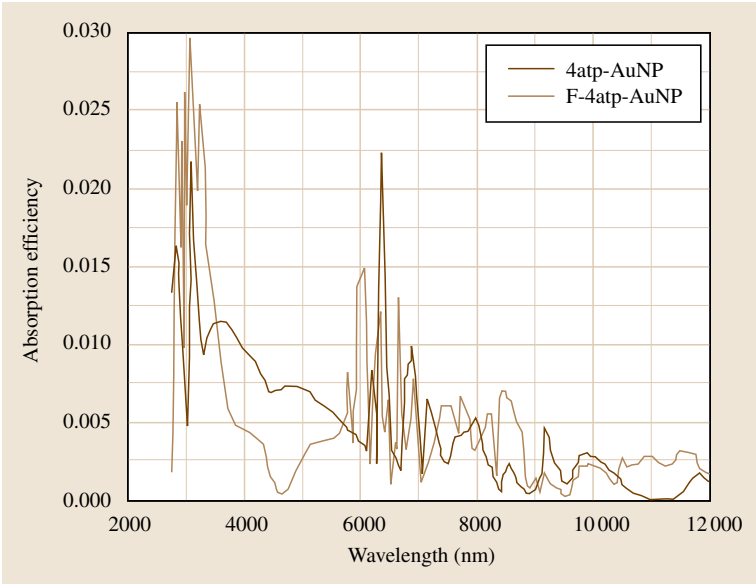


Fig. 30.13 Absorption efficiency for 5 nm aminothiophenol-conjugated gold nanoparticles (4atp-AuNP) and folate-aminothiophenol-conjugated gold nanoparticles (F-4atp-AuNP). The values are calculated with Mie theory using complex index of refraction data for gold from *Shakeri-Zadeh* et al. [30.47]

sorption characteristics of spherical particles in various biomedia, generalized Lorenz–Mie diffraction theory is used (Sect. 30.2), which takes into account the plasmon-resonance absorption effect. Using the complex indices of refraction for the medium and particle (which depend on the wavelength as well as particle size), the theory allows us to determine the absorption efficiency of spherical particles at any wavelength within the bounds of the refractive index values provided. The results of these calculations for the absorption efficiency of AuNP, AgNP, and CuNP are shown in Figs. 30.13 and 30.14 and are listed in Tables 30.1 and 30.2.

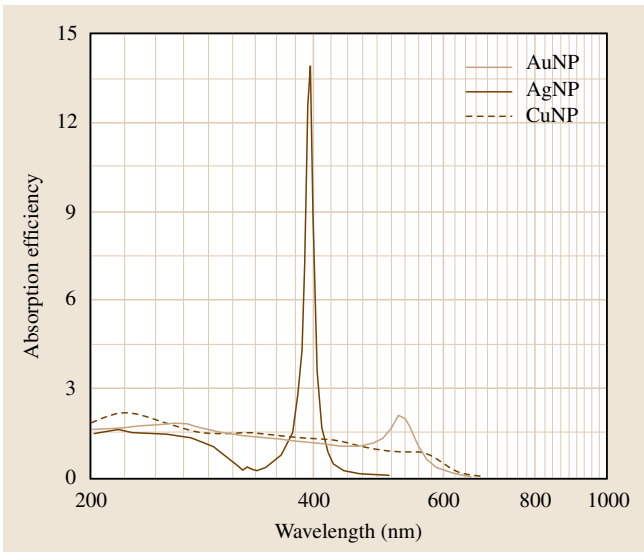


Fig. 30.14 Absorption efficiency for 30 nm-diameter gold, silver, and copper nanoparticles (AuNP, AgNP, CuNP) surrounded by water medium. These values are calculated with Mie theory using complex index of refraction data from *Johnson* and *Christy* [30.48]

Reduction in the size of the spherical nanoparticles lowers the absorption efficiency, as seen when comparing 30 to 5 nm AuNP, where K_{abs} loses an entire order of magnitude. Moving into the IR and

Table 30.11 Parameters for AuNP heating simulation achieving the critical heat of vaporization for bone at the nanoparticle edge

Symbol	Property	Value
d	Nanoparticle diameter	30 nm
E	Pulse energy density	0.788 J/cm^2
λ	Wavelength	520 nm
K_{abs}	Absorption efficiency	2.1

Table 30.12 Parameters for AgNP heating simulation achieving the critical heat of vaporization for bone at the nanoparticle edge

Symbol	Property	Value
d	Nanoparticle diameter	30 nm
E	Pulse energy density	0.119 J/cm^2
λ	Wavelength	394 nm
K_{abs}	Absorption efficiency	13.9

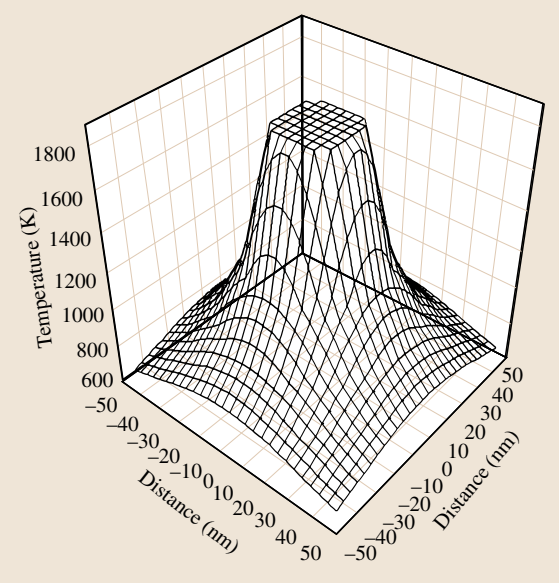


Fig. 30.15 The spatial distribution of the temperature for a 30 nm-diameter Au nanoparticle heated up to the critical temperature of bone vaporization. The simulation parameters are listed in Table 30.11

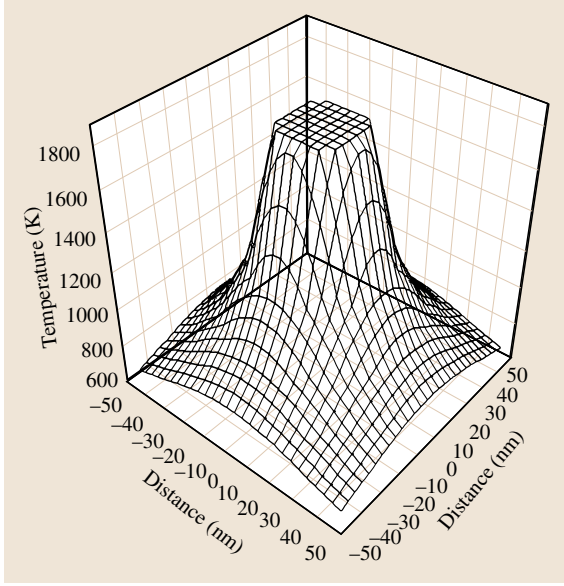


Fig. 30.16 The spatial distribution of the temperature for a 30 nm-diameter Ag nanoparticle heated up to the critical temperature of bone vaporization. The simulation parameters are listed in Table 30.12

longer wavelengths, the absorption efficiency decreases continuously and without any noticeable peaks upon which to capitalize. This means that larger energy densities would be required to heat the nanospheres to the critical temperature. Thus, utilization of silica–gold nanoshells and/or gold nanorods, which absorb IR wavelengths much better than solid nanospheres, is recommended for selective nanothermolysis of bone tissue when working in the longer-wavelength range of the spectrum.

The choices of nanoparticle material, size, and shape used in the model are listed in Tables 30.11 and 30.12 along with the choice of wavelength and corresponding absorption efficiency for that wavelength. The energy densities were chosen to bring the nanoparticle to the melting temperature of hydroxyapatite (1843 K) [30.48] as it is the main constituent of bone tissues. This was considered an appropriate choice for the ablation temperature, as *Fried* et al. showed thermal ablation and expulsion of molten drops in the temperature range of 1473–2273 K [30.49].

The temperature distribution is mainly dependent upon two factors: the thermal conductivities, which affect the slopes of the curves, and the absorption efficiency, which affects the maximum temperature difference reached. In the case of noble-metal nanopar-

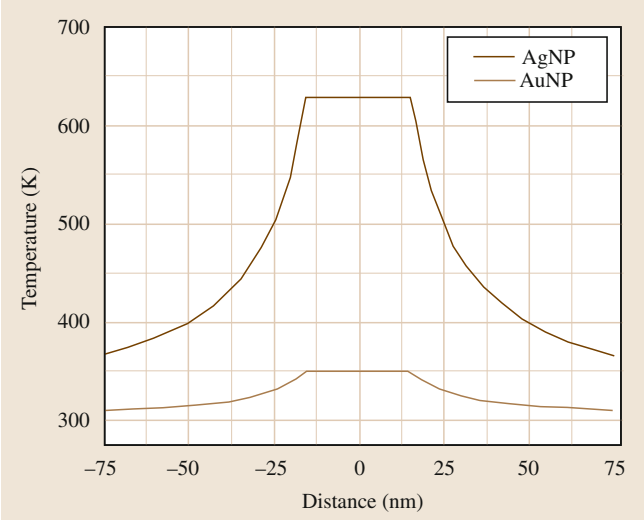


Fig. 30.17 Heat profiles for a 30 nm-diameter AgNP (*solid curve*) heated by a $\lambda = 394$ nm pulse, and a 30 nm-diameter AuNP (*dotted curve*) heated by $\lambda = 520$ nm. Both pulses have equivalent energy densities, and both spheres are within an infinite medium with steady-state temperature 300 K ▶

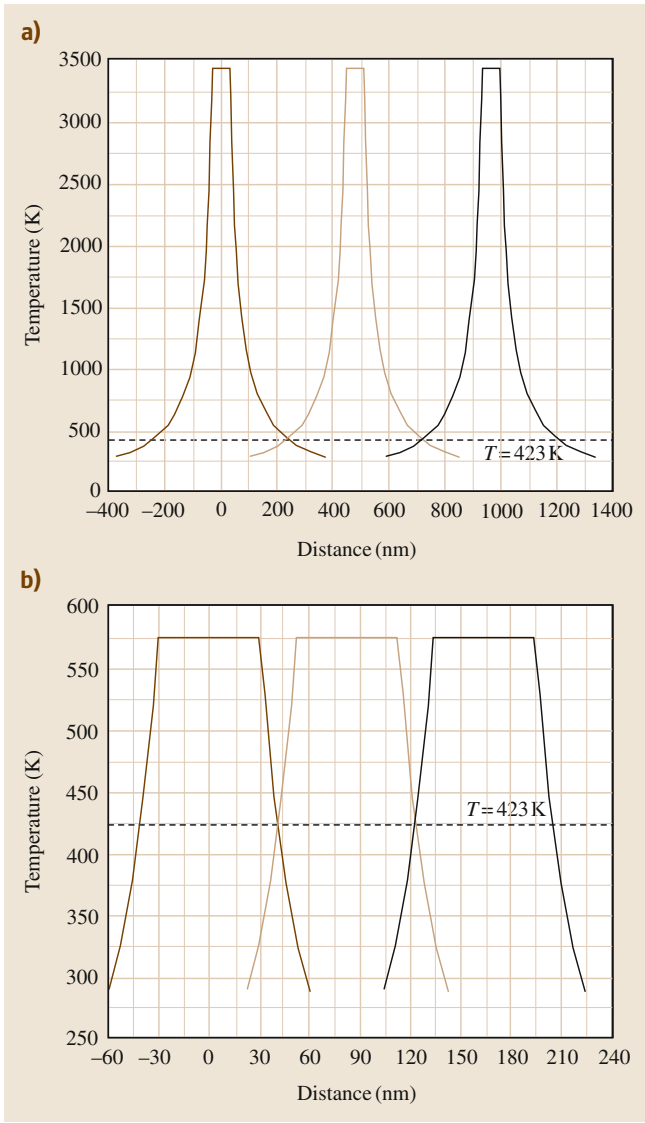


Fig. 30.18a,b Spatial distribution of the temperature fields produced in the blood medium **(a)** by many heat sources irradiated by a single laser pulse with energy density of 2.5 J/cm^2 and pulse duration 8 ns, and **(b)** inside a cluster consisting of 30 nm gold particles irradiated by a 8 ns single laser pulse of energy density 0.42 J/cm^2

ticles, the thermal conductivities of the metals are more than two orders of magnitude greater than that of bone. This leads to an essentially homogeneous temperature distribution within the nanoparticle, with an exponential cooling outside the particle as shown in Figs. 30.15–30.17.

In Fig. 30.17, it is clear that temperature is essentially the same within the nanoparticle radius, with significant cooling outside the radius. Closer inspection shows that the temperature distribution on the plateau varies slightly from the hottest point at the center, to the coolest temperature at the nanoparticle edge. For AgNP this is a variance from 628.1 to 627.8 K, and for AuNP it varies from 349.6 to 349.5 K. Both show less than 0.1% variance from the maximum temperature, and thus the plateau regions can be considered homogeneously heated.

Outside the nanoparticle, the temperatures drop relatively rapidly. In Figs. 30.15 and 30.16 for example, hard-tissue temperatures at the edge of the nanoparticle are at the hydroxyapatite melting temperature (1843 K) and maintain a temperature above 1473 K at a distance 1.05 times the radius of the nanoparticle (i. e., a 31.5 nm-diameter area is heated to this level by the 30 nm nanoparticle). This temperature is the lower bound (1473–2273 K) shown by Fried et al. to produce hydroxyapatite ablation and expulsion of molten drops. The temperature for delayed thermal necrosis of osteocytes (320 K) is maintained for all the tissue up to 75 times the radius, making the cell damage area on the same order of magnitude as the focal spot size.

Thus, we have discussed the method of selective nanophotothermolysis for application to bone tissue cancers. Our simulations for three-dimensional (3-D) thermal fields of plasmonic nanoparticles surrounded by bone medium have shown that alterations to the particle size, particle shape, and material all have effects on the magnitude of the maximum temperature reached in the particle; For example, in the UV and visible ranges of the spectrum, silver and gold solid spherical nanoparticles exhibit a strong plasmonic effect in laser heating of nanoparticles. For longer wavelengths in the transparency window of most biotissues, we recommend utilization of silica–gold nanoshells and/or gold nanorods for selective nanothermolysis of the bone tissue. Additionally, heat loss from the surface of a nanoparticle to the surrounding medium is observed, creating a large thermal damage area in the bone tissue up to 75 times the nanoparticle radius.

30.5.4 Temperature Simulations for Many Heat Sources

The model of (30.15–30.21) can be used for simulations of the spatial distribution of the temperature produced by many heat sources. Figure 30.18a illustrates the temperature fields around closely located nanoparticles in

the surrounding blood medium irradiated by a single laser pulse with energy density of 2.5 J/cm^2 and pulse duration of 8 ns. As follows from these calculations, to provide the threshold temperature 423 K between the particles everywhere in the cell volume (i. e., thermal damage in the cell), the interparticle distance l (i. e., between the centers of neighboring nanoparticles) should not exceed $l \leq 480$ nm.

This criterion can be reached by varying l and the energy density of the incident laser pulse. To find the optimal distance l, where the minimal temperature between the nanoparticles is equal to 423 K, we have conducted calculations of the interparticle temperature distribution for different values of the laser energy density. Results of these simulations, presented in Fig. 30.19, show that an optimum l does not exist in the framework of the thermal calculations: l linearly increases with the energy density of the incident laser pulse. The interparticle distance l sets the lower limit for the nanoparticle concentration n required for cell death (i. e., the number of particles per unit volume) as

$$n = \left(\frac{1}{l^3}\right) . \tag{30.22}$$

Let us estimate n and the absolute number N of nanoparticles to provide the high-temperature distribution inside the cancer cell volume. For $l = 480$ nm, the concentration of $n = 9.0 \times 10^{12}$ cm^{-3} is homogeneously distributed throughout the cell volume. N can be found as $N = nV_{\text{cell}}$, where V_{cell} is the cell volume. In the case of the 10 μm-diameter cells of the MDA-MB-231 breast cancer line, the number of 30 nm gold particles needed to provide the threshold temperature everywhere

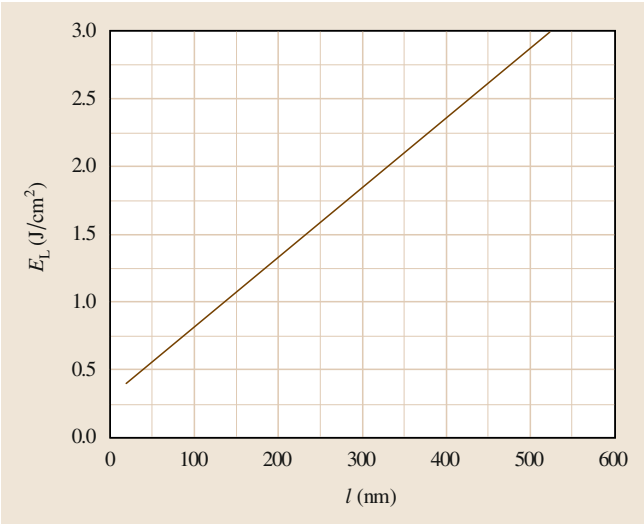


Fig. 30.19 Interparticle distance for different values of the laser energy density

in the cell volume (thermal damage) is $N \approx 4710$. This is a relatively large number of particles per cell, requiring a long incubation time to collect them in the cell or cell membrane. As shown in our experiments [30.12], during this incubation time, the nanoparticles collide with each other, stick together, and form nanoparticle clusters. The temperature distribution inside a cluster is expected to be significantly higher than the threshold temperature 423 K, since the particles in the cluster are compacted much closer to each other. The spatial distribution of the temperature field inside and outside the cluster formed by 30 nm particles conjugated with antibodies is shown in Fig. 30.18.

30.6 New Dynamic Modes in Selective Plasmonic Nanotherapy

30.6.1 Nanocluster Aggregation Mode

Under certain delivery and particle-accumulation conditions, nanoparticles can form clusters in the cancer cell volume or cell membrane surface, as shown in Fig. 30.20. A cluster is a group of closely located nanoparticles (10–30 nm each) separated by the thickness of antibodies with total cluster size of 200–400 nm, which depends on the radii of the nanoparticles and duration of incubation time. This is the time required to collect the appropriate number of nanoparticles in the cell or cell membrane. The presence of nanoclusters may provide further synergistic enhancement of selective nanophotothermolysis due to:

- Increase of the nanocluster's average local absorption
- Red-shifting of absorption to the near-IR range (window of transparency of most biotissues [30.26]) that may be achieved with conventional gold solid nanospheres, which are simpler to prepare, stable, and nontoxic, and cheaper compared with nanoparticles with special design (e.g., rods, shells, etc.)

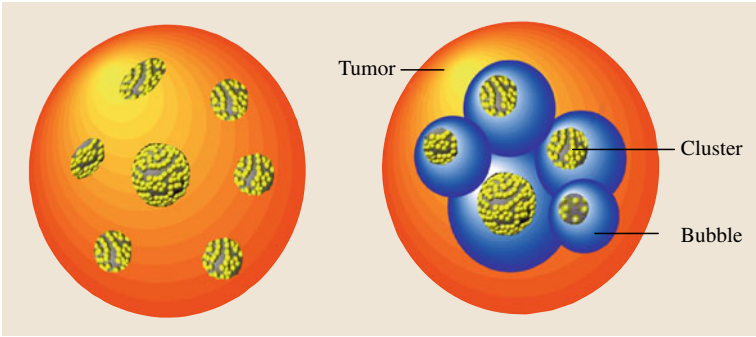


Fig. 30.20 Principle of the nanocluster aggregation mode in selective nanophotothermolysis of cancer

- Better heating efficiency achieved
- Decrease in threshold energy for bubble formation and cell damage.

In this section, we describe theoretically the damage of abnormal cells produced by nanoclusters and then compare this with the single-particle case. Two basic mechanisms of killing of cancer cells in the cluster aggregation mode (CAM) corresponding to a nanosecond laser pulse duration are studied here: thermal damage of abnormal cells by a laser-heated cluster, and bubble generation and their overlapping around the nanoparticles/nanocluster, as shown in Fig. 30.20.

Temperature Distribution Inside the Nanocluster

Our experiments [30.12] show that the distance between the centers of neighboring particles in a cluster is 80 nm, i. e., 20 nm between the surfaces of 30 nm particles. The interparticle distance in the cluster cannot be less than 20 nm, since the particles are covered by antibodies with thickness of about 10 nm. The model described in Sect. 30.4 is used to calculate the temperature distribution inside the cluster consisting of separate gold nanoparticles with radius $r_0 = 30\,\text{nm}$ in the surrounding blood medium irradiated by a single laser pulse of energy density $E = 2.5\,\text{J/cm}^2$ and pulse duration $\tau_\text{L} = 8\,\text{ns}$. As follows from these calculations, the $2.5\,\text{J/cm}^2$ single laser pulse provides an extremely high minimal temperature of 2574 K inside the cluster (minimal temperature between the nanoparticles). The surface temperature of the nanoheaters is 3432 K. So, at the same energy level of the incident laser radiation used for laser heating of the single nanoparticle, the minimal temperature inside the cluster exceeds by six times the threshold temperature for cell killing. Thus, the aggregation of the nanoparticles in clusters gives us a unique possibility to dramatically decrease the incident laser pulse energy with the same efficiency of cell death.

To find the lowest energy level of the incident single laser pulse, we have conducted calculations of the spatial distribution of the temperature inside a cluster consisting of 30 nm gold particles for different laser fluxes. The size of the cluster is chosen to be smaller than that of the laser focal spot. The results of these simulations for the lowest energy providing the threshold temperature of not less than 423 K inside the cluster (between nanoparticles) are illustrated in Fig. 30.18b. As follows from these calculations, an 8 ns single laser pulse with energy density of $0.42\,\text{J/cm}^2$ is enough to heat the 30 nm gold particles inside the cluster up to 577 K and to reach the minimal temperature of 432 K in the cluster volume. There is evidence that specific properties of gold nanoparticles may be the reason for the remarkably low melting temperature (573 K) [30.50]. Thus, clusters aggregated from small nanoparticles can provide thermal damage of cancer cells at the significantly low energy level of $0.42\,\text{J/cm}^2$ of the incident single laser pulse.

Temperature Distribution Outside the Nanocluster

We assume that the cluster is aggregated from 30 nm gold particles with 20 nm interparticle distances, homogeneously compacted in a cylinder of length 380 nm. The cluster is located along the r-axis and surrounded by blood. It is irradiated by a single laser pulse of energy density $1\,\text{J/cm}^2$ and pulse duration of 8 ns at full-width at half-maximum (FWHM). Results of the simulations for the spatial distribution of the temperature field inside and outside the cluster in the surrounding blood medium are displayed in Fig. 30.21a. As follows from these calculations, the temperature inside the cluster oscillates in the range of 1374–1056 K along its length. So, the cluster heated by a single laser pulse of energy

density $1\,J/cm^2$ has a high inside temperature which exceeds by thrice the threshold temperature for cell death. The outside temperature distribution shows us that the cluster provides a large thermal damage area of $\approx 0.5\,\mu m$ within the cell volume at the threshold temperature level of 423 K. To reach the same thermal damage area with a single nanoparticle, a laser pulse with energy density 2.5 times higher than for the cluster case is required.

We note that, since the cluster is treated here as a discrete medium (each particle considered separately), the results obtained above for the cluster temperature and thermal damage area have their lowest values. The upper limit for these values can be found for a homogeneous (continuous) distribution of the medium in the cluster. To keep our notations here the same, we label such a continuously distributed medium as a homogeneous cluster. There are two reasons in support of the homogeneous distribution in the cluster.

The first is the optical area. The size of nanoparticles in a cluster is much smaller than the wavelength of the laser radiation, $r_0 \ll \lambda$. As shown in [30.1], according to the Lorenz–Mie scattering theory, the cross-section of absorption exceeds by four times the geometric cross-section of the gold nanoparticle, $\sigma_{abs} > \sigma_0$. Hence, cross-sections of absorption of each nanoparticle are overlapping in the cluster. Because of this, the light does not distinguish the separate nanoparticles inside the cluster, and the laser energy is distributed homogeneously among the particles.

The second reason is the heat transfer frame. Since the temperature variation inside the nanocluster occurs over a relatively small temperature range of 318 K (45 °C), we can assume that the internal cluster temperature is homogeneous and constant. This means that, from a thermal calculations point of view, the cluster can be treated as homogeneous (continuous) gold particles with the same size.

Let us evaluate the damage area produced by continuous gold *clusters* in the blood medium. The temperature distribution for gold particles of radius 190 nm (cluster diameter 380 nm) in blood irradiated by a single laser pulse of energy density $1\,J/cm^2$ is illustrated in Fig. 30.21b. As follows from these simulations, the upper limit of temperature inside the homogeneous cluster is 2384 K, and the thermal damage area is $2.13\,\mu m$ in diameter at the threshold temperature level of 423 K. Thus, the 380 nm cluster provides a huge thermal damage area with minimum size of $0.5\,\mu m$ (for a discrete cluster) up to a maximal size of $2\,\mu m$ (for a homogeneous cluster) in a cell volume irradiated by a single laser pulse of energy density $1\,J/cm^2$.

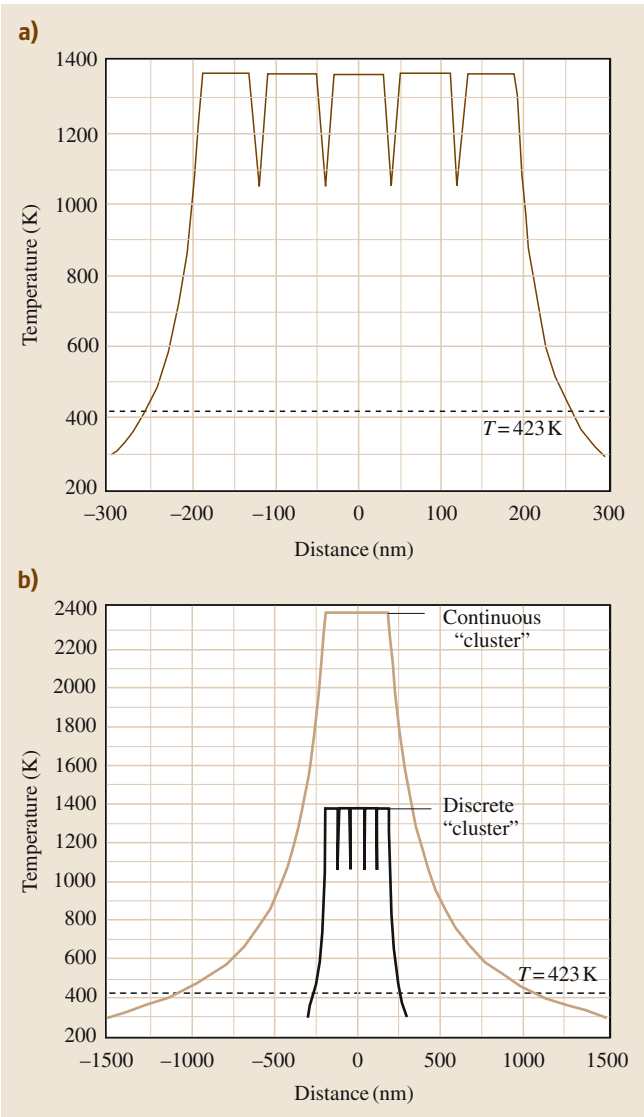


Fig. 30.21a,b One-dimensional distribution of the temperature field inside and outside a discrete cluster **(a)** and continuous cluster **(b)** consisting of 30 nm gold particles in the surrounding blood medium irradiated by a single laser pulse of energy density $1\,J/cm^2$

On the basis of our theoretical modeling, we can conclude that the aggregation of nanoparticles in a cluster mode of nanophotothermolysis raises the efficiency of cancer cell treatment due to the large damage area at

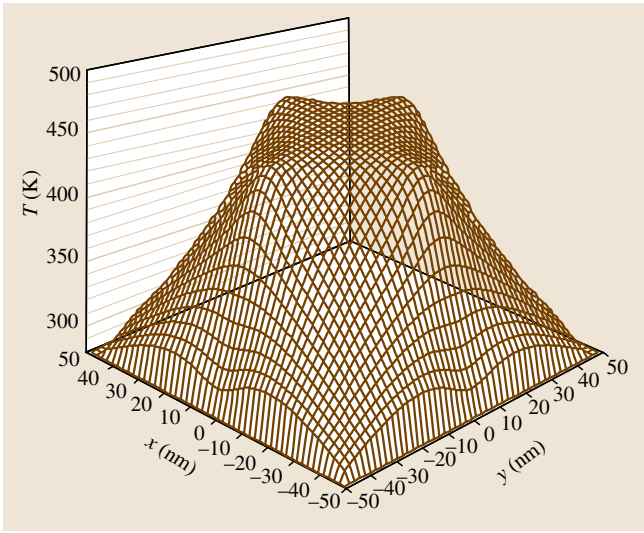


Fig. 30.22 Two-dimensional distribution of the temperature inside and outside a 30 nm gold nanoparticle in surrounding water and blood media irradiated by a single laser pulse of energy density $0.33\,\mathrm{J/cm^2}$ and duration 8 ns

relatively low energy density of the incident single laser pulse. This conclusion is supported by the following results:

- The same laser energy density used for heating a single nanoparticle to the minimal temperature for thermal cell damage provides a temperature six times greater inside the cluster.
- Clusters can produce thermal damage of cancer cells at a significantly lower energy density level of $0.42\,\mathrm{J/cm^2}$ of the incident single laser pulse in comparison with a single particle.
- Clusters provides a larger thermal damage area with minimal size of 0.5 μm (for the discrete cluster case) up to maximal size of 2 μm (for a continuous *cluster*) in a cell volume irradiated by a single laser pulse of energy density $1\,\mathrm{J/cm^2}$ and duration of 8 ns. To reach the same thermal damage area of 0.5 μm by a single nanoparticle, a laser pulse with energy density 2.5 times higher than for the cluster case is required.

We should note that the damage area is estimated here by using the threshold temperature required for the initiation of cell killing effects, i. e., thermal damage. However, the actual damage area is expected to be significantly larger since the damage can occur on the cellular level, for example, due to bubble formation around the nano-absorbers and its expansion in the cell volume. Section 30.5.2 is devoted to the investigation of the microbubble dynamics around nanoparticles/nanoclusters in biological media.

30.6.2 Microbubble Overlapping Mode

As shown in Sect. 30.5.1, significant heat conduction away from a heated nanoparticle requires timescales of the order of microseconds (1.75 μs for water and 1.56 μs for blood). Because of this, for nanosecond laser pulses, most of the pulse energy remains localized at the absorbing nanoparticles/cluster, whose temperature rises high enough to cause vaporization of the immediate surrounding medium. This creates a bubble that then expands outward from the nanoparticle. We now investigate the bubble dynamics resulting from laser pulses with duration of 8 ns at FWHM.

Experiments [30.12] show that it is enough to heat the strongly absorbing nanoparticles above the boiling temperature of water only, or above the critical temperature of the phase transition in water, to generate bubbles around the particles. So, for a relatively low laser flux, the nanoparticle will be surrounded by a rapidly expanding layer of vapor. Let us calculate the threshold energy density of laser pulse deposited into the nanoparticle which is required to raise its surface temperature to the level of the critical temperature for bubble generation.

An experimental nucleation temperature of $T_{\mathrm{thr}} = 150\,^{\circ}\mathrm{C}$ (423 K) for heterogeneous bubble generation on the melanosome's surface was determined by *Kelly* [30.51]. Our calculations (Fig. 30.22) show that a threshold energy density of $0.33\,\mathrm{J/cm^2}$ for the single 8 ns laser pulse is required to reach a surface temperature of 450 K for the 30 nm gold nanoparticles in blood medium. Thus, the bubble mode of photothermolysis can provide a larger damage area at the relatively low optical flux of $0.33\,\mathrm{J/cm^2}$ ($\tau_{\mathrm{L}} = 8$ ns) due to the rapidly expanding nanobubbles around the nanoparticles.

Spherical Bubble Dynamics

Consider a spherical bubble of radius $R(t)$ (where t is time) in an infinite domain of liquid whose temperature and pressure far from the bubble are T_∞ and $p_\infty(t)$, respectively. We will assume that the liquid density ρ_{L} and dynamic viscosity η_{L} are constant and uniform. It will also be assumed that the contents of the bubble are homogeneous, and that the temperature $T(t)$ and pressure $p(t)$ within the bubble are always uniform. The radius of the bubble will be one of the primary

results of the analysis. In the absence of mass transport across the boundary (evaporation or condensation) and with the above assumptions, the bubble dynamics can be described by the generalized Rayleigh–Plesset equation [30.52]

$$\frac{p_V(T_\infty)-p_\infty(t)}{\rho_L}+\frac{p_V(T)-p_\infty(T_\infty)}{\rho_L}+\frac{p_G}{\rho_L} = R\frac{d^2R}{dt^2}+\frac{3}{2}\left(\frac{dR}{dt}\right)^2+\frac{4\eta_L}{\rho_L R}\frac{dR}{dt}+\frac{2S}{\rho_L R}, \tag{30.23}$$

where $p_V(T)$ is the saturated vapor density, and p_G is the partial pressure of the contaminant gas contained in the bubble. The first term on the left side of this equation is the instantaneous tension, or driving term, determined by the conditions far from the bubble. We refer to the second as the thermal term. It will be assumed here that the behavior of the gas in the bubble is polytropic, so that

$$p_G = p_{G_0}\left(\frac{r_0}{R}\right)^{3k}, \tag{30.24}$$

where p_{G_0} is the partial pressure of the contaminant gas contained in the bubble at some reference size $R = r_0$, with k as approximately constant. Clearly, $k = 1$ implies a constant bubble temperature, and $k = \gamma$ would model adiabatic behavior, where γ is the ratio of the specific heat of the vapor at constant pressure to the specific heat at constant volume.

Equation (30.23) can be readily integrated numerically to find $R(t)$ and the rate of bubble growth $v = dR/dt$ given the input $p_\infty(t)$, the temperature T_∞, and the other constants. Initial conditions are also required and, in the context of cavitating flows, it is appropriate to assume that a nanobubble of radius $R = r_0$ is in equilibrium at $t = 0$ in the fluid at a pressure $p_\infty(0)$, so that

$$p_{G_0} = p_\infty(0) - p_V(T_\infty) + \frac{2S}{r_0} \tag{30.25}$$

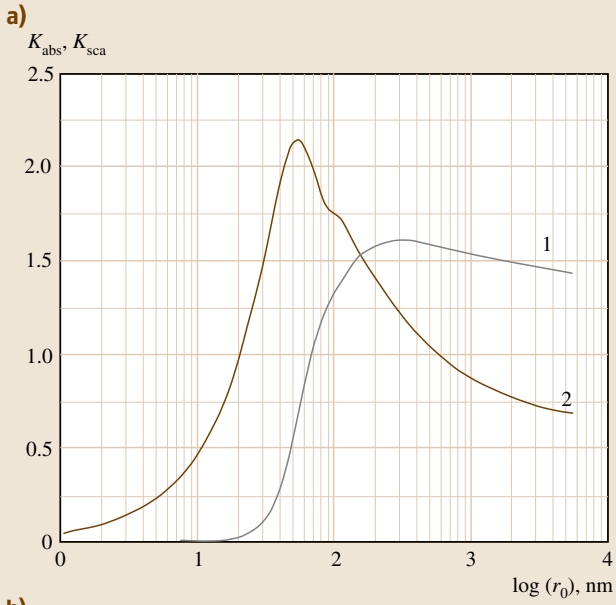
and $(dR/dt)_{t=0} = 0$.

Overlapping Microbubbles

As discussed above, under certain delivery and particle-accumulation conditions, the particles can locate on the membrane surface very close to each other, as shown in Fig. 30.20. In this mode, we can expect the optical, thermal, acoustic, and bubble formation phenomena initiated by laser radiation around each particle to overlap and create some synergistic effects [30.12]; For example, the characteristic radii for these overlapping effects can be defined by an optical radius $R_{opt} = (\sigma_{abs}/\pi)^{1/2}$, thermal diffusion length $R_T = (kt)^{1/2}$, sound transfer distance $R_{ac} = c_s t$, and microbubble radius $R_{bubble} = v_b t$, where σ_{abs} is the cross-section of absorption, k is the heat diffusion coefficient, c_s is the speed of sound, and v_b is the bubble growth velocity. Since for a certain range of gold nanoparticle sizes the optical radius can exceed the geometrical particle radius r_o at the given wavelength of laser radiation, a plasmon–plasmon resonance at $R_{opt} > L$ (where L is the distance between particles) can be achieved. This resonance leads not only to the known *red-shifting* of maximum absorption [30.53], but also increases the integrated absorption coefficient of the particle cluster. The overlapping thermal fields at $R_T > L$ (during or after the laser pulse t_p) lead to a dramatic increase in thermal and accompanying effects (e.g., to sudden appearance of different nonlinear effects such as phase transitions). The interaction of acoustic waves at $R_{ac} > L/2$ significantly changes the local refractive index, which might be crucial for diagnostic purposes. Finally, the interaction of growing bubbles (initially of nanoscale sizes) at $R_{bubble} > L/2$ leads to a substantial increase in the average bubble size, with a decrease in the bubble-formation threshold (which, for single nanoparticles, is relatively high), and probably an increase in the bubble growth velocity. All of these phenomena are crucial when changing the distance between nanoparticles, and they are important for both highly sensitive diagnostics and efficient therapy.

We focus here on therapeutic application of this technology. Indeed, laser-induced overheating effects around nanoparticles may create many therapeutic actions through the microbubble formation phenomena, accompanied by acoustic and cavitation effects, mechanical stress, and laser-induced hydrodynamic pressure arising from the rapid bubble expansion and collapse. In this section, we discuss a dynamic mode for selective cancer treatment by laser-activated nanoheaters, involving the situation where the bubbles are overlapping inside the cell volume. The bubble overlapping mode (BOM) may dramatically increase the efficiency of the cancer treatment by laser-heated nanoparticles as a result of the large damage range.

Since bubbles do not all appear simultaneously, there are few possibilities for bubbles overlapping. The bubbles can overlap at different nucleation times and spreading velocities, or simultaneously with the same spreading velocity when they reach each other midway between neighboring gold particles. In our calculations, we choose stronger criteria than overlapping at



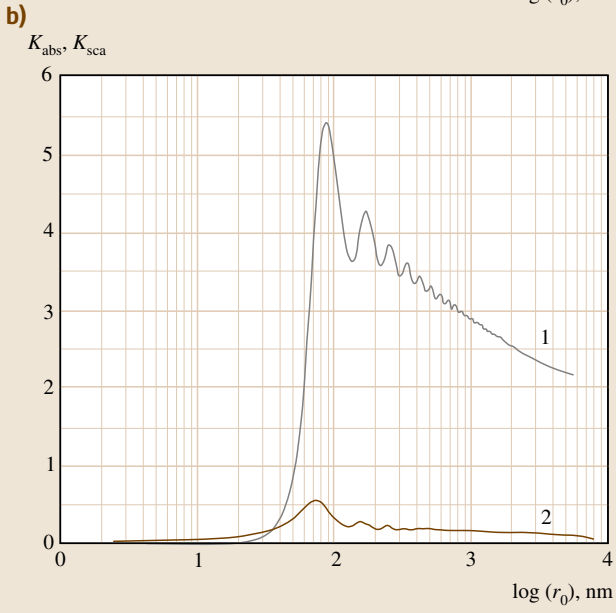


Fig. 30.23a,b Dependences of the scattering K_{sca} (*curve 1*) and absorption K_{abs} (*curve 2*) coefficients at laser wavelength of $\lambda = 450\,\text{nm}$ on the size r_0 of gold particles in water medium ($\tilde{m} = 1.122 - 1.416\,\text{i}$) **(a)** and **(b)** for the case $\lambda = 633\,\text{nm}$ ($\tilde{m} = 0.1126 - 2.5754\,\text{i}$) ◀

midpoints. Effective overlapping with large damage of tumor cells can be achieved if each bubble reaches the neighboring nanoparticles themselves, not just the midpoints between nanoparticles.

Condition for Concentration of Nanoparticles

The criteria for BOM introduced above impose a requirement on the interparticle distance L, the distance between two neighboring nanoparticles. Since the bubble must reach the neighboring particles during the growing time τ_{growth}, the integration of the Rayleigh–Plesset equation (30.23) [30.52] for bubble dynamics at the nucleation temperature T_{nuc} gives the requirement for the interparticle distance L as

$$L \le \sqrt{\frac{2}{3}\frac{P_{sat}(T_{nuc}) - P_\infty}{\rho(T_\infty)}}\,\tau_{growth}\,, \qquad (30.26)$$

where $P_{sat}(T_{nuc})$ is the saturated vapor pressure at the nucleation temperature, P_∞ is the ambient pressure, and $\rho(T_\infty)$ is the water density. This sets the lower limit to that required for the BOM concentration of nanoparticles, the number of particles per unit volume, as

$$n = (1/L^3)\,. \qquad (30.27)$$

Let us now estimate the interparticle distance, the nanoparticle concentration, and their absolute number collected in a tumor cell to provide the BOM by laser-activated nanoheaters. The interparticle distance L calculated by (30.26) for the experimentally measured nucleation temperature of $T_{nuc} = 150\,^\circ\text{C}$ is

$$L \approx 15.8\tau_{growth}\,. \qquad (30.28)$$

The bubble growing time τ_{growth} is limited by the bubble nucleation time t_{nuc} and bubble lifetime τ_{bubble}, i. e., $t_{nuc} \le \tau_{growth} < \tau_{bubble}$. In our experiments [30.12], the nucleation time of the bubbles around isolated gold nanoparticles in aqueous suspension and irradiated by nanosecond laser pulses is $t_{nuc} \approx 100\,\text{ns}$. The bubble lifetime depends on the laser energy and ranges from 100 ns to 2 µs. In the overwhelming majority of experiments, including ours, the bubble lifetime is in the range $\tau_{bubble} = 200–400\,\text{ns}$. So, we can conclude that the bubble growing time is close to the nucleation time, i. e., $\tau_{growth} \sim t_{nuc}$. Then, from the rate equation (30.28), we can estimate the distance between nanoparticles (microbubble radius) required for the BOM as $L = R_{bubble} \approx 1.6\,\mu\text{m}$, which corresponds to the results of our experiments. Thus, (30.27) gives the lower limit of the concentration of nanoparticles to provide the BOM as $n \approx 2.44 \times 10^{11}\,\text{cm}^{-3}$. The absolute number of particles homogeneously distributed inside a tumor cell

Table 30.13 Physical properties of blood at 1 atm pressure used in the simulations

Property	Notation used in the model	Value	Units
Density	ρ_L	998.2	kg/m^3
Viscosity (water)	η_L	1.022×10^{-4}	$kg\,s/m^2$
Surface tension (water-saturated vapor)	S	7.2×10^{-3}	kg/m
Thermal conductivity at $T = 273–373$ K	μ_0	0.48–0.6	W/(m K)
Thermal diffusivity	χ	1.6×10^{-7}	m^2/s
Specific heat at $T = 273–373$ K	c	3645–3897	J/(K kg)
Ratio of specific heats (water/vapor)	γ	1.33	

for this mode can be found as $N = nV_{cell}$, where V_{cell} is the cell volume. For the case of the breast cancer line MDA-MB-231 of 15 μm size, the number of gold nanoparticles providing BOM is $N \approx 430$.

Condition on Nanoparticle Sizes

The optimal range of nanoparticle sizes for effective laser initiation of BOM in tumor cells is governed by the nanoparticle optics described in [30.1]. The optical characteristics of spherical nanoparticles dispersed in a biological medium at a given radiation wavelength λ can be calculated on the basis of Lorenz–Mie diffraction theory in the single scattering approximation discussed in Sect. 30.2. The Mie formalism requires the use of two dimensionless input parameters, $\rho = 2\pi r_0/\lambda$ and $\delta = \rho\tilde{m}$, where $\tilde{m}$ is the relative value of the complex refractive index of the nanoparticles in the surrounding medium at the wavelength λ. Computer calculations of the dependences of the absorption K_{abs} and scattering K_{sca} coefficients at the given laser wavelength on the size of gold nanoparticles in aqueous suspension are plotted in Fig. 30.23. Figure 30.23a shows results for gold particles in water heated by laser radiation of wavelength $\lambda = 450$ nm ($\tilde{m} = 1.122–1.416\,i$), and Fig. 30.23b is for the case of wavelength $\lambda = 633$ nm ($\tilde{m} = 0.1126–2.5754\,i$). It is evident from Fig. 30.23a that the absorption coefficient K_{abs} has a strong maximum at the radius of 50 nm for the gold particle at the given wavelength (for 532 nm wavelength, the maximum radius is 30 nm).

The width of the absorption maximum at the level $K_{abs} \geq 1$ corresponds to the particle radii range of $r_0 = 20–600$ nm. This means that, in this size range, the absorption cross-section of gold particles at the given wavelength $\lambda = 450$ nm exceeds the particle geometric cross-section. Light scattering at $\lambda = 450$ nm by gold nanoparticles in aqueous suspension becomes apparent for particle radii larger than 50 nm. For particles of radii $r_0 \geq 150$ nm, the scattering of laser radiation predominates over the absorption, and the considered suspension containing the nanoparticles becomes a strongly scattering medium at the given wavelength.

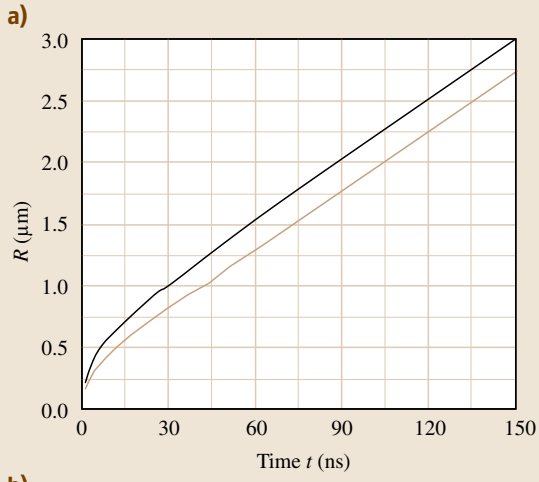
For the particle radius range $r_0 = 1–50$ nm, the absorption coefficient K_{abs} is considerably greater than the scattering coefficient K_{sca}; i. e., the efficiency of laser heating of nanoparticles in this size range is high. Thus, the optimal range of nanoparticle sizes for effective laser initiation of BOM in tumor cells is 1–50 nm. The maximal effect of laser heating of gold particles can be achieved for particles of radii 20–50 nm, where $K_{abs} \geq 1$ and $K_{sca} < 1$.

Figure 30.23b demonstrates the $K_{sca}(r_0)$ and $K_{abs}(r_0)$ curves for the wavelength of $\lambda = 633$ nm. We observe very weak absorption and strong scattering of the light at this wavelength by the gold nanoparticles. The absorption slightly predominates over the scattering for a small range of nanoparticle radii when $r_0 \leq 35$ nm. It follows that laser light with wavelength $\lambda = 633$ nm can be recommended for diagnostic purposes only. However, creation of nanoclusters on a cell surface may lead to shifting the absorption maximum to the near-IR range [30.53], which can also be used for therapeutic purposes.

Thus, the proposed theoretical model for the nanoparticle optics along with bubble dynamics allows us to find the following conditions for BOM realization:

- The maximal effect of laser heating of gold nanoparticles over the wavelength range $\lambda = 450–550$ nm can be achieved for particle radii of 20–50 nm.
- The optimal nanoparticle concentration is $n \approx 2.44\times10^{11}\ cm^{-3}$, which corresponds to an absolute number of nanoparticles in a breast cancer cell volume of 430 (88 on the cell surface).
- The bubble radius providing BOM is $R_{bubble} \approx 1.6$ μm.

These theoretical predictions of the BOM conditions have been confirmed by our experimental re-



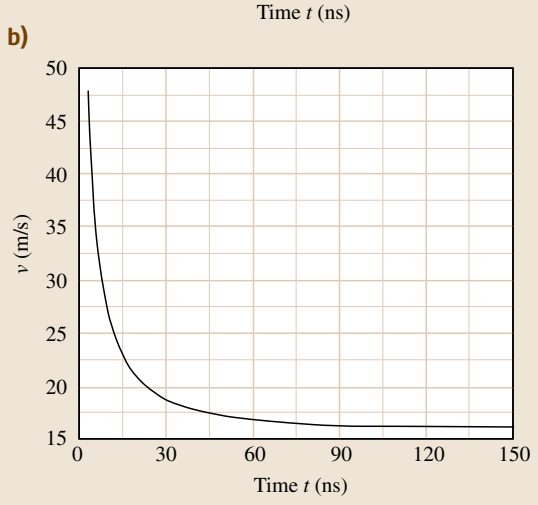


Fig. 30.24 **(a)** Bubble expansion around a 30 nm gold particle in blood irradiated by a laser pulse with energy density $E = 0.33\,\mathrm{J/cm^2}$ and pulse duration $\tau_L = 8\,\mathrm{ns}$ at constant bubble temperature (*upper curve*) and under adiabatic conditions (*lower curve*). **(b)** Bubble expansion rate, $v(t) = \mathrm{d}R/\mathrm{d}t$

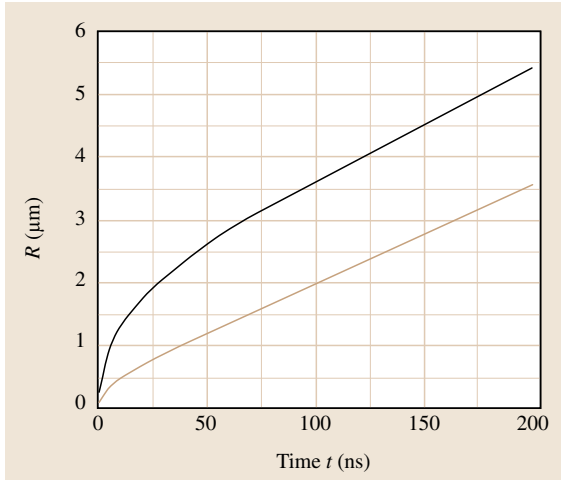


Fig. 30.25 Adiabatic expansion of the bubble produced by a single 30 nm particle (*lower curve*) and 190 nm continuous *cluster* (*upper curve*) irradiated by a laser pulse with energy density $E = 0.33\,\mathrm{J/cm^2}$ and pulse duration $\tau_L = 8\,\mathrm{ns}$

sults [30.12], which include the study of nanocluster-related phenomena as discussed in Sect. 30.5.1 and below.

Microbubble Generation Around Nanoclusters

The model described above has been used to calculate the bubble growth in time around 30 nm gold particles and homogeneous clusters with radius of 190 nm surrounded by blood biomedium when the incident laser pulse has energy density of $E = 0.33\,\mathrm{J/cm^2}$ and pulse duration of $\tau_L = 8\,\mathrm{ns}$. The physical properties of blood used in the calculations are listed in Table 30.13. The results of the simulations are presented in Figs. 30.24 and 30.25. Figure 30.24 illustrates the time behavior of the radius and its rate for the bubble generated around the 30 nm particles heated and cooled in blood. Figure 30.25 demonstrates the difference in the time dynamics of bubble growth caused by the single 30 nm particle and 190 nm homogeneous cluster.

Calculations are performed for both cases at constant bubble temperature ($k = 1$) and for adiabatic conditions ($k = \gamma = 4/3$). Under such conditions, the time dependence of the bubble radius $R(t)$ is a better fit to our experimental results [30.12]. As follows from our calculations, the adiabatic expansion of the bubble provides a final radius of 3.5 μm for the bubble lifetime 200 ns, which agrees well with our experimental observations in [30.12].

The general feature of the simulation results is linear and smooth growth of the bubbles' radius with time when the bubbles' lifetime exceeds 30 ns. The time dynamics of the temperature, as calculated in [30.1] for 30 nm nanoparticles heated by a 8 ns laser pulse, show that the total time for one cycle (heating of the nanoparticles from an initial temperature 300 K to maximum temperature, and then cooling back to the initial temperature) is about 30 ns. Thus, linear growth of the bubble radius with time after 30 ns can be explained by the ab-

sence of an active heat source in the medium. This result is confirmed also by the rate dynamics $v(t) = \mathrm{d}R/\mathrm{d}t$ for the bubble radius shown in Fig. 30.24b. In the time range 0–30 ns, the curves of both $R(t)$ and $v(t)$ have strong nonlinearity due to active heat transfer from the nanoparticle to the surrounding medium. During the first several nanoseconds, the bubble rapidly expands with a high velocity of 40 m/s. Then, the expansion rate drops exponentially and reaches a constant saturation value of 16 m/s for $t > 30$ ns. Since there is no heating source in the system after 30 ns, the microbubble expands uniformly and linearly at a constant rate.

It is important to compare the bubble expansion rate with the thermal conduction rate in the surrounding medium. Using the thermal properties of blood given in Table 30.13 and the size of the locally heated region $l \approx 1\,\mu$m as a focal spot of the laser radiation, we find that the approximate speed for heat conduction is

$$v_{\mathrm{thermal}} \approx \frac{\mu_0}{\rho c l} \approx 0.15\,\mathrm{m/s}\,, \tag{30.29}$$

which is more than two orders of magnitude less than the bubble expansion rate. Here, ρ, c, and μ_0 are, respectively, the density, specific heat, and thermal conductivity of the surrounding medium. So, during a laser pulse of $\tau_{\mathrm{L}} = 8$ ns, thermal damage occurs over a negligible distance from the nanoparticle in comparison with the bubble damage. Thus, bubble expansion occurs on a time scale much shorter than heat loss, which justifies the use of an adiabatic treatment during the expansion. The thermal relaxation time is 1.75 μs for water and 1.56 μs for blood, which is much longer than the bubble lifetime of about 200 ns. This means that, for cell damage by bubble expansion, it is sufficient to heat only the nanoparticles up to the critical threshold temperature for bubble generation (423 K) without having to heat the surrounding cellular medium. Therefore, the relatively low optical flux of 0.33 J/cm^2 ($\tau_{\mathrm{L}} = 8$ ns) is enough for effective cell killing.

Similar bubble expansion dynamics is observed for the bubble produced by a homogeneous cluster, as illustrated in Fig. 30.25. The cluster's curve has both linear and nonlinear parts with notably higher expansion rate of more than 90 m/s in the first 4 ns. During adiabatic expansion of the bubble produced by a homogeneous cluster in blood, the saturated expansion rate is 17 m/s, and the final radius reaches $\approx 5.5\,\mu$m for bubble lifetime of 200 ns. According to our calculations, the heated 380 nm cluster is able to produce one large bubble in the cell volume, whose damage area is comparable to the size of a cancer cell (10–15 μm in diameter). Thus, the formation of just one large bubble around one large nanocluster aggregated in the cell volume is good enough for cancer cell killing.

In conclusion, the bubble mode of photothermolysis decreases the threshold optical flux to 0.33 J/cm^2 ($\tau_{\mathrm{L}} =$ 8 ns) for cancer cell killing and dramatically increases the damage area due to rapid expanding microbubbles around the nanoparticles and cluster:

- The expansion of the bubble has a strong nonlinearity in the time range 0–30 ns due to active heat transfer from nanoparticles to the surrounding medium. During the first several nanoseconds, the bubble produced around a 30 nm particle rapidly expands with a high velocity of 40 m/s. Then, the expansion rate drops exponentially and reaches a constant saturation value of 16 m/s for $t > 30$ ns. Since there is no heating source in the system after 30 ns, the microbubble expands uniformly and linearly at a constant rate.
- The adiabatic expansion of the bubble produced around a single 30 nm particle reaches a final radius of 3.5 μm for bubble lifetime of 200 ns.
- The speed for heat conduction in the cellular medium ($v_{\mathrm{thermal}} = 0.15$ m/s) is more than two orders of magnitude less than the bubble expansion rate ($v_{\mathrm{saturated}} = 16$ m/s), so that, during a laser pulse of $\tau_{\mathrm{L}} = 8$ ns, thermal damage occurs over a negligible distance from the nanoparticle in comparison with the bubble damage.
- A heated 380 nm cluster is able to produce a single large bubble within the cell volume, whose damage area is comparable to the size of a cancer cell (10–15 μm in diameter).

30.6.3 Laser-Induced Thermal Explosion Mode – Nanobombs

In this section, we discuss a new mechanism for selective laser killing of abnormal cells by laser thermal explosion of single nanoparticles – nanobombs – delivered to the cells. Thermal explosion of the nanoparticles is realized for ultrashort laser pulses when the heat is generated within the strongly absorbing target more rapidly than the heat can diffuse away. Laser-induced rapid explosive evaporation of gold nanoparticles (GNs) enables the generation of stress transients, shock waves, and high local pressure. A schematic picture of these complex physical effects is provided in Figs. 30.26 and 30.27. There are two main physical mechanisms

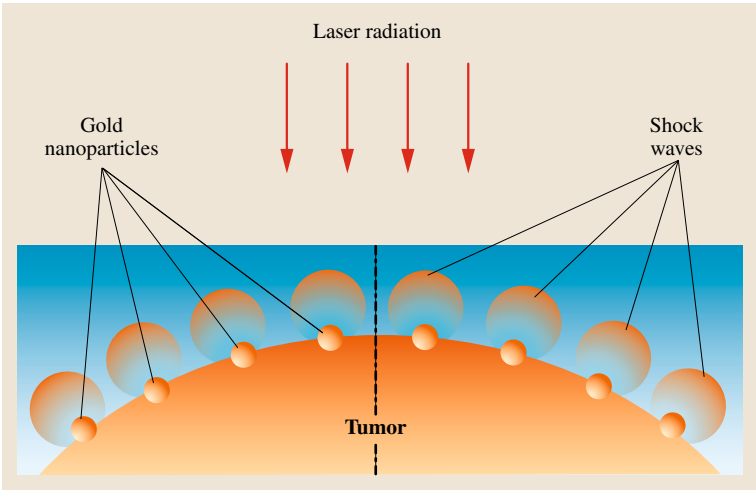


Fig. 30.26 Principle of the thermal explosion mode of nanoparticles – nanobombs – in selective nanophototherapy of cancer

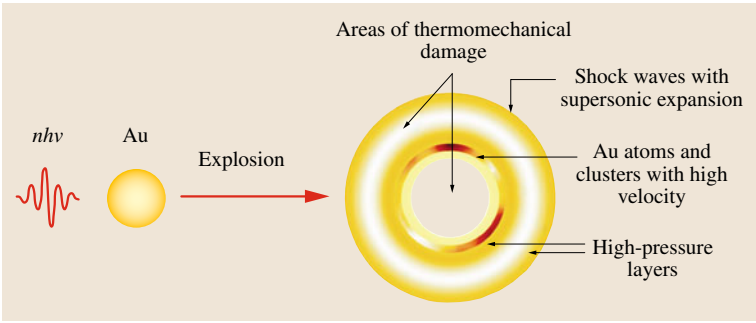


Fig. 30.27 Laser-induced thermal explosion of a gold nanoparticle

that could lead to the laser-induced explosion of GNs: the *thermal explosion mode* through electron–phonon excitation–relaxation, and the *Coulomb explosion mode* through multiphoton ionization.

Thermal Explosion Mode

Under the action of ultrashort laser pulses in the spectral range of the surface plasmon resonances (for a solid spherical GN, the maximum absorption is $\approx 520\,\mathrm{nm}$), GN atoms are excited to upper electronic states owing to the absorption of many photons. Through rapid (picosecond time scale) relaxation, GN atoms decay to their ground state with effective electron–phonon conversion of the absorbed photon energy into thermal energy. Depending on the GN temperature T, the following scenarios, individually or in combination, can occur:

1. $T < T_{\mathrm{LV}}$, where T_{LV} is the liquid vaporization temperature (water in many cases), ≈ 150–$350\,^{\circ}\mathrm{C}$ [30.54]. This is thermal expansion of a single GN and surrounding thin liquid layer, which is accompanied by the generation of linear acoustic waves, known as the *classic* photoacoustic effect.
2. $T_{\mathrm{LV}} \leq T < T_{\mathrm{GNM}}$, where T_{GNM} is the GN melting point, $\approx 1063\,^{\circ}\mathrm{C}$ [30.55]. This is bubble formation with expansion and collapse, which is accompanied by the production of acoustic and shock waves [30.56, 57].
3. $T_{\mathrm{GNM}} \leq T < T_{\mathrm{GNB}}$, where T_{GNB} is the GN boiling point of $\approx 2710\,^{\circ}\mathrm{C}$ [30.55], with GN melting.
4. $T \geq T_{\mathrm{GNB}}$, which is GN boiling with the formation of gold vapor around liquid gold drops.

The photothermal process of scenario 3, and especially scenario 4, may lead to GN fragmentation into smaller parts – nanobullets – and to the thermal explosion of a GN into single atoms.

Coulomb Explosion Mode

For ultrashort laser pulses (e.g., femtosecond time scale) comparable to the time scale of electron–electron

interactions and shorter than the electron–phonon interaction time, a nonphotothermal mechanism of GN explosion can occur through multiphoton ionization when the absorbed photon energy is transferred directly to the electrons, leading to their ejection due to the Coulomb explosion mechanism [30.58, 59]. High GN plasmon-resonance absorption may facilitate this effect due to thermionic electron emission.

Time Scale Approximations

The goal of this theoretical modeling is to estimate the threshold laser energy density E_{expl} required for realization of the thermal explosion mode of GNs, and to compare the calculated data with available experimental results. This mode is realized through rapid overheating of a strongly absorbing target during a short laser pulse when the influence of heat diffusion is minimal. Let us first estimate the time scale for thermal relaxation due to heat diffusion from the surface of the nanoparticle.

In the vicinity of GN $\leq 5R$, where R is the nanoparticle's radius, the thermal relaxation time for a spherical GN can be estimated as $\tau_{\mathrm{T}} = R^2/6.75k$, where k is the thermal diffusivity [30.1]. For $R = 50$, 100, and 200 nm, estimates of τ_{T} (for water, $k = 1.44\times10^{-3}\,\mathrm{cm^2/s}$) are approximately 2.6, 10, and 41 ns, respectively. For a laser pulse duration $t_{\mathrm{P}} \leq \tau_{\mathrm{T}}$, heat is generated within the GN more rapidly than it can be diffused away, so that we can neglect heat losses from the surface of the GN due to heat diffusion into the surrounding medium. This condition for smaller GNs is valid with picosecond and femtosecond laser pulses.

Threshold Intensity for Laser-Induced Thermal Explosion

Consider a nanoparticle selectively delivered to a targeted site (e.g., cancer cell) to be irradiated by a laser of intensity I. The power of the absorbed electromagnetic field is $P = \sigma_{\mathrm{abs}} I$, where σ_{abs} is the GN's cross-section of absorption. If σ_{abs} is large enough, thermal explosion of the GN may occur at certain values of the threshold laser intensity I_{expl}, which is less than the threshold intensity for optical plasma formation in the surrounding medium [30.17, 18]. Under the thermal explosion of GNs, we understand the specific case for which the total energy absorbed by the GN during the time of its inertial retention in vapor state, $\tau_{\mathrm{expl}} = R/u_{\mathrm{s}}$, exceeds the energy required for the GN's complete evaporation, $\rho q V = N_{\mathrm{Au}} q_1 V$. Here, u_{s} is the sound velocity in Au vapor at the critical temperature $T_{\mathrm{cr}} \sim T_{\mathrm{GNB}}$; ρ is the volume density of GN; N_{Au} is the number of Au atoms per unit volume; q and q_1 are the particle's specific heat of evaporation per unit mass and per particle, respectively; and V is the GN's volume. We have a laser pulse duration of $\tau_{\mathrm{L}} > \tau_{\mathrm{expl}} = R/u_{\mathrm{s}}$ (≈ 1 ps for $R \approx 10$ nm), where τ_{expl} is an explosive evaporation time.

To compute I_{expl}, we can use the model described in [30.1]. According to that model, the threshold intensity of the laser radiation for thermal explosion of the spherical GN can be expressed as

$$I_{\mathrm{expl}}(R) \approx \frac{4\rho T_{\mathrm{cr}} q u_{\mathrm{s}}}{3K_{\mathrm{abs}}(R)}\,, \tag{30.30}$$

where K_{abs} is the nanoparticle absorption efficiency. Thus, the solid nanoparticle in a relatively strong laser field with intensity $I \geq I_{\mathrm{expl}}$ during the short time $\tau_{\mathrm{expl}} \approx R/u_{\mathrm{s}}$ transforms into a gas (vapor) sphere of radius $\approx R$, which has high temperature $T \sim T_{\mathrm{GNB}}$ and high pressure $P_{\mathrm{vap}} \gg P_{\infty}$, where P_{∞} is the ambient pressure.

We assume here that thermal explosion of a GN is accompanied by the generation of shock waves that expand with a supersonic velocity $u_{\mathrm{s}} = R/\tau_{\mathrm{expl}} = I_{\mathrm{expl}}/4\Delta H \approx 10^5\,\mathrm{cm/s}$. Here, $\Delta H = \Delta H_{300-\mathrm{vap}} + \Delta H_{\mathrm{vap}}$, where $\Delta H_{300-\mathrm{vap}}$ is the enthalpy change per unit volume for heating the GN from the ambient temperature to the vaporization temperature, and ΔH_{vap} is the vaporization enthalpy per unit volume. The shock waves could be waves of high acoustic or/and water vapor pressure, which spread out over long distances around an epicenter of explosion and produce irreparable mechanical cell damage [30.60–67]. It should be noted that the pressure produced by vaporization of a GN itself (e.g., $\approx 10^{-2}$ atm [30.68]) is less than the water vapor pressure around the hot GNs. Indeed, the number of atoms vaporized per unit of time and per unit of particle surface is given by [30.69]

$$\frac{\mathrm{d}N_{\mathrm{vap}}}{\mathrm{d}t} = u_{\mathrm{s}} N_{\mathrm{Au}} = \frac{I_{\mathrm{expl}}}{4\Delta H} N_{\mathrm{Au}}\,. \tag{30.31}$$

For example, the atomic density of bulk gold is $5.9\times10^{22}\,\mathrm{cm^{-3}}$, while each GN contains approximately 10^9 atoms, leading to an average atom density of $10^{17}\,\mathrm{cm^{-3}}$. Higher gold vapor pressure can only be reached on the front end of the explosion, where explosion products are localized in a thin layer.

Cell Damage Effects

The therapeutic effect of laser-induced explosion of GNs for cancer treatments can be achieved due to one or several phenomena, such as protein inactivation (e.g., through denaturation or coagulation) around hot GNs [30.61], bubble formation [30.12], generation of

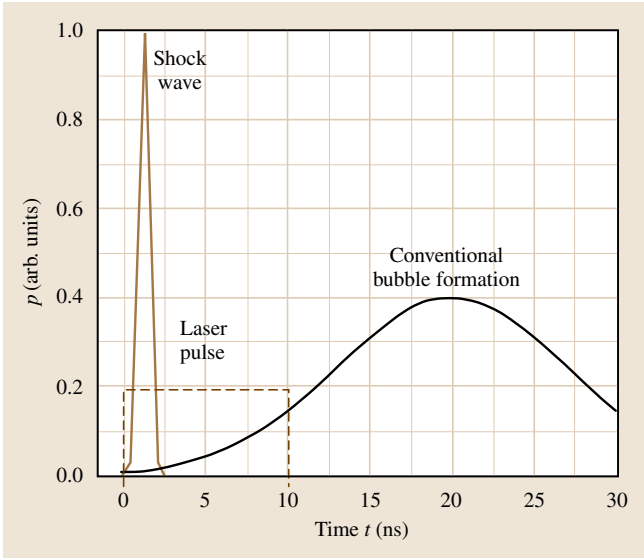


Fig. 30.28 Schematic time scale for shock wave and conventional bubble formation using the thermal explosion mode

acoustic and shock waves [30.62–67], and interaction with GN fragments and atoms. An important damage-related factor is not only the temperature but also the vapor pressure produced by both water and gold vapors, accompanied by the cavitations and shock waves, with local pressure up to gigapascals [30.62–67]. The damage of specific cellular structures (e.g., plasmatic membranes, nuclei, cytoskeletons, and organelles) in the laser explosion mode depends on GN parameters (composition, size, and shape), their number and location, laser parameters (wavelength, fluence, pulse duration, and number of pulses), and properties of the surrounding media (e.g., amount of water).

The time required to destroy an abnormal cell of size d by supersonic expansion of shock waves can be roughly estimated as $\tau_{sw} \approx d/u_s$. In the case of 15 μm-diameter cancer cells [30.12, 17, 18], this is $\tau_{sw} \approx 15$ ns, which is comparable to the lifetime of sound/pressure shock waves in an aqueous medium. We can estimate the lower level of the threshold energy density of a laser pulse required for thermal explosion of the GN using $E_{expl}(R) \approx I_{expl}(R) \times \tau_{expl}$, where the threshold intensity I_{expl} depends on the absorption efficiency of the nanoparticle. For the particular lasers used in the experiments [30.12, 17, 18] ($\lambda = 532$ nm, $\tau_L = 8–10$ ns), the threshold energy density for thermal explosion of a solid gold nanosphere of size $R = 35$ nm (absorption efficiency of $K_{abs} = 4.02$) is $E_{expl} = 38.5\,\mathrm{mJ/cm^2}$. This density strongly depends on the types of nanoparticles (e.g., gold solid nanospheres, nanoshells, and nanorods). For example, gold nanorods have a near-IR resonance absorption efficiency of approximately 14 for an effective radius of 11.43 nm [30.26]. Due to the higher plasmon-resonance absorption efficiency of nanorods, the threshold energy density can be reduced by using gold nanorods to $E_{expl} = 25\,\mathrm{mJ/cm^2}$. It is important to note that the estimated threshold energy densities for thermal explosion of GNs at the given wavelength $\lambda = 532$ nm are 2.5–4 times less than the laser fluence of $100\,\mathrm{mJ/cm^2}$ established as the safety standard for medical lasers [30.70].

The estimated values for E_{expl} are in good agreement with some available experimental results. Indeed, for spherical GNs with average size of 45 nm irradiated with second-harmonic Nd:YAG laser pulses (532 nm for 7 ns), the laser fluence threshold for changing the GN shape and its fragmentation associated with GN melting and boiling phenomena are 16 and $30\,\mathrm{mJ/cm^2}$, respectively [30.55]. The more intense GN fragmentation to small fragments of mainly 5–10 nm in size has been observed for laser fluences in the range $30–140\,\mathrm{mJ/cm^2}$ and higher [30.55]. For a 30 ps pulse, 25 nm GN fragmentation has been observed at $23\,\mathrm{mJ/cm^2}$, with a slight effect on changing the GN shape, even at $2–5\,\mathrm{mJ/cm^2}$ [30.28].

Thus, thermal explosion around GNs may make a significant contribution to cell damage alone or together with conventional water vapor bubble formation in nanophotothermolysis, which is characterized by a higher laser fluence range of $50–500\,\mathrm{mJ/cm^2}$ [30.1]. As previously mentioned, conventional bubble formation usually starts at the end of a nanosecond laser pulse, while the thermal explosion time scale is from 1 ps to a few ns [30.17, 18]. A schematic time scale for shock wave and conventional bubble formation in the thermal explosion mode is shown in Fig. 30.28. Thus, shock waves appear earlier than bubbles induced by the explosive vaporization of GNs in a liquid environment.

The laser-induced explosion effect can explain the experimental results [30.7, 16] with notable cancer damage with 1.4 nm GNs inside viruses on a cell membrane with picosecond laser pulses (30 ps, $50–100\,\mathrm{mJ/cm^2}$) when the probability of classic water bubble formation is very low. We believe that the explosion mode may be essential in selective nanophotothermolysis of DNA, and this mode is definitely becoming dominant in the absence of a sufficient amount of water around GNs. This mode can be combined with a bubble overlapping

mode [30.12] as described above, where the explosion of a few closely located GNs in a gold nanoparticle cluster (GNC) can produce one large bubble with enhanced killing efficiency. The explosion of GNs on smaller particles or single gold atoms during a laser pulse may provide the condition for interaction of the pulse with its atoms, leading to their ionization and plasma formation. However, these effects should appear at relatively high laser fluences that are not safe for normal cells [30.57].

Thus, we have considered a new mechanism for selective laser killing of abnormal cells by laser thermal explosion of single nanoparticles (nanobombs) delivered to the cells. Thermal explosion is realized when heat is generated within a strongly absorbing target more rapidly than the heat can diffuse away. On the basis of simple energy balance, it is shown that the threshold energy density of a single laser pulse required for the thermal explosion of a solid gold nanosphere is approximately 40 mJ/cm^2. The nanoparticle's explosion threshold energy density can be reduced further (to 11 mJ/cm^2) by using large nanorods (and probably nanoshells) and many other advanced GNs whose optical plasmon resonance lies in the near-IR region, where the biological tissue transmissivity is the highest. Additionally, the effective therapeutic effect for cancer cell killing is achieved due to nonlinear phenomena that accompany the thermal explosion of the nanoparticles, such as the generation of GN explosion products with high kinetic energy (nanobullets), as well as strong shock waves with supersonic expansion in the cell volume or production of optical plasma. It is important that most of these phenomena can explain some published experimental results whose interpretation was performed without taking into account this effect.

References

30.1 T.F. George, D. Jelski, R.R. Letfullin, G. Zhang (Eds.): *Computational Studies of New Materials II: From Ultrafast Processes and Nanostructures to Optoelectronics, Energy Storage and Nanomedicine* (World Scientific, Singapore 2011)

30.2 T.M. Fahmy, P.M. Fong, A. Goyal, W.M. Saltzman: Targeted for drug delivery, Nano Today, August 18–26 (2005)

30.3 Y. Fukumori, H. Ichikawa: Nanoparticles for cancer therapy and diagnosis, Adv. Powder Technol. **17**, 1–28 (2006)

30.4 S. Nie, Y. Xing, G.J. Kim, J.W. Simons: Nanotechnology applications in cancer, Annu. Rev. Biomed. Eng. **9**, 257–288 (2007)

30.5 R.R. Letfullin, V.I. Igoshin, A.N. Bekrenev: Thermal calculation of bone-tissue slash modes by laser radiation, Proc. SPIE **2100**, 272–275 (1994)

30.6 R.R. Letfullin, V.P. Zharov, C. Joenathan, T.F. George: Nano-photothermolysis of cancer cells, SPIE Newsroom (2007)

30.7 V.P. Zharov, K.E. Mercer, E.N. Galitovskaya, M.S. Smeltzer: Photothermal nanotherapeutics and nanodiagnostics for selective killing of bacteria targeted with gold nanoparticles, Biophys. J. **90**, 619–627 (2006)

30.8 G.A. Mansoori, P. Mohazzabi, P. McCormack, S. Jabbari: Nanotechnology in cancer prevention, detection, and treatment: Bright future lies ahead, World Rev. Sci. Technol. Sustain. Dev. **4**, 226–257 (2007)

30.9 C.M. Pitsillides, E.K. Joe, X. Wei, R.R. Anderson, C.P. Lin: Selective cell targeting with light-absorbing microparticles and nanoparticles, Biophys. J. **84**, 4023–4032 (2003)

30.10 M.J. Vicent: Polymer-drug conjugates as modulators of cellular apoptosis, Am. Assoc. Pharm. Sci. J. **9**, E200–E207 (2007)

30.11 J. Khandare, T. Minko: Polymer-drug conjugates: progress in polymeric prodrugs, Prog. Polym. Sci. **31**, 359–397 (2006)

30.12 V.P. Zharov, R.R. Letfullin, E.N. Galitovskaya: Microbubbles-overlapping mode for laser killing of cancer cells with absorbing nanoparticle clusters, J. Phys. D **38**, 2571–2581 (2005)

30.13 J.R. Lepock, H.E. Frey, K.P. Ritchie: Protein denaturation in intact hepatocytes and isolated cellular organelles during heat shock, J. Cell Biol. **122**, 1267–1276 (1993)

30.14 C. Yao, R. Rahmanzadeh, E. Endl, Z. Zhang, J. Gerdes, G. Hüttmann: Elevation of plasma membrane permeability by laser irradiation of selectively bound nanoparticles, J. Biomed. Opt. **10**, 064012–1–064012–8 (2005)

30.15 R.R. Letfullin, C.E.W. Rice, T.F. George: Bone tissue heating and ablation by short and ultrashort laser pulses, Proc. SPIE **7548**, 75484K–1–75484K–11 (2010)

30.16 R.R. Letfullin, T.F. George: Laser ablation of biological tissue by short and ultrashort pulses. In: *Computational Studies of New Materials II*, ed. by T.F. George, D. Jelski, R.R. Letfullin, G.P. Zhang (World Scientific, Singapore 2011) pp. 191–218

30.17 R.R. Letfullin, C. Joenathan, T.F. George, V.P. Zharov: Laser-induced explosion of gold nanoparticles: Potential role for nanophotothermolysis of cancer, Nanomedicine **1**, 473–480 (2006)

30.18 R.R. Letfullin, V.P. Zharov, C. Joenathan, T.F. George: Laser-induced thermal explosion mode for selec-

tive nano-photothermolysis of cancer cells, Proc. SPIE **6436**, 643601–1–643601–5 (2007)
30.19 R.R. Letfullin, C.E.W. Rice, T.F. George: Space simulation of thermal fields generated in bone tissue for application to nanophotohyperthermia and nanophotothermolysis, Proc. SPIE **7883**, 78834–L–1–78834–L–10 (2011)
30.20 R.R. Letfullin, T.F. George, G.C. Duree, B.M. Bollinger: Ultrashort laser pulse heating of nanoparticles: Comparison of theoretical approaches, Adv. Opt. Technol. **2008**, 251718–1–251718–8 (2008)
30.21 R.R. Letfullin, T.F. George: Nanomaterials in nanomedicine. In: *Computational Studies of New Materials II: From Ultrafast Processes and Nanostructures to Optoelectronics, Energy Storage and Nanomedicine*, ed. by T.F. George, D. Jelski, R.R. Letfullin, G.P. Zhang (World Scientific, Singapore 2011) pp. 103–130
30.22 R.R. Letfullin, T.F. George: New dynamic modes for selective laser cancer nanotherapy. In: *Computational Studies of New Materials II: From Ultrafast Processes and Nanostructures to Optoelectronics, Energy Storage and Nanomedicine*, ed. by T.F. George, D. Jelski, R.R. Letfullin, G.P. Zhang (World Scientific, Singapore 2011) pp. 131–172
30.23 R.R. Letfullin, C.E.W. Rice, T.F. George: Modeling photothermal heating and ablation of biological hard tissues by short and ultrashort laser pulses, Int. J. Theor. Phys. Group Theor. Nonlinear Opt. **15**, 11–23 (2011)
30.24 R.R. Letfullin, C.B. Iversen, T.F. George: Modeling nanophotothermal therapy: Kinetics of thermal ablation of healthy and cancerous cell organelles and gold nanoparticles, Nanomedicine **7**(2), 137–145 (2011)
30.25 R.R. Letfullin, T.F. George: Nanoscale materials in strong ultrashort laser fields. In: *Computational Studies of New Materials II: From Ultrafast Processes and Nanostructures to Optoelectronics, Energy Storage and Nanomedicine*, ed. by T.F. George, D. Jelski, R.R. Letfullin, G.P. Zhang (World Scientific, Singapore 2011) pp. 37–64
30.26 P.K. Jain, K.S. Lee, I.H. El-Sayed, M.A. El-Sayed: Calculated absorption and scattering properties of gold nanoparticles of different size, shape, and composition: Applications in biological imaging and biomedicine, J. Phys. Chem. B **110**, 7238–7248 (2006)
30.27 V.K. Pustovalov, A.S. Smetannikov, V.P. Zharov: Photothermal and accompanied phenomena of selective nanophotothermolysis with gold nanoparticles and laser pulses, Laser Phys. Lett. **5**, 775–792 (2008)
30.28 Z. Peng, T. Walther, K. Kleinermanns: Influence of intense pulsed laser irradiation on optical and morphological properties of gold nanoparticle aggregates produced by surface acid–base reactions, Langmuir **21**, 4249–4253 (2005)
30.29 V.S. Kalambur, E.K. Longmire, J.C. Bischof: Cellular level loading and heating of superparamagnetic iron oxide nanoparticles, Langmuir **23**, 12329–12336 (2007)
30.30 E.Y. Hleb, D.O. Lapotko: Photothermal properties of gold nanoparticles under exposure to high optical energies, Nanotechnology **19**, 1–10 (2008)
30.31 H. Takahashi, T. Niidome, A. Nariai, Y. Niidome, S. Yamada: Gold nanorod-sensitized cell death: Microscopic observation of single living cells irradiated by pulsed near-infrared laser light in the presence of gold nanorods, Chem. Lett. **35**, 500–501 (2006)
30.32 P. Buffat, J.P. Borel: Size effect on the melting temperature of gold particles, Phys. Rev. A **13**, 2287–2298 (1976)
30.33 T. Torimura, T. Ueno, S. Inuzuka, Y. Kimura, P. Ko, M. Kin, T. Minetoma, T. Majima, M. Sata, H. Abe, K. Tanikawa: Ultrastructural observation on hepatocellular carcinoma: Correlation of tumor grade and degree of atypia of cell organelles by morphometry, Med. Electron. Microsc. **26**, 19–28 (1993)
30.34 G.T. Deans, P.W. Hamilton, P.C.H. Watt, M. Heatly, K. Williamson, C.C. Patterson, B.J. Rowlands, G. Parks, R. Spence: Morphometric analysis of colorectal cancer, Dis. Colon Rectum **36**, 450–456 (1993)
30.35 M.M. Radwan, K.A. Amer, N.M. Mokhtar, M.A. Kandil, A.M. El-Barbary, H.A. Aiad: Nuclear morphometry in ductal breast carcinoma with correlation to cell proliferative activity and prognosis, J. Egypt. Natl. Cancer Inst. **15**, 169–182 (2003)
30.36 D. Ozaki, Y. Kondo: Comparative morphometric studies of benign and malignant intraductal proliferative lesions of the breast by computerized image analysis, Hum. Pathol. **26**, 1109–1113 (1995)
30.37 Y. Cui, E.A. Koop, P.J. van Diest, R.A. Kandel, T.E. Rohan: Nuclear morphometric features in benign breast tissue and risk of subsequent breast cancer, Breast Cancer Res. Treat. **104**, 103–107 (2007)
30.38 N. Campbell, J. Reece: *The Cell: A Tour of the Cell Biology*, 8th edn. (Benjamin Cummings, San Francisco 2007)
30.39 M. Bloom, J. Greenbeerg (Eds.): *BSCS Biology, A Molecular Approach, BSCS Blue Version*, 9th edn. (Glencoe/McGraw-Hill, Columbus 2006)
30.40 D.E. Sadava: *Cell Biology: Organelle Structure and Function* (Jones Bartlett, Boston 1993)
30.41 L.W. Anson, R.C. Chivers: Ultrasonic propagation in mammalian cell suspensions based on a shell model, Phys. Med. Biol. **34**, 1153–1167 (1989)
30.42 D.L. Martin, J. Sampugna: Stimulating Cell Fractionation (Carolina Biological Supply Company 1973), pp. 50–51
30.43 H. Goldenberg, C.J. Tranter: Heat flow in an infinite medium heated by a sphere, Br. J. Appl. Phys. **3**, 296–298 (1952)

30.44 S.R.H. Davidson, D.F. James: Measurement of thermal conductivity of bovine cortical bone, Med. Eng. Phys. **22**, 741–747 (2000)

30.45 P.L. Blanton, N.L. Biggs: Density of fresh and embalmed human compact and cancellous bone, Am. J. Phys. Anthropol. **29**, 39–44 (1968)

30.46 H. Fukushima, Y. Hashimoto, S. Yoshiya, M. Kurosaka, M. Matsuda, S. Kawamura, T. Iwatsubo: Conduction analysis of cement interface temperature in total knee arthroplasty, Kobe J. Med. Sci. **48**, 63–72 (2002)

30.47 A. Shakeri-Zadeh, M. Ghasemifard, G.A. Mansoori: Structural and optical characterization of folateconjugated gold-nanoparticles, Physica E **42**, 1272–1280 (2010)

30.48 P.B. Johnson, R.W. Christy: Optical properties of the noble metals, Phys. Rev. B **6**, 4370–4379 (1972)

30.49 D. Fried, M. Zuerlein, J.D.B. Featherstone, W. Seka, C. Duhn, S.M. McCormack: IR laser ablation of dental enamel: Mechanistic dependence on the primary absorber, Appl. Surf. Sci. **127–129**, 852–856 (1998)

30.50 M.C. Daniel, D. Astruc: Gold nanoparticles: Assembly, supramolecular chemistry, quantum-size-related properties and application toward biology, catalysis and nanotechnology, Chem. Rev. **104**, 293–346 (2004)

30.51 C.P. Lin, M.W. Kelly, S.A. Sibayan, M.A. Latina, R.R. Anderson: Selective cell killing by microparticle absorption of pulsed laser radiation, IEEE J. Sel. Top. Quantum Electron. **5**, 963–968 (1999)

30.52 C.E. Brennen: *Cavitation and Bubble Dynamics* (Oxford Univ. Press, New York 1995)

30.53 K. Aslan, J.R. Lakowicz, C.D. Geddes: Nanogold-plasmon-resonance-based glucose sensing, Anal. Biochem. **330**, 145–155 (2004)

30.54 J. Neumann, R. Brinkmann: Boiling nucleation on melanosomes and microbeads transiently heated by nanosecond and microsecond laser pulses, J. Biomed. Opt. **10**, 024001–024012 (2005)

30.55 A. Takami, H. Kurita, S. Koda: Laser-indiced size reduction of noble particle, J. Phys. Chem. B **103**, 1226–1232 (1999)

30.56 R.R. Anderson, J.A. Parrish: Selective photothermolysis: Precise microsurgery by selective absorption of pulsed radiation, Science **220**, 524–527 (1983)

30.57 V. Venugopalan, A. Gyerra III, K. Nahen, A. Vogel: Role of laser-induced plasma formation in pulsed cellular microsurgery and micromanipulation, Phys. Rev. Lett. **88**, 078103–1–078103–4 (2002)

30.58 A. Vogel, V. Venugolapan: Mechanism of pulsed laser ablation of biological tissue, Chem. Rev. **103**, 577–644 (2003)

30.59 K. Yamada, Y. Tokumoto, T. Nagata, F. Mafune: Mechanism of laser-induced size-reduction of gold nanoparticles as studied by nanosecond transient absorption spectroscopy, J. Phys. Chem. B **110**, 11751–11756 (2006)

30.60 S. Inasawa, M. Sugiyama, S. Noda, Y. Yamaguchi: Spectroscopic study of laser-induced phase transition of gold nanoparticles on nanosecond time scale and longer, J. Phys. Chem. B **110**, 3114–3119 (2006)

30.61 G. Huttmann, B. Radt, J. Serbin, R. Birngruber: Inactivation of proteins by irradation of gold nanoparticles with nano- and picosecond laser pulses, Proc. SPIE **5142**, 88–95 (2003)

30.62 P. Steinbach, F. Hofstadter, H. Nicolai, W. Rossier, W. Wieland: In vitro investigations on cellular damage induced by high energy shock waves, Ultrasound Med. Biol. **18**, 691–699 (1992)

30.63 A.G. Doukas, D.J. McAuliffe, T.J. Flotte: Biological effects of laser-induced shock waves: Structural and functional cell damage in vitro, Ultrasound Med. Biol. **19**, 137–146 (1993)

30.64 T. Douki, S. Lee, K. Dorey, T.J. Flotte, T.F. Deutsch, A.G. Doukas: Stress-wave-induced injury to retinal pigment epithelium cells in vitro, Lasers Surg. Med. **19**, 249–259 (1996)

30.65 T. Kodama, H. Uenohara, K. Takayama: Innovative technology for tissue disruption by explosive-induced shock waves, Ultrasound Med. Biol. **24**, 1459–1466 (1998)

30.66 A. Sonden, B. Svensson, N. Roman, H. Ostmark, B. Brismar, J. Palmblad, B.T. Kjellstrom: Laser-induced shock wave endothelial cell injury, Lasers Surg. Med. **26**, 364–375 (2000)

30.67 E. Faraggi, B.S. Gerstman, J. Sun: Biophysical effects of pulsed lasers in the retina and other tissues containing strongly absorbing particles: Shockwave and explosive bubble generation, J. Biomed. Opt. **10**, 064029–1–064029–10 (2005)

30.68 S. Inasawa, M. Sugiyama, Y. Yamaguchi: Bimodal size distribution of gold nanoparticles under picosecond laser pulses, J. Phys. Chem. B **109**, 9404–9410 (2005)

30.69 L. Boufendi, A. Bouchoule, B. Dubreuil, E. Stoffels, W.W. Stoffels, M.L. deGiorgi: Study of initial dust formation in an Ar-SiH_4 discharge by laser induced particle explosive evaporation, J. Appl. Phys. **76**, 148–153 (1994)

30.70 ANSI Standard Z136.1-2000: American National Standard for safe use of Lasers ANSIZ136.1 (2000)

31. Carbon Nanotube Membrane Filters

Anchal Srivastava, Saurabh Srivastava, Kaushik Kalaga

This chapter provides an overview of different filtration processes (Sect. 31.1) and the mechanism of nanofiltration (Sect. 31.2). In the following sections, we focus on nanofiltration based on carbon nanotube membranes. A brief introduction to carbon nanotubes and their structure and properties is given, with an emphasis on the different kinds of synthesis of membranes; their function in nanofiltration in gas–vapor transport, liquid transport, and some other filtration-like techniques for filtration of bacteria and viruses is also discussed in detail (Sect. 31.3). Finally, an outlook of future research is proposed.

31.1 **Types of Filtration** 1100
31.2 **Mechanisms of Filtration** 1101
31.3 **Carbon Nanotube Membrane Filters** 1102
31.3.1 Structure and Properties of CNTs 1103
31.3.2 Types of CNT Membranes in Nanofiltration 1105
31.4 **Future Research Perspectives** 1112
References 1112

Membrane technology is a widely explored process for separation and filtration of many chemicals, both domestically and commercially. Historically in India, domestic filtration techniques were based on conventional methods using cloth membranes. Different cloth materials were used for filtration of drinking water and separation of various kinds of colloidal solutions. This provided a relatively efficient and inexpensive means for achieving otherwise difficult separations. Starting in the late 1960s, membrane processes gradually found their way into industrial applications to serve as viable alternatives to more traditional processes such as distillation, evaporation or extraction. Membrane and module sales in 1998 were estimated at more than US $ 4.4 billion worldwide, shared by different applications as shown in Fig. 31.1. According to data from 1996, about 45% of these sales were in the USA and 29% in Europe and the Middle East. The market in Asia and South America is also growing fast. The quest for efficient filtration membranes continued, based on the main driving force of accomplishing separation. Many such membrane processes can be distinguished. Pressure-driven membrane processes such as reverse osmosis (RO), nanofiltration (NF), ultrafiltration (UF), and microfiltration (MF) are emerging as key components of water purification systems throughout the world. The majority of the operating cost of membrane systems is associated with the high pressure needed to remove dissolved contaminants (e.g., monovalent ions and small organic molecules). RO and NF are very effective for removing dissolved ions and organic solutes. However, high pressures (100–1000 psi) are required to operate RO and NF membranes. Conversely, UF and MF membranes require much lower pressure (5–60 psi).

Such methods are presently an established part of several industrial processes. Applications of membrane technology include the use of RO and NF for desalination and water purification, electrodialysis (ED) in a chlorine caustic cell, hemodialysis for artificial kidneys, UF in the food industry for protein separation from milk whey and apple juice concentration, pervaporation (PV) for dehydration of ethanol, controlled release of drugs, genetic engineering, etc. [31.1–5]. An overview of the driving forces and the related membrane separation processes is presented in Table 31.1.

Vacuum-driven hollow membranes are also available, commercially known as ZeeWeed membrane. The microfilter, consisting of 0.085 μm pores, operates under a small suction created within the hollow fibers by a permeate pump. The treated water passes through the membrane, enters the hollow fibers, and is pumped out for distribution by the permeate pump. Air flow is intro-

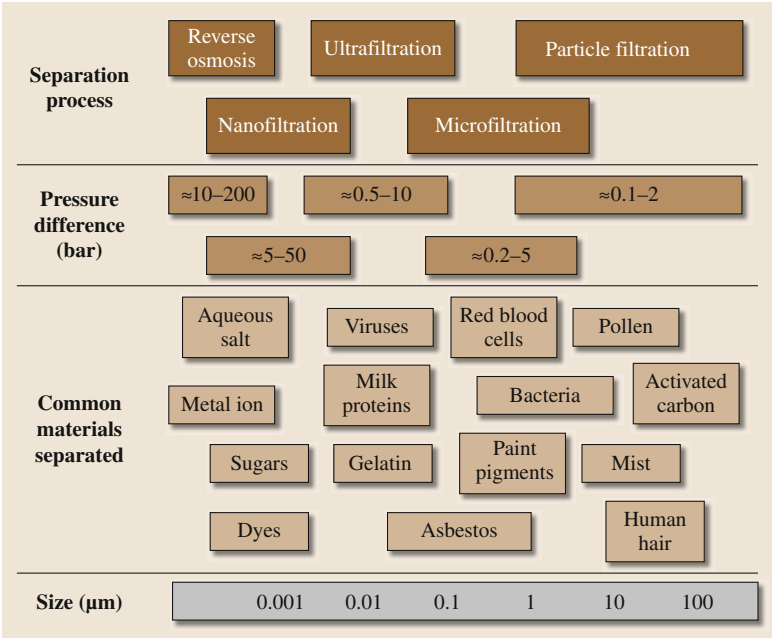


Fig. 31.1 Flowchart showing different filtration applications

Table 31.1 Driving forces and their related membrane separation processes

Driving force	Membrane process
• Pressure difference	Microfiltration, ultrafiltration, nanofiltration, reverse osmosis or hyperfiltration
• Chemical potential difference	Pervaporation, pertraction, dialysis, gas separation, vapor permeation, liquid membranes
• Electrical potential difference	Electrodialysis, membrane electrophoresis, membrane electrolysis

duced at the bottom of the membrane module to create turbulence which scrubs and cleans the outside of the membrane fibers, allowing them to function at high flux rate. This air will also oxidize iron and other, organic compounds, generating better quality water than provided by microfiltration alone.

Access to hygienic water has emerged as one of the most serious problems around the world in the 21st century. Nanotechnology has great potential for providing efficient and environmentally acceptable solutions for improving water quality and for increasing the amount of potable water available. Nanomaterials have a number of key physicochemical properties that make them particularly attractive as separation media for water purification. On a mass basis, they have much larger surface areas than bulk materials. Thus, they are ideal building blocks for developing high-capacity sorbents with the ability to be functionalized to enhance their affinity and selectivity. Nanomaterials can serve as high-capacity and recyclable ligands for cations, anions, radionuclides, and organic compounds. They provide extraordinary opportunities for developing more efficient water-purification catalysts and redox-active media due to their large surface areas and their size- and shape-dependent optical and electronic properties.

31.1 Types of Filtration

Water treatment processes employ several types of membranes. These include microfiltration, ultrafiltration, reverse osmosis, and nanofiltration membranes:

1. Microfiltration (MF) is characterized by a membrane pore size between 0.05 and 2 μm and operating pressures below 2 bar. MF is primarily

used to separate particles and bacteria from other smaller solutes.

2. Ultrafiltration (UF) is characterized by a membrane pore size between 2 nm and 0.05 µm and operating pressures between 1 and 10 bar. UF is used to separate colloids such as proteins from small molecules such as sugars and salts.
3. Nanofiltration (NF) is characterized by a membrane pore size between 0.5 and 2 nm and operating pressures between 5 and 40 bar. NF is used to achieve separation between sugars, other organic molecules, and multivalent salts on the one hand from monovalent salts and water on the other. Nanofiltration, however, does not remove dissolved compounds.

   In recent times, research in the application of nanofiltration techniques has been extended from separation of aqueous solutions to separation of organic solvents to homogeneous catalysis, separation of ionic liquids, food processing, etc. [31.6, 7]. In the literature, two main terms are used to denote this process, viz. organic solvent nanofiltration (OSN) and solvent resistant nanofiltration (SRNF). Two types of membranes are most commonly used: cellulose acetate based and polyamide composites. Membrane configurations typically include spiral wound and hollow fiber. Operational conditions and useful life vary depending on the type of membrane selected, the quality of the feedwater, and the process operating parameters.
4. Reverse osmosis (RO) or hyperfiltration is a physical separation process in which properly pretreated source water is delivered at moderate pressures against a semipermeable membrane. In reverse osmosis, the two solutions are separated by a semipermeable membrane, but pressure is applied to reverse the natural flow of the water as shown in Fig. 31.2. This forces the water to move from the more concentrated solution to the weaker. Thus, the contaminants end up on one side of the semipermeable membrane while the pure water is on the other side. The mechanism of solvent transport in RO is similar to that of NF [31.8].

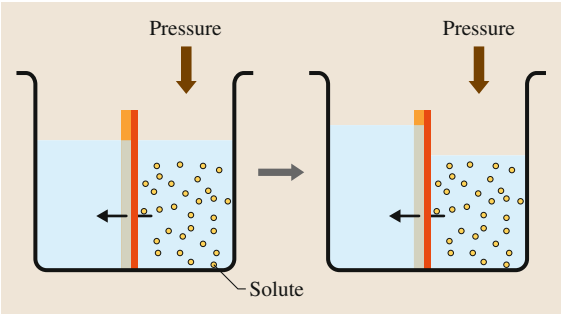


Fig. 31.2 Principle of reverse osmosis

31.2 Mechanisms of Filtration

The basic mechanism of filtration at such a small scale is governed by the Donnan effect of charge balance [31.9, 10]. When different ions diffuse through a membrane, the speed of diffusion varies from ion to ion. Sometimes, a variety of ions are slowed down and others are sped up in order to maintain charge neutrality. This effect becomes more prominent with very small pore sizes and the charge associated with the membranes. Rejection of divalent anions is higher than for monovalent anions because of the charge effect. Because the membrane must still maintain chemical equilibrium on both sides, rejection of monovalent anions will actually decrease as the concentration of divalent anions is increased in a multicomponent feed solution. In some cases this phenomenon can be so pronounced that negative rejection of monovalent anions occurs. Such charge accumulation on the feed end of the membrane leads to concentration polarization. A schematic of this mechanism is shown in Fig. 31.3.

Another proposed mechanism is dielectric exclusion, which generally does not play a role in ultrafiltration or microfiltration but which is of major importance in electrodialysis [31.11, 12]. Due to the charge of the membrane and the dipole moment of water, water molecules will show a polarization in the pore. This polarization results in a decrease of the dielectric constant inside the pore, thereby making it less favorable for a charged solute to enter. However, even in the situation in which the dielectric constant inside the pore is equal to that of water, a change in the electrostatic free energy of the ion occurs when the ion is transferred from the bulk into the pore. This also results in exclusion. The relative importance of these two mechanisms in NF is still a point of debate in the scientific community. Most of the literature on NF

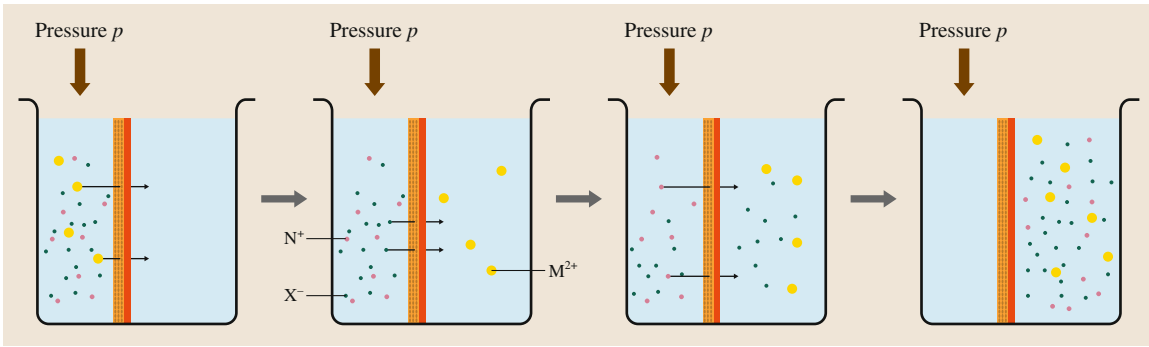


Fig. 31.3 Donnan mechanism of charge balance in nanofiltration

reports the Donnan effect as the distribution mechanism [31.13–15].

Various models have been proposed for the transport of solvent through membranes. These include the Kedem and Katchalsky model, Spiegler and Kedem model, solution-diffusion model, and solution-diffusion imperfection model. Transport of the solvent is accomplished through the free volume between the segments of the polymer of which the membrane is constituted. The operating pressures in RO are generally between 10 and 100 bar, and this technique is mainly used to remove water. Currently, more than 90% of the RO market is in the production of municipal drinking water and ultrapure industrial water. The remaining 10% is used in important separation processes in various applications.

On the basis of their composition and physical nature across the cross-section of the membrane, membranes are also classified as either isotropic or anisotropic. There are two main types of anisotropic membranes: phase-separation membranes and thin-film composite membranes. Anisotropic phase-separation membranes are often called Loeb–Sourirajan membranes, referring to the people who are credited with initially developing them. These phase-separation membranes are homogeneous in chemical composition but not in structure. Loeb–Sourirajan membranes often consist of a rather dense layer of polymer on the surface of an increasingly porous layer. Thin-film composite membranes are both chemically and structurally heterogeneous [31.16]. The most commonly used materials for RO are cellulose acetate, polyamide, and thin-film composites, prepared by interfacial polymerization on the surface of a porous support [31.17–20].

31.3 Carbon Nanotube Membrane Filters

Carbon nanotubes (CNT) are an allotrope of carbon with tubular structure having diameter on the nanometer scale. Carbon atoms in nanotubes are covalently bonded to each other to form hexagonal rings, as in the case of a monolayer of graphite. They exhibit extraordinary strength and unique electrical properties, and are efficient thermal conductors. The chemical bonding of nanotubes is composed entirely of sp^2 bonds, which are stronger than the sp^3 bonds found in diamonds and provide nanotubes with their unique strength. CNTs have attracted considerable interest since their discovery. They have been well investigated in order to exploit their superior properties and multifarious applications owing to their novel properties. CNTs have been extensively used for Li-ion secondary batteries [31.21–25], nanofiltration [31.26–28], hydrogen storage in fuel cells [31.29–32], and supercapacitors [31.33–36]. End/sidewall-localized COOH and NH_2 groups generated by oxidation of CNTs have been exploited for covalent attachment of biomolecular probes [31.37–41], polymers [31.37, 42–44], and metallic particles [31.45–48].

Recently, molecular transport through CNTs and the interstices between vertically aligned CNTs has attracted much attention due to its outstanding mass transport properties. CNTs serve as a suitable membrane that shows an enhanced transport rate of water, by almost four to five orders of magnitude as compared

with other porous materials of similar size, also being very close to that of biological membrane channels such as aquaporin-1 [31.49]. A typical schematic view of this novel phenomenon is shown in Fig. 31.4, where the inner diameter is 7 nm. Molecular dynamics simulation studies predict extremely fast liquid and gas mass transportation through the inner core, as was also experimentally verified [31.50, 51]. Thus, CNT membranes, serving as a technological alternative to the existing reverse osmosis process for desalination, are of great interest [31.52, 53].

For more macroscopic measurements, the flow velocity of a liquid v through a porous membrane can be predicted using the Hagen–Poiseuille equation and is given by

$$v = \frac{\varepsilon_p \mu r^2 \Delta p}{8\mu\tau L}\,, \tag{31.1}$$

where ε_p is the relative porosity, r is the pore radius, p is the applied pressure, μ is the dynamic viscosity, τ is the tortuosity, and L is the pore length. The basic assumptions behind this equation are laminar flow and no slip at the boundary layer (i. e., the velocity of the fluid at the CNT wall is zero). Pressure-driven flow measurements for liquid hexane, decane, water, ethanol, and isopropyl alcohol in CNT membrane were reported by *Majumder* et al. [31.49] based on (31.1), with flow velocity for these liquids of $(5.6, 0.67, 26.1 \pm 17.2, 4.5, 1.12) \times 10^{-2}$ m/s; the enhancement factors obtained for the mentioned liquids were $(1.09, 3.9, 6 \pm 1.6, 3.2, 1.4) \times 10^4$, respectively, calculated as

$$\text{Enhancement factor} = \frac{\text{Experimentally observed flow velocity}}{\text{Hagen–Poiseuille flow velocity}}\,.$$

In addition, there is considerable interest in integrating nanoporous membranes into microfluidic devices, thus enhancing the multiple functionality of such devices [31.54–56].

31.3.1 Structure and Properties of CNTs

A few key studies have explored the structure of carbon nanotubes using high-resolution microscopy techniques, confirming that the nanotubes are cylindrical in structure based on the hexagonal lattice of carbon atoms that forms crystalline graphite. Three types of nanotubes are possible, called armchair, zigzag, and chiral nanotubes, depending on how the two-dimensional graphene sheet is *rolled up*.

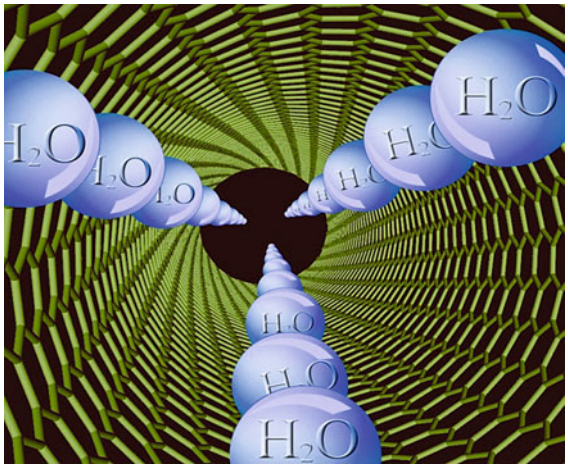


Fig. 31.4 Water molecules passing quickly through the inner core of a carbon nanotube

These different types are most easily explained in terms of the unit cell of the carbon nanotube, i. e., the smallest group of atoms that defines its structure (Fig. 31.5). The so-called chiral vector of the nanotube, $\boldsymbol{C}_h$, is defined by $\boldsymbol{C}_h = n\boldsymbol{a}_1 + m\boldsymbol{a}_2$, where $\boldsymbol{a}_1$ and $\boldsymbol{a}_2$ are unit vectors in the two-dimensional hexagonal lattice, and n and m are integers. Another important parameter is the chiral angle, which is the angle between $\boldsymbol{C}_h$ and $\boldsymbol{a}_1$.

When the graphene sheet is rolled up to form the cylindrical part of the nanotube, the ends of the chiral vector meet each other. The chiral vector thus forms the circumference of the nanotube's circular cross-section, and different values of n and m lead to different nanotube structures. Armchair nanotubes are formed when $n = m$ and the chiral angle is 30°. Zigzag nanotubes are formed when either n or m is zero and the chiral angle is 0°. All other nanotubes, with chiral angle intermediate between 0 and 30°, are known as chiral nanotubes.

The parameters of nanotubes are determined by their diameter and chiral angle, both of which depend on n and m. The diameter d_t is simply the length of the chiral vector divided by π, and we find that $d_t = (\sqrt{3}/\pi) a_{C-C}(m^2 + mn + n^2)^{1/2}$, where a_{C-C} is the distance between neighboring carbon atoms in the flat sheet. In turn, the chiral angle is given by $\tan^{-1}(\sqrt{3}n/2m + n)$.

Multi-walled (MW) CNTs are nanotubes with more than one wall, and their diameters are of the order of

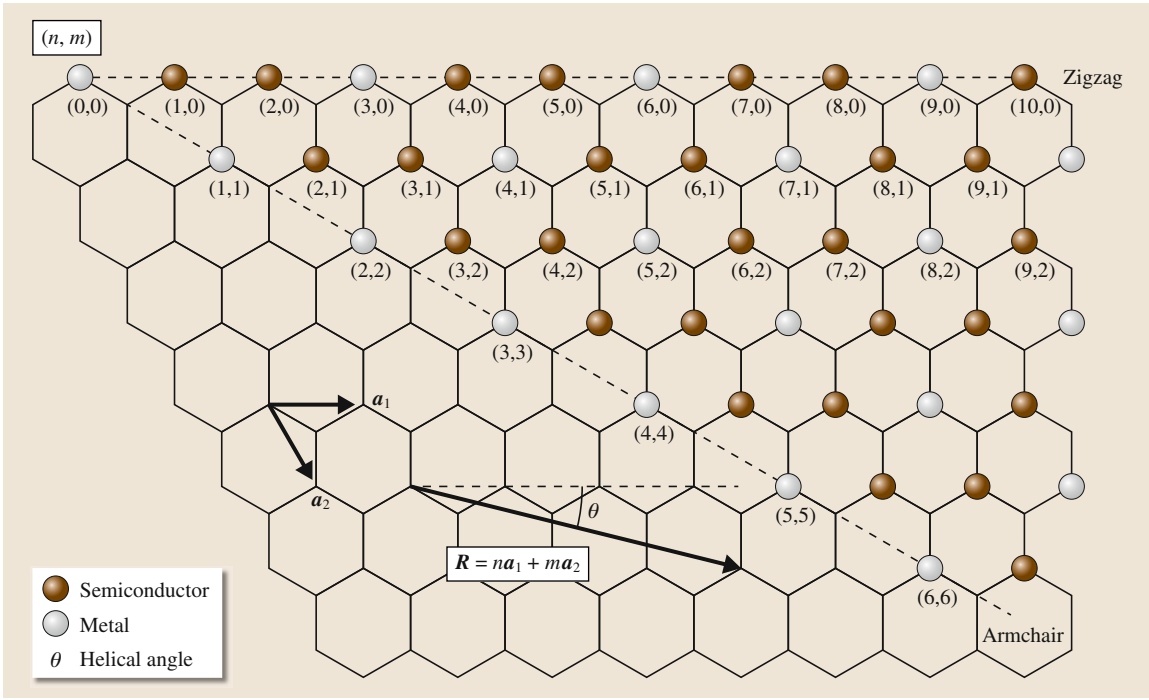


Fig. 31.5 The chiral vector is defined on the honeycomb lattice of carbon atoms by the unit vectors $\boldsymbol{a}_1$ and $\boldsymbol{a}_2$ with respect to the zigzag axis. Along the zigzag axis $\theta = 0°$, and along the armchair axis $\theta = 30°$. Possible vectors are specified by pairs of integers (n, m)

a few tens of nanometers. There are two models which can be used to describe the structures of multi-walled nanotubes. In the Russian doll model, sheets of graphite are arranged in concentric cylinders. In the parchment model, a single sheet of graphite is rolled up around itself, resembling a scroll of parchment or a rolled-up newspaper. The interlayer distance in multi-walled nanotubes is close to the distance between the graphene layers in graphite, approximately 3.4 Å.

CNTs exhibit a wide range of mechanical, optical, and electronic properties. Carbon nanotubes are the strongest and stiffest materials yet discovered in terms of tensile strength and elastic modulus, respectively. This strength results from the covalent sp^2 bonds formed between the individual carbon atoms. In the year 2000, a multi-walled carbon nanotube was tested to have a tensile strength of 63 GPa. Under excessive tensile strain, the tubes will undergo plastic deformation. This deformation begins at strains of approximately 5% and can increase. Geometrical considerations suggest that carbon nanotubes should be much softer in the radial direction than along the tube axis. Indeed, transmission electron microscope (TEM) observations of radial elasticity suggest that even the van der Waals forces can deform two adjacent nanotubes [31.57, 58].

Owing to their unique structure consisting of sp^2 hybridized carbon, CNTs exhibit excellent electrical conductivity along their axial direction. Their conductivity is significantly low along the radial direction. For a given (n, m) nanotube, if $n = m$, the nanotube is metallic, and if $n - m$ is a multiple of 3, then the nanotube is semiconducting with a very small bandgap; otherwise, the nanotube is a moderate semiconductor. Multi-walled carbon nanotubes with interconnected inner shells show superconductivity with a relatively high transition temperature $T_c = 12$ K.

CNTs are good thermal conductors along the axis of the tube and are equally good insulators along the lateral direction to the tube axis. The type of conduction most commonly exhibited by CNTs is known as *ballistic conduction*. A single-walled carbon nanotubes (SWCNTs) has a room-temperature thermal conductivity along its axis of about 3500 $W\,m^{-1}\,K^{-1}$ as compared with 385 $W\,m^{-1}\,K^{-1}$ for copper, which is the most widely used conductor [31.59–61].

31.3.2 Types of CNT Membranes in Nanofiltration

Primarily, there are five approaches to the synthesis of membranes based on CNTs:

1. Deposition of carbonaceous materials inside preexisting ordered porous membranes, such as anodized alumina, also known as template-assisted open-ended CNT membranes [31.62, 63].
2. Membranes based on the interstices between nanotubes in a vertical array of CNTs, subsequently referred to as aligned-array outer-wall CNT membranes [31.64].
3. Vertically aligned open-ended CNTs surrounded by an inert polymer or ceramic matrix, or open-ended CNT/polymer composite membranes [31.65, 66].
4. Membranes composed of nanotubes in the form of a thin mat, also known as buckypaper membranes [31.67–69].
5. Multistacked membranes of aligned CNT bundles.

Template-Assisted Open-Ended CNT Membranes

In this approach, a preexisting ordered porous ceramic membrane (alumina) acts as a template for deposition of carbonaceous materials, usually using chemical vapor deposition (CVD) [31.62, 64–66, 70] at high temperatures, forming pores with reduced dimensions. Ceramic membrane-based templates fabricated by electrochemical anodization of metal films have very low porosity ($< 10\%$), are mechanically very brittle, are often irreproducible (usually having less than 5 nm pore size), and have controllable pore size distribution. These membranes have great potential for application in size-based separation [31.71] and as catalytic membrane reactors [31.72], which upon further modification by carbonaceous materials leads to many possibilities. A schematic representation of carbon nanotubes grown inside an anodized alumina template and a scanning electron micrograph of partially dissolution of the template are shown in Fig. 31.6a,b.

The synthesis and characterization of template-synthesized membranes have been pioneered by Martin's group at the University of Florida. A typical schematic and scanning electron microscopy (SEM) image of a template-synthesized CNT membrane is shown in Fig. 31.6. The carbonaceous materials deposited inside the alumina template by CVD of ethylene can reduce the pore size from ≈ 300 to 200 nm, but further reduction was not observed [31.62]. Since the faster kinetics of this deposition procedure is less controllable for obtaining smaller pore dimension, Martin's later work was dedicated to the use of more well-controlled solution-based electroless deposition techniques for steric separation of small molecules [31.73]. In this context, *Alsyouri* et al. [31.70], used trimethyl ammonium and water for CVD deposition, resulting in a reduction of the porosity of ≈ 20 nm templates and not their pore size.

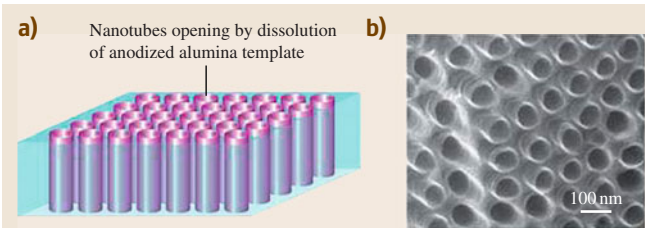


Fig. 31.6 **(a)** Schematic representation of carbon nanotubes grown inside an anodized alumina template; and **(b)** scanning electron micrograph of partial dissolution of the template

CNT membranes synthesized by this method also contain amorphous or partially graphitized CNTs and are chemically different from membranes based on highly ordered graphitic CNTs. They can, however, be graphitized by heat treatment at higher temperature ($> 2000\,^{\circ}\mathrm{C}$) [31.74].

In this regard, it is valuable to point readers to the fabrication of finely controllable, well-branched, and crystallized CNT architectures by *Ajayan* and coworkers [31.75] using this template approach. These have smaller pore dimensions at one end and larger pore structure at the other end, similar to the asymmetric membranes usually used for filtration purposes.

The excellent mass transport properties of these novel nanoscale architectures are of much interest in water vapor/oxygen [31.70] and electroosmotic transport [31.62]. A major advantage of the template synthesis approach is that the modular components of thin-film deposition, electrochemical treatment, and CVD can be integrated into microfluidic device fabrication platforms. However, other approaches using as-formed graphitic CNTs seem to be more realistic for producing CNT membranes for large-scale applications.

Partition of water vapor from air by a membrane was carried out using the apparatus shown in Fig. 31.7 [31.70]. CVD-modified Anopore membranes were carefully fixed in a stainless-steel permeation cell. A 100 cm^3/min mixture of dry air and wet air was established on the upstream side of the sample. Dry

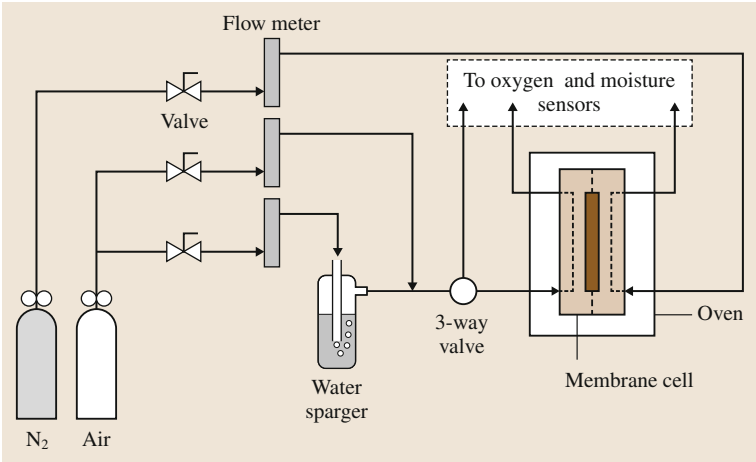


Fig. 31.7 Water vapor separation system

nitrogen from a cylinder was passed at a flow rate of 75 cm^3/min in cross-flow fashion over the downstream side of the sample. Different upstream humidity was acquired by changing the flow rate of dry air and wet air, with the total flow rate kept at about 100 cm^3/min. The temperature was kept at about 25 °C. The relative humidity and oxygen content of the streams were respectively detected by a humidity and oxygen sensors. The occurrence of each species was calculated from the permeation flux of that species divided by its transmembrane partial pressure. Then, the water to oxygen separation factor was obtained from the ratio of water to oxygen molar fraction in the outlet of downstream and that in the outlet of the upstream.

In another example of electroosmotic flow (EOF) across a carbon nanotube membrane (CNM), the membrane separates two electrolyte solutions and an electrode in each solution passes a constant ionic current through the nanotubes [31.62]. EOF was investigated by measuring the flux of a probe molecule (phenol) across the CNM. The as-synthesized CNMs have anionic surface charge, and EOF is in the direction of cation migration across the membrane.

Membranes Formed from Aligned Arrays of CNTs

In the past two decades, production of controlled nanostructure composed of aligned CNTs has become a subject of interest due to its interesting anisotropic properties. Aligned arrays of CNTs can be used as membranes, where transport occurs largely through the interstices between the CNTs, as shown in Figure 31.8a,b. The CNTs in this membrane structure are held together by van der Waals interactions, and the pore size of the membrane is usually in the range of 40–100 nm – suitable for ultrafiltration applications.

The earliest report of aligned MWCNT films was by *deHeer* et al. in 1995 [31.76], using the arc evaporation process. Subsequently, other methods, such as CVD, a scalable and industrially viable process, became popular [31.77]. Aligned MWCNTs were also grown on nickel-coated glass substrates by plasma-enhanced hot-filament CVD from a mixture of acetylene and ammonia below 666 °C [31.78], but considerable bamboo-type structures limit their flowthrough applicability. Efforts have also been focused on ideal and mass production of MWCNT arrays from a continuous source of ferrocene and xylene at ≈ 650 °C [31.79].

CNTs have several unique properties, including high electrical conductivity and elasticity, which have been exploited in creating stimuli-responsive membranes. An account of such demonstrations and how this effect might influence some technologies is presented in this section.

Researchers have demonstrated that superhydrophobic CNT arrays can be rendered hydrophilic by application of an electric potential. These membranes are analogous to dense outer-wall membranes, but are superhydrophobic; water transport through the CNT arrays can be controlled by the application of an electrical bias to the membrane [31.80].

Although this potential-dependent wicking behavior through the CNT membrane is analogous to the well-known phenomenon of electrowetting, the ability to control water transport through a membrane structure by an external stimulus can be useful in applications where controlled transport of water droplets is necessary, for example, in lab-on-chip devices.

In this context, it is worthwhile to discuss the fabrication of freestanding monolithic uniform macroscopic hollow cylinders having radially aligned carbon nanotube walls, with diameters and lengths up to several centimeters, by *Srivastava* et al. [31.64]. The aligned nanotubes that form the uniform nanoporous, cylindrical membrane walls are synthesized from sprayed ferrocene-derived iron catalyst particles; the nanotubes grow in radial directions on the walls of removable silica tube templates. They have been used as filters to demonstrate their utility in two important settings: the elimination of multiple components of heavy hydrocarbons from petroleum – a crucial step in postdistillation of crude oil – with a single-step filtering process, and the filtration of bacterial contaminants such as *Escherichia coli* or the nanometer-sized poliovirus (≈ 25 nm) from water. A major advantage of using nanotube filters over conventional membrane filters lies in the fact that they can be cleaned repeatedly after each filtration process to regain their full filtering efficiency. A simple process of ultrasonication and autoclaving ($\approx 121\,^{\circ}$C for 30 min) was found to be sufficient for cleaning these filters. While conventional membranes are not reusable due to strong bacterial adsorption over the membrane surface, this organized nanotube architecture is reusable and can be operated at temperature of $\approx 400\,^{\circ}$C, which is several times higher than the highest operating temperatures of conventional polymer membrane filters ($\approx 52\,^{\circ}$C). The process of filtration is shown in Fig. 31.9a,b.

Open-Ended CNT/Polymer Composite Membranes

Membranes composed of open-ended CNTs have recently aroused much interest. In this approach, a composite film is synthesized from an aligned array of CNTs and a space-filling polymer [31.65] or ceramic matrix [31.66], with the openings at the ends of the CNTs formed by a plasma oxidation process. These open-ended CNT channels acts as the canal for molecular transport. A schematic and SEM image of a typical nanotube membrane fabricated by such a process is shown in Fig. 31.10a,b. The choice of a suitable polymer is important: among the various polymers, polystyrene is largely explored due to its high wettability with CNTs, resulting in a dense MWCNT array ($\approx 10^{10}$ tubes/cm^2).

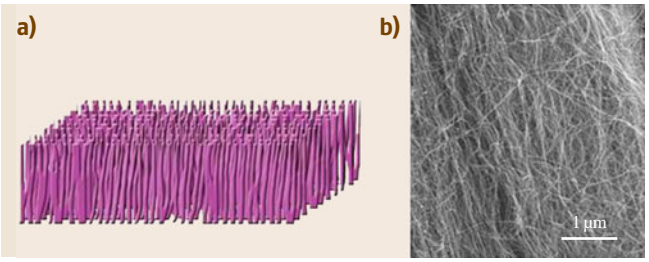


Fig. 31.8 **(a)** Schematic representation of aligned CNTs membrane. **(b)** SEM image indicating aligned array of dense nanotubes. Transport occurs primarily through the interstices between nanotubes; moreover, transport through the inner core of the open nanotubes may also occur

The CNT/polymer film grown over the quartz substrate is removed by a hydrofluoric acid (HF) etch. The vertically oriented CNTs in the polymer matrix often have a graphitic end cap (with a larger concentration of defects and being easily oxidized compared with the side-walls) or a catalyst metal particle sealing the graphitic interiors, which are etched away using mild plasma oxidation without degrading the mechanical structure of the CNTs [31.81, 82].

This plasma oxidation process is advantageous for the membrane fabrication process, since it removes excess polymer by oxidative trimming to make the membrane electrically conducting. Moreover, it also removes amorphous carbon and iron impurities by HCl treatment. Additionally this plasma oxidation process introduces functional groups (mainly −COOH) at the CNT tips, making these membranes suitable for chemical and biological applications.

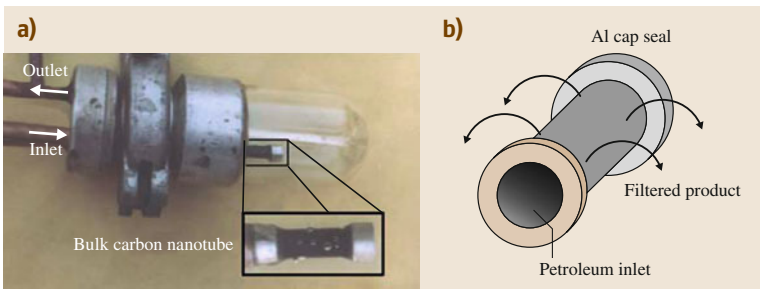


Fig. 31.9a,b Petroleum filtration setup using a nanotube filter. **(a)** Photograph of the arrangement used for heavy hydrocarbon separation. The *inset* shows the bulk tube mounted as a filter. The tube is closed at one end (*right*) with an aluminum cap, and the other end is kept open, serving as an inlet port for injection of petroleum. **(b)** Schematics of the petroleum dynamics through the bulk tubes

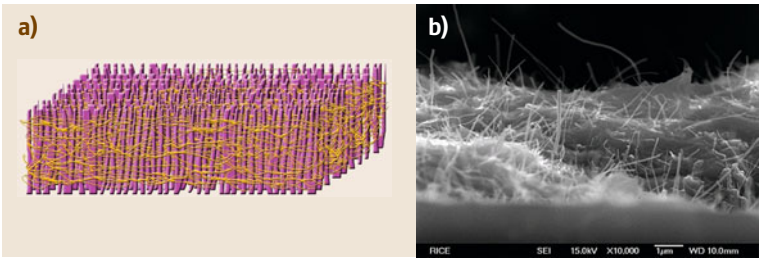


Fig. 31.10 (**a**) Schematic view of an open-ended CNT/polymer composite membrane. (**b**) SEM image representing the cross-section of the membrane with aligned CNTs in an impermeable polymer matrix

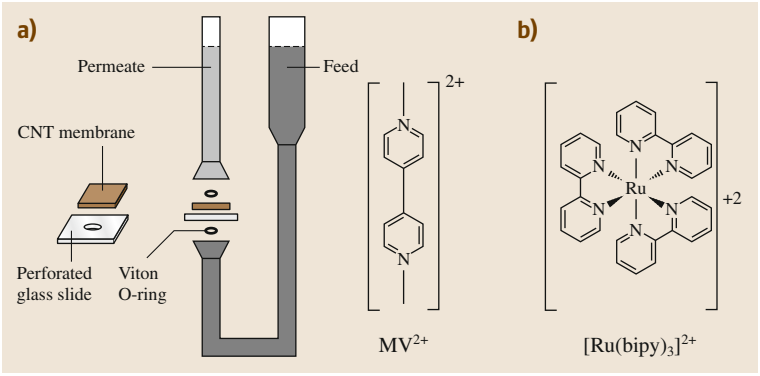


Fig. 31.11 (**a**) Schematic of the permeation cell. The feed solution contains 5 mM $[Ru\text{-}(bipy)_3]^{2+}$ and 5 mM MV^{2+}, the permeate volume is 1.3 ml, and the exposed membrane area is 0.3 cm^2. (**b**) The probe molecules have similar charge but different sizes and shapes. $[Ru\text{-}(bipy)_3]^{2+}$ is a spherical molecule of about 11 Å diameter, and MV^{2+} is a cylindrical molecule of 5 Å equivalent spherical diameter (10 Å long, 3 Å diameter)

The CNT membrane structure after the plasma oxidation process shows a pore size distribution of $\approx (6\pm2)$ nm, which is consistent with TEM observations of the inner core of ≈ 7 nm.

In similar work, aligned CNTs (with < 2 nm diameter) were grown on a Si chip patterned with metal catalyst using a CVD process. The surrounding space between the nanotubes was filled up with a ceramic material (Si_3N_4). Standard etching procedures created openings on the Si chip, and the excess Si_3N_4 and catalyst nanoparticles were removed by Ar-ion milling. Eventually, the CNTs were uncapped by reactive-ion etching [31.66]. The common feature of these two works is that they are based on standard lithography.

More traditional inorganic membrane fabrication research has focused on making robust and cost-efficient CNT membranes, avoiding the use of lithographic tools. In this approach, aligned CNT arrays are grown over macroporous alumina supports and the interstitial space between the CNTs is filled by poly(styrene); however, the viscosity of the polymer is high enough to inhibit its entry into the macroporous alumina support. Mechanical polishing and acid treatment are adopted to remove the polymer overlayer and to open up the CNTs [31.83].

In sum, the fabrication of open-ended CNT membranes is complex, but it offers tighter control over pore size as the transport occurs through the inner cores of the CNTs.

These membranes have been employed mainly in nanoparticle partition and small-molecule separation. Plasma oxidation during the membrane fabrication process establishes carboxylic acid groups on the CNTs' tips that can be modified using carbodiimide-mediated coupling between the carboxylic acid and available amine groups of the functional molecule. Transport through the membrane of two differently sized but equally charged molecules (ruthenium bipyridine and methyl viologen) was quantified in a U-tube permeation cell by UV-Vis spectroscopy [31.84]. The process is depicted in Fig. 31.11a,b.

Owing to their high electrical conductivity, these CNT membranes are used in controlled molecular transport in an effort to mimic the complex functionality of biological voltage-gated membrane channels in an artificial system. In simplified terms, biologists have shown that molecules attached to the walls and entrances of CNT membranes can be actuated electrostatically, thereby selectively occluding the pores and altering the transport of molecules through the pores [31.85].

The CNTs are conductors inside an insulating matrix, allowing for concentration of the electric field at the tips of the CNTs for voltage gating or use as an elec-

trode. In these experiments, the electrically conducting CNT membrane is used as the electrode in a three-electrode electrochemical cell, as shown in Fig. 31.12. To make the aligned CNT membrane an optimal platform for ion channel mimetics, it is essential to increase the functional density of tethered molecules only at the entrances to the CNT cores.

Voltage-gated membrane channels, in which large macromolecules were tethered to the conducting pores of CNTs that can be actuated to selectively occlude the pores. This results in voltage-controlled transport, mimicking biological membranes, for transdermal drug delivery-type applications.

Buckypaper Membrane

CNTs are recognized to have strong affinity to aggregate due to van der Waals interactions, and it is these van der Waals interactions which also hold the CNTs together into cohesive CNT sheets, also known as buckypaper (BP). These have been demonstrated to have various potential applications, e.g., as hydrogen storage materials [31.86], anode materials in lithium-ion batteries [31.87], actuators [31.88], sensors [31.89], and artificial muscles [31.90].

Buckypaper sheets are fabricated by continuous filtration of CNTs suspension in tetrahydrofuran (THF) using a microfiltration setup under high vacuum. A polytetrafluoroethylene (PTFE) membrane is used for the filtration process. After the completion of filtration, the sample is dried in a vacuum oven, and then a thin sheet of buckypaper mat is carefully removed. The process of synthesis of bucky paper membrane,

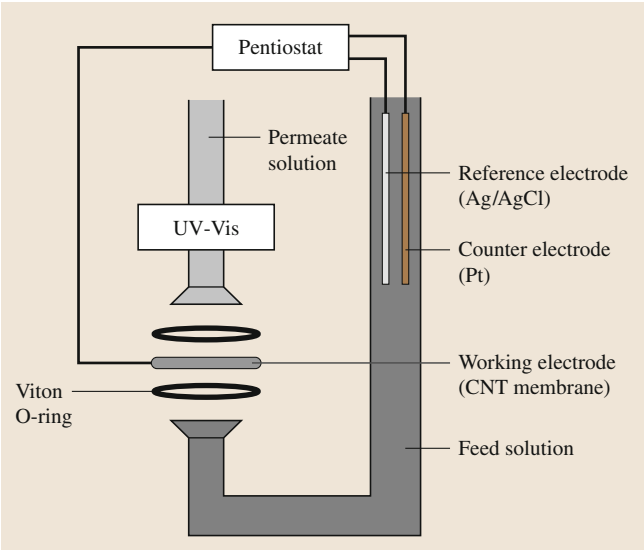


Fig. 31.12 Schematic of the experimental setup for measuring transport through membranes as a function of applied voltage. Note that the CNT membrane placed between the fed and permeate solution is the working electrode. The permeate volume is 0.8 ml, and the exposed membrane area is 0.3 cm^2

an SEM image, and the schematic are shown in Fig. 31.13a–c.

Longer, narrower (fewer walled), and purer nanotubes typically lead to stronger buckypaper with higher tensile strength. With increasing MWCNTs diameter, the attractive van der Waals forces between CNTs become less efficient, leading to buckypaper with lower

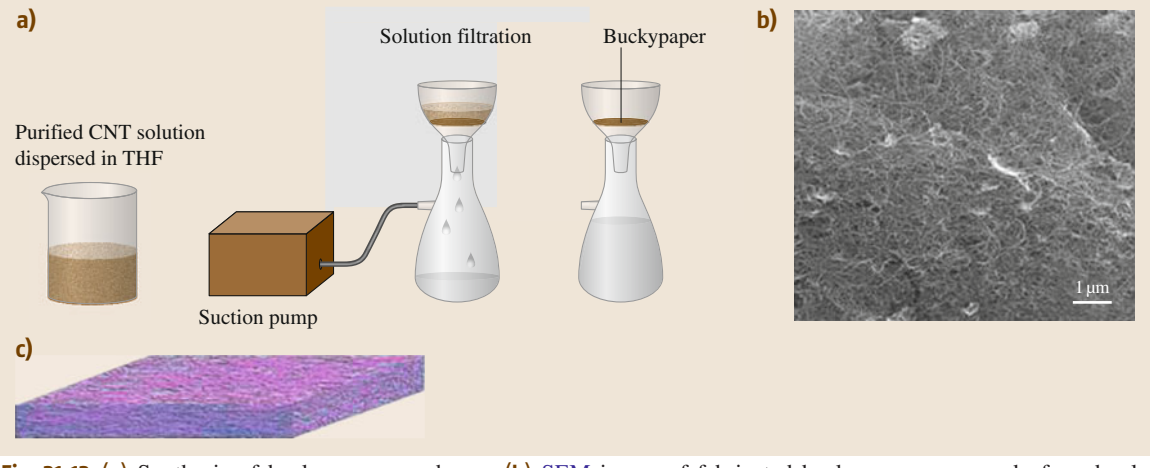


Fig. 31.13 **(a)** Synthesis of buckypaper membrane. **(b)** SEM image of fabricated buckypaper composed of randomly oriented CNTs. **(c)** Schematic representation of buckypaper

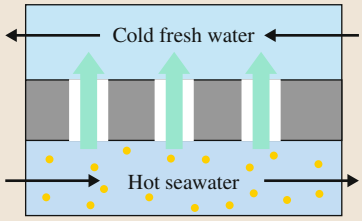


Fig. 31.14 Process of direct contact membrane distillation

tensile strength and reduced cohesiveness. Generally, these are more vulnerable to breakage, so different approaches to strengthen the BPs, such as electron irradiation [31.91], chemical treatment [31.92], polymer intercalation [31.93], and graphitization [31.51], have been theoretically and experimentally investigated, with some positive results.

Recently, a newer technique has been employed, where BPs were infused with polycarbonate (PC) by means of vacuum-aided solution infiltration. This procedure is capable of treating large-size BPs and is readily scalable for mass production [31.94]. A schematic of a buckypaper mat formation and a typical SEM micrograph are shown in Fig. 31.13a,b, where a mat is formed due to the entangled CNTs (Fig. 31.13c). This CNT carpet is so dense that vacuum-assisted filtration can be used to separate desired filtrates.

Buckypapers offer incredible porosity and high specific surface area in a three-dimensional (3-D) network, making them suitable for water purification by a process called direct contact membrane distillation. This technique is an alternative to reverse osmosis and other desalination techniques, particularly when the concentration of solutes is high. As illustrated in Fig. 31.14, the buckypaper is used as a highly hydrophobic membrane to separate a feed of hot sea or salty water from a permeate of cold fresh water. While liquid cannot cross the air gap formed by the membrane, water vapor is able to pass through the pores from the hot feed to the cold permeate, driven by the difference in partial vapor pressure. This vapor then condenses on the permeate side, creating fresh water.

Multistacked Membranes of Aligned CNT Bundles

This process is very similar to that reported by *Andrews* et al. [31.79], where MWCNT arrays are fabricated from a continuous source of ferrocene and xylene using CVD, wherein instead of a single bundle, multistacked bundles can be grown. In this process, a single bundle of aligned CNTs is first grown for a few minutes, then the process is stopped. A successive layer is again grown over this, following the same process. In this way, a membrane composed of the desired number of aligned CNT stacks can be grown. The advantage of this process lies in the fact that, by changing the concentration of ferrocene and by controlling the flow rate of xylene–ferrocene solution, one can tune the density and length of the nanotubes. Therefore, one can produce a desired number of stacks with different density and preferred length of carbon nanotubes during the growth process.

There is also a possibility of sandwiching another thin layer of hydrophilic/hydrophobic materials between the CNT stack to provide desired functionality and specificity to the membrane in filtration processes. A schematic of the growth process and a typical SEM micrograph are shown in Fig. 31.15a,b. A 20 μm-thick membrane formed from 25 stacks of well-aligned CNT bundles has been fabricated. For high-quality filtration, the length of the column is an important parameter. Because of the nanochannels, the column length is reduced and therefore the size of the device is reduced significantly. Nanochannels made up of stacked CNTs will thus provide an advantage for filtering different kinds of pollutants. Another advantage is that, by changing the numbers of stacks, the filtration rate as well as the kind of filtration are modified.

CNT membranes can be widely applied for many potential commercial applications. Extensive research is being conducted in this area, trying to make efficient use of the extraordinary properties of CNTs. There have been attempts to develop functionalized CNT membranes for mass transport, sensors, chemical, and biochemical applications. CNT membranes can be functionalized with various functional groups such as carboxylic acids [31.95], amines, enzymes, and polyelectrolytes containing charged amino and carboxyl groups to achieve separation of ions by electrostatic adsorption [31.96] or proteins by affinity-based separation [31.97].

Experimental results indicate that liquid-phase treatments tend to introduce carboxylic acid groups, whereas gas-phase treatments introduce less oxidized entities such as hydroxyl and carbonyl groups [31.98].

Water plasma treatment for opening CNTs is most likely to introduce carboxyl groups on the tips of the CNT membrane, because the high reactivity of the plasma precludes its entrance deep into the pores, limiting the functionalization to the surface [31.99].

A model of the functionalization of a cylindrical membrane with carboxyl and amino functional groups

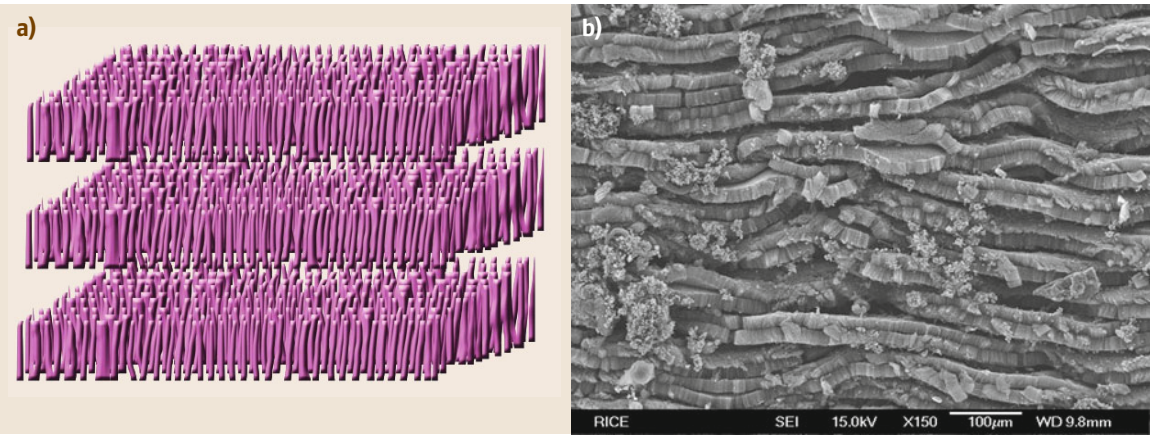


Fig. 31.15 (a) Schematic representation of the formation of multistacked CNT membrane. (b) SEM image shows 25 layers, each 20 μm thick, composed of aligned CNT arrays

is shown in Fig. 31.16b,c. Figure 31.16d presents the nanocomposite structure of this cylindrical membrane and polymer for use in numerous applications. Polymers can also be used as a filler material between the layer. Figure 31.16a shows an SEM image of a fabricated cylindrical membrane.

The concept of membrane reactors, which combine reaction and separation to increase efficiency based on the laws of mass action, is well established [31.100]. The development of electrochemical membrane reactors has been hindered by the lack of electrical conductivity of the membrane materials used to date. As discussed above, the high electrical conductivity and chemical inertness of dense array outer-wall CNT membranes make them a candidate for simultaneous electrochemical reaction and separation, particularly for destruction of hazardous organic compounds [31.101].

The concept of a cross-flow electrochemical membrane reactor based on cylindrically shaped dense array CNT membranes [31.64] with both an open and closed channel is shown in Fig. 31.16e,f.

The organic pollutants containing phenol are fed through the opening of this membrane, using sulfuric acid as the background electrolyte.

Under a constant potential difference between the membrane (anode) and a metallic cathode, the phenol-containing organic pollutants are electrochemically

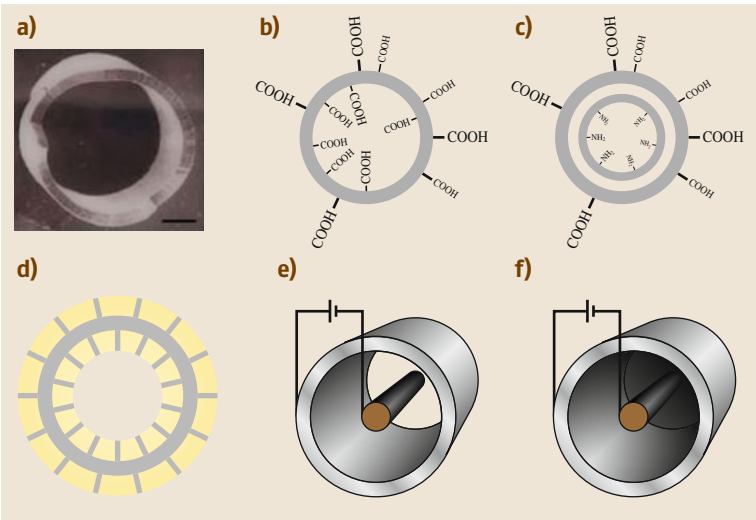


Fig. 31.16 (a) Scanning electron micrograph of a cylindrical CNT membrane. (b) Schematic showing carboxy functionalization of a single layer of this membrane. (c) Stack of two layers with carboxy functional group attached to outer layer and amino terminal groups in inner layer. (d) Membrane filled with polymer composite. (e) Electrochemical oxidation process of organic compounds containing phenol groups to less toxic chemicals such as oxalic acid, CO_2, and H_2O inside the open-channel cylindrical membrane. (f) Closed-channel membrane. The nontoxic chemicals permeate through the wall of the membrane

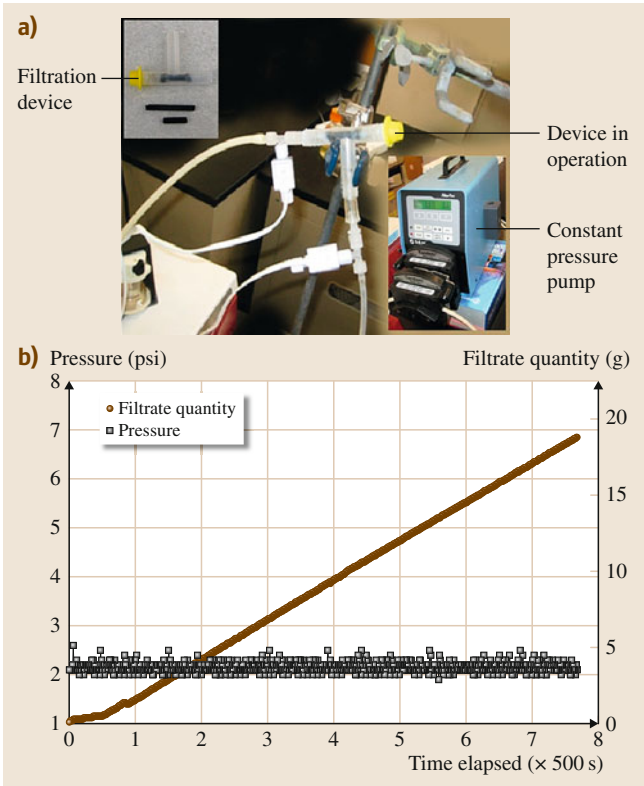


Fig. 31.17 **(a)** Photo of the filtration device, constant-pressure pump, and pressure-driven filtration setup. **(b)** Experimental results of dextran filtration studies. The *black data points* show the constant pressure across the membrane; the *brown data points* show the amount of filtrate increasing with time ◀

oxidized to less toxic compounds such as carbon dioxide, water, and aliphatic compounds such as oxalic acid, which permeate through the wall of the membrane [31.102]. Electrochemical oxidation inside this membrane reactor aims at the mineralization of the contaminants to carbon dioxide, water, and inorganics, or, at least, their transformation into harmless products.

The rate of the filtration process can be further improved by applying a constant pressure along the cylindrical membrane using a constant-pressure pump as shown in Fig. 31.17a. The remaining solution comes out of the membrane from the other end and can be fed again to improve the quality of the filtrate.

The result of dextran (molecular weight 25–35 kDa) filtration studies by applying a constant pressure across a cylindrical CNT membrane is shown in Fig. 31.17b, where the black data points are obtained by continuous monitoring of the pressure difference across the two ends of the membrane during the filtration study, showing that its mechanical strength is high enough to withstand the pressure. The constant-pressure curve shows there is no breakage or distortion in the membrane at this pressure. The other graph shown by brown data points is obtained by measuring the quantity of dextran filtrate against time, showing that the amount of filtrate increases with time, exhibiting linear behavior.

31.4 Future Research Perspectives

In this chapter we have observed that a variety of CNT membranes find different applications in nanofiltration. Research interest in these CNT membranes arose due to their fast mass transport and electrochemical actuation-driven transport and because they represent substitute materials for traditional membranes in the field of membrane technology. These filters may be tailored to specific needs by controlling the nanotube density in the walls and the surface character by chemical functionalization. There are many opportunities for use of these CNT membranes in nanoscale fluidic interconnect-based microfluidic platforms. This wide range of properties, not obvious with traditional membrane materials, is why CNT-based membranes represent a new frontier in membrane science.

References

31.1 M. Takeshi: Progress in membrane science and technology for seawater desalination – A review, Desalination **134**, 47–54 (2001)
31.2 M. Cheryan: *Ultrafiltration and Microfiltration Handbook* (Technomic, Lancaster 1998)
31.3 B. Van Der Bruggen, C. Vandecasteele, T. Van Gestel, W. Doyen, R. Leysen: A review of pressure-driven membrane processes in wastewater treatment and drinking water production, Environ. Progress **22**, 46–56 (2003)

31.4 M. Mulder: *Basic Principles of Membrane Technology* (Kluwer Academic, Dordrecht 1991)
31.5 K. Scott: *Handbook of Industrial Membranes*, 2nd edn. (Elsevier, Amsterdam 1998)
31.6 A.V. Volkov, G.A. Korneeva, G.F. Tereshchenko: Organic solvent nanofiltration: Prospects and application, Russ. Chem. Rev. **77**, 983 (2008)
31.7 C.K. Diawara: Nanofiltration process efficiency in water desalination, Sep. Purif. Rev. **37**, 302–324 (2008)
31.8 J.G. Wijmans, R.W. Baker: The solution-diffusion model: A review, J. Membr. Sci. **107**, 1–21 (1995)
31.9 C. Martin-Orue, S. Bouhallab, A. Garem: Nanofiltration of amino acid and peptide solutions: Mechanisms of Sep, J. Membr. Sci. **142**, 225–233 (1998)
31.10 M.R. Teixeira, M.J. Rosa, M. Nyström: The role of membrane charge on nanofiltration performance, J. Membr. Sci. **265**, 160–166 (2005)
31.11 A.E. Yaroshchuk: Dielectric exclusion of ions from membranes, Adv. Colloid Interface Sci. **85**, 193–230 (2000)
31.12 B. Van der Bruggen, A. Koninckx, C. Vandecasteele: Sep. of monovalent and divalent ions from aqueous solution by electrodialysis and nanofiltration, Water Res. **38**, 1347–1353 (2004)
31.13 T. Tsuru, S.-I. Nakao, S. Kimura: Calculation of ion rejection by extended Nernst–Planck equation with charged reverse osmosis membranes for single and mixed electrolyte solutions, J. Chem. Eng. Jpn. **24**, 511–517 (1991)
31.14 X.-L. Wang, T. Tsuru, S.-I. Nakao, S. Kimura: Electrolyte transport through nanofiltration membranes by the space-charge model and the comparison with Teorell-Meyer-Sievers model, J. Membr. Sci. **103**, 117–133 (1995)
31.15 W.R. Bowen, H. Mukhtar: Characterisation and prediction of Sep. performance of nanofiltration membranes, J. Membr. Sci. **112**, 263–274 (1996)
31.16 A. Sagle, B. Freeman: *Fundamentals of Membranes for Water Treatment*, The Future of Desalination in Texas, Vol. 2 (Texas Water Development Board, Austin 2004) pp. 137–154
31.17 R.J. Petersen: Composite reverse osmosis and nanofiltration membranes, J. Membr. Sci. **83**, 81–150 (1993)
31.18 M. Elimelech, Z. Xiaohua, A.E. Childress, H. Seungkwan: Role of membrane surface morphology in colloidal fouling of cellulose acetate and composite aromatic polyamide reverse osmosis membranes, J. Membr. Sci. **127**, 101–109 (1997)
31.19 S. Kimura, S. Sourirajan: Analysis of data in reverse osmosis with porous cellulose acetate membranes used, AIChE J. **13**, 497–503 (1967)
31.20 S. Belfer, Y. Purinson, R. Fainshtein, Y. Radchenko, O. Kedem: Surface modification of commercial composite polyamide reverse osmosis membranes, J. Membr. Sci. **139**, 175–181 (1998)
31.21 A.S. Claye, J.E. Fischer, C.B. Huffman, A.G. Rinzler, R.E. Smalley: Solid-state electrochemistry of the Li single wall carbon nanotube system, J. Electrochem. Soc. **147**, 2845–2852 (2000)
31.22 E. Frackowiak, S. Gautier, H. Gaucher, S. Bonnamy, F. Beguin: Electrochemical storage of lithium in multiwalled carbon nanotubes, Carbon **37**, 61–69 (1999)
31.23 B. Gao, A. Kleinhammes, X.P. Tang, C. Bower, L. Fleming, Y. Wu, O. Zhou: Electrochemical intercalation of single-walled carbon nanotubes with lithium, Chem. Phys. Lett. **307**, 153–157 (1999)
31.24 H.-C. Shin, M. Liu, B. Sadanadan, A.M. Rao: Electrochemical insertion of lithium into multi-walled carbon nanotubes prepared by catalytic decomposition, J. Power Sources **112**, 216–221 (2002)
31.25 G. Maurin, C. Bousquet, F. Henn, P. Bernier, R. Almairac, B. Simon: Electrochemical intercalation of lithium into multiwall carbon nanotubes, Chem. Phys. Lett. **312**, 14–18 (1999)
31.26 S.T. Mostafavi, M.R. Mehrnia, A.M. Rashidi: Preparation of nanofilter from carbon nanotubes for application in virus removal from water, Desalination **238**, 271–280 (2009)
31.27 Y.L. Li, S. Wang, X. Zhang, J. Wei, C. Xu, Z. Luan, D. Wu, B.Q. Wei: Removal of fluoride from water by carbon nanotube supported alumina, Environ. Technol. **24**, 391–398 (2003)
31.28 M. Yu, H.H. Funke, J.L. Falconer, R.D. Noble: High density, vertically-aligned carbon nanotube membranes, Nano Lett. **9**, 225–229 (2008)
31.29 S. Lee: Hydrogen storage in single-walled carbon nanotubes, Appl. Phys. Lett. **76**, 2877 (2000)
31.30 E. Frackowiak, F. Béguin: Electrochemical storage of energy in carbon nanotubes and nanostructured carbons, Carbon **40**, 1775–1787 (2002)
31.31 N. Rajalakshmi, K.S. Dhathathreyan, A. Govindaraj, B.C. Satishkumar: Electrochemical investigation of single-walled carbon nanotubes for hydrogen storage, Electrochim. Acta **45**, 4511–4515 (2000)
31.32 C. Nutzenadel, A. Züttel, D. Chartouni, L. Schlapbach: Electrochemical storage of hydrogen in nanotube materials, Electrochem. Solid State Lett. **2**, 30–32 (1999)
31.33 K.H. An, W.S. Kim, Y.S. Park, Y.C. Choi, S.M. Lee, D.C. Chung, D.J. Bae, S.C. Lim, Y.H. Lee: Supercapacitors using single-walled carbon nanotube electrodes, Adv. Mater. **13**, 497–500 (2001)
31.34 J.N. Barisci, G.G. Wallace, R.H. Baughman: Electrochemical studies of single-wall carbon nanotubes in aqueous solutions, J. Electroanal. Chem. **488**, 92–98 (2000)
31.35 L. Diederich, E. Barborini, P. Piseri, A. Podestà, P. Milani: Supercapacitors based on nanostructured carbon electrodes grown by cluster-beam deposition, Appl. Phys. Lett. **75**(17), 2662–2664 (1999)

31.36 C. Niu, E.K. Sichel, R. Hoch, D. Moy, H. Tennent: High power electrochemical capacitors based on carbon nanotube electrodes, Appl. Phys. Lett. **70**, 1480–1482 (1997)

31.37 T. Ramanathan, F.T. Fisher, R.S. Ruoff, L.C. Brinson: Amino-functionalized carbon nanotubes for binding to polymers and biological systems, Chem. Mater. **17**, 1290–1295 (2005)

31.38 A. Hirsch: Functionalization of single-walled carbon nanotubes, Angew. Chem. Int. Ed. **41**, 1853–1859 (2002)

31.39 Y.-P. Sun, K. Fu, Y. Lin, W. Huang: Functionalized carbon nanotubes: Properties and applications, Acc. Chem. Res. **35**, 1096–1104 (2002)

31.40 S. Banerjee, M.G.C. Kahn, S.S. Wong: Rational chemical strategies for carbon nanotube functionalization, Chemistry **9**, 1898–1908 (2003)

31.41 D. Tasis, N. Tagmatarchis, V. Georgakilas, M. Prato: Soluble carbon nanotubes, Chemistry **9**, 4000–4008 (2003)

31.42 K.M. Lee, D.W. Chang, F.Y. Yang, L. Dai: Functionalization of carbon nanotubes with polymers, Polym. Prepr. **46**, 197–198 (2005)

31.43 R. Czerw, Z. Guo, P.M. Ajayan, Y.-P. Sun, D.L. Carroll: Organization of polymers onto carbon nanotubes: A route to nanoscale assembly, Nano Lett. **1**, 423–427 (2001)

31.44 M. Moniruzzaman, K.I. Winey: Polymer nanocomposites containing carbon nanotubes, Macromolecules **39**, 5194–5205 (2006)

31.45 R. Zanella, E.V. Basiuk, P. Santiago, V.A. Basiuk, E. Mireles, I. Puente-Lee, J.M. Saniger: Deposition of gold nanoparticles onto thiol-functionalized multiwalled carbon nanotubes, J. Phys. Chem. B **109**, 16290–16295 (2005)

31.46 K. Jiang, A. Eitan, L.S. Schadler, P.M. Ajayan, R.W. Siegel, N. Grobert, M. Mayne, M. Reyes-Reyes, H. Terrones, M. Terrones: Selective attachment of gold nanoparticles to nitrogen-doped carbon nanotubes, Nano Lett. **3**, 275–277 (2003)

31.47 B.M. Quinn, C. Dekker, S.G. Lemay: Electrodeposition of noble metal nanoparticles on carbon nanotubes, J. Am. Chem. Soc. **127**, 6146–6147 (2005)

31.48 V. Georgakilas, V. Tzitzios, D. Gournis, D. Petridis: Attachment of magnetic nanoparticles on carbon nanotubes and their soluble derivatives, Chem. Mater. **17**, 1613–1617 (2005)

31.49 M. Majumder, N. Chopra, R. Andrews, B.J. Hinds: Nanoscale hydrodynamics: Enhanced flow in carbon nanotubes, Nature **438**, 44 (2005)

31.50 G. Hummer, J.C. Rasaiah, J.P. Noworyta: Water conduction through the hydrophobic channel of a carbon nanotube, Nature **414**, 188–190 (2001)

31.51 A.I. Skoulidas, D.M. Ackerman, J.K. Johnson, D.S. Sholl: Rapid transport of gases in carbon nanotubes, Phys. Rev. Lett. **89**, 185901 (2002)

31.52 M.A. Shannon, P.W. Bohn, M. Elimelech, J.G. Georgiadis, B.J. Mariñas, A.M. Mayes: Science and technology for water purification in the coming decades, Nature **452**, 301–310 (2008)

31.53 M. Elimelech, W.A. Phillip: The future of seawater desalination: Energy, technology, and the environment, Science **333**, 712–717 (2011)

31.54 M. Whitby, N. Quirke: Fluid flow in carbon nanotubes and nanopipes, Nat. Nano **2**, 87–94 (2007)

31.55 J.D. Goud, P.M. Raj, J. Liu, R. Narayan, M. Iyer, R. Tummala: Electrochemical biosensors and microfluidics in organic system-on-package technology, Proc. 57th Electron. Compon. Technol. Conf. ECTC'07 (IEEE, Bellingham 2007) pp. 1550–1555

31.56 S. Prasad, Y. Yadav, M. Bothara, V. Kunduru, S. Muthukumar: Nanoporous membrane-based microfluidic biosensors. In: *Microfluidic Devices in Nanotechnology*, ed. by B. Rouge (Wiley, Hoboken 2010) pp. 47–90

31.57 M.-F. Yu, O. Lourie, M.J. Dyer, K. Moloni, T.F. Kelly, R.S. Ruoff: Strength and breaking mechanism of multiwalled carbon nanotubes under tensile load, Science **287**, 637–640 (2000)

31.58 R.S. Ruoff, J. Tersoff, D.C. Lorents, S. Subramoney, B. Chan: Radial deformation of carbon nanotubes by van der Waals forces, Nature **364**, 514–516 (1993)

31.59 R. Saito, G. Dresselhaus, M.S. Dresselhaus: *Physical Properties of Carbon Nanotubes* (World Scientific, Singapore 1998)

31.60 M.M.J. Treacy, T.W. Ebbesen, J.M. Gibson: Exceptionally high Young's modulus observed for individual carbon nanotubes, Nature **381**, 678–680 (1996)

31.61 P. Ajayan, O. Zhou: Applications of carbon nanotubes, Top. Appl. Phys. **70**, 391–425 (2001)

31.62 S.A. Miller, V.Y. Young, C.R. Martin: Electroosmotic flow in template-prepared carbon nanotube membranes, J. Am. Chem. Soc. **123**, 12335–12342 (2001)

31.63 C. Wang, M. Li, S. Pan, H. Li: Well-aligned carbon nanotube array membrane synthesized in porous alumina template by chemical vapor deposition, Chin. Sci. Bull. **45**, 1373–1376 (2000)

31.64 A. Srivastava, O.N. Srivastava, S. Talapatra, R. Vajtai, P.M. Ajayan: Carbon nanotube filters, Nat. Mater. **3**, 610–614 (2004)

31.65 B.J. Hinds, N. Chopra, T. Rantell, R. Andrews, V. Gavalas, L.G. Bachas: Aligned multiwalled carbon nanotube membranes, Science **303**, 62–65 (2004)

31.66 J.K. Holt, H.G. Park, Y. Wang, M. Stadermann, A.B. Artyukhin, C.P. Grigoropoulos, A. Noy, O. Bakajin: Fast mass transport through sub-2-nanometer carbon nanotubes, Science **312**, 1034–1037 (2006)

31.67 G.T. Pham, Y.-B. Park, S. Wang, Z. Liang, B. Wang, C. Zhang, P. Funchess, L. Kramer: Mechanical and electrical properties of polycarbonate nanotube buckypaper composite sheets, Nanotechnology **19**, 325705 (2008)

31.68 L.F. Dumée, K. Sears, J. Schütz, N. Finn, C. Huynh, S. Hawkins, M. Duke, S. Gray: Characterization and evaluation of carbon nanotube Bucky-Paper membranes for direct contact membrane distillation, J. Membr. Sci. **351**, 36–43 (2010)

31.69 S.M. Cooper, H.F. Chuang, M. Cinke, B.A. Cruden, M. Meyyappan: Gas permeability of a buckypaper membrane, Nano Lett. **3**, 189–192 (2003)

31.70 H.M. Alsyouri, C. Langheinrich, Y.S. Lin, Z. Ye, S. Zhu: Cyclic CVD modification of straight pore alumina membranes, Langmuir **19**, 7307–7314 (2003)

31.71 T. Sano, N. Iguchi, K. Iida, T. Sakamoto, M. Baba, H. Kawaura: Size-exclusion chromatography using self-organized nanopores in anodic porous alumina, Appl. Phys. Lett. **83**, 4438–4440 (2003)

31.72 S.-H. Cho, N.D. Walther, S.T. Nguyen, J.T. Hupp: Anodic aluminium oxide catalytic membranes for asymmetric epoxidation, Chem. Commun., 5331–5333 (2005)

31.73 K.B. Jirage, J.C. Hulteen, C.R. Martin: Nanotubule-based molecular-filtration membranes, Science **278**, 655–658 (1997)

31.74 D. Mattia, M.P. Rossi, B.M. Kim, G. Korneva, H.H. Bau, Y. Gogotsi: Effect of graphitization on the wettability and electrical conductivity of CVD-carbon nanotubes and films, J. Phys. Chem. B **110**, 9850–9855 (2006)

31.75 G. Meng, Y.J. Jung, A. Cao, R. Vajtai, P.M. Ajayan: Controlled fabrication of hierarchically branched nanopores, nanotubes, Proc. Natl. Acad. Sci. USA **102**, 7074–7078 (2005)

31.76 W.A. deHeer, W.S. Bacsa, A. Châtelain, T. Gerfin, R. Humphrey-Baker, L. Forro, D. Ugarte: Aligned carbon nanotube films: Production and optical and electronic properties, Science **268**, 845–847 (1995)

31.77 W.Z. Li, S.S. Xie, L.X. Qian, B.H. Chang, B.S. Zou, W.Y. Zhou, R.A. Zhao, G. Wang: Large-scale synthesis of aligned carbon nanotubes, Science **274**, 1701–1703 (1996)

31.78 Z.F. Ren, Z.P. Huang, J.W. Xu, J.H. Wang, P. Bush, M.P. Siegal, P.N. Provencio: Synthesis of large arrays of well-aligned carbon nanotubes on glass, Science **282**, 1105–1107 (1998)

31.79 R. Andrews, D. Jacques, A.M. Rao, F. Derbyshire, D. Qian, X. Fan, E.C. Dickey, J. Chen: Continuous production of aligned carbon nanotubes: A step closer to commercial realization, Chem. Phys. Lett. **303**, 467–474 (1999)

31.80 Z. Wang, L. Ci, L. Chen, S. Nayak, P.M. Ajayan, N. Koratkar: Polarity-dependent electrochemically controlled transport of water through carbon nanotube membranes, Nano Lett. **7**, 697–702 (2007)

31.81 S. Huang, L. Dai: Plasma etching for purification and controlled opening of aligned carbon nanotubes, J. Phys. Chem. B **106**, 3543–3545 (2002)

31.82 I.W. Chiang, B.E. Brinson, R.E. Smalley, J.L. Margrave, R.H. Hauge: Purification and characterization of single-wall carbon nanotubes, J. Phys. Chem. B **105**, 1157–1161 (2001)

31.83 W. Mi, Y.S. Lin, Y. Li: Vertically aligned carbon nanotube membranes on macroporous alumina supports, J. Membr. Sci. **304**, 1–7 (2007)

31.84 M. Majumder, N. Chopra, B.J. Hinds: Effect of tip functionalization on transport through vertically oriented carbon nanotube membranes, J. Am. Chem. Soc. **127**, 9062–9070 (2005)

31.85 M. Majumder, X. Zhan, R. Andrews, B.J. Hinds: Voltage gated carbon nanotube membranes, Langmuir **23**, 8624–8631 (2007)

31.86 C. Liu, Y.Y. Fan, M. Liu, H.T. Cong, H.M. Cheng, M.S. Dresselhaus: Hydrogen storage in single-walled carbon nanotubes at room temperature, Science **286**, 1127–1129 (1999)

31.87 A.S. Claye, J.E. Fischer, C.B. Huffman, A.G. Rinzler, R.E. Smalley: Solid-state electrochemistry of the li single wall carbon nanotube system, J. Electrochem. Soc. **147**, 2845–2852 (2000)

31.88 R.H. Baughman, C. Cui, A.A. Zakhidov, Z. Iqbal, J.N. Barisci, G.M. Spinks, G.G. Wallace, A. Mazzoldi, D. De Rossi, A.G. Rinzler, O. Jaschinski, S. Roth, M. Kertesz: Carbon nanotube actuators, Science **284**, 1340–1344 (1999)

31.89 P. Dharap1, Z.L. Li, S. Nagarajaiah, E.V. Barrera: Nanotube film based on single-wall carbon nanotubes for strain sensing, Nanotechnology **15**, 379 (2004)

31.90 U. Vohrer, I. Kolaric, M.H. Haque, S. Roth, U. Detlaff-Weglikowska: Carbon nanotube sheets for the use as artificial muscles, Carbon **42**, 1159–1164 (2004)

31.91 J.A. Åström, A.V. Krasheninnikov, K. Nordlund: Carbon nanotube mats and fibers with irradiation-improved mechanical characteristics: A theoretical model, Phys. Rev. Lett. **93**, 215503 (2004)

31.92 U. Dettlaff-Weglikowska, V. Skákalová, R. Graupner, S.H. Jhang, B.H. Kim, H.J. Lee, L. Ley, Y.W. Park, S. Berber, D. Tománek, S. Roth: Effect of $SOCl_2$ treatment on electrical and mechanical properties of single-wall carbon nanotube networks, J. Am. Chem. Soc. **127**, 5125–5131 (2005)

31.93 J.N. Colemana, W.J. Blau, A.B. Dalton, E. Muñoz, S. Collins, B.G. Kim, J. Razal, M. Selvidge, G. Vieiro, R.H. Baughman: Improving the mechanical properties of single-walled carbon nanotube sheets by intercalation of polymeric adhesives, Appl. Phys. Lett. **82**, 1682 (2003)

31.94 S. Wang, Z. Liang, G. Pham, Y.-B. Park, B. Wang, C. Zhang, L. Kramer, P. Funchess: Controlled nanostructure and high loading of single-walled carbon nanotubes reinforced polycarbonate composite, Nanotechnology **18**, 095708 (2007)

31.95 H. Peng, L.B. Alemany, J.L. Margrave, V.N. Khabashesku: Sidewall carboxylic acid functionalization of

single-walled carbon nanotubes, J. Am. Chem. Soc. **125**, 15174–15182 (2003)
31.96 A.M. Hollman, D. Bhattacharyya: Pore assembled multilayers of charged polypeptides in microporous membranes for ion Sep, Langmuir **20**, 5418–5424 (2004)
31.97 A.M. Hollman, D.A. Christian, P.D. Ray, D. Galey, J. Turchan, A. Nath, D. Bhattacharyya: Selective isolation and purification of tat protein via affinity membrane Sep, Biotechnol. Prog. **21**, 451–459 (2005)
31.98 H. Ago, T. Kugler, F. Cacialli, W.R. Salaneck, M.S.P. Shaffer, A.H. Windle, R.H. Friend: Work functions and surface functional groups of multiwall carbon nanotubes, J. Phys. Chem. B **103**, 8116–8121 (1999)
31.99 M. Domingo-García, F.J. López-Garzón, M. Pérez-Mendoza: Effect of some oxidation treatments on the textural characteristics and surface chemical nature of an activated carbon, J. Colloid Interface Sci. **222**, 233–240 (2000)
31.100 K.G. Denbigh, J.C.R. Turner: *Chemical Reactor Theory: An Introduction*, 3rd edn. (Cambridge Univ. Press, London 1984)
31.101 C.A. Martinez-Huitle, S. Ferro: Electrochemical oxidation of organic pollutants for the wastewater treatment: Direct and indirect processes, Chem. Soc. Rev. **35**, 1324–1340 (2006)
31.102 M.A. Maluleke, V.M. Linkov: Partial electrochemical oxidation of phenol on ceramic-based flat-sheet type electromembrane reactors, Sep. Purif. Technol. **32**, 377–385 (2003)

32. Nanomaterial Toxicity, Hazards, and Safety

Zuzanna A. Lewicka, Vicki L. Colvin

Manufactured nanoparticles of different chemical compositions are now widely commercially applied. They are found in places as diverse as food packaging and automotive bumpers, where their special nanoscale properties help to lower cost while improving performance. Given these widespread applications, the unintended effects of manufactured nanomaterials on workers, consumers, and the environment have become a focal point for international research. Initially, the human health effects of nanoscale materials were of most interest, but more recently identification of nanoscale particles in wastewater sludge has turned attention towards their environmental impacts. Though the topic of nanomaterial safety has received substantial attention in the literature, many basic questions about nanoparticle transport, fate, and toxicology remain unanswered. A central challenge for researchers has been the definitive characterization of particular manufactured nanomaterials, particularly in commercial products that have significant human or environmental exposure. Careful determination of the physical size, surface chemistry, internal structure, and intermediate stability of manufactured nanomaterials helps investigators compare results, as well as link unwanted biological outcomes to particular material features. This chapter provides an overview of the current exposure and toxicity studies of manufactured (e.g., engineered) nanomaterials. A special emphasis in this chapter is the practice used for nanomaterial characterization as it relates to their biological and environmental properties.

32.1 **Engineered Nanomaterials – General Overview** 1118

32.2 **Occurrence of Engineered Nanoparticles in the Environment** 1119

32.3 **Effects of Nanoparticles on Organisms** 1120
- 32.3.1 Ecotoxicity of Nanoparticles in Aquatic Ecosystems 1121
- 32.3.2 Ecotoxicity of Nanoparticles in Soil Ecosystems 1121
- 32.3.3 Routes of Human Exposure to Nanoparticles and Their Translocation in the Body 1122
- 32.3.4 In Vitro Toxicity of Nanoparticles .. 1124

32.4 **Nanoparticle Physicochemical Characteristics of Relevance for Toxicology** 1124
- 32.4.1 Characterization Methods 1126
- 32.4.2 Electron and Atomic Force Microscopy 1126
- 32.4.3 Brunauer–Emmett–Teller Analysis and X-Ray Diffraction 1127
- 32.4.4 Overall and Surface Elemental Analysis 1128
- 32.4.5 Dynamic Light Scattering (DLS) 1129

32.5 **Special Case – Sunscreens** 1130
- 32.5.1 Regulatory Policy as Related to Sunscreens 1130
- 32.5.2 Photocatalytic Activity of TiO_2 and ZnO Nanoscale Particles 1130
- 32.5.3 Health Effects of Nanoscale Titania and Zinc Oxide 1131
- 32.5.4 Materials Derived from Consumer Products and Their Photochemical Behavior 1131
- 32.5.5 Physicochemical Characteristics of Sunscreen Nanoscale Materials. 1132

32.6 **Conclusions** 1132

References 1133

Nanotechnology has been defined by the American Society for Testing and Materials (ASTM) as [32.1]

> *A term referring to a wide range of technologies that measure, manipulate, or incorporate materials and/or features with at least one dimension between approximately* 1 *and* 100 nm. *Such applications exploit the properties, distinct from bulkmacroscopic systems, of nanoscale components.*

32.1 Engineered Nanomaterials – General Overview

Nanoscale materials (or nanomaterials) have been described as any material having one or more dimension between approximately 1 and 100 nm [32.1, 4]. These materials can be naturally occurring (e.g., volcanic ash), incidentally produced (e.g., diesel exhaust particles) or intentionally manufactured (e.g., carbon nanotubes). Of most relevance to this work is the latter class – manmade (engineered or manufactured) nanoscale materials designed with specific properties (e.g., mechanical, optical, electrical, and/or magnetic) that differ from those of bulk materials. Nanomaterials can exist in various shapes: nanoplates, nanorods, nanotubes or nanoparticles, as presented in Fig. 32.1. According to the British Standards Institution (BSI), nanoplates are objects which have a nanoscale-order thickness while having two other external dimensions significantly larger, nanorods have two similar external dimensions on the nanoscale and the third dimension significantly larger, nanotubes are hollow nanorods, while nanoparticles are defined as particles with all three dimensions within the nanoscale [32.4].

Nanoscale materials are often lighter, stronger, and more reactive than bulk materials and can be applied in industries as diverse as medicine and aerospace [32.2, 5]. One size-dependent property that often motivates incorporation of nanoscale materials is the surface area. As the size of a material decreases, the ratio of surface molecules or atoms to total molecules or atoms increases exponentially [32.6]. Greater surface area means a larger fraction of material is available for chemical reactions, a fact that generally increases nanomaterial overall reactivity as compared with bulk materials (Fig. 32.2) [32.3]. This translates into improved physical, chemical, and biological properties which can be incorporated into many improved applications. Other size-dependent properties may arise from the confinement of electronic excitations, or the enhanced cooperativity of magnetic spins in solids of low dimensions [32.7, 8].

Given their many unique and size-dependent properties, it is not surprising that nanomaterial use in consumer products is increasing rapidly [32.9, 10]. In 2011, the Project on Emerging Nanotechnologies (PEN) inventory identified over 1300 nanotechnology-based consumer products on the market from over 24 countries, including the USA, China, Canada, and Germany [32.10]. The largest group of products (738 products) was within the health and fitness category, which included cosmetics, clothing, personal-care products, sporting goods, sunscreens, and air and water filters. However, the database has not been updated since March 2011. Therefore, the number of consumer

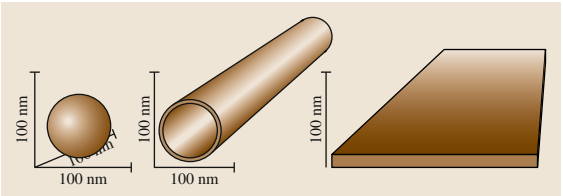


Fig. 32.1 Schematic representations of various forms of nanomaterials, which include nanoparticles (nanoscale in all three dimensions), nanotubes (nanoscale in two dimensions), and nanoplates (nanoscale in only one dimension); nanoscale refers to a dimension between 1 and 100 nm (after [32.2])

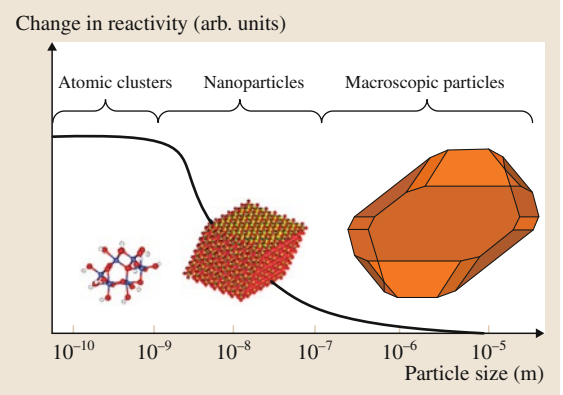


Fig. 32.2 Trend for size-dependent reactivity change of a material as the particle transitions from macroscopic (bulk like) to atomic (after [32.3])

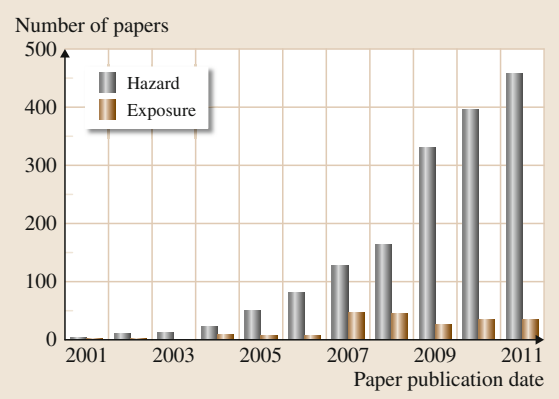


Fig. 32.3 Annual number of articles published in scientific journals, broken down by study topic: nanomaterial hazard versus exposure (after [32.12])

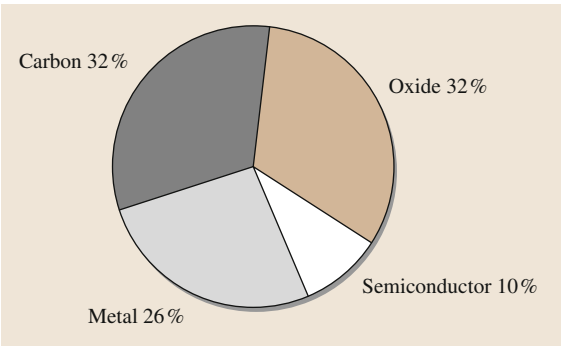


Fig. 32.4 Percentage of scientific papers addressing the hazard and exposure of carbon-based, metal oxide, metal, and semiconductor nanoparticles between 2001 and 2011 (after [32.12])

products having engineered nanomaterials as presented in PEN is only a portion of the nanotechnology-enabled products currently on the market [32.10, 11].

As their use has expanded to include many applications that bring them into contact with people and the environment, significant questions have been raised about their possible biological and environmental interactions [32.13, 14]. As noted by *Simkó* and *Mattsson* [32.15], *A risk can be deduced from exposure data together with the hazard assessment* that results after exposure. As shown in Fig. 32.3, work on hazards has dominated the development of the study of nanomaterial risk, representing 90% of papers published in scientific journals.

Different nanomaterials have been the subject of varying levels of risk-based analysis. These types include carbon-based materials such as fullerenes and carbon nanotubes, metal oxide nanoparticles and rods (iron oxide, cerium oxide, titanium dioxide, silicon dioxide, etc.), metals (gold and silver), as well as semiconductor nanoparticles or so-called quantum dots (typically cadmium sulfide or cadmium selenide) [32.16]. Interestingly, a literature analysis reveals that of these materials the metal oxide and carbon-based systems have been the most examined (Fig. 32.4).

32.2 Occurrence of Engineered Nanoparticles in the Environment

As the number of consumer products containing engineered nanoscale particles grows, so will the chance of environmental exposure of a wide range of organisms [32.17]; For example, it has been estimated that in the USA, based on the reported market size for suncare products, approximately 125 tons of nanoscale TiO_2 and ZnO ultraviolet (UV) blocking agents are used (and released) in commercial products every year [32.18]. Nanoscale TiO_2 and ZnO particles are used in sunscreens because they do not scatter visible light like their larger counterparts and appear transparent when applied to the skin [32.19, 20]. Furthermore, *Hendren* et al. estimated upper and lower bounds for the annual production quantities for five classes of engineered nanomaterials in the USA: titanium dioxide (TiO_2), silver (Ag), cerium oxide (CeO_2), carbon nanotubes (CNTs), and fullerenes, which ranged from 7800–38 000 tons/year for TiO_2, 2.8–20 tons/year for Ag, 35–700 tons/year for CeO_2, 55–1101 tons/year for CNTs, and 2–80 tons/year for fullerenes [32.21]. These estimates were done based on data from academic publications, professional reports, company websites, production process patents, and personal communication with company representatives. The fact that such information was not readily available reflects the lack of labeling and reporting standards for consumer products that contain nanoscale materials.

Nanoparticles can enter the environment during either their manufacture, use, or disposal; studies of nanoparticle fate and transport have concluded that the natural sinks for nanoparticles generally are soil or water [32.22, 23]. So far, no measurements of engineered nanoparticles in the environment have been able to quantify trace concentrations of these mater-

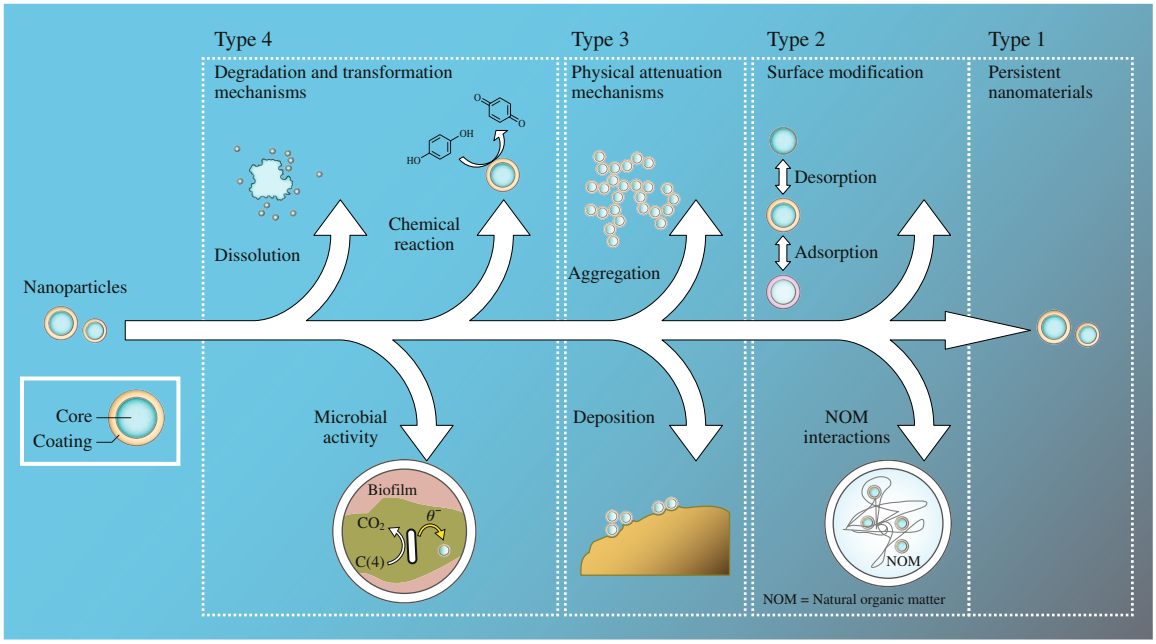


Fig. 32.5 Transformation of nanomaterials as they move through the environment (after [32.28])

ials [32.17]. However, some have found qualitative evidence that nanoscale materials, particularly those from sunscreens, can be detected in the solid waste generated by wastewater treatment plants [32.24]. Due to the lack of quantitative analytical tools for environmental exposures, much of the information about exposure has been derived from relatively coarse-grained environmental exposure models [32.25–27].

To complicate the study of exposure even further, a growing body of research focuses on the fact that nanoparticles can drastically change their behavior and physical characteristics as they move through the environment (Fig. 32.5) [32.28–33].

Changes in physicochemical properties such as surface charge and size can modify environmental fate and transport. As an example, Guzman et al. showed that the mobility of nanoscale materials in aqueous environments is dependent on the size of the nanoparticles. They reported that the point of zero charge (pzc) of TiO_2 nanoparticles changed with their size and that the aggregation state increased as the pH of the solution approached the pzc [32.34]. On the other hand, *Labille* et al. studied the aging and fate of TiO_2 nanoscale particles recommended by the manufacturer (BASF Chemical Company) as sunscreen pigments and discovered that, after contact with water, the TiO_2 nanocomposite dispersed and formed a stable suspension available to microorganisms [32.35]. *Lin* et al. published a thorough review on the fate and transport of nanoscale materials in the environment, which included aggregation and suspension behaviors with emphasis on the influencing factors, including natural colloids, natural organic matter, pH, and ionic strength [32.36]. The authors concluded that there are still many unknowns regarding the environmental fate, transport, exposure, ecotoxicity, and lifecycle of engineered nanomaterials and that future research should focus more on real environments and experiments in the field.

32.3 Effects of Nanoparticles on Organisms

Once released into the environment, nanomaterials will interact with organisms [32.6, 37–39]. Although nanomaterial toxicity is an active area of research, the majority of the published data focus on mammalian toxicity studies using a range of in vitro and in vivo tests to assess the possible toxic behavior of nanoscale materials

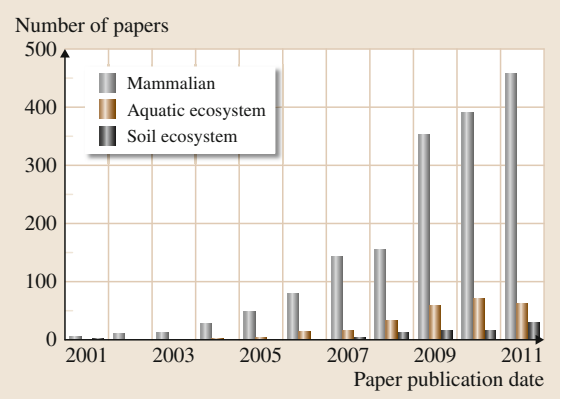


Fig. 32.6 Annual number of articles published in scientific journals by topic: mammalian, aquatic ecosystem, and soil ecosystem toxicity studies (after [32.12])

(Fig. 32.6). On the other hand, study of nanomaterial ecotoxicity, which identifies hazards to the environment in both aquatic and soil ecosystems, is just emerging.

32.3.1 Ecotoxicity of Nanoparticles in Aquatic Ecosystems

In 2004, *Oberdorster* et al. demonstrated for the first time that 0.5 ppm aqueous carbon-based nanoparticles (uncoated fullerenes, C_{60}) can cause oxidative damage and depletion of glutathione (GSH) in vivo in an aquatic species (juvenile largemouth bass) [32.37]. Since that initial report, researchers have studied how nanomaterials affect other freshwater species and marine organisms including trout, fish, waterflea, bacteria, algae, and other aquatic plants [32.40–44]. *Farre* et al. presented a review of ecotoxicological data on carbon-based nanomaterials, metal and metal oxide nanoparticles, as well as quantum dots in the aquatic environment [32.40]. The results indicate that nanoparticles may have ecotoxicological effects which depend sensitively on the physicochemical properties. Factors such as the chemical composition, concentration, size, shape, surface coating, charge, as well as mechanical stability can play a central role in whether a given nanomaterial is toxic or benign [32.45–50]. *Farre* et al. and *Kahru* and *Dubourguier* discussed also challenges in nanoecotoxicological research [32.40, 51]. Both groups agreed that the fate of nanosized materials and in situ investigation of their impact on organisms are of the highest priority for validation of models proposed for environmental risk assessment of nanoparticles. Moreover, physicochemical characteristics of particles before, during, and after experiments were vital to ensure the progress and comparison of research results. Furthermore, a battery of tests with different organisms is recommended to ensure adequate evaluation of the ecological situation; For example, *Kahru* and *Dubourguier* demonstrated that, among organism groups representing the main food-chain levels (bacteria, algae, crustaceans, ciliates, fish, yeasts, and nematodes), algae and crustaceans (daphnids) were the organism groups most sensitive to aquatic exposure of nanoparticles [32.51].

32.3.2 Ecotoxicity of Nanoparticles in Soil Ecosystems

While research on the ecotoxicity of nanoparticles in aquatic ecosystems is not yet complete, it is an extensive dataset compared with the very few studies of nanoparticles in the terrestrial ecosystem (Fig. 32.6). Soil ecosystems are much more complex than aqueous ones. Soils contain a wide variety of colloidal materials, including phyllosilicates, humic acids, iron oxides, and naturally occurring nanosized particles [32.52, 53]. These complexities make it particularly difficult to measure and distinguish between naturally occurring materials and engineered nanoparticles. Moreover, colloidal soil can interact with engineered nanoscale materials and affect their fate, transport, and transformation [32.36, 54]. For this reason, information on the interactions of engineered nanoparticles with soil components is needed to understand the effect of nanoparticles on terrestrial organisms.

Microbes are an important component of the terrestrial ecosystem, yet the antimicrobial activity of nanoparticles largely has been studied with human pathogenic bacteria. There is very little information available on soil microorganisms such as those that promote plant growth (e.g., rhizobacteria, nitrifying and denitrifying bacteria) or those that benefit nutrient cycling in soils [32.55]. Fourteen studies reporting the effects of engineered nanoscale materials on soil microorganisms published between the years 2007 and 2011 were reviewed by *Dinesh* et al. [32.55]. They summarized that fullerenes did not cause any significant toxicity to soil microorganisms while high concentrations (5000 µg/g soil) of multi-walled carbon nanotubes could significantly suppress the activity and biomass of soil microorganisms. Metal nanoparticles such as Al, Si, Pd, Au, and Cu and metal oxides (TiO_2 and ZnO) impacted soil bacterial communities, with silver nanoparticles being highly toxic to these organisms. It is important to note that the mentioned studies were done

using simplified ecosystems, under controlled conditions, far from the actual soil environment. Real-world studies, using components that reflect the complexity of the existing environment, are vital in order to assess the actual risk of manufactured nanomaterials in this environment.

The interactions between engineered nanoparticles and plants are another important area for study. A review of the toxic effects of engineered nanoparticles on plant growth was completed by *Ma* et al. [32.56]. They focused on the toxicity of nanoparticles to plant seedlings and cells, as well as analyzing uptake, translocation, and accumulation of nanoparticles by plants and their interactions with plant cells. Most studies of nanoparticles indicated a certain degree of phytotoxicity to seedlings affecting, e.g., root elongation and seed germination; For instance, *Canas* et al. investigated the effects of the surface properties of single-walled carbon nanotubes on root elongation of six crop species [32.57]. They tested the phytotoxicity of nonfunctionalized and functionalized carbon nanotubes on cucumber, cabbage, carrot, lettuce, tomato, and onion. Nonfunctionalized nanotubes inhibited root elongation in tomato but enhanced that of onion and cucumber. Functionalized nanotubes inhibited root elongation in lettuce, while cabbage and carrots were not affected by either form of nanotubes. On the other hand, *Khodakovskaya* and coworkers did not find any toxic effects of multi-walled carbon nanotubes on root elongation of tomato seedlings up to a concentration of 40 mg/l but observed an increase in seed germination [32.58]. Ma et al. concluded that differences in the toxicity of nanoparticles to plants may arise from the changing physicochemical properties of nanoparticles as they are exposed to the exudates of varying plant species.

Recently, studies have also been performed on terrestrial organisms such as the nematode *Caenorhabditis elegans* [32.59, 60]. Wang et al. did not observe a significant difference in toxicity between nano (TiO_2 of 50 nm, ZnO of 20 nm) and bulk materials (> 200 nm), for example. However, as is the case in many studies, there was a significant difference between the particle compositions as a function of size. On the other hand, Roh et al. demonstrated a relationship between the diameter of TiO_2 nanoparticles and their impact on nematodes. Smaller-sized (7 nm) titania had a more negative impact on *C. elegans* fertility and survival than larger-sized zinc oxide (20 nm). These kinds of inconsistencies in the nanotoxicology literature are more the exception than the rule. *Peralta-Videa* et al. reviewed available literature on the toxicity, fate, and transport of nanoparticles in terrestrial ecosystems for the years between 2008 and 2010 [32.17].

Most analyses of the data suggest that direct comparison between studies is a challenge because the form of the nanomaterials – their size, shape, degree of agglomeration, and composition – was not appropriately defined [32.61]. Thus, studies of nanoscale titania can reach different conclusions because the specific forms of nanoscale titania examined can be different. Furthermore, there are no specific standardized protocols or certified reference materials for nanomaterial testing, which leads to difficulties in comparing results. *Handy* et al. reviewed ecotoxicity test methods for conventional chemicals and presented strategies and modifications to these experimental methods and protocols so they can be applied to nanomaterial testing [32.62].

32.3.3 Routes of Human Exposure to Nanoparticles and Their Translocation in the Body

Human toxicity studies of nanoscale materials are far more common in the research literature (Fig. 32.7). These studies usually start with a perspective about the nanomaterial exposure routes, which include inhalation, skin penetration, and ingestion [32.6, 16, 63, 64]. As shown in Fig. 32.7, inhalation studies are the most prevalent, largely because of the existing work on incidental exposure to exhaust particles.

Respiratory Route

Nanoparticle deposition in the body after inhalation and the factors influencing the fate of inhaled nanomaterials are described in the reviews by *Yang* et al. [32.65] and *Bakand* et al. [32.66]. Once inhaled, these materials will be carried by diffusional motion from the nose or mouth through the various diameters of airways (trachea, bronchi, bronchioles) to the alveoli [32.64, 67]. As a result, particles of different sizes will have different effects in different parts of the lungs [32.6, 63]. Lipid- or water-soluble particles will be dissolved by mucous or serous lining fluid on the walls of the respiratory tract. These soluble components can interact with proteins or subcellular structures and eventually be transferred to the blood. Finally, metabolic products of these solutes may reach other organs and produce toxic effects [32.63]. In case of insoluble particles smaller than 200 nm, neither tracheal mucociliary transport nor digestion by defense cells such as alveolar macrophages would be able to completely remove these particles. Such small materials may be able to translocate through

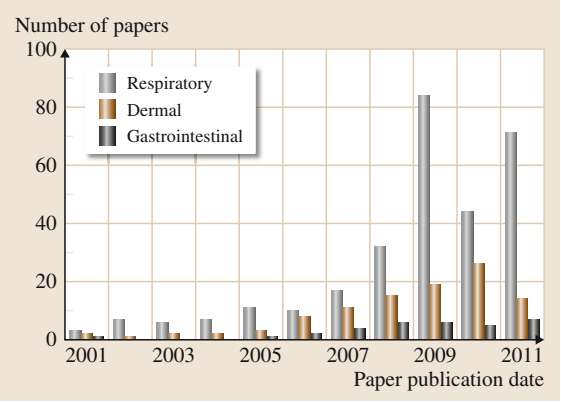


Fig. 32.7 Annual number of articles published in scientific journals by human health topic: respiratory, dermal, and gastrointestinal routes of nanoparticle exposure (after [32.12])

the lymphatic pathways into the blood, resulting in systemic exposure of internal organs [32.6, 63, 64].

For example, in vivo studies by *Kreyling* et al. showed that about 1% of iridium particles (15 and 80 nm) inhaled by rats accessed the systemic circulation and deposited material in organs such as liver, spleen, heart, and brain [32.68]. Moreover, 15 nm particles were deposited at a rate far greater than 80 nm particles. Furthermore, translocation of carbon nanoparticles into the brain via the olfactory nerve system has also been reported [32.69]. Metal oxide nanoparticles such as TiO_2 entered the brain through the olfactory bulb, as well. In the presence of TiO_2 particles, the level of malondialdehyde (MDA), which is a marker of oxidative stress, was elevated and ultrastructural changes of neurons in the hippocampus were observed [32.70]. Wang et al. noticed differences in the responses of the central nervous system to anatase TiO_2 particles versus rutile titania, with lower risk potential for the latter. In summary, different types of inhaled nanoparticles can translocate into the liver, brain, and other organs through blood vessels and the central nervous system. This exposure can produce acute and chronic changes within cells and organisms. Fewer data are available about dermal contact and ingestion exposures [32.2, 71].

Dermal Route

Currently, there is widespread use of nanotechnologies in cosmetic products [32.10, 72, 73]. Most relevant for these topically applied products is the potential for nanoparticles to translocate across the skin. Studies of the skin penetration of cosmetic nanoscale materials have been reviewed by *Nohynek* et al. [32.74, 75]. Researchers found an agreement that such particles can accumulate in hair follicle openings and the stratum corneum but do not reach living cells of the epidermis and dermis. A negligible tendency for penetration into intact and healthy skin, independent of species, has also been reported recently for topically applied nanosized TiO_2, ZnO, and quantum dots [32.76–80].

On the other hand, *Ryman-Rasmussen* et al. reported that spherical quantum dots with diameter 4.6 nm were able to reach the dermis of porcine skin [32.81]. *Baroli* et al. have shown, using human skin pieces, that metallic nanoparticles smaller than 10 nm were able to localize to the epidermal layers [32.82]. *Huand* et al. demonstrated diffusion of 5 nm gold nanoparticles through the stratum corneum of intact mouse skin [32.83]. Other studies performed by *Sonavane* et al. have found that 15, 102, and 198 nm gold nanoparticles penetrated ex vivo rat skin [32.84]. Furthermore, it has been shown that the state of the skin can have a profound effect on its barrier properties; For example, flexed, broken or diseased skin has a greater susceptibility to penetration by nanoparticles [32.78, 80, 85–89].

As noted in prior areas of safety research, these studies are difficult to compare. They differ in methods (for example, tape stripping, scanning or transmission electron microscopy, fluorescent microscopy), type of investigated nanoparticles (elemental composition, size, and shape), and models (e.g., pig, rat, human biopsies). In particular, measuring the penetration of any substance across human skin – whether it is nanoscale or not – is a challenging experiment, and one that is fraught with controversy [32.90–93]. It is not surprising that these unresolved issues in dermal toxicology are reflected in the inconsistent data found in investigations of nanoparticle–skin interactions.

Gastrointestinal Route

Due to the limited number of studies and lack of complete characterization of the nanomaterials studied, there is also no consensus about the behavior of nanomaterials in the gastrointestinal tract [32.2, 94]. Nanomaterials may get into the human body directly via oral ingestion of food, water or drugs that contain nanoscale materials [32.6, 64]. Currently, nanotechnology is mostly used in functional food compounds and delivery systems, food packaging, and food security [32.94, 95]. Food may also be unintentionally contaminated by nanoscale materials through environmental exposure during production [32.94]. Alternatively, exposure to nanoparticles may occur through

hand-to-mouth transfer if products, such as cosmetics, are left on hands [32.64, 96]. Nanoparticles may also be cleaned from the respiratory system through mucociliary transport, where they are swallowed and introduced into the gastrointestinal tract [32.63]. Once in this environment, materials could be eliminated in urine or feces or penetrate the gastrointestinal tract, resulting in translocation to other organs [32.97]; For example, 98% of water-soluble fullerenes when administrated orally to rats were cleared in the feces within 48 h, whereas the rest were eliminated via urine [32.98]. On the other hand, studies by *Jani* et al. have shown that rutile TiO_2 particles of nominal size (500 nm), administered orally as a suspension to female rats, were translocated to systemic organs such as the liver and spleen [32.99]. Furthermore, when mice were exposed to nanoscale particles of copper via he gastrointestinal tract, these materials targeted kidney, liver, and spleen, causing heavy injuries to these organs [32.100].

In summary, current in vivo studies indicate that the target organ for nanomaterial exposure depends on the experimental conditions and nanoparticle physicochemical properties. However, a central and still unanswered question is the rate at which nanoparticles are cleared or degraded. A review discussing the interaction of nanoparticles with living systems has been carried out recently by *Lu* et al. [32.101]. One model anticipates that, should nanoparticles find their way into the body, they would be marked with proteins as foreign agents and consumed by phagocytes (immune cells) [32.102]. After delivery to the lymph nodes, they could be biodegraded into biologically safe components if their constituent material is itself nontoxic. Phagocytosis is a basic defense mechanism against exogenous substances. However, if particles are very stable and difficult to metabolize within the body, they could reside in the body for long time periods and unknown health effects may occur.

32.3.4 In Vitro Toxicity of Nanoparticles

In the past few years many investigators have been developing in vitro model systems using both human and animal cells to simplify the study of the cellular response to nanoparticles [32.103, 104]. While in vitro testing provides a limited view of the responses of only the cell types being tested, it is quick and relatively inexpensive, and allows evaluation of specific mechanisms of action [32.105]. Although nanoparticle-induced cytotoxicity has been reported by several groups, the exact mechanism for toxicity is not well understood [32.106–109]. Nonetheless, studies point to nanoparticle-enhanced generation of reactive oxygen species (ROS) that may result in oxidative stress, inflammation, and consequent damage to proteins, membranes, and DNA [32.110, 111].

Lewinski et al., who reviewed the cytotoxicity of carbon-, metal-, and semiconductor-based nanoparticles, concluded that different data have been published about cytotoxicity due to differences in experimental procedures as well as differing nanoparticle properties [32.106]. Incomplete characterization and lack of protocols and calibration standards in nanoparticle characterization will result in inconsistent and unreliable in vitro toxicity data; For example, in one study, multiwalled carbon nanotubes were reported to be toxic and cause a decrease in mitochondrial membrane potential [32.112], whereas another study reported that these nanotubes were nontoxic [32.113]. Such uncertainties and inconsistencies are likely caused by variations in nanoparticle characteristics and experimental procedures [32.106, 114–116].

Because the physicochemical properties of nanomaterials can influence toxicological endpoints, thorough characterization is vital to this community [32.29, 105, 117, 118]. There is no doubt that nanoscale particles can in some forms be biologically reactive and lead to cell damage; what is less clear is whether these cell culture effects are apparent in animal systems [32.119]. In addition, the risk due to any potentially toxic substance is not only a function of the hazard but also of the chance of exposure. However, lack of exposure data for humans and the environment limits the effective risk assessment of commercially available nanomaterials [32.9, 120].

32.4 Nanoparticle Physicochemical Characteristics of Relevance for Toxicology

The examples provided in human and ecological toxicity studies of engineered nanomaterials highlight that nanomaterial structure is essential for determining biological outcomes. This broad hypothesis certainly

What does the material look like?

- Particle size/size distribution
- Agglomeration state/aggregation
- Shape

What is the material made of?

- Overall composition (including chemical composition and crystal structure)
- Surface composition
- Purity (including levels of impurities)

What factors affect how a material interacts with its surroundings?

- Surface area
- Surface chemistry including reactivity, hydrophobicity
- Surface charge

Overarching considerations

- *Stability*—how do material properties change with time (dynamic stability), storage, handling, preparation, delivery, etc.? Include solubility, and the rate of material release through dissolution.
- *Context/media*—how do material properties change in different media, i.e. from the bulk material to dispersions to material in various biological matrices? ("as administered" characterization is considered to be particularly important)
- *Where possible, materials should be characterized sufficiently to interpret the response to the amount of material against a range of potentially relevant dose metrics, including mass, surface area and number concentration.*

Fig. 32.8 Recommended minimum physical and chemical parameters for characterizing nanomaterials in toxicology studies (after [32.123])

needs refinement, with a specific focus on which physicochemical properties of nanomaterials are the most important in defining their hazard [32.119, 121, 122].

To date, no specific regulation for nanomaterials at the international level exists. The International Standards Organization (ISO) published nanotechnology terminology in 2008 as an outcome of ISO/TC 229 Nanotechnologies: ISO/TS 27687 *Nanotechnologies – Terminology and definitions for nano-objects – Nanoparticle, nanofiber and nanoplate* [32.124]. This international organization continues its work in developing effective regulation for nanotechnology-related products, including *Guidance on physicochemical characterization of engineered nanoscale materials for toxicologic assessment* (ISO/DTR 13014), but writing new rules takes time; hence it will take some time before new standards are completed [32.124].

A minimum set of parameters that accounts for the most important and identifiable nanomaterial characterization in nanotoxicity studies was discussed and proposed at the Woodrow Wilson International Center for Scholars in Washington,DC in 2008 [32.123]. Although there is some variability across the list of ideal properties, most authors agree with the minimum characterization set presented in Fig. 32.8 [32.29, 121, 123, 125, 126]. Definitions of nanoparticle characteristics and techniques suitable for their measurements were described in [32.29, 127].

Characterization of nanoscale particles should begin with the study of as-received samples, which are often shipped as dry powders [32.127]. This primary characterization is useful, particularly for ensuring batch similarity, however study of these powders is not sufficient for safety studies. It is vital to investigate the properties of nanomaterials when they are dispersed in the media used for toxicity studies. Some material properties, such as primary particle size and shape, chemical composition, and crystal structure, are the same in both dry and dispersed phases. However, the composition of the fluid in which nanoparticles are dispersed may affect their agglomeration state, surface charge, and reactivity [32.119, 125]. Also, many of these changes can be slow to occur, and thus samples dispersed in fluids may change over a period of time. Ideally, physicochemical studies should be completed at various time points which reflect the times relevant to the biological questions [32.29].

Technique	Information
Scanning electron microscopy (SEM)	Particle size distributions, shape, agglomeration/aggregation state
Transmission electron microscopy (TEM) Atomic force microscopy (AFM)	Particle size distributions, shape, agglomeration/aggregation state, surface texture
Brunauer–Emmett–Teller (BET) surface area analysis	Specific surface area, porosity, average diameter
X-ray diffraction (XRD)	Crystal structure, crystallite size
Energy-dispersive spectroscopy (EDS)	Overall elemental composition
X-ray photoelectron spectroscopy (XPS)	Surface elemental composition
Inductively coupled plasma mass spectrometry (ICP-MS)	Overall elemental composition
Dynamic light scattering (DLS)	Hydrodynamic size, aggregation/agglomeration state, charge on a particle surface

Table 32.1 Common techniques for investigating nanomaterial properties

32.4.1 Characterization Methods

Physicochemical characterization of nanoparticles generally requires advanced instrumentation. Scanning and transmission electron microscopies can produce high-resolution two-dimensional images of nanoparticles [32.128], while atomic force microscopy (AFM) gives information about nanoparticles in three dimensions [32.129, 130]. Another approach to characterization of nanoparticles involves Brunauer–Emmett–Teller (BET) surface area analysis and x-ray diffraction (XRD). The BET method can analyze dry powders and provide the specific surface area of the nanoparticles [32.131], while XRD yields the atomic structure [32.132]. Energy-dispersive x-ray spectroscopy identifies the elemental composition of the sample [32.128], and x-ray photoelectron spectroscopy (XPS) can be employed to determine the chemical composition at the nanoparticle surface [32.133]. Inductively coupled plasma mass spectrometry (ICP-MS) is a type of MS which is capable of detecting nanoparticles in environmental samples [32.134, 135]. Furthermore, measurement of the nanoparticle hydrodynamic size and zeta potential is useful for getting information about the stability of nanoparticle suspensions with respect to time and medium [32.136, 137]. Common techniques capable of investigating nanomaterial properties are summarized in Table 32.1.

32.4.2 Electron and Atomic Force Microscopy

In vitro and in vivo studies, using carbon, metal oxide, and metal nanomaterials, have all noted various size- and surface-dependent toxicity effects [32.106, 138–144]. These parameters are critical determinants of cellular uptake, distribution through the body, and accumulation in organs.

Direct visualization of nanoparticles by electron or atomic force microscopy allows exact determination of primary particle size and shape. They can also indicate if aggregation or agglomeration is a factor in the sample, an essential issue for safety studies. The agglomeration/aggregation state is likely to differ depending on whether it is determined in powder form or in the experimental media [32.145]; For example, the tendency for airborne nanoparticles to form clusters may limit inhalation exposure to free nanoscale particles, but on the other hand promote locally high concentrations in sediments. Furthermore, depending on the interparticle bond strength, such agglomerates could still undergo deagglomeration once reaching biological fluids. In this case, the primary particles will be of interest for toxicity studies. Therefore, characterization of the size, shape, and agglomeration/aggregation state of nanoparticles in the context of the experimental exposure media (cell culture media, dosing solution, aerosol, etc.) is necessary for informative nanotoxicity studies.

Scanning electron microscopy (SEM) offers the ability to image an area of the order of square millimeters and can be used to observe the formation and arrangement of nanoparticle clusters. However, whether the clusters are formed by nanoparticles in an agglomerated state (weak van der Waals forces between the particles) or aggregated state (strong attractive interactions between the particles) is difficult to establish. Quantitative methods to measure the strength of nanoparticle associations are not routinely available [32.146]. Additionally, it can sometimes be a challenge to fully evaluate aggregated or agglomerated nanomaterials. In the example shown in Fig. 32.9a, some of the individual nanoparticles forming the clusters appear to be visible in higher-magnification SEM

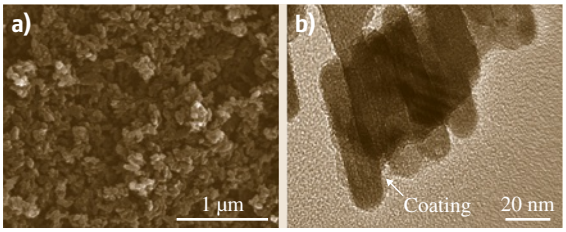


Fig. 32.9a,b Electron microscopy images of TiO_2 nanoparticles coated with SiO_2: **(a)** SEM image showing degree of agglomeration/aggregation in the sample and **(b)** high-magnification TEM image showing surface coating

images. However, given the 20 nm resolution limit of SEM, it is hard to conclude that nanoscale particles are made of one crystallite or several smaller nanoparticles.

Transmission electron microscopy (TEM) analysis provides improved spatial resolution and can, under some circumstances, confirm the presence of nanoscale primary particles in clusters and even measure their size distribution [32.128,147,148]. Moreover, high-resolution TEM can reveal a coating layer on nanoparticle surfaces (Fig. 32.9b) [32.149]. Furthermore, TEM of a cryogenically fresh-frozen sample (cryo-TEM) can produce micrographs of what a biological system, e.g., cell, encounters when exposed to nanoparticles [32.150]. Electron microscopy analysis can be time consuming and expensive, but it provides valuable information in toxicological testing regarding the formation of clusters, primary particle size/size distribution, shapes, and surface coating.

Unlike electron microscopies, AFM does not rely on electron beams to create an image. AFM offers three-dimensional visualization of nanoparticles distributed on a flat surface by measuring the small force between a sharp probe, which is supported on a flexible cantilever, and the surface [32.129]. Therefore, unlike electron microscopies, AFM does not require a vacuum environment or special sample preparation. Such versatility makes it very useful for many questions relevant for nanomaterial safety testing, but it lacks the intrinsic structural sensitivity of electron microscopies [32.130]. Nevertheless, with the appropriate protocols, it can provide information about nanoparticle size, shape, surface texture, and roughness [32.129].

32.4.3 Brunauer–Emmett–Teller Analysis and X-Ray Diffraction

Size-dependent toxic effects of nanoparticles have been correlated with the increased surface-to-volume ratio

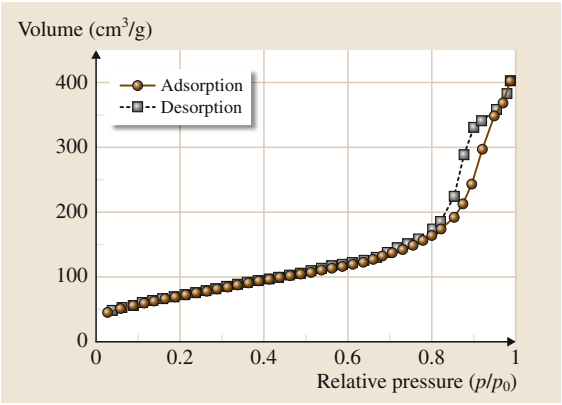


Fig. 32.10 Adsorption–desorption isotherms of nitrogen measured on TiO_2 nanoparticles with surface area of 261 m^2/g that at high relative pressures exhibit a hysteresis loop attributed to the interparticle spaces

of small particles [32.6]. Therefore, the surface area is a physicochemical parameter often considered to be of central importance to nanoparticle toxicity. When the surface area-to-volume ratio increases, there is a greater portion of nanoparticle surface atoms or molecules available to react, and reactivity is generally thought to be a prelude to toxicity [32.127]. This principle has been demonstrated explicitly in several instances where the surface area rather than the particle mass was found to be the best measure of nanomaterial dose [32.151–154]. However, there are also studies that defined the hypothesis of increased toxicity for smaller-surface-area nanoparticles because nanomaterial toxicity depends on several physicochemical parameters that include surface area [32.116,155].

Brunauer–Emmett–Teller (BET) analysis provides specific surface area (SSA) evaluation of nanoscale materials by nitrogen multilayer adsorption measured as a function of relative pressure. Furthermore, the surface area can be related to primary particle size [32.131]. BET analysis can also be used for an indication about aggregation/agglomeration state; For example, if the primary particles form strong aggregates (due to strong bonds between particles), they have lower surface areas than that calculated from TEM images [32.156, 157]. The aggregation/agglomeration state of nanoparticles can also be determined from adsorption–desorption isotherms of nitrogen measured on nanoparticle surfaces (Fig. 32.10), as well as the pore shape, area, and specific pore volume [32.158–160].

The interior crystal structure also determines the toxicity of nanoscale materials; For example, the two

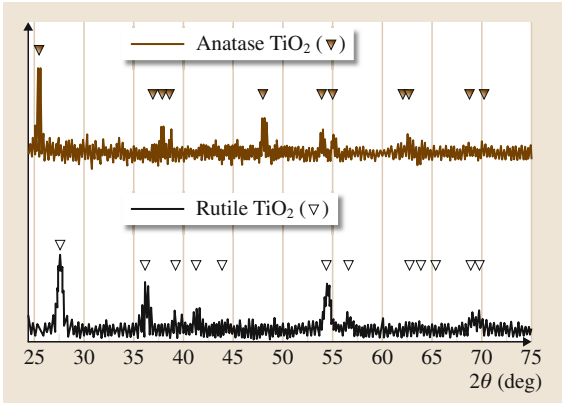


Fig. 32.11 X-ray diffraction patterns of anatase and rutile TiO_2 nanoparticles

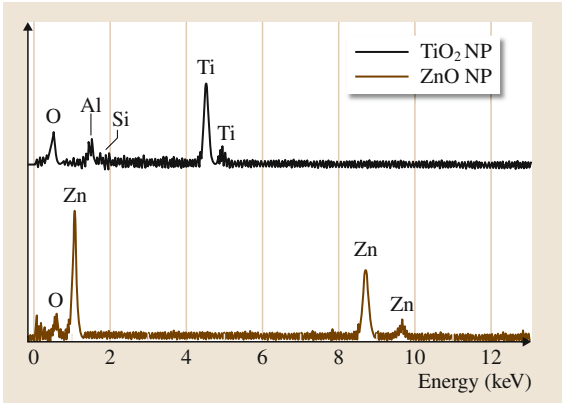


Fig. 32.12 EDS spectra of TiO_2 nanoscale particles (NPs) coated with alumina plus simethicone and uncoated ZnO particles (after [32.18])

most important polymorphs of titania, rutile and anatase (Fig. 32.11), display different photocatalytic activities, with anatase acting as a stronger photocatalyst than rutile [32.161]. Studies have shown that this chemical activity of anatase TiO_2 translates into an increase in biological activity [32.70, 126]. The crystalline structure of nanoparticles can be identified by x-ray diffraction, which is based on the constructive interference of monochromatic x-rays and a crystalline sample. The crystallite size of nanopowders can be determined from the most intense peaks of the XRD patterns according to the Scherrer equation [32.132].

32.4.4 Overall and Surface Elemental Analysis

Several studies have shown that nanomaterials of similar size but differing chemical composition can have varying biological effects [32.115, 116]; For example, *Lanone* et al. demonstrated that, among 24 nanoparticles of similar shape and size but various elemental composition, copper- and zinc-based nanomaterials had the greatest toxicity to human pulmonary cells [32.116]. Furthermore, in addition to the primary material structure, impurities in nanomaterials may also be responsible for biological effects; For example, *Pulskamp* et al. showed that impurities associated with commercial nanotubes caused toxicity in cells [32.112]. Nanomaterials may be contaminated during the preparation process by more toxic, surface-adsorbed surfactants used, for example, to control the size and shape of the particles [32.162]. Unfortunately, manufacturers are not willing to share the details of their proprietary manufacturing methods; hence, in nanotoxicity studies, researchers need to investigate the purity of nanoparticles independently.

For environmental and health studies, the nanoparticles should be free from reactants used in the synthetic steps. Otherwise, toxic impurities can drastically change the results of the toxicity study; For example, for nickel ferrite particles coated with oleic acid prepared by the polyol method, the cytotoxicity significantly increased when one or two layers of oleic acid were deposited as compared with particles without oleic acid prepared by ball milling [32.163].

Moreover, particle surface coatings intentionally designed to optimize use in applications may end up defining the overall toxicity of the nanomaterial. Studies on a number of commercial formulations of TiO_2 particles indicate that different surface treatments can influence the pulmonary toxicity [32.164]. Surface coatings can render noxious particles nontoxic, while less harmful particles can be made highly toxic; For example, in the case of TiO_2 nanoparticles, silica is often used to block access to the titania surface in a solution environment, and consequently reduce its reactivity [32.165, 166].

The overall chemical composition of nanoparticles can be analyzed by energy-dispersive x-ray spectroscopy (EDS) to evaluate impurities; for more surface-specific information, x-ray photoelectron spectroscopy (XPS) is an ideal tool. EDS is commonly coupled with SEM or TEM, where an electron beam scans the surface of the sample and causes emission of x-rays characteristic of the elements present [32.128]. By analyzing the energy of the x-rays from the elements, qualitative analysis of the sample can be

performed in a few minutes (Fig. 32.12). However, EDS has some limitations; For example, elements lighter than sodium are not detectable, and closely spaced lines may not be resolved due to poor energy resolution of the detector [32.128]. Furthermore, EDS does not provide information about chemical bonding. To obtain such detailed chemical characterization of the nanoparticle surface, XPS is often performed.

XPS uses x-rays of sufficient energy to eject core electrons from the sample's various atoms and then measures the energy of the ejected electrons. In addition to chemical state information, XPS spectra can be quantified to provide additional semiquantitative elemental analysis, offering far greater surface sensitivity than EDS or conventional elemental techniques [32.133]. XPS is among the most common analytical methods used in determining the chemical composition of a nanoscale particle's surface. Alternative surface chemical analysis tools for characterization of nanoparticles have been presented recently by *Bear* et al. [32.129].

Analyses by EDS and XPS can provide important information in terms of the chemistry of nanoparticles. Unfortunately, in these cases the samples are analyzed under a vacuum, and thus the results are difficult to apply to the complex environments relevant to nanomaterial safety. ICP-MS has been used as a detection method for nanoparticles in environmental materials [32.134, 135]. It offers sensitive and accurate determination of chemical elements in aqueous media as well as biological samples. A common approach for quantification of nanoparticles by ICP-MS is based on the determination of the total elemental concentrations in a nanoparticle suspension after sample digestion by acid. In an ICP-MS system, a high-temperature argon plasma creates elemental ions, which are separated according to their mass-to-charge ratios, enabling identification and quantification of unknown materials. Another common technique for nanoparticle characterization in solution is dynamic light scattering, which determines the hydrodynamic size.

32.4.5 Dynamic Light Scattering (DLS)

Dynamic light scattering (DLS) involves monochromatic light that interacts with particles undergoing Brownian motion in a fluid. The motion is size dependent (e.g., larger particles move more slowly through the fluid), and this causes a shift in the frequency of the scattered light (Doppler shift). Larger particles, which have lower velocities, cause lower frequency shifts, whereas smaller particles that move rapidly through the fluid cause higher frequency shifts. Therefore, measuring the frequency shift provides the movement of the particles and their hydrodynamic size distribution. Moreover, DLS measurements of nanoparticle hydrodynamic diameter can be used as a method for monitoring the stability of nanoparticle solutions [32.136]. When the stability of the nanoparticles is changing and aggregates/agglomerates form, the DLS spectrum of hydrodynamic diameter increases. DLS can also be used for determining the quality of nanoparticle dispersion by directly measuring the zeta potential, which is a measure of particle interaction. The particles will repel each other and resist the formation of clusters when their zeta potential is large, above +30 mV or below −30 mV [32.137].

Well-characterized hydrodynamic size and zeta potential of nanoparticle dispersions are imperative for toxicological studies. As a result, The International Alliance for NanoEHS (environment, health, safety) Harmonization (IANH) decided to perform round-robin tests on the hydrodynamic size and zeta potential of monodisperse gold, silica, polystyrene, and agglomerated/aggregated ceria nanoparticles [32.167]. *Roebben* et al. concluded that, for highly uniform nanoparticles, DLS provided an excellent measure of hydrodynamic diameter. Therefore, the IANH DLS test protocol can be applied to the characterization of nearly monodisperse nanoparticle dispersions in ecotoxicity studies. However, polydisperse samples, such as ceria that consisted of nanoparticle aggregates, showed large lab-to-lab variations in measured hydrodynamic diameters. Sonication was a difficult process to standardize, and without this preparation the highly aggregated materials sedimented to the bottom of solution vials, yielding nonuniform solutions for DLS analysis. Methods to produce homogeneous dispersions of nanomaterials should use sonication cautiously and with detailed procedures to ensure reproducibility across laboratories [32.167]. There was also a significant difference between round-robin participants in reported zeta potential data. Therefore, IANH protocols for zeta potential require further improvement to enable accurate and precise measurements.

The surface charge of nanoparticles, which can be approximated by zeta potential measurement, and surface composition are not the only surface chemistry properties that need to be measured for safety research. According to *Powers* et al. surface chemistry includes also surface energy (or wettability), solubility, catalytic properties, surface adsorption and desorption of molecules from solution, etc., and quantification of

these characteristics can be difficult [32.127]. Powers et al. listed several common methods for analysis of nanoparticle surfaces that included, for example, contact angle and microcalorimetric measurements for surface energy and reactivity.

In summary, currently, the research literature on nanomaterial safety is inconclusive due to the lack of sufficient detail about characterization and the dearth of standardized laboratory methods for characterization. The IANH developed protocols for measuring nanoparticle hydrodynamic diameter and performed round-robin experiments to ensure that the protocols are reproducible. This one example needs to be replicated and expanded to more critical physiochemical parameters. With such standard tools, it would be possible to integrate the vast amount of safety data to provide a correlation of nanoparticle properties to their toxicological effects.

One topic not highlighted yet is the importance of completing characterization studies directly on the most relevant engineered nanomaterials, i. e., those found directly in consumer products [32.31]. In the next section, an overview of the challenges in risk evaluation of sunscreen nanoparticles is presented as a case study for nanomaterial characterization within consumer products.

32.5 Special Case – Sunscreens

In sunscreens, the size-dependent optical properties of TiO_2 and ZnO nanoparticles make them transparent at visible wavelengths; thus, when applied to the skin, they form clear films as opposed to white, cloudy applications. Moreover, both materials have very strong absorbance and scattering at UVB and UVA wavelengths (290–320 and 320–400 nm, respectively), which makes them effective at protecting skin from the ultraviolet radiation present in sunlight [32.20, 168–170]. SEM and TEM images of TiO_2 and ZnO sunscreen particles are presented in Fig. 32.13.

32.5.1 Regulatory Policy as Related to Sunscreens

In the USA, product labeling regulations have specifically addressed the issue of pigment size in the list of suncare ingredients. Briefly, manufacturers need only list the chemical composition rather than the diameter, form, or crystalline structure of the pigment. Historically, micronized titania and zinc oxide particles have been used in sunscreens for decades. Because of their large size, they scatter visible light and produce a white and chalky appearance when applied. When manufacturers began to shrink the particle size of these inorganic pigments, the US Food and Drug Administration (FDA) reviewed their requirements for labeling of personal care product ingredients. They ruled in 1999 that *micronized* titania and zinc oxide was an appropriate terminology for sunscreen pigments and that it was not necessary to specify whether pigments were truly nanoscale [32.171]. As a result, consumers do not know from the label when the products they are using contain nanoscale materials.

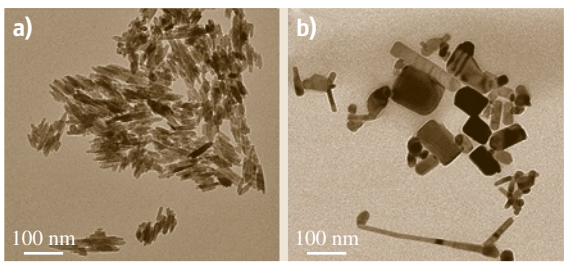


Fig. 32.13a,b TEM images of **(a)** TiO_2 and **(b)** ZnO sunscreen nanoparticles (after [32.18])

32.5.2 Photocatalytic Activity of TiO_2 and ZnO Nanoscale Particles

While the label may not convey the particle size of sunscreen pigments, this does not mean that such information is irrelevant. One specific area of concern has been the native photocatalytic activity of sunscreen pigments. While they are effective at absorbing ultraviolet light, some forms of both titania and zinc oxide are also effective at transforming their photoexcitations into surface-reactive species that generate highly oxidizing products. As a result, in addition to suncare products, nanoscale TiO_2 is also of interest in the ultraviolet-mediated oxidation of organic pollutants and wastewater contaminants [32.172–176]. These applications rely on the ability of TiO_2 nanoparticles to form reactive oxygen species (ROS) such as hydroxyl ($OH^{\bullet}$), superoxide ($O_2^{\bullet -}$), and hydroperoxy ($HOO^{\bullet}$) radicals and hydrogen peroxide (H_2O_2) when excited with UV light [32.177–180].

Critical for these remediation examples is the observation that the generation of ROS by certain forms of nanoscale titania is catalytic: a single particle of titania can generate many hundreds of ROS species under constant ultraviolet illumination [32.108]. While less studied, nanoscale ZnO materials can also catalyze the photooxidation of organic species in water, and may be more efficient photocatalysts than TiO_2 [32.181–188]. However, since zinc oxide is more soluble than titania, the lifetime of these materials is more limited than titania for some applications. However, since zinc oxide is more soluble than titania, the lifetime of these materials is more limited than titania for some applications.

32.5.3 Health Effects of Nanoscale Titania and Zinc Oxide

Reactive oxygen species are generally acutely toxic to living systems because they rapidly react with many cell components (e.g., DNA, proteins, and lipids) and lead to cell damage [32.189–191]. In light of their potential as photocatalytic materials, it is not surprising that toxicology studies have shown that TiO_2 and ZnO nanoparticles have an adverse effect on cellular function when illuminated by UV light. Some studies have shown that TiO_2 nanoparticles are toxic only in the presence of UV light [32.192, 193], while other studies have shown that in the presence of UV irradiation the toxicity is higher than in the dark [32.194–198]. ZnO nanoparticles have also shown photocatalytic effect on cells [32.197, 199–201].

Whether these acute cell effects are relevant to a product applied to skin depends in part on whether the particles translocate across the dermis; studies of TiO_2 and ZnO pigments appear to indicate that, for healthy and intact skin, these nanoscale materials do not penetrate the dermis but can end up in hair follicles, sweat glands, or skin folds [32.74, 75, 202–205]. However, at the seaside, where sunscreens are more likely to be used, the action of sun, water, and sand can irritate or even harm the skin by hydration, infrared (IR) irradiation, peeling or inflammation, consequently enhancing its permeability [32.206]. Furthermore, recent studies demonstrated that the state of skin can have significant effects on its barrier performance [32.78, 80, 85–89]. Therefore, there is still uncertainty regarding skin penetration of sunscreen zinc oxide and titanium dioxide nanoparticles under a variety of real-life conditions. Moreover, to fully assess the toxicological impact of sunscreen nanoparticles, future studies will need to focus on the potential for ROS generation by TiO_2 and ZnO nanoparticles lodged in hair follicles [32.204]. In addition to the potential photocatalytic effect on cells, ZnO and TiO_2 nanoparticles may cause loss of the ultraviolet protection efficacy of sunscreens, due to the enhanced photooxidative degradation of organic sunscreen components [32.165].

Also important in understanding the connection between chemical and biological reactivity are the physicochemical characteristics such as particle size and surface area, crystal structure, surface chemistry, and particle aggregation/agglomeration tendency; For example, photochemical reactivity is quite sensitive to the phase composition of TiO_2, with rutile materials being orders of magnitude less chemically reactive than equivalently sized anatase systems. This trend in chemical reactivity parallels the results of acute in vitro cell toxicology studies, which find anatase to be more toxic than rutile for a range of diameters [32.126]. Additionally, the chemical reactivity of nanoscale oxides can be reduced by modifying their surface with inert inorganic materials such as silica (SiO_2) or alumina (Al_2O_3), and/or by doping with manganese or vanadium [32.165, 207–211]. Due to the great variety of different nanoparticle forms of TiO_2 and ZnO that exhibit different chemical behaviors, it is difficult to generalize the potential ROS generation capacity of inorganic pigments used in sunscreens [32.212].

32.5.4 Materials Derived from Consumer Products and Their Photochemical Behavior

FDA regulations do not require that labels provide information about the diameter, form or photoactivity of inorganic sunscreen ingredients [32.171]; therefore, consumers and researchers have little information about what people are exposed to. Compared with studies of model titania and zinc oxide pigments, there has been comparatively little systematic study of the properties of pigments derived directly from commercial products.

Hidaka et al. showed that ZnO pigments extracted from sunscreen products commercially available in Japan, when illuminated by UV, caused DNA plasmid strand breaks via the generation of ROS [32.199]. The same pigments were also photoactive toward degradation of phenol. A similar effect of rapid photodegradation of methylene blue dye by sunscreen-isolated zinc oxide pigments (uncoated, dimethicone coated, and mixtures of ZnO and TiO_2 particles) was presented by *Rampaul* et al. [32.209]. In the area of the poten-

tial hazard of sunscreen pigments, ZnO has been less studied than TiO_2 [32.213]. Titania is a more commonly used photocatalyst than ZnO, and as a result there has been more concern regarding this material. DNA damage induced by TiO_2 nanoparticles extracted form sunscreens was first noted in 1997 by *Dunford* et al. [32.214]. Then, *Rampaul* et al. found that some TiO_2 particles isolated from sunscreens caused significant cellular damage to cultured human skin and other animal epithelium cells [32.209]. Recently, *Buchalska* et al. tested the photoreactivity of TiO_2 sunscreen components toward degradation of azur B and oxidation of α-terpinene and showed high efficiency of singlet oxygen formation [32.215].

These studies largely relied on *pure* pigments; it is possible that the other constituents in sunscreens may modify or augment the nanoparticle effects. Full sunscreen, including TiO_2 pigments, has also been tested toward the formation of oxygen- and carbon-centered radicals using spin-trap electron paramagnetic resonance (EPR) spectroscopy by Brezova et al. They concluded that some sunscreens generated ROS [32.178]. These observations were confirmed by *Barker* and *Branch*, who showed that sunscreens containing titanium dioxide and zinc oxide nanoparticles were the primary cause of the rapid corrosion of paint surfaces on steel roofing via the production of reactive oxygen species [32.216]. Furthermore, *Lewicka* and *Colvin*, who evaluated the photochemical properties of whole sunscreen emulsions that contained nanoscale components and the inorganic particles derived from these sunscreens using several assays such as dichlorofluorescein fluorescence, decolorization of Congo red dye, and 5,5-dimethyl-pyrroline *N*-oxide (DMPO) spin-trap electron paramagnetic resonance spectroscopy, showed that samples with nanoscale ZnO materials were more photoactive than the samples that contained TiO_2 nanoparticles [32.217].

32.5.5 Physicochemical Characteristics of Sunscreen Nanoscale Materials

A central challenge in assessing the risk of inorganic pigments used in sunscreens has been the great diversity of material types present: both titania and zinc oxide are used, often with different sizes and forms, with different surface coatings and possibly distinct crystal structures [32.18]. Recently, *Lewicka* et al. characterized the inorganic pigments derived from nine commercial products purchased in the USA [32.18]. Nanoscale pigments were apparent in evaporated sunscreen residues from all items that listed TiO_2 or ZnO as active ingredients, and these materials could be isolated further for analysis via water or alcohol washes. Their dimensions, shape, phase, and elemental composition were determined using a suite of methods including TEM, SEM, XRD, EDS, and inductively coupled plasma optical emission spectroscopy. Wurtzite zinc oxide pigments were rod-like in shape with short axes under 40 nm and longer dimension ranging from tens to hundreds of nanometers. TiO_2 materials were generally rutile and exhibited needle-like or near-spherical shapes; they were consistently smaller than the zinc oxide materials, with average length of 25 nm and widths ranging from 7 to 16 nm. The physical and chemical features of pigments derived from commercial sunscreens were notably similar to two commercial sources of TiO_2 and ZnO nanoparticle powders obtained from EMD and BASF [32.18]. Therefore, in some cases, these pure materials may serve as surrogates for ongoing research evaluating the transport, fate, and toxicology of these widely applied engineered nanomaterials.

32.6 Conclusions

Adequate characterization of manufactured nanomaterials in toxicity, ecotoxicity, and exposure studies is central to clear definition and management of their risks. Diameter, shape, aggregation state, and surface area are some of the basic parameters that should be measured, ideally on the most relevant samples in media that reflect the biological or environmental questions of interest. Typically, such characterization should utilize a variety of techniques that provide complementary information about nanoparticles before in vitro or in vivo testing. Moreover, standardized tests and protocols for nanoparticle characterization need to be established for accurate assessment of their physiochemical properties. Ultimately, such data could be held in a public-access *nanoparticle safety database*, which in addition to listing the material composition (e.g., ZnO) could also include its characteristics (e.g., size, shape) and the results of toxicity tests. Then, by asking a specific question (e.g., "How hazardous are ZnO nanoparticles of a certain size and form?"),

the database would provide the result of an experiment that was done on the safety of this specific material [32.11]. Even though characterization of nanomaterials can be complicated, time consuming, and expensive, it is vital in order to define exactly what manufacturers, consumers, and the environment are exposed to during the production, application, and release of nanomaterials.

References

32.1 ASTM (2006) Terminology for Nanotechnology. E2456-06 American Society for Testing and Materials, available online at http://www.astm.org/Standards/E2456.htm (last accessed 7 February 2011)

32.2 H.F. Krug, P. Wick: Nanotoxicology: An interdisciplinary challenge, Angew. Chem. Int. Ed. **50**(6), 1260–1278 (2011)

32.3 N.S. Wigginton, K.L. Haus, M.F. Hochella: Aquatic environmental nanoparticles, J. Environ. Monitoring **9**(12), 1306–1316 (2007)

32.4 BSI (2007) Terminology for nanomaterials. PAS 136: 2007 British Standards Institution, available online at www.bsigroup.com (last accessed 15 February 2010)

32.5 A.D. Maynard: Nanotechnology: The next big thing, or much ado about nothing?, Ann. Occup. Hyg. **51**(1), 1–12 (2007)

32.6 G. Oberdörster, E. Oberdörster, J. Oberdörster: Nanotoxicology: An emerging discipline evolving from studies of ultrafine particles, Environ. Health Perspect **113**(7), 823–839 (2005)

32.7 R. Rossetti, S. Nakahara, L.E. Brus: Quantum size effects in the redox potentials, resonance Raman-spectra, and electronic-spectra of Cds crystallites in aqueous-solution, J. Chem. Phys. **79**(2), 1086–1088 (1983)

32.8 E.A. Schutz-Sikma, H.M. Joshi, Q. Ma, K.W. MacRenaris, A.L. Eckermann, V.P. Dravid, T.J. Meade: Probing the chemical stability of mixed ferrites: Implications for magnetic resonance contrast agent design, Chem. Mater. **23**(10), 2657–2664 (2011)

32.9 S.F. Hansen, E.S. Michelson, A. Kamper, P. Borling, F. Stuer-Lauridsen, A. Baun: Categorization framework to aid exposure assessment of nanomaterials in consumer products, Ecotoxicology **17**(5), 438–447 (2008)

32.10 PEN (2009): The Project on Emerging Nanotechnologies *Woodrow Wilson International Center for Scholars* (Washington 2011), available online from www.nanotechproject. org (last accesses 08 February 2011)

32.11 R. Kessler: Engineered nanoparticles in consumer products: Understanding a new ingredient, Environ. Health Perspect **119**(3), 120–125 (2011)

32.12 ICON (2012) Nano-EHS Database Analysis Tool. International Council on Nanotechnology, Rice University, Houston (2012), available online from http://icon.rice.edu/ report.cfm (last accessed 05 March 2012)

32.13 A.D. Maynard, R.J. Aitken, T. Butz, V. Colvin, K. Donaldson, G. Oberdörster, M.A. Philbert, J. Ryan, A. Seaton, V. Stone, S.S. Tinkle, L. Tran, N.J. Walker, D.B. Warheit: Safe handling of nanotechnology, Nature **444**(7117), 267–269 (2006)

32.14 E. Nielsen: *Human Health and Nanomaterials in Consumer Products. Literature Review for the Region of Peel's Public Health Unit* (EBN Consulting, Richmond 2008)

32.15 M. Simkó, M.O. Mattsson: Risks from accidental exposures to engineered nanoparticles and neurological health effects: A critical review, Part. Fibre Toxicol. **7**, 42 (2010)

32.16 P.J.A. Borm, D. Robbins, S. Haubold, T. Kuhlbusch, H. Fissan, K. Donaldson, R. Schins, V. Stone, W. Kreyling, J. Lademann, J. Krutmann, D. Warheit, E. Oberdorster: The potential risks of nanomaterials: A review carried out for ECETOC, Part. Fibre Toxicol. **3**, 11 (2006)

32.17 J.R. Peralta-Videa, L.J. Zhao, M.L. Lopez-Moreno, G. de la Rosa, J. Hong, J.L. Gardea-Torresdey: Nanomaterials and the environment: A review for the biennium 2008–2010, J. Hazard. Mater. **186**(1), 1–15 (2011)

32.18 Z.A. Lewicka, A.F. Benedetto, D.N. Benoit, W.W. Yu, J.D. Fortner, V.L. Colvin: The structure, composition and dimensions of TiO_2 and ZnO nanomaterials in commercial sunscreens, J. Nanopart. Res. **12**(4), 3607–3617 (2011)

32.19 B.D. More: Physical sunscreens: On the comeback trail, Indian J. Dermatol. Venereol. Leprol. **73**(2), 80–85 (2007)

32.20 A.P. Popov, A.V. Priezzhev, J. Lademann, R. Myllya: The effect of nanometer particles of titanium oxide on the protective properties of skin in the UV region, J. Opt. Technol. **73**, 208–211 (2005)

32.21 C.O. Hendren, X. Mesnard, J. Dröge, M.R. Wiesner: Estimating production data for five engineered nanomaterials as a basis for exposure assessment, Environ. Sci. Technol. **45**(7), 2562–2568 (2011)

32.22 B. Nowack, T.D. Bucheli: Occurrence, behavior and effects of nanoparticles in the environment, Environ. Pollut. **150**, 5–22 (2007)

32.23 N. Musee: Nanowastes and the environment: Potential new waste management paradigm, Environ. Int. **37**(1), 112–128 (2011)

32.24 M.A. Kiser, P. Westerhoff, T. Benn, Y. Wang, J. Perez-Rivera, K. Hristovski: Titanium nanomaterial removal and release from wastewater

treatment plants, Environ. Sci. Technol. **43**(17), 6757–6763 (2009)
32.25 F. Gottschalk, T. Sonderer, R.W. Scholz, B. Nowack: Possibilities and limitations of modeling environmental exposure to engineered nanomaterials by probabilistic material flow analysis, Environ. Toxicol. Chem. **29**(5), 1036–1048 (2010)
32.26 F. Gottschalk, T. Sonderer, R.W. Scholz, B. Nowack: Modeled environmental concentrations of engineered nanomaterials (TiO_2, ZnO, Ag, CNT, fullerenes) for different regions, Environ. Sci. Technol. **43**(24), 9216–9222 (2009)
32.27 B. Nowack, J.F. Ranville, S. Diamond, J.A. Gallego-Urrea, C. Metcalfe, J. Rose, N. Horne, A.A. Koelmans, S.J. Klaine: Potential scenarios for nanomaterial release and subsequent alteration in the environment, Environ. Toxicol. Chem. **31**(1), 50–59 (2012)
32.28 P.J.J. Alvarez, V. Colvin, J. Lead, V. Stone: Research priorities to advance eco-responsible nanotechnology, ACS Nano **3**(7), 1616–1619 (2009)
32.29 V. Stone, B. Nowack, A. Baun, N. van den Brink, F. von der Kammer, M. Dusinska, R. Handy, S. Hankin, M. Hassellov, E. Joner, T.F. Fernandes: Nanomaterials for environmental studies: Classification, reference material issues, and strategies for physico-chemical characterisation, Sci. Total Environ. **408**(7), 1745–1754 (2010)
32.30 S.K. Brar, M. Verma, R.D. Tyagi, R.Y. Surampalli: Engineered nanoparticles in wastewater and wastewater sludge – Evidence and impacts, Waste Manag. **30**(3), 504–520 (2010)
32.31 M.J. McCall: Environmental, Health and Safety Issues; Nanoparticles in the real world, Nat. Nanotechnol. **6**(10), 613–614 (2011)
32.32 J.R. Lead, K.J. Wilkinson: Aquatic colloids and nanoparticles: Current knowledge and future trends, Environ. Chem. **3**(3), 159–171 (2006)
32.33 M. Delay, F.H. Frimmel: Nanoparticles in aquatic systems, Anal. Bioanal. Chem. **402**(2), 583–592 (2012)
32.34 K.A.D. Guzman, M.P. Finnegan, J.F. Banfield: Influence of surface potential on aggregation and transport of titania nanoparticles, Environ. Sci. Technol. **40**(24), 7688–7693 (2006)
32.35 J. Labille, J.H. Feng, C. Botta, D. Borschneck, M. Sammut, M. Cabie, M. Auffan, J. Rose, J.Y. Bottero: Aging of TiO_2 nanocomposites used in sunscreen. Dispersion and fate of the degradation products in aqueous environment, Environ. Pollut. **158**(12), 3482–3489 (2010)
32.36 D.H. Lin, X.L. Tian, F.C. Wu, B.S. Xing: Fate and transport of engineered nanomaterials in the environment, J. Environ. Qual. **39**(6), 1896–1908 (2010)
32.37 E. Oberdörster: Manufactured nanomaterials (Fullerenes, C-60) induce oxidative stress in the brain of juvenile largemouth bass, Environ. Health Perspect **112**(10), 1058–1062 (2004)
32.38 V.L. Colvin: The potential environmental impact of engineered nanomaterials, Nat. Biotechnol. **21**(10), 1166–1170 (2003)
32.39 E. Bergamaschi: Occupational exposure to nanomaterials: Present knowledge and future development, Nanotoxicology **3**(3), 194–201 (2009)
32.40 M. Farre, K. Gajda-Schrantz, L. Kantiani, D. Barcelo: Ecotoxicity and analysis of nanomaterials in the aquatic environment, Anal. Bioanal. Chem. **393**(1), 81–95 (2009)
32.41 V. Matranga, I. Corsi: Toxic effects of engineered nanoparticles in the marine environment: Model organisms and molecular approaches, Mar. Environ. Res. **76**, 32–40 (2012)
32.42 S.J. Klaine, P.J.J. Alvarez, G.E. Batley, T.F. Fernandes, R.D. Handy, D.Y. Lyon, S. Mahendra, M.J. McLaughlin, J.R. Lead: Nanomaterials in the environment: Behavior, fate, bioavailability, and effects, Environ. Toxicol. Chem. **27**(9), 1825–1851 (2008)
32.43 R.D. Handy, F. von der Kammer, J.R. Lead, M. Hassellov, R. Owen, M. Crane: The ecotoxicology and chemistry of manufactured nanoparticles, Ecotoxicology **17**(4), 287–314 (2008)
32.44 A. Kahru, K. Savolainen: Potential hazard of nanoparticles: From properties to biological and environmental effects, Toxicology **269**(2/3), 89–91 (2010)
32.45 J.P. Cheng, E. Flahaut, S.H. Cheng: Effect of carbon nanotubes on developing zebrafish (*Danio rerio*) embryos, Environ. Toxicol. Chem. **26**(4), 708–716 (2007)
32.46 L.K. Adams, D.Y. Lyon, P.J.J. Alvarez: Comparative eco-toxicity of nanoscale TiO_2, SiO_2, and ZnO water suspensions, Water Res. **40**(19), 3527–3532 (2006)
32.47 R.J. Griffitt, R. Weil, K.A. Hyndman, N.D. Denslow, K. Powers, D. Taylor, D.S. Barber: Exposure to copper nanoparticles causes gill injury and acute lethality in zebrafish (*Danio rerio*), Environ. Sci. Technol. **41**(23), 8178–8186 (2007)
32.48 M. Heinlaan, A. Ivask, I. Blinova, H.C. Dubourguier, A. Kahru: Toxicity of nanosized and bulk ZnO, CuO and TiO_2 to bacteria *Vibrio fischeri* and crustaceans *Daphnia magna* and *Thamnocephalus platyurus*, Chemosphere **71**(7), 1308–1316 (2008)
32.49 F. Gagne, J. Auclair, P. Turcotte, M. Fournier, C. Gagnon, S. Sauve, C. Blaise: Ecotoxicity of CdTe quantum dots to freshwater mussels: Impacts on immune system, oxidative stress and genotoxicity, Aquat. Toxicol. **86**(3), 333–340 (2008)
32.50 M.K. Yeo, M. Kang: Effects of nanometer sized silver materials on biological toxicity during zebrafish embryogenesis, Bull. Korean Chem. Soc. **29**(6), 1179–1184 (2008)
32.51 A. Kahru, H.C. Dubourguier: From ecotoxicology to nanoecotoxicology, Toxicology **269**(2/3), 105–119 (2010)

32.52 M.A. Wilson, N.H. Tran, A.S. Milev, G.S.K. Kannangara, H. Volk, G.Q.M. Lu: Nanomaterials in soils, Geoderma **146**(1/2), 291–302 (2008)

32.53 B.K.G. Theng, G. Yuan: Nanoparticles in the soil environment, Elements **4**(6), 395–399 (2008)

32.54 G.V. Lowry, E.M. Hotze, E.S. Bernhardt, D.D. Dionysiou, J.A. Pedersen, M.R. Wiesner, B.S. Xing: Environmental occurrences, behavior, fate, and ecological effects of nanomaterials: An introduction to the special series, J. Environ. Qual. **39**(6), 1867–1874 (2010)

32.55 R. Dinesh, M. Anandaraj, V. Srinivasan, S. Hamza: Engineered nanoparticles in the soil and their potential implications to microbial activity, Geoderma **173**, 19–27 (2012)

32.56 X. Ma, J. Geiser-Lee, Y. Deng, A. Kolmakov: Interactions between engineered nanoparticles (ENPs) and plants: Phytotoxicity, uptake and accumulation, Sci. Total Environ. **408**(16), 3053–3061 (2010)

32.57 J.E. Canas, M. Long, S. Nations, R. Vadan, L. Dai, M. Luo, R. Ambikapathi, E.H. Lee, D. Olszyk: Effects of functionalized and nonfunctionalized single-walled carbon nanotubes on root elongation of select crop species, Environ. Toxicol. Chem. **27**(9), 1922–1931 (2008)

32.58 M. Khodakovskaya, E. Dervishi, M. Mahmood, Y. Xu, Z. Li, F. Watanabe, A.S. Biris: Carbon nanotubes are able to penetrate plant seed coat and dramatically affect seed germination and plant growth, Acs Nano **3**(10), 3221–3227 (2009)

32.59 J.-Y. Roh, Y.-K. Park, K. Park, J. Choi: Ecotoxicological investigation of CeO_2 and TiO_2 nanoparticles on the soil nematode Caenorhabditis elegans using gene expression, growth, fertility, and survival as endpoints, Environ. Toxicol. Pharmacol. **29**(2), 167–172 (2010)

32.60 H.H. Wang, R.L. Wick, B.S. Xing: Toxicity of nanoparticulate and bulk ZnO, Al_2O_3 and TiO_2 to the nematode *Caenorhabditis elegans*, Environ. Pollut. **157**(4), 1171–1177 (2009)

32.61 V.K. Sharma: Aggregation and toxicity of titanium dioxide nanoparticles in aquatic environment – A Review, J. Environ. Sci. Health Pt. A **44**(14), 1485–1495 (2009)

32.62 R.D. Handy, N. van den Brink, M. Chappell, M. Mühling, R. Behra, M. Dušinská, P. Simpson, J. Ahtiainen, A.N. Jha, J. Seiter, A. Bednar, A. Kennedy, T.F. Fernandes, M. Riediker: Practical considerations for conducting ecotoxicity test methods with manufactured nanomaterials: What have we learnt so far?, Ecotoxicology **21**(4), 933–972 (2012)

32.63 W.G. Kreyling, M. Semmler-Behnke, W. Moeller: Health implications of nanoparticles, J. Nanopart. Res. **8**(5), 543–562 (2006)

32.64 C.S. Yah, G.S. Simate, S.E. Iyuke: Nanoparticles toxicity and their routes of exposures, Pak. J. Pharm. Sci. **25**(2), 477–491 (2012)

32.65 W. Yang, J.I. Peters, R.O. Williams: Inhaled nanoparticles – A current review, Int. J. Pharm. **356**(1/2), 239–247 (2008)

32.66 S. Bakand, A. Hayes, F. Dechsakulthorn: Nanoparticles: A review of particle toxicology following inhalation exposure, Inhal. Toxicol. **24**(2), 125–135 (2012)

32.67 W. Hofmann: Modelling inhaled particle deposition in the human lung–A review, J. Aerosol. Sci. **42**(10), 693–724 (2011)

32.68 W.G. Kreyling, M. Semmler, F. Erbe, P. Mayer, S. Takenaka, H. Schulz, G. Oberdörster, A. Ziesenis: Translocation of ultrafine insoluble iridium particles from lung epithelium to extrapulmonary organs is size dependent but very low, J. Toxicol. Env. Health Pt. A **65**(20), 1513–1530 (2002)

32.69 G. Oberdörster, Z. Sharp, V. Atudorei, A. Elder, R. Gelein, W. Kreyling, C. Cox: Translocation of inhaled ultrafine particles to the brain, Inhal. Toxicol. **16**(6/7), 437–445 (2004)

32.70 J.X. Wang, Y. Liu, F. Jiao, F. Lao, W. Li, Y.Q. Gu, Y.F. Li, C.C. Ge, G.Q. Zhou, B. Li, Y.L. Zhao, Z.F. Chai, C.Y. Chen: Time-dependent translocation and potential impairment on central nervous system by intranasally instilled TiO_2 nanoparticles, Toxicology **254**(1/2), 82–90 (2008)

32.71 T.G.M. Smijs, J.A. Bouwstra: Focus on skin as a possible port of entry for solid nanoparticles and the toxicological impact, J. Biomed. Nanotechnol. **6**(5), 469–484 (2010)

32.72 C. Smith (Feature Ed): Nanotechnology in cosmetics analysed, Personal Care Mag. (Nov. 2010), available online from http://www.personalcaremagazine.com (last accessed 08 June 2012)

32.73 L.A. DeLouise: Applications of nanotechnology in dermatology, J. Investig. Dermatol. **132**(3), 964–975 (2012)

32.74 G.J. Nohynek, E. Antignac, T. Re, H. Toutain: Safety assessment of personal care products/cosmetics and their ingredients, Toxicol. Appl. Pharmacol. **243**(2), 239–259 (2009)

32.75 G.J. Nohynek, J. Lademann, C. Ribaud, M.S. Roberts: Grey goo on the skin? Nanotechnology, cosmetic and sunscreen safety, Crit. Rev. Toxicol. **37**(3), 251–277 (2007)

32.76 P. Filipe, J.N. Silva, R. Silva, J.L.C. de Castro, M.M. Gomes, L.C. Alves, R. Santus, T. Pinheiro: Stratum corneum is an effective barrier to TiO_2 and ZnO nanoparticle percutaneous absorption, Skin. Pharmacol. Physiol. **22**(5), 266–275 (2009)

32.77 R.F.V. Lopez, J.E. Seto, D. Blankschtein, R. Langer: Enhancing the transdermal delivery of rigid nanoparticles using the simultaneous application of ultrasound and sodium lauryl sulfate, Biomaterials **32**(3), 933–941 (2011)

32.78 N.A. Monteiro-Riviere, K. Wiench, R. Landsiedel, S. Schulte, A.O. Inman, J.E. Riviere: Safety evaluation of sunscreen formulations containing titanium

ioxide and zinc oxide nanoparticles in UVB sunburned skin: An in vitro and in vivo study, Toxicol. Sci. **123**(1), 264–280 (2011)
32.79 T.W. Prow, J.E. Grice, L.L. Lin, R. Faye, M. Butler, W. Becker, E.M.T. Wurm, C. Yoong, T.A. Robertson, H.P. Soyer, M.S. Roberts: Nanoparticles and microparticles for skin drug delivery, Adv. Drug. Deliv. Rev. **63**(6), 470–491 (2011)
32.80 N.V. Gopee, D.W. Roberts, P. Webb, C.R. Cozart, P.H. Siitonen, J.R. Latendresse, A.R. Warbitton, W.W. Yu, V.L. Colvin, N.J. Walker, P.C. Howard: Quantitative determination of skin penetration of PEG-coated CdSe quantum dots in dermabraded but not Intact SKH-1 hairless mouse skin, Toxicol. Sci. **111**(1), 37–48 (2009)
32.81 J.P. Ryman-Rasmussen, J.E. Riviere, N.A. Monteiro-Riviere: Penetration of intact skin by quantum dots with diverse physicochemical properties, Toxicol. Sci. **91**(1), 159–165 (2006)
32.82 B. Baroli, M.G. Ennas, F. Loffredo, M. Isola, R. Pinna, M.A. Lopez-Quintela: Penetration of metallic nanoparticles in human full-thickness skin, J. Investig. Dermatol. **127**(7), 1701–1712 (2007)
32.83 Y.Z. Huang, F.Q. Yu, Y.S. Park, J.X. Wang, M.C. Shin, H.S. Chung, V.C. Yang: Co-administration of protein drugs with gold nanoparticles to enable percutaneous delivery, Biomaterials **31**(34), 9086–9091 (2010)
32.84 G. Sonavane, K. Tomoda, A. Sano, H. Ohshima, H. Terada, K. Makino: In vitro permeation of gold nanoparticles through rat skin and rat intestine: Effect of particle size, Colloid Surf. B – Biointerfaces **65**(1), 1–10 (2008)
32.85 S.S. Tinkle, J.M. Antonini, B.A. Rich, J.R. Roberts, R. Salmen, K. DePree, E.J. Adkins: Skin as a route of exposure and sensitization in chronic beryllium disease, Environ. Health Perspect. **111**, 1202–1208 (2003)
32.86 J.G. Rouse, J. Yang, J.P. Ryman-Rasmussen, A.R. Barron, N.A. Monteiro-Riviere: Effects of mechanical flexion on the penetration of fullerene amino acid-derivatized peptide nanoparticles through skin, Nano Lett. **7**, 155–160 (2007)
32.87 L.J. Mortensen, G. Oberdörster, A.P. Pentland, L.A. DeLouise: In vivo skin penetration of quantum dot nanoparticles in the murine model: The effect of UVR, Nano Lett. **8**(9), 2779–2787 (2008)
32.88 L.W. Zhang, N.A. Monteiro-Riviere: Assessment of quantum dot penetration into intact, tape-stripped, abraded and flexed rat skin, Skin. Pharmacol. Physiol. **21**(3), 166–180 (2008)
32.89 S. Ravichandran, L.J. Mortensen, L.A. Delouise: Quantification of human skin barrier function and susceptibility to quantum dot skin penetration, Nanotoxicology **5**(4), 675–686 (2010)
32.90 J.R. Bond, B.W. Barry: Limitations of hairless mouse skin as a model for invitro permeation studies through human-skin – hydration damage, J. Investig. Dermatol. **90**(4), 486–489 (1988)
32.91 G.A. Simon, H.I. Maibach: Relevance of hairless mouse as an experimental model of percutaneous penetration in man, Skin. Pharmacol. Appl. Skin. Physiol. **11**(2), 80–86 (1998)
32.92 R.L. Bronaugh, R.F. Stewart, E.R. Congdon: Methods for invitro percutaneous-absorption studies II. Animal-models for human-skin, Toxicol. Appl. Pharmacol. **62**(3), 481–488 (1982)
32.93 N. Otberg, H. Richter, H. Schaefer, U. Blume-Peytavi, W. Sterry, J. Lademann: Variations of hair follicle size and distribution in different body sites, J. Investig. Dermatol. **122**(1), 14–19 (2004)
32.94 B.A. Magnuson, T.S. Jonaitis, J.W. Card: A brief review of the occurrence, use, and safety of food-related nanomaterials, J. Food Sci. **76**(6), R126–R133 (2011)
32.95 C.-Y. Kuan, W. Yee-Fung, K.-H. Yuen, M.-T. Liong: Nanotech: Propensity in foods and bioactives, Crit. Revi. Food Sci. Nutr. **52**(1–3), 55–71 (2012)
32.96 E. Frohlich, E. Roblegg: Models for oral uptake of nanoparticles in consumer products, Toxicology **291**(1–3), 10–17 (2012)
32.97 K.R. Vega-Villa, J.K. Takemoto, J.A. Yanez, C.M. Remsberg, M.L. Forrest, N.M. Davies: Clinical toxicities of nanocarrier systems, Adv. Drug. Deliv. Rev. **60**(8), 929–938 (2008)
32.98 S. Yamago, H. Tokuyama, E. Nakamura, K. Kikuchi, S. Kananishi, K. Sueki, H. Nakahara, S. Enomoto, F. Ambe: In-vivo biological behavior of a water-miscible fullerene – C-14 labeling, absorption, distribution, excretion and acute toxicity, Chem. Biol. **2**(6), 385–389 (1995)
32.99 P.U. Jani, D.E. McCarthy, A.T. Florence: Titanium-dioxide (rutile) particle uptake from the rat GI tract and translocation to systemic organs after oral-administration, Int. J. Pharm. **105**(2), 157–168 (1994)
32.100 Z. Chen, H.A. Meng, G.M. Xing, C.Y. Chen, Y.L. Zhao, G.A. Jia, T.C. Wang, H. Yuan, C. Ye, F. Zhao, Z.F. Chai, C.F. Zhu, X.H. Fang, B.C. Ma, L.J. Wan: Acute toxicological effects of copper nanoparticles in vivo, Toxicol. Lett. **163**(2), 109–120 (2006)
32.101 M. Lu, K.T. Al-Jamal, K. Kostarelos, J. Reineke: Physiologically based pharmacokinetic modeling of nanoparticles, Acs Nano **4**(11), 6303–6317 (2010)
32.102 M. Bartneck, H.A. Keul, G. Zwadlo-Klarwasser, J. Groll: Phagocytosis independent extracellular nanoparticle clearance by human immune cells, Nano Lett. **10**(1), 59–63 (2010)
32.103 V. Stone, H. Johnston, R.P.F. Schins: Development of in vitro systems for nanotoxicology: Methodological considerations, Crit. Rev. Toxicol. **39**(7), 613–626 (2009)
32.104 B. Kong, J.H. Seog, L.M. Graham, S.B. Lee: Experimental considerations on the cytotoxicity of nanoparticles, Nanomedicine **6**(5), 929–941 (2011)

32.105 P. Rivera Gil, G. Oberdörster, A. Elder, V. Puntes, W.J. Parak: Correlating physico-chemical with toxicological properties of nanoparticles: The present and the future, Acs Nano **4**(10), 5527–5531 (2010)

32.106 N. Lewinski, V. Colvin, R. Drezek: Cytotoxicity of nanoparticles, Small **4**(1), 26–49 (2008)

32.107 N. Khlebtsov, L. Dykman: Biodistribution and toxicity of engineered gold nanoparticles: A review of in vitro and in vivo studies, Chem. Soc. Rev. **40**(3), 1647–1671 (2010)

32.108 R. Landsiedel, L. Ma-Hock, A. Kroll, D. Hahn, J. Schnekenburger, K. Wiench, W. Wohlleben: Testing metal-oxide nanomaterials for human safety, Adv. Mater. **22**(24), 2601–2627 (2010)

32.109 A. Dhawan, V. Sharma: Toxicity assessment of nanomaterials: Methods and challenges, Anal. Bioanal. Chem. **398**(2), 589–605 (2010)

32.110 A. Nel, T. Xia, L. Madler, N. Li: Toxic potential of materials at the nanolevel, Science **311**(5761), 622–627 (2006)

32.111 A. Seaton, L. Tran, R. Aitken, K. Donaldson: Nanoparticles, human health hazard and regulation, J. R. Soc. Interface **7**, S119–S129 (2011)

32.112 K. Pulskamp, S. Diabate, H.F. Krug: Carbon nanotubes show no sign of acute toxicity but induce intracellular reactive oxygen species in dependence on contaminants, Toxicol. Lett. **168**(1), 58–74 (2007)

32.113 J. Chlopek, B. Czajkowska, B. Szaraniec, E. Frackowiak, K. Szostak, F. Béguin: In vitro studies of carbon nanotubes biocompatibility, Carbon **44**(6), 1106–1111 (2006)

32.114 S.J. Soenen, P. Rivera-Gil, J.-M. Montenegro, W.J. Parak, S.C. De Smedt, K. Braeckmans: Cellular toxicity of inorganic nanoparticles: Common aspects and guidelines for improved nanotoxicity evaluation, Nano Today **6**(5), 446–465 (2011)

32.115 S.K. Sohaebuddin, P.T. Thevenot, D. Baker, J.W. Eaton, L. Tang: Nanomaterial cytotoxicity is composition, size, and cell type dependent, Part. Fibre Toxicol. **7**, 22 (2010)

32.116 S. Lanone, F. Rogerieux, J. Geys, A. Dupont, E. Maillot-Marechal, J. Boczkowski, G. Lacroix, P. Hoet: Comparative toxicity of 24 manufactured nanoparticles in human alveolar epithelial and macrophage cell lines, Part. Fibre Toxicol. **6**, 14 (2009)

32.117 C.R. Thomas, S. George, A.M. Horst, Z.X. Ji, R.J. Miller, J.R. Peralta-Videa, T.A. Xia, S. Pokhrel, L. Madler, J.L. Gardea-Torresdey, P.A. Holden, A.A. Keller, H.S. Lenihan, A.E. Nel, J.I. Zink: Nanomaterials in the environment: From materials to high-throughput screening to organisms, Acs Nano **5**(1), 13–20 (2011)

32.118 D.B. Warheit: How meaningful are the results of nanotoxicity studies in the absence of adequate material characterization?, Toxicol. Sci. **101**(2), 183–185 (2008)

32.119 G. Oberdörster: Safety assessment for nanotechnology and nanomedicine: Concepts of nanotoxicology, J. Int. Med. **267**(1), 89–105 (2009)

32.120 K.D. Grieger, A. Baun, R. Owen: Redefining risk research priorities for nanomaterials, J. Nanopart. Res. **12**(2), 383–392 (2010)

32.121 J.W. Card, B.A. Magnuson: A method to assess the quality of studies that examine the toxicity of engineered nanomaterials, Int. J. Toxicol. **29**(4), 402–410 (2011)

32.122 D.R. Boverhof, R.M. David: Nanomaterial characterization: Considerations and needs for hazard assessment and safety evaluation, Anal. Bioanal. Chem. **396**(3), 953 (2010)

32.123 A. Maynard: MINChar Initiative, Recommended Minimum Physical and Chemical Parameters for Characterizing Nanomaterials on Toxicology Studies (2008), available online from http://characterizationmatters.org/parameters/ (last accessed 21 May 2011)

32.124 D. Hyde: Technical Committee, TC 229 Nanotechnologies, ISO International Standards for Business, Government and Society (ISO, Geneva 2011), available online from http://www.iso.org/iso/iso_technical_committee?commid=381983 (last accessed 18 May 2011)

32.125 A.D. Maynard, D.B. Warheit, M.A. Philbert: The new toxicology of sophisticated materials: Nanotoxicology and beyond, Toxicol. Sci. **120**, S109–S129 (2011)

32.126 C.M. Sayes, R. Wahi, P.A. Kurian, Y. Liu, J.L. West, K.D. Ausman, D.B. Warheit, V.L. Colvin: Correlating nanoscale titania structure with toxicity: A cytotoxicity and inflammatory response study with human dermal fibroblasts and human lung epithelial cells, Toxicol. Sci. **92**, 174–185 (2006)

32.127 K.W. Powers, S.C. Brown, V.B. Krishna, S.C. Wasdo, B.M. Moudgil, S.M. Roberts: Research strategies for safety evaluation of nanomaterials. Part VI. Characterization of nanoscale particles for toxicological evaluation, Toxicol. Sci. **90**(2), 296–303 (2006)

32.128 P.J. Goodhew, J. Humphreys, R. Beanland (Eds.): *Electron Microscopy and Analysis*, 3rd edn. (Taylor Francis, London 2001)

32.129 D.R. Baer, D.J. Gaspar, P. Nachimuthu, S.D. Techane, D.G. Castner: Application of surface chemical analysis tools for characterization of nanoparticles, Anal. Bioanal. Chem. **396**(3), 983–1002 (2010)

32.130 S. Gupta, P. Brouwer, S. Bandyopadhyay, S. Patil, R. Briggs, J. Jain, S. Seal: TEM/AFM investigation of size and surface properties of nanocrystalline ceria, J. Nanosci. Nanotechnol. **5**(7), 1101–1107 (2005)

32.131 S. Brunauer, P.H. Emmett, E. Teller: Adsorption of gases in multimolecular layers, J. Am. Chem. Soc. **60**, 309–319 (1938)

32.132 B.D. Cullity, S.R. Stock (Eds.): *Elements of x-ray Diffraction* (Prentice Hall, Upper Saddle River 2001)

32.133 J.F. Watts, J. Wolstenholme (Eds.): *An Introduction to Surface Analysis by XPS and AES* (Wiley, Chichester 2003)

32.134 A. Scheffer, C. Engelhard, M. Sperling, W. Buscher: ICP-MS as a new tool for the determination of gold nanoparticles in bioanalytical applications, Anal. Bioanal. Chem. **390**(1), 249–252 (2008)

32.135 B. Fernandez, J.M. Costa, R. Pereiro, A. Sanz-Medel: Inorganic mass spectrometry as a tool for characterisation at the nanoscale, Anal. Bioanal. Chem. **396**(1), 15–29 (2010)

32.136 R.C. Murdock, L. Braydich-Stolle, A.M. Schrand, J.J. Schlager, S.M. Hussain: Characterization of nanomaterial dispersion in solution prior to In vitro exposure using dynamic light scattering technique, Toxicol. Sci. **101**(2), 239–253 (2008)

32.137 Malvern Inc.: Zeta Potential: An Introduction in 30 Minutes, Malvern Tech. Note MRK654-01, available online from http://www.nbtc.cornell.edu/facilities/downloads/Zeta%20potential%20-%20An%20introduction%20in%2030%20minutes.pdf. (last accessed 29 July 2012)

32.138 B.D. Chithrani, A.A. Ghazani, W.C.W. Chan: Determining the size and shape dependence of gold nanoparticle uptake into mammalian cells, Nano Lett. **6**(4), 662–668 (2006)

32.139 B.D. Chithrani, W.C.W. Chan: Elucidating the mechanism of cellular uptake and removal of protein-coated gold nanoparticles of different sizes and shapes, Nano Lett. **7**(6), 1542–1550 (2007)

32.140 K.W. Powers, M. Palazuelos, B.M. Moudgil, S.M. Roberts: Characterization of the size, shape, and state of dispersion of nanoparticles for toxicological studies, Nanotoxicology **1**(1), 42–51 (2007)

32.141 A. Magrez, S. Kasas, V. Salicio, N. Pasquier, J.W. Seo, M. Celio, S. Catsicas, B. Schwaller, L. Forro: Cellular toxicity of carbon-based nanomaterials, Nano Lett. **6**(6), 1121–1125 (2006)

32.142 H.L. Karlsson, J. Gustafsson, P. Cronholm, L. Moller: Size-dependent toxicity of metal oxide particles – A comparison between nano- and micrometer size, Toxicol. Lett. **188**(2), 112–118 (2009)

32.143 A.M. Schrand, M.F. Rahman, S.M. Hussain, J.J. Schlager, D.A. Smith, A.F. Syed: Metal-based nanoparticles and their toxicity assessment, Wiley Interdiscip. Rev.-Nanomed. Nanobiotechnol. **2**(5), 544–568 (2010)

32.144 S. Wang, W. Lu, O. Tovmachenko, U.S. Rai, H. Yu, P.C. Ray: Challenge in understanding size and shape dependent toxicity of gold nanomaterials in human skin keratinocytes, Chem. Phys. Lett. **463**(1–3), 145–149 (2008)

32.145 I. Montes-Burgos, D. Walczyk, P. Hole, J. Smith, I. Lynch, K. Dawson: Characterisation of nanoparticle size and state prior to nanotoxicological studies, J. Nanopart. Res. **12**(1), 47–53 (2010)

32.146 G. Nichols, S. Byard, M.J. Bloxham, J. Botterill, N.J. Dawson, A. Dennis, V. Diart, N.C. North, J.D. Sherwood: A review of the terms agglomerate and aggregate with a recommendation for nomenclature used in powder and particle characterization, J. Pharm. Sci. **91**(10), 2103–2109 (2002)

32.147 E. Vigneau, C. Loisel, M.F. Devaux, P. Cantoni: Number of particles for the determination of size distribution from microscopic images, Powder Technol. **107**(3), 243–250 (2000)

32.148 A.J. Paine: Error-estimates in the sampling from particle-size distributions, Part. Part. Syst. Charact. **10**(1), 26–32 (1993)

32.149 J.T. Nurmi, P.G. Tratnyek, V. Sarathy, D.R. Baer, J.E. Amonette, K. Pecher, C.M. Wang, J.C. Linehan, D.W. Matson, R.L. Penn, M.D. Driessen: Characterization and properties of metallic iron nanoparticles: Spectroscopy, electrochemistry, and kinetics, Environ. Sci. Technol. **39**(5), 1221–1230 (2005)

32.150 S.C. Sahu, D.A. Casciano (Eds.): *Nanotoxicity: From In Vivo and In Vitro Models to Health Risks* (Wiley, Chichester 2009)

32.151 T. Stoeger, C. Reinhard, S. Takenaka, A. Schroeppel, E. Karg, B. Ritter, J. Heyder, H. Schulz: Instillation of six different ultrafine carbon particles indicates a surface area threshold dose for acute lung inflammation in mice, Environ. Health Perspect. **114**(3), 328–333 (2006)

32.152 D.M. Brown, M.R. Wilson, W. MacNee, V. Stone, K. Donaldson: Size-dependent proinflammatory effects of ultrafine polystyrene particles: A role for surface area and oxidative stress in the enhanced activity of ultrafines, Toxicol. Appl. Pharmacol. **175**(3), 191–199 (2001)

32.153 R. Duffin, L. Tran, D. Brown, V. Stone, K. Donaldson: Proinflammogenic effects of low-toxicity and metal nanoparticles in vivo and in vitro: Highlighting the role of particle surface area and surface reactivity, Inhal. Toxicol. **19**(10), 849–856 (2007)

32.154 D. Napierska, L.C.J. Thomassen, V. Rabolli, D. Lison, L. Gonzalez, M. Kirsch-Volders, J.A. Martens, P.H. Hoet: Size-dependent cytotoxicity of monodisperse silica nanoparticles in human endothelial cells, Small **5**(7), 846–853 (2009)

32.155 M.A. Maurer-Jones, Y.S. Lin, C.L. Haynes: Functional assessment of metal oxide nanoparticle toxicity in immune cells, ACS Nano **4**(6), 3363–3373 (2010)

32.156 A.L. Ortiz, W. Osborn, T. Markmaitree, L.L. Shaw: Crystallite sizes of LiH before and after ball milling and thermal exposure, J. Alloy. Compound. **454**(1/2), 297–305 (2008)

32.157 M.K. Naskar: Soft solution processing for the synthesis of alumina nanoparticles in the presence of glucose, J. Am. Ceram. Soc. **93**(5), 1260–1263 (2010)

32.158 M. Khalfaoui, S. Knani, M.A. Hachicha, A. Ben Lamine: New theoretical expressions for the five adsorption type isotherms classified by BET based

on statistical physics treatment, J. Colloid Interface Sci. **263**(2), 350–356 (2003)
32.159 Y.H. Tan, J.A. Davis, K. Fujikawa, N.V. Ganesh, A.V. Demchenko, K.J. Stine: Surface area and pore size characteristics of nanoporous gold subjected to thermal, mechanical, or surface modification studied using gas adsorption isotherms, cyclic voltammetry, thermogravimetric analysis, and scanning electron microscopy, J. Mater. Chem. **22**(14), 6733–6745 (2012)
32.160 S. Lowell, J.E. Shields, M.A. Thomas, M. Thommes (Eds.): *Characterization of Porous Solids and Powders: Surface Area, Pore Size and Density* (Kluwer Academic, Dordrecht 2004)
32.161 P. Bouras, E. Stathatos, P. Lianos: Pure versus metal-ion-doped nanocrystalline titania for photocatalysis, Appl. Catal. B-Environ. **73**(1/2), 51–59 (2007)
32.162 S.G. Wang, W.T. Lu, O. Tovmachenko, U.S. Rai, H.T. Yu, P.C. Ray: Challenge in understanding size and shape dependent toxicity of gold nanomaterials in human skin keratinocytes, Chem. Phys. Lett. **463**(1–3), 145–149 (2008)
32.163 H. Yin, H.P. Too, G.M. Chow: The effects of particle size and surface coating on the cytotoxicity of nickel ferrite, Biomaterials **26**(29), 5818–5826 (2005)
32.164 D.B. Warheit, W.J. Brock, K.P. Lee, T.R. Webb, K.L. Reed: Comparative pulmonary toxicity inhalation and instillation studies with different TiO_2 particle formulations: Impact of surface treatments on particle toxicity, Toxicol. Sci. **88**(2), 514–524 (2005)
32.165 T.A. Egerton, N.J. Everall, J.A. Mattinson, L.M. Kessell, I.R. Tooley: Interaction of TiO_2 nano-particles with organic UV absorbers, J. Photochem. Photobiol. A **193**(1), 10–17 (2008)
32.166 J.-E. Otterstedt, D.A. Brandreth (Eds.): *Small Particles Technology* (Plenum, New York 1998)
32.167 G. Roebben, S. Ramirez-Garcia, V.A. Hackley, M. Roesslein, F. Klaessig, V. Kestens, I. Lynch, C.M. Garner, A. Rawle, A. Elder, V.L. Colvin, W. Kreyling, H.F. Krug, Z.A. Lewicka, S. McNeil, A. Nel, A. Patri, P. Wick, M. Wiesner, T. Xia, G. Oberdörster, K.A. Dawson: Interlaboratory comparison of size and surface charge measurements on nanoparticles prior to biological impact assessment, J. Nanopart. Res. **13**(7), 2675–2687 (2011)
32.168 D. Fairhurst, M.A. Mitchnick: Particulate sun blocks: General principles. In: *Sunscreens*, ed. by N.J. Lowe, N.A. Shaath, M.A. Pathak (Marcel Dekker, New York 1997) p. 313
32.169 N. Serpone, D. Dondi, A. Albini: Inorganic and organic UV filters: Their role and efficacy in sunscreens and suncare product, Inorg. Chim. Acta **360**(3), 794–802 (2007)
32.170 P. Stamatakis, B.R. Palmer, G.C. Salzman, C.F. Bohren, T.B. Allen: Optimum particle-size of titanium-dioxide and zinc-oxide for attenuation of ultraviolet-radiation, J. Coat. Technol. **62**(789), 95–98 (1990)
32.171 FDA: *Sunscreen Drug Products for Over-The-Counter Human Use*, Final Monograph Federal Register **48**(98) (US Food and Drug Administration, Washington 1999)
32.172 J. Cunningham, P. Sedlak: Interrelationships between pollutant concentration, extent of adsorption, TiO_2-sensitized removal, photon flux and levels of electron or hole trapping additives. 1. Aqueous monochlorophenol-TiO_2 (P25) suspensions, J. Photochem. Photobiol. A **77**(2/3), 255–263 (1994)
32.173 J.C. Doliveira, G. Alsayyed, P. Pichat: Photodegradation of 2-chlorophenol and 3-chlorophenol in TiO_2 aqueous suspensions, Environ. Sci. Technol. **24**(7), 990–996 (1990)
32.174 A.L. Linsebigler, G.Q. Lu, J.T. Yates: Photocatalysis on TiO_2 surfaces – principles, mechanisms, and selected results, Chem. Rev. **95**(3), 735–758 (1995)
32.175 G. Mills, M.R. Hoffmann: Photocatalytic degradation of pentachlorophenol on TiO_2 particles – Identification of intermediates and mechanism of reaction, Environ. Sci. Technol. **27**(8), 1681–1689 (1993)
32.176 U. Stafford, K.A. Gray, P.V. Kamat: Radiolytic and TiO_2-assisted photocatalytic degradation of 4-chlorophenol – a comparative-study, J. Phys. Chem. **98**(25), 6343–6351 (1994)
32.177 V. Brezova, D. Dvoranova, A. Stasko: Characterization of titanium dioxide photoactivity following the formation of radicals by EPR spectroscopy, Res. Chem. Intermed. **33**(3–5), 251–268 (2007)
32.178 V. Brezova, S. Gabcova, D. Dvoranova, A. Stasko: Reactive oxygen species produced upon photoexcitation of sunscreens containing titanium dioxide (an EPR study), J. Photochem. Photobiol. B **79**(2), 121–134 (2005)
32.179 M.R. Hoffmann, S.T. Martin, W.Y. Choi, D.W. Bahnemann: Environmental applications of semiconductor photocatalysis, Chem. Rev. **95**(1), 69–96 (1995)
32.180 G. Riegel, J.R. Bolton: Photocatalytic efficiency variability in TiO_2 particles, J. Phys. Chem. **99**(12), 4215–4224 (1995)
32.181 N. Daneshvar, D. Salari, A.R. Khataee: Photocatalytic degradation of azo dye acid red 14 in water on ZnO as an alternative catalyst to TiO_2, J. Photochem. Photobiol. A **162**(2/3), 317–322 (2004)
32.182 C.A.K. Gouvea, F. Wypych, S.G. Moraes, N. Duran, N. Nagata, P. Peralta-Zamora: Semiconductor-assisted photocatalytic degradation of reactive dyes in aqueous solution, Chemosphere **40**(4), 433–440 (2000)
32.183 J.R. Harbour, M.L. Hair: Radical intermediates in the photosynthetic generation of H_2O_2 with aque-

ous ZnO dispersions, J. Phys. Chem. **83**(6), 652–656 (1979)
32.184 V. Kandavelu, H. Kastien, K.R. Thampi: Photocatalytic degradation of isothiazolin-3-ones in water and emulsion paints containing nanocrystalline TiO_2 and ZnO catalysts, Appl. Catal. B **48**(2), 101–111 (2004)
32.185 C. Kormann, D.W. Bahnemann, M.R. Hoffmann: Photocatalytic production of H_2O_2 and organic peroxides in aqueous suspensions of TiO_2, ZnO, and desert sand, Environ. Sci. Technol. **22**(7), 798–806 (1988)
32.186 A. Lipovsky, Z. Tzitrinovich, H. Friedmann, G. Applerot, A. Gedanken, R. Lubart: EPR study of visible light-induced ROS generation by nanoparticles of ZnO, J. Phys. Chem. C **113**(36), 15997–16001 (2009)
32.187 A. Shafaei, M. Nikazar, M. Arami: Photocatalytic degradation of terephthalic acid using titania and zinc oxide photocatalysts: Comparative study, Desalination **252**(1–3), 8–16 (2010)
32.188 J. Villasenor, P. Reyes, G. Pecchi: Photodegradation of pentachlorophenol on ZnO, J. Chem. Technol. Biotechnol. **72**(2), 105–110 (1998)
32.189 B. Balasubramanian, W.K. Pogozelski, T.D. Tullius: DNA strand breaking by the hydroxyl radical is governed by the accessible surface areas of the hydrogen atoms of the DNA backbone, Proc. Natl. Acad. Sci. USA **95**, 9738–9743 (1998)
32.190 K.J.A. Davies: Protein damage and degradation by oxygen radicals I. General-aspects, J. Biol. Chem. **262**(20), 9895–9901 (1987)
32.191 I. Kruk: Environmental toxicology and chemistry of oxygen species: Reactions and processes. In: *The Handbook of Environmental Chemistry*, 2nd edn., ed. by O. Hyutzinger (Springer, Berlin, Heidelberg 1998) p. 261
32.192 Y. Nakagawa, S. Wakuri, K. Sakamoto, N. Tanaka: The photogenotoxicity of titanium dioxide particles, Mutat. Res. Genet. Toxicol. Environ. Mutagen **394**(1–3), 125–132 (1997)
32.193 J.F. Reeves, S.J. Davies, N.J.F. Dodd, A.N. Jha: Hydroxyl radicals ($^{\bullet}OH$) are associated with titanium dioxide (TiO_2) nanoparticle-induced cytotoxicity and oxidative DNA damage in fish cells, Mutat. Res. Fundam. Mol. Mech. Mutagen **640**(1/2), 113–122 (2008)
32.194 T. Uchino, H. Tokunaga, M. Ando, H. Utsumi: Quantitative determination of OH radical generation and its cytotoxicity induced by TiO_2-UVA treatment, Toxicol. Vitro **16**(5), 629–635 (2002)
32.195 C. Wang, S.Q. Cao, X.X. Tie, B. Qiu, A.H. Wu, Z.H. Zheng: Induction of cytotoxicity by photoexcitation of TiO_2 can prolong survival in glioma-bearing mice, Mol. Biol. Rep. **38**(1), 523–530 (2011)
32.196 J. Petkovic, T. Kuzma, K. Rade, S. Novak, M. Filipic: Pre-irradiation of anatase TiO_2 particles with UV enhances their cytotoxic and genotoxic potential in human hepatoma HepG2 cells, J. Hazard. Mater. **196**, 145–152 (2011)
32.197 R.C. Gopalan, I.F. Osman, A. Amani, M. De Matas, D. Anderson: The effect of zinc oxide and titanium dioxide nanoparticles in the Comet assay with UVA photoactivation of human sperm and lymphocytes, Nanotoxicology **3**(1), 33–39 (2009)
32.198 K. Hirakawa, M. Mori, M. Yoshida, S. Oikawa, S. Kawanishi: Photo-irradiated titanium dioxide catalyzes site specific DNA damage via generation of hydrogen peroxide, Free Radic. Res. **38**(5), 439–447 (2004)
32.199 H. Hidaka, H. Kobaysahi, T. Koike, T. Sato, N. Serpone: DNA damage photoinduced by cosmetic pigments and sunscreen agents under solar exposure and artifical UV illumination, J. Oleo Sci. **55**, 205–1212 (2006)
32.200 TGA: A review of the scientific literature on the safety of nanoparticulate titanium dioxide or zinc oxide in sunscreens, Australian Governemt (Therapeutic Goods Administration, Woden 2009), available online from http://www.tga.gov.au/pdf/review-sunscreens-060220.pdf (last accessed 20 July 2012)
32.201 D.T. Tran, R. Salmon: Potential photocarcinogenic effects of nanoparticle sunscreens, Australas. J. Dermatol. **52**, 1–6 (2010)
32.202 M. Crosera, M. Bovenzi, G. Maina, G. Adami, C. Zanette, C. Florio, F.F. Larese: Nanoparticle dermal absorption and toxicity: A review of the literature, Int. Arch. Occup. Environ. Health **82**(9), 1043–1055 (2009)
32.203 M.D. Newman, M. Stotland, J.I. Ellis: The safety of nanosized particles in titanium dioxide- and zinc oxide-based sunscreens, J. Am. Acad. Dermatol. **61**(4), 685–692 (2009)
32.204 M.J. Osmond, M.J. McCall: Zinc oxide nanoparticles in modern sunscreens: An analysis of potential exposure and hazard, Nanotoxicology **4**(1), 15–41 (2010)
32.205 N. Sadrieh, A.M. Wokovich, N.V. Gopee, J.W. Zheng, D. Haines, D. Parmiter, P.H. Siitonen, C.R. Cozart, A.K. Patri, S.E. McNeil, P.C. Howard, W.H. Doub, L.F. Buhse: Lack of significant dermal penetration of titanium dioxide from sunscreen formulations containing nano- and submicron-size TiO_2 particles, Toxicol. Sci. **115**(1), 156–166 (2010)
32.206 B. Baroli: Penetration of nanoplarticles and nanomaterials in the skin: Fiction or reality?, J. Pharm. Sci. **99**(1), 21–50 (2009)
32.207 M.E. Carlotti, E. Ugazio, S. Sapino, I. Fenoglio, G. Greco, B. Fubini: Role of particle coating in controlling skin damage photoinduced by titania nanoparticles, Free Radic. Res. **43**(3), 312–322 (2009)
32.208 L.F. Hakim, D.M. King, Y. Zhou, C.J. Gump, S.M. George, A.W. Weimer: Nanoparticle coating for advanced optical, mechanical and rheological properties, Adv. Funct. Mater. **17**, 3175–3181 (2007)

32.209 A. Rampaul, I.P. Parkin, L.P. Cramer: Damaging and protective properties of inorganic components of sunscreens applied to cultured human skin cells, J. Photochem. Photobiol. A **191**(2/3), 138–148 (2007)
32.210 G. Wakefield, M. Green, S. Lipscomb, B. Flutter: Modified titania nanomaterials for sunscreen applications – reducing free radical generation and DNA damage, Mater. Sci. Technol. **20**(8), 985–988 (2004)
32.211 G. Wakefield, S. Lipscomb, E. Holland, J. Knowland: The effects of manganese doping on UVA absorption and free radical generation of micronised titanium dioxide and its consequences for the photostability of UVA absorbing organic sunscreen components, Photochem. Photobiol. Sci. **3**(7), 648–652 (2004)
32.212 H.J. Johnston, G.R. Hutchison, F.M. Christensen, S. Peters, S. Hankin, V. Stone: Identification of the mechanisms that drive the toxicity of TiO_2 particulates: The contribution of physicochemical characteristics, Part. Fibre Toxicol. **6**, 33 (2009)
32.213 K. Schilling, B. Bradford, D. Castelli, E. Dufour, J.F. Nash, W. Pape, S. Schulte, I. Tooley, J. van den Bosch, F. Schellauf: Human safety review of "nano" titanium dioxide and zinc oxide, Photochem. Photobiol. Sci. **9**(4), 495–509 (2010)
32.214 R. Dunford, A. Salinaro, L. Cai, N. Serpone, S. Horikohi, H. Hidaka, J. Knowland: Chemical oxidation and DNA damage catalysed by inorganic sunscreen ingredients, FEBS Lett. **418**, 87–90 (1997)
32.215 M. Buchalska, G. Kras, M. Oszajca, W. Lasocha, W. Macyk: Singlet oxygen generation in the presence of titanium dioxide materials used as sunscreens in suntan lotions, J. Photochem. Photobiol. A **213**(2/3), 158–163 (2010)
32.216 P.J. Barker, A. Branch: The interaction of modern sunscreen formulations with surface coatings, Prog. Org. Coat. **62**(3), 313–320 (2008)
32.217 Z.A. Lewicka, V.L. Colvin: Photoactivity tests of TiO_2 and ZnO sunscreen ingredients, Mater. Res. Soc. Symp. Proc. **1413**, mrsf11–1413–gg03–03 (2012)

Acknowledgements

A.2 Graphene – Properties and Characterization

by Aravind Vijayaraghavan

The author would like to acknowledge L. Song for his support in preparing this chapter.

A.3 Fullerenes and Beyond: Complexity, Morphology, and Functionality in Closed Carbon Nanostructures

by Humberto Terrones

I acknowledge the École Polytechnique de Louvain of the Catholic University of Louvain for support as visiting professor and the Center for Nanophase Materials Sciences at Oak Ridge National Laboratory for support as invited scientist.

A.8 Nanodiamonds

by Olga A. Shenderova, Suzanne A. Ciftan Hens

Gary McGuire, International Technology Center is acknowledged for his valuable comments.

B.9 Noble Metal Nanoparticles

by Theruvakkattil S. Sreeprasad, Thalappil Pradeep

We thank our coworkers who have contributed to several aspects of our work presented here. Thanks are also due to the Department of Science and Technology, Govt. of India and the Indian Institute of Technology Madras, for constant support for all the research activities presented here.

C.16 Compound Crystals

by Roi Levi, Maya Bar-Sadan, Reshef Tenne

This work was supported by ERC grant INTIF 226639, the Israel Science Foundation, the G. Schmidt Minerva Center for Supramolecular Chemistry, the Irving and Cherna Moskowitz Center for Nano and Bio-Nano imaging, and the Harold Perlman Foundation. Reshef Tenne holds the Drake Family Chair in Nanotechnology and is the director of the Helen and Martin Kimmel Center for Nanoscale Science.

C.18 Glasses on the Nanoscale

by Hellmut Eckert, Sidney J.L. Ribeiro, Silvia H. Santagneli, Marcelo Nalin, Gael Poirier, Younès Messaddeq

Authors acknowledge funding from Brazilian agencies FAPESP, CNPq and CAPES. This chapter summarizes previously published contributions from numerous co-workers, doctoral students and postdoctoral associates. Concerning the NMR part, H. Eckert expresses special thanks to former PhD students H. Deters, C.C. De Araujo, S. Elbers, J.D. Epping, D. Larink, S. Puls, S. Santagneli, M.T. Rinke, and U. Voigt. Scientific contributions made by previous postdoctoral workers J.C.C. Chan and L. Zhang are also most gratefully acknowledged. The same holds for lanthanide containing transparent glass ceramics and S.J.L. Ribeiro thanks L.A. Bueno, A.S. Gouveia-Neto, M. Mortier, V. Briois, M. Poulain, G.F. Sá, M.A.P. Silva, J.P. Donoso, C.J. Magon, L.F.C. Oliveira, I. Kosacki and A. Monteil. H. Eckert's work is supported by the Wissenschaftsministerium Nordrhein-Westfalen and by the Deutsche Forschungsgemeinschaft.

E.21 Nanoporous Metals

by Yi Ding, Zhonghua Zhang

The authors gratefully acknowledge financial support by the National Science Foundation of China (20928003, 90923011, 50971079, 50831003) and the Independent Innovation Foundation of Shandong University (IIFSDU). Y. Ding is a Tai-Shan Scholar supported by the Shandong Natural Science Fund for Distinguished Young Scholars.

F.26 Nanocomposites as Bone Implant Material

by Vinod Kumar, Bipul Tripathi, Anchal Srivastava, Preeti S. Saxena

The authors are thankful to Prof. P.M. Ajayan and Dr. Robert Vajtai, Rice University, for their valuable suggestions. P.S. Saxena acknowledges the CAS program in the Zoology Department and Anchal Srivastava acknowledges the CAS program in the Physics Department, Banaras Hindu University (BHU) funded by the University Grants Commission (UGC).

G.28 Nanostructured Materials for Energy-Related Applications

by Arava L.M. Reddy, Sundara Ramaprabhu

The authors acknowledge the Indian Institute of Technology, Madras, India. The Defence Research and Development Organization (DRDO) India, Department of Science and Technology (DST) India, Ministry of Non-conventional Energy Sources (MNES) India, and Ministry of Human Resource Development (MHRD) India are gratefully acknowledged for their financial support.

About the Authors



Maya Bar-Sadan

Ben-Gurion University
Department of Chemistry
Be'er Sheba, Israel
barsadan@bgu.ac.il

Chapter C.16

Dr. Maya Bar-Sadan is an Assistant Professor in the chemistry department of Ben-Gurion University. She received her PhD in 2007 from the Weizmann Institute of Science where she specialized in characterizing closed-cage structures to the atomic level by high resolution electron microscopy. Dr. Bar-Sadan is currently interested in studying functional interfaces in nanomaterials and their properties by atomic-resolution HRTEM.

Giovanni Barcaro

Italian National Research Council
Institute for the Physical and Chemical Processes
Pisa, Italy
barcaro@ipcf.cnr.it; giobarc@gmail.com



Chapter B.11

Giovanni Barcaro got a degree in Materials Science in 2003 and received his PhD in Chemistry from the University of Pisa, Italy, in 2007. The aim of Dr. Barcaro's research has mainly been centred on the theoretical/computational structural characterization of pure and bimetallic metal nanoclusters, both in the gas-phase and absorbed on oxide supports.

Paolo Bettotti

University of Trento
Department of Physics, Nanoscience Laboratory
Povo, Italy
bettotti@science.unitn.it



Chapter E.24

Paolo Bettotti received his MS in Materials Science at the University of Padova and his PhD in Physics at the University of Trento. He is currently working in the development of optical sensors and analytical tools using both integrated silicon photonic devices and nanoporous materials.



Alfredo Caro

Los Alamos National Laboratory
Materials Science and Technology Division
Los Alamos, NM, USA
caro@lanl.gov

Chapter B.11

Alfredo Caro received his PhD from the Swiss Federal Institute of Technology at Lausanne in 1981. He worked at the Atomic Center at Bariloche, Argentina, at the Paul Scherrer Institute in Switzerland, and at the Lawrence Livermore and Los Alamos National Laboratories in the US. He works now on computational materials science, focused on the thermodynamic aspects of multicomponent.



Eunhyea Chung

Korea Institute of Science and Technology (KIST)
Center for Water Resource Cycle
Seoul, Korea
echung@kist.re.kr

Chapter G.29

Eunhyea Chung received her MS degree in Civil, Urban, and Geosystem Engineering at Seoul National University, Korea and her PhD in Environmental Engineering from the Georgia Institute of Technology. Her research activities include the estimation of colloidal particle and surface interactions in natural or engineered environments through theoretical and experimental approaches using scanning probe microscope or the neutron diffraction technique, and their applications.

Suzanne A. Ciftan Hens

ITC/International Technology Center
Raleigh, NC, USA
shens@itc-inc.org



Chapter A.8

Suzanne Hens received her PhD degree in Chemistry from UNC Chapel Hill. Her work at the International Technology Center (ITC) has encompassed the areas of nanoparticles and microelectronic applications. She has focused on the biological, chemical, and colloidal stability of nanodiamonds, synthesis of nanodiamond conjugates for commercial sales, as well as the design of highly conductive thermal interface materials used in microelectronic applications.

Vicki L. Colvin

Rice University
Office of Research, Chemistry
Houston, TX, USA
colvin@rice.edu



Chapter G.32

Vicki Colvin is Vice Provost of Research and Kenneth S. Pitzer-Schlumberger Professor of Chemistry at Rice University, Houston, USA. She earned her PhD in Chemistry from the University of California at Berkeley in 1994. The focus of her research is the unique behavior of nanoparticles in complex systems such as cells, organisms and the environment and problems related to water purification as well as targeted cell death.



Rodolfo Cruz-Silva

Shinshu University
Research Center for Exotic Nanocarbons
Nagano, Japan
rcruzsilva@shinshu-u.ac.jp

Chapter A.6

Rodolfo Cruz-Silva graduated in Chemical Engineering from Coahuila State University, Mexico, and received his PhD in Polymer Science from the Applied Chemistry Research Center, in Saltillo, Mexico. His research interests are in polymer/carbon nanocomposites and chemistry of nanocarbons. He is currently Associate Professor at the Research Center for Exotic Nanocarbons, at Shinshu University, in Nagano, Japan.



Pratap Kumar Deheri

ShayoNano Singapore Pte Ltd.
Singapore
dehe0001@e.ntu.edu.sg

Chapter B.12

Pratap Kumar Deheri is a PhD student from the School of Materials Science and Engineering, Nanyang Technological University (NTU), Singapore, where he does research in the chemical synthesis of magnetic nanomaterials. He is working as a Research Assistant in ShayoNano Singapore Pte. Ltd., a nanomaterials synthesis based company.

Libo Deng

University of Manchester
School of Materials
Manchester, UK
libo.deng@manchester.ac.uk



Chapter D.19

Libo Deng was educated in China and earned his PhD with work on carbon nanotube composites from the University of Manchester, UK. He presently does post-doctoral studies on the manufacture of carbon fibers by the pyrolysis and graphitization of cellulose fibers. His recent interest is in the behavior of double-walled carbon nanotubes and graphene.

Yi Ding

Shandong University
School of Chemistry and Chemical Engineering
Jinan, China
yding@sdu.edu.cn



Chapter E.21

Yi Ding received his PhD in Materials Science and Engineering from Johns Hopkins University, Baltimore in 2005. He then joined the faculty of Shandong University as a Tai-Shan Scholar and full Professor in Chemistry and Materials Science and Engineering. His research focuses on design and processing of functional nanostructures such as de-alloyed nanoporous metals for advanced energy technology applications.



Huanli Dong

Chinese Academy of Sciences
Institute of Chemistry,
Key Laboratory of Organic Solids
Beijing, China
dhl522@iccas.ac.cn

Chapter F.25

Huanli Dong received her PhD degree in Physical Chemistry from the Institute of Chemistry, Chinese Academy of Sciences in 2009 after she got her MS degree in Inorganic Chemistry from Fujian Institute of Research on the Structure of Materials, Chinese Academy of Sciences in 2006. Her researches are presently focusing on the self-assembling of molecular materials and the application of molecular materials in optoelectronic devices. She is an Associate Professor of the Institute of Chemistry, Chinese Academy of Sciences.



Mildred S. Dresselhaus

Massachusetts Institute of Technology
Physics; Electrical Engineering
Cambridge, MA, USA
millie@mgm.mit.edu

Chapter A.7

Mildred Dresselhaus received her PhD from the University of Chicago in 1958. After two years as an NSF postdoctoral fellow at Cornell, Dresselhaus took permanent positions at MIT, first at Lincoln Labs in 1960 and then as part of the MIT faculty, as Professor of Electrical Engineering in 1967 and in 1983 in the Physics Department. She is known for her contributions to carbon nanoscience.

Dimple P. Dutta

Bhabha Atomic Research Centre
Chemistry Division
Mumbai, India
dimpled@barc.gov.in



Chapter C.13

Dr. Dutta joined Bhabha Atomic Research Centre in 1996 after completing her MSc from Indian Institute of Technology, Kanpur. She did her PhD at Mumbai University and Postdoctoral research from Ruprecht-Karls University Heidelberg, Germany. She has been selected for Young Associate of Maharashtra Academy of Sciences, India in 2008. She is a member of Member of National Academy of Sciences India (NASI), 2011. Her current research interests include synthesis, property evaluation of inorganic phosphor nanomaterials for white light generation, magnetic and multiferroic materials.

Hellmut Eckert

University of Sao Paulo
Department of Physics
Sao Carlos, SP, Brazil
eckert@ifsc.usp.br



Chapter C.18

Professor Eckert obtained his doctoral degree in Physical Chemistry in 1982 from the Westfälische Wilhelms Universität (WWU) Münster. He was a Professor of Chemistry at UC Santa Barbara (1987–1996), before he accepted a Chair in Physical Chemistry at the WWU Münster. He has published some 400 papers on solid state NMR technique development and applications in Materials Science, with a particular focus on glasses. In 2011 he became a faculty member of the Instituto de Física de Sao Carlos, IFSC/USP.



Morinobu Endo

Shinshu University
Research Centre for Exotic Nanocarbons
Nagano, Japan
endo@endomoribu.shinshu-u.ac.jp

Chapter A.7

Morinobu Endo studied Electrical Engineering at Shinshu University, Japan and obtained his PhD from the University of Orleans, France in 1975. In his PhD he had developed the synthesis method of carbon nanotubes and showed that it is a tubular structure for the first time. He is a CEO of the Institute of Carbon Science and Technology and is a Distinguished Professor of the Research Centre for Exotic Nanocarbons at Shinshu University. His current interests are in science and technology of nanocarbons such as carbon nanotubes, and the development of high-performance energy storage devices.



Adam W. Feinberg

Carnegie Mellon University
Department of Biomedical Engineering
Pittsburgh, PA, USA
feinberg@andrew.cmu.edu

Chapter F.27

Professor Feinberg graduated with a BS in Materials Science and Engineering from Cornell University in 1999 and with a PhD in Biomedical Engineering from the University of Florida in 2004. He holds a joint appointment in the Departments of Biomedical Engineering and Materials Science and Engineering at Carnegie Mellon University and is developing biomimetic fabrication strategies that use extracellular matrix proteins to engineer 2-D and 3-D nanofiber scaffolds. Prof. Feinberg has been award the NIH Director's New Innovator Award and holds 10 US patents and patent applications.

Alessandro Fortunelli

IPCF Consiglio Nazionale delle Ricerche
(CNR)
Pisa, Italy
alessandro.fortunelli@cnr.it



Chapter B.11

Alessandro Fortunelli is Senior Researcher at CNR-IPCF which he joined in 1984 after obtaining his degree in Chemistry at Scuola Normale Superiore. He coordinated two European projects, is taking part to others, including COST Action on "Nanoalloys", and is Visiting Associate at Caltech, Pasadena. His research interests focus on structural, optical, catalytic and magnetic properties of nanoalloys and ultrathin oxide-on-metal films. He is author of roughly 150 articles in peer-reviewed journals.

Yogeeswaran Ganesan

Intel Corporation
Hillsboro, OR, USA
yogiganesan@gmail.com



Chapter A.4

Yogeeswaran Ganesan obtained in PhD in Materials Science from Rice University (2011), where he worked on the in situ mechanical characterization of carbon nanotubes and carbon nanotube reinforced composites with Professor Jun Lou. He is currently employed as a lithography engineer at Intel Corp., Hillsboro, USA.



Wei Gao

Los Alamos National Laboratory
Center for Integrated Nanotechnology
Los Alamos, NM, USA
wei.gaofanyi@gmail.com

Chapter C.15

Dr. Wei Gao received her MA (2009) and PhD (2012) in Chemistry from Rice University, Houston, USA. Her research interests include synthesis of carbon nanomaterials and their composites, and their applications in water purification, energy storage and conversion technologies. Currently, she is working on a carbon-based solar cell project at Los Alamos National Laboratory.



Thomas F. George

University of Missouri–St. Louis
Office of the Chancellor, Center for
Nanoscience
St. Louis, MO, USA
tfgeorge@umsl.edu

Chapter G.30

Thomas F. George is Chancellor and professor of chemistry and physics at the University of Missouri – St. Louis. He is an active researcher in chemistry and physics, specializing in chemical/materials/laser physics and nanoscience, including nanomedicine. His work has led to 735 papers, 5 authored and 18 edited books. He has been recognized worldwide, such as being awarded the Marlow Medal by the Royal Society of Chemistry in Great Britain and the Medal of Honor by Gulf University for Science and Technology in Kuwait.

Lei Gong

University of Manchester
School of Materials
Manchester, UK
lei.gong@stud.manchester.ac.uk



Chapter D.19

Lei Gong was educated in China and got an MSc from the University of Sheffield and his PhD upon graphene composites from the University of Manchester. He has published a number of papers on graphene-based composites in high-impact journals and a major review in the mechanics of graphene-based composites.

Takuya Hayashi

Shinshu University
Department of Electrical and Electronic
Engineering
Nagano, Japan
hayashi@endomoribu.shinshu-u.ac.jp



Chapter A.7

Takuya Hayashi received a PhD in 1999 from University of Tokyo, Japan. He is an Associate Professor of Shinshu University and he has published about 150 papers in international journals. His research interests are structural analysis and property measurements of carbon nanomaterials using high-resolution transmission electron microscopy, in-situ physical property measurement of nanostructured carbon materials and simulation of carbon nanomaterial formation, and its property prediction.



Wenping Hu

Key Laboratory of Organic Solids
Institute of Chemistry,
Chinese Academy of Sciences
Beijing, China
huwp@iccas.ac.cn

Chapter F.25

Wenping Hu received his PhD in 1999. Then he joined Osaka University and Stuttgart University as a research fellow of the Japan Society for the Promotion of Sciences and Alexander von Humboldt Research Fellowship, respectively. In 2003 he worked at Nippon Telephone and Telegraph, and then returned to the Institute of Chemistry, Chinese Academy of Sciences. He focuses on molecular electronics and has more than 180 refereed publications. He is now a Professor of the Institute of Chemistry, Chinese Academy of Sciences.



Erik H. Hároz

Rice University
Electrical and Computer Engineering
Houston, TX, USA
enano@rice.edu

Chapter A.4

Erik Hároz is a PhD student in Electrical Engineering with final exams in Spring 2013 from Rice University. At Rice he already earned a BA in Chemistry and a MS in Electrical Engineering. His doctoral work, under the supervision of Professors Junichiro Kono, Robert Hauge and Frank Tittel, has been on carbon nanotube colloid and separation chemistry as well as armchair carbon nanotube photophysics.

Quentin Jallerat

Carnegie Mellon University
Biomedical Engineering
Pittsburgh, PA, USA
qjallera@andrew.cmu.edu



Chapter F.27

Quentin Jallerat received a BS from Ecole Centrale Paris, France and a MS in Biomedical Engineering from Columbia University, New York. He is now a graduate student in the Regenerative Biomaterials and Therapeutics Group at Carnegie Mellon University, Pittsburgh, PA. He is developing new scaffolds that mimic the extracellular matrix of the chick embryonic heart for cardiac tissue engineering.

Heli Jantunen

University of Oulu
Department of Electrical Engineering
Oulu, Finland
heli.jantunen@oulu.fi



Chapter D.20

Heli Jantunen received her Dr. Tech. degree in Microelectronics from the University of Oulu, Finland, in 2001 and is working as Full Professor in Technical Physics in the Microelectronics and Materials Physics Laboratory. Her research interests include novel sensors and RF applications by implementation of advanced functional materials, structures and nanotechnology into multifunctional micromodules and printed electronics devices.



Song Jin

University of Wisconsin–Madison
Department of Chemistry
Madison, WI, USA
jin@chem.wisc.edu

Chapter C.17

Song Jin received his BS from Beijing University in 1997 and his PhD from Cornell University, Ithaca, NY, in 2002. He is currently an Associate Professor of Chemistry at the University of Wisconsin-Madison, WI. With interest in chemistry and physics of nanomaterials, Dr. Jin studies the fundamental formation mechanisms of nanomaterials, their novel physical properties and applications in renewable energy such as solar and thermoelectric energy conversion as well as energy storage, nanospintronics, and nanobiotechnology.



Kaushik Kalaga

Rice University
Department of Mechanical Enginnering &
Materials Science
Houston, TX, USA
kalaga.kaushik@gmail.com

Chapter G.31

Kaushik Kalaga received his B.Tech and M.Tech (Integrated Dual Degree) from Indian Institute of Technology, at Banaras Hindu University, Varanasi. He is currently pursuing his PhD at Rice University, Houston, USA in Mechanical Engineering and Materials Science. He is currently working on carbon nanomaterials and other layered materials for lithium ion battery applications.

Ji-Hee Kim

Rice University
Department of Electrical and Computer Engineering
Houston, TX, USA
withphys@gmail.com



Chapter A.4

Ji-Hee Kim received her PhD from Chungnam National University, Korea, in 2011 under the supervision of Professor Ki-Ju Yee. Her thesis focused on coherent phonons in graphene and single walled carbon nanotubes by ultrafast spectroscopy. She moved to Rice University as a postdoctoral researcher in Professor Junichiro Kono's group. Her current research focuses on many-body processes of excitons in quantum wells under high magnetic fields.

Yoong A. Kim

Shinshu University
Department of Electrical and Electronic Engineering
Nagano, Japan
yak@endomoribu.shinshu-u.ac.jp



Chapter A.7

Yoong Ahm Kim received a PhD in Materials Engineering in 2001 from Shinshu University, Japan. He is an Associate Professor at Shinshu University and has published about 160 papers (H-index = 33). His current research areas are carbon nanotube-based transparent conductive films, optical properties of double-walled carbon nanotubes, fabrication of novel nanofibers by electrospinning, biological compatibility of carbon nanotubes, fabrication of high-quality graphenes, application of nanocarbons in energy storage devices, and nanocarbon-based three dimensional scaffolds for growing cells.



Ian A. Kinloch

University of Manchester
School of Materials
Manchester, UK
ian.kinloch@manchester.ac.uk

Chapter D.19

Ian Kinloch studied Physics at Durham University, UK, and undertook his PhD at the University of Cambridge upon the processing characterization and properties of carbon nanotubes. He was awarded a Royal Academy of Engineering/EPSRC Research Fellowship in Carbon Nanotubes in Advanced Engineering Materials at Cambridge and moved to Manchester University in 2006. His research is now concentrated upon the production, processing and applications of nanomaterials and has recently refocused his interests towards graphene.

Imre Kiricsi (deceased)

Chapter E.22



Junichiro Kono

Rice University
Electrical and Computer Engineering &
Physics and Astronomy
Houston, TX, USA
kono@rice.edu

Chapter A.4

Junichiro Kono received his BS and MS degrees in Applied Physics from the University of Tokyo in 1990 and 1992, respectively, and completed his PhD in Physics at the State University of New York at Buffalo in 1995. He was a postdoctoral research associate at the University of California, Santa Barbara (1995–1997) and a W. W. Hansen Experimental Physics Laboratory Fellow at Stanford University 1997–2000. He joined the Department of Electrical and Computer Engineering of Rice University in 2000 and since 2009 he has been a Professor at Rice University. Kono's current research interests include optical studies of low-dimensional systems; spintronics and quantum information processing; nonlinear, ultrafast, and quantum optics in solids; phenomena in ultrahigh magnetic fields; and terahertz phenomena in semiconductors.

Krisztián Kordás

University of Oulu
Department of Electrical Engineering
Oulu, Finland
lapy@ee.oulu.fi



Chapters B.10, D.20

Krisztián Kordás is a Research Professor at the Department of Electrical Engineering, University of Oulu, where he earned his Dr. Tech. degree in Microelectronics in 2002. Between 2004 and 2008 he held an Academy Research Fellow position of the Academy of Finland. His research is focused on nanomaterials synthesis and modification for (photo)catalysis, sensors and electrical components and devices.

Gábor Kozma

University of Szeged
Department of Applied and
Environmental Chemistry
Szeged, Hungary
kozmag@chem.u-szeged.hu



Chapter A.5

Gábor Kozma graduated in Environmental Science from the University of Szeged, Hungary, in 2007. After graduation he started his PhD studies at the Department of Applied and Environmental Chemistry, where he is now working as Assistant Research Fellow. His research interests include mechanochemical synthesis and kinetics, nanocomposites and nanoscaled materials applications in environmental remediation.



Jarmo Kukkola

University of Oulu
Department of Electrical Engineering
Oulu, Finland
jarmo.kukkola@gmail.com

Chapter D.20

Jarmo Kukkola, after receiving his MSc degree in Theoretical Physics from the University of Oulu, Finland (2008), he joined the Microelectronics and Materials Physics Labs in Oulu, where he is currently a PhD student. His primary research interest are electrical properties of nanostructured materials.



Ákos Kukovecz

University of Szeged
Department of Applied and
Environmental Chemistry
Szeged, Hungary
kakos@chem.u-szeged.hu

Chapters A.5, D.20, E.22

Ákos Kukovecz received his PhD in chemistry from the University of Szeged, Hungary, in 2001 and has done his postdoctoral work at the University of Vienna, Austria. He is now an Associate Professor of Chemistry at Szeged. His current research interests include porous nanocomposites, networks of one-dimensional nanostructures, fluid–nanoparticle interactions, electron microscopy and Raman spectroscopy.

Vinod Kumar

Banaras Hindu University
Department of Zoology
Lanka, Varanasi, India
mail2vinod2@gmail.com



Chapter F.26

Vinod Kumar is a PhD student in the department of Zoology at Banaras Hindu University, India. He received his MSc in Biotechnology from Chhatrapati Shahu Ji Maharaj University (CSJM), Kanpur, India. His current research interests focus on biomedical application of carbon nanomaterials with a special attention to the field of tissue engineering and disease diagnosis.

Zoltán Kónya

University of Szeged
Department of Applied and
Environmental Chemistry
Szeged, Hungary
konya@chem.u-szeged.hu



Chapters A.5, D.20, E.22

Zoltán Kónya received his PhD in Chemistry from the University of Szeged, Hungary (1997). His research interests include inorganic nanostructures, synthesis procedures, spectroscopy and microscopy. Currently he is working on two main fields, one is the synthesis and modifications of new 0-D and 1-D nanostructures for (photo)catalytic applications. The second is the possible environmental applications of nanostructures.



Jaesang Lee

Korea Institute of Science and Technology
(KIST)
Center for Water Resource Cycle
Seoul, Korea
lee39@kist.re.kr

Chapter G.29

Dr. Jaesang Lee is a senior research scientist at the Center for Water Resource Cycle, Korea Institute of Science and Technology. He received his PhD from POSTECH and worked as a postdoctoral researcher at Georgia Institute of Technology and Rice University. His current research interests include environmental photochemistry and photocatalysis, advanced oxidation processes, and environmental fate of nanomaterials.



Seunghak Lee

Korea Institute of Science and Technology (KIST)
Center for Water Resource Cycle
Seoul, Korea
seunglee@kist.re.kr

Chapter G.29

Dr. Seunghak Lee received his PhD in Geoenvironmental Engineering from Seoul National University (2005) and worked as a postdoctoral research associate at University of Wisconsin-Madison. His research interests include subsurface remediation technologies, especially, permeable reactive barriers, contaminant transports in the subsurface and hazardous waste landfills. His current research is focused on estimating fate and transport of nanoparticles in the subsurface.

Renat R. Letfullin

Rose-Hulman Institute of Technology
Physics and Optical Engineering
Terre Haute, IN, USA
letfullin@rose-hulman.edu



Chapter G.30

Renat R. Letfullin is Associate Professor of Physics and Optical Engineering Department at the Rose-Hulman Institute of Technology at Terre Haute, IN. He has extensive academic credentials in nanotechnology and specializes in laser physics, wave and quantum optics, biophotonics and nanomedicine. He published over 150 articles and conference proceedings, including 12 book chapters and 10 authored/edited books. He is an Editor for International Journal of Theoretical Physics, Group Theory and Nonlinear Optics.

Roi Levi

Weizmann Institute of Science
Department of Materials and Interfaces
Rehovot, Israel
roi.levi@weizmann.ac.il



Chapter C.16

Roi Levi received his BSc in Chemical Engineering from the Ben-Gurion University, Israel (2006), the MSc degree in Chemistry from the Weizmann Institute of Science and is currently striving for his PhD in Chemistry at the Weizmann Institute of Science, Rehovot. His research interests include electronic and electro-mechanic properties of inorganic nanotubes and functional devices incorporating inorganic nanotubes.



Zuzanna A. Lewicka

Rice University
Department of Chemistry
Houston, TX, USA
zuzannal@rice.edu

Chapter G.32

Dr. Zuzanna Lewicka received a PhD from Rice University, Houston, USA, in May 2012 and a Master of Science degree from the University of Technology, Wrocław, Poland, in 2005. Her research has centred upon the characterization of engineered nanomaterials prior to their examination in toxicology and environmental studies, as well as the development of methods to produce nanostructure arrays over large areas.



Longtu Li

Tsinghua University
Materials Science & Engineering
Beijing, China
llt-dms@mail.tsinghua.edu.cn

Chapter C.14

Longtu Li is a Professor in the Department of Materials Science and Engineering at Tsinghua University, where he graduated in 1958. He is a member of the Chinese Academic of Engineering and has worked as visiting scholar and visiting Professor at Lehigh University and Penn State University, USA, in 1987 and 1994, respectively. His research fields include piezoelectric, ferroelectric, dielectric, semiconductive, ferrite materials and their applications.

Shaily Mahendra

University of California, Los Angeles
Civil and Environmental Engineering
Los Angeles, CA, USA
mahendra@seas.ucla.edu



Chapter G.29

Dr. Shaily Mahendra is an Assistant Professor in the UCLA Department Civil & Environmental Engineering. She received PhD from University of California, Berkeley, and post-doctoral fellowship from Rice University, Houston. Her research areas are microbial processes in natural and engineered systems, applications of molecular and isotopic tools in environmental microbiology, biodegradation of emerging groundwater contaminants and environmental impacts of nanomaterials.

Balaji P. Mandal

Bhabha Atomic Research Centre
Chemistry Division
Mumbai, India
bpmandal@barc.gov.i



Chapter C.13

Dr. Balaji P. Mandal joined the Bhabha Atomic Research Centre (BARC) in 2004. He was awarded the PhD degree in Chemistry in 2009 by the Mumbai University in recognition of his work on high temperature ceramic materials for futuristic nuclear technologies. He did his postdoctoral research at Wayne State University, Detroit, USA during 2011/2012. His research interest is in synthesis and structural elucidation of inorganic materials based on oxides.



Fei Meng

University of Wisconsin-Madison
Department of Chemistry
Madison, WI, USA
fmeng@chem.wisc.edu

Chapter C.17

Fei Meng received his BS degree in Chemistry from Beijing University in 2005. Now he is pursuing doctoral thesis in the Department of Chemistry in the University of Wisconsin-Madison under the supervision of Professor Song Jin. His research focuses on the screw dislocation-driven growth of nanomaterials.



Guowen Meng

Chinese Academy of Sciences
Institute of Solid State Physics
Hefei, China
gwmeng@issp.ac.cn

Chapter E.23

Guowen Meng is a Professor in the Institute of Solid State Physics, Chinese Academy of Sciences (CAS), Hefei. He obtained his PhD in Materials Science and Engineering from Northwestern Polytechnic University, Xi'an, China (1996) and did his post doc work at the Rensselaer Polytechnic Institute, Troy, NY. His research interests include 1-D nanostructures and environmental applications of nanomaterials. He co-authored more than 150 papers (H-index 38) and was awarded the 2nd class of The State Natural Science Award of the P.R. China.

Younès Messaddeq

Université Laval
Department of Physics
Québec, Québec, Canada
younes.messaddeq@copl.ulaval.ca



Chapter C.18

Younès Messaddeq, who holds a PhD in chemistry and a bachelor's degree in solid-state chemistry from the Université de Rennes 1, France, is a researcher in materials development for optics and photonics. He has published over 290 papers in refereed journals and conferences, and presented several of Invited talks related to glass and advanced materials. In 2010, he was appointed to one of the 19 prestigious Canada Excellence Research Chairs (CERC), providing 28M$ in research funds at Université Laval, Québec, Canada.

Jyri-Pekka Mikkola

Åbo Akademi University
Department of Chemical Engineering
Åbo-Turku, Finland
jyri-pekka.mikkola@chem.umu.se;
jyri-pekka.mikkola@abo.fi



Chapter D.20

Jyri-Pekka Mikkola is a Professor of Sustainable Chemical Technology at Umeå University, Sweden and Åbo Akademi University, Finland. He earned his Dr. Tech. (Chem.Eng.) degree in 1999. Previously he held an Academy Research Fellow position at the Academy of Finland. He received the Incentive Award from the Academy of Finland (2006) and the Umeå University's Young Researcher Award (2009). His research encompasses areas including nanostructured catalysis, ionic-liquid technologies and biorefining.



Melinda Mohl

University of Oulu
Department of Electrical Engineering
Oulu, Finland
memohl@ee.oulu.fi

Chapter B.10

Melinda Mohl received her PhD in Nanotechnology from the University of Szeged, Hungary, in 2011. She performed internships at the Facultés Universitaires Notre-Dame de la Paix, Namur, France (2005–2006) and at Rice University, Houston (2008–2009). Since 2011, she is a postdoctoral research fellow at the University of Oulu, Finland, pursuing research on nanostructures for (photo)catalysis, sensors and electronic devices.



Aarón Morelos-Gómez

Shinshu University
Institute of Carbon Science and Technology
Nagano, Japan
amorelos@shinshu-u.ac.jp

Chapter A.6

Aarón Morelos-Gómez received his doctoral degree in Applied Sciences specialized in Nanoscience and Nanotechnology in 2010 from Institute for Scientific and Technological Research of San Luis Potosi (IPICYT), Mexico. Currently he is a postdoctoral fellow at the Institute of Carbon Science and Technology at Shinshu University in Japan. His research interests are synthesis and physical properties of carbon nanotubes, graphene nanoribbons and carbon inverse opal.

Stephen A. Morin

Harvard University
Chemistry and Chemical Biology
Cambridge, MA, USA
smorin@gmwgroup.harvard.edu



Chapter C.17

Stephen A. Morin received his PhD in Chemistry from the University of Wisconsin – Madison in 2011. His graduate research focused on the synthesis and assembly of functional nanomaterials and enabled the development of the fundamental understandings and strategies for dislocation-driven nanowire, nanotube, and nanoplate growth in the aqueous phase. He is currently a Postdoctoral Fellow at Harvard University in the Lab of Professor George M. Whitesides.

Marcelo Nalin

Federal University of Sao Carlos
Department of Chemistry
Sao Carlos, Brazil
mnalin@ufscar.br



Chapter C.18

Marcelo Nalin is a Professor at the Federal University of Sao Carlos, Brazil. He earned his PhD in Chemistry from both Institute of Chemistry – UNESP (Brazil) and Rennes~ I University (France) in 2002. He did his post-doctoral work at Paris-Sud University (France) and in the Physics Department of Unicamp (Brazil). His research includes the synthesis of glasses and nanoglassceramics for photonics.



Sebastien Nanot

Rice University
Electrical and Computer Engineering &
Physics and Astronomy
Houston, TX, USA
sebastien.nanot@gmail.com

Chapter A.4

Sebastien Nanot received his PhD from Université de Toulouse (France) in 2009 under supervision of Professors Bertrand Raquet and Jean-Marc Broto. His thesis focused on individual carbon nanotube properties under very high magnetic fields. He moved to Rice University where he is appointed as a postdoctoral researcher in Prof. Junichiro Kono's Group. His current research focuses on optoelectronic properties of carbon materials.



Rachelle N. Palchesko

Carnegie Mellon University
Biomedical Engineering
Pittsburgh, PA, USA
rachelle@andrew.cmu.edu

Chapter F.27

Dr. Rachelle Palchesko received her PhD in Surface Chemistry focusing on the covalent attachment of biomolecules to bone replacement materials at Duquesne University, Pittsburgh, PA. She is currently a Postdoctoral Fellow working with Professor Adam Feinberg and James Funderburgh on tissue engineering the corneal endothelium. Her research focuses on the bottom-up engineering of basement membrane mimics utilizing ECM proteins and biomechanics.

Cary L. Pint

Vanderbilt University
Department of Mechanical Engineering
Nashville, TN, USA
Cary.L.Pint@vanderbilt.edu



Chapter A.4

Cary is currently an Assistant Professor of Mechanical Engineering at Vanderbilt University, where he serves as Director of the Nanomaterials and Energy Devices Laboratory. Cary received his PhD in Applied Physics from Rice University in 2010 and authored over 40 publications focused on growth and applications of carbon nanomaterials. Cary also serves as Associate Editor of Advanced Carbon.

Gael Poirier

Federal University of Alfenas
Institute of Science and Technology
Poços de Caldas, MG, Brazil
gael.poirier@unifal-mg.edu.br



Chapter C.18

Professor Gael Poirier obtained his doctoral degree in Physical Chemistry in 2003 from the Université de Rennes 1, France, and Sao Paulo State Univerisity (UNESP), Araraquara, Brazil. Between 2003 and 2006, he also worked in the field of glasses and glass-ceramics for optics also at UNESP in collaboration with Professors Sidney Ribeiro and Younes Messaddeq. He is a Professor of chemistry and solid state science since 2006 at the Federal University of Alfenas, Brazil. He has published 32 papers focusing on new glass-ceramics for optical applications based on germinate and tellurite compositions.



Thalappil Pradeep

Indian Institute of Technology Madras
Department of Chemistry
Chennai, India
pradeep@iitm.ac.in

Chapter B.9

Dr. Pradeep earned his PhD from the Indian Institute of Science in 1991 and had post doctoral training at University of California, Berkeley and Purdue University, West Lafayette. His interests are in molecular and nanoscale materials and he builds instruments to perform several of these studies. He develops affordable technologies for clean water and has authored over 275 publications, four books and several book chapters. He is a Fellow of the Indian Academy of Sciences.



István Pálinkó

University of Szeged
Department of Organic Chemistry
Szeged, Hungary
palinko@chem.u-szeged.hu

Chapter E.22

István Pálinkó is an Associate Professor at the Chemistry Institute, University of Szeged. He earned his PhD and DSc from the Hungarian Academy of Sciences. He did postdoctoral works with Professor Seddon at Queen's University of Belfast and Nobel-Laurate G.A. Olah at the University of South California. He is active in diverse areas like synthetic materials science, physical organic chemistry and solution inorganic chemistry.

Raju V. Ramanujan

Nanyang Technological University
School of Materials Science and Engineering
Singapore
ramanujan@ntu.edu.sg



Chapter B.12

Professor Raju V. Ramanujan is a Fellow of the American Society for Materials. He earned his PhD degree at Carnegie Mellon University (USA). Ramanujan serves on the Editorial Board of Nanomedicine and Materials Science and Engineering C. He serves on the Magnetic Materials Committee of TMS (USA) and is the Vice Chair of the Phase Transformations Committee of TMS and ASM (USA). He received the Nanyang Award for Excellence in Teaching. His research interests include the study of advanced nanomaterials for both functional and structural applications.

Sundara Ramaprabhu

Indian Institute of Technology, Madras
Department of Physics
Chennai, India
ramp@iitm.ac.in



Chapter G.28

After completing PhD in Physics at the Indian Institute of Technology Madras, Chennai, Dr. Ramaprabhu worked at the TU Darmstadt, Germany, for 2 years as an Alexander von Humboldt Fellow and for 5 years at University of Geneva, Switzerland. He joined IITM, Chennai as Assistant Professor and subsequently became Professor. He is a DAAD Fellow, Visiting Fellow to Germany by BMBF & DFG German Science Foundations, Visiting Fellow to South Korea and Japan. He is a member of American Chemical Society and Member of Electrochemical Society. His research areas are nanotechnology, hydrogen energy technology, fuel cell technology, pv, li ion battery, nanofluids, water purification, and CO_2 capture. He has published in 228 International journals of repute and has 32 patents.



Jayshree Ramkumar

Bhabha Atomic Research Centre
Analytical Chemistry Division
Mumbai, India
jrk@barc.gov.in

Chapter C.13

Dr. Jayshree Ramkumar is affiliated to the Analytical Chemistry Division of Bhabha Atomic Research Centre. She is also an Assistant Professor Homi Bhabha National Institute, India. Her area of specialization is the development of new separation procedures for different metal ions and toxic substances using membranes and adsorbents. She was awarded the PhD on her work on ion exchange and related studies using Nafion membrane. She has more than 40 international journal publications and pursued her postdoctoral research in 2009 as an MANA Research Fellow at the National Institute of Materials Science (NIMS), Ibaraki, Japan.



Arava L.M. Reddy

Rice University
Department of Mechanical Engineering and Materials Science
Houston, TX, USA
leela@rice.edu

Chapter G.28

Dr. Arava Leela Mohana Reddy obtained his PhD in Physics from the Indian Institute of Technology Madras, India in 2007. He then spent a year as a postdoctoral fellow at the University of Pittsburgh with Prof. Gilbert Walker. He is currently a Research Scientist in the Department of Mechanical Engineering and Material Science at Rice University. His research focuses on nanostructured materials, particularly hybrid nanoarchitectures for applications in lithium-ion rechargeable batteries, fuel cells and supercapacitors. He has published more than 55 papers.

Vincent C. Reyes

University of California, Los Angeles
Department of Civil and Environmental Engineering
Los Angeles, CA, USA
vincecreyes@ ucla.edu



Chapter G.29

Vincent C. Reyes is a PhD candidate in Civil & Environmental Engineering at the University of California, Los Angeles, where he also received his MS. He got his BS in Genetics from the University of California, Irvine. His current research focuses on understanding the interactions of metal containing nanomaterials with nitrogen cycling microorganisms.

Sidney J.L. Ribeiro

Sao Paulo State University – UNESP
Institute of Chemistry
Araraquara, SP, Brazil
Sidney@iq.unesp.br



Chapter C.18

Professor Sidney J.L. Ribeiro obtained his PhD degree working on glasses and glass-ceramics at Sao Paulo State University (UNESP). Post-doc stages were performed at the École Centrale Paris and the CNET-France Telecom, France. Ribeiro published more than 240 papers and 19 patents were deposited. His research includes inorganic chemistry, materials science and education in chemistry.



William D. Rice

Los Alamos National Laboratory
National High Magnetic Field Laboratory
Los Alamos, NM, USA
wdrice@lanl.gov

Chapter A.4

William Rice obtained his BSc (Honors) in Physics at Brown University focusing on picosecond ultrasonics and coherent phonons in water. His doctoral work at Rice University centred on electronic spin resonance, exciton dynamics, and magnetotransport in carbon nanotubes and quantum wells. Currently, he is a post-doctoral fellow at Los Alamos investigating photo-induced magnetism in quantum dots.



Silvia H. Santagneli

Sao Paulo State University – UNESP
Institute of Chemistry
Araraquara, SP, Brazil
santagneli@iq.unesp.br

Chapter C.18

Silvia Santagneli received her PhD degree in Chemistry from Sao Paulo State University – UNESP, Brazil in 2006. The she spent a post-doctoral period at the same institution. Her research interests include glass materials and solid state NMR technique for applications in materials science. Currently she develops new glasses for photonic and battery devices also at UNESP.

Preeti S. Saxena

Banaras Hindu University
Department of Zoology
Lanka, Varanasi, Uttar Pradesh, India
pssaxena@rediffmail.co



Chapter F.26

Preeti S. Saxena received her PhD from the University of Rajasthan, Jaipur in 2003. At present, she is working as Assistant Professor in the Department of Zoology, BHU. She is doing research in the area of nanobiology, nanotoxicology and biosensing. She has also been a visiting research scholar at Rensselaer Polytechnic Institute, Troy, USA in 2006.

Olga A. Shenderova

International Technology Center
Raleigh, NC, USA
oshenderova@itc-inc.org



Chapter A.8

Olga Shenderova received the PhD degree in Materials Science from the St. Petersburg State Technical University, Russia. She is a Head of the Nanodiamond Laboratory at the International Technology Center and a President of Adámas Nanotechnologies Inc., Raleigh, USA. She works on applied research and commercialization of nanodiamond particles. She authored more than 120 papers and edited 5 books on nanodiamonds.



Rakesh Shukla

Bhabha Atomic Research Centre
Chemistry Division
Mumbai, India
rakesh@barc.gov.in

Chapter C.13

Mr. Rakesh Shukla joined the Solid-State Chemistry Section of the Chemistry Division, Bhabha Atomic Research Centre, Mumbai in 2006. His main research interests are in the chemistry of nanomaterials for various applications. Recently he was a visiting researcher at Wayne State University, Detroit, USA. Presently he is pursuing his PhD (Chemistry) from Mumbai University under the guidance of Dr. A. K. Tyagi.



Shashwat Shukla

Nanyang Technological University
Singapore
shas0002@e.ntu.edu.sg

Chapter B.12

Shashwat Shukla is a PhD student in the School of Materials Science and Engineering, Nanyang Technological University (NTU), Singapore. His research interests include non-equilibrium processing of magnetic nanomaterials, x-ray absorption spectroscopy, electron microscopy, neutron diffraction and kinetic modelling of alloy systems subjected to external driving forces such as mechanical milling and ion irradiation.

Theruvakkattil S. Sreeprasad

Kansas State University
Department of Chemical Engineering
Manhattan, KS, USA
sprasad@k-state.edu



Chapter B.9

Dr. Sreeprasad is a postdoctoral fellow at the Kansas State University. He earned his PhD from the Indian Institute of Technology Madras, India in 2011 and has MSc from the School of Chemical Sciences, MG University, Kottayam, India. His areas of interest include nanosystems and 2-D materials. He has authored/co-authored 26 journal articles, 3 book chapters and is a co-inventor in 8 patent applications.

Anchal Srivastava

Banaras Hindu University
Department of Physics
Lanka, Varanasi, Uttar Pradesh, India
anchalbhu@gmail.com



Chapters F.26, G.31

Anchal Srivastava received his PhD from Banaras Hindu University (BHU), India, in 2002. He continued in the same department as a post doctoral fellow, as a lecturer in 2004 and is currently an Assistant Professor in the Department of Physics, BHU. He specializes in synthesis, characterizations and applications of carbon nanomaterials and has been awarded the Max-Planck India fellowship. He did research at Max-Planck Institute of Solid State Physics, Stuttgart, Germany in Professor von Klitzing's group. He has also been awarded the prestigious BOYSCAST fellowship from the government of India in 2008–2009. He has also been a visiting research scholar at Rensselaer Polytechnic Institute, USA in 2006.



Saurabh Srivastava

National Physical Laboratory
Biomedical Instrumentation Section,
New Rajender Nagar, New Delhi, India
saurabhnpl@gmail.com

Chapter G.31

Saurabh Srivastava received his MSc in Physics from Banaras Hindu University (BHU), Varanasi, India, where he is currently pursuing his PhD in Physics. He is a senior research fellow (CSIR) in the Biomedical Instrumentation Section, National Physical Laboratory, New Delhi, India. He is actively engaged in carbon nanomaterials and their derivatives for biosensing application.



Yan Sun

Beihang University (BUAA)
School of Biological Science and Medical Engineering
Beijing, China
sunyan@buaa.edu.cn

Chapter F.27

Yan Sun received her PhD in Biochemistry and Molecular Biology from the Chinese Academy of Sciences (CAS). She is an Associate Professor in the School of Biological Sciences and Medical Engineering of Beihang University (BUAA), China. Her research activities include biomechanics, effect of microgravity on human cells and microorganisms, anti-tumor research of Chinese herbal medicine, as well as biomicrofluidics and micropatterning.

Mária Szabó

University of Szeged
Applied and Environmental Chemistry
Szeged, Hungary
szmaria@chem.u-szeged.hu



Chapter D.20

Mária Szabó is a PhD student at the University of Szeged in Hungary, where she finished her Chemistry BSc and then MSc before. She has also been working as summer trainee at the University of Oulu, Finland. She focuses on the preparation and characterization of nanoparticles for her PhD thesis where she discusses 1-D nanostructures.

John M. Szymanski

Carnegie Mellon University
Department of Biomedical Engineering
Pittsburgh, PA, USA
jszymans@andrew.cmu.edu



Chapter F.27

John Szymanski earned his BS in Materials Science and Engineering from Johns Hopkins University. John is currently performing his doctoral work under Dr. Adam Feinberg in the Department of Biomedical Engineering at Carnegie Mellon University, Pittsburgh. His research focuses on investigating the mechanosensitive properties of extracellular matrix protein nanofibers and how these properties affect cell behavior.

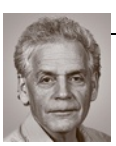


András Sápi

University of Szeged
Department of Applied and Environmental Chemistry
Szeged, Hungary
sapia@chem.u-szeged.hu

Chapter D.20

András Sápi earned his PhD degree in Chemistry at the University of Szeged, Hungary, where he is an Assistant Lecturer in the Applied and Environmental Chemistry Department. His researches mainly focused on 0-D and 1-D nanomaterials, different types of nanocomposites. He has experience in carbon nanotubes, titanate nanostructures, materials science characterization methods and catalytic investigations.



Reshef Tenne

Weizmann Institute of Science
Department of Materials and Interfaces
Rehovot, Israel
Reshef.tenne@weizmnn.ac.il

Chapter C.16

Reshef Tenne earned his PhD in 1976 in Physical Chemistry from the Hebrew University of Jerusalem and joined the Weizmann Institute in 1979. His interests are focused on the synthesis and study of nanotubes and fullerene-like nanoparticles of layered compounds, like WS_2, which he discovered in 1992. He is the Director of the Helen and Martin Kimmel Center for Nanoscale Science at the Weizmann Institute and a member of the Israel Academy of Sciences and Humanities and Academia Europaea and a Fellow of the Materials Research Society and the Royal Society of Chemistry.

Humberto Terrones

Pennsylvania State University
Physics Department
University Park, PA, USA
hzt2@psu.edu



Chapter A.3

Humberto Terrones obtained his PhD from the University of London, UK. Following a posdoctoral position in Cambridge University (UK), he joined UNAM and IPICYT in Mexico. Then moved to UCL in Leuven, Belgium and ORNL, Oak Ridge, USA. Presently, he is Visiting Professor at Pennsylvania State University, University Park, PA and at the Ceara Federal University in Brazil. His main interests involve theory and experiment of 2-D layered nanostructures.

Mauricio Terrones

Pennsylvania State University
Department of Physics and Materials Science and Engineering
University Park, PA, USA
mut11@psu.edu



Chapter A.6

Mauricio Terrones obtained his BSc in Engineering Physics with first class honours at Universidad Iberoamericana. In 1994 he started his doctorate with Sir Prof. Harold W. Kroto (Nobel Laureate, FRS) and received his D.Phil. degree from the University of Sussex in 1998. He has co-authored more than 300 publications in international journalswith an H index of 63. He has numerous awards including: the Alexander von Humboldt Fellowship, the Javed Husain Prize and the Albert Einstein medal from UNESCO, the TWAS Prize in Engineering Physics, the Carbon Prize given by the Japanese Carbon Society, the Somiya Award by the International Union of Materials Research Societies, among others. He is currently Professor of Physics at The Pennsylvania State University (USA) and distinguished Professor at Shinshu University, Japan.



Nicholas A. Thompson

Rice University
Department of Physics & Astronomy
Houston, TX, USA
nt7@rice.edu

Chapter A.4

Nicholas Thompson is a Graduate student in Physics at Rice University working in Prof. Junichiro Kono's research group. His experimental work involves observation of the optical properties of graphene under strong excitations. He obtained his Master's Degree in Mathematics from Idaho State University.



Bipul Tripathi

Banaras Hindu University
Department of Physics
Lanka, Varanasi, Uttar Pradesh, India
bipultripathi@gmail.com

Chapter F.26

Bipul Tripathi received his BSc (Honors) in Physics from Banaras Hindu University (BHU), India and completed the MSc in Physics with specialization in Biophysics from the same department in 2012. His field of interest includes synthesis of advanced functional nanomaterials for application in nanobiotechnology partiularly in tissue enigineering and drug delivery.

Ferdinando Tristán López

Shinshu University
Faculty of Engineering, Research Center for Exotic Nanocarbons
Nagano, Japan
ftristan@shinshu-u.ac.jp



Chapter A.6

Ferdinando Tristan Lopez received his PhD in Chemical Engineering from the Universidad Autonoma de San Luis Potosi, Mexico in 2008. His research interests include catalysis, self-assembly and synthesis of carbon nanostructures. Currently he develops his research at the Research Center for Exotic Nanocarbons in Shinshu University, Japan.

Avesh K. Tyagi

Bhabha Atomic Research Centre
Chemistry Division
Mumbai, India
aktyagi@barc.gov.in



Chapter C.13

Dr. Avesh K. Tyagi joined BARC in 1986. Presently he is heading the Solid-State Chemistry Section. He is a Professor of Chemistry at Homi Bhabha National Institute. His research interests are in nano, functional and nuclear materials. He also awarded a number of prestigious awards such as such as Homi Bhabha Science and Technology Award MRSI Medal; CRSI, Medal; Gold Medal of Indian Nuclear Society; Rheometric-ITAS Award; Dr. Laxmi Award of ISCAS and IANCAS-Dr Tarun Datta Memorial Award, R.D. Deasi Memorial Award of Indian Chemical Society and CRSI-Prof. CNR Rao National Prize for Chemical Sciences. He is a Fellow of the National Academy of Sciences, India, Royal Society of Chemistry, UK, and the Maharashtra Academy of Sciences.



Géza Tóth

University of Oulu
Department of Electrical Engineering
Oulu, Finland
geza@ee.oulu.fi

Chapter D.20

Dr. Tech. Geza Toth is a postdoctoral researcher. After his diploma in Physics from the University of Szeged in 2002, he joined the Microelectronics and Materials Physics Laboratories in Oulu, Finland, where he finished his postgraduate studies in 2007. His primary research field is related to materials physics and characterization (electron microscopy); computational analysis (thermomechanics and fluid dynamics by FEM). He authored 30+ papers on laser-matter interaction, and syntheses/applications of nano-structured materials (CNTs, AAO, porous-Si). He has been active in national (Finnish) and European projects as key personnel and coordinator.



Robert Vajtai

Rice University
Department of Mechanical Engineering and Materials Science
Houston, TX, USA
robert.vajtai@rice.edu

Chapter 1

Robert Vajtai is a Faculty Fellow at Rice University, Houston, Texas, in the Department of Mechanical Engineering and Materials Science. His expertise covers synthesis, processing, characterization of physical and chemical properties of new, advanced material forms and structures. Dr. Vajtai's interests are in nanostructured materials, nanocomposites and nanomaterials; as well as their applications in thermal management, energy storage, microelectromechanical systems, sensors and electronic devices. He received his graduate and PhD degrees from the University of Szeged, then named Jozsef Attila University, Hungary.

Sofia M. Vega Díaz

Shinshu University
Research Center for Exotic Nanocarbons
Nagano, Japan
smvd@shinshu-u.ac.jp



Chapter A.6

Sofia Magdalena Vega-Diaz received the MSc degree in 2003 and PhD in 2009 in Chemical Engineering from Universidad Autonoma de San Luis Potosi, Mexico. Her research activities include synthesis and processing of hybrid materials and polymer nanocomposites with nanoclays and nanocarbon structures. She currently develops her research at the International Research Center for Exotic Nanocarbons in Shinshu University, Japan.

Aravind Vijayaraghavan

University of Manchester
School of Computer Science
Manchester, UK
aravind@cs.man.ac.uk



Chapter A.2

Dr. Aravind Vijayaraghavan is currently a Lecturer at the University of Manchester. He received his PhD (2005) and MEng (2002) in Materials Engineering from Rensselaer Polytechnic Institute, Troy, and BTech (2000) from the Indian Institute of Technology, Madras. He was previously an Alexander von Humboldt fellow at the Karlsruhe Institute of Technology (KIT). His current research explores the production, properties and applications of graphene, carbon nanotubes and related nanomaterials, with particular focus on nanoelectronics and biosensing.



Xiaohui Wang

Tsinghua University
Department of Materials Science & Engineering
Beijing, China
wxh@mail.tsinghua.edu.cn

Chapter C.14

Dr. Xiaohui Wang is a Professor of Department of Materials Science & Engineering at Tsinghua University. She received her PhD in Physical Chemistry from Jilin University in 1994 and did her postdoctoral work at the University of Pennsylvania. Her current research activities include the synthesis and characterization of nanomaterials, sintering of nanoceramics and its applications.



Xuan Wang

Rice University
Department of Electrica and Computer Engineering
Houston, TX, USA
xw13@rice.edu

Chapter A.4

Dr. Xuan Wang got his Bachelor's degree in Physics from Nankai University in China. He finished his PhD program in Physics at Florida State University. His research topic was to develop and use the ultrafast electron diffraction technique to study lattice dynamics. Currently, he is a postdoctoral Researcher at Rice University and his research interest are the transport and optical properties of CNT devices.

Qiaoling Xu

Chinese Academy of Sciences
Key Laboratory of Materials Physics (CAS), Anhui Key Laboratory of Nanomaterials and Nanostructures
Anhui, China
qlxu@issp.ac.cn



Chapter E.23

Qiaoling Xu is an Associate Professor at the Institute of Solid-State Physics, Chinese Academy of Sciences (CAS). She received her PhD degree in Materials Physics and Chemistry from Institute of Solid-State Physics, CAS in 2009. Her current research interests include the fabrication of 1-D nanostructures and their performance and environmental applications of the nanomaterials.

Robert J. Young

University of Manchester
School of Materials
Manchester, UK
robert.young@manchester.ac.uk



Chapter D.19

Professor Young was educated at the University of Cambridge and in 1986 he was appointed as Professor of Polymer Science & Technology in the University of Manchester. He is interested in all aspects of the relationship between the structure and mechanics of polymers and composites. He has recently focused his attention upon structure/property relations in graphene and chemically-modified graphene for use in high-performance polymer-based nanocomposites. He is listed by HighlyCited.Com for his publications in Materials Science and is a Fellow of the Royal Academy of Engineering.



Ling Zhang

Carnegie Mellon University
Department of Biomedical Engineering
Pittsburgh, PA, USA
zling03@gmail.com

Chapter F.27

Dr. Ling Zhang received her PhD in Biophysics from Tsinghua University, China (2008). She has since been a postdoctoral fellow at the University of Pittsburgh and Carnegie Mellon University. Her research interests are using smart biomaterials to manipulate stem cells for tissue repair, especially in neural tissue engineering and neural regeneration. Currently, she is trying to use biomaterials and neural stem cells to treat stroke and traumatic brain injury.



Shaopeng Zhang

Tsinghua University
Department of Materials Science and Engineering
Beijing, China
zspthu@gmail.com

Chapter C.14

Shaopeng Zhang is a PhD course student in the department of Materials Science and Engineering at Tsinghua University. His research works focus on preparation of $(1\text{-}x)BiScO_3\text{-}xPbTiO_3$ and $Pb(Zr_{1-x}Ti_x)O_3$ piezoelectric ceramics, size effects study on the structures and properties of ferroelectric/piezoelectric ceramics.

Zhonghua Zhang

Shandong University
School of Materials Science and Engineering
Shandong, China
zh_zhang@sdu.edu.cn



Chapter E.21

Zhonghua Zhang received his PhD degree in 2003 from the School of Materials Science and Engineering, Shandong University, where he is now a full professor. He has extensive experience in casting, rapid solidification, amorphous alloys, and shape memory alloys. Now he mainly focuses upon preparation, microstructural characterization, and potential applications of nanoporous metals/alloys through dealloying.

Detailed Contents

Foreword by Claes-Göran Granqvist V
Foreword by Neal Lane VII
List of Abbreviations XXIX

1 **Science and Engineering of Nanomaterials**
Robert Vajtai 1
1.1 History and Definition of Nanomaterials 2
1.1.1 History of Nanomaterials 2
1.1.2 Definition of Nanoscale and Nanomaterials 4
1.2 Formation of Nanomaterials 6
1.3 Properties of Nanomaterials 10
1.3.1 Morphology of Nanomaterials 10
1.3.2 Bonds and Structures 10
1.3.3 Mechanical Properties of Nanomaterials 12
1.3.4 Electrical, Magnetic, and Optical Properties 14
1.3.5 Thermal Properties 18
1.3.6 Chemical Properties, Reactivity, and Functionalization 20
1.3.7 Behavior of Nanomaterials in Corrosive Environments 22
1.4 Typical Applications of Nanomaterials 22
1.4.1 Catalysts and Catalyst Templates 26
1.4.2 Energy Conversion and Storage 26
1.4.3 Sensors Based on Nanomaterials 28
1.5 Concluding Remarks 31
1.6 About the Contents of the Handbook 31
References 31

Part A NanoCarbons

2 **Graphene – Properties and Characterization**
Aravind Vijayaraghavan 39
2.1 Methods of Production 42
2.1.1 Micromechanical Cleavage of Graphite (Scotch Tape Technique) 42
2.1.2 Chemical Vapor Deposition (CVD) 43
2.1.3 Decomposition of Carbides 44
2.1.4 Exfoliation by a Solvent 46
2.1.5 Synthetic Production Route 49
2.1.6 Graphene Nanoribbon (GNR) 49
2.1.7 Derivatives of Graphene 50

2.2 Properties 50
2.2.1 Structure and Physical Properties 50
2.2.2 Mechanical Properties 51
2.2.3 Electronic Properties 52
2.2.4 Optical Properties 55
2.2.5 Thermal and Thermoelectric Properties 56
2.2.6 Chemical Properties 56
2.2.7 Properties of Graphene Derivatives 57
2.3 Characterization 58
2.3.1 Optical Characterization 58
2.3.2 Transmission Electron Microscopy 58
2.3.3 Scanning Probe Techniques 60
2.3.4 Angle-Resolved Photoemission Spectroscopy (ARPES) 60
2.3.5 Raman Spectroscopy 61
2.3.6 Electrical Characterization 63
2.3.7 Photocurrent Microscopy 69
2.4 Applications 69
2.4.1 Structural and Electrical Composites 69
2.4.2 Transparent Conducting Films 69
2.4.3 Sensors 72
2.4.4 Electronic Applications 73
2.4.5 Photonics and Optoelectronics 74
2.5 Conclusions and Outlook 74
References 74

3 **Fullerenes and Beyond: Complexity, Morphology, and Functionality in Closed Carbon Nanostructures**
Humberto Terrones 83
3.1 Geometry and Structural Features of Fullerenes 85
3.1.1 The Mathematics of Closed Carbon Nanostructures 85
3.1.2 Carbon Nanostructures with Zero, Positive, and Negative Gaussian Curvature 85
3.1.3 Classical and Nonclassical Fullerenes 86
3.2 Methods of Synthesis of Fullerenes and Proposed Growth Models ... 88
3.2.1 Fullerenes by Laser Vaporization Method 88
3.2.2 Fullerenes by Arc Discharge 88
3.2.3 Fullerenes by Pyrolysis 88
3.2.4 Fullerenes by Combustion in Flames 89
3.2.5 Fullerenes Under Electron Beam Irradiation Inside a Transmission Electron Microscope (TEM) 89
3.2.6 Fullerenes by Concentrated Solar Flux 89
3.2.7 Proposed Mechanisms for Fullerene Growth and Formation 89
3.3 Physicochemical Properties of Fullerenes 90
3.3.1 Mechanical Properties and Phases of Fullerene Crystals ... 90
3.3.2 Electrical Properties and Superconductivity of Fullerites ... 91
3.3.3 Chemical Properties of Fullerenes 91

3.4 Applications of Fullerenes and Beyond 92
3.4.1 Fullerenes and Health 92
3.4.2 Fullerenes in Solar Cells 92
3.4.3 Nested Fullerenes: Carbon Onions 92
3.4.4 Fullerene Peapods and Fullerene Coalescence 94
3.4.5 High-Genus Fullerenes 97
3.4.6 Inorganic Fullerenes (BN, MoS_2, NbS_2, etc.) 97
3.4.7 Nanodiamond 98
3.5 Conclusions 99
References 99

4 **Single-Walled Carbon Nanotubes**
Sebastien Nanot, Nicholas A. Thompson, Ji-Hee Kim, Xuan Wang, William D. Rice, Erik H. Hároz, Yogeeswaran Ganesan, Cary L. Pint, Junichiro Kono 105
4.1 History 106
4.2 Crystallographic and Electronic Structure 106
4.2.1 Crystallographic Structure 106
4.2.2 Electronic Dispersion 107
4.2.3 Phonon Dispersion 109
4.3 Synthesis 111
4.3.1 Substrate-Free Growth Techniques 112
4.3.2 Substrate-Bound Growth Technique 113
4.3.3 Growth Mechanisms 114
4.4 Optical Properties 115
4.4.1 Optical Absorption and Photoluminescence 116
4.4.2 Raman Spectroscopy 118
4.4.3 Resonant Rayleigh Spectroscopy 119
4.4.4 Ultrafast Spectroscopy 120
4.4.5 Excitonic Effects 121
4.5 Transport Properties 123
4.6 Thermal and Mechanical Properties 128
4.6.1 Thermal Properties 128
4.6.2 Mechanical Properties 130
4.7 Concluding Remarks 135
References 135

5 **Multi-Walled Carbon Nanotubes**
Ákos Kukovecz, Gábor Kozma, Zoltán Kónya 147
5.1 Synthesis 148
5.1.1 Arc Discharge 148
5.1.2 Laser Ablation 149
5.1.3 CCVD Methods 149
5.1.4 Exotic MWCNT Synthesis Methods 150
5.1.5 MWCNT Formation Mechanism – Current Understanding 151

5.1.6 Industrial Production 152
5.1.7 Quality Assessment 153
5.2 Chemistry of MWCNTs 153
5.2.1 Purification of Raw MWCNTs Obtained by Various Methods 154
5.2.2 MWCNT Functionalization 155
5.3 Properties 157
5.3.1 Mechanical Properties 159
5.3.2 Electromagnetic Properties 159
5.3.3 Thermal Properties 160
5.3.4 Spectroscopic Properties 160
5.3.5 Health and Environmental Issues 162
5.4 Selected Applications 163
5.4.1 MWCNT Membranes, Filtration, and Adsorption 164
5.4.2 MWCNTs in Catalysis 166
5.4.3 MWCNT Composites 167
5.4.4 Other Selected MWCNT Applications 168
References 169

6 **Modified Carbon Nanotubes**
Aarón Morelos-Gómez, Ferdinando Tristán López, Rodolfo Cruz-Silva, Sofia M. Vega Díaz, Mauricio Terrones 189
6.1 Doped Carbon Nanotubes 191
6.1.1 Endohedral Doping 192
6.1.2 Exohedral Doping 192
6.1.3 In-Plane Doping 193
6.2 Defects in Carbon Nanotubes 193
6.3 Nanotube Chemical Functionalization 197
6.3.1 Covalent Modification 197
6.3.2 Functionalization of Carbon Nanotubes via $\pi-\pi$ Interactions 200
6.3.3 Electrostatic Functionalization of Carbon Nanotubes 201
6.4 Properties of Modified Carbon Nanotubes 203
6.4.1 Electrical Properties of Modified Tubes 203
6.4.2 Electrochemistry of Modified Nanotubes 203
6.5 Characterization of Modified Carbon Nanotubes 208
6.5.1 Transmission Electron Microscopy 208
6.5.2 Atomic Force Microscopy and Scanning Transmission Microscopy 209
6.5.3 Electron Energy Loss Spectroscopy (EELS) 211
6.5.4 X-Ray Photoelectron Spectroscopy 212
6.5.5 Raman Spectroscopy 212
6.5.6 Thermogravimetric Analysis 214
6.6 Applications of Modified Carbon Nanotubes 215
6.7 Toxicity and Biocompatibility 218
6.8 Conclusions 220
6.9 Outlook and Perspectives 221
References 221

7 **Carbon Nanofibers**
Yoong A. Kim, Takuya Hayashi, Morinobu Endo, Mildred S. Dresselhaus 233
7.1 Similarity and Difference Between Carbon Fibers and Carbon Nanofibers 234
7.1.1 Basic Concepts 234
7.1.2 Synthesis and Properties of Carbon Fibers 235
7.1.3 Vapor-Grown Carbon Fibers 236
7.2 Growth and Structural Modifications of Carbon Nanofibers 238
7.2.1 Catalytically Grown Cup-Stacked Type 238
7.2.2 Catalytically Grown Platelet Type 241
7.2.3 Electrospun Carbon Nanofibers 244
7.2.4 Electrospun Porous Carbon Nanofibers 249
7.3 Applications of Carbon Nanofibers 251
7.3.1 Electrode Material in Lithium-Ion Secondary Batteries 251
7.3.2 Electrode Material for Supercapacitors 253
7.3.3 Supporting Material for Metal Nanoparticles 256
7.3.4 Bone Tissue Scaffold 257
7.4 Conclusions 257
References 258

8 **Nanodiamonds**
Olga A. Shenderova, Suzanne A. Ciftan Hens 263
8.1 Stability of Diamond at the Nanoscale 264
8.2 Types of Nanodiamonds and Methods of Nanodiamond Synthesis 267
8.2.1 Nanodiamond Produced by Detonation Shock Wave-Assisted Synthesis 270
8.2.2 Survey of Laboratory-Scale Methods of Nanodiamond Synthesis 275
8.3 Detonation Nanodiamond Processing and Modification 278
8.3.1 Postsynthesis Processing 278
8.3.2 Nanodiamond Deagglomeration and Fractionation 279
8.3.3 ND Surface Functionalization 280
8.4 Fluorescent Nanodiamonds 284
8.5 Applications of Nanodiamond Particles 285
8.5.1 Nanodiamond in Polishing Applications 285
8.5.2 ND Applications in Composites 286
8.5.3 Biomedical Applications 288
8.5.4 Nanodiamonds for Seeding 290
8.6 Future Directions of Production and Applications 292
References 293

Part B NanoMetals

9 **Noble Metal Nanoparticles**
Theruvakkattil S. Sreeprasad, Thalappil Pradeep 303
9.1 Historical Perspective of Gold and Silver NPs 304

9.2 Diverse Nanostructures 307
9.2.1 Physical and Chemical Methods 308
9.2.2 General Issues of Concern 309
9.3 Common Synthetic Routes for the Preparation of Noble Metal NPs 311
9.3.1 Solution Phase Routes by Chemical Reduction 311
9.3.2 The Most Common Methods for Gold NPs 312
9.3.3 Specialized Synthetic Strategies – Anisotropic NPs 314
9.4 Properties of Noble Metal Nanoparticles 322
9.5 Postsynthetic Tuning of Properties 324
9.5.1 Tuning Properties Through Chemical Reactions 324
9.5.2 Modification of Properties – Formation of Superstructures 331
9.6 Functionalized Metal NPs 343
9.6.1 Core–Shell Nanoparticles 343
9.7 Applications of Gold and Silver Nanoparticles 347
9.7.1 Water Purification 348
9.7.2 Bioconjugation and Labeling 357
9.7.3 Optical Contrast Agents 357
9.7.4 Photothermal Therapy 358
9.7.5 Cancer Cell Imaging 359
9.7.6 Surface-Enhanced Raman Scattering Substrates 360
9.7.7 Superhydrophobic Surfaces 360
9.7.8 Mercury Sensor 361
9.7.9 Infrared Absorbing Material 362
9.7.10 Plasmonic Waveguides 362
9.7.11 Biosensors 362
9.7.12 Photovoltaic Devices 362
9.8 New Gold and Silver Materials – Quantum Clusters 363
9.9 Conclusions 366
References 367

10 **Nanostructures of Common Metals**
Melinda Mohl, Krisztián Kordás 389
10.1 Post-Transition Metals 390
10.1.1 Lead, Bismuth, Tin, and Indium 390
10.1.2 Aluminum 392
10.2 Transition Metals 392
10.2.1 Titanium 393
10.2.2 Tungsten 394
10.2.3 Molybdenum 395
10.2.4 Tantalum 395
10.2.5 Zinc 396
10.2.6 Copper 397
10.3 Concluding Remarks 398
References 399

11 **Alloys on the Nanoscale**
Giovanni Barcaro, Alfredo Caro, Alessandro Fortunelli 409
11.1 Concepts and Principles 411
11.2 Preparation and Synthesis 413
11.2.1 Solution-Phase Methods 413
11.2.2 Surface Deposition Methods 416
11.3 Characterization of Nanoparticles and Nanoalloys 417
11.3.1 Scanning Force Microscopy (SFM) 417
11.3.2 Grazing-Incidence Small-Angle X-ray Scattering (GISAXS) . 418
11.3.3 X-ray Absorption Spectroscopy (XAS) 418
11.3.4 Scanning Tunneling Microscopy (STM) 419
11.3.5 X-ray Photoelectron Spectroscopy (XPS) 420
11.3.6 Surface X-ray Diffraction (SXRD) 421
11.3.7 Transmission Electron Microscopy (TEM) 421
11.3.8 Vibrational Sum-Frequency Generation (VSFG) 424
11.4 Properties 424
11.4.1 Structural Properties of Alloyed Nanoparticles 425
11.4.2 Catalytic Properties 437
11.4.3 Optical Properties 442
11.4.4 Magnetic Properties 448
11.5 Nanostructured Bulk Alloys 450
11.5.1 Bulk Materials Incorporating Nanoscale Precipitates of a Different Phase 450
11.5.2 Bulk Nanophase Materials 453
11.6 Applications 457
11.7 Concluding Remarks 458
References 459

12 **Magnetic Nanostructures: Synthesis, Properties, and Applications**
Shashwat Shukla, Pratap Kumar Deheri, Raju V. Ramanujan 473
12.1 Background 474
12.2 Atomic Origin of Magnetism 475
12.2.1 Quantum Mechanics of Ferromagnetism 475
12.2.2 Atomic-Scale Magnetism and Exchange Effect 476
12.3 Magnetic Length Scales and Origin of Nanomagnetic Behavior 478
12.3.1 Domains in Fine Particles 478
12.3.2 Nanomagnetism 479
12.4 Magnetic Nanostructures 483
12.4.1 Processing of Magnetic Nanostructures 483
12.4.2 Characterization of Magnetic Nanostructures 488
12.4.3 Hard Magnetic Nanostructures 492
12.4.4 Soft Magnetic Nanostructures 498
12.4.5 GMR and Spin Valves 502
12.4.6 Applications 503
12.5 Conclusions 505
References 506

Part C NanoCeramics

13 **Nanocrystalline Functional Oxide Materials**
Rakesh Shukla, Dimple P. Dutta, Jayshree Ramkumar, Balaji P. Mandal, Avesh K. Tyagi 517
13.1 Synthesis Methods 518
13.1.1 Solid-State Route 518
13.1.2 Soft Chemical Routes 519
13.2 Optical Properties of Oxide Nanomaterials 524
13.3 Sorbent Properties of Oxide Nanomaterials 532
13.3.1 Sorbents for Environmental Remediation 533
13.4 Catalytic Properties of Oxide Nanomaterials 536
13.5 Oxide Nanomaterials in Ionics 538
13.6 Conclusions 541
References 542

14 **Piezoelectric Nanoceramics**
Xiaohui Wang, Shaopeng Zhang, Longtu Li 553
14.1 Introduction to BSPT 554
14.1.1 Structures and Morphotropic Phase Boundary 554
14.1.2 Ceramic Properties and Grain Size Effects 554
14.2 Synthesis of BSPT Nanopowders via Sol–Gel Method 555
14.3 Sintering of BSPT Nanoceramics 556
14.3.1 Two-Step Sintering 556
14.3.2 Combination of Spark Plasma Sintering and Two-Step Sintering 558
14.3.3 Ultrahigh-Pressure (UHP) Forming and Two-Step Sintering 561
14.4 Grain Size Effect on the Properties of BSPT Ceramics 563
14.4.1 Dielectric Properties 563
14.4.2 Ferroelectric Property 564
14.4.3 Piezoelectric Property 564
14.5 Summary 567
References 568

15 **Graphite Oxide**
Wei Gao 571
15.1 Synthesis of Graphite Oxide 572
15.1.1 Brodie and Staudenmaier Methods 573
15.1.2 Hummers Method and Its Modifications 573
15.1.3 Tour Method and Discussion 574
15.2 Characterization, Chemical Structure and Properties 576
15.2.1 Characterizations 576
15.2.2 Chemical Structure 581
15.2.3 Reactivity and Physical Properties 583

15.3 Applications 589
15.3.1 Platform for RGOs and GO Derivatives/Composites 589
15.3.2 An Anisotropic Proton Conductor 591
15.3.3 Catalyst and an Electron Transparent Window 591
15.4 Concluding Remarks 592
References 592

16 **Compound Crystals**
Roi Levi, Maya Bar-Sadan, Reshef Tenne 605
16.1 Nanostructures 605
16.2 Synthetic Methods 608
16.2.1 IF Synthesis 608
16.2.2 INT Synthesis 614
16.3 Physical Properties 618
16.3.1 Synthesis and Structural Properties 618
16.3.2 Mechanical Properties 622
16.3.3 Electronic and Optical Properties 625
16.3.4 Calculations and Simulations 627
16.4 Applications 628
16.4.1 Tribological Applications 629
16.4.2 Composites 629
16.4.3 Hydrogen and Lithium Adsorption/Desorption in INT 630
16.4.4 Miscellaneous 630
16.5 Conclusions 630
References 631

17 **Growth of Nanomaterials by Screw Dislocation**
Fei Meng, Stephen A. Morin, Song Jin 639
17.1 Classical Crystal Growth Theories 640
17.1.1 Layer-By-Layer Crystal Growth 640
17.1.2 Screw-Dislocation-Driven Crystal Growth 641
17.2 Theories for Screw-Dislocation-Driven Growth of Nanomaterials 642
17.2.1 Eshelby Twist 642
17.2.2 Dislocation-Driven Nanotube Formation 643
17.2.3 Dislocation-Driven Growth of 2-D Nanoplates 644
17.3 Structural Characterization of these Nanomaterials 645
17.3.1 Observation of Dislocation Contrast 645
17.3.2 Determination of Eshelby Twist 646
17.3.3 Lattice Tilt 648
17.3.4 Observation of Nanotubes or Voided NWs 649
17.4 Generality of Dislocation-Driven Nanomaterial Growth 649
17.4.1 Vapor-Phase Synthesis 650
17.4.2 Solution-Phase Synthesis 652
17.4.3 Solution Growth of 2-D Nanoplates 655
17.5 Rational Growth of Dislocation-Driven Nanomaterials – General Strategies 658

17.6 Applications 659
17.7 Summary and Perspectives 660
References 661

18 **Glasses on the Nanoscale**
Hellmut Eckert, Sidney J.L. Ribeiro, Silvia H. Santagneli, Marcelo Nalin, Gael Poirier, Younès Messaddeq 665
18.1 Studying Medium-Range Order in Glasses and Nanoceramics 666
18.1.1 Static Dipolar NMR Spectroscopy 668
18.1.2 Spin-Echo Decay Spectroscopy 669
18.1.3 Spin-Echo Double Resonance 670
18.1.4 High-Resolution Dipolar NMR Spectroscopy 671
18.1.5 Homonuclear *J*-Resolved Spectroscopy 675
18.2 Nanoceramics 676
18.2.1 Lanthanide-Containing Transparent Glass Ceramics 676
18.2.2 Metal Nanoparticles in Glasses 680
18.2.3 Quantum Dots in Glasses 682
18.3 Perspectives and Concluding Remarks 684
References 685

Part D NanoComposites

19 **Carbon in Polymer**
Robert J. Young, Libo Deng, Lei Gong, Ian A. Kinloch 695
19.1 Materials Basics 695
19.1.1 Carbon Nanotubes 696
19.1.2 Graphene 698
19.1.3 Raman Spectroscopy and the Deformation of Carbon Nanomaterials 701
19.2 Carbon Nanotube Composites 702
19.2.1 Preparation and Properties of Bulk Composites 702
19.2.2 Preparation and Properties of Composite Fibers 703
19.2.3 Reinforcement Mechanisms and Modelling 703
19.2.4 Fundamental Aspects of CNT Composites 705
19.2.5 Characterization of CNT Composites 709
19.2.6 Characterization of CNT Composites Using Raman Spectroscopy 712
19.3 Graphene Composites 716
19.3.1 Preparation Methods 716
19.3.2 Mechanical Properties 716
19.3.3 Functional Properties 719
19.3.4 Nanomechanics 720
19.3.5 Model Graphene Monolayer Composites 720
19.4 Conclusions 722
References 722

20 **Nanoparticle Dispersions**
Krisztián Kordás, Jarmo Kukkola, Géza Tóth, Heli Jantunen, Mária Szabó, András Sápi, Ákos Kukovecz, Zoltán Kónya, Jyri-Pekka Mikkola 729
20.1 Stabilization of Nanoparticle Dispersions 730
20.1.1 Shape of Nanoparticles 730
20.1.2 Sedimentation, Ordering, and Coarsening of Nanoparticles in Liquid Dispersions 730
20.1.3 Electrolytes and the DLVO Theory 732
20.1.4 Steric (Nonelectric) Stabilization 734
20.2 Nanoparticle Dispersion in Practice 734
20.3 Dispersions of Carbon Nanomaterials 745
20.4 Drying Dispersions on Surfaces 752
20.4.1 Ring-Stain Effect 752
20.4.2 Self-Organized Structures 756
20.4.3 Inkjet Printing of Nanoparticle Dispersions 757
20.5 Concluding Remarks 758
References 758

Part E Nanoporous Materials

21 **Nanoporous Metals**
Yi Ding, Zhonghua Zhang 779
21.1 Preparation of Nanoporous Metals 779
21.1.1 Alloy Design of Precursors Suitable for Dealloying 780
21.1.2 Formation Mechanisms of Nanoporous Metals by Dealloying 781
21.1.3 Control over Structures of Nanoporous Metals 784
21.2 Properties of Nanoporous Metals 789
21.2.1 Structure and Morphology 789
21.2.2 Catalytic Properties 794
21.2.3 Electrocatalytic Properties 796
21.2.4 Mechanical Properties 799
21.2.5 Optical Properties 802
21.2.6 Sensing and Actuation Properties 805
21.2.7 Electrical, Thermal, and Magnetic Properties 807
21.3 Applications 808
21.4 Concluding Remarks and Prospects 810
References 811

22 **Zeolites**
István Pálinkó, Zoltán Kónya, Ákos Kukovecz, Imre Kiricsi 819
22.1 Common Zeolite Frameworks 822
22.1.1 Zeolites A, X, Y 822
22.1.2 Mordenite 822
22.1.3 Zeolites of Intermediate Pore Size 822
22.1.4 Other Zeolites of Commercial Interest 823

22.2 Zeolite and Zeolite-Related Molecular Sieves 823
22.2.1 Isomorphous Substitution of Si and/or Al Atoms in Zeolite Frameworks 823
22.2.2 New Large-Pore Zeolites 824
22.3 Natural Zeolites: Occurrence and Formation 825
22.3.1 Formation and Occurrence of Natural Zeolites 826
22.4 Methods of Identification and Characterization 828
22.4.1 Determining the Chemical Composition 828
22.4.2 Thermal Analysis Methods 828
22.4.3 Diffraction and Microscopic Techniques 828
22.4.4 Nuclear Magnetic Resonance (NMR) Spectroscopy 828
22.4.5 EPR Spectroscopy 829
22.4.6 Vibrational Spectroscopies 829
22.4.7 UV-Vis Spectroscopy 830
22.4.8 Mössbauer Spectroscopy 830
22.4.9 X-Ray Photoelectron Spectroscopy 830
22.5 Synthesis of Zeolitic Materials 830
22.5.1 Effects of Major Chemical Components and Further Additives 831
22.5.2 Influence of Various Physical Parameters on Zeolite Synthesis 834
22.5.3 Mechanisms of Zeolite Crystallization 835
22.5.4 Alternative Synthesis Procedures 835
22.6 Ion Exchange, Sorption, and Diffusion in Microporous Materials 836
22.6.1 Ion-Exchange Properties 836
22.6.2 Molecular Sieving Properties 837
22.6.3 Diffusion Properties 838
22.7 Acid–Base Properties of Zeolites 841
22.7.1 Acidity of Zeolites 841
22.7.2 Basicity of Zeolites 842
22.8 Stability and Modification of Zeolite Structures 843
22.8.1 Thermal Stability 843
22.8.2 Dealumination of Zeolites 843
22.8.3 Formation of Secondary Pore Structure 843
22.8.4 Isomorphous Substitution 844
22.8.5 Transition-Metal Ions and Metal Particles in Zeolites 845
22.8.6 Coke Formation in Zeolites 845
22.9 Zeolites as Catalysts 846
22.9.1 Zeolites in the Refining and Petrochemical Industry 847
22.9.2 Zeolites in the Fine Chemical Industry 847
22.10 Some Special Applications of Zeolites 848
22.11 Conclusions 850
References 850

23 **Porous Anodic Aluminum Oxide**
Qiaoling Xu, Guowen Meng 859
23.1 Background 859

23.2 Preparation of AAO Templates 860
23.2.1 AAO Templates with Straight Pores 860
23.2.2 AAO Templates with Branched Pores 860
23.2.3 AAO Templates with Step-Shaped Pores 862
23.3 Nanostructures Constructed in AAO Templates 862
23.3.1 One-Dimensional Nanostructures 862
23.3.2 Complex-Shaped 1-D Nanostructures 863
23.3.3 Nanoheterostructures 869
23.3.4 Complex-Shaped Nanoheterostructures 878
23.4 Conclusions and Outlook 879
References 879

24 **Porous Silicon**
Paolo Bettotti 883
24.1 Basics of Porous Silicon Electrochemistry and Formation Models 884
24.1.1 Chemical Dissolution Model 884
24.1.2 *I–V* Curves 885
24.1.3 Porous Silicon Formation Mechanisms 885
24.2 Other Etching Methods 886
24.3 Porous Silicon Structural Properties 887
24.4 Light Emission from Porous Silicon 890
24.5 Thermal and Electrical Properties 891
24.6 The Role of the Surface 891
24.7 Applications of Porous Silicon 892
24.7.1 Porous Silicon Light-Emitting Diodes 892
24.7.2 Porous Silicon-Based Photonic Crystals 893
24.7.3 Optical Sensing 896
24.7.4 Drug Delivery Systems 896
24.7.5 Oxidized Porous Silicon 897
24.8 Conclusions 897
References 898

Part F Organic and Bionanomaterials

25 **Organic Nanomaterials**
Huanli Dong, Wenping Hu 905
25.1 Preparation/Synthesis of Organic Nanomaterials 905
25.1.1 Solution Processes 906
25.1.2 Vapor Processes 909
25.2 Properties of Organic Nanomaterials 910
25.2.1 Structure and Morphology 910
25.2.2 Absorption and Emission Properties 912
25.2.3 Optoelectronic Properties 916
25.2.4 Mechanical Properties 923

25.3 Applications 925
25.3.1 Sensors and/or Detectors 925
25.3.2 Surface Wettability Control 927
25.3.3 Optical Waveguides and Lasers 928
25.3.4 Nanocircuits 928
25.4 Concluding Remarks 930
References 932

26 **Nanocomposites as Bone Implant Material**
Vinod Kumar, Bipul Tripathi, Anchal Srivastava, Preeti S. Saxena 941
26.1 The Quest for a Suitable Bone Implant 942
26.2 Bone 942
26.2.1 Structure and Composition of Bone 942
26.2.2 Limitations of Natural Bone 944
26.3 Existing/Conventional Bone Implant Materials and Their Shortcomings 944
26.3.1 Metallic Implants 945
26.3.2 Polymeric Implants 945
26.3.3 Ceramic Implant 945
26.3.4 Ceramic Polymer Composites as Implants 946
26.4 Major Challenges with Existing/Conventional Implant Materials 949
26.4.1 Mechanical Integrity 949
26.4.2 Incorporation of Biomolecules 949
26.4.3 Long-Term Characterization of Porous Composite Scaffolds 949
26.4.4 Biocompatibility Study 949
26.5 Nanotechnology and Tissue Engineering 949
26.5.1 Unique Properties of Nanomaterials 950
26.5.2 Nanoscaffold Fabrication Techniques 951
26.5.3 Nanomaterial Scaffold for Orthopedic Purposes 954
26.6 Future Perspectives 965
References 965

27 **Nanofiber Biomaterials**
Rachelle N. Palchesko, Yan Sun, Ling Zhang, John M. Szymanski, Quentin Jallerat, Adam W. Feinberg 977
27.1 Methods of Production 980
27.1.1 Fiber Spinning 980
27.1.2 Phase Separation 982
27.1.3 Directed and Self-Assembly 983
27.2 Properties of Nanofiber Biomaterials 986
27.2.1 Structure and Physical Properties 986
27.2.2 Mechanical Properties 988
27.2.3 Electrical Properties 988
27.2.4 Chemical Properties 989
27.2.5 Biological Properties and Cell Response 990

27.3 Characterization of Nanofiber Biomaterials 993
27.3.1 Optical Characterization 993
27.3.2 Electron Microscopy 995
27.3.3 Atomic Force Microscopy (AFM) 995
27.3.4 Mechanical Characterization 996
27.4 Applications 999
27.4.1 Cardiac Tissue Engineering 999
27.4.2 Skeletal Muscle Tissue Engineering 1001
27.4.3 Ophthalmic Tissue Engineering 1002
27.4.4 Neural Tissue Engineering 1004
27.5 Conclusions and Outlook 1005
References 1006

Part G Applications and Impact

28 **Nanostructured Materials for Energy-Related Applications**
Arava L.M. Reddy, Sundara Ramaprabhu 1013
28.1 Energy-Related Carbon Nanotubes 1013
28.1.1 Catalytic Support in Proton Exchange Membrane Fuel Cells (PEMFC) 1013
28.1.2 Electrochemical Supercapacitors 1015
28.1.3 Lithium-Ion Batteries 1015
28.2 CNTs as Support Material for Electrocatalysts in PEMFC 1016
28.2.1 Nonnoble Metal Based Electrocatalysts for Fuel Cells 1020
28.3 CNTs as Supercapacitor Electrode Materials 1023
28.3.1 Cyclic Voltammetry 1025
28.3.2 Galvanostatic Charge–Discharge 1027
28.3.3 Electrochemical Impedance Spectroscopy 1027
28.3.4 Lithium-Ion Batteries 1029
References 1032

29 **Nanomaterials in Civil Engineering**
Jaesang Lee, Seunghak Lee, Eunhyea Chung, Vincent C. Reyes, Shaily Mahendra 1039
29.1 Applications of MNMs in Construction 1041
29.1.1 Concrete and Cement 1041
29.1.2 Steel 1044
29.1.3 Plastic 1044
29.1.4 Window Glass 1044
29.1.5 Coatings 1045
29.1.6 Lighting 1046
29.1.7 Sensors 1046
29.2 Environmental Release of MNMs Used in Construction 1047
29.2.1 Construction Material Manufacturing 1047
29.2.2 Structural Applications 1048

29.2.3 Structural Demolition 1048
29.2.4 Construction Waste Disposal 1048
29.3 Potential Adverse Biological Impacts and Toxicity Mechanisms 1049
29.3.1 TiO_2 1050
29.3.2 Quantum Dots 1050
29.3.3 Carbon Nanotubes 1050
29.3.4 C_{60} Fullerene 1050
29.3.5 SiO_2 1052
29.3.6 Copper/Copper Oxide 1052
29.4 Mitigation of Environmental and Health Impacts 1052
29.4.1 Manufacturing 1052
29.4.2 Application 1053
29.4.3 Recycling/Disposal 1053
29.5 Conclusions 1054
References 1055

30 **Plasmonic Nanomaterials for Nanomedicine**
Renat R. Letfullin, Thomas F. George 1063
30.1 Introduction 1063
30.2 Nanooptics – Lorenz–Mie Formalism 1064
30.3 Optical Properties of Gold Nanoparticles in Biological Media 1065
30.4 Kinetics of Heating and Cooling of Nanoparticles 1067
30.4.1 Time Dynamics of the Nanoparticle Temperature 1067
30.4.2 Comparison of Single-Pulse and Multipulse Modes of Heating 1067
30.5 Spatial Distribution of Temperature Fields Around the Nanoparticle 1076
30.5.1 Theoretical Model 1076
30.5.2 Laser Heating of a Single Nanoparticle in Biomedia 1077
30.5.3 Bone Tissue Ablation by Plasmonic Nanoparticles 1079
30.5.4 Temperature Simulations for Many Heat Sources 1082
30.6 New Dynamic Modes in Selective Plasmonic Nanotherapy 1083
30.6.1 Nanocluster Aggregation Mode 1083
30.6.2 Microbubble Overlapping Mode 1086
30.6.3 Laser-Induced Thermal Explosion Mode – Nanobombs 1091
References 1095

31 **Carbon Nanotube Membrane Filters**
Anchal Srivastava, Saurabh Srivastava, Kaushik Kalaga 1099
31.1 Types of Filtration 1100
31.2 Mechanisms of Filtration 1101
31.3 Carbon Nanotube Membrane Filters 1102
31.3.1 Structure and Properties of CNTs 1103
31.3.2 Types of CNT Membranes in Nanofiltration 1105
31.4 Future Research Perspectives 1112
References 1112

32 **Nanomaterial Toxicity, Hazards, and Safety**
Zuzanna A. Lewicka, Vicki L. Colvin 1117
32.1 Engineered Nanomaterials – General Overview 1118
32.2 Occurrence of Engineered Nanoparticles in the Environment 1119
32.3 Effects of Nanoparticles on Organisms 1120
32.3.1 Ecotoxicity of Nanoparticles in Aquatic Ecosystems 1121
32.3.2 Ecotoxicity of Nanoparticles in Soil Ecosystems 1121
32.3.3 Routes of Human Exposure to Nanoparticles and Their Translocation in the Body 1122
32.3.4 In Vitro Toxicity of Nanoparticles 1124
32.4 Nanoparticle Physicochemical Characteristics of Relevance for Toxicology 1124
32.4.1 Characterization Methods 1126
32.4.2 Electron and Atomic Force Microscopy 1126
32.4.3 Brunauer–Emmett–Teller Analysis and X-Ray Diffraction 1127
32.4.4 Overall and Surface Elemental Analysis 1128
32.4.5 Dynamic Light Scattering (DLS) 1129
32.5 Special Case – Sunscreens 1130
32.5.1 Regulatory Policy as Related to Sunscreens 1130
32.5.2 Photocatalytic Activity of TiO_2 and ZnO Nanoscale Particles 1130
32.5.3 Health Effects of Nanoscale Titania and Zinc Oxide 1131
32.5.4 Materials Derived from Consumer Products and Their Photochemical Behavior 1131
32.5.5 Physicochemical Characteristics of Sunscreen Nanoscale Materials 1132
32.6 Conclusions 1132
References 1133

Acknowledgements 1143
About the Authors 1145
Detailed Contents 1163
Subject Index 1181

Subject Index

C_{60} nanotube 906
γ-butyrolactone (GBL) 734
$\pi-\pi$ interaction 201
$\pi-\pi$ stacking 907, 910
$\pi-\pi^*$ absorption 913
π-conjugated system 917
$\pi-\pi$ interaction 200
$\pi-\pi$ stacking 591, 752
$\sigma-\pi$ coupling 589
β-sheet based nanofiber 985
$n-\pi^*$ absorption 913
^{13}C-labeled GO 579
^{13}C-^{13}C J coherence transfer 579
0-D nanodot 412
0-D particle 413
1,2,3,4,5-pentaphenyl-1,3-cyclopentadiene (PPCP) 915
1,3,5-cyclooctatriene (COT) 314
1,3,5-triphenyl-2-pyrazoline (TPP) 913
1,3-dimethyl-2-imidazolidinone (DMEU) 752
1,5-cyclooctadiene (COD) 314
1,5-diaminoanthraquinone (DAAQ) 925
1-D
– exciton 115
– multicolor emission 915
– nanomaterials 643
– nanostructure 315, 321, 862, 909
– nanostructure, complex shape 863
– nanostructure, metal 862
– nanostructure, polymer 862
– nanostructure, semiconductor 862
– nanosystem 324
– nanosystem, gold nanorod 324
– nanowire 915
– organic nanomaterials 913
– quantum confinement 116
– template 640
– wire model 413
1-cyano-trans-1,2-bis(3′,5′-bis-trifluoromethyl-biphenyl)ethylene (CN-TFMBE) 914
1-phenyl-3-((dimethylamino)styryl)-5-((dimethylamino)phenyl)-2-pyrazoline (PDDP) 912
2,4,5-triphenylimidazole (TPI) 928
2-D
– array detector 323
– graphene 59
– nanocrystal superlattice 332
– nanofabric 915
– nanomaterial 656
– particle 730
2-D NMR (two-dimensional NMR) 828
2-D and 3-D superstructure 313
2-D spectrum 577
2-D/3-D hybrid NPG structure 792
2-pyridine-aldoxime methiodide (2-PAM) 350
3-D
– energy plot 643
– graphite 129
– nanocrystal superlattice 332
– porous media 896
– space 85
– superlattice 341, 343
– thermal field 1082
3-D superlattice-like 336
3-aminopropyltriethoxysilane (APTS) 590
4-hexadecyloxyphenyl (4Hop) 911
5–7 pair 196
5–7–7–5 defect 196
9,10-bis(phenylethynyl)anthracene (BPEA) 928

A

AAO template
– multiple-branched pore 861
– nanochannels 862
– porous 874
– preparation 860
– step-shaped pore 862
– three-branched 864
– Y-branched 864
AB_2 structure nanoparticle 757
ABAB
– stacking 239
aberration correction 422
ablation temperature 1070
– nanorod 1070
ABO3-type perovskite 554
absorption 1065
– coefficient 1065, 1089
– efficiency 1066
– spectrum 1066
accelerated
– decay 670
accumulative heating 1070
acetylcholine esterase (AChE) 350
acetylene/methane over hydrogen $MmNi_3$ 1017
acidic
– zeolite material 847
acoustic pressure 524
activated
– carbon 352
activation
– cycle 1019
– energy 541
active edge 243
actuation
– electrostatic 52
actuator 553, 589
adatom 197
additive to lubricant 287
adhesion
– energy 430
– interfacial 707, 714
– of polymers 849
– plaque 961
adhesive ECM 978
adiabatic implosion 524
adsorption 837
– capability 591
– energy 438
– site 836
advanced fluorescent imaging 994
aerogels 10
aerosil 832
affinity-based separation 1110
AFM
– contact-mode 656
– manipulation 10
– nanoindentation 996
– structure deposition and ink self-assembly 9
Ag
– cluster 365
– crystallite 361
– dendritic film surface 361
– nanocage 358
– nanocube 342, 457
– nanoparticle 583
– nanoplate/GaAs composite surface 361
– nanostructure 793
– shell 327

Ag-Au
– alloy core–shell NP 345
– alloyed nanoparticle 445
– cluster 434
– nanoparticle 434, 441
agglomerated in clusters 731
aggregation
– -caused quenching (ACQ) 914
– -enhanced emission (AEE) 914
– -induced emission (AIE) 914
– -induced enhanced emission (AIEE) 913
aging 890
AgNP 1080
– heating simulation 1080
Ag-ZrO_2 core–shell NP 345
Aharonov–Bohm effect 105
air stabilization 253
air-dry GO 578
air-stabilized
– flameproof 246
– nanofiber 245
– web 246
Al film 392
alcohol oxidase 203
aligned
– array 1107
– carbon nanotube (ACNT) 927
– CNT membrane 1109
– multi-walled nanotube 150
– nanofiber 987
– nanoparticle 731
– nanoparticle viscosity 731
– nanotube 160
alignment of cardiomyocytes 999
alignment of nanofibers 981
alkali
– borate glass 670
– feldspar 827
– -metal oxide 613
alkaline
– fuel cell (AFC) 1013
alkaline metal vapor treatment 829
alkali–zeolite reaction 827
alkylation of aromatics 846
all-aluminate framework 832
allotrope
– carbon 40
alloy
– amorphous 499
– bimetallic 457
– catalyst 440
– chemistry 500
– cluster 366
– design 780
– NP 314
– ordered 434
– phase 152
– surface chemical ordering 421
alloyed
– catalyst 437
– metal cluster 440
– subnanometer 440
– surface 421
alloyed nanoparticle 419, 422
– chemical ordering pattern 433
– crystalline structure 425
– structural properties 425
AlN whiskers 651
AlPO-5
– formation mechanism 824
Alq3 nanowire 909
alumina
– anodized template 1105
– powder dispersion 754
– template 906
– template junctions 9
aluminoborate glass 673
aluminophosphate (AlPO) 823
aluminophosphate glass 673
aluminosilicate
– crystalline 820
aluminum
– nanostructure 392
– removal 843
aluminum membrane
– anodized (AAM) 618
alveolar macrophages (AM) 162
amalgamation of Hg
– gold nanorod 361
– with GNR 361
ambient pressure photoelectron spectroscopy (APPES) 421
ambipolar transport characteristic 923
American Society for Testing and Materials (ASTM) 1118
American Water Works Association (AWWA) 534
amino acid 520
– derivative 343
aminothiophenol conjugated 1080
amorphous
– alloy 499
– calcium phosphate (ACP) 946
– carbon 40, 239
– carbon debris 153
– silicon model 890
– solid 665
amphiphilic self-assembling
– model 984
– structure 869
analcime 843
Andreev reflection 54
– crossed 55
angle-resolved photoemission spectroscopy (ARPES) 60
angular momentum 475
anisotropic 943
– etching mechanism 889
– growth 642
– membrane 1102
– nanomaterial 347, 362, 639, 649
– nanorod 325
– nanostructure 340
– nanosystem 328
– PS formation 888
anisotropy
– energy 481
– field 481
– magnetic 480
– parallel and perpendicular 495
anode material 243, 252
anodic
– etching 887
– oxidation 884
anodic aluminum oxide (AAO) 391, 640, 859, 906
– template 859
anodized
– alumina template 1105
– aluminum membrane (AAM) 618
– nanotubular Ti 954
anomalous loss 499
anthracene 908
antibacterial properties of silver NP 356
antibody (Ab) 1064
anti-epidermal growth factor receptor (anti-EGFR) 359
antiferromagnetically coupled (AFC) media 504
antifriction additive 286
antigen-presenting cells (APC) 992
anti-interference 930
anti-Mackay icosahedron 428
antimicrobial activity 92
antireflection coating 524, 893
application
– of carbon nanofibers 251
APTES-functionalized 339
aqueous environment 1076
aqueous metal ion 314
arc discharge (AD) 88, 132, 148
– growth 112
– technique 614
Arg-Gly-Asp (RGD) 1005

arginine 520
arid region 827
armchair
– axis 1104
– case 589
– layer 619
– nanotube 98, 107
– ribbon 195
– SWNT 131
aromatic organic compound (AOC) 925
aromatization 847
AROMAX process 823
array
– aligned 1107
– dot 8
array detector
– 2-D 323
arrested growth 611
Arrhenius plot 540
Arrhenius–Neel equation 478
artificial muscle 589
artificial peptide 985
as phenol–quinone exchange 582
asbestos exposure 162
ascorbic acid (AA) 325
aspartic acid 520
aspect ratio (AR) 315
assemblies of NP 331
assembly 336
– gold nanorod 332
– involving 334
– layer-by-layer (LBL) 69
– on substrate 339
– through electrostatic force 336
asymmetric reduction 617
atomic absorption spectroscopy (AAS) 828
atomic force microscope (AFM) 8, 42, 60, 120, 133, 208, 209, 220, 490, 555, 580, 656, 700, 732, 789, 832, 833, 979, 995, 1126
– microscopy probe 394
atomic hydrogen adsorption 1018
atomic layer deposition (ALD) 803, 863, 876
atomic mixing
– nanoalloy 411
atomically thin sheet 10
atomic-level blending 521
atom-transfer radical polymerization (ATRP) 591
attenuation
– efficiency 1065
attractive repulsive potential 732
attrition wear 286
Au
– carbon-supported nanoparticle 441
– nanocluster 439, 446
– nanocluster, optical response 445
– nanocube 329
– nanogap electrode 926
– nanooctahedra system 362
– nanooctahedra/glucose oxidase (GOx) system 362
– nanoparticle, plasmonic response 444
– three-branched 865
– Y-branched 864
$Au_{0.18}Ag_{0.82}$ alloy nanowire 809
Au-Ag
– alloy nanosystem 347
– core–shell nanorod 345
– nanobox 329
– nanocrystal 327
Auger electron spectroscopy (AES) 592
Au-layer
– stamping technique 918
Au-Ni particle 440
AuNP 1080, 1081
– heating simulation 1080
Au-Pd
– nanoparticle 434
autograft 944
auto-ignition 519
average
– grain size 557
averaging technique 668
axial nanocompression 624
axial screw dislocation 650
Ayurvedic medicine 306
azobenzene 343

B

back-bone oxidation 892
bacterial killing 1072
bactericid function 849
Bain transformation 17
ballistic
– conduction 1104
– resistance 126
– transport limit 129
bandgap
– photoluminescence 18
bandgap in graphene 46
barium titanate (BT)
– ceramic 553
basic fibroblast growth factor (bFGF) 1004
basin-hopping algorithm 412
battery 1015
– electrode 659
– lithium ion 243, 251, 252
– power density 251
B-doped
– carbon nanofiber 242
B-doped CNT 203
bent
– nanotube 194, 195
benzene alkylation 847
(BET) analysis 1127
Bi shell/Cu core nanocable 877
Bi triangular nanoplate 391
bikitaite 843
bilayer graphene 47, 59
bimetallic
– alloy 457
– cluster 446
– core–shell NP 345
– nanoparticle 798
– nanorod 328
– nanotube 398
binaphthyl 88
binary
– alkali phosphate glass 676
– chemical composition 683
– cluster 442
– metal cluster 432
– metal system 440
– nanowire 913
– structure 757
binder matrix 845
binding energy (E_b) 420
binocular-like structure 196
bioactive
– ceramic 946, 949
– electrospun scaffold 989
– glass 948
– substrate 290
bioactivity 949
biochemical
– sensor 589
biocidal activity
– of silver ions 355
biocide 533
biocompatibility 488, 946, 977
biocompatible and biodegradable coatings 488
biocomposite 947, 948
bioconjugation 357
biodegradable
– polymer 945, 947, 949, 957, 961
– polymer, biocompatibility 949
biodegradation 977, 993
biodegradative properties 993

biofouling 356
biofuel cell 205
biofunctionalization chemistry 284
bioinorganic composite 535
biological
– cell environment 1075
– response 992
– sensing 640
– surrounding 1065
– synthesis 316
– tissue 1095
– toxin 533
biologically-derived polymer 979
biomedical imaging 359
biomedicine 290
biomembrane force probe 998
biomolecular label 504
biopolymer 746, 977
biosensor 290, 362, 503
biotin–streptavidin interaction 334
biphasic calcium phosphate (BCP) 946
Birch reduction 91
bis(phenylethynyl)anthracene (BPEA) 926
bismuth
– nanocrystal 391
– nanocube 391
– nanosphere 391
– nanostructure 391
bismuthtriangular nanoplate 391
black silicon (BS) 887
blend electrospinning 989
block copolymer 10
blocking electrode behavior 254
blood 1066, 1089
– biomedia 1077
– physical property 1089
body-centered-cubic (bcc) 10, 499
Bohr
– condition 667
– exciton diameter 525
– model 475
boiling temperature 1086
Boltzmann distribution 476
bond
– distance 666
– length 12
– length contraction 11
– length relaxation 10
– rotation 196
bonds and structure 10
bone 943, 1079
– augmentation 945
– cancellous 943
– cell function 954
– cement 945
– disease 944
– hydroxyapatite particle 1075
– implant material 944
– ingrowth 945
– making cell 944
– material property 1079
– medium 1082
– mineral component 944
– nanolevel 944
– regeneration 256, 944
– resorbing cell 944
– structure and composition 942
bone implant 941, 944, 948, 956
– conventional 941
– efficacy 956
– material 941
– polymer 948
bone tissue
– ablation 1079
– engineering 958
– growth 961
– scaffold 257
– temperature 1075
bone/cartilage tissue 959
Born repulsion 732
boron nitride (BN) 10, 97
boron-doped
– carbon nanofiber 245
– CNT 211, 214, 216
– SWCNT 203
borophosphate glass 673
bottom-up 698
– approach 9
– paradigm 905
bovine serum albumin (BSA) 949
Bragg peak 711
brain-derived neurotrophic factor (BDNF) 1004
branch diameter 867
branch growth 650
branched
– nanochannel 867
– nanostructure 864
– nanostructure, multiple generations 867
– nanotube network 167
– pore 861, 868
branching
– nanowire 643
branch-like nanostructure 927
breast cancer 1073
brewsterite 843
bridging oxygen 673
Brillouin
– function 476
– zone 108
Brodie
– material 699
– method 46, 573, 699
Brown paradox 482
Brownian motion 731
Brunauer–Emmett–Teller (BET) 791, 1126
Brust method 313
Brust–Schiffrin reduction 312
Brønsted acidity 841
Brønsted base 842
Brønsted–Evans–Polanyi (BEP) 437
BSPT ($(1\text{-}x)BiScO_3\text{-}xPbTiO_3$) 554
– phase diagram 554
BSPT ceramic
– coercive field 564
– dielectric properties 563
– ferroelectric phase 564
– ferroelectric property 564
– hysteresis loop 565
– nanocrystalline 564
– piezoelectric property 564
– sintering 558
– two-step sintering 558
BSPT nanoceramics
– piezoelectric properties 567
– piezoelectric response 567
– sintering 556
BSPT nanopowder 555, 559
bubble
– dynamics 1086, 1088, 1089
– effect 1068
– formation 1079, 1084, 1094
– lifetime 1088
– overlapping mode (BOM) 1087
– polytropic 1087
– radius 1091
– temperature 1090
buckling of carbon nanotube 14
Buckminsterfullerene 83, 112
bucky
– diamond 265, 266
– gold 429
buckyball 695
buckypaper (BP) 164, 165, 1109, 1110
– membrane 1109
bulk
– alloy 425, 450
– carbon 265

– composite 702
– dense ceramic 562
– erosion 947
– glass 683
– graphene 69
– material 4, 450, 626
– metallic glass (BMG) 498
– molybdenum 395
– nanophase material 453
– phase 1, 10
– phase tungsten 394
– Si bandgap 890
– silicon 884, 888
– solid material 10
– structural information 248
Burgers vector
– direction 645
– screw component 643

C

C_{60} 83
– chemistry 91
– fullerene 1050
C_{60}–C_{60} 95
$CaCO_3$ NP 1043
calcined rho zeolite 838
calcium deposition 954
calcium tetraphosphate 945
calculation of phase diagram (CALPHAD) 437
calfskin 954
cancellous
– bone 943
cancer cell 1064, 1075, 1079
– killing 1091
– nanophotothermolysis 1079
– nucleus 1075
cancer treatment 1063
cancerous
– nucleus 1074
cancerous cell organelle 1073
– multipulse heating 1073
cancerous mitochondria 1074
capacitive performance 254
capillary condensation 158
capping agent 522
– chemisorption 735
carbene 589
carbide matrix 267
carbide-derived diamond 278
carbon 859
– activated 352
– allotrope 40
– amorphous 40, 239
– black 39
– bulk 265
– defect 196
– fibrous 253
– hybridized 1104
– management 457
– metal 44
– nanocoil 159
– nondiamond 279
– onion 84, 92, 93
– overcoating 115
– paste electrode 203
– ring 90
– sheet 40
– sorbent 533
– surface 746
carbon fiber 234, 701
– properties 235
– textile 167
carbon material 263
– CVD-based 240
– end planes 242
– mechanical properties 51
carbon nanofiber (CNF) 147, 233, 994, 1044
– application 251
– boron doped 244
– boron-doped 245
– catalytically grown 241
– CNF 960
– composite 963
– defect-free 257
– electrical resistivity 242
– electrode material 251
– electrospun 252
– electrospun-based 244
– Fermi level 243
– large-scale production 238
– physically entangled 254
– platelet type 241
– platelet-type 243
– Raman spectra 244
– thermal treatment effect 244
– thermally treated 253
carbon nanofiber/collagen composite 256
carbon nanohorn 961
carbon nanomaterial 574
– deformation 701
– organic solvent 746
carbon nanoparticle
– stability 265
carbon nanoscience 190
carbon nanotechnology 190
carbon nanotube
– doped 204
– pristine 751
carbon nanotube (CNT) 40, 62, 85, 105, 148, 190, 238, 253, 276, 338, 393, 571, 575, 606, 695, 696, 748, 860, 954, 960, 1013, 1023, 1043, 1050, 1102
– aryl diazonium chemistry 199
– carboxylic acid functionality 199
– catalytic activity 166
– chemically modifying 191
– commercial feasibility 164
– covalent modification 198
– defect 193
– defect introduction 191
– dispersion 158
– doped 206
– doping 191
– doping category 191
– doping type 191
– electrocatalytic performance 207
– electrochemical properties 961
– electrochemistry 206
– electronic properties 192, 203
– electronic transport properties 123
– electrostatic functionalization 201
– exohedral doping 193
– filling 192
– fluorinated 199
– fluorination 199
– functionalization 155, 191
– functionalization technique 199
– heat stability 166
– heterogeneous catalysis 166
– high-modulus 701
– ink 28
– inorganic composites 168
– in-plane doping 193
– intercalated compounds 203
– mechanical properties 706
– membrane (CNM) 1106
– modified 189, 208
– multi-walled 276
– noncovalent modification 201
– orientation 706
– oxidation process 198
– phonons 160
– potential hazard 1050
– properties 191
– radially aligned, remove nicotine and tar 164
– redox-enzyme-modified 203
– remove amorphous carbon 154
– resistance 17
– risk assessment 162
– sensors 31
– solubilization 201

– spectroscopic properties 160
– structure 1103
– support 166
– support and metal 152
– synthesis 148
– synthesis and separation 111
– thermal conductivity 18
– toxicological hazard 162
– undoped semiconductor 128
carbon NM
– risk assessment 1048
carbonaceous
– impurity 535
– material 1105
carbonaceous residue 521
carbon-based
– nanomaterial 696, 964
– nanomaterials, ecotoxicological data 1121
– system 1119
carbon–carbon bond 696
carbon-containing precursor 275
carbon-fiber-reinforced plastic 234
carbonization 241
carboxilation 198
carboxy functional group 1111
carboxylated MWCNT 156
carboxyl-functionalized nanotube 746
carbyne 589
cardiac anisotropy 1000
cardiac tissue
– engineering 999
– fatigue resistance 999
– Young's modulus 999
cardiomyocyte survival 1001
carpet-rolling structure 235
carrier
– –carrier scattering 120
– dynamics 120
– quasirelativistic nature 67
cast assembly 908
catalysis 253, 347, 536, 735
– electronic structure factor 438
– heterogeneous 149, 166, 167, 256, 416, 437, 438, 442, 457, 536
– heterogeneous, metal nanoparticle 438
– heterogeneous, subnanometer metal 440
– homogeneous 149, 437, 1101
catalyst 397, 824, 916
– and catalyst template 26
– cobalt 26, 864
– coke formation 845
– membrane 794
– metal 863
– methanation 441
– nanoparticle 115
– particle 393
– polymerization 591
– quantum cluster 364
– support 154
– tailor-made 847
– $TiSi_2$ 393
– zeolite petrochemical processes 847
– zeolite, pore-opening size 845
– zeolitic 846
catalyst layer composition 591
catalyst-driven mechanism 640, 650
catalytic
– condition 440
– cracking 847
– growth 236
– membrane reactor 1105
– metal particle 237, 239
– properties 537, 794
– site 836
catalytic activity 794
– descriptor 437
– mechanistic path 438
catalytic chemical vapor deposition (CCVD) 149, 252
cathode material 252
cathodically induced sol–gel method 863
cation exchanger resin 535
cation number density 671
cation-exchange properties 821
cavitation 1094
– bubble 523
c-axis ordering length 244
C–C stretching mode 118
C-doped INT-WS_2 627
CdSNW–CNT heterostructure 873
CdS–PPY nanowire 922
cell
– death 1072
– death, critical temperature 1072
– phase contrast 964
– response 991
– response nanofiber scaffold 991
cell damage 1068, 1093, 1094, 1131
cell function
– bone 954
cell membrane 1066
– optical properties 993
– organelles and nanofibers 993
cellular growth 583
cellular refractive index 1076
cement
– bone 945
cement hydrate 1042
cementite phase of steel 1044
centrifuge 731
CeO_2
– Bohr exciton radius 528
– emission spectrum 529
– nanocrystal 529
– nanoparticle 527, 528
– rare-earth-doped 530
ceramic
– barium titanate (BT) 553
– bioactive 946, 949
– ferroelectric 553
– piezoelectric 553
ceramic powder
– nanocrystalline 541
ceramic property 554
ceramic scaffold
– degradability 946
ceramic-polymer composite 946
ceramics 10
– ionic conductivity 538
ceramization 678
ceria
– doped 536
– doped, nanopowder 537
– doped, physicochemical properties 537
ceria nanoparticle
– biocompatibility 528
ceria nanoparticles 527
cerium oxide 527
cetyltributylammonium bromide (CTBAB) 326
cetyltrimethylammonium (CTA) 395
cetyltrimethylammonium bromide (CTAB) 325
chabazite 843
chain formation 12
chalcogenide glass 669
– QD-containing 683
Chapman–Jouguet state 272
characterization
– nanoalloy 417
– nanoparticle 417
– of magnetic nanostructures 488
characterization of nanofibers 993
characterization of single nanofibers 998
characterization technique 58
– magnetic nanostructure 473
charge neutrality point 52
charge transfer (CT) 529, 912

charge transport property 917
charge/discharge curve 252
charge-induced faceting 325
charge-transfer resistance 1028
chemical
– bath deposition 872
– dissolution model 884
– functionalization 592
– mechanical planarization (CMP) 285
– ordering 433, 446, 447
– polymerization 523
– properties, reactivity, functionalization 20
– reactivity 1131
– reduction 311
– sensing 410
– sensor 925
– stability 1023
– structure 985
– synthesis 486
chemical (gas)
– sensor 28
chemical shift 674, 842
– anisotropy (CSA) 577
– calculation 582
– correlation 577
chemical vapor deposition (CVD) 9, 43, 113, 148, 233, 290, 397, 416, 572, 651, 697, 859, 862, 1031, 1105
– low temperature catalytic 132
– technique 523
– transition-metal precursor 167
chemically converted graphene (CCG) 572
chemically functionalized surface 756
chemically modified graphene (CMG) 572
chemically tunable properties 907
chemistry of microorganisms 355
chiral
– angle 107
– branched NW 647
– index 121
– vector 107, 1104
chitosan 948, 965
chitosan-PCL nanofiber scaffold 1002
cholesterol oxidase 203
chromaticity diagram 531
chromatographic separation 849
CIE chromaticity diagram 529
circuit of organic
– thin films 924
citrate
– sol–gel method 555
citrate reduction method 312
citrate route 312
citric acid 520
civil engineering 31
C-labeled graphite oxide 577
classical
– fullerene 86
classical isomer 87
clay 827
clean
– energy 26
cleavage
– micromechanical 42
– of graphite 42
click chemistry using 283
clinoptilolite 843, 848
close packed (cp) 428
closed
– nanoparticle 621
closed-channel
– membrane 1111
closed-system growth 658
closely located
– nanoparticle 1082
cluster 425
– Ag 365
– Ag-Au 434
– bimetallic 446
– binary 442
– CoPt 433, 449
– cross section 433
– discrete 1085
– formation 1127
– free-space 432
– gold 795
– homogeneous 1085
– Ih_{13} 428
– subnanometer 440
– very small 429
cluster aggregation mode (CAM) 1084
CNT (carbon nanotube)
– /polymer composite membrane 1107, 1108
– /polymer film 1107
– aligned membrane 1109
– application 163
– arc-grown 697
– array 863, 1111
– -based biomaterial 168
– -based supercapacitor 1023
– biosensors 28
– carpet 1110
– composite dispersion 712
– conductive polymer doped nanotube 207
– covalently modified nanotube 208
– drug-carrier 218
– electrochemical intercalation of nanotube 208
– growth 111
– hazards 163
– inhalation 162
– membrane 1106
– preparation 697
– production method 149
– properties 697
– reinforced polymer 168
– safe systemic dose 163
– substrate-bound growth 113
– substrate-free growth technique 112
– three-branch-three-subbranch morphology 868
– toxicity 218
– x-ray photoelectron spectroscopy (XPS) 212
CO oxidation 794
CO poisoning 798
CO to CO_2
– conversion 538
$Co(OH)_2$ NW
– dislocation-driven growth 654
coagulation 732
– spinning 703
coated cluster 447
coating 286
– corrosion-proof 1046
coaxial
– nanostructure 1031
– nanotube 1032
coaxial electrospinning 989
coaxial nanotube
– hybrid 1030
cobalt
– catalyst 26, 864
CoCrMo 954
co-electrodeposition 1031
coercivity 480, 808
– of nanostructured materials 480
coffee-drop effect 752
coherent phonon (CP) 120
– oscillation 121
coiled-coil-based self-assembling peptide 986
coin-stacked graphene 575
coke 845
collagen 947, 950, 1066
– -CaP biocomposite 947
– fiber size 953

– fibril 944
– implant 256
– model 986
– nanofiber 981
– –PCL composite nanofiber 995
collagen type I 978
– nanofiber 994, 1002
collapsed nanotube 196
collective electronic state 445
colloidal
– fullerene cluster 746
– nanoalloy coated alloy cluster 437
colloidal metal particle 680
colloidal nanoparticle 416
– gold 312
colloidal soil 1121
columnar array 884
combinatorial method
– electrodeposition and chemical etching 878
combustion 519
– amount of fuel 521
– flameless 520
– in flames, fullerenes by 89
– process parameter 519
– process, characteristics of the fuel 520
– synthesis 527
commercial nanodiamond 269
complex formation 520
complexing 538
– agent in electrodeposition 485
complex-shaped
– nanoheterostructure 878
composite 1023
– bioinorganic 535
– bulk 702
– conductive 750
– electrical 69
– epoxy 706
– fiber 703
– GO-polymer 69
– graphene 721
– material 164
– material surface roughness 962
– material wettabililty 962
– nanoparticle 415
– polymer-CNT 962
– polymeric 234
– reinforcement 696
compound
– semiconductor 524
computational sampling 440
concentrated solar flux 89
concentration quenching 679
concrete
– fiber-reinforced 1043
– mixture of aggregates 1041
– nano-TiO_2-added 1043
– reinforcement material 1044
conductance change 17
conducting
– polymer 989
– polymer NW Y-branched 864
– polymer/metal NT heterostructure 875
conduction
– ballistic 1104
conduction perpendicular to plan (CPP) 68
conductive
– composite 750
– film 749
– graphene 590
– polymer composite 589
– polymer nanofiber 1005
conductivity 810
– Hall 65
cone angle 239
confocal microscopy 994
conical
– graphene sheet 239, 240
constant force method 109
construction
– of nanostructure 860
construction industry 1040
construction material 1053
– manufacturing 1047
– nanoenabled 1049
contact angle 361, 753
contact epitaxy 431
contact-line
– deposit 755
contact-mode
– AFM 656
continuous cluster 1085
continuous flow reactor (CFR) 653, 658
– schematics 658
continuum
– model 454
– plate model 52
contrast agent 94
controlled crystallization 676, 677
controlled pore synthesis 250
conventional
– bone implant 941
conventional implant 949
conventional titania 955
convergent-beam electron diffraction (CBED) 647, 649
conversion
– energy 26
coordination sphere 667
coordination-dependent bond-energy variations (CBEV) 435
copolymer
– block 10
copolymer PA 6/12 nanofiber 1003
copper
– nanostructure 397
copper nanoparticle 51, 397, 1080
– geometry 1079
copper NP 1044
copper oxide
– oxidative toxicity 1052
copper phthalocyanine (CuPc) 909
copper tetracyanoquinodimethane (CuTCNQ) 916
Co-PPY composite 1023
coprecipitation 415
– procedure 522
– reaction 522
CoPt
– cluster 433, 449
– nanoparticle 448
– supported cluster 433
core
– nanoheterostructure 869
core–sheath
– nanofiber 1005
core–shell
– Au–SiO_2 NP 363
– electrospinning 989
– model 266
– nanofiber 993
– nanoheterostructure 875
– nanoparticle 343
– particle 313
– pIh cluster 428
– system 344
core–shell metal/metal
– nanoheterostructure 876
corneal stroma
– tissue engineering 1003
corner atom 28
correlated color temperature (CCT) 530
corrosion
– moisture-induced 1046
– prevention 22
– product 945
– -proof coating 1046
– rebar 1043
– resistance 1044
corrugated
– nanotube 96

cortical bovine bone 955
cosmetic product
– nanoparticle 1123
COSY experiment 829
Coulomb
– blockade 127
– correlation 105
– explosion mechanism 1093
– explosion mode 1092
– interaction 122, 837
countercation 843
coupled metallic nanostructure 447
covalent
– functionalization 156
covalent bond 746
covalent bonding
– GNR 334
covalent chemistry 20
covalent modification 197
coverage fluctuation 439
Cox orientation 707
crack stopper 943
cracking 846
– catalyst 845
Cr-doped 526
cristobalite 827
critical potential 782
critical single-domain size 494
critical temperature 1072, 1082
cross polarization (CP) spectrum 578
cross polarization/magic angle spinning (CP/MAS) 576
cross-flow electrochemical membrane reactor 1111
cross-section of absorption 1085
Cr-Pt nanoalloy 441
cryogenic plasma etching 9
cryo-TEM 1127
cryptic self-binding domain 983
crystal
– zeolitic 839
crystal field
– energy 477
crystal growth
– dislocation-driven 650
– processes, fundamental kinetics 640
– supersaturation 655
– theories 640
crystal inorganic NT 649
crystal violet 10B (CV) 805
crystalline
– graphene layer 243
– nanoribbon 915
– order 40
– silicon 883
– solid 666
crystallization 666
– curve 830
– kinetics 834
– model 675
– of AlPO-5 824
– of CoAPO-5, XRD patterns 831
– of liquid carbon 272
crystallographic discontinuity 325
crystallographic facet 435
crystallographic ordering 517
Cu
– nanocrystal 423
– nanocube 398
– nanoparticle 423
– nanostructure 398
– nanowire 397, 398, 654
– shell/Bi core nanocable 877
– surface 361
cubic
– nanoframe 329
cuboctahedron (CO) 425, 426
Cu-Ni particle 441
CuNP 1080
CuNT–BiNW heterostructure 871
CuPc
– nanowire crystal 924
cup-stacked-type carbon nanofiber 238
Curie law of paramagnetism 476
Curie temperature 479, 554, 555, 564
curled graphite layer 151
curling of graphite sheet 151
current in the plane (CIP) 503
current perpendicular to the plane (CPP) 503
Cu-Ru
– particle 441
curvature 85
– -directed oxidation 326
– -induced strain 156
CuTCNQ nanocone 917
cutoff frequency 73
CVD diamond growth 290
cycle
– activation 1019
cyclic voltammetry (CV) 806, 1025
cyclic voltammogram (CV) 254, 1018
cycloaddition 91, 164
– reaction 582
cyclohexylpyrrolidone (CHP) 751
cylindrical membrane 1107
cytokine therapy 257
cytoplasm 1066, 1073
– property 1073
cytotoxicity 304, 1064

D

DAAQ nanowire 925
– array 926
dachiardite 843
damaged ocular surface 1003
dark-field optical microscopy 359
data storage 473, 503
– density 449
dealloyed depth 800
dealloying 779, 780, 789
dealuminated zeolite 843
Debye
– length 733
– temperature 128
decahedral cluster 427
decay
– accelerated 670
decomposition temperature 519
dedoping process 253
deep-level
– emission 526
defect
– concentration 156
– creation 198
– -free material 700
– -induced mode 241
– model 890
– site 151
definition 411
defluoridation of water 533
degradation 990
dehydrated zeolite 841
Dekany model 582
delivery
– drug 505
– gene 505
demagnetization factor 480
demolition waste 1048
dendritic cells (DC) 992
dendritic growth mechanism 641
density functional theory (DFT) 474
density of defects 214
density of states (DOS) 16, 204, 626
density-functional tight-binding calculation (DFTB) 623, 626
density-functional-based method (DF) 627
density-gradient ultracentrifugation (DGU) 48

dental
– tissue engineering 963
depolymerization 669, 835
deposit
– contact-line 755
Derjaguin, Landau, Verwey, and Overbeek 732
dermal route
– skin penetration 1123
destructive adsorbent 533
destructive immune response 992
detection of pesticide 349
determination
– microscopic technique 828
– zeolite 828
detonation nanodiamond (DND) 263, 265, 266, 284
– seeding 291
detonation shock wave-assisted synthesis 270
detonation soot 272
– synthesis 278
deuterated GO 578
dewaxing 847
dextran filtration 1112
di(propoxyethyl)perylene-3,4,9,10-tetracarboxylic diimide (PTCDI) 910
diamond 93, 94
– bucky 265, 266
– carbide-derived 278
– film growth 290
– -like carbon (DLC) 292
– nanoparticle 275
– nucleation 276
– spherical 266
– synthesis ultrasound cavitation 278
– ultrananocrystalline (UNCD) 268, 292
diamondoid 268
diazonium salt 199, 200
dicalcium phosphate dehydrate (DCPD) 948
dielectric exclusion 1101
dielectric function 443
Diels–Alder reaction 156, 283
diethylene glycol (DEG) 530
die-upset Nd-Fe-B magnet 491
differential electronic density 449
differential interference contrast (DIC) 993
differential scanning calorimetry (DSC) 678, 709
differential thermal analysis 246
diffraction spot 645
diffuse dispersion 730
diffuse reflectance infrared Fourier transform (DRIFT) 578
diffusion 780, 836
– inward 609
diffusivity 731
diluted Nafion 1017
dimensionality 16
dimethylacetamide (DMA) 734
dimethylformamide (DMF) 244, 734, 888
dimethylsulfoxide (DMSO) 281, 291, 888
dip coating 28, 906
dip-and-dry procedure 906
dipolar evolution time 669, 672
dipolar NMR spectroscopy 668, 671
dipolar recoupling technique 668
dipolar second moment 669
dipolar second moment value 670
dipole–dipole coupling 667, 668
dipole–dipole interaction
– heteronuclear 671
– homonuclear 669
dip-pen
– lithography 10
– nanolithography 9
Dirac
– fermion 108
– point 52, 67, 108
direct alcohol fuel cell (DAFC) 1013
direct current (DC) 235
direct ethanol fuel cell (DEFC) 1021
direct hydrogel transformation 835
direct methanol fuel cell (DMFC) 797, 1014, 1021
direct methanol or formic acid fuel cell (DMFC, DFAFC) 808
disassembly 337
disc
– electrode 800
discovery 147
discrete cluster 1085
discrete dipole approximation (DDA) 444
dislocation 791
– activity 454
– contrast 645, 651
– contrast two-beam analysis 646
– crystal growth 654
– -driven mechanism 649
– migration 453
dispersed MWNT 1023
dispersibility 309
dispersion
– carbon nanotube 734
– graphene 734
– of particles 729
– relation 108
– stability 758
displacements per atom (dpa) 452
distributed Bragg mirror (DBR) 893
disulfide
– molybdenum 607
– tungsten 607
DLVO theory 732
DNA 162
– -wrapped MWCNT 210
DND (detonation nanodiamond)
– /plasmid complex 289
– metal impurity 278
– nanoparticle biosensor and biochip 290
– nondiamond carbon 279
– -probe-based array 290
DND (detonation nanodiamond)
– ink 290
domain
– in fine particles 478
domain wall 564
– pinning 491
– width 478
Donnan effect 1101
donor 92
– –acceptor interaction 911
doped
– carbon nanotube 204
– ceria 536
– ceria nanopowder 537
– ceria, physicochemical properties 537
– nanotube electrical resistivity 193
– nanowire 913
doped conducting oxide 524
doped Gd_2O_3 phosphor 530
doped IF (inorganic fullerene-like) 627
doped INT (inorganic nanotube) 627
doped pyrochlore 541
doped ZnO NW
– undoped 653
doping
– concentration 895
– process 253
dorsal root ganglion (DRG) 1004
dot
– array 8
double four ring (D4R) 833

double layer capacitance 1015
double quantum dot device 67
double-layer capacitor 810
double-quantum/single-quantum (2Q/SQ) 577
double-walled carbon nanotube (DWCNT) 190, 192, 696
doxorubicin (DOX) 218, 288
DQ (double quantum) NMR 844
DQ/SQ correlation SSNMR spectrum 579
drag force 731
draw ratio (DR) 714
DRG neurite field 1005
drift of particle 731
drop casting 749, 750, 906
drop-on-demand 757
drop-on-demand inkjet printer 753
drug delivery 92
– targeted 505
drying droplets of liquid 752
ductal breast carcinoma 1073
ductile–brittle transition 799
durability of the concrete 1042
self-assembly 907
dynamic conductivity 106
dynamic light scattering (DLS) 1126, 1129
dynamic nanofiber process 996

E

early transition metal element (TE) 499
e-beam irradiation 613
ECM (extracellular matrices) 952
– protein 1002
– protein basic role 978
ecotoxicity 1120
ectopic bone 256
EDAX line profile 330
eddy current loss 499
edge 197
– loop formation 243
effective anisotropy 478
effective diffusivity 164
effective modulus 704
efficiency
– attenuation 1065
egg white solution 528
Eklund shift 118
elastic stiffness 51
electric double layer 254
electric double layer capacitor (EDLC) 1023
electrical composite 69
electrical conductivity 204, 249, 807, 896
electrical double layer (EDL) 732
electrical gating 54
electrical resistivity 204, 245
electrical transport 891
electrically conducting polymers (ECP) 1023
electroactive
– polymer 1001, 1004
– polymer surface resistance 989
electroactive scaffold 1001
electrocatalyst 442, 1016
– activity 797, 864
electrochemical
– actuation 807
– application 206
– cell 886, 1109
– dealloying 783
– deposition 523
– deposition nanochannel-confined 867
– device 1015
– double layer (ECDL) 1015
– energy storage 253, 640, 1029
– etched silicon 883
– etching 896
– impedance spectroscopy (EIS) 1027
– membrane reactor 1111
– modification 198
– performance 254
– potential 654
– reduction 313
– sensing of biomolecules 350
– sensor 806
– setup 320
– supercapacitor 810, 1015
– synthesis 318
electrochemically active surface area (ECSA) 1018
electrode
– disc 800
– –electrolyte interface 1029
– material 251, 253, 797
electrodeposition 474, 484–486, 792, 863
– in nanochannel 863
– one-step 876
electrodialysis (ED) 1099
electroluminescence (EL) 892
– device 524
– electrode 589
electrolyte 732
– acessibility 255
– decomposition 252
electromagnetic (EM) 286
electromechanical coupling factor 554
electron
– acceptor 92
– analyzer 420
– beam irradiation 89
– beam lithography 484
– biprism 490
– diffraction (ED) 239, 665
– –electron interaction 1093
– energy loss spectroscopy (EELS) 208, 211, 220
– energy-loss spectroscopy (EELS) 592
– field emission electrode 589
– holography 490
– irradiation 88
– microscopy 995
– spin resonance (ESR) 160
– transfer chemistry 57
– transfer theory 57
– transparent window 591
electron paramagnetic resonance (EPR) 160, 264, 284, 424, 829, 846, 1132
electron–hole
– conversion 54
– pair 682
electronic
– application 168
– conduction 540
– device 163
– dispersion 107
– portable device 252
– structure 106
electronically conducting polymer (ECP) 1015
electron–phonon interaction 1093
electroosmotic flow (EOF) 1106
electrophoresis 731, 732
electropolishing 885
electrospinning 247, 252, 703, 953, 980, 1002
– device 981
– method of 249
– setup 980
electrospun
– carbon nanofiber 252
– chitosan 990
– fibrous scaffold 1003
– nanofiber 244, 245, 247, 249
– nanofiber web 246
– PCL blend nanofiber 1002
– PCL scaffold 991

– polyurethane nanofiber 995
– scaffold 987
electrostatic
– actuation 52
– force 336
– force microscopy (EFM) 60
– GNR nanochain formation 335
– interaction 752
– self-assembly 331
electrowetting 1106
element aluminophosphosilicate (ElAP(S)O) 823
elemental doping 787
elongation growth 237
embryonic stem cell (ESC) 1004
emission
– deep-level 526
empirical potential simulation 436
encapsulation 191
endohedral doping 191, 192
endohedral fullerene 20
endosulfan–noble metal NP 350
end-to-end assembly 338
energetic minimum 613
energy
– activation 541
– adhesion 430
– clean 26
– conversion 26
– conversion and storage 28
– crystal field 477
– flux density 1067
– Gibbs 732
– of a nanoalloy 411
– specific battery 251
– storage 26
energy dispersive analysis (EDAX) 1017
energy dispersive x-ray (EDX) 789
energy plot
– 3-D 643
energy-dispersive spectroscopy (EDS) 866, 995, 1126, 1128
engine oil NanoLub 628
engineered nanomaterial 1118
– characterization methods 1126
– consumer product 1130
– effects on organisms 1121
– environmental fate 1120
– in vitro toxicity 1124
– inorganic pigment 1132
– overview 1118
– physicochemical characteristics 1124, 1125
– production quantities 1120
engineered nanoparticle
– phytotoxicity 1122
engineering cell function 978
engineering stress 803
environmental
– nanoparticle 1129
– pollutant removal 504
– remediation 533
– TEM (ETEM) 423
environmental fluoride 533
environmental impact 1117
enzyme inhibition 92
epitaxial
– casting 789
– graphene growth 44
epithelial cells (EPITH) 162
epoxy
– composite 706
– group 590
– nanocomposite 964
– polymer 749
– ring 590
equilibrium configuration 412
equivalent series resistance (ESR) 254, 1028
erionite 823, 843
erosion
– bulk 947
Eshelby twist 642, 646, 652
– pathway 644
etch rate 884, 886
etching
– conditions 889
– parameter 895
ethylenediamine (EDA) 654
– acid (EDTA) 337, 520
Euclidean 85
eucryptite (Li_2O-Al_2O_3-$2SiO_2$) 676
Euler's law 86
evaporated gold (EG) film 803
evaporation
– profile 165
– solvent 487
exchange
– -coupled nanocomposite 496
– coupling 497
– effect 476
– energy 477
– length 478
exciton
– 1-D 115
– Bohr radius 682
– diffusion length 932
excitonic binding energy 122
excitonic state 117
exfoliated
– graphene 66
exohedral
– fullerene 20
exohedral doping 191, 192
exothermic decomposition 519
exotic MWCNT synthesis 150
expandable
– graphite 46
explosive molecule 265
explosive vaporization 1094
exposure 1119
extended surface 438
extended x-ray absorption fine structure (EXAFS) 666, 685
external quantum efficiency (EQE) 890
extinction spectra 327
extracellular matrix (ECM) 950, 978
extracellular polymeric substance (EPS) 1050
extracrystalline diffusion 839
extrusion mechanism 152

F

fabrication
– bottom-up 487
– method 988
– of nanostructures 8
– strategy 977
– technique 989
face-centered
– cubic (fcc) 10, 390, 425, 499, 645, 655
– cubic structure (fcc) 88
– tetragonal (fct) 492
Fano resonance 448
fast atom bombardment mass spectroscopy (FABMS) 828
fast breeder reactor 518
fast Fourier transform (FFT) 28, 120, 239, 756, 789
– image 328
fatigue crack growth 719
faujasite 843
– framework 837
– material 822
– polytype 824
FAU-polytype 832
FAU-X 831
FAU-Y 831
fcc (face-centered cubic) 492
– cluster 430
– lattice 39

– -like particle 449
– -stacked monolayer 790
FePt nanoparticle
– bio-functionalized 457
– vancomycin-coated 458
Fermi energy 28, 53
Fermi velocity 108
ferrierite 835
ferritic
– steel 452
ferritic stainless steel 450
ferro- and ferrimagnetism 518
ferroelectric 553
– ceramic 555
– critical size 555
– transition 563
– transition temperature 564
ferrofluid 17, 18
ferromagnet–graphene
– interface 67
ferromagnetic resonance (FMR) 501
few-domain
– nanoparticle 17
few-layer
– graphite 84
few-layer graphene 60
fiber
– -aligned scaffold 981
– diameter 991
– length 238
– -reinforced concrete 1043
– spinning 979, 980
– -to-fiber bonding 1044
fibroin core–sheath nanofiber 990
fibronectin 957
fibrous
– carbon 253
– nanocarbon 257
Fick's second law 839
field emission device 917
field-effect transistor (FET) 14, 748, 754, 757
– printing 749
field-emission scanning electron microscopy (FESEM) 906
film
– conductive 749
filter architecture 164
filter performance
– cross-linking 164
– interlinked CNT network 164
– nanotube 164
fine chemical industry 847
fine metal
– particle 389
fine structure 236
– constant 55
Finemet 474, 500
finite-size effect 439
fire-protective window glass 1045
first-principles calculation 436
first-principles simulation 442
Fischer–Tropsch 847
– reaction 26
– synthesis 26, 167
flake 391
– thickness 48
flame spray pyrolysis 527
flameless
– combustion 520
flat-panel displays (FPD 530
flexible electronics 71
flow cytometry 358
flowchart
– BSPT powder 556
fluctuation-enhanced sensing (FES) 28
fluctuation-induced tunneling (FIT) 124
fluorene 343
fluorescein isothiocyanate (FITC) 993
fluorescence microscopy 914, 993
fluorescence spectroscopy 709
fluorescent
– nanodiamond 285
fluorescent carboxylated HPHT ND (FND) 288
fluoride
– nanocrystal 666
fluoride anion 884
fluoride crystal phase 677
fluorinated
– MWCNT 212
– SWCNT 203
fluorinated graphite 582
fluorogermanate glass 679
fluorographene 58
fluorophore 993
focused ion beam (FIB) 8
food packaging 1123
food processing 848, 1101
force-based spinning technique 980
formation
– of clusters 1127
– of nanoparticle 682
Förster resonance energy transfer (FRTE) 448
four-branched Ni nanowire 866
four-generation Y-branched CNT 867
Fourier transform mass spectrometry (FTMS) 90
Fourier-transform infrared spectroscopy (FTIR) 994
four-point probe method 242
Fowler–Nordheim (F-N) plot 917
fractional quantum Hall effect (FQHE) 65
fracture mechanism 708
fracture toughness 629
framework
– exchange method 845
– property 829
– type 821
Frank–Kasper bulk phase 428
free corrosion 785
– condition 794
free enthalpy change 836
free induction decay 668
free-space
– cluster 432
free-standing structure 897
Freundlich constant 535
Freundlich equation 535
Friedel–Crafts-type acylation 156
frozen-in properties 665
FTIR spectra 995
fuel
– agent 538
– excess ratio 521
– –oxidant precursor 519
– -to-oxidant ratio 520
fuel cell 527, 1013
– alkaline (AFC) 1013
– application 166
– polymer 591
– stack 1018
full isolation by porous oxidized silicon (FIPOS) 883
fullerene 2, 10, 20, 40, 92, 190, 276, 343, 575, 605, 746
– /P3BT nanowire power conversion efficiency 921
– application 747
– chemical properties 91
– classical 86
– cluster 747
– coalescence 94
– colloidal cluster 746
– drug delivery 92
– electrical properties 91
– exohedral 20
– formation 90
– geometry 85
– giant 93
– high genus 97

– mechanical properties 90
– nested 93, 94
– nonclassical 86
– peapod 92, 94, 95, 192
– physicochemical properties 90
– pioneering experiment 149
– road 90
– solar cell 92
– superconductivity 91
– synthesis 89, 147
fullerene sphere
– half 147
fulleride 91
fullerite 83, 91
– superconducting temperature 91
full-width at half-maximum (FWHM) 1084
functional nanofiber 249
functional food compound
– nanoscale materials 1123
functional materials 517
functional surface 927
functionalization 197, 343
– covalent 156
– electrostatic 201
– mechanochemical 157
– schematic model 200
– technique 199
– with carbene 200
– wrapping 200
functionalized
– membrane 352
– metal nanoparticle 343
– SWCNT (f-SWCNT) 218
– SWCNT (f-SWCNT), biocompatibility 218
fundamental charge transport 923

G

GaAs
– nanowire 10
gadolinia-doped ceria 537
gadolinium oxide (Gd_2O_3) 530
galvanic
– cell 867
– coating 287
– deposition 867
– reaction 328, 329, 793
– replacement 330, 415
– replacement reaction 316
galvanostatic charge–discharge 1027
gas
– atomization 502
– chromatography (GC) 166
– sensing 31
– sensor 524, 749
– sorption separation 838
gas-phase diffusion 611
gastrointestinal route 1123
gate-induced absorption 54
Gauss–Bonnet theorem 86
Gaussian curvature 85, 98
Gaussian decay 669
Gd_2O_3 nanocrystal 530
Gd_2O_3 particle 531
$Gd_2O_3:Eu^{3+}$
– nanotube 531
– nanowire 531
$Gd_2O_3:Tb^{3+}$
– nanoparticle 531
$Gd_2O_3:Tb^{3+}/Eu^{3+}$
– nanosphere 531
$Gd_2O_3:Tb^{3+}:Dy^{3+}$
– nanoparticle 531
gel 519
– combustion 520, 538
– combustion synthesis 519, 521, 541
– formation 519
– precursor 521
gelatin 947
gelatin/collagen scaffold 947
generalized tight binding molecular dynamics (GTBMD) 133
genus 86
geometry 85, 1079
geothermal deposit 827
germanate
– glass 670
giant
– fullerene 93
giant magnetoresistance (GMR) 473
Gibbs
– energy 732
Gibbs free energy 264
Gibbs–Thomson equation 18
gigatechnology 666
gismondine 843
glass 665
– bioactive 948
– bulk 683
– coating 685
– crystallization peak 678
– definition 665
– germanate 670
– medium-range structure 667
– nonoxide 669
– oxyfluoride 666, 670
– phosphate 670, 676
– real 665
– Roman 680
– short-range order 666
– sodium borate 670
– sodium silicate 670
– system 677, 682
– tellurite 670
– theory 666
– thermochromic 1045
– to the crystalline 679
– transition 665
– Venetian 680
– window 1044
glass ceramic 666, 676, 946
– system 673
glass microneedle 998
glass system 677
glass-forming oxide 677
glass-transition
– temperature 665
glassy carbon electrode (NPG/GC) 216, 806
glassy solid 675
glassy state 666
Gleiter schematics 10
glucose detection 806
glucose oxidase 203, 204
glycine 520
glycosaminoglycan (GAG) 978
GMR (giant magnetic resonance) 502
GNP (gold nanoparticle) 305, 325
GNR (gold nanorod) 327
– plasmonic characteristic 327
– preferential growth 327
GO 576
GO (graphite oxide) 46, 571, 579, 699, 750
– antibacterial activity 583
– application 589
– band structure 588
– characterization 576, 577
– chemical composition 573, 578
– chemical structure 581
– chemistry 589
– derivative 589
– edge structure 588
– flake 583
– functional group 587
– nanosheet 575
– NMR spectrum 576
– oxidation degree 573
– physical property 583
– preparation 573, 574
– quantum dot 588
– Raman spectrum 578

– reactivity 583
– reduction protocol 584
– sheet 69, 576
– structure model 581
– synthesis 575
– thermal stability 581
– toxicity 583
– UV-Vis spectrum 578
GO (graphite oxide) fabrication
– graphite source 575
– oxidation reagent 575
GO (graphite oxide) preparation recipe
– comparison of procedures 574
GO (graphite oxide) thin film 70
– electrical 70
– optical properties 70
gold 1071, 1079, 1080
– bucky 429
– cluster 795
– material property 1079
– nanocage 457
– nanocrystal 323
– nanocube 320
– nanooctahedra 362
– nanoparticle (GN) 9, 92, 157, 347, 444, 756, 1066, 1078, 1080, 1086, 1089, 1091, 1123
– nanoparticle (GN), melting point 22
– nanoplate 657
– nanorod (GNR) 337, 1070
– nanorod (GNR) assembly 340
– nanorod (GNR) film 340
– nanosphere 322
– nanowire 9
– QC 364
– refraction data 1080
– rod-shaped 325
– solid nanosphere 1063, 1094
gold and silver 303
gold anion cluster 430
gold ligament 790
gold NP 325, 347
gold particle 1065, 1089
– absorption coefficient 1089
gold–platinum nanocatalyst 26
GO-polymer composite 69
GO-polymethyl methacrylate (GO-PMMA 591
grain
– average size 557
– conductivity–relaxation process 539
– growth 559
– growth inhibitor 522
– resistance 539
– size distribution 561, 563
– size effect 554, 564
– size strengthening 454
grain boundary (GB) 454
– migration 557
grain size
– optimum 12
Gram-positive bacteria 457
granuloma formation 162
graphane 39, 50
graphene 10, 24, 83, 84, 352, 695, 746, 750, 964
– 2-D 59
– AB stacked 62
– bilayer 47
– bulk 69
– characterization 60
– chemical properties 56
– composite 721
– conduction band 52
– conductive 590
– conductivity 71
– conical sheet 239, 240
– crystalline layer 243
– density of states 60
– derivative 57
– dispersion 752
– elastic properties 51
– electrical characterization 63
– electronic structure 53
– exfoliated 66
– few-layer 60
– field-effect transistor 69
– filler particle 718
– film 71, 750
– flake 43, 59
– growth 44
– hexagonal lattice 52
– linear dispersion relation 66
– membrane 60
– molecule 20, 588
– monolayer 699
– nanoribbon (GNR) 42
– noninteracting 55
– optical characterization 58
– oxide (GO) 22, 39, 40, 571, 699
– preparation 698
– production 44
– properties 699
– -Pt composite 69
– quantum dot (QD) device 66
– quasi-2-D derivative 41
– ribbon 195
– sheet 14, 195, 235, 614
– single-layer 701
– solution 750
– spin valve 68
– stiffness 51
– strain 721
– substrate supported 50
– suspension 48
– thin film 69
– tight-binding dispersion 108
– TiO_2 (titanium oxide) 69
– trilayer 47
graphite 40, 234, 237, 239, 270, 746, 750
– 3-D 129
– cleavage of 42
– expandable 46
– few-layer 84
– fiber 235
– fluoride (GF) 46
– intercalated 47
– intercalation compound (GIC) 46
– nanoplatelet (GNP) 698, 716
– oxide (GO) 46, 571, 579, 699, 750, 752
– platelet 750
– powder 1016
– sheet 235
– single-layer 105
– solution 750
– target 613
– whisker 235
graphite-like SWCNT 111
graphitic
– acid 571
– cone 194
– material 196
– nanofiber 239
– nanoribbon 242
– onion 277
– platelet 147, 148
graphitization 155, 240, 241
graphitization accelerator 242
graphitized coated nanofiber 242
graphitized uncoated nanofiber 242
gravimetric capacitance 255
grazing-incidence small-angle x-ray scattering (GISAXS) 418
green fluorescent
– protein (GFP) 993
grinding 519
growth
– environment 643
– kinetics 641
– mechanism 239, 608, 639
– mechanism of carbon fibers 237
– mechanism outside-in 608
– model for fibers 236

– of a vascular network 1001
– of carbon nanofibers 238
– process diffusion limited 522
– process diffusion-controlled 611
G-surface 87
guided growth 618

H

Hagen–Poiseuille equation 1103
Hahn spin-echo
– amplitude 671
– sequence 672
half fullerene sphere 147
half octahedral cluster 431
half-width at half-maximum (HWHM) 240
Hall
– conductivity 65
halloysite additive 22
Hall–Petch relation 454
halogenation 91
Halpin–Tsai approach 717
Hamaker constant 732
Hammett constant 842
hard tissue engineering 960
hard magnetic
– nanostructure 494
hardness 287
– particle size dependence 12
harmotome 843
haversian system 944
hazards
– of CNT 163
hcp
– nanodot morphology 432
hcp lattice 432
hcp monolayer 790
hcp structure 432
healthy mitochondria 1074
healthy nucleus 1074
heat accumulation effect 1074
heat conduction 1086
heat profile 1081
heat transfer 1085
– equation 1067
heat treatment effect 248
heat-affected zone (HAZ) 1044
heating kinetics 1075
heating of bone tissue 1075
heat–mass transfer 1076
heavy metal
– nanoparticle 289
– oxide glass (HMOG) 681
He-induced embrittlement 452
Heisenberg interaction 477
helical carbon
– nanotube 150
helical rosette
– nanotube (HRN) 959
helix-shaped
– nanotube 194
hematite (Fe_2O_3) 1042
Henkel plot 497
hepatocellular carcinoma 1073
heptagonal 93
Herman's orientation factor 710, 714
heterodoped
– nanotube 212
heterogeneous
– catalysis 166, 167, 256, 416, 437, 438, 442, 457, 536
– catalysis metal nanoparticle 438
– catalysis subnanometer metal 440
– nucleation 415
heterojunction
– nanowire 922
heterojunction photovoltaic device 363
heterometallic
– nanorod 330
heteronuclear
– dipole–dipole interaction 671
heteronuclear dipolar coupling 684
heteronuclear dipolar Hamiltonian 672
heteronuclear *J*-coupling 674
heterostructure
– fabrication 869
heulandite 843
hexadecylamine (HDA) 398
hexagonal close packing (hcp) 90, 645
hexagonal polytype 621
hexamethylenetetramine (HMT) 520, 653, 656
hierarchical organization 943
hierarchical structure 927
high coercivity FePt particle 448
high genus
– fullerene 97
high refractive index contrast 896
high resolution scanning electron microscope (HRSEM) 623
high-angle annular dark-field (HAADF) 619
– detector 422
high-angle annular dark-field scanning transmission electron microscopy (HAADF-STEM) 789
high-energy-density
– permanent magnet 492
highest occupied molecular orbital (HOMO) 626
highly charged ion (HCI) 277
highly curved carbon nanostructure (HCCN) 151
highly oriented pyrolytic graphite (HOPG) 42, 200, 571
high-performance
– photodetector 926
high-power
– supercapacitor 253
high-pressure high-temperature (HPHT) 264
high-quality
– nanotube 149
high-resolution electron microscopy (HREM) 828
high-resolution transmission electron microscopy (HRTEM) 151, 190, 220, 273, 417, 555, 578, 619
high-silica
– zeolite 823, 825, 848
high-strength
– steel 1044
high-temperature annealing 1031
high-temperature decomposition 486
high-temperature piezoelectric 554
hip joint
– implant 292
– prostheses 963
HiPCO process 113
HiPCO SWCNT 117
Hitperm 474, 500
H-MOR 846
Hofmann model 581
hole 884
hollow
– core 238
– gold cage 430, 432
– membrane 1099
– nanopipe 652
– nanostructure 328
– nanotube 328, 329, 643, 792
hollow cage
– nanoparticle 432
homogeneous
– catalysis 437, 1101
– cluster 1085
homogeneously dispersed 731
HOMO–LUMO
– gap 626
– interaction 200
– transition 355, 589

homonuclear dipole–dipole interaction 670, 684
homonuclear J-interaction 675
honey comb lattice 1104
honeycomb structure 698
HOPG (highly ordered pyrolytic graphite) 396
horseradish peroxidase (HRP) 806
HRTEM (high-resolution transmission electron microscopy) 784
– image of porous carbon nanofibers 255
human nanoparticle exposure 163
human promyelocytic leukemia (HL60) 218
human skeletal muscle cell (hSKMC) 1002
Hummers method 574
Hund's rule 477
hyaluron 948
hybrid
– coaxial nanotube 1030
– electric vehicles (HEV) 252
– electrode material 1030
– nanoarchitecture 878
– nanocluster 621
– nanomaterial 932
– nanoparticle 752
– NPG structure 792
– structural motif 428
hybridized
– carbon 1104
hydrazinium graphene (HG) 750
hydrocarbon 150
– conversion 846
hydrocracking 847
hydrodesulfurization (HDS) 395
hydrodynamic voltammogram 1018
hydrogel 952
hydrogen
– bonding 336
– -bonding method 331
– propagation 608
– sensor 257
– storage 20
– -terminated diamond 268
hydrogenation 91
hydrogenation–decomposition–desorption–recombination (HDDR) 486
hydroisimerization 847
hydrolysis 652
hydrolyzed poly(styrene-co-maleic anhydride) carrying pyrene (HPSMAP) 158
hydrolyzed poly(styrene-co-maleic) anhydrite (HSMA) 158
hydrophilic
– zeolite 837
hydrophilic conversion 1043
hydrophobic
– CNT surface 166
– gold nanorod 338
– octadecanethiol (ODT) 343
– surface 734
hydrosilylation 892
hydrothermal
– deposit 827
– processing 523
– synthesis 28, 527
– treatment 833
hydrous manganese dioxide (HMO) 535
hydroxyapatite (HAP) 942
hydroxypropylmethyl cellulose (HPMC) 948
hyperbolic 85
hyperfiltration 1101
hyperthermia 505, 1064
hysteresis
– of magnetic nanostructures 481
H-ZSM-5 846

I

icosahedra (Ih) 427
icosahedral 84
icosahedral cluster 427
IF (inorganic fullerene-like)
– aggregation 629
– doping 611
– -iPP nanocomposite 629
– mechanical properties 629
– synthesis 608
– tribological application 629
– -WS_2 nanobud 611
Ih_{13}
– cluster 428
imaging
– biomedical 359
iminopyrrole (IP) 912
immersion–electrodeposition (IE) 797
immobilized
– nanoparticle 872
immune response 992
immunity-promoting signal 992
immuno-Au
– nanocage 358
immunogenic reaction 257
impedance plot 255
impedance spectra 254
impedance spectrum 539
implant
– biocompatible polymer 945
– bone 941, 944, 948, 956
– ceramic material 945
– knee joint 292
– loosening 945
– material 949
– metallic material 945
– metallic nanoscale 954
– surface modification 949
implanted materials 992
impurity
– carbonaceous 535
in vitro study 220
in vivo study 218
In_2O_3
– nanobelt 526
– nanocrystal 526
– nanocube 525
– nanofiber 525
– nanorod 525
– nanotube 526
– particle 527
– powder 525
In_2O_3:Eu particle 527
In_2O_3:Eu^{3+} quantum dots 526
indentation measurement 997
indium tin oxide (ITO) 69, 70, 754, 921, 1045
– nanostructured 1045
induced pluripotent stem cells (iPSC) 1004
inductively coupled plasma (ICP) 783, 828
– mass spectrometry (ICP-MS) 1126
industrial
– wastewater 527, 534
industry
– construction 392
– packaging 392
– transport 392
inert gas deposition technique 2
inflammation 945
infrared (IR) 424
inhalation 1122
inkjet printing 749
inner tube surface 643
Ino decahedron 426
inorganic
– nanotube (INT) 606, 863
– pigment 1132
– –polymer nanocomposite 909
– semiconductor nanocrystal 362

– semiconductor quantum dot 912
– UV filter 1130
inorganic fullerene-like (IF) nanoparticle 606
inorganic nanoparticle
– application 735
– dispersion 735
– solvent 735
in-plane
– doping 193
– magnetization 449
– surface anisotropy 480
– tensile stress 791
insertion alloy 1016
inside nanochannels 869
inside-out mechanism 613
inside-out synthetic method 619
insulating material 897
insulator 518
INT (inorganic nanotube)
– conductivity 626
– mechanical properties 629
– properties 618
– synthesis 614
– transport properties 626
– tribological application 629
integrated circuit (IC) 897
intelligent aggregate 1047
interatomic exchange 477
interband conversion 54
interband excitation 122
intercalated
– graphite 47
intercalation 191
interconnected
– nanofiber 252
interface
– coupling 495
– electrode–electrolyte 1029
– ferromagnet–graphene 67
– polymer–graphene 720
– self-organization at 331
– solid–liquid 732
interface-stabilized morphology 432
interfacial
– adhesion 707, 714
interfacial shear strength (IFSS) 707
interference electron microscopy 490
interference function 418
interfiber forces 997
interfiber spacing 983
interlamellar water 583
interlayer shear modulus 629
intermolecular interaction 916
intermolecular self-assembly 907
internal cluster temperature 1085
internal temperature distribution 1078
International Standards Organization (ISO) 1125
International Zeolite Association (IZA) 821
internuclear distance 669
interparticle
– distance 1083
– interaction 492, 493
– spacing 282
interplanar stacking fault 825
interstitial 197
intertube interaction 111
intraatomic exchange 477
intracellular component 993
intracrystalline
– diffusion 839
– self-diffusivity 839
– transport diffusivity 839
intramolecular
– self-assembly 907
intrinsic
– 1-D function 253
– brittleness 799
– resistance 126
invisibility criterion 645
iodine-doped DWCNT 203
ion
– -conducting channel 670
– exchange 822, 836
– exchanger 848
– imaging 501
– implantation 682
– sieving selectivity 836
– solution 535
ionic conductivity 539, 1030
ionic liquid (IL) 394, 799, 1101
ionic strength 332
ionics 538
ion-track-etched
– membrane 859
IR spectroscopy 829
iron oxide 1071
iron oxyhydroxide 653
irreversible capacity 252
isobar 837
isolated particle 483
isolated pentagon rule (ipr) 88
isomeric precursor 912
isomorphous substitution 823
isostere 837
isotactic polypropylene (iPP) 629
isotherm 837
– distillation 732
isotopical labeling of GO 576
isotropic chemical shift 579
isotropic nanosystem 307
itinerant exchange 479
I–V curve 885

J

Janus particle 434
J-coupling multiplets 675
jellium model 445
Josephson effect 55
Jouguet point 272
J-resolved spectra 675

K

kaliophilite 836
kaolin 827
Kataura plot 18
Keating Hamiltonian 131
Kedem and Katchalsky model 1102
Kelly–Tyson model 709
Kerr rotation 503
Kevlar 167
– matrix 287
Kikuchi bands 648
kink atom 794
Kirkendall effect (KE) 9, 330
kitchenware 676
knee joint
– implant 292
knee ligament 945
Knudsen diffusion 838
Kohn anomaly 63
Kohonen clustering 165
Kramers–Kronig (KK) self-consistency 802
Krätschmer electronic arc discharge 147
KRSR (Lys-Arg-Ser-Arg) 958
Kubelka–Munk units 579

L

labeling 357
lab-on-chip device 1106
laccase 203
Lagergren rate equation 536
lamellar bone 943
lamellar stack 730
laminar flow 1103
laminin derived self-assembling peptide, IKVAV 1004

Landauer law 17
Langmuir equation 535
Langmuir–Blodgett (LB)
– assembly 351
– deposition 70
– technique 341
lanthanide-doped glass 676
Laplace operator 1067
large pore molecular sieve 825
large surface area 254
large zeolitic crystal 839
large-area monolayer of nanosystem 341
large-pore
– material 821
– mordenite (LPM) 843
– zeolite 824
large-scale production 148
Larmor frequency 667
Larson–Miller plot (LMP) 451
laser
– -activated nanoheater 1088
– -grown nanotube 746
– heating 1074, 1077
– host 676
– killing of abnormal cell 1095
– nanoparticle heating 1068
– pyrometry 160
– thermal explosion 1095
– vaporization method 88
laser ablation 89, 149, 613
– growth 112
– liquid 277
laser-induced explosion 1093
– cell damage 1094
– heating 1064
– overheating 1087
– thermal explosion 1091
laser–nanoparticle interaction 1075
late ferromagnetic transition metal element (TL) 499
lateral enlargement 888
lattice mismatch 431
lattice tilt 648
Laue condition 648
laumonite 843
layer-by-layer (LBL) 640, 1047
– assembly 69
– crystal growth 640
– growth 611
– growth mechanism 641
– templating 346
LCD (liquid crystal display) 286
LDA-relaxed geometry 446
lead germanate glass 679
lead nanoparticle 390
Leary tetrahedron 428
– magic number 429
LED (light-emitting diode) efficiency 893
LED/OLED 286
Lehmann formula 886
length of myotubes 1002
length scale
– magnetic 478
– of nanopores 789
Lerf–Klinowski model 582
less noble (LN) 780
level of reinforcement 718
Lifshitz theory 732
ligament length 808
ligament–channel structure 779
ligand exchange reaction 343
ligand-mediated reaction 354
light emission 890
light emission efficiency 893
light-absorption 1065
light-emitting device
– silicon based 883
light-emitting diode (LED) 524, 757, 1046
light-emitting phosphor 530
lightweight nanocomposite plastics 1044
– mechanical properties 1044
limbal stem cell (LSC) 1003
Linde 3A 848
Linde type A (LTA) 822
linear filament 233
lines of defects 195
lipopolysaccharide (LPS) 356
liquid
– carbon 272
– crystal 341
– -crystal display 731
– -phase exfoliation 49
– vaporization (LV) 1092
lithium
– adsorption 244
– –air cell 26
– battery 1031
– borate glass 671
– ion battery 243, 251, 252
– ion battery application 244
– ion battery capacity 245
– ion battery charge–discharge cycle 245
– ion capacitor 169
– –lithium interaction 671
– rechargeable battery 1029
– storage material 589
lithium ion battery 243, 251, 252
lithography 484
local composition variation 521
local density approximation (LDA) 445
local density of states (LDOS) 210
local electronic state 445
local strain 720
localization regime 127
localized electron 479
localized surface plasmon 442
localized surface plasmon resonance (LSPR) 322, 685, 803
Loeb–Sourirajan membrane 1102
logic circuit of NOR
– gate 929
– schematic 929
longitudinal acoustic (LA) 110
longitudinal surface plasmon (LSP) 324
long-range hexagonal order 341
Lorentz
– deflection 488, 489
– image 490
– microscopy 473, 488
Lorenz–Mie
– diffraction 1064
– diffraction theory 1080
Lotus effect 361
low diamondoid 268
low dimensional organic nanomaterials 917
low supersaturation 654
lowest occupied molecular orbital (LUMO) 626
low-supersaturation growth 645
lubricant 629
lubrication 390
luminogen 914, 915
lung exposure data 1050
lung fibrosis 162
Lycurgus cup 2
lymphocytes (LYM) 162

M

M1
– phenotype 992
M2
– phenotype 992
Mackay icosahedron 427
Mackay transformation 17
macromolecule
– nonstoichiometric 572
macropolarization 564
macropore 887
– formation 887

macroporous alumina 1108
macroporous silicon 888
macroscale sample
– tensile testing 997
macroscopic 148
– crystal 9
magic
– angle sample spinning (MAS) 668
– angle spinning (MAS) 828
– cluster 445
– system 447
magnetic
– anisotropy 808
– anisotropy energy (MAE) 448
– biosensor 504
– bit length 503
– characteristic length 478
– dipole–dipole interaction 668, 676
– drug delivery 474
– field sensor 503
– flux density 668
– force microscope 490
– force microscopy (MFM) 473, 474, 490
– hysteresis loop 18
– length scale 473
– moment 475, 479
– multilayer 498
– nanocomposite 497
– nanoparticle 459
– nanostructure 483
– refrigeration 474
– relaxation switch (MRSw) 474
– relaxation switching (MRSw) 504
– resonance imaging (MRI) 457, 474, 504
– separation 458
– soft alloy 486
– switch 503
– tweezer 505
magnetic material
– hard 474
– soft 474
magnetic nanomaterial
– functionalized 504
magnetic nanostructure 486
– application 473, 503
– biocompatibility 488
– characterization techniques 473
– hard 492
magnetic resonance (MR) imaging 504
– contrast agent 504, 747
magnetically separated bacteria 458
magnetism 475
– atomic-scale 476
magnetization
– buckling 494
– coherent rotation 481
– curling 481, 494
– curve 17
magnetization process
– of nanostructured materials 480
magnetization reversal 482
– mechanism 473
magnetocrystalline anisotropy 448, 480
– constant 481
magnetofection 505
magneto-optical Kerr effect (MOKE) 474
magneto-optical spectroscopy 115
magnetoresistance 160
magnetorestivity 474
magnetostatic length 478
magnetotactic bacteria 504
Mama-tube 612
mammalian toxicity 1120
manipulation
– AFM 10
manufactured nanomaterial (MNM) 1039
– actual risk 1122
– adequate characterization 1132
– environmental properties 1117
marine deposit 827
marker gene (mRNA) 959
MAS Hamiltonian 674
MAS-NMR line shape 674
material 517
– Brodie 699
– carbonaceous 1105
– performance 1039
– property 1079
– removal rate (MRR) 285
– to control the immune response 992
maximum contamination limit (MCL) 353
mazzite omega 843
mean curvature 85
mechanical
– alloying (MA) 450
– deagglomeration 280
– milling 487
– properties 237, 802
– property mismatch 993
– reinforcing 750
– vibration damping 731
mechanism
– self-assembly 335
– vapor–solid (VS) 617
mechanochemical functionalization 157
mechanochemical synthesis 487
mechanochemistry 150, 151, 159
mechano-sensor 944
medium
– pore size 822
medium-range order 666
melt spinning 486, 703
melt-assisted template wetting 907
melt-quenching technique 682
membrane
– catalyst 794
– channel 1109
– closed-channel 1111
– distillation 1110
– electrode assembly (MEA) 809, 1014, 1018
– filter 1102
– ion-track-etched 859
– permeability 1064
– pore size 1101
– process 1099
– reactor 1111
– technique 839
mercaptopropyltrimethoxysilane (MPS) 337
mercaptosuccinic acid (MSA) 313
merlionite 843
Mermin–Wagner theorem 50
mesenchymal stem cells (MSC) 991
mesh-like Au layer 863
mesoflower (MF) 362
mesolite 843
mesophase pitch-based carbon fiber (MPCF) 235
mesophase pitch-based fiber 236
mesopore 843
mesoporous
– material 158, 168
– molecular sieve 821
– platinum 789
mesoporous gold film
– optical properties 802
metal
– -assisted Si etching 887
– binary cluster 432
– bioaccumulation 1050
– catalyst 863
– chalcogenide 98
– component 409
– -graphite multilayer (MGM) 396

– –insulator transition 331
– into nanochannel 872
– ion center 677
– -ion intercalation 572
– nanoaggregate 421
– nanoalloy 435
– nanoparticle (NP) 2, 69, 205, 256, 389, 396, 436, 457, 666, 680, 754, 1032, 1071, 1075, 1076
– nanoparticle (NP) aqueous environment 1076
– nanoparticle (NP) biological cell environment 1075
– nanoparticle (NP) catalytic properties 437
– nanoparticle (NP) chemical activity 443
– nanoparticle (NP) optical properties 443
– nanoporous 779
– nanostrutured 954
– nanotube 393
– nanowire 390
– NT growth 871
– oxide/RGO composite 589
– oxyhydroxide 653
– particle decoration 206
– –polymer heterostructure 869
– quantum cluster 364
– –semiconductor electronic transport 871
– skin 809
– –substrate interaction 430
– SWNT 697
metal cluster
– subnanometer 440
metal nanocluster 410, 416, 435, 437
– magnetooptical properties 448
metal oxide nanoparticle 517, 518
– ecotoxicological data 1121
– solid-state reaction mechanism 523
metalaluminophosphate (MAPO) 823
metallic
– Ag 862
– aluminum 392
– bulk glass (BMG) 498
– carbon nanotube 126
– Cu 862
– glas 781
– -like character 626
– nanoparticle 149, 157, 424
– nanoporous material (MNPM) 791
– nanotube 20, 108, 122, 697
– nanowire 157
– NW Y-branched 864
– SWCNT 119, 193
– Zn 862
metallocenes 151
metallofullerene 192
metalloid (M) 499
metallosilicate 823
metal–metal
– interaction energy 430
– junction 871
– oxide core–shell 344
metal-on-insulator 317
metal-on-metal 317
metal-on-semiconductor 317
metal-oxide 653, 1046
– nanofoam 1046
– NP 1045
– scratch-resistant NP 1045
– surface chemistry 532
– wear-resistant NP 1045
methanation
– catalyst 441
methanol electrooxidation 797
methanol fuel cell 69
methanol photoelectrocatalysis 796
method
– of electrospinning 249
method of production
– nanofiber biomaterial 980
method of synthesis 414
– dynamic 269
– static 269
methyl orange (MO) 796
MF-coated glass 362
micro fuel cell 1014
microbial fuel cell (MFC) 1014
microbubble 1063
– generation 1090
– radius 1087
micro-$CaCO_3$ 1043
microcrystal 912
microcrystalline diamond powder 270
microdiamond 275
microdiffraction
– experiment 791
– image 791
microelectromechanical system (MEMS) 474, 1046
microemulsion 486
microextraction material 589
microfibre
– multicolor emission 915
microfiltration (MF) 155, 1099
microfluidic-based sensor 791
microgel 339
micromagnetic modeling 473
micromanipulation technique 998
micromechanical cleavage 40
microorganism 355
micropipe 643
micropore 254
microporous aluminoborate 825
microporous material
– properties 836
microscale surface roughness 962
microscope 89
microsized carbon fiber 1043
microsized fiber 246
microstructure 238
microtubule 1073
microwave 149
– -assisted heating 528
– plasma torch system 277
microwire 908, 927
– array 926
Mie parameter 1065
Mie theory 443, 1080
migration of molecules 839
milled particle 729
mineral 729
minimal surface 86
minimum off-state current 917
mitochondrium 1072
mixed nanoalloy 434
mixed polymer phase 250
MMFX2 steel 1044
MNM (manufactured nanomaterial) 1045
– -containing waste, disposal of 1053
– -containing waste, recycling of 1053
– in glass matrices 1044
– toxicological impact 1047
– vulnerability 1053
mobile ion distribution 670
mobility 840
modes of buckling 14
modified carbon nanotube
– atomic structure 203
– characterization 208
– electrode 205
– electronic device 215
– field emission 215
– metal nanoparticle 205
– properties 203
– sensor 215
– x-ray photoelectron spectroscopy (XPS) 212

modified cellulose 352
modified nanotube 203
modified sensitization–preactivation process 872
modified Staudenmaier method 46
modulus
– Young's 700
moisture-induced
– corrosion 1046
molar flux 838
molding 561
molecular
– aggregation 912
– beam epitaxy (MBE) 473, 484
– diffusion 838
– fluorescence enhancement 805
– magnet 483
– mediated assembly (MBE) 362
– model 94, 194
– modeling 841
– nanomaterial 917
molecular beam epitaxy (MBE) 474
molecular dynamics (MD) 394, 454, 626, 627
– simulation 132
molecular sieve 834
– diffusion properties 838
– pore size dimension 821
– zeolite 823
molten carbonate fuel cell (MCFC) 1014
molybdenum
– nanoparticle 395
– sulfide 97, 395
– sulfide fullerene 626
monoclonal antibody 92
monodispersity 310
monolayer (ML) 71
– flake 42
– -protected clusters (MPC) 313
monolayer graphene 58
– deformation 701
– thermal conductivity 56
Monte Carlo simulation 781, 841
montmorillonite 827
mordenite 822, 843, 848
– /ferrierite family 822
more noble (MN) 780
morphological change 329
morphological transformation 240
morphology of nanomaterial 10, 639
morphology of nanostructure 618
morphotropic phase boundary (MPB) 554
MoS_2 nanooctahedron 620
Mössbauer spectroscopy 473, 830
Mott detector 489
MPTMS-functionalized 339
MRAM (magnetic random-access memory) 503
multication powder 522
multicomponent
– glass 683
– nanosystem 415
– oxide system 522
– system properties 425
multidimensional spectroscopy 668
multi-gas sensor response 165
multilayer 889
– graphene 47
– structure 893
multiloop 242
multinuclear NMR spectroscopy 842
multiphoton ionization 1092
multiphoton microscopy 979, 994
multiple
– -branched nanostructure 864
– -branched pore 861
– branching 868
– ECM protein 984
– generations of branched pore 861
– hollow core 251
multiply twinning structure 266
multipulse 1071
– heating 1073
– heating mode 1071
– mode 1073
– mode of heating 1067
multishell
– nanoalloy 434
– nanotube 151
– onion-like nanoalloy 434
– pattern 412, 435
multispin system 669
multistacked CNT membrane 1111
multistacked membrane 1110
multi-walled carbon nanotube (MWCNT) 10, 111, 147, 148, 168, 190, 254, 286, 338, 531, 748, 960, 962, 993, 1023
– adsorption 164
– analytical application 165
– anchor quantum dot 157
– array 1110
– biosensor applications 168
– buckypaper 164
– buckypaper gas permeability 165
– cantilever 159
– characterization method 153
– chemical functionalization 197
– chemical heterogeneity 153
– chemistry 153
– -coated cellulose fiber filter 165
– composites 167
– conductivity 160
– current issues 169
– density 157
– DNA complex 157
– doping 161
– electrode 1028
– electromagnetic property 159
– electronic applications 169
– end morphology 159
– filling 157
– film, thermal conductivity 160
– filtration 164
– fluorinated 212
– forest 154
– functionalization 155, 156, 160
– growth mechanism 151
– health effects 162
– heavy-metal ion adsorbent 166
– hydrophilic–hydrophobic balance 166
– improvement 155
– impurities 166
– in situ modification 153
– industrial production 152
– intravenous route 163
– irreversible noncovalent functionalization 158
– magnetic moment 160
– mechanical properties 159
– membranes 164
– modification study 153
– nanocomposite 157
– opening 154, 155
– optical characterization 161
– pharmaceutical application 168
– photoluminescence (PL) 161
– polarizability 159
– –polymer nanocomposite 167
– pore diameter 164
– product quality 153
– production capacity 152
– properties 157
– purification 154
– quality assessment 153
– Raman spectrum 160
– safe handling 163
– sensor 31
– solubility 158
– spectroscopic properties 160
– surface functionalization 161
– surface impurities 153
– synthesis 148

– tensile strength 159
– terahertz spectroscopy 161
– vapor-phase growth method 151
– world production capacity 153
– x-ray diffraction 158
multi-walled nanotube 1104
myotube assembly 1002

N

N-(4-aminophenyl)-*N*′-(4′-(3-triethoxysilyl-propyl-ureido)phenyl-1,4-quinonenediimine) (ATQD) 1005
N,*N*′-di(dodecyl)-perylene-3,4,9,10-tetracarboxylic diimide (DD-PTCDI) 910
N,*N*′-di(nonyldecyl)-perylene-3,4,9,10-tetracarboxylic diimide (ND-PTCDI) 910
N,*N*-dimethylamide (DMA) 48
N,*N*-dimethylformamide (DMF) 751
Nafion 591
NAND gate
– dynamic switching characteristics 929
nanoalloy 409, 411
– colloidal, coated alloy cluster 437
– metal 428, 435
– particle synthesis 413
– phase diagram 437
– subcluster segregated 434
Nanoamando 280
nanobelt 307, 391, 605, 910
– In_2O_3 526
– structure 910
– Zn 397
nanobiotechnology 941
nanobomb 1091
nanobox 307, 329
nanobubble 1086
nanobud 611, 619
nanobullet 1092
nanocable
– Bi shell/Cu core 875
– fabrication process 875
– semimetal/metal coaxial 875
– shell thickness 877
nano-$CaCO_3$ 1043
nanocage 307, 329
– Ag 358
– gold 457
– immuno-Au 358
nanocapillarity 192
nanocapsule 26
nanocarbon 190
– cage 190
– chemistry 20
– fibrous 257
nanocatalysis 441
nanocatalyst 424
nanoceramic 666, 676, 957
– dielectric constant 563
– polarization switching 567
nanochain formation 12
nanochannel 861, 862
– branched 867
– -confined electrochemical deposition 867
– Y-branched 864
nanocircuit 928
– architecture 929
– wire 106
nanoclay 1044
nanocluster 422, 628, 667, 950, 1063, 1084
– Ag-Au alloyed 423
– aggregation mode 1083
– Au 445
– gas-phase metal 436
– hybrid 621
– metal 428
– morphology 445
– optical properties 442
– self-assembled 1063
– temperature distribution inside 1084
– temperature distribution outside 1084
nanocomb 307
nanocomposite 629, 676, 685, 699, 708, 923, 957, 962, 1024, 1045
– biocompatibility 961
– bulk metallic glass 498
– CNT/CNF polymer 960
– design 950
– electrode 1015
– exchange-coupled 496
– fiber 942
– filler material 1048
– formation 1111
– metal 1045
– metal oxide 1045
– MWCNT-terpolymer 961
– of Ti/PLGA 959
– phosphate 959
– polymer/calcium phosphate 959
– SWCNT polymer 960
nanocone 917
– array 916, 917
nanocontainer 22
nanocorn 307
nanocrystal 517, 666, 678, 756, 909
– 2-D superlattice 332
– 3-D superlattice 332
– building block 342
– Cu 423
– gold 323
– In_2O_3 526
– network 363
– octahedral gold 316
nanocrystalline (NC) 292
– alloy 455, 499
– –amorphous composite 499
– ceramic 538, 555
– ceramic powder 519
– ceria 536
– cobalt ferrite 535
– compound 534
– diamond 277
– diamond film 291
– ferromagnet 499
– grain size 455
– HAP 958
– indium oxide 526
– metal 312, 923
– powder 538, 555
– soft magnetic alloy 499, 500
nanocube 308
– Ag 342, 457
– Cu 398
– gold 320
– In_2O_3 525
nanocup layer 9
nanodevice 390, 804
nanodiamond 2, 31, 92, 94, 98
– aggregate deagglomeration 280
– aminated 282
– application in composites 286
– biomedical application 288
– classes 270
– cluster structural model 266
– colloidal stability 279
– covalent bonding 282
– CVD 276
– cytotoxicity 288
– deagglomeration 279
– dynamic synthesis 275
– ferromagnetic behavior 17
– fluorescence properties 284
– fluorescent 285
– formation 277
– healthcare product 289
– modeling 265
– noncovalent binding 283
– ozone-modified (NDO) 279
– photoluminescent 284

– physicochemical properties 288
– postsynthesis purification 279
– processing and modification 278
– produced by shock conversion 270
– produced from carbon precursor 271
– produced from explosive mixture 271
– produced from high-energy explosives 271
– stability 272
– structure of different types 273
– surface functionalization 280
– synthesis 275, 276
– toxicity 288
– tumor targeting 98
– Young's modulus 287
nanodiamond particle 267
– application 285
– laser-assisted synthesis 277
– polishing 285
– synthesis 264
nanodomain 567
nanodot
– hcp morphology 432
nanodumbbell 308
nanoecotoxicity 1121
nanoEHS (environment, health, safety) 1129
nanoelectromechanical system (NEMS) 1046
nanoelectronics 392, 640, 756, 917
nanoenabled construction material 1049
nanoenabled product
– lifetime 1053
nanofabric
– 2-D 915
nanofabrication 907, 941
– technology 950, 951
nanofeature (NF) 451
nanofiber 207, 950, 951, 977
– adhesive properties 996
– air-stabilized 245
– aligned 987
– alignment 995
– biological properties 990
– conductive polymer 1005
– core–sheath 1005
– core–shell 993
– electrical conductivity 249
– electrospun 244, 245, 247, 249
– graphitic 239
– heat treatment 249
– hollow core 239
– interconnected 252
– mechanical properties 988
– organic 249
– polymer 990
– properties 981
– RADA16 996
– schematic model 239
– self-assembly 985
– single 996
– single PEO 997
– spun 982
– supramolecular 958
– surface 240
– uncoated 239
– undoped 242
nanofiber biomaterial 977, 979, 990, 992, 995, 999
– chemical and biochemical properties 989
– chemical composition 994
– common properties 986
– electrical properties 988
– fabrication method 982
– fabrication-dependent properties 987
– for skeletal muscle tissue 1002
– formed by phase separation 988
– mechanical characterization 996
– mechanical properties 988
– mesh 1003
– molecular fingerprint 994
– physical properties 986
– scaffold 988, 993
– technique 982
– Young's modulus 988
nanofiber tip 239
nanofiber web composite implant 257
nanofiber web electrode 254
nanofibrous conduit 1004
nanofibrous scaffold 990
nanofilm 950
nanofiltration (NF) 1099
– technique 1101
nanofoam 1046
nanoframe
– cubic 329
nanograin
– ceramics 553
– in aluminum 22
– microstructure 561
– nature 555
nanoheterostructure 862, 869
– complex-shape 878
– complex-shaped 878
– core 869
– core–shell metal/metal 876
– metal–semimetal 869
nanohydroxyapatite (NHAP) 535, 957
nanoindentation 51, 801, 802
– AFM 996
nanolithography 474
– dip-pen 9
nanomagnetic behavior 478
nanomagnetism 479
nanomaterial 363, 366, 524, 538, 905, 1120
– 1-D 643
– 2-D 656
– absorption spectrum 17
– active element 28
– anisotropic 639, 649
– base lubricant 287
– basic mechanical properties 12
– biomimetic feature 950
– bond system 18
– carbon-based 696, 964
– carbon-based, ecotoxicological data 1121
– ceramic 20
– chemical properties 24
– chemistry 20
– classification 11
– definition 2
– electrical properties 14
– formation building blocks 6
– growth 642
– growth kinetics 639
– history 2
– hybrid 932
– hybrid structure 932
– in gastrointestinal tract 1123
– interaction 14
– magnetic features 18
– magnetic properties 17
– manufacturing method 1128
– mechanical properties 12, 923
– metallic 20
– morphology 10, 639
– nanotopography 951
– optical properties 17
– physical properties 10
– polymer 931
– pre-modern era 2
– preparation processes 20
– production 9
– production quantity 1119
– properties 1, 10
– risk 1119
– safety 1117, 1130
– safety testing 1127

– surface chemistry 951
– target organ 1124
– testing 1122
– therapeutic potential 949
– thermal properties 18
– two-dimensional 571
– wettability 951
nanomaterial characterization 1117
– minimum set of parameters 1125
nanomechanics 923
nanomedicine 31, 1063
nanometer-scale precipitate 451
nanometric crystal 670
nanooctahedra 620
– theoretical minimum size 621
nanooptics 1064
nanooxide 517
nanoparticle (NP) 10, 257, 304, 392, 492, 518, 522, 525, 555, 605, 607, 783, 950, 1042, 1064, 1066, 1076, 1086, 1118, 1123
– /nanocluster 1084
– AB_2 structure (0001) 757
– absorption efficiency 1093
– Ag 583
– Ag-Au 434, 441
– antimicrobial activity 1121
– Au-Pd 434
– boiling temperature 1086
– cellular response 1124
– chemical compatibility 310
– closed 621
– closely located 1082
– clustering 682
– composite 415
– concentration 1088
– coprecipitation synthesis 522
– CoPt 448
– cosmetic product 1123
– Cu 423
– deposit 753
– deposition inhalation 1122
– diamond 275
– dispersibility 309
– DND (detonation nanodiamond) biosensor and biochip 290
– few-domain 17
– formation 682, 1126
– $Gd_2O_3:Tb^{3+}$ 531
– $Gd_2O_3:Tb^{3+}:Dy^{3+}$ 531
– gold (GN) 9, 92, 157, 347, 444, 756, 1066, 1078, 1080, 1086, 1089, 1091, 1123
– gold (GN), melting point 22
– heavy-metal 289
– hollow cage 432
– HR-TEM 423
– hybrid 752
– immobilized 872
– in liquid dispersion 730
– indium oxide 525
– ink 752
– manufactured 1117
– metal 2, 69, 205, 256, 389, 396, 436, 457, 666, 680, 754, 1032, 1071, 1075, 1076
– metal, aqueous environment 1076
– metal, biological cell environment 1075
– metal, catalytic properties 437
– metal, chemical activity 443
– metal, optical properties 443
– morphology 425
– Ni 395
– on MWCNTs 166
– optical property 1066
– optics 1089
– ordering and coarsening 730
– oxidation 422
– palladium 257, 313
– Pd-Cu 798
– PdPt, chemical ordering 435
– physicochemical characterization 1126
– properties of bonds 12
– safety database 1132
– sensor 31
– shape 730, 1066
– shape control 493
– silver 49, 347, 353, 681
– single 434, 1077, 1079, 1095
– SiO_2 755
– size 11, 913, 1089
– size-dependent optical properties 1130
– spherical 1080
– spontaneous assembly 756
– STM observation 419
– surface 1127
– surface atom 1127
– surface charge 1129
– surface chemistry 745
– surface energy 1129
– synthesis 735
– thermal stability 309
– TiO_2 (titanium oxide) 393, 796, 1050
– titanium 393
– toxic effect 1127
– trace concentration 1119
– ultrasound synthesis 523
– uptake 1048
– with metallic core 309
– YAM 453
nanoparticle dispersion
– inkjet printing 757
– on surfaces 752
– stabilization 730
nanoparticle temperature 1067
– time dynamics 1067
nanoparticle toxicity 1127
nanoparticulate powder
– sinterability 524
nanopatterning 290, 484
nanopenetration 163
Nanoperm 474, 500
nanophase 453, 954
– material bulk 453
– mechanical response 454
– polymer 956
– scaffold 951
– titania 955
– zinc 958
nanophotothermolysis 1064, 1079, 1084
– of cancer 1092
nanopipe 651
– hollow 652
nanoplate 640, 644, 1118
– gold 657
– hillock 645
– morphology 656
– silver 360
– solution growth 655
– thickness variation 657
nanoplatelet 28
– graphite (GNP) 698, 716
– sensor 31
nanopore
– channel 790
– size 805
nanoporous 10
– alloy 786
– $Au_{0.8}Pt_{0.2}$ 807
– Au/Pt alloy 786
– Au-Pt 798
– Au-Pt alloy 807
– carbon 278
– copper 783, 789, 806
– Cu ribbon 794
– material 883
– membrane 1103
– membrane metal 797
– nanotube (NPNT) 792
– nanowire 787
– nickel 808
– palladium 793

– platinum 784, 805
– Pt-Ru 798
– silicon 885
– silver (NPS) 793
– structure 523
nanoporous gold (NPG) 790, 791, 796, 805
– /MnO_2-based supercapacitor 809
– –alumina film 804
– chemical inactivity 804
– composite (NPGC) 793
– film 802, 803
– film electrode 797
– foam 795
– membrane material 780
– nanowire 809
– pillar 791
nanoporous metal 10, 779, 784, 786
– catalytic properties 794
– electrocatalytic properties 796
– mechanical properties 799
– properties 808
nanopowder 526, 534
– as catalyst 537
nanoprecipitates 652
nanoprism 391
– preparation method 18
nanorattle 307
nanoribbon 242
– assembly 916
– crystal 909
– crystalline 915
– graphitic 242
– photovoltaic solar cell 923
– p–n junction 922
– template 922
nanorice 307
nanorod 322, 327, 339, 444, 523, 605, 639, 644, 872, 911, 950, 1064, 1070, 1081, 1094, 1118
– anisotropic 325
– gold (GNR) 337, 1070
– gold (GNR) assembly 340
– gold (GNR) film 340
– heterometallic 330
– In_2O_3 525
– Pd 329
– temperature profile 1070
nanoscaffold 957
– fabrication technique 951
nanoscale 4
– biological research 457
– building block 931
– carbon phase diagram 265
– ceramic material 1044
– characterization 666
– characterization of biomaterials 979
– characterization of particles 1125
– crossbar latch 928
– heterogeneities 684
– heterogeneous system 681
– interaction 478
– material formation process 912
– morphology 860
– oxidation 8
– oxide 1131
– particle photocatalytic activity 1130
– precipitate 450
– sensing 284
nanoscale materials 278
– human toxicity exposure route 1122
– interior crystal structure 1127
– manmade 1118
– physicochemical properties 1120
– skin penetration 1123
– suspension behavior 1120
– toxic behavior 1121
nanoscale TiO_2 and ZnO
– health effects 1131
– photochemical behavior 1131
nanoscaled photonic device
– construction 928
nanoseashell 620
nanosensor
– synthetic 925
nanoshell 1063, 1081, 1094
nanosized
– alloy catalyst 26
– fiber 246
– material 1042
– metal 389
– oxide particle 534
– Pd cluster 431
– SiO_2 1046, 1052
– SiO_2 toxicity 1052
– TiO_2-coated glass 1045
– tungsten oxide (WO_3) 1044
nanosphere 327, 910, 911, 1070
– $Gd_2O_3:Tb^{3+}/Eu^{3+}$ 531
– lithography 321
nanostructure 105, 307, 414, 605
– 1-D 315, 321, 862, 909
– anisotropic 340
– anisotropic behavior 623
– branched 864
– branched, multiple generations 867
– coaxial 1031
– construction 860
– copper 397
– hard 474
– hard magnetic 494
– hollow 328
– hyperbranched 643
– magnetic 474, 483
– magnetic properties 448
– soft magnetic 498
– step-shaped 868
– template synthesis 523
– Ti 394
– zero- and one-dimensional 605
nanostructured
– alloy 409
– alloy, concepts and principles 411
– carbon material 746
– composite 942, 958
– composite material 950
– ferritic alloy (NFA) 450, 451, 453
– glass 666, 683
– material 11, 518, 607
– metal 390
– polymer 957
– powder 287
– semiconductor glass optical characteristics 683
– SnO_2 film 747
– system 409, 410
– thin film 474
nanostructures of metal 859
nanosystem
– 1-D 324
– anisotropic 328
– multicomponent 440
– plasmonic resonance 442
nanotechnology 942
– definition 1118
nano-TiO_2
– -added concrete 1043
– particle 1043, 1048
– toxicity 1050
nanotoxicology 1122
nanotree 643
nanotube
– open 155
nanotube (NT) 2, 84, 307, 493, 605, 639, 644, 746, 860, 863, 950, 1118
– armchair 98, 107
– bent 194, 195
– centrifugal separation 155
– characterization 119
– chemistry 196
– coaxial 1030, 1032
– conductance mechanism 14
– corrugated 96
– critical length 708

– dislocation-driven formation 643
– doped, electrical resistivity 193
– doping 124
– -electrode junction 123
– fabrication 863
– filter 1107
– forest 167
– formation 95
– functionalization 198, 200
– Gd_2O_3:Eu^{3+} 531
– helical carbon 150
– helical rosette (HRN) 959
– helical shape 150
– helix-shaped 194
– high-quality 149
– hollow 328, 329, 643, 792
– HR-TEM 423
– In_2O_3 526
– length distribution 153
– metal 393
– –metal composite 168
– metallic 108
– morphology 615
– nucleation site 151
– optical properties 107
– oxidation 198
– perylene 907
– reaction product 20
– reactivity 198
– roll-up vector 606
– semiconducting 105, 108, 125
– semiconducting zigzag 108
– semiconductor 20
– soft purification 154
– spiral 150
– surface 196
– transistor 126
– wall defect 161
– WS_2, growth mechanism 615
– Young's modulus 132
– zigzag 107, 697
nanotube composite
– dispersion 709
– orientation 710
– stress 709
nanotubular mesoporous platinum (NMP) 789
nanotubular Ti
– anodized 954
nanotypography 950
nanourchin 307
nanowhisker 615
nanowire (NW) 11, 31, 307, 444, 483, 487, 492, 493, 523, 605, 612, 639, 644, 730, 860, 862, 908, 927, 950, 1029
– 1-D 915
– Al 392
– binary 913
– branching 643
– coaxial 1030
– crystal elasticity 925
– crystal maximum local strain 925
– crystal polymer 920
– Cu 397, 398
– CuPc crystal 924
– DAAQ 925
– DAAQ array 926
– device 809
– doped 913
– formation 395
– GaAs 10
– Gd_2O_3:Eu^{3+} 531
– growth 391
– heterojunction 922
– HR-TEM 423
– magnetic 474
– metal 390
– photovoltaic properties 920
– p–n junction 921
– polycrystalline 397
– semiconductor 906
– single polymer 921
– single-crystal Pb 390
– single-crystalline 927
– superconducting behavior 390
– Ti 393
– transport properties 920
– voided 643
– Zn 397
naphthalene 88
natrolite 843
natural bone 946
– limitation 944
natural graphite 698
natural highly-oriented pyrolytic graphite 396
natural zeolite 826, 848
– genetic type 826
Nb-doped INT-MoS_2 627
Nb-doped nc-Cu 456
nC_{60} toxicity 1052
ND cluster 265
ND particle
– dynamic 269
– EPI ready 285
– static 269
Nd:YAG laser 88
ND–epoxy composite 287
ND–gadolinium complex 289
$NdGdZr_2O_7$
– crystallite size 539
N-doped SWCNT 193
near-band-edge (NBE) 526
near-edge x-ray absorption fine structure (NEXAFS) 587
near-infrared (NIR) 324
– luminescence 684
negative catalyst 536
negative curvature 95, 195
nerve growth factor (NGF) 1005
nested
– fullerene 93, 94
neural stem cell (NSC) 1004
neural tissue engineering 1004
– nerve regeneration 1004
neurite extension of neurons 1005
neuroprotection 527
neuroprotective agent 92
neutron scattering 839
neutrophils (NEUT) 162
Ni
– nanoparticle 49, 395
Ni surface 361
Ni/MgO nanodot 432
$Ni(OH)_2$ nanoplates 657
NiMnCo catalyst 276
NIR-IR absorption
– nanomaterial 362
nitridation 892
nitrogen vacancy (NV) 276, 284
nitrogen-doped CNT 211, 213–215
nitrogen-doped MWCNT 210
nitrogen-doped SWCNT
– conductivity 203
Ni-W system 455
NM-concrete debris
– waste disposal 1048
NM-containing material 1052
– manufacturing 1052
N-methylpyridinium (Nmpd) 911
N-methylpyrrole (Nmpr) 911
N-methyl-pyrrolidone (NMP) 734
N-methylpyrrolidone (NMP) 751
NMR (nuclear magnetic resonance)
– related component 1048
– relaxation 839
– spectroscopy 667, 828
– tracer desorption 840
noble metal (NM) 499
– catalytic activity 443
– nanoparticle 303, 366
– nanoparticle optical properties 322
– nanosystem 308, 363
nonclassical
– fullerene 86
nonclassical isomer 87

noncovalent
– adsorption 746
– functionalization agent 156
– interaction 908
noncrystalline matrix 18
nondephased spin echo 674
nondiamond carbon 279
nonelectrically activated window 1045
nongraphitizable carbon 248
noninteracting
– graphene 55
nonlinear susceptibility 424
nonmetallic photothermal absorber 347
nonoxide
– glass 669
nonradiative decay 678
nonzeolitic material 827
normal cytomorphology 962
NPG (nanoporous gold) 790, 794, 800, 806
– catalyst 795
– nanowire 788
np-Pt foam morphology 785
NR (nanorod)-loaded microgel 339
NT (nanotube)
– production catalyst support 149
– structure 649
nuclear fuel element 848
nuclear isotope 667
nuclear magnetic resonance (NMR) 160, 665, 666, 828
nuclear spin quantum number 667
nucleated particle 522
nucleation 9, 522
– barrier 641
– controlled magnetization 482
– field 496
nucleus 1072, 1075
– cancerous 1074
number of particle 1088
NV centre
– types 284
NW (nanowire)
– Co 862
– Fe 862
– heterojunction array 871
– heterostructure 659
– Ni 862
Nyquist plot 254

O

O_2 reduction 205
OC (graphite oxide) 752
octadecyltrimethoxysilane (ODS) 337
– steel 451
octahedral gold nanocrystal 316
octahedron 425
Office of Basic Energy Sciences 4
offretite 823, 843
olefin isomerization 846
oligodynamic effect 306
oligomerization 846
oligonaphthylene 88
one-dimensional (1-D) 40, 307, 859, 862, 910, 1029
– nanostructure 859
– photonic crystal (1-DPC) 893
– pore system 825
one-temperature model (OTM) 1067
onion-like carbon (OLC) 286
opal 827
open MWCNT 158
open nanotube 155
open pore structure 824
open-circuit potential (OCP) 885
open-core dislocation
– model 643
open-ended CNT membrane 1105
O-phenylenediamine (OPD) 806
ophthalmic tissue engineering 1002
optical
– absorption 193
– characterization 993
– coherence tomography (OCT) 347
– contrast agent 357
– cutoff filter 684
– plasmon resonance 1095
– property 1066
– quality 676
– sensor 896
– sensor materials 925
– transition 119
– transition energy 116
– tweezer 731, 999
optical properties
– In_2O_3 nanoparticle 525
– nanometer-sized In_2O_3 524
optically driven laser 928
optically transparent electrode (OTE) 28
optimum grain size 12
optoelectronic device 524, 905
– p–n junction 921
orbital moment quenching 474
ordered
– alloy 434
ordered microwire 927
organelle 1073, 1074
– property 1073, 1074
organic
– building block 912
– functional compound 928
– light-emitting diode (OLED) 524
– nanofiber 249
– nanoribbon 918
– nanowire array 925
– optoelectronic device 926
– photovoltaic cell 363
– pollutant 1130
– semiconductor 908, 917
– solar/photovoltaic cell (PV) 931
– solvent nanofiltration (OSN) 1101
organic field-effect transistors (OFET)
– electrical characterization 918
organic light-emitting diode (OLED) 913
organic micro- and nanocrystals
– fabrication 918
organic nanomaterial 905, 912, 925, 930
– 1-D 913
– absorption and emission 912
– field-emission property 916
– growth 906
– luminescence efficiency 928
– optoelectronic properties 916
– photodetector/photoswitch 925
– preparation/synthesis 905
– surface functionalization 931
– transport properties 917
– unique properties 910
organic single crystal 924
– logic circuit 929
– transistor 929
organism group
– food-chain level 1121
organometallic 314
– catalyst 845
– complex 442
organophosphorus hydrolase (OPH) 350
orientation distribution function (ODF) 713
orientation efficiency factor 704
orientational quantization 667
orientational quantum number 667
ORR 798, 799
orthopedic 956, 960
– biomaterial 945
– use of nanocomposites 941

osseointegration 946
osteoarthritis 942, 944
osteoblast 942, 944
– adhesion 954
– function 956
– proliferation 956
osteocinductive 958
osteocyte 942, 944
osteogenic scaffold 961
osteolysis 945
osteon 943, 944
osteonectin 944
osteopontin 944
osteoporosis 942
osteosarcoma 963
Ostwald ripening 522, 681, 732
outer diameter distribution 153
out-of-plane anisotropy 480
out-of-plane demagnetization factor 480
outside temperature distribution 1079
outside-in mechanism 613
overlapping thermal field 1087
over-oxidation 575
oxidation
– behavior 238
– catalyst 439
– graphitic oxide 573
– of CO 537
– of GNR 326
– process 198, 573
oxidative
– damage 1121
– digestion 154
– stabilization 245
oxide
– ceramics 538
– heavy metal oxide glass (HMOG) 681
– ion migration 539
– precursor 610
– quantum dot 683
– sheet 47
oxide nanomaterial 538
– catalytic properties 536
– optical properties 524
– sorbent properties 532
oxidized carbon
– chemical functionality 578
oxidized porous silicon 897
oxidized PS (OPS) 897
oxyfluoride
– glass 666, 670
oxygen ionic conduction 540
oxygen reduction catalyst 1014
oxygen reduction reaction (ORR) 798, 1020
oxygen vacancy 526
oxygenated functional group 575
oxygen-containing functional group 156
ozone-modified
– nanodiamond (NDO) 279

P

P3BT nanowire network 921
P3BT/fullerene nanocomposite solar cell 921
PA 6/12 nanofiber scaffold 1003
palladium
– nanoparticle 257, 313
PAN carbon fiber 252
PAN-derived nanofiber 248
PANI nanofiber 987
paramagnetic nanomaterial 731
paramagnetism 668
paraoxon 350
parchment model 1104
parent glass phase 676
Pareto plot 457
partial devitrification 486
partially oriented SWCNT 124
particle
– 2-D 730
– crystal 331
– Cu-Ru 441
– deposition 257
– fine metal 389
– morphology 439
– on solid 752
– size 10, 523
– size distribution 415
parting limit 780
passivation 782
passive optical device 891
paste electrode 919
pattern recognition receptor (PRR) 992
Pauling's minimum radius ratio 845
paulingite 843
Pb 391
Pb nanowire 391
$Pb(Zr,Ti)O_3$ (PZT) 554
p-block element
– Young's moduli of melting point 390
$PbMg_{1/3}Nb_{2/3}O_3$-$PbTiO_3$ (PMN-PT) 554
$PbTiO_3$ (PT) 554
$PbZn_{1/3}Nb_{2/3}O_3$-$PbTiO_3$ (PZN-PT) 554
PC (photonic crystal) structure
– optical properties 896
PCL 953
– blend nanofiber 1002
– -gelatin (PG) 1004, 1005
– mechanical properties 1002
– nanofiber 995
Pd nanorod 329
Pd nanoparticle
– catalytic activity 438
Pd/Au bimetallic nanorod 327
Pd-Cu
– nanoparticle 798
PDDP nanoparticle 913
PdPt
– nanoparticle, chemical ordering 435
peak-splitting behavior 555
peapod 192, 619
– nanostructure 619
Pechini sol–gel process 529
peel strength 629
PEGylated Au nanocage 360
pentacene
– nanotube 907
– nanotube array 907
pentagonal 93
pentagon–heptagon pair 194
pentasil material 822, 835
pentasil-based catalyst 822
peptide amphiphile (PA) 952, 958, 959
percolation threshold 69
periphery diffusion 782
permeation cell 1108
permissible occupational exposure limit (PEL) 162
perovskite 554
peroxidase 203
perpendicular recording 503
pervaporation (PV) 1099
perylene
– nanotube 907
pesticide 350
petroleum dynamics 1107
PGA 953
pH sensitive electrode 394
phase diagram
– size-dependent 437
phase separation 666, 979, 980, 982
– membrane 1102
– technique 952
phase transformation 837
pH-dependent self-assembly 336

phenotype
– M1 992
– M2 992
phenyl rotor 914
phenylalanine 520
phillipsite 843
phonon
– density of states (PDOS) 129, 421
– dispersion 109
– lifetime 242
– mode 109
– sideband 119
phosphate
– glass 670, 676
– nanocomposite 959
phosphate buffered saline (PBS) 1068
phospholipid polyethylene glycol (PL-PEG) 218
phosphoric acid fuel cell (PAFC) 1013
phosphorus-doped carbon nanotube 216
phosphotungstic acid ($H_3PW_{12}O_{40}$) 1045
– UV irradiation 1045
photo/electrochromics 524
photoabsorption 446
photoacoustic
– diagnosis 1064
– effect 1092
photoactive material 527
photoannealing 326
photocatalysis 157, 524
photocatalytic
– material 1131
– oxidation of water 527
– properties 796
photochemical functionalization 198
photochromic coating 1045
photoconversion 920
photodetector 92, 920
– high-performance 926
photodynamic therapy 1063
photoelectrochemical (PEC) 659
– energy conversion 28
photoelectron (PE) 666
– spectroscopy 161
photoluminescence (PL) 115, 117, 157, 525, 890, 928
– bandgap 18
– excitation (PLE) 117
– marker 284
– properties 531
– quantum clusters (QC) 363
– spectrum 528
photonic band gap 893
photonic crystal (PC) 893
– fiber (PCF) 685
– higher dimensional 895
photonic defect state 893
photonic device 525
– nanomaterial 362
photonics 756
photooxidation reaction 845
photosensitive smart window 1045
photoswitching characteristic 926
photothermal
– ablation 1079
– effect 1079
– sensitizer 1064
– therapy 358
– treatment 94
photovoltaic 92, 524
– cell 71
– component 589
– device 363, 887
– Si solar cell 676
– technology 920
phyllosilicate 827
physical vapor deposition (PVD) 416, 909
phytotoxicity 1122
piezoelectric
– ceramic 559, 564
– coefficient 564
– force microscopy (PFM) 567
– grain size effect 555
– hysteresis loop 567
– printing head 757
piezoresistive AFM 997
piezoresponse force microscopy 555
pigmented skin lesions 1077
pillared graphene structure 22
pinning 482
plane-wave (PW) 627
plasma 149
– -enhanced CVD (PECVD) 154
– -enhanced hot-filament CVD 1106
– rotating 148
– treatment 949
plasmon 447
– localized 803
– resonance 447
plasmonic 443, 666, 681, 684
– characteristic 327
– nanoparticle 1063, 1079, 1082
– therapy 1063
– waveguide 362
plasmon-resonance absorption 1064, 1080
plate and sheet 307
platelet-like morphology 243
plating 789
platinum–copper (Pt-Cu) alloy 798
platinum-plated nanoporous gold leaf (Pt-NPGL) 809
Platonic solid 426
PLLA (poly(L-lactic acid))
– /PLGA composite 946
– matrix 983
plot 70
p–n heterojunction nanoribbon 922
p–n junction 921
– nanoribbon 922
– nanowire 921
p-nitrophenol (p-NP) 806
point of zero charge (pzc) 1120
polarization curve 1018
polarization switching 564
polarization–electric field 564
polarization-reversal characteristic 555
poly(ε-caprolactone) (PCL) 979
poly(3-hexylthiophene) (P3HT) 921
poly(3-hydroxybutyrate) 961
poly(diallyldimethyl)ammonium chloride (PDDA) 338
poly(dimethyl siloxane) (PDMS) 286, 715, 983
poly(ether ether ketone) (PEEK) 703, 963
poly(ethylene oxide) (PEO) 711
poly(ethylene terephthalate) (PET) 926
poly(lactic-co-glycolic) acid (PLGA) 945
poly(L-lactic acid) (PLLA) 287
poly(methyl methacrylate) (PMMA) 703
poly(*N*-isopropylacrylamide) (PIPAAm) 983
poly(*p*-phenylene benzobisoxazole) (PBO) 703
poly(vinyl alcohol) (PVA) 702
poly(vinyl pyrrolidone) (PVP) 390
polyacrylamide gel electrophoresis (PAGE) 313, 364
polyacrylic acid (PAA) 979
polyacrylonitrile (PAN) 153, 235, 244, 703

polyalkene 91
polyaminobenzene sulfonic acid (PABS) 749
polyanhydride 945
polyaniline (PANI) 204, 207, 875, 980, 1023
polycarbonate (PC) 703
– membrane 859
polycrystalline
– ceramic material 518
– diamond 273
– nanowire 397
polycyclic aromatic hydrocarbon (PAH) 24, 49, 576
polydisperse system 731
polyethylene (PE) 945
– glycol (PEG) 488, 749, 985
– imine (PEI) 202
polyethylene glycol (PEG) 202
polyglycolic acid (PGA) 945, 979
polyhedral
– Ag nanocrystal 360
– building block 342
– particle 266
– -shaped crystal 640
poly-icosahedra (pIh) 427
polylactic acid (PLA) 945
polylactic acid (PLLA) 979
polylactic/ceramic composite 946
polymer 92, 859
– biodegradable 945, 947, 949, 957, 961
– chain 195
– composite reinforcement 748
– conducting 875, 989
– conducting, NW Y-branched 864
– degradation properties 946
– electrically conductive 719
– electroactive 1001, 1004
– electroactive, surface resistance 989
– electrolyte 591
– epoxy 749
– fiber 701
– fuel cell 591
– graphene-reinforced 717
– matrix 707
– matrix material 695
– matrix reinforcement 717
– mechanical strength 945
– membrane filter 1107
– nanofiber 990
– nanowire crystal 920
– pom-pom 339
– QD 683
– reinforcement 702
– tethering 339
– thermal conductivity 719
– thermal expansion coefficient 720
– thermal stability 720
– thermoresponsive 505
polymer electrolyte membrane fuel cell (PEMFC) 808
polymer nanocomposite 286, 719
– flame-retardant properties 720
– functional properties 719
– gas barrier properties 719
polymer/RGO
– composite 589
polymer-based
– electronic device 921
– nanocomposite 716
polymer-blend solution 249
polymer-capped core–shell NP 346
polymer-ceramic composite
– acid-based 946
– carbohydrate-based 948
– protein-based 947
polymer-coated core–shell NP 346
polymer-dispersed liquid-crystal (PDLC) 71
polymer–graphene
– interface 720
polymeric
– composite 234
– electrospun nanofiber 250
– material 905, 1015
– scaffold 953
– thin film 909
polymerization 91
– catalyst 591
polymer-mediated self-assembly 487
polymer-nanotube composite 746
polymetallic nanoparticle 437
polymethylmethacrelate (PMMA) 58
polymethylmethacrylate (PMMA) 249, 945
polypropylene (PP) 703, 961
polypyrrole (PPY) 864, 989, 1004, 1015, 1023
polystyrene (PS) 328, 703
– sulfonate (PSS) 338
– sulfonate sodium salt (NaPSS) 202
polysulfonate (PSU) 962
polytetrafluoroethylene (PTFE) 945, 961
polyvinyl alcohol (PVA) 964
polyvinyl pyrrolidone (PVP) 528
polyvinyldifluoride (PVDF) 961
pore
– architecture 860
– array geometry 889
– cell diameter 861
– evolution 783
– growth direction 888
– shape 888
– site nucleation 889
– system 158
pore size 885, 889, 896
– diameter 801
– distribution 253, 792
– medium 822
porosity layer 885
porosity of carbon nanofiber 250
porous
– 3-D media 896
– alumina 523
– architecture 953
– carbon 84, 253
– carbon nanofiber 249, 254
– ceramic membrane 1105
– composite scaffold 949
– nanodiamond 290
– nanofiber 251
– nanofiber-based electrode 255
– polymer membrane 952
porous silicon (PS) 883, 893
– applications 892
– electrochemistry 884
– formation 885
– formation model 884
– light emission 890
porous structure 883
– coarsening 787
– fabrication 889
postsynthesis processing 278
postsynthetic purification 149
post-transition metal 390
potential energy surface (PES) 435
potentiostatic dealloying 785
Pourbaix diagram 783
powder
– alloying technique 453
– reaction 519
– x-ray diffraction 1127
power conversion efficiency (PCE) 92
power density 1067
power spectral density 28
PPY (polypyrrole) 922
– -Co-carbon 1020
– Y-branched 864
Prato reaction 283

precession frequency 667
precipitation 150
precursor concentration 640
preferential growth 327
preparation of MWNT
– fundamental principle 149
pretreated MWNT 1024
pretreatment of graphite 573
principal component analysis (PCA) 28
printing ink 749
pristine
– carbon nanotube 751
processing
– of magnetic nanostructures 483
product labeling 1130
product layer 519
production
– nanoframe 329
– nanowire 617
programmed self-assembly 333
Project on Emerging Nanotechnology (PEN) 1118
proliferation 942, 954
propagation of cracks 624
propellant chemistry 520
properties
– of nanomaterial 10
property 1073
proportionality constant 478
propoxyethyl-PTCDI nanobelt 910
propylene fumarate (PPF) 948
protection schemes 654
protein
– adsorption 949
– denaturing 1069
– green fluorescent (GFP) 993
– matrix 950
proteoglycan (PG) 978
proton conductor 591
proton exchange membrane fuel cell (PEMFC) 1013
PS (porous silicon)
– -based sensor 896
– biocompatibility 896
– electrical properties 891
– fabrication 896
– formation model 884
– luminescence properties 892
– microcavity 896
– nanostructure 890
PS (porous silicon) multilayer
– cross section 894
– microcavity 894
– reflectivity 894
pseudocapacitive system 1023
pseudo-ordered structure 578
Pt (platinum)
– /C catalyst 797
– -based material 1020
– bimetallic nanoparticles 799
– -decorated nanoporous gold (Pt-NPG) 789
– -doped GNR 340
– electrode 1020
– nanoparticle 206, 213, 394
– -NPG surface structure 797
– -Ru catalyst 797
p-type silicon 885
pulmonary
– toxicity 1128
pulse electrodeposition 872
pulsed laser ablation (PLA) 392, 393, 525, 614
pulsed-field-gradient (PFG) 839
pump-probe measurement 120
pure carbon MWCNT 203
pure metal nanowire 863
purification method 279
PVP-wrapped CNT 748
pyrene 343
pyrene carboxylic acid (PCA) 749
pyrolytic 88
– carbon 395
– deposition 237
– fullerene 88
– graphite surface 277
– method 151
pyrophyllite 562
pyrrole 849
– hydrogenation reaction 26

Q

QD-containing waveguide 685
quadrant electron detector 489
quadrupole interaction 668
quantum
– 1-D confinement 116
– chemical calculation 627
– cluster 307
– confinement 5, 682
– confinement model 890
– dot (QD) 10, 666, 993, 1045, 1050
– dot (QD) cellular automata 928
– dot (QD) composition 683
– dot (QD) device 66, 67
– dot (QD) graphene device 66
– dot (QD) maximum size 682
– dot (QD) toxicity trial 1050
– dot semiconducting 157
– Hall effect 56
– information 284
– size effect 528, 683
quasiparticle 52
quasiperiodic structure 790
quick EXAFS (QEXAFS) 419

R

R value parameter 248
RADA16
– nanofiber 996
radial breathing mode (RBM) 110, 118, 121, 161, 213, 701
radial compression 623
radially aligned
– carbon nanotube, remove nicotine and tar 164
radiation-induced damage 527
radical-scavenging antioxidant 527
radio-frequency identification (RFID) 918
radioimmunoassay (RIA) 518
radiolytic reduction 313
radiowave region 668
Raman
– active vibrational mode 118
– band 715
– characterization 241, 248
– D-band 161
– G-band 160
– scattering carbon D and G peaks 994
– signal 213
– spectroscopy 115, 118, 213, 578, 622, 695, 712, 720
– spectrum 147
Raman band shift
– rate 715
– stress-induced 721
random anisotropic effect 482
random linkage model 673
Raney catalyst 780
rapid gel combustion route 539
rare earth (RE) 526
rare-earth-doped
– conducting oxide 524
rate law 519
rate of bubble expansion 1090
Rayleigh
– imaging 58
– –Plesset equation 1087, 1088
– –Plesset equation bubble dynamics 1088
– spectroscopy 119
RBM oscillation 121

RCF (rabbit corneal fibroblast) 1003
reactive etching 9
reactive ion etching (RIE) 887, 1108
reactive milling (RM) 487
reactive oxygen species (ROS) 1043, 1124, 1130
reactive sputtering 484
reactivity with HCl 353
real glass 665
real-time detection of biomolecule 360
rebar
– corrosion 1043
receptor-mediated endocytosis 163
recombination process 120
recoupling pulse 671
recrystallization 906
Re-doped IF-MoS_2 627
REDOR
– data analysis 672
– experiment 672
– pulse sequence timing 672
redox
– enzyme 207
– -enzyme modified nanotube 207
– overpotential 655
– peak area 806
– reaction 519, 655
– replacement reaction (RRR) 797
reduced graphene oxide (RGO) 22, 67, 572
reduced temperature 476
reduction
– efficiency 28
– potential 485
– process 311
reference gel 832
reflection coefficient 887
refraction data 1080
refractive index 682
regenerative medicine 941, 958
reinforcement
– bar (rebar) 1043
– material 1044
reinforcing filler 707
remodeling 943
removal of catalyst 154
resistance
– ballistic 126
resistivity 891
resonance Raman spectroscopy 242
resonant Raman absorption 117
resonant Raman scattering (RRS) 118
resorcinarene 343
respiratory route 1122
retinal progenitor cells (RPC) 1004
reverse micelle route 527
reverse osmosis (RO) 1099
reversible binding 343
reversible capacity 252, 253
– thermally treated 253
RF/magnetron sputtering 495
RGD (Arg-Gly-Asp) 958
RGO (reduced graphene oxide) 591
– covalent functionalization 591
– edge structure 588
– quantum dot 588
– toxicity 583
rho zeolite 838
rhodamine 6G (R6G) 805
rhombohedral polytype 621
ribbon 651
– armchair 195
ribosomal 1074
– heating 1074
ribosome 1073
right ventricular myocardium 1000
ring lactol structure 576
ring stain 753
ring-shaped deposit 753
ring-stain formation 752
RIR process 914
risk-based analysis 1119
RKKY (Ruderman–Kittel–Kasuya–Yosida) 478, 503
– interaction 503
Rochelle salt 554
rod-like PMMA phase 250
rod-shaped
– gold 325
rod-shaped gold NP 322
rod-to-sphere conversion 326
rolling-up process 617
roll-to-roll dry transfer process 71
Roman glass 680
room temperature (RT) 17, 1024
ROS-derived toxicity 1050
rotary jet spinning (RJS) 980, 982
rotating bioreactor 952
rotational echo double resonance (REDOR) 671
roughness factor 800, 806
rubrene doping 913
Ruess model 581
Russian doll
– model 1104
– structure 148

S

Sabatier principle 438
SAED 784
– pattern 870
samaria-doped ceria 537
samaria-doped nanoceria 538
sandwich complex 340
saturated calomel electrode (SCE) 1018
saturated vapor pressure 1088
saturation magnetization 478, 499
scaffold 942, 945, 951, 965
– biomaterial 257
– ceramic nanomaterial 954
– material 945
– metallic nanoparticle 954
– polymeric nanomaterial 956
scaling law 801
scanning electron micrograph (SEM) 45
scanning electron microscope (SEM) 489, 861
scanning electron microscopy (SEM) 153, 291, 474, 488, 656, 781, 835, 907, 979, 995, 1017, 1105, 1126
scanning electron spectroscopy (SEM) 709
scanning force microscopy (SFM) 417
scanning photocurrent microscopy 69
scanning probe microscopy (SPM) 555, 567, 623, 711
scanning transmission electron microscopy (STEM) 783
scanning transmission microscopy (STM) 208, 220
scanning tunneling microscopy (STM) 8, 60, 95, 419, 578, 607, 789
scanning tunneling spectroscopy (STS) 60, 95
scattering 1065
– amplitude function 1064
schematic model 200
Scherrer equation 537
Scherzer defocus 620
Scholz–Boehm model 582
Schottky barrier 126
Schwarz 86
schwarzite 86
scintillator materials 530
scolecite 843
Scotch tape method 40
SCR model 886

screw dislocation 639, 642
– axial contrast 655
– degree of tilt 648
– line defects 641
– spiral 657
secondary building unit (SBU) 822
secondary pore 843
secondary-ion mass spectrometry (SIMS) 828
second-step anodization 860
sedimentation 730
SEDOR method 671
Seebeck coefficient 26
seed 415
– crystal 658
– -mediated growth 315
segmented heterostructure 869, 872
segmented heterostructure of BiNT and CuNW 870
segmented nanoheterostructure 869
– fabrication procedure 873
segregated nanoalloy 434
– core–shell 434
– ordering pattern 434
selected-area electron diffraction (SAED) 648, 784, 866, 909, 917
selective
– adsorption 166
– dissolution 780
– laser killing 1091
– nanothermolysis 1081
– oxidation 795
– oxidative coupling 795
– plasmonic nanotherapy 1083
– therapy 1068
selectoforming 847
self-acidifying effect 783
self-assembled 1063
– Co-Pt nanoparticle 448
– monolayer (SAM) 92, 339, 1005
– multilayer thin film 750
– nanofiber 952, 985
– nanometer sized wire 928
– peptide nanofiber 988
– peptide properties 985
– phototransistor 927
– superstructure 331
self-assembling peptide nanofiber
– biochemical properties 990
self-assembly 487, 905
– dynamic 907
– intramolecular 907
– of polypeptides 980
– process 959
– template-assisted (TASA) 756
self-catalyzed VLS 650
self-diffusivity 839
self-healing 802
self-limiting process 889
self-ordering condition 860
self-ordering nanoparticle 391
self-organization
– at interface 331
self-organized nanoparticles 11
self-organized P3HT 921
self-organized structure 756
self-organizing GNR 339
SEM image
– nanofiber 239
semiconducting
– electronic transport 863
– nanomaterials 757
– nanotube 105, 108, 125
– quantum dot 157
– SWCNT 116, 123
semiconductor 627, 859
– compound 524
– core–shell NP 345
– electrochemistry 884
– material 659
– nanocrystal 345, 682
– nanotube 20
– nanowire 906
– sensor 72
– SWCNT 193
– SWNT 697
semimetal/metal coaxial nanocable 875
sensing
– biological 640
sensitization 872
sensor 28, 791
– biochemical 589
– chemical (gas) 28
– electrochemical 806
– gas 524
– microfluidic-based 791
– nanoparticle 31
– optical 896
– semiconductor 72
– Taguchi-type 31
sensorics 157
separating ferromagnetic nanoparticle 731
separation and storage 253
Sepiolite nanoclay 1048
sequential electrodeposition 869, 875
SERS
– activity anisotropic metal NP 360
– effect 805
shadow mask technique 918
shape 414
– anisotropy 493
– change 28
– -controlled nanomaterial 328
– -memory alloy (SMA) 491
shape selectivity
– product 846
– reactant 846
– transition-state 846
shape-selective catalysis 838
shape-selective property 847
shearing force 623
shear-lag theory 720
sheet
– graphite 235
sheet-like shape 730
shell material 995
shell nanoheterostructure 869
shell-by-shell growth 151
shock
– conversion 270
– synthesis 270
shock wave 1092
– assisted synthesis 270
– simulation 456
short-range order of glass 667
Shubnikov–de Haas (ShdH) oscillation 64
side-by-side assembly 332
sidewall addition reaction 156
side-wall functionalization 746
signal-to-noise ratio (SNR) 504
Si–H-terminated surface 884
silenced RNA (siRNA) 284
silica coated GNP 344
silica mineral 827
silica NP 1052
– toxicity 1052
silica-coated GNR 328
silica-coated zeolite 845
silica–gold nanoshell 1066
silicalite-1 terraces 833
silicate glass 670, 683
silicoaluminate 825
silicoaluminophosphate (SAPO) 823
silicon
– bulk 884, 888
– bulk bandgap 890
– bulk properties 891
– crystalline 883
– dissolution 886
– doping content 885
– electrochemistry 889
– nanocrystal (Si-nc) 890
– nanostructure 890

– nanowire 28
– nanowire pore size 885
– needle 887
silole crystal and fiber 915
siloxene model 890
silver 340, 1079, 1080
– cluster 365
– foil dressing 307
– ion biocidal activity 355
– material property 1079
– nanoparticle 49, 347, 353, 681
– nanoparticle ring 754
– nanoplate 360
– nanoprism 20
– nanoshell particle 18
– nanosphere 1066
– nanowire monolayer 342
silver-based product 307
simple cubic (SC) 90
simplified 573
single
– nanoparticle 434, 1077, 1079, 1095
single crystal logic circuit 930
single lattice temperature 1067
single nanofiber
– mechanical properties 996
single nanoparticle
– internal temperature distribution 1078
– laser heating 1077
– laser thermal explosion 1095
– measurement 447
– outside temperature distribution 1079
– surrounding medium 1079
single PEO
– nanofiber 997
single polymer
– nanowire 921
single Y-branched Au nanowire 866
single-crystal transistor 919
single-crystalline
– nanowire 927
single-domain
– configuration 18
– particle 478, 492, 494
single-electron transistor (SET) 14, 66, 127, 928
single-layer
– graphene 701
– graphene sheet 17
– graphite 105
single-particle band gap 122
single-particle rotation 482
single-pulse mode 1070
– of heating 1067
single-walled 10
single-walled carbon nanotube (SWNT) 85, 92, 95, 106, 107, 147, 148, 190, 393, 696, 748, 754, 960, 1016, 1023, 1049
– dispersion 746
sintered bulk ceramic 555
sintering 863
– parameter 556
– spark plasma (SPS) 558
– two-step 553
SiO_2
– nanoparticle 755
size control 310
size exclusion chromatography (SEC) 155, 709
size-dependent reactivity 1118
skeletal muscle
– loss 1001
– tissue engineering 1001
skeletal tissue regeneration 945
skin interaction 1123
slippage of fibers 997
small angle neutron scattering (SANS) 473, 709
small band gap nanotube 117
small molecule 930
small particles
– melting point 6
small-angle neutron scattering (SANS) 451, 474, 789
small-angle x-ray scattering (SAXS) 273
small-pore mordenite (SPM) 843
smart aggregate 1047
smart orthopedic implant 957
Sn and In nanostructure 391
sodalite 831
– cage 822
sodium borate
– glass 670
sodium dodecyl sulfate (SDS) 158, 746
sodium dodecylbenzene sulfonate (NaDDBS) 397, 746
sodium octanoate (SOCT) 158
sodium silicate
– glass 670
soft chemical route 518, 538
soft chemistry 618
soft lithography technique 530
soft magnetic
– nanostructure 498
soft magnetic material 499
soft phase grain diameter 498
soft surface 752
soil
– deposit 827
– ecosystem 1121
– microorganism 1121
solar ablation (SA) 614
solar cell 92, 363, 524, 747
– electrode 750
– nanometric ceria particle 530
solar energy conversion 28, 640, 660
sol–gel
– citrate method 555
– deposition 523
– method 1024
– nanomaterials 523
– process 523, 862
– processing 527
– synthesis 523
– technique 345, 876
– template process 863
solid
– amorphous 665
solid freedom fabrication (SFF) 953
solid nanoparticle 732
solid oxide fuel cell (SOFC) 538, 540, 1014
solid phase offretite 833
solid/liquid (S/L) dispersion 158
solid–electrolyte interphase (SEI) 1031
solid–liquid interface 522, 732
solid-phase diffusion 611
solid-state
– diffusion 518
– ion exchange 837
– NMR (SSNMR) 577, 667, 684
– oxide materials 523
– reaction 528
– route 518, 538
solution
– chemistry technique 519
– -diffusion imperfection model 1102
– -diffusion model 1102
– –liquid–solid (SLS) 391, 640
– -phase route 311
– -phase synthesis 652
– reaction 519
– supersaturated 522
solvated metal atom dispersion method (SMAD) 331
solvent exchange 906
solvent resistant nanofiltration (SRNF) 1101

solvothermal synthesis 493, 523
sonication 583
sonochemical
– effect 523
– synthesis 523, 527
– technique 524
sonolysis 314
sonothermal synthesis 9
soot
– flame generated 89
sorbent technology 533
sorption 535, 836
sound generation 1079
sp^2 carbon 148, 156, 236, 266, 274
– cluster 578, 588
– domain 591
– network 242
sp^3 carbon 151, 156, 266
– matrix 578, 588
space
– 3-D 85
space elevator 164
space quantization 475
space-charge region (SCR) 886
spaced superconducting electrode (SGS) 55
spark plasma sintering (SPS) 558
spatial distribution 1076, 1082
– temperature field 1076
specific battery
– energy 251
specific capacitance 810, 1026
specific heat 1069
specific surface area (SSA) 791, 1127
spectrofluorometry 20
speed of diffusion 1101
spherical
– bubble dynamics 1086
– carbon onion 94
– diamond 266
– nanoparticle 1080
– particle 326
spider silk 703
Spiegler and Kedem model 1102
spin
– coating 747
– –orbit coupling 476
– polarization 479
– qubit 67
– valve 502
– valve device 68
spin-echo
– amplitude 669
– decay spectroscopy 669
– double resonance (SEDOR) 670
– intensity 670
– NMR measurement 840
spin-polarized scanning electron microscopy 488
spin-polarized scanning tunneling microscopy (SP-STM) 474
spintronics 67
spiral nanotube 150
spiral step edge 655
spiropyran-capped GNP 343
splat quenching 502
spray coating 750
spring back phenomenon 498
spun nanofiber 982
sputtered nanocoating 25
sputtering 474
– DC 484
– RF 484
SQUID magnetometry 474
stability of fibrous morphology 250
stable dispersion 732
– clay 733
– silicate 733
stack fuel cell 1018
stacking
– ABAB 239
stacking fault 418
stain etching 886
stain on surface 752
stainless steel (SS) 1025
stamping technique
– Au-layer 918
static growth 658
static self-assembly 907
stationary heat transfer equation 1077
Staudenmaier method 573
steam activation 253
steel
– ferritic 452
– high-strength 1044
stellerite 843
stem
– channel 861
– diameter 867
– nanochannel 866
step pile-up 645
step-free facet 644
step-shaped
– CuNW 869
– nanochannel 862
– nanostructure 864, 868
stick-slip mechanism 755
stiffness
– Young's modulus 51
stilbazolium-like dye 911
stilbene 343
stilbite 825, 843
stochastic optical reconstruction microscopy (STORM) 994
stoichiometric variation 519
Stoner–Wohlfarth (S–W)
– model 481
– particle 481, 492
Stone–Wales (S–W) transformation 132
straight pore 860
strain graphene 721
strain–stress correlation 628
streptavidin–Au conjugate 209
stress corrosion cracking (SCC) 780
stress transfer 624
stress–strain curve 700, 803
stress–strain plot 1000
string-like alignment 338
strong reducing agent 311
structural
– characteristic 238
– composite 69
– defect 194, 196
– demolition 1048
– model 236
– properties porous silicon 887
structure
– of carbon nanotube 1103
– toroidal 97
structure and morphology
– nanofibrous scaffold 987
structure deposition and ink self-assembly
– AFM 9
structure prediction
– theoretical method 435
structure–activity relationship 1052
– surface functionalization 1052
structured illumination microscopy (SIM) 994
structure-directing agent 833
subbranch morphology CNT 868
subcellular localization 995
subnanometer
– metal cluster 440
suboxide nanowhisker 616
sub-ppm sensitivity 896
substitutional doping 191
substrate supported
– graphene 50
subwavelength-sized optical cavity 928
suction casting 502
suitable bone implant 942

suncare ingredient 1130
sunscreen 1130
– emulsion photochemical properties 1132
– nanoparticle 1130
– nanoscale material 1132
– pigment 1120
– pigment photocatalytic activity 1130
superacidity 842
superalloy 22
supercapacitor 94, 254, 1013, 1015
– array 28
– device 28
– electrode 589
– electrode material 253
– high-power 253
– symmetric 1028
superconducting quantum interference device (SQUID) 473
supercritical drying 885
supercritical fluid inclusion process 878
superhydrophobic CNT array 1106
superhydrophobicity 917, 927, 928
superlarge integrated circuit 930
superlattice 28, 756
– 3-D 341, 343
– formation 487
superparamagnetic limit 503
superparamagnetic material 14, 17
superparamagnetism 478
superresolution technique 979
supersaturated solution 522
supersaturation 640, 641
– level 654
– level manipulation 658
superstructure 331, 539
support material 166
supported cluster
– CoPt 433
supported crystal 430
supported nanoalloy
– catalytic properties 421
– chemical composition 421
supported particle
– morphology 429, 439
– silver 439
surface
– -anchored crown ether 340
– anisotropy 480
– area 1127
– area analysis 1126
– area of precursor 245
– -assisted solvent–vapor annealing 906
– biochemistry 990
– catalysis 26
– coating 1127
– -controlled reaction 863
– deposition method 416
– diffusion 782, 784
– diffusivity 786
– dislocation spiral 641
– domain 490
– elemental analysis 1128
– energy 430
– growth 415
– hydrides model 890
– hydrophilization 1045
– hydrophobicity 360
– -initiated assembly 983
– manipulation 310
– morphology 752
– nanopatterning 416
– nondestructive analysis 488
– nucleation 835
– oxidation 891
– pinning 753
– plasmon (SP) 14, 18, 322, 362
– plasmon absorption 444
– plasmon polariton (SPP) 803
– plasmon resonance (SPR) 18, 20, 324, 362, 442, 681, 803, 1092
– potential 60
– properties 253
– reactivity 256, 532
– roughness 951
– scattering 809
– segregation 412
– sol–gel method 863
– stabilization 891
– stabilization technique 891
– states model 890
– temperature 1086
– temperature of gold nanoparticle 1086
– water-repellant 1046
– wettability 951
– Wulff construction 430
– x-ray diffraction (SXRD) 421
surface-enhanced infrared absorption (SEIRA) 447, 797
surface-enhanced Raman scattering (SERS) 323, 347, 443, 447, 804
surfactant 735
surrounding biomedia 1065
surrounding medium 1079
sustainable nanomaterial 659
SWCNT (single-walled carbon nanotube) 106
– absorption spectroscopy 116
– chemical functionalization 197
– crystallographic structure 106
– film 124
– fluorinated 203
– mechanical properties 128
– metal 697
– optical absorption 116
– phonon density 111
– photoluminescence 116
– semiconductor 697
swelling resistance 452
symmetric
– supercapacitor 1028
symmetry 85
– orbit 412
synergetic effect 167
synergistic effect 798
synthesis 518, 530, 572
– method 148, 518
– mixture silica/alumina ratio 831
– of clathrasil 834
– of Cu NW 655
– of DND 272
– of nanocrystalline soft magnetic alloys 502
– route 517
synthetic
– methodology 608
– zeolite 828, 848
synthetic corneal prosthetics 1003

T

Ta nanoparticle 395
– salt-encapsulated 396
Tabor–Winterton approximation 732
Taguchi-type sensor 31
tailor-made
– catalyst 847
– organic nanowire 930
tantalum
– nanoparticle 396
– nanostructure 395
teflon coating 165
telecommunication 684
tellurite
– glass 670
temperature
– distribution 1084
– field 1076, 1082
– field spatial distribution 1082
– profile 1070
– programmed desorption (TPD) 842
– stability 843

template
– 1-D 640
template method 207, 906
template synthesis 523, 1105
template-assisted
– electrodeposition 493
– self-assembly (TASA) 756
template-free method 907
templating 906
templating agent 833
tensile strength 159
tensile test of a nanofiber 998
tensile Young's modulus 131
terahertz spectroscopy 162
terminated surface bond 884
terrace diffusion 782
terrestrial ecosystem 1121
Terrones model 93
tetra(ethylene glycol) (TEG) 390
tetracalcium phosphate (TTCP) 948
– cement 947
tetracyanoquinodimethane (TCNQ) 916
tetragonal Bain cell 18
tetrahydrofurane (THF) 612, 983
tetraphenylethene (TPE) 914
tetrapropylammonium (TPA) 838
the British Standards Institution (BSI) 1118
theranostics 457
thermal
– 3-D field 1082
– analysis 835
– carbonization 892
– conductance quantum 160
– conductivity 1069
– diffusivity 1067
– explosion 1091, 1094
– explosion mode 1091, 1092
– explosion threshold energy density 1094
– gravimetric analysis (TGA) 581
– gravimetry 828
– insulation 891
– motion 731
– necrosis of osteocytes 1082
– threshold 1079
– treatment effect 247
thermally induced phase separation (TIPS) 952
thermally treated
– electrospun nanofiber 251
– nanofiber 250
– web 246
thermochemical barrier 349
thermochromic glass 1045
thermoelectric 659
– coefficient 390
– nanomaterial 26
– power (TEP) 56
thermogravimetric analysis (TGA) 208, 214, 221
thermophoresis 390
thermopolymerization 906
thermoresponsive polymer 505
THF/DMF weight ratio 340
thickness dependant magnetization reversal 496
thin-film 17, 495
– circuits of organic 924
– composite membrane 1102
– field-effect transistor 917
– nanocomposite 498
– nanocrystalline soft magnetic alloy 501
– QD 683
– solar cell 920
– transistor (TFT) 907
– ultracapacitor 591
thin-film interference pattern 656
thin-film transistor (TFT) 750
thin-walled nanotube 644
thioflavin T (ThT) 366
thiophenol-functionalized GO 591
thiourea 611
thomsonite 843
thoria (YDT) 518
three-branched AAO template 864
three-branched Ni nanowire 866
three-dimensional (3-D) 39, 148, 307
– porous silicon 888
– stacking order 240
– stain 754
three-point bending 623
three-stage crystallization model 831
three-way catalyst (TWC) 536
threshold energy 1084
– density 1094
threshold voltage 917
Thrower–Stone–Wales defect (TSW) 195, 196
Ti
– nanostructure 394
– nanowire 393
Ti-doped INT-MoS_2 627
tight-binding model 107
time dynamics 1067
time-dependent
density-functional-theory (TDDFT) 444
time-dependent perturbation theory 668
time–temperature profile 1070, 1071, 1074
– calculated 1070
– multipulse 1071
tin-doped indium oxide (ITO) 524
TiO^2 (titanium oxide) 524
TiO_2 (titanium oxide) 363
– graphene 69
– graphene composite 69
– -modified window 1045
– nanoparticle 393, 796, 1050
– nanoparticle toxicity trial 1050
– photocatalysis 1130
tip geometry 490
tip of nanofiber 240
tip-growth mechanism 152
tissue
– artificial 504
– biological 1095
– engineered implant 982
– engineered scaffold 987
– growth enhancement 954
– regeneration 257
tissue engineering 504, 941, 948, 949, 965, 977, 979, 993, 999
– application 990
– dental 963
– hard 960
titanium
– film 393
– nanosized structure nanowire 393
TNT (2-methyl-1,3,5-trinitrobenzene) 271
tolerance factor 554
toluene disproportionation 847
Tommonaga–Lüttinger liquid model 124
tomographic reconstruction 790
top-down 698
– method 10
topographical analysis 996
topological defect 196
toroidal
– carbon 194
– structure 97
total spin Hamiltonian 668
Tour method 574
toxic gas 575
toxic industrial chemical (TIC) 533
toxicity
– aquatic ecosystem 1121
– effect surface-dependent 1126
– graphene oxide 583
– mammalian 1121

– mechanism 1052
– pulmonary 1128
– reduced graphene oxide 583
– soil ecosystem 1121
toxicological impact 1047
toxicology 31
TPL (two-photon luminescence) microscopy 359
trabecular bone 960
track-etch membrane 523
track-etched polycarbonate (PTCE) 391
traditional
– Chinese medicine 2
– classification 518
– concrete 1041
– implant lifetime 945
transconductance 16
transducer 553
transfer matrix 895
transformable steel
– nanostructured 451
transistor 589
transistor configuration 125
transitional layer 888
transition-metal 499
– element 667
– oxide 613, 1016, 1023
– sulfide 613
transmetallation 779
transmission electron microscope (TEM) 42, 89, 209, 607
transmission electron microscopy (TEM) 58, 208, 421, 474, 488, 490, 526, 645, 697, 780, 835, 864, 979, 995, 1017, 1126, 1127
– sample preparation 153
transmission electron spectroscopy (TES) 709
transmissivity 1095
– biological tissue 1095
transparent
– conducting film 69
– conductive coating 754
– conductive oxide (TCO) 524
– electrode 524, 750
– glass ceramics 676, 677
transverse
– acoustic (TA) 110
– dispersion 129
– overgrowth 327
– surface plasmon (TSP) 324
tree-like branched channel 868
triangular nanoframe 308
tricalcium phosphate (TCP) 945
tridymite 827
trigonal boron 673
trigonal polytype 621
trilayer graphene 47
triple helix
– bundle 944
– formation 986
triple-quantum/single-quantum (3Q/SQ) 577
tris(8-hydroxyquinoline)aluminum (Alq3) 909
truncated
– Ag nanocube 329
– cone 239
– hexagonal bipyramid 426
– icosahedral structure 87
– octahedral cluster 431
– octahedron (TO) 426
trunk growth 650
tryptophan 520
T-site configuration 821
TTF crystal 919
tube axis 118
tube interior 147
tube-on-tube MWCNT 167
tubular filament 236
tumor cell 1072, 1088
– number of particle 1088
tumor damage 1064
tungsten
– nanostructure 395
– nanowire 394
– oxide (WO_3) 1044
– sulfide 98
tuning nanosystem properties 324
tunnel magnetoresistance (TMR) 503
tunneling current 419
Turkevich method 312, 352
turnover frequency (TOF) 794
twin-screw extrusion 946
twist contour analysis 651
twist mode 110
twist of the lattice 642
two-dimensional (2-D) 40, 307
two-photon luminescence (TPL)
– imaging 359
– microscopy 347
two-segment Au–Ni NW 874
two-shell carbon onion 94
two-site jump 583
two-stage precipitation process 528
two-step anodic oxidation 860
two-step sintering 556, 558
two-terminal conductance 124
type-I collagen 942
type-III collagen 954
types of nanofibers 986
typical applications of nanomaterials 22

U

UHP molding 562
– apparatus 561
ultracentrifugation 750
ultracentrifuge 731
ultrafast optical spectroscopy 115
ultrafast spectroscopy 120
ultrafiltration (UF) 1099, 1106
– membrane 134
ultrafine particles 18
ultrahigh pressure (UHP) 561
ultrahigh-vacuum (UHV) 416
ultralong microwire 908
ultrananocrystalline diamond (UNCD) 292
– particle 268
ultrasensitive diagnostic 1063
ultrasonic cavitation 523
ultrasonic treatment 154
ultrasound cavitation 278
ultraviolet radiation (UVR) 290
uncoated nanofiber 239
underpotential deposition (UPD) 791
undoped nanofiber 242
undoped semiconductor carbon nanotube 128
unidimensional channel 844
unreduced GO 591
unstructured silicon sample 888
up-conversion efficiency 679
UPD (underpotential deposition) 792
US food and drug administration (FDA) 1130
UV physical sunscreen filter 1119
UV-induced coloration 1045
UV-Raman spectra 824
UV-Vis spectroscopy 709, 830, 1108

V

vacancy 197
vacuum filtration 750
vacuum pyrolysis carbothermal (VPC) 394
vacuum-aided solution infiltration 1110
valine 520

van der Waals (vdW) 52, 609
– attraction 732
– chain 95
– contact 907
– force 752, 1104
– interaction 591, 837
van Hove
– optical transition 20
– singularity (VHS) 108, 123
van Vleck
– formulae 669
– second moment 669
vapor deposition 909
vapor-grown carbon fiber (VGCF) 233, 236, 237
vaporization temperature 1093
vapor–liquid–solid (VLS) 114, 640
vapor-phase synthesis 650
vapor–solid (VS) growth 397
vapor–solid–solid (VSS) 114, 640
variable range hopping (VRH) 124
Venetian glass 680
very small cluster 429
vibrating sample magnetometry (VSM) 474
vibrational IR-Vis sum-frequency generation (VSFG) 423
vibrational Raman scattering 118
vibrational spectroscopy 669, 829
vibrational sum-frequency generation (VSFG) 424
vibronic spectra 679
viscous liquid 519
vitronectin 957
void formation 993
voided
– nanowire 643
– structure 649
volcano curve 438
voltage-controlled transport 1109
voltammetric dealloying 798
volume anisotropy 480
volume concentration 679
volumetric resistivity 245

W

wairakite 843
Warburg impedance 255
wash and go method 154
waste degradation 1049
waste disposal 1048
wastewater treatment 1120
water 1066
– contact angle 990
– purification 348, 589
– -repellant surface 1046
– softening 822
– -soluble fullerene 1124
– -soluble polymer 949
water-repellent 361
– self-cleaning surface 361
– superhydrophobic surface 361
waveguide (WG) 897
WC-Co cemented carbide 276
W-diamond 287
wettability 360, 927, 951
wetting dispersion 754
whisker 642, 651
wide angle x-ray diffraction (WAXD) 710
Wiedemann–Franz law 808
window glass 1044
wire model 412, 413
– 1-D 413
woodpile 895
working electrode 886
World Health Organization (WHO) 534
woven bone 943
WS_2 nanotube
– growth mechanism 615
Wulff construction 411, 423, 439
– canonical 426
Wulff shape 430

X

xc-functional 445
xenogenicity 257
xenograft 944
x-ray
– characterization 248
– image 256
– magnetic circular dichroism 474
x-ray absorption fine structure (EXAFS) 419
x-ray absorption near-edge spectroscopy (XANES) 419
x-ray absorption spectroscopy (XAS) 418, 783, 789
x-ray diffraction (XRD) 158, 273, 555, 580, 622, 665, 678, 864, 1126
– carbon nanofiber 244
– pattern 560
x-ray microdiffraction 791
x-ray photoelectron spectroscopy (XPS) 22, 208, 212, 220, 242, 417, 420, 580, 830, 1126, 1128
x-ray powder diffraction (XRD) 1017
xylene isomerization 847

Y

$Y_4Al_2O_9$ (YAM) 452
yablonovite 895
Y-Al complex oxide 452
YAM nanoparticle 453
Y-branched
– AAO template 864
– Au nanowire 865, 866
– Bi nanowire 864
– Cu nanowire 864, 865
– nanostructure 864
– pore 860, 861
yield 149
– strength equation 801
Young's modulus 159, 696, 801, 925, 997
– NPG 801
Yttria-doped 518
yugawaralite 843

Z

Z-DNA 985
Zeeman
– energy 481
– Hamiltonian 667
– interaction 668
– splitting 475
zeolite 10, 366
– A 831
– A, X, Y 822
– acid–base property 841
– acidic material 847
– amorphous phase 843
– analysis method 828
– bactericid function 849
– basicity 842
– catalytic activity 846
– channel system 846
– characterization 828
– chemical composition 828
– coke formation 845
– complex ion 830
– dealuminated 843
– dealumination 843
– deodorizing function 849
– diffusion properties 838
– drying agent 848
– fine chemicals 847
– gas purification 849
– high-silica 823, 825, 848
– hydrophilic 837
– intermediate pore size 822
– ion exchange properties 836
– mazzite 823

– metal particle 845
– microcrystal 834
– mineral genetic type 826
– molecular sieving properties 837
– paper industry 849
– petrochemical industry 847
– phase 834
– physicochemical characteristic 827
– pore size dimension 821
– protecting polymers 849
– QD 683
– regeneration 846
– sieve of molecular porosity (ZSM) 822
– small-pore 822
– synthetic 848
– textile industry 849
– thermal stability 843
– voids 821
– ZSM-5 837
zeolite β
– bipyramidal morphology 824
– channel system 824
– crystallization curves 834
zeolite catalyst
– petrochemical processes 847
– pore-opening size 845
zeolite characterization
– Mössbauer spectroscopy 830
zeolite characterization 830
zeolite crystallization
– chemical component 831
– parameter 835
zeolite framework
– construction 820
– structure 821
zeolite lattice
– crystal ionic radii 823
zeolite structure 846
– isomorphous substitution 844
– satbility and modification 843
– secondary pore structure 843
zeolite synthesis 823, 830, 832, 834
– organic additive 833
– physical parameter 834
– procedure 835
– reaction mixture 830
– viscosity 834
zeolite–sorbate interaction 838
zeolitic
– catalyst 846
– crystal 839
– framework 829
zeotype material 821
– NMR measurement 829
zero band gap semiconductor 108
zero-dimensional (0-D) 40, 307, 910
zero-length-column (ZLC) 839
zero-valent iron 348
zeta potential
– surface charge 1129
zigzag
– axis 1104
– case 589
– layer 619
– nanotube 107, 697
– ribbon 57, 195
zinc chloride 253, 254
zinc hydroxydodecylsulfate (ZHDS) 657
Zn
– nanobelt 397
– nanomaterial 397
– nanowire 397
ZnO 363
– photocatalysis 1130
ZSM family 823
ZSM-20 crystallization curves 834
ZSM-39 829
ZSM-5 843
– acidity 842
– channels 841
– structure 822
– zeolite 838
zwitterion intermediates 156
zwitterionic character 520